

Lieping Ye
Peng Feng
Qingrui Yue

Advances in FRP Composites in Civil Engineering

Proceedings of the 5th International Conference on FRP Composites in Civil Engineering (CICE 2010), September 27-29, 2010, Beijing, China

Lieping Ye
Peng Feng
Qingrui Yue

Advances in FRP Composites in Civil Engineering

Proceedings of the 5th International Conference on FRP Composites in Civil Engineering (CICE 2010), Sep 27-29, 2010, Beijing, China

With 1279 figures

Editors

Lieping Ye
Department of Civil Engineering
Tsinghua University
Beijing 100084, P.R. China
Email: ylp@tsinghua.edu.cn

Peng Feng
Department of Civil Engineering
Tsinghua University
Beijing 100084, P.R. China
Email: fengpeng@tsinghua.edu.cn

Qingrui Yue
Science & Technology Dept.
Metallurgical Corporation of China Ltd.
Beijing 100028, P.R. China
E-mail: yueqr@vip.163.com

ISBN 978-7-302-23910-9
Tsinghua University Press, Beijing

ISBN 978-3-642-17486-5
Springer Heidelberg Dordrecht London New York

e-ISBN 978-3-642-17487-2

© Tsinghua University Press, Beijing and Springer-Verlag Berlin Heidelberg 2011

This work is subject to copyright. All rights are reserved, whether the whole or part of the material is concerned, specifically the rights of translation, reprinting, reuse of illustrations, recitation, broadcasting, reproduction on microfilm or in any other way, and storage in data banks. Duplication of this publication or parts thereof is permitted only under the provisions of the German Copyright Law of September 9, 1965, in its current version, and permission for use must always be obtained from Springer. Violations are liable to prosecution under the German Copyright Law.

The use of general descriptive names, registered names, trademarks, etc. in this publication does not imply, even in the absence of a specific statement, that such names are exempt from the relevant protective laws and regulations and therefore free for general use.

Printed on acid-free paper

Springer is part of Springer Science+Business Media (www.springer.com)

Preface

Applications of fiber reinforced polymer (FRP) composites in civil engineering have increased significantly in the past two decades. As FRPs are non-corrosive, high-strength and lightweight, their use in civil infrastructure has extended from the strengthening of existing structures to new construction. FRP therefore has wide application prospects in civil engineering. The Fifth International Conference on Composites in Civil Engineering, CICE 2010 (www.cice2010.net) was held in Beijing on 27-29 September 2010. CICE 2010 was organized by the Department of Civil Engineering, Tsinghua University and China Metallurgical Group Corporation. It is the official conference of the International Institute for FRP in Construction, IIFC (www.iifc-hq.org). The aim of this conference is to provide an international forum for all concerned with the application of FRP composites in civil engineering to exchange and share recent advances in both research and practice. The CICE conference series started with CICE 2001 (www.cse.polyu.edu.hk/cice) in Hong Kong, China, initiated by Professor Jin-Guang Teng. The next conference in the series, CICE 2004 (www.adelaide.edu.au/cice2004) was chaired by Dr Rudi Seracino, held in Adelaide, Australia, in December 2004, followed by CICE 2006 (www.iifc-hq.org/cice2006) chaired by Professors Amir Mirmiran and Antonio Nanni, held in Miami, USA, in December 2006, and CICE 2008 (www.cice2008.org) chaired by Professor Masoud Motavalli, held in Zurich, Switzerland, in July 2008.

This conference is also sponsored by the China Civil Engineering Society (CCES) and its FRP Application Committee, the China Composites Industry Association (CCIA), the Chinese Ceramic Society FRP Committee, and the National Natural Science Foundation of China (NSFC) by Projects No.50978149, 50608047 and 50868004.

A total of 210 papers are included in the proceedings, while 203 papers and 7 keynotes are being presented. All papers are included in two volumes. Volume I, FRP for Future Structures, covered a range of topics including follows focusing on the new construction.

- FRP Materials and Sustainability
- All FRP Structures
- FRP Hybrid Structures and Concrete-Filled FRP Tubes
- Smart FRP Structures
- Concrete Structures Reinforced or Prestressed with FRP
- Long-Term Performance
- Fire, Impact and Blast Loading
- Education, Applications and Design Guidelines

Volume II is FRP Strengthening Structures covering the following topics.

- Bond and Interfacial Stresses between FRP and Concrete
- Confinement of Concrete by FRP in Compression
- Flexural Strengthening of Concrete Beams and Slabs
- Shear Strengthening of Concrete Beams
- Strengthening of Concrete Columns, Walls, and Frames
- Strengthening of Steel Structures
- Strengthening of Masonry and Timber Structures

The papers are authored by experts in the field from 30 different countries around the world, including Argentina, Australia, Belgium, Brazil, Canada, China, Czech Republic, Egypt, France, Germany, Greece, India, Iran, Iraq, Italy, Japan, Korea, Lithuania, Malaysia, Netherlands, Pakistan, Poland, Portugal, Singapore, Spain, Switzerland, Thailand, Turkey, UK, and USA. The technical papers in proceedings not only address analytical and experimental work, but also cover field applications, and design and construction guidelines. Comparing the papers in this set of proceedings with those published in the early CICE conferences, it is clear that we have paid more attention to FRP for new structures, new applications, and long-term behaviors.

The valuable articles in the proceedings would not have been possible without the help, dedication, and collaboration of numerous individuals. First and foremost, we thank the authors for meeting our various submittal deadlines, allowing this document to represent the most current work on the subjects from around the world. We would also like to thank the Organizing Committee and the International Scientific Committee of the conference for their relentless efforts in making this conference to happen. It is also important to thank the Executive Committee, the Advisory Committee, and the Council of IIFC for their support throughout this process.

The Editors

Lieping Ye

Professor

Department of Civil Engineering, Tsinghua University
Beijing, China

Peng Feng

Associate Professor

Department of Civil Engineering, Tsinghua University
Beijing, China

Qingrui Yue

Professor

China Metallurgical Group Corporation
Beijing, China

September 20, 2010

Message from the President of IIFC

Recent years have seen rapidly growing interest in the application of fibre-reinforced polymer (FRP) composites in construction around the world, in terms of both research activities and practical implementations. Indeed, FRP composites are being hailed as a new generation of construction materials, following steel and concrete. Against this background, the International Institute for FRP in Construction (IIFC) was formed in 2003 to promote and coordinate world-wide activities in this area. One of the important activities of IIFC is the organization of a biennial official conference series, as well as biennial regional conferences.

As President of IIFC, I would like to take this opportunity to express my sincere appreciation to Professor Lieping Ye, Chair of CICE 2010, and his team for devoting so much time and energy to make this conference a great success. I would also like to thank all others who contributed to this success in different ways, including members of the Organizing Committee, the International Advisory Committee and many others. The strong support for CICE 2010 shown by the international civil engineering FRP research community is a testimony to the importance and significance of this conference.

There is no doubt that a major impact of IIFC has been the sponsorship of international symposia and conferences. This will continue with this CICE conference and the 6th CICE conference scheduled for 2012 in Rome. Registration fees at such conferences imply that IIFC dues are waived for the year in question. Other advantages of IIFC membership are the FRP International newsletter, complimentary copies of conference proceedings, and participation in various working groups. We are striving to enhance the benefits of IIFC membership, and are open to all suggestions and ideas for doing so. I would like to conclude with a request to all members of the Institute: please inform your colleagues of the activities of IIFC and encourage them to join our vibrant organization.

Kenneth W. Neale

President IIFC

September 20, 2010

Committees

Conference Chairs

Lieping Ye, Tsinghua University, Beijing, China

Qingrui Yue, China Metallurgical Group Corporation, Beijing, China

General Secretary

Peng Feng, Tsinghua University, Beijing, China

International Scientific Committee

Chairman: K.W.Neale (Canada)

B. Bakht (Canada)	P.Y. Huang (China)
C.E. Bakis (USA)	A. Ilki (Turkey)
L.C. Bank (USA)	L.C. Hollaway (UK)
N. Banthia (Canada)	V.M. Karbhari (USA)
J.A. Barros (Portugal)	A. Katz (Israel)
B. Benmokrane (Canada)	T. Keller (Switzerland)
L. Bisby (UK)	R. Kotynia (Poland)
C. Burgoyne (UK)	P. Labossière (Canada)
J.F. Chen (UK)	H. Li (China)
E. Cosenza (Italy)	W.Q. Liu (China)
L. De Lorenzis (Italy)	L.L. Luo (China)
R. El-Hacha (Canada)	Z.T. Lu (China)
A. Fam (Canada)	A. Machida (Japan)
H. Fukuyama (Japan)	U. Meier (Switzerland)
M. Green (Canada)	A. Mirmiran (USA)
J. Grenestedt (USA)	M. Motavalli (Iran)
X.L. Gu (China)	G. Monti (Italy)
I.E. Harik (USA)	A. Mufti (Canada)
K. Harries (USA)	A. Nanni (USA)

D.J. Oehlers (Australia)	L. Taerwe (Belgium)
J.P. Ou (China)	T. Ueda (Japan)
M.D.G. Pulido (Spain)	G. Van Erp (Australia)
S.H. Rizkalla (USA)	P. Waldron (UK)
H. Seliem (Egypt)	J. Wang (China)
R. Seracino (USA)	Z.S. Wu (Japan)
J. Sim (Korea)	Y. Xiao (China/USA)
S.T. Smith (China)	Z.M. Xue (China)
B. Täljsten (Sweden)	W.C. Xue (China)
K.H. Tan (Singapore)	J. Yao (China)
J.G. Teng (China)	X.L. Zhao (Australia)
T.C. Triantafillou (Greece)	J.W. Zhang (China)

Organizing Committee

Y. Bai (Monash University, Australia)

X.B. Chen (China Metallurgical Group Corporation, China)

J.G. Dai (Hong Kong Polytechnic University, China)

J. Deng (Guangdong University of Technology, China)

Z.C. Deng (Beijing University of Technology, China)

P. Feng (Tsinghua University, China)

Y.J. Kim (North Dakota State University, USA)

R. Li (China Metallurgical Group Corporation, China)

X.Z. Lu (Tsinghua University, China)

B.L. Wan (Marquette University, USA)

Y.L. Wang (Dalian University of Technology, China)

G. Wu (Southeast University, China)

Z.H. Yan (California Department of Transportation, Sacramento, USA)

Y.X. Yang (China Metallurgical Group Corporation, China)

CONTENTS

Vol. I FRP for Future Structures

Keynote Papers	1
Innovative Textile-Based Composites for Strengthening and Seismic Retrofitting of Concrete and Masonry Structures <i>Triantafyllou, T.</i>	3
Strengthening of Concrete, Metallic and Timber Construction Materials with FRP Composites <i>Smith, S.T.</i>	13
Multifunctional and Robust Composite Material Structures for Sustainable Construction <i>Keller, T.</i>	20
Hybrid FRP-Concrete-Steel Double-Skin Tubular Structural Members <i>Teng, J.G., Yu, T., Wong, Y.L.</i>	26
Durability of GFRP Reinforcement Bars <i>Bakis, C.E.</i>	33
FRP Design Using Structural Mechanics Models <i>Oehlers, D.J., Haskett, M., Mohamed Ali, M.S., Lucas, W., Muhamad, R.</i>	37
Finite Element Modelling of FRP-to-Concrete Bond Behaviour Using the Concrete Damage Plasticity Theory Combined with a Plastic Degradation Model <i>Chen, J.F., Tao, Y.</i>	45
FRP Materials and Sustainability	51
Fiber Reinforced Cementitious Composites (FRCC) Plate for the Anchoring of FRP Sheet on Concrete Member <i>Jin, Q.X., Leung, C.K.Y.</i>	53
Study of Tensile Behavior for Interval Impregnated Hybrid Carbon/Basalt Fiber Sheet (C/BFS) <i>Wu, G., Jing, W.J., Wu, Z.S.</i>	57
Statistical Studies on Material Behavior of CFRP Sheets under Uniaxial Loads and Its Application in Reliability Analysis..... <i>Wang, W.W., Yang, W.</i>	61
Comprehensive Characterization of BFRP Applied in Civil Engineering <i>Li, H., Xian, G.J., Xiao, B., Wu, J.Y.</i>	65
Influence of Elevated Temperature on the Mechanical and Thermal Performance of BFRP Rebar <i>Wu, J.Y., Li, H., Xian, G.J.</i>	69
Composite Decks and Sustainable Development: a Case Study <i>Drissi-Habti, M., Chapeleau, X., Cournée, S.</i>	73
Matrix and Fabric Impregnation Influence on Textile Reinforcement Concrete Behaviour <i>Contamine, R., Si Larbi, A., Hamelin, P.</i>	77
Discrete Fiber Reinforced Polyurea for Hazard Mitigation <i>Carey, N.L., Myers, J.J.</i>	81
Experimental Research on the Fundamental Mechanical Properties of Presoaked Basalt Fiber Concrete <i>Ma, J.X., Qiu, X.M., Cheng, L.T., Wang, Y.L.</i>	85
All FRP Structures	89
Shear Buckling of GFRP Beam Webs <i>Manshadi, B.D., Vassilopoulos, A.P., Keller, T.</i>	91

Shear Wrinkling of GFRP Webs in Cell-Core Sandwiches	95
..... <i>Manshadi, B.D., Vassilopoulos, A.P., de Castro, J., Keller, T.</i>	
Pin-Bearing Strengths for Design of Bolted Connections in Pultruded Structures	99
..... <i>Zafari, B., Mottram, J.T.</i>	
Development of an Effective Joining Method for a Pultruded Hybrid CFRP/GFRP Laminate	103
..... <i>Nguyen, D.H., Mutsuyoshi, H., Shiroki, K., Ishihama, T.</i>	
A Consistent Design Concept for Bolted Connections in Standardized GFRP-Profiles	107
..... <i>Oppe, M., Knippers, J.</i>	
Composite Behavior of a Pultruded Hybrid CFRP-GFRP Beam with UFC Deck	111
..... <i>Mutsuyoshi, H., Shiroki, K., Nguyen, D.H., Ishihama, T.</i>	
Sensitivity Studies on Local Flange Buckling Equations for Pultruded Beams and Columns	115
..... <i>McCarthy, M.J., Bank, L.C.</i>	
Analytical Study on Buckling Modes of Simply Supported Delaminated Composite Beams	119
..... <i>Zhu, B., Zhou, D., Liu, W.Q.</i>	
Interlaminar Behavior of Paulownia Wood Sandwich Composites with Grooves	123
..... <i>Wan, L., Liu, W.Q., Fang, H., Zhou, D.</i>	
GFRP Structures Subjected to Dynamic Action	127
..... <i>Boscato, G., Russo, S.</i>	
GFRP Members in Free Vibrations Field, Dynamic Parameters of Profiles and 3D Structure	131
..... <i>Boscato, G., Russo, S.</i>	
Experimental Design on Multi Layers of LVL Fiber Reinforced Wood Composite Using Bagasse as Core Structure	135
..... <i>Meekum, U.</i>	
Shear Behavior of Glue-Laminated Composite Sandwich Beams	139
..... <i>Manalo, A., Aravinthan, T., Karunasena, W.</i>	
Flexural Behavior of FRP Reinforced Glulam Beams	144
..... <i>Zhou, Q., Xiao, Y.</i>	
Trial Design of Cable-Stayed Bridges Using Hybrid Composite Girders and Applicability to Free Passage Over Railway	148
..... <i>Nakamura, H., Maeda, K., Mutsuyoshi, H., Yaginuma, K., Matsui, T.</i>	
Performance Based Design of Laminated FRP Box Girders for Short Span Bridges	152
..... <i>Almansour, H., Cheung, M.</i>	
A Design Concept for an All Composite Road Bridge	156
..... <i>Leo, B., Chakraborty, A., Khennane, A.</i>	
Mechanical Model and Analysis of FRP Woven Web Structures	160
..... <i>Qi, Y.J., Feng, P., Ye, L.P.</i>	
GFRP-Polyurethane Sandwich Panels under Reversed Bending Fatigue	164
..... <i>Hale, M., Fam, A.</i>	
Development and Experimental Verification of a Pedestrian Slab Bridge Using GFRP Pultrusion Profiles	168
..... <i>Fujita, S., Maeda, K., Nakamura, H., Kitayama, N., Watanabe, T.</i>	
Study on Dynamic Characteristics of Light-Weight FRP Footbridge	173
..... <i>Jin, F.F., Feng, P., Ye, L.P.</i>	
Honeycomb Fiber-Reinforced Polymer Sandwich Panels for Fish Culture Tanks	177
..... <i>Davalos, J.F., Vantaram, A., Chen, A., Ray, I., Plunkett, J.D.</i>	
FRP Hybrid Structures and Concrete-Filled FRP Tubes 183	
Hybrid FRP-Concrete Structural Member: Research and Development in North America	185
..... <i>Chen, D., El-Hacha, R.</i>	

Hybrid FRP-Concrete Structural Member: Research and Development in Europe and Asia	
.....	<i>Chen, D., El-Hacha, R.</i> 191
Experimental Study on Flexural Behaviour of Hybrid GFRP/ Concrete Bridge Deck	
.....	<i>Liu, Y.Q., He, J., Fan, H.F., Chen, A.R., Dai, L.</i> 197
Experimental Study of GFRP-Concrete Hybrid Beams	
.....	<i>Zhao, F., Chen, C.H., Lou, W.J., Feng, P.</i> 202
In-Situ Load Tests and FE Modeling of Concrete Bridge with FRP Stay-in-Place Forms	
.....	<i>Wan, B.L., Foley, C.M.</i> 207
Structural Performance Evaluation of Precast FRP-Concrete Composite Deck with Concrete Wedge for Cable-Stayed Bridge	
.....	<i>Park, S.Y., Cho, K., Kim, S.T., Cho, J.R., Kim, B.S.</i> 211
Static and Fatigue Behaviors of Precast FRP-Concrete Composite Deck for Cable-Stayed Bridge	
.....	<i>Cho, K., Park, S.Y., Kim, S.T., Kim, B.S.</i> 215
Experimental Studies on FRP-Concrete Composite Deck with FRP Perfobond Shear Connectors	
.....	<i>Xue, W.C., Ge, C., Tan, Y., Wang, Y.S.</i> 219
Numerical and Experimental Investigation of Concrete-Filled FRP Tube	
.....	<i>Chung, W., Jang, H., An, Z.O.</i> 224
An Experimental Investigation into the Behaviour of Filament Wound Hybrid FRP-Concrete Beam	
.....	<i>Chakraborty, A., Khennane, A., Morozov, E.V.</i> 228
Experimental Study on Bending Performances of FRP-Concrete Composite T-Beams with Prefabricated BFRP Shell	
.....	<i>Zhu, H., Zhang, P., Wu, G., Wu, Z.S.</i> 232
A Comparative Study of Various FRP Shear Connectors for Sandwich Concrete Walls	
.....	<i>Woltman, G.D., Tomlinson, D.G., Fam, A.</i> 237
Smart FRP Structures	241
Effectiveness of Smart Dampers for Hybrid FRP Cable in Long- Span Cable-Stayed Bridge	
.....	<i>Wang, X., Wu, Z.S.</i> 243
A Smart FRP-Concrete Composite Beam Using FBG Sensors	
.....	<i>Wang, Y.L., Hao, Q.D., Ou, J.P.</i> 248
Smart CFRP Systems–Fiber Bragg Gratings for Fiber Reinforced Polymers	
.....	<i>Käseberg, S.F., Holschemacher, K.</i> 252
Sensor CFRP-Sheets for the Controlled Strengthening and Retrofitting of Reinforced Concrete Members	
.....	<i>Holschemacher, K., Käseberg, S.F.</i> 256
Electrically Conductive Nanocomposite Coating for Strain and Health Monitoring	
.....	<i>Luo, J.L., Li, H., Xian, G.J.</i> 260
Smart Composites for Durable Infrastructures – Importance of Structural Health Monitoring (SHM)	
.....	<i>Drissi-Habti, M.</i> 264
Concrete Structures Reinforced or Prestressed with FRP	269
Experimental Study on the Tension Stiffening Effect of GFRP RC Elements	
.....	<i>Baena, M., Turon, A., Torres, L., Miàs, C., Barris, C., Barbeta, G.</i> 271
Behavior of High-Strength Concrete Beams Reinforced with Different Types of Flexural Reinforcement and Fiber	
.....	<i>Yang, J.M., Min, K.H., Shin, H.O., Yoon, Y.S.</i> 275
Deflection Behaviour of Concrete Beams Reinforced with Different Types of GFRP Bars	
.....	<i>El-Gamal, S., AbduRahman, B., Benmokrane, B.</i> 279
Behavior of Continuous Concrete Beams Reinforced with FRP Bars	
.....	<i>El-Mogy, M., El-Ragaby, A., El-Salakawy, E.</i> 283

Testing of Large-Scale Two-Way Concrete Slabs Reinforced with GFRP Bars*Dulude, C., Ahmed, E., El-Gamal, S., Benmokrane, B.* 287

Development Length of Glass Fiber Reinforced Plastic (GFRP)/Steel Wire Composite Rebar*Hao, Q.D., Wang, Y.L., Ou, J.P.* 292

Deformation Behavior of Concrete Two-Way Slabs Reinforced with BFRP Bars Subjected to Eccentric Loading*Zhu, H.T., Zhang, Y.K., Gao, D.Y., Xiao, Z.L.* 296

Experimental Study on the Flexural Behavior of Concrete Beam Hybrid Reinforced with FRP Bars and Steel Bars*Ge, W.J., Zhang, J.W., Dai, H., Tu, Y.M.* 301

Study on the Flexural Capacity of Concrete Beam Hybrid Reinforced with FRP Bars and Steel Bars*Zhang, J.W., Ge, W.J., Dai, H., Tu, Y.M.* 304

Experiments According to ETAG to Determine Friction Effects on Deviated CFRP-Strips*Hwash, M., Knippers, J.* 308

Study of Static Load Tests of Bond-Type Anchors for CFRP Tendons*Cai, W.H., Zhang, J.W., Liang, S.T., Tu, Y.M.* 313

Bond Type Anchorage Systems for Permanent High Strength CFRP Ground Anchors*Sentry, M., Al-Mahaidi, R., Bouazza, A., Carrigan, L.* 317

Flexure-Shear Analysis of Concrete Beam Reinforced with GFRP Bars*Ramadass, S., Thomas, J.* 321

Effect of Bond Parameters on Recoverability of RC Bridge Columns Reinforced with Ordinary Rebars and Steel Fiber Composite Bars.....*Fahmy, M.F.M., Wu, Z.S., Wu, G.* 325

Effect of Reinforcement Detailing on the Behavior of GFRP-RC Beam-Column Joints*Mady, M., Hasaballa, M., El-Ragaby, A., El-Salakawy, E.* 330

Long-Term Performance335

Interfacial Crack Growth Behavior on RC Beams Strengthened with Prestressed CFL under Cyclic Bending Loads*Zhou, H., Huang, P.Y., Li, Z.W., Zheng, X.H., Xie, J.H.* 337

Effects on the Fatigue Lives of RC Beams Strengthened with CFL at Elevated Temperature under Cyclic Bending Loads*Huang, P.Y., Wang, H.Y., Zhou, H., Guo, X.Y., Zhou, Z.L.* 341

Fatigue-Loading Effect on RC Beams Strengthened with Externally Bonded FRP*Ferrier, E., Limam, A., Hamelin, P., Quiertant, M.* 344

Box Girders under Extreme Long-Time Static and Fatigue Loading*Meier, U., Müller, R., Barbezat, M., Terrasi, G.P.* 348

Experimental Study of Time-Dependent Behaviour of Concrete Members Reinforced with GFRP Bars*Miàs, C., Torres, L., Turon, A., Baena, M., Vilanova, I., Llorens, M.* 352

Hygrothermal Ageing of Basalt Fiber Reinforced Epoxy Composites*Xiao, B., Li, H., Xian, G.J.* 356

Moisture Diffusion in FRP Adhesively-Bonded Joints under Hot/Wet Environments*Jiang, X., Kolstein, H., Bijlaard, F.S.K.* 360

Durability of CFRP Bonding System under Freeze-Thaw Cycling*Yun, Y.C., Wu, Y.F.* 364

Bond Strength of Glass FRP Bars in Concrete Subjected to Freeze-Thaw Cycles and Sustained Loads*Alves, J., El-Ragaby, A., El-Salakawy, E.* 368

Long-Term Durability of FRP Cables under Maritime Conditions*Nishizaki, I., Sasaki, I.* 372

Temperature Effects on Full Scale FRP Bridge Using Innovative Composite Components*Sirimanna, C.S., Islam, M.M., Aravinthan, T.* 376

Modeling the Effect of Repeated Loading on the Behaviour of CFRP Confined Bond of Corroded Reinforcement	<i>Abbas, S., Rteil, A.</i>	381
Effects of Accelerated Ageing on the Adhesive Bond Between Concrete Specimens and External CFRP Reinforcements	<i>Benzarti, K., Quiertant, M., Marty, C., Chataigner, S., Aubagnac, C.</i>	385
Parametric Analysis for Creep of High-Strength Concrete Columns Confined by AFRP	<i>Ma, Y.S., Wang, Y.F.</i>	390
Fire, Impact and Blast Loading		395
Glassy-Rubbery Transition Behavior of Epoxy Resins Used in FRP Structural Strengthening Systems	<i>Jaipurari, A., Flood, J.P., Bakis, C.E., Lopez, M.M., He, X.J.</i>	397
Fire Tests on RC Beams Strengthened with NSM	<i>Palmieri, A., Matthys, S., Taerwe, L.</i>	401
Fire Performance of Water-Cooled Cellular GFRP Columns	<i>Bai, Y., Keller, T., Hugi, E., Ludwig, C.</i>	405
Flexural and Punching Performances of FRP and Fiber Reinforced Concrete on Impact Loading	<i>Min, K.H., Yang, J.M., Yoo, D.Y., Yoon, Y.S.</i>	410
Protection of Aged Cement Clinker Silo against High Impact and High Temperature Discharge	<i>Lim, B.K., Yang, M.H.</i>	415
Nonlinear Response of Steel-Fiber Reinforced Concrete Beams under Blast Loading: Material Modeling and Simulation	<i>Haido, J.H., Abu Bakar, B.H., Jayaprakash, J., Abdul-Razzak, A.A.</i>	419
Fire Behaviour of CFRP Prestressed High Strength Concrete Slabs	<i>Terrasi, G.P., Stutz, A., Barbezat, M., Bisby, L.A.</i>	423
Finite Element Modeling of Insulated FRP-Strengthened RC Beams Exposed to Fire	<i>Dai, J.G., Gao, W.Y., Teng, J.G.</i>	428
Effect of Fire and High Temperature on the Properties of Self Compacted Concrete	<i>Helal, M.A., Heiza, Kh.M.</i>	433
Educations, Applications and Design Guidelines		441
IIFC Educational Modules on Polymer Composites in Construction	<i>Bisby, L.A.</i>	443
Challenges in the Design and Delivery of an Online Postgraduate Course in Fibre Composites	<i>Aravinthan, T.</i>	447
Virtual Practice with Computer Aided Software toward Better Understanding of RC Beams Strengthened by External Bonded FRP	<i>Ferrier, E., Hamelin, P., David, B.</i>	452
Structural Remediation of Unreinforced Brick Masonry Walls of Heritage Palace Building with Carbon Fibre Reinforced Polymers.....	<i>Savardekar, S.K., Jamaji, R., Raikar, K.R.</i>	456
Inspection, Analysis and Loading Test of a Slab Bridge Strengthened with FRP Laminates	<i>Yan, D.M., Wu, C.L., Li, J.B., Chen, G.D.</i>	460
Structural Performance of Concrete Bridge Deck with Internal FRP Reinforcement	<i>Wan, B.L., Foley, C.M.</i>	464
Guidelines for Design of Honeycomb FRP Sandwich Panels	<i>Chen, A., Davalos, J.F.</i>	468
Load-Bearing Properties of an FRP Bridge after Nine Years of Exposure	<i>Sasaki, I., Nishizaki, I.</i>	474
Cost Optimum Design of Structural Fibre Composite Sandwich Panel for Flooring Applications	<i>Awad, Z.K., Aravinthan, T., Zhuge, Y.</i>	478
Author Index		A-I

Vol. II FRP Strengthening Structures

Bond and Interfacial Stresses Between FRP and Concrete	483
Effect of Load Distribution on IC Debonding in FRP-Plated RC Beams <i>Teng, J.G., Chen, G.M., Chen, J.F.</i>	485
Effect of Bar-Cutoff and Bent-Point Locations on Debonding Loads in RC Beams Strengthened with CFRP Plates <i>Eftekhar, M.R., Mostofinejad, D.</i>	490
Meso-Scale Modelling of FRP-to-Concrete Bond Behaviour Using LSDYNA <i>Li, X.Q., Chen, J.F., Lu, Y.</i>	494
Investigation on Fracture Behavior of FRP-Concrete Interface under Direct Shear <i>An, F.C., Cao, S.Y., Pan, J.L., Ge, Q.</i>	499
Towards a Standard Test Method for Assessing FRP-to-Concrete Bond Characteristics <i>Eveslage, T., Aidoo, J., Bro, W., Harries, K.A.</i>	504
Examination of Interfacial Stresses due to Crack Propagation in FRP Retrofitted RC Beams <i>Kabir, M.Z., Hojatkashani, A.</i>	508
A Rigorous Solution for Interfacial Stresses in Plated Beams <i>Narayanamurthy, V., Chen, J.F., Cairns, J.</i>	512
Evaluation of the Bond Behavior at the Intermediate Crack Element with a Special Test Procedure <i>Finckh, W., Zilch, K.</i>	517
Numerical Modeling of the FRP/Concrete Interfacial Behavior of FRP Shear-Strengthened Beams <i>Godat, A., Labossière, P., Neale, K.W.</i>	521
Analysis of Interfacial Bond Stress of Bonding Anchors for FRP Tendon <i>Zhao, Q.L, Li, F., Chen, H.S.</i>	525
Debonding Behavior of Skew FRP-Bonded Concrete Joints <i>Dai, J.G., Cao, Y.B.</i>	529
Effectiveness of U-Shaped CFRP Wraps as End Anchorages in Predominant Flexure and Shear Region <i>Khan, A.R., Ayub, T.</i>	533
Behavior of an Innovative End-Anchored Externally Bonded CFRP Strengthening System under Low Cycle Fatigue <i>Sadone, R., Quiertant, M., Chataigner, S., Mercier, J., Ferrier, E.</i>	537
Experimental Investigation of CF Anchorage System Used for Seismic Retrofitting of RC Columns <i>Sami, Q., Ferrier, E., Michel, L., Si Larbi, A., Hamelin, P.</i>	541
Experimental Study on Grooving Detail for Elimination of Debonding of FRP Sheets from Concrete Surface <i>Mostofinejad, D., Hajrasouliha, M.J.</i>	545
Interfacial Behavior Between Mechanically Fastened FRP Laminates and Concrete Substrate <i>Martinelli, E., Napoli, A., Realfonzo, R.</i>	548
FRP-to-Concrete Joint Assemblies Anchored with Multiple FRP Anchors: Experimental Investigation <i>Zhang, H.W., Smith, S.T.</i>	553
Temperature and Water-Immersion Effect on Mode II Fracture Behavior of CFRP-Concrete Interface <i>Imani, F.S., Chen, A., Davalos, J.F., Ray, I.</i>	557
Ultrasonic Evaluation of CFRP-Concrete Interface for Specimens under Temperature and Water-Immersion Aging Effects <i>Mahmoud, A.M., Ammar, H.H., Mukdadi, O.M., Ray, I., Imani, F.S., Chen, A., Davalos, J.F.</i>	562
Modified Beam Bond Test on Externally Bonded and Near Surface Mounted FRP Strengthened RC Beams <i>Kotynia, R.</i>	567
Experimental Investigation on Bond of NSM Strengthened RC Structures <i>Palmieri, A., Matthys, S.</i>	572

Bond Strength of BFRP Bars to Basalt Fiber Reinforced High-Strength Concrete	<i>Bi, Q.W., Wang, H.</i>	576
Bond Strength of FRP Rebar to Concrete: Effect of Concrete Confinement	<i>Quayyum, S., Rteil, A.</i>	581
Bond Strength of Fiber Reinforced Polymer (FRP) Bars in Autoclaved Aerated Concrete (AAC)	<i>Ayudhya, B.I.N., Ungkoon, Y.</i>	585
Bond Mechanism of Carbon Fiber Reinforced Polymer Grid to Concrete	<i>Ding, L.N., Rizkalla, S., Wu, G., Wu, Z.S.</i>	589
Confinement of Concrete by FRP in Compression		593
Effect of Geometric Discontinuities on FRP Strain Efficiency in FRP-Confined Circular Concrete-Filled Steel Tubes	<i>Li, S.Q., Chen, J.F., Bisby, L.A., Hu, Y.M., Teng, J.G.</i>	595
The Ultimate Condition of FRP Confined Concrete Columns: New Experimental Observations and Insights	<i>Bisby, L.A., Stratford, T.J.</i>	599
Bearing Strength of CFRP Confined Concrete	<i>Scheffers, C.A., Sri Ravindrarajah, R., Reinaldy, R.</i>	603
Confinement Behaviour of Eccentrically Loaded RCC Columns Using FRP Sheets	<i>Chakrabarti, A.</i>	607
Concrete Column Confinement with Mechanism-Based Composite Bistable Structures	<i>Wan, C., Quon, C., Cheng, L.</i>	610
Confined Circular and Square R.C. Sections: an Analytical Model for the Prediction of Ultimate Strength	<i>Nisticò, N., Monti, G., Lovo, V.</i>	614
Stress-Strain Modeling of Rectangular Concrete Columns Confined by FRP Jacket	<i>Wei, Y.Y., Wu, Y.F.</i>	618
Axial Behavior of FRP Jacketed Extended Rectangular Members Constructed with Low Strength Concrete	<i>Akgun, D., Demir, C., Ilki, A.</i>	622
Nonlinear Micromechanics-Based Finite Element Analysis of FRP-Rapped Concrete Columns Subjected to Axial Load	<i>Baky, A., Demers, M., Yahiaoui, A., Neale, K.W.</i>	626
Compressive Strength of Concrete Cylinders Confined with CFRP Wraps	<i>Khan, A.R., Zafar, N.S.</i>	630
Procedure for the Statistical Determination of the Design FRP-Confined Concrete Strength	<i>Monti, G., Nisticò, N., Lovo, V., Alessandri, S., Santini, S.</i>	634
Performance Evaluation of SFRP-Confined Circular Concrete Columns	<i>Mashrik, M.A., El-Hacha, R., Tran, K.</i>	638
Mechanical Behavior of Concrete Columns Confined by Laterally Pre-Tensioned FRP	<i>Zile, E., Tamužs, V., Daugevičius, M.</i>	642
Effect of CFRP and GFRP Confinement on Behavior of Square Lightweight Concrete Specimens	<i>Oskouei, A.V., Kivi, M.P., Boroujeni, S.T.</i>	646
Confinement of Concrete Piles with FRP	<i>Seliem, H.M., Ding, L.N., Rizkalla, S.</i>	650
Three-Dimensional Finite Element Model for FRP-Confined Circular Concrete Cylinders under Axial Compression	<i>Xiao, Q.G., Teng, J.G., Yu, T., Lam, L.</i>	654
Numerical Analysis of Rectangular Reinforced Concrete Columns Confined with FRP Jacket under Eccentric Loading	<i>Hajsadeghi, M., Alaei, F.J.</i>	658
Flexural Strengthening of Concrete Beams and Slabs		663
Flexural Strengthening of Reinforced Concrete Beams with Textile Reinforced Concrete (TRC)	<i>Si Larbi, A., Contamine, R., Ferrier, E., Hamelin, P.</i>	665

The Flexural Behavior of Beams Strengthened with FRP Grid and ECC	<i>Ding, Y., Chen, X.B., Chen, W.Y.</i>	668
Comparison of Different Repairing Techniques Used for Rehabilitation of Initially Cracked RCC Beams	<i>Qureshi, L.A., Qureshi, K.A., Sultan, T., Munir, J.</i>	672
Analysis on Mechanical Behavior of RC Beams Strengthened with Inorganic Adhesive CFRP Sheets	<i>Zhang, X., Li, S.B., Yang, L.L., Kong, X.F.</i>	676
Experimental Study of Concrete Beams Strengthened with CFRP Sheets under Simulated Vehicles Loads	<i>Wang, W.W., Zhao, G.F., Huang, C.K.</i>	681
A Systematic Study of Rehabilitation of Reinforced Concrete T-beam Structures Using Externally Bonded FRP Composites	<i>Davalos, J.F., Chen, A., Ray, I., Justice, A.</i>	685
Basalt FRPs for Strengthening of RC Members	<i>Serbescu, A., Guadagnini, M., Pilakoutas, K., Palmieri, A., Matthys, S.</i>	691
Load-Carrying Capacity of Flexural Reinforced PC Beams with Pretensioned AFRP Sheet	<i>Kurihashi, Y., Kishi, N., Ali, A.M., Mikami, H.</i>	695
Flexural Performance of RC Beams Strengthened with Prestressed AFRP Sheets: Part I. Experiments	<i>Deng, Z.C., Xiao, R.</i>	699
Flexural Performance of RC Beams Strengthened with Prestressed AFRP Sheets: Part II. Theoretical Analysis	<i>Deng, Z.C., Xiao, R.</i>	704
Numerical Simulation on Flexural Reinforcing Effects of AFRP Sheet for Damaged RC Girders	<i>Kishi, N., Komuro, M., Mikami, H.</i>	708
A Study on the Applicability of ECE Technique on Chloride Contaminated Concrete Retrofitted with FRP Strips	<i>Anderson, M., Ray, I., Chen, A., Davalos, J.F.</i>	712
Finite Element Modeling of RC Beams Strengthened in Flexure with Prestressed NSM CFRP Strips	<i>Omran, H.Y., El-Hacha, R.</i>	718
Advances of Finite Element Analysis for FRP Concrete Beams	<i>Zhang, Y.X., Lin, X.S.</i>	722
Nonlinear Finite Element Analysis of Composite Steel/FRP- Reinforced Concrete Beams Using a New Beam Element	<i>Lin, X.S., Zhang, Y.X.</i>	727
Non-Bolted Anchorage Systems for CFRP Laminates Applied for Strengthening of RC Slabs	<i>Donchev, T., Nabi, P.</i>	731
Arching Action in Laterally Restrained GFRP Reinforced Slabs	<i>Tharumarajah, G., Taylor, S.E., Robinson, D., Cleland, D.J.</i>	735
Flexural Strengthening of RC Continuous Beams Using Hybrid FRP Sheets	<i>Akbarzadeh, H., Maghsoudi, A.A.</i>	739
Comparative Study of Deflection Equations for FRP RC Beams	<i>Vilanova, I., Barris, C., Torres, L., Miàs, C., Baena, M., Garcia, V.O.</i>	744
Experimental Study on Deformation Recovery and Residual Strength of FRP RC Beams	<i>Oh, M.H., Hong, S.N., Kim, T.W., Cui, J., Park, S.K.</i>	748
Shear Strengthening of Concrete Beams		753
Influence of the Concrete Properties in the Effectiveness of the NSM CFRP Laminates for the Shear Strengthening of RC Beams	<i>Dias, S., Barros, J.</i>	755
Experimental Tests on FRP Shear Retrofitted RC Beams	<i>Nuti, C., Santini, S., Sguerri, L.</i>	759
Influence of Transverse Steel on the Performance of RC T-Beams Strengthened in Shear with GFRP Strips	<i>Panda, K.C., Barai, S.V., Bhattacharyya, S.K.</i>	763
Shear Design Equations for Concrete Girders Strengthened with FRP	<i>Murphy, M.S., Belarbi, A., Kuchma, D.</i>	767

The Shear Behavior of Beams Strengthened with FRP Grid	Chen, W.Y., Chen, X.B., Ding, Y.	772
Efficiency of RC T-Section Beams Shear Strengthening with NSM FRP Reinforcement	Kotynia, R.	776
Mechanical Model to Simulate the NSM FRP Strips Shear Strength Contribution to RC Beams	Bianco, V., Barros, J.A.O., Monti, G.	781
Shear Strengthening of RC Beams by Means of NSM FRP Strips: Constitutive Law of a Single Strip	Bianco, V., Monti, G., Barros, J.A.O.	785
Size Effects in Reinforced Concrete Beams Strengthened with CFRP Straps	Nelson, L.A., Lees, J.M.	789
Shear Capacity of Flexural Strengthened Reinforced Concrete Structures with CFRP Materials	Finckh, W., Zilch, K.	794
Strengthening of Concrete Columns, Walls and Frames		799
Emergency Retrofit for Damaged RC Columns by Fiber Belts Prestressing and Plywoods	Kyoda, N., Yamakawa, T., Nakada, K., Javadi, P., Nagahama, A.	801
Seismic Retrofitting by FRP Jacketing and Prediction Method of Ultimate Deformation	Jirawattanasomkul, T., Anggawidijaja, D., Ueda, T.	806
Seismic Performance of FRP-Confined Circular RC Columns	Wang, Z.Y., Wang, D.Y., Sheikh, S.A., Liu, J.T.	810
Cyclic Behaviour of FRP Confined RC Rectangular Columns with High Aspect Ratio	Napoli, A., Nunziata, B., Realfonzo, R.	815
Numerical Simulation of FRP-Jacketed RC Columns Subjected to Cyclic Loading	Teng, J.G., Lu, J.Y., Lam, L., Xiao, Q.G.	820
Concrete Column Shape Modification with FRP and Expansive Cement Concrete	Yan, Z.H., Pantelides, C.P., Duffin, J.B.	824
Flexural Behavior of Concrete Columns Strengthened with Near Surface Mounted FRP Bars	Danesh, F., Noveiri, B.B.	829
Use Near Surface Mounted FRP Rods for Flexural Retrofitting of RC Columns	Sarafraz, M., Danesh, F.	833
Effect of FRP Strengthening on the Behavior of Shear Walls with Opening	Asfa, M., Mostofinejad, D., Abdoli, N.	837
Seismic Assessment of FRP-Retrofitted RC Frames Using Pushover Analysis Considering Strain Softening of Concrete	Mahini, S.S., Hadigheh, S.A., Maheri, M.R.	841
Seismic Performance Analysis of FRP Reinforced Concrete Frame Structure	Peng, Y.P., Ma, M., Dong, G.	845
The Anchorage Behavior of FRP EBR in the Plastic Zone of RC Beams	Ceroni, F., Pecce, M., Bibbò, F.A.	849
Application of FRP for Punching Shear Retrofit of Concrete Slab-Column Connections	Polak, M.A., Lawler, N.	854
Beam-to-Column Connection of a Precast Concrete Frame Strengthened by NSM CFRP Strips	da Fonseca, T.de C.C.S., de Almeida, S.F., de Hanai, J.B.	858
Strengthening of Steel Structures		863
Treatment of Steel Surfaces for Effective Adhesive Bonding	Teng, J.G., Fernando, D., Yu, T., Zhao, X.L.	865
Effect of Surface Preparation on the Strength of FRP-to-Mild Steel and FRP-to-Stainless Steel Joints	Kim, S.J., Smith, S.T., Young, B.	869

Modeling of Steel Beams Strengthened with CFRP Strips Including Bond-Slip Properties	Kim, Y.J., Harries, K.A.	873
Temperature Effect on Adhesively Bonded CFRP and Steel Double Strap Joints	Nguyen, T.C., Bai, Y., Zhao, X.L., Banbach, M.R., Al-Mahaidi, R.	877
Repairing Method for the Steel Members by CFRP Strand Sheets	Hidekuma, Y., Kobayashi, A.i, Tateishi, A., Nagai, M., Miyashita, T.	881
Temperature Effects in Adhesively Bonded FRP Strengthening Applied to Steel Beams: Experimental Observations	Stratford, T.J., Bisby, L.A.	886
Experimental Study on Bond Behaviour between UHM CFRP Laminate and Steel	Wu, C., Zhao, X.L., Al-Mahaidi, R., Duan, W.H.	890
Static Behavior of Tension Steel Plate Strengthened with Pre-Stressed CFRP Laminates	Ye, H.W., Qiang, S.Z., König, C., Plum, R., Ummenhofer, T.	894
Fatigue Life Prediction of Steel Beams Strengthened with a Carbon Fibre Composite Plate	Deng, J.	899
Tests on CFRP Repaired Welded Thin-Walled Cross-Beam Connections	Xiao, Z.G., Zhao, X.L., Tong, L.W.	903
Fatigue Behavior of CFRP Repaired Non-Load Carrying Cruciform Welded Joints	Chen, T., Gu, X.L., Zhao, X.L.	907
Tests on CFRP Strengthened Aluminium RHS Subject to End Bearing Force	Zhao, X.L., Phiphat, P.	911
Lateral Torsional Buckling of Steel I-Beam Retrofitted Using FRP Sheets: Analytical Solution and Optimization	Kabir, M.Z., Seif, A.E.	915
Experimental Study on Behavior of FRP Anti-Buckling Strengthening Steel Members	Bekey, S., Feng, P., Ye, L.P.	919
Effects of FRP Reinforcements on the Buckling and Reduced Stiffness Criteria of Compressed Steel Cylinders	Yamada, S., Bhetwal, K.K., Yanagida, M., Matsumoto, Y.	925
Numerical Simulation of Prestressed CFRP Plate Strengthened Steel-Concrete Composite Girders	Zangeneh, P., Omran, H.Y., El-Hacha, R.	929
Experimental Study on Fatigue Behavior of I-Steel Beam Strengthened with Different FRP Plates	Wu, G., Liu, H.Y., Wu, Z.S., Wang, H.T.	933
Strengthening of Masonry and Timber Structures		937
Experimental Study on Seismic Behavior before and after Retrofitting of Masonry Walls Using FRP Laminates	Oday, A.S., Li, Y.M., Houssam, M.A.	939
Strengthening of Masonry Structures Using FRP – Experimental Research	Witzany, J., Cejka, T., Zigler, R.	943
Improvement of Transverse Connection of Masonry Walls through AFRP Bars	Menegotto, M., Monti, G., Salvini, S., Vailati, M.	947
FRP-to-Softwood Joints: Experimental Investigation	Wan, J., Smith, S.T., Qiao, P.Z.	951
Author Index		A-XI

Vol. I FRP for Future Structures

Keynote Papers

Innovative Textile-Based Composites for Strengthening and Seismic Retrofitting of Concrete and Masonry Structures

Thanasis Triantafillou (triant@upatras.gr)

Department of Civil Engineering, University of Patras, Patras, Greece

ABSTRACT The author reviews experimental studies which have provided fundamental knowledge on the use of a new generation of composite materials, namely textile-reinforced mortars (TRM), as strengthening and seismic retrofitting materials of concrete and masonry structures. TRMs are investigated as a means: to provide confinement in plain and reinforced concrete (RC), to increase the deformation capacity of old-type RC columns subjected to simulated seismic loading, to increase the shear and flexural resistance of RC members and to increase the out-of-plane or in-plane strength of unreinforced masonry walls. In all cases, the effectiveness of TRM systems is quantified through comparison with equivalent fiber-reinforced polymer (FRP) ones. Based on the results it is concluded that TRM jacketing is an extremely promising new technique, which will enjoy the attention of the research community and will be employed in numerous applications in the next decades.

1 INTRODUCTION

The increasing popularity of fiber-reinforced polymers (FRP) as a means of strengthening and seismic retrofitting of existing structures derives from numerous attractive features of these materials, such as: high specific strength (i.e. strength to weight ratio), corrosion resistance, ease and speed of application and minimal change of cross section dimensions. Despite these well-established advantages over other methods, the FRP strengthening technique entails a few drawbacks, which are mainly attributed to the organic resins used to bind and impregnate the fibers. The replacement of organic binders with inorganic ones, e.g. cement-based polymer-modified mortars, would seem as the logical course of action, targeting at the alleviation of all resin-related problems. Nevertheless, the substitution of FRP with fiber-reinforced mortars would be inhibited by the relatively poor bond conditions in the resulting cementitious composite as, due to the granularity of the mortar, penetration and impregnation of fiber sheets is very difficult to achieve. Enhanced fiber-matrix interactions could be achieved when continuous fiber sheets are replaced by textiles, resulting in a new generation of materials, which may be called Textile-Reinforced Mortars (TRM), and may be thought of as an alternative to FRP in the field of strengthening and seismic retrofitting.

Textiles comprise fabric meshes made of long woven, knitted or even unwoven fiber rovings in at least two (typically orthogonal) directions (Figure 1). The quantity and the spacing of rovings in each direction can be

independently controlled, thus affecting the mechanical characteristics of the textile and the degree of penetration of the mortar matrix through the mesh openings. The latter is a measure of the composite action achieved for the mortar-grid structure through mechanical interlock. For the polymer-modified cementitious matrix of externally applied TRM overlays used for strengthening purposes, the following requirements should be met: no shrinkage; high workability (application should be possible using a trowel); high viscosity (application should not be problematic on vertical or overhead surfaces); low rate of workability loss (application of each mortar layer should be possible while the previous one is still in a fresh state); and sufficient shear (hence, tensile) strength, in order to avoid premature debonding. In case E-glass fiber textiles are used, the cement-based matrix should be of low alkalinity.

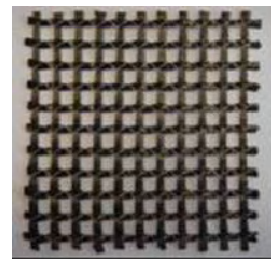


Figure 1 Two-directional carbon fiber-based textile

In this paper, the author reviews experimental studies which have provided fundamental knowledge on the use of TRM as strengthening and seismic retrofitting materials: to provide confinement in plain and reinforced

concrete (RC); to increase the deformation capacity of old-type RC columns subjected to simulated seismic loading; to increase the resistance of RC members in shear and flexure; and to increase the strength and deformation capacity of masonry walls subjected to out-of-plane or in-plane loading. In all cases, the effectiveness of TRM systems is quantified through comparison with equivalent FRP ones. Based on the results it is concluded that TRM jacketing is an extremely promising new technique, which will enjoy the attention of the research community and will be employed in numerous applications in the next decades.

2 CONFINEMENT OF CONCRETE

2.1 Axially loaded concrete

First we study experimentally the effectiveness of TRM versus FRP jackets as a means of confining unreinforced or reinforced concrete members subjected to concentric compression. The test plan included the following groups of specimens: (i) unreinforced cylinders with diameter 150 mm and height 300 mm (Series A); (ii) short column – type prisms of both reinforced and unreinforced concrete, with rectangular cross section 200×200 mm and height 375 mm (Series B). Each specimen series was cast using the same ready-mix concrete batch (but slightly different from series to series, in terms of water to cement ratio). The steel used for both longitudinal and transverse reinforcement in Series B specimens (see configurations in Figure 2) had an average yield stress equal to 560 MPa. The four corners of all rectangular prisms were rounded at a radius equal to 25 mm.

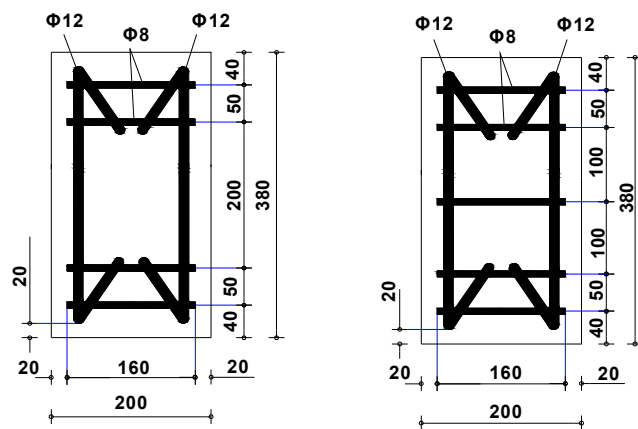


Figure 2 Reinforcement configurations for specimens in Series B (dimensions in mm)

All specimens received textile sheets as externally bonded reinforcement, except for some of the Series B specimens in which the epoxy resin – impregnated jackets consisted of fabrics (unidirectional fiber sheets). All confining systems were applied “as usual”, that is with a single textile (or fabric) sheet wrapped around

each specimen until the desired number of layers was achieved. The bonding agent was either epoxy resin or polymer-modified cement mortar, applied to the concrete surface, in between all layers and on top of the last layer. Application of the mortars was made in approximately 2 mm thick layers with a smooth metal trowel.

Specimens are given the notation Y_XN , where: Y denotes the series designation (A, B); X denotes the type of jacket (C for the unjacketed/control specimens, M_A for Series A cylinders with mortar jackets, M_B for Series B prisms with mortar jackets (mortar quality in this case being different from mortar M_A) and R for resin-based jackets (FRP); N denotes the number of layers.

Two different commercial unwoven textiles with equal quantity of high-strength carbon fiber rovings in two orthogonal directions were used. The mass of fibers in the textile used for all specimens of Series A (Tex1) was 168 g/m^2 and the nominal thickness of each layer (corresponding to the equivalent smeared distribution of fibers) was 0.047 mm. The corresponding values in the textile used in Series B receiving mortar were double (in this case, i.e. in Tex2, the rovings were impregnated with a low strength polymer). The fabric used for specimens of Series B receiving epoxy resin had a unit mass of 300 g/m^2 and a nominal thickness of 0.17 mm. The guaranteed tensile strength of the fiber sheets in each direction was 3350 MPa for Tex1, 3545 MPa for Tex2 (when the nominal thickness is used) and 3790 MPa for the fabric; the elastic modulus for all carbon fiber materials ranged between 225 GPa and 230 GPa. Mortars M_A and M_B were commercial dry polymer-modified cement-based binders with a 28-day compressive and flexural strength equal to 30.6 MPa and 4.2 MPa, respectively, for M_A and 22.1 MPa and 6.8 MPa, respectively, for M_B .

The response of all specimens in uniaxial compression was obtained through monotonically applied loading in displacement control. Loads were measured from a load cell and displacements were obtained using external displacement transducers. From the applied load and average displacement measurements the stress-strain curves were obtained for each test (selected results are given in Figure 3). All stress-strain plots for TRM- and FRP- confined reinforced concrete specimens are characterized by an ascending branch, which nearly coincides with that for unconfined concrete, followed by a second nearly linear one, which drops at a point where the jacket ruptured due to longitudinal bar buckling at specimens’ corners. Past the peak load, FRP-confined specimens exhibited an explosive type of failure which was not preceded by any kind of visible jacket damage, due to the release of a large amount of strain energy stored in the column. On the contrary, prior to strength loss, TRM jackets experienced gradual fracture and a

post-peak behaviour that was distinctively more compliant than their resin-based counterparts.

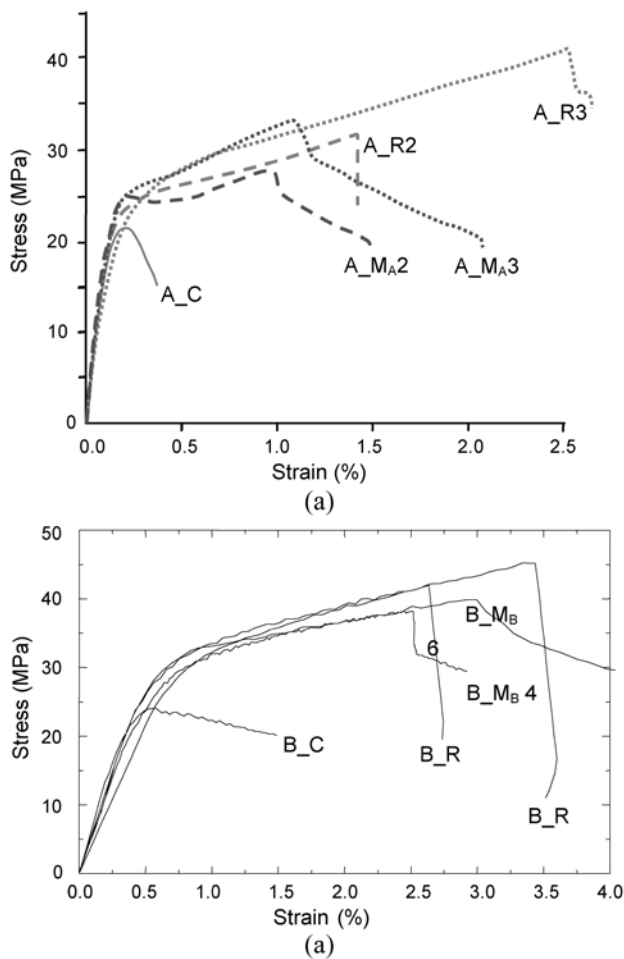


Figure 3 Typical stress-strain curves for (a) Series A (plain concrete cylinders) and (b) Series B (RC prisms with stirrups every 100 mm)

Based on the response of confined specimens made of plain concrete, it is concluded that: (a) TRM confining jackets provide substantial gain in compressive strength and deformation capacity. This gain is higher as the number of confining layers increases and depends on the shear strength of the polymer-modified mortar, which determines whether failure of the jacket will occur due to fiber fracture or debonding. (b) Compared with their resin-impregnated counterparts (FRP), TRM jackets may result in reduced effectiveness, depending on the type of mortar. (c) Failure of mortar-impregnated textile jackets is less abrupt compared to that of their resin-impregnated counterparts, due to the slowly progressing fracture of individual fiber bundles. A more detailed analysis of the results as well as some modeling aspects of TRM-confined concrete may be found in Triantafillou et al. (2006) and Bournas et al. 2007. Generally, similar conclusions apply for the case of reinforced concrete specimens; TRM jackets seem to be slightly less effective in terms of both strength increase and deformation capacity, by approximately 10%.

2.2 Seismic retrofitting

In this section selected results are presented as part of an experimental investigation of the effectiveness of TRM jacketing in plastic hinge confinement of old-type RC columns designed with poorly detailed reinforcement. The increase in ductility provided by TRM jackets is compared with the one provided by equivalent (that is with the same amount of fibers in the circumferential direction) FRP ones. Three full-scale reinforced concrete columns were cast using ready-mix concrete. The columns measured 1.80 m in height and had a cross section of 250 mm×250 mm. Testing was done in a cantilever configuration, with a shear span of 1.60 m. The geometry of the columns, the reinforcement detailing and the general set-up of the test are shown in Figure 4. Details are provided in Bournas et al. (2007) and an in-depth experimental investigation for columns with lap-splices is given in Bournas et al. (2010).

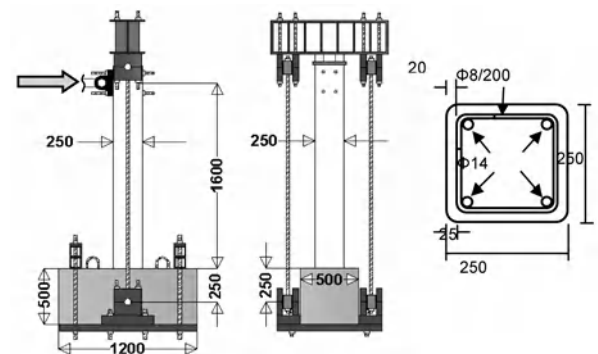


Figure 4 Geometry of columns and details of cross section

The columns were cast using concrete of mean 28-day compressive strength equal to 25 MPa. The steel used for both longitudinal and transverse reinforcement (both smooth) had an average yield stress equal to 372 MPa. Special attention was given to the appropriate anchoring of longitudinal reinforcement into the specimens' footings in order to minimize slippage. One column was unstrengthened (control specimen), another one received a four-layer TRM jacket in the plastic hinge region (jacket height being equal to 430 mm, accounting for the calculated height of the plastic hinge) and a third column was jacketed with two-layers of resin-impregnated carbon fiber fabric (FRP). The materials used for jacketing were identical to the ones used for strengthening specimens of Series B in the previously described experimental investigation. The columns were subjected to lateral cyclic loading under a constant axial load of 460 kN corresponding to 30% of the member's compressive strength. The lateral load was applied using a horizontally positioned actuator and the axial load was exerted by a set of four hydraulic cylinders. Displacements at the plastic hinge region were monitored using six rectilinear displacement transducers. The load versus piston

displacement curves for all specimens are given in Figure 5.

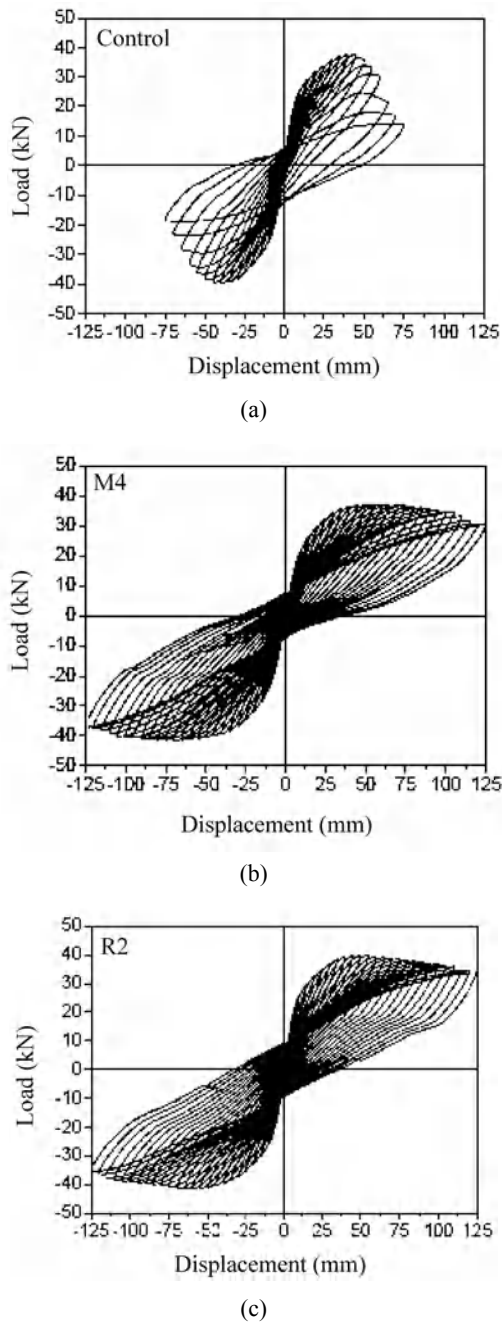


Figure 5 Load-displacement curves for (a) the control specimen, (b) the TRM-confined specimen (M4), and (c) the FRP-confined specimen (R2)

The performance and failure mode of all tested columns was controlled by flexure. The unretrofitted column (Figure 5a) attained a drift ratio (tip displacement divided by height) at failure of about 3.6%. The concrete cover and part of the core over the lower 200 mm of the column disintegrated and bar buckling initiated after the concrete cover spalled off at a drift ratio of about 3%. The behavior of the two retrofitted columns was very similar (Figures 5b and 5c for columns M4 and R2,

respectively), but quite different from and far better than their unretrofitted counterpart. Member deformation capacity increased by a factor of more than two, corresponding to a drift ratio at failure of about 7.5%; peak resistance was practically the same as in the unretrofitted column; and the post peak response was quite stable, displaying gradual strength degradation. Whereas the CFRP jacket in column R2 exhibited limited rupture over the lower 50 mm at 7.2% drift ratio (in the pull direction), the TRM jacket remained intact until the test was terminated at 7.8% drift ratio. When the jackets were removed in both retrofitted columns after the end of the tests, a completely disintegrated concrete core was exposed, one that had been kept in place by the heavy confinement provided by the jackets (both FRP and TRM).

3 SHEAR STRENGTHENING OF RC

The aim of this part of the experimental program was to examine the effectiveness of TRM jackets as strengthening reinforcement of shear-critical RC members. The investigation was carried out on six beams deficient in shear (i.e. with a large spacing of stirrups in the shear span) in four point bending. The beams measured 2.60 m in length and had a cross section of 150 mm×300 mm. The geometry of the beams, the reinforcement detailing and the general set-up of the test are shown in Figures 6a, b. A more detailed description of this study is given in Triantafillou and Papanicolaou (2006).

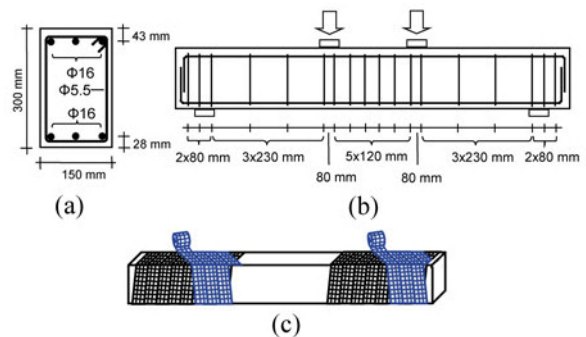


Figure 6 (a)-(b) Geometry of beams, (c) spiral application of strips at the shear spans

The beams were cast using a ready-mix concrete of mean 28-day compressive strength equal to 30.5 MPa. The steel used for transverse and longitudinal reinforcement had an average yield stress equal to 275 MPa and 575 MPa, respectively. Textile, mortar (type M_A) and resin matrices were the same materials as those in the experimental study involving confined specimens made of plain concrete. The influence of three parameters was considered in the experimental investigation, namely the use of inorganic mortar versus resin-based matrix material for the textile reinforcement, the number

of layers (one versus two) and the use of conventional wrapping versus “spirally applied” textiles. Here, “conventional wrapping” corresponds to a single textile sheet being wrapped around the shear span until the desired number of layers is achieved. The bonding agent was either epoxy resin or polymer-modified cement mortar, applied to the concrete surface, in between all layers and on top of the last layer. “Spirally applied” jacketing (Figure 6c) was implemented in one beam only and involved the formation of each layer through the use of a single strip, approximately 150 mm wide. The first strip was wrapped around the member in a spiral configuration, starting from one end of the shear span and stopping at the other; the next strip was wrapped in the same configuration but in a direction opposite to that of the first strip. Both strips formed a 10° angle with respect to the transverse to the member axis.

Four of the beams were tested monotonically and two of them were subjected to cyclic loading. One of the four monotonically tested beams served as a control specimen (C); a second one was wrapped with two layers of mortar-based jacket in the shear span (M2); a third beam was identical to the second but with a resin-based matrix material for the textile reinforcement (R2); and a fourth beam was strengthened with jackets formed by spirally applied strips (M2-s). The next two specimens (subjected to cyclic loading a few months later than the previous four) were identical to the second and third, but with one layer (instead of two) of textile in a mortar-based (M1) and a resin-based (R1) matrix, respectively. Specimens C, M2, R2 and M2-s were tested monotonically, whereas the remaining two were subjected to quasi-static cyclic loading, all in displacement control. The load was applied using a vertically positioned actuator and the displacements were measured at mid-span using two external linear variable differential transducers mounted on both sides of the specimens. The load versus mid-span displacement curves for all specimens are given in Figure 7.

The control beam (C) failed in shear, as expected, through the formation of diagonal cracks in the shear spans; the ultimate load was 116.5 kN. No sudden drop in the load was recorded after diagonal cracking, as considerable contribution to shear resistance was provided by both the stirrups crossing the crack and the strong dowel action (activated by the three $\text{\O}16$ mm longitudinal rebars).

The behavior of beams R2, M2, M2-s and R1 indicated that shear failure was suppressed and that failure was controlled by flexure: cracks in the constant moment region became wide and yielding of the tension reinforcement resulted in a nearly horizontal branch of the force versus displacement curve. The maximum loads in specimens R2, M2 and M2-s were 233.4 kN, 243.8 kN and 237.7 kN, respectively, that is nearly the

same. This confirms the fact that the shear strengthening scheme selected in this study did not affect the flexural resistance. But the increase in shear resistance was dramatic (more than 100%), regardless of the strengthening scheme: two layers of textile reinforcement (either in the form of continuous sheets or in the form of spirally applied strips) with the cementitious binder performed equally well to the epoxy-bonded (FRP) jacket (with two layers of textile reinforcement). Specimen R1 experienced a flexural yielding failure mode with unequal capacities in the push and pull directions (261.9 kN and 201.4 kN, respectively), possibly due to the unintentionally larger concrete cover at the top of each beam compared to the bottom. Specimen M1 failed in shear (at a peak load of 200.1 kN); this was evident by diagonal cracking in the shear span as well as by the rather sudden strength and stiffness degradation. In this case, the application of a single-layer TRM jacket resulted in a substantial increase in the specimen’s shear capacity with respect to the control specimen, in the order of 70%. It should be noted that for specimen M1: (i) fracture of the fibers in the cement-based jacket was gradual, starting from a few fiber bundles and propagating slowly in the neighboring fibers; and (ii) contrary to conventional FRP jackets, beam cracking was clearly visible on the TRM jacket, a feature that facilitates damage assessment.

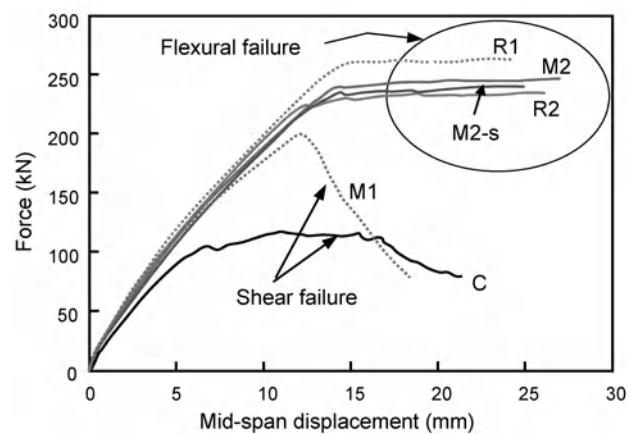


Figure 7 Force – mid-span displacement curves for all beams tested (for beams M1 and R1 subjected to cyclic loading the envelope curves in the push direction are given)

Overall, it may be concluded that the TRM jackets employed in this study were quite effective in increasing the shear resistance of reinforced concrete members. Two layers of textile reinforcement (with a nominal thickness per layer equal to only 0.047 mm in each of the principal fiber directions) were sufficient to prevent sudden shear failure, whereas one layer proved less effective compared to its resin-bonded counterpart, but still sufficient to provide a substantially increased shear resistance.

4 FLEXURAL STRENGTHENING OF RC

4.1 Beams

In this part of the investigation the effectiveness of TRM as externally applied flexural strengthening reinforcement of RC beam-type members was examined. The results reported here refer to testing of three under-reinforced beams in four-point bending, at a span length of 2.0 m and a shear span of 0.75 m. The beams had a cross section of 150×250 mm and were reinforced with 2Ø12 longitudinal rebars on each side (top and bottom), at a cover equal to 25 mm. The shear reinforcement comprised Ø8 stirrups at a small spacing equal to 100 mm, to ensure that failure would be controlled by flexural yielding. Self-compacting concrete was used for casting of the beams (mix design and production were performed in the laboratory within the framework of a parallel experimental investigation); mean 28-day compressive strength was equal to 34.5 MPa. The steel reinforcement had an average yield stress equal to 530 MPa. Textile, polymer-modified mortar (type M_A) and epoxy resin matrices were the same materials as those in the experimental study involving confined cylinders made of plain concrete.

One of the three beams was tested without strengthening, as a control specimen (C_{fl}); a second one was strengthened with four layers of textile bonded with cement-based mortar (M4_{fl}); the third beam was identical to the second but with an epoxy resin-based matrix material for the textile reinforcement (R4_{fl}). The externally bonded reinforcement had a width and a length equal to 120 mm and 1.90 m, respectively, so that its distance from each support was equal to 50 mm. All beams were tested monotonically with the load applied using a vertically positioned actuator and a heavy spread beam; the displacements were measured at mid-span using two external linear variable differential transducers mounted on both sides of the beams. The load versus mid-span displacement curves for all beams are given in Figure 8.

The control specimen (C_{fl}) displayed the standard nearly-bilinear response characteristics of under-reinforced beams. Strengthening with the epoxy-impregnated textile (beam R4_{fl}) resulted in increased strength (by approximately 50%) and increased stiffness, as expected; failure in this case was rather sudden, due to the tensile fracture of the externally bonded reinforcement at mid-span (at a load of 125 kN). The TRM-strengthened beam (M4_{fl}) displayed similar characteristics to its epoxy-bonded counterpart, with four distinct differences: its response was a little more ductile; yielding initiated at a lower load; the ultimate load was lower (111 kN); and the failure mechanism was governed by debonding at the end (anchorage) of the external reinforcement due to inter-laminar shearing. It is believed that the slightly

lower stiffness and higher ductility characteristics of beam M4_{fl} compared to R4_{fl} are attributed to the lower stiffness of the bond between the external reinforcement and the concrete, which may have resulted in reduced composite action. Overall, the TRM-based strengthening system used in this study was approximately 30% less effective in terms of strength but 30% more effective in terms of (displacement) ductility.

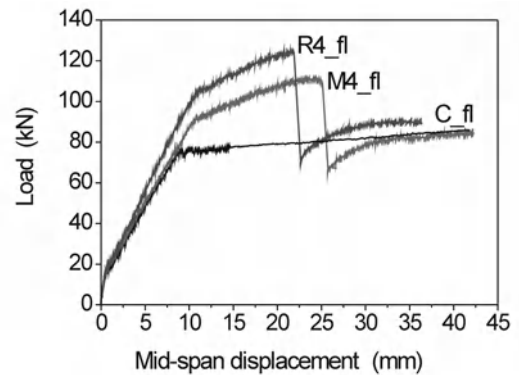


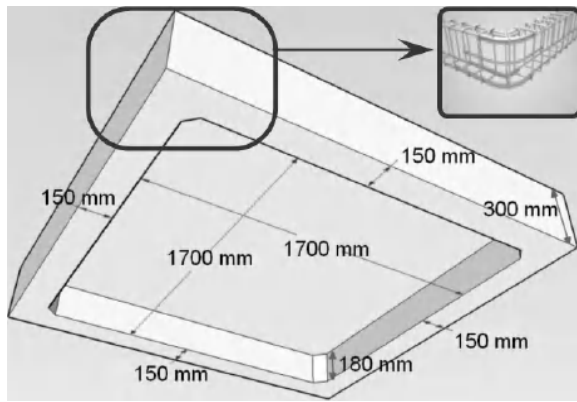
Figure 8 Load – displacement response of beams strengthened in flexure

4.2 Two-way slabs

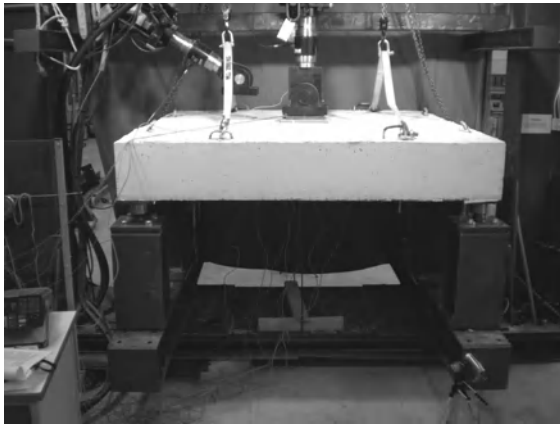
Here we aim to assess the effectiveness of TRM overlays as a measure of increasing the strength and deformation capacity of centrally loaded two-way RC slabs. To examine this, four specimens were tested under monotonic flexure. The specimens were square in plan with a side length of 2000 mm and a slab thickness of 120 mm. The slabs were uniformly cast with perimeter beams measuring 300 mm in height and 150 mm in width; therefore, the slab section of each specimen measured 1700×1700 mm in plan. One specimen was used as a control specimen, and the others were strengthened. Specimens' geometry is shown in Figure 9a.

All slabs were fabricated with identical structural steel reinforcement simulating lightly reinforced or, alternatively, moderately corroded slabs. Two welded wire fabrics (WWF) were used: the first comprised a T139 WWF [i.e. 100 × 100-W13.8 × W13.8 (mm × mm-mm² × mm²)] and was placed at the bottom (tension) surface of the slabs, whereas the second one was a T92 WWF [i.e. 150 × 150-W13.8 × W13.8 (mm × mm-mm² × mm²)] and was placed at their top (compression) surface. The tensile reinforcement ratio was equal to 0.14%. The WWF placed at the compression side of the specimens was regarded as non-structural and was used to avoid cracking during handling and transportation of the slabs to the testing rig.

The slabs were cast using a ready-mix concrete of mean 28-day compressive strength equal to 25.6 MPa (31.2 MPa at the day of testing). The steel had a conventional yield stress of 645 MPa (at plastic strain 0.2%).



(a)



(b)

Figure 9 (a) Geometry of two-way slabs tested, (b) test set-up

For the specimens receiving TRM overlays, commercial textiles with either high-strength carbon or E-glass fiber rovings arranged in two orthogonal directions were used. Both types of textiles shared the same geometry and comprised equal (but different between textiles) quantities of fibers in each direction. Each fiber roving (1650 Tex for carbon and 2400 Tex for E-glass) was 3 mm wide and the clear spacing between rovings was 7 mm. The weight of fibers in the textiles was 350 g/m² and 500 g/m² for the carbon fiber and the E-glass fiber textile, respectively. The nominal thickness of each layer (based on the equivalent smeared distribution of fibers) was 0.18 mm, for both types of textile. The guaranteed tensile strength of the fibers (as well as of the textile, when the nominal thickness is used) in each direction was taken from data sheets of the producer equal to 3500 MPa and 1750 MPa for carbon and E-glass fibers, respectively; the elastic modulus of the fibers was 220 GPa (carbon) and 72 GPa (E-glass). It becomes clear that in terms of axial rigidity one layer of carbon fiber textile is equivalent to three layers of E-glass fiber textile. The inorganic binder had a 28-day flexural and compressive strength equal to 6.5 MPa and 24.6 MPa, respectively.

Three specimens were strengthened in total, whereas one served as the control specimen (designated as CON).

One specimen received one layer of carbon fiber textile (specimen 1C), another one received two (specimen 2C), whereas the third specimen was strengthened with three layers of E-glass fiber textile (specimen 3G) having the same axial rigidity (i.e. equal product of fibers' modulus of elasticity and textile thickness) with the single-layered carbon fiber textile (in both directions). These strengthening schemes were selected in this study so that they would provide useful insight into the effects of the fiber reinforcement ratio and the number of TRM layers (of equivalent axial rigidity).

All specimens were subjected to monotonic compressive loading at mid-span – in a displacement- control mode – using the stiff steel frame and support steelwork shown in Figure 9b. All specimens were simply supported at their corners on ball-bearing hinges (thus, they were free to rotate at these points).

The load versus centre-point deflection for all specimens is shown in Figure 10. All specimens responded in a similar manner in terms of crack development and failure mode. In the uncracked stage the initial stiffness of all strengthened specimens was higher than the one of the control specimen. For all slabs first cracking due to flexure occurred – as expected – directly below the load application area and at approximately the same load value. With increasing imposed displacement, more flexural cracks formed in both directions along the bars of the tensile steel reinforcement grid (this being more visible in the control specimen) and diagonal cracks were generated propagating from the centre of the specimens to the corners. As recorded by strain gauges, yielding of tensile reinforcement in both directions was delayed in all strengthened specimens.

The failure mechanism involved sudden punching out of a pyramid concrete plug at the centre of the slabs, accompanied by immediate and significant drop in load. The punched concrete plug was steeper (in the narrower direction) in the control specimen in comparison to the strengthened ones. Failure is characterised as “flexural

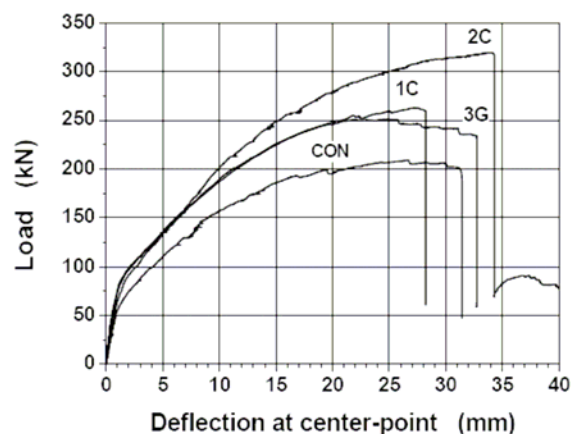


Figure 10 Load – centre point deflection curves

punching” since punching occurred shortly after yielding of the flexural reinforcement (in both directions) near the load application point.

The increase in textile layers (1C to 2C) did not lead to an undesirable failure mode (debonding of the TRM overlays from the soffit - common for FRP strengthening). Furthermore, increasing the overlay thickness while keeping the same axial rigidity resulted in an almost identical response of specimens 1C and 3G; for the latter, premature failure in the form of inter-layer delamination was avoided (this was attributed to the high shear strength of the mortar and to the relatively short span of the slab). Stepwise load reduction following the achievement of maximum load-carrying capacity for specimen 3G denotes gradual fiber fracture, whereas the enhanced deformation capacity of this specimen (in relation to specimen 1C) is the result of inter-laminar slippage. It is notable that the deformation capacities of specimens 1C and 2C are practically identical. The load-carrying capacity of the strengthened slabs was increased by 26%, 53%, and 20% over that of the control specimen for slabs 1C, 2C and 3G, respectively, as the external TRM reinforcement delayed tensile steel yielding. Further details on test results as well as a comparison with analytical predictions are given in Papanicolaou et al. (2009).

It is concluded that TRM overlays are successful in increasing the load-carrying capacity of flexure-critical RC slabs acting as external reinforcement with improved bonding conditions to the substrate. Load-carrying capacity increases with increasing fiber reinforcement ratio, overlays of equal axial rigidity per direction result in comparable increase in elements’ ultimate strength, and inter-layer relative slippage in multi-layered systems seems to enhance the deformation capacity of the slabs. Although all strengthened specimens in this study failed due to flexural punching, the failure mode is likely to change into a brittle shear punching one should TRM overlays of higher axial rigidity be used.

5 SEISMIC RETROFITTING OF MASONRY

Textile reinforced mortar (TRM) has been investigated also as a new method for seismic retrofitting of unreinforced masonry (URM) walls through jacketing. A comprehensive experimental program was carried out on unreinforced masonry wall specimens subjected to cyclic loading which induced in-plane flexure combined with axial force, out-of-plane flexure and in-plane shear with axial force. The walls were strengthened using two-sided jacketing made of TRM materials (Figure 11). The main parameter under investigation was the number of textile layers (one or two), but also comparisons were

made on the response of TRM-strengthened walls and identical specimens strengthened with FRP jackets. The results were obtained in terms of load-displacement diagrams as well as stiffness and cumulative energy plots as a function of the loading cycles.



Figure 11 Strengthening of masonry specimens using TRM jackets

The investigation was carried out on three types of medium-scale, single-wythe, fired clay brick wallettes composed of running bond courses: (a) Specimens type A (shear walls) measured 1300 mm in height and 800 mm in width; (b) Specimens type B (beam-columns) measured 1300 mm in height and 400 mm in width; and (c) Specimens type C (beams) measured 400 mm in height and 1300 mm in width. All specimens were constructed in the laboratory by an experienced mason using perforated bricks (185×85×60 mm), with the perforations running in parallel to the units’ length. Details about the experimental program and the results are given in Papanicolaou et al. (2007, 2008).

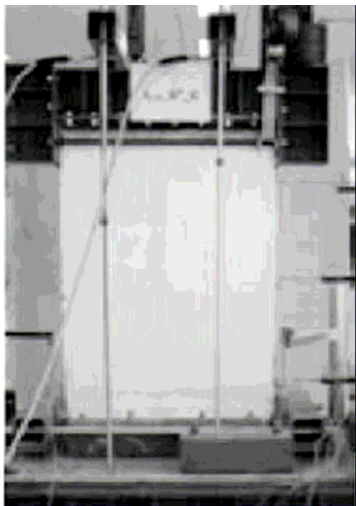
The first part of the investigation comprised testing of Specimen types B and C subjected to *out-of-plane* loading. Those specimens were used so as to assure failure parallel and perpendicular to bed joints, for the former and the latter, respectively. The test set-up is shown in Figure 12a.

The second part of the investigation comprised testing of Specimen types A, B and C subjected to *in-plane* loading. Type A specimens were tested as vertical cantilevers with a concentrated force at the top, at a distance of 1.10 m from the fixed base; type B and C specimens were tested as horizontal beams in three-point bending, at a span of 1.17 m and 1.12 m, respectively. The test arrangement of type B walls aimed at reproducing the in-plane flexure/shear seismic loading of pilasters found in the lower levels of masonry structures, where axial loads may be considerable.

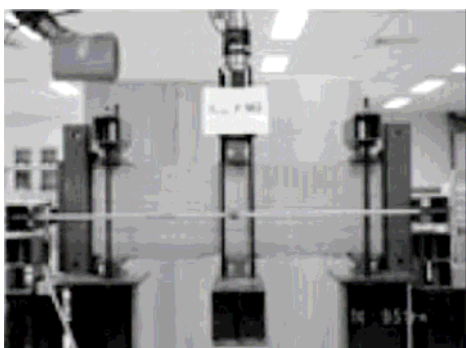
Therefore, during cyclic loading of these specimens an axial load was applied on their outer brick rows and kept constant throughout the duration of the test. For type C specimens, the test arrangement intended to simulate in-plane flexure/shear loading typically applied in lintels during seismic excitations. The test set-up is shown in Figures 12b, c.



(a)



(b)



(c)

Figure 12 Test set-up for (a) out-of-plane loading and (b)-(c) in-plane loading of masonry walls

Main conclusions from this part of the study are as follows: Both TRM and FRP overlays increase the strength and deformation capacity of unreinforced masonry walls by several times. For the case of out-of-plane loading, TRM outperform their FRP counterparts on the basis of maximum load and displacement at failure, whereas if

the failure mechanism involves tensile fracture of the textile reinforcement the effectiveness of TRM versus FRP is slightly reduced. For the case of in-plane loading, TRM (compared with FRP) results in slightly reduced (by no more than 30%) effectiveness for strength, the magnitude of which depends on the type of loading and on the number of textile layers used. In terms of deformation capacity, of crucial importance in seismic retrofitting of unreinforced masonry walls, TRM jacketing is much more effective than FRP. The increased effectiveness is about 15-30% in shear walls, 135% in beam-column type walls and 350% in beam type walls. Moreover, regardless of the matrix material (polymer-modified mortar versus epoxy resin), the strength generally increases with the number of layers and the axial load, at the expense of deformation capacity.

6 CONCLUSIONS

An innovative strengthening technique (TRM) is described in this study for strengthening and seismic retrofitting of reinforced concrete members through confinement; the technique is also used in shear and flexural strengthening. Key feature of this technique is the combination of textiles with polymer-modified cementitious binders, hence it may be considered as an alternative to FRP strengthening. From the results presented in this study it was shown that TRM jacketing of RC is nearly as effective as FRP jacketing. The authors believe that TRM jacketing is an extremely promising solution for increasing the confinement as well as the shear and flexural capacity of reinforced concrete members, of crucial importance in strengthening and seismic retrofitting. Extrapolation of the technique to unreinforced masonry walls resulted in substantial increase in strength and deformation capacity, indicating that this new generation of inorganic binder-based composite materials offers a promising solution in the restoration of masonry structures, including monument-type ones.

REFERENCES

- Bournas, D., Lontou, P., Papanicolaou, C.G. & Triantafillou, T.C. 2007. Textile-Reinforced Mortar (TRM) versus FRP Confinement in Reinforced Concrete Columns. *ACI Structural Journal* 104(6): 740-748.
- Bournas, T.C. & Triantafillou, T.C. 2010. Bond Strength of Lap Spliced Bars in Concrete Confined with Composite Jackets. *ASCE Journal of Composites for Construction*, in press.
- Papanicolaou, C.G., Triantafillou, T.C., Karlos, K. & Papathanasiou, M. 2007. Textile Reinforced Mortar (TRM) versus FRP as Strengthening Material of URM Walls: In-plane Cyclic Loading. *RILEM Materials and Structures* 40(10): 1081-1097.
- Papanicolaou, C.G., Triantafillou, T.C., Papathanasiou, M. &

- Karlos, K. 2008. Textile Reinforced Mortar (TRM) versus FRP as Strengthening Material of URM Walls: Out-of-plane Cyclic Loading. *RILEM Materials and Structures* 41(1): 143-157.
- Papanicolaou, C., Triantafillou, T.C., Papantoniou, I. & Balioukos, C. 2009. Strengthening of Two-Way Slabs with Textile-Reinforced Mortars (TRM), *11th International fib Symposium, London, 22-24 June 2009*.
- Triantafillou, T.C., Papanicolaou, C.G., Zisimopoulos, P. & Laourdekis, T. 2006. Concrete Confinement with Textile Reinforced Mortar (TRM) Jackets. *ACI Structural Journal* 103(1): 28-37.

Strengthening of Concrete, Metallic and Timber Construction Materials with FRP Composites

S.T. Smith (stsmith@hku.hk)

Department of Civil Engineering, The University of Hong Kong, China

ABSTRACT This paper provides a review of research being conducted at The University of Hong Kong (HKU) on the strengthening of concrete, metallic and timber construction materials with externally bonded fibre-reinforced polymer (FRP) composites. The motivation of such research is to enhance our understanding of the interfacial behaviour between the FRP and the three different substrate materials via FRP-to-concrete, -metal, and-timber joint tests. Of the three substrate materials, concrete has clearly experienced the most research activity to date by the wider research community, followed by that of metal and then that of timber. In order to progress the extensive knowledge base of FRP-to- concrete behaviour, research at HKU is aimed at enhancing the bond strength of the FRP via the addition of anchorage. The anchor of choice is the so called FRP anchor and its effectiveness in anchoring FRP flexural strengthening applied to reinforced concrete (RC) slabs is also presented. For the metal and timber substrate materials, HKU research is more focused at this stage on understanding the influence of key fundamental variables affecting interfacial behaviour such as FRP geometry, surface preparation and substrate material characteristics.

1 INTRODUCTION

Reinforced concrete (RC), metal and timber are three very commonly used construction materials. Structures made from these materials may, however, be in need of strengthening or repair or even restoration. Externally bonded fibre-reinforced polymer (FRP) composites offer a viable solution (Hollaway and Teng 2008). Considerable research to date has been conducted on the application of FRP to RC structural elements and such research has shown the propensity of the FRP to debond at strains well below its strain capacity. Our understanding of the debonding phenomenon has been enhanced via FRP-to-concrete joint testing. The same experimental approach has been extended to a lesser extent to FRP to metal interfaces. Application of FRP to timber is comparatively less again.

Research of an experimental, analytical and numerical nature is being conducted at The University of Hong Kong (HKU) which is aimed at enhancing our understanding of the application of FRP to the three very different materials of concrete, metal and timber. Such research is at various stages of development and an overview of selected experimental research to date is provided in this paper. For the case of FRP-to-concrete interfaces, enhancement of the strength of the bond between the FRP and concrete via anchorage with so called FRP anchors is being explored. The proof of the anchorage concept is also demonstrated in tests on FRP-strengthened RC slabs anchored with FRP anchors. Research on the strength

and behaviour of FRP-to-metal and FRP-to-timber joints is also presented. Fundamental variables affecting interfacial behaviour, such as surface preparation and material type for metal joints, as well as natural growth characteristics in the timber for timber joints, are being investigated. Comments regarding suitable analytical modeling approaches are also made in light of the experimental findings obtained to date. Overall comments about the three different materials are also provided.

2 FRP-TO-CONCRETE

It has been well established that FRP plates bonded to concrete surfaces can debond at strains well below the strain capacity of the FRP (Hollaway and Teng 2008). The strain capacity of the FRP can be increased by suppression, or at least delay, of debonding by the addition of anchorage. The anchor of choice by the HKU group is the so called FRP anchor (also known as an FRP spike anchor). An FRP anchor, which is a collection of rolled fibre sheets or bundled fibre strands, is shown in Figure 1a. This figure also shows how the FRP anchor is used to anchor an externally bonded FRP plate.

2.1 FRP-to-concrete joint tests

Tests on single-shear FRP-to-concrete joints, anchored with FRP anchors (Figure 1b, 2a), have proven the effectiveness of FRP anchors. The addition of a single anchor has been shown to increase the strength and slip capacity above that of an unanchored joint by 70% and

800%, respectively. A recent review of research undertaken by the HKU group, as well as other groups, was presented in Smith (2009). Such research on single anchored joints by the HKU group addressed parameters of (i) fibre type (carbon and glass fibres), (ii) method of anchor formation (dry anchor or impregnated anchor), (iii) anchor position, and (iv) installation. In all cases, the anchor consisted of a single anchor fan. As shown in Figure 2a, the fan was oriented in the direction of applied load. More recent studies on single fan FRP anchors have addressed the influence of multiple FRP anchors on FRP-to-concrete joints (Zhang et al. 2010).

The encouraging performance of single fan FRP anchors has paved the way for the development of double fan FRP anchors. Such double fanned anchors, as shown in Figures 1a and 2b, are herein referred to as *bow-tie FRP anchors*.

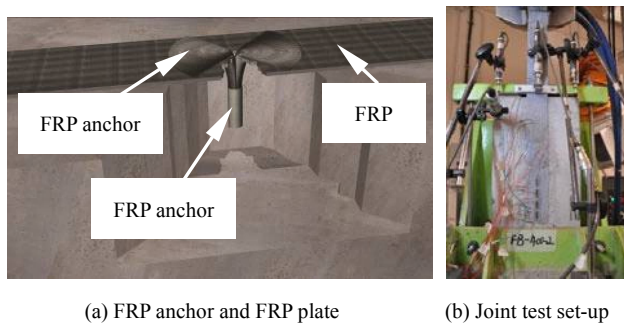


Figure 1 (a) FRP plate anchored with an FRP anchor.

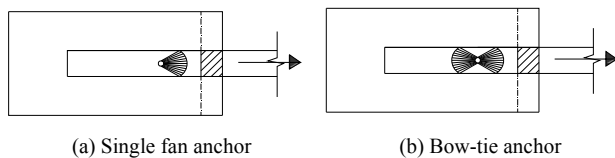


Figure 2 FRP-to-concrete joints anchored with two different types of FRP Anchors

Figure 3 shows the typical load-slip responses of two nominally identical FRP-to-concrete joints. The joints, which were tested in the set-up shown in Figure 1b, were anchored with a bow-tie FRP anchor or no anchor at all. The enhancement in load and slip capacity of the anchored joint is most evident and the three main stages in its load-slip response are herein described. It is important to note that the single and bow-tie anchors behaved in a similar manner for stages A and B. For stage C, the behaviour differed.

Stage A: Debonding initiated at the loaded end of the joint at approximately the same load to initiate debonding in an unanchored joint. The anchor was then engaged once the debonding crack passed by it. At this stage, the enhancement in joint strength above that of an unanchored joint was due to the engaged anchor and the remaining bonded FRP plate. The joint stiffness reduced as the

debonding crack increased in length.

Stage B: The large drop of load at the beginning of this stage was associated with complete debonding of the FRP plate. The load then increased from friction due to sliding between the roughened surfaces of the debonded plate and concrete. In addition, the flexible FRP anchor enabled the debonded FRP plate to remain clamped to the concrete.

Stage C: The load reduced at the beginning of this stage due to partial rupture of the anchor dowel closest to the direction of applied load. A relatively constant load was then maintained from friction and the clamping effect of the remaining intact anchor. The anchor eventually completely ruptured after the slip exceeded over 10 times the slip capacity of an unanchored joint. This stage of behaviour does not occur in joints anchored with single anchor fans due to complete failure of the anchor at the end of stage B.

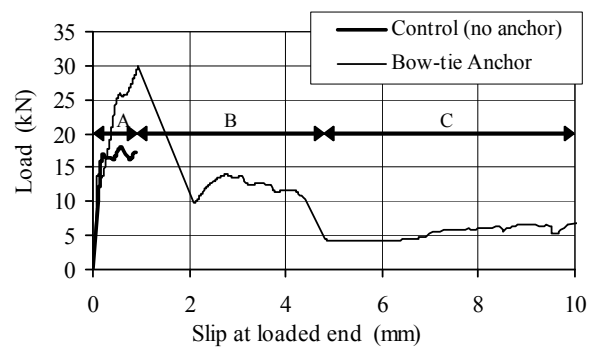


Figure 3 Load-slip responses

2.2 Anchored FRP-strengthened RC slab tests

The effectiveness of the bow-tie FRP anchor in anchoring FRP flexurally-strengthened RC slabs is described in Smith et al.'s (2010) study. A summary of some of the results is presented herein.

Figure 4 is a schematic of Smith et al.'s (2010) slab specimens and test set-up. Figure 5a shows the resulting load-midspan deflection responses for three of the slabs, namely (i) unstrengthened and unanchored control slab (Slab S1), (ii) strengthened but unanchored control slab (Slab S2), and (iii) strengthened and anchored control slab (Slab S5). The FRP plate and bow-tie FRP anchor layout for Slab S5 is also shown in Figure 5b. The load-deflection response for Slab S5 reveals the anchorage to enhance the load carrying capacity and deflection capacity by 24 % and 64 %, respectively, above that of Slab S2 (note: these increases are relative to the peak load – the following large drop in load represents complete debonding of the FRP plate). The optimal layout of anchors produced strength and deflection gains of up to 30% and 110%, respectively, however such results are not presented in this paper. The post-peak response of Slab S5 represents

residual strength offered by sliding friction between the debonded FRP and concrete substrate and clamping from the anchorage. The response of Slab S5 in Figure 5a also demonstrates significant energy absorption capacity. The extent of debonding crack propagation and the conditions of the anchors at complete plate debonding is shown in Figure 5b.

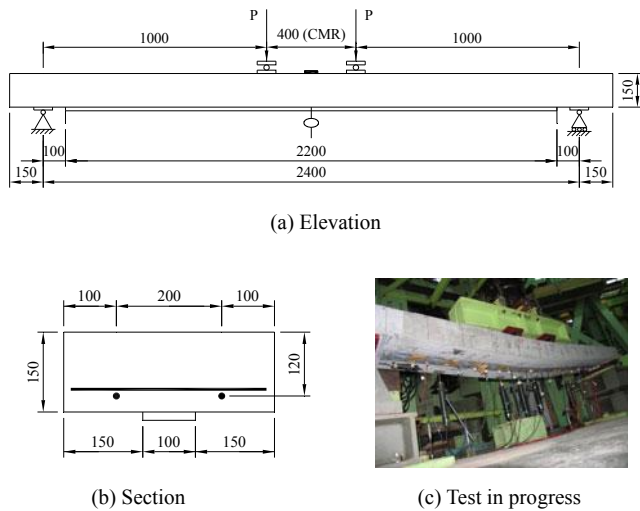


Figure 4 FRP-anchored FRP-strengthened slab test details

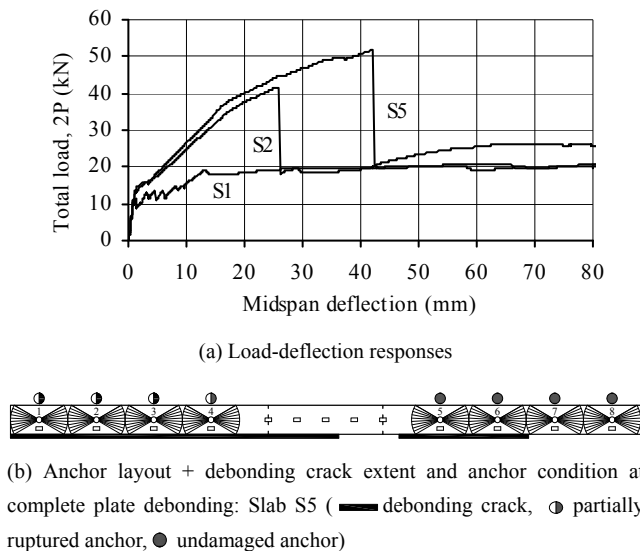


Figure 5 FRP-anchored FRP-strengthened slab test results

3 FRP-TO-METAL

Decidedly less research activity has been directed towards the application of FRP to metal than FRP to concrete. A recent review by Zhao and Zhang (2007) highlighted limitations in our understanding of the interfacial behaviour between the FRP and its metal substrate. Recent efforts by the research community are, however, addressing the bond issue (e.g. Xia and Teng 2005, Akbar et al. 2010). At HKU, experimental investigations are being conducted on the bond strength and behaviour of FRP-to-metal joints. The main test

parameters being systematically investigated, which have received little to no attention to date but which are considered of importance, are

- **Surface preparation:** mechanical (i.e. sanding, grinding, needling), and chemical (i.e. acid etching) treatments,
- **Metal type:** (i.e. non-galvanised mild steel, stainless steel, aluminium), and
- **Geometry:** bond length and identification of effective bond length.

Research efforts are ultimately directed towards the development of bond strength and bond stress-slip models. A brief treatment of some of the surface preparation research, which is contained in more detail in Kim et al. (2010), is presented as follows in addition to some more recent work and a discussion on suitable analytical modeling approaches.

3.1 FRP-to-metal joint tests

The single-shear FRP-to-metal joint test set-up shown in Figure 6 has been utilised to date. In order to minimise bending of the test specimens, the metal plates were stiffened to produce a flexural rigidity ratio between the metal and FRP of 13,000. The set-up is simple, quick to assemble, and easy to test.

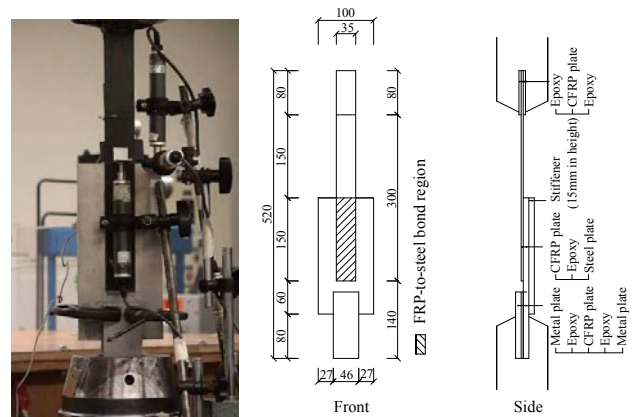


Figure 6 Stiffened single-shear FRP-to-metal joint test set-up

Tests on different mechanical surface preparation techniques of sanding, grinding and needling on mild-steel and stainless steel has enabled identification of the following failure modes:

- Mode 1:* Adherend failure in oxidised layer,
- Mode 2A:* Thin-layer cohesive failure in metal-to-adhesive interface,
- Mode 2B:* Thin-layer cohesive failure in FRP-to-adhesive interface, and
- Mode 2C:* Mixed thin-layer cohesive failure.

Mode 1 (Figure 7a) was typically observed in unprepared mild-steel samples and if the oxidised layer was not sufficiently removed. The strength of the bond between the oxidised layer and the base metal was clearly the

limiting factor and this revealed an important practical issue. In mild steel, the epoxy needed to be applied to the exposed base metal straight after preparation in order to halt/delay oxidation. For specimens exhibiting cohesive failure (e.g. Figure 7b), the effect of surface preparation was less obvious. There, however, appeared to be a correlation between rougher topology of the metal surface and reduced bond strength.

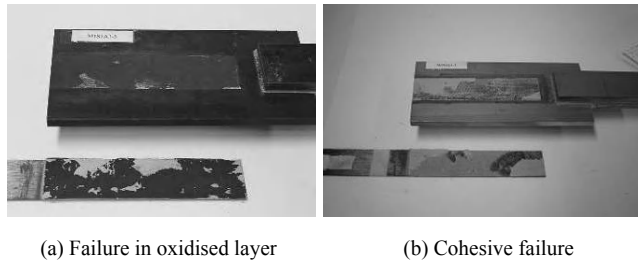
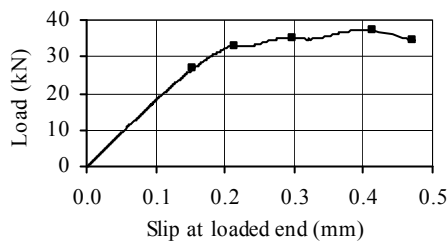
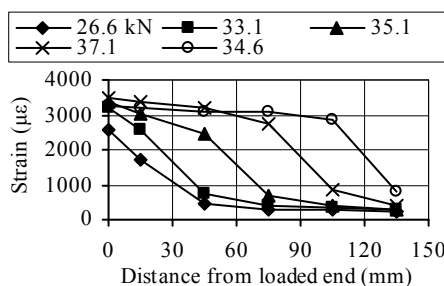


Figure 7 FRP-to-metal joint failure modes

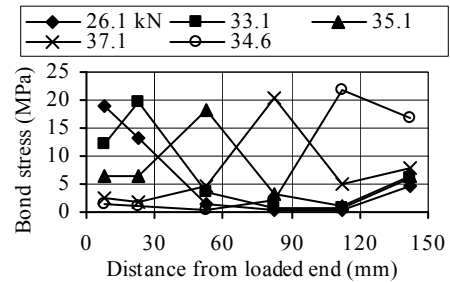
Figure 8 shows slip and stress results obtained from strain gauge readings. Figure 8a shows a typical load-slip response for an FRP-to-stainless steel joint. The peak load plateau, corresponding to propagation of the debonding crack with little increase in load, is obvious. The corresponding strain versus distance at different levels of load is shown in Figure 8b while the bond stress-distance and bond stress-slip relationships are shown in Figures 8c and 8d, respectively. The bi-linear nature of the bond stress-slip curves is evident and the low scatter of results is due to the homogeneity of the steel and the nature of the cohesive failure. This is in contrast the higher scattered FRP-to-concrete and FRP-to-timber joint results. Such scatter is attributed to debonding occurring in the non-homogenous adherends.



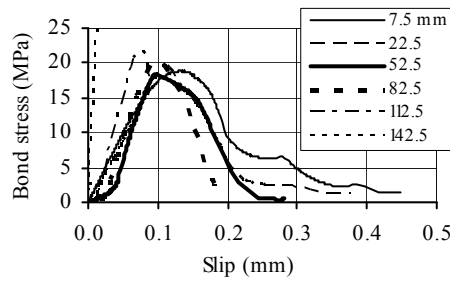
(a) Load-slip



(b) Strain-distance



(c) Bond stress-distance



(d) Bond stress-slip

Figure 8 FRP-stainless steel joint (fine sanding) results

Current work entails more testing and development of bond stress-slip models. Such models can be developed from bond-slip responses directly derived from strain gauges (e.g. Dai et al. 2003). Models can also be developed from measured load-slip responses (e.g. Dai et al. 2003, Zhou et al. 2010), the J-integral based approach, or other means (e.g. partial interaction approach of Akbar et al. 2010).

4 FRP-TO-TIMBER

Timber has been a commonly used construction material in civil infrastructure throughout the world for several millennia and still continues to be a popular construction material today. Externally bonded FRP composites offer strengthening and stiffening solutions to biologically degraded or mechanically overloaded timber members. In addition, the unobtrusiveness of FRP composites, particularly when used as near-surface mounted (NSM) reinforcement, offers tremendous potential for the repair and restoration of historical timber structures. The application of FRP to timber has received the least research activity to date, despite the popularity of timber.

The aim of the HKU research is to enhance understanding of the bonded FRP-to-concrete interface and to develop analytical models. The following is a summary of important aspects requiring investigation and understanding. Some of these issues are receiving attention to date already (e.g. Davalos et al. 2000, Raftery et al. 2009).

4.1 Timber

Species (hard/soft wood), grade, grain direction, density, moisture content (seasoned, unseasoned), pre-aging,

weathering, natural growth characteristics (knots, checks, pith and core wood), existing cracks and damages, stress level (i.e. creep), treated and untreated wood, geometry.

FRP: Fibre type (carbon and glass), resin type (e.g. epoxy, polyester, phenolic), elastic modulus, geometry.

Adhesive: Type (e.g. epoxy, resorcinol-formaldehyde (RF), vinyl ester), compatibility with wood and FRP, and type of primer (coupling agent), elastic modulus, geometry.

Loading direction and type: Parallel or perpendicular to grain, monotonic/cyclic.

Surface preparation: Sanding, planing, needling and wiping with solvents.

Durability: Effect of changing moisture content on FRP-to-timber bond.

4.2 FRP-to-timber joint tests

Tests on the bond strength and behaviour of FRP-to-timber bonds are limited. The majority of tests have utilised a modified block-shear test of ASTM D905-03 (2003). This test, which gives the shear strength of the bond as an average stress over the bonded plate area, has been used to date (e.g. Davalos et al. 2000, Raftery et al. 2009). As the FRP is sandwiched between two pieces of timber, its surface is difficult to monitor. In order to monitor the bonded interface and understand it in more detail, tests on single-shear FRP-to-timber joint specimens are being conducted at HKU (Figure 9).



Figure 9 Single-shear FRP-to-timber joint tests

To date, tests on seasoned pine (moisture content \approx 10%), which have been strengthened with externally bonded wet lay-up carbon fibre sheets, have been undertaken. The main test variables have been (i) length of bonded FRP, and (ii) natural growth characteristics of the timber (i.e. influence of direction of annual growth rings in relation to the bonded surface, and knots). Figure 10 provides a visual summary of many of the test specimens post-test. The failure planes in Figure 10 show that interfacial failure generally occurs in the timber (provided good quality FRP application exists). Such a failure is analogous to interfacial failure in the concrete in FRP-to-concrete joints. A more comprehensive account of these tests can be found in Wan et al. (2010), however, a brief over-view as well as more recent work and comments pertaining to analytical modeling are given as follows.



Figure 10 Debonded FRP plate and timber interfaces

Figure 11 shows the relationship between strength and bonded FRP length for 52 joint tests. The effective bond length phenomenon exists in which the strength of the joint increases until a certain bond length is reached. Sides A and B are distinguished by the location of the harder pith wood in relation to the bonded FRP. This translates to FRP bonded to faces predominately perpendicular (Side A) or parallel (Side B) to the annual growth rings. Side B clearly provides a lower bound strength which is more governed by the interlaminar strength of the annual growth rings. The scatter of results amongst each bond length increases with increased length. Apart from inherent experimental variation, this scatter is also due to the presence of other natural growth characteristics in the timber such as knots. In light of the complexity and variability of timber, as revealed in Figure 11, much more testing is required.

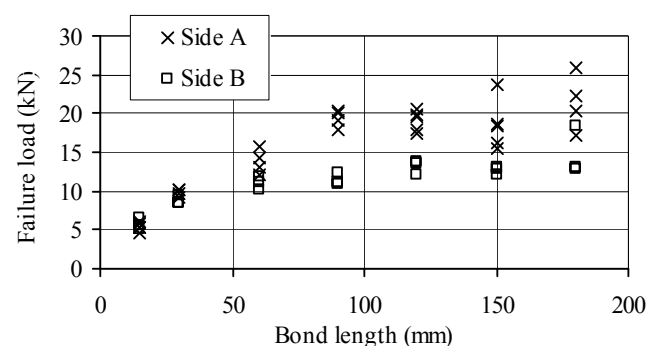
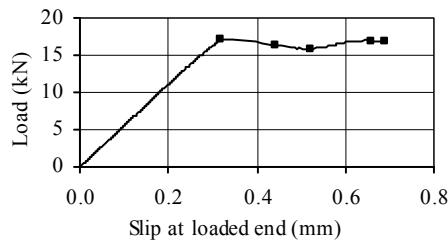


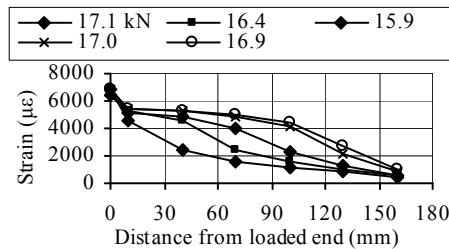
Figure 11 Failure load-bond length of FRP-to-timber joints

The results of a typical joint of long bond length (i.e. 180 mm) are shown in Figure 12 in which slips and stresses are obtained from strain gauge readings. Figure 12a shows a typical load-slip response and Figure 12b the corresponding strain-distance response at selected levels of load. The flattening of the load-slip and strain-distance response indicates propagation of the debonding crack. The propagating debonding crack is also observed from the moving peak in the bond stress-distance responses in Figure 12c. The resulting bond stress-slip response at different positions along the FRP is then provided in Figure 12d. The familiar bi-linear bond stress-slip relation exists, however, the variability of results due to the highly variable nature of timber suggests bond-slip models would

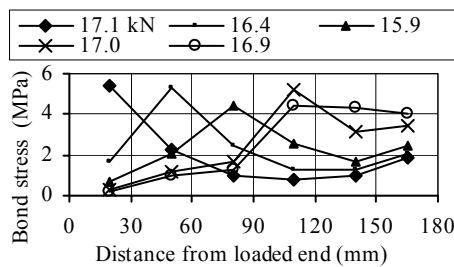
be better derived from the load-slip response (i.e. Dai et al. 2003, Zhou et al. 2010) or other methods (e.g. Akbar et al. 2010).



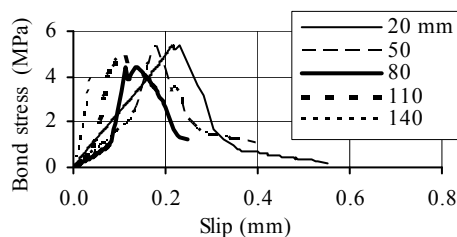
(a) Load-slip



(b) Strain-distance



(c) Bond stress-distance



(d) Bond stress-slip

Figure 12 FRP-timber joint test results

5 DISCUSSION

FRP-to-concrete and FRP-to-timber joints will generally experience interfacial failure in the concrete or timber adherends, respectively. Metal-to-FRP joints generally experience cohesive failure. The test results presented herein are, however, suitable for developing analytical models, via (i) strain gauge, (ii) load-slip, (iv) J-integral, and (v) partial interaction based approaches. It should be noted though that there are limitations in using strain gauge measurements for developing analytical models due to the discrete nature of the measurements.

6 CONCLUSIONS

Selected ongoing experimental research at The University of Hong Kong on the application of FRP to concrete, metal and timber materials has been presented herein. Some similarities and differences in behaviour between FRP bonded to concrete, metal and timber materials have been identified as well as potential analytical modeling approaches.

ACKNOWLEDGEMENTS

The financial assistance of the HK Research Grants Council (grants HKU 716308E, 715907E) and HKU (grants 10208970, 10400354) are acknowledged. The author also thanks his collaborators and graduate students, namely Profs P.Z. Qiao (WSU, USA) and B. Young (HKU); Drs R. Seracino (NCSU, USA) and S.J. Kim (HKU); Messers S.H. Hu, J.Q. Yang and H.W. Zhang; and Miss J. Wan (all HKU).

REFERENCES

- ASTM D 905-03 2003. *Strength Properties of Adhesive Bonds in Shear by Compression Loading*, American Society for Testing and Materials (ASTM), PA, USA.
- Akbar, I, Oehlers, DJ & Mohamed Ali, MS 2010. Derivation of the bond-slip characteristics for FRP plates steel members, *J. of Const. Steel Res.*, in-press.
- Dai, JG, Ueda, T & Sato, Y 2003. Development of the nonlinear bond stress-slip model of fiber reinforced plastics sheet-concrete interfaces with a simple model, *J. Comp. for Const.*, ASCE, 9(1), 52-62.
- Davalos JF, Qiao PZ & Trimble BS 2000. Fiber-reinforced composite and wood bonded interfaces: Part 1. durability and shear strength, *J. Comp. Tech. & Res.*, 22(4), 224-231.
- Hollaway, LC & Teng, JG 2008. *Strengthening and Rehabilitation of Civil Infrastructures using Fibre-reinforced Polymer (FRP) Composites*, Woodhead Publishing, UK.
- Kim, SJ, Smith, ST & Young, B 2010. Effect of surface preparation on the strength of FRP-to mild steel and FRP-to-stainless steel joints, *Proc., Fifth Int. Conf. on FRP Comp. in Civil Eng.*, CICE 2010, Beijing, China.
- Raftery, GM, Harte, AM & Rodd, PD 2009. Bonding of FRP materials to wood using thin epoxy gluelines, *Int. J. Adhesion & Adhesives*, 29, 580-588.
- Smith, ST 2009. FRP anchors: recent advances in research and understanding, *Proc., Second Asia-Pacific Conf. on FRP in Struct.*, APFIS 2009, Seoul, Korea, 35-44.
- Smith, ST, Hu, SH, Kim, SJ & Seracino, R 2010. FRP-strengthened RC slabs anchored with FRP anchors, *Eng. Struct.*, under review.
- Wan, J, Smith, ST & Qiao, PZ 2010. FRP-to-softwood joints: experimental investigation, *Proc., Fifth Int. Conf. on FRP Comp. in Civil Eng.*, CICE 2010, Beijing, China.

- Xia, SH & Teng, JG 2005. Behaviour of FRP-to-steel bonded joints, *Proc., Int. Symp. on Bond Behaviour of FRP in Struct.*, BBFS 2005, Hong Kong, China. 411-418.
- Zhang, HW & Smith ST 2010. FRP-to-concrete joint assemblies anchored with multiple FRP anchors: experimental investigation, *Proc., Fifth Int. Conf. on FRP Comp. in Civil Eng.*, CICE 2010, Beijing, China.
- Zhao. XL & Zhang, L 2007. State-of-the-art review on FRP strengthened steel structures, *Eng. Struct.*, 29, 1808-1823.
- Zhou, YW, Wu, YF & Yun, YC 2010. Analytical modeling of the bond-slip relationship at FRP-to-concrete interfaces for adhesively bonded joints, *Comp. Part B*, in-press.

Multifunctional and Robust Composite Material Structures for Sustainable Construction

Thomas Keller (thomas.keller@epfl.ch)

Composite Construction Laboratory (CCLab), Ecole Polytechnique Fédérale de Lausanne (EPFL), Lausanne, Switzerland

ABSTRACT The multifunctional use of FRP composites offers the potential to contribute to the emergence of a new generation of lightweight engineering structures for an innovative infrastructure that meets the challenges with which today's construction industry is faced. Six axes of development are discussed, which address the potential innovations and the main problems to be overcome to allow the widespread application of multifunctional lightweight FRP composites in civil infrastructure. Three axes are related to the structural robustness of FRP structures. Structural robustness is primarily dependent on a material-tailored structural concept and system ductility and can be obtained particularly thanks to ductile adhesive joints. Further three axes explore the opportunities for innovation through a multifunctional use of FRP materials. Structural functions are combined with building physics functions, energy supply, and architectural functions.

1 INTRODUCTION

Today, almost all types of industry have adopted automated processes to speed up, optimize and economize production, with the exception of one: the construction industry. Bridges and buildings are still cast on-site using scaffolding and formwork and employing cumbersome wet-in-wet processes with increasingly unacceptable consequences regarding cost, quality and safety. The construction industry is therefore now confronted with the challenge of switching from pure on-site prototype production to fully industrialized and modularized made-to-measure prefabrication. This transition will shorten construction times, improve quality and increase overall flexibility and economy.

This challenge coincides with the arrival of new materials in the field of construction such as fiber-reinforced polymer (FRP) composites. These lightweight and high-strength materials are compatible with industrialized prefabrication and rapid installation. FRP composites may also exhibit advantageous environmental characteristics, particularly if glass fibers are used, such as low grey energy consumption and low carbon dioxide emissions. FRP composites can therefore contribute significantly to profound innovations in the construction industry on the environmental and economic levels.

In the past, the implementation of new construction materials occurred, in a first phase, via the simple substitution of traditional materials by new materials – the structural concepts and connection technologies optimized for traditional materials have simply been copied. This substitution phase has been important in

that it has allowed confidence to be gained in the new materials. The full and optimized use of the properties of the new materials, however, has not been possible, resulting in uneconomical practical applications. History clearly demonstrates that new materials are only successful when the substitution phase has been surmounted and when a transition to new material-tailored structural concepts and construction processes occurs (Dooley 2004).

Today, FRP composites are in this substitution phase in new construction and are used in the structural forms of traditional materials such as steel, concrete and timber, as demonstrated by the Pontresina Bridge and the Eyecatcher Building, shown in Figure 1 (Keller 2003). The shapes of isotropic steel profiles are copied exactly using the new anisotropic FRP materials, thus preventing the advantageous properties of the latter from being exploited.

Against this background, an analysis of the advantageous and adverse material properties of FRP composites in new construction presents the basis for reflection. The most important material properties specific to FRP composites that influence a material-tailored design are:

- high specific strength (strength-to-unit weight ratio) and high live-to-dead load ratio of FRP structures.
- comparably low stiffness if economic glass fibers are used (GFRP).
- material anisotropy (one-dimensional fibers embedded in homogeneous matrix).
- material brittleness (linear-elastic stress-strain response up to failure, no dissipation of inelastic energy).

- matrix sensitivity to elevated and high temperatures and fire in particular.
- low thermal conductivity of GFRP.
- optional transparency and translucency of GFRP.

The specific strength and stiffness properties primarily influence the configuration of the structural system while material anisotropy predominately impacts the conception of component joints. The brittleness of FRP composites is a significant disadvantage with regard to the acceptance of FRP structures by structural engineers who are familiar with ductile construction materials such as steel or reinforced concrete. FRP structures must also provide ductility and structural robustness in order to become widely accepted. Furthermore, for a widespread application in building structures, the low fire resistance of FRP composites must be improved.



Figure 1 FRP Pontresina Bridge and FRP Eyecatcher Building, Basel



Figure 2 Multifunctional GFRP sandwich roof of Novartis Campus Main Entrance Building, 2006

On the other hand, properties such as the low thermal conductivity and optional translucency of GFRP offer promising new options, e.g. the integration of building physics and architectural functions into structural components of buildings. Function integration allows a reduction in the number of building components, as shown in Figure 2 (one multifunctional sandwich element), thus shortening construction time and mitigating higher material costs (Keller 2004).

Based on the above analysis, six areas of development are discussed in the following, summarized in Table 1, which address the potential innovations and the main problems to be overcome, in order to allow a widespread application of multifunctional lightweight FRP composites in civil infrastructure.

Three axes are related to the structural robustness of FRP structures and primarily address the problems to be

overcome. Since innovation should not create a risk for the user of the innovation, a high system safety or robustness of FRP structures must be ensured. Structural robustness is primarily dependent on a material-tailored structural concept and system ductility and can particularly be obtained through the use of ductile adhesive joints. Further three axes explore the opportunities for innovation via a multifunctional use of FRP materials. Structural functions are combined with building physics functions (thermal systems), energy supply (energy systems), and architectural functions (light systems). These axes particularly comprise interdisciplinary approaches combining structural engineering, material science, building physics, and architecture.

Table 1 Overview axes of development

Structural robustness	Multifunctionality
Material-tailored concepts	Thermal systems
System ductility	Energy systems
Ductility of adhesives	Light systems

2 MATERIAL-TAILORED STRUCTURAL CONCEPTS

Form-active systems, such as shell or membrane systems, require the lowest material consumption and are therefore in line with sustainability and economy requirements. Existing form-active systems, however, cannot be directly used for lightweight materials due to the resulting high live-to-dead load ratio and associated instability problems. Attempts to directly use form-active systems (suspension and cable-stayed systems) for FRP pedestrian bridges failed – several bridges had to be stabilized retroactively by adding ballast. The family of form-active systems must be developed by adding stabilization components or mechanisms in order to be usable for FRP composites and offer economic solutions for the comparatively expensive materials.

A second family exhibiting relatively low material consumption is comprised by sandwich structures, in which the expensive materials are used for the thin skins only. Since another material is needed for the core, the main problems arise from material compatibility and adherence at the interfaces.

Because FRP composite components may present significant weaknesses if subjected to compression due to a matrix-controlled behavior (e.g. early fiber buckling at elevated temperatures), their sole use in fiber-controlled tension and combination with a material strong in compression is a promising approach (Deskovic et al. 1995). The combination of both lightweight new FRP composites and ultra-high performance fiber-reinforced concrete, the former used in tension and the latter in compression has already been successfully demonstrated; an example is shown in Figure 3 (Schaumann 2008).

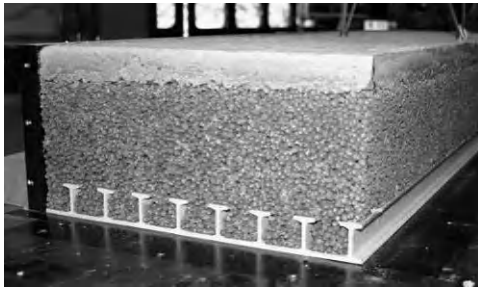


Figure 3 Hybrid-FRP sandwich bridge deck (top layer: ultra-high performance fiber-reinforced concrete; core: ultra-lightweight concrete; bottom layer: GFRP sheet with T-upstands)

3 SYSTEM DUCTILITY

Ductile materials permit a favorable redistribution of internal forces in the case of overloading of the structure (linked with an increase in structural safety), dissipation of energy from impact or seismic actions as well as a warning of a possible structural problem thanks to the large deformations occurring before failure. To compensate for the lacking material ductility of FRP composites, ductility can be provided on the structural system level, known as system ductility, which may offer the same advantages as the aforementioned material ductility. In the case of a combination of purely brittle components in a structural system, system redundancy is required to allow progressive failure and corresponding dissipation of inelastic energy in the components or joints prior to global structural collapse (De Castro 2005).

To compare and quantify the level of structural ductility or structural safety, a multitude of ductility, deformability or robustness factors are proposed in literature (Park et al. 2006, Fu and Frangopol 1990). Van Erp (2001) proposed a robustness factor, applicable to both, ductile and brittle materials or structures, in particular FRP materials, which combines deformability and strength terms. Reinforced concrete and steel beams reach robustness factors of approximately 20, which comprise almost identical deflection factors of approximately 8 and strength factors of 2.5. FRP beams reach almost the same range of values (16 to 25) in a different way however, through almost identical deflection factors and strength factors of approximately 4 to 5 due to their linear-elastic behavior. Experimental results obtained in De Castro (2005) could not confirm these values however. Methods to quantify the system ductility of brittle FRP structures in an appropriate way are still lacking.

The basic feasibility of the concept of system ductility and redundancy for new all-FRP structures has been demonstrated in De Castro (2005) and Gürtler (2004), see Figure 4. In the latter case, it was shown how a redundant FRP bridge deck system with trapezoidal cells could dissipate energy during progressive failure, while a similar but statically determinate system with

triangular cells (without any redundancy) failed in a brittle manner. On the other hand, however, the brittle system provided much higher stiffness and strength than the ductile system.

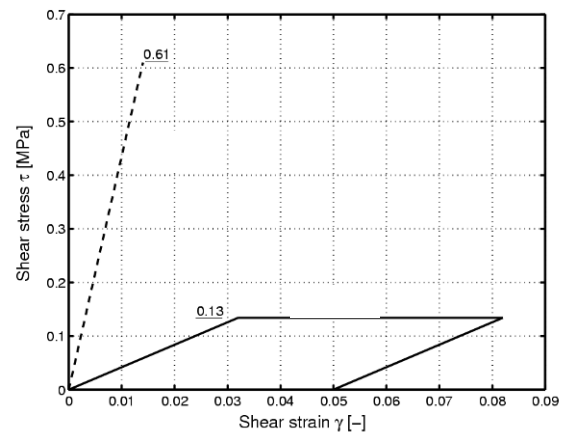
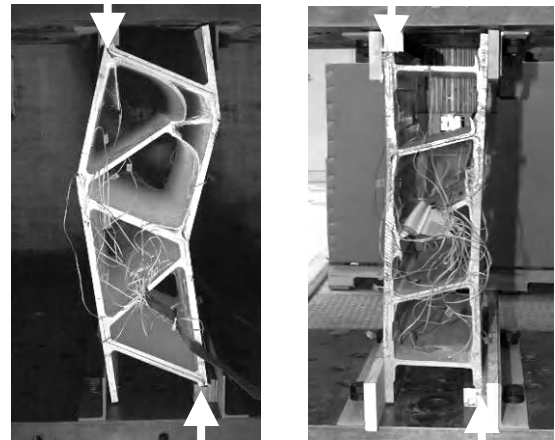


Figure 4 In-plane shear stress-strain system properties of two FRP bridge deck systems: triangular cells (left) brittle, trapezoidal cells (right) exhibiting system ductility

4 DUCTILITY OF ADHESIVES

Adhesive connections, unlike mechanical connectors (e.g. bolts), allow smooth load transfer in the joint and favor lightweight construction. De Castro (2005) has moreover demonstrated that soft adhesives may dissipate inelastic energy, defined as the area between the loading and re-loading path (obtained after unloading and recovery) or by the residual deformation after unloading, as shown in Figure 5.

Based on potential adhesive ductility, the concept of system ductility and redundancy mentioned above can be extended by including ductile adhesive joints to connect brittle components. De Castro (2005) has demonstrated in a simple case of one- and two-span pultruded FRP beams with and without an acrylic adhesive connection that the concept works. The bonded beams showed load distribution prior to global failure and improved structural robustness compared to continuous two-span beams.

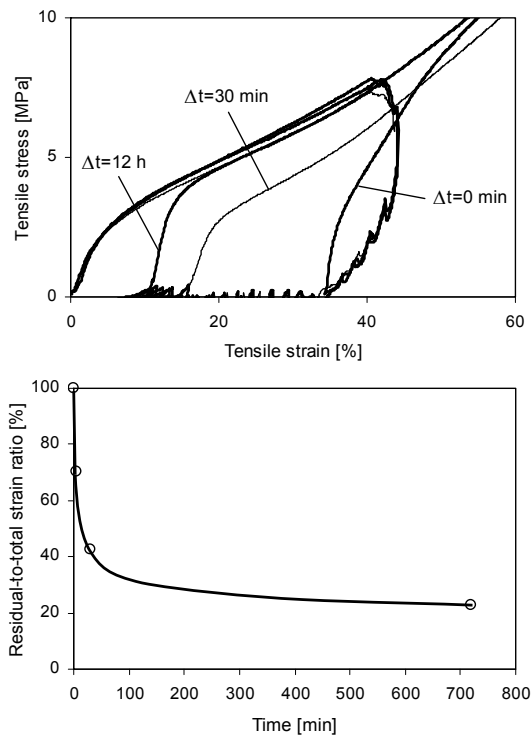


Figure 5 Nominal tensile load-unload-reload stress-strain curves, reloading after 0 and 30 min and 12 hours, and time-dependent ratio of residual-to-total strain for a ductile acrylic adhesive

5 MULTIFUNCTIONAL THERMAL SYSTEMS

FRP composites enable the creation of multifunctional systems that cannot be provided by traditional materials. The low thermal conductivity of GFRP in particular permits the integration of static and building physics functions into single building components. This allows a merging of load-bearing structure and building envelope and therefore leads to a significant reduction in the number of building components, which can be prefabricated under controlled conditions, thus improving quality compared to multilayered on-site production. Due to the lightweight material, components can be large-scale and nevertheless easily transported to the construction site and rapidly installed, as shown in Figure 2, thus shortening construction time and compensating for the higher material costs (Keller 2004). Low-energy standards are easily met while lightweight construction is maintained. A load-bearing envelope further liberates the ground plan from fixed elements and restores to architecture the flexibility of LeCorbusier’s “free plan” as shown in Figure 6. In addition, the load-bearing structure can again be used as an architectural element (as in the Bauhaus era between the 50s and 70s as demonstrated by famous architects such as Mies van der Rohe or LeCorbusier) and no longer needs to be wrapped and hidden by the envelope for energy saving reasons.

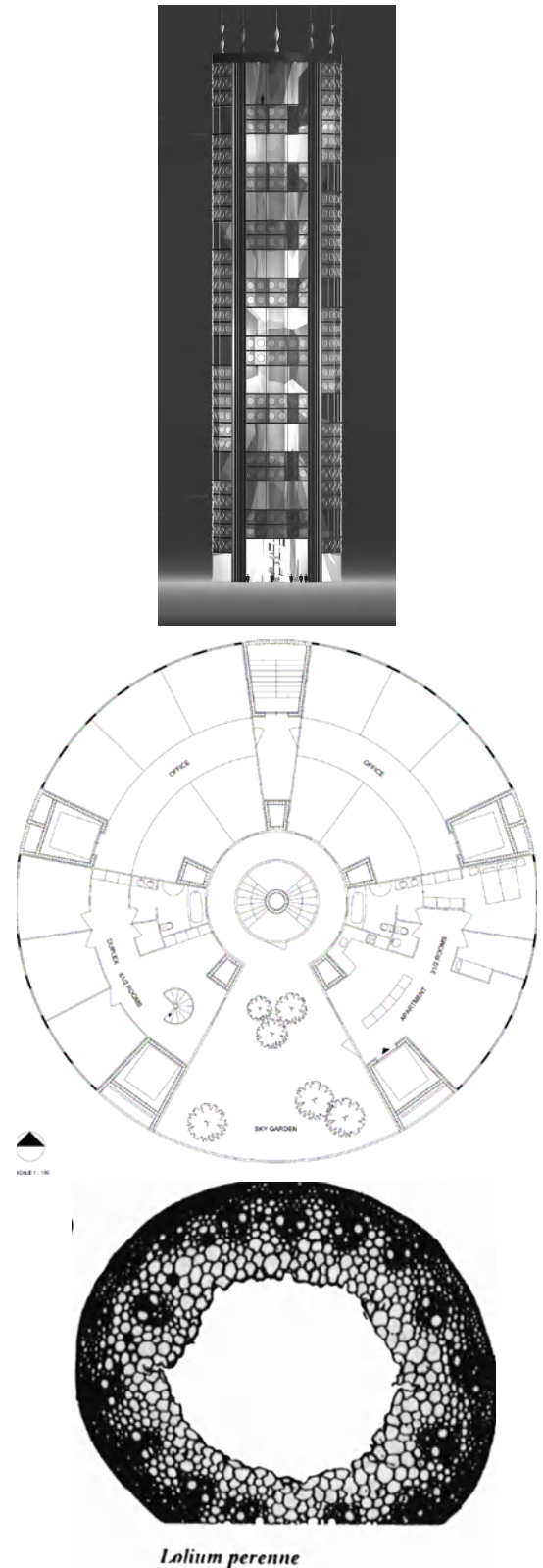


Figure 6 Dock Tower: concept of a self-sustainable lightweight 100-m high-rise GFRP building with multifunctional load-bearing exterior skin and free plan, derived from a plant stem (Keller 2006)

Cellular GFRP wall and slab components furthermore may contain circulating water, as schematically shown in Figure 7, which serves as heat transfer medium for several purposes: fire resistance through storage and

removal of heat, interior room heating during winter and cooling during summer, thermal mass, but also as potential absorber for integrated thermal solar systems or cooling of photovoltaic (PV) cells (see next Section). Furthermore, the extension of the water system to capture geothermal energy is possible.

Combined mechanical loading and fire experiments on full-scale water-cooled cellular slabs (Tracy 2005) and columns (Bai 2009) proved the feasibility of an effective fire protection. Fire endurance durations of up to two hours could be reached at slow water flow rates of between 0.2 to 5 cm/s, as can also be found in floor heating, cooling ceilings and heat pump systems.

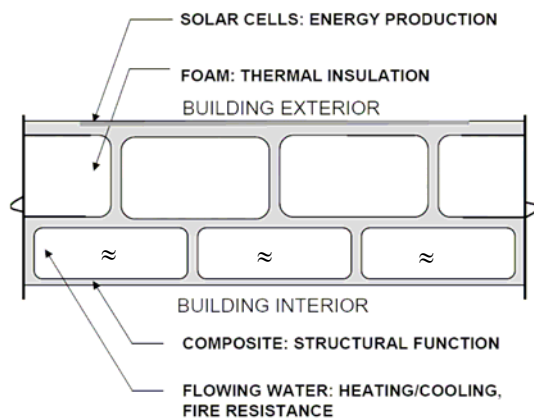


Figure 7 Combined thermal-energy wall concept

6 MULTIFUNCTIONAL ENERGY SYSTEMS

The production of energy by solar cells is of interest in building construction due to the great environmental benefits: no pollution is emitted, no greenhouse gases are produced, and no finite fossil fuel resources are used. Solar cells can be integrated into building elements for electric power generation, designated BIPV (Building Integrated PV), or used as solar thermal systems, designated BIST (Building Integrated Solar Thermal systems). To this date, however, such building elements did not fulfill any primary load-bearing functions.

Rion (2008) recently worked on the encapsulation of PV-cells into the skins of load-bearing ultra-lightweight sandwiches for the Swiss Solar Impulse airplane structure (www.solarimpulse.com). CCLab was involved in this project and started working on the encapsulation of PV-cells into the skins of multifunctional GFRP sandwich structures for building applications, see Figure 8 (Keller et al., in press). A main problem discovered in this preliminary work was a significant temperature increase on the top sandwich surface due to the heat production of the cells during operation. This, combined with the temperature increase caused by sunlight, resulted in the glass transition temperature of the resin being almost

reached. The long-term thermomechanical behavior of such sandwiches, the integrated PV-cells and the material interfaces therefore need further basic investigation. Cooling with integrated water systems, as mentioned in the previous Section, may present an effective measure to control the temperature, see Figure 7.

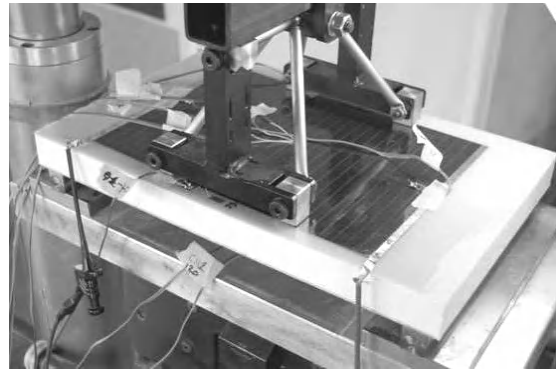


Figure 8 Mechanical loading of thin-film silicon PV-cell sandwich (Keller et al., in press)

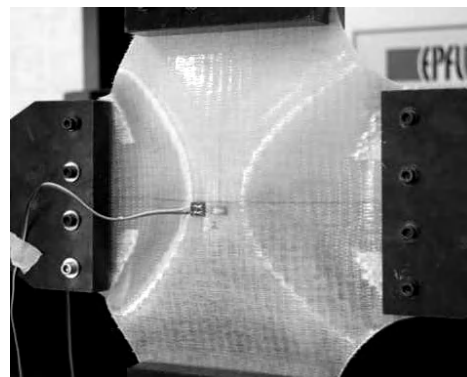


Figure 9 Shear buckling of thin-walled translucent GFRP webs (laminates subjected to bi-axial in-plane compression/tension loading)

7 MULTIFUNCTIONAL LIGHT SYSTEMS

Load-bearing GFRP materials may be translucent or transparent (either natural or colored) and glass fibers may conduct and disperse light (again natural or colored). Transparent and illuminating load-bearing components, along with possible freeform structures, and integration of envelope and structure are exciting new options offered for architecture. For the widespread future application of FRP materials it is crucial to win over architects since it is they (and not structural engineers) who normally select the building materials in building construction. The integration of transparent thermal aerogel insulation opens up horizons towards combined thermal-energy-light wall and slab systems.

The degree of transparency depends on the laminate thickness, fiber architecture (stacking sequence and type of fabrics, etc.), fiber volume fraction, and optical fiber/matrix properties (refraction indices). The mechanical properties themselves depend on the degree of transparency

(higher transparency will result in lower properties). Short-term aspects such as the stability of thin-walled translucent plates, as shown in Figure 9, and long-term aspects such as creep of transparent materials with low fiber content need to be taken into account in the design.

8 CONCLUSIONS AND FUTURE PROSPECTS

The multifunctional use of FRP composites offers the potential to contribute to the emergence of a new generation of lightweight engineering structures for an innovative infrastructure that meets the challenges with which today's construction industry is faced – engineering structures that ideally are multifunctional, safe and reliable, durable, adaptable or mobile, sustainable, economical and beautiful.

Flexible lightweight structures may be developed that will meet the future needs of our society such as, for example, the indispensable densification of urban areas by adding new stories onto existing buildings (a development known as “city lifting”). Lightweight multifunctional and energetically autonomous FRP structures are predestined to meet such challenges. Visions include transparent and luminous bridges and self-sustaining buildings (lightweight passive or zero-energy houses) and all types of multifunctional flexible, modular or convertible structures.

The transition from material substitution to material-tailored application took approximately 70 years for iron/steel (up to the welded steel frame) and 40 years for concrete (up to Robert Maillart's flat slab). With regard to FRP composites, we are still in the substitution phase and, therefore, the widespread implementation of material-tailored use will certainly take another one or two decades.

REFERENCES

- Bai, Y. 2009. Fiber reinforced polymer composites under elevated and high temperatures. EPFL-CCLab PhD-thesis No. 4340.
- De Castro, J. 2005. System ductility and redundancy of FRP structures with ductile adhesively-bonded joints. EPFL-CCLab PhD-thesis No. 3214.
- Deskovic, N., Meier, U., Triantafillou, T. C. 1995. Innovative design of FRP combined with concrete: short term behavior. *Journal of Structural Engineering*, 121/7: 1069-1078.
- Dooley, S. 2004. The development of material-adapted structural form. EPFL-CCLab PhD-thesis No. 2986.
- Fu, G., Frangopol, D. M. 1990. Balancing weight, system reliability and reliability in a multiobjective optimization framework. *Structural Safety* 7/(2-4): 165-75.
- Gürtler, H. 2004. Composite action of FRP bridge decks adhesively bonded to steel main girders. EPFL-CCLab PhD-thesis No. 3135.
- Keller, T. 2003. Use of fiber reinforced polymers in bridge construction. Structural Engineering Documents, No. 7, International Association for Bridge and Structural Engineering IABSE, ISBN 3-85748-108-0.
- Keller, T. 2004. Conceptual design of hybrid-FRP and all-FRP structures. 4th International Conference on Advanced Composite Materials in Bridges and Structures (ACMBS IV), Calgary, Canada, (keynote).
- Keller, T., Vassilopoulos, A.P. & Manshadi, B. D. 2010. Thermomechanical behavior of multifunctional GFRP sandwich structures with encapsulated photovoltaic cells. *Journal of Composites for Construction*, in press.
- Park, G.-J., Lee, T.-H., Lee, K. H., Hwang, K.-H. 2006. Robust design: an overview. *American Institute of Aeronautics and Astronautics* 44/1: 181-192.
- Rion, J. 2008. Ultra-light photovoltaic composite sandwich structures. EPFL-LTC PhD-thesis no. 4138.
- Schaumann, E. 2008. Hybrid FRP-lightweight concrete sandwich system for engineering structures. EPFL-CCLab PhD-thesis No. 4123.
- Tracy, C. 2005. Fire endurance of multicellular panels in an FRP building system. EPFL-CCLab PhD-thesis No. 3235.
- Van Erp, G. M. 2001. Robustness of fibre composite structures loaded in flexure. Proc., International Conference on FRP Composites in Civil Engineering, Elsevier, Amsterdam, 1421-1426.

Hybrid FRP-Concrete-Steel Double-Skin Tubular Structural Members

J.G. Teng (cejgteng@inet.polyu.edu.hk), T. Yu & Y.L. Wong

Department of Civil and Structural Engineering, The Hong Kong Polytechnic University, Hong Kong, China

ABSTRACT Hybrid FRP-concrete-steel double-skin tubular members (DSTMs) are a new form of hybrid structural members composed of an inner steel tube, an outer FRP tube and a concrete infill between them. The two tubes may be concentrically placed to produce a section form more suitable for columns, or eccentrically placed to produce a section form more suitable for beams. These hybrid structural members possess many important advantages over conventional structural members, including their excellent corrosion resistance as well as excellent ductility and seismic resistance. This paper explains the rationale and advantages of this new form of structural members and discusses their potential applications before presenting a summary of the recent and current studies on their structural behaviour and design. These studies form part of a major on-going research programme at The Hong Kong Polytechnic University (PolyU).

1 INTRODUCTION

Hybrid FRP-concrete-steel double-skin tubular members (referred to as hybrid DSTMs) (Figure 1) are a new form of hybrid members proposed by the first author (Teng et al. 2004, 2007). A hybrid DSTM consists of an outer tube made of fiber-reinforced polymer (FRP) and an inner tube made of steel, with the space between filled with concrete. The two tubes may be concentrically placed (Figures 1a and 1b) to produce a section form more suitable for columns, or eccentrically placed to produce a section form more suitable for beams (Figures 1c and 1d). In hybrid DSTMs, the FRP tube offers mechanical resistance primarily in the hoop direction to confine the concrete and to enhance the shear resistance of the member. Hybrid DSTMs may be constructed in-situ or precast, with the two tubes acting as the stay-in-place form. The sections of the two tubes may be both circular (Figures 1a and 1c), rectangular (Figure 1d), or in another shape; they may also have shapes different from each other (Figure 1b). Shear connectors need to be provided between the steel tube and the concrete, particularly in beams, but are generally not needed for the FRP tube which is normally designed to have only a small longitudinal stiffness.

The most important advantage of hybrid DSTMs is their excellent corrosion resistance, as the FRP tube is highly resistant to corrosion while the steel tube is protected by the FRP tube and the concrete. The other main advantages of hybrid DSTMs include (1) excellent ductility, as the concrete is well confined by the two tubes and inward local buckling of the steel tube is constrained by the concrete; (2) a high strength/stiffness-to-weight

ratio as the inner void largely eliminates the redundant concrete; (3) ease for construction, as the two tubes act as a permanent form for casting concrete, and the presence of the inner steel tube and the concrete allows easy connection to other members. More discussions of the rationale and advantages of hybrid DSTMs are available in Teng et al. (2007).

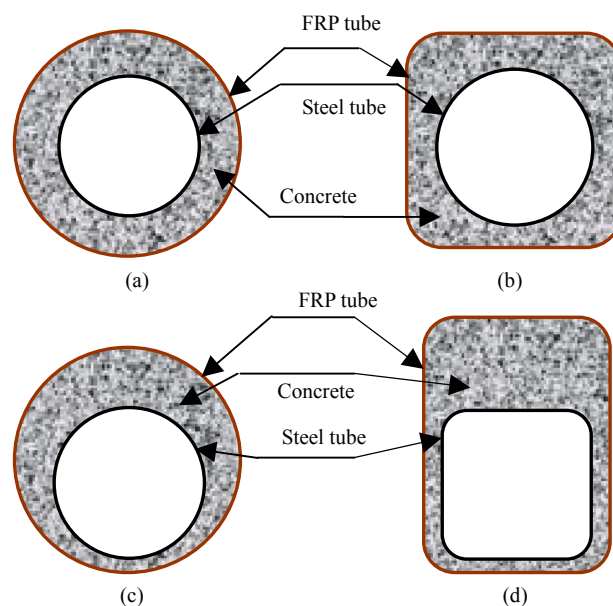


Figure 1 Typical sections of hybrid DSTMs

2 POTENTIAL PRACTICAL APPLICATIONS

2.1 Double-skin tubular columns

Because of their excellent corrosion resistance, hybrid

DSTMs are most suitable for use in outdoor structures such as bridges and coastal structures which are likely to be exposed to a harsh environment. Hybrid DSTMs can be used as compression members, such as piles and bridge piers, various towers (e.g. wind turbine towers, electricity transmission towers and bridge towers) and other similar structures. Hereafter hybrid DSTMs used as compression members are referred to as hybrid double-skin tubular columns or hybrid DSTCs for brevity.

In practical applications, when the length of DSTCs becomes very large (e.g. as wind turbine towers), they can be constructed using a segmental method, which involves the segmental construction of the outer FRP tube and the inner steel tube and the use of the two tubes as the permanent formwork for the in-situ casting of concrete as schematically illustrated in Figure 2. The flanges of the steel tubular segments and the FRP profiles inside the FRP tubular segments serve not only as longitudinal connectors between the segments, but also as (1) shear connectors between the concrete and the tubes; and (2) stiffeners to both tubes, thus improving the structural performance of hybrid DSTCs.

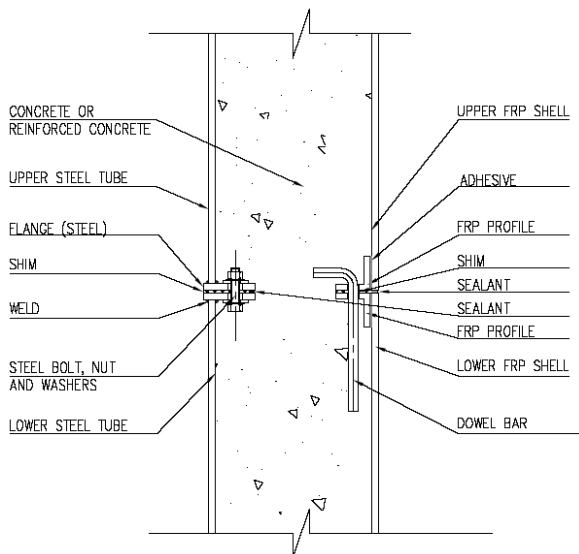


Figure 2 Segmental construction of tall DSTCs

2.2 Double-skin tubular beams

Hybrid DSTMs can also be used as flexural members in bridges, coastal structures and other structures exposed to a harsh environment. Hereafter hybrid DSTMs used as flexural members are referred to as hybrid double-skin tubular beams or hybrid DSTBs for brevity.

As bridge girders, hybrid DSTBs can be used with an all FRP deck (or another form of lightweight and corrosion-resistant deck such as a hybrid FRP-concrete deck or an aluminium deck) to form a light slab-on-girder bridge system (Figure 3a). In Figure 3a, the deck is connected with the hybrid DSTB through an adhesive layer, but this adhesive layer can be replaced by or used

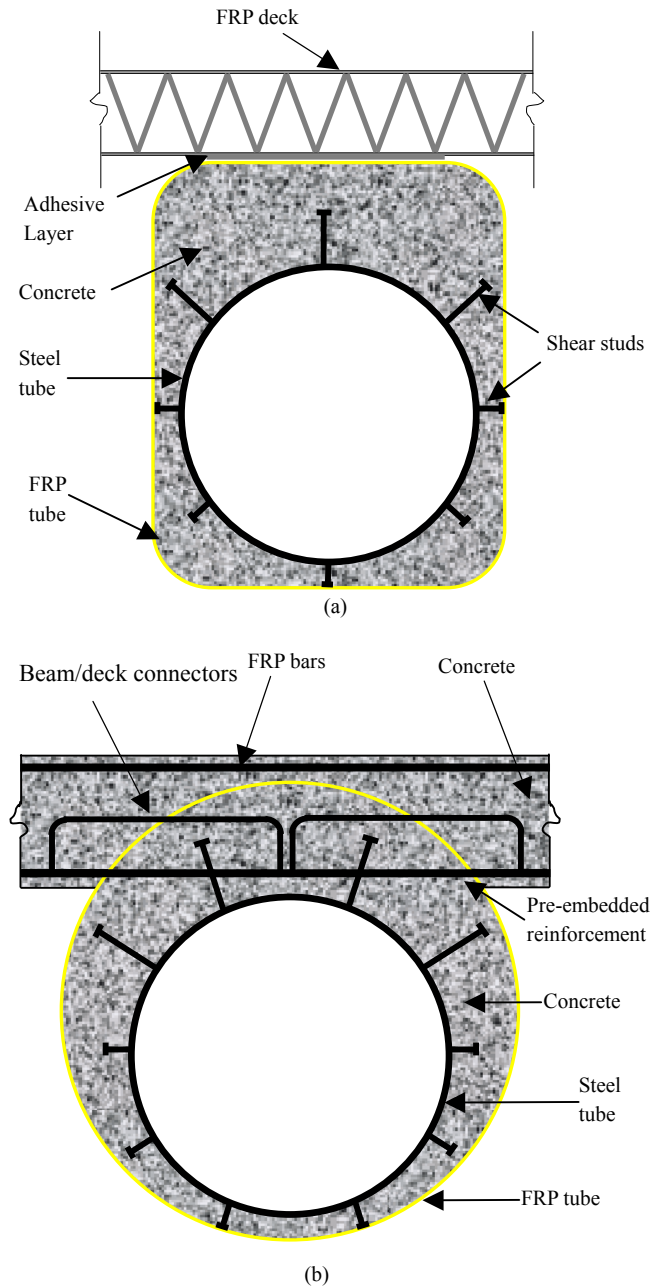


Figure 3 Hybrid DSTB/deck units

together with mechanical joints (e.g. bonded shear keys) when necessary. Hybrid DSTBs can also be integrated into a concrete deck reinforced with FRP bars to form a bridge system (Figure 3b). In such cases, pre-embedded steel (stainless steel may be used here) reinforcement in the DSTB can be spliced with the bottom layer of FRP bars in the deck using mechanical couplers for beam-deck connection (Figure 3b). Additional shear connectors in the form of U-shaped dowels (or other appropriate forms) passing through the FRP tube may also be used to ensure the longitudinal composite action between the beam and the deck (Figure 3b). As the fibres in the FRP tube are close to the hoop direction, the passing of steel bars through the tube is expected to affect little its overall performance.

While hybrid DSTBs with a constant cross-sectional configuration are particularly suitable for simply-supported beams, cost-effective continuous DSTBs can be built by placing the steel inner tube in an inclined position in the longitudinal direction (i.e. the steel tube lies near the bottom of the cross-section in sagging moment zones but near the top of the cross-section in hogging moment zones). For a beam/deck unit as illustrated in Figure 3a, if composite action between the DSTB and the deck is not pursued (e.g. because of the relatively low stiffness/strength in the longitudinal direction of an all FRP deck), the behaviour of the DSTB alone governs the performance in the longitudinal direction of the beam/deck assembly. For a beam/deck unit as illustrated in Figure 3b, the composite action between the beam and the deck typically needs to be considered.

3 EXISTING RESEARCH ON HYBRID DSTMS

At The Hong Kong Polytechnic University (PolyU), a large amount of research has been conducted on hybrid DSTMs. Most of the work undertaken prior to 2007 can be found in Teng et al. (2007), Yu et al. (2006), Wong et al. (2008), and Yu et al. (2010a, 2010b, 2010c, 2010d). Teng et al. (2007) explained in detail the rationale for the new member form together with its expected advantages, and presented preliminary experimental results to demonstrate some of the advantages of this new member form, such as excellent ductility and shear resistance. Yu et al. (2006) presented the results of a systematic experimental study on the flexural behavior of hybrid DSTMs as well as results from a corresponding theoretical model based on the fiber element approach. Yu et al. (2006) showed that the flexural response of hybrid DSTMs, including their flexural stiffness, cracking load and ultimate load, can be substantially improved by shifting the inner steel tube towards the tension zone or by providing FRP bars as additional longitudinal reinforcement. Wong et al. (2008) presented a systematic experimental study on the compressive behavior of hybrid DSTMs and compared the performance of hybrid DSTMs with that of FRP-confined solid cylinder/column (FCSC) specimens and FRP-confined hollow cylinder/column (FCHC) specimens; a good understanding of the behavior of concrete in hybrid DSTMs resulted from this study. Yu et al. (2010a, b) developed a new plastic-damage model for FRP-confined concrete based on a critical review of the previous D-P type plasticity models. A finite element model incorporating the new plastic-damage model was shown to provide close predictions of the test results of hybrid DSTMs (Yu et al. 2010b). Based on the available experimental observations and the results from the finite element model, Yu et al. (2010c) proposed a design-oriented stress-strain model

for the confined concrete in hybrid DSTMs subjected to axial compression. Yu et al. (2010d) presented experimental results on the behaviour of hybrid DSTMs subjected to eccentric compression as well as a so-called “variable confinement model” for the confined concrete to account for the effect of strain gradient on confinement effectiveness. These studies at PolyU have led to a simple design approach for hybrid DSTMs as columns, and this design approach has recently been adopted by the draft Chinese Code for Infrastructure Application of FRP Composites (Teng and Yu 2010). In addition to research carried out at PolyU, work has also been undertaken by Xu and Tao (2005), Yu (2006), Liu (2007) and Han et al. (2010). These studies have further confirmed the good performance of hybrid DSTMs subjected to different loading conditions.

At PolyU, intensive research on the behaviour and design of hybrid DSTMs is continuing. In the remainder of the paper, the latest advances of this ongoing research programme at PolyU are briefly presented, covering: (1) cyclic axial compression tests; (2) hybrid DSTCs with high strength concrete; (3) large-scale column tests; (4) behaviour of hybrid DSTBs.

4 CYCLIC AXIAL COMPRESSION TESTS

Since hybrid DSTCs are particularly suitable for use in seismic regions, their behaviour under cyclic loading is of significant interest. Therefore, a series of cyclic axial compression tests on hybrid DSTCs has recently been completed as part of a comprehensive study aiming at the eventual development of an appropriate procedure for the seismic design of hybrid DSTCs.

In total, eight identical hybrid DSTCs were tested, covering four loading schemes; two specimens were made for each loading scheme. The specimens had an outer diameter (i.e. the outer diameter of the annular concrete section) of 205.3 mm, an inner diameter (i.e. the inner diameter of the annular concrete section and the outer diameter of the inner steel tube) of 140.3 mm, and a height of 400 mm. The void ratio of these specimens (i.e. ratio between the inner diameter and the outer diameter of the annular concrete section) was thus around 0.7. The nominal thickness of the FRP tube formed from fibre sheets via the wet layup process was 0.34 mm while the thickness of the steel tube was 5.3 mm. The use of wet layup FRP tubes with fibres oriented solely in the hoop direction instead of filament-wound FRP tubes with fibres oriented at small angles to the hoop direction was due to difficulties in finding commercial FRP tubes with properties required by the tests. Such use is considered to be acceptable as the main function of the FRP tube is to provide hoop resistance. The four loading schemes included monotonic loading, full unloading/reloading, partial unloading and partial reloading. More details of

the experimental programme are available in Yu et al. (2010e).

The axial load-axial strain curves of the two specimens subjected to full unloading/reloading cycles (i.e. specimens F1 and F2) are compared with those of the two monotonic loading specimens (i.e. specimens M1 and M2) in Figure 4. It is evident from Figure 4 that the envelope curves of the two specimens subjected to cyclic axial compression, which provide an upper boundary of their responses under cyclic loading, are almost the same as the axial load-axial strain curves of the two specimens subjected to monotonic compression. Figure 4 also shows that the unloading/reloading cycles at the same unloading displacement generally do not coincide with each other, indicating that the effect of loading history on the cyclic response of hybrid DSTCs is not negligible. The difference between two consecutive loading cycles is, however, seen to become smaller as the number of repeated cycles increases (Figure 4).

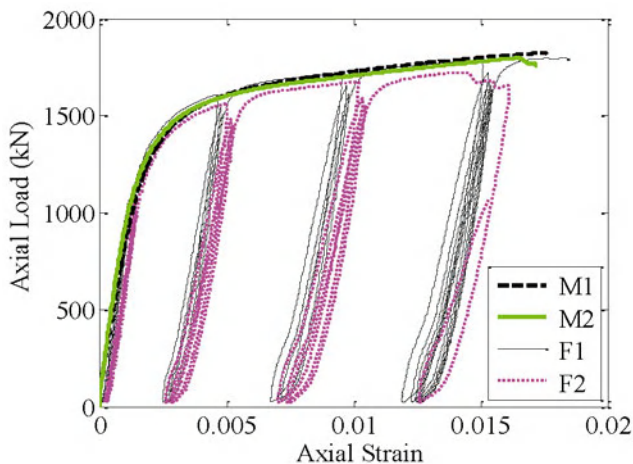


Figure 4 Axial load-axial strain curves of DSTCs under cyclic axial compression

The axial stress-axial strain curves of the confined concrete in specimens M1, M2, F1 and F2 are shown in Figure 5. The axial stress of concrete in a DSTC is defined herein as the load carried by the annular concrete section divided by its cross-sectional area. The load carried by the concrete section is assumed to be equal to the difference between the load carried by the DSTC and that carried by the steel tube; the latter was found from compression tests on hollow steel tubes. These tests on hybrid DSTCs subjected to cyclic axial compression revealed that during unloading, the steel tube unloaded more rapidly than the concrete and reached the zero stress first when considerable compressive stresses still existed in the concrete. As unloading continued, tensile stresses were induced in the steel tube. In deducing the axial stress in the concrete, it was assumed that the ratio of axial stress increment to axial strain increment for the steel is equal to the unloading modulus of steel found

from the cyclic compression test of a hollow steel tube cut from the same original long tube which provided steel tubes for the hybrid DSTCs tested. The above difference in unloading behaviour between the steel tube and the concrete is at least partially due to their different modulus degradations: the unloading modulus of a steel tube is generally the same as its elastic modulus but the unloading modulus of concrete is considerably smaller than its elastic modulus due to degradation.

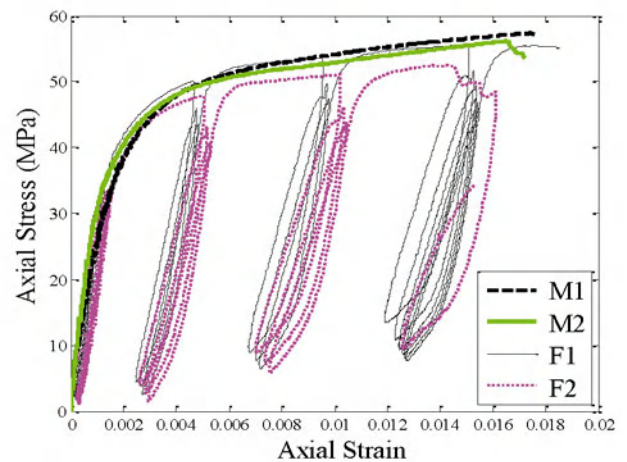


Figure 5 Axial stress-axial strain curves of concrete in DSTCs under cyclic axial compression

Figure 5 shows that the envelope curves of specimens F1 and F2 are almost the same as the axial stress-axial strain curve of specimens M1 and M2. It is also interesting to note that while specimens F1 and F2 were subjected to full unloading/reloading cycles (i.e. unloading was terminated at a very small load), the axial stresses at the termination points of unloading were significantly larger than zero. This phenomenon is due to the development of tensile stresses in the steel tube, as explained earlier.

More details of the test results and discussions of the effect of partial unloading and partial reloading are available in Yu et al. (2010e).

5 HYBRID DSTCS WITH HIGH STRENGTH CONCRETE

High strength concrete (HSC) is normally defined as concrete with a cylinder compressive strength exceeding 50 MPa (Xiao et al. 2010). Hybrid DSTCs offer an ideal opportunity for the use of HSC: the confinement provided by the two tubes ensures a ductile response of the concrete and the absence of any steel bars ensures good-quality casting of HSC.

Six hybrid DSTC specimens with HSC have recently been tested under axial compression at PolyU, as part of a comprehensive study. The concrete of these specimens had a cylinder compressive strength of 83.5 MPa. These

six specimens covered three combinations of void ratio and FRP tube; two identical specimens were prepared for each combination. Two void ratios (i.e. 0.558 and 0.779) within the practical range were adopted. Two types of FRP tubes, namely, one-ply carbon FRP (CFRP) tubes and six-ply glass FRP (GFRP) tubes, were used; the two types of FRP tubes had a similar circumferential stiffness but the GFRP tubes had a much larger ultimate hoop strain (around two times that of the CFRP tubes). All specimens had the same outer diameter of 204 mm and the same height of 400 mm.

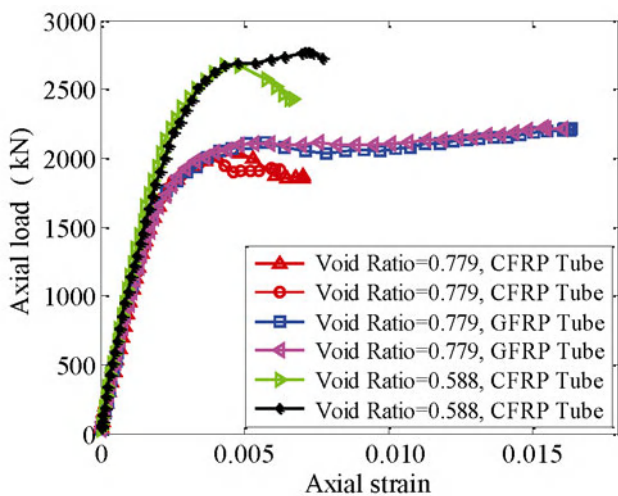


Figure 6 Axial load-axial strain curves of hybrid DSTCs with high strength concrete

The axial load-axial strain curves of all six specimens are shown in Figure 6. While all these curves are close to an approximately elastic-perfectly-plastic curve, the plastic plateau for those specimens with a GFRP tube is much longer than that for specimens with a CFRP tube. The two specimens with a GFRP tube showed a very ductile response with the ultimate axial strain being over 1.6% and around 5 times the strain of unconfined concrete at peak stress (i.e. 0.329%, found from tests on three 152.5 mm × 305 mm concrete cylinders). By contrast, the ultimate axial strain is only around 0.7% for the four specimens with a CFRP tube. The two different void ratios (i.e. 0.558 and 0.779) did not lead to obvious differences in the ultimate axial strain of hybrid DSTCs with a CFRP tube.

These test results suggest that hybrid DSTCs with HSC can have very good ductility when the FRP outer tube has a sufficiently large strain capacity in the circumferential direction. This advantage, however, may be much less pronounced when a relatively brittle FRP tube is used. Further work on hybrid DSTCs with HSC is being conducted at PolyU, covering a larger range of concrete strength and aiming to develop a unified stress-strain model for both NSC and HSC in hybrid DSTCs.

6 LARGE-SCALE COLUMN TESTS

The early experimental studies undertaken at PolyU and elsewhere were limited to the testing of small-scale columns. Whether the conclusions reached on the basis of these small-scale tests are valid for full-scale members is an issue of concern. To address this concern, an experimental study is under way where large-scale columns are tested under pure axial compression or combined axial compression and lateral loading. Preliminary test results of three large-scale hybrid DSTCs under pure axial compression are presented below.



Figure 7 Large-scale hybrid DSTC after test

The three specimens all had an outer diameter of 404 mm and a height of 800 mm. Two of the specimens (i.e. Specimens S325-4 and S325-6) had the same steel tube with an outer diameter of 324 mm and a thickness of 9 mm, leading to a void ratio of 0.80; the two specimens had an FRP tube with a nominal thickness of 0.68 mm (i.e. a 4-ply FRP tube) and 1.02 mm (i.e. a 6-ply FRP tube) respectively. The remaining specimen had a steel tube with an outer diameter of 246 mm and a thickness of 8 mm, a void ratio of 0.61, and a 6-ply FRP tube (i.e. Specimen S245-6). Once again, the FRP tubes were formed from dry fibre sheets in the laboratory using the wet layup method with all fibres oriented in the hoop direction.

Similar to the small-scale specimens tested by Wong et al. (2008), all three large-scale specimens failed by the rupture of the FRP tube as a result of hoop tension. One of the large-scale specimens after test is shown in Figure 7.

The axial load-axial strain curves of these three DSTC specimens are shown in Figure 8, where the strains were found from the readings of displacement transducers covering the mid-height region of 320 mm. All three specimens showed an approximately bilinear axial load-axial strain curve. The slope of the second linear portion

of the curve is seen to increase significantly with the thickness of the FRP tube, but the void ratio does not seem to affect this slope significantly. For the two DSTCs with a six-ply FRP tube, the ultimate axial strains are over ten times the strain at the peak stress of unconfined concrete. The much smaller ultimate axial strain for the specimen with a four-ply FRP tube was partially caused by the unexpected early failure of the FRP tube at a relatively small hoop strain due to a defect arising from the preparation of the specimen.

These preliminary test results suggest that the behaviour of large-scale hybrid DSTCs can be extrapolated from that found from testing small-scale hybrid DSTCs (Wong et al. 2008). While further studies are needed to examine the effect of member size in various terms such as the axial stress-axial strain curve of the confined concrete and the ultimate state of the FRP tube, these preliminary test results have confirmed the good performance of hybrid DSTCs as initially expected.

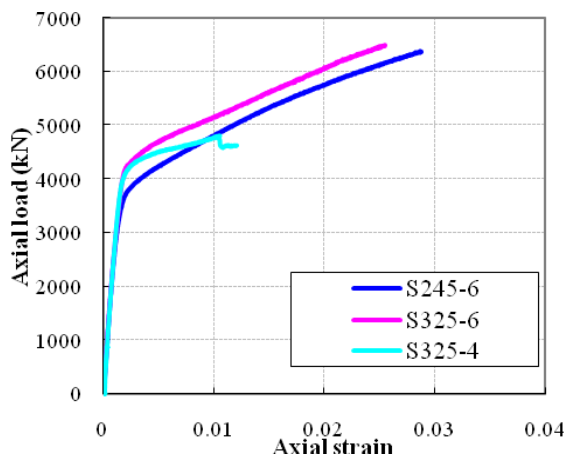


Figure 8 Axial load-axial strain curves of large-scale DSTCs

7 BEHAVIOUR OF HYBRID DSTBS

As mentioned earlier, existing studies at PolyU and elsewhere have been focused on the behaviour of hybrid DSTMs as columns (i.e. hybrid DSTCs). Only a limited number of laboratory tests have been conducted on small-scale hybrid DSTBs without shear connectors and subjected to static loads (Yu et al. 2006; Liu 2007). Among these tests, ten specimens had a section form as shown in Figure 1a (i.e. two concentric circular tubes) and were tested as part of a study to understand the beam-column behaviour of these hybrid members; the other five had a section form as shown in Figure 1c which is more suitable for use in beams. Further research is being pursued to address the issues outlined below.

Yu et al. (2006) showed that shear connectors should be provided between the steel tube and the concrete in hybrid DSTBs to ensure a high degree of composite action between them. Research is therefore needed to establish appropriate forms of shear connectors and to

develop a design method for such shear connectors. In hybrid DSTBs, the compressive concrete is subjected to lateral confinement by the FRP tube and the steel tube, so the behaviour of the shear connectors in hybrid DSTBs is expected to be different from that of shear connectors in traditional hybrid steel-concrete beams with a steel I-section. Existing design methods developed for the latter (e.g. Eurocode 4 2004) are thus not expected to be applicable to the former. To address this issue, appropriately-designed push-out tests need to be conducted to investigate the behaviour of shear connectors and to develop simple design methods for them.

For DSTBs to be used as bridge girders, research on their fatigue behaviour is needed. As fatigue failure of a hybrid beam generally occurs in the shear connectors, the behaviour of these connectors under fatigue loading needs to be understood first through push-out tests. A reliable analysis approach is also needed to predict the fatigue life of hybrid DSTBs, which should appropriately account for partial interaction (Newmark et al. 1951), fatigue-induced material property changes (e.g. softening and/or creep deformation of concrete) (Holmen 1982; Ahmad et al. 2004), and fatigue-induced stiffness reduction of shear connectors.

Although hybrid DSTBs are expected to be very strong in shear because of the presence of an inner steel tube and an outer FRP tube, their high shear strength needs to be confirmed through laboratory testing. A simple design method also needs to be developed for the shear strength of hybrid DSTBs, where the simple additive approach (Teng et al. 2002; Chen and Teng 2003) widely used for FRP-strengthened RC beams may be adopted.

8 CONCLUDING REMARKS

This paper has discussed the rationale and advantages of hybrid FRP-concrete-steel double-skin tubular members (i.e. hybrid DSTMs), provided a brief summary of existing research on hybrid DSTMs, and outlined the issues currently being addressed by the authors' research group in a major on-going research programme at The Hong Kong Polytechnic University. Hybrid DSTMs have a great potential for use as piles, columns and towers as well as beams in structures exposed to harsh environments such as bridges, coastal structures and various tower structures. While existing and current research is mainly concerned with DSTMs as isolated members, exciting opportunities exist for the development of structural systems based on DSTMs. One such example is the development of a bridge system with DSTCs as piers, piles and towers and with DSTBs as girders supporting corrosion-resistant decks. Such a bridge system is highly durable and offers an attractive alternative to existing structural systems in a corrosive environment. Such

system-level research is needed in the near future to realize the full potential of DSTMs.

9 ACKNOWLEDGMENTS

The authors are grateful for the financial support received from the Research Grants Council of the Hong Kong SAR (Project No: PolyU 5278/07E) and The Hong Kong Polytechnic University. They are also grateful to Mr Y.B. Cao, Ms P. Xie and Mr B. Zhang who conducted the tests described in Sections 4 to 6.

REFERENCES

- Ahmad, I., Zhu, Z. and Mirmiran, A. 2008. Fatigue behaviour of concrete-filled fiber-reinforced polymer tubes, *Journal of Composites for Construction*, ASCE, 12(4): 478-487.
- Chen, J.G. and Teng, J.G. 2003. Shear capacity of fiber-reinforced polymer-strengthened reinforced concrete beams: Fiber reinforced polymer rupture, *Journal of Structural Engineering*, ASCE, 129(5): 615-625.
- Eurocode 4 2004, *Design of Composite Steel and Concrete Structures*, European Committee for Standardization (CEN).
- Han, L.H., Tao, Z., Liao, F.Y. and Xu, Y. 2010. Tests on cyclic performance of FRP-concrete-steel double-skin tubular columns, *Thin-Walled Structures*, 48(6): 430-439.
- Holmen, J. 1982. Fatigue of concrete by constant and variable amplitude loading, *Fatigue of Concrete Structures*, ACI SP-75, Detroit, MI, 71-110.
- Liu, M.X. 2007. Studies on Key Behavior of FRP-Concrete-Steel Double Skin Tubular Columns. PhD Thesis, Tsinghua University. (in Chinese).
- Newmark, N.M., Siess, C.P. and Viest, I.M. 1951. Tests and analysis of composite beams with incomplete interaction, *Proceedings, Society for Experimental Stress Analysis*, 9(1): 75-92.
- Teng, J.G. and Yu, T. 2010. Hybrid FRP-concrete tubular columns: design provisions in the draft Chinese code, *Proceedings, International Symposium on Life-Cycle Performance of Bridges and Structures*, Changsha, China, 27-29 June, pp. 387-394.
- Teng, J.G., Chen, J.F., Smith, S.T. and Lam, L. 2002. *FRP-Strengthened RC Structures*, John Wiley and Sons, UK.
- Teng, J.G., Yu, T. and Wong, Y.L. 2004. Behaviour of hybrid FRP-concrete-steel double-skin tubular columns, *Proceedings, Second International Conference on FRP Composites in Civil Engineering*, December 8-10, Adelaide, Australia, 811-818
- Teng, J.G., Yu, T., Wong, Y.L. and Dong, S.L. 2007. Hybrid FRP-concrete-steel tubular columns: concept and behavior, *Construction and Building Materials*, 21(4):846-854.
- Wong, Y.L., Yu, T., Teng, J.G. and Dong, S.L. 2008. Behavior of FRP-confined concrete in annular section columns, *Composites: Part B-Engineering*, 39:451-466.
- Xiao, Q.G., Teng, J.G. and Yu, T. (2010). Behavior and modeling of confined high strength concrete, *Journal of Composites for Construction*, ASCE, 14 (3): 249-259.
- Xu, Y. and Tao, Z. 2005. Key issues of dynamic behavior of hybrid FRP-concrete-steel double skin tubular columns, *Journal of Fuzhou University (Natural Science)*, 33: 309-315 (in Chinese).
- Yu, T., Wong, Y.L., Teng, J.G., Dong, S.L. and Lam, S.S. 2006. Flexural behaviour of hybrid FRP-concrete-steel double skin tubular members, *Journal of Composites for Construction*, ASCE, 10 (5): 443-452.
- Yu, T., Teng, J.G., Wong, Y.L. and Dong, S.L. 2010a. Finite element modeling of confined concrete-I: Drucker-Prager type plasticity model, *Engineering Structures*, 32 (3): 665-679.
- Yu, T., Teng, J.G., Wong, Y.L. and Dong, S.L. 2010b. Finite element modeling of confined concrete-II: plastic-damage model, *Engineering Structures*, 32(3): 680-691.
- Yu, T., Teng, J.G. & Wong, Y.L. 2010c. Stress-strain behavior of concrete in hybrid double-skin tubular columns, *Journal of Structural Engineering*, ASCE, 136(4): 379-389.
- Yu, T., Wong, Y.L. and Teng, J.G. 2010d. Behavior of hybrid FRP-concrete-steel double-skin tubular columns subjected to eccentric compression, *Advances in Structural Engineering*, 13(5).
- Yu, T., Teng, J.G., Zhang, B. and Cao, Y.B. 2010e. Behavior of hybrid FRP-concrete-steel double-skin tubular columns subjected to cyclic axial compression, *in preparation*.
- Yu, X.W. 2006. *Behavior of Hybrid CFRP-Concrete-Steel Double-Skin Tubular Columns under Axial Compression*. MSc Thesis, Harbin Institute of Technology. (in Chinese).

Durability of GFRP Reinforcement Bars

Charles E. Bakis (cbakis@psu.edu)

Department of Engineering Science and Mechanics, Pennsylvania State University, University Park, PA, USA

ABSTRACT Results of a 3-year-long investigation of durability of one type of glass fiber reinforced vinylester composite reinforcement bar are summarized. Bars were cast in concrete beams and subjected to simultaneous sustained load and exposure to one of four different environments: ambient indoor laboratory, natural outdoor weathering in central Pennsylvania, high-alkaline aqueous solution at 60°C, and alternating -17°C dry freeze and room-temperature water immersion. The conditioned beams were tested to determine crack width in the concrete, local bond-slip behavior of the bars, and tensile stress-strain behavior of bars extracted from the beams. Over time, crack widths increased by up to 75% while local ultimate bond strength in the anchorage zone remained essentially constant or increased. Tensile strength decreased by as much as 25% in the high moisture environments and was essentially constant in the indoor and outdoor environments. These results suggest promising durability characteristics of GFRP bars under realistic service conditions.

1 INTRODUCTION

The durability of glass fiber reinforced polymer (GFRP) composite reinforcement bars for concrete structures has been the subject of much research in recent years. For example, several laboratories have investigated the tensile behavior (Bakis et al. 1998, Porter and Barnes 1998, Dejke et al. 2003, Nkurunziza et al. 2005, Chen et al. 2007) and bond behavior (Bank et al. 1998, Bakis et al. 1998) of GFRP bars in aggressive environments. Specific conclusions vary according to the type of bar being tested and the exact combination of stress and environmental conditions applied over time prior to the measurement of tensile or bond strength. The mechanisms of tensile and bond strength reduction are believed to be glass corrosion and fiber/matrix interface degradation, respectively. Elevated temperature, increased access of moisture to the bar, alkalinity of the moisture, and elevated stress exerted on the bar are generally considered deleterious to tensile and bond strength. However, the degradation in longitudinal modulus of elasticity of GFRP bars under these aggressive conditions is relatively minor. Conditions inside of concrete have been found to be more benign than those imposed in many laboratory tests done on bare bars in various aggressive aqueous solutions (Tannous & Saadatmanesh 1999, Nkurunziza et al. 2005). Therefore, it is possible that current design guidelines that limit the maximum sustained tensile stress on GFRP bars may be overly conservative. On the other hand, information on the long-term crack width of GFRP-reinforced beams under sustained loading and environmental conditioning is relatively scarce.

In this paper, a review of the findings of a 3-year-long

investigation of the tensile and bond durability of GFRP bars embedded in loaded concrete beams is given. The purpose of the review is to present the findings together for the first time. Previous publications by the author and his colleagues explain the details of the investigation of tensile behavior (Bakis et al. 2005) and bond behavior (Bakis et al. 2004, 2007). Space limitations prevent the inclusion of all the details in this paper.

2 METHODS

2.1 Experimental

The 10.2-mm-dia. E-glass reinforced vinylester bars, shown in Figure 1, were obtained from the manufacturer in October, 1999. The ingredients of the bars are listed in Table 1. The materials and parameters reported here differ slightly from bars currently made by the manufacturer.



Figure 1 GFRP bar (mm scale)

Beam specimens of 178(H)×89(W)×1830(L) mm dimensions were cast using concrete provided by a local ready-mix plant. A single longitudinal GFRP reinforcement bar was centered 38 mm from the bottom of the section. The actual and balanced reinforcement ratios were 0.66%

and 0.46%, respectively. The cylinder strength was 39.4 MPa. The beams were pre-cracked in 4-point bending to a moment of 2.19 kN·m, which is approximately 50% of the ultimate governed by shear/compression.

Table 1 Bar characteristics (Gremel)

Property and Unit	Value
E-Glass Fiber volume fraction (%)	51
Vinylester matrix volume fraction (%)	49
Styrene (pph wt. matrix)	1
Hydrous kaolin clay (pph wt. matrix)	26
Longitudinal Tensile Modulus (GPa)	41
Longitudinal Tensile Strength (MPa)	700

For each conditioning period, three pairs of pre-cracked beams were placed in 4-point loading jigs under a moment of 850 N·m, which is 20% of ultimate (Figure 2). According to a conventional beam section analysis with parabolic concrete behavior, the sustained stress and strain on the bars were roughly 78 MPa and 2000 $\mu\epsilon$, or 11% of the manufacturer's ultimate listed in Table 1.

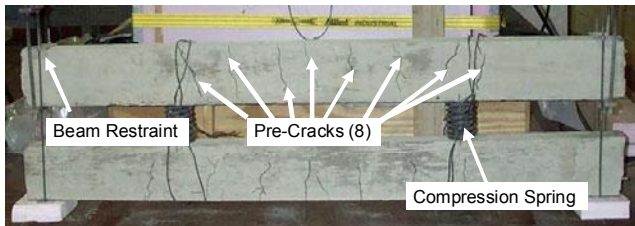


Figure 2 Sustained 4-pt. bending rig.

Loaded beams were placed in four environments: up to ~3 years in an indoor laboratory environment of 23±3°C, 40–60% RH; up to ~3 years outdoors in University Park; up to ~12 months in a sealed, heated immersion tank filled with a saturated solution of Ca(OH)₂ and 60±2°C tap water (pH=12–13); and up to ~12 months of alternating immersion in water 23±2°C (pH=8) and freezing at -17±2°C. The freeze/thaw (F/T) conditioning consisted of cycles that lasted 5.6 days on average, with approximately half the cycle time immersed in water. Roughly 60 F/T cycles accrued in 12 months of conditioning.

Crack widths at the bottom of the beams were measured at irregular intervals using an optical magnifier/reticule with 25 μm resolution. The expression for the maximum crack width, w , according to the current ACI design guide for FRP reinforced concrete (ACI 2006), is as follows:

$$w = \frac{2\beta k_b f_f}{E_f} \sqrt{d_c^2 + \left(\frac{s_b}{2}\right)^2}, \quad (1)$$

where E_f is the Young's modulus of the bar, β is the ratio of the distance between the neutral axis and the bottom of the section to the distance between the neutral axis and the bar (1.308), k_b is a bond-dependent parameter, f_f is

the longitudinal stress on the bar (78 MPa), d_c is the cover depth (38.1 mm), and s_b is the bar spacing (44.5 mm). A value of k_b greater than 1.0 implies wider cracks than the case of deformed steel bars under the same tensile strain. The 90th percentile crack width for each set of beams subjected to a particular duration of conditioning was used to determine k_b versus time under the assumption that all the other terms in Eq. (1) are invariant during conditioning.

After conditioning, beams were unloaded and subjected to eccentric 3-point flexure tests to evaluate bond behavior of the bar in the anchorage zone near one end of each beam (Figure 3). In this test, load, width of the concrete crack under the load point, and free-end slip of the bar were measured for anchorage zone lengths, l , of 314, 364, 414, and 464 mm. Following bond testing, the bars were carefully extracted from the untested portion of the beams by removing the concrete cover. In preparation for tensile testing, portions of the bars within the midspan region subjected to sustained load were fitted with metallic anchors filled with expansive cementitious grout. Three to six bars of each conditioning were tensile-tested in accordance with ASTM D7205.

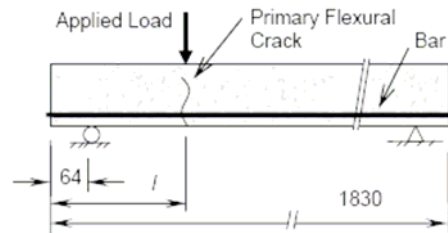


Figure 3 Eccentric 3-pt. flexure test for bond (mm)

2.2 Analytical

Bond behavior was characterized in terms of the local bond-slip constitutive law fitted to the experimental data. The assumed relationship between local bond stress, τ , and local slip, s , is

$$\tau = \begin{cases} Cs^\alpha (1 - s/\bar{s}) & \text{for } 0 \leq s \leq \bar{s} \\ 0 & \text{for } s > \bar{s} \end{cases} \quad (2)$$

where C , α , and \bar{s} are empirical constants that can vary with loading time and environment. The local bond strength, τ_{\max} , and interfacial fracture energy, G_f , defined as the maximum value of τ and the area under the local τ - s curve, respectively, are given by

$$\tau_{\max} = C \left(\frac{\alpha \bar{s}}{1 + \alpha} \right)^\alpha \frac{1}{1 + \alpha}, \quad (3)$$

$$G_f = \frac{C \bar{s}^{\alpha+1}}{(1 + \alpha)(2 + \alpha)}. \quad (4)$$

For loads where the local slip vanishes at some point within the anchorage zone, the equation for bar force, N ,

in terms of the loaded-end slip, s_l , is

$$N = \sqrt{\frac{2CE_f A_f \pi d}{1 + \alpha} s_l^{1+\alpha} - \frac{2CE_f A_f \pi d}{\bar{s}(2 + \alpha)} s_l^{2+\alpha}}, \quad (5)$$

and the predicted bar force, $N_{\bar{s}}$, for $s_l \geq \bar{s}$ is

$$N_{\bar{s}} = \sqrt{2E_f A_f \pi d G_f}. \quad (6)$$

Loaded end slip was equated to half the width of the primary concrete crack (Figure 3), while bar force was calculated using a conventional section analysis with parabolic concrete behavior. Equations (5) and (6) can only be used up to the onset of free-end slip. Parameters C , α , and \bar{s} were found by fitting Eq. (5) to the experimental $N-s_l$ data.

3 RESULTS

Crack width parameter k_b is plotted versus conditioning time in Figure 4. Initial values of k_b are, on average, 1.14. It is observed that k_b , which varies proportionally to crack width, increases by up to 75% in all environments except freeze/thaw, where it is seen to remain roughly constant out to one year. The large amount of scatter in the outdoor measurements could be due to the highly variable temperatures when the measurements were made.

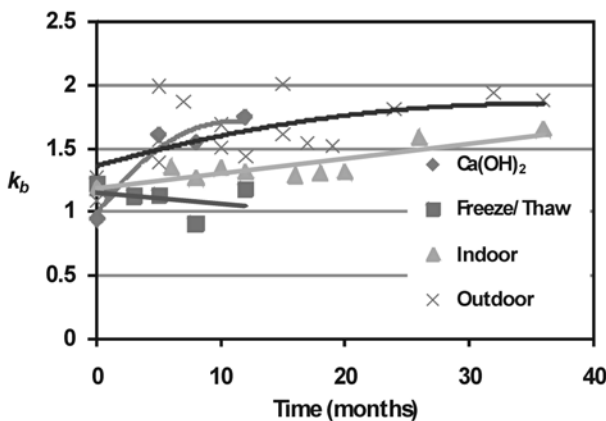


Figure 4 Bond parameter k_b vs. conditioning time

Local bond strength, τ_{max} versus conditioning time is seen in Figure 5 to increase over time in the indoor and outdoor environments. Hardly any change occurs in either of the more aggressive environments. The fracture energy, G_f , was noted to remain roughly constant over time, meaning that little change in the maximum pull-out force occurred with any of the conditionings followed in this investigation. Figure 6 shows the change in shape of the local bond stress-slip curves as a function of conditioning time in the outdoor environment. As seen in this example, it was generally true for all environments that parameters α and \bar{s} decrease slightly with time, making the local $\tau-s$ curves taller, narrower, and almost perfectly rigid at low stress.

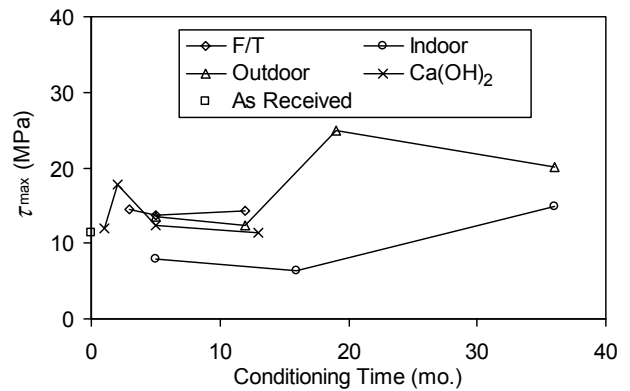


Figure 5 Local bond strength, τ_{max} , vs. conditioning time.

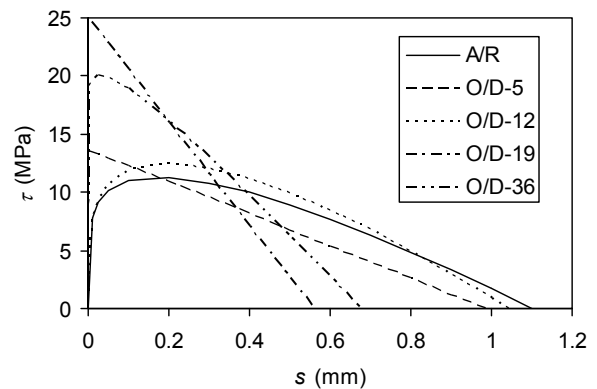


Figure 6 Local bond stress-slip curves for outdoor (OD) environment and as-received (A/R) bars (-n in the legend refers to the number of months of conditioning)

The tensile strength of bars after exposure to various environments and sustained load are shown in Figure 7. The included scatter bars show the range of the individual data points for each conditioning. The “as-received” data point, obtained for bars that were never cast in concrete, shows a strength of 643 MPa—about 8% less than the manufacturer’s value. The strength for zero conditioning time, 627 MPa, was obtained from bars cast in beams, subject to preliminary eccentric 3-pt bond tests, and removed for tensile testing without experiencing any sustained load or special conditioning. This result shows that the casting and extraction processes did not degrade the strength of the bars significantly. Indoor and outdoor conditionings of up to three years did not significantly affect the strength of the bars. The F/T conditioning caused a 15% loss of strength after a half year. This value did not change significantly by the end of F/T testing at one year. In the Ca(OH)_2 environment, the bars steadily lost strength until the end of testing at one year, at which time the strength loss was nearly 25%. On a semi-log scale, strength reductions of roughly 20% per decade exist for the F/T and Ca(OH)_2 conditions. Even in these highly aggressive environments, a linear extrapolation to 50 years predicts a residual tensile strength of ~300 MPa or about half the strength of virgin bar. No appreciable change in elastic modulus was observed in any of the tests.

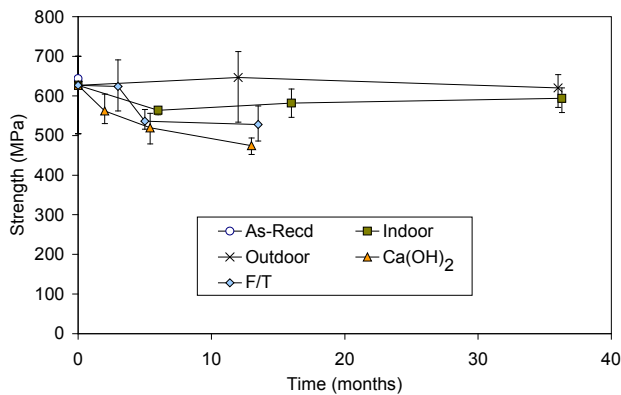


Figure 7 Bar tensile strength vs. conditioning time

4 CONCLUSIONS

GFRP bars were conditioned in concrete beams in various environments with sustained loads of roughly 11% of ultimate. Although crack widths widened by up to 75% for times as long as three years, most of this increase was complete after about one year. While the increase in crack width could be due to bond degradation near the flexural cracks in concrete, it was observed from bond testing that the local bond strength in the uncracked anchorage zone of the beams did not degrade over time and in fact increased slightly in some cases. The local bond-slip curve showed a more brittle type of behavior with increased conditioning time, although the area under the curve remained about the same, leading to essentially the same pullout-force for any conditioning followed in this investigation.

Tensile testing of conditioned bars indicated degradation only in the artificially aggressive environments, which in this investigation contained much exposure to water: dry freeze/wet thaw and 60°C alkaline solution. In these cases, an extrapolation to 50 years predicted a residual strength of about half the initial strength. No strength reduction was seen in the “natural” indoor and outdoor environments for times as long as 3 years.

5 ACKNOWLEDGMENTS

This research was supported by the US National Science Foundation under Grants No. 0219484 and 9908934. Hughes Brothers (Seward, Nebraska, USA) donated the GFRP bars. The author thanks Profs T.E. Boothby of Penn State Univ. and A. Mukherjee of Indian Inst. Tech.-Bombay, who helped plan and execute this research, and the many students who helped with data generation and analysis. The assistance and encouragement of Mr. Doug Gremel

is also appreciated. The opinions, findings, and conclusions expressed in this paper are those of the author and do not necessarily reflect the views of the sponsors.

REFERENCES

- ACI. 2006. Guide for the Design and Construction of Structural Concrete Reinforced with FRP Bars, ACI 440.1R-06. Farmington Hills: American Concrete Institute.
- Bakis, C.E., and Boothby, T.E. 2004. Evaluation of crack width and bond strength in GFRP reinforced beams subjected to sustained loads. In: *Proc. ACMBS-IV*, El-Badry, M. and Dunaszegi, L. (eds.). Paper No. 171. Montreal: Canadian Soc. Civil Engineering.
- Bakis, C.E., Boothby, T.E., and Jia, J. 2007. Bond durability of GFRP bars embedded in concrete beams. *J. Composites for Construction*, 11:269-278.
- Bakis, C.E., Boothby, T.E., Schaut, R.A., and Pantano, C.G., 2005. Tensile strength of GFRP bars under sustained loading in concrete beams. In: *Proc. FRPRCS-7*, Shield, C.K., Busel, J.P., Walkup, S.L. and Gremel, D.D. (eds.), SP-230, Vol. 2, 1429-1446. Farmington Hills: American Concrete Institute.
- Bakis, C.E., Freimanis, A.J., Gremel, D., and Nanni, A. 1998. Effect of resin material on bond and tensile properties of unconditioned and conditioned FRP reinforcement rods. In: Benmorane, B. (ed.), *Proc. CDCC*, 525-535. Sherbrooke: Univ. Sherbrooke.
- Bank, L.C., Puterman, M., and Katz, A. 1998. The effect of material degradation on bond properties of fiber reinforced plastic reinforcing bars in concrete. *ACI Materials J.* 95: 232-243.
- Chen, Y., Davalos, J.F., and Ray, I. 2007. Life-cycle durability prediction models for GFRP bars in concrete under sustained loading and environmental exposure. In: Triantafillou, T.C (ed), *Proc. FRPRCS-8*, 10 p. Patras: Univ. Patras.
- Dejke, V., Poupard, O., Nilsson, L.O., Tefpers, R., and Ait-Mokhtar, A. 2003. Influence of sustained stress on the durability of GFRP bars embedded in concrete. In: Tan, K.H. (ed.), *Proc. FRPRCS-6*, 833-842. London: World Scientific.
- Gremel, D., Hughes Brothers, Seward, NE, USA, pers. comm.
- Nkurunziza, G., Debaiky, A, Cousin, P., and Benmokrane, B. 2005. Durability of GFRP bars: A critical review of the literature. *Progress in Structural Engineering and Materials*, 7(4):194-209.
- Porter, M.L., and Barnes, B.A. 1998. Accelerated aging degradation of glass fiber composites. In: *Proc. ICCI-2*, Saadatmanesh, H. and Ehsani, M.R. (eds.), Vol. II, 446-459. Tucson: Univ. Arizona.
- Tannous, F. E., and Saadatmanesh, H. 1999. Durability of AR glass fiber reinforced plastic bars, *J. Composites for Construction* 3(1):12-19.

FRP Design Using Structural Mechanics Models

D.J. Oehlers, M. Haskett, Mohamed Ali M.S., W. Lucas & R. Muhamad

The University of Adelaide, Adelaide, Australia

ABSTRACT The application and expansion of FRP reinforced concrete has been hindered and obstructed through the misconception and misunderstanding that empirically derived rules developed for steel reinforced concrete in cracked regions can be used either directly or as a guidance for FRP reinforced concrete. This assumption is incorrect because the empirical rules developed for steel reinforced concrete in cracked regions, as with all empirical rules, should only be used within the bounds of the testing regimes from which they were developed, which for steel reinforced concrete is normal strength concrete with high ductile steel that has very good bond. As these bounds do not apply to FRP reinforced concrete, the steel RC empirical rules for cracked concrete are of little or no help for FRP RC. In fact, they are often misleading and as such prevent the widespread use of FRP reinforcement. It will be shown and illustrated in this presentation that generic mechanics based rules can be developed at all load conditions for RC beams that applies to both steel and FRP reinforcement. And, furthermore, that these generic mechanics based design rules allay many of the misconceptions inferred by the empirically based RC design rules such as that moment redistribution cannot occur with brittle FRP reinforced concrete which is simply not the case.

KEY WORDS FRP; reinforced concrete beams; moment rotation; discrete rotation; hinges; flexural capacity; IC theory; shear capacity; moment redistribution; deflection.

1 INTRODUCTION

Reinforced concrete that is subjected to cracking whether by shear or flexure is extremely complex because cracking changes the behaviour from that of a undisturbed region where the Euler-Bernoulli theory applies to a disturbed region where the Euler-Bernoulli assumption of linear strain profiles does not apply (Oehlers et al 2010a and 2010b). To overcome this problem of cracked concrete, empirical approaches have been developed where: at least one major component of the approach, not including the material properties, has to be determined purely through experimental testing; or where the approach is limited to a defined range of material properties. Furthermore because these approaches are determined empirically, by the very nature of empirical models they should only be used within the bounds of the testing regime from which they were developed which for reinforced concrete in national codes or standards is: normal strength concrete; with high ductile steel reinforcement that is steel which on yielding can develop very large strains prior to fracturing; and reinforcement that has a very good bond with concrete such as that which occurs with ribbed steel reinforcing bars. Consequently, these empirical rules in national standards are of little help when using FRP reinforcement which has absolutely no ductility and often a weak bond.

The following are examples of the empirical models

developed for steel reinforced concrete in cracked regions in national standards (Oehlers et al 2010a and 2010b): (1) the rotation at a hinge θ at a cracked section which is based on a full-interaction moment-curvature (M/χ) analysis, and on a hinge length over which the curvature is integrated and which by theory has to be derived empirically; (2) the flexural capacity at a cracked section which relies on a linear strain profile for its M/χ analysis in a cracked region and also on the use of ductile steel reinforcement such that concrete crushing at a strain ϵ_c always controls failure; (3) the shear capacity at a cracked section which relies on ductile steel stirrups so that the shear resisted by the stirrups V_s can be quantified as well as a purely empirically derived concrete component of the shear capacity V_c ; (4) the moment redistribution within a beam that relies on a full interaction M/χ analysis to determine the neutral axis depth factor k_u which has then to be calibrated purely from test results; (5) the crack spacing and crack widths; (6) and finally the deflection of a cracked beam which uses a full-interaction M/χ analysis to determine the flexural rigidities of both the cracked and uncracked sections which have then to be combined empirically to determine an effective flexural rigidity $(EI)_{\text{eff}}$ for calculating the deflection. It can be seen that the common denominator in all of these empirical approaches is the fact that they are dealing with cracked regions.

In this paper, it will be shown that all of the six empirical models listed above, that were derived empirically for steel reinforcement with high ductility and bond, can be replaced by mechanics based discrete rotation models that apply to both reinforced concrete with steel or FRP reinforcement with any degree of ductility and bond. The basis of the model is the discrete rotation mechanism across a crack and this will be first applied to a single crack to obtain the moment-rotation (M/θ) behaviour. This will be followed by the flexural limits to the M/θ that is the flexural capacity followed by the shear limit to the M/θ that is the shear capacity. Having defined the M/θ and its limits, this is then used in a mechanics based approach for moment redistribution. Finally the M/θ approach is applied to beams with multiple cracks to develop a mechanics based approach for crack spacing, crack widths and deflections.

2 DISCRETE ROTATION MODEL

The cross-section of an FRP plated RC beam is shown in Figure 1(a) and the rigid body deformation at an individual crack along the length of the beam of height h_{cr} is shown in Figure 1(b). It has been long recognised (Bachman 1970) that much of the deformation in a cracked beam is associated with the rigid body rotation between crack faces that is 2θ in Figure 1(b) and that this rotation requires slip between the reinforcement and the crack face Δ when

the reinforcement is subjected to an axial force P which in turn relies on the bond-slip properties τ - δ between the reinforcement and the concrete.

The discrete rigid-body moment rotation (M/θ) in Figure 1(b) has been quantified by Oehlers and Liu (Oehlers et al 2005; Liu et al 2007), Oehlers and Mohamed Ali (Oehlers et al 2008; Mohamed Ali et al 2008a), and Oehlers, Mohamed Ali and Haskett (Haskett et al 2009a and 2009b). The discrete rotation θ shown in Figure 1(b) induce the forces P as shown. In the tension region of height h_{cr} , the force in the reinforcement P depends on the slip at the crack face Δ and the relationship P/Δ can be determined from IC theory (Mohamed Ali et al 2008b and 2010; Haskett et al 2008) which in turn depends on the bond-slip material property τ/δ between the reinforcement and the concrete (Seracino et al 2007). In the compression region of height h_{cmp} , at low rotations the force in the concrete P_{asc} can be determined from the ascending branch of the concrete stress-strain relationship. However wedges may eventually form whose resistance is P_{soft} (Mohamed Ali et al 2010). These wedges may eventually slide uncontrollably when the slip of the wedge shown as s reaches a critical value; the slip s is equal to the slip strain $\epsilon_{pk}-\epsilon_w$ across the sliding plane multiplied by the length of the sliding plane L_{soft} where ϵ_{pk} is the strain in the concrete at the peak stress just prior to softening and ϵ_w is the strain in the wedge at P_{soft} .

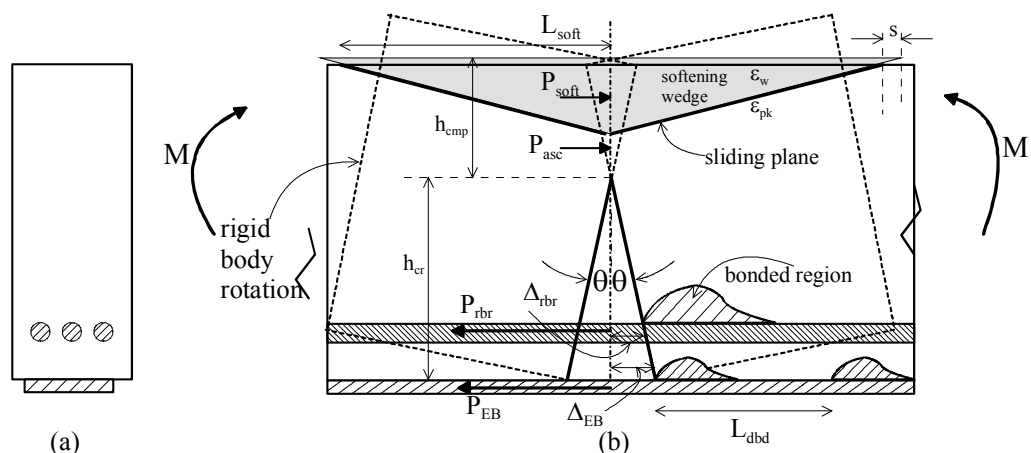


Figure 1 Discrete rotation

It can now be seen that all the parameters required to derive the discrete moment-rotation M/θ can be determined. The limit to this rotation is: uncontrollable sliding of the wedge when s reaches a critical value; the slip in the reinforcement Δ when the reinforcement fractures; and shear failure across the crack plane (Oehlers et al 2010a and 2010b; Lucas et al 2010). There is also a limit to rotation due to debonding. For steel reinforcement with ribbed bars the bond is usually very strong so that fracture of the bar usually occurs before the force to cause intermediate crack (IC) debonding

occurs do that the bonded region remains stationary as for the reinforcing bar in Figure 1b. However for FRP reinforcement such as externally bonded (EB) and near surface mounted (NSM) plates the bond strength and slip is usually low so that debonding can occur before fracture. In this case, the bonded region moves along the reinforcement a distance L_{dbd} as shown in Figure 1(b) so that the slip at the crack face increases by $\epsilon_{IC}L_{dbd}$ where ϵ_{IC} is the maximum strain in the reinforcement associated with IC debonding. Hence debonding improves the ductility and it is a question of determining the debonded

length L_{dbd} over which debonding can occur whilst the reinforcement retains its IC debonding force.

3 FLEXURAL CAPACITY

Figure 2(b) summarises the flexural analysis (Haskett et al 2009a; Mohamed Ali 2010a) for the discrete rotation shown in Figure 1. It can be seen that the slip in the wedge s in the compression region of height h_{cmp} is directly related to the slip in the reinforcement Δ in the tension region of height h_{cr} through a linear displacement. The compression wedge only forms when the concrete is softening that is where the compressive concrete strain

exceeds that which occurs at the peak compressive strength ϵ_{pk} . The angle of the concrete wedge α depends on the shear-friction Mohr-Coulomb frictional component m . Hence there is a direct relationship between L_{soft} and d_{soft} and since s is a function of L_{soft} , the depth of the concrete wedge d_{soft} follows the locus of s which is quantifiable. As previously explained, the reinforcement force and displacement in the tension zone P/Δ is related by IC theory. Hence it is a question of finding the linear displacement profile in Figure 2b where longitudinal equilibrium occurs and where only one slip capacity is exceeded (Haskett et al 2009a; Mohamed Ali et al 2010a).

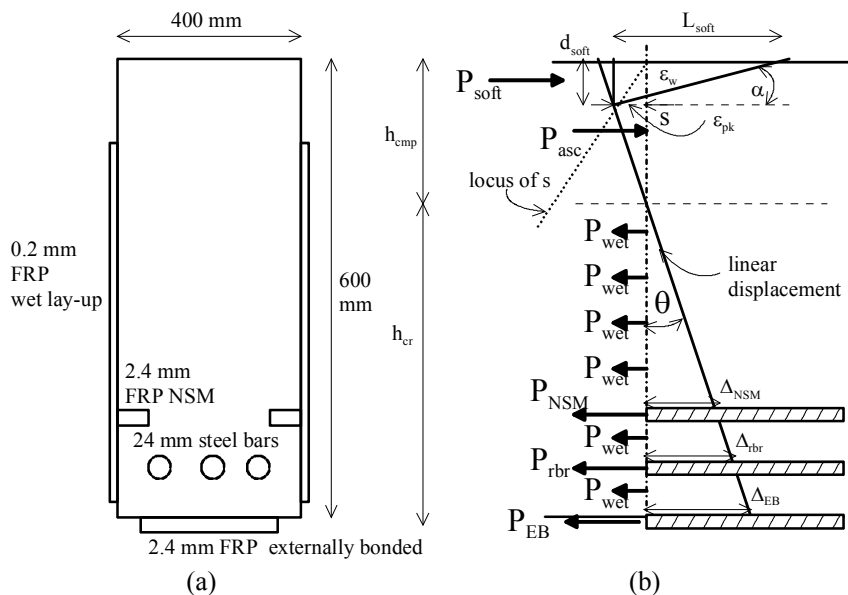


Figure 2 Moment rotation analysis

The compression zone h_{cmp} in Figure 2b only governs failure when the slip s exceeds the slip capacity limit which is given by shear friction theory (Haskett et al 2009a; Mohamed Ali 2010a). In general, this only occurs when L_{soft} is large that is in deep beams and is unlikely to occur in slabs or with ductile concrete such as with fibre reinforced concrete.

In the tension zone in Figure 2b, the reinforcement slip Δ has three components. The slip whilst the reinforcement is elastic Δ_{el} which is inversely dependent on the elastic axial rigidity of the reinforcement $E_{el}A$ (where E_{el} is the reinforcement elastic modulus and A is the cross-sectional area of the reinforcement) which is generally large so Δ_{el} is relatively small. The slip whilst the reinforcement is yielding or strain hardening Δ_{sh} which depends on the strain hardening axial rigidity $E_{sh}A$ which is generally very small so that the strain hardening component of the slip Δ_{sh} can be quite large. The limit to this total slip $\Delta_{el} + \Delta_{sh}$ is fracture of the reinforcement $\Delta_{fract-lmt}$. The third component of slip is that due to debonding Δ_{deb} which as previously described depends on $\epsilon_{IC}L_{dbd}$ where

the limit to L_{dbd} can be taken as half the depth of the beam. The slip at debonding $\Delta_{deb-lmt}$ can be quite large. The slip at debonding depends on the bond-slip τ/δ characteristics. For steel reinforcing bars with ribs the bond is generally very strong and ductile so that reinforcement fracture generally precedes debonding so that most of the slip prior to failure is due to yielding. In contrast, FRP reinforcement does not yield but generally has a weak and brittle bond so that most of the slip prior to failure is due to debonding. It can be seen that the weak and brittle bond attributed to FRP reinforcement is beneficial as it increases the ductility.

The results of the analysis of the cross-section in Figure 2a also shown in Figure 3a are shown in Figures 3b to 3d where Figure 3b shows the variation in crack width used in the analysis as well as the debonding limits for each type of reinforcement. The wet lay-up plate was divided into 50 mm deep increments and each section treated independently for ease of analysis. It was found that the debonding limit of the externally bonded plate at the soffit of the beam occurred before other limits were reached.

Hence, the variation in crack width w_{cr} and consequently reinforcement slip Δ at this debonding limit is that shown in Figure 2b. From this slip distribution, IC theory can be used to determine the forces in the reinforcement as shown idealised in Figure 2b and, therefore, the stresses as shown in Figure 2d. There is a discontinuity in the stress distribution in the wet lay-up plates in Figure 3c. This is because the slip at the discontinuity causes the start of IC debonding in the wet lay-up plate

so that for slips greater than this value the stress in the wet lay-up plate is uniform as shown. From the stress distribution in Figure 2c can be derived the strain distribution at failure in Figure 2d. It can be seen that even though debonding of the EB plate controls the analysis, the strain in the FRP EB plate is the smallest reinforcement strain and there certainly is no linear variation in strain as required in a conventional moment-curvature analysis.

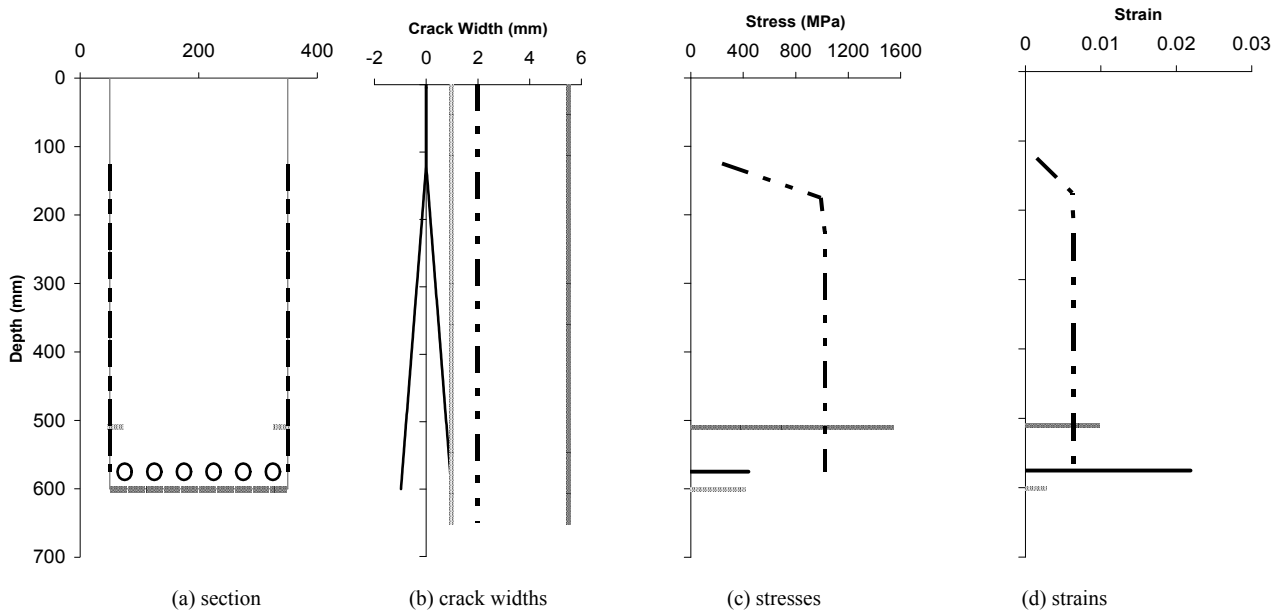


Figure 3 Flexural analysis of FRP plated section

4 SHEAR CAPACITY

The moment-rotation or discrete rotation mechanism illustrated in Figure 1 with the analysis in Figure 2b for a vertical crack with longitudinal reinforcement can also be applied directly to an inclined crack with both longitudinal and vertical reinforcement as in Figure 4 (Lucas et al 2010). Let us consider a cross-section which could comprise of either steel or FRP reinforcement or both. When a crack width w_{cr-fl} (or rotation 2θ) is imposed at the soffit, then the crack widths measured in line with the longitudinal reinforcement w_{lg-fl} and that in line with the stirrups w_{stp-fl} are known. Therefore from IC theory, the forces in both the stirrup and longitudinal reinforcement can be determined and from equilibrium the reaction V and consequently the moment M for that rotation 2θ . Hence a flexural discrete rotation analysis gives the force in the stirrups, that is the shear resisted by the stirrups directly. It is a question of whether the interface shear force S can be resisted that is whether the concrete component of the shear capacity V_c is sufficient.

The shear deformation causes sliding as in Figure 4b which through aggregate interlock or shear friction causes a further widening of the crack by w_{cr-sh} . This increases the slip in the longitudinal reinforcement by

w_{lg-sh} so that the force in the longitudinal reinforcement increases by P_{lg-sh} . Hence by shear-friction an equal, opposite and in-line force is induced across the sliding plane as shown. This is the difference between flexural deformations where the forces are offset to provide a moment, whereas, in shear deformations they are in-line so as not to induce moment. The force across the sliding plane can be resolved into the normal component N_{lg-sh} and the shear component S_{lg-sh} . The same mechanism occurs adjacent to the stirrups inducing a normal force N_{st-sh} and a shear force S_{st-st} . There is already a force across the potential sliding plane from flexure shown as P_{fl} in Figure 4a which has a normal component N_{fl} and shear component S_{fl} .

The resulting normal force across the sliding plane that is $N_{fl}+N_{st-sh}+N_{lg-sh}$ clamps the sliding plane together and hence determines the magnitude of the shear friction resistance or capacity across the sliding plane shown as $(V_c)_\beta$ in Figure 4b. This shear capacity $(V_c)_\beta$ must resist the algebraic sum of the shear forces S_{fl} and S_{st-sh} and S_{lg-sh} such that the resultant of the remainder resolved vertically is the concrete component of the shear capacity shown as V_c . If V_c is greater than S in Figure 4a then shear failure does not occur.

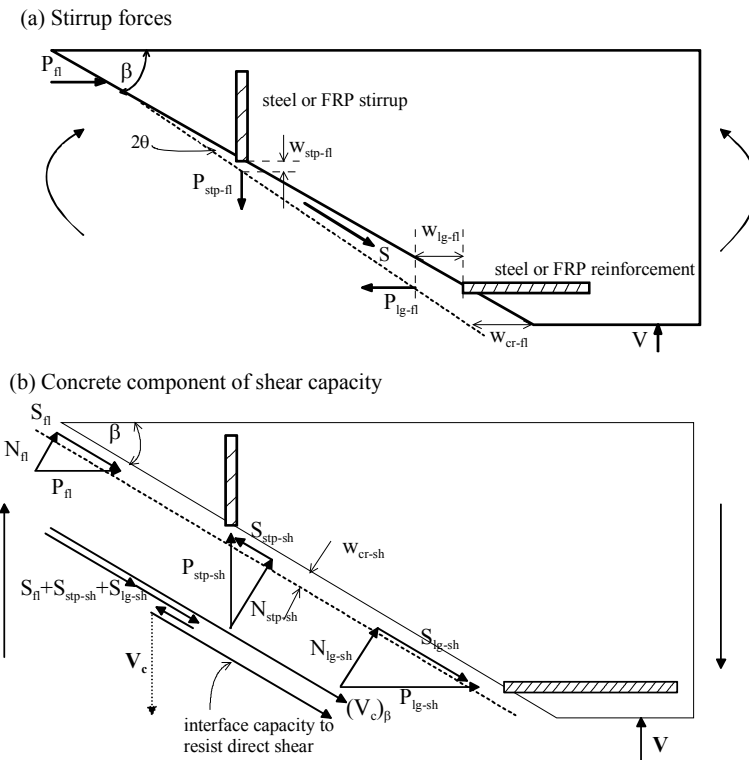


Figure 4 Shear capacity

5 MOMENT-REDISTRIBUTION

Consider the continuous beam in Figure 5a of flexural rigidity EI and length L . The beam is subjected to a uniformly distributed load that induces a static moment M_{st} so that the elastic distribution of moment shown in Figure 5b varies from $(M_{hg})_{el}$ at the supports to $(M_{hg})_{el}/2$ at mid-span. It is common practice to redistribute moment from the hogging region to the sagging region

by reducing the hogging moment by M_{rd} and increasing the sagging moment by M_{rd} . In this case when the beam is first loaded, M_{hg} will first be achieved at the supports as in Figure 5c for the *elastic* case with further increases in the static moment requiring discrete rotation at the supports θ_{hg} until the required sagging moment is achieved. The percentage moment redistribution is often given as $100K_{MR}$ which is equal to $100M_{rd}/(M_{hg})_{el}$.

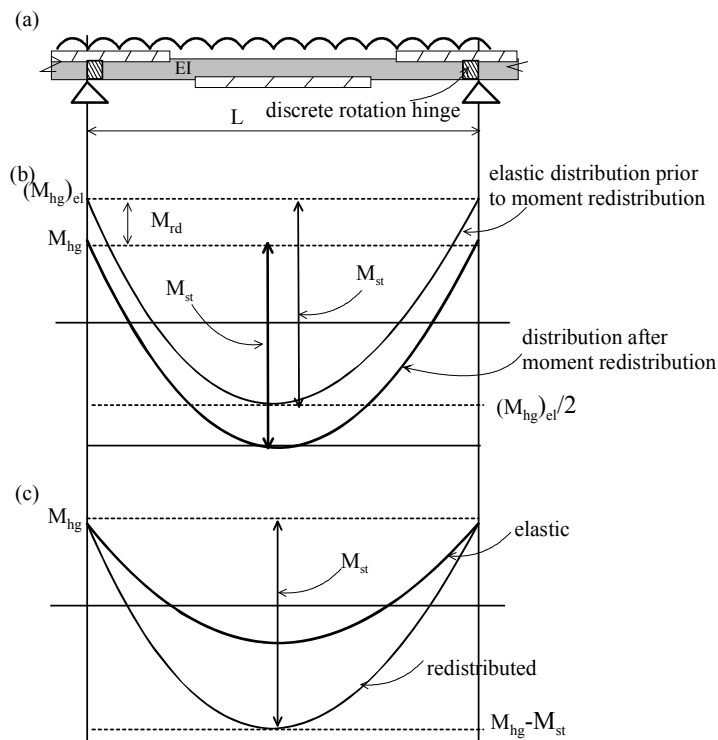


Figure 5 Moment redistribution

From the moment redistribution mechanism in Figure 5c, it can be shown using structural mechanics (Haskett et al 2010; Oehlers et al 2010c) that the moment redistribution factor K_{MR} is given by

$$K_{MR} = \frac{2(EI)\theta_{hg}}{2(EI)\theta_{hg} + M_{hg}L} \quad (1)$$

where the discrete rotation analysis gives M_{hg} and θ_{hg} . Equation 1 is generic and can be applied to both plated and unplated discrete rotation hinges. Tests have shown that FRP plated members can redistribute substantial amounts of moment (Oehlers et al 2004; Liu et al 2006). The major reason for this being the low bond which on progressive debonding allows the crack to widen and rotate as shown on the EB plate in Figure 1b, thereby, increasing θ_{hg} . Equation 1 allows a beam to be designed

specifically for ductility. For example, FRP NSM plates may be used at the hogging regions in Figure 5a where rotation is required and FRP EB plates used in the sagging region where rotation is not required.

6 MULTIPLE CRACKS

Consider the reinforced concrete beam in Figure 6a where an initial crack has developed at mid-span. Once the initial crack has developed, it is common practice to determine subsequent cracking by idealising the behaviour as that of a concentrically loaded prism (Goto 1971; Jiang et al 1984) as in Figures 6b to 6d. Partial-interaction theory, that allows for slip between the reinforcement and the concrete, can now be used to determine the behaviour (Muhamad et al 2010a).

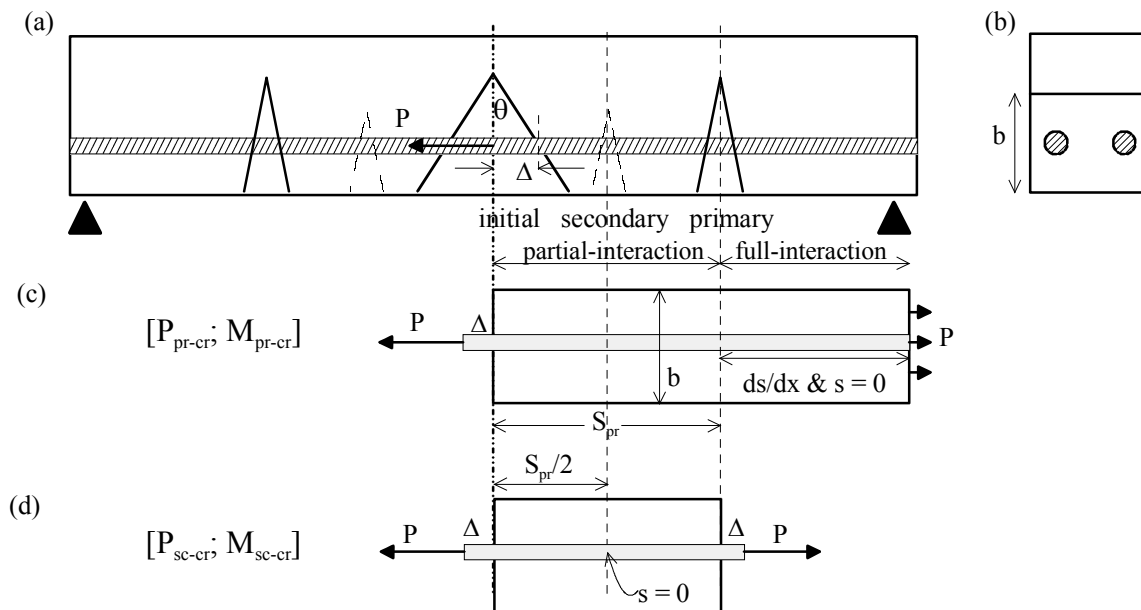


Figure 6 Multiple cracks

When a load P is first applied to the reinforcing bar as in Figure 6c it induces a slip s , which is Δ at the crack face, and slip-strain ds/dx between the reinforcing bar and the concrete, both of which gradually diminish along the length of the reinforcement in the *partial-interaction* region shown (Muhamad et al 2010a). The *full-interaction* region shown which starts at a distance S_{pr} from the initial crack face is where both the slip and slip-strain tend to zero. The tensile stresses in the concrete gradually build up from zero at the crack face to a maximum at S_{pr} from the crack face so that should a crack develop it will occur at the distance S_{pr} and subsequent cracks will occur at this spacing. Hence S_{pr} is the spacing of the primary cracks. The axial load in the reinforcement at which the stress in the concrete reaches its tensile capacity P_{pr-cr} can be determined from partial-interaction theory. Knowing P_{pr-cr} , the moment in the beam at which this occurs which is 2 of the moment at which a primary crack develops

M_{pr-cr} can be determined.

After the primary cracks have formed at a spacing of S_{pr} , the partial interaction problem in Figure 6c changes to that in Figure 6d where the crack width w_{cr} is equal to 2Δ and the boundary condition is that the slip is equal to zero mid-way between crack faces. This analysis can be used to determine the axial load in the reinforcement to cause a secondary crack P_{sc-cr} which by symmetry occurs at a crack spacing of $S_{pr}/2$, should the bond be sufficiently strong to allow this, and subsequently the moment required to form a secondary crack M_{sc-cr} . The partial-interaction analysis in Figure 6d also gives the relationship between P_{cr-pr} and Δ_{cr-pr} when only primary cracks have developed. Hence if the moment at a primary crack is M_{cr-pr} , the force in the bar can be determined P_{cr-pr} and hence the slip Δ_{cr-pr} . It can also be seen that the analysis depicted in Figure 6d after the development of the primary cracks can also be used for the analysis after the

development of the secondary cracks in which case the crack spacing is $S_{pr}/2$. Hence if the moment at a secondary crack is M_{cr-sc} , and the force in the bar is P_{cr-sc} then the slip is Δ_{cr-sc} .

7 DEFLECTION

The partial interaction analysis depicted in Figure 5 can be used to determine the deflection of a beam (Muhamad et al 2010b) as shown in Figure 7. Let M_{serv} in Figure 7a be the distribution of the moment at serviceability. If M_{pr-cr} is the moment to cause the primary cracks then these occur over the length of beam L_{pr-cr} at a crack spacing of S_{pr} . Furthermore, if the moment to cause the secondary cracks is M_{sc-cr} then these occur in the region L_{sc-cr} where the cracks will be spaced at $S_{pr}/2$.

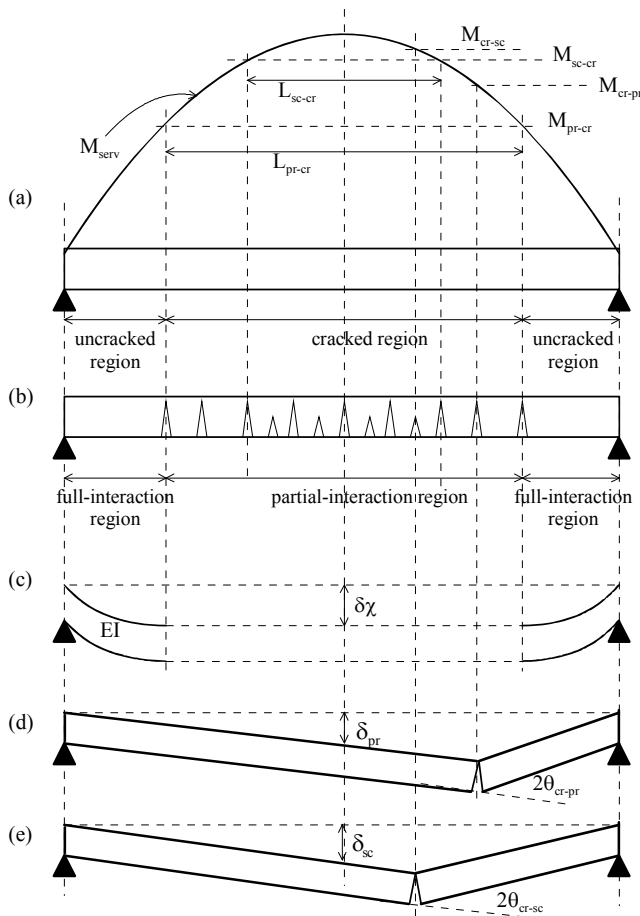


Figure 7 Components of deflection

In the full-interaction uncracked regions adjacent to the supports, the deflection δ_χ at say mid-span can be determined by integrating the curvature over these uncracked regions based on the uncracked flexural rigidity. Within the cracked region all of the deflection is assumed to occur through the accumulation of the discrete rotation from each individual crack. For example, at the primary crack shown in Figure 6d the moment at the crack is M_{cr-pr} from which can be determined the force in the reinforcement P_{cr-pr} . Hence from the analysis

depicted in Figure 6d can be determined the slip Δ_{cr-pr} and consequently the discrete rotation $2\theta_{cr-pr}$ and deflection $\delta_{\theta pr}$ due to the discrete rotation at that particular primary crack. The same approach can be applied to determining the deflection due to the discrete rotation at the secondary crack shown in Figure 6e where the moment is M_{cr-sc} .

8 CONCLUSIONS

Current reinforced concrete design approaches that deal with cracked regions of concrete use empirical solutions that have been developed specifically for concrete that has been reinforced with steel reinforcement that is both ductile and which has very good bond. As these rules are empirical, they can only be used within the bounds of the tests from which they were developed and are, therefore, of little assistance outside these bounds as for example FRP reinforcement which is neither ductile nor has good bond strength. It has been shown that these empirical rules for cracked concrete can be replaced with mechanics rules based on discrete rotation which are generic and, therefore, can be applied to any type of reinforcement with any type of bond characteristics.

REFERENCES

- Bachmann, H. (1970) Influence of shear and bond on rotational capacity of reinforced concrete beams, Publications, IABSE, Zurich, 1970: Vol. 30, Part II, pp. 11-28.
- Goto, Y. (1971). Cracks formed in concrete around deformed tension bars. *J. Amer. Conc. Inst.*, 68(4), 244-251.
- Haskett, M., Oehlers, D.J., and Mohamed Ali M.S. (2008) Local and global bond characteristics of steel reinforcing bars, *Engineering Structures*, Vol. 30, Issue 2, 376-383, Feb.
- Haskett, M., Oehlers, D.J., Mohamed Ali, M.S., and Wu, C., (2009a) Rigid body moment-rotation mechanism for reinforced concrete beam hinges, *Engineering Structures*, 31 (2009) 1032-1041.
- Haskett, M., Oehlers, D.J., Mohamed Ali and Wu, C. (2009b) Yield penetration hinge rotation in reinforced concrete beams. *ASCE Structural Journal*, Vol. 135, Issue 2, Feb., 130-138.
- Haskett, M., Oehlers, D.J., and Mohamed Ali, M.S., (2010) Design for moment redistribution in RC beams retrofitted with steel plates. *Advances in Structural Engineering*. Vol. 13, No.2, pp. 379-391.
- Jiang, D.H., Shah, S.P., and Andonian, A.T. (1984). Study of the transfer of tensile forces by bond. *J. Amer. Conc. Inst.*, 81(3), 251-259.
- Liu, I.S.T, Oehlers, D.J. and Seracino, R., (2006) Tests on the ductility of reinforced concrete beams retrofitted with FRP and steel near surface mounted plates. *ASCE Journal of Composites for Construction*, March/April, Vol.10, No.2, pp. 106-114.
- Liu, I.S.T., Oehlers, D.J., and Seracino. (2007) Study of intermediate crack debonding in adhesively plated beams. *ASCE, Composites for Construction*, Vol.11, No.2, April 1, pp. 175-183.

- Lucas, W., Oehlers, D.J. and Mohamed Ali M.S. (2010) A Shear Resistance Mechanism for Inclined Cracks in RC Beams. Submitted ASCE Journal of Structural Engineering.
- Mohamed Ali, M.S., Oehlers, D.J. and Griffith, M.C. (2008a) Simulation of plastic hinges in FRP plated RC beams. ASCE, Composites for Construction, Vol.12, Issue 6, Nov-Dec, pp. 617-625.
- Mohamed Ali, M.S., Oehlers, D.J., Griffith, M.C., and Seracino, R., (2008b) Interfacial stress transfer of near surface mounted FRP-to-concrete joints, Engineering Structures, Vol. 30, Issue 7, July, 1861-1868.
- Mohamed Ali M.S., Oehlers, D.J., Haskett, M., and Griffith, M.C.. (2010a) The discrete rotation in reinforced concrete beams. Submitted to ASCE Journal of Engineering Mechanics.
- Mohamed Ali, M.S., Oehlers, D.J., and Griffith, M.C. (2010) The residual strength of confined concrete, Accepted Advances in Structural Engineering.
- Muhamad, R., Mohamed Ali, M.S., Oehlers, D.J. and Griffith, M.C., (2010a) Tension stiffening mechanism in reinforced concrete prisms. In preparation.
- Muhamad, R., Oehlers, D.J., and Mohamed Ali M.S. (2010b) Discrete rotation deflection of RC beams. In preparation.
- Oehlers, D.J. Ju, G., Liu, I and Seracino, R. (2004) Moment redistribution in continuous plated RC flexural members. Part 1: neutral axis depth approach and tests, Engineering Structures, 26, pp. 2197-2207.
- Oehlers, D.J., Liu, I.S.T. and Seracino, R. (2005) The gradual formation of hinges throughout reinforced concrete beams. Mechanics Based Design of Structures and Machines, 33, pp. 375-400.
- Oehlers, D.J., Mohammed Ali, M.S., and Griffith, M.C. (2008) Concrete component of the rotational ductility of reinforced concrete flexural members. Advances in Structural Engineering, Vol. 11, No.3, June, 293-303.
- Oehlers, D.J., Mohamed Ali M.S., Griffith, M.C., Haskett, M., and Lucas, W. (2010a) A generic unified reinforced concrete model, Accepted Proc. ICE , Structures and Buildings.
- Oehlers, D.J, Haskett, M., Mohamed Ali M.S., Lucas, W., and Muhamad, R., (2010b) Our obsession with curvature in reinforced concrete modelling. Accepted Advances in Structural Engineering.
- Oehlers, D.J., Haskett, M., Mohamed Ali, M.S. and Griffith, M.C. (2010c) Moment redistribution in reinforced concrete beams. Accepted Proceedings ICE, Structures and Buildings.
- Seracino, R., Raizal Saifulnaz M.R., and Oehlers, D.J. (2007) Generic debonding resistance of EB and NSM plate-to-concrete joints. ASCE Composites for Construction. 11 (1), Jan-Feb, 62-70.

Finite Element Modelling of FRP-to-Concrete Bond Behaviour Using the Concrete Damage Plasticity Theory Combined with a Plastic Degradation Model

J.F. Chen (j.f.chen@ed.ac.uk) & Y. Tao

Institute for Infrastructure and Environment, School of Engineering, The University of Edinburgh, UK

ABSTRACT The technique of externally bonding fibre reinforced polymer (FRP) composites has been becoming popular worldwide for retrofitting existing reinforced concrete (RC) structures. A major failure mode in such strengthened structures is the debonding of FRP from the concrete substrate. The bond behaviour between FRP and concrete thus plays a crucial role in these structures. The FRP-to-concrete bond behaviour has been extensively investigated experimentally, commonly using the pull-off test of FRP-to-concrete bonded joint. Comparatively, much less research has been concerned with the numerical simulation of this bond behaviour, chiefly due to difficulties in accurately modelling the complex behaviour of concrete. This paper proposes a robust finite element (FE) model for simulating the bond behaviour in the entire loading process in the pull-off test. A concrete damage plasticity model based on the plastic degradation theory is proposed to overcome the weakness of the elastic degradation theory which has been commonly adopted in previous studies. The model produces results in very close agreement with test data.

1 INTRODUCTION

Externally bonding fibre reinforced polymer (FRP) has been widely used to upgrade and retrofit concrete structures. One of the main failure modes of flexurally and shear strengthened structures is the debonding failure of the FRP. This has led to extensive research on the bond behaviour between FRP and concrete in the last two decades. This bond behaviour is typically investigated experimentally using the pull-off test of FRP-to-concrete bonded joints (e.g. Yao et al. 2005), although a number of analytical (e.g. Yuan et al. 2004; Chen et al. 2007), and numerical (e.g. Chen & Pan 2005; Lu et al. 2005) studies have been available. This paper is concerned with the numerical modelling of the bond behaviour using the finite element (FE) method.

Typical failure in the pull-off test occurs in the concrete a short distance away from the adhesive-concrete interface. The bond behaviour is thus controlled by the behaviour of the concrete. Existing FE studies on the problem may be classified into three approaches all of which do not explicitly model the thin adhesive layer: a) direct model where the behaviour of concrete is accurately modelled in a meso-scale with an appropriate constitutive model (e.g. Lu et al. 2005, 2006); b) interface model where the bond behaviour is modelled using a layer of interface elements (e. g. Diab & Wu 2007); and c) crack band model which assumes that debonding takes place within a band in the concrete adjacent to the concrete-FRP interface and a modified constitutive law for the

concrete in this band (Coronado & Lopez 2007; Coronado & Lopez 2010). The first approach can be used to predict not only the entire debonding failure process but also the bond-slip relationship for the FRP-concrete interface. The second approach relies on the appropriate use of a bond-slip model which may be developed from either the first approach or from test. This is thus not a predictive approach for the bond behaviour but appropriate for modelling large structures where meso-scale modelling of concrete is unrealistic (e.g. Chen et al. 2009). The third approach requires different material properties for the crack band which including fracture energy, size effect fracture energy and tensile strength, need to be obtained from test. This means that the approach is not truly predictive. Therefore, for simulating the detailed bond behaviour, the first approach is more appropriate.

Lu et al. (2005) adopted the fixed angle crack model available in the FE software MARC, together with a shear retention model for concrete. The bond-slip model (Lu et al. 2006) developed based on this excellent work has been very widely adopted by the research community. One of the disadvantages of the FE model is that it needs to be implemented through a user-subroutine in MARC which not many researchers have the skill nowadays. The results are also sensitive to the choice of the shear retention mode. The purpose of this study is to develop a general predictive model based on the concrete damage plasticity model available in a more widely accessible FE

software ABAQUS, incorporating a plastic degradation model.

2 MODELLING OF CONCRETE BEHAVIOUR

2.1 Crack band theory of concrete fracture

There are two common methods which can be used to approach the computational mechanics of concrete cracking: discrete crack model and smeared crack model (Rots 1991). In the former, a crack is treated as a geometrical identity so it is either pre-embedded in the FE mesh or through continuous re-meshing (Yang et al. 2003, 2005). The latter keeps the geometry fixed and the cracking is modelled through the concrete constitutive law (Rots 1991). The smeared crack approach is adopted in this study as it is impossible to track multiple cracks, especially the numerous micro-cracks in the pull off test where failure occurs within a few millimetres in the concrete adjacent to the FRP.

One of the drawbacks in the smeared concrete model is that it involves the strain localisation phenomenon due to strain-softening, where the energy consumption approaches to zero during crack propagation when the element size approaches to zero (Bažant & Jaime 1998). This is overcome by adopting the crack band theory (Bažant & Oh 1983):

$$w = h \int \varepsilon_{ct} \quad (1)$$

where w is crack opening width, h is the width of the crack band and ε_{ct} is the crack strain caused by the opening of micro-cracks. The crack band width h represents the effective width of the fracture process zone over which micro-cracks are assumed to be uniformly distributed. In FE analysis, the cracking strain is assumed to be uniformly distributed over h which is in turn related to the element size, type and integration scheme.

2.2 Compressive and tensile behaviour of concrete

The concrete is modelled using the isotropic plasticity model available in ABAQUS and an isotropic damage model. The plasticity model adopts the yield function proposed by Lubliner et al. (1989) and modified by Lee & Fenves (1998) and follows a non-associated flow rule. The concrete under uniaxial compression is described by the following stress strain relationship proposed by Saenz (1964):

$$\sigma = \frac{E_0 \varepsilon}{1 + \left(\frac{E_0 \varepsilon_p}{\sigma_p} - 2 \right) \left(\frac{\varepsilon}{\varepsilon_p} \right) + \left(\frac{\varepsilon}{\varepsilon_p} \right)^2} \quad (2)$$

where σ and ε are respectively the compressive stress and strain, σ_p and ε_p are the experimentally determined maximum stress and its corresponding strain which are taken to be the cylinder strength f_c' (MPa) and 0.002

respectively (Chen et al. 2010). The elastic modulus of the concrete E_0 is estimated from $E_0 = 4730 \sqrt{f_c'}$ (MPa) following ACI318 (2002).

Under uni-axial tension, the problem involves tensile cracking. The fracture energy G_F , the energy required to create a unit area of stress free crack, instead of the descending branch of the stress-strain curve, is treated as a material property of the concrete. The stress-crack opening displacement relationship proposed by Hordijk (1991) is adopted:

$$\frac{\sigma_t}{f_t} = \left[1 + \left(c_1 \frac{w_t}{w_{cr}} \right)^3 \right] e^{\left(-c_2 \frac{w_t}{w_{cr}} \right)} - \frac{w_t}{w_{cr}} (1 + c_1^3) e^{(-c_2)} \quad (3)$$

$$w_{cr} = 5.14 \frac{G_F}{f_t} \quad (4)$$

where w_t is the crack opening displacement, w_{cr} is the crack opening displacement at the complete loss of tensile stress, σ_t is the tensile stress normal to the crack direction, f_t is the concrete uniaxial tensile strength, and $c_1 = 3.0$ and $c_2 = 6.93$ are constants determined from tensile tests of concrete. f_t and G_F may be estimated from the CEB-FIB (1993) model:

$$f_t = 1.4 \left(\frac{f_c' - 8}{10} \right)^{\frac{2}{3}}, \text{ MPa} \quad (5)$$

$$G_F = (0.0469 d_a^2 - 0.5 d_a + 26) \left(\frac{f_c'}{10} \right)^{0.7}, \text{ N/m} \quad (6)$$

where d_a is the maximum aggregate size. In the present study, d_a is assumed to be 20mm if no test data is available.

Once the stress-crack opening displacement relationship is known, the stress-strain relationship can be determined for each element based on its size through Equation 1. The Poisson's ratio $\nu = 0.2$ is assumed in the present model.

2.3 Elastic degradation model of concrete

The isotropic scale damaged stiffness is introduced in ABAQUS (2007), which can be represented by the following equation under uniaxial loading:

$$\sigma = (1 - d) D_0 (\varepsilon - \bar{\varepsilon}^p) \quad (7)$$

where σ , ε and $\bar{\varepsilon}^p$ are respectively the stress, total strain and equivalent plastic strain in the loading direction; D_0 is the initial (undamaged) stiffness and d is the damage variable. The degraded stiffness is thus:

$$D = (1 - d) D_0 \quad (8)$$

This is illustrated in Figure 1 for the case of uni-axial tension.

2.4 Plastic degradation model of concrete

Lubliner et al. (1989) stressed that the concept of elastic (stiffness) degradation is associated with the total

deformation but without the necessity of a damage criterion. Furthermore, the concept of effective stress may be appropriate and has a physical basis for metal plasticity but this is not necessary the case for concrete and geomaterials. There are also some critical problems involved in the application of the stiffness (elastic) degradation theory: such as, how to definite the elastic damage variable d , how to decide whether both tensile damage variable and compressive damage variable involved together, what stage of loading the initial damage should start. A plastic degradation theory, in which the stiffness degradation is associated with the plastic deformation instead of the total deformation, was developed to overcome these weaknesses (Lubliner et al. 1989). It has the advantage of relating the plastic degradation variable to the plastic deformation through the plastic flow rule (Lubliner et al. 1989). Lubliner et al. (1989) proposed a simple model that the plastic degradation occurs only in the softening range and that the stiffness $(1-\delta)D_e$ is proportional to the cohesion:

$$\delta = 1 - \frac{c}{c_{\max}} \quad (9)$$

where δ is the plastic degradation variable; D_e is the stiffness after considering elastic stiffness degradation; δ varies from 0 (no stiffness degradation) to 1 (total stiffness degradation); c is the cohesion in the yield criteria which is proportional to stress and c_{\max} is proportional to the strength of the concrete (Lubliner et al. 1989). Under uni-axial tension and uni-axial compression, Equation 9 reduces to:

$$\delta = 1 - \frac{\sigma}{f} \quad (10)$$

in which f is either the tensile or the compressive strength as appropriate.

Lubliner et al.'s (1989) was implemented in ABAQUS to model the bond behaviour in the pull-off test but it did not lead to reasonable predictions in comparison with test data. A new model is thus proposed in this study as follows. Instead of assuming that the stiffness is proportional to the cohesion of the material, it is assumed that the ratio of the plastic strain with stiffness degradation to that without stiffness degradation, ρ is proportional to the cohesion of the material. In the case of uni-axial tension, this ratio is expressed as (Figure 1):

$$\rho = \frac{\bar{\varepsilon}_t^p}{\varepsilon_t^p} = \frac{\sigma_t}{f_t} \quad (11)$$

Assuming that all stiffness degradation is associated with plastic deformation (so $D_e = D_0$), the plastic degradation variable δ can be directly used in place of the damage variable d in Equation (8). For the case of uni-axial tension, the stiffness degradation variable δ_t (which equals the damage variable d_t in this case) can be found

from the geometrical relationships between the variables in Figure 1 as:

$$\delta_t = \frac{(1-\rho)\varepsilon_t^p}{(1-\rho)\varepsilon_t^p + \sigma_t/E_0} \quad (12)$$

The same expression applies under uni-axial compression by replacing the tensile strength with the compressive strength.

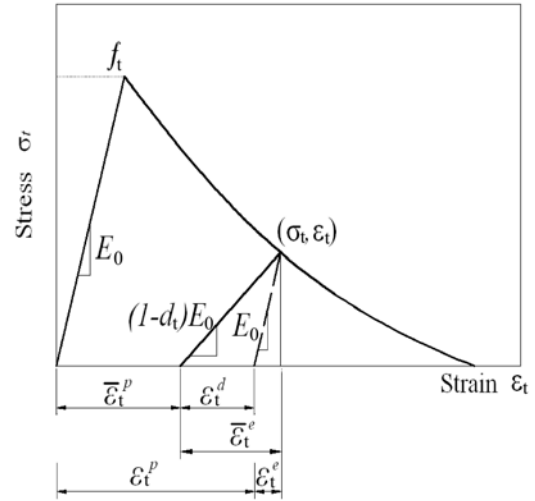


Figure 1 Stress-strain relationship of concrete under uniaxial tension

2.5 Implementation of the plastic degradation model in ABAQUS

Assuming that all stiffness degradation is associated with plastic deformation, the plastic degradation factor δ_t shown in Equation 12 can be used directly in place of the damage factor d in Equation 8 in ABAQUS. Under uni-axial tension, the stress-strain curve for a given element can be obtained from the stress-crack opening displacement curve (Eq. 3) depending on its type and size via Equation 1. The relationship between the plastic strain and tensile stiffness degradation variable (tension damage factor) can then be calculated from Equations 11 and 12. The compression damage versus compressive plastic strain can be calculated from Equations 2, 11 and 12 by replacing the tensile strength with the compressive strength in Equations 11 and 12. Note that the compressive plastic strain is calculated from $\varepsilon^p = \varepsilon - \sigma_c/E_0$. Damage is assumed to occur only after the concrete enters softening in both tension and compression. The two damage factor versus plastic strain curves (tension and compression) are used as user input data in ABAQUS.

3 FE MODELLING OF PULL-OFF TEST

3.1 Geometry

A 45 mm thick concrete prism as shown in Figure 2 has been modelled as a plane stress problem in the FE analysis. This thickness is smaller than most specimens used in the experiments but the rest of the concrete

should have little effect on FE results as the pull-off test commonly fails by debonding in concrete a few millimeters away from the FRP-concrete interface and only this failure mode is concerned in this study. The specimen is restrained vertically along the bottom and horizontally along part of the right edge h_s (Figure 2). For specimens with a free height h_c smaller than 30mm, the actual h_c value is used. For specimens with h_c greater than 30mm, h_c is set to 30mm. The thickness of the FRP plate t_p is set equal to 1 mm but the modulus of elasticity of the plate E_p is modified so that the plate has the actual axial stiffness $E_p t_p$.

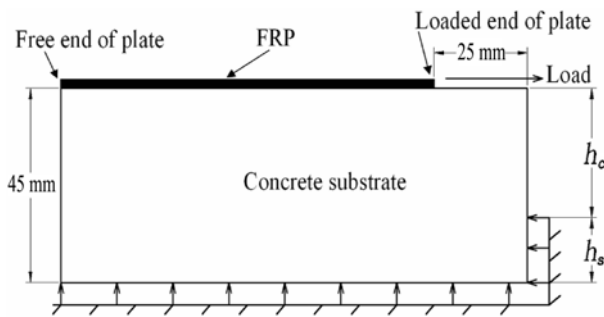


Figure 2 FE model of pull-off test

3.2 Constitutive model of materials

As aforementioned, the concrete damage plasticity model is used to describe the concrete behaviour. The plastic behaviour of concrete is modelled following the compressive and tensile behaviour described in Section 2.2. The damage is modelled using the proposed plastic degradation model in Section 2.4. The FRP is modelled as a linear elastic material.

The concrete is modelled using mono-size square elements with four integration points (CPS4). Rots' (1988) recommendation is adopted that the characteristic length for a square element with 4 integration points is $\sqrt{2}e$ where e is the element side length. The FRP is modelled using the same element with matching mesh.

3.3 Interpretation of numerical results

Because the problem is modelled as a plane stress problem while the actual behaviour is three dimensional (Chen and Pan 2005), the FE predicted load, displacement, stress and strain in the FRP plate are all adjusted following the width ratio factor β_w proposed by Chen & Teng (2001).

3.4 Mesh convergence

Specimen II-5 reported in Yao et al. (2005) was used as a reference case for conducting the mesh convergence study. Figure 3 shows the converging trend of the predicted loading capacity as the element reduces. The difference in the loading capacity between the 0.5mm mesh and the 1mm mesh is 2.8%. On the balance of accuracy and computational economy, the 1mm mesh was used for all the modelling reported in the rest of the paper.

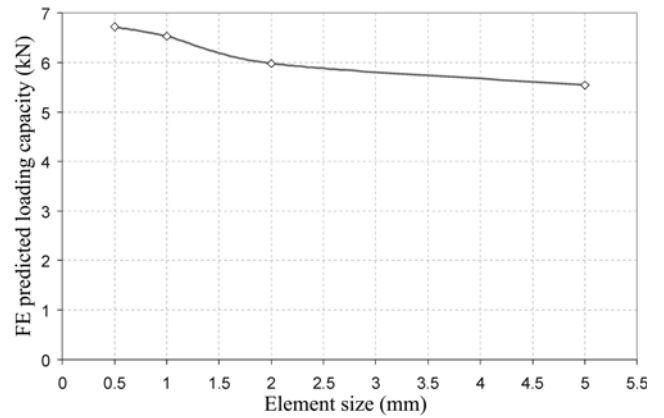


Figure 3 Predicted loading capacity for specimen II-5 in Yao et al. (2005)

4 COMPARISON OF FE PREDICTIONS WITH TEST RESULTS

The proposed FE model has been used to simulate a total of all 56 pull-off test reported in Yao et al. (2005) in which all the geometrical and material properties necessary for the FE modelling are reported. It may be noted that Yao et al. (2005) reported a total of 72 tests but 16 of them failed in other modes rather than debonding in concrete so they were excluded in this study. The concrete cylinder strength for the specimens in Yao et al. (2005) varied from 19 to 27 MPa. To increase the range of concrete strength, specimen No. 1 from Ali-Ahmad et al. (2006) and three specimens (S-CFS-400-25) from Wu et al. (2001) were further simulated. The concrete cylinder strength was 38MPa for the former and 57.6MPa for the latter respectively. Figure 4 shows that the FE predictions are overall in very close agreement with the 60 test data.

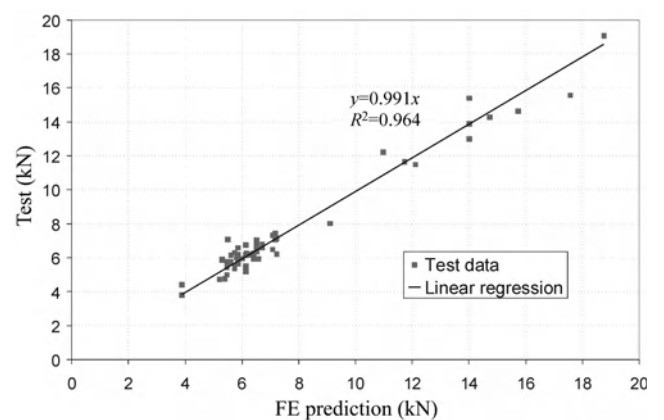


Figure 4 Comparison of FE prediction with test results

Figures 5 and 6 show the predicted and measured load-slip curve at the loaded end for two specimens: specimen II-5 in Yao et al. (2005) which had concrete strength of 23MPa and specimen No. 1 in Ali-Ahmad et al. (2006) which had a concrete strength of 38MPa. Clearly the predictions are in close agreement with test data for both

specimens in the whole loading range.

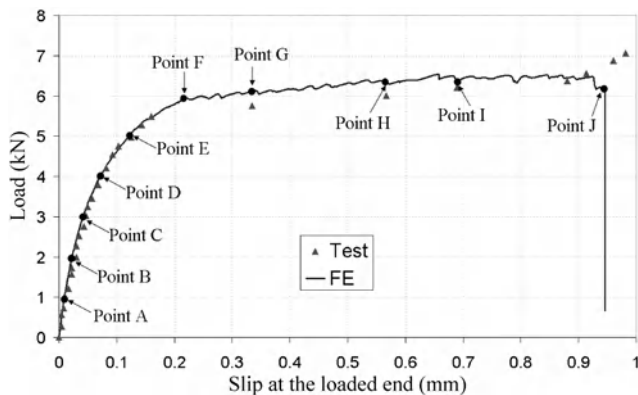


Figure 5 Comparison of FE prediction with test for specimen II-5 in Yao et al (2005)

For the reference specimen II-5 in Yao et al. (2005), a number of points on the FE predicted load-slip curve (marked Point A-I in Figure 5) are chosen to inspect the debonding process. Tensile damage contours in the concrete have been plotted for this purpose. It may be noted that the tensile damage is directly related to the cracking strain so the tensile damage contour closely represent the cracking pattern in the concrete. Due to limit of space, only five damage contours are shown in Figure 7.

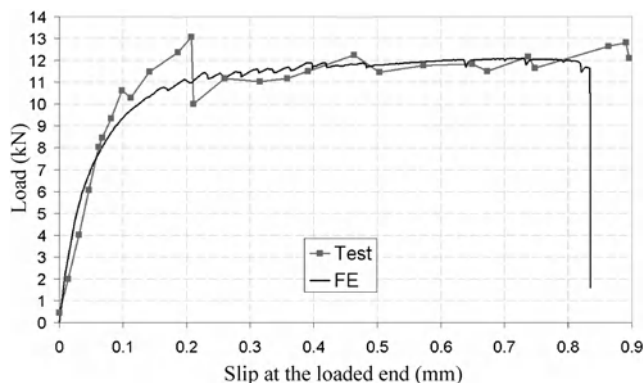


Figure 6 Comparison of FE prediction with test for specimen No. 1 in Ali-Ahmad et al (2006)

The concrete at the loaded end experiences softening in a small horizontal zone immediately under the FRP when the load is 30% of the ultimate load (Figure 7a). The length of this small softening zone has been about doubled and its depth significantly increased when the load increases to about 60% (Figure 7b). Microcracks start to form with an angle of about 45° to the horizontal. A macro crack only appears when the load is about 90% of the ultimate load (Figure 7c) and debonding starts to propagate rapidly thereafter towards the free end of the FRP (Figure 7d) leading to the total separation of the FRP plate from the concrete (Figure 7e).

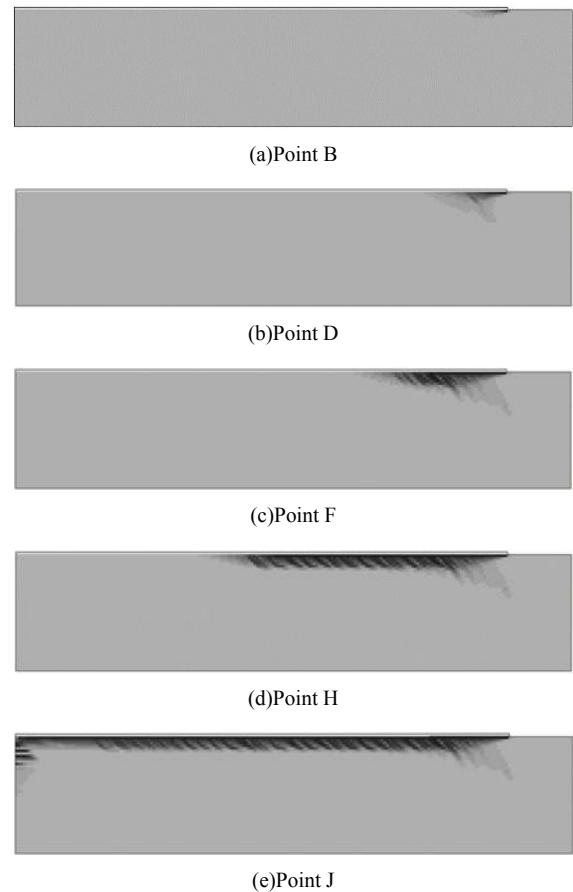


Figure 7 Predicted crack pattern at different stages: specimen II-5 in Yao et al (2005)

5 CONCLUSIONS

A plastic degradation model based the concrete damage plasticity theory has been proposed in this paper to simulate the bond behaviour between FRP and concrete. The plastic degradation is used to describe the damage of the concrete after it enters softening in both tension and compression. The proposed model has been implemented in ABAQUS to model the FRP-to-concrete bond behaviour in the pull-off test. It has been shown that the model can accurately predict the bond behaviour in the whole loading process and the numerical results are in very close agreement with test data from the literature.

6 ACKNOWLEDGEMENTS

The authors would like to acknowledge the support from the Scottish Funding Council for the Joint Research Institute between the University of Edinburgh and Heriot-Watt University which forms part of the Edinburgh Research Partnership in Engineering and Mathematics (ERPem). They would also like to acknowledge the support from the UK Engineering and Physical Sciences Research Council (EPSRC) and Shell for providing the second author the Dorothy Hodgkin Postgraduate Award.

REFERENCES

- ABAQUS. 2007. *ABAQUS Analysis user's manual*. Version 6.7. HKS Corporation.
- ACI318. 2002. *Building Code Requirements for Structural Concrete and Commentary*. ACI Committee 318. American Concrete Institute, Detroit, Michigan.
- Ali-Ahmad, M., Subramaniam, K. and Ghosn, M. 2006. Experimental investigation and fracture analysis of debonding between concrete and FRP sheets. *Journal of Engineering Mechanics* 132(9):914-923.
- Bažant, Z. and Jaime, P. 1998. *Fracture and Size Effect in Concrete and Other Quasibrittle Materials*. CRC Press, Boca Raton, Florida.
- Bažant, Z. and Oh, B. 1983. Crack band theory for fracture of concrete. *Materials and Structures* 16(3):155-177.
- CEB-FIB. 1993. *CEB-FIB MODEL CODE 1990*. Thomas Telford. London, UK.
- Chen, G.M., Teng, J.G. and Chen, J.F. (2010). Finite element modeling of intermediate crack debonding in FRP-plated RC beams. Submitted to *Journal of Composites for Construction, ASCE*.
- Chen, J. F. and Pan, W. K. 2005. Three dimensional stress distribution in FRP-to-concrete bond test specimens. *Construction and Building Materials* 20(1-2):46-58.
- Chen, J. F. and Teng, J. G. 2001. Anchorage strength models for FRP and steel plates bonded to concrete. *Journal of Structural Engineering* 127(7):784-791.
- Chen, J. F., Chen, G. M. and Teng, J. G. 2009. Role of bond modelling in predicting the behaviour of RC beams shear-strengthened with FRP U-jackets. *Proceedings of the 9th International Symposium on Fibre Reinforced Polymer for Concrete Structures (FRPRCS9)*, 13-15 July, Sydney, Australia.
- Chen, J. F., Yang, Z. J. and Holt, G. D. 2001. FRP or steel plate-to-concrete bonded joints: effect of test methods on experimental bond strength. *Steel Composite Structures* 1(2):231-244.
- Chen, J. F., Yuan, H. and Teng, J. G. 2007. Debonding failure along a softening FRP-to-concrete interface between two adjacent cracks in concrete members. *Engineering Structures* 29(2): 259-270.
- Coronado, C. A. and Lopez, M. M. 2007. Damage approach for the prediction of debonding failure on concrete elements strengthened with FRP. *Journal of Composites for Construction* 11(4):391-400.
- Coronado, C. A. and Lopez, M. M. 2010. Numerical modeling of concrete-FRP debonding using a crack band approach. *Journal of Composites for Construction* 14(1):11-21.
- Diab, H. and Wu, Z. 2007. Nonlinear constitutive model for time-dependent behavior of FRP-concrete interface. *Composites Science and Technology* 67(11-12):2323-2333.
- Hordijk, D. A. 1991. *Local Approach to Fatigue of Concrete*. PhD thesis, Delft University of Technology, Delft.
- Lee, J. and Fenves, G. L. 1998. Plastic-Damage Model for Cyclic Loading of Concrete Structures. *Journal of Engineering Mechanics* 124(8):892-900.
- Lu, X. Z., Jiang, J. J., Teng, J. G. and Ye, L. P. 2006. Finite element simulation of debonding in FRP-to-concrete bonded joints. *Construction and Building Materials* 20(6):412-424.
- Lu, X. Z., Ye, L. P., Teng, J. G. and Jiang, J. J. 2005. Meso-scale finite element model for FRP sheets/plates bonded to concrete. *Engineering Structures* 27(4):564-575.
- Lubliner, J., Oliver, J., Oller, S. and Oñate, E. 1989. A plastic-damage model for concrete. *International Journal of Solids and Structures* 25(3):299-326.
- Rots, J. G. 1988. Computational modeling of concrete fracture. PhD thesis, Delft University of Technology, Delft.
- Rots, J. G. 1991. Smeared and discrete representations of localized fracture. *International Journal of Fracture* 51(1):45-49.
- Saenz, L. P. 1964. Discussion of equation for the stress-strain curve of concrete-by Desayi, P. and Krishan, S. *ACI Journal* 61(9):1229-1235.
- Wu, Z. S., Yuan, H., Yoshizawa, H. and Kanakubo, T. 2001. Experimental/analytical study on interfacial fracture energy and fracture propagation along FRP-concrete interface. *ACI International SP201(8)*:133-152.
- Yang, Z.J. and Chen, J.F. 2005. Finite element modelling of multiple cohesive discrete crack propagation in reinforced concrete beams. *Engineering Fracture Mechanics* 72(14): 2280-2297.
- Yang, Z.J., Chen, J.F. and Proverbs, D. 2003. Finite element modelling of concrete cover separation failure in FRP plated RC beams. *Construction and Building Materials* 17(1):3-13.
- Yao, J., Teng, J. G. and Chen, J. F. 2005. Experimental study on FRP-to-concrete bonded joints. *Composites Part B: Engineering* 36(2):99-113.

FRP Materials and Sustainability

Fiber Reinforced Cementitious Composites (FRCC) Plate for the Anchoring of FRP Sheet on Concrete Member

Qingxu Jin & Christopher K.Y. Leung

Department of Civil and Environmental Engineering, Hong Kong University of Science and Technology, Hong Kong, China.

ABSTRACT To increase the bond capacity of FRP sheets employed in the strengthening of concrete members, various anchoring methods have been proposed and used. In this paper, a new anchoring approach with the gluing of precast fiber reinforced cementitious composites (FRCC) plate on top of the FRP sheet will be discussed. The direct shear bond test is employed to measure the failure load and study the failure mechanisms. Several sets of tests have been performed with different FRCC composition and different length of the FRCC plate. Comparison with the control sample shows that the installation of FRCC plate can significantly increase the bond capacity (by up to 100%).

1 INTRODUCTION

When Fiber Reinforced Polymer (FRP) sheets are employed for the flexural or shear strengthening of concrete members, the achievable increase in load capacity is often limited by the sudden debonding of the FRP from the concrete substrate. In order to increase the bond capacity of retrofitted FRP sheets and avoid the brittle structural failure behavior, the anchoring of FRP sheets has been studied for many years. In former investigations, various anchorage devices have been proposed to enhance the load-carrying capacity of FRP. For example, U-shape FRP jackets applied on the sides and tension face of a beam can be employed to 'confine' the FRP strip and hence to delay debonding (Teng et al, 2002). Bond capacity can also be improved with the use of a spike anchor, which can be installed in a hole drilled in the concrete member (Eiswar et al, 2008). In another technique, a groove is cut in the concrete member for the end of FRP to be inserted. After the groove is half-filled with epoxy, a GFRP rod is inserted before the whole groove is filled. With the plate end embedded, the bond capacity is significantly improved (Khalifa and Nanni, 2000).

In this paper, a new anchoring method will be introduced. To resist debonding, a precast FRCC plate is glued on the top of the FRP sheet. The direct shear bond test is employed to study the effects of FRCC composition and plate size on the bond and deformation capacities. The test results for various cases will be presented and the mechanisms for bond improvement will also be briefly discussed.

2 EXPERIMENTAL PROGRAM

2.1 Specimen Preparation and Material Properties

The specimen for direct shear test consists of FRP sheet

bonded on a concrete prism and a FRCC plate glued on the top of the FRP sheet. The size of the concrete prism was 100(width)×100(depth)×500mm (length) (Figure 2). The FRCC plate was precast and its size was 100×15×400 mm, with a middle groove 0.5 mm in depth and 40 mm in width, as shown in Figure 1. Before FRP bonding, both the FRCC and concrete prism were cured for 28 days. The concrete surface was then roughened by a needle-gun to expose the aggregates. Then, epoxy primer was applied. After the primer hardened, four layers of FRP sheets were bonded onto the concrete prism layer by layer using epoxy resin. The bonded FRP sheets were 40 mm in width and 300 mm in length. The initial 50 mm of the FRP from the edge of concrete prism was left un-bonded to avoid wedge failure of concrete caused by shear stress in the test (Figure 2). After the bonding of FRP sheet, a FRCC plate, extending 100mm beyond the free end of the sheet was glued on top of the FRP with another layer of epoxy (Figure 1 & 2). The bond test was performed 7 days after sample preparation to ensure full hardening of the epoxy.

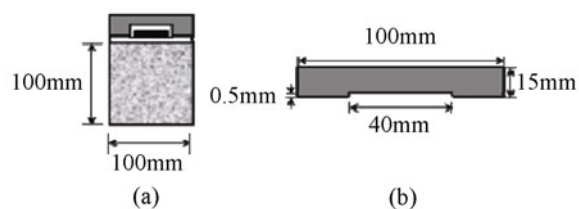


Figure 1 (a) Cross-section of specimen and (b) FRCC plate with detailed dimensions

The FRP used in this test is the Reno Composite Material System (Electric Insulator Co. Ltd. Taiwan, China).

According to the properties provided by the manufacturer, the tensile strength for design is 4200 MPa along the fiber direction and the tensile modulus is 235 GPa. The thickness of the FRP is 0.11mm per ply. The tensile strength of epoxy resin after complete curing (which takes 7 days) is over 30 MPa while the shear strength is more than 10 MPa. The adhesion strength of primer with a dry concrete surface is about 2 MPa and cohesion failure within concrete is observed in the test.

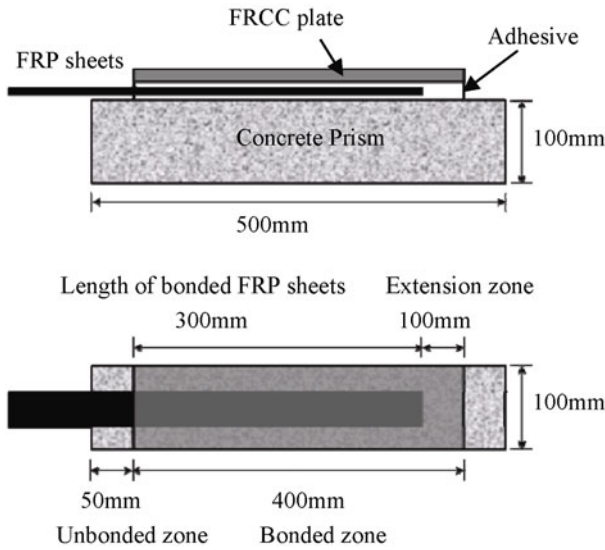


Figure 2 Test specimen with detailed dimensions

To investigate the effect of FRCC plate on the bond capacity of FRP sheets on concrete, 8 groups of samples with different FRCC composition and FRCC plate length were prepared for the test (Table 1). Group A was the control with no FRCC plate. In Group C, the employed FRCC composition can result in pseudo-ductile (or strain hardening) tensile behavior as described in Leung and Cao (2009). To achieve such behavior, only fine sand is used in the mix. The FRCC in Group B is similar in composition but with a lower fiber content. In Groups D to F, normal river sand was used in place of the fine sand. For Group D, no fiber was added to the plate. In Groups E and F, PVA and steel fiber were used respectively. In Groups G and H, the plate is fabricated with high strength fiber reinforced cementitious composites (Cheung and Leung, 2008). Different lengths of FRCC plates were used in these tests.

Based on direct tensile testing, the ultimate tensile strength of the FRCC's used for Group C and Group G/H is about 5 MPa and 8-10 MPa, respectively.

2.2 Setup and procedure of direct shear test

The direct shear bond test is performed and the testing set-up, as shown in Figure 3, was developed by Pan &

Leung (2007). Concrete specimen was first held tightly in a steel frame. To apply a pulling force on the FRP sheet, the whole system was installed in the Material Testing System (MTS). Alignment of the system had to be carefully adjusted to ensure the pulling force to be acting along the vertical plane of the FRP plate so any peeling effect could be prevented. A linear variable differential transformer (LVDT) was placed besides the specimen to measure the displacement of FRP plate (Figure 3) relative to the fixed support. The test was conducted under displacement control at the loading rate of 0.1mm/min.

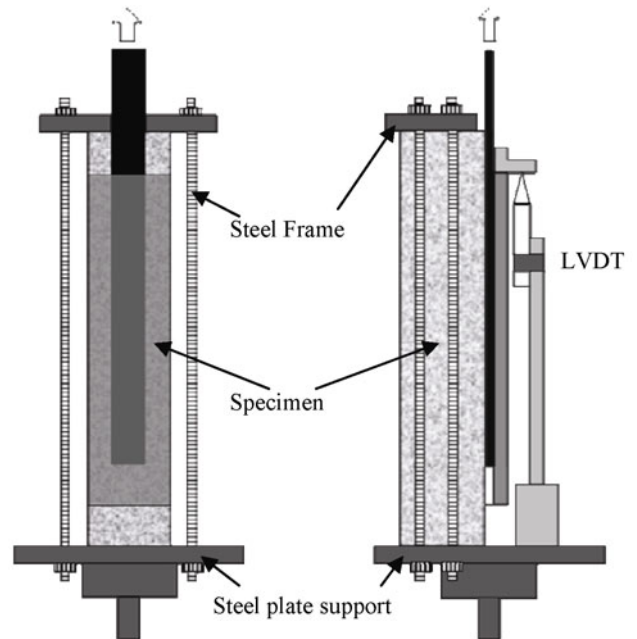


Figure 3 Test set-up for the direct shear test

3 TEST RESULTS AND DISCUSSION

All test results are listed in table 2. Typical load vs displacement curves for Groups A, B, E and G are shown in Figure 4. According to the test results, the bond capacity increased by around 50% to over 100% when

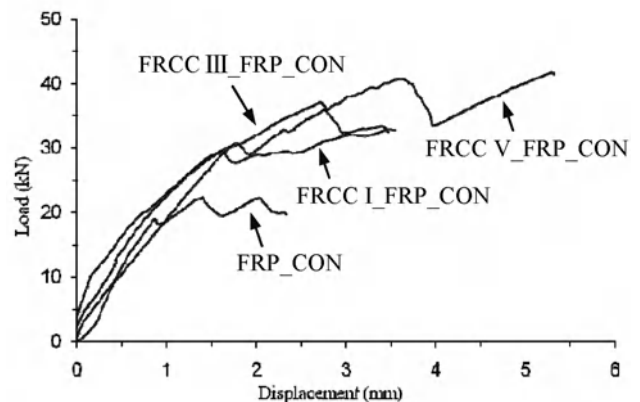


Figure 4 Load vs Displacement Curve

Table 1 Mix Proportion of the FRCC plate

Group No.	Specimen	Cement	Fly Ash	Silica Fume	Silica Sand*			River Sand*	Water	SP*	PVA Fiber	Steel Fiber I*	Steel Fiber II*
					I	II	III						
A	FRP_CON												
B	FRCC I _FRP_CON	0.8	0.18	0.02	0.2			0.22	0.0051	1%			
C	FRCC II _FRP_CON	0.8	0.18	0.02	0.2			0.22	0.0051	2%			
D	Plain Mortar _FRP_CON	1					1.5	0.35					
E	FRCC III _FRP_CON	1					1.5	0.35		1%			
F	FRCC IV _FRP_CON	1					1.5	0.35			0.5%		
G	FRCC V _FRP_CON	1	0.245	0.111	0.139	0.313	0.413	0.257	0.0114			2%	
H	FRCC VI _FRP_CON	1	0.245	0.111	0.139	0.313	0.413	0.257	0.0114			2%	

* Silica sand: Type I: 300 - 1180 μ m Type II: 150 - 600 μ m Type III: 53 - 300 μ m River sand: 80 μ m to 4.75mm SP for B and C: AVDA 105 SP for G and H: BASF Superplasticizer: a) ACE80: 80% b) B211: 20% Steel Fiber I: hooked end, 1.08mm diameter, 50mm in length; Steel Fiber II: straight, 0.16mm diameter, 13mm in length

Table 2 Test Results

Group No.	Length of attached FRC plate on FRP sheets mm	Member No.	Ultimate Load kN	Ultimate Displ. mm	Failure mode**	Perc. of Impr. with contr. group (Aver.)	
						Load	Displ.
A	NA	1	23.4	1.7	Control group		
		2	22.3	2.3			
		3	20.8	2.5			
		Average	22.2	2.2			
B	300	1	32.8	3.5	I	47.7%	44.6%
		2	31.9	3	I		
		3	33.5	2.9	I		
		Average	32.7	3.1			
C	300	1	33.1	3.8	I	54.7%	82.3%
		2	35.5	4.1	I		
		3	25.6	1.8	III		
		Average	34.3	4			
D	300	1	30.1	3.5	I	35.3%	58.5%
		2	33.2	3.8	I		
		3	26.7	3	II		
		Average	30	3.4			
E	300	1	36.8	3.5	I	56.7%	47.7%
		2	30.4	2.8	II		
		3	37	3.3	I		
		Average	34.7	3.2			
F	300	1	50.1	4.5	I	121%	82.3%
		2	46.2	3.3	III		
		3	47.9	3.4	I		
		Average	50	4.5			
G	300	1	41.7	5.3	I	83.3%	106.2%
		2	36.1	4	II		
		3	44.1	4.1	I		
		Average	40.6	4.5			
H	150	1	34.4	5.3	I	58%	101.5%
		2	36	4	I		
		3	34.7	3.8	I		
		Average	35	4.4			

** Failure Mode: I) Formation of a major transverse crack in the FRCC plate around the cut-off location of FRP sheet. II) FRCC plate debonded together with the FRP sheet. III) FRP rupture (Excluded in average calculation)

the FRCC plate was employed as anchoring device. Even an un-reinforced mortar plate could enhance the load capacity by 35%. However, failure occurred by material shattering in this case, so the use of a plain mortar plate in practice is not recommended. The ultimate displacement (defined as the displacement at ultimate load) was found to increase by about 45% for Group B with PVA FRCC plate but was doubled with the use of steel fiber in Groups F to H. Comparing group G to H, it is interesting to see that the shorter plate (with 150mm over the FRP) achieve $35/40.6 = 86\%$ of the ultimate load capacity for the longer plate (with 300mm over the FRP). This high efficiency indicates that the effect of bonded FRCC plate may be more significant around the free end of the FRP.

In the tests, three modes of failure can be observed. In the first mode, ultimate failure occurred with the formation of a major transverse crack in the FRCC plate around the cut-off location of FRP sheet (Figure 5 (a)). As a second failure mode, the bonded FRCC plate debonded together with the FRP sheet (Figure 5 (b)). For failure mode 3, FRP rupture was observed.

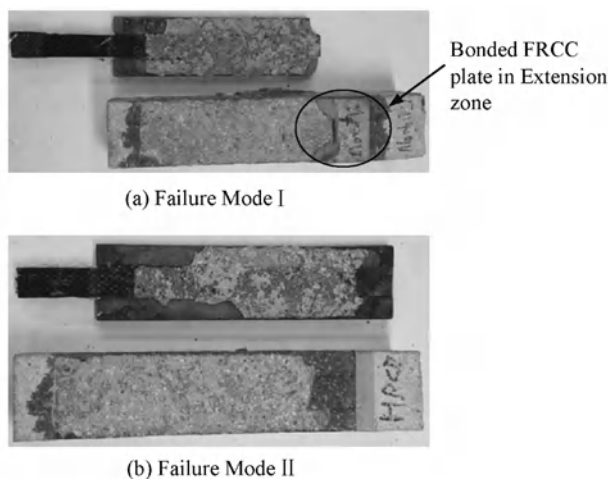


Figure 5 Failure Modes of Specimens

The improvement of bond capacity can be explained by three mechanisms. Firstly, the overall bond area is increased as the FRCC plate is wider than the FRP sheet. Secondly, as debonding occurs within the concrete, the debonded region exhibits an undulating surface. When a debonded plate is pulled, the sliding is coupled with displacements perpendicular to the interface. With the FRP covered by a cementitious plate bonded to the adjacent concrete surface, the normal displacement is resisted and normal compression is induced to increase the friction along the debonded interface. Thirdly, the

tensile load carried by the part of the plate extended beyond the free end of the FRP can enhance the overall bond capacity of the FRP.

As mentioned in the last section, the FRCC in group G has a much high load capacity than that in group C. A correspondingly higher ultimate load capacity and displacement was also obtained. In future work, models will be developed to relate bond capacity to the tensile behavior of the FRCC plate.

4 CONCLUSION

In this paper, a direct shear test was conducted to study if the debonding load capacity of FRP sheets on concrete member can be enhanced by the use of a glued FRCC plate as anchor. The effects of FRCC composition and plate length have been investigated. With the FRCC plate, both the debonding load capacity and ductility are found to increase considerably. The plausible mechanisms for the performance improvement are discussed. Based on our limited test results, the effectiveness of FRCC plate appears to have a correlation with the tensile strength of the FRCC. Also, the part of the plate around the free end of FRP seems to play a more significant role. While further experimental and modeling work is certainly required to clarify the effect of the FRCC plate, its feasibility as a simple anchor for the FRP sheet is demonstrated.

REFERENCES

- Cheung, A.K.F., Leung, C.K.Y. 2008. Experimental study on the bond between steel reinforcement and self-compacting high strength fiber reinforced cementitious composites, *Seventh International RILEM Symposium on Fibre Reinforced Concrete: Design and Applications BEFIB*: 667-678.
- Eshwar, N., Nanni, A. and Ibell, T.J. 2008. Performance of two anchor systems of externally bonded fiber-reinforced polymer laminates, *ACI Mat. J.*, 105(1): 72-80.
- Khalifa, A. and Nanni, A. 2000. Improving shear capacity of existing RC T-Section beams using CFRP composites, *Cem and Conc Comp*, 22: 165-174.
- Leung, C.K.Y. & Cao, Qian. 2009. Development of Strain hardening Permanent Formwork for Durable Concrete Structures, *Mat. & Struct.*, accepted and available on line.
- Pan, J.L. and Leung, C.K.Y. 2007. Effect of Concrete Composition on FRP/Concrete Bond Capacity. *J. Compos. & Cons.*, 11 (6): 611-618.
- Teng, J.G., Chen, J. F., Simith, S. T. and Lam, L., 2002. *FRP strengthened RC structures*, Wiley, West Sussex, U.K.

Study of Tensile Behavior for Interval Impregnated Hybrid Carbon/Basalt Fiber Sheet (C/BFS)

Gang Wu¹ (g.wu@seu.edu.cn), W.J Jing¹, Z.S. Wu^{1,2}

1. International Institute for Urban Systems Engineering, Southeast University, Jiangsu, China

2. Departments of Urban & Civil Engineering, Ibaraki University, Hitachi, Japan

ABSTRACT This paper presents a inter-ply hybrid fiber sheet C/BFS (carbon/basalt fiber sheet) in order to solve the problems encountered in the application of FRP in the present strengthening engineering, such as inconvenient transportation, not ideal adhesive interface and low tension control stress. Interval impregnated inter-ply hybrid method was adopted to enhance the performance of C/BFS, not only increases the adaptability to the structure shape but also raises the utilization ratio of fiber strength. Mechanical tensile tests were conducted on interval impregnated C/BFS with different lengths (2m/5m/10m). Test results show that the prestress degree of C/BFS can be over 50% of its design stress after interval impregnation.

KEY WORDS Hybrid effect; Prestress; Interval impregnation; Tensile behavior; FRP

1 INTRODUCTION

In recent years, Fiber Reinforced Polymer (FRP) has been widely used for the strengthening of concrete structures. However, researchers find that there are still several problems existing in practical application of FRP, such as stress lag, low strength efficiency and not ideal adhesive interface. Extensive research shows that externally bonded prestressed FRP can effectively solve these problems. However, such studies are restricted to full impregnated FRP. The research about un-impregnated and partial impregnated hybrid FRP still seldom involves. But full impregnated FRP is too hard to transport and the adhesive interface is not ideal. Un-impregnated FRP has low tension stress strength, only 30%~40% of full impregnated FRP, so it can only be imposed a low prestress.

From the perspective of hybrid effect and interval impregnation, this paper proposes an new fabrication form of interval impregnated C/BFS to realize its good hybrid effect and achieve a better tension mechanical prosperity of C/BFS by interval impregnation and imposing high prestress. In order to study its mechanic property, a series of longitudinal tension tests are conducted on C/BFS.

2 INTRODUCTION OF CBFHS

C/BFS (carbon/basalt fiber sheet) is a inter-ply hybrid of CFS (carbon fiber sheet) and BFS(basalt fiber sheet). It not only has a good mechanic property but also very economical. The CFS used in the tests is produced by Japanese cooperation Torayaca, and the BFS is produced by Hengdian Group Shanghai E'Jing Ltd. The impregnate

glue uses SK-RN. Some mechanical tests designed according to GB-T 1447-2005 are conducted on these materials. The tests results can be seen in Table 1.

Table 1 Summary of Mechanical Properties

	CFS	BFS	SK-RN
Tensile strength(N/mm ²)	3400	1825	40.6
Elastic modulus(kN/mm ²)	230	70.8	1.9
Elongation (%)	1.48	2.58	3.66
Thickness(mm)	0.111	0.145	/

3 TEST PROGRAM

3.1 Test device

Figure 1 shows the parts of test device. Load value can be achieved by the load cell and strain gauges were longitude applied to the middle of un-impregnated areas. Details of the parts and other application can be seen in Figure 2.

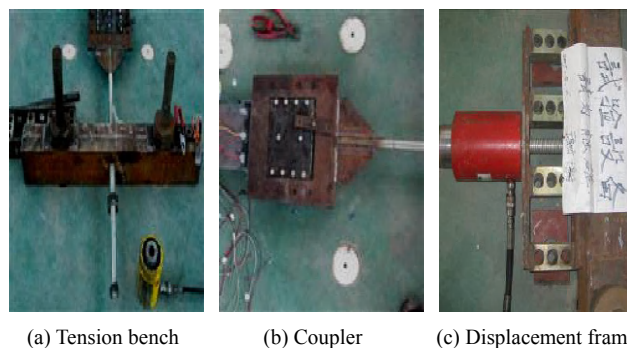


Figure 1 Parts of test device

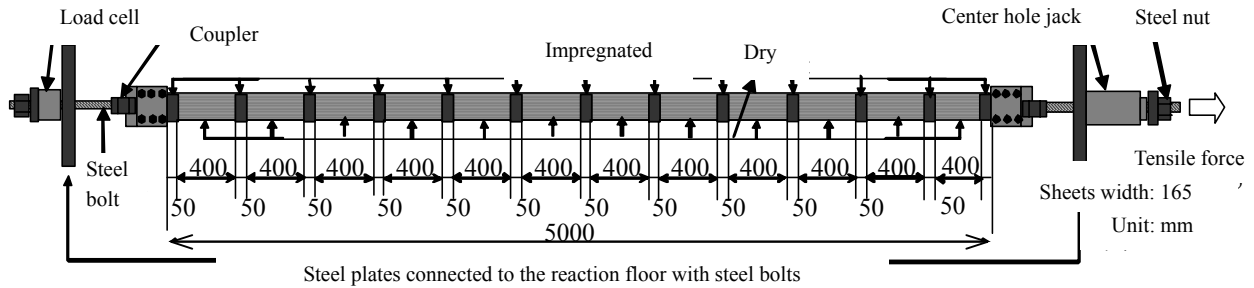


Figure 2 5m length interval impregnated C/BFS

3.2 Test specimens

Three groups of C/BFS with different lengths (2m, 5m, 10m), different hybrid form (inter-ply hybrid of CFS and BFS) and whether or not impregnate were prepared for tensile test. The specimen number can be seen in Table 2. Take 2B1C-D05 for example, 2B means 2 layers of BFS, 1C means 1 layer of CFS, D means un-impregnated and without “D” means interval impregnated, 05 means the length of C/BFS is 5m. All the C/BFS was 165mm width. All the interval-impregnated specimens are in the same interval (400/50). Details of the 5m length interval impregnated C/BFS can be seen in Figure 2.

4 TEST RESULTS AND ANALYSIS

Table 2 presents the test results. P_m means the theoretical ultimate tensile load, calculated by

$$P_m = \varepsilon_{cf} (E_{cf} A_{cf} + E_{bf} A_{bf}) \quad (1)$$

where ε_{cf} is the strain of carbon fiber corresponding to fracture; E_{cf} and E_{bf} , respectively, are the elastic modulus of carbon fiber and basalt fiber; A_{cf} and A_{bf} , respectively, are the areas of carbon fiber and basalt fiber. P_m ratio equals P/P_m .

Table 2 Test results

Specimens parameters		Ultimate load P (kN)	P_m (kN)	Ultimate strain ($\mu\epsilon$)	Ultimate stress (MPa)	P_m ratio (%)
2m length (un-impregnation)	1B-D02	11.2	25.3	9027	468	44.3
	1C-D02	26.6	62.7	7556	1452	42.4
	2B1C-D02	50.7	112.4	7519	1534	45.1
2m length (interval impregnation)	1B-02	12.0	25.3	/	502	47.4
	1C-02	27	62.7	7626	1474	43.1
	1B1C-02	46.7	87.3	7687	1819	53.5
	2B1C-02	60.5	112.4	8640	1831	53.8
5m length (un-impregnation)	1B-D05	11.7	25.3	7497	489	46.2
	1C-D05	18.9	62.7	6075	1032	30.1
5m length (interval impregnation)	1B-05	12.9	25.3	8245	539	51
	1C-05	23.2	62.7	6435	1267	37
	1B1C-05	47.0	87.3	7663	1834	53.8
	2B1C-05-1(2)	57(58.1)	112.4	7685(7252)	1725(1819)	55.1(56.1)
10m length (interval impregnation)	1B-10	12.5	25.3	7317	522	49.4
	1C-10	25.9	62.7	6150	1414	41.3
	1B1C-10	48.0	87.3	7622	1869	55.0
	2B1C-10	56.2	112.4	7591	1701	50.0
	1B2C-10	71.1	149.6	7890	1616	47.5

4.1 Hybrid effect and interval-impregnation

The load-strain curves of 5m C/BFS under tensile load are shown in Figure 3. On the one hand, contrast the load-strain curves of 1B-05 and 1B-D05, 1C-05 and

1C-D05, their load-strain curves almost coincide. It is similar in the comparison types of 2m group. In Table 2, the ultimate load, stress and strain are almost coincide with each other in the comparison types in the groups of 2m and 5m C/BFS. It shows that interval impregnation

has little influence on tensile property for single-laminar FRP sheet. On the other hand, contrast the ultimate load of 2B1C-D02 and 2B1C-02 in Table 2, the later increases 19.3% of the former. It shows that interval impregnation can increase the tensile property of interply hybrid C/BFS.

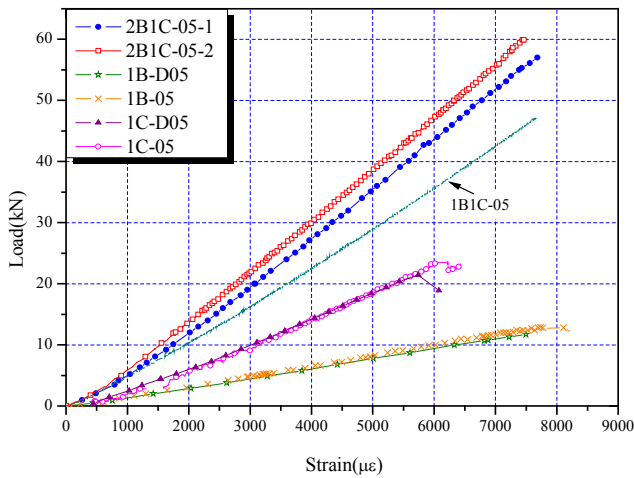


Figure 3 Load-Strain curves of 5m C/BFS

In Table 2, for un-impregnated C/BFS, twice the ultimate load of 1B-D02 and plus the ultimate load of 1C-D02 is 49kN, and the ultimate load of un-impregnated 2B1C-D02 is 50.7kN. The later only increases 3.5% by hybrid effect. For interval impregnated C/BFS, twice the ultimate load of interval impregnated 1B-02 and plus the ultimate load of interval impregnated 1C-02 is 51kN, and the ultimate load of interval impregnated 2B1C-02 is 60.5kN. The later increases 18.6% by hybrid effect. It is similar to the groups of 5m and 10m C/BFS and Figure 3 can give an intuitive grasp. It shows that hybrid effect has little influence on the tensile property of un-impregnated C/BFS, but can increase the tensile property a lot for interval-impregnated CBFHS.

As is known to all, the utilization of un-impregnated carbon FRP is usually 30%~40%, and the P_m ratio of 1C-D05 is only 30.1% in this test. So un-impregnated carbon FRP can only be imposed a small prestress. However, according to interval impregnation and hybrid effect, C/BFS can achieve a good tensile property. Take 2B1C-05 for example, P_m ratio is 56.1% and the utilization of carbon fiber is surely over 50%. The tension control stress of 2B1C-05 can achieve an ideal high value. So interval impregnated C/BFS is suitable for imposing a high prestress and the utilization of carbon fiber is over 50%. Meanwhile, the ultimate strain of 2B1C-02 is 8640 $\mu\epsilon$, and the ultimate strain of 2B1C-D02 is 7519 $\mu\epsilon$. The former increases 14.9% with the later. So it can improve the ductility by interval impregnated C/BFS.

Figure 4 shows the tensile strength- v_{cf} curves. Converse basalt fiber area to carbon fiber area by equivalent rigidity method, it can be seen that although the tensile strength margin of 2B1C-05, 1B1C-05 and 1B2C-5 is narrow

and 1B1C is the biggest one, the v_{cf} of 2B1C is the smallest. It is economics. In addition, the ductility of 1B1C is small. So interval impregnated 2B1C is the ideal C/BFS in this test.

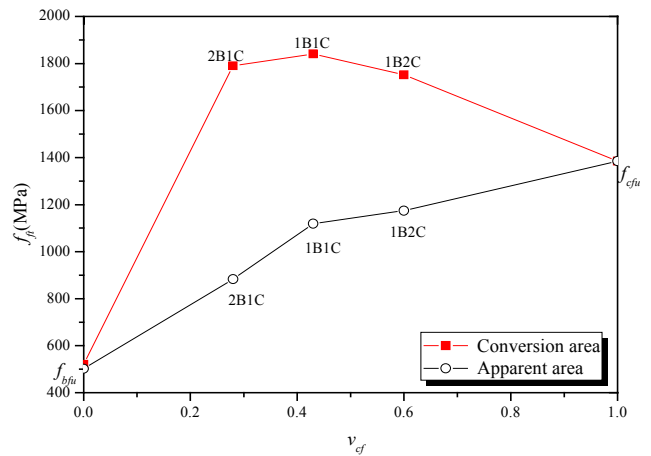


Figure 4 Tensile strength-carbon fiber volume ratio v_{cf} curves

4.2 Length effect of interval impregnated C/BFS

As is known to all, length effect has great influence on un-impregnated FRP based on theory and statistics. The longer the fiber is, the easier the fiber to rupture.

Figure 5 shows the length-strain histogram of interval impregnated C/BFS. It can be seen that length effect has a great influence on the ultimate strain of single-laminar FRP sheet. The strain of 1B decreases 1600 $\mu\epsilon$ from 2m to 10m, 1C decreases 1476 $\mu\epsilon$. However, length effect has little influence on 1B1C. The strains of 1B1C are nearly the same from 2m to 10m, only decreases 65 $\mu\epsilon$. The strain of 2B1C decreases 1049 $\mu\epsilon$ from 2m to 10m, smaller than single-laminar FRP sheet.

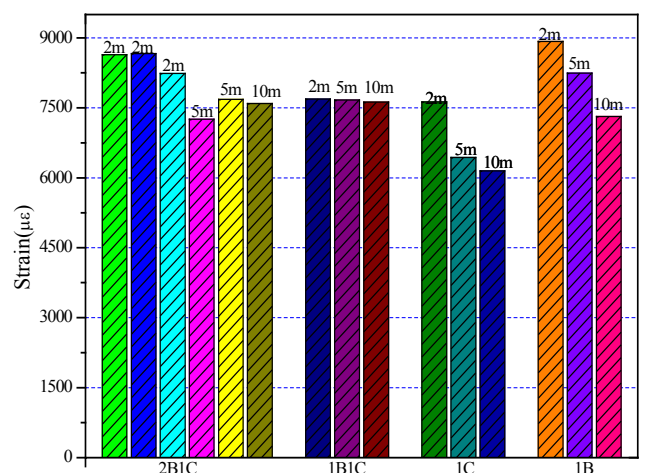


Figure 5 Length-strain histogram of C/BFS

It can be seen in Figure 6 that the influence of length effect on the ultimate load of interval impregnated 2B1C is not obvious. The ultimate load of 2B1C is 57kN or so from 2m to 10m in this paper. The effect of length more

than 10m on interval impregnated C/BFS awaits further study.

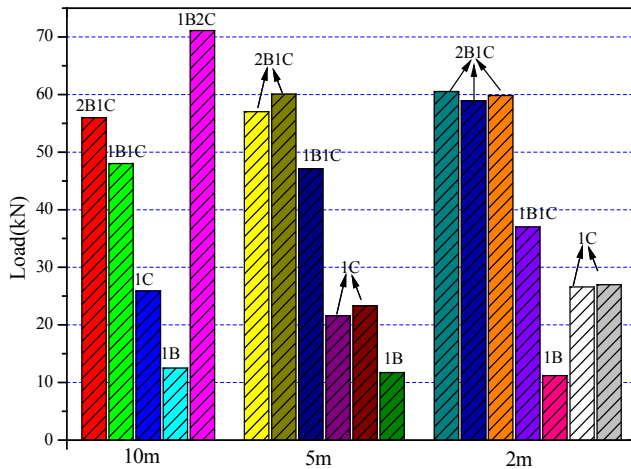


Figure 6 Length-Load histogram of C/BFS

5 CONCLUSIONS

Based on the tensile test on interval impregnated inter-ply hybrid fiber sheet C/BFS and comparisons, the conclusions can be drawn as follows:

- Interval impregnation has little influence on tensile property of single-laminar FRP sheet, but can increase the tensile property of inter-ply hybrid fiber sheet C/BFS.
- Hybrid effect has little influence on the tensile property of un-impregnated inter-ply hybrid fiber sheet C/BFS, but can increase the tensile property efficiently of interval-impregnated inter-ply hybrid fiber sheet C/BFS a lot.

- According to interval impregnation and hybrid effect, the ultimate load of interval impregnated inter-ply hybrid C/BFS can be over 50% of its theoretical ultimate load capacity. In this paper, it is 56.1% for 2B1C-05. So it can impose a high tension control prestress on interval impregnated C/BFS to exert its material properties, especially to increase the utilization of fiber. Meanwhile, its ductility decreases little.
- Length effect has great influence on single-laminar FRP sheet, but has little influence on interval impregnated C/BFS. In this paper, the influence of length effect on interval impregnated C/BFS is not obvious. The effect of length more than 10m on interval impregnated C/BFS awaits further study.

REFERENCES

- Selden RB. Fracography of carbon epoxy angle-ply laminates. IC2CM- IV,1982,1525-1533
- Wu Zhishen, NIU He-dong. Recent Developments in FRP Strengthening Techniques. The 3th China FRP Academic Thesis Album Nanjing: Industrial construction, 2004, 112-118.
- Wu, Z.S., et al., Japanese Conference on Composite Materials, 31, 5, 2005, 230-237
- Alkhrdaji, T. & A. Nanni. Surface Bonded FRP Reinforcement for Strengthening/Repair of Structural Reinforced Concrete. Proc, ICRI-NRCC Workshop, Baltimore, MD, Oct. 30, 1999, 19 pp.
- Wenjun Jing, G WU, Z.S. Wu, et al. Study on Tensile Performance of Small Size Carbon-Basalt Fiber Hybrid Sheets. The sixth national academic exchange conference of FRP, 31, 5, 2009, 230-232

Statistical Studies on Material Behavior of CFRP Sheets under Uniaxial Loads and Its Application in Reliability Analysis

Wenwei Wang (wangwenwei@seu.edu.cn) & Wei Yang

Department of Bridge Engineering, Southeast University, Nanjing, China

ABSTRACT The uniaxial load tests were conducted to investigate the material behavior of CFRP sheets. The results show that the probability distribution of CFRP tensile strength can be described by the three-parameter Weibull distribution. The design formulae for determining flexural capacity of reinforced concrete strengthened with CFRP sheet are proposed. The Monte Carlo procedure is applied to simulate the flexural capacity of reinforced concrete strengthened with CFRP sheet, and the results show that the flexural capacity can be considered to obey the normal distribution. By using the JC method, the reliability index is calculated based on the statistics of flexural capacity and load effect. After the analysis of the effect of the partial factor of CFRP sheet on the reliability index, the results reveal that the reliability index of all design points are the most close to target reliability index overall when the partial factor of CFRP sheet is 1.25, and in this condition the reliability index of three failure modes is larger than the target reliability index. Therefore, the partial factor is suggested to be 1.25, which can meet the requirement of reliability design.

1 INTRODUCTION

The method of strengthening concrete structures with CFRP laminates is becoming increasingly popular because of its efficiency of application, high strength and immunity to corrosion. During the engineering practice and the research of the FRP concrete structures, several design guidelines of the FRP concrete structures have been published [1-5]. However, the existing design guidelines or codes related to the design formulas are empirical, it is necessary to confirm the material partial factor of the CFRP sheet in the design formulas based on reliability theory.

In this paper, the two methods (JC Method and Monte Carlo simulation method) are integrated to analysis the reliability of flexural capacity of CFRP-reinforced concrete beams, and to determine the material partial factor of CFRP sheet in the design formulae.

2 MATERIAL BEHAVIOR TEST

2.1 Specimen Description

The HITEX-C30-CFRP sheet was used in the experiment to achieve the strength and the elongation under unidirectional load. One group (HITEX-C30-CFRP-F), which included 20 specimens, was impregnated manually with impregnated adhesive. Another group (HITEX-C30-CFRP) was composed with 5 specimens without the adhesive. The specimens were made according to *Chinese Test Method for the Directional Tensile Properties of Oriented Fiber Reinforced Plastics* [6]. The shape of

the specimens was shown in Figure 1.



Figure 1 CFRP sheets

2.2 Test Method

The experiments were conducted in Gregory 30kN computer-controlled electronic universal testing system. During the experiment, the CFRP sheets were ensured to be loaded with uniform force by clamping the aluminum plates bonded at the end of CFRP sheets. The loading rate with the deformation control is 2mm/min. All data are recorded by computer-automated data acquisition system.

3 TEST RESULTS

3.1 The failure mode

The tensile stress - strain curves of the CFRP sheet with epoxy resins and the CFRP sheet without the epoxy resins are shown in Figure 2. The tensile stress - strain curve of CFRP sheet is linear, which show the CFRP sheet is a kind of linear-elastic material before it ruptures.

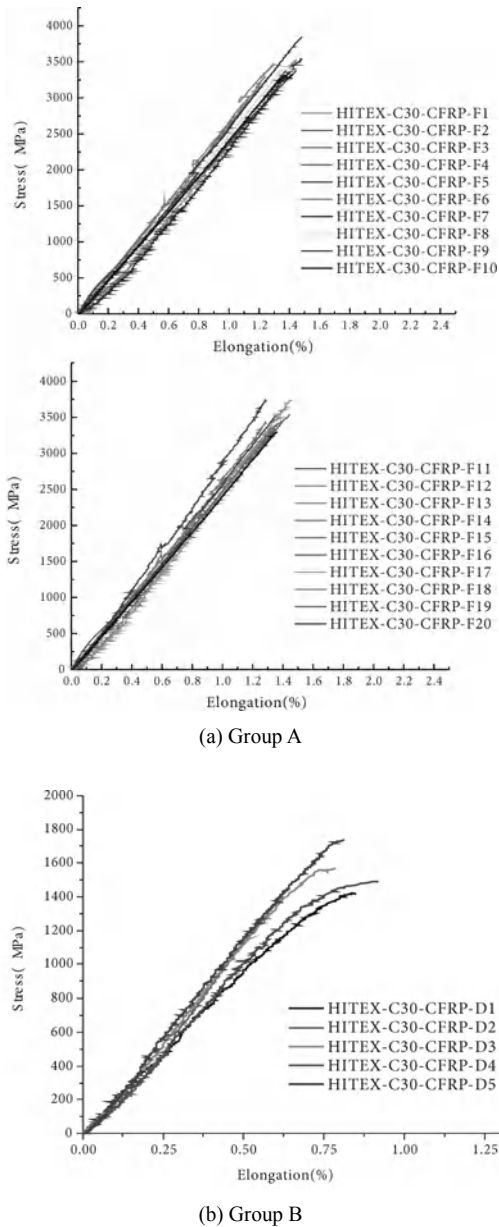


Figure 2 Tensile stress - strain curves

The average ultimate tensile strength of the Group A and B are 3480.5MPa and 1531.92MPa, which shows that the average ultimate tensile strength of Group B is about 50% of the Group A. The tensile strength of standard deviations of two groups is 157.25MPa and 128.51MPa, respectively. The average elastic moduli of two groups are almost the same, which is 258.89GPa and 228.58GPa, respectively. This result shows that only when the CFRP fabric impregnated with epoxy resins to connect each bunch of fiber horizontally into a whole, the CFRP sheet can be ensured to work together better, the characteristics of high strength can be achieved.

3.2 CFRP tensile strength distribution

The comparisons of the probability density curve of CFRP tensile strength calculated according to the three-parameter Weibull distribution and the experimental values are shown in Figure 3. It can be found that the

tensile strength of CFRP obey the three-parameter Weibull distribution.

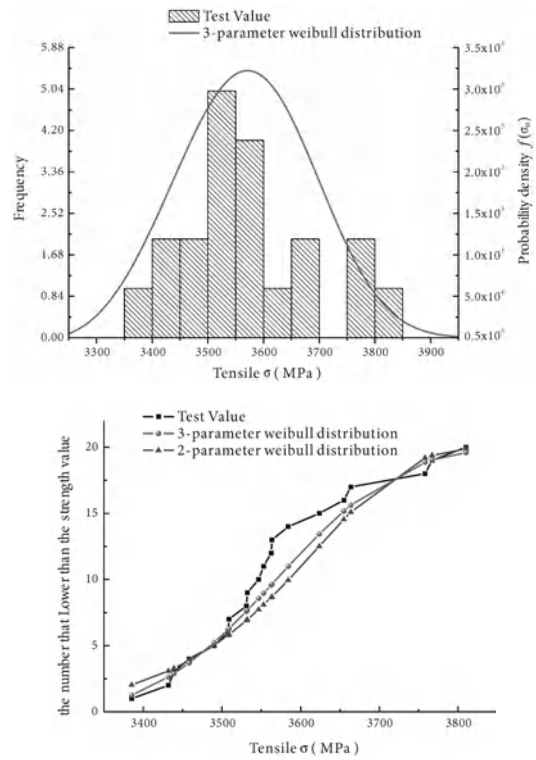


Figure 3 Comparisons of the distribution of tensile strength between experimental and calculated values

4 PARTIAL FACTOR OF THE CFRP SHEET

4.1 Flexural Capacity

Debonding failures are not considered here. The properly designed CFRP-strengthened concrete beams may fail in three failure modes: 1) concrete crushing before the steel rebar yielding; 2) concrete crushing after the steel rebar yielding; 3) CFRP rupture after steel rebar yielding.

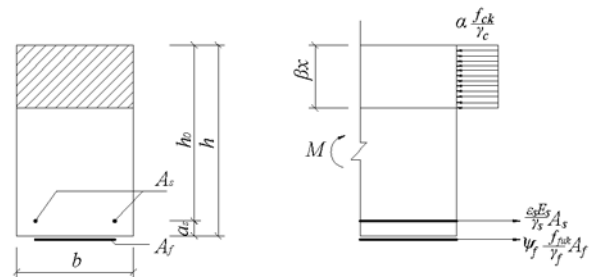


Figure 4 Cross section of reinforced-concrete beam strengthened with CFRP sheet

The ultimate moment capacity M_u is given as follows (Figure 4):

$$M_u \leq \alpha\beta \frac{f_{ck}}{\gamma_c} \left(h_0 - \frac{\beta x}{2} \right) + \psi_f \frac{f_{fuk}}{\gamma_f} A_f a_s \tag{1}$$

$$\alpha\beta \frac{f_{ck}}{\gamma_c} bx = \frac{E_s \varepsilon_s}{\gamma_s} A_s + \psi_f \frac{E_f \varepsilon_{fu}}{\gamma_f} A_f \quad (2)$$

$$\psi_f = \frac{\varepsilon_{cu}(h-x)/x - \varepsilon_{f0}}{\varepsilon_{fu}} \quad (3)$$

$$\varepsilon_s = (\psi_f \varepsilon_{fu} + \varepsilon_{f0}) \left(\frac{h_0 - x}{h - x} \right) \quad (4)$$

$$\varepsilon_{sy} = \frac{f_{sk}}{E_s}; \quad \varepsilon_{fu} = \frac{f_{fuk}}{E_f} \quad (5)$$

Where M_u is the ultimate moment capacity; α and β are the equivalent rectangular stress block coefficients; h and x are the height of cross section and the depth of the concrete compressive stress block; h_0 is the effective depth; A_f is the cross-section area of CFRP sheet; A_s is the cross-section area of steel rebar; ψ_f is the strength coefficient considering that the actual tensile strength of CFRP sheet does not reach the design value; ε_{fu} is the ultimate tensile strain of CFRP sheet; E_f is the elastic modulus of CFRP sheet; ε_s is the tensile strain of steel rebar; ε_{sy} is the yield strain of rebar; ε_{cu} is the ultimate compression strain of concrete; ε_{f0} is the initial strain at the bottom face of the beam; f_{ck} is the standard value of axial compressive strength of concrete; γ_c is the material partial factor of concrete, $\gamma_c=1.45$; f_{sk} is the standard value of the tensile strength of steel rebar, γ_s is the material partial factor of the rebar, $\gamma_s=1.2$; f_{fuk} is the standard value of the tensile strength of CFRP sheet, $f_{fuk} = f_{fum} - 3\sigma_f$, f_{fum} and σ_f are the mean tensile strength and the standard deviation of CFRP sheet tensile strength^[1]; γ_f is the material partial factor of CFRP sheet.

ψ_f and x can be calculated using the equations (2)~(4). when $\psi_f > 1$, the CFRP sheet ruptures failure mode will happen. Then, $\psi_f = 1$ and x will be recalculated by solving the equations (2) and (4). The flexural capacity can be calculated by equation (1).

The design criterion for the CFRP-reinforced concrete beam is as follows:

$$\gamma_0 S_d \leq R_d \quad (6)$$

Where γ_0 is the important coefficient of the structure; S_d is the design value of the load effect; R_d is the design value of the cross-section resistance.

According to the *Chinese Unified Standard for Reliability Design of Building Structures*^[7], S_d can be determined using the following two equations:

S_d is controlled by the live load effect:

$$S_d = \gamma_{G1} S_{Gk} + \gamma_Q S_{Qk} \quad (7)$$

S_d is controlled by the constant load effect:

$$S_d = \gamma_{G2} S_{Gk} + \psi_c \gamma_Q S_{Qk} \quad (8)$$

where S_{Gk} and S_{Qk} are the stand values of the constant

load effect and the live load effect; γ_{Gi} is the partial factor of the constant load, $\gamma_{G1}=1.2$, $\gamma_{G2}=1.35$; γ_Q is the partial factor of the live load, $\gamma_Q=1.4$; ψ_c is the combination coefficient, $\psi_c=0.7$. The statistical parameter of the constant load effect and the live load effect can be valued with reference to the *Chinese Load Code for the Design of Building Structures*^[8].

4.2 Partial factor of the CFRP sheet

The Monte Carlo-JC method^[9~13] used in this paper is the method that combining the JC method and Monte Carlo simulation method to calculate the reliability index β . The cross-section resistance (bending moment capacity) can be simulated using Monte Carlo method according to the equations in section 4.1. Then the probability distribution of resistance can be achieved based on the simulation results. It can be seen that the probability distribution of resistance obey the normal distribution, as shown in Figure 5. The reliability index β can be calculated using JC method according to the equations (6)~(8). The calculated reliability index β should be calibrated with the target reliability β_H ^[8]. Therefore, the material partial factor of CFRP sheet can be achieved in the calibration procedure.

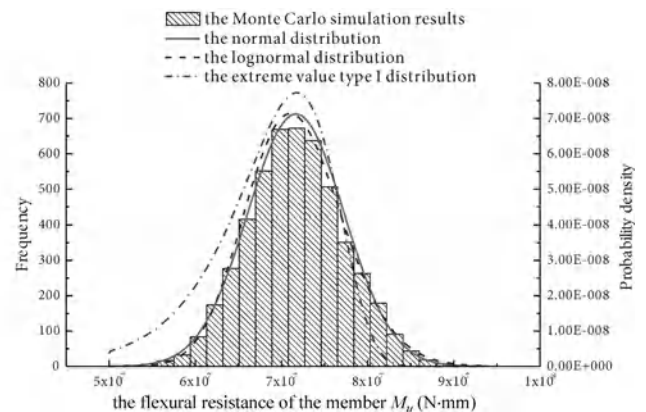


Figure 5 Probability distribution of resistance

Five design variables such as the width b , the height h , the effective height h_0 , the concrete strength f_{ck} and initial strain ε_{f0} are considered to obey the normal distribution. The FRP strength f_{fuk} is considered to obey the Weibull distribution and the steel rebar strength f_{sk} obeys the β distribution. Five ratios of live to dead load were considered, namely 0.1, 0.25, 0.5, 1.0, 2.0 and 2.5^[8].

Figure 6 shows the calibration procedure. It can be seen that value of H_γ is the smallest (0.236) when $\gamma_f = 1.25$. Figure 7 shows the calculated reliability index under different failure modes. The value of β_m is 4.05 under the CFRP rupture failure mode, 4.16 under the failure mode of the concrete crushing after the steel rebar yielding, and 4.31 under the failure mode of the concrete crushing before the steel rebar yielding. They are all larger than the target reliability index. As a result, the

material partial factor of CFRP sheet is recommended to be 1.25, which is according with the basic principles of reliability design.

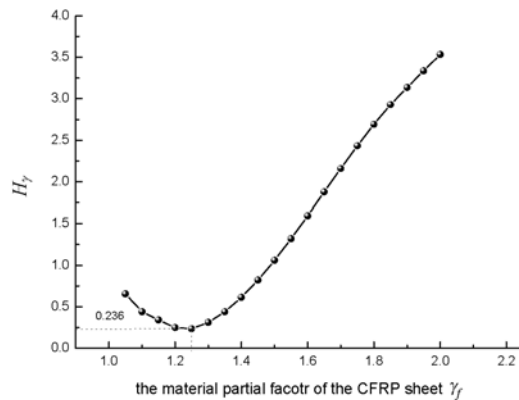


Figure 6 The calibration procedure

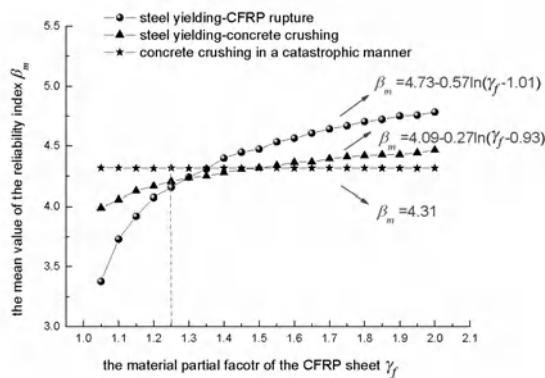


Figure 7 The calculated reliability index under different failure modes

5 CONCLUSIONS

The designed method for determining flexural capacity of reinforced concrete strengthened with CFRP sheet is proposed in this paper. The Monte Carlo simulation method is applied to simulate the distribution of the bending moment capacity, and the results show that bending moment capacity can be considered to obey the normal distribution. By using the JC method, the reliability index is calculated based on the statistics of flexural capacity and load effect. The material partial factor of CFRP sheet in the design formulae is also confirmed. The results reveal that when the partial factor of CFRP sheet is 1.25, the reliability index is larger than the target reliability index. Therefore, the partial factor is suggested to be 1.25, which can meet the requirement of reliability design.

REFERENCE

1. American Concrete Institute ACI 440 2002. Guide for the design and construction of externally bonded FRP systems for strengthening concrete structures. Detroit: American Concrete Institute.
2. Canadian Standards Association International CSA-806-02 2002. *Design and construction of building components with fiber reinforced polymers*. Toronto: Canadian Standards Association International.
3. ISIS Canada Corporation 2001a. *Reinforcing concrete structures with fiber reinforced polymers (FRPs)*. Manitoba: The Canadian Network of Centers of Excellence on Intelligent Sensing for Innovative Structures.
4. ISIS Canada Corporation 2001b. *Strengthening reinforced concrete structures with external bonded fiber reinforced polymers*. Manitoba: The Canadian Network of Centers of Excellence on Intelligent Sensing for Innovative Structures.
5. Ministry of House and Urban-Rural Development of People's Republic of China 2006. *Design code for strengthening concrete structure GB50367-2006*. Beijing: China Architecture & Building Press.
6. Ministry of commerce of People's Republic of China 1999. *Test method for tensile properties of oriented fiber reinforced plastics GB/T 50068-2001*. Beijing: Standards Press of China.
7. Ministry of House and Urban-Rural Development of People's Republic of China 2001. *Unified standard for reliability design of building structures GB 50068-2001*. Beijing: China Architecture & Building Press.
8. Ministry of House and Urban-Rural Development of People's Republic of China 2001. *Load code for the design of building structures GB50009-2001*. Beijing: China Architecture & Building Press.
9. Zheng H. & Cunyong H. 2007. Application of Monte Carlo-JC method to the reliability assessment of flexural capacity of RC beams strengthened with FRP. *ACTA Material Composite Sinica*, 4(1): 117-121(in Chinese).
10. Plevris N., Triantafillou T.C. & Veneziano D. 1995. Reliability of RC members strengthened with CFRP laminates. *Journal of Structural Engineering*, 121(7): 1037-1044.
11. Jinxin G. & Weiwei W. 2007. *Designed theory of reliability of engineering structures*. Beijing: China Machine Press.
12. Giorgio M. & Silvia S. 2002. Reliability-based calibration of partial safety coefficients for fiber-reinforced plastic. *Journal of Composites for Construction*, 6(3): 162-167.
13. Rackwitz R. & Fiessler B. 1978. Structure reliability under combined random sequences. *Computers & Structures*, 9: 489-494.

Comprehensive Characterization of BFRP Applied in Civil Engineering

Hui Li (huili@hit.edu.cn), Guijun Xian, Bo Xiao & Jingyu Wu

School of Civil Engineering, Harbin Institute of Technology, Harbin 150090, China

ABSTRACT In the present study, BFRP rebars for internal concrete reinforcement and wet lay-ups for external rehabilitation have been systematically characterized on the basic physicochemical properties and durability performance of the BFRP materials subjected to hygrothermal ageing, freeze-thaw cycles and elevated temperatures. The basic mechanical performances of BFRP are tested according to ACI 440.3R, which indicates the better modulus and stiffness than GFRP, but inferior to CFRP. Hygrothermal ageing in distilled water and alkaline solution immersion leads to deterioration of both mechanical and thermal properties. The water uptake and thermal properties due to the long term immersion ageing were performed to understand the degradation mechanisms. After extreme freeze-thaw cycles ranging from -30°C to 30°C , no adverse effects were found for the properties of BFRP and the bonding between BFRP and concrete blocks. The elevated temperature leads the mechanical properties BFRP rebars to be reduced remarkably. The residual properties exceed the half room temperature values at the temperature much higher than the glass transition temperature of the system. Compared to the CFRP and GFRP, the promising properties of the BFRP rebar and wet lay-up clearly illustrates the high potential for the application in civil engineering.

1 INTRODUCTION

As a novel reinforcement, basalt fibers are produced directly from basalt rock through a melting process with high mechanical properties and chemical resistance (Sim, Park et al. 2005). Compared to the commonly used carbon fiber reinforced polymer (CFRP) and glass fiber reinforced polymer (GFRP), basalt fiber reinforced polymer (BFRP) composites possess many advantages, such as relative low price, excellent mechanical and thermal properties, good chemical resistance, and environmental friendly, etc. Since BFRP has been applied in civil engineering only for several years, the comprehensive knowledge of the BFRP from the basic physicochemical properties to the long term durability in various civil environments is not completely understood yet. As known, a comprehensive knowledge of basalt fiber and BFRP in terms of basic physic-chemical properties, long term durability under various civil environments, freeze-thaw cycle resistance as well elevated temperature resistance, is prerequisite for its acceptance in the field.

In the past several years, some works have been conducted on the performance and application of BFRP composites in structural strengthening, rehabilitation etc. (Sim, Park et al. 2005; Cerny, Glogar et al. 2007; Deak and Czigany 2008; Wang, Zhang et al. 2008; Yongsheng, Zhishen et al. 2009). Some contradictory results are reported in literature, which may due to the fact that the properties of basalt fiber varied from each other seriously,

dependent on the basalt rock mines and producing process. Without consistent and reliable property data of BFRP, as believed, it may be impossible to design and apply them in real civil engineering practice, especially for some key infrastructures.

In view of this, the present work is focused on a thorough performance investigation of commercial BFRP composites for civil engineering application. GFRP and CFRP bar have already been accepted to replace traditional steel rebars in many applications, while FRP wet layups have been widely used to strengthen, rehabilitate and renew civil structures in the past more than 20 years. Therefore, the current investigation is concentrated on BFRP bar and BFRP wet layups.

The effects of water immersion, alkaline immersion, and extreme freeze thaw as well as elevated temperature on the performance degradation of BFRP bars and wet layups are explored. The study is aimed to evaluate the possible advantage and withdraw of the BFRP application in civil engineering.

2 EXPERIMENT

2.1 Materials

An epoxy resin system, including epoxy resin and hardeners, is developed at our lab used for saturation of fiber clothes to strengthen, repair and rehabilitate concrete or other civil engineering structures. This epoxy resin system has a low viscosity, and thus can easily saturate a

fiber fabric completely. The resin can be cured at room temperature, and reaches a high deflection temperature ($>80^{\circ}\text{C}$).

Unidirectional basalt fiber fabrics are commercially available in China. As indicated, the fiber diameter is 13 micron; the area density of the fabric is 360 g/m^2 ; tensile strength is 2.1 GPa and modulus is 105 GPa .

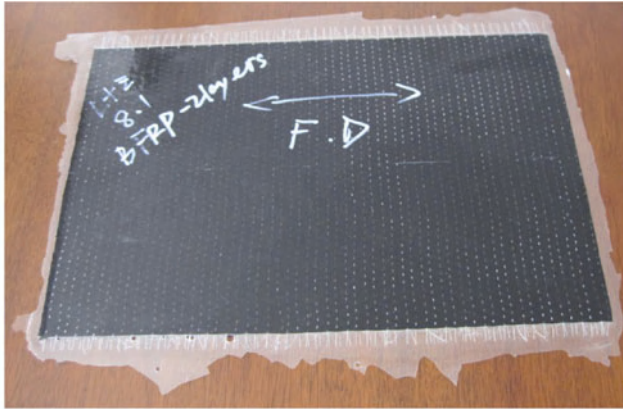


Figure 1 BFRP wet layup plate. (The white edge is cured extra epoxy resin)



Figure 2 BFRP bar (nominal diameter, 8mm) tested in the present study

BFRP prepared with a hand wet layup process. First, a pre-cut fabric, laid on a flat surface, was saturated with enough epoxy resin system. The more resin was pressed out from the fabric with a plastic trowel. Two layers of fabrics were used for a sample with the dimensions of $300 \times 300\text{ mm}^2$.

After cured in the lab (around 23°C) for 7 days, the wet layup plate was cut into $25\text{ mm} \times 250\text{ mm}$ strips completely along the fiber direction. Those strips used for tensile testing will be post-cured at an oven of 110°C for 2 hours.

BFRP bars are also commercial available in China. The bar was spirally wound with glass fiber roving and sand coated to improve the bonding strength to a concrete

structures. The studied bar diameter is 8 mm, and shown in Figure 2.

2.2 Testing

Tensile testing were performed for both BFRP bar and wet layups, according to ACI 440.3R and ASTM D3039, respectively. Note, BFRP bar should be anchored with steel pipes at both of the ends. A high modulus epoxy adhesive developed at our lab was used to bond the rebar with the steel pipe.

For BFRP wet layup samples ($150\text{ mm} \times 20\text{ mm} \times$ nominal thickness of 0.8 mm), the strain was measured with a mechanical strain gauge. For BFRP bar, the strain measurement only be performed less than 0.5% , in order to avoid damage of the strain gauge by the exploring breakage of the BFRP bar.

Freeze-thaw cycle testing was performed with an refrigerator and an oven with a temperature range of $-30^{\circ}\text{C} \sim 30^{\circ}\text{C}$, 24 hours for one cycles. The testing samples are BFRP strips and BFRP bonded concrete block. The temperature profile for two cycles can be seen in Figure 3. As shown, the temperatures on the sample surface and the surrounding are measured, which are almost the same.

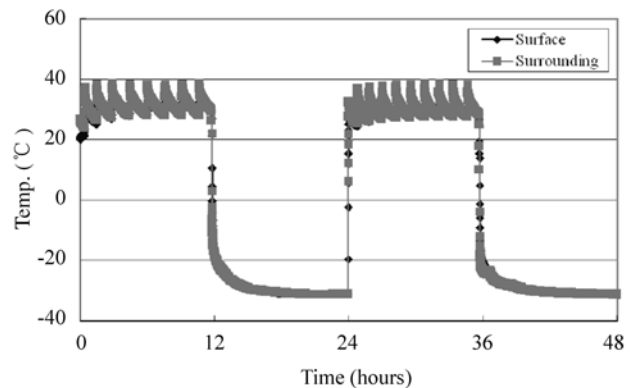


Figure 3 Freeze-thaw temperature cycle profile

Immersion ageing of BFRP bar and wet layup strips were performed with water bath at $23, 40, 60$ and 80°C . Water uptake of the samples was tested with the gravimetric method. The moisture uptake was detected by periodically measuring the mass of the samples. Samples were taken out of the baths, swiped off the surface water using tissue papers and weighted using an electronic balance with an accuracy of 0.01 mg . The presented data are an average for 10 coupons for each condition.

Tensile properties of aged samples were tested using the same procedure as un-aged samples.

The elevated temperature performance of BFRP specimens were conducted on BFRP bar only. One set of samples were tested at elevated temperatures, while one another set of samples were tested after elevated temperature treatment for pre-determined period.

3 RESULT AND DISCUSSION

3.1 Basic properties of BFRP composites

Table 1 & 2 present the basic tensile properties of BFRP wet lay ups and bars. For comparison, similar GFRP and CFRP materials from renowned companies in the world.

As shown in Table 1, BFRP wet layups exhibit a slightly higher tensile strength (by 5%) and modulus (by 11%) than GFRP, but much lower than CFRP. In addition, both BFRP and GFRP have an elongation at break 2.2%, much higher than that of CFRP, ~ 1%.

Table 1 Comparison of tensile properties of BFRP, GFRP and CFRP wet layups

	Tensile strength (MPa)	Tensile modulus (GPa)	Elongation (%)
BFRP	602.9	29.7	2.2
GFRP*	575	26.1	2.2
CFRP*	986	95.8	1

Note. GFRP and CFRP are referred to Tyfo® SEH 51A and Tyfo® SCH 41 composites from Fyfe Co LLC (www.fyfeco.com).

Table 2 Comparison of tensile properties of BFRP, GFRP and CFRP bars

	Tensile strength (MPa)	Tensile modulus (GPa)	Elongation (%)	Bonding to concrete (MPa)
BFRP	899	50.3	1.8	14.8
GFRP*	825	40.8	/	11.6
CFRP*	2100	124	1.7	8.5

Note: GFRP Bar is ASLAN 100; CFRP bar is ASLAN 200. Both are from Hughes Brothers, Inc. USA.

Similar results are also found for BFRP bars (Table 2). BFRP possesses much higher modulus compared to GFRP and a closed strength. Both GFRP and BFRP bars show remarkable inferior to CFRP in tensile properties.

The bonding strength of BFRP bar to concrete block is remarkably higher than those of GFRP and CFRP. This indicates the surface configuration of the current BFRP bar is effective to enhance the bonding to concrete. The lowest bonding strength of CFRP is expected and reported elsewhere.

3.2 Freeze-thaw cycle resistance of BFRP

Freeze-thaw cycle testing in the temperature range of $-30 \sim 30^\circ\text{C}$ was performed for BFRP strip and BFRP bonded concrete blocks. After 88 cycles, there is no any degradation on the tensile properties of BFRP strips. Figure 4 gives variation of the tensile strength of the BFRP as a function of freeze-thaw periods (one day one cycle). The same results are found for tensile modulus and elongation at break, which were not given in the paper.

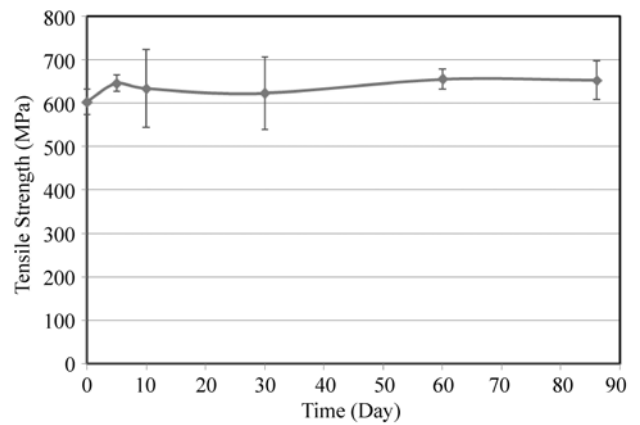


Figure 4 Variation of tensile strength of BFRP subjected to freeze thaw cycles



Figure 5 Pull-off testing of BFRP-concrete block with a pull-off testing machine on the left bottom

Besides of the BFRP composites, more concern is focused on the bonding performance of the BFRP and concrete block. In the present study, after 60 freeze thaw cycles, no any degradation in the bonding strength (measured with pulling off testing) was found. All testing indicates the fail occurred on concrete structures (see in Figure 5) rather than debonding of the FRP plate from concrete.

3.3 Immersion ageing

BFRP bar and wet layup samples are immersed in distilled water and alkaline solutions (simulating concrete alkali environment) at 23, 40, 60 and 80°C. Water uptake and mechanical properties were tracked with immersion time.

As shown, for wet layups, despite remarkable degradation of tensile strength, the tensile modulus of wet layups is only slightly affected. It is interesting to note that the degradation degree of the modulus in alkaline is not readily higher than that in water.

For BFRP bar, due to the improved impregnation quality and high fiber content, less degradation is found for tensile modulus, strength and elongation at breakage. Tensile strength of the BFRP bar, as the same as the wet

layup samples, are also vulnerable to the immersion ageing, showing a remarkable decrease even in the first month immersion. This indicates that the fiber surface modification for improved adhesion of resin to the fibers, and resin modification with improved water insulation, should be conducted for better immersion ageing performance.

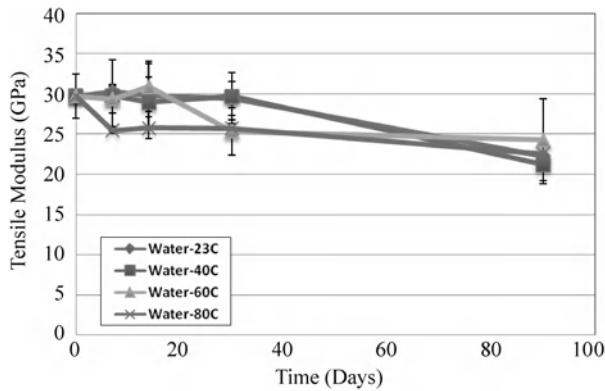


Figure 6 Variation of tensile modulus of BFRP wet lay ups subjected to distilled water immersion at various temperatures.

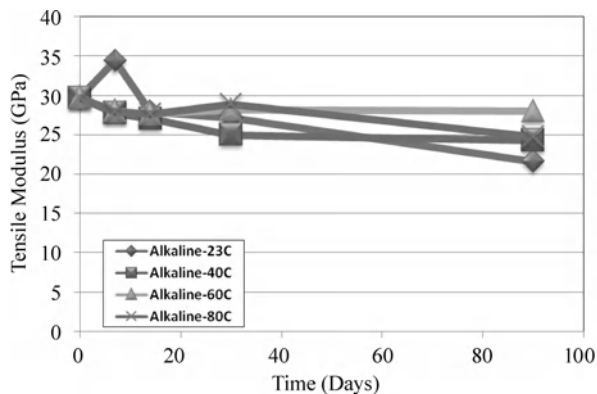


Figure 7 Variation of tensile modulus of BFRP wet lay ups subjected to alkaline solution immersion at various temperatures

3.4 Elevated temperature performance

BFRP composites were aged at elevated temperature for various temperatures and then tested on its tensile

properties. Up to 250°C for 8 hours, both modulus and strength are only slightly decreased, less than 5%, indicating the promising post-fire performance.

With increasing the testing temperatures, the tensile modulus and strength slowly decrease when the temperature less than 200°C, and then dramatically reduce with further more increase of the temperatures. At about 320°C, the tensile strength of the BFRP reduces to its half value at room temperature, while the tensile modulus reaches the half original value at about 250°C.

4 CONCLUSIONS

The basic mechanical properties, freeze-thaw resistance, immersion resistance as well as elevated temperature performance of BFRP bar and wet layups were systematically studied in the present paper. As shown, BFRP composites possess promising mechanical and durability characteristics, which are essential for the application of a new material in civil engineering field.

REFERENCES

- Cerny, M., P. Glogar, et al. 2007. Comparison of mechanical properties and structural changes of continuous basalt and glass fibres at elevated temperatures. *Ceramics-Silikaty* 51(2): 82-88.
- Deak, T. and T. Czigany 2008. Investigation of basalt fiber reinforced polyamide composites. *Materials Science, Testing And Informatics Iv* 589: 7-12.
- Sim, J., C. Park, et al. 2005. Characteristics of basalt fiber as a strengthening material for concrete structures. *Composites Part B-Engineering* 36(6-7): 504-512.
- Wang, M. C., Z. G. Zhang, et al. 2008. Chemical durability and mechanical properties of alkali-proof basalt fiber and its reinforced epoxy composites. *Journal Of Reinforced Plastics And Composites* 27(4): 393-407.
- Yongsheng, T., W. Zhishen, et al. 2009. Development of self-sensing BFRP bars with distributed optic fiber sensors. *Proceedings of the SPIE - The International Society for Optical Engineering*: 729317 (10 pp.).

Influence of Elevated Temperature on the Mechanical and Thermal Performance of BFRP Rebar

Jingyu Wu, Hui Li & Guijun Xian (gjxian@hit.edu.cn)

School of Civil Engineering, Harbin Institute of Technology, Harbin, China

ABSTRACT Compared to glass fiber reinforced polymer (GFRP) rebars, basalt fiber reinforced polymer (BFRP) rebars possess many advantages as internal reinforcement of concrete structures, in terms of the enhanced corrosion resistance. In the present study, mechanical and thermal properties of BFRP rebar at elevated temperatures and after elevated temperature treatment were conducted. The study is believe to offer the basic mechanical and thermal property data of BFRP rebars during and post- fire, which is helpful for the the safe design of BFRP in rehabilitation when considering the fire hazarder. The tensile properties of BFRP rebars were performed in the temperature ranging from room temperature to 350°C. Three stages of deterioration of the tensile strength and modulus are observed based on the degradation rate. It was found that the strength and stiffness of BFRPs still remain high values (e.g., more than half of the room temperature values) even at the temperature much higher than T_g (glass transition temperature) of the system. The deterioration is attributed to the decreased force transferring capacity of the resin. In addition, BFRP rebars were treated at elevated temperatures for various periods in an oven. The oxidation of the resin and the deterioration of the interface between fiber and resin bring in remarkable degradation of the mechanical and thermal properties.

1 INTRODUCTION

Basalt fiber reinforced polymer (BFRP) rebar has many advantages such as high strength, excellent anticorrosion performances, etc. As reported BFRP rebar possesses (Sim et al. 2005, Liu et al. 2006) a good alkali resistance, and thus it may be suitable to replace steel bar, reinforcing concrete structures. Since BFRP composites were applied in civil engineering only for several years, the study of BFRP on its basic physic-chemical properties as well as long term durability performance are very limited. This lack of comprehensive understanding of BFRP composites will hinder its wide and safe application.

In view of this, the FRP composite and structure group at the school of civil engineering, Harbin institute of technology has been conducting a series of researches to illuminate the advantage and disadvantage of BFRP composites used in external or internal strengthening system for concrete structures.

As known, due to the low temperature deflection point of polymer matrix, FRP composites, generally, exhibit a sharp decrease in the stiffness and strength at the temperatures, which exceeds the glass transition temperatures of the polymer matrix, e.g., in the range of 60 ~ 200°C. Besides, it is also very important to evaluate the safety of the FRP related elements / structures which have been undergone a fire.

In the present paper, performances of BFRP rebar at

elevated temperatures or after elevated temperature treatment have been investigated.

2 EXPERIMENT

2.1 Specimen Preparation

The studied BFRP rebar is spirally wound with glass fiber rovings and coated with sand to improve the bonding performance between the rebar and concrete. The tensile properties were tested according to ACI 440.3R-04. The tensile strength is 899MPa, and the elastic modulus is 50.8GPa, which is acquired based on 25 testing specimens. The glass transition temperature (T_g) of the BFRP rebar is 132°C, which is tested with differential scanning calorimetry (Linseis, PT10) at heating rate of 10°C/min.

The gauge length of the specimen is 320 mm, and the anchor length is 140 mm. Gripping anchor is selected as the anchorage system, which consists of binding material (mixture of epoxy resin and plugging compound) and a circular steel tube confined the binding material. This kind of anchorage system can make sure the rupture occurred in the middle of the rebar.

2.2 Elevated temperature testing

The tensile properties of BFRP rebar at various elevated temperatures (ranging from 100°C to 350°C) is tested.

The testing apparatus include following parts: WDW-10E computer controlled electronic universal tensile

machine (UTM), electrically heating kiln, thermocouple and temperature controlling device. The maximum capacity of the UTM is 100 kN and its relative error reading is less than 1%. The electrically heating kiln (Figure 1), which is purpose-built, contains 10 heating rods, which are arranged in a curved line. The kiln can heat rebars up to 500°C. The thermocouple has two probes, which can record the temperature of air in the kiln (T_1) and the temperature of rebar (T_2), which will be fed into computer directly.



Figure 1 The elevated temperature tensile testing setup

To do the elevated temperature testing, the following procedure was followed. Firstly, two thermocouple probes and extensometer was fastened on the rebar, as shown in Figure 2. Then, fix the rebar to the UTM and install the electrically heating kiln. Be sure that the extensometer doesn't contact with the kiln. Thirdly, raise the temperature to the target values. When the rebar reaches the target temperature (T_2), hold this temperature for 10 minutes ($\pm 5^\circ\text{C}$). Then, test the rebar to failure with a speed of 5mm/min. The UTM will record the stress vs. strain curve. The softening of the superficial resin at elevated temperature makes it difficult to get the stiffness of the rebar. In view of this, a high-temperature extensometer is selected to measure the stiffness of rebar. Using high-temperature extensometer, the stress-strain curves at the temperatures ranging from 100°C to 250°C can be obtained. However, at the temperature of 300°C and 350°C, a serious slippage between extensometer and the rebar happens. The modulus was not obtained in the latter cases.



Figure 2 Thermocouple probes and high-temperature extensometer fixed to the rebar

2.3 Elevated temperature treated specimens

The BFRP rebar are kept in an oven at temperatures of 150, 200 and 250°C for 1, 2, 4, 8 hours, respectively. In each condition, 5 specimens were tested. In this test, the UTM and extensometer are the same as used in the above section.

3 RESULT AND DISCUSSION

When BFRP rebars is heated to the temperature above 200°C (Figure 3), a smoke is rising from the kiln. At 250°C and 350°C, the rebar started to burn with flame. The resin at the location of fracture of the rebar above temperature of 300°C is found to be decomposed completely.

The fibers of FRP start to break at much lower stress at high temperatures compared with room temperature. This is obtained from the sound of fiber rupture at elevated temperature which comes out at lower stress levels (before the failure of rebar) than at room temperature. This may be due to the fact that the resin can't transfer tension effectively at such high temperatures.

Figure 4 shows the variation of the tensile strength as a function of temperatures. The initial tensile strength is 899 MPa, which is acquired based on testing date of 25 specimens at room temperature. From the curve, it is founded that below the temperature of 250°C, the strength doesn't suffer from remarkable deterioration. However, when the temperature exceeds 250°C, there is a sharp drop of the strength. The residual strength is less



Figure 3 Smoke comes out from kiln at 200°C

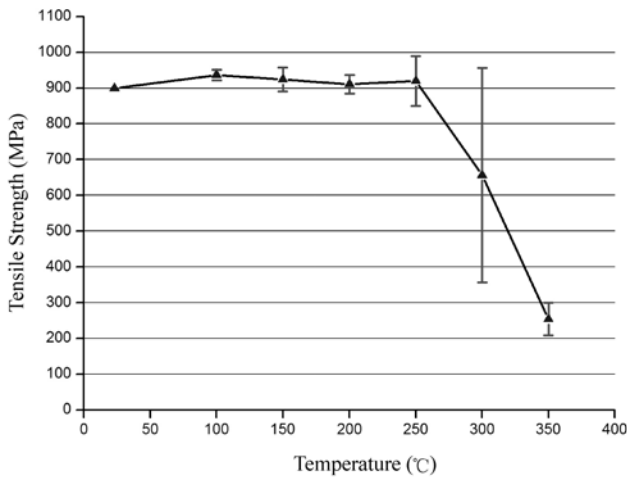


Figure 4 Variation of the tensile strength vs. temperature

than 1/3 at 350°C. In addition, it should be noted that the standard deviation of the testing data rises with the temperature.

Figure 5 Shows the variation of the stiffness as a function of the temperature ranging from 100°C to 250°C. It is found that there are two temperature ranges that the elastic modulus suffers a great loss. At the temperature of 250°C, the residual stiffness of rebar is less than 1/2 of the stiffness at room temperature. Compared with the relationship between strength and temperature, it is noted that the stiffness is much sensitive to the temperature change.

The stress-strain curves at 150°C and 200°C show a linear dependence. While at 250°C, the degree of linear dependence reduced. Figure 6 shows the stress-strain relationships at the temperature of 250°C.

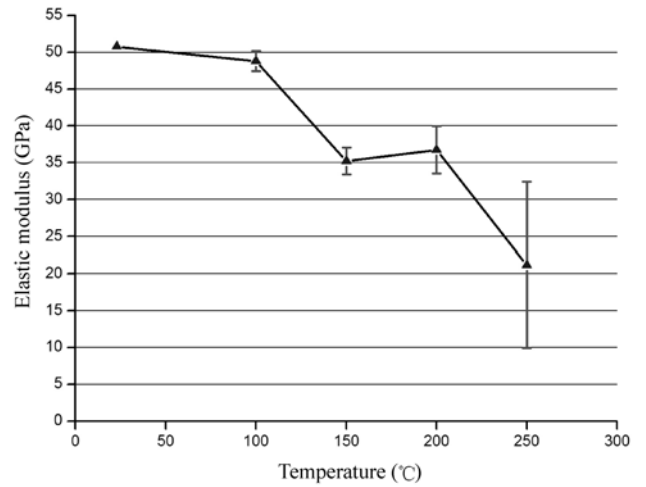


Figure 5 Variation of the elastic modulus as a function of temperature

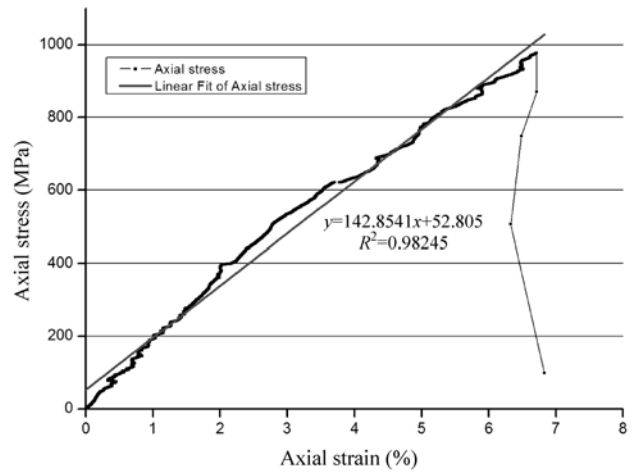


Figure 6 Stress-strain curve of BFRP rebar at 250°C

Figure 7 shows the variation of strength as a function of heating durations. It is found that the strength increases with the duration of 8 hour. This may come from the post-curing effect of the resin at high temperatures, which increases the force transferring capacity of the

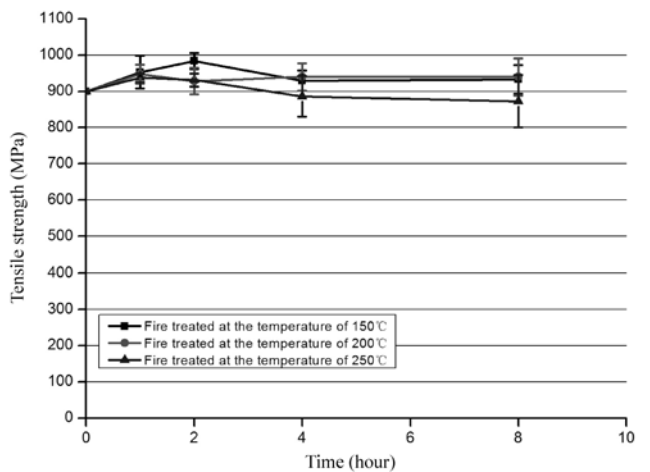


Figure 7 Tensile strength of BFRP rebar after exposed to high temperature for various durations

resin to fibers. While at the temperature of 250°C, the strength decreased due to the oxidation of the resin and possible degradation of the interfaces between fiber and matrix. At temperature of 250°C, a terrible smoke is rising from the oven, which indicates the serious decomposition process of the resin.

4 CONCLUSIONS

From room temperature to 350°C, BFRP rebar exhibits a readily reduction in the tensile modules, and reaches about 40% of the residual modulus at 250°C. The tensile strength of the BFRP shows a better temperature resistance. When the temperature increases up to 250°C, the tensile strength is slightly altered, but dramatic reduce to 1/3 of

its room temperature value at 350°C due to the ignition of the resin at such high temperature.

Treated at elevated temperature for up to 8 hours, BFRP shows a slight decrease of the strength, less than 10% for the temperature ranging from 150 to 250°C.

REFERENCES

- Liu, O. & Shaw, M. T. 2006. Investigation of basalt fiber composite aging behavior for applications in transportation. *Polymer Composites* 27(5): 475-483.
- Sim, J. & Park, C. 2005. Characteristics of basalt fiber as a strengthening material for concrete structures. *Composites Part B-Engineering* 36(6-7): 504-512.

Composite Decks and Sustainable Development: a Case Study

Monsséf Drissi-Habti (monsséf.drissi@lcpc.fr), Xavier Chapeleau & Sébastien Cournée

LCPC, Route de Bouaye, 44341 Bouguenais, France

ABSTRACT Composite materials, based on glass fibers are promising candidates for civil engineering and building applications. Sustainable development issues are of prime importance worldwide. Therefore, new structures made out of new materials as well more conventional materials should be analyzed to provide more precise data about greenhouse gas release. In this work, a short-span bridge deck is used as a case study. Three different cases are considered: a reinforced concrete deck, a steel deck and a composite deck. The three cases are discussed regarding carbon dioxide release.

1 INTRODUCTION

Composite materials have been used extensively in the aerospace industry in large part due to their high strength to weight and high stiffness to weight ratios. In the electrical and marine industries, the lightweight and non-corrosive properties of composite materials have encouraged use, generally in small structures. For industries that do not place a great importance on material weight or corrosion, there is little justification for the added cost of composite materials. However, recent developments in efficient manufacturing technologies, which is the case of pultrusion, the wide use of glass fibers and the growing body of research data, are boosting the integration of large-scale composite structures into civil, construction and off-shoring applications.

In civil engineering, highway bridge systems have been among the first structures to incorporate composite materials. Numerous bridge deck designs have been proposed, developed and tested, mainly in the US, Japan, Switzerland, France, Germany, UK, Danmark and Spain. Some recent composite bridge designs have not only used composite deck systems but also employ composite spanning members. Composite materials can therefore be competitive alternatives for structural applications in civil engineering. Owing to the extensive importance of recent trends worldwide related to sustainable development issues, this article is an attempt to evaluate the environmental impact of using composite structures. This work is based on a real project that was completed in France (Saint Cadarec bridge, Côtes d'Armor, FRANCE) in which we considered the hypothesis of using a composite deck. The profile that was used for the calculation is the one patented by Martin Marietta Composites (Raleigh, NC, USA). It is the same one now in-service in numerous bridges throughout the USA.

2 DEFINITIONS

2.1 Functional Unit

The functional unit of the present work is “the use of pultruded composite materials as structural decks of Saint Cadarec Bridge”.

2.2 Description of the deck of St Cadarec Bridge

The bridge is made of 2 sections. Three parts: 28m, 34m and 28m. Each section is carrying 2 lanes of traffic and a third lane devoted to emergency stopping. The deck consists of steel and concrete. A concrete-made slab supported by double-beam steel columns is used for carrying the lanes.

Description of the composite deck.

Table 1 Characteristics of Duraspan 766

Thickness	Dimension	Weight	Allowed span-distance
195 mm	2,44 - 3,05 m	93 kg/m ²	3,05 m

The composite materials deck used in this bridge is the profile DURASPAN 766, produced by Martin Marietta Composites and Creative Pultrusions Inc., and is basically the same one that is already used for many bridges in USA. A view of this profile is shown in Figure 1, whereas the characteristics are listed in Table 1. The profile is obtained by pultrusion, starting with continuous glass fibers and a thermosetting matrix (epoxy).

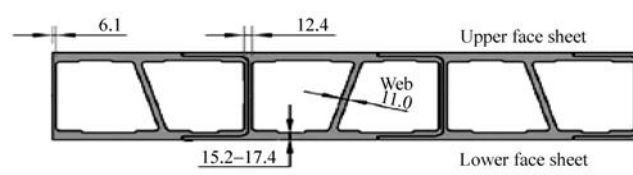


Figure 1 Schematic of the DuraSpan deck panel

Figure 2 shows the steps that are taken into account when conducting the preliminary environmental analysis of the composite deck of the St Cadarec bridge. The system takes into account the fabrication process of glass fibers, the epoxy matrix, the pultruded deck profile and the transport of the deck to the final location. The recycling of the deck is not treated in the present study.

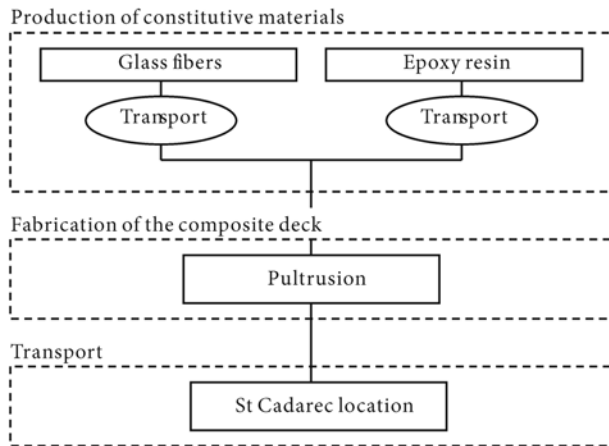


Figure 2 System boundaries

2.3 Flux and environmental impacts

In the present work, the following gas were taken into consideration in the environmental study: CO₂, CH₄, N₂O, NO_x, ...). The environmental impact of composite constituents (glass fibers and epoxy resin), the pultrusion process and transport are evaluated using the indicator of greenhouse gas release over 100 years.

2.4 Environmental effects

2.4.1 Composite constituents

Glass fiber reinforcement production is part of the glass industry, known for its high energy-consumption and carbon dioxide-emission release. According to Ademe (French Environment and Energy Management Agency), the indicator of greenhouse gas emission of glass fibers is 580 kg carbon equivalent (C eq.) per ton of product.

The process route of the epoxy resin is relatively complex and the basic constituents are mainly coming from the oil industry, thus known as generating a high quantity of greenhouse gas. The indicator of greenhouse gas pertaining to the production of epoxy resin is approximately 2.33 kg of carbon equivalent per kilogram of liquid epoxy resin produced. This value has been reported by the European Association of Plastic Producers (APME, Plastics Europe).

Considering 55% as fibers volume fraction in the composite, Table 2 shows the results of the calculation of the indicator of the greenhouse impact of the composite material used in the case of the deck of the St Cadarec

bridge. Calculations are based on a weight of 93 kg per m² of composite deck.

Table 2 Indicator of greenhouse impact of the composite constituents

Constituent	Used quantity (kg)	Carbon equivalent (kg pour 1kg of product)	Total carbon equivalent (kg Ceq.)
Glass fiber ¹	137538	0,58	79772,04
Epoxy resin ²	51958,8	2,3248	120793,82
		Total	200565,86

1 $\rho_f=2.6\text{g/cm}^3$

2 $\rho_r=1.2\text{g/cm}^3$

2.4.2 Pultrusion

Pultrusion is a composite process route known as being highly energy-consuming. Heat is necessary for both curing and cleaning the molds. These two operations are mainly responsible for greenhouse gas emission. In the present study, the shape of the DURASPAN 766 profile requires the fabrication of 60 panels, 3m-large and 11.32m-long, that approximately corresponds to a 680m profile. The relative estimated production time is 57 hours. Table 3 shows the emission of greenhouse gas resulting from the pultrusion process.

Table 3 Greenhouse gas impact indicator of the pultrusion process

	Used quantity	Carbon Equivalent	Total carbon equivalent
Electricity consumption	1140 kW	0,023	26
Acetone	3790 kg	2,33	2274
		Total	2300

Calculations have been carried out considering a pultrusion speed of 20cm/min and a mean consumption of electrical power of 20kW/h (source: DFC Company, Creil, FRANCE). In France, 1 kWh corresponds to an emission of 0,023 kg C eq. (Source : ADEME). In the case of acetone, an average value of 2% of the total composite weight is considered necessary for the composite production and this value is therefore introduced in the calculation. Following the Association of European Plastics, the production of 1 kg of acetone is responsible of 0.6kg of greenhouse gas emission, C eq.

2.4.3 Shipping contribution

Table 4 shows the greenhouse gas release following road-shipping of the products needed to fabricate the deck profile, according to the system considered. Calculations are conducted taking into account the maximum truck load-carrying capacity, regulated by the corresponding French Authority. Calculations are based on ADEME's

inputs (Emissions Factors Guide, 2007) that take into account the part pertaining to the distance over which trucks are driving empty. This distance corresponds to 20% of the total shipping distance. Results also include the part of greenhouse gas release related to the fabrication of trucks (per km of shipping).

Table 4 Impact indicators of greenhouse gas release related to shipping of composite constituents and profiles

Products shipped	Quantity (kg)	Total emissions (kg C eq.)
Glass fibers	137,5	1477
Epoxy resin	52,0	1586
Composite profile	189,5	859
Total		3922

3 RESULTS

Adding the results of the above-mentioned emissions, the overall environmental impact, related to the composite deck of St Cadarec bridge is 758 tons of CO₂. This corresponds to 372 kg of CO₂ per m² of composite profile.

Table 5 Total greenhouse gas release

Emission per product	Emission (kg C eq.)	Emission (kg CO ₂ eq.)	Part (%)
Glass fibers	79772	292205	39
Resin	120794	442468	58
Pultrusion	2301	8426	1
Shipping	3922	14365	2
Total	206789	757464	100

Given the results of Table 5, it follows that the production of the composite constituents represents 97% of greenhouse gas release. This result is not surprising knowing that the production of glass fibers, as well as epoxy resin, are highly energy-consuming, whereas pultrusion is merely a transforming industry that needs much lower energy.

To be able to conduct a preliminary comparative study of the environmental impact following the use of composite materials instead conventional ones, the analysis depicted above should be also conducted when using steel and concrete as deck constitutive materials. In such a comparison, only the fabrication of the deck is considered. Table 6 shows the values of the impact indicator of greenhouse gas release for a deck made out of steel and concrete.

If a steel deck is considered, then greenhouse gas release depends on the process route that led to its production (either refining mined products or recycling

Table 6 Impact indicator of greenhouse gas emission of steel and concrete

Material	Quantity (kg)	C eq. (kg C eq. per ton)	Total (kg C eq.)
Steel ¹	351894	397	139702
Concrete ²	2495500	235	586443

1 $\rho_A = 7850 \text{ kg/m}^3$

2 $\rho_B = 2300 \text{ kg/m}^3$

used steel). However, it should be noted that final recycling is not taken into account in the present study, neither in the case of steel, nor in the case of composite decks. Furthermore, the steel used in the case of the deck is considered partly coming from recycling. Indeed, greenhouse gas release must take into account the percent of recycling in the production of steel, which is 43% worldwide. The impact indicator of greenhouse gas emission is therefore 573 kg C eq. per ton of refined steel and 164 kg C eq. per ton of recycled steel. For steel containing 43% of recycled material, the corresponding greenhouse gas emission is 397 kg C eq. per ton (Source: the International Iron and Steel Institute).

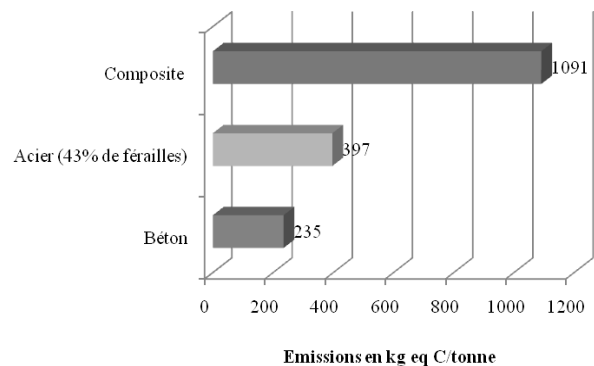


Figure 3 Greenhouse gas release per ton of products

In the case of a concrete deck, the indicator of the impact of greenhouse gas emission considered is 235 kg C eq. per ton of concrete, according to ADEME. This value is including greenhouse gas emissions related to energy consumption following the process route, the non-energetic consumption and the one linked to the degradation of calcium carbonate ($\text{CaCO}_3 \rightarrow \text{CaO} + \text{CO}_2$).

Figure 3 shows that 1 ton of composite is releasing more greenhouse gas than a ton of steel or concrete. However, it is worthwhile to note that the quantities of materials needed to build the deck of St Cadarec bridge are much less important for composites than in the case of concrete or steel (Tab. 7).

Taking into account the quantities of materials that are needed to achieve the deck of St Cadarec bridge, Figure 4 shows that greenhouse gas release following the use of composite are slightly higher than in the case

Table 7 Comparison of the deck weight depending on the constitutive materials

Matériau	Steel	Concrete	Composite
Deck weight (in Tons)	351,9	2495,5	189,5

of steel, but much less than in the case of concrete. However, it should be noted that neither the shipping of steel was taken into account in the calculations, nor the maintenance operations such as painting for corrosion-protection. In the special case of painting, high levels of greenhouse gas release can be recorded due to solvent production. Finally, the present study shows that if up-front cost only has to be considered, construction using composites or steel results in the same greenhouse gas release. If, for example, the maintenance over 10 years exploitation is also considered, then the use of composites as a deck constitutive materials provides obviously more benefit.

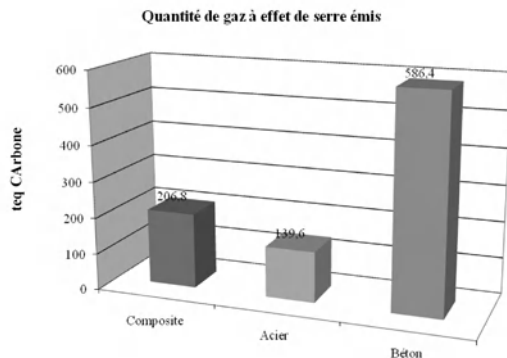


Figure 4 Comparison of greenhouse gas release depending on the constitutive materials, in the case of a bridge deck

4 CONCLUSION

In this article, a preliminary study related to the environmental effect of using composite materials as bridge decks was presented. The calculations show that greenhouse gas release, following composite constituents are prevailing in comparison to shipping and pultrusion. This can be explained when keeping in mind that glass production (in the case of glass fibers) and the chemical industry (in the case of epoxy resin), are among the main energy-consuming and greenhouse gas releasing industries.

A comparative study has been conducted for the deck

of the St Cadarec bridge. It shows that the environmental impact related to a composite-made deck is on the same level as when using steel. In the case of a concrete deck, not only is this solution the highest one in terms of weight, but greenhouse gas release is nearly 2 times higher than in the previous one, using composite or steel. It should be noted however that when Fiber-reinforced polymer composite materials are used, they provide excellent strength-to-weight ratio and can be fabricated for on-command properties. Composite materials can strengthen bridges without any reduction of vertical clearance, and they can be applied in severe exposure environments that may have resulted in the deterioration of the original structure. Also, composite-made decks can be used to enhance the life of girder-system bridges, due to their low dead load that permits an increase in live-load carrying capacity. Composite materials are highly corrosion-resistant and this is of a prime importance in comparison to either steel and/or steel-reinforced structures. These aspects should become prevalent in the near future when not only up-front cost is considered, but also with maintenance over a ten-year period. For the reasons summarized above, the use of composites in civil engineering should be promoted and a deeper analysis of the life cycle should be implemented.

ACKNOWLEDGMENTS

This work has been conducted in the framework of decid 2 project (French Ministry of Industry funded project). It is a part of the 2 Long-Term Research Operations of LCPC : COMPOSI-GeC and EPEES.

REFERENCES

- DuraSpan Bridge Decks by Martin Marietta Composites (w3.martinmarietta.com/Products/duraspan.asp).
- Guide des facteurs d'émissions 2007, Bilan Carbone Entreprises et Collectivités, ADEME (Agence De l'Environnement et de la Maîtrise de l'Energie, France).
- Mémento des Décideurs 2003, Mission Interministérielle de l'effet de serre, France. www.ecologie.gouv.fr/IMG/pdf/memento.pdf.
- Resin Epoxy, Eco profiles: life-cycle analysis, APME (Association of Plastics Manufacturers in Europe). www.plasticseurope.org.
- International Iron and Steel Institute, World Steel Life Cycle Inventory. www.worldsteel.org.

Matrix and Fabric Impregnation Influence on Textile Reinforcement Concrete Behaviour

Raphaël Contamine, Amir Si Larbi (amir.si-larbi@univ-lyon1.fr) & Patrice Hamelin

LGCI Site Bohr, Université Claude Bernard Lyon I, INSA de Lyon, Franc

ABSTRACT This study aims to analyze the textile reinforced concrete tensile (TRC) behaviour. Firstly A tensile test suitable for this type of cracking material is designed and validated. The second phase aims to highlights the influence of several parameters considered as critical (the material, the thickness of the composite, the impregnation of the fibres, the fibre volume ratio) in the textile reinforced concrete (TRC) behaviour in terms of mechanical performance (strength and stiffness) or the amount of damage correlated with the crack opening measured using image correlation analysis.

1 INTRODUCTION

Repairing structural elements with textile-cement composites is a relatively recent procedure, research on this material having begun in the mid-90s (Ohno & Hannant 1994, Peled et al. 1994). Work done to characterise the composite concentrated on its behaviour under tension and various procedures for characterising tensile strength were established. Characterisation in pure tension (Jesse 2004, Hegger et al. 2005, Mobasher et al. 2005) was preferred to flexion (Peled & Bentur 2000), for the latter, owing to the unknown position of the textile in the thickness of the composite as well as the unknown behaviour of the textile-cement composite in compression, was not thought to be appropriate for this type of material.

In the studies already carried out on the behaviour of textile-cement composites in pure traction, the stress-strain curve was usually divided into three zones. The first zone (Zone 1) is linear as seen in (RILEM TC 201-TRC members), and in the ACK model (Aveston et al. 1971), or quasi-linear (Mobasher et al. 2005). At the transition between zones 1 and 2 there is a sudden change in rigidity, linked (Hegger et al. 2005) to the initiation of the first crack in the cement. Zone 1 is then followed by a zone of non-linearity in which the rigidity is much lower and can present considerable oscillation (Zone 2); the rigidity of the third, linear, zone is greater than in the second zone but lower than in the first (Zone 3).

In any case, the quantitative aspect of the tension-strain curve is subject to wide variations depending on such factors as the strength of the fibres and the cement, the proportion of fibres, the type of fibre and of cement (adhesion at the fibre-cement interface, impregnation of the fibres etc.), the configuration and orientation of the

textile... Many studies have been undertaken on the influence of the various parameters of textile-cement; however, most of them were of an exploratory nature and presented a very limited number of tests which led to somewhat tendency conclusions.

The present experimental study is a part of an important experimental campaign that we will undertake to provide experimental information on textile-cement composites and to allow the construction of reliable analytical models. The study involves 14 configurations of composites and its main objectives are to analyse i) the influence of ratio reinforcement on composites of different textile configuration, ii) the influence of matrix nature on the tensile behaviour, and iii) the influence of the roving configuration and roving impregnation used in textile reinforcements of identical mesh on the mechanical behaviour of the composite under tension. To this end, a methodology for comparing the key parameters of stress-strain curves was established.

2 COMPOSITES CONFIGURATION

2.1 Fabric and matrix

Two dissimilar matrix are test in this study i) a thixotropic fine grained concrete (maximum size of 1.25 mm) matrix (TC) alloying contact-moulded "in situ" procedure and ii) a fluid consistency inorganic phosphate cement (IPC) (Promis et al. 2010) adapt to plate prefabrication process. The supplier's characteristic of TC matrix are 8 MPa for flexion strength and 17.6 GPa for E-modulus.

The textile was a warp-knitted fabric with a mesh size of 3×5 mm (5 mm between weft roving). The only variable in the textiles was the configuration of the roving (Table 1) in the direction of tension of the composite (i.e.

in the weft). The warp yarn was a 2200 Tex high-strength polyester (PET).

Table 1 Technical characteristics of reinforcements

Fabric nature	Fibre per roving	Roving titer (Tex)	Diameter of fibre (μm)	Supplier strength of roving " σ_f " (Mpa)	Supplier E-modulus of roving " E_f " (Gpa)
Basalt	4598	1680	13	1835	84
AR-glass	1600	1200	19	1102	74

2.2 Textile reinforced concrete composite

Table 2 shows the composite configurations retained. According to (Häußler-Combe & Hartig 2007, Krüger et al. 2002, Krüger 2004) deeper is the fibre position in the roving, worst is the impregnation. So, in a roving, only very few filaments have a perfect bond quality (Hegger et al. 2005). Fabric impregnation could improve transfer of bond stress among fibre. To test this, composites' fabrics are impregnated with epoxy (E3ep) and with synolit (E3sy).

Table 2 Composite configuration

Name	Thickness of composite (mm)	Fabric nature	Matrix nature	Number of Fabric per composite	Roving volume ratio (%)
B1*	5	Basalt	TC	1	19.5
B2*	5	Basalt	TC	2	39.1
B1	10	Basalt	TC	1	9.8
B2	10	Basalt	TC	2	19.5
B3	10	Basalt	TC	3	29.3
B4*	5	Basalt	IPC	4	
E1*	5	E-glass	TC	1	14.5
E2*	5	E-glass	TC	2	29.1
E1	10	E-glass	TC	1	7.3
E2	10	E-glass	TC	2	14.5
E3	10	E-glass	TC	3	21.8
E4*	5	E-glass	IPC	4	
E3ep	10	E-glass	TC	3	21.8
E3sy	10	E-glass	TC	3	21.8

2.3 Tensile test description

The test specimens used for the characterisation of the textile-cement composites under pure tension consisted of a plate of contact-moulded composite material (5mm or 10mm \times 100mm \times 500mm) and aluminium lugs (4 \times 100 \times 100mm) bonded (sand-blasting + epoxy glue) to the four extremities of the plate. Tension was applied to the extremity of a metal cylinder placed across the lugs of the previously drilled specimen (Figure 1). Specials more were developed to applied pure axial tension

(Figure 2). As in a previous experiment (Jesse 2004), two extensometers (measuring zone - 200 mm) were bonded with flexible glue on the middle of each side of the specimen (Figure 1). Other authors prefer to measure the space between the aluminium lugs (Singla 2004, Hegger et al. 2005, Hegger & Voss 2008), probably in order to record the post-peak behaviour; however, this measurement integrates, in the average strain, any possible perturbations caused by the aluminium lugs. (Hegger et al. 2005) considers a measurement zone of 400 mm, but, given the maximum spacing between the cracks of 20mm that was noted (Hegger et al. 2005, Mobasher et al. 2005), a zone of 200 mm was deemed sufficient. The homogenised stress of the composite is obtained by dividing the tensile-force by the section of a composite sample. The average strain is calculated by averaging the displacements measured for the two faces of the sample, and then dividing this value by the length of the LVDT measuring zone.

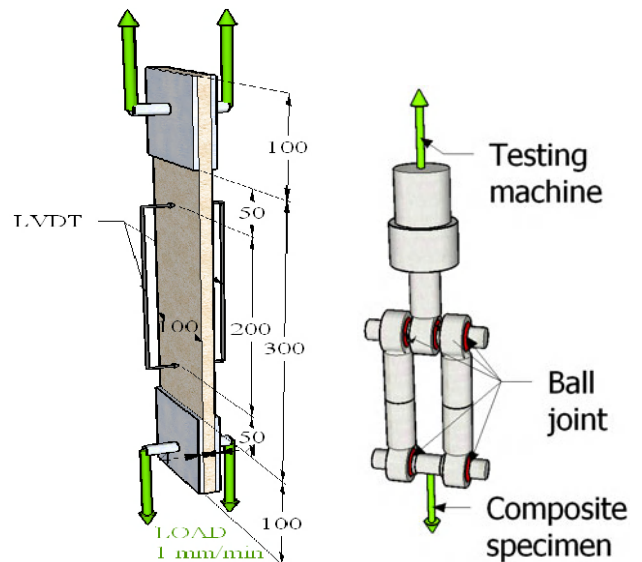


Figure 1 Tensile specimen (geometry, instrumentation and loading)

Figure 2 Tensile specimen (geometry, instrumentation and loading)

3 RESULTS

As noted in the review of the literature in introduction, the stress-strain curves obtained in our series of experiments present three zones. To facilitate the comparison of these curves, three characteristic points between each of the zones and at the point of ultimate constraint have been defined (Figure 3).

Many results were collected during this study, such as the relationships between the volume ratio of fibre reinforcement in the direction of tension and the following values: stress at characteristic point 1, the stiffness of zone 1, the range of strain in zone 2, the stiffness in zone 3, the spacing of cracks at failure and the strength

and ultimate strain of the composite. In the interests of concision, only the results involving strength and stiffness in zone 3 are presented.

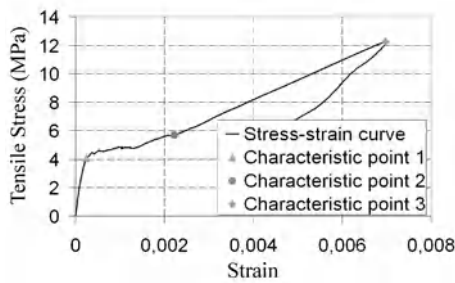


Figure 3 Qualitative comportement type of stress-strain curve and characteristic point position.

The final stiffness of composites is defined by the slope of the stress-strain curves in zone 3 (linear zone). This slope is calculated by the method of least squares between the characteristic points 2 and 3. The curves of composite final stiffness as a function of reinforcement volume (for an identical roving configuration) are linear and their prolongation passes through the origin (Figure 4). Similarly, the composite strength seems to be directly proportional to the composites' reinforcement ratio (Figure 5).

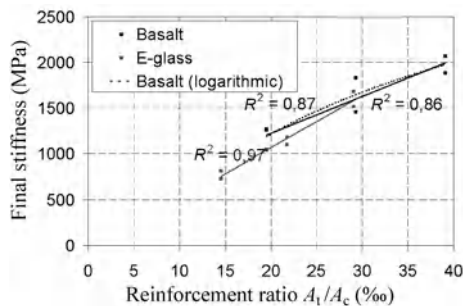


Figure 4 Composite final stiffness-reinforcement ratio linear tendency curves

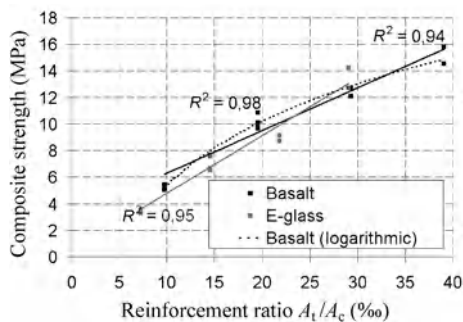


Figure 5 Composite strength-reinforcement ratio linear tendency curves

These results should be qualified, since, with no reinforcement, the strength and stiffness would be that of the matrix. There is, therefore, as a function of the textile and matrix configurations, a threshold level of

reinforcement below which the preceding relationships are not valid. Also, for a more important reinforcement ratio (1 - 3%) Hegger at al. (Hegger at al. 2005) show that for similar type of fabric and fine grained concrete the composite, tensile strength of textile decrease with increasing reinforcement ratio. So, there is probably an other threshold level of reinforcement above which the preceding relationships are not valid. This could mean that above a threshold (that depend of matrix and roving configuration) layers influence each other and cause reduction in bond performance. This is probably the reason for light nonlinearity observed for Basalt roving.

This relationships agree with the ACK model (Aveston et al. 1971) which considers that strength " σ_c " and final stiffness of composite " E_c " are proportional to fibre ratio " f ". Comparison of the experimental results with the ACK model ($E_c = E_f \cdot f$ et $\sigma_c = \sigma_f \cdot f$) shows that the model overestimates the mechanical characteristics of the composite. As the ACK model considers that all the fibres work in a homogenous way until failure, it is interesting to calculate the fibres' rate of work " T_{fE} " and " $T_{f\sigma}$ " using this model (with $E_c = E_f \cdot f \cdot T_{fE}$ and $\sigma_c = \sigma_f \cdot f \cdot T_{f\sigma}$). It then appears that the work level calculated using the rigidity relationship is significantly greater than that calculated using the relationship of composite strength (Table 3)

Table 3 Taux de travail en rigidité et résistance

Configuration	E_f/f (GPa)	σ_f/f (MPa)	T_{fE} (%)	$T_{f\sigma}$ (%)
B	54	472	65	26
B4'	62	697	74	38
E (reference)	54	466	74	34
E4'	63	650	87	47
E3ep	52	640	72	46
E3sy	53	379	73	27

This divergence between the ACK model and the experimental results in strength is probably linked to failure obtained by the textile slipping through lack of anchorage or by a state of non-homogenous stress in the roving. Indeed, ACK model consider a perfect bond of the roving, but according to (Häußler-Combe & Hartig 2007, Krüger et al. 2002, Krüger 2004) deeper is the fibre in the roving, worst is the impregnation. This state of non-homogenous impregnation leads then to great stress concentration (near to the aluminium lugs and out of measurement zone) (Figure 6) leading to premature failure of outer roving's fibres, slipping of central roving's fibres and then failure of composite.

On the other hand, thanks to central fibres bond, further from the aluminium lugs roving is, more homogenous the stress is (Figure 6). Textile slipping through lack of anchorage or homogenisation of stress across the roving explain the divergence between the work level calculated

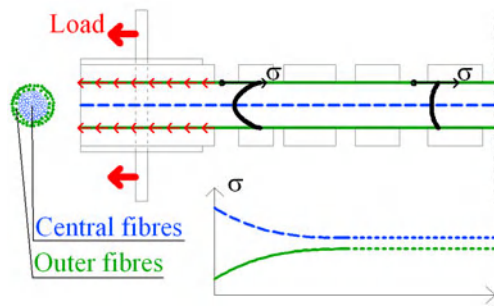


Figure 6 Roving's fibres stress distribution in a composite specimen

using the rigidity and the strength relationship. So it seems pertinent to retain, even as merely an approximate indicator of the ratio of fibres mobilised in the TRC, the ratio resulting from the calculation of the levels of work in rigidity.

Synolit impregnation of fabrics decrease " $T_{f\sigma}$ ". A slip of roving were experimentally noticed. So, bond between mortar and synolit is probably smaller than between mortar and rovings. On the contrary epoxy impregnation improve " $T_{f\sigma}$ ". This is most likely due to a better stress distribution inside roving thanks to epoxy. On the other hand, epoxy impregnation don't improve " T_{fE} ". So like it is showed Figure in the LVDT measurement zone stress is probably uniform inside the roving, even without impregnation. Impregnation seems useless to improve stiffness in the LVDT measurement zone. When IPC matrix is used, improvement of " T_{fE} " is likely due a better stress repartition among fabric. Increase of " $T_{f\sigma}$ " is probably due to a deeper matrix penetration inside the roving. At last, " T_{fE} " and " $T_{f\sigma}$ " are better for E-glass than for Basalte. This is due to a better bond of E-glass with TC and IPC matrix and to a better matrix penetration in E-glass roving thanks to a smaller fibres number per roving and a wider fibres diameter.

4 CONCLUSION

The procedure retained for the characterisation of TRC in traction proved effective. Low dispersion (less than 7%) was observed between the stress-strain curves.

It has been shown in this study that the strength of TRC depends on the surface available to the textile, that is, the surface in contact with cement. A linear correlation has been established between the final stiffness (and strength) of the TRC and the ratio volume of useful fibres (those in the direction of the load). The work level of the fibres as calculated with the ACK model varies according to the parameter calculated (the composite's final stiffness or its strength). It seems more pertinent, in view of the occurrence of failure through lack of anchorage, to calculate the quantity of filaments actually under load by

using the level of work on the basis of the final rigidity of the TRC.

REFERENCES

- Aveston, J., Cooper, G. & Kelly, A. 1971. Single and multiple fracture: the properties of fiber composites, *Proc. Nat. Phys. Lab.*, pp. 15-26. IPC Science and Technology Press Ltd., Surrey.
- Häußler-Combe, U. & Hartig, J. 2007. Bond and failure mechanisms of textile reinforced concrete (TRC) under uniaxial tensile loading, *Cement and Concrete Composites*, Volume 29, Issue 4, pp. 279-289.
- Hegger, J., Will, N., Bruckermann, O. & Voss, S. 2005. Load Bearing Behaviour and Simulation of Textile Reinforced Concrete, *Materials and Structures*.
- Hegger, J. & Voss S. 2008. Investigations on the bearing behaviour and application potential of textile reinforced concrete, *Engineering Structures*, Volume 30, Issue 7, Pages 2050-2056
- Jesse, F. 2005. Tragverhalten von Filamentgarnen in zementgebundener Matrix. PhD Thesis, Dresden : Faculty of Civil Engineering, Technische Universität Dresden, urn:nbn:de:swb:14-1122970324369-39398.
- Krüger, M., Xu, S., Reinhardt, H. W. & Ožbolt, J. 2002. Experimental and numerical studies on bond properties between high performance fine grain concrete and carbon textile using pull out tests. In: Beiträge aus der Befestigungstechnik und dem Stahlbetonbau (Festschrift zum 60. Geburtstag von Prof. Dr.-Ing. R. Eligehausen), Stuttgart, pp. 151-164.
- Krüger, M. 2004. Vorgespannter Textilbewehrter Beton. (*Prestressed textile reinforced concrete.*) Stuttgart, Universität Stuttgart, Fakultät Bau- und Umweltingenieurwissenschaften, Diss.
- Mobasher, B., Peled, A. & Pahaljani, J. 2005. Distributed Cracking and Stiffness Degradation in Fabric-Cement Composites, *Journal of Materials and Structures*.
- Ohno, S. & Hannant, D. J. 1994 Modelling the Stress-Strain Response of Continuous Fiber Reinforced Cement Composites, *ACI Materials Journal*, 1994, Vol. 91, No.3, pp. 306-312.
- Peled, A., Bentur, A. & Yankelevsky, D. 1994. Woven Fabric Reinforcement of Cement Matrix, *Advanced Cement Based Materials Journal*, Vol.1, pp. 216-223.
- Peled, A. & Bentur, A. 2000. Geometrical characteristics and efficiency of textile fabrics for reinforcing cement composites; *Cement and Concrete Research*, Volume 30, Issue 5, pp. 781-790.
- Promis, G., Gabor, A., Maddaluno G. & Hamelin, P. 2010. Behaviour of beams made in textile reinforced mineral matrix composites, an experimental study, *Composite Structures*, In Press, Accepted Manuscript, Available online 13 February 2010.
- RILEM TC 201-TRC members. 2006. *Textile Reinforced Concrete-State-of-the-Art Report of RILEM TC 201-TRC* ; Edited by W. Bramshuber; ISBN: 2-912143-99-3; e-ISBN: 2351580001, p. 135.
- Singla, N. 2004. Experimental and theoretical study of fabric cement composites for retrofitting masonry structures, M.S. Thesis, Arizona State University, 2004.

Discrete Fiber Reinforced Polyurea for Hazard Mitigation

N.L. Carey & J.J. Myers (jmyers@mst.edu)

Civil, Architectural and Environmental Engineering Department, Missouri University of Science and Technology, Rolla, Missouri, USA

ABSTRACT This research investigated the development and characterization of different discrete fiber-reinforced polyurea systems for infrastructure applications. The behavior of various systems consisting of several polyureas with different fiber configurations was evaluated. Polyurea coating systems were previously evaluated for blast mitigation and impact resistance, and showed to be adequate in containing debris scatter from blast and impact (Carey and Myers, 2009a, 2009b). The purpose of further testing was an effort to develop a polyurea system for multi-hazard and/or repair-retrofit applications. The addition of fiber to a polymer coating provides improved stiffness and strength to the composite system while the polyurea base material provides ductility. Coupon tensile testing was conducted to determine the material mechanical properties in this study. The two parameters that were varied throughout testing were fiber volume fraction and fiber length. E-Glass fiber was used during specimen fabrication. Several optimal composite configurations of polyurea and fiber resulted from this coupon testing.

1 INTRODUCTION

Research initiatives have been advanced to investigate new materials that can be used for blast mitigation, seismic, and general repair-retrofit applications. This research investigates the mechanical properties and performance of different discrete fiber-reinforced polyurea systems under development at Missouri University of Science and Technology (Missouri S&T) in Rolla, Missouri. Elastomeric polyurea coating possesses several advantageous characteristics, including elasticity, ductility, and energy absorption. Additionally, polyurea is capable of containing spalling and reducing fragmentation during a blast event (Carey & Myers 2009). The tensile properties of the plain polyurea and composite polymer matrix were determined by conducting coupon testing. In addition, sample ignition loss testing was conducted to determine the fiber reinforcement content. Polyurea material is a two-component 100% solid reactive cure. Polyurea is a low-viscosity liquid, so it bonds very quickly and evenly during application. Several key characteristics of the polyurea coating include chemical and water resistance, excellent elongation, and quick curing. The polyurea coating is capable of withstanding regular thermal or dynamic movement as well. Despite requiring special equipment and experienced operators for mixing, application is easy and the material cures rapidly. Prior to application, the surface should be thoroughly prepared in order to achieve an adequate and strong bond. Also, the material is not very sensitive to temperature and

humidity, which eliminates the need for additional arrangements for application procedures and curing environments. Polyurea also aids in the confinement of post-blast materials in compression loaded structures, which produces a residual load-bearing capability.

2 EXPERIMENTAL STUDY

2.1 Material description

During this experimental program, two polyureas were investigated and tested under tension. Coupon specimens were fabricated using each elastomeric polyurea and E-Glass fiber by varying fiber content and fiber length. Tables 1 and 2 list the mechanical properties for the tested materials as specified on product data sheets.

Table 1 Mechanical Properties of Elastomeric Polyureas

Material	Tensile strength (MPa)	Elongation (%)
Polyurea A	17	480
Polyurea B	14.8	91

Table 2 Mechanical Properties of E-Glass Fiber

Mechanical properties	Dry	Wet
Tensile strength (MPa)	64.8 - 77.2	60 - 71.7
Flexural strength (MPa)	153.8 - 186.2	124.8 - 131

2.2 Test matrix description

Various coupon samples were fabricated by varying matrix material, fiber content, and fiber length. Fiber volume

was adjusted during coupon fabrication by increasing the speed of fiber chopping and integration into the polyurea matrix. Fiber chopping speed was adjusted on the equipment and carefully monitored. Three fiber lengths were investigated for each fiber volume. Fiber length was easily adjusted and maintained consistent throughout testing. Great care was taken to maintain the fiber content consistency for each fiber length. Table 3 provides test matrix description.

Table 3 Test Matrix

Material	Fiber length (mm)	Fiber chopping speed (# of dial turns)
Polyurea A	6	3, 3.5, 3.75, 4, 5
Polyurea A	13	3, 3.5, 3.75, 4
Polyurea A	38	3, 3.5, 3.75
Polyurea B	6	3, 3.5

2.3 Coupon sample fabrication

Coupon specimen fabrication was conducted according to ACI 440.3R-04. In order to obtain coupon samples, the material was sprayed on a steel oiled plate and then peeled off, as shown in Figure 1. Coupon samples were cut out of the peeled sections. Because sample surfaces were slightly uneven, several width and thickness measurements were taken with calipers to obtain average coupon dimensions. Several coupon samples were made from the plain polyurea material and the fiber-reinforced polyurea composite material for benchmarking. Chopped E-Glass fibers were discretely integrated in with the polyurea to develop a fiber-reinforced system. General purpose gun roving fibers were chopped and mixed instantaneously during the application process.



Figure 1 Polyurea application process

The specimen dimensions and modified testing procedure were adopted from the previous study by Carey and Myers (2009a). All test specimens had the same gage length of 127 mm but varied in cross-sectional

geometry. The coating thickness varied from 2.5 to 4 mm with an average specimen width of 40 mm. Figure 2 provides the layout of the polyurea coupon sample. Thin aluminum sheets 51 × 51 mm were glued with epoxy to each end of the specimen in order to ensure a tighter grip for the machine and effective load transfer to the sample. Several coupon test samples are displayed in Figure 3.

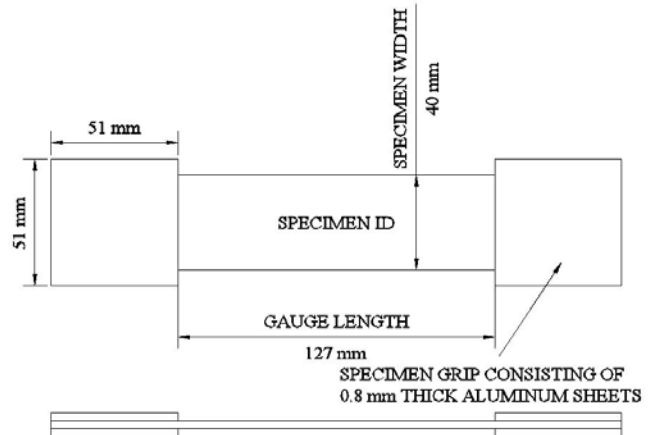


Figure 2 Coupon test specimen layout

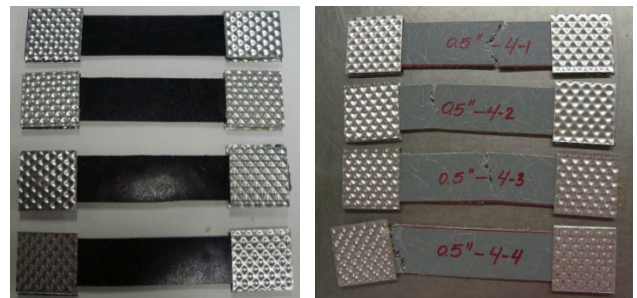


Figure 3 Plain polyurea (left) and discrete fiber-reinforced polyurea (right) coupon test samples

2.4 Coupon tensile testing

Tensile testing was conducted at Missouri S&T. Coupon specimens were tested using an Instron 4485 tensile testing machine, as shown in Figure 4. The stress-strain behavior of the material was determined and evaluated.

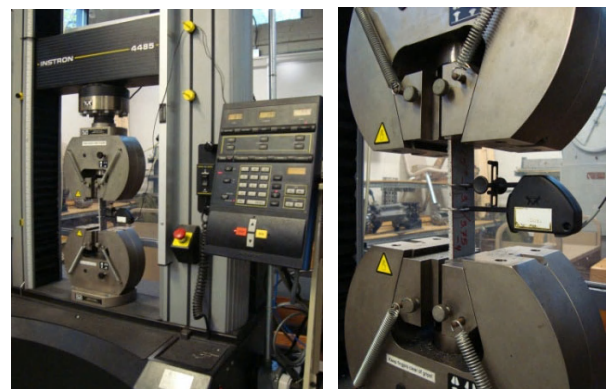


Figure 4 Tensile testing equipment (left) and composite coupon sample undergoing tension (right)

The testing procedure specified by the ACI 440.3R-04 was followed with a few minor modifications. A loading rate of 12.7 mm/min was used. To record the strain data a 25.4 mm extensometer was used, attached at the midpoint of the gage length. To prevent damage to the testing machine and extensometer, the extensometer was removed when a 100% strain value was achieved. Four samples were tested for each material configuration. Some coupon samples exhibited tearing within the tabs which eliminated them from the data analysis.

2.5 Ignition loss testing

Ignition loss testing was conducted according to ASTM D 2584 with a few slight modifications. Initially, a small test sample was weighed, then placed on a glass substrate and reweighed. The samples on glass substrates were heated in the muffle furnace at 600°C until all polyurea resin has disappeared, see Figure 5. The samples were then cooled and weighed again including the substrate. Fiber content was calculated to check and compare to the estimated value. Samples prior and after ignition loss testing are demonstrated in Figure 6.

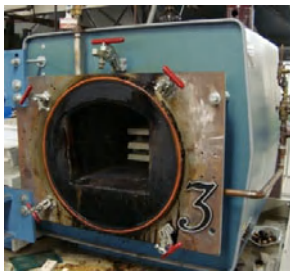


Figure 5 Samples in the muffle furnace prior to heating

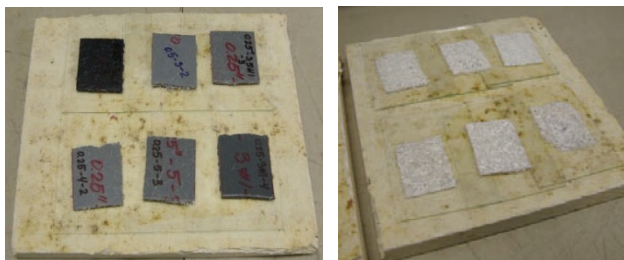


Figure 6 Samples prior (left) and after (right) ignition loss test

3 RESULTS AND CONCLUSIONS

3.1 Results and discussion

Data acquired during coupon tensile testing was graphed and analyzed. For each fiber-reinforced polyurea system four samples were tested. If during testing, the tearing in the sample occurred within the tabs, the sample was eliminated. The most conservative result from each tested combination was graphed. Stress vs. strain behavior for 6 mm, 13 mm, and 38 mm fiber lengths combined with polyurea A are presented in Figures 7, 8, and 9. A few samples with the highest fiber content plotted lower than expected due to delamination. Some samples with long

fibers or high fiber volume content exhibited delamination and high amount of voids leading to lower ultimate strength. Several conclusions were drawn from this study. As the fiber content increased, material strength increased, but ductility decreased. Fiber-reinforced polyurea systems with longer fiber length exhibited decreased ductility. As the fiber content and the fiber length increased, the modulus of elasticity increased as well, as shown in Figure 10. Samples with shorter fibers exhibited higher ductility due to the weaker bond between the fiber and the matrix.

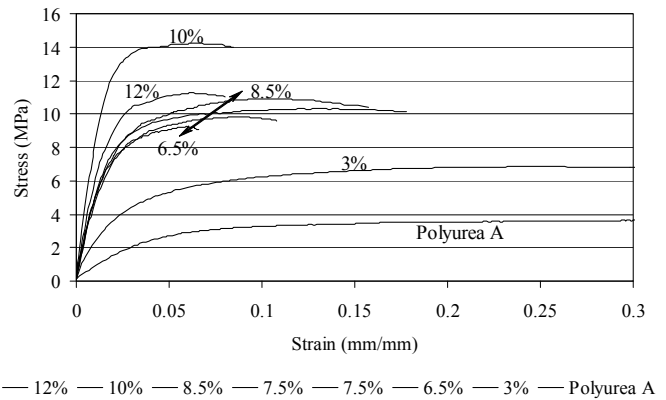


Figure 7 Stress-strain behavior of 6 mm fiber-reinforced polyurea systems

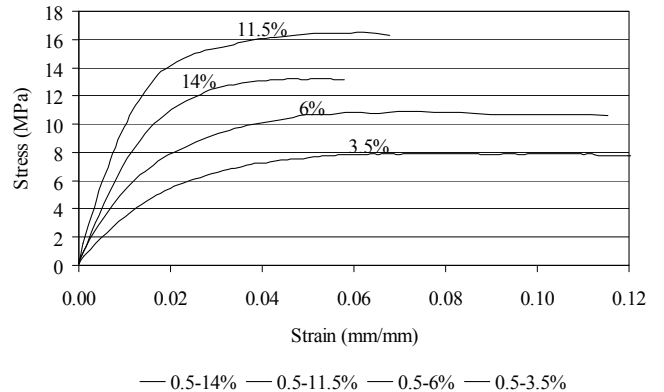


Figure 8 Stress-strain behavior of 13 mm fiber-reinforced polyurea systems

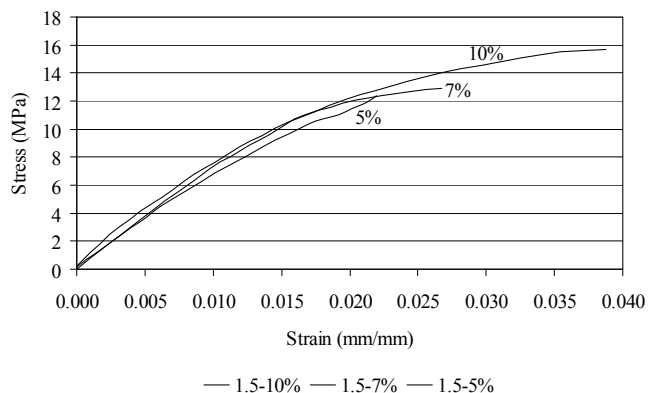


Figure 9 Stress-strain behavior of 38 mm fiber-reinforced polyurea systems

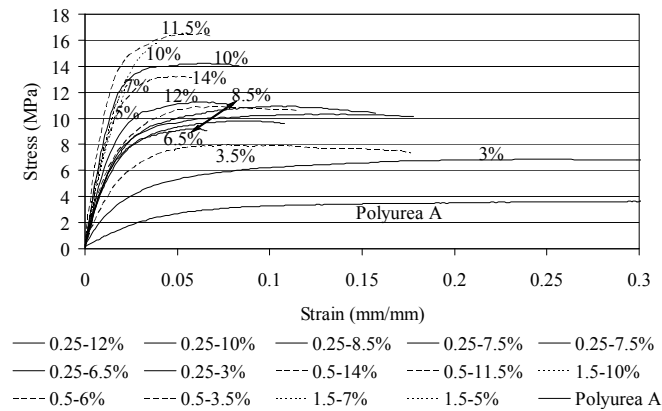


Figure 10 Stress-strain behavior of 6 mm, 13 mm, and 38 mm fiber-reinforced polyurea systems

Stress vs. strain behavior for fiber-reinforced polyurea systems consisting of polyurea B and 6 mm E-Glass fiber are presented in Figure 11. It can be observed that as the fiber volume increased, the strength and modulus of elasticity increased compared to the plain polyurea, as noted previously. Figure 12 demonstrates stress vs. strain graphs for both polyureas and fiber-reinforced systems with fiber content ranging from 5% to 6.5%. Both polyureas with shorter fibers at comparable fiber content showed similar results.

3.2 Conclusions

Coupon tensile testing was conducted to determine mechanical properties and performance of different E-Glass fiber-reinforced polyurea systems. Two various polyureas were tested by varying fiber volume fraction and fiber length. Sample ignition loss testing was conducted to

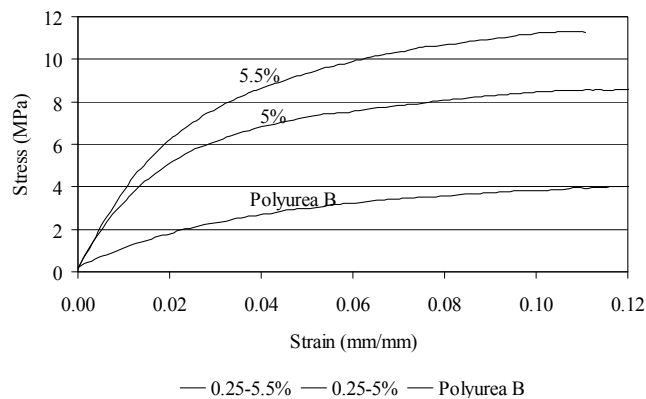


Figure 11 Stress-strain behavior of 6 mm fiber-reinforced polyurea systems

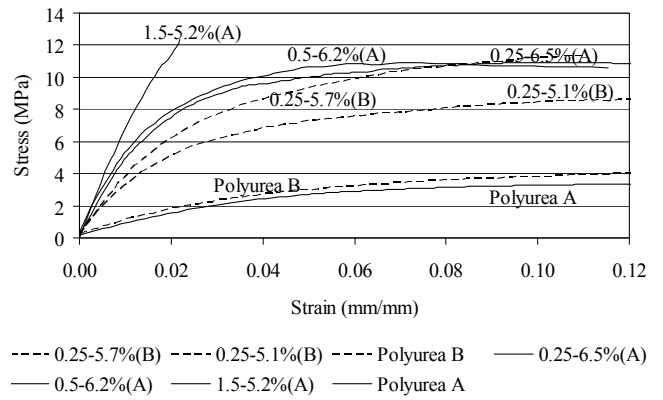


Figure 12 Stress-strain behavior of plain polyureas and fiber-reinforced polyurea systems with fiber content ranging from 5% to 6.5%

determine the fiber volume fraction. Several conclusions resulted from this study:

1. As the fiber content increased for both polyureas fiber-reinforced systems, material strength increased, but ductility decreased.
2. As the fiber content and the fiber length increased for polyurea A composite systems, the modulus of elasticity increased. In addition, fiber-reinforced polyurea systems with longer fiber length exhibited decreased ductility.
3. Both polyureas reinforced with shorter fibers at comparable fiber content showed similar results.

Further testing currently in progress, examines four polyureas reinforced with 6 mm E-Glass fiber by varying fiber content and tested under tension. Shorter fibers were selected for testing due to the increase in ductility of the material. In addition, higher fiber volume fractions have been fabricated and are currently being tested. Other work in progress is simultaneously examining the repair effectiveness on reinforced concrete members for flexure and shear.

REFERENCES

Carey, N.L. & Myers, J.J. 2009a. Full scale blast testing of hybrid barrier systems. American Concrete Institute (ACI) Special Publication Journal. (Currently under review)

Carey, N.L., Myers, J.J. 2009b. Impact Testing of Polyurea Coated Reinforced Concrete and Hybrid Panels (9th FRPRCS, Sydney Australia).

Experimental Research on the Fundamental Mechanical Properties of Presoaked Basalt Fiber Concrete

Jianxun Ma (majx@mail.xjtu.edu.cn), Xuemei Qiu, Litao Cheng & Yunlong Wang

Department of Civil Engineering, Xi'an Jiaotong University, Xi'an, China

ABSTRACT Presoaked basalt fiber concrete (PBFC) is a new kind of concrete reinforced with random short presoaked basalt fibers. In the paper, the applicability of the presoaked basalt fiber (PBF) as a strengthening material was investigated through various experimental works for mechanical characteristics and strengthening effects by changing its dosage and length, and compared with ordinary concrete. Experimental researches showed that: adding the presoaked basalt fiber on the condition of constant in matrix concrete, the influence on compressive strength was not noteworthy, but tensile strength was improved significantly. Form the results of the tests, it is concluded that presoaked basalt fiber can significantly reduce the brittleness of concrete, improving the toughness and deformation resistance. The presoaked basalt fiber can be regarded as a strengthening material for concrete structures.

1 INTRODUCTION

Studies had shown that fiber reinforced concrete can significantly improve inherent defects of traditional concrete, such as tensile strength, low energy absorption. For the time being, Polypropylene fiber, Steel fiber, Carbon fiber and Glass fiber have been widely researched in fibers used to strength concrete. But without exception, its wide application was limited because of its flaws. Presoaked basalt fiber as the 21st century natural green and environmental protection and high-tech material presents many advantages in terms of high tensile strength, corrosion resistance, high temperature, lower price and other advantages, becoming a good alternative methodology among the FRP strengthening systems. The experimental research about presoaked basalt fiber has become a hot at home and abroad.

This research investigated the effect and its degree on the fundamental mechanical properties of concrete with presoaked basalt fiber, by changing its dosage and length, hoping that the research will provide the scientific evidences and methods for future references of engineering applications.

2 EXPERIMENT

2.1 Materials

Cement: 32.5 ordinary Portland cement;

Sand: river sand, medium sand;

Rock: 5~31.5 mm diameter continuous gradation pebbles;

Water: drinking water;

Presoaked basalt fiber: the technical performance index see Table 1.

Table 1 Mechanical properties of presoaked basalt fiber

Density (g/m ³)	Elasticity modulus (GPa)	Tensile strength (MPa)	Elongation rate (%)
2.8	79.3~93.1	0.324100~4840	3.1

2.2 Test design

This research mainly studied the influence on compressive strength, splitting tensile strength and flexural strength of presoaked basalt fiber concrete with three different lengths (10mm, 20mm, 30mm) and three different dosages (3, 5, 7 kg/m³). The strength of matrix concrete is 30 MPa, its mix proportion seeing in table 2.

Table 2 Mix proportion of matrix concrete per stere

Cement (kg)	Sand (kg)	Stone (kg)	Water (kg)	Water-cement ratio (%)
425	542	1263	170	0.4

According to «Standard for test method of mechanical properties on ordinary concrete» (GB/T 50081-2002), 150mm×150mm×150mm standard cube specimens are used to test cube compressive strength and splitting tensile strength, 150mm×150mm×300mm standard specimens are used to test elastic modulus and direct compressive strength, and 150mm×150mm×550mm standard beam specimens are used to test flexural performance in the experiment.

3 RESULTS AND ANALYSIS

3.1 Workability

One of the most important indicators of concrete performances is workability. It is a composite indicator

reflecting technology, refers to the uniform stability of composition and the performance of flow deformation in the operations of concrete mixing, transportation, construction, tamping, and so on.

From the test results presented that there was influence on workability by adding presoaked basalt fiber into concrete. The slump reduced with increasing fiber dosage and fiber length (see Figure 1), The reasons are chiefly as follows: For one thing, because of greater specific surface area, rough surface and high coefficient of friction, the relative friction increased when concrete mix flowing; For another thing, as presoaked basalt fiber in concrete adsorbed certain moisture, causing the slump to reduce. Also it was found that, while reducing the slump of concrete, the permeability and viscosity of concrete had been obviously advanced.

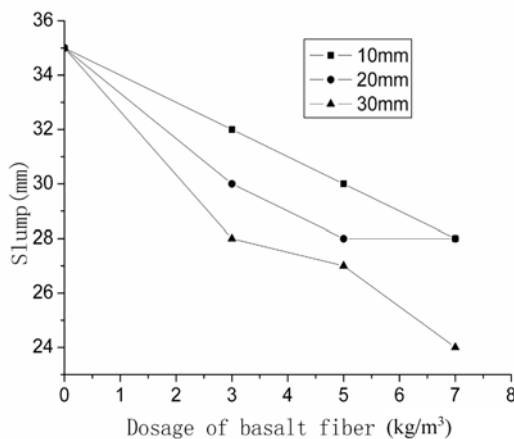


Figure 1 Influence of PBF on slump of PBFC

3.2 Mechanical properties

3.2.1 The influence of presoaked basalt fiber upon compressive strength of concrete

As showing in the figure 2-3, the effect of enhancing concrete compressive strength is not prominent by adding presoaked basalt fiber, the change was within 7 percentage points of the amplitude of ordinary concrete. The reason is that the compressive strength of concrete depends mainly on the compressive strength of cement matrix. There are more the poor areas of interface in the system after adding presoaked basalt fiber. The poor areas of interface first break when compressed, they may cancel the improvements. Adverse effect by poor areas minimized when there is a better adherence between presoaked basalt fibers and concrete, this may lead to a higher compressive strength. People should endeavor to make a further step change in improving the interfacial bonding between fiber and concrete matrix to improve the compression properties of fiber reinforced concrete.

Though the effect of enhancing concrete compressive strength is not prominent by adding presoaked basalt fiber, it was found that the broken shapes were all basically

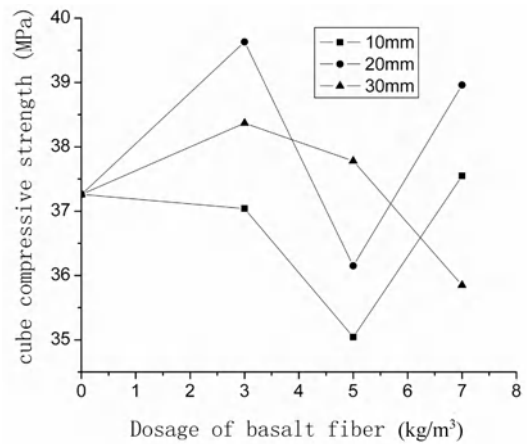


Figure 2 Influence of PBF on cube compressive strength of PBFC

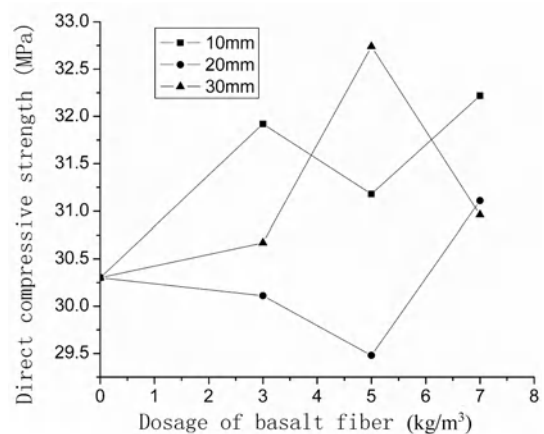


Figure 3 Influence of PBF on direct compressive strength of PBFC

maintained its form for only appeared many cracks and spallings, not like ordinary concrete which crushed when reached the ultimate compressive strength, still had a big bearing capacity. This is because the fiber has the effect of bridging in the cracks, preventing the process of deep development of cracks.

3.2.2 The influence of presoaked basalt fiber upon tensile strength of concrete

As showing in the figure 4-5, the tensile strength of concrete is obviously improved by adding presoaked basalt fiber, with the increase from 2% to 26%. The splitting tensile strength and flexural strength of presoaked basalt fiber concrete increased with the dosage and the length of presoaked basalt fiber. The main reason is that the matrix is in a dominate position to bear loads when fiber reinforced concrete loaded in initial stage. With the increase of fiber strain, stress which fiber bears increases, postponing the formation of initial crack. After the matrix cracked, fibers which bridged cracks transfer the loads to the flanks of crack, bringing stress redistribution between cracks to suffer loads continually, slowing down the crack velocity and keeping crack in a stable state. The more fibers which transfer tensile stress, the longer time which crack develops in a stable state and the

higher peak tensile Stress finally reaches.

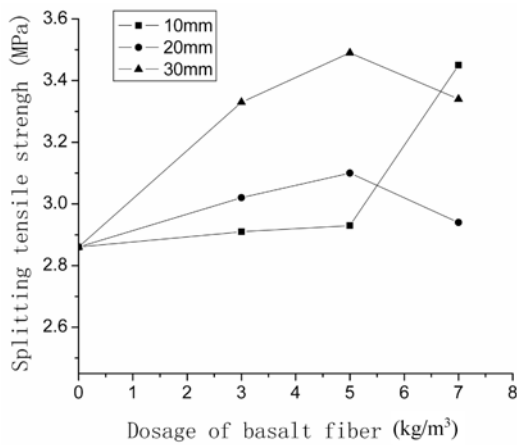


Figure 4 Influence of PBF on splitting tensile strength of PBFC

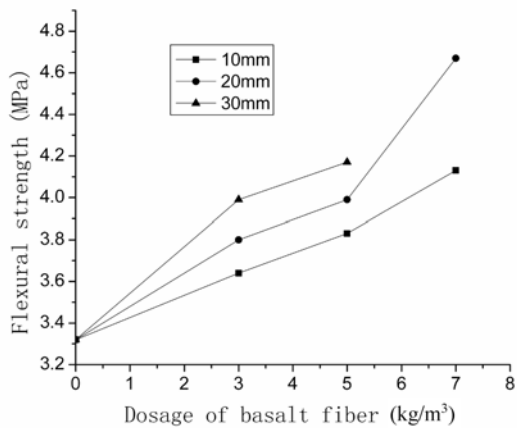


Figure 5 Influence of PBF on flexural strength of BFRC

In the experiment of splitting tensile strength, there are several secondary cracks, except one central principal crack. Perhaps this is because after adding presoaked basalt fiber, stress redistributed after appeared the initial crack, the weakest area didn't necessarily appear in the middle of concrete section.

In flexural experiment, ordinary concrete broken when cracked. After added fiber, the bottom of concrete cracked first and developed to top, the fiber which bridged cracks can still suffer loads, preventing the development of cracks and minimizing the crack width.

3.2.3 The influence of presoaked basalt fiber upon the brittleness of concrete

The ratio of tension and compression is one of indexes which reflect the brittleness of concrete. It means the ratio of tensile strength to cubic compressive strength of concrete at the same mixture ratio, the value reflects tensile properties. The smaller ratio of tension and compression, the greater brittleness, it also means the smaller toughness.

As can be seen from the figure 6-7, after adding presoaked basalt fiber, the ratio of tension and compression

of concrete had been greatly improved, a maximum 56.3%. From the test, we can see the highest ratio of tension and compression is reached when the fiber content was 5kg/m^3 and the fiber length was 20mm. So we can predict that presoaked basalt fiber can decrease the brittleness, improve the tensile toughness and flexural performances to improve the toughness of concrete.

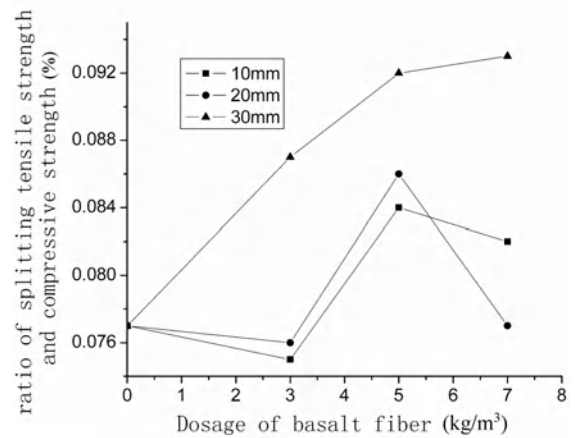


Figure 6 Influence of PBF on the ratio of splitting tensile strength and compression strength of PBFC

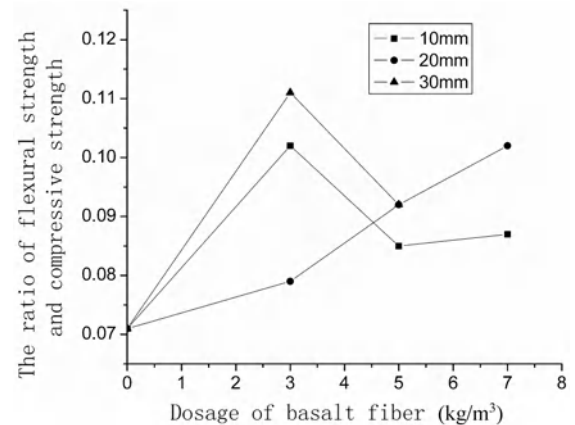


Figure 7 Influence of PBF on the ratio of flexural strength and compression strength of BFRC

4 CONCLUSIONS

In the study herein, the applicability of the presoaked basalt fiber as a strengthening material was investigated through various experimental works for mechanical properties and strengthening effects.

The slump of concrete reduces with adding presoaked basalt fiber, but the permeability and viscosity of concrete are obviously advanced.

From the compression test, the effect of enhancing concrete compressive strength is not prominent by adding presoaked basalt fiber, even might is reduced. But the failure model is modified; the integrity of fiber concrete is kept when the tensile failure occurs. It illustrated that the

fracture pattern of concrete is changed from brittleness to toughness with presoaked basalt fiber, improving the compression toughness.

From the tensile test, the effect of enhancing concrete tensile strength is obvious by adding presoaked basalt fiber, and the crack extension slows down, and the toughness and the deformation performance improve. The tensile strength of presoaked basalt fiber concrete is increased with the increase of the dosage and the length of presoaked basalt fiber. When the fiber content is 5kg/m^3 and the fiber length is 20mm, the toughness of presoaked basalt fiber concrete is the best.

So we can believe that the presoaked basalt fiber can be regarded as a strengthening material for concrete structures. The presoaked basalt fiber will be a good

alternative material among the fiber concretes.

REFERENCES

- Wu, Gang et al. 2007. The application research and development of basalt fiber in civil engineering field. *Industrial buildings*: 410-414.
- Hu, Xianqi & Shen, Tunian 2005. The application of continuous basalt fiber in Military and civilian fields. *Hi-Tech Fiber & Application* 30(6): 7-13.
- GB/T50081-2002. Standard for test method of mechanical properties on ordinary concrete. Beijing: China Standards Press.
- Liu, Q et al. 2006. Investigation of basalt fiber composite mechanical properties for applications in transportation. *Polymer Composite* (10): 41-48.

All FRP Structures

Shear Buckling of GFRP Beam Webs

Behzad D. Manshadi, Anastasios P. Vassilopoulos & Thomas Keller (thomas.keller@epfl.ch)

Composite Construction Laboratory (CCLab), Ecole Polytechnique Fédérale de Lausanne (EPFL), Lausanne, Switzerland

ABSTRACT Slender webs of glass fiber-reinforced polymer (GFRP) beams are sensitive to shear buckling. Shear buckling can be seen as an in-plane biaxial compression-tension buckling problem. The transverse tensile load thereby delays the onset of buckling and increases the ultimate load. Thin-walled GFRP plates of two different fiber stacking sequences, [0/90]_S and [90/0]_S, were subjected to in-plane biaxial compression-tension loading. The buckling loads were almost duplicated by increasing the tensile load while the ultimate loads were increased by up to 20%. The fiber stacking sequence thereby had significant effects on buckling mode shape and buckling and ultimate loads.

1 INTRODUCTION

FRP composite materials are increasingly applied in civil engineering. Structural components primarily used are beams and cellular slabs (Upadhyay & Kalyanaraman 2003, Keller & Schollmayer 2004). In many cases webs of open or closed beam cross-sections are slender and therefore sensitive to shear buckling. Shear buckling thereby can be seen as an in-plane biaxial compression-tension buckling problem. The diagonal compression stress field is crossed by a transverse tension stress field, whose stresses increase with the out-of-plane deformation and, in this way, produce a stabilizing effect. Several analytical and numerical studies have been carried out on the buckling and post buckling of flat composite panels subjected to general loading conditions. However, most of them concern biaxial compression-compression buckling (Romeo & Frulla 1994, Kim & Hoa 1995). Only one study was found, which concerns the buckling behavior of composite panels subjected to in-plane biaxial compression-tension loading (Tuttle et al. 1999). In this work, the buckling loads increase with an increase of the transverse tensile loads. However, large discrepancies between experimental and numerical results are reported.

In this paper, the results of an experimental investigation of the buckling and the post-buckling behavior of GFRP laminates subjected to in-plane biaxial compression-tension loading are presented. The influence of increasing transverse tension load on the buckling and post-buckling behavior is investigated. Panels with two different fiber architectures were used in order to evaluate the effect of different orthotropic stacking sequences.

2 EXPERIMENTAL SET-UP

An Instron planar biaxial cruciform testing system of 63 kN capacity in both axes directions was used, see

Figure 1. Compression loads were applied horizontally and tension loads vertically.

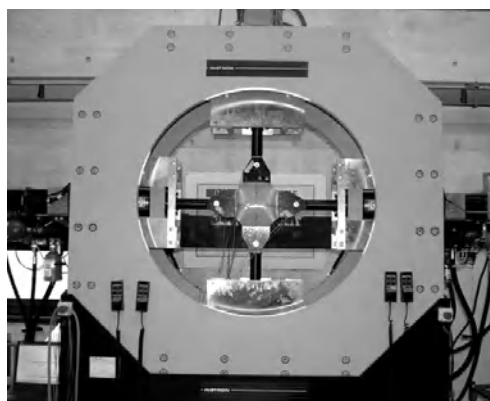


Figure 1 Instron planar biaxial cruciform testing systems

Composite panels of $350 \times 350 \text{ mm}^2$ and nominal thickness of 3.6 mm were prepared by hand-lay-up. Four layers of unidirectional E-glass fibers (0° : 960 g/m^2 , 90° : 50 g/m^2) and polyester resin were used. Specimens with stacking sequences of [0/90]_S and [90/0]_S were cut from the panels with an aspect ratio of 1, as shown in Figure 2. To prevent interfering of grip motions during loading and to smoothen load introduction the corners were truncated. Nine linear strain gages were applied in the specimen axes in order to record the in-plane strains (see Figure 2). Gages (1)-(5) and (7)-(9) were on one side while gage (6) was on the opposite specimen side. Moreover, the out-of-plane displacement was recorded by using an LVDT transducer located on the back side at the center point (see Figure 2).

The tensile load was first applied in vertical direction at a loading rate of 0.3 kN/s and then kept constant throughout the test. Compression was then applied in displacement control at a rate of 0.017 mm/s up to

specimen failure. Tensile loads were selected in 5 kN steps from 0 to 30 kN. Two specimens were tested for $[0/90]_s$ laminates at each load level while only one specimen was used for $[90/0]_s$.

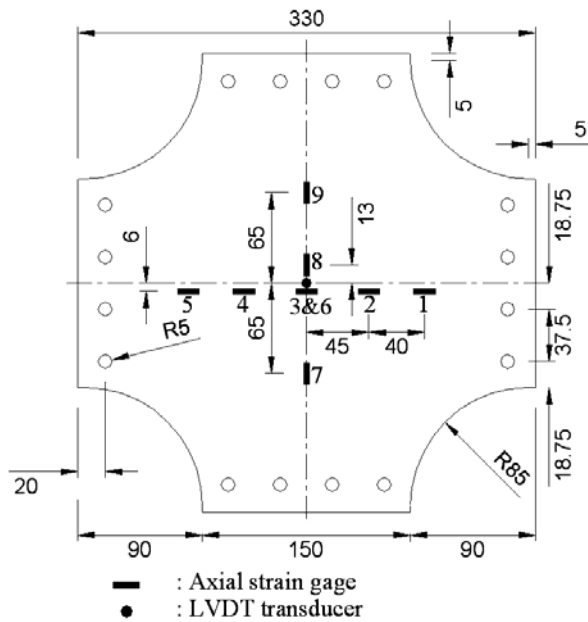


Figure 2 Specimen geometry in [mm] and instrumentation

3 EXPERIMENTAL RESULTS

3.1 $[0/90]_s$ specimens

Independent of the applied tension load, an almost half-sine wave buckling mode shape was observed, as shown in Figure 3. Typical strain responses, at a tension load of 15 kN, are presented in Figure 4. Gages (3) and (6), on opposite sides, had the same compressive behavior up to the onset of buckling. Subsequently, gage (3) changed to tension while gage (6) continued measuring compressive strains. Gages (1) to (6) showed symmetric results in accordance with the observed mode shape. The effect of the tension load on the buckling and the post buckling behavior is shown in Figure 5. The curves move upwards with increasing tension load.

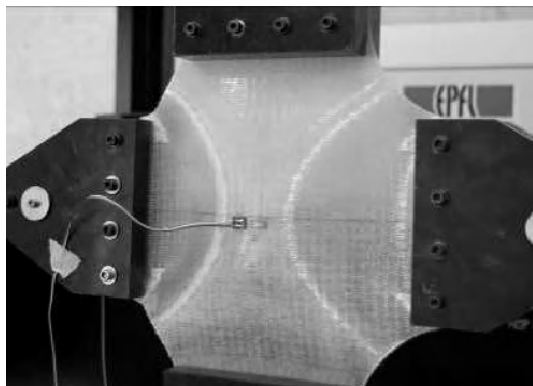


Figure 3 Buckling mode shape of a $[0/90]_s$ specimen

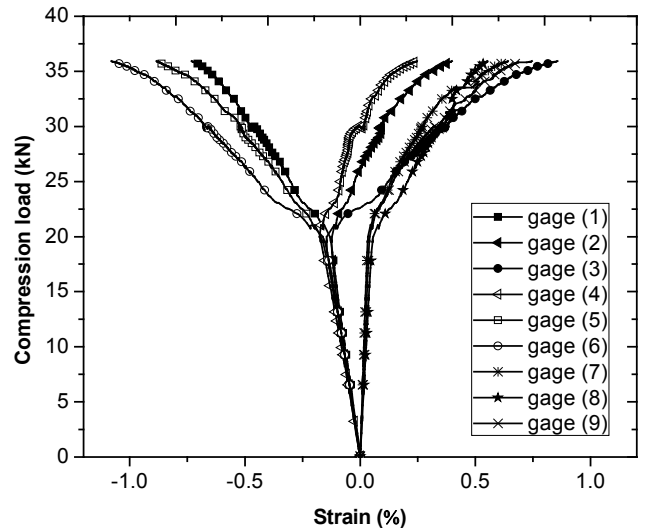


Figure 4 Compression load vs. strain responses of $[0/90]_s$ specimen at 15 kN tensile load

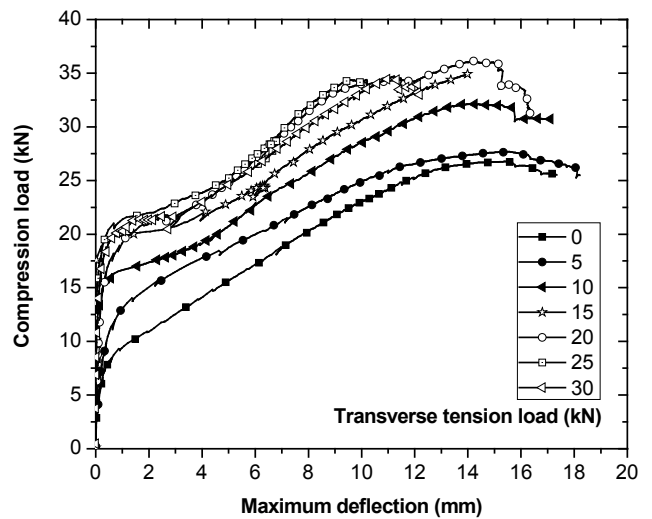


Figure 5 Compression load vs. maximum out-of-plane displacement responses of $[0/90]_s$ specimens at different tension loads

3.2 $[90/0]_s$ specimens

A half-sine wave buckling mode was observed at 0 kN tension load only. Applying tension loads let the mode shape change to a full-sine wave, as shown in Figure 6. Strain responses were again in accordance with the observed mode shape, as shown in Figure 7 for a 20 kN tension load. Gages (2) and (4) were on the concave and convex part of the two half-waves and, accordingly, showed tension and compression. Symmetry of the shape was confirmed by gages (1)-(3) and (4)-(6).

The effect of transverse tension on the buckling load is illustrated in Figure 8, which shows the gage (2) responses. The reversal point of the strain curves, which normally is associated with the buckling load, is moving up by applying higher tensile loads.

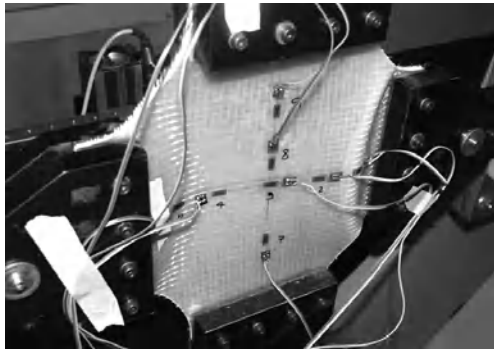


Figure 6 Buckling mode shape of a $[90/0]_s$ specimen

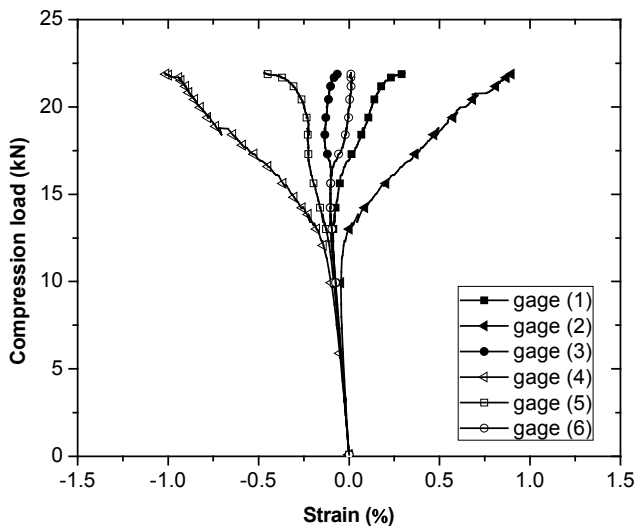


Figure 7 Compression load vs. strain responses of $[90/0]_s$ specimen at 20 kN tensile load

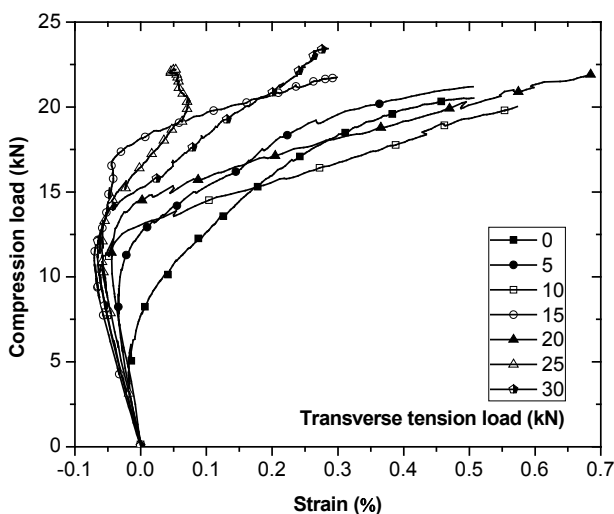


Figure 8 Comparison of gage (2) load-strain responses of $[0/90]_s$ specimens at different tension loads

4 DISCUSSION AND CONCLUSION

In order to derive the buckling loads, the load vs. maximum out-of-plane displacement curves of $[0/90]_s$ specimens,

shown in Figure 5, were fitted with the numerical fitting method proposed by Fok (1984). This method was not applicable for specimens $[90/0]_s$ because center point out-of-plane displacements were almost zero due to the full-sin wave. The strain reversal method (Singer et al. 1998) was used in this case based on the load-strain responses shown in Figure 8.

The resulting buckling loads as a function of the transverse tension loads are shown in Figure 9. Fitting curves were added to the experimental results. The buckling loads show an increasing trend at lower tension loads and approach a plateau for higher tension loads. An increase of almost 155% was observed for the $[90/0]_s$ specimens, while the buckling load of the $[0/90]_s$ specimens was almost duplicated.

The pure shear buckling load, determined as the intersection point of the pure shear buckling line (corresponding to equal tension and compression loading) with the fitting curves in Figure 9 was 20.5 kN for $[0/90]_s$ specimens and 9.8 kN for $[90/0]_s$ specimens.

The positive effect of the increasing transverse tension load on the ultimate compression loads was less pronounced in both cases, see Figure 10. Nevertheless, the ultimate compression loads increased up to 20% for $[0/90]_s$ specimens and 15% for $[90/0]_s$ specimens. Both, the increase of buckling and ultimate loads, confirmed the significant and increasing stabilizing effect provided by the increasing transverse tension load.

Figures 9 and 10 demonstrate that the stacking sequence had a significant effect on the results. In the $[0/90]_s$ configuration, the fibers parallel to the compression axis were on the outer side in the cross-section, while they were in the center in the $[90/0]_s$ configuration. The bending stiffness along the compression axis was therefore much higher in the $[0/90]_s$ configuration than in the $[90/0]_s$ configuration. The resulting increased resistance against buckling in the $[0/90]_s$ configuration, caused by the effect of the fiber architecture, explains therefore the much higher buckling and ultimate compression loads of this configuration. In beam webs, therefore, the fiber architecture should be conceived in such a way that maximum bending stiffness is obtained in the direction of the compression diagonal.

Similar effects of the fiber architecture were observed on the buckling mode shape. The $[90/0]_s$ configuration had the higher bending stiffness in tension direction. Applying furthermore stabilizing tension loads prevented out-of-plane deformations of the tension axis and led to the change of the buckling mode from a half-sine wave (at zero tension) to a full-sine wave when applying transverse tension.

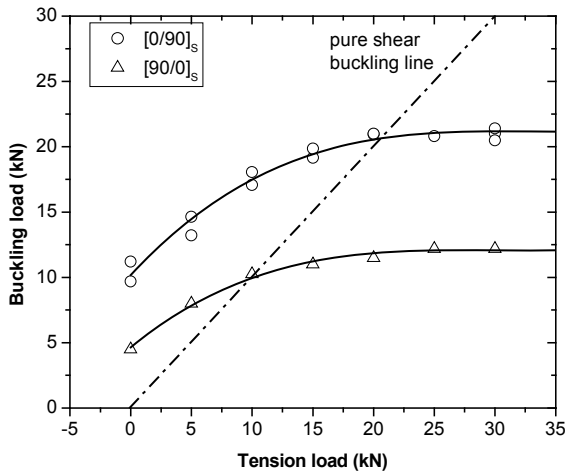


Figure 9 Buckling load vs. transverse tensile load

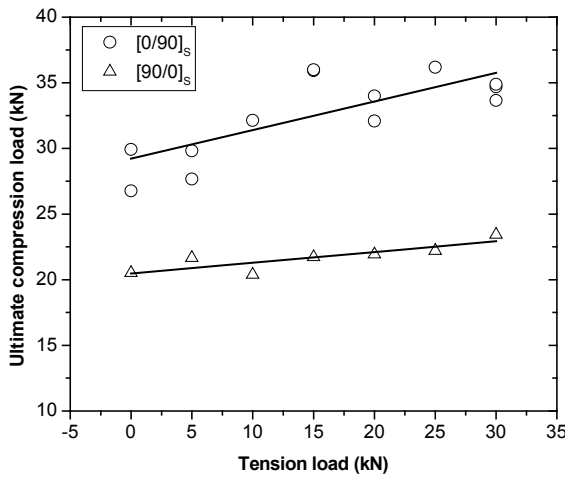


Figure 10 Ultimate compression load vs. transverse tensile load

5 ACKNOWLEDGEMENTS

The authors would like to thank the Swiss Innovation Promotion Agency CTI for its financial support (Grant No. 9121.1 PFIW-IW), Scobalit Composites, Winterthur, Switzerland for fabricating the composite plates, and the EPFL LMAF Laboratory for use of the biaxial test machine.

REFERENCES

Fok, W.C. 1984. Evaluation of experimental data of plate buckling. *J Struct Eng-ASCE* 110(4):577-588.

Keller, T. & Schollmayer, M. 2004. Plate bending behavior of a pultruded GFRP bridge deck system. *Compos Struct* 64: 285-295.

Kim, Y.S. & Hoa, S.W. 1995. Bi-axial buckling behavior of composite rectangular plates. *Compos Struct* 31(4):247-252.

Romeo, G. & Frulla, G. 1994. Nonlinear analysis of anisotropic plates with initial imperfections and various boundary conditions subjected to combined biaxial compression and shear loads. *Int. J. Solids Struct* 31(4):763-783.

Singer, J., Arbocz, J. & Weller, T. 1998. *Buckling Experiments: Experimental Methods in Buckling of Thin-Walled Structures- Volume I*. New York: John Wiley & Sons Inc.

Tuttle, M., Singhatanadgid, P. & Hinds, G. 1999. Buckling of composite panels subjected to biaxial loading. *Exp Mech* 39(3):191-201.

Upadhyay, A. & Kalyanaraman, V. 2003. Simplified analysis of FRP box-girders. *Compos Struct* 59(2):217-225.

Shear Wrinkling of GFRP Webs in Cell-Core Sandwiches

Behzad D. Manshadi, Anastasios P. Vassilopoulos, Julia de Castro & Thomas Keller (thomas.keller@epfl.ch)

Composite Construction Laboratory (CCLab), Ecole Polytechnique Fédérale de Lausanne (EPFL), Lausanne, Switzerland

ABSTRACT Glass fiber-reinforced (GFRP) cell-core sandwich structures are increasingly used in bridge deck and roof construction. GFRP cell-core sandwiches are composed of the outer GFRP face sheets, a foam core and a grid of GFRP webs integrated into the core in order to reinforce the shear load capacity. One of the critical failure modes is shear wrinkling, a local buckling failure in the sandwich webs due to shear loading. Shear wrinkling is a biaxial compression-tension wrinkling problem and, for this reason, the numerous results of pure compressive wrinkling research are not necessarily applicable. The details and results of in-plane biaxial compression-tension wrinkling experiments on GFRP sandwich laminates, stabilized by a polyurethane foam core, are presented. It is shown that an increasing transverse tension load significantly decreases the wrinkling load. These results are confirmed by finite element calculations.

1 INTRODUCTION

Foam-core based sandwich structures, reinforced by an internal grid of webs, and denominated cell-core sandwiches, are increasingly used in applications requiring high bending stiffness and strength combined with low weight such as aerospace and marine structures. Nowadays, the advantageous use of glass fiber-reinforced polymer (GFRP) materials in sandwich construction is also being explored in civil applications, e.g. building construction. Keller et al. 2008 showed that FRP composites assembled in large-scale cell-core sandwich structures enable the prefabrication of lightweight, single-layer and function-integrated roof structures for rapid on-site installation, as shown in Figure 1. In this particular building, structural functions, building physics functions (thermal insulation, water proofing), and architectural functions (complex shapes) were integrated into single components by using GFRP sandwich construction.



Figure 1 Novartis Campus Main Gate Building with GFRP cell-core sandwich roof (Keller et al. 2008)

As the design of this GFRP sandwich roof structure demonstrated, one of the critical failure modes is shear wrinkling, a local buckling failure in the GFRP webs of

the cell-core sandwich due to shear loading, as shown in Figure 2. In contrast to uniaxial compression wrinkling, for which several theoretical models and a large amount of research work and available experimental data exists (Plantema 1966, Allen 1969, Ley et al. 1999), only a small amount of information on shear wrinkling is available. Shear wrinkling is a biaxial compression-tension wrinkling problem and, therefore, the results of compressive wrinkling research are not directly applicable. Only a few models exist for the analysis of face wrinkling of sandwich laminates under biaxial loading (Fagerberg & Zenkert 2005, Birman & Bert 2004, Hadi & Matthews 2000, Sullins et al. 1969, Vonach & Rammerstorfer 2000), which, however, concern biaxial compression and not compression-tension loading. Only



Figure 2 Shear wrinkling failure of web and subsequent failure of upper face sheet of GFRP sandwich beam subjected to four-point bending (Keller et al. 2008)

one experimental study on shear wrinkling of composite sandwiches (Lake et al. 2007) was found. In this study, however, no comprehensive model was presented.

This paper presents the details and results of in-plane biaxial compression-tension wrinkling experiments on GFRP sandwich panels stabilized by a thick polyurethane (PU) foam core. The influence of an increasing tension load on the wrinkling load is investigated.

2 EXPERIMENTAL SET-UP

An Instron planar biaxial cruciform testing system with 4 advanced 63 kN servo-hydraulic actuators, mounted in-plane and perpendicular to each-other, was used, see Figure 3. Compression and tension loads were applied horizontally and vertically, respectively.

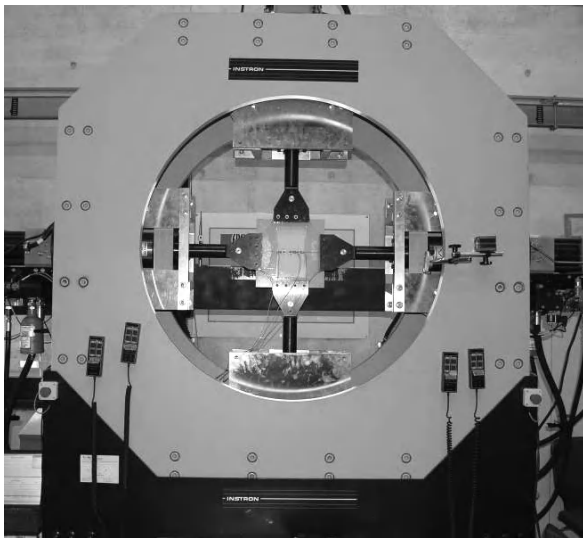


Figure 3 Instron planar biaxial cruciform testing system

Sandwich panels of 400×400 mm² with one thin face sheet stabilized by thick PU foam were prepared by hand-lay-up. The face sheet of 1.2 mm thickness consisted of two unidirectional E-glass fiber layers (470 g/m² each) arranged in [90/0] stacking sequence and polyester. The core of 60 mm thickness consisted of polyurethane foam of 60 kg/m³ density (PU-60). The main mechanical properties of foam core and UD glass-polyester laminates used for face sheet are summarized in Table 1. The specimens were cut from the sandwich panels with an aspect ratio of 1, as shown in Figure 4. To prevent interfering of grip motions during loading and to smoothen load introduction the corners were truncated. The foam from the edges which were clamped in the steel grips was removed. A supporting frame, consisting of a GFRP laminate, was bonded on each specimen to avoid any grip failure and to impose the wrinkling failure to occur in the part subjected to the transverse tension load, see Figure 5. In addition, an aluminum plate was placed behind the foam to prevent the out-of-displacement of the specimen. This set-up with

these dimensions simulated the wrinkling of sandwich panels with infinite foam core thickness. According to Ley et al. 1999, a core is assumed infinite when

$$\left(\frac{t_f}{t_c}\right)\left(\frac{E_f}{E_c}\right)^{1/3} < 0.2 \tag{1}$$

where E_c and E_f are the elastic modulus of foam and face sheets (given in Table 1); and t_c and t_f are the thicknesses of foam core and face sheet, respectively.

Table 1 Mechanical properties of foam core and UD glass-polyester laminates used for face sheet

Properties	Core (PU-60)	Face sheet (GFRP)
Longitudinal Elastic Modulus (MPa)	17.5	17100
Transverse Elastic Modulus (MPa)	17.5	6040
Shear Modulus (MPa)	6.5	2000

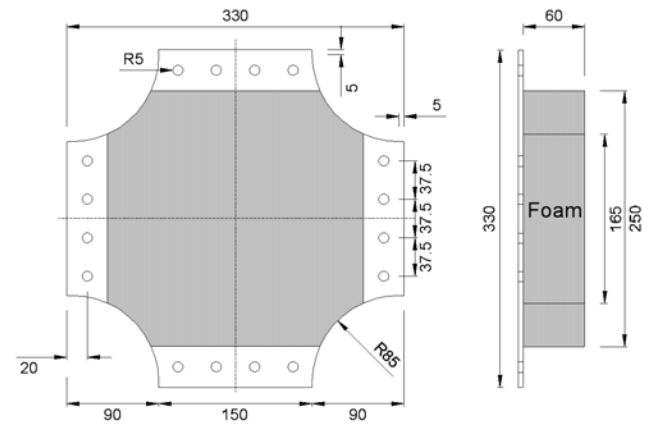


Figure 4 Specimen geometry in [mm]

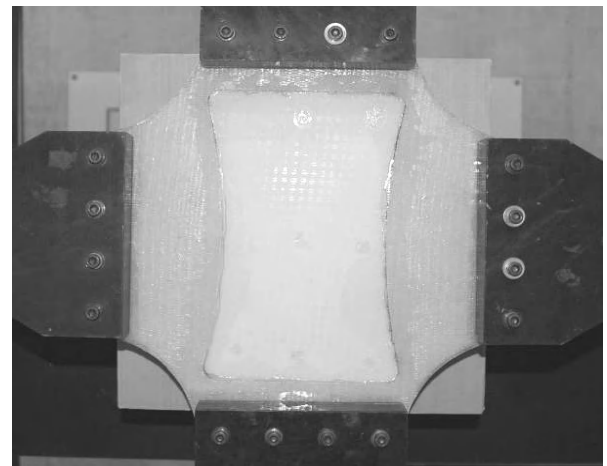


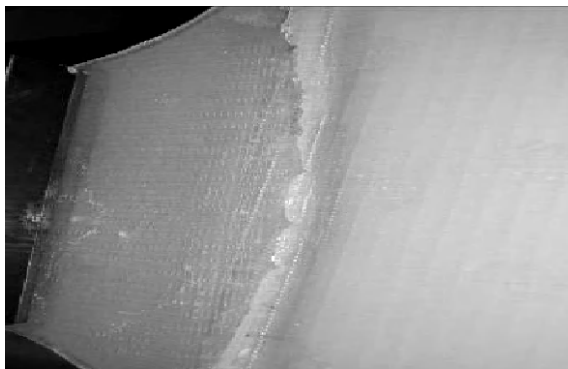
Figure 5 Biaxial compression-tension test set-up

The tension load was first applied in vertical direction at a loading rate of 0.25 kN/s and then kept constant throughout the test. Compression was then applied in displacement control at a rate of 0.017 mm/s up to

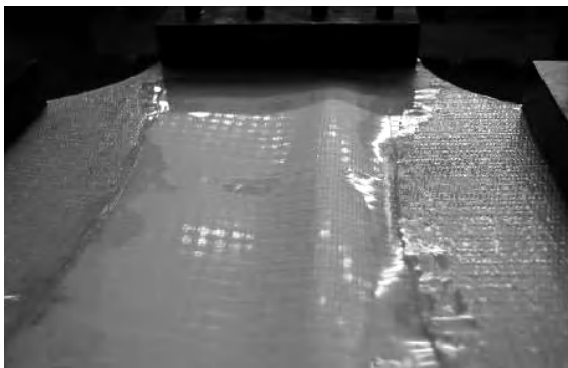
specimen failure. Tension loads were selected in different steps from 0 to 20 kN. One specimen was tested at each load level, except at 0 kN tension load for which two specimens were used.

3 EXPERIMENTAL RESULTS

Two typical wrinkling failure modes were observed, as shown in Figure 6. Either the face sheet's wrinkling wave went inside the foam (case (a)) or the wrinkling wave came out of foam (case (b)). Table 2 presents the wrinkling loads recorded at the different tension loads. The average wrinkling load (ultimate compressive load) in the case without any tension load was 20.5 kN while this value decreased in the case of 20 kN tension load to 14.9 kN, which corresponds to a decrease of 27%.



(a)



(b)

Figure 6 Wrinkling failure modes, (a) wrinkling wave went inside foam, (b) wrinkling wave came out of foam

Table 2 Experimental wrinkling loads at different tension loads

Tension load (kN)	Wrinkling load (kN)
0	21.0
0	19.9
3	19.0
5	17.1
10	15.8
11.2	15.9
17.7	15.3
20	14.9

4 FINITE ELEMENT MODELING

Linear elastic finite element (FE) analysis on wrinkling stability has been performed by using ANSYS software. The specimens were modeled using 8-node layered shell elements (Shell-91) for the face sheets and 20-node structural solid elements (Solid-95) for the foam. Figure 7 shows the mesh; 5432 elements were used in total. The material properties given in Table 1 were applied.

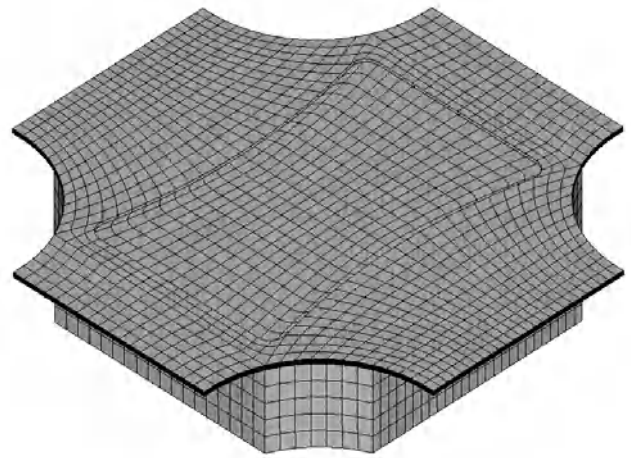


Figure 7 Finite element model of specimen

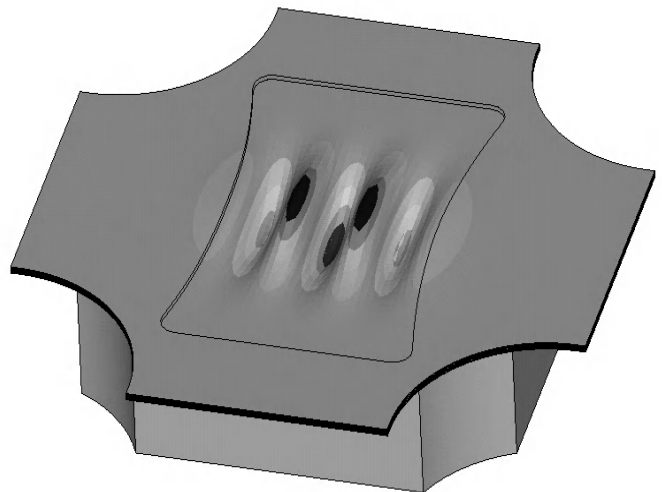


Figure 8 First mode of eigen-value buckling solution

The wrinkling load was calculated as a local buckling load by performing the eigen-value buckling solution. A plot of the first buckling mode shape is shown in Figure 8. The buckling mode consists of several parallel local waves. In reality, one of these local waves grows fast up to ultimate failure, as it was observed in the experiments. The other waves could not be detected.

5 DISCUSSION AND CONCLUSIONS

The resulting wrinkling loads as a function of the transverse tension loads are shown in Figure 9. Fitting

curves were added to the experimental results. The wrinkling loads show a pronounced decreasing trend at lower tension loads which slows down for higher tension loads and approaches a plateau. A decrease of almost 27% was observed by applying 20 kN tension load. The FE results, also shown in Figure 9, confirm the negative effect of the increasing transverse tension load on the wrinkling loads. However, they overestimate the experimental results and do not clearly show the plateau.

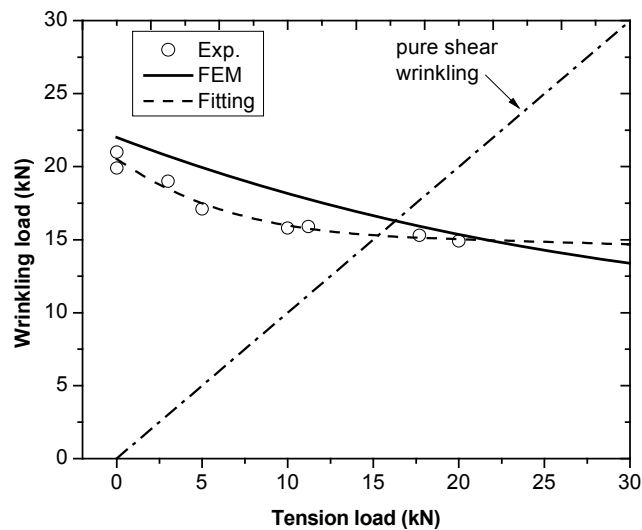


Figure 9 Comparison experimental and numerical wrinkling loads at different transverse tension loads

The pure shear wrinkling load, determined as the intersection point of the pure shear wrinkling line (corresponding to equal tension and compression loading) with the fitting curve was 15.3 kN.

The study is still in progress. Further investigations with different foam core densities and fiber architectures of face sheet will be performed and an analytical model will be developed to predict the wrinkling load as a function of the transverse tension load.

6 ACKNOWLEDGEMENTS

The authors would like to thank the Swiss Innovation Promotion Agency CTI for its financial support (Grant No. 9121.1 PFIW-IW), Scobalit Composites, Winterthur, Switzerland for fabricating the sandwich plates, and the EPFL LMAF Laboratory for use of the biaxial test machine.

REFERENCES

- Allen, H.G. 1969. *Analysis and Design of Structural Sandwich Panels*. Oxford: Pergamon Press.
- Birman, V. & Bert, C.W. 2004. Wrinkling of Composite-facing Sandwich Panels under Biaxial Loading. *Journal of Sandwich Structures and Materials* 6:217-237.
- Fagerberg, L. and Zenkert, D. 2005. Effects of Anisotropy and Multi-Axial Loading on the Wrinkling of Sandwich Panels. *Journal of Sandwich Structures and Materials* 7:177-194.
- Hadi, B.K. & Matthews, F.L. 2000. Development of Benson-Mayers Theory on the Wrinkling of Anisotropic Sandwich Panels. *Composite Structures* 49:425-434.
- Keller, T., Haas, Ch. & Vallée, T. 2008. Structural Concept, Design and Experimental Verification of a GFRP Sandwich Roof Structure. *Journal of Composites for Construction* 12(4):454-468.
- Lake, S., Saunders, M. & Anderson, J. 2007. Shear Wrinkling of Composite Sandwich Stiffener Webs. SAMPE-2007, Baltimore, MD.
- Ley, R.P., Lin, W. & Mbanefo, U. 1999. *Facesheet Wrinkling in Sandwich Structures*. NASA: Langley Research Center.
- Plantema, F.J. 1966. *Sandwich Construction*. New York: John Wiley & Sons Inc.
- Sullins, R.T. Smith, G.W. & Spier, E.E. 1969. *Manual for Structural Stability Analysis of Sandwich Plates and Shells*. 1969, NASA-Contractor Report No. 1467.
- Vonach, W.K. & Rammerstorfer, F.G. 2000. Wrinkling of Thick Orthotropic Sandwich Plates under General Loading Conditions. *Archive of Applied Mechanics* 70:338-348.

Pin-Bearing Strengths for Design of Bolted Connections in Pultruded Structures

B. Zafari (B.Zafari@warwick.ac.uk) & J. T. Mottram

Civil Research Group, School of Engineering, University of Warwick, Coventry, UK

ABSTRACT Presented in this paper are pin-bearing strengths of pultruded FRP materials that are required to check for bearing resistance when designing bolted connections. Bearing failure is the distinct failure mode with a strength formula that requires its ‘own’ material strength property, which we call the bearing strength. Using a test method developed at the University of Warwick a series of pin-bearing strength tests have been conducted to characterise the web material from a 203 mm × 203 mm × 9.53 mm wide flange standard shape. Testing is performed with the loading oriented at either 0, 45 or 90° to the direction of pultrusion. Reported are the salient test results and characteristic values determined using the guidance in Annex D to Eurocode 0.

1 INTRODUCTION

If we consider a single bolted connection subjected to double-lap shear the various distinct modes of failure are shown in Figure 1, in terms of their stress distributions, when bolting is of steel and the plate material is of pultruded fibre reinforced polymer (Mottram and Turvey, 2003). Connection designs failing with the bearing mode (Figure 1(a)) can provide the connection with a degree of damage tolerance and this is desirable because it imparts a degree of structural integrity (Mottram and Turvey, 2003, Thoppul et al., 2009). It is also the distinct failure mode with a strength formula (Bank, 2006) that requires its ‘own’ material strength property (F_{θ}^{br}), and the formula is

$$R_{br} = tdF_{\theta}^{br} \quad (1)$$

t is plate thickness, d is the bolt diameter and F_{θ}^{br} is the specified pin-bearing strength for the orientation (θ) of the resultant force at the bolt/FRP contact with respect to the direction of pultrusion. Figure 1 shows the plate for a single bolted connection to have constant width, which because the bolt is centrally placed is twice the edge distance e_2 . Another relevant geometric parameter is the hole diameter d_n , which due to a hole clearance is greater than d .

It is recognised from previous double lap-shear single bolted tests (Mottram and Turvey (2003)), that to promote failure in the bearing mode (at room temperature) the geometric ratios e_1/d and $2e_2/d$ need to be at least four when the material is pultruded and loading is tensile.

The pin-bearing strength by Equation 1 is given by the projected area of bolt bearing times the relevant specified pin-bearing strength. For the purpose of design

this relevant strength is the characteristic value. To establish the bearing strength of a particular connection we sum the appropriate R_{br} s (using Equation 1) times the number of bolts for each of R_{br} s calculated. To obtain the design strength for a bolted connection the bearing strength is then multiplied by a factor that is < 1 . The question of what this factor is to be is not an issue for this paper.

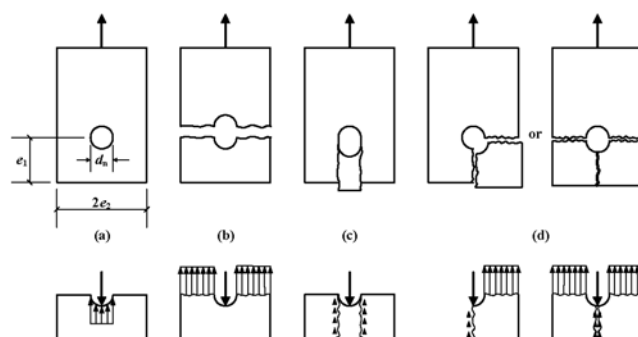


Figure 1 Plate-to-plate distinct modes of failure with a single steel bolt; (a) bearing, (b) net-tension, (c) shear-out, (d) cleavage

When the connection force is aligned with the longitudinal direction of pultrusion we have $\theta = 0^\circ$, and F_0^{br} is the highest pin-bearing strength. If $\theta = 90^\circ$, the force is parallel to the transverse direction of pultrusion and F_{90}^{br} is the lowest pin-bearing strength. In the American pultruders’ manuals (Anon, 2010a,b) the 0° direction is referred to as lengthwise (LW) and the 90° direction as crosswise (CW). Depending on how orthotropic the pultruded material is, it was believed (Mottram, 2009) that, prior to the new test results given in Tables 1 and 3 of this paper, the strength ratio F_0^{br} / F_{90}^{br}

lies within the range 1.2 to 1.5.

By definition the pin-bearing strength is the mean stress at bearing failure, when the maximum load is attained (Mottram, 2009) and there is no lateral restraint. It is further assumed that when measuring this property there is no bolt thread bearing against the FRP material. It is important to emphasize that for the bearing strength to be the pin value there must be no tightening of the bolting. It is well-known that bearing strength increases significantly on tightening because a torqued bolt provides stiffness to oppose the 'free' through-thickness deformation (Cooper and Turvey, 1995; Mottram, 2004). Other factors not already mentioned that influence the bearing strength are; the fibre reinforcement architecture and material thickness, the bolt-flexibility, the presence of thread over the bearing surface, the bolt diameter-to-thickness (d/t) ratio, the size of the clearance hole and the environmental conditioning.

2 MATERIAL AND TEST PROCEDURE

Test results for 0, 45 and 90° material orientations are obtained from a series of pin-bearing strength tests, at room temperature, using the so-called Warwick University (WU) test method, which is described in Mottram (2009). Figure 2 shows an in-house compression die set with fixtures to apply the compressive loading to semi-notched specimen via a steel pin. The anti-buckling holder for the nominal 9.53 mm thick material requires a specimen width of 100 mm. Because bearing failure will occur when the end distance (e_1) is $4d$ the specimen height is set at 100 mm.

The WU method (Mottram, 2009) is employed for this series of tests because it is suitable for specimens cut from the web of a 203 mm × 203 mm × 9.53 mm wide flange shape having a web depth of 180 mm. This pultruded shape is from Creative Pultrusions Inc. (Anon, 2010a) and the standard 1525 series product range. Reported (Anon, 2010a) maximum bearing strengths are $F_0^{\text{br}} = 206 \text{ N/mm}^2$ and $F_{90}^{\text{br}} = 124 \text{ N/mm}^2$. They were determined in accordance with standard test method ASTM D953 and are therefore representative pin values for a bolt of 6.35 mm diameter and without a clearance hole.

Number of nominally identical specimens per batch is six when the loading is either at 45 or 90° to the direction of pultrusion. For the tests load at 0° the batch size was higher at 11. For each of the three orientations there are four batches, comprising the following pairs of nominal hole diameters (d_n) and nominal pin diameters (d): 12 mm and 10 mm; 15 mm and 12.7 mm; 21 mm and 19 mm and 28 mm and 25.4 mm. The four pins were cut from standard steel bolts. The mean measured diameters (d and d_n) and mean hole clearance ($d_n - d$) are given in rows two to four in Tables 1 to 3. It is to be

noted that the minimum clearance of 1.9 mm is above the 1.6 mm given in the pultruders' design manuals (Anon, 2010a,b).

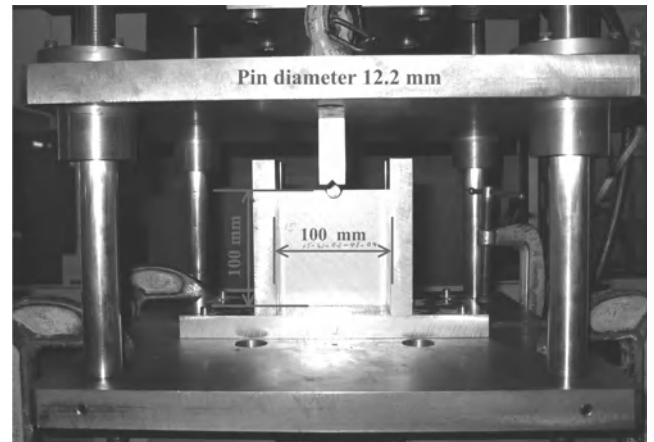


Figure 2 The larger Warwick University (WU) pin-bearing strength test rig (Mottram, 2009)

Web thickness per specimen was measured to the nearest 0.05 mm with an outside micrometer, and t is found to have a mean in the range of 9.07 to 9.18 mm. The mean thicknesses per batch are given in the first row in Tables 1 to 3.

Compression load is applied under a constant stroke rate of 0.01 mm/s using a DARTEC 9500 hydraulic testing machine with a 250 kN load cell. To establish the maximum compressive force at failure, 0.338 kN is added to the maximum machine reading to allow for the dead weight of the top plate (seen in Figure 2) and rocker transfer fixture.

A Solartron SI 3531 data acquisition system is used to monitor the load and stroke in real time, at the rate of one pair of readings every two seconds. To reach the failure load the duration of testing can be 110 seconds.

Table 1 Statistical test results for longitudinal pin-bearing strengths using the WU test approach with web material from a 203 mm × 203 mm × 9.53 mm wide flange shape

Longitudinal web material				
Mean web thickness, t (mm)	9.16	9.14	9.12	9.14
Mean notch diameter, d_n (mm)	11.8	14.8	20.9	27.9
Mean pin diameter, d (mm)	9.7	12.2	18.8	25.4
Mean clearance, $d_n - d$ (mm)	1.9	2.6	2.1	2.5
Number of nominally identical specimens	11	11	11	11
Mean pin-bearing strength	188	170	154	136
SD (N/mm^2)	6.2	9.1	12.7	14.8
CV (%)	3.3	5.3	8.4	10.9
Characteristic value* (N/mm^2)	177	155	133	111
Mean d/t ratio	1.06	1.34	2.05	2.78

* Mean - 1.72SD

Table 2 Statistical test results for 45° pin-bearing strengths using the WU test approach with web material from a 203 mm × 203 mm × 9.53 mm wide flange shape

45° web material				
Mean web thickness, t (mm)	9.14	9.10	9.11	9.07
Mean notch diameter, d_n (mm)	11.8	14.8	20.9	27.9
Mean pin diameter, d (mm)	9.7	12.2	18.8	25.4
Mean clearance, $d_n - d$ (mm)	1.9	2.6	2.1	2.5
Number of nominally identical specimens	6	6	6	6
Mean pin-bearing strength	174	158	113	118
SD (N/mm ²)	10.3	8.4	7.5	4.4
CV (%)	5.9	5.3	5.6	3.7
Characteristic value* (N/mm ²)	156	143	121	111
Mean d/t ratio	1.06	1.34	2.06	2.80

* Mean – 1.77SD

Table 3 Statistical test results for transverse pin-bearing strengths using the WU test approach with web material from a 203 × 203 × 9.53 mm wide flange shape

Transverse web material				
Mean web thickness, t (mm)	9.09	9.10	9.17	9.18
Mean notch diameter, d_n (mm)	11.8	14.8	20.9	27.9
Mean pin diameter, d (mm)	9.7	12.2	18.8	25.4
Mean clearance, $d_n - d$ (mm)	1.9	2.6	2.1	2.5
Number of nominally identical specimens	6	6	6	6
Mean pin-bearing strength	168	146	120	110
SD (N/mm ²)	10.5	13.7	10.1	7.2
CV (%)	6.2	9.3	8.5	6.6
Characteristic value* (N/mm ²)	149	122	102	97
Mean d/t ratio	1.07	1.34	2.05	2.77

* Mean – 1.77SD

3 TEST RESULTS AND DISCUSSION

Tables 1 and 3 present a summary of the test results, with, respectively, the table ordering of longitudinal (0°), 45° and transverse (90°). Strengths are given in units of N/mm² (MPa). The number of specimens is given in row five. For each batch the mean, standard deviation and Coefficient of Variation (CV) are given in rows six to eight on the assumption that the strength population fits the Gaussian distribution. Characteristic values in row nine are determined using the guidance in Annex D7 (General principles for statistical evaluation) of Eurocode 0 (BS EN 1990:2002), and they may be associated with a pin-bearing strength when using Equation 1 to design a bolted connection. The CV is typically between 5 and 10%; with the higher values linked to the largest hole diameter of 28 mm. The final row entries in the tables give the mean pin diameter-to-material thickness ratios (d/t).

Plotted in Figure 3 are typical stress-stroke curves at the three material orientations of 0, 45 and 90° for tests with the 28 mm hole and 25.4 mm pin diameters. Their

characteristic shapes are similar with the maximum load occurring at a stroke of about 1.0 mm and in descending magnitude with increase of material orientation (θ). After the initial embedding stage the slope of the linear part of load-stroke curve should be proportional to the modulus of elasticity. The ratio of gradients (for stroke between 0.4 and 0.8 mm) for the 0 and 90° tests is 1.72; very close to 1.7 given by the moduli reported in the PhD thesis by Lane (2002) that were determined using the resin burn-off method and micromechanical modelling.

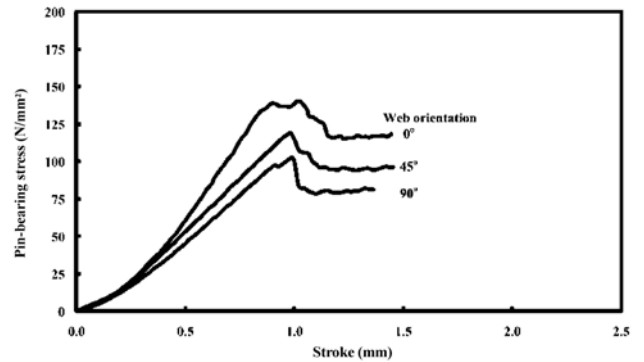


Figure 3 Pin-bearing stress with stroke curves for web material at the three orientation of 0, 45 and 90° with nominal hole diameter of 28 mm ($d/t = 2.77$ to 2.80)

Using the gradient for the 45° test in Figure 3 we find that the 45° modulus of elasticity is 11.2 kN/mm², which is 12% higher than in the transverse direction. For the pin-bearing strengths not governed by UD roving reinforcement we find the ratio F_{45}^{br}/F_{90}^{br} is 1.13 using the mean of the four characteristic strengths in Tables 2 and 3. This suggests that for orientations away from 0° there may be a correlation between the modulus of elasticity and the pin-bearing strength.

In Figure 4 the characteristic strengths from Tables 1 to 3 are plotted against the mean bolt diameter-to-material thickness ratio (d/t). It is assumed that there is a linear variation between the data points. The legend defines the plots that are for the three web material orientations. The d/t ratio increases from 1.06 to 2.80. The pin-bearing strength is seen to reduce with increase in d/t . The trend of the strength decrease in Figure 4 might be linear, but confirmation does require more test results. Based on the lowest characteristic value (with biggest pin diameter) the strength is found to reduce by between 50% and 60% as the pin diameter increases from 9.7 to 25.4 mm.

From the characteristic value in Tables 1 and 3 the lowest value to the ratio F_0^{br}/F_{90}^{br} is 1.13 (mean of the four values is 1.23), and this is lower than the previously understood lower bound ratio of 1.2 (Mottram, 2009). Given that the ratio of the directional modulus of elasticity is 1.7 (Lane, 2002) it is observed that this pin-bearing strength ratio is not proportional to the modulus ratio. An explanation for this finding could be that the

mechanism for the bearing mode of failure has changed with orientation, and this is the subject of research.

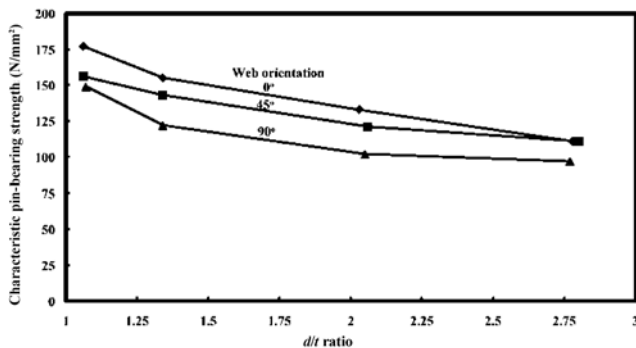


Figure 4 Characteristic pin-bearing strengths (in N/mm^2) of 9.1 mm thick web material with d/t ratio and hole clearance of 1.9 mm or larger

4 CONCLUDING REMARKS

In this paper new pin-bearing strengths are reported for the web material in a standard wide flange shape from the 1525 series of shapes pultruded by Creative Pultrusions Inc. Because the length of the 90° specimen coupon is limited by the web having a depth of 180 mm the load is applied using a test method developed recently at University of Warwick (Mottram, 2009).

Mean and characteristic values for pin-bearing strengths at the three material orientations of 0° , 45° and 90° are given for mean bolt diameter-to-material thickness ratios from 1.06 to 2.80. To represent site application a clearance hole (minimum of 1.9 mm) is present. By plotting the characteristic values it is found that the strength decreases (up to 60% based on lowest value) with increase of this ratio. The trend might be linear, but confirmation will require more test results (with a minimum of 10 nominally identical specimens per batch).

It is found that the minimum characteristic values are for the test parameters with the 28 mm hole and 25.4 mm steel pin (bolt). These minimum test values at $111 \text{ N}/\text{mm}^2$ (0°), $111 \text{ N}/\text{mm}^2$ (45°), and $97 \text{ N}/\text{mm}^2$ (90°), cannot easily be linked to the maximum bearing strength values of $206 \text{ N}/\text{mm}^2$ (0° or lengthwise), and $124 \text{ N}/\text{mm}^2$ (90° or crosswise) given in the pultruder's design manual (Anon, 2010a). The main reason for this finding is that the test parameters are different, thereby highlighting the requirement that pin-bearing strengths must be determined

with test parameters that correspond to those found in bolted connections in practice.

To complement the room temperature values reported in this paper it shall be necessary to know how pin-bearing strengths change when the connection is subjected to environmental conditioning that impacts degradation to the material around a bolt hole equivalent to what could occur over the service life of a pultruded structure.

It is because of the uncertainty on how every possible influence could affect a bearing strength that the authors strongly recommend using the pin-bearing value (i.e. there is no lateral restraint) when carrying out resistance design calculations for the design of bolted connections using Equation 1.

REFERENCES

- Anonymous, 2010a. The New and Improved Pultrex® Pultrusion. *Design Manual (Metric version)*. Creative Pultrusions Inc.: Alum Bank, PA. //www.creativepultrusions.com/rd.html (Literature library) 2nd June 2010.
- Anonymous, 2010b. *Strongwell Design Manual*. Strongwell: Bristol, VA. //www.strongwell.com/ (Literature) 2nd June 2010.
- Bank, L. C. 2006. *Composites for Construction - Structural Design with FRP Materials*, John Wiley & Sons, New Jersey.
- BS EN 1990:2002. *Eurocode 0 - Basis of Structural Design*. United Kingdom: British Standards Institution
- Cooper, C. & Turvey G. J. 1995. Effects of joint geometry and bolt torque on the structural performance of single bolt tension joints in pultruded GRP sheet material. *Composite Structures* 32(1-4): 217-226.
- Lane, A. 2002. *An Experimental Investigation of Buckling Mode Interaction in PFRP Columns*. PhD thesis. Coventry, UK: University of Warwick.
- Mottram, J. T. 2004. Friction and load transfer in bolted joints of pultruded fibre reinforced polymer section. *Proceedings of the 2nd International Conference on FRP Composites in Civil Engineering*. Adelaide. 845-850. Lieden: Balkema.
- Mottram, J. T. 2009. Determination of pin-bearing strength for the design of bolted connections with standard pultruded profiles. *Proceedings of the 4th International Conference on Advanced Composites in Construction (ACIC 2009)*. Edinburgh. 483-495. Chesterfield: NetComposites Ltd.
- Mottram, J. T. & Turvey, G. J. 2003. Physical test data for the appraisal of design procedures for bolted joints in pultruded FRP structural shapes and systems. *Progress in Structural Engineering and Materials* 5(4): 195-222.

Development of an Effective Joining Method for a Pultruded Hybrid CFRP/GFRP Laminate

Nguyen Duc Hai, Hiroshi Mutsuyoshi, Kensuke Shiroki & Tatsuya Ishihama

Department of Civil and Environmental Engineering, Saitama University, Saitama, Japan

ABSTRACT This paper presents results from an experimental investigation on the tensile behavior of double lap joints in pultruded hybrid CFRP/GFRP laminates. A number of hybrid FRP coupon specimens with bolted-only and bonded-and-bolted joints were tested. The results show that a combined use of steel bolts, adhesive bonding and V-notch splice plates in double lap joints was found to be an effective method for joining hybrid FRP laminates. The rough surface of V-notch splice plates and adhesive bonding contributes to improve the stiffness of joints.

1 INTRODUCTION

FRP composites have been increasingly used in civil infrastructure applications due to their advantageous properties such as high specific strength, lightweight, and corrosion resistance. Recently, a hybrid FRP girder consisting of carbon and glass fibers have been developed. The idea is to use the superior strength of CFRP in the flanges while keeping the material costs low by using GFRP in the flanges and web. A number of laboratory tests have been conducted to investigate the structural performance of hybrid FRP beam and the results showed a possibility of utilizing this beam as a bridge component (N.D. Hai et al. 2009). However there are still two major issues needed to be further investigated before applying hybrid FRP beam for real bridge application. One is development of joining for hybrid FRP laminates. The other is evaluation of environmental aspects such as amount of carbon dioxide emission (CO_2) and life cycle cost of hybrid FRP bridges. As the second step of the ongoing FRP research project supported by Japanese government, this study focuses on the first issue with emphasis on developing an effective joining method for hybrid FRP laminates.

Joining of FRP laminate is commonly achieved by adhesive bonding, mechanical fastening or a combination of the two methods. The combination of adhesive bonding and mechanical fastening is often employed as a safeguard against defects within the adhesive layer which may lead to premature or catastrophic failure (Kelly 2006). Numerous experimental and analytical investigations on joining of FRP laminates have been conducted which mainly focused on aerospace applications (Hart-Smith 1985, Camanho 1997). However, limited published works exist in the field of civil infrastructure applications. In addition, previous studies cover a wide range of FRP

laminates with various fiber architect and matrix types, fiber lay-up and stacking sequences, etc., which result in different behavior of joints. Thus, additional investigations are required to fully understand the characteristics of joints. This study focuses on experimentally determined behavior of bolted/bonded joints for hybrid CFRP/GFRP laminates. A number of coupon specimens with double lap bolted-only and bonded-and-bolted joints were tested to examine their strength and behavior. The effects of end distance, V-notch splice plates and the contribution of adhesive bonding to the joint strength and failure modes are discussed.

2 TEST PROCEDURE

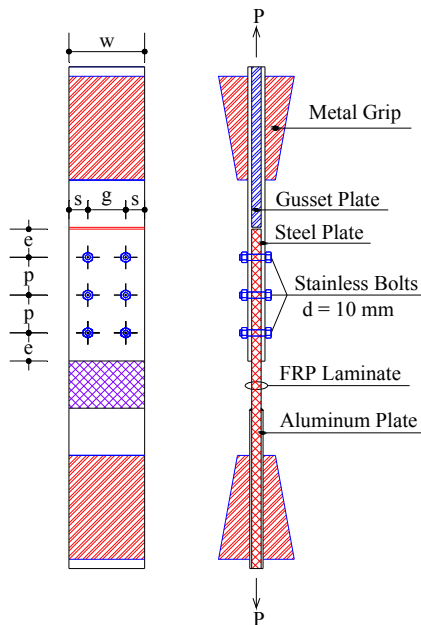
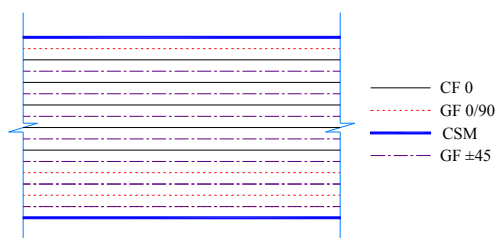
2.1 Test specimen

A series of hybrid FRP coupon specimens with bolted/bonded double lap joints were tested under tensile loading as shown in Figure 1. Typical specimens have the same width of $w = 80$ mm, end distance of $e = 30$ mm, side distance of $s = 20$ mm, longitudinal and transverse hole spacing of $p = g = 40$ mm. The nominal thickness of the FRP laminates is 14 mm. The FRP laminates consist of CFRP and GFRP. The angle of CFRP was fixed to be zero degree while the angle of GFRP was 0, 90, ± 45 degree or Continuous Strand Mat (CSM). All specimens were manufactured using pultrusion process. Layer composition of hybrid FRP coupon specimens is shown in Figure 2. Material properties of the FRP laminae are listed in Table 1.

Typical specimens were configured with the same ratios of end distance to bolt diameter ($e/d = 3$), laminate width to bolt diameter ($w/d = 8$), side distance to bolt diameter ($s/d = 2$), longitudinal spacing (pitch) to bolt diameter ($p/d = 4$), transverse spacing (gage) to bolt diameter ($g/d = 4$), bolt diameter to splice plate thickness

Table 1 Material properties of FRP laminae

Parameters	Notation	Unit	CF 0	GF 0/90	GF ± 45	GF CSM
Young's Modulus	E_{11}	GPa	128.1	25.9	11.1	11.1
	E_{22}	GPa	14.9	25.9	11.1	11.1
Shear Modulus	G_{12}	GPa	5.5	4.4	10.9	4.2
Poisson's Ratio	ν_{12}	-	0.32	0.12	0.29	0.31

**Figure 1** Test configuration**Figure 2** Layer composition of hybrid FRP laminate

($d/t_{sp} = 1.1$), washer diameter to bolt diameter ($d_w/d = 2.5$) and hole clearance ($d_h - d = 0.05d$). Stainless steel bolts were used with a nominal diameter of 10 mm. The yield and ultimate strength of bolts are 450 MPa and 700 MPa, respectively. Holes were machined in the specimens using diamond tips. The specimens were lateral clamped with bolts through 9 mm thick splice plate in both sides. The torque was applied exactly at distinct values by controlling the presetting torque wrench. The same configuration was set for specimens with bolted-only and bonded-and-bolted joints. For the bonded-and-bolted joint specimens, the adhesive was pasted on both sides of the FRP laminates before applying the torque. The adhesive was cured in the experimental room for 24 hours before each test. The mechanical properties of adhesive are shown in Table 2. A number of coupon

specimens with double lap bolted-only and bonded-and-bolted joints were tested to examine their strength and behavior. The effects of end distance, V-notch splice plates and the contribution of adhesive bonding to the joint strength and failure modes are discussed. Coupon test variables are listed in Table 3.

Table 2 Mechanical properties of adhesive

Parameters	Curing condition	Properties after curing (MPa)
Bending strength	20 \pm 2 $^{\circ}$ C	50
Compressive strength		70
Compressive modulus		4000
Tensile strength		20
Tensile shear strength		10

Table 3 Coupon test variables

Specimen	Type of joint	Type of splice plate	No. of bolts	Torque (Nm)	1 TAL (mm)	2 ED
A0	\dagger B	Flat	6	20	n/a	3d
A1	$\dagger\dagger$ BB	Flat			0.1	
A2	$\dagger\dagger$ BB	V-notch			0.1	
E2d-B	\dagger B	Flat	2	20	n/a	2d
E3d-B						3d
E4d-B						4d
E2d-BB	$\dagger\dagger$ BB	Flat	2	20	0.1	2d
E3d-BB						3d
E4d-BB						4d

\dagger B = Bolted-only; $\dagger\dagger$ B = Bonded-and-bolted; 1 TAL = Thickness of adhesive layer; 2 ED = End distance

2.2 Test setup and measurement

All tests were conducted using a Universal Testing Machine (UTM) with a load capacity of 500 kN. The data logger was used to record load, displacement and strain data. The specimens were clamped by the grips of the testing machine at both ends and the tensile force was applied at the top and bottom end.

Clip gages were attached on the both sides of the specimen to measure the relative displacement between the FRP laminate and the splice plates. Each specimen was instrumented with back-to-back strain gages attached on the FRP laminate and the splice plates. The test setup is schematically illustrated in Figure 3.

3 TEST RESULT AND DISCUSSION

3.1 Load and displacement curve

The comparison of load-relative displacement curves of specimens with configuration of 6-bolt double lap joints is shown in Figure 4. For identification purpose, the specimen with bolted-only will be referred to as specimen

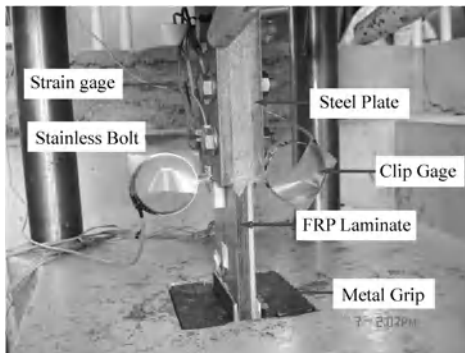


Figure 3 Test setup

A0 and the specimen with bonded-and-bolted will be referred to as specimens A1 and A2 as shown in Table 3.

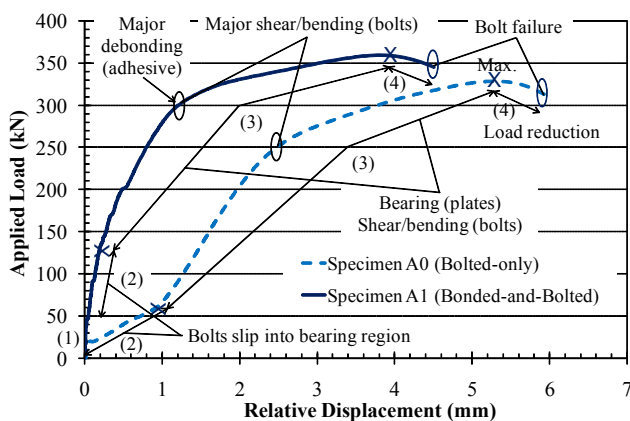


Figure 4 Load-relative displacement curve

Note that the relative displacement in the figure indicates the difference in the averaged elongation of clip gages attached on both sides of the specimen (one end of the clip gage is attached on the splice plate and the other end is attached on the specimen). As can be seen, the load-displacement curve of the specimen A0 can be subdivided into four stages. For the first stage (1), there was no slip between the splice plates and the FRP laminates when the load in the range of 0 to 15 kN. This is due to the effect of the bolt-torque applied to the bolts. For the second stage (2), the load-displacement curve behaves linearly when the load increases from 15 to 60 kN corresponding to the relative displacement of 0.0-1.0 mm. This indicates that the bolts gradually slipped into bearing region around the holes of FRP laminates. The third stage (3) shows the nonlinear behavior of the load-displacement curve with the range of relative displacement from 1.0-5.5 mm. This might be due to the development of bearing failure in the FRP/splice plates combined with shear/bending of the bolts. The final stage (4) is the load reduction after excessive failure strength of bolts.

Similarly, the load-displacement curve of the specimen A1 can be subdivided into four stages. The first stage shows the slip resistance of joints when the load is approximately 50 kN. This value is three times higher

than that of the specimen A0 due to the contribution of adhesive bonding. The second stage indicates linear behavior of load-displacement curve when the load increases from 50-130 kN corresponding to the relative displacement of 0.05-0.2 mm. It is noted that the maximum displacement of specimen A1 in this stage is much smaller than that of specimen A0 because the hole clearances are filled with adhesive during the preparation of specimen A1. The behavior of bolts filled with adhesive seems to be similar to that of precision fit bolts. Therefore specimen A1 can effectively reduce slip in the joint. The third stage (3) exhibits a gradual development of bearing failure in the FRP/splice plates together with local debonding of the adhesive layer and shear/bending of bolts when the load increases from 130-360 kN corresponding to the relative displacement of 0.2-3.5 mm. The final stage shows the sudden failure of the specimen A1 at about 345 kN. It is clear from Figure 4 that the stiffness of the load-displacement curve of the specimen A1 is much higher than that of the specimen A0. This suggests that adhesive bonding can improve considerably the slip resistance and the stiffness of joints.

3.2 Effect of V-notch splice plate

To examine the effect of splice plates on the strength of bonded-and-bolted joints, two specimens with the same configuration but different types of splice plates were tested. The specimen A1 using flat splice plates while specimen A2 using V-notch splice plates (height and spacing of V-notches are 0.5 mm and 1.0 mm, respectively). The original idea of using V-notch splice plate is to provide more clamping force between the splice plates and the hybrid FRP specimen (splice plates bite the specimen) with an appropriate amount of torque that will not lead to damages at the outermost surface of the specimen. Figure 5 shows the comparison of the load-relative displacement relationship between specimens A1 and A2. The figure shows that the stiffness of load-displacement curve of these specimens is almost the same up to 130 kN. However, with the continuing increases of load, specimen A2 shows higher stiffness than that of specimen A1. The differences in stiffness tend to increase with the increases of load. This may be due to rough surface of the splice plate in specimen A2 contributed to improve bonding between the splice plates and the hybrid FRP specimen. Indeed, the load at which major debonding of adhesive layer and major shear/bending of bolts happen of specimen A2 is approximately 14% higher than specimen A1. This indicates that adhesive layer may carry almost the load before major debonding occurs. When the adhesive layer fails, the load is carried solely by bolts. Finally, both specimens A1 and A2 fail due to shearing of bolts.

3.3 Effect of end distance

To investigate the effect of end distance to the failure strength of joints, a number of specimens with 2-bolt

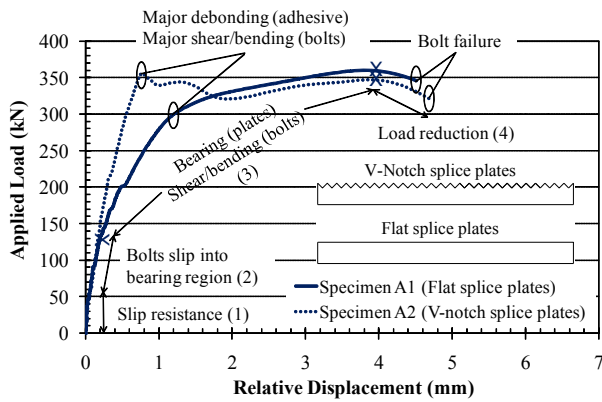


Figure 5 Effect of splice plates

configuration varying end distances (e) from $2d$ to $4d$ (where d is nominal diameter of bolt) were conducted. Two series of specimens with bolted-only and bonded-and-bolted joints were investigated. Figure 6 shows the relationship between load and displacement of bolted-only joint specimens. It can be seen that the specimen E2d-B (with end distance of $2d$) has lowest failure load and failed due to shear-out failure of the FRP laminate as shown in Figure 7. The specimens E3d-B and E4d-B (with end distance of $3d$ and $4d$, respectively) have almost the same failure load but different failure modes. The failure mode of specimen E3d-B was shear-out failure while the failure mode of specimen E4d-B was bearing failure. This indicates that specimen E4d-B is the most appropriate for the bolted-only joints. However, all specimens with bonded-and-bolted joints (E2d-BB, E3d-BB and E4d-BB) showed the same failure load and failure mode although the end distance was varied as same as bolted-only specimens. The load-displacement curve of bonded-and-bolted specimens is shown in Figure 8. The failure mode of these specimens was bearing failure. The differences in failure mode of bolted-only and bonded-and-bolted specimens were due to the present of adhesive layer. As previous discussion, adhesive may carry almost the load before major debonding occurs. The load is then transmitted to the bolts but they could

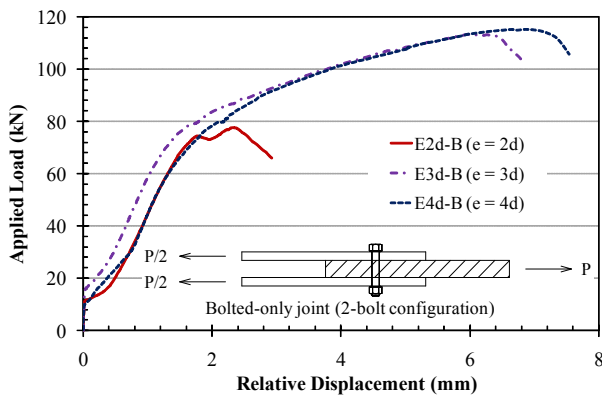


Figure 6 Effect of end distance to bolted-only joint

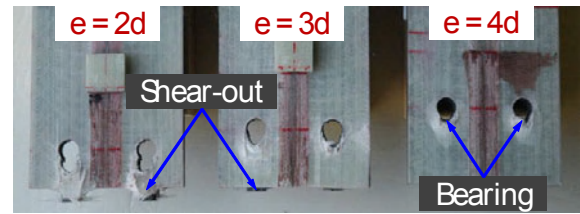


Figure 7 Failure mode of bolted-only specimens

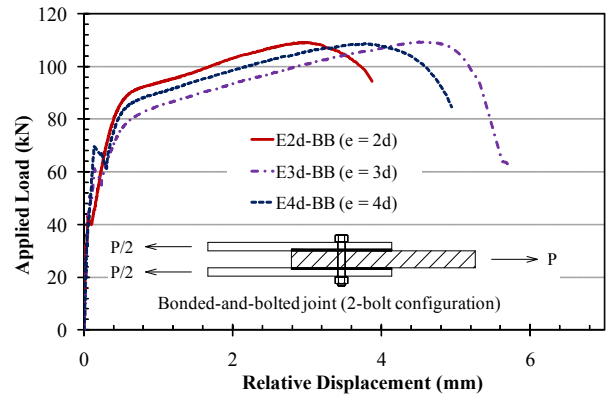


Figure 8 Effect of end distance to bonded-and-bolted joint

not cause the shear-out failure as bolted-only specimens. This suggests that shear-out failure was developed gradually but not suddenly. It is concluded that the effect of end distance on the failure strength of bonded-and-bolted joints is not sensitive as that of bolted-only joint and the failure mode of bonded-and-bolted specimens is of desirable failure mode. The end distance of $3d$ is minimum requirement for designing of joints for hybrid FRP laminates.

4 CONCLUDING REMARK

The combined use of steel bolts, adhesive bonding and V-notch splice plates in double lap joints was found to be an effective method for joining hybrid FRP laminates. The rough surface of V-notch splice plates and adhesive bonding contributes to improve the stiffness of joints.

REFERENCES

Nguyen Duc Hai, Hiroshi Mutsuyoshi, Shingo Asamoto, and Takahiro Matsui (2009). Structural Behavior of Hybrid FRP Composite I-Beam, *Journal of Construction and Building Materials*, Vol. 24, June 2010, pp. 956-969.

G. Kelly, 2006. Quasi-Static Strength and Fatigue Life of Hybrid (Bonded/Bolted) Composite Single-Lap Joints, *Compos Structure* (72): 119–129.

Camanho P. P., Matthews F. L., 1997. Stress Analysis and Strength Prediction of Mechanically Fastened Joints in FRP: a Review, *Composites Part A* (28A): 529-547.

L.J. Hart-Smith, 1985. Bonded-bolted Composite Joints, *J. Aircraft* (22): 993–1000.

A Consistent Design Concept for Bolted Connections in Standardized GFRP-Profiles

Matthias Oppe (M.Oppe@knippershelbig.com)

Knippers Helbig Inc., New York, USA

Jan Knippers

Knippers Helbig – Knippers Helbig GmbH, Stuttgart, Germany

ABSTRACT This paper presents a consistent design concept for bolted connections of standardized GFRP-profiles. All test specimens have been taken either from pultruded flat-profiles or the webs of standard pultrusion I or U-profiles from Fiberline Composites A/S. At first the orthotropic material properties of the laminates were determined by experimental tests, including short term and long term properties as well as influence of temperature and media. Experimental results have been confirmed by numerical simulations; taking the complex limit state conditions into account introducing the fracture criteria of Puck. Afterwards relevant functions to determine resistances have been developed for different limit state conditions. To obtain characteristic values, these functions have been calibrated according to the reliability requirements of EN 1990. Using simplified engineering models for the practical design of bolted connections therefore a complete and consistent design concept is provided.

1 INTRODUCTION

The design of bolted connections within GFRP-profiles is much more complex than for standard structural materials such as steel. Bolted connections, which are the most practical connection for civil applications, not only sever the reinforcing fibers and therefore reduce the overall strength of the composite, but also introduce high stress concentrations, which promote fracture.

A lot of research has been carried out on bolted connections loaded in shear. However, there is only few information on ultimate resistance and failure criteria for connections, where the bolts are subjected to tension loads. The EUROCOMP Design Code (1996) includes a simplified resistance model, whereas Morsi (1994) and Turvey (2009) present the results of tests conducted on different types of GFRP connections and fasteners.

So far design rules, which exist in international and national guidelines, are far from being complete and consistent.

2 EXPERIMENTAL INVESTIGATIONS

2.1 Material Properties

At first several experimental investigations were performed in order to verify the different short-term material properties. Including determination of in-plane shear strength according to the Iosipescu-method. Subsequently long-term properties, influences of temperature and media respectively have been determined within numerous

experimental investigations.

2.2 Bolts loaded in shear

The intention of the test-programme on mechanically fastened connections subjected to shear loading was to modify the existing resistance formula by

- determination and introduction of stress concentration factors k_{cc} and k_{lc} ,
- investigations on angle ν for load-distribution in front of the bolt,
- determination of in-plane shear strength $f_{\tau,xy}$ and pin-bearing strength f_p .

Therefore 70 tests with different specimen dimensions, number of bolts etc. have been carried out with action in direction of pultrusion as well as perpendicular to direction of pultrusion.

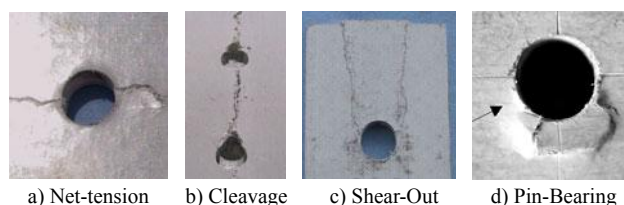


Figure 1 Failure modes observed within tests

Four typical failure modes examined during the tests are presented within Figure 1. A complete summary of all tests and corresponding evaluations of results can be found within Oppe (2009a).

2.3 Bolts loaded in tension

Since there is a lack of information on the load-bearing capacity of connections, in which the bolts are subjected to tension loads those connections were specially focused.

The intention of the comprehensive test-series was to verify the validity of the resistance formula for bolts subjected to tension loads proposed by EUROCOMP Design Code. Therefore 42 tests with different dimensions for the test specimens (e.g. distance to support a , laminate thickness t , diameter of hole d_0 and washer d_w).

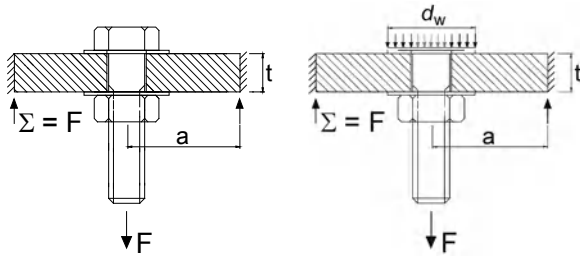


Figure 2 Test setup (1st test series on bolts in tension)

The load situation (Figure 2) refers to applications where e.g. single loads are introduced via the flanges of hollow sections. Figure 3 presents the two different failure modes observed within the tests. Depending on the dimensions of the specimens either delamination or pull-through failure was governing.

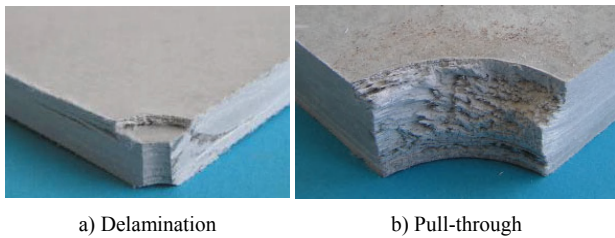


Figure 3 Failure modes observed within 1st test series

A second test series has been carried out using a modified test setup in order to fulfill the orthotropic material requirements and investigate the load-deformation behaviour of a typical beam-to-column connection. In addition to the global normal stresses, caused by bending, there is a local load introduction into profile flanges.

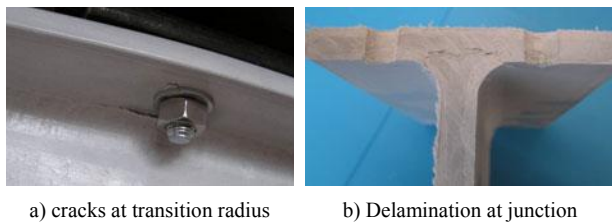


Figure 4 Failure modes observed within 2nd test series

The first cracks were observed at the edge of the transition radius between web and flange (Figure 4a).

Where as final failure occurred due to a complete delamination at the joint between the web and flange (Figure 4b). Oppe (2009a) describes all tests in detail.

3 NUMERICAL MODELLING

The stress- and strength analysis for composite materials is done in different steps while each lamina is idealised as a homogeneous unidirectional ply.

Using a special subroutine, the state of the art strength criterion defined by Puck (2002), based on the mechanical principles of Coulomb and Mohr for brittle material, can be used within the Finite-Element Software MSC MarcMentat (Oppe, 2008) instead of conventional global strength criterions by e.g. Tsai-Wu and Tsai-Hill.

Beyond successful verifications by recalculation of small-scaled coupon tests on several unidirectional plies and complex laminates under various loading situations (Figure 5).

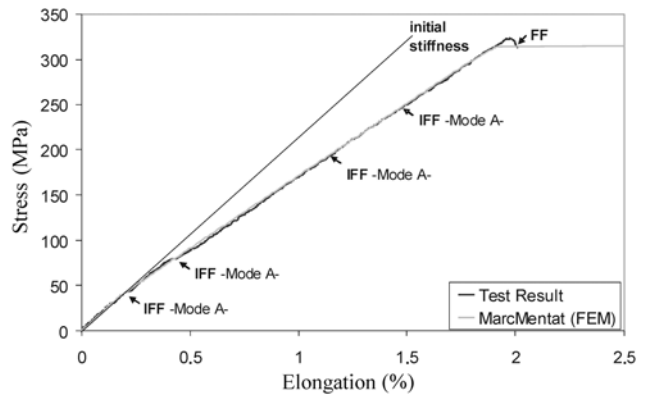


Figure 5 Comparison for tension coupon test

The FE-models have been extended subsequently to allow for the analyses of load-displacement behaviour for bolted connections.

4 DESIGN MODEL

4.1 General

Following dimensions have to be guaranteed within design of bolted connections.

The holes within groups of bolts have to be fabricated with small tolerances in order to make sure, that the load is carried by all of the bolts within the connection.

Table 1 Minimum requirements for dimensions

	e	c	p_1	p_2
0°	$3,5d_0$	$2d_0$	$4d_0$	$4d_0$
90°	$2,5d_0$	$2,5d_0$	$4d_0$	$4d_0$

A maximum of five bolts within loading direction and two bolts in perpendicular direction shall not be exceeded.

Figure 6 presents the general approach to determine ultimate resistance of bolted connections subjected to various loading and environmental conditions respectively.

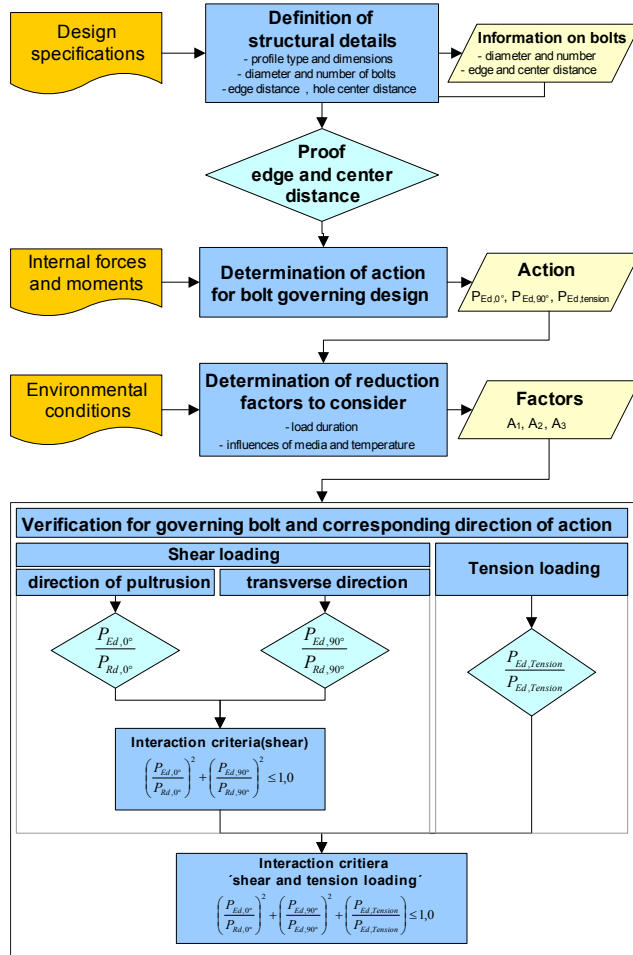


Figure 6 General approach to determine resistance

Reduction factors $A_1 - A_3$ can be considered on action or resistance side respectively.

$$P_{Rd} = P_{Rk} / (\gamma_M \times A_1 \times A_2 \times A_3) \quad (1)$$

where P_{Rd} = ultimate resistance; P_{Rk} = characteristic resistance; γ_M = partial safety factor and $A_1 - A_3$ reduction factors.

4.2 Bolts loaded in shear

The four distinct failure modes of single-bolted double-lap joints in concentric tensile loading experienced within this test series can be predicted by means of the following stress distribution (Figure 7) and corresponding formulas.

Within wide standardized cross-sections the decisive width w^* and corresponding edge distance c^* is controlled by minimum distance to the edge of the profile to the hole center distance (Figure 8).

Minimum resistance determined for the four different failure modes governs design of bolts subjected to shear loading.

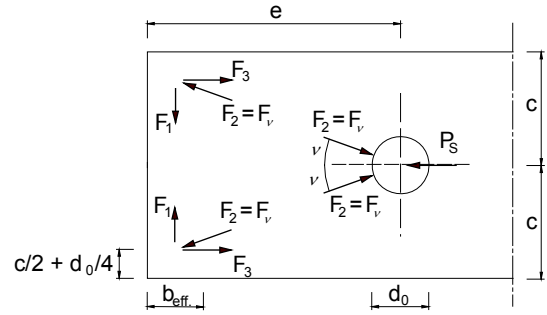


Figure 7 Distribution of stresses within connection

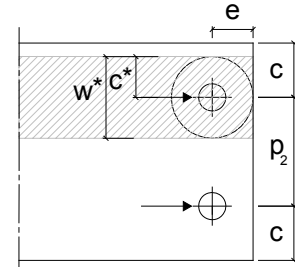


Figure 8 Decisive width w^* and edge distance c^*

– Net-tension failure

$$P_S = P_{Rk} = 2(c - d_0/2) \times t \times f_{t,i} / k_{tc} \quad (2)$$

where P_S = shear force within bolt; c = edge distance; d_0 = diameter of bolt hole; t = laminate thickness; $f_{t,i}$ = tension resistance and k_{tc} = stress concentration factor.

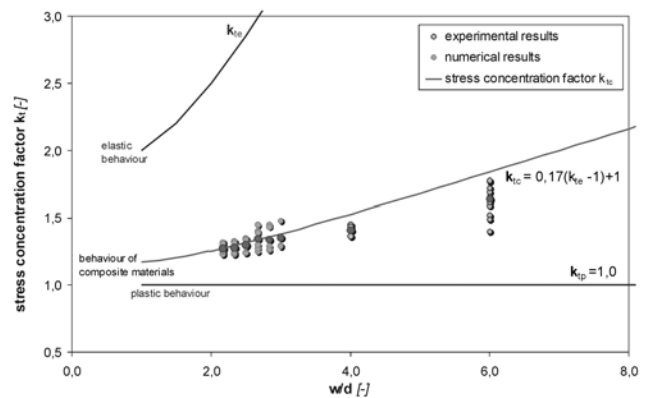


Figure 9 Determination of stress concentration factor k_{tc} .

– Cleavage failure

$$P_S = P_{Rk} = 2b_{eff} \times t \times f_{t,i} / \tan v \quad (3)$$

where b_{eff} = effective width and v = angle of load distribution.

Table 2 Relation between angle v and dimensions e/w .

e/w	0,375	0,500	0,750	1,000	$\geq 1,125$
0°	30,63	28,28	25,67	23,51	23,20
90°	36,60	33,83	31,20	30,00	29,80

$$\tan v = \frac{c/2 + d_0/4}{e - b_{eff}/2} \quad (4)$$

where e = edge distance

– Shear-out failure

$$P_S = P_{Rk} = 2(e - d_0/2) \times t \times f_{\tau,xy} \quad (5)$$

where $f_{\tau,xy}$ = in plane shear strength.

– Bearing failure

$$P_S = P_{Rk} d \times t \times f_{p,i} / k_{cc} \quad (6)$$

where d = bolt diameter, $f_{p,i}$ = pin bearing strength and k_{cc} = stress concentration factor

$$k_{cc} = (d_0/d)^2 \quad (7)$$

Whenever the force is not acting in direction of pultrusion or transverse direction, it has to be distributed within two parts. Resistance determined for each of those two has to be combined by means of the following interaction criteria.

$$\left(\frac{P_{Ed,0^\circ}}{P_{Rd,0^\circ}} \right)^2 + \left(\frac{P_{Ed,90^\circ}}{P_{Rd,90^\circ}} \right)^2 \leq 1,0 \quad (8)$$

where $P_{Ed,0^\circ}$ = action in 0° -dir., $P_{Rd,0^\circ}$ = Resistance in 0° -dir., $P_{Ed,90^\circ}$ = action in 90° -dir., and $P_{Rd,90^\circ}$ = Resistance in 90° -dir.

4.3 Bolts loaded in tension

Minimum resistance determined for the three different failure modes, observed within experimental investigations, governs design of bolts subjected to shear loading (Oppe, 2009b).

– Delamination

$$P_t = P_{Rk} = \frac{2}{3} f_\tau \times \pi \times d_w \times t \times (m_\lambda) \quad (9)$$

$$\lambda = \left(a - \frac{d_w}{2} \right) / t \quad (10)$$

where P_t = tension force within bolt, f_τ = shear strength, d_w = diameter of washer, m_λ = modification factor and a = distance to support.

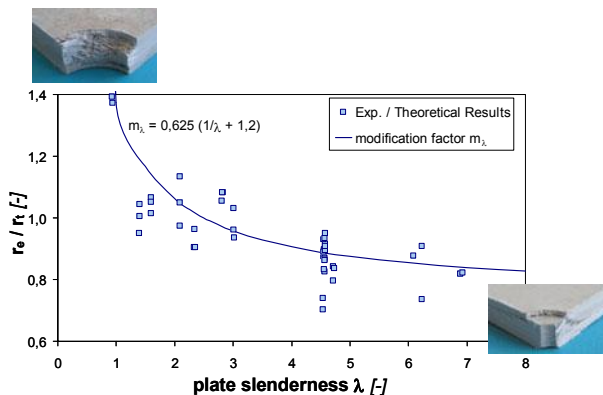


Figure 10 Modification factor m_λ

– Punching

$$P_t = P_{Rk} = \frac{2}{3} f_{\perp II} \times \pi \times d_w \times t \quad (11)$$

where $f_{\tau,\perp}$ = shear strength of UD-ply

– Interaction 'shear and bending'

$$\frac{f_{by,Ed}}{f_{by,Rd}} + \frac{f_{\tau,Ed}}{f_{\tau,Rd}} \leq 1 \quad (12)$$

where $f_{by,Ed}$ = transverse bending stress, $f_{by,Rd}$ = transverse bending strength, $f_{\tau,Ed}$ = shear stress and $f_{\tau,Rd}$ = shear strength.

4.4 Determination of partial safety factor

The final design models for bolted joints subjected to shear loads and tension loads respectively have been evaluated by means of statistical evaluations according to Annex D of EN 1990 (2001). Safety factors based on the evaluation procedure are stated to $\gamma_{M,Shear} = 1,35$ and $\gamma_{M,Tension} = 1,33$ respectively.

5 CONCLUDING REMARKS

So far design rules, which exist in international and national guidelines, are far from being complete and consistent.

Using simplified engineering models for the practical design of bolted connections including also environmental conditions (temperature and media) a complete and consistent design concept is provided.

REFERENCES

- EN 1990, 2001. Basis of Structural Design, *CEN European Committee for Standardization*, Brussels, Belgium.
- EUROCOMP Design Code and Handbook, 1996. Structural Design of Polymer Composites, The European Structural Polymeric Group; E & FN Spon, London, UK.
- FIBERLINE Design Manual, 2002. *Design- und Konstruktionshandbuch für Konstruktionsprofile aus Verbundwerkstoffen*, Fiberline Composites A/S; Kolding.
- Morsi, E., Larralde, J. 1994. Characteristics of Mechanical Connectors for Construction of FRP Structures, *Proceedings of ASCE Conference*, San Diego CA, ASCE NY, 991-1000.
- Oppe, M. 2009 Zur Bemessung geschraubter Verbindungen von pultrudierten faserverstärkten Polymerprofilen, *Dissertation, Schriftenreihe Stahlbau, Heft 66*, Shaker-Verlag Aachen, ISBN: 978-3-8322-8247-9.
- Oppe, M., Feldmann, M. 2008. Load Bearing Behaviour of Detachable Connections in Glass-Fibre Reinforced Polymers, *Fourth International Conference on FRP Composites in Civil Engineering (CICE2008)*, ISBN: 978-3-905594-50-8, Zurich, Switzerland.
- Oppe, M., Knippers, J. 2009. Behaviour of bolted connections in GFRP subjected to tension loads, *Advanced Composites in Construction ACIC '09 (Edinburgh)*, NetComposites Ltd, Chesterfield, 2009, 495-506.
- Puck, A., Kopp, J., Knops, M. 2002. Guidelines for the determination of the parameters in Puck's action plane criterion, *Composite Science and Technology* 62.
- Turvey G. J. 2009. An experimental investigation on bolt pull-through failure in pultruded GRP plate, *Advanced Composites in Construction ACIC '09 (Edinburgh)*, NetComposites Ltd, Chesterfield, 2009, 462-472.

Composite Behavior of a Pultruded Hybrid CFRP-GFRP Beam with UFC Deck

Hiroshi Mutsuyoshi, Kensuke Shiroki, Nguyen Duc Hai & Tatsuya Ishihama

Department of Civil and Environmental Engineering, Saitama University, Saitama, Japan

ABSTRACT Hybrid Fiber Reinforced Polymer (HFRP), which is composed of Carbon FRP (CFRP) and Glass FRP (GFRP), has many advantages over conventional materials such as light weight, high specific strength, and corrosion resistance. HFRP is expected to find its application in severe corrosive environments or where light-weight rapid construction is required. This paper presents the development of a composite beam using an HFRP I-beam and precast Ultra-high strength Fiber reinforced Concrete (UFC) slab. UFC has high strength and high ductility, so it allows for reduction of the cross-section area and self weight. Full-scale flexural beam tests were conducted with different geometry of UFC slab and shear connection methods between the UFC slab and HFRP beam. For the composite beams with bolted-only connection, slip occurred between the HFRP beam and the UFC slab. On the other hand, slip was not observed in the composite beams with bonded-and-bolted connections. The flexural stiffness of beam specimens with bonded-and-bolted connection increased significantly compared with that of bolted-only connection specimens. Delamination failure was not observed in the compressive flange of the composite beams and the high tensile strength of the CFRP in the bottom flange could be utilized effectively by addition of the UFC slab on the top flange.

1 INTRODUCTION

Fiber Reinforced Polymer (FRP) has many advantages over conventional materials such as high specific strength, light weight and corrosion resistance. In recent years, FRP materials have been applied to structural members in many pedestrian and road bridges. Presently, a hybrid FRP (HFRP) composite beam for bridge applications is being developed. This beam optimizes the combined use of Carbon Fiber Reinforced Polymer (CFRP) and Glass Fiber Reinforced Polymer (GFRP) in HFRP beam cross section. While CFRP has high tensile strength and higher stiffness, it is relatively expensive, whereas GFRP is comparatively less expensive but its mechanical properties are lower than those of CFRP. In a beam subjected to bending about the strong axis, the top and bottom flanges are subjected to high axial stress. In the HFRP beam, these flanges are fabricated using a combination of CFRP and GFRP layers. On the other hand, the web is composed entirely of GFRP because it is not subjected to the same high stresses. The hybrid FRP beam therefore utilizes the advantages of both CFRP and GFRP for strength, stiffness and economy. Hybrid FRP is expected to find application in severe corrosive environments or where lightweight and rapid construction is required. The application of hybrid FRP composites could also contribute to a reduction of life cycle costs (LCC) and environmental load.

In previous laboratory studies of HFRP beams, it was

reported that the design was governed by deformation rather than strength limitations due to the low elastic modulus of FRP materials compared with equivalent steel or reinforced concrete beams. In addition, the HFRP I-beams subjected to flexural loading failed in the compressive flange due to delamination at the CFRP and the GFRP interface (N.D. Hai et al. 2009). These prior studies suggest that individual HFRP beams could not utilize the high tensile strength of the CFRP in the tension flange. To fully utilize this strength, the delamination failures in the compression flange must be avoided. One approach to accomplish this is to reduce the stresses in the HFRP compression flange by adding a concrete topping slab to resist the compression. This is analogous to composite steel construction where compression buckling failure of the steel top flange can be avoided by using the concrete topping slab to carry compression.

This research aims to develop a composite beam using HFRP I-beams and a UFC topping slab. It is expected that the composite beam system will increase beam stiffness, prevent buckling and delamination in the HFRP compressive flange and more effectively utilize the high tensile strength of the CFRP in the HFRP tension flange. Since the UFC slab will carry the majority of compression, it is no longer necessary to include CFRP in the HFRP top flange. However, during manufacturing of the HFRP I-beam, it was determined that both flanges must have the same properties to avoid initial beam curvature.

In order to maintain the light weight and high corrosion resistance of the HFRP beam in the composite beam, ultra high strength fiber reinforced concrete (UFC) was selected for the topping slab. The UFC used in this study had a compressive strength of 180N/mm^2 and a tensile strength 8.8N/mm^2 , with high ductility in both tension and compression due to the crack-bridging effect of the high strength steel fibers included in the UFC. Therefore steel bars are not necessary to reinforce the UFC slab for shrinkage and temperature effects, thereby reducing the slab thickness and overall self-weight of the composite HFRP-UFC beam system.

This paper discusses the flexural behavior of HFRP-UFC composite beams. Full-scale bending tests were performed using distinct shear connection methods to verify the performance of the overall HFRP-UFC beam system.

2 EXPERIMENTAL PROCEDURE

2.1 Material

a. Hybrid Fiber Reinforced Polymers (HFRP)

The HFRP beams were manufactured by pultrusion process using the FRP layer composition as shown in Table 1. The flanges are composed of CFRP and GFRP in order to increase flexural strength and beam stiffness. The angle of the CFRP is fixed to 0 degree, meaning that all CFRP fibers are aligned in the longitudinal direction. The GFRP is oriented at 0, 90 and ± 45 degrees to provide integrity across the flange width, and to avoid strong anisotropic behavior. The web is composed entirely of GFRP because of the lower stresses, and to reduce cost. The overall height of the HFRP beam is 250 mm and the flange width is 95 mm. The flange thickness is 14 mm and the web thickness is 9 mm (Figure 1). Mechanical properties of the HFRP laminae are shown in Table 2.

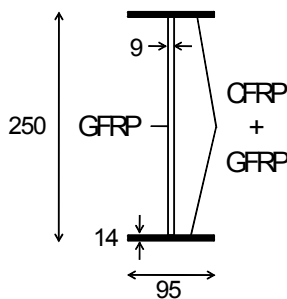


Figure 1 Dimensions of HFRP girder (unit: mm)

Table 1 Layer composition of HFRP laminates

Lamina	Flange (%)	Web (%)
CFRP 0	33	0
GFRP 0/90	17	43
GFRP 45	41	43
CSM	9	14

Table 2 Mechanical properties of HFRP laminae

Parameters	Notation	Unit	CF 0	GF 0/90	GF ± 45	GF CSM
Young's Modulus	E_{11}	GPa	128.1	25.9	11.1	11.1
	E_{22}	GPa	14.9	25.9	11.1	11.1
Shear Modulus	G_{12}	GPa	5.5	4.4	10.9	4.2
Poisson's Ratio	ν_{12}	-	0.32	0.12	0.29	0.31

b. Ultra High Performance Fiber Reinforced Concrete (UFC)

Mixture proportions of the UFC are shown in Table 3. The UFC is composed of water, premixed cementitious powder, sand, water reducing agent and steel fibers. The premixed cementitious powder includes ordinary Portland cement, pozzolanic materials (usually silica fume) and ettringite according to Japanese standards for blended cement. The steel fibers have a tensile strength of $2,000\text{N/mm}^2$ and lengths of 22 mm and 15 mm. The fibers were added at approximately 1.75% volume ratio with 50% by weight of each fiber length. The UFC slabs were precast and cured at 85 degrees Celsius for 24 hours after casting. They were then exposed to laboratory conditions for at least 7 days until installation on the HFRP beams in preparation for testing.

Table 3 Mix proportions of UFC

Air Content (%)	Unit quantity (kg/m^3)				Steel Fiber (kg/m^3)
	Water	Premix Cement	Sand	W.R. Admixture	
2.0	205	1287	898	32.2	137.4

2.2 Test variables

Test variables for the full-scale beam flexural tests are shown in Table 4. Five specimens were tested with different dimensions for the UFC slab, different types of shear connector and with/without epoxy bonding. The geometry of the test specimens and dimensions of the beam cross-sections are shown in Figures 2 and 3. The total length of each specimen is 3500 mm and flexural and shear spans are 1000 mm as shown in Figure 2. Timber stiffeners were installed at 500 mm intervals on both sides of the web to prevent web buckling. The

Table 4 Flexural beam test variables

Beam	Shear connector	Epoxy adhesive	Width/thickness of UFC slab (mm)	Embedded length of bolt (mm)
^a B1	Bolt M16	No	135/50	35
^b B2	Slab anchor	No	135/50	35
^c B3	Bolt M16	Yes	95/50	35
^d B4	Bolt M16	Yes	135/35	30
^e B5	Bolt M16	Yes	135/50	35

^aB1 = B-135-50, ^bB2 = SA-135-50, ^cB3 = BE-95-50, ^dB4 = BE-135-35, ^eB5 = BE-135-50

stiffeners were bonded to the HFRP specimens using epoxy adhesive. The spacing of headed bolts and slab anchors was determined from the shear connection tests to prevent premature bolt shear failure as shown in Figure 4. A torque wrench was used to apply 20 Nm torque to the bolts in all specimens.

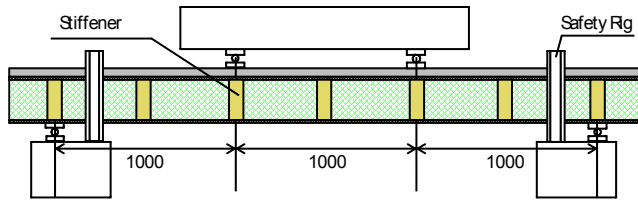


Figure 2 Geometry of flexural test specimen

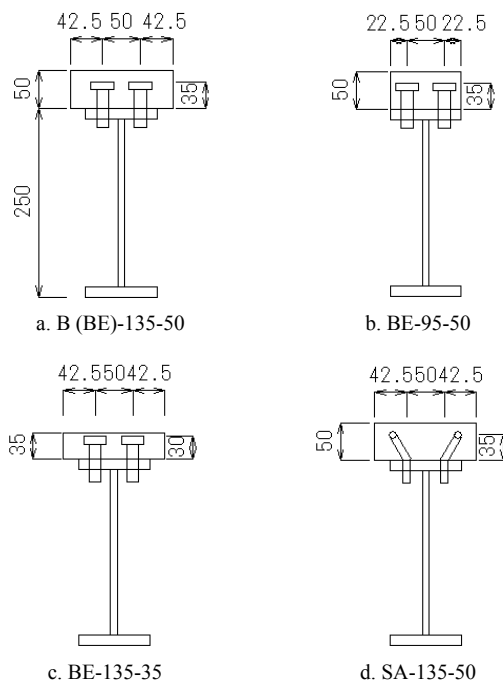


Figure 3 Dimensions of beam cross-sections

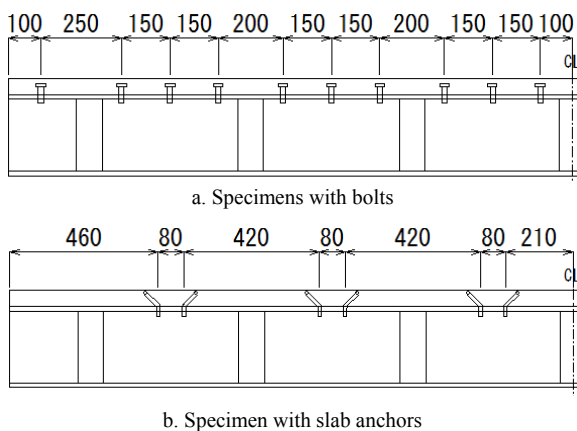


Figure 4 Locations of shear connectors

2.3 Test setup

Four point bending tests were conducted on all specimens. The experimental setup is shown in Figure 5. The load

was applied by a manually operated hydraulic jack until beam failure. The applied load, deflection at mid-span, and strains in the HFRP beam were measured throughout each test.



Figure 5 Flexural beam test setup

3 RESULTS AND DISCUSSION

Figure 6 shows the relationship between load and mid-span deflection of each specimen. The load-deflection relationship for a simple HFRP beam without UFC slab (control beam) is also shown in Figure 6 for comparison. Every specimen with bolt shear connectors shows higher stiffness and loading capacity compared with the simple HFRP beam. In particular, the stiffness of specimens with epoxy bonding was increased by approximately 15% compared with that of specimens without adhesive bonding. Specimen SA-135-50 with shear anchors did not perform as well as the specimens with headed bolts.

Relationships between load and longitudinal strain through the depth of the composite beam at mid-span are shown in Figure 7 for various load levels, including failure. As shown in Figure 7(a), the specimens without adhesive bonding show slipping at the interface between the UFC slab and the HFRP beam. On the other hand, the specimens with epoxy bonding (Figure 7(b)) show a linear strain distribution through the cross-section. This indicates that specimens with bonded-and-bolted connection show full composite action until final failure. The specimens with shear anchors (Figure 7(c)) showed even larger slip than the specimens with bolts.

All specimens with headed bolts failed due to crushing of the UFC slab at a loading point as shown in Figure 8(a). Crushing of the HFRP beam flange occurred after the UFC failed. Delamination of the top flange of the HFRP beam was observed in specimen SA-135-50 with shear anchors (Figure 8(b)). This failure mode was the same as that for the simple HFRP beam, however failure was not brittle because the UFC slab carried compressive load after delamination failure occurred. In addition, a few of the slab anchors failed in shear, while others caused bearing failure of the HFRP flange.

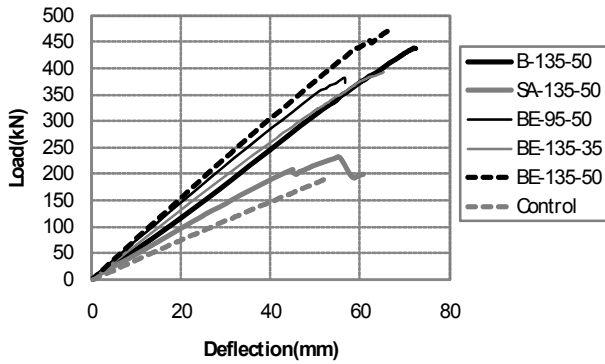
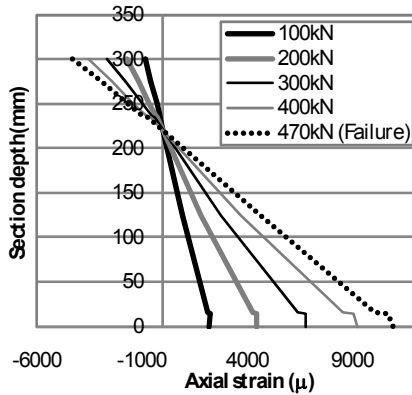


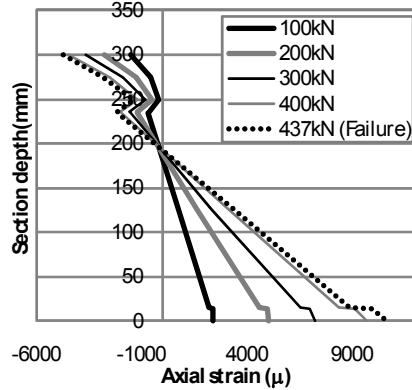
Figure 6 Load-deflection relationships



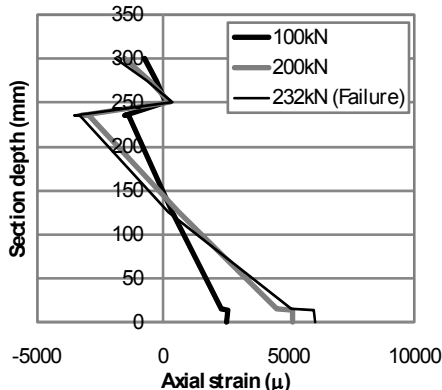
(a) Crushing of UFC slab



(a) BE-135-50



(b) B-135-50



(c) SA-135-50

Figure 7 Longitudinal strain distributions



(b) HFRP flange delamination failure

Figure 8 Flexural beam failure modes

4 CONCLUDING REMARKS

This paper presents an experimental study of a new composite beam system composed of HFRP I-beams and UFC slabs connected by bolts or slab anchors. The main concluding remarks from the study are withdrawn as follows:

1. Composite beams composed of HFRP I-beams and UFC slabs can utilize fully the superior properties of the HFRP laminates.
2. HFRP-UFC composite beams with headed bolt shear connectors provide considerable stiffness and strength increase compared with simple HFRP beams.
3. Specimens with epoxy bonding between the UFC slab and HFRP top flange showed approximately 15% increase in ultimate flexural strength.

REFERENCES

Concrete Committee of Japan Society of Civil Engineers (JSCE-2004). Recommendations for Design and Construction of Ultra High Strength Fiber Reinforced Concrete Structures.

Nguyen Duc Hai, Hiroshi Mutsuyoshi, Shingo Asamoto, and Takahiro Matsui (2009). Structural Behavior of Hybrid FRP Composite I-Beam, *Journal of Construction and Building Materials*, Vol. 24, June 2010, pp. 956-969.

Sensitivity Studies on Local Flange Buckling Equations for Pultruded Beams and Columns

M. J. McCarthy (mjmccarthy2@wisc.edu) & L. C. Bank (bank@enr.wisc.edu)

Department of Civil Engineering, University of Wisconsin, Madison, United States of America

ABSTRACT The objective of this research was to investigate the sensitivity of a proposed design equation for local flange buckling in pultruded I sections to the mechanical properties of the elements of the section and to determine the accuracy of the equation that includes the effect of the rotational restraint at the web-flange junction. The web-flange junction stiffness is shown to contribute significantly to the flange buckling resistance of the cross-section and it is more significant in beams than in columns. The predicted buckling loads were compared with the results of tests and professional factors for LRFD calibrations have been developed. The sensitivity study was performed with respect to the orthotropic in-plane stiffness properties of the pultruded material in an effort to determine to what degree they contribute to the calculated buckling resistance of the section. Finally, the practicality of using the equation for the design of macroscopically non-homogeneous members is discussed.

1 INTRODUCTION

1.1 Background

This paper presents a study on the sensitivity of a proposed design equation for local flange buckling in pultruded I sections to the mechanical properties of the elements of the section. It also compares the predicted buckling load obtained from the proposed equation that accounts for the rotational restraint at the web-flange junction to results of tests. The predictions are made using the mechanical and geometric properties measured from the actual section which was tested (not the manufacturer reported nominal properties) to ensure that any variation in the design equation is only a function of the design equation's accuracy and not from any other source (such as variation in the mechanical properties).

Local flange buckling has been observed in beams by several researchers including Bank et al. (1994), Lopez-Anido et al. (1996), and Qiao & Zou (2002), and has also been observed in columns by several researchers including Yoon et al. (1993), Tomblin & Barbero (1994), and Lane & Mottram (2002). This failure mode has also been discussed theoretically by Qiao et al. (2001), Kollár (2003), and Mottram (2004). Whether in beams or columns, whenever local flange buckling occurs experimentally several wavelengths are formed along the length of the beam or column provided the member is long enough for this to occur. If the flange was only simply supported at the web then the entire flange would form one buckled half wave along the entire length of the beam or column, in a fashion similar to how a simply

supported plate would buckle due to an in plane load. This experimental evidence suggests that the web-flange junction must provide more restraint than just a simple support.

1.2 Previous work

Qiao et al. (2001) proposes a simplified design equation to predict the local flange buckling stress with the flange modeled as a plate with one free and one rotationally restrained unloaded edge. This work is then expanded by Kollár (2002) for plates and summarized in Kollár (2003) for different cross sections and stress states. This paper includes a closed form equation for the local buckling critical stress with the web-flange junction modeled as rotationally restrained. Mottram (2004) expanded on this work by comparing several different design equations for local flange buckling using experimental results from several researchers. His conclusion was that equations which do *not* include the effect of the rotational restraint are the most conservative and least accurate when compared to the experimental results, therefore in order to correctly model the physics of local flange buckling the effect of the rotational restraint provided by the web-flange junction must be included. Mottram also discusses Kollár's method which has the ability to distinguish between flange buckling in beams subjected to transverse loads (flexure) and flange buckling in columns subjected to axial loads (pure compression). This is because the web restraint is given as a function of the end conditions of the restraining plate. None of the other existing equations have this ability.

2 PROPOSED EQUATIONS

Based on orthotropic plate theory, the local buckling stress for a plate with one free and one simply supported unloaded edge subjected to uniform axial compression is given by Equation 1 (Lekhnitskii 1968).

$$f_{cr}^{LFB} = \frac{4t_f^2}{b^2} G_{LT} \quad (1)$$

where t_f = flange thickness; b = flange width; and G_{LT} = in-plane shear modulus.

The only parameters are the flange slenderness and in-plane shear modulus of the flange. Nothing accounts for any other part of the cross-section including the restraint provided by the web-flange junction.

2.1 Rotationally restrained web-flange junction

Equation 2 gives the local buckling stress for a flange modeled as free and rotationally restrained along its unloaded edges subjected to uniform axial compression. (Kollár 2003).

$$f_{cr}^{LFB} = \frac{4t_f^2}{b_f^2} \left(\frac{7}{12(1-\nu_L\nu_T)} \sqrt{\frac{E_L^c E_T^c}{1+4.12\xi_f}} + G_{LT} \right) \quad (2)$$

where ν_L , ν_T = Longitudinal and transverse Poisson's ratios; E_L^c , E_T^c = Longitudinal and transverse compressive moduli; and ξ_f = coefficient of restraint.

It can be seen that when rearranged Equation 2 contains all of Equation 1 plus an additional term. This additional term accounts for the rotational restraint provided by the web-flange junction and will be shown to contribute significantly to the calculated critical stress.

Equation 3 gives the coefficient of restraint.

$$\xi_f = \frac{2}{b_f} \frac{E_T^c t_f^3}{k_f 12(1-\nu_L\nu_T)} \quad (3)$$

where k_f = rotational constant. The rotational constant is different for different cross-sections and stress states. For I shaped cross-sections the rotational constant is given by Equation 4.

$$k_f = \frac{c E_T^c t_w^3 (1 - \sigma_f^{SS} / \sigma_w^{SS})}{12h(1-\nu_L\nu_T)} \quad (4)$$

where h = section depth; σ_f^{SS} = simply supported flange buckling stress; σ_w^{SS} = simply supported web buckling stress; and c = stress distribution coefficient. For beams subjected to flexural stresses $c = 4$, and for columns subjected to axial compression $c = 2$. The c term describes how the web restrains the flange as a function of the deformed shape of the web. Figure 1 shows the different values of c based on the different end conditions of the web. The case of $c = 4$ applies to beams because the tension flange stays in its original plane during buckling while only the compression flange buckles.

The case of $c = 2$ applies to columns because both of the flanges buckle.

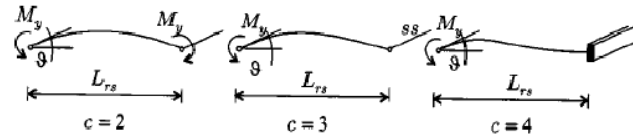


Figure 1 Values of c in the rotational constant (Kollár 2003)

The rotational constant is higher in beams than in columns because the web does a better job of restraining the flange against buckling. Therefore, the rotational stiffness of the web-flange junction should contribute more to the local flange buckling resistance of beams than columns.

3 EXPERIMENTAL CORRELATION

3.1 Professional factors

In order to compare the equations the predicted strengths of the equations are compared with experimental results. This is done by calculating a professional bias, defined by Equation 5.

$$\text{Professional Bias} = \frac{\text{Experimental Strength}}{\text{Predicted Strength}} \quad (5)$$

If the professional bias for an equation is equal to 1 it means the equation correlates perfectly with the experimental result, if it is greater than 1 it means the equation is conservative and less than 1 means non-conservative. In general, the closer the professional bias value is to 1 the more accurate the equation is. After a set of data is collected the professional bias values can be averaged to calculate the professional factor for a proposed design equation.

3.2 Experimental data

In order to accurately calculate professional factors for design equations all of the parameters in the equation must be measured and reported along with any experimental results. If any parameters of an equation are approximated then it will be impossible to tell if any variation from the experimental result is a function of the equation's accuracy or the accuracy of one of the parameters in the equation. There is a limited amount of published data on local buckling in pultruded beams and columns, and this requirement has reduced the available data even more. All 10 experimental data points used for beams were taken from one source (Bank et al. 1994) and all 11 experimental data points used for columns were also taken from one source (Yoon 1993). The professional factors and coefficients of variation for Equations 1 and 2 are presented in Table 1. For more details see McCarthy (2009).

Table 1 Professional factors for Equations 1 and 2

	Number of specimens	Coefficient of variation	Professional factor
Equation 1*			
Beams	10	0.19	2.68
Columns	11	0.19	1.64
Equation 2**			
Beams	10	0.15	1.20
Columns	11	0.12	1.07

* Web-flange junction modeled as simply supported-free

** Web-flange junction modeled as rotationally restrained-free

Table 1 shows that Equation 2 has lower coefficients of variation and professional factors closer to 1.0 for both beams and columns. This suggests that modeling the web-flange junction as rotationally restrained correlates best with experimental results that achieved local flange buckling in pultruded beams and columns. The results also show that the inclusion of the rotational stiffness of the web-flange junction is more significant in beams than in columns, as discussed in section 2. Based on the experimental data used in Table 1, the web-flange junction rotational stiffness accounts for 55% of the local flange buckling resistance in beams and 35% of the local flange buckling resistance in columns. The web-flange junction stiffness is more significant in beams but still important for columns.

4 SENSITIVITY OF TERMS IN EQUATION 2

In order to confidently calculate the local flange buckling resistance of a pultruded member all of the terms of the equation need to be known. However, this is not always possible because of the number of mechanical tests required to obtain all of the material properties. Therefore, because Equation 2 was shown to be the more accurate design equation the sensitivity of its terms will be examined to study how they affect the calculated outcome of the equation. Because the web-flange junction stiffness is more significant in beams the sensitivity of the terms in Equation 2 will be examined just using the experimental data from beams. In all cases, all parameters were held constant except for the term of interest which was scaled by various factors from 25% of its actual value to 200% of its actual value. The sensitivity of the term was then shown by graphing the calculated resistance of the equation as the term varies.

The sensitivity of the longitudinal compressive modulus, E^c_L , is shown in Figure 2.

If E^c_L is input 125% higher than it actually is for a given beam the equation would only predict a 6% higher critical stress, and if the modulus was input as 200% higher than it actually was the equation would only predict a critical stress that is 21% higher.

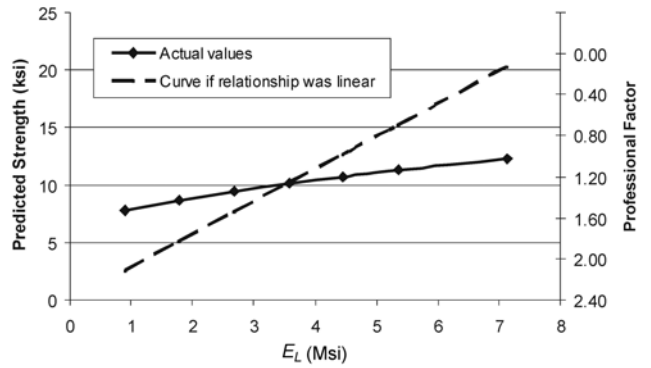


Figure 2 Sensitivity of E^c_L in Equation 2 (McCarthy 2009)

The sensitivity of the transverse compressive modulus, E^c_T , is shown in Figure 3.

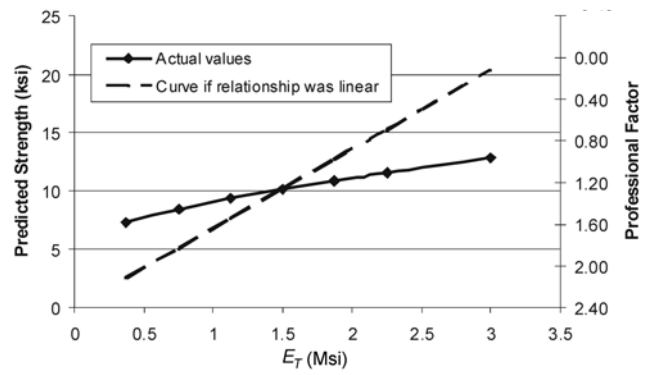


Figure 3 Sensitivity of E^c_T in Equation 2 (McCarthy 2009)

If E^c_T is input 125% higher than it actually is for a given beam the equation would only predict an 8% higher critical stress, and if the modulus was input as 200% higher than it actually was the equation would only predict a critical stress that is 27% higher.

The sensitivity of the shear modulus, G_{LT} , is shown in Figure 4.

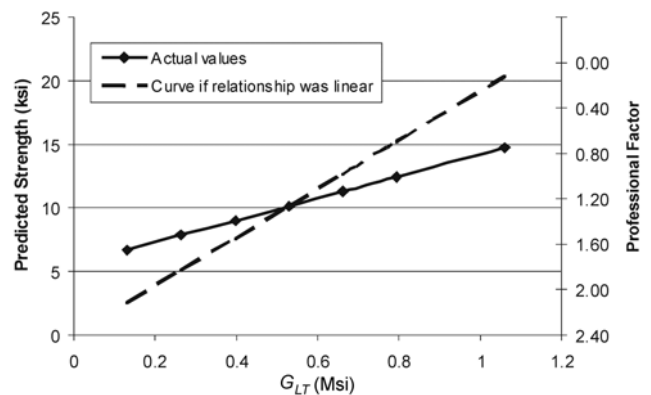


Figure 4 Sensitivity of G_{LT} in Equation 2 (McCarthy 2009)

If G_{LT} is input 125% higher than it actually is for a given beam the equation would only predict a 12% higher critical stress, and if the modulus was input as 200% higher than it actually was the equation would predict a

critical stress that is 45% higher.

Figures 2-4 show that Equation 2 is most sensitive to variations in G_{LT} , then E^c_T and finally E^c_L . Therefore, if material properties need to be approximated to evaluate Equation 2 it is desirable to approximate E^c_L first, then E^c_T and lastly G_{LT} .

The final parameter to be examined is the product of the Poisson's ratios, $\nu_L \times \nu_T$. The sensitivity is shown in Figure 5.

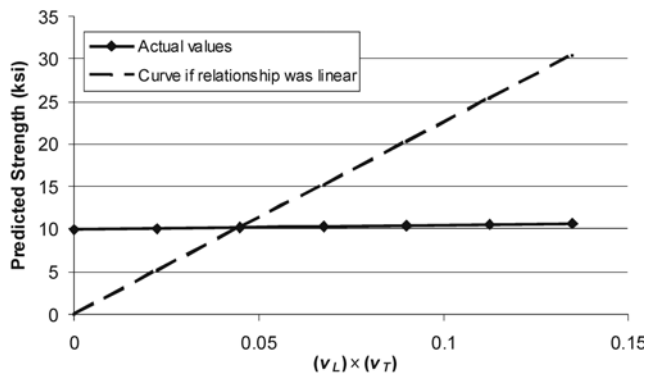


Figure 5 Sensitivity of $\nu_L \times \nu_T$ in Equation 2 (McCarthy 2009)

Figure 5 shows that Equation 2 is almost independent of the product of the Poisson's ratios because their product is close to 0 and the term is always subtracted from 1 making the term $(1 - \nu_L \nu_T)$ very close to one. For simplicity the term $(1 - \nu_L \nu_T)$ can be removed from Equation 2 as well as Equations 3 and 4 with negligible consequences. After this simplification, in beams the coefficient of variation remains at 0.15 and the professional factor changes to 1.23. In columns the coefficient of variation changes to 0.14 and the professional factor changes to 1.12. In both instances the equation becomes slightly more conservative but considerably more easy to work with.

5 NON-HOMOGENEOUS MEMBERS

In an effort to optimize the cross-section many pultruded beams are intentionally manufactured to be macroscopically non-homogeneous by putting a larger fraction of unidirectional fibers in the flange for bending and a larger fraction of bidirectional mats in the web for shear. However, in spite of this most manufacturers simply report one value for strengths or moduli for the entire cross-section. If only one value is reported for each mechanical property the longitudinal moduli will usually come from the flange and the shear modulus will usually come from the web. As discussed in section 4, Equation 2 is most sensitive to G_{LT} so careful consideration should be taken if only one shear modulus is reported for an entire cross-section because Equation 2 is

written in terms of properties of the flange. If Equation 2 is evaluated using a higher shear modulus than is actually present in the flange the predicted buckling stress will vary according to Figure 4.

6 CONCLUSIONS

Modeling the web-flange junction as rotationally restrained as opposed to simply supported for local flange buckling correlates better with experimental results. The junction provides more stiffness in beams than in columns because the entire cross-section is subjected to compressive axial stresses in columns. The rotationally restrained junction equation is more sensitive to the shear modulus than the longitudinal or transverse moduli of the flange.

REFERENCES

- Bank, L. C., Gentry, T.R. & Nadipelli, M. 1994. Local Buckling of Pultruded FRP Beams – Analysis and Design. *Composites Institute Conference: Proc., Cincinnati, 7-9 February 1994: Session 8-D, p. 6.*
- Kollár, L.P. 2002. Buckling of Unidirectionally Loaded Composite Plates with One Free and One Rotationally restrained Unloaded Edge. *Journal of Struct. Engr: 128(9): 1202-11.*
- Kollár, L.P. 2003. Local Buckling of Fiber Reinforced Plastic Composite Structural Members with Open and Closed Cross Sections. *Journal of Struct. Engr: 129(11): 1503-13.*
- Lane, A. & Mottram, J. T. 2002. The influence of modal coupling upon the buckling of concentrically PFRP columns. *Inst. Mech. Engrs. Part L: 216(12): 133-44.*
- Lopez-Anido, R., Bendidi, R., GangaRao, H.V.S. & Al-Megdad, M. 1996. Local Buckling Experiments on Pultruded Composite Beams. *Materials Engineering Conference: Proc., 2: 914-23.*
- Lekhnitskii, S. G. 1968. *Anisotropic Plates*, New York: Gordon and Breach Science.
- McCarthy, M. J. 2009. Professional Factors for an LRFD Standard for Pultruded Beams. *MS Thesis*. University of Wisconsin.
- Mottram, J. T. 2004. Determination of Critical Load for Flange Buckling in Concentrically Loaded Pultruded Columns. *Composites, Part B: Engineering. 35(1): 35-47.*
- Qiao, P. & Zou, G. 2002. Local Buckling of FRP Structural Shapes – Explicit Analyses. *Composites in Infrastructure: Proc. Intern. conf. 109: 12.*
- Qiao, P., Davalos, J. F., & Wang, J. 2001. Local buckling of composite FRP shapes by discrete plate analysis. *Journal of Structural Engineering. 127(3): 245-255.*
- Tomblin, J. & Barbero, E. 1994. Local buckling experiments on FRP columns. *Thin-Walled Structures. 18: 97-116.*
- Yoon, S.J. 1993. Local Buckling of Pultruded I-Shape Columns. *PhD Thesis*. Georgia Institute of Technology.

Analytical Study on Buckling Modes of Simply Supported Delaminated Composite Beams

Zhu Bo (zhubo1999@126.com), Zhou Ding, Liu Weiqing

Advanced Engineering Composites Research Center, Nanjing University of Technology, Nanjing, China

ABSTRACT Based on the two-dimensional elasticity theory, the buckling modes of delaminated composite beams are studied in this paper. Firstly, critical buckling loads are obtained. Then, the displacement modes of the beam are given by substituting the critical loads back to the eigenvalue equations. The possible contact between the delaminated interfaces is considered, and “Free” and “contact” modes are separately computed. According to the situations of the vertical displacements and normal stresses on the delaminated interfaces, the real buckling modes can be judged.

1 INTRODUCTION

Fiber reinforced plastic composites are widely used because of their superior specific strength and stiffness over most metallic engineering materials. However, composite structures are susceptible to delaminations under axial loads. Once delamination occurs, stresses within the composites will be redistributed. This will then lower the compressive load carrying capacity of the composite laminates.

One-dimensional buckling analysis of a through width delaminated composite laminate plates was studied by Simitzes et al. [1]. This model was believed to be sufficient to describe the behavior of the laminate plates. Shu [2] identified ‘free mode’ and ‘constrained mode’ of buckling for a beam with multiple delaminations by an exact solution. All above works were based on classical beam theory, without considering transverse shear effects. Considering this effect, Chen [3] studied the elastic buckling and post-buckling analysis of an axially loaded beam plate having an across-the-width delamination by a variational-principle. Lim and Parsons [4] used Rayleigh-Ritz method to analyze the buckling analysis of multiple delaminated beams.

Contact effect is an important problem in buckling analysis of delaminated structures. In previous studies [1-4], one-dimensional model with an across-the-width delamination were usually used, without considering contact problems. When two-dimensional model is applied, the contact is tended to find, which can not be ignored. Yeh et al. [5] investigated the bending behavior and local buckling phenomenon of the delaminated plates with contact effects by using a two-dimensional nonlinear finite element method. Whitcomb [6] analyzed the behavior of a laminate with postbuckled embedded delamination using three-dimensional geometrically nonlinear finite element analysis with approximate contact

constraints. Hu et al. [7] conducted the buckling analysis of laminates with an embedded delamination employing the finite element method based on the Mindlin plate theory.

In this paper, two-dimensional elasticity solution is obtained on buckling modes of delaminated composite beams. The possible contact on the delaminated interfaces is considered in the study. “Free” and “contact” modes are separately computed. According to the situations of the vertical displacements and normal stresses on the delaminated interfaces, the real buckling modes can be judged.

2 FORMULATION

Consider an I -layer delaminated beam with the length L and the thickness H , as shown in Figure 1. The thickness of the i th ($i = 1, 2, \dots, I$) layer of the beam is defined as H_i . Suppose that there contains J_i delaminations between the i th layer and $(i+1)$ th layer of the beams. And the delamination length is L_2 , the length of continuous segment at the left hand of the delamination is L_1 . The axial force P is applied, which is located at the neutral axis of the beam. The axial force P can be replaced by a

static equivalent distributed stress $\sigma_{x0}^i = \frac{E_i P}{\sum_{k=1}^I E_k H_k}$, in

which only the stresses near the end are affected.

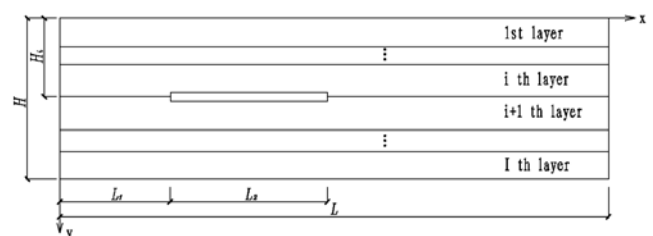


Figure 1 Multi-layered laminated beam with arbitrary delaminations

The equilibrium differential equation of buckling with the displacements for the plane stress state in the xy plane of element i is given by

$$\frac{E_i}{2(1+\mu_i)}\nabla^2 u_i + \frac{E_i}{2(1-\mu_i)}\left(\frac{\partial^2 u_i}{\partial x^2} + \frac{\partial^2 v_i}{\partial x\partial y}\right) = \sigma_{x0}^i \frac{\partial^2 u_i}{\partial x^2} \quad (1)$$

$$\frac{E_i}{2(1+\mu_i)}\nabla^2 v_i + \frac{E_i}{2(1-\mu_i)}\left(\frac{\partial^2 v_i}{\partial y^2} + \frac{\partial^2 u_i}{\partial x\partial y}\right) = \sigma_{x0}^i \frac{\partial^2 v_i}{\partial x^2}$$

Where u_i is the displacement in the x direction of element i , as well as v_i , the displacement in the y direction. The symbols E_i and μ_i denote the elastic modulus and Poisson's ratio respectively.

For the simply supported beam, considering the boundary conditions at two ends, assume that the displacement distributions have the following form:

$$u_i(x, y) = \sum_{m=1}^{\infty} U_m(y) \cos \frac{m\pi x}{l} \quad (2)$$

$$v_i(x, y) = \sum_{m=1}^{\infty} V_m(y) \sin \frac{m\pi x}{l} \quad (3)$$

Substituting equations (2) and (3) into equation (1), the solution of $u(x, y)$ and $v(x, y)$ can be derived out as follows

$$\text{Case 1: When } \frac{2\sigma_{x0}^i}{E_i}(1+\mu_i) > 1 > \frac{\sigma_{x0}^i}{E_i}(1-\mu_i^2),$$

assume that

$$\alpha_m^i = \left(\frac{m\pi}{l}\right) \sqrt{1 - \frac{\sigma_{x0}^i}{E_i}(1-\mu_i^2)}, \beta_m^i = \left(\frac{m\pi}{l}\right) \sqrt{\frac{2\sigma_{x0}^i}{E_i}(1+\mu_i) - 1}, \text{ then}$$

$$v_i(x, y) = \sum_{m=1}^{\infty} (A_m^i \text{sh} \alpha_m^i y + B_m^i \text{ch} \alpha_m^i y + C_m^i \sin \beta_m^i y + D_m^i \cos \beta_m^i y) \sin \frac{m\pi x}{l} \quad (4)$$

$$u_i(x, y) = \sum_{m=1}^{\infty} (B_m^i \frac{m\pi}{l\alpha_m^i} \text{sh} \alpha_m^i y + A_m^i \frac{m\pi}{l\alpha_m^i} \text{ch} \alpha_m^i y - D_m^i \frac{l\beta_m^i}{m\pi} \sin \beta_m^i y + C_m^i \frac{l\beta_m^i}{m\pi} \cos \beta_m^i y) \cos \frac{m\pi x}{l} \quad (5)$$

$$\text{Case 2: When } \frac{2\sigma_{x0}^i}{E_i}(1+\mu_i) > \frac{\sigma_{x0}^i}{E_i}(1-\mu_i^2) > 1 \text{ and}$$

$$1 > \frac{2\sigma_{x0}^i}{E_i}(1+\mu_i) > \frac{\sigma_{x0}^i}{E_i}(1-\mu_i^2), \text{ has similar equations.}$$

In above equations, $A_m^i, B_m^i, C_m^i, D_m^i$ are the unknown coefficients, determined from the boundary conditions along the upper and lower surface of the i th layer. Equations (4) and (5) are already satisfied the boundary conditions at two ends for a simply supported beam.

$$\sigma_x^i = 0, v_i = 0 \text{ at } x = 0 \text{ and } x = L$$

The above boundary conditions are applicable to each element in the y direction.

3 BOUNDARY CONDITIONS

The boundary conditions on the upper surface of element 1 can be written as

$$\sigma_y^1 = 0, \tau_{xy}^1 = 0 \quad (0 \leq x \leq L, y = 0) \quad (6)$$

The boundary conditions on the lower surface of element I can be written as

$$\sigma_y^I = 0, \tau_{xy}^I = 0 \quad (0 \leq x \leq L, y = H) \quad (7)$$

For the delaminated structures, when delaminations located at different interfaces. "Free" and "contact" modes may both occur between upper and lower surfaces of the delaminations. Without considering the possibility of contact between the delaminations in analysis, the buckling modes would be physically impossible, in some cases. Such as delamination interfaces may run through such other. For convenience, the points N are selected with the equal distance distribution along the length of the beam. The coordinate values are $L/(N+1), 2L/(N+1), \dots, NL/(N+1)$, respectively. The interface boundary conditions of each point are as follows

Continuous segments ($0 \leq x \leq L_1, L_1+L_2 \leq x \leq L, y = H_i$)

$$u_i = u_{i+1}, v_i = v_{i+1}, \sigma_y^i = \sigma_y^{i+1}, \tau_{xy}^i = \tau_{xy}^{i+1} \quad (8)$$

Delamination segments ($L_1 \leq x \leq L_1+L_2, y = H_i$)

'Free' mode:

$$\sigma_y^i = 0, \tau_{xy}^i = 0, \sigma_y^{i+1} = 0, \tau_{xy}^{i+1} = 0 \quad (9a)$$

'Contact' mode:

$$\sigma_y^i = \sigma_y^{i+1}, v_i = v_{i+1}, \tau_{xy}^i = 0, \tau_{xy}^{i+1} = 0 \quad (9b)$$

4 COEFFICIENTS EQUATION

Without loss of generality, a two-layer composite laminated beam with single delamination is considered here. Substituting equations (4) and (5) into equation (6) to (9), the coefficients equation can be obtained. It is not difficult that derivation and method above can extended to solving buckling of laminated composites with more than two layers or multiple delaminations.

The number of points N is selected with the equal distance distribution along the length of the beam. According to upper and lower surface conditions as well as delamination interface conditions, one has a $8 \times I \times N$ order homogeneous linear equation. The existence of nonzero solutions of this equation is that the value of coefficient determinant is zero. The eigenvalues are obtained by using the FORTRAN program, among which the first eigenvalue is namely the critical buckling load P_{cr} .

5 MODAL IDENTIFICATION

Substituting above buckling load P back to above linear equation, the stress and displacement distributions of the beam under this load can be obtained. According to the situations of the vertical displacement and normal stress on the delaminated interfaces, the real buckling modes can be judged as follow

a. When using the ‘free mode’, vertical displacement at every point along the delaminated interfaces can be judged. If $v_i > v_{i+1}$, then the upper and lower interfaces of the delamination at this point may run through each other. Which is physically impossible, and ‘contact mode’ should be used here instead. Contrarily, when $v_i < v_{i+1}$, the deformation of delamination interface at this point is non-interfered. Which show that it is appropriate in the description of ‘free mode’.

b. When using the ‘contact mode’, relationship between normal stresses at every point along the delaminated interfaces can be judged. If $\sigma_y^i = \sigma_y^{i+1} > 0$, tensile stress is generated at this point along the upper and lower interfaces of the delamination. Which is also physically impossible for the non-adhesive delamination, and ‘free

mode’ should be used here instead. Else if, stress between delamination interface at this point is pressure. Which show it appropriate using ‘free mode’ in calculation.

6 NUMERICAL EXAMPLES

Take a three-layer laminated beam with double delaminations for example. These two delaminations located at different interlayer and overlapped in position. The elastic modulus and thickness of upper and lower panels are both defined as E_1 and H_1 . While E_2 and H_2 denoting the elastic modulus and thickness of the core layer respectively. Comparisons of the results for a simply-supported laminated beam using two different delaminated interface models are shown in Table 1. It can be seen from the table that the results of two models differ from each other. And critical buckling loads obtained from ‘free mode’ always less than that from ‘contact mode’. Modal identification method mentioned above is needed in order to get the real mode. Effect of delamination thickness on the non-dimensional buckling load for different delamination lengths are shown in Figure 2.

Table 1 Comparisons of the results for a simply-supported laminated beam using two different delaminated interface models

L_2/L	$H_1/H=0.20$		$H_1/H=0.30$		$H_1/H=0.40$		$H_1/H=0.50$	
	Free	Contact	Free	Contact	Free	Contact	Free	Contact
$E_1/E_2 = 1.2$								
0.20	0.705	0.789	0.804	0.851	0.914	0.932	0.983	0.999
0.40	0.404	0.517	0.662	0.726	0.863	0.908	0.961	0.991
0.60	0.218	0.334	0.451	0.547	0.720	0.795	0.883	0.934
0.80	0.102	0.233	0.245	0.358	0.535	0.632	0.706	0.787

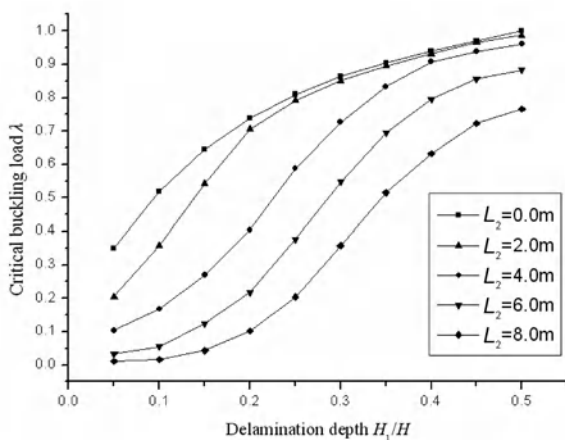


Figure 2 Effect of delamination thickness on non-dimensional buckling load for different delamination lengths

It can be seen from the figure, the critical buckling loads increase as the thickness ratio H_1/H increases when the delamination length L_2 is invariable. Buckling modes go from ‘free mode’ to ‘contact mode’ gradually with the turning point at $H_1/H = 0.25$.

Figure 3 and 4 give the buckling mode of the beam with delamination depth $H_1/H = 0.25$ and $H_1/H = 0.4$ respectively, at the delamination length is 6.0m. In Figure 3, no contact occur between upper and lower surfaces of both the two delaminations, namely the delaminations are free deformation. While in Figure 4, one of the delaminations interface is ‘contact mode’ while another one is ‘free mode’.

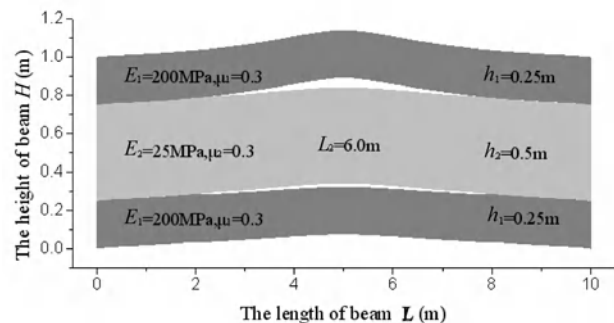


Figure 3 The buckling displacement mode of the beam with delamination depth $H_1/H = 0.25$

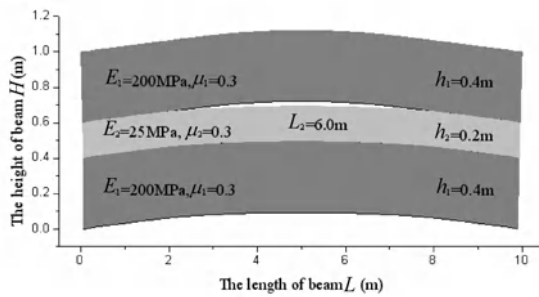


Figure 4 The buckling displacement mode of the beam with delamination depth $H_1/H = 0.4$

We can draw the following conclusions from the results:

- When the laminated beam with only one delamination, it is found that ‘free mode’ are always appeared in buckling.
- When more than one delaminations occur at different layers, ‘contact mode’ and ‘free mode’ may appear at the same time. Contacts generate or not depend on the thickness of each layer and the material properties of beam.

7 CONCLUSIONS

The buckling modes of delaminated beams with multiple delaminations located at different layers are studied in this paper. Two-dimensional elasticity theory is used as well as point collocation technique. The possible contact on the delaminated interfaces is considered in present

work. “Free” and “contact” modes are separately computed at each point. According to the situations of the vertical displacements and normal stresses between the delaminated interfaces, the real buckling modes can be judged.

REFERENCES

- [1] Simites G J, Sallam S, Yin W L. Effect of delamination of axially loaded homogeneous laminated plates [J]. AIAA Journal, 1985, 23(9): 1437–1444.
- [2] Shu D. Buckling of multiple delaminated beams [J]. Int J Solids Structures, 1998, 35(13): 1451–1465.
- [3] Chen H P. Shear deformation theory for compressive delamination buckling and growth [J]. AIAA Journal, 1991, 29(5): 813–819.
- [4] Lim Y B, Parsons I D. The linearized buckling analysis of a composite beam with multiple delaminations [J]. Int J Solids Structures, 1993, 30(22): 3085–3099.
- [5] Yeh M K, Fang L B, Kao M H. Bending behavior of delaminated composite plates with contact effects [J]. Composite Structures 1997, 39(3/4): 347–356.
- [6] Whitcomb J D. Analysis of a laminate with a postbuckled embedded delamination, including contact effects [J]. Journal of Composite Materials 1992, 26(10): 1523–1535.
- [7] Hu Ning, Hu Bin, Yao Zhenhan. Contact problem in buckling analysis of delaminated laminates [J]. Chinese Journal of Theoretical and Applied Mechanics, 1998, 30(6): 700–710. (in Chinese)

Interlaminar Behavior of Paulownia Wood Sandwich Composites with Grooves

Wan Li (sloman@126.com), Liu Weiqing, Fang Hai, Zhou Ding

Advanced Engineering Composites Research Center, Nanjing University of Technology, Nanjing, China

ABSTRACT Some grooves were arranged on the surface of the paulownia wood core, with the resins fulfilled. After solidifying, the resins left in the grooves strongly bonded the faces and core together. Therefore, the adhesive capacity between the faces and the core was enhanced. VARIM process was used to manufacture the specimens with different groove widths, depths and distances, and the DCB method was used to test the interfacial strength of the sandwich beams. Based on the energy release ratios from the test data, some factors are analyzed. It was found that the grooves can improve both the processing and interfacial properties. The present analysis provides the basis for the wide applications of paulownia wood sandwiches in future.

1 INTRODUCTION

A sandwich structure is a three-layer structure comprising a low density and low modulus core material between two high modulus face sheets. This arrangement provides a structure with a high bending stiffness^[1]. The sandwich structures have been applied among aircraft, ships, automobiles, rail cars, wind energy systems, and bridge construction.

Face sheets and core are bonded by some adhesive. In adhesive joints, the thickness of the adhesive is typically much smaller than the thickness of the adherents. But adhesive is very relevant to sandwich's mechanical behavior. Zenkert (2009) studied foam sandwich under circular loads, and the crack started from the interface^[2]. Somers (1992) found sandwich's buckling and post-buckling behavior were very sensitive to its interlaminar property^[3]. In Suvorov's research (2005), the low impact behavior could be improved by higher interfacial energy release ratio^[4].

Due to the high price of balsa wood, Advanced Composites Research Center of Nanjing Univ. of Tech. started the research of paulownia wood at 2006, which was a proper replacement of balsa wood^[5]. To improve the mechanics of paulownia wood sandwich and expand its application, the interface behavior was studied.

2 INTERFACE OF PAULOWNIA SANDWICH

2.1 Test method

Srinivas (1994) used cantilever beam to measure the energy release ratio of aluminum face sheets and PVC, PMI foam sandwich^[6]. ASTM also proposed a method for

mode I interlaminar fracture toughness of unidirectional fiber-reinforced polymer matrix composites. With a standard DCB pre-cracked specimen, after the crack propagated 3-5mm, the interfacial energy release ratio should be the mode I interlaminar fracture toughness. But there were grooves on the surface in the grooved paulownia wood sandwich, standard DCB method cannot satisfy the facial structures. Pan (2007) used the DCB method to test the interfacial properties of the honeycomb sandwich^[12].

In this paper, sandwich specimens comprise paulownia wood core(25.4mm) and 2 face sheets(four 800g glass fibers $[0^\circ/90^\circ, \pm 45^\circ, 0^\circ/90^\circ, \pm 45^\circ]$, vinyl ester resin). The dimension of the specimens was 200mm (length) \times 60mm (width). The core thickness was 25mm and face sheet thickness was 3.5mm. The overall thickness was 32mm. In Figure 1, a 50mm pre-crack was between the top face sheet and paulownia wood core. With two perforated metal solid, the cracks propagates along the pre-crack. The interlaminar properties were analyzed by the propagation speed and propagation energy.

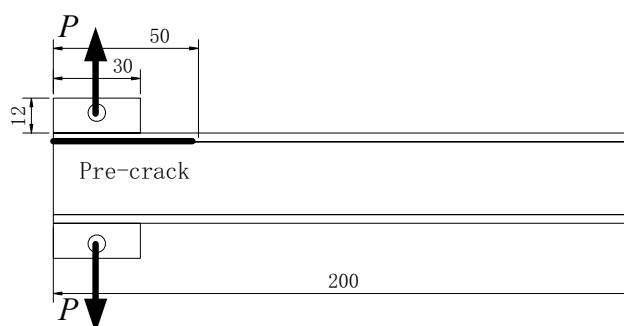


Figure 1 Double cantilever beam specimens

Figure 2 were the apparatus and specimen sample. An electric servo universal testing machine was used to pull the metal blocks bonded on the face sheets. The tensile force P and load displacement were recorded at 50Hz. At the same time, a camera was used to record the process of propagation. On the specimen, a paper staff was pasted to indicate the crack length in the test video.



Figure 2 Apparatus and specimen of DCB test

2.2 Paulownia wood sandwich

The energy release ratio could be calculated by the Eq.(1)^[9].

$$G = -\frac{1}{b} \frac{dU}{da} \quad (1)$$

In Eq.(1), U is the total elastic strain energy, b is the width of the specimen and a is the crack propagation length. U could be integrated from the $P-\Delta$ curve, while a could be measured with the paper staff on the specimens.

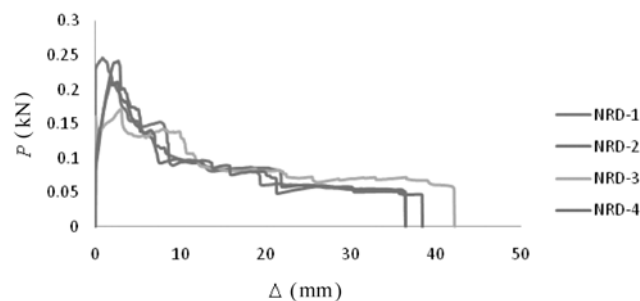


Figure 3 $P-\Delta$ curve of the hand lay-up specimens

In Table 1, the energy release ratios of four specimens were listed. NRD indicated the specimen type which was a Non-Reinforced Double cantilever specimen. There was little difference among the four specimens. DCB test method showed good reliability.

Table 1 Interfacial energy release ratio of handy lay-up paulownia wood sandwich

	NRD-1 (N/m)	NRD-2 (N/m)	NRD-3 (N/m)	NRD-4 (N/m)	Average (N/m)	Coefficient of Variance
Energy Release Ratio	380	364	426	379	374	2%

3 GROOVED PAULOWNIA WOOD CORE SANDWICH

DIAB's ProBalsa and Alcan's BALTEK are typical balsa wood core with grooves. The balsa wood was cut into pieces and bonded along its transverse direction. The grooves are 0.8mm width, 3mm height, with the distance of 20mm, which provides flow path for the resins^{[10],[11]}.

According to the usual saw blade, three typical groove widths were provided. Orthogonalization and nondimensionalization method were used in the experiment design. Eight dimension combinations were proposed in Table 2 with the 1mm, 3mm, 5mm in width, and 10mm, 20mm,

Table 2 Interfacial energy release ratio of grooved paulownia wood sandwich

	Grooves			Energy Release Ratio G (N/m)
	Width b (mm)	Height h (mm)	Distance d (mm)	
GCD-1	0.8	1.0	40	395
GCD-2	0.8	3.0	40	783
GCD-3	1.3	3.0	20	745
GCD-4	1.3	5.0	20	797
GCD-5	2.2	3.0	20	803
GCD-6	2.2	5.0	20	805
GCD-7	1.3	5.0	10	864
GCD-8	2.2	5.0	10	1002
GD-X	0.8	3.0	20	791

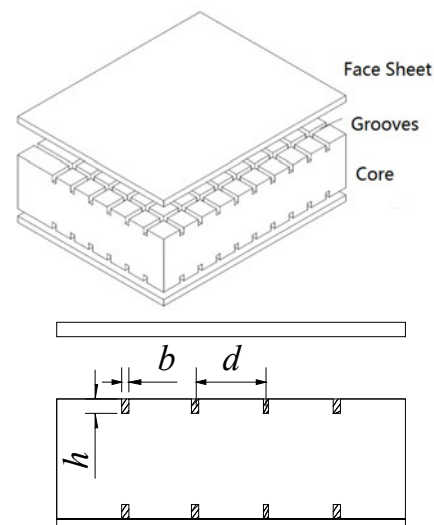


Figure 4 Grooved paulownia wood sandwich

40mm in distance. The fiber plies were the same with the handy lay-up specimens. The thickness was 31mm, slightly thinner than the handy specimens because of the manufacture process.

To ensure the impregnation of the resins in the grooves, vacuum assisted resin infusing molding (VARIM) process was used to manufacture all the specimens in Figure 5. By the vacuum pump, the air was driven out of the specimens, while the resin were infused under atmospheric pressure.



Figure 5 Manufacture process of grooved paulownia wood sandwich

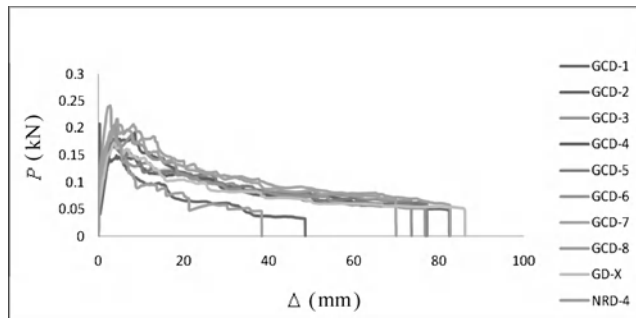


Figure 6 The P - Δ curve of grooved paulownia wood sandwich specimens

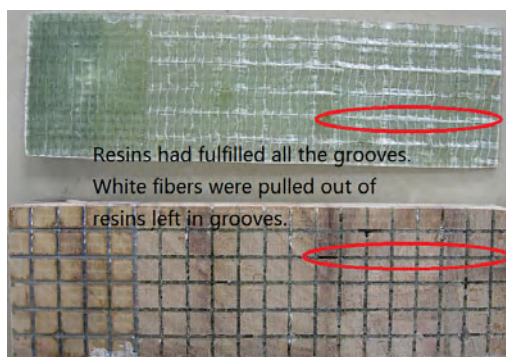


Figure 7 Face sheets and grooved wood after delamination

Figure 7 was the GCD-7 after delamination. It was found that the resins had fulfilled all the grooves completely. Additionally, there were some white fibers pulled out of the matrixes in the grooves. This kind of fiber-resin interfacial failure could be easily observed in all the grooved specimens. Because the interface between the glass fibers and resins was much more available than

the interface of wood and face sheet. Therefore, the adhesion of grooved sandwich was enhanced by the resins left in the resins. And different energy release ratio in Table 2 showed the accurate reinforcing effect of different grooves.

In Table 2, G in GCD was short for “Grooved”, while D was short for “DCB test”. And C indicated this was the 3rd group. Because the VARIM method was very sensitive and unstable for the small specimens, three groups of specimens were manufactured. Only in group C, all the grooves were fulfilled with resins. The energy release ratios had been listed in Table 2. GCD-1 showed the worst interfacial property. The energy release ratio was only 395N/m, far below other specimens. The 1mm groove height should be responsible for this. The lowest height made the grooves much easier to be blocked by the woven fibers and the resins could not fulfill all the grooves. Most grooves were empty. While, comparing with the handy lay-up specimens, the other 8 specimens improved 100% above.

4 DISCUSSION

4.1 Parameter analysis

GCD-1 was ignored, because of its blocked resin paths and imperfect resin grooves. The left eight specimens were analyzed. In Figure 6, P - Δ curves of all the specimens were printed. With the same groove width and distance, the groove height gave little influence to the energy release ratio. The P - Δ curves of GCD-3 and GCD-4 or GCD-5 and GCD-6 were almost the same. The most improvement of energy release ratio was less than 1%. There was no additional effect when the groove height increased from 3mm to 5mm. To increase the groove width from 1.3mm to 2.2mm, the energy release ratio grew more effectively (GCD-3 and GCD-5, GCD-4 and GCD-6, GCD-7 and GCD-8). The least improvement was 1%, while the most could be 16%. Decreasing the distance between grooves was the most effective method (GCD-2 and GD-X, GCD-4 and GCD-7, GCD-6 and GCD-8). The most remarkable improvement was 24%, least was 1% and average was 11%. Although the improvement was instable, it was figured that the interfacial properties were affected only by the groove width and groove distance.

Eq.(2) was the fitting equation, with related coefficient factor $r = 0.9857$.

$$G = 790 - 454\left(\frac{b}{d}\right) + 6476\left(\frac{b}{d}\right)^2 \quad (2)$$

4.2 Manufacture process and grooves

According to Eq. (2), it was found that the real factor was the surface area of the grooves in the core. The grooves played two roles in the sandwich. First, they were the necessary paths for resins. Second, the grooves

could be interfacial reinforcing structures. The resins left in the grooves could bond the face sheets and core strongly.

The constant in Eq. (2) was very similar to the energy release ratio of GCD-2. And in GCD-2, the area of grooves was only 4% of the total core surface, so the constant could be recognized as the energy release ratio without any grooves. These improvements were the effect of the VARIM.

Total G could be rewritten as Eq.(3). The total energy release ratio was divided into two parts. In Eq.(3), G_v was the energy release ratio because of the VARTM process, and G_g was the energy release ratio because of the resins left in grooves.

In Eq.(4), $(bd-4b^2)/d^2$ was percent of the groove area in the core. Then G_g and G_v could be expressed in Eq.(4) and Eq.(5). And G_g/G was the percent of the resin grooves' contribution. In GCD-8, grooves' was 25%.

$$G = G_v + G_g \quad (3)$$

$$G_v = 790\left(1 - \frac{bd - 4b^2}{d^2}\right) \quad (4)$$

$$G_g = 329\left(\frac{b}{d}\right) + 5693\left(\frac{b}{d}\right)^2 \quad (5)$$

Additionally, the delamination caused some white areas on the face sheet, in Figure 7. And the white areas were just the position of the grooves. That meant the delamination between face sheet and paulownia was partly because of the microscopical debonding of glass fibers and resins left in the grooves. It needed further proof. If there was another way improve the interfacial properties of the glass fibers and resins, the interlaminar behavior might be better.

5 CONCLUSION

Grooves in the paulownia wood could improve the interlaminar behavior of sandwich effectively. Both the process and interfacial structure would be benefitted. The

energy release ratio would be promoted as the increase of the resin groove width and decrease of the groove distance. So groove could be considered as a reinforcing method to improve the interlaminar properties of paulownia wood sandwich.

REFERENCE

- [1] Jones, R. M. 1999. Mechanics of composite materials[M]. Taylor & Francis, Inc.
- [2] Zenkert D, Burman M. 2009. Tension, Compression and shear fatigue of a closed cell polymer foam[J]. Composites Science and Technology (69): 785-792.
- [3] Somers M., Weller T., Abramovich H. 1992. Buckling and postbuckling behavior of delaminated sandwich beams[J]. Composite Structures, 21(4): 211-232.
- [4] Suvorov A P, Dvorak G J. 2005. Enhancement of low velocity impact damage resistance of sandwich plates[J]. International Journal of Solids and Structures, (42):2323-2344.
- [5] Fang Hai, Liu Weiqing, Wan Li. 2009. Research on innovative composite matting for rapid parking ramp expansion [J]. Journal of China & Foreign Highway, 29(6): 222-225. (In Chinese)
- [6] Srinivas Prasad, Leif A. Carlsson. 1994. Debonding and crack kinking in foam core sandwich beams—I. Analysis of fracture specimens[J]. Engineering Fracture Mechanics, 47(6): 812-824.
- [7] Cantwell W.J, Davies P. 1996. A Study of Skin-Core Adhesion in Glass Fibre Reinforced Sandwich Materials. Applied Composite Materials, (3), 407-420.
- [8] Carlsson L.A., Matteson R.C., Aviles F., Loup D.C. 2005. Crack path in foam cored DCB sandwich fracture specimens. Composites Science and Technology, 65(15-16): 2612-2621.
- [9] Standard Test Method for Mode I Interlaminar Fracture Toughness of Unidirectional Fiber-Reinforced Polymer Matrix Composites[S]. ASTM, D5528-01, 2007.
- [10] ProBalsa Technical Manual[R]. <http://www.diabgroup.com>.
- [11] Data sheet of Baltek[R]. <http://www.corematerials.alcancomposites.com>.
- [12] Pan Shidong, Wu Linzhi, Sun Yuguo. 2007. Analysis of fracture behavior of honeycomb sandwich specimens[J]. Chinese Journal of Theoretical and Applied Mechanics, 39(5): 610-617. (In Chinese)

GFRP Structures Subjected to Dynamic Action

Giosuè Boscato & Salvatore Russo

University Iuav of Venice, Venice, Italy

ABSTRACT The good ratio between strength and dead load defines the composite material as an efficacious solution for structural rehabilitation of historical buildings. The composite material with polymeric matrix, known with FRP acronym (Fiber Reinforced Polymers), is widely used in civil engineering as sheets, bars and strips. Recently a new technology was adopted to improve the structural response – with limited increment of dead load – with reversible and independent solution. The GFRP pultruded profiles allow the building of all-composite structure both for over elevation frame, structures and beams for increment of flexural stiffness of deck. The present work proposes and analyses the solution for seismic behaviour GFRP (Glass Fiber Reinforced Polymers) applications to evaluate the performances respect to dynamic actions considering the global effect on historical structure.

1 INTRODUCTION

The lightness of the FRP material guarantees a good structural behaviour respect to dynamic actions thanks to the reduced incidence of mass participation on the inertial forces. Despite the lightness and transversal deformability of the GFRP pultruded elements, they must be controlled so as to avoid excessively flexible structures unable to check the buckling phenomena due to $P-\Delta$ (load-deformation) effects.

To analyse the dynamic behaviour of GFRP structures in this work has been evaluated the stiffening effects of the braced systems, the different rotational stiffness of joint and the comparison with similar solutions built through traditional material.

In spite of the favorable properties of this new technology in dynamic engineering field the themes that define the possible applications are not completely developed.

While the study of static behaviour is still now in-depth (ASCE 1984, CNR-DT 205/2007 2008, Russo 2007) the researches on dynamic response are still inadequate. To regards recent studies were carried out on profiles - with different cross section – panels (Boscato and Russo 2009), two-dimensional and three-dimensional structures (Boscato 2009) in free vibration field to define the frequencies of flexural and torsional modes of vibration, the damping ratio and related displacements. In the past Holloway e Farhat (1990) studied the dynamic response of two models made by perspex and fiber-reinforced composite. Subsequently the study of Mosallam et al. (1994) developed the node problem between pultruded structural elements highlighting the better dissipative response of bolted solution than glued connections.

Based on the research results is possible to consider the FRP structural elements as reinforcement application, structural rehabilitation and seismic improvement. From the experimental analysis about the structural elements and 3D structures subjected to free vibrations (Boscato 2009) has been possible to calibrate the numerical model that simulates the structural response of all-GFRP structure with dynamic action. In reference to all-GFRP constructions, the analysis carried out on three-dimensional frame, allowed to define the dynamic parameters of GFRP structures with steel bolts and, then, the effects on the global behaviour of different configurations subjected to dynamic action.

The research develops, moreover, a comparison between the models of building with different roof elements – configuration with wood, steel, RC (Reinforced Concrete) or GFRP roof truss – subjected to seismic main shock recorded at April 6, 2009 in L'Aquila, Italy.

2 STRUCTURAL RESPONSE TO SEISMIC ACTIONS

2.1 Dynamic behavior of GFRP structure

Through the modal and spectral response analysis - using the dynamic parameters defined by experimental tests (Boscato 2009) – has been possible to define, through the finite element method, the effects of variations of structural design approaches and technology solutions to evaluate the global behaviour of GFRP systems subjected to seismic action.

In particular the modal analysis defines the dynamic characteristics of analyzed configurations; while the spectral response analysis individuates the structural performances respect to seismic action.

The modal and spectral analysis of the 3D framework was carried out considering different configurations - three external constraints, clamped, pinned and clamped-pinned and three internal restrains, rigid, semi-rigid and pinned – to evaluate the mode of vibration upon variation of the stiffness, with or without braces (Table 1).

The rotational stiffness of semi-rigid internal node of 3D frame was calculated as average value of Eurocode 3 interval - considering the beam length equal to 4961mm - braced $100.66 \leq K_{\phi} \leq 1610$ with $K_{\phi} = 755$ kNm/rad and unbraced $100.66 \leq K_{\phi} \leq 5033$ with $K_{\phi} = 2466$ kNm/rad.

The structural elements made of different profiles were modeled as perfectly collaborating; the dimensions and characteristics of structure are shown in Figure 1, (Boscato 2009). The analysis of the GFRP structure response to the dynamic action it has been considered only an earthquake excitation which ignores the non-linear behaviour, ductility and failure mode. The different structural typologies reported in Table 1 were analysed via spectral response approach for zone 2 (average seismicity with $a_g = 0.25g$) and category of soil B according to what is defined by Eurocode 8 (2003).

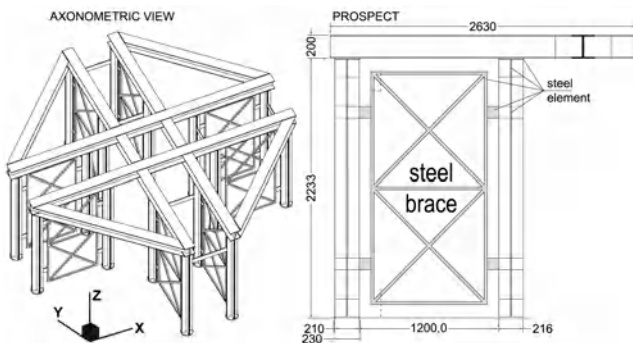


Figure 1 General view, mm dimensions

Table 1 3D frame braced and unbraced, first frequency

External joint	Int. joint K_{ϕ} (kNm/rad)		BRACED		UNBRACED	
			Hz	Mass part. (%)	Hz	Mass part. (%)
Clamped	Rigid	∞	23.82	67.76	13.31	81.56
	Semirigid	755	23.69	67.43	13.01	81.26
	Pinned	0	23.68	67.38	12.96	81.22
Pinned-Clamped	Rigid	∞	22.39	65.89	9.07	82.694
	Semirigid	755	22.29	65.52	9.624	84.517
	Pinned	0	22.27	65.46	9.59	84.486
Pinned	Rigid	∞	21.8	65.92	6.62	88.22
	Semirigid	755	21.71	65.46	6.43	88.04
	Pinned	0	21.69	65.37	6.4	88

The global behaviour and performances regarding the two principal directions of dynamic action that were analysed are shown in Figure 2.

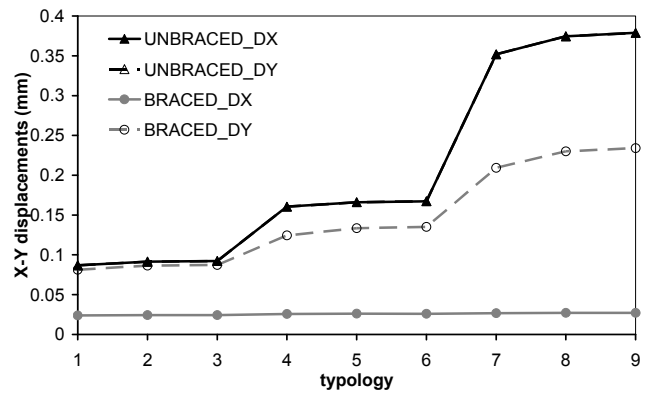


Figure 2 3D frame, displacements

For the unbraced configuration with the dynamic action along y direction, the increment of displacements is equal to 45% from Clamped to Pinned-Clamped configuration and equal to 55% from Pinned-Clamped to Pinned configuration.

As regards the braced configuration – for the same direction - the increment of displacements is 35% from Clamped to Pinned-Clamped and equal to 42% from Pinned-Clamped to Pinned configuration. The relationship between the braced and unbraced configurations shows a similar behaviour for the Clamped external joint and the increment of displacement values - of the unbraced configuration compared to the braced configuration – equal to 20% and 40%, respectively.

The structural response of the framework with unbraced configuration respect to the dynamic action, applied in directions x and y, is coincident.

Figure 3 illustrates the maximum level of stress reached by the elements with regards to compression axial stress.

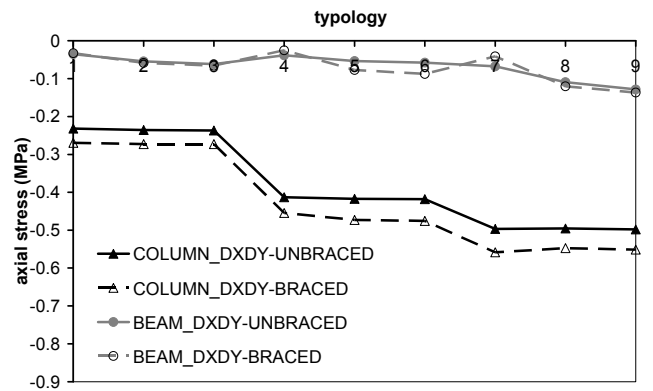


Figure 3 3D frame, stress behaviour

The variation of the external constraint conditions influences the stress level of the columns; from the Clamped to Pinned-Clamped configuration the stress value increases of about 43%, while for the next step – from the Pinned-Clamped to the Pinned configuration – the increment is equal to 16%.

2.2 Dynamic behavior of GFRP elements for structural rehabilitation of existing buildings

The evaluation of dynamic response of the masonry structure, with different roof solutions, subjected to the seismic actions has been carried out by dynamic linear analysis.

The analyzed model is a structure 12m width, 18m length and 15m high (Figure 4). The span between the roof truss is equal to 2m; the thickness of longitudinal walls and facade wall are 0.6m and 1m respectively. From analysis is important to highlight the different effect on masonry wall – considered with equal mechanical characteristics (Attached 11.D of OPCM 3431/2005, Tab. 11.D.1) – with roof truss for material and cross section of constitutive elements (Figure 4).

The configurations analysed are 5, the traditional solution with wood roof truss (cfgW, Figure 4 scheme a) directly on masonry wall, while the solutions for structural rehabilitation propose the steel (cfgSTEEL), RC (cfgRC, cfgRCa) and GFRP (cfgGFRP) roof truss. In particular the solutions with steel and GFRP roof truss propose a perimeter profile at levels of roof truss (Figure 4 scheme b), while for the solutions with RC structural elements the roof truss rest on directly on masonry wall (cfgRC, Figure 4 scheme a) or on RC curb (cfgRCa, Figure 4 scheme c).

The finite element analysis is carried out considering the masonry modeled by three-dimensional elements, the roof truss with mono-dimensional elements while the panels roof were modeled with plate elements. For the boundary condition the model is fully clamped at the plane xy of base (Figure 4).

From preliminary modal analysis were determined the frequencies of the first mode of vibration of each analyzed configuration, Table 2.

Table 2 shows, moreover, the physic-mechanical characteristics of analyzed solutions; considering the optimized cross section obtained by structural equivalence defined in serviceability state is evident the low dead load effect of GFRP configuration.

Table 2 Characteristics of analysed configurations (Cfg.) and fundamental frequency

Cfg.	Area (cm ²)	J _{max} profile (cm ⁴)	Dead of truss (kg)	Dead of beam (kg)	E (MPa)	f ₀ (Hz)
W	320	10666	4592	/	10500	5.16
GFRP	137	11084	6444	737	23000	3.24
STEEL	45	1208	9021	3217	210000	4.14
RC	150	5040	9394	/	24768	3.46
RCa				13163		3.45

Table 2 highlights the greater fundamental frequency of the solution with wood roof truss (cfgW) - due to low dead load – than the others configuration.

As regards the seismic analysis, the structure has been developed applying the same acceleration recorded during the mainshock of april 2009, accelerometric station AQV, <http://itaca.mi.ingv.it/ItacaNet>.

The results regard the maximum displacements of global system and the stress state of masonry of different configurations considering the first 10 seconds of seismic event.

Three components of seismic acceleration have been considered following North-South, East-West direction and the up component applied contemporarily along X, Y and Z respectively (see Figure 4).

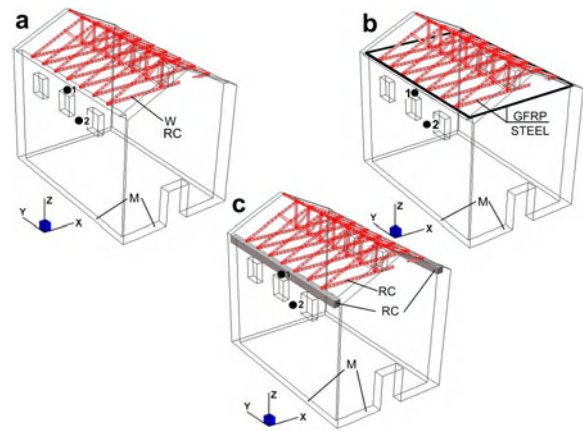


Figure 4 Configurations of FEM model

The stabilizing effect and uniform distribution of loads, assured through presence of perimeter profile, is highlighted through GFRP configuration with greater displacements correspondent to peak of acceleration and, subsequently, with exponential decrement. Nevertheless the presence of perimeter profile on cfgSTEEL configuration causes a progressive increment and constant trend of displacement values of point 1, (see Figure 4 scheme b).

The similar behaviour, at the start of maximum displacements, was recorded with different entity by solutions proposed with wood (cfgW), RC with curb (cfgRCa) and without (cfgRC).

The maximum displacements to the acceleration peak of event (3.9 sec), recorded by GFRP configuration, is 60-90% greater than the other solutions; however, in the same time, the capacity of GFRP configuration to comeback at initial condition is better than the other configurations, Table 3.

Table 3 Displacements of Point 1 to 3.9 and 9.6 sec

Cfg	Displ.(mm) to 3.9 sec	Displ.(mm) to 9.6 sec
W	0.7	1.59
GFRP	4.09	1.02
STEEL	1.8	2.29
RC	0.7	1.71
RCa	0.43	0.84

To evaluate the possibility to realize the solution with composite structural elements, for seismic improvement of existing structure, is necessary to analyse the displacements (Point 1, Table 3) with the main stress (Point 2, Table 4).

The better behaviour of masonry wall with cfgGFRP configuration - characterized by the good ratio between the strength properties and the low dead load of composite material - enable to reduce the entity of stress values along ZZ direction, (see Figure 4). At acceleration peak the stress level of GFRP configuration highlights a similar response to STEEL solution and lower than the other configurations, Table 4.

At the end of analyzed period the recorded values of cfgGFRP solution are 10 times less than the other configurations.

Table 4 StressZZ of Point 2 to 3.9 and 9.6 sec

Cfg.	Stress ZZ(MPa) to 3.9 sec	Stress ZZ(MPa) to 9.6 sec
W	0.056	0.097
GFRP	0.032	0.007
STEEL	0.035	0.057
RC	0.042	0.096
RCa	0.040	0.046

3 CONCLUSIONS

For the 3D GFRP structure subjected to seismic action the higher stiffness of the system does not seem to be affected by the presence, or otherwise, of the braces. The same variation of internal restrain conditions influences in negligible way the global dynamic response.

Considering the all applications evaluated for seismic improvement the solution with pultruded elements are an interesting alternative respect to traditional technologies. The configuration with GFRP element offers, besides the favorable characteristics of composite material – the high durability, low dead load, easiness to transport and assembling phases – the good behaviour respect to steel and RC solutions. In particular the GFRP configuration records the elevated displacements in the initial phase but

a better capacity to dissipate the accumulated acceleration than the other solutions.

The damping ratio of GFRP roof truss is equal to 1.4% while for the other solutions is 0.07% with wood, 0.15% with steel, 0.31% with RC and 0.87% with RC together RC curb.

At the maximum peak the stress condition of the masonry with roof truss of GFRP configuration is similar to steel solution and, although, 30% lower than the other configurations; at 10 seconds the stress level is reduced of 10 times.

For the themes proposed by this research is necessary further studies to consider the non linear behaviour of GFRP material, the ductility absence and the rotational stiffness of joint considered as rigid.

REFERENCES

- ASCE 1984. Structural Plastic Design Manual. American Society Civil Engineering, ASCE, Volume 1 and 2.
- Boscato, G., 2009. Numerical analysis and experimental tests on dynamic behaviour of GFRP pultruded elements for conservation and architectural and environmental heritage, PhD thesis, University of Nova Gorica, Graduate School, Venice, 2009.
- Boscato, G. & Russo, S. 2009. Free Vibrations of Pultruded FRP Elements: Mechanical Characterization, Analysis, and Applications. Journal of Composite for Construction, ASCE, Vol. 13 No. 6, December 2009.
- CNR-DT 205/2007, 2008. Istruzioni per la Progettazione, l'Esecuzione ed il Controllo di Strutture realizzate con Profili Sottili Pultrusi di Materiale Composito Fibrorinforzato (FRP), Roma CNR. CNR-DT 205/2007.
- Holloway, L. and A. M. Farhat. 1990. Vibrational analysis of a double-layer composite material structure. Composite Structure, 16(4): 283-304.
- Mosallam, A. S.; Abdelhamid, M. K.; Conway, J. H., 1994 performance of pultruded frp connections under static and dynamic loads, Journal of reinforced plastics and composites, vol. 13, issue 5, pp. 386-407.
- Russo, S., 2007. Strutture in Composito: Sperimentazione, Teoria e Applicazioni. Edited by Ulrico Hoepli, Milano, Italy.

GFRP Members in Free Vibrations Field, Dynamic Parameters of Profiles and 3D Structure

Giosuè Boscato & Salvatore Russo

University Iuav of Venice, Venice, Italy

ABSTRACT The study examines the topic of dynamic identification of the pultruded elements and GFRP (Glass Fiber Reinforced Polymers) structural systems starting from the definition and quantification of the fundamental parameters of dynamic engineering, natural frequencies, modes of vibration and damping. The research illustrates the results of an extended campaign of experimental tests on mono-dimensional elements, panels and framework systems, subject to free vibration. The boundary conditions for the structural elements are simply supported, for the 3D structure are supported configuration. The tests concern profiles with open cross-sections with one or two axis of symmetry, tubular sections and panel. As regards the all-GFRP structures have been investigated the three-dimensional frame (5m × 5m for the plan and 2.5m for the high), it is an auxiliary floor built in historical building of Vicenza, Italy.

1 INTRODUCTION

The dynamic behavior of pultruded profiles and all-FRP structure is, actually, a topic not enough studied. The main characteristic of good ratio between self weight-strength – greater than steel and aluminum, 4 and 2 times respectively – defines, together the important aspect of durability, the specific application fields (Russo 2007). More than temporary and emergency structures, superimposed constructions, frame and solutions as support for structural rehabilitation of existing structures, the GFRP system can be take into account as opposed to dynamic action. As regards it's necessary, first of all, to define the dynamic parameters of GFRP profiles and structures. These properties were examined via micro-mechanical considering the matrix, the fibrous reinforcing and the fiber-matrix interface, (Sun and Lu 1995).

Gibson and Plunkett (1976) defined the interval of frequencies from 0 to 500Hz on unidirectional composite laminate and the dependence of the mechanical characteristics on the variation of the vibration frequency. For pultruded profile Nori et al. (1996) studied the influence of percentage and fibers type on dynamic behavior. To regards the numerical approach the FE analysis was conducted at a macro-mechanical level was developed by Qiao and Zou (2002), Turvey and Mulcahy (2004). As regards models for natural frequency analysis of pultruded FRP elements, the research compares the results obtained by Timoshenko's shear-deformable beam theory (Timoshenko 1921, Nowinski 1969) and Euler-Bernoulli's beam theory. The present work is a part of wide study on dynamic behavior, of GFRP profiles and structures carried out by Boscato and Russo (2009),

Boscato (2009). The research defines the variation of dynamic parameters in free vibration field – modal shape, frequencies, damping ratio – of GFRP material from structural element to three-dimensional frame.

2 CHARACTERISTICS OF GFRP PROFILES

The GFRP profiles are built by pultrusion manufacturing process with standard cross section. The basic components are, E-glass fibers and vinylester matrix. In particular the cross section is similar to laminate configuration with external layer (mat), where the fibers are short and randomly distributed on more layers, and core layer (roving) with the continuous and unidirectional fibers parallel to main axis of mono-dimensional element. The physic and mechanical characteristics of material and profile are shown by Boscato and Russo (2009).

3 GENERAL DESCRIPTION

Modal analysis methodology to define the dynamic parameters was carried out with same procedure both on profiles and structures.

For mono-dimensional elements the analysed cross sections are shown in Figure 1 whereas the different configurations and geometrical characteristics are listed in Table 1. The boundary condition of GFRP profiles is simply supported.

As regards the GFRP structures built by columns of 4 "L" shape profile assembled together and "H" beams linked by bolts and joints made by steel, Table 2 and Figure 2 (Boscato 2009). The three-dimensional frame

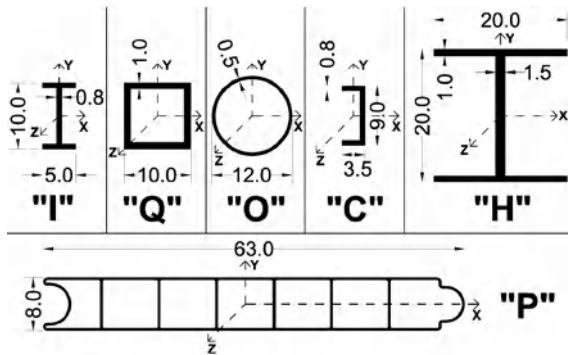


Figure 1 Shapes of GFRP profile, cm dimensions

Table 1 Characteristics of GFRP profiles

Element	$J(\text{cm}^4)$	L (cm)	Area(cm^2)	Weight(kg)
“I”, J_{max}	209.22	300	14.72	8.65
“I”, J_{min}	17.02			
“Q”	492	240	36	14.87
“O”	299.20	240	18.06	7.85
“C”, J_{min}	11.27	200	11.52	4.2
“H”, J_{max}	4342.3	500	67	62
“H”, J_{min}	1338.4			
“P”	808.66	420	74.57	57.3

Table 2 Characteristics of GFRP profiles, 3D structure

Structural Elements	A (cm^2)	J_{xx} (cm^4)	J_{yy} (cm^4)
Beam	67	4342.3	1338.4
Column	61.44	1260.1	



Figure 2 3D structure, axonometric and detail views

is simply supported on the floor of historical building.

Figure 3 illustrates the analysed beams with excitation points and positions of accelerometers.

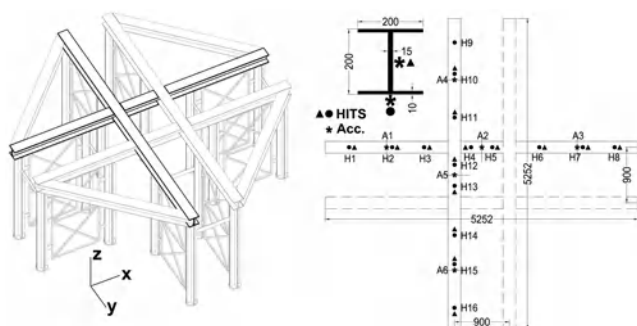


Figure 3 Axonometric view and detail of analysed beams

For both experimental tests the instruments was determined considering the masses and stiffness of profiles and 3D system.

The excitation pulse of the structural element was generated by a Dytran 5850A instrumented hammer with a particular stiffness in order to obtain complete broad oscillation periods. The structural responses were recorded by using BBN accelerometers, model 507Lf, with a mass of 10 grams and a frequency field of between 0.1 and 12 kHz, compatible with the mechanical characteristics of elements. Both hammer and sensors used are piezoelectric sensing elements featuring a cylindrical shear stress configuration with integral charge preamplifier and are connected to a data acquisition system through high stability coaxial cables that minimize the environmental influence on the test results.

4 DYNAMIC RESPONSE IN FREE VIBRATIONS FIELD

Through the modal analysis carried out on pultruded profiles and GFRP structures in free vibrations field the values of fundamental frequency obtained by experimental and numerical approach and the damping ratio are shown.

4.1 Mono-dimensional structural elements

Figure 4 shows the comparison between the fundamental frequencies of all profiles considering the different configurations, J_{min} e J_{max} .

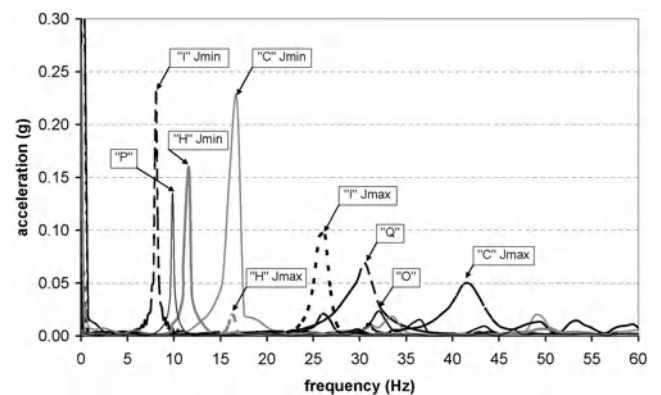


Figure 4 Fundamental frequency of all structural element

Figure 4 highlights the better response of profiles with greater flexural stiffness (“H” J_{max} , “I” J_{max} , “C” J_{max} , “Q” and “O”). The comparison is particularly interesting if analysed with different capacity to dissipate the initial acceleration, Figure 5, illustrated by the exponential curve that interpolates the peek points of accelerograms in time domain.

Although the stiff profiles with a greater fundamental frequency (Figure 4) show a better capacity to dissipate the initial acceleration (Figure 5). For example in the same time for the “I” shape profile the decrement of

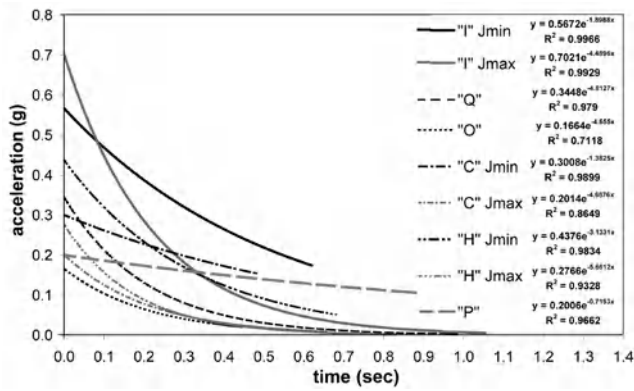


Figure 5 Comparison between structural element

acceleration is 10 times respect the initial acceleration whereas “P” element reduces the initial acceleration of 1.4 times. Table 3 compares the frequencies of first mode of vibration obtained by experimental, numerical and finite element method. To concerns the numerical analysis the effects of two approaches were considered, Euler-Bernoulli’s beam theory (EB) and Timoshenko’s shear-deformable beam theory (T) to consider or not the influence of shear deformability and torsional effect. Table 3 shows, moreover, the damping ratio calculated by decrement logarithmic approach.

Table 3 Frequencies of first mode and damping ratio ξ , structural elements

Structural element	FEA (Hz)	Th (Hz) by eq. (EB)	Th (Hz) by eq.(T)	Exp (Hz)	ξ (%)
“I”, J_{min}	7.07	7.01	6.54	7.02	0.96
“I”, J_{max}	24.38	24.59	22.81	24.41	2.59
“Q”	37.66	38.34	34.71	35.09	2.72
“O”	41.48	42.21	38.46	38.14	2.26
“C”, J_{min}	15.14	14.37	13.52	14.49	1.45
“H”, J_{min}	9.97	10.21	9.75	10.5	1.18
“H”, J_{max}	18.80	18.39	17.54	16.47	3.40
“P”	11.93	10.74	10.22	11.9	0.97

For the slender structural elements (“I”, “C”, “H” with J_{min} and “P”) the range of damping ratio is between 0.9-1.5%. The damping values for the profiles with low slenderness (“I”, “H” with J_{max} and tubular profiles) are included in the interval between 2.25-3.5%. An important analysis to consider the influence of torsional effect of GFRP pultruded profile is shown in Figure 6; scheme (a) the analysis of section regards the excitation S0 near the support, scheme (b) with excitation S4 to L/2, scheme (c) excitations S5 horizontal to L/2 and S6 vertical asymmetrical to L/2.

To analyse the torsional and transversal effect on pultruded profile is important to consider the displacements difference between the half flanges, caused by S6 excitation (scheme c of Figure 6), with the maximum displacement

equal to 0.059mm and the minimum displacement equal to 0.021mm.

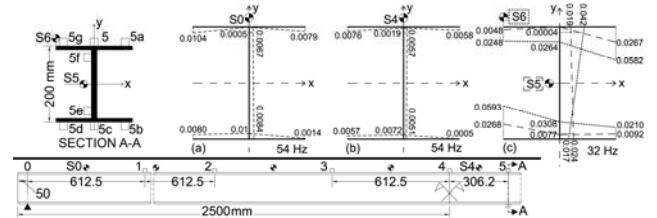


Figure 6 Displacements (mm) of section A-A

4.2 3D Structures

Starting from global analysis of dynamic behavior of all-GFRP structure (Boscato 2009) are shown only the beams to focus the different response of “H” profile, evaluated both as structural element (Figure 6) and part of 3D system (Figure 3). Considering the first flexural mode of vibrations - induced by excitation H1 J_{max} (Figure 3) - the fundamental frequencies of beams are 20.34Hz and 20.75 for the beam parallel to x and y axis respectively.

Figure 7 shows the different capacity of beams to dissipate the initial accelerations induced by excitation H4 J_{max} , see Figure 3.

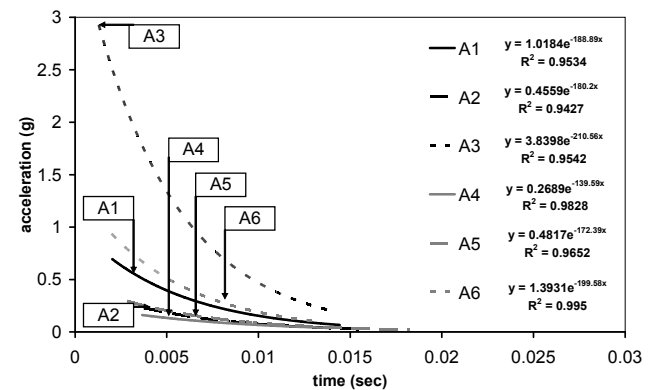


Figure 7 Comparison between beams, excitation H4 J_{max}

4.3 Results comparison

The comparison between the dynamic response of structural element with “H” cross section analysed in the configuration both as simply supported (Table 4) and as the beam in the 3D structure (Figure 7) is proposed. This comparison, made possible by the equal dimensions of the static scheme of beams (same section and length slightly different, 5m for the mono-dimensional structural element and 5.2m for the beam considering a span of 5m between the two external constraints) allows to identify the influence on the dynamic response of the various boundary conditions. As regards the damping ratio are almost similar, 3.15% for the beam in the 3D structure and 3.4% as structural element. The comparison between all the analysed configurations enables to interpret the

obtained experimental results of the modal analysis (Table 4) in order to identify the solution with the best dynamic performances. With reference to “H” shape profile the geometry of the structure 3D always allows to have similar parameters of the dynamic response with respect to the configuration simply supported without undergoing important decrement of the fundamental frequency, see Table 4.

Table 4 Comparison between profiles and 3D structure

Elements and structure	Direction of excitations	Hz	T (s)
“I”	J_{max}	24.41	0.04
“Q”	/	35.09	0.028
“H”	J_{max}	16.47	0.06
“P”	J_{max}	11.9	0.08
3D structure	x	20.34	0.05
	y	9.36	0.1

4.4 Comparison with traditional materials

The results of the study carried out on the damping of the mono-dimensional elements and of the GFRP structures are particularly interesting when compared with the values recorded in the following table defined by Chopra (1995) which refers to traditional materials, Table 5.

Table 5 Damping ξ value of traditional materials

Structures with elements below of 50% than elastic limit	
Welded steel structures	2-3%
Bolted or nailed steel structures	5-7%
Bolted or nailed wood structures	
GFRP structures	
Bolted GFRP structures	2.2%

5 CONCLUSIONS

Through the comparison between the dynamic response of GFRP profile and 3D structure, in free vibration field, the first considerations to be drawn: The modes of vibration analysis of open cross-section GFRP longer pultruded elements can be developed with available theories and computational methods for isotropic materials. On the other side, formulations accounting for the transverse shear deformation and torsional effect are generally more suitable to the investigation of dynamic behavior of GFRP elements. For the simply supported condition the damping ratio ξ – considering only the maximum moment of inertia – came from 2.25% to 3.5%. The damping ratio of 3D structure is equal to 3.15%. For the same profile and different boundary condition,

the fundamental frequency of “H” structural element change from 16.5Hz to 20.34Hz. Considering “H” profile the damping ratio decreases of 7% from the structural element configuration to the beam configuration in the structure. The incidence of torsional phenomena is evident in the dynamic response of “H” shape profile excited asymmetrically. Through these first results and the characteristics of GFRP material it is possible to consider the application of structure all-composite in dynamic engineering field. Defined the dynamic parameters of GFRP profiles and structure in free vibration field is necessary, then, to analyse the structural response respect to dynamic action.

REFERENCES

- Boscato G., 2009. Numerical analysis and experimental tests on dynamic behaviour of GFRP pultruded elements for conservation and architectural and environmental heritage, PhD thesis, University of Nova Gorica, Graduate School, Venice, 2009.
- Boscato, G.& Russo, S. 2009. Free Vibrations of Pultruded FRP Elements: Mechanical Characterization, Analysis, and Applications. *Journal of Composite for Construction, ASCE*, Vol. 13 No. 6, December 2009.
- Chopra, A.K. 1995. Dynamics of Structures-theory and applications to earthquake engineering, Prentice-Hall, Englewood Cliffs, New Jersey.
- Gibson, R.F., Plunkett, R., 1976. Dynamic Mechanical Behaviour of Fiber-Reinforced Composites: Measurement and Analysis, *Journal of Composite Materials*, Vol.10.
- Nori, C.V., McCarty, T.A., Mantena, P.R., 1996. Experimental and Finite Element Analysis of Pultruded Glass-Graphite/Epoxy Hybrids in Axial and Flexural Modes of Vibration, *Journal of Composite Materials*, Vol.30.
- Nowinski, J. L., 1996. On the Transverse wave Propagation in Orthotropic Timoshenko Bars. *International Journal of Mechanical Science*, Vol. 11, 689-693.
- Qiao, P., Zou, G., 2002. Analytical and Experimental Study of Vibration Behaviour of FRP Composite I-Beams, *15th ASCE Engineering Mechanics Conference*, Columbia University, New York .
- Russo, S. 2007. *Strutture in Composito: Sperimentazione, Teoria e Applicazioni*. Edited by Ulrico Hoepli, Milano, Italy.
- Sun, C. T., Lu, Y. P., 1995. Vibration Damping of Structural Elements, Prentice Hall PTR, New Jersey.
- Timoshenko, S. P., 1921. On the correction for shear of the differential equation for transverse vibrations of prismatic bars. *Philosophical Magazine*, Ser. 6, 41(245), 744-746.
- Turvey, G.J., Mulcahy, N., 2004. Free Vibration of Clamped Pultruded GRP Circular Plates with Central Circular Cut-Outs, *Fourth International Conference on Thin-Walled Structures*.

Experimental Design on Multi Layers of LVL Fiber Reinforced Wood Composite Using Bagasse as Core Structure

Meekum U. (umsut@g.sut.ac.th)

School of Polymer Engineering, Suranaree University of Technology, Nakorn Ratchasima, Thailand

ABSTRACT The multi layers of laminated veneer lumber(LVL) fiber reinforced wood composite were constructed. It was comprised of peeled rubber and eucalyptus woods sheet obtained from commercial forest. Epoxy and vinyl ester cured bagasse were used as core and the fiber glass woven as reinforcement. Those constituents were alternately laid and bonded with epoxy and vinyl ester resins and compression molded. The 2k experimental design method was applied to study the effect of those parameters on the mechanical properties by mean of flexural properties It was found that, within the statistical result, there is no significant effect of those parameters on the flexural properties of the LVL. It would be contributed from the less brittle bagasse core. Then, the over all strength would not be enhanced and no contribution from the other strong constituents.

1 INTRODUCTION

As global warming is concerned, wood is one of the precious natural resources. It is not only the most effective CO₂ scavenger but also the most important raw materials for many of industries such as building construction. There are several engineering materials to substitute this resource but they are still incompletely satisfactory, especially in the sense of artistically. There are several common ways to manipulate the materials to substitute the natural wood including wood polymer composite (WPC) and engineered wood. The later is normally called man made wood. They are usually derived from pieces of fast grow wood and manufactured into stronger ones by mean of engineering composite methods.

The examples of engineered wood are plywood, oriented stand wood(OSW), glulam, laminated veneer lumber (LVL), etc. The LVL is produced by bonding thick/thin wood veneer together into a larger billet. The LVL billet then sawn into desired dimension. The strength of the billet can increased by using fiber reinforced materials such as fiber glass and carbon fiber. The maximum loading of the reinforced wood also is depended on the adhesive used. Urea and phenol formaldehyde are commonly and commercially used. Colak and co-worker reported that flexural strength of LVL obtained from spruce veneers using phenol formaldehyde is prox. 98.4 MPa [1]. The strength of beech and alder veneer was 100 to 79 MPa using melamine urea formaldehyde [2]. There is document published on glass fiber and carbon fiber reinforced timber beam. It was found that carbon had shown more significant improve in flexural strength than glass fiber [3]. Thermoplastic adhesives such as poly(vinyl acetate)

(PVAc) is also the most conventional one. This glue is less water resistance.

In this work, the LVL derived from the multi layers core sandwich-like structure were investigated. The bagasse fiber from sugar cane factory was used as cores. Epoxy and vinyl ester resins are used as adhesives. Rubber and eucalyptus peeled sheet were used and fiber glass woven was exploited as reinforced materials. The results of parameters that effect to the strength of the LVL beam were analyzed by design of experiment(DOE) method.

2 EXPERIMENTAL PROCEDURE

2.1 Materials

The main materials used in this study can be classified into 4 categories; (i) the wood veneers, (ii) the fiber reinforced materials, (iii) bagasse fiber and (vi) adhesives. Wood veneers; rubber and eucalyptus, were peeled at thickness of approx. 2.5 mm. The young teak veneer, approx. 15 yrs, was sliced at the thickness of 0.5 mm. The moisture of woods was controlled at around 6-14% by drying in oven at 105°C. The woven E-glass with the areal density of 821 g/m² was employed. The bagasse fiber was prepared by soaking in 0.5%(w/v) NaOH solution over night, autoclaving for 4 hours and crushed in non-intermeshing twin screw extruder. The fiber that passed thru the twin screw 2 times was classified as *long fiber*. The fiber thru the screw 4 times resulted in shorted L/D ratio and was called as *short fiber*. The room temperature amine cure epoxy system and vinyl ester resin were used. The bisphenol A epoxy was formulated in house. Vinyl ester resin was purchased

from Thai Mitsui Co. Ltd. All chemical for adhesives were commercial grade and used as received.

The bagasse core was prepared by thoroughly mixing the fiber with the given adhesive using mechanical mixer. The sticky pulp was then smoothly spread in the rectangular compression mold and pressed at 10 psi and 120°C for 30 mins. 250×250×2 mm sheet was obtained and then cut into required dimension.

2.2 Multi Layers LVL Core Sandwich Preparation

Ten layers of peeled wood sheets, bagasse cores and glass woven were gathered for manufacturing the LVL composite specimen. The teak veneers were laminated on both faces of the sample. The layers were alternately stacked and bonded using the assigned adhesive. It was cured at 120°C and 5 psi for 45 mins. The LVL sandwich composite with dimension of approx. 120×120×50 was obtained. The specimen was machine saw cut into the required test sample, paper sand polished and post cured at 70°C for 8 hours.

2.3 Design of Experiment

There are 3 parameters of the 2^K DOE to verify their effect to flexural properties. There are adhesive type(A), peeled wood type(B) and L/D ratio of bagasse fiber(C) corresponding to rubber wood, epoxy adhesive and short bagasse fiber(Low L/D ratio), respectively. For each high and low level parameter was spit into 2 sub levels as shown in table 1. The percentage is referred to fraction of 10 layers used. Therefore 1 layer is equivalent to 10%. The matrix of the DOE is summarized in table 2. The flexural properties by mean of strength, modulus and their specific figures were engaged as experimental respond.

Table 1 The DOE parameters and their level

Parameters	(-)Low Level(%)	(+)High Level(%)
Adhesive(A)	20	30
Wood(B)	20	30
L/D ratio(C)	20	30

Table 2 The DOE Matrix

Run No.	Factors		
	A(Adhesive)	B(Woods)	C(L/D Ratio)
1	2(-20)	2(-20)	2(-20)
2	3(-30)	3(-30)	6(+60)
3	2(-20)	6(+60)	3(-30)
4	3(-30)	7(+70)	7(+70)
5	6(+60)	3(-30)	3(-30)
6	7(+70)	2(-20)	6(+60)
7	6(+60)	7(+70)	2(-20)
8	7(+70)	6(+60)	7(+70)

2.4 Material Testing

Flexural testing by mean of three point bending was conducted according to ASTM 790. The 50 kN load cell

InstronTM 5569 were employed. The span length of 100 mm was resumed and displacement speed of 5.5 mm/min was electronically controlled. Six specimen were tested. The average values were reported.

3 RESULTS AND DISCUSSION

Flexural properties of the LVL derived from the DOE are summarized in Table 3. By calculating the density of the specimen, kg/m³, and use it for determining the specific flexural values, the results are shown in table 4.

Table 3 Flexural Properties of LVL composite

Test No.	Responds#1(Flexural Properties)		
	Strength (MPa)	Modulus (MPa)	Toughness (kJ/m ²)
1	16.60±0.86	105.20±9.16	31.35±5.43
2	20.88±0.76	130.41±12.96	33.17±6.33
3	19.28±2.28	148.15±19.94	28.17±7.41
4	19.41±0.82	160.51±19.91	32.47±16.65
5	21.88±3.21	167.53±10.28	27.37±10.84
6	21.87±1.97	176.31±39.14	27.25±6.14
7	16.41±2.28	114.24±2.01	31.38±18.14
8	33.84±1.47	224.73±20.16	44.14±4.24

Table 4 Specific Flexural Properties of LVL composite

Test No.	Responds#2(Specific Flexural)		
	Strength(MPa)	Modulus(MPa)	Toughness(kJ/m ²)
1	0.017±0.001	0.111±0.009	0.033±0.006
2	0.022±0.000	0.136±0.015	0.034±0.007
3	0.020±0.003	0.153±0.019	0.030±0.008
4	0.020±0.001	0.165±0.020	0.033±0.017
5	0.023±0.003	0.174±0.011	0.028±0.011
6	0.023±0.002	0.184±0.011	0.028±0.006
7	0.017±0.002	0.119±0.021	0.032±0.019
8	0.035±0.001	0.233±0.021	0.045±0.004

Roughly observation, it is found that the 8th run, high epoxy adhesive, high rubber wood and high L/D ratio of bagasse fiber, exhibit the highest values. This preliminary indicates that rubber wood, epoxy adhesive and short fiber give rise to the superior flexural properties. In order to conclude the effect of those parameters on the flexural properties of LVL composite, the Design ExpertTM with 95% degree of confidential, p = 0.05, was employed.

Table 5 and 6 summarize the ANOVA result for both normal flexural properties and the specific properties. The tables show that all of the models used to evaluate the effect of those assigned parameters are not significant, within 95% degree of confidential, p-values are greater than 0.05. These conclusions are confirmed by the normal plots and pareto chart as selectively given only for the flexural strength and the specific flexural strength in Figure 1. The rest of the plots show the similarity. As

Table 5 ANOVA analysis for Flexural Properties of DOE

Source	Sum of Square	df	Mean Square	F value	P value	Conclusion
Respond: <i>Flexural Strength</i> (MPa)						
Model	59.57	1	59.57	2.35	0.1763	Not significant
C	59.57	1	59.57	2.35	0.1763	
Residual	152.71	6	25.36			
Cor Total	211.74	7				
Respond: <i>Flexural Modulus</i> (MPa)						
Model	3739.17	3	1246.39	0.76	0.5711	Not significant
A	2399.17	1	2399.17	1.47	0.2923	
B	581.06	1	581.06	0.36	0.5831	
AB	758.94	1	758.94	0.46	0.5330	
Residual	6536.72	4	1634.18			
Cor Total	10275.89	7				
Respond: <i>Toughness</i> (kJ/m ²)						
Model	112.94	4	28.23	0.890	0.5623	Not significant
A	3.05	1	3.05	0.096	0.7772	
B	36.04	1	36.04	1.13	0.3654	
C	44.18	1	44.18	1.39	0.3237	
BC	29.65	1	29.65	0.930	0.4957	
Residual	95.51	3	31.84			
Cor Total	208.43	7				

Table 6 ANOVA analysis for Specific Flexural Properties of DOE

Source	Sum of Square	df	Mean Square	F value	P value	Conclusion
Respond: <i>Specific Flexural Strength</i>						
Model	7.23E-05	2	3.61E-05	1.15	0.3874	Not significant
B	6.13E-06	1	6.13E-06	0.20	0.6768	
C	6.61E-05	1	6.61E-05	2.11	0.2060	
Residual	1.57E-04	5	3.13E-05			
Cor Total	2.29E-04	7				
Respond: <i>Specific Flexural Modulus</i>						
Model	3.90E-03	3	1.30E-03	0.75	0.5768	Not significant
A	2.63E-05	1	2.63E-03	1.52	0.2856	
B	5.28E-04	1	5.28E-04	0.30	0.6103	
AB	7.41E-04	1	7.41E-04	0.43	0.5488	
Residual	6.93E-03	4	1.73E-03			
Cor Total	0.011	7				
Respond: <i>Specific Toughness</i>						
Model	3.61E-05	1	3.61E-05	1.28	0.3003	Not significant
C	3.61E-05	1	3.61E-05	1.28	0.3003	
Residual	1.69E-04	6	2.81E-05			
Cor Total	2.05E-04	7				

indicated in figure that all of the effects and also their interacted ones are lined on the trend line, and below the critical t-values as shown in the pareto chart, respectively. It is obviously seen that those effects are positive affect

to the flexural properties. Except for the flexural modulus where the interaction parameter AB is shown the negative effect to the respond properties. It is meant that if high content of rubber wood(+B) is employed, the low level of epoxy adhesive(-A) must be used and vice versa.

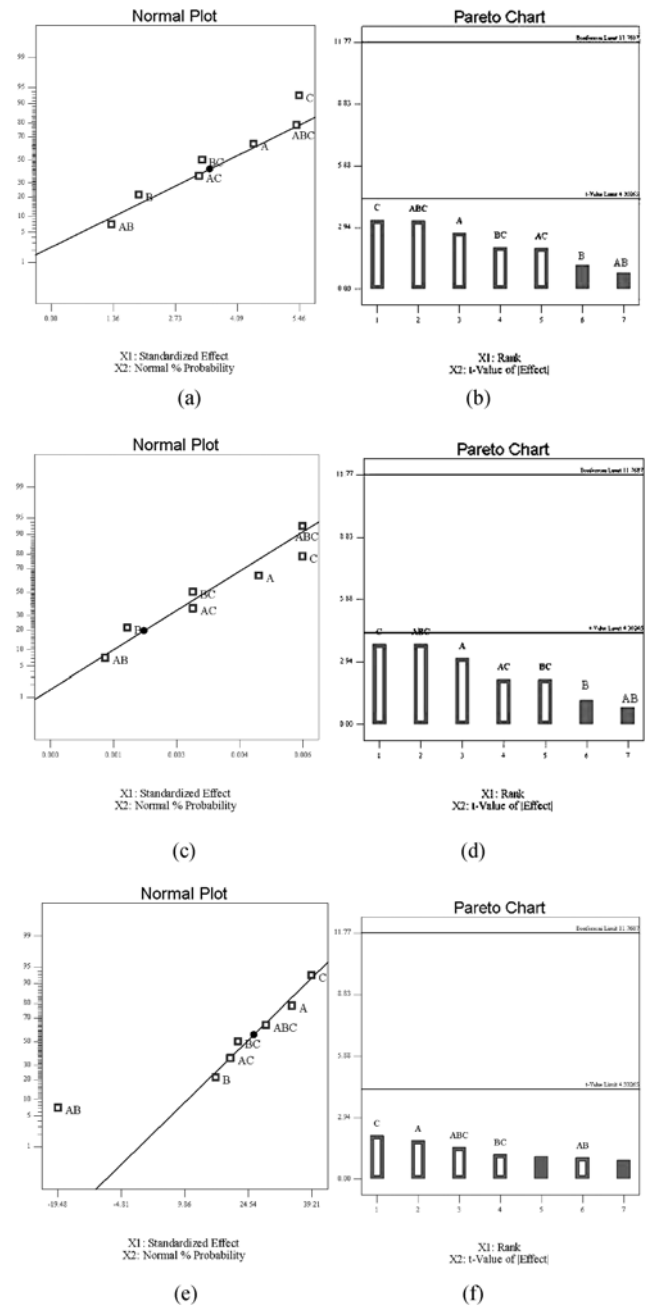


Figure 1 The normal plot and pareto chart of (a) – (b) flexural strength, (c) – (d) specific flexural strength and (e) – (f) flexural modulus of the DOE analysis, respectively

From the above statistically analyzed results, it can be concluded that epoxy and vinyl ester adhesives, rubber and eucalyptus woods and the L/D ratio of bagasse fiber used as core sandwich LVL composite does not any significant effect of the properties by mean of flexural bending of the LVL wood. However from the previous work studied the fiber reinforced LVL composite, it was

indicated that rubber wood with room temperature cure epoxy adhesive exhibit the superior properties than eucalyptus wood[4]. Their strengths are much higher than the values observed in this sandwich material. This might be the fact that the bagasse cores are worst brittle and then they significantly contribute to inferior flexural properties. Adding more tougher constituent would not enhance the properties.

4 CONCLUSIONS

By using the DOE approach to evaluate the effect of adhesive, epoxy and vinyl ester, wood types, rubber and eucalyptus, and core material derived from bagasse fiber with different in L/D ratio, for preparing the multi layers core sandwich LVL composite, it was found that those parameters do not have any significant to the responded properties by mean of flexural bending. The statistical

means showed the analyzed values are more than the critical p-value.

REFERENCES

- Colak, S. Colakoglu, G. and Aydin, I. (2007). Effect of log steaming veneer drying and aging on the mechanical properties of laminated veneer lumber(LVL). *Building and Environment*. 42: 93-98.
- Toksoy, D., Colakoglu, G., and Aydin, I. (2006). Technological and economic comparison of the usage beech and alder wood in plywood and laminated veneer lumber manufacturing. *Building and Environment*. 41: 872-876.
- Johns, K.C., and Lacroix, S. (2000). Composite reinforcement of timber in bending. *Canadian J. of Civil Eng.* 27:899-906.
- Mingmongkol, Y. (2009). Experimental design on engineered wood: Laminated veneer lumber(LVL) reinforce composites. M.S. thesis, Suranaree University of Technology, Thailand.

Shear Behavior of Glue-Laminated Composite Sandwich Beams

Allan Manalo (manalo@usq.edu.au), Thiru Aravinthan & Warna Karunasena

Centre of Excellence in Engineered Fibre Composites (CEEFC), Faculty of Engineering and Surveying, University of Southern Queensland, Toowoomba, Queensland, Australia

ABSTRACT The shear behaviour of a new generation composite sandwich structure made up of glass fibre reinforced polymer skins and modified phenolic core material was investigated in view of using this composite material as a shear loading component in structural glue-laminated beams. Characterisation of the shear strength and stiffness of the fibre composite skins and the modified phenolic core material was conducted following the ASTM-D5379/D5379M-93 test standard. The shear behaviour of the individual and the glue-laminated composite sandwiches was investigated under asymmetrical beam shear test. The results of the experimental investigation showed that the asymmetrical beam shear test gives a good estimation of the shear strength and stiffness of the glue-laminated composite sandwiches. A theoretical prediction of the shear strength of the composite sandwich beams with high strength core material was proposed and comparison with experimental results showed a good correlation. The results of the study suggest the high possibility of using composite sandwich construction in the development of structural laminated beams to carry shear.

1 INTRODUCTION

The main driver for fibre composite research in Australia is finding a suitable alternative for replacing deteriorating timber structures as hardwood timber is becoming more expensive, less available and is of inferior quality compared to the timber previously available. Recently, a new generation composite sandwich panel made up of glass fibre composite skins and modified phenolic core material has been developed (Van Erp and Rogers, 2008). Several studies have shown that these sandwich panels are appropriate for structural beam applications (Manalo et al 2010). This material can be engineered to have stiffness and strength compatible with structural timber. As these sandwich panels are produced in limited thicknesses, a structural beam can be manufactured by gluing several sandwiches together. The flexural behavior of these glue-laminated sandwich beams has shown that gluing these composite sandwiches resulted in a more stable and stronger section. Another important consideration when designing structural beams from composite sandwich panels is the shear strength of the core material. Typically, the brittle nature of the core causes the sudden collapse of the sandwich structure and could become the limiting factor in designing such structures.

In this paper, the shear behavior of an innovative sandwich structure is investigated in view of using this composite material as a shear loading component in glue-laminated beams. Iosipescu shear test (ASTM-D5379) was conducted to characterize the shear strength and modulus of the fibre composite skin and the phenolic core material. Asymmetrical beam shear test was then

performed to determine the shear behavior of the glue-laminated composite sandwich beams. The shear behavior in the flatwise and in the edgewise positions was investigated in an attempt to improve the structural performance of the sandwich beams by making the non-horizontal skins carry the shear usually carried by the core material.

2 EXPERIMENTAL PROGRAM

2.1 Material properties

The composite sandwich beams tested in this study are made up of glass fibre composite skins co-cured onto the core material using a toughened formaldehyde resin. The skin is made up of 2 plies of stitched bi-axial (0/90) E-CR glass fibre fabrics while the modified phenolic foam core is a proprietary formulation by LOC Composites, Pty. Ltd. Australia. The effective mechanical properties (in the main direction) of the fibre composite skin and the core material determined from flexural test are listed in Table 1.

Table 1 Effective mechanical properties of the skin and core

Property	Skin	Core
Young's modulus (MPa)	14280	1350
Nominal thickness (mm)	1.8	16.4

2.2 Iosipescu shear test

The shear test of the fibre composite skin and the modified phenolic core material was conducted following the ASTM D5379/D5379M-93 standard. Coupon specimens with symmetrically located v-notches at the centre were

loaded in a universal testing machine by a modified Wyoming test fixture at a constant head speed of 1mm/min. Resistance strain gauges oriented at $\pm 45^\circ$ to the loading axis were bonded in the middle of the specimen to determine its shear response during the entire loading regime. The average shear strain, γ_{ave} is then determined from the strain gauges using the relation:

$$\gamma_{ave} = \varepsilon_{+45} - \varepsilon_{-45} \quad (1)$$

where the ε_{+45} is the strain measured by the $+45^\circ$ gauge and the ε_{-45} is the strain measured by the -45° gauge. The average shear stress, τ_{ave} is then determined by dividing the applied load P by the area of the cross section between the notches. The apparent shear modulus, G_{ave} is then calculated by:

$$G_{ave} = \frac{\tau_{ave}}{\gamma_{ave}} \quad (2)$$

2.3 Asymmetrical beam shear test

The shear test of the composite sandwich beams was performed using an asymmetrical beam shear test. This test setup is a modification of the Iosipescu shear test for composites. The test setup for the asymmetrical beam shear of composite sandwich beams is illustrated in Figure 1. The specimen was eccentrically loaded at two trisected points and the supports were placed at the remaining two points. The load was applied through a 100kN servo-hydraulic testing machine. Strain gauges were attached to the specimen to evaluate the shear strain during loading and until final failure. The applied load and strains were obtained using a data logger. All specimens were tested up to failure to determine the shear strength and the mode of failure. The details of the composite sandwich beam specimens for asymmetrical beam shear test are listed in Table 2.

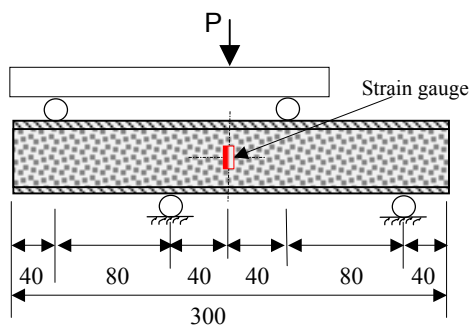


Figure 1 Schematic diagram of asymmetrical beam shear test

3 RESULTS AND DISCUSSION

3.1 Shear behavior of the skin and the core

The shear properties of the fibre composite skins and the modified phenolic core are listed in Table 3. The shear modulus was determined from the slope of the linear elastic portion of the shear stress-strain diagram of the

skin and the core. The experimental results showed that the skins exhibit non-linear behaviour under shear loading while the core material behaved linearly up to failure.

Table 2 Details of specimen for asymmetrical beam shear test

Specimen	Illustration	Number of specimens	B	D
			(mm)	(mm)
AS-1LSW-F		5	50	20
AS-1LSW-E		5	20	50
AS-2LSW-F		5	50	40
AS-2LSW-E		5	40	50
AS-3LSW-F		2	60	60
AS-3LSW-E		2	60	60
AS-4LSW-F		2	80	80
AS-4LSW-E		2	80	80

Table 3 Shear properties of the skin and core

Property	Skin		Core	
	Ave	Std dev	Ave	Std dev
Shear modulus (MPa)	2465	105	528	4.97
Shear stress (MPa)	22.82	0.69	4.25	0.19
Strain at peak (%)	3.11	0.11	0.81	0.03

3.2 Shear behavior of composite sandwich beams

Table 4 shows the maximum load carried by the composite sandwich beams in the flatwise and the edgewise positions. As expected, the results show that the capacity of the glue-laminated beams increases with increasing number of sandwich laminations. The results

also show that the specimen tested in the edgewise position failed at a higher load than in the flatwise position. The maximum load carried by the specimen in the edgewise position is almost double than that in the flatwise position. Interestingly, the load when the first crack was observed in the edgewise specimen is significantly higher than the failure load recorded for the flatwise specimen.

Figures 2 and 3 show the failure mode of composite sandwich beams under asymmetrical beam shear test. The experiment shows that the specimens tested in the flatwise position failed after the formation of the first shear crack in the core. In this position, a diagonal shear crack propagates through the core at the location of maximum shear (Figures 2a and 3a). However, the presence of fibre composite skins inhibits the development of shear cracks in the core of specimens in the edgewise position. When shear cracks in the core was observed, a drop in the stiffness was noticed but the skins prevented the crack width from increasing. The specimen then continued to carry load before shear cracking of the skin was observed. With increasing load, the shear failure became obvious due to the scaling of the resin at the skins (Figures 2b and 3b). Based on these observations, it

can be concluded that the non-horizontal skins increase the shear capacity of the composite sandwich by preventing the widening of cracks in the core thereby increasing the maximum load of the specimens tested in the edgewise position.

4 THEORETICAL EVALUATION OF SHEAR STRENGTH OF COMPOSITE SANDWICH

In this section, some of the available equations used in predicting the shear strength of structural plywood and structures strengthened for shear with fibre composites were used to calculate the shear strength of sandwich beams. An empirical equation is also proposed by taking into account the basic shear strength and stiffness properties of the fibre composite skins and the modified phenolic core material.

4.1 American Plywood Association (APA), 1995

The APA (1995) recommended that the effective modulus under edgewise shear, G_{sw} for plywood panel could be obtained using equation 3 below. The effective shear modulus is then multiplied with the homogenous cross sectional area and the shear strain observed in the plywood. The shear capacity, P_{sw} can then be estimated using equation 4.

$$G_{sw} = \frac{1}{b} (2t_s G_s + t_c G_c) \quad (3)$$

$$P_{sw} = nbDG_{sw}\gamma_{sw} \quad (4)$$

where n is the number of sandwich laminations, b is the total thickness of the composite sandwich, t_s and t_c are the thicknesses of the skin and the core, respectively, G_s and G_c are the shear moduli of the skin and core, respectively, D is the depth of the composite sandwich, and γ_{sw} is the shear strain in the composite sandwich beams.

4.2 Triantafillou, 1998

Triantafillou (1998) concluded that the analysis of the shear strength of wood members reinforced with fibre composite laminates or fabrics can be determined by transforming the fibre reinforcement into equivalent wood using the ratio of the fibre composite elastic modulus to wood elastic modulus in the longitudinal direction. Using this definition, the shear capacity of the composite sandwich beams when all the materials are transformed into equivalent core, P_{swc} can be estimated using equation 5 while the shear capacity when all the materials were transformed into an equivalent skin material, P_{sws} is estimated using equation 6.

$$P_{swc} = n\tau_c \left(t_c + 2t_s \frac{E_s}{E_c} \right) D \quad (5)$$

Table 4 Failure load of composite sandwich under shear test

Specimen	Flatwise (N)		Edgewise (N)	
	Peak load	Load at 1 st crack	Peak load	Peak load
AS-1LSW	10523	16568	17606	
AS-2LSW	19717	33170	40347	
AS-3LSW	37446	57790	78350	
AS-4LSW	70622	99328	–	

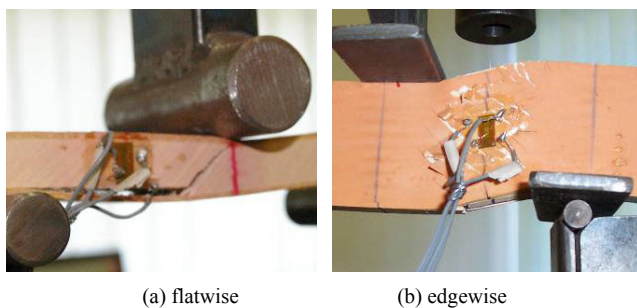


Figure 2 Failure behavior in shear of specimen AS-1LSW

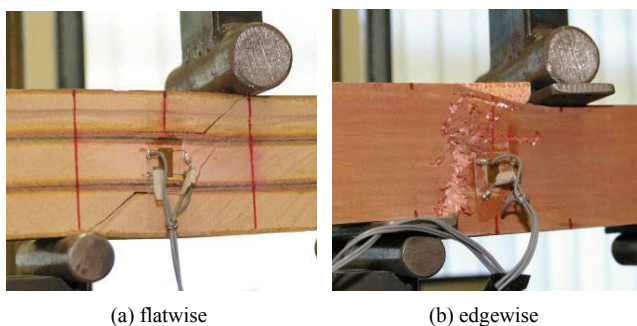


Figure 3 Failure behavior in shear of specimen AS-3LSW

$$P_{sws} = n\tau_s \left(t_c \frac{E_c}{E_s} + 2t_s \right) D \quad (6)$$

where τ_c and τ_s are the shear strength of the core and skin, respectively, and E_s and E_c are the modulus of elasticity of the skin and the core, respectively.

4.3 Proposed equation

A theoretical prediction to calculate the shear strength of composite sandwich beams is proposed. Based on this prediction, the shear capacity of the composite sandwich beams is calculated similar to the equation provided by Triantafillou (1998) with the modulus of elasticity of the skin and the core replaced with its corresponding shear modulus. A transformation factor n_G , defined as the ratio of the shear modulus of the core to that of the skin is introduced. The failure load of the composite sandwich beam, P_{sws} when transformed into an equivalent skin material can be calculated by equation 7 while the failure load when transformed into an equivalent core material, P_{swc} by equation 8.

$$P_{sws} = n\tau_s (2t_s + n_G t_c) D \quad (7)$$

$$P_{swc} = n\tau_c \left(\frac{2t_s}{n_G} + t_c \right) D \quad (8)$$

4.4 Comparison with experiments

Table 5 summarises the predicted failure load of the composite sandwich beams given by equations 4 to 8. The results suggest that the shear strength of the beams tested in the flatwise position can be predicted accurately when all the materials are transformed into an equivalent skin material using the ratio of the elastic moduli (Equation 6). The difference between the predicted and the actual load (Table 4) is only 5-14%. For specimens tested in the edgewise position, the predicted shear strength using Equation 8 gives an almost 30% lower load than the actual failure load. It can be observed however that this predicted load is comparable to the load when the first shear crack on the specimen was observed. This result shows that the maximum shear strength of the composite sandwich beam in the edgewise position could be predicted based on the shear properties of the skin as the failure of specimens tested in this position is due to the shear failure of the skin.

Figure 4 shows that the shear behaviour of the glue-laminated sandwich beams in the edgewise position is similar to that of the fibre composite skins and individual sandwiches but slightly stiffer at higher level of shear stress. This difference in stiffness is not significant but could be attributed to the reinforcing effect of the epoxy adhesives between the sandwich laminations. The maximum shear stress recorded for all composite sandwich beams is at least 23 MPa. It is interesting to note that this shear strength is comparable to the maximum shear strength of the fibre composite skin established

from coupon testing as reported in Table 3. This result also shows that the contribution of the fibre composite skin in the shear strength has a dominant effect and should be included to determine the overall shear behavior of the composite sandwich beams.

Table 5 Predicted shear capacity of sandwich beams

Specimen	Failure load (N)				
	Eq. 4	Eq. 5	Eq. 6	Eq. 7	Eq. 8
1LSW-F	12778	21982	11116	13110	15021
1LSW-E	14178	23724	11996	14546	16666
2LSW-F	27984	45121	22816	27446	31445
2LSW-E	27948	45026	22768	27410	31404
3LSW-F	50170	82074	41502	49934	57211
3LSW-E	51886	84993	42978	51641	59165
4LSW-F	90588	148833	75260	90622	103827
4LSW-E	90622	148867	75277	90656	103866

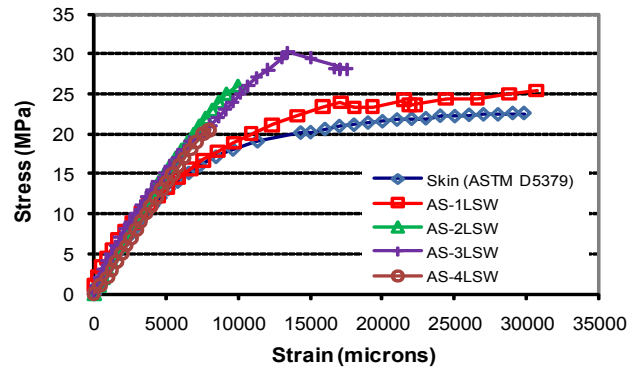


Figure 4 Shear stress-strain relationship of edgewise beams

5 CONCLUSIONS

The results of the study showed that the asymmetrical beam shear test is effective in inducing shear failure in the composite sandwich beams. The results also show that the shear behaviour of the composite sandwich beams is significantly influenced by the shear strength and modulus of the fibre composite skins. The proposed theoretical prediction using the shear moduli of the constituent materials and taking into account the homogenization of the section into an equivalent skin material gives a good estimation of the shear strength of the composite sandwich beams. The results showed a significant improvement on the shear strength of structural composite sandwiches in the edgewise position. This result suggests the high potential of composite sandwiches as a shear loading component in structural beams.

REFERENCES

- American Plywood Association, 1995. Design and fabrication of all-plywood beams. *APA*. Tacoma, Washington.
- Manalo, A.C., Aravinthan, T., Karunasena, W. & Islam, M. 2010.

- Flexural behaviour of structural fibre composite sandwich beams in flatwise and edgewise positions. *Composite Structures* 92(4): 984-995.
- Triantafillou, T.C. 1998. Composites: A new possibility for the shear strengthening of concrete, masonry and wood. *Composite Science and Technology* 58: 1285-1295.
- Van Erp, G. & Rogers, D. 2008. A highly sustainable fibre composite building panel. *Fibre composites in Civil Infrastructure – Past, present and future; Proc. intern. workshop, 9-11 December 2009*. USQ Toowoomba, Australia.

Flexural Behavior of FRP Reinforced Glulam Beams

Quan Zhou (quanzhou516@163.com)

Institute of Modern Bamboo, Timber and Composite Structures (IBTCS), Hunan University, Changsha, 410082, Hunan, China

Yan Xiao (yanxiao@usc.edu)

Department of Civil Engineering, University of Southern California, Los Angeles, CA, 90089, USA

Institute of Modern Bamboo, Timber and Composite Structures (IBTCS), Hunan University, Changsha, 410082, Hunan, China

ABSTRACT A new type of rectangular glued laminated bamboo (glulam) beam had adopted in the world first truck-safe modern bamboo bridge in Leiyang, Hunan, by the authors. The glulam beams can further be enhanced by FRP. This paper analyzes the effect of some parameters, such as FRP thickness, span-depth ratio, strengthen measures, types of node on bending properties. The basic mechanical model is established to predict the failure. Through the experimental work, the flexural stiffness and ultimate load of FRP reinforced beams are compared with those of unreinforced beams. The result show that the analytical model can forecast the flexural behavior of FRP reinforced glulam beams well.

1 INTRODUCTION

From the beginning of last century, due to the energy-saving, environmental protection, excellent structural performance, etc., wood has been widely used in building structures. However, because of the shortage of domestic timber resources, wood structure has been developed slowly in China. Despite the high tariffs for imports of timber, a large number of Europe, the United States, Japan's wooden houses have been brought in as a result. But, most of timber is used only for the expensive villas.

The research on wood and timber structures also falls behind, while the national wood-structure standard often referring to foreign standards. For the limitations of traditional wooden structures, some experts and scholars began to research the bamboo as a substitute of wood, which would alleviate the shortage of fine structural timber. China is in abounding with bamboo, but most of it remains in the original bamboo stage. In recent years, researchers continue to explore new types of manufactured bamboo production all over the world. S.Rittironk & M. Elnieiri investigate Laminated Bamboo Lumber as an alternative structural material. It takes a different approach from conventional raw bamboo structure, which is an alternative manufactured bamboo. They proposed that LBL's structural properties and superior quality compared to wood lumber in terms of higher strength, higher density, lower shrinkage, and dimension stability, have been proven through many studies. J. Correal & L. Lopez introduced another type of structural bamboo material, glued laminated Guadua (GLG), which has comparable mechanical properties to structural Colombian wood. In some case, the mechanical properties of the GLG are better than those of the best structural wood in Colombia.

The Institute of Modern Bamboo, Timber and Composite Structure (IBTCS) conducted a comprehensive research program, with the goal to develop modern bamboo structures for building and bridge. A modern bamboo pedestrian bridge had been completed, using glued bamboo (glulam®) as the main material. The bridge had much lighter superstructure and was easier to construct compared with conventional steel or concrete in terms of same load condition. After the successful completion of the first modern bamboo pedestrian bridge in 2006 [Zhou et al. 2007], the authors were given the opportunity to design and construct a truck loaded 10 m long bridge in the Village of Daozi, Leiyang, Hunan Province. The bridge was a single lane bridge to cross the Xunjiang river and connect the rural roadway network in the local region, as a part of the agriculture infrastructure development by the local government. Different from the former bridge, the girders of this bridge were glulam beams with FRP reinforcement.

In this paper, flexural behaviors of glulam beams were studied through tests, compared with those of FRP reinforced beams, which could be taken as a reference of production, design and application of this kind of structure.

2 EXPERIMENT DESIGN

The glulam was made from *Phyllostachys edulis*, which was sourced from Yiyang city of Hunan province. The resin used in glulam was domestic glue named ESA-T, particular for FRP bonding. Some small clear specimens of glulam had been tested to obtain the main physical and mechanical properties of glulam, in which the values

was the mean tested value, while the other materials referring to literatures (see Table 1). In addition, Elastic modulus of CFRP was 220Gpa and tensile strength was 2.6Gpa as obtained by test.

Table 1 Basic material properties of laminated bamboo

Materials	In-plane compressive strength (MPa)	In-plane tensile strength (MPa)	Bending strength (MPa)	Elastic (GPa)	Density (kg/m ³)
Plybamboo	54	80	75	9.4	880
Typical Bamboo Clum	55	124	-	17	650~880
Douglas Fir	48	-	83	12	497
West White Pine	35	-	64	10	398

Table 2 Details of large tested beams

	Cross-section dimension (mm×mm)	Span (mm)	Reinforcement rate (ρ^*) (%)	a^{**} (mm)
B1	100×600	3500	0.037	1250
B2	100×600	3500	-	1250
B3	100×600	3500	-	1250
B4	100×600	4500	-	1750
B5	100×600	4500	-	1750
B6	100×600	4500	-	1750
B7	100×600	4500	-	1750
B8	100×600	4500	-	1750
B9	100×600	4500	0.037	1750
B10	100×600	4000	-	1500
B11	100×600	4000	-	1500
B12	100×600	4000	-	1500
B13	100×600	4000	-	1500

* the cross-section rate of FRP to bamboo,

** the length between bearing plate and nearest load point.

There were two groups of glulam beam, and first group had 11 non-reinforced specimens and 2 FRP reinforced specimens. All of those were produced by researched in laboratory under 25 centigrade, while heaters were employed to stabilize the temperature. FRP reinforced beams were tested about one month after they cohered. The specimens design was developed referring to the code ASTM D3737-03, ASTM D7199-07, ASTM D7341-08 and GB/T 50329–2002.

There were some assumptions in experiments: 1) the cross-section of girder remain plane after bending; 2) the adhesive layer between FRP and bamboo was linear-elastic body, without regard to its thickness, and bond connects bamboo sheets well; 3) FRP was considered a linear-elastic material; 4) the theoretical value mentioned

in this paper was base on the hypothesis of ideal joint in bamboo beams

This paper analyzes the effects of several parameters, such as FRP reinforcement, span to depth ratio, strengthen measures, types of node and so on, on bending properties. Table 2 shows the details of the former group, all of which were large scale beams ranged from B1 to B13, while another group stating the small scale beams ranged from S1 to S15. And then, qualitative analysis of large specimens is carried out.

3 RESULT AND ANALYSIS

3.1 Experimental results

The length of pure bending zone is one meter in large tested beams. All of non-reinforced specimens broke in the tensile zone when its tensile strain reached maximum. At the beginning of test, bamboo was in elastic stage. With the load increasing, it showed some plastic behaviors and the flexural stiffness decreased. When bamboo beams cracked, noises came from the bottom and deflection was obvious. The beams collapsed quickly at the moment of failure. On the other hand, FRP reinforcement increased the ultimate strength of the glulam beams. Moreover, cracking noises came later than former and the failure didn't happen only in the compressive zone. Some crack came up in the top of beams, and the deflection of mid-span was less than non-reinforced beams.

The ultimate design condition was checked based on the following simple procedure:

$$M_u = f_y S \tag{1}$$

$$P_{max} = M_u / a \tag{2}$$

where P_{max} = the ultimate design strength; M_u = moment of flexure subject to P_{max} ; a = length between bending plate and nearest load point; f_y = bending strength of plybamboo.

3.2 Analysis of experimental results

3.2.1 Results of 3.5m span beam tests

Ultimate strength of 3.5m span beam calculated from formula (1) and (2) was 360kN, and that of B1 was 340kN which was close to the theoretical value. Finger-zone prematurely approached to failure in tension, resulting in the compression zone of bamboo quickly reached the limits of strain.

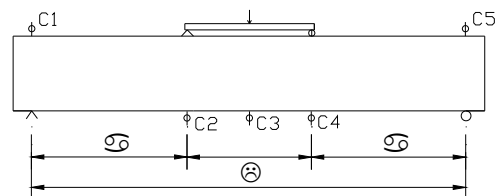


Figure 1 Experiment equipments

Table 3 Test results of 3.5m-span beams

	Joint-length (mm)	Bolt Reinforcement	FRP	Initial stiffness (kN/mm)	Ultimate load (kN)
B1	20	✓	✓	7.556	390
B2	30	-	-	7.096	260
B3	20	✓	-	6.189	237.86

Joint effect factor J was took into calculation, and revision formula was showed below:

$$P_j = P_{\max} \times J \quad (3)$$

where $J = 0.75$ when there is two finger-area overlap in bending zone, else $J = 1$ when other conditions.

The theoretical result of B2 multiplied 0.75 is 270, close to test result. Moreover, bearing capacity of B3 was close to B2, but 20mm finger-joint lead to deflection increased quickly after cracking. However, it presented good ductility when the specimen stiffness decreased gradually.

In addition, initial stiffness of B1 was 7.556 kN/mm, higher than other two beams, due to the strengthening of FRP. As the cracks increasing, FRP reached the strain limit. When load reached 340 kN, a sudden failure occurred. The effect of FRP reinforcement was not obvious for capacity, but it could significantly improve the specimen stiffness. B2, with 7.096 kN/mm initial stiffness, implied that 30mm length finger-joint performance was better than 20mm, also the cracks developed slower than B1, obviously. However, with no bolts to strengthen nodes, resistant ability to shear between sheets extremely decreased, and a sharp increase turned up in the deflection. As a result, after the specimen had been loaded exceed 200 kN, stiffness was declining as the finger-joint cracks expanding. Finally when the load reached 260 kN, the cracks at the bottom suddenly expanded near the vicinity of the neutral axis. After that the specimen broke and the experiment ended. The initial stiffness of B3 was 6.189, lowest in this group.

3.2.2 Results of 4.5m span beam tests

Calculated load carrying capacity of 4.5 m clear span beam was 257.1kN. Because finger-zone existed in B4 and B6, their capacity reduced to 192.9kN according to equation (1)~(3). Initial stiffness, damage loads and mid-span deflection of each specimen's are listed in Table 2. Specimens B5 and B9 were the counterpart testing cases with the main difference being the existence of FRP reinforcement in B9. As a result, initial stiffness of B9 exceeded 21.5% over B5 and 15.7% of ultimate load. Obviously, FRP played a significant role in improving the stiffness and slowing the destruction.

B5 held the lowest initial stiffness and load carrying ability due to short finger-joint. Moreover, Despite of FRP reinforcement enhanced the joint strength in B9,

stress-concentration subject to large force in compressive zone led to the crush of bamboo beam and specimen damage quickly and this behavior belongs to brittle failure. In the other hand, the experiment data of 30mm finger-joint beam B7 and B8 surpassed theoretical values by 26.98% - 27.18% of initial stiffness and 16.1% - 28.53% of ultimate load.

Table 4 Test results of 4.5m-span beams

	Joint-length (mm)	Bolt Reinforcement	FRP	Initial stiffness (kN/mm)	Ultimate load (kN)
B4	30	✓	-	8.791	222.5
B5	20	✓	-	6.220	168.5
B6	30	✓	-	4.722	242.5
B7	30	✓	-	9.113	298.54
B8	30	✓	-	9.128	330.5
B9	20	✓	✓	7.556	195

Through comparison of specimens, it could be seen that ductility of glulam beams of 30mm finger-joint was better than 20 mm finger-joint. In addition, the ductility of B5 was not poor but its bearing ability was worse than others and it destructed too early in the experiment, which attributed to short length of joint. B4, B6, B7, B8, with 30mm length joint, put out fine ductility, even better than the FRP reinforced B9, and possessed higher ultimate load. Although joint-finger cracked early in B6, the crack exploded for a long time until it was crushed. To sum up, all of above implied that longer finger-joint performed better ductility in the bending condition.

3.2.3 Results of 4m span beam tests

It is can be seen from the experiments that each of tested initial stiffness was similar to calculated results. In addition, as there was no joint-fault overlapped in this group of beams, we only took the finger length into consider. Then, the initial stiffness and carrying ability of 30 mm beams exceeded 20mm beams by 3.72%-9.96% and 60.4% - 42%, respectively. Moreover, those of FRP reinforced glulam beams surpassed non-reinforced by about 10% and 42%. Obviously, members which did not reinforced with bolt and FRP had poor characteristics, extremely inappropriate to be adopted in practice and design, since their abilities were poorer than others.

Table 5 Test results of 4 m-span beams

	Joint-length (mm)	Bolt Reinforcement	FRP reinforcement	Initial stiffness (kN/mm)	Ultimate load (kN)
B10	20	✓	-	10.462	212
B11	20	✓	-	10.462	239.5
B12	30	✓	-	11.504	340
B13	30	-	-	10.851	170.5

3.2.4 Small cross-section beam

A four point load method, was used to test specimens. The clear distance between the edges of the bearing plate and the nearest loading point was about one-third of the length of beam, equal to those between load points. Moreover at least a lateral support located at space between the reaction and the load point.

Deflectometers fixed at the position of load points, reactions and mid-span, where five strain gauges located throughout the depth. All the measured data were record simultaneously by the static strain measurement system.

Some parameters of small beams were listed in Table 6, such as cross-section dimension, span, reinforcement-rate and so on. Through Comparison with three types of beams, the quantitative reinforce effects of FRP was obtained accurately. The results showed that load carrying ability of FRP reinforced beams were higher than non-reinforced beams with a range from 2.95% - 28.77%, and larger thickness resulted in more increase of ultimate load. Further tests are still underway in this testing series.

Table 6 Test results of small volume beams

Beam number	Cross-section dimension (mm×mm)	Span (mm)	Reinforcement rate (%)	type	F _{max} (kN)
S1, 2, 3	56×112	2016			27.12
S4,S5	56×112	2016		H*	13.95
S6	56×112	2016	0.1		28
S7	56×112	2016	0.5		32
S8,9,10	84×160	2240			73
S11S12	84×160	2240		H*	28.5
S13	84×160	2240	0.21		74
S14	84×160	2240	0.35		78
S15	84×160	2240	0.69		94

* Load is perpendicular to the plane of bamboo sheet

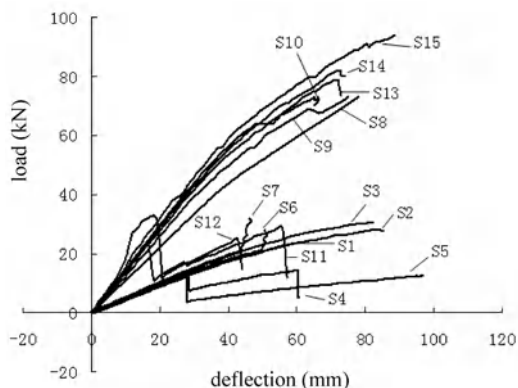


Figure 2 Load-deflection curve of small volume beam

4 CONCLUSION

Loading tests were conducted on glue-laminated bamboo

(GluBam®) beams with or without CFRP strengthening. Some observations can be made through the preliminary examination of the testing results.

Longer finger-length and bolt reinforcements contributed to increase of the initial stiffness, load carrying capacity and deformability of glubam beams.

Through the analysis on FRP reinforced glubam beam, it was found that FRP reinforcement could effectively improve the specimen stiffness. Appropriate FRP thickness should be chosen while enhancing the load carrying capacity of glubam beam, in order to avoid over-reinforcement.

Since different batches of specimens were produced in different period and the process and gluing environment is not the same, resulting in their various characteristics in bending, it is advised that the same process and quality control means should be applied to ensure uniform performance in structure.

Due to the presence of finger-zone which may reduce the load bearing capacity of glubam beams, the joint effect factor J was adopted in the calculation of load bearing capacity of components. However, more studies are required to improve the accuracy of prediction. Therefore, more researches and studies are needed to be done in order to improve the factor of J in future.

PREFERENCES

- Moody, R., Falk, R., and Williamson, T. (1990), *Strength of Glulam Beams – Volume Effects*, Sugiyama, H. ed. Proceedings of the 1990 International Timber Engineering Conference, October 23-25, Tokyo, pp.176-182. Vol. 1.
- Xiao, Y., Inoue, M., and Paudel S., *Modern Bamboo Structures: Proceedings of first international conference on modern bamboo structures*, CRC Press, Taylor and Francis, London, 2008. ISBN-13: 9780415475976 (hbk), 9780203888926(ebook), 299p.
- Xiao, Y., Shan, B., Chen, G., Zhou, Q., and She, L.Y. (2008), *Development of A New Type of Glulam – GluBam*, Modern Bamboo Structures, Xiao et al. edited, CRC Press, UK, 299p.
- Zhou, Q., Shan, B., and Xiao, Y. 2007. *Design and Construction of a Modern Bamboo Pedestrian Bridge*. Proceedings of the International Conference on Modern Bamboo Structures. ICBS-2007. Changsha. China. Oct. 28-30.
- Xiao, Y., Zhou, Q., and Shan, B., *Design and Construction of Modern Bamboo Bridges*, ASCE Journal of Bridge Engineering, (in press)
- Yang, Huifeng, Liu, Weiqing (2008), *Study on flexural behavior of FRP reinforced glulam beams*. Journal of Building Structures. 64-71. Vol.28.1.
- Liu, Weiqing, Yang, Huifeng (2008), *Experimental study on flexural behavior of engineered wood beams*. Journal of Building Structures. 90-95. Vol.29.1.

Trial Design of Cable-Stayed Bridges Using Hybrid Composite Girders and Applicability to Free Passage Over Railway

Hitoshi Nakamura (hnaha@tmu.ac.jp), Ken-ichi Maeda & Hiroshi Mutsuyoshi
Dept. of Civil and Environmental Engineering, Tokyo Metropolitan University, Japan

Kenji Yaginuma
East Japan Railway Company, Japan

Takahiro Matsui
Toray Industries, Inc., Japan

ABSTRACT A pultruded hybrid composite girder is being developed consisting of carbon and glass fibers. The innovative feature is the optimum use of CFRP and GFRP in the flanges to maximize structural performance while reducing the overall cost by using glass fibers in the web section. In this paper, the cable-stayed bridges were trially designed using the developed hybrid composite girders. In order to utilize the lightweight of FRP, the construction site was selected to the free passage over the busy railway as a case study. The cable-stayed bridges were two continuous-span bridges with the span lengths of 5.5 m and 24.0 m. As a result, the feasibility of the proposed structures and the reduction of total cost were confirmed.

1 INTRODUCTION

In the design of FRP footbridges, it is a subject that the deflection limitation becomes dominant. It is desired that the development of the FRP composite girders with high bending rigidity and the structure systems which can control bending deflections effectively.

In this study, in order to solve reasonably such a problem, the applicability of the developed hybrid composite girders to the free passage over railway was examined. The hybrid composite girder is being developed consisting of carbon and glass fibers. The innovative feature is the optimum use of CFRP and GFRP in the flanges to maximize structural performance while reducing the overall cost by using glass fibers in the web section and it can also be manufactured by pultrusion. The hybrid composite girders have been investigated experimentally by the material tests and bending tests of girders and their connections (Mutsuyoshi, H. et al. 2007, 2008, Nakamura, H. et al. 2007, Manalo, A. C. et al. 2008).

As a case of the construction site under very severe restriction in erection, the free passage over two or more rail tracks of an urban trunk railway was selected to demonstrate effective practical use of lightweight FRP. Aiming at large shortening of construction period by weight saving and longer span, the cable-stayed bridges using hybrid composite girders were proposed and trially designed.

2 APPLICABLE CONDITION AND TRIAL DESIGN TO CABLE-STAYED SYSTEM

2.1 Set up of alternative model

The general views of the free passages over an urban trunk railway are shown in Figure 1. Figure 1 (a) is an example of the reference bridge, whose superstructure consists of three main steel girders of the I-shaped section, PC slab, walls, and sheds (slate material).

The case research has reported that the bridge piers of P3 and P4 were in particular constructed in rail tracks, and the construction period became remarkably long, and also increased construction cost considerably since construction work was limited to nighttime operation in the urban trunk railway.

In such a situation, shortening drastically construction period is predicted by minimizing the construction work in rail tracks, and the total cost reduction of construction is expected, even if the material cost increases considerably.

Therefore, it was investigated that the span length is longer by reducing a bridge pier, and the superstructure is made lightweight using the hybrid composite girders for main girders in order to perform easily the large block erection of superstructure by a crane.

Since the bending rigidity of the main girder is not enough against the vertical deflection when the span length becomes longer, the cable-stayed system is adopted. As a result of considering the arrangement of span and

foundation, as shown in Figure 1 (b), the trial design for the two continuous-span cable-stayed bridge was performed as an alternative model. The cable-stayed bridge has the main span length of 24 m, four main girders, and the cross beam located at approximately 2 m spacing based on the reference bridge.

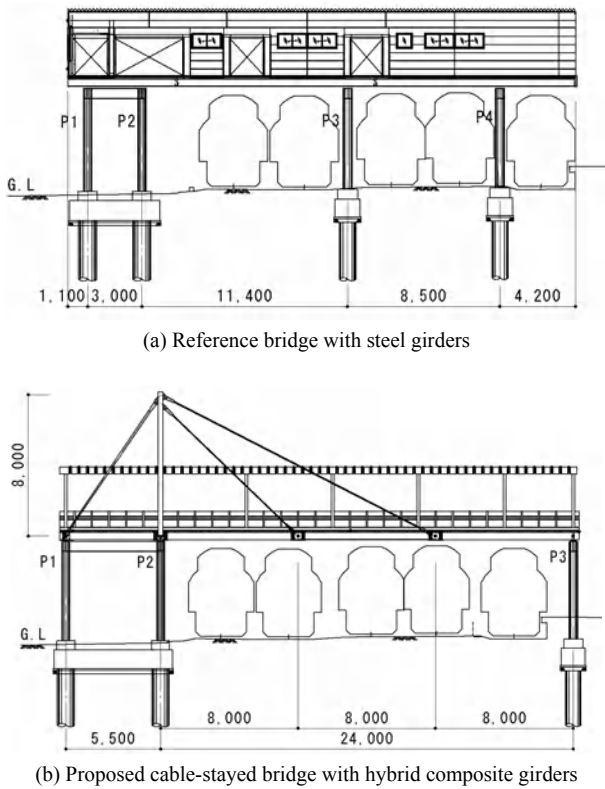


Figure 1 General views of free passages over an urban trunk railway

2.2 Cross-sectional properties of hybrid composite girders

The hybrid composite girder is premised on manufacture by pultrusion, has the upper and lower flanges made of CFRP and GFRP to increase bending rigidity efficiently, and the web made of GFRP including many grass fibers of ± 45 degree to increase shear rigidity also. The cross-section of hybrid composite girder is shown in Figure 2. The cross-sectional size of the girder is the same as that of the reference bridge for comparison examination.

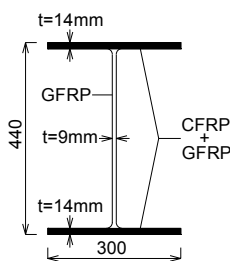


Figure 2 Cross-section of hybrid composite girder

Four cases of Case A to D, where the laminated constitution and the volume ratio of CF and GF changed

in the flange, were set up, as shown in Table 1. The equivalent elastic moduli of flange and web are theoretical values based on the lamination theory of laminated constitution listed in Table 1.

Table 1 Material properties of hybrid composite girders

Part	Case	Laminated constitution (volume ratio: %)					Elastic modulus E (GPa)	Shear elastic modulus G (GPa)
		CF 0 (deg.)	CF 0/90 (deg.)	GF 0 (deg.)	GF 45 (deg.)	GF Mat		
Flange	A	52	0	10	13	25	65.7	4.4
	B	33	10	19	13	25	52.9	
	C	33	0	29	13	25	48.8	
	D	14	0	48	13	25	32.0	
Web	-	0	0	32	42	25	15.7	6.7

2.3 Constituent members and design conditions

As mentioned above, in the reference bridge, conventional materials, such as steel, concrete and slate, were used, and dead load was also large. The constituent members of superstructure were made lightweight to aim at slimming substructure and shortening construction period by the large block erection.

The shed was changed into the steel folded-plate from the slate plate. The materials of slab and felloe guard were changed into GFRP from PC and concrete. In addition, the wall was omitted and the GFRP railing was installed. And the others, such as towers, cables and cross beams including the brackets fixed stay cables, were steel members. However, the general cross beams except for rigid members anchored stay cables were made of GFRP, and they were the same cross-sectional size as the main girder. The cross-sectional properties of constituent members are shown in Table 2. The elastic moduli of the hybrid composite girder were calculated as the composite sections using the elastic moduli of flange and web as shown in Table 1. The schematic view of the hybrid composite girder and the GFRP slab is shown in Figure 3.

Table 2 The cross-sectional properties of constituent members

Constituent members	Cross sectional area A ($\times 10^{-2} \text{ m}^2$)	Torsional constant J ($\times 10^{-7} \text{ m}^4$)	Geometrical moment of inertia		Elastic modulus E (GPa)	Shear elastic modulus G (GPa)
			I_{in} ($\times 10^{-4} \text{ m}^4$)	I_{out} ($\times 10^{-5} \text{ m}^4$)		
Main girder	Case A	1.21	6.51	4.34	6.30	59.7
	Case B					48.4
	Case C					44.8
	Case D					30.0
Cross beam (general)	1.21	6.51	4.34	6.30	25.0	4.5
Slab (GFRP panel)	1.52	205	0.064	15.1	25.0	4.5

The calculation of the cable tension including the prestress was based on the calculation technique as a conventional cable-stayed bridge. The cable pre-stresses were calculated so that the vertical deflections under dead load become zero at the cable anchor point. Main girders, cross beams and towers were modeled with beam elements, and cables were modeled with the axial elements.

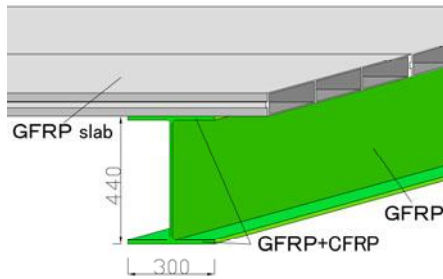


Figure 3 Schematic view of hybrid composite girder and GFRP slab

In trial design, the required cross-sectional areas of cables were calculated so that the vertical deflections of main girders become 1/500 or less of span length under the live load of 3.5 kN/m² (Japan Road Association 1979).

3 RESULTS OF TRIAL DESIGN AND DISCUSSIONS

3.1 Weight comparison of superstructure

As a part of trial design results, the weight comparison of constituent member is shown in Figure 4. In the cable-stayed bridge, the weight of towers, cables and steel cross beams for the cable anchor increases compared with the reference bridge. Because the weights of the other members were reduced drastically, the total weight of the cable-stayed bridge was below half of the reference bridge.

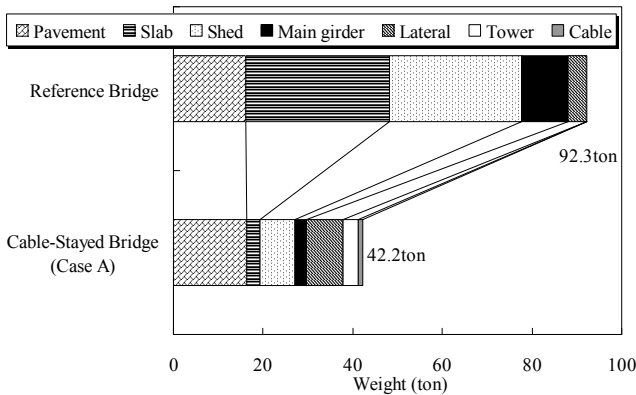


Figure 4 Weight comparison of constituent member

3.2 Cross-sectional area and tensile stresses of stay cables

The cross-sectional areas and the maximum tensile stress of cables vs. the elastic moduli of hybrid composite girders are shown in Figure 5. Since the vertical deflections of main girders increases so that the elastic moduli is low, it was found that it is necessary to increase the cross-sectional areas of cables.

Moreover, the maximum stresses of cables became small with lowering the elastic moduli of girders. And in the case D, where a cross-sectional area is the largest, the maximum stress was 247MPa. Generally, since the tensile strength of steel cables is high, and the tensile stress is small enough, it was confirmed that the required

cross-sectional areas are also governed by the deflection limitation.

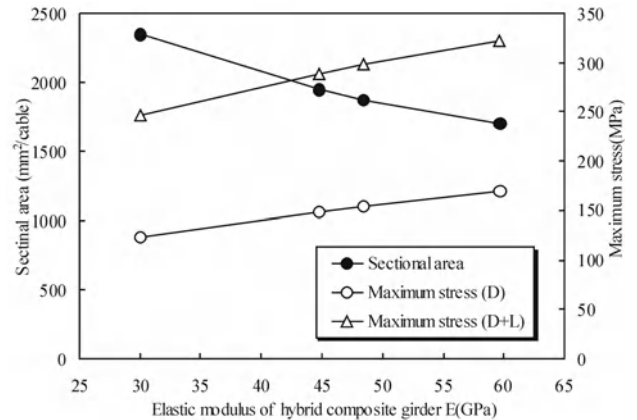


Figure 5 Cross-sectional areas and maximum tensile stress of cables vs. elastic moduli of hybrid composite girders

3.3 Flexural characteristics of girders

The vertical deflections of main girders under dead load are shown in Figure 6. Because the cable prestress were determined in the design condition, where the deflections at those points are zero under dead load, the deflections hardly occurred at the cable anchor points. However, except the cable anchor points and the supported points, it was also found that the deflections increase with lowering the elastic moduli of main girders.

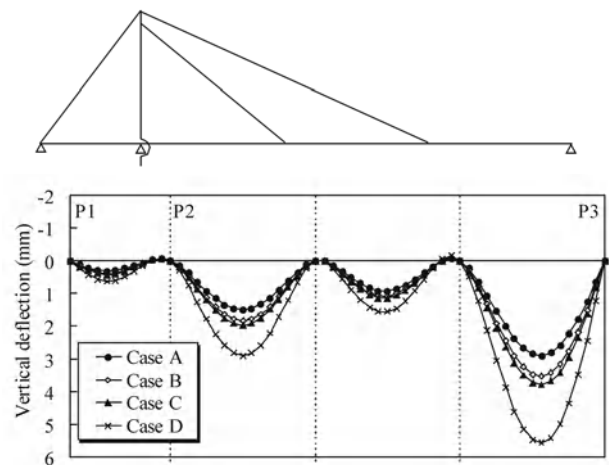


Figure 6 Vertical deflection distribution of girder under dead load

Figure 7 shows deflection distribution under live load. It was found that the deflection limitation (L/500) is satisfied in all cases.

3.4 Stress checks of girders

The results of the stress check are shown in Figure 8. This figure shows the stress distribution of the main girder in Case A, where the stresses become the highest under dead and live load. The stress under dead load was small enough, and the stress under dead and live load were also from -50 to 30 MPa.

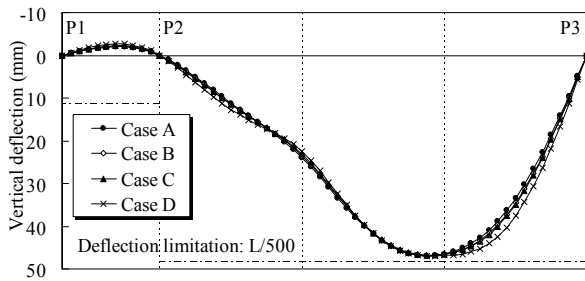


Figure 7 Vertical deflection distribution of girder under live load

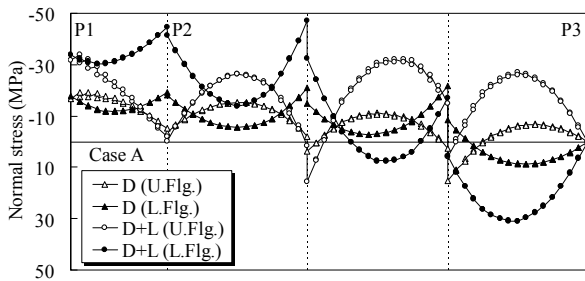


Figure 8 Normal stress distribution of girders under dead and live loads

Therefore, it was confirmed that the stresses are sufficiently small compared with the material strength of the hybrid composite coupon specimen (Manalo, A. C. et al. 2008).

3.5 Natural frequency and vibration serviceability

The relationships between the elastic moduli of hybrid composite girders and natural frequencies are shown in Figure 9. Although the frequencies of the symmetrical deflection modes were the smallest, the vibration serviceability in the Japanese standard for pedestrian bridges (Japan Road Association 1979) was satisfied. The frequencies lower modes were almost constant regardless of the elastic moduli of main girders. The cable tensile rigidity designed due to the deflection limitation has contributed the frequencies of deflection modes.

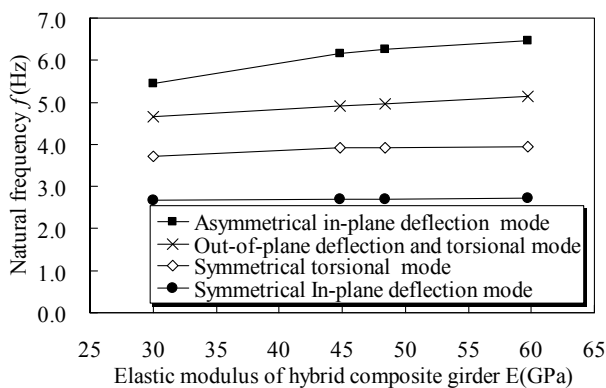


Figure 9 Relationships between elastic moduli of hybrid composite girders and natural frequencies

On the other hand, the frequencies were higher in proportion to the elastic moduli of main girders as the higher order mode. In addition, it was also confirmed that

the frequencies of the torsional modes and out-of-plane deflection modes were comparatively high.

3.6 Selection of laminated constitution

Although the deflection limitation became dominant in the design, it was confirmed that the cable-stayed bridge with any laminated constitution is feasible by using the cables of the required sectional area.

In the selection of laminated constitution, when the elastic modulus is adopted more than 45 GPa (equivalent to Case C), there is no problem for practical use, because the deflection of the main girder of Case D, which is the lowest elastic modulus, is partially large under dead load.

4 CONCLUSION

The cable-stayed bridges were trially designed using the developed hybrid composite girders. In order to utilize the lightweight of FRP, the construction site was selected to the free passage over the busy railway as a case study.

Consequently, the deflection limitation became dominant in the structural design. However, the normal stresses under design loads were very small and the vibration serviceability due to the Japanese standard for pedestrian bridges was also satisfied. Moreover, It was found that the weight saving contributes to large shortening of the construction period. Therefore, the feasibility of the proposed structures and the reduction of total cost were confirmed compared with a typical steel girder bridge.

ACKNOWLEDGEMENT

This research is financially supported by MLIT (Ministry of Land, Infrastructure and Transport in Japan) grant-in-aid for scientific research of construction technology, which is greatly acknowledged.

PREFERENCES

- Mutsuyoshi, H. et al. 2007. Development of New Hybrid Composite Girders Consisting of Carbon and Glass Fibers. *COBRAE conference 2007 Benefits of composites in civil engineering*, 2, University of Stuttgart.
- Nakamura, H. et al. 2007. Shear Deformation Characteristics and Web-Crippling of New Hybrid Composite Girders. *Proc. of Asia-Pacific Conference on FRP in Structures, APFIS 2007*, Hong Kong, 12-14 December 2007: 459-464.
- Manalo, A. C. et al. 2008. Mechanical behavior of hybrid FRP composites with bolted joints, *Proc. of 20th Australasian Conference on the Mechanics of Structures and Materials, ACMSM20, Toowoomba, Queensland, Australia, 2-5 December 2008*. London: Taylor & Francis Group, 47-53.
- Mutsuyoshi, H. et al. 2008. Composite Behavior of Hybrid CFRP-GFRP Bridge Girders, *Proc. of 20th Australasian Conference on the Mechanics of Structures and Materials, ACMSM20, Toowoomba, Queensland, Australia, 2-5 December 2008*. London: Taylor & Francis Group, 61-67.
- Japan Road Association. 1979. Japanese standard for pedestrian bridges and underpasses, Tokyo: Maruzen. (in Japanese)

Performance Based Design of Laminated FRP Box Girders for Short Span Bridges

Husham Almansour (husham.almansour@nrc-cnrc.gc.ca)

National Research Council Canada, Institute for Research in Construction, Ottawa, Canada

Moe Cheung

Department of Civil and Environmental Engineering, Hong Kong University of Science and Technology, Hong Kong, China

ABSTRACT All-advanced composite bridge superstructure represents a significant advance in the use of advanced composites in civil-structures. However, one of the critical obstacles to extensive use of advanced composites in construction is the lack of simplified and practical design guidelines. In this paper, an iterative performance based multi-scale analysis and design approach for all-advanced composite bridge superstructure is proposed. The bridge superstructure is formed from laminated FRP box girder and chopped FRP top surface plate. Several laminate designs are examined and the performance of the most efficient material and structural design of the proposed bridge is compared to a slab on prestressed concrete bridge. The results show that the proposed procedure leads to an efficient use of the materials with highest structural performance.

1 INTRODUCTION

One of the obstacles to the extensive use of advanced composites (AC) such as fiber reinforced polymers (FRP) in construction is the lack of simplified and practical design approaches and guidelines.

Typical applications of AC in civil engineering are in strengthening, retrofitting and reinforcing of concrete structures. Advanced composites in such applications are assumed to act as isotropic materials and traditional design approaches of the structures build using traditional construction materials are extended to design AC elements. However, an efficient use of advanced composites that take into account the anisotropic nature of the material, the need to relate the material micro/macro design to the structural performance of the system are still not sufficiently developed and evaluated.

Unlike standard materials, advanced composites (AC) are anisotropic, and the structural analysis and design of AC structures needs more complicated computations. The material properties are coupled with the structural geometry and deformations. For example, while changes in the geometry of AC structures is related to changes in the material stiffness, changes in the material constituents could not lead to obvious changes in the stiffness in a specified direction of the structure. In addition, shear deformations in pultruded FRP composite materials are usually significant and, therefore, modeling of FRP structural components should account for various shear

effects. For the applications of AC in bridge superstructures, there is a need to develop a simplified design procedure, which should provide accurate predictions of the bridge behavior and be easily implemented by practicing engineers. In design of AC structural members, stiffness and strength properties are equally important and depend on the coupled material and geometry of the AC structural system [Mosallam et al, 1992].

Davalos et al [1996] presented a comprehensive approach for the analysis and design of pultruded FRP beams in bending. The research was based on Barbero's [1991] proof that the material architecture of pultruded FRP shapes can be efficiently modeled as a layered system. Salim et al [1997] presented a comprehensive study on the analysis and design of FRP deck-and-stringer bridge deck. Qiao and Davalos [2000] presented a systematic approach for the analysis and design of all-FRP-deck-stringer bridges. Aref and Parsons [2000] presented an integral FRP bridge structural system. The bridge was manufactured using the filament winding process. Burgueno et al [2001] tested, at large scale, a system comprised of concrete filled, filament wound, circular carbon/epoxy girders and an E-glass/polyester deck.

The objective of this paper is to propose a performance based multi-scale analysis and design approach for all-advanced composite (AAC) bridge superstructure. The procedure would lead to an efficient use of the materials with highest structural performance.

2 PERFORMANCE BASED ANALYSIS-DESIGN PROCEDURE

An iterative analysis and design procedure is proposed in this paper. The procedure includes three phases, two initial service and safety checks, and two performance checks. In the first phase, a micro design is performed for each independent AC material then a macro level design of the lamina is performed. The second phase includes a macro design of the laminate and then design of the laminated box girder and the top chopped layer. Two checks are following the first two phases, which consist of the material failure criteria and the serviceability and ultimate limit states for the bridge super structure.

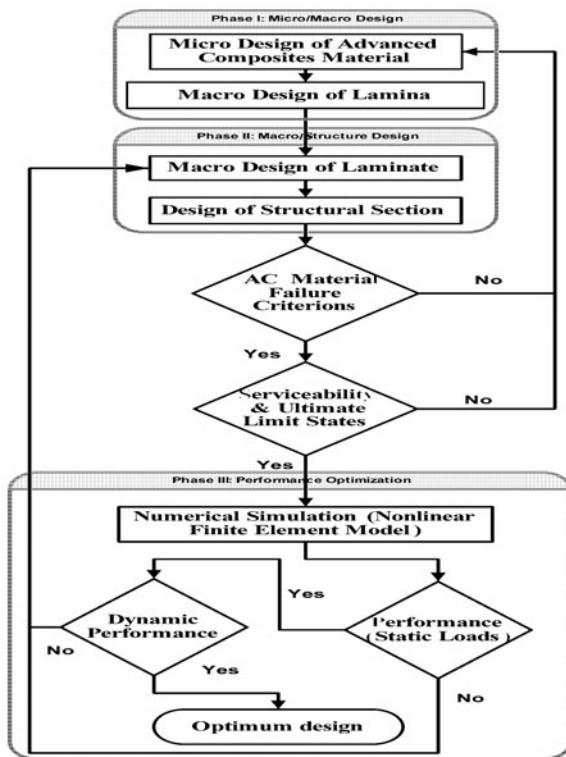


Figure 1 Multi scale analysis and design procedure

The third phase include the numerical simulation of the AAC bridge superstructure and two performance checks for structural performance under static and dynamic loading conditions. Figure 1 shows the proposed procedure.

3 SUPERSTRUCTURE AND DESIGN LOADS

All-advanced-composite box girder bridge formed from laminated FRP box girder and chopped FRP top surface plate is proposed in this paper (Figure 2). The bridge deck section consists of a series of inner FRP box cells surrounded by an outer FRP binding box. A filament winding process is to be used in manufacturing this deck section. In addition to its ability to distribute the concentrated load the chopped FRP plate smoothes stresses when they are transferred to the laminated box girder to minimize punching failure occurrence, local buckling or delamination. The internal proportions and thicknesses of the section are complicated functions of the material properties and the structural analysis.

In contrast with the relatively simple stage of selecting a traditional material from a well-defined list, more complicated micro-macro material design process is needed for advanced composite materials.

Optimizing the stiffness and strength of the laminated box girder is a complicated multi-task process includes deciding: (i) laminate structure and thickness; (ii) the box-girder cells shapes dimensions and then number of cells; (iii) level of stress concentration at cell corners; and (iv) the interaction between inner cells and outer binding box. The laminated cells and outer box dimensions and laminates thicknesses and lay-up, are complex variables contributing to the stiffness of the overall bridge section. The thickness of the “deck slab” or the top surface plate is a function of punching stresses due to vehicle wheel loads and the chopped FRP material properties. Tsai-Hill criterion [Jones 1999] for anisotropic materials is used to check for the first ply failure.

The bridge has two lanes of 3.75 m each, two shoulders of 2.5 m each (including the barrier), and the design traffic speed is 100 km/hr. The traffic load model of the Canadian Highway Bridge Design Code CHBDC [CSA S06-2006] is used. For short span bridges, the truck load rather than the lane loading leads to maximum stresses in the bridge superstructure.

It has been found that truck loading conditions, rather than the lane are critical for the design.

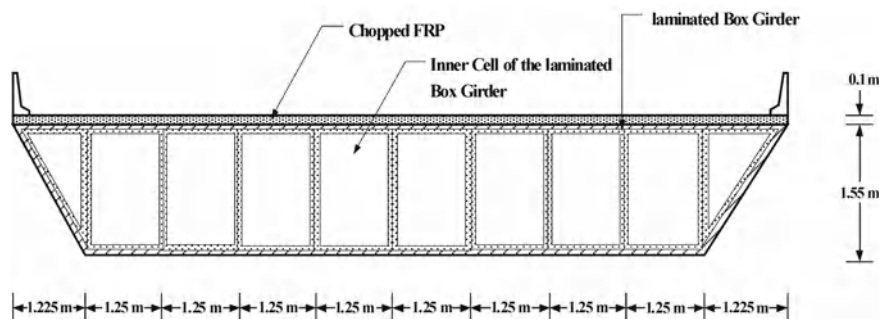


Figure 2 Deck Section of the simply supported advanced composite bridge superstructure sections

4 OPTIMUM MACRO DESIGN OF LAMINATES

Homogenized materials properties of chopped FRP of the “deck slab” are: (i) modulus of elasticity is 9.32 GPa; (ii) Poisson ratio is 0.276; and (iii) ultimate strength is 139 MPa. The lamina is formed from E-Glass fiber and Vinylester Matrix (GFVM) with material properties shown in Table 1.

Table 1 Mechanical properties of the lamina - E-Glass fiber and Vinylester Matrix (GFVM)

Longitudinal modulus of elasticity, E_1	36.61 GPa
Transverse modulus of elasticity, E_2	12.83 GPa
In-Plane Poisson Ratio, ν_{12}	0.279
In-Plane shear modulus	4.013 GPa
Longitudinal Tensile strength	1020 MPa
Longitudinal Compressive strength	620 MPa
Transverse Tensile strength	40 MPa
Transverse compressive strength	140 MPa
In-Plane shear strength	70 MPa

Efficient laminate macro design is investigated by examining seven different designs with 4, 8 and 12 laminas, either for the inner boxes or for the outer binding box laminates. The lamina thickness is assumed to be constant in every design. Three different laminate thicknesses are studied. All the studied laminate designs are shown in Table 2.

Table 2 Different designs of internal and external laminates

Lamina	Lamina Alignment						
	LAA ⁽¹⁾	LAB	LAC	LAD	LAE	LAf	LAG
	Deg	Deg	Deg	Deg	Deg	Deg	Deg
	IL ⁽²⁾ OL ⁽³⁾	IL & OL	IL & OL	IL & OL	IL & OL	IL & OL	IL & OL
1	-10, -10	10	30	45	10	10	10
2	30, 45	-10	-30	-45	30	45	30
3	10, 10	-10	-30	-45	-10	-10	45
4	-30, -45	10	30	45	-30	-45	-10
5	10, 10	-	-	-	-30	-45	-30
6	45, 90	-	-	-	-10	-10	-45
7	45, 90	-	-	-	30	45	-45
8	10, 10	-	-	-	10	10	-30
9	-30, -45	-	-	-	-	-	-10
10	10, 10	-	-	-	-	-	45
11	30, 45	-	-	-	-	-	30
12	-10, -10	-	-	-	-	-	10
LTh ⁽⁴⁾ -a	1.5	4.5	4.5	4.5	2.5	2.5	1.5
LTh-b	2.25	6.75	6.75	6.75	3.37	3.37	2.25
LTh-c	3.0	9.0	9.0	9.0	4.5	4.5	3.0

(1) LA: Laminate Alignment (Deg); (2) IL: Inner Laminate Box; (3) OL: Outer Binding Laminate Box; (4) LTh: Laminate Thickness (mm)

5 STRUCTURE MODELING & RESULTS

The proposed AAC bridge is modeled using nonlinear

anisotropic finite element model. The finite element mesh is refined in the regions where the applied wheel loads result in high stress concentration. Figure 3 shows the mesh for the bridge superstructure.

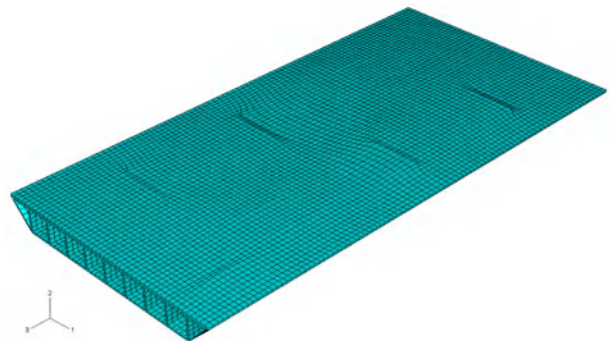


Figure 3 Finite element mesh for the advanced composite bridge

Maximum deflection of the bridge for all the examined cases of all the laminate designs is within the acceptable range.

Figures 4 shows the effect of laminate thickness on the maximum deflection of the bridge deck. Figure 5 shows the effect of laminate thickness on the first vertical natural frequency for different laminate designs. Figure 6 shows the maximum Tsai-Hill Failure Function (THFF) for different laminate thicknesses.

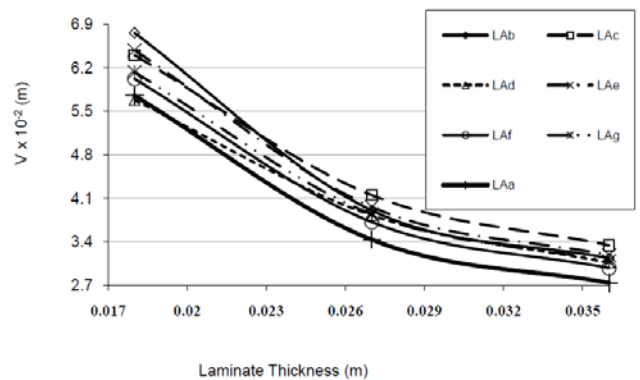


Figure 4 Maximum deflection of the deck top surface of the bridge versus the laminate thickness, under dead and traffic loads

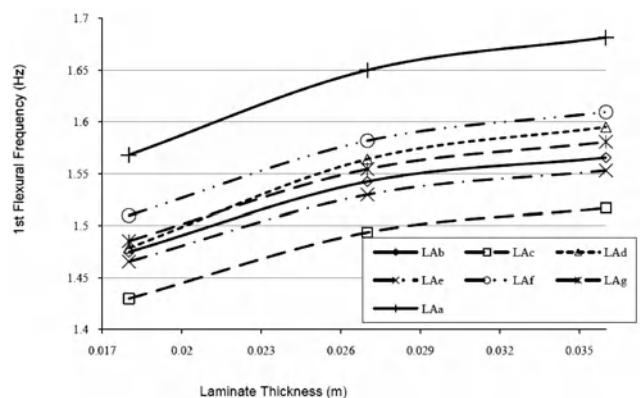


Figure 5 First Vertical Flexural Natural Frequencies versus laminate thickness of the bridge

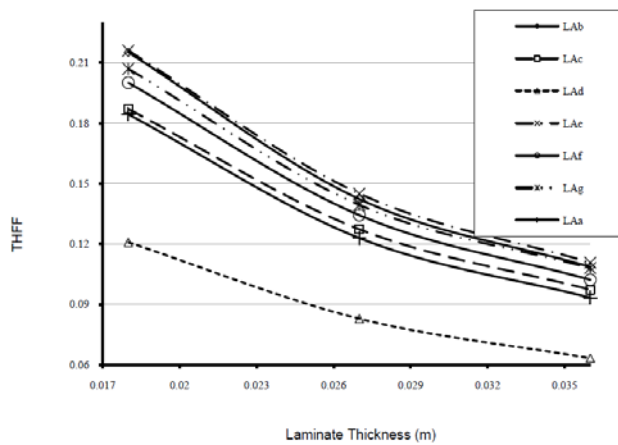


Figure 6 Tsai-Hill Failure Function for different laminate thickness of the bridge

Comparing the results of single-orientation-angle laminate arrangements (i.e. LAb, LAc, and LAd), it is observed that LAb ($\pm 10^\circ$) gives minimum lateral displacement and reasonably low deflection, LAc ($\pm 30^\circ$) gives minimum longitudinal displacement, and LAd (or $\pm 45^\circ$) gives minimum deflection, minimum Tsai Hill Failure Function and the highest flexural natural frequency.

LAF gives lower deflection; lower Tsai-Hill Failure Function, lower longitudinal displacement for low or high thickness, and higher vertical natural frequencies. The triple-angle-orientation laminate design LAg gives medium deformations, medium flexural natural frequency and high Tsai-Hill Failure Function.

The increase of the laminate thickness results in decreasing the resultant displacement field, increasing natural frequencies and decreasing the Tsai-Hill Failure Function.

6 STRUCTURAL PERFORMANCE COMPARED TO PRECAST-PRESTRESSED CONCRETE BRIDGE

The proposed AAC bridge deflection is comparable to long term deflection of a typical slab on prestressed concrete bridges. The slab thickness is 0.25 m and its concrete compressive strength is ($f'_c = 30$ MPa). The five prestressed concrete girders of this bridge are standard PCI-1400 Girders with concrete compression strength of ($f'_c = 40$ MPa). Each girder has a prestressing reinforcement of eighteen strands (low relaxation, size designation 13, grade 1860 and diameter 12.7 mm), which are straight and lie at the bottom of the girder and ten strands that are linearly varied. The maximum static deflection is calculated to be 15.4 mm and the first flexural natural frequency is 3.81 Hz. The final deflection (including creep, shrinkage, etc) is calculated to be 72 mm. The results of AAC Bridge show higher deflection than

the short term deflection but close to the long term deflection of the slab on prestressed girder bridge.

7 CONCLUSIONS

In this paper, an iterative performance based multi-scale analysis and design approach for all-advanced composite bridge superstructure is proposed. The bridge superstructure is formed from laminated FRP box girder and chopped FRP top surface plate. Several laminate designs are examined and the performance of the most efficient material and structural design of the proposed bridge is compared to a slab on prestressed concrete bridge. The results show that the proposed procedure leads to an efficient use of the materials with highest structural performance.

8 ACKNOWLEDGMENTS

The authors wish to acknowledge the financial support of Hong Kong Research Grant Council #611908 for the Performance and Dynamic Characteristics of Composite Long-span Cable-stayed Bridges

REFERENCES

- Almansour, H.H. 2006. *The performance of hybrid long span cable stayed bridges using advanced composites*. Ph.D. Thesis, U of Ottawa.
- Almansour, H.H. & Cheung, M.S. 2003. *Finite element modeling of a CFRP composite deck for long span cable-stayed bridge*. Proc JCJC-III, Ueda, Nagano, JAPAN.
- Aref, A.J. & Parsons, I.D. 2000. *Design and performance of a modular fiber reinforced plastic bridge*. Composites: Part B, 31, 619-628.
- Barbero, E.J. 1991. *Pultruded structural shapes: from the constituents to the structural behavior*. SAMPE J., 27(1), 25-36.
- Burgueno, R., Karbhari, V.M., Seible, F., Kolozes, R.T. 2001. *Experimental dynamic characterization of an FRP composite bridge, superstructure assembly*. Composite Structures, 54, 427-444.
- Canadian Standards Association. 2006. *Canadian Highway Bridge Design Code*. CSA S06-06.
- Davalos, J.F., Salim, H.A., Qiao, P., Lopez-Anido, R., Barbero, E.J. 1996. *Analysis and design of pultruded FRP shapes under bending*. Composites: Part B, 27B, 295-305.
- Jones, R.M., 1999. *Mechanics of composite materials*. Second Edition, Taylor & Francis.
- Mosallam, A.S. & Bank, A.S. 1992. *Short-term behavior of pultruded fiber-reinforced plastic frame*. J. of Struct. Engrg, 118(7), 1937-1944.
- Qiao, P., Julio, Davalos, F., Brown, B. 2000. *A systematic analysis and design approach for single-span FRP deck/stringer bridges*. Composites: Part B 31, 593-609.
- Salim, H.A., Davalos, J.F., Qiao, P., Kiger, S.A. 1997. *Analysis and design of fiber reinforced plastic composite deck-and-stringer bridges*. Composite Structures, 38(1), 295-307.

A Design Concept for an All Composite Road Bridge

Benedict Leo, Anup Chakraborty & Amar Khennane (a.khennane@adfa.edu.au)

School of Engineering and Information Technology, UNSW@ADFA, Canberra, Australia

ABSTRACT The present paper describes a design concept for an all composite road bridge. Most of the components, including the deck to girder connection, are made entirely using the pultrusion process. The stiffness of the girders is tailored to meet the deflection requirements. The analysis results have shown that the structure can carry the specified loads with safety.

1 INTRODUCTION

Despite many advantages over conventional materials, composites are making limited progress in the field of highway structures, where the only niche markets is in FRP deck construction over steel girders and externally bonded FRP repair. Indeed, there are few all composite bridges. The reason is to be found in the low stiffness of the GFRP girders. Using GFRP typically results in a very thick girder cross section as shown on Figure 1 depicting the Tech21 Bridge built in 1997. The alternative is to use hybrid girders combining GFRP, CFRP, and concrete (Deskovic et al, 1995; Canning et al, 1999; van Erp et al, 2002). However, the design of such girders was based on that of reinforced concrete in the sense that the carbon laminate, the stiffest material, was designed to fail first to serve as a warning sign of collapse, thus playing the role of steel yielding in a reinforced concrete beam. As a result, such girders suffer from an inherent lack of stiffness, and when used in a bridge, they had to be put side by side as shown on Figure 2.

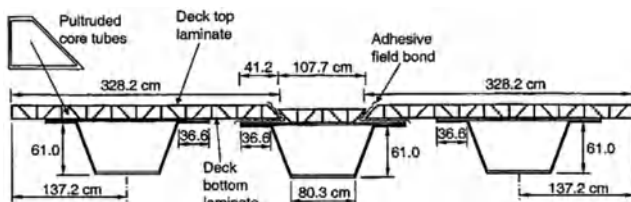


Figure 1 Cross section of the Tech21 all composite bridge (Farhey 2005)



Figure 2 Bridge Cross-Section of FCDD Proposal (van Erp et al 2002)

2 PROPOSED DESIGN

2.1 Description

Using the newly developed filament wound hybrid beam as detailed in the sequel (Chakraborty et al. 2010), a design concept for an all FRP bridge is presented. A typical cross section of the girder is shown on Figure 3. The girder consists of a pultruded profile, a CFRP laminate, and a concrete block wrapped in a filament wound GFRP laminate. The particularity of this design is that the CFRP laminate is not designed to fail first but rather to tailor the stiffness of the girder.

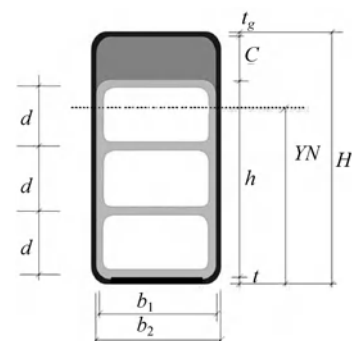


Figure 3 Typical girder cross section

The Strongwell deck system was selected for this bridge. Researchers at Virginia Tech have evaluated the performance of this multi-cellular modular FRP deck system produced using pultruded components (Liu et al. 2008). The mechanical properties are readily available in the design manual, and the orthotropic properties of the square tube assembly and of the equivalent deck have been calculated and published by Liu et al (2008).



Figure 4 Strongwell deck system

With steel girders, the FRP deck is usually attached using shear studs. However, this type of mechanical deck-to-girder connections shows several disadvantages. The concentrated load introduction points can lead to high local stress concentrations and the necessity of cutting holes in the decks can affect the durability (Keller, 2009).

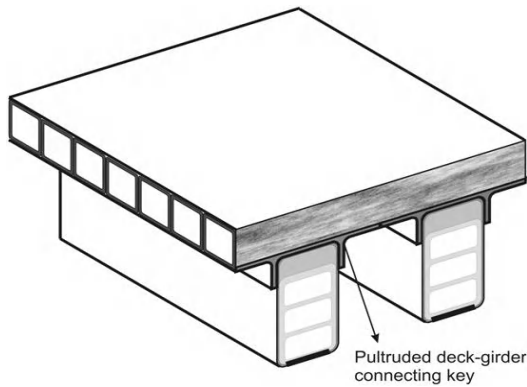


Figure 5 Deck-girder connection

In the present case, it is even more difficult to attach the studs to the hybrid girder. Therefore, a new deck-to-girder attachment made entirely of adhesive bonding is proposed. The system shown on Figure 5 consists of a pultruded key that takes the shape of the girder. It provides enough bonding area between the deck and the girders to ensure stability of the deck girder system

2.2 Design

2.2.1 Design loads

In addition to self weight, the Australian bridge design code AS 5100 recommends the use of the M1600 moving traffic loading and S1600 stationary traffic loading shown on Figures 6 and 7.

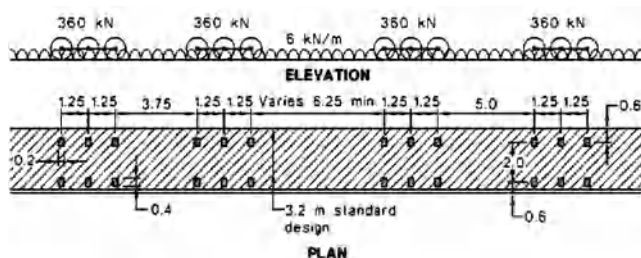


Figure 6 M1600 moving traffic load (AS 5100.2, 2004)

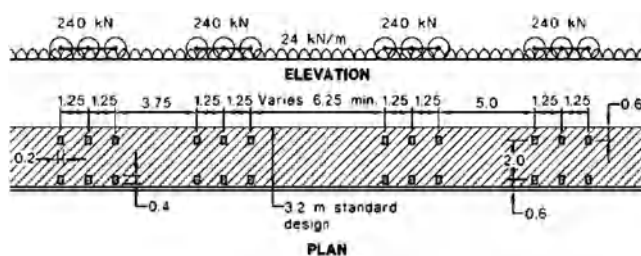


Figure 7 S1600 stationary traffic load (AS 5100.2, 2004)

Table 1 gives the various load factors for the load combinations under ULS and SLS.

Table 1 Load factors for ULS and SLS

Type of load factor	Symbol	ULS	SLS
Dead load (DL)	γ_D	1.2	1.0
Superimposed dead load (SDL)	γ_{SD}	2.0	1.0
Traffic load	γ_T	1.8	1.0

2.2.2 Determination of the number of girders

A unit length of the deck in the transversal direction is chosen as the model to determine the girders' spacing. The strip of the bridge deck is idealised as a continuous beam with the girders considered as simple supports as shown in Figure 8. A total of nine girders are first assumed and the spacing between each girder is 875 mm. Four axle loads, P , are applied at appropriate distances according to the design traffic models shown in Figures 6 and 7. The UDL, w is also applied across the whole beam. The largest deflections of the bridge deck, ΔT obtained from the two traffic load conditions, M 1600 and S 1600 are 0.97 mm and 0.66 mm respectively. When compared to the allowable deflection, 11.7 mm, these values are very small. This indicates that there is a possibility of further reducing the number of girders. However, it must be noted that the lesser the number of girders, the larger the load on each girder will be. This means that the girder has to be designed with a deeper section and reinforced with a thicker CFRP laminate and/or concrete section to achieve sufficient flexural stiffness. With the above consideration, and after further trials, the total of nine girders was selected for this proposed bridge structure with a girder to girder spacing of 875 mm.

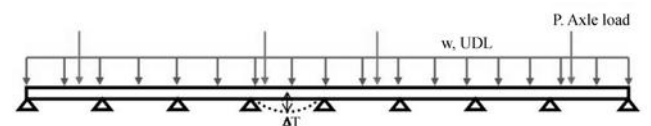


Figure 8 Model for the determination of girders' spacing

2.2.3 Design of the Hybrid Beam

2.2.3.1 Sizing of the beam

The hybrid beam consists of a high strength concrete (HSC) block with thickness C and width b , a GFRP pultruded box sectional profile of height h with uniform thickness t_w , a CFRP laminate of thickness t , and an outer filament wind GFRP wrap of thickness t_g with fibres orientated at $\pm 45^\circ/90^\circ$. The cross section of this hybrid beam is shown in Figure 3. The overall height of the hybrid beam is H and width b_2 . As a starting point, certain initial dimensions of the hybrid beam are chosen based on recommendations for a reinforced concrete beam while other dimensions are chosen via trial and

error so as to allow for the design process to continue. In reinforced concrete design, the span to depth ratio varies between 10 and 20. The lower limit of 10 is chosen so that a deeper beam can be achieved and the problem of a lack of stiffness of a thin walled GFRP box section can be addressed. Thus, for a span of 8 m, the depth of the hybrid beam, H is chosen as 800 mm. The concrete block should not be too thin otherwise it might fail prematurely through punching failure. But, it should not be too thick either, otherwise the self weight of the beam will increase greatly since concrete is the heaviest constituent in this beam. The ratio of the depth of the GFRP pultruded profile to the thickness of the concrete layer is chosen to be 4, i.e. $c = h/4$. Since $c + h = H$, the concrete depth is calculated as $c = 160$ mm and that of the pultruded profile as $h = 640$ mm with a width, $b = 300$ mm. The thickness of the GFRP pultruded profile is set to $t_w = 10$ mm since this is limited by the pultrusion process. The only unknown is the thickness of the CFRP laminate.

2.2.3.2 CFRP thickness

To determine the CFRP thickness, which controls the stiffness of the girder, the total deflection is written as function of the laminate thickness, t , and compared to the deflection criterion recommended by AS 5100, which states that the deflection limit of a road bridge under traffic for SLS under live loading shall not be greater than $L/600$.

$$\delta_{\text{total}}(t) = \delta_{\text{bend}}(t) + \delta_{\text{shear}}(t) \leq L/600 \quad (1)$$

where δ_{bend} is the deflection due to bending in a four point loading case and δ_{shear} is the deflection due to transverse shear effects.

Solving equation (1) under the worst SLS load scenario using Maple yielded a CFRP thickness of 11.92 ~ 12mm.

2.2.3.3 Failure analysis

The beam can fail in a number of ways; crushing of the concrete, buckling of the webs, or local bearing failure at the support. The later is quite premature, and can be averted using adequate local support. The ideal scenario is for the beam to fail through concrete crushing.

– Lateral stability

In general, pultruded box sections have high resistance to lateral torsional buckling. However, limits are often imposed on the section's height to width ratio to prevent lateral instability and also to satisfy other design requirements (Deskovic, 1995). The beam's height to width ratio is often checked by the following equation, $(C + h) < k$, where k is a constant to be chosen by the designer. Deskovic et al. (1995) has recommended a value of $k = 3$ for composite sections and thin walled hybrid sections. Using the trailed initial width, $b = 300$ mm, gives a value of $k = 2.67$ which is well within the accepted value.

– Web buckling load

Another possible failure of the beam is through buckling of the webs of the pultruded box section. To ensure that the webs of the hybrid beam are stiff enough to take the load and not buckle, the theoretical web shear buckling stress is calculated using the method given in (Holmes and Just, 1983, Deskovic et al. 1995). The web buckling load was estimated to 3545 kN which is far greater than the applied load under ULS which is equal to 719 kN.

– Strength capacity

The ideal scenario is for the beam to fail through concrete crushing. Using strain compatibility, as shown on Figure 9, the moment capacity of the beam and the load at which the concrete should crush are calculated and compared to the external applied loads under ULS.

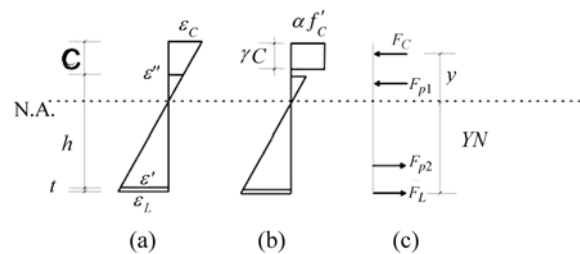


Figure 9 Strain compatibility

The calculated moment of 2270 kN·m is far greater than the applied moment of 959 kN·m under ULS.

3 FINITE ELEMENT ANALYSIS

Once all the components of the bridge are designed, the finite element software ANSYS was used as a design check. The whole of the bridge superstructure is modelled as shown on Figure 10. The bridge deck is modelled as a slab using the SHELL 91 element, which is a layered structural shell element that can be used for modelling thick sandwich structures. It is defined by eight nodes, layer thicknesses, layer material direction angles and orthotropic properties, and has six degrees of freedom at each node. The top and bottom plates of the girder have a

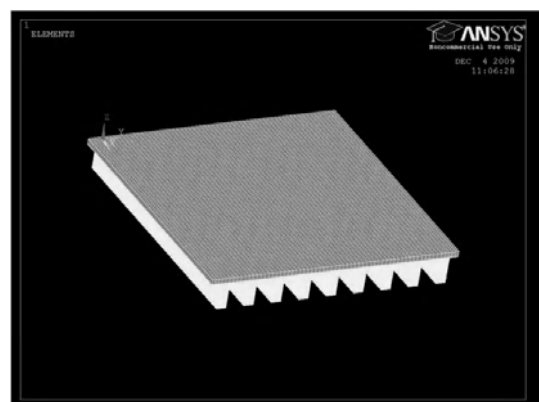


Figure 10 Finite element model of the bridge

thickness of 9.5 mm each while the square tube assembly has a thickness of 152.4 mm.

The hybrid girders are modelled using BEAM 189 element with a meshed cross section. This allows the user to create any cross sectional profile and assign different material models to represent the different constituents of a composite beam. Another important feature of the element is that it can be offset from any chosen location. The element is based on the Timoshenko beam theory, and has six degrees of freedom at each node.

Figure 11 shows the deflected shape of the bridge under the worst SLS load combination. The maximum deflection recorded is equal to 13.085 mm, which is less than $L/600$ as specified in the code.

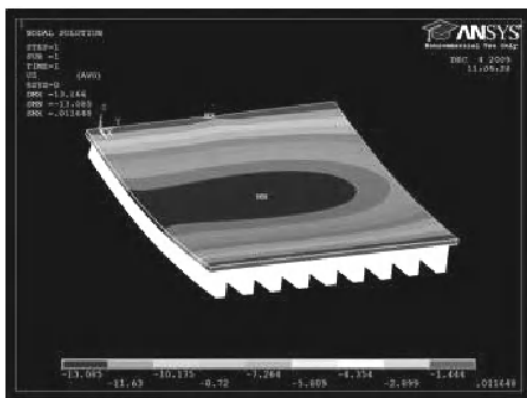


Figure 11 Deflected shape of the bridge superstructure

Figure 12 shows a contour plot of the von-Mises stress in the deck. It can be seen that the stresses are very low. This confirms once more that the design of composite structures is deflection driven.

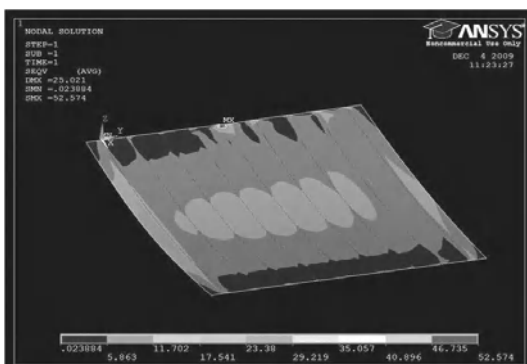


Figure 12 Plot of the von Mises stress in the deck

4 CONCLUSION

The present study has shown that it is possible to design an all-composite bridge that meets the deflection requirements without the encumbrance of very thick girder cross sections. The stiffness of the girders is tailored to meet the deflection requirements. Most of the components, including the deck to girder connection, are made entirely using the pultrusion process. The analysis results have shown that the structure can carry the specified loads with safety. Future work will emphasise on the economics of the bridge, and its dynamical behaviour.

REFERENCES

- AS 5100, Australian Standards, Bridge Design Code, 2004.
- Canning, L., Hollaway, L. and Thorne A.M. 1999, Manufacture, testing and numerical analysis of an innovative polymer composite/concrete structural unit. *Proceedings – Institution of Civil Engineers, Structures and Buildings*, 134, pp. 231-241.
- Chakraborty, A. Khennane A. Morozov E. An experimental investigation into the behavior of filament wound FRP-HSC hybrid beams. *CICE2010, Beijing, China*
- Deskovic, N., Triantafillou, T.C. & Meier, U. 1995. Innovative design of FRP combined with concrete: short term behavior. *ASCE Jou. Struct. Engrg* 121(7). 1069-1078.
- Farhey N. 2005. Long-Term Performance Monitoring of the Tech 21 All-Composite Bridge. *ASCE Jou. Comp. for Construction*, 9(3) 255-262.
- Holmes, M. & Just, D.J. 1983. GRP in Structural Engineering, *Applied Science Publishers, UK*.
- Keller T. (Accessed November 2009). Fiber-Reinforced Polymer Bridge Decks–Status Report and Future Prospects. <http://www.cobrae.org/afbeeldingen/paperkeller.pdf>
- Liu, Z., Cousins, T.E., Lesko, J.J. & Sotelino, E.D. 2008. Design recommendations for a FRP bridge deck supported on steel superstructure. *ASCE Jour. Comp. Construction*, 12(6) 660-668.
- Van Erp, GM, Heldt, TJ, Cattell, CL, & Marsh, R, 2002 ‘A new approach to fibre composite bridge structures’, Proceedings of the 17th Australasian conference on the mechanics of structures and materials, ACMSM17, Australia 37-45.

Mechanical Model and Analysis of FRP Woven Web Structures

Yujun Qi, Peng Feng(fengpeng@tsinghua.edu.cn), & Lieping Ye

Department of Civil Engineering, Tsinghua University, Beijing, China

ABSTRACT The fiber-reinforced polymer (FRP) woven web structure (WWS) is an innovative large-span spatial structure composed of FRP strips. The FRP strips are crossed each other and woven to form a flexible web plane, and the web is stressed integrally in out-of-plane. The WWS is a tensegrity spatial structure system made of flexible members, which has four mechanical statuses. The basic assumptions and the 3D fundamental mechanical model of the simple FRP WWS which has ring beams and central symmetry FRP strips are studied. The mechanical equations are drawn. Based on the equations, three load cases of FRP WWS including integrally pre-stressed in out-of-plane, full span load and half span load are analyzed in theoretical method. The fundamental mechanical model of FRP WWS is established that provides the theoretical approach for analyzing FRP WWS.

The fiber-reinforced polymer (FRP) woven web structure (WWS) is an innovative large-span spatial structure composed of FRP strips, as show in Figure 1. In the WWS, the high strength of FRP in tension is used efficiently, as all FRP strips are in tensile stage. The FRP WWS can make the lager span than the traditional structures.

The WWS is a flexible spatial structure system made of FRP members, which have the similar mechanical behavior to cables. In this paper, the fundamental mechanical model and equations are proposed and studied, for simple FRP WWS which has ring beams and central symmetry FRP strips.

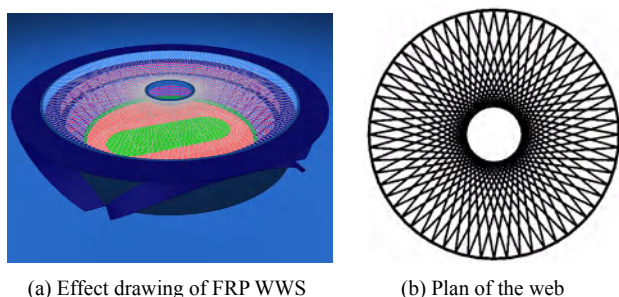


Figure 1 FRP WWS

1 BASIC ASSUMPTIONS FOR FRP WWS

FRP WWS has stronger geometric stiffness by integrally pre-stressed in out-of-plan direction. If the simple FRP WWS which has ring beams and central symmetry FRP strips, to can create fundamental mechanical model, the basic assumptions are proposed as flowing.

(1) The FRP strips are connected to ring beams by hinges. The beams have greater stiffness and are assumed to be rigid body.

(2) FRP strips are only tensioned in all load cases. FRP

strips have large slenderness ratio, they can not resist compression and bending.

(3) FRP strips are liner elastic on tension stages.

(4) Interaction of FRP strips on intersection is neglected. There is no connection between FRP strips at the intersections, only the friction force is smaller relatively to the axial tension force.

2 BASIC EQUATIONS OF SINGLE FRP STRIPS

The above basic assumptions of FRP strips are same as assumptions of single cable in single cable theory. The equations of single FRP strips can use equations of single cable. In single cable theory, the basic equations are following.

$$H \frac{d^2 z}{dx^2} + q_z = 0 \quad (1)$$

$$z = \frac{M}{H} + \frac{c}{l} x \quad (2)$$

$$H - H_0 = \frac{EA}{2l} \left(\frac{D}{H^2} - \frac{D_0}{H_0^2} \right) + EA \frac{c^2 - c_0^2}{2l^2} + EA \frac{u_B - u_A}{l_0} - EA\alpha\Delta t \quad (3)$$

$$D = \int_0^l \left(\frac{dM}{dx} \right)^2 dx \quad (4)$$

3 FUNDAMENTAL MECHANICAL MODEL OF SINGLE LAYER WWS

The mechanic model of the single layer WWS is studied in Figure 3. For single FRP trip, anchor point A is on out-

ring-beam, and anchor point B is on inner ring beam., tension stiffness of FRP strips is EA , self-weight load intensity of FRP strips is p , horizontal span is l , radius of out-ring-beam is R , radius of inner ring beam is r . For No. i of strip on No. j of stage, the mechanic equations are found as following.

$$z_{i,j} = \frac{M_{i,j}}{H_{i,j}} + \frac{c_{i,j}}{l_{i,j}}x \quad (5)$$

$$H_{i,j} - H_{i,0} = \frac{EA}{2l_0} \left(\frac{D_{i,j}}{H_{i,j}^2} - \frac{D_{i,0}}{H_{i,0}^2} \right) + EA \frac{c_{i,j}^2 - c_{0,j}^2}{2l_0^2} + EA \frac{u_{i,j}}{l_0} \quad (6)$$

There are $3i$ of unknown variables, $H_{i,j}$, $c_{i,j}$ and $u_{i,j}$ in above equations.

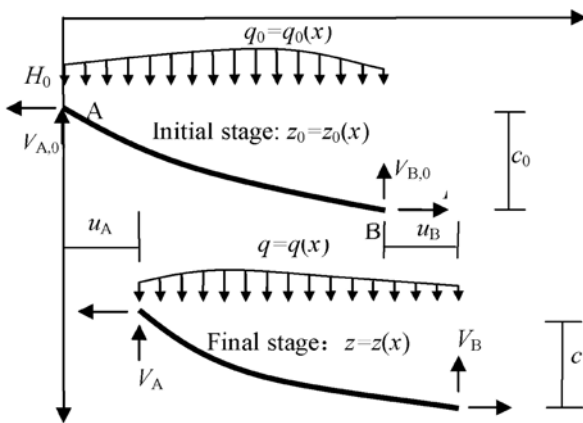


Figure 2 Mechanical analysis of single FRP trip

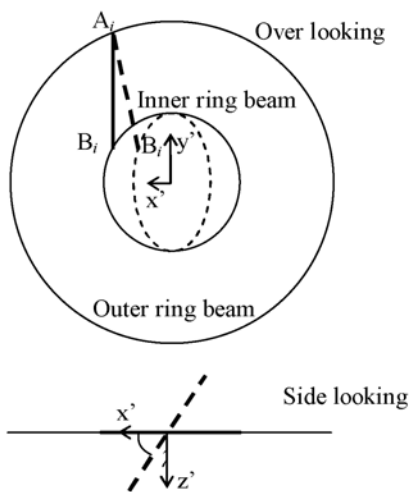


Figure 3 Analysis schematic diagram of WWS

All strips must satisfy the conditions of compatibility of displacement and force equilibrium, as they are linked to the rigid inner ring beam. The inner ring beam can not rotate in web plan as the symmetric condition, but can only translate and rotate in out-of-plan of web. The axis of rotation in out-of-plan called y' , and the integral coordinate system $x'-O-y'$ is created as Figure 3. The

initial angle of line OA_i and x -axis is called α_i , and the initial angle of line OB_i and x -axis is called β_i . The angle of rotated plan and initial plan of inner ring beam is called γ . The translated displacements of inner ring beam are u_x , u_y and u_z .

The coordinate of point A_i calculated as follows:

$$\begin{cases} x_{A_i} = R \cos \alpha_i \\ y_{A_i} = R \sin \alpha_i \\ z_{A_i} = 0 \end{cases} \quad (7)$$

The initial coordinate of point B_i calculated as follows:

$$\begin{cases} x_{B_i} = r \cos \beta_i \\ y_{B_i} = r \sin \beta_i \\ z_{B_i} = c_{i,0} \end{cases} \quad (8)$$

The final stage coordinate of point B_i calculated as follows:

$$\begin{cases} x_{B_i} = r \cos \gamma \cos \beta_i + u_x \\ y_{B_i} = r \sin \beta_i + u_y \\ z_{B_i} = c_{i,0} + r \cos \beta_i \sin \gamma + u_z \end{cases} \quad (9)$$

Combining Eqs. (8)-(10), the parameters can be determined as follows:

$$c_{i,j} = c_{i,0} + r \cos \beta_i \sin \gamma + u_z \quad (10)$$

$$u_{i,j} = l_{i,j} - l_{i,0} \quad (11-a)$$

$$l_{i,j} = \sqrt{(x_{B_i} - x_{A_i})^2 + (y_{B_i} - y_{A_i})^2} \quad (11-b)$$

Based on the equilibrium conditions, the following equations can be established:

$$\text{x-axis: } \sum_i H_{i,j} \frac{x_{A_i} - x_{B_i}}{l_{i,j}} = 0 \quad (12-a)$$

$$\text{y-axis: } \sum_i i H_{i,j} \frac{y_{A_i} - y_{B_i}}{l_{i,j}} = 0 \quad (12-b)$$

$$\text{z-axis: } \sum_i H_{i,j} \frac{z_{A_i} - z_{B_i}}{l_i} + G = 0 \quad (12-c)$$

where, G is vertical force at inner ring beam.

As The force moment equilibrium for y -axis, the following equation can be established.

$$\begin{aligned} & \sum_i H_{i,j} \frac{x_{A_i} - x_{B_i}}{l_{i,j}} r \cos \beta_i \sin \gamma \\ & + \sum_i H_{i,j} \frac{z_{A_i} - z_{B_i}}{l_{i,j}} r \cos \gamma \cos \beta_i b = 0 \end{aligned} \quad (12-d)$$

Substitute Eqs. (7)-(12) in Eq. (6), eliminate $c_{i,j}$ and $u_{i,j}$, and obtain i equations which only included $i+4$ unknown parameters. Then, combining Eqs.(12-a)-(12-d), the all

unknown parameters can be determined. Substitute above results in Eqs.(10) and (5), the geometrical deformation $z_{i,j}=z_{i,j}(x)$ of all strips can be found.

This above solutions can be applied to generic load case. If the load is regular, example of central symmetry or axial symmetric FRP strips, the solutions can be predigested. As following, the simply solutions on typical stages for single web WWS is studied.

4 ANALYSIS OF SINGLE LAYER WWS

The FRP WWS have four typical mechanical stages, initial prestressed stage, out-of-plane tensioned stage, full span loaded stage, half span loaded stage, as illustrated in Figure 4. The first two are the key stages in the construction process, the last two are the key stages in the service.

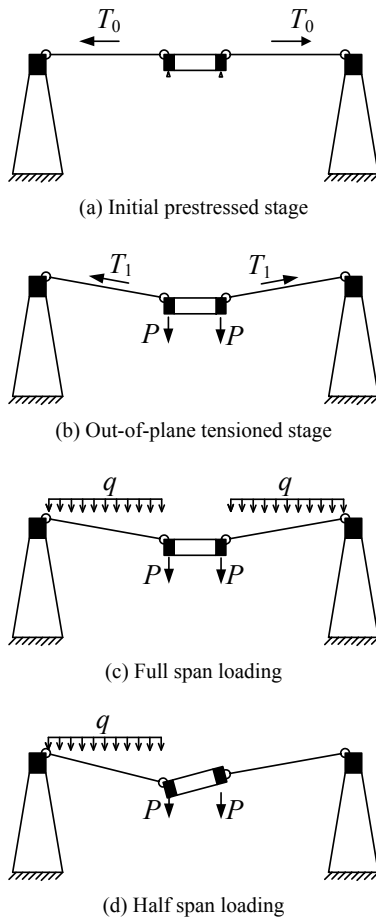


Figure 4 Stages of FRP WWS

4.1 Stage I - Initial prestressed stage

In this stage, there is an initial prestressed force T_1 in all FRP strips (Figure 5). The results can be easily established as following.

$$M_1 = \frac{qx(l-x)}{2}, D_1 = \int_0^l \left(\frac{dM}{dx}\right)^2 dx = \frac{q^2 l^3}{12} \quad (13)$$

$$z_1 = \frac{qx(l-x)}{2H_1}, H_1 = \sqrt{T_1^2 - (ql/2)^2} \quad (14)$$

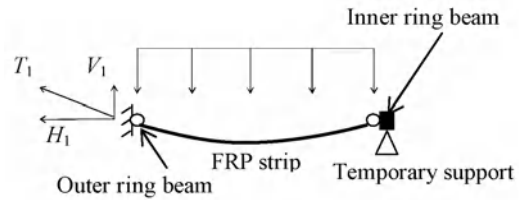


Figure 5 Stage I- initial prestressed stage

4.2 Stage II - Out-of-plane tensioned stage

The out-of-plan tensioned method mainly is two ways: only using self-weight of inner ring beam and using additional prestressed tendons.

In this stage as Figure 6, the vertical displacement is assumed c_2 , when out-of-plan tension force is P .

Compare with stage I, the distributed load q is not change. Thus, $M_2=M_1$ and $D_2=D_1$ is calculated. The following equations can be direct obtained.

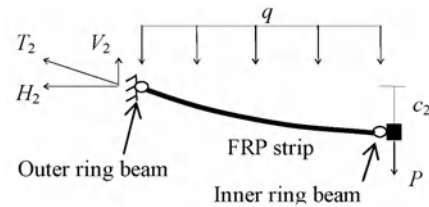


Figure 6 stage II - out-of-plane tensioned stage

$$z_2 = \frac{qx(l-x)}{2H_2} + \frac{c_2}{l}x \quad (15)$$

$$H_2 - H_1 = \frac{q^2 l^2 EA}{24} \left(\frac{1}{H_2^2} - \frac{1}{H_1^2} \right) + EA \frac{c_2^2}{2l^2} \quad (16)$$

Combining above two equations, the horizontal component H_2 of FRP trip axis force and geometrical shape of FRP trip can be established.

Besides, the rotated angle at inner ring beam must be satisfied as following.

$$\frac{dz_2}{dx} \Big|_{x=l} = \frac{P}{H_2} \quad (17)$$

the out-of plan tension force P is as following.

$$P = H_2 \frac{c_2}{l} - \frac{ql}{2} \quad (18)$$

4.3 Stage III - full span loaded stage

In Figure 7, the load on the FRP strips is trapezoidal load because of that the load on the web is uniform load. The value of trapezoidal load at the inner ring beam is called q_l and the value of trapezoidal load at the outer ring beam is called q_r .

$$M_3(x) = \frac{1}{2}q_l(lx - x^2) + \frac{1}{6}(q_r - q_l)(2lx - 3x^2 + \frac{1}{l}x^3) \quad (19)$$

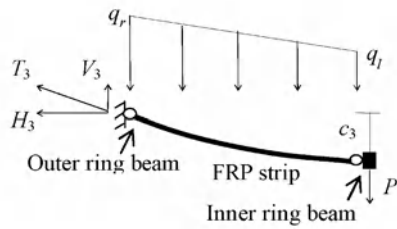


Figure 7 stage III - full span loaded stage

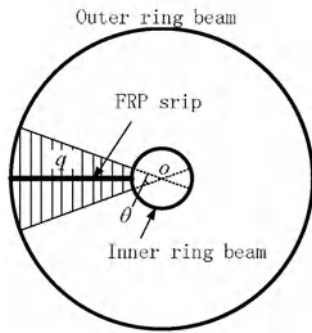


Figure 8 Equivalent load of FRP strips on full span load

Besides, the conditions of rotated angle at inner ring beam is

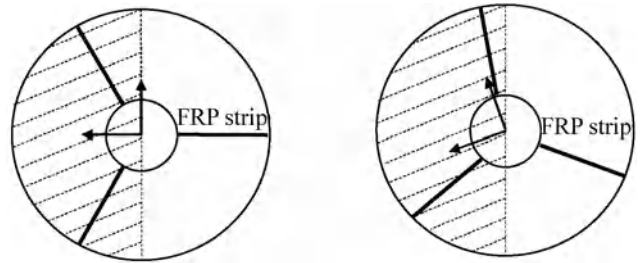
$$\frac{dz_3}{dx} \Big|_{x=l} = \frac{P}{H_3} \quad (20)$$

$$c_3 = \frac{l}{H_3} \left(P + \frac{l}{6} (q_r + 2q_l) \right) \quad (21)$$

Substitute D_3 and c_3 in Eqs.(3) and (2), the H_3 and z_3 can be calculated.

4.4 Stage IV - half span loaded stage

In half span loaded stage, the mechanical acting of FRP strips is different. The analysis can not only study single FRP strip, and must study the whole web that is the all FRP strips. If symmetry axis of the half span loads coincide with symmetry axis of the web (Figure 9), the displacement of inner ring beam in the direction of the y' -axis is zero. That is $u_y=0$. In this time, to reduce the numbers of unknown parameter, can only study the half span WWS.



(a) symmetry axis coincide (b) symmetry axis do not coincide

Figure 9 Diagram of WWS on half span load

5 CONCLUSION

(1) Theoretical equations of single FRP strip are proposed.

(2) Based on the basic assumptions of the FRP WWS, the fundamental mechanical model is proposed. For simply FRP WWS which has a single web, the theoretical analysis is studied, and the solution equations are established.

(3) The calculation formula of geometrical shape and force of FRP strips on four typical load cases are derived.

6 ACKNOWLEDGMENTS

The authors gratefully acknowledge the financial supports from the National Natural Science Foundation of China (No. 50608047).

REFERENCES

- Peng Feng, Lie-ping Ye, J. G. Teng. 2007. Large-Span Woven Web Structure Made of Fiber-Reinforced Polymer. *Journal of composites for construction*. 11(2): 110-119
- Peng Feng, Lieping Ye, Rui Bao, Yujun Qi. 2007. Concepts, forms and basic analysis of FRP woven web structure. *Journal of Building Structures*, 28(4):109-116
- Shizhao Shen, Chongbao Xu, Chen zhao et. 2006. *The design of cable structure*. Beijing: China architecture & building press
- Ruizhao Shen. 1996. Calculation Methods for Design and Erection of Cable Curve of Suspension Bridge. *China Civil Engineering Journal*. 29(2): 3-9

GFRP-Polyurethane Sandwich Panels under Reversed Bending Fatigue

Mathieson, Hale

Doctoral Student, Department of Civil Engineering, Queen's University, Kingston, Canada

Fam, Amir

Professor and Canada Research Chair in Innovative and Retrofitted Structures, Department of Civil Engineering, Queen's University, Kingston, Canada

ABSTRACT Sandwich panels composed of lightweight polyurethane core and GFRP skins have a great potential for a variety of applications. Some of the promising applications include cladding of buildings, in which the lightweight panels are used to provide the building envelope in terms of insulation and protection from the elements, and in lightweight decking applications of pedestrian bridges or platforms. In cladding applications, although the panels are not of the load-bearing type, they are subjected to a strong wind pressure or suction. In this case the panels are repeatedly loaded in cyclic bending, which may cause fatigue problems. This study investigates sandwich panels in four point reversed cyclic bending. The panels were exposed to various stress levels and for each level; the number of cycles to failure was established. Stiffness degradation characteristics were also measured at various stages of loading. It was shown that at a cyclic load of $\pm 30\%$ of the ultimate monotonic flexural strength, the panels were able to sustain over 2 million cycles.

1 INTRODUCTION

Glass fiber reinforced polymer (GFRP) materials have been used in a variety of forms in structural applications. The advantages of GFRPs include their high specific strength combined with moderate cost, relative to other composites. Barbero (1993) explored the concept of sandwich panels and pointed out the need for proper fatigue investigation of this system. Composite sandwich panels consist of FRP exterior skins and a lightweight soft foam core made of materials such as polyurethane. The premise is the panel will resist flexure in the same way a steel W-section does. In this way, the flexural resistance will be provided by the top and bottom skins similar to the flanges. The core material will then provide shear resistance, analogous to the web of the W-section, except that shear deformations of the rather soft core are significant and may not be ignored. As explained by Halfpenny (2005), fatigue is a specific response all materials experience where minor and microscopic failures initiate and propagate while experiencing less than ultimate loading. The fatigue loading ratio (R) represents the minimum applied load divided by the maximum applied load. Generally, a 100% reverse loading case (R-value is -1) results in the lowest number of cycles per amplitude. This is when the minimum applied load is the equivalent of the maximum applied load in the

opposite direction. This is considered the worst case scenario and is important in fatigue design of certain structures such as exterior walls subjected to wind pressure or suction.

Experiments have been performed on FRP sandwich panels to investigate the differences in loading ratio (Burman, 1998). Investigation into the individual elements of sandwich structures has revealed that the rate of loading could change material properties. Sheno (1995) and Challis (1986) reported that too much increase of the loading rate reduces the stiffness of the foam by causing the temperature to rise. Challis (1986) found that changing loading frequency from 1 Hz to 5 Hz resulted in a difference of 16°C. The resulting decrease in shear properties was 10% at 5 Hz. However, from 0.33 Hz to 0.91 Hz, it was found that no measurable change occurs. This paper explored FRP-polyurethane sandwich panels under fully reversed high cycle fatigue. The objective is to establish their S-N curve in flexure and any degradation of stiffness during cyclic loading.

2 EXPERIMENTAL PROGRAM

2.1 Test Specimens and Material Properties

To date, four sandwich panels have been tested. The general structure of the panel is displayed in Figure 1. Each panel is comprised of a polyurethane foam as the

core material, with two parallel sheets of GFRP acting as the top and bottom skins.

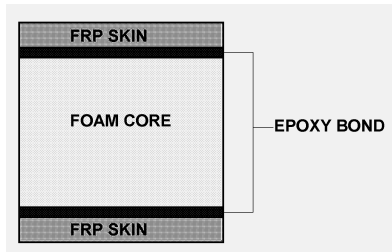


Figure 1 General FRP sandwich panel cross section

The type of polyurethane foam is Corafoam U020 and was produced by DUNA-USA Foams & Chemicals, Inc. GFRP skins are fabricated from 54 oz 3 weave E-glass 2022 silane sized and CoPoxy 4281A resin with Copoxy 4284 hardener. All specimens were constructed by Comtek Advanced Structures Inc. The dimensions of the specimens are provided in Table 1. Note that bonding region is considered negligible thickness.

Table 1 Test specimens dimensions and loading level

Spec. ID	Load % ultimate	Dimensions			
		Length (mm)	Width (mm)	Foam (mm)	Skin (mm)
A1	100%	1221	634	75	1.55
A2	50%	1220	635	75	1.56
A3	30%	1222	635	75	1.55
A5	40%	1221	634	74	1.55

2.2 Test Setup and Procedure

A special test frame was designed to apply four-point bending on a simple beam with the capability to completely reverse loading (Figure 2). The machine used was an *Instron 8800*, with hydraulic grips to hold the supporting and loading components of the setup (Figure 3).

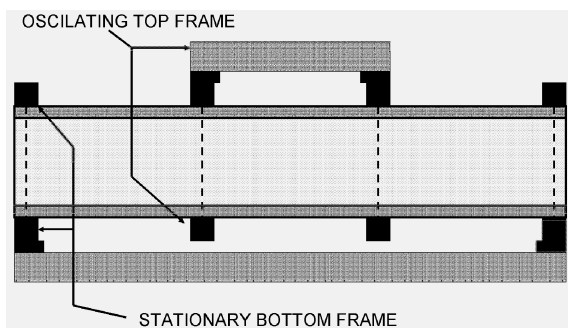


Figure 2 Schematic of reversed loading setup

Figure 2 shows the end supports and loading points on the top and bottom faces of the panel. At each point the steel sections on both skins were connected through

a specialized bolts that allow rotation independently of the rest of the frame to provide the simple beam conditions. The loads were applied at one third of the span.

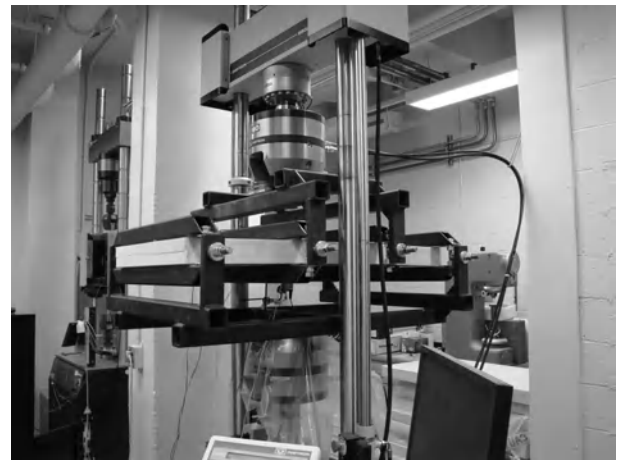


Figure 3 Generalized loading during testing

As mentioned, four tests have been completed. In the first test a specimen was monotonically loaded to failure as a control specimen. Using this initial test, loading levels of 50%, 40% and 30% of the ultimate strength were selected for the remaining specimens. The loading was applied equally in both directions, resulting in a loading ratio (R-value) of -1 . First, the specimen was subjected to a quasi-static loading at a stroke control rate of 1 mm/min from zero loading to the maximum positive load, then reversing to the maximum negative load, followed by unloading back to zero. The objective was to establish the initial stiffness of the panel. The fatigue cycles were then applied under load control with a loading rate of 0.6 Hz to 0.7 Hz. The cyclic loading was periodically halted at pre-determined number of cycles additional quasi-static tests were conducted to establish any change in stiffness. For each specimen, this testing procedure continued until fatigue failure of the sandwich panel occurred. Two important sets of data were obtained at the same time. The first is the number of cycles to reach failure for each sample. Video surveillance and computer sensors were running continually to be sure to capture this final stage and total cycles to failure. Also, the periodic quasi-static load-deflection curves were obtained to check for changing stiffness of each specimen.

3 TEST RESULTS AND DISCUSSION

3.1 Failure Mode

Shear failure of the soft foam core occurred in the high shear region of all four specimens. It was determined that the fatigue crack propagation initiated in the foam. Upon investigation after failure, the propagation could be observed to advance within the foam fairly close to the bond line between the skin and the foam (Figure 4).

After a number of cycles, the crack advances to a point where the remaining connected foam is insufficient to resist the shear within the system and failure occurs rapidly within one to two cycles for each direction of bending.



Figure 4 Shear failure at end of cycles

3.2 The S-N Curve

Table 2 shows the upper loading levels and their percentage of ultimate, along with the number of cycles to failure.

Table 2 Fatigue test results

Loading Amplitude		Cycles to Failure
Metric Value (kN)	% of Ultimate	
14.44	100%	Failure within 1 st cycle
7.22	50%	46,208
5.78	40%	134,500
4.33	30%	2,358,795

The S-N curve using the data in Table 2 is shown in Figure 5. The vertical axis represents the load as percentage from ultimate, while the horizontal axis is a logarithmic scale. The point of fatigue failure is the point when the first direction of bending fails.

To establish a useful model, a general equation was formulated for this particular data. Three known facts were used to establish this mathematical model. First, all relevant cycles will be between 1 and infinite number of cycles. Secondly, the load value can not exceed 100% of ultimate, and will have a minimum that is greater than or equal to zero that will never fail at infinite cycles. Third, Halfpenny (2005) and Sheno (1995) have suggested the shape of the graph on a log plot will be an s-shape, so a sigmoid function is used in this case (Equation 1).

$$f(x) = \frac{1}{1 + e^{-x}} \quad (1)$$

Through transformation of this basic equation and simplification and rearrangement of constants, Equation 2 was derived.

$$S(N) = \frac{A}{1 + B \times N^m} + C \quad (2)$$

For Equation 2, m = a logarithmic conversion constant, 0.434; C = fatigue limit as a fraction of ultimate (0.23); N = number of cycles to failure, $S(N)$ = stress amplitude as fraction of ultimate; A & B are undefined material constants = 0.788 and 0.018 respectively, through curve fitting.

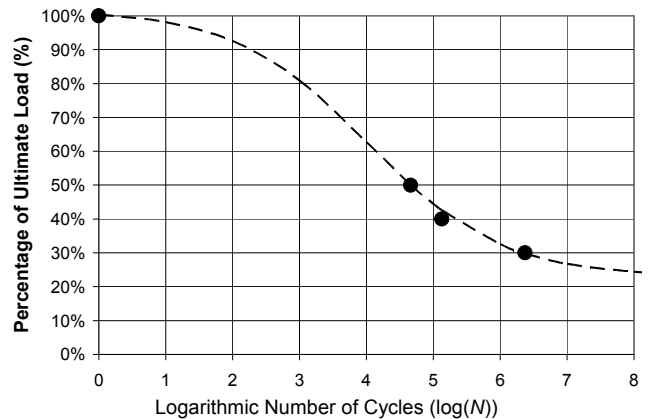


Figure 5 S-N curve of tested GFRP sandwich panel

As shown in this graph, the fatigue limit is determined to be 23% of ultimate. This means any amplitudes less than 23% will never cause the sample to fail. Future testing will determine how accurate this value is. Further analysis will compare the material properties of each sample to the damage induced by less the failure cyclic loading. From this, a practical analytical approach will be constructed determining the values of A and B , rather than curve fitting.

3.3 Stiffness Degradation

Each cycle could cause some micro-crack initiation or propagation. This propagation could result in a decreased shear transfer region. In turn, this could result in a decrease in the global resisting shear stiffness of each specimen as cyclic loading progresses.

In this study the recorded strains remained generally constant, However some change in deflections were measured. Figure 6 displays results of maximum mid-span deflection versus the applied load at specified points of interest. The loading axis and the number of cycles axis have been normalized for all three cyclic tests (30%, 40%, and 50%) to ease comparisons.

As displayed in Figure 6, all cycling tests have a some change in deflection, ranging from a small increase of about 5% to over 25% increase, depending on loading level. This observation, combined with the insignificant change in skin strains, suggests that the increase in deflection is likely attributed to the considerable effect of shear deformation of the soft core. Future work will be looking at shear properties of the CORAFOAM core within the system to explain the variance of maximum deflections.

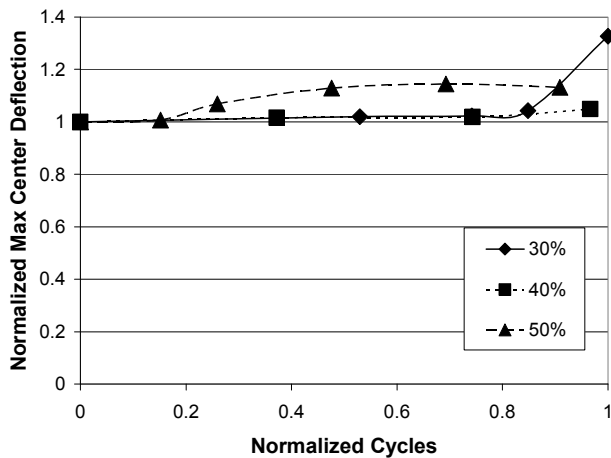


Figure 6 Changing deflection per cyclic test

4 SUMMARY AND CONCLUSIONS

For the GFRP skin-polyurethane core sandwich panels studied in this paper, the S-N fatigue curve has been established under fully reversed bending, using a rather few but quite informative data points. Compared to most sandwich panel specimens studied in literature, the panels tested in this study are considered relatively large scale (1220×635×75 mm). The reversed cyclic loading represents the effect of wind pressure and suction on exterior cladding walls or the effect of moving loads on a continuous decking system.

The study showed that under a load of $\pm 30\%$ of the ultimate quasi-static load, the panels can resist about 2.3 million cycles, whereas at 50% load, only 46,000 cycles could be sustained to failure. Also, the increase in deflection with loading cycles could increase to over 25% near failure, due to stiffness degradation. Furthermore, contribution of the soft foam shear deformation to deflection is likely quite significant.

By observing the failure modes and viewing the current recorded data it is concluded that the failure initiation and propagation during cyclic loading is a diagonal tension

shear failure of the soft foam core. This propagation occurs near the contact of the foam and skin and will progress until the remaining intact foam fails in shear.

Future work will include more tests to establish more data points on the S-N curve. Also, the effect of internal GFRP ribs of various configurations on the fatigue behavior will be studied.

5 ACKNOWLEDGMENTS

The authors wish to acknowledge the financial contributions of the Ontario Centre of Excellence (OCE) and Future composites Products Ltd, for their in kind contributions. The authors are also grateful to Jamie Escobar of Queen's University.

REFERENCES

- Barbero, E.J., Lopez-Anido, R. & Davalos, J.F. 1993. On the mechanics of thin-walled laminated composite beams. *Journal of Composite Materials* 29(18): 806-829.
- Burman, M. 1998, Fatigue crack initiation and propagation in sandwich structures. Doctoral Thesis, report No.98-29. ISSN 0280-4646. Stockholm, Sweden: Kungliga Tekniska Högskolan (Royal Institute of Technology)
- Challis, K.E., Hall, D.J. & Paul, D.B. 1986. A novel method for determining the temperature dependence of shear properties of structural foams. *Cellular Polymers* 5: 91-101.
- Chambers, R.E. & Fellow, P.E. 1997. ASCE design standard for pultruded fiber-reinforced-plastic (FRP) structures. *Journal of Composites in Construction* 1(1): 26-38.
- Daniel, I.M. & Abot, J.L. 2000. Fabrication, testing and analysis of composite sandwich beams. *Composites Science and Technology*.
- Halfpenny, A. 2005. A practical introduction to fatigue. Sheffield UK: company publication for nCode International Ltd.
- Shenoi, R.A., Clark, S.D., & Allen, H.G. 1995. Fatigue behaviour of polymer composite sandwich beams. *Journal of Composite Materials* 29(18): 2423-2445.

Development and Experimental Verification of a Pedestrian Slab Bridge Using GFRP Pultrusion Profiles

Seigo Fujita, Ken-ichi Maeda & Hitoshi Nakamura (hnaka@tmu.ac.jp)

Department of Civil and Environmental Engineering, Tokyo Metropolitan University, Tokyo, Japan

Nobuhiko Kitayama

IHI Infrastructure Systems Co., Ltd., Tokyo, Japan

Tetsuya Watanabe

AGC Matex Co., Ltd, Kanagawa, Japan

ABSTRACT This paper deals with the development and the experimental verification of a newly proposed pedestrian slab bridge using GFRP pultrusion profiles bonded together by adhesive layers. The innovative feature is the appropriate adoption of semi-fixed support conditions with anchor bolts at both ends, in order to sharply reduce the bending deflection. By the drastic reduction of the bending deflection which often becomes dominant in the design of GFRP pedestrian bridges, the economic efficiency is also drastically due to be improved.

1 INTRODUCTION

FRP has drawn attention as a new construction material. Recently, in the civil engineering field, studies on pedestrian bridges developed using FRP as structure materials have become very active (Keller et al. 1999, 2002), and many actual bridges have already been constructed (JSCE 2004, 2006).

This paper deals with the development of a newly proposed pedestrian slab bridge using GFRP pultrusion profiles bonded together by adhesive layers, which can significantly improve the economic efficiency (Maeda et al. 2007). The innovative feature is the appropriate adoption of semi-fixed support conditions with anchor bolts at both ends, in order to sharply reduce the bending deflection. By the drastic reduction of the bending deflection which often becomes dominant in the design of GFRP pedestrian bridges, the economic efficiency is also drastically due to be improved.

In the study by the authors, at the beginning, material tests were done in order to measure the material properties of GFRP pultrusion profiles. Next, based on the material properties, a trial design of the new pedestrian slab bridge was carried out.

Then, three types of real size specimens were made as partial models of the trial design bridge, and the following three experiments were done using loading tests. The first experiment was for investigating the bending deformation characteristics considering the shear deformation, and for exactly calculating the applicable effective span length. The second was for confirming the reasonability and the

safety of semi-fixed support systems using anchor bolts. Moreover, the third was for examining the designing method of slab girder connections by blind rivets, which enables the long span of bridge.

In this paper, the validity of the development is verified from these research results, and the possibility of the practical application is discussed considering the construction workability and the economic efficiency.

2 MATERIAL PRPERTIES

The newly proposed pedestrian slab bridge, shown in Figure 1, has adopted the tall I-section profile called I300 and the wide sheet-like profile called F1000.

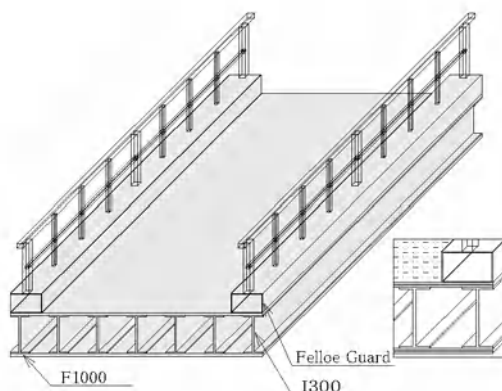


Figure 1 Overview of New pedestrian slab bridge

Sectional sizes and material arrangements of I300 and F1000 are shown in Figure 2. The reinforcement fibre

was the E-glass fibre, and the polymer matrix was the unsaturated polyester resin.

As adhesive layers what bond these GFRP pultrusion profiles, the so-called mat-in consisted of the unsaturated polyester resin and the E-glass fibre CSM (Chopped Strand Mat) was used in order to absorb the unevenness on each adhesion surface.

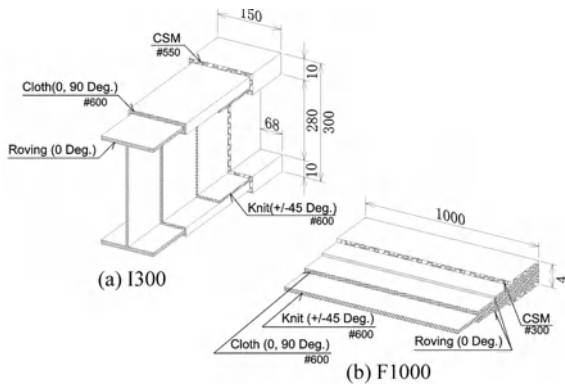


Figure 2 Arrangement of GFRP pultrusion profiles

Material tests were done based on JIS (Japanese Industrial Standard) for FRP. Typical material properties are shown in Table 1. Then, it was also proven that attention is necessary, because the tensile shear strength of the adhesive layer was quite small at 4.6 MPa by single-lap-joint tensile tests using F1000.

Table 1 Material properties

	F1000	I300		Adhesive layer (Mat-in)
		Flange	Web	
Tensile elastic modulus E_{xt} (GPa)	28.3	34.0	27.1	9.1
Compressive elastic modulus E_{xc} (GPa)	29.7	36.0	30.5	-
Tensile strength σ_{tu} (MPa)	409.0	406.8	253.0	151.9
Compressive strength σ_{ct} (MPa)	429.6	484.1	439.7	-
Density (kN/m ³)	17.99	17.55	17.55	13.01

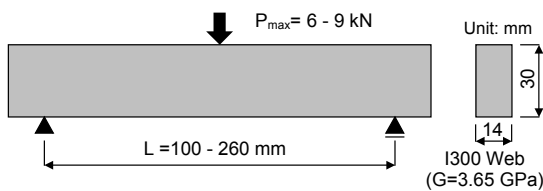


Figure 3 Measurement of elastic shear modulus

In the design of GFRP pedestrian bridges, it is well known that the influence of shear deformation on the bending deflection cannot be disregarded. Therefore, the authors applied the special test method called “the short

beam method” specified as JIS K7057 shown in Figure 3. The evaluated elastic shear modulus of the web in I300, which governs most of the shear deformation, was 3.65 GPa also shown in Figure 3.

3 TRIAL DESIGN

A trial design was carried out in making the effective span length and width to be 16 m and 1.5 m, respectively. All the components except the mortar pavement are GFRP pultrusion profiles. The general view is shown in Figure 4. The authors have also proposed semi-fixed support conditions using anchor bolts at both ends. This was because such support conditions can almost reduce the bending deflection to one fifth compared with the simple support conditions, and significantly improve the economic efficiency, since the bending deflection often becomes dominant in the design of GFRP pedestrian bridges.

The details of the cross-sectional composition and the sectional view are shown in Figures 5 and 6. The design conditions of the applied loads and the values of serviceability limit are shown in Table 2 according to the Japanese Standard (JRA 1979).

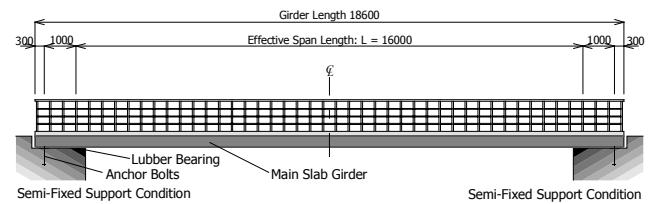


Figure 4 General view of pedestrian slab bridge

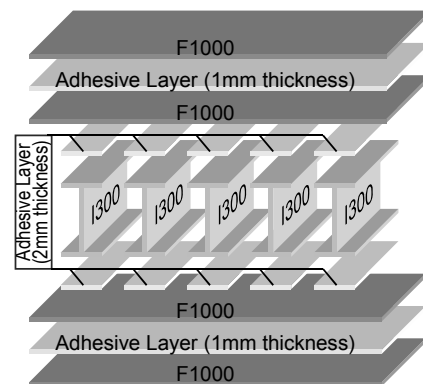


Figure 5 Details of cross-sectional composition

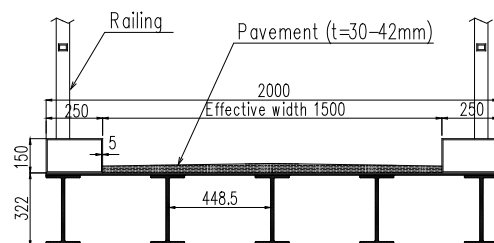


Figure 6 Sectional view of trial design bridge

Table 2 Design conditions

Dead Load	Structural cross-section (kN/m)	1.308
	Felloe guard (kN/m)	0.126
	Railing (kN/m)	0.56
	Pavement (kN/m)	1.202
Live Load (kN/m ²)		3.5
Temperature change (Degree of C)		-30 ~ +30
Deflection limitation (L: effective span length)		L/600
Limit value for structural frequencies (Hz)		1.5 ~ 2.3

To simplify the trial design, the analytical calculation was conducted using a Bernoulli-Euler beam model fixed perfectly at both ends. As the result, the maximum deflection of the mid-span was 22.74 mm, and was slightly smaller than $L / 600$ ($L = 16$ m).

The maximum absolute value of vertical bending stresses was 23.96 MPa at the fixed end, and the maximum stress was generated on the upper or lower edge of the I300 flange with the highest elastic modulus. Consequently, it was confirmed that the exceedingly sufficient safety was achievable considering the absolute value 10.50 MPa of temperature stress.

4 BENDING DEFIRMATION CHARACTERISTICS

As a partial model of the trial design bridge, a real size specimen was fabricated, and the four-points bending load test was carried out to evaluate the plane conversation based on the Bernoulli-Euler theory and the effect of shear deformation.

The side view, the sectional view and test set-up of the specimen are shown in Figures 7, 8 and 9. The applied load P was increased to 300 kN.

As compared with the test results, three kinds of analysis methods were applied as shown in Table 3.

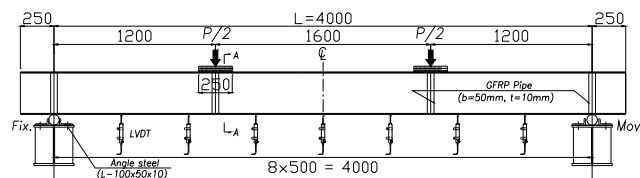


Figure 7 Side view of specimen

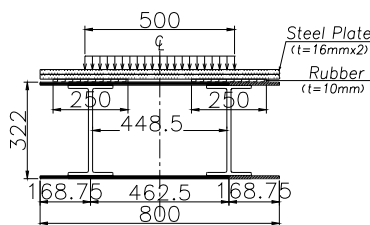


Figure 8 Sectional view of specimen



Figure 9 Test set-up of specimen

Table 3 Analysis methods

Method	Analytic theory
3D FEA	3D FE analysis using orthotropic solid elements
Timoshenko Th.	The framed structure analysis using fiberelements based on the Timoshenko beam theory
B.-E. Th.	The framed structure analysis based on the Bernoulli-Euler beam theory

From the distributions (the figures are omitted) of normal strains and stresses in noticed cross-sections, it was confirmed that the plane conversation based on the Bernoulli-Euler theory was satisfied under the action of pure bending moment. Moreover, it was proven that the analytic values agreed with the experimental values very well. Naturally, the analytic value by the Timoshenko Th. method also agreed perfectly with the B.-E. Th. method.

Figure 10 shows a comparison of the vertical deflection distribution from each analysis method under the applied load P of 300 kN. It was proven that the analytic values by the 3D FEA method agreed with the experimental values very well, and that the difference with the 3D FEA method of the Timoshenko Th. method was slightly on the safe side. However, compared with the experimental value at the mid-span, it was also proven that the analytic value was about 18% smaller when evaluated by the B-E Th. method in which the shear deformation was disregarded, unlike the Timoshenko Th. method.

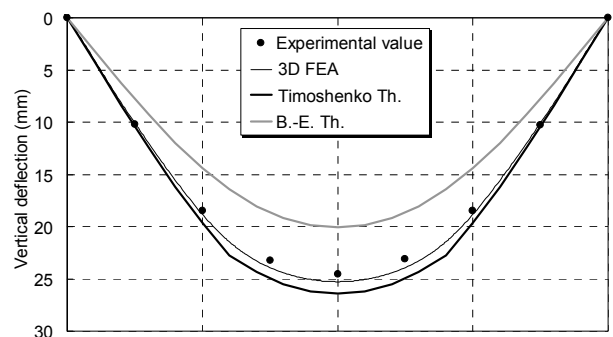


Figure 10 Vertical deflection distribution of specimen

Using the three kinds of analysis methods shown in Table 3 and models with the semi-fixed support conditions

at both ends, analytical examinations of the static bending deformation characteristics were carried out for the trial design bridge.

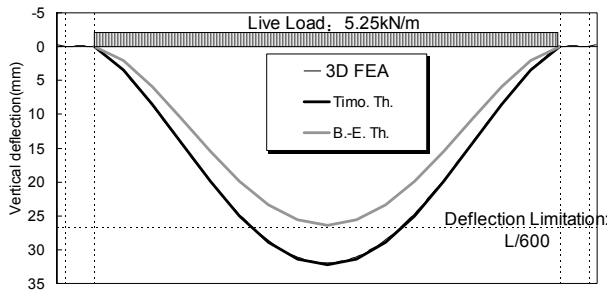


Figure 11 Vertical deflection distribution of bridge

Figure 11 shows a comparison of the vertical deflection distribution under the live load in the effective span. It was proven that the maximum deflection by the Timoshenko Th. method was about 1% larger than the one by the 3D FEA method, and about 17% larger than the one by the B.-E. Th. method.

Therefore, it was confirmed that the effect of shear deformation on the bending deflection cannot be disregarded in the calculation of the applicable span length, and that the framed structure analysis based on the Timoshenko beam theory can be used to evaluate at sufficiently accurate level to be safe. Consequently, the applicable effective span lengths were exactly calculated based on the Timoshenko Th. Method. Table 4 shows the applicable effective span lengths for the deflection limitation.

Table 4 Applicable effective span lengths of bridge

Deflection limitation	Applicable effective span length
L/600*	14.956 m
L/450*	16.627 m
L/300*	19.321 m

* Deflection Limitation L/600 (Japanese Standard)
L/450, L/300 (EUROCOMP)

5 SAFETY OF SEMI-FIXED SUPPORT SYSTEM

To examine the safety of the semi-fixed support system, a peculiar loading test was conducted using a partial model of the trial design bridge. The side view, the sectional view and test set-up of the specimen are shown in Figures 12, 13 and 14.

The maximum load P to the failure was 207.1 kN, and the safety factor against the design load was about 7.4. Therefore, it was proved that the semi-fixed support systems can ensure the very sufficient safety, and that the partial strengthening for shear by blind rivets can effectively increase the safety.

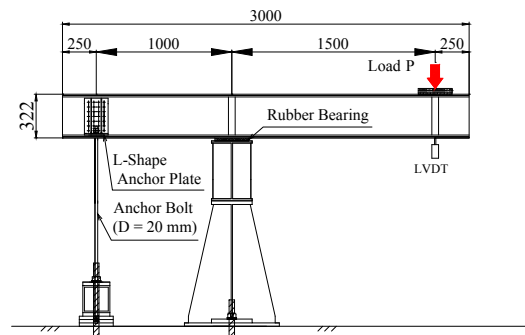


Figure 12 Side view of specimen

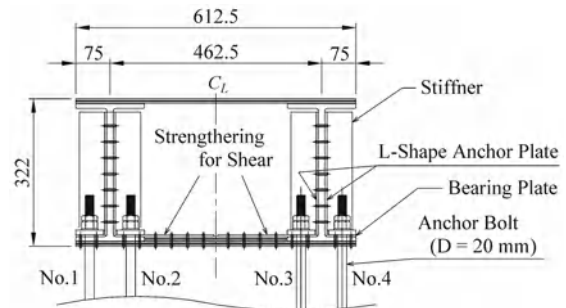


Figure 13 Sectional view of specimen

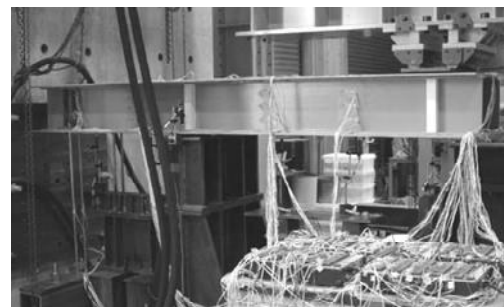


Figure 14 Test set-up of specimen

6 SAFETY OF SLAB GIRDER CONNECTION

To examine the safety of the slab girder connections by blind rivets, the four-points bending load test was conducted using a partial model of the trial design bridge. The side view and the enlarged view of the specimen are shown in Figures 15 and 16.

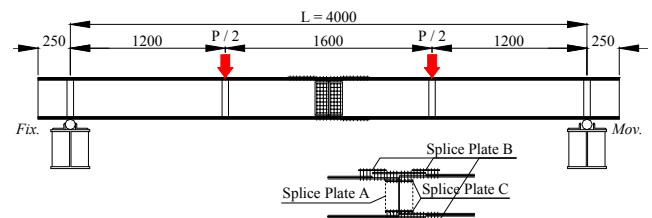


Figure 15 Side view of specimen

As the test result, the local failure in the connection was generated from the time in which the load P exceeded 500 kN. Afterwards, a cross-section near the connection

failed perfectly, when the load P reached 727.8 kN. The safety factor against the design load became about 7.7 and very high value even in the case with former. Therefore, it was proven that the slab girder connections for the long span can ensure the exceedingly high safety.

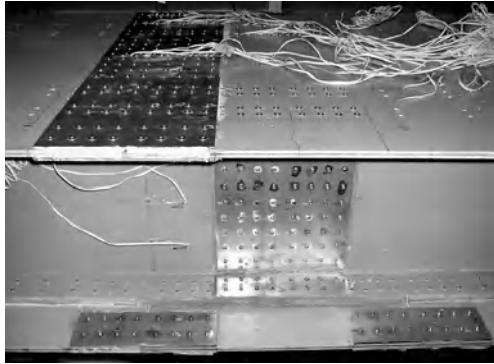


Figure 16 Enlarged view of specimen

7 CONCLUSION

From all the research results, the possibility of the practical application of the newly proposed GFRP pedestrian slab bridge was proven to be very high.

Also, it was confirmed that the effect of shear deformation on the bending deflection cannot be disregarded

in the calculation of the applicable effective span length, and that the framed structure analysis could evaluate at a sufficient accuracy to be safe.

Moreover, it was proven that the semi-fixed support systems could ensure the very sufficient safety, and significantly improve the economic efficiency. Finally, it was also proven that the slab girder connections for the long span could ensure the exceedingly high safety.

REFERENCES

- T. Keller et al. 1999. Advanced materials, *Structural Engineering International*, IABSE, Vol.9, No.4, 250-301.
- T. Keller et al. 2002. Advanced materials, *Structural Engineering International*, IABSE, Vol.12, No.2, 66-116.
- JSCE 2004 (in Japanese), 2006 (in Chinese). K. Maeda (ed.), FRP bridges - Technologies and their future, *Structural Engineering Series 14*, Japan Society of Civil Engineers, Tokyo: Maruzen.
- K. Maeda et al. 2007. Development of a pedestrian slab bridge using GFRP pultrusion profiles. In S.T. Smith (ed.), *Proceedings of the Asia-Pacific Conference on FRP in Structures (APFIS 2007)*, IIFC, Vol. II, 1093-1099, Hong Kong, 12-14 December 2007.
- JRA 1979 (in Japanese). Japanese standard for pedestrian bridges and underpasses, Japan Road Association, Tokyo: Maruzen.

Study on Dynamic Characteristics of Light-Weight FRP Footbridge

Feifei Jin (jff0505@163.com), Peng Feng & Lieping Ye

Department of Civil Engineering, Tsinghua University, Beijing, China

ABSTRACT Comparing to footbridges made of traditional materials, FRP (fiber reinforced polymer) footbridges have many advantages, such as rapid installation, corrosion resistance, waterproof property, pleased appearance, lasting color, overloading resistance, good fatigue performance, good seismic performance, and potential capacity to build greater span. A tentative FRP cable-stayed bridge is investigated, in which the design method and the design indices for FRP footbridges are studied. It is found that the vibration comfort of FRP footbridge are the main controlling factors for structural design. The indices for the pedestrian vibration comfort requirements are also summarized, and the frequency limit, acceleration limit and excitation load are analyzed. Considering the finite element analysis and the field measurement results, it is concluded that the acceleration should be the controlling indicator, and a simplified excitation load model and the calculation method for acceleration are proposed. For the cable-stayed FRP footbridge, the results of finite element analysis and field measurement show that it can't meet the designing requirements. Hence, the improvement of overlaying a concrete layer is proposed. After it, the behaviors of the FRP footbridge meet the requirements. All these works make out the design approach and the design indices for FRP footbridges, which are proved practical and reasonable through the actual FRP footbridge.

1 INTRODUCTION

In recent years, FRP (fiber reinforced polymer) is becoming a new engineering material which is successfully used in civil engineering structures. With its light-weight, high strength capacity, corrosion resistance and easy construction modeling, FRP become an important complement to the traditional structural materials such as concrete, steel, etc (Ye, Lieping et al. 1996). It has been an important developing direction that using FRP into various types of engineering structures. Comparing to footbridges made of traditional materials, FRP bridges have many advantages, such as rapid installation, corrosion resistance, waterproof property, pleased appearance, lasting color, overloading resistance, good fatigue performance, good seismic performance, and potential capacity to build greater span.

For the early FRP bridges are mainly made by hand lay-up, the stability and reliability of FRP quality are not good with low fiber content, also the mechanical properties dispersion is very large. In recent years, as the pultrusion, winding and RTM technics upgrading, combined with the development of fiber and resin materials, more stable mechanical properties and performance of large-size, high performance FRP components can be produced. These high-performance FRP bridge structures and components with the industrialization and standardization characteristics can meet the needs of large amount of engineering construction.

For the FRP's capacity of strength is high enough, FRP bridges' bearing capacity is also relatively high, so the bearing capacity is usually not the main control parameter, and as in the actual construction, the footbridge can be inverted arch, which can balance the deformation, the pedestrian comfort are the major control parameters. In 2008, China built an industrial FRP experimental footbridge using pultruded profiles. With this footbridge as the background, high-performance of FRP footbridge structural performance and the key indicators were studied in this paper.

2 PROJECT OVERVIEW

This cable-stayed FRP experimental footbridge has 4.0m width, 24m main span length, and 5.5m headroom, it's 39m full long, as shown in Figure 1. The GFRP (glass fiber reinforced polymer) girder section is 0.5m high made of pultruded profiles paralleling one by one, as shown in Figure 2. The cable is made of GFRP pultruded rod with 32mm diameter. The inclined pylon is made of steel with the bottom rigid connection to the ground. The side columns are all GFRP tube concrete columns with 600mm diameter. Live loads for design is 5kN/m².

The Pultruded GFRP for the cable-stayed footbridge is orthogonal anisotropy with 45GPa longitudinal elastic modulus, and 9GPa transverse elastic modulus. The ultimate tensile strength in longitudinal direction is 500MPa, and the density of FRP is 2000kg/m³.

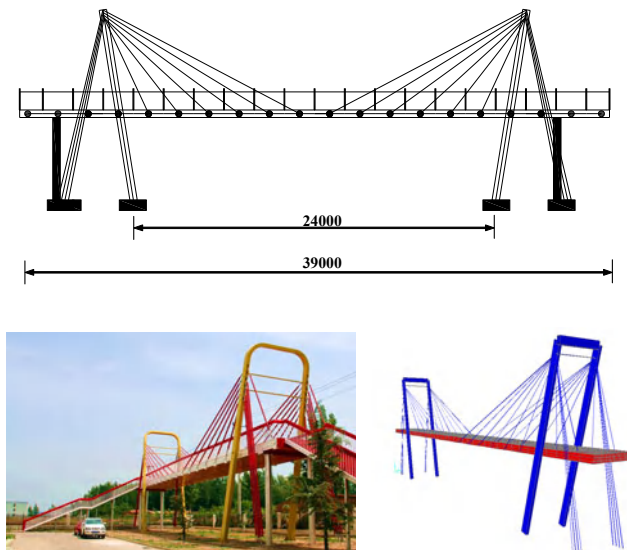


Figure 1 The FRP footbridge and FEA modeling

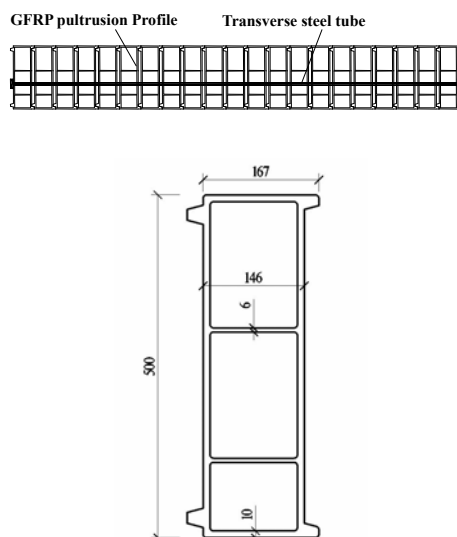


Figure 2 The cross sectional drawing of FRP footbridge girder

The FEA modeling is constructed using SAP2000 in actual size, as shown in Figure 1, it's been calculated under the maximum load combination and the greatest longitudinal stress of the structure were all less than 60MPa, which is much smaller than its ultimate strength, so the bearing capacity of FRP footbridge is enough safe.

Through the design and calculation progress, as mentioned above, the bearing capacity of FRP footbridge is not usually a controlling design parameter, while the deflection and vibration comfort are the main controlling design factors, but in the actual construction, the footbridge deformation can be balanced through inverted arch. Therefore, this paper below will mainly discuss its vibration comfort's design and controlling methods.

3 VIBRATION INDICATOR

3.1 Specification Requirement

In order to ensure the pedestrians' vibration comfort and

prevent large deformation caused by resonance, the vibration characteristics of the footbridge is required to meet some limits, mostly the vibration frequency of footbridge is required to avoid pedestrians step frequency to avoid resonance. Therefore, the specification of China require that the vertical vibration frequency as the main control target. In fact, the vibration acceleration is the direct mechanical characteristic that pedestrians can feel, which affect the pedestrians' comfort, so some specifications use the acceleration as the direct controlling indicator, which are showed as below:

(1) China(Industry Standards of China. 1996): the vertical vibration frequency should be designed over 3Hz;

(2) Europe(European Committee for Standardization. 2002): When the vertical vibration frequency is less than 5.0 Hz, the horizontal or twisting vibration frequency is less than 2.5 Hz, the vibration of the bridge should be checked, acceptable maximum vertical acceleration is 0.7m/s^2 , horizontal 0.2m/s^2 ;

(3) USA (AASHTO. 2004): to avoid the vertical vibration frequency below 3Hz;

(4) Switzerland (A. Zhou et al. 2005): to avoid the first-order frequency falling between 1.6 Hz and 2.4 Hz, while the second-order between 3.5 Hz and 4.5 Hz;

(5) Japan (Fujino Y et al. 2006): to avoid the first-order vertical frequency falling between 1.5Hz and 2.3Hz;

(6) United Kingdom (British Standards Association. 1978.): to avoid the vertical vibration frequency less than 5 Hz, when the horizontal vibration frequency is less than 1.5 Hz, detailed dynamic characteristics should be analyzed ;

(7) Canada (Standards Council of Canada. 2000.): to avoid the vertical vibration frequency below 4Hz;

(8) Russia (Industry Standards of Russia. 1984): the first two order vibration periods should not fall in the scope as follows: 0.45-0.60s in the vertical direction; 0.9-1.2s in the horizontal direction.

It can be seen that the requirement for the traditional footbridge is not yet unified. The vibration requirements differs from direction and limit value, and frequency and acceleration are the main indicators.

The crowd is the most important source of vibration of footbridge. The first-order vibration mode is usually vertical vibration, the horizontal vibration and reverse vibration is usually appeared in high order. From the basic principles of structural dynamics, the basic vibration equation can be obtained:

$$[M]\{\ddot{u}(t)\} + [C]\{\dot{u}(t)\} + [K]\{u(t)\} = \{F(t)\} \quad (1)$$

Where: $[M]$ for the mass matrix; $[C]$ for the damping matrix; $[K]$ for the stiffness matrix; $\{F(t)\}$ for outside motivation; $\{\ddot{u}(t)\}$ for structural acceleration; $\{\dot{u}(t)\}$ for structural velocity; $\{u(t)\}$ for structure displacement.

According to the basic dynamic principles, footbridge reaction under the foot load is depended on the incentives,

structure stiffness, structure mass, and the structure damping. Only controlling the self-vibration frequency of the structure is not reasonable, considering the light quality of FRP footbridge and the low damping ratio, even if the requirements of 3Hz frequency is meet, the comfort of pedestrians may still not meet the requirements.

3.2 Acceleration and Excitation Load

In recent years, most researchers have generally reached the agreement that pedestrians' vibration comfort is closely relative with the vibration acceleration of the footbridge. There are two main kinds of acceleration that describe the vibration, one is maximum acceleration(a_{\max}), the other is root mean square acceleration(a_{rms}).

a_{rms} is defined as:

$$a_{rms} = \sqrt{\frac{1}{T} \int_0^T a_w^2(t) dt} \quad (2)$$

Where: T for the vibration time (s); $a_w(t)$ for the acceleration time history.

For the acceleration is different under different excitation load, the input excitation load of the footbridge must be determined before using the acceleration as the vibration characteristics.

The pedestrian loads have been study in the early times. Some researchers have found that the frequency of pedestrian excitation load is 2.0Hz (Y. Matsumoto et al. 1972, S.C. Kerr et al. 2001), and some analyze the force time history of one step(T.P. Andriacchi et al. 1977) (Figure 3) and jumping.

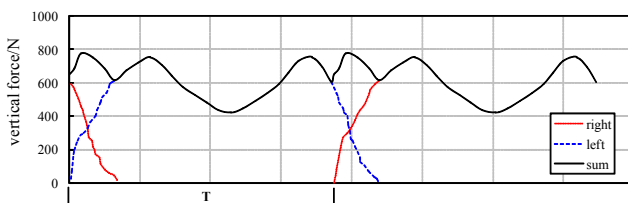


Figure 3 Periodic walking time history in vertical direction

For the pedestrian excitation load is very complicated and influenced by many factors, it is difficult to determine a relatively simple expression, most researchers use the time-domain force model to give the expression which is made of a fourier series, but it's not very convenient used in engineering design. Some specifications also give the excitation load expression to be applied in design, such as the British bridge code BS 5400 giving the excitation load as below:

$$F(t) = \begin{cases} 180 \sin(2\pi f_0 t) & f_0 < 4\text{Hz} \\ [1 - 0.3(f_0 - 4)] \times 180 \sin(2\pi f_0 t) & 4\text{Hz} \leq f_0 \leq 5\text{Hz} \end{cases} \quad (3)$$

This excitation load will move with the speed $0.9f_0$ m/s along the bridge to stimulate one person walking on a bridge.

For calculating the acceleration under those excitation load is not convenient, in order to study the dynamic response of FRP footbridge under a forced vibration, a crouching excitation load is proposed. It is used to stimulate a single person crouching up and down in the middle of the footbridge, and the expression is given as below:

$$F(t) = G[1 + \sin(2\pi ft)] \quad (4)$$

Where: $G = 650\text{N}$, f is the person's crouching frequency, which can be defined as natural vibration frequency of footbridge f_0 .

Crouching excitation load can make the structure reach the resonance state, the dynamic response will quickly reaches a steady state for the structure damping, then the a_{\max} is obtained. This a_{\max} can be used to evaluate the vibration comfort. This load modeling took both the vibration characteristics of structure and human load features into account, so it's a standardized and practical engineering method.

3.3 Test Measurement and calculation of the FRP experimental foot bridge

After the completion of the FRP footbridge, the dynamic characteristics was measured. The vertical natural vibration frequency is 3.13Hz, compared with the calculated result 3.17Hz, the error is only 1.44%. Although the vertical natural frequency is more than 3Hz, while walking, crouching and running, the vibration are all obvious.

According to the finite element analysis, this FRP cable-stayed footbridge's vibration frequency is 3.17Hz. The crouching excitation load is expressed as below:

$$F(t) = 650[1 + \sin(2 \times 3.17\pi t)] \quad (5)$$

Applying this crouching excitation load in the finite element modeling, the obtained a_{\max} is 0.65m/s^2 , which mean that the footbridge will vibrate obviously if one person is crouching in the middle of the footbridge.

4 THE VIBRATION CHARACTERISTICS IMPROVEMENT OF FRP EXPERIMENTAL FOOTBRIDGE

As mentioned above, the vertical vibration frequency of FRP footbridge is 3.13Hz, meet regulatory requirements, but in fact vibration is still obvious during used state. Therefore, in this paper, it's suggested that pave a layer of 60mm concrete surface on the deck to improve the mechanical properties of the structure.

After paving a layer of concrete, the vibration frequency is reduced to 2.72Hz. Then the crouching excitation load can be expressed as below:

$$F(t) = 650[1 + \sin(2 \times 2.72\pi t)] \quad (6)$$

After the same way to calculation, the obtained a_{\max} is reduced to 0.378m/s^2 .

The acceleration time history under the two different calculation modeling are both shown in Figure 4.

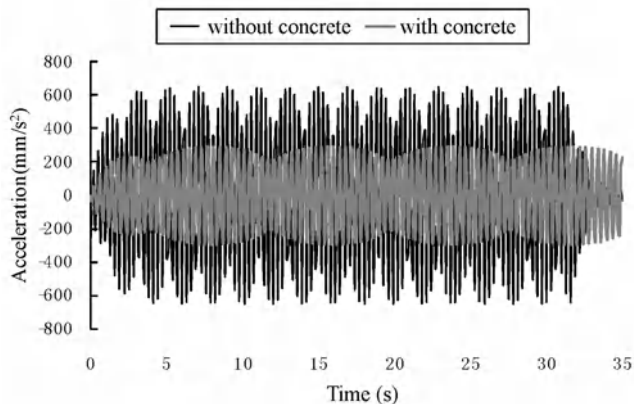


Figure 4 Acceleration time history

The results showed that after paving a layer of concrete, the a_{\max} decreased 55.4% under crouching excitation load, which is consistent with the people's feeling on the bridge. Hence, it can be concluded that for light-weight FRP footbridge, the frequency isn't the only evaluation indicator controlling the vibration comfort, the acceleration should also be considered. The proposed crouching excitation load can reflect the FRP footbridge vibration comfort reasonably.

5 CONCLUSIONS

The following conclusions are obtained in this paper.

1. The dynamic characteristics of lightweight FRP footbridge is very important in design, frequency and deflection, these two indicators are both relative to the lightweight FRP footbridge's length.

2. The dynamic characteristics include two main indicators: frequency and acceleration. Through test measurement it can also be found that the acceleration is more important than frequency to evaluate the vibration comfort.

3. Crouching excitation load is proposed to calculate the vibration acceleration. This maximum acceleration can be used to evaluate the dynamic characteristics of light bridges, which are proved practical and reasonable through the actual FRP footbridge.

4. Suggestion is proposed to the FRP cable-stayed footbridge for vibration characteristics improvement: a layer of concrete is paved on to the deck. Although the frequency decrease, but the acceleration response is reduced obviously, it's an effective method.

ACKNOWLEDGMENTS

The authors gratefully acknowledge the financial supports from the International Cooperation Project (2010DFR50400) of China MOST.

REFERENCES

- Ye Lieping and Feng, Peng. 2006. Applications and Development of Fiber-Reinforced Polymer in Engineering Structures. *China Civil Engineering Journal*, 39 (3)24-36.
- Industry Standards of China, 1996. Urban footbridge and tunnel specification.
- European Committee for Standardization. 2002. Basis of Structural Design. EN 1990: 2002
- American Association of State Highway and Transportation Officials (AASHTO). 2004. LRFD bridge design specifications.
- Zhou, Y. Bai and T. Keller. 2005. Dynamic characteristics of bridge superstructure with FRP composite structural Elements. *Third International Conference Composites in Construction*.
- Fujino Y, Pacheco B, Nakamura S, et al. 2006. Synchronization of human walking observed during lateral vibration of a congested pedestrian bridge. *Earthquake Engineering & Structural Dynamics*, 22(9): 741-758
- British Standards Association. 1978. BS5400.
- Standards Council of Canada. 2000. National Standard of Canada. Canadian Highway Bridge Design Code. CAN/CSA-S6-00.
- Industry Standards of Russia. 1984. Roads, railways, urban roads and bridges specification.
- Y. Matsumoto, S. Sato, T. Nishioka, H. Shiojiri. 1972. A study on design of pedestrian over-bridges. *Transactions of JSCE*, 1972(4): 50-51.
- S.C. Kerr, N.W.M. Bishop. 2001. Human induced loading on flexible staircases. *Engineering Structures*, 23: 37-45.
- T.P. Andriacchi, J.A. Ogle, J.O. Galante. 1977. Walking speed as a basis for normal and abnormal gait measurements. *Journal of Biomechanics*, 1977(10): 261-268.

FRP Hybrid Structures and Concrete-Filled FRP Tubes

Honeycomb Fiber-Reinforced Polymer Sandwich Panels for Fish Culture Tanks

Julio F. Davalos (julio.davalos@mail.wvu.edu) & Avinash Vantaram & An Chen (an.chen@mail.wvu.edu) & Indrajit Ray
Department of Civil & Environmental Engineering, West Virginia University, Morgantown, WV 26506, USA

Jerry D. Plunkett
Kansas Structural Composites Inc. (KSCI), Russell, Kansas 67665, USA

ABSTRACT The U.S. aquaculture gross revenues have grown from \$350 million in 1985 to nearly \$900 million in 1996, and while large overseas markets are available for native products, the national aquaculture production was only about 3 percent of world production value. It is argued that the utilization of impaired mine waters abundant in West Virginia (WV) and the other mid-Appalachian states for fish culture can substantially increase aquaculture economic development. Approximately 878.12 million L of water per day are discharged in WV from both active and abandoned mines, and if only 30% of these water resources were used for aquaculture, the expansion of this industry in WV would be significant. The primary limitation to the effective utilization of discharged waters is the lack of suitable fish culture tanks that can be easily installed in rugged terrains surrounding mine water treatment plants. Such topographical constraints do not easily permit the construction of cast-in-place concrete tanks, and therefore, FRP sandwich materials offer an economical alternative for production of modular, transportable, light, and durable fish culture raceway systems. This study is concerned with the development and evaluation of prototype fish culture tanks using a honeycomb FRP (HFRP) sandwich panel with sinusoidal core geometry, which is produced by KSCI by the contact-molding process. Based on defined functional requirements, a raceway system consisting of four staggered tanks is designed, and each tank is 1.83×9.14×0.91m, with a middle partition along the 9.14m length to carry out parallel aquaculture studies. Representative panel samples of the side and bottom walls as well as the side-to-bottom panel connections are tested within the linear range and eventually to failure. The linear response of the samples is analyzed by the finite element method.

1 SIGNIFICANCE

Aquaculture, the science of growing aquatic plants and animals, continues to develop worldwide at a rapid pace. In West Virginia (WV), USA, coldwater species like rainbow trout dominate commercial production, with a potential estimated output of 4.0 to 2.72 million kg annually (Jenkins et al. 1995). Two focus areas for aquaculture economic development have been identified: (1) production of fish utilizing water discharged from abandoned and active coalmines; and (2) production of farm-raised fish for recreational and tourism purposes. Most commercial trout producers utilize raceways as a culture unit. In these systems water flows through a series of long rectangular tanks usually made of concrete. Fish in these raceways swim against the current much as they would in a stream, and are fed complete rations in pellet form.

Of major significance is the effective treatment and subsequent use of impaired mine waters for fish production in WV, where it is estimated that 878.12 million L of

water per day are discharged from both active and abandoned mines, and if only 30% of these water resources were used for aquaculture, the expansion of this industry in WV is expected to increase dramatically. However, the primary limitation for the effective utilization of discharged waters is the lack of suitable fish culture tanks that can be easily installed in rugged terrains surrounding mine water treatment plants. Such topographical constraints do not easily permit the construction of cast-in-place concrete tanks, and therefore, advanced composite materials offer an economical alternative for production of modular, transportable, light, and durable fish culture raceway systems.

Our overall research work on fiber-reinforced polymers (FRP) is directed to the worldwide interest in development and application of new materials and methods for rehabilitation and new construction of industrial and public works, more commonly termed civil infrastructure.

We present in this paper the development of a fish-culture raceway system (Figure 1) manufactured from Honeycomb Fiber-Reinforced Polymer (HFRP)

panels, 0.05 to 0.1 meters thick, using E-glass fibers and a polymer resin (Davalos et al. 2001). The core consists of sinusoidal corrugations and vertical components sandwiched between the face sheets (see Figure 2), with smooth finished exposed faces that will permit easy cleaning and virtually eliminate algae growth. A dark green pigment is selected and added to the resin to achieve a permanent color that will not require painting over the service-life of the structure. Also, the resin is formulated to have a UV resistance for outdoor applications of over 30 years. The resin used can resist nearly any chemical exposure and wet-dry cyclic environments at low and high temperatures, making the honeycomb panels highly durable. The raceway system consists of four 9.14m by 1.83m tanks staggered vertically to permit gravity flow of water. Each of the 1.83-meter wide tanks has a longitudinal partition panel to allow for parallel fish culture studies (Figure 1). The weight of the panels are approximately 5.97 kg/m^2 to 8.95 kg/m^2 , which is about 12 times less than the weight of a comparable concrete material. Thus, the HFRP tanks can be easily transported and installed.

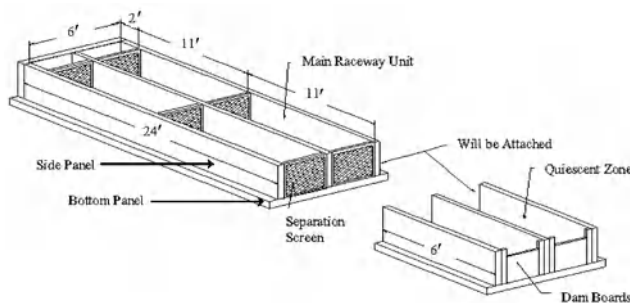


Figure 1 3-D view of the fish tank (1ft = 0.3m)

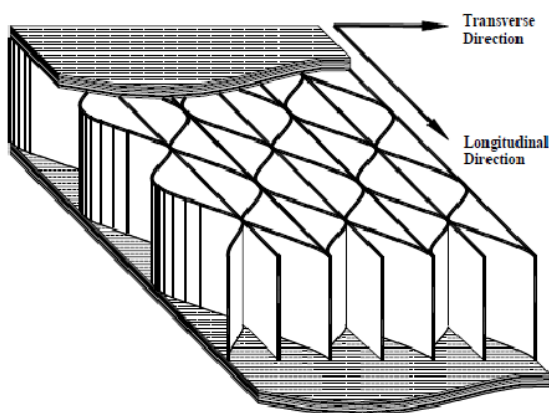


Figure 2 Core geometry of HFRP panel

2 OBJECTIVE AND SCOPE

This study is concerned with the design, manufacturing, and experimental and numerical evaluations of HFRP sandwich panels and panel-to-panel connections for applications of fish culture tanks to be installed as raceway systems in WV for fish growth utilizing both

treated coalmine waters and fresh spring waters. The component panels are tested as beams and their measured displacements and strains are correlated with finite element analyses with ABAQUS (2009). Similarly, two designs of side-to-bottom panel connections are evaluated experimentally and modeled as cantilever beams to study their relative rotational stiffness of the connected joints. General details of the design of the fish tank are presented, and an overview of three projects is given.

3 DESIGN OF HFRP RACEWAY

The design of the HFRP raceway system is based on requirements established by future users of the system, who defined the height, length and width of the tanks. The strength and stiffness of the HFRP structural components was then determined jointly by the research team and the manufacturer.

The requirements of the tanks were partially based on current concrete raceway systems, but also on specific needs of the future users. A schematic view of the tank is shown in Figure 1. The tank must have two parallel channels of constant cross-section, allowing for simultaneous comparative aquaculture studies. The channels are 0.91m wide by 1.07m high, to allow for a depth of water of 0.91m. The tank is divided into two separate components. There is a main raceway unit which is 7.32m long, and is used for raising fish. There can be separation screens placed along the tank to allow for the possibility of raising different species or sizes of fish in the same channel. The second part of the tank is a quiescent zone. The fish will be restricted from this area, which will be used for collecting and disposing of fish waste and debris, using a drain located on the bottom panel of the quiescent zone. Dam boards are placed at the end to control the elevation of the water in the tank. The two sections of the tank are connected using a bolted structural fastening system.

In order to establish appropriate stiffness and strength properties for the component panels, several functionality requirements had to be considered. The tanks should not have any obstructions on the outside that would impede easy access. Also, the interior cross-section of the channels must have normal corners. Thus, the connection of the bottom-to-side panels must be stiff enough to meet deflection and strength criteria, while also satisfying the prescribed requirements. There are two proposed connection details, which are discussed in a following section.

After the initial design of the raceway tank, the required structural capacity of the panels could be determined. Based on past experience, the research team and the manufacturer determined an appropriate size and lay-up. The loads were based on 0.91m of water pressure and other loads possibly from people leaning against the side panels.

The deflection limit is based on the separation screen openings, which was determined to be 9.53×10^{-3} m.

A 3-D view of the sandwich panel geometry is given in Figure 2, showing the top and bottom face sheets and the core consisting of sinusoidal and straight components. The constituent materials are chopped E-glass fibers and polyester resin. The side panels have a thickness of 0.61m with the top and bottom face sheets consisting of three layers of chopped strand mat (ChSM), each being 9.1×10^{-3} m thick. The core is produced from two layers of ChSM. The bottom panels have the same face sheet and core thickness and same materials, but the panel thickness is 1.22m.

4 EVALUATION OF COMPONENTS

The structural components of the HFRP raceway system consist of the side and bottom panels and their connection. The sinusoidal core orientation is in the “longitudinal direction” (see Figure 2) along the length of the tank. Beam samples representing these panels are experimentally tested to evaluate deflections and strains and to correlate results with finite element analyses. Also, two proposed side-to-bottom panel connections are tested and analyzed by the finite element method.

4.1 Experimental Testing of Beam Samples

The beam samples used in the experimental protocol

consist of five bottom panel samples and five side panel samples. For both panels, there are two longitudinal (sinusoidal wave along the length) and two transverse (sinusoidal wave along the width) samples, each 0.2m wide by 1.52m long. In addition, there are two 0.31m wide by about 2.13m long panels, one with transverse core orientation for the side panel and one with longitudinal core orientation for the bottom panel.

The beams are tested in a 3-point loading configuration, and the span-length depends on the overall length of the sample. Strains are measured on the top and bottom face sheets of the sample. On the top, there are three gages spaced equally across the width at a distance of 0.15m from the midspan. The bottom face sheet is instrumented with one strain gage at the midspan and mid-width of the beam. Deflections are measured at the midspan and at third points with respect to the span-length. The beams are loaded to approximately 136.2kg, staying well within their linear range.

Data is recorded by a computerized data acquisition system and later reduced using a spreadsheet. The data presented in Table 1 are obtained from the linear regression recorded for each sensor for a maximum load of 45.4kg. The reported deflection values for L/3 are the averages of the symmetric values at L/3 and 2L/3. The maximum and minimum strains, as well as the average of the three values, are shown for the top face sheet.

Table 1 Experimental results for beam samples

Panel type	Core orientation	Width, meters	Span, meters	Sample number	Deflection, 10^{-4} m		Strain, microstrain			
					@ L/3	@ L/2	Bottom	Top		
								Max.	Min.	Avg.
Bottom	Longitudinal	0.31	1.82	1	5.436	6.248	106	-67	-110	-90
				2	2.997	3.505	119	-102	-107	-105
		0.2	1.22	1	3.048	3.505	115	-98	-105	-101
	Transverse	0.2	1.22	1	3.658	4.166	128	-102	-123	-112
				2	5.41*	6.096*	122	-111	-122	-116
				1	13.03	14.834	–	-226	-249	-238
Side	Longitudinal	0.2	1.22	2	13.03	15.189	255	-215	-257	-236
				1	18.009	21.996	268	-228	-269	-249
				0.31	1.67	1	13.487	16.129	296	-239
	Transverse	0.2	1.22	1	13.487	16.129	296	-239	-254	-244
				2	13.564	16.662	326	-231	-286	-256
				1	13.564	16.662	326	-231	-286	-256

* These higher values may be due to experimental errors

4.2 Finite Element Analysis of Beam Samples

Finite element beam models are created to correlate predictions with the experimental results. These models are intended to simulate the actual geometry of the beam samples. The beam models are created using 3- and 4-node layered shell element with ABAQUS (2009). The face sheets are composed of three layers of quasi-isotropic chopped strand mat and the core walls are composed

of two layers of the same material. Using the pre- and post-processor FEMAP (2009) program, the models are generated using a copy-and-paste method, in which a 0.1m by 0.1m “cell” of the specific panel is defined and copied to produce a beam of any length, width and core orientation. Symmetry is exploited to decrease the computational effort, by defining a shear-release boundary condition at the midspan of the models, and the load is applied along the width as a line load. Further details on

finite element modeling are discussed in Davalos et al. (2001), Robinson et al. (2001) and Robinson et al. (2002). Table 2 shows the results for 45.4kg of load. The strain data is found by examining the element average values across the width at the desired location with

respect to the midspan. Because of the coarseness of the mesh, strain data varies somewhat. Thus, the maximum and minimum strain values are reported, along with the average of the two. The strain results are given in microstrain, while deflections are given in meters.

Table 2 Finite element results

Panel type	Core orientation	Width, meters	Span, meters	Deflection, 10^{-4} m		Strain, microstrain					
				@ L/3	@ L/2	Bottom			Top		
						Max.	Min.	Avg.	Max.	Min.	Avg.
Bottom	Longitudinal	0.31	1.82	4.978	5.893	103	73	88	-63	-91	-77
		0.2	1.22	2.286	2.743	96	67	82	-57	-81	-69
	Transverse	0.2	1.22	2.79	3.404	128	109	119	-87	-103	-95
Side	Longitudinal	0.2	1.22	10.363	12.192	227	172	200	-148	-191	-170
		0.31	1.67	17.983	21.844	217	197	207	-195	-212	-204
	Transverse	0.2	1.22	11.43	13.538	278	222	250	-210	-235	-222

4.3 Comparison of Results for Beam Samples

A comparison of experimental and finite element analysis results shows good correlations in strains and displacements. The finite element models show stiffer behaviors than in actuality, predicting lower strains and deflections than recorded in the experimental tests. However, for the cases of longer span-lengths with samples of 0.31m width, particularly the side panels with transverse core orientation, the predicted deflections are much closer to the experimental values. An observation of the results indicate that both deflections and strains can be predicted by the finite element method with reasonable confidence, and based on these favorable results, the side-to-bottom panel connection is studied in the next section.

4.4 Experimental Testing of the Connection

Two different designs for the connection of the side panel to the bottom panel were proposed, and samples for each connection type were produced and tested. The goal of the experimental testing is to evaluate the two connections and suggest the best design for production of the tank. The unstiffened connection, shown in Figure 3, is designed for the side panel to be embedded into the bottom panel a distance of 0.03m. The panels are then joined with a polyester resin. The bottom panel extends 0.1m beyond the outside face of the side panel to allow for a better distribution of stresses at the corner. The stiffened connection, shown in Figure 4, is similar to the previous connection, with the exception of a triangular stiffener placed on the outside edge of the embedded panels. The stiffener, which extends 0.1m up the side wall and 0.1m out to the edge of the bottom panel, is produced by a core section of triangular cross-section covered by a face sheet. The stiffener is co-cured to the side and bottom panels. In both cases, the inside corner remains normal

as required by the design. Each of the two connection samples is 0.31m wide. The bottom panel extends 0.46m from the interior edge of the side panel, with the longitudinal core orientation along its length. The side panel extends 1.1m from the top of the bottom panels, with the longitudinal core orientation along its length.



Figure 3 Unstiffened connection design

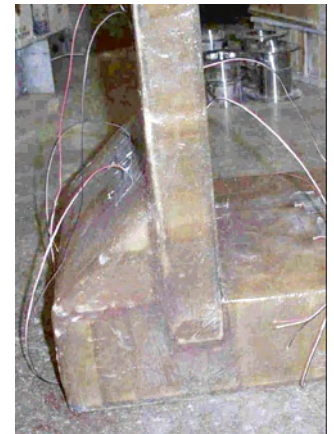


Figure 4 Stiffened connection design

The experimental testing of the connection is performed by mounting the bottom panel of the sample to a fixed steel vertical column. A tip load is applied to the side panel at a distance of 0.91m from the interior face of the bottom panel, as shown in Figure 5, and deflections are recorded at distances of 0.61 and 0.91m. Strains are measured at 11 locations on each of the samples, with 5 gages bonded to the bottom panel (#1, #2, #3, #6 and #7), which is fixed to the steel column, and 6 gages bonded to the side panel (#4, #5, #8, #9, #10 and #11). Each gage is bonded in the same respective location for each sample to allow for easy comparisons. The

exception being gages #8 and #9 for the stiffened sample, which are offset a distance of 0.05m because of the location of the stiffener. The data is reduced using

the same method as for the beam samples, and the strains and deflections for 45.4kg of loading are shown in Tables 3 and 4, respectively.

Table 3 Strain comparisons

Connection sample	Strain locations, microstrain										
	#1	#2	#3	#4 ^a	#5 ^a	#6	#7	#8 ^a	#9 ^a	#10 ^a	#11 ^a
Unstiffened	83	180	165	416	388	-15	18	-406	-417	–	-51
Stiffened	42	–	91	428	433	-196	-173	-366	-392	-222	-61
FE model ^b	–	–	–	394	394	–	–	-407 ^c , -366 ^d	-407 ^c , -366 ^d	-219	-73

a Gages on the side panel, which is the one loaded.

b Values obtained for clamped boundary condition (closer to stiffened connection).

c Value corresponds to location for unstiffened sample.

d Value corresponds to location for stiffened sample.

Table 4 Deflection comparisons

Connection sample	Deflection location, 10 ⁻⁴ meters	
	@ 0.61m	@ 0.91m
Unstiffened	44.882	78.886
Stiffened	31.064	54.204
FE Model	27.686	53.34

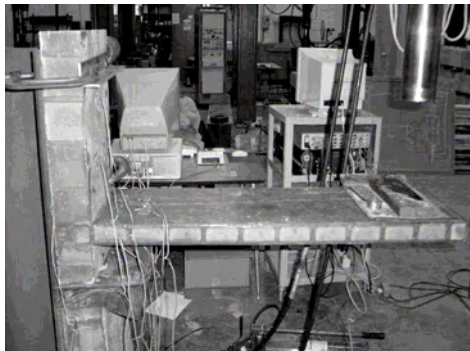


Figure 5 Experimental setup for connection

4.5 Finite Element Modeling of the Connection

A finite element model of the side panel was conceived as a 0.31m wide by 0.91m long cantilever beam, which assumes complete fixity at the location of the bottom-to-side panel. This simplified boundary condition is used as a baseline to evaluate, by comparison, the relative rotational stiffness of the connection, for both types of connection design. The core geometry of the model corresponds to the actual sample, with the longitudinal core orientation along the length. The beam model is fixed at one end, and a tip line load is applied at the opposite end. The magnitude of the resulting load is 45.4kg. The strains and deflections are shown in Tables 3 and 4, respectively, corresponding to the same locations as in the experiment. The predicted strain values are obtained using the same procedure as for the 3-point bending beam models. For gages #8 and #9, the two strain values given in Table 3 correspond to locations on the unstiffened and

stiffened panels, as noted in the table. Figure 6 shows the deformed shape of the cantilever beam model.

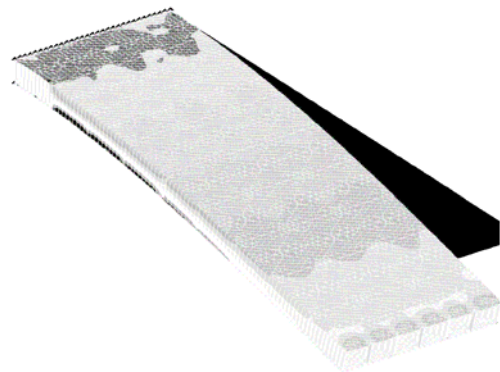


Figure 6 Deformed shape of FE model of cantilever side panel

4.6 Comparison of FE and Experimental Results for the Connection

In relation to the finite element model, which assumes a fixed boundary condition, the stiffened connection design approaches this condition. The unstiffened connection is more flexible, showing a relative rotation at the joint. Examining the maximum displacement values in Table 4, we can see significant differences between the two designs. The deflections of the unstiffened sample are about 42% greater than those of the stiffened sample. Since the strains of the side panel (the panel on which the load is applied) for both connection types are approximately the same, we can infer that the joint rotation of the unstiffened sample is significantly greater than that of the stiffened sample.

The finite element model predicts strain values for the side panel of approximately the same magnitude as recorded for both connection designs, but generally closer to those of the stiffened sample. However, for displacements there is a 44% difference between the FE model and the experimental results for the unstiffened sample, but only a negligible difference for the stiffened sample.

While there are larger displacements for the unstiffened connection design, both connection types are adequate for use in the production of the tank. The stiffened connection will be used for the exterior panels, and the unstiffened connection will be used for the interior partition panel (see Figure 1).

5 APPLICATION OF HFRP RACEWAY SYSTEMS

Two projects have been completed in which modular HFRP tanks were installed. One site is located at the Dogwood Lakes water treatment facility near Morgantown, WV, which is owned by Consolidated Coal Company. The other site is Reymann Memorial Farm in Wardensville, WV, a university-run research facility. While the terrain and water source at these two sites are different, they both share the need for a removable raceway system.

Dogwood Lakes is a water treatment facility, in which treated mine water is channeled to a settling pond from which the water discharges into a stream. The goal of the aquaculture project at this site is to capture the water from the outlet of the pond, and divert it into a raceway system consisting of four HFRP tanks, which will be staggered along the hillside to grow trout and study the commercial feasibility of treated mine water for fish production. The terrain at Dogwood Lakes is very rugged, making it nearly impossible to use conventional concrete tanks. Moreover, the coal company will not allow permanent structures to be built at this site.

The second site is the Reymann Memorial Farm, owned by West Virginia University. The tanks will be located on a pasture field below a permanent spring of abundant fresh water. Part of the spring water would flow through a 4-tank raceway system and empty into either a pond or an adjacent creek. While the terrain at this site has a gentle slope, the modular HFRP raceway system is preferred because of its mobility and versatility.

In addition to these two sites, there is a third project in which a HFRP tank will be used as an in-pond floating system. The tank will be submerged in a pond and will be fitted with adjustable ballast to permit the tank to float above the water level, which is needed to safely keep the fish inside the tank and to dispose of the fish waste without contaminating the pond. This floating unit will be installed at the Warwick Mine Water Treatment Plant in Greene County, Pennsylvania.

6 CONCLUDING REMARKS

This paper presents an overview of the design of a fish raceway system, consisting of several tanks in series manufactured from HFRP sandwich panels. The design is based on functionality requirements, and accordingly, structural members are sized and corresponding samples are manufactured and experimentally tested to evaluate their linear response, which is also investigated using finite element models with ABAQUS (2009).

Several projects utilizing this new product have been completed. Thus, it is expected that demand for the HFRP tanks will increase. Future field evaluations by the research team and users of the raceway system will define further refinements to the overall design of the individual tanks. Furthermore, additional experimental testing will be performed, including failure of the samples discussed in this paper. A finite element analysis of the entire tank, based on equivalent panel properties, will be conducted to assist in the optimization of the structural components and connections.

REFERENCES

- ABAQUS, Standard Users Manual, 2009, version 6.7. Hibbitt, Karlsson and Sorensen, Inc., USA.
- Davalos, J.F. & Qiao, P.Z. & Xu, X.F., Robinson, J. & Barth, K.E. 2001. *Modeling and characterization of fiber-reinforced plastic honeycomb sandwich panels for highway bridge applications*, J. Comp. Struct. 52(2001): 441-452.
- FEMAP Users Manual, 2009, version 8.3. Enterprise Software Products, Inc., Exton, PA.
- Jenkins, M.R. & Wade, E.M. & Fletcher, J.J., & Hankins, J.A. 1995. *Economic analysis of non-traditional water resources for aquaculture in West Virginia*. The Conservation Fund's Freshwater Institute, Shepherdstown, WV.
- Robinson, J. & Davalos, J.F. & Xu, X.F. & Qiao, P.Z., & Barth, K.E. 2001. *FRP honeycomb composite sandwich beams under bending*, Proceedings of the ASC 16th Annual Technical Conference, American Society of Composites (ASC), Blacksburg, VA, Sept. 9-12 (in CD-ROM, Paper#111, 12 pages).
- Robinson, J. & Davalos, J.F. & Qiao, P.Z., 2002. *Modeling and characterization of FRP honeycomb composite sandwich beams*, Proceedings of the 3rd International Conference on Composites in Infrastructure (ICCI'02), San Francisco, CA, June 10-12.

Hybrid FRP-Concrete Structural Member: Research and Development in North America

Donna Chen & Raafat El-Hacha (relhacha@ucalgary.ca)

Department of Civil Engineering, University of Calgary, Calgary, Alberta, Canada

ABSTRACT In recent years, fibre reinforced polymers (FRPs) have become the focus of numerous research projects in the field of civil engineering. FRPs are a structural material known to possess high strength, high resistance to corrosion and high strength-to-weight ratio. It is also easy to install in both new as well as existing structures. Hybrid FRP-concrete structural members, in particular, have shown significant promise in a wide range of applications. This paper will investigate and discuss in detail the research performed on hybrid FRP-concrete structural members in North America. Emphasis will be placed on the design philosophies and results from both experimental and analytical testing.

1 INTRODUCTION

Considerable research has been performed on Fibre Reinforced Polymers (FRPs) as a viable alternative to reinforced concrete, which is the primary material currently used in construction today. Over the years, it has been found that reinforced concrete structures require a great deal of maintenance, repairs, strengthening and other engineering works throughout its design span due to its susceptibility to corrosion. This leads to the increasing spending that is directly dedicated to maintaining existing structures.

FRP material exhibits high strength, high strength-to-weight ratio as well as exception corrosion resistance qualities. In addition, the nature of the material allows for easy installation in both new construction and existing structures. Many different types of hybrid FRP-concrete structural members have been investigated internationally with the objective of replacing reinforced concrete as the main structural material in a variety of applications. Current research performed on hybrid FRP-concrete structural members in Europe and Asia was presented in the companion paper (Chen and El-Hacha, 2010). This paper will focus on the research that has been completed in North America. For each research, design details and results from experimental tests and analytical modeling will be explained and summarized.

2 CURRENT RESEARCH AND DEVELOPMENT

2.1 Hybrid Concrete-Filled GFRP Tubes - University of Manitoba

Fam and Rizkalla (2000) tested the performance of concrete-filled GFRP tubes under axial loadings for

applications as piles, poles, highway overhead signs and bridges. The GFRP tube serves three main functions: 1) stay-in-place concrete formwork, 2) non-corrosive reinforcement and 3) concrete confinement. The concrete mixes were prepared with CONEX, an expansive additive that prevents separation to occur between the concrete and the FRP tube as a result of shrinkage. For a period of seven weeks after casting of concrete, the hoop strains were monitored in the specimen. Regardless of the type of configuration, maximum hoop strains were recorded at approximately 20 days after curing, showing that the period of expansion is smaller than the period of shrinkage. A large variety of tubes were tested, incorporating different combinations of tubes sizes, fabrication types as well as concrete shapes, with a total of 11 different specimens.

In general, concrete filling significantly improved the strength of the specimen. Increases of 49.5%, 212% and 250% were obtained for the steel tube, the filament wound GFRP tube and the pultruded GFRP tube, respectively, when compared to their hollow strength capacities. The increases can be partially attributed to the elimination of large deformations, buckling and ovalization that occurs with the hollow tubes. Depending on the orientation of the fibres in the GFRP tube, different failure modes occurred. GFRP tubes, left hollow without concrete, failed due to local buckling. Concrete-filled GFRP tubes with fibres oriented close to the hoop and axial direction failed in tension by fibre rupture in its axial direction. Concrete-filled GFRP tubes with fibres oriented in larger angles failed in compression due to cracking of the matrix and buckling of the fibres. Pultruded GFRP tubes, where all the fibres were aligned in its axial direction, failed in horizontal shear.

The effect of cross-sectional configuration was analyzed. Test results confirmed that under pure flexural loading, the presence of a solid core does not significantly increase the strength of the specimen. There is a slight increase in strength if the concrete is confined between two GFRP tubes, given all other parameters are maintained the same. Strength could further be increased if the inner tube is positioned off center towards the tension side. However, due to the fact that most loadings are expected to occur in a variety of directions, this type of design was not considered feasible for applications. The fabrication process of the GFRP tube also has an effect on the strength, stiffness and failure mode experienced by the hybrid member. Fibres in the pultruded tubes were all aligned in the axial direction and therefore allowed for greater stiffness along its length; however, due to this property, shear failure in the horizontal direction is more likely to occur. The concrete strength obtained in the filament wound specimen was 32% greater than specimens with pultruded FRP tubes.

2.2 Three-Dimensionally Woven Hybrid GFRP/Concrete Bridge Deck - North Carolina State University

Johnson et al., (2008) researched the structural performance of Glass FRP-only bridge decks as well hybrid GFRP-concrete bridge decks fabricated using the 3-D weaving process. The weaving process uses E-glass FRP to produce fabric skins, where each skin is made up of two layers of fabric. During fabrication, one layer of skin was cut, detached and folded until it was parallel to the z-axis. By assembling two of these sections together, one inverted over the other, the folds became the webs of the deck system. To complete the FRP section, balsa wood cores were inserted in the openings along with other final preparation details such as vacuum infusion with epoxy resin and post curing. By applying the 3-D weaving technique, it was expected that delamination, particularly at section joints, would be greatly reduced, compared with the use of unidirectional and bidirectional FRP material. Figure 1 is a series of diagrams graphically depicting the fabrication steps.

The hybrid GFRP-concrete bridge deck system was composed of the 3-D woven GFRP section with a 46mm thick layer of concrete cast on top, and anchored together by a series of shear connector placed throughout the width of the deck. The concrete topping included internal steel reinforcement; however, it was explicitly stated that for real applications where exposure to the elements may occur, it would not be recommended to include any steel reinforcement. The total depth of the deck slab section was 163mm. A diagram of the hybrid section is shown in Figure 2.

Two hybrid deck specimens were tested, one to examine the shear effects under flexural loading and the other to study the behaviour of the deck under a predominately

flexural load. The first specimen failed by shear failure in the concrete, with visible signs of cracking and delamination of concrete from the top skin of FRP over more than 50% of the span. For the second specimen, through the loading scheme up to failure, partial delamination of the concrete topping progressed from midspan outwards towards the ends, until complete detachment at the ends occurred at failure. Both specimens behaved linearly without exhibiting large deformations under service conditions.

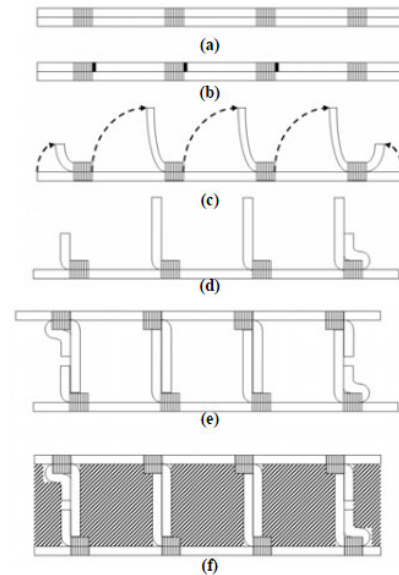


Figure 1 Assembly steps for FRP-only panels (Johnson et al., 2008)

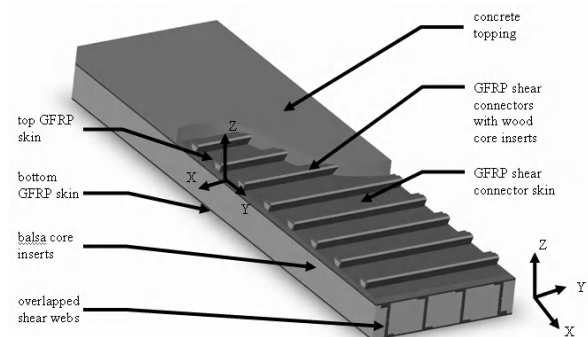


Figure 2 Schematic of GFRP/concrete hybrid deck panel (Johnson et al., 2008)

From the experimental results, delamination of the concrete from the top of the GFRP showed that the bond at the interface was inadequate. It was recommended that, for future studies, roughening the surface of the GFRP or the additional application of a bonding agent be used to reach the full flexural potential of the hybrid deck system. It was estimated based on the concrete strain prior to delamination that enhancing the bond strength would increase the section strength by approximately 50%.

2.3 Analysis of Hybrid FRP-Concrete Multi-cell Bridge – The State University of New York

Aref et al., (2005) developed a finite element model intended to predict the behaviour of hybrid FRP-concrete bridge superstructure system and tested its accuracy using comparisons with experimental data. The focus of the project was to establish a quick and simplistic method to determine the expected flexural behaviour of other hybrid bridge superstructures. The trial section consisted of three trapezoidal, filament-wound box beams, with a concrete layer above and a CFRP sheet bonded at the base. The member experimentally tested was designed as an 18.3m one-span bridge, with one lane. The final hybrid section is shown in Figure 3.

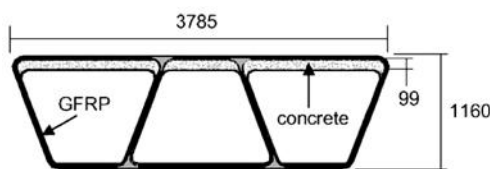


Figure 3 Cross-section of bridge superstructure (Aref et al., 2005)

Two flexural loading cases were examined by applying either on-center or off-axis loadings in the transverse directions. The finite element model was developed based on the assumption that no deformation would occur in the cross-sectional direction with longitudinal restraint at one end and vertical restraint at both to simulate an idealized simply supported structure. Focus was placed on observing, at midspan, the force-displacement behaviour as well as the deformed shape at the bottom surface under different levels of applied loads and comparing the experimental and analytical results.

In general, the linear finite element model yielded load displacement, strain values and predictions of the member's deformed shape that greatly resembled the flexural behaviour exhibited in experiments. Significant discrepancies were noted when evaluating the twisting rotation, where the finite element analysis results were considerably less than those obtained experimentally. This finding could be attributed to the defined boundary conditions, where in experiments, the specimen was supported on elastomeric bearing and permitted small degrees of vertical movement, unlike the idealized simply supported parameters used in analysis. Non-linear finite element analysis for modeling at higher, near failure loads also correlated closely with experimental data, with a 5.6% difference in midspan displacement at failure; however, the developed model did not factor in material failure thresholds and therefore was not capable of predicting the load magnitude at failure.

On the whole, it was found that linear finite element analysis predicted very well the elastic behaviour of hybrid members. Non-linear analysis also produced

suitable results but it was suggested that the model required more consideration towards material properties with particular attention to the material behaviour under tension, compression and cyclic loading as well as various possible failure modes.

2.4 Steel-Free Hybrid FRP Stiffened Panel-Concrete Deck System - University of California, San Diego

Cheng and Karbhari (2005) tested a composite FRP-concrete deck panel system, fabricated with a bottom plate, end hooks for the slab-girder connection along with stiffeners and interfacial ribs, and a layer of concrete slab cast over the panel. The deck panel was produced from 8 layers of unidirectional carbon fabric and 4 layers of E-glass chopped strand mat placed in a specific pre-designated layering sequence to a total thickness of 6.3mm. Rectangular stiffeners constructed from unidirectional carbon fabric and foam core were bonded onto the bottom plate. A picture of the FRP deck panel only is given in Figure 4.

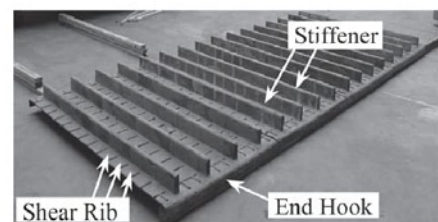


Figure 4 FRP deck panel (Cheng and Karbhari, 2005)

Five specimens, each with different combinations of stiffener and rib spacing, were tested under static loading. For analysis of the section under fatigue loading, two of the sections used for the static loading were placed side-by-side with a layer of concrete slab cast on top. A supplementary layer of carbon fibre reinforced mesh was provided near the top surface of the concrete in the negative moment region within the middle one-third span region to act as tensile reinforcement. Three additional specimens, for shear bond tests, were made. Reinforced concrete blocks were cast at the ends of the specimens tested under static and fatigue loading, to simulate the rigidity and fixity of girder supports.

When tested under static load, the magnitude of rib spacing on the top of the panel did not significantly influence the behaviour and load carrying capacity of the section. Doubling stiffener spacing as well as removing stiffeners completely resulted in a decrease in flexural resistance of 17% and 43%, respectively. Additionally, experimental results from shear bond tests showed that when shear ribs are provided, flexural-shear cracks were present at failure; without shear ribs, the specimen exhibited almost purely flexural failure. It was shown that the presence of shear ribs, regardless of spacing, was required to provide adequate load transfer

resistance between the slab and the panel. Failure of all five statically loaded specimens occurred when an abrupt flexure-shear crack formed in the slab.

During fatigue tests, the specimen was subjected to service load for 2 million cycles, followed by 250,000 cycles under double service loads and an additional 10,000 cycles using triple service loads. The specimen was loaded to failure after completing the series of cycles. The specimen did not experience any significant reductions in stiffness during the first 2 million cycles; however, once the fatigue load was doubled and tripled, stiffness of the section reduced by 37.6% and 44%, respectively. The specimen behaved elastically and no significant residual deformations resulting from fatigue loading. In addition, no slippage occurred at the interface between slab and deck. Tensile cracks did not appear on the specimen's vertical sides and compressive and tensile strains were within allowable limits. It was found that the presence of the carbon fibre composite mesh controlled the degree of cracking in the negative bending moment areas and it was recommended by the authors that minimum amount of mesh to resist tensile stresses be provided in future specimens.

2.5 Pultruded GFRP Sections as Stay-in-Place Open Structural Formwork - Queen's University, Kingston Ontario

Honickman (2008) performed experimental and analytical investigations into the use of pultruded GFRP sections in hybrid FRP-concrete members, acting as stay-in-place formwork, capable of resisting both positive and negative moment loading. Hybrid slabs and girders were tested.

2.5.1 Hybrid Slabs

Eight specimens, consisting of concrete cast on top of a GFRP plate, were tested. A steel welded wire mesh was also placed in the upper surface of the slab for shrinkage crack control. The first four slabs tested different bonding mechanisms, such as concrete cast on wet adhesive, coarse aggregates bonded to the GFRP plate prior to concrete casting, GFRP shear connectors and steel shear connectors. The latter four slabs had different concrete depths. By varying the concrete depth while maintaining the same GFRP plate thickness, these slabs were designed to test the effect of FRP reinforcement ratio.

All specimens failed due to debonding, and the full effect of the bonding method or reinforcement ratio on the flexural strength could not be evaluated. Strain values obtained at failure indicate that compressive failure of the samples may be expected if debonding failure did not occur first. Adhesive-type bonding through wet adhesive and coarse aggregates provided continuous bonding over the entire concrete-FRP interface. No progressive shear slip at the interface or flexural cracks occurred up to failure, when diagonal shear cracks developed and spread towards the interface, causing abrupt debonding. The use of shear

studs resulted in the formation of flexural cracks which traversed vertically through the section. Failure occurred due to horizontal shearing of the shear studs, though the use of steel shear studs produced higher ultimate resistance due to the higher modulus of elasticity of the steel shear studs as compared to GFRP shear studs. It was also determined that adhesive type bonding exhibited cracking at higher loads when compared to mechanical bonding methods due to the fact that in the immediate area adjacent to shear studs, concrete is displaced, producing local areas of weakness. The GFRP reinforcement ratio was determined to be directly proportional to the flexural stiffness achieved in the slab. Increasing the reinforcement ratio by 33% and 96% resulted in flexural stiffness increases of 22% and 65%, respectively.

2.5.2 Hybrid Girders

The pultruded GFRP sheet pile section had an open trapezoidal shape. Nine girders, categorized into three types based on the geometric configuration and relationship between the GFRP section and the concrete, were tested. Type 1 girders (girders 1, 2 and 3) were cast with a concrete slab as well as a concentric void located beneath the neutral axis; these were tested for the evaluation of different bonding methods. Type 2 girders (girders 4 and 5) were completely filled with concrete and each tested under either positive or negative bending moment to determine its use in a continuous beam. Type 3 girders (girders 6, 7, 8 and 9) used built-up box sections produced from pultruded GFRP sheets bonded to the top of the pultruded GFRP sheet piles section. A concrete slab was cast on top of girders 6, 7 and 8; girder 9 was tested alone without a concrete slab. Figure 5 illustrates the configuration of the different specimen types.

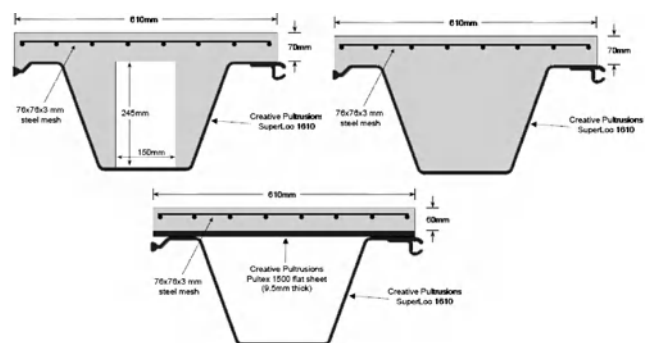


Figure 5 Configuration of type 1, type 2 and type 3 specimens (Honickman, 2008)

Experimental tests showed similar results to those obtained from tests of hybrid slabs in terms of the effect of the type of bonding mechanism used. Adhesive type bonding created near perfect composite behaviour between the concrete and GFRP prior to failure. Using a combination of both adhesive bonding as well as headed

shear studs increased the flexural capacity of the girder by 45% when compared to using solely the adhesive system. It was also determined that built-up box section girder systems achieved between 30 – 70 percent higher flexural resistance while obtaining a 50 – 60 percent reduction in weight. In general, the hybrid girders performed better when subjected to positive bending compared to when under negative bending by 45 – 90 percent.

2.6 Hybrid FRP-UHP Concrete Deck System – University of Calgary

Elmahdy et al., (2008a, 2008b) tested the behaviour of hybrid FRP-UHPC sections. Four beams were fabricated, two as short beam and the remaining two as long beams. The hybrid section consisted of a Glass FRP (GFRP) pultruded hollow box section with ultra high-performance concrete (UHPC) cast on top; the specimens either had one layer of Steel Reinforced Polymer (SRP) sheet or two layers of Carbon FRP (CFRP) sheet applied at the base of the section. Moisture insensitive epoxy was applied on top of the GFRP box section in addition to GFRP shear studs, for bonding with the wet UHPC and moisture tolerant epoxy was used to bond the SRP and CFRP sheets to the GFRP section. The cross-section detail of the beams is shown in Figure 6.

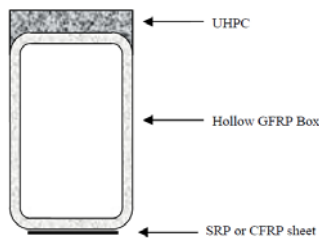


Figure 6 Cross-section of hybrid FRP-UHPC beams (Elmahdy et al., 2008a)

Although both long specimens were initially the same length (6.0m long), testing of the SRP-reinforced beam failed prematurely due to web crippling failure at the support. The damaged portion was removed and the intact portion was tested as a slightly shorter beam (5.1m long) with thicker bearing plates at the supports.

The long specimens failed under concrete crushing and shear failure, followed by concrete delamination at the location of initial failure. Behaviour of both long beams up to failure was linear-elastic and the location of the neutral axis remained relative constant throughout the entire loading duration. It was determined through testing that the application of UHPC and tensile reinforcement sheets increased the flexural capacity of the hybrid section by approximately 3.7 times when compared to the strength of the GFRP hollow section alone. The moisture insensitive epoxy used for bonding at the interface between the box section and the UHPC was

quite effective and, combined with the shear studs, augmented the shear capacity along the interface five times above that provided solely by the shear studs.

The short beams (0.7m and 0.5m long for the CFRP and SRP reinforced specimens, respectively) failed due to debonding along the interface between the UHPC and the GFRP hollow box section. After debonding occurred, failure of the UHPC at the loading points resulted. At failure, cracks were formed at the bottom of the concrete layer due to the large concentration of longitudinal tensile stress present.

In general, the hybrid FRP-UHPC beams maintained satisfactory lateral torsional stability throughout testing. Limited ductility was shown by all specimens and failures occurred suddenly and without significant warning. Continuing research is being performed on these hybrid beams, with particular focus on providing pseudo-ductile failures through the designed initial failure of the CFRP or SRP sheets.

2.7 Seismic Performance of Hybrid FRP-Concrete Pier Columns - Florida International University

Shi and Li (2007) studied the performance of different hybrid concrete-FRP columns, known also as concrete-filled FRP tube (CFFT), under reverse cyclic loading. Six specimens were tested. All specimens except for Specimen LC had the same length; Specimen LC was 60% longer. The columns were also internally reinforced with longitudinal and transverse steel reinforcement bars. The number and type of sheets used in each specimen were selected in order to closely match the expected final tensile strength of the cured laminate for all columns. The structural details of the specimens are:

- Specimen RC – Reinforced concrete column;
- Specimen Y – Off -the-shelf filament wound tube with 17 layers of $\pm 55^\circ$ E-glass fibres;
- Specimen SC and LC – Laboratory-made tube with 2 layers of bi-directional CFRP;
- Specimen G – Laboratory-made tube with 3 layers of bi-directional GFRP; and,
- Specimen H – Laboratory-made tube with 2 layers of uni-directional CFRP longitudinally and 3 layers of uni-directional GFRP in the hoop direction.

Prior to testing, gravity loads on the column equivalent to approximately $0.04f'_cA_g$ were simulated using external prestressing. The testing regime involved the application of reverse cyclic loading in incremental steps. The column drift loading was applied up to a ductility ratio of 6, where ductility ratio is defined as “the ratio of the imposed displacement to a reference displacement”, with the reference displacement taken as the displacement in the control reinforced concrete column when yielding of steel reinforcement first occurred. Upon reaching each level of ductility, 2 cycles of reverse lateral loading were applied.

From the research, it was confirmed that hybrid columns using GFRP tubes produced smaller residual deflections, an important feature for seismic load resistance. Of the CFFT tubes, it was found that Specimens H, SC and LC all exhibited significantly larger residual deflections both at zero loading and neutral position. Specimen H also exhibited the greatest energy dissipation potential as well as the largest moment resistance capacity, followed by Specimen G, while the other specimens showed very similar results. Additionally, factors such as shear span ratio as well as the combined effect of shear and moment on CFFT columns were proven to have marginal effects on its performance. The failure mode of Specimens SC and LC occurred due to sudden cracking of the FRP tube at ductility ratios of 3 and 2, respectively, after which load resistance dropped dramatically. The other CFFT tubes (Specimens Y, G and H) did not fail at a ductility ratio of 6 and did not show any significant cracking of the matrix.

3 CONCLUSIONS

This literature review has shown that the bond strength provided at the FRP-concrete interface plays a very important role in ensuring optimum performance. Hybrid FRP-concrete structural members are shown to display higher load carrying abilities than its individual components, though a significant range of strength variability is present depending on the orientation of the FRP fibres in relation to the load as well as its method of fabrication. Attempts at modeling these hybrid members have shown that linear finite element analysis could predict linear elastic behavior whereas additional considerations may be required in non-linear analysis. It is also important to note that GFRP can improve ductility for seismic applications. In addition, it was suggested that a carbon fibre composite mesh, in place of steel, could control cracking in a bridge deck.

REFERENCES

- Aref, A.J., Kitane, Y., and Lee, G.C. 2005. *Analysis of Hybrid FRP-Concrete Multi-Cell Bridge Superstructure*. Composite Structures, Vol. 69, No. 3, July 2005, pp. 346-359.
- Elmahdy, A., El-Hacha, R., and Shrive, N. 2008. *Flexural Behavior of Hybrid Composite Girders for Bridge Construction*. Proceedings of the ACI Special Publication on FRP Stay-in-Place Forms for Concrete Structures: Research Activities, Case Studies, and Field Applications, sponsored by ACI Committee 440 during the ACI Spring 2008 Convention in Los Angeles, CA, USA, April 3, 2008 (CD-Rom, 19).
- Elmahdy, A., El-Hacha, R., and Shrive, N. 2008. *Flexural and Shear Behaviour of Hybrid FRP-Concrete Composite Beams*. Proceedings of the 2nd Canadian Conference on Effective Design of Structures. McMaster University, Hamilton, Ontario, Canada. May 20 – 23, 2008, (CD-Rom, 10.)
- Fam, A., and Rizkalla, S. 2000. *Hybrid FRP/Concrete Structural Members*. Proceedings of the 2nd ACUN International Composites. Sydney, Australia, February 14-18, 2000, pp. 191-197.
- Fam, A., Greene, R., and Rizkalla, S. 2003. *Field Applications of Concrete-Filled FRP Tubes for Marine Piles*. Proceeding of ACI Special Publication SP-215-9 on Field Applications of FRP Reinforcement: Case Studies, sponsored by ACI Committee 440 during the ACI Fall 2003 Convention in Boston, MA, September 27 – October 1, 2003 (pp. 161-180).
- Honickman, H. N. 2008. *Pultruded GFRP Sections as Stay-in-Place Structural Open Formwork for Concrete Slabs and Girders*. MSc Thesis, Queen's University, Department of Civil Engineering, Kingston, Ontario.
- Johnson, C., Mohamed, T., and Rizkalla, S. 2007. *Behavior of Three-Dimensionally Woven Glass Fiber Reinforced Polymeric Bridge Deck*. Composites Research Journal, Volume 1, pp. 27-42.
- Cheng, L., and Karbhari, V.M. 2005. *Steel-Free Hybrid FRP Stiffened Panel-Concrete Deck System*. Proceeding from ACI Special Publication SP-230-37 at the 7th International Symposium on Fibre Reinforced Polymer Reinforcement for Concrete Members during the ACI Fall 2005 Convention in Kansas, MO, November 6-10, 2005 (pp. 631-650).
- Shi, Y., Li, B., and Miramiran, A. 2007. *Seismic Performance of FRP-Concrete Pier Columns*. A report for the NSF NEESR-SG Award #0420347 Seismic Performance of Bridge Systems with Conventional and Innovative Design by the Department of Civil and Environmental Engineering at Florida International University, December 2007.

Hybrid FRP-Concrete Structural Member: Research and Development in Europe and Asia

Donna Chen & Raafat El-Hacha (relhacha@ucalgary.ca)

Department of Civil Engineering, University of Calgary, Calgary, Alberta, Canada

ABSTRACT Approximately 40% of Canadian bridges currently in service were constructed forty to fifty years ago. Many existing structures suffer from structural integrity problems, such as corrosion, and require significant repairs. In some cases, complete replacement of the structure is necessary. Fibre reinforced polymers (FRPs) have shown great potential as a structural material due to its high strength, resistance to corrosion, light weight and ease of construction. Hybrid FRP-concrete structural members have become of particular interest. This paper will investigate the different applications of hybrid FRP-concrete structural members and the experimental research studies performed on these members in Europe and Asia. Summaries of results from experimental tests and analytical investigations are provided with a focus on the effect of factors such as the type of shear bond used at the FRP-concrete interface and FRP fabrication methods on the ultimate load resistance and failure mode.

1 INTRODUCTION

Reinforced concrete is the most commonly used building material today; however, despite its widespread use, frequent problems occur. Over the duration of a typical reinforced concrete structure's lifespan, maintenance, repairs and sometimes rehabilitation would be required due to corrosion of the steel reinforcement bars within the concrete. In Canada, the municipal infrastructure deficit, as calculated in 2007, is approximately \$124 billion dollars, with \$44.5 billion dollars directly related to the areas of transportation and transit (Mirza, 2007). In addition, it is estimated that \$115 billion dollars will be required to accommodate the changing needs of new and growing communities through the construction of new infrastructure or the expansion of existing ones (Mirza, 2007).

Research conducted within the past 20 years investigating the performance of Fibre Reinforced Polymers (FRPs) in Civil Engineering applications has shown that FRP materials have great potential for use in structures due to its high strength, resistance to corrosion, light weight and ease of construction. More recently, studies have been performed to investigate the replacement of reinforced concrete members with hybrid FRP-concrete members in structures, leading to the construction of several structures using the new hybrid system. This paper will present experimental details of current developments in the research of hybrid FRP-concrete structural members. A brief overall summary of the findings will also be provided at the end.

2 CURRENT RESEARCH AND DEVELOPMENT

2.1 FRP-Concrete Composite Deck - Korea Institute of Construction Technology, Korea

Kim et al. (2005) tested a unique modular hybrid FRP-concrete deck system. To address failure in earlier models at the interface between adjacent modules, individual modules were fabricated by pultrusion, with male-female socket-shapes present at the extremities. Shear connecting plates perpendicular to the upper face of the module were produced monolithically with the FRP module in lieu of bonding using epoxy at a later stage to prevent failure at the bond interface. Though it was suspected that coarse sand coating alone would provide sufficient bond strength, the development of bond between the concrete and the FRP was achieved through the use of both the shear connecting plates as well as the coarse sand coating. Steel reinforcement bars, provided in the concrete deck, were supported either on top of the shear connection plates or through pre-fabricated holes through the plates. Figure 1 shows the section details.

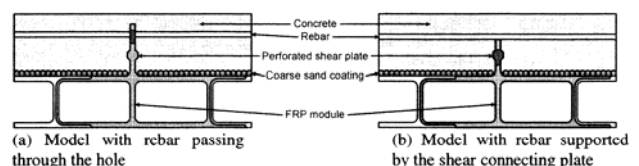


Figure 1 Section detail of modular hybrid FRP-concrete deck system (Kim et al., 2005)

Disregarding the small degree of slip that took place between adjacent modules, it was assumed for analysis that a linear strain distribution was present through the deck section. The section was designed to initially act as a perfect composite section until failure of the concrete under fatigue; after concrete failure, the section was expected to act solely as a FRP section. At failure of the FRP section, the safety factor was designed to exceed 2, thus preventing brittle failure.

Shear strength tests were performed to determine the effect of the shear connecting plates and the coarse sand coating. In the case where both systems were used, the failure shear strength in the transverse and longitudinal directions was 4.47 and 4.44 times the strength when only the coarse sand coating was used. Static tests were performed on a 2.5m span hybrid deck section. Punching failure occurred in the concrete. After punching failure, the load resistance of the deck reduces incrementally as the deflection of the deck section increases. Final failure of the section occurred at the connection points between FRP modules. Fatigue tests performed showed that the integrity and load resistance of the deck system could be maintained up to 2 million cycles. Static load tests were performed every 50,000 cycles in order to ascertain the degree of damage sustained due to fatigue loading.

2.2 Hybrid FRP-Concrete-Steel Double-Skin Tubular Columns - The Hong Kong Polytechnic University, Hong Kong

Yu et al., (2004) tested a new hybrid FRP-concrete-steel double-skin tubular column, composed of an interior steel tube, exterior FRP tube and concrete in the space between the two tubes, for use in seismic applications. The steel tube acted as longitudinal reinforcement; the FRP tube, prepared using the wet lay-up process with its fibres oriented in the circumferential direction, confined the concrete.

Six specimens, with varying FRP tube thicknesses, were tested under concentric axial loading. For all specimens, failure occurred due to FRP rupture, after which the load resistance of the column dropped dramatically. Evaluation of the performance of the hybrid structural member and the effect of FRP confinement compared the ultimate resistance achieved through experimental testing with the expected individual axial capacities of the concrete and steel tube assuming no interaction occurred between the two components. It was found that application of one layer of FRP did not increase the axial resistance of the member. Two layers and three layers of applied FRP tube resulted in 27% and 48% increases in load capacities, respectively. The behaviour of the hybrid member approximated elastic-near plastic behaviour with higher ductility achieved when compared with unconfined concrete columns. Axial strains measured at failure for one-, two-, and three-ply FRP tubes were 5.53, 7.69, and 8.96 times that of the unconfined concrete

members.

Flexural testing was performed on six specimens, with varying concrete strength, steel tube thickness and FRP tube thickness. Due to the limited amount of headroom clearance available in the loading frame used, testing was only performed to an approximate mid-span deflection of 150mm and not to failure. This is shown in more detail in Figure 2.



Figure 2 Failure of hybrid FRP-concrete-steel column (Yu et al., 2007)

For pure bending applications, it was advised that additional strengthening and modifications to the hybrid member be provided. The thickness of the FRP tube used, based on the number of plies applied, did not greatly affect the load capacity of the member; however, the thickness of the inner steel tube did exert a significant influence. All the specimens showed a high degree of ductility. Due to the fact that none of the specimens were loaded to failure, it was concluded that greater ductility could be expected from the hybrid members.

2.3 Laboratory and Field Performance of Cellular Fiber-Reinforced Polymer Composite Bridge Section – Swiss Federal Institute of Technology and Other Institutions

Zhou et al., (2005) researched the development of composite bridge deck systems made from off-the shelf pultruded FRP sections. FRP structural square tubes were placed side-by-side spanning in the transverse direction of the bridge and linked together using adhesives and steel rods. FRP plates were placed on both the top and bottom of the assembled structure after which all the components were bonded using the vacuum bagging process. Four phases of the bridge deck system were developed, using different combinations of properties such as material quality, dimensions, adhesive type and level of environmental exposure. The completed deck section was then supported by three steel wide flange beams, spaced evenly apart about the center, leaving the section edges unsupported to create the worse load case scenario. During laboratory testing, loading patches were placed at designated locations so that loads designed to simulate the truck axle loads could be applied in different combinations and orientations to obtain the greatest load effect. Field testing of the bridge deck was

put into operation at an environmentally exposed weigh station, which is expected to under approximately 0.5 million loading cycles at month.

It was discovered that the cutout areas intended for insertion of the steel rods attracted higher concentrations of stress. Where the holes were placed in the web, loss of bearing resistance resulted, leading to shear cracks when more than many rods are located in close proximity to each other. To minimize cost and maintain the structural integrity of the section, it was suggested that only three rods, the minimum amount required to prevent movement of the FRP square tubes during curing, be provided. Additionally, when tested under the same applied load, larger deflection and strains were detected from the unsupported edges as compared to the centre of the deck. In real application, it was advised to avoid leaving the edges of the cellular FRP bridge deck section without support unless absolutely necessary; where unavoidable, supplementary transverse support along the edges must be provided. Through both laboratory and field testing, the cellular FRP bridge deck system has proven to be resilient to the effects of fatigue loading and did not display any signs of lowered strength or stiffness after 7 million cycles. As a result of the experimental data, Zhou et al., (2005) believed that the use of the FRP deck design for practical applications in highway bridges could a feasible possibility.

2.4 Innovative Design of FRP Combined with Concrete: Short and Long Term Behaviour

Deskovic and Triantafillou (1995a, 1995b) designed and investigated the short and long term performance of composite flexural structural members to optimize the combined use of concrete, GFRP and CFRP based on their individual material properties. GFRP pultruded shapes generally perform well as a structural beam but do not possess high compressive strengths or stiffness and are vulnerable to sudden failure. For the hybrid section tested, concrete was cast above the GFRP box section, which also acted as a stay-in-place formwork. CFRP sheet, with a failure strain smaller than that of the GFRP, was applied at the base of the beam to provide additional tensile reinforcement. The CFRP was designed to be the first element of the composite section to fail, allowing for the beam to fail in a pseudo-ductile manner by giving advanced warning of complete section failure. A cross-sectional view of the hybrid member is shown in Figure 3.

Three hybrid FRP-concrete beams were tested for short term flexural behaviour. The first specimen failed due to debonding of the concrete and GFRP; as a result the remaining two specimens were fabricated with steel bolts to act as shear connectors, which then both failed in the intended pseudo-ductile manner. It was found that experimentation and finite element analysis provided very similar results.

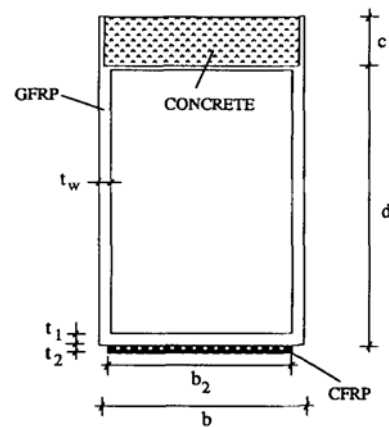


Figure 3 Configuration of hybrid beam using concrete, GFRP box section and CFRP sheets (Deskovic and Triantafillou, 1995a)

Investigation into long term behaviour, such as creep and shrinkage, of the hybrid design was conducted by testing four specimens. Two beams were first tested under one-day creep with the application of constant load. After the initial full day of sustained loading, the beams were then tested under alternating loading at a rate of 4.2Hz. The loads which were applied to the first two beams were different during both stages of testing. The latter two specimens were used to test environmental effects, where one was tested indoors under constant humidity and temperature while the other was placed outdoors and subjected to weathering. At the time when the paper was published, six months of data was available for examination. From the creep and fatigue test results, it was found that under lower loads, deflection was governed primarily by the fatigue loading rather than the initial sustained load whereas higher applied loads reflect a greater importance on the initial load on the final deflection and response of the hybrid member. This phenomenon was attributed to the loss of stiffness over time as a result of sustained and cyclic loading, which becomes more apparent as the level of load applied increases. In addition, it was concluded that temperature variations between -5°C to 35°C resulted in negligible effects on the behaviour of the hybrid members.

Two analytical models were used for comparison, based on the laminate theory as well as semi-empirical. Overall, the semi-empirical proved to be the more accurate of the two methods although at lower loads, the predictions made through the laminate theory were more exact. Both methods showed satisfactory correlation with actual experimental data collected.

2.5 Innovative Externally Bonded FRP-Concrete Hybrid Flexural Members – Ibaraki University, Japan and Tongji University, China

Wu et al., (2005) experimented with a new hybrid FRP-concrete beam design. The cross-section consisted of a concrete beam, prepared with rounded edges on all four corners, reinforced longitudinally with CFRP sheets

at the bottom and then encased in the hoop direction by GFRP/CFRP sheets for the purpose of providing supplementary anchorage to the CFRP sheets as well as concrete confinement. Six specimens were tested, where Type A beams were fabricated with no steel reinforcement bars and Type B beams included four steel bars; neither categories included the use of steel stirrups. The effect of CFRP reinforcement ratio and the number and type of FRP layers used in the hoop direction were tested.

It was found through experimentation that the stiffness of the hybrid beam in the stage after initial cracking and prior to debonding of the FRP sheets is proportionally related to the CFRP reinforcement ratio. By increasing the CFRP reinforcement ratio, the failure mode of the hybrid beam transitions from a tensile to compressive failure. Without the presence of steel reinforcement bars in the Type A specimens, a sudden and catastrophic style of failure occurred. Due to these findings, for safety reasons, steel reinforcement bars equal to the minimum reinforcement ratio should be provided to control the development and growth of cracks. Overall, of the six specimens tested, the one that showed the greatest flexural strength contained the minimum required steel reinforcement ratio with equal application of both GFRP and CFRP sheets in the hoop direction. When compared to a reinforced concrete with similar dimensions and a reinforcement ratio of 2.5%, the specimen mentioned above outperformed by 60% in regards to flexural strength. Comparison between analytical models, which characterized the concrete either as confined or unconfined, showed that confinement as a result of FRP sheets applied in the hoop direction does occur. Whereas the unconfined model predicted compression failure and a significantly lower flexural strength that that exhibited through experimentation, the confined concrete model correctly predicted a balanced failure mode with concrete crushing and CFRP rupturing almost simultaneously.

2.6 Composite GFRP Composite Decks – School of the Civil and Environmental Engineering, Kookmin University, Korea

Lee and Hong (2009) developed modular composite GFRP deck cross-sections with different connections details. In the first stage, decks using tongue-and-groove connections were tested. The deck profile consists of three adjacent trapezoidal cells, fabricated by pultrusion, with 8800 Tex E-glass roving in the longitudinal direction and stitched fabric woven at 90 and 45 degrees to the primary fibres. The resin used was unsaturated polyester. The deck design with its connection detail is shown in Figure 4.

Through testing, it was discovered that the above design problems during application. Firstly, due to the fact that the modules are required to be assembled by horizontal sliding adjacent deck sections together, shear studs cannot be inserted until after all of the decks are

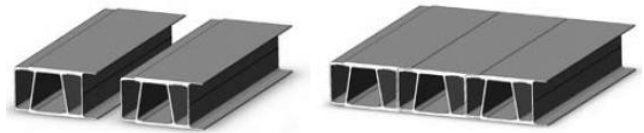


Figure 4 GFRP composite deck with tongue-and-groove connection (Lee and Hong, 2009)

placed in position. This causes a high potential for mismatch and misalignment between the pre-drilled shear stud holes, making it difficult for assembly. Additionally, the design requires for the shear studs to be welded on-site to either steel girders or the steel plates, which are attached to concrete girders. The limited workspaces as well as the size of the shear stud holes make welding quite difficult to performing.

As a result, a new type of composite GFRP deck was created with snap-fit connections. The cross-section is shown in Figure 5.

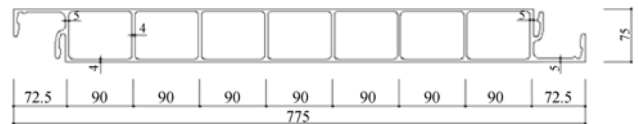


Figure 5 GFRP composite deck with snap-fit connection (Lee and Hong, 2009)

In this design, adjacent deck modules are connected vertically, which greatly increases workability while allowing for shear studs to be inserted with better accuracy since vertical assemblage reduces the amount of horizontal discrepancy between the pre-drilled holes for shear studs. A diagram showing the module assembly is given in Figure 6.

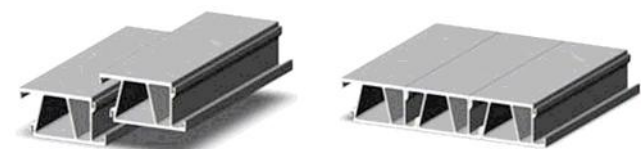


Figure 6 Vertical assembly of GFRP composite deck with snap-fit connection (Lee and Hong, 2009)

With this connection design, it can also be used in curved bridge construction, which was not an option for the previous tongue-and-groove connection design. Additionally, the modules can be constructed with adhesives at the connection interface, allowing for ease in disassembling and reuse of the GFRP composite deck section if required, as in the case of temporary bridge constructions.

The application of both the tongue-and-groove connection and snap-fit connection GFRP composite bridge deck sections have been seen in more than 20 traffic, pedestrian and walkway expansions bridges located in Korea. In the future, more bridges using this

type of technology are planned for use in Taiwan, China.

2.7 Use of Uni-Axial Pseudo-Ductile Hybrid FRP Sheet to Strengthen Existing Reinforced Concrete Flexural Members – HanKyong National University, Korea

Choi et al., (2009) investigated methods of strengthening existing reinforced concrete structures using hybrid FRP sheets using varying volumetric ratios between E-glass fibres (GF) and high-strength carbon fibres (CF). Using previous research performed by Manders et al. (1981) relating the optimum ratio between GF and CF to allow for a pseudo-ductile failure where the CF are designed to fail first, leaving the remaining GF to carry the applied load, the GF:CF ratio used to manufacture the hybrid FRP sheets in this research was 4.62. The load-elongation behaviour of this type of hybrid FRP sheet is shown in Figure 7.

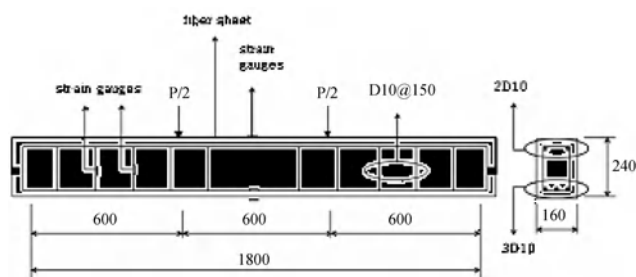


Figure 7 Load-elongation behaviour of the hybrid GF/CF sheet (Choi et al., 2009)

Five reinforced concrete beams were prepared for flexural testing, with one beam left unreinforced as a control, three beams reinforced with 1-, 2- and 3-ply of the hybrid sheet and the last beam reinforced with only CF tensile sheets. To avoid premature debonding failure during loading tests, special design considerations were put into a new anchorage mechanism for the sheets. The loading setup for the beam is shown in Figure 8.

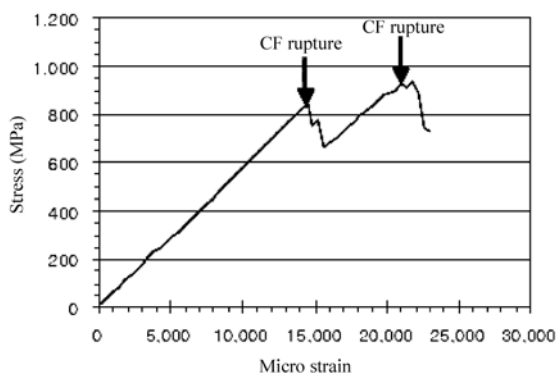


Figure 8 Load setup and section details of reinforced concrete beams strengthening with the hybrid sheet (Choi et al., 2009)

From tests, the results showed that applying one ply of the hybrid sheet showed the best outcome in regards to improved strength and ductility while taking into

consideration economic feasibility. It was found that though both the structural behaviour of the beam strengthened with one ply of the hybrid sheet performed similarly to that strengthened with CF only up until failure, the latter loses strength abruptly past the peak, resulting in the beam to exhibit the same load-strain behaviour of the control beam. Additionally, the amount of carbon fibres used to achieve the same load resistance up to failure in the two strengthening configuration is approximately 5 times greater in the CF strengthened reinforced beam, significantly increasing the cost of construction in practical applications. When the number of hybrid sheets is increased, it results in higher peak load resistance, equal to 88.9kN and 96.5kN from 79.6kN for the reinforced concrete beam, for the 1-ply and 2-ply strengthened beams, respectively. It also results in less ductility. In the case of the reinforced concrete beams reinforced with three sheets of the hybrid sheet, collapse was caused due to anchorage failure and debonding despite the additional considerations made in the design of the special anchorage mechanism.

3 CONCLUSIONS

In this literature review, it was shown that FRP material can fulfill the roles of a stay-in-place formwork, non-corrosive reinforcement as well as concrete confinement in columns, simultaneously when used in hybrid structural members. When used in the hoop direction around columns, the confinement effect is achieved, resulting in an associated increase in axial load resistance; furthermore, the increase in ductility with every additional layer of FRP applied is incredibly substantial. In regards to flexural members, linear elastic failure due to the natural physical property of FRP material can be avoided in lieu of a pseudo-ductile failure mode by using hybrid FRP sheets manufactured from a combination of high-strength carbon fibres and E-glass fibres, with a recommended ratio of 1 to 8.8. It is also important that adequate bond strength is provided, particularly in flexural members, to prevent early failure due to debonding. Under long-term loading, there is a loss in stiffness in hybrid FRP-concrete structural members causing larger deflections to occur. This becomes more apparent as the magnitude of the applied load increases. Analytical models formed using the laminate theory as well as semi-empirically did show good correlation to experimental data, where the laminate theory provided more accurate results at lower loads.

REFERENCES

- Choi, D., Ha, S., and Kim, K. 2009. Use of Uni-Axial Pseudo-Ductile Hybrid FRP Sheet to Strengthen Existing Reinforced Concrete Flexural Members. Proceedings of the 2nd International Conference of International Institute for FRP in Construction

- for Asia-Pacific Region. Seoul, Korea, December 9-11, 2009, pp. 563-569.
- Deskovic, N., Triantafillou, T. C., and Meier, U. 1995a. Innovative Design of FRP Combined with Concrete: Short-Term Behavior. *Journal of Structural Engineering*, 121(7), pp. 1069-1078.
- Deskovic, N., Meier, U., and Triantafillou, T. C. 1995b. Innovative Design of FRP Combined with Concrete: Long-Term Behavior. *Journal of Structural Engineering*, 121(7), pp. 1079-1089.
- Kim, B.-S., Cho, J.-R., Park, S. Y., and Cho, K. 2006. Toward Hybrid Bridge Deck: An Innovative FRP-Concrete Composite Deck. *Proceedings of International Joint Seminar of the KSCE and the JSCE: 2006 KSCE Annual Conference on "Recent Progress of Concrete-Steel-FRP Hybrid Structures."* Gwangju, Korea, October 13, 2006, pp. 63-78.
- Lee, S and Hong, K-J. 2009. The Current and Future Applications of FRP Decks. *Proceedings of the 2nd International Conference of International Institute for FRP in Construction for Asia-Pacific Region.* Seoul, Korea, December 9-11, 2009, pp. 29-34.
- Mirza, S. 2007. *Danger Ahead: The Coming Collapse of Canada's Municipal Infrastructure.* A report prepared for the Federation of Canadian Municipalities, Ottawa, Ontario, November 2007.
- Wu, Z., Li, W., and Sakuma, N. 2006. Innovative Externally Bonded FRP/Concrete Hybrid Flexural Members, *Composite Structures*, Vol. 72, No. 3, March 2006, pp. 289-300.
- Yu, T., Wong, Y.L., Teng, J.G., and Dong, S.L. 2004. Structural Behaviour of Hybrid FRP-Concrete-Steel Double-Skin Tubular Columns. *Proceeding from 2004 ANCER Annual Meeting.* Honolulu, Hawaii, July 28-30, 2004 (CD-Rom, 11p).
- Zhou, A., Coleman, J.T., Temeless, A.B., Lesko, J.J., and Cousins, T.E. 2005. Laboratory and Field Performance of Cellular Fiber-Reinforced Polymer Composite Bridge Deck Systems. *Journal of Composites for Construction*, ASCE, September-October 2005, pp. 458-467.

Experimental Study on Flexural Behaviour of Hybrid GFRP/Concrete Bridge Deck

Yuqing Liu (yql@mail.tongji.edu.cn), Jun He, Haifeng Fan & Airong Chen
Department of Bridge Engineering, Tongji University, Shanghai, China

Liang Dai
Shenzhen Municipal Design & Research Institute Co. Ltd, Shenzhen, China

ABSTRACT A novel cost-effective hybrid GFRP/Concrete deck system consists of the corrugated pultruded GFRP plate with T-upstands for the tension part and concrete with distributing reinforcing bars for the compression part was proposed. Static tests on six full-scale models with different influence factors such as penetrating bars and surface treatment under sagging moments were conducted and observed to evaluate the load-carrying capacity and failure modes of proposed hybrid deck system. Results from experimental work indicate that both surface treatment and penetrating bars improve the connection between GFRP plate and concrete, also promote the ultimate strength and whole rigidity of hybrid deck; moreover the effect of surface treatment is better than that of penetrating bars. The overall investigation showed that the presented hybrid GFRP/concrete concept is a viable option for beam-and-slab bridges.

1 INTRODUCTION

Glass Fiber Reinforced Polymer (GFRP) decks have emerged as a promising solution to the premature deterioration and structural deficiency problems associated with conventional bridge decks, owing to their several advantageous properties including high strength, lightness, ease of installation, good thermal and electromagnetic insulation properties, low maintenance requirements (Keller T. 2002).

The world's first FRP vehicular bridge, albeit with only FRP box girders, was built in China in 1982 (Ye L.P. 2003), after that time, many bridges with FRP deck systems have been developed and built in the United States and worldwide (Bakis C.E. 2002; Karbhari, V. M. 2000). Experimental (both model and field test) and analytical work on FRP bridge decks with various materials, configurations, and connection detailing, mechanical characteristics including stiffness, strength, and stability, etc, have been widely reported (Turner M.K. 2004; Naaman, A. E.2004; Cheng L 2005; Stiller, W. B. 2006; Ghosh, K. K.2007).

However, the largest concern regarding FRP decks in the bridge involves the initial higher price of an FRP deck compared to that of a concrete deck presently (Nystrom, H. E. 2003). In the long run, the higher cost of FRP may be justified by considering life-cycle costs. On the other hand, compared with concrete decks, the further significant drawback are the low stiffness in the main girder direction, the brittle behaviour and the susceptibility to instability

phenomena (Keller T. 2006).

To overcome such disadvantages and to make the best use of materials, combinations of FRP and conventional materials as concrete with low cost but high compressive performance have recently been widely used (Keller T. 2007). The main problems that occurred were premature web buckling of hollow FRP sections, insufficient interface capacity to provide full composite action between the FRP and concrete. A new hybrid FRP - concrete bridge deck system is proposed here that should allow preventing some of these problems. The proposed hybrid bridge deck consists of the corrugated pultruded GFRP plate with T-upstands for the tension part and concrete with distributing reinforcing bars for the compression part, as shown in Figure1. A 6 mm thick GFRP sheet with T-upstands, acts both as structural formwork as well as the flexural reinforcement. The hybrid deck should behave with sound connection between concrete and GFRP. There are two bonding mechanisms, i.e. mechanical bonding at the intersection of the main GFRP T-sections and cross rebars, and the physicochemical (natural) bonding on the surface of the main T-sections.

Static tests on six full-scale models with different influencing factors such as penetrating bars (types and presence or absence) and surface treatment (with or without sand coating) under sagging moments were conducted and observed in order to evaluate the load-carrying capacity and failure modes. And the presented hybrid GFRP/concrete concept was verified as a viable option for beam-and-slab bridges.

2 EXPERIMENTAL PROGRAM

2.1 Test specimen

The experimental program consisted of six 3000mm long (2500mm for clear span), 1000mm wide and 200mm deep hybrid GFRP/concrete decks. Figure 1 shows the cross-section of the decks. For the GFRP layer, the standard corrugated pultruded GFRP plate was used, the height of the T-upstands is 143mm, and their distance is 250mm in transversal direction.

Furthermore, two types of GFRP/Concrete interface were investigated: unbonded (Concrete directly cast on the GFRP) and bonded with surface treatment (Sand coating). The sand coating was applied on both GFRP sheet and T-upstands.

The corrugated pultruded GFRP plate with high tensile strength was replaced for the tensile reinforcement in the bottom layer, and the arrangement of reinforcing bars in the top layer of the deck was the same as the conventional concrete deck. The reinforcing steel bars or GFRP bars with diameter of 20mm were used for longitudinal main bars, while the reinforcing steel bars or GFRP bars with diameter of 16mm were used for erection bars, and the distance of main bars and erection bars were 125mm.

The specimens were defined according to the parameters with the penetrating bar presence or not, bar type and interface condition, as show in Tab.1.

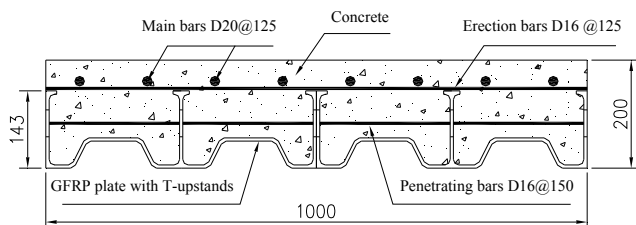


Figure 1 Cross section of test specimen /mm

Table 1 Experimental series

Specimen	Penetrating bars	Interface(GFRP/C)
S-V-1	Without	Un-bonded
S-V-2	Without	Sand coating
S-S-1	Penetrating steel bar	Un-bonded
S-S-2	Penetrating steel bar	Sand coating
S-G-1	GFRP bar	Un-bonded
S-G-2	GFRP bar	Sand coating

2.2 Material properties

The GFRP material, matrix resin and pultrud technique of the GFRP plates were designed specifically according to the requirements, E-glass in the form of a woven fabric was chosen as the reinforcement of FRP. Vinyl ester resin was chosen as the matrix. To determine the mechanical properties of a laminate made of E-glass woven fabric

and vinyl ester, tensile tests were performed using MTS universal testing machine. The tensile strength parallel to the fiber direction of T-upstands at the middle and in the edge was 509MPa and 480MPa respectively, and the tensile strength of corrugated GFRP plate was 488MPa. The Young's modulus of T-upstands at the middle and in the edge was 30MPa and 32MPa respectively, and the Young's modulus of corrugated GFRP plate was 34MPa. In addition, the tensile strength of GFRP bars with diameter of 16mm and 20 mm are 655MPa and 620MPa, while the Young's moduli are from 35 to 41GPa. The measured compressive strengths and Young's modulus for concrete slab were 35.6MPa and 30.7GPa respectively.

2.3 Experimental set-up and instrumentation

The loading set-up of flexural behaviour test for hybrid GFRP/concrete deck was shown in Figure 1. The test specimen was simply supported by steel girders at two ends. Two point concentrated load with the distance about 1/3 of the clear span were applied symmetrically by the hydraulic jack. And the deck between two loading points was assumed to be suffered pure bending moment, while the parts between the loading and support point endure combined shear force and bending moment. The experiments were performed over the ultimate load till the failure of the specimen.

During the test, load displacement relationship, stress distribution of GFRP plate, strain distribution along the depth of hybrid deck were measured and investigated to study the mechanical behavior of hybrid deck under positive moment. Displacement transducers LVDTs were used to measure the vertical deflection at the mid-span and 1/4 span of the decks, as shown in Figure 2. At critical sections, the strains were measured using 50 mm electrical gauges for the concrete slab and 5 mm electrical gauges for the GFRP plate. All the information obtained from the transducers, gauges, and load cells were automatically recorded by a data acquisition system at regular intervals during the test.

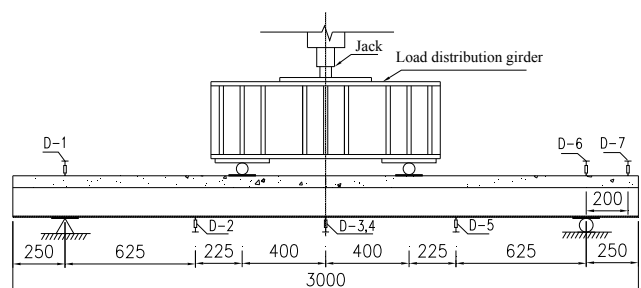


Figure 2 Test setup and LVDTs arrangement /mm

3 EXPERIMENTAL RESULTS AND DISCUSSION

3.1 Failure modes

Two typical failure modes of the six specimens under

ultimate load for flexural behaviour were obtained: one is that the T-upstand at the edge de-bonded, obviously relative slip appeared at the both end, and the shearing break took place at the position below the holes of T-upstands, the crack initiated at the mid-span of concrete, but the concrete slab can still carry about 80% of ultimate load and showed good ductility for specimens S-V-1, S-G-1 and S-S-1(Group1); The other is that the top concrete crushed under ultimate load, the diagonal crack occurred between loading and support point, and showed shear compression failure for specimens S-V-2, S-G-2 and S-S-2 (Group2). No obvious slip between GFRP plate and concrete was observed under ultimate load, the soundness of connection on the interface was improved by the sand coating. The failure modes and relative slip at the end of specimen under ultimate load for flexural test were shown in Figure 3.



Figure 3 Failure modes and relative slip at the end of specimen

3.2 Load-displacement Relationship

The relationship between load and displacement at mid-span until failure was shown in Figure 4. And the deflection along longitudinal direction under ultimate load was shown in Figure 5. Comparison the curves with different test parameters, the results were concluded as follows:

(1) The sand coating for Specimen S-V-2, S-G-2 and S-S-2 improved the ultimate load and the rigidity of the entire deck in comparison with others without surface treatment.

(2) In Group1, the penetrating bars improve the strength and stiffness in comparison with the specimen without them obviously, but the type of penetrating bars influence the strength and rigidity slightly when the Specimen S-S-1 with steel bars comparing with S-G-1 with GFRP bars. In group2, the penetrating bars did not improve the strength in comparison with the specimen without them.

(3) Both surface treatment and penetrating bars improve the connection between GFRP plate and concrete, and promote the strength and whole rigidity of hybrid deck. However, the effect of surface treatment was better than that of penetrating bars based on the comparison of Specimen S-V-2 and S-G-1 or S-S-1.

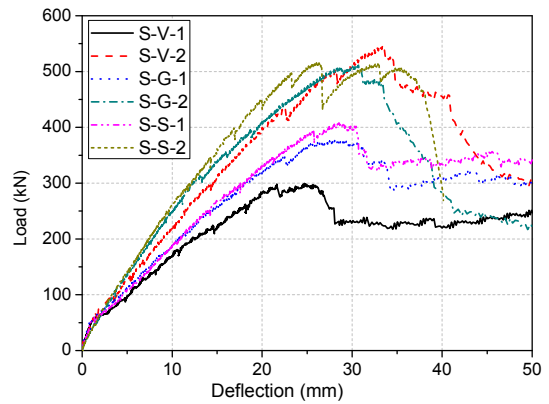


Figure 4 Comparison of load-deflection curves at mid-span

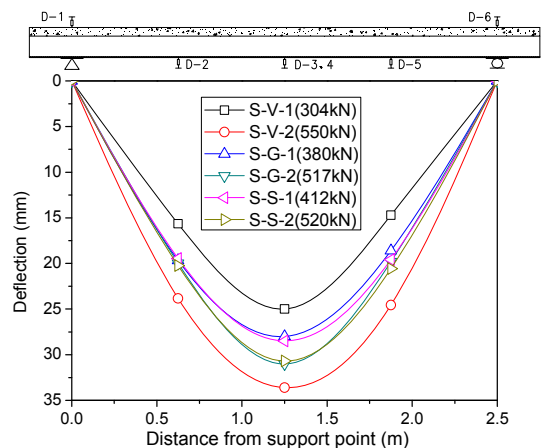
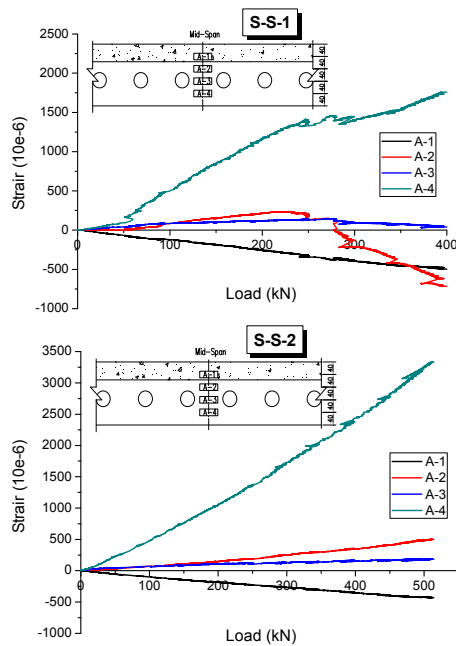


Figure 5 Deflection along longitudinal direction

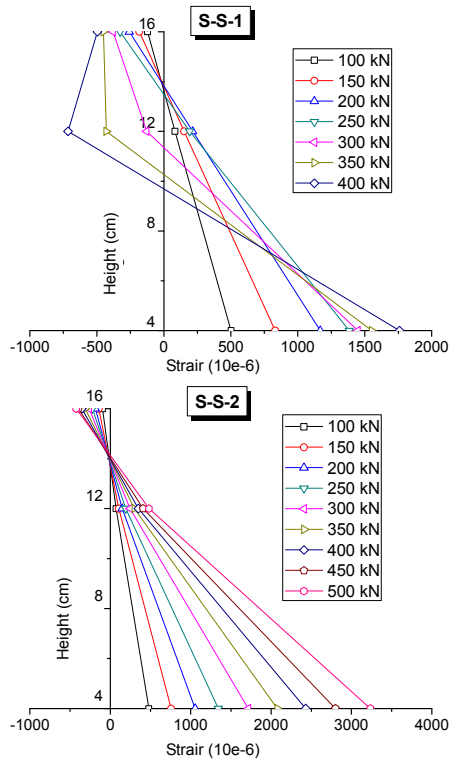
3.3 Strain results on lateral face of hybrid deck

Figure 6 (a) showed the relationship between load and strain on lateral face of hybrid deck at mid-span. It was found that the value of strain changed slightly at the initial loading state (0~60kN), but the slope increased after the load of 60kN, and the strain increased nonlinearly after the load of 250kN for specimen S-S-1, while the strain increased linearly approximately until ultimate load for specimen S-S-2.

Figure 6 (b) showed the strain distribution along depth of hybrid deck at mid-span under different load stage. The value of strain gauge A-3 at the axis position of the holes for the perforated plate was ignored due to strain concentration. It was found that the strain of A-1, A-2 and A-4 showed linearly along the depth of hybrid deck at the initial load stage. However, the location of the neutral axis obtained from the test moved down from 14cm to 9.7cm with the load increased for specimen S-S-1, as the stiffness reduced due to the occurrence of relative slip between GFRP plate and concrete. While the strain values remain plane along the depth of hybrid deck at all load stages, and the neutral axis kept at the distance of about 14cm from the bottom for specimen S-S-2. It was considered that the hybrid deck could be assumed as the full composite section until the ultimate state.



(a) Load-strain relationship



(b) Stress distribution along depth at mid-span

Figure 6 Load-stress relationship and stress distribution along depth

Figure 7 showed the relation between position of neutral axis in the mid-span and the applied load. Two groups were classified according to the different failure mode.

For Specimens in Group1, the neutral axis moved down with the load increased, the stiffness reduced due to the relative slip occurred between GFRP plate and concrete.

For Specimens in Group2, the strain distribution basically corresponded with plane section assumption

under all load stages. The neutral axis kept at the distance of about 14.5cm, 13.5 and 14cm from the bottom for Specimen S-V-2, S-G-2 and S-S-2 respectively. The hybrid deck could be assumed as the full composite section until the ultimate state.

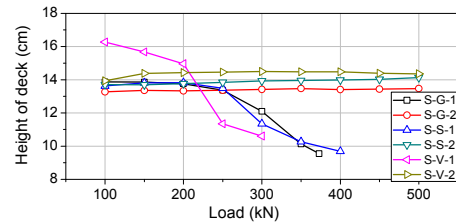


Figure 7 Load-neutral axis relations

4 CONCLUSION

The flexural behaviour of hybrid GFRP/concrete decks considering influencing factors of penetrating bars (types and presence or absence) and surface treatment (with or without sand coating) has been experimentally investigated in this study. The following conclusions may be drawn from the present study:

(1) The surface treatment affects the connection between GFRP plate and concrete, flexural behaviour of hybrid deck obviously.

(2) The influence of the penetrating bars type to the strength and rigidity of the hybrid deck with the same surface treatment condition was comparatively slight. The existence of penetrating bars improved the bending stiffness to some extent, while increased ultimate flexural resistance only for specimens without surface treatment.

(3) Both surface treatment and penetrating bars improve the connection between GFRP plate and concrete, and promote the strength and whole rigidity of hybrid deck. However, the effect of surface treatment was better than that of penetrating bars.

(4) The surface treatment improve the connection performance, and the neutral axis position did not change with the load increased, while neutral axis position moved down without sand coating as the load increased due to stiffness reduction and slip occurrence.

ACKNOWLEDGEMENTS

This research is sponsored by National High-tech R&D Program under Grant No. 2006AA11Z103. This support is gratefully acknowledged. Assistance for experimental studies from State Key Laboratory for Disaster Reduction in Civil Engineering (SLDRCE) in Tongji University is also appreciated.

PREFERENCES

Bakis CE, Bank LC, Brown VL, Cosenza E, Davalos JF, Lesko JJ, et al. 2002. Fiber-reinforced polymer composite for construction-state-of art review. *ASCE, J Compos Constr.* 6(2):73–87.

- Chen L, Zhao, L., Karbhari, V. M., Hegemier, G. A., and Seible, F. 2005. Assessment of a steel-free fiber reinforced polymer composite modular bridge system. *J. Struct. Eng.* 131(3): 498–506.
- Ghosh, K. K., and Karbhari, V. M. 2007. Evaluation of strengthening through laboratory testing of FRP rehabilitated bridge decks after in-service loading. *Compos. Struct.* 77(2): 206–222.
- Karbhari, V. M., and Zhao, L. 2000. Use of composites for 21st century civil infrastructure. *Comput. Methods Appl. Mech. Eng.* 185(2–4): 433–454.
- Keller T. 2002, Fiber reinforced polymer materials in bridge construction. In: *IABSE symposium, towards a better built environment - innovation, sustainability, information technology.*
- Keller T, Gürtler H. 2006. In-plane compression and shear performance of FRP bridge decks acting as top chord of bridge girders. *Compos. Struct.* ;72(2):151 – 162.
- Keller T, Schaumann E, Vallée T. 2007. Flexural behavior of a hybrid FRP and lightweight concrete sandwich bridge deck. *Composites Part A* 38(3): 879-889.
- Naaman, A. E., and Chandransu, K. 2004. Innovative bridge deck system using high-performance fiber-reinforced cement composites. *ACI Struct. J.* 101(1): 57–64.
- Nystrom, H. E., Watkins, S. E., and Nanni, A. 2003. Financial viability of fiber-reinforced polymer bridges. *J. Manage. Eng.* 19(1), 2–8.
- Standardization Administration of the People's Republic of China (SA of P. R. C.) 1983. Test method for tensile properties of glass fiber-reinforced plastics, GB/T1447-1983, Beijing: China Building Material Industry Publishing House, (In Chinese).
- Stiller, W. B., Gergely, J., and Rochelle, R. 2006. Testing, analysis, and evaluation of a GFRP deck on steel girders. *J. Bridge Eng.* 11(4): 394–400.
- Turner MK, Harries KA, Petrou MF, Rizos D. 2004. In situ structural evaluation of a GFRP bridge deck system. *Compos. Struct.* 65(2):157–165.
- Ye LP, Feng P, Zhang K, Lin L, Hong WH, Yue QR, et al. 2003. FRP in civil engineering in China: research and applications. In: Tan KH editor. *Proceedings of fiber reinforced polymer: reinforcement for concrete structures.*

Experimental Study of GFRP-Concrete Hybrid Beams

Fei Zhao^{1,2}, Chaohe Chen¹ (chech@hainu.edu.cn), Wenjuan Lou²

1. College of Civil Engineering and Architecture, Hainan University, Haikou, China

2. College of Civil Engineering and Architecture, Zhejiang University, Hangzhou, China

Peng Feng³

3. Department of Civil Engineering, Tsinghua University, Beijing, China

ABSTRACT A new design concept that led to a hybrid beam is proposed. It comprises a U-shaped GFRP pultruded profile in which concrete was casted. Results are presented from 6 beams tested to ultimate failure, four of which having a fiber-reinforced plastic(FRP)-reinforced concrete construction of combined tensile reinforcement and permanent shuttering, while the others are conventional reinforced concrete beams as a comparison. It is shown that in comparison with an equivalent reinforced concrete beam, hybrid beam gives a great increase in bearing capacity but decrease in ductility.

1 INTRODUCTION

Conventional reinforced concrete is widely applied in the construction industry owing to the availability and low cost of steel and concrete, the knowledge regarding design, and the vast experience of its use in practice. The deterioration of many structures built 40 or 50 years ago is due to the susceptibility of steel reinforcement to corrosion, and this is now a major engineering and economic problem. In the last few decades there has been considerable progress made to establish the emerging construction technology of using fiber-reinforced plastic (FRP) as a material for reinforcing concrete. FRP has many advantages such as high tensile strength, low weight, corrosion immunity, high fatigue strength, high damping, and electromagnetic neutrality (Hull 1981). An important application of FRP in structural engineering involves the use of lightweight components such as framing, walkways and bridges in corrosive environments, chemical and water treatment plants, cooling towers and non-electromagnetic interference buildings [e.g. McCormick(1978), Starr(1983), Sims et al.(1987), Bakeri (1989), Bank and Mosallam(1990), Hollaway(1990), Plecnik et al.(1990), Head(1992), Johansen et al.(1992), and Deskovic(1995a,1995b)].

Some innovative FRP-concrete hybrid members have been proposed by several researchers [e.g. Hillman and Murray(1990), Deskovic et al.(1995a, 1995b), Hall and Mottram(1998), Ribeiro(2001), Nordin and Täljsten(2004) etc.] They considered the combination of FRP pultruded profiles and concrete to form lightweight, high strength and stiffness, and cost-effective structural systems. The idea of combining FRP and concrete was to utilize the

high tensile strength from FRP and high compressive strength from concrete.

The work presented herein is an experimental study on mechanical properties of hybrid beams composed by U-shaped GFRP pultruded profiles and reinforced concrete. The GFRP profile provides tensile reinforcement and permanent shuttering for the system. Results from the tests showed that in comparison with an equivalent reinforced concrete beam, hybrid beam gives a great increase in bearing capacity but decrease in ductility.

2 EXPERIMENTAL PROCEDURE

2.1 Fabrication

For the convenience of adjustment to the cross section size of beam, an L-shaped GFRP pultruded profile was first fabricated, then two L-shaped profiles were connected with GFRP bar to form a U-shaped profile. To ensure an efficient section, composite action between the GFRP permanent shuttering and the concrete is essential. So the mechanical bond is provided with some T-up-stands on the GFRP internal surface which was covered with a curing epoxy mortar, as shown in Figure 1.

A total of four hybrid beams (named as FB1, FB2, FB3 and FB4 respectively) and two conventional reinforced concrete beams (named as RB1 and RB2 respectively) were fabricated with the specifications (including the reinforcement arrangement and method of loading) given in Table 1. The two conventional reinforced concrete beams were used as reference to the hybrid beams. All specimens were 2 m long with 250-mm-deep and 150-mm-wide cross sections (outside dimensions).

All the beams were cast with a normal weight, grade 25, concrete mix of cement: water: fine aggregate: coarse aggregate proportions 1:0.56:1.68:2.99 by weight. Composite portland cement was used and the maximum aggregate size was 15 mm. Three 150-mm cubes for each beam were cast at the same time.

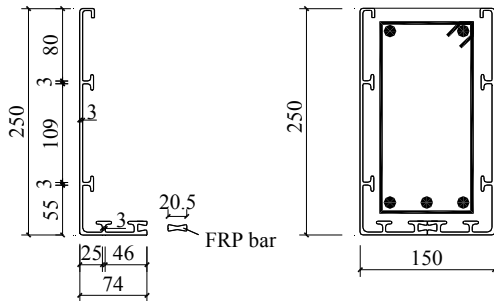


Figure 1 Pultruded GFRP profile and beam cross section (dimensions in mm)

Table 1 Beam specimens specification

Beams	Longitudinal steel rebar	Stirrup	GFRP	Loading method
FB1	3 12	6@100	Yes	Four-point bending
FB2	3 12	6@100	Yes	Three-point bending
FB3	2 10	6@80	Yes	Three-point bending
FB4	–	–	Yes	Three-point bending
RB1	3 16	6@100	No	Four-point bending
RB2	2 10	6@80	No	Three-point bending

2.2 Testing

Tests on all the six beams were carried out. Beams FB1 and RB1 were tested in four-point bending over a span of 1800 mm, the constant moment length was 800 mm and the shear span was 500 mm, while the other four beams in Three-point bending. Load was gradually increased up to failure at the increment of 10kN. To avoid local failure, the supports were made of 200-mm-long and 10-mm-thick steel plates on which the beams were grouted using a fast-curing epoxy-motar mix. Load was measured with a load cell, and deflection at midspan and supports were measured with displacement meters. Strains in the GFRP web face and bottom flange at midspan were recorded using 15-mm-long strain gauges bonded externally to the GFRP outer faces. And strains in the tensile longitudinal steel bar at midspan were also recorded using 3-mm-long strain gauges. The testing apparatus is schematically illustrated in Figure 2.

The material properties were established from test on specimens subjected to uniaxial loading. The compressive strength of the concrete in the hybrid beams was obtained by testing three 150-mm cubes for each beam on the same day that beam was tested. GFRP testing in uniaxial tension was performed on a series of 30×400mm specimens.

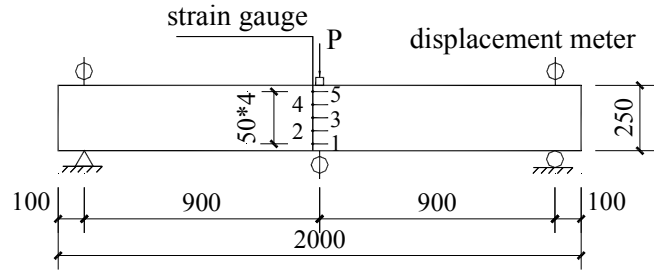


Figure 2 Schematic illustration of test setup

Testing took place by bonding 2-mm-thick aluminum plates at the end of each specimen on both sides, to facilitate anchoring. A computerized testing machine imposed deformations at a rate of 5mm/min, while a strain gauge attached to the middle of each specimen was used to measure strains.

3 TEST RESULTS

3.1 Mechanical properties of materials

The mechanical properties of concrete, steel rebars and GFRP obtained from uniaxial tests are presented in Table 2-4.

Table 2 Mechanical characteristics of concrete

Beams	Concrete strength f_{cu} (MPa)
FB1	29.1
FB2	27.3
FB3	23.1
FB4	23.6
RB1	29.1
RB2	27

Table 3 Mechanical characteristics of steel rebars

Diameter	Yield strength f_y (MPa)	Ultimate strength (MPa)
6	325	550
10	347.5	482.5
12	368	560
16	370	568

Table 4 Mechanical characteristics of GFRP

	Tensile strength f_{frp} (MPa)	Tensile elasticity modulus E_{frp} (GPa)	Tensile elongation ϵ_{frp}
GFRP	680	4.1	4%

3.2 Failure modes

All the hybrid beams failed in shear. The transverse strength and shear strength of GFRP profile were low, so it was susceptible to appearing horizontal cracks first in the profile lateral surface. With the increase of load, it

could be seen that the shear crack had propagated along the GFRP concrete interface. Finally, the web fractured due to shear stresses, resulting in shear failure, and the slip between GFRP surface and concrete occurred. Longitudinal reinforcements yielded in most of beams except FB1, and no concrete crush occurred in compression zone. The mode of failure is shown in Figure 3. In a well-designed hybrid FRP-concrete section, the bottom GFRP flange fails first at a certain moment. The stresses are then redistributed and the section continues to carry an increasing moment until the concrete crushes in compression when its maximum compressive strain equals the ultimate failure strain of concrete. When treating the FRP as a replacement for steel rebars, conventional reinforced concrete analysis shows that all the tested hybrid beams were overreinforced relative to a balanced design.



Figure 3 Beam FB2 after test: shear mode of failure is visible

3.3 Flexural behavior of hybrid beams

The moment-versus-midspan deflection, the moment-versus-FRP tensile extreme surface strain at midspan, the strain distribution profile on FRP web surface at midspan and the moment-versus-longitudinal steel rebar tensile strain at midspan for the four hybrid beams tested are illustrated in Figures 4 – 7. At initial loading stage, the moment with deflection response at midspan was linear and elastic. At ultimate failure the central deflection was in the span/127-span/103 range, the nonlinear behavior of the flexural members above serviceability is apparent. The strain distribution profiles on FRP web surface at midspan for beam FB1 (Due to space limitations, the similar profiles for beams FB2, FB3 and FB4 are not shown) show that the midspan section remains plane after loading.

The comparison on serviceability moment (referred to the moment when central deflection equals to $\text{span}/250=7.2\text{mm}$, a serviceability limit on deflection from “Code for design of concrete structures”), ultimate moment and the corresponding central deflection between hybrid

beams and conventional reinforced concrete beams are given in Table 5. It could be seen that the experimental ultimate moment/serviceability moment ratio for hybrid beams was in the 1.4-1.6 range, and the equivalent ratio for central deflection was higher at 2.0-2.4. From Table 5, it is shown that the ultimate moment capacity of FB3 is 6 times as much as RB2 which has the same reinforcement arrangement. It is also concluded that with the increase of longitudinal steel rebars areas, the bearing capacity of hybrid beams also increase, although the increment is not as high as the steel rebars areas. This means FRP plays a major role in carrying capacity.

Table 5 Response of beam specimens

Beams	Serviceability moment (kN · m)	Ultimate moment (kN · m)	Central deflection* (mm)
FB1	47.5	72.5	15
FB2	64	90	14
FB3	49	79	17
FB4	45	67.5	15
RB1	43	47.5	8
RB2	—	13.5	3

* Central deflection referred to the deflection corresponding to the ultimate moment.

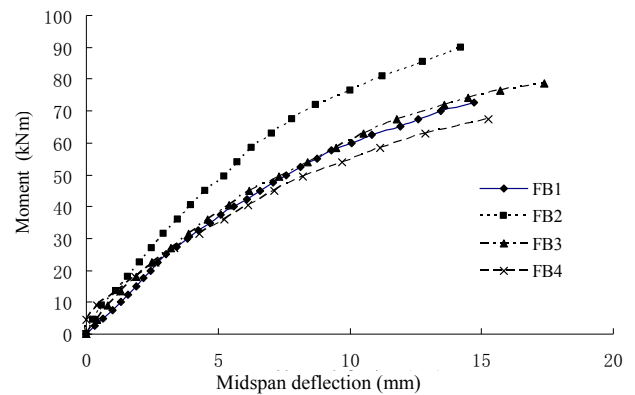


Figure 4 Maximum moment-versus-central deflection

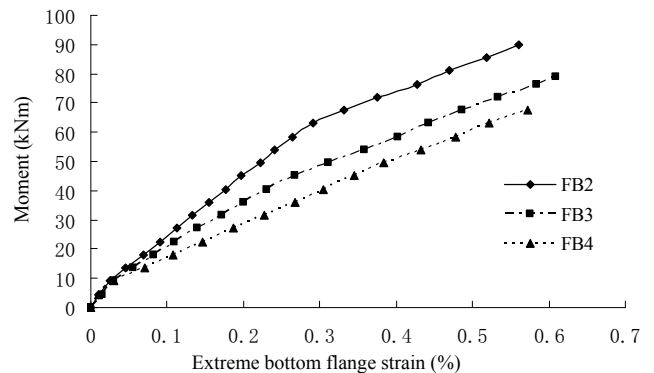


Figure 5 Maximum moment-versus-extreme surface tensile strain at midspan(bottom flange strain in FB1 was not measured)

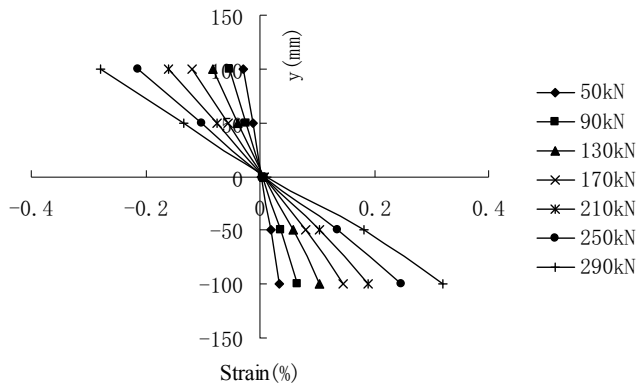


Figure 6 The strain distribution profile on FRP web surface at midspan for beam FB1

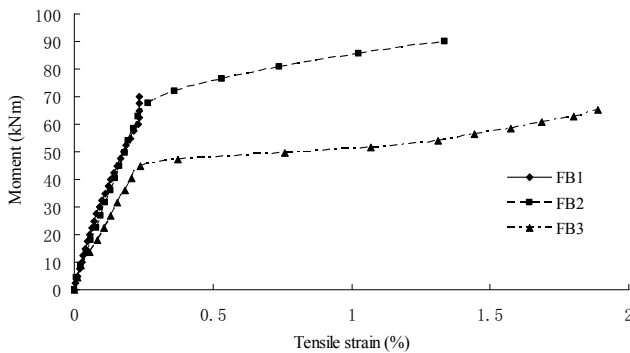


Figure 7 Maximum moment-versus-longitudinal steel rebar tensile strain at midspan

4 CONCLUSION

The study presented here has focused on short-term behavior of concrete with composite material providing combined permanent shuttering and tensile reinforcement. Four hybrid beams and two conventional reinforced concrete beams have been tested in flexure. Results from the experimental program showed the following:

(1) A comparison of hybrid beam with an equivalent reinforced concrete beam of the same specifications (including dimensions and reinforcement arrangement) gives a great increase in bearing capacity but decrease in ductility.

(2) When treating the FRP as a replacement for steel rebars, conventional reinforced concrete analysis shows that all the tested hybrid beams were overreinforced relative to a balanced design.

(3) With the increase of longitudinal steel rebars areas, the bearing capacity of hybrid beams also increase, although the increment is not as high as the steel rebars areas. This means FRP plays a major role in bearing capacity.

(4) Failure of connection between two L-shaped profiles was not found in all tested hybrid beams, this indicates that the connection is efficient and reliable.

(5) All the tested hybrid beams failed in shear due to the low transverse strength and shear strength of GFRP

profile. The desired flexural failure could hardly be achieved. Therefore, it is essential to refabricate the GFRP profile to promote the transverse strength and shear strength of webs.

The durability and corrosion resistance of advanced polymer composite materials is generally good. They have superior properties to the current conventional materials used in reinforced concrete construction. This has particular implications for hostile environments, e.g. marine applications.

Fiber-reinforced composite material is more expensive than reinforced concrete materials of the equivalent load capacity, however, when the whole-life costing of the fabrication, erection and maintenance of the beam is considered, the overall costs will be comparable to those of a reinforced concrete beam.

Further theoretical analysis on mechanical behavior for hybrid beam will be undertaken.

ACKNOWLEDGEMENTS

The authors are grateful to the National Natural Science Foundation of China (Project No. 50868004) for the financial support. Thanks are also due to associate professor Hong Wang and postgraduate Yefan Chen for their support and assistance during the experimental program.

REFERENCES

- Bakeri, P.A. 1989. *Analysis and design of polymer composite bridge decks*. MS thesis, Dept. of Civ. Engrg., Massachusetts Inst. of Technol., Cambridge, Mass.
- Bank, L.C. & Mosallam, A.S. 1990. Structural performance of a fiber reinforced plastic pultruded frame. *Proc., 8th Struct. Cong. 90, ASCE, New York, N. Y.*, 509-510.
- Deskovic, N., Triantafillou, T.C., Meier, U. 1995a. Innovative design of FRP combined with concrete: short-term behavior. *Journal of Structural Engineering* 121(7): 1069-1078.
- Deskovic, N., Triantafillou, T.C., Meier, U. 1995b. Innovative design of FRP combined with concrete: long-term behavior. *Journal of Structural Engineering* 121(7): 1079-1089.
- Hall, J.E. & Mottram J.T. 1998. Combined FRP reinforcement and permanent formwork for concrete members. *Journal of Composites for Construction* 2(2): 78-88.
- Head, P.R. 1992. Design methods and bridge forms for the cost effective use of advanced composites in bridges. *Proc., 1st Int. Conf. on Adv. Composite Mat. in Bridges and Struct., Can. Soc. For Civ. Engrg.*, Montreal, Canada, 15-30.
- Hillman, J.R. & Murray, T.M. 1990. Innovative floor systems for steel framed buildings. *Proc., IABSE. symp., Mixed Struct., including New Mat.*, Brussels, 60, IABSE, Zurich, 672-675.
- Hollaway, L. ed. 1990. *Polymers and polymer composites in construction*. T. Telford, London, England.
- Hull, D. 1981. *An introduction to composite materials*. Cambridge, England: Cambridge University Press.

- Johansen, G.E., Wilson, R., Pope, D.A., Goss, G., Ritchie, P., and Mellen, J. 1992. Spanning "devil's pool" with a prestressed cable/FRP tube structural system. *Proc., 1st Int. Conf. on Adv. Composite Mat. in Bridges and Struct.*, Sherbrooke, Canada, 435-444.
- McCormick, F.C. 1978. Laboratory and field studies of a pedestrian bridge composed of glass reinforcement plastic. *Transp. Res. Rec. 665*, Transp. Res. Board, Washington, D.C., 99-107.
- Nordin, H. & Täljsten, B. 2004. Testing of hybrid FRP composite beams in bending. *J. Composites: Part B* 35(1): 27-33.
- Plecnik, J.M., Azar, W., and Kabbara, B. 1990. Composite applications in highway bridges. *Proc., First Mat. Engrg. Cong. 90, ASCE, New York, N. Y.*, 986-995.
- Ribeiro, M.C.S., Tavares, C.M.L., Ferreira, A.J.M., Marques, A. T. 2001. Static flexural performance of GFRP-polymer concrete hybrid beams. *Proceedings of the International Conference on FRP Composites in Civil Engineering. Hong Kong:Elsevier Science Ltd*, 1355-1361.
- Sims, G.D, Johnson, A.F., and Hill, R.D. 1987. Mechanical and structural properties of a GRP pultruded section. *Composite Struct.* 8(3): 173-187.
- Starr, T.F. 1983. Structural applications for pultruded profiles. *Composite Struct. 2:Proc., 2nd Int. Conf. on Composite Struct.*, 193-213.

In-Situ Load Tests and FE Modeling of Concrete Bridge with FRP Stay-in-Place Forms

B. Wan (baolin.wan@marquette.edu) & C.M. Foley

Department of Civil and Environmental Engineering, Marquette University, Milwaukee, WI, USA

ABSTRACT Two in-situ load tests were performed on a highway bridge with FRP Stay-in-Place (SIP) formwork that also serves as positive flexural reinforcement for the bridge deck as part of a long-term monitoring program. The load tests conducted consisted of positioning a wheel of a tri-axle dump truck with calibrated loading at a series of target locations in a line parallel to the girders at mid-span of the deck. Portable strain sensors were used to determine the distribution of the wheel loads within the FRP-SIP bridge deck and draw-wire transducers were used to measure deck deflections. Wheel load distribution widths are calculated using the measured strain values and the results are compared with wheel load distribution widths found in the AASHTO-LRFD and AASHTO Standard specifications. A 3-D finite element model was created to analyze the performance of the bridge subjected to traffic load and concrete shrinkage.

1 INTRODUCTION

The state of Wisconsin recently constructed a highway bridge with a novel deck system as part of the FHWA Innovative Bridge Research and Deployment Program. The bridge has been in service for over five years. The bridge superstructure is composed of traditional precast concrete I-girders acting compositely with the bridge deck and FRP Stay-in-Place (SIP) formwork that also serves as positive flexural reinforcement for the deck (Bank et al. 2005). The bridge is Bridge B-20-133 on U.S. Highway 151 in Waupun, Wisconsin and it is a typical precast, pre-tensioned two-span continuous superstructure system (two simple spans at time of construction and two-continuous spans under live loading) as shown in Figure 1. In order to monitor its long-term performance, a five-year program was established including two in-situ load tests with two-year interval and field inspections. During field inspections, it was found that transverse cracks formed around the negative moment regions above the central piers shortly after the bridge serviced the traffic (Martin 2006). A 3-D finite element model was built to study the potential causes of the deck cracking.

2 IN-SITU LOAD TESTS

2.1 Instrumentation

The portable strain sensors developed by Schneeman (2006) were utilized to measure normal strain in various bridge superstructure components (e.g. bridge deck, girders). Mounting the portable strain sensors in the field required that two wedge-type expansion anchors be

drilled into the cover concrete (25.4-mm of embedment). Calibration of the sensors for this mounting is discussed in Schneeman (2006). Commercially available draw wire transducers (DWT's) were used to measure the deflection of the bridge deck relative to the bridge girders.

A schematic illustrating the instrumentation in plan is shown in Figure 1. The instrumentation in this bridge structure was focused on measuring the distribution of wheel loads within the bridge deck and the deflection of the bridge deck relative to the girders.

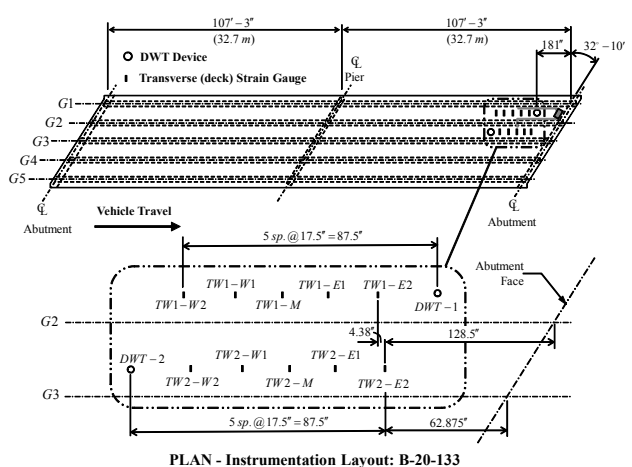


Figure 1 Instrumentation layout for B-20-133 (1 in. = 25.4 mm)

2.2 Loading Protocol

Calibrated (i.e. weighed) tri-axle dump trucks were utilized during all load tests. The truck used in July 2007 had gross vehicle weight of 254,184 N and the one used in

July 2009 was 288,360 N. Two loading protocols were used to examine the wheel load distributions within the bridge deck. Loading protocol 1 (Travel path 1) as shown in Figure 2 was intended to generate larger strains in the TW1 sensors (relative to the TW2 sensors) to evaluate the exterior deck span strain and deflections. Therefore, the left front wheel of the truck is positioned along a longitudinal line at mid-span of this exterior bridge deck span. Loading protocol 2 (Travel path 2) was intended to generate larger strains in the TW2 sensors (relative to the TW1 sensors) measure deck deflection and wheel load distribution within the first interior deck span in the superstructure.

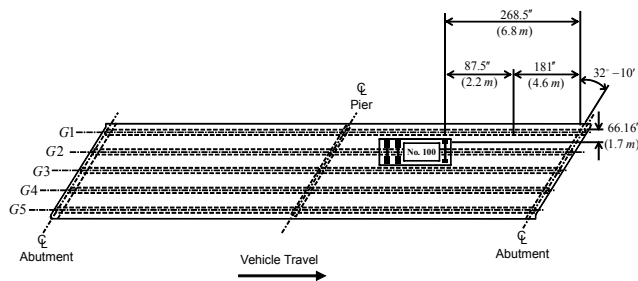


Figure 2 Loading protocols used to examine wheel load distribution in the exterior deck spans within the deck

During the test for load protocol 1, the truck was slowly brought onto the superstructure and temporarily stopped at the first sensor location (TW1-W2 in Figure 1). The truck then proceeded forward at a slow (controlled) pace with additional stops at locations corresponding to the remaining four strain sensors and one draw wire transducer (DWT). The truck left the bridge and then followed the path for load protocol 2 to do the same creep-forward-with-stop motion. The data acquisition system kept record the strains and deflections when the truck was on the bridge.

2.3 Load Testing Results and Discussion

Two load tests were conducted as part of the monitoring effort. The first occurred in July 2007 and the second occurred in July 2009. Peak deck deflections measured by DWT-1 during the two load tests are comparable to one another with the peak magnitudes on the order of 0.381 mm. The peak deformations do not illustrate any significant difference over the two year period and therefore, one can conclude that there has been no significant change in the flexure load transfer mechanism in the bridge deck. Therefore, there is a very low likelihood of degradation within time.

Figure 3 illustrates the wheel load strain distribution at mid-span of the exterior deck span (TW1 sensors) obtained during the July 2007 load test when truck travel path 1 was implemented. It illustrates the expected stepped variation in strain readings from sensor TW1-E2 through TW1-W2. When the vehicle wheel is intended

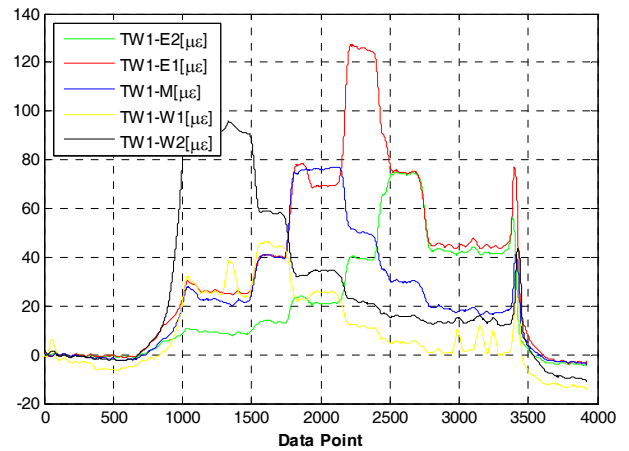


Figure 3 Wheel load strain distribution measurements in the exterior bridge deck span

to be placed over TW-W2, this sensor experiences the largest tensile strain. When the wheel is intended to be over TW1-E2 (far right of Figure 1), sensor TW1-W2 reads the smallest tensile strain. This is consistent with the sensor layouts within the exterior deck span shown in Figure 1.

3 WHEEL LOAD DISTRIBUTION WITHIN BRIDGE DECK

The load testing conducted afforded the opportunity to evaluate wheel load distribution widths within the novel FRP-SIP bridge deck system used in B-20-133. The strain measurements from the July 2007 load test were used as the basis for computing estimates for the amount of bridge deck width that resists wheel loading. The strain readings were used to generate equivalent bending moment magnitudes assuming fully-composite behavior between the FRP-SIP formwork and the concrete deck. Preliminary FEA indicated that this is a reasonable assumption for service-level loads (Martin 2006). The strain readings at the bottom surface of the FRP-SIP formwork were converted to moments using Bernoulli beam theory assumptions,

$$M = \frac{E_{comp} \varepsilon I_{comp}}{y_{bot}} \quad (1)$$

where E_{comp} is the modulus used for the transformed section assuming that the concrete material has been transformed to equivalent FRP material (39.5 GPa). I_{comp} is the second moment of area for the composite cross-section ($197.4e6 \text{ mm}^4$). Its magnitude was computed using a 444.5-mm width and data related to the FRP grid and the FRP-SIP formwork panels (Berg 2004). The total height of the in-situ bridge deck is 203.2 mm. ε is the measured strain and y_{bot} is the distance from the centroid of the transformed composite deck cross-section to the bottom surface of the FRP-SIP formwork (103.9 mm).

The strain readings from Figure 3 are used to generate bending moment magnitudes acting in the vicinity of the strain sensor and these magnitudes are assumed to be an average across the 444.5-mm width adjacent to the strain sensor. The total positive moment resisted within the linear influence surface adjacent to the wheel loads is simply the summation of all moment magnitudes computed using the measured strains. The total moments are then divided by the linear distance defining the area of influence to generate an average positive bending moment per unit width. The total and average moments calculated by using the measured strains are given in Table 1.

Table 1 Bending moment calculated from measured strains

Stop Location	M_T^+ (kN-m)	M_{avg}^+ (kN-m/m)
Exterior Span		
TW1-W2	20.4	5.1
TW1-W1	19.1	6.1
TW1-M	17.0	7.7
TW1-E1	21.3	6.8
TW1-E2	24.5	6.1
Interior Span		
TW2-W2	14.5	3.6
TW2-W1	12.1	3.9
TW2-M	10.4	4.7
TW2-E1	13.1	4.2
TW2-E2	12.6	3.2

Standard specification design procedure for bridge deck analysis (AASHTO 2002) was also used to calculate the live load bending moment for this bridge subjected to the truck load. The bending moment per unit width for continuous bridge deck, M_{LLM} , is calculated by

$$M_{LLM} = 0.8P_w \frac{S+2}{32} \quad (2)$$

where P_w is the wheel loading; and S is the span of the bridge deck. For this bridge, the deck span is 2.6 m and the wheel loading was 48.6 kN. By using these data, the Standard specification design method (Equation 2) results 12.99 kN-m/m for the bending moment per unit width. Compared with the results calculated from measured strains (Table 1), the Standard specification (AASHTO 2002) methodology conservatively estimates the bending moment per foot of width that would be seen in the deck. As expected, the exterior span would control the positive bending moment magnitude used for design and the Standard specification procedure is more conservative for the interior span. One could use the Standard specification procedure (AASHTO 2002) to conservatively analyze the FRP-SIP bridge deck at load levels slightly above service-level loading.

The LRFD procedure includes definition of a strip width used to facilitate use of bending moments computed using one-dimensional analysis (AASHTO 2006). Strip widths were computed using the measured strain data

and compared with the calculated results using LRFD procedure (Foley et al 2008). The average positive moment strip width for the exterior span computed using the measured strains is approximately 3.2 m. The positive moment strip width computed using the LRFD specifications (AASHTO 2006) is 2.1 m. The average positive bending moment strip width for the interior span condition computed using the field-measured strain magnitudes is larger indicating a greater width of bridge deck resisting wheel loads. Therefore, LRFD specifications are also conservative for analyzing this innovative FRP-SIP bridge deck.

4 FINITE ELEMENT ANALYSIS

A 3-D finite element model of the bridge superstructure was created using ANSYS to determine the relationship between traffic loading on bridge decks, and the possibility of transverse cracking over interior piers. The model was first calibrated by the in-situ load test data, and then loaded with two HL-93 trucks to represent the traffic loading on the bridge. The HL-93 truck loads were placed on the bridge at the locations at which the maximum negative moment would result in the deck over the interior pier (Komp 2009).

To examine the probability of transverse cracking over the interior pier, nine nodes of the finite element model were selected at the top of the deck surface, over the interior pier of the bridge (shown in Figure 4), to examine the longitudinal stresses. The maximum longitudinal tensile stress in the deck is 0.79 MPa which is much less than the concrete modulus of rupture (3.7 MPa). Therefore, the normal traffic load itself will not cause concrete deck cracking.

The transverse cracks did appear in the deck (Martin 2006). The possible reason is concrete shrinkage. Concrete shrinks after it is cured as a result of water being consumed during the hydration process and evaporation. If this volume change of concrete is restrained, tensile stresses will be developed and may cause cracking. Shrinkage cannot be directly modeled by ANSYS. Therefore, temperature load was applied the bridge to represent the shrinkage in the concrete in a finite element analysis. The detail of the finite element modeling for concrete shrinkage can be found in Komp (2009). The finite element analysis indicated that maximum tensile stress (4 MPa) in bridge deck due to concrete shrinkage was higher than the modulus of rupture of the concrete (3.7 MPa) as early as the age of 10 days after casting. The longitudinal normal stress contour in the deck over the interior pier is shown in Figure 5.

The FEA shows that the HL-93 loading caused tensile stress is approximately equal to 21.6% of the modulus of rupture of the concrete, and 19.4% of the stress caused by concrete shrinkage. In modeling the traffic loading, only two HL-93 trucks were statically placed on the

deck's surface. In reality, varying traffic loading would have a dynamic component as vehicles move across the bridge deck. Therefore, even if the deck is not cracked due to concrete shrinkage, the combination of traffic load and concrete shrinkage will cause transverse cracking in the bridge deck over the interior support as is seen in the bridge.

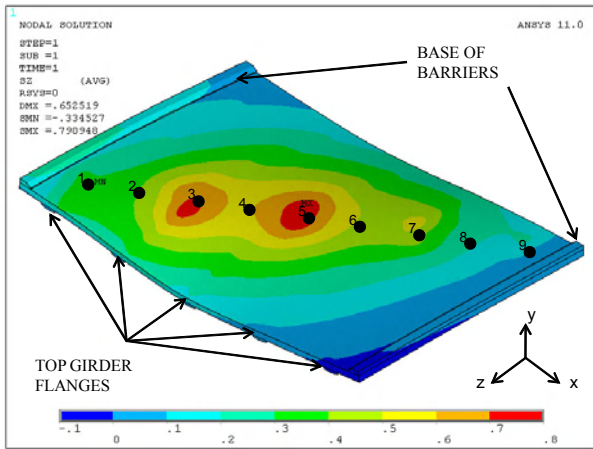


Figure 4 Longitudinal stress contour on top of deck due to two HL-93 truck loads

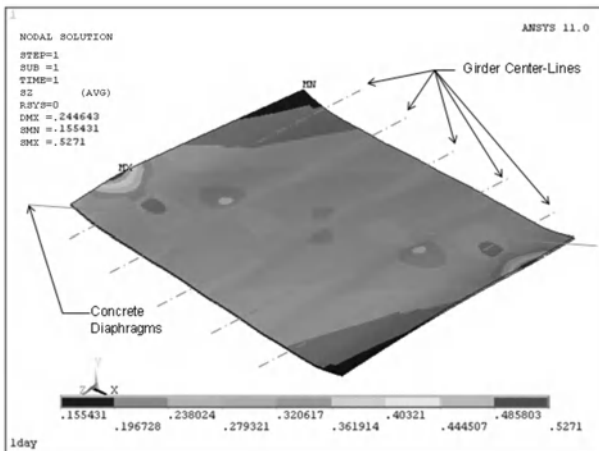


Figure 5 Longitudinal stress contour on top of deck due to concrete shrinkage

5 CONCLUSIONS

Following conclusions can be drawn from this research:

1. The Standard and LRFD procedures for estimating bending moment load-transfer mechanisms in bridges are conservative to predict the load distribution width for this FRP-SIP deck system.

2. Traffic load itself will not cause deck cracking in this bridge. However, traffic load combined with concrete shrinkage will likely cause transverse cracking in the deck over the interior piers.

REFERENCES

- AASHTO (2002). *Standard Specifications for Highway Bridges, Customary Units*, 17th Edition, American Association of State Highway and Transportation Officials, Washington, DC.
- AASHTO (2006). *AASHTO LRFD Bridge Design Specifications Including 2006 Interim Revisions*, Customary U.S. Units, 3rd Edition, American Association of State Highway and Transportation Officials, Washington, DC.
- Bank, L.C., Oliva, M.G., and Russell, J. S. (2005). *In-Situ Load Testing of IBRC Bridge*, Wisconsin Department of Transportation, Federal Highway Administration, Madison, WI.
- Berg, A. C. (2004). *Analysis of a Bridge Deck Built on U.S. Highway 151 with FRP Stay-In-Place Forms, FRP Grids, and FRP Rebars*, MS Thesis, University of Wisconsin at Madison, Madison, WI.
- Foley, C.M., Wan, B. and Liu, J. (2008). Wheel Load Distribution in Concrete Bridge Decks with FRP Stay-in-Place Forms, *ACI SP-257: FRP Stay-In-Place Forms for Concrete Structures CD-ROM*, SP-257-3.
- Martin, K.E. (2006). *Impact of Environmental Effects on and Condition Assessment of IBRC Bridge Decks in Wisconsin*, M.S. Thesis, Marquette University, Milwaukee, WI.
- Schneeman, C.L. (2006). *Development and Evaluation of a Removable and Portable Strain Sensor for Short-Term Live Loading of Bridge Structures*, M.S. Thesis, Marquette University, Milwaukee, WI.

Structural Performance Evaluation of Precast FRP-Concrete Composite Deck with Concrete Wedge for Cable-Stayed Bridge

S. Y. Park (syPark@kict.re.kr), K. Cho, S. T. Kim, J. R. Cho & B. S. Kim

Korea Institute of Construction Technology (KICT), Gyeonggi-do, Republic of Korea

ABSTRACT Despite of the large contribution of the deck in the whole weight of the superstructure, the deck occupies a small portion of the construction costs in cable-stayed bridges. The application of high performance materials for the deck can represent a fair alternative to reduce the weight of the deck and improve the economic efficiency of the bridge even if high performance materials are costly. Accordingly, KICT developed a precast FRP-concrete composite deck to provide solution. The self-weight of this new-type deck is reduced to 60% compared to the conventional precast concrete deck. In this study, experiments on several beams were performed in order to investigate the behavioral characteristics of the deck and verify its structural performance.

1 INTRODUCTION

The weight of the superstructure is a determinant factor in the design of long-span bridges like cable-stayed bridges. Figure 1 compares the weight and construction costs of the superstructure of steel composite cable-stayed bridges built in Korea. The deck is responsible of 69% of the weight of the superstructure while occupies merely 15% of the whole construction cost (KICT Reports, 2007).

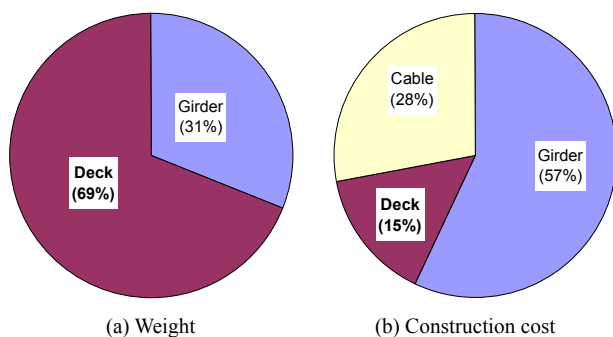


Figure 1 Example of the contribution of the superstructure in the weight and construction cost of cable-stayed bridges

From such observation, it can be easily stated that effective reduction of the construction cost to an acceptable level can be achieved through the reduction of the quantity of the other members like cables by realizing lightweight deck through the use of high-performance materials. Accordingly, Korea Institute of Construction Technology (KICT) started the development of decks for cable-stayed bridges using FRP since 2007.

Figure 2 depicts the precast FRP-concrete composite deck adopted in this study. This deck modifies the previous FRP-concrete composite deck developed by KICT by

surrounding the 4 edges of the FRP panel by concrete and be being fabricated through precasting. The optimal design and economical efficiency of the deck have already been implemented for the deck considering a target span of 4m through the preceding study (Cho et al., 2009).

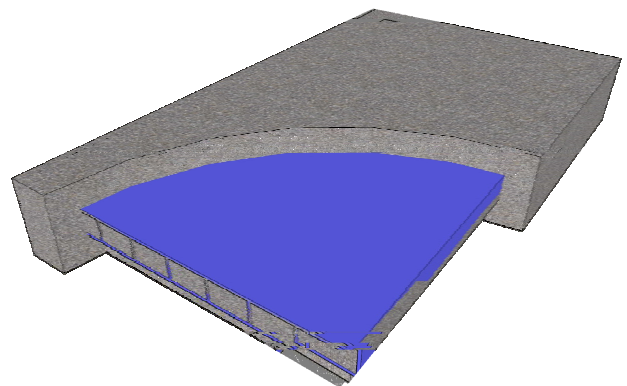


Figure 2 Conceptual scheme of the FRP-concrete composite deck for cable-stayed bridges

This study conducts static tests on specimens to evaluate the structural performances of optimized precast FRP-concrete composite deck applying concrete wedge as a bridge deck. The performance of the concrete wedge for the composition of FRP and concrete has been already been demonstrated in a former paper (Park et al., 2009).

2 EXPERIMENTAL STUDY

2.1 Design and fabrication of the specimens

Differently from normal girder bridge decks, the span length of the deck of cable-stayed bridges is determined by the spacing of the cross-beams and the traveling direction

becomes the principal direction of the deck. Figure 3 presents the results of the optimal design of the deck for cable-stayed bridge with a span length of 4m satisfying the Korea Highway Bridge Design Code (2005). The height of the FRP module is 150mm and the thickness of the upper and lower flanges is 6mm and 12mm, respectively. The web thickness of FRP is 8mm with a

spacing of 200mm. The height of concrete is 100mm above the FRP module and is 330mm at the supports including the haunch of 80mm. Figure 3(c) shows the details of the concrete wedge introduced to strengthen the connection between FRP and concrete. Table 1 lists the mechanical characteristics of the FRP used. The design strength of concrete is 40MPa.

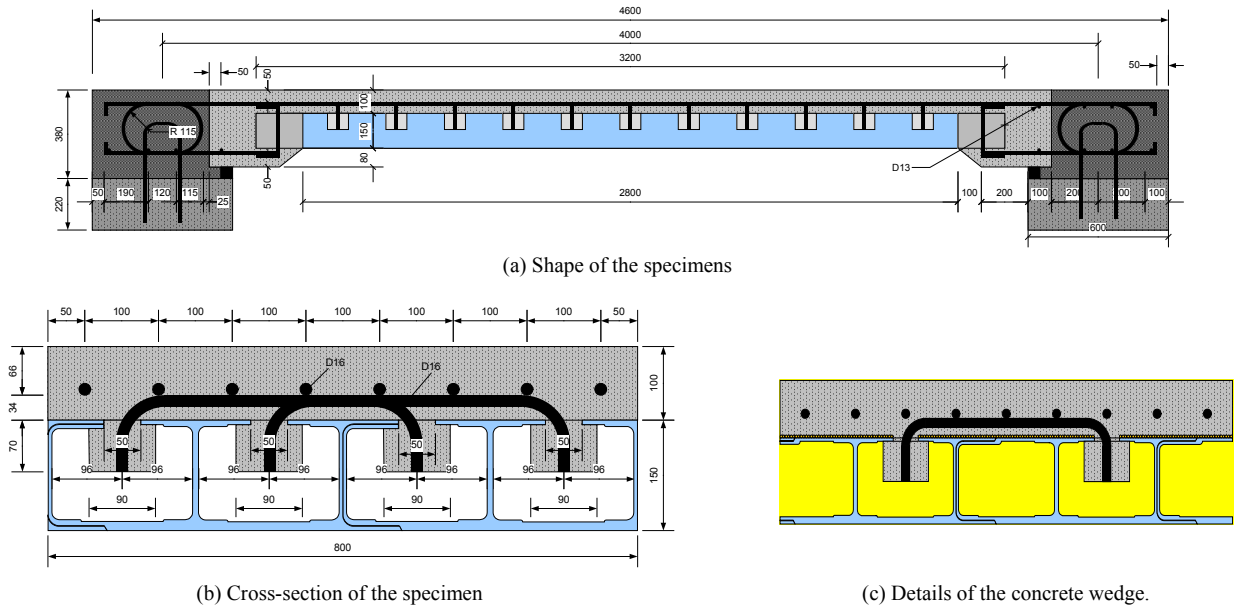


Figure 3 Shape and dimensions of the specimens

Table 1 Mechanical properties of FRP

Characteristics		Unit	Lower flange	Web	Upper flange
Pultrusion direction	Tensile strength	MPa	305	317	312
	Tensile elastic modulus	GPa	28.9	29.1	21.5
	Compressive strength	MPa	512	450	383
	Compr. elastic modulus	GPa	5.60	169	–
Direction perpendicular to pultrusion	Tensile strength	MPa	5.38	–	87.7
	Tensile elastic modulus	GPa	9.37	–	15.4
	Compressive strength	MPa	163	183	166
	Compr. elastic modulus	GPa	2.51	–	–

Besides, the specimens were fabricated following a sequence reproducing conditions similar to field that is, the precast part is manufactured at first and composed with the end blocks that have been fabricated separately. Reinforcing bars with diameter of 16mm were arranged at spacing of 100mm to strengthen the negative moment zones (Figure 4). The extremities were fabricated with a loop shape so as to enable the application of loop joint of the precast concrete deck. By adopting such scheme, the section of this deck presents a reduction of its weight by 60% compared to common precast concrete decks for cable-stayed bridges.



Figure 4 Fabrication of the precast FRP-concrete composite deck specimens (after assembling of rebars)

2.2 Test results

A total of 6 specimens were fabricated with total length of 4.8m and width of 0.8m. However, the first two specimens exhibited problems during the test process and were discarded from the analysis of the results. Figure 5 illustrates the boundary conditions of the specimens. The specimens were fixed using support blocks and hydraulic jacking bolts so as to obtain results more conservative than any actual bridge deck in terms of the negative moment.

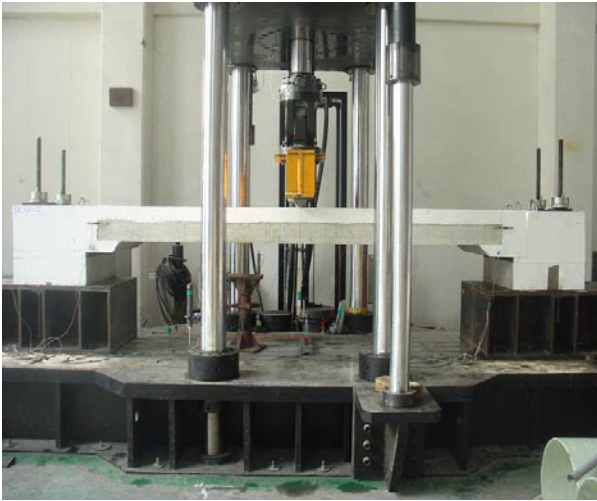


Figure 5 Testing of the precast FRP-concrete composite deck specimens

Cracks initiated first with increasing load at the top of concrete near the supports. Thereafter, the number of cracks augmented gradually at the supports to result finally in the failure of the specimen through the debonding of the web of the FRP module from the upper flange. Figure 6 presents a typical failure mode where debonding occurs between the web of the FRP module and the upper flange.

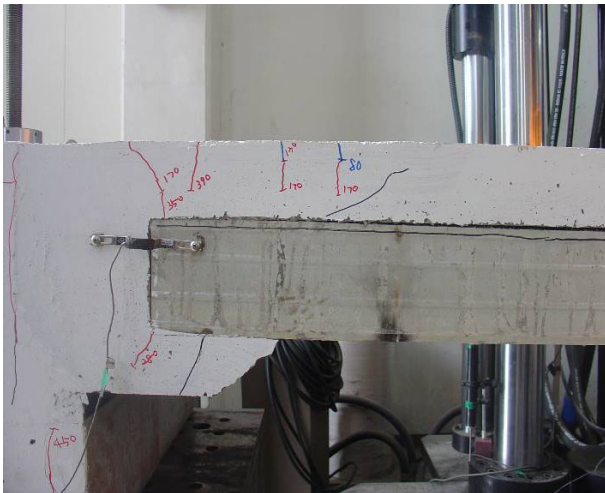


Figure 6 Typical failure mode of the precast FRP-concrete composite deck

On the other hand, problems like concrete spalling did not occur at the haunches of all the specimens until final failure. Furthermore, debonding between the FRP module and concrete could not be observed at the extremities of the FRP module near the supports nor the parts in contact with concrete. Accordingly, the reinforcement details at the haunches applied during the design of the specimens can be said to be appropriate. Figure 7 shows the cracks that occurred in the deck at proximity of the supports due to the negative moment. Here also, the crack gage installed in the construction joints revealed that additional cracks

maintained constant spacing and presented evenly distributed pattern. This result also confirms the appropriateness of the design of the reinforcement details.

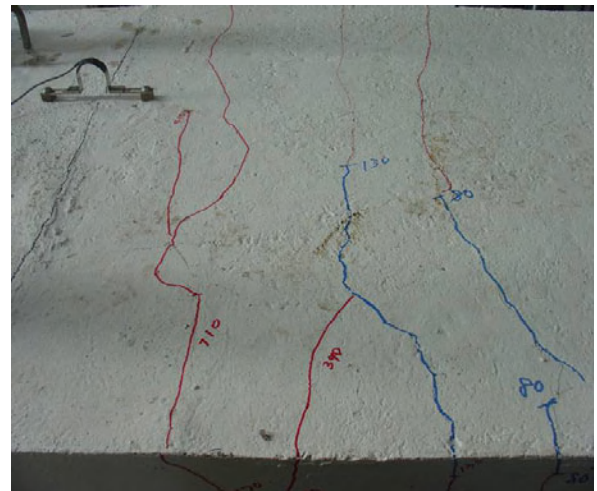


Figure 7 Crack pattern at supports

3 STRUCTURAL PERFORMANCES

Figure 8 plots the load-deflection curves of each specimen together with the design criteria. It can be seen that all of the 4 specimens which were named BCSF-3 to BCSF-6 failed between 510 and 620kN. The corresponding mean values are used to verify the deflection, strength and crack width with respect to the Korea Highway Bridge Design Code (KHBDC, 2005).

For the deflection, the deflection measured in the specimens remained below 3mm, which satisfies the criterion ($L/800 = 5\text{mm}$) of KHBDC. Besides, the satisfaction of the design criterion for the ultimate strength depends on the application of the strength reduction factor. In the present study, the negative moment zones of the specimens apply a strength reduction factor of 0.85 since these parts are not using FRP. However, the final failure pattern occurred with the failure of the FRP module as shown in Figure 6. In such case, a strength reduction factor of 0.55 should be adopted (ACI 440.1R, 2006). The ultimate strength required by KHBDC (2005) being 345kN, the mean value of 561kN for the ultimate failure strength developed by the specimens becomes 477kN when applying the strength reduction factor of 0.85 and satisfies this design criterion. Besides, the application of a strength reduction factor of 0.55 leads to a value of 309kN, which does not satisfy the design criterion. This problem can be solved by two alternatives that are, increasing the ultimate strength of the section itself or improving the failure mode. Figure 9 plots the load-crack width curves of the specimens together with the design loads. The mean value of the maximum crack width occurring under service load is 0.13mm, which is satisfying the maximum crack width of 0.14mm. By the way, the specimens were reloaded after the first crack was

found. Sensors for measuring crack width were installed crossing the found cracks before the reloading stage.

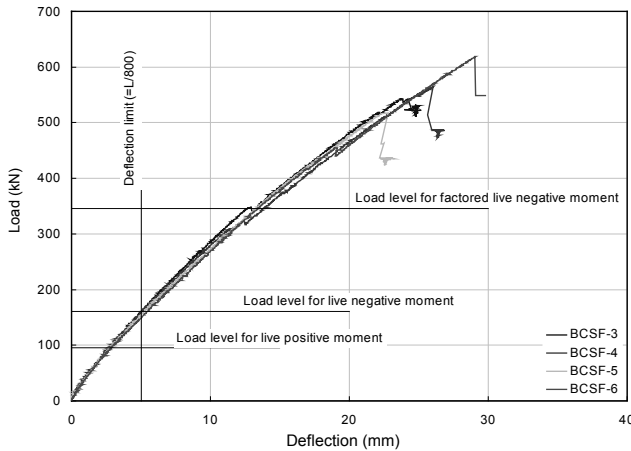


Figure 8 Comparison of the load-displacement curves of the specimens with the design criteria

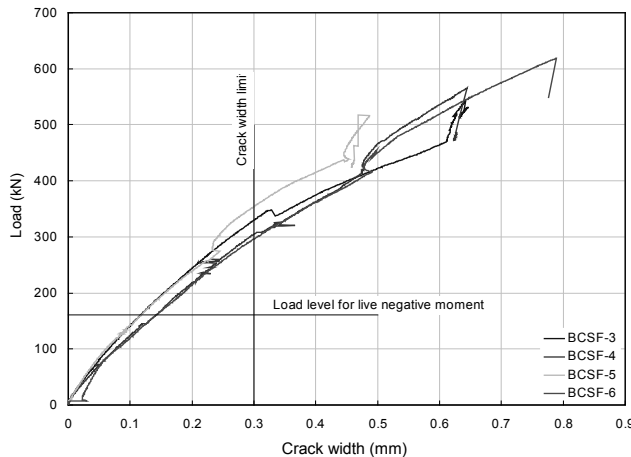


Figure 9 Comparison of the load-crack width curves of the specimens with the design criteria

4 CONCLUSIONS

FRP-concrete composite deck specimens were fabricated at the beam scale in order to develop lightweight decks to be applied for cable-stayed bridges. The so-fabricated specimens exhibit a span length of 4m (spacing of cross-beams) and present reduced weight reaching 60% of that of common precast concrete decks for cable-stayed bridges.

The results of the static tests performed on the specimens revealed that the specimens developed ultimate

strength with mean value of 516kN, which satisfies the design requirement (345kN) when applying a strength reduction factor of 0.85. However, the final failure of the specimens occurred through the failure of the FRP module near the supports, which is not satisfying the design strength requirement when applying the corresponding strength reduction factor of 0.55 prescribed by ACI 440.1R. On the other hand, the deflection and crack width secured sufficient safety factor in terms of serviceability.

Considering these features, the FRP-concrete composite deck developed in this study can be assumed to provide sufficient applicability for its use as deck for cable-stayed bridges. However, further studies should modify the details of the cross-section to improve the failure pattern or increase the cross-section in order to satisfy the strength requirement of the design code.

ACKNOWLEDEMENTS

This study has been supported through the “Development of Technology for Low-Cost and Durable Hybrid Cable-Stayed Bridge – Development of Deck Systems for Hybrid Cable-Stayed Bridge” project, an in-house project of the Korea Institute of Construction Technology. The authors express their gratitude for the support.

REFERENCES

- ACI 440.1R. 2006. Guide for the Design and Construction of Structural Concrete Reinforced with FRP Bars, ACI Committee 440.
- Cho, K., Park, S.Y., Kim, S.T., Cho, J.R., and Kim, B.S. 2009. Development of FRP-Concrete Composite Deck with Long Span, *9th International Symposium on Fiber Reinforced Polymer Reinforced for Concrete Structures (FRPRCS), Sydney, 13-15, July 2009*.
- Korea Institute of Construction Technology (KICT). 2007. System Integration for Hybrid Cable-Stayed Bridge, Research Report (in Korean).
- Ministry of Construction and Transportation. 2005. Korea Highway Bridge Design Code (KHBDC).
- Park, S.Y., Cho, K., Kim, S.T., Cho, J.R., and Kim, B.S. 2009. Structural Behavior of FRP-Concrete Composite Deck with Concrete Wedge, *9th International Symposium on Fiber Reinforced Polymer Reinforced for Concrete Structures (FRPRCS), Sydney, 13-15, July 2009*.

Static and Fatigue Behaviors of Precast FRP-Concrete Composite Deck for Cable-Stayed Bridge

Keunhee Cho (kcho@kict.re.kr), Sung Yong Park, Sung Tae Kim, Byung-Suk Kim

Korea Institute of Construction Technology, Goyang, Korea

ABSTRACT The precast FRP-concrete composite deck enables a reduction of the weight by 50% compared to reinforced concrete decks owing to the composition of a FRP panel with concrete. Therefore, the application of such deck in cable-stayed bridge will reduce effectively the weight of the superstructure leading also to substantial savings of the materials required for the superstructure and substructure and, subsequently, to achieve significant improvement of the economic efficiency. In view of these advantages, a precast FRP-concrete composite deck is selected and newly designed as a deck economically applicable to cable-stayed bridge. The applicability of the deck system is verified through static and fatigue tests.

1 INTRODUCTION

FRP-concrete composite deck is a deck combining FRP and concrete. Such composition enables to reduce the weight of the deck by 50% compared to common reinforced concrete decks. The reduction of the weight offered by the FRP-concrete composite deck represents a very attractive alternative for bridges of which economic efficiency is sensitive to the weight of the superstructure like cable-stayed bridges. Figure 1 illustrates the distribution of the weight and construction cost per element constituting the superstructure of a cable-stayed bridge with steel composite edge girder.

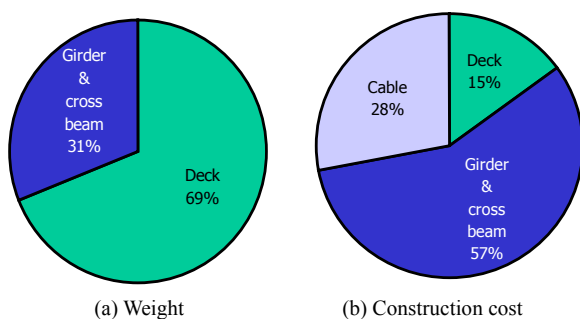


Figure 1 Contribution of the elements constituting the superstructure of cable-stayed bridge in the weight and construction cost

It can be observed that the deck contributes merely to 15% of the construction cost of the superstructure but occupies approximately 70% of the weight of the superstructure. This means that reducing the weight of the deck would result in savings of the relatively costlier cables and girder. Cho et al (2009) demonstrated that the application of FRP-concrete composite deck in cable-stayed bridge would increase the construction cost of the

deck by about 50% while decrease the construction cost of the whole superstructure by about 10%.

The economically efficient application of this advantageous FRP-concrete composite deck could not be achieved when the spacing between the cross-beams supporting the deck is narrow. Narrow spacing requires larger number of relatively costlier cross-beams leading to the increase of cost. Therefore, this paper adopts a cross-beam spacing of 4m identically to that of former RC decks.

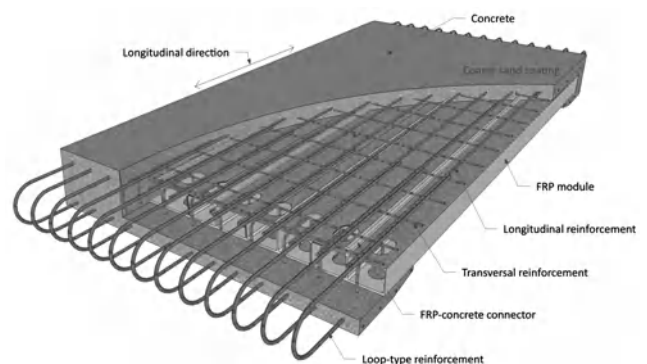


Figure 2 Basic configuration of precast FRP-concrete deck

Furthermore, it seems advisable to fabricate precast deck in order to shorten the construction period in view of its impact on the economic efficiency. In such case, connection should be realized between the deck segments above the cross-beams constituting the supports of the deck. However, achieving strong connection of two different materials is difficult. Therefore, the 4 edges of the deck were covered with concrete as shown in Figure 2 so as to apply the loop connection known to be a verified connection method. This deck is referred to as

precast FRP-concrete deck (PFC deck) to distinguish it from the previous FRP-concrete composite deck.

This study intends to investigate the applicability of the PFC deck for cable-stayed bridge by examining its static and fatigue behaviors.

2 DETAILS OF THE PROTOTYPE

Figure 3 outlines the shape of the deck prototype. Coarse sand coating and FRP shear keys are adopted for the composition of FRP and concrete. The height of the section is 350mm at the haunch and 270mm at the center of the span. The height of the FRP panel is 150mm.

Cross-beams are included in the prototype in order to examine not only the behavior at the positive moment zone in the center of the span but also the behavior at the negative moment zone of the supports. The compressive strength of concrete is 30.1MPa, the tensile strength ranges from 265 to 314MPa and the tensile stiffness from 19.4 to 22.5MPa in the FRP panel.

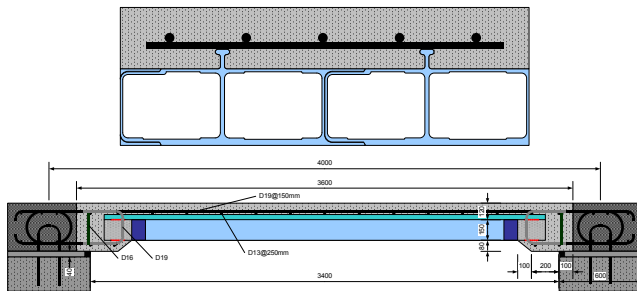
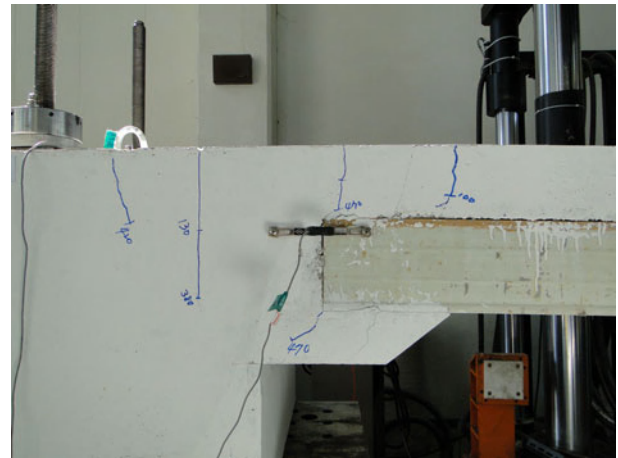


Figure 3 Shape of the deck prototype

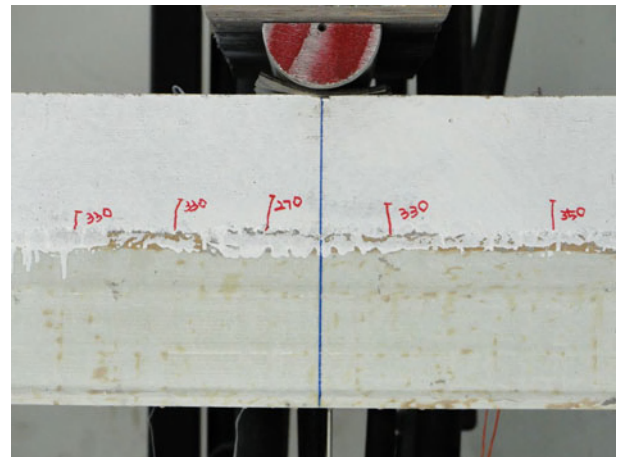
The prototype was fabricated following a sequence and method identical to those of real construction so as to secure a behavior similar to a real bridge. The construction process started with the fabrication of the precast deck and cross-beams followed by the installation of the deck above the cross-beams. A bedding layer was then formed by placing non-shrinkage mortar and the construction ended by placing the connections above the bedding layer.

3 STATIC PERFORMANCE

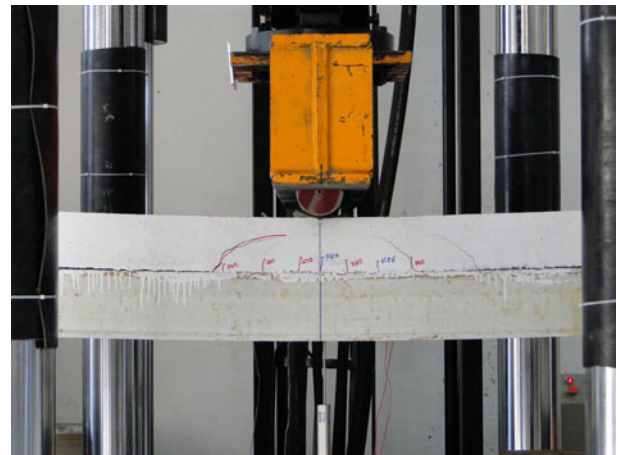
The evaluation of the static performance was conducted on a series of 3 prototypes (BCSF2). Figure 4 illustrates the typical failure pattern of the prototypes. Cracks initiated first in the negative moment zones and occurred later in the positive moment zones with increasing loads. Failure occurred through the propagation of inclined cracks together with debonding of the interface. The even distribution of the cracks and the failure mode of the positive moment zones indicated the appropriateness of the details of the arrangement of the reinforcing bars in the prototypes.



(a) Crack pattern at the negative moment zone



(b) Crack pattern at the positive moment zone

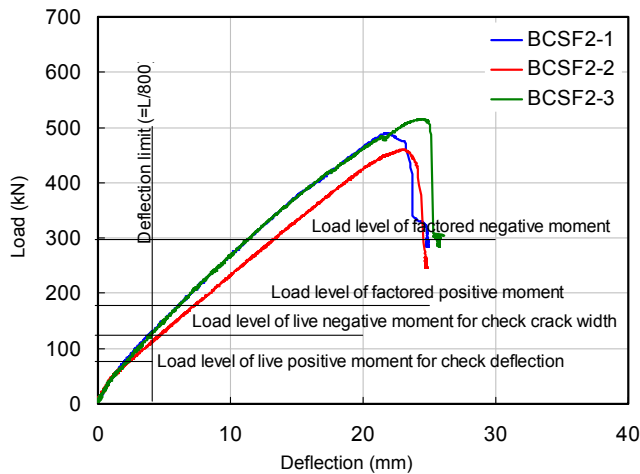


(c) Final failure pattern

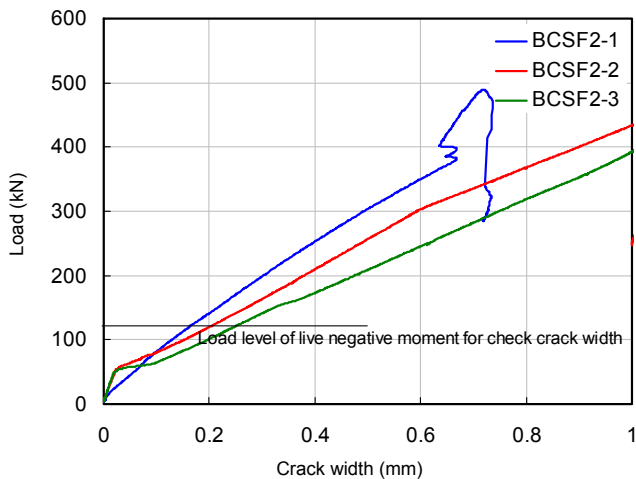
Figure 4 Failure pattern of static specimen

Figure 5 plots the load-deflection curves and load-crack width curves together with the design criteria for the 3 prototypes. It can be observed that even the deflection criterion $L/800$ (L : span length) under live load is sufficiently satisfied. The mean failure strength of the 3 prototypes reached 488kN (standard deviation: 28kN), which corresponds respectively to 269kN and 415kN when applying strength reduction factors of 0.55 for the positive moment zone and 0.85 for the negative moment

zone. These static strengths satisfy sufficiently the factored loads of 175kN for the positive moment zone and 294kN for the negative moment zone. Moreover, the allowable crack width of 0.3mm for service load is also satisfied. The prototypes are thus satisfying sufficiently the static design criteria.



(a) Load-deflection curves



(b) Load-crack width curves

Figure 5 Comparison of the static performance of the prototypes with the design criteria

4 FATIGUE PERFORMANCE

The evaluation of fatigue performance was conducted on 2 prototypes (BCSF2F). Prototype BCSF2F-1 was subjected to cyclic fatigue loading of 10~200kN and prototype BCSF2F-2 to cyclic fatigue loading of 10~250kN. These ranges of the fatigue load correspond to approximately 40% and 50% of the static failure load of 488kN and 166% and 208% of the service load of 120kN.

Cracks initiated first at the negative moment zone of prototype BCSF2F-1 during the first fatigue cycles, which complies with the trend observed in the static prototypes. At about 50,000 cycles, 5 to 6 flexural cracks occurred at the center of the span. Thereafter, cracks propagated

slightly with ongoing fatigue cycles but by a very small amount. No particular sign of failure could be observed until 2 million loading cycles.

For prototype BCSF2F-1 subjected to a fatigue load with maximum larger by 50kN compared to prototype BCSF2F-1, numerous cracks developed at the positive and negative moment zones during the static test executed before cyclic loading. These cracks propagated together with additional cracks at 10,000~20,000 cycles and final failure occurred at 438,000 cycles through simultaneous occurrence of inclined cracks and interface failure as shown in Figure 6.

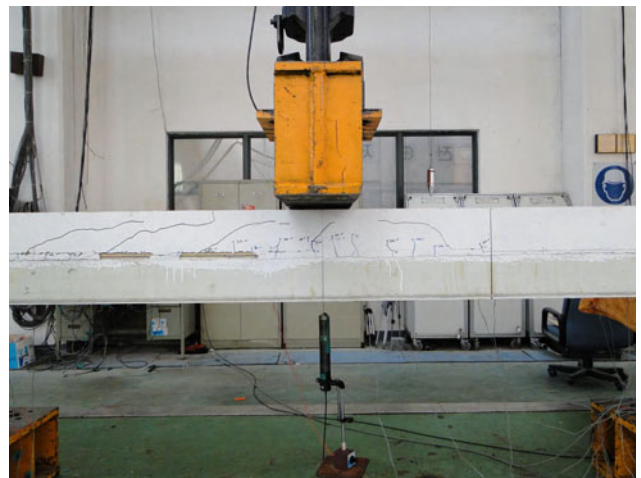


Figure 6 Fatigue failure pattern

Static failure test was carried out for prototype BCSF2F-1, which did not fail even after 2 million fatigue loading cycles in order to examine the residual static strength. The final failure pattern in the static test occurred through the development of inclined cracks followed by failure of the interface. This failure pattern corresponds to that of the static test prototype for which failure test was not conducted. Figure 7 plots the load-deflection curves and load-crack width curves together with the design criteria for comparison. At early loading, the sectional rigidity tends to be slightly smaller than that of the static loading test prototype because of damages due to the occurrence of cracks induced by the fatigue load. However, the final failure strength shows a level comparable to the static loading test prototype. This result proves that the resistance performance to static loading of prototype BCSF2F-1 satisfies sufficiently the design criteria even after having been subjected to 2 million fatigue loading cycles.

Furthermore, the load-crack width curve shows that larger crack widths developed compared to the static loading test prototype. However, prototype BCSF2F-1 also satisfies the design criterion since these cracks are smaller than the allowable crack width of 0.3mm.

These results indicate that the PFC deck secures sufficient fatigue performance.

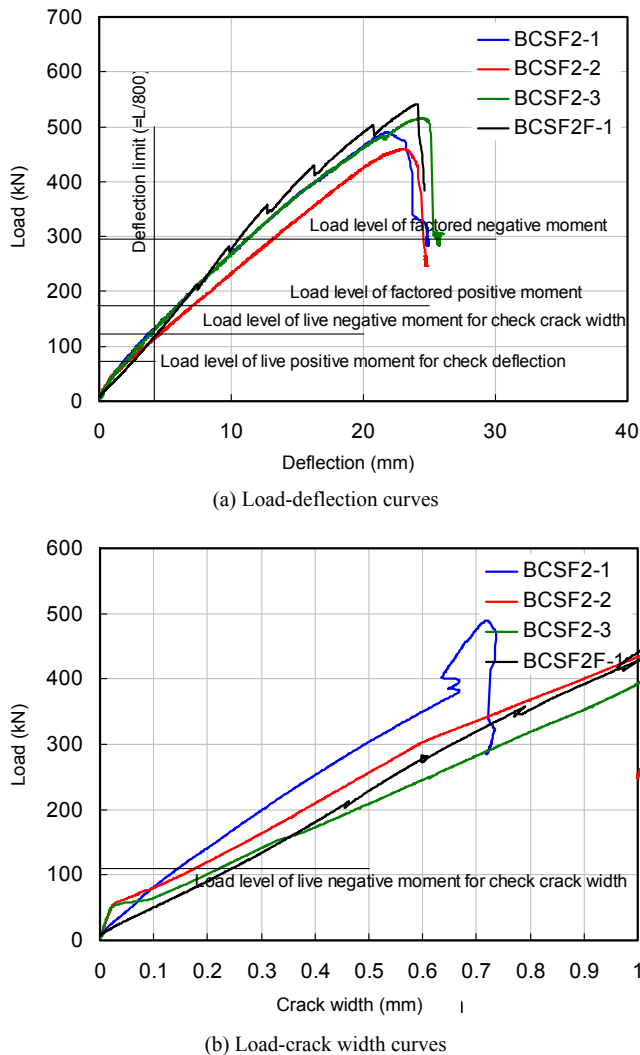


Figure 7 Comparison of the fatigue performance of the prototypes with the design criteria

5 CONCLUSION

The precast FRP-concrete deck (PFC deck) has been selected as a type of deck providing economic efficiency when applied to cable-stayed bridges. The static and

fatigue performances of the deck have been investigated experimentally.

The static test prototypes exhibited evenly distributed cracking in the positive and negative moment zones, and final failure occurred through a desirable pattern at the concrete of the positive moment zone. All the prototypes showed deflections, crack widths and resistance strength satisfying the design criteria.

The prototypes subjected to cyclic fatigue load of 208% of the service load failed at about 438,000 cycles. On the other hand, the prototypes subjected to cyclic fatigue load of 166% of the service load did not fail even after 2 million cycles. In addition, the static tests conducted on the prototypes that did not fail verified that all the design criteria were satisfied.

These experimental results prove that the PFC deck developed in this research secures sufficient performances for future applications for cable-stayed bridges.

ACKNOWLEDGEMENT

This study has been supported through the “Development of Technology for Low-Cost and Durable Hybrid Cable-Stayed Bridge – Development of Deck Systems for Hybrid Cable-Stayed Bridge” project, an in-house project of the Korea Institute of Construction Technology. The authors express their gratitude for the support.

REFERENCES

- Cho, K., Park, S.Y., Kim, S.T., Cho, J.R., Kim, B.S. 2009. Development of FRP-Concrete Composite Deck with Long Span, 9th International Symposium on Fiber Reinforced Polymer Reinforced for Concrete Structures, Sydney, 13-15, July 2009. Ministry of Homeland and Maritime Affairs. 2009. Development of High Performance Construction Material, Research Report, 678pages. (in Korean)
- Korea Institute of Construction Technology. 2008. System Integration for Hybrid Cable-Stayed Bridge, Research Report.

Experimental Studies on FRP-Concrete Composite Deck with FRP Perfobond Shear Connectors

Weichen Xue (xuewc@tongji.edu.cn), Chang Ge, Yuan Tan, Yongsheng Wang

Department of Building Engineering, Tongji University, Shanghai, China

ABSTRACT Push-out tests were conducted to investigate the shear performance of FRP perfobond shear connectors. Shear failure was observed on the ribs of connectors at ultimate. Based on test results, the FRP perfobond connectors showed relatively high shear capacity and could be applied to the FRP-concrete composite deck. Then the simply supported FRP-concrete composite deck with FRP perfobond shear connectors was tested under monotonic load. The load versus mid-span deflection response of composite deck behaved linearly up to the ultimate load. Shear failure occurred on the webs of FRP deck near the upper flange, while the FRP perfobond shear connectors remained intact without any damage. The measured maximum mid-span deflection was 25.4 mm, corresponding to 1/63 of the simply supported span, which demonstrated the large deformability of FRP-concrete composite deck.

1 INTRODUCTION

The application of fiber-reinforced polymer (FRP) materials combined with concrete has been proposed to reduce the initial costs, enhance the structural stiffness and make more effective use of each constituent material (Deskovic et al. 1995). One innovative FRP-concrete composite member developed in bridge engineering is the FRP-concrete composite deck, which consists of FRP deck in tension and concrete slab in compression. To make insure the composite action between FRP deck and concrete slab, some shear transfer methods have been provided and investigated, including bond with epoxy adhesive, installation of bolts or FRP perfobond shear connectors etc (Zhou & Keller 2005). Based on the experimental work carried out by Nam et al. (Nam et al. 2007), the FRP perfobond shear connectors exhibited the advantages of high shear capacity and easy of construction.

The Miyun bridge of China built in 1982, was a road traffic bridge, in which the FRP-concrete composite deck systems were firstly employed (Ye & Feng 2008). In 1990s, Deskovic et al. provided the conception of lightweight composite beam consisting of a glass fiber-reinforced polymer (GFRP) filament wound box section with a concrete layer on the top side and a carbon fiber-reinforced polymer (CFRP) strap on the bottom flange (Deskovic et al. 1995). In 1998, Hall & Mottram performed tests on the FRP-concrete composite beams, which were composed of pultruded GFRP panels with T-upstands and normal or lightweight concrete slabs (Hall & Mottram 1998). In addition, experimental work on the FRP-concrete composite deck systems was also

conducted by other researchers (Van Erp et al. 2002; Kitane et al. 2004; Keller & Gurtler 2005).

In summary, existing studies mainly focused on the feasibility and structural behavior of FRP-concrete composite beam/deck bonded with epoxy adhesive, or connected with bolts, while limited research was reported regarding to the FRP-concrete composite deck with FRP perfobond shear connectors. Herein, this paper presents the push-out tests on FRP perfobond shear connectors and the pilot experimental studies on the FRP-concrete composite deck with FRP perfobond shear connectors.

2 PUSH-OUT TESTS ON FRP PERFOBOND SHEAR CONNECTORS

2.1 Test design

2.1.1 Specimens

Push-out tests were conducted on two identical specimens, numbering PS-1 and PS-2, respectively. The FRP perfobond shear connectors used are shown in Figure 1. The FRP perfobond shear connectors had several parallel

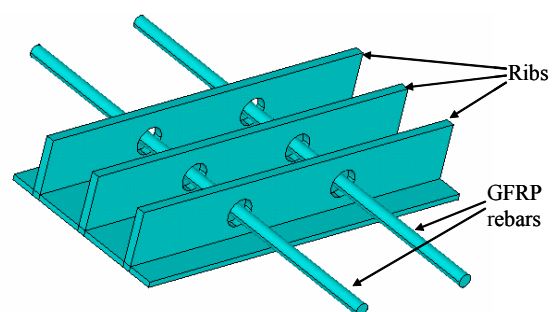


Figure 1 FRP perfobond shear connectors

ribs with six 20 mm-diameter holes. The holes were drilled at the middle height of the ribs, and spaced with 100 mm. The GFRP rebars installed through the holes were 360 mm long and 9.5 mm in diameter. For each push-out specimen, a 176 mm-width FRP deck is attached with the FRP perfobond shear connectors at each side and then held by two identical reinforced concrete slabs, as illustrated in Figure 2.

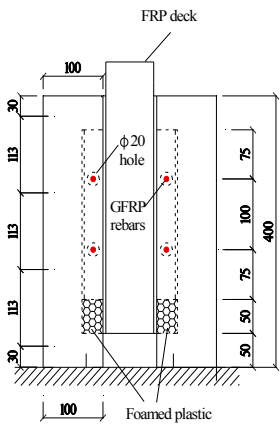


Figure 2 Details of push-out specimen

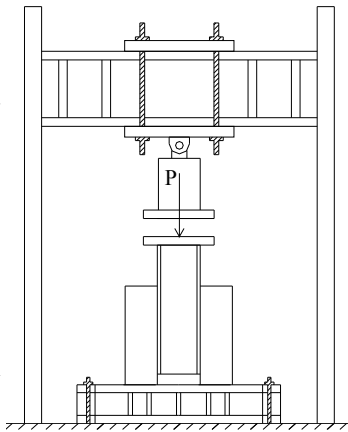


Figure 3 Test setup

2.1.2 Loading and measurements

The push-out specimens were tested to failure under monotonic loading. Figure 3 shows the test setup.

Two displacement transducers were positioned at each side of the specimen to measure the relative slip between the FRP deck and concrete slab. For each push-out specimen, six strain rosettes in all were used to measure the strains of FRP perfobond shear connectors. The strains on two of the three ribs of FRP perfobond shear connectors, the middle one and a side one, were recorded during the tests.

2.2 Test results and analysis

2.2.1 Failure pattern

Shear failure on the ribs of FRP perfobond shear connectors was observed in the push-out tests, as shown in Figure 4. During test loading, no damage occurred on the surrounding concrete and the GFRP rebars installed through the holes.



Figure 4 Shear failure on ribs of perfobond shear connectors

2.2.2 Load versus slip curves

The measured load versus slip curves of push-out specimens are plotted in Figure 5. Note the slip represents the average relative slip between FRP deck and concrete slab recorded by the displacement transducers.

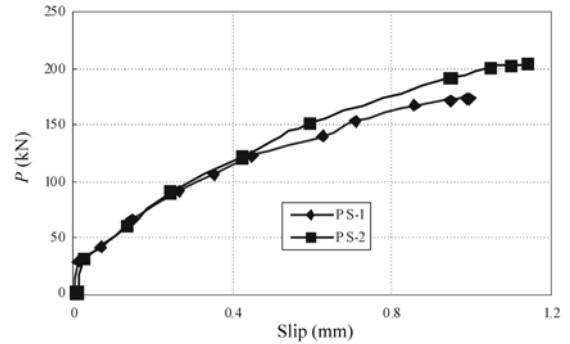


Figure 5 Load versus slip curves of push-out specimens

The measured load versus slip curves of push-out specimens exhibit the elastic stage and plastic stage under loading. As the applied loads were less than 0.2 time the ultimate loads, specimens showed an almost linear-elastic responses, and the slip between the FRP deck and concrete slab was small. Some fine damage might begin to form at the FRP perfobond shear connectors when the applied loads reached 0.2 time the ultimate loads, and the stiffness of FRP perfobond shear connectors decreased as the applied loads increased. The load versus slip curves are nonlinear after 0.2 time the ultimate loads. At ultimate, the relative slip developed rapidly with little increase of applied loads.

2.2.3 Load versus strain curves

Figure 6 and Figure 7 show the measured load versus strain curves of specimens. Note ϵ_1 and ϵ_2 denote the normal strain parallel to and perpendicular to the direction of loading, respectively, and γ_{12} denotes the converted shear strain. Seen from the figures:

(1) The load versus strain curves are similar for the two specimens. The strains on ribs of FRP perfobond connectors developed linearly up to 0.4 time the ultimate loads. When shear failure occurred, the shear strains on ribs of FRP perfobond connectors are 8113 $\mu\epsilon$ and 7898 $\mu\epsilon$, respectively.

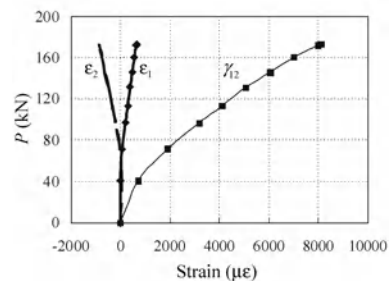


Figure 6 Load versus strain curves of PS-1

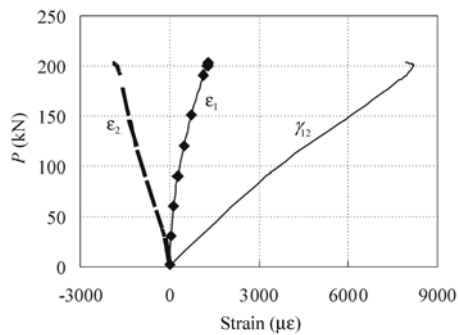


Figure 7 Load versus strain curves of PS-2

(2) The normal strains measured at the same position are much smaller than the shear strains, which indicates that the FRP perfobond connectors are mainly subjected to the shear forces in the push-out tests.

2.2.4 Shear capacity

The measured ultimate loads were 173.1 kN and 203.3 kN for specimen PS-1 and PS-2, respectively. Based on the test results, the shear failure on ribs of FRP perfobond shear connectors was observed. So the load carrying capacity of push-out specimens was mainly controlled by the shear capacity of FRP perfobond connectors, P_s , which can be calculated by:

$$P_s = \tau_u A_{sn} \quad (1)$$

where τ_u = shear strength of ribs (MPa); A_{sn} = total area of ribs with deducting the area of holes (mm^2). The predicted shear capacity of FRP perfobond connectors is 243.0 kN according to Eq. (1), which is higher than the measured ultimate loads. It may be due to the fact that FRP perfobond connectors were under the combined forces of shear and flexure in push-out test. Based on test results, the FRP perfobond connectors showed promising behaviors and could be used to the FRP-concrete composite deck.

3 STATIC TEST ON FRP-CONCRETE COMPOSITE DECK

3.1 Test design

The specimen of FRP-concrete composite deck was 1800 mm long and had a cross-sectional area of 500×140 mm, consisting a 80 mm-depth FRP deck and 60 mm-depth concrete slab. The FRP perfobond connectors were applied to transfer shear. Note the materials of FRP perfobond connectors, FRP deck and GFRP rebars used in the static test were identical with those used in the push-out tests, while with different dimensions.

The simply supported composite deck was loaded monotonically to failure. Figure 8 shows a diagram of the loading configuration. A hydraulic jack and distribution beam produced two point loads at equal distances of 200 mm from the center of the composite deck.

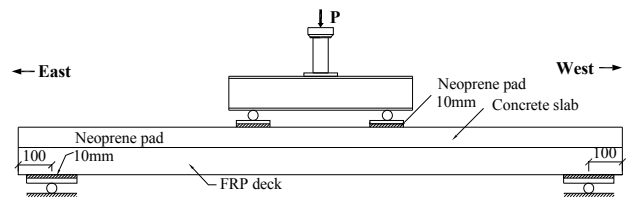


Figure 8 Loading configuration

3.2 Overall response

The initial cracking was observed at the bottom of concrete slab beneath the west load point when the applied load, P , increased to about 0.1 time the ultimate load, P_u . The formed cracks propagated upwards and several new cracks developed within the constant moment region as the applied load increased. Under the load of $0.7P_u$, the relative slip between the FRP deck and concrete slab was 0.6mm and the sounds of fiber fracture from FRP deck could be heard sporadically. The relative slip between the FRP deck and concrete slab was increased to about 1.1 mm at ultimate, and the measured shear stresses on FRP webs were 52.4 MPa, which exceeded the shear strength of FRP deck obtained from the tests of mechanical properties. Figure 9 shows the failure pattern of FRP-concrete composite deck. Shear failure occurred on the webs of FRP deck near the upper flange accompanied with a loud sound, while the FRP perfobond shear connectors remained intact without any damage.



Figure 9 Failure pattern of FRP-concrete composite deck

3.3 Test results analysis

3.3.1 Strain distributions of mid-span section

The strain distributions through depth of mid-span section under different load levels are plotted in Figure 10. Seen from the figure, the strains approximately exhibit a linear distribution along the height of section, while the short fold lines reflect the relative slip developed between concrete slab and FRP deck.

3.3.2 Load versus deflection curves

As illustrated in Figure 11, the measured curves of load versus deflection at mid-span behave linearly up to P_u . The initial concrete crack was observed at about $0.1P_u$, while it seemed that the concrete cracking had limited influence on the stiffness of the composite deck. The measured mid-span deflection was 25.4 mm at ultimate, corresponding to 1/63 of the simply supported span, which

demonstrates the large deformability of FRP-concrete composite deck.

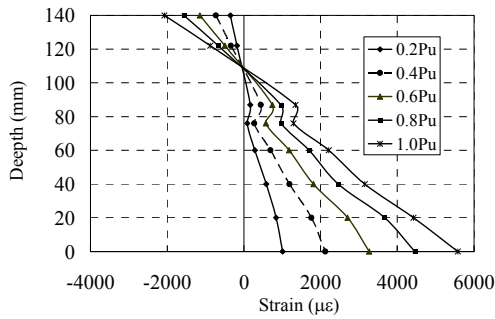


Figure 10 Strain distributions of mid-span section

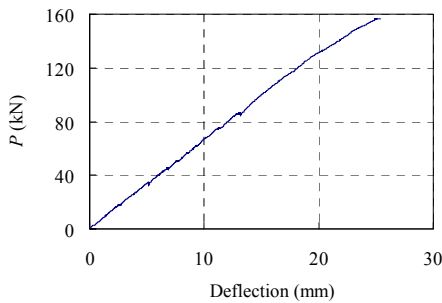


Figure 11 Load versus deflection curves

3.3.3 Load versus slip curves

Three displacement transducers were used to record the relative slips between the FRP deck and concrete slab at the ends of composite deck (s_1), the middle of shear span (s_3) and at the position beneath the west loading point (s_2), respectively. Figure 12 shows the measured load versus slip curves of composite deck. No slip was observed under the applied load of $0.1P_u$. The relative slips between the FRP deck and concrete slab began to develop after $0.1P_u$, and the load versus slip responses exhibited an approximate linear relationship up to P_u . The maximum average relative slip reached 1.1 mm at ultimate, and it was observed that the values of relative slip at the middle of shear span were larger than those measured at the ends of composite deck or the middle of shear span during test.

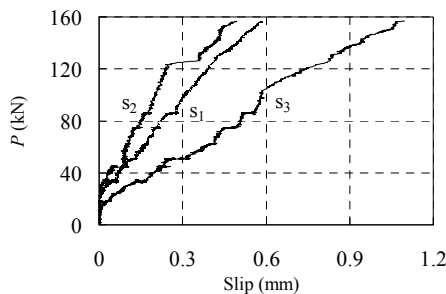


Figure 12 Load versus slip curves

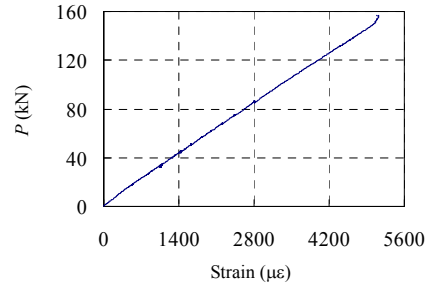


Figure 13 Strains developed at the bottom of FRP deck

3.3.4 Strains developed in FRP deck

As shown in Figure 13, the longitudinal strains at the bottom of FRP deck in mid-span section are increased linearly up to the ultimate load. The measured strains of FRP deck web at the distance of 330 mm from the specimen center and at the distance of 15 mm from the FRP deck upper flange are shown in Figure 14, where ϵ_1 and ϵ_2 represent the normal strain parallel to and perpendicular to the longitudinal direction of composite deck, respectively, and γ_{12} denotes the converted shear strain. Seen from Figure 14, the normal strains developed linearly under the applied loads, while some nonlinear characteristics could be observed in the response of load versus shear strain. In addition, the shear strains are higher than the normal strains at the position, which may be caused by the fact that webs of FRP deck mainly resist the shear forces. The shear strains developed in the web of FRP deck were 10691 $\mu\epsilon$ at ultimate load, and the corresponding shear stresses were 52.4 MPa, which led to the shear failure on webs of FRP deck.

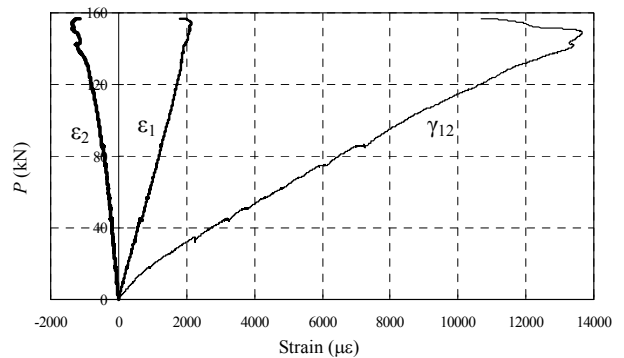


Figure 14 Strains developed at the web of FRP deck

3.3.5 Load carrying capacity

Based on test results, shear failure was observed on the webs of composite deck and concrete in compression remained intact. So the load carrying capacity of FRP-concrete composite deck could be controlled by the shear capacity of FRP deck. Furthermore, the shear capacity of FRP deck was mainly contributed to the shear capacity of its webs according to the principles of material mechanics. By this means, the shear capacity of FRP-concrete

composite deck was calculated as 129.8 kN, corresponding to 83% of the measured ultimate load.

4 CONCLUSION

The following conclusions can be drawn from the experimental studies:

(1) Shear failure on the ribs of FRP perfobond shear connectors was observed in the push-out tests, while no damage occurred on the surrounding concrete and the GFRP rebars installed through the holes. The FRP perfobond connectors showed promising behaviors and could be used to the FRP-concrete composite deck.

(2) For the FRP-concrete composite deck, shear failure occurred on the webs of FRP deck near the upper flange at ultimate, and the FRP perfobond shear connectors remained intact without any damage. The strains approximately exhibit a linear distribution along the height of section, and the average relative slip reached 2.5 mm under the ultimate load. The measured mid-span deflection was 25.4 mm at ultimate, corresponding to 1/63 of the simply supported span, which demonstrates the large deformability of FRP-concrete composite deck.

ACKNOWLEDGMENTS

This work was supported by the Fund of Western Communications Construction Scientific and Technological Project by the Ministry of Communications of the P.R. China (No.20063188 2244) and the National Natural Science Foundation of China (No. 50008012 & No. 50978193).

REFERENCES

- Deskovic, N., Triantafillou, T.C. & Meier, U. 1995. Innovative design of FRP combined with concrete short-term behavior. *Journal of Structural Engineering* 121(7):1069-1078.
- Hall, J.E. & Mottram, J.T. 1998. Combined FRP reinforcement and permanent framework for concrete members. *Journal of Composites for Construction* 2(2):78-86.
- Keller, T., Gurtler, H. 2005. Composite action and adhesive bond between FRP bridge decks and main girders. *Journal of Composites for Construction* 9(4):360-368.
- Kitane, Y., Aref A.J. & Lee, G.C. 2004. Static and fatigue testing of hybrid fiberreinforced polymer–concrete bridge superstructure. *Journal of Composites for Construction* 8(2):182-190.
- Nam, J.H., Yoon, S.J., Ok, D.M. & Cho, S.K. 2007. Perfobond FRP Shear Connector for the FRP-Concrete Composite Bridge Deck. *Key Engineering Materials* 334-335 I: 281-284.
- Van Erp, G.M., Heldt T., McCormick, L., Carter, D. & Tranberg, C. 2002. An Australian approach to fiber composite bridges. In Gowripalan, N., Sri Bandyopadhyay, S. & Rizkalla, S.H. (eds), *Composite systems: macro composites, micro composites, nano composites; Proc. ACUN-4 international composites conference, 21-25 July 2002*, University of New South Wales: Sydney.
- Ye, L.P. & Feng P. 2008. Applications and development of fiber-reinforced polymer in engineering structures. *China Civil Engineering Journal* 39: 24-36. (in Chinese)
- Zhou, A. & Keller, T. 2005. Joining techniques for fiber reinforced polymer composite bridge deck systems. *Composite Structures* 69(3): 336-345.

Numerical and Experimental Investigation of Concrete-Filled FRP Tube

Wonseok Chung (wschung@khu.ac.kr), Hoon Jang & Zu-Og An

Department of Civil Engineering, Kyung Hee Univeristy, Korea

ABSTRACT This study is to investigate nonlinear failure behavior of the concrete-filled FRP (CFFRP) hybrid tube structure. This study consists of two phases. First, a CFFRP tube is fabricated and tested to investigate the flexural failure behavior of CFFRP tube. Second phase involves practical nonlinear finite element analysis of the CFFRP tube up to failure. FRP tube is modeled by layered shell elements and filled concrete is idealized by fiber beam element. Failure theory for the prediction of the strength of unidirectional composite materials is considered. Uniaxial constitutive models for the concrete and steel material are selected in this study. The adopted material model is integrated into the ABAQUS elements through a user-defined material subroutine (UMAT). Within a developed nonlinear finite element framework, the FE results have been compared to experimental results. It has been found that the proposed finite element model is capable of predicting the initial cracking load level, the yield load, and the ultimate load with acceptable accuracy.

1 INTRODUCTION

The main objective of this research is to develop a concrete-filled FRP (CFFRP) tube and to evaluate the structural performance of the proposed system. Experimental and numerical investigation is conducted to investigate the structural performance of CFFRP structure. In recent years, there has been an increasing number of research towards the experimental and numerical studies of CFFRP tube structures (Cole and Fam 2006; Fam and Rizkalla 2001; Shao and Mirmiran 2005; Son and Fam 2008).

Numerical studies generally adopt solid element-based finite element model. The solid element-based model requires a large amount of computational resources. In this study, simplified nonlinear finite element (NLFE) model of the CFFRP tube has been developed. The proposed modeling technique utilizes fiber beam elements for the in-filled concrete. This model is expected to minimize computation costs while maintaining the accuracy of the FE solution. As a part of NLFE modeling, the material model for concrete is integrated into ABAQUS through a user-defined material subroutine. The CFFRP tube is tested under flexural loading conditions. The test results are then compared to numerical results proposed in this study. Finally, the applicability of the proposed NLFE model will be discussed.

2 FRP-CONCRETE HYBRID TUBE

A FRP tube with an outside diameter of 360 mm and a wall thickness of 3 mm is fabricated. The FRP tube is

filament wound with glass fibers all oriented in the hoop direction. The stacking sequence of the FRP tube is $[(\pm 45)_3]$. The steel cage system is then inserted inside the FRP tube and concrete was filled. The length of the CFFRP tube specimen is 4.5 m. Figure 1 shows the test unit of CFFRP tube. The vendor-supplied ply properties are given in Table 1.

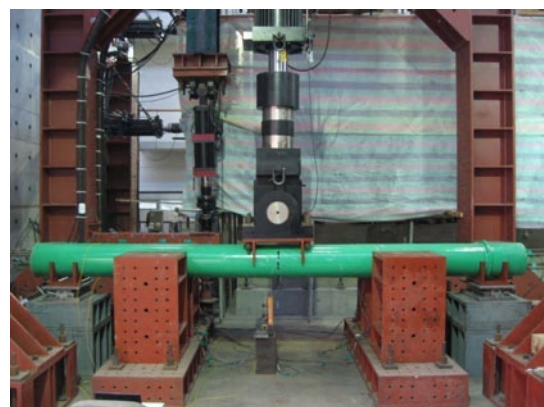


Figure 1 Test unit of CFFRP tube

3 TEST PROGRAM

Test program involved the measurement of the nonlinear static behavior until failure under to investigate the failure mechanism of the CFFRP tube. Several strain gauges are installed on the surface of test unit in both longitudinal and hoop direction as shown in Figure 2 and Figure 3. Strain gauges were also embedded in the steel cages before pouring concrete.

The CFFRP tube was then tested with a clear span of 4.5m and loaded symmetrically and monotonically in four-point bending to failure. Deflections were directly measured at the mid-span and quarter-span using displacement transducers. A measurement setup is shown in Figure 4. The CFFRP tube is loaded to the point at which all load carrying capacity is lost. Figure 5 shows the test unit after loading test.

Cylinder splitting and crushing tests on concrete cores were performed to identify the uniaxial tensile and compressive strengths of the concrete. Tensile tests on samples of the reinforcing bars were also undertaken. Table 1 presents the material properties for the test unit.

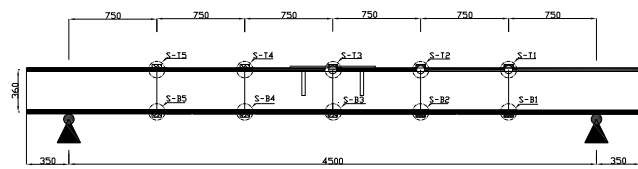


Figure 2 Sensor layout (longitudinal direction)

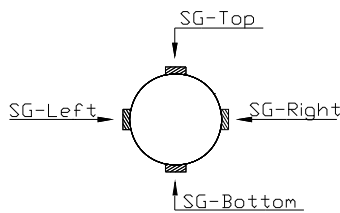


Figure 3 Sensor layout (hoop direction)



Figure 4 Loading setup and displacement transducer



Figure 5 Configuration of failure

Table 1 Material Properties

Material	Properties	Value
GFRP Composite	E_1	53.2 GPa
	E_2	10.75 GPa
	ν_{12}	0.288
	G_{12}	8.59 GPa
Concrete	F_t	3.98 MPa
	f'_c	40 MPa
	E_c	28.6 GPa
	ν	0.2
Steel	f_y	400 MPa
	E_s	210 GPa
	ν	0.3

4 NUMERICAL STUDY

This study presents the ultimate behavior of CFFRP tube by means of practical NLFE analyses. The numerical simulations are performed using the general-purpose finite element software package ABAQUS (2001). In FE modeling, the in-filled concrete is typically modeled by solid elements. However, this study utilizes three-dimensional fiber beam element (B33) to reduce the amount of computational resources. Steel cage is also modeled by beam elements. The FRP shell is idealized by layered shell elements available in ABAQUS. The composite properties given in Table 1 are considered in each layer. Rigid links through multi-point constraints (MPCs) are then imposed to each component to ensure the full composite action. Figure 6 and Figure 7 show the finite element model used in this study.

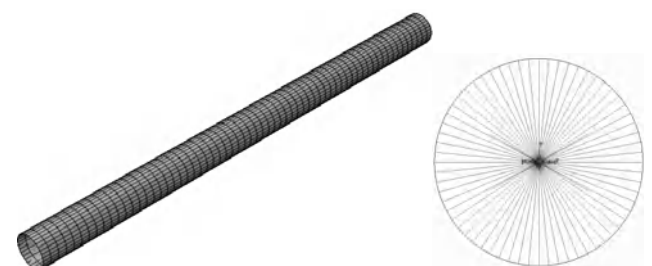


Figure 6 Finite element model

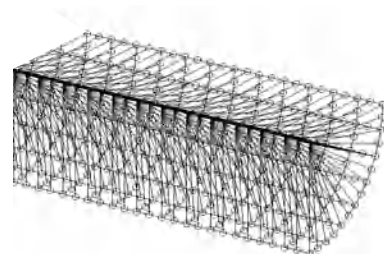


Figure 7 Rigid link

Many concrete material models have been proposed for the NLFE analysis of reinforced concrete structures. Majority of analytical models require higher level of

understanding in the field of plasticity (Chung and Sotelino 2005). In this study, uniaxial constitutive models for the concrete and steel material are selected for the practical purpose. The scope of this study is restricted to cracked reinforced concrete model on a continuum level. The cracks are assumed to be smeared in the element rather than discrete, since the overall load deformation relationship of the structure is of interest.

Concrete uniaxial model is composed of six states as shown in Figure 8. Line 1 represents the linear elastic tensile behavior with the stiffness of concrete modulus (E_{co}) and Line -1 represents nonlinear elastic compressive behavior of concrete (Hognestad 1951) which is defined by

$$\sigma = f'_c \left[2 \left(\frac{\varepsilon}{\varepsilon_{cc}} \right) - \left(\frac{\varepsilon}{\varepsilon_{cc}} \right)^2 \right] \quad (1)$$

where f'_c is concrete compressive strength and ε_{cc} is corresponding concrete strain.

$$\varepsilon_{cc} = \frac{2f'_c}{E_{co}} \quad (2)$$

where E_{co} is initial stiffness of concrete.

At the instant of crack formation it is commonly assumed that the tensile stresses across the crack surface are released due to the brittle nature of concrete. In reinforced concrete model, however, the tensile stress across the crack is not immediately dropped to zero due to the effect of tension stiffening. This is modeled by adding a linear unloading curve (Line 2) in the concrete material model as shown in Figure 8. The tensile strain limit is defined by

$$\varepsilon_t = \frac{2G_f}{f_t l} \quad (3)$$

where G_f is fracture energy, l is characteristic length, and f_t is tensile strength of concrete. The simplified material model is integrated into a fiber beam element through a user-supplied material subroutine (UMAT).

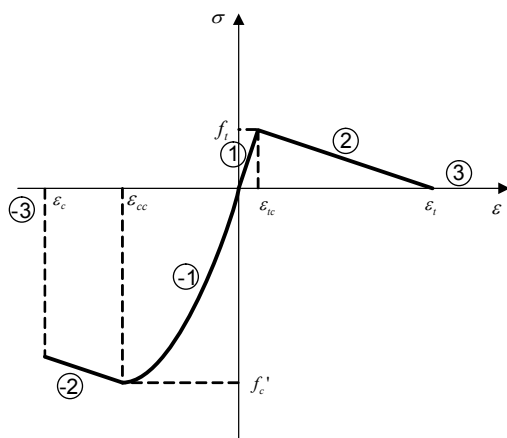


Figure 8 Uniaxial idealization of concrete material

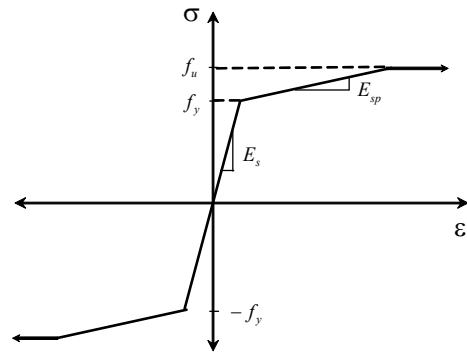


Figure 9 Uniaxial idealization of steel material

Hill-Tsai failure criterion is adopted as the strength criterion for composite materials. In this study, the following strength limits are applied for the composite materials; tensile stress limit in fiber direction (490 MPa); compressive stress limit in fiber direction (300 MPa); tensile stress limit in transverse direction (100 MPa); compressive stress limit in transverse direction (415 MPa); in-plane shear strength (100 MPa).

The main solution strategy used in ABAQUS is a Newton-Raphson (N-R) method. The ABAQUS N-R strategy is broken into two parts: increment and iteration. The total applied load is broken into several increments. At the end of each increment the equilibrium should be satisfied. In each increment, iterations are required to satisfy the equilibrium at the end of the increment. ABAQUS employs an advanced technique to avoid the damaged iterations (Crisfield, 1991).

The predicted load–deflection curve at the mid-span is plotted with the experimental results in Figure 10. It is clear from the numerical model that the response of the model is linear until the first crack has formed at the bottom part of the concrete at approximately 30 kN. Beyond this point significant nonlinear behavior occurred due to the progress of concrete cracking. The initial yielding of the reinforcing bar was predicted at 90 kN. The difference between the predicted strength (131 kN) and measured strength (138 kN) is about 5%. The maximum deflection of the predicted result and the test result at the final load level was 54 mm and 69 mm, respectively. The discrepancy of the deflection may come from the assumption of full composite action between the in-filled concrete and FRP shell regardless of the load level. Figure 11 shows the load–deflection response at the quarter-span. As can be seen, the response is captured accurately by the numerical simulation. Figure 12 shows the configuration after final load stage.

In general, the FE predictions are in close agreement with the corresponding experimental results. Therefore, the proposed FE model used in the analysis is found to be capable of predicting the nonlinear behavior of the CFRP tube.

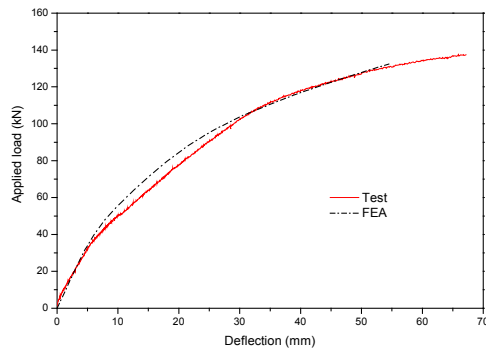


Figure 10 Deflection at mid-span

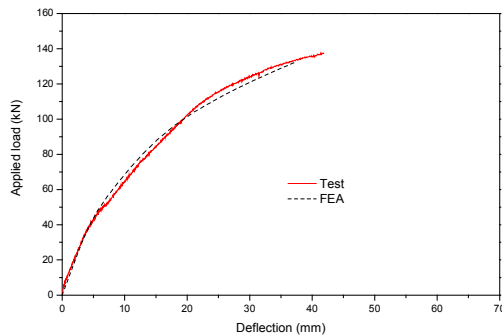


Figure 11 Deflection at quarter-span

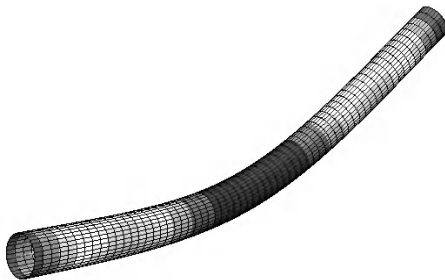


Figure 12 Deformed configuration

5 SUMMARY & CONCLUSIONS

This study is to investigate nonlinear failure behavior of the concrete-filled FRP (CFFRP) tube structure. This study consists of two phases. First, a CFFRP tube is fabricated and tested. Span centered loads are applied to investigate the flexural failure behavior of CFFRP tube.

Second phase involves practical nonlinear finite element analysis of the CFFRP tube up to failure. FRP tube is modeled by layered shell elements and filled concrete is idealized by fiber beam element. Failure theory for the

prediction of the strength of unidirectional composite materials is considered. Uniaxial constitutive models for the concrete and steel material are selected in this study. The adopted material model is integrated into the ABAQUS elements through a user-defined material subroutine (UMAT).

The FE results have been compared to experimental results. In general, the proposed model is capable of predicting the initial cracking load level, the yield load, and the ultimate load with acceptable accuracy. The discrepancy may come from the assumption of full composite action between the in-filled concrete and FRP shell regardless of the load level. It has been found that the proposed simplified model provides a rational tool for the understanding of the behavior of CFFRP tube structures.

ACKNOWLEDGMENT

This paper was supported by National Research Foundation of Korea (2009-0065990).

REFERENCES

- ABAQUS, Inc. 2001, ABAQUS/Standard User's Manual -Version 6.2., Pawtucket, R.I., USA.
- Chung, W. and Sotelino, E.D. 2005. Nonlinear Finite-Element Analysis of Composite Steel Girder Bridges. *Journal of Structural Engineering* 131(2): 304-313.
- Cole, B. and Fam, A. 2006. Flexural Load Testing of Concrete-Filled FRP Tubes with Longitudinal Steel and FRP Rebar. *Journal of Composites for Construction*. 10(2):161-171.
- Crisfield, M.A. 1991. Non-linear Finite Element Analysis of Solids and Structures, *John Wiley & Sons Ltd*. U.K.
- Fam, A. and Rizkalla, S.H. 2001. Flexural Behavior of Concrete-Filled Fiber-Reinforced Polymer Circular Tubes. *Journal of Composites For Construction*. 6(2):123-132.
- Hognestad, E.A. 1951. A Study of Combined Bending and Axial Load in Reinforced Concrete Members, *University of Illinois Engineering Experiment Station*, Bulletin No. 399.
- Shao, Y. and Mirmiran, A. 2005. Experimental Investigation of Cyclic Behavior of Concrete-Filled FRP Tubes. *Journal of Composites for Construction*. 9(3):263-273.
- Son, J. and Fam, A. 2008. Finite element modeling of hollow and concrete-filled fiber composite tubes in flexure: Model development, verification and investigation of tube parameters. *Journal of Engineering Structures* 30(10):2656-3313.

An Experimental Investigation into the Behaviour of Filament Wound Hybrid FRP-Concrete Beam

A. Chakraborty, A. Khennane (a.khennane@adfa.edu.au), & E.V. Morozov

School of Engineering and Information Technology, UNSW@ADFA, Canberra, Australia

ABSTRACT This study presents the results of an experimental investigation into the performance of hybrid beams wrapped with filament winding. A cost-effective pultruded profile was used to reduce the high initial cost of the beam. High strength concrete was cast on top of the pultruded profile to take the compressive forces and CFRP laminate at the bottom to take the tensile forces. The whole system was then wrapped with GFRP using filament winding to eliminate the debonding of the concrete from the pultruded profile. Two different lay-up types of wrapping $\pm 45^\circ$ and $90^\circ/\pm 45^\circ$ were used. The experimental results show that the wrapping did not only eliminate the debonding of concrete from the pultruded profile but also increased the overall stiffness and the load carrying ability of the beam. As a result, the beams carried a significant amount of load before failure.

1 INTRODUCTION

If in the past the use of composite materials in the field of construction was predicated on improved performance attributes, better enviro-mechanical durability, and ease of transportation and construction, then in the near future, it is very likely that it will be on energy efficiency. A study was done to compare the energy consumption of using various materials such as steel, aluminum, composites and reinforced concrete for construction from the stages of extraction of raw materials, production and fabrication of the material, delivery of the material to the construction site and maintenance throughout the design life of the structure (Daniel, 2003). It was found that composites consume approximately half the total amount energy as any other construction material considered. In this manner, FRP material promises to be a greener construction option over concrete and steel. Despite these advantages over conventional materials, composites are making limited progress in the field of highway structures, where the only niche markets for composites is in FRP deck construction over steel girders and externally bonded FRP repair. One of the main reasons of this limited progress is their expensive production cost (Hota et al. 2002). Cost-effective manufacturing processes such as pultrusion and filament winding can help considerably in reducing this initial cost of FRP's when produced in large volumes.

The present study presents the results of an experimental program into the behaviour of hybrid FRP-concrete beams using a pultruded profile and wrapped with filament winding. It also proposes a new design method where the CFRP laminate is used to tailor the

stiffness of the beam rather than serves as a warning sign of failure.

2 DESIGN

2.1 Description of the beam

We propose to design and test a series of beams, whose typical cross section is shown on Figure 1. The beam consists of a pultruded profile, a high strength concrete block, a CFRP laminate, and a filament wound GFRP wrapping. The concept in itself is not new, it has already been trailed by (Deskovic et al, 1995; Canning et al, 1999; van Erp et al, 2002) to cite only a few, but the wrapping using filament winding, and designing the CFRP laminate to tailor the stiffness of the beam is not reported.

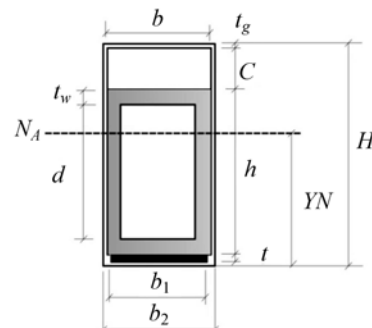


Figure 1 Hybrid beam cross section

The beams are designed to carry a minimum load of 50 kN over a span 1.29 m in four point bending and deflect less than $L/600$ as recommended in AS5100 for reinforced concrete beams.

2.2 Section dimensions

In reinforced concrete design, the span to depth ratio varies between 10 and 20. The lower limit of 10 is chosen so that a deeper beam can be achieved and the problem of a lack of stiffness of a thin walled GFRP box section can be addressed. Thus, for a span of 1.29 m, the depth of the hybrid beam, H is chosen as 200 mm. The height and width of the pultruded profile are imposed and respectively equal to 152 mm and 102 mm. The height of the concrete block is chosen as 40 mm. The thickness of the wrapping is variable as different lay-up will be tested. However, for initial dimensions, we choose it to be equal to 2 mm.

CFRP laminate thickness.

Total maximum mid span deflection of a simply supported beam under four point bending can be expressed as:

$$\delta_{Max} = \delta_{Bend} + \delta_{Shear} \quad (1)$$

where δ_{Bend} represents the deflection due to bending and expressed as:

$$\delta_{bend} = Pa(3L^2 - 4a^2)/24EI \quad (2)$$

and δ_{Shear} obtained as:

$$\delta_{shear} = (Pa/\sum GA) f_s \quad (3)$$

where a represents the shear span and f_s represents the shear factor, see (Hulatt et al. 2003).

Expressing the stiffness rigidity and the neutral axis of the beam respectively as:

$$\begin{aligned} EI = & E_c \left(bc \left(\frac{c}{2} + h + t + t_g - YN \right)^2 + \frac{bc^2}{12} \right) \\ & + E_p \left(bt_w \left(h + t + t_g - \frac{t_w}{2} - YN \right)^2 + \frac{bt_w^2}{12} \right) \\ & + 2E_p \left(dt_w \left(\frac{d}{2} + t_w + t + t_g - YN \right)^2 + \frac{t_w d^2}{12} \right) \\ & + E_p \left(bt_w \left(YN - \frac{t_w}{2} - t - t_g \right)^2 + \frac{bt_w^2}{12} \right) \\ & + E_g \left(b_2 t_g \left(H - \frac{t_g}{2} - YN \right)^2 + \frac{b_2 t_g^2}{12} \right) \\ & + 2E_g \left((H - 2t_g) t_g \left(\frac{H - 2t_g}{2} + t_g + YN \right) \right. \\ & \left. + \frac{t_g (H - 2t_g)^2}{12} \right) \\ & + E_g \left(b_2 t_g \left(YN - \frac{t_g}{2} \right)^2 + \frac{b_2 t_g^2}{12} \right) \\ & + E_L \left(b_1 t \left(YN - \frac{t}{2} - t_0 \right)^2 + \frac{b_2 t_g^2}{12} \right) \end{aligned} \quad (4)$$

and

$$\begin{aligned} YN = & \frac{1}{p} \times \left(E_c bc \left(\frac{c}{2} + h + t + t_g \right) + E_p bt_w \left(h + t + t_g - \frac{t_w}{2} \right) \right) \\ & + 2E_g t_w d \left(\frac{d}{2} + t_w + t + t_g \right) + E_p bt \left(\frac{t_w}{2} + t + t_g \right) \\ & + E_L b_2 t \left(\frac{t}{2} + t_g \right) + E_g b_2 t_g \left(H - \frac{t_g}{2} \right) \\ & + 2E_g (H - 2t_g) t_g \left(\frac{H - 2t_g}{2} + t_g \right) + \frac{E_g b_2 t_g^2}{2} \end{aligned} \quad (5)$$

with

$$\begin{aligned} D = & E_c bC + 2E_p bt_w + 2E_p t_w d + E_L b_1 t \\ & + 2E_g b_2 t_g + 2E_g t_g (H - 2t_g) \end{aligned}$$

where, E_c , E_p , E_L and E_g are the elastic modulus of concrete, pultruded profile, CFRP and GFRP laminate respectively, and solving the equation

$$\delta_{max} = \delta_{bend} + \delta_{shear} = L \quad (6)$$

for t using Maple yields the thickness of the CFRP laminate, which is obtained as 1.14 mm. A CFRP laminate of 1.2 mm thickness is chosen as this is a standard thickness.

2.3 Load carrying capacity

2.3.1 Lateral stability

Generally pultruded box sections have high resistance to lateral torsional buckling. However, to satisfy the design requirements and to prevent lateral instability, height to width ratio is often checked by the following relation (Deskovic et al. 1995),

$$(C + h)/b < k \quad (7)$$

According to Deskovic (1995), for thin-walled composite hybrid sections the value of k is around 3. For this beam cross section the value of k is obtained as 1.88, which is well within the accepted value.

2.3.2 Web buckling load

Another possible mode of failure of this beam is through buckling of the pultruded box section webs. To make sure that the beam's webs are stiff enough to take the design load and would not buckle, theoretically the web buckling load was calculated using the formulas given in (Holmes and Just, 1983, Deskovic et al. 1995).

The web buckling load was obtained as 1303 kN, which is well above the assumed design load.

2.3.3 Flexural capacity

The ideal scenario is for the beam to fail through concrete crushing. Using strain compatibility, as shown on Figure 2, the moment capacity of the beam at which the concrete should crush is calculated and compared to the external applied moment caused by the 50 kN load. Based on a crushing strain of concrete, equal to $\varepsilon_c = 0.0026$ measured on a cylinder, the ultimate moment capacity of the section was found to be equal to 40.9 kN.m, which is four times greater than the design moment of 10.75 kN.m.

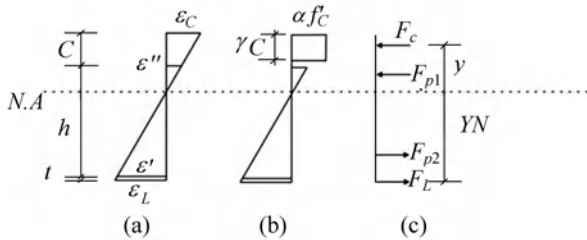


Figure 2 Strain compatibility

3 EXPERIMENTAL PROGRAMME

To investigate the effect of filament wound wrapping on the performance, three beams were wrapped with different lay-ups. The first beam, labeled A, had no CFRP reinforcement and was wrapped up with a $\pm 45^\circ/90^\circ$ lay-up. The second and third beams labeled B and C, were reinforced with a 1.2 mm thick CFRP laminate, and wrapped up with $\pm 45^\circ$ and $\pm 45^\circ/90^\circ$ lay-ups respectively. All the beams were tested in four point bending.

Figure 3 shows the load-displacement curves for the beams. For the sake of comparison, an extra curve for a beam with a hand lay-up wrapping (Khennane, 2009) is added. It can be clearly seen that filament wound wrapping increases not only the stiffness but also the load carrying ability of the beams. The beam without any CFRP reinforcement displays enough stiffness when compared to the beam having a hand lay-up process, which had CFRP reinforcement.

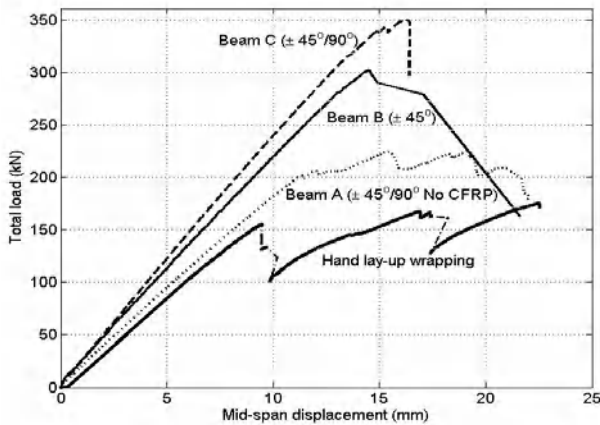


Figure 3 Mid-span load displacement curves

The beam without CFRP reinforcement failed through local bearing capacity at the support. Even though this constitutes a premature failure, the load displacement curve for this beam still shows that dissipation of energy can be obtained through tearing and splitting of the pultruded profile as previously reported by Bank et al. (2001) when testing pultruded profile for use as safety crash barriers.

To avoid this sort of premature failure, the remaining beams B and C were reinforced at the support as shown on Figure 5 with a block made of Delrin, a plastic material

that is easily machined and having similar stiffness properties as a pultruded profile. This inhibited the failure at the support and allowed the beams to fail through concrete breaking in the zero shear area. The concrete did not crush, but rather failed in a sudden fashion accompanied by a loud sound. Figures 6 and 7 show the failure of the beam. The brittleness of the high strength concrete apparently did not allow for energy dissipative behavior.

A total of 18 strain gauges were placed on each beam. Figure 8 shows the strains in the top and bottom fibres at mid-span for beam B.



Figure 4 Failure of beam A



Figure 5 Support reinforcement with a plastic block

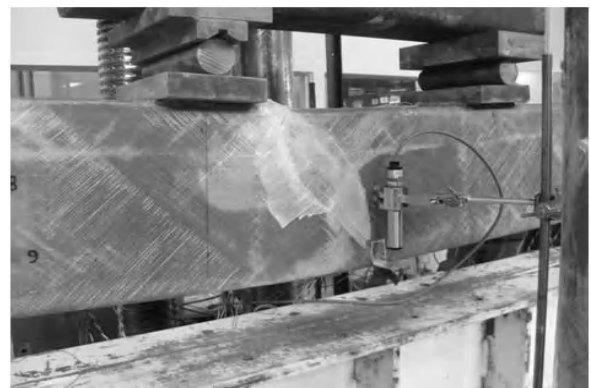


Figure 6 Failure of the beam

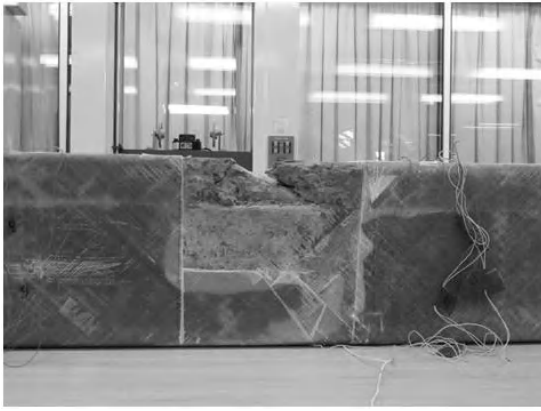


Figure 7 Failure of the concrete block

At peak load, the top fibre recorded a compressive strain of 0.0033. Although this strain is recorded on the wrapping, it does suggest that the strain in the concrete top fibre is within the vicinity of this value. This proves that the wrapping does confine the concrete since the ultimate compressive strain of the concrete recorded in a standard compressive test was only 0.0026. However, the confinement hence introduced is not enough as to provide ductility to the concrete. Current research is focused on using high strength concrete reinforced with steel fibers to improve the pseudo-ductility of the beam.

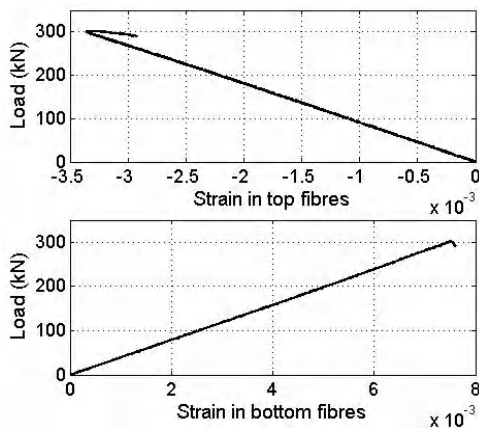


Figure 8 Strains in top and bottom fibres for beam B

In terms of stiffness and load carrying ability, the beam C with $\pm 45^\circ/90^\circ$ performed extremely well reaching a load of 350 kN, which is seven times the deflection governed design load. This corresponds to a moment of 75.25 kN-m, which is nearly twice the predicted ultimate moment of 40.9 kN-m. It is clear that the developed analytical theory based on a crushing strain of concrete of 0.0026 is very conservative as the confinement effect, albeit small, is not taken into account. Further theoretical developments are warranted.

4 CONCLUSION

The results obtained from the experimental data and analyses enable the following conclusions to be drawn:

- the wrapping of a hybrid beam using filament winding not only enhance the stiffness but also the load carrying ability;
- when a pultruded profile is subject to concentrated loads, the local bearing capacity should be improved as to inhibit premature failure through tearing and splitting of the profile;
- the wrapping does introduce some form of confinement to the concrete but not sufficient enough as to induce a ductile behavior;
- future research should focus on improving the ductility of the concrete block through the introduction for example of steel fibres (an experimental investigation is currently underway), and the development of reliable theoretical models to predict the ultimate load carrying capacity.

REFERENCES

- Bank L.C. & Gentry T.R. 2001, Development of a pultruded composite material as a highway guardrail. *Composites: Part A*, 32, 1329-1338.
- Canning, L., Hollaway, L. and Thorne A.M. 1999, Manufacture, testing and numerical analysis of an innovative polymer composite/concrete structural unit. *Proceedings – Institution of Civil Engineers, Structures and Buildings*, 134, pp. 231-241.
- Daniel, R.A. 2003, Environmental considerations to structural material selections for a bridge, *European Bridge Engineering Conference*, pp. 1-10.
- Deskovic, N., Triantafillou, T.C. & Meier, U. 1995. Innovative design of FRP combined with concrete: short term behavior. *ASCE Jou. Struct. Engrg* 121(7), 1069-1078.
- Holmes, M., and Just, D. J. (1983). *GRP in Structural Engineering*, Applied Science Publishers, UK.
- Hota., G. R. V. S., and Hota., S. R. V. (2002). Advances in fibre-reinforced polymer composite bridge decks. *Prog. Struct. Engg. Mater.*, 4, 161-168.
- Khennane, A. 2009, Manufacture and testing of a hybrid beam using a pultruded profile and high strength concrete. *Australian Journal of Structural Engineering*, Vol. 10, No. 2.
- van Erp, GM, Heldt, TJ, Cattell, CL, & Marsh, R, 2002 ‘A new approach to fibre composite bridge structures’, Proceedings of the 17th Australasian conference on the mechanics of structures and materials, ACMSM17, Australia 37-45.
- Hulatt, J., Hollaway, L., and Thorne, A. 2003. Short term testing of hybrid T beam made of new prepreg material. *Journal of Composites for Construction*, 7(2), 135-144.

Experimental Study on Bending Performances of FRP-Concrete Composite T-Beams with Prefabricated BFRP Shell

Hong Zhu(alice_zhuhong@seu.edu.cn), Pu Zhang, Gang Wu, Zhishen Wu

*Key Laboratory of Concrete and Prestressed Concrete Structures, Ministry of Education, China
International Institute for Urban Systems Engineering, SEU, Nanjing, 210096, China*

ABSTRACT FRP-Concrete composite beams with prefabricated BFRP shell are further studied in this paper. Based on previous research experience, several specimens of FRP-Concrete composite T-beams were designed with steel bar as the main reinforcement and lower FRP participation proportion than before to improve the performance, in which the FRP-concrete interface was wet-bonding combined with a new type of FRP shear Key (FSK-WB), and the prefabricated BFRP section was made by the vacuum infusion molding technique and then filled with freshly-cast concrete. Bending experiments of six composite beams and two RC beams, under either static or cyclic load, were conducted. The experiment results indicate that this kind of FRP-concrete composite beam has the advantages of higher bearing capacity, proper post-yield stiffness, better recoverability, and at the same time without reducing the ductility. On the other hand, these beams will use less FRP materials to obtain durability, thus reduce the materials cost. The FSK-WB interface is proved to be safe and reliable.

1 INTRODUCTION

In order to reduce LCC (Life cycle cost), advanced fiber composite polymer is more and more frequently combined with conventional materials to develop new structures^[1-3]. For the purpose of high durability and ease of construction, Wu et al.^[4-5] proposed an innovative hybrid FRP-concrete composite system, in which special FRP bonding technique termed as “wet-bonding”(WB) was adopted. The first group of the specimens focus on the minimum steel reinforcement ratio, and the results indicate that the WB bonding technique is proved effective but these beams are unsatisfactory due to the low ductility and local premature peeling. In further studies, composite beams with increased steel reinforcement ratio are studied, in which FRP sheet and steel bar have approximately equal load capacity^[6-7]. The results show that the ductility is improved, but the cost is still not widely acceptable. Based on the previous research experience, several composite beams with lower FRP participation proportion than before are recommended and studied in this paper. The U-shape basalt fiber reinforced polymer (BFRP) shell made by the vacuum infusion molding technique is filled with the freshly-cast concrete, thus forming a whole girder. In addition, the interface of the composite beam is wet-bonding, combined with a new type of FRP shear key (FSK-WB), and both ends of vertical BFRP are directly anchored into the flange concrete. Bending

experiments of eight beams, under either static or cyclic load, are conducted. Among them, two pieces are conventional reinforced concrete (RC) beams for comparison, and the others are new type FRP-concrete composite T-beams, in which the reinforcement ratio of steel and FRP are designed to optimize the performance of the beams. One composite beam is specially designed for verifying the reliability of FSK-WB. Results prove that the interface is reliable, and the flexural performance of this kind of innovative FRP-concrete composite beam is promising.

2 EXPERIMENTAL PROGRAM

2.1 Specimen preparations

The properties of FRP sheets and the design parameters of beams are listed respectively in Table 1 and Table 2. To ensure the reliability of the interface, FSK-WB interface is developed. The beam span, l , is 3000mm. The sizes and components of beams with the same cross-section, along with the loading equipment are shown in Figure 1. The U-shape BFRP section was made by the vacuum infusion molding technique, in which BFRP sheets were axially laid at the bottom of the beams in order to improve bearing capacity, and hoop-directionally laid at the lateral side of the beams with the advantages of improving the shear resistance, protecting the steel bars from corrosion, and preventing the premature debonding of tensile FRP

at the bottom. All beams are designed with relatively weak bending capacity and enough shear capacity.

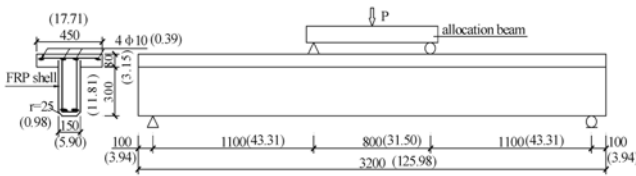


Figure 1 Sizes and components of the composite beams unit:mm(in)

The measured average cylinder compression strength, f'_c of the C40 concrete is 36.6MPa. Tensile steel bar is made of HRB335; while other steel bars are made of HPB235. The measured average yield strength, f_y of HPB235 and HRB335 are 328MPa and 445MPa respectively.

Table 1 Properties of axially laid BFRP sheets

Type of FRP	b_f (mm)	t_f (mm)	f_{tu} (MPa)	E_f (GPa)	ϵ_{fu} ($\mu\epsilon$)
BFRP sheet	100	0.148	1902	73.7	26920

Table 2 The parameters of FRP-concrete composite beams

Specimen	Steel bar	ρ_s	Tension FRP	R_f	Interface mode	Loading style
B1	2 Φ 22	1.47%	—	—	—	C
B2	2 Φ 20	1.21%	—	—	—	C
B3	2 Φ 20	1.21%	1B	9.8%	SK-WB	C
B4	2 Φ 28	2.41%	2B	10.4%	SK-WB	C
B5	2 Φ 20	1.21%	4B	30.1%	SK-WB	C
B6	2 Φ 20	1.21%	4B	30.1%	WB	M
B7	2 Φ 20	1.21%	4B	30.1%	SK-WB	M
B8	2 Φ 20	1.21%	10B	51.7%	SK-WB	C

Notice: 1B represents one layer of BFRP sheet, 2B represents two layers, and so on. ‘M’ represents monotonic loading and ‘C’ represents cyclic loading. R_f is the ratio of fiber participation proportion of ultimate moment.

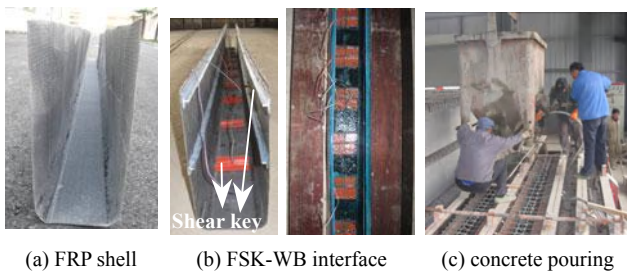


Figure 2 Manufacture process of composite beams

The manufacture process of FRP-concrete composite beams is shown in Figure 2. Firstly, FRP shells were produced by the vacuum infusion molding technique. Secondly, the FRP shear keys were bonded at the bottom and the two lateral sides of the inner surface of the FRP shell using the FRS-type epoxy resin. After the shear

keys were firmly bonded, the epoxy resin was coated on the inner surface of the FRP shell, and then the shell was placed into the mould. Then, the reinforcement cage was put into the FRP shell immediately. About 20~120 minutes later, fresh concrete was poured into the FRP shell.

2.2 Test equipment and loading system

The beams were under four-point bending, and the test load is controlled by means of the pressure sensor and displacement sensor. Load level was 10kN per level until failure except for changing to 2kN per level near cracking. The cyclic loading system is shown in Figure 3. Force control was used before steel yielding, while displacement control was used after yielding. $0.75P_y$ was taken as the unloading points prior to yielding to measure the unloading stiffness and the deflection, 15mm, 20mm, 25mm, and 40mm were taken as the control points after yielding.

3 EXPERIMENT RESULTS

3.1 Axial strain distributions of the beams

Compressive (tensile) strains at different height of middle section of each beam were measured, such as B7 in Figure 4. Figure 4 shows that the plane section of the beam remains plane under the increasing load.

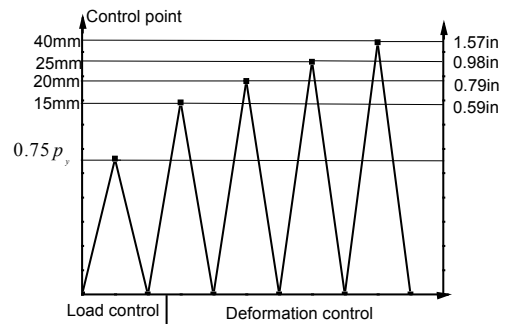


Figure 3 Cyclic loading system

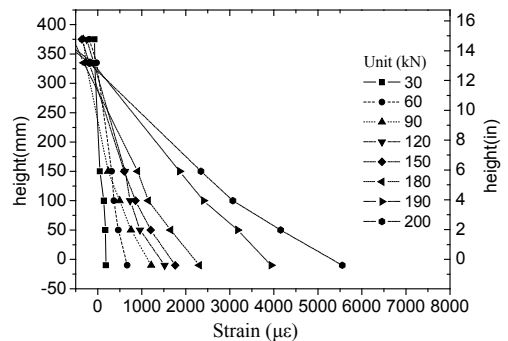


Figure 4 strain distributions of middle section (B7)

3.2 Summary of experiment results

The failure modes of all FRP-concrete composite beams are the axially tensile FRP sheets rupture after the steel yielding, and finally the concrete crushed, as shown in

Figure 5. The experimental results are summarized in Table 3.



Figure 5 The failure modes of B3-B8

Table 3 Experiment results

Specimen	P_{cr} (kN)	P_y (kN)	P_u (kN)	$P_{u,c}$ (kN)	P_u ($P_{u,c}$)	Δ_y (mm)	Δ_u (mm)	μ_Δ
B1	36.0	196.0	258.2	234.1	0.91	12.2	90.4	7.43
B2	38.2	163.0	198.5	200.0	1.01	9.3	87.4	9.44
B3	42.1	180.2	211.4	205.4	0.97	9.6	90.6	9.46
B4	48.0	300.4	360.3	348.3	0.97	12.2	63.0	5.16
B5	45.2	169.0	241.9	263.1	1.09	10.4	65.7	6.32
B6	41.9	185.9	256.3	263.1	1.03	10.4	46.1	4.45
B7	41.1	178.8	241.2	263.1	1.09	9.9	52.6	5.29
B8	40.0	195.1	383.1	376.3	0.98	10.2	85.1	8.35

" P_{cr} " is the cracking load, " P_y " is the yield load; " P_u " is the ultimate load; " $P_{u,c}$ " is the calculated loading capacity.

3.3 Ultimate bending capacity

Using the principles of strain compatibility and equilibrium equations, an iterative analytical model is developed to predict the flexural behavior of the FRP-concrete beams. The assumptions include: (1) Euler–Bernoulli beam theory; (2) Plane sections remain plain under the increasing load; (3) No slip between the longitudinal reinforced steel and the surrounding concrete occurs; (4) No slip between the externally bonded FRP shell and concrete occurs; (5) No debonding or shear failure is accounted for.

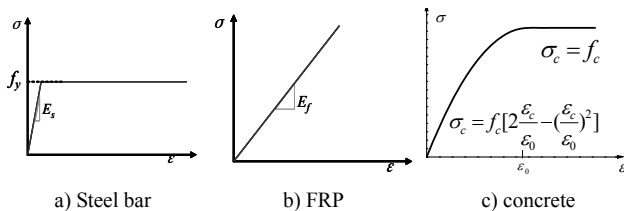


Figure 6 Constitutive relationships for materials

The materials constitutive models can be seen in Figure 6. Reinforced steel is modeled by the ideal Elastic-Plastic curve in tension and compression, and FRP materials are assumed to behave linear elasticity until failure. Classical laminate theory and maximum strain failure criterion of the composite materials are adopted. Unconfined concrete is assumed to follow the model in the Chinese code [8].

The ultimate moment of the FRP-concrete composite beam, M can be calculated by the following equations;

$$M = A_s f_y (h_0 - x/2) + A_f f_{f,u} (h - x/2) + A'_s \sigma'_s (a'_s - x/2) \quad (1)$$

$$x = \beta_1 x_0 \quad (2)$$

In which,

h_0 — sectional effective height;

x — height of equivalent rectangular concrete compression zone;

x_0 — height of concrete compression zone;

A_s, A'_s, A_f — Areas of tensile steel bar, compressive steel bar and tensile FRP;

f_y — yield strength of tensile steel bar;

σ'_s — stress of compressive steel bar;

$f_{f,u}$ — ultimate strength of tensile FRP;

β_1 — equivalent coefficient of the concrete compression zone height.

The calculation methods for β_1 , σ'_s and x_0 have been proposed by the authors in reference [7]. The ultimate load, $P_{u,c}$ is equal to $2M$ divided by $l/3$. The calculated values, $P_{u,c}$ of the model mentioned above are listed in Table 3. Data in Table 3 indicates that a good agreement is observed between the calculated values and the measured, and the maximum error is 9%. Therefore, this analytical model which considers the tension stiffening effect of FRP is proved to be effective.

3.4 Ductility

Ductility is an important structure performance indicator for the FRP-concrete composite beams due to the sudden rupture of the FRP material. Displacement ductility coefficient can be calculated by Equation (3).

$$\mu_\Delta = \Delta_u / \Delta_y \quad (3)$$

Δ_u — ultimate deflection of the beam;

Δ_y — deflection of the beam when yielding;

As shown in Table 3, the displacement ductility coefficient of RC contrastive T-beam is 9.44, while for the FRP-concrete composite beams, its range is from 4.45 to 8.35. Although the ductility of FRP-concrete composite beams is not as good as that of RC beams good, however it is still satisfactory. It is much better than those beams in literature 9, where the ductility coefficient drops rapidly from 5.28 to (1.66, 1.99) after strengthened by CFRP plates. The test results of B3 and B4 show that lower fiber participation proportion can get higher ductility. Because the fiber participation proportion of ultimate moment is less than 15% in these beams, when FRP ruptures, the capacity of these beams will reduce but will still be higher than 85% of its maximum ultimate capacity.

4 RESULTS DISCUSSION

4.1 B1/B2/B5

Specimens B1 and B2 are RC beams, and B2 is the basic one. The load-displacement curves of B1, B2 and B5 are

shown in Figure 7a). The capacity load of B5 is almost equal to that of B1, as it was designed. Compared with B2, the post-yield stiffness of B5 is obviously greater than RC beams, and the ductility is satisfactory, and more importantly, the durability is much better than that of RC beams.

4.2 B2/B3/B4

Specimens B3, B4 are FRP-concrete composite beams designed with the steel bar as the main reinforcement. The fiber participation proportion of ultimate moment is about 10%. The load-displacement curves are shown in Figure 7b). Although the post-yield stiffness is not significant, it is still considerable. Load decreasing after FRP rupture in the load-displacement curve is not obvious, and the beam can bear the load till the concrete in the compression zone is crushed. Compared with RC beams, composite beams designed with steel bars as main reinforcement and some FRP to improve the performance have the advantages of higher bearing capacity, proper post-yield stiffness, better recoverability, and better durability and at the same time without reducing the ductility. On the other hand, these beams will use less FRP materials, thus reduce the materials cost.

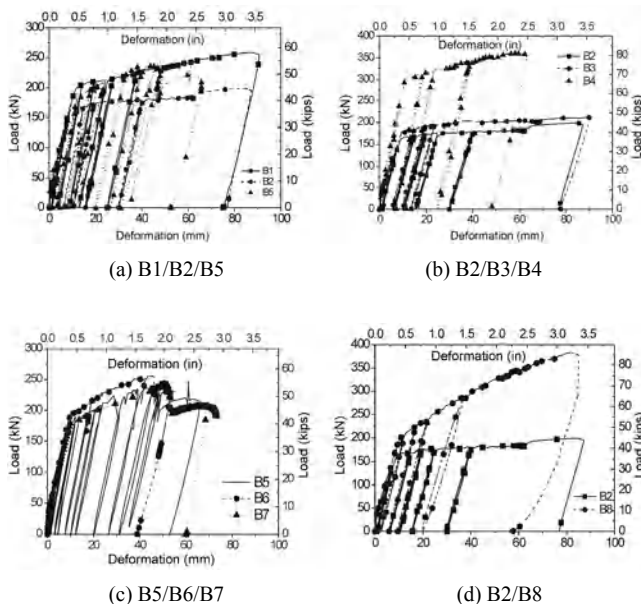


Figure 7 Load-displacement curves

4.3 B5/B6/B7

Specimens B5, B6, and B7 are the same, except for the difference in interface mode and in the loading systems. B5 and B7 are both the FSK-WB interface specimens, while the interface of B6 is wet-bonding without FSK at the beam bottom. B5 is under the cyclic loading, while B6 and B7 are under the monotonic loading. The load-displacement curves are shown in Figure 7c). The failure modes of B5, B6 and B7 are all BFRP rupture. However, when load reaches 200kN, a small hollowing area appears

on the side of the FRP shell of B6 at the loading point, and finally, the hollowing area is increased to 300mm×400mm.

The residual displacement after yielding is much larger than that before yielding. It is observed that when the number of cycles is small, the bending capacity under the cyclic load is not significantly weakened than that under the monotonic load because B5 and B7 have almost the same performance.

4.4 B2/B8

The load-displacement curves of B2 and B8 are shown in Figure 7d). After steel yielding of B8, there is significant post-yield stiffness and 93% increase of the ultimate load compared with B2. The load-displacement curve of B8 shows obvious recoverability than B2. The failure mode of B8 is BFRP rupture immediately followed by the concrete crushing in compression zone. The interface of the beam is reliable, no hollowing or peeling is found. It indicates that the FSK-WB interface is reliable enough even when there are 10 layers BFRP sheets in the bottom of the shell.

5 CONCLUSION

1) FRP-concrete composite beam composed by prefabricated FRP shell and freshly-cast concrete through the FSK-WB interface is an innovative type of composite beam. Test results prove that the interface is safe and reliable enough even when there are 10 layers FRP sheets in the bottom of the shell.

2) FRP-concrete composite beams designed with steel bar as the main reinforcement and with suitable FRP participation proportion to improve the performance are recommended for their good integrated performance, including high bearing capacity, proper post-yield stiffness, good recoverability, good durability, high ductility and low materials cost.

3) When the number of cycles is small, the bending capacity of the composite beam under cyclic load is not weakened than that under monotonic load. But the reliability of the FSK-WB interface should be further studied by the fatigue test.

6 ACKNOWLEDGMENTS

The authors gratefully acknowledge the financial supports from the National Key Technology R&D Program of China (No.2006BAJ03B07), National Natural Science Foundation of China (No.50908045).

REFERENCE

- Cheng LJ & Karbhari VM. 2006. New bridge systems using FRP composites and concrete: A state-of-the-art review. *Progress in Structural Engineering and Materials*. V. 8, No. 4, Oct-Dec.

- pp.143-154.
- A.A. Mufti, P. Labossière and K.W. Neale, 2002. Recent bridge applications of FRPs in Canada, *Struct. Eng. Int.* V. 12, No. 2. pp.96–98.
- C. E. Bakis; L. C. Bank, V. L. Brown, E. Cosenza, J. F. Davalos, A. & et.al. 2002. Fiber-Reinforced Polymer Composites for Construction—State-of-the-Art Review. *Journal of composites for construction / MAY.*:73-87.
- Wu ZS, Li WX, Sakuma N. 2006. Innovative externally bonded FRP/concrete hybrid flexural members[J]. *Composite Structures*. Mar,72(3):289-300.
- K.Iwashita, Z.S.Wu, H. Zhu, H. Mishima, 2006. Flexural behavior of FRP-RC hybrid structures with wet-bonding technique, Proc. of 58th Annual Convention of JSCE, CS02-045, 157-158.
- Z.S.Wu, K.Iwashita, C.Q.Yang et al. 2007. Experimental Investigation on Damage-Control Hybrid FRP-RC Girders with Wet-Bonding. *2-nd International Conference on Advances in Experimental Structural Engineering*. Tongji University, Shanghai, China, pp.144-151.
- Zhang Pu, Zhu Hong, Meng Shaoping, Lei Yun, Wu Gang, Wu Zhishen. 2010. Experimental study on bending performances of Hybrid FRP-Concrete composite T-beams. *Journal of Southeast University(Natural Science Edition)*. V. 40, No. 3, pp.548~553.
- National standard of the People's Republic of China.2002. Code for design of concrete structures. Beijing: China Architecture & building press.
- Toutanji, H., Zhao, L., and Zhang, Y. 2006. Flexural behavior of reinforced concrete beams externally strengthened with CFRP sheets bonded with an inorganic matrix. *Engineering Structures*, V.28, No.4. pp.557-566.

A Comparative Study of Various FRP Shear Connectors for Sandwich Concrete Walls

G.D. Woltman, D.G. Tomlinson, A. Fam (fam@civil.queensu.ca)

Department of Civil Engineering, Queen's University, Kingston, Ontario, Canada

ABSTRACT There is a great demand to improve both the structural and thermal characteristics of insulated precast concrete sandwich panels. This paper addresses the potential of using a number of Glass Fibre Reinforced Polymer (GFRP) connectors developed in this research program as an alternative to metallic connectors. The objective is to reduce thermal bridging in the sandwich panels, while transferring shear forces to develop composite action within the panel. The panel incorporates a new system of concrete wythes and studs connected by the GFRP connectors, where the studs are not in direct contact with the wythes. The load-slip response of the system has been established through shear tests. It was also shown that adhesion between the insulating foam and concrete provides significant shear resistance prior to engaging the GFRP connectors.

1 INTRODUCTION

Precast concrete sandwich panels have been used reliably in the construction industry for over a half century. Sandwich panels traditionally consist of two concrete wythes separated by a layer of insulation. The wythes are then connected by either solid concrete regions or metal ties (PCI 1997).

In a composite or partially composite sandwich panel, the connectors transfer shear forces between the concrete wythes, but they also create a thermal bridge through the insulation layer. The transfer of shear forces allows both wythes of the panel to act together to resist applied loads, giving the panel a higher stiffness and greater structural efficiency. However, the thermal bridge created by the connectors, whether stainless steel or concrete, can reduce the thermal performance of a panel by as much as 40% (McCall 1985).

Significant research has been conducted to determine the effect of shear connectors on the structural and thermal properties of sandwich panels, and to develop new panel geometries to improve these properties (Lee and Pessiki 2008a,b). Other research has developed a limited number of Glass Fibre Reinforced Polymer (GFRP) connectors, to take advantage of the relatively low thermal conductivity of GFRP materials (Salmon et al. 1997). The previously mentioned research has shown that GFRP connectors are feasible for use in sandwich panels, and can develop significant composite strength with minimal reductions in thermal efficiency.

This study aims to develop a simple yet reliable GFRP connector, and combine it with modified structural geometry of the concrete wall to create a more thermally

and structurally efficient sandwich panel. The project is work in progress, with preliminary testing of the various FRP shear connectors reported in this paper. Future work includes more testing focused on repeating these preliminary tests to establish a statistically sound and reproducible results. Also, full scale panels will be tested under in-plane and out-of-plane loading to determine their thermal and structural characteristics.

2 EXPERIMENTAL STUDY

2.1 Test Parameters

This experimental study involved testing fourteen test specimens in double-shear push-out tests. All specimens comprised two concrete wythes and a concrete stud in between. The studs were not in direct contact with the wythes and were separated by a 25 mm layer of extruded polystyrene (XPS) insulation foam, however, the FRP shear connectors run through the stud and the two wythes. Also, the space between the wythes around the stud was filled by the same foam. Test parameters included the FRP type, diameter, and end treatment. No attempt was made to eliminate the bond (adhesion) between the concrete and the insulation layers. As will be shown, test results showed that the concrete-insulation bond was quite significant but rather brittle, and the effect of this bond could easily be isolated from the resistance of the connector.

The specimens were loaded on the concrete stud and supported on the two wythes, in a double-shear test configuration. The objective was to measure the relative displacement of the stud and wythes, and the applied load until failure.

2.2 FRP Connector Details

Various connector patterns were tested as part of this initial phase of the study. These included GFRP pultruded bars from three different manufacturers, referred to here as types A, B and C. Two of the GFRP bars, A and B, are commercially available sand-coated concrete reinforcement bars in North America. Two nominal diameters of type A bars, 9.5 and 12.7 mm, and three nominal diameters of type B bars, 6.4, 9.5 and 12.7 mm, were used. The third connector, C, is a commercially available 12.7 mm diameter GFRP threaded rod that can be used with a commercially available nut. Additionally, three commercially available polypropylene connectors, referred to as type D, of three nominal diameters of 9, 12.5 and 14.5 mm, were included in the test matrix, for comparison with the GFRP samples. The reported longitudinal tensile strengths of type A bars ranged from 690 to 760 MPa depending on diameter. Similarly the tensile strength of type B bars ranged from 708 to 874 MPa. For type D connectors the tensile strength was 40 MPa. No data on tensile strength of type C rods is available.

Selected end treatments of the GFRP bar connectors in some of the specimens involved notching circumferential grooves, the use of lock washers, nuts, and nuts and washers in combination. The goal was to enhance mechanical interlock of the connector within the rather short embedded in the 51 mm thick wythe. The preliminary test matrix is shown in Table 1. Specimens are given certain designations. For example, C-13N indicates connector type C of 12.7 mm nominal diameter with an end treatment of using a nut. Table 1 also shows the number of connectors, their spacing and their total cross-sectional area in each specimen.

2.3 Specimen Details

The test specimens were 900 mm in height, and 250 mm x 250 mm in cross-section, including the two 51 mm x 250 mm wythes and the 51 mm x 100 mm stud. The specimens were cast using 35 MPa concrete, directly against the insulation boards. The wythes were reinforced with conventional steel welded wire mesh.

The GFRP connectors were placed horizontally, spanning the two wythes and through the concrete stud. To compare different diameters of connectors, the total cross sectional area of the connectors was kept as close to constant as possible. This required that the number of connectors be varied, with a minimum of three connectors used, and a maximum of eleven, as shown in Table 1.

2.4 Test Setup and Instrumentation

All fourteen specimens were mounted with the exterior wythes supported by steel HSS sections, and tested by loading the middle stud using a 1000 kN Reihle machine. Care was taken to centre both the samples and the load ram in all three axes.

Table 1 Details of test specimens

Spec. ID	Number of connectors	Spacing (mm)	Connectors area (mm ²)	End treatment
A-10	5	180	356	-
A-10A*	7	128	498	-
A-10C	5	180	356	Notch
A-10W	5	180	356	Washer
A-13	3	300	380	-
B-6	11	82	348	-
B-10	5	180	356	-
B-13	3	300	380	-
C-13	3	300	380	-
C-13N	3	300	380	Nut
C-13NW	3	300	380	Nut & Washer
D-9	3	300	382	-
D-12	3	300	368	-
D-14	3	300	495	-

* Added to match area of D-14

The specimens were loaded at a rate of 1 mm/min, with the load applied over the 100 mm x 50 mm stud.

Relative displacements (slip) between the wythes and stud were measured using two 100 mm Linear Potentiometers (LPs) in order to provide a reliable average. Figure 1 shows a picture of the test setup. Loading continued until the connectors sheared off.



Figure 1 Test setup

3 TEST RESULTS AND DISCUSSION

3.1 Preliminary Test Results

The goal of the preliminary testing phase was to assess the relative performance of the four potential shear connector materials, as well as the effect of end treatments on connector strength and ductility in shear transfer. The

relative performance of different diameters of the same connectors was also assessed.

Figures 2 and 3 show selected load-deflection responses of some of the specimens. Because no attempt was made to eliminate the bond between the XPS insulation and the concrete, the load-deflection curves exhibit a distinct double peak pattern. The first load peak reflects the effect of adhesion bond between the concrete and the insulation. This bond was observed to be brittle, and failed after a displacement of only 2 to 3 mm, which is represented by the load drop. At this point, the load was fully transferred through the shear connectors and started rising until it reached a second peak at a displacement of about 7 to 20 mm, depending on the connector system. The insulation adhesion bond strength was shown to vary significantly as evident by the first load peak ranging from about 40 to 80 kN. It is also unlikely that this strength is sustainable over a long time under various temperature and mechanical loading cycles. As such it should not be relied upon for long term applications. Additional tests are being planned with the insulation bond eliminated to experimentally isolate the strength based on the shear connectors only.

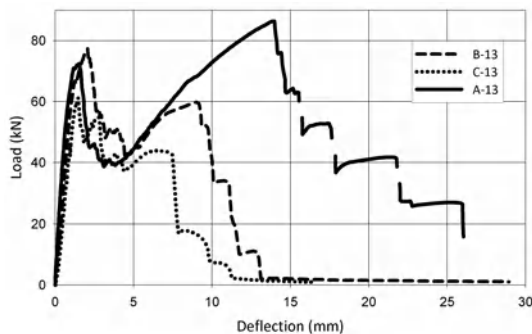


Figure 2 Test results for specimens of equal diameter GFRP connectors types A, B and C.

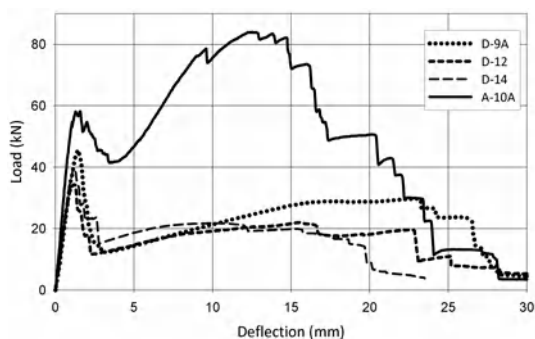


Figure 3 Test results for specimens of different diameter type D polypropylene connector, in comparison to type A GFRP connector

The difference in relative strength of the different materials was considerable. For example, the three GFRP connectors varied in strength by up to 47%, despite having the same bar diameter and total cross sectional area, as shown in Figure 2. Type A GFRP bars showed

the highest shear strength. These results were consistent, and varied very slightly with different bar diameters and end treatments. In all cases, changing the bar diameter or end treatment did not change the relative order of the connectors when comparing strength or ductility. While additional testing of each material is planned to confirm these results, little change is anticipated.

All three diameters of the type D polypropylene connectors demonstrated considerably lower strengths than the GFRP ones, as expected. However, these connectors demonstrated a considerable ductility, as shown in Figure 3.

Of particular note is that the largest polypropylene connector did not outperform the two smaller connectors, though it had a greater total cross sectional area. As the results for all three connectors were relatively similar, and significantly underperformed the GFRP connectors, they will not be carried forward for further testing.

End treatment appeared to have little effect upon the strength of the connectors in this application. In some cases the end treatment appeared to increase the ductility of the connector, but this remains to be confirmed. In the preliminary results obtained so far, bar diameters did not significantly change the strength and ductility of the specimens, provided the total cross section area of connectors was equal.

3.2 Connector Failure Mode

All three GFRP materials failed in the same manner. First the connectors would begin to delaminate internally due to the combined flexural and shear stresses within the connector as the concrete stud moves relative to the wythes, with the 25 mm gap in between. Eventually, the connectors ruptured, as shown in Figure 4. It appears that the peak load is attained and then the load drops gradually as a result of the progressive failure. Also, the peak load appears to be reached, without any bond failure from the surrounding concrete.



Figure 4 Failure of GFRP connectors

4 CONCLUSIONS

The following conclusions can be drawn from the preliminary test results:

1. GFRP sand-coated bars used conventionally for concrete reinforcement have a great potential as shear connectors.

2. GFRP shear connectors are considerably stronger than polypropylene connectors, however, the polypropylene ones should have considerable ductility.

3. Failure of GFRP connectors may be progressive and gradual over a large displacement.

4. Bar diameter and end treatment of the connectors appear to have an insignificant effect on overall strength of the panels. However, further tests will be conducted for confirmation.

5. The adhesion between concrete and insulation material is quite considerable and is very significant initially. However, since it is brittle and unlikely to be sustainable under repeated thermal or loading cycles, it should not be relied upon in design.

5 ACKNOWLEDGMENT

The authors wish to acknowledge the financial and in-kind support of Ontario Center of Excellence (OCE) and Anchor Concrete Products Ltd.

REFERENCES

- Lee, B & Pessiki, S. 2008a. Experimental Evaluation of Precast, Prestressed Concrete, Three-Wythe Sandwich Wall Panels. *PCI Journal* 53 (2).
- Lee, B & Pessiki, S. 2008b. Revised Zone Method R-value Calculation for Precast Concrete Sandwich Panels Containing Metal Wythe Connectors. *PCI Journal* 53 (5).
- McCall, W.C. 1985. Thermal Properties of Sandwich Panels. *Concrete International* 7(1): 35-41.
- PCI Committee on Precast Sandwich Wall Panels. 1997. State-of-the-Art of Precast/Prestressed Sandwich Wall Panels. *PCI Journal* 42 (2): 92-134.
- Salmon, D.C., Einea, A., Tadros, M.K. & Culp, T.D. Full Scale Testing of Precast Concrete Sandwich Panels. *ACI Structural Journal* 96 (4): 354-362.

Smart FRP Structures

Effectiveness of Smart Dampers for Hybrid FRP Cable in Long-Span Cable-Stayed Bridge

Xin Wang

*International Institute for Urban Systems Engineering, Southeast University, Nanjing, Jiangsu, China
College of Civil Engineering, Southeast University, Nanjing, Jiangsu, China*

Zhishen Wu (zswu@mx.ibaraki.ac.jp)

*Department of Urban and Civil Engineering, Ibaraki University, Hitachi, Ibaraki, Japan
International Institute for Urban Systems Engineering, Southeast University, Nanjing, Jiangsu, China*

ABSTRACT This paper presents a theoretical evaluation of modal damping of hybrid FRP cable with smart dampers for long-span cable-stayed bridge. Based on previous studies of FRP and hybrid FRP cables, hybrid FRP cable exhibited advantages in static and dynamic behavior compared with conventional steel cables and newly developed CFRP cables. One of the advantages is its designable sectional structure that can improve internal damping and benefit vibrational control of stay cable under various excitations. To validate the effectiveness of hybrid FRP cable with smart damper design, the principle and design consideration of smart dampers were first described. Based on the energy principle, the theoretical expression on modal damping was derived for in-plane vibration. Finally, in terms of a detail designed hybrid FRP cable with smart damper, the damping ratio was evaluated which demonstrated the effectiveness of smart damper design.

1 INTRODUCTION

Stay cables in cable-stayed bridge are potentially prone to vibrate due to their deficiency of structural damping compared with the other structural components (Fujino and Hoang 2008). The vibration of stay cable will become even evident with increasing of length. In one hand, the lower natural frequency of longer cable may be easier to excite vibration and the enlarged dimension will suffer from larger wind effect; on the other hand, long span cable-stayed bridges usually locate nearby the sea bay or large rivers and connect heavy traffic line, the effect of strong wind and traffic becomes even dominant.

Various types of treatments have been adopted to suppress potential vibration of cable such as aerodynamic, structural and mechanical control (Caetano 2007). Among them, the internal dampers do not require optimization of position or proper tuning, and can suppress different kinds of vibration effectively. Due to this characteristic, the internal damper can also be called smart damper. However, in practical the internal dampers mentioned above were found to be not very effective due to the limited deformation of internal damping in conventional steel cables (Yamaguchi and Adhikari 1995). Focusing on the advantages of internal damper, a new type of smart damper will be introduced and evaluated in this paper in terms of newly developed

hybrid basalt and carbon fiber-reinforced polymer (B/CFRP) cables (Wang and Wu 2010a).

FRP composites characterized by high ratio of strength to weight and durability have been widely applied in civil infrastructure. As a stay cable, FRP composites exhibit essential advantages in long-span cable-stayed bridge aiming at the deficiency of conventional steel cable such as large sag effect and durability (Wang and Wu 2010a). CFRP cables were initially investigated to replace steel cables (Meier 1987). Although superior static and dynamic performances of long-span cable-stayed bridge with CFRP cables were proven by theoretical analysis and FEM simulation, the constantly high cost still restricted their practical and large amount of application. Moreover, CFRP cables are also sensitive to wind effect due to its extremely high ratio of strength to weigh. Therefore, hybrid B/CFRP cables were developed to replace steel cable and also overcome the limitations of CFRP cables in long-span cable-stayed bridge, by which not only high static and dynamic performances were achieved but also the overall cost can be lowered (Wang and Wu 2010b). Furthermore, focusing on the general deficiency in damping of stay cables, a special structure of hybrid FRP cable section can be designed to enhance its internal damping in terms of different characteristics of two kinds of material in the whole cable, which is also the objective of this paper.

2 SMART DAMPER DESIGN

2.1 Principle and sectional structure

For hybrid B/CFRP cable, a special arrangement of section can be designed focusing on enhancing internal damping as shown in Figure 1. BFRP tendons are arranged inside the cable and forming inner cable, while hybrid FRP tendons are arrayed around inner cable based on the inner sleeve. A gap is retained between inner and outer cable where the viscoelastic material can be inserted. The objective of this design is to generate an interaction between inner BFRP tendons and outer hybrid FRP tendons when the entire cable is excited to vibration because of the different dynamic characteristic of these two tendon materials as shown in Figure 2. This interaction can compress the inserted viscoelastic material that will result in dissipation of vibrational energy.

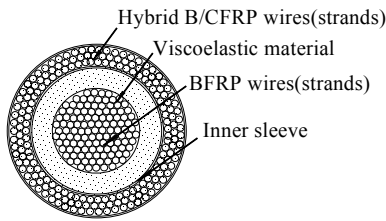


Figure 1 Section of hybrid FRP cable

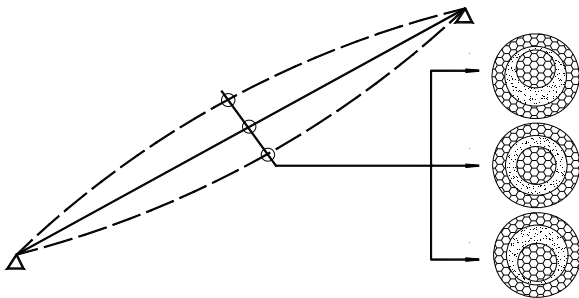


Figure 2 Relative motion between inner and outer cables

2.2 Arrangement along the cable

Since the inserted viscoelastic damping is equivalent to the additional load applied along the cable, the larger amount inserted will lead to more apparent effect of sag. For instance, for 575 m length hybrid B/CFRP 25% cable with a 30 mm thickness of continuous viscoelastic damping, the sag at the middle span will increase 42% and λ^2 (a integrated parameter defined by Irvine and Caughey 1974) of the entire will increase 100%. Moreover, this influence will become even critical with increase of cable length. Thus, a continuous distribution of viscoelastic damping along the cable may not a suitable choice so that a discontinuous distribution is suggested herein, by which the volume of inserted damping will be reduced greatly and the corresponding

influence to cable mechanical property will be minimized. The most important is the dissipated energy by discontinuous distribution can be equivalent to that by continuous way, which can be proven by the following equations.

The energy dissipated by viscoelastic material per unit volume in one cycle can be presented by the following equation (Meyers and Chawla 2009)

$$Q = \oint \sigma d\varepsilon = \int_0^T \sigma_0 \frac{d\varepsilon}{dt} dt = \pi \omega E'' \varepsilon_0^2 \quad (1)$$

where E'' is the storage modulus of viscoelastic material. ε_0 and σ_0 are the maximum strain and stress in one cycle. ω is circular frequency of vibration.

For continuous and discontinuous distribution, the total energy dissipated by viscoelastic material can be expressed by Eq. (2) and (3), respectively,

$$Q_1 = V_1 \pi \omega E_1'' \varepsilon_0^2 = A_c L \pi \omega E_1'' \left(\frac{F}{E_1' L b} \right)^2 \quad (2)$$

$$Q_2 = V_2 \pi \omega E_2'' \varepsilon_0^2 = A_c n l \pi \omega E_2'' \left(\frac{F}{E_2' n l b} \right)^2 \quad (3)$$

where A_c is the cross sectional area of viscoelastic material, and L is the length of cable. E' is elastic modulus, b is the depth of viscoelastic material in transversal direction of cable, l is the length of individual viscoelastic damping, n is the number of viscoelastic damping.

Due to the limitation of gap between inner and outer cable, the maximum strain of viscoelastic material is certain. Assuming the total interaction force F between inner and outer cable is constant because it is only dependent on the property of inner and outer cable. To achieve allowable maximum strain of viscoelastic material, the elastic modulus of E_1' must be much lower than that of E_2' .

$$\text{Let } \frac{F}{E_1' L b} = \frac{F}{E_2' n l b}, \text{ thus } E_1' L = E_2' n l \quad (4)$$

Substitute Eq. (4) into Eq. (2) and (3), the ratio of Q_1 and Q_2 is

$$\frac{Q_1}{Q_2} = \frac{E_2' n l}{E_1' L} = 1 \quad (5)$$

From Eq. (5), the dissipated energy of discontinuous damper is equivalent to that of continuous damper by changing elastic modulus of viscoelastic material.

3 THEORETICAL DERIVATION OF MODAL DAMPING RATIO

3.1 Assumptions

It is generally more convenient and physically reasonable to define the damping of a MDOF system using the

damping ratio for each mode rather than to evaluate the coefficients of the damping matrix because the modal damping ratios can be determined experimentally or estimated with adequate precision (Clough and Penzien 2003). Based on the previous study of dynamic characteristic of hybrid B/CFRP cable for long-span cable-stayed bridge, only the first order of cable mode has potential risk of resonance between cable and bridge (Wang and Wu 2010a), and additionally, in-plane vibration is more common and important (Caetano 2007) so that in this study, the first order in-plane vibration is considered to evaluate damping effect of smart damper of hybrid B/CFRP cable.

Since the objective is to evaluate the damping effect of hybrid B/CFRP cable with smart damper, only the internal damping generated by inserted viscoelastic material will be considered, and the other sources of damping including material damping of cable, friction among each wires and aerodynamic damping are not taken into consideration. The energy dissipated by axial and bending deformation of viscoelastic material will be neglected due to their discontinuous distribution inside the cable.

3.2 Derivation of dynamic equilibrium equations

The dynamic response of cable directly described by logarithmic decrement damping of cable can be derived by applying the Hamilton's principle (Clough and Penzien 2003)

$$\int_{T_1}^{T_2} \delta(\Pi_T - \Pi_V) dT = - \int_{T_1}^{T_2} \delta W dT \quad (6)$$

where Π_T , Π_V , W denote the cable kinetic energy, cable potential energy and the work done by nonconservative force, respectively. The cables in cable-stayed bridge are applied with initial tension in order to maintain static equilibrium. This initial tension gives rise to the geometrical stiffness which constitutes a dominant part in the total stiffness of the cable. Therefore, the potential energy of cable is consisted of strain energy generated by initial tension and vibration, and gravitational potential energy. Herein, when we use free-vibration decay method to determine modal damping ratio, the work done by nonconservative force is equivalent to the energy dissipated by viscoelastic material as show below,

$$- \int_{T_1}^{T_2} \delta W dT = \int_{T_1}^{T_2} Q(t) dT \quad (7)$$

The potential energy Π_V can be presented by the summation of Π_S and Π_G .

$$\Pi_S = \Pi_S^i + \int_0^L (P\varepsilon_d + \frac{1}{2}EA\varepsilon_d^2) dS \quad (8)$$

$$\Pi_G = \Pi_G^i + \int_0^L -mgU_v dS \quad (9)$$

where Π_S^i and Π_G^i are strain energy and gravitational

potential energy under static equilibrium, respectively (Perkins 1992). P is the static cable force. E and A are elastic modulus and cross-sectional area of cable, respectively. ε_d is the dynamic strain generated by vibration. mg is cable weight per unit length. U_v is displacement along vertical direction. L is the cable length.

Π_T can be expressed as

$$\Pi_T = \int_0^L \frac{1}{2}m(V_1^2 + V_2^2 + V_3^2) dS \quad (10)$$

where V_1 , V_2 , V_3 are velocity of differential element in three directions, respectively.

The energy dissipated by viscoelastic material per unit volume in one cycle is presented by Eq. (3).

Considering the difference of amplitudes within n cycles, the dynamic equilibrium equation in Eq. (6) can be expressed as

$$\int_0^{nT} (\Delta\Pi_T - \Delta\Pi_V) dT = \int_0^{nT} Q(x) dT \quad (11)$$

The start point is set to be the first maximum amplitude of vibration after release of external force/displacement, and the end point is chosen to be the maximum amplitude of vibration after n cycles. Because the kinetic energy maintains zero at both of the status, the only variation of potential energy lies in strain energy and gravitational potential energy which are only related to the start and end status because they both belong to conservative force. Thus, the variation of cable potential energy can be presented by

$$\Delta\Pi_S = \int_0^L \left[P(\varepsilon_{d,1} - \varepsilon_{d,n}) + \frac{1}{2}EA(\varepsilon_{d,1}^2 - \varepsilon_{d,n}^2) \right] dS \quad (12)$$

$$\Delta\Pi_G = \int_0^L -mg(U_{v,1} - U_{v,n}) dS \quad (13)$$

where $\varepsilon_{d,1}$ and $\varepsilon_{d,n}$ represent the dynamic strain at first cycle and at n cycles, respectively. $U_{v,1}$ and $U_{v,n}$ represent the vertical displacement at first cycle and at n cycles, respectively.

The first order vibration mode shape is presented by (Caetano 2007)

$$U_i(x) = U_{m,i} \left(1 - \tan(\omega'/2) \sin(\omega'x/L) - \cos(\omega'x/L) \right) \quad (14)$$

where $U_{m,i}$ is maximum amplitude at the middle span in i cycles, ω is given by $\omega' = \omega L / (P/m)^{1/2}$.

In terms of in-plane equilibrium, the dynamic stain can be expressed as

$$\varepsilon_{d,i} = \eta U_{m,i} \quad (15)$$

where

$$\eta = \frac{mg \cos \theta}{P\omega'(1+8(d/L)^2)} \left(\omega' + \tan\left(\frac{\omega'}{2}\right) \cos\left(\frac{\omega'}{2}x\right) - \sin\left(\frac{\omega'}{2}x\right) \right)$$

Considering the dynamic equilibrium of a segment of inner cable in y direction, the equilibrium equation is

(Clough and Penzien 2003):

$$P \frac{\partial^2 u}{\partial x^2} + h_\tau \frac{\partial^2 y}{\partial x^2} = m \cos \theta \frac{\partial^2 u}{\partial t^2} - f_i \quad (16)$$

h_τ is dynamic force induced by vibration, and the transversal motion with respect to time is assumed

$$u(x, t) = u(x) e^{i\omega t} \quad (17)$$

The static configuration is described by

$$y = 4d \frac{x}{L} \left(1 - \frac{x}{L} \right) \quad (18)$$

Substitute Eq (17) and (18) into Eq (16)

$$f_i = -[\alpha e^{i\omega t} + \beta] \quad (19)$$

where

$$\alpha = m U_{m,i} \omega^2 \left(\frac{\cos \theta + (\tan(\omega' / 2) \sin(\omega' x / L) + \cos(\omega' x / L)) (1 - \cos \theta)}{\cos(\omega' x / L)} \right) \quad (19a)$$

$$\beta = \frac{mgEAU_{m,i}\eta \cos \theta}{H} \quad (19b)$$

Therefore, Eq. (11) can be expressed as follows

$$\left[P\eta(U_{m,0} - U_{m,n}) + \frac{1}{2} EA\eta^2(U_{m,0}^2 - U_{m,n}^2) \right] L + \frac{2}{\pi} mgL \cos \theta (U_{m,0} - U_{m,n}) = \sum_0^n \int_0^L Q(S) dS \quad (20)$$

Let $U_{m,n}/U_{m,0} = \xi$ and introduce it into Eq (20) and finally lead to

$$\xi = \frac{-B' + \sqrt{B'^2 - 4A'C'}}{2A'} \quad (21)$$

$$A' = -\frac{1}{2} EA\eta^2 LU_{m,0}^2$$

$$B' = -P\eta LU_{m,0} - \frac{2}{\pi} mgLU_{m,0} \cos \theta$$

$$C' = P\eta LU_{m,0} + \frac{1}{2} EA\eta^2 LU_{m,0}^2 + \frac{2}{\pi} mgLU_{m,0} \cos \theta - \sum_0^n \int_0^L Q(S) dS$$

Thus, logarithmical damping is

$$\delta = \ln \left(\frac{U_{m,0}}{U_{m,n}} \right) \frac{1}{n} = \ln \left(\frac{1}{\xi} \right) \frac{1}{n} \quad (22)$$

4 EVALUATION OF MODAL DAMPING

The longest cable in a 1088 m span cable-stayed bridge is selected for evaluation (Wang and Wu 2010a). The smart damper design and corresponding dimension are shown in Figure 3 and Table 1. A total of nineteen sections of smart-dampers are installed along the longitudinal direction of cable. Generally, the Young's modulus of

viscoelastic material is found in the range from 1×10^4 to 5×10^9 N/m². thus, thus, thus, 6×10^5 N/m² of the elastic modulus of viscoelastic material are adopted for this particular calculation, considering a loss factor of 1.

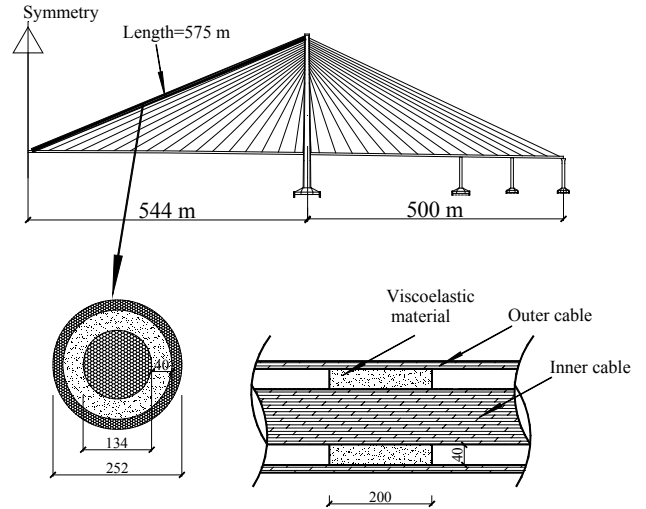


Figure 3 Design parameters of smart dampers

The initial amplitude of vibration $U_{m,0}$ is assumed to be 2 m according to the practical observation. Based on Eq. (21) and (23), the first order of modal damping ratio contributed by viscoelastic material is calculated to be 0.52%, which proves the effectiveness in comparison with less than 0.2% of damping ratio of general cables (even lower for long length of cable). It should be mentioned that this damping ratio is contributed only by smart damper, whereas other sources of damping are not taken into account.

Table 1 Parameters of viscoelastic material

Type of cable	Proportion	Sectional area (mm ²)*	Cable force (N)	Diameter (mm)**
Original cable	C 25%	19692	1.19×10^7	189
	B 75%			
Cable with smart damper	Inner cable C 50%	9846	7.59×10^6	134
	Outer cable B 50%			
smart damper	Outer cable B 100%	9846	4.31×10^6	252

* 35% volume of matrix is taken into account.

** Consider 70% packing efficiency.

5 CONCLUSIONS

Focusing on the characteristic of hybrid FRP cable, a smart damper design was proposed to improve cable's internal damping. Theoretical derivation on damping ratio was conducted in terms of energy principle and the evaluation of a smart damper designed cable demonstrated its effectiveness.

REFERENCES

- Clough R. W., Penzien J., 2003, *Dynamics of Structures-2nd Edition*, Computers and Structures, Inc., USA
- Caetano de Sa E., 2007, Cable Vibrations in Cable-stayed Bridges, *Structural Engineering Documents 9*, Zurich: IASBSE-AIPC-IVBH
- Fujino Y., Hoang N., 2008, Design formulas for damping of a stay cable with a damper, *Journal of structural engineering*, 134(2):269-278
- Irvine H. M., Caughey T. K., 1974, The linear theory of free vibrations of a suspended cable, *Proceedings of the Royal Society of London, Series A*, 341: 299-315
- Meier U., 1987, Proposal for a carbon fibre reinforced composite bridge across the Strait of Gibraltar at its narrowest site, *Proceedings of the Institution of Mechanical Engineers*, 201(B2): 73-78.
- Meyers M. A., Chawla K. K., 2009, *Mechanical Behavior of Materials*, second edition, Cambridge University Press, USA
- Perkins N.C., 1992, Modal interactions in the non-linear response of elastic cables under parametric/external excitation, *International Journal of Non-linear Mechanics*, 27(2):233-250
- Wang X., Wu Z., 2010a, Integrated High-Performance Thousand-metre Scale Cable-Stayed Bridge with Hybrid FRP Cables, *Composites Part B: Engineering*, 2010, 41(2): 166-175
- Wang X., Wu Z., 2010b, Evaluation of FRP and hybrid FRP cables for super long-span cable-stayed bridges, *Composite Structures*, 92(10): 2582-2590
- Yamaguchi H, Adhikari R, 1995, Energy-based evaluation of modal damping in structural cables with and without damping treatment, *Journal of Sound and Vibration*, 181(1): 71-83

A Smart FRP-Concrete Composite Beam Using FBG Sensors

Yanlei Wang (wangyanlei@dlut.edu.cn)

School of Civil Engineering, Dalian University of Technology, Dalian, China

Qingduo Hao & Jinping Ou

School of Civil Engineering, Harbin Institute of Technology, Harbin, China

ABSTRACT A new kind of smart FRP-concrete composite beam, which consists of a FRP box beam combined with a thin layer of concrete in the compression zone, was developed by using two embedded FBG sensors. The fabrication process of the smart FRP-concrete composite beam was introduced. The proposed smart composite beam was tested in 4-point bending to verify the operation of the embedded FBG sensors. The experimental results indicate the output of embedded FBG sensors in the smart beam agrees well with that of surface-bonded strain gauges over the entire load range. The proposed smart FRP-concrete composite beam can reveal the true internal strain from 0 to the failure of the beam and will have wide applications for long-term monitoring in civil engineering.

1 INTRODUCTION

Fiber reinforced polymer (FRP) composites have found increased applications in bridge structures in recent years (Bakis et al. 2002). One of the main reasons preventing greater implementation of FRP composites into the civil infrastructure is the lack of performance data and accepted engineering standards. Using sensors and instrumentation, data can be obtained that will provide information on the behavior of the structure over a given time. The integrity of the structure can be established at any phase during the service life of the structure to compensate for other parts of it that are weakening. Smart structures will be employed to a greater extent in the future than they are currently (Hollaway 2003). In most designs, crushing of concrete in compression defines the flexural failure of FRP-concrete composite beam. The failure will be sudden and the composite beam did not show any ductility (Wang & Ou 2006). For load bearing elements, the brittle failure is not anticipated because there is no safety pre-warning before the structure failure. So, a strain monitoring of FRP-concrete composite beam is essential.

Compared with electric resistance strain gauge, the fiber Bragg grating (FBG) sensor has the advantages of electromagnetic insensitivity, wavelength multiplexing, capability, miniature size, high sensitivity, good long-term stability and high reliability (Wang et al. 2007). However, there are some problems in applications because the bare FBG sensors are very thin and frangible. They should be packaged or protected before application. FRP materials lend themselves as prime candidates for the rapidly expanding field of research of “smart

structures” (Kalamkarov et al. 1994). FRP structures are good candidates for making smart structures because their fabrication technique inherently allow for the embedding of sensors and communication lines.

In this paper, two FBG sensors will be embedded in FRP-concrete composite beam during the fabrication process. Embedment of FBG sensors in FRP-concrete composite beam leads the beam to be smart FRP-concrete composite beam. 4-point bending test will be carried out to assess the overall behavior of the smart FRP-concrete composite beam and compare the performance of the embedded FBG sensors with that of strain gauges.

2 FBG SENSING PRINCIPLE

The fiber Bragg grating is an optical fiber with a periodic variation in the refractive index in the core. The Bragg grating acts as light reflector with maximum reflection at a certain wavelength. The Bragg wavelength is described as follows (Zhou et al. 2002):

$$\lambda_B = 2n_{eff}\Lambda \quad (1)$$

where λ_B = the Bragg wavelength; n_{eff} = the effective index of refraction, and Λ = the grating periodicity.

According to eq.1, it can be seen that the effective index of refraction and the grating periodicity are two main parameters influencing the Bragg wavelength. Any external perturbation that can change the two parameters will alter the Bragg wavelength. Strain and temperature are two main external perturbations that can induce changes in the effective index of refraction and the grating periodicity, and the change in Bragg wavelength with strain and temperature can be expressed as follows:

$$\frac{\Delta\lambda_B}{\lambda_B} = (1 - p_e)\Delta\varepsilon + (\alpha + \zeta)\Delta T \quad (2)$$

where $\Delta\lambda_B$ = the Bragg wavelength shift, $\Delta\varepsilon$ and ΔT = changes in strain and temperature, respectively, p_e = the strain optic coefficient, α and ζ = thermal-expansion and thermo-optic coefficients, respectively.

3 EXPERIMENTAL PROGRAM

3.1 Specimen preparation

The photograph, the geometry of cross-section and the locations of FBG sensors and electric resistance strain gauges (SG) of the proposed smart FRP-concrete composite beam are shown in Figure 1. The composite beam consists of a FRP box beam combined with a layer of concrete in the compression zone. Two FBG sensors were designed to be embedded into the top and bottom flange of the FRP box beam in the mid-span section on the longitudinal direction, respectively, to form the intelligent FRP-concrete composite beam. The FBG sensors were used to monitor the internal compressive and tensile strain of the beam, respectively.

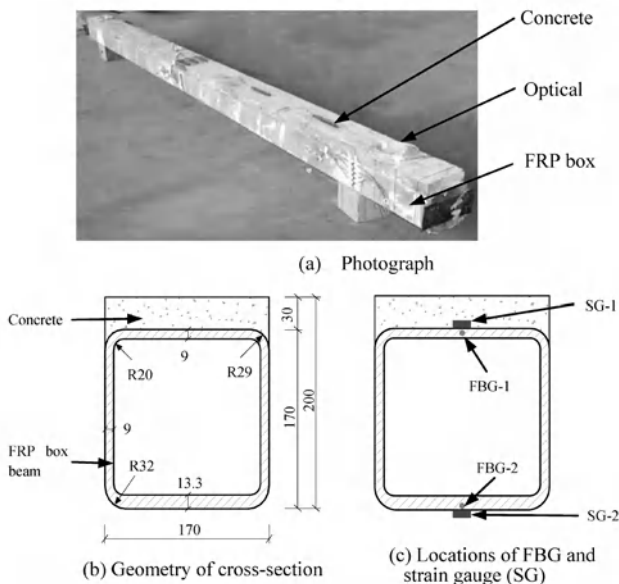


Figure 1 Smart FRP-concrete composite beam (Units in mm)

Two types of stitched bidirectional E-glass fabric with a weight of 600 g/m^2 , $(0^\circ/90^\circ)$ and $(\pm 45^\circ)$, were selected as the primary continuous reinforcement in this study. Vinyl ester resin, Swancor 901, was selected as the matrix for the composite beam. It has also been widely documented that for optimum transfer of strain from host material to sensor, the sensor should be aligned parallel to the reinforcing fiber (Moloney et al. 2005). When sensors were embedded parallel to the direction of reinforcing fiber, resin rich areas around the sensor gage were prevented. It was assumed that this placement minimized non-uniform stress fields around the sensor,

which could reduce measurement accuracy.

The top flange and two webs of FRP box beam have the same fiber architecture, which consists of 13 layers of bidirectional fabric reinforcement. However, the bottom flange consists 19 layers of fabric to increase the global stiffness of the composite beam. Stacking sequence of the top flange with FBG sensor was $[(0^\circ/90^\circ)_3, (\pm 45^\circ)_2, (0^\circ/90^\circ)_2, (90^\circ/0^\circ), (\mp 45^\circ)_2, (90^\circ/0^\circ), \{\text{FBG-}0^\circ\}, (90^\circ/0^\circ)_2]$. Stacking sequence of the bottom flange with FBG sensor was $[(0^\circ/90^\circ)_3, (\pm 45^\circ)_2, (0^\circ/90^\circ)_2, (90^\circ/0^\circ), (\mp 45^\circ)_2, (90^\circ/0^\circ), (0^\circ/90^\circ)_3, (90^\circ/0^\circ)_3, \{\text{FBG-}0^\circ\}, (90^\circ/0^\circ)_2]$. The average fiber volume fraction of the FRP part is about 0.3. Stitching/bonding FBG sensors to the fabric reinforcement was the least invasive method to prevent sensor slippages. The FRP box beam was fabricated by hand lay-up at present.

To develop a good bond between FRP box beam and concrete, 5~10 mm aggregate was applied to the top flange of GFRP beam with epoxy adhesive. Applying too much or too little aggregate could create insufficient bond between FRP and concrete for the two materials to act compositely. The aggregate distribution percentage was recommended to be 35%~45% to obtain the optimal bond. Due to the size of the test specimens, coarse aggregates with maximum size of 10 mm were used in the concrete. The compressive strength of the concrete on the day of test is 51 MPa.

3.2 Test set-up and loading protocols

As mentioned in section 3.1, two FBG sensors were embedded into the mid-span section of FRP-concrete composite beam. Two surface-bonded electrical strain gauges (shown in Figure 1c) were also used to check the accuracy of the output of the embedded FBG sensors. A four-point bending test was conducted to investigate the flexural behavior and the strain response measured from FBG sensors in the proposed smart FRP-concrete composite beam. Figure 2 shows the loading configuration of the composite beam and the location of the cross-section with embedded FBG sensors. Test setup of the 4-point bending test for the composite beam is illustrated in Figure 3. The composite beams were simply supported on rollers with a span length of 3333 mm. The spacing between the inner loading points was 467 mm.

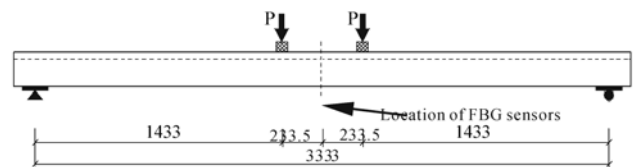


Figure 2 Loading configuration of the smart composite beam

The strain sensing performances of the embedded FBG sensors were recorded by the Micron Optical

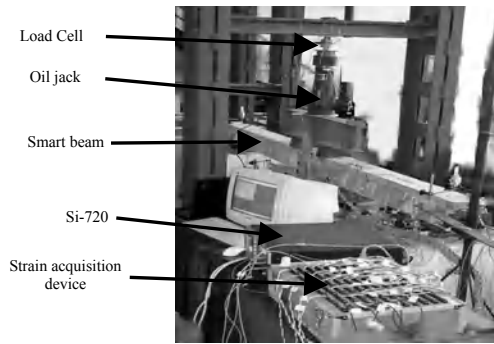


Figure 3 Test setup of the 4-point bending test

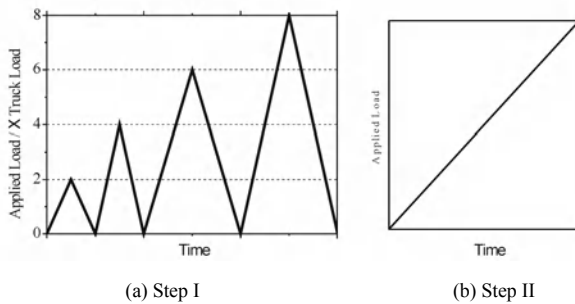


Figure 4 Loading protocols of the test

Sensing Interrogator (MOI Ltd, si-720). And the data of the electric resistance strain gauges were gathered using the Static Strain Acquisition Device (DongHua Test Inc.). In this test, the change of temperature wasn't considered for the test time was short and the temperature of the laboratory almost didn't change during the test.

This flexural test was performed by force control, and it was divided into two steps: Step I and Step II, shown in Figure 4, in order to evaluate their performance and meet the objectives of the research. In the first step (Step I), force history of a triangular shape with the load amplitude gradually increased was applied to examine the deflection stabilization. In Step II (Step II), force had been increased monotonically until the test specimen failed. In Figure 4, "Truck Load" means a scale truck load for the smart FRP-concrete composite beam to investigate the performance of the beam subjected to a simulated truck load.

4 RESULTS AND DISCUSSIONS

4.1 Failure mode

The first noise from the beam was heard at about 10× truck load during step II, and subsequently snapping sounds were heard from the beam all the way until failure. The failure occurred at 13.5×truck load when the concrete crushed inside one of the loading points, shown in Figure 5. Crushing of concrete in compression between the two loading points defines flexural collapse of the beam. However, the FRP part was found to be intact. This can be described as follows. As concrete failed,

large deflection occurred immediately due to the low stiffness of FRP part in comparison to the composite specimen, along with instantaneous reduction of the load due to the quick increase of deflection, and the combined compression capacity of the FRP part and the residual strength of the concrete enable the specimen to carry the residual load. After unloading the residual load, the deflection of the specimen almost came back. The failure was sudden due to the nature of the concrete. However, the obtained failure mode is considered to be favorable because it did not lead to collapse of the entire structure and the structure can be retrofitted easily by the replacement of the concrete layer.



Figure 5 Failure mode of test specimen

There was no visual failure in the connection between FRP and concrete. This phenomenon reflects that using aggregate coating is an efficient method to ensure composite action between FRP and concrete for the proposed composite beam.

4.2 Smart Performance

The locations of embedded FBG sensors and strain gauges in the smart FRP-concrete composite beam are illustrated in Figure 1c. Strains from two FBG sensors and two strain gauges of the smart beam during step I are shown in Figure 6. The strains of FBG sensors are obtained based on the strain sensing coefficients, which is 1.16 $\mu\text{m}/\mu\text{ε}$. This figure shows that there is a good agreement between FBG sensor and strain gauge in tensile status at bottom flange of the FRP beam, as well as in compressive status at top flange of the FRP beam. And we can see that the repeatability and consistency of embedded FBG sensors and strain gauges are remarkable. From this figure, we can find that the outputs of FBG sensors are slightly smaller than those of strain gauges. The reason is that the locations of them are different in the cross-section of the smart beam (shown in Figure 1c). So the outputs of them should be slightly different based on the assumption of plane section.

Figure 7 shows the measured strains from FBG sensors and strain gauges in the smart FRP-concrete composite beam during step II. There is an excellent agreement between FBG sensors and strain gauges in tensile and compressive status over the entire load range. Because

of the same reason mentioned above, the outputs of FBG sensors are slightly smaller than those of strain gauges. And the maximum tensile and compressive strains recorded by the embedded FBG sensors are 0.79% and -0.11% at failure of the composite beam, respectively.

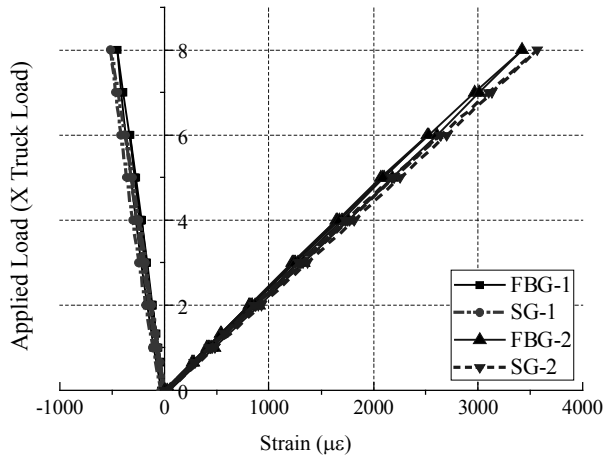


Figure 6 Strains from FBG sensors and strain gauges in the smart beam subjected to the load of step I

We can conclude that the embedded FBG sensors can monitor the internal strain of the proposed smart FRP-concrete composite beam over the entire load range from zero to the failure of the beam. It indicates that the embedded FBG sensors can monitor the internal strain of the composite beam in normal service state as well as in limit state.

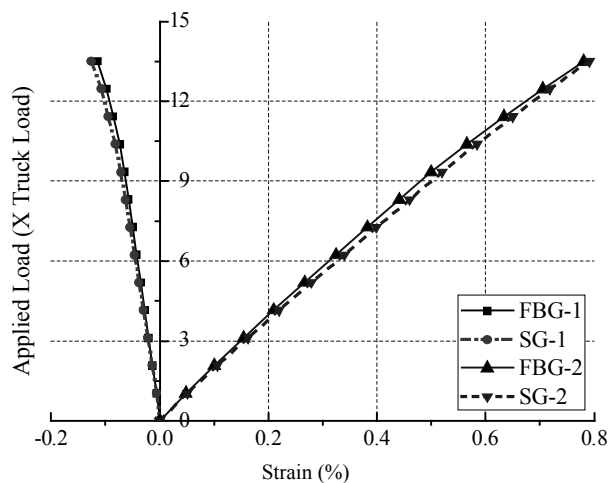


Figure 7 Strains from FBG sensors and strain gauges in the smart beam subjected to the load of step II

5 CONCLUSIONS

A new kind of smart FRP-concrete composite beam was developed by embedding two FBG sensors into the

mid-span section of the FRP box beam to monitor the longitudinal internal strains of the composite beam. Four-point bending test was carried out to assess the flexural behavior of the proposed smart FRP-concrete composite beam and the feasibility of strain monitoring of the embedded FBG sensors. There is an excellent agreement between FBG sensor and strain gauge in tensile status at bottom flange of the FRP beam over the entire load range, as well as in compressive status at top flange of the FRP beam. And the embedded FBG sensors can reveal the true internal strain of the smart composite beam over the entire load range from 0 to the failure of the beam. The smart FRP-concrete composite beam has a good capability of monitoring internal strain in service and is very suit for the long-term monitoring.

6 ACKNOWLEDGEMENTS

The authors gratefully acknowledge the financial support provided by the Natural Science Foundation of China (Project No. 50908030), the National Key Technologies R&D Program of China (Project No. 2006BAJ03B07) and China Postdoctoral Science Foundation (Project No. 20080441118).

REFERENCES

- Bakis, C.E., Bank, L.C., Brown V.L., et al. 2002. Fiber-reinforced polymer composites for construction—state-of-the-art review. *J. Compos. Const.* 6(2):73-87.
- Hollaway, L.C. 2003. The evolution of and the way forward for advanced polymer composites in the civil infrastructure. *Constr. and Build. Mater.* 17:365-378.
- Kalamkarov, A.L., Fitzgerald, S.B., MacDonald, D.O., et al. 1994. Smart pultruded composite reinforcements incorporating fiber optical sensors. *Proc. SPIE 3400*, 94-105, San Diego, 13-17 March 1994.
- Moloney, S., Connelly, M.J. & Butler P.A. 2005. Strain sensing in carbon composite material using embedded fibre Bragg grating sensors. *Proc. SPIE 5826*, 645-653, Long Beach, 6-9 March, 2005.
- WANG, Y.L. & OU J.P. 2006. Fundamental mechanical behavior of innovatively designed hybrid FRP-concrete beams. *J. Xi'an Univ. of Arch. & Tech.* 38(4):455-462.
- Wang, Y.L., Zhou, Z. & Ou J.P. 2007. Study on fabrication of smart FRP-OFBG composite laminates and their sensing properties. *Proc. SPIE 6595*, 65952W1-6, Harbin, 4-7 July 1996.
- Zhou, Z., Tian, S.Z., & Zhao, X. F. et al. 2002. Theoretical and experimental studies on the strain and temperature sensing performance of optical FBG. *Journal of Functional Materials.* 33(5):551-554.

Smart CFRP Systems—Fiber Bragg Gratings for Fiber Reinforced Polymers

Stefan Käseberg & Klaus Holschemacher

HTWK Leipzig, University of Applied Sciences, Faculty of Civil Engineering, Leipzig, Germany

ABSTRACT Since 1970 the development of optical fiber measurement systems has begun. Especially the measuring of strain and temperature with Fiber Bragg Gratings (FBG) is interesting, because there are a large number of advantages in opposite to electrical measuring methods. Examples are small dimensions, low weight, high static and dynamic resolution of measured values, corrosion resistance, variable forms, multiplex behavior, long distance monitoring and high durability. In the past there were several attempts to use optical systems for monitoring of concrete structures. One example is the strain measurement in bar reinforcement. Another possibility is the embedding of optical fibers with FBG in Carbon Fiber Reinforced Polymers. Fiber Re-inforced Polymers (FRP) have got more and more important during the last decade. In civil engineering the main usage of FRP is the repair of concrete structures. CFRP systems for retrofitting of concrete structures with optical sensors have already been discussed in several publications. It could be shown, that the reinforcing function of the CFRP can be ideally connected with the measurement and monitoring functions of the optical sensors like FBGS. The main problem is the fixing of the glass fiber and the small FBG at the designated position. In this paper the possibility of setting the glass fiber with embroidery at the reinforcing fiber material will be presented. Experiments will show the functionality of the method.

1 MONITORING AND SMART COMPOSITE STRUCTURES

1.1 Monitoring in Civil Engineering

The fields of activity in civil engineering are subjected to a constant change. Thereby maintenance, strengthening and monitoring of existing buildings have become more and more important. This tends to result in smaller investment for new buildings and significant increase for cost for maintenance and observation. For permanent measurement rugged measurement systems are needed. Electrical systems like strain gauges are not the best alternative. Hence optical measurement systems move over to the foreground.

1.2 From FRP to Smart Composite Structures

Fiber Reinforced Polymers (FRP) have got more and more important during the last decade. In civil engineering one of the main usages of FRP is the repair of concrete structures. In the majority of cases Carbon fibers are used as reinforcing material. Reasons are the superior technical properties of Carbon fibers compared to other high-strength fibers like Glass fibers or Aramid fibers. The number of products of Carbon Fiber Reinforced Polymer (CFRP) for reinforced concrete (RC) constructions is huge. Examples are at the surface bonded CFRP laminates or sheets as well as laminates which are placed in slots at the concrete surface. Furthermore it is possible to prestress CFRP laminates.

Main fields of application are strengthening of RC beams under flexural tension and shear as well as the retrofitting of columns with wrapped CFRP sheets.

Failure types of FRP materials can differ. Principle forms of failure can be the crack of the reinforcing fiber or matrix and the bond failure or delamination between fiber and matrix. The stiffness of the fiber material, form, amount and orientation of fiber, the bond between fiber and epoxy matrix as well as the matrix properties affect the stiffness and resistance of the FRP material. Besides the forms of failures of the composite material thereby the bond behaviour between FRP and concrete surface is very important. In particular this contact zone is critical for the design of CFRP strengthened concrete structures. Above all in structures under bending moment the small tensile strength of concrete is the most important parameter for the bond bearing strength. Figure 1 shows the delamination of a CFRP sheet during a displacement controlled four point bending test. The delamination started in this case at the last bending crack.

In Figure 2 the failure mode of a wrapped concrete column can be seen. In this case the crack of the reinforcing fiber (after reach of ultimate strain) was the failure type. The described failure types go on very fast and often without any previous notice. A ductile behaviour of the strengthened structural element can not be achieved under this term. But assurance is essential in civil engineering. Furthermore it is not comprehensively

clarified if the constancy of the bonding between the different partners will be assured over a long decade or under dynamic load.

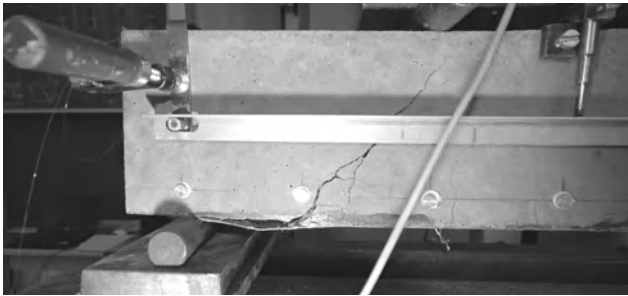


Figure 1 Debonding failure between concrete and CFRP sheet



Figure 2 Short concrete column confined with CFRP sheets after failure

With adequate measurement systems it is might possible to realise a safe monitoring to control the powerful but brittle CFRP strengthening systems. With optical measurement systems, which base on Glass fibers, you can integrate the sensor system in the FRP material. The name of such materials is smart composite. These structures have the ability to measure their own mechanical behaviours and to give a solid feedback. The most important representatives under the fiber optic measurement systems are the Fiber Bragg Grating Sensors (FBGS).

2 PROPERTIES OF FIBER BRAGG GRATINGS

2.1 Configuration and Assembly

A Bragg Grating consists of a periodic sequence of artificial and equidistant refraction switches in the core of an optical fiber. It can be produced over emblazing of an interference pattern of ultraviolet light. The core is surrounded by cladding. The refraction index of both is different and this results in total reflection of inducted light λ .

For mechanical protection the Glass fiber gets an additional coat of synthetic material. This coating can consist of polyimide and inhibits the infiltration of water and hydrogen. The maintenance of the safety function is very important, in order to guarantee an error free and durable FBG unit. For the production of FBG in optical fibers it is necessary to have powerful ultra violet laser with wavelength of circa 240 ... 250 nm. These will be apportioned in two bales. This generates a pattern with a period Δ . This period is addicted by the angle of the laser. Δ describes thereby the distance between two interference maxima in the pattern. At every maximum a change of the refraction index will happen, whereby the actual pattern develops. The coating must be removed before producing the FBG. This means an additional stress for the optical fiber. Particularly a decrease of strength in these areas might be possible.

2.2 Theoretical background

Because of the emblazed interference pattern a reflection of inducted appointed light wavelength is possible. Light with the Bragg wavelength λ_B will be reflected. This means that the light of inducted spectrum will be reflected which abides equation 1.

$$\lambda_B = 2 \cdot n_{eff} \cdot \Delta \quad (1)$$

where λ_B = Bragg wavelength, n_{eff} = effective refraction index and Δ = period of diffraction grating.

This term of the light spectrum will be missing in the penetrated array. With equation 1 it is possible to clarify the measuring principle of FBG. A change of the period of diffraction grating results in an adjustment of the Bragg wavelength. Now other spectra of light will be reflected. These modifications can be activated by strain or temperature and then changes can be measured. The change of strain in the optical fiber can be explained with equation 2.

$$\Delta\lambda_B = \lambda_B \cdot (1 - p_e) \cdot \Delta\varepsilon \quad (2)$$

where $\Delta\lambda_B$ = change of Bragg wavelength, p_e = photo elastic component ≈ 0.22 and $\Delta\varepsilon$ = change of strain.

3 USE IN FRP FOR CONCRETE STRUCTURES

3.1 Advantages of Fiber Bragg Gratings

The advantages of fiber-optic measurement systems compared to classical electric measurement procedures are great.

In Figure 3 the proportions of different strain gauge and a glass fiber for FBG are shown. One big advantage of the fiber-optic measurement system, the small dimensions, can be seen clearly. Furthermore there is the possibility to distribute several Bragg Gratings at one optical fiber. The analysis of the reflected light spectrums can be done with only one spectral measurement system.

Other advantages are the insensibility towards to electromagnetic radiance and the most chemicals as well as the high static and dynamic resolution of measurement values.

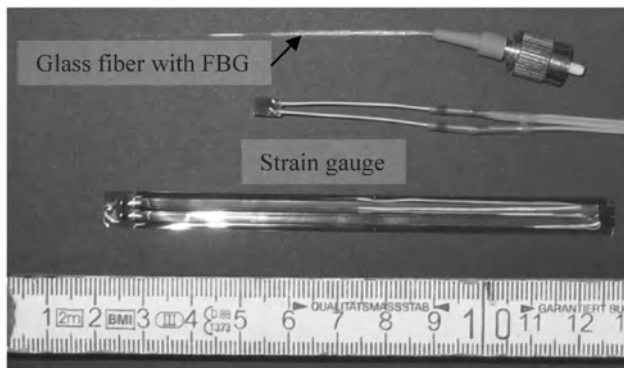


Figure 3 Proportion of a typical Glass fiber and Strain gauge

3.2 FBGS in FRP

The direct embedding of optical fibers with FBG in the epoxy resin of FRP materials allows exact strain measurement in the material. So mistakes are minimized during the monitoring. The epoxy resin is thereby an effective protection for the optical fiber.

CFRP systems for retrofitting of concrete structures with optical sensors have already been discussed in several publications. It could be shown, that the reinforcing function of the CFRP can be ideally connected with the measurement and monitoring functions of the optical sensors like FBGS. Lu and Xie (2007) accomplished strain measurements in smart CFRP sheets with FBGS.

It also was possible to get first results with fiber optical measurement systems at real constructions. Bastianini et al. (2005) were able to localize and monitor failures between concrete surface and the used CFRP system at inaccessible sites.

4 SETTING THE GLASS FIBER WITH EMBROIDERY

4.1 Sensor-based textile clutch

For an effective production of smart structures, it is very important to fix the optical fiber sufficiently during the production and the lamination of the FRP material. Especially the placing of the fiber in a particular design is complex and must be done carefully.

One possibility to realize any designs of sensor arrangements can be seen in embroidering the optical fiber directly on a carrier material. In this case the carrier materials are the reinforcing fibers which are often arranged as webs or clutches. The direct embroider of the optical fiber (and the FBGS) simplifies the fixing clearly. An embroidery machine, using computerized support, is able to fix the fiber optical system accurately fitting at the carbon fiber material.

By using of computer-controlled machines it is possible to achieve a very high degree of prefabrication as well as a high productiveness. The economic industrial fabrication of smart structures can be realized. In Figure 4 the direction of an optical fiber with FBG for strain and temperature measurement on a Carbon-fiber sheet is demonstrated.

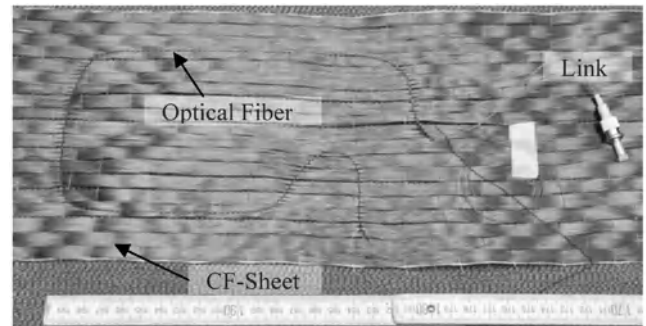


Figure 4 Course of an optical fiber with FBG on CF-Sheet by using embroider technique

With this method it is possible, to fix the Fiber Bragg Gratings close to these locations where strain monitoring should take place. Through the embroidery method the direct mechanical bound between optical fiber and Carbon fiber clutch (sheet) is possible. Now the sensor based Carbon fiber textile can be easily industrial laminated. Another possibility is the direct converting at the building site by hand made lamination.

4.2 Own Experiments with confined short concrete columns

To test the new smart CFRP system different concrete members were strengthened and tested. So for example short concrete columns were confined and the significant changes of strength and strain (of the used concrete) researched.

In Figure 5 the test set up and the main properties of the columns can be seen. The compression tests were deflection controlled. To get the axial strain, LVDT were used. For the lateral stress strain curves with embroider integrated optical fibers (2 FBG at the fiber) and strain gauges could be monitored. Totally 3 short columns were wrapped with the sensor based CFRP sheets.

In Figure 6 the stress strain curves of the first specimen are shown. It can be seen, that an efficient monitoring of the strain development inside of the CFRP sheet was possible. The curves present a very good convergence between electrical and optical measurement methods. Thereby only the FBG-system guaranteed a save measurement till the ultimate strain of the Carbon fibers at nearly 1,5% (see also Table 1 $\epsilon_{l,FBG}$). Furthermore it also works to find out the area of failure inside the CFRP material, like shown in Figure 7. In this case the ultimate strain inside the CFRP material was reached near FBG 2.

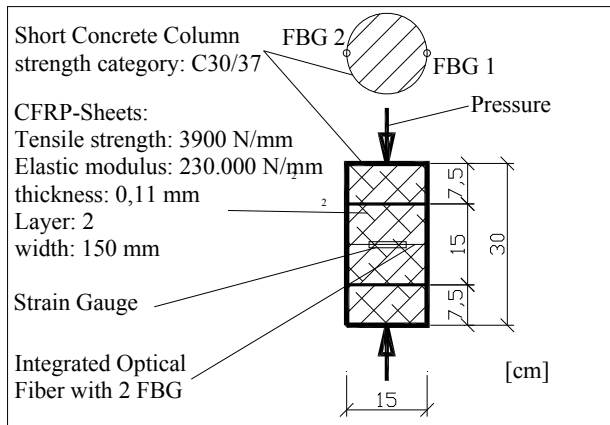


Figure 5 Test set-up of the deflection controlled compression test

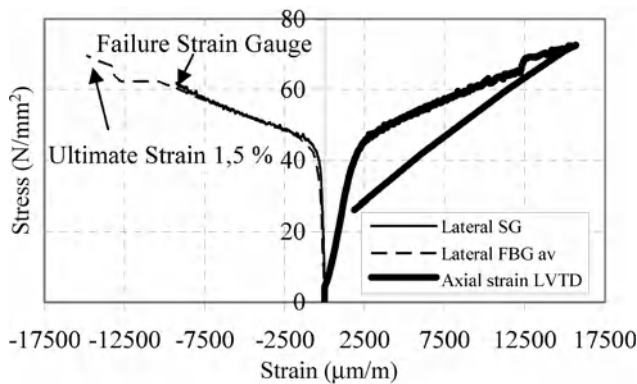


Figure 6 Lateral stress strain curves of Strain Gauge (SG) and FBG average (FBG av) and Axial strain of Column 1

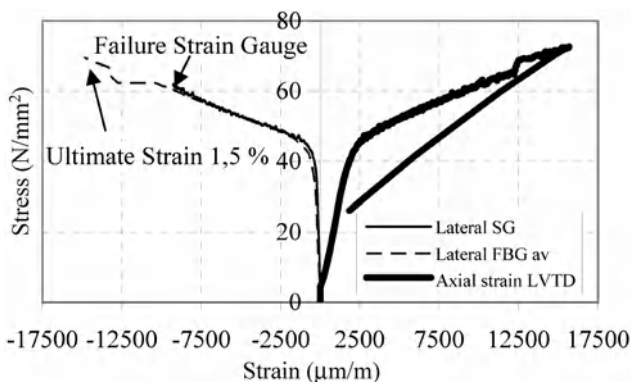


Figure 7 Lateral stress strain curves of Strain Gauge (SG) and Fiber Bragg Grating (FBG) and Axial strain of Column 2

In Table 1 the ultimate stress (f_{cc}) and strain (ϵ_{cc}) of the three specimen in opposite to the results of plain concrete columns (f_{co} , ϵ_{co}) are shown. It clearly can be seen, that an high raise of strength and strain is possible with the used sensor based CFRP sheets.

Table 1 Experimental results

	f_{cc}	f_{cc}/f_{co}	ϵ_{cc}	$\epsilon_{cc}/\epsilon_{co}$	$\epsilon_{l,FBG}$
	[N/mm ²]	[-]	[%]	[-]	[%]
Specimen 1	72.7	1.74	15.69	7.57	14.87
Specimen 2	66.4	1.59	12.40	5.99	14.1
Specimen 3	68.2	1.63	14.00	6.76	16.54

5 CONCLUSION

One possibility to monitor and reinforce existing concrete structures is given by the embedding of optical fibers with FBG in Carbon Fiber Reinforced Polymer (smart composite). The small proportions of optical glass fibers allow very flexible strain and temperature measurements inside of the CFRP material. Advantages like the high tensile strength of the CFRP material will not be influenced by the FBG sensor system. With the presented embroider method an accurate and reproducible fixing method could be shown.

6 ACKNOWLEDGEMENT

The study which is the base for the presented paper was part of the research project: “Sensorbasierte Textilarmierung” of the “Wachstumskern HighStick” and is supported by the Federal Ministry of Education and Research of the Federal Republic of Germany. We thank the Federal Ministry of Education and Research for the financial advancement.

Still special thanks to H. Kieslich and T. Müller.

REFERENCES

- Mehrani, E. Ayoub, A. and Ayoub, A. 2009. Evaluation of fiber optic sensors for remote health monitoring of bridge structures. *Materials and Structures* 42, p. 183 – 199.
- Moerman, W. Waele, W. Coppens, C. Taerwe, L. Degrieck, J. Baets, R. and Callens, M. 2001. Monitoring of a Prestressed Concrete Girder Bridge with Fiber Optical Bragg Grating Sensors. *Strain* 37, p. 151 – 153.
- Lu, S. and Xie, H. 2007. Strengthen and real-time monitoring of RC beam using “intelligent” CFRP with embedded FBG sensors. *Construction and Building Materials* 21, p. 1839 – 1845.
- Bastianini, F. Corradi, M. Borri, A. and Tommaso, A. 2005. Retrofit and monitoring of an historical building using “Smart” CFRP with embedded fibre optic Brillouin sensors. *Construction and Building Materials* 19, p. 525 – 535.

Sensor CFRP-Sheets for the Controlled Strengthening and Retrofitting of Reinforced Concrete Members

Klaus Holschemacher & Stefan Käseberg

HTWK Leipzig, University of Applied Sciences, Faculty of Civil Engineering, Leipzig, Germany

ABSTRACT The reinforcement of bearing structures with secondary glued reinforcement has been practiced successfully for a long time. Thereby steel plates have been used for circa 50 years and FRP plates have been used for circa 25 years. Compared to steel the carbon fiber has some important advantages, for example the higher elastic modulus (up to 50%) and the higher tension strength. The load bearing behavior of Carbon Fiber Reinforced Polymer (CFRP) is significantly influenced by the properties of the matrix, the fiber and the interface between both. Thereby some important disadvantages of the brittle materials must be considered, for example the low ductility of the bond between CFRP and concrete and brittle failure of FRP. With embedded sensor systems it is possible to measure crack propagation and strains. In this paper a sensor based CFRP system will be presented, that can be used for strengthening and measuring. On the basis of four point bending tests on beams (dimensions of 700×150×150 mm) the potential of the system is introduced. Primarily a comparison of two different measurement methods (Strain Gauge and Fiber Bragg) is shown.

1 CARBON FIBER REINFORCED POLYMER

1.1 Development status

The strengthening and retrofitting of reinforced concrete structures become an increasing importance in the modern reinforced concrete construction. Reasons are the rising age of existing buildings as well as the necessity for change of use. For the rehabilitation of concrete structures there are different effective possibilities like the additional reinforcement of cross section, the change of the static system, injections and the prestress of the reinforcement. Particularly the additional reinforcement of the cross section is interesting, because it is possible to avoid complex changes at the static system. Besides shotcrete or concrete topping the use of glued reinforcement has become very popular. In many cases the reinforcement are plates which consist of steel or Fiber Reinforced Polymer (FRP). The bond between reinforcing plate and the structural element can be realized with a cold-curing resin. If steel plates are used, the reinforcement will be consistent to the normal reinforced concrete concerning bearing capacity and deformation behavior. One disadvantage of steel plates can be seen in the warranty of the durability. This is caused by the high risk of corrosion in the area of contact between steel and adhesive. Accuracy and the execution of metallic bright steel surfaces must be realized for good achievements. By the use of fiber reinforced polymer plates it is

possible to minimize the risk of corrosion. Thereby these plates have a high tensile strength and low weight. The mainly used raw materials for the reinforcing fibers are glass and carbon. These fibers are embedded and fixed in an epoxy resin. But the use of glass fibers causes some problems. Compared with steel Glass Fiber Reinforced Polymers (GFRP) has only a small elastic modulus. It results in huge cross sections of the plates to assure the same extensional stiffness like in steel plates. The high tensile strength of glass fibers can not be accomplished. An economical use in the field of reinforcement is not possible in many cases. However, it is possible to avoid this problem if carbon fibers are the reinforcing material.

1.2 Field of application for CFRP

The reinforcement of bearing structures with secondary glued reinforcement (like delineated in chapter 1.1) has been practiced successfully for a long time. Thereby steel plates have been used for circa 50 years and FRP plates have been used for circa 25 years. Compared to steel the carbon fiber has some important advantages, for example the higher elastic modulus (up to 50%) and the higher tension strength. Furthermore carbon fibers are free of corrosion, they are resilient under dynamic load, and they do not creep and have good shrinkage behavior. On the other hand stands a high material price as well as a high sensitivity towards to side pressure and failures at the surface. For the reinforcement of horizontal and vertical concrete elements different alternatives of

CFRP systems can be used. Thereby the products which are glued in slots have been not able to succeed till now. On the one hand the slot is very advantageous for the bond between concrete and CFRP. On the other hand only the distance from surface up to the first reinforcement layer is available for the depth of the slots. So bulky sounding is necessary as well as many slots to get the required cross section of CFRP material. This is the reason why the biggest part of uses of CFRP systems under bending are at the surface glued CFRP plates or CFRP sheets as tensile reinforcement. Main problem is the bond between concrete surface and CFRP. The debonding processes go fast and without advance notice. In cases of failure the composite shows no ductile behaviour. So it was thought about a durable monitoring of the CFRP structures.

2 SENSOR BASED CFRP

2.1 General configuration

In sensor based CFRP optical measuring units are embedded, which rest on glass fiber telecommunications. Especially the use of Fiber Bragg Gratings (FBG) is very popular because of diverse advantages. Through this technology it is possible to measure strains at every point inside of the FRP material. The small FBG will be baked into the glass fiber by laser. They are able to reflect particular spectrums of light and changes of these spectrums which are caused by strain or temperature changes. Thereby it is possible to arrange several FBG at only one glass fiber. Against the arrangement of glass fiber and FBG it is possible to measure uniaxial or biaxial strain conditions inside of the CFRP system. Their advantages are the long term durability and the small proportions of the fiber optic measurement systems. The epoxy resin of the FRP is an effective protection for the glass fiber and assures the bond between optical fiber and FRP material. If the reinforcing carbon fibers are arranged as clutch or canvas (CFRP sheets) it is possible to embroider the fiber optic sensor system directly on these sheets before the laminating with the epoxy resin starts. The effectiveness of those smart structures will be shown in the next topics.

2.2 Test program 1

In the context of the “regional Wachstumskern highStick” technical textiles like carbon fiber sheets (CF-clutches) are to be embroidered with optical fibers, to test the effectiveness of the strain measurement of the developed smart composites. For this purpose it was necessary to create reinforced concrete beams. The length of this specimens conducted 70 cm (dimensions of 700×150×150 mm) and they consisted of high strength concrete C 60/75 and two reinforcing bars (diameter 6 mm) as

bending reinforcement. All in all three beams were produced. At first the test beams were loaded in a deflection controlled four point bending test up to a crack width of 0.40 mm. Thereby it was possible to simulate a realistic measure of redevelopment and to bring the beams into the cracked status.

Thereafter the application of the sensor based CF-clutches (Tensile strength: 3900 N/mm², Elastic modulus: 230.000 N/mm², Thickness: 0.11 mm) followed with an epoxy resin at the surface of the tensile zone of the concrete beams.

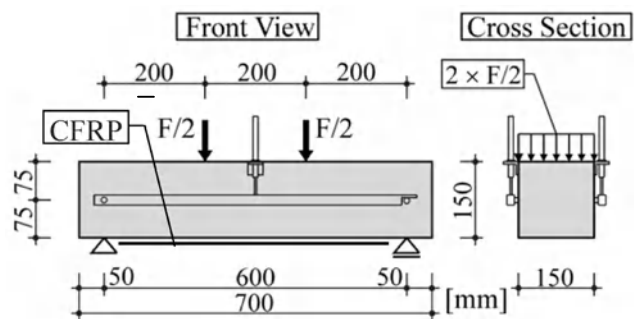


Figure 1 Test set-up of the four point bending test

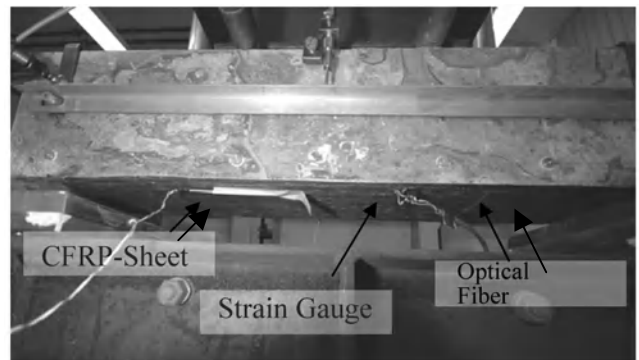


Figure 2 Real four point bending test

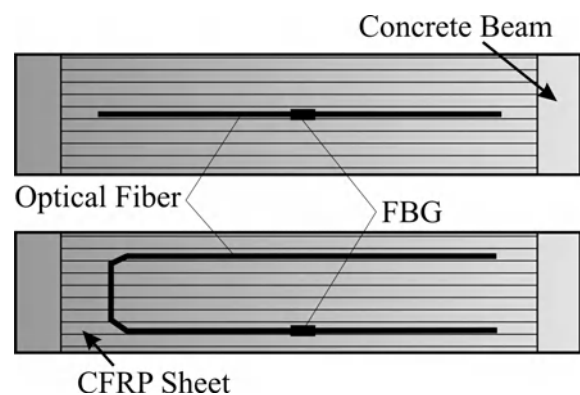


Figure 3 Arrangement of the optical fiber measurement system (test program 1)

For the deflection controlled tests displacement transducer were used as well as load cells to get load deflection curves and load strain curves of the bending

tests. Figure 1 explains the whole test set-up and the used equipment. The CFRP Sheets were glued (like shown in Figure 2) at the underside in the tensile zone of the concrete beams. The CFRP material was appointed with an optical fiber with one FBG by use of the embroider technique. The orientation of the optical fibers carried out in longitudinal direction in the middle of the sheet. Furthermore the optical fiber was arranged parallel by use of a kink as turning point (beam 1). For checking of the optical strain measurement strain gauges were used additionally. They can be seen in Figure 2 at the right side. Every strain gauge was ranged alongside the particular FBG. Furthermore the nitriding optical fibers and the arrangement of the used FBG can be seen. It is also possible to recognize the good integration in the epoxy matrix. The comparison of the results of the FBG strain measurement with the results of the strain gauges led to the load strain curves, presented in Figure 4 for the beams 1 and 2. It can be seen, that an efficient monitoring of the strain development inside of the CFRP sheets was possible. The curves present a good convergence between electrical and optical measurement methods at the test beams. The achieved results clarify the capability of the nitrogenized FBG sensor system. A damage or detraction of the optical glass fiber because of embroider or of the laminating did not appear.

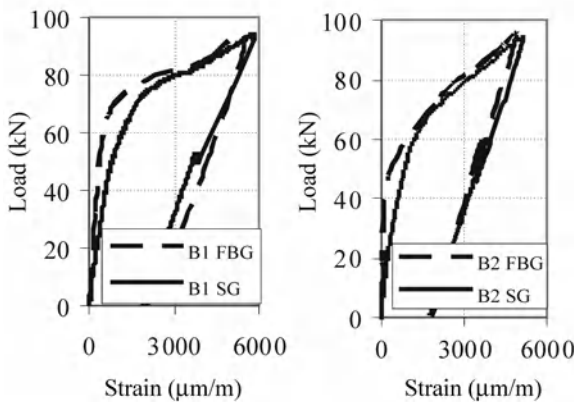


Figure 4 Load strain curves of Strain Gauge (SG) und Fiber Bragg Grating (FBG)

Furthermore the load displacement behaviour (measured with displacement transducer) of the test beams before and after reinforcement can be seen in Figure 5. The curves clarify the strong ascent of bearing strength because of the CFRP reinforcement with the modified CF clutches. A detraction because of the embedded optical sensor systems could not be noticed. It also can be recognized that the load displacement curves of the three reinforced beams point a very good agreement in the trend. This is a good argument for the repeatability of by hand laminated CFRP systems.

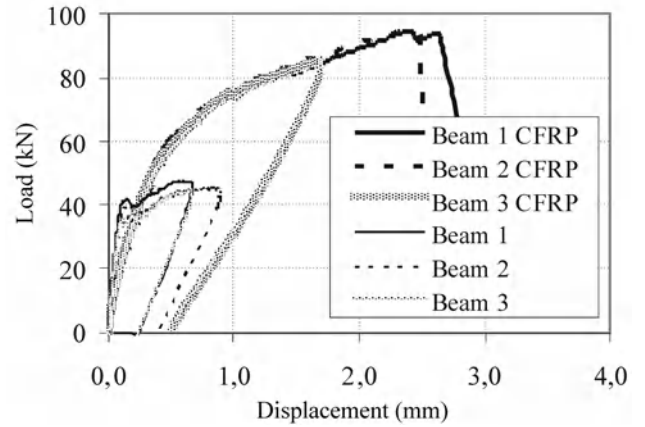


Figure 5 Load displacement curves of series 1

The refractory failure of the beams 1 and 2 emanated from the end of the plate, show clearly, that there is no announcement in the case of collapse.

2.3 Test program 2

After the satisfying tests with optical fibers with only one FBG, new experiments with three FBG at one fiber should be investigated at three concrete beams with same setting as in chapter 2.2. For this purpose the optical fiber was again arranged parallel by use of a kink as turning point. The control of the optical strain measurement was once more realized with a strain gauge, which was arranged in the middle of the CFRP-sheet.

Figure 6 presents the sensor arrangement of optical fiber and FBG at the CFRP sheet. FBG 1 and 2 were used for strain measurement in the middle of the beam at each side. The FBG 3 was arranged in the turning point to realize temperature compensation. Thereby it was to analyze if the arrangement in the breaking point assures an adequate mechanical decoupling to realize an independent temperature measurement.

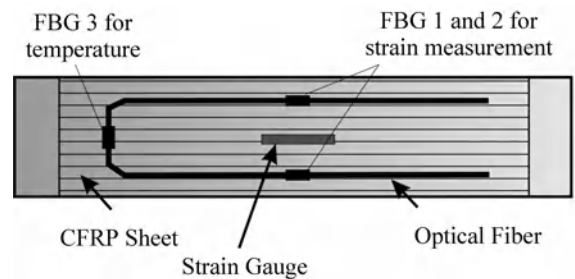


Figure 6 Sensor arrangement of test series 2

The load strain curves explained in Figure 7 show a good agreement between the results of the strain gauges and the average values (FBG av) of the two in lengthwise placed FBG 1 and 2.

However between the FBG 1 and 2 arranged at beam 1 irregularities between the measurement results were assessed. Reasons for these results can be bending cracks near the FBG position, which create different strain

states at the FBG measurement points because of the non-linear behaviour of the reinforced concrete beams (concrete, reinforcing bars, CFRP material). The results attest that it is possible to nitrogenize several FBG, grouped at one optical fiber, at a CF-clutch free of failure. The analysis of all FBG was possible. Thereby it worked to create temperature compensation by the use of FBG 3 in the breaking point.

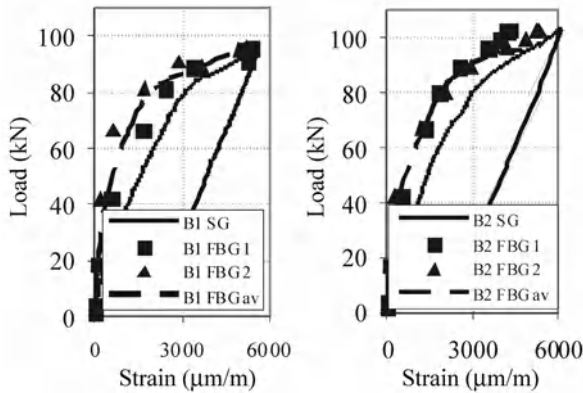


Figure 7 Load strain curves of Strain Gauge (SG) and Fiber Bragg Grating (FBG) (test series 2)

2.4 Test program 3

In test series 3 the effects of a concrete with normal strength (C30/37) were monitored. Furthermore a new sensor arrangement at the CF-Sheet was sampled. This fact and a very careful laminating of the CFRP-system guaranteed the very good agreement between the results of the strain gauges and the average values (FBG av) shown in Figure 8. The comparison of the load displacement curves of normal and high performance concrete (Figure 9) explain the high importance of the compressive strength and the Elastic modulus (of concrete) for the stiffness and the ultimate load of a CFRP-reinforced beam.

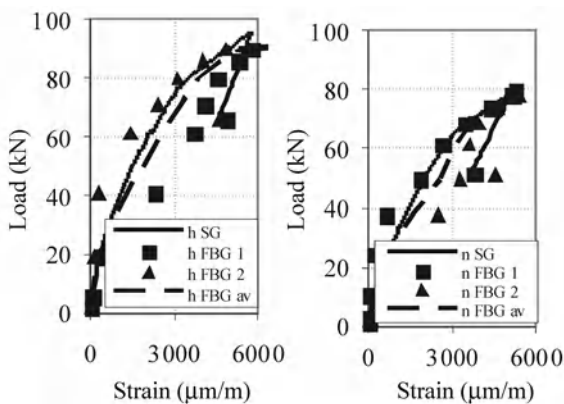


Figure 8 Load strain curves of Strain Gauge and FBG by use of Concrete C60/75 (h) and C30/37 (n) (test series 3)

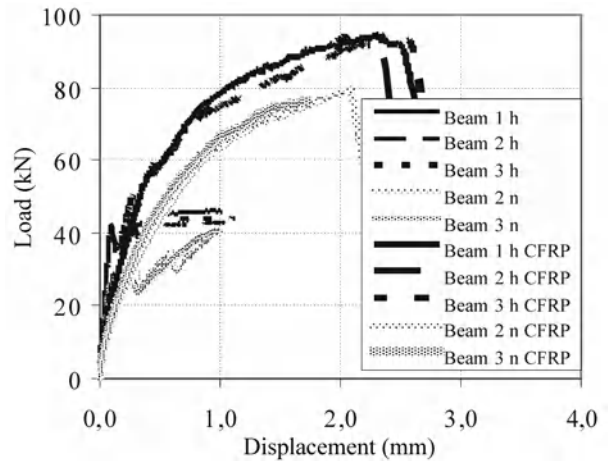


Figure 9 Load displacement curves of series 3 with beams of Concrete C 60/75 (h) and C30/37 (n)

3 CONCLUSIONS

CFRP Systems are a very effective method for reinforcing and retrofitting of existing reinforced concrete structures. They allow a strong growth of bearing strength without big interventions into the basic structure of a building. Nevertheless also this method of rehabilitation causes problems. Examples are the low ductility of the CFRP reinforced concrete structure as well as the long-term behaviour under constant high load. By using of embedded fiber optic measurement systems, like Bragg Gratings, it is possible to realize an integral monitoring of the CFRP material.

4 ACKNOWLEDGEMENT

The study which is the base for the presented paper was part of the research project: “Sensorbasierte Textilarmierung” of the “Wachstumskern HighStick” and is supported by the Federal Ministry of Education and Research of the Federal Republic of Germany. Furthermore special thanks for the project partners and to Hubertus Kieslich and Torsten Müller.

REFERENCES

Yao, J. and Teng, J.G. 2007. Plate end debonding in FRP-plated RC beams – I: Experiments. *Engineering Structures* 29, p. 2457 – 2471.

Lau, K. T. Zhou, L. M. Tse, P. C. and Yuan, L. B. 2002. Applications of Composites, Optical Fibre Sensors and Smart Composites for Concrete Rehabilitation: An Overview. *Applied Composite Materials* 9, p. 221 – 247.

Lu, S. and Xie, H. 2007. Strengthen and real-time monitoring of RC beam using “intelligent” CFRP with embedded FBG sensors. *Construction and Building Materials* 21, p. 1839 – 1845.

Electrically Conductive Nanocomposite Coating for Strain and Health Monitoring

Jianlin Luo^{1,2}, Hui Li¹ & Guijun Xian¹ (gjxian@hit.edu.cn)

1. School of Civil Engineering, Harbin Institute of Technology, Harbin 150090, China

2. School of Civil Engineering, Qingdao Technological University, Qingdao 266033, China

ABSTRACT FRP bridge decks are designed to withstand high load levels and a lifetime of several ten years, facing an extremely high number of load cycles. The fatigue life and degradation of the mechanical properties are needed to be essentially considered during the service of the FRP deck. In the present study, a novel electrically conductive coating was developed with a function of strain monitoring for the FRP bridge deck. An epoxy resin was modified with multi-walled nanotube (MWCNT) in order to achieve electrical conductivity. Processing, structure and properties of the MWCNT-epoxy nanocomposite were optimized, and the correlation between the strain level and electrical conductivity of the coating was set up. The conductivity of the coating on the FRP bridge deck is tracked with a simple electrical measurement, and the strain of the FRP bridge deck is obtained through the determined conductivity ~ strain relationship. It is worth noting that the damage modes of the coatings (also the coated FRP surface) can be determined from the conductivity curves. Together with the easy application and data collection, such coating has a high potential for the application in stress/strain and health monitoring.

1 INTRODUCTION

Fiber reinforced polymer (FRP) composites can be used as novel construction materials for sustaining high load levels but with light weight. The fatigue life and degradation of the mechanical properties are needed to be essentially considered during the service of the FRP deck, it's urgent to develop practical and effective sensors application in in-situ monitoring of damage development and/or apparent stresses and strains of FRP-structures.

Since first document found by Iijima (Iijima 1991) in 1991, carbon nanotube (CNT) has been intensively investigated. Its exceptional properties make it potential candidate for lots of applications. The superior conductivity of either individual single-wall CNT (SWCNT) or multi-wall CNT (MWCNT) can be used to monitor the delamination or matrix cracking under static and dynamic loading of CNT-based composites (Li 2008a, Luo 2009, Han 2009, Lu 2005, Zhang 2009). Thereby, this "piezoresistive" effect of reinforcement CNT in nonconductive matrix allows a sensing of the mechanical deformation and possible damage of the composite material and structure.

In present study, some conductive MWCNT with different loading is filled in epoxy resin with the dispersion technique of surfactant-decoration, high-intensive shear mixing, and bath sonication process. This kind of conductive functional resin coating will be

simply brushed on the surface of the FRP sheet. The percolation threshold and DC I-V characteristic of the cured nanocomposite coating will be explored by measuring its volume resistivity with four-electrode method. The change in its electrical resistivity will be simultaneously monitored under three-point bending, attempt to develop a novel sensor for condition monitoring for FRPs materials.

2 EXPERIMENTAL

2.1 Materials and masterbatch preparation

MWCNT used in this work was purchased from Chengdu organic chemicals Co. Ltd. (Chengdu, China). Its main physical properties are listed in Table 1.

Nonionic surfactant Triton x100 (Tx100, imported subpackage, AR), was purchased from Shanghai chemical reagent co. Ltd. (Shanghai, China). Epoxy resin, E-51, Shandong Tianmao chemicals Co. Ltd., and epoxy reactive diluents (AGE, Liaoning Dalian Liansheng trading Co.) were used. The curing agent is Tyfo s-part B, kindly offered by FYFE Co. LLC (USA). The coupling agent KH-560 γ is bought from Harbin institute of chemical industry. The antifoaming agent was BYK-141, imported subpackaged, Byk chemie Co..

The MWCNT/epoxy masterbatch was prepared by the following procedure. AGE (20.0 wt.%, with respect to the epoxy addition, the same reference as followed if no mention) and surfactant Tx100 (1.0 wt.%) was mixed

into 300 g epoxy. MWCNT (5.0 wt.%) was slowly stirred into the solution. The mixture was mixed at a speed of 5,000 rpm for 30 min, and then the slurry was sonicated (100 W, 40 kHz) for 12 hours. Finally, the mixture was vacuum dried at 60 °C and -0.08 MPa for 12 hours.

Table 1 Qualification and physical properties of MWCNT.

External Diameter	Length	Mass fraction	BET surface area	Conductivity
(nm)	(μm)	(wt.%)	(m^2/g)	(S/m)
10-20	~30	≥ 95	100-300	$>10^{-2}$

2.2 Nanocomposite coating preparation

Nanocomposites were prepared with different weight loadings of MWCNT (w/M) (0.5, 1, 2, 3, 4, 5 wt.%), and specially with the w/M being 2.3, 2.5, and 2.8 wt.%. Hereafter Tyfos-B hardener, the coupler KH-560 γ (0.8 wt.%), and the defoamer BYK-141 (0.2 wt.%) was added. The mixture was stirred for 5 min, and then vacuum dried for 10min. Hereafter, the slurry was brushed into the rectangular space on the FRP sheet. The space was enclosed with three layers adhesive tapes (each layer has 0.15 mm thickness) adhered on the FRP sheet, its dimension was $180 \times 20 \times 0.45 \text{ mm}^3$. It is noting that two pairs of electrodes were symmetrically pre-adhered onto the surface of the FRP sheet at 100 mm and 140 mm intervals, the sized electrode was made of copper foil after coarsened. Figure 1 was the configuration image of the FRP sheets before and after brushed on the nanocomposite slurry. The third step, the nanocomposite was cured at room temperature (RT) for 12 hours, hereafter, the nanocomposite was post-cured at 110°C for 2 hours, and then nature cooled to RT. Two duplicates were fabricated for each composition.

The volume resistivity (ρ) of the cured nanocomposite coating was obtained from performing 4-terminal DC measurements of the resistance. To investigate DC I - V characteristic of the nanocomposite coating, the signals were obtained from performing 4-terminal voltage measurements of the inner-pair electrodes of the coating and the in-series standard resistor with a DC power applied with a range of 0~32 V. The corresponding ρ , electrical conductivity (σ) or DC current (I) can be derived from the equation 1.

$$\rho = \frac{U \cdot S}{U_0 / R_0 \cdot L} = \frac{U \cdot S}{I \cdot L} = \frac{1}{\sigma} \quad (1)$$

where, U = DC 2-terminal voltage (V) of the coating; U_0 = 2-terminal voltage (V) of the standard resistor, R_0 = the resistance value of the resistor (here, 50 k Ω), I = DC current of the in-series circuit (mA), S = the cross-section area (mm^2), and L = the spacing of the inner-pair electrodes (mm).

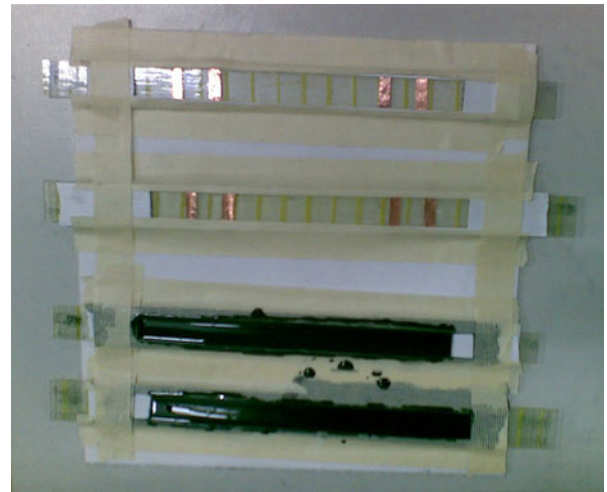


Figure 1 FRP sheets before and after coated with nanocomposites

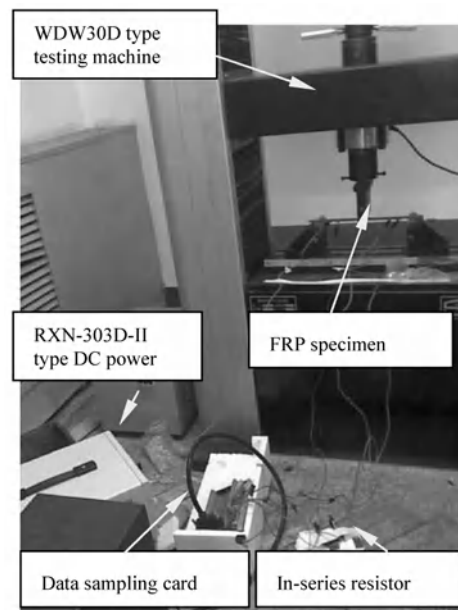


Figure 2 Data acquisition system setup for strain-sensitive testing

As for its strain-sensitive property under three-point bending, the voltage signals were recorded with similar four-electrode method with 4.0 V DC power applied, the crosshead displacement (δ) at the mid-span was simultaneously recorded by a multifunctional digital material testing machine at a speed of 2.0 mm/min loading rate, with a range of 0~10 kN. Figure 2 is the data collection setup for strain-sensitive property of the coating brushed on the bottom surface of the FRP sheet.

3 RESULTS AND DISCUSSIONS

3.1 The percolation threshold

As shown in the ρ - w/M relation curve (Figure 3), the ρ of the coating steadily falls down with the increment of w/M .

As known, the pure epoxy resin is a kind of insulator, its ρ generally is much above 10^6 k Ω .cm. When

MWCNT is added in, the conductivity drops to the value of 10^6 k Ω .cm, and steadily descends with w/M . The ρ with 5.0 wt.% w/M reaches 8.54×10^3 k Ω .cm. As reveals in Figure 3, the ρ - w/M relationship roughly divides into three ranges: 0.5–2.0 wt.%, 2.0–3.0 wt.%, and 3.0–5.0 wt.% span. The ρ has relatively slow descending trend at the first and last stage, while the ρ of the nanocomposite sharply drops from 2.19×10^5 k Ω .cm to 4.46×10^4 k Ω .cm with the change of w/m from 2.0 to 3.0 wt.%. Hereby it can be derived that the onset percolation threshold of this type of nanocomposite is around 2.0 wt.% of w/m .

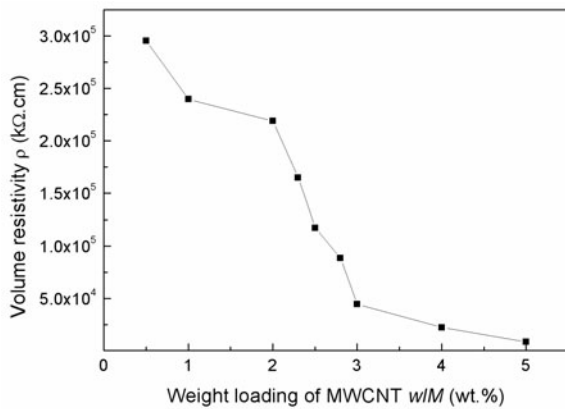


Figure 3 ρ vs. w/M of the nanocomposite coatings

3.2 DC I-V characteristic

As shown in the DC I - V curves (Figure 4), a little nonlinearity can be found, especially when the voltage is in-between ± 1.5 V.

The I - V characteristic curve of the coating with 2.0 wt.% w/M begins to sharp rise in contrast to that with 0.5 wt.%, or 1.0 wt.% w/M , and that with 3.0 wt.% w/M rises much obviously. This also can reflect on the percolation effect happened on the nanocomposite when the w/M is between 2.0 wt.% and 3.0 wt.%. When the w/M is up to 4.0 wt.%, the I - V characteristic shows more linear and smooth, which implies that some physical contacts with conductive MWCNT fibers have been happened within the epoxy matrix, which benefits for the further enhancement of the slope of the I - V curve and the bulk conductivity.

In fact, the maximal current is less than 0.03 mA even with the applied voltage up to 20 V (the power supply is up to 30 V), which demonstrates that there is almost no resistance-heating effect happened amongst the coating. So if the suitable voltage level is chosen, the electrical parameters can be conveniently and accurately measured during long-term monitoring.

3.3 The strain-sensitive property

Figure 5 shows the fractional change in resistivity ($\Delta\rho$) as a function of the tensile strain (ϵ) of the coating, just

which of the bottom layer of the FRP sheet under bending.

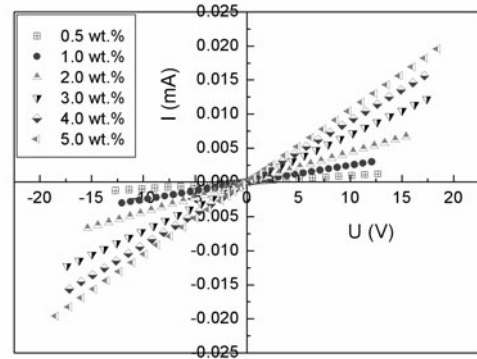


Figure 4 DC I - V curves of five compositions nanocomposite coatings

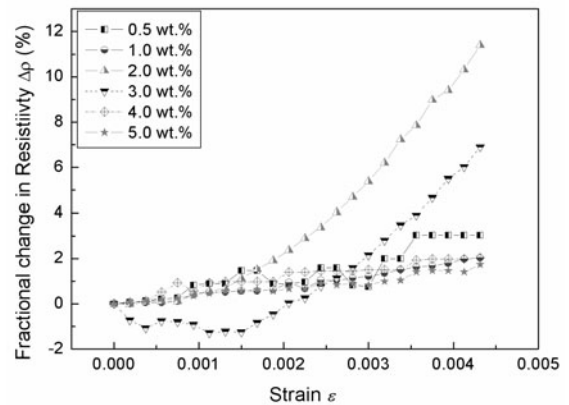


Figure 5 The $\Delta\rho$ - ϵ curves of the combined system of six coatings and the corresponding FRP sheets

As shown in above six curves, the $\Delta\rho$ of the coating at 2.0 wt.% w/M exhibits most even and dramatical response to the corresponding ϵ . The ρ steadily increases along with the ϵ , and has maximal amplitude 11.4% at 0.0043 strain with respect to the initial value, the maximal strain sensitivity arrives up to around 30, about 15 times than that of common strain gauge; where as other $\Delta\rho$ either exist fluctuatations or low sensitivity to the change of ϵ .

MWCNT has superior macroscopic quantum tunneling-through capability, which may result in some conductive pathways formation after overcoming possible potential barriers between MWCNTs isolated by epoxy resin film. At low w/M (such as 0.5 wt.%, 1.0 wt.%), in one hand, the chances of physical contacts of MWCNT fibers is lack owing to well-distribution of MWCNTs within epoxy matrix after sufficient dispersion, on the other hand, the potential barriers between well-distributed but relatively far-apart MWCNTs are hardly tunneled-through (Simmons 1963). Two above contribute to the high resistivity, low and uneven sensitivity of ρ upon the bending tension. At high w/M (such as 4.0 wt.%, 5.0

wt.%), the chances of physical contacts of MWCNTs may greatly increase, yet the distribution of MWCNTs among high viscous mix system becomes somewhat bad. Lots of MWCNTs may form micro-size, even macro-size local clumps (seen in Figure 6), which do harm to the network formation. As a result, the conductive pathways of physical contacts between local agglomerations are frequently found, yet the tunneling-through pathways of close but isolated MWCNTs are seldom found. These lead to the low value, yet small and smooth increment of the ρ with increment of ε (Li 2008b).

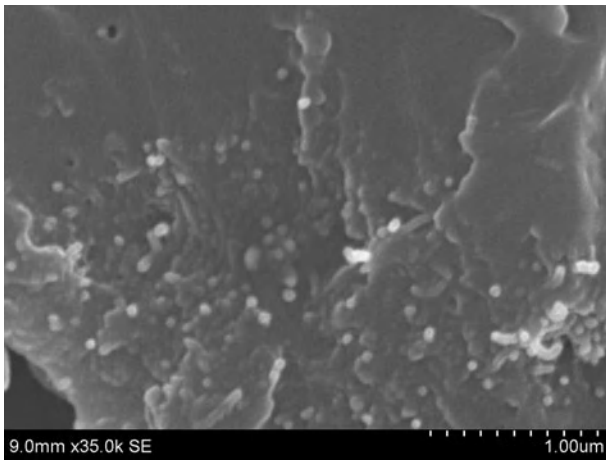


Figure 6 The fracture section of the nanocomposite with relative high w/M

When w/M stays between 2.0-3.0 wt.%, the counterpoise of two above factors contributes to the necessary numbers of conductive pathways and formation of tunneling-through meshwork of close but isolated MWCNTs. With increment of the sheet's bending deformation, the coating is extended with the ε enhancing, and the conducting MWCNTs are correspondingly deviated from each other. Physical contact chances between MWCNTs become less and less, and potential barriers become wider and wider, therefore, the effective conductive pathways get less and less, the field current density becomes thinner and thinner, as a result of that, the ρ gets higher and higher with the ε increasing. It's worth to noting that, at the endset percolation threshold (3.0 wt.%), the ρ of the corresponding coating has somewhat descending trend at initial bending stage before steadily going-up.

Obviously, the intrinsic parameter $\Delta\rho$ of the coating

with w/M being around the onset percolation threshold can well response and diagnose the bending strain of FRP sheet, and the sensitivity is much higher than that of the common strain gauge. The strain-sensitive property of the nanocomposite coating implies that in addition to reinforcing mechanical properties (strength, modulus, structural damping, etc.), this type of multifunctional material presents the potential to provide real-time traffic monitoring and self-diagnostic functionalities to FRP decks.

4 CONCLUSIONS

An epoxy resin was modified with MWCNT using surfactant-decoration, high-intensive shear mixing, and bath sonication process. The nanocomposite can be used as a coating onto the bottom surface of the FRP sheet. At the onset percolation threshold (2.0 wt.%), the coating possesses a linear $I-V$ characteristic, superior strain-sensitive property with high strain-sensitivity. With this function, the coating can be used as a novel self-sensing element to monitoring traffic impact or long term durability of a FRP structure, e.g., a FRP bridge deck.

REFERENCES

- Iijima, S. 1991. Helical microtubes of graphitic carbon. *Nature* 354 (7): 56-58.
- Li, X., Levy, C., and Elaadil, L. 2008. Multiwalled carbon nanotube film for strain sensing. *Nanotechnology* 19: 045501.
- Luo, J.L., and Duan, Z.D. 2009. The dispersivity of multi-walled carbon nanotubes (NMWNTs) and pressure-sensitive property of NMWNTs reinforced cement composite. In *1st International Conference of the Chinese Society of Micro/Nano Technology, Beijing, China, 2008*. Switzerland: TTP publisher.
- Han, B.G., Yu, X. and Kwon, E. 2009. A self-sensing carbon nanotube/cement composite for traffic monitoring. *Nanotechnology* 20:445501.
- Lu, J.W., Wang, W.L., Liao, K.J. and Wan, B.Y. 2005. Strain-induced resistance changes of carbon nanotube films. *Int J Modern Physics B* 19: 627-629.
- Zhang, W., Suhr, J. and Koratkar N. 2009. Carbon nanotube-polycarbonate composites as multifunctional strain sensors. *Smart Mater Struct* 18: 055010.
- Simmons, J. G. 1963. Electric tunnel effect between dissimilar electrodes separated by a thin insulating film. *J Appl Phys* 34 (9): 2581-2589.

Smart Composites for Durable Infrastructures – Importance of Structural Health Monitoring (SHM)

Monssef Drissi-Habti (monssef.drissi@lpc.fr)
LCPC, Route de Bouaye, 44341 Bouguenais, France

ABSTRACT The goal of this contribution is to share some ideas that can bring heavier discussion among the population of bridge researchers and engineers about SHM. For existing infrastructures, an emphasis will be made on how critical the detection of the onset of corrosion as well as its rate of proliferation within steels. In the case of new bridges, design and conception should include smart materials and structures. Smart composites, that are integrating embedded sensors, can bring significant advances in civil engineering applications. So is the case of nano-sensors, that will surely offer additional valuable solutions in the mid-term future. The issues related to standards in using composites in civil engineering are also addressed.

1 INTRODUCTION

For existing infrastructures, corrosion and stress-corrosion are detrimental for reinforcing steels. The challenge of how efficiently we can protect steels against corrosion has been for a long time critical. However, knowing how advanced are corrosion protecting techniques used nowadays, is it still relevant to concentrate solely on protecting steel structures or should we focus mostly on structural health monitoring that would enable us identifying the onset of corrosion within steel structures and its rate of extension (which in turn would make us start the pre-maintenance at the right time) ? In the case of new infrastructures, new materials developed in the last three decades as well as the significant advances recorded in various engineering fields, are currently enabling challenging smart structures to be included as key-parts of bridges. So, how can we proceed to make smart structures increasingly used in bridges?

In previous articles (Drissi-Habti et al., 2008, 2009a, 2009b), loading conditions of critical cable parts were discussed, emphasizing the influence of environmentally-assisted degradation (corrosion and stress-corrosion). The focus was on inspection issues and the struggle for reliable data fusion procedures. As alternative materials for bridge cables, continuous carbon fiber-reinforced-polymer matrix composites were introduced, along with suitable structural health monitoring (SHM) techniques. In this article, the objective is to provide the readers with an opinion on how structural health monitoring techniques can help inspection of bridge cables. The cables are used as a working example of structures available in existing bridges. In the case of new bridges, structures based on composites will be briefly introduced

as well as nano-sensors that will surely bring a significant technological jump in the near future unless some issues are overcome.

2 EXISTING BRIDGES: CRITICAL ASPECTS OF CABLE BRIDGE SAFETY

To avoid corrosion, thus increasing cable life, valuable efforts have been undertaken in various countries. The current strategy is based on various methods to protect against corrosion. To show how far corrosion-protection techniques have advanced, two examples of the most advanced corrosion-protection technologies are presented hereafter.

The work of Freyssinet, reported by Lecinq et al., (2005), introduced the individually protected parallel strand system (PSS), with a higher durability, called Cohestrand. The individual protection of cable strands is insured through the use of polymers. The Cohestrand is new seven-wire strand released in year 2000, protected with a polyethylene sheath fully bonded to the steel wires. The system was reported to be applicable to the largest suspension bridges as well as to smaller structures. Cohestrand was applied to Sungai Muar bridge (132m, Malaysia) and Kanne bridge (96m, Belgium). The authors however reported that the application of PSS system on cable-stayed bridges with a slender pylon using a deviation saddle, or on the main cables of suspended bridges, implied singular points through the saddle or the hanger collars with reduced durability. Indeed, to prevent the collars from sliding, a high clamping force is necessary, requiring direct steel to steel contact. Hence, any addition corrosion protection of the main cable, such as zinc paint, outer sheath or

wrapping with wires, is always interrupted at the collar level. It is therefore premature to conclude about the reliability of this technology, because of the lack of in-field durability data (Yanev, 2009).

In Japan, new cables are built with shop-fabricated strands, composed of 127 straight galvanized wires with yield strength up to 1800 N/mm². The shop-fabricated cable strands are anchored with sockets. Most anchorages (including old ones) are being equipped with dehumidification systems. On several record-breaking bridges in Japan, such as the Kurushima and Akashi-Kaikyo, managed by the Honshu-Shikoku Bridge Authority, pressurized dry air is injected under the cable wrapping (Yanev, 2007). It must be noted however than even with dehumidification, how can we make sure that corrosion is not present in such cables ?

- The corrosion-protection techniques listed above show clearly the tremendous efforts undertaken to keep water and corrosive agents far away from cables. Despite that, evidence of corrosion is still being reported: Therefore, corrosion should better be considered as an inherent part of the game when using steels, knowing that two points are critical for inspectors, namely the onset of corrosion and its rate of propagation. This opinion seems to be in accordance with some published works (see for example, Betti et al., 2005, 2008).

SHM: THE SOLUTION ?

Rather than concentrating solely on corrosion-protection techniques only, researchers and engineers, involved in bridge technologies, should consider corrosion as an intimate part of using steel. Corrosion is insidiously developing in steel parts, whatever the corrosion protection. Corrosion-protection techniques can reduce corrosion rate significantly, but never fully arrest it. Therefore, ongoing applied research should rather concentrate on how finely corrosion initiation and development inside cables can be detected and finely monitored. This, of course, will not prohibit continuing the design of new corrosion-protection techniques.

3 NEW BRIDGES – CHALLENGES FOR COMPOSITE STRUCTURES

Bridge cables are made out of steel that “naturally” suffers from corrosion. Consequently, engineers and researchers focus mainly on corrosion-protection. In planning future bridges, using cables made out of new structural materials, inert to corrosion would be a very attractive option. Carbon fiber-reinforced-epoxy matrix composites can be considered as appropriate candidates for cable bridge technology. Their health monitoring and anchoring, is discussed herein.

Fiber-reinforced polymer (FRP) composite materials show great potential for integration into highway

infrastructures (Figure 1). Typically, they provide excellent strength-to-weight ratio (five times lighter than steels) and can be fabricated for on-command strength, stiffness, geometry, and other properties. Composite materials can strengthen bridges without reduction of vertical clearance, and they can be applied in severe exposure environments that may have resulted in the deterioration of the original structure. Also, composite-made decks can be used to enhance the life of girder-system bridges, due to their low dead load that permits an increase in live-load carrying capacity.

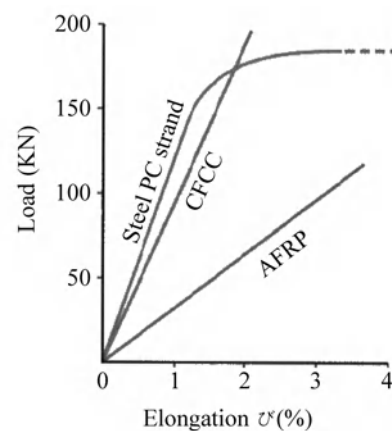


Figure 1 Stress-strain curves of carbon fiber-reinforced epoxy matrix composites and steel (Courtesy of Tokyo Rope Inc., JAPAN)

High tensile strength and stiffness as well as high fatigue life, low weight and excellent chemical resistance are material properties of carbon fibre composites (CFRP) which make these materials interesting for stay cable systems. The key problem to which the application of stay cables as well as tendons is faced is the anchoring. In the present work, we will be summarizing the properties of CFRP, the requirements to stay cables or tendons and the development of such systems.

Despite the widespread use of carbon fiber composites in the aerospace and defense industry, applications in the construction industry were limited for many years primarily due to economic reasons. Key advantages of advanced composites, such as design freedom and tailored characteristics, high strength/weight ratios (which significantly exceed those of conventional civil engineering materials) and a high corrosion-resistance in most civil engineering environments, are lost in high material and manufacturing costs (particularly in direct comparison with conventional structural materials such as steel, concrete, or masonry).

Several developments have changed this scenario over the past few years: advances in manufacturing (pultrusion is an example), the need for mass-production markets in civil engineering and construction and the conception of integrated structural applications fully made out of composites rather than on conventional

structural materials have drawn significant advances both technically and financially.

3.1 NDT OF CARBON FIBER COMPOSITES

To be more convincing for end-users, it is of a prime importance to use composites as smart structures, *ie* by embedding/bonding SHM sensors. The sensors can be used as strain sensors and/or crack extension ones.

When developing new structural materials, the issue of detecting initiation of damage as well as its extension is always present. Extensive work was devoted to detecting damage in carbon fiber-reinforced polymer matrix composite structures. The main damage mechanisms are matrix cracking, fiber-matrix debonding and fiber failures. Acoustic Emission (AE), for example, was used successfully at either laboratory and/or structural scales (Rizzo et Lanza di Scalea, 2001). These authors used AE for monitoring damage during large-scale failure tests of three types of cables of potential use in the new UCSD I-5 composite bridge. Good potential of an effective use of in-situ AE for real-time health monitoring of similar CFRP stay cables in bridges during service life was reported.

Owing to their particular process route, in-situ sensors can be embedded into the final structures, to provide structural health monitoring. Optical fiber sensors used as strain sensors and ultrasonic patches used as crack-growth monitoring techniques (<http://www.nrc-cnrc.gc.ca>) can bring significant interest for structural health monitoring. However, even if in-situ embedded sensors are implemented successively in various composite structures, other issues however remain. Most of them relate to installation, physico-chemical compatibility, durability, joining and bonding and data transmission.

It is interesting to note that strain sensors and flaw extension sensors can be both used to ensure a better control of composite structures. Such concept (Drissi-Habti, 2008b) may boost the use of smart structures in the field of civil engineering.

3.2 NANOMATERIALS – NANOSENSORS

Another topic that will bring a strong interest in the field of infrastructures is the development of sensors based on nano-materials. Indeed, carbon nanotubes, since been firstly discovered by Iijima in 1991, have drawn the most research interests because of their unique geometry, morphology and properties. Carbon nanotubes (CNT) are a new form of carbon, configurationally equivalent to two dimensional graphene sheet rolled into a tube. It is grown now by several techniques and is just a few nanometers in diameter and several microns long. CNT exhibits extraordinary mechanical properties: the Young's modulus is over 1 TPa. It is stiff as diamond. The estimated tensile strength is 200 GPa. These properties are ideal for reinforced composites and nano-electromechanical systems. Besides, the very high

surface-to-volume ratio and hollow structure of nano-materials is ideal for gas molecules adsorption and storage. Theoretical and simulation works have also been conducted to understand this nano-scaled material and related phenomenon (Meyyappan, 1996).

The structure of carbon nanotubes (CNTs) provides them with inherently unique electrical, physical, and chemical properties. Mechanically, CNTs are the strongest and stiffest fibers that are known currently. Thermally, CNTs have high thermal stability in both vacuum and air. In terms of electrical properties, CNTs can be either metallic or semi-conducting. Due to the conductivity of CNTs, they are also under focus to build up new nano-sensors. Accordingly, temperature sensors, paint-like substances based on CNTs, strain sensors, gaz-sensors, are among the most promising ongoing research. For example, a layer-by-layer (LBL) method was proposed by Kenneth et al., (2007) to develop a multifunctional material for measuring strain and corrosion processes (Figure 9). LbL fabrication of carbon nano-tube composites yields mechanically strong thin films in which multiple sensing transduction mechanisms can be encoded. By selecting carbon nanotube concentrations and polyelectrolyte matrices, yield thin films that exhibit changes in their electrical properties to strain and pH, were achieved. The authors showed that while thicker films sensors can provide additional mechanical strength, more layers decrease the overall sensitivity of the film. Therefore, a trade-off must be found between mechanical and electrical properties (Kenneth et al., 2007).

The use of nano-sensors can be extended to cables and decks. The issues would be the durability of the bonding between the sensors and the substrates as well as the reliability of the sensors themselves.

4 STANDARDS ISSUES

It is a secret that standardization is usually regarded as a dull, but unavoidable part of a given industry. Absence of standardization leads to extra costs to industry and can be a source of fiasco, while the inability to meet international standards may hinder a company entering a new market. Good standardization can protect the industry finance and open up new applications. In the case of composites for example, the design and the conception are based primarily upon well established constituent mechanical and physical properties. Their reliability is also an issue for standards. Therefore, protecting composite markets through the establishment of standards will obviously boost the applications, especially in civil engineering and construction that are promising mass-production markets.

Fiber-reinforced polymer composites, which have been chosen for advanced industries (aerospace, military, marine, and automotive), now are beginning to be

introduced in civil engineering and construction, where their desirable properties can boost performance. As emphasized by Ellingwood, 2003, a load and resistance factor design (LRFD) standard for composites would facilitate their use in civil infrastructures, creating a market for new composite building materials by providing a basis for structural design that is comparable with existing LRFD standards for other common construction materials. Such a specification must take into account the specific features of polymer composites: Their orthotropic nature, sensitivity to environment (moisture, temperature, and ultraviolet radiation effects, dependence of strength and stiffness on the rate of application and duration of structural loads, and uncertainties in their mechanical and structural properties. Given the existing theories related to testing and modeling the behavior of composite materials, time maybe has come for working all together to establish round-robin tests, thus supporting the development of ISO standards, to be implemented for civil engineering and construction. The opportunity of the CICE conference should be taken at least to launch a future plan, to be further deepened.

5 CONCLUSION

As a summary, 2 main points should be pointed out. The first one is pertaining to existing bridges and more specifically to steel structures. For this case, concentrating solely on corrosion protection is no more topical since significant technological advances have been got and they are showing that the rate of corrosion can only be decreased and never fully stopped. Hence, structural health monitoring enabling the precise monitoring of the 2 issues listed above is critical.

In the case of new materials-based structures, composites can, for example, be largely used as stay-cables. Embedment of sensors serving as “nerves” in such structures should be a positive advance since both the strain and eventually the extent of any damage can be dynamically and continuously monitored. This will obviously bring more confidence for end-users, thus opening the doors for larger applications of composites in civil engineering and construction. Furthermore,

recent advances in nano-sensors may bring important advances in the mid-term future, given their low intrusive character and their high sensitivity, over available sensing techniques.

An issue of main concern in using composite structures in civil engineering is related to standards. It is well known that some trials towards the extension of the LRFD standards to composites were implemented, but are still not worldwide adopted. Therefore, either working out standards based on the extension of LRFD or thinking about new approach-based ones, one must keep in mind that civil engineering and construction industries are mass-production markets potentially, unless well established standards are available and adopted.

REFERENCES

- Betti R., West A.C, Vermaas G, and Cao Y., *Corrosion and embrittlement in high-strength wires of suspension bridge cables*, Journal of Bridge Engineering, 2005, vol. 10, pp. 151-162.
- M. Drissi-Habti, *Smart composite materials for civil engineering works and more generally mechanical based structures*, JEC Composites Magazine, N°42, July-August 2008.
- Drissi-Habti M., Gaillet L., Tessier T., Le Cam V., SMT Conference, NDE/NDT for Highways & Bridges, Oackland (CA), September 2008.
- Drissi-Habti M., Yanev B., Betti R., Materials Evaluation, November 2009, 1285.
- Ellingwood B.R., J. Struct. Engrg. 2003, Vol. 129, Issue 4, pp. 449-458.
- Iijima S., *Helical microtubules of graphitic carbon*, Nature, 1991, vol. 354, no. 6348, pp. 56-58.
- Lecinq B., Petit S., Zivanovic I., *Keep Concrete Attractive*, Budapest 2005.
- Kenneth J Loh K.J., , Kim J., Lynch J.P., Wong N. S., Kotov N.A., Smart Mater. Struct. 16 (2007) 429-438.
- Meyyappan M., *Carbon Nanotubes: Science and Applications*. CRC Press, Boca Raton, Fla, USA.
- Rizzo,Lanza di Scalea. *Acoustic emission monitoring of carbon-fiber-reinforced-polymer bridge stay cables in large-scale testing*. Experimental Mechanics, 2001, vol. 41, n°3, pp. 282-290.
- Yanev B., *Bridge Management*, Wiley 2007.

Concrete Structures Reinforced or Prestressed with FRP

Experimental Study on the Tension Stiffening Effect of GFRP RC Elements

M. Baena (marta.baena@udg.edu), A. Turon, Ll. Torres, C. Miàs, C. Barris, G. Barbeta
Analysis and Advanced Materials for Structural Design (AMADE), Universitat de Girona, Spain

ABSTRACT Direct tension test experiments are accepted to be adequate to study the tension stiffening effect of fibre reinforced polymer reinforced concrete (FRP RC) members. In this paper, an experimental program on direct tension tests on GFRP RC is presented. Four different reinforcing ratios were considered; the ties were instrumented to analyze the member behaviour (load-strain relationship and crack width). Measured member deformation and crack widths are compared with those calculated using the procedures of available codes for steel reinforced concrete, like EC-2 and ACI 224, as well as with ACI 440 for FRP reinforced concrete structures.

1 INTRODUCTION

Deformations and crack width at service loads are usually larger for GFRP RC compared to steel RC. Therefore, their prediction plays an important role in the design of GFRP RC structures. The ability of concrete between cracks to carry tensile stresses, commonly referred as tension stiffening effect, has great influence in the member global serviceability response. Although some studies have been carried out to investigate the tension stiffening effect in FRP RC structures, the differences in behaviour between steel RC and FRP RC, and between existing models and experimental behaviour, have not been completely explained and further research is needed.

The preliminary results of an experimental program on FRP RC ties are presented in this paper. Experimental measures on member behaviour and crack width are compared with predictions based on codes for steel RC structures (EC-2 (CEN 1992) and ACI224.2R-92 1992), which were modified with specific coefficients for their application to FRP RC structures. Moreover, experimental crack width is also compared with ACI 440.1R-03 (2003) for FRP RC structures.

2 EXPERIMENTAL PROGRAM

2.1 Test program

Several GFRP-RC ties axially loaded in tension were tested. All specimens were 1300mm long and had a square concrete cross section (variable). Bond between concrete and reinforcement was in the central 1200mm because a fifty millimeter de-bonded length was maintained on either side of all specimens to avoid local concrete tensile failure at the ends.

A specially designed gripping system was used to

apply the load at the ends of the protruding bars without causing any damage to the bar. Load was applied by means of a hydraulic jack at the specimen's life end, and a rigid reaction structure was used to connect the specimen's dead end, as shown in Figure 1. The load was applied under displacement control and an automatic data acquisition system was used to collect the data. Load steps were not predefined, as the test was stopped anytime a new crack appeared at the concrete surface; after each increment the evolution of cracks and strains was recorded. Crack widths were measured with an optical magnifier with an accuracy of 0.05mm. A linear variable differential transformer (LVDT) was used to measure the member axial deformation. Additionally, member strains were measured at the height of the reinforcement by means of a mechanical extensometer with a gauge length of 150mm between Demec points; both the automatically and manually read deformations were measured over the 1200mm bonded length.

Three different sizes of GFRP bars ($d_b = \#4, \#5$ and $\#6$, where # stands for eighths of an inch) and two cross section sizes ($b = 170$ and 110mm) were considered. One reinforcing bar was placed in the center of the cross sections and four different reinforcing ratios were obtained ($\rho = 0.44, 0.68, 0.98$ and 1.63%), as shown in Table 1.

The ties specimen were identified as DD-SSS, where DD stands for the rebar designation (13, 16 and 19 standing for #4, #5 and #6, respectively) and SSS stands for the square section size (110 and 170mm).

2.2 Materials

Ready-mix concrete, with a maximum aggregate size of 20mm and a target compressive strength of 50MPa, was used to cast the specimens in two batches.

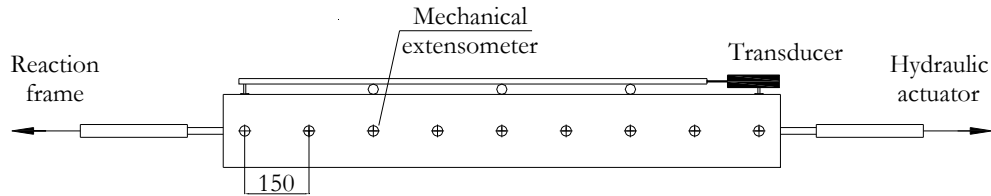


Figure 1 Test setup

Table 1 Geometric characteristics of the ties

Tie designation	Nominal bar diameter, d_b (mm)	Section width, b (mm)	Reinforcement ratio, ρ (%)
13-170	12.7	170	0.44
16-170	15.9	170	0.68
19-170	19.1	170	0.98
16-110	15.9	110	1.63

The GFRP reinforcing bars were manufactured by Hughes Brothers Inc. and had a helical wrapping surface and some sand coating (Figure 2). Normalized measurements were conducted to determine the cross-sectional areas of the rebars, according to ACI440.3R-04 (2004). Mean values of mechanical properties obtained from uniaxial tension tests are shown in Table 2.

Table 2 GFRP rebars geometrical and mechanical properties

Rebar designation	Experimental bar diameter, d_b (mm)	Rupture tensile strength, f_{tu}^* (MPa)	Modulus of Elasticity, E^* (MPa)
13	13.73	659 (690)	37418 (40800)
16	16.11	732 (655)	38758 (40800)
19	19.14	635 (620)	40595 (40800)

* Values provided by manufacturer in brackets



Figure 2 Helical wrapped GFRP rebar

3 TEST RESULTS AND DATA ANALYSIS

3.1 Load-deflection

The load, P , applied to the tie versus member elongation, δ , is shown in Figures 3a, b. The elongation continuously recorded by the LVDT has been compared with the sum of the elongations obtained by the lectures of the

mechanical extensometer between Demec points. Good agreement between the two measurements is observed.

As shown in Figure 3, the tension response of a RC member can be defined with three different regions. In the pre-crack stage the concrete and reinforcement are acting compositely and, therefore, the global stiffness corresponds to the combination of the two materials stiffness. Once cracking takes place, large increments in member strain are visible, making the specimen's global stiffness very low. When stabilized cracking is attained, and depending on bond deterioration or splitting cracks propagation, the overall specimen response tends to be parallel to the bare bar response.

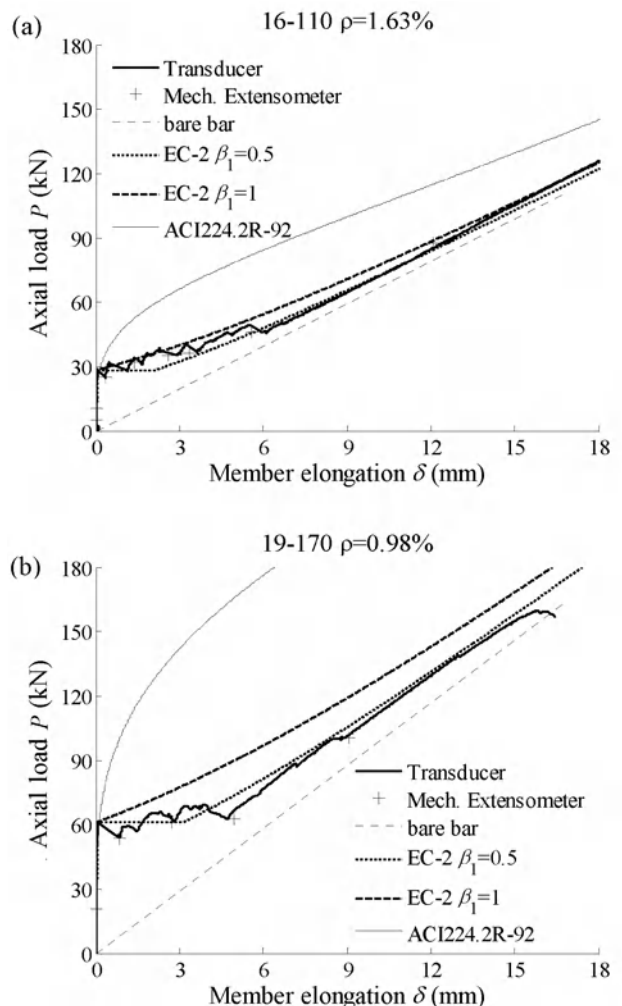


Figure 3 Experimental and predicted load-elongation curves (a) Tie 16-110, (b) Tie 19-170

3.2 Prediction of tension stiffening influence

Guidelines are provided in different code publications like EC-2 (CEN 1992) and ACI224.2R-92 (1992) to predict the general response of reinforced concrete in tension.

ACI224.2R-92 (1992) proposes to study the tension stiffening behaviour for steel RC elements with an analogous approach to that of the effective moment of inertia used in flexural behaviour. Hence, ACI224.2R-92 (1992) proposes an expression for an effective cross-sectional area (A_e) that varies gradually from the gross sectional area (A_g) to the cracked cross sectional area (A_{cr}), as loading of the member increases beyond the cracking point:

$$A_e = \left(\frac{P_{cr}}{P_a}\right)^3 A_g + \left[1 - \left(\frac{P_{cr}}{P_a}\right)^3\right] A_{cr} \leq A_g \quad (1)$$

where P_{cr} = cracking axial load, and P_a = actual axial load. In ACI440.1R-03 (2003), the code for flexural FRP RC elements, a reduction coefficient β_d was used to modify equation for steel reinforced concrete and adapt it to the FRP characteristics. Likewise, several authors have introduced a coefficient in Equation 1, in order to obtain a relationship, for the calculation of the effective cross-sectional area (A_e), similar to that employed for predictions of flexural member deflections (Aiello et al. 2004, Sooriyaarachchi et al. 2005, 2007):

$$A_e = \left(\frac{P_{cr}}{P_a}\right)^3 \beta_d A_g + \left[1 - \left(\frac{P_{cr}}{P_a}\right)^3\right] A_{cr} \leq A_g \quad (2)$$

$$\beta_d = 0.5 \left[\frac{E_{FRP}}{E_s} + 1 \right] \leq 1 \quad (3)$$

where E_{FRP} = FRP elastic modulus, and E_s = steel elastic modulus.

EC-2 (CEN 1992) proposes a method to calculate the average strain in the reinforcement by decreasing the difference between the strain in the crack section and the average strain of the specimen with increasing load. Within this approach, the average strain in the reinforcement, for steel RC structures, is described as follows:

$$\varepsilon_{sm} = \varepsilon_s \left[1 - \beta_1 \beta_2 \left(\frac{\sigma_{cr}}{\sigma_s} \right)^2 \right] \leq \varepsilon_s \quad (4)$$

where β_1 = bond characteristics factor (1 for ribbed and 0.5 for smooth bars), β_2 = loading type factor (1 for first loading and 0.5 for repeated or sustained loading), σ_{cr} = tensile stress in the steel bar at cracked section when the first crack occurs ($\sigma_{cr} = P_{cr}/A_s$), and σ_s and ε_s = stress and strain in the steel bar at the cracked section at the actual load. No specific data is available for β_1 factor of the rebars used in this experimental program. Therefore,

extreme values of $\beta_1=0.5$ and $\beta_1=1$ have been considered.

Although the reduction coefficient β_d , firstly introduced for flexural behaviour of FRP RC structures, has been considered in ACI approach (Eqs 2-3), the prediction of tension stiffening effect clearly underestimates the strain of the FRP RC specimen, as it is observed in Figure 3. This overestimation of the tension stiffening effect is directly linked with the underprediction of computed deflections for flexural elements observed by others in the past. On the contrary, EC-2 (CEN 1992) predictions are closer to experimental results.

3.3 Cracking analysis

Experimental values of mean and maximum crack width, $w_{m,exp}$ and $w_{max,exp}$, measured at the height of the reinforcement once crack maturity was attained, are given in Table 3.

Table 3 Maximum and mean experimental crack width

Tie designation	Crack width	
	Maximum, $w_{max,exp}$ (mm)	Mean, $w_{m,exp}$ (mm)
13_170	2.20	1.95
16_170	4.10	2.20
19_170	2.20	0.98
16_110	2.50	1.51

For comparison purposes, EC-2 (CEN 1992), ACI224.2R-92 (1992) and ACI440.1R-03 (2003) provisions have been considered to predict cracks width (Figure 4). In particular, EC-2 (CEN 1992) calculates the characteristic crack width value as $w_k = \beta_k \varepsilon_{sm} s_{rm}$ where β_k = factor that relates the mean crack width value to design one (equal to 1.7) and s_{rm} = mean crack spacing, defined as:

$$s_{rm} = 50 + 0.25k_1 k_2 \frac{d_b}{\mu_s} \quad (5)$$

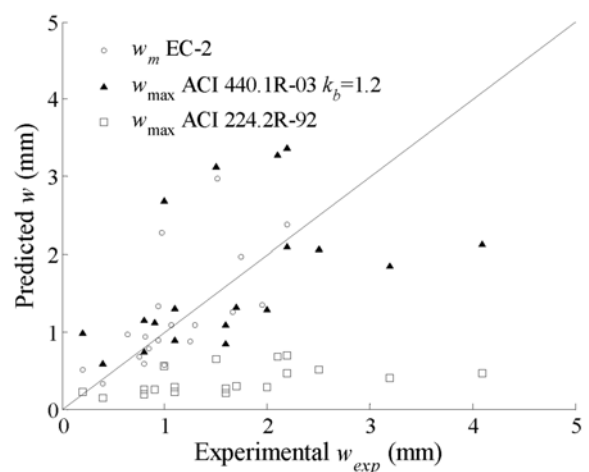


Figure 4 Comparison of experimental and code provisions for mean crack width (w_m) and maximum crack width (w_{max})

where k_1 = bond coefficient, k_2 = loading type coefficient, and μ_s = ratio of the internal reinforcement to the effective area of concrete in tension, $A_{c,eff}$. No indication on how to calculate $A_{c,eff}$ for the case of tension members is available. Therefore, an area surrounding the reinforcing bar with a radius of 3 times the diameter of the bar, previously proposed in Ceroni & Pecce (2009), was assumed in this study. In ACI224.2R-92 (1992) an empirical formula is proposed to evaluate directly the maximum crack width in steel RC ties, without evaluation crack spacing:

$$w_{max} = 0.0145\sigma_s \sqrt[3]{d_c A} \times 10^{-3} \quad (6)$$

where d_c = distance from the center of bar to extreme tension fiber (i.e. concrete cover), and A = area of concrete symmetric with reinforcing steel divided by number of bars. In ACI440.1R-03 (2003) a corrective coefficient k_b is introduced to adapt the formula proposed to calculate the most probable maximum crack width in steel RC elements and account for the differences in bond behaviour in FRP RC elements:

$$w = 2.2\alpha k_b \frac{\sigma_{FRP}}{E_{FRP}} \sqrt[3]{d_c A} \quad (7)$$

where α = ratio of the distance from the neutral axis to extreme tension fiber to the distance from the neutral axis to the center of tensile reinforcement. According to ACI 440.1R-03 (2003) provisions, a design value of $k_b=1.2$ is proposed for those cases where no data is available for a given rebar.

Although being a steel RC code, EC-2 (CEN 1992) provisions for mean crack width ($\beta_k=1$) compare well with experimental data. The lack of a specific coefficient for GFRP RC members in ACI224.2R-92 (1992) code leads to underestimations in the crack width provision, however, although being developed for predicting crack width in flexural FRP RC members, accurate provisions of maximum crack width in GFRP RC ties are obtained with ACI440.1R-03 (2003).

4 CONCLUSIONS

Preliminary results of an experimental program on GFRP-RC members subjected to axial tension have been presented. The following conclusions can be drawn:

- ACI224.2R-92 (1992) approach overestimates tension stiffening effect when predicting load-elongation relationship, even when corrected with β_d factor, previously introduced for flexural study. On the contrary, EC-2 (CEN 1992) provisions follow nearly well the experimental behaviour observed.

- Good mean crack width provisions are obtained with EC-2 (CEN 1992).
- ACI code for tensile members is not accurate in predicting maximum crack widths. However, good predictions are obtained with ACI code for flexural FRP RC members.

5 ACKNOWLEDGEMENTS

The authors acknowledge the support provided by the Spanish Government (Ministerio de Educación y Ciencia), Project BIA-2007-60222. The first author acknowledges the support from the Catalan Government (Generalitat de Catalunya) for the FI pre-doctorate grant supported by European Social funds and for the mobility grant (BE-DGR 2008).

REFERENCES

- ACI 224.2R-92 1992. *Cracking of concrete members in direct tension* (Committee 224). Detroit, Michigan: American Concrete Institute.
- ACI 440.1R-03 2003. *Guide for the design and construction of concrete reinforced with FRP bars* (Committee 440). Detroit, Michigan: American Concrete Institute.
- ACI 440.3R-04 2004. *Guide test methods for fiber-reinforced polymers (FRPs) for reinforcing or strengthening concrete structures* (Committee 440). Detroit, Michigan: American Concrete Institute.
- Aiello, M., Leone, M. & Ombres, L. 2004. Cracking analysis of fibre-reinforced polymer-reinforced concrete tension members. Thomas Telford Services Ltd., *Proceedings of the Institution of Civil Engineers-Structures and Buildings* 157(1):53-62.
- CEN 1992. *Eurocode 2: Design of concrete structures. Part 1-1: General rules and rules for buildings* (BS EN 1992-1-1:1991): European Committee for Standardisation, Brussels.
- Ceroni, F. & Pecce, M. 2009. Design provisions for crack spacing and width in RC elements externally bonded with FRP. *Composites: Part B* 40(1):17-28.
- Sooriyaarachchi, H., Pilakoutas, K. & Byars, E. 2005. Tension Stiffening Behavior of GFRP-Reinforced Concrete. In Shield et al. (ed.), *7th International Symposium on Fiber-Reinforced Polymer (FRP) Reinforcement for Concrete Structures (FRPRCS-7)*, Kansas, 6-9 November 2005.
- Sooriyaarachchi, H., Pilakoutas, K. & Byars, E. 2007. Models for tension stiffening for deflections of GFRP-RC. In Thanasis C. Triantafillou (ed.), *8th International Symposium on Fiber-Reinforced Polymer (FRP) Reinforcement for Concrete Structures (FRPRCS-8)*, Patras, 16-18 July 2007.

Behavior of High-Strength Concrete Beams Reinforced with Different Types of Flexural Reinforcement and Fiber

J. M. Yang, K. H. Min, H. O. Shin & Y. S. Yoon (ysyoon@korea.ac.kr)

School of Civil, Environmental & Architectural Engineering, Korea University, Seoul, Korea

ABSTRACT Six high-strength concrete beam specimens reinforced with different types of flexural reinforcement were constructed and tested. All beam specimens consisted of two layers of flexural reinforcements. Three types of conventional steel bars, CFRP bars, and GFRP bars were used as a flexural reinforcement. While three beam specimens were reinforced with single type of flexural reinforcement, the other three beams were reinforced with combination of two types of flexural reinforcement. In addition, four more high-strength concrete beam specimens were constructed and tested to investigate the influence of fibers on the behavior of FRP bar-reinforced concrete beams. Two types of hooked steel fiber and crimped synthetic fiber were used.

1 INTRODUCTION

Recently, there has been a rapid increase in the use of fiber-reinforced polymer (FRP) bars substituting for conventional steel bars for concrete structures, due to the advantages of noncorrosive characteristic, high strength, and light weight of FRP bars (ACI 2006). Direct substitution with FRP bars, however, is not possible without consideration of the total system response. The elastic modulus of FRP bars is much less than that of steel bars. This low elastic modulus leads to higher deflection and larger crack width in FRP bar-reinforced concrete beams that have an equivalent reinforcement ratio to steel-reinforced concrete beams. In addition, while steel bars behave inelastically after yield strength, FRP bars show perfect elastic behavior up to failure, and fail in a brittle manner. To avoid brittle failure, failure by concrete crushing (over-reinforced beams), which is generally avoided in steel-reinforced concrete design, is preferred in FRP bar-reinforced concrete design (ACI 2006, Bank 2006). However, because concrete itself is a brittle material and high-strength concrete is even more brittle, the ductility of FRP bar-reinforced high-strength concrete beams is much less than that conventionally reinforced concrete beams.

In order to overcome the problems in terms of deformability and ductility of concrete beams reinforced with FRP bars, alternative solutions of hybrid reinforcing with FRP and steel bars, and using fiber reinforced concrete (FRC) were presented in this paper. Hybrid reinforcing involves positioning the FRP bars in the outer layer near the concrete cover in the tensile zone and arranging the steel bars in the inner layer. The steel bars in the inner layer play the part of a control material

for deflection, crack width and ductility, and can be protected from aggressive agents by the large concrete cover thickness after cracking (Aiello 2002). It is now well established that the addition of steel fibers improve the mechanical properties of concrete members. Steel fibers offer increased toughness, durability, and impact resistance, and control initiation and growth of cracks (ACI 1996). Furthermore, because the failure of over-reinforced beams with FRP bars is controlled mainly by the concrete compressive strain, the increased and softened postpeak strain of FRC may highly improve the ductility of FRP beams.

2 EXPERIMENTAL PROGRAM

2.1 Details of test specimens and test setup

Ten high-strength concrete beam specimens reinforced with different types of flexural reinforcement and fiber were constructed and tested. Figure 1 and Table 1 show the details of ten beam specimens. All specimens were 2300 mm long with a rectangular cross section of 230 × 250 mm. These were reinforced with two layers of reinforcement, and the effective depths of the outer layer (d_1) and the inner layer (d_2) were 206 mm and 162 mm, respectively. Each specimen had different combinations of flexural reinforcement of conventional steel bars, CFRP bars, and GFRP bars. Specimens SS, CC series, GG series were each reinforced with a single type of reinforcement and specimens CS, GS, GC were reinforced with two different types of reinforcement. The first letter and the second letter in the specimen names indicate the type of outer and inner layer reinforcement, respectively. The 1.0% by volume of hooked steel fibers were added to specimens CC-ST and GG-ST, and 2.0% by volume

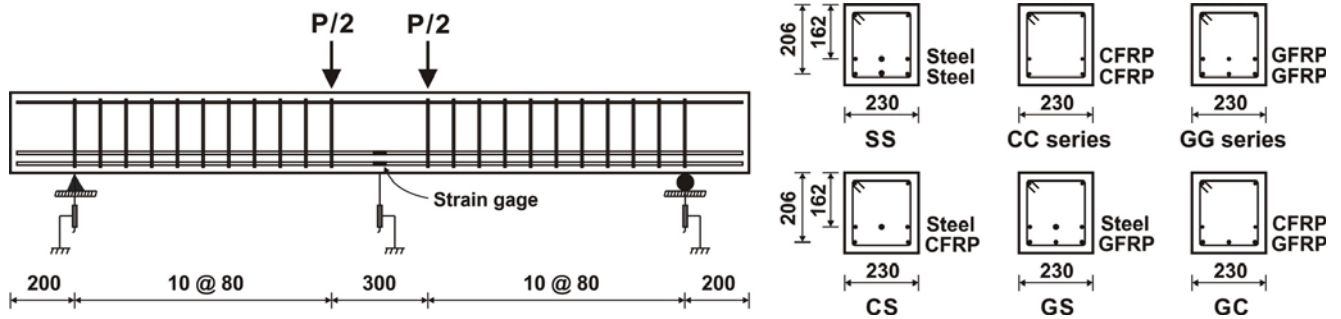


Figure 1 Details of test specimens and test setup (dimensions in mm)

Table 1 Details of test specimens

Specimen	E_{r1} , (GPa)	E_{r2} , (GPa)	A_{r1} , (mm ²)	A_{r2} , (mm ²)	$A_r E_r$, (MN)	Fiber content by volume
SS	200.0	200.0	485	485	194.0	–
CC	146.2	146.2	128	128	37.4	–
CC-SN	146.2	146.2	128	128	37.4	2.0% synthetic
CC-ST	146.2	146.2	128	128	37.4	1.0% steel
GG	48.1	48.1	381	381	36.7	–
GG-SN	48.1	48.1	381	381	36.7	2.0% synthetic
GG-ST	48.1	48.1	381	381	36.7	1.0% steel
CS	146.2	200.0	128	485	115.7	–
GS	48.1	200.0	381	485	115.3	–
GC	48.1	146.2	381	128	37.0	–

of crimped synthetic fibers were added to specimens CC-SN and GG-SN. In order to provide similar nominal flexural strength for all specimens, D10, D13 and D19 steel was used in the steel bar layers, two 9 mm CFRP bars were used in the CFRP bar layers, and three 13 mm GFRP bars were used in the GFRP bar layers. All specimens with FRP bars were designed to fail by concrete crushing to avoid brittle failure. A 25 mm concrete cover was used, and D10 steel bars were used as closed stirrups at 80 mm spacings and as longitudinal compression reinforcements for all specimens.

Four-point static loading was applied by a 500 kN universal testing machine for all specimens, as shown in Figure 1. The loading was applied monotonically in small increments, while the loads, deflections and strains were recorded at each increment. At each load stage, the crack pattern and crack widths were also recorded. The crack widths were measured using a crack width comparator. The midspan deflection and support settlements were measured with linear voltage differential transformers (LVDTs). Electrical resistance strain gages were glued to the center of all flexural reinforcements.

2.2 Material properties

The mechanical properties of the steel reinforcing bars, of which average values of steel bars were determined by testing three random samples for each bar size, and the properties of FRP bars, which were supplied by the manufacturer, are shown in Table 2. In this study, the

manufacturer's guaranteed design properties were used for the FRP bars. Both types were manufactured by Dongwon Construction in Korea.

The bundled type hooked steel fibers and crimped polyolefin synthetic fibers made from polypropylene macro-monofilament were added to the SFRC and SNFRC, respectively, and the properties of these fibers are presented in Table 3.

Table 4 summarizes the material properties of the concrete. The residual strength at net deflection of $L/600$, f^D_{600} , and $L/150$, f^D_{150} , and toughness, T^D_{150} , defined in ASTM C 1609 (ASTM), for steel fiber-reinforced concrete (SFRC) and synthetic fiber-reinforced concrete (SNFRC) are presented in Table 4. The toughness performance level method proposed by Morgan et al. (1995) was also used to determine the toughness of the SFRC and SNFRC. The SFRC and SNFRC were found

Table 2 Properties of steel and FRP bars

Type of reinforcement	Area, (mm ²)	E_r , (GPa)	f_y , (MPa)	f_u , (MPa)
D10 steel	71	200.0	477	594
D13 steel	127	200.0	470	612
D19 steel	287	200.0	469	598
9 mm CFRP bar	64	146.2	–	2130
13 mm GFRP bar	127	48.1	–	941

Table 3 Properties of steel and synthetic bars

Type of fiber	l_f , (mm)	Dimension, (mm ²)	Density, (kg/m ³)	Elastic modulus, (GPa)	Tensile strength, (MPa)	Ultimate elongation, (%)
Steel fiber	30	Φ 0.5	7.85	200.0	1195.5	0.6
Synthetic fiber	40	1.4×0.7	0.91	46.3	470.5	15.3

Table 4 Concrete properties

Concrete	f'_c , (MPa)	f_{sp} , (MPa)	f_r , (MPa)	f^D_{600} , (MPa)	f^D_{150} , (MPa)	T^D_{150} , (Nm)
Plain concrete	75.9	5.62	7.21	–	–	–
SNFRC	89.3	9.03	9.02	5.77	8.40	48.00
SFRC	104.4	9.29	10.39	8.25	2.65	40.00

to have a toughness performance level of IV, based on a design flexural strength of 5.88 MPa.

3 TEST RESULTS AND DISCUSSIONS

3.1 General behavior of test specimens

Figure 2 shows the applied load versus midspan deflection responses, while Table 5 summarizes the loads and midspan deflections at the formation of the first flexural crack as well as the failure mode for all beam specimens. The specimens with fibers showed higher first cracking loads than those without fibers. In particular, the first cracking loads of specimens CC-ST and GG-ST, which were fabricated with SFRC, were twice as high as those of specimens CC and GG, respectively. This indicates the

Table 5 Summary of test results

Specimen	P_{cr} (kN)	Δ_{cr} (mm)	P_u (kN)	Δ_u (mm)	μ_e	Failure mode
SS	26	0.43	198	17.85	6.05	Compression
CC	21	0.68	212	43.82	1.84	Shear compression
CC-SN	27	0.52	218	36.59	1.64	FRP bar rupture
CC-ST	42	0.83	225	36.81	1.84	FRP bar rupture
GG	23	0.67	207	38.85	1.92	Compression
GG-SN	35	0.65	230	50.88	3.24	Compression
GG-ST	39	0.79	259	56.19	3.43	Compression
CS	25	0.61	194	34.03	3.25	Compression
GS	25	0.62	205	28.76	4.10	Compression
GC	22	0.71	203	37.61	1.74	Compression

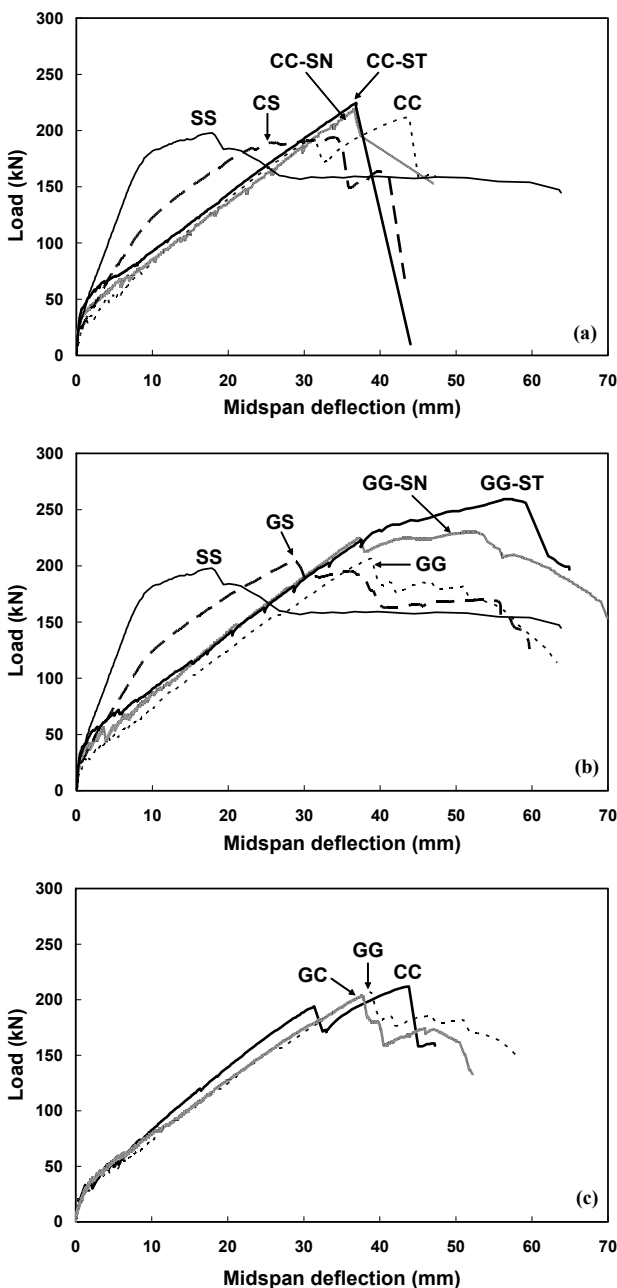


Figure 2 Load versus midspan deflection responses

tensile strength of concrete increased due to the addition of fibers.

After first flexural cracking, the stiffness of the cracked beams was reduced, and each specimen started to behave differently depending on the combination of the flexural reinforcement. The stiffness of specimen SS was the highest after cracking, and was reduced remarkably after general yielding of the steel bars. The post cracking stiffnesses of the CC series and the GG series were much lower than those of specimen SS. This is attributed to the low elastic modulus of FRP bars and the low reinforcement ratio. In addition, the post cracking stiffnesses of the CC series and the GG series were similar due to the similar longitudinal rigidities, $E_r A_r$, which are tabulated in Table 1. The influence of fibers on the post cracking stiffness was negligible. Specimens CS and GS, which were hybrid reinforced with steel and FRP bars, showed better post cracking behavior than specimens CC and GG, respectively, due to the effect of steel bars in the inner layer, but the stiffness was reduced to even lower than the previous stiffness and lower than that of specimens CC and GG after general yielding of steel bars, as can be seen in Figure 2. This result indicates that low stiffness and large deflection of FRP bar-reinforced beams can be controlled by the hybrid reinforcing with steel bars. In the case of the GC, the behavior was not significantly different from the behaviors of the CC series and the GG series, and was more similar to the behavior of the GG because concrete beams are more affected by the outermost layer reinforcements.

The failure behaviors differed significantly depending on the addition of fibers. In the case of the specimens without fibers, the ultimate loads carried by all specimens were almost the same, the specimens failed by the crushing of concrete between the point loads with the exception of specimen CC which failed by the shear compression failure mode, as shown in Table 5. This shear compression failure occurred due to the deep propagation of cracks in the FRP bar-reinforced beams.

The CC series specimens with fibers failed by FRP bar rupture, although all specimens had been designed as over-reinforced beams which lead to concrete compression failure. This can be attributed to the increased ultimate compressive strain of FRC. In research on the stress-strain behavior of FRC in compression, the strain at failure of FRC exhibited a value higher than 0.0035 (Bencardino et al. 2008, Nataraja et al. 1999). This indicates that it is prudent to consider and determine the increased ultimate concrete strain in order to prevent abrupt FRP bar rupture failure when FRP bar-reinforced beams with fibers are designed. The GG series with fibers failed by the crushing of concrete. Specimens GG-SN and GG-ST showed significant inelastic deformations and ductile behavior near failure. This is due to the increased ultimate compressive strain and improved and more softened postpeak behavior of FRC (ACI 1996). The ultimate loads of specimens GG-SN and GG-ST were approximately 11% and 25% higher, respectively, than that of specimen GG.

3.2 Cracking responses

The depth of cracks in specimen SS was very short, while the cracks in specimens CC, GG and GC propagated quite deeply into the compression zone. This indicates that immediately after the formation of the first cracks the neutral axis shifted up very near the top compression fiber of the FRP bar-reinforced beams. Cracks in hybrid reinforced specimens with steel bars, and in fiber reinforced specimens were shallower than those in specimens CC, GG and CG. This indicates that the deep propagation of cracks in the FRP bar-reinforced beams can be restrained by fibers and steel bars. Furthermore, the maximum crack width of FRP bar-reinforced beams was controlled by the addition of fibers and hybrid reinforcing with steel bars.

3.3 Ductility

In order to evaluate the ductility of FRP reinforced members, the ductility index, μ_e , proposed by Naaman & Jeong (1995) was used and presented in Table 5. The ductility index of the FRP bar-reinforced beams was much smaller than that of steel-reinforced beam. However, the low ductility of FRP bar-reinforced beams was improved by the addition of fibers and hybrid reinforcing with fibers. The ductility indexes of specimens CC-SN and CC-ST were either similar or smaller than the ductility index of specimen CC due to the brittle FRP bar rupture failure of specimens CC-SN and CC-ST.

4 CONCLUSIONS

1) The lower stiffness and higher deflection of FRP bar-reinforced beams were controlled and improved by hybrid reinforcing with steel bars.

2) Because of the increased ultimate concrete compressive strain, the GFRP bar-reinforced beams with steel and synthetic fibers displayed inelastic and ductile behavior near the failure, and higher ultimate flexural strength than the beam with no fibers.

3) The steel fibers in concrete and hybrid reinforcing with steel controlled the propagation of cracks and the crack width of FRP-bar reinforced beams.

4) Addition of fibers and hybrid reinforcing with steel bars can be possible methods to overcome the low ductility of FRP bar-reinforced beams.

5 ACKNOWLEDGEMENTS

The work presented in this paper was funded by the Center for Concrete Corea (05-CCT-D11), supported by the Korea Institute of Construction and Transportation Technology Evaluation and Planning (KICTTEP) under the Ministry of Construction and Transportation (MOCT).

PREFERENCES

- ACI committee 440. 2006. Guide for the design and construction of concrete reinforced with FRP bars (ACI 440.1R-06). Farmington Hills, MI: American Concrete Institute.
- ACI committee 544. 1996. Report on fiber reinforced concrete (ACI 544.1R-96). Farmington Hills, MI: American Concrete Institute.
- Aiello M.A. & Ombres L. 2002. Structural performances of concrete beams with hybrid (fiber-reinforced polymer-steel) reinforcements. *Journal of Composites for Construction* 6(2): 133-140.
- ASTM International. 2007. Standard test method for flexural performance of fiber-reinforced concrete (using beam with third-point loading) (ASTM C1609-07). West Conshohocken, PA: ASTM International Standard Worldwide.
- Bank, L.C. 2006. Composites for construction – structural design with FRP materials. Hoboken, NJ: John Wiley & Sons.
- Bencardino F., Rizzuti L., Spadea G. & Swamy R.N. 2008. Stress-strain behavior of steel fiber-reinforced concrete in compression. *Journal of Materials in Civil Engineering* 20(3): 255-263.
- Morgan D.R., Mindess S. & Chen L. 1995. Testing and specifying toughness for fiber reinforced concrete and shotcrete. In Banthia N & Mindess S (ed.), *Fiber-Reinforced Concrete - Modern Developments; Proceedings of 2nd University - Industry Workshop on Fiber-Reinforced Concrete and Other Advanced Composites*, Toronto: 29-50.
- Naaman A.E. & Jeong S.M. 1995. Structural ductility of concrete beams prestressed with FRP tendons, In *Proceedings of the second international RILEM symposium (FRPRCS-2): Non-metallic (FRP) for concrete structures*, Ghent, Belgium: 379-386.
- Nataraja M.C., Dhang N. & Gupta A.P. 1999. Stress strain curve for steel-fiber reinforced concrete under compression. *Cement and Concrete Composites* 21(5-6): 383-390.

Deflection Behaviour of Concrete Beams Reinforced with Different Types of GFRP Bars

S. El-Gamal, B. AbdulRahman, & B. Benmokrane (Brahim.Benmokrane@USherbrooke.ca)
NSERC Research Chair, Department of Civil Eng., University of Sherbrooke, Sherbrooke, Quebec, Canada

ABSTRACT GFRP bars are non noncorrosive reinforcing materials having relatively lower tensile modulus compared to steel. The design of flexural concrete members reinforced with GFRP bars are usually governed by serviceability limits, deflection, and crack width. This paper describes an experimental study conducted to investigate the deflection behavior of concrete beams reinforced with GFRP bars. The bars came from three different manufacturers. A total of 8 beams measuring 4250 mm long \times 200 mm wide \times 400 mm deep were built and tested up to failure under four-point bending. The study's main parameters were reinforcement type (GFRP and steel) and amount (three reinforcement ratios). The midspan deflection of all the beams tested were recorded and compared. The test results were used to assess the equations in different FRP codes and guidelines.

1 INTRODUCTION

GFRP reinforcing bars offer advantages not available with steel reinforcement due to their noncorrosive nature and magnetic transparency. Special considerations should be made in the design of GFRP reinforcing concrete members resulting from the relatively lower modulus of elasticity of GFRP bars compared to steel bars. As a result, GFRP-reinforced concrete members after cracking have relatively less stiffness than steel-reinforced members. Consequently, deflection and crack width calculations under service loads usually govern the design. North American codes and guidelines for designing FRP-reinforced concrete require that deflection be computed. The deflection calculation of flexural members provided in these codes are mainly based on equations derived from linear elastic analysis using an effective moment of inertia, I_e , given by Branson's formula, first published in 1965. Many researchers have suggested different modifications to Branson's equation to make it more suitable for FRP-reinforced concrete members.

This paper presents an experimental investigation into the deflection behavior of concrete beams reinforced with different types and ratios of FRP bars. In addition, the deflection equations provided in CSA S806-2002, ACI 440.1R-2006, and the ACI 440-2010 ballot were evaluated.

2 CURRENT DEFLECTION PROVISIONS

2.1 CAN/CSA S806-02

Clause 8.3.2 in the CAN/CSA S806-02 (CSA S806 2002) states that deflections that occur immediately on

application of load shall be computed by methods based on the integration of curvature at sections along the span. The moment-curvature relation of FRP reinforced concrete members shall be assumed to be tri-linear with the slope of the three segments being $E_c I_g$, zero, and $E_c I_{cr}$. For the case of two-point loading of $P/2$ on a simple span, L , with a shear span, a , the deflection is calculated according to Eq. 1.

$$\delta_{\max} = \frac{PL^3}{48E_c I_{cr}} \left[3 \left(\frac{a}{L} \right) - 4 \left(\frac{a}{L} \right)^3 - 8\eta \left(\frac{L_g}{L} \right)^3 \right] \quad (1a)$$

$$\eta = 1 - \left(\frac{I_{cr}}{I_g} \right) \quad (1b)$$

where δ_{\max} is the midspan deflection (mm), L is the span (mm), a is the shear span (mm), E_c is the modulus of elasticity of concrete (MPa), I_{cr} is the moment of inertia of cracked section transformed to concrete (mm^4), and L_g is the uncracked length (mm).

2.2 ACI 440.1R-06

ACI 440.1R-06 uses an effective moment of inertia formulation, I_e , to compute the deflection of cracked FRP-reinforced-concrete beams and one-way slabs based on an empirical expression originally developed for steel-reinforced concrete. The procedure entails calculating a uniform moment of inertia throughout the beam length and uses deflection equations derived from linear elastic analysis. The effective moment of inertia, I_e , is based on semi-empirical considerations and, despite some doubt about its applicability to conventional reinforced-concrete members subjected to complex

loading and boundary conditions, it has yielded satisfactory results in most practical applications over the years. ACI 440.1R-06 uses Eq. 2 to calculate the deflection of FRP-reinforced concrete members:

$$I_e = \left(\frac{M_{cr}}{M_a} \right)^3 \beta_d I_g + \left[1 - \left(\frac{M_{cr}}{M_a} \right)^3 \right] I_{cr} \quad (2a)$$

$$\beta_d = \frac{1}{5} \left(\frac{\rho_f}{\rho_{fb}} \right) \leq 1 \quad (2b)$$

where I_e is the effective moment of inertia (mm^4), M_{cr} is the cracking moment (N mm), M_a is the applied moment (N mm), I_g is the moment of inertia of gross section (mm^4), and ρ_f and ρ_{fb} are the actual and balanced reinforcement ratio, respectively.

2.3 ACI 440 2010 ballot

Based on the work of Bischoff and Scanlon (2007), a ballot taken by ACI 440 Committee (February 2010) proposed using Eq. 3 to calculate deflection:

$$I_e = \frac{I_{cr}}{1 - \gamma \left(\frac{M_{cr}}{M_a} \right)^2 \left[1 - \frac{I_{cr}}{I_g} \right]} \leq I_g \quad (3a)$$

$$\gamma = 1.72 - 0.72(M_{cr} / M_a) \quad (3b)$$

All parameters are as in Eq. 2.

2.4 Materials

Three different types of GFRP bars referred to as GFRP-1 (V-ROD Standard) (#5, #6, and #7), GFRP-2 (#5) (Aslan-100) and GFRP-3 (#5) (Combar),—manufactured by Pultrall, Hughes Brothers, and Schöck respectively—were used. Figure 1 shows the three types of GFRP bars used in this study. No. 15M steel bars were used in one beam for comparison.



Figure 1 The three types of GFRP bars used in the study

The mechanical properties of the FRP reinforcement bars were determined by tensile testing of representative specimens in accordance with ACI 440 3R-04. Table 1 summarizes these properties.

Based on the values of modulus of elasticity, the three tested types of GFRP bars were classified as Grade I (GFRP-1 and GFRP-2) and Grade III (GFRP-3) according to the new CSA S807-09 (2010) specification for fibre-reinforced polymers. Grade I requires a minimum modulus of elasticity of 40 GPa, while Grade III requires 60 GPa.

Table 1 Mechanical properties of the reinforcing bars

Bar Type	db	Area	Modulus of Elasticity	Guaranteed Strength ⁺
	(mm)	(mm ²)	(GPa)	(MPa)
Steel	15M	16	200	$f_y^* = 453$
	#5	16	199	684
GFRP-1	#6	19	284	656
	#7	22	387	693
GFRP-2	#5	16	199	660
GFRP-3	#5	16	199	1130

^{*} f_y is the yield strength of the steel bars.

⁺ Average tensile strength – 3 times the standard deviation.

2.5 Beam specimens and test setup

Eight full-scale concrete beams, measuring 4250 mm long × 200 mm wide × 400 mm deep (see Figure 1), were constructed. All the beams were reinforced in the compression side with two steel bars (ϕ 10 mm). On the tension side, the beams were reinforced with different types and numbers of reinforcing bars. The beams were divided into four groups. Each group was designed to investigate one parameter among 1) bar type, 2) reinforcement ratio with a similar bar diameter and different spacing, 3) reinforcement ratio with different diameters and similar spacing, and 4) beams of similar axial stiffness (see Table 2).

Table 2 Test matrix

Group	Parameter	ID	Type of Bars	No. of Bars	Area (mm ²)	ρ (%)
1	Type of reinf.	G-V-3#5	GFRP-1	3#5	594	0.84
		G-A-3#5	GFRP-2	3#5	594	0.84
		G-Co-3#5	GFRP-3	3#5	594	0.84
		St-3#5	Steel	3#5	600	0.84
2	Reinf. Ratio (same diameter)	G-V-2#5	GFRP-1	2#5	396	0.56
		G-V-3#5		3#5	594	0.84
		G-V-4#5		4#5	792	1.12
3	Reinf. Ratio (different diameters)	G-V-2#5	GFRP-1	2#5	396	0.56
		G-V-2#6		2#6	570	0.81
		G-V-2#7		2#7	776	1.11
4	Similar axial stiffness	G-V-3#5	GFRP-1	3#5	594	0.84
		G-V-2#6		2#6	570	0.81
		G-V-4#5		4#5	792	1.12
		G-V-2#7		2#7	776	1.11

Five linear variable displacement transducers (LVDTs) were installed on each beam to measure deflections at different beam locations (Figure 2). In addition, one high-accuracy LVDT was installed at the position of the first crack to measure crack width. Furthermore, several electrical-resistance strain gauges were used to measure

strain in the reinforcing bars and at the top surface of the concrete.

All beams were tested under four-point bending. The load was monotonically applied with a displacement control rate of 1.2 mm/min. During loading, crack formation on the side surface of the deck slabs were marked and recorded. Figure 2 illustrates the test setup, while Figure 3 is a photo of a beam during testing.

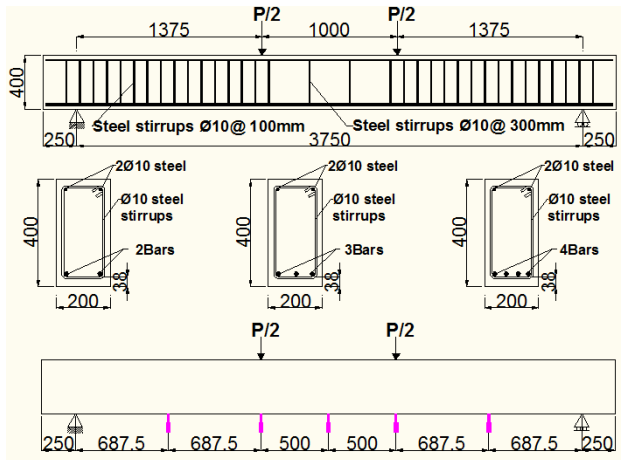


Figure 2 Dimensions and instrumentation of tested beams



Figure 3 View of beam during testing (Beam G-V-2#7)

3 TEST RESULTS AND DISCUSSION

3.1 Load–deflection curves

The experimental load to midspan deflection curves of the steel and GFRP reinforced concrete beams are presented in Figures 4 to 7. Each curve represents the average of two deflection readings obtained from two LVDTs at beam midspan. The load–midspan deflections curves were bilinear for all FRP-reinforced beams. The first part of the curve up to cracking represents the behavior of the uncracked beams. The second part represents the behavior of the cracked beams with reduced stiffness. The cracking loads for all FRP-reinforced beams ranged from 15 to 20 kN. The value was slightly higher for the steel-reinforced beam: 26.3 kN.

For the beams in group 1, the GFRP-reinforced

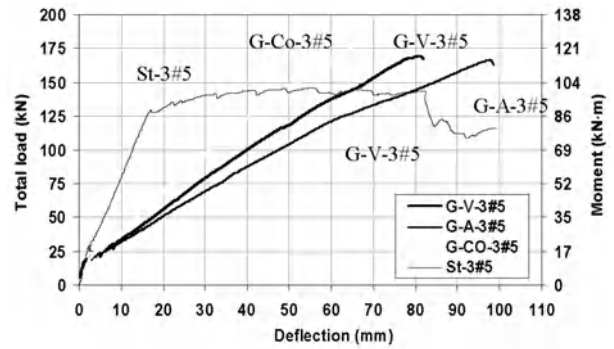


Figure 4 Load–midspan deflection of beams in group 1

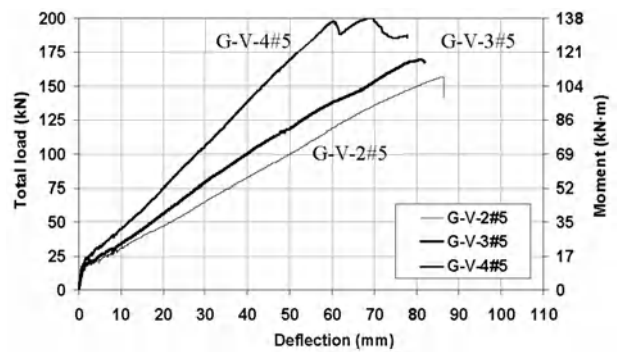


Figure 5 Load–midspan deflection of beams in group 2

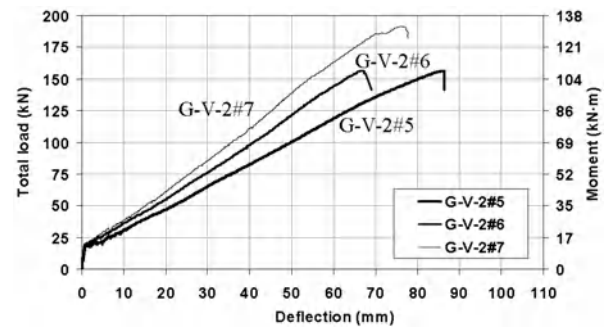


Figure 6 Load–midspan deflection of beams in group 3

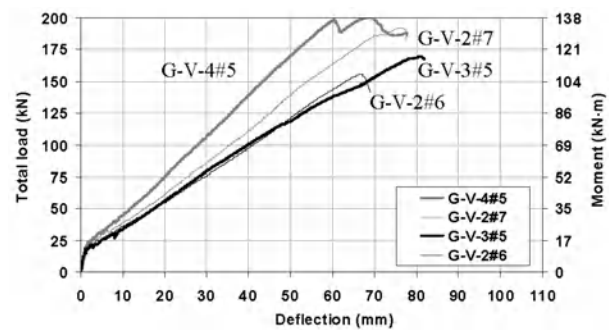


Figure 7 Load–midspan deflection of beams in group 4

concrete beams evidenced wider cracks than the steel-reinforced concrete beam. Consequently they exhibited greater midspan deflections (see Figure 4). It can also be seen that, as the modulus of elasticity of the GFRP bars decreased, the reinforcement’s axial stiffness decreased, leading to increased midspan deflections. At 35 kN—about twice the cracking load—the midspan deflections

were 3.6, 11.7, 10.6, and 8.8 mm for beams St-3#5, G-A-3#5, G-V-3#5, and G-Co-3#5, respectively.

Figure 5 and 6 show that, for the same type of bars, the midspan deflection increased as the reinforcement ratio decreased. Increasing the reinforcement ratio, however, increased the ultimate capacity of the beams.

At about twice the cracking load, increasing the tensile reinforcement from 2 #5 bars to 3 and 4 #5 bars decreased the midspan deflection from 12.5 to 10.6 and to 6.3 mm, respectively. For the beams in group 3, increasing the reinforcement from 2 #5 bars to 2 #6 and to 2 #7 bars decreased the midspan deflection from 12.5 to 9.5 and 8.2 mm, respectively. Figure 7 shows a comparison between midspan deflections of two pairs of beams whose tension reinforcement evidenced similar axial stiffness (G-V-3#5 and G-V-2#6) and (G-V-4#5 and G-V-2#7). Beams G-V-3#5 and G-V-2#6 had similar load–midspan deflection up to failure. Beam G-V-4#5, however, showed less midspan deflection than beam G-V-2#7. This indicates that using more bars of smaller diameter was more efficient than a smaller number of larger bars. This phenomenon could be explained by enhanced bond, better cracking performance by lowering reinforcement spacing, and the higher tension stiffening provided by FRP bars of smaller diameter. These factors contributed to beam stiffness, which was evidenced in lower mid-span deflection.

3.2 Predicted Deflections

Table 3 shows a comparison between the midspan deflections of the tested beams and those predicted from Eqs. 1, 2, and 3. The accuracy of the calculated cracking moment, M_{cr} , is key to the accuracy of the deflection calculations. The controlling variable for predicting cracking moment is the modulus of rupture of concrete, f_r . The modulus of rupture used to calculate the M_{cr} in Eqs. 1, 2, and 3 was taken from the corresponding code or guideline as given below in Eq. (4):

$$\text{For Eq. 1, } f_r = 0.6\lambda\sqrt{f'_c} \quad (4a)$$

$$\text{For Eqs. 2 and 3, } f_r = 0.62\lambda\sqrt{f'_c} \quad (4b)$$

where f_r is the modulus of rupture (MPa); f'_c is the concrete compressive strength (MPa); and λ is a factor accounting for concrete density. For normal-density concrete, $\lambda = 1$.

The moment due to beam self-weight (3.17 kN·m) was included in the analysis. Table 3 shows that, at 1.2 M_{cr} (applied moment right after cracking) and at 2.0 M_{cr} (around the service-load level), Eq. 1 (the CSA/S806 equation) gave very good yet conservative predictions of deflection compared to the measured values. Equations 2 and 3 (the current ACI 440.1R-06 equation and that proposed by ACI 440), however, underestimated deflection at 1.2 M_{cr} and 2.0 M_{cr} .

Table 3 Experimental and predicted deflections

Beam ID	Measured Midspan Deflection, (mm)		Predicted Midspan Deflection, (mm)					
	Deflection, (mm)		Eq.1 (Pred./Exp.)		Eq.2 (Pred./Exp.)		Eq.3 (Pred./Exp.)	
	1.2 M_{cr}	2 M_{cr}	1.2 M_{cr}	2 M_{cr}	1.2 M_{cr}	2 M_{cr}	1.2 M_{cr}	2 M_{cr}
G-V-3#5	8.5	17.2	9.1 (1.07)	17.5 (1.02)	5.9 (0.69)	15.3 (0.89)	3.95 (0.46)	13.17 (0.77)
G-A-3#5	8.7	19.3	10.1 (1.16)	19.5 (1.01)	5.6 (0.64)	16.2 (0.83)	4.31 (0.50)	14.6 (0.76)
G-Co-3#5	6.6	13.7	6.9 (1.05)	13.3 (0.97)	3.3 (0.5)	10.4 (0.76)	3.18 (0.48)	10.12 (0.74)
G-V-2#5	9.7	21.5	13.0 (1.34)	25.2 (1.17)	8.7 (0.90)	22.3 (1.04)	5.36 (0.55)	18.73 (0.87)
G-V-4#5	4.6	11.1	6.1 (1.32)	13.3 (1.20)	3.9 (0.85)	11.2 (1.01)	4.31 (0.94)	9.53 (0.86)
G-V-2#6	6.9	17.3	8.6 (1.24)	17.8 (1.03)	5.3 (0.77)	15.0 (0.87)	2.71 (0.39)	12.47 (0.72)
G-V-2#7	5.6	15.0	6.7 (1.19)	13.7 (0.91)	3.9 (0.70)	11.5 (0.77)	2.27 (0.41)	9.73 (0.65)
Average (Pred./Exp.)			1.19	1.04	0.72	0.88	0.53	0.77

* For comparison, M_{cr} was taken as the average experimental value from all beams (17 kN·m – without $M_{self\ weight}$).

4 CONCLUSIONS

The use of smaller-diameter GFRP bars yielded better deflection enhancement than larger-diameter bars for the same reinforcement ratio. Higher beam stiffness was observed when increasing the reinforcement ratio, either by using more bars or larger-diameter bars. In terms of deflection prediction, CAN/CSA S806-02 showed very good agreement with the experimental results for the three types of GFRP bars. Based on the comparison at 1.2 M_{cr} and 2.0 M_{cr} , both ACI.440.1R-06 and ACI 440 ballot underestimated the deflection values, although the former gave a better prediction.

REFERENCES

- ACI 2006. ACI 440.1R-06: Guide for the design and construction of concrete reinforced with FRP bars, American Concrete Institute, Farmington Hills, Michigan, USA.
- CSA 2002. Standard CAN/CSA-S806-02: Design and Construction of Building Components with Fibre-Reinforced Polymers, Canadian Standards Association, Toronto, Ontario.
- CSA 2010. Standard CAN/CSA-S807-09: Specification for Fibre-Reinforced Polymers, Canadian Standards Association, Toronto, Ontario.
- Bischoff, P.H., and Scanlon, A. 2007. Effective Moment of Inertia for Calculating Deflections of Concrete Members Containing Steel Reinforcement and FRP Reinforcement, ACI Structural Journal, V. 104, No. 1, pp. 68–75.

Behavior of Continuous Concrete Beams Reinforced with FRP Bars

Mostafa El-Mogy, Amr El-Ragaby & Ehab El-Salakawy (ehab_elsalakawy@umanitoba.ca)

Department of Civil Engineering, University of Manitoba, Winnipeg, Manitoba, Canada

ABSTRACT Continuous concrete beams are commonly used elements in structures such as parking garages and overpasses which might be exposed to extreme weather conditions and the application of de-icing salts. Therefore, the use of the non-corrodible fiber reinforced polymer (FRP) bars in these types of structures is beneficial. However, due to the linear-elastic behavior of FRP materials up to failure, the ability of such materials to redistribute loads and moments in continuous beams is questionable. To date, unlike simply supported structures, very few experimental studies investigated the behavior of continuous concrete beams reinforced with FRP bars. Due to the lack of research, recently published design guidelines for FRP-reinforced structures provided limited provisions regarding continuous beams. The objectives of this research are to investigate the behavior of continuous concrete beams reinforced with carbon and glass FRP bars and provide design guidelines to predict the failure load and failure location. This paper presents the experimental results of two reinforced concrete beams with rectangular cross section of 200×300 mm continuous over two spans of 2800 mm each. One beam was reinforced with CFRP longitudinal bars while the other reinforced with GFRP bars. Both beams were reinforced with steel stirrups and provided with different reinforcement configurations at critical sections. Beams were tested under concentrated monotonic loads applied at the mid-point of each span. It is concluded that the FRP-reinforced concrete beams were able to redistribute the connecting moment over the intermediate support. Also, the Canadian code CSA-S806-02 could reasonably predict the failure load of the tested beams; however, it fails to predict the failure location.

1 INTRODUCTION

Statically indeterminate elements such as continuous beams are common in structures that might be exposed to harsh weathering and the use of deicing salts. Using FRP reinforcement in such structures is a viable alternative to traditional steel to overcome the corrosion problems. In general, steel-reinforced statically indeterminate beams are capable of redistributing bending moment between critical sections. Such distribution gives the structure a favorable ductile behavior and ample warnings before failure. Due to the linear-elastic behavior of FRP materials up to failure, the ability of FRP-reinforced continuous concrete beams to redistribute moments needs to be investigated.

2 BACKGROUND

In the last ten years, extensive research studied the behavior of simply-supported concrete beams reinforced with FRP (Grace et al. 1998; Toutanji and Saafi 2000; Vijay and GangaRao 2001). On the other hand, very limited number of studies investigated the behavior of FRP-reinforced continuous concrete beams. These previous experimental and analytical studies showed signs of moment redistribution in continuous beams

reinforced with FRP. Grace et al. (1998) reported experimental results of seven continuous concrete beams with T-section. The specimens were reinforced with different combinations of steel, glass FRP (GFRP) and carbon FRP (CFRP) for both longitudinal and shear reinforcement. It was concluded that FRP-reinforced beams demonstrated similar load capacity as their steel-reinforced counterparts; however, the failure modes and ductility were different. Also, Razaqpur and Mostofinejad (1999) presented experimental results of four continuous concrete beams reinforced with CFRP. The research concluded that section over-reinforced with FRP bars in continuous beams exhibit a semi-ductile behavior. Moreover, Habeeb and Ashour (2008) introduced experimental results of three GFRP-reinforced continuous concrete beams with different reinforcement ratios. Signs of moment redistribution were observed. On the analytical side, Gravina and Smith (2008) presented a theoretical study that investigates the flexural behavior of statically indeterminate FRP-reinforced concrete beams. The authors developed a local deformation model to predict the bending moment distribution, flexural cracks, crack spacing and crack width. The theoretical results were found to be dependent on the bond characteristics of the FRP bars and the

surrounding concrete.

3 EXPERIMENTAL PROGRAM

3.1 Test specimens

Two reinforced concrete beams continuous over two spans were tested in flexure. Beam CS1 was reinforced with top and bottom longitudinal CFRP bars while beam GS2 was reinforced with GFRP bars. The beams were 6.0 m long with a rectangular cross-section of 200 mm width and 300 mm depth. The beams were continuously supported over two equal spans " l " of 2800 mm each as shown in Figure 1. As part of the same project, a similar steel-reinforced control beam was tested and reported by El-Mogy et al. (2009).

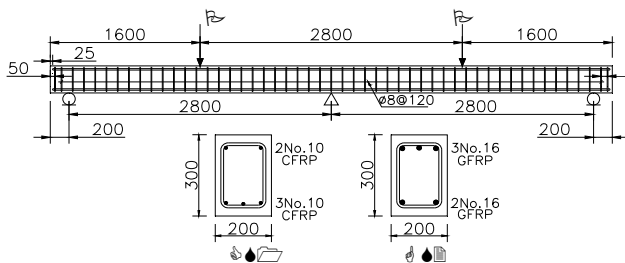


Figure 1 Details of tested beams

Both beams were designed to achieve similar failure load capacity in flexure. The tested beams were designed to have compression failure at both critical sections as recommended by the CSA/S806-02 code (CSA 2002). Therefore, both mid-span and middle support sections were provided with reinforcement ratios higher than the balanced reinforcement ratio (ρ_b) as show in Table 1.

Table 1 Reinforcement details of the tested beams

Beam	Bar type	Top reinforcement		Bottom reinforcement		ρ_b^* (%)
		Bars	Ratio(%)	Bars	Ratio(%)	
CS1	CFRP	2 No.10	0.28	3 No.10	0.42	0.22
GS2	GFRP	3 No.16	1.18	2 No.16	0.79	0.47

* ρ_b is the balanced reinforcement ratio.

For the loading configuration used in this study, the connecting moment over the middle support and the mid-span moment based on elastic analysis are $0.188Pl$ and $0.156Pl$ respectively. It can be seen that moment over middle support is higher than that at mid-span. Beam GS2 was designed to satisfy the elastic moment distribution by providing reinforcement ratio at middle support higher than mid-span. On the other hand, beam CS1 was designed assuming 20% redistribution of middle support moment into mid span. This resulted in changing the design moment to be $0.15Pl$ and $0.175Pl$ for the sections at middle support and mid-span, respectively. Therefore, the flexural reinforcement in

this beam was designed to provide flexural strength at mid-span higher than middle support considering the moment redistribution. Table 1 shows the provided top and bottom reinforcement at critical sections of the tested beams. Both beams were provided with 8-mm diameter steel stirrups spaced at 120 mm all over the entire length of the beam.

3.2 Materials properties

Table 2 lists the mechanical properties of the reinforcing bars as determined by tensile tests on representative specimens in accordance with ACI 440.3R-04 (ACI Committee 440 2004). It should be mentioned here that some of the experimentally obtained material properties in Table 2 are different from those provided by the manufacturer and used in the design. The nominal tensile strength and associated ultimate strain for CFRP bars according to the manufacturer were 1590 MPa and 0.0128 respectively. Based on compressive and splitting testing on standard concrete cylinders, the used concrete had an average compressive and tensile strengths of 26 MPa and 2.7 MPa, respectively.

Table 2 Mechanical properties of the reinforcing bars used in this study.

Bar Type	Bar Diameter (mm)	Bar Area (mm ²)	Modulus of Elasticity (GPa)	Tensile Strength (MPa)	Ultimate Strain (%)
Stirrups	8	49.4	190	$f_y = 300^*$	$\epsilon_y = 0.0016^*$
GFRP	15.9	198	46±1	731±9	0.016± 0.0005
CFRP	9.5	71	116±2	1388±62	0.012± 0.0007

* f_y and ϵ_y is the yield stresses and yield strain respectively.

3.3 Instrumentations and Test set-up

The tested beams had two equal spans supported on one hinged and two roller supports in the middle and both ends respectively. Monotonic concentrated load was applied at mid-point of both spans using a 1000-kN hydraulic actuator and a rigid steel spreader beam. The end reactions were measured using two load cells at the end-supports. Deflection was measured, using linear variable differential transformers (LVDTs), at three different locations in each span, at one-quarter, mid-point and three-quarters of the span length. To measure the strain at critical locations, 6-mm gauge length electrical strain gauges were attached to the top and bottom longitudinal reinforcement at both positive and negative moment regions. Data was electronically recorded during the test using a data acquisition system monitored by a computer.

4 RESULTS AND DISCUSSIONS

4.1 General behavior and modes of failure

It was observed during testing of both beams that first

cracks were always vertical flexural cracks at the middle support section followed by similar cracks at mid-span. New cracks continued to form while existing ones propagated vertically toward the compression zone up to approximately 50% of the maximum load, then the rate of formation of new cracks significantly decreases at higher loading stages. At this stage, existing cracks grow wider and deeper, and then become inclined following compression stresses trajectories, and finally the beams failed in shear. The failure mode of beam CS1 was compression failure at both middle support and mid-span sections immediately followed by bar rupture at middle support. Beam GS2 failed by concrete crushing at mid-span and the final shear failure occurred close to the mid-span section. This is because the mid-span section had a flexural capacity less than middle support section. The failure shapes of all tested beams are shown in Figure 2.



a- Beam CS1



b- Beam GS2

Figure 2 Failure shapes of tested beams

4.2 Cracking pattern and strains in reinforcement

The first crack in beam CS1 was observed in the vicinity of the middle support at a load of 20 kN followed immediately by a crack at the mid-span. Very few but wider cracks were observed at the middle support section indicating poor bond strength between the used No.10 CFRP bars and surrounding concrete. The first crack in beam GS2 was observed at the middle support at 13 kN, followed by a crack at mid-span at 20 kN. In both beams, the number of cracks in positive and negative moment regions increased as the load increased and the spacing of these cracks ranged between 130 and 260 mm. At high loading stages close to failure, diagonal cracks between middle support and mid-span propagated towards the loading point. Figure 3 shows the measured tensile strains in the longitudinal reinforcement against the applied load for the test beams. It can be seen that the strains in FRP bars increased suddenly after concrete cracking. It can be also observed that the section at middle support, in all tested beams, cracked before the mid-span section. This is due to the

higher elastic moment at the middle support section. It can also be noted that maximum tensile strains in FRP bars in beam GS2 did not reach the ultimate value as this beam was designed as over reinforced to have concrete crushing failure. On the other hand, it can be seen that CFRP bars in tension at middle support section reached the ultimate strain value listed in Table 2. This is due to the fact that this beam became under-reinforced considering the actual properties of CFRP bars, obtained from standard tensile tests carried in the lab, which were less than the properties provided by the manufacture that were used in the design .

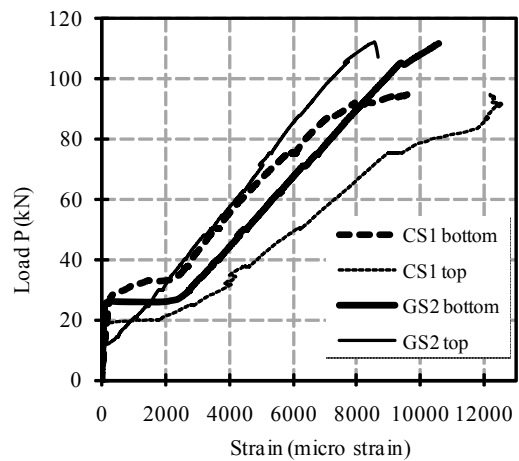


Figure 3 Load-strain relation for tested beams

4.3 Load-deflection response

The relation between the applied load at each span and the recorded deflection at mid-span is shown in Figure 4.

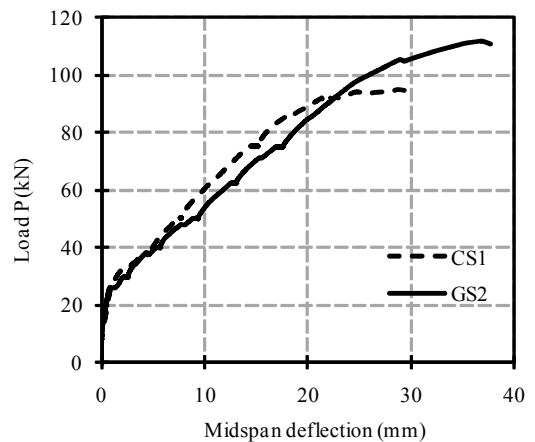


Figure 4 Load-deflection response of the tested beams

The tested beams demonstrated linear load-deflection behavior before cracking. Upon cracking, stiffness was reduced however the beams maintained a post-cracking linear behavior too. It can also be observed that beam GS2 demonstrated higher deflections compared to CS1. This is because beam CS1 had positive FRP reinforcement

with axial stiffness (EA) 1.4 times higher than beam GS2. Even though both beams were designed to have the same failure load, beam CS1 could not develop the expected ultimate flexural capacity at the negative moment region. This may be attributed to significant slippage between the top CFRP bars and the surrounding concrete.

4.4 Load redistribution

As the beams were statically indeterminate, the measured reactions from load cells were used to calculate the actual internal forces at any location along the length of the specimens. Figure 5 shows the variation of end reactions versus the applied load for all tested beams. The elastic end reaction with the value $R = 0.312 P$ was also plotted to evaluate the amount of load redistribution, where R is the end support reaction. For beam CS1, signs of load redistribution were observed from the negative moment at the middle support section to the mid-span as the actual end reactions were higher than elastic reactions at the same load. This might be attributed to the difference in stiffness between mid-span and middle support sections. As the reinforcement ratio in mid-span section is higher than that in middle support section, stiffness of the beam cross-section at mid-span is higher. Beam GS2 demonstrated load redistribution from the mid-span to the middle support section. This is due to the higher stiffness at middle support section provided by the higher reinforcement ratio compared to the mid-span section.

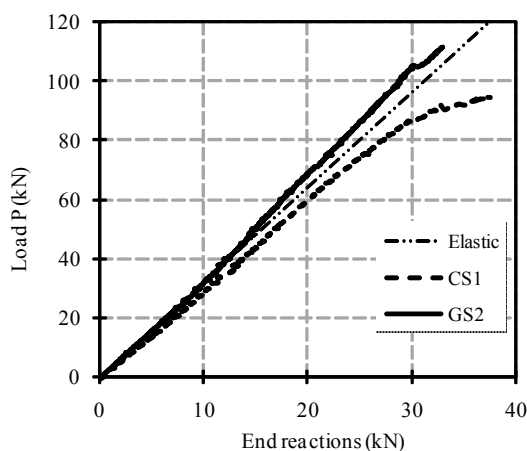


Figure 5 Load-end reactions relationship for the tested beams

5 CONCLUSIONS

Based on the results of this investigation, the following conclusions can be drawn:

(1) Using reinforcement configuration that allows for moment redistribution in FRP-reinforced continuous beams had a positive effect on deflection;

(2) Continuous beams reinforced with FRP bars showed ample warnings before failure in the form of

large deflections and wide cracks;

(3) The CFRP reinforced beam (CS1) demonstrated redistribution of the connecting bending moment, which exceeded the flexural strength at middle support, to the mid-span section.

(4) The Canadian code CSA-S806-02 could reasonably predict the failure load for the GFRP-reinforced beam (GS2) provided with reinforcement configuration satisfying the elastic moment distribution.

6 ACKNOWLEDGEMENT

The authors wish to express their gratitude and sincere appreciation for the financial support received from the Natural Science and Engineering Research Council of Canada (NSERC), through Canada Research Chairs program. The help received from the technical staff of the McQuade Heavy Structural Laboratory in the department of civil engineering at the University of Manitoba is also acknowledged.

REFERENCES

- ACI Committee 440. 2004. Guide Test Methods for Fiber Reinforced Polymers (FRPs) for Reinforcing or Strengthening Concrete Structures. ACI 440.3R-04, American Concrete Institute, Farmington Hills, Mich., 40 p.
- CSA. 2002. Design and construction of building components with fibre-reinforced polymers. *CSA Standard S806-02*, Canadian Standards Association, Rexdale (Toronto), Ontario, Canada, 177 p.
- El-Mogy, M., El-Ragaby, A. and El-Salakawy, E.F. (2009). Behaviour of Continuous Beams Reinforced with GFRP Bars and Stirrups. Proceedings on CD-ROM, Asian-Pacific Conference on FRP in Structures, Seoul, Korea, December 9-11, pp. 331-336.
- Grace, N. F., Soliman, A. K., Abdel-Sayed, G. and Saleh, K. R. 1998. Behavior and Ductility of Simple and Continuous FRP Reinforced Beams. *ASCE Journal of composites for construction*, 2(4), 186-194.
- Gravina, R.J. and Smith, S. T. 2008. Flexural behaviour of indeterminate concrete beams reinforced with FRP bars. *Journal of Engineering Structures*, 30(9), 2370-2380.
- Habeeb, M. N. and Ashour, A. F. 2008. Flexural Behavior of Continuous GFRP Reinforced Concrete Beams. *ASCE journal of composites for construction*, 12(2), 115-124.
- Razaqpur, A. G. and Mostofinejad, D. 1999. Experimental Study for Shear Behavior of Continuous Beams Reinforced with Carbon Fiber Reinforced Polymer. *Fiber Reinforced Polymer Reinforcement for Reinforced Concrete Structures*, Proceedings of the Fourth International Symposium, 169-178.
- Toutanji, H. A. and Saafi, M. 2000. Flexural Behaviour of Concrete Beams Reinforced with Glass Fiber-Reinforced Polymer (GFRP) Bars. *ACI structural journal*, 97(5), 712-719.
- Vijay, P. V. and GangaRao, H. V. 2001. Bending Behaviour and Deformability of Glass Fiber-Reinforced Polymer Reinforced Concrete Members. *ACI structural journal*, 98(6), 834-842.

Testing of Large-Scale Two-Way Concrete Slabs Reinforced with GFRP Bars

C. Dulude, E. Ahmed, S. El-Gamal & B. Benmokrane (Brahim.Benmokrane@USherbrooke.ca)

NSERC Research Chair, Department of Civil Engineering, University of Sherbrooke, Sherbrooke, Quebec, Canada

ABSTRACT Few studies were conducted to investigate the structural behavior of GFRP-reinforced concrete two-way slabs. This paper presents preliminary results of an extended research project aims to developing the FRP technology reinforcing bar for parking garage structures and to introducing design guidelines for such structures. The results of five full-scale isolated interior parking flat slabs which are part of a 20-specimen experimental program are presented and discussed. Four slabs were reinforced with GFRP bars and one reference slab was reinforced with steel. The test parameters are: (i) reinforcement type and ratio; (ii) slab thickness; (iii) column size; and (iv) compressive reinforcement. The test results showed that there was no significant difference between the specimens in term of general behavior and mode of failure.

1 INTRODUCTION

In North America, most reinforced concrete parking garage structures are constructed using flat slab systems to minimize the height and facilitate the construction of such structures. Design of such structures with non-corrosive reinforcement is now of interest due to the need to reduce the deterioration and repairing costs of steel reinforced ones. However, few studies have investigated the punching shear of two-way slabs reinforced with GFRP bars (Razaqpur et al. 1995; El-Ghandour et al. 1999, 2003; Ospina et al. 2003; Hussein et al. 2004; Zaghoul and Razaqpur 2004; Zhang et al. 2005; Lee et al. 2009). Thus, through this investigation, the main objective is to develop the FRP composite reinforcing bar technology to the parking structures and to provide design guidelines and recommendations for such structures. Besides, the CAN/CSA S806 is being updated and there is a proposed equation developed by Razaqpur (2009) for calculating the punching strength of GFRP-RC two-way slabs. The accuracy of this equation will be evaluated considering the experimental results of this study.

This paper presents results of five full-scale two-way slabs reinforced with GFRP and steel bars. Those slabs are part of a 20-slab experimental program which is planned to investigate the effect of the following parameters on the punching behavior: (i) the reinforcement type and ratio; (ii) the concrete strength; (iii) the slab thickness; (iv) the column size; (v) the compressive reinforcement effect; and (vi) shear reinforcement. The results will contribute to using the GFRP bar technology in three parking garages in Quebec (Canada) in 2010.

2 EXPERIMENTAL PROGRAM

2.1 Test specimen

The test parameters of the five slabs presented in this paper are: (i) the reinforcement type (steel or GFRP bars); (ii) the column size (300×300 mm or 450×450 mm); (iii) the reinforcement ratio (0.34 to 1.66%); (iv) the slab thickness (200 or 350 mm) and (v) the compressive reinforcement effect. Four specimens reinforced with GFRP bars and one reference specimen reinforced with steel bars were constructed and tested. The slabs were reinforced with sand-coated GFRP bars of the properties presented in Table 1. The dimensions of the slabs were 2.5×2.5 m and a column stub extended 300 mm above and below the slab. The test specimen properties are summarized in Table 2. The slab specimens were labeled by a letter denotes the reinforcement type (G for GFRP and S for steel bars) followed by the column size (300 or 450 mm), the slab reinforcement (No. of bars and diameter) and ended by the letter “B” when the slab was provided with bottom reinforcement (four GFRP bars No. 25 in each direction) or by the letter “T” when the slab thickness was 350 mm (otherwise the slab thickness was 200 mm). For example, the specimen G450-12#15T was reinforced with twelve GFRP bars No. 15 in each direction with a column size of 450×450 mm and with a slab thickness of 350 mm. Figure 1 shows the dimensions and the reinforcement of the test specimen G450-18#20B and Figure 2 shows the fabrication of a slab specimen. The concrete cover was 50 mm for the top and bottom reinforcement.

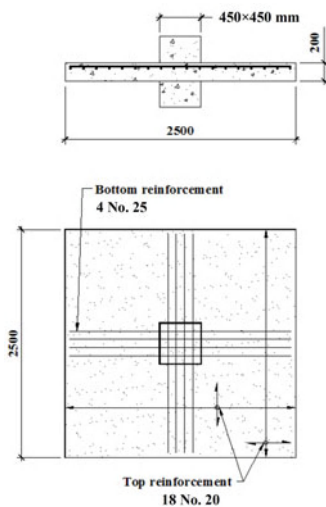
Table 1 GFRP bars properties (Pultrall 2007)

GFRP Bar size	Area (mm ²)	Tensile Modulus (GPa)	Tensile Strength (MPa)	Ultimate Strain (%)
No. 15	198	48.2	751	1.56
No. 20	285	47.6	728	1.53
No. 25	507	51.9	675	1.30

Table 2 Properties of the test specimens

Specimen	Thickness (mm)	f'_c (MPa)	Type of Reinf.	Column Size (mm)	Top Reinf.
G450-12#15T	350	48.6	GFRP	450	12 #15
G450-12#15	200	44.9	GFRP	450	12 #15
G450-18#20B*	200	39.4	GFRP	450	18 #20
G300-18#20	200	38.7	GFRP	300	18 #20
S300-18#20	200	45.5	Steel	300	18 #20

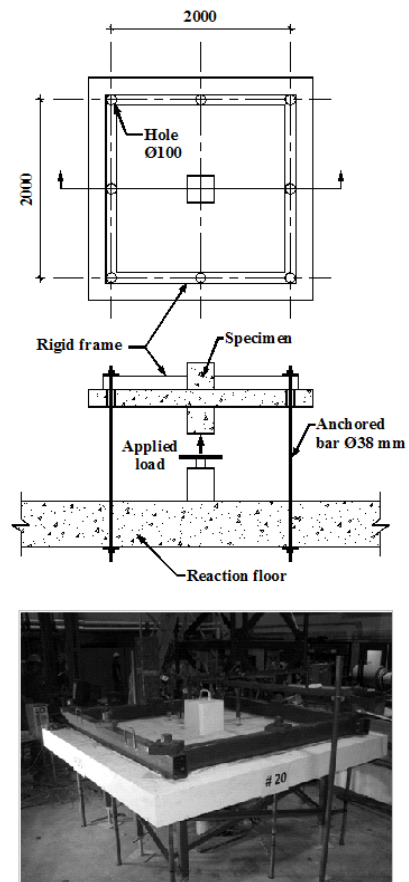
*This specimen has 4 GFRP bars No. 25 in each direction as bottom reinforcement

**Figure 1** Dimensions of test specimen G450-18#20B**Figure 2** Fabrication of a test specimen

2.2 Test setup

The specimens were tested under monotonic loading at a rate of 5 kN/min until failure. A hydraulic jack placed under the column stub of the specimen providing an upward loading. The reaction was resisted by eight steel bars anchored to the strong floor of the laboratory in the department of civil engineering at the University of Sherbrooke. The edges of the slab were free to rotate and the displacement at the edges, if any, is related to

the strain in the supporting anchors. Figure 3 shows the details of the test setup. To measure deflections, linear voltage differential transformers (LVDTs) were installed along the principal directions. The concrete surface and also the reinforcing bars were instrumented with electrical resistance strain gauges to capture the strains during the test. The strain gauges and the LVDTs as well as the load cell were connected to a data acquisition system to record the measurements during the test.

**Figure 3** Test setup

3 RESULTS AND DISCUSSION

3.1 Punching shear capacity

All the slabs failed in punching shear failure with the same brittleness. Figure 4 shows a typical crack pattern for one of the slab specimens (G450-18#20B) at failure. Table 3 presents the punching shear capacities of the five slabs. It can be noticed that the specimen G300-18#20 reinforced with GFRP bars has a normalized capacity about 68% of that of its counterpart S300-18#20 reinforced with the same amount of steel. Replacing the steel bars with GFRP bars reduced the punching strength with about 32%. The lower modulus of the GFRP reduced the resistance provided by the aggregate interlock due to wider cracks. Moreover, the lower stiffness reduced the depth of the neutral axis, and thus the shear resistance provided by a smaller uncracked concrete in

the compressive zone.

As expected, the effective depth of the slab has a strong effect on the punching capacity. The higher the effective depth, the higher the punching shear strength. Increasing the effective depth of the G450-12#15T specimen with a ratio of 112% greater than that of the G450-12#15 specimen increased the punching strength with about 119%.



Figure 4 Typical crack pattern of test specimen (G450-18#20B) at failure

The results confirmed also that, the column size is an important parameter because it increases the surface of the failure which increases the punching capacity. The specimen G450-18#20B showed 18% increase in the punching strength than the specimen G300-18#20. This is due to a combined effect of the bigger column size and the presence of structural integrity reinforcement (compression reinforcement). However, in a previous study, Dulude et al. (2010) concluded that, the contribution of the compressive reinforcement to the normalized capacity of similar specimens of 350 mm thickness and a 300 mm column was 2.4% which is very small. Also, the specimen G450-18#20B showed a 37% higher capacity than the specimen G450-12#15. This increase is due to the higher reinforcement ratio rather than the compression reinforcement which confirms that the higher the reinforcement ratio, the higher the punching strength of the slab.

Table 3 Punching capacity of the test specimens

Specimen	Ultimate Capacity, P_u , (kN)	Normalized capacity, $P_u / \sqrt{f'_c}$
G450-12#15T	911	130.7
G450-12#15	400	59.7
G450-18#20B	511	81.5
G300-18#20	431	69.3
S300-18#20	688	102.1

3.2 Slab deflection

The load-deflection relationships of the five slabs are

shown in Figure 5. The specimen with a 350-mm thickness showed the lowest deflection at the same load level than the other four specimens with 200-mm thickness. It can be noticed that, the four specimens with a slab thickness of 200 mm shows a similar behavior until cracking. After cracking, the specimens reinforced with GFRP bars showed higher deflection than S300-18#20 (reinforced with steel), as expected, due to the lower modulus of the GFRP bars. As can be seen in the same figure, the specimens G300-18#20 and G450-18#20B have a very similar slab deflection relationship. This implies the minimum effect of the compression reinforcement on the deflection of the test specimens.

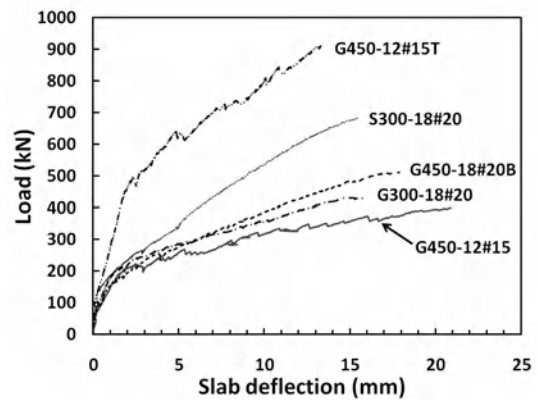


Figure 5 Load - deflection relationships

3.3 Strain

The strain distribution along the distance from the center of the slab in the top reinforcement for the specimens S300-18#20 and G300-18#20 (steel and GFRP-reinforced, respectively, with the same reinforcement ratio) is shown in Figure 6. From the figure, it can be noticed that, the two slabs showed the same strain distribution profile along the reinforcing bar and the strains were proportional to the distance from the centerline of the slab. Besides, it can be also noticed that there was no slippage of the reinforcing bars.

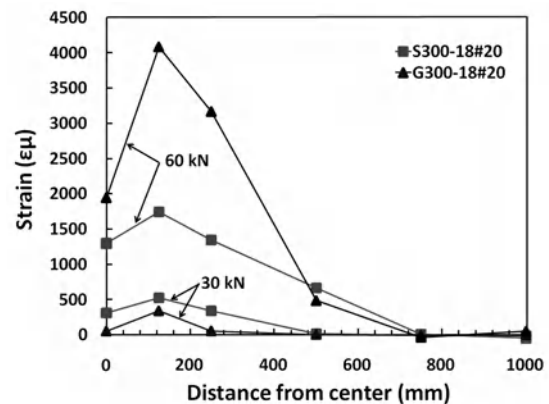


Figure 6 Strain distribution of test specimens S300-18#20 and G300-18#20

4 PREDICTION OF PUNCHING STRENGTH

The punching shear capacity of the test specimens was predicted using the JSCE (1997), the ACI 440.1R-06 (ACI 2006) and Eq. [1] which is being incorporated in the updated draft of the CAN/CSA S806 (2010). Eq. [1] is proposed by Razaqpur (2009) through private communication.

$$V_c = 0.3 \left[(f'_c)^{1/3} + 0.184 \sqrt{f'_c} (E_{FRP} \rho)^{0.42} \right] \left(\frac{d}{b_o} \right)^{0.55} b_o d \quad (1)$$

where b_o is the perimeter of the critical section at a distance of $d/2$ from the concentrated load; d is the effective depth; E_{FRP} is the modulus of elasticity of FRP bars; ρ is the average values for the reinforcement ratio in both directions.

The ratios between the measured and predicted punching strength are presented in Table 4. From this table, it can be noticed that the ACI 440.1R-06 is very conservative with an average ratio for V_{exp}/V_{pred} of 1.85. On the other hand, the JSCE (1997) equation yielded good and conservative prediction with an average V_{exp}/V_{pred} of 1.08. Moreover, Eq. [1] proposed by Razaqpur (2009), shows good agreement with the experimental results with an average ratio for V_{exp}/V_{pred} of 1.13.

Table 4 Measured to predicted punching strength (V_{exp}/V_{pred})

Reference	G450-12#15T	G450-12#15	G450-18#20B	G300-18#20	Average
JSCE (1997)	1.11	1.04	1.06	1.13	1.08
ACI 440.1R-06 (2006)	2.08	1.75	1.67	1.91	1.85
Razaqpur (2009)	0.91	1.15	1.24	1.21	1.13

5 CONCLUSION

Based on the experimental results of this study, the following conclusions can be drawn:

- Generally, there was no significant difference between the test specimens in term of general behavior and mode of failure.
- As expected, shear strength of G300-18#20 (GFRP) with the same reinforcement amount as the S300-18#20 (Steel) showed lower punching shear strength than the steel-reinforced one (68%).
- The strain profile in the test specimens was similar to that of a steel reinforced slab. The strain in the FRP bar was proportional to the distance of the gauge from the column face.
- The 440.1R-06 yielded very conservative prediction with an average V_{exp}/V_{pred} of 1.85. Both of the JSCE (1997) and Razaqpur (2009) showed reasonably

conservative predictions. Razaqpur equation, which is being incorporated in the updating draft of the CAN/CSA S806 (2010), showed good agreement with the experimental results with an average V_{exp}/V_{pred} of 1.13.

6 ACKNOWLEDGMENTS

The authors would like to express their special thanks and gratitude to the Natural Science and Engineering Research Council of Canada (NSERC), and The Ministère du Développement économique, de l'Innovation et de l'Exportation of Quebec (MDEIE). The authors are also grateful to the company Pultrall Inc. (Thetford Mines, Quebec), and the consultant engineering firm EMS ingénierie Inc. (Quebec City, Quebec). The authors would like also to thank the technical staff of the structural laboratory in the Department of Civil Engineering at the University of Sherbrooke.

REFERENCES

- ACI 440.1R-06. 2006. Guide for the Design and Construction of Concrete Reinforced with FRP Bars. Farmington Hills: American Concrete Institute.
- CSA-S806-02 2002. Design and Construction of Building Components with Fibre Reinforced Polymers. Rexdale: Canadian Standard Association.
- Dulude, C., Ahmed, E., and Benmokrane, B. 2010. Punching Shear Strength of Concrete Flat Slabs Reinforced with GFRP Bars. *2nd International Structural Specialty Conference (ISSC-02)*, CSCE, Winnipeg, MB, Canada, 9-12 June, 10 p. (CD-ROM).
- El-Ghandour, A.W., Pilakoutas, K., and Waldron, P. 1999. New Approach for Punching Shear Capacity Prediction of Fiber Reinforced Polymer Reinforced Concrete Flat Slabs. *ACI journal*, SP 188-13, pp. 135-144.
- El-Ghandour, A.W., Pilakoutas, K., and Waldron P. 2003. Punching Shear Behavior of Fiber Reinforced Polymers Reinforced Concrete Flat slabs: Experimental Study. *Journal of Composites for Construction*, 7(3): 258-265.
- Hussein, A., Rashid I., and Benmokrane B. 2004. Two-Way Concrete Slabs Reinforced with GFRP Bars, *Advanced Composite Materials in Bridges and Structures*, 4th International Conference on Advanced Composite Materials in Bridges and Structures, CSCE, Calgary, Alberta, Canada.
- Japan Society of Civil Engineers. JSCE 1997. *Recommendation for Design and Construction of Concrete Structures Using Continuous Fibre Reinforcing Materials*. Machida: Concrete Engineering Series 23.
- Lee, J.H., Yoon, Y.S., and Mitchell D. 2009. Improving Punching Shear Behavior of Glass Fiber-Reinforced Polymer Reinforced Slabs. *ACI Structural journal* 106(4): 427-434.
- Ospina, C.E., Alexander, S.D. B., and Roger Cheng, J.J. 2003. Punching of two-way concrete slabs with fiber-reinforced polymer reinforcing bars or grids. *ACI structural Journal*, 100(5): 589-598.

- Razaqpur 2009. Private communications.
- Razaqpur, A.G., Svecova, D., and Cheung, M.S. 1995. Failure Criteria for FRP Rods Subjected to a Combination of Tensile and Shear Forces. *Non-Metallic (FRP) Reinforcement for Concrete Structures, Proceedings of the 2nd International RILEM Symposium (FRPRCS-2)*, London, Great Britain, pp. 26-33.
- Zaghloul, A., and Razaqpur, A.G. 2004. Punching Shear Strength of Concrete Flat Plates Reinforced with GFRP Grids. *4th International Conference on Advanced Composite Materials in Bridges and Structures*, CSCE, Calgary, Alberta, Canada, 8p.
- Zhang, Q., Marzouk, H., Hussein, A. 2005. A Preliminary Study of High-Strength Concrete Two-Way Slabs Reinforced with GFRP Bars. *33rd CSCE Annual Conference: General Conference and International History Symposium*, CSCE, Toronto, Ontario, Canada, 10p.

Development Length of Glass Fiber Reinforced Plastic (GFRP)/Steel Wire Composite Rebar

Qingduo Hao (haoqingduo@163.com)

School of Civil Engineering, Harbin Institute of Technology, Harbin, China

Yanlei Wang & Jinping Ou

School of Civil & Hydraulic Engineering, Dalian University of Technology, Dalian, China

ABSTRACT The bond between glass fiber reinforced plastic (GFRP)/steel wire composite rebars and concrete is the key problem to the performance of concrete structures reinforced with GFRP/steel wire composite rebars. In this study, pull-out test was tested to experimentally investigate the bond strength of GFRP/steel wire composite rebars to concrete. The test variables were the nominal diameter, the embedded length, the concrete compressive strength, the concrete cover thickness and the concrete cast depth. Based on the two modification factors of 1.2 and 1.6 to account for the top rebar effect and concrete cover effect, respectively, a new formula is proposed for the calculation of development length for GFRP/steel wire composite rebars.

1 INTRODUCTION

Based on the hybrid theory, GFRP/steel wire composite rebars were manufactured to enhance the ductility and elastic modulus of GFRP rebars. The tensile strength of non-corrosion GFRP/steel wire composite rebar is larger than that of ordinary steel rebar, and the typical stress-strain relationship of GFRP/steel wire composite rebar exhibits the similar yielding characteristics to that observed for ordinary steel rebar. Therefore, GFRP/steel wire composite rebars offer a superior alternative to ordinary steel rebars in concrete structures (ACI 440 2001, Hao 2006).

So far, few studies recommending design guidelines for bond of GFRP/steel wire composite rebars to concrete have been reported in the literature. And the lack of information and design guidelines on their bond properties to concrete is one of the important factors limiting the filed application of GFRP/steel wire composite rebars to civil engineering. Moreover, the direct utilization of design guidelines for RC structures for the calculation of development length of GFRP/steel wire composite rebars is unwarranted because of the inherent differences between steel rebars and GFRP/steel wire composite rebars in terms of their tensile strength, modulus of elasticity, and surface configurations (Hao 2007a,b, Ehsani 1997).

Thus, pull-out specimens were tested to investigate the effect of nominal diameter, embedded length, concrete compressive strength, concrete cover thickness, and concrete cast depth on bond behavior of GFRP/steel

wire composite rebars to concrete. The primary objective of this research project was to study the bond behavior and develop design recommendations for anchorage of GFRP/steel wire composite rebars to concrete. The present paper focuses on the development of a new formula for the calculation of development length for GFRP/steel wire composite rebars (Ehsani 1996, Tastani 2006).

2 GFRP/STEEL WIRE COMPOSITE REBAR

The GFRP/steel wire composite rebars used in this test are supplied by Harbin Tider Science & Technology Inc.. These rebars had nominal diameter (d) of 8, 10, 12, and 14mm. They were generally manufactured using the so-called pultrusion process, and were made of continuous longitudinal glass fibers, steel wire, and epoxy resin. Two kinds of steel wire in nominal diameter of 1.5mm and 2.0mm were used. The cross section of GFRP/steel wire composite rebars can be seen in Figure 1.

During manufacturing, surface treatment was adopted to enhance the bond between GFRP/steel wire composite rebar and concrete. The longitudinal fibers and steel wire were wrapped in a helical pattern with two small strand fibers which were tight to induce indentations on the surface before heat-curing. The surface configurations and the rib geometries of GFRP/steel wire composite rebars can be seen in Figure 2.

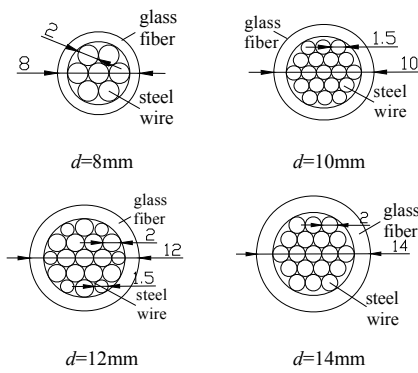


Figure 1 Schematic of cross section of GFRP/steel wire composite rebars

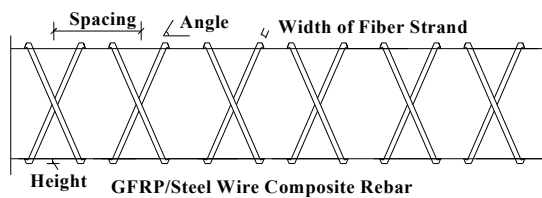


Figure 2 Schematic of rib geometries of GFRP/steel wire composite rebars

3 ANALYSIS OF TEST RESULTS

3.1 Modification factor

3.1.1 Modification factor of concrete cover

The failure mode for all specimens with concrete cover ranging from one to three times of rebar diameters was found to be due to concrete splitting. The distribution of the ratios of measured bond strength in specimens with concrete cover more than three rebar diameters to those with three rebar diameter is shown in Figure 3. A confinement factor of 1.2 will cover all cases when the concrete cover is three rebar diameter or less. Thus, according to the analysis on the determination of concrete cover thickness (ACI 440 2006), the basic development length must be multiplied by a confinement factor of 1.2 for cases with a concrete cover of two rebar diameter of smaller, and 1.0 when the cover is greater than two rebar diameter to account for the influence of concrete cover.

3.1.2 Modification factor of top-bar

The casting position has been shown to significantly influence bond strength under monotonic static loading. The top-bar modification factor is defined as the ratio of the ultimate bond strength reached when pulling out the bottom rebar to that reached when pulling out the top rebar. Test results indicate 12 pairs of specimens in which pullout failure rather than rebar rupture controlled. All values are less than 1.6. Therefore, it is recommended that a factor of 1.6 be used to account for the top-bar effect (ACI 440 2006).

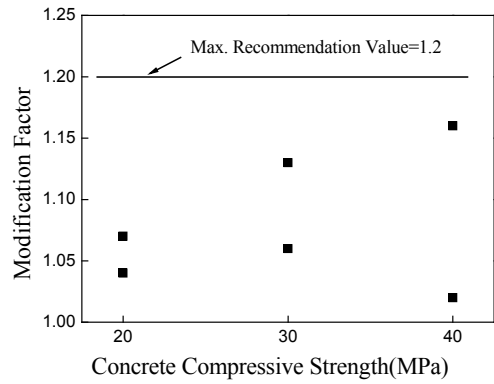


Figure 3 Modification factor of concrete cover

3.2 Critical value of slip

The above slip limitations for ordinary steel rebars cannot be directly utilized in evaluation of GFRP/steel wire composite rebars which differ from ordinary steel rebars in two important aspects (Achillides 2004). First, lower modulus of elasticity of GFRP/steel wire composite rebars results in greater elongation and contributes to the loaded-end slip. Second, the surface configurations of GFRP/steel wire composite rebars cannot resist large bond stresses and result in greater loaded-end and free-end slips. Thus, new criteria for bond of GFRP/steel wire composite rebars needed to be developed. These criteria were developed based on load-slip relationships and are presented in the following section.

The typical load-slip relation curves for specimens with different embedment lengths shown that various embedment lengths have only a minor influence on the load values until the loaded-end slip is 0.41 mm. It can be seen that various embedment lengths have only a minor influence on the load values until the free-end slip is 0.183 mm. A similar trend was observed in most of the other specimens. Thus, the critical slip value at the free and loaded ends is 0.183mm and 0.41mm, respectively. (Cairns 1995, CSA 2002, Tighiouart 1998)

3.3 Basic development length

The transmission of bond stress between GFRP/steel wire composite rebars and concrete is shown in Figure 4. Under the assumption of constant distribution of bond stress τ , the problem of a diameter d GFRP/steel wire composite rebar embedded in the concrete member for a length l_a and subjected to a pull-out force is governed by the following equilibrium equation (Cosenza 2002):

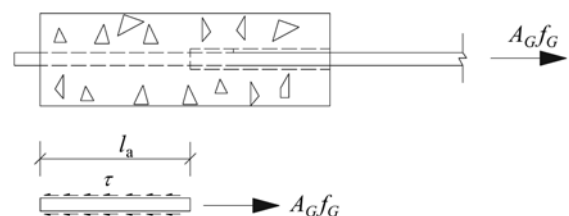


Figure 4 Schematic of transmission of bond stress

$$\tau \pi d l_a = A_G f_G \quad (1)$$

From Eq. (1), it follows:

$$l_a = \frac{A_G f_G}{\tau \pi d} \quad (2)$$

Where, τ is average bond strength in MPa; d is diameter of the rebar in mm; l_a is embedded length in mm; A_G is the cross section area of the rebar in mm²; and f_G is the normal tensile stress of the rebar in MPa.

For GFRP/steel wire composite rebars, it has been found that the average bond strength τ is a linear function of the square root of the concrete compressive strength f'_c :

$$\tau = k \sqrt{f'_c} \quad (3)$$

Where, k is a constant.

Therefore, from Eqs. (2) and (3):

$$l_a = \frac{A_G f_G}{\pi d k \sqrt{f'_c}} \quad (4)$$

And setting $K = \frac{1}{\pi d k}$, it follows:

$$l_a = K \frac{A_G f_G}{\sqrt{f'_c}} \quad (5)$$

Where, K is the bond factor reflecting the effect of rib spacing, rebar diameter, embedded length, concrete compressive strength, concrete cover thickness, and concrete cast depth on bond behavior of GFRP/steel wire composite rebars to concrete.

The basic development length is defined as the minimum embedded length required to develop the ultimate strength of the rebar. Hence, the basic development length l_{bd} can be calculated by the following equation:

$$l_{bd} = K \frac{A_G f_y}{\sqrt{f'_c}} \quad (6)$$

Where, f_y is the design tensile strength of GFRP/steel wire composite rebar considering reductions for service environment, and can be calculated as:

$$f_y = 0.7 f_u^* \quad (7)$$

Where, f_u^* is guaranteed tensile strength of the GFRP/steel wire composite rebar, defined as the mean tensile strength of a sample of test specimens minus three times the standard deviation.

From Eqs. (1) and (6), the factor K listed in column 9 of Table 3 was calculated as:

$$K = \frac{\sqrt{f'_c}}{\tau_c \pi d} \quad (8)$$

Where, τ_c is the critical bond stress in MPa. The value of τ_c was calculated from (1), when the applied

tensile force was replaced with T_c .

The next objective was to determine the bond factor K , such that after the application of the relevant factors for top-bar, concrete cover thickness, etc., the resulting equations would yield a conservative development length. Therefore, the basic development length equation was modified for the use of GFRP/steel wire composite rebars as:

$$l_{bd} = 0.028 \frac{A_G f_y}{\sqrt{f'_c}} \quad (9)$$

which was based on the pull-out test results. The 0.028 coefficient ensures that all development lengths calculated based on (9) will be larger than the measured ones.

3.4 Bond strength

From Eqs. (1) and (9), the bond strength of GFRP/steel wire composite rebars to concrete can be calculated as:

$$\tau = 11.37 \frac{\sqrt{f'_c}}{d} \quad (10)$$

The bond strength calculated from Eq. (10) must be adjusted by three steps (Chaallal 1993). First, all stresses corresponding to top rebars were divided by 1.6 to account for the top-bar effect. Second, the stresses for those specimens with concrete cover of two bar diameter or smaller were divided by 1.2 to account for the small cover. Even with these conditions, some of the bond stresses were still too high, resulting in unconservative development length calculation. Therefore, the third modification was to impose a maximum bond stress limit on these values. Analysis of the data indicated that an upper limit of 6.0 MPa for GFRP/steel wire composite rebars could ensure that all development lengths calculated based on adjusted bond stresses will be larger than the measured ones.

The above bond stress limit of 6.0 MPa can be incorporated into (1) and rewritten in another form, which is more familiar to design engineers as

$$l_{bd} = 0.0417 d f_y \quad (11)$$

4 CONCLUSIONS

Pull-out specimens were tested to develop design guidelines for bond of GFRP/steel wire composite rebars to concrete. Based on the theoretical analysis of the test results, the following conclusions were drawn:

(1) The embedment length has little effect on the bond stresses attained by GFRP/steel wire composite rebars until the loaded-end slip reaches 0.41 mm or the free-end slip reaches 0.183 mm. Therefore, it is recommended that the allowable slips at the loaded-end and free-end of GFRP/steel wire composite rebars be limited to 0.41 mm and 0.183 mm, respectively.

(2) The effect of concrete cover and top-bar on bond behavior of GFRP/steel wire composite rebars to concrete is significant. Therefore, it is recommended that one factor of 1.2 to account for the effect of concrete cover and the other factor of 1.6 to account for the top-bar effect.

(3) For straight GFRP/steel wire composite rebars, the development length, l_d should be computed as a product of (9) multiplied by top-bar modification factor and concrete cover modification factor. This figure shall not be less than the values obtained from (11). Finally, a minimum development length of 381 mm or 20 times the rebar diameter must be provided.

REFERENCES

- Achillides, Z., Pilakoutas, K.. Bond behavior of fiber reinforced polymer bars under direct pullout conditions. *Journal of Composites for Construction*, 2004, 8(2): 173-181.
- ACI 440 Committee. 2001. Guide for the design and construction of concrete reinforced with FRP bars. *American Concrete Institute*, Detroit, Michigan, USA.
- ACI 440.1R-06. Guide for the design and construction of concrete reinforced with FRP bars. Farmington Hills (MI, USA): *American Concrete Institute*, 2006.
- Cairns, J., and Abdullah, R.. 1995. An evaluation of bond pullout tests and their relevance to structural performance. *Struct. Eng.* 73(11): 179–185.
- Chaallal O., Benmokrane B.. 1993. Pullout and bond of glass-fiber rods embedded in concrete and cement grout. *Materials and Structures* 26: 167-175.
- CSA S806-02. 2002. Design and construction of building components with fiber reinforced polymers. *Canadian Standards Association*. Toronto (Ont., Canada).
- Cosenza E., Manfredi G., Realfonzo R.. 2002. Development length of FRP straight rebars. *Composites: Part B* 33: 493–504.
- Ehsani M. R., Saadatmanesh H., Tao S.. 1996. Design recommendations for bond of GFRP rebars to concrete. *Journal of Structural Engineering* (3): 247-254.
- Ehsani, M.R., Saadatmanesh, H., Tao, S.. 1997. Bond behavior of deformed GFRP rebars. *Journal of Composites Materials* 14:1413-1430.
- Hao, Q.D., Wang, B., Ou, J.P.. 2006. Fiber reinforced polymer rebar's application to civil engineering. *Concrete* 9(1): 38-40 (in Chinese).
- Hao, Q.D., Zhang, Z.C., Wang, Y.L., Ou, J.P.. 2007a. Comparison experimental study on bond behavior of deformed GFRP rebars with different outer surface. *FRP/CM* (2):37-39 (in Chinese).
- Hao, Q. D., Wang, Y. L., Ou, J. P. et al.. 2007b. Bond Strength Improvement of GFRP Rebars with Different Rib Geometries *Journal of Zhejiang University Science* A9(8): 1356-1365.
- Tastani, S. P., Pantazopoulou, J.. 2006. Bond of GFRP bars in concrete: experimental study and analytical interpretation. *Journal of Composites for Construction* 10(5):381-391.
- Tighiouart, B., Benmokrane, B., Gao, D.. 1998. Investigation of bond in concrete member with fiber reinforced polymer FRP bars. *Construction and Building Materials* 12:162-453.

Deformation Behavior of Concrete Two-Way Slabs Reinforced with BFRP Bars Subjected to Eccentric Loading

Haitang Zhu (htzhu@zzu.edu.cn), Yakun Zhang, Danying Gao & Zhilong Xiao
School of Water Conservancy&Environment, Zhengzhou University, Zhengzhou, China

ABSTRACT Based on the punching shear test results of 9 simply supported concrete two-way slabs reinforced with basalt fiber reinforced polymer (BFRP) bars subjected to eccentric concentrated loading, the deflection distribution and the load-deflection characteristics of test slabs are investigated. The test results show that the deformations of test slabs before punching shear failure are caused by bending moments. The concrete strength, the ratio of FRP bars reinforcement, the location of concentrated load and the ratio of punching span are the main factors that affect the load-deflection curves and the energy dissipations capacity of concrete two-way slabs reinforced with FRP bars under eccentric concentrated load.

1 INTRODUCTION

Load-deflection curve of concrete two-way slab reflects many aspects of performance, including bearing capacity, deformation, ductility, energy absorption capacity and so on. Study on the Load-deflection curve (P-w curve) of concrete two-way slabs is of very importance because it is related to the interpretation of punching failure mechanism and the establishment of punching shear failure mode. However, specialized research on deformation of concrete punching shear slab was often overlooked in the past, especially on concrete two-way slab reinforced with FRP bars. In this paper, deformations and load-deflection curves of concrete two-way slabs reinforced with FRP bars under concentrated eccentric load were analyzed based on the test.

2 TEST DESCRIPTION

Concrete two-way slab members reinforced with basalt FRP bars in the single-sided configuration are designed. Specimens are designed as shown in Figure 1, and the design parameters of specimens are shown Table.1. The designed concrete strength grade of specimens S-7, S-5 and S-8 are respectively C20, C30 and C40. Actual measured strength of BFRP bar and steel bar is respectively 987MPa and 468MPa.

Test Features are as follows: bearing with four sides simply supported, clear span of 1500mm, single or double-direction eccentric concentrated loads which loading area of 150mm × 150mm square (Figure 1). The displacement measuring points of slab surface are set through load centerline and others shown in Figure 6 below.

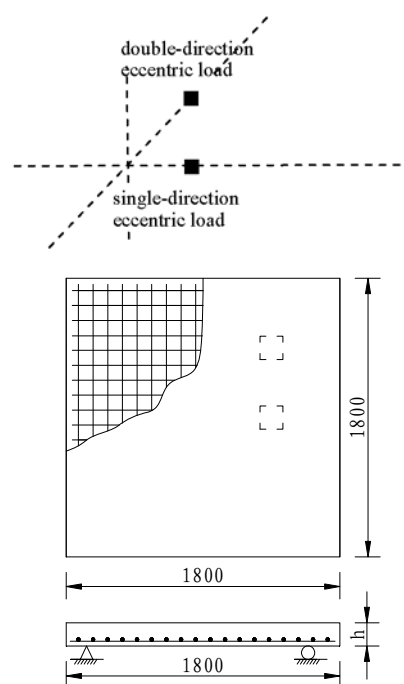


Figure 1 Schematic diagram of two-way slabs

Table 1 Design parameters of specimens

No	Eccentric loading location	Span (mm)	Depth of Slabs (mm)	Effective depth (mm)	Concrete compressive strength (MPa)	Ratio of Rebars	
						FRP	Steel (%)
S-1	double-direction	1500	150	135	36.8	—	0.97
S-2	double-direction	1500	150	135	36.0	0.29	0.30
S-3	double-direction	1500	150	135	33.5	0.29	—

(Continued)

No	Eccentric loading location	Span (mm)	Depth of Slabs (mm)	Effective depth (mm)	Concrete compressive strength (MPa)	Ratio of Rebars	
						FRP	Steel (%)
S-4	double-direction	1500	150	135	35.6	0.55	—
S-5	double-direction	1500	150	135	32.8	0.42	—
S-6	single-direction	1500	150	135	32.5	0.42	—
S-7	double-direction	1500	150	135	22.6	0.42	—
S-8	double-direction	1500	150	135	41.8	0.42	—
S-9	geometric center	1500	150	135	40.6	0.42	—

3 DEFORMATIONS OF CONCRETE TWO-WAY SLABS

3.1 Load-deflection curves of test specimens

According to the failure process and the failure mode, punching failure manner of the two-way slabs reinforced with FRP bars in this experiment can be divided into bending-type failure and punching-type failure. When the load is small, test slabs are basically in the stage of flexible working, and deflection increases linearly with the increases of loading. Since the first cracks, the curvature of the load-deflection curves (P-w curve) reduce and the P-w curves gradually deviate from the loading axis but still exhibit approximate linear change. About 80% of the damage load, load-deflection curve begins to bend shaft deflection. When reaching limit load, the punching cone comes up, and at the same time bearing capacity of the test lab reduced in vast scale. After punching failure, load gradually stabilizes at 10% to 30% of the limit load. The deflection is about 3 to 4 times as large as its destroyed deflection. Deformation of the test slab continues to develop under the effect of residual load until the eventual loss of its bearing capacity.

The shape, highest point and slop of load-deflection curve are closely related with concrete strength grade, FRP bars reinforcement ratio and load location, etc.

It is not difficult to see from Figure 2 that the higher the concrete strength grade, the smaller its deflection under the same load, however the higher its carrying capacity when destroyed. This is due to that the stiffness of the components increased with the increase of concrete strength under other conditions being equal. Concrete strength changes from C20 to C30, C40, the ultimate bearing capacity of corresponding test specimens

increased by 37% and 39%. The area surrounded by P-w curve and deflection axis is equal to the ability for test component to absorb energy throughout the entire process of the test slab occurring punching damage.

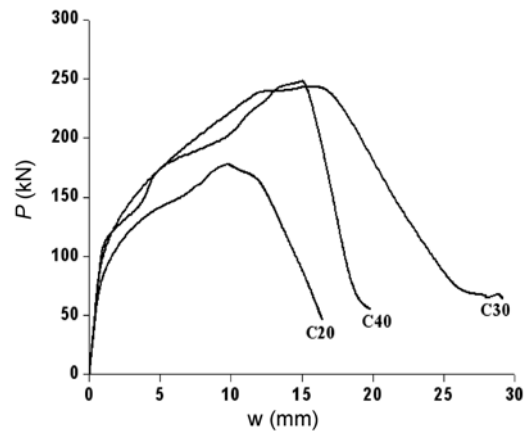


Figure 2 Influence of concrete strength on P-w curves

Figure 2 shows that with the increase in concrete strength, the energy dissipation capacity of concrete two-slab reinforced with FRP bars grows.

Figure 3 tells us that the greater the ratio of FRP bars reinforcement, the smaller its deflection under the same load, however the higher its carrying capacity when destroyed. With the ratio of FRP bars reinforcement increasing, the punching ultimate bearing capacity shows increasing trend. As the load increases, the deflection is still approximately linear increase. Ratio of FRP bars reinforcement changes from 0.29% to 0.42%, 0.55%, the ultimate bearing capacity of corresponding specimens increased by 45% and 68%. It also shows that the energy dissipations capacity of the higher ratio of FRP reinforcement as specimen S-4 is less than the lower ratio of FRP bars reinforcement as S-5.

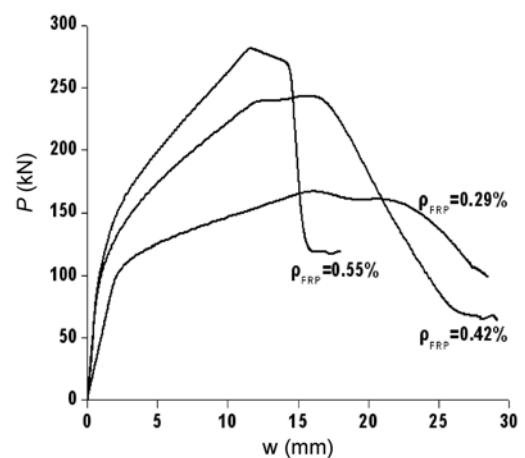


Figure 3 Influence of FRP bars ratio on P-w curves

As can be seen from Figure 4, comparing with the test slabs subjected to center loading as specimen S-9, the deflection of two-way slab reinforced with FRP bars

subjected to eccentric loading as specimen S-5 and S-6 is smaller and the punching ultimate bearing capacity is higher. It also indicates that deflection and ultimate bearing capacity of the specimen subjected to single-direction eccentric loading is lower than that of the specimen subjected to double-direction eccentric loading. The different areas surrounded by P-w curve and deflection axis according to Figure 4 tell that the deformation and energy dissipations capacity of two-way slabs reinforced with FRP bars under eccentric load have little to do with load location, but the test slab under center load has the worst energy dissipations capacity of all.

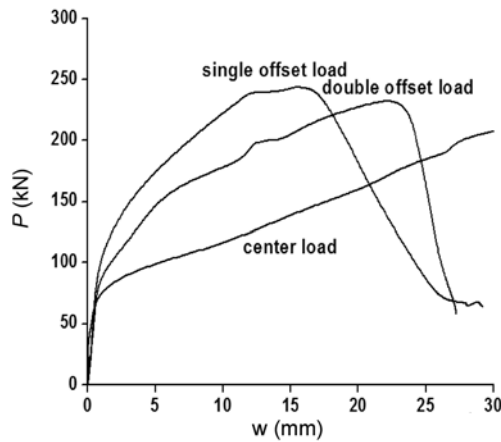


Figure 4 Influence of load location on P-w curves

As can be seen from Figure 5, when reinforced with FRP bars in replacement part of the steel bars, the test slabs with the greater ratio of FRP bars reinforcement, the larger of its deflection under the same load, however the lower of its carrying capacity when destroyed. From Figure 5, the different areas surrounded by P-w curve and deflection axis suggest that deformation and energy dissipations capacity of the two-way slab reinforced with steel bars during its punching shear failure process is the worst in all of the 8 test slabs. With the increasing

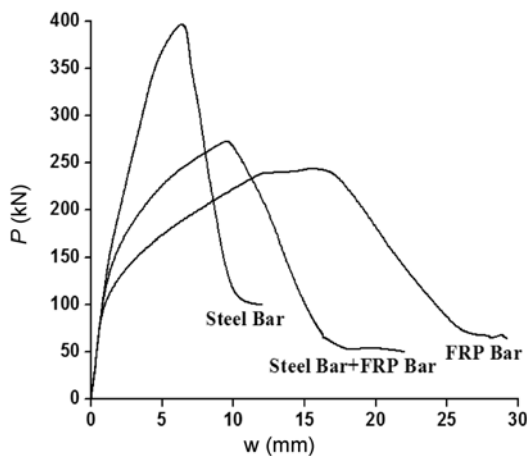


Figure 5 Influence of amount of steel bars and FRP bars on P-w curves

number of steel bars replaced by FRP bars, the deformation and energy dissipation capacity of the two-way slabs grow in the process of punching damage occurring.

3.2 Deformation distribution of test slabs' surface

Deformations of the two-way slabs before occurrence of punching shear failure are caused by bending moments. There is no significant relative rotation on the punching cone and its vicinity, and there is no significant relative dislocation too. The typical measured displacement of specimens is shown in Figure 6.

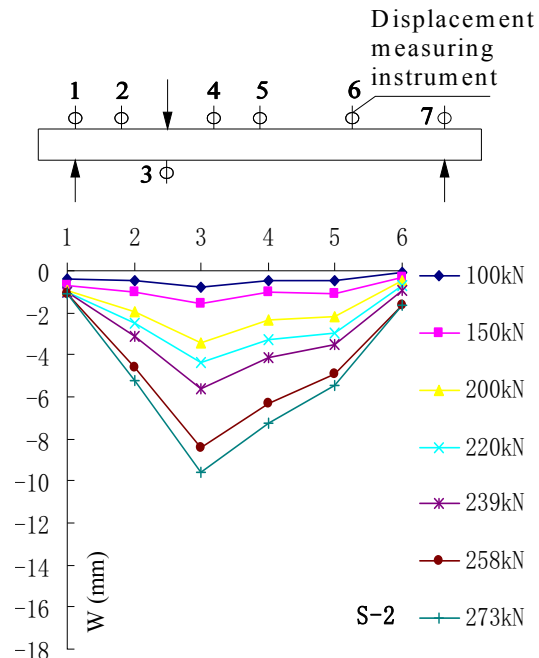


Figure 6 measured typical displacement distribution on the surface of test slabs

Designed concrete strength of test two-way slabs as specimens S-7, S-5 and S-8 are respectively C20, C30 and C40, and other parameters of them are all the same. As can be seen from deflections Data measured in the tests, the maximum deflection value of test slab S-7 compared with those of test slabs S-5 and S-8 decrease by 55.7% and 52.7% when their occurring punching damage. When the concrete strength is at a lower level, the tensile strain of the concrete in the center and its local vicinity of the two-way slabs reinforced with FRP bars subjected to concentrated loading, which is in multi-dimensional stress state, can easily exceed the limit strain of the concrete. Thus the cross intersection cracks occur in the center of load location. As the load continues to increase, cracks develop continuously. The punching shear capacity is provided by concrete of the test two-way slabs. As the strength of concrete is low, the punching shear damage occurs when the load is not too large. As the damage load is low, the deflection of the test slab does not fully develop, resulting in the deflection in the center of load is small. Moreover, concrete strength

changes from C30 to C40, the maximum deflection value of the test slab S-8 reduces by 1.91%. This is because the higher the concrete strength, the greater the brittleness of the concrete component. Thus S-8 is more of a sudden than S-5 while damaging. So the maximum deflection value of S-8 is smaller than that of S-5 when their damaging.

The ratio of FRP bars reinforcement of test two-way slabs as specimens S-3, S-5 and S-4 is respectively 0.29%, 0.42% and 0.55%, and their other parameters are all the same. Based on the test measured data we can see that the maximum deflection values of S-3 whose ratio of FRP bars reinforcement is 0.29% compared with those of S-3 and S-5 whose ratio of FRP bars reinforcement is 0.42% and 0.55% reduce by 7.68% and 29.23% when destroyed. This shows that as the ratio of FRP bars reinforcement increases, the trend of deflection decreases while punching shear damaging. Because as the amount of FRP bars increases in the two-way slabs reinforced with FRP bars, the stiffness of the two-way slabs increases, so that deformability of test two-slabs under concentrate load diminishes.

Test slab S-1 reinforced only with steel bars, and S-5 reinforced only with FRP bars, and S-2 reinforced synchronously with steel bars and FRP bars. It can be seen from the test results that with the FRP bars increasing in the number to replace the steel bars, the maximum deflection value of S-2 and S-5 compared with that of S-1 increases by 67.66% and 165.91% when punching damage occurs. Deformation ability of concrete two-way slab reinforced with FRP bars compared with concrete two-way slab reinforced with steel bars improves far a lot. As the elasticity modulus of steel bars is larger than that of FRP bars, the flexural stiffness of concrete two-way slab reinforced with FRP bars is smaller than that of test slabs reinforced with steel bars when other conditions are all the same, so joining FRP bars in concrete two-way slab can improve the deformation performance to a large extent when punching damage occurs.

According to Figure 6, we can see that deflection at the center of the slabs surface is the largest and surface deflections gradually descend from the load center to the edge of the test slabs. Deflection value of measuring point close to the load center is relatively large, whereas that of measuring points far from load center is relatively small. It is not hard to determine that the destruction of the test two-way concrete slabs reinforced with FRP bars subjected to eccentric concentrated load is done in partial, and damage occurs in the concentrated loads center and its nearby areas.

The bending of test two-way slabs is mainly caused by the development of cracks in the edge area of concentrated load and the rotation of various rigid plates on the center of concentrated load and its surrounding

areas. It can be confirmed through the test observations that development and width of ring cracks closed to the center of concentrated load and its surrounding areas are much larger than that of the cracks outside areas until the punching cone pushes out at last.

4 CONCLUSIONS

In order to discuss the deformation performance of the concrete two-way slab reinforced with FRP bars, punching shear tests of 7 concrete two-way slabs reinforced with FRP bars, 1 concrete two-way slab reinforced with steel bars, and 1 concrete two-way slab reinforced synchronously with FRP bars and steel bars are carried out, and get the following conclusions:

(1) The failure modes of bending and punching commonly exit in the tests of concrete two-way slabs.

(2) The concrete strength grade, the ratio of FRP bars reinforcement, the location of concentrated load and ratio of punching span are the main factors that affect the load-deflection of the concrete two-way slabs reinforced with FRP bars under eccentric concentrated load.

(3) The destruction of the concrete two-way slab reinforced FRP bars subjected to concentrated load occurs in the center of load area and its nearby areas, which belongs to partial punching shear damage. The carrying capacity of concrete two-way slab reinforced FRP bars while their punching shear destruction occurring is mainly controlled by the concrete of the two-way slab.

(4) The concrete strength, the ratio of FRP bars reinforcement are the main factors that affect the deformation ability and the energy dissipations capacity of the concrete two-way slab reinforced FRP bars.

(5) The maximum deformation of the test two-way slabs is in the center of load, and with the distance to the loading center increasing, the deformation of slab surface decrease.

5 ACKNOWLEDGMENTS

The research reported herein was supported by National Science Foundation of China (No.50879082) .

REFERENCES

- Ayman S.M. & Khalid M.M. 2003 Strengthening of two-way concrete slabs with FRP composite laminates. *Construction and Building Materials* (17):43-54.
- Carlos E. O. & Scott D. B. et al. 2003 Punching of Two-Way Concrete Slabs with Fiber-Reinforced Polymer Reinforcing Bars or Grids. *Structural Journal* 100(5): 589-598.
- Gao, D.Y. & Li, S.H. et al. 2009. Experimental research on basic mechanical properties of GFRP bars. *Fiber Reinforced Plastics/Composites*,(3): 28-32.
- Jiang, D.H. & Shen, J.H. 1986. Strength of concrete slabs in punching shear. *ASCE*,112(12):2578-2591.

- Kinnunen, S. 1963. Punching of concrete slabs with two-way reinforcement. *Meddelande Nr. 41, (Institutionen for Byggnadsstatik, Stockholm)*.
- Kinnunen, S. & Nylander, H. 1960. Punching of concrete slabs without shear reinforcement. *Meddelande Nr. 38, (Institutional for Byggnadsstatik, Stockholm)*.
- Samay, R.N. & Ali, S.A.R. 1982. Punching shear behavior of reinforced slab-column connections made with steel fiber concrete. *ACI Journal*,79(5):392-406.
- Xu, T. 2009. The structural property research of concrete flexural members reinforced with fiber reinforced polymer bars. *Ph.D thesis of Xi'an University of Architecture and Technology*.
- Zhan, Y.K. & Fang, G.G. et al. 2009. Bonding performance of FRP rebar with concrete: A review of the state-of-the-art. *Industrial Building Supplement*: 148-153.
- Zhou, Y.W. 2009. Analytical and experimental study on the strength and ductility of FRP reinforced high strength concrete beam. *Ph.D thesis of Dalian University of Technology*. 2009.

Experimental Study on the Flexural Behavior of Concrete Beam Hybrid Reinforced with FRP Bars and Steel Bars

Wenjie Ge (jshagwj@yahoo.cn), Jiwen Zhang, Hang Dai & Yongming Tu

College of Civil Engineering, Southeast University, Nanjing, China

Key Laboratory of Concrete and Prestressed Concrete Structure of Ministry of Education, Southeast University, Nanjing, China

ABSTRACT The hybrid reinforced concrete structure combine the advantages of reinforced concrete structure and FRP structure together, it could resolve the problem of the durability of RC structure and brittle failure of FRP structure. In order to investigate the flexural behavior of concrete beam hybrid reinforced with FRP bars and steel bars, three different area ratio of FRP bar to steel bar hybrid reinforced concrete beams, one FRP reinforced concrete beam and one reinforced concrete beam static flexural test were made. Mechanics characteristic, flexural capacity of normal section and deflection of hybrid reinforced beams were analyzed. The results show that the average concrete strains of different height keep plane, the flexural capacities calculate by proposed formula was close to the tested value. The load-deflection curve decreased gradually after steel bars yielded.

1 INSTUCTION

The fiber reinforced polymer bar (FRP bar) as a substitute for steel bar used in concrete structure is an effective method which could resolve the problem of concrete durability aroused by corrupt of steel bars and meet the requirement of special structure such as protecting electromagnetic interference. Recent years, researching about the capability of FRP bar and concrete structures reinforced with FRP bar are focus of the civil engineering; New structures are widely used in the coastal structures and the subway engineering. But FRP bar have characteristics of high strength, low elasticity modulus and linear deformation, these characteristics lead to the phenomenon of brittle failure, larger crack width and deflection which restrict the application of FRP structure in civil engineering.

The hybrid reinforced concrete structure combine the advantages of reinforced concrete structure and FRP structure together, it could resolve the problem of the durability of RC structure and brittle failure of FRP structure by laying the FRP bar in the corner area where concrete easy corrupted, and it still need to keep on loading to up to the ultimate load after the steel bars yield and shows certain safety factor and good ductility. So it is a goodish reinforced format.

2 EXPERIMENTAL TEST

Three different area ratios of FRP bar to steel bars hybrid reinforced concrete beams, one FRP reinforced concrete beam and one reinforced concrete beam static

bending test were made. The size of the member was $b \times h \times l = 200 \text{ mm} \times 300 \text{ mm} \times 2500 \text{ mm}$, C35 fine aggregate concrete was used, domestic BFRP bar of diameter 8 mm and steel bars of diameter 10 mm were used as the longitudinal main bars, steel bar of diameter 8 mm was used as stirrup bars. Member geometric parameter was list in Table 1.

Table 1 Member geometric parameter

Specimen	FRP bar (mm)	Steel bar (mm)	A_f/A_s
FS1	4	6	0.96
FS2	5	5	0.64
FS3	6	4	0.43
F1	0	9	—
S1	10	0	—

Before bending test, strength and elastic modulus of concrete, tensile strength and elastic modulus of BFRP bar, yield strength, tensile strength and elastic modulus of steel bar should determinate firstly. Relative bond coefficient of the BFRP bar considered as 1.0 according to the bond-slip experiment. Mechanical performance of concrete was list in Table 2, mechanical performance of BFRP bar and steel bars was list in Table 3 and test set-up was show in Figure 1.

Table 2 Mechanical performance of concrete (MPa)

f_{cu}	E_c	f_c	f_t
42	3.3×10^4	28.1	2.4

Table 3 Mechanical performance of BFRP bar and steel bars

Bar	Diameter (mm)	E_f (GPa)	f_y (MPa)	f_u (MPa)
Steel	10	180	360	533
Steel	8	180	423	585
BFRP	8	55	—	880

* The Steel bars surface form of diameter 8 mm and 10 mm is screwed; the surface form of BFRP bar is screwed.

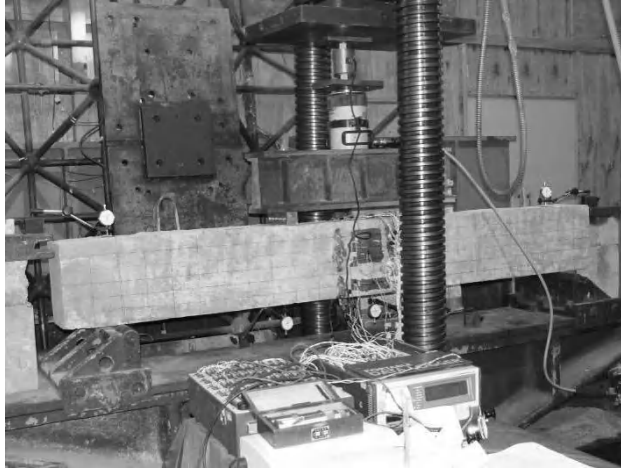


Figure 1 Test set-up

3 EXPERIMENTAL STUDY

3.1 Plane section assumption

Theory of normal concrete flexural member was on the base of plane section assumption. Strain gauges were laid on the side of the beams and TDS303 was used to measure the strain value of each steps. Figure 2 shows the FS1 member's concrete strain of different height vary to the changing of load, as can be seen from the figure, concrete strain linear distribution along the height, neutral axis upward gradually as the load increasing, the concrete strain accord with plane section assumption.

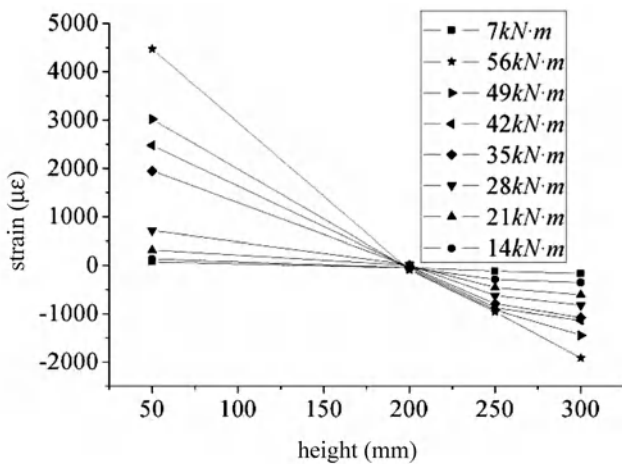


Figure 2 Average concrete strain of different height

3.2 Ultimate bearing capacity

According to the simplified calculate formula proposed by literature 2.

$$M_u = f_c b h_0^2 \xi (1 - \xi / 2) \tag{1}$$

$$\xi = \frac{A - B + \sqrt{(A - B)^2 + 3.2B}}{2} \tag{2}$$

As $A = \frac{f_y \rho_s}{f_c}$, $B = \frac{0.0033 E_f \rho_f}{f_c}$, b section width, h_0

section effective height, f_c axis compression strength of concrete, f_y yield strength of steel bars, ρ_s reinforcement ratio of steel bars, ρ_f reinforcement ratio of FRP bars, E_f elastic modulus of FRP bar, 0.0033 ultimate compression strain of concrete.

Flexural capacity $M_{u,t}$ calculate by simplified formula using the measured strengths of bars and concrete and flexural capacity $M_{u,e}$ measured by the test were list in table 4. As can be seen from the table, average value of $M_{u,t}/M_{u,e} = 1.04$ and coefficient of variation $\delta = 0.002$.

Table 4 Comparison of theory value and tested value of Ultimate bearing capacity

Specimen	$M_{u,e}$ (kN·m)	$M_{u,t}$ (kN·m)	$M_{u,t}/M_{u,e}$
FS1	74.4	70.2	1.06
FS2	73.5	70.9	1.04
FS3	72.8	71.5	1.02
F1	67.6	69.5	0.97
S1	67.9	71.3	0.95

3.3 Load-deflection curve of tested member

As can be seen from the load-deflection curve of tested member shown in Figure 3, for hybrid reinforced beams, the curves have three turning point, the first point corresponding to the crack load, the second point corresponding to the yield of steel bars and the third point corresponding to the flexural capacity, the load-deflection decreased gradually after the steel bars yielded; for FRP

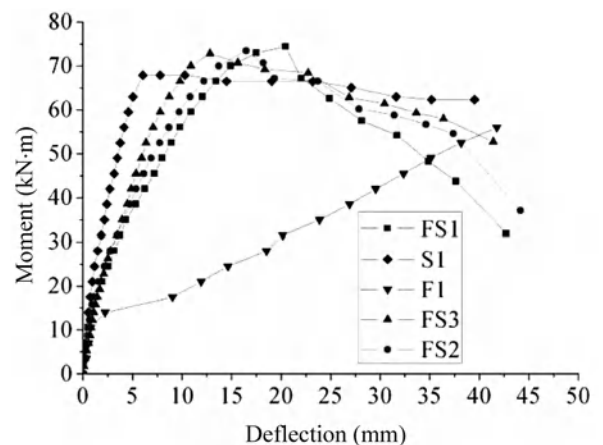


Figure 3 Load-deflection curve of tested member

beam, just one turning point corresponding to the crack load, the load-deflection curve of FRP beam keeping linear till failure, but its stiffness decrease quickly after crack; for reinforced beam, the curve has two turning point, the first point corresponding to the crack load, the second point corresponding to the yield of steel bars; with the same load, the deflection of FRP beam is maximum and the deflection of reinforced beam is minimum; for hybrid reinforced beams with the same load, the deflection of beam FS1 is maximum and the deflection of beam FS3 is minimum, so the deflection decrease as the value A_f/A_s , (area ratio of FRP bars to steel bars) decrease.

4 CONCLUSIONS

Mechanics characteristic of hybrid reinforced beams was similar to normal reinforced beam, the average concrete strain of different height keep plane; flexural capacities calculate by proposed formula was close to tested value; the load-deflection curves of hybrid reinforced beam have three turning point, the first point corresponding to the crack load, the second point corresponding to the yield of steel bars and the third point corresponding to the flexural capacity; the load-deflection decreased gradually after the steel bars yielded.

5 ACKNOWLEDGEMENTS

This work is supported by the National Natural Science Foundation of China (50808039), the Chinese National High Technology Research and Development Program (2007AA03Z550), the Natural Science Foundation of Jiangsu Province, China (BK2008148, SBK200921303),

the Doctoral Foundation of Ministry of Education, China (20070286095), and the State Key Laboratory of Subtropical Building Science, South China University Of Technology, China (2008KB24).

REFERENCE

- ACI Committee 400. 2001. Guide for the Design and Construction of Concrete Structure Reinforced with FRP Bars, *American Concrete Institute*. Michigan: Detroit.
- Ge, W.J. 2009. Experimental Study and Theoretical Analysis on Concrete Beams Reinforced with FRP Bars Blend with Steel Bars or FRP and Steel Composite Bars, *Southeast University*. China: Nanjing.
- Ge, W.J & Zhang, J.W. & Tu, Y.M. & Lv, J.P. 2009. Experimental study on the bond behaviour between BFRP bar and concrete. *Innovation & sustainability of structures proceeding of the international Symposium on Innovation & Sustainability of Structures in Civil Engineering*: 696-700. South China University of Technology, China: Guangzhou.
- Ge, W.J & Zhang, J.W. & Tu, Y.M. & Lv, J.P. 2009. Study on the crack spacing of concrete flexural member hybrid reinforced with BFRP bars and steel bars. *Proceeding of shanghai international Conference on Technology of Architecture and Structure*: 115-119. Tongji university press: China: Shanghai.
- Lan, Z.J. & Liang, S.T. & Meng, S.P. 2002. Design Theory of Concrete Structure. *Southeast University*. China: Nanjing.
- Masmoudi, R. & Theriault, M. & Benmokrane, B. November-December 1998. Flexural behavior of Concrete Beams Reinforced with Deformed Fiber-Reinforced Plastic Rods, *ACI Structural Journal*, p665-676.
- Zhou, M.H. 2002. Civil Engineering Structural Testing and Inspection. *Southeast University*. China: Nanjing.

Study on the Flexural Capacity of Concrete Beam Hybrid Reinforced with FRP Bars and Steel Bars

Jiwen Zhang (jwzhang@vip.163.com), Wenjie Ge, Hang Dai & Yongming Tu

College of Civil Engineering, Southeast University, Nanjing, China

Key Laboratory of Concrete and Prestressed Concrete Structure of Ministry of Education, Southeast University, Nanjing, China

ABSTRACT Two Nominal reinforcement ratios and three failure modes were put forward according to the characteristic of FRP bar and the criterion of appropriate hybrid reinforcement beam was given. Flexural capacity of appropriate hybrid reinforcement beam was analyzed according to the theory of reinforcement concrete and flexural capacities simplified calculate formula of appropriate hybrid reinforcement beam was proposed. three different area ratio of FRP bar to steel bar hybrid reinforced concrete beams, one FRP reinforced concrete beam and one reinforced concrete beam static flexural test were made and the tested results show that the flexural capacities calculate by proposed simplified formula was close to the tested value.

1 INSTUCTION

The fiber reinforced polymer tendons (FRP tendons) as a substitute for steel bars used in concrete structure is an effective method which could resolve the problem of concrete durability aroused by corrupt of steel bars and meet the requirement of special structure such as protecting electromagnetic interference. Recent years, researching about the capability of FRP tendons and concrete structures reinforced with FRP tendons are focus of the civil engineering, new structures are widely used in the coastal structures and the subway engineering. But FRP tendons have characteristics of high strength, low elasticity modulus and linear deformation, these characteristics lead to the phenomenon of brittle failure, larger crack width and deflection which restrict the application of FRP structure in civil engineering.

The hybrid reinforced concrete structure combine the advantages of reinforced concrete structure and FRP structure together, it could resolve the problem of the durability of RC structure and brittle failure of FRP structure by laying the FRP tendons in the corner area where concrete easy corrupted, and it still need to keep on loading to up to the ultimate load after the steel bars yield and shows certain safety factor and good ductility. So it is a goodish reinforced format.

2 BASIC ASSUMPTION

1) Plane section assumption, the section keep plane under load and the strain of concrete and bars were linear to its distance to neutral axis.

2) The bars and concrete has good bond behavior, the strain of steel bar was the same with FRP bar in the same place.

3) Neglect concrete tensile force after crack.

4) Constitutive relationships were simplified.

Constitutive relationships of steel bar was simplified as two line model, when $\epsilon_s < \epsilon_y$, $\sigma_s = E_s \epsilon_s$, when $\epsilon_y \leq \epsilon_s \leq \epsilon_u$, $\sigma_s = f_y$. f_y yield strength of steel bars, E_s elastic modulus of steel bars, ϵ_u ultimate tensile strain of steel bar and it was consider as 0.001.

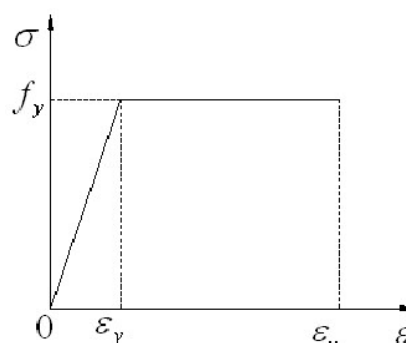


Figure 1 Stress-strain curve of steel bar

Constitutive relationship of concrete was simplified as follows:

$$\epsilon_c \leq \epsilon_0, \sigma_c = f_c (1 - (1 - \epsilon_c / \epsilon_0)^n) \quad (1)$$

$$\epsilon_c > \epsilon_0, \sigma_c = f_c \quad (2)$$

$$\epsilon_0 = 0.002 + 0.5 (f_{cu,k} - 50) \times 10^{-5} \quad (3)$$

$$\epsilon_{cu} = 0.0033 - (f_{cu,k} - 50) \times 10^{-5} \quad (4)$$

$$n = 2 - (f_{cu,k} - 50) / 60 \quad (5)$$

ϵ_c compressive strain of concrete, σ_c concrete compressive stress corresponding to ϵ_c , f_c axis compressive strength of concrete, ϵ_0 concrete compressive strain while the stress up to f_c , consider it as 0.002 while the calculate value less than 0.002, ϵ_{cu} ultimate compressive strain of concrete, consider it as 0.0033 while it calculate more than 0.0033, $f_{cu,k}$ characteristic value of compressive strength of concrete cube, n coefficient, consider it as 2.0 while it calculate value more than 2.0.

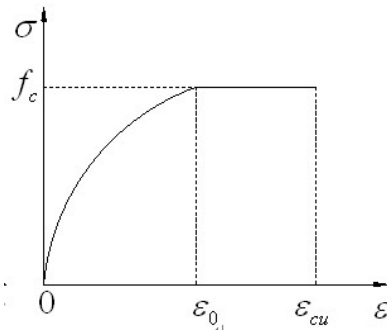


Figure 2 Stress-strain curve of concrete

The stress-curve of FRP keep linear, $\sigma_f = E_f \epsilon_f$, E_f elastic modulus of FRP bars, ϵ_{fu} ultimate strain of FRP bar, f_{fu} ultimate strength of FRP bar, ϵ_{fd} design strain of FRP bar, f_{fd} design strength of FRP bar.

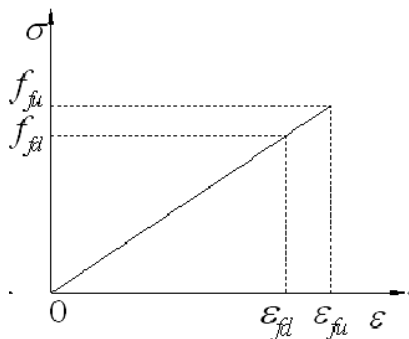


Figure 3 Stress-strain curve of FRP bar

3 REINFORCEMENT RATIO

Three kinds of reinforcement ratio were put ward for the different elastic modulus and ultimate strength between steel bar and FRP bar

1) Practical reinforcement ratio: ρ

$$\rho = \rho_s + \rho_f \tag{6}$$

$\rho_s = A_s / (bh_0)$, $\rho_f = A_f / (bh_0)$, A_s area of steel bars, A_f area of FRP bars, b section width, h_0 section effective height.

2) Nominal reinforcement ratio conversion by strength: ρ_1 .

$$\rho_1 = \rho_s + \rho_f f_{fd} / f_y \tag{7}$$

3) Nominal reinforcement ratio conversion by elastic modulus: ρ_2 .

$$\rho_2 = \rho_s + \rho_f E_f / E_s \tag{8}$$

4 FAILURE MODES OF NORMAL SECTION

Failure modes of normal section could divide into three kinds as following according to the constitutive relationships of steel bar and FRP bar.

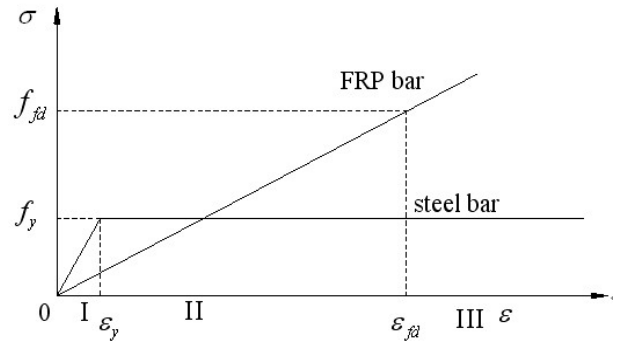


Figure 4 Failure modes of normal section

1) $\epsilon_c = \epsilon_{cu}$, $0 < \epsilon_s = \epsilon_f < \epsilon_y$

Failure characteristics: the steel bar has not yield and the stress of FRP bar is small while the concrete up to the ultimate compressive strain, this situation similar to the over bar of concrete beam and it was not allowed for its brittle failure.

2) $\epsilon_c = \epsilon_{cu}$, $\epsilon_y < \epsilon_s = \epsilon_f < \epsilon_{fd}$

Failure characteristics: the steel bar had yield and the stress of FRP bar is just a little small than or equal to design stress while the concrete up to the ultimate compressive strain, this situation was expected for its ductile failure.

3) $\epsilon_c < \epsilon_{cu}$, $\epsilon_{fd} < \epsilon_s = \epsilon_f$

Failure characteristics: the steel bar had yield and the stress of FRP bar is more than design stress or the concrete up to the maximum compressive strain, this situation was not allowed for its brittle failure.

Boundary relative neutral axis height could define according to plane section assumption and the given value of ϵ_{cu} .

Boundary failure 1:

$$\xi_{nb1} = x_{n1} / h_0 = \epsilon_{cu} / (\epsilon_{cu} + \epsilon_y) = 1 / (1 + f_y / (E_s 0.0033)) \tag{9}$$

Boundary failure 2:

$$\xi_{nb2} = x_{n2} / h_0 = \epsilon_{cu} / (\epsilon_{cu} + \epsilon_{fd}) = 1 / (1 + \epsilon_{fd} / 0.0033) \tag{10}$$

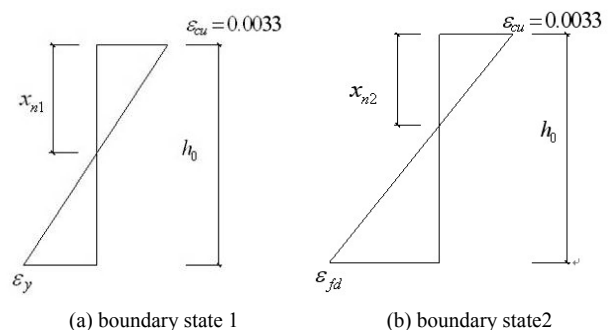


Figure 5 Boundary state

Assume the height of neutral axis is x_c , h_0 section effective height, so boundary relative neutral axis height $\xi = x_c/h_0$, when $\xi > \xi_{nb1}$, failure mode 1 occurred, when $\xi_{nb2} \leq \xi \leq \xi_{nb1}$ failure mode 2 occurred, when $\xi < \xi_{nb2}$ failure mode 3 occurred.

According to internal force equilibrium:

$$\int_0^{x_c} b\sigma_c dx = f_s A_s + f_f A_f \quad (11)$$

$x_c = \varepsilon_{cu} h_0 / (\varepsilon_{cu} + \varepsilon_{fd})$, for concrete grade less than C50, formula 11 could rewrite as follows according to formula 1-5,

$$f_c b h_0 \frac{2\varepsilon_0}{3(\varepsilon_{cu} + \varepsilon_f)} = f_s A_s + f_f A_f \quad (12)$$

For boundary failure 1:

$$\rho_s + \frac{E_f}{E_s} \rho_f = \frac{f_c}{f_y} \cdot \frac{2\varepsilon_0}{3(\varepsilon_{cu} + \varepsilon_y)} \quad (13)$$

For boundary failure 2:

$$\rho_s + \frac{f_{fd}}{f_y} \rho_f = \frac{f_c}{f_y} \cdot \frac{2\varepsilon_0}{3(\varepsilon_{cu} + \varepsilon_{fd})} \quad (14)$$

So appropriate reinforcement should meet the following requirement simultaneously:

$$\rho_1 = \rho_s + \frac{f_{fd}}{f_y} \rho_f > \frac{f_c}{f_y} \cdot \frac{2\varepsilon_0}{3(\varepsilon_{cu} + \varepsilon_{fd})} \quad (15)$$

$$\rho_2 = \rho_s + \frac{E_f}{E_s} \rho_f < \frac{f_c}{f_y} \cdot \frac{2\varepsilon_0}{3(\varepsilon_{cu} + \varepsilon_y)} \quad (16)$$

5 APPROPRIATE HYBRID REINFORCEMENT BEAM

In order to calculate convenience, assume k_1 ratio of average compressive stress to compressive strength of concrete, k_2 ratio of the distance of the compressive force point to the compressive edge to the height of compress zone.

$$k_1 f_c b x_n = \int_0^{x_n} \sigma(\varepsilon) b dy \quad (17)$$

$$k_2 x_n = x_n - \frac{\int_0^{x_n} \sigma(\varepsilon) b y dy}{k_1 f_c b x_n} \quad (18)$$

k_1, k_2 could obtain according to the for the Constitutive relationship of concrete for the maximum compressive strain ε_c .

$$\varepsilon_c \leq \varepsilon_0, k_1 = \frac{\varepsilon_c}{\varepsilon_0} \left(1 - \frac{\varepsilon_c}{3\varepsilon_0} \right), k_2 = \frac{1 - \varepsilon_c / 4\varepsilon_0}{3 - \varepsilon_c / \varepsilon_0} \quad (19)$$

$$\varepsilon_c > \varepsilon_0, k_1 = 1 - \frac{\varepsilon_c}{3\varepsilon_0}, k_2 = \frac{6 - (\varepsilon_c / \varepsilon_0)^2}{12 - 4(\varepsilon_c / \varepsilon_0)} \quad (20)$$

Concrete compressive stress figure was transferred into equal rectangle stress figure. The height of rectangle

is $\gamma_1 x_c$, the compressive stress is $\gamma_2 f_c$, keeping the force and its location unchanged, $\gamma_1 = 2k_2$, $\gamma_2 = 2k_2/k_1$, when $\varepsilon_c > 0.003$, ε_c has no obvious effect on γ_1 and γ_2 , taken the ultimate concrete compressive strain as 0.0033 could obtain $\gamma_1 = 0.823$, $\gamma_2 = 1.03$, consider $\gamma_1 = 0.8$, $\gamma_2 = 1.0$ for simplified. So boundary relative neutral axis height could obtain $\xi_{b1} = 0.8\xi_{nb1}$, $\xi_{b2} = 0.8\xi_{nb2}$, according to internal force equilibrium:

$$f_c b x = f_y A_s + E_f \varepsilon_f A_f \quad (21)$$

$$\varepsilon_f = 0.0033(0.8/\xi - 1) \quad (22)$$

Taken equation 22 to equation 21 and assume

$$A = \frac{f_y \rho_s}{f_c}, B = \frac{0.0033 E_f \rho_f}{f_c}, \text{ so flexural capacity of}$$

appropriate hybrid reinforcement beam could simplify calculate as following:

$$M_u = f_c b h_0^2 \xi (1 - \xi/2) \quad (23)$$

$$\xi = \frac{A - B + \sqrt{(A - B)^2 + 3.2B}}{2} \quad (24)$$

6 EXPERIMENTAL VERIFICATION

Three different area ratios of BFRP tendons to steel bars hybrid reinforced concrete beams, one BFRP reinforced concrete beam and one RC beam static bending test were made. The size of the member was $b \times h \times l = 200 \text{ mm} \times 300 \text{ mm} \times 2500 \text{ mm}$, C35 fine aggregate concrete was used and the concrete cover was 23 mm, BFRP tendons of diameter 8 mm and steel bars of diameter 10 mm were used as the longitudinal main bar, steel bar of diameter 8 mm was used as stirrup bars. Mechanical performance of concrete was list in Table 1, mechanical performance of BFRP bar and steel bars was list in Table 2 and test set-up was show in Figure 1.

Table 1 Mechanical performance of BFRP bar and steel bars

Bar	Diameter (mm)	E_f (GPa)	f_y (MPa)	f_u (MPa)
Steel	10	180	360	533
Steel	8	180	423	585
BFRP	8	55	—	880

* The Steel bars surface form of diameter 8 mm and 10 mm is screwed; the surface form of BFRP bar is screwed.

Table 2 Mechanical performance of concrete (MPa)

f_{cu}	E_c	f_c	f_t
42	3.3×10^4	28.1	2.4

Flexural capacity $M_{u,t}$ calculate by proposed simplified formula using the measured strength of bars and concrete and ultimate bearing capacity $M_{u,e}$ measured by the test were list in Table 3. As can be seem from the table, average value of $M_{u,t} / M_{u,e}$ $u = 1.04$, coefficient of

variation $\delta=0.002$.



Figure 6 Test set-up

Table 3 Comparison of theory value and tested value of flexural capacity

Specimen	FRP bar	Steel bar	$M_{u,t}$	$M_{u,e}$	$M_{u,e}/M_{u,t}$
FS1	4	6	68.9	74.4	1.08
FS2	5	5	68.8	73.5	1.07
FS3	6	4	68.7	72.8	1.06
F1	0	9	66.5	67.6	1.02
S1	10	0	69.8	67.9	0.97

* Unit of $M_{u,t}$ and $M_{u,e}$ is kN·m.

7 CONCLUSIONS

Based on the constitutive relationships of materials, two Nominal reinforcement ratios, three failure modes were put forward and the criterion of appropriate hybrid reinforcement beam was given. Flexural capacity of appropriate hybrid reinforcement beam was analyzed and simplified calculate formula was proposed. three different area ratio of FRP bar to steel bar hybrid reinforced concrete beams, one FRP reinforced concrete beam and one reinforced concrete beam static flexural test were made and the tested results show that the flexural capacities calculate by proposed simplified formula was close to the tested value.

8 ACKNOWLEDGEMENTS

This work is supported by the National Natural Science Foundation of China (50808039), the Chinese National High Technology Research and Development Program (2007AA03Z550), the Natural Science Foundation of

Jiangsu Province, China (BK2008148, SBK200921303), the Doctoral Foundation of Ministry of Education, China (20070286095), and the State Key Laboratory of Subtropical Building Science, South China University Of Technology, China (2008KB24).

REFERENCE

- ACI Committee 400. 2001. Guide for the Design and Construction of Concrete Structure Reinforced with FRP Bars, *American Concrete Institute*. Michigan: Detroit.
- Antoine E. Naaman. 1995. Unified Bending Strength Design of Concrete Members: AASHTO LRFD Code. 964-970. *Journal of Structural Engineering*.
- Ge, W.J. 2009. Experimental Study and Theoretical Analysis on Concrete Beams Reinforced with FRP Bars Blend with Steel Bars or FRP and Steel Composite Bars, *Southeast University*. China: Nanjing.
- Ge, W.J & Zhang, J.W. & Tu, Y.M. & Lv, J.P. 2009. Experimental study on the bond behaviour between BFRP tendon and concrete. *Innovation & sustainability of structures proceeding of the international Symposium on Innovation & Sustainability of Structures in Civil Engineering*: 696-700. South China University of Technology, China: Guangzhou.
- Ge, W.J & Zhang, J.W. & Tu, Y.M. & Lv, J.P. 2009. Study on the crack spacing of concrete flexural member hybrid reinforced with BFRP tendons and steel bars. *Proceeding of shanghai international Conference on Technology of Architecture and Structure*: 115-119. Tongji university press: China: Shanghai.
- Lan, Z.J. & Liang, S.T. & Meng, S.P. 2002. Design Theory of Concrete Structure. *Southeast University*. China: Nanjing.
- Masmoudi, R. & Theriault, M. & Benmokrane, B. November-December 1998. Flexural behavior of Concrete Beams Reinforced with Deformed Fiber-Reinforced Plastic Rods, 665-676. *ACI Structural Journal*.
- Saatcioglu, M. & Sharbatdar, K. 2001. Use of FRP Reinforced in Column of New Structures. *Proceedings of International Conference on FRP Composites in Civil Engineering*, 1219-1226. China: Hong Kong.
- Vistasp M Karbhari. 1998. WTEC Monograph on Use of Composite Materials in Civil Infrastructure in Japan. *ITRI Word Technology Division*.
- Zhou, M.H. 2002. Civil Engineering Structural Testing and Inspection. *Southeast University*. China: Nanjing.

Experiments According to ETAG to Determine Friction Effects on Deviated CFRP-Strips

Mohamed Hwash (m.hwash@itke.uni-stuttgart.de) & Jan Knippers

Institute of Building Structures and Structural Design, University of Stuttgart, Stuttgart, Germany

ABSTRACT In recent years the Institute of Building Structures and Structural Design, University of Stuttgart (ITKE), has undertaken a large amount of experimental work to determine the load bearing capacity, strain responses up to failure and the failure mode of CFRP-Strips at different deviation saddle geometries. Several tests with different deviation angles and deviation saddle radii were carried out. The results have shown that the tensile strength of the CFRP-Strip is reduced significantly by deviation, even if the deviation radius in proportion to the thickness of the CFRP-Strips is comparatively large. Further tests were carried out to determine the influence of other important parameters on the load bearing capacity of the strip such as surface properties of the saddle including the friction of the saddle surface. The results of these tests show that, with the help of a polyethylene layer (HD-PE) between the CFRP-Strip and the deviation saddle friction could be reduced, which lead to an increase in tensile strength. The effect of these parameters on the load bearing capacity of the CFRP-Strip is published in this paper.

1 INTRODUCTION

CFRP-Materials have been the focus of much attention in the engineering community since the development of lightweight fibres with high stiffness in the 1940's. In the last two decades, the use of CFRP composites as a reinforcement for concrete members has emerged as one of the most exciting and promising technologies in materials / structural engineering. Due to the high price of CFRP-Strips its application today is mostly found in buildings, where its strength is highly utilized and the strips are needed in small quantities, e.g. for the strengthening and rehabilitation of reinforced concrete structures.

In the meantime the new developments/researches focuses on direct gluing of pre-stressed CFRP-Strips on reinforced concrete constructions in order to improve their stability. The applied pre-stress rises the degree of utilization for the CFRP-Strip, at the same time the pre-stressed CFRP-Strips need to anchor their force locally into the concrete. This is not easy due to the sensitivity of the carbon fibers to transverse loads. The development of CFRP-Strip anchorage is presently under investigation in many research institutions and universities.

This strip could also be used for external prestressing of bridges or for unstrained ceilings in high building structures. Because of the flat and broad cross section of a CFRP-Strip, the lateral strain at the bearing saddle and the end anchorages are smaller than induced by circular tension members, this may be of advantage. At present

knowledge of the deviated CFRP-Strips is still missing. How does load bearing capacity change, if the CFRP-Strip is deviated on a saddle and stressed?

The following section shows part of a comprehensive experimental program which is running on CFRP-Strips on a deviation saddle. The effect of the deviation angle and the contact surface between the CFRP-Strip and the deviation saddle on the load bearing capacity and the deformational behaviour of the CFRP-Strips will be investigated.

2 EXPERIMENTAL WORK

2.1 Background of previous Tests

The first research investigations were conducted at the Institute of Building Structures and Structural Design (ITKE) at the University of Stuttgart. Several tests with different deviation angles and deviation saddle radii were carried out. The results have shown that the tensile strength of the CFRP-Strip is reduced significantly by deviation, even if the deviation radius in proportion to the thickness of the CFRP-Strip is comparatively large.

An initial test was carried out on a CFRP-Strip 90×1.4 mm with a deviation angle of 110°, In order to have a basic idea of the ultimate load of the used anchorages and the deviated CFRP-Strip. After the hardening phase, the CFRP-Strip is loaded and released up to certain load-level. Then the CFRP-Strip is loaded gradually to 400 kN (max. load capacity of the testing machine). So that approximately 55% of the ultimate load (characteristic) is applied. The maximum measured

strain was 1.1%, which is 55% of the rupture strain of the CFRP-Strip. As the result of this test, it was recognized that the deviated CFRP-Strips can be loaded up to 55% of their characteristic breaking load without reaching failure mode. As a result, the required test loads were limited by reducing the CFRP-Strip outside the Anchorage area. Further tests with angle 110° and 30° respectively, deviation radius 150 mm and the reduced strip were carried out. It was recognized that increasing the contact area between the strip and the saddle and larger the deviation angles lead to higher forces between the strip and the saddle, which causes more restraining of the strip and consequentially earlier failure. According to the tests, the ultimate strength of deviated strip was reduced up to about 75% for angle 110° and was increased up to 89% of the ultimate strength of a straight strip by angle 30°.

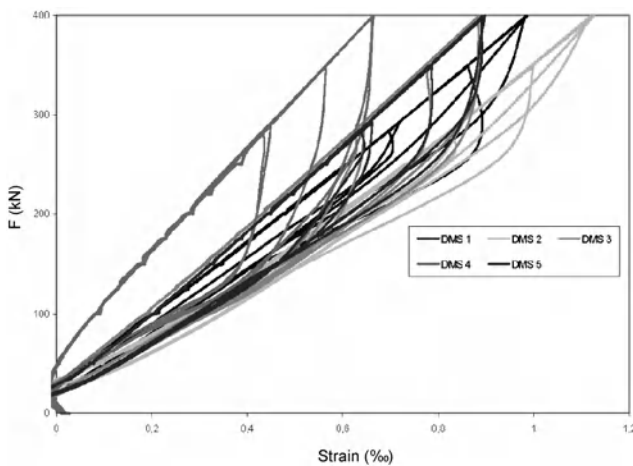


Figure 1 Load-Strain curves

By using a bending radius of 1000 mm for deviation angle 30° the reduction factor was increased up to 92%. For all tests the acceptance criteria for mandatory requirements, which are listed in the guideline for European technical approval of post-tensioning kits for prestressing of structures (ETAG 013), are not satisfied, i.e. reduction factor 95%. More results and test set-up can be found in the earlier references.

2.2 Experiments with smaller angle

Other experiments were carried out with a deviation angle of 15° and bending radius 1000 mm in order to determine the influence of this parameter on the load bearing capacity of the strip. The strain gauges are positioned similarly as the tests above. The obtained results have shown significant improvement compared to above tests. A breaking load of 250 kN was reached, which is about 97% of the breaking load of a straight strip. This value is above the value of 95% which is listed in the ETAG 013. According to the new angle, the first contact line between the strip and deviation saddle

was at gauge 3. Therefore the largest strain occurred at gauge 3, while due to friction the lowest strain was measured at gauge 4. Figure 2 shows the load strain diagram.

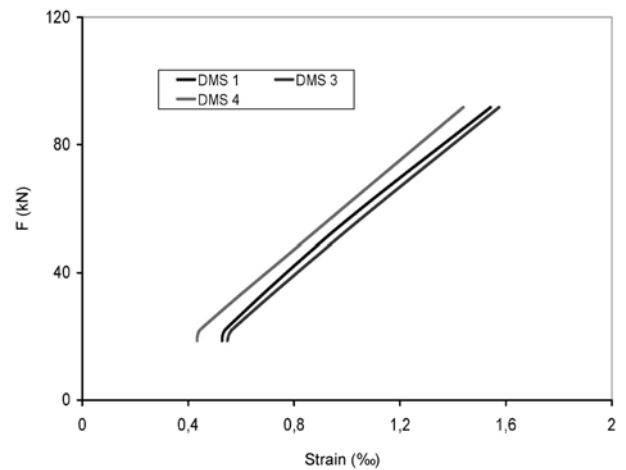


Figure 2 Load-Strain curves on strip 50*1.4 mm; F = Force of the testing device

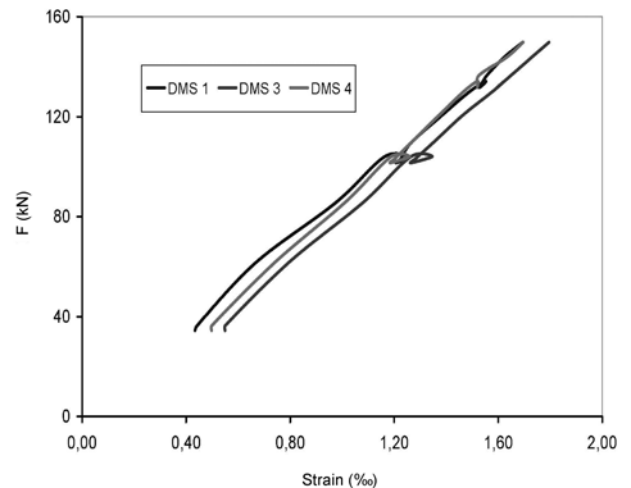


Figure 3 Load-Strain curves on strip 50x1.4 mm for saddle surface with CFRP-strip; F = Force of the testing device

2.3 Friction effect on the load bearing capacity

The friction between the strip and the saddle is an important design parameter. Therefore, further tests were carried out in order to obtain the effect of the saddle surface on the Load bearing capacity of the strip. Two groups, saddle surface with CFRP-strip and Polymer sheath, were tested.

The results of the tests show that by reducing the friction the tensile strength of the strip were increased. The breaking force of the strip was increased to about 97% in compare with the same test group without reducing the friction between the saddle and the strip. Figure 3 shows the load-strain diagrams for test with saddle surface CFRP-strip as example.

3 EXPERIMENTS WITH RELATIVE MOVEMENT TO DEVIATION SADDLE

3.1 Test set-up and test program

A very important effect was not being captured by the experiments in step 1, namely the movement of the strip on the deviation saddle during the prestressing process. Furthermore, the deformation of the strip which occurs under loading can influence the fracture load. In order to capture this effect, experiments with relative strip movement to deviation saddle were carried out according to the ETAG 013, Annex B5.1. Table 1 summarizes the test program.

Table 1 Test program

Group	Surface	Saddle Radius (mm)	Angle
I	Steel	1000	15°
II	CFRP-strip	1000	15°
III	PE-HD	1000	15°
V	Steel	150	15°

The experimental setup for the friction tests is shown in figure 4, and their schematic is shown in Figure 5.



Figure 4 Experimental setup for the friction tests

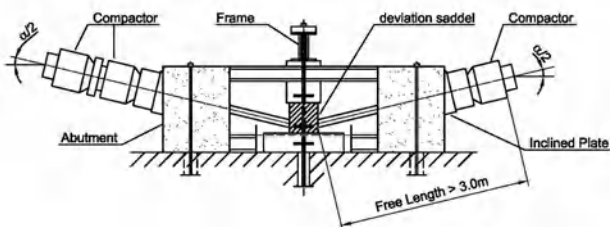


Figure 5 Schematic setup

Notwithstanding ETAG 013 the deflection angle was set at 15 degrees to allow, however, for comparability with the results of step 1. The CFRP-strip and anchoring are chosen similar to step 1.

3.2 Test procedure

With the help of temporary anchor clamps, a tensioning load is applied in 10% increments in order to prestress

the CFRP-strip up to 40% of its characteristic strength. Meanwhile, a permanent anchor was installed (Figure 6). The prestressing force is held constant for 24h to allow for the entire hardening of the permanent anchor. After curing process of the permanent anchor, the strip is pulled over the deviation saddle with a constant load of 40% while simultaneously increasing the tension on one side and decreasing it on the opposite side. The movement distance is at least 800 mm with a speed of 1mm/sec.

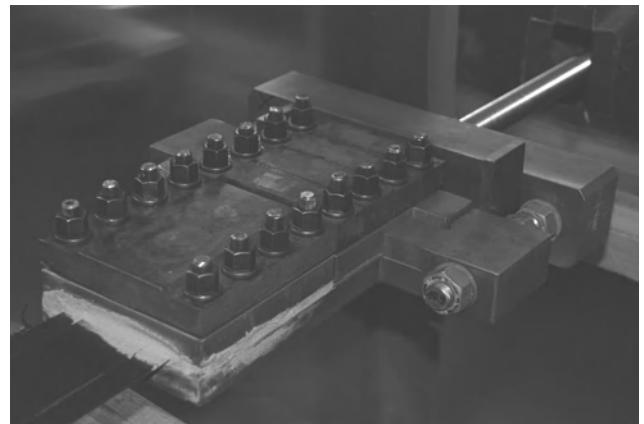


Figure 6 Anchor of the CFRP-strip

The same process is repeated at load levels of 60% and 80% of the strength of the CFRP-strip. At each load level, the tensioning is held constant after the movement for at least 1 h. Then the strip is loaded until failure. The experiment is carried out at room temperature ($20^{\circ}\text{C} + / - 5^{\circ}\text{C}$).

Figure 7 shows the setup of the hydraulic stressing jacks during the prestressing of the strip (left photo) and after the movement (right photo). There are two hydraulic jacks on each side with double hollow chamber. One of them has a stabilizer to apply the prestressing force and the second one to apply the necessary pressure differential for the movement of the strip. The strain in the strip was measured at several positions along the strip length using electrical strain gauges. All measurements were



Figure 7 Setup of the hydraulic stressing jacks

recorded automatically at each loading level. Figure 8 shows the arrangement of the gauges over the deviation saddle area. The automatic program, which controls the measuring instruments was connected to a computer system for data acquisition.

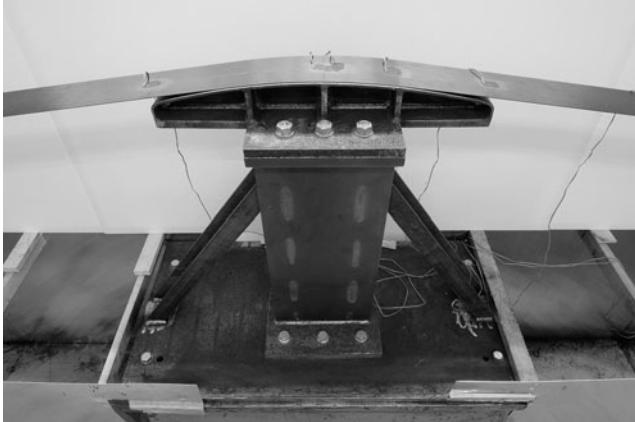


Figure 8 Arrangement of the gauges over the saddle

4 FIRST RESULTS

The first results show that the tensile strength of the CFRP-strip is affected by saddle friction. The movement of the strip under prestressing on the saddle leads to higher friction forces and reduces the fracture force of the strip.

Figure 9 shows exemplary a screen shot of the measurements while moving the CFRP-strip over the saddle as part of test group I. The prestressing force in kN, the moving distance in mm, the strain in $\mu\text{m}/\text{m}$ and time in second were measured. The movement was under prestressing force of 80% of the strip while taking this screen shot. The speed of the movement is influenced by prestressing force and friction. High forces in the strip lead to higher friction on the saddle and slow movement

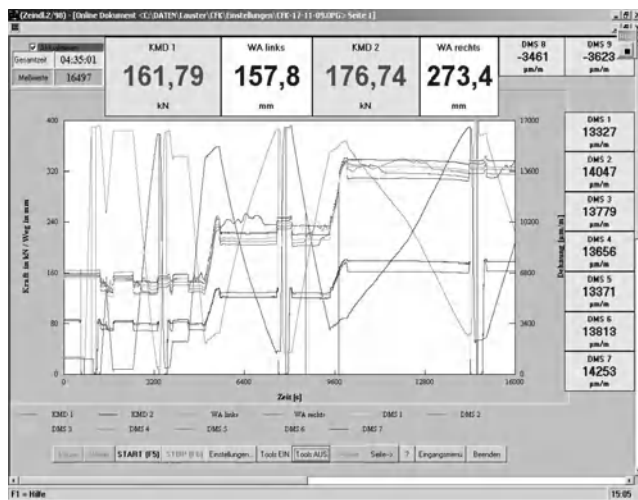


Figure 9 Screen shot of the measurements while moving

of the strip over the saddle. The force differential between the right and the left hydraulic jacks gives the friction force over the saddle which was about 15 kN as shown in the figure. More test results will be presented in later publications. The end failure shape of the strip can be seen in figure 10. The failure of the strip is an explosion form, setting free a fine dispersible dust. Therefore, it was necessary to build a room around the test setup in order to collect the dust carefully.



Figure 10 The end failure shape of the CFRP-strip

5 CONCLUSION

The use of CFRP-Strips as freestanding elements for bridge constructions seem to be promising; The high tensile strength of carbon fibre reinforced polymers, combined with the high compression strength of the concrete offer a durable construction system. The results of the current experimental work showed that the ultimate strength of the deviated CFRP-Strips is significantly affected by the bending radius, the deviation angle and friction, so that the following recommendations can be drawn.

- For small deviation angel of 15° the reduction factor of the deviated strip was increased up to 97% without any need for a Polyethylene layer, i.e. there is low contact pressure as well as a low friction effect on the breaking force of the strip.
- With the help of Polyethylene layer (HD-PE) for a deviation angle of 30° and by using a bending radius of 1000 mm the acceptance criteria for mandatory requirements, which are listed in the Guideline for European Technical Approval of post-Tensioning Kits for Prestressing of Structures, can be satisfied , i.e. reduction factor up to 95%.
- For deviation angles between 30° and 110° an ultimate strength reduction factor up to 86% should be considered in the design.

REFERENCES

- Hwash, M., Knippers, J. & Saad, F. 2007. Experiments on deviated CFRP-Strips for external prestressing. In COBRAE Conference, Benefits on Civil Engineering, Stuttgart, Germany
- ETAG 013, Edition June. 2002. Guideline for European Technical Approval of post-Tensioning Kits for PRESTRESSING OF Structures; EOTA, Brussels
- Hwash, M., Knippers, J. & Saad, F. 2008. Behaviour of Deviated CFRP-Strips. In Fourth International Conference on FRP Composites in Civil Engineering, CICE2008, Zurich

Study of Static Load Tests of Bond-Type Anchors for CFRP Tendons

Wen-hua Cai

College of Civil Engineering, Key Laboratory of Concrete and Prestressed Concrete Structure of Ministry of Education, Southeast University, Nanjing 210096, China; Civil Engineering of Yancheng Institute of Technology, Yancheng, 224003, China

Ji-wen Zhang, Shu-ting Liang & Yong-ming Tu

College of Civil Engineering, Key Laboratory of Concrete and Prestressed Concrete Structure of Ministry of Education, Southeast University, Nanjing 210096, China

ABSTRACT As a novel type of bond-type anchors, straight pipe plus inner cone bond-type anchors for CFRP tendons have a better development prospect, because which have advantages of both straight pipe bond-type anchors and inner cone bond-type anchors. However, the study at home and abroad is very little. In this paper, through carrying out static load tests for four groups of anchor assemblies, the failure modes, load-slip behavior and the strain development of CFRP tendons in the loading process are researched. The results showed that straight pipe plus inner cone bond-type anchors for CFRP tendons had a good anchorage performance. The research work done for bond-type anchors of CFRP tendons used in pilot project of suspended construction had provided reliable basis.

1 INSTRUCTIONS

Carbon Fiber Reinforced Polymer (CFRP) is a new type of composite material, which is based on resin matrix, and added adjuvant, and then shaped by drawing and surface treatment. Carbon fiber composite materials due to high-strength, lightweight, corrosion resistance, etc, are increasingly widely used in practical engineering, especially in civil engineering fields. At home and abroad, the research and application of the prestressed CFRP tendons, bars, cables used for reinforcement and enhancement are also more and more. The study and application show that CFRP tendons and cables are being gradually replaced steels and strand in traditional building structure and large-span bridge structure, and have increasingly become major force components. However, due to the axial and transverse different properties of CFRP, resulting in the ultimate bearing capacity of prestressed CFRP tendons structure will be more dependent on anchorage system than the strength of CFRP tendons themselves. These show that selection or design of economic, practical, safe and efficient anchor is crucial. At present, various forms of anchors and cable anchor system have been developed at home and abroad, according to the different anchoring mechanism which can be divided into three categories, namely, mechanical clamp-type anchor, bond-type anchor and mixed-type anchor. The bond-type anchor has the best anchorage properties and most widely used

for transferring shear and avoiding biting geosynthetics through the bond strength, friction, and mechanical force on the interface.

At present, in home and broad the study of bond-type anchor focused on the anchorage performance test of a single CFRP tendon anchorage system, while for dragon CFRP tendons is very few. In this paper, the test of four CFRP tendons anchorage system encapsulated with epoxy is carried out.

2 TESE CONTENT

Reference to the relevant provision, the test method is determined. Then, the influencing factors affecting the anchorage performance, different surface of CFRP tendons and different bond length, will be discussed.

2.1 Anchorage design

Bond-type anchor according to the different shape of the internal sleeve can be divided into straight-type, inner cone and the straight plus cone. Straight-type diameter is small, but the anchorage length is large, cone diameter is larger, while the anchorage length can be smaller, the slip is large. However, straight pipe plus inner cone bond-type anchorage with the advantages of straight-type and cone has better application prospect. The experiment is exactly on the straight pipe plus inner cone anchorage, and its basic structure is shown in Figure 1.

The CFRP tendons used in the experiment are

produced by Nanjing Equipment Manufacturing Co.Ltd, and the raw silk is imported from Japan, according to 65% of fiber volume fraction the tendons are formed. The diameter of CFRP tendon is 8 mm, and its surface shape is shown in Figure 2.

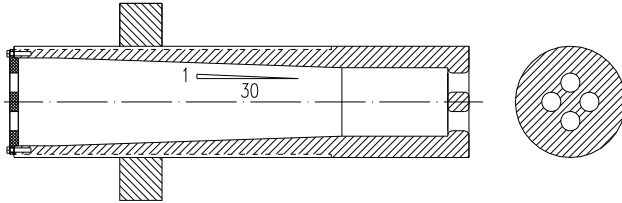


Figure 1 Geometrical parameters and structure of bond-type anchor

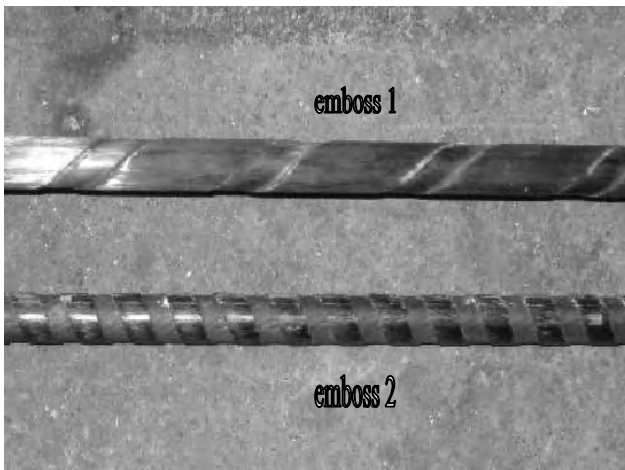


Figure 2 Surface shape of CFRP tendons

The epoxy resin used, namely, LICA structure adhesive is produced by Nanjing Hightop Limited Liability Company.

2.2 Loading method and measuring contents

The static load tests of anchor system for anchorage performance were carried out on the 3 m pedestal of prestressed laboratory of Southeast University. In the process of test the tension is provided by hydraulic jacks, the strain development of CFRP tendons can be measured through the strain gauges pasted on the CFRP tendons, and the relative slip between the CFRP tendons and anchor can be measured through dial indicators. Test device is shown in Figure 3 and four anchor specimens are listed in Table 1.

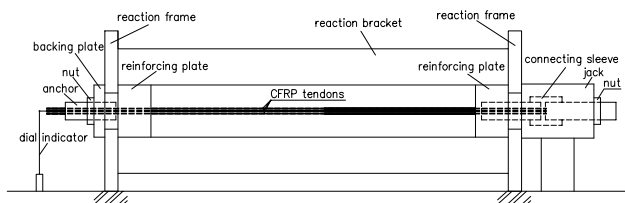


Figure 3 Test set-up

Table 1 Anchor system specimens

Specimen No.	Surface shape of tendons	Anchorage length (mm)
1	Emboss 1	300
2	Emboss 1	350
3	Emboss 2	300
4	Emboss 2	350

3 TESTS RESULTS AND ANALYSIS

3.1 Failure modes

The typical failure modes of bond-type anchors are mainly three: pull-out destruction, the CFRP tendons fractured just in front of anchor, pull-off damage, in which the first two failure modes may appear at the same time. In this static load test of bond-type anchor for CFRP tendons, mainly failure modes are the above-mentioned three kinds of failure modes, as shown in Figure 4.



(a) Pull-out destruction and the CFRP tendons fractured just in front of anchor



(b) Pull-off damage

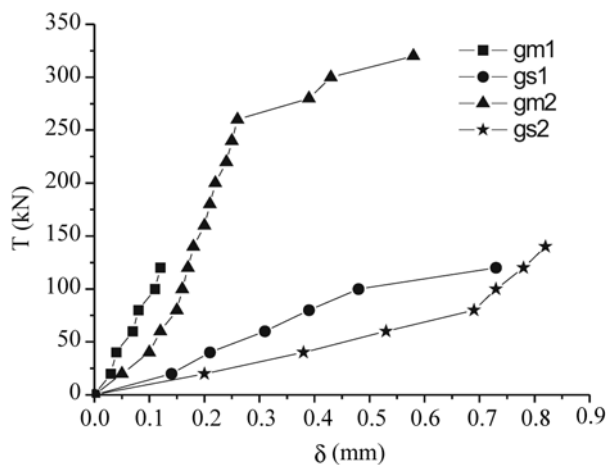
Figure 4 Failure modes of anchor assemblies

The failure modes shown in Figure 4(a) are disadvantage and should be avoided. The reasons for these failure modes may be that due to the position deviations and weight of CFRP tendons, vary lengths between the two anchors were appeared, then the initial eccentricity was produced, which induced to asynchronous face of CFRP tendons and made the CFRP tendons not in pure axial

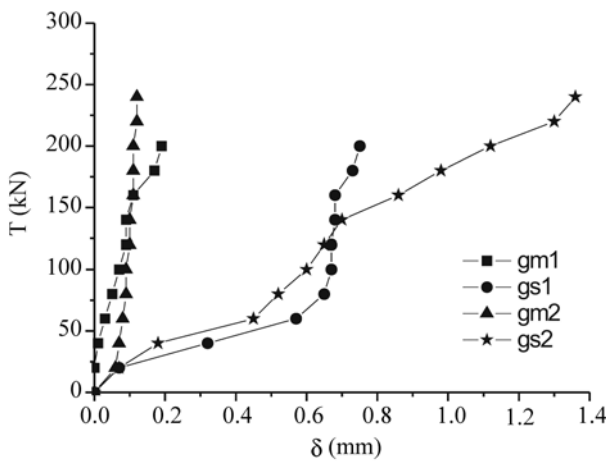
tension under service load, but in complex stress state, and lead to the CFRP tendons broken just in the front of anchors.

3.2 Load-slip curve

Load-slip curve is an important indicator of anchorage performance. Tension-side in this experiment was lengthened by connecting sleeve, so the slip of CFRP tendons was mainly measured from the fixed-side, which is classified into the beginning end and the terminal end, and the slip of beginning end should deduct the elastic elongation of CFRP tendons. The load-slip curves of specimens are shown in Figure 5 (For safety, when the load add to a certain value, dial indicators were retreated, so a full load-slip curve can not be given,)



(a) 300 mm length anchor



(b) 350 mm length anchor

(symbolic significance: g-fixed side, m-terminal end, s-beginning end, 1-emboss 1, 2-emboss 2)

Figure 5 Load-slip curve

As can be seen from Figure 5, with the load increasing, the whole load-slip curves of anchor specimens show non-linear. When the load reaches a certain value, the ratio of load and sliding will be changed, that is the slope of curve changed. The terminal end slip significantly less than the beginning end, analyze the reason may be

that, with the tension load increasing, the stress of the epoxy resin near the beginning end of anchor is gradually increasing, and eventually the stress exceeds the strength, then the cracking and failure appear, thus result in more axial force transforming to the terminal end of anchor, and at this time the stress of epoxy resin gradually play a pole. In addition, figure 5 and observation show that the slips at the beginning end and terminal end of the anchor are small in initial and middle stage, while nearly destroyed load and failure, larger slips produce, which indicates that the spin-off section is large and the reserves strength yet to be further improved.

3.3 Strain of CFRP tendons

For the bond-type anchor of CFRP tendons is concerned, the anchorage performance can be evaluated from the uniformity of the force suffered by the CFRP tendons.

The idea anchor of multi-CFRP tendons should try to ensure that all CFRP tendons suffered uniform force, otherwise it will be because of the early damage of part CFRP tendons caused the anchor assembly suffered eccentric force, and thus makes the anchor low bearing capacity and inefficient.

The strain of each CFRP tendon in anchor assembly was measured in this experiment, and the stress distribution was shown in Figure 6.

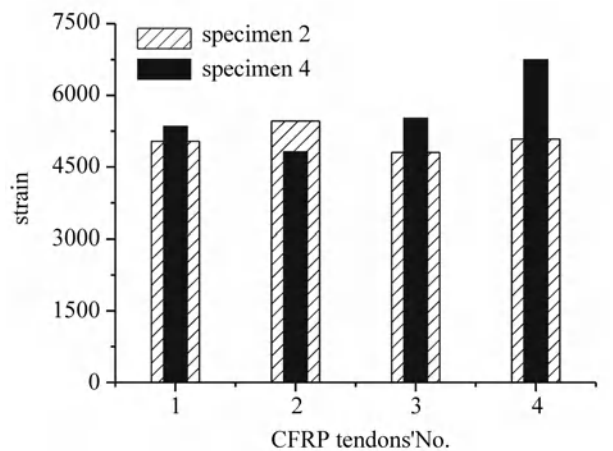
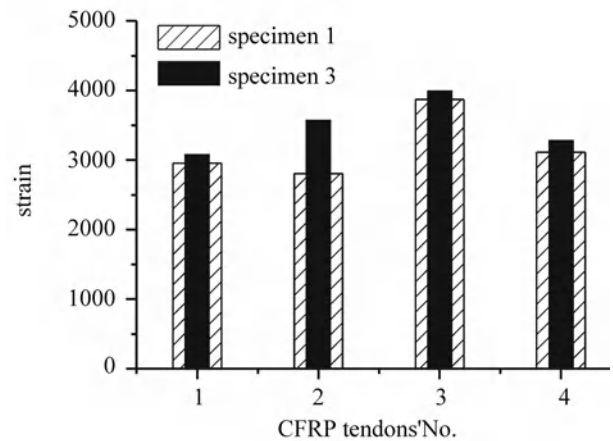


Figure 6 Strain of four anchor assemblies respectively at load of 120kN, 200kN, 320kN, 400kN

As can be seen from Figure 6, there is a certain difference of strain between each CFRP tendons in the same anchor assembly. This difference indicates that there are asymmetry forces of CFRP tendons in the process of tension, but the difference is not significant. All CFRP tendons working together or not will directly affect the anchorage performance of bond-type anchor.

4 CONCLUSION

(1) In this experiment, the anchor assembly of CFRP tendons destructed in typical failure modes.

(2) The slips at the beginning end and terminal end of the anchor are small in initial and middle stage, while nearly destroyed load and failure, larger slips produced, which indicated that the spin-off section is large and the reserves strength yet to be further improved.

(3) There is a certain difference of strain between each CFRP tendons in the same anchor assembly, but the difference is not significant.

REFERENCES

- Lang,D.2004. Experimental study on the static behavior of anchorage system for CFRP tendons[D] Changsha: *master thesis of Hunan University*.
- Zhang,J.W, & Zhu,H. & Lu,Z.T. & Zhao,K.Z. 2004. Development of anchor devices of prestressed FRP tendon[J].Beijing: *Industrial Architecture*(supplement).
- Mei,K.H.& Lu Z.T.& Zhang,J.W.& Zang,H. 2005. Study of static load tests of CFRP stay cable anchors[J].*Bridge Construction*, 20-23.
- Zhu,M.J. & Liu,H.W. 2002 A research of fiber reinforced plastics (CFRP) and its applications[J].Liangyungang: *Journal of Huaihai Institute of Technology*, 64-67.
- Gu,Q.& Zhang,X.S.& Peng,S.M. 2003. General introduction of the study and application of new FRP materials[J]. Wuhan: *Journal of Huazhong University of Science and Technology*, 88-92.
- Jiang,T.Y.& Fang,Z.2008. Experimental investigation of wedge-type anchors for CFRP tendons[J].*China Civil Engineering Journal*, 60-69.
- Cai,W.H. etc. 2009. Analysis of Mechanical Behavior of Bonding Anchorages for CFRP Tendons[J]. England: *World Journal of Modelling and Simulation*.
- Cai,W.H. etc. 2009.The Finite Element Analysis on Bond-type Anchorages for High Strength CFRP Tendons[J]. England: *World Journal of Modelling and Simulation*.
- Zhang,Y.C. & Xu, D.X. 2005. The application and prospects of new CFRP material in bridge construction[J].Chongqing: *Journal of Chongqing Jiaotong University*, 28-30.
- Fang,Z.& Liang,D.& Jiang,T.Y.2006. Experimental investigation on the anchorage performance of CFRP tendon in different bond mediums[J]. Beijing: *China Civil Engineering Journal*, 47-51.

Bond Type Anchorage Systems for Permanent High Strength CFRP Ground Anchors

Matthew Sentry (matthew@geotech.net.au)

Department of Civil Engineering, Monash University, Clayton, Australia & Geotechnical Engineering, Tullamarine, Australia

Riadh Al-Mahaidi

Faculty of Engineering and Industrial Sciences, Swinburne University, Hawthorn, Australia

Abdelmalek Bouazza

Department of Civil Engineering, Monash University, Clayton, Australia

Len Carrigan

Geotechnical Engineering, Tullamarine, Australia

ABSTRACT CFRP ground anchors have an integral place in the ground anchor industry, providing designer and contractors with a corrosion resilient anchor which minimises the labour intensive corrosion protection required when using steel strands. Successful anchoring of long strand lengths in a confined ground anchor environment has been the greatest constraint in the development of CFRP ground anchors. Recent research undertaken at Monash University and Geotechnical Engineering has developed a reliable and compact bond type anchorage head system, practical for permanent ground anchor applications. Laboratory and full scale testing has been successfully carried out. This paper provides tests results on a four and ten strand CFRP modified bond type anchor head system with a reduced bond length. Results showed failure of specimens were within the CFRP fibres due to tensile rupture. Negligible movement at the bond anchor head were recorded.

1 INTRODUCTION

The applied tensile force to a ground anchor system requires to be locked off, generally at the surface of the substructural member. There are many methods to lock this applied load off, ensuring a tensile/resistive force is held, depending on structural situation. Unfortunately not all anchor head systems are applicable to FRP applications, in particular ground anchored structures.

Lateral pressures applied using a barrel and wedge system is acceptable for homogenous materials that can distribute high forces over a short length with minimal deformity and impact on performance. The barrel and wedge anchoring devices are not as acceptable to heterogeneous materials such as FRP. Due to the unidirectional strength of FRP's, applied lateral pressures can cause over stressing of the composite structure resulting in premature rupture of individual fibre tows effectively over loading the surrounding fibres and causing a premature failure within the barrel/wedge system. As presented, modification to enable the use of barrel and wedges have been investigated and developed by manufacturers. These systems rely on using a combination of soft metals sleeves bonded to the strand and oversized soft metal, variable stiffness, or

non-metallic wedges to support the highly concentrated bi-directional stresses at the anchor head (Shrive et al., 2000, Reda and Shrive, 2003, Sentry et al., 2009).

Bond type anchor head systems are a successful anchoring method for FRP applications (Zhang and Benmokrane, 2004). To date, bond type anchor head systems have been large and cumbersome for ground anchor projects where area restrictions at the anchorage zone is quite common. Minimum required bond lengths for an FRP anchor head system is in excess of 500mm (ACI, 2004, Zhang and Benmokrane, 2004). Various mediums have been used including cementitious and resin based annulus with limited success in reducing these bond lengths. Research has shown that resins with low modulus of elasticity can potentially limit the peak shear stress during load transfers, while high modulus resins are more efficient at long-term creep control (Benmokrane et al., 1997). Cementitious based grouts with expansive additives perform better than standard cementitious grouts (Zhang and Benmokrane, 2002, Xue et al., 2008).

A limited number of lock-off systems have been established for bond type anchor heads, which primarily centre around using a locking nut configuration

(Benmokrane et al., 2000). This paper presents alternative bond type anchoring systems that can reduce the overall bonded anchor head length.

2 MODIFIED BOND TYPE ANCHR HEAD ASSESSMENT

The patented modified bond type CFRP anchor head system (Sentry and Carrigan, 2009) was developed to ensure ultimate failure was within the CFRP strand and not the anchor head whilst minimising bond length requirements and the overall physical anchor head dimensions. The modified anchor head also established an easy method for fabrication by use of common materials including cementitious and epoxy based grouts as the primary bond agent (this paper looks only into cementitious based grout results). Tests presented are for a four and ten strand CFRP modified anchor head. Each test was conducted to ultimate capacity.

2.1 Modified bond type anchor head materials

The modified bond type anchor head system utilised a 15.2mm diameter CFRP strand (CFCC – Tokyo Rope) with material properties as per Table 1 (comparisons made to steel strand). The anchor head system has been manufactured from both plastics and metals; However, results presented herein are for the metallic based anchor head components (bearing plate and anchor head casing) (Figure 1).

Tests are presented on a four and ten strand CFRP modified bond type anchor head system with a maximum bond length of 500mm. Bond lengths shorter than 500mm has been successfully achieved using the modified method of fabrication (Sentry, 2010).

Table 1

Property	CFCC	Steel
Dimensions		
Diameter (mm)	15.2	15.2
Cross Sectional Area (mm ²)	113.6	143
Linear Weight (g/m)	226	1125
Carbon Fibre		
Minimum fibre volume ratio	0.62	–
Density (g/cm ³)	1.5	–
Tensile strength (MPa)	4200	–
Elastic modulus (GPa)	240	–
Resin		
Type	Epoxy	–
Density (g/cm ³)	1.6–2.0	–
Tensile strength (MPa)	80	–
Product		
Tensile strength (MPa)	2200	1830
Elastic modulus (GPa)	141	195

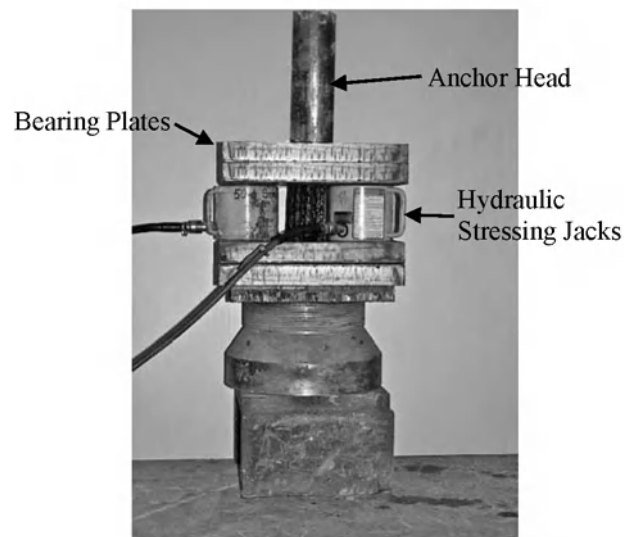


Figure 1 Test set up of modified bond type anchor head system

2.2 Method of Assessment

Test procedure was adopted for both four and ten strand anchor head test and comparisons made against laboratory based single strand results. Specimens were tested as per figure 1. Load was increased gradually in 7% increments of estimated ultimate load (T_{ult}). Each increment was sustained for up to five minutes prior to increasing to next increment to make observations. Test was carried out until a failure occurred. A 50mm-travel dial gauge was located on top of the anchor head to record any movement of the top anchor head unit during testing. Due to destructive nature of test, a measuring marker was located on one hydraulic jack's extension ram to record jack extensions at each load increment. Measurements were readable to 0.5mm. High speed cameras were used to visually record failure mode of the ten strand anchor head. Image speed of camera was 500 frames per second.

3 RESULTS

3.1 Anchor head bond agent strength results

A cementitious grout mix was used as the bond agent in the anchor head. A 28 day unconfined compressive strength tests were carried out on 50mm³ grout cubes taken during the casting of the four and ten strand anchor head. Results showed a density of 2123kgm⁻³ and an unconfined compressive strength of 81.3MPa after 28 Days. Minimum unconfined compressive strength of 60MPa was reached after just over 48 hours.

3.2 Four strand modified bond type anchor head

Specimen failure was due to catastrophic rupture of the strands within the free length and at the surface of the anchor heads proximal end (Figure 2). Failure was sudden across all four strands at a peak load of 1120kN (280kN/strand). Failure occurred at the peak of the

elastic zone at the estimated ultimate strand system capacity (Figure 3). There were no signs of radial cracking of the grout at the distal ends of the anchor head, indicating stresses within anchor head had not exceed the confined compressive strengths of the grout and the bond stresses between grout and tendon.

Peak anchor extension of 0.49mm at a load of 1040kN was recorded. Extension at peak load was unobtainable due to the destructive rupturing of the test specimen at ultimate capacity.

The measured extension results show linear elastic behaviour of the test specimen up to ultimate load (Figure 3). The linear extension indicates no strand slippage was observed.

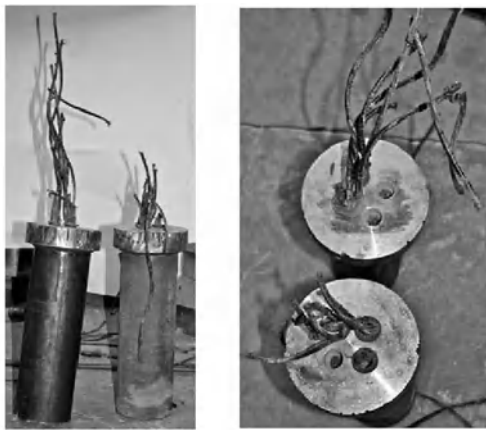


Figure 2 Failure of CFRP strand due to rupture within free length

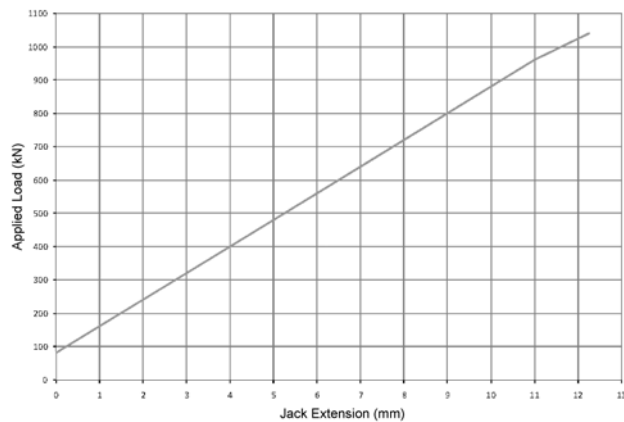


Figure 3 Applied load versus extension result for four strand CFCC anchor head test

When comparing the applied stresses-strain against the control single strand results (Sentry, 2010) (Figure 4), ultimate strain per strand in the four strand anchor head test is comparable with the single strand control results. Elasticity results are also comparable.

3.3 Ten strand modified bond type anchor head

Specimen failure was due to catastrophic rupture of the strands within the free length at the anchor heads proximal end. Failure occurred at a peak load of 2786kN

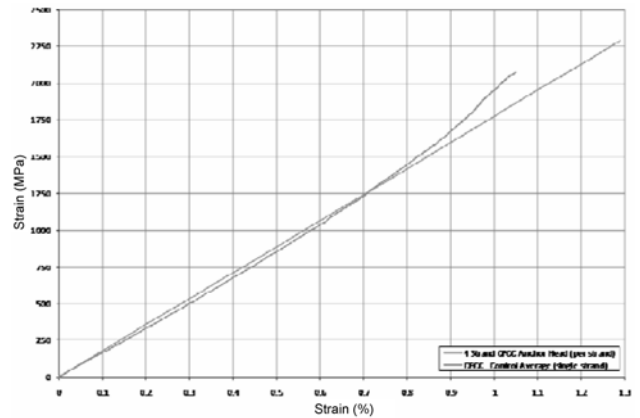


Figure 4 Stress versus strain comparison between four strand anchor head test and average single strand control specimen results

(278.6kN/strand). Ultimate stand load is comparable with the four and single strand results (Sentry, 2010).

Due to the extreme destructive nature of the ten strand test no load-extension or stress-strain results were obtainable.

Figure 5 shows the progressive rupture of strands during the final stages of loading. As one strand commenced its explosive failure, the stored energy was transferred to the surrounding strands. As these strand become over loaded, they too commenced rupturing in the same manner until complete rupture of all strands occurred. In addition to this observed phenomenon, flying debris also applied additional point load impact forces on the highly strung strands assisting in increasing the applied stresses to individual strands.

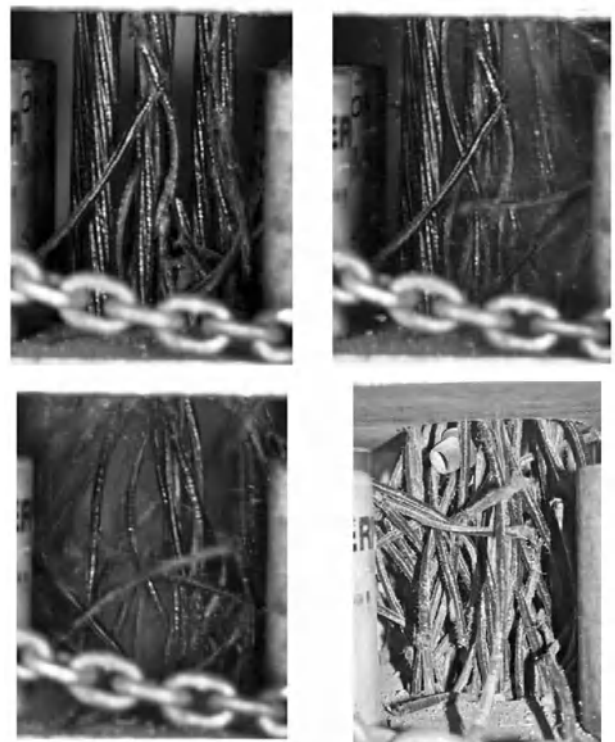


Figure 5 High speed camera images of progressive failure of ten strand modified CFRP anchor head test specimen

Non uniform load transfer between strands within the anchor test arrangement was captured on the high speed camera during the final loading stages of the test specimen. It was observed that this non-uniform load transfer was absorbed within the anchor head system right up to failure of the strands without any signs for bond stress failure, grout failure or CFRP failure within the anchor head unit itself.

4 CONCLUSION

The results from the four strand CFCC anchor head experiment shows that the modified bond type anchor head system (Sentry and Carrigan, 2009) is a successful anchor head system for FRP material whereby effective minimising of bond length is achievable.

The 10 strand anchor head test results provided a greater visual understanding in the progressive failure at ultimate strand capacity. Observations were recorded for the transfer of energy between strands as progressive strand failure occurred in the final moments prior to complete specimen strand rupture.

The cementitious grout mix used as the bonding annulus within the anchor head proved flowable enough to fully bond the strand configuration within both the four and ten strand samples with minimal voids present. Unconfined compressive strength tests were consistent between the two tests with strengths exceeding 70MPa after seven days curing. No bond stress failure was observed in both samples and no significant cracks were generated whilst specimens were under load. The cementitious grout mix provided a sound grout annulus to be able to fully anchor the required number of strands in a permanent ground anchor whilst under sustained loading.

In both tests, manufacture stand capacity was exceeded prior to fibre rupture further confirming that the 'Modified Bond Type Anchor Head' system is efficient and reliable at sustaining required loads without movement at the anchor head.

5 ACKNOWLEDGEMENTS

The authors would like to express their gratitude to

Monash University and the civil engineering laboratory and the project sponsor Geotechnical Engineering.

REFERENCES

- ACI 2004. ACI 440.3R-04: Guide Test Methods for Reinforcing or Strengthening Concrete Structures. *In*: RIZKALLA, S. H. & BUSEL, J. P. (eds.). American Concrete Institution.
- BENMOKRANE, B., XU, H. & NISHIZAKI, I. 1997. Aramid and Carbon Fibre-Reinforced Plastic Prestressed Ground Anchors and Their Field Applications. *Canadian Journal of Civil Engineering*, 24, 968.
- BENMOKRANE, B., ZHANG, B., CHENNOUF, A. & MASMOUDI, R. 2000. Evaluation of Aramid and Carbon Fibre Reinforced Polymer Composite Tendons for Prestressed Ground Anchors. *Canadian Journal of Civil Engineering*, 27, 1031.
- REDA, M. M. & SHRIVE, N. G. 2003. New Concrete Anchors for Carbon Fibre-reinforced Polymer Post-Tensioning tendons - Part 1: State-of-the-Art Review/Design. *Acı Structural Journal*.
- SENTRY, M. 2010. *An investigation into the durability and performance effects of CFRP strand in permanent ground anchors*. PhD, Monash University.
- SENTRY, M., BOUAZZA, A., AL-MAHAIDI, R., LOIDL, D., BLUFF, C. & CARRIGAN, L. 2009. Carbon Fibre Reinforced Polymer (CFRP): An Alternative Material in Permanent Ground Anchors. *Journal of Australian Geomechanics*, 44.
- SENTRY, M. & CARRIGAN, L. 2009. *An Anchorage System*. Australia patent application 2009906252.
- SHRIVE, N. G., SOUDKI, K. A., CAMPBELL, T. I., AL-MAYAH, A., KEATLEY, J. P. & REDA, M. M. 2000. Design and evaluation of wedge-type anchor for fibre reinforced polymer tendons. *Canadian Journal of Civil Engineering*, 27, 985.
- XUE, W., WANG, X. & ZHANG, S. 2008. Bond Properties of High-Strength Carbon Fiber-Reinforced Polymer Strands. *ACI Materials Journal*, 105, 11-19.
- ZHANG, B. & BENMOKRANE, B. 2002. Pullout Bond Properties of Fiber-Reinforced Polymer Tendons to Grout. *Journal of Materials in Civil Engineering*, 14, 399-408.
- ZHANG, B. & BENMOKRANE, B. 2004. Design and Evaluation of a New Bond-type Anchorage System for Fibre Reinforced Polymer Tendons. *Canadian Journal of Civil Engineering*, 31, 14-26.

Flexure-Shear Analysis of Concrete Beam Reinforced with GFRP Bars

Ramadass S & Job Thomas (job_thomas@cusat.ac.in)

Civil Engineering Division, School of Engineering, Cochin University of Science and Technology, Cochin, Kerala, India

ABSTRACT This paper gives the details of flexure-shear analysis of concrete beams reinforced with GFRP rebars. The influence of vertical reinforcement ratio, longitudinal reinforcement ratio and compressive strength of concrete on shear strength of GFRP reinforced concrete beam is studied. The critical value of shear span to depth ratio (a/d) at which the mode of failure changes from flexure to shear is studied. The failure load of the beam is predicted for various values of a/d ratio. The prediction show that the longitudinally FRP reinforced concrete beams having no stirrups fail in shear for a/d ratio less than 9.0. It is expected that the predicted data is useful for structural engineers to design the FRP reinforced concrete members.

1 INTRODUCTION

The fiber reinforced plastic (FRP) is a high strength, light weight material transparent to magnetic fields and radio frequencies. Due to its non-corrosive nature, the use of FRP bars in concrete is becoming popular when the structure is exposed to deicing or marine salts and other chemicals. As the modulus of elasticity of FRP bars are lower than the conventional steel bars, the structures reinforced with FRP bars show increased deflection when compared to similar structures reinforced with steel bars. The usage of FRP bars is limited due to the fact that it is to be cast in required shape at the manufacturing plant itself and cannot be bent at the work site (AslanFRP 2010). To account for the possible catastrophic failure in the FRP bars, the most FRP reinforced structures are recommended to design as over-reinforced sections. The design of FRP reinforced structures is often controlled by serviceability limits on deflection and crack width. Due to the superior corrosive resistance of FRP bars, the permissible crack widths in beams reinforced with FRP bars are higher when compared to that in steel reinforced concrete beams (Bank 2006). The recommendations for the design of FRP reinforced concrete structure are given in ACI 440.1R (2006). The codes of practice for the design of steel reinforced concrete structures are ACI318 (2008) and IS456 (2000).

El-Sayed, El-Salakawy and Benmokrane (2005) observed that shear strength of the concrete slabs reinforced with FRP bars increases with the increase in the amount of longitudinal reinforcements. Wegian and Abdalla (2005) found that the neutral axis depth of GFRP reinforced concrete beams is very small. El-Sayed,

El-Salakawy and Benmokrane (2006) showed that the shear strength of concrete beams increases with the increase in reinforcement ratio. Nehdi, Chabib and Said (2007) stated that the code of practice (ACI 440.1R 2006) estimates the conservative results for the computation of shear strength of FRP reinforced concrete beam. Hoult, Sherwood, Bentz and Collins (2008) indicated that a strong correlation exists between strain effect and the shear capacity of the beam. Tavares, Giogno and Paultre (2008) found that the strength of GFRP reinforced concrete beams is lesser than the strength of corresponding steel reinforced concrete beams. Ahamed, El-Salakawy and Benmokrane (2010) found that the shear strength of the beams is greater in beams with lesser spacing of GFRP stirrups. The flexure shear analysis of the FRP reinforced concrete beams is limited. This study addresses this gap in the literature.

2 ANALYTICAL MODEL

The details of the analytical model proposed in ACI440.1R(2006) are given.

2.1 Shear strength

The nominal shear strength (V_n) of the concrete section is computed by

$$V_n = V_c + V_f \quad (1)$$

where V_c is the shear strength of concrete section without stirrups and V_f is the shear resistance offered by GFRP stirrups. The V_c is computed by

$$V_c = 5(f'_c)^{1/2} b c \leq 8 (f'_c)^{1/2} b d \quad (\text{psi \& in}) \quad (2)$$

$$V_c = 0.4 (f'_c)^{1/2} b c \leq 0.66 (f'_c)^{1/2} b d \quad (\text{MPa \& mm})$$

where f'_c is the cylinder compressive strength, b is the

width of the beam, c is the depth of neutral axis in the cracked elastic section and d is the effective depth of the beam. f'_c is computed by

$$f'_c = 0.8 f_{ck} \quad (3)$$

where f_{ck} is the characteristic compressive strength of concrete based on cube specimens. c is computed by

$$c = k d \quad (4)$$

$$k = [(\rho_f \eta_f)^2 + 2(\rho_f \eta_f)]^{1/2} - (\rho_f \eta_f) \quad (5)$$

where k is the neutral axis depth ratio, ρ_f is the FRP longitudinal reinforcement ratio and η_f is the modular ratio

$$\rho_f = A_f / bd \quad (6)$$

$$\eta_f = E_f / E_c \quad (7)$$

where E_f is the longitudinal modulus of FRP bar and E_c is the modulus of elasticity of concrete. E_c is given by

$$E_c = 57000 (f'_c)^{1/2} \quad (\text{psi}) \quad (8)$$

$$E_c = 4700 (f'_c)^{1/2} \quad (\text{MPa})$$

V_f is computed based on 45 degree crack angle and is given by

$$V_f = \rho_v f_{fv} b d \quad (9)$$

$$\rho_v = A_{fv} / (b s_v) \quad (10)$$

where ρ_v is the vertical reinforcement ratio, A_{fv} is the area of the vertical stirrups across the shear crack, f_{fv} is the stress in the FRP stirrups and s_v is the spacing of vertical stirrups measured along the beam axis. f_{fv} is computed by

$$f_{fv} = \text{MIN} [0.004 E_f, f_{fb}] \quad (11)$$

where f_{fb} is the tensile strength of FRP rebar with a bend and is given by

$$f_{fb} = f_{fu} [0.05(r_b/d_b) + 0.3] \quad (12)$$

where f_{fu} is the design tensile strength of FRP bar, r_b is the inside radius of the bend of the stirrup and d_b is the diameter of the FRP rebar of the stirrup. In Eq. (12), the magnitude of (r_b/d_b) shall not be less than 3.0. f_{fu} is given by

$$f_{fu} = C_E f_{fu}^* \quad (13)$$

where C_E is the environmental reduction factor and f_{fu}^* is the guaranteed tensile strength of FRP bar. The value of C_E depends on the exposure conditions and the type of fibers and is given in ACI440.1R (2006).

2.2 Flexure strength

The nominal shear resistance (V_n^*) corresponding to the flexural capacity of a reinforced concrete beam subjected to concentrated load is given by

$$V_n^* = M_n / a \quad (14)$$

where M_n is the nominal moment of resistance of the section and a is the shear span. M_n is computed by

$$M_n = A_f f_f (d - a^*/2) \quad (15)$$

where A_f is the area of the longitudinal FRP bars, f_f is

the stress in the longitudinal bar and a^* is the depth of Whitney's stress block. f_f is given by

$$f_f = [(E_f \varepsilon_{cu})^2 / 4 + 0.85 \beta_1 f'_c (E_f \varepsilon_{cu}) / \rho_f]^{1/2} - 0.5 (E_f \varepsilon_{cu}) \quad (16)$$

where ε_{cu} is the ultimate strain in concrete and is equal to 0.003. β_1 is a factor depending on the concrete strength (f'_c) and is given by

$$\beta_1 = 0.85 \quad \text{when } f'_c < 4000 \text{ psi} \quad (17)$$

$$\beta_1 = 0.85 - 0.05 (f'_c - 4000) / 1000 \geq 0.65$$

$$\text{when } f'_c \geq 4000 \text{ psi}$$

$$\beta_1 = 0.85 \quad \text{when } f'_c < 28 \text{ MPa}$$

$$\beta_1 = 0.85 - 0.05 (f'_c - 28) / 7 \geq 0.65$$

$$\text{when } f'_c \geq 28 \text{ MPa}$$

In Eq. (15), a^* is given by

$$a^* = A_f f_f / (0.85 f'_c b) \quad (18)$$

2.3 Failure load

The failure load of the beam (P) subjected to four point bending as shown in Figure 1 is computed by

$$P = 2 * \text{MIN} (V_n, V_n^*) \quad (19)$$

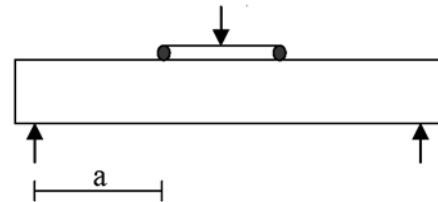


Figure 1 Schematic of loading in RC beam

The influence of various parameters on the failure load predicted based on the model proposed by ACI440.1R (2006) is analysed.

3 DETAILS OF BEAM

A concrete beam of size 600mm×220mm having an effective depth of 500mm is used. The cross sectional details of the beam are given in Figure 2. The guaranteed tensile strength of GFRP bars in the transverse direction is taken as 760 MPa and strength of bar in the longitudinal direction is 655 MPa (AslanFRP 2010).

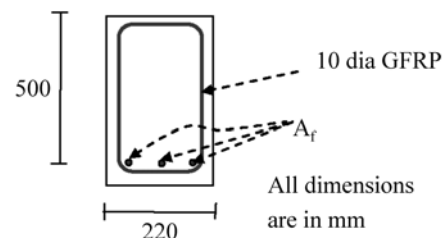


Figure 2 Cross sectional details of the RC beam

The variables considered for the study are longitudinal reinforcement ratio (ρ_f), vertical reinforcement ratio (ρ_v),

and concrete compressive strength (f_{ck}) and shear span to depth ratio (a/d). GFRP longitudinal reinforcement ratio (ρ_f) is varied between 1 and 4 percent. The vertical GFRP reinforcement ratio (ρ_v) of 0 to 1 percent is considered. The grade of the concrete (f_{ck}) is varied between 25 and 75 MPa. Failure load of the reinforced concrete beams with a/d ratio varying between 1.0 and 12.0 is predicted.

4 RESULTS AND DISCUSSIONS

The nominal shear strength and failure load of the beam of size 220mm×600mm has been computed using the model proposed in ACI 440.1R (2006). The influence of FRP reinforcement ratio on the shear strength of normal strength concrete beam has been evaluated ($f_{ck} = 25$ MPa) and is given in Figure 3(a). The shear strength of the beam with GFRP reinforcement increases with the increase in the vertical and longitudinal reinforcement ratio. The influence of longitudinal reinforcement on shear strength of FRP reinforced concrete beam is nominal.

The influence of concrete strength (f_{ck}) on the shear strength of beam reinforced with GFRP bars is given in Figure 3(b). The magnitude of vertical reinforcement ratio is taken as 0.5 percent for the prediction of shear

strength of beam given in Figure 3(b). The influence of concrete strength on the shear strength of FRP reinforced beam is limited.

The flexure shear analysis of the FRP reinforced beam is carried out and the results are given in Figure 4. The failure load (P) of the beam is predicted corresponding to the different values of shear span to depth ratio (a/d). The horizontal plateau of the graph shown in Figure 4 indicates the shear failure and the sloped portion indicates the flexure failure in the beam. The starting point of sloped regime represents the a/d ratio at which the mode of failure changes from shear to flexure. The

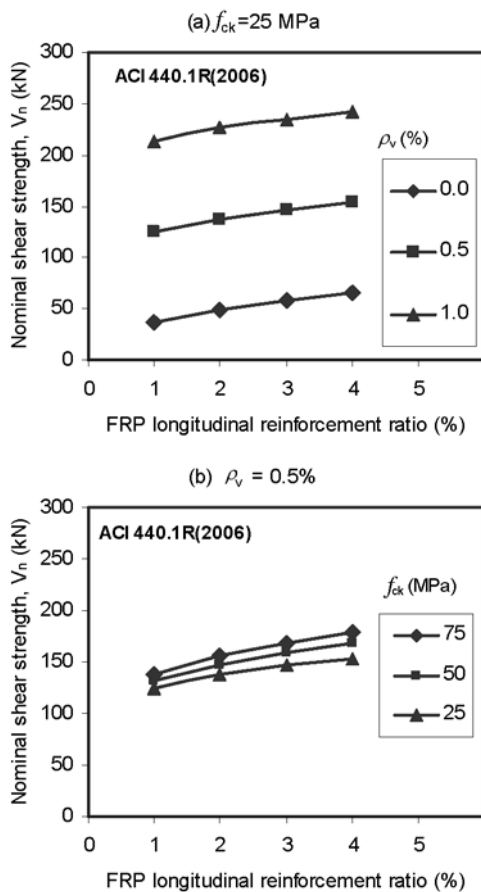


Figure 3 Predicted nominal shear strength of GFRP reinforced concrete beam

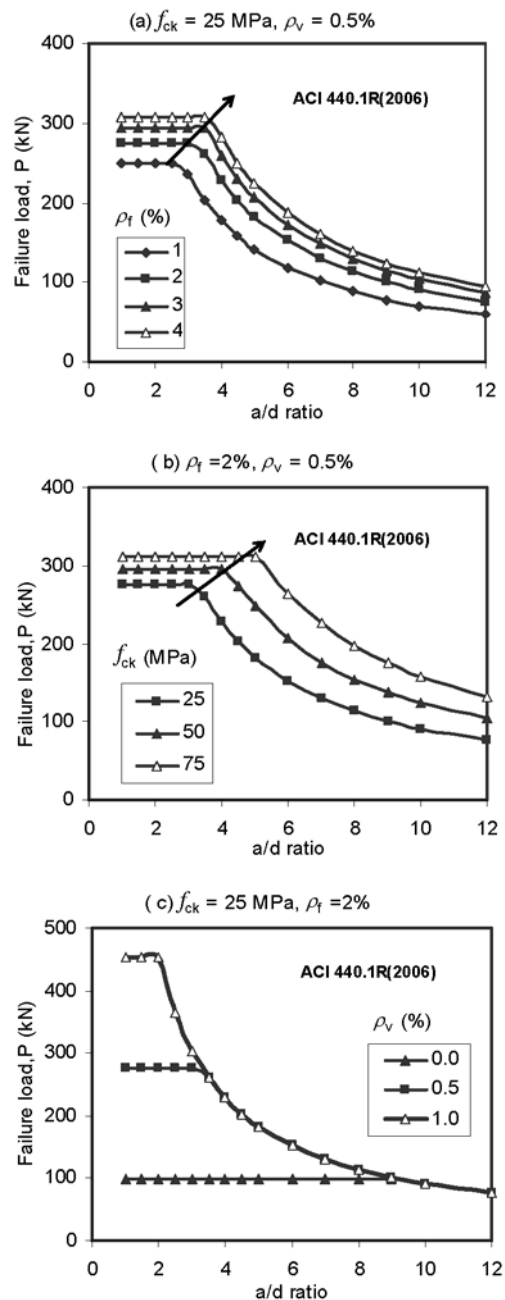


Figure 4 Predicted failure load of GFRP reinforced concrete beam

influence of the FRP longitudinal steel reinforcement ratio is given in Figure 4(a). The failure load of the beam increases with the increase in FRP longitudinal reinforcement ratio. The a/d ratio at which the mode of failure changes from shear to flexure increases with the increase in FRP longitudinal reinforcement ratio.

The influence of concrete strength (f_{ck}) on failure load of the beam (P) is given in Figure 4(b). The failure load of the beam increases with the increase in the concrete strength. The a/d ratio at which the mode of failure changes from shear to flexure increases with the increase in concrete strength.

The variation of the failure load of the beam (P) corresponding to various values of vertical reinforcement ratio (ρ_v) is given in Figure 4(c). For initial values of a/d ratio, the failure load in beams having 1 percent vertical reinforcement is found to be greater in magnitude when compared to the corresponding beam having 0.5 percent vertical reinforcement. The a/d ratio corresponding to the change in mode of failure from shear to flexure depends on the amount of vertical reinforcement. The predicted failure load of the beam corresponding to the higher values of a/d ratio is found to be equal in magnitude for all the values of vertical reinforcement ratio (ρ_v) and is represented by a single line in the inclined regime. This is expected because the flexural failure load depends on the amount of longitudinal reinforcement and not on the vertical reinforcement.

5 CONCLUSIONS

Based on the present study the following conclusions are arrived at.

- Effect of FRP reinforcement in the transverse direction on the shear strength of reinforced concrete beam is significant.
- Influence of FRP reinforcement in the longitudinal direction on the shear strength of FRP reinforced beam is nominal.
- The increase in shear strength of beam with the increase in concrete strength is limited.
- The a/d ratio corresponding to the change in mode of failure increases with the increase in the longitudinal or transverse FRP reinforcement.
- The prediction based on the model proposed by ACI 440.1R (2006) indicates that the FRP reinforced concrete beams having no transverse reinforcement fails in shear if the a/d ratio is less than 9.0.

6 ACKNOWLEDGMENT

Dr. Job Thomas thanks for the financial support rendered by Department of Science and Technology, Government of India under the scheme Fast Track Project.

REFERENCES

- ACI318. 2008. Building code requirements for structural concrete, American Concrete Institute, Farmington Hills, MI, 465p.
- ACI440.1R. 2006. Guide for the design and construction of structural concrete reinforced with FRP bars, American Concrete Institute, Farmington Hills, MI, 44p.
- Ahmed, E. A. El-Salakawy, E.F. & Benmokrane, B. 2010. Performance evaluation of Glass fiber reinforced polymer shear reinforcement for concrete, *ACI structural Journal*, 107(1): 53-62.
- AslanFRP. 2010, http://www.hughesbros.com/aslan100/Aslan%20100_GFRP_rebar_Flyer.pdf, 4p, 2010.
- Bank, L.C. 2006. Composites for construction: Structural design with FRP materials, John Wiley & Sons Inc., NJ, 551p.
- El-Sayed, A. El-Salakawy, E. & Benmokrane, B. 2005. Shear strength of one-way concrete slabs reinforced with fiber-reinforced polymer composite bars, *ASCE Journal of composites for construction* 9(2): 147-157.
- El-sayed, A.K. El-Salakawy, E.F. & Benmokrane, B. 2006. Shear strength of FRP-reinforced concrete beams without transverse reinforcement, *ACI Structural Journal* 103(2): 235-243.
- Haoult, N. A. Shewood, E.G. Bentz E.C. & Collins, M.P. 2008. Does the use of FRP reinforcement change the one way shear behaviour of reinforced concrete slab, *ASCE Journal of materials in civil engineering* 12(2): 125-133.
- IS456. 2000. Plain and reinforced concrete- code of practice-fourth revision, Bureau of Indian Standards, New Delhi, 100p.
- Nehdi, M. Chabib, H. El. & Said, A.A. 2007. Proposed shear design equations for FRP reinforced concrete beams based on genetic algorithms approach, *ASCE Journal of materials in civil engineering* 19(12): 1033-1042.
- Tavares, D.H. Giongo, J.S. & Paultre, P. 2008. Behavior of reinforced concrete beams reinforced with GFRP bars, *IBRACON structures and materials journal* 1(3): 285-295.
- Wegian, F.M. & Abdalla, H.A. 2005. Shear capacity of concrete beams reinforced with fiber reinforced polymers, *Elsevier Composite Structures* 71: 130-138.

Effect of Bond Parameters on Recoverability of RC Bridge Columns Reinforced with Ordinary Rebars and Steel Fiber Composite Bars

Mohamed F.M. Fahmy (mfmf1976@yahoo.com) & Z.S. Wu
Department of Urban & Civil Engineering, Ibaraki University, Hitachi, Japan

G. Wu
International Institute for Urban Systems Engineering, Southeast University, Nanjing, China

ABSTRACT In this study, effects of bond parameters on post-earthquake recoverability of RC bridge columns reinforced with ordinary deformed bars and innovative composite bars: steel fiber composite bars (SFCBs), are studied. A computer program is employed to investigate the effect of bond parameters on column post-yield stiffness and residual deformations. Then, the required recoverability is examined for experimentally tested columns with different unbonded length of longitudinal ordinary rebars, available from literature, and two tested scale-model RC bridge columns reinforced with different products of SFCBs, i.e. steel basalt-fiber composite bars (SBFCBs) and steel carbon-fiber composite bars (SCFCBs). The study showed that weaken bond between deformed bars and the surrounding concrete has no clear effect on column residual deformations, however, mitigation of residual deformations could be when columns are reinforced with SFCBs. Furthermore, bond effect could play an important role in the recoverability of structures reinforced with SFCBs, where both the achieved post-yield stiffness and residual deformations could be controlled.

1 INTRODUCTION

New seismic design philosophies for bridges recommend that important bridges subject to a near-land-large-scale interplate earthquake or an inland earthquake near the structure should be able to sustain the expected maximum lateral force in the inelastic stage with limited damages: structure should realize the existence of post-yield stiffness and its permanent deformations (residual deformations) should be limited, to ensure quick post-earthquake recoverability (Fahmy et al. 2009). The 1996 Seismic Design Specifications of Highway Bridges in Japan specifies that the residual displacement should not be greater than 1% of the piers height, JSCE (2000).

Bond between longitudinal reinforcement and concrete is a key factor controlling the performance of reinforced concrete (RC) structures. Because bond between the longitudinal bars and concrete results in concentration of damage at a specific localized interval of longitudinal bars where the local buckling occurs, Takiguchi et al. (1976) suggested mitigating this concentration of damage through unbonding of the longitudinal bars from concrete at plastic hinge zone. This suggestion was experimentally studied by Kawashima et al. (2001), where RC columns reinforced with different lengths of

unbonded bars at the plastic hinge zone were tested.

In light of the requirements of the new codes and the limited studies on bond controlled structures, this paper examines how is the performance of RC bridge piers could be affected by altering bond conditions between longitudinal steel reinforcement (deformed bars and SFCBs) and concrete.

2 ANALYTICAL INVESTIGATION

2.1 Fiber-Based Analysis of RC Columns with zero-length section element

Cyclic loading analysis is conducted using a computer program, Mazzoni et al. The confined concrete properties were based on Mander's model. The widely used Giuffrè-Menegotto-Pinto model is employed in this study to represent the hysteretic stress-strain behavior of longitudinal steel reinforcement. To find the effect of different bond conditions of longitudinal bars anchored into footing on performance of structures, the developed constitutive model by Zhao & Sritharan (2007) for the steel fibers is adopted here. This model for the steel fibers of the zero-length section element expresses the bar stresses (σ) versus loaded-end slip response (S). Hence, for well anchored rebar, the main parameters of this model are the yield and ultimate strengths of the

reinforcing bar (f_y and f_u) and the corresponding loaded-end slips S_y and S_u , respectively.

2.2 RC bridge column with deformed bars

Using these four parameters of Zhao and Sritharan model, effects of bond condition between steel reinforcement and concrete are studied here. Scale-model bridge column (Specimen A) tested by Kawashima et al. (2001) is considered in this study to reflect the effect of these parameters on column performance. The tested specimen had square cross-section of 400×400mm and 1450-mm-height. Specimen A was reinforced with twelve longitudinal rebars of 13-mm-diameter, lateral reinforcement consisted of 6-mm-diameter ordinary bars with spacing of 50mm. The tested compressive strength of the concrete cylinder was 20.6 MPa. The column was tested under constant axial load (160kN) and reversed cyclic lateral load.

The ultimate achieved strength of steel bars is function of steel bond condition with the surrounding concrete, e.g. when steel bars are unbonded to the surrounding concrete, it may not approach the ultimate strength and slip deformations would increase. Consequently, four cases are studied, Table 1, where the first case is that proposed by Zhao & Sritharan (2007) to consider the effect of strain penetration of longitudinal bars into foundation, second-fourth case studies examine the effects of poor bond between ordinary rebars and the adjoining concrete.

From the view point of post-earthquake recoverability of structures, it could be concluded from Figure 1 that weaken of bond strength with limited slip deformations is accompanied by a decrease of column strength after yielding, namely, zero or negative post-yield stiffness is the expected performance in the inelastic stage (Figures. 1 b & c, respectively), without any clear effect on column residual deformations. But, increase of steel slippage would be favored, where column permanent deformations could be reduced (Figure 1d).

Table 1 Studied bond properties of column reinforced with ordinary rebars

Case	Bond properties			
	S_y (mm)	σ_y (MPa)	S_u (mm)	σ_u (MPa)
1	S_y	f_y	S_u	$1.5f_y$
2	S_y	f_y	S_u	f_y
3	S_y	f_y	S_u	$0.8f_y$
4	$2S_y$	f_y	$2S_u$	f_y

2.3 RC bridge column with SFCBs

To guarantee a controlled hardening performance of steel reinforcement in the inelastic stage, it was approved by Wu et al. (2010) that hybridization of steel bar in its longitudinal direction with fiber reinforced polymers

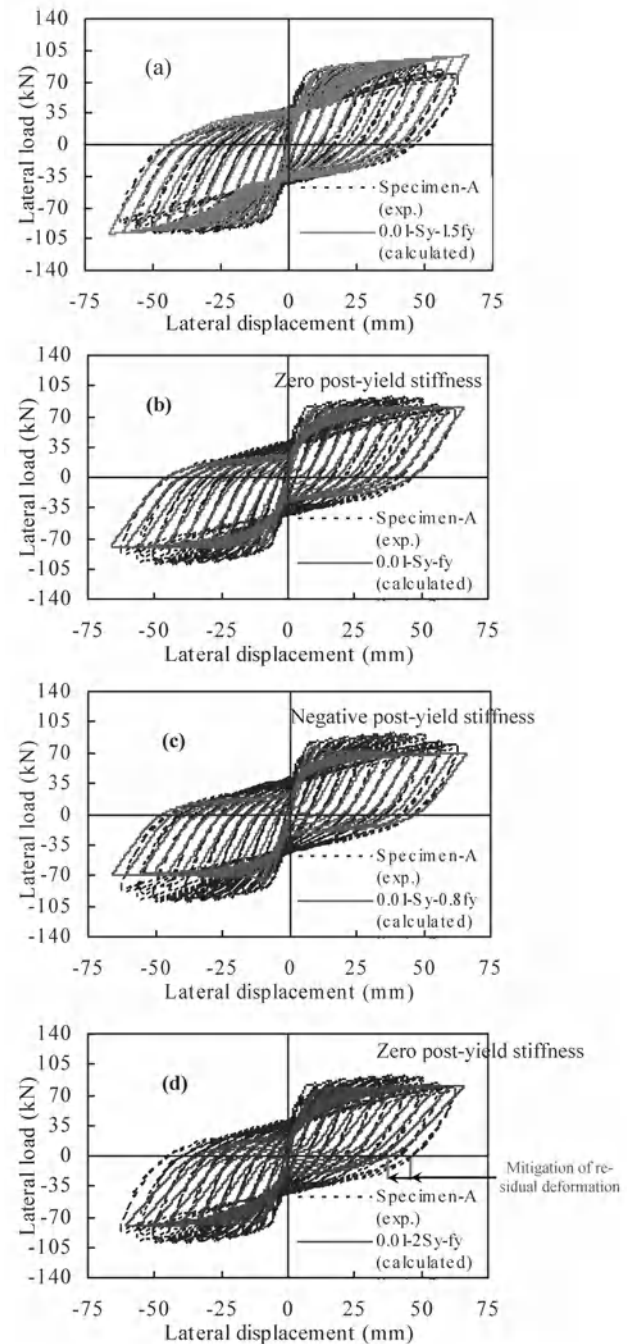


Figure 1 Bond effects on the performance of RC columns reinforced with ordinary rebars

(FRP) is a reasonable concept; where, the slope of post-yielding stiffness and end point of this stage could be define based on the type and amount of FRP used. Two types of the innovative rebars (SFCBs) were produced, where the longitudinal reinforcement consisted of inner steel rebar of 10-mm-diameter and outer fibers, i.e., 30 bundles of basalt fibers (Figure 2) and 40 bundles of carbon fibers. Mechanical properties of SFCBs are given in Table 2 for both products of SFCBs.

To investigate the effect of bond properties on the performance of RC bridge columns reinforced with the innovative rebars, four cases are considered in this study

for concrete column reinforced with SBFCBs, Table 3. Of course, the column performance is function of concrete-to-SBFCBs bond capacity. Consequently, three cases are studied here to examine the effect of achieved ultimate strength of SBFCBs on the performance of RC bridge columns. Last case study (case No. 4) considers the effect of the increase of rebars slippage when merely 60% of their ultimate strength could be achieved. The studied column has square cross-section of 300x300mm and 1300-mm-tall. It is typified CS10-B30 and reinforced with twelve SBFCBs, Table 2. The concrete compressive strength is ~38 MPa. The columns are analyzed under the effect of constant axial load (12% of column axial strength) and reversed cyclic lateral load.

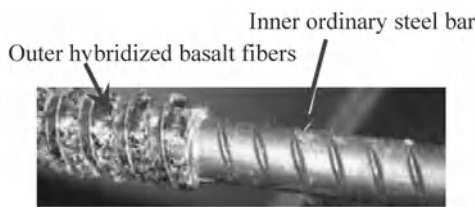


Figure 2 Product of steel basalt-fiber composite bar (SBFCBs)

Table 2 Properties of SFCBs and ordinary rebar

Type	Diameter (mm)	Elastic modulus (E_1) (GPa)	Yield strength (MPa)	Post-yield stiffness (E_2) (GPa)	Ultimate strength (MPa)	E_2/E_1 (%)
Φ10+30B (SBFCB)	13.2	142	312.4	16.6	691.3	11.7
Φ10+40C (SCFCB)	12.9	155.5	342.2	30.2	641.8	19.7
Φ14	14	200	340	-	340	-

Table 3 Studied bond properties of column reinforced with SFCBs

Case	Bond properties			
	S_y (mm)	σ_y (MPa)	S_u (mm)	σ_u (MPa)
1	S_y	f_y	S_u	f_u
2	S_y	f_y	S_u	$0.8 f_u$
3	S_y	f_y	S_u	$0.7 f_u$
4	$2 S_y$	f_y	$2 S_u$	$0.7 f_u$

Figure 3 shows the effect of bond properties on column post-yield stiffness (its slop and end point) and residual deformations. For instance, Figure 3.a shows that the highest achieved inelastic stiffness which ends at lateral drift of 40-mm (due to rupture of the outer basalt fibers) with the minimum residual deformations could be when SBFCBs achieve the ultimate strength.

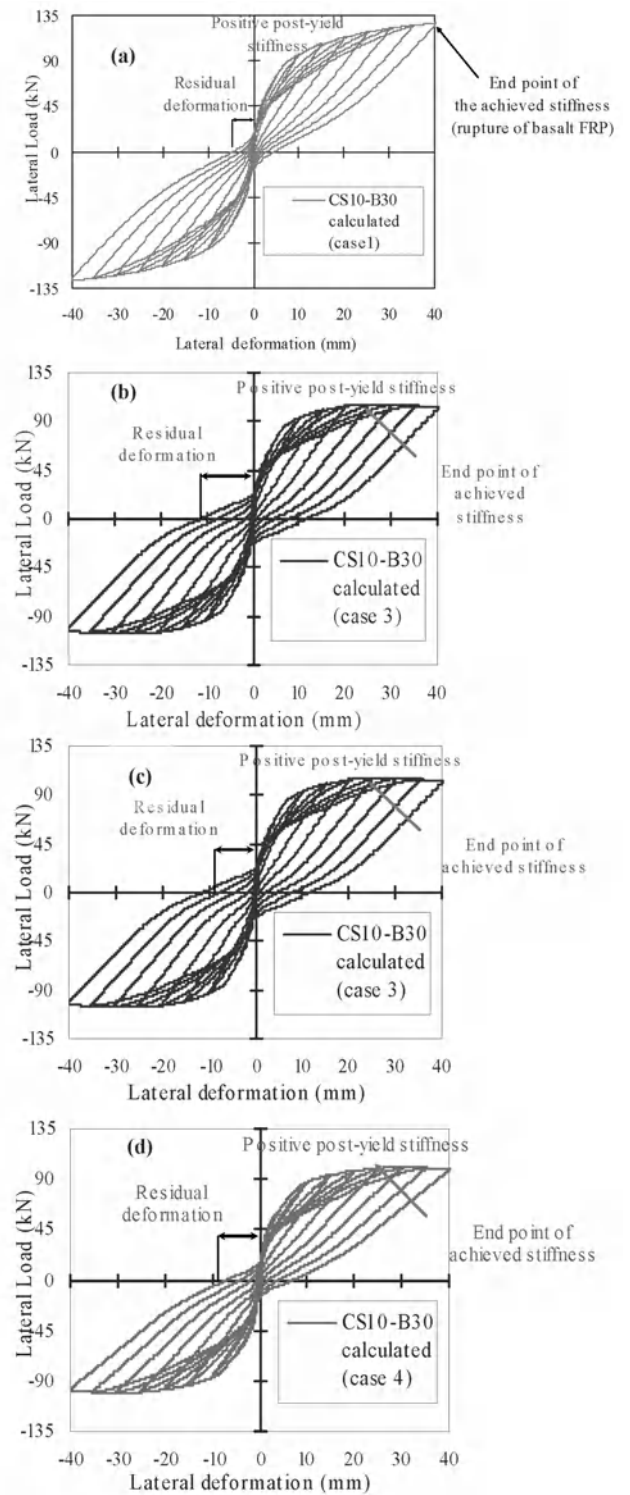


Figure 3 Bond effect on performance of RC column reinforced with SBFCBs

But, when bond between SBFCBs and concrete is weakened and rebars can not achieve the ultimate strength, the hysteretic response after column yielding divides to two parts: the first shows that the column can still carry the load even after the SBFCBs yields and hardening behavior has been exhibited and then column shows the ability to keep its achieved strength demonstrating a favorable ductility. Finally, it is clear from Figures 3. c&d

that the increase in slip deformations would be favorable for the required recoverability after seismic action, where the residual deformations could be mitigated.

3 EXPERIMENTALLY TESTED COLUMNS REINFORCED WITH ORDINARY REBARS AND SFCBs

Kawashima et al. (2001) conducted an experimental study on RC columns reinforced with different lengths of unbonded ordinary bars at the plastic hinge zone. Those columns are restudied from the view point of the required post-earthquake recoverability. Figure 4 shows that the increase of the length of the unbonded zone has no clear effect on column residual deformations. Besides, unbonding of rebars is accompanied by a reduction of the achieved strength. These results have good agreement with the analytical results presented in Figure 1. Although, it was reported by Kawashima et al. (2001) that the failure of concrete was much less in the unbonded column than standard column, unbonding of ordinary deformed rebars is not a reasonable tool to have a recoverable structure. Since bridge piers should keep their ultimate strengths in the inelastic stage with minimum residual deformations.

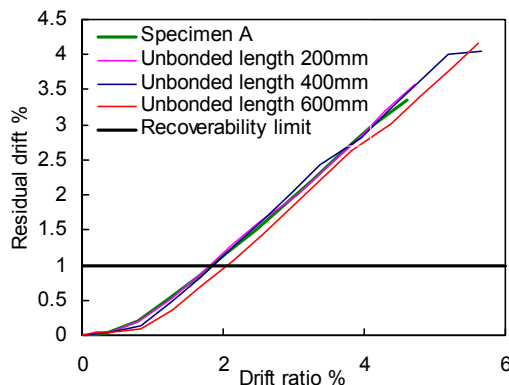


Figure 4 Residual deformations of bonded and unbonded columns reinforced with ordinary rebars

To investigate the recoverability of bridge columns reinforced with SFCBs in place of the ordinary reinforcement. Two columns were tested: the first typified CS10-B30 and the latter is CS10-C40 with previously defined materials and details in section (2-3). Moreover, one column (CS14) reinforced with twelve 14-mm diameter deformed rebars was tested, Table 2.

Figure 5 shows that the residual drift in columns reinforced with SFCBs was considerably lower than that of CS1. For instance, the conventionally reinforced column CS14 could not achieve a lateral drift at the recoverability limit, i.e. residual deformation equal to 1% of column height, over 1.91%, but hybridization of the longitudinal steel reinforcement with FRPs shifted

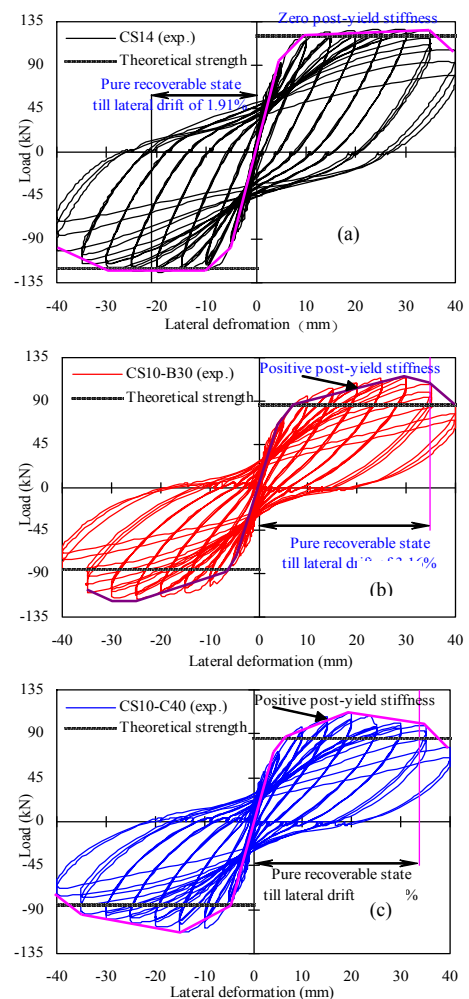


Figure 5 Hysteretic responses of RC columns reinforced with SFCB

the end of the recoverable state of columns CS10-B30 and CS10-C40 to 3.16% and 3.06%, respectively. Furthermore, the innovative columns had clear existence for post-yield stiffnesses, but column CS14 had a zero post-yield stiffness.

4 CONCLUSIONS

Unbonding of ordinary rebars is not a reasonable tool to have a recoverable structure.

Hybridization of steel rebars with FRP would be a reasonable protecting technology for important bridges.

REFERENCES

- Fahmy, M.F.M., Wu, Z.S., Wu, G. 2009. Seismic performance assessment of damage-controlled FRP-retrofitted RC bridge columns using residual deformations. *Journal of Composites for construction*; 13(6): 498-513.
- JSCE Earthquake Engineering Committee 2000. Earthquake resistant design codes in Japan. Japan Society of Civil Engineers (JSCE), Tokyo, Japan:150 pp.
- Takiguchi, K., Okada, K., and Sakai, M. 1976. Ductility capacity of bonded and unbonded reinforced concrete members. *Proc.*

- Architectural Institute of Japan. 249, 1-11.
- Kawashima, K., Hosoi, K., Shoji, G., & Sakai, J. 2001. Effects of unbonding of main reinforcements at plastic hinge region on enhanced ductility of reinforced concrete bridge columns. *Structural and Earthquake Engineering, Proc. JSCE*, 689/I-57, 45-64.
- Mazzoni, S., McKenna, F., Scott, M.H., Fenves, G.L., et al. *Open System for Earthquake Engineering Simulation User Manual version 2.1.0*. Pacific Earthquake Engineering Center, University of California, Berkeley, CA.
- Zhao, J., Sritharan, S. 2007. Modeling of strain penetration effects in fiber-based analysis of reinforced concrete structures. *ACI Struct. J.* 104(2): 133-141.
- Wu G, Wu ZS, Luo YB, Sun ZY, Hu XQ. 2010. Mechanical properties of steel fiber composite bar (SFCB) under uniaxial and cyclic tensile loads. *Journal of Materials in Civil Engineering, ASCE*, (Accepted).

Long-Term Performance

Effect of Reinforcement Detailing on the Behavior of GFRP-RC Beam-Column Joints

Mohamed Mady, Mohamed Hasaballa, Amr El-Ragaby & Ehab El-Salakawy (ehab_elsalakawy@umanitoba.ca)

Department of Civil Engineering, University of Manitoba, Winnipeg, Manitoba, Canada

ABSTRACT The behavior of FRP bars under tension-compression load reversals in RC beam-column joints and frame structures has not yet been fully explored. This research project is attempting to partially fulfill this gap by investigating the structural performance and ultimate capacity of concrete beam-column connections totally reinforced with FRP bars. A total of three full-scale exterior beam-column joint (T-shaped) prototypes were constructed and tested under simulated seismic load conditions. The main test parameter was the detailing of the beam longitudinal bars within the joint by using either straight bars or bent bars. Test results are presented in terms of load vs. drift ratio, and strains in longitudinal reinforcement. The experimental results showed a superior performance for the GFRP reinforcement when bar slippage within is prevented through proper detailing of the beam bars within the joint.

1 INTRODUCTION

The fiber reinforced polymer (FRP) reinforcement is currently being used as an innovative material in new concrete structures especially those in harsh environments such as bridges and parking garages. The main driving force behind this effort is the superior performance of FRP in corrosive environments due to its non-corrodible nature. FRP reinforcements, in general, offer many advantages over the conventional steel such as high strength-to-weight ratio, favourable fatigue performance and high electro-magnetic transparency. However, the FRP material exhibits linear-elastic behavior up to failure with relatively low modulus of elasticity (40–50 GPa for glass FRP “GFRP” and 110–140 MPa for carbon FRP “CFRP” compared to 200 GPa for steel). Moreover, they have different bond characteristics, relatively low strength under compression stresses, and some concerns still exist about their performance under load reversal conditions (CSA 2002). In seismic zones, moment-resisting frames require sufficient ductility to dissipate the seismic energy. Due to the non-ductile linear elastic characteristics of FRP reinforcements, concerns still exist among researchers on the validity of using FRP in such structural members that require the inelastic behavior (ductility) of reinforcement.

2 ACKGROUND

Very little research has been conducted to study the behavior of concrete columns and frame structures internally reinforced with FRP bars subjected to seismic loading. Fukuyama et al. (1995) noticed the elastic behavior of concrete frames reinforced with longitudinal

aramid FRP bars until failed by concrete crushing. Sharbatdar et al. (2007) reported that exterior beam-column joints reinforced with carbon FRP longitudinal bars and carbon FRP grids were able to achieved a lateral drift ratio exceeds 3.0%. This drift capacity exceeds the 2.5% drift ratio recommended by the National Building Code of Canada (NBCC 2005).

The focus of this research is to further investigate the effect of the beam reinforcement detailing within the joint on the ultimate and service performance of the beam-column joints in RC frames subjected to seismic loading. The most critical zone in moment resistant frames is the exterior joints due to the unsymmetrical conditions and restraints associated with providing limited anchorage length for the beam longitudinal reinforcement. As a common practice in case of exterior beam-column joints reinforced with conventional steel, top and bottom beam longitudinal reinforcement are usually bent inside the joint to enhance their bond strength to concrete, prevent slippage, and to provide more confinement to the joint. In case of FRP reinforcement, some restrictions still exist when using bent bars. The FRP bars have to be formed to the required shape during the manufacturing process, which currently limiting the straight part length of a bent bar. Moreover, due to relatively low lateral strength, the tensile strength of FRP bars is reduced by up to 50% at the bend location (ACI 2006).

3 EXPERIMENTAL PROGRAM

3.1 Test specimens

An experimental program is carried out in the McQuade

Heavy Structural Laboratory at the University of Manitoba to investigate the performance of GFRP reinforcement in RC frames subjected to seismic loading. The experimental program includes construction and testing of a number of full-size exterior (T-shape) beam-column joint prototypes. Three full-size beam column joint prototypes were constructed and tested. All test prototypes were reinforced with No. 16 (15.9 mm diameter) GFRP longitudinal bars for both beams and columns. Figure 1 shows the overall dimensions of a typical test prototype. Table 1 shows the details of test specimens.

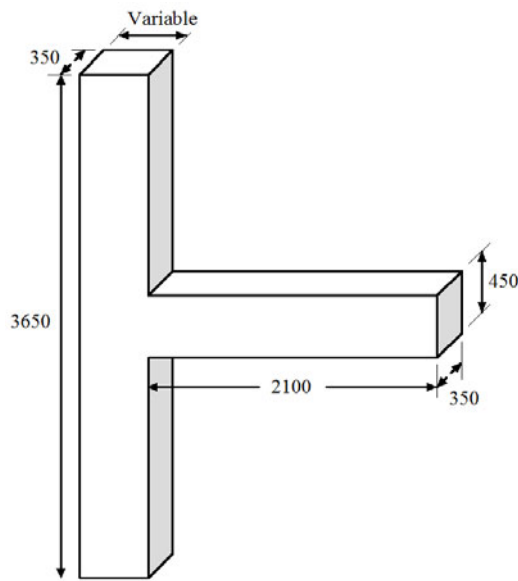


Figure 1 Geometry of beam-column joint specimens

Table 1 Specimens details

Specimen	G1	G2	G3
Column depth (mm)	350	350	500
Beam reinforcement	5 No. 16	6 No.16	5 No.16
Column reinforcement	8 No.16	8 No.16	8 No.16
Actual/Balanced reinforcement ratio (Beam)	1.15	0.83	1.15
Column/Beam flexural strength ratio	1.12	1.12	2.00

The first specimen (G1) had a column depth of 350 mm with straight top and bottom beam bars within the joint. This reinforcement configuration resulted in embedment length for the beam top and bottom reinforcement within the joint of 20 times bar diameter ($20 d_b$). The second specimen (G2) has the same column depth of 350 mm but the beam top and bottom longitudinal reinforcement was bent into the joint. Due to manufacturing limitations, the bent GFRP bars could not be produced in lengths longer than 1500 mm.

Therefore, the beam bars were spliced 460 mm away from the joint face with a 640 mm splice length ($40 d_b$). The third specimen (G3) is similar to (G1); however the column depth was increased to 500 mm; achieving an embedment length of $30 d_b$.

3.2 Materials properties

All test specimens were designed and constructed using normal weight, ready-mixed concrete with a targeted 28-day concrete compressive strength of 35 MPa. The reinforcing bars used in this study are sand-coated GFRP V-ROD™ (Pultrall Inc. 2007). Table 2 shows the mechanical properties of the used GFRP bars.

Table 2 Mechanical properties of the used GFRP bars

Bar Type	Tensile Modulus (GPa)	Tensile Strength (MPa)	Ultimate Strain
Straight	48.2	751	0.0156
Bent*	39.5	512	0.0130

* Properties of straight portion of GFRP bent bar

3.3 Test set-up and instrumentations

All specimens were tested while the column was lying horizontally and the beam was standing vertically; 90-degree rotated from the actual condition, as shown in Figure 2. A fully dynamic actuator was utilized to apply the reversed quasi-static cyclic loading to the tip of the beam following the loading scheme shown in Figure 3 (ACI, 2005; Ghobarah & El-Amoury, 2005, Chun et al., 2007). A hydraulic jack was used to apply a constant axial compression force to the columns during testing equal to 15% of the column ultimate capacity (670 kN for specimens G1 and G2 and 800 kN for specimen G3).



Figure 2 Test set-up

Several electrical resistance strain gauges were installed on the GFRP reinforcement, linear variable displacement transducers (LVDTs) to measure the beam and column rotations, the joint distortion, and crack width. A data acquisition system, monitored by a computer

was used to monitor and record the readings during the test.

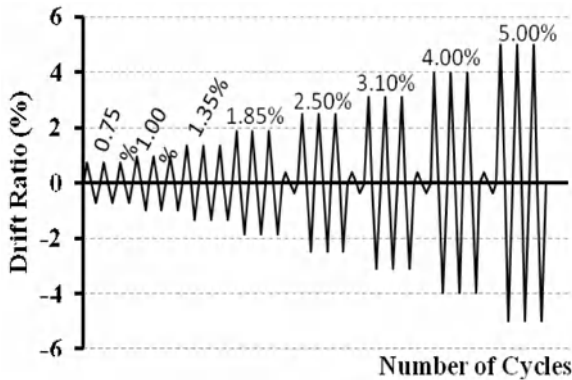


Figure 3 Seismic loading Scheme

4 RESULTS AND DISCUSSIONS

4.1 General behavior and modes of failure

Generally, test results showed that the behavior of all test specimens was satisfactory according to the requirements of the National Building Code of Canada (NBCC 2005) for earthquake resistant structures. The three test specimens exceed the 2.50% drift ratio before failure. All specimens exhibited a deformable behavior with minimal damage in the joint area. The failure of the three specimens took place in the beam near the column face with no damage to the joint area. Specimen G1 failed due to insufficient anchorage length of beam reinforcement ($20d_b$) at 3.0% drift ratio before reaching the design strength. Specimen G2 exhibited failure due to slippage at the spliced portion of the beam reinforcement at 3.0% drift ratio after achieving the design capacity. This indicates the feasibility of using GFRP bent bars inside the joint to avoid the slippage problem within the joint. For specimen G3, the observed failure was a concrete crushing immediately followed by rupture of the beam GFRP bars at 5% drift ratio, after achieving the anticipated design capacity.

4.2 Strain measurements

Figure 4 shows the measured strains in the beam flexural reinforcing bars at the column face for the three test specimens. The strains in the GFRP bars remain, as expected, linear-elastic up to failure with maximum measured strains of approximately 12,000, 15,800 and 15,000 micro-strains for G1, G2 and G3, respectively. It can be seen that the GFRP bars were capable of exhibiting large elastic strains which indicates the feasibility of using GFRP bars in such joints based on replacing typical yielding of steel reinforcement with the large elastic deformations of FRP. The maximum strain recorded in specimen G3 (15,000 micro-strains) is less than the ultimate strain, which is in good agreement with design procedure as G3 was designed to fail by

concrete crushing; over-reinforced. However, specimen G1 did not achieve the targeted strain due to early slippage failure (not enough anchorage).

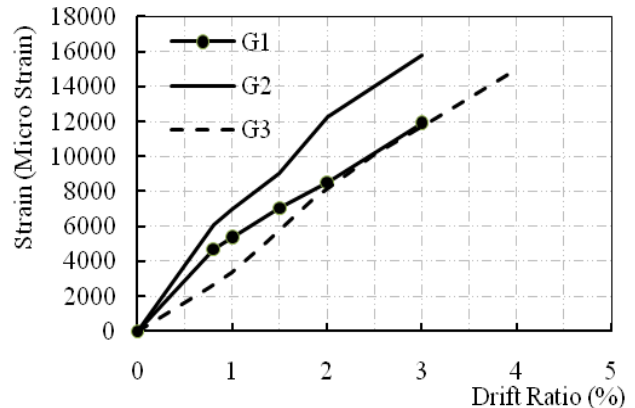


Figure 4 Maximum strain in beam longitudinal bars-drift ratio relationship

Moreover, the measured strains in the longitudinal column reinforcement of the three tested specimens remain elastic up to failure. The maximum strains developed in the column bars were around 3800, 4000 and 4900 micro-strain for G1, G2 and G3, respectively, which is still much less than the rupture strain of the FRP material (15,600 micro strains).

4.3 Load-lateral drift response

Figure 5 shows the typical relationship for the horizontal load applied at the beam tip versus lateral drift (load-drift behavior). For all specimens, the lateral load capacity continued to increase up to failure. No significant pinching appeared through the whole test. It can be noticed that all specimens had elastic-stable behavior without any significant stiffness degradation observed up to failure. Figure 6 shows comparison of the behavior of each specimen before failure. For G1 specimen, the failure occurred after completing 3 cycles at 3.0% drift ratio at a load of 90 kN due to slippage of beam bars. For specimen G2, the failure occurred during the first loading cycle at 3.0% drift ratio at a load of 118 kN, which is close to the design capacity (125 kN). For

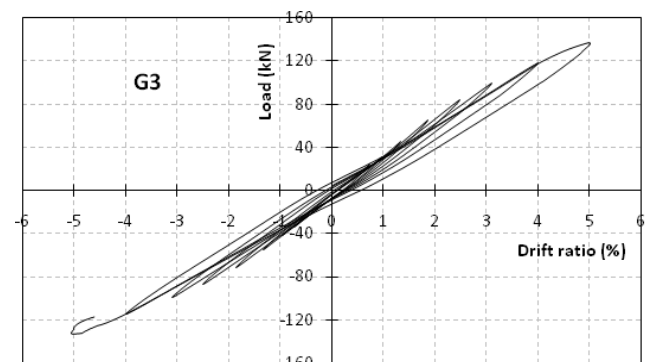


Figure 5 Load-lateral drift relationship

specimen G3, the joint failed at a drift level of 5.0% at 135 kN. This obtained capacity is close to the design capacity of 125 kN.

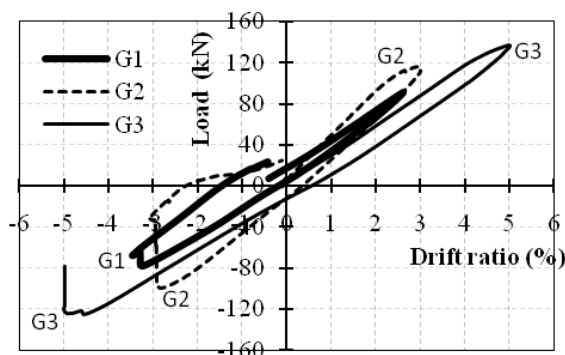


Figure 6 Load-lateral drift relationship

5 CONCLUSIONS

Based on the results of the tested specimens, the following conclusions can be drawn:

- When enough anchorage length within the joint is provided, it is evident that the GFRP-reinforced joint can safely reach 5.0% drift capacity under reversed cyclic loading. This drift capacity is more than the 2.5% required by the National Building Code of Canada (NBCC 2005).
- Test results showed that anchorage length of 30 times bar diameter for the beam straight top and bottom longitudinal reinforcement (specimen G3) is enough to prevent slippage (bond failure).
- It is feasible to use GFRP bent bars to avoid bar slippage within the joint provided that bent bars are spliced with a lap splice greater than 40 times bar diameter

6 ACKNOWLEDGEMENT

The authors wish to express their gratitude and sincere appreciation for the financial support received from the Natural Science and Engineering Research Council of Canada (NSERC), through Canada Research Chairs program. The equipment funds provided by Canada Fund for Innovation (CFI) and the Manitoba Research

Innovation Fund (MRIF) are greatly appreciated. The help received from the technical staff of the McQuade Heavy Structural Laboratory in the department of civil engineering at the University of Manitoba is also acknowledged.

REFERENCES

- ACI Committee 440. 2006. Guide for the Design and Construction of Concrete Reinforced with FRP Bars. *ACI 440.1R-06*, American Concrete Institute, Farmington Hills, Mich., 44 p.
- ACI Committee 374. 2005. Acceptance Criteria for Moment Frames Based on Structural Testing and Commentary. *ACI 374.1-05*, American Concrete Institute, Farmington Hills, Mich., 9 p.
- Canadian Standards Association (CSA). 2002. Design and Construction of Building Components with Fibre-Reinforced Polymers. *CAN/CSA S806-02*, Canadian Standards Association, Ontario. 177 p.
- Chun, S. C., Lee, S. H., Kang, T. H. K., Oh, B., and Wallace, J. W. 2007. Mechanical Anchorage in Exterior Beam-Column Joints Subjected to Cyclic Loading. *ACI Structural Journal*. 104(1): 102-112.
- Ghobarah, A. and El-Amoury, T. 2005. Seismic Rehabilitation of Deficient Exterior Concrete Frame Joints. *Journal of Composites for Construction, ASCE*. 9(5): 408–416.
- Fukuyama, H., Masuda, Y., Sonobe, Y., and Tanigaki, M. 1995. Structural Performances of Concrete Frame Reinforced with FRP Reinforcement. *Non-Metallic (FRP) Reinforcement for Concrete Structures, Proceeding of the Second International RILEM Symposium (FRPRCS-2)*, London. 275-286.
- National Building Code of Canada (NBCC). 2005. *National Research Council of Canada, Ottawa, Ontario*. 1167p.
- Pultrall Inc. V-ROD™, Technical Data Sheet. 2007. *ADS Composites Group Inc* <http://www.pultrall.com>, Thetford Mines, Quebec, Canada.
- Sharbatdar, M. K., Saatcioglu, M., Benmokrane, B., and El-Salakawy, E. 2007. Behavior of FRP Reinforced Concrete Beam-Column Joints under Cyclic Loading. *3rd International Conference on Durability & Field Applications of Fibre Reinforced Polymer (FRP) Composites for Construction, (CDCC-07)*, Quebec City, Quebec, Canada. 541-548.

Interfacial Crack Growth Behavior on RC Beams Strengthened with Prestressed CFL under Cyclic Bending Loads

Hao Zhou, Peiyan Huang (pyhuang@scut.edu.cn), Zhengwei Li & Xiaohong Zheng
School of Civil School and Transportation, South China University of Technology, Guangzhou, China

Jianhe Xie
Faculty of Civil and Transportation Engineering, Guangdong Univ. of Technology, Guangzhou, China

ABSTRACT The interfacial fatigue crack growth behavior on the interface between prestressed FRP and concrete of the strengthened beams under cyclic bending loads were studied by fracture mechanics theoretical method and fatigue crack growth testing method. The results showed that the interfacial crack growth process on the RC beams strengthened with prestressed carbon fiber laminate (CFL) under cyclic bending loads could be divided into three stages: 1) rapid growth stage; 2) steady growth stage; 3) unstable growth stage. In the rapid growth stage and steady growth stage, the interfacial fatigue crack growth rate could be described effectively with Paris-Erdogan expression. Where, the stress intensity factor of the interfacial crack, K_{II} , could be obtained by calculating the energy release rate of the interfacial crack, G_{II} , with the fracture mechanics theoretical method.

1 INTRODUCTION

Since the cracks are always existed and allowed in reinforced concrete (RC) bridges, it has become a new technique which the cracked RC members were strengthened with fiber reinforced polymer (FRP) in civil engineering [1-5]. However, the new technique brings a problem on the durability of the strengthened cracked RC structure. Therefore, it is necessary to study fatigue behavior and durability of the strengthened cracked RC structure.

In this paper, the experimental and theoretical studies on interfacial fatigue crack propagation of the RC beam strengthened with prestressed carbon fiber laminate (prestressed CFL) under three-point bending loads are carried out, and then the calculating method of stress intensity factor for the interfacial crack and the semi-experience formula for the fatigue crack propagation rate are proposed.

2 FATIGUE CRACK PROPAGATION EXPERIMENTS

2.1 Experimental materials and specimens

Specimen was RC beam with size of 1850×100×200 mm, and affixed with a new type of FRP which was called as carbon fiber laminate (CFL) to the bottom [6]. The Ordinary Portland cement, locally available sand, crushed granite rock and water with the ratio of 1.0:0.5:2.06:3.66 by weight were used for making the concrete. The steel bar used in the RC beam was shown

in Figure 1. The Young's modulus, yield strength, ultimate strength, and percentage of elongation of the steel bar at failure were found respectively to be 210 GPa, 318 MPa, 478MPa and 32.56%. The reinforcement ratio in the concrete was 0.981%.

TA25 type of CFL was made with carbon fiber of T300-3k by our research group [6], and the size was 1600×100×0.23 mm. According to the national standard of China (GB/T 3354-1999), fourteen typical samples representing the CFL were tested. The Young's modulus, tension strength, percentage of elongation at failure, and density of CFL were found to be 230 GPa, 3500 MPa, 1.5% and 1.76 g/cm³ respectively.

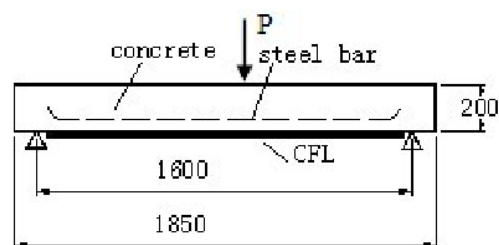


Figure 1 Three-point bending RC beam strengthened with carbon fiber laminate (CFL)

The method of applying prestress was assisted by steel strands outside (Figure 2). The anchorages and clamps were devised for rectangle RC beams. The steel strands outside the beam were tensioned to the stress level needed. The surface of compression side of the

beam was burnished and cleaned. Then the CFL was bonded to the surface of the beam. The electrical resistances strain gauges were bonded to the CFL. The steel strand was released when the CFL was bonded fully. Then CFL gets prestress indirectly up to about 10% of the tension strength.



Figure 2 Anchorages and clamps for applying prestress to the CFL and RC beams

2.2 Experimental method

The three-point bending RC beams strengthened with prestressed CFL were tested in the Material Testing System (MTS 810 Hydraulic Actuator) and dynamic strain measurement system (Wauebook516E). The testing data, such as mid-span deflection, load, time, strain, and corresponding fatigue loading cycles, were recorded automatically. Fatigue loads applied by force control mode with sinusoidal wave, and a frequency of 10 Hz and a stress ratio of 0.1. P_{max} and P_{min} denote the peak load and valley load respectively, corresponding to N cycles applied on the specimen. The specimens were applied to the maximum load, P_{max} , as 32.5kN.

In order to measure the crack length and width, the concrete surface at range of 300mm in mid-span of the beams was selected. It was polished and painted with emulsion, and then painted with 4 mm-interval reticule prior to the experiment. During the experiment, MTS stopped shortly for measuring length, a , and width, w , when it is necessary. Crack length and width measurement adopted DJCK-2 microscope, and which the enlarge multiplier was 40 times, and the measurement range was from 0.02mm to 2.00mm, degree of accuracy was 0.01mm.

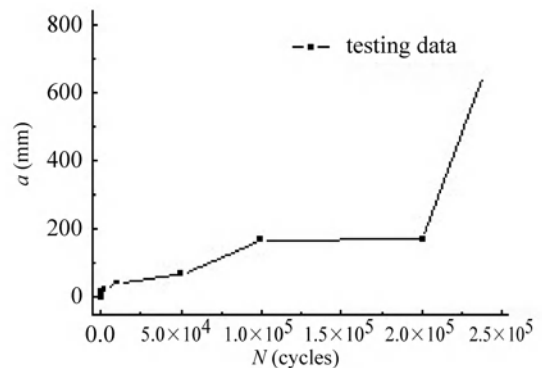
3 INTERFACIAL CRACK PROPAGATION BEHAVIOR

Two specimens (PX-1, PX-2) were tested in fatigue crack propagation experiments by adopting experimental method in Chapter 2, and propagation curves (a - N curves) of the interfacial crack of each specimen were obtained as shown in Figure 3. From the previous work done by our research group [7], and from Figure 3, the main crack propagation on the strengthened beam could

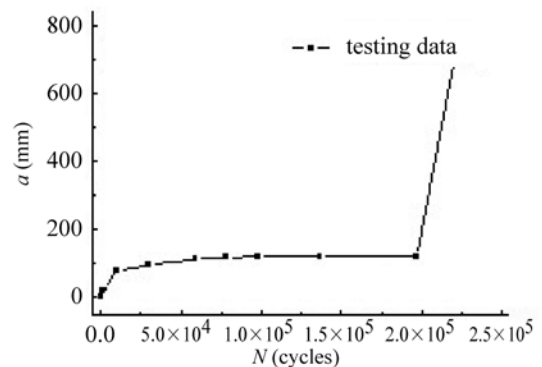
be summarized into three stages:

3.1 Rapid propagation stage

Since the maximum load P_{max} at the test was close to cracking load of the interface between the concrete and prestressed CFL of the specimen, interface experienced crack initiation process, propagation process and fast grow as through-crack process after several hundreds cycles. Fatigue interfacial crack was generated near the mid-span of the RC beam. Once the interfacial crack was generated, the propagation became fast, and the crack propagation direction was along the interface, i.e. the interfacial crack could be assumed as mode II crack.



(a) specimen PX-1



(b) specimen PX-2

Figure 3 Experimental a - N curves

3.2 Steady propagation stage

Specimens were continually applying cyclic loads. Because the rigidity of the specimen reduced after cracking, the fatigue damage of the interface was accumulating and increasing, elastic modulus of interface decreased, thus results in continued propagation of fatigue interfacial crack, then transited to a relatively steady and slow propagation stage. In this stage, the length of interfacial crack presented a small range of increase. The second stage took up 95% of the fatigue interfacial crack propagation lives.

3.3 Unstable propagation stage

At the normal situation, tensile strain of main steel bar was bigger than limit pressure strain of the concrete,

and results in concrete of pressure area reached limit pressure strain and parts crushing failure occurred prior to the main steel bar. This led to the rigidity of the beam decreased rapidly; the speed of tensile strain of the main steel bar increased fast, and the speed of the interfacial crack growth increased rapidly. When the main steel bar was pulled fracture, or prestressed CFL was debonded from the RC beams along the interfacial crack growth, the specimen was failed at last.

4 FORMULA OF INTERFACIAL CRACK PROPAGATION RATE

Since the interfacial crack propagation Stage 1 and Stage 2 (the rapid propagation stage and steady propagation stage) took up 95% of its lives, it was apparent that study on the fatigue interfacial crack propagation in stage 2 was very important for the durability research of the RC beams strengthened with prestressed CFL. Hence, we researched on the fatigue interfacial crack propagation rate in Stage 1 and Stage 2 in this paper.

Based on the research results from the metal materials and pure concrete materials, we assumed that the propagation rate, da/dN (mm/cycles), of the interfacial crack of the RC beams strengthened with prestressed CFL in the Stage 2 could be described by Paris formula [8] as,

$$\frac{da}{dN} = C \cdot (\Delta K_{II})^m \quad (1)$$

where, ΔK_{II} (MPa \cdot m^{1/2}) was amplitude value of the stress intensity factor of the interfacial crack ($\Delta K_{II} = K_{II,max} - K_{II,min}$), whereas stress intensity factor, K_{II} , could be obtained by calculating the energy release rate of the interfacial crack, G_{II} , with the fracture mechanics theoretical method, and the expression equation [9-10] was as follows,

$$K = \sqrt{\frac{E_c}{b} \left\{ \begin{aligned} & \left[\frac{[M_c(x)]^2}{2D_c} + \frac{[M_f(x)]^2}{2D_f} - \frac{[M^T(x)]^2}{2D_t} + \frac{3[Q_c(x)]^2}{5K_c} \right. \\ & \left. + \frac{3[Q_f(x)]^2}{5K_f} - \frac{3[Q^T(x)]^2}{5K_t} + \frac{[N_c(x)]^2}{2W_c} + \frac{[N_f(x)]^2}{2W_f} \right] \end{aligned} \right\}} \quad (2)$$

where, E_c was Young's modulus of concrete, b was the width of RC beam; $M^T(x)$ and $Q^T(x)$ stood for the bending moment and shearing force acted on the whole section of the strengthened beam when the crack length was a ; $M_c(x)$, $Q_c(x)$ and $N_c(x)$ denoted the bending moments, shearing force and axial force acted on the section of RC beam when the crack length was $a+da$; $M_f(x)$, $Q_f(x)$ and $N_f(x)$ represented the bending moment, shearing force and axial force acted on the section of FRP respectively when the crack length was $a+da$; D_e , D_f and D_t were flexural rigidity of RC section, FRP

section and whole section of the strengthened beam respectively; K_c , K_f and K_t represented the shear rigidity of RC section, FRP section and whole section of the strengthened beam; W_c and W_f were compression rigidity of RC section and FRP section respectively.

For the crack propagation coefficient, C , and crack propagation exponent, m , we could obtain the relationship curves of da/dN (mm/cycles) and ΔK (MPa.m^{1/2}) in Figure 4, and then confirmed them in the regression analysis. The value of da/dN was obtained from experimental a-N curves, and the value of ΔK_{II} was obtained from putting parameters of relevant specimen into Equation (2).

Once the values of C and m were established, a semi-experience formula for the interfacial crack propagation rate of the RC beams strengthened with prestressed CFL under constant amplitude cyclic bending loads could be written as:

$$\frac{da}{dN} = 1.30 \times 10^{-6} (\Delta K)^{5.54} \quad (3)$$

By using equation (3), it described the propagation rate of the interfacial crack on the RC beams strengthened with prestressed CFL well in Stage 1 and Stage 2.

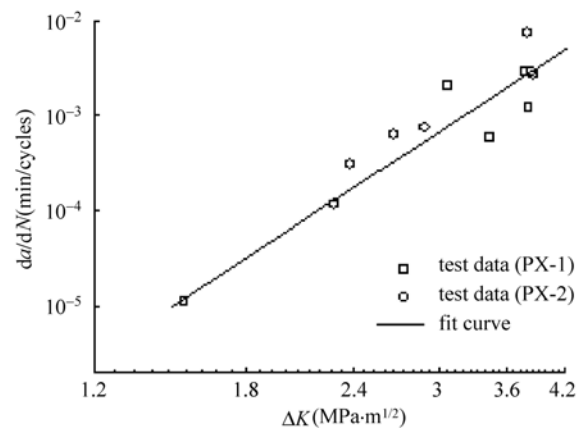


Figure 4 Relationship between da/dN and ΔK

5 CONCLUSIONS

The research on fatigue crack propagation rate of reinforced concrete (RC) beams strengthened with prestressed carbon fiber laminate (CFL) was carried out in this paper. The experimental results showed that, the interfacial crack propagation on the strengthened beams were summarized into three stages, and this was consistent to the crack on metal materials. However, the regular pattern of the crack propagation rate was different.

In the fatigue interfacial crack propagation Stage 1 and Stage 2, its propagation rate was described by adopting the Paris formula. Furthermore, amplitude value of stress intensity factor, ΔK_{II} , was derived from fracture mechanics theory, and the crack propagation

coefficient, C , and crack propagation exponent, m , were obtained from the experimental curves of da/dN and ΔK_{II} and the regression analysis. Using the semi-experience formula of the interfacial crack propagation rate, we could better describe the propagation rate of the interfacial crack of the RC beams strengthened with prestressed CFL in the Stage 1 and Stage 2, and then established the fatigue crack propagation lives of the strengthened RC beams.

6 ACKNOWLEDGEMENTS

The project is supported by National Natural Science Foundation of China (No.10672060) and Guangdong Province Natural Science Foundation of China (No.9251064101000016).

REFERENCES

- Huang P. Y., Long Z. Q., Lou Y., Zhang G. S., Hu S. M., 2002, Experimental study on load-carrying capacity of carbon fiber-Sheet-reinforced concrete three-point bending specimen with a V notch. *Proc. SPIE* Vol.4537: 95-98.
- Huang P. Y., Jin M., Luo L. F., Zhang G. S., Hu S. M., 2002, Effect of length of carbon fiber-sheet on the stress field of the reinforced concrete 3-point bending specimen with a V-notch, *Proc. SPIE* Vol.4537: 111-114.
- Heffernan PJ, Erki MA. 2004, Fatigue behavior of reinforced concrete beams strengthened with carbon fiber reinforced plastic laminates. *J. Compos. for Constr.* 8 (2): 132-140
- Wu Z. J., Bailey C. G., 2005, Fracture resistance of a cracked concrete beam post-strengthened with FRP sheets. *International Journal of Fracture.* 135: 35-49
- Yao Guo-wen, Huang Pei-yan, Zhao Chen. 2006.4, Flexural Fracture and Fatigue Behavior of RC Beams Strengthened with CFRP Laminates under Constant Amplitude Loading. *Key Engineer Materials*, v306-308: 1343-1348
- Huang Peiyan, Zeng Jingcheng. 2006, Fiber laminates and Applications [P]. China Patent No. ZL200410026742.8.
- Guo Xinyan, Huang Peiyan, Liu Guangwan, Xie Jianhe. 2008.11, Fatigue test of RC beams strengthened with prestressed CFLs. *Proceedings of SPIE*, Vol.7375: 737519-1-737519-4
- Paris P C and Erdogan F.A. 1963, Critical Analysis of Crack Propagation Laws. *Journal of Basic Engineering ASME (Series D)*, 85: 528-534
- Xie Jianhe. 2009, Study on flexural fatigue properties of RC beams strengthened with prestressed CFL under bending cyclic loads. *A Dissertation Submitted for the Degree of Doctor of Philosophy, South China University of Technology.* (in Chinese)
- Xie Jianhe, Huang Peiyan, Deng Jun, Yang Yi. 2008, Study on Interfacial Shear Stress in RC Beams Strengthened with Prestressed FRP Laminates. *Advanced Materials Research*, 33-37: 507-514

Effects on the Fatigue Lives of RC Beams Strengthened with CFL at Elevated Temperature under Cyclic Bending Loads

Peiyan Huang (pyhuang@scut.edu.cn), Haiyang Wang, Hao Zhou, Xinyan Guo & Zhilin Zhou

School of Civil Engineering and Transportation, South China University of Technology, Guangzhou, China

ABSTRACT The fatigue behavior of RC beams strengthened with carbon fiber laminate (CFL) was experimental studied and theoretical analyzed under cyclic bending loads in several different temperatures (5°C, 20°C, 50°C and 80°C), which the temperatures approached the weather in subtropical zone such as southern China. The effect of the temperature on fatigue lives of the RC beams strengthened with CFL was discussed. Furthermore, a calculation equation of the fatigue lives of the strengthened beams was proposed under the coupling action from the temperature and the load conditions. Using the equation, the fatigue lives and fatigue limits of the RC beams strengthened with CFL were estimated accurately from the coupling action from the temperatures and the bending loads. The preliminary validity check was completed with the verify tests.

Fatigue behavior and durability of RC beams strengthened with fiber reinforced polymer (FRP) was a cutting edge subject in civil engineering field [1-9]. Temperature variation affected the integration fatigue lives of RC beams strengthened with FRP in practical service environment and the research in this area was seldom mentioned in China and abroad. This paper discussed the fatigue behavior of RC beams strengthened with carbon fiber laminate (CFL) mainly with experimental method under cyclic bending loads in several different temperatures, which the temperatures approached the weather in subtropical zone such as southern China.

1 TEMPERATURE FATIGUE EXPERIMENTS OF RC BEAMS STRENGTHENED WITH CFL

Forty-eight RC beams of the size 1850×100×200mm strengthened with CFL [10] were taken as the samples of the experiment (Figure 1) and CFL was a new type of CFRP invented by our research team. The fatigue behavior of RC beams strengthened with CFL was experimental studied under cyclic bending loads in five different stress levels and in four different temperature environments. The materials, equipments, experimental conditions and methods were as follows.

1) Experimental materials. RC beams strengthened with CFL were composed of concrete, steel bars and CFL three parts. Composition proportion of concrete is mc: mw: ms: ma=1.0: 0.5: 2.06: 3.66. Grade II Φ10 round steel bar was used as the main steel bars and Grade I Φ8 round steel bar was used in the other bars. CFL of 1600mm long, 100mm wide, 0.23mm thick pre-immersion

laminates was fabricated of T300-3k carbon fiber silk produced by Tolei corporation in Japan in which, the fundamental material was epoxy resin, the splice between concrete and CFL was A and B glue of Shenliling brand.

2) Experimental equipments. The experimental equipments were divided into three parts: MTS810 test system, DH3817 dynamic strain collection system, custom-made environmental temperature box.

3) Experimental conditions and methods. The experiments were divided into two parts, except the environmental temperature in the tests and verification experiments of formula in calculating fatigue lives of strengthened beams was set as 50°C, the experimental conditions and methods of both parts were the same. The other three environmental temperatures were set as 5°C, 20°C and 80°C. In order to get five stress levels, the maximum loads were separately set as 25.0 kN, 27.5 kN, 30.0 kN, 32.5 kN and 35.0kN. The three point bending was taken as the loading method, which the span was 1600mm, loading frequency was 10Hz, stress ratio R=0.2 and frequency of strain data collection was 100Hz.

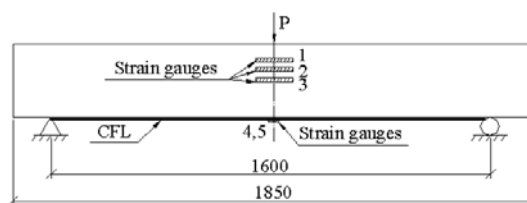


Figure 1 Fatigue testing sample in different temperatures under three-point bending load

2 EFFECTS ON FATIGUE LIVES OF RC BEAMS STRENGTHENED WITH CFL BY ENVIRONMENTAL TEMPERATURES

The bending fatigue experimental $S-N$ curves in environmental temperature of separately 5°C , 20°C and 80°C were shown in Figure 2. Environmental temperature had an obvious impact on fatigue lives of RC beams strengthened with CFL according to Figure 2. The fatigue limits of strengthened beams decreased as the environmental temperature increased in the temperature range of this experiment, furthermore, when the stress level increased, the decrease range of fatigue limits became larger.

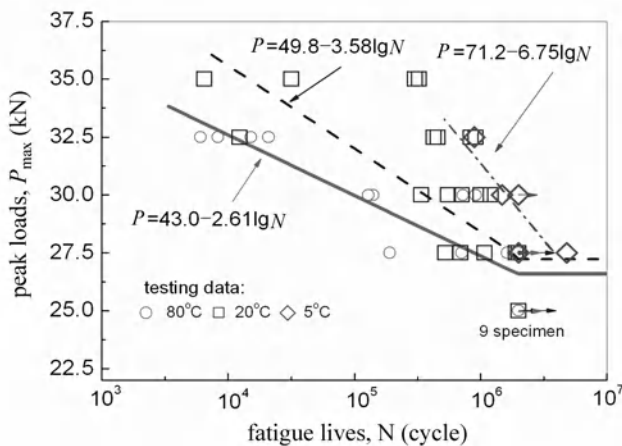


Figure 2 $S-N$ curves in different temperatures.

According to different experimental temperatures, experimental data was dealt with regression method. $S-N$ simulation equations of the beams in environmental temperature of 5°C , 20°C and 80°C were formed as follows:

$$P = 71.2 - 6.75 \lg N \quad (1)$$

$$P = 49.8 - 3.58 \lg N \quad (2)$$

$$P = 43.0 - 2.61 \lg N \quad (3)$$

The relevant factors R in equation (1), equation (2) and equation (3) were separately 0.76, 0.84 and 0.86. P (kN) was the maximum value of cyclic loads, and N (cycles) was the fatigue life of the experimental beam.

According to equation (1) to (3), fatigue strength of the experimental beams at the level of $N=2 \times 10^6$ in environmental temperature of 5°C , 20°C and 80°C were calculated, and the values were 28.6kN, 27.2kN and 26.6kN. Therefore, fatigue limits of strengthened beams decreased as the environmental temperature increased in the temperature range of this experiment. Fatigue limits of strengthened beams at 5°C increased 5.1% and it decreased 2.2% at 80°C compared with fatigue limits of the beams in room temperature.

3 FATIGUE LIVES CALCULATION FORMULA OF STRENGTHENED BEAM UNDER TEMPERATURE AND LOAD COMBINATION

3.1 Formula of fatigue lives

From analyzing the fatigue experimental data and the content in above section, the fatigue limits of strengthened beams decreased as the environmental temperature increased in the temperature range of the experiments. The reasons were listed as follows. 1) The fatigue failure modes of all strengthened beams were debonding, i.e. CFL debonded from the beams at interface between CFL and concrete. Among main factors of fatigue failure at interface, the shear strength of interface (including the penetration layer) was the key factor besides stress levels. 2) Shear strength of the interface which composed of concrete layer and glue layer was decided by shear strength of penetration layer. 3) Temperature effect to shear strength of glue reflected shear strength of penetration layers in temperature changes, higher the temperature is, larger the decrease range of shear strength of the glue. 4) As shear strength decreased in interface, the load carried by main steel bars increased. This accelerated damage of main steel bars in earlier time and caused decreasing of load carrying capacity of the beams. Because of the damage of main steel bars, the load in interface increased and accelerated the fatigue damage in the interface. Due to the reasons above, CFL debonded from the beams in earlier time and fatigue lives of beams decreased. Therefore, the combination of maximum load and temperature should be considered in formulas of calculating fatigue lives of RC beams strengthened with CFL when environmental temperature changed.

From the above, referenced the formula structure from formula (1) to (3), formulas of calculating fatigue lives of RC beams strengthened with CFL under combination of maximum load and temperature was listed as follows:

$$P = C_1 + C_2 f_1(T) + C_3 f(N) + C_4 f_2(T) f(N) \quad (4)$$

where, $C_1 \sim C_4$ were constant coefficients to be determined by experiments, $f_1(T)$ and $f_2(T)$ were temperature functions and $f(N)$ was fatigue life function to be determined by theoretical assumption and simulation of experimental data.

The detail calculation formulas of function $f_1(T)$, $f_2(T)$ and $f(N)$ were assumed as:

$$f_1(T) = e^{C_5 T} \quad (5)$$

$$f_2(T) = e^{C_6 T} \quad (6)$$

$$f(N) = \lg N \quad (7)$$

Using the direct exploration method, $C_1 \sim C_6$ were determined by taking equation (5) to (7) into equation (4)

and take into account of fatigue experimental data in three different temperatures of 5°C, 20°C and 80°C. Then, the formula of calculating fatigue lives of RC beams strengthened with CFL under combination of maximum load and temperature was as follows:

$$P = 45.3e^{(-T/10.56)} + 43.0 - [6.72e^{(-T/10.35)} + 2.61] \lg N \quad (8)$$

From formula (8), the fatigue lives and fatigue limits of strengthened beams considering practical environmental temperature influence were conveniently estimated.

3.2 Experimental Verification

In order to verify the effectiveness of fatigue life calculating formula (8), a new experimental condition which $T=50^\circ\text{C}$, $P=27.5\text{kN}$ was established. Using the same experimental method in section 1, bending fatigue experiments of four RC beams strengthened with CFL were done. Their fatigue lives were respectively 1007789, 119724, 1584468 and 2010000 from the experimental results. Take $T=50^\circ\text{C}$ into formula (8), then:

$$P = 43.4 - 2.66 \lg N \quad (9)$$

From formula (9), when $P=27.5\text{kN}$, the fatigue life was $N = 949388$. The average fatigue life of four experimental beams was 1180495. The relative error compared with calculation results was 19.6%. Therefore, the fatigue life of RC beam strengthened with CFL which considering combination of maximum bending loads and practical environmental temperature influence was predicted using formula (8), and the fatigue limit was effectively estimated.

4 CONCLUSIONS

This paper analyzed the fatigue behavior of RC beams strengthened with carbon fiber laminate (CFL) using experimental study and theoretical analysis under cyclic bending loads in several different temperatures (5°C, 20°C, 50°C and 80°C). The formula of calculating fatigue lives of RC beams strengthened with CFL under combination of maximum load and temperature was established. The fatigue lives of RC beams strengthened with CFL which considering combination of maximum bending load and practical environmental temperature influence was predicted and the fatigue limit was effectively estimated by using the formula. The effectiveness of this formula was preliminarily verified by experiments. The further discussion of the applied range and precision of the formula would be based on accumulation of experimental data.

ACKNOWLEDGEMENTS

The project is supported by National Natural Science Foundation of China (No.10672060) and Guangdong Province Natural Science Foundation of China (No.9251064101000016).

REFERENCES

- Meier U., Farshad M. 1996, Connecting high-performance carbon-fiber-reinforced polymer cables of suspension and cable-stayed bridges through the use of gradient materials [J]. *Journal of Computer-Aided Materials Design*, 3(1-3): 379-384.
- Sherif El-Tawil, Cahit Ogunc, Ayman Okeil et al. 2001, Static and fatigue behavior of reinforced concrete beams strengthened with carbon fiber reinforced plastic laminates [J]. *Compos. for Constr.*, 5(4): 258-267.
- Green Mark F., Bisby Luke A., Fam Amir Z., et al. 2006, FRP confined concrete columns: Behavior under extreme conditions [J]. *Cement & Concrete Composites*, 28:928-937.
- Huang Pei-yan, Zhang Bo-lin, Yang Yi. 2007, Effect on load carrying capacity of carbon fiber laminates strengthened RC beams in elevated temperature. [J]. *Journal of South China University of Technology (Natural Science)*, 35(2):1-5.
- Niu Peng-zhi, Huang Pei-yan, Yang Yi. 2007.11, Experimental study of fatigue strength of carbon fiber laminates strengthened RC beams [J]. *Journal of Engineering Mechanics*, 24(11): 132-135.
- Yang Yi, Hang Pei-yan, Deng Jun. 2008, Experimental Study on the Fatigue Properties of RC Beam Strengthened with Prestressed CFL [J]. *Advanced Materials Research*, 33-37: 169-174.
- Huang Pei-yan, Zhou Xu-ping, Yang Yi, Niu Peng-zhi, Zheng Shun-chao. 2007, Fatigue lives of RC beams Strengthened with carbon fiber laminates under bending loads [J]. *Journal of South China University of Technology (Natural Science)*, 35 (10): 198-204.
- Zhou Zhi-Lin, Huang Pei-Yan, Deng Jun. 2008, Degradation rule of bending stiffness of RC beams strengthened with carbon fiber laminates [J]. *Journal of South China University of Technology (Natural Science)*, 36(10): 16-19.
- Zhou Zhi-lin, Huang Pei-yan, Deng Jun. 2008.8, Fatigue behavior of carbon fiber laminates strengthened RC beams in elevated temperature [J]. *J. of PLA University of Science and Technology (Natural Science Edition)*, 9(4):351-356.
- Huang Pei-yan, Zeng Jing-cheng. 2006.8, Application of Carbon Fiber Laminate [P]. Chinese Patent No. ZL200410026742.8, China Patent Administration.

Fatigue-Loading Effect on RC Beams Strengthened with Externally Bonded FRP

E. Ferrier (Emmanuel.Ferrier@univ-lyon1.fr), A. Limam, P. Hamelin
LGCIE Site Bohr, Université Claude Bernard Lyon I INSA de Lyon, Lyon, France

M. Quiertant
Université Paris-Est, Laboratoire Central des Ponts & Chaussées (LCPC), Paris, France

ABSTRACT External bonding of fiber reinforced polymers (FRP) on concrete beams is particularly attractive for the strengthening of civil engineering structures in order to increase their mechanical resistance. The composite material is generally bonded on the tensile part of the beam. In order to design these bonded reinforcements, an iterative computational method based on section equilibrium and material properties (concrete, steel, adhesive and composite) has been developed: this method can be extended to describe the fatigue behavior of RC beams. This paper focuses on the damage behavior of concrete structures subjected to fatigue loading. A specific modeling coupled with an experimental investigation on large-scale beams made it possible to compare the theoretical and experimental fatigue behaviors of RC beams with and without composite reinforcements. Results showed that the beam deflection and the strain in each material could be calculated with a sufficient accuracy, so that the fatigue behavior of the FRP strengthened beams was correctly estimated by the model.

1 INTRODUCTION

Externally bonded carbon-epoxy fiber-reinforced polymers (CFRPs) have been widely used to restore or increase the capacities of reinforced concrete beams (Meier et al., 1992; Neale and Labossière, 1997; Varastehpour and Hamelin, 1997). A typical reinforced concrete bridge deck may experience up to 7×10^8 stress cycles during the course of a 120-year life span (Barnes and Mays, 1999), while an overpass on a typical highway with a design life of 40 years can experience a minimum of 58×10^8 loading cycles of varying intensities. In contrast to the fairly extensive experimental and analytical studies conducted on the monotonic behavior of FRP-strengthened RC members, relatively little research has been carried out on the fatigue behavior of concrete beams strengthened with FRPs. However, some key research (Barnes et al. 1999, Gheorghiu et al. 2006, Ferrier et al. 2005) has clearly shown that FRP-strengthened structures present better fatigue performances than unstrengthened ones. In most cases, it has been observed that the failure of the structure is initiated by successive yielding of the reinforcing steel in tension, in one or several locations. When debonding of the FRP laminate occurred, it was considered to be a secondary failure mode resulting from yielding and failure of the steel rebars. For serviceability limit state

considerations, the overall behavior of a reinforced concrete beam strengthened with FRPs has to be evaluated. In the present work, this behavior is studied using a model which was designed for the evaluation of the beams' mechanical properties. The fatigue modelling of beams strengthened by FRP is then validated thanks to an experimental investigation on 6 large scale beams.

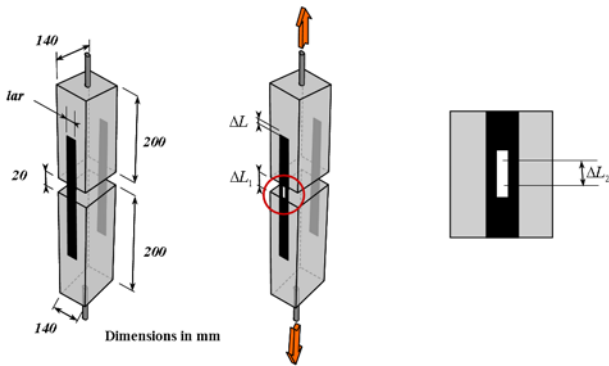
2 PROPERTIES OF THE FATIGUED MATERIALS

Fatigue analysis of the adhesive was done using a tensile shear test which informs on the loading level to be applied to the adhesive to guarantee the durability of the reinforcement. In the present study, the standard double-lap shear test proposed by the Japanese Concrete Institute (1998) was retained for our investigation. In this test, two concrete blocks are attached by two parallel composites strips (Figure 1). A tensile load applied on the concrete blocks produces shear stress in the adhesive. The shear test method has been extensively described in previous papers by Ferrier et al. (2005). The CFRP strip connects two concrete blocks separated by 20 mm. Specimens are tested until failure with cyclic shear stresses (Ferrier et al. 2005). The composite is made of unidirectional carbon fiber (30% in volume) and epoxy polymer (70% in volume) with a glass temperature

value of 55°C. The adhesive layer polymer thickness is 0.20 mm (Table 1). The FRP thickness is 0.8 mm. Static tests on samples show that failure occurs for an average shear stress of 1.5 MPa with cohesive delamination of the composite plate.

Table 1 Material characteristics

	Fibers	Polymer	FRP
E (GPa)	235	3.2	80.0
R (MPa)	3500	40	890



Lc: bonding length; Nb: stress applied in the concrete; x: bonding position; γ : shear strain

Figure 1 Test principle and shear strain distribution along the double lap joint test

An alternate load is applied with a frequency of 1 s^{-1} . The tensile speed is about 10 kN/s. The variation of cycle loading is between 0.10 MPa and the maximum shear stress assessed with static tests. The shear modulus as a function of the number of cycles curve (Ferrier et al. 2005) is a double-sloped curve: the first corresponds to the decrease in adhesive properties and the second to the beginning of the adhesive layer failure. The $\Delta\tau-N$ and $G=f(N)$ curves are assessed using the evolution of strain on bonded FRP (Ferrier et al. 2005) in function of fatigue loading to obtain the shear modulus as a function of number of cycles (Ferrier et al. 2005).

Concerning fatigue strength of the concrete to composite interface (Ferrier et al. 2005), the data suggest a linear relation between the maximum strength ($\Delta\tau_{adh}$) of concrete to FRP interface and the logarithm of the number N of load cycles to failure. This linear relation follows equation 8.

$$\Delta\tau_{adh} = m \cdot \log(N) + b \quad (1)$$

with $m = -0.07$ and $b = 0.98$

Parameters m and b are fitted with experimental data. The average shear stress permits the calculation of the anchorage length to take into account a flexural design. The $\Delta\tau-N$ curve for double lap joints reveals that the shear stress should be limited to 0.80 MPa to ensure a lifetime of 10^6 cycles for a 1 s^{-1} frequency.

3 FATIGUE BEHAVIOR OF THE RC BEAM STRENGTHENED BY COMPOSITE PLATE

3.1 Modeling principle

For this part of the research, a specific software developed by Varasthepour and Hamelin (1997) is used. The modeling method takes into account all the material mechanical behavior laws as well as the section equilibria. The software has been validated in the framework of static tests performed on several RC beams reinforced by composites. Triantafillou and Plevris's (1994) method for modeling the creep behaviour of RC beams reinforced with FRP, uses the delayed properties of each constitutive material to assess the beam section equilibrium. The same principle is used here for modeling the fatigue behaviour. It means that the modeling method takes into account the decreasing mechanical properties of all the materials subjected to fatigue (steel, concrete, polymer adhesive and composite). Modeling of the RC beam fatigue behavior using the above mentioned computational process can be achieved in three steps. A first step based on literature review allows to obtain fatigue strength and Young modulus of material in function of numbers of loading cycles $E = f(N)$. Such relation are available for concrete (Jakobsen et al., Balagru et al. Gao et al. 1998), for steel (Mender et al. 1994), and for the FRP to concrete interface (Horris et al. 1996) In a second step, the damaging process of the RC beam subjected to cyclic load is modeled using Hamelin and Varasthepour's software (1997). Fatigue strength and Young modulus laws of the various materials are computed in a new version of the software. The iterative calculation process allows to consider the value of material strength and Young modulus for each step of cyclic load. The iterative computational method allow then the moment-curvature or load-deflection relation calculation as a function of cyclic loading.

3.2 Fatigue of concrete and steel rebars

For concrete, Gao et al. (1998) have shown that fatigue strain can be divided into three contributions: (i) irreversible strain caused by cyclic creep under the action of average stress; (ii) irreversible strain caused by fatigue cracks; and (iii) fatigue strain. Relations (2) and (3) have been proposed by Jakobsen and Balagru in order to evaluate the decreases in strength and Young modulus, respectively.

$$E_{c_N} = \frac{\sigma_{c_{max}}}{\frac{\sigma_{c_{max}}}{E_c} + \epsilon_{c_N}} \quad (2)$$

$$\frac{f_{c_{N_{max}}}}{f_c} = 1 - 0.0685 \left(1 - \frac{\sigma_c'}{2}\right) \cdot \log(N) \quad (3)$$

The value of concrete compressive strain (ε_{cN}) as a function of numbers of cyclic load (N) is given by relation (4) and allows to calculate the Concrete Young Modulus as a function of N .

$$\varepsilon_{cN} = 8.417 \cdot 10^6 \cdot \left(\frac{\sigma_c^m}{f_c} \right) \cdot \left[\left(\frac{N}{w} \right)^{\frac{1}{3}} + 3.87 \cdot \left(\frac{\sigma_c^r}{f_c} \right) \cdot \left(\frac{N}{9.75} \right)^{\frac{1}{3}} \right] \quad (4)$$

With w : Cycles frequency, N : Number of cycle, f_c : concrete strength $\sigma_c^m = (\sigma_{\max} - \sigma_{\min})^2$: Average loading stress, $\sigma_c^r = \sigma_{\max} - \sigma_{\min}$: Stress cycles amplitude

As regards steel, a fatigue study on 16 mm steel rebars was performed by Mander (1994). Equation (5) represents the steel strain (ε_{sN}) as a function of the number of cycles at failure (N_f), steel strength (f_y) and steel ultimate strain (ε_{su})

$$\varepsilon_{sN} = \frac{f_y}{E} \cdot (2 \cdot N_f)^b + \varepsilon_{su} \cdot (2 \cdot N_f)^c \quad (5)$$

With b, c : constant

With regard to the composite plate, the fatigue tensile strength was investigated in the literature (Horris et al. 1996). It was found that the decrease in ultimate strength may be neglected in the case of carbon/epoxy composites.

3.3 Beam description

For this study, five beams were tested under flexural cyclic loading at four points. The first three beams (1000 mm×100 mm×170 mm) were reinforced by one layer of composite. The next three beams were larger (2000 mm×150 mm×250 mm). The fourth beam was not reinforced by composite (Beam 4), the fifth was reinforced (Beam 5) by three layers of FRP. The sixth was damaged by a load corresponding to 60% of the failure load (Beam 6) and then repaired with three layers of FRP (Figure 2).

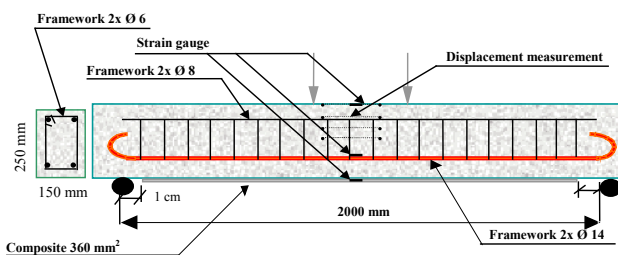


Figure 2 Geometrical description of beam

Suitable ranges of loads are established to ensure the fatigue life of the reinforced concrete beams; the load range for beam testing is set in two categories.

For the first category the objective is to evaluate the effect of maximal fatigue loading level on cyclic loading behaviour (beam 1 to 3). The three first beams, the

maximal fatigue applied load was 30% (Beam 1), 50% (Beam 2) and 80% (Beam 3) of the failure load of CFRP strengthened beams with a frequency of 1 Hz. For the second set of beam, the purpose is to evaluate the efficiency of FRP under high numbers of fatigue loads (10^6 cycles). The loading levels to be applied on the beams (4, 5 and 6) are calculated using the computational process, and the maximal load in each beam is fixed in order to have the same levels of strain in the concrete for the strengthened and unstrengthened beams and the steel and to have 2/3 of the value of steel yielding (F_y) in steel rebars. For Beams 5 and 6, the cyclic load, is increased by 40% compared to Beam 1, due to the FRP strengthening. All beams were instrumented with strain gauges in the middle of the beam section. An LVDT sensor placed on the neutral axis position measured deflection.

3.4 Influence of beam fatigue loading level

The theoretical study was conducted using the computational process described above and the delayed mechanical properties. With this computational method and the results of the test, it was calculated that with one layer of composite plate. The use of CFRP strengthening reduces the stress in the steel and in the concrete.

The experimental results show that the deflection of the concrete beams do not increase during cyclic loading for beam 1 and 2. It can be concluded that with a fatigue load, the behavior of the adhesive layer is not affected by fatigue. In this case, the CFRP and the adhesive layer behave well. Although in the case of Beam 3 (75% of failure load), the increased in deflection is more important and the failure is rapidly obtained by splitting off of steel rebars. This is no doubt because of the concrete cracking and the damage to the steel to concrete interface. This last result showed that steel rebar yielding in FRP strengthened RC beams should not be permitted in the design because of the fatigue failure of the steel and the premature cracking of the concrete.

3.5 Influence of composite on mechanical fatigue behavior

The main results of the tests are shown in Table 2. The fatigue behavior of the three beams can now be compared. The use of composite under fatigue loading reduces the strain in the concrete and in the steel. In the case of the damaged beam 6, the reduction in strain is not as great. This is because the concrete is already cracked when the composite is applied. This conclusion is important because most of the reinforced structures are already pre-cracked.

However, in the case of Beam 6, the strain in the concrete is reduced by 30% compared to Beam 4, after 250,000 cycles.

The mid-span deflection is reduced by 12%, also compared to Beam 4 (Figure 3). These results show that the

composite reinforcement increases the fatigue durability of the beam because the cyclic loads on Beams 5 and 6 represent 84% of the failure load of an RC beam without composite. The use of composite reinforcement in our case increases the service load by 40% and reduces the beam deflection and the steel and concrete strains (Table 2). With the software, the deflection of the beam and the strain in each material are calculated with acceptable accuracy. Using the fatigue mechanical law behavior of each material under cyclic loading and also using the software, the fatigue behavior of RC beam properties with FRP can be accurately calculated.

Table 2 Fatigue results on several beams

			BEAM 4	BEAM 5	BEAM 6
Maximal load (kN)			60	84	84
Minimal load (kN)			10	10	10
Theoretical dead load (kN)			100	170	170
ϵ_{steel} (%)	Cycle	1	0.11	0.11	0.11
		250 000	0.18	0.18	0.13
ϵ_{CFRP} (%)	Cycle	1	0	0.13	0.13
		250 000	0	0.18	0.12
$\epsilon_{\text{concrete}}$ (%)	Cycle	1	-0.06	-0.04	-0.04
		250 000	-0.10	-0.07	-0.055
Deflection (mm)	Cycle	1	4.6	3.8	3.8
		250 000	6.8	6	6.1

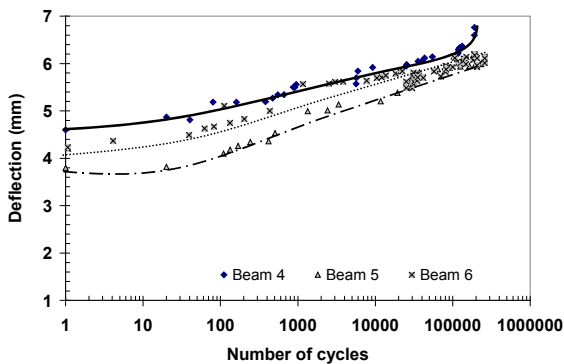


Figure 3 Deflection-Number of cycles curve beams 4 to 6

4 CONCLUSION

The material properties that limit the load in case of fatigue are those of concrete and steel strength. Using the fatigue mechanical law behavior of each material under cyclic loading and also using the software, the fatigue behavior of RC beam properties with FRP is can be accurately calculated. Tests on several beams confirm the model's results. The first tests conducted on small beams for several levels of loads showed that steel yielding should not be allowed in the design because of

failure in the concrete or the steel. According to the design code for steel-reinforced concrete, the service load should be limited to the load corresponding to steel rebars yielding. The use of FRP does not permit to have a cyclic load higher than the load corresponding to the steel rebars yielding. The results for the test on larger beams shows that the overall behavior of the concrete structure is improved with the use of composite: the fatigue behavior of the beam is better, with a 40% increase in the service load.

REFERENCES

- Barnes, R.A., and Mays, G.C, 1999. Fatigue performance of concrete beams strengthened with CFRP plates., *Journal of Composites for Construction*, ASCE; 3; (2); 63-72
- Balagru B. and Shah S.P. A method of predicting crack width and deflections for fatigue loading. *Fatigue of concrete structures ACI publications*, SP-75
- Ferrier E., Bigaud D., Hamelin P., Bizindavyi L., Neale K. W. 2005. Fatigue Reliability of External Bonded CFRP Used for Concrete Structure. *Materials and Structures*, Volume 38; No. 275; 39 – 46
- Gao L. et al. 1998. Fatigue of concrete under uniaxial compression cyclic loading. *ACI Materials Journal*,; vol 95; n°5; 575-581
- Gheorghiu C., Labossière P., Proulx J. 2006. Fatigue and monotonic strength of RC beams strengthened with CFRPs, *Composites Part A: Applied Science and Manufacturing*, August; vol. 37; Issue 8; 1111-1118
- Horris B., Gathercole N., Reiter H. and Adm T. 1996. Constant-stress of fatigue response and life prediction for carbon fiber composite. *Progress in Durability Analysis of Composite Systems*, Edited by A. Cardon, H. Fukada nad K. Reisner; 63-74
- Jakobsen A.K, Fatigue of concrete beams and columns, Bulletin n°70-1, NTH Institut for beton konstruksjoner, Trondheim
- Japanese Concrete Institute, 1998. Report II of Research Committee on Continuous Fiber-Reinforced Concrete. *Japanese Concrete Institute*,; vol. 5
- Mander J. B. et al, 1994. Low cycle fatigue behavior of reinforcing steel. *Journal of Material in Civil Engineering*,; vol.6; n°4; 453-469
- Meier, U., Dearing, M., Meier, H., and Schwegler, G. 1992. Strengthening of structures with CFRP laminates: research and applications in Switzerland. *Advanced Composite Materials in Bridges and Structures*, K.W. Neale and P. Labossière, Eds., Canadian Society for Civil Engineering, Montreal, Canada; 243-251
- Neale, K.W., and Labossière, P. 1997. State-of-the-art report on retrofitting and strengthening by continuous fibre in Canada. *Non-Metallic Reinforcement for Concrete Structure*, *Japan Concrete Institute*,; 25-39
- Plevris N., Triantafillou T.C. 1994. Time dependent behavior of RC members strengthened with FRP laminates. *Journal of Structural Engineering*, March; vol 120; n°3; 1016-1042
- Varastehpour, H., and Hamelin, P. 1997. Strengthening of concrete beams using fiber-reinforced plastics. *Materials and Structures*, RILEM,; 30; 160-166

Box Girders under Extreme Long-Time Static and Fatigue Loading

Urs Meier, Robert Müller, Michel Barbezat & Giovanni Pietro Terrasi

EMPA, Swiss Federal Laboratories for Materials Science and Technology, Dübendorf-Zürich, Switzerland.

ABSTRACT This paper discusses aspects of the extreme long-time behavior of filament wound E-glass fiber reinforced epoxy box girders. Theoretical and experimental data are compared and show good agreement. The performance of these GFRP box girders during 25 years of static loading and 100 million fatigue cycles is excellent.

1 INTRODUCTION

In 1975 EMPA, the Swiss Federal Laboratories for Materials Science and Technology and the Ciba Corporation developed jointly a GFRP box girder system for demonstration experiments during the annual conference of the Swiss Society of Civil Engineers (SIA). This event was so successful that EMPA and Ciba decided to undertake a research and development (R&D) project with the goal of proving the long-time reliability of such GFRP composite box girders (Meier et. al 1983).

2 GFRP BOX GIRDER FABRICATION

The construction of the box girders is seen in Figures 1 and 2. The flanges are fabricated of unidirectional profiles, and the webs of filament-wound laminates. E-glass rovings, Type OCF 859-2360 tex were employed as reinforcement fibers and epoxy resin, XB 2878 A+B as the matrix.

The core of the box girder consists of epoxy resin foam. It served as a lost mandrel for the helical winding process. The $\pm 45^\circ$ laminate of the webs is fabricated of two plies having a nominal thickness of 3 mm. During the filament winding process the inner plies lie directly on the mandrel. The outer plies surround the unidirectional flanges, each of which is produced of 864 rovings. The winding tape consists of four rovings. The actual average laminate thicknesses and the volume-percentage of glass are given in Table 1. The density of the webs is 1.71 g/cm^3 , that of the flanges (incl. $\pm 45^\circ$ plies) 1.76 g/m^3 .

The loading zones were reinforced with a 2 mm thick glass-fabric type, QT 57 having a width of 80 mm wound around the box girder. A smooth surface was produced at the loading points by pressing on a mold, thus assuring an optimum transmission of forces. The test results from the girders No. 1 and No. 2 suggested that an additional reinforcement of the loading zones would result in an increase of the ultimate flexural

load-carrying capacity. Therefore girders No. 3 to 6 were provided with an 8 mm thick laminate on the internal sides of the compression and tension flanges in these zones, extending over a length of 120 mm and tapering off on both sides over a length of 50 mm.

3 STATIC LOADING EXPERIMENTS

The box girders were tested in four-point bending with a span of 2800 mm. The distance between the loading points and the supports was 700 mm. In the design of the test set-up, consideration was given, above all, to the expected large deflections of the girders. This was not to impose any constraints. The test girders with simply supported ends were not placed between fixed and movable hinges, but were suspended between two pendulums.

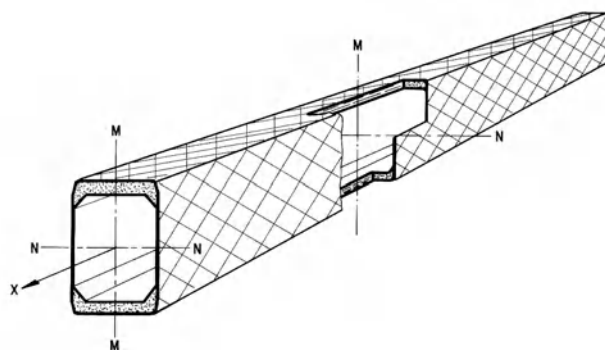


Figure 1 Perspective view of GFRP box girder. The flanges consist of unidirectional E-glass/epoxy profiles surrounded by the $\pm 45^\circ$ plies of the webs

This arrangement permits free rotation at both girder ends as well as horizontal displacement. The two servo-hydraulic actuators, each of which applies a load F at the quarter-points, provide for centering of the girders. In the static loading tests, girders No. 1 to 4 were subjected

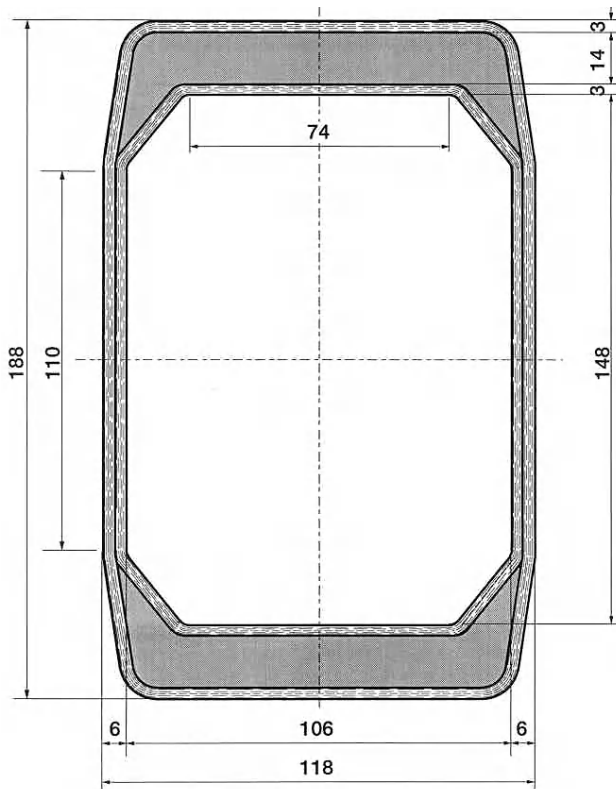


Figure 2 Typical cross section of the GFRP box girder. The finely dotted area designates the unidirectional flanges, the dashed area the $\pm 45^\circ$ filament-wound laminates. All measurements in [mm]

Table 1 Description of the laminates

Laminate	Thick-ness (mm)	Fiber Volume (%)
Flanges (unidirectional)	13.8	42
Outer filament-wound laminates (region of the flanges)	2.5	44
Inner filament-wound laminates (region of the flanges)	1.7	66
Filament-wound laminates $\pm 45^\circ$ plies (region of the webs)	5.8	41

Table 2 Deflections and ultimate loads

Deflections	load F (kN)	Girder 1 (mm)	Girder 2 (mm)	Girder 3 (mm)	Girder 4 (mm)
at mid-span	50	38.7	37.7	35.0	36.0
in mm	100	79.5	75.7	73.3	73.6
	150	121.3	118.2	114.2	116.2
	200	—	—	152.9	162.5
relative	50	5.30	—	4.99	4.99
over	100	11.10	—	10.60	10.40
1000 mm	150	17.23	—	16.51	16.00
in mm	200	—	—	22.94	22.43
Ultimate load	—	157.0	164.8	196.2	209.9
kN					

to a loading rate of 30 kN per minute at each loading point. Up to a load of $F = 50$ kN per loading point, corresponding to a constant bending moment of 35 kNm between the loading points, the girders behaved ideally elastic. Between $F = 50$ and 100 kN, a barely detectable bend was observed in the load-deflection diagram (in direction of higher deflection). The flexural stiffness (Table 2) decreased in this loading range by an average of 4.5% for the girders 3 and 4. From $F = 100$ to 125 kN, the first crackling noises were experienced. These changed into loud snapping noises in the region of 150 to 160 kN. At the same time, delamination between the $\pm 45^\circ$ filaments and the 0° unidirectional flanges could be seen in the compression zone along the rounded upper girder edges. These delaminations grew with further loading until failure.

For all the girders, failure occurred in the compression flanges near one or both loading points (Figure 3). Girders No. 1 and 2 exhibited one single failure, girders No. 3 and 4 double failures. The mean values for the girders 3 and 4 were 26% higher than those for the girders No. 1 and 2 as a result of the additional reinforcement at the loading points. These values are comparable with the moment at yielding of a HEA 200 steel girder ($M_u = 150$ kNm). The steel girder, however, has a mass of 42.3 kg/m^1 compared to only 10.1 kg/m^1 for the GFRP box girder.



Figure 3 Typical compressive failure in unidirectional top flange. Picture taken from longitudinal cross section of girder No.1

After the loading experiments, all the girders exhibited very fine cracks along the $\pm 45^\circ$ filaments in the web-halves subjected to tension. In contrast, no cracks or delaminations could be observed on the tension flanges.

The total deflection at mid-span at failure was 173.3 mm. The relative deflection at failure over a measuring length over 1000 mm at mid-span (region of the constant moment) was 24.16 mm. This data is not available for the girders No. 1 to 3.

Detailed information about strain measurement are given by Meier et. al (1983). A quantitative analysis of those results confirms the assumption that the cross-

sections which were originally planar remain so.

4 LONG-TIME FATIGUE LOADING

The girders No. 5 and 6, which are of the same design as the girders No. 3 and 4 were subjected to sinusoidal loading at 23°C and 50% R.H.

Girder No. 5 was tested for 100 million cycles (1.6 years) with a frequency of 2.0 Hz, with a lower load limit of $F_{\min} = 10$ kN and an upper load limit of $F_{\max} = 40$ kN per loading point. Under the given conditions, no damage or change in the bending stiffness could be observed over the entire course of the test. This is not too surprising, since the calculated load for first ply failure was 60 kN per loading point.

For the girder No. 6 $F_{\min} = 10$ kN remained unchanged but F_{\max} was raised to 60 kN corresponding to the first ply failure load. After four million cycles, cracks appeared on the matrix-rich surface of the tensile flange perpendicular to the x-axis very similar to reinforced concrete girders. These cracks were studied with a stereo microscope while under upper load $F_{\max} = 60$ kN. It was found that the cracks were confined to the matrix surface and did not involve the fibers. The outside $\pm 45^\circ$ filaments bridged the cracks. After 38 million cycles, the first delamination zones, approximately finger-nail size appeared, similar to those occurring due to static loading. These were located in the region of the load points between the unidirectional compression-flange and the outside $\pm 45^\circ$ plies. Up to 100 million cycles these delamination zones enlarged further by approximately 70% (Figure 4). At this stage a decrease of bending stiffness of about 2% was observed.

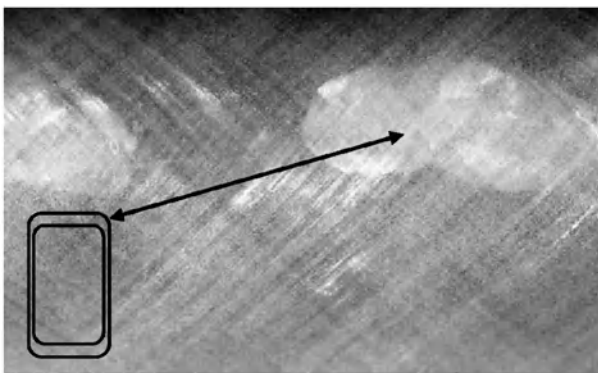


Figure 4 Typical delamination zone between the unidirectional compression-flange and the outside $\pm 45^\circ$ plies

After an interruption of five years (during that time the girder was unloaded) a new test was started with girder No. 5 which had already been loaded for 100 million cycles (see second section above). F_{\max} was doubled to 80 kN and the test frequency reduced to 1.0 Hz. Similar observations have been made as with girder No. 6. Surface cracks at the tensile-flange were developing

and slow growing delamination zones at the interface of the compression-flange and the outside $\pm 45^\circ$ plies. However even this high amplitude with an F_{\max} which was 33% higher than the load for first ply failure, did no harm to the load carrying capacity of the girder. However there was more and more harm to the servo hydraulic testing equipment. The fatigue experiments had several times to be interrupted due to fatigue failures in metallic bearings of the equipment. Beside that the experiment was going to be extremely expensive. Therefore it was decided to stop it after 47 million cycles with an F_{\max} of 80 kN. These last 47 million cycles caused a loss in bending stiffness EJ of 9%. Delamination between the $\pm 45^\circ$ filaments and the 0° unidirectional flanges in the compression zone along the rounded upper girder edges reached in average 15 by 50 mm. The largest delamination had the dimension of 20 by 100 mm. These delaminations are an important reason for the softening of the girder No. 5 in flexure.

5 LONG-TIME STATIC LOADING

After completion of 100 million fatigue cycles with $F_{\max} = 60$ kN the girder No. 6 was subjected to a extreme long-time creep test. The loading arrangement was (and is even now, since the experiment is still going on) also four-point bending, similar to the monotonous static and the fatigue loading. The load $F = 60$ kN = constant was accomplished with a dead load (lead ingot) arrangement. During the first 20,000 hours there were relative high creep rates, as shown in Figure 5. Now after 25 years of constant loading these creep rates are diminishing to zero. The deflections given in Figure 5 have been measured in the center of the girder in the region of the constant bending moment over a gauge length of 1000 mm. These deflections can be correlated with the curvature of the girder. The first 11.4 mm of deflections at “zero time” have been contributed by the elastic deformation during loading.

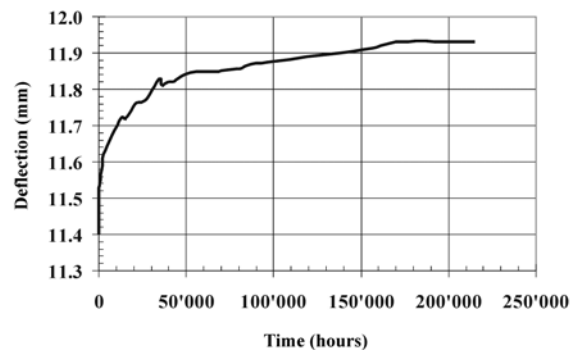


Figure 5 Creep behavior of girder No. 6 for a constant loading of $F = 60$ kN in each loading point during 25 years

The creep calculations made by Themis (1993) are based upon the isochronous stress-strain diagram for the epoxy resin XB 2878 A+B of Ciba Corporation. For the E-glass fiber it was assumed that there is no creep. In Table 3 a comparison is given for the predicted and the experimental relative stiffness of the girder No. 6 due to creep. The calculated values slightly overestimate the creep but from an engineering point of view the agreement with the experimental data is good.

Table 3 Relative bending stiffness EJ versus elapsed time

Elapsed time Hours (h)	Relative Stiffness	
	calculated (%)	experimental (%)
0.1	100.0	100.0
1	100.0	99.6
10	98.8	98.9
100	97.5	98.0
1,000	95.6	96.8
10,000	92.1	94.7
50,000	90.8	92.2

6 CONCLUSIONS

The excellent long-time static and fatigue behavior is due to the fiber-dominated design of the described box girder system. In no situation does the matrix have a primary load carrying function. All girder failures are ruled by the behavior of the fibers and not of the matrix. This is the reason for the high reliability of this GFRP box girder system. The outstanding experimental results of this R&D project are perfectly suited to build up confidence into highly loaded FRP girders over a very long period of time.

7 ACKNOWLEDGEMENTS

A R&D-project like “Box Girders under Extreme Long-Time Static and Fatigue Loading” as described above with 35 years duration takes a lot of energy and determination. However it also takes a tremendous amount of support. Therefore the authors would like to acknowledge the following persons who directly or indirectly contributed to this work: Prof. Dr. Alfred Rösli who had the courage to organize as early as 1975 a civil engineering conference about polymers for structural applications, Prof. Dr. Theodor Erismann (1969–1988 president of EMPA) for the outstanding financial support, Prof. Dr. Alfred Puck for the basic concept of the FRP box girders and the support during fabrication, Mr. Peter Voirol for the filament winding part of the production, Dr. Christoph Rüegg for technical advice, Mr. Peter Flüeler (head of the polymer and composites laboratory of EMPA 1979–2005), Prof. Dr. Masoud Motavalli, Ms. Brigitte Wagner, Mr. Erwin Rindlisbacher, and Mr. Daniel Völki for the supervision of the experiments during three and a half decades.

REFERENCES

- Meier, Urs, Müller, Robert & Puck, Alfred, 1983. FRP-Box Beams under static and fatigue loading. In Feest T. (ed), Testing, Evaluation and Quality Control of Composites, *Proc. intern. conf., Surrey University, Guildford, England, 13-14 September 1983*: 324-336
- Puck, Alfred, 1969. Einführen in das Gestalten und Dimensionieren. In Ehrenstein G.W. & Martin H.-D. (eds), *Konstruieren und Berechnen von GFK-Teilen*: 63-65. Beiheft zur Fachzeitschrift Kunststoffberater. Frankfurt Umschau-Verlag.
- Themis, Marios G., 1993. Model calculation for the creep behaviour of a beam made of E-glass fibre reinforced epoxy matrix, Postgraduate thesis in the Department of Civil Engineering at Swiss Federal Institute of Technology in Zurich.

Experimental Study of Time-dependent Behaviour of Concrete Members Reinforced with GFRP Bars

C. Miàs (cristina.mias@udg.edu), Ll. Torres, A. Turon, M. Baena, I. Vilanova & M. Llorens
Analysis and Advanced Materials for Structural Design (AMADE), University of Girona, Spain

ABSTRACT This study presents the results and discussion of an experimental tests program in which 8 concrete beams reinforced with glass fibre reinforced polymer (GFRP) were maintained under a constant load for a period of 150 days. Two different ratios of reinforcement and two different levels of sustained load were used. The beams were instrumented and monitored to analyze the time-dependent behaviour due to concrete creep and shrinkage.

The measured deflections are compared with those calculated using methodologies available for steel reinforced concrete structures as CEB procedure, as well as with ACI 440.1R-06 and CSA-S806-02 for FRP reinforced concrete structures. The comparisons of the theoretical and experimental long-term deflections indicate that CEB procedure gives reasonable predictions in all 8 beams. However, some differences can be found when ACI 440.1R-06 or CSA-S806-02 procedures are applied.

1 INTRODUCTION

Due to the lower stiffness of glass fibre reinforced polymer (FRP) bars compared to steel, the design of concrete beams reinforced with FRP materials is often governed by the serviceability limit state, where deflections play an important role. Deflections are larger, and the instantaneous and time-dependent parts have a different weight in the total deflection.

Several studies have shown that procedures based on the same principles used for the deflection prediction of steel reinforced concrete structures (SRCS) can be applied to FRP reinforced concrete structures (FRPRCS). This leads to similar expressions to those of the steel, but it is necessary to include some modifications to account for their different characteristics (Brown & Bartholomew 1996, Brown 1997, Arockiasamy et al. 2000).

Hence, ACI 440.1R-06, based on tests carried out by Brown (1997), proposes multiplying the factor used for SRCS by 0.6; although the code recognizes that further work is necessary to validate the coefficient. However, the Canadian standard CSA S806-02 proposes a more conservative approach, adopting the same coefficients as for steel.

The study reported here has been conducted with the aim of analysing the time-dependent behaviour due to creep and shrinkage in eight GFRP reinforced concrete beams. Tests and analytical prediction on the long-term deflection of GFRP reinforced concrete beams are performed using methodologies available for steel reinforced concrete structures as CEB procedure, as well

as with ACI 440.1R-06 and CSA-S806-02 for FRP reinforced concrete structures.

2 EXPERIMENTAL TEST PROGRAM

2.1 Beams specifications

A total of 8 concrete beams of 140×190×2450 were prepared for this study, with a clear concrete cover equal to 20mm. The beams were reinforced with 2Ø12 or 2Ø16 GFRP rebars placed at the tension side. No upper reinforcement was used. The shear-span was reinforced with steel stirrups (d8mm/80mm) in order to minimize shear effects. In the pure bending zone no stirrups were provided, as shown in Figure 1.

The GFRP bars used in these experiments were type E-CR GFRP ComBAR (Schöck Bauteile GmbH) with nominal modulus of elasticity of 60MPa.

Concrete consisted of 185 kg/m³ of water, 880 kg/m³ of fine aggregate, 875 kg/m³ of coarse aggregate (maximum size: 12mm), 320 kg/m³ of Ordinary Portland Cement (OPC) and a 0.58 water/cement ratio, for a target compressive strength of 30MPa.

2.2 Test setup and instrumentation

To represent de service conditions, the beams were subjected to short-term cyclical loading before applying the sustained load. The maximum load corresponded approximately to the theoretical service moment. The sustained load applied to the specimens was designed to obtain top fiber concrete compressive stresses of $0.3f_c$ and $0.4f_c$.

The specimens were identified as Lx-Gyy, where x

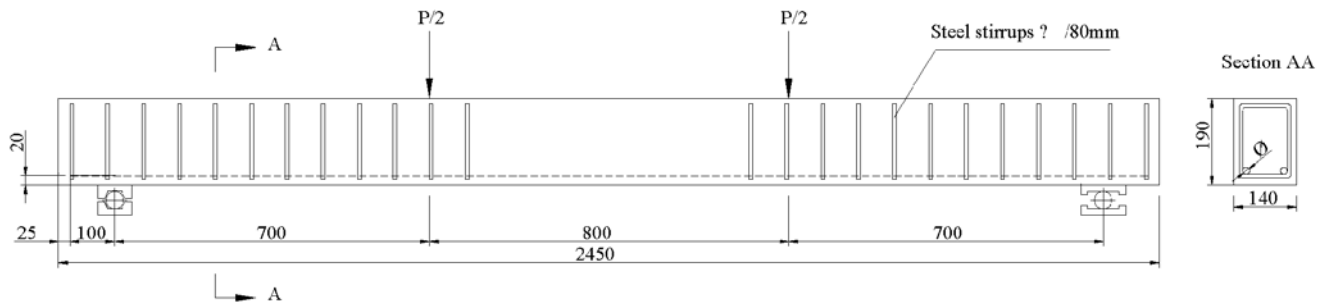


Figure 1 Geometric and reinforcement details

stands for the level of the sustained load and y the diameter of the GFRP bar. Specimen type *a* had a pre-crack in the mid-span section to ensure the creation of a crack in a known specific position. Specimen type *b* was initially uncracked. The relevant details are given in Table 1.

Table 1 Geometric properties and instantaneous compressive concrete stress level

Beam	Ø bar (mm)	ρ (%)	σ_c (MPa)
L1-G12	12	1.0	$0.3f_c$
L2-G12	12	1.0	$0.3f_c$
L1-G16	16	1.8	$0.4f_c$
L2-G16	16	1.8	$0.4f_c$

The sustained load set-up is shown in Figure 2. The beams were simply supported with a testing span of 2200mm. The load was applied by suspending concrete blocks from the beam (constant moment region equal to 800mm).



Figure 2 Loading frames

In order to determine the time-dependent material properties for concrete, concrete cylinders which were cast from the same batches of concrete as the beams were tested to determine the creep coefficient and the value of the free shrinkage. The temperature and relative humidity were registered.

Displacements transducers were used in order to

control the deflections of the tested beams at the mid-span section.

Two dial gauges were placed at 400mm distance from the mid-span. In addition, demec points were installed to measure horizontal strains by means of a mechanical extensometer over a gauge length of 200mm along the beam.

In beams type *a*, the mid-span cross section was instrumented with two concrete strain gauges at the surface of the beam (one on the top surface and the other at 20mm from the top) and a strain gauge on the GFRP bar to control the evolution of the concrete and GFRP strain with time.

3 ANALYTICAL PREDICTION OF TIME-DEPENDENT DEFLECTIONS

Many methods have been developed to try to predict the long-term deflections of steel reinforced concrete structures due to creep and shrinkage.

The CEB procedure, described and illustrated in Ghali & Favre (1994) to obtain time-dependent curvatures due to creep is general for SRCS. Moreover it has been proved to be suitable for other reinforcing materials such as FRP (Hall & Ghali 2000).

In the present analysis, the mentioned method together with two methods for available codes for GFRP, ACI440.1R-06 and CSA-S806-02 are used to calculate theoretical deflections.

3.1 CEB procedure

Based on the approaches developed in CEB Manual on Cracking and Deformations (1985), and incorporated in CEB-FIB Model Code 1990 and Eurocode 2, the mid-span long-term deflections can be obtained from double integration of the long-term curvatures, $\Delta\psi(t, t_0)$, along the member.

The long-term curvature can be determined at each section by interpolation between uncracked and cracked states, denoted as $\Delta\psi_1$ and $\Delta\psi_2$, respectively:

$$\Delta\psi(t, t_0) = (1 - \xi)\Delta\psi_1(t, t_0) + \xi\Delta\psi_2(t, t_0) \quad (1)$$

$$\xi = 1 - \beta \left(\frac{M_{cr}}{M} \right)^2 \quad (2)$$

where ξ is the interpolation coefficient to account for

tension stiffening; M_{cr} is the cracking moment; M is the applied moment; and β is a coefficient taking account of the influence of the duration of loading (1 for a single short-term load, and 0.5 for sustained or repeated loads).

The long-term curvatures at the time t is the sum of the curvatures due to creep and shrinkage (Ghali and Favre 1994):

$$\Delta\psi_{i,creep}(t, t_0) = \varphi(t, t_0)\kappa_{\varphi,i}\psi_i(t_0) \quad (3)$$

$$\Delta\psi_{i,cs}(t, t_0) = \varepsilon_{cs}(t, t_0)\frac{\kappa_{cs,i}}{d} \quad (4)$$

where the subscript i takes a value of 1 for uncracked transformed sections and 2 for fully cracked transformed sections; $\psi(t, t_0)$ is the creep coefficient at age t , $\varepsilon_{cs}(t, t_0)$ is the free shrinkage and d is the effective depth; κ_{φ} and κ_{cs} are the dimensionless coefficients depending upon properties of the section:

$$\kappa_{\varphi,i} = \frac{I_c + A_c y_c \Delta y}{\bar{I}} \quad \kappa_{cs,i} = -\frac{A_c y_c d}{\bar{I}} \quad (5)$$

In Equation 5, I_c is the moment of inertia of the concrete area A_c about an axis through the centroid of the age-adjusted transformed section, y_c is the centroid of the A_c , Δy is the y-coordinate of the centroid of the age-adjusted transformed section, measured downward from the centroid of the transformed section at t_0 , and \bar{I} is the moment of inertia of the age-adjusted transformed section. The age-adjusted transformed section is calculated from the age-adjusted elastic modulus of concrete (Bazant 1972), $\bar{E}_e(t, t_0)$:

$$\bar{E}_e(t, t_0) = \frac{E_c(t_0)}{1 + \chi(t, t_0)\varphi(t, t_0)} \quad (6)$$

where $E_c(t_0)$ is the elastic modulus at the initial time and $\chi(t, t_0)$ is an ageing coefficient.

3.2 ACI 440.1R-06 procedure

The long-term deflection due to creep and shrinkage can be obtained by multiplying the immediate deflection caused by sustained load by the factor, λ :

$$\Delta d(t, t_0) = d(t_0)0.6\lambda \quad \lambda = 0.6\frac{\xi}{1 + 50\rho'} \quad (7)$$

where ρ' is the compression reinforcement ratio and ξ , the time-dependent factor for sustained loads, which value depends on duration of load.

3.3 CSA-S806-02 procedure

The long-time deflection for flexural members is obtained applying the time-dependent factor S , which takes the same values as ξ .

$$\Delta d(t, t_0) = d(t_0)S \quad (8)$$

4 TEST RESULTS

In Figure 3-6, the experimental deflections at the

mid-span are compared with the analytical predictions based on CEB procedure, ACI 440.1R-06 and CSA-S806-02. The total deflection includes immediate and long-term deflections due to creep and shrinkage.

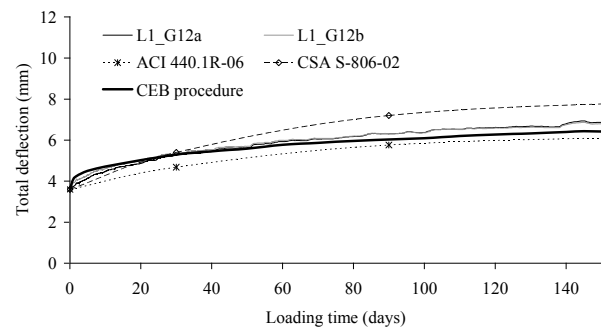


Figure 3 Total mid-span deflection (Series L1-G12)

It can be seen that the theoretical total deflections calculated using ACI 440 procedure are in reasonable agreement with the experimental data of beams L1-G12 and L2-G12 (Figures 3-4), however, underestimate the experimental deflections of beams L1-G16 and L2-G16 (Figures 5-6). In the case of using CSA-S806 procedure, the phenomena is opposite; although, the procedure fits quite well from a loading time greater than 60 days in beams L1-G16 and L2-G16 (Figures 5-6), it overestimates the values of deflections in beams L1-G12 and L2-G12 (Figures 3-4).

The predicted deflections using CEB procedure present reasonable accuracy in all the beams.

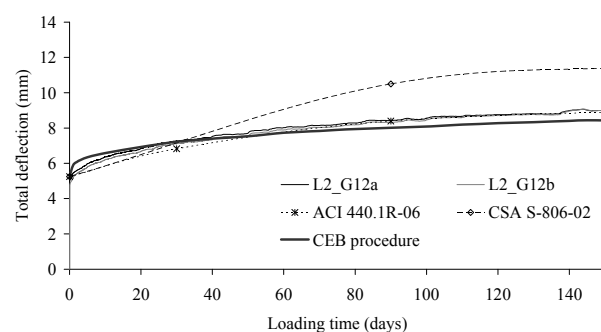


Figure 4 Total mid-span deflection (Series L2-G12)

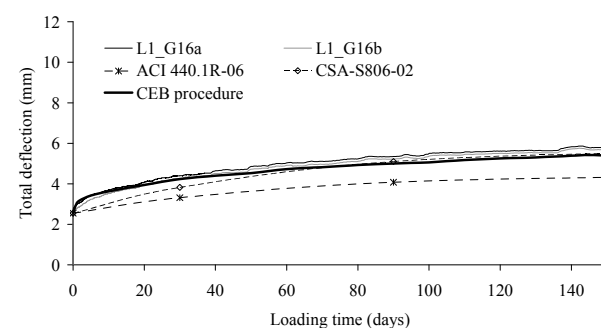


Figure 5 Total mid-span deflection (Series L1-G16)

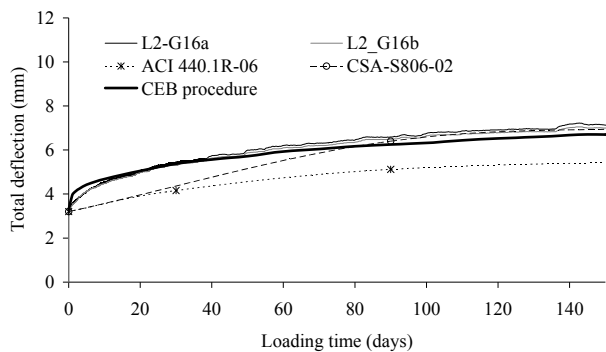


Figure 6 Total mid-span deflection (Series L2-G16)

5 CONCLUSIONS

Preliminary results of an experimental program conducted at University of Girona, for a period of 150 days, on time-dependent behaviour of GFRP reinforced concrete beams have been presented. For the analyzed period, the calculated deflections using procedures available in guidelines for FRPRCS give some differences depending on the reinforcement ratio; however, the comparison with CEB procedure has shown a reasonable agreement.

6 AKNOWELEGEMENTS

The authors acknowledge the support provided by the Spanish Government (Ministerio de Educación y Ciencia), Project ref. BIA2007-60222 and also the support of Schök Bauteile GmbH for the GFRP rebars supply. The first author thanks the Ministerio de Educación y Ciencia for Grant BES-2008-005740.

REFERENCES

- ACI 440.1R-06 2006. *Guide for the Design and Construction of Concrete Reinforced with FRP Bars*, ACI Committee 440. American Concrete Institute, Farmington Hills.
- ACI 318-05 2005, *Building Code Requirements for Reinforced Concrete*, ACI Committee 318. American Concrete Institute, Detroit, Michigan, 2005. CEB- FIP 1990, Model code for concrete structures.
- Arockiasamy M., Chidambaram S., Amera A., Shahawy M. 2000. *Time-dependent deformations of concrete beams reinforced with CFRP bars*. Composites Part B: Engineering, 31: 577-592.
- Brown V. 1997. *Sustained Load Deflections in GFRP- Reinforced Concrete Beams*, Proceedings of the Third Int. Symposium on Non-Metallic (FRP) Reinforcement for Concrete Structures (FRPRCS-3), V. 2, Japan Concrete Institute, Tokyo, Japan, pp. 495-502.
- Bazant Z.P. 1972. *Prediction of concrete creep effects using age-adjusted effective modulus method*. American Concrete Institute Journal, 69 , 212-217.
- Brown V. and Bartholomew C. 1996. *Long-term deflections of GFRP-reinforced concrete beams*. First International Conference on Composites in Infrastructure, (ICCI-96), H. Saadatmanesh and M. R. Ehsani, eds., Tucson, Arizona, pp. 389-400.
- Eurocode 2 1992. *Design of concrete structures. Part 1-1: General rules and rules for buildings (EN 1992-1-1:1991)*: Comité Européen de Normalisation.
- CEB-FIB Model Code 1990. Comité Euro-International du Béton. Fédération Internationale de la Précontrainte, Thomas Telford House, London, England.
- CSA-S806-02 2002. *Design and construction of building components with fibre-reinforced polymers*. Canadian Standards Association, Mississauga, Ontario, Canada, 2002.
- Ghali A. and Favre R., 1994. *Concrete Structures: Stresses and Deformations*. Ed. Chapman and Hall, London.
- Hall T. and Ghali A. 2000. *Long-term deflection prediction of concrete members reinforced with glass fibre reinforced polymer bars*. Canadian Journal of Civil Engineering, 27(5): 890-898.
- Manual on Cracking and Deformations 1985. *Butletin d'Information n° 158-E*. Comité Euro-International du Béton.

Hygrothermal Ageing of Basalt Fiber Reinforced Epoxy Composites

Bo Xiao, Hui Li & Guijun Xian (gjxian@hit.edu.cn)

School of Civil Engineering, Harbin Institute of Technology, Harbin, China

ABSTRACT Due to its low price and high chemical resistance, basalt fiber is emerging as a novel reinforcement for fiber reinforced polymer (FRP) composites used in civil engineering in recent years. Compared to widely applied glass fiber based FRP (GFRP) and carbon fiber based FRP (CFRP), however, much less research works on the durability performances of basalt fiber reinforced polymer (BFRP), have been done by now, which seriously hinders its wide and safe application. In the present study, unidirectional basalt fiber fabric reinforced epoxy composites were prepared with a wet lay-up process. Such BFRP materials are expected to be used for external rehabilitation, strengthening or renewal of structures. Durability studies were performed on cured BFRP strips through water, alkali solution immersion at various temperatures. The evolution of the water uptake and mechanical properties with the ageing time was investigated. The aim of the study is to demonstrate the feasibility of using BFRP in severe civil environments, and to disclose the possible degradation mechanisms. As shown, tensile strength of the BFRP samples shows remarkable degradation due to water and alkaline solution immersion, while the tensile modulus is affected slightly. In addition, the mechanical property degradation of the BFRP samples in water is much less than that in alkaline solutions. The results indicate the current basalt fiber need to be modified in its chemical compositions, surface treatment for enhanced durability performance.

1 INTRODUCTION

In recent more than twenty years, FRP composites have been widely applied in civil engineering as internal strengthening or external reinforcement for civil structures. The most successful application is externally wrapped or bonded FRP systems to strength, rehabilitate or renew various concrete, even steel structures. The commonly used fiber reinforcements for FRP composites are carbon fiber, glass fiber and Aramide fiber. The basic physical and chemical performances of the above FRP composites have been well demonstrated in various design codes, and published papers.

Basalt fiber (BF) is produced from basalt rock through melting process, generally without any other additives in a single process (Sim et al. 2005). The performance of the basalt fiber, which is critically dependent on the basalt rock mine, may be less consistent than the synthetic fibers, such as glass fiber, carbon fiber etc.

Up to date, some durability studies in various environmental conditions have been conducted to facilitate the application of BF and BF reinforced FRP (BFRP). Sim et al. studied chemical resistance, elevated temperature performance and tensile properties of BF (produced in Russia) and BF reinforced BFRP (Sim et al. 2005). As reported, BF shows similar alkaline resistance to glass fibers, and far inferior to carbon fibers, while

BF possesses the best fire resistance, even than the carbon fiber. As concluded, BF can be a promising alternative reinforcement among the commonly used fibers. It was found that basalt fiber reinforced epoxy FRP shows a good water and salt solution resistance up to 240 days at room temperatures (Liu et al. 2006). At elevated temperature (i.e., 40°C), however, the ageing in the above conditions resulted in remarkable decrease of the shear strength, may due to the degradation of the interracial strength. As found in a study on the chemical resistance of BF in acid and alkaline solution, after 3 hours boiling treatment, the remaining strength ratio is about 65.5% in 2 mol/L HCl solution and 81.6% in 2 mol/L NaOH solutions (Wang et al. 2008). In 90 days' alkaline immersion, epoxy based BFRP shows a remarkable reduction in the flexural strength and a relative stable modulus at room temperature. The maximum strength reduction is about 40% of the original value. In addition, the studied BFRP shows a relatively better alkaline solution resistance compared to the acid solution.

In the present paper, BF reinforced epoxy BFRP plates were prepared with a hand wet layup process. After fully curing, BFRP plates were immersed into distilled water, alkaline solution at 23, 40, 60 and 80°C. The tensile properties were tracked as a function of ageing time. Based on the degradation rate of the

mechanical properties, the service life of the BFRP under the above conditions was evaluated using Arrhenius model. The study is to assess the application of BFRP in civil engineering under severe environmental conditions.

2 EXPERIMENTAL

2.1 Materials

An epoxy resin system, including epoxy resin and hardeners, is developed at our lab used for saturation of fiber clothes to strengthen, repair and rehabilitate concrete or other civil engineering structures. This epoxy resin system has a low viscosity and thus can easily saturate fiber fabrics. The resin can be cured at room temperature and reach a high deflection temperature.

Unidirectional basalt fiber fabrics are commercially available. As indicated, fiber diameter is 13 micron; the area density of the fabric is 360 g/m²; tensile strength is 2.1GPa and modulus is 105GPa.

BFRP prepared with a hand wet layup process. First, a pre-cut fabric, laid on a flat surface, was saturated with enough epoxy resin system. The more resin was pressed out from the fabric with a plastic trowel. Two layers of fabric was used for a samples of the dimensions of 300×300 mm².

After cured in the lab (around 23°C) for 7 days, the plate was cut into 25mm×250mm strips completely along the fiber direction. Those strips used for tensile testing will be post-cured at an oven of 110°C for 2 hours.

Figure 1 shows cut strip for following testing.



Figure 1 BFRP strips used for tensile testing

2.2 Testing

Water uptake testing: The cured sample coupons were cut into 25×25 mm² with the original thickness for water sorption tests. Samples were soaked in distilled water baths or alkaline solution at 23, 40, 60 and 80 °C, respectively. Figure 2 shows the samples immersion in the distilled water. The moisture uptake was detected by periodically measuring the mass of the samples. For specimens aged in water, samples were taken out of the baths, swiped off the surface water using tissue papers and weighted using an electronic balance with an accuracy of 0.01 mg. The presented data are an average

for 5 coupons for each condition.

Tensile testing: The tensile properties of the strips are tested according to ASTM D3039 with a WDW-100D electronic tensile machine, which produced by Shandong Shidai Company. The tensile strain was measured with a strain gauge.

The alkaline solution is prepared according to ACI 440 standards, whose pH value about 13.5.

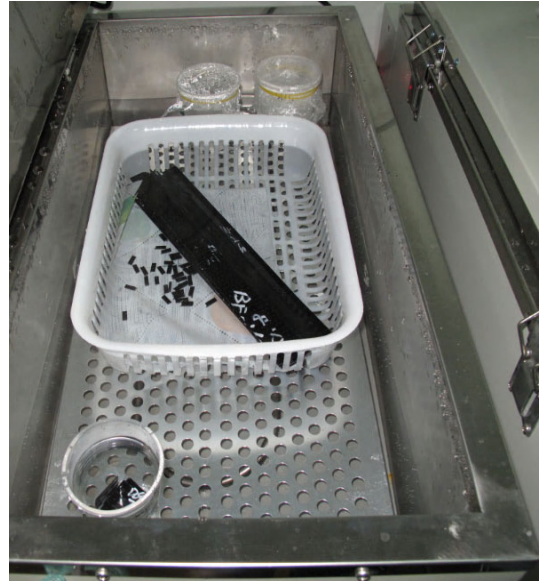


Figure 2 Caption of a typical figure. Photographs will be scanned by the printer. Always supply original photographs

3 RESULT AND DISCUSSION

3.1 Basic physical and mechanical properties

The fiber volume content of the cured samples was determined through burning method. As calculated that the fiber content is about 47 vol.%.

The glass transition temperature of the BFRP is determined with differential scanning calorimetry (DSC) technology with 10°C/min heating rate. The fully cured system has a glass transition temperature 82°C.

Figure 3 shows a typical tensile curve of a BFRP strip,

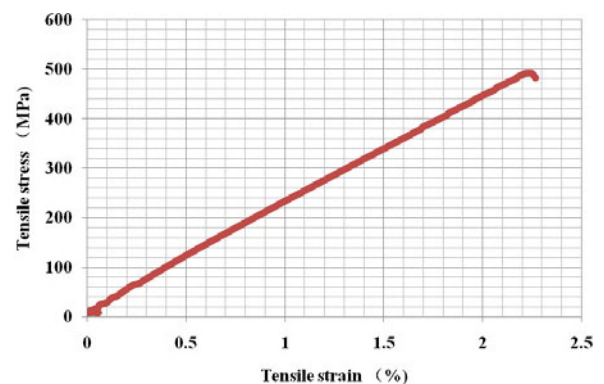


Figure 3 Typical tensile stress vs. strain curve of BFRP according to ASTM D3039

which exhibits a good linearity. The tensile strength, modulus and elongation are averaged from 10 samples, listed in Table 1.

Table 1 Tensile properties of BFRP tested according to ASTM D3039

Strength (MPa)	STD	Modulus (GPa)	STD	Elongation at break (%)	STD
602.9	29.2	29.7	2.8	2.2	0.22

It is worth noting that the tensile properties of BFRP wet layups are about 10% higher than the glass fiber reinforced FRP composites, which using the same epoxy resin system and curing process.

3.2 Water uptake

Figures 4 and 5 give the water uptake curves of the BFRP samples immersed in water or alkaline solutions at various temperatures. As shown, some important phenomena can be found and summarized below.

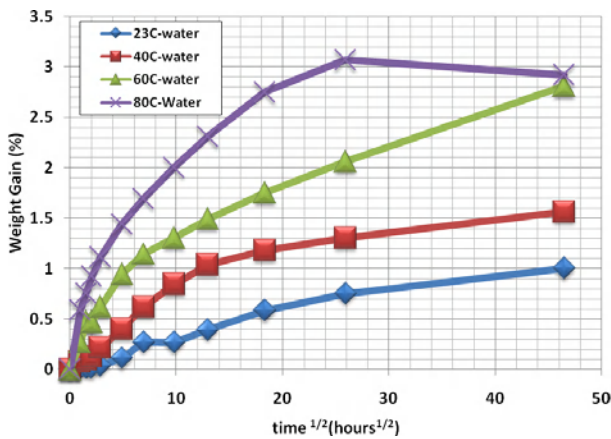


Figure 4 Water uptake vs. square time of BFRP samples immersed in distilled water

With increased immersion temperature, the water uptake in the same period increased also. It is because the water diffusion process is thermal activated. The higher immersion temperature, the high water diffusion rate reaches (Xian et al., 2007, Wrosch et al., 2008, Karbhari et al., 2009).

At the same immersion temperature (except 80°C), the sample immersed in water shows a less water uptake ratio compared to the sample immersed in alkaline solution. This indicates that BFRP suffered more degradation in alkaline solutions.

At 80°C, BFRP samples reach the maximum water uptake after one month immersion, and display an observable weight loss (Figure 4 and 5). More weight loss is found in the case of alkaline immersion. As believed, such weight loss is related to the hydrolysis of epoxy resin or the fibers (Wrosch et al. 2008). More remarkable weight loss of the sample in alkaline solution

indicates that the degradation of the BFRP samples is faster in alkaline solution than in water. The result further supports the aforehand state.

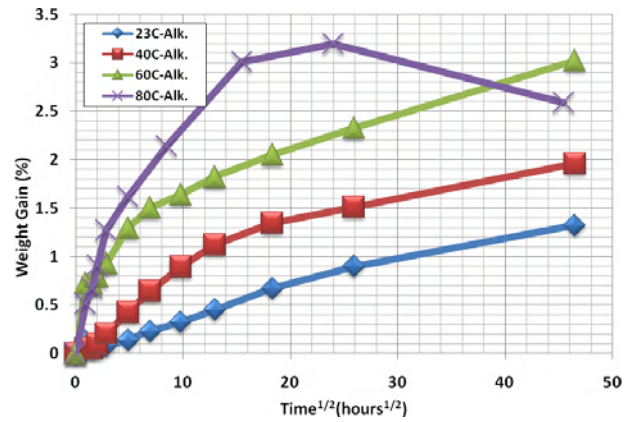


Figure 5 Water uptake vs. square time of BFRP samples immersed in distilled alkaline solution

3.3 Degradation of the tensile properties

The variation of the tensile strength and tensile modulus of BFRP samples immersed in alkaline solution are presented in Figures 6 and 7, respectively. Clearly, alkaline solution immersion brings in a dramatically reduction of the tensile strength, especially at elevated temperatures (Figure 6). After 3 months immersion, the remaining tensile strength only about 1/3 of the original value at high immersion temperatures. Even at room temperature, the strength decreased by about 23%.

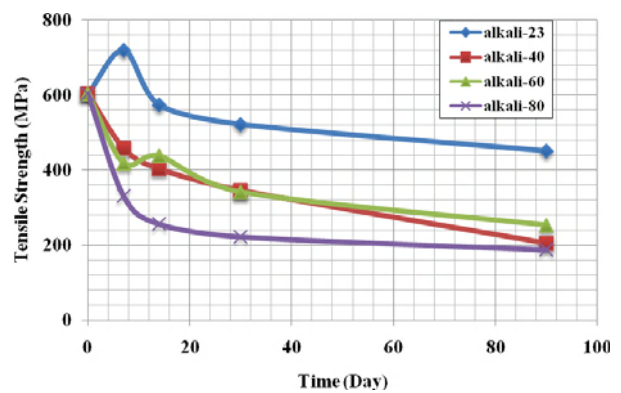


Figure 6 Variation of tensile strength of BFRP samples as a function of immersion time in alkaline solution

During the beginning immersion period (e.g., less than one month), the tensile strength degraded quickly at high temperatures. After that, the degradation slows down. For 23°C alkaline solution immersion condition, the tensile strength firstly increases after first 7 days immersion, which is attributed to the possible stress release effect.

As regarding the tensile modulus, on the contrary, alkaline solution immersion shows a slightly effect.

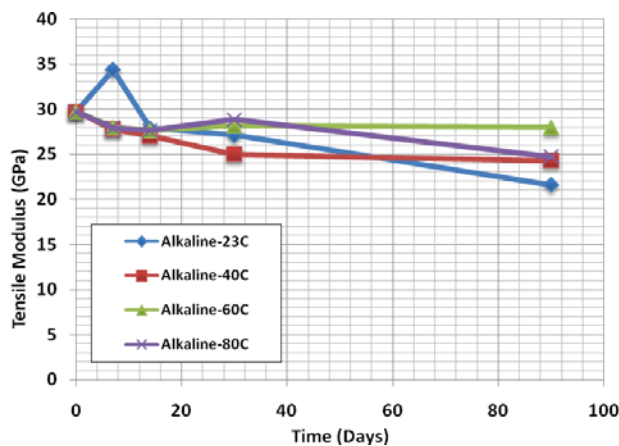


Figure 7 Water uptake vs. square time of BFRP samples immersed in distilled alkaline solution

Especially, there is no a clear temperature effect. The 60°C alkaline solution aged samples do not exhibit decreases in the modulus, while 23°C alkaline solution aged ones display the lowest modulus. As believed, the modulus are measured in the low strain range, e.g., <0.4%. The possible damage of the fiber surface or the resins may not affect the stiffness in this stage.

Similar trends of the tensile properties are found for BFRP samples immersed in distilled water at various time. It should be noted that the degradation degree is much less than that immersed in alkaline solution. This is consistent with the result of water uptake testing. The resin or the fibers may be vulnerable to the alkaline solution attack, which is responsible for the above results.

4 CONCLUSIONS

BFRP wet layups were prepared with an epoxy resin system and basalt fiber fabric. The tensile properties of un-aged samples are superior to those of glass fiber reinforced FRP composites. When immersed in distilled

water or alkaline solution, the water uptake increased with immersion temperature. The weight loss after maximum absorption of water at 80°C indicates a possible hydrolysis of resin system and damage of basalt fibers.

BFRP samples shows a remarkable decrease in tensile strength after immersion in distilled water or alkaline solutions for a short period (e.g., 1 month), while the modulus is less affected. In addition, BFRP is vulnerable to the alkaline solution attack, which is reflected by a more serious degradation in the tensile properties and more water uptake when immersed in alkaline solution.

REFERENCES

- Karbhari, V. M. and Xian, G. J. (2009). Hygrothermal effects on high V-F pultruded unidirectional carbon/epoxy composites: Moisture uptake. *Composites Part B-Engineering* 40(1): 41-49.
- Liu, O., Shaw, M. T., Parnas, R. S and McDonnell, A. M. (2006). Investigation of basalt fiber composite aging behavior for applications in transportation. *Polymer Composites* 27(5): 475-483.
- Sim, J., Park C. and Moon D. Y. (2005). Characteristics of basalt fiber as a strengthening material for concrete structures. *Composites Part B-Engineering* 36(6-7): 504-512.
- Wang, M. C., Zhang Z. G, Li, Y., Li, M. and Sun, Z. J. (2008). Chemical durability and mechanical properties of alkali-proof basalt fiber and its reinforced epoxy composites. *Journal Of Reinforced Plastics And Composites* 27(4): 393-407.
- Wrosch, M., Xian, G. J. and V.M.Karbhari. (2008). Moisture absorption and Desorption in a UV cured urethane acrylate adhesive based on radiation source. *Journal Of Applied Polymer Science* 107(6): 3654-3662.
- Xian, G. J. and Karbhari, V. M. (2007). DMTA based investigation of hygrothermal ageing of an epoxy system used in rehabilitation. *Journal of Applied Polymer Science* 104(2): 1084-1094.

Moisture Diffusion in FRP Adhesively-Bonded Joints under Hot/Wet Environments

Xu Jiang (Xu.Jiang@tudelft.nl), Henk Kolstein & Frans S.K. Bijlaard

Section of Structural and Building Engineering, Department of Design and Construction, Faculty of Civil Engineering and Geosciences, Delft University of Technology, Delft, The Netherlands

ABSTRACT Fibre Reinforced Polymer (FRP) bridge deck systems are finding increasing usage in the constructions of new bridges and renovations of old bridges. Especially hybrid structures are competitive, i.e. steel girders combined with a pultruded FRP bridge deck. Adhesive bonding which provides smoother load transition is often the most attractive joining technique for the connection between steel girders and FRP decks. However, the long-term performance of this connection is not clearly defined. So the durability modelling and life-time prediction of the adhesively bonded joint are still issues which designers and engineers have to face. As a first step of the PhD research, moisture diffusion in FRP adhesively bonded joints is discussed and analyzed numerically. The moisture concentration distribution of FRP adhesively bonded joints after 70 years was obtained, which can subsequently be used as input for the next step stress-strain analysis allowing for the incorporation of moisture-dependent mechanical properties in the FE model.

1 INSTRUCTIONS

Due to the various advantages (rapid installation, low maintenance and low weight) offered by FRP bridge decks, they have been widely used in the bridge construction industry in the past two decades. While several pedestrian bridges have already been constructed entirely of FRP composite material, most road bridges still need main steel girders to be cost-effective. Furthermore, one conspicuous use of FRP composite to steel girder system is the rehabilitation of historic concrete-steel composite bridges. The concrete decks can be replaced with FRP decks. Reducing the deck load to 20% of concrete decks may permit increased load rating without altering the original state of the bridge. The rapid installation of FRP decks also reduces bridge closure time. For the connection between FRP composite deck and steel girders, adhesive bonding technique is usually the excellent choice. Comparing to bolted connections, adhesively-bonded joints can reduce construction time, save weight by eliminating fasteners, introduce more uniform load transfer and provide better long-term performance. Herbert Gurtler (Gurtler, 2004) and Martin Schollmayer (Schollmayer, 2009) have investigated this type of adhesively-bonded joint in the longitudinal bridge direction and transverse direction respectively (Figure 1), combining the results obtained in both directions, proposes the basis for a design method of such joints.

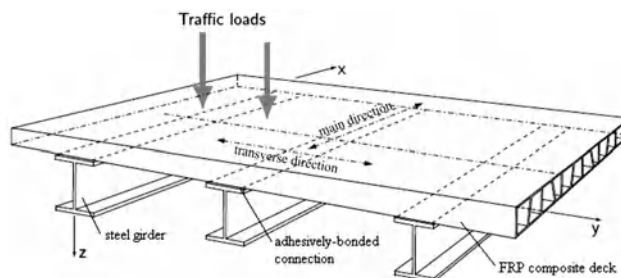


Figure 1 FRP deck to steel girder system (Schollmayer, 2009)

But a longer service-life of FRP composite structures is specially challenged by environmental effects (moisture and temperature). Degradation due to moisture absorption may significantly reduce the service-life of FRP composites and adhesive. The influence that moisture absorption has on the mechanical properties of GFRP composites is well documented (Shao, 2002; Shen, 1976; Garcia, 1998; Prian, 1999; Phifer, 2003). Absorbed moisture can cause pronounced changes in modulus, strength, and strain to failure (Springer, 1980). Moisture content of submerged FRP composites increases through diffusion. The absorbed moisture can act as a plasticizer of the composite resin, and can cause matrix cracking, fiber-matrix debonding, and corrosion of glass fibers (stress corrosion) (Garcia, 1998). These effects result in a reduction of strength and stiffness of the FRP composite. For example, Phifer (Phifer, 2003) recorded tensile strength and stiffness reductions on the order of

60 percent and 10 percent, respectively, for E-glass/vinyl ester composites submerged in fresh water for a period of about 2 years. Swelling of the adhesive can also affect the adhesively bonded joint durability as it can induce significant strains. What’s more, as the amount of water absorbed by the FRP composite increased over time, reductions in the glass transition temperature (T_g) were observed (Tsai, 2009). In this paper, moisture diffusion in FRP composite and adhesive materials are discussed and analyzed numerically. By comparing the result of experiment and numerical analysis, the FEM model was validated, and help predict the moisture concentration distribution of the FRP adhesively-bonded joint under the hot/wet environment in the service-life of 70 years.

2 MOISTURE DIFFUSION THEORY

Berens and Hopfenberg (Berens, 1977) proposed a moisture absorption model for polymeric materials, which was a linear superposition of independent contributions from Fickian diffusion and polymeric relaxation. The total amount of absorption at time t , M_t , may be expressed as

$$M_t = M_{t,F} + M_{t,R} \quad (1)$$

where $M_{t,F}$ and $M_{t,R}$ are the contributions of the Fickian and relaxation processes, respectively, at time t . The purely Fickian process is expressed as:

$$M_{t,F} = M_{\infty,F} \left\{ 1 - \frac{8}{\pi^2} \sum_{n=0}^{\infty} \frac{1}{(2n+1)^2} \exp \left[-\frac{D_z t}{h^2} \pi^2 (2n+1)^2 \right] \right\} \quad (2)$$

where $M_{\infty,F}$ is the equilibrium amount of absorption in the unrelaxed polymer, D_z is the diffusion coefficient, and h is the normal thickness, in direction of diffusion. The relaxation process is assumed to be first order in the concentration difference which drives the relaxation. The differential equation for the relaxation process is therefore:

$$\frac{dM_{t,R}}{dt} = k(M_{\infty,R} - M_{t,R}) \quad (3)$$

where k is the relaxation-rate constant and $M_{\infty,R}$ is the ultimate amount of sorption due to relaxation. Integration of equation (3) leads to:

$$M_{t,R} = M_{\infty,R} [1 - \exp(-kt)] \quad (4)$$

Substitution of equations (2) and (4) into equation (1) results in:

$$M_t = M_{\infty,F} \left\{ 1 - \frac{8}{\pi^2} \sum_{n=0}^{\infty} \frac{1}{(2n+1)^2} \exp \left[-\frac{D_z t}{h^2} \pi^2 (2n+1)^2 \right] \right\} + M_{\infty,R} [1 - \exp(-kt)] \quad (5)$$

Equation (5) is plotted in Figure 2 as a linear superposition of the first term (Fickian diffusion) and the second term

(polymeric relaxation) of the equation. The linear portion of the total absorption is almost identical to that of Fickian absorption until the Fickian curve starts to bend over, indicating that the effect of relaxation on the initial absorption is not significant. The second part of the combined absorption starts at about the maximum Fickian absorption, when the diffusion rate is substantially decreased and the contribution of the polymeric relaxation to the absorption is steadily increased. The final saturation at equilibrium is represented by the sum of the maximum Fickian absorption, $M_{t,F}$ and the maximum relaxation absorption, $M_{t,R}$.

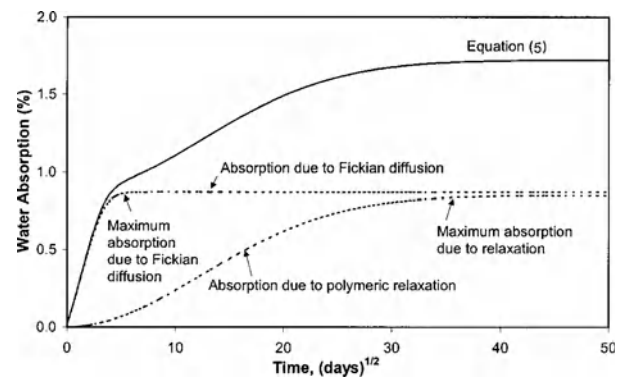


Figure 2 Theoretical absorption curves due to Fickian diffusion and polymeric relaxation (Shao, 2002)

Results of many experimental investigations show that Fickian diffusion behaviors of polymeric materials are dominant, and considered as the relatively rapid first stage of absorption. The penetrant diffuses into pre-existing and available vacancies or sites in the polymer. The relaxation process, which is relatively slow and long-term absorption, may be related to a structural reordering or redistribution of free-volume elements to provide additional sites of suitable size and accessibility to accommodate more penetrant molecules.

3 FEM ANALYSIS OF MOISTURE DIFFUSION IN THE FRP ADHESIVELY- BONDED JOINTS

Mechanical behaviors of adhesively-bonded connection between FRP composite decks and steel girders are usually dominant in the design of the whole girder system. Force transmission capacity of this connection will affect the composite action of FRP to steel girder system. So it is imperative to investigate the mechanical behaviors of FRP composite to steel adhesively-bonded joints under hostile environments, and predict the service-life of them.

There are usually three main steps to model the environmental degradation of FRP composite adhesively-bonded joints (Croccombe, 2008):

- the first step is modeling moisture transport through

the joint in order to determine the moisture concentration distribution through the joint as a function of time.

- the second step involves evaluation of the transient mechanical-hygro-thermal stress-strain state resulting from the combined effects of hygro-thermal effects and applied loads.
- the final step involves incorporation of damage processes in order to model the progressive failure of the joint and hence enable the residual strength or lifetime of a joint to be predicted.

As the first step of modeling, moisture diffusion analysis was conducted in the FEM package ABAQUS. Material parameters required are the diffusion coefficient and the solubility coefficient (Table 1), which can be obtained from gravimetric experiments. The FRP composite material is an epoxy resin (DGEBA-DDA) reinforced by glass fiber and autoclaved by Hexcel Composites from a XE85AI/7781 prepreg (Pierron, 2002). AV119 adhesive was chosen for the study. This is a one-part rubber toughened epoxy adhesive produced by Vantico, which is a multi-purpose, heat curing thixotropic (no flow during cure) paste adhesive of high strength and fracture energy (Loh, 2005). The aging condition is selected to be 50°C and 96% relative humidity, which is a little higher than normal bridge service condition. It ascribed to limited experimental data. But it is conservative for the long-term design of FRP composite bridges. Further details of the specimens and experimental process can be found in Pierron, 2002 and Loh, 2005.

Table 1 Moisture diffusion property of FRP composite and adhesive used in FEM analysis

Material	Condition	D_z (mm^2s^{-1}) $\times 10^{-7}$		M_∞ (%)
AV119 adhesive	50°C,96%RH	2.4		4.99
XE85AI/7781 FRP composite	50°C,96%RH	D_1 4.85	$D_2=D_3$ 1.3	0.605

To validate the FEM model of adhesively-bonded joints, numerical models (single plates) with the same dimensions as experimental specimens were built and analyzed firstly. Figure 3 and Figure 4 show the comparison of results. Time 1 is the moisture saturation level got from FEM analysis, which only considered the Fickian behavior of FRP composite and adhesive material, while time 2 is the final moisture saturation level got from considering both Fickian and non-Fickian behaviors of material. It can be seen that the moisture saturation time-points from FEM analysis agree well with the experimental results and also in accordance with the moisture diffusion theory discussed above.

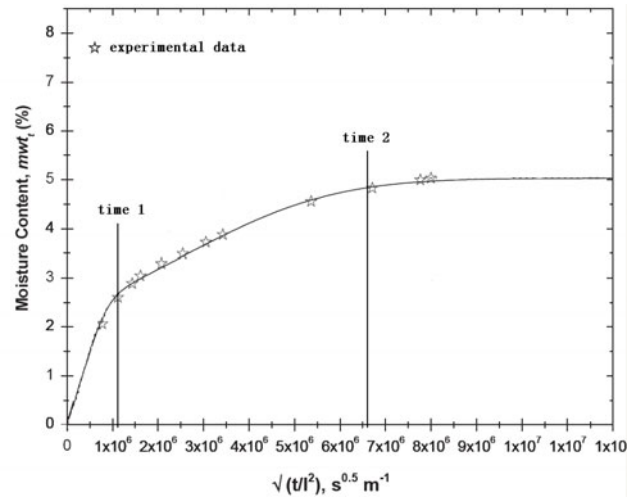


Figure 3 Comparisons of results between experiments and FEM analysis of AV119 adhesive

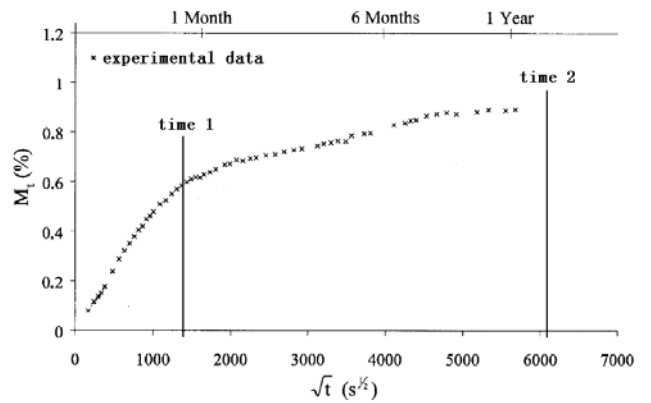
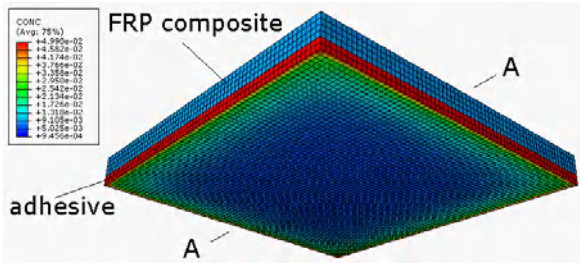


Figure 4 Comparisons of results between experiments and FEM analysis of FRP composite plate

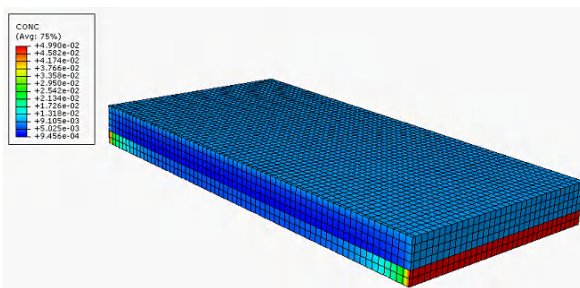
Base on this FEM model, a typical FRP composite to steel adhesively-bonded joint was built and analyzed in ABAQUS to predict the moisture concentration distribution under 50°C and 96% relative humidity condition after 70 years. But the steel plate was not built, because steel material is impermeable. The interface between adhesive layer and steel plate was set to be impermeable and moisture content of other faces were set to be saturation levels as the boundary conditions of FEM model. Depending on the practical experience, the dimension of the FRP composite plate is selected as 260mm×260mm×16mm, and adhesive layer is 260mm×260mm×8mm. Moisture concentration distribution of this joint identified from FEM analysis is shown in Figure 5.

The results of FEM analysis show that moisture absorption of the adhesive layer is much more than FRP composite, because M_∞ of adhesive is about 9 times as that of FRP composite. And moisture diffused through the whole adhesive layer. The lowest moisture concentration in the middle part of adhesive is about 0.5%, which is just a little less than the moisture saturation level of FRP

composite (0.605%). For the FRP composite, moisture has also diffused through mostly the whole plate after 70 years, but the moisture content is relatively low. Thus, moisture dependent behaviors of adhesive layer will affect dominantly the long-term performance of FRP adhesively-bonded joints under hot/wet environments.



(a) Global view of FEM analysis



(b) View from section A-A

Figure 5 Moisture concentration distribution of FRP composite to steel adhesively-bonded joint after 70 years

4 CONCLUSION AND FUTURE WORK

The moisture diffusion theory of FRP composite and adhesive material is introduced succinctly, which form the basic background of the FEM analysis. Depending on the validated FEM model, moisture concentration distribution of a typical FRP composite to steel adhesively-bonded joint under 50°C and 96% RH condition after 70 years was obtained. It was found that M_{∞} of FRP composite and adhesive controlled the amount of moisture absorption in each layer after 70 year service life.

But there are some improper aspects of the parameter selection for the FEM analysis. In fact, AV119 adhesive is a typical adhesive used in the application of aerospace engineering, but not in civil engineering. The adhesive layers for aerospace or aircraft structures are usually thin (0.1–1 mm), while in bridge and building structures adherends and adhesive layers are usually comparatively much thicker (2–20 mm). Furthermore, curing conditions are also different. Adhesives used in civil engineering are cured in ambient environments, but the temperatures of curing conditions in aerospace engineering are usually more than 100°C, which will lead to higher glass transition temperatures and the joints tend to be more durable. In order to address the above limitations, more

experimental investigations of environmental dependent properties of FRP composite and adhesive materials will be planned in the future. Systemic experimental data will be available and lead to the formulation of design guides of FRP composite structures in the application of civil engineering.

REFERENCE

- Berebs, A.R. and Hopfenberg H.B. 1977. Diffusion and relaxation in glassy polymer powders: 2. Separation of diffusion and relaxation parameters. *POLYMER*, 19, 489-495.
- Crocombe AD, Ashcroft IA, Abdel Wahab MM. 2008. Modeling of Adhesively Bonded joints: Chapter 8 Environmental Degradation. Springer-Verlag Berlin Heidelberg.
- Garcia, K., M.D. Hayes, N. Verghese, and J.J. Lesko. 1998. The effects of cycling moisture aging on glass/vinyl ester composite system. *Proceedings of 3rd International Conference on Progress in Durability Analysis of Composite Systems*, pp. 173-179.
- Herbert G. 2004. Composite Action of FRP Bridge Decks Adhesively Bonded to Steel Main Girders. PhD thesis. Lausanne, Ecole Polytechnique Federale de Lausanne.
- Lok WK, Crocombe AD, Wahab MM, Ashcroft IA. 2005. Modeling anomalous moisture uptake, swelling and thermal characteristics of a rubber toughened epoxy adhesive. *International Journal of Adhesion & Adhesives*, 25,1-12.
- Pierron, F., Poirrette Y. and Vautrin A. 2002. A Novel Procedure for Identification of 3D Moisture Diffusion Parameters on Thick Composites: Theory, Validation and Experimental Results. *Journal of Composite Materials*, 36(19), 2219-2243
- Phifer, S.P. 2003. Hygrothermal evaluation of pultruded polymer composite laminates—Experimentation, analysis, and prediction. PhD dissertation, Department of Engineering Science and Mechanics, Virginia Tech, Blacksburg, VA.
- Prian, L., and A. Barkatt. 1999. Degradation mechanism of fiber-reinforced plastics and its implications to prediction of long-term behavior. *Journal of Materials Science*, 34(16), 3977-3989.
- Schollmayer M. 2009. Through-Thickness Performance of Adhesive Connections Between FRP Bridge Decks and Steel Main Girders. PhD thesis. Lausanne, Ecole Polytechnique Federale de Lausanne.
- Shao Y and Kouadio S. 2002. Durability of Fiberglass Composite Sheet Piles in Water. *Journal of Composites for Construction*, 6(4), 280.
- Shen, C.-H., and G.S. Springer. 1976. Moisture absorption and desorption of composite materials. *Journal of Composite Materials*, 10, 2-20.
- Springer, G.S., et al. 1980. Environmental effects on GFRP polyester and vinyl ester composites. *Journal of Composite Materials*, 14, 213-223.
- Tsai Y.I, Bosze E.J., Barjasteh E., Nutt S.R. 2009. Influence of hygrothermal environment on thermal and mechanical properties of carbon fiber/fiberglass hybrid composites. *Composites Science and Technology* 69, 432-437.

Durability of CFRP Bonding System under Freeze-Thaw Cycling

Yanchun Yun & Yufei Wu (yfwu00@cityu.edu.hk)

Department of Building and Construction, City University of Hong Kong, Hong Kong, China

ABSTRACT This paper presents the results of an experimental study on the behavior of externally-bonded fiber reinforced polymer (EB-FRP) joints under freeze-thaw cycling. Four series of single shear tests were conducted on 26 specimens. The parameters considered were the exposure condition, concrete grade, and the number of freeze-thaw cycle. The behavior of the CFRP-concrete interface in the shear direction was investigated. The test results demonstrate that the bond strength, bond stiffness, interfacial fracture energy, and maximum slip of the joints decrease with the increase in the number of freeze-thaw cycle, and also are affected by the testing environment. It is also found that the depth of the cracking and the effective bond length increase with an increase in the cycle number, and thus affecting the bond stiffness and strength. The deterioration of the bond strength is considered due to the damage of the concrete under the freeze-thaw cycling.

1 INTRODUCTION

In recent years, the research community has made great progress in identifying and quantifying the bond characteristics of the FRP composite materials that are used in retrofitting concrete structures. However, the long-term durability of the FRP bonding system is still a serious concern. In particular, the deterioration of bond under freeze-thaw cycling is not well understood and yet has received little attention (Pavel 2006; Karbhari et al. 2003; Bonacci and Maalej 2000). Freeze-thaw cycling can cause differential thermal expansion between the FRP laminate and the substrate concrete, leading to bond damage, premature plate separation hence resulting in premature failure of the member. Therefore, the long-term durability of the FRP strengthening systems is crucial to ensure the safety of structures in cold climate regions.

Kolluru et al. (2008) found from their experimental tests that freeze-thaw cycling caused a decrease in the ultimate bond strength. However, others reported that the bond strength was either unchanged (Green et al. 1997) or even improved (Green et al. 2000; Pavel 2006) by the freeze-thaw cycling process. It is therefore unclear and difficult to draw general conclusions from these studies. A further investigation on the problem is thus very much needed.

Based on the analyses of previous works, the significant parameters that affect the durability of bond were identified and studied experimentally in this work, including the exposure condition, concrete grade, and the number of freeze-thaw cycle. The behavior of the bond strength, bond stiffness, interfacial fracture energy, maximum slip at the loaded end and the effective bond

length of the FRP-concrete bonded joints were investigated in this work.

2 EXPERIMENTAL PROGRAM

2.1 Freeze-thaw cycling

Since there is no available standard for testing FRP-concrete interface under freeze-thaw condition, the following two standards for concrete were referred: ASTM C672/C672M (2003) and ASTM C666 (2003). These two standards have been used in previous works for designing the freeze-thaw test methods of FRP-concrete joints in salt water and tap water, respectively. In this work, the specimens were subjected to an accelerated freeze-thaw cycling in an environmental chamber. The FRP-concrete joint was placed in salt or tap water with FRP facing downward and approximately 6 mm of concrete being submerged. A complete freeze-thaw cycle was as follows: starting at +4°C, the temperature decreased to -18°C in 110 minutes and was held constant for 10 minutes; it was then increased to 4°C in 115 minutes and held for 5 minutes. The specimens were subjected to 17, 33 50, or 67 cycles in different groups. The solution of 4% NaCl was used as the salt water.

2.2 Specimen preparation

The common single shear pull-off test was used for the bond tests. The dimensions of the concrete block were 370×150×150 mm³. Two different concrete grades with cube strengths of 30 MPa and 45 MPa were used. In order to avoid variation of concrete strength in the process of freeze-thaw cycling, all the specimens were left in the lab for more than 500 days. The C30 and C45

concrete had an average 500-day cube strength ($100 \times 100 \times 100 \text{ mm}^3$) of 36.9 MPa and 48.6 MPa, respectively. TORAYCA Cloth with a nominal thickness of 0.167 mm and a tensile modulus of 230 GPa was utilized as the FRP fabric in the tests. Two plies of CFRP were attached to each concrete specimen using Sikadur 300 as both primer and saturating resin. The bonded area was $300 \times 50 \text{ mm}^2$. The test specimens were cured in the lab for double prescribed period of time (7×2 days) before the freeze-thaw cycling.

A total of 30 specimens were prepared. Details of the specimens are listed in Table 1 and Table 2. The first character in the specimen ID in Table 2 indicates the solution, i.e. S for salt water, T for tap water and N for specimens without exposure to freeze-thaw cycling. The number follows the first character specifies the grade of concrete, followed by the number of freeze-thaw cycle. The last number shows the first or the second specimen for each type of design. A pair of specimens was tested for each type of bond design. Four specimens were damaged in the tests, giving a total of 26 useful specimens.

2.3 Test setup and instrumentation

Following the environmental exposure, the specimens were tested using a 250 kN computer controlled MTS frame. The specimens were tested monotonically up to failure, and a loading rate of approximately 0.005 mm/s was adopted. For each test, the surface strain of the CFRP composite and the concrete were obtained using the digital image correlation (DIC) technique. This technique offers the advantage of obtaining spatially continuous measurements of displacements. The strain field can be calculated from the gradients of a set of displacement.

Table 1 Details of bond test

Concrete type	Test number	Test method	Cycles
C30	8	ASTM-672	0,17,33,50
C30	8	ASTM-666	17,33,50,67
C45	8	ASTM-672	0,17,33,50
C45	6	ASTM-666	17,33,50

3 RESULTS AND DISCUSSIONS

3.1 Load-slip curves

A typical set of load-slip response curves for the S30 series is given in Figure 1. Figure 2 shows the variation of the peak load with cycle number for C30 series. Table 2 summarizes the load and the maximum loaded-end slip (at bond failure). The interfacial fracture energy between the bonded surfaces is also provided in Table 2. The interfacial fracture energy G_f can be calculated using Equation (1).

$$G_f = \frac{P_{\max}^2}{2b^2 E_f t_f} \tag{1}$$

From Table 2 and Figures 1-2, it can be seen that the peak load (bond strength), bond stiffness, maximum slip, and the interfacial fracture energy decrease with the increase in the number of freeze-thaw cycle.

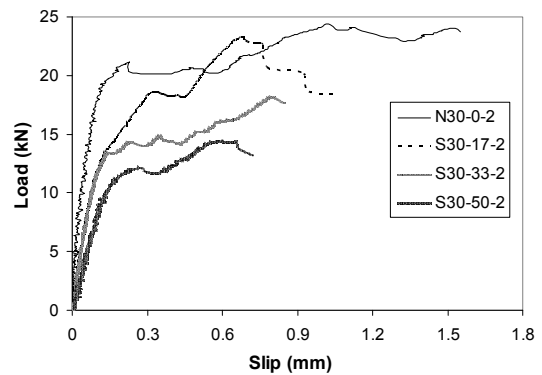


Figure 1 Load-slip responses

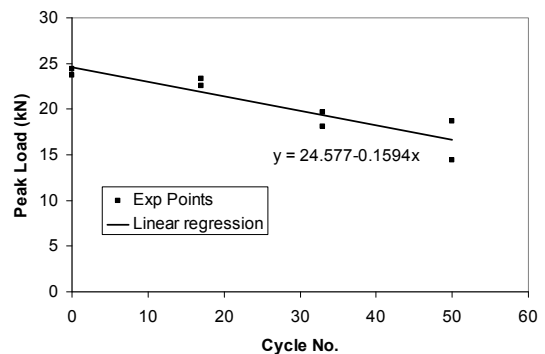


Figure 2 Peak loads of C30 concrete in salt water

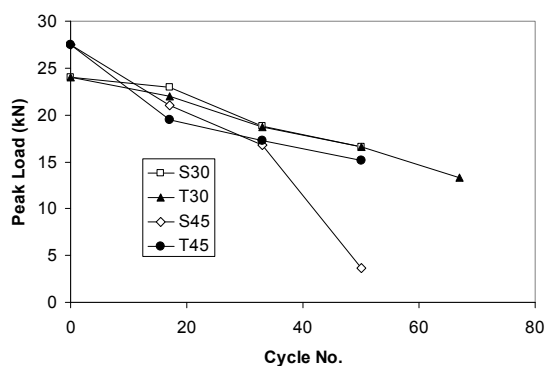
Under normal test conditions without freeze-thaw exposure, the debonded face of an EB-FRP system is uniform and the thickness of concrete peeled off by the FRP strip is about 3~5 mm. It was observed in this study that the thickness of the concrete peeled off by the CFRP strip increased with the increase in the number of freeze-thaw cycles. It is further judged based on our test observation that the drop in the bond strength was caused by the damage in concrete under the environmental exposure, rather than the damage to the polymer between the concrete and the CFRP.

3.2 Solution effect

Figure 3 shows the degradation of bond strength for all series. It can be seen that, for S30 and T30 series, the rates of strength degradation under the two different solutions are almost the same, which indicates that the influence of the freeze-thaw solution is not significant for this grade of concrete. For the two series of S45 and T45, however, the decreasing rates of the bond strength under different solutions show significant difference;

Table 2 Peak loads and max slips

Specimen ID	Peak load (kN)	Max slip at loaded end (mm)	G_f (N/mm ²)
N30-0-1	23.7	1.413	1.480
N30-0-2	24.4	1.552	1.568
S30-17-1	22.6	1.059	1.345
S30-17-2	23.3	1.06	1.430
S30-33-1	19.6	0.791	1.012
S30-33-2	18.1	0.85	0.863
S30-50-1	18.7	0.957	0.921
S30-50-2	14.4	0.722	0.546
T30-17-1	22.0	1.006	1.275
T30-33-1	18.7	0.917	0.921
T30-50-1	16.6	0.764	0.726
T30-67-1	10.3	0.216	0.279
T30-67-2	16.3	0.362	0.700
N45-0-1	27.7	1.70	2.021
N45-0-2	27.4	–	1.978
S45-17-1	22.0	1.111	1.275
S45-17-2	20.1	1.086	1.064
S45-33-1	16.8	0.672	0.743
S45-50-1	4.11	0.057	0.044
S45-50-2	3.2	0.064	0.026
T45-17-1	19.9	0.80	1.043
T45-17-2	19.0	0.953	0.951
T45-33-1	15.6	0.434	0.641
T45-33-2	18.96	0.542	0.947
T45-50-1	15.7	0.587	0.649
T45-50-2	14.6	0.483	0.561

**Figure 3** Average peak load for each series

and the bond deterioration in salt water is clearly much faster than that in tap water after 33 cycles. For specimens with a cycle number less than 33, the difference in bond degradation under the two solutions is not apparent.

3.3 Effect of concrete grade

It has been reported that the internal damage of concrete increases as the W/C ratio decreases under freeze-thaw

cycling (Penttala 2006). For relatively high strength concrete when W/C ratio is below 0.5, the internal damage caused by freeze-thaw cycling in salt water is the major deterioration mechanism. From Figure 3, it can be seen that, in salt water, the decreasing rate of the bond strength between the CFRP and the C45 concrete (W/C ratio 0.4) is faster than that for C30 concrete (W/C ratio 0.53). After 50 cycles, the pull-off failure plane of the two S45-50 specimens was at the depth of the water surface, i.e. it failed by stripping off the whole part of concrete submerged in water rather than the peel-off of the concrete skin. This reflects a fact that the failure was caused by the damage to the concrete material inside rather than the damage of the surface bonding layer. This also confirms the conclusion that the internal damage by freeze-thaw testing in salt water is more significant for concrete with a lower W/C ratio. In tap water, the decreasing rate of bond for T45 specimens is faster than that of the T30 specimens in the early stage of cycling (cycle number less than 17); however, they have a similar rate after 17 cycles. Apparently, the internal damage in the concrete with a lower W/C ratio is severer in the early stage of freeze-thaw cycling in tap water.

3.4 Strain field

Using the DIC technique, the surface strain of the CFRP composite and the concrete is produced. The axial strain along the length of the CFRP strip at the peak load for specimens N30-0-2 and S30-50-2 are shown in Figure 4. At the peak load, the observed strain distributions can be divided into three main regions: (a) the unstressed region; (b) the effective bond zone; and (c) the fully debonded zone, as shown in Figure 4. The effective bond zone that has an effective bond length L_e bears the shear stress. Within the effective bond zone, the strain distribution is approximately “S” shaped (Kolluru et al. 2008). Stress transferred outside the effective bond zone is regarded as negligible because slips between the CFRP and concrete over those locations are either too small or too large to produce bond stress effectively. Based on Dai et al. (2006), L_e can be expressed as a distance between two locations x_1 and x_2 ($L_e=x_1-x_2$) which bears 96% of the peak pull force.

The wobbling in the measured strain is largely caused by the presence of material inhomogeneities in the concrete (Ali-Ahmad et al. 2006) and cracking. In order to find out the overall variation of strain distribution, the wobbled strain measurements are regressed to the following expression that is considered as a general strain distribution for an EB-FRP joint (Kolluru et al. 2008):

$$\varepsilon(x) = \varepsilon_0 + \frac{\alpha}{1 + e^{\left(\frac{x-x_0}{\beta}\right)}} \quad (2)$$

The two regressed strain distributions in Figure 4 are plotted by the solid lines, from which L_e can be calculated and listed in Table 3. It can be seen from Table 3 that the effective bond length increases with the increase in the freeze-thaw cycles, which agrees with the finding by Mukhopadhyaya et al. (1998). Also, it can be seen in Figure 4 and Table 3 that the maximum strain ϵ_x in the CFRP at the loaded end decreases when the number of cycle increases. This change can be attributed to the damage in concrete induced by the freeze-thaw cycling.

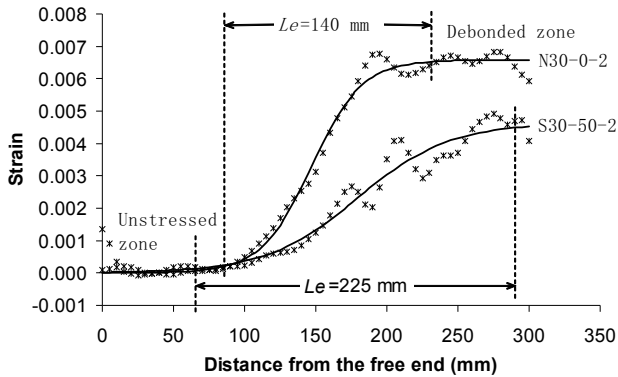


Figure 4 Effective bond length L_e

Table 3 Strain field at peak load

Specimen	L_e	ϵ_x	R^2
N30-0-2	140	6578	0.9968
S30-17-2	200	6195	0.9870
S30-33-2	210	4543	0.9796
S30-50-2	225	4521	0.9751

4 CONCLUSIONS

It can be concluded from the experimental work that the bond strength, bond stiffness, interfacial fracture energy, and maximum slip decrease with an increase in the number of freeze-thaw cycle. The drop of the bond strength is mainly due to the damage in concrete under freeze-thaw cycling. The effective bond length also increases with the increase in the cycle number. The influence of the solution is not clear to the rate of bond deterioration for concrete with a high W/C ratio (above 0.5). However, this rate is significantly larger for specimens in salt water than that in tap water for

concrete with a low W/C ratio (below 0.4). With the concrete strength increasing, the bond strength deteriorates faster.

REFERENCES

Ali-Ahmad, M. Subramaniam, K.V. & Ghosn, M. 2006. Experimental investigation and fracture analysis of debonding between concrete and FRP. *ASCE J. Eng. Mech.*, 132(9): 914-923.

Bonacci, J. F. & Maalej, M. 2000. Externally bonded FRP for service-life extension of RC infrastructure. *J. Infr. Syst.*, 16(1): 41-51.

Chajes, M.J. Thompson, T.A. Farschman, C.A. & Farschman, C.A. 1995. Durability of concrete beams externally reinforced with composite fabrics. *Constr. Bulid. Mater.*, 9(3): 141-148.

Dai J.G. Ueda T. & Sato Y. 2006. Unified analytical approaches for determining shear bond characteristics of FRP-concrete interfaces through pullout tests. *J. Adv. Conc. Tech.*, 4(1): 133-145.

Green, M.F. Soudki, K.A. & Johnson, M.M. 1997. Freeze-Thaw Behaviour of Reinforced Concrete Beams Strengthened by Fibre Reinforced Plastic Sheets. *Proc. Canadian Soci. Civ. Eng., Sherbrooke, 27-30 May 1997.*

Green, M.F. Bisby, L.A. Beaudoin, Y. & Labossiere, P. 2000. Effect of freeze-thaw cycles on the bond durability between fibre reinforced polymer plate reinforcement and concrete. *Canadian J. Civ. Eng.*, 27: 949-959.

Karbhari, V.M. Chin, J.W. Huston, D. Benmokrane, B. Juska, T. Morgan, R. Lesko, J.J. & Sorathia, U. 2003. Durability gap analysis for fiber-reinforced polymer composites in civil infrastructure. *J. Comp. Constr.*, 7(3): 238-246.

Kolluru V. Ali-Ahmad M. & Ghosn M. 2008 Freeze-thaw degradation of FRP-concrete interface: Impact on cohesive fracture response. *Eng. Fra. Mech.*, 75: 3924-3940.

Mukhopadhyaya, P. Swamy, R.N. & Lynsdale, C.J. 1998. Influence of aggressive exposure conditions on the behaviour of adhesive bonded concrete-GFRP joints. *Constr. Bulid. Mater.*, 18(12): 427-446.

Pavel D. 2006. Environmental Durability of FRP bond to concrete subjected to freeze-thaw action. *Master thesis, Massachusetts Institute of Technology.*

Penttala, V. 2006 Surface and internal deterioration of concrete due to saline and non-saline freeze-thaw loads. *Cem. Conc. Res.*, 36: 921-928.

Bond Strength of Glass FRP Bars in Concrete Subjected to Freeze-Thaw Cycles and Sustained Loads

Juliana Alves, Amr El-Ragaby & Ehab El-Salakawy (ehab_elsalakawy@umanitoba.ca)

Department of Civil Engineering, University of Manitoba, Winnipeg, Manitoba, Canada

ABSTRACT In reinforced concrete structures, temperature-induced stresses can be a major concern in regions of drastic temperature changes. FRP reinforced concrete elements are specially susceptible to more damage due to temperature changes because of the mismatching thermal properties between FRP bars and concrete. Furthermore, sustained loads may also damage the bond between FRP bars and concrete and can lead to an unexpected increase of the required anchoring length. Therefore, this research program is designed to investigate experimentally the durability of FRP bond to concrete elements subjected to the effects of freeze-thaw cycles and sustained loads. A FRP-reinforced concrete specimen was developed to apply axial-tension sustained loads to GFRP bars eccentrically located within the concrete environment. Test specimens were subjected simultaneously to the dual effects of 250 freeze-thaw cycles along with sustained load. A total of six test specimens were constructed and tested. The test parameters included bar diameter and concrete cover. After conditioning, each test specimen was sectioned to two replicates (halves) for pull-out test. Another series of twelve unconditioned standard pull-out specimens were constructed and tested as control. Test results are presents in terms of bond-slip relationships and ultimate pull-out strength. Test results showed that freeze-thaw cycles along with sustained load resulted in increase in the bond strength of GFRP bars to con-crete.

1 INTRODUCTION

In North America, bridge deck slabs and parking garages are prime example where GFRP reinforcements are currently used. These elements are continuously subjected to wide combinations of fatigue and/or sustained load from traffic as well as thermal loads due to freeze-thaw cycles and temperature fluctuations. Significant amount of information is currently available on the structural performance of FRP-reinforced concrete elements and short-term properties of composite materials. However, experimentally validated data regarding bond durability of FRP bars to concrete elements under long-term exposure to certain harsh environmental and loading conditions are still lacking.

2 BACKGROUND

In a FRP-concrete composite system, self-equilibrating stresses develop when the FRP and concrete differentially expand or contract due to temperature fluctuations. In the longitudinal direction, GFRP bars tend to have a similar coefficient of thermal expansion to hardened concrete. However, in the transverse direction, GFRP can experience an expansion of 3 times greater than concrete. The difference in thermal expansion in the transverse direction can cause bursting stresses to build up in the concrete surrounding the reinforcement or

separation of the bars from the concrete under temperature decrease. Under freeze-thaw cycles, freezing and crystalline of moisture exists at the interface between FRP and concrete leads to further deterioration of the FRP bond to concrete and the overall ultimate capacity (Aiello 1999, Koller et al. 2006, Mashima and Iwamoto, 2004). FRP bars are also susceptible to creep and stress relaxation since polymers are visco-elastic materials. The effects of these properties become more severe when the bar is exposed to moisture, which accelerates the degradation. (Micelli and Nanni, 2004).

3 EXPERIMENTAL PROGRAM

3.1 Test specimens

This research program is designed to investigate the influence of concrete cover and bar diameter on the bond strength of glass FRP bars embedded in concrete through testing pullout specimens after being simultaneously conditioned by freeze-thaw cycles and sustained loads. The experimental program is divided into two series: (C) Control (unconditioned) specimens; (I) Freeze-thaw cycles along with sustained loads.

A FRP-reinforced concrete specimen for Series I was developed. The specimen consists of three concrete blocks; the test portion (middle block) and two end anchor blocks. The three portions were connected together by

the GFRP bar as shown in Figure 1. The middle block had 200-mm square cross section to meet the requirement of standard pull-out test specified by the Canadian Standard CSA-S806-02 (CSA 2002). The length of the middle block was 405 mm such that after conditioning, each specimen was split into two 200-mm cube replicates for pullout test (considering a 5-mm clearance for the cutting saw). The GFRP bar was always eccentric in the middle block, while the end anchors were always adjusted to be concentric with respect to the GFRP bar. Each anchor contained six 16 mm-diameter threaded rods placed perpendicular to the axis of the GFRP bar to apply the specified loads.



Figure 1 Details of test specimen for Series I

Series C contained 12 unconditioned control specimens to assess the bond characteristics of the used GFRP bars as well as to provide a datum for the other test specimens using a standard procedure provided by the CAN/CSA-S806-02 (CSA 2002). The control specimen consists of a 200-mm concrete cube with a $5d_b$ embedment length with eccentric placement of the bar. Steel pipes were used as anchors, and were cast with expansive grout prior to the casting of the specimens.

The test parameters included the GFRP bar diameter and the concrete cover. Two bar diameters, No.16 and No. 19 GFRP bars (15.9 and 18.9 mm in diameter, respectively) were investigated. Also, three different concrete covers of $1.5d_b$, $2.0d_b$, and $2.5d_b$ were studied. Table 1 gives the details of the test program.

Table 1 Details of test specimen

Series	Name	Bar Diameter	Concrete Cover
C	C.16.15		$1.5d_b$
	C.16.20	No. 16	$2.0d_b$
	C.16.25		$2.5d_b$
	C.19.15		$1.5d_b$
	C.19.20	No. 19	$2.0d_b$
	C.19.25		$2.5d_b$
I	S.FT.16.15		$1.5d_b$
	S.FT.16.20	No. 16	$2.0d_b$
	S.FT.16.25		$2.5d_b$
	S.FT.19.15		$1.5d_b$
	S.FT.19.20	No. 19	$2.0d_b$
	S.FT.19.25		$2.5d_b$

It should be noted that S – stands for sustained load and FT – stands for freeze-thaw cycles.

3.2 Materials properties

The specimens were fabricated using normal weight concrete with an average 28-day compressive strength of 50 MPa. Since the concrete was cast on several stages, it was mixed in the McQuade Heavy Structures Laboratory at the University of Manitoba using a mechanical mixer to obtain consistent concrete properties. The GFRP bars used in this study (V-ROD™) had a sand-coated surface and were made of continuous longitudinal fibres impregnated in a thermosetting vinyl-ester resin with a fibre content of 73% by weight (Pultrall Inc. 2007)

3.3 Loading and Environmental Conditioning

The conditioning scheme consisted of applying dual effects of sustained load and freeze-thaw cycles simultaneously to the test specimens of Series I. the sustained load level was selected to respect the limits permitted by the available FRP design codes and guidelines. Accordingly, a sustained load of 30% of the guaranteed tensile strength (GTS) of the GFRP bar was selected (CSA 2002). The applied sustained loads were 42 and 54 kN for No.16 and No. 19 GFRP bars, respectively. Furthermore, for freeze-thaw conditioning, the environmental chamber was programmed to ramp the temperature from -25°C to $+15^{\circ}\text{C}$ and maintain the freezing period (at -25°C) for five hours and the thawing period (at $+15^{\circ}\text{C}$) for 3 hours to satisfy the ASTM C666-03 requirement. A total of 250 cycles were applied in approximately 4 months. The relative humidity was forest to 50% during freezing and 95% during thawing.

3.4 Instrumentations and Test set-up

The sustained load was applied to the specimens of Series I through a prestressing bed. A set of steel plates was used to apply the load. Steel angles and two 38-mm diameter thread rods were used to hold the anchors in place, thus sustaining the load. To avoid relative movement between concrete and the steel angles, nuts were used in both sides of the angles. During prestressing, the load was monitored by a load cell, while the strains in the GFRP bars were monitored through strain gauges.



(a) Sustained Load

(b) Pull-out test

Figure 2 Details of test Set-up

Thermocouples were attached to the GFRP bars to verify the temperature inside the specimens during the freeze-thaw cycles. A universal 1000-kN MTS machine was utilized to apply the monotonic pull-out loading at load-controlled rate of 10 kN/min in accordance with standard test method of CAN/CSA-S806-02 (CSA 2002). A high accuracy LVDT was used to record the free-end slip of GFRP bars during the pull-out test. Figure 2 shows details of the sustained loading and pull-out tests set-up.

4 RESULTS AND DISCUSSIONS

In this section, test results regarding bond strength and slip measurements are presented in terms of bond stress versus free-end slip.

Figure 3 shows typical bond-slip relationship obtained from the pull-out tests carried on the conditioned specimens. Specimens in Series I sustained load + freeze-thaw “SFT” with 2.5 d_b concrete cover, S.FT.16.25 and S.FT.19.25 showed an increase in the bond strength by about 40% without any changes in the measured slip compared to the control test specimens (Series C). Therefore, it can be concluded that the freeze-thaw and sustained load conditioning enhanced the bond properties of test specimens. This can be explained as the GFRP bar absorbed moisture, especially during thawing, and enlarged in cross-sectional area, thus enhancing the friction mechanism, which improves bond resistance. The manufacturer data sheet (Pulltrall Inc 2007) shows values for moisture absorption of 0.42% and 0.21% for bars No. 16 and No. 19, respectively. The thermal stresses probably degrade the concrete surrounding the bar. However, such deterioration was not enough to reduce the resistance to the shear forces at the interface.

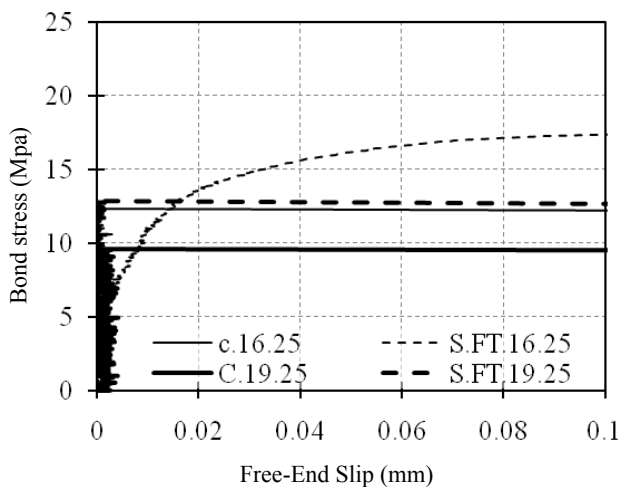


Figure 3 Effect of freeze-thaw and sustained load conditioning on the bond-slip behaviour of GFRP bars

Figure 4 shows comparisons of the bond-slip behaviour of test specimens with different concrete covers after being conditioned under freeze-thaw cycles and sustained load. It can be noticed that the concrete cover seems to play an important role. From Figure 4, it is clear that the degree of increase in the bond strength due to freeze-thaw conditioning depends on the concrete cover. Increasing the concrete cover by about 33% (from 1.5 d_b to 2.0 d_b) and 25% (from 2.0 d_b to 2.5 d_b) increased the bond strength by about 15 and 25%, respectively. However, this percentage was constant (about 15%) for the counterpart control specimens, when increasing the concrete cover from 1.5 d_b to 2.0 d_b or from 2.0 d_b to 2.5 d_b . This can be explained as increasing the concrete cover increases the confinement pressure on the bar which improves the bond strength. Also it plays an important role in decreasing the temperature gradient effects at reinforcement level which reduces the thermal effects due to temperature fluctuation.

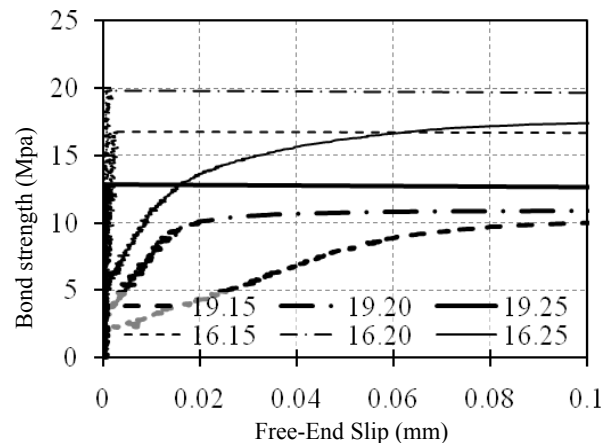


Figure 4 Effect of concrete cover on the bond-slip behaviour of GFRP bars

Figure 5 shows comparisons of the bond strength of GFRP bars to concrete after conditioning. In case of specimens with No. 19 GFRP bars, the bond strength values obtained for Series I were similar to those obtained for Series C for 1.5 and 2.0 d_b concrete covers. However, for the concrete clear cover of 2.5 d_b , the bond strength values were higher than those from Series C. This may be due to the effect of thermal stresses on the expansion of the bar cross section, which is more pronounced for the larger bar diameter (No. 19). Therefore, the largest cover, 2.5 d_b , appears to have resisted the thermal loads and was capable of promoting significant increase in bond resistance. For smaller covers (1.5 and 2.0 d_b), the enlargement in the bar diameter may have caused damage in the surrounding concrete. From these figures, it can be concluded that using concrete cover of 2.0 d_b and 2.5 d_b resulted in the highest bond strengths for GFRP bars No. 16 and No. 19,

respectively, either for the control or the conditioned specimens.

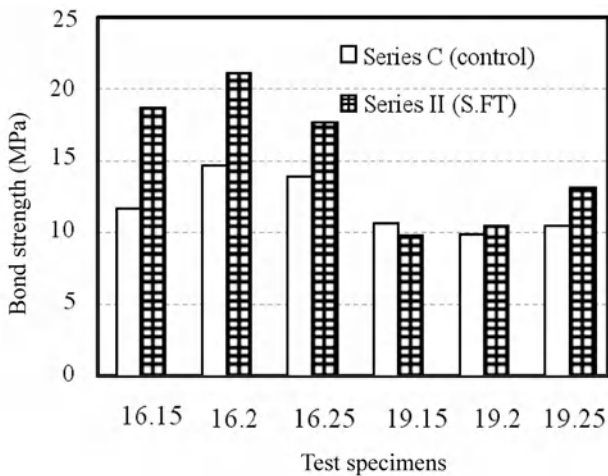


Figure 5 Comparison of the bond strength of GFRP bars to concrete after sustained load and freeze-thaw conditioning

5 CONCLUSIONS

This research program investigated the influence of concrete cover and bar diameter on the bond strength of glass FRP bars embedded in concrete subjected to freeze-thaw cycles along with a sustained axial tensile load. Based on the experimental results, the following conclusions can be drawn:

- Freeze-thaw cycles along with the sustained load conditioning enhanced the bond strength for bars No. 16 with the three concrete covers used and No. 19 with concrete cover of $2.5d_b$ only. Such conditioning resulted in significant increase in the peak slip (decrease in bond stiffness) for bars No. 19, while for bars No. 16, only specimens with concrete clear cover of $2.5d_b$ showed increase in slip.
- It seems that a concrete clear cover of $2.0d_b$ is an optimum for sand-coated GFRP bars. However, if subjected to the effect of freeze-thaw cycles, bar No. 19 presented 25% higher bond resistance than

unconditioned specimens for the larger concrete cover of $2.5d_b$.

6 ACKNOWLEDGEMENT

The authors wish to express their gratitude and sincere appreciation for the financial support received from the Natural Science and Engineering Research Council of Canada (NSERC), through Canada Research Chairs program. Also, the equipment provided by a Canada Foundation for innovation (CFI) grant is greatly appreciated. The help received from the technical staff of the McQuade Heavy Structural Laboratory in the department of civil engineering at the University of Manitoba is also acknowledged.

REFERENCES

- Aiello, M. 1999. Concrete cover failure in FRP reinforced beams under thermal loading. *ASCE, Journal of Composites for Construction*, 3(1): 46-52.
- ASTM C666/C 666m-03. 2003. Standard Test Method for Resistance of Concrete to Rapid Freezing and Thawing. *American Society for Testing and Materials*, Pennsylvania, USA.
- CSA. 2002. Design and construction of building components with fibre-reinforced polymers. *CSA Standard S806-02*, Canadian Standards Association, Rexdale (Toronto), Ontario, Canada, 177 p.
- Koller, R., Chang, S. and Xi, Y. 2006. Fibre-reinforced polymer bars under freeze-thaw cycles and different loading rates. *Journal of Composite Materials*, 41(1): 5-25.
- Mashima, M. and Iwamoto, K. 2004. Bond characteristics of FRP rod and concrete after freezing and thawing deterioration. *ACI Structural Journal*, 138: 51-70.
- Micelli, F. and Nanni, A. 2004. Durability of FRP rods for concrete structures. *Elsevier, Construction and Building Materials*, 18: 491-503.
- Pulltral Inc. V-ROD. 2007. Product guide specification. Thetford Mines, Quebec.

Long-Term Durability of FRP Cables under Maritime Conditions

Itaru Nishizaki (nisizaki@pwri.go.jp) & Iwao Sasaki

Advanced Materials Research Team, Public Works Research Institute, Tsukuba, Ibaraki, Japan

ABSTRACT Six types of FRP cables were subjected to an exposure test lasting more than fifteen years under maritime conditions, and the retrieved cables were evaluated mainly by SEM and FT-IR microscopy. Loss of surface resin was observed for all the tested FRP cables; however, deterioration between the fiber and matrix resin was not found by SEM. Observation by FT-IR microscopy detected surface deterioration of AFRP cables, and the feasibility of this method for evaluating the deterioration of some FRP cables was indicated.

1 INTRODUCTION

The application of FRP cables such as carbon (CFRP) and aramid (AFRP) to the tendons of prestressed concrete members has been studied since the early 1980s. Their application has also spread to ground anchors and rebars (Benmokrane et al. 1989). Design methods and codes have been established for applying FRP cables to tendons, but actual application is limited to less than two hundred examples, and most of these were trial construction. The main reasons for this are the lack of evaluation of (1) cost-benefit effects and (2) durability. The main application of FRP cables in construction today is for PC tendons, but other applications, such as for external reinforcing cables or suspension cables for bridges, also seem promising.

FRP cables applied to PC tendons are exposed to strong alkalis present in the concrete under tensile load conditions, and there are many studies on the durability of FRP cables under these conditions (Nanni et al. 1992; Takewaka et al. 1996). When considering the application of FRP cables for external reinforcing cables or suspension cables for a bridge, the main deterioration factor is the outdoor environment including maritime conditions. To evaluate the durability of FRP cables under these conditions, outdoor exposure tests are indispensable. Several studies have focused on this area (Uomoto et al. 1996; Tomosawa et al. 1997); however, the reported data is not sufficient for evaluating the durability of this material.

We conducted a series of outdoor exposure tests on FRP cables mainly under maritime conditions, and obtained durability data on the materials (Katawaki et al. 1992; Sasaki et al. 1997). This report presents some of the results on the chemical deterioration of FRP cables based on the tests.

2 METHODS

2.1 Exposure location

The selected exposure site was a platform steel deck facility located in Suruga Bay, Shizuoka prefecture, Japan, facing the Pacific Ocean. The distance from the platform to the coast is about 250 m. Figure 1 shows a view of the platform. The platform is of square dimensions (15×15 m) and has three decks.

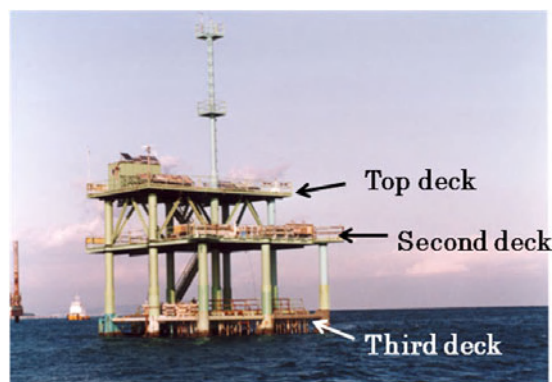


Figure 1 Platform used for the exposure test

The top (first) deck is 13.9 m in height from the tidal point, the middle (second) deck is 8.9 m in height and the bottom (third) deck is 1.9 m in height. The climate of the location is moderate, but there is high exposure to corrosion from sea salt.

2.2 Tested materials

We tested six types of FRP cables: CFRP (two), AFRP (two), glass (GFRP) (one) and vinylon (VFRP) (one). Although the GFRP and VFRP cables were not considered for application to tendons at this time, they were included in the study to acquire knowledge on their durability. Table 1 shows the details of each type of cable tested in this study. The values for tensile strength

Table 1 Specifications of the FRP cables used in the test

Code	CFRP1	CFRP2	AFRP1	AFRP2	GFRP	VFRP
Shape	Strand	Rod	Rod	Woven	Rod	Rod
Fiber type	Carbon	Carbon	Aramid	Aramid	E-Glass	Vinylon
Matrix resin	Epoxy	Epoxy	VE	Epoxy	VE	Epoxy
Vf (%)	64	65	66	65	65	72
Diameter (mm)	12.5	8.0	6.0	8.0	6.0	6.0
Ultimate load (kN)	141	70.6	52.4	65.4	36.3	19.6
Modulus (GPa)	145	168	55.6	62.1	52.9	28.6
Anchor system	Adhesive	Wedge	Adhesive	Adhesive	Adhesive	Adhesive

and modulus were measured at the beginning of the exposure test using the anchor systems suggested by the manufacturers of the cables.

2.3 Exposure test

The exposure test reported here was carried out on the second deck of the platform where the height is 8.9 m from the tidal point. We conducted the test under both loaded and unloaded conditions; however, the results reported here are only on the unloaded cables. Each FRP cable was cut to a length of 2000 mm, and then the six types of cables were set in a steel frame rack using rubber spacers. Figure 2 shows the placement of FRP cables in the steel frame for exposure. Nine sets of steel frames were prepared. In order to evaluate the effect of the difference in environment on the deterioration of the FRP cables, two different places were selected on the second deck of the platform. One was at the handrail well exposed to sunshine (Figure 3 a)), and the other was under a large concrete beam where there is less sunshine (Figure 3 b)). We labeled these as place-W (well exposed) and place-L (less exposed) respectively. Five steel frames with FRP cables were set at place-W and four were set at place-L in March 1994.

**Figure 2** Steel frames for exposure test using six FRP cables

(a) Place-W (at the handrail)

(b) Place-L (below the beam)

Figure 3 Placement of cables for exposure test

Each of the two sets was retrieved in November 1996, and the results on the FRP cables exposed for 2 years and 8 months have already been reported (Sasaki et al. 1997). The remaining steel frames with FRP cables, three at place-W and two at place-L, were retrieved in July 2009. The exposure time for these FRP cables was 15 years and 4 months. This report presents the results on these cables.

2.4 Retrieval and evaluation

Evaluation for the retrieved FRP cables was carried out by appearance check, surface and cross-section observation by scanning electron microscopy (SEM), cross-section observation by Fourier transform infrared (FT-IR) microscopy and chemical analysis by differential scanning calorimetry (DSC) on the material obtained from the surface and interior of the cables. We will also evaluate the mechanical properties in future.

3 RESULTS

3.1 Appearance

All of the retrieved FRP cables showed a decrease in the original surface gloss exhibited by the unexposed cables. Even in the case of CFRP2, where the initial unexposed cable did not have much surface gloss, the retrieved CFRP2 showed less gloss. GFRP cables showed remarkable change in color to brown whereas the unexposed cable was white. GFRP cable also showed fiber blooming on the cable surface.

There was no clear difference between place-W and place-L for CFRP1 and AFRP2; however, VFRP and GFRP showed more remarkable deterioration at place-W than at place-L. CFRP2 and AFRP1 at place-W showed slightly yellowed surfaces, but it is not clear whether this discoloration was due to deterioration or to rust from the steel frame used for the exposure test.

3.2 SEM

Resin loss and fiber blooming on the cable surface was also observed from SEM images. Figure 4 shows an example of AFRP2. CFRP1 has a protective layer of polyester fiber; the carbon fiber does not appear on the surface, but fiber blooming of the polyester fiber was observed. On the other hand, the carbon fiber of CFRP2 is exposed on the surface of the cable. Figure 5 is SEM

images of the CFRP2 surface, which shows the degradation of surface resin to small particles on the surface of the retrieved cable. These changes seem to be the reason for the reduced gloss in the appearance evaluation.

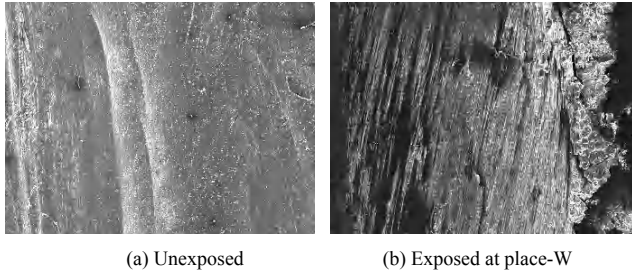


Figure 4 Observation by SEM (AFRP2, ×30)

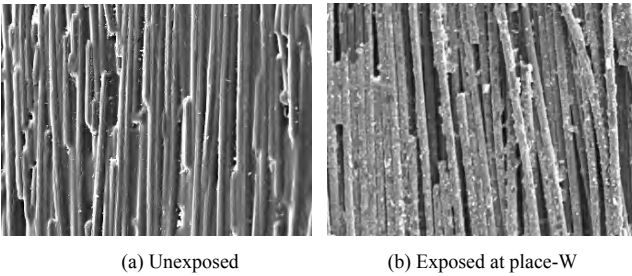


Figure 5 Observation by SEM (CFRP2, ×500)

Figures 6 and 7 show examples of SEM images of cross sections of the cables. We searched for deterioration between the fiber and matrix resin of small cracks that were not present in the unexposed cables; however, we did not find any clear difference between the unexposed and retrieved cables.

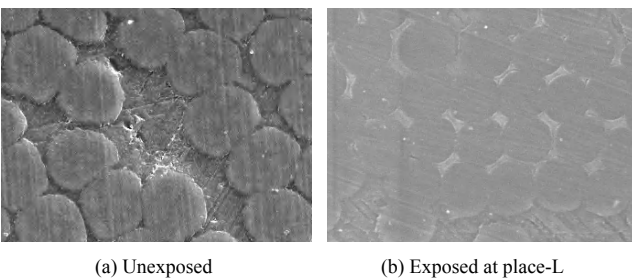


Figure 6 Observation by SEM (AFRP1, ×2000)

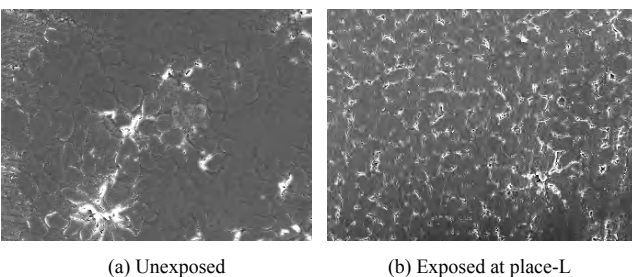


Figure 7 Observation by SEM (VFRP, ×500)

3.3 FT-IR microscopy

FT-IR microscopy was applied to three types of the unexposed and place-W cables. CFRP2, AFRP1 and AFRP2 were selected for the three types. Figure 8 shows the results for AFRP1.

Figure 8a) is a photograph of the cross section of AFRP1 (place-W) using the optical microscope, which shows the evaluation part of the cable (inside the white lines). Figure 8d) shows the IR spectra at two points in the evaluation part: the surface region and the interior region. A new peak at 1715 cm^{-1} was observed in the spectra for the surface region (shown with an arrow in the figure). This peak was not observed in the spectra for the interior region, and is considered to indicate the presence of a C–O double bond, according to the wavenumbers. Details of the chemical reaction behind this peak are not yet clarified, but it is likely related to the oxidation of resin or fiber. The peak at 1656 cm^{-1} (C–C double bond) was used as the interior reference. The peak area ratio ($1715/1656\text{ cm}^{-1}$) of each point (0.1 mm mesh) in the evaluation was measured by FT-IR microscopy. Figure 8b) shows the results for place-W. The results suggest a large peak area ratio region around the surface area of the cross section. Figure 8c) shows the same observation for the unexposed AFRP1. There was no specific region on the surface that suggested a large peak area ratio for the unexposed AFRP1.

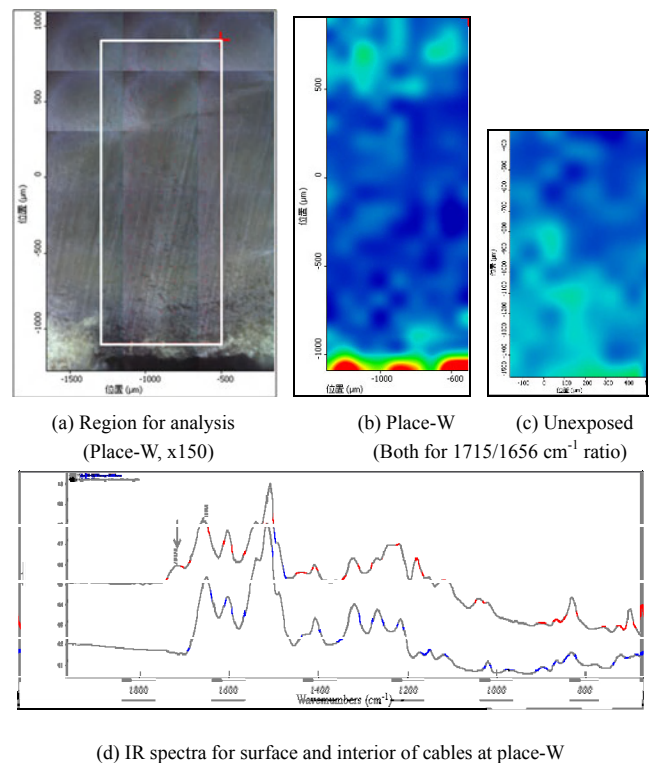


Figure 8 Results of FT-IR microscopy for AFRP1

Figure 9 shows the results of FT-IR microscopy for AFRP2. Figure 9a) shows the evaluation area for

place-W. From the observation of IR spectra at several points in the evaluation region, we decided to measure the peak area ratio of $1747/1652\text{ cm}^{-1}$. Figure 9b) shows the results of mapping the peak area ratio of $1747/1652\text{ cm}^{-1}$ inside the evaluation region. Figure 9c) shows the same measurement for the unexposed AFRP2. There was a large peak area ratio of $1747/1652\text{ cm}^{-1}$ in the surface region of the cross section of place-W, which was not found in the unexposed cable. This result indicates that the surface region of the AFRP2 (place-W) cable was oxidized.

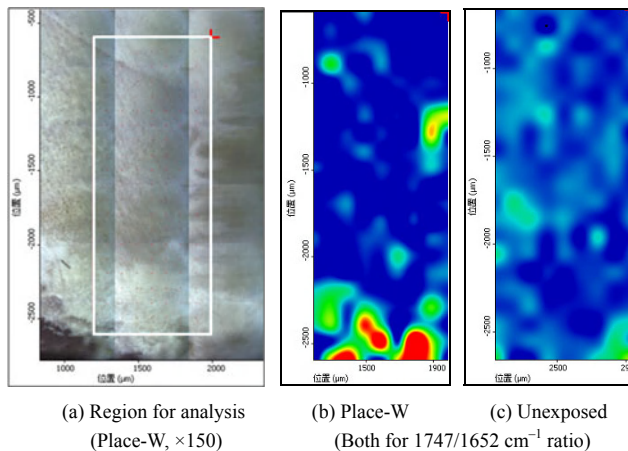


Figure 9 Results of FT-IR microscopy for AFRP2

The same measurement was performed for CFRP2 (both unexposed and place-W); however, no specific deteriorated region was observed even for the CFRP2 place-W cable.

3.4 DSC

DSC was performed for several cables. Small pieces were sampled from the surface and interior region of the cables, and the glass transition point for each sample was measured using DSC, and then compared with the initial values. The glass transition point of the exposed CFRP2 was 110.9°C where the equivalent initial value was 94.6°C . The exposed GFRP also showed a higher glass transition point (136.8°C) compared with the initial value (126.4°C).

4 CONCLUSIONS

An exposure test for six types of FRP cables was carried out for more than fifteen years under maritime conditions, and the retrieved cables were evaluated mainly by SEM and FT-IR microscopy. Loss of surface resin was observed for all the tested FRP cables; however,

deterioration between the fiber and matrix resin was not found by SEM. Observation by FT-IR microscopy detected the deterioration on the surface of AFRP cables, and the feasibility of this method in evaluating the deterioration of some FRP cables was indicated. We plan to evaluate the mechanical properties of the retrieved cables in the future, and to clarify the relationship between the chemical deterioration and mechanical properties.

5 ACKNOWLEDGMENTS

This work was supported by JSPS KAKENHI (21360209), which is gratefully acknowledged. The authors also would like to acknowledge the support by the manufacturers of FRP cables and the Shizuoka River Office of the Ministry of Land, Infrastructure and Transport of Japan (MLIT).

REFERENCES

- Benmokrane, B. et al. 1997. Aramid and carbon fibre-reinforced plastic prestressed ground anchors and their field applications, *Canadian Journal of Civil Engineering*, 968-985.
- Katawaki, K. et al. 1992. Evaluation of the Durability of Advanced Composites for Applications to Prestressed Concrete Bridges, *Proceedings of the First International Conference on Advanced Composite Materials in Bridges and Structures (ACMBS-1)*, 119-127.
- Nanni, A. et al. 1992. Durability of Braided Epoxy-Impregnated Aramid FRP Rods, *Proceedings of the First International Conference on Advanced Composite Materials in Bridges and Structures (ACMBS-1)*, 101-109.
- Sasaki, I. et al. 1997. Durability Evaluation of FRP Cables by Exposure Tests, *Proceedings of the Third International Symposium on Non-Metallic (FRP) Reinforcement for Concrete Structures*, 131-137.
- Takewaka, K. & Khin, M. 1996. Deterioration and Stress-Rupture of FRP Rods in Alkaline Solution Simulating a Concrete Environment, *Proceedings of the Second International Conference on Advanced Composite Materials in Bridges and Structures (ACMBS-2)*, 649-656.
- Tomosawa F. et al. 1997. Evaluation of the ACM Reinforcement Durability by Exposure Test, *Proceedings of the Third International Symposium on Non-Metallic (FRP) Reinforcement for Concrete Structures (2)*, 139-146.
- Uomoto, T. & Ohga, H. 1996. Performance of Fiber Reinforced Plastics for Concrete Reinforcement, *Proceedings of the Second International Conference on Advanced Composite Materials in Bridges and Structures (ACMBS-2)*, 125-132.

Temperature Effects on Full Scale FRP Bridge Using Innovative Composite Components

C. S. Sirimanna, M. M. Islam (mainul.islam@usq.edu.au) & T. Aravinthan

Centre of Excellence in Engineered Fibre Composites, University of Southern Queensland, Toowoomba, Queensland 4350, Australia

ABSTRACT Numerous large-scale demonstrator projects around the world have shown the viability of composite materials for bridge applications. Most of the projects have been directed towards the better understanding of bridge behaviour in strength and serviceability. However, the behaviour under different environmental conditions and longer term effects on durability are yet to be fully understood. This paper presents the results of an investigation on effects of temperature change into the structural behaviour of a FRP demonstrator trial bridge. It was installed at the University of Southern Queensland, Toowoomba Campus using innovative sandwich composites. It has been found that temperatures in different locations of the bridge vary for different locations within the bridge. The variation is found to reverse during day and night time. Based on the measured temperature variation, some important recommendations are provided on the effects of temperature for innovative fibre composite bridge.

1 INTRODUCTION

During the past decade, many large-scale demonstrator projects around the world have shown that fibre composites are viable structural materials for bridge applications. Advantages of these new materials over traditional bridge materials include low weight and high strength, greatly improved corrosion resistance and durability, ease of transportation and installation and lower energy consumption during manufacture. A technological development in Australia was the construction of a prototype bridge at the University of Southern Queensland (USQ). This new generation fibre composite bridges using sandwich panels could potentially increase the span by two folds. This new technology has been realised through partnership with Department of Transport and Main Roads, Queensland and LOC Composites Pty Ltd, which is a start-up company based in Toowoomba (Aravinthan & Heldt 2008).

Most of the projects have been directed towards the better understanding of the bridge behaviour in terms of strength and serviceability. For example, Epaarachchi et al. (2008) investigated the dynamic behaviour of the girder for the above mentioned fibre composite bridge. However, the behaviour under different environmental conditions and its long-term effects on durability are yet to be fully understood. A previous relevant study (Shahrooz et al. 2007) showed some investigation on the thermal characteristics of FRP panels for bridge decks. Unlike traditional construction materials such as

concrete, which has got good thermal behaviour, temperature variation in a fibre composite bridge structure could have some influence in thermal stresses due to low stiffness of fibre composites (Ho & Liu 1991).

This paper presents the initial results of an investigation on the effects of temperature changes into the structural behaviour of a fibre composite demonstration bridge at USQ, Toowoomba Campus.

2 EXPERIMENTAL PROGRAMME

The full scale fibre composite trial bridge installed at USQ is 10m long and 5m wide (bridge beck). Figure 1 schematically shows the cross-section of the bridge. Temperature monitoring was conducted over twelve months starting from June 2008 before the winter, covering the extreme temperature conditions including spring, summer and autumn. Five temperature sensors were installed in the critical section of the bridge at different depths. The locations include top and bottom of the bridge deck, top and bottom of a bridge girder and a controlled one for the ambient temperature. Figure 2 shows the sensors' locations in details with the dimensions.

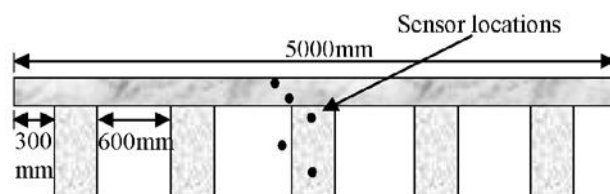
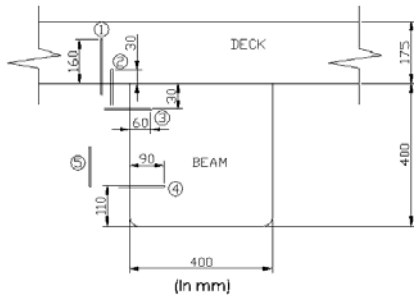


Figure 1 Cross-section of the fibre composite bridge.

Figure 3 shows the photographs of the sensors during temperature monitoring.



Sensor locations	Description
1	Top of the bridge Deck
2	Bottom of the bridge deck
3	Top of the bridge Girder
4	Bottom of the bridge girder
5	Ambient temperature (under the bridge)

Figure 2 Bridge cross section and temperature sensors locations



Figure 3 Temperature monitoring through the sensors

Each sensor gave 96 temperature measurements per day with 15 minute intervals. Over the twelve month period, each location has approximately 32,500 temperature data.

3 TEMPERATURE ANALYSIS

Temperature variation over the sensor point was identified with respect to seasons. Figure 4 illustrates a sample seasonal temperature variation over the sensor points during summer.

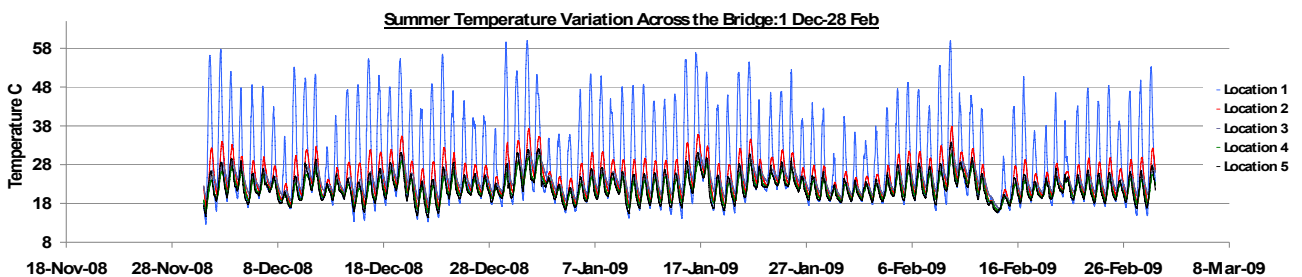


Figure 4 Temperature variation across the bridge - Summer (1st Dec - 28th Feb)

Observing temperature variation in all four seasons, location 1 had high temperature variation throughout year. Bitumen based material was used as surfacing of the FRP trial bridge. Also the bridge deck was fully exposed to direct sunlight. As a result the rapid temperature variation was predominant in location 1. In summer, locations 2, 3 and 4 had almost steady temperature variation operating in between 18°C and 38°C range.

Then each day maximum and minimum temperature was identified over the year with respect to sensor locations.

Again, Figure 5 shows that location 1 had comparatively high temperature variation. After careful analysing some critical dates identified throughout the year to get temperature behaviour over the bridge. Table 1 shows these critical days.

As shown in Table 1, 9-Feb-2009 was a critical date; because it shows maximum temperature difference in location 2 and 4 as well as maximum temperature in location 2, 4 and 5. In addition 29-July-2008 gave minimum temperature in location 2, 3, 4 and ambient. In

all locations, maximum temperature occurred in summer season and minimum temperature occurred in winter season. Therefore, when dealing with FRP related structural design, this summer and winter seasonal variation must be taken into consideration, because thermal stresses can give significant contribution throughout the structure.

According to Figure 6, location 1 always reached maximum temperature before ambient temperature got its maximum. After getting in maximum ambient temperature, other locations 2, 3 and 4 reached maximum temperature. Likewise in the night, locations 2, 3 and 4 got to minimum temperature after reaching minimum ambient temperature. Additionally in day time, for some time period, location 3 and location 4 approximately coincided with each other. This implies that at this period, there was negligible temperature gradient in bridge girder.

Considering seasonal variations, the ratio between maximum and minimum temperature for all locations over ambient temperature were calculated. Figure 7

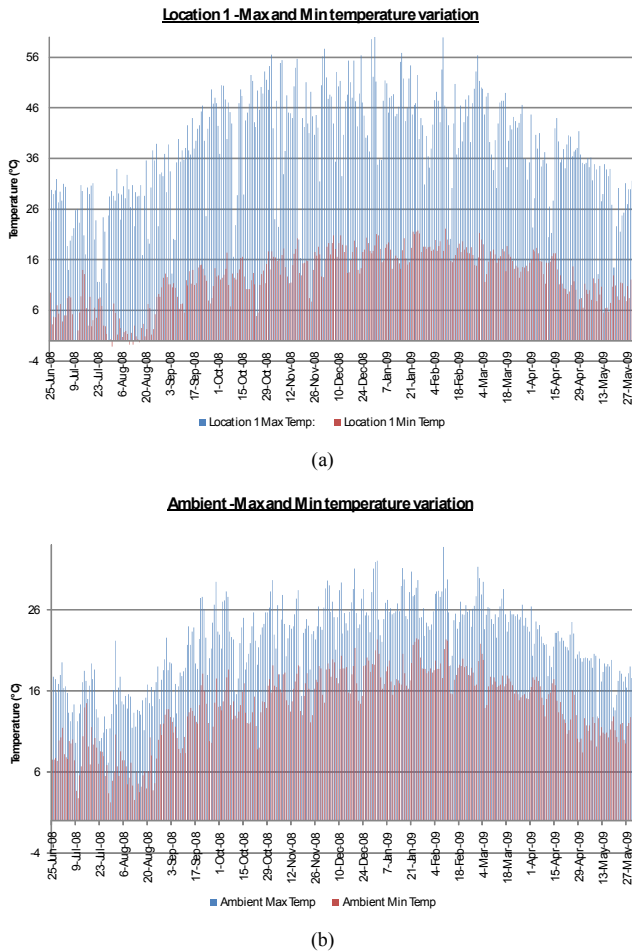


Figure 5 Maximum and minimum temperature variation in (a) location 1 and (b) ambient over the year

Table 1 Critical dates over the year with respect to locations

Sensor location	Max.temperature difference (°C)	Date of max. temperature difference	Max. temperature (°C)	Date of max. temperature	Min. temperature (°C)	Date of min. temperature
1	43.909	24-Oct-08	60.013	31-Dec-08	-1.126	31-Jul-08
2	15.871	9-Feb-09	37.851	9-Feb-09	2.327	29-Jul-08
3	8.033	17-Nov-08	31.823	1-Jan-09	3.435	29-Jul-08
4	9.170	9-Feb-09	30.923	9-Feb-09	3.096	29-Jul-08
5	12.837	27-Sep-08	33.788	9-Feb-09	2.272	29-Jul-08

indicates that only location 1 variation with respect to seasons.

Table 2 lists the ratios of maximum to ambient temperatures for all locations. It shows that location 1 had drastic variation in absorption and emission temperature over the ambient temperature.

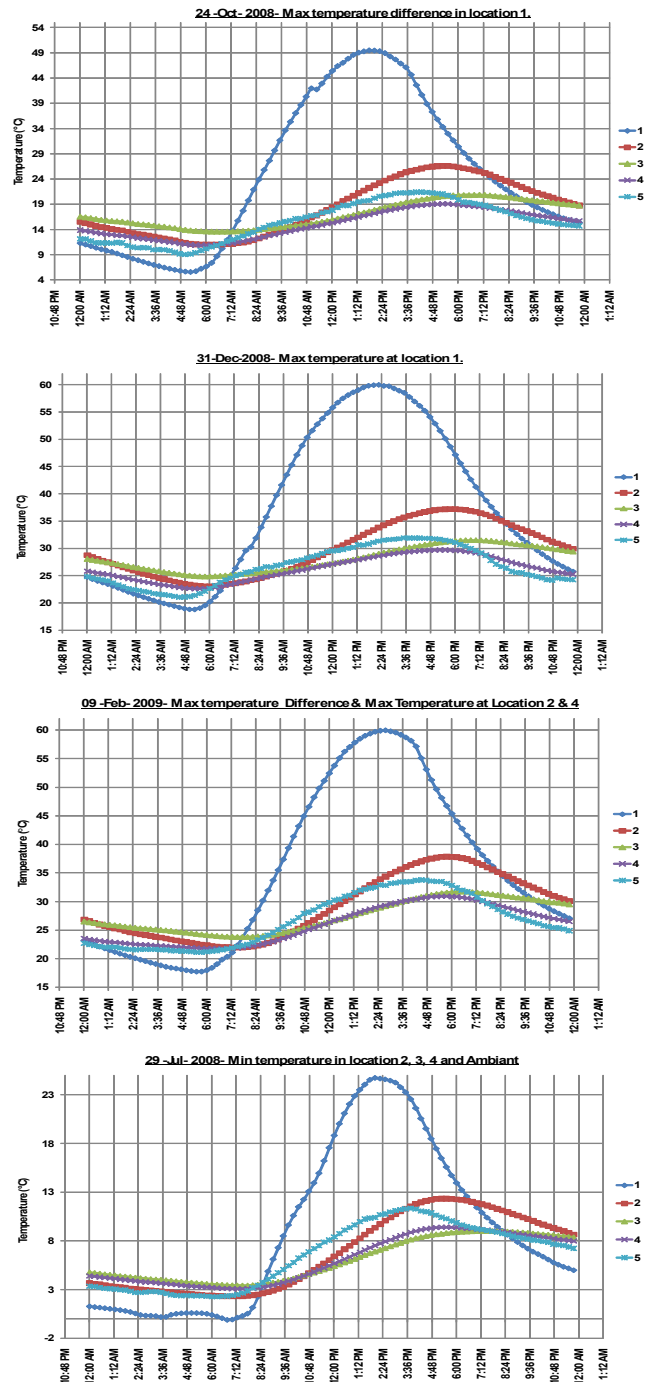


Figure 6 Temperature variation on 24-Oct-2008, 31-Dec-2008, 9-Feb-2009 and 29-Jul-2008 (respectively)

Figure 8 shows that locations 1, 2 and 3, 4 acted separately. In actual situation locations 1 and 2 lied on bridge deck and 3 and 4 lied on bridge girder. There was construction discontinuity between point 2 and 3. Therefore, region in between locations 2 and 3 acted as transition region, which allowed transferring temperature absorption gradient from FRP deck to FRP girder. As per Figure 8, the bridge girder had approximate uniform temperature absorption gradient throughout the year.

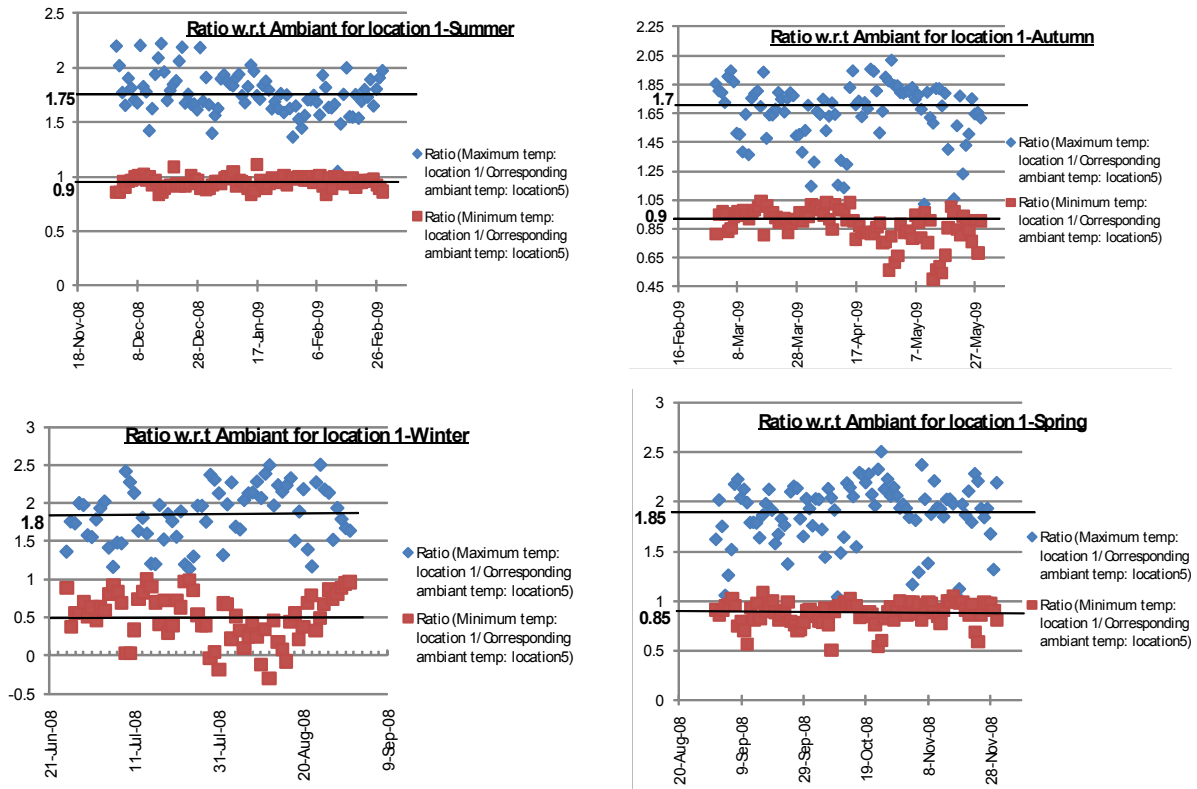


Figure 7 Ratio between maximum and minimum temperature over ambient temperature

Table 2 Summary of the ratios of maximum to ambient temperatures for all locations

Location	Distance from top of deck (mm)	Summer		Autumn		Winter		Spring	
		Ratio of max temp/ambi. temp.	Ratio of min temp/ambi. temp.	Ratio of max temp/ambi. temp.	Ratio of min temp/ambi. temp.	Ratio of max temp/ambi. temp.	Ratio of min temp/ambi. temp.	Ratio of max temp/ambi. temp.	Ratio of min temp/ambi. temp.
1	15	1.75	0.9	1.7	0.9	1.8	0.5	1.85	0.85
2	145	1.15	1.035	1.175	1.02	1.18	0.98	1.17	1.04
3	205	1.04	1.125	1.05	1.1	0.98	1.13	1.05	1.13
4	465	0.95	1.035	0.97	1.05	0.95	1.12	0.94	1.03

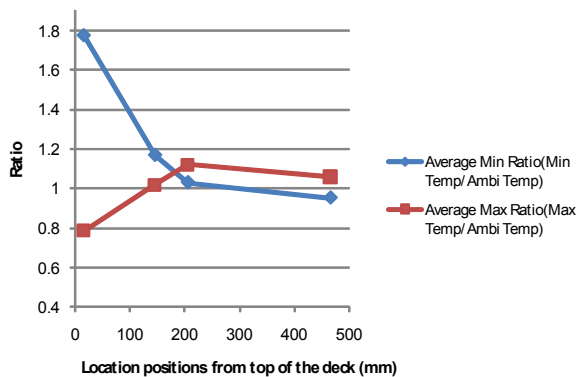


Figure 8 Average ratios from Table 2 vs. location positions from top of the deck for entire year

4 CONCLUSIONS

Temperature monitoring in an actual fibre composite

bridge was conducted. It was found that the temperature in different locations on the bridge vary for different locations within the bridge. The following conclusions can be drawn based on this study:

- Location 1 experiences higher temperature variation, because of bitumen type surfacing and exposing to sunlight directly. Therefore in FRP bridge structures, surfacing materials cause significant temperature effect compared to other locations.
- Based on ratio analysis (Figure 8), bridge deck faces significant ratio variation. However, girder varies by around 1. Therefore, bridge deck causes high thermal stress compare to girder, provided that other factors than temperature variation may also be involved in stress variation.
- In the night time, FRP components get to minimum temperature after reaching minimum ambient

temperature.

- In the day time, FRP components get to maximum temperature after reaching maximum ambient temperature.

The above information is important as it provides a benchmark on which the effects of the temperature variation could be related into the structural behaviour of the fibre composite bridge. Further studies should be conducted to determine the effects of thermal stresses on the fibre composite bridge due to the temperature variation.

5 ACKNOWLEDGEMENTS

Authors gratefully acknowledge the support of Mr. Wayne Crowell in installing the temperature sensors. They also thank Mr. Allan Manalo for some assistance in data collection.

REFERENCES

- Aravinthan, T. & Heldt, T.J. 2008. R&D on Engineered Fibre Composites – Past, Present and Future. *Proceedings of Fibre Composites in Civil Infrastructure – Past, Present and Future (FCCI)*, Toowoomba, Australia, 1-2 December 2008, 3-10.
- Ho, D. & Liu, C.H. 1991. Temperature distribution in concrete bridge decks. *Proceedings of Institution of Civil Engineers, Part 2*, September 1991, 451-476.
- Epaarachchi, J.A., Karunasena, W. & Aravinthan, T. 2008. Dynamic Behaviour of Hybrid Composite Bridge Girder. *Proceedings of the 20th Australasian Conference on the Mechanics of Structures and Materials (ACMSM20)*, Toowoomba, Australia, 3-5 December 2008, 75-78.
- Shahrooz, B.M., Neumann, A.R. & Reising, R.M.W. 2007. Durability of FRP Composite Bridge Decks – Construction and Temperature Effects. *International Journal of Materials and Product Technology*, 28, 1/2, 66-88.

Modeling the Effect of Repeated Loading on the Behaviour of CFRP Confined Bond of Corroded Reinforcement

Safeer Abbas & Ahmad Rteil (ahmad.rteil@ubc.ca)

School of Engineering, The University of British Columbia, Kelowna, Canada

ABSTRACT In steel-reinforced concrete, the transfer of forces between concrete and reinforcing steel bars dictates the general behaviour of the structure. This transfer is affected by several factors such as the corrosion of steel reinforcement, the presence of FRP confinement and the loading regime. This study used design of experiment methodology to examine the experimental data available on the behaviour of corroded steel-FRP confined concrete bond under repeated loading. The fatigue bond life of a CFRP wrapped bond critical zone was studied as a function of the corrosion level and the repeated applied load range. The analysis of the unbalanced experimental data concluded that the loading range, accounting for 52.4% of the total variability, is the significant factor that affects the performance of the CFRP confined tested specimens. Based on the statistical analysis, a model was developed that relates the fatigue bond life of a CFRP confined bond critical zone to the corrosion level and the applied loading range. The proposed model satisfactory predicts the experimental behaviour.

1 INTRODUCTION

1.1 Steel-Concrete Bond

The behaviour of reinforced concrete (RC) structure under both static and cyclic loading depends on the bond between steel and concrete. A transfer of tensile forces from the concrete to the reinforcing steel requires an adequate bond between the two materials (concrete and steel). Bond deterioration interrupts the force transfer mechanism and results in an increased deflection, cracks and a decreased load carrying capacity, causing a brittle and abrupt failure (ACI 408, 2003).

Corrosion is one of the most serious problems affecting the service life of RC structures. Corrosion of reinforcement in RC structures cost the US economy almost 1% of its gross domestic product (Whitmore and Ball, 2004). The consequences of corrosion in RC structures are: 1) loss of reinforcing steel cross sectional area and 2) cracking of concrete cover, which leads towards concrete spalling, and loss of bond between steel and concrete. The reduction in the area of the steel bars decreases the load carrying capacity of the RC structures. The cracking and spalling of the concrete cover, resulting from the splitting tensile forces acted by the rust volume on the concrete (ACI 222, 2001), lead to the deterioration of the bond due to the loss of friction and mechanical anchorage provided by the ribs as well as the loss of concrete cover confinement.

Marine structures and bridges are more liable to corrosion and are also subjected to repeated rather than static loading. The live to dead load ratio is high in these

structures due to the use of high strength material which reduces the dead load. Therefore, fatigue loading may govern the design at the serviceability limit state (ACI 215, 1974). The repeated loading can cause damage in the form of increased number of cracks, crack width and deflection. The bond between steel and concrete directly or indirectly affects these aspects (Oh and Kim, 2007).

Fibre reinforced polymer (FRP) system has achieved a worldwide acceptance over other strengthening systems due to its high strength to weight ratio, favourable behaviour in harsh environments, improved fatigue behaviour, ease of handling in application, and non corrosive nature (ACI 440, 2002). Also, the FRP repair system controls the corrosion activity and hence increases the strength of RC structures (El Maaddawy et al., 2005a). Research has also shown that FRP wrapping increases the bond strength by providing confinement to the concrete, which does not allow the cracks to propagate further (Harajli et al., 2004; Rteil et al., 2005).

The existing analytical models that account for the bond fatigue strength are very few and used pullout specimens, which does not capture the true bond behaviour of real RC structures. In addition, the analytical studies were conducted without considering the effect of corrosion or confinement with FRP sheets.

1.2 Design of Experiment Methodology

“Design of experiments is a sequence of tests in which decisive changes are made to the input variables of a system and the effects on the response variables are measured” (Telford, 2007). Factorial design method

varies all the factors/variables simultaneously and orthogonally such that the effects due to each factor and to combinations of factors are estimated (Telford, 2007).

This study is based on the design of experiment methodology to develop a model which examines the basic influence of the cyclic loading on the bond behaviour between the corroded steel reinforcement and carbon fibre reinforced polymer (CFRP) confined concrete. In this study factorial design was used in order to analyze the unbalanced (unequal number of replicates for each run) experimental data.

2 EXPERIMENTAL DATA

The experimental data used in this study was reported by Rteil (2007). He studied the effect of carbon fibre reinforced polymer (CFRP) on the bond behaviour of corroded beams under fatigue loading. The experimental results indicated that the CFRP wrapped beam specimens attained more fatigue bond life than the unwrapped beam specimens did at all corrosion levels. The increase in fatigue bond strength was up to 31%. In addition, the slip behaviour of the steel rebar relative to CFRP wrapped concrete was different from that of the unwrapped concrete. This was due to the CFRP confinement of the concrete in the bond anchorage zone (Rteil, 2007).

3 ANALYSIS OF EXPERIMENT USING FACTORIAL DESIGN APPROACH

Full factorial design or 2^k design of the experimental result was used in order to study the effects of two factors, namely corrosion level and loading rate, on the fatigue bond life. The two levels are normally referred to as low (L) or level 1 and a high (H) or level 2.

The test variables in this study were 1) the time of corrosion exposure (C) when the beams were tested and 2) the load level range applied (P) as shown in Table 1. Uncorroded and corroded reinforcement bar are defined here as the low (C_L) and high (C_H) level for the corrosion factor (C) respectively. Load range less than or equal to 62% of the static load capacity was selected as the low level of the load factor (P_L) and greater than 62% was considered as the corresponding high level (P_H) for the CFRP wrapped specimen. These ranges for the loading range were selected in order to make a complete factorial design. The number of cycles till failure (Fatigue bond life) was the response in this study.

Table 1 Factors and their corresponding level.

Factors	Name	low level (L)	High level (H)
Corrosion	C	uncorroded (C_L)	corroded (C_H)
Loading range	P	$\leq 62\%$ (P_L)	$> 62\%$ (P_H)

For any 2^k experiment, all combinations of the k

factors must be considered. With two factors, there will be four combinations of the low and high values. The geometric view for the 2^2 factorial design can be conveniently laid in the form of a rectangle as shown in Figure 1.

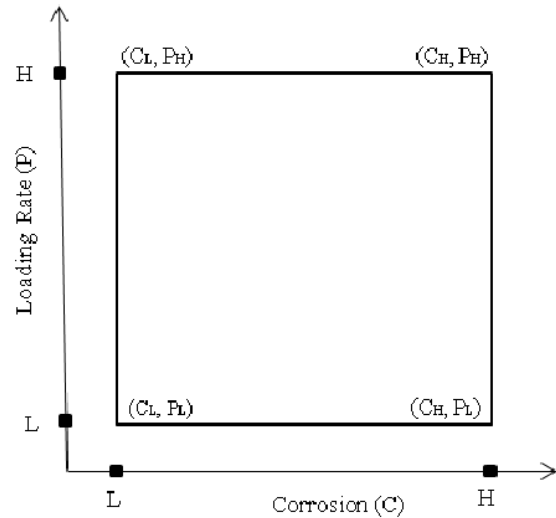


Figure 1 Geometric view of 2^2 factorial design

Four treatment combinations [(C_L, P_L) , (C_H, P_L) , (C_L, P_H) , (C_H, P_H)] are required for 2^2 factorial design.

Table 2 summarizes the effect estimates and percentage contribution. The column labelled "percent contribution" measures the percentage contribution of each model term to the total sum of squares. Note that the main factor P (loading rate) dominates, accounting for 52.40% of the total variability while corrosion contributes 41.71%. The analysis of variance (F-value) confirms the magnitude of these effects (Table 2). The effect of corrosion (C) is negative (Table 2); this suggests that increasing corrosion level from the low level (uncorroded) to the high level (corroded) will decrease the fatigue bond life. Also the effect of the load range (P) is negative which suggests that increasing the loading rate will decrease the fatigue bond life.

Table 2 Effect estimate and percent contribution

Factor	Effect estimate	Sum of square	Percentage contribution	F-value
C	-1.56	0.61	41.71	0.53
P	-1.75	0.77	52.40	0.67
CP	-0.59	0.09	5.88	0.07

In order to check the adequacy of the underlying model, a residual analysis was performed. Figure 2 shows the normal probability plot of residuals and Figure 3 shows the plot of the residuals versus the predicted fatigue bond life. It is seen that the normality assumption of the data is valid as the plot of normal probability of residual (Figure 2) forms a straight line.

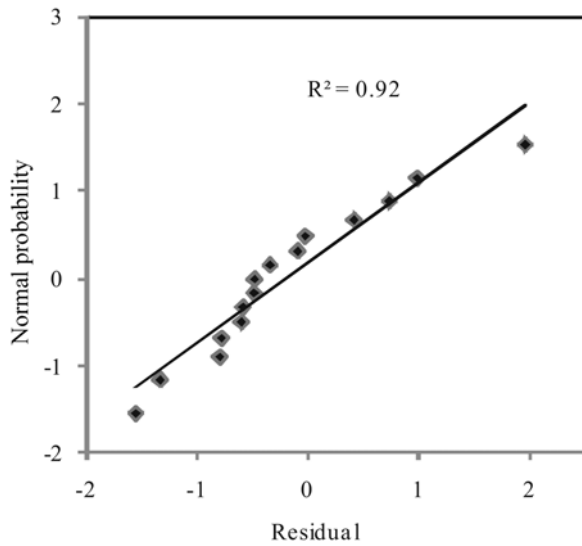


Figure 2 Normality plot of residual

Also the residual versus predicted values (Figure 3) shows a scattered data which implies that the errors are randomly distributed.

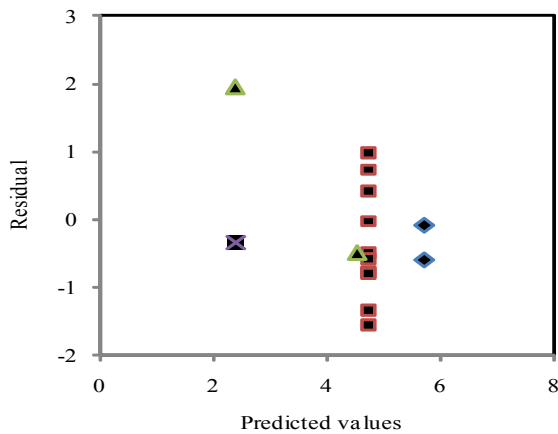


Figure 3 Residual versus predicted values

Since the normality assumption of the data was validated (Figure 2) and the errors were shown to be randomly distributed (Figure 3), then the 2^2 factorial regression could be used to predict the fatigue bond life. The 2^2 factorial regression model for predicting the fatigue bond life was conducted and the following equation was determined.

$$\log N_f = 11 - 10.17C - 10.10P \quad (1)$$

Where N_f , C and P are the fatigue bond life, percentage mass loss due to corrosion and percentage range of loading applied respectively.

Figures 4, 5 and 6 compare the experimental and the predicted fatigue bond life for 0%, 5% and 9% mass loss due to corrosion for CFRP wrapped specimens. The proposed model was able to satisfactory predict the experimental results.

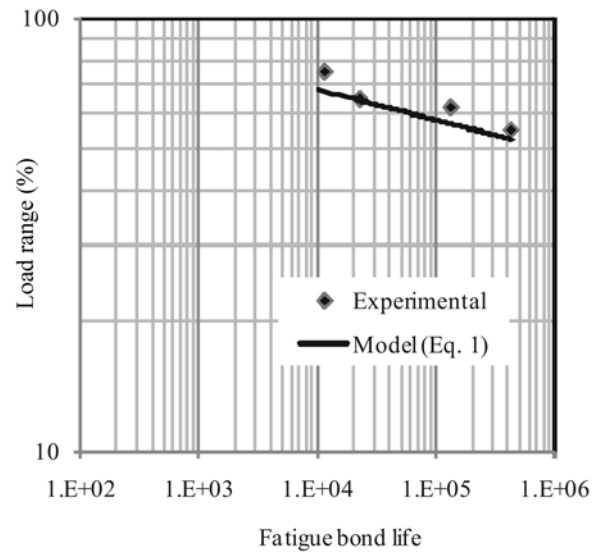


Figure 4 Model prediction versus experimental result for uncorroded wrapped beams

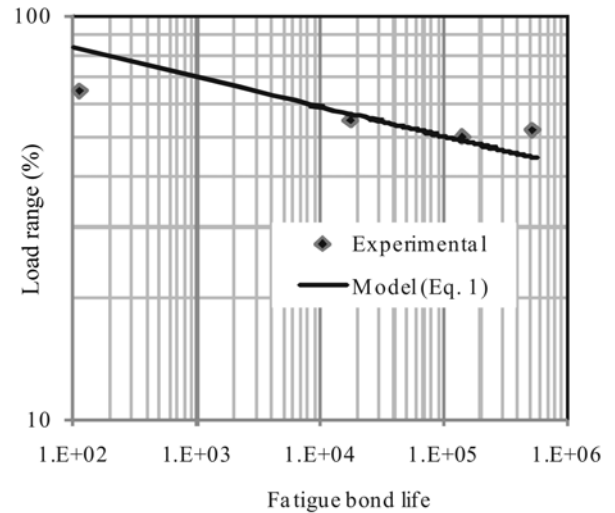


Figure 5 Model prediction versus experimental results for 5% corroded wrapped beams

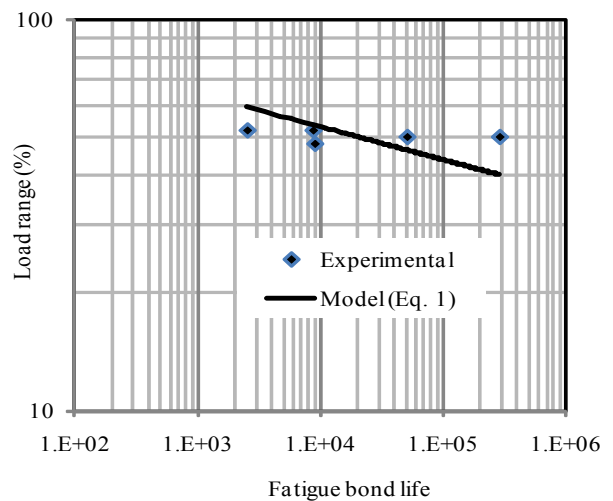


Figure 6 Model prediction versus experimental results for 9% corroded wrapped beams

4 CONCLUSIONS

The following conclusions can be drawn from the above presented study:

- Loading range affects the fatigue bond strength of CFRP wrapped bond regions more than corrosion.
- As predicted, the analysis result shows that the fatigue bond life decreases as the corrosion level and loading rate increases.
- A 2² factorial regression model was proposed that satisfactory predicts the experimental behaviour.

5 ACKNOWLEDGEMENT

The authors gratefully acknowledge the input of Dr. Sadiq. The first author would like to thank the University of Engineering and Technology Lahore, Pakistan for its financial support through “Faculty Development Program”.

REFERENCES

- ACI Committee 215, 1974. Considerations for Design of Concrete Structures Subjected to Fatigue Loading (ACI 215-74, Reapproved 1999). *American Concrete Institute, Farmington Hills, MI*, 24p.
- ACI Committee 222, 2001. Protection of Metals in Concrete against Corrosion (ACI 222-01). *American Concrete Institute, Farmington Hills, MI*, 41 p.
- ACI Committee 408, 2003. Bond and Development of Straight Reinforcing Bars in Tension. *American Concrete Institute, Farmington Hills, MI*, 49 p.
- ACI Committee 440, 1996. State of the Art Report on Fiber Reinforced Plastic (FRP) Reinforcement for Concrete Structures (ACI 440-96, Reapproved 2002). *American Concrete Institute, Farmington Hills, MI*, 68 p.
- El Maaddawy, T. and Soudki, K., 2005a. Carbon-Fiber-Reinforced Polymer Repair to Extend the Service Life of Corroded Reinforced Concrete Beams, *ASCE Journal of Composites in Construction* 9(2): 187-194.
- Harajli, M.H. and Rteil, A.A. 2004. Effect of Confinement Using Fiber-Reinforced Polymer or Fiber-Reinforced Concrete on Seismic Performance of Gravity Load-Designed Columns. *ACI Structural Journal* 101(1): 47-56.
- Oh, H. B. and Kim, H. S. 2007. Realistic Models for Local Bond Stress-Slip of Reinforced Concrete under Repeated Loading. *Journal of Structural Engineering* 133(2): 216-224.
- Rteil, A., Soudki, K. and Topper, T. 2005. Effect of CFRP sheets on concrete steel bond strength. *1st CSCE specialty conference on infrastructure technologies, management and policy*, June 2-4.
- Rteil, A. 2007. Fatigue bond behavior of corroded reinforcement and CFRP confined concrete. PhD thesis, University of Waterloo, Waterloo, Ontario, Canada.
- Telford, J.K. 2007. A brief introduction to design of experiment. *Johns Hopkins apl technical digest* 27(3).
- Whitmore, D.W. and Ball, J.C. 2004. Corrosion Management. *ACI Concrete International* 26(12): 82-85.

Effects of Accelerated Ageing on the Adhesive Bond Between Concrete Specimens and External CFRP Reinforcements

K. Benzarti (benzarti@lpc.fr), M. Quiertant & C. Marty

Université Paris-Est, Laboratoire Central des Ponts et Chaussées (LCPC), Paris, France

S. Chataigner & C. Aubagnac

Laboratoire Régional des Ponts et Chaussées d'Autun, Autun, France

ABSTRACT CFRP strengthened concrete specimens were submitted to accelerated ageing conditions (40°C and 95% R.H.) and the time evolution of the adhesive bond strength was monitored using either pull-off or shear loading tests. In a parallel investigation, effects of hydrothermal ageing on the microstructure of the bulk epoxy adhesives were assessed by means of thermal analyses and tensile tests. From those experiments, it was found that the property evolution of the concrete/FRP bonded interface is primarily dependent on the sensitivity of the polymer to ageing conditions, but also on the type of test used for the mechanical characterizations. These trends were supported by numerical modeling based on finite element analysis.

1 INTRODUCTION

Applications of Fiber Reinforced Polymer (FRP) composites to the strengthening of civil infrastructures have met a growing popularity in the last decade. If the effectiveness of the technique is now widely recognized (Pendari et al. 2008, Hamelin 2002), many questions remain regarding durability issues (Karbhari et al. 2003). In a more general way, durability aspects are still to be addressed for structural assemblies involving adhesively bonded joints (Cognard 2006).

Design guidelines for FRP strengthened concrete structures usually introduce safety coefficients on the FRP properties, to account for possible deteriorations of both the composite reinforcement itself and the adhesive bond under service conditions (Gangarao et al. 2006, Karbhari et al. 2007). In recent years, extensive researches were undertaken to investigate the environmental ageing behavior of FRP/concrete bonded interfaces (Grace et al. 2005, Yang et al. 2008, Silva et al. 2008, Marouani et al. 2008). Most of these studies showed significant effects of wet environments (direct immersion or exposure to water saturated air) on the long-term performances.

The present study focuses on two FRP reinforcement systems commercially available on the French market, both based on a unidirectional pultruded carbon plate associated to a bi-component/room temperature curing epoxy adhesive.

Concrete specimens were strengthened using these two systems, and the ageing behavior of both the constitutive materials (concrete, epoxies, CFRP plates)

and the bonded interfaces were investigated. In this regard, specific ageing conditions were chosen, i.e., a temperature of 40°C and a relative humidity of at least 95%. Such conditions were intended to accelerate the moisture sorption phenomenon, while keeping the temperature value just below the usual glass transition temperature (T_g) range of ambient cured epoxies used in construction.

The present paper is structured as follows:

- sample preparation and storage conditions are first briefly recalled.
- ageing behaviors of the constitutive materials are then presented, with a special emphasis on epoxy adhesives.
- another section is devoted to the property-evolutions of the ageing FRP/concrete interfaces, which were assessed using two different characterization methods: the usual pull-off test and a single lap shear test. Apparent evolutions are discussed in the light of the previous results obtained for individual constituents.
- in the final part, a finite element approach is implemented to validate the experimental study.

2 SAMPLES AND STORAGE CONDITIONS

2.1 Samples

The two FRP systems under study (denoted $S1$ and $S2$) are commercialized by two different manufacturers. $S1$ and $S2$ are based on unidirectional pultruded carbon plates of respective widths 100 and 80mm, respective

thicknesses 1.4 and 1.2mm, and respective Young's moduli of 163 and 165GPa. Specific bi-component epoxy adhesives (denoted *Epo1* and *Epo2*) are respectively used for bonding of systems *S1* and *S2*, according to the product datasheets.

FRP strengthened concrete blocks were specifically designed to enable multiple mechanical characterizations, as shown in Figure 1: concrete compressive strength can be measured on samples cored from the previous specimens, according to EN 12 390-3 standard (2003); adhesive bond characterizations of the concrete/FRP interfaces can be performed either by the pull-off test according to EN 1542 standard (1999), or by a single lap shear test previously detailed in (Chataigner et al. 2009).

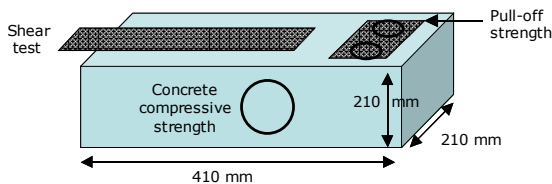


Figure 1 Detail of the CFRP strengthened specimens

Concrete blocks were prepared from CEM II 32.5 cement and silico-calcareous aggregates with a w/c ratio of 0.55. A maturing period of 28 days was observed before the application of FRP reinforcements.

For each FRP system, a series of 39 reinforced concrete specimens was prepared; this number was intended for 13 test sessions corresponding to different periods of ageing (3 repeated tests per session). Bonding of the FRP systems was achieved by a professional staff according to the guidelines. The bonded length was 200mm on each specimen.

Besides, samples of the bulk epoxies were also fabricated, either parallelepiped or dumbbell shaped, in order to study the moisture sorption and perform thermal analyses and tensile tests. Figure 2 shows some pictures of the various samples.

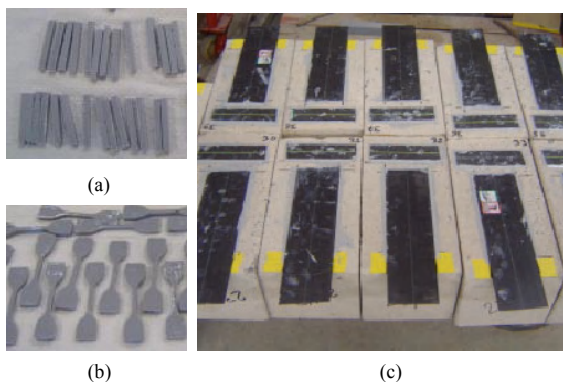


Figure 2 Test samples for bulk epoxies (a) and (b) and CFRP strengthened blocks (c)

2.2 Ageing conditions

A curing period of 15 days at room temperature was observed before the first test session. Then, samples were placed in a climatic room under ageing conditions (temperature of 40°C and relative humidity higher than 95%), for a total duration up to 20 months (628 days). Series of 3 specimens were periodically removed from the chamber in order to be tested. Results of the various characterizations will be presented in the next sections. In all cases, the first test session corresponds to the initial state of the specimens, just before starting the ageing treatment.

3 AGEING BEHAVIOURS OF CONSTITUTIVE MATERIALS

3.1 Evolution of the concrete compressive strength

Compressive strength of the concrete material was measured on cylindrical samples cored from the CFRP strengthened specimens, at each test session. With ageing time, a slight and progressive increase was observed in the compressive strength values (from 35 MPa in the initial state to about 43 MPa after 20 months). Such a trend was expected due to the continuation of the hydration process in the warm and wet ageing environment.

3.2 Evolution of the CFRP plate properties

Tensile tests performed on CFRP plates from systems *S1* and *S2* did not reveal any significant evolution of the material stiffness over ageing time. Young's moduli remained unchanged with values around 160 GPa.

3.3 Ageing behaviors of the bulk epoxies

Mass uptakes of the two ambient temperature cured epoxies *Epo1* and *Epo2* were first monitored as a function of ageing time (Figure 3 a). Fickian behaviors were observed for the two systems, but with a much higher saturation level for *Epo1* (~2%-2.5%) than for system *Epo2* (~0.8%).

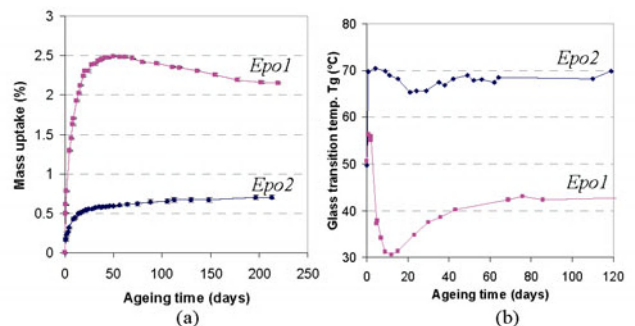


Figure 3 Mass uptakes (a) and evolution of the glass transition temperature (b) versus ageing time for bulk adhesives *Epo1* and *Epo2*.

Changes in the glass transition temperature (T_g) induced by ageing were determined using a modulated differential scanning calorimetry (MDSC). Observed variations (Figure 3 b) were ascribed to the competition between two antagonistic phenomena: the post-curing of the adhesive leading to an increase in T_g , and the plasticization effect which produces the opposite trend. The two systems exhibited very different behaviors: a large drop of T_g was observed for *Epo1* (down to 30°C), which indicates an extensive plasticization due to moisture sorption; differently, *Epo2* showed much more limited plasticization and kept its T_g value higher than 60°C.

Tensile tests were also performed and the stress-strain curves obtained after various periods of ageing are plotted in Figure 4. Tensile characteristics of the two ageing epoxies both evolved from an elastic behavior toward an elasto-plastic behavior, with a decrease in strength and an improved ductility. However, ductilization was much more pronounced for *Epo1* than for *Epo2* in line with the extensive plasticization revealed by sorption and DSC experiments.

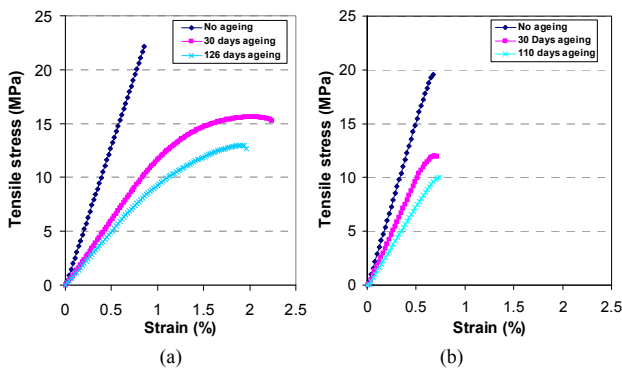


Figure 4 Tensile stress-strain curves for bulk epoxies *Epo1* (a) and *Epo2* (b), after various ageing periods

4 AGEING BEHAVIOURS OF CONCRETE/FRP INTERFACES

This part investigates the property evolutions of the adhesive bond during ageing as determined using the pull-off and single-lap shear tests.

4.1 Pull-off characterizations

Figures 5 and 6 depict respectively the evolutions of the pull-off strengths and failure modes for ageing CFRP strengthened specimens of type *S1* and *S2*.

Systems *S1* and *S2* exhibited very different ageing behaviors: a large decrease in the pull-off strength and an evolution of the failure mode from a substrate failure towards a cohesive failure within the glue were observed for system *S1*, whereas no significant evolution was observed for system *S2*. This point will be discussed further in the next section.

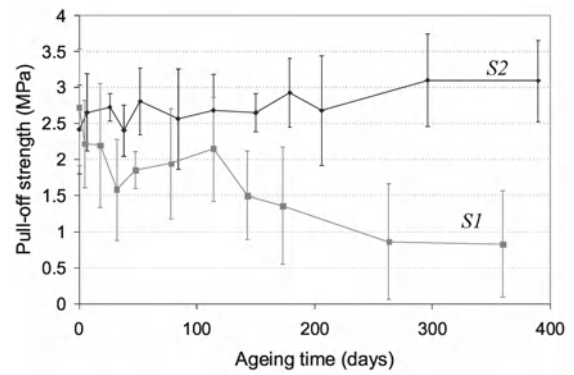


Figure 5 Evolution of the pull-off strengths versus ageing time for specimens strengthened by CFRP systems *S1* and *S2*

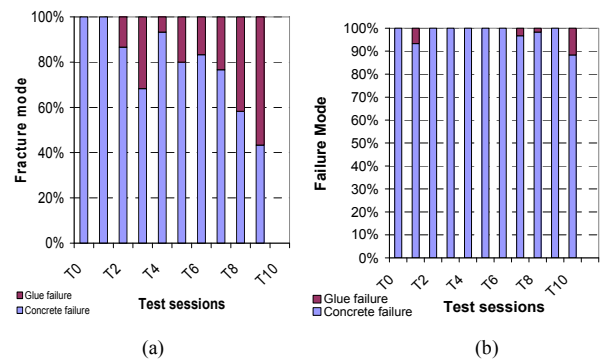


Figure 6 Evolution of the failure mode for specimens of type *S1* (a) and *S2* (b) after pull-off tests

4.2 Single-lap shear tests

Figures 7 and 8 display respectively the evolutions of the maximum shear loads and failure modes for ageing specimens of type *S1* and *S2*.

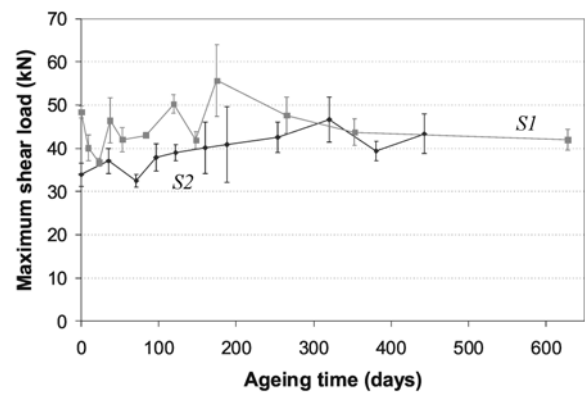


Figure 7 Evolution of the maximum shear load versus ageing time for specimens strengthened by CFRP systems *S1* and *S2*

Failure mode of the shear tested interfaces evolved for both systems *S1* and *S2*, from a concrete failure toward a failure within the glue layer. This is consistent with a deterioration of the glue properties after ageing, as shown previously on samples of the bulk epoxies. Surprisingly, no significant evolution of the maximum shear load was obtained for the two systems, despite the

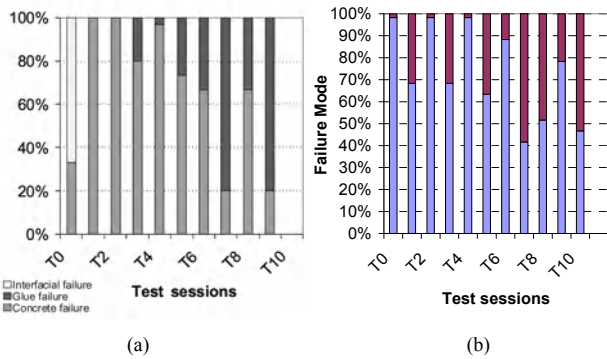


Figure 8 Evolution of the failure mode for specimens of type *S1* (a) and *S2* (b) after single lap shear tests

change in the fracture mode. Complementary data provided by a strain gage instrumentation revealed that the shear load transfer along the joint is affected by ageing (increase of the transfer length due to the plasticization of the glue), which might explain the unchanged shear capacity.

Another point is the divergence between the pull-off and shear test results. The pull-off method clearly showed a deterioration of the adhesive bond characteristics for system *S1* (based on glue *Epo1*, which undergoes a large plasticization during ageing), but not for system *S2*. Differently, the shear test revealed a marked evolution of the failure mode for the 2 systems, suggesting bond deterioration in both cases.

It is believed that the pull-off test is less sensitive than the shear test to ageing induced changes in the adhesive bond properties.

5 FINITE ELEMENT MODELING

Finite element approaches were then implemented using CESAR-LCPC software (CESAR 2010), in order to confirm some of the experimental trends.

5.1 Modeling of the pull-off test

In a first step, a modeling of the pull-off configuration (not detailed here) showed that the test is not based on a pure tensile loading of the bonded joint, and revealed local stress concentrations within the substrate due to the partial coring of concrete around the test zone. This finding supports that the pull-off test might exhibit a low sensitivity to actual changes in the bond properties.

5.2 Modeling of the single lap shear configuration

A modeling was finally proposed in order to simulate the single lap shear test in the case of a non aged CFRP reinforced specimen (considering a glue layer with a pure elastic behavior) or an aged specimen (with an elasto-plastic behavior of the glue similar to that of *Epo1* after ageing).

Simulations confirmed the increase in the load transfer length for the aged specimen due to the plastic deformation of the polymer adhesive, and pointed out a

better diffusion of the shear stress within the aged specimen, as shown in Figure 9. These findings are consistent with experimental observations.

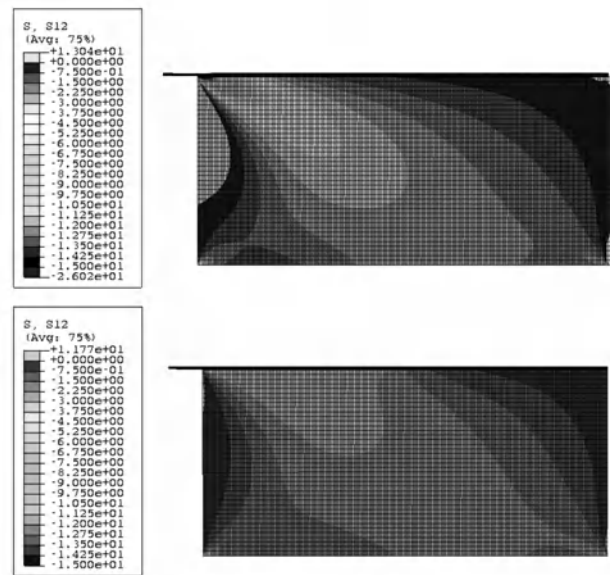


Figure 9 Representation of the stress field within a shear tested CFRP reinforced specimen. Results in the initial state (a) and after ageing (b)

6 CONCLUSION

In this work, ageing behaviors of two FRP strengthening systems based on pultruded carbon plates have been investigated. Ageing conditions consisted in exposing specimens at 40°C and 95% RH.

Investigations on the bulk materials revealed that both adherents (concrete, carbon plates) did not notably evolve during ageing, whereas epoxy adhesives underwent more or less severe plasticization effects depending on their formulation.

Adhesive bond characterizations relied on pull-off and single lap shear tests. It was found that results of the two methods were not always correlated. The shear test revealed a clear evolution of failure modes for the 2 FRP plate systems. The weakest part of the assembly, initially assigned to the concrete substrate, became progressively the polymer joint. A strain gage equipment made it possible to detect a major change in the load transfer mechanism along the joint (increase in the transfer length). These findings were finally supported by finite element simulations.

REFERENCES

- CESAR-LCPC website. 2010. <http://www.cesar-lcpc.com>
- Chataigner, S. Caron, J.F. Benzarti, K. Quiertant, M. & Aubagnac, C. 2009. Characterization of composite to concrete bonded interface: Description of the single lap shear test. *Eur. J. Environ. Civ. Eng.* 13 (9):1073-1082.

- Cognard, J. 2006. Some recent progress in adhesion technology and science. *Comptes-Rendus de Chimie* 9: 13-24.
- EN 1542. 1999. Products and systems for the protection and repair of concrete structures. Test methods. Measurement of bond strength by pull-off.
- Gangarao, H. Taly, N. & Vijay P.V. 2006. *Reinforced concrete design with FRP composites*. Taylor & Francis, CRC Press.
- Grace, N.F & Singh, S.B. 2005. Durability Evaluation of Carbon Fiber-Reinforced Polymer Strengthened Concrete Beams: Experimental Study and Design, *ACI Structural Journal* 102 (1): 40-51.
- Hamelin, P. 2002. Renforcement des ouvrages d'art par matériaux composites. *Tech. de l'Ingénieur* AM5615: 1-10.
- Karbhari, V.M. & Abanilla, M.A. 2007. Design factors, reliability, and durability prediction of wet layup carbon/epoxy in external strengthening. *Composites: Part B* 38: 10-23.
- Karbhari, V.M. Chin, J.W. and al. 2003. Durability gap analysis for fiber-reinforced polymer composites in civil infrastructure. *J. of Composites for Construction* 7(3): 238-247.
- Marouani, S. Curtil, L. & Hamelin, P. 2008. Composites realized by hand lay-up process in civil engineering environment: initial properties and durability. *Materials and Structures* 41(5): 831-851.
- NF EN 12390-3. 2003. Testing hardened concrete. Part 3: Compressive strength of test specimens.
- Pendari, S.S. Kant, T. & Desai, Y.M. 2008. Application of polymer composites in civil construction: A general review. *Composite structures* 84: 114-124.
- Silva, M.A.G. & Biscaia, H. 2008. Degradation of bond between FRP and RC beams. *Compos. Struct.* 85: 164-174.
- Yang, Q.A. Xian, G.J. & Karbhari, V.M. 2008. Hygrothermal ageing of an epoxy adhesive used in FRP strengthening of concrete. *J. of Applied Polymer Science* 107(4): 2607-2617.

Fire, Impact and Blast Loading

Parametric Analysis for Creep of High-Strength Concrete Columns Confined by AFRP

Yishuo Ma & Yuanfeng Wang (cyfwang@bjtu.edu.cn)

School of Civil Engineering, Beijing Jiaotong University, Beijing, China

ABSTRACT This paper investigates the effect of various material and geometric parameters on the creep of axially loaded fiber-wrapped high-strength concrete column (FWHSCC). For this purpose, a total of twenty-eight FWHSCCs, classified into nine groups, with different intrinsic factors such as the type and amount of fiber reinforced polymer (FRP), the creep of FRP, the water-cement ratio, the aggregate-cement ratio, the silica fume content and the compressive strength of high-strength concrete (HSC) core, and extrinsic factors including the level of loads applied to columns and the radius of column section, were analyzed by the model for predicting the creep of FWHSCC. The results of this parametric study indicate that the creep of FWHSCC is mainly affected by the composition and compressive strength of the concrete core, while the others only have slight influence on the compliance function of creep of FWHSCC.

1 INTRODUCTION

Wrapping fiber reinforced polymer (FRP) around high-strength concrete (HSC) columns is a structural technique employed for new constructions and restorations of existing buildings. While the short-term behavior of FRP wrapped concrete columns is studied intensively, concerns on long-term behavior, especially for FRP wrapped HSC column (FWHSCC), are limited.

Directed at gaining improved understanding of the properties of FWHSCC under sustained axial load, this paper investigates the contribution of nine parameters on the creep of FWHSCC. Nine groups of twenty-eight FWHSCCs with different intrinsic and extrinsic factors were analyzed by the model for the creep of FWHSCCs (Wang & Ma unpubl.).

2 CREEP MODEL FOR AXIALLY LOADED FWHSCC

In summary, the creep model for axially loaded FWHSCC is developed by incorporating the creep models for HSC and FRP into the mechanical equilibrium and strain compatibility in the composite section, and considering the confinement effect and the interaction stress history. The development of the FWHSCC creep model consists of two steps: short-term (static) and long-term (creep) analyses.

Short-term analysis is based on the mechanical characteristic of concrete core bearing the entire axial load, the geometric compatibility condition of the hoop strain in FRP being equal to the radial strain in concrete, and the axial stress-strain relationship for circular

concrete columns confined by FRP developed by Teng et al. (2002). The axial and radial strains of concrete and the lateral confining pressure at the moment of loading can be determined through the short-term analysis.

Long-term analysis turns complex since both HSC and FRP have creep behaviors and their creep properties are different. The confining pressure results from the concrete core pushing out against the AFRP wraps. Clearly, the extent to which the concrete core and the FRP deform in hoop direction compatibly under the sustained load is an important determinant of the lateral pressure capable of being mobilized. The lateral confining pressure so induced, therefore, must vary constantly over time within the long-term deformation process.

Long-term analysis for the creep of FWHSCC involves the modified Model B3 for HSC (Wang & Ma unpubl.), the autogenous shrinkage model for HSC (Mazloom et al. 2004, Mazloom 2008), the power law for FRP (Findley 1960), the effective creep Poisson's ratio of concrete (Zhong 1994), the calculating approaches for the creep of concrete under triaxial variable stresses (Gopalakrishnan et al. 1970) and creep of FRP under an uniaxial variable stress (Findley 1960), and the conditions of static equilibrium for stress increment and geometric compatibility for total strain at any time (Wang & Ma unpubl.).

3 EFFECTS OF INTRINSIC FACTORS ON CREEP OF FWHSCC

In order to investigate the effect of the type and amount of FRP, the creep of FRP, the water-cement ratio,

aggregate-cement ratio, silica fume content, and compressive strength of concrete core on the creep of axially loaded FWHSCC, seven groups of specimens were analyzed with the model for the FWHSCC creep. The diameters of all the specimens are 150mm, and the heights are 450mm. At the age of 28 days, all the specimens were subjected to a sustained compressive stress of 21MPa which corresponded to the stress-strength ratio of 20~30%.

Tables 1 and 2 present the type and number of layers (n_{FRP}) of FRP in Groups A and B, and the material parameters of FRP respectively. Composition of the HSC cores in the two groups is identical. The content of cement, water, aggregate and silica fume are 470.5kg/m^3 , 155kg/m^3 , 1691.75kg/m^3 and 83.04kg/m^3 respectively, and the measured 28-day cube compressive strength is 76.2N/mm^2 . Figures 1, 2 show the compliance functions of creep $J(t, t')$ of the two groups of FWHSCCs with different types or n_{FRP} of FRP. It is clear there is little or no effect of the type and amount of FRP on the creep of FWHSCC. Therefore, in the following analyses, two layers of AFRP laminates can be selected representatively as the jacket for all FWHSCCs.

Table 1 Type and number of layers of FRP in Groups A and B

Groups	Specimens	Types of FRP	n_{FRP}
A	A1	AFRP	2
	A2	CFRP	
	A3	GFRP	
B	B1	AFRP	1
	B2		2
	B3		3

Table 2 Material parameters of FRP

Material parameters	AFRP	CFRP	GFRP
Elastic modulus (MPa)	118,000	230,000	75,000
Tensile strength (MPa)	2006	3430	1800
Thickness per layer (mm)	0.286	0.167	0.169

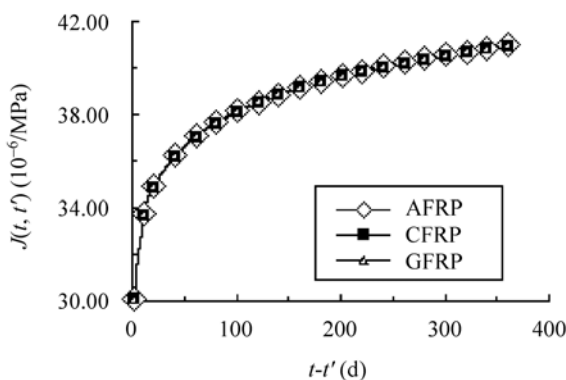


Figure 1 $J(t, t')$ of FWHSCCs with different FRP

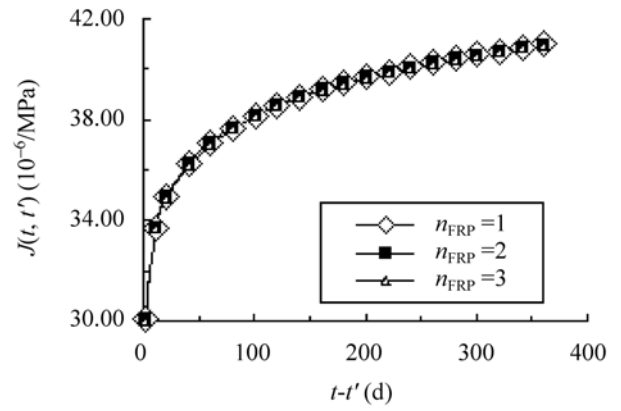


Figure 2 $J(t, t')$ of FWHSCCs with different n_{FRP}

The influence of FRP creep upon FWHSCCs is investigated in Group C. Details are given in Table 3. Figure 3 presents the curves of $J(t, t')$ of FWHSCCs under the condition of considering FRP creep or not. For the same FWHSCCs, $J(t, t')$ calculated under the condition of not considering FRP creep are lower slightly than that calculated under the condition of considering FRP creep. Accordingly, in order to simplify the calculating procedure, FRP can be regarded as an elastic material without creep when calculating the compliance function of creep of FWHSCC.

The water-cement ratio (w/c), aggregate-cement ratio (a/c) and silica fume content (s) of the concrete cores in Groups D, E and F are shown in Table 4. Figures 4–6 illustrate $J(t, t')$ of the three groups of FWHSCCs with different parameters.

Table 3 Details of FWHSCCs in Group C

Specimens	C1	C2	C3	C4
Cement (kg/m^3)	470.5	470.5	451.6	451.6
Aggregate (kg/m^3)	1691.75	1691.75	1689.87	1689.87
Water (kg/m^3)	155	155	170	170
Silica fume (kg/m^3)	83.04	83.04	79.69	79.69
$f_{cu, 28}$ (N/mm^2)	76.2	76.2	73.0	73.0
Considering FRP creep or not	No	Yes	No	Yes

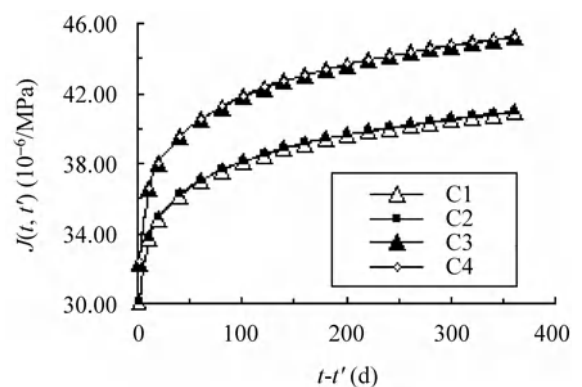


Figure 3 $J(t, t')$ of FWHSCCs involving FRP creep or not

Table 4 Composition of concrete cores in Groups D, E and F

Groups	Specimens	c (kg/m ³)	w/c	a/c	s (kg/m ³)
D	D1	470.5	0.27	3.6	83.04
	D2		0.30		
	D3		0.33		
	D4		0.36		
E	E1	470.5	0.33	2.6	83.04
	E2			3.6	
	E3			4.6	
	E4			5.6	
F	F1	470.5	0.33	3.6	78.04
	F2				83.04
	F3				88.04
	F4				93.04

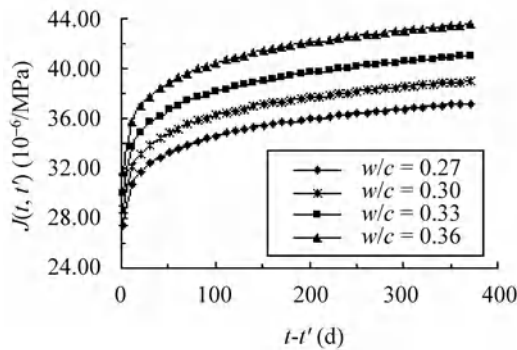


Figure 4 $J(t, t')$ of FWHS CCs with different w/c

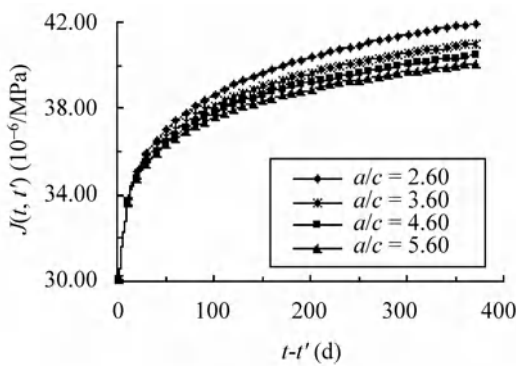


Figure 5 $J(t, t')$ of FWHS CCs with different a/c

As shown in Figure 4, the general effect of increasing w/c is to increase $J(t, t')$ of FWHS CC. With w/c of 0.27, 0.30, 0.33 and 0.36, the percent increases of $J(t, t')$ at the age of 370 days are 4.78%, 5.28% and 6.11% from D1 to D4. Figure 5 indicates that when w/c and s remain constant, increasing a/c decreases $J(t, t')$. With a/c of 2.6, 3.6, 4.6 and 5.6, from E1 to E4, the percent decreases of $J(t, t')$ at the age of 370 days are 2.16%, 1.37% and 0.95%. Figure 6 demonstrates there is an obvious decrease in $J(t, t')$ at high levels of silica fume content. With the silica fume of 78kg/m³, 83kg/m³, 88kg/m³ and

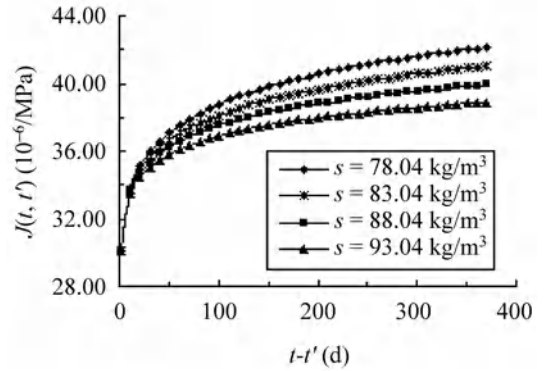


Figure 6 $J(t, t')$ of FWHS CCs with different s

93kg/m³, at the age of 370 days, the percent decreases of $J(t, t')$ are 2.67%, 2.65% and 2.64% from F1 to F4. Therefore, it is important to consider the noticeable effect of concrete composition on the creep of FWHS CC.

Besides, for studying the effect of compressive strength of concrete core on the creep of FWHS CC and comparing the creep of FWHS CC with that of FRP wrapped normal strength concrete column (FWNSCC), $J(t, t')$ of three specimens in Group G with different 28-day cube compressive strengths of concrete core ($f_{cu,28}$) are calculated, as shown in Figure 7. Details of the concrete cores in Group G are shown in Table 5. Among the three specimens, the concrete core of G3 is normal strength concrete (NSC) without silica fume. Hence, the calculation for G3 is based on Model B3 (Bažant & Baweja 2000) in the framework of the analytical model for the creep of FRP-wrapped concrete columns.

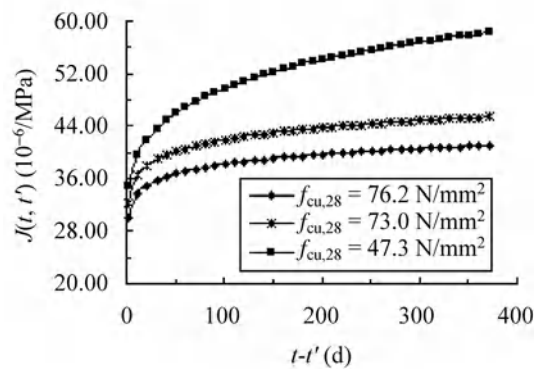


Figure 7 $J(t, t')$ of FWHS CCs with different $f_{cu, 28}$

Table 5 Composition and $f_{cu, 28}$ of concrete cores in Group G

Specimens	G1	G2	G3
Cement (kg/m ³)	470.5	451.6	394.7
Aggregate (kg/m ³)	1691.75	1689.87	1874.67
Water (kg/m ³)	155	170	150
Silica fume (kg/m ³)	83.04	79.69	0.00
$f_{cu, 28}$ (N/mm ²)	76.2	73.0	47.3

Figure 7 shows that the compressive strength of concrete core affects $J(t, t')$ considerably. As $f_{cu,28}$ decreases, $J(t, t')$ increase in evidence. When $f_{cu,28}$ of concrete cores are 76.2MPa, 73.0MPa and 47.3MPa, the percent increases of $J(t, t')$ are 10.54% and 28.41% at the age of 370 days from G1 to G3. Figure 7 also illustrates that for FWHS CCs containing silica fume, the curves of $J(t, t')$ remain almost stable in the later period of loading. Compared with FWNSCC without silica fume, this phenomenon appears more prominent. It is clear silica fume has an important influence on reducing creep.

4 EFFECTS OF EXTRINSIC FACTORS ON CREEP OF FWHS CC

Creep of two groups (Groups H and I) of FWHS CCs made out of the same concrete with the variable parameter of f_c/f'_{cc} or r are studied, where f_c is the axial stress applied on FWHS CC, f'_{cc} is the compressive strength of FWHS CC and r is the radius of concrete core. The parameters used in Groups H and I are listed in Table 6. The composition of HSC cores in Groups H and I is identical to that used in Groups A and B. Figures 8, 9 demonstrate that f_c/f'_{cc} and r do not obviously affect $J(t, t')$ of FWHS CCs. In fact, $J(t, t')$ of the three FWHS CCs with different f_c/f'_{cc} or r in each group are basically the same.

Table 6 Parameters f_c/f'_{cc} and r used in Groups H and I

Groups	Specimens	f_c/f'_{cc}	r (mm)
H	H1	20%	75
	H2	30%	
	H3	40%	
I	I1		55
	I2	20%	75
	I3		95

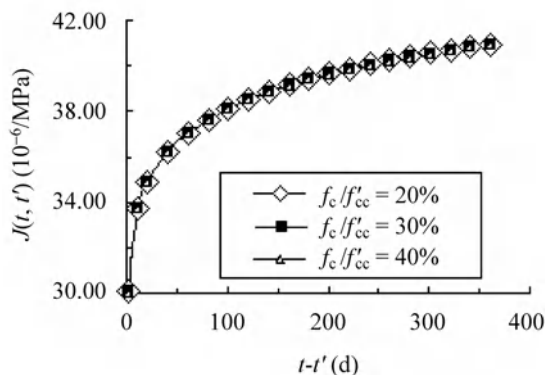


Figure 8 $J(t, t')$ of FWHS CCs with different f_c/f'_{cc}

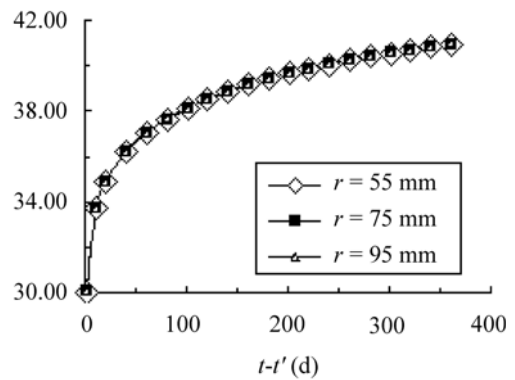


Figure 9 $J(t, t')$ of FWHS CCs with different r

5 CONCLUSIONS

From the analysis about the effect of intrinsic and extrinsic factors on the creep of FWHS CC, the main conclusions are:

- The type and amount of FRP, and the creep of FRP have little or no effect on the creep of FWHS CC.
- There is an important influence of the composition and compressive strength of concrete core on the creep of FWHS CC. As water-cement ratio increases, or aggregate-cement ratio, silica fume content, and compressive strength of concrete decrease, the compliance function of creep of FWHS CC increase obviously.
- There exists a great difference between the creep of FWHS CC and FWNSCC. The creep of FWNSCC grows rapidly during the later period of loading, while that of FWHS CC develops slowly. The supplementary binder of silica fume reduces the creep of FWHS CC obviously during the later period.
- The effects of the axial stress level and the radius of column section on the creep of FWHS CC are negligible.

REFERENCES

Bazant, Z.P. & Baweja, S. 2000. Creep and shrinkage prediction model for analysis and design of concrete structures: Model B3. In Al-Manaseer, A. (ed.), *Creep and shrinkage-Structural design effects; Adam Neville symp., Michigan, 2000*.

Findley, W.N. 1960. Mechanism and mechanics of creep of plastics. *SPE journal* 16(10): 57-65.

Gopalakrishnan, K.S., Neville, A.M. & Ghali, A. 1970. A hypothesis on mechanism creep of concrete with reference to multiaxial compression. *ACI Journal Proceedings* 67(1): 29-35.

Mazloom, M., Ramezani-pour, A.A. & Brooks, J. J. 2004. Effect of silica fume on mechanical properties of high-strength concrete. *Cement and Concrete Composites* 26(4): 347-357.

Mazloom, M. 2008. Estimating long-term creep and shrinkage of

- high-strength concrete. *Cement and Concrete Composites* 30(4): 316-326.
- Teng, J.G., Chen, J.F., Smith, S.T. & Lam, L. 2002. *FRP-Strengthened RC Structures*. Chichester: John Wiley and Sons.
- Wang, Y.F. & Ma, Y.S. unpubl. Creep of high-strength concrete columns confined by AFRP under axial load. *Submitted to Advances in Structural Engineering*.
- Zhong, S.T. 1994. *Concrete-Filled Steel Tubular Structures*. Harbin: Heilongjiang Science and Technology Press..

Glassy-Rubbery Transition Behavior of Epoxy Resins Used in FRP Structural Strengthening Systems

Anurag Jaipuria¹, Jeffrey P. Flood², Charles E. Bakis¹ (cbakis@psu.edu), Maria M. Lopez², & Xiongjun He³

¹ Department of Engineering Science and Mechanics, Pennsylvania State University, USA

² Department of Civil and Environmental Engineering, Pennsylvania State University, USA

³ School of Transportation, Wuhan University of Technology, China

ABSTRACT The glass transition behavior of five different epoxies, commercially available as primers and saturants for FRP strengthening systems, have been investigated using dynamic mechanical analysis. Glass transition temperatures, T_g , were assigned using three methods: storage modulus onset, loss modulus peak, and $\tan \delta$ peak. Based on the T_g values, a comparison of the five epoxies as well as the three different methods of T_g assignment were made. It was observed that post-curing during the DMA test procedure can have a dramatic effect on the glass transition behavior, with T_g values increasing up to 22°C on two short exposures to the maximum test temperature. For a given product, the difference in T_g values as a function of test method ranged from 12°C to 42°C on the first thermal cycle. Two T_g values were observed for one of the products, indicating the presence of secondary polymer as a blend or copolymer. Epoxy polymers used as saturants showed a higher transition temperature than those used as primers and adhesives.

1 INTRODUCTION

Over the past two decades, FRP (fiber reinforced polymer) strengthening systems have evolved as a viable alternative to conventional strengthening techniques. With the continuous development of design guidelines for FRP strengthened structures (e.g., ACI 2008, CAN/CSA-S806-02 2007, CECS 146 2003), there has also been interest in the high temperature capability of these strengthened structures.

Preliminary durability studies conducted at Penn State University on notched plain concrete beams with externally bonded carbon FRP (CFRP) tensile reinforcement under a constant flexural load of about 50% of the fiber ultimate showed a catastrophic de-bonding mode of failure at the epoxy/concrete interface in the ambient summer weather (~40°C surface temperature and ~80% relative humidity) following 1 to 6 days of exposure (Bakis, 2008). The reduction in physical properties of epoxy resins over a temperature range associated with the so-called glass transition temperature, T_g , was suspected to be the cause of the loss of bond strength. It is therefore critical to understand the bond behavior FRP bonded to concrete at elevated temperatures and sustained loads. To do this, an important first step is to understand the mechanical properties of the epoxy polymer at elevated temperatures and the transition between glassy and rubbery behavior at T_g .

This paper describes an experimental investigation of the T_g of five different commercially available resins

used as adhesives and matrices in FRP strengthening systems. The specific objective is to determine the T_g following a “maximum likely” cure temperature that might be seen in the field and also the T_g following a short exposure to an even higher temperature to observe the maximum T_g potential of the materials.

The glass transition phenomenon is observed by measuring electrical, mechanical, thermal, or other physical properties which change significantly over the transition temperature range. For example DSC (differential scanning calorimetry) assigns T_g based on changes in specific heat capacity; TMA (thermo-mechanical analysis) assigns T_g based on changes in coefficient of thermal expansion, and DMA (dynamic mechanical analysis) assigns T_g by measuring changes in the dynamic stress-strain behavior.

In the current study, DMA was chosen for investigating T_g because of the ease with which this method depicts the T_g and because of the dependence of the results on the stress-strain behavior of the polymer, which in the authors' opinion is closely related to the mechanical performance capability of the polymer at elevated temperatures.

2 EXPERIMENTAL PROGRAM

2.1 Materials

The five resin products selected for investigation are two-component epoxies that are commercially available

as primers, adhesives, and saturants for FRP strengthening systems. Epoxy-based polymers are thermosetting polymers having a cross-linked structure after curing. The identification codes and functions of the products are listed in Table 1.

Table 1 Products investigated

Product	Function
MBP	Primer for substrate.
MBS	Fiber saturant or adhesive.
TS	Fiber saturant.
TTC	Tack coat for vertical and overhead surfaces.
S30	Adhesive. Suitable for vertical and overhead surfaces. Contains calcium carbonate and silica.

2.2 Specimen preparation

The materials were all mixed according to the manufacturers' recommended procedure. DMA specimens were approximately 30 mm long, 5 mm wide and 0.2 mm thick. Since the specimens were only 0.2 mm thick, maintaining a uniform thickness and minimizing voids took on extra importance.

Materials of relatively low viscosity (TS, MBP, and MBS) were molded between two spray-release-coated aluminum plates held together by two layers of 0.1-mm-thick double sided tape as shown in Figure 1. These plates were submerged inside a polytetrafluoroethylene (PTFE) container filled with the material and then degassed in a vacuum chamber.

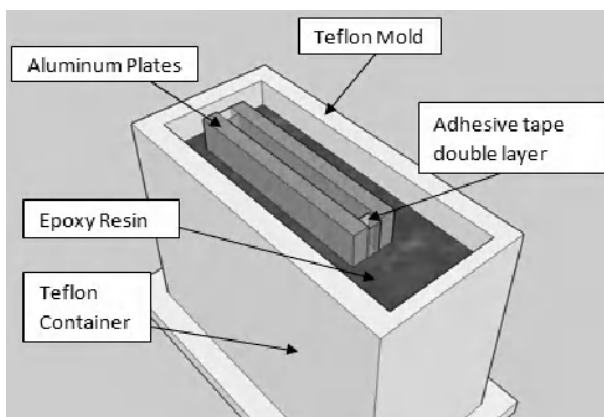


Figure 1 Schematic diagram showing arrangement of sheet mold for low viscosity epoxy resins

Higher viscosity materials (TTC and S30) were compressed into open PTFE sheet molds using plastic spatulas and two layers of 0.1-mm tape to form sides in order to maintain a uniform thickness. After the molds were filled with liquid resin, the entire setup was placed and leveled in an oven and set at the cure temperature of 50°C. This temperature was selected as an upper-bound cure temperature that might be experienced in the field

with these materials, without consideration of the manufacturers' recommended cure temperatures. The materials were left in the oven to cure for 7 days. Following de-molding, the sheets of epoxy were surface-ground (no liquid coolant was used) to a uniform thickness where necessary, cut to size for the DMA, and stored in desiccators at 23°C for 14 days before testing commenced.

2.3 Instrumentation and test method

In this investigation, a TA Instruments Q800 dynamic mechanical analyzer was used in the tensile mode. The tests were run using a constant sinusoidal strain excursion of 0.05% and a loading frequency of 5 Hz. The T_g test sequence was determined according to ASTM E1640 (2004).

The specimens were equilibrated at -20°C and temperature was ramped at the rate of 3°C per minute until 120°C was reached. Three sequential heating/cooling cycles were run for each specimen to study the effect of post curing on T_g . A second set of specimens was tested with a minimum temperature of -50°C to investigate the presence of a second T_g which is discussed in the results.

When viscoelastic materials such as epoxy are loaded dynamically, the stress and strain are not perfectly in phase. The in-phase ratio of stress to strain is known as the storage modulus, E' , while the 90-deg. out-of-phase ratio is the loss modulus, E'' . As temperature increases through the transition from glassy to rubbery behavior, E' decreases dramatically as indicated by a change of E' vs. temperature slope. Likewise, E'' reaches a distinct local peak on the E'' vs. temperature plot. The loss factor (also known as $\tan \delta$), which is the ratio of the loss to the storage modulus, also peaks towards the upper end of the DMA T_g range. In the current investigation, the T_g has been assigned using each of the following three methods:

- Onset of decrease of the storage modulus, E' , versus temperature plot—i.e., the midpoint of the temperature range over which the rate of decrease of E' with increasing temperature dramatically increases.
- Peak of the loss modulus, E'' , versus temperature plot.
- Peak of the $\tan \delta$ versus temperature plot.

3 EXPERIMENTAL RESULTS

The variation of storage modulus, loss modulus and $\tan \delta$ with temperature are shown in Figures 2, 3 and 4, respectively, for one of the five products. In these figures R1, R2 and R3 represent three consecutive runs on the same specimen.

The construction lines used to find the storage modulus onset T_g are shown in Figure 2. Since the E' vs.

temperature curves are not perfectly linear before and after the transition, T_g determination by the E' onset

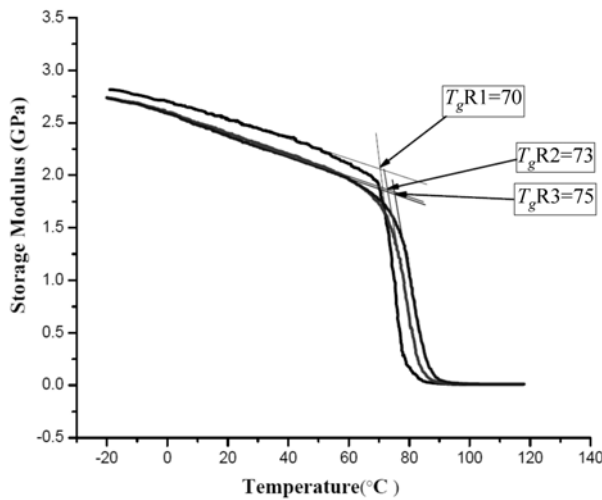


Figure 2 Storage modulus vs. temperature for TS-1

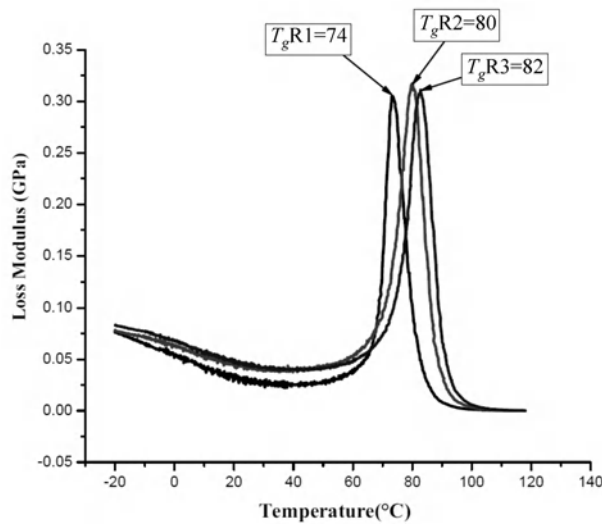


Figure 3 Loss modulus vs. temperature for TS-1

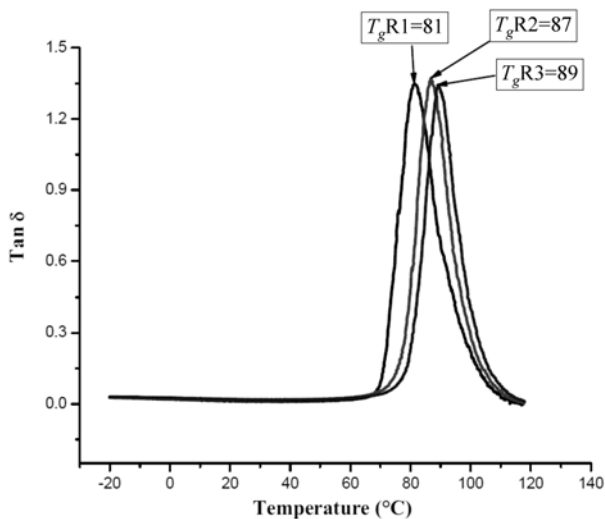


Figure 4 Tan δ vs. temperature for TS-1

method is prone to a certain degree of subjectivity. On the other hand, the E'' and $\tan \delta$ peaks are relatively easy to discern unambiguously. The E'' and $\tan \delta$ methods provide T_g values slightly greater than the midpoint of the temperature range over which transition in E' takes place. From the structural engineer's point of view, the E' onset T_g may be the more relevant temperature, rather than T_g determined by the peak of E'' or $\tan \delta$, at which the storage modulus has been diminished to almost half its value at the E' onset T_g .

The phenomenon of post-curing can be further observed from Figures 2–4 as the T_g increases with consecutive runs. This is because, as the specimen is exposed to a temperature higher than its cure temperature during the first run, previously unreacted polymer sites are able to cross-link owing to the available thermal energy. In the TS1 specimen shown in Figures 2–4, the increasing T_g after sequential DMA runs was easy to detect. This was not the case with all specimens. Across the five products, it is typical that the rubbery storage modulus is essentially nil in comparison to the glassy storage modulus.

The T_g values for different products based on storage modulus, loss modulus and $\tan \delta$ are summarized in Table 2. Specimens with a minimum run temperature of -20°C and -50°C have a suffix “-1” and “-2” respectively.

Table 2 Summary of assigned glass transition temperatures, T_g , in $^\circ\text{C}$

Specimen	E' onset			E'' peak			$\tan \delta$ peak		
	R1	R2	R3	R1	R2	R3	R1	R2	R3
MBP-1	*	69	73	59	73	77	69	90	93
MBP 2	36	47	54	50	62	69	69	89	91
MBS-1	72	68	69	79	81	83	92	97	98
MBS-2	72	68	64	78	82	83	91	96	99
TS-1	70	73	75	74	80	82	81	87	89
TS-2	66	70	74	70	78	80	79	85	88
TTC-1	68	65	67	73	75	78	80	83	90
TTC-2	69	65	70	72	74	76	79	83	85
S30-1	57	60	62	72	76	77	86	86	85
S30-2	45	*	*	55	*	*	87	*	*

*incomplete or erroneous run

Comparison of T_g values for the first run shows that, among saturants, MBS has a higher T_g compared to TS. It also shows that saturants, in general, have a higher T_g compared to primer and adhesive products. Based on the average T_g for the first run, the trend among all five products is: MBS $T_g >$ TS $T_g \approx$ TTC $T_g >$ S30 $T_g >$ MBP T_g . Specimen MBP2 shows a distinctly low T_g of 36°C based on storage modulus onset.

The TTC specimen tested with the lower minimum

sweep temperature of -50°C (TTC-2) showed two glass transitions—one at around -20°C and another at around 70°C (Figure 5). The lower T_g is believed to represent a second (more flexible) polymer either integrated into the epoxy network as a copolymer or blended as a distinct phase, while the upper T_g is believed to be the predominant epoxy constituent. Only the higher of the two T_g values for the TTC material is listed in Table 2.

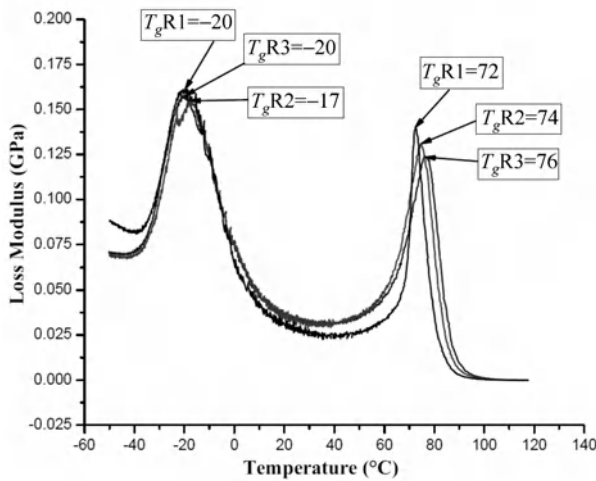


Figure 5 Loss modulus vs. temperature for TTC-2

4 CONCLUSIONS

The glass transition phenomenon was studied for five different epoxy resins used in commercial FRP strengthening systems. In general, saturants showed a higher T_g in comparison to primer and adhesive products. The T_g increased with multiple short exposures to a temperature in excess of the initial cure temperature of 50°C which was held for 7 days prior to testing. Most notable in this regard was the 22°C increase seen in the MBP epoxy according to the $\tan \delta$ peak method. While further investigation is needed to determine how quickly the T_g increases over time at various temperatures, a conservative outlook in design would employ the T_g found on the first DMA thermal excursion. As expected, the three DMA methods for assigning the T_g gave differing results. The lowest (most conservative) values were obtained by storage modulus onset and the highest

by $\tan \delta$ peak. On the first thermal cycle, the maximum difference in T_g values assigned according to the storage modulus onset and $\tan \delta$ peak methods ranged from as much as 42°C in the S30 system to as little $12\text{--}13^{\circ}\text{C}$ in the TTC and TS systems. Two T_g phenomena were observed in the TTC system, with the lower one believed to be evidence of a secondary polymer present as a copolymer or blend. Further investigation should include epoxies cured at lower temperatures which may be appropriate for certain FRP strengthening applications.

5 ACKNOWLEDGEMENTS

The authors gratefully acknowledge the financial support of the National Science Foundation through grant CMMI-0826461 and an REU supplemental grant. The authors would also like to thank the manufacturers for generously providing samples for testing: BASF Construction Chemicals, Fyfe Co., and Sika Corp.

REFERENCES

- ACI Committee 440. 2008. *Guide for the Design and Construction of Externally Bonded FRP Systems for Strengthening Concrete Structures*. ACI 440.2R-08. Farmington Hills: American Concrete Institute.
- ASTM Standard E1142. 2007. *Standard terminology relating to thermo physical properties*. In *Annual Book of ASTM Standards*. West Conshohocken: ASTM International.
- ASTM Standard E1640. 2004. *Standard test method for assignment of the glass transition temperature by dynamic mechanical analysis*. In *Annual Book of ASTM Standards*, West Conshohocken: ASTM International.
- Bakis, C.E. 2008. *Elevated temperature capability of epoxy resins: issues and developments*. In M. M. Lopez (ed.), *Proc. US-South America Workshop on Innovative Materials for Civil Infrastructure*, Research and Education, Santiago, Chile, 13-15 Oct. 2008. Washington DC: National Science Foundation.
- CAN/CSA-S806-02 R2007. 2007. *Design and Construction of Building Components with Fibre-Reinforced Polymers*. Mississauga: Canadian Standards Association.
- CECS 146. 2003. *Technical Specification for Strengthening Concrete Structure with Carbon Fiber Reinforced Polymer Laminate*. Beijing: China Planning Press (in Chinese).

Fire Tests on RC Beams Strengthened with NSM

A. Palmieri, S. Matthys & L. Taerwe (Aniello.Palmieri@ugent.be, Stijn.Matthys@ugent.be, Luc.Taerwe@ugent.be)
Magnel Laboratory for Concrete Research, Department of Struct. Eng., Gent University, Gent, Belgium

ABSTRACT The use of Near Surface Mounted (NSM) FRP for strengthening and rehabilitation of reinforced concrete structures has been the subject of various research projects in recent years. FRP strengthening systems are known to perform weak at elevated temperatures. This can be attributed to the relatively poor performance of both adhesive and FRP matrix polymers at temperatures in the range of their glass transition temperatures. Hence, there is a need for thermal protection of such elements. An investigation on the fire endurance of NSM FRP concrete beams under standard fire conditions was undertaken. Six reinforced concrete beam were strengthened in flexure with NSM bars and insulated with different insulation system. Temperatures and deflections were measured during fire testing. Test results indicated that insulated NSM FRP strengthened beams can achieve a fire endurance of at least two hours.

1 INTRODUCTION

In recent years Near Surface Mounted (NSM) FRP is becoming a promising technology for enhancing the flexural strength and shear resistance of deficient reinforced concrete (RC) and prestressed concrete (PC) members. It consists of placing the FRP reinforcing rebars or strips into grooves pre-cut into the concrete cover in the tension side of the strengthened concrete member filled with high strength adhesive (epoxy or mortar). While the structural behavior of RC members strengthened with NSM under normal environmental conditions is getting more and more documented, few researches are available on their behaviour at elevated temperature and under fire conditions. Of the constituent materials, the fibres in FRP materials perform significantly better at elevated temperatures than the polymer binder of these composites (Bisby et al. 2005). Indeed, the interaction between the glued composite bar and the concrete will be lost very quickly in a fire, due to weakening of the adhesive (epoxy resin), which has a low glass transition temperature, T_g (the T_g of epoxies are usually in the range of 50-100°C. Several studies on the high temperature properties of FRP are available in the literature (Blontrock et al. 1999; Bisby et al. 2005; Matthys et al. 2006; Kodur et al. 2007). They generally show that the material properties of FRPs can significantly deteriorate at relatively moderate increases in temperature. Beyond the T_g , the strength and stiffness of a polymer decreases rapidly.

Concerning the fire resistance of FRP strengthened elements (with fire protection) limited data has been reported in the literature. Furnace tests were carried out by Blontrock et al. 2001 on insulated slabs and beams strengthened with externally bonded carbon FRP, to

evaluate their fire endurance. The insulation schemes varied several parameters including protection thickness, location, method of bonding, and overall length. The main conclusion reached in this study is that thermal protection is required in order to maintain the interaction between the FRP and the concrete. Rein et al. 2007 performed fire test by using two different fire protection system: a paint intumescent coating and a gypsum board box. Two types of bonded FRP strengthening were used: EBR and NSM. The main conclusion was that the NSM strengthening system provided a better performance than the EBR strengthening system.

The current paper discusses one component of a larger study investigating the behaviour of NSM FRP strengthened and insulated members under fire conditions. In order to investigate the problem in more detail a test program on six beams protected with different thermal protection systems was performed at Ghent University. The fire protection was applied in different ways with respect to thickness and shape.

2 EXPERIMENTAL PROGRAMME

2.1 Tests specimens

The dimensions of the tested beams were: height of 300 mm, width of 200 mm and a length of 3150 mm. Figure 1 represents the geometry of the beams, the reinforcement arrangement and the number and position of the FRP bars or strips. The testing programme involved the design and fabrication of ten beams. Four reference beams (an unstrengthened one and three strengthened beams) were tested at room temperature (more details about reference beams in terms of test set-up, mechanical properties of concrete, properties of FRP and reinforcement application can be found in Palmieri et al. 2010).

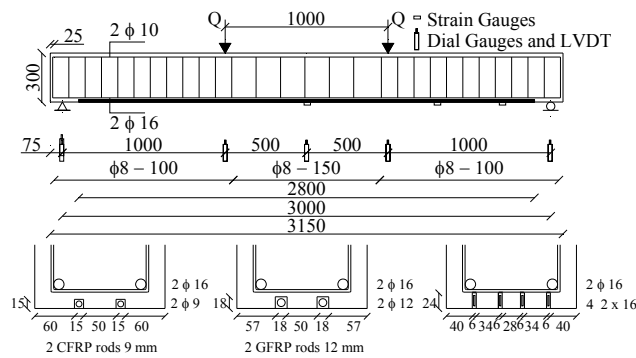


Figure 1 Test set-up reference beams

Six beams were tested in a fire test: one unprotected and unstrengthened beam and five protected and strengthened beams. An overview of the fire test matrix is given in Table 1 in terms of FRP reinforcement, FRP size D_f , concrete compressive strength f_c and age of testing.

Table 1 Test-matrix

Beam	FRP	D_f (mm)	Epoxy resin	f_c (MPa)	Age at testing (days)
B0-F1	–	–	–	48.0	111
B1-F1-1	Combar GFRP	12.0	Sikadur 30	50.0	109
B1-F1-2	Combar GFRP	12.0	Sikadur 30	50.0	109
B2-F1-1	Aslan 200 CFRP	9.0	Fortresin	48.0	111
B2-F1-2	Aslan 200 CFRP	9.0	Fortresin	49.0	105
B3-F1-1	Aslan 500 CFRP	2x16	Fortresin	49.0	105

Three passive fire protection systems were investigated: Aestuver (Xella), Promatect H (Promat) and Super VG system (Fyfe Co).

Aestuver is a cement-bonded glass-fiber fire protection board with a density of $\rho = 980 \text{ kg/m}^3$ and a thermal conductivity of $\lambda = 0.185 \text{ W/mK}$. Promatect H is a steam-hardened silicate plate with a density of $\rho = 870 \text{ kg/m}^3$ and a thermal conductivity of $\lambda = 0.164 \text{ W/mK}$. The third fire protection system is a two-component system. The insulation consisted of a layer of Super VG insulation (a lightweight fire resistant cementitious plaster), applied to the exterior of the specimen beam, along with an impermeable surface hardening topcoat (type EI-R). The fire system protections were applied to the beams for a total length of 2950 mm. Figure 2 provides the lay out of the different fire protection systems.

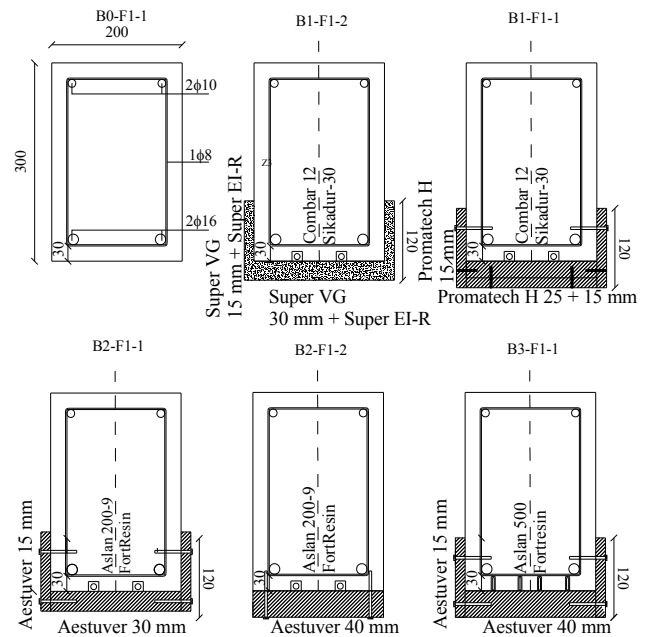


Figure 2 Lay out of protection system

Beam B1-F1-1 was protected with Promatect H fixed in a U shaped form. The thickness of the plate at the bottom was 40 mm (composed of two plates Promatect H with thickness 25 and 15 mm, stapled together), the thickness of the plates at the side faces of the element was 15 mm. The bottom plate was fixed with staples (with a distance of 200 mm) to the sideplates, that were mechanically fixed in the concrete with a spacing of 250 mm. Super VG on B1-F1-2 was manually applied (towed) to a thickness of 30 mm on the bottom and 15 mm to the sides. Beam B2-F1-1 was protected with Aestuver fixed in a U shaped form. The protection system was composed by two boards of 1400 mm length joined by an extra board of 150 mm length in the middle. The joints were closed by an intumescent strip (type Aestuver band DSB). The bottom plates (30 mm thick) were connected by screws to the side plates (thickness of 15 mm) that were mechanically fixed in the concrete with a spacing of 250 mm. Beam B3-F1-1 had the same protection of beam B2-F1-1 but the bottom plate is 40 mm thick. Beam B2-F1-2 was protected with Aestuver plate (thickness 40 mm). As for the previous beams the protection system was composed by two boards of 1400 mm and one of 150 mm. The joints were closed by an overlap with an additional board (thickness 40 mm) of 300 mm. The bottom plates were mechanically connected to the concrete by screws with a spacing of 250 mm.

2.2 Test procedure fire tests

The beams were tested simultaneously in a horizontal furnace of 6 m long by 3 m wide. A reaction frame, by which the tested elements were supported, was placed above the furnace, the opening between the beams were closed by aerated concrete slabs. Therefore, the beams

were exposed to fire from below, and the top surface was exposed to ambient temperature. The beams were all placed in the transverse direction of the furnace (the clear span of the beams being 3.0 m). Fire testing standards require that structural elements need to resist only service loads during fire. Thus, before starting the fire tests beam B0-F1 was loaded to the service load of the un-strengthened beam ($Q_{sl} = 30,66$ kN), while the protected beams to the service load of the respective strengthened beams ($Q_{sl} = 40.73$ for beam B2-F1-1, B2-F1-2 and B3-F1-1 and $Q_{sl} = 36.22$ for beams B1-F1-1 and B1-F1-2). A calculation of the maximum service load was made in accordance to Eurocode 2. This load was kept constant during fire test. Per service load a separate hydraulic unit was used, so that the beams were loaded in 3 groups (B0-F1-1; B1-F1-1 and B2-F1-2; B2-F1-1, B2-F1-2 and B3-F1-1). The beams were unloaded when one of the beams connected to the same pump reach the span/deflection ratio of about 1/30 and/or when reaching a total time of 120 min for the fire tests. The fire test is executed according to ISO 834 (Fire Resistance: Test-Elements of Building Construction). This standard prescribes the heating by the combustion gases function of the time and is given by equation 1:

$$T_{gs} = T_0 + 345 \log_{10}(8t + 1) \quad (1)$$

Where T_{gs} = the temperature of the combustion gases [$^{\circ}\text{C}$], T_0 = the initial temperature [$^{\circ}\text{C}$] and t = the time [min]. Twenty thermocouples were placed inside the concrete at two different locations along the span of the beams. In each concrete section ten thermocouples were placed: one is placed at the bottom face of concrete beam, one on the FRP reinforcement, two are placed on the lower steel reinforcement, one at the unexposed surface and the remaining in the concrete section. An LVDT was located at the unexposed surface of each beam to measure the deflection at mid-span during testing.

3 TESTS RESULTS AND DISCUSSION

A number of small view ports were located around the furnace walls that allowed observations during fire tests. Time-deflection and time-temperature curves for the FRP reinforcement can be found in Figure 3.

Beam B0-F1-1 (unstrengthened and unprotected) was unloaded when the increase of deflection was about 52 mm, the temperature of the internal steel was about 570°C at that moment. At 20 minutes the fire protection system of beam B1-F1-2 fell off completely and cause a sudden increase of temperature at the FRP reinforcement. At 37 minutes a sudden increase of time-deflection denotes the reduced capacity of the epoxy adhesive to transfer bond stresses from the FRP reinforcement to the concrete, at that time the epoxy adhesive was not longer

protected. The unexpected behaviour of this fire protection system can be related to an incorrect preparation of the cementitious plaster during its application. Therefore the fire protection system did not possess sufficient bond adhesion to withstand fire exposure.

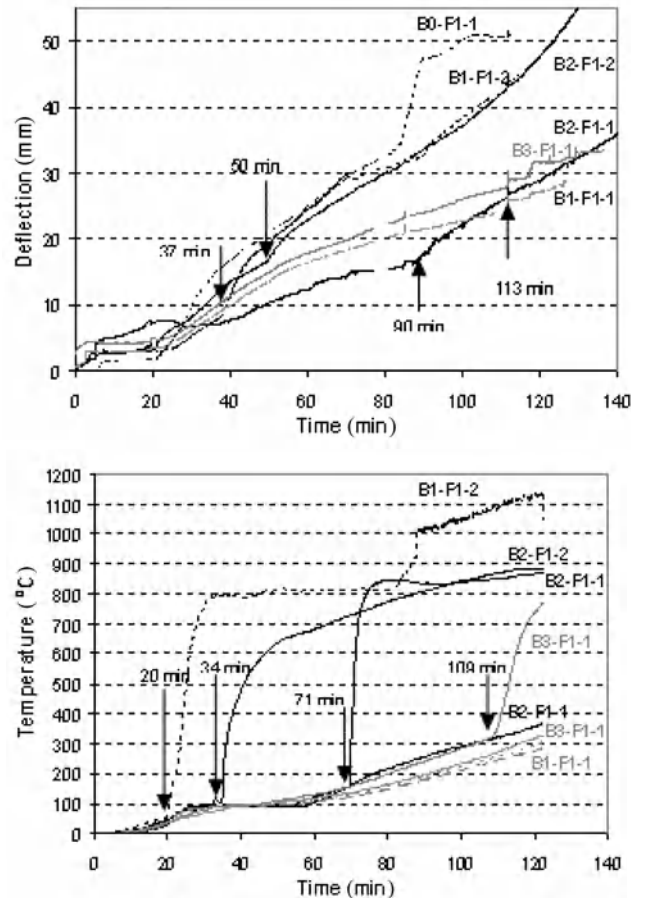


Figure 3 Time-deflection and time-temperature of FRP curves

In beam B2-F1-2 the quick increase of temperature of the FRP reinforcement after 34 minutes was caused by the protection plate that started to fall off the concrete beam. At 50 minutes flaming of bonding agent was observed and at same time also an increase in time-deflection curve was observed. After fire tests the FRP reinforcement was still in the grooves without showing any visual detachment.

Fire board protection of beam B3-F1-1 is the same of beam B2-F1-2 but additional boards with a thickness of 15 mm were provided at both sides along the entire length of the beam. In the first 113 minutes the midspan deflection increased slightly with increasing fire exposure time (no sudden increase of time-deflection curve was observed). The maximum midspan deflection was 30 mm. The intumescent strip, used to close the joints between the boards, performed well for the desired time of the fire test. The temperature in the FRP increased to 100°C within 38 minutes, followed by a constant temperature plateau lasting until 60 minutes, caused by

the evaporation of the free water in the concrete. After almost 2 hours of fire exposure, the maximum recorded FRP temperature was about 300°C (a sudden increase of temperature was observed in the section where the fire board fell off). Beam B2-F1-1 has the same fire protection system of beam B3-F1-1 but the bottom board thickness was reduced from 40 mm to 30 mm. Again a sudden increase of temperature in the FRP reinforcement was observed at 71 minutes when part of the protection board fell off, with a subsequent increase in time–deflection curve at 90 minutes. The maximum recorded temperature of the FRP in the protected side was about 300°C.

Time–deflection curve of beam B1-F1-1 increases slightly with increasing fire exposure time during fire test. The maximum midspan deflection was 29 mm. The maximum recorded temperature in the FRP was beyond 300°C. No damages to the fire protection board were observed at the end of the fire test.

4 CONCLUSIONS

Based on the results of fire tests discussed herein, the following conclusions can be made. Despite the higher service load of the strengthened beams, and despite the failure of fire protection of some beams, all beams appeared to withstand 2 hours of fire. The U shaped protection was more efficient in protecting the FRP reinforcement than the flat protection applied only on the bottom face of the beams. The insulation system maintained low temperatures in the beam such that they did not fail under service load levels during fire exposure. Further tests, at room temperature, on the fire exposed beams will be performed at Ghent University to study their residual strength.

5 ACKNOWLEDGEMENTS

The authors wish to acknowledge the support of the

FWO and the companies Hughes Brothers, Fortius, Schoeck, Promat, Xella and Fyfe for providing testing materials. Fire tests has been conducted in cooperation with Warrington Fire Ghent.

REFERENCES

- Bisby L., Williams B., Kodur V., Green M, Chowdhury E. 2005, Fire Performance of FRP Systems for Infrastructure: a state-of-the-art report. *Research report (IRC-IR-179)*, Institute for Research in Construction, National Research Council Canada, RR 179.
- Blontrock H., Taerwe L., Matthys S. 1999, Properties of Fibre Reinforced Plastics at Elevated Temperatures with Regard to Fire Resistance of Reinforced Concrete Members, *Fiber Reinforced Polymer Reinforcement for Reinforced Concrete Structures. American Concrete Institute*, Detroit, Michigan, pp. 43-54.
- Kodur, V., Bisby, L., Green, M. 2007, Preliminary guidance for the design of FRP strengthened concrete members exposed to fire, *Journal of Fire Protection Engineering*, v 17, February, pp. 5-16.
- Leone M., Matthys S., Aiello M.A. Effect of elevated service temperature on bond between FRP EBR system and concrete, *Journal Composites Part B: Engineering, Elsevier* (under publication).
- Blontrock H., Taerwe L., Vandeveldel, P. ,2001, Fire Testing of Concrete Slabs Strengthened with Fibre Composite Laminates. *In The Fifth Annual Symposium on Fibre-Reinforced-Plastic Reinforcement for Concrete Structures (FRPRCS-5). Edited by C. Burgoyne, Thomas Telford*, London, pp. 547-556.
- Rein G., Abecassis Empis C., Carvel R. 2007, The Dalmarnock Fire Tests: Experiments and Modelling, *Published by School of Engineering and Electronics*, University of Edinburgh.
- Palmieri A., Matthys S., Taerwe L., 2010, Strenghaghtening with Near Surface Mounted reinforcement: structural and fire behaviour, *proceeding of 3rd fib international congress*, Washington D.C., USA.

Fire Performance of Water-Cooled Cellular GFRP Columns

Yu Bai & Thomas Keller (thomas.keller@epfl.ch)

Composite Construction Laboratory (CCLab), Ecole Polytechnique Fédérale de Lausanne (EPFL), Lausanne, Switzerland

Erich Hugi & Carsten Ludwig

Swiss Federal Laboratories for Materials Testing and Research (EMPA), CH-8600 Dübendorf, Switzerland

ABSTRACT Structural fire endurance experiments were conducted on full-scale cellular glass fiber reinforced (GFRP) columns under axial compression and subjected to ISO 834 fire exposure from one side. Unprotected columns could resist fire for more than 30 min, which is sufficient for occupants to be evacuated from smaller buildings. The closed cellular cross section prevented the rapid heating of the webs, which could therefore continue stabilizing the face sheet on the cold side against buckling. Water cooling was proved to offer an effective active fire protection system. The structural function of the column could be maintained for two hours. Previously developed models were capable of predicting the time-dependent temperature responses, modulus degradation and time-to-failure.

1 INTRODUCTION

In recent years, fiber-reinforced polymer (FRP) composite materials have been increasingly considered particularly in bridge construction. In building construction, however, FRP composites have not yet met with the same success, although they also offer promising material properties for this application. Glass fiber-reinforced polymers (GFRPs), for instance, provide the added benefit of low thermal conductivity that enables GFRP load-bearing components to act as insulating elements (Keller et al. 2008). However, the polymer component of FRP composites is particularly sensitive to elevated and high temperatures and the fire performance of FRP structures for building applications thus requires special attention.

Investigations carried out on FRP laminates showed that mechanical properties (modulus and strength) degrade considerably at glass transition, a temperature range much lower than the decomposition temperature, T_d (Feih et al. 2007; Bai et al. 2008b). Especially in compression, FRP components are much more vulnerable because of early polymer softening and subsequent fiber buckling (Wong et al. 2004) or global buckling (Asaro and Dao 1997). Furthermore, full-scale structural fire endurance experiments (Keller et al. 2006) on cellular GFRP panels in a four-point bending setup and subjected to an ISO 834 fire from the underside (which was in tension), showed that failure occurred not on the (tensioned) fire side but on the (compressed) cold side at a temperature close to the glass transition temperature, T_g . The results confirmed that FRP structural components are much more sensitive to elevated and high temperatures

on the compression than on the tension side.

This work focuses on column or wall components (with both sides - also the fire side - in compression) and reports on the results (thermal responses, stiffness degradation, time-to-failure) obtained from cellular GFRP columns subjected to axial compression and an ISO 834 fire from one side. Both non-cooled and water-cooled specimens were investigated.

2 EXPERIMENTAL INVESTIGATION

2.1 Material and specimens

Three pultruded four-cell cross sections of the Dura Span[®] 766 system were used, which are composed of two face sheets and alternating vertical and inclined webs of different thicknesses. A detailed material description can be found in (Keller et al. 2006).

2.2 Experimental scenarios and set-up

Specimen NC was tested without any fire-protection measures up to failure. Specimens WC1 and WC2, subjected to one and two hours of heating, were equipped with a water-cooling system. Water circulated in the cells at a low flow rate of 2.5 cm/s. Figure 1 shows the experimental setup. First, an axial compressive load of 145 kN (corresponding to a uniform stress level of 5 MPa) was applied and kept constant during the subsequent thermal loading. Then the water flow (if used) was started. When all the flow meters and thermocouples gave stable values, thermal loading was applied following the ISO 834 fire curve until structural failure occurred or the planned time duration was attained.

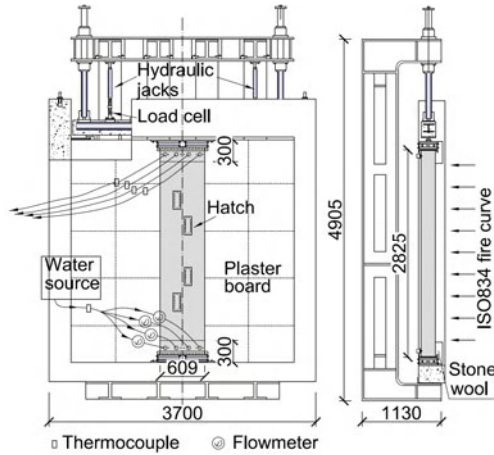


Figure 1 Experimental set-up and configuration of water cooling system

2.3 Instrumentation

Thermocouples were placed at different depths through the thickness and designated T1, T2, etc. Strain gages (S1, S2, etc.) were placed in the pultrusion direction on the outer face sheets and the two outside webs to measure the axial strains, as indicated in Figure 2.

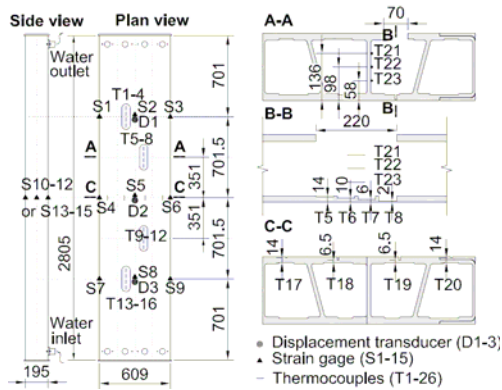


Figure 2 Specimen instrumentation

3 EXPERIMENTAL RESULTS

3.1 Non-cooled specimen NC

During the (pre-fire) mechanical loading, the lateral deflection at mid-height remained small: 1.4 mm towards the fire side. When fire exposure started (at time $t = 0$), lateral deflection towards the fire side started to increase due to the thermal expansion of the inner fire-exposed face sheet and reached a maximum of 8.1 mm after 20 min, see Figure 3. From this point on, lateral deflections started to decrease due to the loss of decomposed material on the inner face sheet, which moved the cross section's centroid towards the outer face sheet and resulted in an eccentricity that produced a deflection away from the fire side. Specimen ultimate failure occurred after 49 min at a lateral deflection of 2.0 mm towards the fire side.

The temperature progressions are shown in Figure 4. After less than 15 min the temperature through the whole inner face sheet exceeded T_g (117°C) and T_d was exceeded at the hot face, suggesting that the inner face sheet completely lost its stiffness and decomposition started at the hot face. At ultimate failure, approximately 70% (12 of a total of 16.8 mm) of the inner face sheet depth had reached a temperature of above 300°C and therefore decomposed.

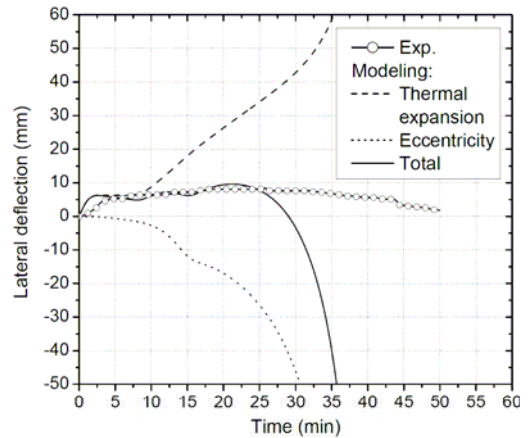


Figure 3 Measured mid-height lateral deflections with time and comparison to modeling results, non-cooled specimen NC

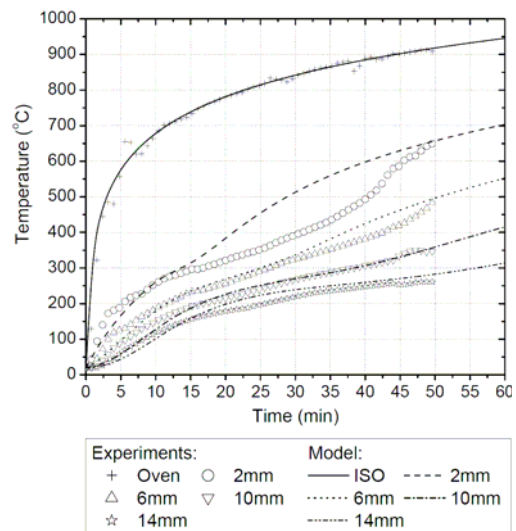


Figure 4 Temperature progression at different depths of inner face sheet of specimen NC and comparison to modeling results

3.2 Water-cooled specimens WC1 and WC2

The pre-fire mechanical responses of WC1 and WC2 were almost the same as for the NC specimen. Again similarly to the NC specimen, lateral deflections started increasing towards the fire side with increasing temperature and then decreasing after decomposition started on the hot face, as shown in Figure 5 for WC1 (WC2 results were similar). The maximum lateral deflection, however, was only approximately half that of NC specimen (4.8 mm for WL1 and 4.1 mm for WL2)

since decomposition was delayed by the water cooling. After approximately 15 min, the lateral deflection of WC1 stabilized at 4.2 mm (3.0 mm for WC2) and remained almost constant up until the end of the experiment (60/120 min for WC1/2).

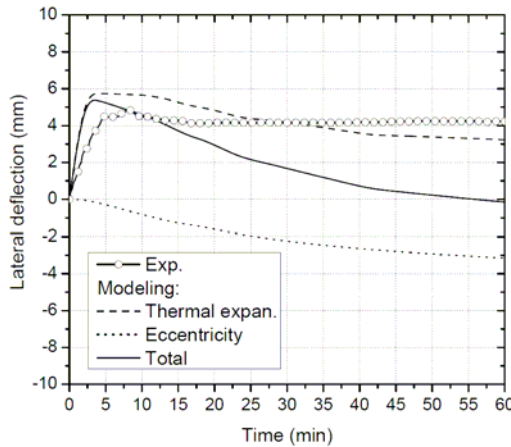


Figure 5 Measured mid-height lateral deflections with time and comparison to modeling results, water-cooled specimen WC1

The temperature progressions are shown in Figure 6 for WC2 (WC1 results were similar). The temperature development close to the hot face (at 2 mm remaining depth) was similar to that of the non-cooled specimen. A significant increase occurred after approximately 50 min close to the hot face (which was similarly visible in the NC specimen at 40 min) where the material was in the decomposition process and the resin above the first fiber layer almost burnt away. The easier heat transfer through this fiber layer might have caused this temperature increase. In contrast to specimen NC, the temperatures at the cold face of the inner face sheet (at 14 mm remaining depths of inner face sheet of WC2 and comparison to modeling results depth) clearly remained below T_g throughout the experiments (duration of up to 120 min).

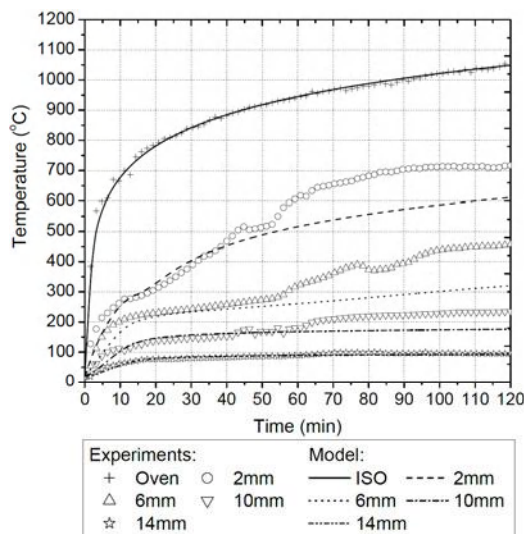


Figure 6 Temperature progression at different

4 MODELING RESULTS AND DISCUSSION

4.1 Temperature responses

To obtain the through-thickness thermal responses of the inner and outer face sheets, the one-dimensional thermal response model proposed by the authors in (Bai et al. 2008a) was applied. The NC modeling results are presented in Figure 4, while the WC2 results are shown in Figure 6. Generally, the predicted thermal responses compared well to the experimental results. The greatest differences were observed at the thermocouples closest to the hot face for layers where the resin had decomposed or was in the decomposition process. The subsequent significant temperature increase could not be captured in the model. The best predictions were obtained for layers below the glass transition temperature.

4.2 Time-dependent lateral deflection

During the thermal loading process, lateral deflections changed because of thermal expansion and load eccentricity resulting from the centroid shift due to material degradation. In view of the change of the non-dimensional specimen slenderness, second-order effects occurred.

Assuming the specimen as a hinged column, the time-dependent Euler buckling load $P_E(t_i)$ can be expressed as

$$P_E(t_i) = \frac{\pi^2 \cdot EI(t_i)}{L^2} \quad (1)$$

where L is the specimen height (2825 mm) and $EI(t_i)$ is the time-dependent effective bending stiffness of the specimen. Based on the thermomechanical property model presented in (Bai et al. 2008b), the shift of the neutral axis and the decrease of the Euler buckling load were obtained, see Figure 7.

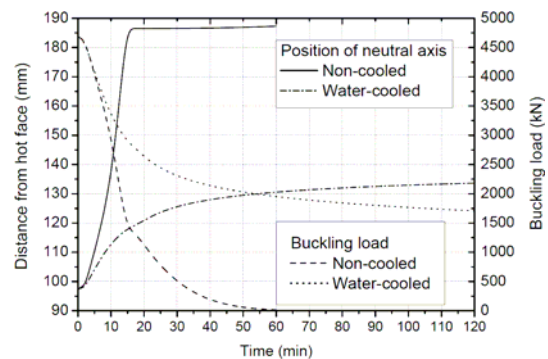


Figure 7 Modeling results for shift of neutral axis and decrease of Euler buckling load with time

Based on the predicted temperature gradients, the mid-height lateral second-order deflection due to thermal expansion $wT(t_i)$ at time step t_i was approached by:

$$w_T(t_i) = \frac{\lambda_{c,e}(t_i) \cdot L^2}{8} \cdot \left(\frac{\Delta T}{h} \right)_{t_i} \cdot \frac{1}{1 - P/P_E(t_i)} \quad (2)$$

where $\lambda_{c,e}(t_i)$ is the temperature-dependent effective coefficient of thermal expansion at time step t_i , and P is the applied compressive load.

Assuming that the compressive load always was uniformly distributed over the cross-section, the mid-height lateral second order deflection due to load eccentricity, $w_e(t_i)$, was estimated as follows:

$$w_e(t_i) = e_0(t_i) \left[\frac{1}{\cos\left(\left(\frac{\pi}{2}\right) \cdot \sqrt{P/P_E(t_i)}\right)} - 1 \right] \quad (3)$$

where $e_0(t_i)$ is the eccentricity at time t_i , corresponding to the shift of neutral axis from the initial position due to material degradation.

The calculated second-order lateral deflections due to thermal expansion and eccentricity are shown in Figure 3 for specimen NC and Figure 5 for WC1. The total lateral deflections were obtained by superposing both contributions. The total deflection agreed well with measurements of NC specimen during the first 25 min, but then, in contrast to the measurements, the predicted values greatly increased. For the WC specimen, only a moderately good agreement was found during the first 5-10 min and subsequently the measurements were underestimated. Several reasons may exist for these discrepancies. First of all, the lateral deflections were small, less than 10 mm for the NC and less than 5 mm for the WC specimens. In view of the scale of the experiments, the corresponding measurement accuracy and the complex processes which occurred during the fire exposure, it is difficult to accurately predict such small values. Furthermore, the slenderness of the NC specimen due to material loss largely increased. The corresponding amplification of small values due to second order effects can easily lead to large discrepancies. This may explain why the sharp increase of deflections was predicted to early, after 25 min and not after 49 min where failure occurred.

4.3 Time-to-failure

Figure 8 shows that, at ultimate failure, the buckling load of the non-cooled specimen approached the applied load. The 145 kN load level was reached after 43 min, which represents an underestimation of the measured time-to-failure (49 min) of 12%. The buckling load of the water-cooled specimens approached a value of 1007 kN, marked in Figure 8, which represents the buckling load of a specimen which completely lost one face sheet. After the maximum experimental duration (120 min), however, this critical load is still exceeded by almost 70%.

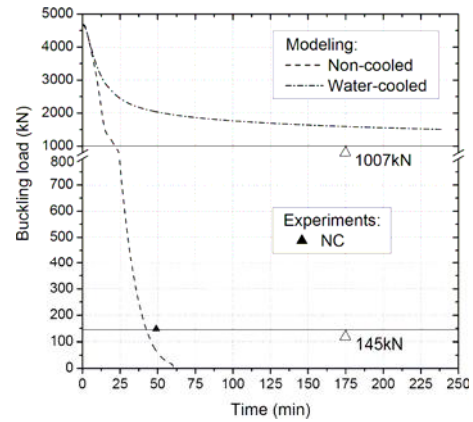


Figure 8 Modeling results for shift of neutral axis and decrease of Euler buckling load with time

5 CONCLUSION

Structural fire endurance experiments were conducted on full-scale cellular GFRP columns under axial compression and subjected to ISO 834 fire exposure. The following conclusions can be drawn:

- 1) It was demonstrated that unprotected cellular GFRP columns can resist for more than 30 min to an ISO 834 fire from one side. This time-to-failure normally is sufficient for smaller buildings to evacuate occupants.
- 2) Lateral deflections, which normally accelerate the buckling process, remained small in all the cases due to two counteracting effects: deflections caused by an increasing eccentricity due to material loss were almost compensated by deformations due to thermal expansion.
- 3) Water-cooling proved to offer an effective active fire protection system. The structural function of the column could be maintained during two hours in the experiments and could easily be extended to four or five hours according to the model prediction.
- 4) Previously developed models can well describe the time-dependent temperature responses and modulus degradation in both the non-cooled and water-cooled cases, as well as the time-to-failure.

REFERENCE

- Asaro, R.J. & Dao, M. 1997. Fire degradation of fiber composites. *Marine Technology*, 34(3): 197-210.
- Bai, Y., Vallée, T. & Keller, T. 2008a. Modeling of thermal responses for FRP composites under elevated and high temperatures. *Composites Science and Technology*, 68(1): 47-56.
- Bai, Y., Keller, T. & Vallée, T. 2008b. Modeling of stiffness of FRP composites under elevated and high temperatures. *Composites Science and Technology*, 68: 3099-3106.
- Feih, S., Mathys, Z., Gibson, A.G. & Mouritz, A.P. 2007. Modeling the tension and compression strengths of polymer laminates in fire. *Composites Science and Technology*, 67: 551-564.

Keller, T., Haas, Ch. & Vallée, T. 2008. Structural concept, design and experimental verification of a GFRP sandwich roof structure. *ASCE Journal of Composites for Construction*, 12(4): 454-468.

Keller, T., Tracy, C. & Hugi, E. 2006. Fire endurance of loaded and liquid-cooled GFRP slabs for construction. *Composites*

Part A, 37(7): 1055-1067.

Wong, P.M.H., Davies, M.J. & Wang, Y.C. 2004. An experimental and numerical study of the behavior of glass fiber reinforced plastics (GRP) short columns at elevated temperatures. *Composite Structures*, 63: 33-43.

Flexural and Punching Performances of FRP and Fiber Reinforced Concrete on Impact Loading

K. -H. Min, J. -M. Yang, D. -Y. Yoo & Y. -S. Yoon (ysyoon@korea.ac.kr)
School of Civil, Environmental & Architectural Engineering, Korea University, Seoul, Korea

ABSTRACT In this study, in order to observe the behaviors of fiber reinforced polymer (FRP) strengthened and steel fiber reinforced concrete specimens for impact and static loads, flexural and punching tests were performed. For the one-way flexural and two-way punching tests, concrete specimens with the dimensions of 50×100×350 mm and 50×350×350 mm were fabricated. The steel fiber reinforced concrete specimens showed much enhanced resistance on two-way punching of static and impact loads. Also, the FRP strengthening system provided the outstanding performance under punching resistance. Because of large tensile strength and toughness of ultra high performance concrete (UHPC) in itself, the UHPC specimens retrofitted with FRP showed marginally enhanced strength and energy dissipating capacity.

1 INTRODUCTION

The addition of fiber reinforcement is one of the most effective methods for enhancing the performances of concrete (Bindganavile et al., 2002; Rao et al., 2010; Sukontajukkul et al., 2001). Conventional fiber reinforced concrete was developed in the 1960s and has been improved with the addition of high performance fiber reinforced cementitious composites. However, the required properties of fiber reinforced cementitious composites are not provided by the simple method of merely adding the fibers to concrete matrices. Today, construction structures demand higher resistances to impacts, blasts, earthquakes, and extreme fires. Because of the significant benefits with high strain rate loads, many researchers are paying attention to fiber reinforced polymers (FRPs) for the reinforcement of construction structures (Chen & Li, 2005; Min et al., 2009). Apart from the cost, the most essential problem in the FRP system is the “bond” between the FRP and concrete.

Hence, in this study, in order to assess the performances of FRP strengthened and steel fiber reinforced concrete specimens for impact and static loads, one-way flexural and two-way punching tests were carried out.

Table 1 Mix proportions of concrete

W/C (%)	S/a (%)	Unit weight (kg/m ³)				SP.
		Water	Cement	Fine agg.	Coarse agg.	
50.0	50.4	204	408	876	863	2.04

2 MATERIALS AND VARIABLES

Table 1 shows the mix proportions for 40 MPa design

strength concrete with ordinary Portland cement used in this study. Aggregates were crushed gravels with a maximum size of 13 mm and sea sands. In order to achieve workability, a liquid type super-plasticizer (SP) was injected. On the SFRC, 0.75% volume fraction of steel fiber was applied into the normal concrete mixture. Also, the UHPC was tested in this study (Joh et al., 2008). Test variables are summarized in Table 2, and the glass fiber reinforced polymer (GFRP) was used with the normal concrete only, while the carbon fiber reinforced polymer (CFRP) was used with the three matrices. The mechanical properties of matrices and FRP materials are summarized in Table 3.

Table 2 Test variables

Variable	Details	Notation
Concrete	Normal concrete	NC
	Steel fiber reinforced concrete	SFRC
	Ultra high performance concrete	UHPC
FRP	Not retrofitted	N
	GFRP	G
	CFRP	C

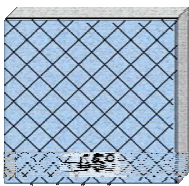
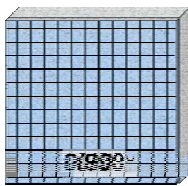
Angle of fabrics			±45 0/90

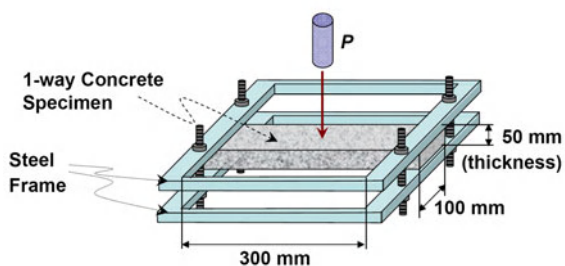
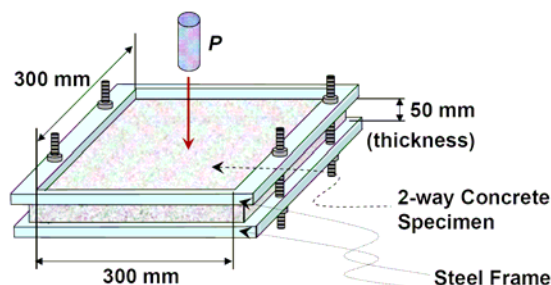
Table 3 Properties of materials

Concrete	NC	SFRC	UHPC
Compressive strength(MPa)	47.8	46.7	179.8
Flexural strength (MPa)	6.0	7.7	29.5
FRP	Glass	Carbon	Epoxy
Tensile strength (MPa)	2,300	4,900	90
Elastic modulus (MPa)	76	230	3.0
Ultimate strain (%)	3.0	2.1	8.0
Thickness (mm)	0.350	0.111	–

3 EXPERIMENTAL PROGRAM

For the one-way flexural tests and two-way punching tests, concrete specimens with the dimensions of 50×100×350 mm and 50×350×350 mm were made, respectively. The casted specimens were stored in water at 20±3°C until tested. 14 days after casting, the FRPs were adhered and then cured for 14 days more at 50% relative humidity and at a temperature of 20°C.

The restrain conditions of flexural and punching tests were illustrated in Figures 1 and 2. The span of each specimen was 300 mm and the point loads were applied in the center of specimens. For flexural specimens, the loading was applied gradually using a 2,700kN capacity UTM (universal testing machine) under displacement control at a loading rate of 0.01 mm/s. The deflection at the center and a fourth of span were measured with LVDTs (linear variable differential transformers).

**Figure 1** Test setup for one-way flexure**Figure 2** Test setup for two-way punching

Impact tests were carried out with a drop weight test machine that has a maximum capacity of about 800

Joules. Considering the high energy dissipation ability of reinforced specimens, a 33.62 kg weight was dropped with air pressure along a 0.7 m clear height. The load cell in the tub, with the attached speedometer, measured the impact load and velocity. Then the computer calculated the impact velocity and load, impact energy, and displacement, etc.

4 RESULTS AND DISCUSSIONS

4.1 One-way flexural tests

The results of the one-way static and impact flexural tests are summarized in Table 4 and 5, respectively. Figure 3 show the load-deflection relationships of specimens in the static tests. Also, Figure 4 shows the load-deflection relationships of specimens in the impact tests.

Table 4 Test results of one-way static flexure

Specimen	Maximum load (kN)	Defl. at max load (mm)
NC-N	6.32	0.83
NC-G-±45	8.24	3.22
NC-G-0/90	13.21	1.22
C-C-±45	9.27	2.94
NC-C-0/90	10.31	2.43
SFRC-N	8.75	8.68
SFRC-C-±45	16.92	6.28
SFRC-C-0/90	17.17	1.70
UHPC-N	27.90	10.07
UHPC-C-±45	33.34	5.31
UHPC-C-0/90	40.79	4.49

Table 5 Test results of one-way impact flexure

Specimen	Max. load (kN)	Defl. at max load (mm)	Total energy (J)
NC-N	38.63	1.77	77.76
NC-G-±45	47.23	2.27	114.44
NC-G-0/90	49.23	2.33	162.60
NC-C-±45	46.49	2.27	98.79
NC-C-0/90	45.39	2.35	154.07
SFRC-N	44.93	1.83	87.35
SFRC-C-±45	50.16	2.33	212.84
SFRC-G-0/90	52.49	2.86	168.75
UHPC-N	69.99	1.39	643.89
UHPC-C-±45	72.46	1.55	694.38
UHPC-C-0/90	72.82	1.61	671.89

While the maximum load of SFRC specimens were marginally more improved than the NC specimens, the toughness of SFRC increased significantly. The FRP strengthening in the NC and SFRC series increase the

resistance of static and impact loads. Because large tensile strength and toughness of UHPC in itself, the UHPC specimens retrofitted with FRP showed marginally enhanced strength and energy dissipating capacity.

4.2 Two-way punching tests

The results of the two-way punching tests are summarized in Tables 6 and 7. Figures 5 and 6 show the load-deflection relationships of specimens in the static and impact tests, respectively. Also, Figure 7 shows the representative failure patterns of two-way specimens under impact punching tests.

The SFRC specimens showed much enhanced resistance on static and impact loads of two-way punching. Also, the FRP strengthening system provided the outstanding performances under two-way punching loads. The UHPC, FRP reinforced SFRC and UHPC members did not fail by one blow.

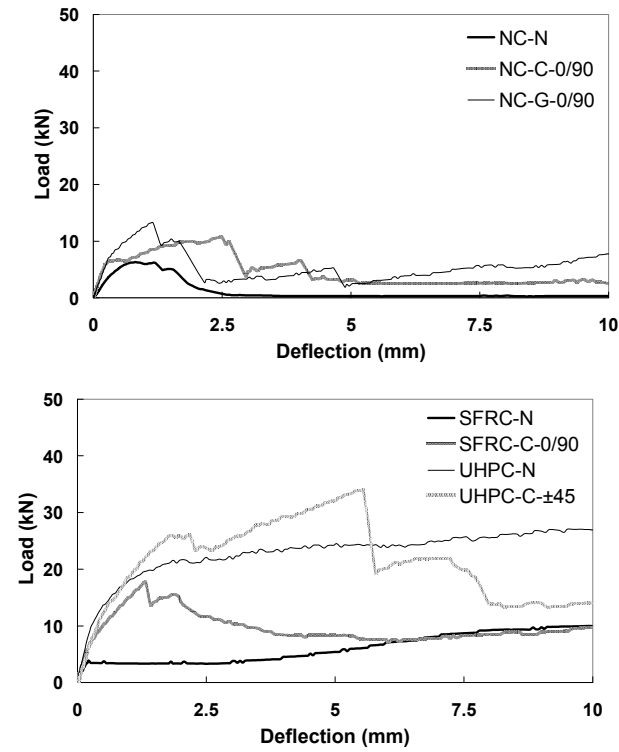


Figure 3 Static load-deflection relationships of one-way flexural tests

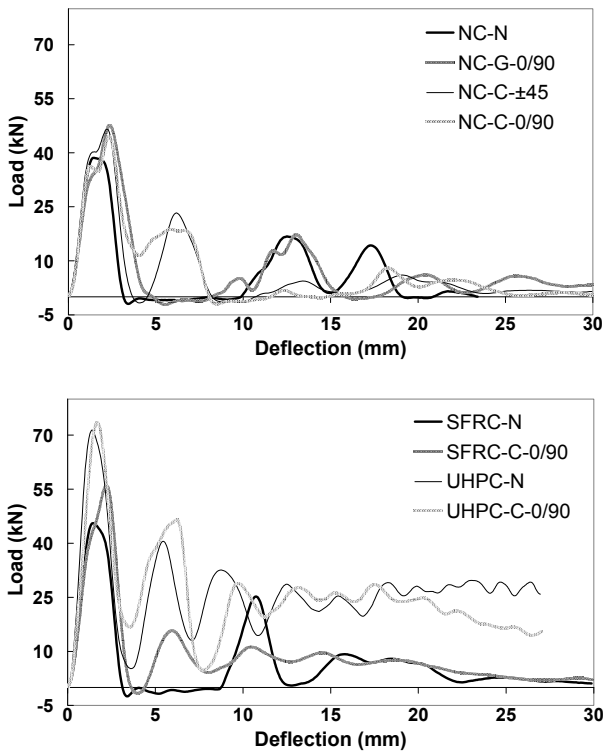


Figure 4 Impact load-deflection relationships of one-way flexural tests

Table 6 Test results of two-way static punching

Specimen	Maximum load (kN)	Defl. at max load (mm)
NC-N	14.90	0.29
NC-G-±45	43.05	1.14
NC-G-0/90	45.18	1.33
NC-C-±45	39.48	1.11
NC-C-0/90	44.66	1.36
SFRC-N	22.24	5.74
SFRC-C-±45	63.13	1.25
UHPC-N	64.70	4.28
UHPC-C-±45	97.05	2.03
UHPC-C-0/90	98.42	1.41

Table 7 Test results of two-way impact punching

Specimen	Max. load (kN)	Defl. at max. (mm)	Total energy (J)
NC-N	53.23	2.54	128.08
NC-G-0/90	71.19	4.55	522.52
NC-C-±45	70.30	3.61	534.07
NC-C-0/90	70.13	4.53	653.28
SFRC-N	63.48	2.09	405.85
SFRC-C-±45	1 st blow: 73.40 2 nd blow: 16.03	3.16 9.23	767.33 106.99
UHPC-N	1 st blow: 75.16 2 nd blow: 45.69	1.70 2.36	778.09 424.66
UHPC-C-±45	1 st blow: -* 2 nd blow: 35.32	-* 15.17	794.62 383.42
UHPC-C-0/90	1 st blow: 75.00 2 nd blow: 47.19	1.71 5.09	808.68 512.64

* Acquired data are not available.

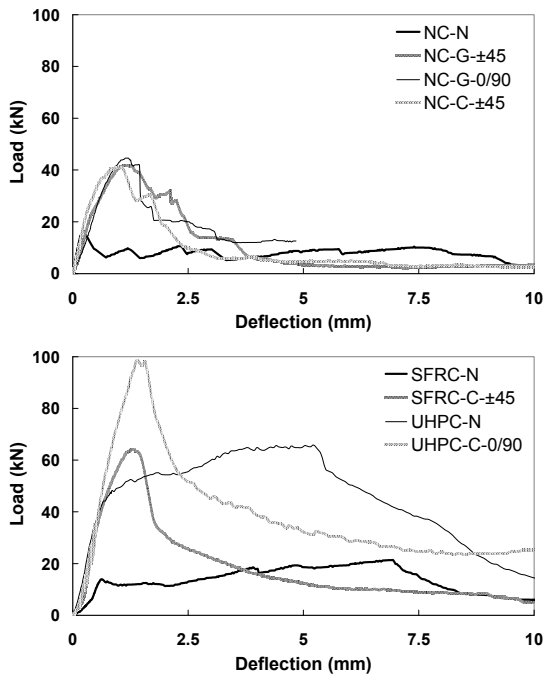


Figure 5 Static load-deflection relationships of two-way punching tests

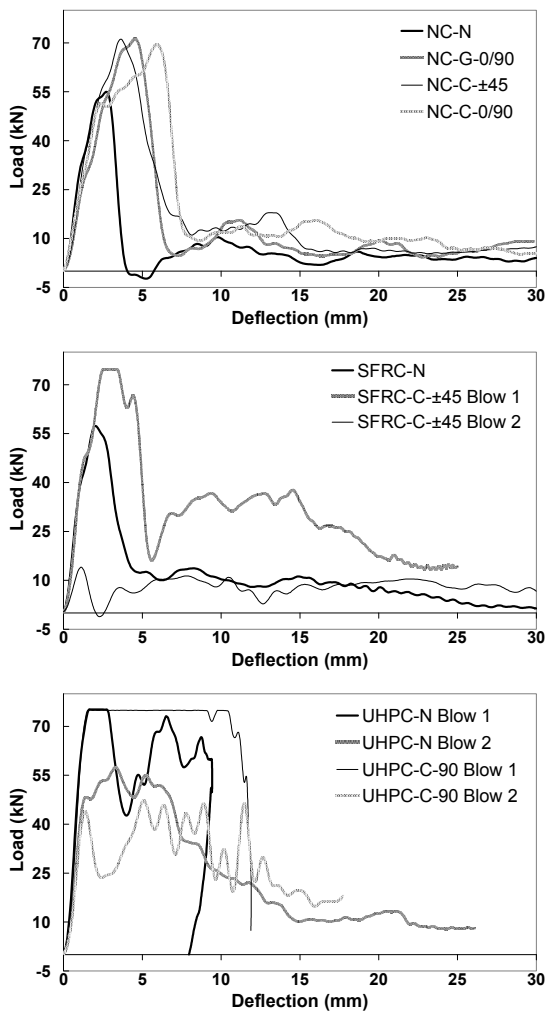


Figure 6 Impact load-deflection relationships of two-way punching tests

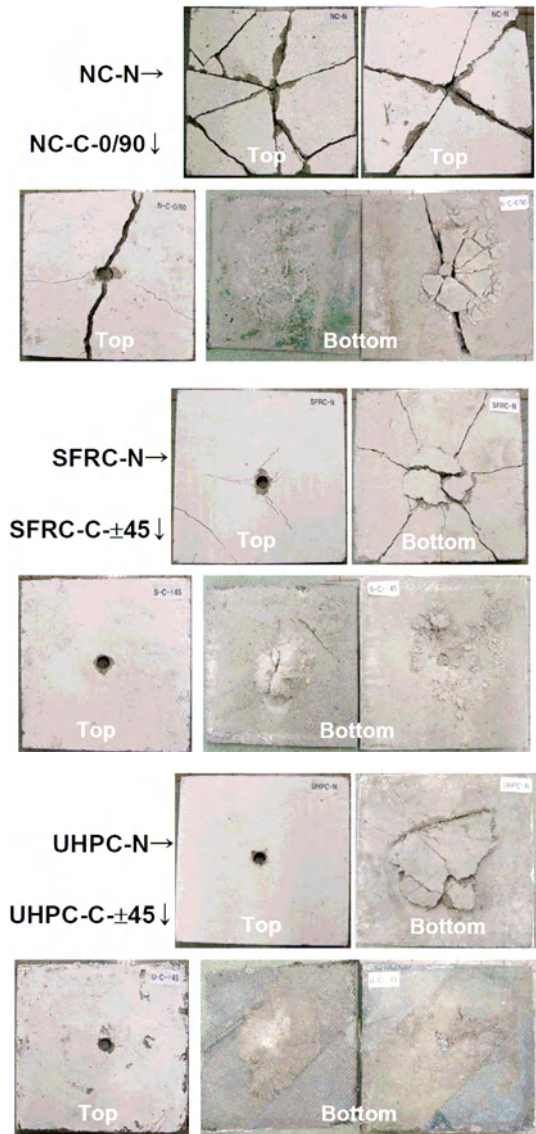


Figure 7 Representative failure patterns of two-way specimens on impact punching loads

5 CONCLUSIONS

To observe the behaviors of FRP strengthened and steel fiber reinforced concrete specimens for impact and static loads, flexural and punching tests were performed. The one-way flexural capacity of SFRC specimens were marginally more improved than the NC specimens, however the FRP strengthening in the one-way specimens of NC and SFRC series increase the resistance on static and impact loads. The strength and toughness of the FRP retrofitted UHPC specimens showed marginally enhanced. The SFRC specimens showed much enhanced resistance on two-way punching on static and impact loads. Also, the FRP strengthening system provided the outstanding performances under punching loads.

ACKNOWLEDGEMENT

This work was supported by the National Research Foundation of Korea (NRF) grant funded by the Korea

government (MEST) (No. 2007-0056796).

REFERENCES

- Bindiganavile, V., Banthia, N. & Aarup, B. 2002. Impact response of ultra-high-strength fiber-reinforced cement composite. *ACI Mater J.* 99(6):543-548.
- Chen, C.C. & Li, C.Y. 2005. Punching shear strength of reinforced concrete slabs strengthened with glass fiber reinforced polymer laminates. *ACI Struct J.* 102(4):535-542.
- Joh, C., Hwang, H., Choi, E.S, Park, J.J. & Kim, B.S. 2008. Punching shear strength estimation of UHPC slabs. *Proc. 2nd Int Symp UHPC.* Kassel: Univ. of Kassel.
- Min, K.H., Cho, S.H., Kim, Y.W., Shin, H.O. & Yoon, Y.S. 2009. Assessment on impact resisting performance of HPFRCCs using hybrid PVA fibers. *Proc PROTECT 2009.* Yokohama: Nat'l Defense Academy Protect Workshop.
- Rao, H.S., Ghorpade, V.G, Ramana, N.V. & Gnanwsvar, K. 2010. Response of SIFCON two-way slabs under impact loading. *Int J Impact Eng.* 37(4):452-458.
- Sukontajukkul, P., Mindess, S., Banthia, N. & Mikami, T. 2001. Impact resistance of laterally confined fibre reinforced concrete plates. *Mater Struct.* 34(10):612-618.

Protection of Aged Cement Clinker Silo against High Impact and High Temperature Discharge

Lim Boon Kok, Yang Ming Hui
Fyfe Asia Pte Ltd

ABSTRACT Located in the outskirts of Lhasa (the capital of Tibet) at an altitude of more than 4000 meters above sea level, this cement clinker silo is a cylindrical, reinforced concrete structure measuring 45m high. An annual maintenance service discovered extensive cracks and severe concrete spalling within the clinker's inner walls. Some of the beams have been badly damaged and even fractured. In several areas, the concrete cover had already spalled to such depth that the rebars were exposed. The damage to the concrete cover was caused by the highly abrasive effect of the clinker during discharge operations while the constant impact force on the inner concrete walls and beams was the cause of the extensive structural cracks and fracture in some beams. Moreover, the operating temperature in the silo is about 150 deg C, a high temperature dry heat environment which accelerated the concrete spalling process. A strengthening scheme using TYFO[®]SEH 51 and TYFO[®]T, a high temperature resistant epoxy was adopted to strengthen the damaged beams. The TYFO[®]T was proposed in view of the constant high operating temperature of 150 deg C. Since the structural members were constantly exposed to recurring high impact and abrasive actions, a mixture of high temperature resistant TYFO[®]T and silicon carbide powder was used as an external protective layer. Despite the harsh and unforgiving environment, the project took only one month to complete and the silo resumed production in January 2009 and has been incident-free to date.

1 GENERAL

1.1 Introduction

The affected clinker silo is one of several in Lhasa owned by the Tibet Cement Corporation, a major local cement manufacturer. Lhasa is situated in one of the highest regions in the world, with an average elevation of 4000 meters and is subjected to high temperatures in the summer and intense cold in the winter. The extensive damage to the cement clinker storage silo was a result of a combination of continuous internal exposure to high working temperature of 150 degree Celsius, plus high abrasion and impact forces from the discharge of cement clinker onto the structural members as well external exposure to the harsh environmental conditions.

Earlier in 2007, another cement storage silo at the same site had been successfully strengthened by Fyfe China using similar methods. It was completed at a lower cost and proved to perform much better than the traditional steel plate bonding technique done by the previous contractor, which had caused frequent shutdowns due to the steel plates occasionally debonding and obstructing the discharge chute.

1.2 The Tibet Cement Clinker Storage Silo

The aged silo had been in operation for several years under high differential temperature gradient, wide fluctuations in seasonal and daily temperatures as well

as earthquakes in the vicinity. These factors were not properly addressed during the design stage which not only led to monetary losses incurred due to frequent repair works but also posed a danger to the silo workers.

The three main factors that contributed to the deterioration rate of the aged clinker silo are (i) high and fluctuating operating temperatures, (ii) high abrasion and (iii) impact forces during discharge of clinkers. In order to overcome these problems caused by both natural and operational processes, the design engineer and the contractor's engineer held several discussions on possible solutions to lengthen the life span of the clinker silo.

2 TEMPERATURE EFFECTS

2.1 Clinker Silo High Temperature

Reinforced concrete cracks formation is a concrete deterioration mechanism developed under severe conditions mainly due to both environmental and loading effects. Crack formation will lead to a decrease in strength and other physical properties of the reinforced concrete structure. Concrete is porous in nature and deterioration occurs mostly due to the complex processes in its capillary- porous structure.

Coupled with widely fluctuating temperatures during operation, the silo is simultaneously exposed to constantly changing differential temperature gradients in the silo

walls. Meteorological temperature changes will also cause the external concrete to expand and contract accordingly. In summer, the daytime temperature can reach as high as 25 degree Celsius while the night time temperature can drop to as low as 8 degree Celsius while in winter, the maximum daytime temperature is 8 deg C with night time temperatures at minus 10 deg C (refer to Figure 1).

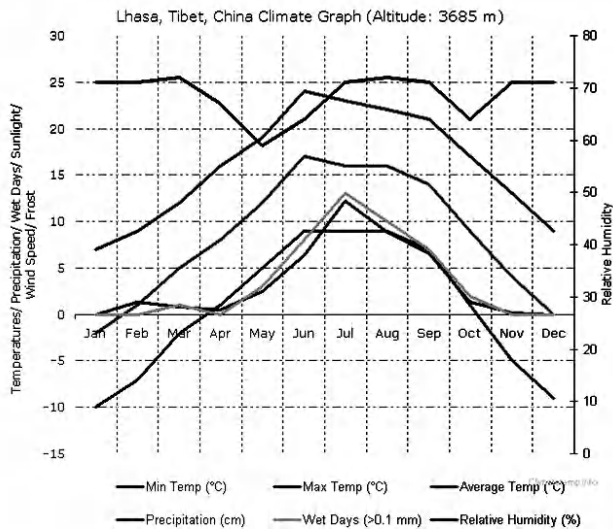


Figure 1 Lhasa, Tibet, China Climate Annual Graph

Also, when the internal concrete is exposed to high temperatures during operation, dehydration of calcium silicate hydrate (C-S-H) will cause the cement paste to shrink, while the aggregates expand. Therefore, exposing the internal concrete to high temperatures for a long time will cause its cover to spall. Being continuously exposed to the above mentioned process, the clinker silo's internal concrete cover first weakens while the continuous impact/ abrasive forces during the discharge operations gradually dislodge the concrete cover through the path of weakest resistance.

2.2 Condensation Due to Cooler Atmospheric Temperature and Warmer Clinker Silo's Surface

Condensation occurs when the surface of a warmer clinker silo comes in contact with a cooler atmospheric temperature. This causes moisture to build over a long period of time, whereby the water molecules will slowly seep into the porous concrete body. Moisture content in concrete contributes significantly to expansion and contraction stresses during temperature changes.

When the concrete gains moisture through surface condensation or rain, it will expand. As concrete drying process occurs, the surface will dry faster than the inner portion of the concrete causing contraction. The action of contraction and expansion will cause the straining of concrete cover. Development of tensile stresses at the surface will accelerate and leads to the formation of cracks.

3 CARBONATION EFFECTS

In normal circumstances, the reinforcing steel in the concrete does not corrode. The initial corrosion reaction forms a passive oxide film on the surface of the steel and with the introduction of high alkalinity from the freshly placed concrete; it stabilizes the oxide film ensuring steel protection.

However, once the carbon dioxide (CO_2) from the atmosphere diffuses through the porous concrete and neutralizes the alkalinity of concrete, carbonation of the steel reinforcement starts again. Without suitable remedies, extensive corrosion of the steel reinforcement will lead to structural failure in the worst case scenario.

4 FREEZE-THAW EFFECTS

Temperatures in Tibet frequently fluctuate above and below freezing point. When water that has entered the concrete surface cracks freezes, the ice formed strains the cracks and causes them to deepen and widen. When the ice thaws, water can flow further into the concrete surfaces cracks. When the temperature drops below freezing point and the water freezes again, the ice enlarges the cracks further causing more strain to the concrete cover. Extensive weakening of the concrete will expose the reinforcement steel.

5 MECHANICAL EFFECTS CAUSED BY OPERATIONAL HAZARD: HIGH ABRASION AND IMPACT FORCES

After the heating process at the kiln, the molten cement clinker is being cooled by cooler to a temperature of about 150°C . It is then being transported and stored in the clinker silo for further grinding processes. The working temperature in the clinker silo throughout the year is maintained at about 150 degree Celsius. As the clinker is being discharged into the storage silo, the molten clinker rolls and grinds against the concrete surfaces and supporting beams.

The constant high impact forces from the discharge weaken the concrete cover while the abrasive forces from the clinker will eventually wear off the concrete cover if there is no proper anti-abrasion and impact treatment. Therefore, to prevent the concrete cover from eventually wearing off completely and resulting in the beams' significant loss in load bearing capacity, an anti abrasion and anti impact protective coating is needed to mitigate the effect.

6 PREVIOUS STRENGTHENING METHOD UNSUCCESSFUL

The aged clinker storage silo had earlier been strengthened using the steel plate epoxy bonding technique. The disadvantage of using this technique is that the set up is

very bulky and time consuming. Tailor made steel plates are required and it is highly labour intensive, time consuming and dangerous considering heavy lifting works required in oxygen deprived working conditions. After the previous strengthening works was carried out by another contractor, major problems started to surface once the silo commenced full production. Due to the high working temperature of 150 degree Celsius, some steel plates debonded from the concrete surfaces over several occasions.

From examination of the dislodged steel plates and the debonded areas of the concrete surfaces, it was found that the epoxy used to bond steel plates to the concrete was not capable of withstanding the high working temperature. Furthermore, problems caused by impact and abrasive forces from the discharge were not addressed. Instead of providing the solution to the problems, the traditional strengthening technique caused further substantial downtimes and monetary losses. There was an urgent need to explore new methods of retrofitting the clinker silo at the shortest possible time.

7 TYFO[®] FIBRWRAP METHOD

Following the successful retrofitting of a similar silo in Tibet in year 2007, Fyfe China Pte Ltd was once again called upon to provide a feasible and economical solution to address the factors listed in section 1.1 above. In order to withstand the high working temperature of 150 degree Celsius, the TYFO[®]T epoxy was selected.

TYFO[®]T is a high performance epoxy that has been used on concrete, metallic and other structural materials. It has excellent chemical resistance towards chemicals such as sulfuric acid, hydrochloric acid, nitric acid, chromic acid, phosphoric acid etc. With its heat resistance property of 149°C at continuous high working temperature to as high as 177 °C at intermittent temperatures, the epoxy is well suited to withstand the working temperature of the clinker storage silo. Its glass transition temperature has been tested according to the ASTM D4065-01, where cured specimens were placed in mechanical oscillation either at fixed or natural resonant frequencies. Elastic or loss moduli, or both of the specimens are measured while varying time, temperature of the specimen or frequency, or both, of the oscillation. Plots of the elastic or loss moduli, or both, are indicative of viscoelastic characteristics of the specimen. Rapid changes in viscoelastic properties at particular temperatures, times, or frequency are normally referred to as transition regions.

Beams and columns- damaged concrete cover is first removed and patch repair done while corroded reinforcements were treated and damaged ones replaced with new ones welded onto existing ones. Previously installed protective steel angles along the edge lines of beams and columns were inspected and all gaps between

the steel angles and concrete surfaces were grouted with high strength mortar. The same mortar is then troweled throughout to form a flush surface after which 200mm strips of TYFO[®] SEH 51 composite system were wrapped over the steel angles at the ends and mid spans of these members (ref to Figure 2) to provide a more robust anchorage. A unique mixture of silicon carbide power and preheated TYFO[®]T High Temperature Resistance Epoxy is then trowelled over the entire beams and columns to form a high impact/abrasion protection layer.

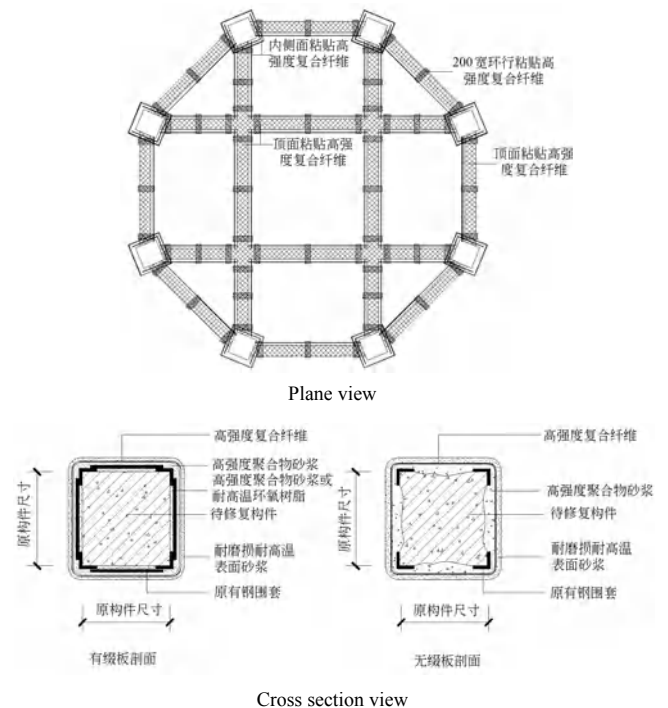


Figure 2 Views of Internal Beams and Columns

Silo walls-steel plates previously installed were replaced by circumferentially wrapping with the TYFO[®] SEH 51 composite system to compensate for estimated 20% loss of the original hoop reinforcement tensile strength due to corrosion. These were originally designed to resist the maximum hoop stresses developed in the silo walls during the silo operation.

The TYFO[®] SEH 51 composite system has a higher tensile strength than steel plate and yet has a unit weight of only a fraction of steel plates. It is an ICC ER-5282 listed material and has been used since 1988 to add strength and ductility to structural members. Due to such high strength to weight ratio, it has proven to be a more cost effective method compared to traditional strengthening techniques.

To address the issue of high abrasive and impact forces occurring during discharge operations, a mixture of silicon carbide powder and the TYFO[®] T epoxy was used as a final protective layer. Silicon carbide is one of the hardest substances and is usually used as an abrasive and heat-refractory material and in single crystals as

semiconductors, especially in high-temperature applications. The hardness of the silicon carbide is approximately value 9 on the mohs hardness scale (Diamond has a value of 10 on the same scale).

The abrasion resistance property of the silicon carbide also makes it an appropriate solution for the anti-abrasion coating for the clinker silo. Silicon carbide powder is premixed with TYFO[®] T (mix ratio of 3:1 by weight) to form a high temperature resistance anti-abrasion and anti-impact protective coating. The coating is then applied at minimum 5 mm thickness onto surfaces wrapped with the TYFO[®] SEH 51 composite as well as exposed surfaces subject to clinker impact. This coating provided effective abrasion and impact resistance to all affected surfaces as well as helps prevent formation of structural cracks in surfaces areas not strengthened with the TYFO[®] SEH 51 composite system.

Due to the high-cost of shutdown, only one annual inspection is conducted during the coldest period of winter. An inspector would hammer at and visually evaluate the strengthened areas of the structure to test whether air voids or delaminations have occurred. Any voids or delaminations greater than 6" in diameter must be repaired according to the procedures detailed in the project specifications. Voids less than 6" in diameter must be repaired by injecting with TYFO[®] epoxy. Any delaminations less than 2 in² do not require any means of repair, as they do not adversely affect the performance of the jacket. Small entrapped voids which naturally occur in mixed resin systems do not require attention. To date, there has been zero occurrence of blockage to the discharge chute and no remedial works as described above have been necessitated.

8 CONCLUSION

After the failure of a traditional strengthening technique done previously, a new and innovative approach to strengthening the aged clinker silo was introduced into Tibet. Based on site investigations, the core problems were first correctly identified and an economical and yet more effective method was proposed and implemented successfully.

A unique combination of TYFO[®] T epoxy and TYFO[®] SEH51 glass/kevlar fiber fabric was used to form a high temperature resistant composite system. This system not only increased the strength of the clinker silo, but also increased its durability as well as extended its useful lifespan. An innovative combination of TYFO[®] T epoxy and silicon carbide powder was then used as a

lasting and durable abrasion and impact resistant final protection coating.

Table 1 TYFO[®]SEH 51 Composite System

COMPOSITE GROSS LAMINATE PROPERTIES		
PROPERTY	ASTM METHOD	TYPICAL TEST VALUE*
Ultimate Tensile Strength in primary fiber direction, Psi	D-3039	83,400 psi (575MPa)
Elongation at break	D-3039	2.2%
Tensile Modulus, psi	D-3039	3.79×10 ⁶ psi (26.1GPa)
Ultimate Tensile Strength 90 degrees to primary fiber, psi	D-3039	6,250 psi (43Mpa)
Laminate Thickness	0.05 in. (1.3mm)	0.05 in. (1.3mm)

Table 2 TYFO[®]T- High Temperature Resistant Epoxy

PROPERTY	TYPICAL TEST VALUE*
Pencil hardness	3H
Impact Resistance, lbs (direct /Reverse)	10/0
Abrasion Resistance 1,000 cycles wt loss gram	0.030
Service Temperature (continuous/ Intermittant)	149°C/ 177°C
Chemical Resistance	

Table 3 Silicon Carbide Powder

SILICON CARBIDE PROPERTIES		
PROPERTY	UNITS	
Flexural strength	MPa	550
Elastic Modulus	GPa	410
Compressive Strength	Mpa	3900
Hardness	Kg/mm ²	2800
Fracture Toughness	Mpa•m ^{1/2}	4.6
Coefficient of Thermal Expansion	10 ⁻⁶ /°C	4.0

REFERENCES

- M.K.Kassir, K.K. Bandyopadhyay & M. Reich. (1996): Thermal Degradation of Concrete in The Temperature Range from Ambient to 315°C (600°F)
- ICC Evaluation Service Inc. (1996): Proposed Acceptance Criteria for Concrete and Masonry Strengthening Using Fiber-Reinforced Composite Systems, AC125-R1-0197, ICC Evaluation Service Inc., Whittier, California
- ASTM Standards: D4065-01, Plastics: Dynamic Mechanical Properties: Determination and Report of Procedures

Nonlinear Response of Steel-Fiber Reinforced Concrete Beams under Blast Loading: Material Modeling and Simulation

James H. Haido (almayee_eng@yahoo.com), Abu Bakar B. H. & J. Jayaprakash
School of Civil Engineering, University Sains Malaysia, Penang, Malaysia

Ayad A. Abdul-Razzak
Department of Civil Engineering, College of Engineering, University of Mosul, Mosul, Iraq

ABSTRACT Steel fiber reinforced concrete (SFRC) is widely used in the constructional field especially in defense related structures which often subjected to various types of static and dynamic forces. This paper describes the experimental investigation results of SFRC specimens under the effect of compressive and tensile loading. Variables considered are type, aspect ratio and percentage volume of fractions of steel fibers. New mathematical general material constitutive stress-strain relationship for fibrous and conventional concrete were predicted statistically by using SPSS-program, this by basing on the present experimental data. Nonlinear transient dynamic analysis of reinforced concrete beams subjected to blast loading using the finite element method is presented. Eight-node serendipity degenerated plate elements have been used to represent the concrete beam structures. Implicit Newmark with corrector-predictor algorithm is employed for time integration of the equation of the motion. A computer program coded in FORTRAN language is written to implement the present study to give a complete listing of stress and deformation in every concrete or steel layer at any time. The numerical results show good agreement with other published studies' results which include deflections.

1 GENERAL INSTRUCTIONS

The reinforcement of concrete by means of fibers has proved to be an efficient and economic way to mitigate this short-coming (Elser et al, 1996). The finite element method has enabled to model of complexities that arise due to nonlinear behavior of reinforced concrete. While many available material nonlinear models showed good agreement with test results from which the equations were derived, there was no such good agreement when models the models were applied to other test data which proved by Bencardino F. et al (2008). Based on a correlation study on applicability evaluation on published empirical models for SFRC material and the regression analysis on experimental data of mechanical properties of SFRC, Xu and Shi (2009) found that the applicability of the many tensile behavior models to SFRC material and recommended to formulate further constitutive relationships for this material by considering multi-variables in regression analysis. Hence, further investigations in this direction are considered essential. Especially in determination of suitable material constitutive relationships proper for both conventional and steel fibrous reinforced concrete structures. It is with this objective that a nonlinear analysis of SFRC beams under dynamic loading is presented and blast loading was adopted as loading case study using new

material constitutive relationships.

2 MATERIAL NONLINEARITIES

Cubic and cylindrical specimens were prepared for uni-axial testing using plain concrete and SFRC mixes containing crimped, one end paddled and two end paddled steel fibers have volume fractions V_f of 0.5% and 1% and different aspect ratios (fiber length L_f / fiber diameter D_f) (as in Table 1). The mix proportion of

Table 1 Total Number of Specimens in compression or splitting test

Type of Concrete	Fiber type	L_f/D_f	$V_f\%$	Number of specimens
Plain	–	–	0	3
Fibrous	Crimped (I)	50	0.5	3
			1.0	3
	One End Paddled (II)	16	0.5	3
			1.0	3
	One End Paddled (III)	20.5	0.5	3
			1.0	3
	Two Ends Paddled (IV)	34	0.5	3
			1.0	3
			1.0	3

cement, water, sand and gravel per cubic meter of the concrete mix is 300kg, 150kg, 600kg, 700kg respectively. Compressive stress-strain curves for each mix were obtained from testing 150mm cubes. While tensile concrete behavior has been investigated from splitting test of cylindrical specimens have diameter 150mm and height 300mm. Number of specimens per test was illustrated in Table 1. All specimens required for aforementioned experiments were tested at age 28 days. The average results for 30 specimens (Table 1) per test are presented in Figure 1.

The compressive strength (f'_c) of ordinary concrete will be improved and increased by addition of steel fibers which lead to improve the fibrous concrete strain value (ϵ_{pf}) at the compressive strength of steel fibrous concrete and consequently improve the maximum compressive strain value (ϵ_{cuf}). The influence of steel fiber content (V_f %) and its length to diameter ratio of fibers (i.e. aspect ratio (L_f / D_f)) on compressive strength and strain of fibrous concrete can be investigated depending on present experimental data, by performing a regression analysis of these data in SPSS program the relations 1, 2 and 3 for fibrous concrete compressive strength f_{cf} , ϵ_{pf} and ϵ_{cuf} have been obtained with suitable index of determinations about 98.7%, 97.8% and 97.5% respectively.

$$f_{cf} = 14.169V_f.L_f / D_f + 0.984f'_c \tag{1}$$

$$\epsilon_{pf} = 0.002242 + 0.001V_f.L_f / D_f \tag{2}$$

$$\epsilon_{cuf} = 0.021114(0.001 + V_f.L_f / D_f)^{1/3} - 0.00918V_f.L_f / D_f + 0.000918 \tag{3}$$

These two compressive strain values can be used successfully in compressive stress-strain relations for finite element nonlinear analysis and for investigating the case of concrete crushing in the case of both fibrous and ordinary concrete. Three rules or conditions should be used to study the uni-axial and bi-axial compressive response of concrete which are yield condition, hardening rule, flow rule and crushing condition. The yield condition defines the magnitude of the compressive stress at which is the onset of plastic strain, the plastic behavior of concrete compression strain can be represented in two models which are perfectly plastic and strain hardening models. In the perfectly plastic model the plastic behavior will be started when the effective stress reached to the value of compressive strength (f_{cf}) and is continued until crushing status occurs. While in strain hardening model the plastic simulation of strain will be began directly at $\sigma=0.3f_{cf}$. By using nonlinear regression analysis of current experimental stress (σ)-strain (ϵ) data in SPSS program the expression (4) can be formulated (with good index of determination=95.47%).

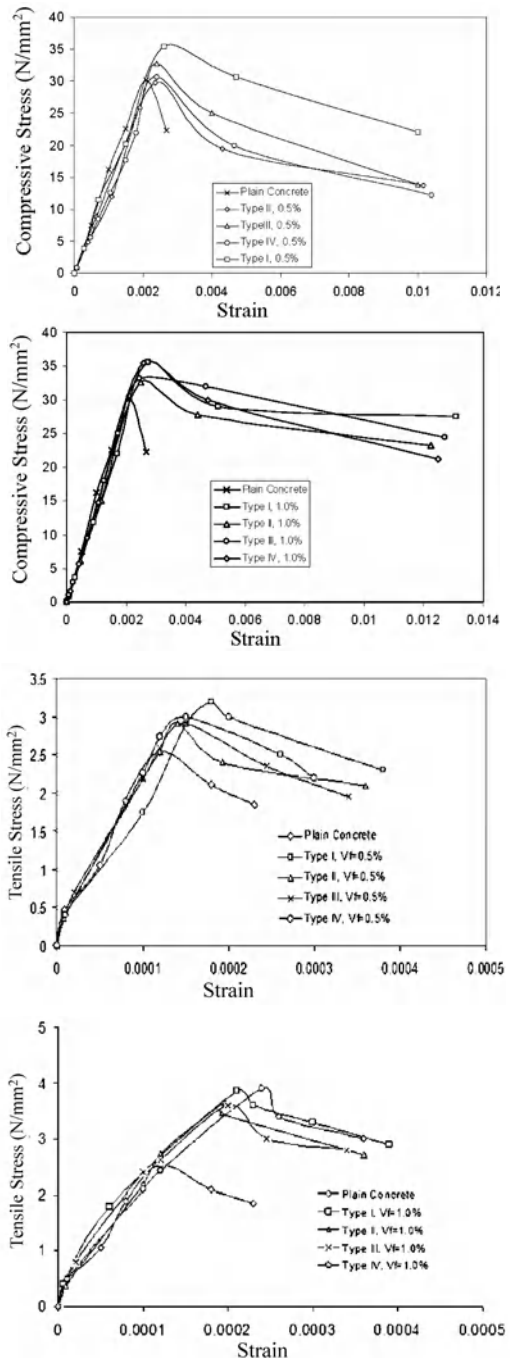


Figure 1 Compression and tension stress-strain curves

$$\sigma = 0.53 f'_c \left(\frac{\epsilon}{\epsilon_{pf}} \right) \left[\left(\frac{\epsilon}{\epsilon_{pf}} \right) + e^{V_f} \right] \tag{4}$$

To propose a model for tensile stress-strain relation of steel fiber concrete, it is better to separate it into two regions, namely, the pre and post peak regions. For representing the relation of pre- and post-peak tensile stress-strain relations, regression analysis of present splitting test results has been carried out and expression 5 and 6 determined with index of determination=99.1% and 95.6% respectively.

$$\sigma = f_{cf} (\epsilon / \epsilon_{cf})^{0.664} \quad \dots \text{for pre-peak zone} \tag{5}$$

$$\sigma = f_{tf}((\varepsilon + \varepsilon_m)/(\varepsilon_{tf} + \varepsilon_m))^{-1.150} \dots \text{for post peak zone} \tag{6}$$

where f_{tf} , ε_{tf} are the composite tensile strength and the strain at tensile strength respectively, ε_m is the ultimate tensile strain.

Cracked shear modulus (G') can be formulated using tension stiffening function (Post-Peak region tensile stress). According to this approach, the cracked shear modulus can be proposed as a function of un-cracked shear modulus as follows:

$$G' = 0.25G((\varepsilon + \varepsilon_m)/(\varepsilon_{tf} + \varepsilon_m))^{-1.150} \tag{7}$$

where (G) is the un-cracked shear modulus in (MPa).

To investigate the reliability of proposed model (eq. 4) of concrete behavior under compression action, a critical comparative study has been performed between the proposed theoretical compressive stress values and the experimental stress values measured by Bencardino et al. (2008), Ezeldin and Balaguru (1992), Mansur et al. (1999), Nataraja et al. (1999), and Soroushian and Lee (1989). A comparison illustrates good agreement of the present model results with other experimental data as shown in Figure 2. Figures 3 and 4 depict the matching of present pre- and post-tension zone model with the available tensile stress values determined by Abdull-Ahad and Abbas (1989), and Cho and Kobayashi (1976, 1979). It is obvious that the mean value of the ratio of theoretical to experimental values close to one. Thus, the suitability of the compressive and tensile behavior models has been proved for plain concrete and various type of specimens contain different shapes of steel fibers such as straight, hook ends...etc. This indicates the reliability of the present proposed models for representing the behavior of various types of SFRC.

3 FINITE ELEMENT ANALYSIS

Eight-node two-dimensional plate finite element was used to discrete the spatial structures. The layered approach is used to represent nonlinear stress behavior of concrete. Geometrical nonlinearity in the layered approach is considered in the mathematical model, which is based on the total lagrangian approach considering Von Karman assumptions. The nonlinear dynamic equilibrium equation in semi-discrete form is given as follows (Kappos, 2004):

$$Ma + Cv + p(d) = f_e \tag{8}$$

where d , v and a are vectors of nodal displacements, velocities and accelerations, respectively. M and C are the global mass and damping matrices, $p(d)$ is the vector of internal resisting forces, and f_e is the vector of external applied forces.

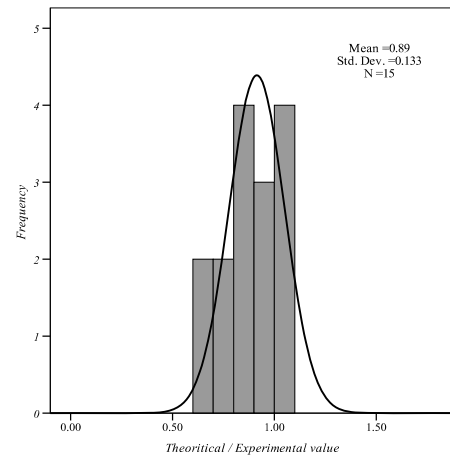


Figure 2 Validity of eq. 4

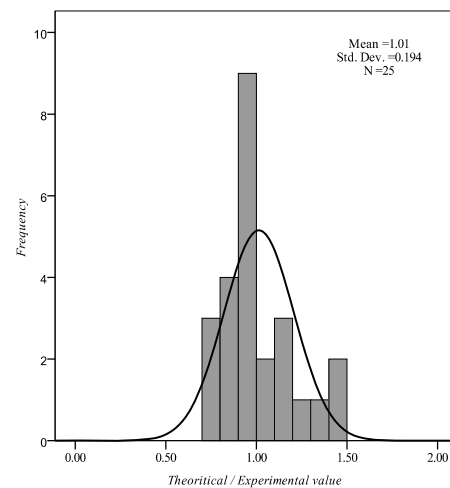


Figure 3 Validity of eq. 5

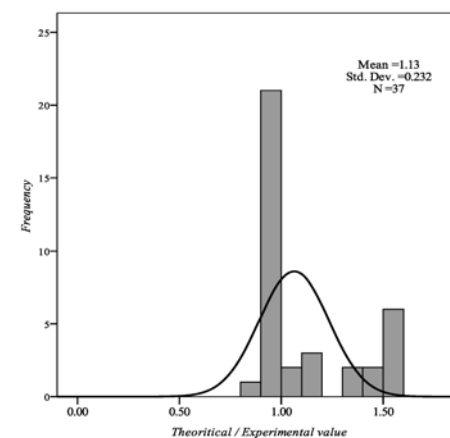


Figure 4 Suitability of eq. 6

In present study the unconditionally stable Newmark's implicit integration method (was adopted together with the predictor-corrector scheme for solving eq. 8). A computer program coded in FORTRAN was implemented for the non-linear dynamic analysis of steel fibrous concrete beams structures subjected to dynamic loading, using the proposed material nonlinear models.

4 VALIDITY OF THE PROPOSED NUMERICAL FORMULATION

The validity of the proposed finite element formulation was proved via analysis of SFRC simply supported beam its dimensions $1.5\text{m}\times 0.3\text{m}\times 0.16\text{m}$; subject to a blast loading and tested by Magnusson (1998). The magnitude of this loading is 380 kPa and its duration 0.04s. The concrete properties used in the analysis are $f_{cf} = 95.0\text{ MPa}$, $f_{ff} = 6.82\text{ MPa}$, $\varepsilon_{ff} = 0.00014$, $\varepsilon_m = 0.0004$, $\rho = 2400.0\text{ kg/m}^3$. And steel fiber properties are $V_f = 1.0\%$, $L_f = 60\text{mm}$, $L_f / D_f = 80$. Due to symmetry, only one half of the beam was considered in the present finite element procedure. The beam was divided into six eight-node finite elements, three elements per each half of the beam. Six concrete layers were used in analysis. The effect of compressive models was investigated as shown in Figure 5, while Figure 6 depicts the influence of dynamic response by the number of concrete layers used in analysis.

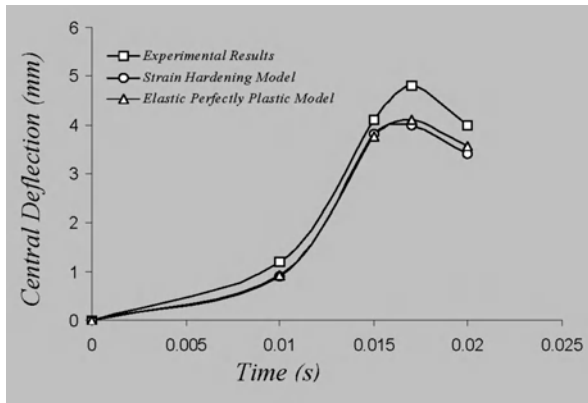


Figure 5 Influence of the compression models

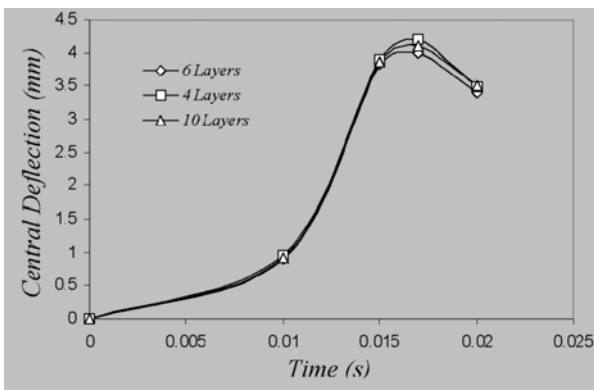


Figure 6 Effect of number of layers in dynamic analysis

5 CONCLUSION

Present study comprises of formulation of new material constitutive relationships of steel fibrous concrete materials. Various nonlinear material models were proposed depending on experimental data for compression and tension behavior tests of SFRC specimens. The validity of these models was demonstrated statistically via determining suitable index of determination more

than 90% and also by comparison with other experimental data available in literature. Finite element procedure was developed depending on present new material nonlinearities, eight-node degenerated plate elements were adopted in analysis. Finally, numerical application was presented and a comparison was carried out between numerical and other experimental results, good agreement was found. No significant difference was observed in numerical dynamic analysis outputs when strain hardening and elastic perfectly plastic models were used. Also close results were found by using different number of layers of concrete in analysis.

REFERENCES

- Abdull-Ahad, R.B. & Abbas, J.M. 1989. Behavior of steel fiber reinforced concrete under biaxial stresses. Proc. of the Inter. Conf. on recent developments in fiber reinforced cements and concrete, Cardiff (U.K.), Eds. Swamy and Barr, Elsevier Applied Science, publishers Ltd., Essex:126-135.
- Bencardino F, Rizzuti L, Spadea G, & Swamy R N. 2008. Stress-strain behavior of steel fiber reinforced concrete in compression. *Journal of Material in Civil Engineering* 20(3):255-263.
- Cho, R. & Kobayashi, K. 1976. Load deformation properties of steel fiber reinforced concrete. *Concrete Journal*, University of Tokyo, 28(9):20-23.
- Cho, R. & Kobayashi, K. 1979. Testing method for tensile strength of steel fiber reinforced concrete. *Concrete Journal*. JCI, 17(9):87-95.
- Elser, M., Tschegg E.K., & Stanzl-Tschegg S.E. 1996. Fracture behavior of polypropylene-fiber reinforced concrete under biaxial loading: an experimental investigation. *Composites Science and Technology* 56:933-945.
- Ezeldin, A.S. & Balaguru, P.N. 1992. Normal- and high-strength fiber reinforced concrete under compression. *J. Mater. Civ. Eng.* 4(4):415-429.
- Kappos A.J. 2004. *Dynamic Loading and Design of Structures Taylor & Francis e-Library*.
- Magnusson, J. 1998. Fiber reinforced high strength concrete beams subjected to transient load. *Defense Research Establishment, FOA-R--98-00808-311--SE, Stockholm-Sweden*.
- Mansur, M.A., Chin, M.S., & Wee, T.H. 1999. Stress-strain relationship of high-strength fiber concrete in compression. *J. Mater. Civ. Eng.* 11(1):21-29.
- Nataraja, M.C., Dhang, N. & Gupta, A.P. 1999. Stress strain curve for steel-fiber reinforced concrete under compression. *Cem. Concr. Compos* 21:383-390.
- Newmark, N.M. 1959. A method of computation for structural structural dynamics. *ASCE Journal of Engineering Mechanics Division* 85:67-94.
- Soroushian, P. and Lee, C.D. 1989. Constitutive modeling of steel fiber reinforced concrete under tension and compression. *Fiber reinforced cements and concretes, recent developments*, R. N. Swamy and B. Barr. Eds.: 363-377.
- Xu B.W., Shi H.S. 2009. Correlations among mechanical properties of steel fiber reinforced concrete. *Construction and Building Materials* 23:3468-3474.

Fire Behaviour of CFRP Prestressed High Strength Concrete Slabs

Giovanni P. Terrasi (giovanni.terradi@empa.ch) Alex Stutz & Michel Barbezat
Mechanical Systems Engineering, EMPA, Dübendorf, Switzerland

Luke A. Bisby
BRE Centre for Fire Safety Engineering, University of Edinburgh, Scotland

ABSTRACT More sustainable precast concrete elements are emerging utilizing high-performance, self-consolidating, fibre-reinforced concrete (HPSCC) reinforced with high-strength, lightweight, and non-corroding prestressed carbon fibre reinforced polymer reinforcement. One example of this is a new type of precast carbon FRP pretensioned HPSCC member intended as load-bearing elements for building envelopes. Their performance in fire must be understood before they can be widely used with confidence. It is known that the bond strength between both steel and FRP reinforcing bars and concrete deteriorates at elevated temperature and that high strength concrete tends to an explosive spalling failure when subjected to a fire. The bond strength reductions in fire, their impacts on the load-bearing capacity of prestressed concrete elements, and the spalling behaviour of HPSCC remain largely unknown. This paper gives insight in the fire behaviour of CFRP prestressed HPSCC slabs and presents selected results of an experimental fire test study on thin-walled slabs.

1 INTRODUCTION AND MATERIALS

The prestressing reinforcements chosen for this work were 5.4 mm Ø pultruded and quartz sand-coated CFRP rods with circular cross-section that were used as tendons for pretensioning thin concrete slabs. Their design tensile strength was 2000 MPa and the elastic modulus was about 150 GPa. The tendons were unidirectionally reinforced by carbon fibres of type Tenax UTS, that were embedded in an epoxy matrix (with a high glass transition temperature, $T_g = 121^\circ\text{C}$). The low density, excellent stress-corrosion resistance, and low creep and relaxation (see for example the studies by Uomoto 2001) of CFRP are well known. The above properties make unidirectional CFRP profiles particularly suitable as prestressing reinforcements for concrete elements (Burgoyne 1997). For the reference slab an indented prestressing steel tendon 6 mm Ø of type Nedri 1470/1670 was used (measured tensile strength was 1749 MPa).

The study focussed on a HPSCC of strength class C90 (concrete with a minimum 150mm cube strength after 28 days of 90 MPa), a material that is becoming popular for producing slender precast elements in Switzerland. The HPSCC is characterized by a precise grain size distribution of selected 0–8 mm limestone aggregates. The cement content is typically in the order of 450 kg/m³. Silica fume and high performance superplasticizers play a key role in the mix design of the HPSCC, which shows self-compacting properties at water/cement ratios of 0.39-0.4. Short polypropylene

fibres of length 20 mm at a dosage of 2 kg/m³ were used to prevent shrinkage cracking and to increase resistance against spalling in fire. Curing consisted of a simple covering of the moulds to keep the HPSCC humid for 36 hours before prestress release and demoulding. After demoulding the elements were kept under a polyethylene sheet for 5 days, after which they were left to cure under ambient conditions.

The combination of CFRP and HPSCC, along with an appropriate interface between them (sand-coating of the CFRP), make it possible to minimise the weight of prestressed bending elements by reducing concrete cover and wall thickness while providing excellent serviceability (no susceptibility to corrosion, high bending stiffness, and high fatigue strength). However, the performance of these elements during fire is essentially unknown.

2 EXPERIMENTAL SPECIMENS

For the present study, 9 thin walled (45–75 mm total thickness) slabs with rectangular cross-section were produced by the precaster SACAC AG in Lenzburg, Switzerland. The CFRP and steel tendons were stressed to an initial prestress of 1200 MPa and were located in the mid-plane of the slabs to obtain a central prestress. To study the temperature profiles of the tendons and through the depth of the HPSCC, 3–19 Type K thermocouples (TCs) were placed at several locations along the lower edge of the tendons and in the HPSCC

at slab midspan at a height of half the concrete cover (10 mm, 13.5 mm or 17.5 mm) from the fire-exposed surface.

2.1 Small-scale fire pre-test

A first small-scale fire test (pre-test) was performed on two HPSCC slab specimens of 45 mm thickness (giving a clear cover of 20 mm to the CFRP tendons) \times 175 mm width \times 1080 mm length. These were prestressed by four CFRP tendons that had a lateral cover of 25 mm and a tendon-to-tendon clear spacing of 35 mm. A preconditioning storage of the small-scale slabs followed their construction for eight weeks in an oven at 40°C and 15% relative humidity (r.H.). They were then kept at 23°C and 50% r.H. for two weeks prior to testing.

2.2 Full-scale fire tests

In the main fire tests six full-scale CFRP prestressed HPSCC slabs of cross-section 45, 60 or 75 mm depth \times 200 mm width with a length of 3360–3600 mm were centrally prestressed by four CFRP tendons in the mid-plane (Table 1: Slabs 4, 7, 8, 5, 9, 6). A single steel prestressed slab of cross-section 75 mm depth \times 200 mm width with a length of 3360 mm was also tested as a reference. Again, the slab was centrally prestressed by 4 tendons at its mid-plane. The tendons had a lateral cover of 22.5 mm and a tendon-to-tendon clear distance of 45 mm.

Table 1 Experimental programme and selected test results

Specimen	Age mts	Tendon type	Cover (mm)	Overhang (mm)	Failure time (min)	Failure mode*
A	2.5	CFRP	20	30	26	lb→c
P	2.5	CFRP	20	30	26	lb→c
4	9.3	CFRP	20	160	26	sp→c
7	8.8	CFRP	20	280	34	sp→c
8	8.4	CFRP	27.5	280	24	sp→c
5	8.4	CFRP	27.5	160	47	sp→c
9	9.3	CFRP	35	280	60	sp→c
6	9.3	CFRP	35	160	91	sp→c
40	1.0	steel	35	160	29	sp→c

* lb→c = bond loss → crushing; sp→c = spalling → crushing

After demoulding all slabs were stored for between 1 and 7.5 months in the SACAC production hall before being delivered to the Empa fire lab, where they were stored outside under a covered storage area for maximally 2 months. As usual with fire tests of reinforced concrete structural elements, the authors aimed to age the slabs as long as reasonably possible before testing them to avoid explosive concrete spalling due to an unrealistically high moisture content. This was unfortunately not possible for the steel prestressed reference slab. The moisture content of the slabs was

determined by mass loss during dehydration of 50 g of crushed material with two samples taken from the core of an additional slab after 1 and 7.8 months from casting. The moisture content after 1 and 7.8 months was 4.8% and 4.4%, respectively.

3 FIRE TEST SETUP

An ISO 834 fire (ISO 1999) was considered to represent a worst-case scenario for a façade element (a typical real application of the thin-walled CFRP prestressed HPSCC slabs being studied). This produces a furnace temperature, for example, of $T \approx 850^\circ\text{C}$ after 30 minutes. The primary result of interest for the tests was the time to failure of the slabs in fire under service load.

3.1 Small-scale fire pre-test

The test span of the simply supported slabs was 1020 mm, so that they had only 30 mm of (cold) overhang per side. A three-point bending loading condition was selected with a central line-load at midspan of 3040 N causing a bending stress at the tensile edge of $\sigma_{c,bottom} = 1.3$ MPa (slight tension, corresponds to a typical service load state, no bending cracks visible at the start of testing). Mid-span deflection was measured during testing with an accuracy of ± 0.5 mm.

3.2 Full-scale fire tests

The main fire tests of the CFRP prestressed HPSCC slabs consisted of exposing six simply supported slabs (span = 3040 mm) to an ISO 834 fire while simultaneously loading the slabs in four-point bending (Figure 1) to reach decompression at the tension fibre of the slabs in the constant moment region (i.e. $\sigma_{c,bottom} = 0$ MPa).

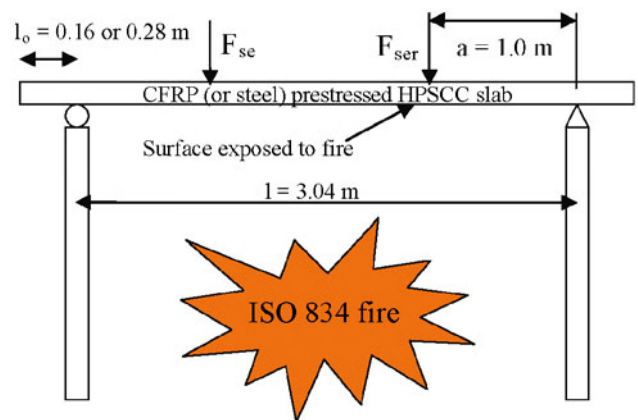


Figure 1 ISO 834 fire test setup for CFRP or steel prestressed HPSCC slabs under service load (F_{ser})

This loading condition corresponds to a typical service load condition for CFRP prestressed façade elements (Terrasi 2007). In addition, a single steel prestressed slab was tested with the same test protocol. The slabs had two possible overhang lengths, l_o , of 160 mm or 280 mm, giving a total slab length of 3360 mm or 3600 mm.

When planning the fire tests, the overhang length, l_0 , was felt likely to be a critical parameter (along with possible cover spalling) for fire survivability. It was hypothesized that loss of tendon bond would be severe at temperatures in the range of the resin's T_g (121 °C in this case). Note that the pultruded CFRP tendons' matrix (epoxy) was used to coat the tendons with a bond-enhancing quartz sand layer directly after pultrusion. The decision was taken that (within the experimental limits given by Empa's furnace dimensions) the overhang length would be a key parameter studied. An overhang length at least as long as the room temperature prestress development length was considered as a minimum requirement for the slabs' design; this prestress development length for the 5.4 mm \varnothing CFRP tendons was assumed to be approximately 30 bar diameters, or 160 mm. Therefore the minimum length of the overhang of the slabs was fixed to 160 mm (short overhang). Keeping in mind that the overhang would experience some heating due to heat transfer along the slab, and that CFRP has a relatively high thermal conductivity in the fibre direction, it was decided to consider the maximum possible overhang length of 280 mm (long overhang), which was limited by the furnace's width. This corresponds to 1.75 times the room temperature prestress development length assumed for the CFRP tendons at an initial prestress, $\sigma_{p0} = 1,200$ MPa. Both overhang lengths are considered realistic for building façade applications for which these elements are envisioned (Terrasi 2007). The test parameters considered are given in Table 1.

For monitoring the time dependent deflection increase one LVDT with range 450 mm (and accuracy of ± 0.5 mm) was placed at midspan for every slab. A maximum of 5 slabs was tested in parallel per fire test. The load introduction devices for the sustained service loads are depicted in Figure 2.

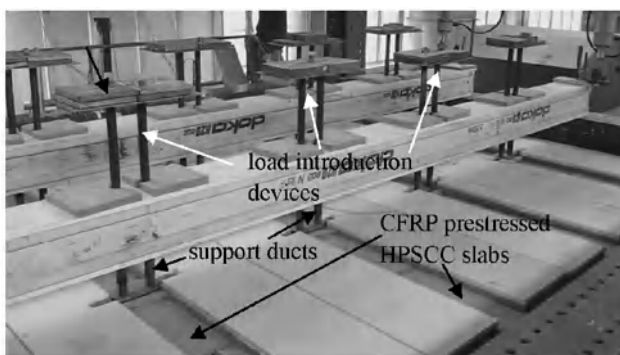


Figure 2 Load introduction devices used to apply sustained service loads during exposure to the ISO 834 fire

All furnace's openings were covered with fire protection plates.

4 RESULTS

4.1 Small-scale fire pre-test

The time to failure was 26 minutes for both small-scale slabs; they collapsed at almost the same instant (Table 1). The failure mode observed (see Figure 3) was a central crack at midspan in both cases that opened because of loss of prestress caused by bond degradation between the CFRP tendon and the concrete; at the end of testing tendon slippages ranging between 1.5 mm and 8 mm were measured at the slabs' end faces. Crushing of the HPSCC at the compression fibre (see Figure 4) subsequently occurred. The testing load was released about 1 minute after failure and the CFRP tendons were still able to keep the slabs in one piece. The residual deflection of the specimens after unloading was about 50 mm (see Figure 4). No concrete spalling was observed in either of these specimens; although the fire exposed surfaces showed small pores that were opened by melting of the short PP fibres.

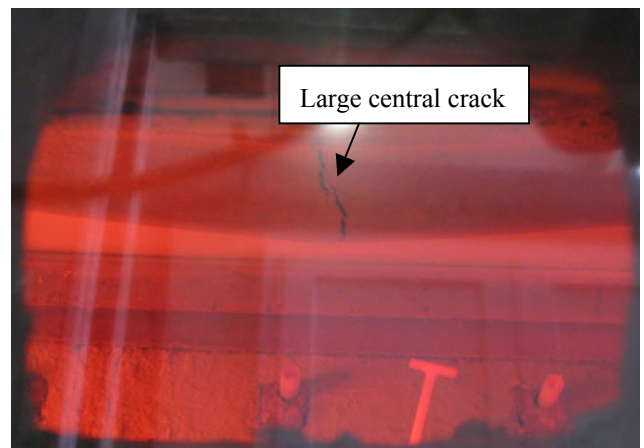


Figure 3 Failure of Slab P (view of the fire exposed surface)

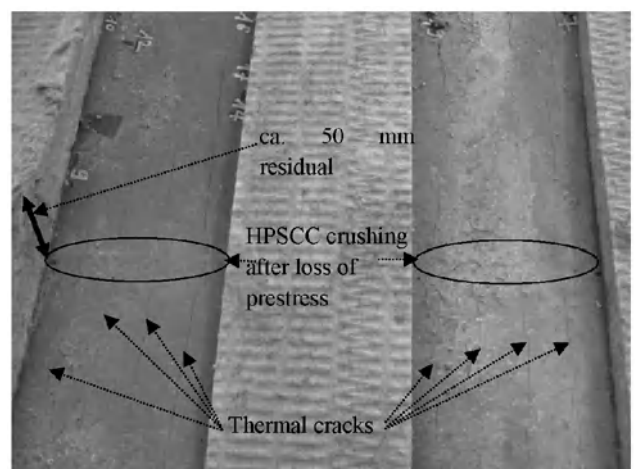


Figure 4 Longitudinal thermal incompatibility (splitting) cracks on the slabs' top surfaces after fire pre-test

The steady increase of the central deflection of both slabs during the fire test is shown in Figure 5. The increase in deflection, due to a combination of thermal

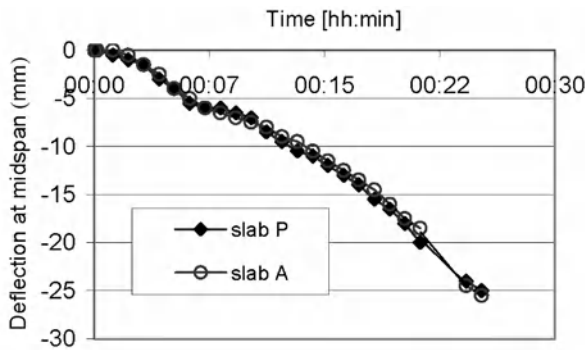


Figure 5 Deflection vs. time curves during small-scale fire test

bowing, loss of flexural stiffness, and bond reductions leading to tendon slippage, was gradual. The simply-supported slabs showed a reasonable deformation capacity, with measured midspan deflection values corresponding to $\text{span}/40$ (≈ 25 mm) 1.3 minutes before failure.

After failure of the slabs several longitudinal splitting cracks running along all four CFRP tendons were observed over the slabs' top surfaces (Figure 4) and, to a lesser extent, on their fire exposed surfaces. These splitting cracks were probably caused by thermal incompatibility of the orthotropic CFRP tendon with the HSPCC. At temperatures between 10–100 °C the coefficient of thermal expansion of the CFRP tendons transverse to the fibre direction is about 2.7-times higher than that of concrete. These cracks eased the slippage of the tendons during the loss of bond. In terms of temperature distributions, the following observations were made: 18 seconds before failure the beginning of the CFRP tendons' anchorage zone (i.e. 20 mm from the slabs' end surface) showed temperatures in the range of 115–153 °C. This is in the range of T_g (121 °C) of the CFRP tendons. At the same instant the temperature in the concrete at midspan, 10 mm from the exposed surface, was in the range of 392–450 °C. The CFRP-TC at 160 mm from the slab's end (i.e. at the end of the tendons' anchorage length at room-temperature) measured about 330 °C. The CFRP-TCs at midspan showed temperatures in the same range.

4.2 Full-scale fire tests

The failure times of the prestressed slabs studied in the full-scale tests are given in Table 1. For all slabs the failure mode was sudden collapse due to "accumulated" HSPCC spalling that reduced the cross-section until the slab failed in bending (due to crushing of the remaining concrete) under the sustained service load. The first spalling occurred at 9'50" from the start of the fire test with the first spalling from Slab 6. It is interesting to note that the first spalling was localized in the slabs' near the supports, where the bending moment is low and the concrete is most highly precompressed. It is well known that concrete spalling is exacerbated by compressive stress, which explains why the decompressed

central span of the slabs was less affected by spalling. Figure 6 shows typical spalling areas of Slab 5 near the support.

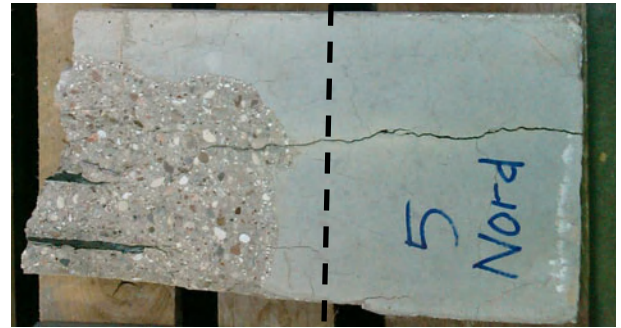


Figure 6 Concrete spalling areas of a section of Slab 5 after fire testing (the support line is dotted on the slab and the fire-exposed side is on the left)

The following remarks can be made from Table 1:

1. The overhang length, l_0 , of 160 or 280 mm did not appear to influence the fire resistance of the slabs. An overhang of 160 mm seemed to be sufficient for anchoring the CFRP tendons, as long the concrete did not spall near to the support. Almost all tendons monitored with TCs near the slab's end were at room temperature in the overhanging zones during the test up until failure. A temperature increase in the overhang zone was measured only for Slab 6 (which failed after more than 90 minutes); this despite temperatures at 200 mm from the tendons' ends reaching 138–199 °C without any slippage of either of the monitored CFRP tendons observed after the test.

2. The two 45 mm thick slabs showed a limited failure time between 26 minutes (Slab 4) and 34 minutes (Slab 7). The 60 mm slabs with failure times of 24 minutes (Slab 8) to 47 minutes (Slab 5) did not show a relevant increase in fire resistance when compared to the thinner slabs (Slabs 4 and 7). The 75 mm thick slabs showed the highest fire resistances with failure times of 60 minutes (Slab 9) to 91 minutes (Slab 6).

3. The steel prestressed reference Slab 40 showed a limited fire resistance of only 29 minutes, which is however not particularly surprising considering the young age of this slab of approx. 1 month at testing. The still humid concrete (with moisture in the range of 4.8%) showed a high spalling rate and collapsed rapidly. This reference test is being repeated on an identical slab but with an age of 12 months in May 2010.

The deflection versus time behaviour of the seven full-scale slabs is given in Figure 7. The slabs' deflection increased rapidly during the first 3–4 minutes of heating, probably due to thermal bowing arising from the temperature gradient over the slab thickness (with furnace temperatures having reached 549–591 °C), and then increased more slowly until a stabilisation was

attained. Thereafter localized concrete spalling could cause small decreases of midspan deflection through cross-section reduction of the now eccentrically prestressed slab's region of spalling (see Slab 4 in Figure 7). Finally the collapse was often preceded by a second steady increase of the midspan deflection.

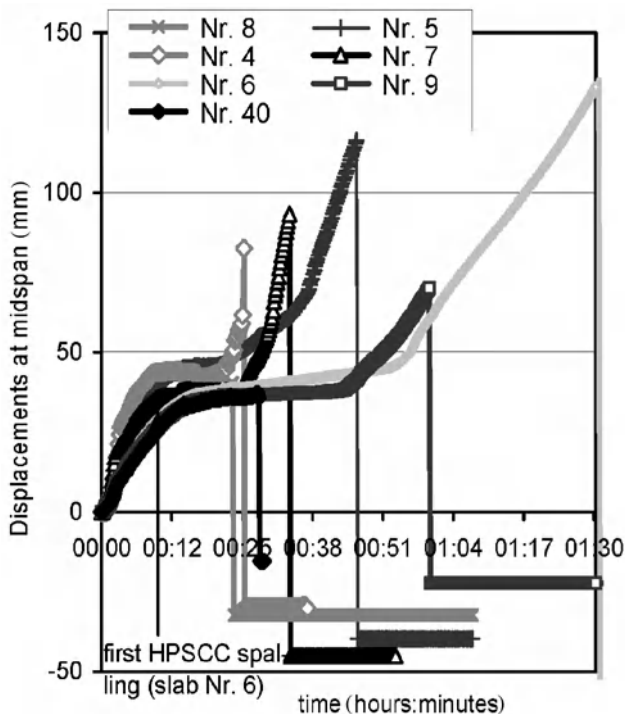


Figure 7 Midspan deflections of the six CFRP and one steel full-scale prestressed HPSCC slabs during the fire tests

5 DISCUSSION AND CONCLUSIONS

5.1 Small-scale fire pre-test

The failure time of the two CFRP prestressed HPSCC slabs with cover $c = 20$ mm under service load conditions (in three-point bending) was 26 minutes. The determining factors were the particular support, prestress development, and slab drying conditions at 40°C and 15% r.H. (which precluded spalling). The observed failure mode was rather gradual, and a brittle failure with separation of the slabs' concrete cover did not occur. In this case the slabs were kept in one piece despite the smoothly sliding debonded tendons until crushing of the compressive zone occurred. The loss of bond in the CFRP tendons' anchorage zones was the reason for the prestress loss, that allowed the opening of the central crack that led to failure (Figure 3).

5.2 Full-scale fire tests

From the full-scale fire tests the following conclusions

can be drawn:

- A fire resistance of R30 (which is an important prerequisite for the design of façades in Switzerland) is achievable for CFRP prestressed HPSCC slabs when a concrete cover of 35 mm is provided. This conclusion is valid for the prestressing level considered herein (1200 MPa) in conjunction with a HPSCC concrete mix containing at least 2 kg/m^2 of short PP fibres.
- The fire resistance of a one month old reference steel wire prestressed HPSCC (with PP fibres) slab was less than 30 minutes. This is not surprising considering the high moisture content (4.8%) of the HPSCC after one month.
- The moisture content of the slender prestressed slabs made of HPSCC with 2 kg/m^2 of short PP fibres was high ($>4\%$) after 8 months from casting, leading to widespread spalling, cracking, and collapse of the slabs in fire. Spalling appears to be a critical issue for these types of members in fire.
- Longitudinal splitting cracks (Figure 4) caused by thermal incompatibility of the orthotropic CFRP tendons with the HPSCC were observed extensively for the two 45 mm thick slabs (Slabs 4 & 7) and, to a smaller extent, for the 60 mm thick slabs (Slabs 5 & 8). Even for the thicker slabs (75 mm wall thickness) single longitudinal cracks were observed.
- Additional research is needed to understand and prevent both concrete cover spalling and longitudinal splitting cracking. Such research is currently underway.

REFERENCES

- Burgoyne, C.J. 1997. Rational Use of Advanced Composites in Concrete. In Japan Concrete Institute (ed.), *Non-Metallic (FRP) Reinforcement for Concrete Structures (FRPRCS-3)*, Proc. intern. Symp., Sapporo, 14-16 October 1997: pp. 75-88. Tokyo: Japan Concrete Institute.
- Terrasi, G.P. 2007. Prefabricated thin-walled structural elements made from high performance concrete prestressed with pultruded carbon wires. In Thanasis Triantafyllou (ed.), *Non-Metallic (FRP) Reinforcement for Concrete Structures (FRPRCS-8)*, Proc. intern. Symp., Patras, 16-18 July 2007. University of Patras.
- Uomoto, T. 2001. Durability Considerations of FRP Reinforcement. In Chris Burgoyne (ed.), *Non-Metallic (FRP) Reinforcement for Concrete Structures (FRPRCS-5)*, Proc. intern. Symp., Cambridge, 16-18 July 2001: pp. 17-32. University of Cambridge.
- ISO 834-1 standard, 1999. Fire-resistance tests—Elements of building construction—Part 1: General requirements. Int. Organisation for Standardisation.

Finite Element Modeling of Insulated FRP-Strengthened RC Beams Exposed to Fire

J. G. Dai (cejgdai@polyu.edu.hk), W.Y. Gao & J.G. Teng

Department of Civil and Structural Engineering, The Hong Kong Polytechnic University, Hong Kong, China

ABSTRACT This paper presents a finite element (FE) model for the thermo-mechanical analysis of insulated FRP-strengthened reinforced concrete (RC) beams exposed to fire. In the model, the effects of loading, thermal expansion of materials, and degradations in both the mechanical properties of materials and the bond behavior at FRP-to-concrete and steel-to-concrete interfaces due to elevated temperatures are all considered. The validity of the FE model is demonstrated through comparisons of FE predictions with results from existing standard fire tests on insulated FRP-strengthened RC beams.

1 INTRODUCTION

Despite its great success in the past two decades, the fiber reinforced polymer (FRP) strengthening technology suffers from one major limitation when indoor applications are considered. FRP composites show poor performance in fire as the polymer matrix typically has a low glass transition temperature, T_g . The polymer transforms into a soft and viscous material with severe stiffness and strength degradations when it is subjected to temperatures close to T_g . In addition, the polymer matrix may ignite under high heat fluxes, resulting in the generation of smoke and the spread of flames. Therefore, a layer of insulation material is often applied on the bonded FRP reinforcement to maintain the fire safety of the strengthened reinforced concrete (RC) member.

A direct approach for evaluating the fire endurance of an RC member strengthened with FRP is to conduct a standard fire test. Limited standard fire tests (Bisby et al. 2005a; Gao et al. 2010; Williams et al. 2008) have indicated qualitatively that FRP-strengthened RC members with appropriate design and insulation can achieve satisfactory fire performance. However, such standard fire tests are usually very expensive and time-consuming and therefore, their usefulness is limited in providing a comprehensive, quantitative understanding of the fire performance of insulated FRP-strengthened RC members covering wide ranges of various design parameters.

As an alternative to standard fire tests, numerical models for the fire resistance analysis of FRP-strengthened structural members have been developed. Bisby et al. (2005b) proposed a sectional model for the fire resistance analysis of FRP-confined RC columns. Hawileh et al. (2009) employed a nonlinear finite element (FE)

model to study the heat transfer and deformation mechanisms in an insulated FRP-strengthened RC T-beam which was tested by Williams et al. (2008). In their work, both the external FRP and the internal reinforcing bars were assumed to be fully bonded with the concrete although bond failure between FRP and concrete is a common failure mode in FRP-strengthened RC beams. Indeed, the bond between FRP and concrete may degrade more rapidly than FRP itself under elevated temperatures.

The fire endurance analysis of insulated FRP-strengthened RC members is more challenging than that of un-protected FRP-strengthened RC members as for the latter the contribution of FRP can be simply ignored [e.g. Han et al. (2006)]. Additional aspects that need to be considered in the former include the temperature-dependent behavior of FRP and interactions among FRP, concrete and steel reinforcement at elevated temperatures. This paper presents a generic and advanced FE model based on ABAQUS to simulate the thermal and structural responses of insulated FRP-strengthened RC members exposed to fire.

2 THE FE MODEL

2.1 Thermal and mechanical properties of steel, concrete and FRP at elevated temperatures

The thermal conductivity, specific heat and thermal expansion of steel and concrete are defined following EN 1992-1-2 (2004). The thermal properties of carbon FRP sheets at elevated temperatures are determined according to Griffis et al. (1981) but the longitudinal thermal expansion coefficient of carbon FRP sheets is assumed to be zero based on ACI 440.2R-08 (2008).

The uni-axial compressive stress-strain model for

concrete at elevated temperatures given in EN 1992-1-2 (2004) is adopted; this model already includes the temperature and transient creep effects. The tension-softening behavior of concrete is represented by a tensile stress-crack displacement relationship based on the fracture energy and crack band concepts. Concrete is modeled using a damaged plasticity model, in which the yield surface developed by Lee and Fenves (1998) and the Drucker-Prager flow potential function are employed. The uni-axial tensile stress-strain relationship of reinforcing steel at elevated temperatures is also defined according to EN 1992-1-2 (2004).

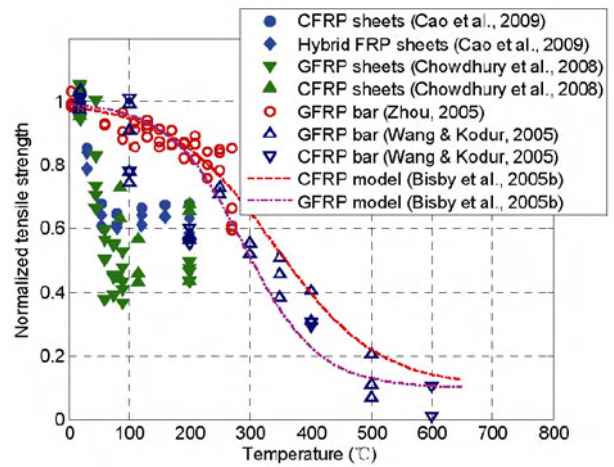
Little information is available on the mechanical behavior of FRP plates/sheets for structural strengthening applications at elevated temperatures in the published literature. Bisby et al. (2005b) collected existing test data and proposed a sigmoid function model for the strength and stiffness degradations of FRP composites at elevated temperatures. It should be noted that most of the test data collected by Bisby et al. (2005b) were from the tensile tests of FRP bars or tendons. Therefore, Bisby et al.'s (2005b) model may not be suitable for FRP sheets commonly used to strengthen RC beams as such FRP sheets are usually formed via a wet lay-up process and possess a much lower T_g than pre-cured FRP products.

Figure 1a presents the available tensile strength test data for FRP sheets at elevated temperatures (Cao et al. 2009; Chowdhury et al. 2008). The test data from Wang and Kodur (2005) and Zhou (2005) for FRP bars and the models proposed by Bisby et al. (2005b) are also shown in the figure for comparison. In the figure, the tensile strengths of FRP bars/sheets at different temperatures are normalized by that obtained at room temperature. It is clearly seen that the tensile strength degradation of FRP sheets is more severe than that of FRP bars. As the performance of FRP sheets/bars depends predominately on the glass transition temperature, T_g , of the polymer matrix, the value of T_g needs to be taken as a key parameter in any mathematical relationship representing the degradation of tensile strength with elevated temperature. A sigmoid function as given below and used by Bisby et al. (2005a) seems appropriate for the tensile strength degradation of both FRP bars and FRP sheets:

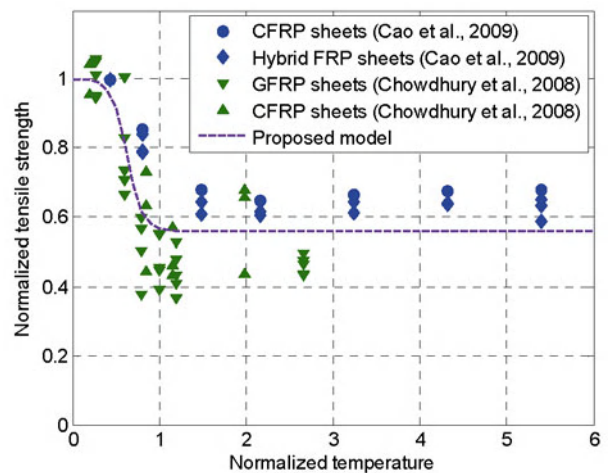
$$\frac{f_T}{f_0} = \left(\frac{1-a_1}{2} \right) \times \tanh \left(-a_2 \times \left(\frac{T}{T_g} - a_3 \right) \right) + \left(\frac{1+a_1}{2} \right) \quad (1)$$

where f_0 and f_T are the tensile strengths at ambient temperature and at an elevated temperature T , respectively; and $a_1 = 0.556$, $a_2 = 5.624$ and $a_3 = 0.630$ are empirical factors. Figure 1b shows this proposed relationship where the tensile strength is normalized by the tensile strength at ambient temperature and the temperature by the T_g value of the polymer matrix. Due

to a lack of test data, it is assumed that relationship described by Eq. 1 can be also used to evaluate the degradation of elastic modulus of FRP sheets at elevated temperatures.



(a) Normalized strength vs. temperature



(b) Normalized strength vs. normalized temperature

Figure 1 Tensile strength degradations of FRP sheets at elevated temperatures

2.2 Bond models for interfaces

For insulated FRP-strengthened RC members exposed to fire, the bond behavior of FRP-to-concrete and reinforcing steel-to-concrete interfaces becomes important. Bond deteriorations at both interfaces with elevated temperature may significantly affect the cracking behavior of concrete and the occurrence of debonding failure in the insulated system. However, such bond deteriorations have received little attention in existing work. In the present FE model, the bond-slip responses at FRP-to-concrete and steel-to-concrete interfaces at elevated temperatures are explicitly represented through the use of nonlinear spring elements. A perfectly rigid contact condition is assumed for the normal direction between reinforcing steel bars and concrete. In the tangential direction, the CEB-FIP (1993) bond-slip model is

adopted as the ambient temperature model for steel-to-concrete interfaces; appropriate bond strength and interfacial energy reductions are incorporated into this model to reflect bond deteriorations at elevated temperatures (Dai et al. 2010).

For FRP sheets-to-concrete interfaces, Gao et al. (2010) conducted double-lap shear tests to investigate bond deteriorations at elevated temperatures. The carbon fiber sheets (0.167 mm thick) used had a tensile strength of 2900 MPa and an elastic modulus of 230 GPa. The bond length and width of the FRP sheets were 120 mm and 100 mm, respectively. The compressive strength of concrete was 34.5 MPa. As shown in Figure 2, the failure load of the FRP-to-concrete interface at 40°C is slightly higher than that at 4°C but then decreases as the temperature further increases. For the current FE model, the bond-slip model proposed by Lu et al. (2005) for FRP-to-concrete interfaces at room temperature was modified to describe the temperature-dependent bond behavior described above. The interfacial fracture energy (the area underneath the bond-slip curve) of the FRP-to-concrete interface at an elevated temperature was derived from the temperature-dependent interfacial failure load (i.e. the pull-off load of the FRP sheet as shown in Figure 2), based on the fact that the failure load is proportional to the square root of the interfacial fracture energy. As a result, a temperature-dependent local bond stress-slip model for FRP sheets-to-concrete interfaces at elevated temperatures was established for use in the FE model (Figure 3) (Dai et al. 2010).

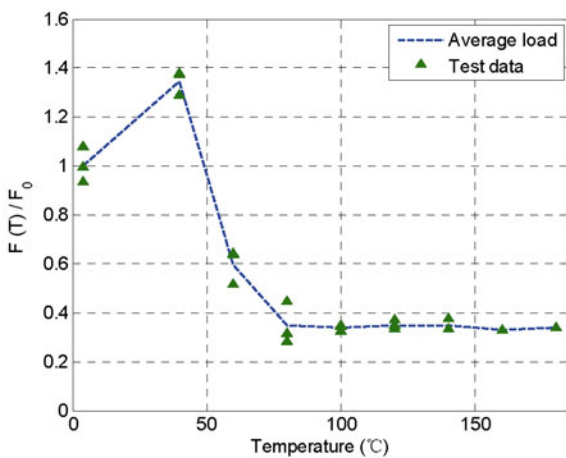


Figure 2 Failure load of FRP-to-concrete bonded joints versus temperature

3 VERIFICATION OF THE FE MODEL

The FE model described above was implemented using ABAQUS and deployed to analyze full-scale fire tests conducted on three RC beams strengthened with CFRP sheets, which were protected with different insulation materials (Gao et al. 2010). Due to space limitation, only results for one RC beam insulated with a 40 mm

calcium silicate board are presented herein. In the test, the temperatures at the FRP sheet-to-concrete interfaces at the mid-span and quarter-span cross-sections were measured by Type-K thermocouples. Other details of the tests, such as the arrangements of steel reinforcement and thermocouples, can be found in Gao et al. (2010).

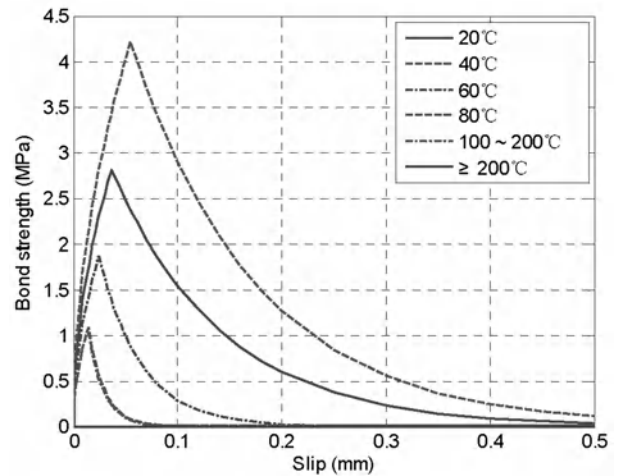
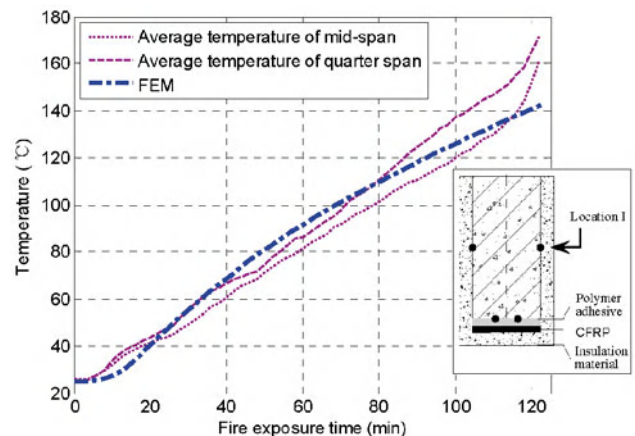
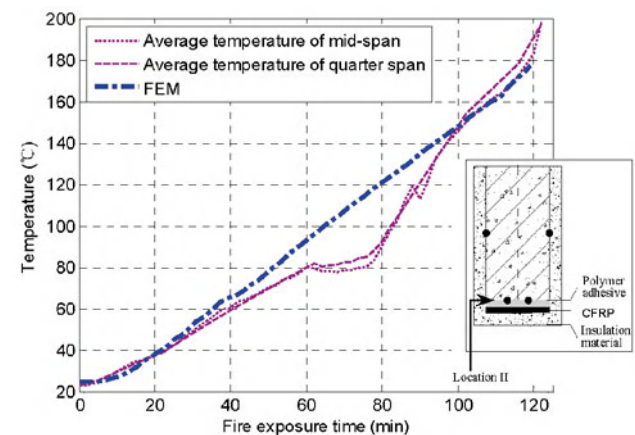


Figure 3 Proposed bond-slip curves of FRP-to-concrete interfaces at elevated temperatures



(a) Location I (at the mid-height of the beam and between the insulation layer and the concrete)



(b) Location II (at the soffit of the beam and between the FRP and the concrete)

Figure 4 Temperatures versus fire exposure time

Figure 4 shows experimental and predicted temperatures at various sectional depths as a function of fire exposure time. At the mid-height of the beam, a close agreement between experimental and predicted temperatures is seen. At the soffit of the beam, the predicted temperatures at the FRP-to-concrete interface differ significantly from the experimental values at fire exposure times of 60 and 80 minutes; otherwise, there is reasonable agreement between the two sets of results. In the test, the temperature experienced a plateau 60 minutes after the fire test commenced and a more rapid increase between 80 minutes and 100 minutes. However, the FE modeling could not capture these variations. This plateau was possibly due to the migration of moisture from the insulation material to the surface of the FRP sheet due to the better moisture-resistance of the latter. In Figure 5, the test and predicted mid-span deflections of the insulated FRP-strengthened RC beam are shown as a function of the fire exposure time. It is seen that the predicted results agree very closely with the test results. It can thus be concluded that the FE model is capable of providing reasonably accurate predictions for both the temperature field and the structural response of an insulated FRP-strengthened RC beam.

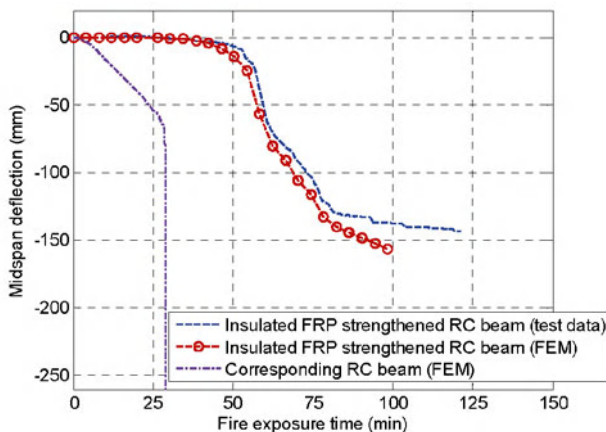


Figure 5 Mid-span deflections versus fire exposure time

4 CONCLUDING REMARKS

In this paper, an advanced FE model has been presented for the evaluation of fire performance of insulated FRP-strengthened RC beams. In the model, the bond-slip responses of FRP-to-concrete and steel-to-concrete interfaces at elevated temperatures are explicitly represented. The accuracy of the FE model has been verified through comparisons between predicted results and results from a standard fire test on an insulated FRP-strengthened RC beam conducted by Gao et al. (2010). FE predictions for both the temperature field and the structural response are in reasonably close agreement with the test data. The model is being exploited in parametric studies for the development of fire endurance

design guidelines for insulated FRP-strengthened RC beams.

5 ACKNOWLEDGEMENT

The authors would like to thank The Hong Kong Polytechnic University and the Innovation and Technology Commission of the Hong Kong SAR Government (Project No: ITS/084/08) for their financial support. They are also grateful to Mr G.M. Chen who assisted in the FE modeling work.

REFERENCES

- ACI 440.2R-08. 2008. Guide for the design and construction of externally bonded FRP systems for strengthening concrete structures. Michigan: Farmington Hills.
- Bisby, L.A., Kodur, V.K.R. & Green M.F. 2005a. Fire endurance of Fiber-reinforced polymer-confined concrete columns. *ACI Structural Journal*, 102(6): 883-891.
- Bisby, L.A., Green M.F. & Kodur, V.K.R. 2005b. Modeling the behavior of Fiber reinforced polymer-confined concrete columns exposed to fire. *Journal of Composite for Construction*, ASCE, 9(1): 15-24.
- Cao, S.H., Wu, Z.S. & Wang, X. 2009. Tensile properties of CFRP and hybrid FRP composites at elevated temperatures. *Journal of Composite Materials*, 43(4): 315-330.
- CEB-FIP. 1993. CEB-FIP model code 1990, Thomas Telford, London, UK.
- Chowdhury, E.U., Eedson R., Bisby, L.A., Green, M.F., Benichou, N. & Kodur, V.K.R. 2008. Mechanical characterization of fibre reinforced polymers for numerical fire endurance modelling. In K.H.Tan, V.K.R.Kodur and T.H.Tan (eds.), *Proceeding of the Fifth International Conference-Structures in Fire*, 28-30 May 2008, Singapore.
- Dai, J.G., Gao, W.Y. & Teng, J.G. 2010. Finite element modeling of reinforced concrete beams exposed to fire, in preparation.
- EN 1992-1-2. 2004. Eurocode 2: Design of concrete structures - Part 1-2: General rules - Structural fire design. Brussels: CEN.
- Gao, W.Y., Hu, K.X. & Lu, Z.D. 2010. Fire resistance experiments of insulated CFRP strengthened reinforced concrete beams. *China Civil Engineering Journal*, 43(3): 15-23.
- Griffis, C.A., Masmura, R.A. & Chang, C.I. 1981. Thermal response of graphite epoxy composite subjected to rapid heating. *Journal of Composite Materials*, 15(5): 427-442.
- Han, L.H., Zheng, Y.Q. & Teng, J.G. 2006. Fire resistance of RC and FRP-confined RC columns, *Magazine of Concrete Research*, 58(8), 533-546.
- Hawileh, R.A., Naser, M., Zaidan, W. & Rasheed, H.A. 2009. Modeling of insulated CFRP-strengthened reinforced concrete T-beam exposed to fire. *Engineering Structures*, 31(12): 3072-3079.
- Lee, J. & Fenves, G. 1998. Plastic damage model for cyclic loading of concrete structures. *Journal of Engineering Mechanics*, ASCE, 124(8): 892-900.
- Lu, X.Z., Teng, J.G., Ye, L.P. & Jiang, J.J. 2005. Bond-slip models

- for FRP sheets/plates bonded to concrete. *Engineering Structures*, 27(6): 920-937.
- Wang, Y.C. & Kodur, V.K.R. 2005. Variation of strength and stiffness of fibre reinforced polymer reinforcing bars with temperature. *Cement & Concrete Composites*, 27(9-10): 864-874.
- Williams, B., Kodur, V.K.R., Green M.F. & Bisby, L. 2008. Fire endurance of Fiber-reinforced polymer strengthened concrete T-beams. *ACI Structural Journal*, 105(1): 60-67.
- Zhou, C.D. 2005. Fire performance of GFRP reinforced concrete. Research Report, Department of Civil Engineering, Tongji University, Shanghai, China.

Effect of Fire and High Temperature on the Properties of Self Compacted Concrete

M. A. Helal¹ (mahelal54@yahoo.com) & Kh. M. Heiza² (khheiza@yahoo.com)

1. Housing & Building National Research Center, Cairo, Egypt

2. Civil Engineering Dept., Faculty of Engineering, Minoufiya University, Egypt

ABSTRACT The use of self-compacted concrete increased significantly during the last few decades. Self-compacted concrete exhibits significantly higher compressive strength than normal concrete, which allows structural members to carry higher loads. The influence of elevated temperature on the properties of concrete is important for fire resistance studies. Fire remains one of the most serious potentials hazardous to any building. In this study, the effect of high temperature on the properties of self-compacted concrete (SCC) compared with the ordinary concrete (NC) was investigated. The effect of cooling technique on the properties of SCC and NC was discussed. The properties of SCC and NC were measured after exposed to 200°C, 400°C and 600°C for two hours. Results from these tests show that the mechanical properties decreased with increasing temperatures. The mechanical properties of SCC cooled gradually are better than that cooled suddenly by water.

1 INTRODUCTION

The high temperatures due to fire have a significant effect on the strength and deformation characteristics of the various structural components, such as columns, beams, slabs, shear-walls, etc [1–2]. The degree of damage depends on the properties of the constituent materials of concrete. Malhotra reported that concrete partially loses its strength at temperature of 200°C to 250°C, but cracks start to occur at about 300°C where the concrete loses 30% of its compressive strength, and the loss of strength continues with the increase in the temperature. All concrete loses strength at elevated temperatures, but the rate of reduction differs with the type of aggregate used [3–5]. High performance concrete has been shown to have greater risks of deterioration during fire exposure compared to ordinary and self compacted concrete. The same high performance concrete conditions are applied for when self-compacted concrete is susceptible to fire damage. It is also important to address any additional conditions that may arise for self-compacted concrete behavior [6–7]. Fire performance of both normal and self compacted reinforced concrete loaded columns was studied [8]. Spalling effect is clear in SCC than NC. The highest compressive strength was recorded for SCC using dolomite aggregate [9]. Also, the porosity increased with the exposure time from 1–3 hours and SCC with dolomite has the maximum values compared to the other. The structural elements have to be protected or sealed after exposure to fire to prevent moisture penetration due to the increase

in porosity[10]. Behavior of thermally treated SCC was studied using X-ray diffraction (XRD) and the phase composition (DSC) to investigate the internal decomposition of SCC subjected to fire at different intervals [11]. It shows that the high temperature has a clear effect on both physico-mechanical and microstructure characteristics of SCC. The phase composition and microstructure indicate an increased degree of crystallinity of formed hydrates upon thermal treatment at 200 °C with a marked decomposition at 600 °C [12-13-14].

2 EXPERIMENTAL PROGRAM

The mixes properties constituents are reported in tables (1).

Table 1 Mix proportions by weight (kg) for NC and SCC

	Cement	Dolomite	Sand	Water	Fly ash	VEA	W/C
NC	400	1100	720	180	–	–	0.45
SCC	400	800	980	145	40	8	0.36

Concrete was mixed, cast in the molds and curing according to the standard specifications. For hardened properties all specimens were kept in molds for 24 hours. The influence of high temperature on the microstructure and physico-mechanical properties of SCC was studied. The experimental program is performed to investigate the behavior of concrete exposed to uniform temperature for two hours, and then cooled by different cooling techniques. The specimens are heated

up to 200 °C, 400 °C and 600 °C and the centers temperatures are measured and recorded with time for two hours, then the furnace is switched off. The specimens cooled gradually or suddenly until the temperature of specimen reaches the ambient temperature. Gradual technique: the specimens were removed from the furnace at the end of the required heat interval and allowed into air-cooled gradually in the laboratory atmosphere. Sudden technique: the specimens were removed from the furnace at the end of the required heat interval and quenched by tap water until reaching the laboratory atmosphere.

3 ANALYSES AND DISCUSSION OF TEST RESULTS

3.1 Effect of temperature on the mechanical properties

Figure (1) shows the variation of the compressive strength with the temperature for SCC and NC at 28 days. For different treatment. For SCC, it is clear that; for gradually cooling the compressive strength at 200 °C was increased with (5.7%) of its reference compressive strength. The figure shows also, with increasing the temperature of furnace up to 400 °C and 600 °C decreasing the compressive strength with (9.34% and 27.73%) respectively compared with the compressive strength of the control mix. The figure also indicates that reduction of the compressive strength using the suddenly cooling higher than the gradually cooling. The percentage of the reduction of compressive strength was (10.33%, 24.56% and 40.78%) of its initial compressive strength at 200 °C, 400 °C and 600 °C respectively. For NC the compressive strength at 200 °C was increased with (4.47%) of its reference compressive strength for gradually cooling. The figure shows also, with increasing the temperature of furnace up to 400 °C and 600 °C decreasing the compressive strength with (16.15% and 49.32%) respectively compared with the compressive strength of the control mix. The figure also indicates that reduction of the compressive strength using the suddenly cooling higher than the gradually cooling. The percentage of the reduction of compressive strength was (21.09%, 37.44% and 63.14%) of its initial compressive strength at 200 °C,

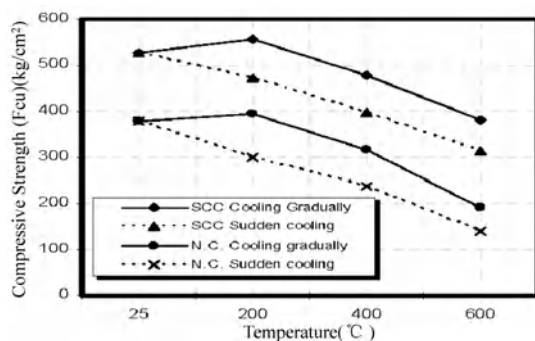


Figure 1 Relationship between temperature and ultimate compressive strength (Fcu) for concrete at 28 days

400 °C and 600 °C respectively. It can be concluded that, using fly ash improved the performance of self-compacted concrete at elevated temperature compared to normal concrete. Using suddenly cooling decrease the compressive strength compared with gradually cooling. The percentage of reduction of compressive strength for normal concrete is more than the self-compacted concrete. At high temperature, the strength of self-compacted concrete was still in the safe limits and did not reach to critical strength after two hours.

Figure (2) shows the relationship between the splitting tensile strength with the temperature for the SCC and NC at 28 days for different treatment. For SCC, for gradually cooling the reduction in splitting tensile strength were 26.67%, 44.17% and 58.46% of its initial splitting tensile strength at 200 °C, 400 °C and 600 °C respectively. The figure also indicates that reduction of the splitting tensile strength using the suddenly cooling higher than the gradually cooling. The percentage of the reduction of splitting tensile strength were 30.97%, 48.51% and 66.47% of its initial splitting tensile strength at 200 °C, 400 °C and 600 °C respectively. For NC for gradually cooling the reduction in splitting tensile strength were 24.91%, 40.28% and 63.42% of its initial splitting tensile strength at 200 °C, 400 °C and 600 °C respectively. The figure also indicates that reduction of the splitting tensile strength using the suddenly cooling higher than the gradually cooling. The percentage of the reduction of splitting tensile strength were 34.87%, 52.8% and 67.37% of its initial splitting tensile strength at 200 °C, 400 °C and 600 °C respectively. In general, the splitting tensile strength for self-compacted concrete using 10% fly ash as an addition to cement content decrease with increase the temperature of the furnace. It can be concluded that, the reduction in splitting tensile strength for self-compacted concrete cooling gradually was less than the splitting tensile strength for normal concrete. Also the reduction in splitting tensile strength for self-compacted concrete cooling suddenly was higher than the splitting tensile strength for normal concrete for samples cooling suddenly, the reduction in splitting tensile strength higher than cooling gradually.

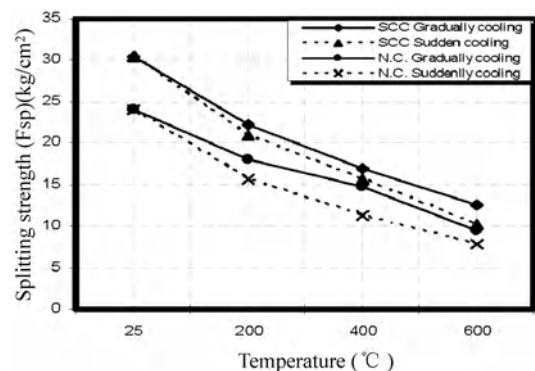


Figure 2 Relationship between temperature and splitting tensile strength (Fsp) for concrete at 28 days

Figure (3) illustrates the relationship between the flexural strength (F_f) with the temperature for the SCC and NC at 28 days for different treatment. For SCC, the results observed that, the flexural strength decreases with increases the temperature of the furnace using gradually cooling. The reduction in flexural strength was 33.52%, 58.36% and 81.11% of its initial flexural strength at 200°C, 400°C and 600°C respectively. The figure also indicates that reduction in the flexural strength using the suddenly cooling was higher than the gradually cooling. The percentage of the reduction in flexural strength was (42.9%, 66.20% and 88.87%) of its initial flexural strength at 200°C, 400°C and 600°C respectively. For NC, The results observed that, the flexural strength decreases with increases the temperature of the furnace using gradually cooling. The reduction in flexural strength was 28.46%, 71.57% and 83.11% of its initial flexural strength at 200°C, 400°C and 600°C respectively. The figure also indicates that reduction in the flexural strength using the suddenly cooling was higher than the gradually cooling. The percentage of the reduction in flexural strength was (48.55%, 79.07% and 88.30%) of its initial flexural strength at 200°C, 400°C and 600°C respectively. From these curves, it can be observed that, the flexural strength for self-compacted concrete using 10% fly ash as an addition to cement content decrease with increase the temperature of the furnace. The reduction in flexural strength for self-compacted concrete which cooling gradually was less than the flexural strength for normal concrete. Also the reduction in flexural strength for self-compacted concrete cooling suddenly was higher than the flexural strength for normal concrete. For samples cooling suddenly, the reduction in flexural strength higher than cooling gradually.

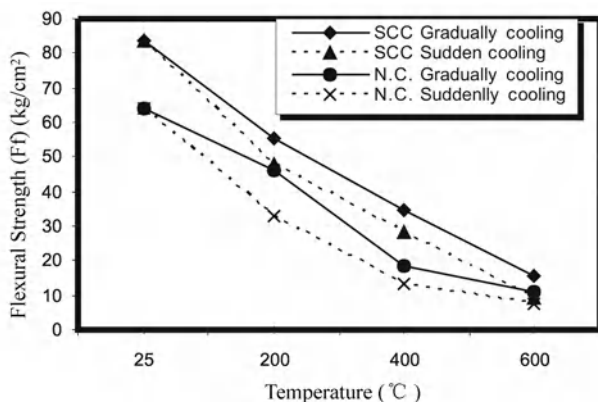


Figure 3 Relationship between temperature and flexural strength (F_f) for concrete at 28 days

Figure (4) shows the variation of the bond strength (F_b) with the temperature for the SCC and NC at 28 days for different treatment. For SCC, the bond strength decreases with increases the temperature of the furnace

using gradually cooling. The reduction in bond strength was 7.39%, 16.94% and 29.74% of its initial bond strength at 200°C, 400°C and 600°C respectively. The figure also indicates that reduction in the bond strength using the suddenly cooling was higher than the gradually cooling. The percentage of the reduction in flexural strength was (14.75%, 34.31% and 41.41%) of its initial bond strength at 200°C, 400°C and 600°C respectively. For NC, the bond strength decreases with increases the temperature of the furnace using gradually cooling. The reduction in bond strength was 13.82%, 23.19% and 42.54% of its initial bond strength at 200°C, 400°C and 600°C respectively. The figure also indicates that reduction in the bond strength using the suddenly cooling was higher than the gradually cooling. The percentage of the reduction in bond strength were (34.93%, 53.52% and 60.26%) of its initial bond strength at 200°C, 400°C and 600°C respectively. From these curves, it can be observed that, the bond strength for self-compacted concrete using 10% fly ash as an addition to cement content decrease with increase the temperature of the furnace. The reduction in bond strength for self-compacted concrete which cooling gradually was less than the bond strength for normal concrete. Also the reduction in bond strength for self-compacted concrete cooling suddenly was higher than the bond strength for normal concrete. For samples cooling suddenly, the reduction in bond strength higher than cooling gradually.

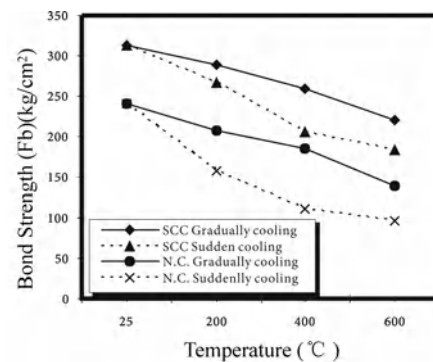


Figure 4 Relationship between temperature and bond strength for concrete at 28 days

3.2 Variation of the center temperature

The center temperature of the samples is affected by the thermal properties of the mixes materials. The moisture movement through the samples, is explained as, most of water thus formed will go to the colder interior of the samples and reabsorbed in the voids. The movement of the moisture through the samples depends on the materials microstructure and the pore system inside the materials.

Figure (5) illustrates the variation in the temperature inside the center of the cube with the time of exposure at

different temperature (200°C, 400°C and 600°C) for SCC and NC. It is clear that, the temperature of the cube center from SCC exposed to 200°C reaches to about 55°C after 60 min while reaching at the same time to 95°C for NC. By increasing the exposed temperature to 400°C, the temperature of the cube center reaches to about 105°C and 305°C for SCC and NC respectively after 60 min. Also, by increasing the exposed temperature to 600°C, the temperature of the cube center reaches to about 245°C and 465°C for SCC and NC respectively after 60 min. Finally at 120 min, the temperature of the cube center from SCC exposed to 200°C, 400°C and 600°C reached to about 80°C, 150°C and 345°C respectively while reached to about 105°C, 355°C and 560°C for NC respectively. It can be concluded that, the variation in temperature inside the cube for SCC less than the variation in temperature for NC because of the permeability in SCC is less than that in NC and generally, the temperature inside the cube increasing with the time.

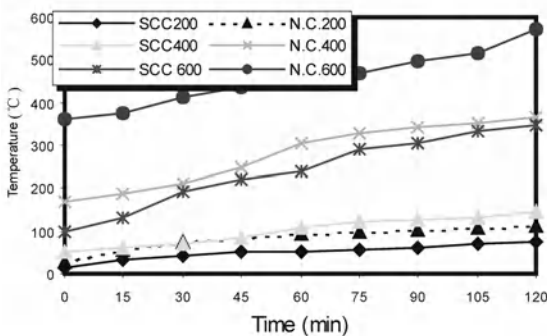


Figure 5 Relationship between the temperature and the time inside the cube at 28 days

Figure (6) shows the variation in the temperature inside the center of the cylinder with the time of exposure at different temperature (200°C, 400°C and 600°C) for SCC and NC. It is clear that, the temperature of the cylinder center from SCC exposed to 200°C reaches to about 45°C after 60 min while reaching at the same time to 55°C for NC. By increasing the exposed temperature to 400°C, the temperature of the cylinder center reaches to about 195°C and 255°C for SCC and NC respectively after 60 min. Also, by increasing the exposed temperature to 600°C, the temperature of the cylinder center reaches to about 295°C and 425°C for SCC and NC respectively after 60 min. Finally at 120 min, the temperature of the cylinder center from SCC exposed to 200, 400 and 600°C reached to about 60,250 and 425°C respectively while reached to about 80, 330 and 475°C for NC respectively. It can be concluded that, the variation in temperature inside the cylinder for SCC less than the variation in temperature for NC because of the permeability in SCC is less than that in NC and generally, the temperature inside the cylinder increasing

with the time.

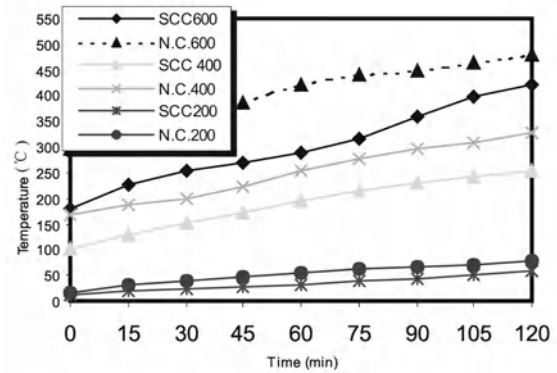


Figure 6 Relationship between the temperature and the time inside the cylinder at 28 days

Figure (7) illustrates the variation in the temperature inside the center of the prism with the time of exposure at different temperature (200°C, 400°C and 600°C) for SCC and NC. It is clear that, the temperature of the prism center from SCC exposed to 200°C reaches to about 50°C after 60 min while reaching at the same time to 60°C for NC. By increasing the exposed temperature to 400°C, the temperature of the prism center reaches to about 55°C and 150°C for SCC and NC respectively after 60 min. Also, by increasing the exposed temperature to 600°C, the temperature of the prism center reaches to about 250°C and 375°C for SCC and NC respectively after 60 min. Finally at 120 min, the temperature of the prism center from SCC exposed to 200, 400 and 600°C reached to about 70,110, and 340°C respectively while reached to about 85, 230 and 460°C for NC respectively. It can be concluded that, the variation in temperature inside the prism for SCC less than the variation in temperature for NC because of the permeability in SCC is less than that in NC and generally, the temperature inside the prism increasing with the time.

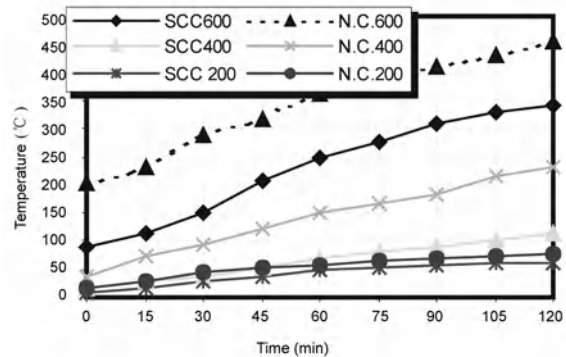


Figure 7 Relationship between the temperature and the time inside the prism at 28 days

Figure (8) shows the variation in the temperature inside the center of the cylinder with steel with the time of exposure at different temperature (200°C, 400°C and

600°C) for SCC and NC. It is clear that, the temperature of the cylinder with steel bear in center from SCC exposed to 200°C reaches to about 50°C after 60 min while reaching at the same time to 55°C for NC. By increasing the exposed temperature to 400°C, the temperature of the cylinder with steel bear in center reaches to about 200°C and 225°C for SCC and NC respectively after 60 min. Also, by increasing the exposed temperature to 600°C, the temperature of the cylinder with steel center reaches to about 340°C and 370°C for SCC and NC respectively after 60 min. Finally at 120 min, the temperature of the cylinder with steel center from SCC exposed to 200, 400 and 600°C reached to about 75, 260 and 440°C respectively while reached to about 90, 285 and 490°C for NC respectively. It can be concluded that, the variation in temperature inside the cylinder with steel for SCC less than the variation in temperature for NC because of the permeability in SCC is less than that in NC and generally, the temperature inside the cylinder with steel bear in center increasing with the time.

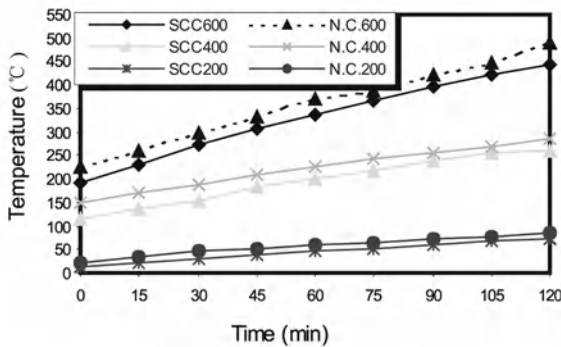


Figure 8 Relationship between the temperature and the time inside the cylinder with steel bear in center at 28 days

By analysis the results of the variation of the center temperature of different samples, it can noted some important remarks. In the case of the cube, the temperature of the cube center from NC exposed to 200, 400 and 600°C equal 1.72, 2.9 and 1.89 times the temperature of the cube center from SCC respectively after 60 min while equal 1.31, 2.36 and 1.62 times respectively after 120 min. In the case of the cylinder, the temperature of the cylinder center from NC exposed to 200, 400 and 600°C equal 1.22, 1.3 and 1.44 times the temperature of the cylinder center from SCC respectively after 60 min while equal 1.33, 1.32 and 1.11 times respectively after 120 min. In the case of the prism, the temperature of the prism center from NC exposed to 200, 400 and 600°C equal 1.2, 2.72 and 1.5 times the temperature of the prism center from SCC respectively after 60 min while equal 1.21, 2.09 and 1.35 times respectively after 120 min. In the case of the cylinder

with steel bear in center, the temperature of the cylinder with steel bear in center from NC exposed to 200, 400 and 600°C equal 1.1, 1.12 and 1.08 times the temperature of the cylinder with steel bear in center from SCC respectively after 60 min while equal 1.2, 1.09 and 1.11 times respectively after 120 min. From this analysis, it can be concluded that the important effect of the shape of the samples regarding to the temperature distribution inside the samples where the largest value were observed in the cube case for every exposure temperature (200°C, 400°C and 600°C). Also, the steel bear in center leads to that the temperature difference between SCC and NC is small relative to the cylinder without bear in center steel. The couture line temperature with time for both the self-compacted concrete and the normal concrete were illustrated in Figure (9) and Figure (10). When exposed the concrete to high temperature, we find that the amount of heat absorbed by concrete increases because the increasing in the temperature difference between the temperature of concrete and the surrounding (ΔT). Using fly ash in self-compacted concrete provided fire resistance. The amount of heat absorbed at the same temperature for self-compacted concrete lower than the amount of heat absorbed for normal concrete because of the thermal conductivity for self-compacted concrete less then normal concrete.

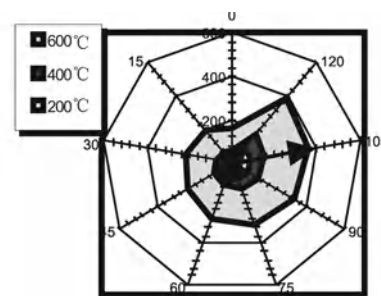


Figure 9 Couture line of temperature inside the cube with time for self-compacted concrete

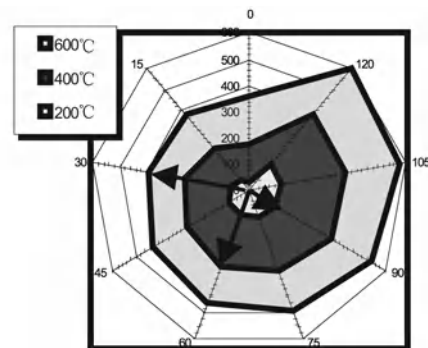


Figure 10 Couture line of temperature inside the cube for normal concrete

3.3 Phase Composition

Firstly, it is important to make a comparison between the phase composition of SCC and NC at room temperature and after exposure to high temperature.

Figure (11) shows the DSC thermo grams of NC and SCC at room temperature and after exposure to high temperature. The thermo grams of NC and SCC illustrate three main endothermic peaks around 140, 460 and 580°C respectively. The first peak located around 140°C represents to the decomposition of the tobermrite gel as well calcium and sulphoaluminate or carbonate hydrates. The second peak is located around 460°C represents to the decomposition of calcium hydroxide (CH). The third peak is located around 580°C is due to the conversion of quartz. The figure demonstrated that the enthalpy of Ca(OH)₂ phase reached to 16.36 and 13.62 J/g in the case of NC at room temperature and after exposure to high temperature respectively. Also, the figure demonstrated that the enthalpy of Ca(OH)₂ phase reached to 17.27 and 9.37 J/g in the case of SCC at room temperature and after exposure to high temperature respectively.

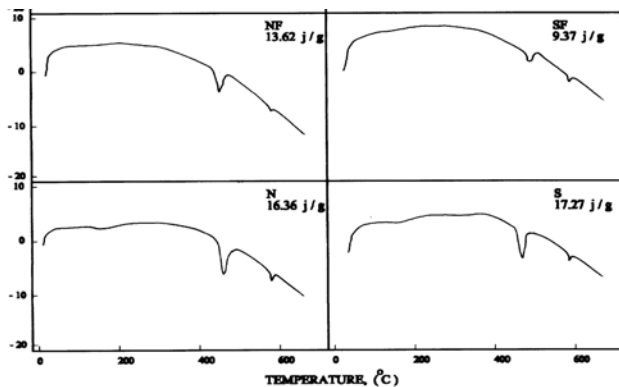


Figure 11 DSC thermo grams of NC and SCC columns after exposure to fire

Fig (12) shows the DSC thermo grams of SCC after thermal treatment at 200°C, 400°C and 600°C. The thermo grams of the SCC illustrate three main endothermic peaks around 120, 460 and 580°C respectively. The first peak located around 120°C represents to the decomposition of the tobermrite gel. The second endothermic peak observed around 460°C represents to the decomposition of calcium hydroxide (CH). The third endothermic peak is located around 580°C is due to the conversion of quartz. Also, it can be seen that, the peak intensities of the main endotherms characteristic for calcium hydroxides and calcium silicate hydrates increase with increasing temperature from 200 to 400°C. This result is mainly due to the accelerated autoclaved hydration within the internal pore system of the SCC. Thermal treatment up to 600°C, however, results in a marked decrease in the peak intensity of calcium

hydroxide with a complete disappearance of the endotherms characterizing the calcium silicate hydrates; this result leads to a marked reduction in the strength values after 400°C.

3.4 XRD patterns

Figure (13) shows the XRD patterns of SCC after thermal treatment at 200°C, 400°C and 600°C. The figure shows that all treated samples contain quartz, CH, calcite, feldspar, and dolomite. The intensity of the peak characteristic for the CH phase appeared in the samples thermally treated up to 400°C and then disappeared in the samples thermally treated up to 600°C. This is due to the decaying of Ca(OH)₂ into CaO+H₂O, where the H₂O evaporated at this temperature. The decrease in intensity of hydration products at 600°C is due to decomposition of those hydration products.

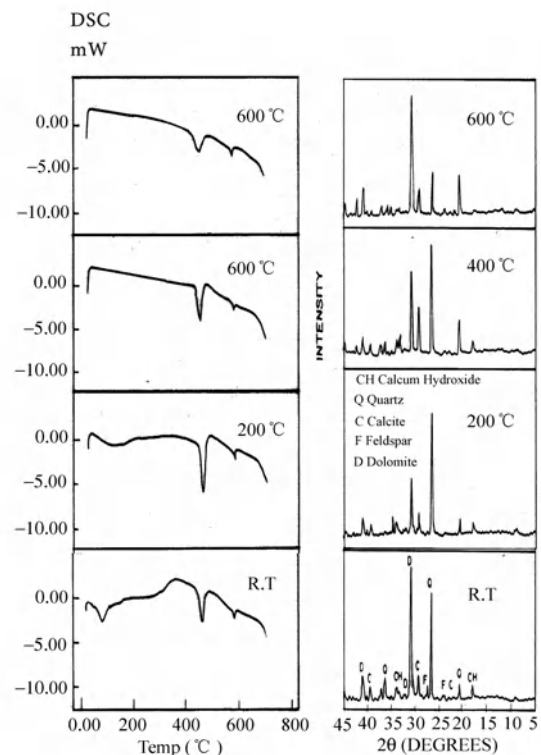


Figure 12 The DSC thermograms of SCC after thermal treatment at 200°C, 400°C and 600°C

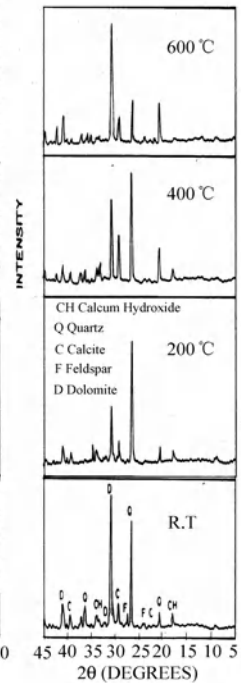


Figure 13 The XRD patterns of SCC after thermal treatment at 200°C, 400°C and 600°C

The intensity of the main peak characteristic for the quartz increase by increasing temperature up to nearly 400°C and then decrease sharply at 600°C. Also it can be seen from the figure that, the intensity of the main peak characteristic for the dolomite decrease in the samples thermally treated up to 200°C and then increase up to 600°C. This is due to that, increasing temperature lead to increasing rate of losing of CO₂ i.e. part of dolomite [calcium magnesium carbonate Ca Mg CO₃] covert to

calcium magnesium oxide Ca Mg O. The molecular weight of Ca Mg Ca₃ is greater than Ca MgO. Also, at 600°C, the organic compounds decomposed at this degree, i.e. the dolomite ratio increase at this degree (600°C). The intensity of the peak characteristic for the calcite was nearly constant up to 200°C. Then it increases at 400°C after which it decreases at 600°C. The results of DSC thermo grams are in a good agreement with those of X-ray diffraction analysis.

4 CONCLUSION

(1) More damage was observed for SCC specimens in comparison with NC when subjected to fire.

(2) The mechanical properties of SCC cooled by air (slowly cooling) are better than that cooled by water (sudden cooling).

(3) Regarding to the temperature distribution inside the sample, the specimen shape has an important effect.

(4) In case of constant shape (cylinder), the presence of the steel rod decreases the difference of temperature distribution between NC and SCC.

(5) The phase composition of SCC mixes was related as much as possible to physico-mechanical characteristic of SCC mixes which exposed to 200, 400 and 600°C for two hours.

REFERENCES

- J. R. Lawson, L.T. Phan, and F. Davis, Mechanical Properties of High Performance Concrete after Exposure to Elevated Temperatures, March 2000. <http://fire.nist.gov/bfrlpubs/fire00/PDF/f00014.pdf>.
- T. A. Elsayed, effect of fire on behavior of concrete. International conference future vision and challenges for urban development Cairo, Egypt: 20:22 December 2004.
- M.M. Abdel-Razek , A.M. Ragab, H.A. Hodhod and A. M. Rashad, coating protection of loaded RC columns against elevated temperature. International conference future vision and challenges for urban development Cairo, Egypt: 20:22 December 2004.
- H. L. Malhotra, Design of Fire Resisting Structure, Chapman and Hall, New York, 1982.
- Abrams, M. S., Compressive Strength of Concrete at Temperature to 1600 °F Temperature and Concrete, SP-25, American Concrete Institute, Detroit,1971, 33-58.
- E. Holt, Self-Compacting Concrete, State-Of-The-Art Part IV. Fire Resistance internal report RTE40-IR-15/2003. <http://www.betoni.com/404.html>.
- Z. A. Etman, Effect of High Temperature and Fire on the Behavior and Strength of Reinforced Concrete Members Cast with Self-Compacting Concrete. PhD. thesis, Faculty of Engineering, Menofiya University, Egypt, 2008.
- Kh. M. Heiza and M. A. Helal, Fire performance of both normal and self compacted reinforced concrete loaded columns, 11th International colloquium on Structural and Geotechnical Engineering (ICSGE), Ain Shams University May 17-19, 2005.
- M. A. Helal and Kh. M. Heiza, Effect of aggregate type on the behavior of thermally treated SCC, Egyptian Journal of Applied Science, Vol. 21, pp .68-82, 2006.
- M. A. Helal, Physico-mechanical properties of NC and SCC loaded columns Subjected to Fire, Ain Shams University Journal, Vol. 40,No. 4, December, 2005.
- M. A. Helal, Kh. M. Heiza and H. Allam, New Building Technology: Properties of Self Compacting Concrete (SCC) with High Temperature, World Renewable Energy Congress VIII (WREC2004), Denver, Colorado, USA, August 29-September3, 2004.
- M. A. Helal, Physico-Mechanical and Microstructural Characteristics of Thermally Treated Cement Pastes Containing Limestone, 23rd International Conference on Cement Microscopy, New Mexico, USA, April 29- May 3, (2001).
- M. A. Helal. Effect of Curing Time on The Physico- Mechanical Characteristics of The Hardend Cement Pastes Containing Limestone, Cement Concrete Research, 32, 447-450, (2002).

Educations, Applications and Design Guidelines

IIFC Educational Modules on Polymer Composites in Construction

Luke A Bisby (Luke.Bisby@ed.ac.uk)

The Institute for Infrastructure and Environment, The University of Edinburgh, Scotland, UK

ABSTRACT The next generation of engineers, faced with rapidly deteriorating infrastructure, is destined to face many difficult decisions in maintaining and preserving our civil infrastructure systems. The International Institute for FRP in Construction (IIFC) recognizes the need for the development, advancement, and application of fibre reinforced polymers (FRPs) in construction applications. Many FRP technologies are recognized as important tools for construction and repair of buildings, bridges, and infrastructure. However, these technologies will not become commonplace until the broader civil engineering community is aware of their benefits and potential applications. A key group that will play a role in shaping the future of the construction industry is the next generation of civil engineers. As such, the IIFC Working Group on Education is, in conjunction with the ISIS Canada Research Network, in the process of developing a series of educational modules on FRP technologies for use in engineering curricula. The overarching goal of these modules is to enable and encourage the teaching of FRP technologies in curricula where such topics are not currently covered. This non-research paper presents a brief overview of the educational modules that are being developed by the IIFC Working Group on Education and which will be made freely available for use by all interested parties.

1 INTRODUCTION

The sustainability and longevity of our infrastructure is currently in danger. Civil infrastructure systems around the world are aged, dense, complex, and interconnected, especially in urbanized areas where ever greater proportions of society choose to live. To maintain what we have as we plan and build for the future, engineers will need to apply innovative technologies and creative solutions; education of the next generation of engineering practitioners will need to evolve accordingly. In the last few decades, many novel structural technologies have emerged from the civil/structural engineering research community, and while many of these technologies have been shown to be both effective and efficient, many of them will never see widespread implementation unless the new generation of civil engineers is aware of their existence. Indeed, the use of fibre reinforced polymer (FRP) composites in construction is but one example of an emerging technology which has yet to make significant inroads into undergraduate engineering curricula.

FRP technologies are now in widespread use around the world, and design codes and/or recommendations are widely available to support their use. However, in spite of the fact that both research and demonstration projects and numerous field applications of FRP materials in construction have shown FRPs offer attractive solutions to some of the civil engineering

community's most challenging problems, FRPs are not yet considered mainstream materials in practice. A key factor hindering the wide-spread application of FRPs remains lack of awareness and confidence among practicing engineers.

This non-research paper describes a series of educational modules on FRP technologies for use in engineering curricula that are currently under development by the IIFC Working Group on Education, in conjunction with the ISIS Canada Research Network. The modules are intended to enable and promote teaching about FRP construction technologies in undergraduate engineering curricula globally. It is hoped that the modules will be taken up and used by both university and professional educators.

2 PHILOSOPHY & APPROACH

Increased use of novel technologies in engineering requires a basic understanding and awareness of these technologies by all members of the civil/structural engineering profession; not simply those with graduate level or research degrees. Hence, in 2001 the ISIS Canada Research network created an Educational Committee with a mandate to develop a suite of teaching materials; the initial focus was on undergraduate civil engineering students, since this was deemed the area in which the greatest impact could be expected. ISIS subsequently developed a successful series of educational

modules (ISIS 2009) devoted to Canadian design methodologies for FRP (and Structural Health Monitoring) technologies in construction; these are now widely used not only in Canada but around the world.

In 2007, the IIFC Education Working Group (WG) was formed with similar objectives, i.e. to:

- develop strategies to attain the educational and training objectives of the IIFC;
- provide guidance for the organization of special sessions, workshops, and seminars;
- develop educational modules on the use of FRP composites in construction; and
- provide a forum for exchange, discussion and consolidation of ideas and educational best-practices through the organization of specialist workshops and special sessions at conferences.

A decision was made to initially focus the IIFC Education WG efforts on the development of IIFC educational modules, similar in motivation to and based on the pre-existing ISIS educational modules, which could be used within typical existing undergraduate civil engineering courses globally. The overarching philosophy of the IIFC modules, in recognition of the fact that altering existing courses is a time consuming and difficult task, is that it should be as easy as possible for course instructors to take up and use the modules in a way that enhances learning, builds awareness of alternative engineering materials and solutions, and increases motivation.

As was the case for the previously developed ISIS modules, it was decided to present material that would augment conventional information that is currently delivered in civil engineering curricula. As they are completed, the modules are being made available free of charge to engineering educators via the IIFC website (<http://www.iifc-hq.org>).

3 OBJECTIVES

The educational modules are being developed to enable and encourage teaching of FRP technologies in undergraduate curricula at universities, colleges, or in professional skills training courses where these technologies may or may not currently be covered. Rather than proposing full courses FRP technologies, the preferred strategy is to slot this new material into various existing courses with three or four lecture units on topics related to FRPs. Every attempt is being made to make integration of the new teaching material as seamless as possible. An attempt is also being made to provide educational materials that can be easily modified and/or updated and used together as a suite of material that can be used as a launch pad for full term-length courses on FRP technologies. A difficult issue that is not addressed here is the question of how to fit new material into an already overcrowded

undergraduate civil engineering curriculum; individual instructors must tackle this common problem on a case-by-case basis.

4 SPECIFIC MODULE TITLES

As already noted, a total of six educational modules are currently under development by the IIFC Education WG. The development of the modules is being led by an international group of experts, with each specific module under the leadership of a different member of the IIFC Education WG, as follows:

1. “Module 1: FRP Composites for Construction – Materials and Mechanics” is being led by Dr Luke Bisby, University of Edinburgh, luke.bisby@ed.ac.uk.

2. “Module 2: Reinforcing Concrete Structures with FRPs” is being led by Dr Fabio Matta, University of Miami, fmatta@miami.edu.

3. “Module 3: Strengthening Concrete Structures with FRPs” is being led by Dr Scott Smith, Hong Kong University, stsmith@hku.hk.

4. “Module 4: Strengthening Metallic Structures with FRPs”, is being led by Dr Tim Stratford, University of Edinburgh, tim.stratford@ed.ac.uk.

5. “Module 5: Strengthening Masonry Structures with FRPs”, is being led by Dr Enzo Martinelli, Università degli Studi di Salerno, e.martinelli@unisa.it.

6. “Module 6: Durability of FRP Composites for Construction”, is being led by Dr Raafat El-Hacha, University of Calgary, relhacha@ucalgary.ca.

First editions of these six initial modules are expected to be available for use by fall 2010. The Education WG is of course happy to accept new IIFC members who are interested in actively contributing to the ongoing development of the IIFC’s suite of teaching resources. Interested individuals are encouraged to contact the specific leader for each of the given topic areas.

Table 1 shows a possible integration matrix for the first six educational modules. This table outlines the various (typical) existing undergraduate courses into which each of the modules could be inserted. Clearly, the modules could also be used in combination to develop entirely new courses (undergraduate or graduate) on the use of FRP composites in construction; this has been done in at least one Canadian civil engineering program to

Table 1 Implementation matrix for the IIFC educational modules

Module #	1	2	3	4	5	6
Mechanics of Materials	✓					
Civil Engineering Materials	✓					✓
Structural Design / Analysis		✓	✓	✓	✓	
Reinforced Concrete Design		✓				✓
Infrastructure Rehabilitation			✓	✓	✓	✓
Structural Design with FRPs	✓	✓	✓	✓	✓	✓

create a new graduate course on reinforcement and strengthening of concrete structures with FRP materials.

The modules are being developed in fully-modifiable (i.e. non-write-protected) PowerPoint format to ensure easy incorporation into pre-existing lecture notes. Figure 1 below provides examples of the typical content which has been created in the modules, in this case with slides taken directly from IIFC Educational Module 1.

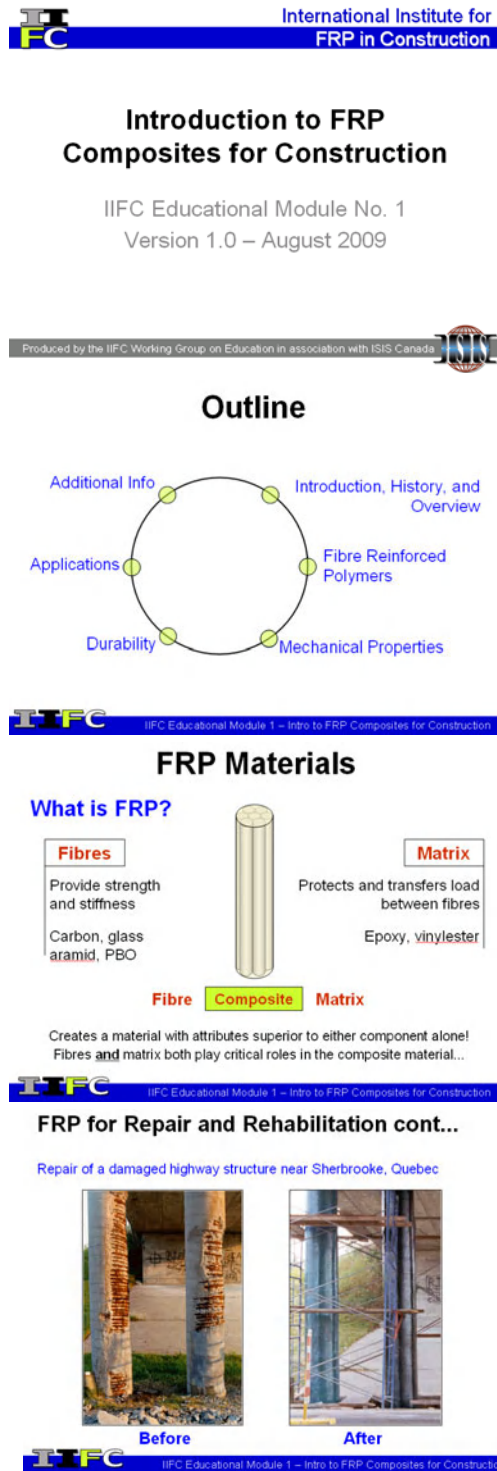


Figure 1 Example powerPoint slides taken from IIFC Educational Module 1

5 PEDAGOGICAL (& OTHER) BENEFITS

There are numerous potential pedagogical benefits, direct and indirect, associated with teaching undergraduate engineering students about FRP technologies.

Exposing engineering students to state-of-the-art or innovative information makes these students feel as though they are active participants in the greater engineering community. In the experience of the author, this contributes greatly to the excitement, motivation, and inspiration of undergraduate students which has been shown to directly contribute to student success in undergraduate courses (Baillie & Fitzgerald 2000).

An increased depth of student understanding is realized when students are exposed to FRP materials. These technologies offer opportunities for instructors and students to consider important issues in the in-service behaviour of structures. For instance, the use of FRP reinforcement for concrete creates interesting discussions about strength, serviceability, ductility, deformability, and the philosophical underpinnings of structural design which are particularly enlightening for undergraduate structural engineering students. Examination of FRP materials in conjunction with other engineering materials, such as concrete and steel, results in a more complete understanding of concepts such as linear elasticity, isotropy, and homogeneity.

Additional benefits arise from the fact that an awareness of the full suite of potential infrastructure solutions makes graduates more attractive to employers and more successful in industry. In addition, when used appropriately, FRP technologies have the potential to substantially increase the sustainability of our infrastructure systems, thus allowing public funds to be used for other important initiatives.

6 CONCLUSIONS & HOW TO GET INVOLVED

The future use of FRP construction technologies in civil/structural engineering applications depends to a considerable degree on the timely and widespread education and awareness of the engineering community with respect to these promising technologies. The IIFC Education WG, in collaboration with ISIS Canada, is developing a series of six targeted Educational Modules covering various aspects of the use of FRPs in construction. Among other educational benefits, these modules, when integrated into existing undergraduate engineering curricula, provide engineering graduates with the tools to make educated decisions regarding the potential use of FRP technologies in civil infrastructure applications.

7 ACKNOWLEDGEMENTS

The author gratefully acknowledges the efforts made by the members of the IIFC Working Group on Education in developing the Educational Modules discussed herein. The author would like to acknowledge the contributions of the ISIS Canada Education Committee in developing the initial teaching materials on which the IIFC Educational Modules are based, and would also like to thank ISIS Canada for supporting to extension of the ISIS Modules for use by the IIFC. The author would

also like to acknowledge the ongoing support of The Ove Arup Foundation, the Royal Academy of Engineering, and The University of Edinburgh.

REFERENCES

- Baillie, C. & Fitzgerald, G. 2000. Motivation and attrition in engineering students. *European Journal of Engineering Education* 25(2): 145-155.
- ISIS 2009. ISIS Canada Educational Modules. Winnipeg: Intelligent Sensing for Innovative Structures Canada.

Challenges in the Design and Delivery of an Online Postgraduate Course in Fibre Composites

Thiru Aravinthan (aravinthant@usq.edu.au)

Centre of Excellence in Engineered Fibre Composites (CEEFC), Faculty of Engineering and Surveying, University of Southern Queensland, Toowoomba, Queensland, Australia

ABSTRACT Practicing engineers seek to enhance their careers through upgrading skills. Coursework based postgraduate programs are being offered by various institutions targeting these engineers. While face-to-face lectures are feasible in certain circumstances, these courses are ideally suited for web-based delivery, due its flexibility in learning and teaching. Due to industry driven demand, a postgraduate certificate program was introduced recently at the University of Southern Queensland (USQ), Toowoomba, Australia. One of the courses that was introduced as part this program is the Mechanics and Technology of Fibre Composites (ENG8803). With the expertise developed over the years at USQ through the Centre of Excellence in Engineered Fibre Composites (CEEFC) and the experience of providing online and distance courses at USQ, this was an ideal course within the postgraduate program. One of the major challenges faced in the design and delivery of this course is the need to cater for a diverse student cohort with varying industry experience. This course was successfully delivered for the first time in 2008 and employed a variety of online assessment tools. The experiences of the author in developing the course on fibre composites within the graduate program and an evaluation on the effectiveness of the diverse assessment strategies from a student learning perspective are presented in this paper. Enhancement to the course materials through multi-media resources is also discussed.

1 INTRODUCTION

In recent years, several large-scale structures have been constructed to demonstrate the potential of fibre reinforced polymer (FRP) composite materials in major civil engineering applications. Yet, despite the strong indications of the potential of these materials, composites continue to be slow in penetrating the mainstream civil engineering marketplace. Currently, one of the main factors that is impeding the widespread implementation of FRP composites in the civil infrastructure is the lack of performance data and accepted engineering standards (Hollaway and Head, 2001). Another reason for this continued lack of penetration and growth of fibre composites in construction is that civil engineers have not possessed the information and design tools to truly exploit the advantages of composite materials. While several international and national conferences, workshops and symposia are being held to disseminate information on the recent advances in materials, manufacturing techniques and design of fibre composite materials for civil infrastructure, these information are contained mostly to academic and researchers working in universities and research institutions, and not to practicing engineers.

2 THE NEED FOR A COURSE IN FIBRE COMPOSITES

The lack of curricula and training for engineers on composite materials has slowed the progress of its application in the mainstream civil engineering structures. To improve this situation, it is imperative that effective steps be taken to disseminate the knowledge of composite materials in the civil engineering community. This goal could be achieved through teaching composites design and application in engineering schools (Taly, 1998). Though there have been considerable amount of research, conferences, workshops and symposia on this area, it has not been yet fully translated into teaching curricula and the classrooms are still lagging behind. Civil engineering graduates for the most part are not sufficiently trained to design and specify FRPs for construction (Mirmiran et al 2003). In the recent APFIS Conference in Korea, Prof Rizkalla of the North Carolina State University highlighted the importance of education in this area.

Many institutions and foundations are now taking the initiative to answer this need. The National Science and Foundation in the US has sponsored a number of integrated research and educational programs, with a few focusing on developing undergraduate and graduate

courses on FRP composites in civil engineering curricula (Davalos and Quiao, 2001). The working group on Education of the International Institute for FRP in Construction also aims to develop Education Modules on FRP composites in construction to be used globally in undergraduate (and eventually also in graduate and professional) engineering curricula. The ISIS Canada Education Committee, on the other hand, has developed a series of Educational Modules on fibre composites to be used in engineering education curricula by any interested parties. The Queensland Department of Employment, Economic Development and Innovation has recently funded the production of an introductory guide on fibre composite materials for engineers, designers and those new to the technology in the mining, mineral and chemical and corrosion industries. Though there have been short courses on fibre composites offered in some universities and institutions, internationally accepted curriculum has not been drafted. Training, education, skills and knowledge development is therefore important to fill the industry's needs and shortages in this leading edge technology and sustainability.

This paper presents the experiences of the author in developing a course on fibre composites delivered in an online environment. Evaluation on the effectiveness of the diverse assessment strategies from a student learning perspective is also discussed.

3 ENG8803 – MECHANICS AND TECHNOLOGY OF FIBRE COMPOSITES

The technical nature of the topic and the lack of a University-accredited program in Australia on composites have led to the difficulty of incorporating it in an undergraduate course. The option is to offer this in postgraduate programs or for continuing professional development for several engineers who have had minimal or no exposure to fibre composites in their training curriculum. Another is to make this an elective course for undergraduate engineering students in their last year in the university.

3.1 Course content

The course on ENG8803 – Mechanics and Technology of Fibre Composites aims to address the need for the improved understanding of composite materials and their behavior within the civil engineering context. This course is intended for practicing civil and structural engineers who need to acquaint themselves in the principles, recent structural design techniques and the latest utilization of the advanced composite materials in the civil infrastructure. In 2009, this course was also offered as an elective course for undergraduate engineering students, who are in their last year in the university. The foundation of this course is based on the

study book on fibre composites authored by Van Erp (2008). Table 1 lists the study modules for ENG8803.

Table 1 Course content of ENG8803

Module	Topics
1	The application of composite materials in civil engineering structures
2	Polymer matrix materials for civil and structural engineers
3	Fibre reinforcement for composite materials
4	Composite material behaviour
5	Structural design of fibre composites in civil engineering environment
6	Lamina design properties
7	Flexural behavior and robustness
8	Determination of characteristic lamina properties by physical testing
9	Durability of fibre composites

3.2 Design methods and delivery

For postgraduate students and professionals, the course delivery can become an issue. Face to face delivery may not be feasible and sustainability of the course can become a problem. With USQ being known as Australia's leading e-learning provider for online and distance education, web-based delivery is the best option to go. It could provide the convenience and flexibility for students to complete the course at their own pace at a time and place that fits in with their other commitments as most are already employed in some capacity.

The ENG8803 is being offered every first semester that runs from the beginning of March to end of July. This course is entirely web-based using the Moodle system. The study materials for this course are regularly uploaded through the course homepage on the StudyDesk.

3.3 Assessment

Table 2 summarizes the assessment criteria for the ENG8803. The table shows that during in 2008, the assessment only includes 2 major assignments: Assignment 1 which covers modules 1-4 and Assignment 2 which covers modules 5-9. In every assignment, each student is given a different set of design parameters to avoid any collusion and uniqueness of the answer. Submission of all these assignments was a compulsory requirement for the subject assessment. In 2009, online quizzes and discussion are introduced and included in the assessment criteria.

Table 2 Assessment criteria and weighting for ENG8803

Criteria	2008	2009
Assignment 1	40	30
Assignment 2	60	50
Quizzes	0	10
On-line discussion	0	10
Total	100	100

4 E-LEARNING INNOVATIONS

The sustainability due to low enrollment rate is always a concern for newly introduced engineering courses. Innovative teaching methods and new learning resource should therefore be developed to increase course attractiveness and produce better educational outcomes. For ENG8803, several innovative teaching techniques are implemented and a number of developed resource are made available to enhance student's learning.

4.1 Online quizzes

Online quizzes which are composed of formative assessment items are set-up on the StudyDesk to enhance student's learning. Most are multiple-choice type questions with a few fill in the blanks to test the student's understanding on each module of the course. Students are given unlimited attempts to answer these quizzes but only their first attempt for each set of quiz is marked. While these online quizzes are available throughout the semester, students are encouraged to attempt as soon as they are released as deadline is set for the first attempt.

4.2 On-line discussions

Electronic discussion facilities in the StudyDesk are used extensively for communication amongst students and lecturer. Online discussions (but not marked) on each topic module are conducted providing an equivalent experience of face-to-face teaching and learning. In 2009, discussion topics covering selected areas on fibre composites for civil infrastructure are introduced periodically throughout the semester. The participation of the students on these online discussion topics, is assessed based on the quality and quantity of their contribution. This assessed on-line discussion is designed such that students have to give their comments and answer first on the relevant topic before they can see others contribution.

4.3 Guest lectures

Selected lectures and papers presented in workshops and conferences on fibre composites were uploaded in the StudyDesk. These were made available to the student to increase their awareness and understanding of the technological progress in Australia and overseas on fibre composites in civil infrastructure. Video and PowerPoint presentations and some of the paper presented in the International workshop on Fibre Composites in Civil Infrastructure held in USQ Toowoomba in December 2008 and the Composites Australia Conference and Trade Show in March 2009 were recorded and uploaded. These are accomplished with the assistance of the professional services of video and audio recording as well as multi-media services at USQ through its Distance and e-Learning Centre (DeC).

4.4 On-line videos

Video clips on manufacturing and testing of fibre composite and polymer materials are also uploaded on the StudyDesk. These instructional videos were developed by CEEFC and PARTEC Institute, with support of the Australian Flexible Learning Framework. This provides a more enhanced course delivery on fibre composites in a flexible learning environment.

4.5 Electronic submission and marking

Electronic assignment submission through electronic submission boxes is encouraged for all assignments. Similarly, Tablet PC's are used for marking and providing electronic feedback for assessment items. This enabled the markers to provide feedback in the electronic environment and in a timely manner. Results of the assignments were quickly returned to all students interstate and even, overseas. This is a great accomplishment compared with mail delivery processes as turnaround times of three weeks or more are not uncommon at USQ.

5 STUDENT PERFORMANCE IN 2 YEARS

The ENG8803 has already been offered for 2 years, 2008 and 2009.

5.1 Number and demography of students

An initial survey at the beginning of semester was conducted to get a better understanding of the student's expectations in the course. The survey includes the program that the students are taking, location, organization and familiarity with composites. A summary of this survey is listed in Table 2.

Table 3 Location of students

State	2008	2009
New South Wales	1	2
Queensland	3	7
Tasmania	0	1
Victoria	0	2
South Australia	1	1
Western Australia	1	1
Overseas	0	1
Total	7	15

The results show that there is a significant increase in the number of students from 2008 to 2009. From only 7 postgraduate students who took the course in 2008, this number increased to 15 (10 postgraduates and 5 undergraduates) in 2009. The flexibility of teaching delivery resulted to at least 1 student enrolled from each state in Australia in 2009. On the same year, a student from the US also took the ENG8803. The results of the

survey show that most of the students who took the course are working in the construction and consulting industries but more than half of them have poor knowledge in fibre composites. The main reason for taking the course is to have a more complete understanding on fibre composite materials and to effectively use this material in real world situations. One mature student, who is working as a bridge engineer, took the course as fibre composite was not part of the syllabus at the university where he completed his civil engineering studies. He is interested in gaining insights into fibre composites and its applications in the bridge industry.

5.2 Student participation

Figure 1 shows a normalized value of the level of participation of students (total number of participation per student) during the course of the semester. It can be seen from the figure that the students logged in the StudyDesk the least in March. During this month, the students are just starting to familiarize themselves with the StudyDesk and the course. As the course progresses, students logged in the StudyDesk and studied the course modules more often. In 2008, the students logged in the StudyDesk the most during the months of June and July. It is important to note that Assignments 1 and 2, which are the only basis for assessment, are due on these months. In 2009, the level of participation is at its most in July when Assignment 2 is due. Interestingly, the level of participation by students remains the same for the months of April to June. This is due to the introduction of the quizzes, online discussions, guest lecture and online videos which keeps the level of interest on the course. In general, students logged in to the StudyDesk more frequently in 2009 than in 2008.

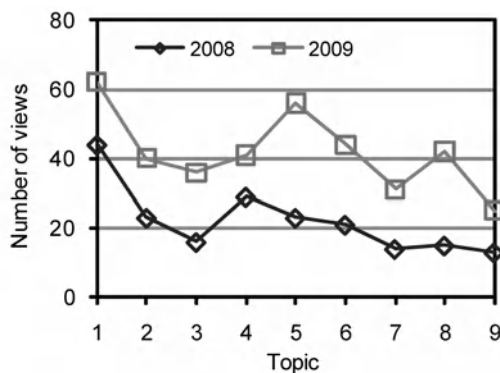


Figure 1 Participation of ENG8803 students

Figure 2 shows the number of times the students viewed each module. The figure shows that the most read topic is the review on developments and application of fibre composites in civil infrastructure. There is also a high level of interest in the understanding the behavior of fibre composite materials and designing structures from these advanced materials. This is compatible with the

result of the survey on the interest of students taking the course. However, the topic on durability seems to be the least interesting.

Figure 3 shows the number of posts made by each student on the different discussion topics and the number attempts made for each quiz. All of the students shared their view and opinions on every discussion topics posted. Similarly, all the students, except for one, tried answering the online quizzes. Even though only the first attempt on the online quizzes is being marked, some of the students have tried answering the online quizzes more than once. Similarly, each student viewed the all the guest lectures and online videos at least once during the course.

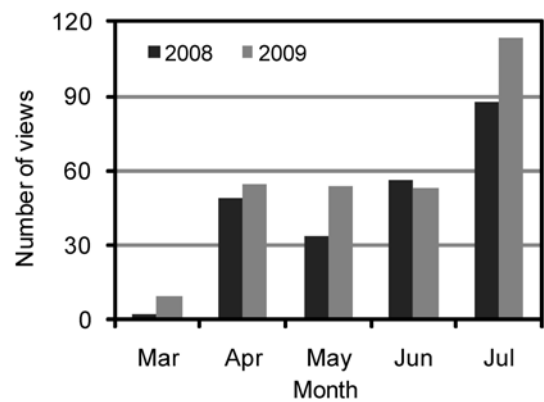


Figure 2 Number of views per topic

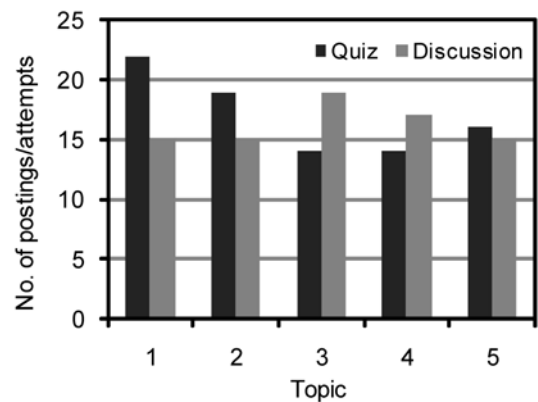


Figure 3 Numbers of discussion posts and quiz attempts

5.3 Student performance

All students passed the course even though initial survey showed that most of the students who took the course have little knowledge on fibre composites. This result shows the effectiveness of the delivery of the course.

6 CONCLUSIONS

The time has now come to convey the collective knowledge and innovative efforts of many researchers on fibre composites to the construction industry and the civil engineering community to increase its application

to civil infrastructure. At the same time, practicing engineers should be trained and taught on this new material to keep up with the skills demand on this emerging industry. This task is not easy to perform but with the introduction of courses on fibre composites in a flexible learning environment and development of innovative learning resource, practicing engineers can continue their professional development in this new technology and could provide valuable information to those who are not exposed much to fibre composite materials. This effort can only be realized by multidisciplinary collaborations among researchers, academes and the composites community.

REFERENCES

- Davalos, J. F., and Qiao, P. Z. 2001. Innovative teaching guides for composite materials in civil engineering curricula. Proc. ASEE North Central Regional Conf., Cleveland.
- Hollaway, L.C. & Head, P.R. 2001. Advanced polymer composites and polymers in the civil infrastructure. Elsevier Science Ltd., UK.
- ISIS Canada Research Network. Educational Modules. <http://www.isiscanada.com/education/education.html>.
- Mirmiran, A., Bank, L.C., Neale, K.W., Mottram, T.B., Ueda, T., & Davalos, J.F. 2003. World Survey of Civil Engineering Programs on Fiber Reinforced Polymer Composites for Construction. *J. Prof. Issues in Engrg. Educ. and Pract.* 129 (3), pp. 155-160.
- Taly, N. 1998. Structural design with FRP composites. Proc., Int. SAMPE Symp. and Exhibition, Covina, CA, 43(2), 1229–1237.
- Van Erp, G. 2008. Mechanics and technology of fibre composites. University of Southern Queensland, Toowoomba, Australia.

Virtual Practice with Computer Aided Software toward Better Understanding of RC Beams Strengthened by External Bonded FRP

Ferrier Emmanuel (Emmanuel.Ferrier@univ-lyon1.fr), Hamelin Patrice
LGCI Site Bohr, Université Claude Bernard Lyon I - INSA de Lyon, Lyon, France

Bigaud David
IMIS-ESTHUA, Université d'Angers, Angers, France

ABSTRACT This paper focuses on a computer solution that proposes the non-linear behaviour analysis of reinforced concrete beams strengthened by means of external bonded FRP. This analysis considers actual material behaviour laws. It takes into account the sliding effect at the composite-to-concrete interface and the durability of the strengthened structure via the study of the materials fatigue and the interface visco-elastic properties. After research development, this software is currently used in Lyon 1 University by student at a Master level. In the case of FRP strengthening course deliver in the university, students are asked to practice FRP virtually thanks to modelling to better understanding the effect of those materials of RC beams strengthening. Parametrical studies are carried out in order to understand the influence of FRP properties on the beams me-chemical behaviour.

1 INTRODUCTION

The Civil Engineering Master of LYON 1 University deliver 60 hours of teaching on FRP used in construction and 30 of the 60 hours are devoted to RC strengthening using external strengthening FRP. About 25 students follow this course each year since 2004. 12 hours on the 30 are devoted to practice with 8 hours of test on real RC beams and 8 hours on modelling thanks to specific software develop first for research by the team of the Lab.

The estimation of the instantaneous and deferred performances of reinforced structures strengthened by FRP is of a great interest. The characteristics of the materials and their interactions, which influence the strengthening capability, need to be understood and defined on an experimental basis. Because experimental investigation with a lot of parameters variation are always difficult to do with student during a short time period, a software is used to model the moment-curvature or loading/displacement curve response of a RC beams strengthened by FRP. The Beam Compo Design (BCD) software has been developed with this aim and follows the previous works of Varastehpour (1995) and Nasser (1997). BCD is a program devoted to the determination of the behaviour law, the ultimate capacity and the failure mode of concrete beams strengthened by FRP sheets. Built on a non-linear formulation of the moment-curvature theory, its purpose is to describe the non-linear behaviour of concrete beams by taking into

account the actual materials behaviour laws. This method takes also into account the initial deformation of the beam at the time of strengthening. Thus, the loading story before the strengthening (damage and ageing) and the durability of the strengthened structure is considered via the study of the materials fatigue and of the time dependency behaviour of the composite-to-concrete bond. Various failure criteria of the beams, further to the classical ones (concrete crushing, steel yielding), are taken into account; in particular, the failure due to peeling-off, the failure of the composite-to-concrete interface and the tensile failure of the composite plate. The criteria can present specific modifications associated with the deferred behaviours.

2 PRESENTATION OF BCD

The software is developed under a personal computer (PC) platform and compute in Visual Basic interface. It is subdivided in three main parts as illustrated in Figure 1.

2.1 Data

The first step consists in collecting the mechanical and geometrical data of the problem. These are listed below:

- The instantaneous or deferred (or damaged) behaviour laws of the materials involved (Figure 2). As far as the instantaneous behaviours are concerned, we consider:
 - a bi-linear elastic tensile behaviour of the concrete

with a post-peak strength,

- a Sargin-type law for the compressive behaviour of concrete,
- an elasto-plastic law for the steel,
- a linear elastic behaviour for the composite,
- a bi-linear shear behaviour of the interface,

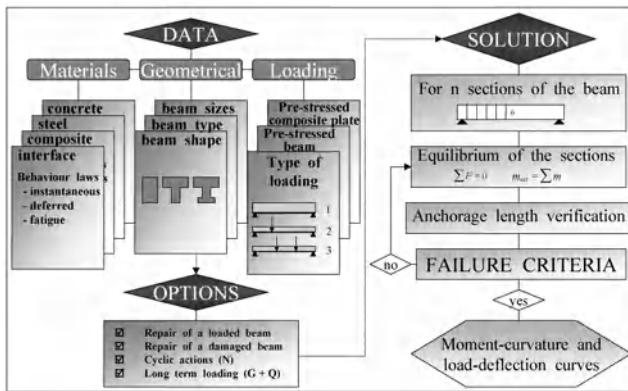


Figure 1 General overview of BCD

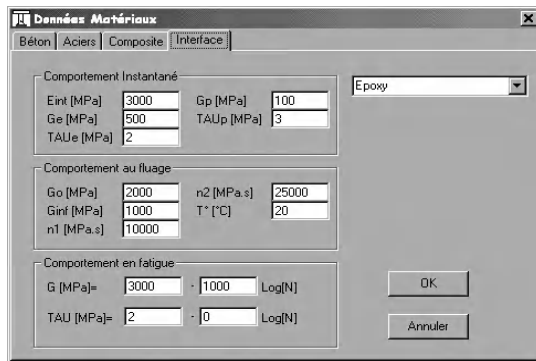


Figure 2 Example of interface instantaneous and deferred mechanical properties

Ferrier (2000a, 2000b) details the effects of fatigue and creep on the reduction of these characteristics.

The type of shape and size of the beam: either steel reinforced or pre-stressed beam can be calculated. The study of rectangular or T-shape beams is possible.

- The loading type: It may be considered as uniform or of three or four-point bending type.
- The number of layers of steel reinforcement, their length, area, position and possible pre-stressing.
- The number of composite plies applied on lower and lateral surfaces, their width, length and thickness.
- The number (n) of consecutive section considered (for purpose of anchorage length assessment): the number of composite plies and their sizes may vary all along the beam length (Figure 3).

2.2 Options

This second step pre-requests the last options before calculation. It is essentially a question of load scheme definition. The choices are:

- Strengthening of a beam under loading: the initial

deformation at the time of repair is considered.

- Cyclic loading: the characteristics at N fatigue cycles of a strengthened beam are calculated and then considered as a new initial state of deformation.
- Long-term loading: the purpose of this option is to define the mechanical characteristics of a strengthened beam subject to a long-term loading (ageing or creep effects) before repair. Using the time-temperature superposition principle, the effect of an increasing temperature can also be investigated (Ferrier, 1999).

One or several simultaneous choices among these options allow the study of various configurations. For example, if the objective is to consider the remaining characteristics of a RC beam after N fatigue cycles and taking into account the actual deformation at the strengthening time, we should choose the two first options.

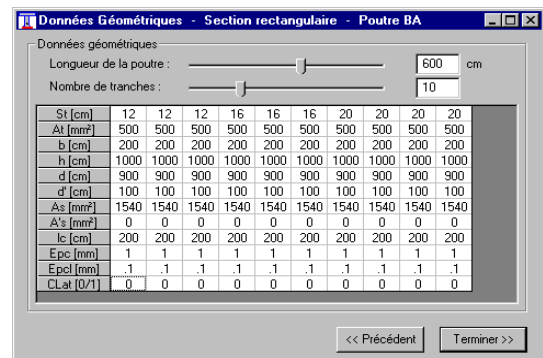


Figure 3 Definition of geometrical and reinforcement parameters for ten consecutive sections of the beam

2.3 Solution

The third step consists in the solving of the problem defined at the end of the two prior steps. For the n consecutive sections all along the beam, equilibrium conditions are ensured, and, stress and strain diagrams are determined according to the non-linear calculation method (with consideration of the sliding effect).

Sliding at the composite-to-concrete interface:

This is a consequence of two phenomena: the transverse deformation of the adhesive layer and the horizontal cracking at the adhesive/concrete and adhesive/ composite interfaces. The first phenomenon depends on the quality and the thickness of the adhesive layer. On the other hand, the latter depends only on the bonded surface treatment.

For each iteration of the calculation method (by assuming the Bernoulli hypothesis for the first iteration), the unit strain of the composite plate is determined. Once the shear stress at the interface is calculated, it is possible to reduce the plate deformation proportionally to the sliding, knowing the mechanical behaviour of the interface. This behaviour is experimentally determined

by mean of a double-lap joint shear test whose procedure is presented by Ferrier (2000a).

Failure criteria: different failure modes of beams, further to classical ones (concrete crushing, steel yielding), are considered (Figure 4):

- Failure of the composite-to-concrete interface: it is a premature failure mode, essentially due to the concentration of shear stress within the adhesive and the plate end. The shear stress distribution all along the plate length is determined analytically by taking into account the mechanical and geometrical characteristics of the adhesive joint. The equation [1] presents the evolution of this interfacial shear stress in the case of a four-point bending test. It is inspired from the formalism developed by Täljsten (1997) in the case of three-point bending.
- Failure of the interface is considered when the maximum shear at the plate end reaches the ultimate shear stress $\tau_{ult.int.}$ of the joint (Eq. [2]).

$$\tau(x) = \frac{GP(d_p - y_{cr})}{2sE_c I} \left[\left\{ \frac{a}{\lambda} \tanh(\lambda b) - \frac{1}{\lambda^2 \cosh(\lambda b)} \right\} \cosh(\lambda x) - \frac{a}{\lambda} \sinh(\lambda x) + \frac{1}{\lambda^2} \right] \quad (1)$$

$$\tau_{max} = \tau(0) = \frac{GP(d_p - y_{cr})}{2sE_c I} \left[\frac{a\lambda \sinh(\lambda x) + \cosh(\lambda b) - 1}{\lambda^2 \cosh(\lambda b)} \right] < \tau_{ult.int.} \quad (2)$$

$$\text{with } \lambda^2 = \frac{Gb_p}{s} \left[\frac{1}{E_p A_p} + \frac{1}{E_c A_c} + \frac{(d_p - y_{cr})^2}{E_c I} \right]$$

Where P : total applied load, G : shear modulus of the interface, E_c , E_p , A_c , A_p : Young modulus and section area of concrete and composite plate, I : homogeneous inertia of the strengthened beam. Geometrical parameters s , b_p , d_p , y_{cr} , a and b are illustrated in Figure 5.

- Failure of the concrete layer between longitudinal steels and the composite plate (peeling-off): it is also a premature failure of the beam occurring by combination of normal and shear stress at the composite plate ends. It is considered as a failure criterion of Mohr-Coulomb type where the shear stress is the maximum shear expressed above.

$$\tau_{max} + \sigma_n \cdot \tan \phi = C \quad (3)$$

Where σ_n : normal stress, C : cohesion parameter, ϕ : internal friction angle.

- Failure of the composite plate in tension: it is the ideal failure mode. However, it is rarely reached because of the high tenacity of the reinforcement used. This criterion is expressed by using the tension behaviour of the composite.

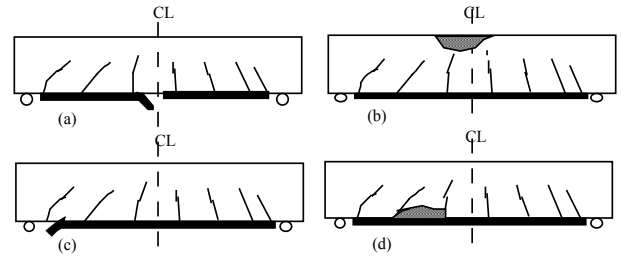


Figure 4 Different failure modes in Rc beam strengthened with FRP plate

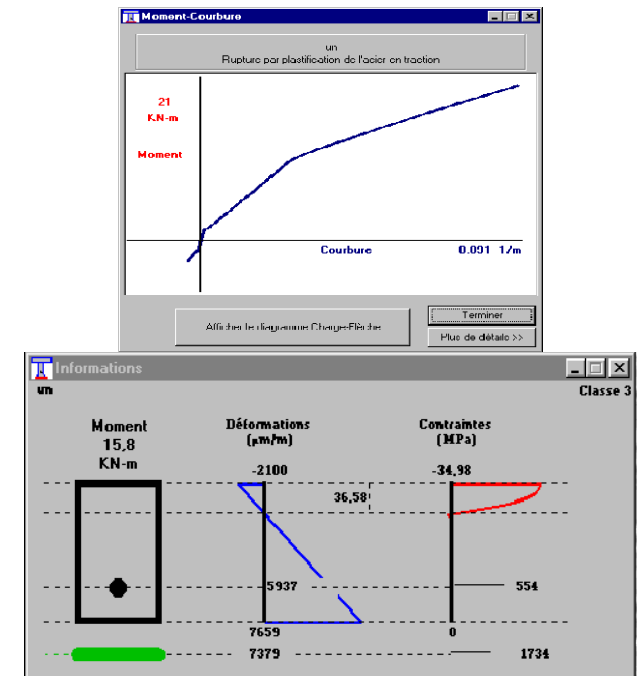


Figure 5 Non-linear behaviour law and information on deformation and stress levels

Examples of studies done by students

We study the case of RC beams with externally bonded FRP consisting of 30% volume fraction high strength unidirectional carbon fibres within an epoxy matrix. The FRP modulus of elasticity and ultimate tensile strength are given by table 1. The thickness layer is 3.2 mm. The composite is applied by wet lay up method.

The geometry of this beam is given in Figure 6.

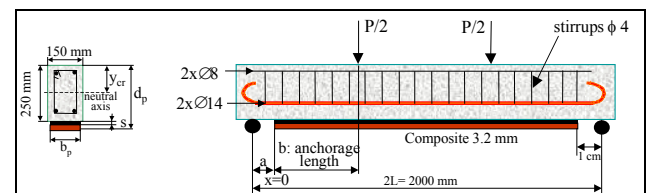


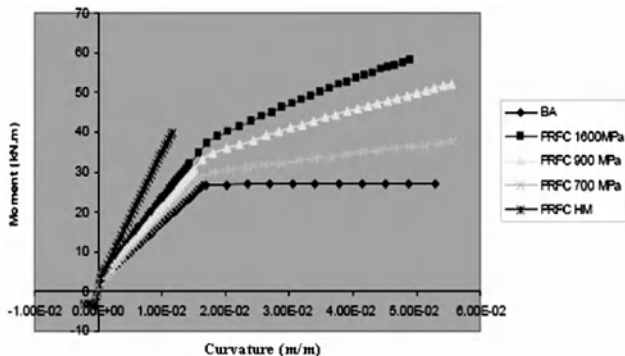
Figure 6 Geometrical and strengthening Characteristics of RC beams

Base on calculation of 6 cases studies student are able to consider the effect of FRP Young Modulus and ultimate strength of the moment-curvature behaviour (Table 1).

Table 1 Example of case studies

Case study		Tensile strength f_t (MPa)	Young modulus E_f (GPa)	Serviceability Moment (kN·m)	Ultimate Moment (kN·m)
1	BA	–	–	18.5	27.05
2	PRFC 1600	1600	120	20.1	37.55
3	PRFC 900	900	80	23.7	52.08
4	PRFC 700	700	30	26.4	58.22
5	PRFC 3000	3000	400	39.8	39.8

Figure 7 shows Moment-curvature for several case studies of FRP strengthening. This calculation allows to show the combined effect of increasing the Young modulus of FRP (increased of bending stiffness, brittle behaviour) and the increase of FRP ultimate strength which can not be so useful if debonding occurs.

**Figure 7** Examples of obtained results by students

Others case studies and comparison with experimental work done in laboratory or field case studies are also proposed during this course.

3 CONCLUSIONS

A software devoted to the design of reinforced and pre-stress beams strengthened by FRP has been developed for research purpose and is now regularly used for teaching at a Master level. Its main objective is the prediction of instantaneous and deferred properties

(behaviour laws and failure modes) of repaired structures. The calculation method is based on a non-linear formulation of the moment-curvature theory that takes into account the actual properties of materials and the sliding at the composite-to-concrete interface.

The use of computer aided calculation process allows student to better understand the interest and the limit of FRP strengthening and coupled with a short experience on RC testing contribute to a better analysis of RC strengthening. Comparison with design approach is also introduced in this course. This teaching is particularly well appreciated by student because it's combine light experimental work and computer used.

REFERENCES

- Ferrier, E. & Hamelin, P. (1999). *Influence of time-temperature loading on carbon epoxy reinforcement for concrete structure*, Fourth international symposium on fiber reinforced polymer (FRP) for reinforced concrete structures (FRPRCS-4), Baltimore, Maryland, US, 31 octobre – 5 novembre 1999.
- Ferrier, E. & Hamelin, P. (2000a). *FRP for civil engineering structure: effect of creep in the adhesive layer*, Third international conference on Advanced Composite Materials in Bridges and Structures, Ottawa, August 15-18, 2000.
- Ferrier, E. & Hamelin, P. (2000b). *Evolution of bending stiffness of RC beam strengthened by FRP under fatigue loading*, Third international conference on Advanced Composite Materials in Bridges and Structures, Ottawa, August 15-18, 2000.
- Ferrier E., Nasser H., Hamelin P., *Fatigue behavior of composite reinforcement for concrete structure*, ACI publications, SP-188-48, P.535-546, novembre 1999.
- Täljsten, B. (1997). *Defining anchor length of steel and CFRP plates bonded to concrete*, International journal of adhesives, Vol.17, N°4.
- Varastehpour, H. & Hamelin, P. (1995). *Structural behaviour of reinforced concrete beams strengthened by epoxy bonded FRP plate* Second international symposium on non-metallic (FRP) reinforcement of concrete structures, pp. 559-567, Ghent, Belgique.

Structural Remediation of Unreinforced Brick Masonry Walls of Heritage Palace Building with Carbon Fibre Reinforced Polymers

S. K. Savardekar (fyfeindia@vsnl.net)
FYFE (India) Pvt. Ltd., Mumbai, India

R. Jamaji
FYFE Asia Pte. Ltd., Singapore

K. R. Raikar
Structwel Designers & Consultants Pvt. Ltd, Mumbai, India

ABSTRACT A sprawling palace complex built in the year circa. 1893 and belonging to the Nizam family, rulers of the erstwhile princely state of Hyderabad in India, is currently being developed as a luxury heritage palace hotel by a leading hotel group from India. Various functional buildings are integrated to form the palace complex of around 940,000 square meters area. The original construction of the palace features mainly of a load bearing masonry structure comprising of burnt brick masonry with lime mortar. Years of disuse and exposure to environmental vagaries had resulted in various distresses to the structures. The present developers thought it prudent to conduct a structural audit of the palace complex to assess the present condition of the various structures. Subsequent to a structural audit, it was noted that, amongst other anomalies, various sections of the load bearing masonry walls of various buildings were non-compliant to the allowable values of slenderness ratios. This necessitated certain remediation measures to the deficient masonry wall panels. A remediation scheme using carbon fibre reinforced polymer (CFRP) bands as localised intermediate stiffeners onto the walls was found appropriate and thus adopted considering various advantages it offered. This paper describes the site case study on the installation of a particular proprietary CFRP system in achieving the desired objective of carrying out structural remediation of masonry walls.

1 INTRODUCTION

1.1 Project description

A leading hotel group in India had recently commenced development of an existing old palace complex to be converted into a luxury heritage hotel. The palace complex belonged to the Nizam royal family, of the erstwhile princely state of Hyderabad in southern India. The construction had commenced in the year 1884 and is said to have been completed in various stages over a period of nine years. The palace complex comprises of various functional buildings such as the main palace, Gol bungalow, Zanani mahal and various other ancillary buildings all integrated to form a sprawling complex covering around 940,000 square meters. Refer Figure 1.

1.2 Need for structural remediation

The various buildings of the palace complex are predominantly load bearing type and constructed of burnt brick masonry with lime mortar rendering. Certain sections of the walls at the ground level are noted to be of stone masonry with lime mortar. Over the years the palace complex was in state of disuse and had been exposed to environmental vagaries.



Figure 1 Front façade view of the main palace building

Certain sections of the palace buildings exhibited distresses in the form of cracks in the masonry and even partial collapses of the masonry walls at few locations were evident. The developers have therefore considered it prudent to conduct a structural audit of all the palace buildings to determine its suitability for their proposed use and the resulting loading conditions. The developers had thus appointed structural engineers for this purpose. Various surveys, visual inspections, non destructive and

partially destructive tests and analysis had been conducted by the structural engineers. Based on their evaluation, the structural engineers had identified certain structural anomalies. One amongst the various anomalies having relevance to this paper was that, certain masonry walls of the various buildings of the palace complex being slender. This necessitated localized structural remediation to address the issue.

2 STRUCTURAL REMEDIATION DETAILS

2.1 Structural remediation approach

To appropriately address this particular anomaly at hand, the use of various remedial options using different conventional techniques such as, section enlargement and introduction of steel sections as substitute framing systems were explored by the structural engineers. However, at certain locations, the age, aesthetic and heritage nature of the existing structures governed the choice of a remedial technique. As such it was imperative that a retrofit system to be executed should have essentially been minimal invasive, quick and discreet. Prime deterrents to the use of the above mentioned conventional techniques were that they were invasive, would aesthetically alter the walls appearance and were time consuming. Thus, the use of CFRP for structural remediation measures in order to appropriately address the above issues was recommended by the structural engineers.

2.2 Strengthening basis

Certain wall panels that were identified by the structural engineers to be non-compliant to the specified slenderness limits were recommended for structural remediation. Two criteria of slenderness had been checked for, viz. the ratio of;

- a. wall height / wall thickness
- b. wall length / wall thickness.

The structural remediation detail was based on the concept of providing CFRP strips in the horizontal and vertical directions and at certain specified spacing and bonded coincident onto either sides of the masonry walls, anchored with fibre anchors. This was designed to act as vertical and horizontal stiffeners by locally plating or sandwiching the masonry walls thereby increasing the stiffness. These CFRP stiffeners would then essentially act as intermediate pilasters/columns so as to reduce the effective wall height / length and thus bring the slenderness ratios within acceptable limits. Based on this concept shop drawings for individual wall panels were prepared taking into account factors such as openings and aesthetic features. Figure 2 shows an actual wall panel at site and Figure 3 shows part print of a shop drawing of the CFRP installation details for that wall panel.



Figure 2 A wall panel at site identified for structural remediation

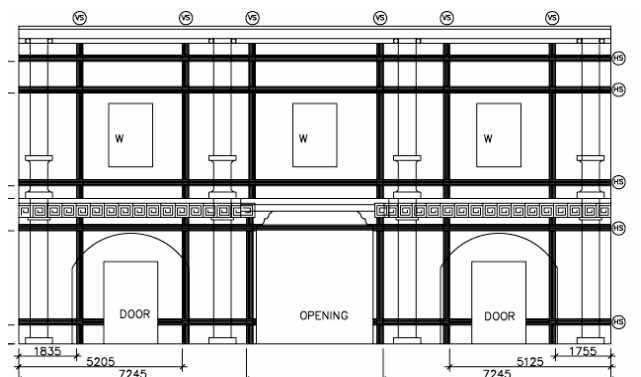


Figure 3 CFRP installation detail for the identified wall panel

2.3 CFRP system properties

The CFRP system selected for installation was a proprietary system from a reputed FRP system manufacturer. This system was selected on the criteria of material characterization, system performance and environmental durability as specified by structural engineer. The CFRP system comprised of a unidirectional carbon fibre fabric as the reinforcement and a compatible two component epoxy resin as the matrix. The key properties of the CFRP system used for carrying out the structural remediation are as shown in Table 1.

Table 1 Properties of CFRP system used for structural remediation

Property	Test Method	Typical Test Value*
Ultimate tensile strength in main fibre direction	ASTM D-3039	986.0 MPa.
Elongation at break	ASTM D-3039	1.0%
Tensile modulus	ASTM D-3039	95.8 GPa.
Laminate thickness		1.0 mm

* Values reported by CFRP system manufacturer based on gross laminate properties.

3 STRUCTURAL REMEDIATION PROCESS

3.1 Preparatory Works

The preparatory works commenced with identifying on site, wall panels marked for structural remediation from the drawings. Locations of the vertical and horizontal CFRP strips were then marked onto the walls ensuring that the CFRP strip locations are coincident on the internal and external faces of the walls. The lime plaster rendering was carefully chipped off at these marked locations to expose the brick masonry. Figure 4 shows the CFRP strip locations and removal of lime plaster. A polymer modified cementitious skim coat was then applied onto the exposed masonry to level off all concavities and depressions, so as to provide for a level substrate to receive the CFRP application. After adequate water curing, the leveled surface was then sanded using sand paper to smoothen out any protrusions and make the surface ready to receive CFRP application. Holes for fibre anchors were drilled at locations as indicated on the drawings. Figure 5 shows a wall panel with the prepared surface ready to receive CFRP strips.



Figure 4 Marking of CFRP strip locations and removal of lime mortar rendering



Figure 5 View of a wall panel with prepared surface ready to receive CFRP strips

3.2 CFRP Installation

The installation of the CFRP was wet wrapping type process as recommended by the system manufacturer. The installation process commenced with sizing and cutting of the carbon fibre fabric to the required dimensions that were obtained from site measurements. The two components of the saturant resin matrix were mixed together in the ratio as per manufacturer's specifications. The sized fabric was then manually saturated from both sides with the mixed resin matrix. The saturation was carried out manually using fabric rollers. The saturated fabric was then rolled onto spools and taken to site for installation. Prior to installation of the CFRP strips, the prepared surface was first wet primed with a coat of saturant resin. The saturated fabric was then installed onto the primed surface by evenly rolling out the spool along the primed surface. The CFRP strips were adhered onto the surface using uniform hand pressure along the main fibres. This also ensured to remove any entrapped air voids behind the CFRP strip. At a given wall panel all the vertical CFRP strips were installed followed by the horizontal CFRP strips. Figure 6 shows the installation of vertical CFRP strip.

The fibre anchors were then installed by first saturating the anchors into the saturant resin matrix and inserting one end of the anchor into the pre-drilled holes.



Figure 6 Installing vertical CFRP strip onto a wall panel

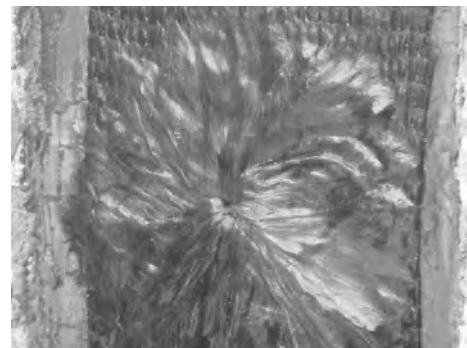


Figure 7 Closeup view of fibre anchor installed over CFRP strip

The outer end of the fibre anchor was then splayed over the CFRP strips as shown in Figure 7.

Upon the CFRP strip achieving a tacky stage of the curing process, quartz sand was sprinkled over it. This acted as a key for further lime plaster render finish.

4 CONCLUSION

The use of CFRP for structural remediation of the masonry walls of the palace buildings was found to be an appropriate technique to achieve the desired objective and at the same time being minimal invasive, quick and discreet as compared to conventional strengthening

techniques.

REFERENCES

- ACI Committee 440, Guidelines for the design and construction of externally bonded FRP system for strengthening concrete structures. American Concrete Institute, Detroit, 2000.
- ICC AC125, Interim criteria for concrete and reinforced and unreinforced masonry strengthening using fibre reinforced polymer (FRP) composite systems. ICC Evaluation Service Inc. Whittier, California, 2003.
- Technical Datasheet, Tyfo® SCH41 composite using Tyfo® S epoxy. Fyfe Co. LLC, San Diego, CA. 2006.

Structural Performance of Concrete Bridge Deck with Internal FRP Reinforcement

B. Wan (baolin.wan@marquette.edu) & C.M. Foley

Department of Civil and Environmental Engineering, Marquette University, Milwaukee, WI, USA

ABSTRACT In-situ load tests were performed for a highway bridge with deck containing a novel FRP grillage system. Strains under the deck and top and bottom flanges of girders at various locations were recorded when dump trucks were placed on the bridge. Loading protocols were designed to evaluate: (a) the bridge deck deflection relative to the girders; (b) girder lane load distribution factors; (c) transverse wheel loading distribution widths; and (d) strain distribution over the height of the girder-deck composite section. It was found that lane load distribution factors for wide-flange bulb-tee composite bridge girder systems can be computed accurately with standard design/analysis procedures found in modern bridge specifications. The strain gradients over the height of girders clearly exhibit composite behavior. There was no significant degradation of this bridge from 2005 to 2007.

1 INTRODUCTION

A novel FRP grillage system was used as bridge deck reinforcement in a highway bridge in the state of Wisconsin as part of the FHWA Innovative Bridge Research and Deployment Program. The bridge is B-20-148 which is part of the City of Fond du Lac bypass (US 151) in Fond du Lac County Wisconsin. It contains (approximately) 33.55 m simple-span pretensioned 54W girders. Support for the girders consists of bench-type abutments supported on steel piles. The bridge deck contains a novel FRP grillage system for both top and bottom reinforcement layers within the deck. Transverse reinforcement consists of FRP "I-shape bars" and longitudinal reinforcement consists of FRP rods passing through the bars. FRP "shear" struts are provided between the mats as required to preserve proper alignment of the reinforcement layers. There is a slight deck overhang beyond the edge of the 54W girder flange and mild-steel reinforcement is contained in this overhanging portion of the deck.

The FRP grillage used for primary reinforcement of the concrete bridge deck is a new material and structural system. Significant laboratory testing has been conducted to date (Bank et al. 1992), but in-situ validation is lacking. In this research, the in-situ load testing was conducted with a two-year separation with the goal being to evaluate changes in response over this period, which may indicate degradation in the superstructure. Performance parameters evaluated through the load testing to track degradation include: wheel load distribution within the bridge deck, composite action in the girders, and bridge deck deflections relative to the girders.

2 IN-SITU LOAD TESTS

2.1 Instrumentation

Innovative removable strain sensors (Schneeman (2006) were utilized to measure strains. Wiring of the strain sensors was accomplished using 6-pin mini-DIN connectors. This facilitated plugging and unplugging the sensors as the load tests were initiated and completed, respectively. Commercially available draw wire transducers (DWT's) were used to measure the deflection of the bridge deck and girders. This study is aimed at evaluating the long term behavior of the bridge and as a result, permanent equipment (e.g. wiring, junction boxes, NEMA 6P enclosures with screw terminals) were installed and left in place thereby reducing effort for the load tests performed in this research and possible future tests. The mounting bolts for strain gauges, lead wires for the instruments, protective PVC piping and an electrical enclosure box were installed on the bridge. The PVC wiring runs and the Mini-DIN connectors are shown in Figure 1, and the enclosure box and the data acquisition system are shown in Figure 2.

The focus of the load testing on this bridge is to experimentally determine the following: (a) bridge deck deflection relative to the girders (DWT instruments); (b) girder lane load distribution factors (LM and LT instruments); (c) transverse wheel loading distribution widths (TW instruments); (d) strain distribution over the height of the girder-deck composite section (LM and SP instruments).

Longitudinal distribution of load between the girders was conducted by attaching individual strain sensors to the underside of bridge girders at mid-span (LM strain



Figure 1 Mini-DIN plugs and PVC wire runs used in the field instrumentation



Figure 2 Image of laptop-based DAQ system.

gauges) and a third-point of the span (LT strain gauges). As there are seven girders, fourteen individual sensors were installed with each sensor being centered transversely on the girder. The location and distribution of these sensors in the superstructure is shown in Figures 3 and 4.

The strain profile of the bridge deck and girders is important to verify that composite action of exists between the deck and girders. The B-20-148 super-structure was

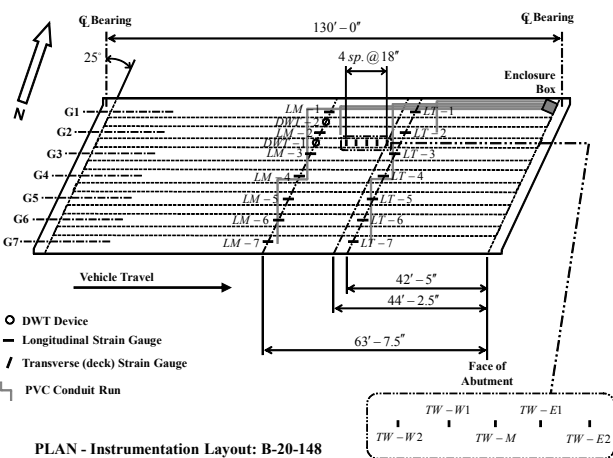


Figure 3 Instrumentation layout for B-20-148 (1 ft = 0.305 m and 1 in. = 25.4 mm)

designed assuming composite action and verification of such behavior is required. Additionally, any degradation of this composite behavior over time needed to be measured. By locating the strain sensors at the girder bottom flange, girder top flange, and on the FRP-reinforced deck as indicated in Figure 5, the strain variation over the height was recorded.

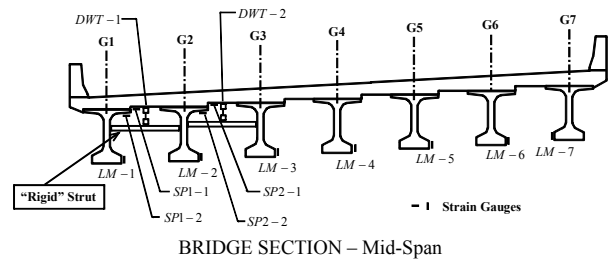


Figure 4 B-20-148 cross-sections with instrumentation locations and layout

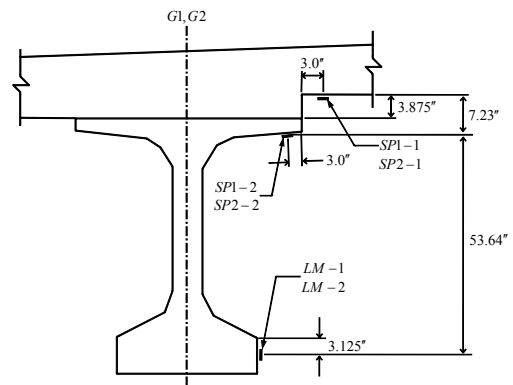


Figure 5 B-20-148 strain sensor locations used to measure strain distribution over height of girders (1 in. = 25.4 mm)

2.2 Loading Protocol

Calibrated (i.e. weighed) tri-axle dump trucks were utilized during all load tests. Four loading protocols were used for in-situ tests. Loading protocol 1 was used to establish maximum deflections relative to the girder due to front wheel loads in the exterior bridge deck span by placing the front left wheel of a dump truck at the center of exterior span. Loading protocol 2 was used to establish maximum deck deflections in the first interior span of the bridge deck by placing the front right wheel of a dump truck at the center of this span. Loading protocol 3 was established to examine the distribution of wheel loading within the bridge deck in the first interior bridge deck span by locating the front right wheel of a dump truck at the center of this span and moving with four stops at every 18 inches. The final loading protocol (number 4) used for this bridge is shown in Figure 6. Three dump trucks placed bumper to bumper on the bridge created a loading scenario that allowed lane loading distribution factors for the bridge superstructure to be determined.

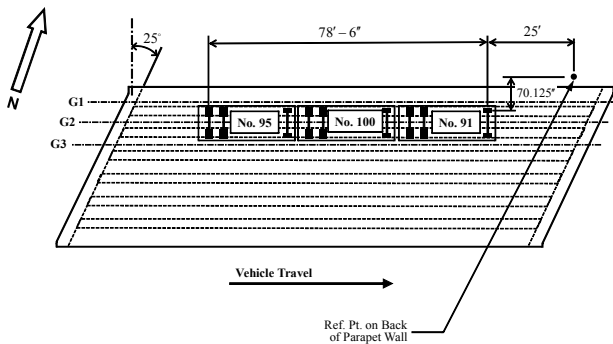


Figure 6 Loading protocol used to examine lane load distribution among the girders in Bridge B-20-148 (1 ft = 0.305 m and 1 in. = 25.4 mm)

During load tests, dump trucks were brought to the bridge and stopped at designated locations. A data acquisition system was used to record the strain and deflection data.

3 LANE LOADING DISTRIBUTION FACTORS

The tension strains measured across all girders in the superstructure can be used to evaluate a lane load distribution factors, mg_i , as follows (Turner et al 2003):

$$mg_i = \frac{\varepsilon_i}{\sum_{n=1}^N \varepsilon_n} \quad (1)$$

where ε_i is the strain measured in girder i ; and N is the total number of girders.

Using the girders' tensile strain data measured at mid-span, the lane load distribution factor for girder G2 at the mid-span location can be computed as,

$$mg_{LM} = \frac{62}{62 + 55 + 37 + 37 + 16 + 10} = 0.29$$

Using the strain data at the third-span, the lane load distribution factor for girder G2 at the third-span location can be computed as,

$$mg_{LT} = \frac{58}{58 + 52 + 42 + 25 + 25 + 10} = 0.27$$

The moment distribution factor at mid-span is slightly larger than that at the 1/3 points and this is consistent with the known behavior for skews nearing 30-degrees (AASHTO 2006).

A distribution factor was also computed as part of the baseline load testing conducted after B-20-148 was completed (Hernandez et al 2005). This distribution factor was computed using beam deflections across the superstructure and its magnitude was reported to be 0.23. This is very close and agreeable to the data obtained through the present research effort. As a result, one can say that the lane load distribution factor did not change

from 2005 to 2007 and therefore, there has been no degradation or change in the load transfer mechanism in the superstructure in this regard.

The AASHTO (2006) specifications also contain procedures for estimating how much of the design lane will be carried by a single girder within the bridge superstructure. For a single lane loaded situation, the calculation performed for girder G2 in the present system is as follows,

$$mg_{ml}^S = \frac{1}{1.2} \left[0.06 + \left(\frac{S}{14} \right)^{0.4} \left(\frac{S}{L} \right)^{0.3} \left(\frac{K_g}{12Lt_s^3} \right)^{0.1} \right] = 0.31 \quad (2)$$

where S is the center to center spacing of the longitudinal girder; L is the total span length of girder; K_g is the longitudinal stiffness parameter; and t_s is the depth of the deck. The distribution factors computed using strain readings in the present research are in excellent agreement with the distribution factor estimated using bridge specification expression (AASHTO 2006).

4 COMPOSITE ACTION

It is very important to quantify the change in strain readings over the height of the composite girders within the superstructure with time. This would give yet another indication that the load transfer mechanisms within the bridge superstructure were changing with time.

The peak strain data were transcribed onto a strain diagram over the height of the cross-section as shown in Figures 7 and 8. A theoretical composite section should have a linear strain diagram over the height of the cross-section. Furthermore, if the girders and deck were NOT acting compositely with one another, the underside of the deck would not be in compression. Figure 7 clearly indicates that composite behavior is occurring in these girders. The data for girder G1 indicates virtually no change in composite behavior from July 2007 to July 2009. Furthermore, the strain readings above the neutral axis for girder G2 had virtually no change from July 2007 to July 2009 as shown in Figure 8. The strain readings at the bottom flange of girder G2 were unexpected. While the July 2007 load test yielded expected strain readings, the July 2009 load test results were surprising. A reading of 155 microstrains would indicate significant behavioral change within the system. However, the response seen in girder G1 during this same load test suggests that this extreme strain reading was caused by improper installation of the strain gauge (Foley et al 2010).

Overall, the data in Figures 7 and 8 support the conclusion that there has been no change in the composite stringer-deck load transfer mechanism from July 2007 to July 2009 and therefore, there has been no degradation in the system in this regard.

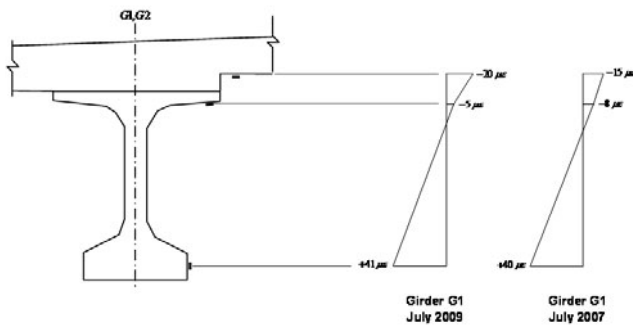


Figure 7 Strains over girder height for girder G1 for truck position 4 (Figure 6)

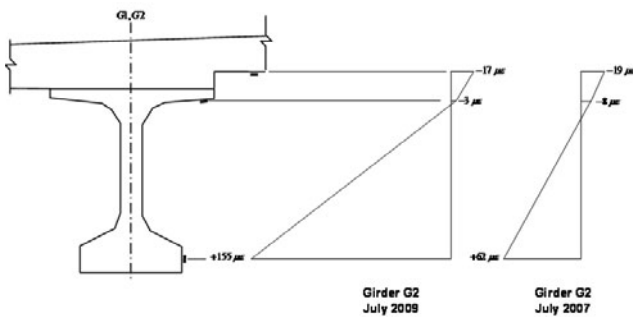


Figure 8 Strains over girder height for girder G2 for truck position 4 (Figure 6)

5 CONCLUSIONS

Lane load distribution factors for wide-flange bulb-tee composite bridge girder systems with FRP reinforced concrete deck (e.g. that used in B-20-148) can be computed accurately with standard design/analysis procedures found in modern bridge specifications (AASHTO 2006). Furthermore, these lane load distribution factors did not change from July 2005 (Hernandez et al 2005) and the July 2007 load test in

this research study. As a result, there was no degradation measured in this regard.

Strain gradients over the height of the girders clearly exhibit composite behavior. Furthermore, the strain gradients did not significantly (if at all) change with time and therefore, one can conclude that there was no change in the composite beam load transfer mechanism within bridge B-20-148 over the two-year monitoring period and therefore, no degradation in this regard.

REFERENCES

- AASHTO (2006). *AASHTO LRFD Bridge Design Specifications Including 2006 Interim Revisions*, Customary U.S. Units, 3rd Edition, American Association of State Highway and Transportation Officials, Washington, DC.
- Bank, L., Xi, Z., and Munley, E. (1992). Performance of Doubly-Reinforced Pultruded Grating/Concrete Slabs, *Advanced Composite Materials in Bridges and Structures*, Canadian Society for Civil Engineering: 351-360.
- Foley, C.M., Wan, B., Schneeman, C.L., Martin, K.E. and Komp, J. (2010). *In-Situ Monitoring and Testing of IBRC Bridges in Wisconsin*, Wisconsin Highway Research Program 0092-05-02, Wisconsin Department of Transportation, Federal Highway Administration, Madison, WI.
- Hernandez, E., Galati, N., Nanni, A. (2005). *In-Situ Load Testing of Bridges B-20-148 and B-20-149, Fond du Lac, WI*, Center for Infrastructure Studies, University of Missouri – Rolla.
- Schneeman, C.L. (2006). *Development and Evaluation of a Removable and Portable Strain Sensor for Short-Term Live Loading of Bridge Structures*, M.S. Thesis, Marquette University, Milwaukee, WI.
- Turner, M.K., Harries, K.A., Petrou, M.F., Rizos, D. and Wan, B. (2003). *In-Situ Evaluation of Demonstration GFRP Bridge Deck System Installed on South Carolina Route S655*, University of South Carolina, Department of Civil and Environmental Engineering Report No. ST 03-02.

Inspection, Analysis and Loading Test of a Slab Bridge Strengthened with FRP Laminates

Dongming Yan (yando@mst.edu), Chenglin Wu, Jianbo Li & Genda Chen

Center for Infrastructure Engineering Studies, Missouri University of Science and Technology, Missouri, USA

ABSTRACT The advantages of FRP as a strengthening material have been widely recognized in recent years. Typical applications of FRP have extended from repairing of cracked columns, beams, bridge decks to enhancing the load capacity of critical structural components. As a demonstration of application of FRP laminates in concrete bridge decks with no transverse reinforcement, the Rolla Bridge in Missouri is selected for this study, which is a two-span simply supported reinforced concrete slab with no transverse steel reinforcement. The original construction combined with the presence of very rigid parapets caused the formation of a wide longitudinal crack which resulted in the slab to behave as two separate elements. The strengthening scheme was designed to avoid further cracking and such that the transverse flexural capacity be higher than the cracking moment. An initial load test, to evaluate the structural behavior, was performed prior the strengthening. The retrofitting of the structure was employed after the major cracks were injected to allow continuity in the cross section. Once the repair work was completed, another load test, identical in procedure to the previous one, was performed to evaluate the efficiency of the strengthening. No additional cracking was observed in the concrete decks as a result of the strengthening program.

1 INTRODUCTION

The overall objective of the paper was to demonstrate the feasibility of externally bonding fiber reinforced polymer (FRP) reinforcement for the flexural strengthening of existing concrete bridge structures with a wide open longitudinal crack.

The bridge selected for demonstration of the FRP strengthening technology is located on County Road 8010, in Phelps County, Missouri. The bridge is a two-span simply-supported reinforced concrete slab. The total bridge length is 36 ft (10.98 m) and the edge-to-edge width of the bridge deck is 30 ft (9.15 m). This bridge represents an ideal case for the application of FRP composites since its deficiency is due primarily to a lack of transverse reinforcing steel (Stone et al. 2002). Based on the initial inspection, the area where the FRP was to be installed showed excellent surface conditions. A single crack extends longitudinally through the two spans along the centerline. The crack was more than 1.0 inch (2.54 cm) wide at some locations. There was no significant cracking elsewhere and only minor corrosion of the reinforcement was detected.

Fiber-reinforced polymer (FRP) material systems, composed of fibers embedded in a polymeric matrix, exhibit several properties suitable for their use as structural reinforcement (ACI Committee 440 2008, Nanni 2001). FRP composites are anisotropic and

characterized by excellent tensile strength in the direction of the fibers. They do not exhibit yielding, but instead are elastic up to failure. FRP composites are corrosion resistant, and therefore should perform better than other construction materials in terms of weathering behavior.

2 NON-DESTRUCTIVE EVALUATION AND BRIDGE ANALYSIS

2.1 Non-Destructive Testing Results

Based on the visual and Non-Destructive Testing (NDT) evaluation, it was determined that the superstructure is a solid concrete slab 9 in (22.86 cm) thick, running from pier to pier. It was longitudinally reinforced with #10 (31.75 mm) bars spaced at 6 in (12.7 cm) center-to-center. No transverse reinforcement was observed. Based on the compressive tests of four cylindrical concrete cores (3in×6in or 7.62cm×15.24cm), the average compressive strength of the concrete was determined to be 4,100 psi (28.27MPa). The yield strength of the steel reinforcement was 32ksi (220.63MPa) based on the tension test of one bar.

2.2 Load Calculation Based on Non-Destructive Test Results

According to AASHTO 3.5.1, the dead load shall include the weight of all components of the structure, appurtenances and utilities attached thereto, earth cover,

wearing surface, future overlays, and planned widening.

The bridge was analyzed for a design truck load condition and for a design lane load condition. The design truck load has a front axle load of 8.0 kips (55.12MPa), a second axle load of 32.0kips (220.63MPa) located 14.0 ft behind the drive axle and a rear axle load also of 32.0 kips (220.63MPa). The rear axle load is positioned at a variable distance ranging between 14.0 ft (4.2m) and 30.0 ft (9.0m). A dynamic load allowance shall be considered as specified in Article 3.6.2. The calculated ultimate moment (M_u) and shear (V_u) resistant capacities are 353.25 k-ft and 83.71 kips (576.7MPa), respectively.

Ultimate values of the bending moment and shear force were obtained by multiplying their nominal values by the dead and live load factors and by the impact factor: The calculated nominal moment (ϕM_n) and shear (ϕV_n) resistant capacities are 568.3 k-ft (153kN-m) and 153 kips (1057.3MPa).

3 BRIDGE STRENGTHENING

3.1 Objectives and Technical Approach

The objective of the strengthening is to provide the necessary transverse reinforcement. Since no reinforcement was provided in the transverse direction, minimal strengthening is needed to ensure that the transverse design moment capacity is larger or equal to the cracking moment, in order to avoid further crack openings and deterioration of the concrete due to water percolation through the cracks. In this study, a commercially available externally bonded Carbon Fiber Reinforced Polymers (CFRP) laminates were adopted to strengthen the bridge in the transverse direction by a manual wet lay-up installation technique. Before FRP installations, the longitudinal crack along the centerline of the bridge was first repaired in order to re-establish material continuity and assure no water percolation through the crack. For this purpose, the crack was sealed using an epoxy-paste and then injected with a very low viscosity resin. FRP was then applied.

The FRP laminates was designed according to ACI 440.2R-08, referred to ACI 440 thereafter. The properties of the FRP composite materials used in the design are summarized in Table 1. They are the guaranteed values by manufacturers.

The ϕ factors used to convert nominal strengths to design capacities were obtained as specified in AASHTO (2007) for the as-built bridge members and from ACI 440 for the strengthened members. The FRP material properties reported by manufacturers, such as the ultimate tensile strength, typically do not consider long-term exposure to environmental conditions, and should be considered as initial properties. They are modified in all design equations as in ACI 440. The FRP

design modulus of elasticity is the average value as reported by the manufacturer, which is listed in Table 1.

Table 1 Properties of CFRP Laminate Constituent Materials

Materials Strength	Primer	Putty	Saturant	High Strength Carbon Fiber
f_{fu}^* ksi	2.5	2.2	8.0	550
f_{fu}^* ksi	40	7.0	7.0	0.017
E_f ksi	104	260	260	33000
t_f in.	---	---	---	0.0065

3.2 External Bonded CFRP Laminates

To avoid further cracking in the bridge deck, a total of five, 12 in (30.48 cm) wide, 28 ft (8.53 m) long, two-ply CFRP strips are required. The final design of the CFRP laminates was to evenly space five strips over the span length of 18 ft (5.49 m) and run the entire width of the slab, as shown in Figure 1. The CFRP laminates were applied by a certified contractor in accordance to manufacturer’s specification (Watson Bowman Acme Corp., 2002) (see Table 1).

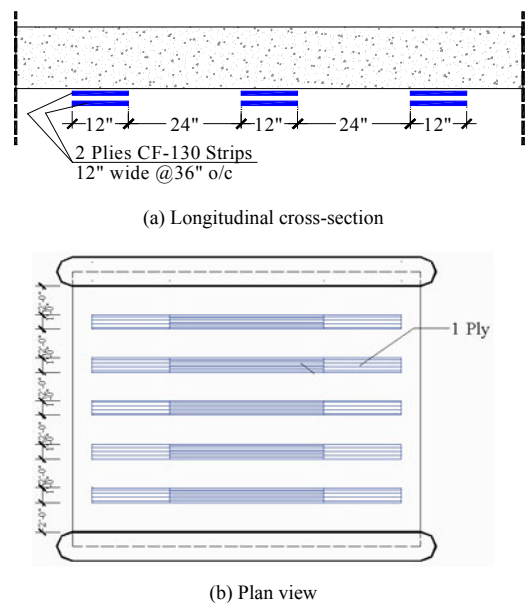


Figure 1 Laminate locations and dimensions

3.3 Field Evaluation

Although in-situ bridge load testing is recommended by AASHTO (2007) as an “effective means of evaluating the structural performance of a bridge,” no guidelines currently exist for bridge load test protocols. In each case the load test objectives, load configuration, instrumentation type and placement, and analysis techniques are to be determined by the organization conducting the test.

In order to validate the behavior of the bridge, static load tests were performed with a dump truck. The bridge was tested under three passes of the truck: one central and two side passes as illustrated in Figure 2. For

each pass, four stops were executed with the truck having its rear axle centered over the center pier, at the quarter point, at the mid-span, and over the end pier, which were clearly marked on the asphalt pavement for the side pass.

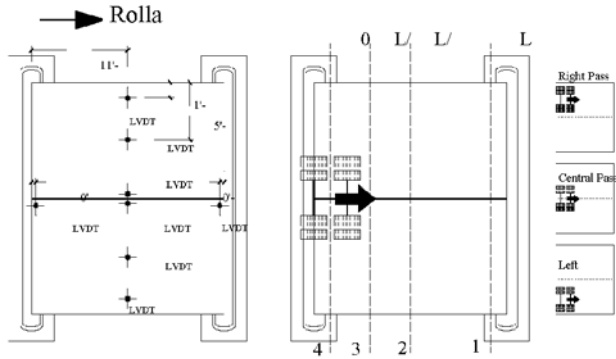
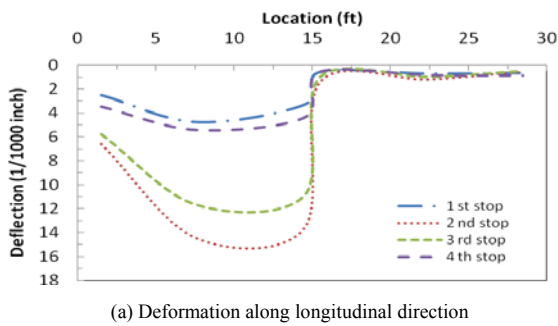


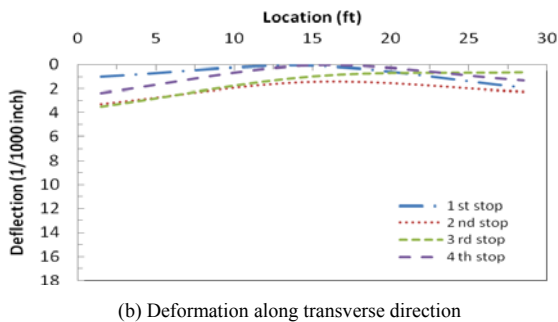
Figure 2 LVDT locations and stop locations of the truck rear axle

During each stop, the truck stationed for at least two minutes before proceeding to the next location to allow stable readings. Vertical displacements were measured with eight Linear Variable Differential Transformers (LVDT as shown in) that were distributed along the traffic direction and its perpendicular direction.

Note that Figure 3, Figure 4 and Figure 5 correspond to the loading cases that the truck ran from Location 1 to 4 as marked in Figure 2. Also note that the LVDTs along the transverse centerline were located closer to the left side. That explains why the transverse distributions of the bridge deck deflection for the left and right passes differ as illustrated in Figure 3 and Figure 5.

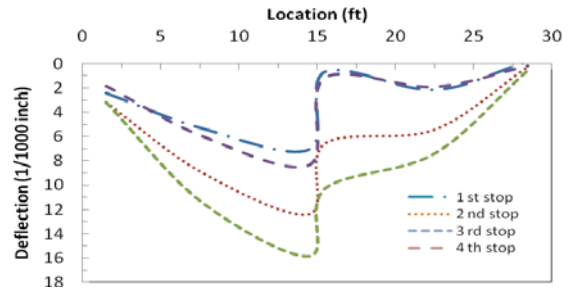


(a) Deformation along longitudinal direction

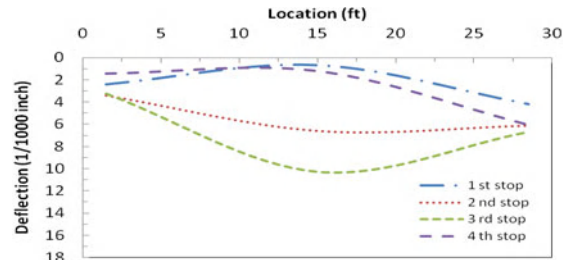


(b) Deformation along transverse direction

Figure 3 Deflection along the longitudinal and transverse direction (left pass)

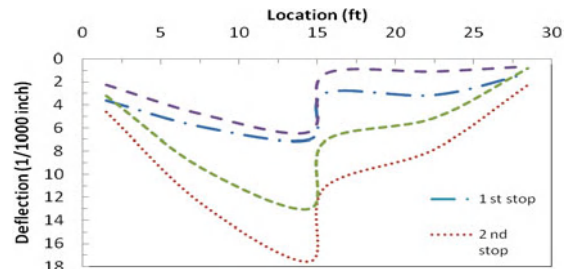


(a) Deformation along longitudinal direction

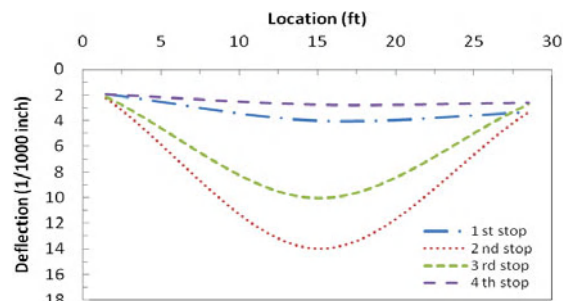


(b) Deformation along transverse direction

Figure 4 Deflection along the longitudinal and transverse directions (central pass)



(a) Deformation along longitudinal direction



(b) Deformation along transverse direction

Figure 5 Deflection along the longitudinal and transverse directions (right pass)

When crack initiates along the centerline of the bridge deck, only half of the deck supported the truck passing on that side, resulting in a greater deflection. The lateral FRP laminate will not only restrict the further development of the crack, but also improve the integrity of the bridge deck.

The instrumentation layout was designed to understand the deflection distribution of the bridge deck. In theory, the bridge acted symmetrically. Therefore, the instrumentation system was concentrated on one half of

the bridge deck. The results of the load tests are presented in Figure 3 to Figure 5. These results consistently show the discontinuity of deflection along the centerline of the bridge as a result of the longitudinal crack. This was probably the first bridge application with a significant longitudinal crack. Therefore, although an effort was made to seal the crack, the two sides of the bridge deck still did not perform as one unit. Overall, the bridge performed well in terms of the maximum deflection. In fact, the maximum deflection measured during the load test is below the allowable deflection prescribed by the 2007 AASHTO, Section 8.9.3. That is $\delta_{\max} \leq L/800 = 0.27\text{in} (6.86\text{mm})$.

4 CONCLUSIONS

Based on the load tests and numerical simulations, the following observations can be made:

- An externally bonded FRP laminate system is a feasible solution to upgrade the obsolete bridge to meet the current design requirement for transverse reinforcement;
- The load tests indicate that the FRP strengthening of the concrete bridge meets the deflection requirement stipulated in the 2007 AASHTO Specifications;
- The test results indicates that the lateral FRP laminate will not only restrict the further development of the crack, but also improve the integrity of the bridge deck.

5 ACKNOWLEDGE

The participation of Antonio Nanni, Galati Nestore, Cox Jason, Xing Tao in the design, strengthening and/or testing process is highly appreciated.

REFERENCES

- AASHTO (2007): Standard Specifications for Highway Bridges, 17th Edition, Published by the American Association of State Highway and Transportation Officials, Washington D.C.
- ACI 440.2R-08, 2008: Guide for the Design and Construction of Externally Bonded FRP Systems for Strengthening Concrete Structures, Published by the American Concrete Institute, Farmington Hills, MI.
- ACI 318-02, 2002: Building Code Requirements for Structural Concrete and Commentary (318R-02), Published by the American Concrete Institute, Farmington Hills, MI.
- De Lorenzis, L. (2002), Strengthening of RC Structures with Near Surface Mounted FRP Rods, Ph.D. Thesis, Department of Innovation Engineering, University of Lecce, Italy, 289 pp. <http://nt-lab-ambiente.unile.it/delorenzis>.
- Nanni, A. (2001), Relevant Applications of FRP Composites in Concrete Structures, Proc., CCC 2001, Composites in Construction, Porto, Portugal, Oct. 10-12, 2001, J Figueiras, L. Juvandes and R. Fúria, Eds., (invited), pp. 661-670.
- Yang, X. (2001), The engineering of construction specifications for externally bonded FRP composites, Doctoral Dissertation, Department of Civil Engineering, University of Missouri-Rolla, Rolla, Missouri, 166 pp.

Guidelines for Design of Honeycomb FRP Sandwich Panels

An Chen (an.chen@mail.wvu.edu) & Julio F. Davalos (julio.davalos@mail.wvu.edu)

Department of Civil and Environmental Engineering, West Virginia University, Morgantown, WV, USA

ABSTRACT Honeycomb Fiber-Reinforced Polymer (HFRP) sandwich panels with sinusoidal core geometry have shown to be successful both for new construction and rehabilitation of existing bridge decks. The development of standards and guidelines is needed in order to promote wider acceptance of composite sandwich products in construction. Much effort has been devoted to the modeling, optimization, and strength evaluation of the HFRP panel at West Virginia University, in terms of both experimental investigations and analytical solutions. This paper first summarizes all the findings, including out-of-plane compression failure and buckling, shear buckling, shear failure, and delamination at interface due to shear-tension coupling of out-of-plane shear; and progressive failure of laminated facesheet. And then, using the analytical models obtained, parametric studies are carried out and equations are provided to describe the influence of such parameters as interface bonding layer numbers, core wall thicknesses, and facesheet configurations. Next, through correlations with existing experimental results, design guidelines are proposed considering various failure modes. Finally, the proposed guidelines are used to evaluate the strength of HFRP sandwich panels and verify their applicability in practice. All methods presented in this paper can be extended to study other types of sandwich panels.

1 INTRODUCTION

In recent years, the demands in civil infrastructure have provided opportunities for development and implementation of Fiber-Reinforced Polymer (FRP) bridge panels, both in rehabilitation projects and new constructions. Primary benefits of FRP decks include: durability, lightweight, high strength, rapid installation, lower or competitive life-cycle cost, and high quality manufacturing processes under controlled environments.

However, in contrast to its increasing applications, the design process is not in a code format. Rather, individual decks are designed on a job-by-job basis using a combination of sample testing, Finite Element (FE) technique, and empirical judgment, and such approaches have likely hampered the wider acceptance of relatively new and innovative FRP bridge decks.

In the second part, using the analytical and numerical models obtained, parametric studies are carried out and equations are provided to describe the influence of such parameters as interface bonding layer numbers, core wall thicknesses, and facesheet configurations. Next, through correlations with existing experimental results, design guidelines are proposed considering various failure modes as mentioned above.

Finally, the guidelines are used to evaluate the strength of HFRP sandwich panels and verify their applicability in practice.

2 EVALUATION OF CORE AND FACESHEET COMPONENTS

Core materials for sandwich structures are primarily subjected to out-of-plane compression and shear, and therefore, research has been directed to three areas: out-of-plane compression, out-of-plane shear, and study on facesheet laminates. All studies were carried out through combinations of analytical solutions and experimental investigations.

2.1 Out-of-plane Compression

Based on various studies (Chen, 2004; Davalos and Chen, 2005; Chen and Davalos 2009), it was concluded that there are two failure modes for HFRP sandwich panels under out-of-plane compression: pure compression and buckling failures, which were also observed by Zhang and Ashby (1992). Thus, two analytical models, corresponding to pure compression and elastic buckling failures, respectively, were provided.

Compression tests were carried out to evaluate the effect of the bonding layer thickness and core thickness, and the experimental results correlated closely with analytical and FE predictions (Chen and Davalos, 2009).

2.2 Out-of-plane Shear

The study for out-of-plane shear (Chen, 2004; Chen and Davalos, 2007; Chen and Davalos, 2005; Chen and Davalos, 2009) provided analytical models, including delamination considering skin effect, shear buckling,

and shear crushing.

Four-point bending tests were carried out according to ASTM standards to study shear strength and shear stiffness of the core materials, and the thickness of interface bonding layers and core elements were varied to study their effect on strength (Chen and Davalos, 2009). Two types of beam samples were manufactured by orienting the core sinusoidal wave shown in Figure 1, as: (1) along the length (“longitudinal”), and (2) along the width (“transverse”). Equations were provided to predict the failure load due to different failure modes and good correlations were obtained.

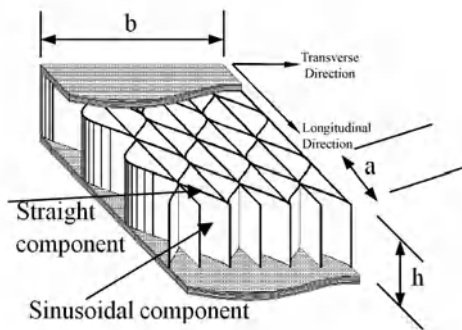


Figure 1 HFRP panel with sinusoidal core configuration

2.3 Facesheet Study

For facesheet configurations (Chen, 2004; Chen and Davalos, 2004; Chen and Davalos, 2009), a progressive failure model was developed using FE method to predict the behavior of laminated composite plates up to failure.

In order to further investigate the behavior of facesheet experimentally, coupon samples on selected configurations to evaluate compressive and bending strengths were tested in accordance with ASTM standards. The strength properties both in the longitudinal and transverse directions were evaluated.

3 PARAMETRIC STUDY

Using the analytical models described in the previous section, parametric studies are carried out to describe the influence of such parameters as bonding layer numbers, core wall thicknesses, and facesheet configurations. The naming conventions for all parameters are shown in the Appendix, Figure A.1. The results will also be used to derive design guidelines in the following section.

3.1 Out-of-plane Compressive

In practice, it is common to vary the core height to meet the requirement for the panel depth. The critical buckling stress vs. core height curve is illustrated in Figure 2 for the straight core component of width $a=102$ mm (4 inches) (Figure 1). From which it can be seen that the buckling stress is quite sensitive to variation of cell height up to about $a=102$ mm (4-inch), and within

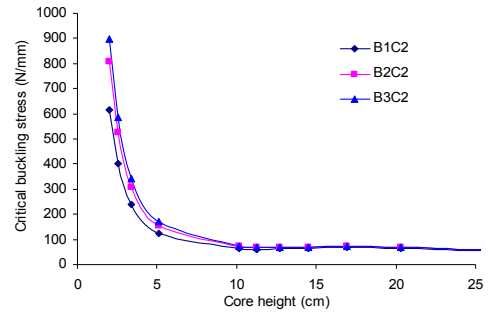


Figure 2 Critical buckling stress vs. core height (See Figure. A.1 for naming convention)

this range there is a notable difference among the buckling stresses for different number of bonding layers. The buckling stress decreases as the core height increases, and the stress reaches nearly a plateau when the core height is higher than 203 (8-inch). Beyond this limit point the bonding layer thickness does not affect the result much. Figure 2 also illustrates the relationship between the critical buckling stress and the aspect ratio of the core wall. Based on Figure 2, the buckling strength can be calculated using the regression formula:

$$\sigma = 4.45 \times \frac{A_1 e^{-h/(B_1 \times 25.4)} + A_2 e^{-h/(B_2 \times 25.4)} + F_0}{A} \quad (1)$$

where h is the height of the panel, and all the other parameters are listed in Table 1.

Table 1 Parameters for Eq. (1)

	A_1	B_1	A_2	B_2	F_0
One bonding layer	957515	0.2363	124742	0.7464	8081
Two bonding layers	87639	1.0105	954711	0.2917	8136
Three bonding layers	1038189	0.2985	88384	1.0765	8152

3.2 Out-of-plane Shear

Figure 3 plots shear stiffness vs. aspect ratio for C2 (two core thickness), where the aspect ratio is defined as h/a (see Figure 1). The lower bound was given by Davalos et al. (2001) without considering skin effect. From Figure 3, we can observe that the analytical solution, considering shear warping, corresponds to hinge connection. There is a significant difference between hinge and rigid cases when the aspect ratio is low, whereas all the solutions approach the lower bound value as aspect ratio increases. This proves that, as pointed out by several researchers (e.g., Davalos et al., 2001), the skin effect is localized, and its effect on stiffness, which is a global parameter, is negligible when the core is high enough. To more accurately describe shear stiffness, the results from analytical solution (shear warping) can be used for design purpose. Based on the curve for analytical solution considering shear warping from Figure 3, the following equation can be

used to calculate equivalent shear modulus

$$G_{xz} = 314 + 5.23e^{-\frac{R-0.1113}{0.7987}} + 0.99e^{-\frac{R-0.1113}{20}} \quad (2)$$

where R is the aspect ratio.

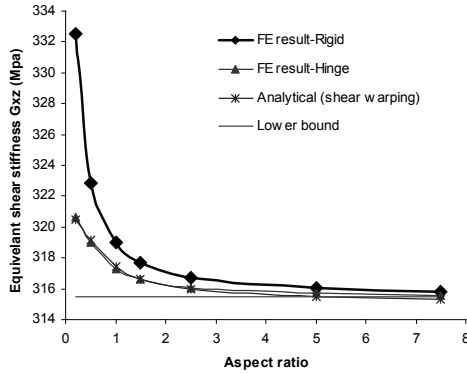


Figure 3 Stiffness vs. aspect ratio

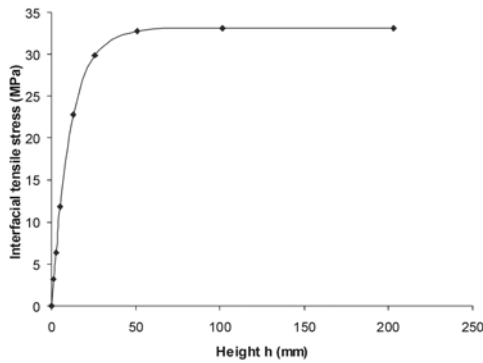


Figure 4 Normal interfacial stresses vs. height

A parametric study is carried out for the interfacial normal stress, $\sigma_{\text{interface}}$, at the panel intersection under a shear strain of 0.02, as shown in Figure 4, from which we can observe that $\sigma_{\text{interface}}$ increases as the aspect ratio increases, and reaches a constant value beyond a certain limit, for instance, $h \approx 51$ mm (2 inch) for this case. Based on the curve shown in Figure 4, we find the interfacial tensile stress for the curved core component as

$$\sigma_{\text{interface}} = \gamma(1656 - 1656e^{-[0.09123h]^{1.0221}}) \quad (3)$$

where γ is the shear strain, and h is the height of the panel.

The critical buckling stresses for different bonding layers are shown in Figure 5, from which we can observe that the bonding layers effect on shear buckling capacity is negligible for aspect ratio used in practice. Based on Figure 5, the shear buckling strength can be calculated using the following regression formula:

$$\tau = 0.175 \times \left(\frac{A_1}{t} e^{\frac{R}{B_1}} + \frac{A_2}{t} e^{\frac{R}{B_2}} + \frac{N_0}{t} \right) \quad (4)$$

where R is the aspect ratio, t is the thickness of the core wall, and all other parameters are given in Table 2.

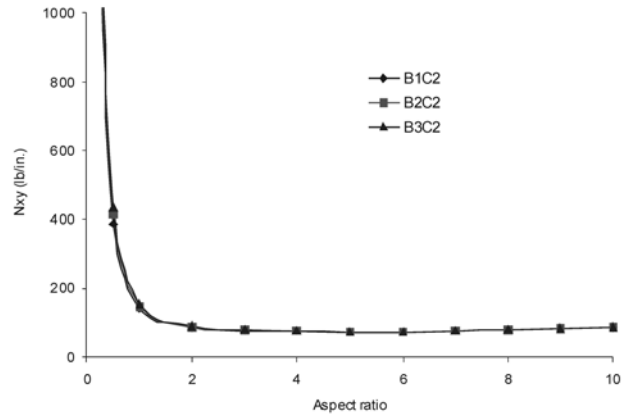


Figure 5 Normal interfacial stresses vs. height

Table 2 Parameters for Eq. (4)

	A_1	B_1	A_2	B_2	N_0
One bonding layer	2103	0.5326	34611	0.1388	448
Two bonding layers	2661	0.5097	37093	0.1355	449
Three bonding layers	3015	0.4970	38734	0.1339	450

4 DESIGN GUIDELINES*

Based on the results from analytical models and experimental investigations from previous studies, and the parametric study given in the previous section, design guidelines are proposed considering various failure modes as follows. Out-of-plane Compression.

Figure 6 can be used to predict compression failure load. The following method is proposed:

1) In relation to the interface bonding layer thickness (number of layers), a transition height h_T is defined, above which the core undergoes buckling failure. Thus, we compare the height of the panel h with the transition height h_T , as shown in Table 3. If $h < h_T$, the failure mode is pure compression failure, and we use material compressive strength f_c , which can be obtained from coupon test (Chen and Davalos, 2009), as controlling strength; otherwise, buckling dominates the failure, and we evaluate strength according to Eq. (1).

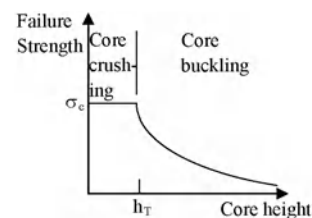


Figure 6 Design diagram for compression and shear

* The units used in this section are N, mm, MPa, and N-mm unless otherwise mentioned.

2) We calculate the compressive stress based on the most critical loading condition, and compare this stress with the compressive strength obtained from previous step 1 to find the safety factor.

Table 3 Transition height (mm)

	One bonding layer	Two bonding layers	Three bonding layers
h_T	32	36	38

Three distinct failure modes may occur for a panel under out-of-plane shear: shear crushing and shear buckling for the flat component, and interface debonding for the sinusoidal component, where the final failure load depends on the lowest value from these failure modes. Figure 6 can be schematically used to define failure strength for the flat core component. The following method is proposed:

1) We compare the height of the panel h with the transition height h_T , as shown in Table 4. If $h < h_T$, the failure mode is pure shear failure, and we use the material shear strength as controlling strength; otherwise, buckling dominates the failure, and we define strength as provided in Eq. (4). The debonding needs to be evaluated separately in Step 3;

2) Eq. (2) can be used to calculate equivalent shear modulus G_{xz} . Next, we calculate shear strain based on induced shear load per unit transverse core area. Then we find the shear stress for the flat core component, and we compare this stress with the shear strength obtained from step 1 to get the safety factor;

3) Using shear strain obtained from Step 2, we can find the interfacial tensile stress for the curved core component from Eq. (3). We then compare the interfacial tensile stress $\sigma_{interface}$ with the nominal interfacial tensile strength in Table 5 (Chen, 2004) to define the safety factor.

Table 4 Transition height (mm)

	One bonding layer	Two bonding layers	Three bonding layers
h_T	88	94	98

Table 5 Nominal interfacial tensile strength (MPa)

	B1C2	B2C2	B3C2	B2C1	B2C3	B3C1	B3C3
$\sigma_{interface}$	8.3	12.1	15.1	8.8	11.8	11.8	20.7

5 APPLICATION

Using the design guidelines provided in the previous section, we can evaluate the strength of an HFRP sandwich panel for a bridge under a patch load. The height of the panel $h=254$ mm (10 inch), the core wall thickness for both curved and flat is $t=2.3$ mm (0.09 inch), the length of the component $a=102$ mm (4 inch), and the aspect ratio $R=h/a=2.5$. One bonding layer is used at the interface between core and facesheet. The

HFRP panel can be treated as one way slab, with two sides simply-supported and two sides free, as shown in Figure 7. The maximum applied load, considering AASHTO HS20-44 (AASHTO, 2007) design truck wheel load [71,171 N (16,000 lb)] with a dynamic load allowance of 33%, is

$$P_{max} = 71,171 \times 1.33 = 94,658 \text{ N} \quad (5)$$

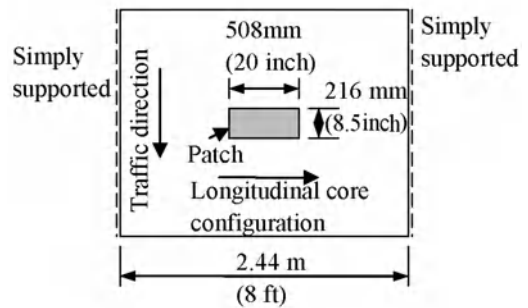


Figure 7 Panel layout

According to AASHTO LRFD Specifications (2007), the width of the contact area between wheel and bridge deck is 508 mm (20”), and the length can be calculated as (AASHTO Sect. 3.6.1.2.5):

$$\begin{aligned} \ell &= 6.4\gamma(1 + IM/100) = 6.4(1 + 33/100) \\ &= 8.512 \text{ inch} = 216 \text{ mm} \end{aligned} \quad (6)$$

where γ , the load factor, is assumed to be 1.0 for safety reasons; IM =dynamic allowance percent. It is assumed that the wheel load is evenly distributed over the contact area. It is worth pointing out that, when designing a bridge deck, further distribution along the longitudinal direction is allowed (AASHTO Sect. 4.6.2), which is not considered because the purpose of this example is to illustrate how to evaluate the strength of the panel for a given loading condition. Proper code/specifications shall be followed in order to calculate the design forces, which is beyond the scope of this paper.

5.1 Compressive Strength

The compressive stress can be calculated as,

$$\sigma_c = \frac{P_{max}}{216 \times 508} = \frac{94,658}{216 \times 508} = 0.86 \text{ MPa} \quad (125 \text{ psi}) \quad (7)$$

The panel height is 254 mm (10 inch). From Table 3, we find that the transition height for one bonding layer is 32 mm (1.25 inch), which is less than 254 mm (10 inch), and therefore, buckling controls the design. Substituting all the values into Eq. (1), the buckling strength is found to be 3.48 MPa (505 psi), which gives a safety factor of $3.48/0.86=4.0$. The calculation can be repeated for other core heights, and the results are given in Table 6.

5.2 Shear Strength

For convenience, we define a 25.4 mm (1 inch) wide beam

Table 6 Compressive strength check

Core height (mm)	Pure compressive strength (MPa)	Buckling strength (MPa)	Controlling strength (MPa)	Safety factor
13	15.9	80.7	15.9	18.5
51	15.9	7.3	7.3	8.4
102	15.9	3.7	3.7	4.3
203	15.9	3.5	3.5	4.0
254	15.9	3.5	3.5	4.0
305	15.9	3.5	3.5	4.0
508	15.9	3.5	3.5	4.0
1016	15.9	3.5	3.5	4.0

with a distributed load q acting at mid-span, i.e., $b=25.4$ mm, as shown in Figure 8. The distributed load q can be calculated as

$$q = \frac{P_{max}}{216 \times 508} = \frac{94,658 \times 25.4}{216 \times 508} = 21.9 \text{ N/mm (125 lb/in)} \quad (8)$$

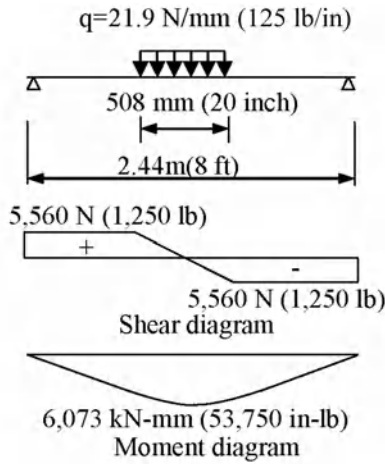


Figure 8 Unit width panel loading condition

The shear and moment diagrams are given in Figure 9. It is noted that when designing a bridge deck, diagrams of moment and shear envelop shall be used to check for moment and shear capacity, which is not considered for the same reason as stated in the previous section.

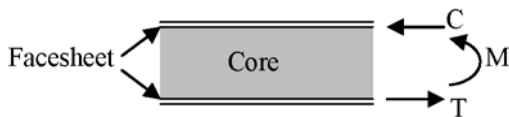


Figure 9 Forces acting on facesheet

The height of the panel is 254 mm (10 inch), and therefore, aspect ratio $R=254/102=2.5$. Using Eq. (2), we can find the equivalent shear stiffness $G_{xz}=315$ MPa (45,689 psi). The shear strain can be approximated as,

$$\gamma = \frac{V}{G_{xz}bh} = \frac{5560}{315,000 \times 25.4 \times 254} = 0.002736 \quad (9)$$

Therefore,, the shear stress in the flat core component is $\tau_{12} = G_{12}\gamma = 4,206 \times 0.002736 = 11.5$ MPa (1,669 psi) (10)

where G_{12} [4,206 MPa (610 ksi)] is the material shear modulus from material test data (Chen and Davalos, 2009). From Table 4, we find $h_T=88$ mm (3.48”), and thus $h>h_T$, and buckling controls the design. From Eq. (4), the shear buckling strength is found to be 35.8 MPa (5,192 psi), giving a safety factor of 3.11.

To find whether interface delamination is of concern, the shear strain is substituted into Eq. (3), and the interfacial shear stress is found to be 4.5 MPa (657 psi). Comparing with the nominal interfacial strength of 8.3 MPa (1,210 psi) from Table 5, it gives a safety factor of 1.84. The procedures can be repeated for other core heights, as shown in Table 7.

Table 7 Shear strength check

Height mm	Aspect ratio R	Shear stiffness (MPa)	Shear strain	Shear stress in flat panel (MPa)	Buckling Strength (MPa)
13	0.125	320.0	0.026933	113.3	1238.8
51	0.5	318.1	0.013549	57.0	169.5
102	1	316.5	0.006807	28.6	60.9
203	2	315.3	0.003417	14.4	38.1
254	2.5	315.0	0.002736	11.5	35.8
305	3	314.9	0.002281	9.6	34.9
508	5	314.7	0.001369	5.8	34.3
1016	10	314.5	0.000685	2.9	34.3

Material strength (MPa)	Controlling strength (MPa)	Safety factor for flat panel	Interfacial normal stress (MPa)	Safety factor for curved panel
70.6	70.6	0.62	30.6	0.27
70.6	70.6	1.24	22.2	0.37
70.6	60.9	2.13	11.3	0.74
70.6	38.1	2.65	5.7	1.47
70.6	35.8	3.11	4.5	1.84
70.6	34.9	3.64	3.8	2.21
70.6	34.3	5.96	2.3	3.68
70.6	34.3	11.91	1.1	7.35

5.3 Facesheet check

As composite action with supporting beams is generally not accounted for FRP bridge decks, the bending moment is carried through the membrane forces of the facesheet, as shown in Figure 9. From Figure 8, we have

$$M = 6,073 \text{ kN – mm} \quad (11)$$

And the compressive and tensile force (Figure 9) can be calculated as,

$$C = T = \frac{M}{h} = \frac{6,073}{254} = 23.9 \text{ kN (5,375 lb)} \quad (12)$$

From experimental results, the compressive strength for the facesheet with current configuration is 116.1 kN (36,670 lb) for b=25.4 mm (1-inch) (Chen, 2004; Chen and Davalos, 2004), giving a safety factor of 4.9. Safety factors for other laminate lay-ups (Table A.1) are given in Table 8, from which we can see that, even when ChSM layer is introduced into the facesheet, compressive strength of facesheet is still not a concern for design.

Table A.1 Plate configurations for facesheet laminate

Laminate 1(current)	Laminate 2	Laminate 3
2 layers 900 g/m ² ChSM*	2 layers 900 g/m ² ChSM*	2 layers 900 g/m ² ChSM
1 layer Bi-axial*	1 layer Bi-axial	8 layers Bi-axial
9 layers Uni-axial	1 layer 900 g/m ² ChSM	
1 layer Bi-axial	1 layer Bi-axial	
	1 layer 900 g/m ² ChSM	
	1 layer Bi-axial	
	1 layer 900 g/m ² ChSM	
	1 layer Bi-axial	
	1 layer 900 g/m ² ChSM	
Thickness (in)		
0.59	0.65	0.56

* Bi-axial: CDM 3208; Uni-axial: CM 1708; ChSM: Chopped Strand Mat

In conclusion, the example panel configuration, which is similar to the current design, is sufficient to sustain the given patch load. It is interesting to note that several other panel heights, as shown in Table 7 in shaded areas, will fail due to interface delamination.

Table 8 Facesheet check (See Table A.1 for laminate descriptions)

	Laminate 1L	Laminate 1T	Laminate 2	Laminate 3
Failure load (kN)	118.6	62.0	104.0	97.4
Safety factor	4.9	2.6	4.4	4.1

Table 9 Comparison between current and recommended configuration

Core height (mm)	Buckling load (Current) (MPa)	Safety factor	Buckling load (Recommended) (MPa)	Safety factor
51	7.3	8.4	17.2	19.9
102	3.7	4.3	8.9	10.3
203	3.5	4.0	8.3	9.6
508	3.5	4.0	8.3	9.6
1016	3.5	4.0	8.3	9.6

6 CONCLUSIONS

Based on research conducted by the authors, design guidelines are provided for HFRP sandwich panel with sinusoidal core geometry, and an example is given to illustrate the application of guidelines. Recommendations

to improve the strength of HFRP panels are presented. It is expected that this study will not only contribute to the development of design specifications and facilitate the acceptance of this innovative light weight structure, but also provide a base for developing design guidelines for other types of FRP sandwich structures.

REFERENCES

AASHTO 2007. Load Resistance and Factor Design, Bridge Design Specifications (4th Edition), *AASHTO, Washington, D.C.*

Bakis, C.E., Bank, L.C., Brown, V.L., Cosenza, E, Davalos, J.F., Lesko, J.J., Machida, A., Rizkalla, S.H., and Triantafillou, T.C. 2002. Fiber-reinforced Polymer Composites for Construction-State-of-Art Review. *Journal of Composites for Construction, ASCE*, 6(2), pp. 73-87.

Chen, A. 2004. Strength Evaluation of Honeycomb Sandwich FRP Panels with Sinusoidal Core Geometry, *Ph.D. Dissertation, Dept. of Civil and Environmental Engineering, West Virginia University, Morgantown, WV, USA.*

Chen, A. & Davalos, J.F. 2004. Development of Facesheet for Honeycomb FRP Sandwich Bridge Deck Panels. *Proceedings of 4th International Conference on Advanced Composite Materials in Bridges and Structures, ACMBS IV, Calgary, Canada, July 20-23, 2004.*

Chen, A. & Davalos, J.F. 2005. A Solution including Skin Effect for Stiffness and Stress Field of Sandwich Honeycomb Core. *International Journal of Solids and Structures*, Vol 42/9-10, pp. 2711-2739.

Chen, A. & Davalos, J.F. 2007. Transverse Shear with Skin Effect for Composite Honeycomb Sinusoidal Core Sandwich. *Journal of Engineering Mechanics, ASCE*, 133(3), pp. 247-256.

Chen, A. & Davalos, J.F. 2009. Strength Evaluations of Sinusoidal Core for FRP Sandwich Bridge Deck Panels. Accepted by *Composite Structures*, in press.

Davalos, J.F. & Chen, A. 2005. Buckling Behavior of Honeycomb FRP Core with Partially Restrained Loaded Edges under Out-of-plane Compression. *Journal of Composite Materials*, 39 (16), pp. 1465-1485.

Davalos, J.F., Qiao, P., Xu, X.F., Robinson, J., and Barth, K.E. 2000. Modeling and Characterization of Fiber-reinforced Plastic Honeycomb Sandwich Panels for Highway Bridge Applications, *Composite Structures*, 52, 441-452.

Plunkett, J.D. 1997. Fiber-reinforced Polymer Honeycomb Short Span Bridge for Rapid Installation, *IDEA Project Report.*

Zhang, J. & Ashby, M.F. 1992. Out-of-plane Properties of Honeycombs, *International Journal of Mechanical Sciences*, 34(6), pp. 475-489.

APPENDIX

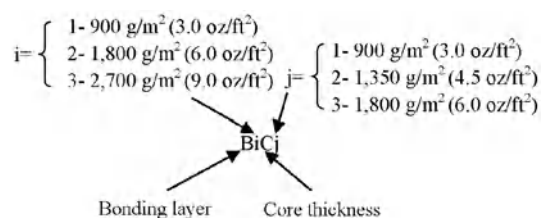


Figure A.1 Naming conventions for specimen type

Load-Bearing Properties of an FRP Bridge after Nine Years of Exposure

Iwao Sasaki (isasaki@pwri.go.jp) & Itaru Nishizaki

Advanced Materials Research Team, Public Works Research Institute, Tsukuba, Ibaraki, Japan

ABSTRACT FRP is used for corrosion protection and/or as structural members utilizing its anti-corrosion properties. Moreover, since the weight of a superstructure can be significantly reduced due to its specific strength, FRP is expected to offer structural functionalities such as rapid construction, substructure downsizing, and improved seismic performance. We constructed an FRP bridge made entirely of pultruded and hand-lay-up GFRP materials, and have been monitoring its functionality and durability. This paper reports the changes in structural load-bearing behavior during nine years of field exposure. Loading response of the FRP bridge after long-term exposure was almost the same as that just after its completion and deterioration in structural performance has not been observed in nine years. The results prove that FRP materials have good durability and functionality for long-term field exposure as structural materials for bridges.

1 INTRODUCTION

Utilizing the favorable material properties of FRP composites such as light weight, mechanical processability, and corrosion resistance, FRP is increasingly being used for civil engineering structures. Various studies are proceeding on durability issues, with numerous reports on the evaluation of FRP durability through exposure tests (e.g. Nishizaki et al. 2007). However, the majority of previous studies are test-panel-based material investigations. Although there are several reports on the applicability and durability inspections of actual structures (Bank et al. 2007; Keller et al. 2007), research on structural behavior and durability has not been sufficient. In order to establish FRP as a major structural material, it is necessary to accumulate cases of validated long-term structural durability.

The authors have been studying the applicability of FRP as a structural material. In the development study, an FRP truss bridge was built as a trial structure for post-disaster emergency restoration, utilizing the advantages of lightweight and corrosion-resistant properties. The all-FRP bridge has been exposed for nine years in a material test facility.

This paper explains the outline of the FRP bridge and the results of loading tests just after its completion as well as after nine years of exposure.

2 METHODS

2.1 FRP truss bridge

A truss bridge made entirely of FRP, as shown in Figure 1, was built in 2000 in a material test facility in Shizuoka,

Japan. The emergency bridge has a span of 8.0 meters and a superstructure weight of 3.8 tons.



Figure 1 FRP truss bridge (in 2000)

2.2 Test procedure

The bridge was used to examine FRP material requirements, applicability, design procedures, and construction works (PWRI et al. 2000).

Regarding structural load-bearing behavior, we carried out a loading test just after the bridge was completed and then again after nine years of exposure (see Figure 2), in order to evaluate its long-term durability as a whole bridge structure. Moreover, we relocated the FRP bridge to another site (see Figure 3) to evaluate its applicability as an emergency bridge. The outline of the bridge is as follows:

- Factory fabrication (processing, block assemble)
- Site selection (installation workability evaluation)

- 2000 loading test (2-ton truckload)
(Site exposure: 9 years 3 months)
- 2009 loading test (2-ton, 5-ton)
(Bridge relocation by crane)
- 2009 relocation loading test (2-ton)



Figure 2 Loading test (5-ton, 2009)



Figure 3 Bridge relocation

2.3 Design conditions

Figure 4 shows a general view of the FRP truss bridge. As an emergency structure, the bridge was designed in accordance with the conditions listed in Table 1. *Specifications for Highway Bridges in Japan* was used as the design standard, although it is not necessarily applicable to FRP bridges.

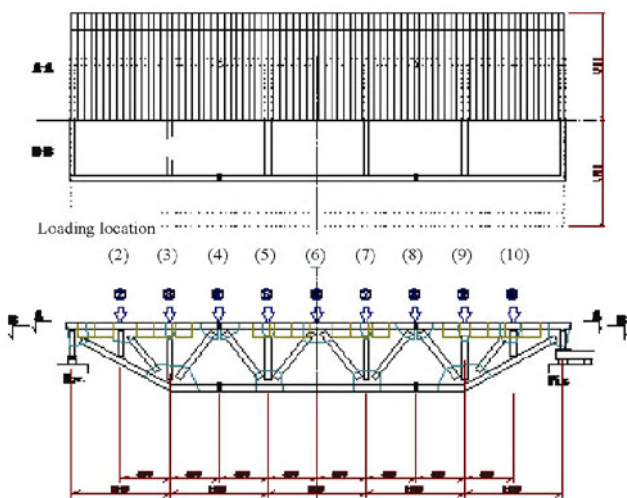


Figure 4 FRP truss bridge: general view

In the structural design, the stress, strain, and deflection were checked through rigid frame analysis of a truss girder. At the member where compressive (Euler buckling) load or tensile load reaches maximum,

sectional stress was calculated and checked using a safety factor of 3.0. Sway bracing members were checked under wind load and seismic load.

Table 1 Structural design conditions of FRP truss bridge

Item	Condition	Reference
Structure type	Deck truss	
Live load,	T-4,	2-ton truckload
Seismic coefficient	Kh = 0.25, Kv = 0.0	
Length, Span, Width	8.3 m, 8.0 m, 3.5 m	
Block shape, Erection	Transfer: 10-ton truck, Erection: 25-ton crane	

Pultruded GFRP hollow square pipe was used for the truss members. Table 2 shows the design properties of pultruded FRP materials. U-section-shaped pultruded GFRP was used for sway bracing and cross beams. Hand-lay-up molded GFRP was used for the gusset and fixing plates. The calculated total weight of the FRP truss bridge superstructure was 3.8 tons.

Table 2 FRP material properties

	Truss member	Deck
Material	Pultruded GFRP	Pultruded GFRP
ection shape	103 × 103 × t9.3 mm	103 × 103 × t9.3 mm
Fiber arrangement	80:20:0 % *	43:19:38 % *
Tension	σ = 518 MPa, E = 24.0 GPa	σ = 141 MPa, E = 23.5 GPa
Compression	σ = 430 MPa, E = 30.0 GPa	σ = 134 MPa, E = 30.0 GPa
Bending	σ = 413 MPa, E = 11.9 GPa	σ = 129 MPa, E = 12.0 GPa
Shear	τ = 183 MPa	
Weight	358 kg	1,776 kg

* Fiber arrangement = Unidirectional roving, : Nondirectional mat., : 0/90° cloth

Blind rivets were used at panel points to joint a truss beam and gusset plate. The required number of rivets was calculated by applying the rivet shear strength (4.9 kN) and a safety factor of 3.2. Resin adhesive was used complementary, but adhesion strength was not considered in the structural design.

As for the connections between a truss beam and sway bracing/cross beam, stainless steel M20 bolts were used. As an emergency bridge, the block system was adopted to allow a choice of total bridge length by changing the number of intermediate truss modules. In order to provide in-situ quick installation, stainless steel sockets with flange and high-tension bolts were applied to the truss-block connections.

The deck comprises five 3.5×1.6-m panels and is made of pultruded GFRP hollow square pipe. To enable human installation, three square pipes were preliminary

joined into a small panel and five small panels were connected to a deck panel 1.6 m in length. These five deck panels are jointed to the upper truss chord with guide fixtures, but are not structurally linked.

2.4 Loading test

As stated in Section 2.2, we conducted loading tests three times in total. Intending a comparative analysis particularly for long-term durability, the loading and measuring conditions were basically the same.

Measurement items are truss beam stress where compressive or tensile load reaches maximum, deflection of each panel point of truss girders, shoe movement, and out-of-plane displacement at the center of the span.

Normal truck vehicles as described in Table 3 were used for static load.

Table 3 Loading vehicle

Name	2-ton	5-ton
Vehicle	Pickup truck	Truck with crane
Front axle load	10.7 kN (1,090 kgf)	22.8 kN (2,320 kgf)
Rear axle load	8.14 kN (830 kgf)	28.0 kN (2,858 kgf)
Wheelbase	1,920 mm	3,840 mm

3 RESULTS

3.1 Deformation under loading at the center of the span

Figure 5 shows the deflection under loading at the center of the span as the mean of loading locations (7) and (8). Measured deflection under 2-ton loading almost corresponds to the calculated value. Measured deflection under 5-ton loading is 2.5–2.8 times greater than that under 2-ton loading, confirming that the FRP truss bridge exhibits elastic deformation.

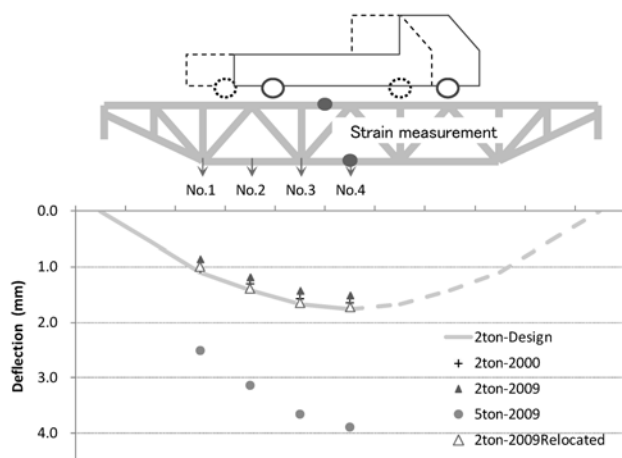


Figure 5 Deflection under loading at the center of span

Figure 6 shows the strain of truss girders under loading at the center of the span. Measured strain values of the lower chord indicate full consistency with the calculated strain; moreover, measured strain under 5-ton

loading is about 2.5 times that of the 2-ton loading results. On the other hand, measured strain of the upper chord indicates somewhat small values, and the strain under 5-ton loading is about 2.0 times greater. This means that the neutral axis climbs upward in accordance with the load increase. This is likely due to the effect of the deck panel, because the lower chord bearing stress never changes but the upper chord bearing stress decreases. Thus, the deck bears part of the compressive load of the bridge.

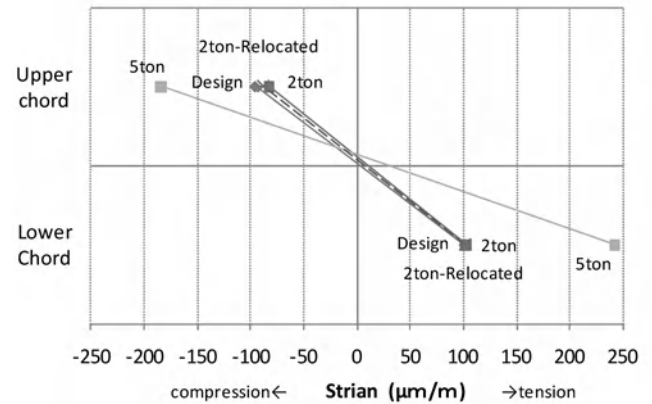


Figure 6 Truss girder strain under loading at the center

As stated in Section 2.3, the deck panels are simply placed on the upper chord of the truss and only their dead load is considered in the structural design. However, an increase in load produces friction that induces a composite girder effect on the deck. After long-term exposure, a type of adhesive link may emerge due to dust particles, mossy substance, local creep deformation, and so on. Actually, in Figures 5 and 6, the 2-ton relocation loading (i.e. after 5-ton loading that causes a large deformation) shows slightly recovered strain in comparison with the 2-ton loading just after long-term exposure.

Regarding structural changes during the nine years of exposure, except for the load distribution to the deck, no signs of change were observed in the loading tests. Connections for the truss members were still rigid, although load distribution to the deck may develop under large loading. It was confirmed that there is no hardening or deterioration of FRP material.

3.2 Loading location and deformation behavior

Figure 7 shows the deflection behavior under different locations of the loading vehicle. The deflection just after long-term exposure shown in Figure 7(a) does not match completely, but the deflection after relocation shown in Figure 7(b) indicates a fairly good match. For the reason of this difference, load distribution to the deck is definitely a major cause, as pointed out in the previous section. However, shoe movement may affect the restriction of deflection just after long-term exposure,

because the deformation of the truss girder end on a shoe was less than 0.01 mm under 2-ton loading and about 0.05 mm even under 5-ton loading. In fact, the shoe base was corroded after long-term exposure, and the roller shoe was not likely to slip easily. Therefore, in addition to the composition effect on the deck, long-term exposure and/or large load may induce a reduction in deflection because of increasing restraining effect.

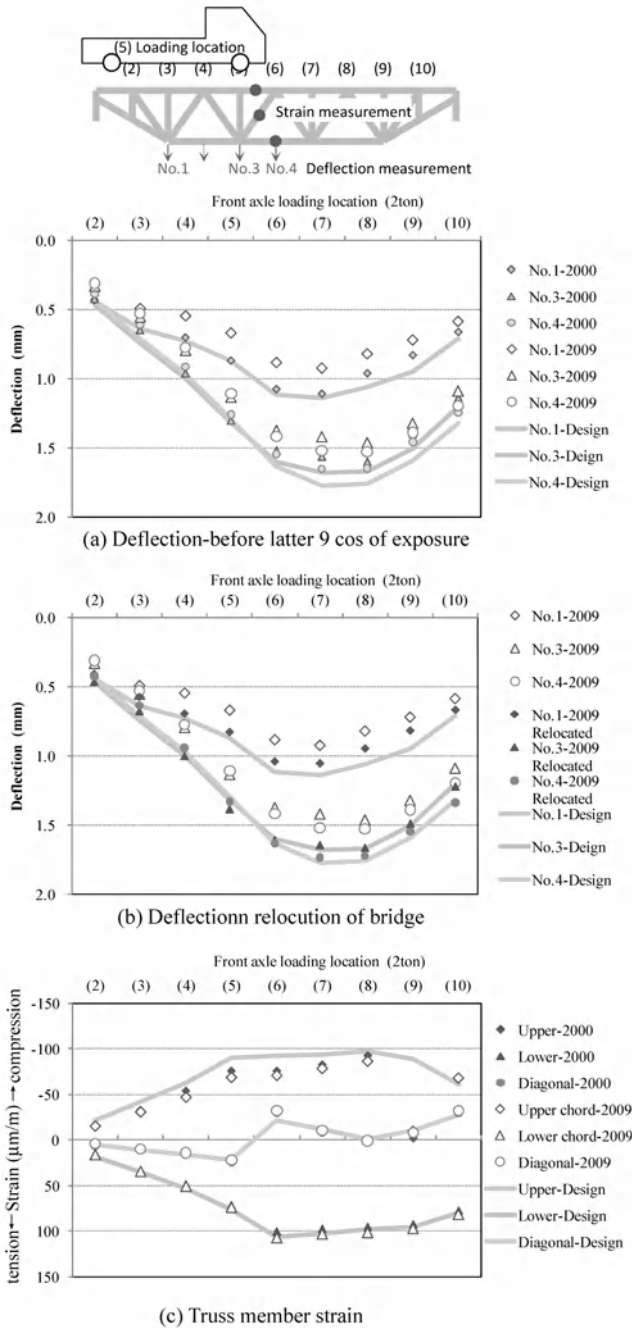


Figure 7 Loading location and deformation behavior

As shown in Figure 7(c), the measured strain results for the truss members correspond to the calculated values. Upper chord strain also exhibits a large value around (7) and (8) where the deflection reaches maximum. Diagonal member strain turns from tension

to compression between (5) and (6) where the rear axle of the loading vehicle passes over the measured member. Moreover, when the measured truss member is between the front and rear axle (i.e. (5)–(8) for the upper chord, (6)–(9) for the lower chord), the strain is almost constant because the loading conditions reach four-point bending.

Figure 8 shows the strain under 5-ton loading. All measured results show 2.5-fold values.

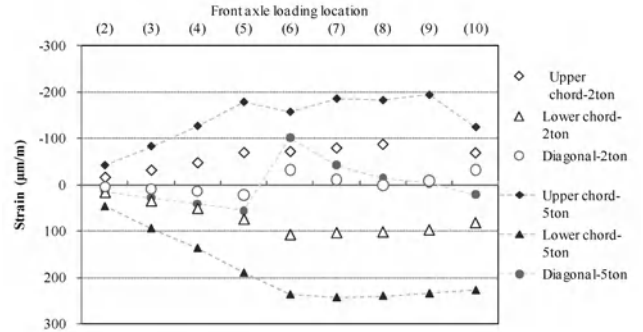


Figure 8 Truss member strain and applied load

4 CONCLUSIONS

After nine years of exposure, the loading response of the FRP truss bridge exhibited almost the same behavior as that just after completion; thus, it has been confirmed that there is no deterioration in structural performance. The results prove that FRP materials have good durability and functionality during long-term field exposure as structural material for bridges.

Fatigue performance of this FRP bridge remains to be proven because live load is rarely applied. However, a determining factor of FRP structures is usually the deflection limit, and allowable stress tends to be redundant. As a future task, structural fatigue performance should be examined with particular focus on the connections of structural members.

This work was conducted in a PWRI cooperative research with JRPS and construction companies, which is gratefully acknowledged.

REFERENCES

Bank, L. et al. 2007. Long-term performance of pultruded light frame canopy structure, Proceedings of the Third International Conference on Durability and Field Applications of FRP Composites for Construction (CDCC 2007), 91-100.
 Keller, T. et al. 2007. Long-term performance of the Pontresina GFRP pedestrian bridge, Proceedings of CDCC 2007, 345-352.
 Nishizaki, I. et al. 2007. Deterioration of mechanical properties of pultruded FRP through exposure tests, Proceedings of CDCC 2007, 159-166.
 PWRI et al. 2000. Cooperative Research Report of PWRI, No. 252.

Cost Optimum Design of Structural Fibre Composite Sandwich Panel for Flooring Applications

Ziad K. Awad (awad@usq.edu.au), Thiru Aravinthan & Yan Zhuge
CEEFC, University of Southern Queensland (USQ), Queensland, Australia

ABSTRACT A new type of FRP composite panel suitable for civil engineering constructions has been invented by the Australian manufacturers. This new type of FRP structural sandwich Panel is made of fibre glass skins and modified phenolic core material with a density relatively higher than the normal sandwich panel. This panel is used for civil engineering applications of flooring system and glue laminate FRP beams. The extensive experimental work has been carried out by the Centre of Excellence in Engineered Fibre Composites (CEEFC) at the University of Southern Queensland to find the strength parameters of this new sandwich panel. This research aims to develop an optimum design of the new FRP sandwich floor panel by using Finite Element (FE) and Genetic Algorithm (GA) method. The numerical FE shows a relatively accurate simulation for the behaviour of the FRP panel. The materials cost was regarded as an objective function with the EUROCOMP design constraints. The optimization shows that the skins orientations 0/90 would produce the best design for one-way spanning floor panel.

1 INTRODUCTION

Fibre composite material has been attracted by many industrial sectors due to its robust characteristics such as high strength and high stiffness to weight ratio. The sandwich structures are used by engineers due to its ability to carry high flexural load, less weight and good thermal insulation. In contrast, it has low fire resistance and suffers from the buckling failure (Gay et al. 2003). Murthy and Munirudrappa (2006) presented an optimization of strength and stiffness for the honeycomb sandwich panel. It was concluded that the maximum bending stiffness occurred at the core to skin weight ratio equal to 2.04. Walker and Smith (2003) presented multi-objective design optimization of fibre composite structure by using FE and genetic algorithms (GA). It was found that the weight and deflection as multi-objective could be optimized by the GA to suite the design engineer. Australian manufacturers have fabricated a new structural sandwich panel for the applications such as pedestrian bridges and railways (Van-Erp & Rogers 2008). The sandwich panel is made from ECR-glass fibre for the skin materials and modified phenolic solid core as shown in Figure 1. The FRP sandwich panel is expected to be used in the civil engineering applications instead of the traditional ply-wood panel. The experimental investigation of this type of sandwich structures was carried out by Manalo et al. (2010).

However, standards specification and codes for FRP in civil engineering is not available yet except British standard code for the design of composite BS4994

(Bank 2006) and the EUROCOMP design code (Clarke 1996). Optimization of FRP plate represents a good practice for the designer to find the configuration of plies thickness and orientation angles. This paper discusses the optimum cost design of the FRP sandwich panel for the domestic floor system.

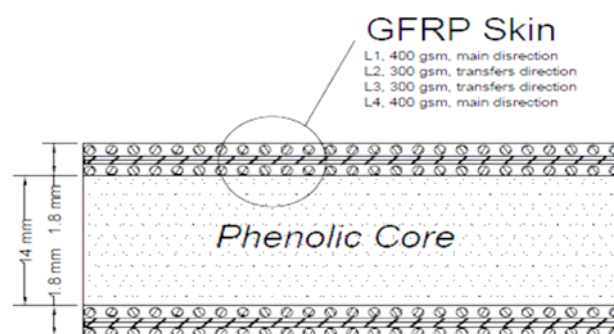


Figure 1 FRP sandwich panel

2 ANALYSIS OF FRP SANDWICH PANEL

The FE simulation is formulated for the analysis FRP composite sandwich panel by using ABAQUS commercial software. The behaviour of this panel is complicated due to the linear behaviour of the FRP skin and the non-linear behaviour of core material in compression, while the core behaviour is approximately linear in tension. The tension and compression behaviour curves of the core were found by the experimental work done by CEEFC, while the softening part is assumed for the analysis. The behaviour of the elastic skin is assumed

linear up to failure at stress 336 MPa (Awad et al. 2009). The material specifications are shown in Table 1. The top and bottom skin are formulated by using shell element type S8R (8- node doubly curved shell element). The core is meshed by using 3D solid element type C3D20R. The total number of elements for half of the panel is 2400. The interaction between skin and core is assumed to be full. Hashin elastic failure model was used to find the failure part through the FRP skin plies. The damage of FRP materials is considered and it depends on Hashin failure theory. Hashin theory considers four types of failure: fibre tension, fibre compression, matrix tension and matrix compression (Hashin 1980).

Table 1 Material properties

Material type	Density (kg/m ³)	Elastic modulus (Mpa)	Poisson ratio	Ultimate tensile strain (%)	Tensile strength (MPa)
FRP Skin	1800	24000	0.25	0.018	336
Core	850	1000	0.2	0.006	6.2

The damage initiation criteria (F) in the four cases are:

Fibre in tension:

$$F_f^t = \left(\frac{\sigma_{11}}{X^T} \right)^2 + \alpha \left(\frac{\tau_{12}}{S^L} \right)^2 \quad (1)$$

Fibre in compression:

$$F_f^c = \left(\frac{\sigma_{11}}{X^C} \right)^2 \quad (2)$$

Matrix in tension:

$$F_m^t = \left(\frac{\sigma_{22}}{Y^T} \right)^2 + \left(\frac{\tau_{12}}{S^L} \right)^2 \quad (3)$$

Matrix in compression:

$$F_m^c = \left(\frac{\sigma_{22}}{Y^C} \right)^2 + \left[\left(\frac{Y^C}{2S^T} \right)^2 - 1 \right] \frac{\sigma_{22}}{Y^C} + \left(\frac{\tau_{12}}{S^L} \right)^2 \quad (4)$$

Where X^T = tension and X^C = compression strength in longitudinal direction. Y^T = tension and Y^C = compression strength in transverse direction. S^L and S^T are shear in longitudinal and transverse directions. α =factor represents shear contribution in the tensile fibre initiation (0 or 1.0). σ_{11} and σ_{22} = normal stresses; τ_{12} = shear stress. Core material is considered relatively same as concrete behaviour. So, the plasticity concrete model was used to simulate the nonlinear behaviour of the core.

2.1 FE model of flat-wise panel

This test is made in a form of the major fibre direction along the longitudinal X-axis of the panel as shown in

Figure 2. Half of the panel is simulated due to symmetry. The load deflection curve is shown in Figure 3. It can be noticed that the behaviour of the panel is approximately linear up to the failure. It is realized from the analysis that the first failure occurred in the top layer of the top skin under compression. The stress analysis of four layers top skin shows that the most of stresses were carried by the 0° plies compared to the 90° plies. The failure of the 0° fibre was noticed under the load position. The failure of the matrix in 90° fibre was noticed in the top and bottom skins due to tension at the bottom and compression at the top. On the other hand, bottom skin 0° fibre stile under the ultimate load by about 20%. There are few cracks developed through the bottom face of the core.

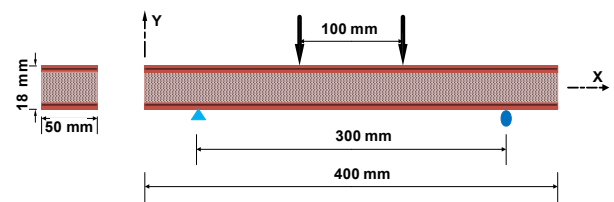


Figure 2 The FRP panel dimensions

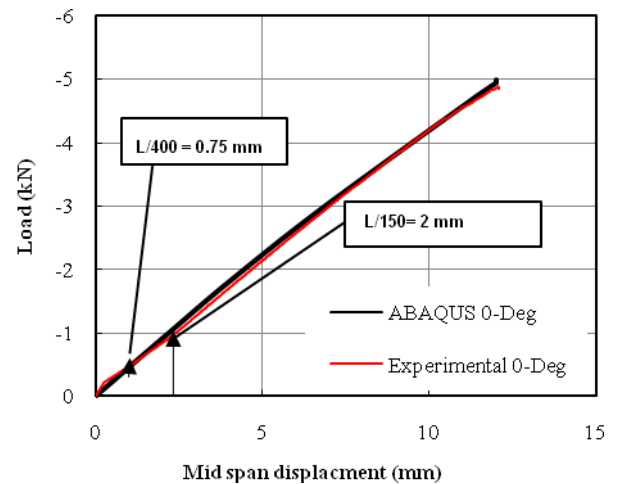


Figure 3 Load deflection curve of FRP panel

3 OPTIMIZATION METHODOLOGY

EUROCOMP is specified the allowable deflection in the service load conditions equal to span/250. The serviceability limit of the civil engineering structure might include few considerations such as the deformation of the structure should not cause any damage for the finishing and non- structural elements. Also, the structure under service load should not have any form of uncomfortable vibration (Clarke 1996). The initial analysis described above shows that the maximum allowable working load of sandwich panel is approximately 520 N. In comparison, the failure load of the sandwich panel is around 4855 N. The failure load is about nine times the

allowable working load. The ratio of the ultimate load to the working load represents the safety factor of the structure. Gay et al. (2003) explained the design factors for the composite structure were around two for short term loading and four for long term loading as shown in Table 2. The aim of this research is to reduce the cost of material used in the production of the sandwich panel.

Table 2 Design parameters

Loads	Point Live Load		Dead Load	
		1.335 kN		1 kN/m ²
Factor of safety (Clarke 1996)	<ul style="list-style-type: none"> • Dead Load= 4 • Live load + Dead load= 2 			
Allowable Stresses	Dead Load		Live + Dead Load	
	Skin	Core	Skin	Core
	90 MPa	5.5 MPa	180 MPa	11 MPa

Design methods could be sophisticated to avoid the material wastage and it is recommended to optimize any form of composite structure to reduce the FRP material in the structures (Bank 2006). The design procedure depends on the cost of the two materials. The estimated cost of the ECR glass fibre composite is 5 times the estimates cost for the core. The design variables are the thicknesses and orientations of the four layers skin at top and bottom and the thickness of the core. The initial design was made on the simply supported one-way sandwich panel as shown in Figure 5. The design variables are the thickness of the skin plies (TT) and thickness of the core (TC).

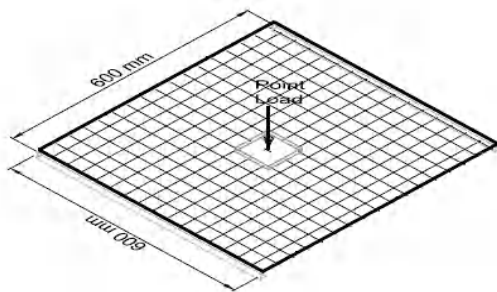


Figure 4 One-way FRP sandwich panel

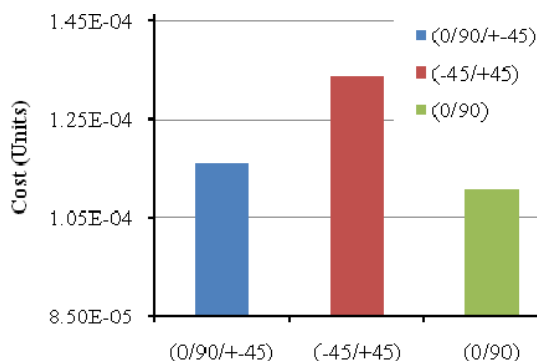


Figure 5 Cost comparison for three layers orientations

The GA is one of the efficient design techniques (Almeida & Awruch 2009), which it is available in the mode FRONTIER. A genetic algorithm is started with random variables called parents which it is a form of the variables population (Walker & Smith 2003) and it is a probability based algorithm in the process of natural selection (Kang et al. 2008). The objective function and design constraints are explain below:

$$\text{Objective} = \text{Minimize} (Vol_{skins} * 5 + Vol_{core} * 1) \quad (5)$$

$$\text{Variables} = \begin{cases} TT_i \\ TC_i \end{cases} i = 1 \rightarrow n_{plies}$$

EUROCOMP constraints:

$$\sigma_{Tf} \leq \frac{\sigma_{Tfu}}{F.S} \quad (6)$$

$$\sigma_{Cf} \leq \frac{\sigma_{Cfu}}{F.S} \quad (7)$$

$$\sigma_{TC} \leq \frac{\sigma_{TCu}}{F.S} \quad (8)$$

$$\sigma_{CC} \leq \frac{\sigma_{CCu}}{F.S} \quad (9)$$

$$\delta \leq \text{Span} / 250 \text{ mm} \quad (10)$$

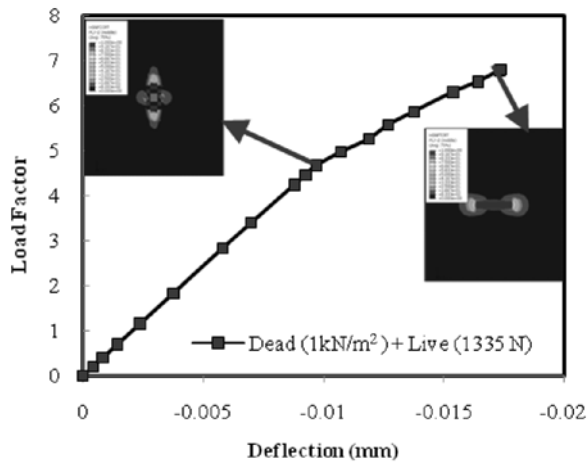
Where, σ_{Tf} = allowable tensile and σ_{Cf} = allowable compressive stress of FRP skin material; σ_{TC} = allowable tensile and σ_{CC} = allowable compressive stresses of the core material; σ_{Tfu} = tension and σ_{Cfu} = compression strength of the FRP skin. σ_{TCu} = tension and σ_{CCu} = compression strength of the core materials; $F.S$ = design factor of safety, which is assumed equal to four in the step one of the dead load and it represents the long term load factor. The factor of safety equal to two is assumed for the total load cases (live and dead load) as explained in Table 2; δ = the total vertical deflection.

4 OPTIMUM DESIGN OF ONE-WAY PANEL

The design optimization was made on minimizing the cost of one-way sandwich panel with 600 mm span (two edges supports) as shown in Figure 4. The minimum cost design was considered for three different layers orientations 0/90°, ±45° and 0/90/±45°. The optimization shows that the 0/90° configuration gives a minimum cost design as shown in Figure 5 and the optimum design results described in Table 3. The FE analysis was considered to find the actual behaviour of the designed sandwich panel. It was found that the behaviour of the sandwich one-way panel is non-linear up to failure. The top skin is failed at the load factor approximately equal to five. While, the complete failure of the FRP panel at load factor seven is shown in Figure 6.

Table 3 Design optimization results

Plies configuration	Core Thick. (mm)	0°- Skin Thick. (mm)	90°- Skin Thick. (mm)	45°-Skin Thick. (mm)	-45°-Skin Thick. (mm)
0/90	19.47	1.09	0.05	No	No
-45/45	31	No	No	0.31	0.31
0/90/+45/-45	19.3	0.73	0.40	0.071	0.071

**Figure 6** Load deflection for optimum One-way FRP panel

5 CONCLUDING REMARKS

This paper demonstrates that the FE method is capable of developing a reliable and acceptable behaviour of the FRP sandwich panel. The optimum design is the target point for the using of FRP sandwich panel in civil engineering applications. The present research gives the civil engineers ability to understand the behaviour of the sandwich panel in terms of failure load and the structural configuration. In addition, the cost showed a good objective function to control the design variable selection. The 0/90° configuration is most appropriate for one way panel. The authors recommend extending this study to cover a comprehensive investigation on the effect of different spans design. In addition, an optimization work should be done on the combinations

of different objective functions including materials selection.

REFERENCES

- Almeida, F.S. & Awruch, A.M. 2009. Design optimization of composite laminated structures using genetic algorithms and finite element analysis. *Composite Structures*, 88 (3), 443-454.
- Awad, Z.K., Aravinthan, T. & Zhuge, Y. 2008. Finite element analysis of fibre composite sandwich panel. *Southern Engineering Conference*, Springfeild, QLD, Australia.
- Bank, L.C. 2006. *Composite for construction: Structural design with frp material*. New Jersey: JOHN WILEY & SONS.
- Clarke, J.L. ed. 1996. *Structural deisgn of polymer composite-eurocomp design code and handbook*. UK: E&FN Spon.
- Van-Erp, G. & Rogers, D. 2008. A highly sustainable fibre composite building panel. *Sustainable Procurement Conference*. Brisbane.
- Gay, D., Hoa, S. & Tsai, S. 2003. *Composite materials: Design and applications*. Florida: CRC Pr I Llc.
- Hashin, Z., 1980. Failure criteria for unidirectional fiber composites. *Journal of Applied Mechanics*, 47 (2), 329-334.
- Kang, B.-K., Park, J.-S. & Kim, J.-H. 2008. Analysis and optimal design of smart skin structures for buckling and free vibration. *Composite Structures*, 84 (2), 177-185.
- Manalo, A.C., Aravinthan, T., Karunasena, W. & Islam, M.M. 2010. Flexural behaviour of structural fibre composite sandwich beams in flatwise and edgewise positions. *Composite Structures*, 92, 984-995.
- Murthy, O., Munirudrappa, N., Srikanth, L. & Rao, R. 2006. Strength and stiffness optimization studies on honeycomb core sandwich panels. *Journal of Reinforced Plastics and Composites*, 25 (6), 663.
- Walker, M. & Smith, R.E. 2003. A technique for the multiobjective optimisation of laminated composite structures using genetic algorithms and finite element analysis. *Composite Structures*, 62 (1), 123-128.

Vol. II FRP Strengthening Structures

Bond and Interfacial Stresses Between FRP and Concrete

Effect of Load Distribution on IC Debonding in FRP-Plated RC Beams

J.G. Teng (cejgteng@polyu.edu.hk) & G.M. Chen

Department of Civil and Structural Engineering, The Hong Kong Polytechnic University, China

J.F. Chen

Institute for Infrastructure and Environment, The University of Edinburgh, UK

ABSTRACT Intermediate crack debonding (IC debonding) is a common failure mode for RC beams flexurally-strengthened with externally bonded FRP reinforcement. Although numerous studies have been carried out on IC debonding, the vast majority of them have been concerned with beams subjected to three- or four- point bending despite the fact that a uniformly distributed load (UDL) is a more common loading condition in practice. This paper presents the first ever finite element study into the effect of load distribution on IC debonding failure. A recently developed FE model was employed to simulate the IC debonding failure of three beams tested by other researchers under different load distributions and then to simulate the IC debonding failure of a beam under UDL. The numerical predictions are found to be in close agreement with the test re-sults and confirm the experimental observation that the IC debonding strain in the FRP plate (and hence the IC debonding moment of the strengthened section) increases as the load distribution becomes more uniform.

1 INTRODUCTION

Over the past two decades, the method of strengthening an RC beam by the bonding of a fibre-reinforced polymer (FRP) plate to the soffit of the beam has become widely accepted in practice. The flexural strength of such a strengthened beam is often governed by debonding of the FRP plate from the original RC beam (Teng et al. 2002, Teng and Chen 2009). Two types of debonding failure modes are possible: (1) intermediate crack (IC) debonding which initiates at a major flexural or flexural-shear crack and propagates towards a plate end; (2) plate end debonding which occurs at or near a plate end. Extensive research on these debonding failure modes has been conducted, but the vast majority of the existing studies have been concerned with beams subjected to either a single point load (i.e. three-point bending) or two point loads (i.e. four-point bending). Consequently, most of the existing strength models proposed by researchers (e.g. Teng et al. 2003, 2004, Lu et al. 2007, Wu and Niu 2007, Teng and Yao 2007, Rosenboom and Rizkalla 2008) have been based on theoretical and experimental studies conducted on beams subjected to three- or four-point bending. For the same reason, design provisions adopted in design guidelines (e.g. fib 2001, JSCE 2001, Concrete Society 2004, CNR-DT 2004, HB-305 2008, ACI-440.2R 2008) have also been based on the three-point or four-point bending conditions.

The three- or four-point bending conditions have been used in existing research primarily due to convenience of laboratory testing. In practice, a uniformly-distributed load (UDL) is much more common and other loading patterns are also often encountered. A different load distribution leads to different distributions of moment and shear force in a beam and thus a different crack pattern, which may significantly alter the debonding process and the debonding strain of the FRP plate (i.e. the strain value reached at the critical location of the FRP plate when debonding occurs). The limited existing test results (Pan et al. 2009) have demonstrated that as the load uniformity increases, the IC debonding strain increases; furthermore, the debonding mode may shift from IC debonding to plate end debonding for which the debonding strength decreases as the load uniformity increases. Therefore, the existing debonding strength models developed based on the three- and four-point bending conditions can be either unsafe or over-conservative (Pan et al. 2009). Assuming that plate end debonding can be suppressed by appropriate end anchorage measures (e.g. U-jackets), an IC debonding strength model that accounts for the effect of load distribution can lead to more efficient use of the expensive FRP material in many practical applications where a UDL dominates the loading condition.

The effect of load distribution on IC debonding strength has not been completely ignored in existing

research. The IC debonding strength models of fib (2001) and Chen et al. (2006), based on the mechanism of interaction between two adjacent cracks, have the potential to consider the effect of load distribution, but they are yet to be validated against test results for loading conditions other than three- or four-point bending.

The above overview reveals a lack of research into the effect of load distribution on the debonding behaviour and strength of FRP-plated RC beams. This lack of research can be more efficiently addressed using numerical simulations than laboratory tests in which the realization of some load distributions such as a UDL can present a significant challenge. Naturally, such numerical investigations often need to be supported by a small number of high-quality tests on large-scale beams to ensure their accuracy.

This paper presents a preliminary finite element (FE) study on FRP-plated beams subjected to loads of different distributions with two objectives: (a) to show that an accurate FE model can predict the effect of load distribution on IC debonding strength; (b) to explore how a UDL affects the IC debonding behaviour and strength. The FE model employed in this study is presented in detail in Chen et al. (2010) and Chen (2010).

2 TEST BEAMS

Numerical results for three FRP-plated beams tested by Pan et al. (2009) are presented herein. These three beams formed part of a larger experimental programme of Pan et al. (2009) and were selected for discussions here because they all failed by IC debonding and their load-displacement curves and crack patterns were reported by Pan et al. (2009). They were named D2-P2-L2, D3-P4-L2 and D4-P6-L2 by Pan et al. (2009) but are referred to as beams A, B and C for brevity in the remainder of this paper.

These three beams were identical except that they were subjected to three different distributions (Figure 1): (a) two point loads (beam A), (b) four point loads (beam B), and (c) eight point loads (beam C) respectively. The loads were applied using a waffle tree system. They each had a clear span of 1800 mm, two deformed steel bars of 10 mm in diameter as the tension reinforcement and was strengthened with a 150 mm x 1650 mm CFRP plate. The cylinder compressive strength of concrete was 59 MPa for all the specimens. Further details are given in Table 1 and full details can be found in Pan et al. (2009). All three beams failed by IC debonding.

These beams were modelled as a plane stress problem using ABAQUS (2004). Only half of the beam span was modelled by taking advantage of symmetry. The plane stress element CPS4 was used to model concrete while the truss element T2D2 was used to model both the steel

and the FRP reinforcements. The cohesive element COH2D4 was used to model the bond-slip behaviour of both the steel-to-concrete and the FRP-to-concrete interfaces. The properties of these interfacial elements were determined according to the CEB-FIP (1993) bond-slip model for the steel reinforcement and Lu et al.'s (2005) bond-slip model for the FRP reinforcement. A dynamic solution approach (Chen et al. 2009, Chen 2010) with direct load control was adopted to follow the deformation process.

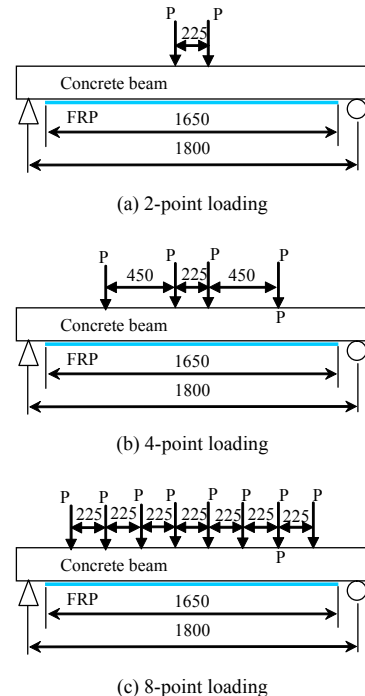


Figure 1 Three load distributions (all dimensions in mm)

Table 1 Details of beams tested by Pan et al. (2009)

Beam	Beam width and height		Elastic modulus and thickness of FRP plate		Number of point loads	Ultimate moment (kNm)	
	b_c (mm)	h_c (mm)	E_f (GPa)	t_f (mm)		Test	FE
A	150 (mm)	200 (mm)	235 (GPa)	0.22 (mm)	2	26.3	25.7
B					4	29.7	28.8
C					8	31.0	30.5

A mesh convergence study showed that the numerical results change very little when the maximum concrete element size is less than 5 mm. As a result, an element size of 5 mm for the concrete was adopted in all the numerical simulations presented in this paper. Matching element sizes were employed to represent the FRP plate and the steel bars.

All three beams were predicted by the FE model to fail by IC debonding. In Figure 2, the predicted relationship between the maximum moment in the beam

and the mid-span displacement is compared with that from the test for each beam. It is seen that the numerical predictions are in very close agreement with the test results for all three beams (i.e. all three load distributions). The ultimate moment of the strengthened section increases significantly as the number of load increases, and this experimental trend is accurately predicted by the numerical model (Figure 2 and Table 1). The predicted crack patterns (plotted using the maximum principal strain) for the three specimens at the ultimate state of IC debonding failure (i.e. when the peak load was reached) (Figure 3) are also in close agreement with the experimental crack patterns (Pan et al. 2009). In particular, it can be seen from Figure 3 that the FE model captures the effect of load distribution on the crack pattern at the ultimate state; that is, as the load uniformity (i.e. the number of point loads) increases, the cracks in the RC beam become more distributed as observed in the tests (Pan et al. 2009). As the IC debonding strain of the FRP plate (and hence the IC debonding moment) is directly affected by the widening of the most critical crack and the crack adjacent to it (Teng et al. 2006, Chen et al. 2007), a more distributed crack pattern means that the stresses in the FRP plate at the two adjacent cracks are closer to each other. As a result, the debonding strain in the FRP plate increases, as explained in Teng et al. (2006) and Chen et al. (2007).

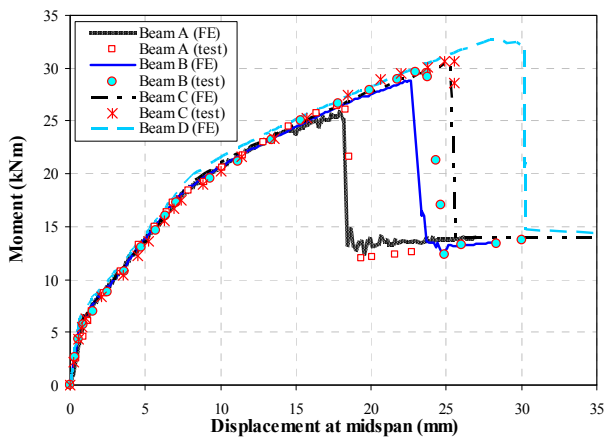


Figure 2 FE vs. test moment-displacement responses

This phenomenon is clearly illustrated in Figure 4 where the predicted FRP strain distributions at the ultimate state for the three beams are shown. It can be seen there that when the number of point loads increases from 2 to 8, the IC debonding strain of the FRP increases from 9,010 $\mu\epsilon$ to 10,640 $\mu\epsilon$. Figure 4 also shows that for each beam a region of constant FRP strain away from the plate end exists, which corresponds to a debonded region of zero interfacial shear stress. Shortly after the ultimate state, debonding rapidly propagates to the plate end, causing the FRP plate to detach completely from the beam.

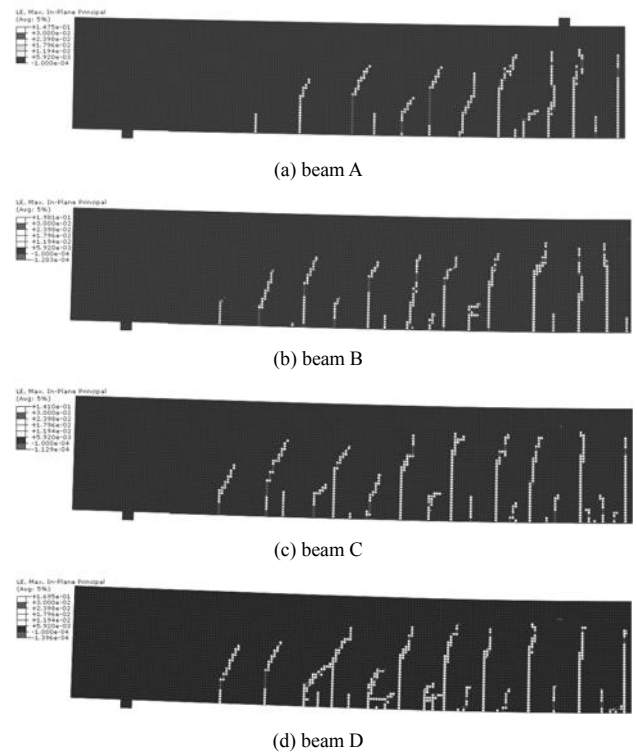


Figure 3 Numerical crack patterns at the ultimate state

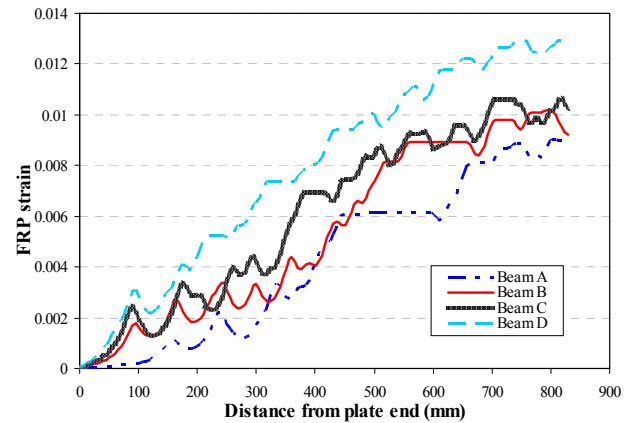


Figure 4 Strain distributions in FRP at the ultimate state

Based on the results discussed above, it can be concluded that the present FE model (Chen et al. 2010) can accurately predict IC debonding failure in FRP-plated RC beams subjected to different load distributions. This FE model can thus be employed as a useful tool to study the IC debonding behaviour of FRP-plated RC beams under other load distributions such as a UDL. As a first step, a fourth beam (i.e. beam D) was analysed using the present FE model to study IC debonding behaviour under UDL; all other parameters of the fourth beam are the same as those of the three test beams (Table 1). The predicted moment-displacement response, the crack pattern at the ultimate state, and the FRP strain distribution at the ultimate state of beam D are given in Figures 2, 3(d) and 4 respectively. These figures indicate that although the predicted crack pattern

of beam D is similar to that of beam C, the predicted ultimate moment (32.8 kNm) and the IC debonding strain of the FRP plate (12,960 $\mu\epsilon$) of the former are higher than those of the latter. The numerical simulation predicted the development of wider cracks in the beam at IC debonding due to a reduced overall strain gradient in the FRP plate under UDL than that under 8-point loading (Figure 4).

3 CONCLUDING REMARKS

This paper has presented an FE study into the effect of load distribution on IC debonding in FRP-plated RC beams. A recently developed FE model was first employed to simulate the IC debonding failure of three beams tested by Pan et al. (2009) under three different load distributions (2-, 4- and 8-point loading respectively). The FE predictions have been shown to be in close agreement with the test results, in terms of all examined aspects including the failure mode, the load-displacement response, and the crack pattern. The FE model was then employed to simulate a fourth beam which is subjected to a uniformly distributed load. The FE results show that the IC debonding strain of the FRP plate and hence the benefit of the FRP plate is significantly higher under UDL than under a single point load (i.e. three-point bending) or two point loads (i.e. four-point bending). The FE model thus provides a useful tool to conduct further investigations into the effect of load distribution on IC debonding for the eventual establishment of an IC debonding strength model that accounts for the effect of load distribution.

4 ACKNOWLEDGEMENTS

The authors are grateful for the financial support received from the Research Grants Council of the Hong Kong Special Administrative Region (SAR) (Project Nos: PolyU 5173/04E and PolyU 5315/09E).

REFERENCES

- ABAQUS 2004. *ABAQUS 6.5 User's Manual*, ABAQUS, Inc., Rising Sun Mills, 166 Valley Street, Providence, RI 02909-2499, USA.
- ACI-440.2R 2008. *Guide for the Design and Construction of Externally Bonded FRP Systems for Strengthening Concrete Structures*, ACI Committee 440, American Concrete Institute, Farmington Hills, MI, USA.
- Concrete Society 2004. *Design Guidance for Strengthening Concrete Structures with Fibre Composite Materials*. Second Edition, Concrete Society Technical Report No. 55, Crowthorne, Berkshire, UK.
- CNR-DT200 2004. *Guide for the Design and Construction of Externally Bonded FRP Systems for Strengthening Existing Structures*. Advisory Committee on Technical Recommendations for Construction, National Research Council, Rome, Italy.
- Chen, G.M., Teng, J.G. and Chen, J.F. 2009. Finite element simulation of IC debonding in FRP-plated RC beams: a dynamic approach. *Proceedings, Ninth International Symposium on Fiber Reinforced Polymer Reinforcement for Concrete Structures (FRPRCS-9)*, Sydney, Australia, July 13-15. 2009.
- Chen, G.M. 2010. *Behaviour and Strength of RC Beams Shear-Strengthened with Externally Bonded FRP Reinforcement*. PhD thesis, Department of Civil and Structural Engineering, The Hong Kong Polytechnic University, Hong Kong, China.
- Chen, G.M., Teng, J.G. and Chen, J.F. 2010. Finite element modeling of intermediate crack debonding in FRP-plated RC beams. Submitted to *Journal of Composite for Construction*, ASCE.
- CEB-FIP 1993. *CEB-FIP Model Code 90*, Thomas Telford Ltd., London, UK.
- Chen, J.F., Teng, J.G. and Yao, J. 2006. Strength model for intermediate crack debonding in FRP-strengthened concrete members considering adjacent crack interaction, *Proceedings, Third International Conference on FRP Composites in Civil Engineering (CICE 2006)*, 13-15 December, Miami, Florida, USA.
- Chen, J.F., Yuan, H. and Teng, J.G. 2007. Debonding failure along a softening FRP-to-concrete interface between two adjacent cracks in concrete members. *Engineering Structures* 29(2): 259-270.
- FIB 2001. *Externally Bonded FRP Reinforcement for RC Structures*, The International Federation for Structural Concrete, Lausanne, Switzerland.
- JSCE 2001. *Recommendations for Upgrading of Concrete Structures with Use of Continuous Fiber Sheets*. Concrete Engineering Series 41, Japan Society of Civil Engineers, Tokyo, Japan.
- HB-305 2008. *Design Handbook for RC Structures Retrofitted with FRP and Metal Plates: Beams and Slabs*. Standards Australia, GPO Box 476, Sydney, NSW 2001, Australia.
- Lu, X.Z., Teng, J.G., Ye, L.P. and Jiang, J.J. 2005. Bond-slip models for FRP sheets/plates bonded to concrete. *Engineering Structures*, 27(6): 381-389.
- Lu, X.Z., Teng, J.G., Ye, L.P. and Jiang, J.J. 2007. Intermediate crack debonding in FRP-strengthened RC beams: FE analysis and strength model, *Journal of Composite for Construction*, ASCE 11(2):161-174.
- Pan, J.L., Chung, T. and Leung, C.K.Y. 2009. FRP debonding from concrete beams under various load uniformities. *Advances in Structure Engineering* 12(6): 807-819.
- Rosenboom, O. and Rizkalla, S. 2008. Modeling of IC debonding of FRP-strengthened concrete flexural members. *Journal of Composites for Construction*, ASCE 12(2): 168-179.
- Teng, J.G. and Chen, J.F. 2009. Mechanics of debonding in FRP-plated RC beams, *Proceedings of the Institution of Civil Engineers – Structures and Buildings* 162(5): 335-345.
- Teng, J.G., Chen, J.F., Smith, S.T. and Lam, L. 2002. *FRP-strengthened RC Structures*, Chichester, UK: John Wiley and Sons, Inc.
- Teng, J.G., Lu, X.Z., Ye, L.P., and Jiang, J.J. 2004. Recent

- research on intermediate crack-induced debonding in FRP-strengthened RC beams. *Proceedings, 4th International Conference on Advanced Composite Materials in Bridges and Structures, ACMBS IV*, Calgary, Alberta, Canada.
- Teng, J. G., Smith, S.T., Yao, J. and Chen, J.F. 2003. Intermediate crack-induced debonding in RC beams and slabs, *Construction and Building Materials* 17(6-7): 447-462.
- Teng, J.G. and Yao, J. 2007. Plate end debonding in FRP-plated RC beams— II : Strength model. *Engineering Structures* 29(10): 2472-2486.
- Teng, J.G., Yuan, H. and Chen, J.F. 2006. FRP-to-concrete interfaces between two adjacent cracks: theoretical model for debonding failure. *International Journal of Solids and Structures* 43(18-19): 5750-5778.
- Wu, Z.S. and Niu, H.D. 2007. Prediction of crack-induced debonding failure in R/C structures flexurally strengthened with externally bonded FRP composites. *Journal of Materials, Concrete Structures, and Pavements*, JSCE 63(4): 620–639.

Effect of Bar-Cutoff and Bent-Point Locations on Debonding Loads in RC Beams Strengthened with CFRP Plates

Eftekhari M. R. (mreftekhari@yahoo.com) & Mostofinejad D.

Department of Civil Engineering, Isfahan University of Technology, Isfahan, Iran

ABSTRACT In recent years, the use of Fibre Reinforced Polymer (FRP) composites for external strengthening of concrete structures has emerged as one of the most promising technologies in material and structural engineering. Although bonding of FRP to the soffit and side faces of reinforced concrete beams increases their flexural and shear capacities, debonding of FRP layers from the concrete substrate frequently happens and decreases the expected failure capacity. Over the last two decades, many parameters such as surface preparation of concrete specimens, compressive strength of concrete and geometrical dimensions of the FRP plate including bonded length, thickness and width, number of plies, and taper end effects have been shown to affect the debonding failure of RC beams strengthened with FRP laminates. An experimental study was performed to determine the effects of bar-cutoff or bend-point location on design debonding loads of RC beams strengthened with CFRP sheets. A total of seven 3-m long beams were produced, strengthened and tested under a 3-point loading. Two specimens served as control, while two had two different types of bar-cutoff locations and two had two different types of bend-point locations. Finally, the last one with four U-shaped strips to prevent debonding of the FRP sheet was used as a bar-cutoff specimen. The analysis of the experimental results was focused mainly on crack distribution and crack widths. The results of the experimental program showed distinct effects of bar-cutoff and bend-point on the total beam behaviour and debonding load, which will be discussed in the full paper.

1 INTRODUCTION

A simple method to strengthen RC beams is to use steel or fibre reinforced polymer (FRP) plates, which can be even employed for operating members in constructions. Certain unique properties of composite fibre plates such as their high resistance in moist and corrosive environments or their light weight and ease of application have made them even more attractive than their conventional metal counterparts. The basic concern, however, with bonding composite fibre plates onto concrete members is their premature debonding off the concrete surface, which normally takes place at points prior to the ultimate design load or typically beyond the reinforcement yield point, or as a result of small deflections below expected levels. A number of factors may be involved in this behaviour of CFRP plates that include type of surface conditioning, concrete tensile strength, plate thickness, number of wrappings, and taper end point. Crack propagation and crack growth are included among the most important causes cited in the literature for this debonding behaviour.

The arrangement of reinforcement in strengthened RC beams can alter the patterns of cracks created in the

specimen with respect to crack spacing and debonding [4]. In this study, the effects of bar cut-off and bend point locations on the debonding of strengthening plates and the pattern of crack propagation have been experimentally investigated in RC beams strengthened with CFRP plates.

2 SPECIFICATION OF THE EXPERIMENTAL SPECIMENS

For the purposes of the present study, a number of bending tests were performed on 7 actual-sized RC beams. The 300×350mm beams 3.3 m in length were simply supported at the ends and tested under a three-point loading up to failure. After each load increment, strain gauge, load and LVDT readings were recorded using an electronic data acquisition system. Table (1) summarizes the beam details along with the specifications of both embedded steel bars and external strengthening. According to the Table, specimen I500 is not retrofitted with CFRP plates, which is used as control. The other beams listed in Table 1 are retrofitted with two strengthening plates 0.12 mm thick and 150 mm wide externally on the underside of the beam using

the wet lay up method. Table (2) summarizes the specifications of the materials used in the beams.

Table 1 Specifications of experimental specimens

Specimen	Tensile reinf.	No of cut-off or Bent bars	L* (mm)	No of plys
I500	5Φ14	—	—	—
I521	5Φ14	—	—	2
B1I521	5Φ14	1	900	2
B3I521	5Φ14	3	2100	2
C1I521	5Φ14	1	1200	2
C3I521	5Φ14	3	2400	2
C3UI521	5Φ14	3	240	2

*: Direct length of cut-off or bend bar at the tensile region (mm)

Table 2 Properties of materials

FRP	Type	Thickness per layer (mm)	Tensile strength (MPa)	Elastic modulus (GPa)	Ultimate tensile strain (%)
	SikaWrap Hex 230C	0.12	4100	231	1.7
adhesive	Type	Thickness per layer (mm)	Tensile strength (MPa)	Tensile modulus (MPa)	Flexural Modulus (MPa)
	Sikadur-300	0.4	45	3500	3000
concrete	Max. Agg. Size (mm)	Concrete Cylinder Strength (MPa)	Elastic modulus (GPa)	Tensile strength (MPa)	
	10	34.6	26.6	2.4	

In the specimens B1I521 and B3I521, respectively, 20% and 60% of the tensile reinforcement were bent at an angle of 45° and extended to the end of the beam in the opposite face at the same level as the compression reinforcement. In C1I521 and C3I521, 20% and 60% of the tensile bars were cut off in the middle of the beam and adjacent to the support point, respectively.

The specimen C3UI521 (Figure 1) is exactly identical to C3I521 in terms of bar arrangement. In addition to the two strengthening plates, 4 U-shaped FRP strips 50 mm wide have also been used in this specimen to control the middle and taper end debonding of the strengthening plate. The strips are joined to the two ends of the plate and at beam mid-span of the specimen normal to the longitudinal axis of the beam. Figure 2 shows two samples of the beams tested.

In all the specimens strengthened with two CFRP plates, the general rule of setting back the second plate by 150 mm from the first has been observed (Tapper end) [5]. Table 2 presents the specifications of the materials used in the specimens.



Figure 1 C3UI521 specimen

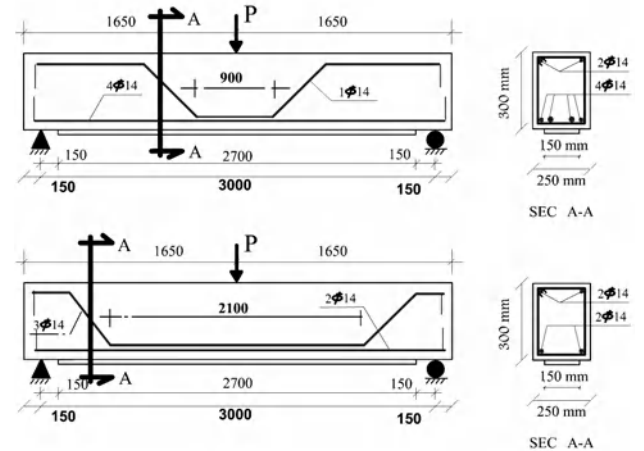


Figure 2 two samples of the bend point location beams

3 CRACK PROPAGATION AND GENERAL BEHAVIOR OF THE SPECIMENS

Upon initial loading, the first flexural crack appears in the specimens at a loading equal to nearly 30 kN. Table (3) presents the details of crack propagation in the bar cut-off and bend specimens.

Upon the creation of the first flexural crack and as a result of exerting a load on the beam, other flexural and flexural-shear cracks may also appear in the beam, which ultimately leads to the debonding of the strengthening plate and to beam failure. It is clear from Table (3) that at around the yield load of the tensile reinforcement, which is almost equal to 75% of the ultimate load of the test specimens, the beams experience around 90% of their ultimate number of cracks. In the specimen I521 in which none of the tensile bars is bent or cut off, the numbers of recorded cracks are 21 and 27 at the tensile bar yield point and at the crack stabilization point, respectively. It may be claimed that bar cut-off and bend generally lead to altering the shear and flexural capacities of the specimen adjacent to the cut-off and bend point locations. This leads to an increased number of cracks in the beam compared to the case when no bar cut-off or bend occurs. Additionally, crack width is also affected by the longitudinal bar cut-off and bend.

Figure (3) illustrates the width of the largest flexural crack typically occurring in the middle of the beam. Clearly, under identical load levels, the width of the

largest flexural crack is greater in specimens with bar bends than in those with bar cut-offs. Bent bars seem to prevent the widening of cracks at the bar bend point and, consequently, the crack width in specimens with bar bending exceeds that in specimens with bar cut-off in order to attain identical peeling at beam mid-span. Comparison of the crack widths in Figure 3 reveals that the more bars are cut-off or bent, the lower will be the flexural crack width. In other words, the location of bar bending or cut-off at the point of larger flexural moments leads to greater crack widths.

Table 3 Crack propagation in specimens

specimen	First crack point	Bar yield point		Crack stabilization point	
	Load (kN)	Load (kN)	No. of cracks	Load (kN)	No. of cracks
B11521	20	150	29	183	36
B31521	28	150	30	182	34
C11521	30	150	32	179	34
C31521	33	150	33	160	34
C3UI521	28	150	26	182	29

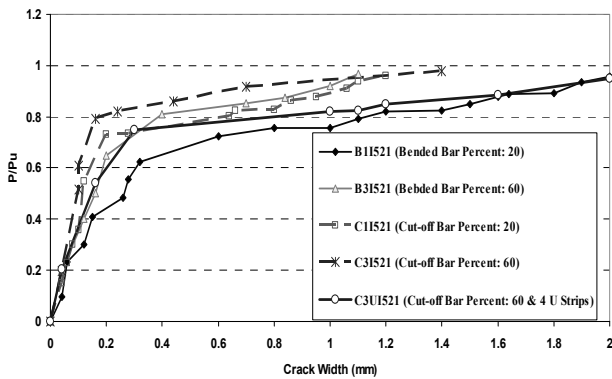


Figure 3 Effects of bar-cutoff and bent-point location on widening of the largest flexural crack

4 LOAD-DISPLACEMENT BEHAVIOR

Figure 4 depicts the load-displacement curve at the mid-span of the beam for bar cut-off and bar bend specimens. All the specimens exhibited almost similar behaviors prior to the bar yield point with the major differences lying in the debonding load of the strengthening plate and the corresponding displacement. This Figure also shows a magnified view of the end portion of the load-displacement curve. The rupture in all the strengthened specimens was due to the debonding of the CFRP plate.

As seen in the Table 4, the debonding of the plate in all the specimens was of the IC type, except for the specimen C31521 in which initially a shear-flexural crack occurred under a load of 137 kN at the longitudinal bar cut-off point (at a distance of 1200 mm from the

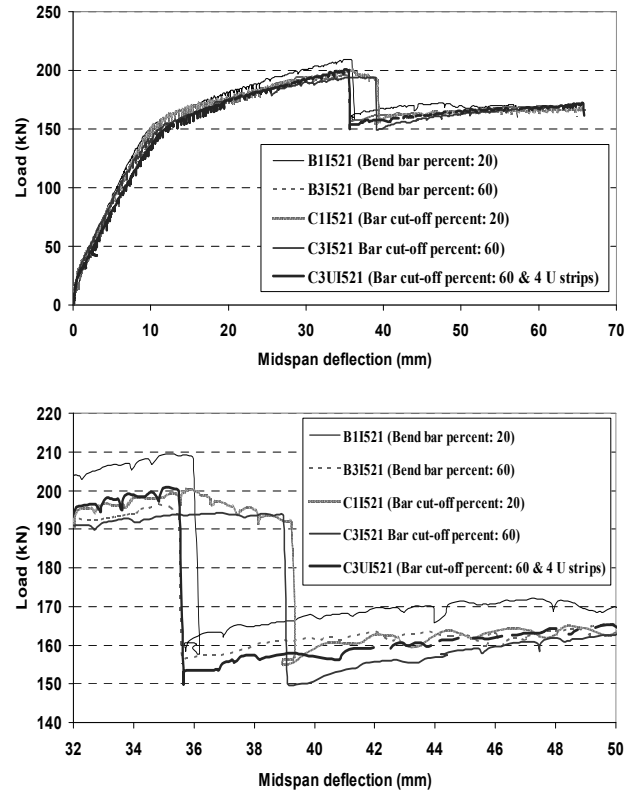


Figure 4 load-deflection curves for strengthened RC beams

mid-span). The crack then rapidly propagated up to the neutral axis of the section. The width of this crack at the time of its creation and at its first reading was recorded as 0.2 mm, while the width of flexural cracks at the first reading was 0.02 mm. The rapid widening of the crack causes relative displacements on its two sides, which may exert additional stresses on the strengthening plate on the two sides of the crack. This event at a load of 167 kN in the specimen C31521 caused part of the taper end to suddenly break away from the beam end (PE debonding). PE debonding is shown in Figure 5 where the bonding of part of the concrete at the end of the strengthening plate is clearly seen.

It is seen in this figure that the cut-off specimens enjoy a higher load bearing capacity while the bar bend ones exhibit a higher formability. Since crack growth is one of the main causes for the sudden debonding of the strengthening plate, rupture occurs more rapidly in bar

Table 4 Specification of debonding type for tested specimens

specimen	Plate debonding point		
	Deflection (mm)	Load (kN)	Type of debonding
B11521	35	210	IC
B31521	36	197	IC
C11521	39	200	IC
C31521	18	167	PE
	39	194	IC
C3UI521	36	201	IC



Figure 5 Plat end debonding in specimen C3I521

bend specimens due to the wider cracks created. As already mentioned above, the greater load bearing capacity of the specimen can also be attributed to the continuity of the tensile reinforcement and the greater uniformity of bar bend specimens as compared with bar cut-off specimens. The results presented in Table 3 and 4 and comparison of the load-displacement curves reveal the very similar behaviors of the two B3I521 and C3UI521 specimens so that both have ruptured under the debonding of the plate at the middle of the beam. This indicates that application of traverse FRP strips at the bar cut-off point can satisfactorily control the PE debonding of the plate and improve the performance of the specimen.

5 RESULTS

This paper investigated the effects of bar-cutoff and bent-point locations in RC beams strengthened with CFRP plates on the peeling load and their cracking behavior. Based on the experiments, the following

results were obtained:

- The debonding of CFRP plate is affected by bar cut-off percent.
- Crack growth is the cause of the debonding of the strengthening plate in specimens with various tensile bar cut-off percentages; however, quite different mechanisms are involved in the formation of cracks that lead to rupture in these specimens.
- Traverse strengthening plates cannot prevent their debonding at the middle of the beam.
- Under identical load levels, the width of the largest flexural crack is larger in bar bend specimens than that in bar cut-off specimens.
- Bar cut-off or bend increases formability but reduces crack distances.

REFERENCES

- Saadatmanesh, H., and Ehsani, M. R., RC Beams Strengthened with GFRP Plates. I: Experimental Study, *J. Struct. Engrg.*, ASCE, Vol. 117, No. 11, 1991, pp. 3417-3433.
- Lu, X. Z., Teng, J. G., Ye, L. P., and Jiang, J. J., Intermediate Crack Debonding in FRP-Strengthened RC Beams: FE Analysis and Strength Model, *Journal of Composites for Construction*, Vol. 11, No. 2, 2007, pp. 161-174.
- Pham, H., and Al-Mahaidi, R., Assessment of Available Prediction Models for the Strength of FRP Retrofitted RC Beams, *Composite Structures*, 66, 2004, pp. 601-610.
- Eftekhari, M. R., and Mostofinejad, D., Effects of Steel Bar Arrangement on Cracking Pattern and Peeling Load in RC Beams Strengthened with CFRP Plates, *FRPRCS-9*, Sydney, Australia, 2009.
- ACI 440.2R-02, Guide for the Design and Construction of Externally Bonded FRP Systems for Strengthening Concrete Structures, *American Concrete Institute*, Farmington Hills, Mich., 2002.

Meso-Scale Modelling of FRP-to-Concrete Bond Behaviour Using LSDYNA

X.Q. Li, J.F. Chen (j.f.chen@ed.ac.uk) & Y. Lu

Institute for Infrastructure and Environment, School of Engineering, University of Edinburgh, Scotland, UK

ABSTRACT This paper presents a preliminary investigation into the modelling of FRP-to-concrete bond behaviour using the K&C concrete damage model in LSDYNA explicit. The proposed FE model adopts the first order eight node hexahedron 3D solid element with one integration point and a sub-millimetre mesh. Results show that the model can simulate the static FRP-to-concrete bond behaviour with good accuracy and mesh objectivity. Further research is being undertaken to investigate its suitability for modelling the dynamic FRP-to-concrete bond behaviour.

1 INTRODUCTION

Fibre reinforced polymer (FRP) composite materials have been used for strengthening concrete structure since the early 1990s and the technique is now very popular worldwide. More recently, FRP has been used to retrofit concrete structures for blast protection (Buchan & Chen 2006). However, much of the existing research on blast retrofitting has been concerned on either experimental investigation or numerical modelling on macro scale of the structures. Little attention has been paid to the bond behaviour between FRP and concrete under blast loading which could be significantly different due to the effects of high strain rate and damage resulting from the blast waves. An ongoing research project at the University of Edinburgh aims to quantify these effects. The finite element (FE) analysis package LSDYNA Explicit is employed due to its capability in modelling high energy events such as blast. This paper reports the first stage of this investigation which focuses on the modelling of the static FRP-to-concrete bond behaviour and its validation. In particular, a number of issues in the FE modelling such as representation of fracture energy, Hourglass control and loading time are discussed.

2 FE MODEL

The FRP-to-concrete pull-off test specimen S-CFS-400-25 reported in Wu et al. (2001) was adopted as the reference case in this study. The test specimen consisted of a 275×100×100 mm (length × width × depth) concrete prism bonded with a 0.22mm thick and 40mm wide FRP sheet with a bond length of 250mm. The concrete had a cylindrical compressive strength of 57.6MPa. The FRP had a modulus of elasticity of 230GPa.

The same FE geometry and boundary conditions as Lu et al.'s (2004) FE model were adopted (Figure 1). The test was modelled as a 2D plane stress problem but the predicted results including loads, stresses, strains and slips are corrected according to Chen and Teng's (2001) width effect factor so that they can be compared with the test results.

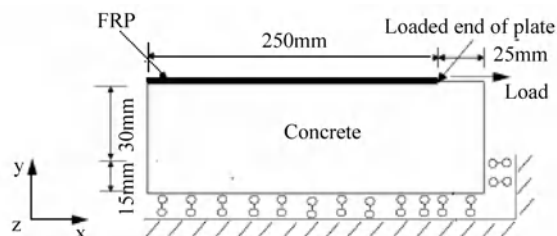


Figure 1 Pull-off test FE model geometry

Both the FRP plate and the concrete were modelled using the eight node hexahedron 3D solid element. The width direction of the test specimen (z direction in Figure 1) was represented by a single element. The model thus consists of a single layer of elements. All nodes on one face of this layer of elements (at $z=0$) were restrained for displacement in z direction to simulate the plane stress condition.

The FRP was modelled as an isotropic linear elastic material with a thickness $t_f=1\text{mm}$ and Young's modulus $E_f = 50.6\text{ GPa}$ so that its axial rigidity $E_f t_f$ remains the same as in the test. Because debonding of FRP in the pull off test usually occurs at a small distance away from the adhesive-concrete interface in the concrete, the FRP is assumed to be perfectly bonded to the concrete prism as in Lu et al. (2004). The specimen was loaded with a time dependent displacement at the loaded end in the FE model.

The concrete was modelled using the K&C concrete damage model (Malvar et al. 1997). It may be noted that this concrete damage model in LSDYNA is a smeared crack band model with a default localisation width l_w equal to 25.4mm. However, if the default l_w is adopted and the element size is small (less than 25.4mm for a first-order cubic element), no mesh objectivity can be achieved. Instead, the l_w should be set equal to the element characteristic length h_c , so that the Mode I fracture energy G_f^I remains a material constant in each element:

$$\int \sigma d\varepsilon = \frac{G_f^I}{h_c} \quad (1)$$

Equation 1 shows that the fracture energy is controlled by the uniaxial tensile stress strain curve.

There is a parameter b_2 in K&C concrete damage model which governs the softening branch of the concrete uniaxial tension. The default value of b_2 is equal to 1.35 according to a comparison between the laboratory material characterization of a class of 45.6MPa concrete, which is commonly used as the ‘standard concrete’ in many numerical simulations (Schwer and Malvar 2005). The default value may not produce the correct fracture energy G_f^I when the concrete strength is different so the user need change b_2 value. Generally, a reduction in b_2 increases G_f^I . In the reference case, $G_f^I = 102\text{N/m}$ calculated according to CEB-FIP (1993). To produce this value, b_2 needs to be changed to 0.45.

3 INTEGRATION SCHEME AND HOURGLASS CONTROL

All solid elements in LSDYNA are first order elements. For modelling structures under impulsive loads, e.g. blast load or impact, first order elements with single integration point are recommended to avoid internal vibration inside the elements during a high energy event and save computational cost. A disadvantage of the one-point integration scheme is that it involves zero energy modes, the so-called hourglassing modes, which must be controlled. Hourglass deformations are orthogonal to the directions in which strain calculations are performed. Work done by the hourglass resistance is thus neglected in the energy equation, leading to the loss of energy (LSDYNA 1998). If zig-zag mesh deformation is seen, hourglass can be a serious problem in the FE model leading to inaccurate results in terms of both stiffness and load carrying capacity.

An alternative option is to use the full integration scheme. However, severe shear locking can occur for the first order eight node hexahedron solid element. When the full integration scheme was trialled in modelling the pull-off test, it led to unrealistically stiff

behaviour and automatic termination. Therefore, the one point integration scheme was adopted for the concrete elements. The full integration scheme was adopted for the FRP elements as they did not result in the shear locking phenomenon.

The effect of hourglass deformation (HD) may be controlled in LSDYNA by a user defined hourglass coefficient, which has a default value of 0.1. A large hourglass coefficient usually corresponds to large hourglass resisting forces. In an FE model with reduced one integration point elements, the ratio of the hourglass energy to the internal energy of the structure should be smaller than 5% (LSDYNA 1998). Otherwise the results are unreliable.

There are two hourglass control methods which may be applied to solid elements: the stiffness hourglass control method and viscosity hourglass control method. Both types were trialled in this study and their effects on the simulated load-slip behaviour are respectively shown in Figures 2 and 3. Note that in these runs the loading was applied via a constant velocity at the right loaded end (Figure 1) with a loading time of 5T, where T is the fundamental period of the structure from a free vibration analysis. It is seen that the stiffness hourglass control method is more effective than the viscosity hourglass control method in the sense that the stiffness hourglass coefficient strongly affects the loading capacity. When the hourglass coefficient is very small such as 0.001, the predictions from both methods are very close to the test results. Further analysis has shown

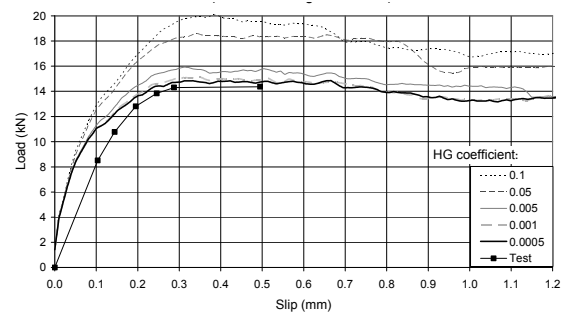


Figure 2 Effect of stiffness hourglass coefficient on the load-slip behaviour

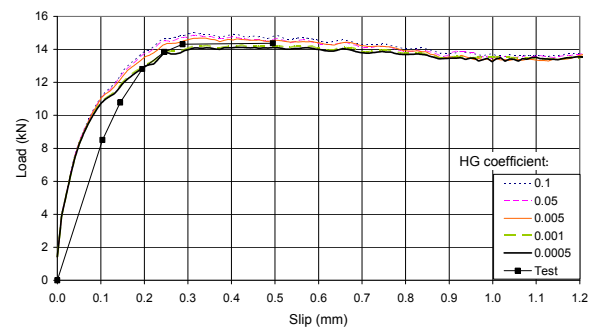


Figure 3 Effect of viscosity hourglass coefficient on the load-slip behaviour

that the hourglass to internal energy ratio is well below 5% for both cases when the hourglass coefficient is 0.001. The viscosity hourglass control method was adopted in all the analyses in the rest of the paper because the insensitivity of the predictions to the hourglass coefficient. A coefficient of 0.001 was adopted.

4 LOADING TIME AND LOADING SCHEMES

In modelling static problems with the explicit integration method, the loading time should be long enough to avoid dynamic effects but it is also preferable to be sufficiently short and with a large time step for computational efficiency. The largest possible time step Δt_{cr} without causing numerical instability is usually the time for the P-wave to travel through the smallest element in the model:

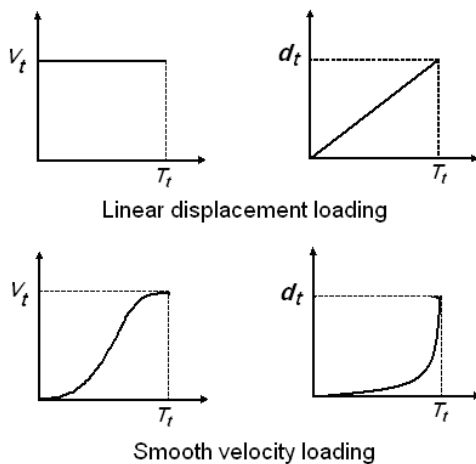
$$\Delta t_{cr} = \frac{L_e}{c} \tag{2}$$

where L_e is the smallest element size and c is the P-wave speed in the concerned material:

$$c = \sqrt{\frac{E}{\rho}} \tag{3}$$

in which E is the Young’s modulus of the material and ρ is its density.

Two different loading schemes have been trialled in modelling the pull off test with 1mm mesh: linear displacement loading and smooth velocity loading (Figure 4). The linear displacement loading is equivalent to a step velocity loading, which imposes an infinite initial acceleration. This can induce large inertia forces at the beginning especially when the loading rate is fast (loading time is short) (Figure 5). For the reference case, the dynamic effect becomes negligible when the total



(d_T = maximum loading displacement; T_t = total loading time; V_t = maximum loading velocity)

Figure 4 Two loading schemes

loading time is greater or equal to 5T as seen in Figure 5. The smooth velocity loading is advantageous in terms of that initial displacement, velocity and acceleration are all equal to zero. However, a longer loading time ($\geq 10T$) is required to achieve results with negligible dynamic effects because the loading increases very slowly initially (Figure 6). The smooth velocity loading scheme with a loading time of 10T was adopted in the rest of the paper. A maximum displacement of 1.6mm was applied in both cases.

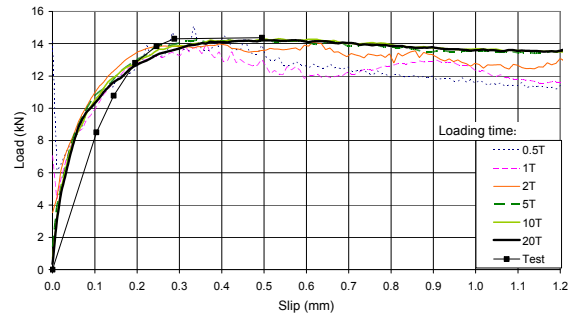


Figure 5 Effect of loading time: linear displacement loading

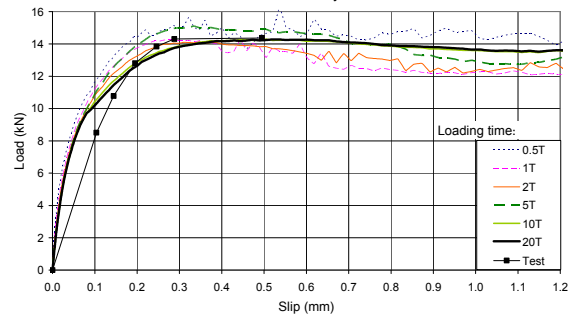


Figure 6 Effect of loading time: smooth velocity loading

5 MESH CONVERGENCE

Figure 7 shows that the predicted loading capacity increases with a reduction of the mesh size in general but the difference is very small between those predicted using the 1mm and 0.5mm meshes. The ultimate load-carrying capacity predicted from the 0.5mm mesh (14.5kN) is in close agreement with the test result (14.1kN), Lu et al.’s (2004) FE prediction (13.8kN) and Chen and Teng’s (2001) prediction (11.4 kN).

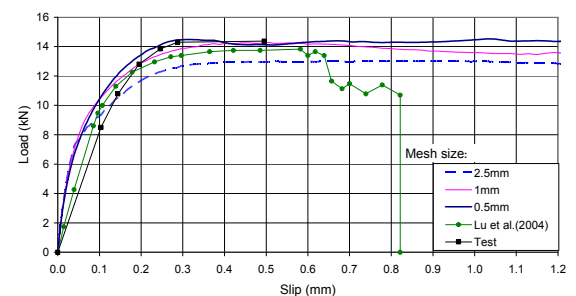


Figure 7 Mesh convergence (smooth velocity loading)

6 FRP STRAIN DISTRIBUTION AND BOND-SLIP RELATIONSHIP

The FE results from the 0.5mm mesh is further analysed here in terms of the FRP strain distribution and the bond-slip relationship. Figure 8 shows that the FRP strain distributions at different loading levels are in close agreement with the test strain observations and Lu et al.'s (2004) FE predictions. Note that the load is normalised in Figure 8 by their respective ultimate load P_u from the three studies.

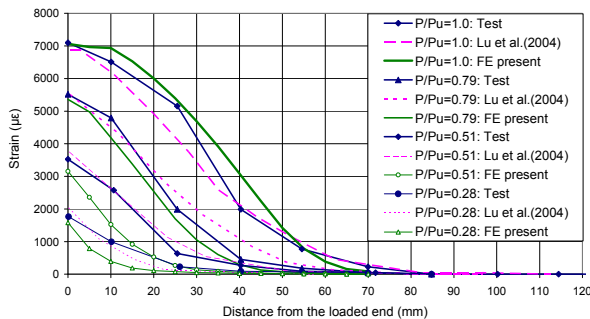


Figure 8 FRP strain distribution

Figure 9 shows the local bond-slip relationship obtained at 19.5mm from the loaded end via the following equation:

$$\tau = \frac{\Delta\sigma_f}{\Delta x} t_f \quad (4)$$

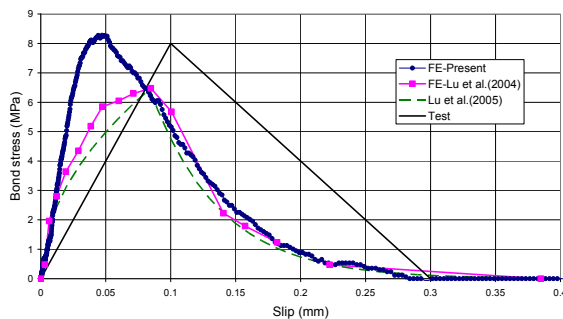


Figure 9 Local bond-slip curve

in which τ is the local bond stress; $\Delta\sigma_f$ is the difference of axial stress between two adjacent FRP elements; Δx is the length of the FRP element; and t_f is the thickness of the FRP plate. The bond-slip curve deduced by Wu et al. (2001) from test, that from Lu et al.'s (2004) FE analysis and Lu et al.'s (2005) "simplified model" are also shown for comparison. It is seen that the area under the local bond-slip curve is slightly larger than Lu et al.'s (2004) prediction, but similar to that under the bi-linear curve deduced by Wu et al. (2001) from the test data. However, it should be noted that the local bond-slip curve obtained from an FE

analysis is different at different locations, depending on their relative position to the micro-cracks in the concrete. The bi-linear bond-slip curve in Figure 9 was deduced based on the global load-displacement response of the pull-off test, so it represents to certain degree an average of the local bond-slip relation over the bond length. Therefore, some differences between the curves predicted from different FE models at a particular position does not necessarily mean that one model is inferior than another.

7 CONCLUSIONS

This paper has presented a preliminary investigation into the modelling of the FRP-to-concrete bond behaviour using the K&C concrete damage model in LSDYNA using the explicit integration scheme. The proposed FE model adopts the first order eight node hexahedron 3D solid element with one integration point and sub-millimeter mesh. It has been shown that the model can simulate the static FRP-to-concrete bond behaviour, in terms of the load-carrying capacity, load-displacement behaviour and local bond-slip behaviour with reasonable accuracy and mesh objectivity subjected to that:

- 1) the localised width (the crack band width) is set as the element characteristic length to ensure mesh objectivity under such a stress condition;
- 2) the model parameter b_2 governing the tensile softening behaviour of concrete is adjusted according to the concrete being modelled to ensure that the correct tensile fracture energy is achieved;
- 3) the hourglass deformation mode is properly controlled to ensure that the hourglassing deformation is negligible and the hourglass energy is small compared with the internal energy of the structure (e.g. less than 5%) during the entire loading process; and
- 4) the loading time is sufficiently large relative to the fundamental period of the structure to minimise the dynamic effect.

Further research is being conducted to investigate its suitability for modelling dynamic FRP-to-concrete bond behaviour.

8 ACKNOWLEDGEMENTS

The authors are grateful for funding provided to the first author by EPSRC and Royal Dutch Shell plc through a Dorothy Hodgkin Postgraduate Award.

REFERENCES

- Buchan, P.A., & Chen, J.F. 2006. Blast resistance of FRP composites and polymer strengthened concrete and masonry structures – a state-of-the-art review. *Composites: Part B* 38:509–522.
- CEB-FIP. 1993. *Model Code 90. Lausanne.*

- Chen, J.F. & Teng, J.G. 2001. Anchorage strength models for FRP and steel plates bonded to concrete. *Journal of Structural Engineering*, ASCE 127(7):784–791.
- Flanagan, D.P. & Belytschko, T. 1981. A uniform strain hexahedron and quadrilateral and orthogonal hourglass control. *Int. J. Numer. Meths. Eng.* 17:679-706.
- Kwak, H.G. & Filippou, F.C. 1990. Finite element analysis of reinforced concrete structures under monotonic load. *Research report of Department of Civil Engineering, U. C. Berkeley, No. UCB/SEMM-90/14.*
- Lu, X.Z., Ye, L.P., Teng, J.G. & Jiang, J.J. 2004. Mesoc-scale finite element model for FRP sheets/plates bonded to concrete, *Engineering structures*, 27:564-575.
- Lu, X.Z., Teng, J.G., Ye, L.P. & Jiang, J.J. Bond–slip models for FRP sheets/plates bonded to concrete, *Engineering Structures*, 27:920–937.
- LS-DYNA. 1998. *Theory manual*, Livermore software technology corporation, California.
- Malvar, L.J., Crawford, J.E., Wesevich, J.W. & Simons, D. 1997. A plasticity concrete material model for DYNA3D, *International Journal of Impact Engineering*, 19(9-10): 847-873.
- Malvar, L.J, Crawford, J.E. & Morrill, K.B. 2000. K&C Concrete material model release 3 - automated generation of material model input. *K&C Technical Report TR-99-24-B1*, Karagozian & Case Structural Engineers, CA.
- Schwer, L.E. & Malvar, L.J. 2005. Simplified concrete modeling with *mat_concrete_damage_rel3, *JRI LS-Dyna User Week*, Nagoya, Japan.
- Wu, Z.S., Yuan, H., Yoshizawa, H. & Kanakubo, T. 2001. Experimental/analytical study on interfacial fracture energy and fracture propagation along FRP-concrete interface. *ACI International SP-201-8*, 133–152.

Investigation on Fracture Behavior of FRP-Concrete Interface under Direct Shear

Feng-Chen An, Shuang-Yin Cao(cao@public1.ptt.js.cn), Jin-Long Pan & Qian Ge

Department of Civil Engineering, Southeast University, Nanjing, Jiangsu Province, China

ABSTRACT In this study, the existing researches on debonding performance of FRP-Concrete Interface under direct shear are reviewed and compared at first, and then the hypothesis is put forward that ultimate bearing capacity of FRP-Concrete Interface under pure shear is combined of fracture-resisting force at the undamaged area and friction stress transferred along the already debonded surface. Following that, the formulae on fracture energy and friction stress for FRP-Concrete Interface under pure shear are deduced, through which the values for fracture energy and friction stress at the FRP-Concrete Interface are obtained based on the experimental results of eight specimens with FRP-Concrete Interface. On the basis of theoretical analysis mentioned above, such conclusions can be reached that the friction-resisting stress transferred along the already deteriorated bi-material interface is independent of length of FRP bonded onto concrete substrates and concrete strength, but relies on the tension rigidity; on the contrary, cohesive fracture energy is dependent on length and tension stiffness of FRP bonded to concrete substrate. Besides, the percentage of the fracture-resisting force in the ultimate debonding load for the interface decreases with the bonding length of FRP increasing, but increases with the increase of the layers of the FRP.

1 INTRODUCTION

The method of externally bonding fiber reinforced polymer (FRP) plates to the tension faces of concrete beams to retrofit the structural elements has become increasingly popular in today's strengthening industry. In this strengthening system, the bonding performance of FRP-Concrete Interface plays a predominant role in the ultimate bearing capacity of the beams retrofitted with FRP strips. However, scholars in the worldwide are still confused by the debonding phenomenon around the FRP-Concrete Interface in the flexural span of one reinforced concrete beam, which occurs mainly due to high stress concentration in the vicinity of flexural crack. Also, this phenomenon happens in one-way slabs in large possibilities, which can be explained using the theoretical approach similar to the former one. In most circumstances, the RC beams or one-way slabs serve with some initial cracks, which will initiate the debonding in the bottom of retrofitted beams with FRP strips, thereby resulting in the failure of the retrofitted beams. Therefore, the bonding performance of FRP-Concrete Interface plays a pivotal role in the ultimate failure of the beams retrofitted with FRP strips, which has attracted an increasing number of researchers to investigate.

Numerous academics in the worldwide conducted a large amount of investigation in numerical and

experimental methods. The experimentations in the field can be classified in to single-direct method((Täljsten (1994, 1997), Chajes et al.(1995, 1996), Bizindavyi & Neale(1999)) and double-direct method (Swamy et al.(1986), Brosens & Van Gemert (1997), Fukuzawa et al.(1997), Maeda et al.(1997), Neubauer & Rostásy(1997)), according to different designation of specimens for experiments. Based on the experimental results through the setups mentioned above, lots of theoretical models are established to describe the debonding performances on FRP-Concrete Interface, namely empirical models (Tanaka(1996), Maeda et al.(1997)), strength-based models(Triantafillou & Plvrvis(1992), Täljsten(1997), Yuan & Wu(1999), Yuan et al.(2001), Malek et al(1998), Smith & Teng(2002)), fracture-based models (Hearing (2000), Gunes(2004)).

However, there is no one of them who can combine the merits of the strength-based models and the fracture-based models successfully, and avoid the demerits of them in the mean time. The strength-based models investigate the mechanical conditions of FRP-Concrete Interface in the perspective of stress, but dependent on the geometry parameters seriously. In contrast, the fracture-based models investigate them in the perspective of energy and independent of geometry parameters, but neglect presence of friction-resisting stress (or interlock effects) along the already debonded

surface. The paper elaborates that fracture energy is not determined by the ultimate debonding force, but instead by the initial debonding force of interface, based on which the authors deduced the relevant formulae of fracture energy of the bi-material interface. Therefore, the ultimate bearing capacity of the bi-material interface is determined by the combination of the fracture-resisting force in the bonded region (i.e. equal to initial debonding force of the interface) and the friction-resisting force in the already debonded region of the interface.

2 THEORETICAL ANALYSIS

As is mentioned above, the ultimate debonding load for the bi-material interface is combined of the fracture-resisting force in the undamaged region and the friction-resisting force in the already debonded surface, both of which will be explained in the chapter below.

2.1 Nonlinear fracture mechanics

When fracture occurs to FRP-Concrete Interface, the release energy of the bi-material interface obtained in the experimentation is fracture energy of the interface, and the corresponding load is called debonded load at the instant when debonding failure occurs initially, which can be obtained from initial debonding load P_{ini} in the experimentation. The initial bonding length of FRP-Concrete Interface is set as l ; the length of 'a' was left unbonded to avoid the wedge failure of concrete induced by shear stress concentration around the bi-material interface of the specimens during testing (Pan et. al. 2007). This means that FRP-Concrete Interface has the bonding zone with the actual length of $l-a$.

Täljsten(1996) has derived that the shear expression shown as follows (The end of FRP-Concrete Interface is referred to as origin of horizontal axis, shown in Figure 1):

$$\tau(x) = \frac{P_{\max} \omega}{b} \cdot \frac{\cosh(\omega x)}{\sinh(\omega(l-a))} \quad |0 \leq x \leq l-a| \quad (1)$$

where, $\omega^2 = \frac{G_s}{s} \left(\frac{1}{E_1 t_1} + \frac{1}{E_2 t_2} \right)$, s =thickness of adhesive layer, G_s =shear modulus of adhesive layer, $E_1 t_1$, $E_2 t_2$ =tension stiffness for FRP and compression stiffness for concrete respectively.

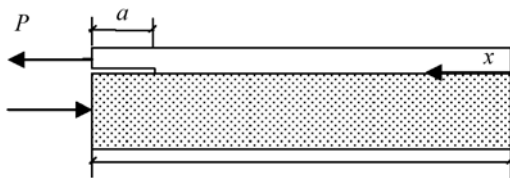


Figure 1 Crack model for shear of FRP-concrete interface

When the length of crack propagates from a to $a+da$, it requires import of work W_e done by external load. The work W_e can be expressed as follows:

$$W_e = \int_{l-(a+da)}^{l-a} \left[\int_0^{\gamma(x)} b\tau(\gamma)sd\gamma \right] dx \quad (2)$$

Then, the equation of energy release rate G can be written as follows:

$$G = \frac{W_e}{bda} = \frac{1}{bda} \cdot \int_{l-(a+da)}^{l-a} \left[\int_0^{\gamma(x)} b\tau(\gamma)sd\gamma \right] dx \quad (3)$$

Equation (3) can be simplified as follows, according to Mean Value Theorem for Integral.

$$G = \frac{\{l-a-[l-(a+da)]\}}{bda} \cdot \int_0^{\gamma(l-a)} b\tau(\gamma)sd\gamma \quad (4)$$

$$= s \int_0^{\gamma(l-a)} \tau(\gamma)d\gamma$$

Consider the correlation between shear stress τ and strain γ , namely $\tau(\gamma) = G_s \gamma$, in the case that the bonding zone is linear and elastic, thus equation (4) can be written as

$$G = \frac{sG_s}{2} \cdot \gamma_1^2 \quad (5)$$

Where, γ_1 = the value of shear strain in the crack tip, equal to $\gamma(l-a)$.

Consider $x=l-a$, $\tau = G_s \cdot \gamma$ and equation (1), equation(5) can be simplified as

$$G = \frac{s}{2G_s} \cdot \frac{\omega^2 P^2}{b^2} \cdot \frac{1}{\tanh^2(\omega(l-a))} \quad (6)$$

Here, we define the fracture release energy G as cohesive fracture energy (i.e. employed to distinguish from other definitions of fracture energy, which was obtained through the ultimate debonding load of the interface), when initial debonding failure occurs at the FRP-Concrete Interface ($P=P_{ini}$), which is denoted as $G_{II,b}$.

$$G_{II,b} = \frac{s}{2G_s} \cdot \frac{\omega^2 P_{ini}^2}{b^2} \cdot \frac{1}{\tanh^2(\omega(l-a))} \quad (7)$$

In which, P_{ini} is denoted as tension load of the interface when the initial debonding failure occurs at the FRP-Concrete Interface. The derivation mentioned above is based on such fact that in the bonded zone of FRP-Concrete Interface, except the zone where the second debonding behavior occurs, interfacial stress maintains at very low level of stress or even zero, when debonding happens in the interface.

However, if ductility of the adhesive at the FRP-Concrete Interface is so good that the interfacial stress can distribute uniformly along the whole bonded joint before debonding. And then, the shear stress at the FRP-Concrete can be expressed as follows:

$$\tau_f \approx \frac{P_{\max}}{b \cdot (l-a)} \quad (8)$$

Hence, this sort of interfacial failure mechanism can not be explained by fracture theory, but instead by strength theory. In fact, there is no such adhesive with so good ductility in today's market, so eq.(8) only expressed one extreme case in the level of theory.

2.2 Analysis on friction-resisting force between debonded surfaces

In the subsection, the friction force in the damaged surfaces will be described.

As is shown in the Table 1, the parameter of $k=P_{ini}/P_{max}$ declines steadily, with the increase of bonding length of the bi-material interface. The parameter of k maintains constant, when the bonding length is unchangeable, which has nothing in relation to the concrete strength. The decrease of the parameter k , immediately means that the composition of friction-resisting force in the ultimate debonding capacity of FRP-Concrete Interface tends to increase due to increase of the FRP length bonded to concrete substrate. It is also found that the friction-resisting force constitutes approximately one third of the total ultimate debonding capacity of the FRP-Concrete Interface, when the bonding length exceeds the length of 450 mm. Viewed from this perspective, the presence of friction-resisting force cannot be neglected while calculating the total debonding capacity of FRP-Concrete Interface.

Besides, the parameter k for FRP-Concrete Interface with four layers of FRP grows by a wide margin, comparing to that with two layers of FRP strips; in other words, the contribution of the friction force in debonded region decreases accordingly. The friction-resisting force is produced by the relative displacement of the already debonded regions of FRP-Concrete Interface, but the tension stiffness of FRP-Concrete Interface was enhanced due to increase in the layers of the FRP strips, which will immediately reach such conclusion that the relative displacement of bi-material specimens with four layers of FRP strips will be smaller than its counterpart with two layers after debonding. Therefore, the friction-

resisting load at the FRP-Concrete Interface with four layers of FRP strips turns to be larger than that with two layers of FRP strips.

Discussion about the value of friction-resisting stress along the already debonded surface: Suppose that the friction stress is distributed uniformly along the whole already debonded FRP-Concrete Interface, and that the length of FRP debonded from concrete substrates for every time is constant (denoted as x). Then, there is such equation shown as follows:

$$\frac{F_{N1}}{l_1 - x} = \frac{F_{N2}}{l_2 - x} \quad (9)$$

Where F_{N1} and F_{N2} are the values for friction force in the already debonded region of the bi-material interface before debonding and after debonding respectively; l_1 and l_2 represents the already debonded length of FRP strips; x represents the length of FRP strips bonded to concrete prism before the last debonding occurs to the bi-material specimens.

All results obtained through the foregoing equation, will be listed in Table 1.

3 EXPERIMENT PROGRAMME

3.1 Testing specimens

In this paper, single-shear tests were selected to investigate fracture performance on the FRP-Concrete Interface. The concrete prisms were cast into the dimensions of 150mm×150mm×550mm. The width of FRP bonded onto the concrete prisms was 50 mm; the length of it is designed within the range of 150mm, 300mm, 450mm and 500 mm with two or four layers respectively. The details of the parameters of the specimens are listed in Table 1. Besides, the length of 100 mm was left unbonded to avoid the wedge failure of concrete at the top of specimens induced by shear stress concentration during testing, which was called virtue crack in this study.

Table 1 Test results for FRP-concrete interface under direct pull test

Specimen	Layer	L (Mm)	f_c (MPa)	f_a (MPa)	f_{CFRP} (MPa)	P_{ini} (kN)	P_u (kN)	k	l_e (mm)	l_f (mm)	τ_f (MPa)	$G_{II,b}$ (N/m)
M II -1	2	150	61.6	44.5	4667	10.79	12.03	0.90	62.68	87.32	0.2840	906.06
M II -2	2	300	61.6	44.5	4667	9.71	13.08	0.74	62.68	237.32	0.2840	733.76
M II -3	2	450	61.6	44.5	4667	8.55	13.4	0.64	62.68	387.32	0.2504	568.91
M II -4	2	500	40.3	44.5	4667	7.64	13.9	0.55	62.68	437.32	0.2863	454.26
M II -5	2	150	40.5	44.5	4667	10.61	11.86	0.89	62.68	87.32	0.2863	876.08
M II -6	2	300	61.6	44.5	4667	12.47	16.64	0.75	62.68	237.32	0.3514	1210.17
M II -7	2	450	40.5	44.5	4667	9.74	14.51	0.67	62.68	387.32	0.2463	738.30
M II -8	4	450	40.5	44.5	4667	15.36	18.13	0.85	—	—	—	1836.10

Remark: l = bonding length of FRP-Concrete Interface; f_c = Compression Strength of concrete; f_a = tensile Strength of Adhesive; f_{CFRP} = tensile Strength of Adhesive; P_{mi} = Load for initial debonding; P_u = Ultimate load; ϵ_u = Ultimate strain of FRP; G_f = for Fracture energy; k = the value of P_{mi}/P_u ; l_e = the bonding length of the FRP-to-Concrete Interface before the last debonding occurs to the interface(i.e. referred to as the effective length of FRP-Concrete Interface); l_f = the debonding length of the FRP-to-Concrete Interface before the last debonding occurs to the interface; τ_f = the friction stress due to the presence of the interlock effect between the aggregates in the debonding region.

3.2 Mechanical properties of materials

For each batch of concrete, the compressive strength of concrete was measured after the concrete was cured for 28 days in the standard curing condition. Samples of adhesive were tested under tension and shear respectively, following standard procedures [ASTM 2005c, d]. The properties of the carbon fibre-reinforced polymer (CFRP) were determined using the procedures recommended in ASTM D 3039 [ASTM 2005b]. The properties of these materials are listed in Table 1.

3.3 Test procedures

One steel slab with the size of 800mm×800mm put on the base plate of MTS (i.e. Material Test System) is fixed with bolts firstly; and then the bi-material specimen is fixed on the steel plate using four nuts and four steel sticks with screw thread. Following that, the free end of FRP strips of the bi-material specimen is fitted to loading setup, which is fixed on the loading end of the MTS.

Before loading, draw a line as a mark on the joint between loading device and FRP material to monitor the relative slip of the bi-material interface.

4 CONCLUSION

In sum, we can reach such conclusion that the ultimate debonding capacity of the FRP-Concrete Interface is composed of the fracture-resisting force and the friction-resisting force.

Through comparison between MII-7 and MII-8 in terms of fracture energy, such conclusion is reached that increase in the layers of FRP strips bonded to concrete prism immediately leads to increase of interfacial fracture energy and initial debonding force, while the friction force will decrease to large extent in the mean time, due to the fact that the enhancement of the stiffness of the bi-material interface will lead to the decline of FRP strain while being loaded under the same level of load, which will immediately render the concrete strain smaller. Therefore, the fracture-resisting force is determined by the tensile strength of concrete to a great extent and will increase when the layers of FRP strips increase, due to the fact that Smith & Teng (2002) has demonstrated that concrete delamination has been the most observed debonding mode from large scale beam tests and mesoscale shear and peel tests, regardless of where debonding is initiated.

Besides, the friction force is produced through relatively large displacement, we can also see from Table 1 that the friction force of the FRP-Concrete Interface will decline accordingly, due to the increase of stiffness of the FRP strips bonded to the concrete prism.

The fracture-resisting force is also determined by the bonded length of the FRP-Concrete Interface before debonding occurs at the FRP-Concrete Interface in the

last time, which is also equal to the value of initial debonding load of the joint.

Also, it is found that fracture energy is determined by the combination of bonded length of FRP and concrete strength, but the length of FRP is the major determinant showed in the Table 1. Perhaps, the value for fracture energy may maintain constant if the bonded length of FRP exceeds certain length, but now we cannot get such conclusion due to limit of the number of the specimens having done in the experimentation.

Besides, although the emphasis of the paper is on the FRP-Concrete Interface, the analytical approach is general and also applicable to other bi-material interfaces between thin plates (e.g. FRP, steel, aluminium) and a substrate of various materials (Chen et al 2006) (e.g. concrete, steel, rock and aluminium).

REFERENCES

- Bizindavyi L. & Neale K.W. 1999. Transfer length and Bond strengths for composites bonded to concrete. *Journal of composites for construction*, Vol. 3, No. 4. pp.153-160.
- Brosens K. & Van Gemert D. 1997. Anchoring stresses between concrete and carbon fiber reinforced laminates Non-Metallic (FRP) Reinforcement for concrete structures. *Proceeding of the Third International symposium*, Sapporo, Japan, pp. 271-278.
- Chajes M.J., Januszka T.F. & Finch W.W. 1995. Shear strengthening of reinforced concrete beams externally applied composite fabrics. *ACI Structural Journal*, Vol. 92, pp. 295-303.
- Chajes, M.J., Finch, W.W. Januszka T.F. & Thomosh, T.A. 1996. Bond and force transfer of composite material plates bonded to concrete. *ACI Structural Journal*, Vol. 93, No. 2, pp. 231-244.
- Chen J.F., Yuan H. & Teng J.G. 2006. Debonding failure along a softening FRP-to-concrete interface between two adjacent cracks in concrete members. *Eng Struct*, Vol 04, No.017.
- Fukuzawa K, Numao T., Wu Z, Yoshizawa H. & Mitsui M. 1997. Critical strain energy release rate of interfacial debonding between carbon fiber sheet and mortar. *Non-metallic (FRP) Reinforcement for Concrete Structures, Proceeding of the Third International symposium*, Sapporo, Japan, pp.295-302.
- Gunes, O. 2004. A Fracture Based Approach to Understanding Debonding in FRP bonded Structural Members. *Ph.D. Thesis*, Massachusetts Institute of Technology, Cambridge, MA.
- Hearing, B. 2000. Delamination in Reinforced Concrete Retrofitted with Fiber Reinforced Plastics. *Ph.D. Thesis*, Massachusetts Institute of Technology, Cambridge, MA.
- Maeda, T., Asano, Y., Sata, Y., Ueda, T. & Kakuta, Y. 1997. A study on bond mechanism of carbon fiber sheet. *Non-metallic (FRP) Reinforcement for Concrete Structures, proceedings of the Third International Symposium*, Sapporo, Japan, pp. 279-285.
- Maeda, T., Asano, Y., Sata, Y., Ueda, T. & Kakuta, Y. 1997. A study on bond mechanism of carbon fiber sheet. *Non-metallic (FRP) Reinforcement for Concrete Structures, proceedings of*

- the Third International Symposium, Sapporo, Japan*, pp. 279-285.
- Malek, A.M., Saadatmanesh, H. & Ehsani, M.R. 1998. Prediction of Failure Load of RC Beams Strengthened with FRP Plate Due to Stress Concentration at Plate End *ACI Structural Journal*, No.2, pp.142-152.
- Neubauer U. & Rostasy F. S. 1997. Design aspects of concrete structures strengthened with externally bonded CFRP plates. *Proceeding of the Seventh International conference on structural Faults and Repairs*, Edited by M.C. Forde, Engineering Technics Press, Edinburgh, UK, pp.109-118.
- Pan J.L. & Leung Christopher K. Y. 2007. Effect of Concrete Composition on FRP/Concrete Bond Capacity. *Journal of Composites for Construction*, Vol. 11, No.6, pp.611-618.
- Smith, S.T. & Teng, J.G. 2002. FRP-strengthened RC beams I: Review of Debonding Strength models. *Engineering Structures*, 24, pp.385-395.
- Swamy R.N., Jones R. & Charif A. 1986. Shear adhesion properties of epoxy resin adhesive. *Adhesion Between Polymers and Concrete, Proceedings of an International symposium*, Edited by H.R. Sasse, Paris, France, pp. 741-755.
- Täljsten, B. 1994. Plate bonding: Strengthening of existing concrete structures with epoxy bonded plates of steel or fiber reinforced plastics. *Doctorial Thesis*. Lulea University of Technology, Sweden.
- Täljsten, B. 1996. Strengthening of concrete prisms using the plate-bonding technique. *International Journal of Fracture* 82: pp.253-266.
- Täljsten, B. 1997. Strengthening of beams by plate bonding. *J. Mat. in Civ. Engrg., ASCE*, 9(4), pp.206-212.
- Tanaka, T. 1996. Shear Resisting Mechanism of Reinforced Concrete Beams with CFS as Shear Reinforcement. *Graduation Thesis*, Hokkaido University.
- Triantafillou, T. C. & Plevris, N. 1992. Strengthening of R/C beams with epoxy-bonded fiber-composite materials. *Mater. Struct.*, 25, pp.201-211.
- Yuan, H. & Wu, Z. 1999. Interfacial fracture theory in structures strengthened with composite of continuous fiber. *Proceedings of Symposium of China and Japan, Science and Technology of 21st Century*, Tokyo, Japan, pp.142-155.
- Yuan, H. Wu, Z.S. & Yoshizawa, H. 2001. Theoretical solutions on interfacial stress transfer of externally bonded steel/composite laminates. *Journal of Structural Mechanics and Earthquake Engineering*, JSCE, No. 675/1-55, pp.27-39.

Towards a Standard Test Method for Assessing FRP-to-Concrete Bond Characteristics

Troy Eveslage, John Aidoo & William Bro

Department of Civil Engineering, Rose-Hulman Institute of Technology, Terre Haute, IN, USA

Kent A. Harries (kharries@pitt.edu)

Department of Civil and Environmental Engineering, University of Pittsburgh, Pittsburgh, PA, USA

ABSTRACT It is well established that debonding of adhesive-applied FRP retrofit materials from their concrete substrate often is a critical limit state. This paper adopts the use of a simple concrete beam specimen similar to that used to determine the modulus of rupture of concrete. To achieve controlled debonding behaviour, the beam is notched to represent cracked concrete. This paper addresses specific issues associated with standardising such a test specimen including a) the width of the FRP relative to the concrete substrate width; b) the geometry of the induced notch; and c) the effect of providing an initially unbonded region in the vicinity of the notch. Conclusions provide recommended specimen geometry which satisfies the objectives of such a standardised test.

1 INTRODUCTION

Debonding of externally applied FRP materials from concrete substrates is well established as being a critical mode of behaviour in many applications. In reinforced concrete beams having relatively long shear spans debonding of the FRP initiates at flexural (FIC) and flexural/shear (SIC) cracks near the region of maximum moment (Oehlers 2005). Under loading, these cracks open and induce high interfacial shear stress (Mode II) accompanied by a small amount of peeling stress (Mode I) causing delamination, which propagates across the shear span in the direction of decreasing moment. Although FIC/SIC is dominant in many structures, the mixed mode nature of such debonding is complex and behaviour varies with concrete and FRP geometry and with the applied moment-to-shear ratio. As such, axial intermediate cracking (AIC), having no such mixed mode behaviour, is viewed as a characteristic behaviour or property of a bonded system (Oehlers 2005).

The objective of the present work is to promote the development of a practical standardised test method for assessing FRP-to-concrete bond characteristics. For a test method to be practical, and therefore universally adopted, it must a) provide a reliable and repeatable engineering property that describes bond behaviour; b) be sufficiently compact to be easily handled and allow repetition; and c) have a form that is both suitable for environmental exposure and accelerated aging tests while also capturing the general geometry of *in situ* applications.

2 TEST SPECIMEN DETAILS

A standard test method must be “acceptable” to the community of users. Additionally, leveraging methodology from existing long-standing methods that have been universally adopted strengthen the case for a new method, easing the way to its acceptance and adoption. For this reason, the adoption of a beam-style test specimen having dimensions similar to those used for standard concrete modulus of rupture tests (ASTM C78 2008): 152 mm square, tested over span of 450 mm is proposed. This unreinforced test specimen is familiar to test technicians and well supported in terms of standardised forms and test apparatuses.

To adapt the test specimen to FRP bond testing the specimen is notched at midspan. Debonding initiates at concrete cracks and this notch represents such a crack. By “initiating” the crack, the location of debonding is known thereby simplifying instrumentation. Additionally, a three point bend test (rather than the four point test used by ASTM C78) is adopted. This is done because a) the presence of the notch eliminates the need for a constant moment region; and b) the shear span is increased thus reducing the likelihood of a shear failure in the flexurally strengthened test specimens.

In order to develop a standard specimen, details of the test specimen must be specified. Specimen detail requirements must be relatively simple to achieve while nonetheless permitting to user a variety of means of achieving these ensuring that the test method is relatively universal, accommodating a variety of FRP materials. Additionally, the effect on test results of

variation in these details where they are unavoidable must be understood. With this in mind, this paper undertakes to address the impact of the following specimen details: a) the width of the FRP relative to the concrete substrate width; b) the geometry of the induced notch; and c) the effect of providing an initially unbonded region in the vicinity of the notch. The following sections address these details in turn. In all discussions, the adoption of the ASTM C78 test specimen having a 152 mm square section tested in midpoint flexure over a 450 mm span is assumed as shown in Figure 1.

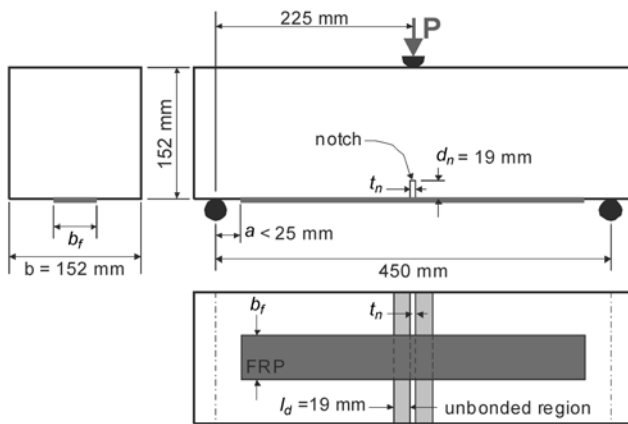


Figure 1 Test specimen details

2.1 Width of FRP on concrete substrate

FRP materials that may be applied to concrete come in a variety of forms and it has been shown that the ratio of FRP width to concrete substrate width, b_f/b , affects the efficiency of the bonded system and therefore the test results (Harries et al. 2007; Ramanathan and Harries 2008). These effects are partly attributed to the shear lag effect in the very thin FRP strip and have been shown very clearly both analytically (Thomsen et al. 2004) and experimentally (Harries and Webb 2009). Interaction of stress fields between adjacent FRP strips and at the edge of the concrete substrate have also been shown to affect the efficiency of bonded FRP systems (Oehlers and Seracino 2004).

A number of standards and recommendations address these effects of FRP geometry with the inclusion of the so-called k_b factor, which is a function of b_f/b , in the determination of an allowable FRP strain used for design (most are based on Teng et al. 2003). For a standard test method, however, this process must be “reversed” and k_b used as a ‘correction factor’ to results obtained from a standard b_f/b ratio. Thus it is necessary to select this standard FRP geometry. In general, it has been shown that thinner FRP strips – smaller values of b_f/b – result in greater FRP stresses thereby implying greater bond stress.

Other practical considerations must be considered in

selecting a standard FRP width: a) the amount FRP must not be too large as to change the mode of failure of the test specimen from flexure to shear; and b) the amount of FRP must be practical in relation to available commercial products. In the present study FRP widths of $b_f = 25, 51$ and 102 mm were used on the 152 mm wide substrate resulting in b_f/b ratios of $0.17, 0.33$ and 0.67 .

2.2 Notch geometry

The notch serves to initiate the FIC debonding which will then propagate in the direction of one of the supports. The notch may be formed in one of two manners: a) an insert in the formwork; or b) saw cutting following specimen curing. An insert may be of any width (t_n) or depth (d_n) and the only requirement is that it results in a straight and uniform slot. In the present study, greased steel shim stock was used to form 1.3 and 2.5 mm wide notches. Saw cutting will generally be easier and will result in uniform slots. However, the notch width in this case is a function of the kerf of blade used. The smallest practical kerf for a concrete saw is 3.8 mm and larger is likely in a commercial operation.

The depth of the notch in the present study was limited to $d_n = 19$ mm. This results in an unretrofit beam flexural capacity 76% of the gross 152 mm square section which was felt to be a reasonable limit. While increasing the depth of the notch does reduce the capacity of the unretrofit specimen, within reasonable limits it will not affect the capacity of the retrofit specimen since the concrete compression block in the reinforced specimen is generally quite small.

It is critical in the preparation of the specimen that the adhesive used to bond the FRP not work its way into the notch. For specimens where a debonded region is provided adjacent the slots (see following section), this is easily accomplished. If no such region is to be provided, the authors found that filling the notch with sprayed foam insulation prior to FRP installation worked very well. In the present study, all slots had $d_n = 19$ mm and had widths provided by inserts of $t_n = 1.3$ and 2.5 mm and by saw cutting of $t_n = 3.8$ and 7.6 mm.

2.3 Unbonded region adjacent to notch

When bond is assessed using a pull-off test, typically, the leading edge of the FRP is left unbonded to the concrete substrate in order to avoid shear failure of a wedge of concrete at this leading edge (Figure 2a). This type of failure is also exhibited in notched beam tests at the notch (Figure 2b) and in other beam tests adjacent to the crack that initiates debonding (Figure 2c). In pull-off and notched beam tests the size of the shear wedge is affected by the test or notch geometry. The presence of longitudinal reinforcing steel usually defines the wedge in a beam test.

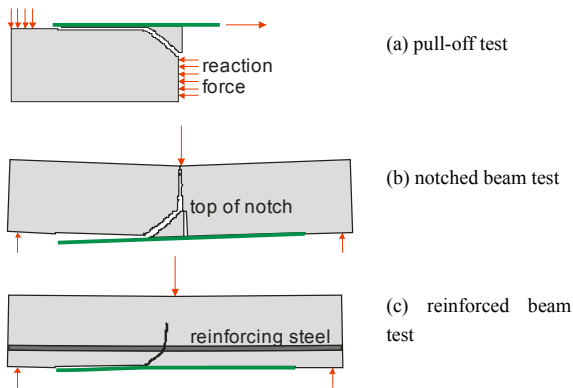


Figure 2 “Shear wedge” in various test arrangements

To produce the unbonded region, it is typically sufficient to simply tape the unbonded region (described as a length l_d extending either side of the notch) prior to FRP application. In the present work, some specimens were provided an unbonded region extending $l_d = 19$ mm to either side of the notch.

3 EXPERIMENTAL PROGRAM

As shown in Table 1, 27 beam tests having the geometry shown in Figure 1 were conducted. The concrete compressive strength was $f'_c = 36.1$ MPa. As determined from the control specimens, the modulus of rupture of the concrete was $0.86\sqrt{f'_c} = 5.2$ MPa. The preformed CFRP strip used had a thickness, $t_f = 1.4$ mm, $E_f = 155$ GPa and $f_{fu} = 2800$ MPa. The adhesive used had a tensile modulus and strength of 4480 MPa and 25 MPa, respectively; the modulus of rupture was 47 MPa and the shear strength was 25 MPa. The adhesive had a reported bond capacity is 22 MPa and the bondline was approximately 1 mm thick.

Table 1 Matrix of test specimens

b_f (mm)	b_f/b	t_n (mm); $d_n = 19$ mm					
		none	1.3	2.5	3.8	3.8 ¹	7.6
none	–	3	–	–	3	–	–
25	0.17	–	–	–	3	–	–
51	0.33	–	3	3	3	3	3
102	0.66	–	–	–	3	–	–

¹ initially unbonded specimens: $l_d = 19$ mm

As described previously, 19 mm deep notches were provided using steel shims inserted into the forms ($t_n = 1.3$ and 2.5 mm) and by saw cutting ($t_n = 3.8$ and 7.6 mm). Prior to CFRP installation, the notches were filled with expansive sprayed foam insulation and trimmed flush. Duct tape was used to provide a 19 mm unbonded region (l_d) on both sides of the 3.8 mm notch for the three specimens indicated in Table 1. The concrete substrates were mechanically abraded and cleaned with compressed air to expose the aggregate and remove any

laitance. The FRP strips were installed based on the manufacturer’s instructions. The adhesive was allowed to cure at room temperature for seven days prior to any further specimen preparation.

The tests were carried out in midspan bending over a 450 mm span (Figure 1). Loading was applied at a rate of approximately 90 N/sec, consistent with the requirements of ASTM C78 (2008).

4 RESULTS OF EXPERIMENTAL PROGRAM AND DISCUSSION

Test results in terms of the applied load and calculated CFRP strain at failure are presented in Table 2. The un-notched control specimens yield the modulus of rupture of the concrete to be $0.86\sqrt{f'_c} = 5.2$ MPa. A similar calculation based on the notched control beams yields $0.69\sqrt{f'_c} = 4.1$ MPa. The difference in these results reflects the stress intensifying effect of the notch. The capacity of the notched control specimen is the basis for the strength ratio, reflecting the increase in capacity resulting from the CFRP, given in Table 2.

Table 2 Test results

b_f (mm)	t_n (mm)	P (N)	ϵ_{fd} ($\mu\epsilon$)	σ_{bond} (MPa)	failure mode
none	none	26910	–	–	crack
none	3.8	16500	–	–	crack
25	3.8	27421	2890	3.30	debond
51	1.3	48020	2890	3.30	debond
51	2.5	53580	3320	3.79	debond
51	3.8	48080	2900	3.31	debond
51	3.8 ¹	54190	3370	3.85	debond
51	7.6	50080	3050	3.48	debond
102	3.8	68190	2180	2.49	shear

¹ $l_d = 19$ mm

Due to a computer malfunction, measured strain data was corrupted for all specimens. In this case, CFRP debonding strain (ϵ_{fd}) is estimated from a fibre section analysis at the failure load. The analysis was conducted using Program RESPONSE (Bentz 2000) assuming a modified parabolic stress strain relationship for the concrete (Bentz 2000) and a linear relationship for the CFRP. The estimated debonding strains are comparable to those reported elsewhere for similar CFRP/adhesive/concrete systems. For example, Harries et al. (2007) report $\epsilon_{fd} = 3550$ and 3200 $\mu\epsilon$ for large scale beams having 51 and 25 mm CFRP strips, respectively.

The apparent bond stress at failure shown in Table 2 is calculated assuming that CFRP stress spanning the notch is developed over a length equal to the ‘effective bond length’ of the CFRP, defined by Teng et al. (2003) as:

$$L_e = \sqrt{E_f t_f / \sqrt{f'_c}} = 190 \text{ mm in this study} \quad (1)$$

Thus, the apparent bond stress at failure reported in Table 2 is determined as $\sigma_{\text{bond}} = E_f \varepsilon_{fd} t_f / L_e$.

All specimens having $b_f = 25$ or 51 mm exhibited debonding failures. The specimens having $b_f = 102$ mm were over-strengthened to an extent beyond which their shear capacity was exceeded. Thus the results for these specimens reflect the shear capacity of the concrete specimen – found to be $0.25\sqrt{f'_c} = 1.5$ MPa.

4.1 FRP width

Within the parameters investigated, the FRP width does not appear to affect bond stress results. This result is inconsistent with previous research based on which one would expect the 25 mm strip to develop greater bond stress than the 51 mm strip. The stress intensifying effect of the notch may negate this expected behaviour to some extent.

Clearly, the 102 mm CFRP strip over-reinforces the beam resulting in the failure mode no longer being controlled by debonding. Thus the thinner strips are preferable although with different FRP materials the strip size leading to over-reinforcement will vary.

4.2 Notch width

In the present work, the notch width does not have a significant effect on the observed behaviour. Certainly the presence of the notch is important to serve as a location for the initiation of debonding, but the width itself is not important within reasonable bounds. Thus, from a practical perspective, saw cutting the notch with a normal concrete saw blade is acceptable practice.

4.3 Unbonded region

The apparent bond capacity is improved by providing an unbonded region (l_d) adjacent to the notch. In the context of the beam test, this increase can be partially explained by the fact that the unbonded region effectively ‘shifts’ the base of the ‘shear wedge’ (Figure 2b) away from the notch so that it must engage more concrete to form. However, such behaviour is not representative of *in situ* applications since there is no such unbonded region adjacent a crack in the concrete substrate. Additionally there is some concern with the unbonded region acting as a ‘crevice’ and affecting results of specimens subject to environmental condition. Thus it is proposed that the unbonded region is not necessary in a beam test such as that proposed here.

4.4 Derived results

In the present work, due to failure of strain data, it was necessary to estimate the CFRP strain at failure. In any application of the test it is necessary to estimate the apparent bond stress based on the effective bond length

(Eq. 1) which is an empirical formulation. Thus it is argued that this test method may be used as a basis for comparing comparable FRP systems or for assessing relative effects of environmental conditioning or other externality. Due to the use of derived results, however, the use of the proposed test method to directly obtain engineering design values must be approached with caution.

5 CONCLUSIONS

The results of the study reported here support the development of a standard test method for assessing FRP-to-concrete bond. The authors recommend the adoption of a test specimen a) as described in Figure 1; b) having a 51 mm wide FRP strip; and c) a sawcut notch 19 mm deep. The specimen satisfies the basic objectives for a universal test method and is well suited to studies requiring environmental exposure or accelerated aging conditioning.

REFERENCES

- ASTM 2008. C78-08 Standard Test Method for the Flexural Strength of Concrete, ASTM, West Conshohocken, PA.
- Bentz, E. 2000. RESPONSE-2000 RC Sectional Analysis using the Modified Compression Theory version 1.0.5.
- Harries, K.A., & Webb, P. 2009. Experimental Assessment of Bonded FRP-to-Steel Interfaces, *Proceedings of ICE: Structures and Buildings* 162(5): 233-240.
- Harries, K.A., Reeve, B. & Zorn, A. 2007. Experimental Evaluation of Factors Affecting the Monotonic and Fatigue Behavior of FRP-to-Concrete Bond, *ACI Structural Journal*, 104(6): 667-674.
- Oehlers, D.J. 2005. Generic Debonding Mechanisms in FRP Plated Beams and Slabs, *Proc. International Symposium on Bond Behaviour of FRP in Structures*: 35-44.
- Oehlers, D.J. & Seracino, R. 2004. *Design of FRP and Steel Plated RC Structures*, Elsevier, 228 pp.
- Ramanathan, K. & Harries, K.A. 2008. Influence of FRP Width-To-Concrete Substrate Width (b_f/b) on Bond Performance of Externally Bonded FRP Systems. *Proc. 12th International Conference on Structural Faults and Repair*.
- Teng, J.G., Smith, S.T., Yao, J. & Chen, J.F. 2003. Intermediate Crack Induced Debonding in RC Beams and Slabs, *Construction and Building Materials*, 17(6-7): 447-462.
- Thomsen, H., Spacone, E., Limkatanyu, S. & Camata, G. 2004. Failure Mode Analyses of Reinforced Concrete Beams Strengthened in Flexure with Externally Bonded Fiber-Reinforced Polymers, *Journal of Composites for Construction*, 8 (2): 123-131.

Examination of Interfacial Stresses due to Crack Propagation in FRP Retrofitted RC Beams

Mohammad Zaman Kabir (mzkabir@aut.ac.ir)

Department of Civil Engineering, Amirkabir University of Technology, Tehran, Iran
Center of Excellence for Retrofitting and Optimizing of Structures and Lifelines

Ata Hojatkashani (ata_hojat@aut.ac.ir)

Department of Civil Engineering, Amirkabir University of Technology, Tehran, Iran

ABSTRACT The present study investigates the stresses on the concrete substrate at the vicinity of the FRP fabrics. In this experimental research, 4 RC beams are prepared from which 2 beams are unstrengthened and 2 beams are strengthened with CFRP fabrics. Dimensions of the beams are 150mm×150mm×1000mm, and all of them are precracked at the middle section of the beam. The aim of the research is to identify the effect of the cracks on the stresses at the bond region between the FRP layer and the concrete substrate. An innovative experimental process is proposed in order to observe these stresses, which are critical parameters in debonding mode of failure in FRP retrofitted RC beams.

1 INTRODUCTION

The use of composite materials for strengthening of concrete structures has become a common practice in structural rehabilitation industry since last decade. Considering externally bonded Fiber Reinforcement Plastics (FRP), due to their high strength to weight ratio, easy installation and cost effectiveness, the use of them seems to be advantageous in repairing and retrofitting of RC beams. Therefore, high strength carbon, glass and aramid composites are being promoted as an alternative to steel plate. [American Concrete Institute(ACI) 1996; Toutanji & Gomez 1997]. Carbon-fiber reinforced polymers have been used extensively to strengthen reinforced concrete beams both in field and laboratory (Labossiere et al. 2000) From flexural tests on steel-to-concrete joints, as well as on composite-to- concrete joints, it was concluded that plate separation was due to high local interfacial bond stresses and peeling forces at the end of plates(Jones et al. 1980; Van Gemert 1980; Oehlers & Moran 1990; Considering the high tensile strength of adhesives, these stresses were found to depend on the tensile strength of the concrete (Triantafillou & Plevris 1992), the concrete surface preparation(Ziraba et al. 1995), and the strength and thickness of the adhesive(Quantrill et al. 1996b) .

2 EXPERIMENTAL

2.1 Properties

In the present research, 4 beams are prepared for the

monotonic testing. 2 beams are RC beams and the other 2 are retrofitted with CFRP, and the strengthening procedure is wet lay up. with two layer unidirectional CFRP sheets at the tension face of the concrete beam. Also, U wrap CFRP are implemented at the supports. The carbon fibers used are Sika Wrap-200C and the adhesive used for building the CFRP sheets and bonding them to the concrete substrate, is Sikadure-300 epoxy resin. The specifications of the carbon fiber, epoxy resin, and the produced CFRP sheet are presented in the following table.

Table 1 Mechanical properties of the CFRP composite

	Tensile Strength (MPa)	Tensile Modulus of Elasticity (MPa)	Failure Strain (%)
Fibers	3000	230000	1.5
Epoxy Resin	45	3500	1.5
CFRP Composite	500	73715	1.2

As mentioned, all the specimens were precracked at the middle section of the beam. The retrofitted specimens were strengthened with 2 layers CFRP at the tension face of the specimens. Also, U wraps were applied at the support. The schematic of the retrofitted RC beams is illustrated as the following. The notch dept in this figure is 2cm.

2.2 Test setup

The instrument used for the testing is the servo-hydraulic Dartec1900kN with the capacity of 1000kN.

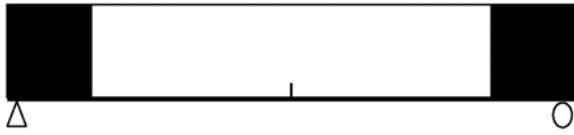
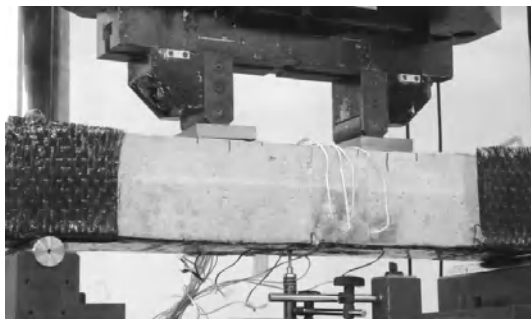


Figure 1 The schematic of the CFRP strengthened RC beam

The beams were tested under four point bending, and the mode of loading was displacement control with the rate of 0.005mm/s. The test setup is illustrated as below.



(a)



(b)

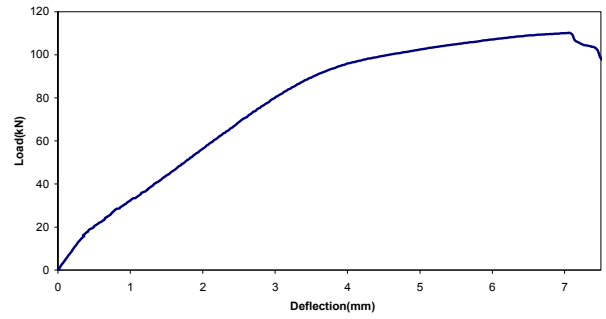
Figure 2 The four-point loading (a) the intact RC beam (b) the CFRP strengthened RC beam

3 RESULTS

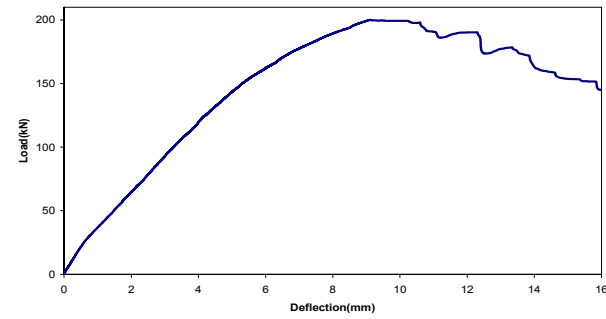
The results collected from the tests contained strains at the critical regions and the load-deflection diagrams.

The load carrying capacity of the plain RC beam was about 110kN, and that for the strengthened RC beam was increased up to about 200kN, which is about 80%. The load-deflection diagrams for both specimens are presented as below:

For both intact and retrofitted RC beams, the cracks pattern are shown in Figure 4. As can be seen in this figure, the cracks in the retrofitted RC beam are more than the intact one and they are distributed all along the beam. Also, at the location of the notch at the middle section of the beams, it is observed that the crack propagation for the retrofitted beam is smaller than the one for the intact beam. The mentioned results in Figure 4, show the difference between the retrofitted and the intact RC beams under four-point bending. The variation of the strain in the concrete portion at the top compression and bottom tension surfaces are illustrated and studied in details. Figure 5 shows the compression

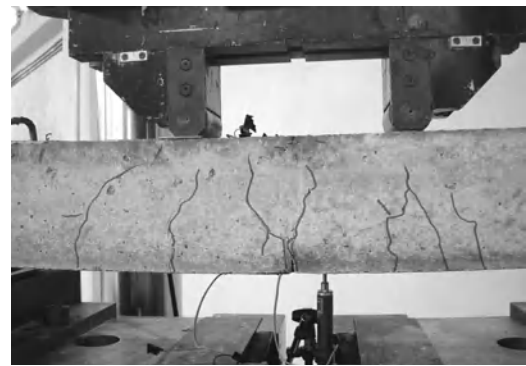


(a)



(b)

Figure 3 The Load-deflection diagrams under monotonic loading: (a) intact beam (b) strengthened beam



(a)



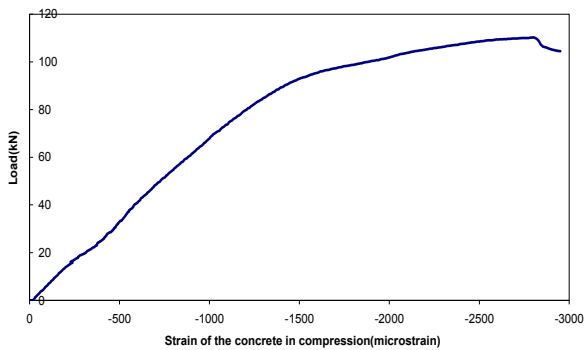
(b)

Figure 4 Crack pattern under four- point loading (a) intact (b) retrofitted

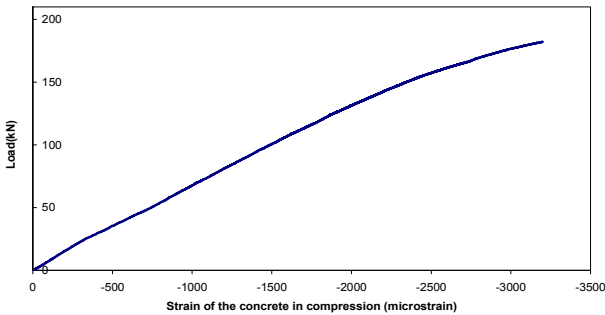
strains at the top surface of the concrete for both intact and retrofitted RC beam. The curve is almost linear for strengthened beam compare to intact one indicating the performance in elastic domain.

In the retrofitted specimens, according to the high tensile strength of the epoxy adhesive used, the probability of the debonding failure would be due to high stresses at the tension concrete at the vicinity of the CFRP plate. Thus, in order to observe these strains, strain gauges are placed at the mentioned location.

Figure 6 shows the location of mounted strain gauges in CFRP retrofitted RC beam. Channel 1 and 2 indicate the strain rosette at the tension zone about 130 mm far from the pre-cracked position. However, the channel 3 gives the information of strains at the middle part of the FRP sheet on the bottom tension surface.



(a)



(b)

Figure 5 Variation of measured strain in compression surface versus applied load (a) intact beam (b) CFRP strengthened beam

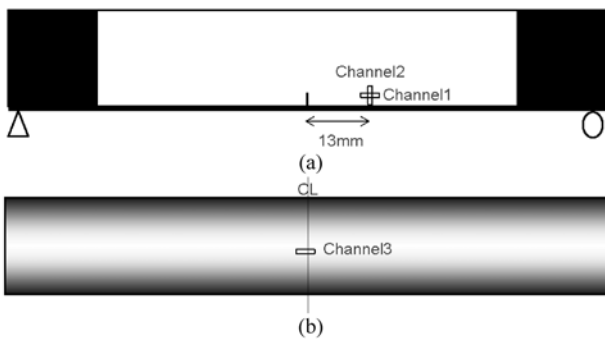
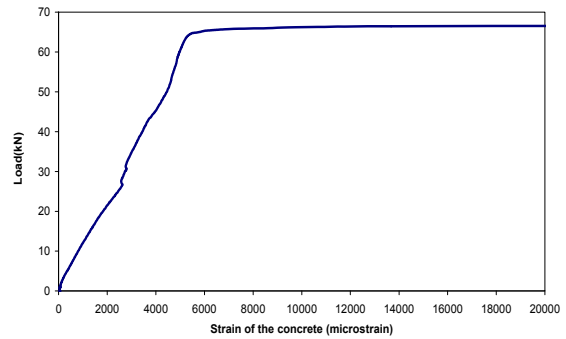


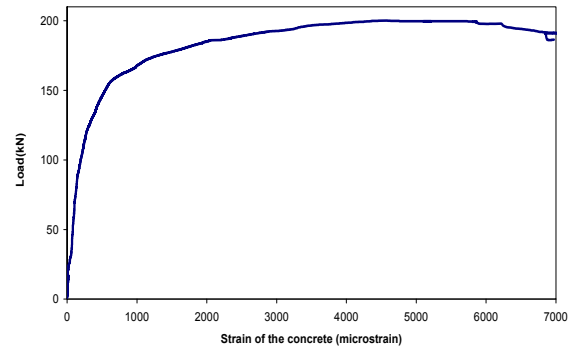
Figure 6 Position of strain gauges for the FRP strengthened RC beams on tension surface (a) Concrete bottom substrate: channels 1 and 2. (b) On the FRP sheet; channel 3

The channel 1 of rosette is 90°, see Figure 6a, shows the possible flexural cracking at the mentioned area,

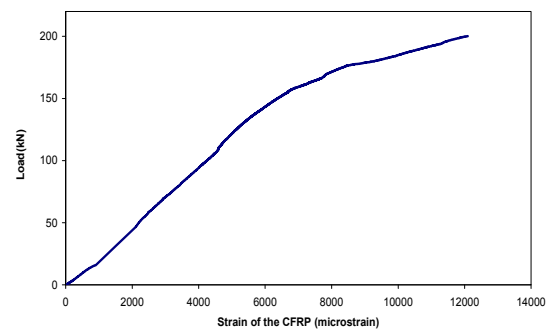
whereas the vertical gauge of this rosette, channel 2 as illustrated in Figure 6a, shows the possible CFRP-concrete substrate debonding failure due to the stresses beyond the concrete tensile strength which is the usual cause of the debonding failure mode in FRP strengthened RC structures. The variation of tensile strains versus loading is shown in Figure 7.



(a)



(b)



(c)

Figure 7 Applied load versus tensile strains: (a) channel 1, (b) channel 2, (c) on the FRP sheet, channel 3

It can be observed that in the CFRP strengthened RC beam, the strains on the concrete near the CFRP are considerably high so that the crack formation in both horizontal and vertical directions is inevitable. The applied load versus strains are shown in Figure 7. In Figure 7a, the applied load versus longitudinal strains measured by the strain gauge at the channel 1 shown in Figure 6, is illustrated. This strain is useful for the prediction of the possible flexural cracking at the location of the channel 1. In Figure 7b the remarkable

elongation of the CFRP sheet is observable. In Figure 7c, the applied load versus transverse strains measured by the strain gauge at the channel2 shown in Figure 6, is illustrated. This strain is useful for the prediction of the possible separation of the CFRP sheet from the concrete substrate due to the tensile stresses at the vicinity of the CFRP-concrete junction zone.

The failure modes of the test of the retrofitted beams were crushing of the compressive concrete, rupture of the CFRP sheet and debonding of the CFRP sheet from the concrete substrate. The failure modes were almost simultaneous. The failure is illustrated in the figure below.



Figure 8 Failure of the CFRP strengthened RC beams

4 CONCLUSIONS

In the present study, an investigation was made on the CFRP retrofitted RC beams. The following conclusion remarks can be drawn:

- Applying CFRP reinforcement sheet at the bottom tensile surface of RC beam under monotonic loading makes load deflection curve stronger for bearing of higher flexural loading and the variation of load deflection curve becomes linear in majority part. This phenomenon is much obvious for variation of compression strain versus applied load in CFRP retrofitted RC beam.

- Considering the monotonic loading as the primary stage, the crack formation was obliged into transverse direction at the bottom substrate.
- Due to the high tensile strength of the epoxy resins, the tensile stresses at the junction of the CFRP sheet to the concrete substrate are significant. The variation of such strains was monitored.

REFERENCES

- American Concrete Institute (ACI) Committee 440. (1996). State of the art report on fiber reinforced plastic reinforcement for concrete structures, Detroit.
- Toutanji, H., and Gomez, W. (1997). Durability of concrete beams externally bonded with FRP sheets in aggressive environments. *Cem. Concr. Compos.*, 19(4), 351-358.
- Labossiere P, Neale KW, Rochette P. Fiber reinforced polymer strengthening of the Saint-Emelie-de-l Energie Bridge: design, instrumentation, and field testing. *Can J Civil Eng* 2000; 27(5):916-927.
- Jones, R., Swamy, R.N. and Bouderbalah, A. (1980). Composite behavior of concrete beams with epoxy bonded external reinforcement. *Int. J. Cement Composites*, 2(2),91-107.
- Van Gemert, D.-A.(1980). Repairing of concrete structures by externally bonded steel plates. *Int. J. of Adhesion*, 2, 67-72.
- Oehlers, D. J., and Moran, J. P. (1990). Premature failure of externally plated reinforced concrete beams. *J. Struct. Engrg.*, 116(4),978-995.
- Triantafillou, T.C., and Plevris, N.(1992). Strengthening of RC beams with epoxy bonded fiber composite materials. *Mat. And Struct.*, 25, 201-211.
- Zibara, Y.N., Baluch, M.H. and Sharif, A.M.(1995). Combined experimental-numerical approach to the characterization of the steel-glue-concrete interface. *Mat. And Struct.*, 28, 518-525.
- Quantrill, R. J., Hollaway, L. C. and Thorne, A. M. (1996b). Prediction of the maximum plate and stresses of FRP strengthened beams: Part II. *Mag. Concrete Res.*, 48(177), 343-351.

A Rigorous Solution for Interfacial Stresses in Plated Beams

V. Narayanamurthy^{1,2}, J. F. Chen¹ (j.f.chen@ed.ac.uk) & J. Cairns²

¹ Institute for Infrastructure and Environment, The University of Edinburgh, Edinburgh, UK

² School of the Built Environment, Heriot Watt University, Edinburgh, UK

ABSTRACT A significant increase in the strength and performance of RC, timber and metallic beams can be achieved by bonding an FRP composite, steel or metallic plate on the tension face of a beam. One of the major failure modes in these plated beams is the premature debonding of the plate from the original beam in a brittle manner. This failure is often attributed to the interfacial shear and normal stresses developed between the adherends, which has led to the development of many analytical solutions over the last two decades. Most of the previous solutions have failed to include the effect of the adherend shear deformation due to difficulties in arriving at the exact solution, although a very few solutions have considered this effect in different approximate methods. The few solutions which included the effect of shear deformation of adherends are limited to one or two specific loading conditions. This paper presents a rigorous analytical solution for predicting the interfacial stresses in plated beams under an arbitrary loading with the axial, bending and shear deformations of the adherends considered simultaneously in closed form using Timoshenko's beam theory. The solution is applicable for any prismatic cross section with any linear elastic material for the adherends and thin or thick plates bonded either symmetrically or asymmetrically to the beam. The present solution is compared with previous analytical solutions.

1 INTRODUCTION

Any RC, concrete, metal or timber beam with a tension face soffit plate made of FRP composite or metal bonded using an adhesive is referred as a plated beam in this paper (Figure 1). This external plate enhances the strength and structural performance of the original beam. The technique of plating beams has gained wide acceptance and popularity in structural engineering for retrofitting and rehabilitation of existing structures. Under external loading on a plated beam, interfacial shear and normal stresses are generated in the adhesive layer between the adherends. The concentration of these stresses is high at the plate ends due to the presence of a geometric discontinuity. Their combination often leads to a premature debonding failure of the plate from the original beam in a brittle manner well before the full flexural strength of the plated beam is achieved.

Consequently, the interfacial stresses between the plate and the original beam have attracted a great interest in the last few decades and many analytical solutions have been developed to quantify them (Vilnay 1988, Roberts 1989, Roberts and Haji-Kazemi 1989, Liu and Zhu 1994, Taljsten 1997, Malek et al. 1998, Rabinovich and Frostig 2000, Smith and Teng 2001, Shen et al. 2001, Deng et al. 2004, Yang et al. 2004, Stratford and Cadei 2006, Narayanamurthy et al. 2010). Very few studies considered the effect of shear deformation of the adherends (Abdelouahed 2006, 2008,

Yang and Wu 2007 and Narayanamurthy et al. 2009), but this effect was considered in different approximate methods. The effect of shear deformation has been found to be considerable for plates made of FRP composites due to their low shear modulus as also in some other cases depending on the elastic modulus of the adhesive, thickness of the adhesive layer, thickness of the plate etc. (Tsai et al. 1998, Yang and Wu 2007).

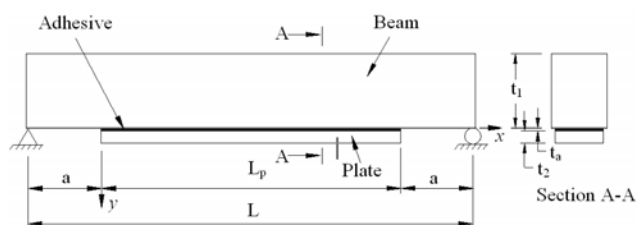


Figure 1 Plated beam

The objective of this research is to develop a rigorous solution considering the simultaneous effect of axial, bending and shear deformation of adherends in both interfacial stresses using Timoshenko's beam theory, and to solve the coupled governing differential equations of interfacial shear and normal stresses to obtain the general solutions by employing the appropriate conditions of the plated beam. The solution is based on the principle of superposition and deformation compatibility between the adherends, considering invariant stresses

through the adhesive layer. A comparison of the present solution with previous analytical solutions is given through an illustrative example to show the effect of shear deformation in adherends.

2 METHODOLOGY

Consider a simply supported beam symmetrically or asymmetrically strengthened with a soffit plate as in Figure 1. The plated beam under an arbitrary loading as shown in Case-1 (Figure 2) may be decomposed into Case-2 and Case-3. Case-2 includes all the external loading plus an axial force, a shear force and a bending moment at each end of the plate. The magnitude of these forces and moments are determined from the deformation of the un-plated beam so that both ends of the plate deform compatibly with the unplated beam under the external loading, and the case can be analysed using the classical composite beam analysis. Case-3 is the plated beam under the same but opposite plate end loading as in Case-2. The combined solution from Cases 2 and 3 gives the solution for the original problem in Case-1. In Figure 2, N , V and M are applied axial forces, shear forces and moments respectively on the beam, subscripts pl and pr refer respectively to the left and right plate ends.

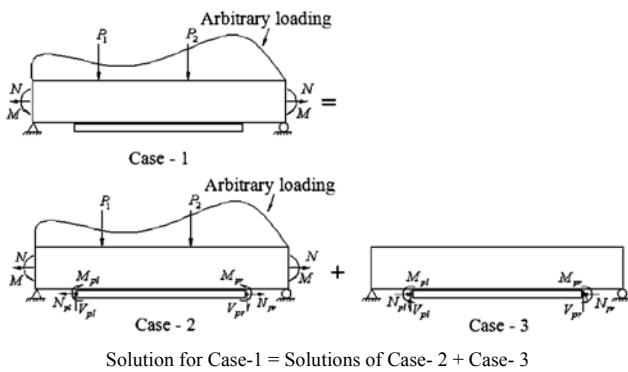


Figure 2 Principle of super position in the interfacial stress analysis of a plated beam

3 SOLUTION FOR CASE-2

The interfacial stress in Case-2 can be obtained from the classical composite beam theory. Considering a point in the adhesive layer at a distance y from the beam to adhesive interface (so y ranges from 0 to t_a within the adhesive). The shear stress at the considered position within the adhesive layer is

$$\tau(x, y) = m_c(y)V_{Tc}(x) \quad (1)$$

where $V_{Tc}(x)$ is the total shear force on the composite beam section at a distance of x from the left plate end due to all the loading in Case-2 (including the contribution from plate end loadings) and $m_c(y)$ is a function of the first and second moments of area of the equivalent composite beam section and breadth of

the plate.

The interfacial normal stress from this theory is negligible, i.e. $\sigma(x) \approx 0$.

4 SOLUTION FOR CASE-3

The governing differential equations (GDE) and general solutions for the interfacial shear and normal stresses between the adherends for Case-3 (Figure 2) are derived considering a differential segment of the plated beam with axial, bending and shear deformations in the adherends together with equilibrium and compatibility of deformations between the three layers of the beam (original beam, adhesive and plate). The GDE for the interfacial shear stress $\tau(x)$ is given by

$$\frac{d^2\tau(x)}{dx^2} - \lambda^2\tau(x) + m_1\lambda^2V_T(x) + \alpha_1\frac{d\sigma(x)}{dx} = 0 \quad (2)$$

The GDE for the interfacial normal stress $\sigma(x)$ is given by

$$\frac{d^4\sigma(x)}{dx^4} - \beta_1\frac{d^2\sigma(x)}{dx^2} + \beta_2\sigma(x) + n_2\frac{d\tau(x)}{dx} = 0 \quad (3)$$

These two governing equations are coupled and need to be uncoupled to find the general solutions for the interfacial stresses. The uncoupled GDE for the interfacial shear stress is given by

$$\frac{d^6\tau(x)}{dx^6} - \alpha_2\frac{d^4\tau(x)}{dx^4} + \alpha_3\frac{d^2\tau(x)}{dx^2} - \alpha_4\tau(x) + \alpha_5V_T(x) = 0 \quad (4)$$

where the parameters λ , m_1 , β_2 , n_2 account for the effects of flexural and axial deformations; α_1 and β_1 take care of the adherend shear deformations; and $\alpha_2 - \alpha_5$ are the functions of the above parameters.

The general solution for the GDE of the interfacial shear stress in Eq. 4 can have the following two forms depending on the parameter Δ ;

$$\Delta = \alpha_6^3 + \alpha_7^2 \quad (5)$$

$$\tau(x) = \begin{cases} B_1e^{\psi_1x} + B_2e^{-\psi_1x} + e^{-\psi_2x}(B_3\cos(\psi_3x) + B_4\sin(\psi_3x)) \\ + e^{\psi_2x}(B_5\cos(\psi_3x) + B_6\sin(\psi_3x)) + \alpha_{15}V_T \quad ; \Delta \geq 0 \end{cases} \quad (6)$$

and

$$\tau(x) = \begin{cases} B_7e^{\psi_4x} + B_8e^{-\psi_4x} + B_9e^{\psi_5x} + B_{10}e^{-\psi_5x} + B_{11}e^{\psi_6x} \\ + B_{12}e^{-\psi_6x} + \alpha_{17}V_T \quad ; \Delta < 0 \end{cases} \quad (7)$$

Applying boundary conditions in terms of axial forces, bending moments and shear forces in beam and plate at the plate ends leads to the formation of a system of simultaneous equations as given in Eqs 8-9 from which the constants of integration B_1 to B_{12} can be determined.

$$\begin{bmatrix} \psi_1 & -\psi_1 & -\psi_2 & \psi_3 & \psi_2 & \psi_3 \\ m_4 & m_4 & m_5 & -2\psi_2\psi_3 & m_5 & 2\psi_2\psi_3 \\ m_6 & -m_6 & m_7 & m_8 & -m_7 & m_8 \\ m_9 & -m_{10} & -m_{11} & m_{12} & m_{13} & m_{14} \\ m_{15} & m_{16} & m_{17} & m_{18} & m_{19} & m_{20} \\ m_{21} & -m_{22} & -m_{23} & m_{24} & -m_{25} & -m_{26} \end{bmatrix} \begin{bmatrix} B_1 \\ B_2 \\ B_3 \\ B_4 \\ B_5 \\ B_6 \end{bmatrix} = \begin{bmatrix} c_1 \\ c_2 \\ c_3 \\ c_4 \\ c_5 \\ c_6 \end{bmatrix} \quad (8)$$

$$\begin{bmatrix} \psi_4 & -\psi_4 & \psi_5 & -\psi_5 & \psi_6 & -\psi_6 \\ p_1 & p_1 & p_2 & p_2 & p_3 & p_3 \\ \psi_4 p_1 & -\psi_4 p_1 & \psi_5 p_2 & -\psi_5 p_2 & \psi_6 p_3 & -\psi_6 p_3 \\ p_4 & -p_5 & p_6 & -p_7 & p_8 & -p_9 \\ p_{10} & p_{11} & p_{12} & p_{13} & p_{14} & p_{15} \\ \psi_4 p_{10} & -\psi_4 p_{11} & \psi_5 p_{12} & -\psi_5 p_{13} & \psi_6 p_{14} & -\psi_6 p_{15} \end{bmatrix} \begin{bmatrix} B_7 \\ B_8 \\ B_9 \\ B_{10} \\ B_{11} \\ B_{12} \end{bmatrix} = \begin{bmatrix} c_1 \\ c_{2m} \\ c_3 \\ c_4 \\ c_{5m} \\ c_6 \end{bmatrix} \quad (9)$$

The general solution for the GDE of the interfacial normal stress given in Eq. 3 can have the following three forms depending on the parameter δ ;

$$\delta = 4\beta_2 - \beta_1^2 \quad (10)$$

$$\sigma(x) = e^{-\eta_1 x} [C_1 \cos(\eta_2 x) + C_2 \sin(\eta_2 x)] - n_3 \frac{d\tau(x)}{dx} \quad ; \delta > 0 \quad (11)$$

$$\sigma(x) = C_3 e^{-\eta_3 x} + C_4 e^{-\eta_4 x} + n_8 \frac{d\tau(x)}{dx} + n_9 \frac{d^3\tau(x)}{dx^3} \quad ; \delta < 0 \quad (12)$$

$$\sigma(x) = [C_5 + C_6 x] e^{-\eta_5 x} \quad ; \delta = 0 \quad (13)$$

where $C_1 - C_6$ are the constants of integration derived using the appropriate boundary conditions and are given as

$$C_1 = \frac{E_a}{t_a E_2 I_2} [R_b (n_4 V_{Tm} + n_5 M_1(0)) + n_5 M_{pl}] - n_{2m} n_4 \tau(0) - n_3 n_5 \left(\beta_1 \frac{d\tau(0)}{dx} - \frac{d^3\tau(0)}{dx^3} \right) - n_3 n_4 \left(\beta_1 \frac{d^2\tau(0)}{dx^2} - \frac{d^4\tau(0)}{dx^4} \right) \quad (14)$$

$$C_2 = \frac{E_a}{t_a E_2 I_2} [R_b (n_6 V_{Tm} - n_6 n_7 M_1(0)) - n_6 n_7 M_{pl}] - n_{2m} n_6 \tau(0) + n_3 n_6 n_7 \left(\beta_1 \frac{d\tau(0)}{dx} - \frac{d^3\tau(0)}{dx^3} \right) - n_3 n_6 \left(\beta_1 \frac{d^2\tau(0)}{dx^2} - \frac{d^4\tau(0)}{dx^4} \right) \quad (15)$$

$$C_3 = \frac{E_a n_{10}}{t_a E_2 I_2} \left(R_b \left[\frac{V_{Tm}}{\eta_4} + M_1(0) \right] + M_{pl} \right) - \frac{n_{2m} n_{10}}{\eta_4} \tau(0) + n_8 n_{10} \beta_1 \left(\frac{d\tau(0)}{dx} + \frac{1}{\eta_4} \frac{d^2\tau(0)}{dx^2} \right) + (n_9 \beta_1 - n_8) n_{10} \left(\frac{d^3\tau(0)}{dx^3} + \frac{1}{\eta_4} \frac{d^4\tau(0)}{dx^4} \right) \quad (16)$$

$$C_4 = \frac{E_a n_{11}}{t_a E_2 I_2} \left(R_b \left[\frac{V_{Tm}}{\eta_3} + M_1(0) \right] + M_{pl} \right) - \frac{n_{2m} n_{11}}{\eta_3} \tau(0) + n_8 n_{11} \beta_1 \left(\frac{d\tau(0)}{dx} + \frac{1}{\eta_3} \frac{d^2\tau(0)}{dx^2} \right) + (n_9 \beta_1 - n_8) n_{11} \left(\frac{d^3\tau(0)}{dx^3} + \frac{1}{\eta_3} \frac{d^4\tau(0)}{dx^4} \right) \quad (17)$$

$$C_5 = \frac{E_a n_{13}}{t_a E_2 I_2} \left(R_b [n_{12} V_{Tm} + M_1(0)] + M_{pl} \right) - n_{2m} n_{12} n_{13} \tau(0) \quad (18)$$

$$C_6 = \frac{(\eta_5^2 - \beta_1)}{2\eta_5} C_5 - \frac{E_a}{2\eta_5 t_a E_2 I_2} (R_b M_1(0) + M_{pl}) \quad (19)$$

The parameters $\alpha_6 - \alpha_7, \psi_1 - \psi_6, m_1 - m_{34}$ and $p_1 - p_{27}, \eta_1 - \eta_5, n_3 - n_{13}$ are influenced by the material and geometric properties of the adherends and adhesive and $c_1 - c_{12}$ are influenced additionally by the loading. The parameters E, G, A, I, b, t and V_T are the elastic modulus, shear modulus, cross sectional area, second moment of area about the centroid of the adherends, breadth, thickness and the total shear force in case-3 of the plated beam respectively; subscripts 1, a and 2 respectively refer to the original beam, adhesive and plate; y_1 and y_2 are the distances from the bottom of the original beam and the top of the plate to their respective centroids; and V_{Tm} is an expression related to V_T, V_{pl} and the bending stiffness ratio of plate to beam R_b .

5 SOLUTION FOR CASE-1

The solutions from Case-2 and 3 are combined to give the solution for the original problem in Case-1. The interfacial shear stress is given by

$$\tau(x, y) = \begin{cases} m_c(y) V_{Tc}(x) + B_1 e^{\psi_1 x} + B_2 e^{-\psi_1 x} + \\ e^{-\psi_2 x} (B_3 \cos(\psi_3 x) + B_4 \sin(\psi_3 x)) + \alpha_{15} V_T + \\ e^{\psi_2 x} (B_5 \cos(\psi_3 x) + B_6 \sin(\psi_3 x)) \quad ; \Delta \geq 0 \end{cases} \quad (20)$$

$$\tau(x, y) = \begin{cases} m_c(y) V_{Tc}(x) + B_7 e^{\psi_4 x} + B_8 e^{-\psi_4 x} + B_9 e^{\psi_5 x} + \\ B_{10} e^{-\psi_5 x} + B_{11} e^{\psi_6 x} + B_{12} e^{-\psi_6 x} + \alpha_{17} V_T \quad ; \Delta < 0 \end{cases} \quad (21)$$

The interfacial normal stress is given by Eqs 11, 12 or 13 depending on the value of δ in Eq. 10.

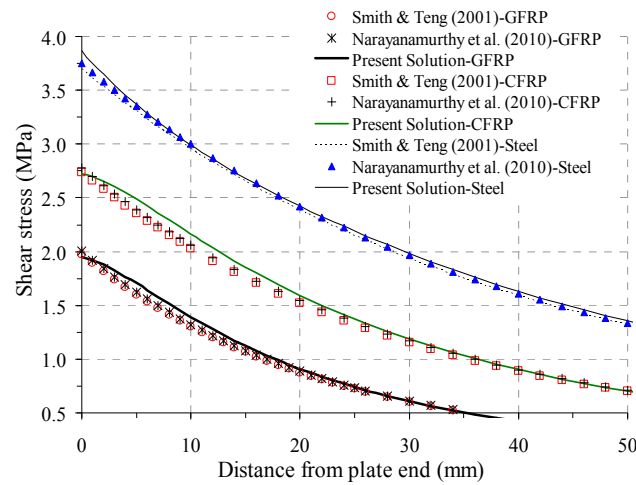
6 COMPARISON OF ANALYTICAL SOLUTIONS

A comparison of the interfacial stresses from the present and a number of the previous closed form solutions is carried out. A RC beam of rectangular cross section plated respectively with GFRP, CFRP composite and steel plate are taken as illustrative examples. This beam has already been analysed by previous researchers and the geometric and material properties listed in Table 1 are taken from Smith & Teng (2001). The beam is simply supported and subjected to an UDL of 50 kN/m.

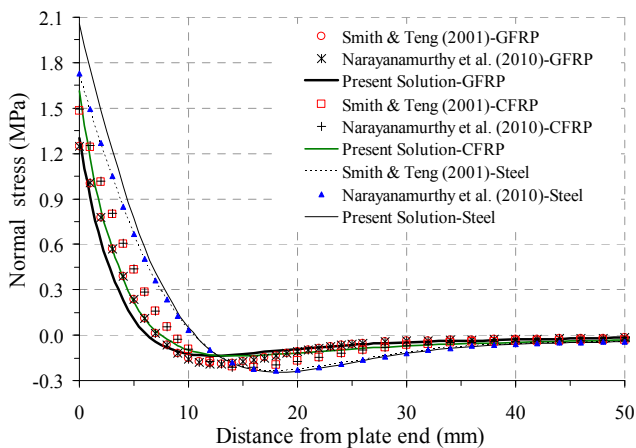
The peak interfacial stresses $\tau(x)$ and $\sigma(x)$ from different solutions are compared in Table 2. The closed form solutions of Smith & Teng (2001) and Narayanamurthy et al. (2010) are taken as reference solutions among all the previous solutions due to their reasonable accuracy in predicting the interfacial stresses and used for comparison with the present solution (Figure 3). For the GFRP and CFRP plated beams, the

Table 1 Geometric and material properties of plated beam

Component	Width (mm)	Depth (mm)	Length (mm)	Elastic Modulus (GPa)	Shear Modulus (GPa)
RC beam	200	300	3000	30	12.82
Adhesive	200	2	2400	2	0.74
GFRP plate	200	4	2400	50	3.50
CFRP plate	200	4	2400	100	3.80
Steel plate	200	4	2400	200	76.92



(a) Interfacial shear stress



(b) Interfacial normal stress

Figure 3 Comparison of analytical solutions for interfacial stresses in a plated RC beam subjected to an UDL

present solution predicts smaller peak $\tau(x)$ (2.4%) but higher peak $\sigma(x)$ (3.9% and 11.1% respectively) than the reference solution, but the difference becomes negligible after 30mm and 45 mm respectively away from the plate end. For the steel plated beam, the present solution predicts 2.4% and 18.3% higher $\tau(x)$ and $\sigma(x)$ respectively than the reference solution and the differences become insignificant after 10mm away from the plate end. The GFRP plate undergoes more shear deformation due to its lower shear rigidity compared to the CFRP plate. The steel plate has a very high shear stiffness so its rigidity

relative to the original beam is increased when the shear deformation of the both the beam and the plate is considered. The shear deformation can have a significant effect on the interfacial stresses when the geometric and material properties of the adherends and adhesive change.

Table 2 Peak interfacial stresses in a plated RC beam, in MPa

Theory	GFRP plated		CFRP plated		Steel plated	
	$\tau(x)$	$\sigma(x)$	$\tau(x)$	$\sigma(x)$	$\tau(x)$	$\sigma(x)$
Roberts & Haji-Kazemi (Solution-1)(1989)	2.001	1.425	2.776	1.668	3.745	1.902
Roberts & Haji-Kazemi (Solution-2) (1989)	1.813	1.256	2.591	1.500	3.567	1.733
Roberts (1989)	1.945	1.386	2.604	1.567	3.302	1.683
Malek et al. (1998)	1.943	1.384	2.597	1.563	3.287	1.675
Smith & Teng (2001)	1.975	1.244	2.740	1.484	3.696	1.714
Narayanamurthy et al. (2010)	2.002	1.249	2.778	1.495	3.748	1.729
Yang & Wu (2007)	1.955	1.227	2.684	1.472	3.592	1.695
Present	1.955	1.299	2.712	1.660	3.836	2.045

7 CONCLUSIONS

The concentration of interfacial stresses at the plate ends has been attributed to some of the premature debonding failures in plated beam. This paper has presented a rigorous analytical solution including the simultaneous effects of axial, bending and shear deformations in the adherends considering the plate and the original beam as two Timoshenko beams for the first time. The principal advantage of the solution is that it is applicable to any beam cross sections under any loading arrangement. An example plated beam has been analysed. The results have shown that the shear deformation in the adherends can have a small effect on both the interfacial normal and shear stresses at the plate ends but this effect can be significant for other geometric and material properties.

8 ACKNOWLEDGEMENTS

The University of Edinburgh and the Heriot-Watt University are thankfully acknowledged for providing the ERP-JRI fellowship to the first author.

REFERENCES

Abdelouahed, T. (2006). Improved theoretical solution for interfacial stresses in concrete beams strengthened with FRP plate. *International Journal of Solids and Structures*, 43, 4154-4174.

Malek, A.M., Saadatmanesh, H. and Ehsani, M. R. (1998). Prediction of failure load of RC beams strengthened with FRP plate due to stress concentration at the plate end. *ACI Structural Journal*, 95(1), 142-152.

Narayanamurthy, V., Chen, J. F. and Cairns, J. (2009). A solution for plated beam including shear deformation effect. *Proceedings of ACIC-09, Edinburgh, 1-3 Sept. 2009*.

Narayanamurthy, V., Chen, J. F. and Cairns, J. (2010). A general analytical method for the analysis of interfacial stresses in plated beams under arbitrary loading. *Advances in Structural Engineering*, in press.

- Roberts, T.M. (1989). Approximate analysis of shear and normal stress concentrations in the adhesive layer of plated RC beams. *The Structural Engineer*, 67(12), 229-233.
- Roberts, T.M. and Haji-Kazemi, H. (1989). Theoretical study of the behaviour of reinforced concrete beams strengthened by externally bonded steel plates. *Proceedings of the Institution of Civil Engineers*, 87(2), 39-55.
- Smith, S.T. and Teng, J.G. (2001). Interfacial stresses in plated beams. *Engineering Structures*, 23, 857-871.
- Taljsten, B. (1997). Strengthening of beams by plate bonding. *ASCE In. J. of Mat. in Civil Engineering*, 9(4), 206-212.
- Tsai, M.Y., Oplinger, D.W. and Mortson, J. (1998). Improved theoretical solutions for adhesive lap joints. *International Journal of Solids and Structures*, 35 (12), 1163-1185.
- Yang, J., Teng, J.G. and Chen, J.F. (2004). A high order closed-form solution for interfacial stresses in soffit plated RC beams under arbitrary loads. *ICE Proceedings: Structures and Buildings*, 157(SB1), 77-89.
- Yang, J. and Wu, Y.F. (2007). Interfacial stresses of FRP strengthened concrete beams: Effect of shear deformation. *Composite Structures*, 80, 343-351.

Evaluation of the Bond Behavior at the Intermediate Crack Element with a Special Test Procedure

Wolfgang Finckh (finckh@mb.bv.tum.de) & Konrad Zilch

Department of concrete structures, Technische Universität München, Germany

ABSTRACT The bond behavior of externally bonded reinforcement is one main parameter for the load bearing capacity of strengthened reinforced concrete structures. Because of the low bond force transfer at the outmost bending crack, the bond forces have also been transferred to elements between the cracks in order to effectively utilize the permissible stress of the CFRP strip. Two different experimental series on the bond behavior on the intermediate crack element were carried out. Small tests on an idealized intermediate crack element were made to evaluate the bond stress increase. In the second series parts of a structural element, which had the length of an intermediate crack element were tested to find out about other effects which only occur in the structural element. Based on these experimental data and the differential equation of the sway bond a new concept for the bond behavior of externally bonded reinforcement has been found out.

1 INTRODUCTION

The strengthening of existing structural elements is a frequently occurring problem to which one solution is the application of additional reinforcing. An established method for achieving this is the strengthening of the flexural resistance by gluing CFRP strips to the structure. However, the bond properties characterized mainly by the tensile strength of the surface concrete layers are very distinctive. The end anchorage checks that are commonly used in conventional reinforced concrete constructions are insufficient by themselves for structural elements with externally bonded CFRP strips. The high tensile capacity of the strips cannot be fully anchored in a single section. With externally bonded CFRP strips the tensile forces of the strip must be transferred to the concrete in various bond areas separated by cracks.

2 MECHANICAL BASED BOND MODEL

2.1 Principles

The bond of externally bonded CFRP-strips is treated by the procedure developed by Holzen-kämpfer (1994) who neglects any concrete deformations. The differential equation of a sway bond as shown in Equation 1 is described by the strip's slippage s_L , thickness t_L and elastic modulus E_L as well as the bond stress/slippage relationship $\tau(s_L)$. A serviceable approximation of the bond stress/slippage relationship for the idealized end anchorage experiment is the bilinear bond approach as shown in Figure 1. It consists of an initial elastic ascending curve and a plastic descending curve.

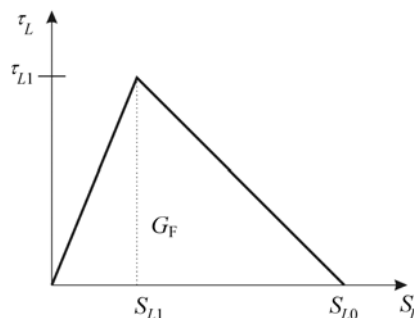


Figure 1 Bilinear bond stress to slippage relationship

$$s_L'' - \frac{1}{E_L \cdot t_L} \cdot \tau(s_L) = 0 \quad (1)$$

2.2 At the end anchorage

The parameters of the bilinear bond approach were determined by Zehetmaier (2006) out of end anchorage tests. From here the bond fracture energy for the mean values can be determined using Equation 2.

$$G_F = 0,046 \cdot \sqrt{f_{cm} \cdot f_{ctm,surf}} \quad (2)$$

By calculating back linearly the strip's maximum resisting stress at the idealized end anchorage can be determined using Equation 3.

$$\max \sigma_L = \sqrt{\frac{E_L \cdot 2 \cdot G_F}{t_L}} \quad (3)$$

When evaluating equation 3 it is apparent that the full tensile resistance – significantly higher than 2000 N/mm² for CFRP strips – cannot even be anchored.

2.3 At the intermediate crack element

For this very reason the end anchorage check commonly used in conventional reinforced concrete design is insufficient for structural elements with externally bonded reinforcement and additional checks are necessary. A more realistic bond check must be performed. This means that bond stresses must be verified at those points where they actually occur which in turn is only possible through a continuous check. A suitable approach is the bond check between flexural cracks at the aforementioned intermediate crack elements.

In this case Niedermeier (2001) solves the differential equation of the sway bond (Equation 1) using the bilinear bond approach according to Figure 1 for boundary values as they would apply for idealized elements between cracks.

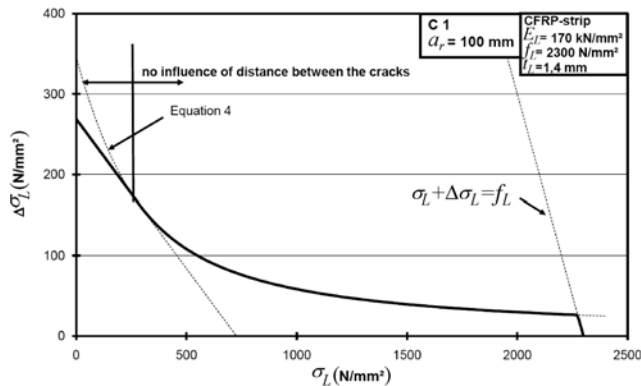


Figure 2 Bond force transfer at inter-crack elements for CFRP strips

The result is a relationship at the intermediate crack element that can be used to calculate the additional resisting stress for the strip in relationship to the base stress. This relationship is two-tiered. The first section has a lower base stress which is influenced by the length of the crack element. In the second section, however, the bond stress resistance is no longer affected by the length of the crack. Through linearization of the bilinear approach Niedermeier (2001) obtains the additional resisting stress in the strip $\Delta\sigma_L$ for section 2 (Equation 4) which only depends on the bond fracture energy and the strip characteristics.

$$aufn.\Delta\sigma_L = \sqrt{\frac{2 \cdot G_F \cdot E_L}{t_L} + \sigma_L^2} - \sigma_L \quad (4)$$

For conventional CFRP strips and typical crack distances the crack distance is negligible, so we must only look at part 2. Additionally the tensile strength of the CFRP strip limits the strip's resisting stress through bonding. Figure 3 shows a representation of this relationship for a typical CFRP strip and a typical length of an intermediate crack element.

3 MATERIALS

The experimental investigation was performed with the same concrete, the same EBR system and the same steel reinforcement as in Finckh and Zilch (2010).

4 BOND TEST ON THE IDEALIZED ICE

4.1 Conception

In order to verify the relation on the intermediate crack element empirically, Thorenfeld (2003) Schilde (2005) and Zilch et. al (2010) performed tests on an idealized intermediate crack element with a schematic set-up as shown in Figure 3. In this experiment, CFRP strips are applied to both sides of a concrete specimen. On either side differing forces are applied until the CFRP strip detaches completely. From every force-controlled test one can then enter a value into the diagram shown in Figure 4.

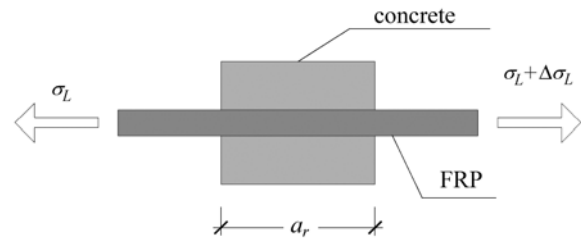


Figure 3 Test on an idealized intermediate crack element

Using different force differentials yields results for different sections in the curve. In the various tests and test series the element length, concrete strength and load levels differ. There are also differences in concept. In the tests made by Zilch et al. (2010) it was ensured that the loading history of the tests based on a proportional control of the forces corresponded to the loading history of the specimen. Table 1 shows the conducted tests on the idealized intermediate crack in dependence of the length of the intermediate crack element, the load ratio and the concrete mixture. All tests were performed with the strengthening System EBR1 from Finckh and Zilch (2010). On every side of the intermediate crack element the strain of strip and the deformation to the concrete was measured. This is needed for a back calculation with differential equation of a sway bond.

Table 1 Tests conducted on the idealized intermediate crack element

Length*	200		300	
	Load ratio**	3-1.5	1.5-1	3-1.5
C1	7	14	1	5
C2	2	3	-	1

* Distance between the cracks

** Ratio between σ_L and $\sigma_L + \Delta\sigma_L$

4.2 Results

For all test series a significantly higher level was achieved than the simplified theoretical approach would predict. This can be traced to the friction effect between the bond fracture surfaces that form even before the bond completely fails which is not included in the bilinear bond approach. This bond friction results from the jagged grain of the rough fracture surfaces which normally run through the concrete surface layer and can reach a maximum depth corresponding to the maximum grain diameter of the concrete. The test results of the single tests are plotted together with the simplified theoretical approach in Figure 4.

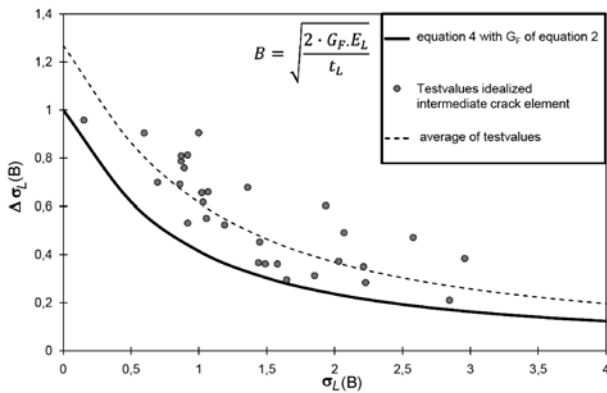


Figure 4 Result of the test on idealized intermediate crack element

5 TESTS FOR THE INTER-CRACK ELEMENT ON A STRUCTURAL ELEMENT

5.1 Conception

Aside from the currently disregarded friction effect, there are other effects acting on the structural element that are generally favourable. In order to investigate these effects in more detail Zilch et. al (2010) performed tests on the intermediate crack element on a structural element. This test set-up (shown in Figure 5) always tests different parts of the beam while on the remainder a bond break-up is prevented by actively pressing onto the strip. Through measurements of the strip strain the uncoupling of the bond may then be observed. At that point where the difference between the strip strain and both sides of the crack drops the strip starts to uncouple. The uncoupling can also be shown through an increase in the sway between strip and concrete which in the tests was determined by optical deformation measurements.

This set-up has the advantage that on a single beam several experiments with varying ratios of shear and bending can be performed so that the proportions of base stress and additional stress increase also differ. The test parameters and number of test conducted on one beam are listed in Table 2. The material properties can

be found in Finckh and Zilch (2010).

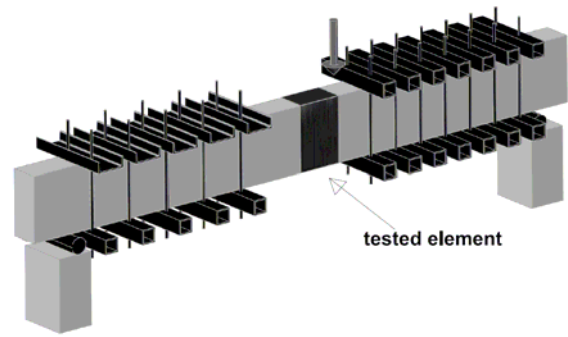


Figure 5 Test set-up for intermediate crack elements on a structural element

Table 2 Tests conducted on the intermediate crack elements on a structural element

Name*	C	TR	FRP	CS	PT
BT-S-1	C1	2xD16	1xEBR1	450x200	3
BT-S-2	C1	2xD16	1xEBR1	450x200	3
BT-B-1	C1	4xD10	1xEBR2	200x500	3
BT-B-2	C1	4xD10	1xEBR2	200x500	3

* Name: C: Concrete mixture; TR: tensile reinforcement FRP: strengthening reinforcement; CS: Cross section (height x width); PT: Preformed tests

5.2 Results

In the experiments there was a significant increase in the bond force compared to both the current approach and the previously described tests on the idealized flat intermediate crack element. The strip stresses from the structural element tests and from the approach based on Figure 1 are shown in Figure 6 alongside the mean values of the intermediate crack element tests. Figure 6 also shows that thinner structural elements act more favourably than thicker ones. This shows the positive effect of the larger deflection curvature. It is also evident in the much lower values for the pre-bent slab. The positive effect of the curvature can also be observed in tests on other structural elements. This curvature creates a self-induced contact pressure comparable to the contact

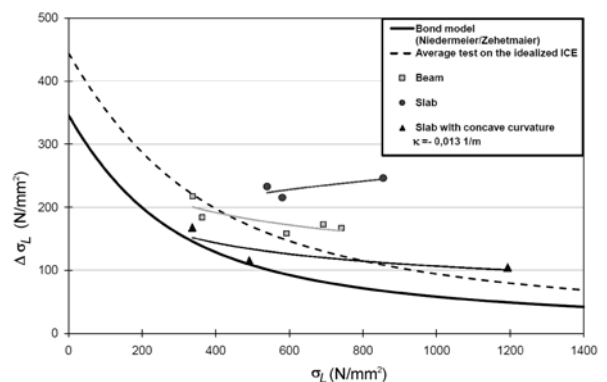


Figure 6 Comparison of the test results on the structural element and the inter-crack element

pressure that Husemann (2009) shows when bracing the CFRP strips by gluing stirrups around them.

6 NEW BOND MODEL

To describe the increase in bond force due to self-induced contact pressure this effect should be incorporated directly into the bond equations. Thus the effects from curvatures and additional friction effects must be introduced into the bond stress/slippage relationship as shown in Figure 7. The bond energy at the inter-crack element on the structure is composed of the bond energy from the bilinear bond approach (G_F) which was determined using end anchorage bonding tests, a bond friction from the grain interlock at the idealized inter-crack element ($G_{FF,ICE}$) as well as the increased bond energy resulting from the structural element's curvature ($G_{FF(\kappa)}$)

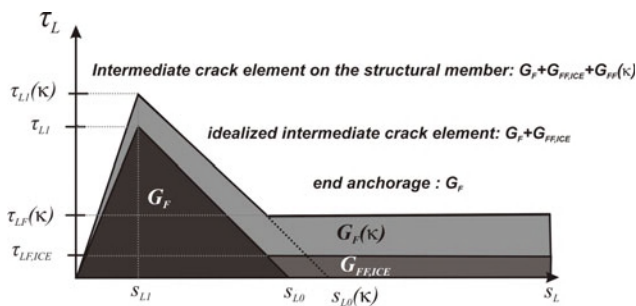


Figure 7 Bond fracture energy at the inter-crack element in relation to the curvature

When entering this bond stress/slippage relationship into the differential equation of the sway bond one obtains a system of three coupled differential equations. These can be solved individually by using the boundary conditions of the intermediate crack element but the resulting system of equations no longer offers a closed description for the resisting strain of the strip due to the bond at the intermediate crack element. The individual parameters of the bond stress/slippage relationship can be determined from deformations seen in the tests when considering the interaction with the curvature. Based on the following parameter study a simplified check is then created.

7 CONCLUSION

Through the combination of end anchorage tests with the tests on the idealized intermediate crack element tests and the test on the intermediate crack element on the structural element a bond model can be created that

takes all possible effects into account.

The end anchorage tests are needed to determine the basic value of the bond and the tests on the idealized intermediate crack element are needed to determine the bond friction.

With the test on the intermediate crack elements on a structural element it is possible to evaluate the effects of the curvature.

8 ACKNOWLEDGEMENTS

The authors would like to thank the Bundesamt für Bauwesen und Raumordnung for the research funding within the scope of the research project “practical design approaches for an economic strengthening of concrete structural elements with adhesive reinforcements” of the Deutscher Ausschuss für Stahlbeton. Further thanks go to the companies Bilfinger Berger AG, Laumer Bautechnik GmbH, Ludwig Freytag GmbH & Co. KG, MC-Bauchemie Müller GmbH & Co. KG, S&P Clever Reinforcement Company AG, Sika Deutschland GmbH, and Stocretec GmbH.

REFERENCES

- Holzenträger P. (1994): Ingenieurmodelle des Verbunds geklebter Bewehrung für Betonbauteile, Dissertation, TU-Braunschweig
- Husemann U. (2009): Erhöhung der Verbundtragfähigkeit von nachträglich aufgeklebten Lamellen durch Bügelumschließungen, Dissertation, TU-Braunschweig
- Finckh W., Zilch K. (2010): Shear capacity of flexural strengthened reinforced concrete structures with CFRP materials, CICE 2010
- Niedermeier R. (2001): Zugkraftdeckung bei klebarmierten Bauteilen, Dissertation, Technische Universität München
- Thorenfeld E. (2002): Anchor capacity of tension loaded CFRP plates bonded to concrete, in Bond in Concrete – From Research to Standards, Proceedings, Budapest, Budapest University of Technology and Economics, November 2002, S 638-647
- Schilde K. (2005): Untersuchungen zum Verbund zwischen Beton und nachträglich aufgeklebten CFK-Lamellen am Zwischenrisselement, Dissertation, Universität Kassel
- Zehetmaier G. (2006): Zusammenwirken einbetonierter Bewehrung mit Klebarmierung bei verstärkten Betonbauteilen, Dissertation, Technische Universität München
- Zilch K. Finckh W. Niedermeier R. (2010): Praxisgerechte Bemessungsansätze für das wirtschaftliche Verstärken von Betonbauteilen mit geklebter Bewehrung – Verbundtragfähigkeit unter statischer Belastung, DAFStb-Heft 592, Beuth Verlag, Berlin

Numerical Modeling of the FRP/Concrete Interfacial Behavior of FRP Shear-Strengthened Beams

Ahmed Godat, Pierre Labossière & Kenneth W. Neale (Kenneth.Neale@USherbrooke.ca)

Département de génie civil, Université de Sherbrooke, Sherbrooke, Canada

ABSTRACT In this paper, we compare the validity of two approaches to simulate the FRP/concrete interfacial behavior of FRP shear-strengthened beams. In the first approach, the FRP/concrete interfacial behavior is modeled with two-dimensional interface elements. These elements are provided in directions parallel and perpendicular to fibers orientation. In this case, the bond-slip behavior between concrete and FRP is established on the basis of experimental results obtained from shear-lap specimens. In the second approach, the slip between concrete and FRP is simulated by one-directional truss elements aligned in a discrete manner. In this case, the bond-slip model of the FRP/concrete interface is a bilinear relationship. The accuracy of each approach to simulate the FRP/concrete interfacial behavior is investigated by comparing them with experimental results. The significance of both approaches is discussed.

1 INTRODUCTION

The success of a finite element model to simulate the behavior of FRP shear-strengthened beams depends on the approach used to simulate the FRP/concrete interfacial behavior. This behavior is very important because debonding of FRP sheets bonded to external faces of a reinforced concrete beam can be a critical failure mode. Unfortunately, the debonding phenomenon is very difficult to measure in experimentally because the position of the critical shear crack is unknown a priori and because the failure process is fast and brittle. With finite element modeling, it is possible to investigate the initiation of debonding and its propagation between the FRP and concrete.

In this paper, the validity of two approaches to simulate the FRP/concrete interfacial behavior of FRP shear-strengthened beams is compared. To evaluate both methods, a three-dimensional finite element model was developed to simulate the behavior of FRP shear-strengthened beams. In the first approach, the DIANA finite element package was used. This analysis was performed by Lee (2003). The FRP/concrete interfacial behavior was modeled with two-dimensional interface elements were provided in directions parallel and perpendicular to fiber orientation. In this case, the bond-slip behavior between the concrete and FRP sheets was established on the basis of experimental results obtained from shear-lap specimens (Lee 2003). In the second approach, the slip between the concrete and FRP was simulated by two-node unidirectional truss elements aligned in a discrete manner. The discontinuities

of the discrete truss elements allow each truss to fluctuate from negative to positive stresses depending on their location from the shear crack. For this method, the bond-slip model of the interface between the concrete and FRP was a bilinear bond-slip relationship proposed by Lu et al. (2005). This bond-slip model represents the overall FRP/concrete interfacial behavior. The ADINA finite element software was used for this approach. The main details of this method are described in Godat et al. (2007).

The accuracy of each approach to simulate the FRP/concrete interfacial behavior is investigated by comparing them with experimental results published by Lee (2003).

2 NUMERICAL MODELING

The beams investigated in this study were externally strengthened in shear with U-wrap CFRP strips, with fibers oriented in the vertical direction. The details of the material and geometrical modeling of concrete, longitudinal and transverse steel, FRP strips, and FRP/concrete interfacial behavior are summarized below for the two methods investigated.

2.1 Modeling with two-dimensional interface elements

For this approach, the DIANA finite element package was employed. Three-dimensional 8-node solid brick elements (HX24L) with three degrees of freedom were employed to model concrete. Steel reinforcing bars were modeled by 3-nodes truss elements, which were connected directly to the concrete nodes. The CFRP plates were simulated using 4-node quadrilateral isoperimetric plane

stress element (Q8MEM). The FRP/concrete interfacial behavior was modeled with two-dimensional interface elements (L8IF), as shown in Figure 1. These elements were provided in directions parallel and perpendicular to the beam axis.

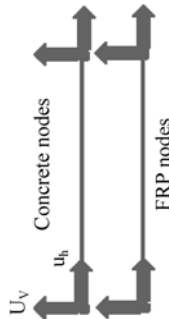


Figure 1 Two-dimensional interface elements (Lee 2003)

The DIANA concrete model follows the implementation of modified compression field theory by Vecchio and Collins (1986). The model represents concrete cracking with a smeared fixed-crack approach and can simulate the post-peak response of concrete. The concrete constitutive model is fully defined in compression and in tension. Both the hardening and softening behavior of the concrete in compression are described by the function of Thorenfeldt et al. (1987). Concrete tension stiffening in the analysis and the nonlinear descending portion of the tensile stress-strain curve is based on mode-I fracture energy.

For the internal steel reinforcement for the beams, a uni-axial isotropic linear elastic material up to the yield point was employed. This accurate since failure of FRP shear-strengthened beams usually occurs without yielding. An orthotropic linear elastic relationship was adopted for the CFRP. The bond-slip behavior between concrete and CFRP was based on experimental results from shear-lap specimens and is shown in Figure 2. In addition, to simulate the peeling off failure of the concrete layer immediately below the CFRP strips, a fine mesh was used for the concrete layer found between the outer surface and the transverse steel.

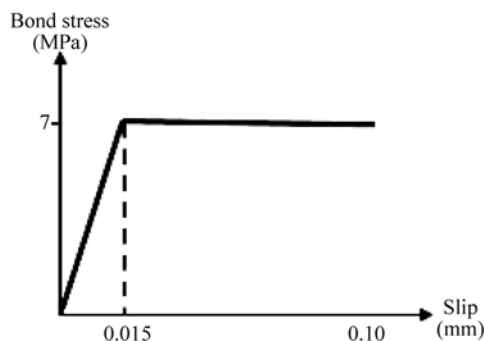


Figure 2 The bond-slip model for 2-D interface elements (Lee 2003)

2.2 Modeling with unidirectional interface elements

The ADINA finite element software (2005) was used for the second approach. Three-dimensional brick elements with three degrees of freedom per node were used to discretize the concrete. The steel reinforcement embedded in the concrete was represented by 3-node truss elements. Since experimental observations usually indicate a perfect bond between steel reinforcement and the surrounding concrete, no interface elements were required along the steel-concrete interface. Shell elements were used to model the CFRP strips and their orthotropic nature was accounted for in the constitutive relations corresponding to fiber orientations.

To represent the bond-slip between concrete and CFRP, unidirectional truss elements aligned in a discrete manner were employed, as shown in Figure 3. The interface elements were arranged parallel to the fiber orientation and full strain compatibility was assumed in the other directions. Each interface element connected the CFRP nodes and the corresponding concrete nodes; the interface elements were totally independent from each other. The discontinuities of the discrete truss elements allowed the stresses in the interface elements to fluctuate from negative to positive depending on their location from shear crack. The difference in displacement between corresponding nodes of concrete and CFRP represents the slip at the interface. It is necessary to emphasize that these link elements do not directly represent the adhesive. They represent the overall concrete/FRP interfacial response, which depends on the concrete, the FRP, as well as the adhesive. The details of the implementation of this approach are provided in Godat et al. (2007).

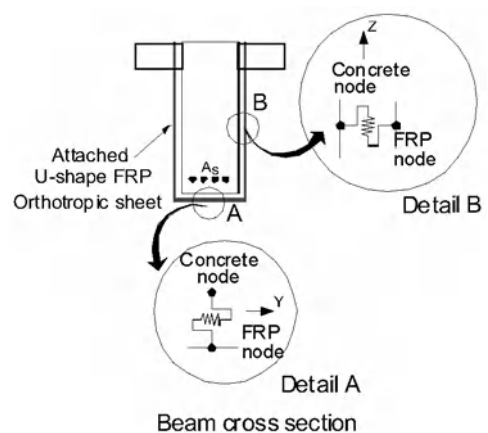


Figure 3 The discrete truss element approach

The constitutive law used to model the concrete is based on an elastic nonlinear stress-strain relation. It utilizes failure envelopes that define both failure in either tension by cracking or compression by crushing. It also features a strategy to model the post-cracking and post-crushing behavior of the material. The tensile

behavior of concrete takes into account cracking, shear modulus degradation, fracture energy and tension stiffening. Tension stiffening is modeled as a linearly descending branch in the stress–strain relationship after the peak point at which concrete has cracked.

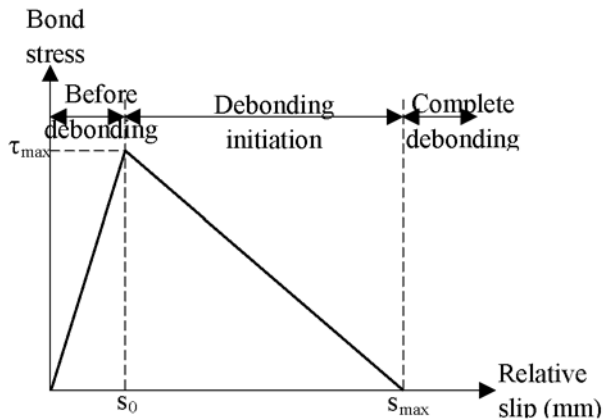


Figure 4 The bond–slip model for unidirectional interface elements (Lu et al. 2005)

Steel reinforcement was represented by an elastic-plastic constitutive relation with linear strain hardening. The ratio between the slopes in the elastic range to the plastic range was taken from 100 to 200. A linear elastic tensile model until failure was assumed to represent the CFRP strips. The bilinear bond–slip model developed by Lu et al. (2005) was incorporated into the finite element model (Figure 4). In this model, the behavior of the FRP/concrete interface is simulated by a bilinear relationship between the bond stress, τ , and the relative slip, s .

3 SPECIMENS INVESTIGATED

In order to validate the accuracy of the numerical models, the beams tested by Lee and Al-Mahaidi (2008) were considered. Their experimental program included four full-scale RC-beams with a T-shaped cross-section. The dimensions of the T-beams were based on the Kiewa Valley Highway Bridge located in the north-east of Victoria, Australia (Lee 2003). Three of these beams were shear-strengthened with CFRP L-shape laminates at various spacing, while the fourth was kept as a reference beam. For the strengthened specimens, the 40 mm wide CFRP strips were spaced at 0.75D, 0.6D and 0.5D centre-to-centre, where D is the overall depth of the beam. The cross section dimension of these specimens is shown in Figure 5. The U-wrap CFRP strips were extended through the flange up to the top face. This was accomplished through rectangular holes drilled at the flange corresponding to the locations of the CFRP strips. The specimens were loaded under four point loading, and the shear span to effective depth ratio was 3.0.

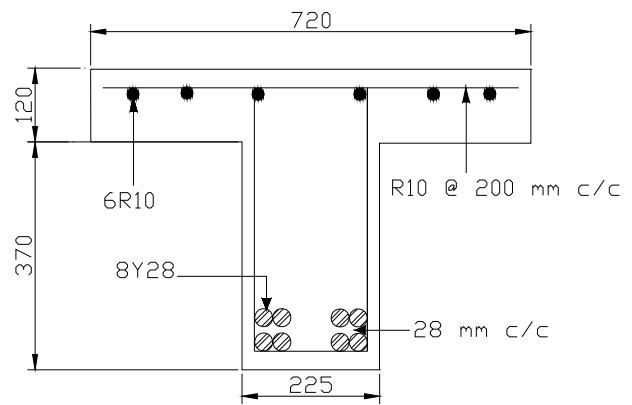


Figure 5 Specimen cross-section

4 NUMERICAL RESULTS

The comparison between the two approaches is presented in terms of load–deflection relationships, and failure modes. For both numerical approaches, the nonlinear load–deformation behavior of the structure was simulated under displacement-controlled loading conditions, as was the case for the laboratory experiments. In view of the geometrical and loading symmetries, only one quarter of the beam was simulated. In this paper, the results of the control specimen and one specimen strengthened with U-wrap CFRP strips spaced at 0.75D are presented in Figures 6 and 7, respectively.

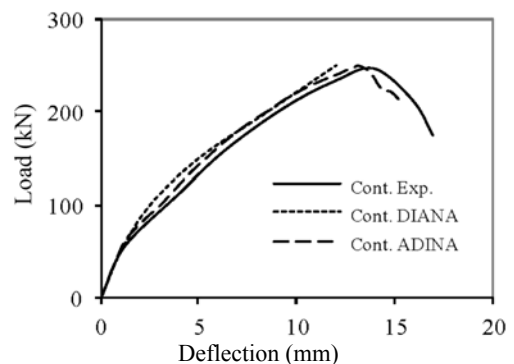


Figure 6 Load–deflection relationships for the control specimen

Before cracking of the control specimen, both finite element approaches exhibit similar behavior compared to the experimental results, as shown in Figure 6. Small discrepancies in the load–deflection curves are observed in the cracking zone. The deflection values corresponding to the maximum load-carrying capacity are 13mm and 14mm for the first and second approaches, respectively, while that measured experimentally was 11.5mm. The load-carrying capacity predicted by the two numerical approaches is essentially identical to the experimental results. Failure of the control specimen obtained by the two numerical models is dominated by concrete crushing; it is the same as what was observed experimentally.

For the CFRP strengthened specimen, the CFRP strips were embedded into the flange to reduce debonding. In

the first modeling approach, full strain compatibility was assumed between the CFRP strips and the concrete along the depth of the flange. In the second modeling approach, the CFRP strips are stopped at the top of the web of the beam. At this location, full contact bond is assumed between the concrete and CFRP strips.

From Figure 7, it can be observed that the responses of the numerical models are similar to their respective experimental curve before cracking. When cracks occur, it can be seen that the numerical methods slightly overestimated the stiffness of the load–deflection curve. The first approach predicts load carrying capacity 10% higher than the experimental value. The deflection corresponds to the maximum load is identical to the experimental one. The second approach estimates ultimate load carrying capacity higher than the experimental value by 6%. Besides, the deflection is higher than the experiments by 5%.

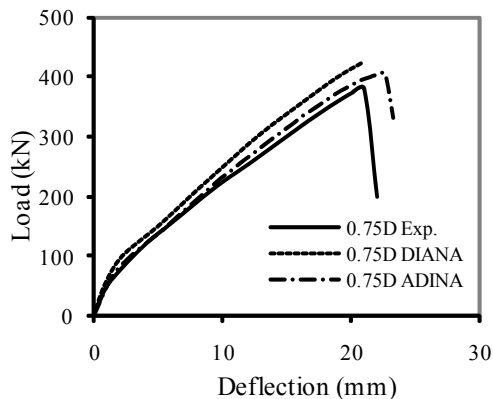


Figure 7 Load–deflection relationships for the strengthened specimen

For the CFRP-strengthened specimens, it is important to mention that the first numerical approach is not able to capture similar failure mode as that observed experimentally. In fact, the failure mode reported experimentally was debonding of the CFRP strips, while concrete crushing is obtained numerically. By contrast, the second numerical approach can predict typical failure mode as that observed experimentally. In addition, the second approach is able to show similar debonding progress as that in the experiment.

5 CONCLUSIONS

This study examined the accuracy of two numerical approaches to simulate the FRP/concrete interfacial behavior of FRP shear-strengthened beams. The first approach employed two-dimensional interface elements with bond–slip behavior established on basis of experimental results of shear-lap specimens. In the second approach, one-directional discrete truss elements with a bilinear bond–slip model were employed. Although, both numerical approaches were able to predict load–deflection relationships close to the experimental ones, the first numerical approach could not identify the failure mode reported experimentally. By contrast, the second numerical approach was able to predict the typical failure modes observed in the experiments.

REFERENCES

- ADINA 2005. *Automatic dynamic incremental nonlinear analysis*. Finite element software, version 8.3, ADINA R&D Inc. Watertown: MA.
- DIANA 2000. *DIANA release 7.2*. Division of engineering mechanics and information technology, TNO building and construction research. Delft: Netherlands.
- Godat, A., Neale, K.W. & Labossière, P. 2007. Numerical modeling of FRP shear-strengthened reinforced concrete beams. *Journal of Composites for Construction* 11(6): 640-649.
- Lee, T.K. & Al-Mahaidi, R. 2008. An experimental investigation on shear behaviour of RC T-beams strengthened with CFRP using photogrammetry. *Composite Structures* 82(2):185-193.
- Lee, T.K. 2003. *Shear strengthening of reinforced concrete T-beams strengthened using carbon fibre reinforced polymer (CFRP) laminates*. M.Sc. thesis, department of civil engineering, Monash University. Victoria: Australia.
- Lu, X.Z., Teng, J.G., Ye, L.P., & Jiang, J.J. 2005. Bond–slip models for FRP sheets/plates bonded to concrete. *Engineering Structures* 27(6): 920-937.
- Thorenfeldt, E., Tomaszewics, A. & Jensen, J.J. 1987. Mechanical properties of high-strength concrete and application in design. *Utilization of high strength concrete; Proc. int. symp.* Stavanger: Norway.
- Vecchio, F. & Collins, M. 1986. The modified compression field theory for reinforced concrete elements subjected to shear. *ACI Structural Journal* 83(2): 219-231.

Analysis of Interfacial Bond Stress of Bonding Anchors for FRP Tendon

Qilin Zhao, Fei Li (lifei609@163.com), Haosen Chen

Engineering Institute of Engineer Corps, PLA University of Science and Technology, Nanjing 210007, China

ABSTRACT An analytic interfacial bonding stress solution of bonding anchors for FRP tendon, loaded by axial force, is studied in this article. Based on the assumptions and differential equations of force equilibrium, the distribution of shear stress through the thickness of the anchors is derived, the calculating formula of interfacial bonding Stress is obtained. The presented calculating formula agrees well with the result of finite element analysis (FEA). Furthermore, based on the analytic solution, the factors affecting the distribution of interfacial bonding stress are discussed, including elastic modulus of material and geometry parameters.

1 INTRODUCTION

To the bond anchor for FRP tendon, many researchers focus on measuring the interfacial bond stress distribution and ultimate tensile strength etc by experiment. The research suggests: the bond anchors transfer the load by interfacial shear stress, the shear failure of tendon material close to or within the anchorage zone is most common mode of failure, this failure is induced mainly by the anchorage geometry and the degree of stress concentration exerted by the anchorage on the tendon. this mode of failure decreases greatly the efficiency of transfer load^{[1][2][3]} Therefore, the research on distribution of bond stress and how to decrease the degree of concentration stress are very important. The experimental research is basic and essential; However, using a great deal of experiment to optimize and develop anchorage systems is too expensive and time-consuming. In the field of analytic theory, However the recent analysis not only simplify the columned anchors to the plate problem^{[4][5]}, but also the effect of grouted material and steel tube to interfacial bond stress are not considered. In this paper, considering the effect of grouted material and steel tube, according to the cylindrical coordinate, the distribution of the shear stress through the thickness of anchors was derived; The calculating formula of interfacial bond Stress of grouted material, FRP tendon and steel tube was obtained.

2 ANALYTIC SOLUTION OF INTERFACIAL BOND STRESS

As shown in Figure 1, the bond anchor loaded by axial force is comprised of FRP tendon, steel tube and grouted material.

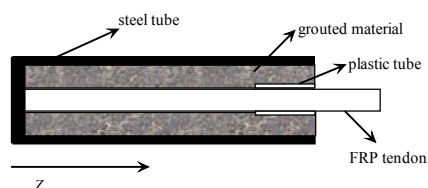


Figure 1 FRP tendon anchor loaded axial force

In the of analysis process of shear stress, the assumptions are taken as follows:

- (1) The steel tube, grouted material and FRP tendon keep linear elastic;
- (2) The tensile stress of FRP tendon and steel tube are uniformly distributed in thickness direction;
- (3) The change of shear stress of grouted material is considered in the thickness direction;
- (4) The effect of the circumferential stress and normal stress are ignored.

Based on the assumptions, the calculating model can be obtained, as shown in Figure 2.

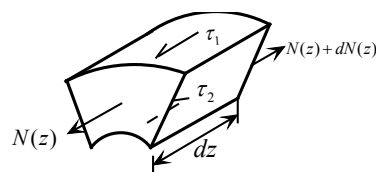


Figure 2 Calculating model

The equilibrium of the element can be written as:

$$\frac{dN_g(z)}{dz} = \tau_1(z)R_2 - \tau_2(z)R_3 \quad (1)$$

Where $N_g(z)$ is the axial force which is loaded in the unit radian of grouted material; R_3 and R_2 is the inner and outer radius of grouted material; $\tau_1(z)$ is the bond stress between steel tube and grouted material; $\tau_2(z)$ is the bond stress between FRP tendon and grouted material.

Based on assumption 2, we can get:

$$\frac{d\sigma_g(z)}{dz} = \frac{dN_g(z)}{(R_2 - R_3)dz} = \frac{\tau_1(z)R_2 - \tau_2(z)R_3}{R_2 - R_3} \quad (2)$$

Substituting equation (2) into differential equations of force equilibrium:

$$\frac{\partial \tau_g}{\partial r} + \frac{\tau_g}{r} + \frac{\partial \sigma_z}{\partial z} = 0 \quad (3)$$

Yield:

$$\tau_g(r, z) = -\frac{\tau_1(z)R_2 - \tau_2(z)R_3}{2(R_2 - R_3)} \cdot r - \frac{c}{r} \quad (4)$$

Where $\tau_g(r, z)$ is the shear stress of grouted material;

$$\tau_g(r = R_3, z) = -\tau_1 \quad (5)$$

Through equation (5), we can get the shear stress of grouted material:

$$\tau_g(r, z) = \frac{\tau_2 R_3 - \tau_1 \cdot R_2}{R_2 - R_3} \cdot r - \frac{\tau_1 R_2}{r} - \frac{\tau_2 R_3 - \tau_1 \cdot R_2}{2(R_2 - R_3)} \frac{R_2^2}{r} \quad (6)$$

We also can get the shear stress of steel tube and FRP tendon:

$$\tau_s(r, z) = \frac{\tau_1(z) \cdot R_2}{2(R_1 - R_2)} \cdot r - \frac{\tau_1 R_2}{r} - \frac{\tau_1 R_2^3}{2(R_1 - R_2)} \frac{1}{r} \quad (7)$$

$$\tau_p(r, z) = -\frac{\tau_2}{2R_3} \cdot r \quad (8)$$

Where $\tau_s(r, z)$ is the shear stress of steel tube; $\tau_p(r, z)$ is the shear stress of FRP tendon; R_1 is the outer radius of steel tube.

The shear stress of steel tendon can be expressed as:

$$\tau_s(r, z) = G_s \gamma_s(r, z) \approx G_s \frac{\partial U_s(r, z)}{\partial z} \quad (9)$$

Where G_s is the shear modulus of steel tube; $\tau_s(r, z)$ is the shear strain of FRP tendon; $U_s(r, z)$ is the displacement along the direction of Z of steel tube.

Through equation (7) and equation (9), the displacement between grouted material and steel tube can be written as:

$$U_s(r = R_2, z) = U_s(r = (R_2 + R_1)/2, z) - \frac{1}{G_s} \frac{1}{16} \tau_1 R_2 (R_1 + 3R_2) - \frac{1}{G_s} \ln \left(\frac{2R_2}{R_1 + R_2} \right) \left(R_2 \tau_1 + \frac{R_2^3 \tau_1}{2(R_1 - R_2)} \right) \quad (10)$$

The displacement between grouted material and FRP tendon also can be written as:

$$U_p(r = R_3, z) = U_p(r = 0, z) - \frac{3\tau_2 R_3}{16G_p} \quad (11)$$

Meantime, the interfacial displacement also can be expressed by the displacement of grouted material:

$$U_g(r = R_2, z) = U_g(r = (R_2 + R_3)/2, z) + \frac{1}{G_g} \left[\frac{\tau_2 R_3 - \tau_1 \cdot R_2}{8} \left(\frac{3R_2 + R_3}{2} \right) + \tau_1 R_2 \ln \left(\frac{R_2 + R_3}{2R_2} \right) + \frac{\tau_2 R_3 - \tau_1 \cdot R_2}{2(R_2 - R_3)} R_2^2 \ln \left(\frac{R_2 + R_3}{2R_2} \right) \right] \quad (12)$$

$$U_g(r = R_3, z) = U_g(r = (R_2 + R_3)/2, z) - \frac{1}{G_g} \left[\frac{\tau_2 R_3 - \tau_1 \cdot R_2}{16} [R_2 + 3R_3] + \tau_1 R_2 \ln \left(\frac{2R_2}{R_2 + R_3} \right) + \frac{\tau_2 R_3 - \tau_1 \cdot R_2}{2(R_1 - R_2)} R_2^2 \ln \left(\frac{2R_2}{R_2 + R_3} \right) \right] \quad (13)$$

Because of the same deformation, equation (10) equals to equation (12), equation (11) equals to equation (13)

$$U_s(r = R_2, z) = U_g(r = R_2, z) \quad (14)$$

$$U_p(r = R_3, z) = U_g(r = R_3, z) \quad (15)$$

The tensile strain of steel tube, FRP tendon and grouted material can be written as:

$$\frac{dU_s \left(z, r = \left(\frac{R_1 + R_2}{2} \right) \right)}{dz} = \varepsilon_s = \frac{N_s(z)}{E_s t_s} \quad (16)$$

$$\frac{dU_p(z, r = 0)}{dz} = \varepsilon_p = \frac{N_p(z)}{E_p t_p} \quad (17)$$

$$\frac{dU_g(z, r = (R_2 + R_3)/2)}{dz} = \varepsilon_g = \frac{N_g(z)}{E_g t_g} \quad (18)$$

Through equation (7) and equation (16) (17) (18), we can get:

$$U_s \left(z, r = \left(\frac{R_1 + R_2}{2} \right) \right) = \frac{N_s(z)}{E_s t_s} = \iint \frac{-\tau_1(z) R_2}{((R_1 + R_2)/2)^2 (R_1 - R_2) E_s} dz \quad (19)$$

$$U_p \left(z, r = \left(\frac{R_1 + R_2}{2} \right) \right) = \iint \frac{2\tau_2(z) R_2}{E_p \cdot R_3^2} dz \quad (20)$$

$$U_g \left(z, r = \left(\frac{R_3 + R_2}{2} \right) \right) = \frac{N_g(z)}{E_g t_g} = \iint \frac{\tau_1 \cdot R_2 - \tau_2 R_3}{E_g \left(\frac{R_3 + R_2}{2} \right)^2 (R_2 - R_3)} dz \quad (21)$$

The conditions of equilibrium of grouted material are:

$$U_{\text{上}} - U_{\text{下}} = \iint 2 \frac{R_2 \tau_1 - \tau_2 R_3}{E_g (R_2^2 - R_3^2)} dz \quad (22)$$

$$\tau_1 = \frac{N}{2\pi R_2} \frac{\lambda_1}{1 - ch(\lambda_1 l)} sh(\lambda_1 z) \quad (23)$$

$$\tau_2 = \frac{N}{4\pi R_3} \frac{\lambda_2}{1 - sh(\lambda_2 l)} ch(\lambda_2 z) \quad (24)$$

Based on associated boundary conditions: $x=0$, $N_s(x)=0$, $N_p(x)=0$; $x=1$, $N_s(x)=N/2$, $N_p(x)=N/2$. The interfacial bonding stress of grouted material-FRP tendon, and grouted material-steel tube can be obtained:

Where: $A=R_1-R_2$, $B=R_2-R_3$, $C=R_1+R_2$, $D=R_2+R_3$

$$\lambda_1^2 = \frac{\left(\frac{4R_3}{E_g AB^2} R_3 / R_2 - \frac{4R_2}{E_s AC^2} - \frac{4R_2}{E_g AB^2} \right) \left(\frac{4R_3}{E_g AB^2} \left(\frac{E_g}{4G_g} R_3 BD + \frac{E_g}{G_g} R_3 R_2^2 \ln \frac{R_3}{R_2} \right) / R_3 + \frac{1}{8G_g D} (R_3 + 3R_2) R_3 + \ln \left(\frac{D}{2R_2} \right) \frac{R_2^2 R_3}{BD} \right)}{\left(\frac{1}{8G_g D} (R_3 + 3R_2) R_3 + \ln \left(\frac{D}{2R_2} \right) \frac{R_2^2 R_3}{BD} + \frac{4R_3}{E_g AB^2} * \frac{E_g}{4G_g} R_3 BD + \frac{E_g}{G_g} R_3 R_2^2 \ln \frac{R_3}{R_2} / R_3 \right)}$$

$$\lambda_2^2 = \frac{\left(\left(-\frac{4R_2}{E_s AC^2} - \frac{4R_2}{E_g AB^2} \right) R_3 / R_2 + \frac{4R_3}{E_g AB^2} \right) \left(-\frac{1}{8G_g C} (R_1 + 3R_2) R_2 + \ln \left(\frac{2R_2}{C} \right) \left(R_2 + \frac{R_2^3}{AC} \right) / G_s + \frac{1}{8G_g D} (R_3 + 3R_2) R_2 + \ln \left(\frac{D}{2R_2} \right) \left(\frac{R_2}{BD} - R_2 \right) / G_g \right)}{\left(-\frac{1}{8G_g C} (R_1 + 3R_2) R_2 + \ln \left(\frac{2R_2}{C} \right) \left(R_2 + \frac{R_2^3}{AC} \right) / G_s + \frac{1}{8G_g D} (R_3 + 3R_2) R_2 + \ln \left(\frac{D}{2R_2} \right) \left(\frac{R_2}{BD} - R_2 \right) / G_g + \ln \left(\frac{D}{2R_2} \right) \frac{R_2^2 R_3}{BD} + \frac{4R_3}{E_g AB^2} * \frac{E_g}{4G_g} R_3 BD \right)}$$

3 EXAMPLE AND ANALYSIS

A bond anchor is shown in Figure 1, the elastic modulus of steel tube is $E_s = 210\text{GPa}$; the elastic modulus of grouted material is $E_g = 5.4\text{GPa}$; the elastic modulus of FRP tendon is $E_p = 45\text{GPa}$ (along the fiber direction); and the associated dimensions are as follows: $l=150\text{mm}$, $R_1=15\text{mm}$, $R_2=10\text{mm}$, $R_3=5\text{mm}$. In this section, a three-dimensional finite element method is employed to determine the bonding stress of the example, where the element solid45 is used. The numerical results of shear stress in the adhesive Layer obtained by the finite element method are compared with the analytical solution, Equation (23) (24) derived in Section 2. The comparison presented in Figure 3, 4 are shown. From these results one can observe: The results agree well in overall, the maximum bonding stress in the analytical Solution is higher 8% than in the finite element analysis.

4 PARAMETRIC STUDY

After deducing the analytical formulation of bonding stress, the factors affecting the maximal bonding stress are discussed. Based on equation (23), (24), two factors are studied. They are: E_g/E_p (the ratio of elastic modulus of grouted material and FRP tendon), R_2/R_3 (the ratio of radius of grouted material and FRP tendon). where E_g/E_p represent the effect of the material properties on the maximum of bonding stress, while R_2/R_3 represent the effect of the geometrical properties.

(1) E_g/E_p (the ratio of elastic modulus of grouted material and FRP tendon) changes, while other factors remain constant. As shown in Figure 5 with the ratio of modulus increasing, the maximum of bonding stress τ_1 and τ_2 increase. In detail, the maximum of bonding stress between steel tube and grouted material τ_1 increase by 58%, and the maximum of bonding stress between FRP tendon and grouted material τ_2 increase by

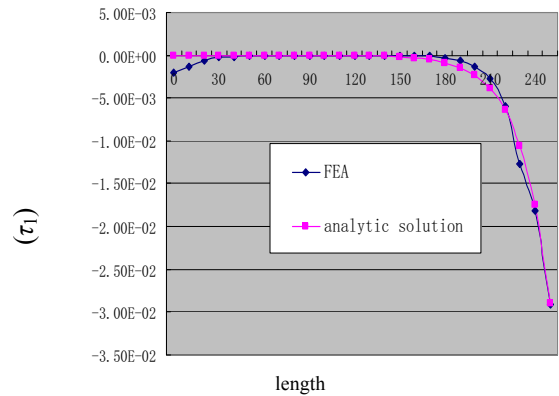


Figure 3 The distribution of τ_1 along length

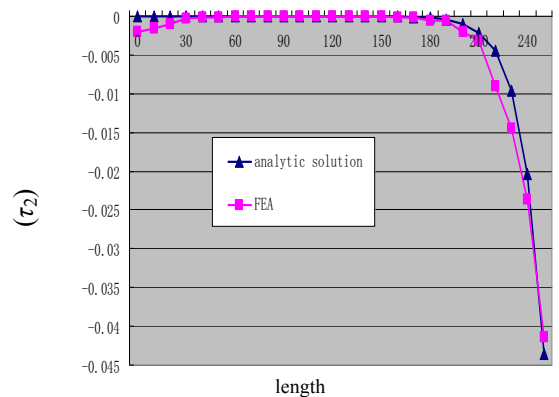


Figure 4 The distribution of τ_2 along length

15%, when the ratio change from 1 to 5. This is why decreasing the modulus of the grouted material can reduce the stress concentration, this factor is primary importance.

(2) R_2/R_3 (the ratio of radius of grouted material and FRP tendon) changes, while other factors remain constant. As shown in Figure 6 with the ratio increasing, the bonding stress decreases. In detail, the maximum of bond stress between steel tube and grouted material τ_1 increase by

100%, and the maximum of bonding stress between FRP tendon and grouted material τ_2 increase by 88% when the ratio change from 0.2 to 1.8. It means: increasing the radius of the grouted material can reduce the stress concentration, so this factor is primary importance.

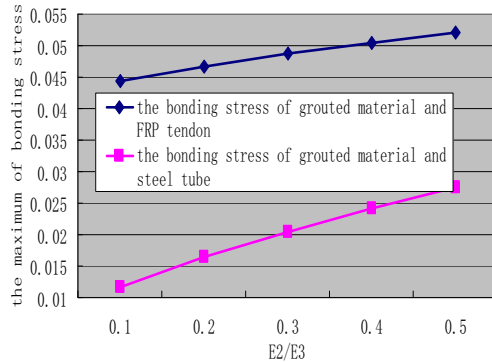


Figure 5 Influential factor E_g/E_p

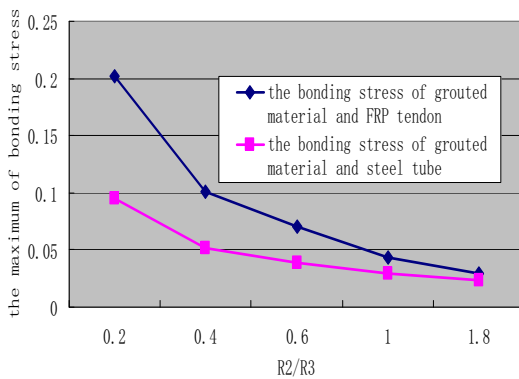


Figure 6 Influential factor R_2/R_3

5 CONCLUSION

In this paper, the calculating formula of interfacial bonding Stress is obtained. And the presented calculating formula

agrees well with the result of finite element analysis (FEA), this proves that: this calculating model is reliable. Furthermore, based on the analytic solution, two factors affecting the distribution of interfacial bonding stress are discussed, including elastic modulus of material and geometry parameters. it is indicated that: the primary factors are the ratio of elastic modulus of grouted material and FRP tendon and the ratio of radius of grouted material and FRP tendon, thickening the grouted material or reducing the elastic modulus can depress the stress concentration.

REFERENCE

- W.C. Tang, T.Y. Lo and R.V. 2008. Bond performance of polystyrene aggregate concrete (PAC) reinforced with glass-fibre-reinforced polymer (GFRP) bars. *Building and Environment*.43(1):98-107.
- READ, M., SAYED-AHMED, E. Y., and SHRIVE, N. G. Toward a new nonmetallic anchorage system for post-tensioned application with carbon fibre reinforced plastic and tendons. *Proceeding of 42 International SAMPE Symposium and Exhibition*, 42 (1):288-297.
- Burong Zhang, Brahim Benmokrane, Adil Chennouf, et al. 2001. Behavior of FRP Tendons for Prestressed Ground Anchors. *Journal of Composites for Construction*, 5(2):85-93.
- Brahim Benmokrane, Burong Zhan, Adil, Chennouf. 2000. Bond Properties and Pullout Behavior of AFRP and CFRP Rods for Grouted Anchor Applications. *Construction and Building Materials*, 14(3):157-170.
- Burong Zhang, Brahim Benmokrane. 2002. Bond Properties of Fiber Reinforced Polymer Tendons to Grout. *Journal of Materials in Civil Engineering*, 14(5): 399-408.

Debonding Behavior of Skew FRP-Bonded Concrete Joints

J. G. Dai (cejgdai@polyu.edu.hk) & Y. B. Cao

Department of Civil and Structural Engineering, The Hong Kong Polytechnic University, Hong Kong, China

ABSTRACT In fibre reinforced polymer (FRP) shear-strengthened RC beams, the fiber orientation in FRP may not coincide with the crack opening direction of concrete (the pullout direction of FRP). FRP under such a stress condition is hereafter termed “skew FRP”. The issue of how to predict the bond strength between a concrete substrate and a skew FRP remains unsolved. This paper presents both experimental and predicted results on the pullout strength of FRP in a series of skew FRP-bonded concrete joints, in which the angle between the fibre orientation and the pullout direction of FRP varied from 0° to 45°. Both FRP plates and FRP sheets were used in the tests. It was found that the above-mentioned angle influences significantly the pullout strength of FRP, in other words, the debonding stress of fibers, due to the skew effects existing in the bond interface. Such effects should be appropriately considered particularly when evaluating the shear contribution of FRP in FRP shear-strengthened RC beams.

1 INTRODUCTION

Debonding of fiber reinforced polymer (FRP) is a dominating failure mode in FRP flexurally and shear-strengthened reinforced concrete (RC) members. In the past decade extensive research has been conducted on the debonding mechanisms of FRP-to-concrete interfaces based on an assumption that the fiber orientation of FRP coincides with the pullout direction of FRP (e.g. Chen and Teng, 2001; Dai et al. 2005). This assumption has been widely adopted because of the anisotropic nature of FRP materials. When they are applied for structural strengthening their fiber orientations are usually arranged in coincidence with the direction (e.g. perpendicular to a concrete crack) of pull-out force that they are expected to bear, so as to take full advantage of their tensile stiffness and strength. However, in some cases, such as in FRP-shear strengthened of RC beams, the fiber orientation of FRP usually may not be perpendicular to a potential shear crack (see Figure 1). FRPs subjected to such a stress condition are hereafter termed “skew FRPs”. Very little research has been conducted to investigate the debonding behavior of skew FRP-bonded concrete joints.

In an FRP-shear strengthened RC beam the following equation has been widely adopted to evaluate the shear contribution of FRP following the traditional truss analogy (see Figure 1):

$$V_{frp} = 2 f_{frp,e} t_{frp} w_{frp} \frac{h_{frp,e} (ctg\alpha + ctg\beta)}{s_{frp}} \sin\beta \quad (1)$$

where V_{frp} is the shear contribution of externally bonded FRP sheets/strips (bonded at two sides of the beam); α

is the angle of the potential shear crack (the diagonal compressive strut); β is the angle between the fiber orientation and the longitudinal direction of the RC beam, t_{frp} is the thickness of FRP sheets/strips; w_{frp} is the width of each FRP sheet/strip; s_{frp} is the spacing of FRP strips/sheets ($s_{frp} = w_{frp} / \sin\beta$ if continuous FRP plates are used); $f_{frp,e}$ is the effective stress of the FRP.

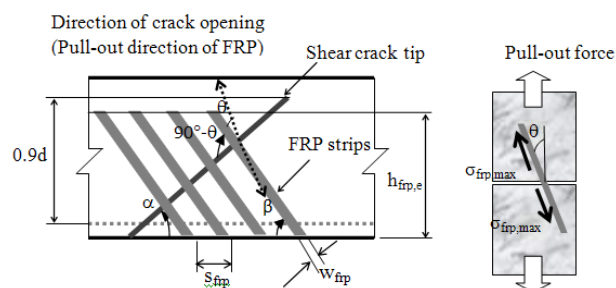


Figure 1 Fiber direction in an FRP-shear strengthened RC beam

Equation 1 adopts an assumption that the shear contribution of FRP is the vertical component of the tensile force in fibers that bridge the shear crack. Therefore, an important issue is how to evaluate the effective stress, $f_{frp,e}$, of the fibers at the ultimate limit state (ULS). Determination of $f_{frp,e}$ relies on whether the shear failure is controlled by FRP rupture or debonding at the ULS and should consider appropriately the un-uniform stress distributions in the fibers along the shear crack. For example, Chen and Teng (2003) adopted the following equation to calculate the effective stress in the fibers:

$$f_{frp,e} = D_{frp} \sigma_{frp,max} \quad (2)$$

where D_{frp} is stress distribution factor to take account of the non-uniform stresses in the fibers bridging the shear crack; $\sigma_{frp,max}$ is the maximum tensile stress that can be reached in the fiber direction (see Figure 1).

If FRP rupture occurs at the ULS, $\sigma_{frp,max}$ needs to be calculated using the tensile strength of FRP or a decreased tensile strength of FRP considering corner effects when the FRP is U-shaped. By contrast, if FRP debonding occurs at the ULS, $\sigma_{frp,max}$ should be taken as the debonding stress of fibers and was usually determined through pull-out tests of FRP-bonded concrete joints, in which the fibers are arranged in coincidence with the pullout force direction. However, this is only true when the FRP is perpendicular to the shear crack ($\alpha+\beta=90^\circ$ or $\theta=0$ in Figure 1). It remains unknown whether or not the debonding stress of fibers, $\sigma_{frp,max}$, remains unchanged when θ is not 0° .

Against the above background, the objective of this research project is to investigate the pullout strength of FRP in skew FRP-bonded concrete joints and the corresponding fiber debonding stress.

2 EXPERIMENTAL OUTLINE

2.1 Materials

Concrete was made with a cube compressive strength of 45.5 MPa at 28 days curing. Two types of carbon FRP (CFRP) composites were used. One was the Sika CarboDur plate, with elastic modulus of 165 GPa, a rupture strain of 1.2% and a thickness of 1.2 mm. Another was the Sika Wrap-600C/120 sheets with elastic modulus of 242 GPa, a design thickness of 0.337 mm per layer and a rupture strain of 1.55%. A two-part epoxy-based adhesive, Sika-330, with tensile modulus of 4.5 GPa and elongation of 0.9% was used as the primer, the bonding adhesive for the FRP plates and the impregnating resins for the FRP sheets.

2.2 Details of specimens

A total of 12 specimens were prepared, with six bonded with Sika CarboDur plates and the remained six bonded with two layers of Sika Wrap-600C/120. Each specimen consisted of two concrete blocks, Block 1 and Block 2, with a 50 mm gap in between (see Figure 2). Each block was 350 mm long, 300 mm wide and 150 mm high. The purpose of setting a gap between two blocks was to accommodate a 30 mm thick steel reaction wall for Block 1. The FRP plates/sheets bridging the gap were strengthened with steel plates underneath, leaving a small gap between them and Block 2 to simulate a concrete crack. The FRP plates/sheets attached onto Block 1 were firmly anchored so that the debonding of FRPs would occur only in its counterpart, Block 2. The length of FRP plates/sheets bonded to each block was 150 mm. Two FRP bond widths (150 and 300 mm) and four different angles (0° , 15° , 30° and 45°) between the

fiber direction and the pullout direction were used. Details of all the specimens are summarized in Table 1.

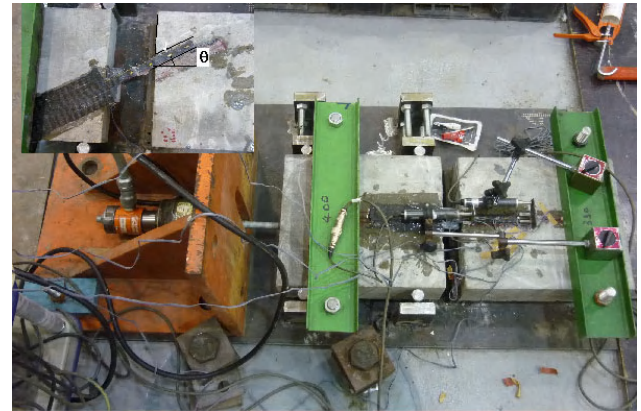
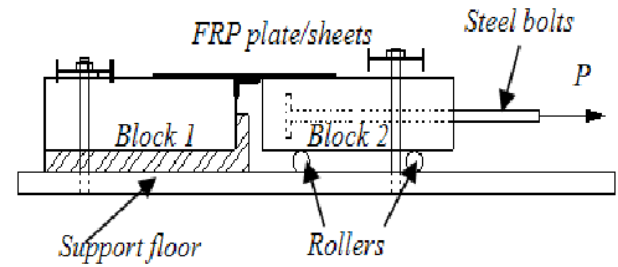


Figure 2 Test setup

Table 1 Summary of specimens and test results

Code of Specimens	Maximum pullout load of FRP				$P_{pred.}/P_{exp.}$	$K_{pred.}/K_{exp.}$
	Experimental		Predicted			
	$P_{exp.}$ (kN)	$K_{exp.}$	$P_{ana.}$ (kN)	$K_{pred.}$		
P-15-0*	9.52	1.00	7.61	1.00	0.80	1.0
P-15-15	7.48	0.79	7.35	0.97	0.98	1.23
P-15-30	7.27	0.76	6.59	0.87	0.91	1.14
P-15-45	4.68	0.49	5.38	0.71	1.15	1.45
P-30-0	16.40	1.00	14.68	1.00	0.90	1.00
P-30-30	12.37	0.75	12.72	0.87	1.03	1.26
S-15-0	9.02	1.00	7.82	1.00	0.87	1.00
S-15-15	7.51	0.83	7.56	0.97	1.01	1.17
S-15-30	7.08	0.78	6.78	0.87	0.96	1.12
S-15-45	3.97	0.44	5.53	0.71	1.39	1.61
S-30-0	18.08	1.00	15.09	1.00	0.83	1.00
S-30-45	14.15	0.78	13.07	0.87	0.92	1.12

*X-Y-Z: X means the type of FRPs (P: plates; S: sheets); Y means the bond width (mm); Z means θ . $P_{exp.}$ and $P_{pred.}$ are the experimental and analytical maximum pullout loads of FRPs, respectively. $K_{exp.}$ and $K_{pred.}$ are the experimental and predicted ratios of the pullout load of skewed FRP plates/sheets ($\theta \neq 0^\circ$) to that of normal FRP plates/sheets ($\theta = 0^\circ$).

2.3 Test setup and instrumentations

Figure 2 shows the test setup used in this study. A high strength steel bar was firmly anchored in Block 2 and pulled to introduce tensile force into FRP plates/sheets. Block 1 was fixed during the tests. Some steel rods were

arranged at the two sides and the bottom of Block 2 to guide its movement while minimizing the friction. A steel frame was installed above (not contacted with) Block 2 for a safety purpose. During the tests, pullout loads and loaded and free end slips parallel to the pullout direction and strain distributions along the fibers were recorded.

3 RESULTS AND DISCUSSION

3.1 Pullout load-slip relationships

All FRP-bonded concrete joints failed due to the debonding between FRP and concrete. The failure was observed in a very thin concrete layer beneath the adhesives. Figure 3 and Figure 4 present the typical pullout load vs. slip relationships of FRP plates and sheets, respectively, at the loaded and free ends. “LE” and “FE” in the figures represent the loaded end and the free end, respectively. A clear tendency is seen in two figures that the initial slope of the pullout load-slip relationships decreases with the increase value of θ , which is the angle between the fiber direction and the pullout force. At the ultimate state, the maximum pullout load of FRP plates/sheets decreases significantly with the increase of θ but the corresponding slip increases. The increased slip was caused by the additional shear in the bond interface caused by the skew effect of FRPs.

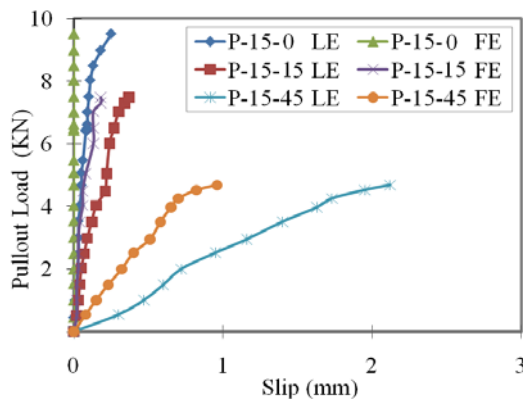


Figure 3 Pullout load ~ slip relationships (FRP plates)

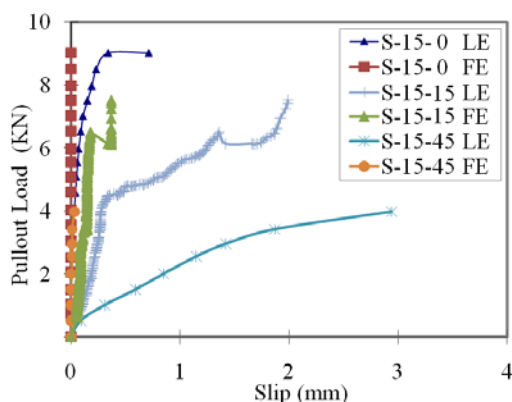


Figure 4 Pullout load ~ slip relationships (FRP sheets)

Compared to FRP sheets-bonded joints, FRP plates-bonded joints exhibited early free end slips and a more brittle debonding behavior. This was mainly because that the tension stiffness of FRP plates was larger than that of FRP sheets and so was their effective bond length. As a result, the debonding of FRP sheets could propagate more progressively along the given bond length. The decrease of the maximum pullout force of FRP with the increase of θ is considered due to the following two factors: (1) the projection value of the debonding stress of fibers on the pullout direction of FRP decreased with the increase of θ ; (2) the skew FRP decreased the debonding stress of fibers as discussed later on.

3.2 Strain distributions

Figure 5 and Figure 6 present typical strain distributions of FRP along the fiber direction in normal and skew FRP plates-bonded concrete joints, respectively. In the former case, the strain gauge attached nearest to the loaded end increased with the pullout load and always exhibited the maximum value along the bond length. However, in the latter case, the value of that strain gauge was quite lower compared to that of the adjacent one although it kept increasing with the pullout load. This is considered to be caused by a combined action of bi-directional interfacial shear and in-plane bending of the skew FRP. Further analysis is being conducted to capture the stress complexity in the bond interface as well as in the FRP.

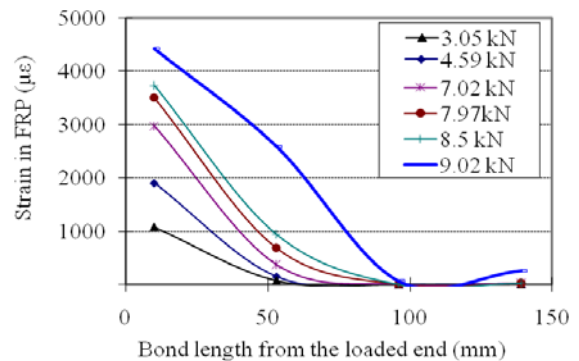


Figure 5 Strain distribution along fibers (P-15-0)

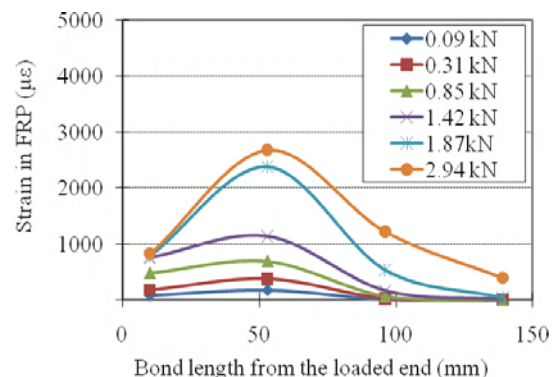


Figure 6 Strain distribution along fibers (P-15-45)

4 PREDICTION MODEL

For normal FRP-bonded concrete joints ($\theta = 0^\circ$), Chen and Teng (2001) proposed the following models to predict the maximum pullout load of FRP:

$$P_u = 0.427 \beta_p \beta_L \sqrt{f'_c} b_{frp} L \quad (3)$$

$$\beta_L = \begin{cases} 1 & \text{if } (L \geq L_e) \\ \sin \frac{\pi L}{2L_e} & \text{if } (L < L_e) \end{cases} \quad (4)$$

$$\beta_b = \sqrt{\frac{2 - b_{frp}/b_c}{1 + b_{frp}/b_c}} \quad (5)$$

$$L_e = \sqrt{\frac{E_{frp} t_{frp}}{\sqrt{f'_c}}} \quad (6)$$

where b_c = width of concrete member; b_{frp} = width of bonded FRP; E_{frp} = Young's modulus of FRP; f'_c = concrete cylinder compressive strength; L = bonded length; L_e = effective bond length; P_u = ultimate pull out load of FRP; t_{frp} = thickness of FRP.

Assuming that the pullout strength of a skew FRP is the projection of the tensile force in all fibers on the pullout direction, the maximum pullout load of a skew FRP can be calculated by slightly modifying Eq. (3) to the following equation:

$$P_{u,skew} = 0.427 \beta_p \beta_L \sqrt{f'_c} b_{frp} L \cos \theta \quad (7)$$

in which $P_{u,skew}$ is the ultimate pullout strength of a skewed FRP; θ is the angle between the fiber direction and the pullout direction as previously mentioned.

The predicted pullout strength of FRPs in all the test specimens by Eq. (6) are summarized in Table 1 and compared with the experimental ones. The ratios of the predicted values to the experimental values varied between 0.8 and 0.9 when $\theta = 0^\circ$, while varied between 0.91 and 1.39 when θ increased from 0° to 45° . This implies that Eq. (6) tends to overestimate the pullout strength of skew FRPs. For an easy comparison of all the specimens regardless of the FRP type, both the experimental and predicted pullout strengths of skew FRPs were normalized by those of normal FRPs with the same bond width. Figure 7 presents the ratio of the normalized predicted pullout strength of skew FRPs to the normalized experimental one of skew FRPs. It is clearly seen that the pullout strength of skew FRPs is generally overestimated by Eq. (6). The overestimation increases non-linearly with the value of θ and may reach up to 60% when $\theta = 45^\circ$. To predict the experimental results correctly, the debonding stress, $\sigma_{fp,max}$, of the fibers should be decreased with the increase θ value, indicating a significant skew effect on the debonding stress of fibers.

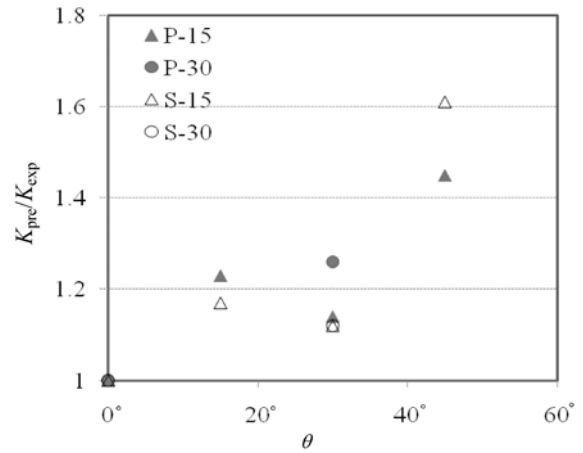


Figure 7 Skew effects on the pullout strength of FRPs

5 CONCLUSIONS

The following conclusions can be made based on the experimental study and analysis on the test results:

(1) Debonding behavior of FRP in skew FRP-bonded concrete joints is significantly different from that in normal FRP-bonded concrete joints.

(2) If the fiber orientation is different from the pullout direction of FRP, the debonding stress of fiber decreases with the increase of the angle between two of them due to the skew effect on the interface debonding.

(3) Without considering the skew effect in the FRP-to-concrete bond interface, the pullout strength of skews FRP will generally be overestimated. When the angle between the fiber orientation and the pullout direction is 45° , the overestimation may reach up to about 50%.

6 ACKNOWLEDGEMENT

The author is grateful to The Hong Kong Polytechnic University and the Innovation and Technology Commission of the Hong Kong SAR Government (Project No: ITS/084/08) for the financial support. The authors also would like to thank two final year students, Mr S.O. Chan and Mr K.M. Kwong, for their assistance in conducting the experimental tests.

REFERENCES

- Chen, J.F. and Teng, J.G. (2001), Anchorage strength models for FRP and steel plates bonded to concrete, *Journal of Structural Engineering*, ASCE, 127(7), 784-791.
- Chen, J.F. and Teng, J.G. (2003), Shear capacity of FRP strengthened RC beams: FRP debonding, *Construction and Building Materials*, 17(1), 27-41.
- Dai, J.G., Ueda, T. and Sato, Y. (2005), Development of the nonlinear bond stress-slip model for fiber reinforced plastics sheet-concrete interfaces with a simple method, *Journal of Composites for Construction*, ASCE, 9(1), 52-62.

Effectiveness of U-Shaped CFRP Wraps as End Anchorages in Predominant Flexure and Shear Region

A. A. R. Khan (asadkhan@neduet.edu.pk) & Tehmina Ayub

Department of Civil Engineering, NED University of Engineering and Technology, Karachi, Pakistan

ABSTRACT U-shaped external anchorage have been used to enhance the shear resistance and performance of RC beams strengthened by externally bonded CFRP plates but the reported results are not adequate yet to draw rational conclusions. One factor that could affect the ultimate strength and mode of failure is the depth of the end anchorage used. Varying end anchorage depths were considered in this study to investigate the effectiveness of U-shaped end anchorages along with determining ultimate load carrying capacity and failure modes of strengthened beams in predominant flexure and shear loading regions. Full depth U-shaped anchorages at plate cut-off points were found to be effective in strengthened RC beams in the predominant shear loading region while depth of the end anchorage was not found to be factor that affects the load carrying capacity of the strengthened RC beams.

1 INTRODUCTION

Strengthening of RC beams in flexure and shear with FRP materials is a fascinating domain for researchers to observe the structural behaviour. Many studies across the world are conducted to study structural behaviour of RC beams with FRP laminates and strip bonded to the tensile face of the RC beam and subjected to shear and/or flexural dominant loading regimes. Prior to strengthening in flexure, shear capacity of the beams must be checked as increase in the flexural capacity after strengthening may lead to more severe as well as undesirable shear failure. Use of CFRP strip with end anchorages is one of the practically efficient strengthening techniques used to strengthen RC beams in flexure and shear respectively (Khan & Ayub 2009a, b). Appropriate positioning of CFRP wraps throughout the beam length does not only enhance the load carrying capacity of the beam but it also improves the performance of strengthened beams by avoiding debonding/ delamination of strip prematurely (Khan & Ayub 2009b).

Uji (1992) and Sato et al. (1996) carried out tests on rectangular RC beams strengthened in shear by CFRP and concluded that fibre-reinforced polymer (FRP) wraps used as anchorages can improve the capacity of rectangular beam sections having less shear capacity than flexural capacity or require added load capacity and can also modify the failure mode of the strengthened RC beams under predominant shear forces from brittle to ductile. According to Bencardino et al. (2007), bonding a CFRP laminate without end anchorages to the tension face of RC beams, weak in shear, is not an adequate structural solution either to increase their load carrying

capacity or to change their mode of failure.

Reinforced concrete members strengthened in bending by bonding of FRP may fail due to failure of material (reinforcing steel, concrete and composite material) or failure of the interface between concrete adhesive or adhesive-FRP. Experimental results confirm that in most cases delamination prevails over the other possible rupture modes (Casas & Pascual 2007). These delamination failure modes can be classified into two main types: due to high interfacial stresses near plate ends and due to flexural or flexural-shear crack (intermediate crack) away from the plate ends (Teng et al. 2003).

The endeavor of this paper is on investigating the effectiveness of U-shaped anchorages on ultimate load carrying capacities, failure modes and performance evaluation of normal and strengthened RC beams in predominant flexure and shear loadings by varying depth of U-shaped anchorages provided at the ends.

2 EXPERIMENTAL PROGRAM

Beams were cast into two groups: Group "A" and Group "B". Each group have total of three beams including one control beam. All beams were 1800 mm long having 150 mm × 200 mm cross section and were cast by mixing cement, fine aggregates and coarse aggregates with a mix proportion of 1:2:4 and water cement ratio of 0.5. All beams were detailed with two 12 mm dia. bars as tension reinforcement, two 6 mm dia. bars as hanger reinforcement and 6 mm dia. mild bar spaced at 100 mm uniformly throughout beam length.

One beam of each group, serving as control beam, was tested to failure with loading spans of 550 mm and

400 mm respectively. All beams were strengthened with CFRP strips and wraps, and tested under four point bending with same loading span as that of control beams. Material Properties of concrete, steel, CFRP strip and wrap are shown in Table 1. Nomenclature of all strengthened beams is described in Table 2, whereas strengthening detail and experimental program is shown in Figure 1.

Table 1 Material properties

Materials		Material Properties	
Concrete	Compressive Strength f'_c (MPa)	20.7	
	Long. Steel Yield Strength f_y (MPa)	420	
	Stirrup Steel Yield Strength f_y (MPa)	318	
Steel	Stirrup diameter (mm)	6	
	Thickness (mm)	1.4	
CFRP Strip	Width (mm)	50	
	Ultimate tensile strength (MPa)	2500	
	Young's modulus (GPa)	150	
CFRP Wrap	Thickness (mm)	0.117	
	Ultimate tensile strength (MPa)	3800	
	Young's modulus (GPa)	240	

Table 2 Nomenclature of strengthened beams

Loading Span	Beam ID	Description
Group "A" 550 mm (a/d= 3.08)	A1	Beam strengthened with CFRP strip and full depth anchors (anchor height = 200 mm)
	A2	Beam strengthened with CFRP strip and Partial depth anchors (anchor height = 150 mm)
	A3	Beam strengthened with CFRP strip and Partial depth anchors (anchor height = 100 mm)
Group "B" 400 mm (a/d= 2.46)	B1	Beam strengthened with CFRP strip and full depth anchors (anchor height = 200 mm)
	B2	Beam strengthened with CFRP strip and Partial depth anchors (anchor height = 150 mm)
	B3	Beam strengthened with CFRP strip and Partial depth anchors (anchor height =100 mm)

3 RESULTS AND DISCUSSIONS

Load carrying capacities of control and strengthened beams for both the groups are summarized in Table 3. Control beam of group "A" failed at a load of 79 kN in conventional ductile flexure mode with yielding of the main reinforcing steel, where as control beam of group "B" failed at a load of 93 kN in pure shear mode with a

prominent diagonal tension crack starting from the support and moving towards the load.

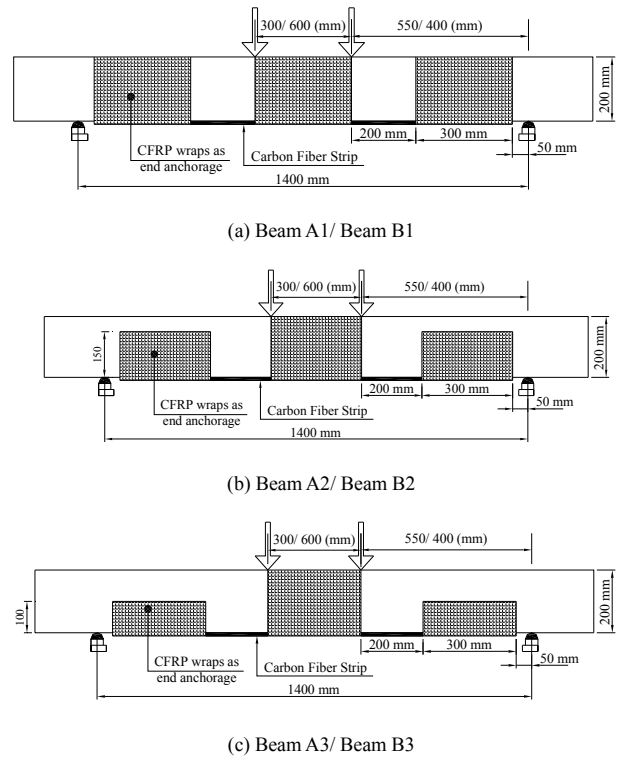


Figure 1 Strengthening schemes of beams

Beams A1, A2 and A3 of Group "A", strengthened with CFRP strip and anchor heights of 200 mm, 150 mm and 100 mm respectively, failed in conventional ductile flexure mode with yielding of the main reinforcing steel followed by crushing of concrete and carried an additional load of 26 kN, 36 kN and 28 kN respectively (33%, 46% and 35% increase in load carrying capacity). It was observed in the case of all the beams of Group "A" that failure was initiated by extensive flexural cracking in the flexure zone leading to delamination of the CFRP strip. This is also reflected by sudden drop in load carrying capacity in load-deflection curves shown in Figure 2. A very marginal difference in load carrying capacities of strengthened beams is noticed indicating that the depth of end anchorages has no significant effect on the load carrying capacities and failure modes of strengthened beams.

Beam B1, strengthened with CFRP strip and anchor height of 200 mm, failed in conventional ductile flexure mode with yielding of the main reinforcing steel followed by crushing of concrete and carried an additional load of 4 kN, showing a marginal increase in load carrying capacity. Presence of end anchorages helped transform the failure mode from brittle to ductile. It was observed that failure was initiated by extensive flexural cracking in the flexure zone leading to delamination of the CFRP strip.

Beam B2, strengthened with CFRP strip and anchor

height of 150 mm, failed in mixed flexure and shear mode and carried an additional load of 37 kN, showing 40% increase in load carrying capacity. Extensive flexural cracking in the flexure zone was observed near failure but failure was ultimately due to the shear cracks in the portion above the end anchorage. The failure was transforming to flexure mode due to the presence of end anchorages but excessive shear cracking in the shear span led to the shear failure of concrete at end anchorages as can be seen in Figure 3.

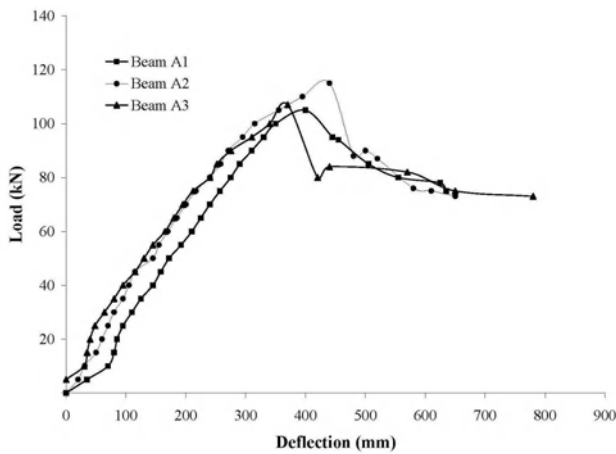


Figure 2 Load deflection curves of group “A” beams

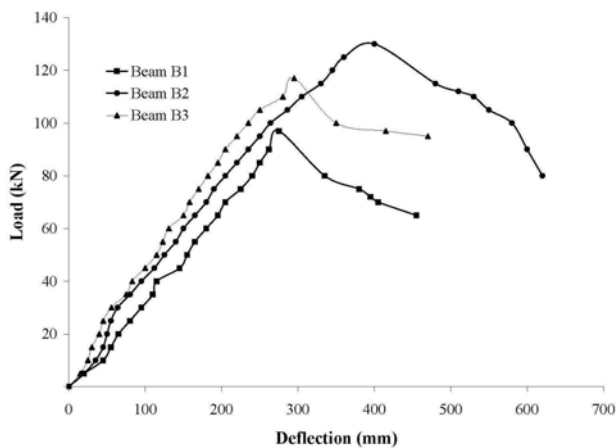


Figure 3 Load deflection curves group “B” beams

Table 3 Ultimate failure loads of beams

Beams		Experimental Failure Load (kN)	Increase in ultimate load after strengthening (%)
Group “A”	Control	79	—
	A1	105	32.9
	A2	115	45.6
	A3	107	35.4
Group “B”	Control	93	—
	B1	97	4.3
	B2	130	39.8
	B3	117	25.8

Beam B3, strengthened with CFRP strip and anchor height of 100 mm, failed in pure shear mode and carried an additional load of 24 kN (26% increase in load carrying capacity). Failure was due to the shear cracking in the shear span especially in the portion above the end anchorage. Shear failure of beam was indicative of the fact that end anchorages of smaller depths are not enough in predominant shear loading regions.

Load-deflection curves for all strengthened beams are shown in Figures 2, 3. It is clear from all the curves that there is a sudden drop in load carrying capacity of beams indicating that failures were initiated by delamination of either CFRP strips and/or wraps caused by excessive flexure, shear or flexure-shear cracking. In the case of Group “A” beams it was excessive flexural cracking in the flexure zone whereas in the case of Group “B” beams it was excessive flexure, shear or flexure-shear cracking depending on the height of end anchorage.

4 CONCLUSIONS

The main conclusions drawn from this study are summarized as follows:

(1) U-shaped anchorages provided at ends and at midspan improved the structural performance of the RC beams strengthened with externally bonded CFRP strips through enhanced strength and greater ductility as can be seen in the case of all the beams.

(2) Observed mode of failure was pure flexure in the case of Group “A” beams while it varied from flexure to flexure-shear and pure shear in the case of Group “B” beams.

(3) In the case of beams of Group “A” U-shaped anchorages, irrespective of their heights, allowed the concrete in the compression zone to reach its ultimate strain capacity leading to crushing of concrete in compression indicating that height of end anchorages does not affect the load carrying capacities and failure modes in predominant flexural loading regions.

(4) In the case of beams of Group “B” full depth U-shaped anchorages at plate cut-off points were found to be most effective in strengthened RC beams in the predominant shear loading region. It is therefore recommended that in predominant shear loading regions full depth anchorages are used to avoid premature and brittle failure modes.

5 ACKNOWLEDGEMENT

The authors are indebted to the Department of Civil Engineering at NED University of Engineering & Technology, Karachi, Pakistan and the University itself, in the pursuit of this work.

REFERENCES

- Bencardino, F., Spadea, G. & Swamy R.N. 2007. The problem of shear in RC beams strengthened with CFRP laminates. *Construction and Building Materials* 21(11): 1997-2006.
- Casas, J.R. & Pascual, J. 2007. Debonding of FRP in bending: Simplified model and experimental validation. *Construction and Building Materials* 21: 1940-1949.
- Khan, A. R. & Ayub, T. 2009a. Performance of RC Beams Strengthened in Shear by Externally Bonded U-shaped Wraps. *Proceedings of 1st International Conference on Sustainable Built Environment Infrastructure in Developing Countries (1st SBEIDCO), 12-14 October, 2009, Oran, Algeria.*
- Khan, A. R. & Ayub, T. 2009b. Role of U-shaped Anchorages on Performance of RC Beams Strengthened by CFRP Plates. *Proceedings of Asia-Pacific Conference on FRP in Structures (APFIS 2009), 9 - 11 December 2009, Seoul, Korea.*
- Sato, Y., Ueda, T., Kakuta Y. & Tanaka T. 1996. Shear reinforcing effect of carbon fibre sheet attached to side of reinforced concrete beams. *Advanced composite material in bridges and structures*: 621-627.
- Uji, K. 1992. Improving shear capacity of existing reinforced concrete members by applying carbon fiber sheets. *Transactions of the Japan Concrete Institute* 14: 253-266.
- Teng, J. G., Chen, J.F., Smith, S.T. and Lam, L. (2003). Behaviour and strength of FRP-strengthened RC structures: a state-of-the-art review. *Proceeding of Institute of Civil Engineering, Structures and Buildings* 156(1): 51-62.

Behavior of an Innovative End-Anchored Externally Bonded CFRP Strengthening System under Low Cycle Fatigue

R. Sadone (raphaelle.sadone@lpc.fr) & M. Quiertant

Université Paris-Est, Laboratoire Central des Ponts et Chaussées, Paris, France

S. Chataigner

Laboratoire Régional des Ponts et Chaussées d'Autun, Autun, France

J. Mercier

Freyssinet International, Velizy, France

E. Ferrier

Laboratoire Mécanique, Matériaux et Structures, Université Claude Bernard, Villeurbanne, France

ABSTRACT Building and bridge columns are particularly vulnerable when earthquakes occur. Retrofit of deficient reinforced concrete columns with CFRP jackets and bonded CFRP plates is an efficient method to increase their strength and ductility and then to enhance their seismic resistance. However, issues related to anchorage of the plates can be a concern when strengthening flexural concrete members. This study presents specific end-anchors reinforcement systems which were designed and tested under monotonic and low cycle fatigue loading and compared with a reference system commercially available. A total of 16 specimens were tested up to failure, to check the performances of these anchors. It appears that anchors increase the ultimate capacity and ductility of bonded plates.

1 INTRODUCTION

The use of fiber-reinforced polymer (FRP) material to reinforce concrete structure by increasing their flexural and shear resistance has been proven to be an effective method today. However, issues related for example to bond length or anchorage may be a concern for the strengthening of structures. Then, to prevent or delay the delamination of the FRP, anchorage of the composite may be necessary. Several anchorage systems have been proposed and tested. For example, mechanically fastened fiber-reinforced polymer strengthening systems have been proposed to increase the load capacity (Elsayed et al. 2009); those fasteners can be shot fasteners (directly embedded into the concrete surface) or screwed fasteners (into shallow predrilled holes in the concrete). Another way to enhance the capacity of externally bonded CFRP can be the utilization of Near Surface Mounted (NSM) end anchor or spike anchor (Eshwar et al. 2008).

The main objective of the present research was to characterize performances of new end-anchored CFRP plates. Such characterization was achieved by comparing performances of the proposed innovative anchored reinforcement system with a commercially available system made of a non-anchored externally bonded FRP plate (considered here as a reference system). The

experimental program examines anchor performances under both monotonic and cyclic loading.

2 EXPERIMENTAL INVESTIGATION

2.1 Test specimens

Test specimens were small reinforced concrete blocs, reinforced with an externally bonded CFRP Strengthening Systems.

2.1.1 Reference strengthening system

In this study, the reference reinforcement system was a commercially available CFRP Strengthening System of Freyssinet. It consisted of a unidirectional pultruded plates with a thickness of 1.2 mm and a width of 50 mm. The tensile modulus of these laminates was 160 GPa.

2.1.2 End-anchored strengthening systems

The anchored strengthening system was fabricated with the previously described pultruded carbon plate from which the end has been modified; then, the anchorage system and the CFRP strengthening system (the plate) were a single continuous element. The end of the plate has been modified to become a cylinder of about 13 cm long and with a diameter of 16 mm. Two types of anchors have been tested, as shown on Figure 1: a plain anchor and a ribbed anchor, on which notches have been

realized. These end-anchored plates were developed and patented by Freyssinet (certificate n°FR0955642).

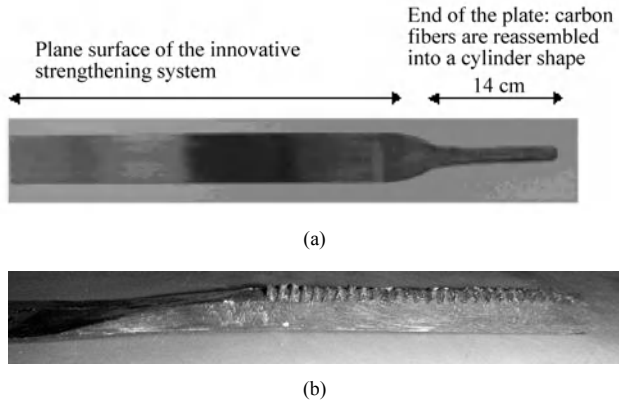


Figure 1 Anchorage system details. (a) Simple version. (b) Optimized version with notches

2.1.3 Reinforced concrete blocs

The reinforcement systems were installed on small reinforced concrete blocs, adapted to the test setup as shown on Figure 2, and internally reinforced to prevent premature failure of the bloc caused by embedded anchorage (Figure 3).

The average compressive strength of concrete blocks, determined from compression test on cylinders, was 38 MPa (NF EN 12 390-4).

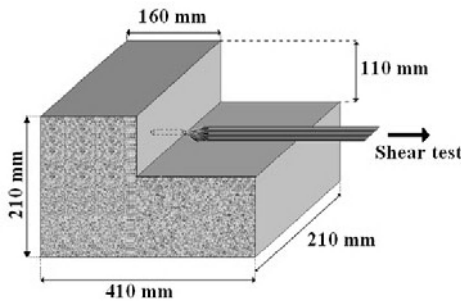


Figure 2 Dimensions of test specimens

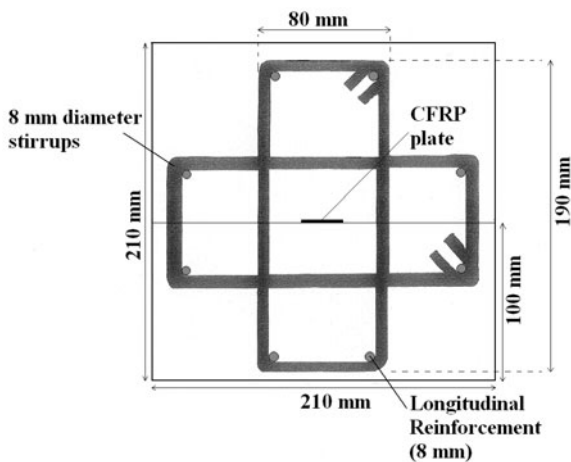


Figure 3 Details of reinforcement

2.2 Strengthening systems installation procedure

The reference strengthening system was bonded in accordance to manufacturer installation procedure including a substrate preparation (abrasive grinding with a diamond wheel). Grinding surface preparation was also carried out to bond the regular (i.e. plane) part of innovative strengthening systems. A concrete drilling machine was used to create the hole for the anchor in the concrete (the hole was aligned with the axis of fibers). Loose material was then removed from the hole thanks to pressurized air, and then the hole was filled with resin. A layer of resin was also applied on the laminate and on the concrete surface to bond the plate on it when introducing the anchorage into the hole. Finally, a bubble roller was rolled over the plane surface of the laminate in order to eliminate trapped air.

2.3 Test setup and testing procedure

The testing was performed by applying a tension on CFRP plates, bonded on concrete blocks, thanks to a hydraulic jack. The force was applied along the plate axis, thanks to conical grips clamping the end of the CFRP plate, inducing a direct shear stress on the adhesive joint.

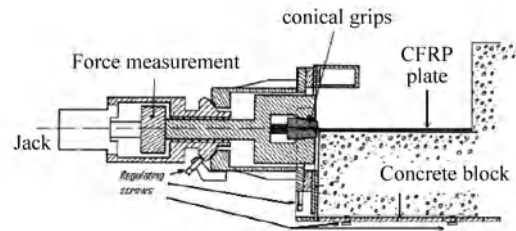


Figure 4 Scheme of the test setup

Three configurations of CFRP strengthening systems (simple plates, plain end-anchored plates and ribbed end-anchored plates) have been tested under monotonic loading and under low cycle fatigue. For each strengthening systems, 3 monotonic tests and 2 low cycle fatigue test have been realized. Simple plates tested under monotonic loading were labeled MP1, MP2, MP3i (“M” for monotonic, “P” for plate and “i” meaning instrumented) and CP1 and CP2i (“C” for cycle) under low cycle fatigue. An additional plain end-anchored plate was monotonically tested because of dispersion on the three previous one; then, plain end-anchored plates samples were labeled MAP1, MAP2, MAP3 and MAP4 (“AP” meaning Anchored Plate) for monotonic test, and CAP1 and CAP2i for low cycle fatigue. Ribbed end-anchored plates tested under monotonic loading were labeled MAPn1, MAPn2 and MAPn3i (“n” for notches) and CAPn1 and CAPn2i for low cycle fatigue.

Concerning the low cycle fatigue loading, series of ten cycles were run at the same amplitude. For CP1 and

CP2i, the first level was 15kN, and then amplitude was increased by 1.5kN every ten cycles. It appears that this test procedure was exceedingly time-consuming while the testing machine didn't permit to apply cycles in an automatic way. The low cycle fatigue testing procedure has then been changed for other series (CAP and CAPn). For end-anchored plates (plain and ribbed), the cycle level of the first series was equal to $[0.9 (F - 2\xi)]$, where F and ξ are respectively the average value of maximal load and the standard deviation observed during monotonic test of the corresponding end-anchored plates (plain or ribbed). Then the second level was equal to $[0.9 (F - \xi)]$, the third one to $0.9 F$, the fourth one to F and the last one to $1.1 F$ (10 cycles being applied for each level). Cycles have been run at 100N/s until failure.

2.4 Instrumentation

During tests, applied force, grips displacement and axial strains on the surface of the plate (or plane part of the end-anchored system) were recorded. The applied force was recorded via a load cell unit, grips displacement via a LVDT, and strains via strain gauges (10 mm length) bonded on the composite. The location of the strain gauges is shown on Figure 5 ; an additional gauge was also bonded on the anchor itself.

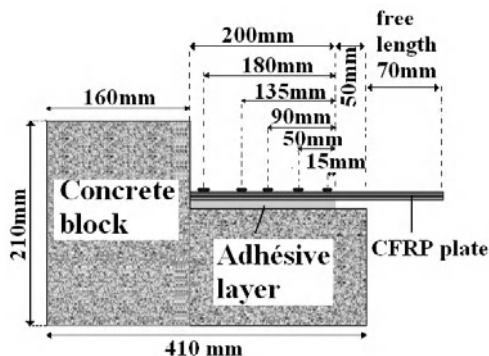


Figure 5 Position of strain gauges on CFRP plates

3 TEST RESULTS

3.1 Plates without any anchorage

Monotonic tests performed on MP1, MP2, MP3i showed an average maximal load of 22.34 kN, with a standard deviation of 1.28 kN. For each sample, the failure mode was cohesive in the concrete

For the samples CP1 and CP2i, the failure mode was also in a cohesive way in the concrete. Loading applied on CP1 was: 10 cycles at 15kN, 10 cycles at 16.5kN, 10 cycles at 18 kN, 19 cycles at 19.5 kN, 10 cycles at 21 kN, 10 cycles at 22.5 kN and 9 cycles at 24 kN (failure during the 9th cycle). Loading applied on CP2i was: 10 cycles at 15kN, 10 cycles at 16.5kN, 10 cycles at 18 kN, 19 cycles at 19.5 kN, 10 cycles at 21 kN, 10 cycles at 22.5 kN and 4 cycles at 24 kN (failure during the 4th cycle). Eventually, in both cases the average maximal

load of samples under static loading has been reached; it seems that low fatigue cycle didn't really affect the behavior of plates.

3.2 End-anchored plates

For end-anchored systems, two phases were observed during testing. The first one was the debonding of the plane part of the CFRP plate from the concrete block. The shear load was then transferred to the anchorage, which started being solicited, making up the second phase.

The plane part of MAP1 debonded for a tensile loading of 22.7 kN, and then failure of the anchorage occurred at an applied load of 43.3 kN, by tensile failure of fibers, at the beginning of the anchorage. The plane part of MAP2 debonded for a shear test of 19 kN. The ultimate capacity of the anchorage was 32.15 kN, followed by several slidings of the anchorage in his embedding hole. The failure of the plane part was cohesive in the concrete (debonding of the CFRP plate with a thick layer of concrete attached on it), but occurred in the adhesive for the anchored part.

MAP3i showed similar failure to that of MAP2; the plane part of the plate failed for a shear test of 21.56 kN and the ultimate capacity of the anchorage was 28.8 kN. Figure 6 shows that gauges situated at 15, 50 and 90mm (near the grips) were the most solicited until the bonded joint failed, and then gauges on the anchorage side started recording deformations. This confirms that the transfer of the shear load from the plane part of the plate to the anchorage only occurred after debonding of the plane part. Furthermore, after the debonding of the plate, gauges (the nearest to the grips) register strains similar to strains corresponding to a typical tensile strength on the plate. MAP4 showed the same kind of failure as MAP1; the plane bonded joint failed for a loading of 21.67 kN and the anchorage failed for a load of 41 kN (tensile failure). Finally, the average maximal load obtained from this set of testing was 36.2 kN with a standard deviation of 6.8 kN. It can be then concluded that the plain end-anchored reinforcement systems exhibits an average ultimate loading capacity increase of about 62% respect to the reference system.

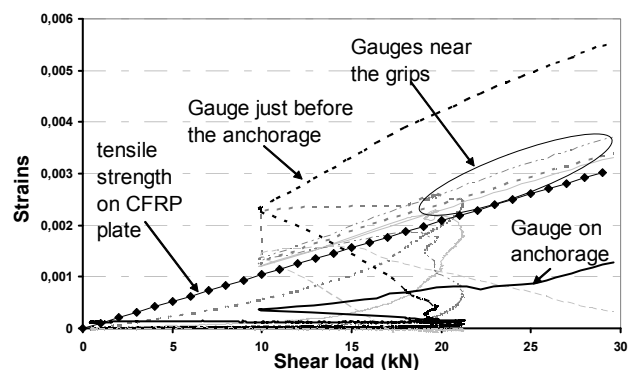


Figure 6 Load-strains curves for SPA3i test

Concerning specimens tested under low cycle fatigue, both kinds of failure were also observed. Loading applied on CAP1 was (based on average values obtained from monotonic loading): 10 cycles at 20.3 kN (and the plane part of the reinforcement system failed during the 1st cycle), 10 cycles at 26.5 kN, 10 cycles at 32.6 kN, 10 cycles at 36.2 kN and 6 cycles at 39.8 kN. Failure of the anchorage occurred during the 7th cycle at 39.8 kN: it slid in his embedding hole. CAP2i was submitted to the same loading procedure, except that the anchorage failed during the first cycle at 39.8 kN, by tensile failure of fibers.

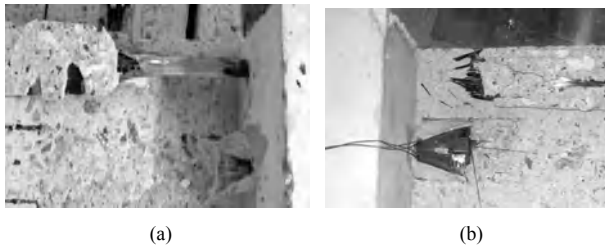


Figure 7 Failure mode for CAP1 (a) and CAP2i (b)

An average failure of 39.8kN was observed for series CAP. Considering the average value of MAP series, it can be concluded that applied cyclic loading generated no detrimental effect.

3.3 Anchored plates with notches

MAPn1, MAPn2 and MAPn3i exhibited similar failure mode to series MAP: a first failure mechanism corresponding to the debonding of the plane part of the reinforcement system, followed, after load increase, by major cracking of reinforced concrete surrounding the anchorage, and partial rupture of carbon fibers. Concerning MAPn1, the plane bonded joint failed at 26 kN and the ultimate capacity of the anchorage was 41 kN. The plane bonded joint of MAPn2 failed at 22 kN and the ultimate capacity was 39.2 kN. For the last monotonic test on ribbed end-anchored plates, MAPn3i, the plane bonded joint failed at 27.2 kN, and the anchorage at 32.9 kN. Finally, the average value of maximal load for these three tests was 37.7 kN with a standard deviation of 4.25 kN. Consequently, the ribbed end-anchored reinforcement systems exhibited an average ultimate loading capacity increase of about 69 % respect to the reference system.

According to average values obtained from monotonic tests, the following loadings were applied for tests on CAPn1 and CAPn2i. CAPn1 went through 10 cycles at 26.3 kN, 10 cycles at 30.1 kN, 10 cycles at 33.9 kN and failure occurred during the first cycle at 37.7 kN. In that case, cycles didn't really damage the plate (failure at the average monotonic maximal load), even if it was noticed that some fibers were severely damaged during this test. CAPn2i didn't reach such a loading capacity: failure occurred for a load level of 27.3 kN (the average maximal

load for monotonic test was 37.7 kN) after 10 cycles at 26.3 kN. A shear failure of notches was observed after testing.

A very promising result of the monotonic tests on ribbed end-anchored plates was the significant increase of the ultimate capacity and ductility of these systems without modifying their initial stiffness (see Figure 8). Such characteristics are essential for seismic retrofitting.

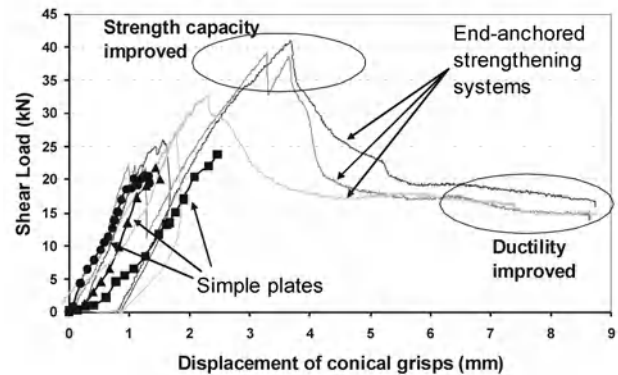


Figure 8 Performances of anchored plates with notches, compared to simple plates

4 CONCLUSIONS

Two specific end-anchored reinforcement systems were tested under monotonic and low cycle fatigue loading. Significant enhancement of ultimate strength and ductility has been obtained from monotonic tests with the innovative anchored system. Best performances were obtained for the anchor with notches. No particularly detrimental effect was observed from cyclic tests. Consequently, the proposed anchorage system seems to be an interesting constructive disposition for seismic strengthening.

REFERENCES

- Chataigner, S., Caron, J.-F., Quiertant, M., Benzarti, K. & Aubagnac, C. 2008. Characterization of composite-to-concrete interface: use of the cohesive zone approach. *Fourth International Conference on FRP Composites in Civil Engineering*, 22-24 July 2008. Zurich, Switzerland.
- Chataigner, S., Caron, J.-F., Benzarti, K., Quiertant, M., & Aubagnac, C. 2008. Characterization of composite-to-concrete interface –Description of the single lap shear test. *European Journal of Environmental and Civil Engineering*, Vol. 13, 1073-1082, 2009.
- Elsayed, W.E., Ebead, U.A. & Neale K.W. 2009. Studies on Mechanically Fastened Fiber-Reinforced Polymer Strengthening Systems. *ACI Structural Journal*. Title no. 106-S06. Jan-Feb 2009.
- Eshwar N., Nanni A. & Ibell T.J. 2008. Performance of two Anchor Systems of Externally Bonded Fiber-Reinforced Polymer Laminates, *ACI Materials Journal*. Title no. 105-M09. Jan-Feb 2008.

Experimental Investigation of CF Anchorage System Used for Seismic Retrofitting of RC Columns

Q. Sami, E. Ferrier (Emmanuel.Ferrier@univ-lyon1.fr), L. Michel, A. Si-Larbi, P. Hamelin

LGCIE Site Bohr, Université Claude Bernard Lyon I INSA de Lyon, Lyon, France

ABSTRACT This paper investigates the suitability and effectiveness of CF anchorage system in strengthening the bond in between the CFRP retrofit sheet and structure junction. i.e. column beam or column slab junction. For this purpose, a detailed experimental program was conducted, which is presented here briefly. Five different anchorage systems are discussed here. Results of the experimental observations are discussed in the form of load-slip curves, ultimate capacity and failure modes. The test result, in general indicates that the use of CF anchor provides an enhancement in the overall seismic capacity of strengthened specimen.

1 INTRODUCTION

Recent earthquakes in urban areas have repeatedly demonstrated the vulnerabilities of older reinforced concrete columns to seismic deformation demands. Failure of these columns occurred due to insufficient provision of longitudinal and transverse reinforcement in the earlier design codes. To account this problem, the most common retrofitting methods adopted round the globe are concrete and steel jacketing. But in recent years fiber reinforced polymers (FRP) materials are used extensively to replace the steel for jacketing. The most common techniques for FRP retrofit are to apply it either in the form of longitudinal strips or to wrap it around the exterior surface in order to improve the flexural and shear capacity respectively. However in recent seismic studies, it is highlighted that when this strengthening technique is applied to RC column, failure occurs either by development of cracks at the junction in between the column and supporting structure element (Figure 1 failure mod 1) or debonding of FRP strips at the end (Figure 1 failure mod 2), thus negating the effectiveness of retrofitting technique as the strength of FRP is not fully utilized. It is thus important to develop an anchor system to have load transfer in between FRP and supporting structure element. i.e. beam, slab or foundation. To remedy this sort of cracking failure, some work has been done in the recent past by providing local reinforcement in the form of small CFRP anchors as shown in Figure 1 [Freyssinnet (2004), Matsuzaki and Al. (2001), Xi Huang and Al. (2005)], with emphasis, to have additional bending moment at the column beam junction or to develop higher stresses in longitudinal FRP strips. These anchorage systems provide an overall increase in the stress development

within CFRP material during loading and behave itself as an additional local reinforcement.

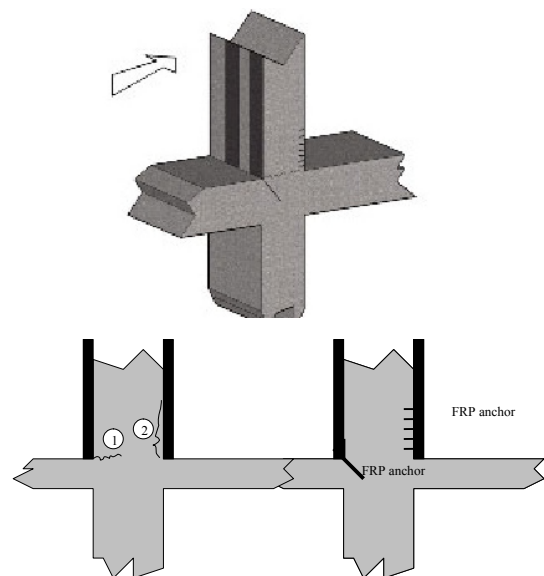


Figure 1 Reinforced column beam junction. Cracking pattern and anchorage system

Since some years this technology has been well adopted by many Civil Engineering companies and research work is already in progress to find out its efficiency [Cannon, R. and all. (1981), Cook, R. A.(1993, 1994)]. Xi Huang and Genda Chen in 2005 developed a technique, named as carbon fiber (CF) anchor dowels. The basic idea of this system is to embed the lower end of CFRP strip, used for confining column, within the concrete basement in order to have load transfer in between CFRP strip and supporting frame member i.e. beam, slab or foundation.

In this work, four different testing techniques have been utilized, in order to evaluate the efficiency of the anchor dowels: (a) direct pull-out test, (b) diagonal pull-out test, (c) bending test (d) double lap shear test. Anchors are fabricated by first drilling a small hole in the basement with an angle ranging from 0 to 90°, then it is filled with epoxy and one end of CFRP strip is dipped in. The other end of the strip is bonded to the column surface followed by the column strengthening layer of carbon fabric (CF), in order to have an increase in the bonding surface area and overall improvement in the bending capacity of the structure. The CFRP strengthening material is made of a layer of UD high modulus of carbon fiber, applied with a hand lay up method. The nominal thickness of the FRP is 0.45 mm with Young's modulus of 140 GPa and strength of 825 MPa.

2 EXPERIMENTAL PROGRAM

2.1 Tests set-up

In order to develop ultimate strength with in the anchorage system and avoid failure due to development of cracks within concrete block, 150 × 250 mm concrete blocks were utilized in experimental analysis. Block dimensions were assessed on the basis of tensile properties of the anchorage material (Considering ultimate tensile strength of CFRP material and concrete as 825 MPa and 3 MPa respectively).

For each system, four specimens were tested thus a total of sixteen specimens were fabricated. The pull-out test setup was made up of concrete blocks assembled by means of mesh anchorage system. A tensile force was applied directly on the first block while the second one being fixed on a strong framework (Figure 2.a and b). The first block was used to represent foundation, and the second one as a column or wall. The specific arrangement of the measurement apparatus allowed to calculate the lateral displacement in between the FRP strip and retrofitted surface as a function of applied load. The bending load test allowed examining the anchorage having an angle of inclination 15 to 25° with respect to embedded foundation. It also allowed reproducing the loading of anchor in the real column where the anchor would be submitted to pull-out force and a bending moment (Figure 2 c). The last testing device was fruitful in evaluating the efficiency of the anchor when it was applied right at the end of CFRP plate at an angle of 90°, in order to improve the bonding capacity of a CFRP plate.

2.2 CFRP anchors manufacturing and placement

CFRP anchors were made up of carbon fibres having a length of 200 mm. The CFRP fibres were first whipped then introduced into a hole drilled in concrete with a specific angle of inclination, depending on the

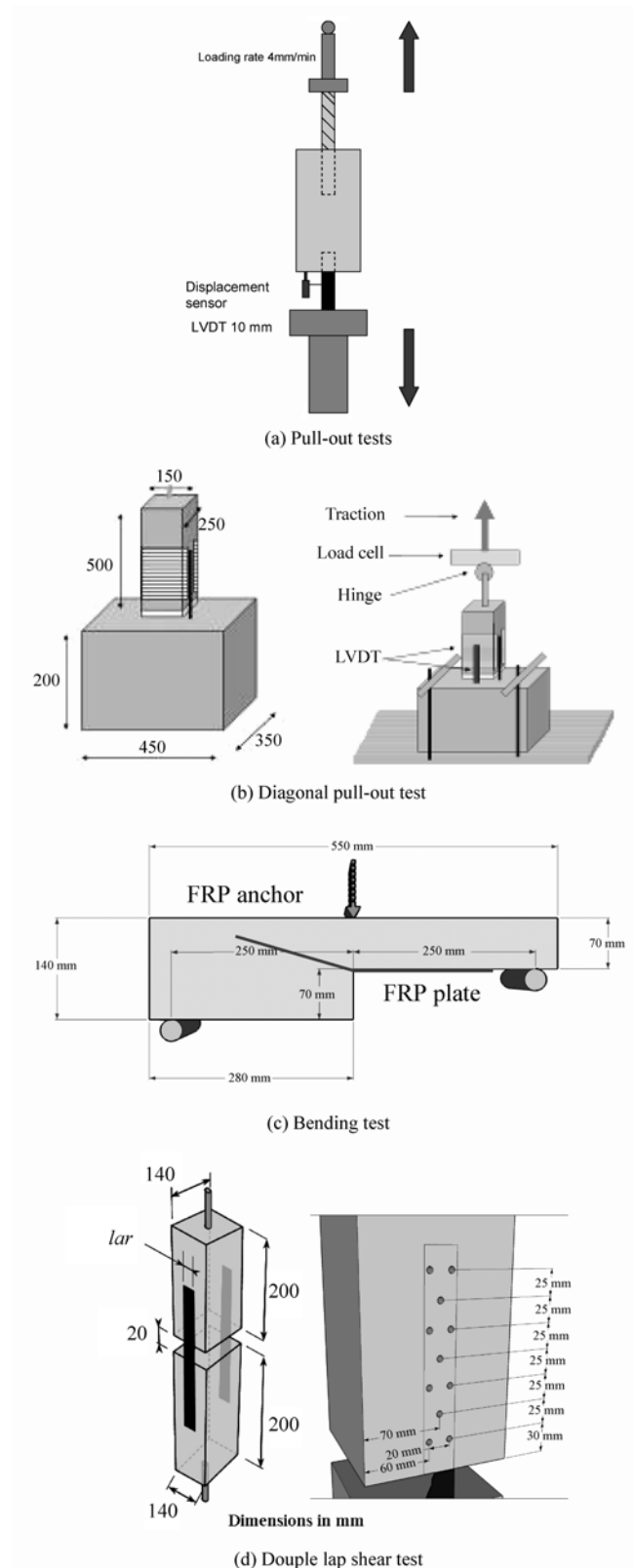


Figure 2 Tests principle

strengthening pattern and the technical feasibility of drilling. The minimal angle that can be retained when the anchors are placed within the column basement is 15°. This angle corresponds to the angle that can be formed in between the electric drill and the structure element to be reinforced. To obtain a perfect bond in

between concrete and resin the holes were first cleaned up with an air blower before filling it with resin. Finally anchors were dipped in risen impregnated holes (Figure 3).



Figure 3 Anchorage system

For system1 an electric heating device (6 V,120 W) was used to reduce the curing time of the anchorage system, with the help of which full curing of the anchor was obtained within 30 min at 130°C. For system 2 to 4 curing was done at 20°C in 7 days. The cross sectional area of the anchors utilized here varied within a range of 28-153 mm², from one system to another (Table 1).

Table 1 Anchorage system description

	Anchorage material	Area (mm ²)	Tests
1	CFRP prepreg with electrical curing	153	Pull-out
2	CFRP anchor	78	Diagonal pull-out and bending pull out
3	3 CFRP anchor	28	Double lap shear
4	11 CFRP anchor	28	Double lap shear

2.3 Instrumentation

The load cell was placed between the loading frame and the specimen and two displacement sensors (LVDT) were placed in order to measure the relative lateral displacement in between the anchors and sealing holes. In order to notify the experimental data load cell and displacement sensors were connected to a data acquisition system. Displacement controlled loading test were conducted with the help of a universal testing machine by applying load at a rate of 1 mm/min.

3 TEST RESULTS

Anchorage systems performances were analyzed on the basis of load-displacement curves and failure modes. The ultimate load capacities of the anchorage system and connection stiffness are derived from the respective load displacement curves.

3.1 Pull-out test

The direct pull out tension tests, enhanced the possibility of having a tension failure within an anchor length, if provided bond length in between anchor and retrofitted concrete surface is of 150 mm (Table 2). For anchorage system 2, the CFRP anchors exhibited a brittle behavior.

Table 2 Results for double lap shear test

Samples	b _f (mm)	L _f (mm)	Average Load (kN)	Total slip (mm)
Direct pull-out test	–	–	60.00 ± 2	0.21
Diagonale pull-out test	50	200	49.98 ± 2.83	1.32
Bending pull-out test (ref)	50	200	12.00 ± 1.50	–
Bending pull-out test	50	200	19.00 ± 3.50	–

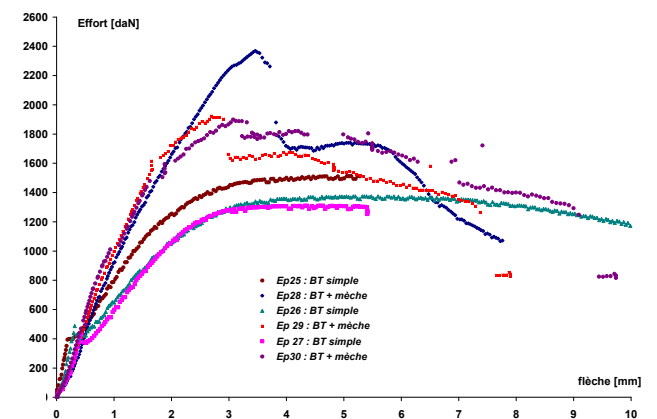


Figure 4 Bending pull-out tests curves

It was noted that specimens failure occurred due to tension failure of composite material right at the junction of the two concrete blocks. It was noted that failure took place prematurely at an average stress of 310 MPa developed with in the anchor. This low efficiency can be explained by the fact that the composite anchors were not loaded in pure tension and there was indeed a local punching phenomena related to the angle of drilling.

3.2 Shear tests

For all anchorage systems the mechanical response of the connection is bi-linear. The first stage corresponds to a linear elastic behavior; the increase in displacement is essentially due to the increase in stress within the anchor. The second stage with lower curve slop corresponds to the beginning of shear failure of the first anchor of the bonded CFRP. When only three anchors were bonded at the end of the plate, full debonding occurred, with a

100% increase in the ultimate load capacity. In the third case when eleven anchors were regularly spaced on the bonded area, the specimen failure was out come of tension failure with in the CFRP anchor.

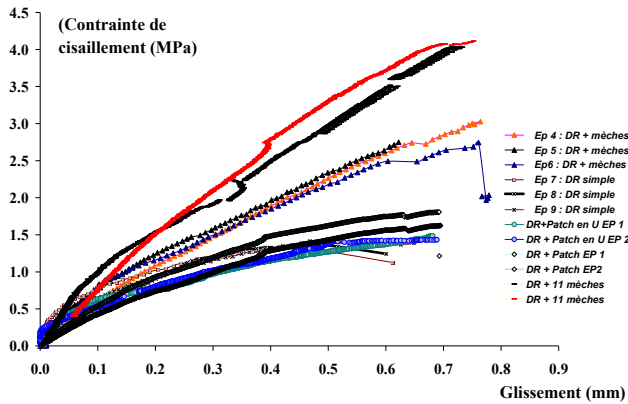


Figure 5 Load-slip curves

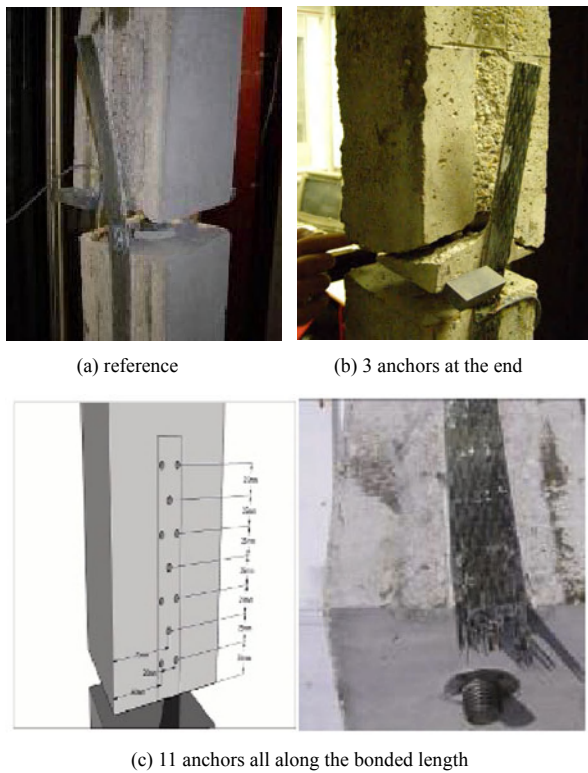


Figure 6 Mode of failure

Experimental calculations are tabulated in the form of Table 3.

Table 3 Results for double lap shear test

Samples	b_f (mm)	L_f (mm)	Average Load (kN)	Total slip (mm)
reference	30	200	15.4	0.6
Anchor N°3	30	200	33.76	0.62
Anchor N°4	30	200	48.89	0.73

4 CONCLUSIONS

Introduction of CFRP anchor systems results in an overall improvement in the performance of external FRP bonded reinforcement.(a) by having an increase in the ultimate strength of the specimens (b) by changing the specimen behavior from brittle to elastic. The test setup helped in figuring out the stress developed with in the anchors depending on the type of anchoring system and the angle in between the anchor and the axial reinforcement. Different failure modes were obtained depending on the efficiency of the CF anchor. Main conclusion is that CF anchoring may be considered as reliable as steel rebar sealing. Further study needs to be done under cyclic loading in order to evaluate the efficiency under seismic loading.

REFERENCES

Cannon, R. W., Godfrey, D. A., and Moreadith, F. L. (1981), Guide to the Design of Anchor Bolts and Other Steel Embedments, *Concrete International*, 3(7).

Cook, R. A. (1993), Behavior of Chemically Bonded Anchors, *Journal of Structural Engineering*, Vol. 119, No. 9, September, pp. 2744-2762.

Cook, R. A., Klingner, R. E. (1992), Ductile Multiple-Anchor Steel-to-Concrete Connections, *Journal of Structural Engineering*, Vol. 118, No. 6, June, pp. 1645-1665.

Freyssinet, Avis Technique (n°3/04-424) du procédé de renforcement TFC®.

Gökhan ÖZDEMİR (2005), Mechanical properties of CFRP anchorages, *thesis submitted to the graduate school of natural and applied sciences of middle east technical university*.

Lynch, T. J., Burdette, E. G. (1991), Some Design Considerations for Anchors in Concrete, *ACI Structural Journal*, Vol. 88, No. 1, pp. 91-97.

Matsuzaki et Al. (2001) Advanced Wrapping system with CF-Anchor, shear strengthening of RC columns with spandrel wall, *Fibre reinforced plastics for reinforced concrete structures, FRPRCS-5 – Vol.2*, Cambridge (UK), 16-18 July 2001, pp. 813-822.

Xi Huang and Genda Chen (2005) Bonding and anchoring characterization between frp sheets, concrete, and viscoelastic layers under static and dynamic loading, *Proceedings of International Symposium on Bond Behaviour of FRP in Structures (BBFS 2005)*, Chen and Teng (eds) 2005.

Zhang, B., Benmokrane, B., and Chennouf, A. (2000), Prediction of Tensile Capacity of Bond anchorages for FRP Tendons, *Journal of Composites for Construction*, Vol. 4, No. 2, pp. 39-47.

Experimental Study on Grooving Detail for Elimination of Debonding of FRP Sheets from Concrete Surface

D. Mostofinejad

Associate Professor of Civil Engineering, Isfahan University of Technology (IUT), Isfahan, Iran

M. J. Hajrasouliha (mj.hajrasouliha@cv.iut.ac.ir)

MSc. Student of Civil Engineering, Isfahan University of Technology (IUT), Isfahan, Iran

ABSTRACT Debonding of FRP sheets from concrete surface has been a challenging phenomenon attracting many researches in recent years. Surface preparation of concrete before attaching FRP sheets is considered a suitable method to postpone debonding, but with limited effects. Grooving is an innovative technique to overcome debonding of FRP laminates from concrete surface, which has been recently used in Isfahan University of Technology (IUT). In this paper, the effect of different factors influencing the grooving capability is addressed aiming at reducing the debonding potential of FRP sheets from the concrete surface. These factors include the width and the depth of the grooves. The laboratory specimens included about thirty 100×100×500 mm plain concrete beams. Having been grooved on the surface, the specimens were reinforced with CFRP sheets and underwent the four-point flexural test so as to measure the ultimate loading capacity. The outcomes demonstrate that, debonding can be completely averted or at least to a large extent limited by considering specified width and depth for the grooves.

1 INTRODUCTION

Structural repairing and strengthening have always been a dynamic area of activity in construction works. Among the reasons for structural strengthening are included increased loading capacity and improved operation of structures [1]. One of the materials which has been used for rehabilitation and strengthening of structures in recent years is FRP composites (Fiber Reinforced Polymer). Employment of fiber reinforced polymer (FRP) composites to repair and retrofit concrete elements has been steadily increasing. In general, FRP is externally bonded to concrete by means of adhesives while transfer of the interfacial stresses to concrete is governed through bond [2]. Their numerous advantages such as high tensile strength, ease of application and corrosion resistance have given rise to their application in strengthening a wide array of structures especially reinforced concrete members. The ultimate load carrying capacity of the retrofitted members is directly influenced by bond, which is the reason that subject has received much attention.

Before installation of FRP laminates, the surface of concrete must be prepared [3]. Laboratory observations reveal that the most significant cause of premature debonding is the lack of surface preparation to create an appropriate interface for the bonding of FRP composite strips. It is, therefore, essential to provide an appropriate interface between the concrete surface and the FRP

composite sheets for flexural strengthening of beams. Preparation of the tensile side of the beam is accomplished by removing a surface layer of the weak and deteriorated concrete and exposing the coarse aggregates so as to enhance the lamination by creating an even interface. Surface preparation before bonding FRP sheets creates a greater interfacial consistency and continuity between the FRP sheet and concrete surface. This, in turn, delays debonding and yields a higher ultimate rupture strength compared with specimens lacking such preparation [4]. Therefore, a high standard surface preparation is essential for promoting long term bond performance [5]. Nevertheless, some difficulties in preparation of concrete surface such as pollution and high cost of surface preparation make it necessary to work on some new alternative methods.

Recently, in Isfahan University of Technology (IUT), Iran, Grooving method has been introduced as an innovative technique to overcome the debonding of FRP laminates from concrete surface instead of conventional surface preparation [6-8].

2 EXPERIMENTAL STUDY

2.1 Specimens detail and material characteristics

In this paper, the effect of different factors influencing the grooving capability aiming at reducing the debonding potential of FRP sheets from the concrete surface is addressed. These factors include the width and the depth

of the grooves. The specimens used in this study were used as beams with dimensions of 100×100×500 mm. To obtain an equivalent compressive strength of around 40 MPa for the cylindrical concrete specimen, 485 kg/m³ of cement, 867 kg/m³ of sand, 736 kg/m³ of coarse aggregate, and 228 kg/m³ of water were used. The concrete specimens were de-molded and cured for 28 days in the moisture bath. Unidirectional CFRP sheets with net fiber thickness of 0.12 mm were cut into 40 mm wide and 360 mm long strips and then adhered to concrete test beams. The mechanical properties of the fabric provided by manufacturer were 231 GPa modulus of elasticity and 1.7 percent ultimate strain.

2.2 Classification of experimental specimens

Overall, specimens were classified in order to be examined in the following ways:

1) examining the effect of increasing groove depth on the ultimate rupture strength of FRP sheets.

2) examining the effect of increasing groove width on the ultimate rupture strength of FRP sheets.

To examine these two, three different depths, i.e., 7.5, 10, and 12.5 mm and three widths, i.e., 4, 6, and 8 mm were considered. It must be mentioned that there were just two grooves, and grooves length was the same as that of sheet. Furthermore, distance between 2 grooves (external to external) was kept constant at 10 mm. each test was carried out 3 times.

2.3 Experimental procedure

In grooving, first the place where grooves are supposed to be made is decided. Then, using a grinding machine, the grooves are made on the surface of concrete. The surface of grooves is totally cleaned by an air blasting so that no dirt or dust would be left. The grooves were filled by Epoxy Dur 31 N in such a way that specimen surface would be quite smooth and uniform. Having filled the grooves with the right Epoxy, another Epoxy called Epoxy Dur 300 was used to install FRP sheet to specimen surface (Figure 1). After removing the extra epoxy, the specimens were allowed to be cured for at least 7 days prior to testing.

The loading setup shown in Figure 2 was used for bending test under four-point loading.

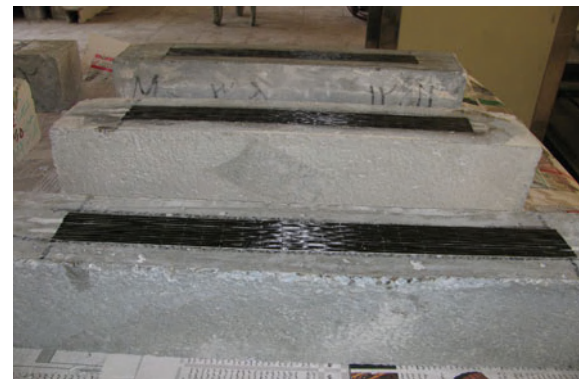
2.4 Discussion on test results

About 30 concrete specimens with dimension of 100×100×500 mm were loaded in test machine up to failure. Full response for each specimen was expressed by plotting the ultimate load versus corresponding depth of grooves (Figure 3) and width of grooves (Figure 4).

As can be seen in Figure 3, in all widths of grooves, there is an increase in ultimate rupture strength of FRP sheet as a result of increasing groove depth from 7.5 to 10 mm. However, if the depth is increased up to 12.5 mm, there is a decrease in ultimate rupture strength. This means that a depth of 10 mm would be optimal for



(a)



(b)

Figure 1 Creating of grooves on concrete surface

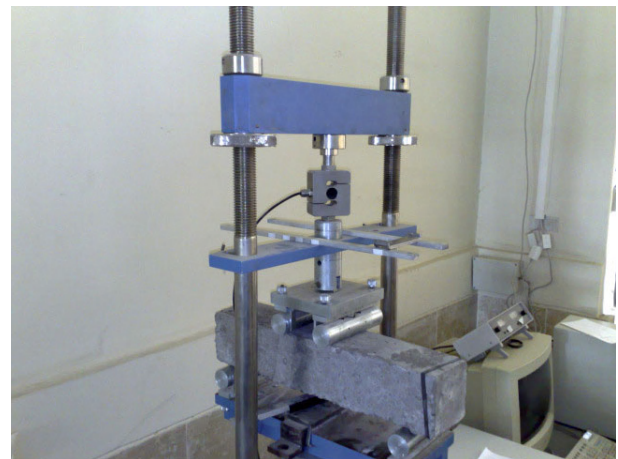


Figure 2 Test setup

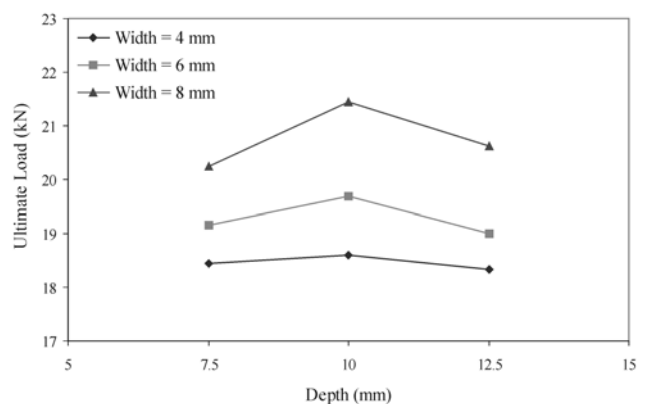


Figure 3 Ultimate load-depth curves

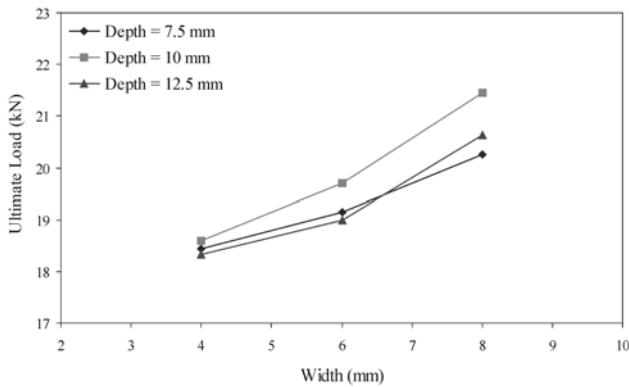


Figure 4 Ultimate load-width curves

all widths as the maximum ultimate rupture strength would be achieved. For the width of 4 mm, the increase in depth has a little effect on ultimate rupture strength as can be seen in the more linear shape of the graph. As the width of the grooves increases, however, the effect of increasing the depth is rising too so much so that its effect on ultimate rupture strength could be clearly seen in a width of 8 mm. Figure 4, shows that at a fixed depth, the increase in groove width results in an increase of the ultimate rupture strength and the rate of this increase is more perceptible in a depth of 10 mm.

All of the specimens bonded with FRP laminates were failed in the same manner. In most of the specimens, no debonding was observed until rupture of FRP laminates. However, in the width of 8 mm and in all depths, full rupturing occurred and there was no sign of debonding of FRP sheet as shown in Figure 5.



Figure 5 Rupture mechanism in most of specimens

It can be concluded that in comparison to an increase in depth, an increase in width has a higher effect on promoting the ultimate rupture strength. It must be mentioned that one of the main concerns among the experts in the field is finding some new ways to delay the debonding of FRP sheets even to a limited extent. The results of this study show that debonding can be completely averted or at least to a large extent limited by considering specified width and depth for the grooves.

REFERENCES

- Fukuyama, H. & Sugano, S., Seismic Rehabilitation of RC Building, *Cement and Concrete Composites*, Vol. 22, No. 3, 2000, pp. 59-79.
- Kamada, T. & Wictor, C.Li., The Effects of Surface Preparation The Fracture Behavior of ECC/Concrete Repair System, *Journal of Cement and Concrete*, 2000, pp. 423-431.
- Hutchinson, A.R., Review of Methods for the Surface Treatment of Concrete, MTS Project 4, Report No 2 on the Performance of Adhesive Joints, Dept. of Trade and Industry, London, 1993.
- Toutanji, H. & Ortiz, G., The Effect of Surface Preparation on the Bond Interface between FRP Sheets and Concrete Members, *Journal of Composite Structures*, Vol. 53, pp. 457-462, 2001.
- Hutchinson, A.R., Strengthening of Reinforced Concrete Structures, London, 1993, P.70.
- Mostofinejad, D. & Mahmoudabadi, E. Grooving as an Alternative Method of Surface Preparation to Postpone Debonding of FRP Laminates in Concrete Beams, *Journal of composites for construction*, ASCE, [http://dx.doi.org/10.1061/\(ASCE\)CC.1943-5614.0000117](http://dx.doi.org/10.1061/(ASCE)CC.1943-5614.0000117), 2010.
- Mostofinejad, D. & Mahmoudabadi, E. Effect of Elimination of Concrete Surface Preparation on the Debonding of FRP Laminates, *3th International Conference on Concrete Repair, Concrete Solutions- Grantham Majorana & Salomoni (Eds)*, Taylor and Francis Group, Venice, Italy, 2009, pp. 357-361.
- Mahmoudabadi, E. & Mostofinejad, D. An Alternative Method to Surface Preparation To Postpone Debonding of FRP Laminates, *Proceedings of the 9th International Symposium on Fiber-Reinforced Polymer Reinforcement for Concrete Structures*, Sydney, Australia, 2009.

Interfacial Behavior between Mechanically Fastened FRP Laminates and Concrete Substrate

E. Martinelli, A. Napoli (annapoli@unisa.it) & R. Realfonzo

Department of Civil Engineering, University of Salerno, Fisciano (SA), Italy

ABSTRACT This study addresses the interfacial behavior between Mechanically Fastened FRP (MF-FRP) laminates and concrete substrate. For this purpose, a simplified numerical model is formulated with the aim of developing a suitable bearing stress-slip relationship to model the mechanical behavior of the FRP/concrete interface. The proposed relationship is significantly different from another proposal found in the literature as it was calibrated using experimental results from tests on MF-FRP connections realized with multiple fasteners.

1 INTRODUCTION

The use of Mechanically Fastened (MF) Fiber Reinforced Polymer (FRP) laminates is emerging as a promising means for the flexural strengthening of reinforced concrete (RC) members. This technology relies on pre-cured hybrid (carbon and glass) FRP laminates with enhanced bearing strength, connected to the concrete substrate by means of steel anchors. Attractive applications are those for emergency repairs where constructability and speed of installation are critical requirements.

Experimental tests performed on RC slabs strengthened in flexure with MF-FRP laminates have recently shown the occurrence of significant slips at concrete-FRP interface which are mainly due to the bearing of the fasteners onto the laminate (Napoli 2008). As a result, the effect of the partial interaction between concrete and FRP laminate cannot be neglected in the analysis and design of MF-FRP strengthened members, whereby the assumption of conservation of plane sections may lead to inaccurate predictions. To address this issue, preliminary studies were recently performed by some authors (Lee et al. 2008; Napoli et al. 2009, 2010).

This paper presents an analytical investigation on the interfacial behavior between MF-FRP laminates and concrete substrate. A simplified numerical procedure is implemented by the authors with the aim of identifying a suitable bearing stress-slip relationship to model the mechanical behavior of the FRP/concrete interface. The accuracy of the proposed formulation is checked by comparing the numerical predictions with experimental results from direct shear tests performed by Elsayed et al. (2009) on MF-FRP strips connected to concrete blocks.

2 THE SIMPLIFIED NUMERICAL MODEL

2.1 Basic assumptions and definitions

A simplified numerical model is formulated to simulate the global behavior of a MF-FRP strip connected to a concrete block and tested in pull-out.

Figure 1 represents a schematic of the mentioned structural system and introduces some of the basic quantities and symbols utilized in the formulation of the present simplified numerical model.

In particular, the strip is connected by n fasteners and the $n-1$ spaces between two adjacent ones are denoted by a number in square brackets.

The force $H^{(k)}$ is considered as the external action applied in the axial direction (namely, z -axis) at the k -th step of the analysis procedure.

Since no distributed action is applied throughout the strip (neither in axial nor in transverse direction), the internal axial force $N^{(k)}(z)$ has a step-wise shape throughout the strip axis. In particular, the constant value assumed for $N^{(k)}(z)$ between the fastener i -th and $(i+1)$ -th is denoted as $N_i^{(k)}$ (Figure 2).

In correspondence of the same analysis step, the fasteners are supposed to transfer to the FRP strip a series of point forces $F_i^{(k)}$ (with $i=1..n$), assumed positive rightwards, as a consequence of the global reference system introduced in Figure 1.

The effect of the possible eccentricity between the axial forces $N_i^{(k)}$ and the fastener actions $F_i^{(k)}$ is neglected in the following, as a result of the assumption of very small thickness of the FRP strip. Such an assumption is needed for formulating a 1D-model considering only the membrane stress regime and neglecting the bending in transverse direction as well as

any possible non-uniform stress-strain distribution across the strip width in the out-of-plane direction.

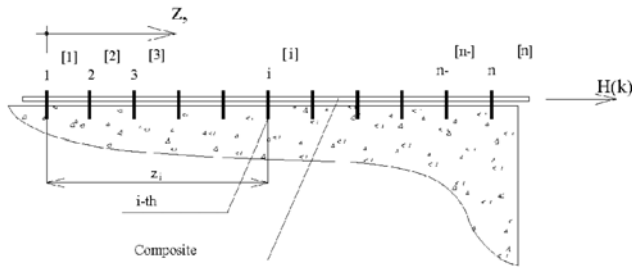


Figure 1 Schematic of the simplified 1D model

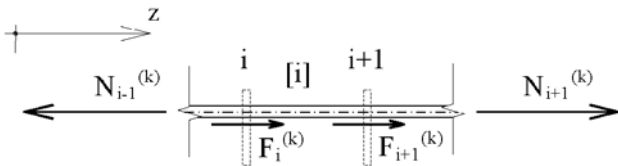


Figure 2 Internal stresses in the composite strip

The same assumption results in considering the axial displacement field $w^{(k)}(z)$ of the i -th fastener throughout the strip centroidal axis, as the unique displacement component of interest. The discrete nature of the mechanical fastening system results in the possibility of considering as main displacement parameters the n displacement values $w_i^{(k)}$ (Figure 3) attained by the displacement field $w^{(k)}(z)$ in correspondence of the n fasteners, whose position is described by the abscissa z_i (Figure 1).

2.2 Formulation of the numerical model

The step-wise shape of the internal axial forces $N_i^{(k)}$ implies a similar shape for the axial strains, whose constant value within the generic $[i]$ -th space between two fasteners can be easily derived as:

$$\varepsilon_i^{(k)} = \frac{N_i^{(k)}}{E_f A_f} \quad \text{for } i=1, n \quad (1a)$$

where E_f is the Young modulus of the composite strip and A_f the area of its transverse section.

It is worth to note that:

$$\varepsilon_n^{(k)} = \frac{N_n^{(k)}}{E_f A_f} = \frac{H^{(k)}}{E_f A_f} \quad (1b)$$

The same axial strain values depend on the strip displacements in the relevant fastener locations:

$$\varepsilon_i^{(k)} = \frac{w_{i+1}^{(k)} - w_i^{(k)}}{\Delta z_i} \quad \text{for } i=1, n-1 \quad (2)$$

where $\Delta z_i = z_{i+1} - z_i$.

The following n equilibrium equations can be written considering the axial forces $N_i^{(k)}$ and the forces $F_i^{(k)}$ transferred by the fasteners:

$$N_i^{(k)} - N_{i-1}^{(k)} + F_i^{(k)} = 0 \quad \text{for } i=1, n \quad (3)$$

being $N_0=0$.

The equilibrium equations can be written in terms of axial strain by dividing by $(E_f A_f)$ eqs. (3):

$$\varepsilon_i^{(k)} - \varepsilon_{i-1}^{(k)} = -\frac{F_i^{(k)}}{E_f A_f} \quad \text{for } i=1, n \quad (4)$$

being $\varepsilon_0=0$.

These equations can be transformed in terms of axial displacements by introducing eqs. (2), thus obtaining the following $n-1$ equations:

$$w_2^{(k)} - w_1^{(k)} = -\frac{F_1^{(k)} \cdot \Delta z}{E_f A_f}$$

$$w_{i+1}^{(k)} - 2w_i^{(k)} + w_{i-1}^{(k)} = -\frac{F_i^{(k)} \cdot \Delta z}{E_f A_f} \quad \text{for } i=2, n-1 \quad (5)$$

having assumed a constant spacing Δz between the fasteners.

A further equation can be introduced for implementing a procedure in displacement control:

$$w_n^{(k)} = \bar{w}_n^{(k)} \quad (6)$$

where $\bar{w}_n^{(k)}$ is the displacement imposed to the n -th fastener at the k -th step of the analysis.

Finally, a general relation can be introduced between the axial displacement $w_i^{(k)}$ and the corresponding force in the i -th fastener $F_i^{(k)}$:

$$F_i^{(k)} = F_i \{ w_i^{(k)} \} \quad \text{for } i=1, n \quad (7)$$

in the general hypothesis that each fastener has an independent behavior described by the function $F_i(w)$.

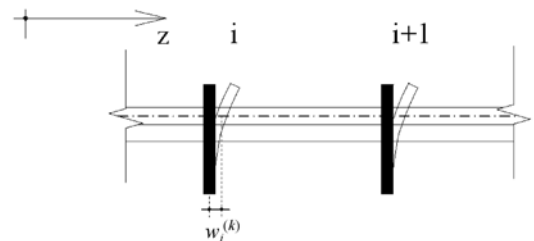


Figure 3 Axial displacement component

2.3 Numerical procedure

The numerical procedure is based on solving the set of nonlinear equations described by (5) and (6). In particular, the following set of simultaneous equations can be written in matrix form by using eqs. (7) for transforming the right hand term of eqs. (5):

$$A w^{(k,j)} = b^{(k,j)} \quad (8)$$

where \mathbf{A} is a n -th order square matrix collecting the coefficients on the left hand terms of eq. (5) and (6), $\mathbf{w}^{(k,j)}$ is the vector collecting the n displacements at the j -th numerical iteration of the k -th analysis step, and $\mathbf{b}^{(k,j)}$ is a vector collecting the right-hand terms of equations (5) and (6), the former being evaluated by means of the displacements $\mathbf{w}^{(k,j-1)}$:

$$\mathbf{b}^{(k,j)} = - \left[\frac{F_1^{(k,j-1)} \cdot \Delta z}{E_f A_f}, \dots, \frac{F_{n-1}^{(k,j-1)} \cdot \Delta z}{E_f A_f}, -\bar{w}_n^{(k)} \right] \quad (9)$$

An iterative procedure is required for handling the nonlinear nature of eq. (8) until the variation of the vector $\mathbf{w}^{(k,j)}$ with respect to the previous iteration is smaller than a given tolerance δ :

$$\frac{|\mathbf{w}^{(k,j)} - \mathbf{w}^{(k,j-1)}|}{|\mathbf{w}^{(k,j)}|} \leq \delta \quad (10)$$

Then the value of external force $H^{(k)}$ corresponding to the imposed displacement $\bar{w}_n^{(k)}$ can be derived by means of the following general equilibrium condition:

$$H^{(k)} = - \sum_{i=1}^n F_i [w_i^{(k,j)}] \quad (11)$$

3 NUMERICAL ANALYSES AND POSSIBLE CALIBRATION OF “LOCAL” STRESS-SLIP RELATIONSHIPS

The accuracy of the implemented procedure has been checked by considering experimental results from direct-shear tests performed by Elsayed et al. (2009) on MF-FRP/concrete connections. In particular, the configurations considered for the experimental-numerical comparisons refer to FRP-concrete joints connected with multiple screwed fasteners, namely: test SC03, where the fastening was realized with three connectors; test SC04, with four fasteners, and tests SC05 and SC06 with five and six connectors, respectively. In such configurations, the screwed fasteners had a 4.76 mm shank diameter (d_s), while the dimensions of the FRP strip were: $t_f = 3.2$ mm, $b_f = 50$ mm and $L = 650$ mm. A constant fastened length of 250 mm was kept for these specimens, while for the outer fasteners (i.e. fasteners at the locations $i=1$ and $i=n$ in Figure 1) a clear distance of 75 mm was left at each end of the concrete block.

From the previous section it is noted that the proposed algorithm can be applied once a relationship between the force in the i -th fastener $F_i^{(k)}$ and the axial displacement $w_i^{(k)}$ is defined, as expressed by eq. (7). In particular, $F_i^{(k)}$ can be approximated as:

$$F_i^{(k)} = -\sigma_{f,i}^{(k)}(w_i^{(k)}) \cdot t_f \cdot d_s \quad (12)$$

where $\sigma_{f,i}^{(k)}(w_i^{(k)})$ is the “local” bearing stress produced

by the single fastener in the FRP laminate which is associated with the axial displacement $w_i^{(k)}$ (or “slip”). The general nonlinear relationships $[\sigma_f(w)-w]$ illustrated in Figure 4 was considered in the numerical modeling:

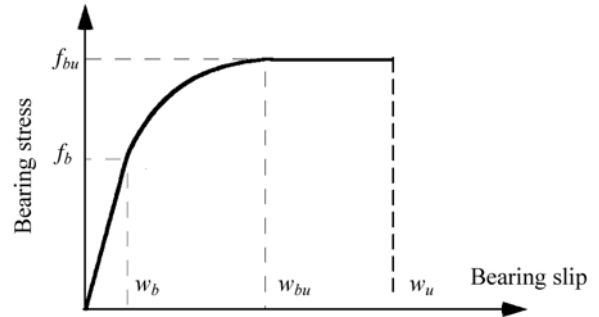


Figure 4 Modeling of the “local” bearing stress-slip

$$\begin{cases} \sigma_f(w) = \frac{f_b \cdot w}{s_b} & \text{if } w \leq w_b \\ \sigma_f(w) = f_b \cdot A^{\exp(-\alpha A^\beta)} & \text{if } w_b \leq w \leq w_{bu} \\ \sigma_f(w) = f_{bu} & \text{if } w \geq w_{bu} \end{cases} \quad (13)$$

where f_b identifies the stress in the FRP laminate at the onset of bearing, resulting in a deviation from linearity of the stress-slip relation, and w_b is the associated slip; f_{bu} is the bearing strength of the FRP laminate, and w_{bu} is the associated slip; w_u is the ultimate slip. The parameter $A = w/w_b$, while α and β define the nonlinear increasing branch.

It is noted that the framework of eq. (13) is that proposed by Elsayed et al. (2009). The parameters f_b , w_b , f_{bu} , w_{bu} , w_u , β , instead, are calibrated through a least-square minimization procedure between the value of the external force $H^{(k)}$ obtained by the numerical procedure and the experimental result corresponding to the associated displacement $w_n^{(k)}$. Such procedure is described in the following by equations:

$$\mathbf{q} = (f_b, w_b, f_{bu}, w_{bu}, w_u, \beta) \quad (14)$$

$$\Delta(\mathbf{q}) = \sum_k \left[H^{(k)}(w_n^{(k)}, \mathbf{q}) - H^{(k, \text{exp})} \right]^2 \quad (15)$$

$$\bar{\mathbf{q}} = \text{argmin} \Delta(\mathbf{q}) \quad (16)$$

while the parameter α relies on the values assumed by the other parameters of the vector \mathbf{q} .

Figure 5 shows the four bearing stress-slip relationships for a single screw yielded by the least-square procedure performed for the tests SC03, SC04, SC05 and SC06.

By comparing the four curves, similar trends can be observed. In particular, it is noted that the bearing strength is not highly sensitive with the number of

fasteners and an average value of about 323 MPa is estimated.

Conversely, the bearing strength of a MF-FRP/concrete joint connected with a single fastener is significantly greater than the corresponding value attributed to a single screw when the connection is realized with multiple fasteners.

This consideration can be drawn by comparing the four local stress-slip relationships illustrated in Figure 5 with the corresponding law proposed by Elsayed et al. (2009), where a value of the bearing strength of 385 MPa was estimated. The latter was in fact obtained through a best fit analysis between numerical simulation and experimental curves obtained for tests on a single screw. In this way, the effect of multiple interactions among fasteners – which may yield to a reduced bearing strength of the MF-FRP connection – was not taken into account.

The mismatch observed both in elastic and post-elastic branch between the relationship proposed by Elsayed et al. and the numerical curves may be attributed to the same reason.

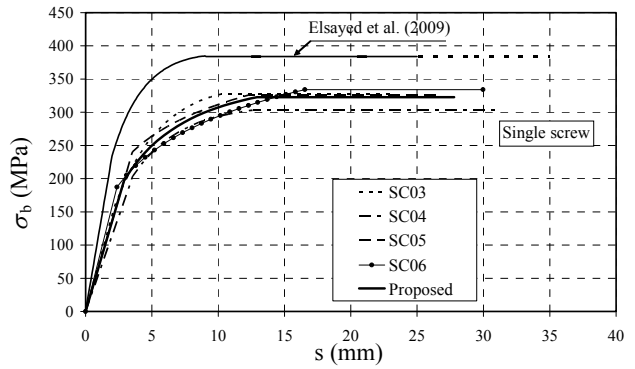


Figure 5 Bearing stress-slip relationships for a single fastener

In Figure 5 the bearing stress-slip relationship proposed by the authors is finally plotted, where the components of the vector \vec{q} assume the following values: $f_b = 197$ MPa, $w_b = 2.9$ mm, $f_{bu} = 323$ MPa, $w_{bu} = 12.9$ mm, $w_u = 27.8$ MPa, $\beta = 0.31$; $\alpha = 0.69$. Such relationship has been obtained by averaging the values of each parameter calibrated through the four numerical simulations.

Figure 6 shows the experimental-numerical comparisons in terms of external force-maximum displacement for the four considered tests. In these plots the numerical

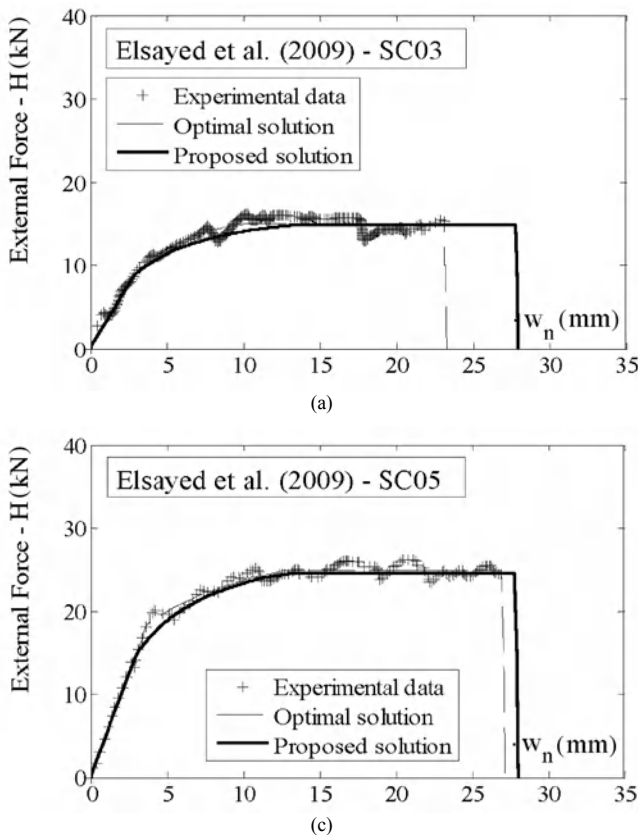


Figure 6 Experimental-numerical comparisons

simulations have been performed by using both the proposed bearing strength-slip relationship and the solution of the optimization problem in eqs.(14-16)

It is noted that the implementation of the developed relation yields force-displacement curves that are in a

good agreement with the experimental ones, with slight differences only in terms of ultimate displacements.

Consequently, although further studies are required for its validation, the proposed bearing stress-slip relationship may be considered to model the interfacial behavior

between MF-FRP laminate and concrete substrate.

4 FINAL REMARKS

In this paper, a simplified numerical model has been presented by the authors to simulate the global behavior of MF-FRP strips connected to concrete a block and tested tested in pull-out. In particular, the implemented algorithm has also pointed out useful indications for the development of an accurate local stress-slip relationship which may be used to model the behaviour of the FRP-concrete interface.

REFERENCES

- Elsayed, W.E., Ebead U. A. & Neale, K. W. 2009. Studies on mechanically fastened fiber-reinforced polymer strengthening system. *ACI Structural J*, 106 (1): 49-59.
- Lee, H.L., Lopez, M.M. & Bakis, C.E. 2007. Flexural behavior of reinforced concrete beams strengthened with mechanically fastened FRP strip. In *Proc. of FRPRCS-8*, Patras, Greece, July 16-18, (on CD).
- Napoli A. 2008. RC Structures strengthened with Mechanically Fastened FRP systems. MSc thesis, University of Miami: 1-78
- Napoli, A., Matta, F., Martinelli, E., Nanni, A. & Realfonzo R. 2009. Flexural RC members strengthened with mechanically fastened FRP laminates: test results and numerical modeling, In *Proc. of Asia-Pacific Conference on FRP in Structures*, APFIS, Seoul, Korea, December 9-11.
- Napoli A., Matta F., Martinelli E., Nanni A. & Realfonzo R. 2010. Accepted for publication to *Magazine of Concrete Research*, a Thomas Telford Journal (in press).

FRP-to-Concrete Joint Assemblies Anchored with Multiple FRP Anchors: Experimental Investigation

H.W. Zhang & S.T. Smith (stsmith@hku.hk)

Department of Civil Engineering, The University of Hong Kong, China

ABSTRACT Higher strains can be developed in fibre-reinforced polymer (FRP) composites which are bonded to the surfaces of concrete members if the FRP is anchored. Anchors made from FRP (also known as FRP spike anchors but herein referred to as FRP anchors) are a promising type of anchorage as they can be applied to a variety of different shaped structural elements and they have been shown to be effective in enhancing the strain capacity of externally bonded FRP. Limited research, however, has been conducted on understanding and quantifying the strength and behaviour of such anchors in isolation and research to date has been on mainly single anchors. A series of tests is therefore reported in this paper on FRP-to-concrete joints anchored with two FRP anchors with the main test variable being the relative position of the anchors. Displacement controlled tests have enabled the complete load-slip responses of the joints to be captured which in turn provides valuable insights to be gained in understanding the behaviour of the anchored joint over the complete loading range. The tests reported in this paper advance our understanding of FRP anchor groups in anchoring externally bonded FRP strengthening systems.

1 INTRODUCTION

Numerous studies have proven the effectiveness of strengthening concrete with externally bonded fibre-reinforced polymer (FRP) composites (e.g. Hollaway and Teng 2008). Numerous studies have also shown the FRP to debond from the concrete at strains substantially lower than the rupture strain of the FRP (Hollaway and Teng 2008). Recent studies have shown the effectiveness of the externally bonded FRP to be increased upon the addition of anchorage (Smith 2009, Zhang et al. 2010). Anchors made from FRP (herein FRP anchors) have been proven to be a most effective form of anchorage as tests have shown the strength of FRP-to-concrete joints to be increased up to 80 % by the introduction of a single FRP anchor (Smith 2009). The bulk of tests conducted to date have, however, been confined to FRP-to-concrete joints with a single FRP anchor. In reality, multiple anchors may need to be installed to the strengthening system and hence our current limit of knowledge needs to be expanded.

This paper reports the results of a series of tests on FRP-to-concrete joints which have been anchored with two anchors. The main test variable is the relative position of the two anchors. These tests reported herein form part of a much larger testing program being conducted at The University of Hong Kong on the characterisation of FRP anchors.

2 EXPERIMENTAL SET-UP AND DETAILS

The single shear test set-up utilised in the experimental programme is shown in Figure 1. The main test variables of number of anchors and relative anchor positions are shown in Figure 2. In addition, three control tests were conducted on unanchored FRP-to-concrete joints (not shown in Figure 2) possessing the same concrete and FRP plate geometrical properties as the anchored joints tests.

All FRP plates were formed from three layers of carbon fibre sheet in a wet lay-up procedure (0.131 mm nominal carbon fibre sheet thickness) and a 40 mm unbonded zone was maintained at the loaded free end of the concrete prism. The impregnated carbon FRP anchors used in this study, which were formed by hand in the laboratory from rolling 200 mm wide carbon fibre sheets (i.e. same sheet used for plate and anchors), are fully described in Zhang et al. (2010). All anchors were embedded to a constant depth of 40 mm and the anchor fan component was oriented to the direction of load as shown in Figure 1. Additional details of the anchors are provided in Figure 3 with selected photographs of the installation of the FRP anchor and FRP plating in Figure 4.

The concrete cube compressive strength of the unanchored control joints was 50.3 MPa and that of all the anchored joints was 51.9 MPa. The FRP mechanical properties, derived from tests on flat coupons, were

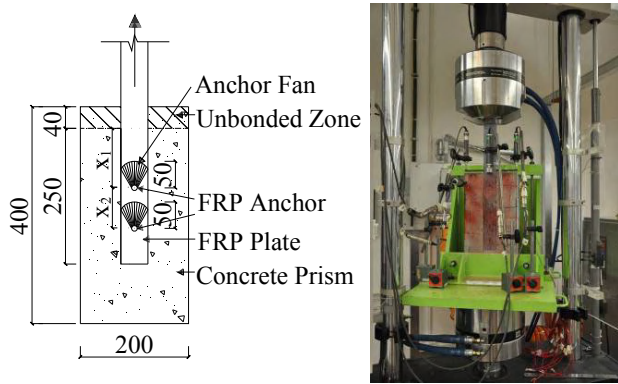


Figure 1 Test set-up

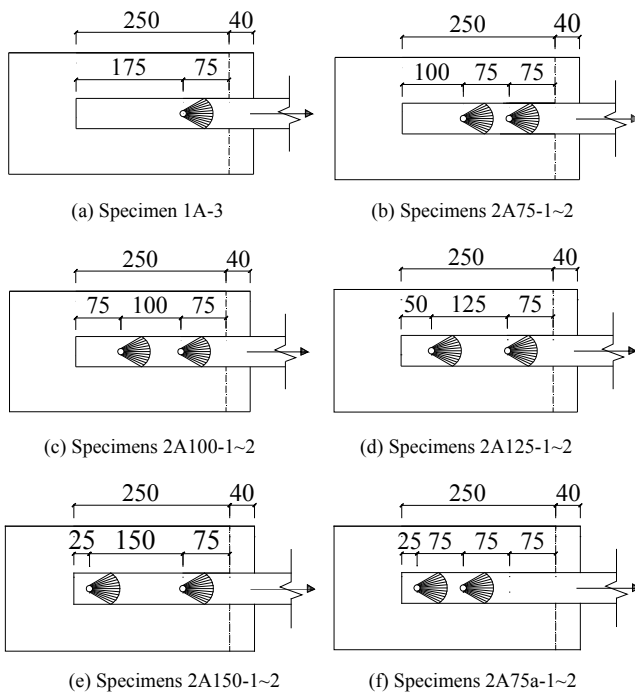


Figure 2 Anchor layout (e.g. 2A100-1~2 represents specimens 1 and 2 for joints with 2 anchors spaced at 100 mm)

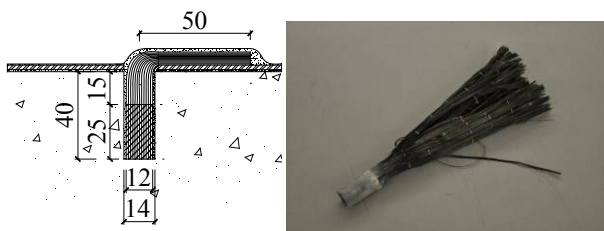


Figure 3 Impregnated carbon FRP anchor details

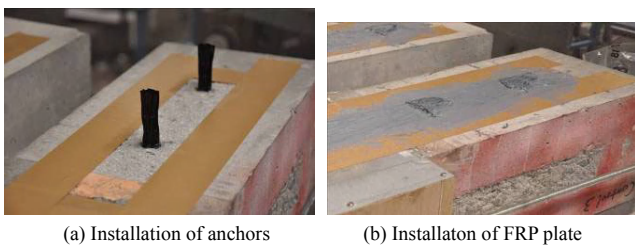


Figure 4 Construction of test specimens

elongation = 15,172 $\mu\epsilon$ (standard deviation, sd. = 126 $\mu\epsilon$), tensile strength = 3,090 MPa (sd. = 38 MPa) and elastic modulus = 201.4 GPa (sd. = 29 GPa).

Several linear variable differential transformers (LVDTs) were used as shown in Figure 5. The slip at the free end of the bonded FRP is in turn calculated from the difference between LVDT 1 and the average of LVDTs 2 and 3 in addition to consideration of the elastic deformation of the unbonded region of FRP and concrete between. Several electric resistance strain gauges were also installed on the surfaces of the strengthening plates however such strain gauge results are not reported in this paper. Load was applied monotonically by displacing the ram of the universal testing machine shown in Figure 1 at a constant rate of 0.3 mm/min.

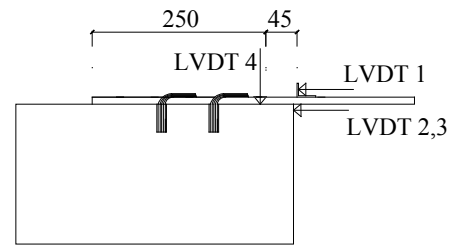


Figure 5 Instrumentation

3 TEST RESULTS

The following is a brief summary and discussion of the results. A much more detailed account is presented in Zhang and Smith (2010).

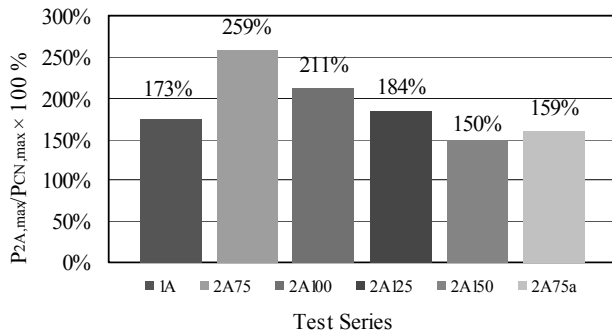
3.1 Strength and effect of anchor position

A summary of the average increase in joint strength for each anchor configuration, relative to the average of the unanchored control joints, is provided in Figure 6a. The increase in joint strength relative to the single anchored joint strength is provided in Figure 6b. The average strength of the unanchored control joints is 18.0 kN and the strength of the single anchored control joints is 31.1 kN.

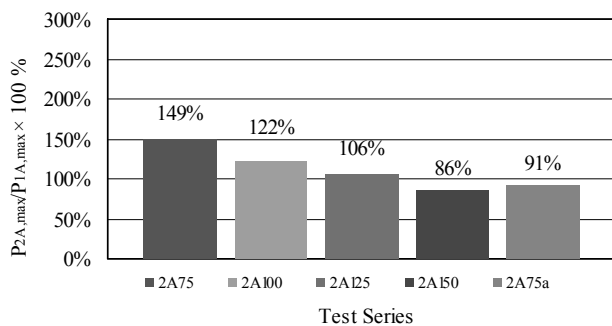
The effect of the different anchor positions is evident in Figure 6 in which the effectiveness of the second anchor decreases as it is positioned further away from the loaded end. It is currently not clearly understood why the strength of specimen 2A150 dropped below that of the average of the single anchored control joint.

3.2 Failure modes

The three unanchored joints failed by debonding which initiated at the loaded end of the joint. Debonding occurred at the interface of the FRP and the concrete with a thin layer of concrete remaining attached to the surface of the FRP (Figure 7a). This desirable mode of failure has been reported numerous times in the literature (e.g. Yao et al. 2005).



(a) Relative to unanchored control joint average result



(b) Relative to single anchored control joint average result

Figure 6 Strength enhancement of multiple anchored joints

The single anchored joints failed by debonding of the plate followed by rupture of the anchor fibres in the bend region. Plate debonding initiated at the loaded end of the joint and the anchor failed after significant slip occurred between the FRP plate and concrete substrate.

For all joints anchored with multiple FRP anchors, the plate completely debonded and then the remaining anchored plate failed in different modes. The following description provides a more detailed account for the majority of the tests.

(1) Plate debonding initiated at approximately the capacity of the unanchored control joints. This is particularly evident in the load-slip responses presented in the following sub-section. Such debonding initiated at the loaded end of the plate and generally extended to the anchor fan region of the first anchor (i.e. the anchor nearer to the loaded end of the joint).

(2) After the debonding crack propagated to the anchor fan region of the second anchor, the curved edge of the first anchor fan cracked but not in all cases.

(3) The remaining bonded portion of the plate then debonded upon which a noticeable drop in the load carrying capacity of the joint was noticed. Most joints then experienced a reserve of strength (and slippage) primarily due to shear resistance provided by sliding of the roughened debonded FRP-to-concrete interface. Such shear resistance was assisted by clamping of the FRP plates by the FRP anchors. In most cases, this reserve of strength was less than the load to cause

complete plate debonding, however, not always; as observed in the case of specimens 2A125-1~2 (in the following sub-section). In some cases, longitudinal splitting was observed which originated at the anchor dowel.

(4) The joints eventually failed by rupture of the FRP plate with debonding of the anchor fan (Figure 7b) closet to the loaded end or otherwise by rupture of the anchor fibres in the same anchor (Figure 7c). In most cases, the anchor located furthest away from the loaded end was relatively undamaged but not always.



(a) Debonded plate

(b) Plate rupture and fan debond



(c) Anchor rupture

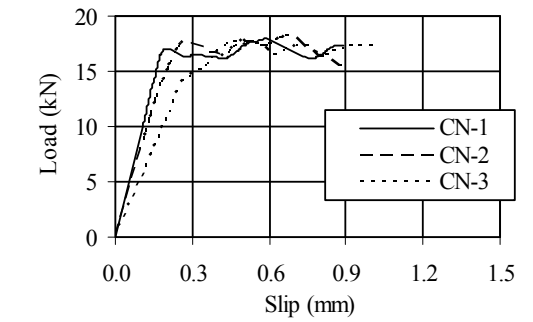
Figure 7 Typical FRP anchor and plate failures

3.3 Load-slip responses

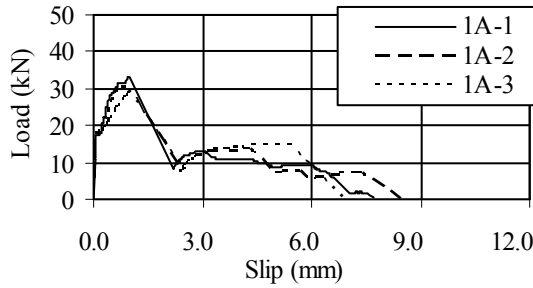
The load-slip responses for all specimens are shown in Figure 8. On account of the long bond length (about double the effective bond length), the control joints exhibited a peak load plateau (Figure 8a). For all of the anchored joints, the peak load at approximately 1 to 2 mm of slip represents complete debonding of the plate. After debonding, the load generally reduced or remained about the same. In most cases, the multiple anchored joints enjoyed strengths larger than the single anchored joints. Even though the slip capacity of the multiple anchored joints was not in excess of the single anchored joints, the deformability of the former was established.

4 CONCLUSIONS

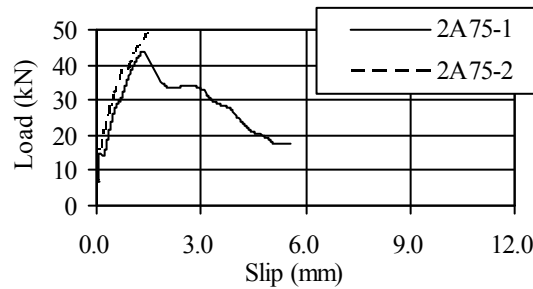
The results of a series of tests on FRP-to-concrete joints which have been anchored with multiple anchors have been presented in this paper. In most cases, the strength of the joint was increased above that of the single anchored joint. Load-slip responses have enabled the post-strength reserve of strength offered by the anchors after complete debonding of the strengthening plate to be observed and quantified and the significant slip capacity of the anchored joints to be established.



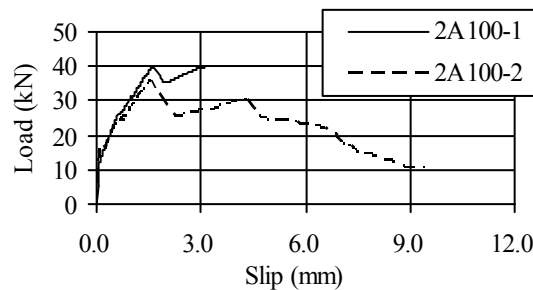
(a) Control joints



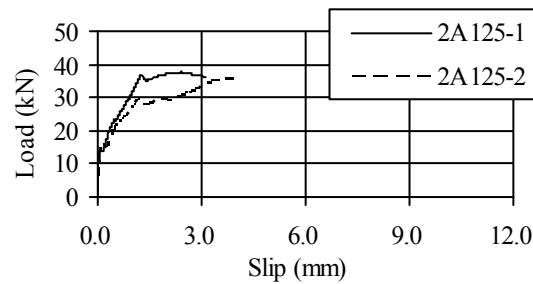
(b) Single anchored joint



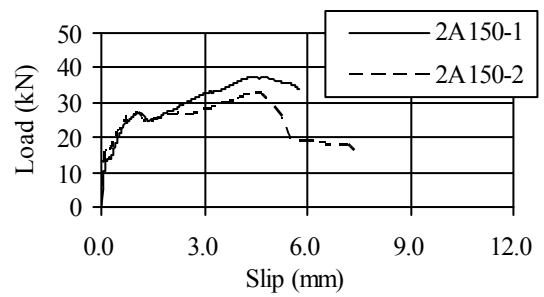
(c) Double anchored joints: spacing = 75 mm



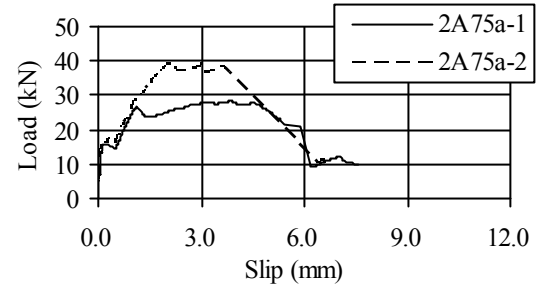
(d) Double anchored joints: spacing = 100 mm



(e) Double anchored joints: spacing = 125 mm



(f) Double anchored joints: spacing = 150 mm



(g) Double anchored joints: spacing = 75 mm

Figure 8 Load-slip responses

5 ACKNOWLEDGEMENTS

Funding provided by the Hong Kong Research Grants Council's General Research Fund Grant HKU 715907E is gratefully acknowledged

REFERENCES

Hollaway, LC & Teng, JG 2008. Strengthening and rehabilitation of civil infrastructures using fibre-reinforced polymer (FRP) composites, Woodhead Publishing, UK, China.

Smith, ST 2009. FRP anchors: recent advances in research and understanding, Second Asia-Pacific Conference on FRP in Structures, APFIS 2009, Korea, 9-11 December, pp. 35-44.

Yao, J, Teng, JG & Chen, J. 2005. Experimental study on FRP-to-concrete bonded joints, Composites: Part B, 36, 99-110.

Zhang, HW, Smith, ST & Kim, SJ 2010. Optimisation of carbon and glass FRP anchor design, under review.

Zhang, HW & Smith, ST 2010. Strength and behaviour of FRP anchor groups in FRP-to-concrete joints, in preparation.

Temperature and Water-Immersion Effect on Mode II Fracture Behavior of CFRP-Concrete Interface

Fatemeh Sedigh Imani, An Chen (An.Chen@mail.wvu.edu), Julio F. Davalos (Julio.Davalos@mail.wvu.edu),
& Indrajit Ray

Department of Civil and Environmental Engineering, West Virginia University, Morgantown, WV 26506-6103, USA

ABSTRACT Rehabilitation and retrofit of concrete structural members using externally bonded Fiber Reinforced Polymer (FRP) strips has been gaining steadily use in recent years because of its many advantages, such as ease and speed of construction, low cost, low maintenance, and high strength to weight ratio. An important design issue with significant performance and safety implications is the debonding of externally bonded FRP strips in flexural members, where the delamination is primarily due to Mode II failure. A lot of research has been done in this area, but there are concerns about interface durability. This study is based on a fracture mechanics approach using Mode II single shear test to evaluate the durability of Carbon FRP (CFRP)-concrete interface subject to two combined environmental conditioning variables: (1) immersion in deionized water varying from 0 to 15 weeks; and simultaneously (2) controlled temperatures varying from 25°C to 60°C of the same samples immersed in water. A new method to obtain the fracture energy release rate and the cohesive law is proposed based on J-integral, by measuring load and slip at the debonding end only, which was verified by the traditional strain-based method. The durability of the interface is characterized by the fracture energy release rate. By comparing the results with those from unconditioned companion specimens, it is found that considerable degradation of the interface integrity resulted with increased moisture duration and temperature. The test results will be further used to develop a model to predict the long-term behaviour of the interface based on Arrhenius or other relations.

1 INTRODUCTION

In the past two decades, the use of Fiber Reinforced Polymer (FRP) composites has become the most popular method of rehabilitating and retrofitting concrete structures, especially bridges. In a typical repair, the FRP plate or strip is bonded to the tension side of the structure improving its load carrying capacity. Therefore, the quality and durability of the FRP-concrete interface are the major concerns for providing long-term performance, and preventing delamination or debonding of FRP strips from the concrete substrate.

Despite the extensive studies on understanding the interface fracture under shear loading (Xu and Needleman, 1993; Nakaba et al., 2001; Högberg, 2006; Wang, 2006; Ferracuti, 2006; and Wang, 2007), and also durability studies on the composite materials, surprisingly, only a few studies can be found in the literature focusing on durability issues in relation to interfacial Mode II fracture.

The objective of the present study are: (1) Developing a Fracture Mechanics Model to characterize the FRP-concrete interfacial behavior under Mode II loading; and (2) extending the aforementioned fracture mechanics model to study the durability of FRP reinforcing technique

in case of exposure to simulated environmental conditions. The following simultaneous environmental effects are considered as exposure conditions: (1) immersed in deionized water varying from 0 to 13 weeks; and (2) controlled temperatures varying from 25°C to 60°C (77°F to 140°F) of samples while immersed in water.

2 EXPERIMENTAL PROGRAM

2.1 Materials

Normal concrete was used for all the specimens. The concrete mix proportions by weight with respect to the cement weight were: 2.5 (coarse aggregates, gravel): 1.82 (fine aggregates, sand): 0.5 (water). In order to obtain better workability, 800 mL/yd³ of air entraining admixture (MB-AE™ 90) was also added to the mix. The average 28-day compressive strength of the concrete determined per ASTM-C39 was 4500 psi (31 MPa). MBrace® CF130 carbon fabrics provided by BASF were used. The nominal tensile strength, modulus of elasticity and effective thickness of the laminates were: 3000 MPa (435 ksi), 230 GPa (33360 ksi), and 0.165 mm (0.0065 in), respectively. A water-based releasing agent was used to coat the inside surface of the concrete mold in order to avoid the surface contamination and

obtain a better surface finish.

2.2 Testing Plan

Concrete prisms with nominal dimensions of $330 \times 127 \times 102 \text{ mm}^3$ ($13 \times 5 \times 4 \text{ in}^3$) were casted using the above mentioned normal concrete. FRP laminates of $160 \times 46 \text{ mm}^2$ ($6.3 \times 1.8 \text{ in}^2$) were bonded to the concrete prisms at the age of 90 days. The concrete specimens were demolded after 24 hours and cured for 28 days in lime saturated water, and then allowed to dry until 90 days in an environmental chamber with 25°C (77°F) and 50% relative humidity to minimize the shrinkage effect which could adversely affect the bond behavior. The concrete surface profile was obtained by sandblasting at the age of 90 days until obtaining a level of CPS 3-4, as defined by ICRI/ACI (1999) by visual inspection, i.e., until the coarse aggregates were exposed. After cleaning off the prism surface using pressurized air, the FRP strip was bonded over the concrete prism using the dry-layup method as recommended by the manufacturer (MBrace® Installation Procedure 2006). A predefined notch was introduced at one end of the concrete prism by placing a wax paper over that area of the prism before bonding. The FRP was extended beyond the concrete prism as shown in Figure 1, to apply the load. After FRP application, the specimens were cured for 7 days in the laboratory ambient, and then were immersed in temperature-controlled deionized water until tested.

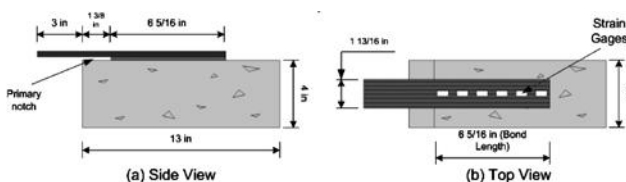


Figure 1 Specimen specifications (1 in=25.4 mm)

A total of 212 specimens were tested. Four were un-conditioned control specimens and the others were tested after being conditioned in deionized water in four custom-made temperature-controlled tanks with $T_1=25^\circ\text{C}$ (77°F), $T_2=36^\circ\text{C}$ (96.8°F), $T_3=48^\circ\text{C}$ (118.4°F), and $T_4=60^\circ\text{C}$ (140°F), respectively; where 52 specimens were used for each temperature. Starting from the end of third week of conditioning, four samples were tested for each temperature in two weeks intervals until the 13th week. In case the coefficient of variance (COV) of calculated fracture energy exceeded 20%, the corresponding sample was disregarded in data analyses. Tensile test was performed on one of the delaminated FRP laminates for each group in order to obtain the modulus of elasticity.

The tests were conducted in a 98 kN (20,000 lbf) capacity Material Testing Machine (MTS) utilizing a custom-made testing fixture as shown in Figure 2. The strain field in the FRP laminate was obtained by 6 strain

gages mounted on the FRP along the fiber direction. A linear variable displacement transformer (LVDT) with a range of $\pm 25.4 \text{ mm}$ ($\pm 1 \text{ in}$) was used to measure the displacement at the crack opening. The tests were performed under displacement control at a rate of 0.002 mm/s up to failure.

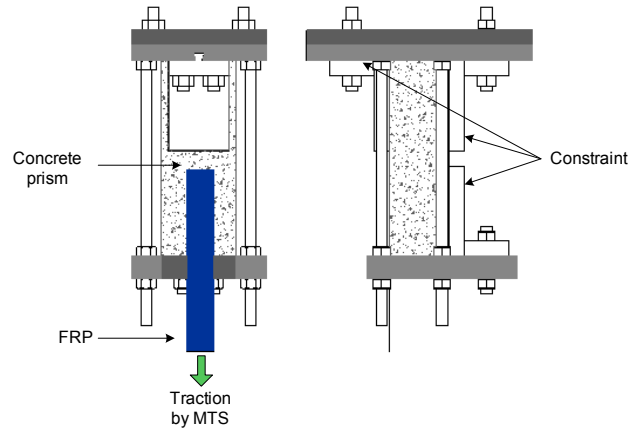


Figure 2 Test setup

3 ANALYTICAL METHODS

3.1 Traction separation law

The traction-separation law is obtained by two approaches: J-integral method based on fracture mechanics, and the traditional method using strain field. The following assumptions are adopted for data analyses:

- Both concrete and FRP to be elastic materials.
- Thickness variation of FRP laminate is neglected.
- Normal stress at the interface is neglected, i.e., assuming that the interface is subjected only to shear stress.

3.1.1 J-Integral approach

The J-integral for elastic materials under uniaxial loading is defined as follows (Rice, 1968):

$$J = \oint_{\Gamma} \left(W dz - \vec{T} \cdot \frac{\partial \vec{u}}{\partial x} ds \right) \quad (1)$$

where u is the displacement vector; T is the traction vector acting outward, normal to Γ , and defined as $T_i = \sigma_{ij} n_j$; ds is an element of infinitesimal length along Γ ; and W is the strain energy.

Based on the closed path shown in Figure 3, and considering that except for sections BA and DC , the J-integral for all the other sections is zero (Fraisse and Schmit, 1993), equation (1) reduces to:

$$J = J_{DC} + J_{BA} \quad (2)$$

where:

$$J_{DC} = - \int_0^{t_c} \left(w dz - \vec{T} \frac{\partial \vec{u}}{\partial x} ds \right) = \frac{1}{2} \left(\frac{N_c^2}{A_c^2 E_c} \times t_c \right) \quad (3)$$

$$J_{BA} = -\int_0^{t_p} \left(wdz - \bar{T} \frac{\partial \bar{u}}{\partial x} ds \right) = \frac{1}{2} \left(\frac{N_p^2}{A_p^2 E_p} \times t_p \right) \quad (4)$$

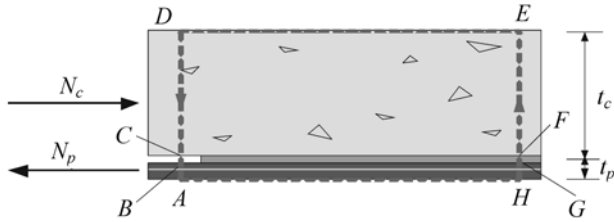


Figure 3 J-integral Path

Since the axial stiffness of FRP laminate is much smaller than concrete, i.e., $E_p A_p \ll E_c A_c$, J_{DC} (concrete) becomes negligible comparing to J_{BA} (FRP). Therefore, the J-integral corresponding to the system shown in Figure 3 is reduced to:

$$J = \frac{1}{2} \frac{N_p^2}{A_p^2 E_p} \times t_p \quad (5)$$

As the J-integral defines the Energy Release Rate (ERR) at the debonding tip, the interfacial shear stress will be:

$$\tau = \frac{dJ}{d\delta} \quad (6)$$

Substituting Equation (5) into Equation (6), the following relation between the interfacial shear stress and the slip at the tip of the notch can be obtained:

$$\tau = \frac{1}{2A^2 E t} \frac{d}{d\delta} (N^2) = \frac{1}{A^2 E t} \left(N \frac{dN}{d\delta} \right) \quad (7)$$

When N is equal to the maximum load, J becomes fracture energy release rate, G_f . From Equation (5), we have:

$$G_f = \frac{1}{2} \frac{N_{\max}^2}{A_p^2 E_p} \times t_p \quad (8)$$

Other researchers (Taljsten, 1996; Yuan et al., 2001; Wu et al., 2002) have obtained the same equation using LEFM approach. Therefore, ERR of the interface, which is also defined as the area under the shear stress-slip curve, can be found by obtaining the maximum applied load only. Thus, Equation (8) can be used to verify the obtained traction-separation law.

3.1.2 Traditional method using mounted strain gages

Taljsten (1997) initiated using the strain field on a plate (FRP/steel) bonded to concrete substrate in order to obtain the constitutive law of the interface. This method has been adopted afterwards by many researchers throughout the years (Nakaba et al., 2001; Pham and Al-Mahaidi, 2006; Ferracuti, 2006; and Ali-Ahmad et al., 2006). The relative slip at location of the gage at a

distance x from the loaded end can be obtained by integrating the strain distribution:

$$s(x) = s(x_{i+1}) + \frac{1}{2} \frac{\varepsilon_{i+1} - \varepsilon_i}{x_{i+1} - x_i} (x - x_i)^2 + \varepsilon_i (x - x_i);$$

$$x_i \leq x \leq x_{i+1} \quad (9)$$

Assuming that the FRP laminate is perfectly bonded to the concrete, $s(x_n) = 0$, the slip at each strain gage location can be calculated. The average slip in the middle of two successive strain gages, $s_{i+1/2}$, can be expressed as:

$$s_{i+1/2} = \frac{s(x_{i+1}) + s(x_i)}{2} \quad (10)$$

The constant shear stress between two successive strain gages can also be calculated based on the strain gradient as:

$$\tau_{i+1} = t_{FRP} E_{FRP} \frac{\varepsilon_{i+1} - \varepsilon_i}{x_{i+1} - x_i} \quad (11)$$

Therefore, the traction-separation law can be plotted as $\tau_{i+1/2}$ versus $s_{i+1/2}$.

4 TESTING RESULTS

4.1 Traction separation law

In order to use the first analytical model (J-integral), an exponential curve in the form of equation (12) was fitted to the experimental data points.

$$N = a(e^{b\delta} - 1) \quad (12)$$

where a and b are empirical constants. A typical load-slip curve is shown in Figure 4. For all the samples, the load increased linearly up to 60%-70% of the ultimate load (Point A in Figure 4). The load-slip relationship was nonlinear until the load became constant for a while before the final failure (Point B in Figure 4).

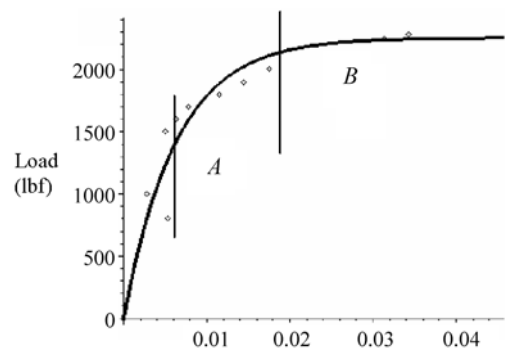


Figure 4 Typical load-slip curve

For the J-integral, based on equations (7) and (8), and as an illustrative example, the traction separation law for samples immersed in 25 °C water for 13 weeks is obtained as follows:

$$\tau = -1154.96(e^{-157.96\delta} - 1)e^{-157.96\delta} \quad (13)$$

This traction separation law along with the corresponding law obtained using the traditional method is shown in Figure 5. Their corresponding Energy Release Rates (ERR) are 0.67 N/mm (3.82 lbf/in) and 0.64 N/mm (3.65 lbf/in), respectively, which are very close to 0.65 N/mm (3.74 lbf/in) as calculated directly from equation (8). Since all the three methods give approximately the same ERR, equation (8) will be used in section 4.2 to calculate the ERR.

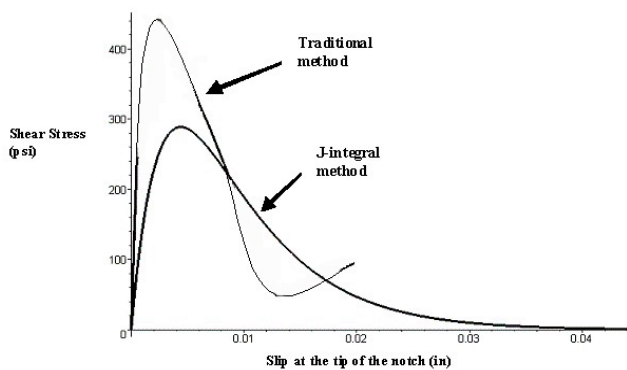


Figure 5 Traction –separation laws obtained by J integral and the traditional method

Although ERR from the two methods are in good agreement, the obtained maximum shear stresses and maximum slips are quite different; 1.98 MPa (288 psi) for the J-integral method and 2.85 MPa (414 psi) for the traditional method, which can be attributed to experimental error in LVDT measurements. As shown in Equation (7), any error in slip at the tip δ will affect shear stress τ . Since the reading from LVDT is normally larger than the actual slip, the maximum shear stress calculated from J-integral method is lower than that from the traditional method, as shown in Figure 5.

However, based on past study (Qiao and Chen, 2008), it was concluded that ERR is more important than the shape of the traction-separation law, which will also be verified by a follow up Finite Element study. Therefore, the results obtained from the J-integral method can be used to describe the FRP-concrete interface behavior.

4.2 Decay of fracture energy due to water-immersion and temperature effects

Figure 6 shows, as expected, the decrease in fracture energy with respect to increase in time and also temperatures. For T1 through T3, there was a significant reduction in fracture energy when the immersion duration was from 0 to 3 weeks. After the specimens were submerged in water for 5 weeks, the average G_f value remained relatively constant.

However, for $T_4=60^\circ\text{C}$ (140°F), even after 5 weeks of immersion, the EER continued to decrease. As shown in Figure 6, the G_f value for T_4 is about 65% of that of the control specimen at the end of 15 weeks of immersion,

which is significantly lower than that of T_1 with about 23%, T_2 with 34%, and T_3 with about 43%.

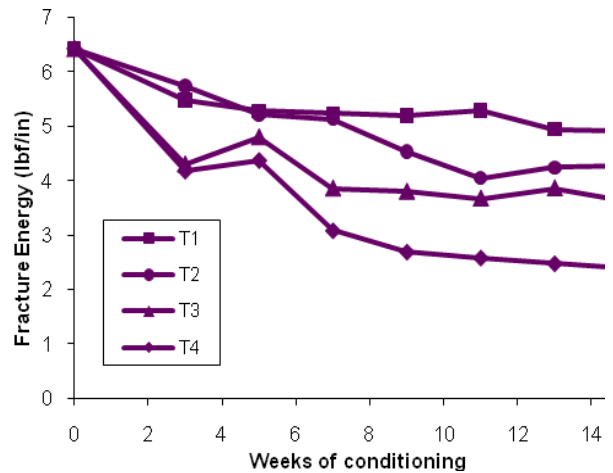


Figure 6 Decay of fracture energy for different durations and temperatures

4.3 Failure mode

The failure occurred suddenly for all the samples. With the increase of the applied load, debonding initiated from the predefined notch followed by a complete separation of the FRP laminate from the concrete substrate, showing a thin layer of concrete attached to the FRP and indicating a cohesive failure as shown in Figure 7. After failure, some of the delaminated FRP laminates were subjected to tensile test. All the laminates behaved linearly until failure and no apparent damage was observed compared to the pristine samples. It was observed that the thickness of the concrete attached to the FRP decreased with the increase of conditioning time for a given temperature.

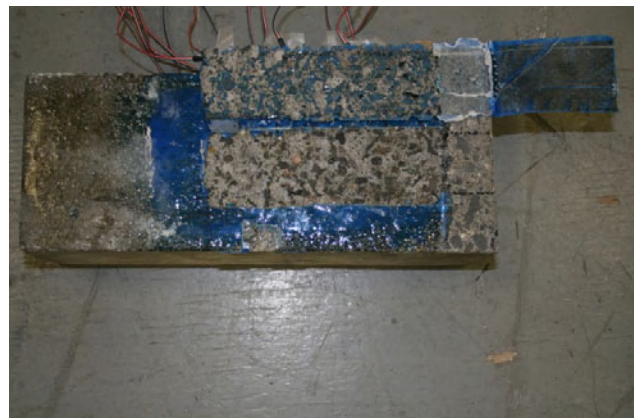


Figure 7 A typical fractured sample

5 CONCLUSIONS

In this paper, the interface durability of concrete with externally bonded FRP laminate is studied under Mode-II loading using a single shear test specimen. Accelerated

aging was achieved by exposing the specimens to both water immersion and elevated temperature. The following conclusions can be drawn based on this study:

- The fracture energy decreases with respect to the increasing conditioning time of the specimen.
- The elevated temperature has a more significant effect on interface degradation than the water-immersion effect. There is a threshold temperature beyond which the degradation mechanism of the interface significantly changes.
- The proposed path-independent J-integral is an effective method for evaluating the interfacial behavior, which only requires the measurements of the relative slip at the tip of the notch and the corresponding load, whereby the effort of bonding strain gages as for the traditional method can be omitted. It can accurately describe the fracture energy; however, the traction-separation law seems to be affected by the accuracy of measuring the relative slip.
- The failure modes for most of the specimens were cohesive. As the exposure duration and the temperature increased, the failure mode shifted from cohesive to adhesive, with less concrete attached to the FRP laminates.

The test results will be further used to develop a model to predict the long-term behavior of the interface based on Arrhenius or similar relation, which can in turn be used to study the durability of concrete structures reinforced with externally bonded FRP laminates.

REFERENCES

- Ali-Ahmad, M., Subramaniam, K., and Ghosn, M. 2006. Experimental Investigation and Fracture Analysis of Debonding between Concrete and FRP Sheets. *Journal of Engineering Mechanics*, 132(9), 914-923.
- Ferracuti, B. 2006. Strengthening of RC structures by FRP: Experimental Analysis and Numerical Modeling. *University of Bologna*, Bologna.
- Fraisse, P., and Schmit, F. 1993. Use of J-integral as Fracture Parameter in Simplified Analysis of Bonded Joints. *International Journal of Fracture*, 63, 59-73.
- Högberg, J. L. 2006. Mixed mode cohesive law. *International Journal of Fracture*, 141, 549-559.
- ICRI guideline No. 03732, Jan 1997.
- Nakaba, K., Kanakubo, T., Furuta, T., and Yoshizawa, H. 2001. Bond Behavior between Fiber-Reinforced Polymer Laminates and Concrete. *ACI Structural Journal*, 98(3), 359-367.
- Pham, H. B., and Al-Mahaidi, R. 2006. Modelling of CFRP-concrete shear-lap tests. *Construction and Building Materials*, 21(4), 727-735.
- Qiao P, Chen Y. Cohesive fracture simulation and failure modes of FRP-concrete bonded interfaces. *Theoretical and Applied Fracture Mechanics*. 2008;49:213-225.
- Rice, J. R. 1968. A Path Independent Integral and the Approximate Analysis of Strain Concentration by Notches and Cracks. *Journal of Applied Mechanics*, 35, 379-386.
- Taljsten, B. 1997. Defining anchor lengths of steel and CFRP plates bonded to concrete. *International Journal of Adhesion and Adhesives*, 17(4), 319-327.
- Wang, J. 2006. Debonding of FRP-plated reinforced concrete beam, a bond-slip analysis. I. Theoretical formulation. *International Journal of Solids and Structures*, 43, 6649-6664.
- Wang, J. 2007. Cohesive zone model of FRP-concrete interface debonding under mixed-mode loading. *International Journal of Solids and Structures*, 44, 6551-6568.
- Xu, X. P., Needleman A. 1993. Void nucleation by inclusion debonding in a crystal matrix. *Modeling and Simulation in Materials Science and Engineering*, 1(2):111-132
- Yuan H, Wu Z, Yoshizawa H. Theoretical solutions on interfacial stress of externally bonded steel/composite laminates. *Structural Engineering/ Earthquake Engineering*. 2001;18(1): 27-39.

Ultrasonic Evaluation of CFRP-Concrete Interface for Specimens under Temperature and Water-Immersion Aging Effects

A. M. Mahmoud, H. H. Ammar & O. M. Mukdadi (sam.mukdadi@mail.wvu.edu)

Department of Mechanical and Aerospace Engineering, West Virginia University, Morgantown, USA

I. Ray, F. Imani, A. Chen & J. F. Davalos

Department of Civil and Environmental Engineering, West Virginia University, Morgantown, USA

ABSTRACT Ultrasonic non-destructive evaluation (NDE) techniques are widely used for structural health monitoring of concrete/FRP structures. In this study, experimental and processing schemes of surface acoustic waves (SAW) are described for assessing concrete/CFRP specimens subjected to accelerated aging conditions. Ultrasonic waves are generated and received at one side using narrow-band transducers of 110 kHz center frequency. The received signals are filtered and amplified then digitized and processed to extract various parameters in both time and frequency domains. These parameters include ultrasound propagation speed, maximum amplitude, total power, and the slope at maximum power spectrum. Changes in these parameters due to water immersion aging at different temperatures were monitored over 10 weeks. Results indicated a notable decrease in measured ultrasonic parameters over time, particularly after the first 2 weeks. This may indicate a debonding or deterioration in the concrete/FRP samples. This behavior showed good agreement with the findings of a parallel destructive study on Mode-II fracture loading of CFRP-concrete samples, tested to obtain fracture energy and define traction-separation response under temperature and water-immersion aging effects.

1 INTRODUCTION

Composite materials made of fibers impregnated in polymeric, mostly epoxy, resin which are also known as fiber-reinforced polymers (FRP) are increasingly used as an alternative to conventional repairing and rehabilitation materials (ACI 440.2R-08). The most commonly used FRP system in rehabilitation consists of fabric made of carbon fiber sheets and epoxy resins. The carbon fiber sheets are externally bonded to concrete surfaces using epoxy resin to rehabilitate and strengthen the structures for bond-critical applications. In such applications, the quality of the FRP-concrete interface bond is the most critical parameter affecting the structural performance and durability of retrofitted structures (Chajes et al. 1996, Davalos et al. 2006). Many studies have been conducted to evaluate the interface durability of FRP-concrete composites against freezing, thawing, acidic and or alkaline attacks, and temperature effects. However, the moisture effects in the form of wet-dry cycles or continuous exposure were found to be the most significant (Ouyang and Wan 2008) and realistic environmental factors affecting the bond in a real structure. Therefore, a sound understanding of these moisture effects on the deterioration of FRP-concrete interface is a key for predicting the interface performance of FRP-concrete composites. Moisture causes several deterioration mechanisms, including plasticization, loss

of stiffness, debonding stresses across fiber-resin interfaces, chemical attack on the fiber-resin bond, and dilatation and swelling pressure from concrete at the interface (Nkurunziza et al. 2005). Concrete retains moisture in its pore solutions which can easily migrate toward the FRP-concrete interfacial region, initiating the degradation process.

To elucidate the durability of FRP-concrete interface within a reasonable time, an accelerated test method is generally adopted by the researchers. In recent work, Chen et al. (2007) successfully used an accelerated aging protocol for evaluations of durability performance to develop a prediction model for long-term performance of an FRP bar-concrete interface bond. In this study, a similar approach was followed for externally bonded FRP-concrete beams immersed in water at four elevated temperatures to accelerate the chemical reaction.

Ultrasonic non-destructive techniques for concrete evaluation have been widely used since the late 1940's (Malhotra and Carino 1991). Different techniques based on pulse velocity measurement, impact echo, guided and surface wave analyses and laser-generated ultrasound could be used to provide quantitative assessments of concrete (Popovics and Rose 1994). Other ultrasonic techniques have been described for imaging the defects via providing a one-dimensional view (A-scan), two-dimensional view (B-scan), or surface view (C-scan)

(Buyukozturk 1998). Ultrasonic techniques have also been used to assess FRP-concrete structures and their possible deteriorations due to various factors (Kaiser et al. 2004). Such acoustic testing methods are considered among the favorite techniques for their safety, low-cost, and flexibility, in addition to the high sensitivity and the single-sided testing capability they provide (Ekenel and Myers 2007, Kaiser et al. 2004). For example, ultrasonic pulse velocity has been utilized to assess damages within FRP-encased concrete (Mirmiran and Wei 2001). The possibility of using ultrasonic guided waves to assess FRP-reinforced concrete structures was investigated by Trovillion et al. (2004). They explained theoretically and experimentally that guided waves could be used to detect cracks and debonds in concrete/FRP structures. However, most of the assessments were based on qualitative observations of the received ultrasound signals.

In this work, experimental and processing schemes of surface acoustic waves (SAW) are described to assess CFRP-concrete specimens undergoing accelerated aging conditions. It provides quantitative parameter to predict the performance of CFRP-concrete interface. Concrete preparation and aging procedures, in addition to descriptions for the experimental set-up and signal processing procedures are described in the following section. Results are then shown and discussed in section 3 followed by a conclusion of the work.

2 METHODS

2.1 Concrete preparation

The normal strength concrete prisms with outer dimensions of 127 mm × 101.6 mm × 330 mm were prepared using Type I portland cement, water, river sand, and # 8 limestone coarse aggregate as substrates. The average 28-day standard cylinder strength was 4500 psi. After casting, specimens were covered with wet burlap and a layer of plastic sheet to maintain the moisture. Specimens were demolded after 24 hours and immersed in lime-saturated water for 28 days to be cured. After curing in water, the prism specimens were transferred to a 50% humidity chamber at 23°C up to 90 days to adequately dry the top surface on which the carbon fiber reinforced polymer (CFRP) was bonded. The 0.508 mm thick × 46.04 mm wide × 260.3 mm long CFRP fabric were used to bond 160.3 mm length on concrete prism along its length. Commercial epoxy resins were used to bond the CFRP on concrete specimens. Before bonding CFRP, the concrete surface was sandblasted to achieve a surface profile of # 5 according to the International Concrete Repair Institute, which provides adequate surface roughness for FRP bonding. Bonding the CFRP was performed according to the manufacturer's application guideline. The two-part primer was mixed first and then

applied to the concrete substrate using a normal paint brush. The detailed sequence for bonding CFRP using the dry lay-up method after priming is provided as follows:

1. The first coat of saturant was applied on top of the primer while it was still tacky using a paint roller.

2. While the saturant was still wet, dry fabric was placed onto the concrete substrate and pressed by means of a squeegee and hand pressure in the fiber direction. Using a paint roller, the composite was rolled starting from the middle of the sheets to push out all the air bubbles, ensuring that the fabrics were completely saturated.

3. After all air bubbles were removed from the fabric, a second layer of saturant was applied using a paint roller and again rolling only in the fiber direction. Any excess amount of the saturant was removed from the system using a squeegee.

After placement, the FRP system was allowed to cure for 7 days at 23°C according to the manufacturers' recommendation. The lower part of Figure 1 illustrates the sample geometry.

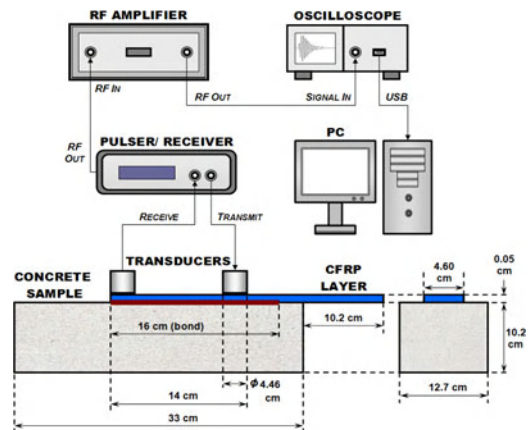


Figure 1 Schematic diagram for the FRP-concrete ultrasound testing experimental set-up, showing the instruments used and relevant dimensions of the concrete sample

2.2 Accelerated aging

In this study, a total of 16 concrete samples were used and divided equally into 4 groups according to the aging temperature. Each sample was initially tested before submerging in heated water tanks. Then, samples were inserted and extracted by hand using thermal protection. The specimens were fully immersed in de-ionized water in four custom-designed temperature-controlled tanks made of one-piece molded high-density polyethylene with 380-liter capacity. Each double-walled tank includes a Teflon-coated immersion heater (500 watts/ 120 V) with a digital temperature control accurate to 0.5°C. Four temperatures labeled T1, T2, T3 and T4 were fixed at 25°C, 36°C, 48°C and 60°C, respectively. The immersed specimens were maintained in such a way that

each specimen was in direct contact with water throughout the immersion period.

2.3 Experimental set-up

Each sample was tested before immersion in the water tanks and every 2 weeks thereafter for a period of 10 weeks. On each testing date, samples were removed from the tank and allowed approximately 2 hours to dry before testing. The experimental setup (Figure 1) was used to generate SAWs in the samples. A main bang of negative impulse was used as the excitation signal for the ultrasound transducer. This signal was generated and amplified using an ultrasonic pulser-receiver (Olympus NDT Inc., Waltham, MA, USA). Both the transmitter and the receiver are placed on the surface of the CFRP layer over the concrete sample at a horizontal center to center spacing of 95.4 mm. Both the transmitter and receiver have 44.6 mm outer diameters with a 110 kHz center frequency and -6 dB bandwidth of approximately 10 kHz. These transducers are used to convert the electrical energy into acoustical energy and vice versa. The received signals were amplified and filtered by the ultrasonic pulser-receiver, then further amplified by 75-W RF power amplifier (Amplifier Research, Souderton, PA, USA). The filtered and amplified signal was then fed to a high-speed digital oscilloscope (Tektronix Inc., Beaverton, OR, USA) that digitized received signals using a rate of 1 MHz. The acquisition process was controlled and acquired by a high performance PC-based system for further signal processing (Signatec Inc., Newport Beach, CA, USA). The data was then transferred to Matlab7.1 (The MathWorks, Inc., Natick, MA, USA) for post-processing and data analysis in time and frequency domains.

2.4 Signal processing and data analysis

After ultrasound propagation from the transmitter to receiver, different parameters were extracted from the received signals. Time-domain parameters, such as the speed of sound (c), peak amplitude (V_{max}), and average power (P_{Avg}), were calculated using the time domain response. Other parameters such as the maximum power-frequency ratio ($(P/F)_{max}$), and the frequency at maximum ratio (F_{max}), were evaluated using the power spectral density (PSD) of the ultrasound signal in the frequency domain. In this paper, the PSD was estimated via Burg's method of representing the power distribution per unit frequency. The autoregressive spectrum was calculated using a fast Fourier transform (FFT) to obtain the spectral parameters of the transmitted signal. During testing each excitation was repeated 3 times, with all parameters being evaluated each time along with the average parameter value. These parameters were estimated every 2 weeks from acquired ultrasound signals to study the abovementioned aging effects.

3 RESULTS AND DISCUSSION

When the ultrasound transmitting transducer (Figure 1) is excited, an ultrasound wave propagates through the concrete sample for approximately 95.4 mm before reaching the receiver transducer. This signal is sensitive to the media and carries important information about the CRFP layer, bond with concrete, and the concrete beyond the interface. Hence, any mechanical or structural change within these regions will affect the signal trend and any extracted parameter. Figure 2 shows both the time- and frequency-responses of a typical ultrasound signal received after propagation through the CFRP-concrete structure. The pulser-receiver generates a synchronization pulse as a flag at the time of excitation (TOE), as shown in Figure 2(a). After a short period, the ultrasound signal reaches the receiver where it is identified as the first arrival signal (FAS), lasting approximately 0.7 ms. Figure 2(b) describes the PSD curve calculated using the time response shown in Figure 2(a). The curve experimentally shows the narrow bandwidth of the transducer (~ 10 kHz) as well as the center frequency occurring at approximately 103.5 kHz.

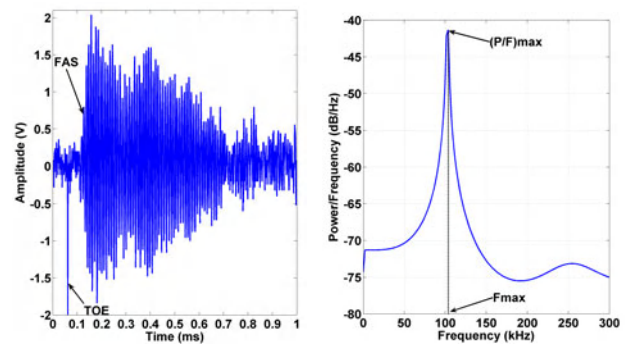


Figure 2 Typical ultrasound signal received after travelling via CFRP-concrete structure. Time response (left) and frequency spectrum (right)

In this study, we observed that ultrasonic parameters including V_{max} , P_{Avg} and $(P/F)_{max}$ showed significant changes due to the aging effect. Figure 3 describes how these three ultrasonic parameters changed due to the temperature water-immersion aging. Over the 10-week period, values of all parameters decreased for all temperatures. The rate of ultrasonic parameter reduction clearly increased with temperature, suggesting greater CFRP-concrete sample deterioration at higher temperature. For further validation, a statistical study was performed to estimate how these ultrasonic parameters extracted using this non-destructive study are correlated with the fracture energy parameter evaluated in a previous destructive study performed by our group (Imani et al. 2010).

Table 1 shows values of the correlation coefficient r between the ultrasonic parameters and the fracture

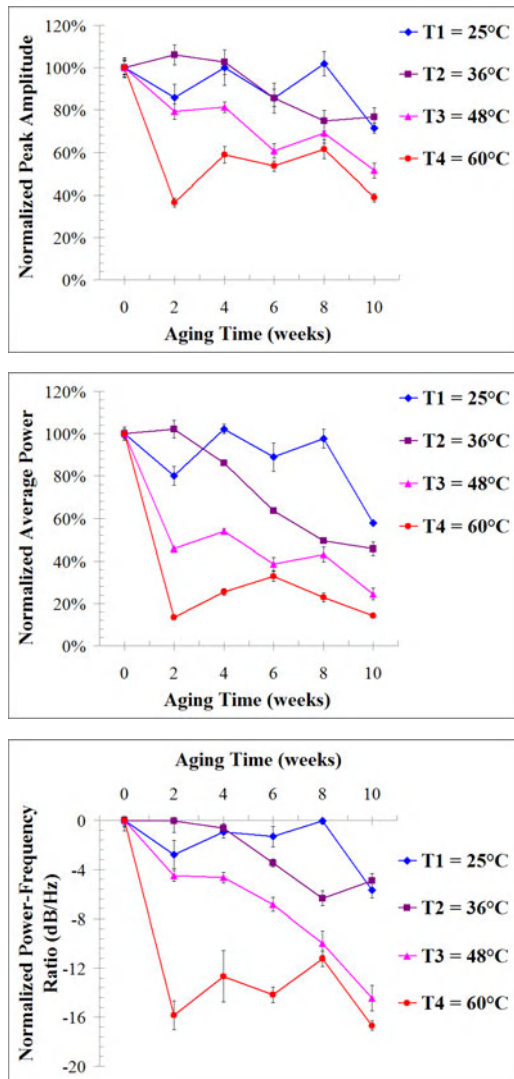


Figure 3 Change in ultrasonic parameters due to temperature and water-immersion aging over 10 weeks; (top) Peak Amplitude (V_{max}), (middle) Average Power (P_{Avg}); and (bottom) Maximum Power-Frequency Ratio ($(P/F)_{max}$)

Table 1 Correlations (r ; $P < 0.05$) between ultrasonic parameters and fracture energy at different temperatures. Average correlation with each parameter is evaluated in the last column.

Parameter	T1	T2	T3	T4	Avg.
V_{max}	0.34	0.79	0.76	0.67	0.64
P_{Avg}	0.35	0.91	0.93	0.77	0.74
$(P/F)_{max}$	0.37	0.83	0.77	0.73	0.68

energy at each of the four temperatures. Generally, it was observed that most ultrasonic parameter responses and the fracture energy results exhibited good correlation ($|r| > 0.5$, $P < 0.05$). Average correlations of $r = 0.64$, $r = 0.74$, and $r = 0.68$ were found between the fracture energy and peak amplitude, average power, and maximum power-frequency ratio, respectively. All responses at T1 showed low correlation ($|r| < 0.5$), reducing the average correlation reported in Table 1.

This low correlation could be due to the minor changes occurring at T1. However, when temperature increases, correlations values showed higher values, particularly for the average power response.

4 CONCLUSION

A non-destructive ultrasonic evaluation technique using surface acoustic waves was described to assess CFRP-concrete structures undergoing temperature and water-immersion aging conditions. Both the experimental and processing procedures were reported in detail. Results indicated an obvious decrease due to aging in various parameters extracted from the ultrasonic received signals. This behavior showed a good correlation with the fracture energy change of a parallel destructive study undergoing the same aging, which offers great potential for NDT evaluations and predictions of CFRP-concrete interface performance.

REFERENCES

ACI 440.2R-08 2008. Guide for the design and construction of externally bonded FRP systems for strengthening concrete structures. Reported by ACI committee 440.

Buyukozturk, O. 1998. Imaging of concrete structures. *NDT & E International* 31: 233-243.

Chajes, M., Januska, T., Mertz, D., Thompson, T., and Finch, W. 1995. Shear strengthening of reinforced concrete beams using externally applied composite fabrics. *ACI Structural Journal* 92(3): 295-303.

Chen, Y., Davalos, J.F., Ray, I. & Kim, H.Y. 2007. Accelerated aging testes for evaluations of durability performance of FRP reinforcing bars for concrete structures. *Composite Structures* 78(1): 101-111.

Davalos, J.F., Kodkani, S.S. & Ray, I. 2006. Fracture mechanics method for mode-I interface evaluation of FRP bonded to concrete substrate. *J. of Mat.in Civil Eng.* 18(5): 732-742.

Ekenel, M. & Myers, J.J. 2007. Nondestructive evaluation of RC structures strengthened with FRP laminates containing near-surface defects in the form of delaminations. *Science and Engineering of Composite Materials* 14: 299-315.

Imani, F. S., Chen, A., Davalos, J. F., & Ray, I 2010. Temperature and Water-Immersion Effects on Mode II Fracture Behavior of CFRP-Concrete Interface. Proceedings of *5th International Conference on FRP Composites in Civil Engineering*, Beijing, China, 27-29 September, 2010.

Kaiser, H., Karbhari, V.M. & Sikorsky, C. 2004. Non-destructive testing techniques for FRP rehabilitated concrete. II: an assessment. *International Journal of Materials and Product Technology* 21: 385-401.

Malhotra, V.M. & Carino N.J. 1991. CRC Handbook on Nondestructive Testing of Concrete. *CRC Press*.

Mirmiran, A. & Wei, Y.M. 2001. Damage assessment of FRP-encased concrete using ultrasonic pulse velocity. *Journal of Engineering Mechanics-Asce* 127: 126-135.

- Nkurunziza, G., Debaiky, A., Cousin P. & Benmokrane B. 2005. Durability of GFRP bars: A critical review of the literature. *Progress in Struc. Eng. and Materials* 7: 94-209.
- Ouyang, Z. & Wan, B. 2008. Modeling of moisture diffusion in FRP strengthened concrete specimens. *Journal of Composites for Construction* 12(4): 425-434.
- Popovics, J.S. & Rose J.L. 1994. A survey of developments in ultrasonic NDE of concrete. *IEEE Transactions on Ultrasonics Ferroelectrics and Frequency Control* 41: 140-143.
- Trovillion, J.C., Godinez-Azcuaga, V.F. & Finlayson, R.D. Dec. 2004. A Nondestructive evaluation technique for fiber reinforced polymer (FRP) composites using acoustic guided waves (AGW). *US Army Engineer Research and Development Center, Construction Engineering Research Laboratory Champaign, IL* 61822-1076.

Modified Beam Bond Test on Externally Bonded and Near Surface Mounted FRP Strengthened RC Beams

Renata Kotynia (renata.kotynia@p.lodz.pl)

Department of Concrete Structures, Technical University of Lodz, Poland

ABSTRACT The paper concerns bond behavior between composite carbon fibre reinforced polymer (CFRP) materials and concrete in externally bonded (EB) and near surface mounted (NSM) FRP strengthened reinforced concrete (RC) beams. Bond mechanism was investigated on the modified bond test in aspect of six parameters: beam's span and depth, longitudinal steel reinforcement ratio, type of the CFRP strips/sheets, CFRP bond length, and concrete compressive strength. In order to confirm the influence of the existing steel reinforcement ratio on the FRP-to-concrete bond conditions, the longitudinal steel bars in some beams were cut through at the mid-span. The test confirmed an important rule of the internal steel bars on the FRP-to-concrete interfaces and the final failure modes.

1 INTRODUCTION

The bond strength between FRP and concrete is a key factor controlling various debonding failure modes in EB and NSM FRP strengthened members. The experimental and theoretical studies investigated bond mechanisms commonly based on direct shear tests (Hassan & Rizkalla 2003, Yao et al. 2005, Seracino et al. 2007) while modified beam tests, which considered the effect of the flexural cracks on the bond behavior of the FRP/concrete interface were performed very seldom (De Lorenzis & Nanni 2002, Sena-Cruz & Barros 2004, Kotynia 2009).

To the author's knowledge almost all except two (Taher Khorramabadi & Burgoyne 2009, Kotynia et al. in prep.) previous EB and NSM FRP bond tests ignored the influence of internal steel bars on the FRP-to-concrete bond conditions. The effect of longitudinal steel reinforcement, its cross section area, mutual location of FRP and steel bars on the FRP-to-concrete bond is the aim of the present test program.

2 EXPERIMENTAL PROGRAM

The experimental tests consisted of fifty single-span, modified simply supported RC beams. The RILEM standard model (1982) originally proposed for steel reinforcement-to-concrete bond tests was adapted to the present CFRP-to-concrete bond tests. The test program considered two basic Series of beams differed in the strengthening technique: Series "E" (11 beams) – with CFRP strips/sheets externally bonded on the tension surface of the beams and Series "N" (39 beams) – with CFRP strips mounted inside the longitudinal grooves made in the concrete cover of the beams. The beams of

Series "E" were strengthened with two different techniques subdivided into "wet lay-up" 3 layers of CFRP sheets (1 layer 90 mm wide and 0.13 mm thick, the elasticity modulus of 231 GPa and the tensile strength of 2714 MPa) and prefabricated CFRP strips (90 mm wide and 1.4 mm, the elasticity modulus of 171 GPa and the tensile strength of 2911 MPa), denoted by "3m" and "S", respectively. Series "N" beams were strengthened with NSM CFRP strips of 15 mm wide and 2.4 mm thick (the elasticity modulus of 169 GPa and the tensile strength of 1893 MPa), bonded into concrete cover grooves of 17 mm deep and 6 mm wide.

The two-component epoxy adhesive Sikadur30 (compressive strength of 88 MPa) was used for bonding of the prefabricated strips to the concrete but the EB sheets were bonded with the Sikadur330 adhesive (compressive strength of 82 MPa).

The next two criterions of the tested beams division was the beam depth and span. A symbol "I" for low and "II" for high beams, corresponding to the cross-sections of 150 × 200 mm and 150 × 400 mm, respectively. Different spans were introduced to investigate the effect of the bending moments distribution along the span ("S" and "L" for short beams of 1350 mm and long beams of 2000 mm length).

Subsequent investigated parameters contained the internal longitudinal steel reinforcement. Symbols "A" and "B" correspond to the steel ribbed bars of nominal diameter 8 mm or 16 mm, respectively (Figure 1). The experimental yield strength and the tensile strength of the steel reinforcement were 543 MPa and 637 MPa for 8 mm diameter bars, and 542 MPa and 636 MPa for 16 mm bars.

The next two investigated parameters referred to the

compressive concrete strength (ranged from 20 MPa to 50 MPa) and the CFRP bond length of 200 mm for the EB CFRP strips/sheets and ranged from 80 mm to 160 mm for the NSM CFRP strips. The last two or three numbers in the specimen ID of NSM strengthened beams correspond to the real bond length of the strip (Figure 2).

2.1 Test specimens

The test specimen was built of two separate concrete blocks with the continuous longitudinal steel bars in the tension zone, and with a steel hinge in the midspan compression zone of the beam (Figure 1).

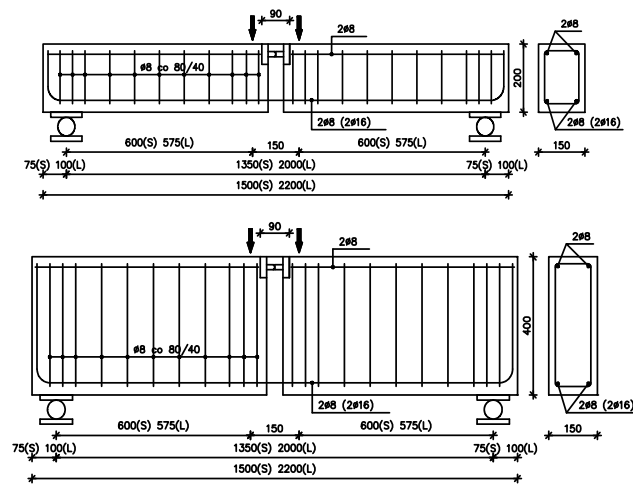


Figure 1 Steel reinforcement in low (I) and high (II) beams

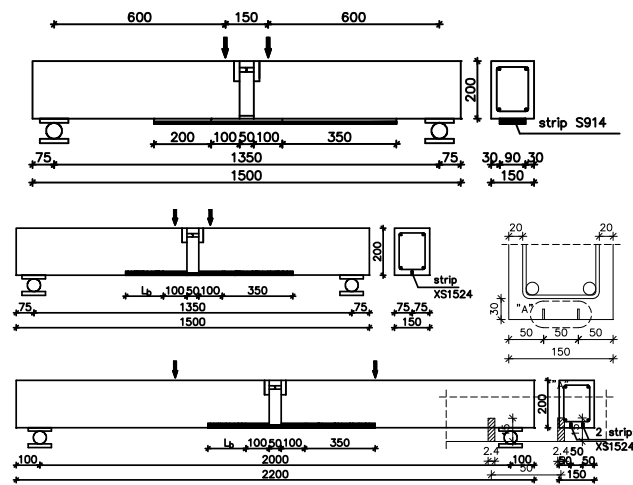


Figure 2 Strengthening modes

All beams were tested in four point bending in the upside down position in order to facilitate access to the strengthened surface. Strengthening modes are shown in Figure 2 and listed in Table 1 and Table 2.

To investigate an effect of a number of the FRP strips on the FRP-to-concrete bond strength, two of beams were strengthened with double NSM strips bonded on the 80 mm length (e.g. NIISB/40/2 × 80). In some beams (denoted with index “s”), the internal steel bars were cut at the beam midspan in order to investigate an effect of

the continuity of the internal steel bars on the FRP-to-concrete bond behavior.

Table 1 Characteristics of series “E” beams

Series	Beam ID	Tensile Reinf.	f'_c (MPa)	CFRP Type
EIS	EISA/20/S	2 ϕ 8	20	strip S914
h=200mm	EISA/20/3m			3 × sheet
$L_o=1350$ mm	EISA/50/S		50	strip S914
	EISB/50/3m			3 × sheet
	EISB/40/S	2 ϕ 16	40	strip S914
	EISB/40/3m			3 × sheet
EIL	EILA/30/S	2 ϕ 8	30	strip S914
h=200mm	EILA/30/3m			3 × sheet
$L_o=2000$ mm	EILB/30/Ss	2 ϕ 16		strip S914
EIIL	EIILB/30/S			strip S914
h=400mm	EIILB/30/3m			3 × sheet
$L_o=2000$ mm				

Table 2 Characteristics of Series “N” beams

Series	Beam ID	Tensile Reinf.	f'_c Mpa	L_b mm
NIS	NISA/20	2#8	20	—
h=200mm	NISA/20/85			85
$L_o=1350$ mm	NISA/20/130			130
	NISA/20/170			170
	NISA/20/85p			85
	NISA/20/120p			120
	NISA/20/160p			160
	NISA/30		30	—
	NISA/30/80			80
	NISA/30/120			120
	NISB/20	2#16	20	—
	NISB/20/85			85
	NISB/20/130			130
NIL	NILA/40	2#8	40	—
h=200mm	NILA/40/120			120
$L_o=2000$ mm	NILA/40/160			160
	NILA/40/120p			120
	NILA/40/120s			120
	NILA/40/120pp			120
	NILA/40/120sp			120
	NILB/40	2#16		—
	NILB/40/90			90
	NILB/40/120			120
	NILB/40/120p			120
	NILB/40/130pp			130
	NILB/40/120s			120
	NILB/40/120sp			120
	NILA/50	2#8	50	—
	NILA/40/100		40	100

(Continued)

Series	Beam ID	Tensile Reinf.	f'_c (MPa)	L_b (mm)
	NILA/40/120			120
	NILA/50/2×80		50	2×80
NIIS	NIISB/40/80	2#16	40	80
h=400mm	NIISB/40/2×80			2×80
$L_o=1350$ mm	NIISB/40/120			120
	NIISB/40/160			160
NIIL	NIILB/40/80			80
h=400mm	NIILB/40/80p			80
$L_o=2000$ mm	NIILB/40/2×80			2×80
	NIILB/40/120			120

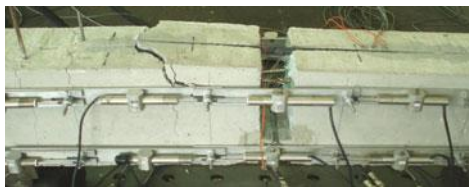
2.2 Test results

The process of cracking proceeded similarly in all NSM strengthened beams with continuous steel reinforcement. Almost all strengthened beams failed due to CFRP debonding, together with the adjacent concrete cover, along or slightly above the level of the longitudinal steel reinforcement. The flexural crack initiated in the concrete at the end of the strip, and then propagated along the internal steel in a cone-shaped (Figure 3a) or crossed the entire beam’s width (Figure 3b), that was typical for the end plate debonding in RC beams strengthened in flexure.

The long span beams and the beams with low height exhibited much more intensive flexural cracks than the



(a)



(b)



(c)

Figure 3 Crack pattern and failure mode of the beams (a-b) Series “N”, (c) Series “E”

rest specimens. The beams strengthened with EB strips/sheets demonstrated much less intensive cracking and CFRP debonding that proceeded in the thin concrete cover (Figure 3c).

In the beams with steel reinforcement cut, the failure occurred as a result of CFRP bond loss in the contact layer of the strip and the epoxy adhesive.

2.3 Analysis of FRP-to-concrete bond conditions

The strain measurements registered in the beams of Series NISA, on the CFRP bond length of 120 mm, confirmed the influence of the concrete strength on the CFRP debonding strain (Figure 4). This effect was visible in both the short span beams ($\epsilon_{fb} = 2.33\%$ and 3.16% for the beams NISA/20/120p and NISA/30/120, respectively), and the long span ones. Similar observation concerning the concrete strength effect was registered in the beams with the steel reinforcement cut in the mid-span.

The increase in the compressive strength of concrete in the beams of Series EISA with the externally bonded strips/sheets affected the increase in the CFRP debonding strain ($\epsilon_{fb} = 1.24\%$, 1.97% , 3.39% and 4.32% for the beams EISA/20/S, EISA/40/S, EISA/20/3m and EISA/50/3m, respectively, Figure 4). The ultimate strain of EB sheets were significantly greater compared to the strains of the prefabricated CFRP strips independently on the internal steel ratio.

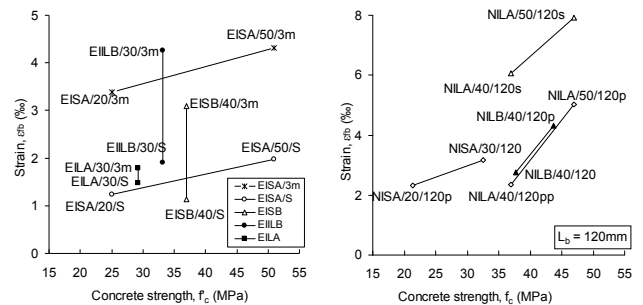


Figure 4 Influence of the concrete strength on the CFRP bond strain in the NSM and EB strengthened beams

Cutting the steel reinforcement (NILA/50/120s, NILA/40/120s) significantly delayed the CFRP debonding, that confirmed a great effect of the steel bars on the CFRP-to-concrete bond behavior.

The flexural failure controlled the ultimate load of the strengthened beams and caused no effect of the bond CFRP length on the load capacity. This is why the test results confirmed a minor influence of the CFRP bond length on the ultimate load (Figure 5).

The CFRP debonding strain in the beams with the high height and reinforced with 16 mm bars (Series NIIB) were by 67% (for $L_b = 80$ mm) and 49% (for $L_b = 120$ mm) greater than those in the low beams height and the same

steel percentage (Series NIB) (Figure 6).

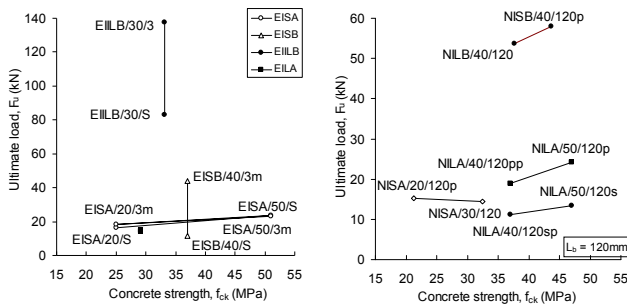


Figure 5 Effect of the concrete strength on the ultimate load

The test results of the long beams reinforced with 16 mm steel bars demonstrated greater single CFRP debonding strains than the double ones (Figure 7).

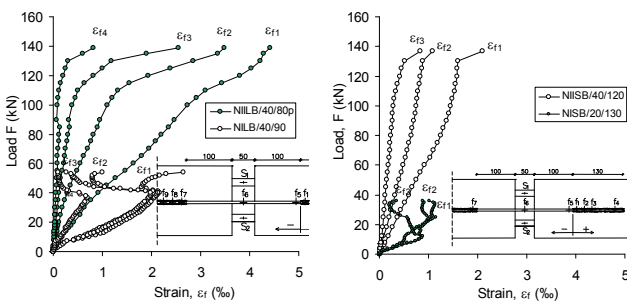


Figure 6 Influence of the beam height on the CFRP strain

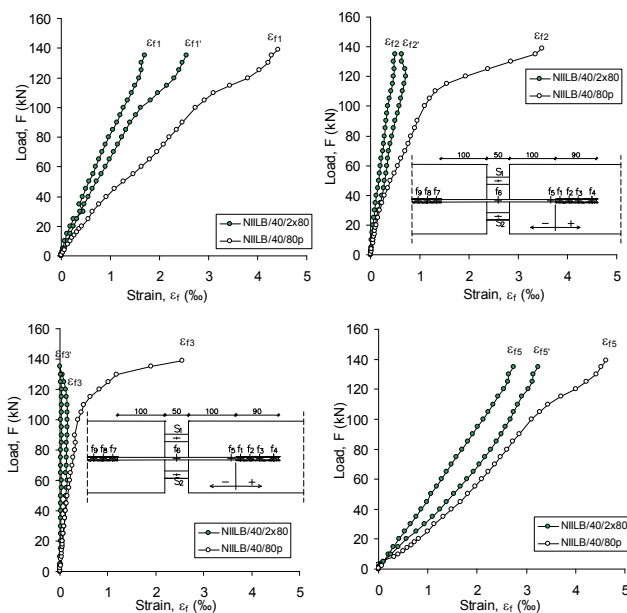


Figure 7 Effect of the CFRP ratio on its strain

3 CONCLUSIONS

Based on the analysis of the test results, the following conclusions may be drawn:

- The increase in the concrete strength delays the CFRP debonding and increases the debonding CFRP strain;

- Steel yielding and flexural failure proceeded by the concrete cover splitting controlled the ultimate load of the strengthened beams and did not affect the bond failure at the FRP/concrete interface in the beams with longitudinal steel reinforcement. This is why the concrete strength has an insignificant influence on the ultimate load of the tested beams, both in the case of beams NSM strengthened as well as externally strengthened;
- Unlike in the specimens with cut steel bars, the slippage between the CFRP and the concrete occurred;
- A favorable influence of the concrete strength on the CFRP strain in beams with steel bars cut was observed; Cutting the longitudinal steel reinforcement delayed the CFRP debonding;
- The beams externally strengthened with the prefabricated strips indicated greater CFRP bond strain in comparison to those strengthened with the sheets;
- If the bond length was situated in the pure bending region, the CFRP debonding occurred later, than in case of the bond length located in the shear–bending region;
- The increase in the composite reinforcement ratio resulted in decrease of the CFRP debonding strain;
- The internal steel reinforcement has the crucial effect on the FRP/concrete bond behavior. Presence of the steel bars changed the concrete failure plane from the trapezoidal one to almost horizontal, along or slightly below the longitudinal steel reinforcement.

The experimental analysis of the present test results persuaded to undertake, further tests to investigate the bond between composite and concrete in aspect of the internal steel reinforcement on the RC specimens designed as strengthened reinforced concrete ties, subjected to the pure tension. The new ongoing author's FRP/concrete bond test aim investigation of the bond conditions under control of the internal steel strain below and at the yield loading.

REFERENCES

- De Lorenzis, L. & Nanni, A. 2002. Bond between near-surface mounted fiber-reinforced polymer rods and concrete in structural strengthening. *ACI Struct J* 99(2):123-132.
- Hassan, T. & Rizkalla, S. 2003. Investigation of bond in concrete structures strengthened with near surface mounted carbon fiber reinforced polymer strips. *J Compos Const* 7(3):248-257.
- Kotynia, R. 2009. Bond between composite materials and concrete in reinforced concrete members strengthened with CFRP composites. *Rep. No. 16, Dept of Concr Struct Tech Univ of Lodz*, Lodz, Poland.
- Kotynia, R., Abdel Baky, H. & Neale, K. W. Bond behaviour of near surface mounted strips in modified reinforced concrete beams - experimental investigation and numerical simulations

- (in prep.).
- Sena-Cruz, J.M.S. & Barros, J.A.O. 2004. Bond between near surface mounted carbon-fiber-reinforced polymer laminate strips and concrete. *J Compos Constr* 8(6):519-527.
- Seracino, R., Jones M., Ali M., Oehlers, J.D. 2007. Bond strength of near surface mounted FRP strip-to-concrete joints. *J Compos Constr* 11(4):401-409.
- Taher Khorramabadi, M. & Burgoyne, C.J. 2009. Tests on FRP-concrete bond behaviour in the presence of steel. *Advanced Composites in Construction; Proc. intern. conf., University of Edinburgh*, London, CD.
- Yao, J., Teng, J.G. & Chen, J.F. 2005. Experimental study on FRP-to-concrete bonded joints. *Compos. Part B Engin.* 36:99-113.

Experimental Investigation on Bond of NSM Strengthened RC Structures

A. Palmieri & S. Matthys (Aniello.Palmieri@ugent.be, Stijn.Matthys@ugent.be)

Magnel Laboratory for Concrete Research, Department of Struct. Eng., Gent University, Gent, Belgium

ABSTRACT Near Surface Mounted (NSM) FRP reinforcement is being increasingly recognized as a valid alternative to externally bonded reinforcement (EBR) for enhancing the flexural strength and shear resistance of deficient reinforced concrete members. As this technology emerges, the structural behaviour of NSM FRP strengthened elements needs to be characterized, and bond between NSM FRP bars and concrete is the first issue to be addressed. This paper presents, as part of a study in the framework of a Round Robin Testing (RRT) programme, the results of a series of 27 double shear bond tests on NSM FRP strengthened concrete. Aim of this project is to investigate the feasibility of the adopted test method and to investigate the mechanism of bond between NSM reinforcement and substrate material. Experimental results confirm the efficiency and re-liability of the test method and the bond effectiveness of the NSM technique for strengthening RC members.

1 INTRODUCTION

The technique of Near Surface Mounted (NSM) FRP bars/strips is receiving more attention recently due to a number of advantages over the externally bonded technique (EBR) such as a better anchoring capacity of the FRP, better bond characteristic, more ductile behaviour, good performance under cycling load, better protection to fire, acts of vandalism and mechanical damage. The NSM technique consists of placing the FRP reinforcing bars into grooves pre-cut into the concrete members and embedding the bars with a high strength adhesive (epoxy or mortar). This method is relatively simple and considerably enhances the bond of the FRP reinforcements, thereby using the material more efficiently. Bond between FRP and concrete is a critical issue for the efficiency of NSM FRP reinforcement. Previous researches have been performed to investigate the performance of different NSM strengthening systems in various applications (Blaschko 2003; De Lorenzis 2002, 2004; Hassan et al 2003; Sena Cruz et al 2004; Koczynia 2005; Seracino et al 2007), focusing on the effects of various system parameters, such as groove characteristics, adhesive types, FRP shapes, FRP surface treatment, and bond length on both overall member performance and bond performance. Based on the still limited data published in the literature, in this paper, as part of a study in the framework of a Round Robin Testing programme, the results of double shear bond tests on specimens strengthened with NSM FRP rods/strips are presented and discussed. Objective of testing was to investigate the feasibility of the test set-up

and the influence of different variables on the bond behaviour of NSM FRP bars (type and shape of the NSM bars/strips and NSM FRP surface treatment).

2 EXPERIMENTAL PROGRAMM

2.1 Specimens and test configuration

The experimental program comprises 27 double-face bond shear tests. The test set-up is shown in Figure 1. The concrete specimen ($150 \times 150 \times 800 \text{ mm}^3$) is formed by two concrete prisms ($150 \times 150 \times 400 \text{ mm}^3$), with a square groove in the middle at both sides, for embedment of the NSM rod/strip. A thin metal plate separates the two concrete prisms. The height of this plate is at both sides 15 mm less than the height of the

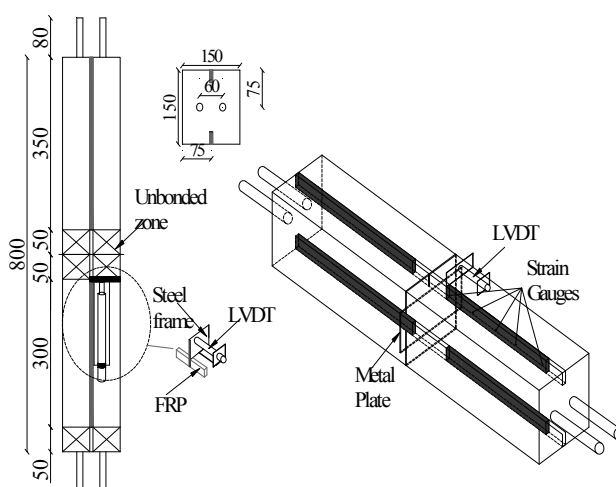


Figure 1 Test-setup

prisms, so that both prisms remain aligned during specimen manipulation and FRP application. Two steel bars with a diameter of 16 mm are embedded into each prism to transfer the load from the tensile test machine to the specimen (these bars do not connected the two concrete prisms). The FRP reinforcement is left un-bonded over a central zone of 100 mm (where the two concrete prisms connect each other). Extra steel clamps are used to prevent debonding from happening at one of the two concrete blocks.

For all the specimens the same concrete type was used, showing a mean compressive cylinder strength f_{cm} at 28 days of 34 MPa. The properties of the FRP reinforcement in terms of bar type, dimensions, FRP tensile strength f_f , modulus of elasticity E_f and the groove sizes in which the FRP is inserted are reported in Table 1.

Table 1 Test- matrix

Name	Bar Type	D_f (mm)	Groove (mm)	f_f (MPa)	E_f (GPa)
C-6-SC	Sand coated CFRP	6.0	12×12	2068	124
B-6-SC	Sand coated BFRP	6.0	12×12	1413	50
B-8-SC	Sand coated BFRP	8.0	14×14	1208	50
G-8-R	Ribbed GFRP	8.0	14×14	1500	60
C-2.5×15-S	Smooth CFRP	2.5×15	8×25	3100	165
C-8-S	Smooth CFRP	8.0	14×14	2800	155
G-8-SW	Spirally Wound GFRP	8.0	12×12	1333	52
C-10×10-S	Smooth CFRP	10×10	15×15	2000	155

* f_f (FRP tensile strength) and E_f (modulus of young) are according to manufacturers values.

The specimen code refers to the following variables: fiber type (C: carbon, G: glass, B: basalt), bar dimension and bar surface. For instance specimen C-6-SC has a carbon FRP bar, diameter 6 mm and sand coated surface. Three specimens for each product have been tested.

2.2 Specimens preparation and testing

The FRP NSM rods/strips were applied according to the procedures specified by the manufacturers. After hardening of the concrete, the grooves were saw-cut and then air-blasted to remove the powdered concrete

produced by cutting. The grooves were filled half way with epoxy resin and the bars were then positioned and lightly pressed. More material was applied if needed and the surface was levelled. Curing of FRP NSM was allowed for at least 7 days under laboratory environment. No pressing devices were applied during curing. Specimens were equipped with five strain gauges on each NSM FRP rod/strip to measure the strains along the bonded length. The gauges were applied at 10, 80, 150, 220 and 290 mm from the end of the rod/strip (Figure 1). The specimen was instrumented also with two linear variable differential transducers (LVDTs), one for both monitored sides, to monitor relative displacement between the FRP reinforcement and the concrete (Figure 1). Testing was conducted in displacement control mode on a 1000 kN universal testing machine with a 0.1 mm/min cross-head displacement rate.

2.3 Test results

The main tests results are reported in Table 2 where Q_{max} is the ultimate load of one bar/strip debonding; σ_u/f_f is the ratio between the recorded ultimate stress and the ultimate tensile strength of the bar (according to manufacturer values); τ_m is the average bond stress, S_{max} is the maximum slip recorded by the LVDTs and τ_{max} the maximum relative bond stress (see section 2.4). Four

Table 2 Test- matrix

Name	Q_{max} (kN)	f_u/f_f (%)	τ_m (MPa)	S_{max} (mm)	τ_{max} (MPa)	Failure Mode
C-6-SC-1	31.5	51.0	2.9	1.5	10.8	DB-C
C-6-SC-2	30.6	49.4	2.8	1.5	12.5	DB-C
C-6-SC-3	36.8	59.5	3.4	1.3	10.8	DB-C
B-6-SC-1	26.7	63.1	4.7	3.2	16.6	DB-SP
B-6-SC-2	30.8	72.9	5.4	2.9	4.2	DB-SP
B-6-SC-3	27.7	65.5	4.9	2.5	15.4	DB-SP
B-8-SC-1	46.1	76.1	6.1	3.1	6.8	DB-SP
B-8-SC-2	37.6	61.9	5.0	3.2	9.9	DB-SP
B-8-SC-3	35.8	59.1	4.7	2.8	8.9	DB-SP
G-8-R-1	55.6	74.2	7.4	2.5	7.8	DB-SP
G-8-R-2	56.3	75.1	7.5	2.4	4.9	DB-SP
G-8-R-3	43.3	57.7	5.7	2.6	11.0	DB-SP
C-2.5×15-S1	60.6	52.1	5.8	1.4	12.5	DB-PO
C-2.5×15-S2	60.9	52.4	5.8	1.8	8.9	DB-PO
C-2.5×15-S3	58.1	50.0	5.5	1.9	11.6	DB-PO
C-8-S-1	56.8	40.4	7.5	1.7	13.0	DB-PO
C-8-S-2	51.4	36.6	6.8	-	8.7	DB-PO
C-8-S-3	62.5	44.5	8.3	-	15.1	DB-PO
G-8-SW-1	43.3	64.7	3.4	0.3	5.5	DB-C
G-8-SW-2	43.2	64.5	3.4	0.5	4.3	DB-C
G-8-SW-3	44.6	66.6	3.5	0.4	4.5	DB-C
C-10×10-S1	65.1	32.6	4.8	0.4	7.8	DB-CL
C-10×10-S2	58.1	29.1	4.3	0.7	9.7	DB-C
C-10×10-S3	59.6	29.8	4.4	0.5	8.6	DB-CL

different failure modes were observed depending on the tests variables: pull-out at the interface between bar and resin (DB-PO); splitting of the resin and/or fracture of the surrounding concrete (DB-SP); debonding at the epoxy-concrete interface with a layer of concrete attached to the NSM FRP bar (DB-CL) and debonding at the epoxy-concrete interface without a concrete layer (DB-C) (Figure 2). The average bond stress was obtained respectively by Equation 1 and Equation 2 for failure type DB-PO or DB-SP and failure DB-CL or DB-C.

$$\tau_m = Q_{\max} / (\pi d_b l_b) \quad (1)$$

$$\tau_m = Q_{\max} / (3d_g l_b) \quad (2)$$

Where d_b is the bar diameter, d_g is the dimension of the groove and l_b the bond length.

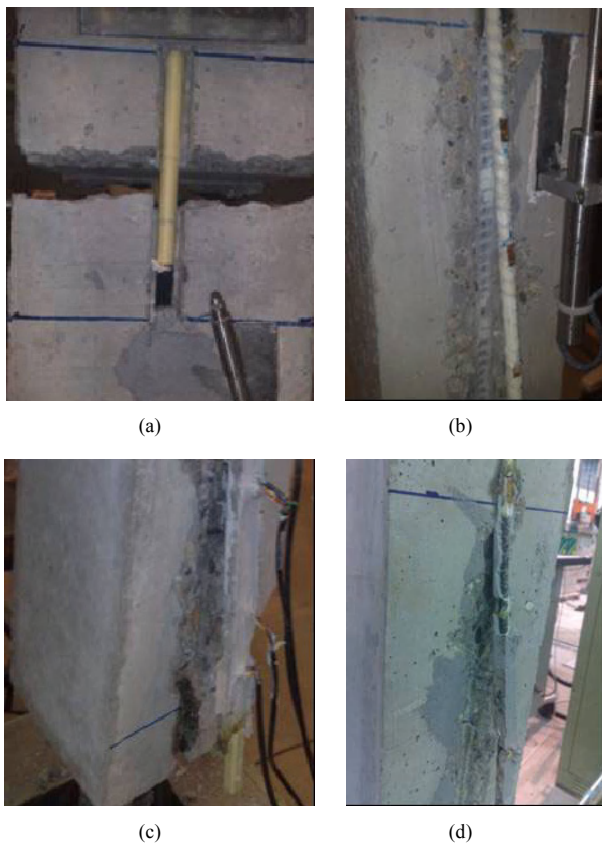


Figure 2 Failure aspects (a) pull-out FRP; (b) resin splitting; (c) debonding at resin-concrete interface with concrete layer; (d) debonding at resin-concrete interface without concrete layer

Splitting of resin was the predominant failure mode of ribbed and sand coated bars, except for specimens C-6-SC in which the failure mode was the debonding of the NSM FRP reinforcement at epoxy-concrete interface. The maximum load was reached after propagation of longitudinal crack along the epoxy cover. The epoxy cover was expelled when the ultimate cracking pattern formed uniformly along the entire bonded length. After

failure, no epoxy adhesive remained attached to the bar. This failure mode appears to be more common for NSM bars than for strips.

The behaviour was different between specimens with different types of bars. In specimen with sand coated BFRP bars the failure was due to epoxy splitting without cracking of the concrete surrounding the grooves. In specimen with GFRP the ribbed area of the bars led to a more brittle failure with respect to sand coated bars. In this case once the longitudinal crack had developed along the bond length, the epoxy cover was suddenly split along with a portion of concrete surrounding the grooves (Figure 2b). In this case the tensile stresses in the epoxy cover were higher than the concrete tensile strength, causing fracture along inclined planes. Furthermore, experimental results shown that the bond failure load of BFRP bars was always lower than GFRP bars, due to the lower modulus of elasticity of the first bars type.

The failure mode of specimens C-6-SC and G-8-SW is characterized by debonding at the epoxy-concrete interface without a layer of concrete (DB-C). After failure a layer of groove-filling adhesive remained attached to the bar. This type of failure may occur as pure interfacial failure, or as a cohesive shear failure in the concrete.

Due to the lower degree of surface deformation the average bond stresses of specimens with spirally wound bars (G-8-SW) were lower than the specimens with ribbed bars (G-8-RB) at the same values of the remaining parameters.

The pull-out of the NSM FRP reinforcement at the bar-resin interface was observed for specimens strengthened with bars and strips with a smooth surface. This failure mode occurs as either pure interfacial failure, or as a cohesive shear failure in the epoxy. This type of failure is identified by the virtual absence of adhesive attached to the bar surface after failure (figure 2 a). During testing at low load levels no cracks were visible on epoxy and neither on concrete. Increasing the load, the internal micro cracking of the epoxy produced by the radial components of the bond stresses accelerates the occurrence of the interfacial failure. The failure mode is characterized by an abrupt slipping of the bar/strip due to its smooth surface. The high values of average bond stresses can be due to the residual friction between the perimeter of the rod/strip and the adhesive. The failure mode of specimens C-10×10-S was different than all the others strengthened with NSM FRP with smooth surface. Failure mode was characterized by debonding at epoxy-concrete interface with a layer of concrete attached to the bars.

Finally specimens strengthened with NSM strip evidenced a bond failure load [Q_{\max}] equal or even higher than specimens strengthened with NSM round bars.

2.4 Stress analysis

Local bond stresses were evaluated based on experimentally recorded strains along the NSM FRP bar/strip (the maximum bond stress, τ_{\max} , for the different tests specimens is reported in Table 1). Referring to two consecutive strain gauges, ranging Δx_i , the equilibrium equation assuming uniform distribution of the bond stress in the analysed discrete interval, gives:

$$\tau_x = E_f \frac{A}{u} \frac{\Delta \varepsilon_i}{\Delta x_i} \quad (3)$$

with, τ_x the bond stress in the FRP reinforcement between two consecutive strain gauges, E_f the modulus of elasticity FRP NSM bars/strip, A the section area, u the bar perimeter and $\Delta \varepsilon_i$ the FRP strain difference between the two considered strain gauges.

For reference, the distribution of bond stresses along the NSM FRP for specimen C6-SC-2 is shown in figure 3. The results for other specimens are not shown as the behaviour is similar.

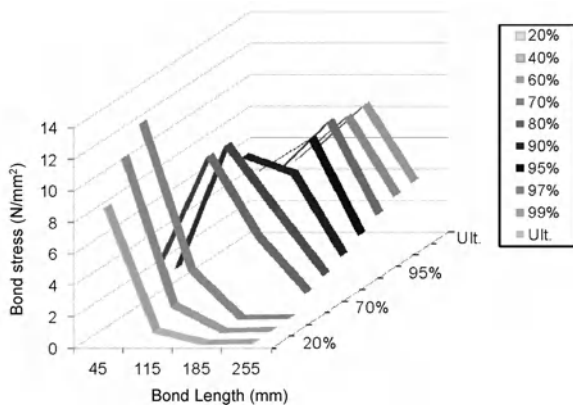


Figure 3 Bond stress distribution

In this figure, each curve corresponds to a specific load level given as a percentage of the ultimate load.

The x axis starts from the zone in between the bonded and un-bonded zone of FRP NSM (loaded end) and ends at the end of the concrete block (free end). At low load levels the bond stresses at free end are close to zero, as the load increases, the peak of the bond stress gradually shifts towards the free end and the entire bond length is mobilized to resist the pulling force.

3 CONCLUSION

A series of 27 double shear bond tests were carried out in order to investigate the effect of different parameters on the bond performance of NSM FRP bars in concrete. Experimental results confirm the efficiency of the test method and the bond effectiveness of the FRP NSM technique. The bar surface configuration proved to be crucial to the specimen failure mode. Failure mode of sand coated bars and ribbed bars was due to the splitting of epoxy adhesive, while specimens with smooth bars mostly failed by bars/strip pull out. It can be concluded that the superficial pattern of FRP NSM reinforcement yet should be sufficiently rough to avoid failure by pull-out at bar-epoxy interface, should generate radial stresses as low as possible to delay splitting phenomena.

REFERENCES

- Blaschko, M. (2003). Bond behaviour of CFRP strips glued into slits, *Proc. of 6th Int. Symposium on FRP Reinforcement for Concrete Structures (FRPRCS-6)*, K. H. Tan, ed., World Scientific, Singapore, pp. 205-214.
- De Lorenzis, L., Rizzo, A., La Tegola, A. 2002. A modified pull-out test for bond of near-surface mounted FRP rods in concrete, *Composites Part B: Engineering*, 33(8), 589-603.
- De Lorenzis, L., Lundgren, K., and Rizzo, A. (2004). Anchorage length of near-surface mounted FRP bars for concrete strengthening – Experimental investigation and numerical modeling, *ACI Structural Journal*, 101(2), 269-278.
- Hassan, T. and Rizkalla, S. (2003). Investigation of bond in concrete structures strengthened with near surface mounted carbon fiber reinforced polymer strips, *ASCE Journal of Composites for Construction*, 7(3), 248-257.
- Kotynia, R., (2005). Strain Efficiency of Near-Surface Mounted CFRP-strengthened Reinforced Concrete Beams, *Proc. Of International Conference on Composites in Construction*, Lyon, July 11-13, 2005.
- Sena Cruz, J., and Barros, J. (2004). Bond between near-surface mounted carbon-fiber reinforced polymer laminate strips and concrete, *Journal of Composites for Construction*, v 8, n 6, December, 2004, pp. 519-527.
- Seracino, R., Saifulnaz M. R. R. and Oehlers, D.J. (2007). Generic Debonding Resistance of EB and NSM Plate-to-Concrete Joints, *Journal of Composites for Construction*, ASCE, Vol. 11, No. 1, January/February 2007, pp. 62-70.

Bond Strength of BFRP Bars to Basalt Fiber Reinforced High-Strength Concrete

^{1,2}Qiaowei Bi (biqiaow@sina.com) & ²Hui Wang

¹ School of Civil & Hydraulic Engineering, Dalian University of Technology, Dalian, China

² School of Civil & Safety Engineering, Dalian Jiaotong University, Dalian, China

ABSTRACT In order to study the bonding characteristic of the BFRP (Basalt Fiber Reinforced Plastics for short) bars and the basalt fiber reinforced high-strength concrete, we embedded the BFRP bar into the cubic concrete specimen which mixed the element of the basalt fiber sized 150mm×150mm×150mm. The diameter of the BFRP bars used for experiment were differentiated into 10mm, 14mm and 18mm. The BFRP bonding length was differentiated into 40mm, 70mm and 100mm. The basalt fiber volume content of high-strength concrete was differentiated into 0%, 0.1%, 0.15% and 0.2%. By changing the diameter of the BFRP, the bonding length of the BFRP and the basalt fiber volume content of the basalt fiber reinforced high-strength concrete, we can research the bonding capacity between the BFRP and the basalt fiber reinforced high-strength concrete. The experimental results indicate that the average bonding strength decreased while the bonding length increased and it become weaker while the diameter of the BFRP was bigger, and we have the best effect of the bonding strength when its fiber content was 0.2% comparing with three kinds of fiber content.

1 INTRODUCTION

Basalt fiber reinforced concrete has the remarkable advantages on excellence of crack resistance, impact resistance, freeze thaw, anti-shrinkage and impermeability; it is beneficial to improve the durability of concrete and to prolong the service life of concrete structure^[1]. Inorganic basalt fiber is superior to organic fiber in anti-aging performance, and it also can improve mechanical behavior of concrete.

Basalt Fiber Reinforced Polymer (BFRP) has been extensively researched as a new type material because of its advantages of high strength, light quality, linear elasticity, corrosion resistance, easy cutting, low relaxation, non-magnetic performance, anti-fatigue and so on in the worldwide in recent years^[2-3]. There are research reports on substituting ordinary reinforcements for the BFRP bars in order to solve the durability problem of reinforcement corrosion in the worldwide.

Study of bonding behaviors of FRP bars to concrete have been researched widely^[4-12]. However, the bonding problems of the BFRP bars to the basalt fiber reinforced high-strength concrete have not been reported. Whether or not the BFRP and the basalt fiber reinforced high-strength concrete can work together effectively was based on the bonding strength of the two materials. This paper adopts three kinds of diameter, three kinds of bonding length, three kinds of fiber volume content considered as the centric pullout bonding strength test parts. Based on the 108 pullout specimens, this paper

has been used the pullout test to study the bonding behaviors of ribbed bars of basalt fiber reinforced polymer (BFRP) to the basalt fiber reinforced high-strength concrete, and conclude the primary result of the bonding strength as references for engineering application.

2 EXPERIMENTAL PROGRAM

2.1 BFRP bar

The BFRP bars which were used in this research program in nominal diameters of 10mm, 14mm and 18 mm provided by Zhe Jiang Shi Jin Basalt Fiber Ltd were made of ribs in helical pattern on the rebar surface. The main technical specifications of the BFRP bars are described in Table 1.

Table 1 Main technical specifications of BFRP bars

Diameter (mm)	Ultimate tensile load (kN)	Ultimate tensile strength (MPa)	Elastic modulus (GPa)
10	61.31	781	40.6
14	109	708	36.8
18	171.93	676	35.2

2.2 Pullout specimen

For the experimental determination of the bond-slip relationship between bar and concrete, pullout specimens with centric bar placement can be used. This method is

popular because it provides a simple means of comparing the relative bonding behavior developed by different bars. A sketch of the pullout specimen is shown in Figure 1. Each bar was embedded in the center of an 150mm×150mm×150mm concrete cube, and each embedded length of them was 40mm, 70mm and 100mm. All the bars were 500mm long. The length of the BFRP bars have 300mm left from its bottom end, in order to meet the load requirements and left 50mm of the length from its top which call free end, so that we can measure the slip on the free end.

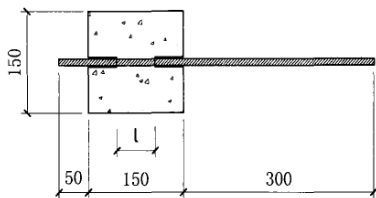


Figure 1 Sketch of pullout specimen (mm)

Contacting surface boundaries between the concrete and the bar were separated by using a PVC tube to reduce the influence of the stress coming from the free end. The basalt filament volume fraction was 0%, 0.1%, 0.15% and 0.2%. Three nominally identical specimens were tested for each bar to check the reliability of the test setup and the scatter of the test results. The concrete and the BFRP bar were cast vertically. After molding, place the specimens in the standard curing room for 28 days.

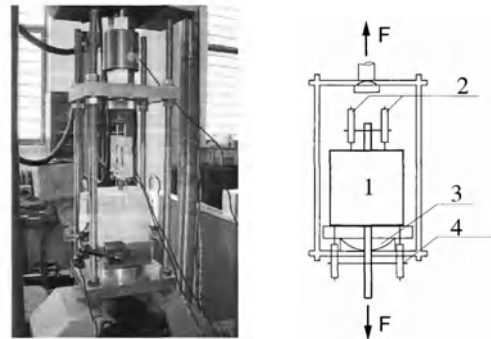
2.3 Testing equipment

The load frame used in this test was made according to CSA [9], which is shown in Figure 2. The bonding specimen was put into the frame, and the frame could be connected with the testing machine using a sleeving made specially. The steel plate had a hole through which the BFRP bar could pass. A spherical seat was put between the channel steel plate and the lower plate, which ensured that the deformed the BFRP bar was subjected to the axial loads, not the torsional or flexural loads.

The slips of the bar relative to concrete at the loaded end and at the free end were measured with four displacement meters. On the loaded end, two displacement meters were clamped to the bar using the gripper rack, which measured the relative displacement. The other two displacement meters were located on the free end to measure the relative displacement between the concrete and the unloaded end of the bar.

The testing machine for pullout tests must be capable of accurately applying the prescribed load. The load applied to the bar must be at a rate not more than 22 kN/min or at a speed of the testing machine head that must not be greater than 1.27 mm/min. In this test, the

testing machine was the INSTRON Series WAW-2000 electronic universal material testing machine with a capacity of 2000 kN. All the tests were carried out in displacement control mode at a speed of 0.5 mm/min so as to obtain the peak behavior. The output load from the testing machine and the four displacement meters were recorded using by an automatic data acquisition system. Loadings and readings were continued until: (1) pull-through or rupture of the BFRP bar occurs; (2) the enclosing concrete splits; or (3) slippage of at least 5 mm has occurred at the loaded end with the load nearly remaining the same.



1. pullout specimen; 2. displacement meters; 3. spherical seat; 4. displacement meters

Figure 2 Setup of pullout test

3 EXPERIMENTAL RESULTS

3.1 Mode of failure

By observing each test, the type of failure is given in Table 2. In some cases, the specimens failed to pull out. Pullout failure occurred because the energy of shearing bonding strength between the bar and the concrete was exceeded over the bonding capacity. In most cases the specimens failed due to the exfoliation of the deformation. The ultimate bonding strength of the specimens was dictated by the shearing strength of the concrete where the bar.

3.2 Average bond strength

Assuming that the uniform of bonding strength distribute along the embedded length in the concrete, the average bonding strength is defined as the shear force on the per unit surface area of the bar. This is given by the relationship:

$$\tau = P / \pi \cdot d \cdot l_a \quad (1)$$

Where τ = average bonding strength in MPa; P = applied pullout load in kN; d = diameter of the bar in mm; and l_a = embedded length in mm.

3.3 Slip at the free end

S is the average slip of the two displacement meters at the free end in mm. The results of the test for all the bonding specimens are given in Table 2.

Table 2 Experimental results of bond strength of BFRP bars in high-strength concrete

Test parameters			Test results				
d (mm)	BF (%)	l_a (mm)	f_c (MPa)	P (kN)	τ (MPa)	S (mm)	Failure mode
10	0	40	60.21	35.07	27.92	5.00	CS
		70	60.21	46.87	21.32	2.28	CD
		100	60.21	53.28	16.97	0.26	DD
	0.1	40	62.89	42.15	33.56	1.00	CD
		70	62.89	51.25	23.32	0.16	DD
		100	62.89	39.79	12.67	0.11	DD
	0.15	40	54.07	37.77	30.07	12.68	CS
		70	54.07	48.22	21.94	0.24	DD
		100	54.07	51.93	16.54	0.98	DD
	0.2	40	57.77	45.86	36.51	2.22	CD
		70	57.77	52.95	24.09	0.78	DD
		100	57.77	55.64	17.72	0.80	DD
14	0	40	60.21	69.80	39.70	10.01	CS
		70	60.21	82.27	26.74	1.57	CD
		100	60.21	48.80	11.10	0.23	DD
	0.1	40	62.89	49.23	28.00	16.03	CS
		70	62.89	72.83	23.67	15.01	CS
		100	62.89	61.71	14.04	0.11	DD
	0.15	40	54.07	40.36	22.95	20.88	CS
		70	54.07	61.71	20.05	22.51	CS
		100	54.07	81.26	18.48	0.13	DD
	0.2	40	57.77	60.69	34.51	9.82	CS
		70	57.77	75.87	24.66	0.55	DD
		100	57.77	87.32	19.86	0.29	DD
18	0	40	60.21	44.51	19.69	22.43	CS
		70	60.21	77.89	19.69	22.89	CS
		100	60.21	73.17	12.95	0.09	DD
	0.1	40	62.89	50.77	22.46	12.88	CS
		70	62.89	76.54	19.35	7.98	CD
		100	62.89	72.16	12.77	0.11	DD
	0.15	40	54.07	61.37	27.15	0.62	DD
		70	54.07	63.39	16.02	0.13	DD
		100	54.07	79.58	14.08	0.11	DD
	0.2	40	57.77	62.00	27.42	34.73	CS
		70	57.77	78.07	19.73	0.13	DD
		100	57.77	83.62	14.79	0.07	DD

d : BFRP diameter; BF : basalt fiber volume fraction; l_a : embedded length; f_c : the concrete compressive strength;

τ : average bond strength; P : applied pullout load; S : the slip at the free end; CS: the shear of bar slip (The pullout specimen occurred a relatively longer bond-slip move from the BFRP bar under the pullout load); CD: the shear of the deformation with the bar being slightly slip (The pullout specimen occurred a relatively shorter bond-slip move from the BFRP bar under the pullout load then it split off very soon); DD: the splitting failure (The pullout specimen almost didn't occur bond-slip move from the BFRP bar under the pullout load, but the specimen split off directly)

4 ANALYSIS OF EXPERIMENTAL RESULTS

4.1 Effect of the BFRP embedded length

The bond-slip curves of the BFRP bars embedded in the different length are shown in Figure 3. From Figure 3 it can be seen that the bonding strength decreased when the embedded length of the bar increased based on the fixed condition of fiber volume fraction. From Figure 3 and Table 2, it can be seen that the failure mode in series 40mm are most the shearing of bar slipping; only one group is the splitting failure and two groups are the shearing of the deformation with the bar slightly slipping then splitting thoroughly; three groups in series 70mm are the shearing of bar slipping and three groups are the shearing of the deformation with the bar slightly slipping then splitting thoroughly, six groups in series 70mm are the splitting failure. The failure mode in series 100mm are all the splitting failure.

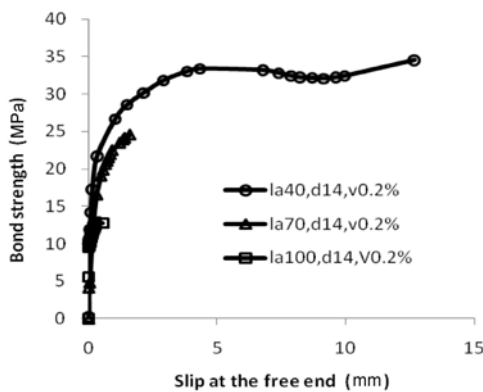


Figure 3 Effect of BFRP embedded length

4.2 Effect of basalt fiber volume fraction

The bond-slip curves of bars embedded in the different basalt fiber volume fraction are shown in Figure 4. It can be seen that the bonding strength of bars in series of 0.2% is higher than the other series in Figure 4. It is explained by the lower of water-cement ratio and more cement in high-strength concrete. So the fiber filaments were fully encapsulated by the cement and the BFRP bars were encapsulated sufficiently by the cement fiber filaments.

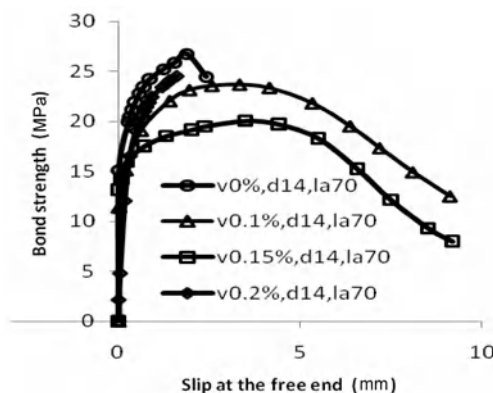


Figure 4 Effect of basalt fiber volume fraction

4.3 Effect of bar diameter

The bond-slip curves of the BFRP bars are shown in Figure 5. It can be seen that when the bonding length was fixed, the bonding strength decreased as the diameter of the bar increased. The reason was that the bigger the diameter of the BFRP bar, the more the quantity of mixed water beneath the bar overflowed so that created greater space. This space reduced the contact surface between the bar and the concrete and hence the bonding strength decreased.

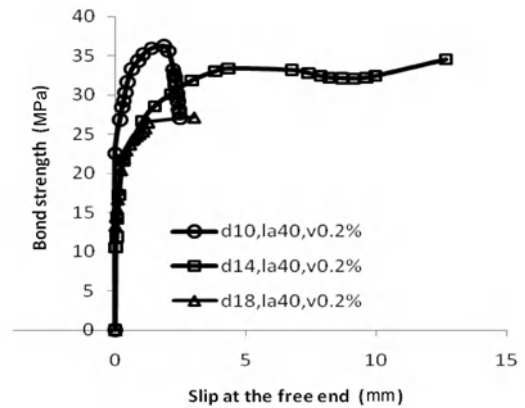


Figure 5 Effect of BFRP diameter

5 CONCLUSIONS

We study the bonding length, the diameter of the BFRP and the influence of basalt fiber volume content on the bonding strength between the BFRP and the basalt fiber reinforced high-strength concrete by comparing with the results of the test of 108 pullout specimens, we can make the conclusions as follow:

- (1) The bonding strength of the BFRP bar depended primarily on mechanical interaction between the bar and the concrete where it was embedded. However, the bonding strength and bond-slip relationship of the BFRP bars did not vary with the compressive strength of the concrete.
- (2) The bonding strength of the BFRP bar embedded in 0.2% volume fraction of basalt fiber was superior to those which were in other volume of the fiber fraction.
- (3) The bonding strength of the BFRP bar varied with the diameter of the bar. The bonding strength decreased due to the increase of the bar diameter.
- (4) The average bonding strength between the BFRP bar and the basalt fiber concrete decreased as anchorage length of the BFRP bar increased.

REFERENCES

XIE Er-gai, LI Zhongying.2003. Application prospect of basalt fiber (in Chinese). *Fiber Composite* 3:15-18 .
 HU Xianqi; LUO Yifeng; SHEN Tunian. 2002. Basalt continuous fiber and its reinforcing composite material (in Chinese).

- Hi-tech Fiber & Application 2: 3-7.
- HU Xianqi, SHEN Tunian. 2005. The Applications of the CBF in War Industry & Civil Fields [J] (in Chinese). *Hi-tech Fiber & Application* 6: 11-17.
- Okelo, R., Yuan, R.L. 2005. Bond strength of fiber reinforced polymer rebars in normal strength concrete. *Journal of Composites for Construction* 9 (3): 203-213.
- San-José, T.J., Manso, J.M. 2006. Fiber-reinforced polymer bars embedded in a resin concrete: Study of both materials and their bond behavior. *Polymer Composites* 27 (3): 315-322.
- Achillides, Z., Pilakoutas, K. 2006. Bond behavior of fiber reinforced polymer bars under direct pullout conditions. *Journal of Composites for Construction* 8 (2): 173-181.
- Benmokrane, B., Tighiouart, B., Chaallal, O. 1996. Bond strength and load distribution of composite GFRP reinforcing bars in concrete. *ACI Materials Journal* 3: 246-253.
- Benmokrane, B., Zhang, B.R., Chennouf, A. 2000. Tensile properties and pullout behavior of AFRP and CFRP rods for grouted anchor applications. *Construction and Building Materials* 14 (3): 157-170.
- CSA (Canadian Standard Association). CSA S806 02. 2002. *Design and Construction of Building Components with Fibre Reinforced Polymers*. Canadian Standards Association International, Toronto, Canada.
- Hao, Q.D., Wang, B., Ou, J.P. 2006. Fiber reinforced polymer rebar's application to civil engineering (in Chinese). *Concrete* 9: 38-40.
- Hao, Q.D., Wang, B., Ou, J.P. 2007a. Bond behavior between FRP rebar and concrete (in Chinese). *Architecture Technology* 1: 15-17.
- HAO Qingduo, WANG Yanlei, ZHANG Zhichun, OU Jin-ping. 2007. Bond strength improvement of GFRP rebars with different rib geometries. *Journal of Zhejiang University SCIENCE A* 8(9): 1356-1365.

Bond Strength of FRP Rebar to Concrete: Effect of Concrete Confinement

Shahriar Quayyum & Ahmad Rteil (ahmad.rteil@ubc.ca)

School of Engineering, The University of British Columbia, Kelowna, BC, Canada

ABSTRACT According to ACI 440.1R-06, the presence of transverse reinforcement does not affect the bond strength of fiber reinforced polymer (FRP) rebar to concrete. This conclusion was based on a limited number of data (19 confined beam tests) available in literature at the time. In the present study, 177 beam bond test data, failed by concrete splitting, was collected to investigate the effect of concrete confinement on the bond strength with FRP rebar. Of these 177 beam-type specimens, 105 specimens had transverse reinforcement. It was observed that the presence of transverse reinforcement increased the bond strength of FRP rebar to concrete by 10%-15%, which eventually decreases the development length needed for attaining the tensile strength of FRP rebar. A linear regression was performed on the collected data to develop an equation to determine the bond strength of FRP rebar to concrete in presence of transverse reinforcement and the equation was compared with the ACI 440.1R-06 equation and the experimental results. Based on the analysis, it was found that the proposed equation is in good agreement with the experimental results and it yields a better estimate of bond strength than the ACI 440.1R-06 equation.

1 INTRODUCTION

Studies on bond behavior of steel reinforcement have demonstrated that the presence of transverse reinforcement confines developed and spliced bars by limiting the progression of splitting cracks and, thus, increases the bond force required to cause failure (Tepfers 1973; Orangun et al. 1977; Darwin and Graham 1993a, b). ACI 408R-03 proposed an equation for estimating the bond strength of steel rebar based on the study of Orangun et al. (1975) which takes into account the effect of transverse reinforcement. Fiber reinforced polymer (FRP) rebars have been recently used in concrete to increase its durability. However, there are only few literature studies available on the effect of concrete confinement of FRP rebar. Due to the limited availability of experimental data, no definite relationship can be established between transverse reinforcement and bond strength for FRP rebar. ACI 440.1R-06 proposed the following bond strength equation of FRP rebar to concrete (in SI units):

$$\frac{u}{\sqrt{f'_c}} = 0.33 + 0.025 \frac{c}{d_b} + 8.3 \frac{d_b}{l_{embed}} \quad (1)$$

where u is the bond strength of FRP rebar to concrete, f'_c is the compressive strength of concrete, c is the lesser of the cover to the center of the bar or one-half of the center-on-center spacing of the bars being developed, d_b is the bar diameter and l_{embed} is the embedment length of

the rebar in concrete. This equation was developed from the study by Wambeke and Shield (2006) in which a linear regression was performed on 67 beam-type specimen data which failed by concrete splitting. Forty eight (48) of these specimens were unconfined and 19 were confined. From this study, it was found that the bar surface did not appear to affect the results, nor surprisingly did the presence of confining reinforcement. Darwin et al. (1996) found that confining steel used in beams that had steel reinforcing bars with a high relative rib area had more of a beneficial increase in the bond force over the same-size steel bars with moderate rib area. The counterargument was proposed in Wambeke and Shield's (2006) study. The GFRP bars have a very low relative rib area and, therefore, the presence of confinement may not increase the average bond stress. Additional research into the effect of confining reinforcement on bond of FRP bars, however, was recommended.

The study reported herein provides an investigation on the effect of the presence of transverse reinforcement on the bond strength of FRP rebar to concrete based on 177 beam test data (105 confined and 72 unconfined) which included carbon, glass and aramid FRP rebars with different surface texture (sand coated, spiral wrap, helical lug) and which failed by concrete splitting.

2 DESCRIPTION OF THE DATABASE

In this study, a database of 177 beam-type specimen was

created from the available literature. Only beam-type specimens that failed by concrete splitting were considered. These specimens consisted of beam end specimens, beam anchorage specimens, and splice specimens. The data included glass, carbon and aramid FRP rebars with different surface textures such as sand coated, spiral wrap and helical lugs. Table 1 shows the breakdown of the database with respect to type of FRP and surface texture. A complete listing of all the data for each test can be found in Quayyum (2010).

Table 1 Classification of the specimens with respect to type of FRP and surface texture of rebar

	GFRP	CFRP	AFRP	Total
Spiral wrap	56	1	3	60
Helical lug	62	12	3	77
Sand coated	10	28	2	40
Total	128	41	8	177

The nominal diameter of the rebars ranged from 8 mm (0.3 in) to 29 mm (1.2 in). The compressive strength of the concrete for the beam tested ranged from 27 MPa (3900 psi) to 66 MPa (9600 psi). Eighty five percent (85%) of the specimens had concrete cover between one and three bar diameters and the embedment lengths of all the specimens ranged between 4 to 116 bar diameters. The database included both confined and unconfined beam tests on top and bottom bars (105 confined bottom, 50 unconfined bottom and 22 unconfined top bars). There were 105 beam tests that contained transverse reinforcement. The nominal diameter of the steel stirrups used in the specimens varied between 8 mm (0.3 in) to 11.3 mm (0.6 in) with a spacing between 78 mm (3 in) and 150 mm (6 in) and all of the tests were performed on bottom bars. Thus the database contains an adequate representation of the different parameters that appear to influence bond performance of FRP rebar to concrete and therefore, the data can be thought to be sufficient to perform statistical analysis.

3 UNCONFINED BEAM TESTS WITH SPLITTING FAILURES

There were 72 unconfined beam tests that failed by splitting of the concrete. Of these 72 tests, 22 tests were performed on specimens where the bars were cast as top bars. These 22 tests were not used to develop the bond strength equation. Using the same approach as Orangun et al. (1975), a linear regression analysis on the normalized cover (cover to the center of the bar divided by the nominal bar diameter) and the inverse of the normalized embedment length was used to develop Equation (2) from the 50 beam tests on bottom bars.

$$\frac{u_c}{\sqrt{f'_c}} = 0.03 + 0.14 \frac{c}{d_b} + 9.0 \frac{d_b}{l_{embed}} \quad (2)$$

where u_c is the bond strength of unconfined FRP rebars to concrete (i.e. due to concrete cover only). When the predicted values were plotted with the experimental values (Figure 1), it was found that the bond strength values obtained from the proposed equation are very close to the actual test results. The ACI equation is also in close proximity to the proposed equation. The average of the ratio of experimental to predicted values was found to be 0.92 with a standard deviation of 0.22 which is quite reasonable. Thus, Equation (2) can provide a reasonable estimate of bond strength of FRP rebar to concrete.

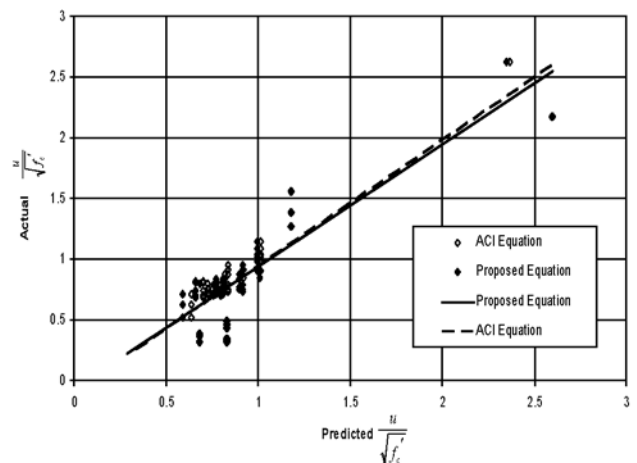


Figure 1 Test vs predicted average bond stress for unconfined bottom bar specimens failed by concrete splitting

4 CONFINED BEAM TESTS WITH SPLITTING FAILURES

In this study, there were 105 beam-type specimens which had transverse reinforcement and failed by concrete splitting. From the accumulated data, it was found that the presence of transverse reinforcement had certain positive impact on the bond behavior of the specimens. Figure 2 shows the normalized average bond stress plotted against normalized embedment length for both confined and unconfined specimens which failed by concrete splitting. Figure 2 clearly shows that the presence of transverse reinforcement increased the overall bond strength of FRP rebar to concrete.

The increase in bond strength can be regarded as the strength of an unconfined rebar plus the strength contributed by the transverse reinforcement (Orangun et al. 1975). The transverse reinforcement contribution (u_{tr}) to bond stress was calculated by subtracting u_c , as determined from equation (2), from the total bond stress achieved in a confined splice test, $u_{confined}$ i.e. $u_{tr} = u_{confined} - u_c$. The value of u_{tr} normalized by square root of f'_c was plotted against $A_{tr}/s n d_b$ for the bars considered

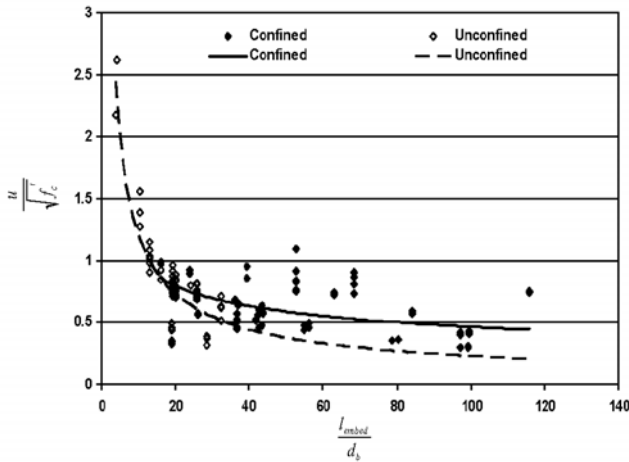


Figure 2 Normalized average bond stress plotted against normalized embedment length for bottom bar specimens failed by concrete splitting

(Figure 3). The straight line fit proposed led to the following equation:

$$\frac{u}{\sqrt{f'_c}} = 2.9 \frac{A_{tr}}{s n d_b} \tag{3}$$

Where A_{tr} is the area of transverse reinforcement normal to the plane of splitting through the bars, s is the center to center spacing of the transverse reinforcement and n is the number of bars being developed along the plane of splitting.

The total bond strength of a FRP bar with transverse reinforcement was determined by combining Equations (2) and (3) as follows:

$$\frac{u}{\sqrt{f'_c}} = 0.03 + 0.14 \frac{c}{d_b} + 9.0 \frac{d_b}{l_{embed}} + 2.9 \frac{A_{tr}}{s n d_b} \tag{4}$$

Equation (4) gives bond strength values for FRP rebar to concrete for splitting mode of failure. Figure 4 presents comparison of the proposed equation against the ACI 440.1R-06 equation and the test results.

It was observed that ACI 440.1R-06 equation underestimates the bond strength of FRP rebars to concrete in presence of transverse reinforcement which has not been taken into consideration for the development of the ACI 440.1R-06 equation. On the other hand, the proposed equation takes into account the effect of transverse reinforcement and hence, it gives less conservative estimate of bond strength than the ACI 440.1R-06 equation. Also, the proposed equation shows good agreement with the test results and the perfect fit line which gives indication about the satisfactoriness of the equation. The proposed equation results in shorter development length required to achieve the tensile strength of FRP rebar because it takes advantage of the presence of confinement. It was found that the proposed equation can increase the bond strength (or reduce the

required development length) by 10-15%. This will reduce the amount of FRP material to be used in construction and hence, decrease the overall cost of construction. This in turn will encourage the use of FRP rebars in construction projects.

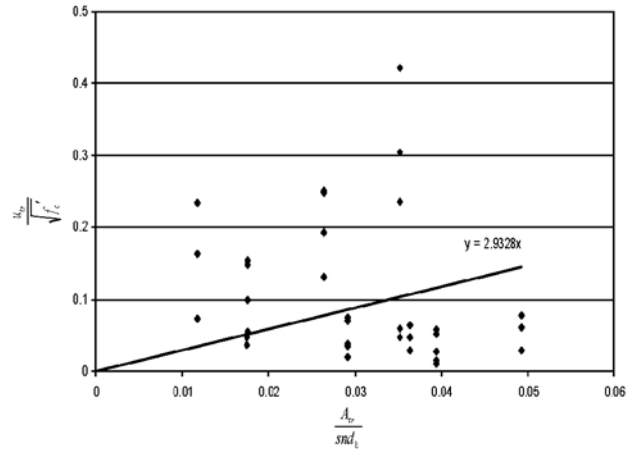


Figure 3 Effect of transverse reinforcement for 105 confined tests with splitting failures

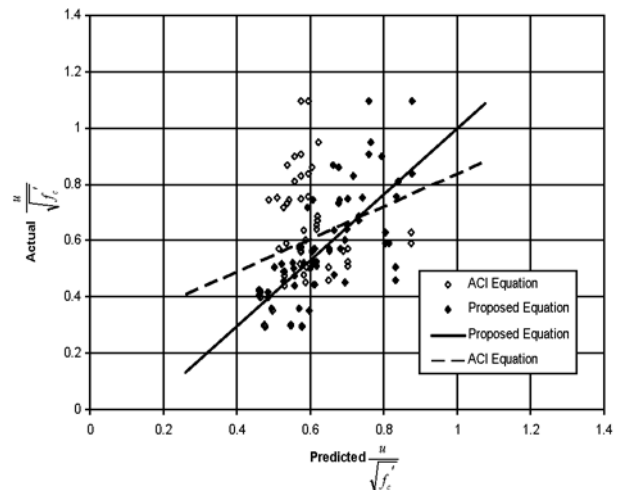


Figure 4 Test vs predicted average bond stress for confined bottom bar specimens failed by concrete splitting

5 CONCLUSION

The study reported herein provides an investigation on the effect of transverse reinforcement on the bond strength of FRP rebar to concrete. It was observed that the presence of transverse reinforcement increases the bond force of FRP rebar to concrete. The increase in bond force was about 10-15% which eventually will decrease the development length needed to acquire the desired tensile strength of the rebar. Hence, the presence of transverse reinforcement should be taken into consideration while calculating the development length of FRP rebar. Based on the analysis, an equation was developed for evaluating the bond strength of FRP rebar to concrete and it was found that the proposed equation

is in good agreement with the actual test results and it gives less conservative estimate of bond strength than the equation proposed by ACI 440.1R-06 in presence of transverse reinforcement. In short, the proposed equation can provide a more cost effective design than the equations reported in the current literature.

REFERENCES

- ACI Committee 408, 2003. Bond and development length of straight reinforcing bars in tension (ACI 408R-03). American Concrete Institute, Farmington Hills, MI, 49 pp.
- ACI Committee 440, 2006. Guide for the design and construction of structural concrete reinforced with FRP bars (ACI 440.1R-06). American Concrete Institute, Farmington Hills, MI, 44 pp.
- Darwin, D., Zuo, J., Tholen, M., and Idun, E. 1996. Development length criteria for conventional and high relative rib area reinforcing bars. *ACI Structural Journal*, V. 93, No. 3: 347-359.
- Darwin, D., and Graham, E. K. 1993a. Effect of deformation height and spacing on bond strength of reinforcing bars. *ACI Structural Journal*, V. 90, No. 6: 646-657.
- Darwin, D., and Graham, E. K. 1993b. Effect of deformation height and spacing on bond strength of reinforcing bars. *SL Report 93-1*, University of Kansas Center for Research, Lawrence, Kans., 68 pp.
- Orangun, C. O., Jirsa, J. O., and Breen, J. E. 1975. The strength of anchor bars: a reevaluation of test data on development length and splices. *Research Report 154-3F*, Center for Highway Research, The University of Texas Austin, Austin, Tex., 78 pp.
- Orangun, C. O., Jirsa, J. O., and Breen, J. E. 1977. Reevaluation of test data on development length and splices. *ACI Journal, Proceedings* V. 74, No. 3: 114-122.
- Quayyum, S. 2010. Bond-slip modeling of FRP rebars in concrete. *MS Thesis (in progress)*. The University of British Columbia, Kelowna, BC, Canada.
- Tepfers, R. 1973. A theory of bond applied to overlapping tensile reinforcement splices for deformed bars. *Publication 73:2*. Division of Concrete Structures, Chalmers University of Technology, Goteborg, Sweden, 328 pp.
- Wambeke, B. W., and Shield, C. K. 2006. Development length of glass fiber-reinforced polymer bars in concrete. *ACI Structural Journal*, V. 103, No. 1: 11-17.

Bond Strength of Fiber Reinforced Polymer (FRP) Bars in Autoclaved Aerated Concrete (AAC)

B. Israngkura Na Ayudhya (ayudhya2003@yahoo.com)

Department of Civil Engineering, Rajamangala University of Technology Krungthep, Bangkok, Thailand

Y. Ungkoon

Research and Development Department of Superblock Ltd., Bangkok, Thailand

ABSTRACT The use of fiber reinforced polymer (FRP) composites is significantly growing in civil engineering works where maintenance cost of structure is concerned. They have excellent properties on highly corrosion resistance, high strength and lightweight. This research studies bond strength of autoclaved aerated concrete (AAC) reinforced with FRP bars. It is compared with autoclaved aerated concrete reinforced with mild steel bars. The concentric pullout method is implemented in order to find the bond strength. The bond strength including the mode of failure and bond strength is studied with varying type, surface treatment and embedment length of reinforcing bars. The result reveals that bond strength is found increased with embedment length. In particular, sand-coated Carbon fiber bar gives the most promising results with the highest bond strength in synthetic fiber bars.

1 INTRODUCTION

Autoclaved aerated concrete (AAC) is a brittle material which is strong in compression but relatively weak in tension. The ability to carry compression and tensile loads are lesser than concrete. In order to compensate the weakness of AAC's behaviour, steel bars are commonly used in AAC panels and lintels. Steel bars are used for carrying the tensile loads. The used of steel bars as reinforcement embedded in AAC is susceptible to corrosion problems. This is due to high porosity of AAC. Nonetheless, the efforts still may not project the best way of solution to the problems, as their long-term effectiveness is still questionable in the working field experience. Lately, fiber reinforced polymer (FRP) reinforcing bars have been developed and introduced in beam, slab, coastal and offshore environment conditions and structure wherein magnetic properties are employed such as the guideway for linear motor vehicles Aramid fiber reinforced polymer (AFRP) and carbon fiber reinforced polymer (CFRP) bars present many advantage such as lightweight materials, high strength-to-weight ratio, electromagnetic neutrality, and ease of handling. Most beneficial is that, they are not affected by the electro chemical corrosion (Dolan, C.W. 1990). Unfortunately, the surface deformation and mechanical properties of mentioned materials are dissimilar to those of steel reinforcing bars.

2 PREVIOUS STUDY

In this research, the literature reviews are stressed

mainly on the bond performance of FRP bars in both concrete and AAC. The relevant literature for AFRP is reviewed by Saafi M & Toutanji H. Since the substantial material and surface deformation of FRP bars are different from that of steel bars, it is expected that the bond performance between FRP bars and AAC is also different from that of steel reinforced concrete. The deformation of FRP reinforcing bars, however, contain a large amount of resin with a low shear modulus and thus contribution of the ribs in FRP bars to the resistance mechanism is significantly lower when compared to the of steel bars. Consequently the bonding and friction may then be the important bond stress components in those concrete reinforced with FRP bars.

3 EXPERIMENT PROGRAMME

3.1 Details of reinforcing bars

In this study, three types of FRP reinforcing bars were investigated: (1) AFRP bar (2) CFRP bar and (3) Fiberglass bar. Mild steel bar was used for comparison. In case of the sand-coated FRP bar, its surface was coated with uniform size of quartz sand using epoxy resin. The AFRP and GFRP bar were made of continuous longitudinal fiber strands impregnated in a thermosetting epoxy resin using the braided process. The fiberglass was made by using pultrusion process. The properties of mentioned FRP are shown in Table 1.

3.2 Preparation and testing methods

All AAC specimens were made by according to Thailand

Industrial Standard (TIS) 1505 – 2541. The AAC specimens were kept at the pressure of 10 – 12 bars, temperature of 180 – 190 °C for 8 hours. The specimens were cut into required test amount by electric cutting device. The bonding strength tests, an adopting testing pullout setup proposed in the Danish Standard DS 2082 (DS 2082, 1980) has been used in this study. In set-up stage, the specimen consists of an AAC prism in which two rods were embedded at the opposite ends. The two rods have different embedment lengths so that pullout was restricted to the shorter one. The beneficial of this set-up was that the compression on the concrete face could be removed. As a result, a similar set-up was used for the present study as illustrated in Figure 2.

Table 1 Properties of FRPs and rebars

Materials	Diameter (mm)	Tension (kN)	Young's modulus (kN/mm ²)	Elongation percent
Aramid fiber	13.7	172	68.6	1.6
Carbon fiber	12.7	264	156.8	1.9
Fiberglass	12.1	163	–	3
Rounded bar	12	400	203.4	12
Deformed bar	12.2	400	203.4	12



Figure 1 Type of FRP bars

In this bonding strength test, AAC specimens of 150 mm diameter by 300 mm long were cast with the FRP bars. The effect of embedment lengths of the shorter bar was investigated (i.e. 125 and 100 mm). A 12 mm diameter of deformed HY steel bar was used as the longer bar to improve the bearing capacity and minimize the slip between the longer bar and AAC. As a result, the pullout was designed to be investigated to the shorter one. The adjustment of embedment length and alignment of the bars were carefully made to the AAC casting as shown in Figure 2.

The bond slip between the AAC and the reinforcing bar was measured by using a Digimatic indicator. This indicator was mounted on the FRP bar and measured from the reference level (surface of specimen). The extensometer was also used and mounted on FRP bar

and measured elongation of the FRP bar. The actual slip was obtained by subtracting the elongation of the shorter bar from the total slip measured. The pullout-loading rate for all the pullouts was 10 N/s. The slip was recorded in each increment of 0.05 kN load. The average bond stress was computed assuming a uniform bond stress distribution along the embedded length of the bar. The average bond stress was computed assuming a uniform bond stress distribution along the embedded length of the bar. The equation used for the computation was

$$f_{av.b} = \frac{P_{max}}{\pi d_b l_d} \quad (1)$$

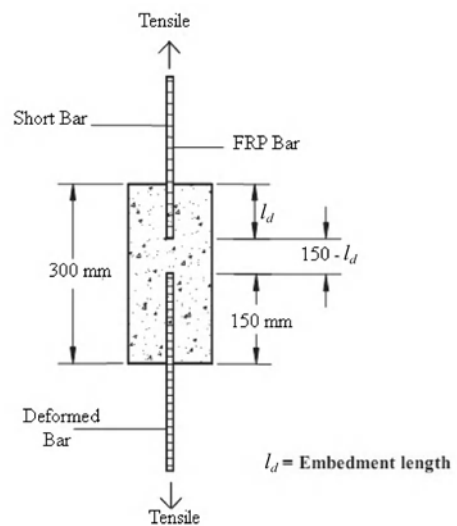


Figure 2 Concentric pullout test specimen used in this study

Where $f_{av.b}$ is the average bond stress; d_b the nominal bar diameter; P_{max} the maximum applied tension load; l_d the embedded length of the shorter bars.

4 RESULT AND DISCUSSION

In this studied, the bond performance of FRP bars reinforced AAC can be characterized by their mode of failure, bond strength and bond-slip relationship. In this paper, the discussions are concentrated on their mode of failure, bond strength and development length. The bond-slip relationship can be found in Balendran, et al. (Balendran, R.V. et al. 2003)

4.1 Mode of failure

The mode of failure of AAC reinforced with FRP can be categorized into 3 types. (1) Pullout failure without tensile splitting or cracking on AAC (2) Pullout with tensile splitting or cracking on AAC (3) AAC tensile splitting failure as shown in Figure 3.

4.1.1 Pullout failure without tensile splitting and cracking on AAC

The pullout type of failure occurred in the majority of

specimens embedded with smooth bars. Pullout failure was characterized by the fact that the AAC surrounding the reinforcing bar was well confined to withstand the splitting stress, the composites generally failed when the bars were pulled out from the AAC specimens. This may be an indication of low bearing stresses produced by the action of a smooth FRP reinforcing bar and as long as the adhesion is broken, the bar moves as a rigid body (Larralde, J & Silva Rodriguez, R. 1993).

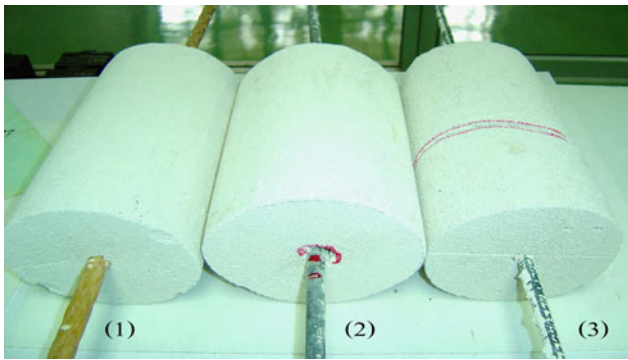


Figure 3 Pattern of failure of AAC

4.1.2 Pull out failure with tensile splitting crack around FRP AAC

The result of experiment showed that specimens bonded with sand-coated FRP bar, an AAC splitting type of failure occurred. This type of failure was mainly observed in sand-coated FRP bars. There was only one type of AAC splitting crack pattern. It was a splitting failure around reinforcement. The occurrence of splitting failure indicates that there was insufficient lateral resistance of the specimen to withstand the pullout force applied. The FRP bar coated with sand creates sufficient radial force components that split the AAC before bond failure. Since the splitting occurred in a tension mode, the failure is brittle. As a result, the splitting failure can be generally characterized by the formation of tensile cracks and accompanied by a large sudden drop in the load-slip curve as shown in Figure 4.

4.1.3 AAC tensile splitting failure

This type of tensile splitting failure occurred with deformed bars. The failure is caused similar to pull out failure with tensile splitting crack around FRP AAC but the degree of failure is higher. The lateral resistance of the specimen to withstand the pullout force is greater than the pullout failure mode. Therefore, there was one type of AAC splitting crack patterns. It was splitting failure without side longitudinal cracks. The splitting was mostly occurred around middle of specimen. Nonetheless, splitting at very top of specimen was occasionally happened. The result showed that bond strength was increased rapidly when slippage is less. Therefore, bond strength of FRP depends on pull out strength which

caused from surface of FRP bar and concrete matrix (Larralde, J. & Silva Rodriguez, R. 1993).

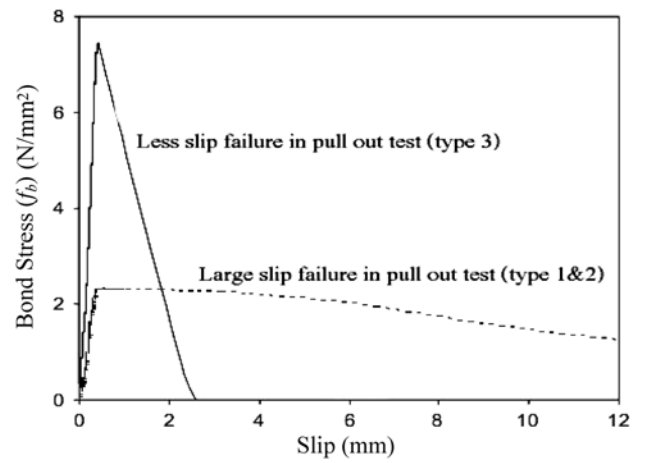


Figure 4 The relationship between bond stress and slippage (Larralde, J & Silva Rodriguez, R. 1993)

4.2 Influence of bar embedment length on bond strength

The influence of embedment length on bond strength of AAC was shown from Table 2. It can be seen that bond strength of reinforcing bar was increased as the length of embedment of reinforcing bar was increased. Nonetheless, the applied value of pull out tensile load can not be

Table 2 Bond strength of FRPs and rebars

Materials	Diameter (mm)	Embedment (mm)	Bond strength (kN)	Mode**
Aramid fiber	13.7	125	5.4	1
Carbon fiber	12.7	125	5.6	2
Fiberglass	12.1	125	3.8	2
Rounded bar	12	125	7.1	2
Deformed bar	12.2	125	10.0	3
Aramid fiber*	13.7	125	6.8	1
Carbon fiber*	12.7	125	8.2	2
Fiberglass*	12.1	125	–	–
Rounded bar	12	125	7.2	2
Deformed bar	12.2	125	10.2	3
Aramid fiber	13.7	100	5.1	1
Carbon fiber	12.7	100	5.2	2
Fiberglass	12.1	100	3.3	2
Rounded bar	12	100	6.9	2
Deformed bar	12.2	100	8.8	3
Aramid fiber*	13.7	100	6.4	1
Carbon fiber*	12.7	100	7.9	2
Fiberglass*	12.1	100	–	–
Rounded bar	12	100	7.3	2
Deformed bar	12.2	100	8.6	3

* Sanded surface ** Mode type (1) Pullout failure without tensile splitting or cracking on AAC (2) Pullout with tensile splitting or cracking on AAC (3) AAC tensile splitting failure.

approached to the tensile strength of the reinforcing bar. This may be due to high porosity structure of AAC. Furthermore, the difference in development lengths between FRP and mild steel bars was very large. Especially, when fiberglass bars were compared with mild steel bars.

4.3 Average bond strength

(1) In figure 5 and 6 showed the bond strength of FRP reinforced in AAC. It has been found that the maximum bond strength for FRP was about 23-47% of ribbed rebars, depending on the values of the embedment length. The resin rich surface layer of FRP bars and their roughness are the critical factors in accounting for the relatively low bond strength.

(2) Bond strength of CFRP sanded was highest among FRP. The bond strength is around 21 percent higher than sanded aramid fiber.

(3) Regarding to mild steel, the bond strength of deformed bar was higher than rounded bar for 41 and 14 percent for 125 mm and 100 embedment respectively.

(4) The sanded surface of FRP helps lateral confinement force around FRP which caused from quartz sand on FRP surface. However, lateral confinement force of FRP was less than deformed bar.

5 CONCLUSIONS

(1) The bond strength of carbon fiber polymer bars gave the highest bond strength when it was compared with others FRP bars.

(2) The bond strength of FRP increased when the depth of reinforcement had been increased.

(3) With identical material, sanded surface bars gave higher bond strength than smooth surface bars.

6 ACKNOWLEDGEMENT

Authors wish to acknowledge the financial support provided by National Science and Technology Development agency (NSTDA).

REFERENCE

- Balendran R.V, Tang W.C, Leung H.Y, Nadeem A. 2003. Bond stress-slip relationships of glass-fibre-reinforced polymer (GFRP) bars embedded in polystyrene aggregate concrete (PAC). In: *28th international conference on our world in concrete&structures, August, 223-232.*
- Danish Standards Organization 1980. Pull Out Test (DS 2082), Copenhagen, Denmark, December: 2.
- Dolan C.W. 1990. Developments in non-metallic prestressing tendons concrete. *PCI J* 35: 80-88.
- Larralade J, Silva-Rodriguez R. 1993. Bond and slip of FRP reinforcing bars in concrete. *Journal of Materials in Civil Engineering* 5(1): 30-40.
- Ritchie Pa, David At, Le-Wu L, Guy MC. 1991. External reinforcement of concrete beams using fiber reinforced plastics. *ACI Structural Journal*: 88(4): 490-500.
- Shelar K. 2006. Manufacturing and design methodology of hybrid fiber reinforced polymer (FRP)- Autoclaved Aerated Concrete (AAC) Panels and its response under low velocity impact. M.S. thesis. CCEE Department, University of Alabama at Birmingham.
- Saafi M, Toutanji H. 1998. Flexural capacity of prestressed concrete beams reinforced with aramid fiber reinforced polymer (AFRP) rectangular tendons. *Construction and Building Materials* 12: 245-249.

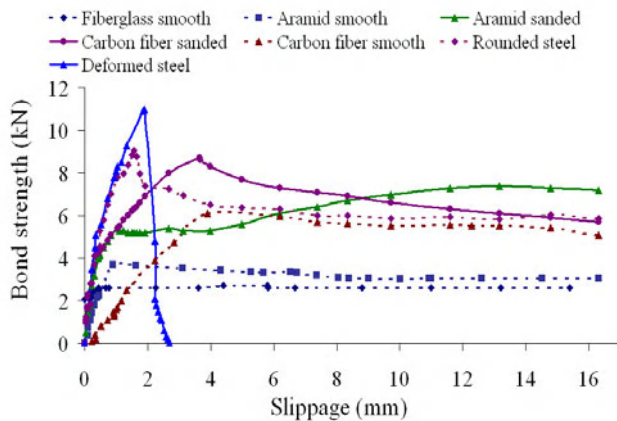


Figure 5 The relationship between bond strength and slippage of FRP materials reinforced in AAC for 125 mm depth

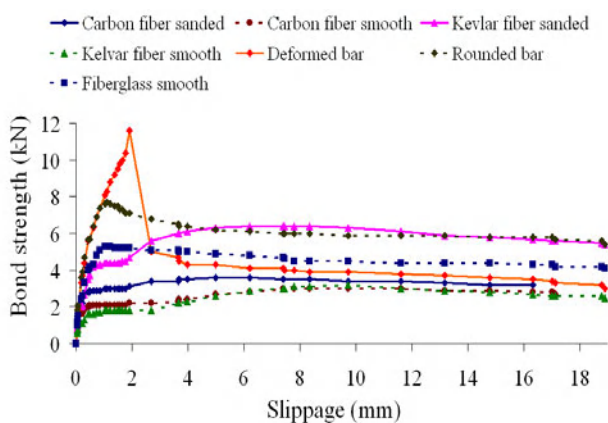


Figure 6 The relationship between bond strength and slippage of FRP materials reinforced in AAC for 100 mm depth

Bond Mechanism of Carbon Fiber Reinforced Polymer Grid to Concrete

L. Ding (carolinedln@126.com)

Department of Civil Engineering, Southeast University, Nanjing, Jiangsu, China

Department of Civil, Construction and Environmental Engineering, North Carolina State University, Raleigh, NC, USA

S. Rizkalla

Department of Civil, Construction and Environmental Engineering, North Carolina State University, Raleigh, NC, USA

G.Wu & Z.S. Wu

Department of Civil Engineering, Southeast University, Nanjing, Jiangsu, China

International Institute for Urban Systems Engineering, Southeast University, Nanjing, Jiangsu, China

ABSTRACT Carbon Fiber Reinforced Polymer (CFRP) Grid provides alternative reinforcing material for concrete structural elements. To implement its use for different structure applications, this paper summarize a research under taken to study the bond properties of CFRP Grid to concrete. The research includes an experimental program consist of eight specially designed specimens, each consist of two concrete blocks, used to apply pure tension loads to the CFRP Grid using hydraulic jacks. The specimens included different embedment length of the CFRP Grid with and without transverse wires. The experimental program included also four one way reinforced concrete slabs with different spliced lengths at mid span to determine the effective development lengths of the CFRP Grid subject to flexural stresses. Research funding provided general design guideline for the use of these types of grids as reinforcements for concrete structures.

1 INTRODUCTION

Fibre Reinforced Polymer (FRP) products become recently more popular as reinforcement for precast concrete structural elements, especially for marine structure, due to their non-corrosion resistance characteristics and high strength to weight ratio. Carbon Fibre Reinforced Polymer (CFRP) orthogonal Grids have been selectively used as an alternative reinforcement for several precast concrete elements.

During the past five years, the use of FRP grids as reinforcement of several precast concrete precast concrete products has been investigated (Rizkalla 2009, Matthys 2000). Research funding indicated that FRP can be used as alternative flexural reinforcement for slab and beam as well as hoop reinforcement for concrete column (Matthys 2000, Saafi 2000). Very few researchers paid attention to the bond mechanism of FRP grid in concrete. Since the strength of reinforced concrete members are governed by the bond, it is essential to study the bond characteristics of the proposed CFRP Grid before its use as reinforcement for concrete flexure members or as confinement reinforcement for concrete piles.

This paper examines the required development length to achieve the full tensile strength as well as the

effectiveness of the presence of the transverse wires on the bond characteristics. The experimental program consisted of two phases which were conducted to explore these two parameters.

The first phase consisted of eight specially designed specimens, each of which consisted of two concrete blocks to subject the grids to pure tension force. Different embedment length with and without transverse wires were used as variables, the load was applied in certain configuration to induce axial tension on the main wires of the CFRP Grid up to failure by using hydraulic jack located between the two concrete blocks. The second phase consisted of four one-way concrete slabs reinforced with the same type of CFRP Grid used in the first phase, spliced within the constant moment region corresponding to the same embedment lengths used in the first phase. All the slabs were tested under four-point bending configuration to determine the flexural capacity resulted by the selected splice lengths.

2 TYPE OF CFRP GRID

The selected CFRP grid used in this investigation was identified C100- 2.36× C25-4.0 Grid. In this paper, C100 wires were used as the main wires subject to pure tensile force, while C25 wires were the transverse wires.

Details of this CFRP grid used are shown in Figure 1.

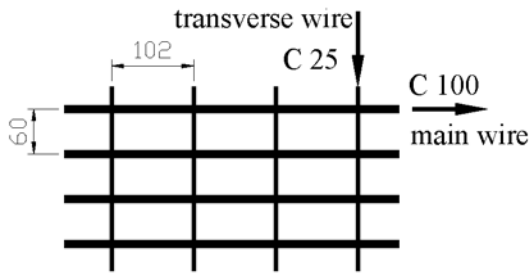


Figure 1 Configuration of C-grid

Eight CFRP Grid coupons were used to determine the material properties of main wires (C100), as shown in Figure 2. Summary of the measured properties are given in Table 1.

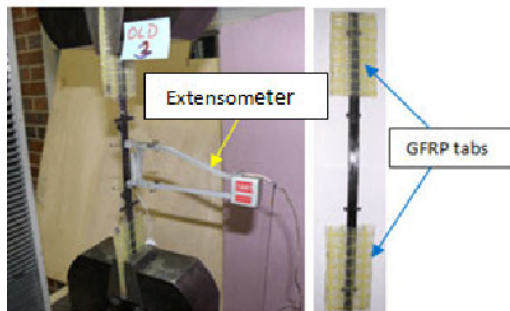


Figure 2 Tensile test of C-grid main wire coupons

Table 1 Material properties of C-grid main wires

Average Max Tensile Force (N)	11,099
Average ultimate Tensile Strain (ϵ)	0.01314
Average Cross Section Area of Composite (mm^2)	8.97
Average Tensile Strength (MPa)	1237
Average Modulus of Elasticity (MPa)	94,140

3 EXPERIMENTAL PROGRAM

The following section summarizes the two phases of the experimental program presented in this paper.

3.1 First phase

In the first phase, a total of eight specimens were manufactured, each of which was composed of two pieces of C-Grid embedded into the two concrete blocks. The measured compressive strength of the concrete was 23 MPa. The embedment length on each side of CFRP grid, in the direction of main wires, were varied in length and used with and without transverse wires as shown in Figure 3(a) and 3(b) respectively.

Construction of typical specimens and location of the grid with respect to the cross section of the block are shown in Figure 4(a) and 4(b) respectively.

Test specimens were identified as “SP-a-b”, where “a” is the embedment length used which was varying

from 4, 8, 12 to 16 inches(102mm, 203mm, 305mm and 406mm). The letter “b” refer to the number of transverse wires included within embedment region. For example specimen SP-8-2 represent specimen with embedment length of 8 inches (203mm) and two transverse wires.

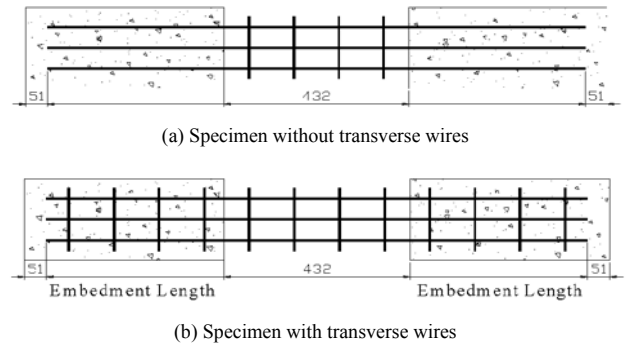


Figure 3 Embedment length of the CFRP grid

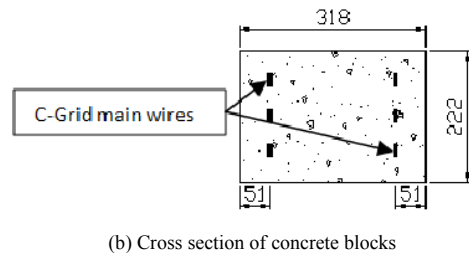
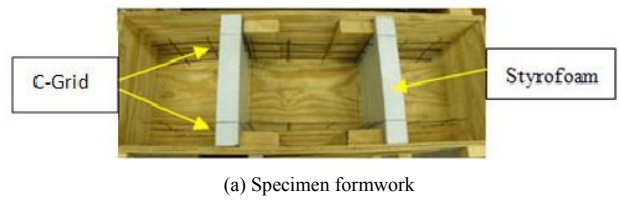


Figure 4 Specimen details in the first phase

The overall test setup is shown in Figure 5. One of the concrete blocks was supported by steel rollers to allow horizontal movement, while the other block was supported by a steel plate. The hydraulic jack in between the concrete blocks was used to measure the applied load. Two linear variable differential transformers (LVDT) were used to measure the horizontal displacement. The load was applied in increments using hand pump and the response was recorded by data acquisition system. The specimen was loaded up to failure.

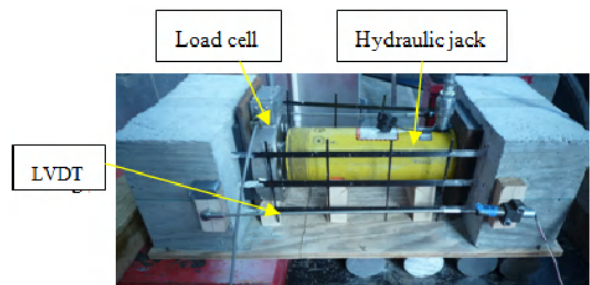


Figure 5 Test setup of concrete blocks

3.2 Second phase

In the second phase, four one-way concrete slabs, reinforced with different splice lengths at mid-span, were tested. The splice lengths tested were the same as the values of the embedment length used in the first phase. Configuration and splice details are shown in Figure 6.

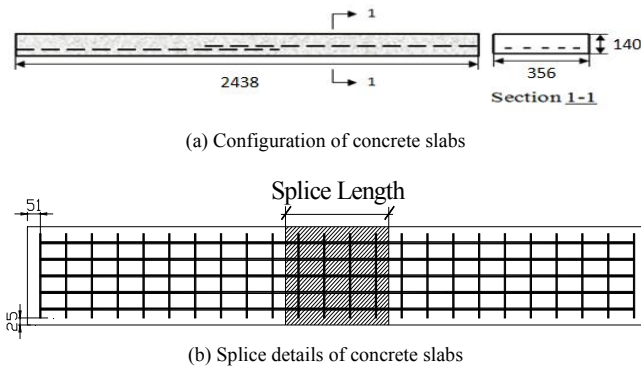


Figure 6 Details of concrete slabs

The slabs are identified as “S-a”, in which “a” is the splice length which was varied from 4, 8, 12 to 16 inches (102mm, 203mm, 305mm and 406mm).

All the slabs were tested under four-point loading configuration. The load was applied by a large hydraulic jack. One load cell was used to measure the applied load. Six gauges were installed to measure concrete strain. And five transducers were used to measure the displacement at the loading points and at the support points during the test process, as shown in Figure 7.

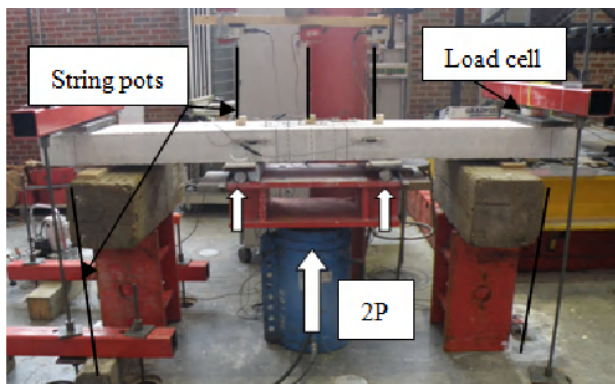


Figure 7 Test setup of slabs

4 TEST RESULTS AND DISCUSSION

The following section briefly present test results of the two phases of the experimental program.

4.1 First phase

The maximum measured load at failure and the failure mode for each tested specimen are given in Table 2.

Test results of the eight specimens are compared in Figure 8.

Table 2 Testing results of the first phase

Identification	Max Load (N)	Failure Mode
SP-4-0	28,452	FRP slip
SP-4-1	31,942	FRP slip
SP-8-0	57,936	FRP rupture
SP-8-2	52,158	FRP rupture
SP-12-0	62,377	FRP rupture
SP-12-3	58,745	FRP rupture
SP-16-0	62,319	FRP rupture
SP-16-4	63,435	FRP rupture

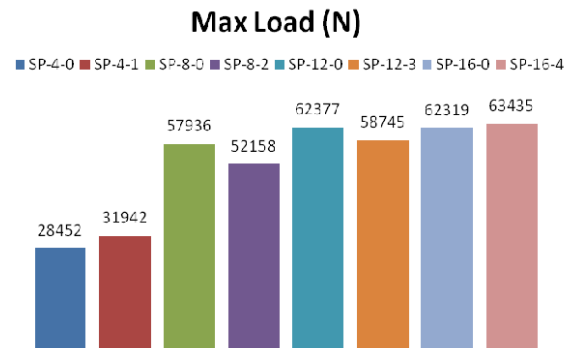
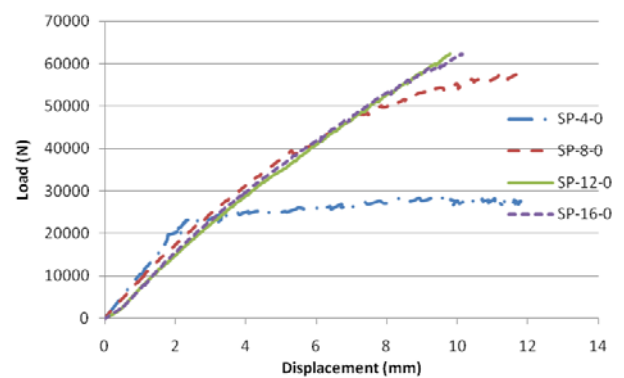
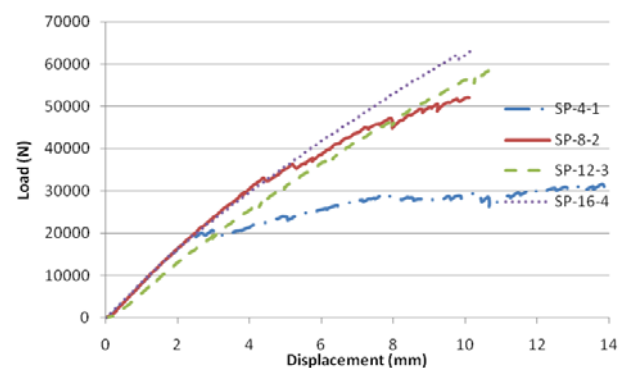


Figure 8 Comparison of maximum loads

The Load-Displacement relationship of the specimens tested without the transverse wires and with transverse wires are shown in Figure 9(a) and 9(b) respectively.



(a) SP-4-0, SP-8-0, SP-12-0 and SP-16-0



(b) SP-4-1, SP-8-2, SP-12-3 and SP-16-4

Figure 9 Load-displacement curves of specimens

The two observed modes of failure of FRP slip and FRP rupture are shown in Figure 10(a) and 10(b) respectively.

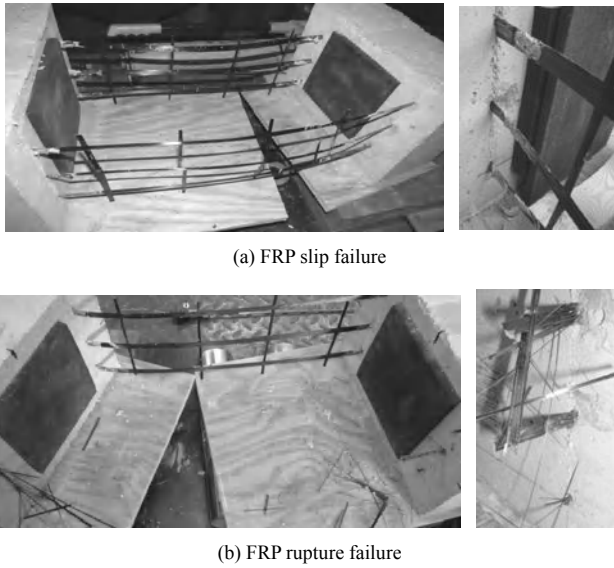


Figure 10 Observed failure modes of the concrete blocks

Test results suggest that a development length of 8 inches (203mm) is sufficient to develop the full tensile strength of the grid and the effect of the transverse wires has insignificant effect on the bond characteristics for this particular grid.

4.2 Second phase

Test results of the four tested slabs and their failure mode are listed in Table 3.

Table 3 Testing results of the second phase

Identification	Max Load (N)	Failure Mode
S-4	6223	FRP rupture
S-8	4223	FRP rupture
S-12	4667	FRP rupture
S-16	5654	FRP rupture

* Max Load is half of the maximum force applied by hydraulic jack.

The load-deflection relationships of the four tested slabs are shown in Figure 11.

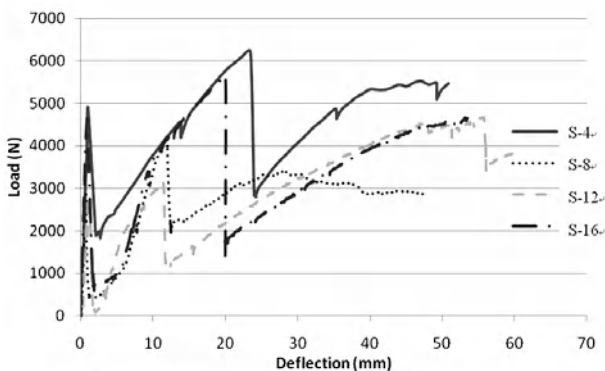


Figure 11 Load-deflection curves for all slabs

The measured flexural cracks were relatively large and the slabs failed due to rupture of the main wires of the CFRP grid, as shown in Figure 12 for the four tested slabs.

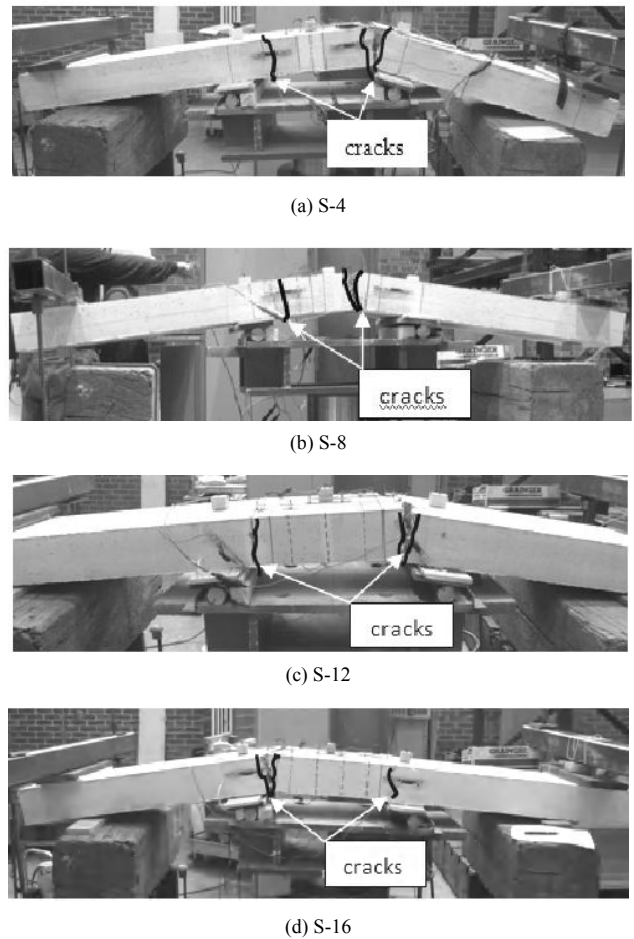


Figure 12 Failure modes of concrete slabs

5 CONCLUSIONS

(1) An embedment length of 8 inches (203mm) is sufficient to develop the full tensile strength of selected CFRP grid.

(2) The presence of transverse wires has insignificant effect on the bond mechanism for this specific type of C-Grid.

(3) A splice length of 4 inches (102mm) is enough to develop the full flexural capacity of the selected CFRP grid.

REFERENCES

Rizkalla, S., Hassan, T. and Lucier, G. 2009. FRP shear transfer mechanism for precast concrete sandwich load bearing panels. ACI Special Publication 265:607-627.

Matthys, S. & Taerwe, L. 2000. Concrete slabs reinforced with FRP Grids I: One-way bending. *Composites for Construction*, Vol.4, No.3:145-153.

Saafi, M. 2000. Design and fabrication of FRP grids for aerospace and civil engineering applications. *Aerospace Engineering*, Vol.13, No.2:144-149.

Confinement of Concrete by FRP in Compression

Effect of Geometric Discontinuities on FRP Strain Efficiency in FRP-Confined Circular Concrete-Filled Steel Tubes

S. Q. Li, J. F. Chen (j.f.chen@ed.ac.uk) & L. A. Bisby

Institute for Infrastructure and Environment, Joint Research Institute for Civil and Environmental Engineering, School of Engineering, The University of Edinburgh, Edinburgh, Scotland, UK

Y. M. Hu & J. G. Teng

Department of Civil and Structural Engineering, The Hong Kong Polytechnic University, Hong Kong, China

ABSTRACT The confinement of concrete columns using FRP jackets/wraps has become a popular retrofitting technique. More recently, the benefit of FRP confinement of concrete-filled steel tubes has been also explored by researchers. Failure of such FRP-wrapped concrete-filled steel tubes is usually governed by rupture of the FRP in the hoop direction. However, the observed FRP hoop strain at failure is typically lower than the ultimate strain in a flat coupon test. Many factors contribute to this phenomenon, one of which is the geometrical discontinuities at the ends of FRP wraps. This paper examines the effect of these geometrical discontinuities on the hoop rupture strain of FRP wraps. Detailed finite element (FE) analyses conducted using both linear elastic and elastic-perfectly plastic adhesive constitutive models are presented. Comparison between the FE predictions and available test results shows that the strain efficiency predicted by FE analysis using an elastic-perfectly plastic adhesive model are in reasonable overall agreement with the test results.

1 INTRODUCTION

There has been extensive research into the use of FRP wrapping to strengthen concrete columns (Teng et al. 2002; Lam and Teng 2004; Jiang and Teng 2007). More recently, Xiao et al. (2005) and Teng and Hu (2006) have explored the benefit of using FRP wraps to provide additional confinement to concrete-filled steel tubes. In such an innovative system, the inward buckling deformation of the steel tube is prevented by the concrete core while the outward buckling deformation is restrained by the FRP jacket. As a result, FRP wrapping can increase both the strength and ductility of concrete-filled steel tubes (Xiao 2004).

The typical failure mode of FRP-confined concrete-filled steel tubes is the tensile rupture of FRP wraps in the hoop direction. It is commonly assumed that this rupture occurs when the hoop strain in the FRP reaches its ultimate tensile strain, which is normally determined from flat coupon tests (ASTM 1995). However, existing experiments (Xiao et al. 2005; Teng and Hu 2006) have all shown that the wrap is observed to rupture at a hoop strain considerably lower than the FRP ultimate strain determined from flat coupon tests. This phenomenon of premature rupture failure of FRP wraps has been widely observed in FRP-confined concrete columns. The ratio of hoop strain in the FRP wrap at rupture to the flat coupon rupture strain was first investigated by Pessiki

et al. (2001).

Many factors may contribute to the lower rupture strain of FRP in FRP-confined concrete-filled steel tubes, such as: geometrical imperfections in the steel tube, geometric discontinuities in the FRP wrap, a 3D stress state in the FRP wrap, and non-uniform support in the test setup. A comprehensive discussion of these factors for FRP-confined concrete columns can be found in Chen (2009) and Chen et al. (2010). A few of these factors have been examined previously studied for FRP-confined concrete columns. For instance, a finite element (FE) study (Chen et al. 2007; Chen et al. 2010) showed that high stress concentrations exist at both ends of an FRP wrap in FRP-confined concrete columns, but the FE results have not been experimentally verified.

This paper investigates the effect of geometrical discontinuities at the ends of an FRP wrap on its strain efficiency when used to confine a concrete-filled steel tube. A detailed FE study is presented. The FE predictions are shown to be in reasonable agreement with test results.

2 EXPERIMENTS

Nine specimens of FRP-confined concrete-filled steel tubes were recently tested under concentric axial compression at The Hong Kong Polytechnic University (Hu 2010) in which the strains in the FRP wraps were carefully measured. The steel tubes all had a length of

400mm and an FRP overlapping zone of 200mm. The concrete cores had a diameter of 200mm. The average values of the elastic modulus and tensile strength from five coupon tests for the GFRP, calculated on the basis of a nominal ply thickness of 0.17mm, are 80.1GPa and 1,826MPa, respectively, leading to an ultimate tensile strain of 0.0228. The ultimate strain of FRP provided by the manufacturer is 0.028.

All of the specimens failed by the rupture of the FRP jacket due to hoop tension (Figure 1). Once rupture of the FRP jacket occurred, the confinement effect of the FRP disappeared and the load carried by the tube reduced immediately and rapidly. With further loading, local buckling of the steel tube occurred where the FRP also ruptured. Among the nine specimens, the FRP jacket ruptured near the outside end of the overlapping zone in four specimens. Figure 1 shows the locations of FRP rupture in two of these four specimens. Therefore, geometric discontinuities at the ends of an FRP wrap may be a significant factor determining the hoop rupture strain of FRP wraps in FRP-confined concrete-filled steel tubes, similar to the phenomenon observed in FRP-confined concrete columns (Chen et al. 2010). It should be noted that once FRP rupture starts, it can propagate to different locations.

The other five specimens failed away from the ends of the overlapping zone. Many possible causes exist for this phenomenon, such as non-axisymmetric deformation of the steel tube due to geometrical imperfections in the tube and localized deformation of the concrete core. Further information and discussion of possible causes can be found in Chen (2009) and Chen et al. (2010).

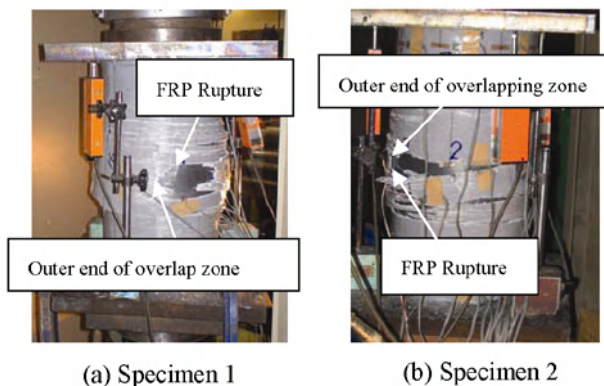


Figure 1 FRP rupture near the finishing end of overlapping zone

3 FINITE ELEMENT MODELLING

3.1 Geometry

A circular column confined with a single continuous FRP wrap comprising N layers/plies was considered (Figure 2). A polar coordinate system was used to describe positions (Figure 2), with the circumferential angular coordinate denoted by θ . The FRP wrap starts at

$\theta = 0^\circ$ (the inner end) and finishes at $\theta = 360N + \alpha$ (the outer end), giving an overlapping zone of α .

The change in radius necessary for the outer layer of FRP to overlap the inner layer occurs within a transition zone of β . The shape of the transition is assumed to be sinusoidal as in Chen et al. (2010).

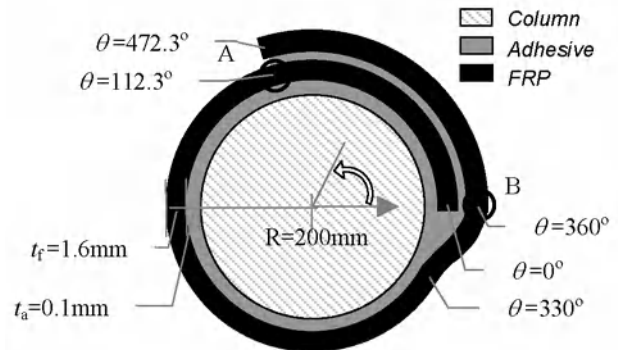


Figure 2 Cross-section of an FRP-confined concrete-filled steel tube

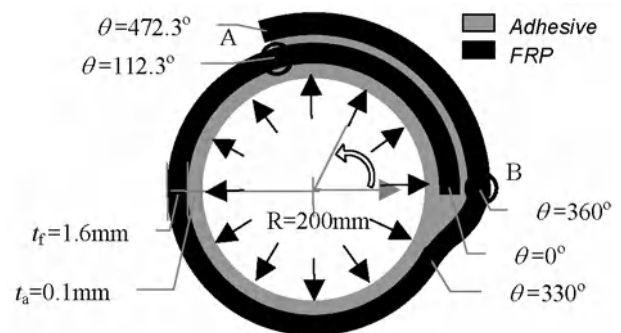


Figure 3 Simplified FE model of an FRP-confined concrete-filled steel tube

3.2 FE modelling

The general finite element analysis package ANSYS (2007) was used to conduct all the analyses in this study. Only the FRP wrap together with the adhesive between the layers was modeled as in Chen et al. (2010). For simplicity, the specimens were modelled as a plane strain problem using eight-node quadrilateral elements though the actual specimens were in three dimensional stress state. The FRP wrap was assumed to be under a uniform internal pressure (Figure 3) which shall be close to the actual pressure distribution between the FRP wrap and the steel tube near the ultimate state when both the steel tube and the concrete had experienced plastic deformation under uniform compression. It was further assumed that there was no slip between the steel tube and the adhesive outside it, meaning that the circumferential displacement at the interface between the steel tube and the adhesive was restrained. The implications of these treatments are being investigated in an ongoing study.

3.3 Properties of adhesive and FRP

The properties of the adhesive provided by the supplier show that the adhesive was nearly linear elastic-brittle in uniaxial tension. However, if a linear elastic-brittle material model is adopted for the adhesive, the FE model predicts that debonding failure occurs at an early stage, but this clearly contradicts what was observed in the tests. There are several reasons why a linear elastic-brittle adhesive model cannot predict the actual failure mode. Firstly, there exist stress singularities at the bi-material wedges at both ends of the FRP wrap. A linear elastic analysis predicts huge (and non-converging) stresses at these locations, leading to failure of the adhesive and thus debonding of the FRP at very low load levels. In practice the precise geometry of the adhesive is more complicated, and even the presence of micro-cracks in the adhesive at these locations would not necessary result in debonding failure. Secondly, the adhesive may well exhibit some post-peak softening behavior, but this is very difficult to observe in a uniaxial tensile test. Thirdly, the adhesive was under triaxial loading in the tests and its behaviour may be rather differently from that under uniaxial tension. Two different adhesive constitutive models, representing two extreme cases, were adopted in this study: (1) a linear elastic model and (2) an elastic-perfectly plastic model. The tensile tests conducted at The Hong Kong Polytechnic University showed that the elastic modulus and the strength of the adhesive were 4.82GPa and 31.3 MPa respectively. The Poisson’s ratio was taken as 0.35.

The concrete-filled steel tubes were strengthened with wet lay-up GFRP where the FRP wrap was formed from the impregnation of fibres with epoxy resin. The actual layer thickness of 1.6mm was adopted in the FE model, with the fibres assumed to be evenly distributed across the FRP layer. This FRP layer thickness was measured from the flat tensile test coupons.

An adhesive layer of 0.1mm in thickness was assumed to sit between the inner and the outer layers of the FRP. It should be noted that most of the adhesive was included in the actual layer thickness of the FRP.

3.4 Predicted FRP strain distributions

Figure 4 shows the predicted distributions of FRP hoop strain on the inner and outer surfaces of the FRP when the maximum FRP hoop strain reaches its ultimate tensile strain obtained from the authors’ flat coupon tests for the elastic-plastic adhesive model. It clearly shows that stress concentrations occur in two locations in the FRP wrap: (a) on the outer surface of the inner layer of the FRP adjacent to the outer end of the wrap (Location A) and (b) on the inner surface of the outer layer of FRP adjacent to the inner end of the wrap (Location B). These two locations are marked in Figure 3. Figure 4 also shows that the predicted stress concentration is more

severe at Location A than at Location B, which is in agreement with the experimental observation that the former is a more critical location for rupture failure than the latter.

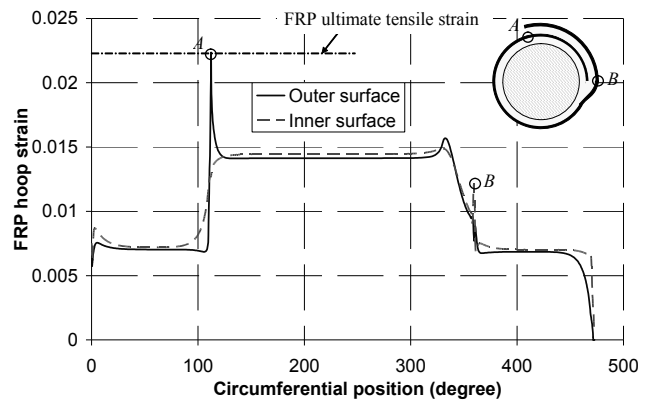


Figure 4 Distributions of hoop strain on the inner and outer surfaces of FRP wrap

4 COMPARISON BETWEEN TEST RESULTS AND FE PREDICTIONS

FRP rupture was assumed to occur when the predicted maximum FRP hoop strain at location A reaches the ultimate tensile strain of the FRP. A predicted strain efficiency factor was obtained by dividing the predicted FRP hoop strain outside the overlapping zone by this peak strain. A test strain efficiency factor was obtained by dividing the average FRP hoop strain outside the overlapping zone by the FRP ultimate tensile strain. Two ultimate tensile strain values were explored for the FRP: 2.28% and 2.8%. The former was from the authors’ flat coupon tests while the latter was provided by the manufacturer. These gave two sets of test strain efficiency values (for the two FRP ultimate strains) and four sets of predicted values (two ultimate FRP strains and two adhesive constitutive models). Figure 5 shows the

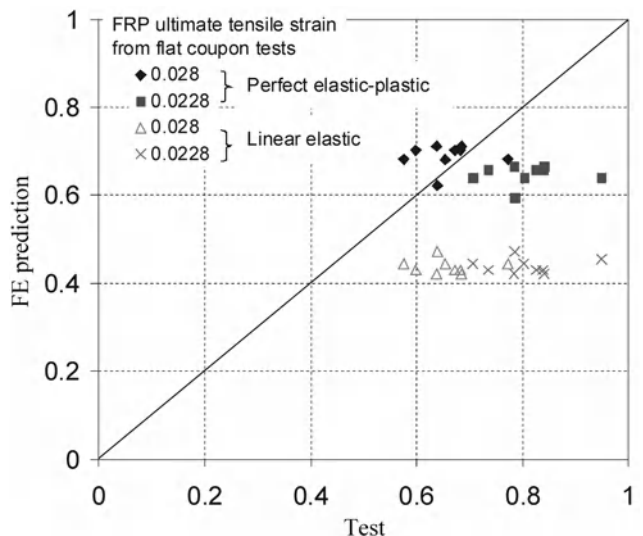


Figure 5 Predicted versus test strain efficiency factors

comparison between the predicted and test FRP strain efficiency factors for all the nine specimens.

Figure 5 shows that the strain efficiency factors predicted using the elastic-perfectly plastic adhesive model are much closer to the test results than those predicted using the linear elastic adhesive model. Most of the test results are located between the two sets of FE results obtained using the elastic-perfectly plastic adhesive model, which suggests that the actual ultimate tensile strain of the FRP might lie somewhere between the two ultimate strains mentioned above.

5 CONCLUSIONS

This paper has presented a finite element (FE) study on the effect of geometrical discontinuities at the ends of FRP wraps in FRP-confined concrete-filled steel tubes on the apparent FRP rupture strain. The FE results have shown that severe FRP hoop strain concentrations occur in very small zones near the ends of the FRP wrap which cannot be measured using conventional strain measurement techniques. This offers one plausible explanation to the phenomenon that the observed FRP hoop rupture strain is typically lower than the rupture strain obtained from flat tensile coupon tests. This conclusion is supported by the experimental observation that of the nine FRP-confined concrete-filled steel tubes tested, four failed at the finishing end of the FRP wrap, demonstrating the importance of geometric discontinuities on the ultimate condition of FRP-confined columns. Furthermore, the FE strain efficiency factors based on an elastic-perfectly plastic adhesive model are in reasonable agreement with the test results.

6 ACKNOWLEDGMENTS

The authors acknowledge the support from the Scottish Funding Council for the Joint Research Institute with Heriot-Watt University which is a part of the Edinburgh Research Partnership in Engineering and Mathematics (ERPem). They have also received support via the UKIERI (UK India Education and Research Initiative) project (IND/CONT/07-08/E/133) funded by the British Council, the UK Department for Innovation, Universities and Skills (DIUS), Office of Science and Innovation, the FCO, Department of Science and technology, Government of India, The Scottish government, Northern Ireland, Wales, GSK, BL, Shell and BAE for the benefit of the India Higher Education Section and the UK Higher Education Sector. S.Q. Li was further supported by a China/University of Edinburgh Joint Scholarship. The

views expressed in this paper are not necessarily those of the funding bodies.

REFERENCES

- ANSYS 2007. *Release 11.0 documentation for ANSYS*. Ansys, I.N.C., Canonsburgh, PA, USA.
- ASTM 1995. *Standard test method for tensile properties of polymer matrix composite materials. D3039/D3039M*, West Conshohocken, USA.
- Chen, J.F., Ai, J. and Stratford, T.J. 2007. FRP strains in FRP wrapped columns. *Proceedings, Third International Conference on Advanced Composites in Construction (ACIC 2007)*, 2–4 April, Bath, UK, 107-115.
- Chen, J.F. 2009. Contributory factors to the reduction of apparent rupture strain in FRP wrapped circular concrete columns. *Proceedings, 6th National Conference on FRP in Construction*, 11-13 October 2009, Zhengzhou, China (*Industrial Construction*, Vol. 39, No. 433, 15-22).
- Chen, J.F., Li, S.Q. and Ai, J. 2009. Relationship between FRP fracture strains in flat coupon tests, split disk tests and FRP wrapped columns. *Proceedings, Second Asian-Pacific Conference on FRP in Structures (APFIS 2009)*, Seoul, Korea, 517-524.
- Chen, J.F., Ai, J. and Stratford, T.J. 2010. Effect of geometric discontinuities on strains in FRP wrapped columns. *Journal of Composites for Construction*, ASCE, in press.
- Hu, Y.M. (2010) *Behaviour and modelling of FRP-confined hollow and concrete-filled steel tubular columns*, PhD thesis, Department of Civil and Structural Engineering, The Hong Kong Polytechnic University, China, in preparation.
- Jiang, T. and Teng, J.G. 2007. Analysis-oriented stress-strain models for FRP-confined concrete. *Engineering Structures*, 29(11): 2968-2986.
- Lam, L. and Teng, J.G. 2004. Ultimate condition of fiber reinforced polymer-confined concrete. *Journal of Composites for Construction*, ASCE, 8(6): 539-548.
- Pessiki, S., Harries, K.A., Kestner, J.T., Sause, R. and Ricles, J.M. 2001. Axial behavior of reinforced concrete columns confined with FRP jackets. *Journal of Composites for Construction*, ASCE, 5(4): 237-245.
- Teng, J.G., Chen, J.F., Smith, S.T. and Lam, L. 2002. *FRP-strengthened RC structures*, John Wiley and Sons, Chichester.
- Teng, J.G. and Hu, Y.M. 2006. Theoretical model for FRP-confined circular concrete-filled steel tubes under axial compression. *Proceedings, Third International conference on FRP Composites in Civil Engineering (CICE 2006)*, Miami, Florida, USA.
- Xiao, Y. 2004. Applications of FRP composites in concrete columns. *Advances in Structural Engineering*, 7: 335-343.
- Xiao, Y., He, W., and Choi, K.K. 2005. Confined concrete-filled tubular columns. *Journal of Structural Engineering*, ASCE, 131(3): 488-497.

The Ultimate Condition of FRP Confined Concrete Columns: New Experimental Observations and Insights

Luke A Bisby (Luke.Bisby@ed.ac.uk) & Tim J Stratford

The Institute for Infrastructure and Environment, The University of Edinburgh, Scotland, UK

ABSTRACT A large body of research is available on FRP confinement of concrete. Many hundreds of tests have been performed and dozens of empirical models are available. However, some of the key mechanics of FRP wrapped concrete are still not understood. Research is needed to understand, quantify, and rationally account for the hoop strain variation in FRP wraps at failure; since failure is fundamentally defined by hoop rupture of the FRP in tension. In this paper, a digital image analysis technique is used to quantify the variation of axial and hoop strain over the surface of FRP wrapped concrete cylinders. Tests on FRP wrapped cylinders of varying aspect ratio are presented to study factors influencing strain variability. The first ever quantified statistical description of hoop strain variability is provided, and the consequences of this variability are discussed.

1 INTRODUCTION

Confinement of circular concrete columns by circumferential wraps is one of the most widely accepted applications of fibre reinforced polymers (FRPs) for repair and strengthening of structures (Bisby & Take 2009). FRPs are wrapped, with fibres oriented in the hoop direction, around the perimeter of columns and bonded in place with an epoxy adhesive; the effect of this is to restrain dilation of the concrete when loaded in compression, creating a triaxial stress condition and drastically improving the concrete's strength and deformability. This has clear benefits for axial strengthening and seismic enhancement which have led to FRP wraps being applied to many thousands of columns around the world. However, key aspects of the mechanics of FRP confined concrete remain poorly understood (Bisby & Take 2009); one area is in understanding the variability of strains in FRP wraps at failure.

1.1 Background

The ultimate compressive strength of FRP confined concrete is reached when the FRP wrap ruptures in hoop tension. Available research (Lam & Teng 2004) suggests that this occurs at hoop strain values between 30% and 50% less than expected on the basis of direct tensile tests on the FRP. The ratio of the tensile hoop strain in the FRP at failure to the average failure strain observed in direct uniaxial tensile coupon tests is termed the strain efficiency, η . From numerous observations, Jiang & Teng (2006) have suggested $\eta = 0.5$ for carbon FRP wraps and $\eta = 0.7$ for glass FRP wraps for design. ACI 440 (2008) suggests $\eta = 0.55$ for circular FRP wrapped

columns.

Various causes have been suggested to explain strain efficiencies of less than 1.0 (Lam & Teng 2004), despite the fact that much higher strain efficiencies have been observed (even exceeding 1.0). None of these have been satisfactorily proven. Furthermore, all available empirical hoop strain data on which current design procedures are based were obtained using localized foil strain gauges, which provide no real insights into the variation of strains over the surface of FRP wraps. This issue is fundamental to the development of accurate and rational confinement models (Lam & Teng 2004).

1.2 Observing strain variation

Bisby & Take (2009) have recently presented the first ever detailed experimental measurements quantifying the axial and hoop strain variation on the surface of short FRP confined concrete cylinders under concentric axial compressive loads. This was accomplished using a digital image analysis technique to optically measure strain distributions using high-resolution image correlation. Their observations clearly showed that accurate measurement of hoop and axial strains on FRP confined concrete cylinders is possible using image analysis and that good correlation was observed between the optical technique and conventional bonded foil strain gauges; hoop strains vary over the surface of FRP confined short circular concrete cylinders at failure by as much as 50% of the coupon failure strain, even away from the frictional confinement provided by the loading platens; and the coupon failure strain is, in fact, achieved in virtually all cases, albeit only very locally.

A recent numerical study by Tabbara & Karam (2008)

suggests that hoop strain variations may be due to localization of shear failure planes within the concrete followed by movement of solid concrete wedges along those failure planes. Using this hypothesis, they numerically predicted hoop strain localizations of similar overall shapes and magnitudes to those experimentally observed by Bisby & Take (2009). This suggests that one mechanism causing much of the hoop strain variation is localization of shear failure planes. Notably, Tabbara & Karam's (2009) study also suggests that cylinders of 2:1 aspect ratios (as used in the majority of testing on FRP confined concrete) may be insufficiently slender to avoid the influence of frictional confinement from the loading platens. A large proportion of the available data on hoop and axial strains in FRP confined concrete may therefore be corrupted by end effects. Hence, there is a need for a detailed comparison of strain variation for 2:1 cylinders against that observed for cylinders with larger aspect ratios.

2 EXPERIMENTAL PROGRAM

Table 1 shows details of the experimental program. Concentric uniaxial compression tests were performed on 16 unreinforced concrete columns, each 150 mm in diameter and 300 mm, 600 mm, or 900 mm tall. Nine of the cylinders (three at each length) were wrapped in the hoop direction over their full height with a single layer of a unidirectional carbon/epoxy FRP strengthening system (SikawrapTM Hex 230C). The wraps were applied using hand lay-up procedures with a hoop overlap of 100 mm. The concrete's compressive strength was 29.8 ± 0.5 MPa at the time of testing (based on three cylinder tests).

The test setup is shown in Figure 1. Digital images with the fields of view shown in Figure 1b were captured every five seconds during testing as each cylinder was loaded to failure. Because only two cameras were available and it was important to maintain similar image resolution for all cylinders during testing, strains were only recorded over the bottom two-thirds of the 900 mm long columns.

After testing, a bespoke image processing algorithm was used to calculate virtual (optical) hoop strains along a single vertical line for each cylinder. Details of the image analysis technique are discussed by Bisby & Take (2009). The technique defines particular regions of interest, called patches, in the first image of each set, and then tracks the displacements of patches in subsequent images, allowing optical measurement of hoop strains by strategically-located patches. Each patch must contain sufficient variation in the intensity and distribution of colours to be unmistakable in subsequent images. A high-contrast texture was thus applied to each cylinder before testing. The gauge length for the optical strain gauges was 15 mm in the current analysis. A

validation of the technique is given by Bisby and Take (2009).

Table 1 Details of experimental program and selected results

ID	Length, H (mm)	H/D	Repeats	Ave. strength (MPa)	Std. dev. (MPa)
U300	300	2	3	29.8	0.5
W300	300	2	3	38.5	2.1
U600	600	4	1	29.0	-
W600	600	4	3	37.1	0.9
U900	900	6	3	28.9	0.4
W900	900	6	3	39.1	1.5

* H = Column length (mm), D = Column diameter (mm)

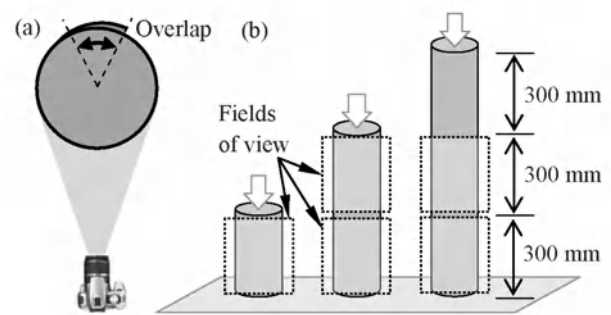


Figure 1 (a) Plan view of test setup; (b) Imaging locations

3 RESULTS & DISCUSSION

The purpose of the testing described above was to study the variability of hoop strains for FRP confined concrete cylinders of increasing aspect ratios, and subsequently to determine if end effects arising from frictional confinement in standard 2:1 cylinders influence hoop strain variability near the cylinders' mid-heights. The goal was to determine if data from 2:1 cylinders are appropriate for calibrating empirical FRP confinement models. It was also desired to study the hoop strain variability in cylinders of realistic slenderness to determine if this has any effect of strain variability at failure.

Table 1 shows the average axial compressive strength observed for both unconfined and FRP confined cylinders. These data show that all unconfined cylinders of different lengths displayed similar strengths, as did FRP confined cylinders of different lengths. This suggests that second-order (slenderness) effects did not influence the results. This is expected since the columns tested herein would be classified as "short" according to most available concrete design codes, assuming an effective length of $0.7H$. The FRP strengthening increased the cylinders' strength by about 30%, which agrees well with predictions of available design models for FRP confined concrete (e.g. ACI 440 2008).

Figure 2 show typical vertical hoop strain profiles recorded during the 25 seconds leading up to failure for

selected tests, along with post-failure photographs to show the correlation between hoop strain peaks and failure initiation locations. Included on the profiles are markers indicating the average axial compressive stress at the instant that each strain profile was recorded. Black profiles represent the final data recorded before failure (these may have preceded failure by up to five seconds).

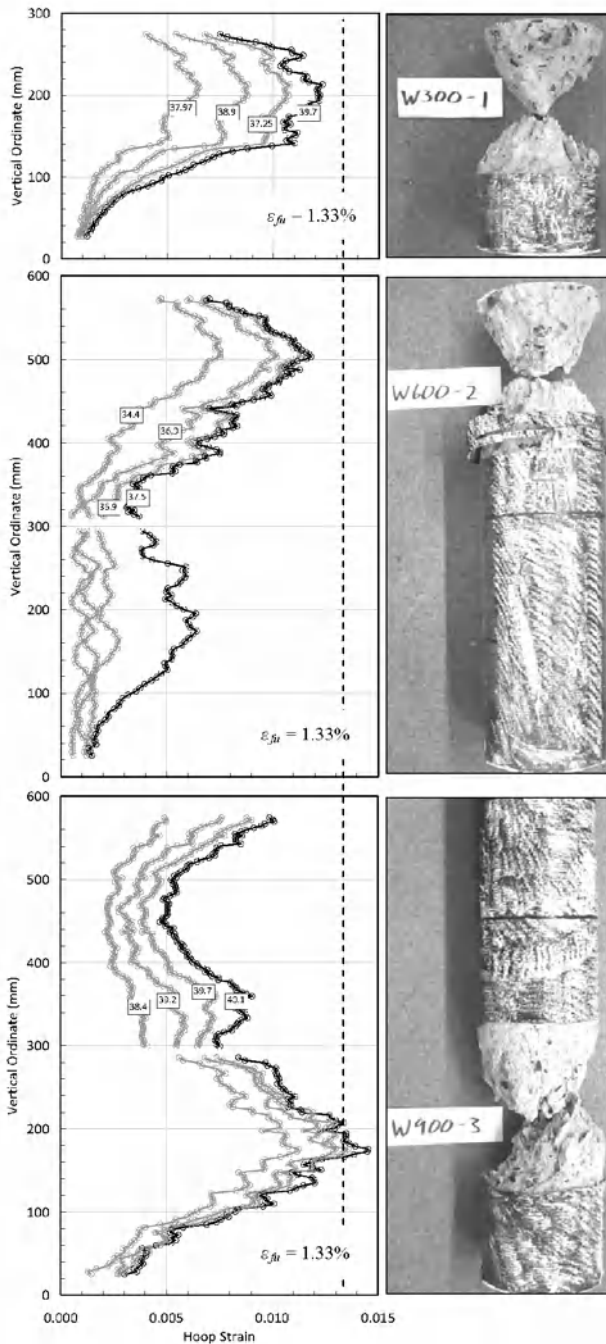


Figure 2 Vertical hoop strain profiles recorded during the 25 seconds prior to failure for selected cylinders

Several features of Figure 2 (and all of the data) are noteworthy. Considerable hoop strain variation was observed in all tests. The shape of the hoop strain profiles and the amount of variability appeared to be random phenomena and it is unlikely that generalizations can be

made with respect to these issues.

The hoop strain profiles evolved rapidly near ultimate, and again generalizations are difficult to make. The rapid, apparently random evolution of strain profiles suggests non-uniform deformations occurring inside the confined concrete cylinders, which lends support to the Tabbara & Karam (2008) hypothesis mentioned previously.

For the 2:1 cylinders (W300) hoop strains were largest close to mid-height. This is expected given that frictional confinement from the loading platens is almost certainly active within the top and bottom 75 mm of the specimens. However, even within the middle 150 mm where this effect can be assumed absent, hoop strain still varied by up to 70% of the coupon failure strain. For 4:1 and 6:1 cylinders (W600 & W900) the hoop strain variation outside the top and bottom 75 mm was random, and generalizations are not possible. Up to 75% hoop strain variability was observed outside the end regions.

As in previous tests by Bisby & Take (2009) on 2:1 cylinders, the average coupon failure strains for the FRP ($\epsilon_{fu} = 1.33\%$) were nearly achieved in most tests (even exceeded in one case), albeit only locally. Bisby & Take (2009) have shown that hoop strains vary radially as well as vertically by up to 50% of the average coupon failure strain. Measuring hoop strains along a single vertical line thus provides no guarantee that the maximum hoop strain is observed.

Comparison of the hoop strain profiles with images of the cylinders taken after failure shows a striking correlation between locations of maximum hoop strain and locations of failure initiation.

3.1 Statistical Variability & Consequences

In the authors' view, it has now been convincingly proven that considerable hoop and axial strain variability exists in FRP wrapped concrete cylinders, both longitudinally and circumferentially. The practical consequences of this variability for existing empirical confinement models, all of which have been calibrated (or validated) on the basis of apparently incomplete, localized strain measurements, remain unclear. While the current work makes no serious attempt to address consequences, by providing a quantified statistical description of the observed hoop strain variability it is hoped that the uncertainty inherent in the available test data can be explicitly included in the calibration of confinement models.

Figure 3 shows a statistical summary of hoop strain efficiencies recorded for each FRP confined cylinder (only strains recorded outside the top and bottom 75 mm of the cylinders are included). The data shown represent by far the most detailed statistical description of hoop strain variability ever presented. For the W300 specimens, each population represents ≈ 175 readings (525 in total), whereas the W600 & W900 populations contain ≈ 200 individual readings for each cylinder (600 in total).

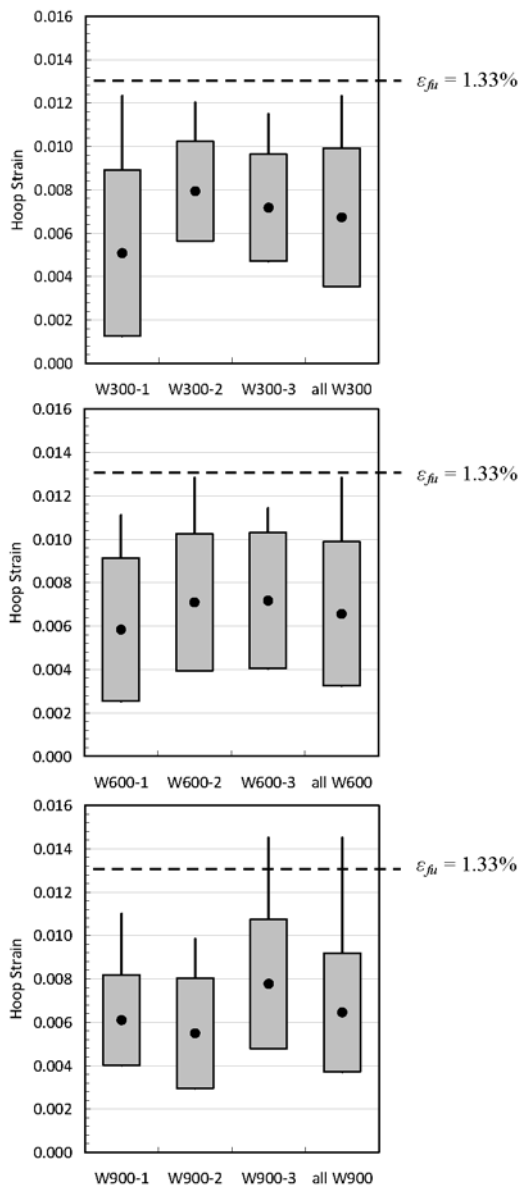


Figure 3 Summary plots for observed hoop strains at failure for FRP wrapped cylinders (mean, mean \pm 1 std. dev., max. value)

Figure 3 shows that the distributions of hoop strains were similar from one cylinder to the next, and also between cylinders of different aspect ratios. The mean hoop strain varied between 0.51% and 0.78% ($\eta = 0.38$ and $\eta = 0.59$) for individual specimens, but was almost uniformly ≈ 0.66 for each cylinder length group ($\eta = 0.50$). This agrees with the value of $\eta = 0.5$ recommended by Jiang & Teng (2006) for carbon FRP wraps, which makes sense given that even isolated strain gauges on multiple columns (as used by Jiang & Teng) should yield the same statistical populations of hoop strain data as given in Figure 3. It therefore appears that currently recommended hoop strain efficiencies are close to the mean hoop strain values which are actually achieved in practice. Interestingly, the standard deviation of hoop strain efficiency is also fairly consistent and ranges between 0.18 and 0.31. These data could be used to calibrate available FRP confinement models with a

prescribed level of statistical confidence. Such a calibration is currently underway.

4 CONCLUSIONS

The data presented in this paper show that considerable hoop strain variability exists in FRP confined concrete at loads approaching failure. In combination with prior work by others (Tabbara & Karam 2008), the data suggest that the observed strain variation is caused at least in part by localization of shear failure planes within the concrete. Zones of high hoop strain localization correlate well with observed locations of failure, indicating that failure of FRP confined concrete is indeed initiated by tensile rupture of the FRP wraps at strains close to (or exceeding) the coupon failure strain, albeit locally. A statistical summary of the observed hoop strains has shown that the hoop strain variability is similar for cylinders of aspect ratios from 2:1 to 6:1, so that empirical confinement models derived on the basis of localized strain measurement from 2:1 cylinders may be used in model calibration. Considering all hoop strain measurements presented herein (1667 hoop strain readings) gives a mean hoop strain efficiency, η , of 0.50 with a standard deviation of 0.30. This agrees exactly with the strain efficiency of 0.5 recommended by Jiang and Teng (2006) for carbon FRP confined concrete and can be used in future reliability studies on empirical confinement models.

5 ACKNOWLEDGEMENTS

The authors would like to thank MEng students M Webster and D Sinclair, who performed the tests described herein, and to acknowledge the support of The Ove Arup Foundation, the Royal Academy of Engineering, and The University of Edinburgh.

REFERENCES

- ACI 440. 2008. Design and Construction of Externally Bonded FRP Systems for Strengthening Concrete Structures. Farmington Hills, USA: American Concrete Institute.
- Bisby, L. A. & Take, W. A. 2009. Strain Localizations in FRP Confined Concrete: New Insights. *Structures and Buildings* 162(5): 301-309.
- Jiang, T. & Teng, J. G. 2006. Strengthening of short circular RC columns with FRP jackets: A design proposal. In Mirmiran & Nanni (eds.), 3rd Intern. Conf. on FRP Composites in Civil Eng., Miami, 13-15 December 2006.
- Lam, L. & Teng, J. G. 2004. Ultimate condition of fiber reinforced polymer-confined concrete. *Journal of Composites for Construction* 8(6): 539-548.
- Tabbara, M. & Karam, G. 2008. Numerical investigation of failure localization and stress concentrations in FRP wrapped concrete cylinders. In Mufti & Neale (eds.), 5th Intern. Conf. on Advanced Composite Materials in Bridges and Structures, Winnipeg, 22-24 September 2008.

Bearing Strength of CFRP Confined Concrete

Craig A. Scheffers (craig.scheffers@aecom.com)
AECOM Australia Pty Ltd, Sydney, New South Wales, Australia

Dr. R. Sri Ravindrarajah & Rhesa Reinaldy
School of Civil and Environmental Engineering, University of Technology, Sydney, New South Wales, Australia

ABSTRACT Concrete sections may be subjected to compressive loads in a concentrated part of the total area. The bearing strength of concrete is related to the compressive strength and the ratio of the total surface area to load bearing area (known as bearing ratio). The bearing strength of concrete can be increased by providing external lateral confinement. This paper reports and discusses the results of experimental investigations into the bearing strength of laterally confined concrete, using Carbon Fibre Reinforced Polymer (CFRP). The parameters of the investigations included the bearing ratio (2, 4 and 6) and bearing shape (square and circular). Results demonstrated the bearing strength of concrete is increased by up to 74% through CFRP confinement. It was found the shape of the bearing area had marginal influence on the bearing strength of concrete.

1 INTRODUCTION

Fibre Reinforced Polymer (FRP) composites can achieve high strength and strain capacity under direct tension. FRP composites have been primarily used to strengthen damaged and deteriorated reinforced concrete members in rehabilitation and remedial work.

Reported research investigations have demonstrated that the strengthening of concrete structures using FRP composites improves the compressive, flexural and shear strength as well as increases the ductility of concrete elements (Teng et al. 2002, Nezamian et al. 2002). However, only limited investigations have been reported on the behaviour of FRP confined concrete under a bearing load condition (Scheffers et al. 2009). This paper reports and discusses the results of experimental investigations into the bearing strength of CFRP confined concrete under different bearing ratios and bearing shapes.

2 BEARING STRENGTH OF CONCRETE

2.1 Mechanisms of the bearing failure of concrete

Concrete is able to resist high direct stress over a localised area compared to compressive strength. Numerous studies have been carried out to analyse the mechanisms of bearing failure for unconfined concrete (Shelson 1957, Tung et al. 1960, Hawkins 1968, Haagsma 1969, Niyogi 1973, Lieberum et al. 1989). Most of these studies are based on the Coulomb/Mohr theory of rupture which suggests failure of concrete subjected to a bearing load condition is due to sliding action along planes that are inclined to the direction of

principal stresses. The investigations by Shelson (1957) demonstrated an inverted pyramid failure in concrete under bearing loads using small bearing plates. Lieberum et al. (1989) reported that it was understood from early experimentation the strength of concrete increases when the lateral strain is confined.

2.2 International standards and codes

Australian Standards AS3600 (2001) and American Concrete Institute (ACI) Committee 318 (1989) suggest the design bearing strength is a function of the characteristic compressive strength of concrete and a square root function between the bearing area and total surface area. It is noted that provision for confinement reinforcement (internal or external) is not considered in these relationships and such considerations are yet to be published in design standards or codes. The relationship to determine the design bearing stress for unconfined concrete as specified by the Australian Standards AS3600 (2001) is outlined in Equation 1.

$$f_b \leq \phi 0.85 f'_c \sqrt{\left(\frac{A_2}{A_1}\right)} \leq \phi 2 f'_c \quad (1)$$

where f_b = bearing strength of unconfined concrete, MPa; ϕ = 0.6 (strength reduction factor); f'_c = compressive cylinder strength of unconfined concrete at 28 days, MPa; A_1 = bearing load area, mm²; and A_2 = total surface area of concrete, mm².

The ACI (1989) also specify a relationship to establish the allowable bearing stress for unconfined concrete as shown by Equation 2.

$$f_b = 0.85\phi \sqrt{\left(\frac{A_2}{A_1}\right)} f'_c \leq 1.19 f'_c \quad (2)$$

where f_b = bearing strength of unconfined concrete, MPa; $\phi = 0.7$ (strength reduction factor); f'_c = compressive cylinder strength of unconfined concrete at 28 days, MPa; A_1 = bearing load area, mm²; and A_2 = total surface area of concrete, mm².

AS3600 (2001) and ACI (1989) equations are design relationships which incorporate a factor of safety in the allowable bearing stress value.

Previous researchers including Hawkins (1968), Haagsma (1969) and Niyogi (1973) derived empirical relationships between the bearing strength and compressive strength for concrete. Comparing the ratio of the bearing strength to compressive strength with respect to the bearing ratio, it is evident that AS3600 (2001) and the ACI (1989) standards are conservative in the design for allowable bearing strength of concrete in comparison to published research. Conservatism in these design standards is evident in the limitation of the ratio of bearing strength to compressive strength to a value of 1.20 and 1.19 respectively.

3 EXPERIMENTAL INVESTIGATION

The primary aim of the investigations carried out by Scheffers (2008) and Reinaldy (2009) was to analyse the effect of lateral confinement on the bearing strength of concrete using an externally bonded CFRP composite wrap. Scheffers (2008) tested the bearing strength of CFRP confined concrete under a square bearing area whereas Reinaldy (2009) tested circular bearing areas. Unconfined concrete control specimens were tested to compare results with that of the CFRP confined concrete specimens. The bearing ratio, defined as the ratio of total surface area to bearing area of the concrete specimen, was varied by using different sized steel bearing plates. The bearing ratio values tested were 2, 4 and 6. Square and circular bearing plates were tested to determine the influence of the bearing shape on the bearing strength of CFRP confined concrete. The bearing plates were considered to be rigid plates as the load applied in the tests was uniformly distributed over the entire bearing plate, as opposed to flexible plates which are loaded over a portion of the plate subjecting the plate to flexure and shear.

The concrete used in the investigations was a ready mixed concrete with a 28 day compressive strength of approximately 32 MPa. A number of concrete cube specimens of 150 mm were cast for the bearing strength tests. Concrete cylinders of 100 mm diameter by 200 mm high were cast to determine the compressive strength of CFRP confined and unconfined concrete.

Neale (2001) reports that the effectiveness of

confinement pressure is significantly less for rectangular sections in comparison to circular sections due to stress concentrations at the sharp corners of a rectangular section. ACI Committee 440 (2002) and Campione et al. (2003) agreed with this principle and outline the confining pressures in a circular section are circumferentially uniform. Therefore, the cube specimens to be confined with CFRP required the corners to be filleted in order to reduce stress concentration at these locations. Filleting was performed using an angle grinder equipped with a diamond tipped concrete grinding wheel. The required radius for the corner filleting was 25 mm and was designed in accordance with recommendations for the application of externally bonded FRP confinement to short rectangular columns by Neale (2001).

Specimens were laterally confined with two layers of unidirectional CFRP sheet in the hoop direction, formed in a wet lay-up procedure. A tensile lap length of 150 mm was applied to ensure adequate bond and continuity of the CFRP sheet in the hoop direction. The mechanical properties of the proprietary CFRP strengthening system used in the experimental investigations are outlined in Table 1. These values were adopted from the CFRP manufacturers' technical data sheet.

Table 1 Mechanical properties of the CFRP system

Carbon fibre – elastic modulus	240 GPa
Ultimate tensile strength	3800 MPa
Ultimate tensile elongation (strain)	1.5 %

4 RESULTS AND DISCUSSION

4.1 Bearing strength test results

For each confinement condition, bearing ratio and bearing shape, three bearing strength specimens were tested. Table 2 summarises the mean bearing strength values for CFRP confined and unconfined concrete with bearing ratios of 2, 4 and 6, for both square and circular bearing areas. The effectiveness of the CFRP confinement has been determined by calculating the ratio of confined bearing strength (f_{bc}) to unconfined bearing strength (f_b) for a given bearing ratio and bearing shape. The effectiveness of CFRP confinement is outlined in Table 2. The results outlined in Table 2 demonstrate externally bonded CFRP confinement significantly increased the bearing strength of concrete by 58% - 74%, depending on the bearing ratio and bearing shape. It is also evident the shape of the bearing area has marginal influence on the bearing strength of CFRP confined concrete as the load is applied over the same bearing area regardless of the bearing shape.

The relationship between the bearing strength of CFRP confined and unconfined concrete, the bearing ratio and bearing shape is shown in Figure 1. The results illustrate CFRP confined concrete has a significantly

Table 2 Bearing strength of CFRP confined concrete

Bearing ratio	Confinement condition	Bearing shape	f_c (MPa)	Bearing strength (MPa)	$\frac{f_{bc}}{f_b}$
2	Unconfined	Square	40.5	49.0	-
2	Confined	Square	75.0	77.5	1.58
2	Unconfined	Circle	46.4	59.8	-
2	Confined	Circle	91.5	97.6	1.63
4	Unconfined	Square	40.5	54.5	-
4	Confined	Square	75.0	95.0	1.74
4	Unconfined	Circle	46.4	76.4	-
4	Confined	Circle	91.5	123.1	1.61
6	Unconfined	Square	40.5	70.0	-
6	Confined	Square	75.0	115.0	1.64
6	Unconfined	Circle	46.4	86.2	-
6	Confined	Circle	91.5	139.1	1.61

f_c = Compressive strength (MPa).

f_{bc} = CFRP confined bearing strength (MPa).

f_b = Unconfined bearing strength (MPa).

greater bearing strength compared to unconfined concrete. It is also evident as the bearing ratio is increased, the bearing strength also increases for both CFRP confined and unconfined concrete. As the bearing area increases, the bearing ratio decreases and less transverse confinement of the concrete core is available to resist the bearing load. When there is limited transverse confinement of concrete, the element is not able to restrain itself with the same ability to when the bearing area is small and greater transverse confinement of the concrete core is available to sustain load.

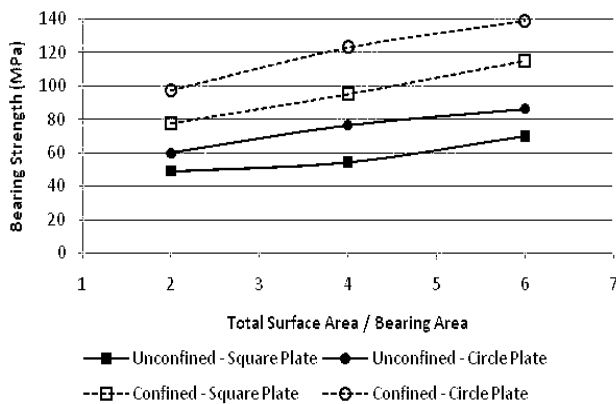


Figure 1 Relationship of bearing strength and bearing ratio

Comparison between the data shown in Table 2 and Figure 1 demonstrates that although specimens tested with a circular bearing area resulted in higher bearing strength compared to those tested with a square bearing area, the ratio of confined to unconfined bearing strength was not necessarily greater for all bearing ratios for the circular bearing area in comparison to the square bearing area. It is assumed a square bearing area would

be less efficient compared to a circular bearing area caused by the adverse effect of stress concentrations induced in the loading due to the sharp corners of a square bearing load. Any discrepancy between the assumed superiority of a circular bearing area over a square area may be due to minor differences in the concrete mix parameters used in the experimental investigations by Scheffers (2008) and Reinaldy (2009).

It is recognised further experimental investigation incorporating full scale prototype testing is required to verify the results that indicate the bearing shape has marginal influence on the bearing strength of CFRP confined concrete. The experimental results would be relevant to conventional steel reinforced concrete elements as the volume fraction of steel reinforcement is insignificant compared to the volume of concrete. External confinement is more critical to enhance the bearing strength, although steel reinforcement provides some extent of resistance to crack development of a concrete element.

4.2 Load-displacement under bearing load

A linear variable differential transformer (LVDT) was used to measure cross-head displacement under the applied bearing load. Readings were recorded for typical specimens and a relationship between the bearing load and displacement was developed. Figure 2 shows this relationship for different bearing ratios tested with a circular bearing area for both unconfined concrete (dark lines) and confined concrete (dotted lines). It is evident that unconfined concrete experienced significantly less cross-head displacement in comparison to the CFRP confined concrete under bearing load. This is due to the CFRP confinement actively resisting the applied bearing load after dilation of the concrete core occurred.

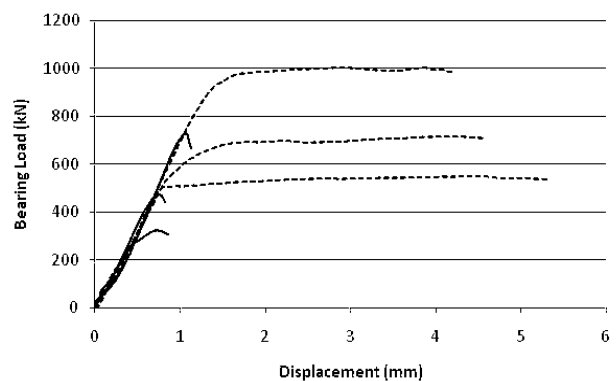


Figure 2 Load-displacement behaviour under bearing load

Figure 2 demonstrates the CFRP confined concrete experiences a more ductile failure compared to unconfined concrete, evident by the gradual strain hardening shown by the dotted lines. Specimens tested under square and circular bearing areas had similar load-displacement behaviour hence the bearing shape

did not have significant influence on the relationship between the bearing load and displacement.

4.3 Crack development and failure mechanisms

Observations on the failure of the bearing strength specimens indicated prior to failure, cracking initiated from the corner of the square bearing plates and radial cracking initiated from the circular bearing plates. These cracks spread across the top surface of the specimens and propagated downward on each of the specimen faces. This crack development represented splitting of the concrete core and shear failure resulted. The maximum bearing load of the unconfined concrete specimens was reached shortly after cracks developed and propagated.

The CFRP confined concrete specimens resisted bearing load beyond failure of the concrete core as the CFRP confinement actively provided lateral support after the concrete had failed. Failure of the CFRP confined concrete occurred in a brittle and explosive manner with loud acoustic emission as the CFRP confinement experienced excessive tension in the hoop direction.

4.4 Application of CFRP in bearing load conditions

Externally bonded CFRP confinement could be applied to strengthen concrete elements subject to bearing load conditions such as beams, columns or slabs with localised compression loads, pad footings, bridge headstocks, end blocks of pre-stressed and post-tensioned structural elements and seismic isolation elements.

5 CONCLUSIONS

Based on the results of the investigations on the bearing strength of CFRP confined concrete, the following conclusions could be made:

- The externally bonded CFRP confinement significantly increased the bearing strength of concrete by up to 74%.
- Bearing strength of concrete is dependent upon the ratio of total surface area to bearing area by changing the state of transverse confinement of the concrete core.
- Comparing square and circular bearing load areas, the shape of the bearing load area has marginal influence on the bearing strength of concrete and on the load-displacement behaviour of concrete.
- CFRP confined concrete resisted load beyond failure of the concrete core and failed in a brittle and explosive manner with a loud acoustic emission as the CFRP confinement experienced excessive tension in the hoop direction.
- The failure of CFRP confined concrete is more ductile than unconfined concrete as the CFRP confinement experiences strain-hardening.
- Externally bonded CFRP confinement could be used to strengthen various types of concrete elements subject to bearing load conditions.

REFERENCES

- ACI Committee 318. 1989. *Building Code Requirements for Reinforced Concrete and Commentary (ACI 318-89/ACI 318 R-89)*. Farmington Hills, United States of America: American Concrete Institute.
- ACI Committee 440. 2002. *Guide for the Design and Construction of Externally Bonded FRP Systems for Strengthening Concrete Structures (ACI 440.2E-02)*. Farmington Hills, United States of America: American Concrete Institute: 440.2R8-440.2R29.
- Campione, G. & Miraglia, N. 2003. Strength and Strain Capacities of Concrete Compression Members Reinforced with FRP. *Cement & Concrete Composites* 25 (1). Elsevier Science Ltd: 32-41.
- Haagsma, T. 1969. *The Ultimate Strength of Unreinforced Concrete Specimens Subjected to Concentrated Load*. Delft, the Netherlands: Technische Hogeschool Delft.
- Hawkins, N.M. 1968. The Bearing Strength of Concrete Loaded Through Rigid Plates. *Magazine of Concrete Research* 20 (62): 31-40.
- Lieberum, K.H. & Reinhardt, H.W. 1989. Strength of Concrete on an Extremely Small Bearing Area. *Journal of the American Concrete Institute* 86(S8): 65-67.
- Mandal, S., Hoskin, A. & Fam, A. 2005. Influence of Concrete Strength on Confinement Effectiveness of Fibre-Reinforced Polymer Circular Jackets. *ACI Structural Journal* 102(3): 383-392.
- Neale, K. 2001. *Strengthening Reinforced Concrete Structures with Externally Bonded Fibre Reinforced Polymer – Design Manual No. 4*. Sherbrooke, Canada: Université de Sherbrooke, ISIS Canada Corporation: 5.1-5.19.
- Nezamian, A., Setunge, S., Lokuge, W., et al. 2002. *Review of Strengthening Techniques Using Externally Bonded Fibre Reinforced Polymer Composites: Report 2002-005-C-01*. Australia: Construction Innovation: 1-48.
- Niyogi, S.K. 1973. Bearing Strength of Concrete – Geometric Variations. *Proceedings of the American Society of Civil Engineers, Journal of the Structural Division* 99(ST7): 1457-1490.
- Reinaldy, R. 2009. *The Effect of Bearing Area on Fibre Reinforced Polymer Concrete*. Sydney, Australia: University of Technology, Sydney.
- Scheffers, C. 2008. *Bearing Strength of Confined Concrete*. Sydney, Australia: University of Technology, Sydney.
- Scheffers, C. & Sri Ravindrarajah, R. 2009. Bearing Strength of Concrete with and without FRP Confinement. *Proceedings of the 24th Biennial Conference of the Concrete Institute of Australia, 17-19 September 2009*. Sydney: Australia.
- Shelson, W. 1957. Bearing Strength of Concrete. *Journal of the American Concrete Institute* 54(5): 405-414.
- Standards Association of Australia. 2001. *Australian Standard AS3600 Concrete Structures*: 127-128.
- Teng, J.G., Chen, J.F., Smith, S.T. & Lam, L. 2002. *FRP-Strengthened RC Structures*. United Kingdom: John Wiley & Sons.
- Tung, A. & Baird, D. 1960. Bearing Strength of Concrete Blocks. *Journal of the American Concrete Institute* 56(48): 869-879.

Confinement Behaviour of Eccentrically Loaded RCC Columns Using FRP Sheets

Anupam Chakrabarti (anupam1965@yahoo.co.uk)

Department of Civil Engineering, IIT Roorkee, Roorkee, India: 247667

ABSTRACT The use of Fiber Reinforced Polymer (FRP) confined reinforced concrete columns are increasing rapidly for new construction as well as rebuilding of concrete structures. Design of these FRP confined concrete columns requires an accurate estimate of the performance enhancement due to the confinement mechanism. Therefore, key issue is to develop a confinement model, which relates the confined concrete strength with the unconfined concrete strength. In the present study, a 3-D finite element model of FRP confined reinforced concrete column under axial and eccentric loading has been developed. The finite element model was developed using the finite element software, ANSYS. Different important parameters have been studied in the present paper: namely, unconfined concrete strength, thickness, orthotropic properties and orientation of FRP layers. The present study has focused on some interesting aspects of these parameters on the confinement effectiveness and has also generated many new results for future reference.

1 INTRODUCTION

The effectiveness of FRP wrapping on concrete elements such as columns has been proven by several researchers. It is clear that there is a need to investigate the behavior of columns under eccentric loads, as most of the columns in buildings especially those at the edges and corner are subjected to uniaxial or biaxial bending.

The present study aims at adding new database for the proper understanding of FRP applications in eccentrically loaded Reinforced concrete columns. A nonlinear FE analysis has been used to evaluate the effects of different parameters on the confinement effectiveness of FRP in circular reinforced concrete columns using the FE software ANSYS (Ref. 1).

2 FINITE ELEMENT MODELLING

Feng et al. (2002) analyzed square concrete columns confined by FRP sheets under uni-axial compression using FEA package ANSYS (Ref. 1). They used William-Warnke (1975) model with five parameters to model the failure criterion of concrete. Li et al. (2003) used ANSYS to simulate the behavior of FRP confined concrete columns. In the present FE model, FRP wrapped RC column with diameter 205 mm and height 1000 mm is considered. Due to symmetry in cross-section of the column and loading only one half of the column was modeled. The SOLID65, SOLID46, LINK8 and SOLID45 elements are used to model the concrete, FRP, steel and stiff loading plate respectively. Tavarez (2001) discussed three techniques to model steel reinforcement in FE modeling of reinforced concrete: the discrete

model, the embedded model, and the smeared model. Fanning (2001) modeled the response of the reinforcement using the discrete model and the smeared model for reinforced concrete beams. It was found that the best option is to use the discrete model and this has been adopted in the present work.

3 MATERIALS AND MODELLING

3.1 FRP composites

In the present study, thickness of one layer was 1.2 mm and it is kept constant for all the cases and up to three numbers of layers have been considered with different fiber orientations.

3.2 Concrete

The SOLID65 element used which requires linear isotropic and multi-linear isotropic material properties to model the von-Misses failure criterion along with the William and Warnke (1975) model to define the failure of the concrete.

3.3 Steel

The LINK8 element is used for all the steel reinforcement (bilinear isotropic) in the column. Elastic modulus equal to 200000 MPa and Poisson's ratio of 0.3 has been used. Tensile strengths of 500 MPa and 250 MPa are used for longitudinal and tie bars respectively. The columns have tie bars with diameter of 10 mm at a spacing of 80 mm and six longitudinal steels with diameter of 12 mm.

3.4 Meshing

Concrete was modeled first as a volume then changed to

a FE model by a controlled (mapped) meshing followed by elemental modeling of the steel (both longitudinal and tie bars). Finally the FRP was modeled as a volume then changed to finite element model by mapped meshing followed by modeling of the loading stiff solid which is 150 mm long placed and merged to the top of the concrete model. In the present work, the number of elements used for each of the element types for a FRP wrapped (one layer) RC column are shown in Table 1.

Table 1 Number of elements used for different types of elements

Element Type	SOLID65	SOLID46	LINK8	SOLID45
No. of element	7500	490	1000	1200

3.5 Boundary conditions and loadings

In the present model, the Y-axis of the coordinate system coincides with the axis of the column. The boundary conditions are:

- 1) One end of the surface was fixed;
- 2) As the concentrated forces cause stress concentration at around point of application of the load, they are applied as an equivalent compressive pressure.

3.6 Simulation

A nonlinear FE analysis was performed to include the nonlinear material behavior of concrete and FRP. In the present analysis automatic load stepping feature has been activated and the analysis is force controlled. In the present study the pressures are incrementally applied till the columns reached their collapse state which corresponds to breaking state.

4 PARAMETRIC STUDY

For axially loaded FRP wrapped RC circular columns, the results obtained by using the present finite element model are compared with those of Chakrabarti et al. (2008) and found to be perfectly matching. There is scarcity of sufficient data for comparison in case of eccentrically loaded FRP wrapped RC columns. As such in this section, independent results are presented to show the effects of different parameters on the behaviour of eccentrically loaded columns.

4.1 Effect of unconfined compressive strength

FRP wrapped RC column with diameter 205 mm and height 1000 mm is considered here. The material properties used for the models are given in Table 2. Analyses results for the models are presented in Table 3. The load deflection curve of the models with M 25, M 40 and M 60 grade of concrete, under eccentric loadings are shown in Figure 1. It can be seen from Table 3 that FRP is most effective in confining the reinforced concrete columns having lower grade of concrete for both axially and eccentrically loaded columns. The results in Table 3 show that the FRP oriented in the hoop direction do not

add significantly to the confinement of eccentrically loaded columns.

Table 2 Material properties used in the models

Material	Comp. Strength (MPa)	Tensile Strength (MPa)	Elastic Modulus (MPa)	Poisson's ratio
Concrete	25	3.114	23665	0.2
	40	3.939	29934	0.2
	60	4.824	36668	0.2
Bars	Longbar Strength (MPa)	Tiebar Strength (MPa)	Elastic Modulus (MPa)	Poisson's ratio
	500	250	2.0×10^5	0.3
FRP composite $t = 1.2$ mm	Elastic Modulus (MPa)	Poisson's Ratio	Shear Modulus (MPa)	Ult. Tensile Strength (MPa)
	$E_x = 96032$	$\nu_{xy} = 0.29$	$G_{xy} = 2001$	1353
	$E_y = 5400$	$\nu_{yz} = 0.43$	$G_{yz} = 1882$	
$E_z = 5400$	$\nu_{zx} = .016$	$G_{zx} = 2001$		

Table 3 Summary of analyses results for varying grade of concrete

Concrete grade	Eccentricity (mm)	P_{cure} (kN) (RC)	P_{cc} (kN) (FRP wrapped RC)	P_{cure}/P_{cc}
M25	0	1234.08	2490.00	2.02
M40	0	1741.31	2287.00	1.31
M60	0	2363.67	2836.40	1.20
M25	50	845.16	972.40	1.15
M40	50	1193.93	1351.03	1.13
M60	50	1578.43	1767.89	1.12

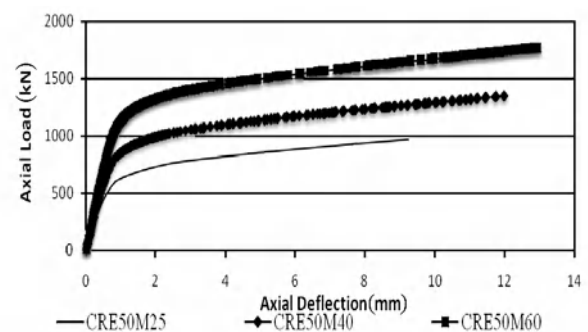


Figure 1 Effect of grade of concrete on load deflection curve ($e = 50$ mm)

4.2 Effect of fiber orientation of FRP sheets

Six circular specimens 205 mm \times 1000 mm having same grade of concrete (25MPa) and FRP composite material ($E_{frp} = 96032$ MPa) but varying FRP fiber orientation have been analyzed. Fiber orientations of 0, 45 and 90 degrees respectively have been tried in the analyses. Table 4 summarizes the analysis results for varying fiber

orientation of FRP composite wrapped columns under pure axial and eccentric loading ($e = 50\text{mm}$). Figure 2 shows when these models are subjected to eccentric loading, 90 degrees fiber orientation has been observed to enhance the load carrying capacity the most. Figure 3 shows the variation of confinement effectiveness with the variation in fiber orientation.

Table 4 Summary of analyses results for variation in fiber orientation

Fiber orientation (deg)	Eccentricity (mm)	P_{curc} (kN) (RC)	P_{cc} (kN) (FRP wrapped RC)	P_{cc}/P_{curc}
0	0	1234.08	2490.00	2.02
45	0	1234.08	1261.71	1.02
90	0	1234.08	1257.64	1.01
0	50	845.16	971.93	1.15
45	50	845.16	1039.55	1.23
90	50	845.16	1183.22	1.40

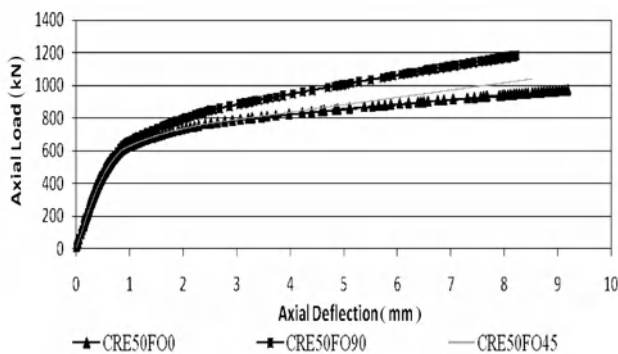


Figure 2 Effect of fiber orientation on load deflection curve ($e=50\text{mm}$)

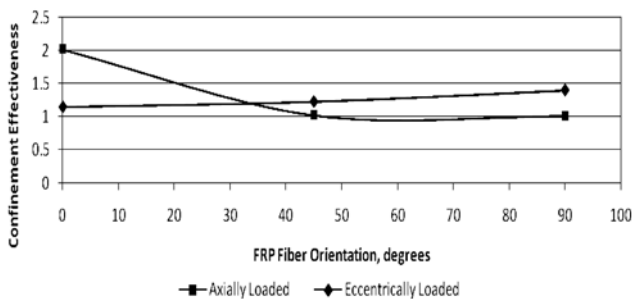


Figure 3 Effect of variation in FRP fiber orientation on confinement effectiveness

5 CONCLUSIONS

The following conclusions can be made for the analysis results investigated in this work:

- The confinement effectiveness is found to be smaller with increase in grade of concrete.

- Zero degree fiber orientation has been observed to be the most effective for models under pure axial load and 90 degrees fiber orientation was the most effective for eccentric loading.
- External confinement with FRP composites significantly increases the strength of concrete column. However, when the eccentric load is introduced the strength loss is obvious and to a greater extent.

NOMENCLATURE

- P_{curc} Ultimate load of reinforced concrete model (without FRP)
- P_{cc} Ultimate load of FRP wrapped reinforced concrete
- CRE50M25 FRP wrapped RC column (M25) under eccentric loading
- CRE50M40 FRP wrapped RC column (M40) under eccentric loading
- CRE50M60 FRP wrapped RC column (M60) under eccentric loading
- CRE50FO0 FRP wrapped (0 degree) RC column under eccentric loading
- CRE50FO45 FRP wrapped (45 degrees) RC column under eccentric loading.
- CRE50FO90 FRP wrapped (90 degrees) RC column under eccentric Loading.

REFERENCES

ANSYS *User's Manual*, Release 10.0, ANSYS, Inc., 2005.

Chakrabarti, A., Chandra A. & Bhargava P. 2008. Finite Element Analysis of Concrete Columns confined with FRP sheets. *Journal of Reinforced Plastics and Composites* 27 (12): 1349-1373.

Fanning, P. 2001. Nonlinear Models of Reinforced and Post-tensioned Concrete Beams. *Electronic Journal of Structural Engineering*, University College Dublin, Earlsfort Terrace, Dublin 2, Ireland, 12 September.

Feng, P., Lu, X.Z. & Ye, L.P. 2002. Experimental research and FE analysis of square columns confined by FRP sheets under uniaxial compression. *Proc. 17th Australasian Conference on the Mechanics of Structures and Materials*. Gold Coast, Australia: 71-76.

Li, G, Hedlund, S., Pang, S., Alaywan W., Eggers, J. & Abadie, C. 2003. Repair of damaged RC columns using fast curing FRP composites. *Composite Part B: Engineering* 34: 261-271.

Tavarez, F.A. 2001. Simulation of Behavior of Composite Grid Reinforced Concrete Beams Using Explicit Finite Element Methods. *Master's Thesis*, University of Wisconsin-Madison, Madison, Wisconsin.

William, K. J. & Warnke, E. P. 1975. Constitutive Model for the Triaxial Behavior of Concrete. *Proceedings of International Association for Bridge and Structural Engineering* 19, ISMES, Bergamo, Italy.

Concrete Column Confinement with Mechanism-Based Composite Bistable Structures

C. Wan & C. Quon

Graduate Researcher, Dept. of Civil & Environmental Engineering, University of California, Davis, CA, USA

L. Cheng (dawcheng@ucdavis.edu)

Assistant Professor, Dept. of Civil and Environmental Engineering, University of California, Davis, CA, USA

ABSTRACT The application of fiber reinforced polymer (FRP) composites in civil engineering has advanced drastically in recent years, especially in the area of retrofitting concrete bridge columns. However, composite's non-ductile (brittle) behavior is one of the concerns that have yet to be fully addressed. The objective of this research is to investigate a mechanism-based bistable composite structure as the wrapping system to improve the confinement in concrete columns. It consists of energy-absorbing "links", main link and waiting link with the former being the primary load carrier and the latter as the secondary after the main link fails. A series of testing on cylindrical concrete members wrapped with the bistable structure made of hybrid carbon and glass FRP were conducted to investigate the effect of link geometry on the behavior. The results showed that a controlled failure was achieved in the structure and the ductility and energy absorption were enhanced. The effectiveness of the confinement was found to be affected by the number of links and the energy absorption relied on the size of the links.

1 INTRODUCTION

Fiber reinforced polymer (FRP) composites have been more and more used in the field of civil engineering such as concrete bridge column retrofitting and rehabilitation projects due to their high strength-to-weight ratio and good corrosion resistance. Extensive research has been done on the behavior of FRP confined concrete columns, including analytical modeling (Samaan et al. 1998; Spoelstra and Monti 1999; Teng and Lam 2004), experimental testing (Fardis and Khalili 1981; Saadatmanesh et al. 1994; Xiao and Wu 2000; Karantzikis et al. 2005), and design guideline development (Nanni and Bradford 1995; Toutanji 1999). The major findings of these studies are further summarized and compared in the recent references (Teng and Lam 2004; Rocca et al. 2008). It is shown that the compressive strength of concrete columns is increased due to the additional confinement provided by the FRP wrapping; however, the ductility is not increased as significantly as the strength and sometimes even decreased. The objective of this research is to improve such ductility in the FRP concrete wrapping method through the development of a new mechanism-based composite "Bistable Structure" system.

The idea of bistable structure was first introduced by Cherkaev and Slepyan (1995), who proposed a mathematical model of systems consisting of "main links" and "waiting links". The main link is designed to

fracture first while the waiting link is intended to continue carrying the load as the main link fails. The synergistic combination of the main link and the waiting link allows the overall bistable structure to have a more controlled fracture and a desired fail-safe mechanism. Moreover, the bistable structure is expected to absorb a larger amount of energy than just the materials alone.

During 2005 and 2006, a pilot study by Whitman and La Saponara (2007a) demonstrated that the bistable structure is capable of increasing the energy absorption in a metal-link system. Figure 1a illustrates such a typical 3-link metallic bistable structure under tension, where the straight metal pieces are the main links and the curved ones are the waiting links. As the system undergoes tensile loading, the main links serve as the primary load carriers and the waiting links do not carry much load until the main links start to fail. Bistable structures made of polymer composites are also investigated in a follow-up study (Whitman and La Saponara 2007b; Kim 2008), as shown in Figure 1b. The original concept behind this design is to mechanically enhance the ductility of the structure made of linear elastic materials such as carbon FRP and glass FRP. Foam cores are utilized to maintain the rounded shape in the waiting link elements and Kevlar stitching is used between the waiting links to enhance the integrity of the structure.

This bistable concept has been adopted in this research

project in developing an effective concrete column wrapping system with much more improved ductility and energy absorption capability in the system. The feasibility of this concept is first investigated and the preliminary results are presented in this paper. Analytical studies and continuing experiments are still in progress and will be discussed in a future paper.

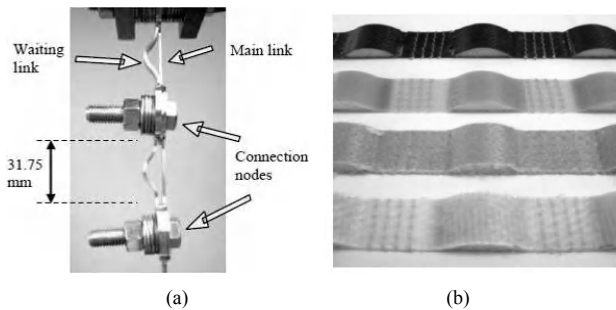


Figure 1 Illustration of bistable concept: (a) metal links (Whitman and La Saponara 2007a); (b) FRP links (Whitman and La Saponara 2007b)

2 EXPERIMENTAL PROGRAM

2.1 Materials

A series of standard plain concrete cylinders with a diameter of 15.2 cm and a height of 30.5 cm were prepared for the testing program. The 28-day compressive strength of the concrete was experimentally obtained as 32.4 MPa, following the ASTM C39/C39M (ASTM 2005). Due to the fact that it is essentially important that the main link fails before the waiting link so that the bistable mechanism can be activated, a stiffer material with less ductility is desired for the main link. On the other hand, the waiting link needs to be more flexible (larger deformability) in order to be engaged at a later stage of failure. Under these considerations, unidirectional carbon fiber composite material (CFRP) was selected for the main link (inner layer) and unidirectional glass fiber composite (GFRP) was chosen for the waiting link (outer layer). The ultimate tensile strength of the CFRP and GFRP material was 849 MPa and 612 MPa, respectively, and their corresponding ultimate tensile strain was 1.12% and 2.45%, respectively (per manufacturer's data). Kevlar thread was used to stitch the layers together, which has a much higher tensile strength (about 3600 MPa) than both CFRP and GFRP. Commonly used styrene foam was inserted in the round-shaped segments in order to form the configuration of the waiting links in the structure. The maximum compressive strength of the foam was about 0.17 MPa based on the data provided by the local material supplier in the region.

2.2 Design

The typical layout of the bistable composite wrap is illustrated in Figure 2 and Figure 3, where the design

example composes of three bistable segments (can be more than 3) connected by lines of Kevlar stitching. The main links are directly bonded onto the concrete cylinder surface and the waiting links contain the foam cores. Each main link consists of one ply of CFRP and the waiting link is made of two plies of GFRP. The overlap region of each structure consists of one layer of GFRP and one layer of CFRP with the length approximately equal to one bistable segment, as illustrated in Figure 2 and Figure 3. The purpose of this is to prevent the undesired premature debonding failure in the specimen at the joint region. The overlapping length of at least one-quarter of the circumference is supported by several other researches (e.g., Lam et al. 2006).

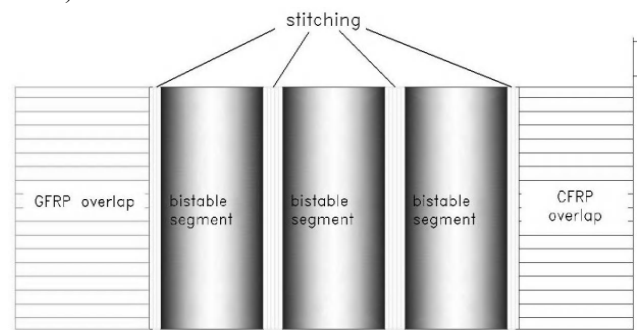


Figure 2 Layout of a typical 3-link composite bistable wrap

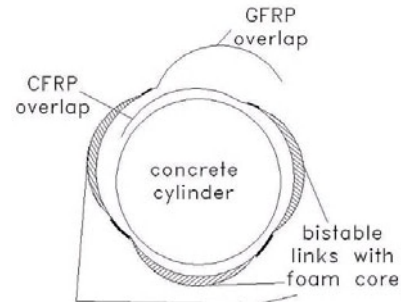


Figure 3 Cross-section of a typical 3-link composite bistable wrap

The major testing parameters in this study include: (a) the total number of the bistable segments (i.e., 3-link, 4-link and 5-link); and (b) the dimension of the waiting link which is designated as “%wait” in this paper. The term “%wait” was first introduced by Whitman and La Saponara (2007a) and is defined by equation 1 below. This percentage corresponds to how much longer the waiting link is with respect to the length of the main link. 2%wait (small), 5.5%wait (medium), and 9%wait (large) are the specimen sizes formed in this study. The specimen with 2%wait was designed such that once the main link broke; the waiting link would immediately take on the load the main link was carrying. The other two types of specimens would have a slight lagging period before the waiting links take load from the main link.

$$\%wait = \left[\frac{\text{waiting link's length}}{\text{main link's length}} - 1 \right] \times 100\% \quad (1)$$

To further compare the FRP bistable wrap with the conventional FRP wrap, two other types of specimens were prepared. The first set used exactly the same type and number of plies of CFRP and GFRP but in a continuous form (designated as “Baseline”). The second set was only wrapped with one ply of CFRP and was designated as “1-ply CFRP”.

2.3 Manufacturing

Crescent shaped foam cores were first cut using a hot wire machine in the laboratory. E-glass and carbon fabric plies were cut into appropriate sizes and were stitched together using needles and Kevlar threads. After each stitching section was completed, the foam core was inserted between the glass and carbon layers and clamped in place using paper clips. The same procedure was then repeated several times to create the desired configuration for the bistable structure. Upon completion, the bistable wrap was then applied onto the concrete cylinders that were cured for 28 days. A typical wet lay-up process was applied for the installation. Twelve sets of different concrete specimens were prepared with 3 specimens in each set, as shown in Table 1.

Table 1 Test results on baseline and bistable specimens

Specimen	Max. load (kN)	Max. displacement (mm)	Energy absorbed (kJ)
Unconfined	741.1	1.04	0.8
Baseline	1701.4	7.57	12.9
1-ply CFRP	1375.1	3.38	4.7
3-link 2%wait	828.4	15.90	13.2
5.5%wait	866.7	24.08	20.9
9%wait	688.8	24.42	16.8
4-link 2%wait	1021.6	15.38	15.7
5.5%wait	931.3	26.40	24.6
9%wait	747.5	34.28	25.6
5-link 2%wait	967.6	11.47	11.1
5.5%wait	853.0	25.96	22.1
9%wait	906.0	31.68	28.7

3 TEST RESULTS AND DISCUSSIONS

All concrete specimens were capped on top and bottom ends using sulfur capping material to create smooth surfaces per ASTM recommendation (ASTM 2005). They were then tested under uniaxial compression via a universal testing machine in the laboratory. Two linear potentiometers (LP) were placed on the left and right hand side of the specimen to measure the vertical displacement. Load and displacement were recorded through a National Instruments Data Acquisition System. Table 1 summarizes the test results (average values) of

the maximum load, the maximum displacement and the total energy absorbed in each set of specimens with different design parameters.

The baseline specimens failed in a very sudden and explosive manner. The bistable specimens were found to all experience the main link failure first followed by the waiting link failure. The failures were much less sudden at the ultimate level comparing to the baseline specimens. A loud “popping” sound was noticed as each main link ruptured, where the load was found to drop as shown in the load-displacement response curve from Figure 4. After the main link failed, the waiting link took on the load and the final failure arrived as the waiting links reached their ultimate strain limit in the hoop direction. When compared with the baseline design and the specimens wrapped with one ply of CFRP, the bistable specimens had an unexpectedly lower load-carrying capacity. A close examination on the failed specimens revealed that small gaps existed between the FRP wrap and the cylinders next to the stitching lines, causing much a earlier debonding in the FRP wrap which reduced the effectiveness of the FRP confinement to concrete. This is expected to be improvable by adding extra clamping onto the specimen to eliminate the gaps during the fabricating process, which is under current investigation. It can be seen from Table 1 that, for each bistable design (3-link, 4-link and 5-link), the 5.5%wait seemed to provide the highest load-carrying capacity with reasonable ductility and energy absorption in the specimen.

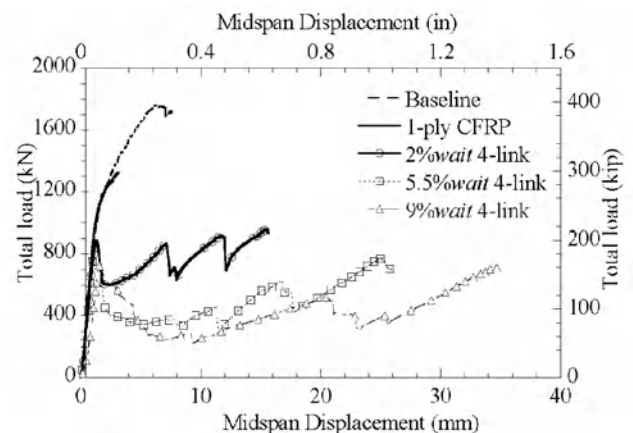


Figure 4 Comparison of load-displacement response for baseline and 4-link bistable specimens

In terms of the displacement level, the bistable specimens displayed significantly more deformation (ductility) before the final failure than the baseline specimens (Figure 4). Among all the bistable designs, the specimens with 2% wait appeared to have the least displacement and 9% wait had the most. It can be seen from Table 1 that almost all the bistable specimens absorbed much more energy than the baseline specimens

and the ones wrapped with 1 ply of CFRP. This higher energy absorption capacity in the bistable structures contributed to the less sudden failure mode in the specimens (more progressive) and provided a safer failure mechanism than the baseline ones. Among all the bistable specimens tested so far, the ones wrapped with the 4-link of 5.5%*w*ait system were found to absorb the most amount of energy.

4 CONCLUSIONS

A mechanism-based composite bistable structure was investigated in this study as the new wrapping material for concrete column rehabilitation purpose. The design concept was explored through a set of experimental tests on cylindrical concrete specimens. Although the current bistable design did not achieve as high of the load-carrying capacity as the baseline specimens, they provided much improved ductility and energy absorption in the structure, which has been one of the most challenging issues in the existing application field. More importantly, the bistable structure created a safer and more controlled failure than the baseline specimens using the existing wrapping method. Based on the current results, the design of bistable structures using 4-link with 5.5%*w*ait showed the best performance among all.

To further improve the bistable design so that a more effective confinement (comparable load-carrying capacity to the baseline design) can be achieved, several alternative manufacturing methods are under current investigation, such as eliminating the gaps between the stitching areas through extra clamping. Analytical modeling is also paralleled to assist achieving such an optimal design in the system. Other design parameters such as the types of FRP reinforcement, smaller bistable configuration and larger structural members (higher aspect ratio) can also be included in the future study.

REFERENCES

- ASTM Standard C39/39M. Standard test method for compressive strength of cylindrical concrete specimens. *ASTM International*, West Conshohocken, PA, 2005.
- Cherkaev, A. & Slepyan, L. 1995. Waiting element structures and stability under extension. *Int. J. Damage Mech.* 4(1): 58-82.
- Fardis, M.N. & Khalili, H. 1981. Concrete encased in fiber glass reinforced plastic. *ACI Journal* 78: 226-241.
- Karantzikis, M., Papanicolaou, C.G., Antonopoulos, C.P. & Triantafillou, T.C. (2005). Experimental investigation of nonconventional confinement for concrete using FRP. *Journal of Composites for Construction* 9(6): 480-487.
- Kim, S. 2008. Design, development, and analysis of a hybrid bistable structure for energy absorption. Master Thesis, Department of Mechanical and Aeronautical Engineering, University of California, Davis.
- Lam, L., Teng, J.G., Cheung, C.H. & Xiao, Y. 2006. FRP-confined concrete under axial cyclic compression. *Cement and Concrete Composites* 28(10): 949-958.
- Nanni, A. & Bradford, N.M. 1995. FRP jacketed concrete under uniaxial compression. *Construction Building Materials* 9(2): 115-124.
- Rocca, S., Galati, N. & Nanni, A. 2008. Review of design guidelines for FRP confinement of reinforced concrete columns of noncircular cross sections. *Journal of Composites for Construction* 12(1): 80-92.
- Saadatmanesh, H., Ehsani, M.R. & Li, M.W. 1994. Strength and ductility of concrete columns externally reinforced with fiber composite straps. *ACI Structural Journal* 91(4): 434-447.
- Samaan, M., Mirmiran, A. & Shahawy, M. 1998. Model of concrete confined by fiber composites. *Journal of Structural Engineering* 24(9): 1025-1031.
- Spoelstra, M. & Monti, G. 1999. FRP-confined concrete model. *Journal of Composites for Construction* 3(3): 143-150.
- Teng, J.G. & Lam, L. 2004. Behavior and modeling of fiber reinforced polymer-confined concrete. *Journal of Structural Engineering* 130(11): 1713-1723.
- Toutanji, H. 1999. Stress-strain characteristics of concrete columns externally confined with advanced fiber composite sheets. *ACI Materials Journal* 96(3): 397-404.
- Whitman, Z. & La Saponara, V. 2007a. Bistable structures for energy absorption I: metallic structures under tension. *Journal of Mechanics of Material and Structures* 2(2): 347-358.
- Whitman, Z. & La Saponara, V. 2007b. Bistable structures for energy absorption II: composite structures under tension. *Journal of Mechanics of Material and Structures* 2(2): 359-376.
- Xiao, Y. & Wu, H. 2000. Compressive behavior of concrete confined by carbon fiber composite jackets. *Journal of Materials in Civil Engineering* 12(2): 139-146.
- Yan, Z., Pantelides, C. & Reaveley, L. 2007. Posttensioned FRP composite shells for concrete confinement. *Journal of Composites for Construction* 11(1): 81-90.

Confined Circular and Square R.C. Sections: an Analytical Model for the Prediction of Ultimate Strength

Nicola Nisticò (nicola.nistico@uniroma1.it), Giorgio Monti, Valentino Lovo

Department of Structural Engineering and Geotechnics, "Sapienza" University of Rome, Rome, Italy

ABSTRACT An analytical model is proposed for the prediction of ultimate strength of square sections confined by FRP. Since the model considers the corner radius influence, circular sections are automatically included as a particular case. The simplified model has been tested against a set of experimental values available in the literature: the comparison was satisfactory and its accuracy is discussed. The performance of the model is validated in terms of average absolute error and its standard deviation. The model is based on a revision of the classical strength criterion proposed by Ottosen.

1 INTRODUCTION

The classical assumptions adopted to justify the effect of confinement in square sections are those well known as "arching effect": many proposals for predictive equations are based on it, even if according the authors this effect is not very well justified in terms of confinement principal stress.

In a previous work (Monti & Nisticò, 2008a) the phenomenology has been studied and a prediction equation has been proposed and matched against the experimental results proposed in literature.

The analytical solution is based on simplified strength criterion assumed but not justified.

Further on the confinement stress field has been simplified by means of simple distributions here revised in order to improve the capability of the model.

2 EXPERIMENTAL RESULTS AND PHENOMENOLOGICAL ASPECT

Experimental investigations on square sections date back to the tests proposed in Mirmiran et al. (1998) where the effects of the corner radius were clearly described, influencing both strength and ultimate strain. After that work, other contributions focussed either on the prediction of ultimate parameters or on the development of constitutive models by means of tests on small specimens.

Recently, the effects of the corner rounding radius has been extensively investigated in Wang & Wu, (2007), where compression tests were performed on 108 concrete specimens (300 mm tall). The section of all specimens can be considered as inscribed in a square section (150×150 mm) with six values of the corner radius: 0, 15, 30, 45, 60, and 75 mm (so that circular sections have been included in the tests). Two different

concrete types (C30 and C50) and two jacket thicknesses (0.165 and 0.33 mm) have been considered, so that 36 classes of specimens have been tested (including the unwrapped specimens) and for each class 3 tests have been performed. Based on the experimental results of the Wang & Wu investigations it is possible (as has been done in this work) a) to evaluate the fiber ultimate strain value as function of the corner radius of the square section b) to calibrate a local strength criterion for confined concrete c) to evaluate the local strength increase and consequently the section strength increase.

All the previous aspects will be discussed in the following.

3 ULTIMATE FIBER STRAIN PREDICTION

The ultimate fiber strain reduction has been evaluated starting from the results of the investigations carried out by Wang & Wu; the ratio between "real" ultimate strain (ε_f) and the one obtained from coupon test (ε_{coupon}) has been expressed by means of a function of the corner radius normalized with respect to the radius of the circular section inscribed inside the square section side length ($r = r_c/R = 2r_c/L$), with the aim of minimizing the global error between the function and the experimental results.

The obtained final relationship is the following:

$$\frac{\varepsilon_f}{\varepsilon_{coupon}} = f(r) = 0.31 + 0.47(r)^{0.1} \quad (1)$$

with a global error (sum of absolute errors) of 0.1262 with respect to the mean curve (see Figure 1).

From Figure 1 it can be observed that, for $r = 0$, $\varepsilon_f/\varepsilon_{coupon}$ is nearly 0.31; then, a significant increase is observed if the corner radius increases, while beyond $r = 0.2$ the ratio between real ultimate strain ε_f and ε_{coupon}

reaches a nearly constant value and tends to the value 0.78 for $r = 1$ (circular sections).

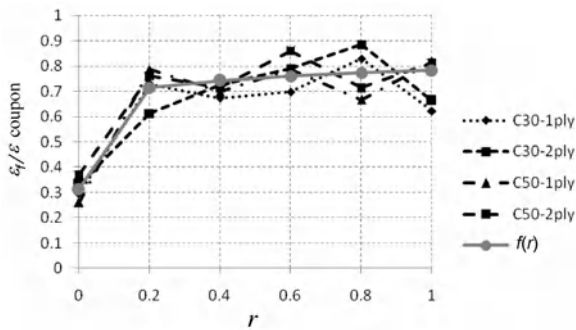


Figure 1 Ultimate fiber strain reduction due to corner radius.

4 ULTIMATE STRENGTH PREDICTION

The classical approach proposed in the literature for the ultimate strength prediction is based on the modification of expressions obtained for circular sections having equal confinement stress (f_{lu}): it can be schematically described through Equation (2), where the strength incremental increase is obtained introducing modification factors (k_i) in order to modify the increase $F(f_{lu})$ obtainable in case of equal confinement stress:

$$f_{cc} = C_1 \cdot f_{co} + \Pi_i k_i \cdot F(f_{lu}) \quad (2)$$

The introduction of the above-mentioned modification factors can be regarded as a shortcut to encapsulate the mechanical behaviour in a simple expression, usable for both circular and square/rectangular sections. Nonetheless, a sound mechanical justification is needed. In this work, a simple yet robust analytical expression is developed starting from some numerical investigations performed on square sections with different corner radii, as explained in the following sections, where starting from the stress field obtainable by means of numerical analyses: a) a simplified strength local criterion has been calibrated b) a simplified stress field has been assumed c) the global strength of the confined section has been evaluated by means of an analytical approach.

4.1 Numerical approach

The model is based on the approach proposed in Monti and Nisticò (2008b), where a methodology is presented to predict the section's stress-strain relationship, based on the following steps: 1) the non-uniform Confinement Stress Field (*CSF*) applied by the confining device are numerically evaluated, 2) the local (position-dependent) axial stress-strain relationships are evaluated at each discretized point within the section, and 3) they are appropriately combined to obtain the global axial stress-strain curve of the section.

Under the assumption of path-independence, if one knew the *CSF* at an ultimate condition (e.g., FRP failure), then the corresponding ultimate strength can be

evaluated in each region of the section, based on a strength criterion (e.g., Ottosen, 1977). By discretizing the section in n regions (see Figure 2), the section strength can be evaluated as:

$$f_{cc} = \frac{\sum_{i=1}^n f_{cc,i} \cdot A_i}{\sum_{i=1}^n A_i} \quad (3)$$

where A_i and $f_{cc,i}$ are the area and ultimate strength of each region, respectively.

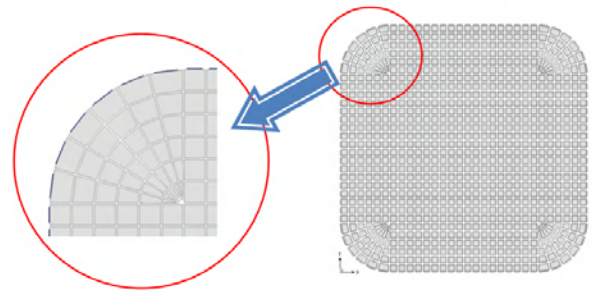


Figure 2 FEM analyses: section model

It can be assumed that, for a boundary condition given in terms of confinement stresses, the *CSF* is independent of the mechanical properties of the section material (in this case, Young's modulus and Poisson's coefficients of concrete). Thus, given the *CSF* for a known FRP axial strain field (E), the proportionality principle applies as follows:

$$CSF(c \cdot E) = c \cdot CSF(E) \quad (4)$$

Though the strain field E varies along the section side, parametric numerical analyses have shown that the maximum/average ratio varies less than 10%. Thus, a control point at mid-side is chosen that allows to reduce the problem to a one-parameter one.

4.2 Adopted strength criterion

Starting from the strength criterion proposed by Ottosen (1977), a simplified criterion has been formalized in terms of minimum and maximum principal confinement stress; it is:

$$\frac{f_{cc}}{f_{co}} = 1 + A \cdot \frac{\sigma_{\min}}{f_{co}} \cdot \frac{\sigma_{\max}}{\sigma_{\min}} + \left(1 - \frac{\sigma_{\max}}{\sigma_{\min}}\right) \cdot \left(a \frac{\sigma_{\min}^2}{f_{co}} + b \frac{\sigma_{\min}}{f_{co}}\right) \quad (5)$$

The previous expression, in case of hydrostatic case $\sigma_{\max} = \sigma_{\min}$ (e.g., for circular sections), becomes:

$$\frac{f_{cc}}{f_{co}} = 1 + A \cdot \frac{\sigma_{\min}}{f_{co}} \cdot \frac{\sigma_{\max}}{\sigma_{\min}} = 1 + A \cdot \frac{f_{lu}}{f_{co}} \quad (6)$$

The coefficient A in Equation (6) has been calibrated with the aim of minimizing the mean global error between predicted values and experimental ones, considering

circular sections only. The result is $A = 2.67$, with a mean global error of 11.8%.

Having calibrated the coefficient A , in order to calibrate the parameters a, b in Equation (6), each of the sections considered in the experimental campaign carried out in Wang & Wu (2007), has been analyzed by means of FEM analyses (Figure 2): the CSF has been evaluated at ultimate condition of the composite, whose ultimate strain has been evaluated through Equation (1).

For each sub-region, knowing σ_{\max} and σ_{\min} , Equation (5) has been applied in order to evaluate a and b with the purpose of minimizing the mean global error. Thus the coefficients a and b have been fixed as follows: $a = -0.02$; $b = 0.5$, obtaining a mean global error of 14.3%, considering both circular and square sections.

Such local strength criterion for confined concrete is represented in Figure 3 together with the results, obtainable by means of Ottosen strength criterion: the normalized strength increase has been evaluate for different values (0; 0.25; 0.5; 0.75; 1) of the ratio between the maximum and minimum confinement principal stress.

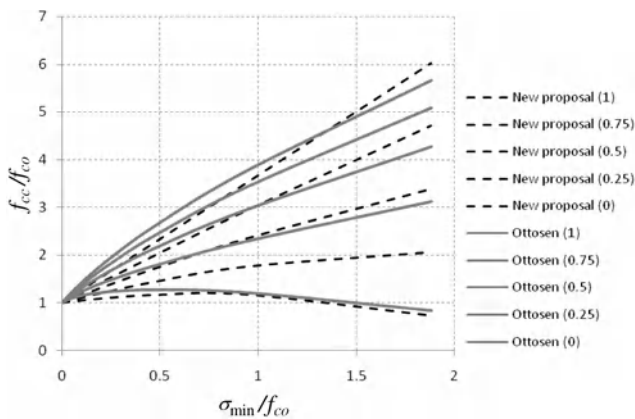


Figure 3 Comparison between Ottosen strength criterion and new proposal ($A = 2.67$; $a = 0.02$; $b = 0.5$)

The same error becomes 15.1%, if a and b are chosen both null. In this case, the strength criterion becomes linear, and consists of a bundle of straight lines, as represented in Figure 4.

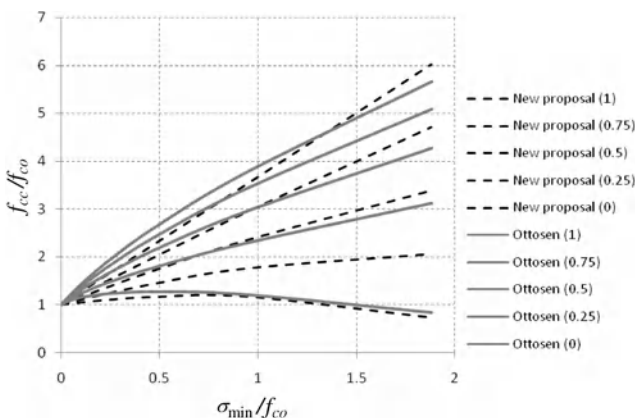


Figure 4 Comparison between classical Ottosen strength criterion and simplified new proposal ($A = 2.67$; $a = 0$; $b = 0$)

4.3 Analytical approach

Alternatively, the section strength can be evaluated based on an analytical closed-form expression. The formulation here proposed is based on a simplified strength criterion that expresses the strength increase of a concrete element in terms of the Principal Stress Field (PSF) and Principal Stress Ratio (PSR), as follows:

$$f_{cc} = f_{co} + F(\sigma_{\min}) \cdot \frac{\sigma_{\max}}{\sigma_{\min}} \quad (7)$$

where σ_{\min} is the minimum PSF, $\sigma_{\max}/\sigma_{\min}$ is the max/min PSR, and $F(\sigma_{\min})$ is a function giving the strength increase when $\sigma_{\min} = \sigma_{\max}$ (i.e., in circular sections).

By integrating the previous expression over the section area, the global ultimate strength can be found. In order to obtain a viable expression for it, some simplifications are introduced in the definition of the PSF.

The minimum PSF is considered as constant inside the *core*. The minimum PSF in the *corner* regions reaches its max absolute value at the section edge and its min absolute value at the core boundaries. For both *core* and *corners* the PSF depends on the ratio between the *corners* rounding radius r_c and the *core* radius R (half of the section side: $R = 0.5 L$).

The *core* minimum PSF $(\sigma_{\min})_{core}$ is assumed equal to the stress field in a circular section:

$$f_l = 2 \frac{t_f}{L} E_f \varepsilon_l \quad (8)$$

where L = square section side length, t_f = FRP thickness, E_f = FRP Young's modulus, ε_l = FRP strain at mid-side (control point).

The *corner* minimum PSF $(\sigma_{\min})_{corner}$ (evaluable at the centroid of it) depends on the corner radius as follows:

$$(\sigma_{\min})_{corner} = \left(2 - \frac{r_c}{R}\right)^\beta \cdot (\sigma_{\min})_{core} \quad (9)$$

Inside the *core*, the min/max PSR (ratio between min and max principal stresses) can be assumed as inversely proportional to the distance (d) of the considered point from the core centre (having an axially symmetric field), according to the following expression:

$$\alpha_{core} = \frac{\sigma_{\max}}{\sigma_{\min}} = \left(0.8 + 0.2 \frac{r_c^2}{R^2}\right) - \frac{d}{R} \cdot \left(1 - \frac{r_c}{R}\right) \quad (10)$$

The previous expression implies that α_{core} is equal to $(0.8 + 0.2r^2)$ (almost equal confinement stresses) in the centre of the core ($d = 0$), and it is 1 everywhere if $r_c = R$ (that is the case of the circular section).

Inside the *corners* (at the centroid), the min/max PSR is assumed to depend on the corner/core radii ratio, as follows:

$$\alpha_{corner} = 1 - \gamma \cdot \left(1 - \frac{r_c}{R}\right) \quad (11)$$

The previous expression implies that: 1) if $r_c = R$, α_{corner} is equal to 1 (equal confinement stresses); 2) if $r_c = 0$, α_{corner} is equal to $(1 - \gamma)$.

Having defined the PSF, Equation (6) is then applied to core and corner regions and integrated over the relevant regions in order to obtain the section strength. It holds:

$$f_{cc} = \frac{(F_{cc})_{core} + (F_{cc})_{corners}}{A} \quad (12)$$

where:

$$\begin{aligned} (F_{cc})_{core} &= \int_{A_{core}} [f_{co} + F(\sigma_{min})_{core} \cdot \alpha_{core}] \cdot dA = \\ &= A_{core} \cdot \left[f_{co} + F(\sigma_{min})_{core} \cdot \left(\frac{1}{5}r^2 + \frac{2}{3}r + \frac{2}{15} \right) \right] \end{aligned} \quad (13a)$$

$$\begin{aligned} (F_{cc})_{corner} &= \int_{A_{corner}} [f_{co} + F(\sigma_{min})_{corner} \cdot \alpha_{corner}] \cdot dA = \\ &= A_{corner} \cdot \left\{ f_{co} + F(\sigma_{min})_{corner} \left[1 - \gamma \left(1 - \frac{r_c}{R} \right) \right] \right\} \end{aligned} \quad (13b)$$

Further on, $F(\sigma_{min})$ can be assumed as proportional to the minimum principal confinement stress (f_{lu}) as:

$$F(\sigma_{min}) = A \cdot f_{lu} \quad (14)$$

where a) the reduction (Equation 1) accounting for the ultimate strain reduction when considering coupon test failure strains is applied; b) $A = 2.67$.

5 RESULTS AND DISCUSSIONS

The above-presented analytical approach has been validated against the experimental results contained in

the data bank. The accuracy of the model has been evaluated based on: 1) the average absolute errors (AE), 2) the average ratio (AR) between experimental and predicted values, 3) its dispersion σ .

The analytical approach fits well ($AE = 0.124$ for both circular and square sections, $AE = 0.118$ for circular sections only, $AR = 0.98$, $\sigma = 0.14$) the experimental results, by assuming the coupon ultimate strain and adopting: $\beta = 1.7$, $\gamma = 1$. Thus, the equivalent strength for the rectangular section can be evaluated according to the following expression (adopting the approach formally expressed through Eq. 2):

$$f_{cc} = f_{co} + k_e f_l \quad (15)$$

where the value of k_e (efficiency factor) is given by:

$$k_e = \frac{\pi \left(\frac{1}{5}r^2 + \frac{2}{3}r + \frac{2}{15} \right) + (4 - \pi)(1 - r^2)r}{4 - (4 - \pi)r^2} \quad (16)$$

REFERENCES

- Mirmiran, A., Shahawy, M., Samaan, M., El Echary, H., Mastrapa, J.C., and Pico, O. (1998). Effect of column parameters on FRP-confined concrete, *Journal of Composites for Construction*, ASCE, 2(4), 175-185.
- Monti, G., Nisticò, N. (2008a). Analytical modelling of square and rectangular concrete sections confined by FRP: ultimate strength prediction, Fourth International Conference on FRP Composites in Civil Engineering (*CICE 2008*), 22-24 July 2008, Zurich, Switzerland.
- Monti, G., Nisticò, N. (2008b). Square and rectangular concrete columns confined by C-FRP: experimental and numerical investigation, *Mechanics of Composite Materials* 44(3).
- Otosen, N.S., (1977). A failure criterion for concrete, *J. Eng. Mech. Div.* 103, EM4, 527-533.
- Wang, L-M., and Wu, Y-F. (2007). Effects of corner radius on the performance of CFRP-confined square concrete columns: Test, *Engineering Structure*, 16(4), 1-13.

Stress-Strain Modeling of Rectangular Concrete Columns Confined by FRP Jacket

Yoyi Wei & Yufei Wu (yfwu00@cityu.edu.hk)

City University of Hong Kong, Hong Kong, China

ABSTRACT The stress-strain behavior of fiber reinforced polymer (FRP)-confined concrete under axial compression has been extensively studied. However, most of the existing models deal with circular and square columns. This paper presents a unified stress-strain model for rectangular, square and circular concrete columns confined by FRP jackets. The model is based on a large database that includes both data from the authors' own tests and those collected from the literature. A difficult task for the stress-strain modeling is the determination of the ultimate strain for which existing models present a larger scattering of results. Different models for the prediction of the ultimate stress and strain of FRP-confined concrete are reviewed, and more accurate expressions are proposed. The proposed stress-strain model is compared with other existing models, which shows a reasonable agreement with the experimental results and an improved performance.

1 INTRODUCTION

Numerous models have been proposed to quantify the behavior of FRP-confined concrete columns. Whereas the stress-strain behavior of FRP confined concrete for circular columns has been extensively studied, the investigations on FRP-confined rectangular columns are scarce, largely due to the many parameters associated with the problem.

In this paper, an experimental and analytical investigation is reported on evaluating the stress-strain behavior of FRP-confined columns, focusing on rectangular columns. Different models for the prediction of the ultimate stress and strain of FRP-confined concrete are reviewed, and more accurate expressions are proposed. Based on the results of this investigation, a new unified stress-strain model that is applicable to circular, square and rectangular columns is proposed.

2 THE PROPOSED MODEL

2.1 Mathematical model

Different mathematical forms have been proposed to describe the stress-strain behavior of FRP-confined concrete. The early stress-strain models based on models for steel-confined concrete do not feature the characteristic bilinear shape of the stress-strain curve. After that, bilinear and tri-linear stress-strain models were proposed to study the behavior of concrete columns confined by FRP. Two of the frequently used expressions in modeling FRP-confined concrete are Richard & Abbott's (1975) four-parameter curve and

Hognested's (1951) parabola. An advantage of the four-parameter curve is that a bilinear shape of stress-strain curve can be characterized using a single expression. The deficiency of Hognested's parabola is that it cannot connect with the second portion smoothly. As a result, Lam & Teng (2003) proposed a new parabola, while Youssef et al. (2007) used a polynomial curve, for the first portion. In the second portion, most of the existing models use a straight line, except the model by Harajli et al. (2006). Although the stress-strain curve exhibits a nonlinear behavior in the second portion, especially for square and rectangular columns with a low confinement ratio, it is difficult to accurately simulate the nonlinear behavior for a descending type of the second portion. Therefore using straight line in the second portion is currently a simple yet effective way for the stress-strain modeling.

The basic assumptions for the proposed model are: 1) the stress-strain curve consists of a parabolic first portion and a straight-line second portion, as shown in Figure 1; 2) the slope of the parabola at $\varepsilon_c=0$ is the same as the elastic modulus of unconfined concrete E_c ; 3) the parabolic first portion meets the linear second portion smoothly with the same slope. Therefore, the proposed model is given in the following general form:

$$\begin{cases} f_c = E_c \varepsilon_c + \frac{f_o - E_c \varepsilon_o}{\varepsilon_o^2} \varepsilon_c^2 \\ f_c = f_o + E_2 (\varepsilon_c - \varepsilon_o) \end{cases} \quad (1)$$

The requirement of an identical slope at the transition point A leads to the following equation

$$\varepsilon_o = \frac{(f_o + f_{cu} + E_c \varepsilon_{cu}) - \sqrt{(f_o + f_{cu} + E_c \varepsilon_{cu})^2 - 8f_o E_c \varepsilon_{cu}}}{2E_c}, \quad (2)$$

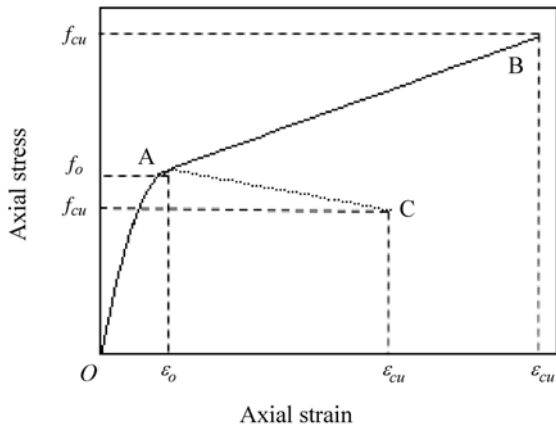


Figure 1 Stress-strain model

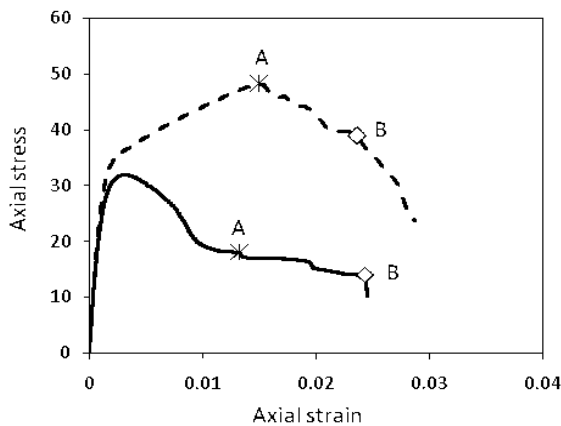


Figure 2 Definition of ultimate point

where E_2 is the slope of the second portion, given by

$$E_2 = \frac{f_{cu} - f_o}{\varepsilon_{cu} - \varepsilon_o}. \quad (3)$$

For the value of ε_{co} , the equation proposed by Popovics (1973) is used: $\varepsilon_{co} = 0.000937 \sqrt[4]{f_{co}}$.

To develop the proposed model, three parameters need to be determined: the ultimate stress f_{cu} , the ultimate strain ε_{cu} and the transitional stress f_o .

2.2 Database

A database is compiled to determine the three parameters, f_{cu} , ε_{cu} and f_o , which contains test results of 315 FRP-wrapped plain concrete columns, including 169 circular columns, 111 square columns and 35 rectangular columns. Among the 315 columns, 101 are from the authors' own tests and the rest are collected from the literature. A summary of the database is given in Table 1.

The criterion used to evaluate the performance of a model is defined as

$$\omega = \frac{\sum |Theo. - Expe. |}{\sum Expe.} \quad (4)$$

where *Theo* and *Expe* are the theoretical and experimental stress or strain, respectively.

Table 1 Outline of database

Feature	Circular section	Square section	Rectangular section	Total
CFRP	124	94	35	253
GFRP	30	7	0	37
AFRP	7	10	0	17
HMCFRP	8	0	0	8
Total	169	111	35	315

The definition of the ultimate point in the stress-strain curve is clear: the point at FRP rupture. However, the rupture of FRP does not occur at one point of the response curve sometimes. Instead, it could be a process, as shown in Figure 2. Noticeable rupturing of FRP initiates at point A of the curves and the final rupture (explosion) occurs at points B. In this work, the first point of significant rupturing (point A) is defined as the ultimate point. This definition is based on the judgment that the rupturing process after point A is unstable that varies significantly from specimen to specimen even all conditions of the test are identical, while the starting point of rupturing (or the end point of steady increase in confinement) is more stable and consistent.

2.3 Ultimate stress

The ultimate stress of FRP-confined concrete f_{cu} is the compressive strength of the confined concrete f_{cc} when the stress-strain curve is monotonically ascending. Many models have been proposed to predict the strength for circular and square columns. Wu & Wang (2009) presented a unified strength model that contains a shape factor as a function of the corner radius ratio $2r/b$. When $2r/b = 0$, it is for square columns with sharp corners; whereas when $2r/b = 1$, it is for circular columns. Therefore the model unifies the strength models for square (with arbitrary corner radius) and circular columns. This model is extended by Wu & Wei (2010) to rectangular columns by including the cross-sectional aspect ratio h/b as another parameter.

However, the ultimate strength f_{cc} is different from f_{cu} for stress-strain responses with a descending branch. Therefore, a new model is required for f_{cu} . Following the same method by Wu & Wei (2010) and based on the regression analysis using the database, the ultimate stress model is obtained as follow

$$\frac{f_{cu}}{f_{co}} = 0.48 + 3.8 \left(\frac{2r}{b} \right)^{0.4} \left(\frac{f_l}{f_{co}} \right)^{0.7} \left(\frac{h}{b} \right)^{-1.1} \quad (5)$$

The confining pressure f_l in Eq. (5) is calculated by

$$f_l = \frac{2f_{frp}t}{b} = \frac{2E_{frp}\epsilon_{frp}t}{b}, \tag{6}$$

where b is the width of column, and equal to the diameter for circular columns or the length of the shorter side for rectangular columns. $\epsilon_l = k \epsilon_{frp}$, where ϵ_{frp} is the ultimate strain of FRP and k is a material reduction factor and equal to 0.6, 0.85, 0.62 and 0.79 for CFRP, AFRP, GFRP and HMCFRP, respectively, in accordance with the values derived by Lam and Teng (2003) and Teng et al. (2009).

The prediction by Eq. (5) and the other four models given in Table 2 are compared using the database in Figure 3 and Table 3. It can be concluded that all the models exhibit a reasonably good performance in predicting the ultimate stress of FRP-confined concrete. The proposed model can accurately predict the ultimate stress with a well balanced scatter, while Lam & Teng’s model predict well for strain-hardening type of response.

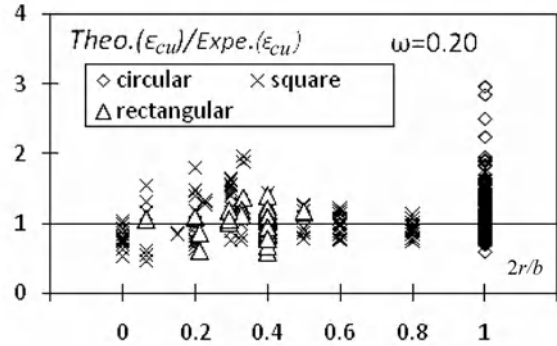
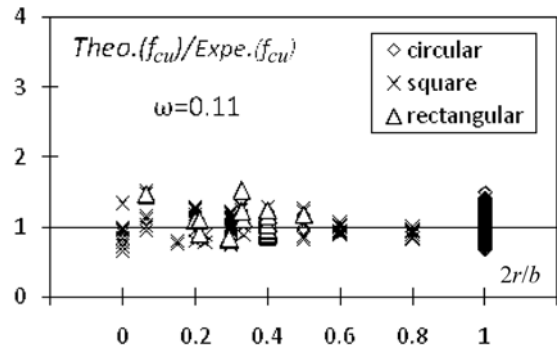
Table 2 Existing models

Model	Ultimate stress and strain
Lam and Teng	$\frac{f_{cu}}{f_{co}} = 1 + k_1 k_{s1} \frac{f_l}{f_{co}}$ $\frac{\epsilon_{cu}}{\epsilon_{co}} = 1.75 + k_2 k_{s2} \frac{f_l}{f_{co}} \left(\frac{\epsilon_{h,FRP}}{\epsilon_{co}} \right)^{0.45}$
Harajli et al.	$f_{cc} = f_{co} + k_1 f_l$ $\epsilon_{cu} = \epsilon_{co} \left[1 + k_2 \left(\frac{f_{cu}}{f_{co}} - 1 \right) \right]$
Wu et al.	$f_{cu} = k_3 f'_{cu}, \epsilon_{cu} = k_4 \epsilon'_{cu}$
Youssef et al.	$\frac{f_{cu}}{f_{co}} = \alpha + \beta \left(\frac{f_l}{f_{co}} \right)^\gamma$ $\epsilon_{cu} = \lambda + 0.26 \left(\frac{f_l}{f_{co}} \right) \left(\frac{f_{ju}}{E_j} \right)^{0.5}$

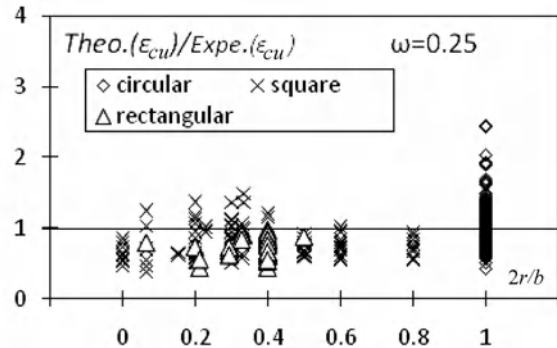
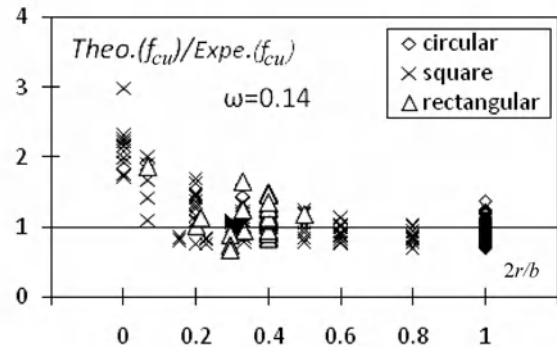
Note: f'_{cu} and ϵ'_{cu} are the ultimate stress and strain of FRP-confined equivalent concrete cylinder.

Table 3 Summary of comparisons

	Proposed model	Lam & Teng’s model	Harajli et al.’s model	Youssef et al.’s model	Wu et al.’s model
Ultimate stress	0.11	0.14	0.24	0.19	0.20
Ultimate strain	0.20	0.25	0.57	0.29	0.28



(a) The proposed model



(b) Lam & Teng’s model

Figure 3 Predictions of ultimate stress and strain

2.4 Ultimate strain

Ilki et al. (2008) pointed out that none of the existing model could predict the ultimate strain with reasonable accuracy. Based on a carefully analysis of the test results, it is found that the ultimate strain is largely affected by the following factors: the confinement ratio (f_l/f_{co}), the

stiffness ratio (E_{ft}/E_{30b}), the corner radius ratio ($2r/b$), the aspect ratio (h/b), and the concrete strength f_{co} , where E_{30} is the elastic modulus of grade C30 concrete. Through the regression analyses, the following equation for the ultimate strain is obtained, which is applicable simultaneously to rectangular, square and circular columns:

$$\frac{\varepsilon_{cu}}{\varepsilon_{co}} = 1.75 + 7.2 \left(\frac{f_l}{f_{co}} \right)^{1.1} \left(\frac{E_{ft}}{E_{30b}} \right)^{-0.34} \left(\frac{f_{30}}{f_{co}} \right)^{0.23} \left(0.43 \frac{2r}{b} + 0.57 \right) \left(\frac{h}{b} \right)^{-1.31} \quad (7)$$

The prediction of the ultimate strain by the proposed model and the other four models in Table 2 are compared in Figure 3 and Table 3. It can be seen from the comparisons that the proposed model performs better than the four existing models.

2.5 Transitional stress

By best fitting Eq. (1) to an experimental stress-strain curve, the transitional stress, f_o , can be determined for all the available test curves. The obtained results are subsequently used for the regression analysis from which the following equation is obtained:

$$f_o = 0.7 \left(\frac{2r}{b} \right)^{0.91} \left(\frac{h}{b} \right)^{0.55} f_l + 1.18 f_{co} - 7.48 \quad (8)$$

3 PERFORMANCE OF MODELS

Through extensive comparison with test curves, the performance of the proposed model is found generally better compared with the other four. Due to the page length limit, only two test results are compared in Figure 4. It can be seen in Figure 4 that all models apart from that by Harajli et al. perform well for circular columns, whereas Harajli et al.'s model give conservative prediction of the ultimate strain which causes a poorer performance of the stress-strain curve. For the rectangular column, the performance of the proposed model is also relatively better, while Wu et al.'s model over predicts the stress, and Youssef et al.'s model gives a relatively conservative prediction.

4 CONCLUSION

A new stress-strain model is proposed for rectangular, square and circular concrete columns confined by FRP jackets. One of the advantages of this model is that it gives a unified expression for circular, square and rectangular columns. The proposed model is validated using both the experimental results obtained from the author's own tests as well as those collected from the literature. The comparisons from this study show that the proposed model can satisfactorily predict the stress-strain relationship for columns with all cross-sectional shapes, with particular improvement in curves with a descending branch.

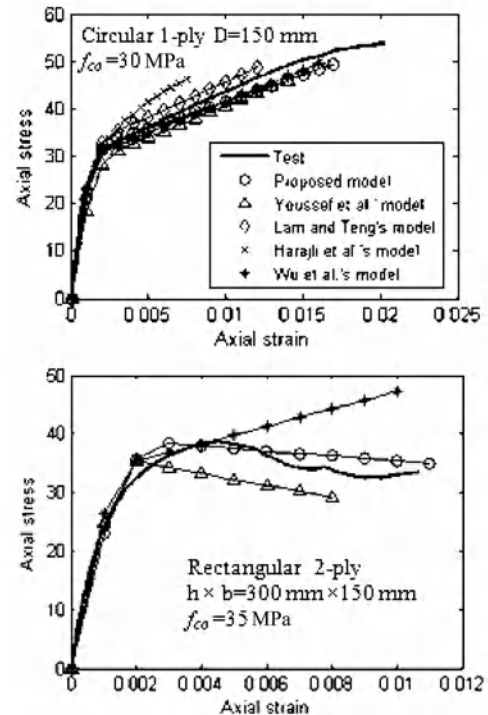


Figure 4 Performance of models

REFERENCES

- Harajli, M.H. Hantouche, E & Soudki, K. 2006. Stress-strain model for fiber-reinforced polymer jacketed concrete columns. *ACI Struct. J.* 103(5):672-682.
- Hognest, E. 1951. A study of combined bending and axial load in reinforced concrete members. *Bulletin Series No. 399*, Urbana: Engineering Experiment Station, Univ. of Illinois.
- Ilki, A. Peker, O. Karamuk, E. Demir, C. & Kumbasar, N. 2008. FRP retrofit of low and medium strength circular and rectangular reinforced concrete columns. *J. Mater. Civ. Eng. ASCE* 20(2):169-188.
- Lam, L. & Teng, J.G. 2003. Design-oriented stress-strain model for FRP-confined concrete in rectangular columns. *J. Reinf. Plast. Compos.* 22(13): 1149-1186.
- Popovics, S. 1973. Numerical approach to the complete stress-strain relation for concrete. *Cem. Concr. Res.* 3(5):583-99.
- Richard, R.M. & Abbott, B.J. 1975. Versatile elastic-plastic stress-strain formula. *J. Eng. Mech. Div.* 101(4):511-515.
- Teng, J.G. Jiang, T. Lam, L. & Luo, Y.Z. 2009. Refinement of a design-oriented stress-strain model for FRP-confined concrete. *J. Compos. Constr. ASCE* 13(4):268-278.
- Wu, G. Wu, Z.S. & Lu, Z.T. 2007. Design-oriented stress-strain model for concrete prisms confined with FRP composites. *Constr. Build. Mater.* 21:1107-1121.
- Wu, Y.F. & Wang, L.M. 2009. Unified strength model for square and circular concrete columns confined by external jacket. *J. Struct. Eng. ASCE* 135(3):253-261.
- Wu, Y.F. & Wei, Y.Y. 2010. Effect of cross-sectional aspect ratio on the strength of CFRP-confined rectangular concrete columns. *Eng. Struct.* 32: 32-45
- Youssef, M.N. Feng, Q. & Mosallam, A.S. 2007. Stress-strain model for concrete confined by FRP composites. *Composites Part B* 38:614-628.

Axial Behavior of FRP Jacketed Extended Rectangular Members Constructed with Low Strength Concrete

Dogan Akgun

Akgun Engineering, Istanbul, Turkey

Cem Demir & Alper Ilki (ailki@itu.edu.tr)

Istanbul Technical University, Istanbul, Turkey

ABSTRACT While extensive experimental data is present on the axial behavior of FRP jacketed concrete members with circular cross-section, only few data is available for the members with square and rectangular cross-sections. Furthermore, the data is particularly scarce for extended rectangular cross-sections, where the cross-sectional aspect ratio is over two. In addition, most of the existing codes and/or guidelines limit the cross-sectional aspect ratio with 1.5-2.0 due to significantly reduced efficiency of FRP confinement beyond these cross-sectional aspect ratios. In this study, specimens with the cross-sectional aspect ratio of 3.0 are tested under axial compression by using a displacement-controlled 5000 kN-capacity Instron testing system. While keeping the thickness of external FRP jacket same in all specimens, the arrangement of FRP sheets, which are used in the form of cross-ties are changed. The concrete quality of the specimens is intentionally poor for representing existing weak structural members. Experimental results showed that the efficiency of FRP jacketing was quite high for the extended rectangular cross-sections in case of low strength concrete. In addition, the efficiency of FRP jacketing could further be increased by the use of additional FRP sheets in the form of cross-ties. In the analytical part, the increased efficiency of the FRP jacketing due to presence of FRP cross-ties is explained using the concept of efficiently confined cross-section developed before for concrete confined with steel rectilinear stirrups and cross-ties.

1 INTRODUCTION

1.1 Previous studies

While there are many studies on the behavior of fiber reinforced polymer (FRP) confined circular specimens, there are very few studies focusing on the axial behavior FRP-confined concrete members with extended rectangular cross-section (Tan 2002, Tanwongsvat et al. 2003, Ilki et al. 2004, Prota et al. 2006, Ilki et al. 2008, Tao et al. 2008, Wu & Wei 2010). The research on the specimens with relatively low strength concrete, particularly carried out on relatively large scale specimens, is even more scarce.

1.2 Significance of the study

In this preliminary experimental study, relatively large size extended rectangular specimens, which were intentionally constructed with low strength concrete, were externally jacketed with three plies of carbon fiber reinforced polymer (CFRP) sheets. The reason of usage of low strength concrete is to demonstrate the poorly constructed existing deficient structures, particularly in developing countries. The cross-sectional aspect ratio was 3 for all specimens. For increasing the effectiveness of external CFRP jacketing for extended rectangular

cross-sections, different amounts of cross-ties made from CFRP sheets were used. The only test variable in this study is the amount and configuration of these CFRP cross-ties.

2 EXPERIMENTAL STUDY

2.1 Testing program

In this preliminary study, test results of five specimens are outlined. The dimensions of all specimens were 200 mm×600 mm×625 mm (width×depth×height) and all specimens were confined with three plies of CFRP sheets. The only test variable was the amount of CFRP cross-ties, which were used for increasing the efficiently confined cross-sectional area. Otherwise, due to very low flexural strength of CFRP sheets, like steel stirrups, the efficiency of external CFRP sheet jacketing is thought to be low in case of extended rectangular cross-sections. The configurations of CFRP cross-ties are shown in Figure 1. All specimens were constructed using low strength concrete with approximately 12.5 MPa compressive strength at the day of tests. The concrete mix-proportion and experimental stress-strain relationships of unconfined concrete are presented in

Table 1 and Figure 2, respectively. The characteristics of CFRP sheets are taken from the manufacturer. According to the manufacturer, the thickness of one ply of sheet is 0.117 mm, tensile strength and elasticity modulus of fibers are 3800 and 240000 MPa, respectively, and the ultimate elongation is 1.55 %.

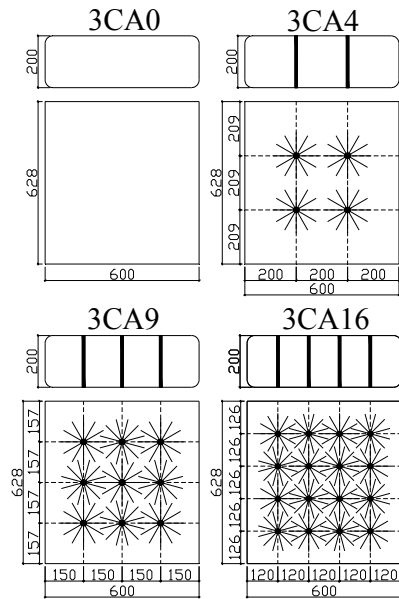


Figure 1 Configurations of CFRP cross-ties (dimensions are in mm)

Table 1 Concrete mix-proportion (kg/m³)

Cement	Water	Agg. (No.1)	Sand	Powdered stone
197	231	852	563	272

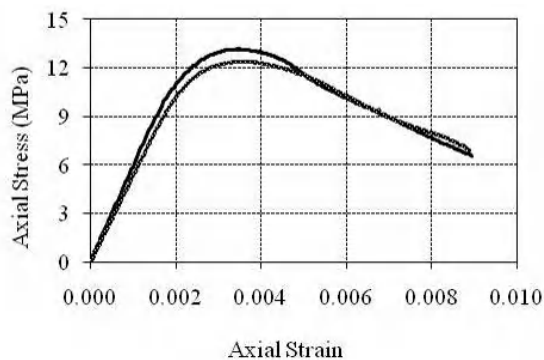


Figure 2 Stress-strain relationships for unconfined standard cylinders

2.2 Construction of specimens

The specimens were constructed using specially designed low strength ready-mixed concrete. After specimens were taken out of the wooden formworks, holes were drilled through the short side of the specimens considering the cross-tie configurations presented in Figure 1. After temporarily capping these holes and application of epoxy based primer on the surface, three plies of continuous CFRP sheets were wrapped and

bonded on the specimens using an epoxy based adhesive. Finally, the cross-ties prepared by using CFRP sheets were impregnated with epoxy adhesive and placed in the holes with two parts of sheets projecting from two sides of the holes. The widths of CFRP sheets used for cross-ties were 200 mm, while their lengths were 500 mm, leaving 150 mm lengths projecting from two sides. These 150 mm projecting parts of the CFRP cross-ties were bended and bonded on the surface of the external CFRP jacket with epoxy adhesive. It should be noted that the corners of the specimens were rounded to the radius of 30 mm before application of CFRP sheets. The construction phases are shown in Figure 3.

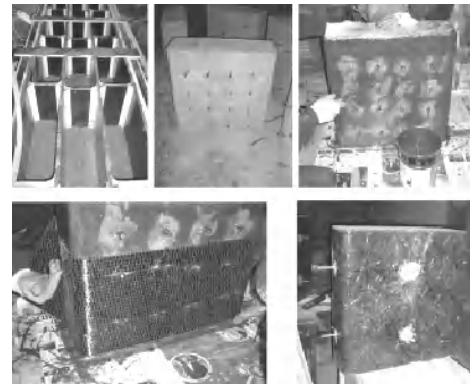


Figure 3 Construction stages of specimens

2.3 Testing setup

All tests were carried out using a 5000 kN capacity Instron testing machine in a displacement controlled manner. Besides the internal load cell and displacement transducer of the Instron testing device, vertical and horizontal deformations were measured by external displacement transducers placed in different gage lengths and strain gages with gage lengths of 30 mm (for horizontal and vertical strain measurements on long sides of specimens with cross-ties) and 60 mm (for horizontal and vertical strain measurements on short sides of specimens with cross-ties and for all strain measurements of specimens without cross-ties). All data was collected and stored by a TML TDS-303 data logger. An appearance of the test setup is shown in Figure 4.

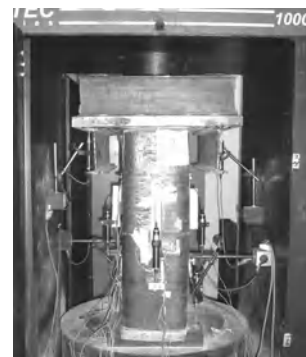


Figure 4 An appearance during tests

While the vertical strain gages and displacement transducers placed at the mid-height of specimen with approximately 300 mm gage length measured almost identical average vertical deformation values before the formation of severe damage, both types of sensors could not work reliably after damage level was increased.

In addition, it was seen that after the formation of severe damage, the measurements of internal displacement transducer of Instron testing device and the average vertical displacement measured by external displacement transducers at full height of specimens were almost same. Therefore, the test results are presented through a combination of measuring devices. Up to 0.0015-0.0020 axial strain level, the strains are taken from the measurements of strain gages and after this level, the axial strains are calculated by considering the global shortening of specimens in full height.

2.4 Test results

Basic test results are presented in the form of axial stress-axial strain relationships of specimens (Figure 5). It should be noted that axial strains given in Figure 5 are obtained as explained above.

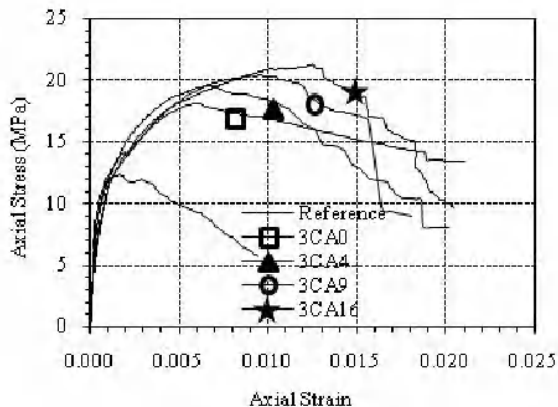


Figure 5 Axial stress-axial strain relationships

The first significant finding was the unexpectedly enhanced behavior of specimen 3CA0, which was externally confined with 3 plies of CFRP sheets and did not have any cross-ties for increasing the efficiency of the jacketing. Both strength and deformability were remarkably better with respect to unconfined reference specimen. The reason of this quite efficient enhancement can be attributed to the damage of the specimen, which demonstrated that a large part of the cross-section behaved as efficiently confined. The damage was not accumulated at one section through elevation, but distributed, thus allowing a larger cross-section to resist axial stresses all through the height of the specimen. In addition, the apparent effectively confined area was much larger than the area defined by second order parabolas with the initial tangent slope equal to 45 degrees. The apparent efficiently confined cross-sectional area was

much larger than defined by ACI440.2R-08 or fib bulletin 14.

As seen in Figure 5, introduction of CFRP cross-ties further enhanced the behavior both in terms of strength and deformability. It is apparent in Figure 5 that an increase in the number of CFRP cross-ties ended up with an increase in the performance of the specimen. It should be noted that the damage was not accumulated at a single section in elevation for the specimens with cross-ties, like specimen 3CA0 without cross-ties. Consequently, contrary to the expectations before the test, the damage was not concentrated around the zones between the cross-ties. As mentioned before, this may be attributed to the imperfect application of cross-ties, as well as the non-uniform quality of low strength concrete. However, these defects seem to permit a more distributed damage than one would assume theoretically, thus leading a more preferable behavior.

2.5 Damage formation

Before carrying out the tests, it was expected that the maximum damage would occur between the cross-ties in elevation and in plan. However, the damage was quite sophisticated, which prevented a clear description. The imperfect performance of CFRP cross-ties partly debonded from the CFRP jacket surface may have caused this irregular damage pattern. Damages of specimens 3CA4 and 3CA16 are shown in Figure 6. It should be noted that the figures on the right side are photographs taken after removal of the CFRP sheets after tests are completed. It is clear from Figure 6 that the angles of fracture surfaces are significantly small leading a larger efficiently confined area. This unexpected type of damage may be related with more ductile characteristics of low strength concrete.

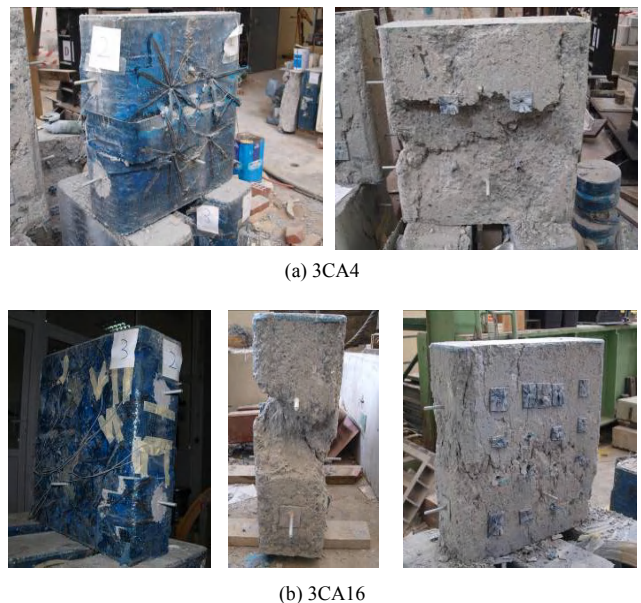


Figure 6 Damaged specimens

3 A SIMPLE PREDICTION METHOD OF STRENGTH

While it is clear that the fracture surface is not regular neither in plan nor in elevation and the visible angles of fracture surfaces are significantly less than 45 degrees, an attempt is made for predicting the strengths of specimens using the common assumption of effectively confined cross-section as defined by Sheikh and Uzumeri (1982) and Mander et al. (1988). It should once more be noted that while the main assumptions made by these researchers are not in good agreement with the experimental observations, for utilizing the simplicity of their approach, the efficiently confined cross-sectional areas are defined as explained in these references with minor modifications (Figure 7).

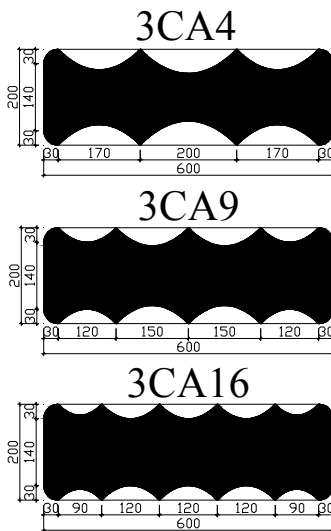


Figure 7 Assumption about effectively confined cross-section

The efficiently confined cross-section was assumed to exist exactly at the level of CFRP cross-ties rather than between the cross-ties in elevation. In addition, concrete adjacent to short sides was assumed to be effectively confined totally. These exceptional assumptions were made considering the experimental observations. For determining the experimental efficiently confined cross-section, the predicted strength was assumed to be equal to the experimentally obtained strength. The efficiently confined cross-sectional area was then calculated by using Ilki et al. (2004) model. The predicted efficiently confined cross-sectional areas determined by the approaches proposed by Sheikh and Uzumeri (1982) and Mander et al. (1988), and the efficiently confined areas back-calculated considering the experimental results are presented in Table 2. As seen in this table, the predictions and experimental findings are quite similar.

Table 2 Comparison of predicted and experimentally determined effectively confined cross-sections (mm²)

	3CA4	3CA9	3CA16
Experimental	83373	91561	99874
Predicted	86627	94627	99427

4 CONCLUSIONS

This preliminary experimental study demonstrated the efficiency of external CFRP jacketing in case of low strength concrete even when the cross-sectional aspect ratio was three. The efficiency of external CFRP confinement was further improved by the introduction of CFRP cross-ties.

5 ACKNOWLEDGMENTS

The valuable comments of Prof.Dr. N. Kumbasar and Prof.Dr. M.A. Tasdemir, and in-kind supports of BASF Turkey, Art-Yol Engineering and ISTON Ready Mixed Concrete Companies are gratefully acknowledged.

REFERENCES

- Ilki, A., Kumbasar, N. & Koc, V. 2004. Low strength concrete members externally confined with FRP sheets. *Structural Engineering and Mechanics*, 18(2): 167-194.
- Ilki, A., Peker, O., Karamuk, E., Demir, C. & Kumbasar, N. 2008. FRP retrofit of low and medium strength circular and rectangular reinforced concrete columns. *ASCE Jour. Mat. Civ. Eng.*, 20(2): 169-188.
- Mander, J.B, Priestley, M.J.N. & Park, R. 1988. Theoretical stress-strain model for confined concrete. *ASCE Jour. Struct. Div.*, 114(8): 1804-1826.
- Prota, A., Manfredi, G. & Cosenza, E. 2006. Ultimate behavior of axially loaded RC-wall-like columns confined with GFRP. *Composites Part B*, 37(7-8): 670-678.
- Sheikh, S.A. & Uzumeri, S.M. 1982. Analytical model for concrete confinement in tied columns. *ASCE Jour. Struct. Div.*, 108(ST12): 2703-2722.
- Tan, K.H. 2002. Strength enhancement of rectangular reinforced concrete columns using fiber-reinforced polymer. *ASCE Jour. Compos. Const.*, 6(3): 175-183.
- Tanwongsva, S., Maalej, M. & Paramasivam, P. 2003. Strengthening of RC wall-like columns with FRP under sustained loading. *Materials and Structures*, 36(259): 282-290.
- Tao, Z., Yu, Q. & Zhong, Y.Z. 2008. Compressive behavior of CFRP-confined rectangular concrete columns. *Mag. Conc. Res.*, 60(10): 735-745.
- Wu, Y.F. & Wei, Y.Y. 2010. Effect of cross-sectional aspect ratio on the strength of CFRP-confined rectangular concrete columns. *Engineering Structures*, 32(1): 32-45.

Nonlinear Micromechanics-Based Finite Element Analysis of FRP-Rapped Concrete Columns Subjected to Axial Load

Abdel Baky (Hussien.El.Baky@USherbrooke.ca)

Department of Civil Engineering, Helwan University, Egypt

Demers & Yahiaoui & Neale (Kenneth.Neale@USherbrooke.ca)

Department of Civil Engineering, University of Sherbrooke, Quebec, Canada

ABSTRACT In this research work, new modifications for the microplane constitutive law are first presented to precisely simulate concrete behaviour under various levels of lateral confinement pressure. A key feature of the suggested formula is to make the microplane theory valid to represent concrete behaviour under both low and high lateral confining pressures. An analysis is then carried out using two different numerical procedures. The first procedure is the use of a three-dimensional finite element analysis with the modified microplane formulations as a user-supplied subroutine into the FE commercial software ADINA to model the concrete behaviour under various stress and strain histories. Here, the sub-objective is to validate the formulated microplane approach that is proposed in the first phase of the research program. In the second analysis; the confinement behaviour is simulated using an in-house code. The code uses the proposed formulations for the microplane theory to represent the concrete characteristics to predict the stress–strain relationships of FRP-wrapped concrete columns up to failure. An accurate equation correlating the axial stiffness of the FRP laminates and the lateral strain of the concrete columns to the confining pressure is incorporated in the in-house code. The two analyses give almost the same predictions, with minor discrepancies due to some numerical aspects. An experimental program consisting of testing thirty eight concrete cylinders under various lateral confinement pressures is carried out to assess the accuracy of the numerical predictions. In the experimental program, the lateral pressure is designed to give almost the same lateral confinement behaviour as that resulting from applying FRP sheets. The numerical predictions are finally compared to experimental results for FRP-wrapped and un-wrapped concrete columns under various levels of lateral pressure. This paper gives an overview for the whole research program with a special emphasis on the theoretical part.

1 INTRODUCTION

A survey of the literature reveals that nonlinear finite element analyses of FRP-wrapped concrete columns are generally restricted to simulate the axial stress–axial strain and axial stress–lateral strain of FRP-wrapped columns. These analyses adopt two concrete constitutive laws; namely, nonlinear elastic, and elastoplastic formulations (Deniaud and Neale 2006; Malver et al 2004; Mirmiran et al. 2000; Parent and Labossière 2000; Spoelstra and Monti 1999; Toutanji 1999). Both of these approaches have been used, whether simulating the hardening behaviour of confined concrete or the softening branch of unconfined columns. Recently, the microplane model has come to be a powerful constitutive model that simulates three-dimensional concrete behaviours. This is attributed to the fact that the microplane theory is capable of capturing both the hardening and softening behaviour of the concrete (Caner, F.C. and Bažant 2000, Neale et al. 2008).

However it has been concluded, through several numerical simulations, that the microplane theory has inconsistent predictions for the concrete behaviour when applying low confinement lateral pressures, as is the case of FRP-wrapped concrete cylinders (Ghazi et al., 2002). Ghazi et al. (2002) observed that the microstructure coefficients of the M4 model do not suitably predict the behaviour of concrete with different uniaxial compressive strengths and different confinement levels. To provide better simulations for an axially loaded FRP-wrapped concrete column using the microplane theory, Ghazi et al. (2002) proposed a new formula for the adjustable micromechanics variables (k_1 to k_4) and for the fixed micromechanics constant (c_{10}) as a function of the level of the confinement lateral pressure (Ghazi et al., 2002). They introduced the factors affecting the post-peak steepness and the stress and strain at the peak of the stress–strain curve of confined concrete as functions of the concrete strength and confinement levels to give a better fit between analytical results and

experimental data. These adjustments in the coefficients of the M4 model were very successful to show excellent agreement between numerical predictions and experimental data of axially loaded FRP-wrapped columns. However, their new proposed coefficients restricted the microplane theory to represent the hardening behaviour of axially loaded concrete cylinders. With that the microplane with the new Ghazi et al. formula has a new challenge to capture the softening behaviour of unconfined concrete cylinders. Furthermore, these adjustments cannot be looked as a unified constitutive law that can describe the characteristics of FRP-wrapped concrete columns under a wide range of complex stress and strain histories. For example, in the finite element analysis of eccentrically loaded FRP-wrapped concrete cylinders, the lateral confinement pressure is not constant for all nodes in the finite element mesh, depending on their relative horizontal and vertical locations from the neutral axis. In this paper and the research work at the University of Sherbrooke, we aim to develop consistent modifications of the M4 model to successfully simulate the concrete behaviour under low and high lateral confinement pressures and maintain the consistency with the existing microplane model for un-confined concrete.

In this research work, new modifications are first proposed for the microplane constitutive law to precisely simulate the concrete behaviour under various levels of lateral confinement pressure. Then the new formulations are implemented to represent the stress–strain behaviour of FRP-wrapped concrete columns up to failure using nonlinear finite element analysis. The existing microplane model M4 is not suitable for concrete behaviour under low confinement pressures. The analysis results show that an additional nonlinear function should be introduced in the existing deviatoric boundaries of the M4 model. In relation to the dilation behaviour of the microplane model, the nonlinearity in the shear boundary of the M4 theory affects the accuracy of predicting the lateral strain of the concrete. The proposed new formulations for the microplane model successfully describe the hardening behaviour of the concrete subjected to low confinement pressure, and it is consistent with an existing microplane model to capture softening responses.

The analyses in this research work were carried out using two different numerical procedures. The first is the use of a three-dimensional finite element analysis with the modified microplane formulations as a user-supplied subroutine in the finite element package ADINA. In the second analysis, the confinement behaviour is simulated using an in-house code. The code uses the proposed modified formulations for the microplane model to represent the concrete characteristics

and the arc-length iterative technique for the numerical implementations to predict the stress–strain relationships of columns up to failure. An accurate equation correlating the axial stiffness of the FRP laminates and the lateral strain of the concrete columns to the confining pressure was incorporated in the in-house code.

2 EXPERIMENTAL PROGRAM

The experimental program consisted of testing three different specimen groups. The objective of the first group is to calculate the parameters of the microplane concrete theory. For that, uniaxial compressive tests ($\sigma_2 = \sigma_3 = 0$) and hydrostatic tests ($\varepsilon_1 = \varepsilon_2 = \varepsilon_3$) were carried out. The second set of specimens aimed to validate the accuracy of the numerical results. In this set, FRP-wrapped and steel-encasted concrete cylinders were tested. The last experimental group was tested under applied lateral confinement pressures. The lateral pressures were applied manually and it was designed to have approximately the same pressure resulting from the confining FRP sheets used in the second part of the experimental program.

The experimental program was carried out on concrete cylinders of circular cross-section of 152 mm diameter and 300 mm height. Two different concrete batches were used in the experimental program with an average actual cylinder compressive strengths after 28-days of 35 MPa and 45 MPa. The experimental program was carried out on thirty eight specimens divided into two main groups according to their uniaxial compressive strength. Each group included testing three uniaxially loaded concrete cylinders, six specimens subjected to three different lateral confinement pressures, two specimens under hydrostatic compressive stresses, three steel-encasted concrete cylinders and two FRP-wrapped concrete cylinders as shown in Table 1.

Table 1 Configuration and characteristics of the tested specimens

Confinement pressure level	Hydrostatic test	Steel-confinement cylinders	FRP-wrapped cylinders	Unconfined cylinders
$0.1 f'_c$		$t = 1/4$ in		
$0.2 f'_c$	$\varepsilon_1 = \varepsilon_2 = \varepsilon_3$	$t = 1/2$ in	$E_{FRP} = 73$ GPa $t = 0.154$ mm	Three tested specimens
$0.3 f'_c$		$t = 3/4$ in		

In the third specimen group of the experimental program, the lateral confinement pressures (first column in the Table 1) were applied manually using a hydraulic pump. First the axial displacement was applied on the specimens until reaching an applied load level corresponding to 80% of the uniaxial concrete compressive strength then the applied lateral pressure was activated. The detailed experimental results will be published in future manuscripts.

3 THEORETICAL STUDY

The M4 Bažant formulations for the microplane model accurately represent the mechanical characteristics of concrete under high confining states of stress (Caner and Bažant 2000). However, as mentioned in the literature, various problems occurred in the simulations of concrete subjected to low confining lateral pressures. The numerical inconsistency of the Bažant formulations occurs under low lateral confining states of stress, where the M4 model could not capture the hardening branch of the uniaxial stress–strain profiles.

We found that this problem arises from the function of the deviatoric boundaries (F_D^+ , F_D^-) and the shear boundary F^T . The deviatoric boundaries are used to characterize the behaviour of lateral cracks normal to the microplane, while the shear boundary physically represents the friction between these cracks. The key problem is the degree of the nonlinearity of these boundaries function and their dependency on the low lateral confining pressure and the associated volumetric stresses. To overcome this problem and to introduce unified formulations that are able to simulate concrete behaviour under various states of stress, we multiplied these boundaries by a nonlinear function $f(\sigma_v)$. This function was expressed as a function of the volumetric stress σ_v and the material adjustable parameters (k_1 to k_4). These modifications are:

3.1 Deviatoric boundaries (spreading, splitting):

$$\sigma_D \geq 0 : \sigma_D^b = F_D^+(\varepsilon_D) = \frac{Ek_1c_5}{1 + \left[\frac{\langle \varepsilon_D - c_5c_6k_1 \rangle}{k_1c_{18}c_7} (1 + g(\sigma_v)) \right]^2} f(\sigma_v) \quad (1)$$

where

$$f(\sigma_v) = 1 + \frac{\langle -\sigma_v \rangle \langle 3.755k_1E + \sigma_v \rangle}{|\sigma_v| 3.755k_1E} \quad (2)$$

$$e^{0.1 \langle 3.755k_1E + \sigma_v \rangle} \frac{\langle 2.75k_1E - \sigma_v \rangle}{2.75k_1E}$$

and

$$g(\sigma_v) = 1 + \frac{\langle -2.75k_1E - \sigma_v \rangle \langle -\sigma_v \rangle}{|\sigma_v|} \quad (3)$$

$$\text{For } \sigma_D \leq 0 : \sigma_D^b = F_D^-(\varepsilon_D) = \frac{Ek_1c_8}{1 + \left[\frac{\langle -\varepsilon_D - c_8c_9k_1 \rangle}{k_1c_7} (1 + g(\sigma_v)) \right]^2} \quad (4)$$

3.2 Frictional yield surface (shear boundary):

$$\sigma_T^b = F_T(-\sigma_N) = \frac{E_Tk_1k_2c_{10} (1 + f_1(\sigma_v)) \langle -\sigma_N + \sigma_N^0 \rangle}{E_Tk_1k_2 + c_{10} (1 + f_1(\sigma_v)) \langle -\sigma_N + \sigma_N^0 \rangle}, \quad (5)$$

$$\sigma_N^0 = \frac{E_Tk_1c_{11}}{1 + c_{12} \langle \varepsilon_v \rangle}$$

where:

$$f_1(\sigma_v) = 0.37 / (3.755k_1E) \langle 3.755k_1E + \sigma_v \rangle \frac{\langle -\sigma_v \rangle}{|\sigma_v|} \quad (6)$$

3.3 Numerical implementations using the new formulation

Four-node tetrahedral solid elements with three translational degrees of freedom per node were used to represent the concrete, FRP laminate and adhesive layers in the finite element simulations. Due to the geometrical and loading symmetries, only one eighth of the FRP-wrapped column was modelled. Symmetrical boundary conditions were placed along the planes of symmetry. A displacement-controlled numerical procedure was used in the finite element analysis to capture the softening branch of the load–displacement curve and the post-debonding behaviour. The finite element mesh of one eighth of a concrete cylinder is shown in Figure 1. All details concerning the in-house code and the related formulations will be presented in future publications.

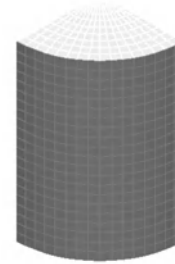


Figure 1 Finite element mesh

The comparison between experimental results and numerical predictions is depicted in Figures 2 and 3 for the application of one and six CFRP sheets, respectively. The experimental results were taken from the research work of Lahlou et al. (1992). From Figures 2 and 3, it was concluded that the microplane approach with the new modifications accurately simulate the stress–strain relationships of concrete under both low (one CFRP sheet) and high (six CFRP sheets) lateral confinement

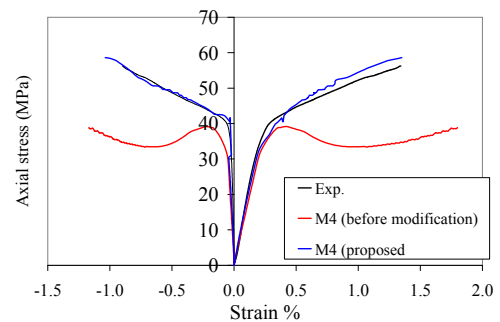


Figure 2 Comparisons between experimental results and numerical predictions using one sheet of CFRP

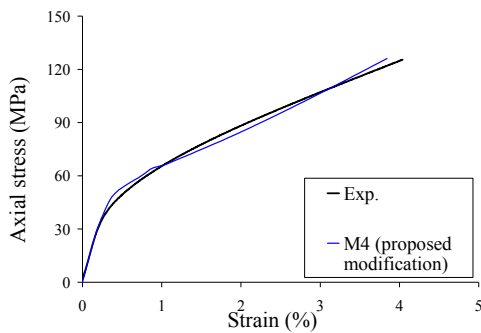


Figure 3 Comparisons between experimental results and numerical predictions using six sheets of CFRP

pressures. The M4 model of Bazant without including the proposed modification has an obvious difficulty to simulate the hardening behaviour of CFRP-wrapped concrete cylinders with one sheet (Figure 2).

4 CONCLUSION

In part of this study, an experimental program has been carried out to investigate the behaviour of concrete cylinders subjected to low confining lateral pressures. The lateral pressures were designed to give the same lateral and axial responses resulting from using FRP wraps. In another part of the paper, nonlinear micromechanics-based finite element analysis have been developed using the microplane concrete theory to simulate the behaviour of FRP-wrapped concrete columns. The analysis was carried out based on our proposed modifications of the original M4 model. Nonlinear functions were multiplied to the deviatoric and shear boundaries functions to overcome the numerical problems encountered when using the old formulations.

In the application of FRP-wrapped columns, the finite element analysis with the microplane concrete theory after considering the proposed modifications was shown to accurately represent the stress–strain relationships of the concrete under both low and high lateral confinement pressures. The key advantage of the

proposed formulations is the ability to adequately represent the concrete behaviour under low lateral confinement pressure and maintaining the consistency with the existing microplane model for un-confined concrete.

REFERENCES

- Caner F. & Bažant Z. 2000. Microplane model M4 for concrete. II: Algorithm and calibration. *Journal of Engineering Mechanics, ASCE*, 126(9), 954-961.
- Deniaud C. & Neale K.W. 2006. An assessment of constitutive models for concrete columns confined with fibre composite sheets. *Composite Structures*, 73(3), 318-330.
- Ghazi M. & Attard M. & Foster S. 2002. Modelling triaxial compression using the microplane formulation for low confinement. *Computers and Structures*, 919-934.
- Lahlou K. & Aitcin P. & Chaallal C. 1992. Behaviour of high strength concrete under confined stresses. *Cement and Concrete Composites*, 14, 185-193.
- Malver J. & Morrill K. & Crawford J. 2004. Numerical modelling of concrete confined by fiber-reinforced composites. *Journal of Composites for Construction, ASCE*, 8(4), 315-322.
- Mirmiran A. & Zagers K. & Yuan W. 2000. Nonlinear finite element modelling of concrete confined by composites, *Finite Element Analysis and Design*, 35(1), 79-96.
- Neale K.W. & Abdel Baky H. & Yahiaoui A. & Ebead U. 2008. Micromechanical modelling of FRP-strengthened concrete structures. *Sixth International Conference on Analytical Models and New Concepts in Concrete and Masonry Structures (AMCM)*, Kotynia, R. & Gawin, D. (Eds.) Lodz, Poland, 109-124.
- Parent S. & Labossière P. 2000. Finite element analysis of reinforced concrete columns confined with composite materials. *Canadian Journal of Civil Engineering*, 27(3), 400-411.
- Spoelstra M. & Monti G. 1999. FRP-confined concrete model. *Journal of Composites for Construction, ASCE*, 3(3), 143-150.
- Toutanji H. 1999. Stress–strain characteristics of concrete columns externally confined with advanced fibre composite sheets. *ACI Materials Journal*, 96(3), 397-404.

Compressive Strength of Concrete Cylinders Confined with CFRP Wraps

A. R. Khan (asadkhan@neduet.edu.pk) & N. S. Zafar

Department of Civil Engineering, NED University of Engineering and Technology, Karachi, Pakistan

ABSTRACT It is well established that the confinement of concrete with fiber reinforced polymers (FRP) composites can lead to a significant increase in both the compressive strength and ultimate strain of concrete. Most of the studies focused on normal-strength concretes with strengths in the range of 35 to 60 MPa, and research on FRP-confined low-strength concrete has been very limited. This paper presents the results of an experimental study on the compressive strengths of FRP-confined concrete cylinders with unconfined concrete strength in the range of 21 MPa. Different confinement schemes were used to determine the effect of schemes on the compressive strength of concrete. All the cylinders were tested in uniaxial compression to determine the load carrying capacities of the confined and unconfined cylinders. Compressive strength of FRP-confined concrete was enhanced in all confinement schemes indicating that confinement of concrete using CFRP strips is an efficient method to improve strength of concrete.

1 INTRODUCTION

Deterioration in Reinforced concrete (RC) columns has been a major problem for the aging infrastructure hence needs special methods for repair and retrofit. RC columns are strengthened by several methods like concrete jacketing, steel jacketing, and fiber-wrapping. Both Concrete and Steel jacketing are labor intensive. But FRP (fiber reinforced polymer) is one of less labor intensive and offers high strength, low-weight, and corrosion-resistant jacket with easy and rapid installation and minimal change in the column geometry. This composite material has become commercially active material for repair and strengthening of deteriorated concrete structure. FRP is characterized by high strength fibers embedded in polymer resin. FRP offers such advantages as high strength and stiffness, low density, chemical stability, high durability, and ease of installation. The most common types of FRPs used are made with carbon, aramid or glass fibers. Researches have been performed to find various ways to apply FRP for the retrofit of RC members either by externally bonding FRP sheets to concrete members or by constructing new concrete structural members by filling concrete into FRP tubes (Fam et al. 2003, Youssef et al. 2007, Shahawy et al. 2000, Park 2008, Camille et al. 2009).

RC structures in the coastal areas of Pakistan are vulnerable to deterioration well before their expected life and this issue needs to be addressed properly. Need of strengthening and retrofitting of RC structures exposed to harsh marine and coastal environments using some viable alternatives was realized at the Department

of Civil Engineering, NED University of Engineering and Technology, and research in this direction was initiated. FRP materials were considered to be a viable alternative but their potential is not yet explored in Pakistan. This study presents the gain in compressive strength of concrete cylinders with unconfined concrete strength in the range of 21 MPa when confined with externally bonded Carbon Fibre Reinforced Polymer (CFRP) wraps. This range of compressive strength was selected as this is representative of average compressive strength of the concrete used in local construction. Confinement was provided using different wrapping schemes. Overall thirty cylinders (twenty seven plain concrete (PC) cylinders and three RC cylinders) were tested. Compressive strength of FRP-confined concrete was enhanced in all confinement schemes used during the study and use of CFRP wraps to confine concrete was found to be an efficient method to improve strength of concrete.

2 EXPERIMENTAL STUDY

A total of 30 cylinders 150 mm in diameter and 300 mm in height were cast out of which 27 were of plain concrete and 3 were of reinforced concrete. Three unconfined plain and reinforced concrete cylinders each were used as control specimens. RC cylinders were reinforced with four 10 mm dia. bars with rings spaced at 3 in. centers. Specimens were cured for 28 days before applying confinement by externally bonded CFRP wraps. Different confinement schemes were used to determine the effect of wrapping schemes on the compressive strength of

concrete. Confinement was provided by using CFRP wraps of different heights and spacing. Wraps of 300 mm and 100 mm heights were used with / without CFRP wraps bonded as spirals with varying spacing. Confinement schemes are summarized in Table 1.

Table 1 Nomenclature of plain and reinforced concrete cylinders

Reference	Description
P-1	Control Unwrapped PC cylinders
P-2	PC Cylinders wrapped with 300 mm high wraps
P-3	PC Cylinders Wrapped with 100 mm wraps in the middle
P1S-1	PC cylinders wrapped with 25 mm wide wraps with 25 mm (1 in.) c/c spacing
P1S-2	PC cylinders wrapped with 25 mm wide wraps with 50 mm (2 in.) c/c spacing
P1S-3	PC cylinders wrapped with 25 mm wide wraps with 75 mm (3 in.) c/c spacing
P3S-1	PC cylinders wrapped with 25 mm wide wraps with 25 mm (1 in.) c/c spacing along with 100 mm wrap in the middle
P3S-2	PC cylinders wrapped with 25 mm wide wraps with 50 mm (2 in.) c/c spacing along with 100 mm wrap in the middle
P3S-3	PC cylinders wrapped with 25 mm wide wraps with 75 mm (3 in.) c/c spacing along with 100 mm wrap in the middle
R-1	Control Unwrapped RC cylinders

Prior to wrapping, the cylinders were made dry and surface was prepared. Orientation of fibres of the installed sheets was along circumferential direction of the cylinders. Wrapping was carried out as prescribed by the manufacturer using the appropriate primer and saturant. First the primer was prepared using adequate ratios and applied on the prepared cylinders which were left for approximately 15 minutes for drying. After this saturant was prepared using adequate ratio and is applied to the CFRP wraps. These CFRP wraps were then wrapped accordingly on the cylinders and were left for air curing.

After curing, all the control and confined cylinders were tested under uniaxial compression in Universal Testing Machine.

3 RESULTS AND DISCUSSIONS

Compressive strengths and failure modes of unconfined and confined cylinders are summarized in Table 2. Following mode of failures were observed for the different categories of the plain and reinforced concrete cylinders wrapped with externally bonded CFRP:

(1) Explosive: the CFRP wraps were totally damaged.

(2) Non-explosive: the fiber carbon was partially damaged. (Particularly in cylinders wrapped with 300 mm and 100 mm wraps)

(3) Crushing of concrete on both ends of the cylinder.

Comparative analysis was performed on the basis of these results, to determine the variation in strength of plain and reinforced concrete cylinders as per the type of the CFRP wrapping used. Reported values are the average of the three tested cylinders.

Table 2 Compressive strengths and failure modes

Sample #	Compressive Strength (ksi)	Mode of failure
P-1	2.346	Crushing of Concrete
P-2	3.73	Fracture of CFRP (Non-Explosive)
P-3	2.73	Crushing of Concrete (Non-Explosive)
P1S-1	5.267	Fracture of CFRP (Explosive)
P1S-2	4.1667	Fracture of CFRP (Explosive)
P1S-3	3.634	Fracture of CFRP (Explosive)
P3S-1	5.833	Fracture of CFRP (Explosive)
P3S-2	4.36	Fracture of CFRP (Explosive)
P3S-3	3.43	Fracture of CFRP (Explosive)
R-1	2.86	Fracture of CFRP (Non-Explosive)

Comparison of compressive strengths of concrete of unconfined and confined cylinders is shown in Figures 1-5. Figure 1 shows the comparison of compressive strengths of control PC cylinders with cylinders wrapped with 100 mm wrap in the middle and 300 mm wrap. Maximum gain in strength (59%) was found to be in PC cylinders with 300 mm wrap.

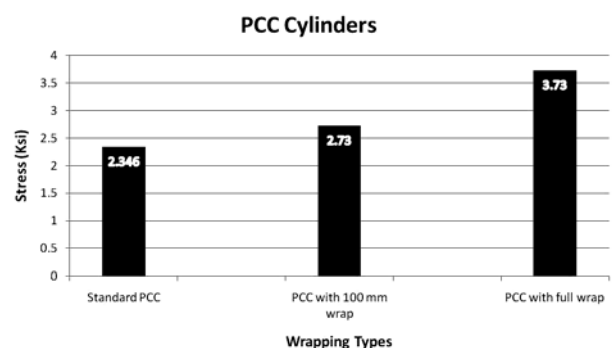


Figure 1 Comparison of PC cylinders

Figure 2 compares the variation in compressive strengths of RC cylinders with 100 mm wrap in the middle and 300 mm wrap. Again maximum gain in strength (126%) was found to be in PC cylinders with 300 mm wrap.

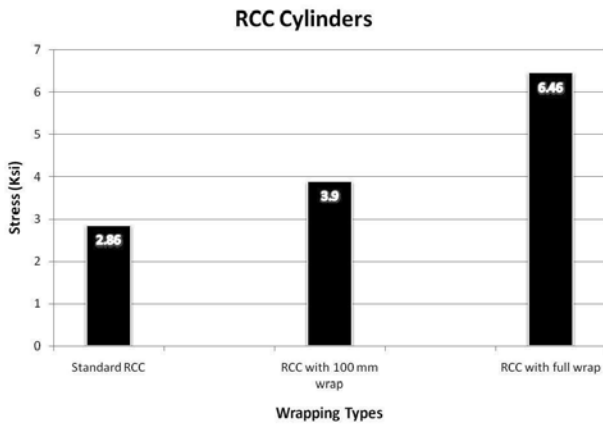


Figure 2 Comparison of RC cylinders

Comparison of gain in strength due to internal confinement (provided by internal reinforcement) and external confinement (provided by CFRP wraps) is shown in Figure 3. It is clear that all the external confinement schemes were more effective than internal confinement. Maximum gain in strength (125%) was found to be in the case of 25 mm (1 in.) c/c spirals, followed by 50 mm (2 in.) c/c spirals, 75 mm (3 in.) c/c spirals and internal confinement respectively (78%, 55% and 22%). Gain in strength compared to RC cylinders was 84%, 46% and 22% respectively for 25 mm (1 in.), 50 mm (2 in.) and 75 mm (3 in.) c/c spirals.

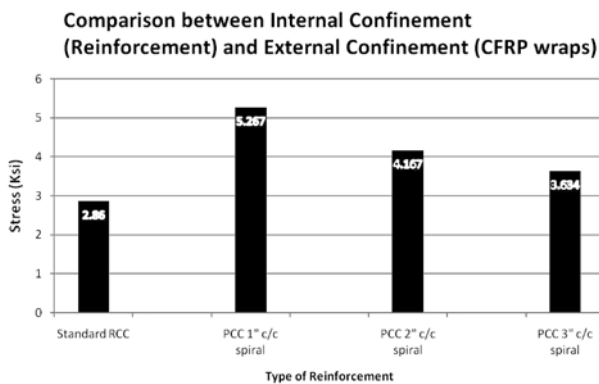


Figure 3 Comparison between internal confinement (Reinforcement) and external confinement (CFRP wraps)

Figure 4 compares the gain in strength in specimens which were reinforced with an additional 100 mm wrap in the middle along with 25 mm (1 in.), 50 mm (2 in.) and 75 mm (3 in.) c/c spirals. Same trend was observed as was in Figure 3 with maximum gain was for the case of 25 mm (1 in.) c/c spiral with 100 mm wrap in the

middle i.e. 189% followed by 86% and 46% respectively for 50 mm (2 in.) and 75 mm (3 in.) c/c spirals. Gain in strength compared to RC cylinders was 104%, 52% and 20% respectively for 25 mm (1 in.), 50 mm (2 in.) and 75 mm (3 in.) c/c spirals.

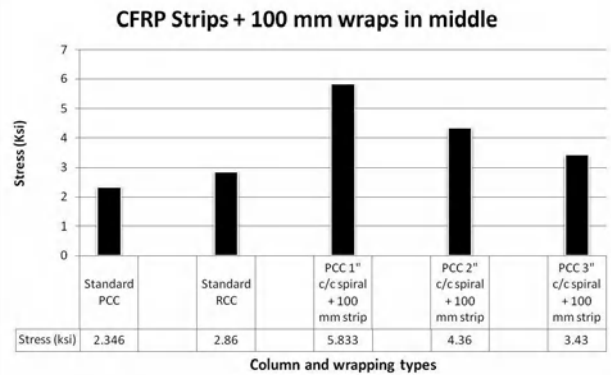


Figure 4 Comparison with CFRP strips +100mm wraps in the middle

Figure 5 shows an overall picture of gain in strengths compares with PC and RC control specimens. Maximum gain in strength was found to be for the case of 25 mm (1 in.) c/c spiral with 100 mm wrap in the middle. It was observed that contribution of 100 mm wrap in the middle was not significant. Maximum (19%) gain was observed in the case of 25 mm (1 in.) c/c spiral with 100 mm wrap in the middle followed by 11% gain in strength in the case of 50 mm (2 in.) c/c spiral with 100 mm wrap in the middle while no gain was observed for the case of 75 mm (3 in.) c/c spiral with 100 mm wrap in the middle.

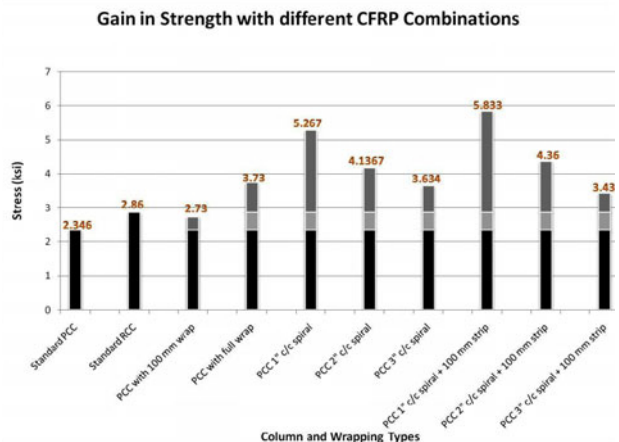


Figure 5 Gain in strength with different CFRP combinations

4 CONCLUSIONS

On the basis of the results of compressive strengths PC cylinders confined with externally bonded CFRP wraps main conclusions drawn from this study are

summarized as follows:

(1) Maximum gain in was observed in PC cylinders wrapped with 300 mm wraps when compared with the cylinders wrapped with 100 mm wrap in the middle. There was only slight increase in strength when wrapped with 100mm CFRP wrap in the middle.

(2) It was assumed that RC Cylinders have an internal confinement in the form of Steel Reinforcement ring while CFRP wraps in the form of spirals provided an external confinement. Externally bonded CFRP spirals proved to be a more effective option for confinement as the compared to the internal reinforcement.

(3) As the center-to-center spacing between the CFRP strips was increased, the strength of the cylinder decreases. The gain in strength increases from 55% to 125% when the spacing between the strips was reduced from 75 mm (3 in.) c/c to 25 mm (1 in.) c/c.

(4) Very little gain in strength was observed when 100 mm strips are wrapped over the spirals. However the trend remains the same i.e. Strength increases as the spacing between the strips is reduced.

(5) It was observed that cylinders confined with 25 mm (1 in.) c/c spacing have the highest gain in strength i.e. 125% when compared to the control PC cylinder which increases to 149% when reinforced with additional 100 mm wrap in the middle.

ACKNOWLEDGEMENT

The authors are indebted to the Department of Civil Engineering at NED University of Engineering & Technology, Karachi, Pakistan and the University itself, in the pursuit of this work.

REFERENCES

- Fam, A., Flisak, B. & Rizkalla, S. 2003. Experimental and analytical modeling of concrete filled fiber-reinforced polymer tubes subjected to combined bending and axial loads. *ACI Structural Journal* 100(4):499-509.
- Youssef, M., Feng, M. Q. & Mossalam, A. Stress-strain model for concrete confined by FRP composites. *Composites Part B: Engineering* 2007 38(5-6):614-628.
- Shahawy, M., Mirmiran, A. & Beitelman, T. 2000. Tests and modeling of carbon-wrapped concrete columns. *Composites Part B: Engineering* 31(6):471-480.
- Park, T. W., Na, U. J., Chung, L. & Feng, M. Q. 2008. Compressive behavior of concrete cylinders confined by narrow strips of CFRP with spacing, *Composites Part B: Engineering* 39:1093-1103.
- Issa, C. A., Chami, P. & Saad, G. 2009. Compressive strength of concrete cylinders with variable widths CFRP wraps: Experimental study and numerical modeling. *Construction and Building Materials* 23 (6): 2306-2318.

Procedure for the Statistical Determination of the Design FRP-Confined Concrete Strength

Giorgio Monti (giorgio.monti@uniroma1.it), Nicola Nisticò, Valentino Lovo
Department of Structural Engineering and Geotechnics, "Sapienza" University of Rome, Rome, Italy

Silvia Alessandri, Silvia Santini
Department of Structures, University "Roma Tre", Rome, Italy

ABSTRACT Worldwide research has now reached a level of integration where an effort towards the harmonization of procedures is absolutely needed. Such harmonization may regard, for example, the various steps that lead to the definition of capacity models to be included in design codes, specifically: definition of the test setup, quantities to be measured, identification of the basic variables influencing the phenomenon, distinction between average values and other fractiles, disaggregation of the model in different parts accounting for mechanics, fine-tuning and randomnesses, and, finally, assessment of the model against the experimental results. Test results and ensuing model developed according to this procedure would naturally lend themselves to be easily shared among the scientific community and would facilitate the task of calibrating the partial coefficients, with the ambitious aim of attaining a uniform reliability level among all capacity equations. This paper, based on previous author works, proposes the application of a procedure for the development of capacity design equations to the capacity model of concrete confined with FRP. The procedure has been applied, with some improving, to a new capacity model proposal and to the one included in the Italian Instructions CNR DT 200-2004. The comparison has the aim of evaluating the uncertainties of the assumed model (both of the mechanical model and of the basic variables) to obtain a constant level of structural reliability and to outline the implication that a not very well calibrated equation could have in the definition of the characteristic value.

1 INTRODUCTION

This paper follows the original approach firstly defined in Monti et al. (2008), where a general procedure was presented with the long-term objective of developing code equations having uniform reliability, that is, having the same probability of underestimating the capacity. The approach stems from what in Eurocode 0 is called "design-by-testing".

The main idea is that, once a new model is conceptually developed, its parameters should be adequately calibrated on collected experimental results, following a given procedure.

The procedure clearly separates the modeling phase from the statistical phase, in order to avoid the typical error by which a model is said to predict a certain phenomenon "on the safe side", thus inappropriately mixing modeling and reliability issues.

Marginally, a fundamental principle is stated, by which any capacity model should describe the physics of the phenomenon through analytical formulations, whenever possible. This implies that all models should be developed *a priori*, as opposed to developing them *a posteriori*, based on the outcomes of experiments, as is

the case of several regression-based models.

In principle, a sound capacity equation should be endowed with the following features:

- It should predict the phenomenon on the average (*i.e.*, it should pass through the centre of the experimental "cloud"). No reliability-related issues should be introduced at this stage.
- The dispersion of the theoretical predictions with respect to the experiments should always be given (the relative error of the model), *e.g.*, in terms of coefficient of variation. This will serve for a subsequent calibration of the equation's reliability.
- The transformation of the predictive model into a design model should be carried out in a rigorous manner, with due consideration of the probability distribution of the capacity model, so that the desired fractile is correctly attained.

The overall procedure can be sketched as follows: a) theoretical development, which should be physics/mechanics-based; b) statistical considerations, where the probability aspects of the formulation (dispersion, errors, fractiles, etc.) are treated.

2 APPLICATION OF THE PROCEDURE

2.1 Development of theoretical strength model

The procedure is here applied for developing a consistent formula for the characteristic peak strength of an FRP-strengthened concrete. It is understood that it can be applied to any formula describing a capacity.

Several formulations have been proposed in the past for the peak strength of concrete reinforced by means of FRP wrapping. Here, two different ones are chosen, for demonstration purposes only.

One is that presented in Nisticò et al. (2010), where the peak strength is given by the following predictive equation:

$$f_{cc} = f_{c0} + k_H \cdot A \cdot f_l \quad (1)$$

In case of circular sections ($k_H = 1$), for a given diameter (D), the confinement stress (f_l) can be expressed in terms of: a) fiber Young modulus (E_f), b) ultimate “real” strain, c) the ultimate coupon strain (ε_c), and d) the fiber width (t_f):

$$f_l = \frac{2E_f \varepsilon_f t_f}{D}; \quad \varepsilon_f = 0.78 \cdot \varepsilon_c; \quad k_H = 1 \quad (2)$$

The calibration of coefficient A in Eq. (1) was performed in Nisticò et al. (2010), with the purpose of minimizing the mean global error. The result was $A = 2.67$, with a mean global error of 11.8%.

The other formulation considered is that reported in CNR DT-200 (2004):

$$\frac{f_{cc}}{f_{c0}} = 1 + 2.6 \cdot \left(\frac{f_l}{f_{c0}} \right)^{2/3} \quad (3)$$

The mechanical parameters assumed as basic random variables are E_f , ε_f , f_{c0} , whereas the geometrical parameters (D , t_f) are considered as deterministic.

The experimental results considered for the purpose of this work have been selected among those proposed in the literature.

2.2 Evaluation of model error variable

The procedure of Monti et al. (2008) requires the evaluation of the model error, defined as the ratio between experimental and theoretical values of the capacity quantity at hand:

$$\delta_i = \frac{f_{cc,i}^{exp}}{f_{cc,i}^{th}} \quad (4)$$

Thus, mean δ_m and standard deviation σ_δ of δ are obtained from usual statistical elaborations. Moreover, a check of error properties should then be performed, essentially, normality and homoscedasticity tests.

The normality hypothesis of residuals has been checked by means of the Kolmogorov-Smirnov test,

performed at 5% significance level. For samples > 35 , the critical value at the 5% level is approximately $1.36 / \text{SQRT}(n)$, where $n =$ sample size. The maximum discrepancy between empirical and theoretical cumulative functions is 0.068 for both formulas, which is less than the critical value 0.123 (for $n = 123$). Thus, in both cases the normal distribution hypothesis is verified at 5% significance level (Figures 1-2).

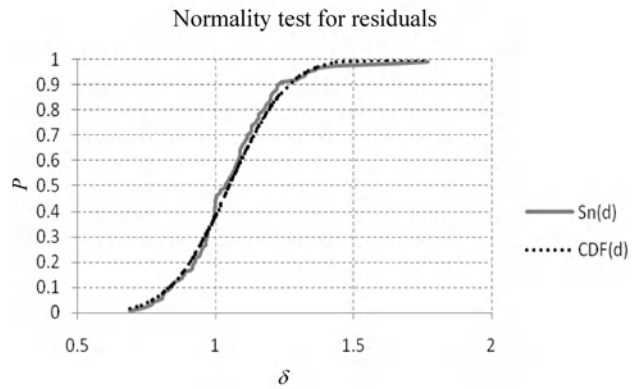


Figure 1 Normality test for residuals – new proposal. Empirical and Theoretical cumulative distributions

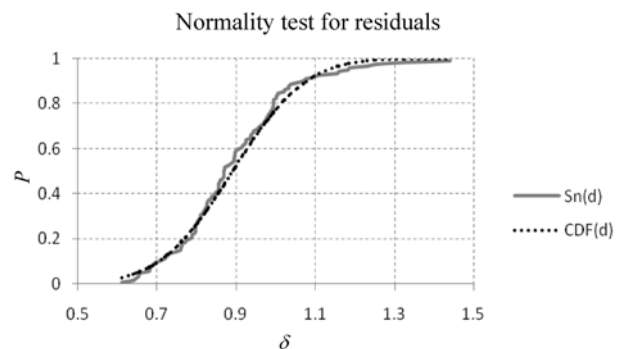


Figure 2 Normality test for residuals – CNR formula. Empirical and Theoretical cumulative distributions

To verify the hypothesis of homoscedasticity of error, the residuals are plotted vs. the theoretical peak strength. For the case of the first formula, the points on the graph cover an homogeneous area around the horizontal line at $\delta_m = 1.05$ (Figure 3); this means that the variance of the residuals does not vary with respect to the independent variable and thus the model is well specified. On the other hand, for the case of the second formula, a systematic error is found, since the points cover a homogeneous area around the horizontal line at $\delta_m = 0.89$ (Figure 4).

2.3 Definition of the probabilistic capacity model

For the first equation, the assumed probabilistic model for the capacity is:

$$f_{cc} = [f_{c0} + A \cdot f_l] \cdot \delta = \left[f_{c0} + A \cdot \frac{2E_f \cdot 0.78 \varepsilon_{coupon} t_f}{D} \right] \cdot \delta \quad (5)$$

where δ is the random error in (Eq. 4). In this case, comparing with the tests results available in the literature, while assuming the basic random variables as statistically independent, the mean value turns out to be $\delta_m = 1.05$ and the variance:

$$\sigma_\delta = \text{Var}\left(\frac{f_{cc}^{\text{exp}}}{f_{cc}^{\text{th}}}\right) = 0.028 \quad (6)$$

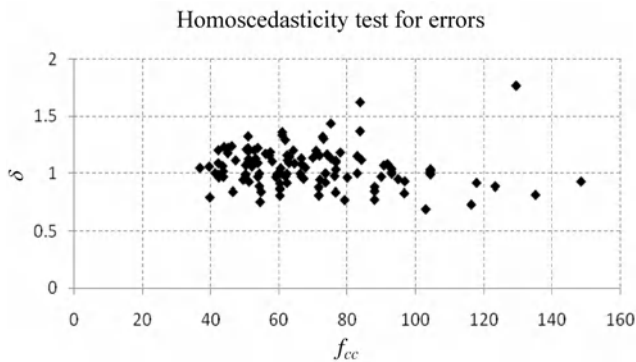


Figure 3 Homoscedasticity test for errors – new proposal. The model is well specified

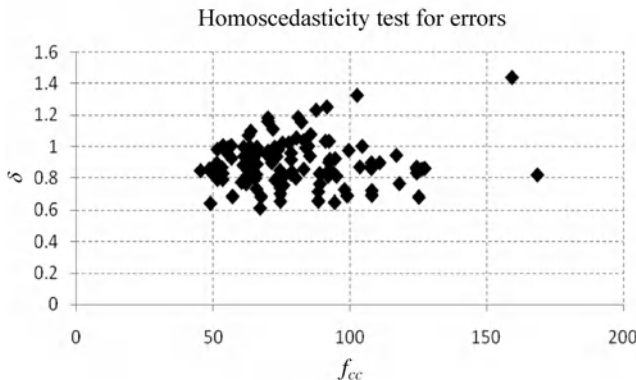


Figure 4 Homoscedasticity test for errors – CNR formula. The model is affected by a systematic error

2.4 Estimation of mean and variance of the capacity model

The mean value of the peak strength can be approximately evaluated by means of the formula:

$$f_{ccm} = \left[f_{com} + A \cdot \frac{2E_{fm} \cdot 0.78\varepsilon_{cm}t_f}{D} \right] \cdot \delta_m \quad (7)$$

The variance of the random variable f_{cc} is given by:

$$\begin{aligned} \text{Var}(f_{cc}) = & \left. \frac{\partial f_{cc}}{\partial f_{co}} \right|_m^2 \cdot \text{Var}(f_{co}) + \left. \frac{\partial f_{cc}}{\partial E_f} \right|_m^2 \cdot \text{Var}(E_f) \\ & + \left. \frac{\partial f_{cc}}{\partial \varepsilon_{coup}} \right|_m^2 \cdot \text{Var}(\varepsilon_{coup}) + \left. \frac{\partial f_{cc}}{\partial \delta} \right|_m^2 \cdot \text{Var}(\delta) \end{aligned} \quad (8)$$

where the coefficients $\left. \frac{\partial f_{cc}}{\partial x_i} \right|_m$ are the values of the partial derivatives of the function f_{cc} with respect to the basic variables x_i , calculated at the mean values of the basic variables and $\left. \frac{\partial f_{cc}}{\partial \delta} \right|_m$ is the value of the partial derivative of the function f_{cc} with respect to the error variable δ .

2.5 Estimation of the characteristic value of the capacity model

Starting from mean and variance of the capacity model, it is possible to evaluate the characteristic value of f_{cc} in a rigorous way, by applying the following equation (under the additional hypothesis of normality of the dependent variable):

$$f_{cck} = f_{ccm} - 1.64 \cdot [\text{Var}(f_{cc})]^{1/2} \quad (9)$$

Alternatively (not correctly, though), the desired percentile can be also obtained, by inserting the characteristic values of the basic variables into the model expression:

$$f'_{cck} = \left[f_{cok} + A \cdot \frac{2E_{fk} \cdot 0.78\varepsilon_{coupon,k}t_f}{D} \right] \quad (10)$$

The same procedure has been applied for the CNR predictive formula (3), subsequently evaluating the fractiles f_{cck} and f'_{cck} as functions of the moments of the basic variables f_{co} , E_f , ε_f . The conclusions are: the mean value of the ratios between the two fractiles, namely f_{cck} / f'_{cck} , is less than 1 (0.985 for the new proposal, 0.84 for the CNR formula). This means that the rigorous fractile is, on the average, lower than the one calculated by inserting into the model the characteristic values of the random variables (then, unsafe situation).

Moreover, by increasing the variability (*i.e.*, the number of random variables involved in the model), the ratio f_{cck} / f'_{cck} becomes higher, even if still less than 1, though with a significant increase in its dispersion: this conclusions are valid for both equations.

Having applied the procedure and having defined the values needed for implementing the model, in the following the consequences of a systematic error in a predictive equation are shown if the 5% fractile is sought for.

As an example, three different circular sections have been considered, evaluating the ratio between the characteristic values of peak strength according to the two equations here considered. The analysis has been carried out with different diameters ($D = 100, 200, 400$ mm) and fiber thicknesses ($t_f = 0.22, 0.44, 0.88$ mm). Some conclusions can be drawn: a) the fractile obtainable

with the first equation is always larger than the fractile obtainable with the second equation (if f_{co} is less than 30 MPa), b) the ratio between the two fraciles is almost 1, if f_{co} is greater than 30 MPa, c) the ratio is not affected by the diameter dimension if the fiber percentage does not change, and d) the ratio increases if the fiber percentage increases.

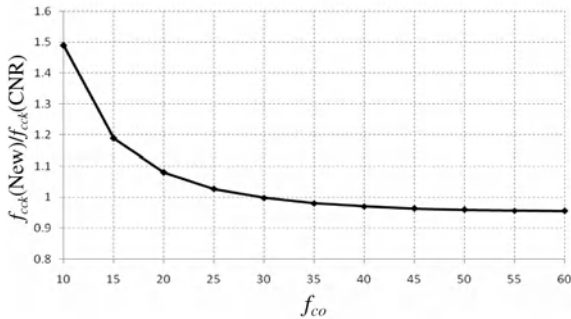


Figure 5 Ratio between characteristic values of peak strength according to new proposal and CNR formula – $D = 100$ mm, $t_f = 0.22$ mm (1 ply)

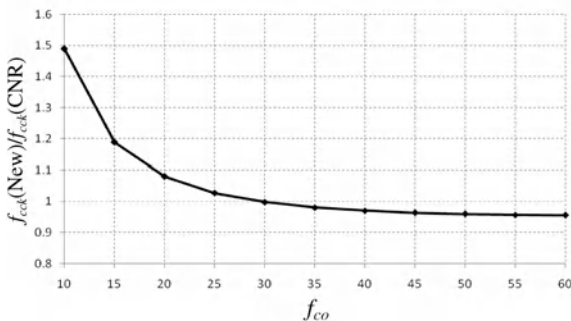


Figure 6 Ratio between characteristic values of peak strength according to new proposal and CNR formula – $D = 200$ mm, $t_f = 0.44$ mm (2 plies)

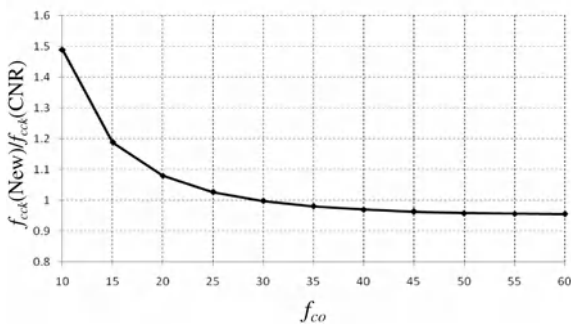


Figure 7 Ratio between characteristic values of peak strength according to new proposal and CNR formula – $D = 400$ mm, $t_f = 0.88$ mm (4 plies)

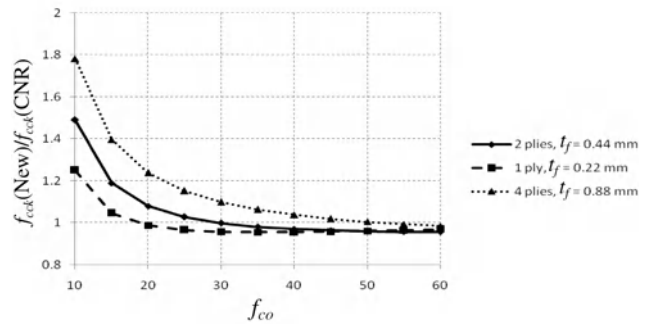


Figure 8 Ratio between characteristic values of peak strength according to new proposal and CNR formula – $D = 200$ mm

3 CONCLUSIONS

A procedure originally defined in Monti et al. 2008 has been here applied to two example equations, to show how to develop, in a consistent manner, design equations that predict the capacity of resisting mechanisms with controlled reliability.

Ideally, any capacity model should be developed on the basis of theoretical considerations and subsequently fine-tuning through a regression analysis based on test results. The formulation here followed includes in the theoretical model a new variable that represents the model error. This variable is assumed to be normally distributed with mean value and standard deviation to be evaluated from comparisons to experimental results. Once the statistical parameters of the model error are known, the statistical parameters of the capacity model can be defined and its characteristic value can be correctly evaluated.

The procedure is applied to two different equations defining the peak strength of FRP-strengthened concrete.

The most important finding is that a non-rigorous procedure can yield non-conservative values of the capacity fractile used in design.

REFERENCES

Monti, G., Alessandri, S., Santini, S. (2009). Design by Testing: A Procedure for the Statistical Determination of Capacity Models. *J. of Construction and Building Materials, Special Issue on FRP Composites*, Volume 23, Elsevier, pp. 1487-1494.

CNR DT-200/2004, Guide for the Design and Construction of Externally Bonded FRP Systems for Strengthening Existing Structures. CNR Rome, July 13th, 2004. (www.cnr.it).

Nisticò N., Monti G., Lovo V., Confined circular and square r.c. sections: an analytical model for the prediction of ultimate strength (2010).

Performance Evaluation of SFRP-Confined Circular Concrete Columns

Mohammad A. Mashrik, Raafat El-Hacha (relhacha@ucalgary.ca) & Khoa Tran

Department of Civil Engineering, University of Calgary, Calgary, Alberta, Canada

ABSTRACT This paper presents the results of an experimental investigation that evaluates the effectiveness of using Steel Fibre Reinforced Polymer (SFRP) sheets to confine small-scale plain concrete circular columns. Different parameters were investigated including: number of SFRP layers (1, 2, and 3) and concrete compressive strength (25, 30, and 35 MPa). A total of thirty-five circular specimens (150 mm diameter \times 300 mm height) were tested and divided into three groups according to concrete compressive strength. In each group, two/three specimens were tested without wrapping for comparison purposes, and two/three specimens for each number of layers. The specimens were tested under monotonic concentric uni-axial compressive load. Results showed that SFRP confinement improved the performance of the concrete cylinders in terms of axial strength, stress-strain behaviour, and ductility.

1 INTRODUCTION

Deterioration of concrete structures due to aging, weathering, overloading, design or construction defects, seismic activity, poor maintenance etc is a significant problem all around the world. The cost of replacing the deteriorated structures is prohibitive. In this regard, Fibre Reinforced Polymer (FRP) sheets can provide an economic and efficient solution to repair and rehabilitate the deteriorated structures. FRP sheets can be bonded onto flexural members to increase flexural and shear capacity, or wrapped around the axial members (columns) to improve axial strength and ductility (El-Hacha et al., 2010). Recently, Steel Fibre Reinforced Polymer (SFRP) sheets have been introduced as an alternative to more conventional Carbon and Glass Fibre Reinforced Polymer (CFRP and GFRP) sheets. SFRP sheets are advantageous over CFRP or GFRP sheets in a way that the steel cords that make up the SFRP sheets have some inherent ductility (Minnaugh, 2006). The behaviour of small-scale circular plain concrete columns wrapped with SFRP sheets, is the focus of this paper.

2 OBJECTIVE

The main objective of this study is to investigate the effectiveness of using SFRP sheets to confine small-scale plain concrete circular columns.

3 EXPERIMENTAL PROGRAM

3.1 Test Specimens

The experimental program involved testing 35 circular plain concrete columns (150 mm diameter by 300 mm

height) under monotonic concentric uni-axial compressive load until the ultimate strength of concrete and SFRP sheets was reached.

3.2 Materials

3.2.1 Concrete

Three types (based on concrete compressive strength) of ready mix Portland cement concrete was used to cast the cylinders. The target compressive strengths at 28 days were 25, 30, and 35 MPa.

3.2.2 Strengthening materials

Steel Fibre Reinforced Polymer (SFRP) sheet was used to wrap the concrete cylinders using epoxy adhesive. The SFRP sheet is made of unidirectional brass coated ultra high strength twisted steel wires forming cords that are assembled into a sheet that can be impregnated using various resin systems. The SFRP wraps used to strengthen the specimens in this project were Hardwire type 3 \times 2-20 manufactured by Hardwire LLC. The thickness of the sheet was 1.23 mm giving net area per width 0.38 mm²/mm. The ultimate tensile strength and effective Modulus for the 1.23 mm thick SFRP sheet were 985 MPa and 66.2 GPa, respectively (Hardwire, 2009).

Sikadur[®] 330 epoxy adhesive was used to bond the SFRP sheets around the specimens. It is a two moisture-tolerant, high strength, and high modulus structural thixotropic epoxy resin. The epoxy consists of two components (Hardener: A, and Resin: B) with a mixing ratio of 4:1 by weight (Sikadur[®] 330).

3.3 Strengthening procedure

The concrete cylinders and the SFRP sheets were

cleaned of any dust or particles before the sheets were bonded on the cylinders. The SFRP sheets were cut in desired lengths allowing an overlap of 100 mm, representing $D/1.5$ where D is the diameter of the cylinders. The sheets were applied to 27 of the 35 cylinders.

3.4 Instrumentation and test set-up

Strain gages were installed at mid-height of the cylinders to measure axial and circumferential strains. The SFRP wrapped cylinders were instrumented with two strain gages on two opposite sides of the cylinders, as far as possible from the overlap, to measure circumferential strains. The unwrapped cylinders were instrumented with two strain gages to measure axial strains. The specimens were tested under monotonic concentric uni-axial compressive load until the specimen failed. The axial load, longitudinal and circumferential strains were recorded.

3.5 Test matrix

The cylinders were divided into three groups according to the concrete compressive strength (25, 30, 35 MPa). As shown in Table 1, each group consisted of four subgroups according to the number of SFRP layers (0, 1, 2, and 3). Each subgroup consisted of three cylinders except for 30 MPa unwrapped, 25 and 35 MPa concrete with 1 layer of SFRP sheet, Table 1 shows two specimens only due to a problem in the data acquisition system during the tests. To identify each specimen, group and specimen index were introduced. Table 1 shows the test matrix.

Table 1 Test matrix

Group Index	Specimen Index	Concrete Strength (MPa)	No. of Layers	No. of Specimens
C25	UW	25	Unwrapped	3
	W1		1 Layer	2
	W2		2 Layers	3
	W3		3 Layers	3
C30	UW	30	Unwrapped	2
	W1		1 Layer	3
	W2		2 Layers	3
	W3		3 Layers	3
C35	UW	35	Unwrapped	3
	W1		1 Layer	2
	W2		2 Layers	3
	W3		3 Layers	3

4 EXPERIMENTAL RESULTS

In this section the results are reported and discussed in terms of ultimate strength, modes of failure, stress-strain behaviour, and ductility of the SFRP confined concrete cylinders.

4.1 Ultimate strength

Results of all the tested cylinders in terms of compressive strength are presented in Table 2.

Table 2 Summary of axial capacity results of tested cylinders

Group Index	Specimen Index	Avg. Compressive Stress (MPa)	Standard Deviation (MPa)	% Increase w.r.t UW Specimens
C25	UW	35	0.2	—
	W1	89	6.5	154
	W2	142	4.9	307
	W3	177	7.2	405
C30	UW	39	1.8	—
	W1	100	2.3	156
	W2	144	4.2	269
	W3	181	0.6	364
C35	UW	42	2.5	—
	W1	100	0.9	138
	W2	146	5.6	248
	W3	186	3.3	343

Figure 1 compares the average axial strengths of all tested cylinders. The axial strengths of wrapped cylinders were much superior to that of the unwrapped cylinders. One layer of SFRP increases the capacity of the columns by 138%-156%. For two and three layers the percent increase varies between 248%-307% and 343%-405%, respectively. It proves the effectiveness of SFRP layers on axial capacity of the columns. It was observed from Table 2 and Figure 1 that in case of two and three layers of SFRP sheets, the percent increase in strength decreases with increasing concrete strength for the same number of SFRP layers.

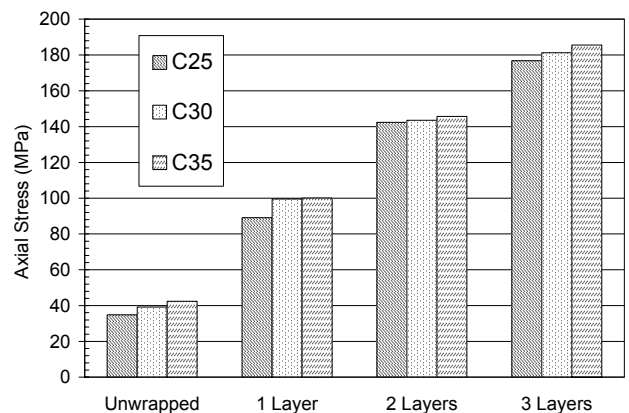


Figure 1 Comparison of average axial compressive strengths

4.2 Modes of failure

In this study the modes of failure of the specimens showed high consistency. All the unwrapped specimens failed in conventional cone or shear failure. For the

wrapped cylinders, the modes of failure were the tension failure by rupture of the SFRP wraps. All specimens wrapped with one layer of SFRP sheet, the sheet ruptured right at the beginning of the overlap. The specimens wrapped with two layers of SFRP sheets showed a combination of rupture and debonding. The only exception was in one specimen from the group C30W2, the SFRP sheets entirely debonded at the overlap without any sign of rupture. This might be due to poor wrapping and/or lack of enough epoxy between the SFRP layers. All specimens wrapped with three layers of SFRP sheets, the sheets debonded at the overlap completely without rupture. When the SFRP sheets ruptured, failure was sudden and in a brittle manner with loud crushing sound without any prior warning except for some creeping sound of concrete cracking. In almost all the wrapped cylinders a conical mode of failure of concrete was observed. It was also observed that when some portion of SFRP sheets departed from the cylinders, a layer of concrete was attached to the sheets. It indicates that good bond existed between concrete and SFRP sheet. Typical modes of failure are shown in Figure 2.

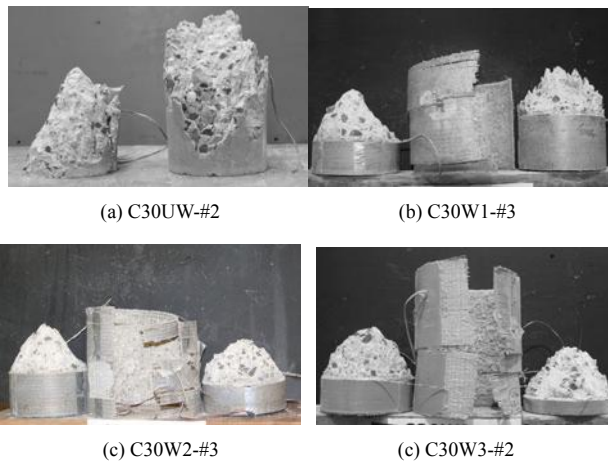


Figure 2 Typical failure modes of unwrapped and SFRP wrapped concrete cylinders. Unwrapped: (a) 30MPa–shear failure; Wrapped: (b) one layer–SFRP rupture; (d) two layers–rupture/debonding; (e) three layers–debonding at the overlap

4.3 Stress-strain behaviour

Figure 3 represents typical axial stress-circumferential strain curves of the 30 MPa concrete cylinders wrapped with different number of SFRP layers. The figure shows that stress-strain curves of SFRP-confined cylinders can be characterized with three regions. First region, an initial linear elastic zone which is observed approximately up to stress level of 30 MPa. Second region, a non-linear transition zone which is observed approximately between stress level of 30 and 60 MPa. Third region, a final linear zone which is observed up to failure stress. The regions can be explained as follows: though the

circumferential strains of the unwrapped cylinders were not measured, it is expected that the slope of first linear zone of stress-strain curves of wrapped cylinders is similar to that of unwrapped cylinders, as found out by Manni et al., (2005). It implies that most of the load in this region is carried by the concrete and the SFRP sheets do not have any significant effect. When the concrete reaches its unconfined strength, transverse strain activates the confining pressure of the SFRP sheets and the curve enters its second transition zone. In this region small increase in the loads results in large lateral expansion, and consequently the confining pressure of SFRP sheets. Finally, the curve enters its third region and again exhibits linear response due to elastic behaviour of the SFRP materials. The slope of the third region is substantially less than the first region.

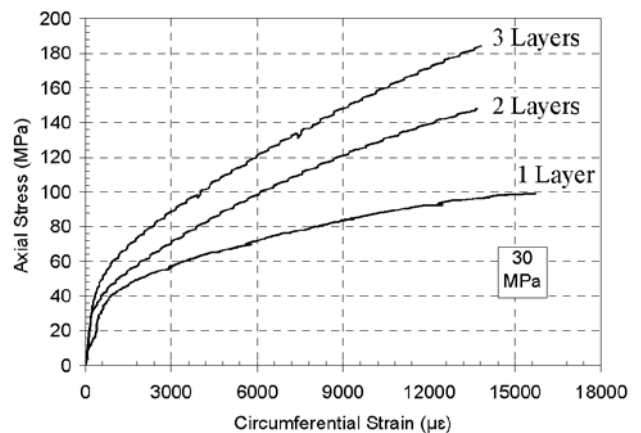


Figure 3 Stress-strain response of 30 MPa concrete cylinders with different number of SFRP layers

Figure 4 shows typical axial stress-circumferential strain curves of the 25, 30, and 35 MPa concrete cylinders wrapped with three layers of SFRP sheets. The stress-strain curves are identical regardless the concrete compressive strength with slight difference in the failure stress.

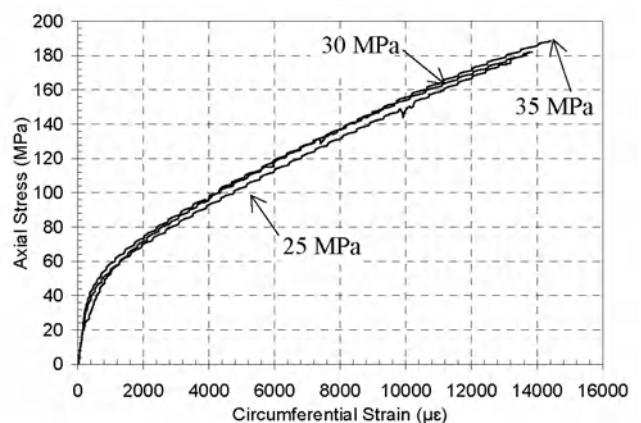


Figure 4 Stress-strain response of 25, 30, and 35 MPa concrete cylinders with 3 layers of SFRP sheets

4.4 Ductility

Ductility is an essential characteristic through which one can determine the suitability and degree of the reliability of the FRP material for civil applications (Alsayed and Alhozaimy, 1999). Different methods are available in the literature to calculate the ductility index. Ductility can be defined as the ability to absorb inelastic energy without losing its load capacity (Wang and Belardi, 2005). In this study, the “energy ductility index” is determined as the area under the stress-strain curve up to ultimate load. Table 3 shows that the addition of SFRP sheet(s) improves the system’s ductility index.

With the addition of SFRP sheets, the axial strength behaviour exhibits an improved ductility index. As the number of SFRP layers increases, the energy ductility indices increase regardless the concrete compressive strength. However, for the same concrete compressive strength, as the number of SFRP sheets increases, the energy ductility index increases slightly with respect to the wrapped cylinders with one layer. As the concrete compressive strength increases, and for confined cylinders with the same number of layers of the SFRP sheets, the increase in the energy ductility indices with respect to the unwrapped cylinders decreases slightly.

Table 3 Energy ductility index

Group Index	Specimen Index	Average Energy Ductility (MPa- $\mu\epsilon$)	% increase w.r.t. UW Specimens	% increase w.r.t. W1 Specimens
C25	UW	54×10^3	—	—
	W1	1022×10^3	18.9	—
	W2	1272×10^3	23.5	1.24
	W3	1513×10^3	28.0	1.48
C30	UW	72×10^3	—	—
	W1	1167×10^3	16.2	—
	W2	1301×10^3	18.0	1.11
	W3	1518×10^3	21.0	1.30
C35	UW	81×10^3	—	—
	W1	1269×10^3	15.6	—
	W2	1367×10^3	16.8	1.08
	W3	1516×10^3	18.6	1.19

5 CONCLUSIONS

This paper presents the results of an experimental investigation that examined the effectiveness of wrapping small-scale circular plain concrete columns with SFRP sheets tested under monotonic concentric uni-axial compressive load. Parameters investigated were different concrete compressive strength and number of layers of the SFRP sheets. Based on the test results, the following conclusions were drawn:

- SFRP wraps improve the axial capacity, stress-strain behaviour, and ductility of the concrete cylinders.
- Irrespective of the concrete strength and number

of layers of the SFRP sheets, the axial stress-circumferential strain curves of the confined cylinders show similar path until failure.

- Increasing the number of SFRP layers for the same concrete strength increases the axial concrete compressive strengths.
- Increasing the concrete compressive strength for the same number of SFRP layers reduces the corresponding percent increase in strength with respect to the unwrapped specimens.
- The addition of the SFRP sheets improves the system’s ductility. For the same concrete compressive strength, increasing the number of SFRP layers improves further the ductility.
- The results indicate that confining concrete columns with SFRP sheets is a very effective and efficient method to improve the axial strength of the concrete cylinders. The only drawback of the method is that SFRP sheets fail in a brittle manner without prior warning.

6 ACKNOWLEDGEMENTS

The authors wish to acknowledge Sika Canada for providing the epoxy adhesive, and Hardwire LLC for providing the SFRP sheets.

REFERENCES

- Alsayed, S.H., and Alhozaimy, A.M., 1999, Ductility of concrete beams reinforced with FRP bars and steel fibers, *SAGE Journal of Composite Materials*, 1999, Vol. 33, No.19, pp. 1792-1806.
- El-Hacha, R., Green, M., Wight, G. 2010. Effect of severe environmental exposures on CFRP wrapped concrete columns. *Journal of Composites for Construction, ASCE*, Vol. 14, No.1, January-February, 2010. pp. 83-93.
- Hardwire. 2009. What is hardwire? (accessed: Feb. 15, 2010) <http://www.hardwirellc.com/solutions/reinforcements.html>
- Manni, O., Micelli, F., Modarelli, R. 2005. FRP-confinement of hollow concrete cylinders and prisms. *Proceedings of the 7th International Symposium on Fibre-Reinforced Polymer Reinforcement for Concrete Structures (FRPRCS-7)*, ACI Special Publications SP-230, Kansas City, USA, November 6–9, 2005, paper SP-230—58, Vol.2, pp. 1029–46.
- Minnaugh, P.L. 2006. The experimental behaviour of steel fiber reinforced polymer retrofit measures. *MSc thesis, University of Pittsburgh, Pittsburgh, USA*.
- Sikadur[®] 330, Product Data Sheet, High-modulus, high-strength, impregnating resin, (accessed date: Feb. 15, 2010) <http://www.sikaconstruction.com/tds-cpd-Sikadur330-us.pdf>
- Wang, H. and Belarbi, A., 2005, Flexural behavior of fiber-reinforced-concrete beams reinforced with FRP rebars, *Proceedings of the 7th International Symposium on Fibre-Reinforced Polymer Reinforcement for Concrete Structures (FRPRCS-7)*, ACI Special Publications SP-230, Kansas City, USA, November 6–9, 2005, paper SP-230—51, Vol. 2, pp. 895-914.

Mechanical Behavior of Concrete Columns Confined by Laterally Pre-Tensioned FRP

E. Zīle (edmunds@pmi.lv) & V. Tamužs
Institute of Polymer Mechanics, University of Latvia, Riga, Latvia

M. Daugevičius
Dept of Reinforced Concrete and Masonry Structures, Vilnius Gediminas Technical University, Vilnius, Lithuania

ABSTRACT This paper presents the results of an experimental investigation of concrete columns confined by a wound pre-tensioned carbon filament yarn. Yarn winding equipment was developed in the Institute of Polymer Mechanics with the ability to set the desired pre-tension force and thereby producing confined concrete specimens with different initial lateral pressure. It is shown that initial lateral pressure increases the axial stress at which intense internal cracking of the concrete develops.

1 INTRODUCTION

One application of the FRP is as confinement for concrete columns subjected to axial compressive loading. Confined concrete possesses greatly enhanced strength and ultimate strain (Tamužs et al. 2006a). FRP has a linearly elastic behavior up to the failure and when it is used as a confinement it creates an ever increasing lateral confining pressure on the concrete. As a result, tri-axial compressive stress state is created in the concrete. Axial stress-axial strain curves of the confined concrete show bilinear behavior. First part of the curve corresponds to the undamaged concrete. When the transition point or knee point is reached, intense internal cracking of the concrete develops. Due to the confinement concrete does not fail and loading curve continues with a greatly reduced slope.

Axial stress at the knee point can be increased by laterally pre-tensioning the confinement, so that there is initial lateral stress acting on the column.

The main objective of this work is to study the mechanical behavior of confined concrete columns, if the confinement is created by winding initially pre-tensioned carbon filament yarn onto a rotating concrete specimen.

2 EXPERIMENTAL PROGRAM

2.1 Concrete properties

The concrete was prepared in the laboratory and was allowed to cast in forms at laboratory conditions for 28 days. Six plain concrete columns were tested under monotonic compressive loading to estimate the unconfined column compressive strength. Diameter of all columns

(confined and unconfined) was 152mm, length – 300mm. Table 1 reports plain concrete strength f_{co} , ultimate axial (ε_{co}) and lateral (ε_{lo}) strain, elastic modulus E_b and Poisson ratio ν .

Table 1 Concrete properties

f_{co} (MPa)	ε_{co} (%)	ε_{lo} (%)	E_b (GPa)	ν
18.7	0.30	0.16	24.1	0.21
38.1	0.26	0.15	29.7	0.20
44.6	0.24	0.10	32.6	0.20

2.2 Composite confinement properties

Concrete specimens were confined by winding them tangentially with a yarn (*Tenax – J UTS 7731*), impregnated with epoxy resin. Mechanical properties, given by the manufacturer, are as follows: tensile strength – 5193MPa; tensile modulus – 244GPa; elongation at break – 2.13%; filament diameter – 7 μ m; number of filaments – 24000. These data are usually exaggerated and therefore cannot be used directly for the estimation of the strength of the composite. Split-disk tests according to the ASTM D 2290 standard were performed to estimate the hoop properties of the composite jacket. It was found that the ratio of experimental strength to manufacturer's data is 0.67, experimental modulus to manufacturer's data is 0.97 and experimental ultimate tensile strain to manufacturer's data is 0.57.

2.3 Winding process and confined specimens

Yarn winding is a technique for confining with FRP, which involves winding resin-coated fibers onto a rotating concrete specimen. Schematic diagram of the

yarn winding process is shown in Figure 1. Continuous flow of the yarn is supplied from the bobbin to the pre-tension device. Pre-tension device is composed of four rubber-coated wheels. Each wheel is separately adjustable to obtain the desired pre-tension force. The placement of the yarns was controlled by traversing the pre-tension device along the longitudinal axis of the specimen at a step of 8 mm per rotation.

The resin was applied on the concrete surface and yarns before winding. The winding process was conducted carefully in order not to damage the yarns in the course of winding. Confined specimens were left to dry for a 10 day period at the temperature of 22°C.

26 confined specimens were tested in this study. The confinement consisted of 2 and 4 layers of wound yarns. Pre-tension force of the yarn P equal to 0N, 245N and 490N was produced. The loading rate was 10MPa/min, following the ASTM C 39/C39M – 99 standards.

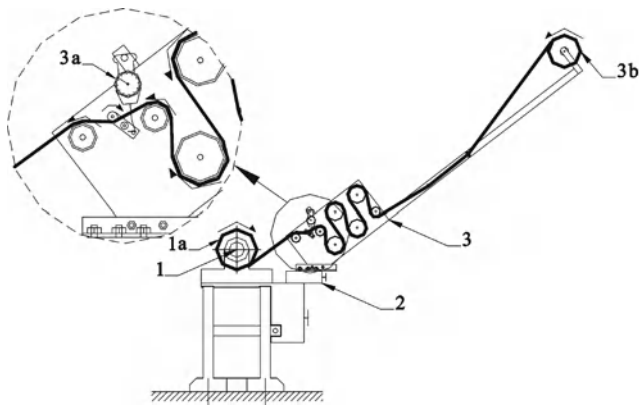


Figure 1 Schematic diagram of the yarn winding equipment. 1-rotating specimen fixture; 1a-specimen; 2-horizontal platform, moving along the longitudinal axis of the specimen; 3-pre-tension device attached to the platform 2; 3a-dynamometer; 3b-yarn bobbin

3 ESTIMATION OF THE EFFECT OF THE LATERAL PRE-TENSIONING OF FRP

It was shown in (Tamužs et al. 2006b) that the compressive strength increase due to the confinement can be well estimated by a simple formula:

$$f_{cc}/f_{co} = 1 + K_{\sigma} \cdot (f_{lu}/f_{co}) \quad (1)$$

where f_{cc} – confined concrete strength and K_{σ} is defined as:

$$K_{\sigma} = (1 - \nu)/\nu \quad (2)$$

A typical value of the initial Poisson ratio is 0.2. In this case $K_{\sigma} = 4$. f_{lu} is the ultimate lateral pressure:

$$f_{lu} = (E_j h / R) \varepsilon_{ju} = E_{lat} \varepsilon_{ju} \quad (3)$$

where E_j – elastic modulus of the FRP jacket, h – thickness of the FRP jacket, R – radius of the column, ε_{ju} – ultimate hoop strain of the FRP jacket in confined specimen tests and E_{lat} is the so called “lateral modulus”.

The ultimate lateral strain of the confined concrete ε_{lu} is equal to the ultimate hoop strain of the FRP jacket: $\varepsilon_{lu} = \varepsilon_{ju}$. If the FRP jacket is made from wound yarn, then thickness is:

$$h = nS_o/t \quad (4)$$

where S_o – average cross sectional area of the yarn, t – step of the winding of the yarn and n – number of wound yarn layers.

It can be shown that, assuming Hook’s law for concrete, slope of the initial loading path in the stress space is:

$$d\sigma_z/d\sigma_l = [1 + k(1 - \nu)]/[k\nu] \quad (5)$$

where σ_z – axial stress, σ_l – lateral stress, and $k=(E_j h)/(E_b R)$ – parameter, which characterizes the stiffness of the confinement.

When the initial loading path reaches the strength line (Equation 1), intense internal cracking of the concrete develops. The confinement acts in such a way that instead of the concrete column failure the loading path bends and becomes roughly parallel to the strength line. Now concrete failure occurs when the hoop stress in the composite jacket reaches its ultimate value. The intersection point of the initial loading path and strength line is called knee point or limit of the linearity. An example of the loading paths in a non-dimensional space of normalized axial stress σ_z/f_{co} and normalized lateral stress σ_l/f_{co} for specimens with different plain concrete strengths and different confinement thicknesses are shown in Figure 2 (Tamužs et al. 2006c).

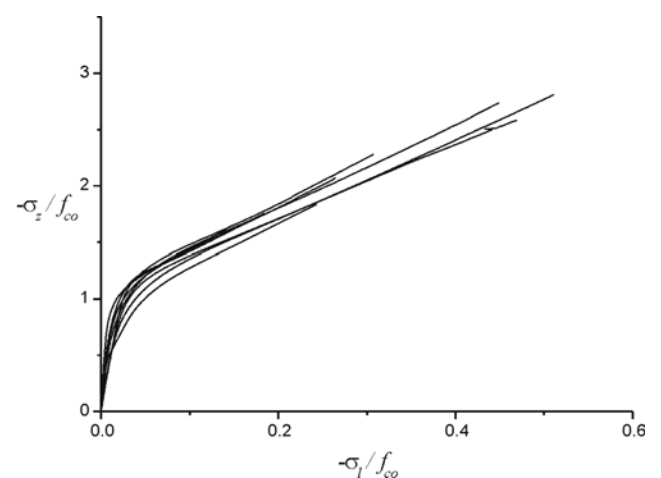


Figure 2 Loading paths of the confined concrete specimens

It is remarkable that all loading paths follow a single master curve, described by:

$$|\sigma_z|/f_{co} = 1 + K_{\sigma} \cdot (|\sigma_l|/f_{co}) \quad (6)$$

From Equation 5 follows that lateral stress in the elastic regime is:

$$\sigma_l = [k\nu\sigma_z]/[1 + k(1 - \nu)] \quad (7)$$

Insertion of Equation 7 in Equation 6 leads to the expression for the axial stress at the knee point:

$$|\sigma_z^*| = [1 + k(1 - \nu)] \cdot f_{co} \quad (8)$$

Axial stress at the knee point can be increased by laterally pre-tensioning the FRP jacket. Pre-tensioning creates initial lateral stress σ_{lo} , therefore the initial loading path will intersect the strength line at higher axial stress. Initial lateral stress can be written as:

$$\sigma_{lo} = -\frac{nP}{Rt} \quad (9)$$

Now, the lateral stress in the elastic regime is:

$$\sigma_l = [k\nu\sigma_z] / [1 + k(1 - \nu)] + \sigma_{lo} \quad (10)$$

Insertion of Equation 10 in Equation 6 leads to the expression for the axial stress at the knee point for pre-stressed concrete:

$$|\sigma_z^*|' = [1 + k(1 - \nu)] \cdot \left[f_{co} + \frac{1 - \nu}{\nu} \cdot \frac{nP}{Rt} \right] \quad (11)$$

In reality, there is no sharp transition between the first and second part of the loading path, therefore knee point is defined as the axial stress at the intersection of the continuations of the linear sections of the first and second part of the loading path.

4 RESULTS

Typical stress-strain curves of the confined concrete specimens are shown in Figure 3. Table 2 reports ultimate axial (ε_{cc}) and lateral (ε_{lu}) strain of the confined concrete, normalized axial stress at the knee point $|\sigma_z^*|^{exp}/f_{co}$ and estimated normalized axial stress at the knee point $|\sigma_z^*|^{est}/f_{co}$.

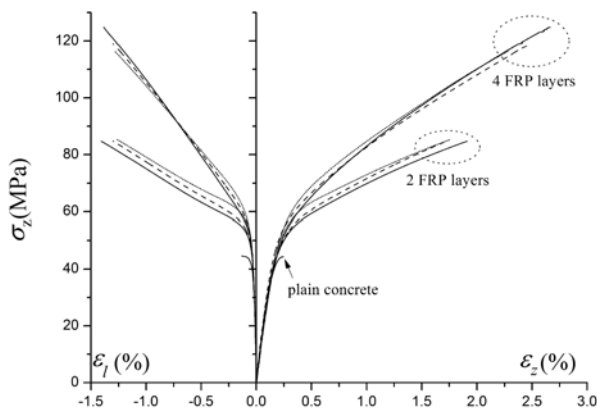


Figure 3 Stress-strain curves of the confined concrete columns. Plain concrete strength $f_{co} = 44.6$ MPa. Solid line – $P = 0$ N, dashed line – $P = 245$ N, dotted line – $P = 490$ N (the compressive stresses and strains are assumed to be positive)

Relative increment of the axial stress at the knee point due to the initial pre-stress Δ^* is calculated as follows:

$$\Delta^* = \left(\frac{|\sigma_z^*|' - |\sigma_z^*|}{|\sigma_z^*|} \right) \quad (12)$$

Estimated relative increment Δ^{*est} is obtained by inserting Equation 8 and 11 in Equation 12:

$$\Delta^{*est} = \frac{1 - \nu}{\nu} \cdot \frac{nP}{Rt} \quad (13)$$

Experimental and estimated relative increments of the axial stress at the knee point due to the initial pre-stress for all tested confined specimen configurations is shown in Figure 4.

Table 2 Experimental results

f_{co} (MPa)	$ \sigma_{lo} $ (MPa)	ε_{cc} (%)	ε_{lu} (%)	f_{cc}/f_{co}	$ \sigma_z^* ^{exp}/f_{co}$	$ \sigma_z^* ^{est}/f_{co}$
18.7	0	3.15	1.29	3.36	1.04	1.02
	0.81	3.15	1.33	3.31	1.08	1.20
	1.61	2.99	1.23	3.21	1.16	1.38
18.7	0	4.39	1.41	5.26	1.00	1.05
	1.61	3.74	1.09	4.45	1.11	1.41
	3.22	4.08	1.17	4.74	1.24	1.77
38.1	0	2.28	1.50	2.10	1.06	1.02
	0.81	1.96	1.26	2.05	1.16	1.10
	1.61	1.82	1.28	1.94	1.16	1.19
38.1	0	2.88	1.39	2.70	1.05	1.04
	1.61	2.91	1.23	2.89	1.16	1.21
	3.22	2.90	1.23	2.88	1.27	1.39
44.6	0	1.91	1.41	1.90	1.19	1.02
	0.81	1.73	1.30	1.90	1.24	1.09
	1.61	1.76	1.26	1.91	1.29	1.17
44.6	0	2.66	1.38	2.80	1.24	1.04
	1.61	2.49	1.30	2.67	1.29	1.19
	3.22	2.28	1.28	2.61	1.40	1.34

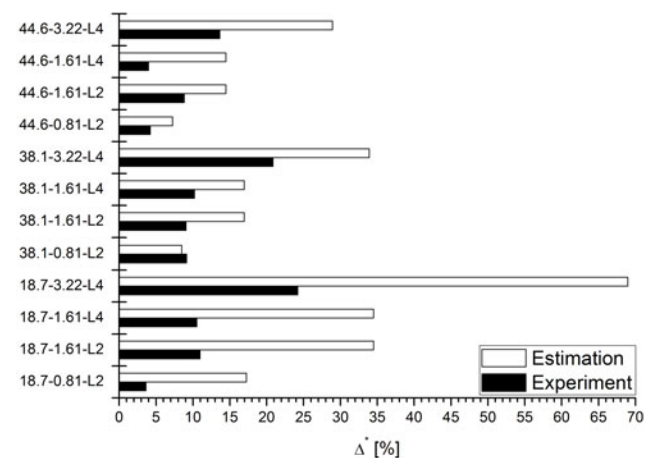


Figure 4 Relative increments of the axial stress at the knee point due to the initial pre-stress. The following confined specimen labeling is used: (plain concrete strength [MPa]) – (initial lateral stress [MPa]) – L(number of confinement layers)

5 DISCUSSION

There is a significant difference between the estimated and experimental increments of the axial stress at the knee point for some of the tested configurations (Figure 4). This indicates that the achieved pre-stress level was much lower than intended. Possible explanation of this is both the stress relaxation and creep in wound specimens during the drying period which led to the reduction of the pre-stress level. This effect is especially pronounced for the lower strength concrete ($f_{co} = 18.7$ MPa).

The drawback of the initial FRP pre-tension is the reduction of the composite deformational capacity because pre-tensioned FRP contains already pre-stretched fibers. It is seen from Table 2 that most of the pre-stressed confined specimens have lower ultimate lateral strain than the specimens without initial pre-stress. Lowered deformational capacity of the FRP leads to lower strength and ultimate axial strain. However, this has no meaning in practical applications because service load of structural concrete elements is lower than the axial stress at the knee point.

The compressive strength depends on the ultimate hoop strain of the FRP jacket (see Equation 1). It was found (Tamužs et al. 2006a, c) that the ultimate FRP hoop strain in the confined concrete tests is about 40% lower than the ultimate hoop strain obtained in the split-disk test if the concrete is manually confined by wrapping continuous carbon fiber tape impregnated with epoxy resin around the column. Tests show, that for concrete confined by wound carbon yarn, the ultimate hoop strain is about the same or even higher than the value from the split-disk test. This means that yarn winding produces higher quality confinement by providing better fiber distribution and minimizing fiber waviness.

If f_{cc}^* and ε_{ju}^* is the compressive strength and ultimate hoop strain of the manually wrapped concrete column ($\varepsilon_{ju}^* = 0.6\varepsilon_{ju}^d$, where ε_{ju}^d is ultimate hoop strain in the split disk test), and f_{cc} is the compressive strength of the wound concrete column, then according to the Equation 1,

the relative increase of the compressive strength due to the yarn winding technique can be roughly estimated by the following formula:

$$\frac{f_{cc} - f_{cc}^*}{f_{cc}^*} = \frac{0.67 \cdot K_{\sigma} E_{lat} \varepsilon_{ju}^*}{f_{co} + K_{\sigma} E_{lat} \varepsilon_{ju}^*} \quad (14)$$

For example, if $f_{co} = 27$ MPa, $\varepsilon_{ju}^d = 1.2\%$, $E_{lat} = 2730$ MPa (Tamužs et al. 2006a, c), then the relative increase of the compressive strength due to the yarn winding technique could be about 50%.

6 CONCLUSIONS

FRP pre-tension creates initial lateral stress which delays the start of intense internal cracking of the confined concrete.

It was demonstrated that FRP pre-tensioning increases the axial stress at the knee point for up to 24% compared with no pre-tensioning. This means that pre-stressed structural concrete elements can be subjected to higher service loads than the non pre-stressed elements.

To fully utilize the deformational capacity of the FRP yarn winding is recommended instead of manual wrapping of resin impregnated tape around the column. For the given plain concrete strength and lateral modulus, wound specimen will have higher compressive strength than the manually wrapped specimen.

REFERENCES

- Tamužs, V., Tepfers, R., You, C.S., Rousakis, T., Repelis, I., Skruls, V. & Vilks, U. 2006a. Behavior of concrete cylinders confined by carbon-composite tapes and prestressed yarns. 1. Experimental data. *Mechanics of Composite Materials* 42(1): 13-32.
- Tamužs, V., Tepfers, R. & Spāmiņš, E. 2006b. Behavior of concrete cylinders confined by a carbon composite. 2. Prediction of strength. *Mechanics of Composite Materials* 42(2): 109-118.
- Tamužs, V., Tepfers, R., Zile, E. & Ladnova, O. 2006c. Behavior of concrete cylinders confined by a carbon composite 3. Deformability and the ultimate axial strain. *Mechanics of Composite Materials* 42(4): 303-314.

Effect of CFRP and GFRP Confinement on Behavior of Square Lightweight Concrete Specimens

A. Vatani Oskouei (asvatani@gmail.com), M. Pirgholi Kivi & S. Taghipour Boroujeni

Department of Civil Engineering, Shahid Rajaei University, Tehran, Iran

ABSTRACT For improving of the structural properties of lightweight concrete, confinement by Fiber Reinforced Polymer (FRP) can be used. Effect of Fiber Reinforced Polymer on confined lightweight concrete elements is one of the most important research fields. In this study, behavior of confined and unconfined lightweight concrete specimens under uniaxial loading has been discussed. For decreasing of stress concentration and to prevent the fiber from being folded, corners of specimens were chamfered to a radius of 5 to 25 mm. The Carbon Fiber Reinforced Polymer (CFRP) and Glass Fiber Reinforced Polymer (GFRP) were used to confine lightweight concrete specimens. The stress-strain curve of specimens is compared. The result was shown that, Confinement of specimens with CFRP has more ultimate strength than the specimens confined with GFRP.

1 INTRODUCTION

Different parameters affect compressive strength of LWC. Except specific weight, aggregate strength, confinement can also lead to increase of axial load bearing and ductility capacity of elements. Confined circle cross section has better performance than square and rectangular specimen.

The sharpness edges of the specimens' affect the behavior of square cross section element and the failure of concrete confinement would be delayed. Although influence of the number of CFRP layers on ductility has been more than strength, confinement with CFRP in addition of increasing the axial load capacity, also increases ductility.

Increasing number of layers, the loading carrying capacity of column has been increased.

Many researchers have suggested a confined model including shape of specimens (circle and square specimens with different edge radius), strength, and the kind of used laminate (GFRP and CFRP).

Stress-strain relationship of confinement concrete specimen based upon results from circle, square and square rectangular specimens in large scale were also proposed.

Many experimental and analytical works were done on normal weight concrete, but less valuable studies of LWC have been presented.

The experimental part of the study was achieved by testing a total of 45 column specimens. All of specimens were short square lightweight concrete columns with rounded edges and different in their corner radius.

2 MATERIAL PROPERTIES

2.1 Fibers

FRP composite materials consist of fibers embedded in, or bonded to a matrix with distinct interfaces between them. In general, fibers are the principal load-carrying members, while the surrounding matrix keeps them in the desired location and orientation, acts as a load transfer medium between them, and protects them from environmental effects.

Commercially, the principal fibers come in various types of glass and carbon as well as aramid.

FRP composite materials exhibit high tensile strength in the fiber direction although they are not always rigid as metals. Because of their low specific gravities, the strength-weight ratios of FRP composite materials are significantly superior to those of metallic materials.

In this research used carbon & glass fibers reinforcement polymer (CFRP & GFRP) had a tensile strength of 4170 MPa & 1750 MPa, respectively. Mechanical properties of CFRP & GFRP are summarized in Table 1.

Table 1 Mechanical properties of CFRP & GFRP

Characteristic	CFRP	GFRP
Tensile strength (MPa)	4170	1750
Tensile modulus (GPa)	245	75
Tensile strain (mm/mm)	0.017	0.025
Thickness (mm)	0.176	0.299

2.2 Concrete

A ready-mix concrete was used. The nominal 28-day

strength of the concrete used about is 25 MPa, also the concrete has a specific weight of 1720 kg/m³, an elasticity modulus 16 GPa to 20 GPa and Poisson coefficient are 0.2. The quantities of ingredients used in the concrete mix are shown in Table 2.

Table 2 Proportions of ingredients used for concrete mix

Ingredients	Quantity (kg/m ³)
Cement (Type 1)	500
Silica Fume	50
Water	150
Lightweight aggregate	340
Normal sand	663.18
Super plasticizer	5

3 EXPERIMENTAL WORK

3.1 Specimen

For experimental work square cross sections with different edge radius were used. The radius of specimens' edge is varied from 0.5 cm to 2.5 cm (See Table 3).

Total number of specimens is 45 and specimens are confined by CFRP and GFRP. These specimens are confined with different number CFRP and GFRP layers. The numbers of these layers are brought in Table 3.

Table 3 Specification of specimens

Specimen	r* (cm)	No. Layer	No. Specimen**
r(0.5)GFRP	0.5	1-2	2
r(0.5)CFRP	0.5	1-2	4
r(1.0)GFRP	1.0	1-2	6
r(1.0)CFRP	1.0	1-2	3
r(1.5)GFRP	1.5	1-2	5
r(1.5)CFRP	1.5	1-2	4
r(2.0)GFRP	2.0	1-2	4
r(2.0)CFRP	2.0	1-2	8
r(2.5)GFRP	2.5	1-2	4
r(2.5)CFRP	2.5	1-2	5

* r = the radius of the corner of the square specimen

** Number of experimented specimens

3.2 Specimen preparation

Forms for the square column specimens were prepared using 20 mm plywood sheets cut and assembled to provide 90° corners with a plywood formed bottom. The forms were cut and assembled very carefully to ensure accurate vertical sides and 90° corners. In order to round off the corners of the square specimens, foam inserts with the desired radius were glued to the corners of the boxes.

Figure 1 shows the specimens before and after jacketing with Carbon and Glass fibers.

The concrete specimens, after 28 days of curing, were

carefully sandblasted. The surface of concrete must be smooth, for this purpose putty and grinding have been used (Figure 2).

In the specimens a 100 mm overlap was used, to insure the development of full composite tensile strength.

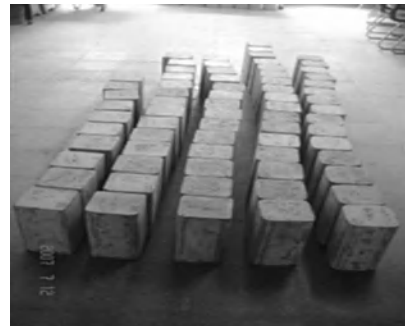


Figure 1 Tested specimens



Figure 2 Preparing of specimens

3.3 Instrumentation

All specimens were instrumented with two strain gauges bonded at mid-height of confined specimens. The strain gauges measure the lateral strains (Figure 3).

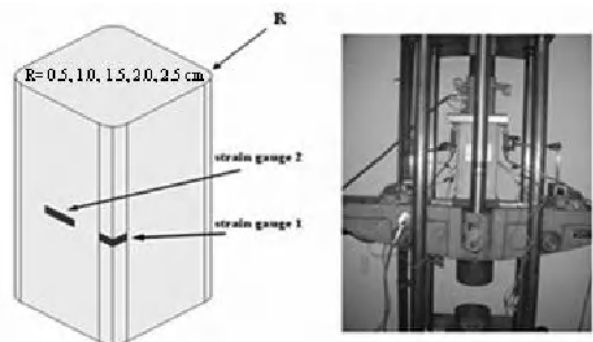


Figure 3 Test set up of loading and value of radiuses

In addition to the strain gauges, two LVDTs (linear variable differential transducers) were mounted to capture the vertical displacements. Load cell under the specimen was used to capture the axial load readings.

The wires for strain gauges, the load cell and the LVDTs were attached to data logger system and checked for readings. The instrumentation of the square specimen is shown in Figure 3.

The axial strains are obtained from average value of the two LVDTs divided by the gauge length.

4 DISCUSSION

Figures 4a-4e, stress-strain curve referring to confined specimens has been presented that in each of the curves value of edge radius would be fixed and number of confining layers has changed that the results is observable.

The stress-strain curve for concrete confined by FRP composites behaves bilinearly. The first portion of the stress-strain curve traces that of unconfined concrete until the jacket start to get activated. At this point, the curve became either ascend or descend, depending on the geometry of the cross-section and the confinement ratio provided.

Experimental results showed that for specimens with a certain corner radius, the concrete strength increases with an increase in the number of plies of CFRP & GFRP.

Also it showed that increase in specimen's edge radius, would increase the compression load carrying capacity of confined specimens. The ultimate strains in specimens with 2.5 cm radius are more than other specimens with smaller edges radius. (See Figures 4a-4e).

Also it showed that the ductility capacity of specimens with larger edge radius is more than other specimen because in specimens with fewer corner radiuses, there is stress concentration on edges and the sharpness of that area leads to reduction of performance quality.

At the begging of loading all load was carrying by concrete, then the concrete reaches to its compression capacity and a reduction occurs in stress-strain curve as a result of crashing in light weight aggregate, but with continuation loading on specimens, confining fibers of CFRP & GFRP work and lead stress-strain curve tangent to ascend. Thus specimen ultimate strength and strain would increase.

The experimental results show that important variables that affect the ductility parameters of a square column include the level of axial load and the amount of confining reinforcement. The proposed procedure relates the confinement design parameters such as the amount of FRP reinforcement and FRP strength to the column's ductile performance.

Figure 5–7 show the failed specimens after have been tested. As it is shown, regardless of its shape, the failure of the specimens took place within the middle half of the specimen.

In these specimens, as the corner radius increases the splitting of concrete becomes uniform along the height.

Confinement of specimens with CFRP has more ultimate strength than the specimens which confined with GFRP. Also for lightweight concrete wrapping the specimens by GFRP have more axial strain than specimen which confined with CFRP.

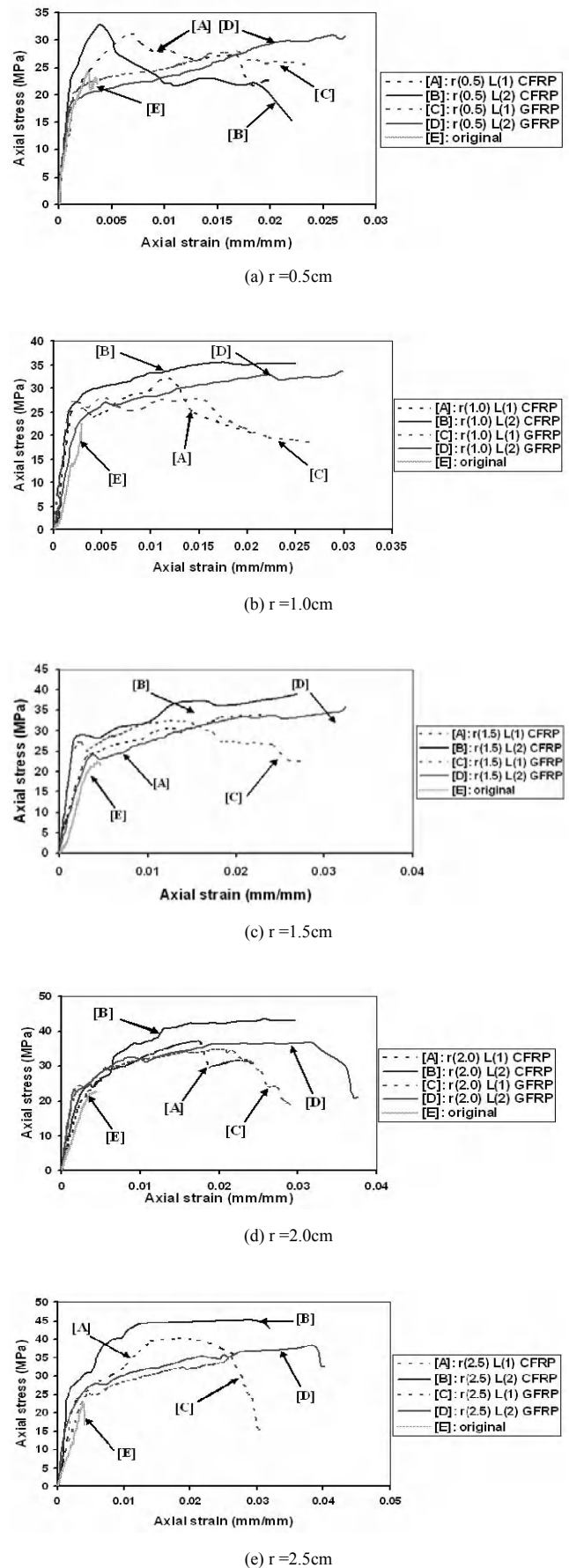


Figure 4 Stress-strain curve of specimens

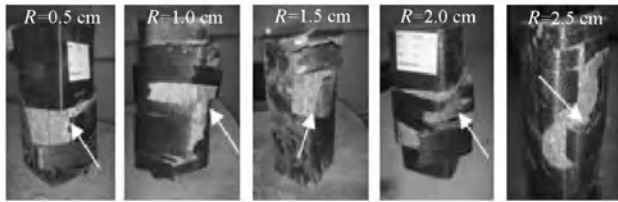


Figure 5 Failure modes for confinement with CFRP

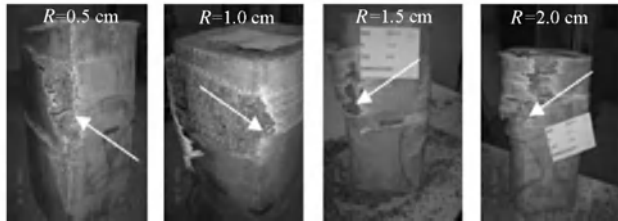


Figure 6 Failure modes for confinement with GFRP



Figure 7 Failure mode for original specimen

5 RESULTS & CONCLUSIONS

This work was conducted to study the compressive strength of FRP confined specimen. The experimental program included testing under pure axial load, 45 square concrete columns with 5 mm, 10 mm, 15 mm, 20 mm and 25 mm corner radius. These specimens are confined by CFRP & GFRP. It is to be mentioned that these specimens are confined with different numbers of CFRP & GFRP layers.

The main purpose was to investigate the effect of corner radius on the behavior of confined lightweight concrete elements by CFRP & GFRP.

The following conclusions are drawn based on the test results of this research:

- Increase of the number of confining layers in confined specimens leads to enhancement of the ultimate strength and strain.
- With increase of wrapping layers' number, stiffness of the specimens to be increased.

- With increase of corner radius, value of ultimate strength and strain increases in two states as same as normal weight concrete.
- Stress strain curve of confined specimens in two states, is the same as bilinear form.
- For lightweight concrete, wrapping the specimens in GFRP has more axial strain than specimen which is confined with CFRP.
- For lightweight concrete wrapping the specimens by GFRP have more axial strain than specimen which is confined by CFRP.
- The required amount of confining FRP increases with the increase in ductility demand, and in the level of axial load applied and also with the reduction of FRP strength.
- The failure of the carbon/epoxy jacketed specimens was explosive in nature releasing tremendous amount of energy.
- The failure of the square columns always starts at one of the corners proving that the stress concentration occurs at the corners.

REFERENCES

- Harmon, K.S. 2003. Recent Research on the Mechanical Properties of High Performance Lightweight Concrete, *In Theodore Bremner Symposium on High-Performance Lightweight Concrete. Tessaoniki, Greece* :131-150.
- Bisby, Luke A., Dent, Aaron J.S. & Green, Mark F. 2005. Comparison of Confinement Models for Fiber-Reinforced Polymer-Wrapped Concrete, *ACI Structural Journal*.
- Harajli, Mohamed H. 2006. Axial stress–strain relationship for FRP confined circular and rectangular concrete columns, *Cement & Concrete Composites* 28:938-948.
- Sheikh, Shamim A. & Li, Yimin. 2007. Design of FRP confinement for square concrete columns, *Engineering Structures* 29:1074-1083.
- Mitchell, D.W. & Marzouk, H.2007. Bond Characteristics of High-Strength Lightweight Concrete, *ACI Structural Journal*, V. 104, No. 1.
- Wu, G, Wu, Z.S. & Lu, Z.T. 2007. Design-oriented stress–strain model for concrete prisms confined with FRP composites, *Construction and Building Materials* 21:1107-1121.
- Youssef, Marwan N., Feng, Maria Q. & Mosallam, Ayman S. 2007. Stress–strain model for concrete confined by FRP composites, *Composites: Part B* 38:614-628.
- Al-Salloum, Yousef A. 2007. Influence of edge sharpness on the strength of square concrete columns confined with FRP composite laminates, *Composites: Part B* 38:640-650.

Confinement of Concrete Piles with FRP

Hatem M. Seliem (hmseliem@gmail.edu)

Department of Civil Engineering, Helwan University, Cairo, Egypt

Lining Ding & Sami Rizkalla

Constructed Facilities Laboratory, North Carolina State University, Raleigh NC, USA

ABSTRACT Precast piles are typically reinforced with steel spiral to provide confinement for the concrete core to increase the load carrying capacity as well as ductility of the pile. Confinement is particularly critical within the top region of the pile to resist the impact forces during driving. Due to direct exposure of piles to soils and harsh minerals, corrosion of outer spiral can compromise the long-term durability of typical piles. Since carbon fiber reinforced polymer (CFRP) materials are non-corrosive, they provide a promising alternative to the spiral steel for precast piles. This paper summarizes test results of an experimental program undertaken to evaluate the performance of specially designed CFRP Grid to replace the steel spirals for piles. Seven short columns, representing a 914 mm long section at the top of a pile were tested up to failure to study the effectiveness of the proposed CFRP Grid as reinforcement for confinement.

1 INTRODUCTION

1.1 General

Precast piles are typically reinforced with steel spiral to provide ductility and to enhance its load carrying capacity. Confinement is particularly critical within the top region of the pile to sustain the impact forces resulting from driving the pile into the ground. However, direct exposure of piles to the soil and other harsh environment may cause corrosion of the outer steel spirals which could compromise the long-term durability of the piles. This paper explores the use of a specially designed carbon fiber reinforced polymer (CFRP) Grid as an alternative to steel spirals for confining precast concrete piles due to the non-corrosive nature of FRP materials. The research included an experimental investigation to evaluate the effectiveness of the proposed CFRP Grid as a replacement of steel spirals. In addition, the bond strength of the proposed CFRP Grid is evaluated using a modified pull-out specimens.

1.2 Mechanical properties of CFRP Grid

The CFRP Grid used had C50 strands and spacing of 44.5 mm in both directions of the grid. The dry fiber area of each strand reported by the manufacturer is 1.71613 mm^2 . The reported ultimate tensile strength and tensile modulus of the fibers are 2800 MPa and 207 GPa, respectively.

To verify the values reported, twenty-four tension coupons from both directions were tested using the universal MTS testing machine and a 50mm extensometer. Each coupon included one strand from the direction under consideration. The average measured

maximum load for the main and transverse strands was 5060 N, respectively. An average ultimate elongation of minimum of 0.01 was recorded for both directions. In addition, a digital caliper and a micrometer were used to measure the width and thickness of the impregnated strands of the tension coupons before testing. An average width and thickness of 7.544 mm and 1.0516 mm were measured, respectively. Using the average measured area of 7.933 mm^2 , the tensile strength of the CFRP strands is 638 MPa.

2 TESTING OF PILE SPECIMENS

2.1 Test specimens and test setup

Seven short columns subjected to concentric axial compression up to failure. The typical dimensions of the test specimens are shown in Figure 1. The specimen is designed to represent a 914 mm long section at the top of a precast pile. The specimens had a 356 mm square cross-section with an overall height of 1143 mm. In addition to a control specimen made of plain concrete, two specimens were confined with 203 mm square steel spirals to provide a reference to evaluate the effectiveness of the proposed CFRP Grid. The remaining four specimens were confined with different reinforcement ratio of the proposed CFRP Grid with various overlap length.

The steel square spirals were made of W3.5 steel wire (cross-sectional area is 22.6 mm^2) provided a clear concrete cover of 76 mm, while the CFRP Grid was circular in shape with a diameter of 318 mm providing a clear cover of 19 mm. Details of test specimens and

concrete compressive strength at the day of testing are given in Table 1. It should be noted that only the two columns confined with steel spirals had 410 mm bars as longitudinal reinforcement to maintain the pitch of the spirals. Steel collars were provided at each end of the columns to prevent premature local crushing.

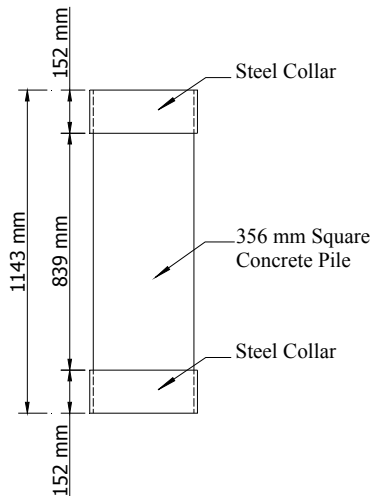


Figure 1 Typical pile specimen

Table 1 Confinement details of test columns

Specimen	Confinement Details	f'_c (MPa)
CN	No confinement	38.3
S@6*	Steel spirals with a pitch of 152 mm	37.9
S@3*	Steel spirals with a pitch of 76 mm	39.4
1C-8	1 layer W/ 203 mm Overlap	37.9
1C-16	1 layer W/ 406 mm Overlap	38.7
2C-C-8	2 continuous layers W/ 203 mm overlap	38.7
2C-S-8	2 separate layers W/ 203 mm overlap	37.9

* Columns had 410 mm bars as longitudinal reinforcement

The columns were tested using 8900 kN compression machine and were loaded concentrically. The columns were capped using Gypsum Cement to ensure parallel loading surfaces and uniform distribution of load to the bearing surfaces. The compression machine was operated in a displacement-controlled mode, maintaining the rate of loading of 4.45 kN/sec.

Linear potentiometers were used to measure the axial deformation of the columns. Electrical resistance strain gages were attached to the outer surfaces of the columns to measure the axial and lateral strain of concrete. For validation purposes, PI gages were also used to measure the axial and lateral strain of the concrete on the surface of the columns. In addition, strain gages were attached to the steel spirals or the CFRP Grid prior to casting of concrete to measure the strain in the confining material.

2.2 Test results

Behavior of the tested columns is assessed in light of

their load carrying capacity, load-deflection relationship, and measured axial concrete strain.

2.2.1 Axial load-carrying capacity

The ultimate axial load-carrying capacities of the seven tested columns are given in Table 2 along with the ratio of the axial capacity of each column to that of the control column (plain concrete). Test results given in Table 2 indicate that the column confined with one layer of CFRP Grid had the same axial load carrying capacity as that confined with steel spirals with a pitch of 76 mm. In addition, using a second layer of CFRP Grid did not enhance the axial capacity of the columns. It should be noted also that using two continuous layers had a better effect in comparison to two separate layers. Furthermore, increasing the overlap length from 203 mm to 406 mm did not affect the confinement level.

Table 2 Axial load-carrying capacity of test columns

Specimen	Axial Load (kN)	P/PCN
CN	2755	1.00
S@6	3413	1.24
S@3	4681	1.70
1C-8	4681	1.70
1C-16	4428	1.61
2C-C-8	4263	1.55
2C-S-8	3720	1.35

All the columns failed suddenly in a brittle manner due to the loss of the outer concrete shell. Failure shape of column 2C-C-8 at the conclusion of the test is shown in Figure 2(a), which is the typical failure exhibited by all test columns. During testing of the specimens confined with CFRP Grid, a popping noise was typically heard at high levels of loading. After completion of each test, the concrete cover was carefully removed and the CFRP Grid was inspected. It was found that strands of the CFRP Grid in both directions were ruptured at various locations as shown in Figure 2 (b) for column 2C-C-8. It is anticipated that rupture of the strands of the CFRP Grid was due to the pre-cracking of the strands which happened during the fabrication process in addition to



Figure 2 Column 2C-C-8 at the conclusion of the test

utilization of the material at high levels of loading. Rounding of the CFRP Grid introduces curvature in the strands which might cause cracking, therefore, using the CFRP Grid in small diameters may not be recommended.

2.2.2 Load-deflection behavior

The load-deflection relationships for all tested columns are shown in Figure 3. It is seen from Figure 3 that the type of confining reinforcement did not affect the initial axial stiffness of the columns. In addition, after reaching the peak load, the load capacity was significantly dropped and a second peak of loading was not achieved. This behavior is attributed to the small amount of spirals used for both the steel confined and CFRP Grid confined columns. It should be noted that the specimens were designed mainly to provide a closed comparison between the two confining materials and to explore the effectiveness of the proposed CFRP Grid.

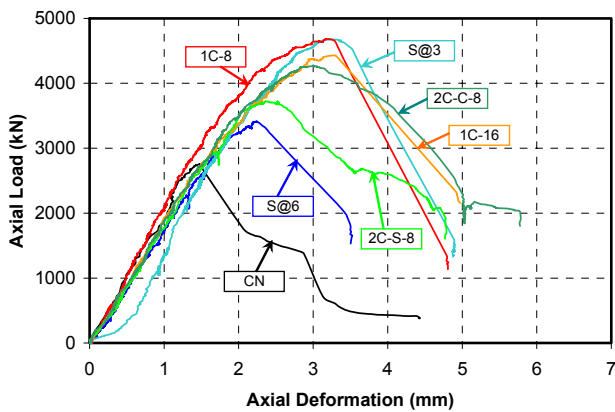


Figure 3 Load-deflection behavior of test columns

2.2.3 Axial strain

The measured axial load versus the measured axial surface strain of the concrete is shown in Figure 4 for six tested specimens. The axial strain reported herein are those measured using PI gages which were in close agreement to those measured using strain gages.

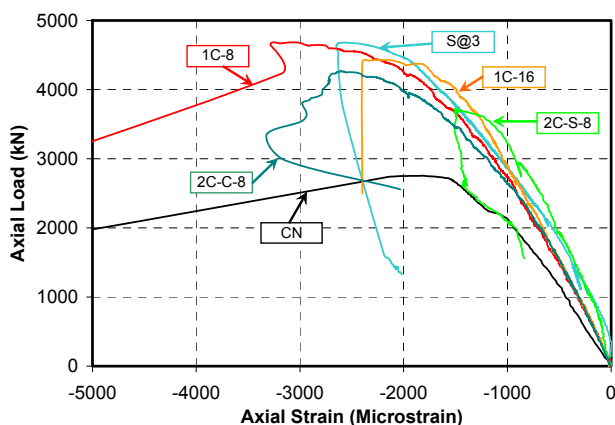


Figure 4 Measured axial strain for test columns

It can be seen from Figure 4 that the control column (without confinement) lost its carrying capacity when the axial strain reached a value of approximately 0.002, while the confined columns achieved an axial strain beyond the 0.002. The two columns 1C-8 (confined with one layer of CFRP Grid) and S@3 (confined with steel spiral with a pitch of 76 mm) who had the highest axial capacity were able to reach an axial concrete strain of approximately 0.003 before failure. The increase in the concrete axial strain is attributed to the confinement effect.

3 MODIFIED PULL-OUT TEST

To examine the required development length of the proposed CFRP Grid, the experimental program included eight modified pull-out specimens.

3.1 Test specimens and test setup

The parameters investigated included the embedment length (L) and the presence of the transverse strands. The modified pull-out specimen is composed of two layers of the CFRP Grid embedded on each end into two concrete blocks. The load was applied in the direction of the main strands. The embedment length (L) varied from 2 times the grid spacing (89 mm), 3 times the grid spacing (133 mm), 5 times the grid spacing (222 mm), and 10 times the grid spacing (445 mm). Figure 5 shows details of the test specimens. Two duplicate specimens with the same embedment length, one with transverse strands (WT) and the other without transverse strands (NT), were tested. For specimens without transverse strands, the transverse strands were cut carefully to avoid any damage of the longitudinal strands.

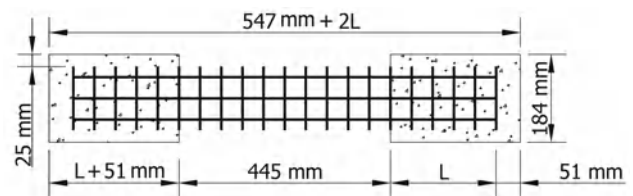


Figure 5 Details of modified pull-out test specimens

The embedment lengths of 5 and 10 times the grid spacing were selected to match the overlap lengths used in the column specimens. The 2 and 3 times the grid spacing were selected to examine the behavior of small development lengths. The selected concrete cover of 19 mm represented the clear cover used for constructing the column specimens. The measured concrete compressive strength of all tested specimens was 27.8 MPa.

The test setup included a hydraulic jack placed between the two concrete blocks to apply forces to the blocks, therefore subjecting the main strands of the CFRP Grid to tension as shown in Figure 6. The concrete

blocks were supported on rollers to allow for the movement of the blocks under the effect of the applied load. A load cell was mounted to the hydraulic jack to measure the applied load. Two linear potentiometers were mounted to the two sides of the concrete blocks to measure the relative displacement between the blocks.

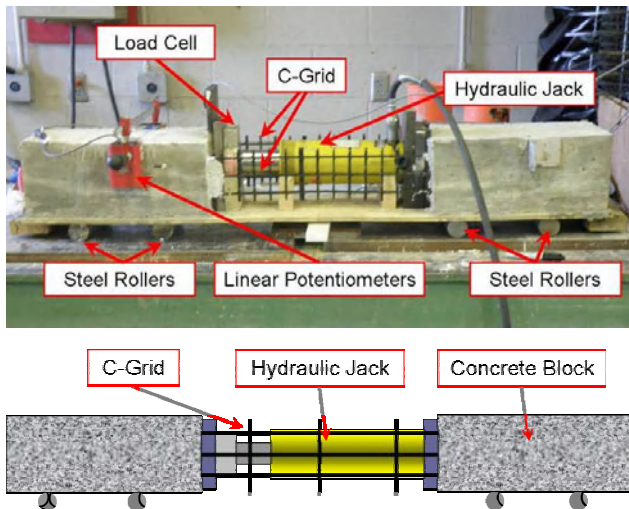


Figure 6 Modified pull-out test setup

3.2 Test Results

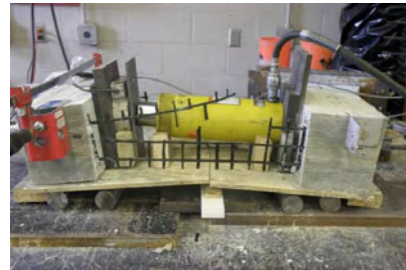
The maximum measured load for all tested specimens is presented in Table 3. The eight specimens failed by rupture of the strands of the CFRP Grid outside the concrete blocks as shown in Figure 7 for specimens 2S-WT and 3S-NT. Accordingly, it can be concluded that using an embedment length of twice the grid spacing (89 mm) can develop the full tensile strength of the strands of the CFRP Grid. However, since all the specimens failed in rupture of the strands, the effect of the transverse wires on the bond strength of the CFRP Grid to concrete in direct tension could not be evaluated.

Table 3 Failure of load of pull-out specimens

Specimen	Maximum load (kN)
2S-NT	23.8
2S-WT	23.0
3S-NT	15.8
3S-WT	17.0
5S-NT	16.8
5S-WT	15.8
10S-NT	18.2
10S-WT	12.8



2S-WT



3S-NT

Figure 7 Pull-out specimens at the conclusion of the test

4 CONCLUSIONS

The findings of this research program can be summarized as follows:

Use of CFRP Grid for confinement of precast piles is a promising alternative to steel spirals. However, it is not recommended to use the CFRP Grid with diameters less than that used in this study ($D=318$ mm), unless additional testing is performed. It was observed that rounding the CFRP Grid in small diameters causes cracking in the strands due to the curvature introduced.

The column confined with one layer of CFRP Grid had the same axial load capacity of that confined with steel square spirals with a pitch of 76 mm.

Use of a second layer of CFRP Grid did not enhance the load carrying capacity of the columns.

The two continuous layers of the CFRP Grid were more effective than using two separate layers of the CFRP Grid. This behavior is attributed to the inefficiency of the second separate grid layer and possible pre-cracking of CFRP strands due to fabrication effort.

Increasing the overlap length from 203 mm to 406 mm did not affect the confinement.

Bond length of twice the grid spacing can develop the full tensile strength of the strands of the CFRP Grid.

5 ACKNOWLEDGMENT

The authors gratefully acknowledge Altus Group for providing the material used in this study and funding of the project.

Three-Dimensional Finite Element Model for FRP-Confined Circular Concrete Cylinders under Axial Compression

Q.G. Xiao, J.G. Teng (cejgteng@inet.polyu.edu.hk), T. Yu & L. Lam

Department of Civil and Structural Engineering, The Hong Kong Polytechnic University, Hong Kong, China

ABSTRACT This paper presents a 3D FE model for FRP-confined circular concrete cylinders based on a plastic-damage constitutive model for concrete recently proposed by Yu et al. (2010b). This 3D model is capable of modeling deformation non-uniformity in the axial direction due to factors such as end restraints. Numerical results obtained using the FE model for FRP-confined cylinders with end restraints or with a vertical gap in the FRP jacket conform to expected trends although their quantitative accuracy awaits confirmation by laboratory tests. This FE model has the potential for extension to more general cases of FRP-confined concrete columns (e.g. rectangular concrete columns) and can provide a useful tool for the exploration of confinement mechanisms in the development of simple stress-strain models for design use.

1 INTRODUCTION

A number of studies exist on the finite element (FE) modeling of fibre-reinforced polymer (FRP)-confined concrete using a Drucker-Prager (D-P) type plasticity model for the concrete (e.g. Mirmiran et al. 2000; Rousakis et al. 2007). In a recent study, Yu et al. (2010a, b) developed a new plastic-damage model for FRP-confined concrete in which the deficiencies of the previous D-P type plasticity models are eliminated. This model was formulated within the theoretical framework of the concrete damaged plasticity model (CDPM) provided in ABAQUS and was implemented in ABAQUS for the analysis of concrete cylinders whose deformation is assumed to be uniform along the height. This assumption means that the FE model needs to include only a horizontal slice of the column represented by a single-layer of solid elements. Such a slice model can closely represent the mid-height region of an FRP-confined cylinder but is incapable of capturing axial non-uniformity in deformation and stresses due to end constraints and other factors such as steel hoops. Provided axial non-uniformity is unimportant, this slice model provides an efficient approach for modeling interactions in the transverse plane. Yu et al. (2010b) has successfully employed the slice model in the nonlinear FE analysis of hybrid FRP-concrete-steel double-skin tubular columns (DSTCs).

In a slice model, the axial direction is always one of the principal directions for both stresses and strains, and the other two principal directions (i.e. lateral directions) are always perpendicular to the column axis. In addition, the principal stress and strain in the axial direction are normally larger than the principal stresses and strains in

both lateral directions. This paper presents an extension of Yu et al.'s (2010b) slice model to a truly three-dimensional (3D) model for FRP-confined circular concrete cylinder with end effects appropriated captured. The necessary refinements to the plastic-damage model of Yu et al. (2010b) are first discussed. Numerical results from the 3D FE model are then presented to examine the capability of the FE model in capturing the effects of restraints against horizontal movements at the ends of the circular cylinder in an axial compression test. The effect of the existence of a mid-height vertical gap between the upper and lower parts of the FRP jacket on the behavior of confined concrete is also discussed using numerical results from the 3D FE model. In this paper, compressive stresses and strains are defined as positive while tensile stresses and strain are negative, unless otherwise specified.

2 PLASTIC-DAMAGE MODEL FOR CONFINED CONCRETE

In the plastic-damage model proposed by Yu et al. (2010b), the damage parameter, the strain-hardening/softening rule and the flow rule are all confinement-dependent and the yield surface reflects the effect of the third deviatoric stress invariant. In addition, the characteristics of non-uniformly confined concrete are included in this model by defining an effective confining pressure as follows:

$$\sigma_{1,eff} = \frac{2(\sigma_2 + 0.039f'_{co})(\sigma_3 + 0.039f'_{co})}{\sigma_2 + \sigma_3 + 0.078f'_{co}} - 0.039f'_{co} \quad (1)$$

where f'_{co} is the compressive strength of unconfined concrete while σ_2 and σ_3 are the two principal lateral

stresses respectively. Two methods have been explored in Yu et al. (2010b) for the flow rule of non-uniformly confined concrete, with the second method being adopted in the present study as it was deemed by Yu et al. (2010b) to be the more reliable approach. This method relates the flow rule to both the equivalent plastic strain and the term $2\sigma_{l,eff}/(\varepsilon_2 + \varepsilon_3)$ whose absolute value represents confinement stiffness, with ε_2 and ε_3 being the two principal lateral strains respectively.

In a 3D FE model of an entire FRP-confined concrete cylinder/column, shear stresses generally develop between adjacent horizontal slices as a result of axial non-uniformity in deformation due to end constraints and other factors. As a result, the axial direction is not necessarily one of the principal directions. For a such more general stress state, the following assumptions are made in implementing Yu et al.'s (2010b) plastic-damage model without compromising the generality of the model for practical applications: (a) σ_2 and σ_3 in Eq. 1 are the two smaller principal stresses while ε_2 and ε_3 used in the flow rule are the two smaller principal strains; (b) σ_2 (or σ_3) is ignored in calculating $\sigma_{l,eff}$ if it becomes negative (i.e. $\sigma_2 < 0$ or $\sigma_3 < 0$), as the effect of tensile stresses on confined concrete is unclear; (c) the term $\varepsilon_2 + \varepsilon_3$ is normally negative (i.e. tensile strains) due to the expansion of concrete, but if it is found to be positive or zero, it is taken as a very small negative value in determining the flow rule.

It should be noted that the analysis-oriented stress-strain model of Teng et al. (2007) was used in Yu et al. (2010b) in deriving the parameters for the plastic-damage model, while in the present study, Jiang & Teng's (2007) model, which provides closer predictions for weakly confined concrete, was used.

3 FE MODEL

The FE model was implemented in ABAQUS to simulate the behavior of FRP-confined concrete cylinders. Circular concrete cylinders with a diameter (D) of 152 mm and a length (L) of 304 mm were initially considered; cylinders with other lengths were also considered in studying the effect of end restraints. The unconfined concrete had a compressive strength f'_{co} of 30 MPa with a corresponding axial strain ε_{co} of 0.0025. The plastic-damage model as described in the previous section was adopted as the constitutive model for concrete in the FE simulations. The confining FRP jacket was modeled as an orthotropic elastic shell with the stiffness being mainly in the hoop direction; the axial elastic modulus of the FRP was assigned a very small value (1×10^{-5} MPa). The Poisson's ratio was set to be zero. The modulus of elasticity in the hoop direction E_{frp} , the thickness t_{frp} , and the hoop rupture strain $\varepsilon_{h,rupt}$ of the FRP jacket were 80.1 GPa, 0.34 mm, and 1.3%, respectively. This simplified model for the FRP jacket means that it functions as a confining device

in the FE model.

Considering the symmetry conditions of FRP-confined circular cylinders under axial compression, an axisymmetric model was used and only half of the column height was included in the FE simulation. The axisymmetric solid element CAX4 and the axisymmetric shell element SAX1 in ABAQUS were adopted for the concrete and the FRP jacket respectively. The concrete and the FRP jacket were tied together at their common nodes so that no relative slides were allowed at their interface. Both the concrete and the FRP jacket had elements size of about 5 mm chosen on the basis of a mesh convergence study. In all the FE analyses, axial displacements were uniformly imposed on the top surface of the concrete cylinder until the maximum lateral strain within the FRP jacket reached its rupture strain (i.e. 1.3%)

4 RESULTS AND DISCUSSIONS

4.1 Effect of end restraints

Circular concrete cylinders confined with a continuous FRP jacket, with or without end restraints, were analyzed. Figures 1 and 2 show that without end restraints, the distributions of both axial displacements and stresses are uniform; however, when the horizontal displacements at the end are prevented with restraints, the distributions of both axial displacements and axial stresses become highly non-uniform. The latter case is close to the actual situation of a laboratory test due to frictions between the end surfaces of the cylinder and the loading platens.

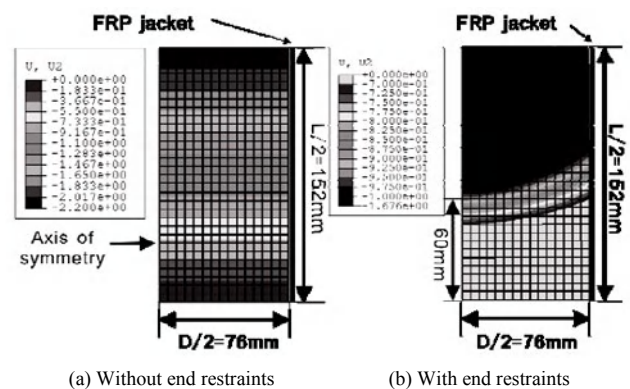


Figure 1 Distributions of axial displacements in FRP-confined circular concrete cylinders

Figure 3 shows the axial stress-axial strain curves (referred to as stress-strain curves hereafter) and axial strain-lateral strain curves obtained from the FE analyses. For the case with end restraints, the FE results shown in Figure 3 are based on the following definitions: (a) the axial stress is the average axial stress over the cross-section; (b) the lateral strain is that of the outer surface of the concrete core at mid-height; and (c) the

axial strain is the average strain defined in one of three different ways. The three definitions of the average axial strain are as follows: (I) the axial displacement of the outer surface node of the concrete core at 60.8 mm divided by 60.8 mm; (II) the average axial displacement of all nodes of the concrete core at 60.8 mm divided by 60.8 mm; (III) the total axial shortening of the cylinder divided by the cylinder height.

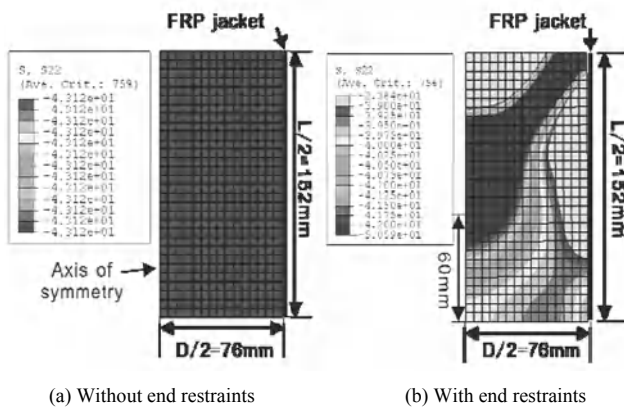
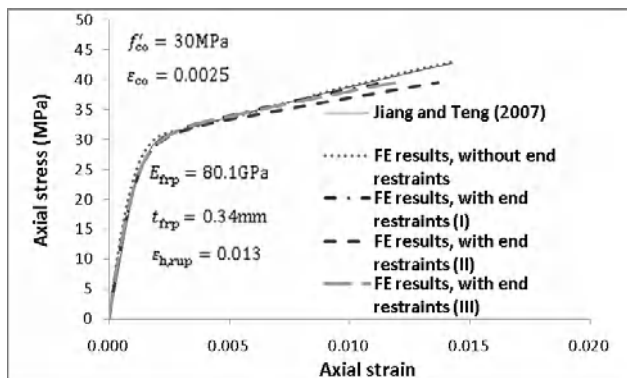
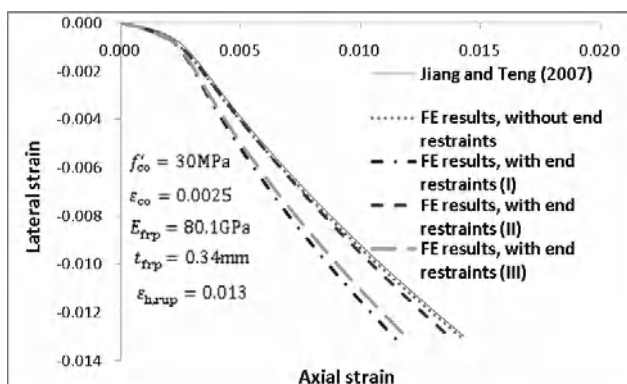


Figure 2 Distribution of axial stresses in FRP-confined circular concrete cylinders



(a) Axial stress-axial strain curves



(b) Axial strain-lateral strain curves

Figure 3 Behavior of FRP-confined circular concrete cylinders

It can be seen from Figures 3(a) and 3(b) that for the case without end restraints, the FE analysis produced almost the same stress-strain curve and axial strain-lateral strain

curve as predicted by Jiang & Teng's (2007) model. For the case with end restraints, the stress-strain curves based on axial strains of definitions (I) and (III) almost coincide with that predicted by Jiang and Teng's (2007) model, but terminate at smaller ultimate axial strains. By contrast, the curve based on axial strains of definition (II) falls below that predicted by Jiang and Teng's (2007) model, but the ultimate axial strain is nearly the same as that from Jiang and Teng's (2007) model.

The FE results indicate that the compressive strength of confined concrete with end restraints is lower than that without end restraints (Figure 3(a)). This is not in agreement with experimental results of unconfined concrete. It has been well established by laboratory tests that end restraints increase the observed compressive strength of concrete and this effect becomes more significant as the L/D ratio decreases (Sangha and Dhir 1972). However, FE results from the present study not shown here indicated that end constraints lead to a reduced confined concrete compressive strength for L/D ratios from 1 to 3, but this unfavorable effect of end restraints becomes insignificant when the L/D ratio exceeds 3.

The adverse effect of end restraints on the compressive strength of FRP-confined concrete cylinders can be explained as follows. End restraints prevent the FRP-confined cylinder from lateral expansion at the ends and lead to non-uniform straining of the FRP jacket along the height. When the FRP jacket reaches its hoop rupture strain at the mid-height, its hoop strain is still much smaller away from the mid-height and is equal to zero at the ends. As a result of this non-uniform straining of the jacket, the FRP-confined concrete reaches its ultimate axial stress earlier at a reduced total axial displacement [i.e. a smaller value of axial strain of definition (III), as shown in Figure 3(b)]. Laboratory tests are needed to confirm the correctness of the above explanation.

4.2 Effects of a gap in the FRP jacket

In certain practical applications (e.g. a column with a transverse beam), the column surface cannot be fully covered by a continuous FRP jacket and instead a vertical gap exists between the upper and lower parts of the FRP jacket. In addition, columns may be strengthened using discrete FRP rings (e.g. Wu et al. 2009) instead of a continuous FRP sheet where vertical gaps exist between rings. The FE model, being a truly 3D model, was employed to study the effect of a single vertical gap in the FRP jacket on the behavior of confined circular concrete cylinders. End restraints were not specified in these FE analyses to simplify the situation based on the results discussed above. Two gap heights, 38mm and 76mm, were considered in the FE simulations.

Figure 4 shows that the distribution of axial stresses is highly non-uniform due to the presence of a vertical gap

at the mid-height of the FRP jacket although the cylinder was uniformly loaded without end restraints. The effect of the gap on the stress-strain curve is shown in Figure 5, where the results for a continuous FRP jacket and for an unconfined cylinder are also shown for comparison. The axial strain is the average strain over the entire height of the cylinder. Figure 5 clearly indicates that a larger gap height leads to a greater reduction in the compressive strength of FRP-confined concrete. The stress-strain curve features a softening branch when the gap height is 76 mm. The results given in Figures 4 and 5 conform to expected trends and provides an initial indication that the FE model has captured the mechanics of the problem at least qualitatively. The quantitative accuracy of the FE results await confirmation by laboratory tests.

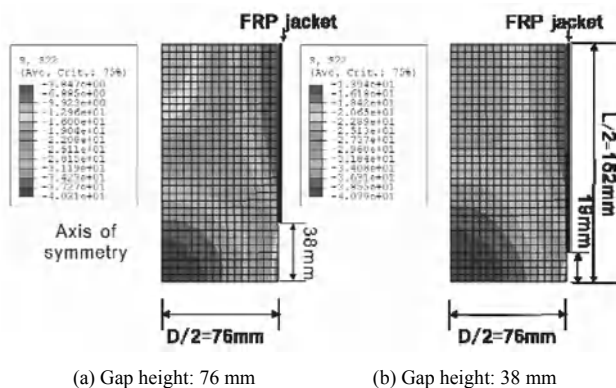


Figure 4 Distribution of axial stresses in FRP-confined circular concrete cylinders with a mid-height gap in the jacket

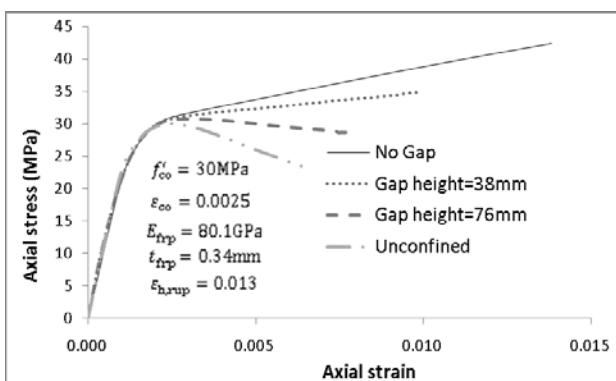


Figure 5 Axial stress-axial strain curves of FRP-confined circular concrete cylinders with a mid-height gap in the jacket

5 CONCLUDING REMARKS

A 3D FE model for FRP-confined circular concrete cylinders based on Yu et al.'s (2010b) plastic-damage model has been presented in this paper. This 3D model is capable of modeling deformation non-uniformity in the axial direction due to factors such as end restraints

and a vertical gap in the FRP jacket. Numerical results obtained using the FE model have revealed that end restraints lead to highly non-uniform distributions of stresses and strains. FE results have also shown that a vertical gap in the FRP jacket leads to non-uniform distributions of stresses and strains and a reduction in the axial compressive strength. The FE model is currently being extended to more general cases of FRP-confined concrete columns such as FRP-confined rectangular concrete columns and eccentrically loaded concrete columns. The FE model with suitable verification can provide a useful tool for the exploration of confinement mechanisms in various FRP-confined concrete columns in the development of simple stress-strain models for use in design.

6 ACKNOWLEDGEMENTS

The authors gratefully acknowledge the financial support provided by the Research Grants Council of the Hong Kong Special Administrative Region, China (Project No: PolyU 5289/08E) and The Hong Kong Polytechnic University.

REFERENCES

- Mirmiran, A., Zagers, K. & Yuan, W.Q. 2000. Nonlinear finite element modeling of concrete confined by fiber composites. *Finite Elements in Analysis and Design* 35(1): 79-96.
- Jiang, T. & Teng, J. G. 2007. Analysis-oriented stress-strain models for FRP-confined concrete. *Engineering Structures* 29(11): 2968-2986.
- Rousakis, T.C., Karabinis, A.I. & Kioussis, P. D. 2007. FRP-confined concrete members: Axial compression experiments and plasticity modelling. *Engineering Structures* 29 (7): 1343-1353.
- Sangha, C.M. & Dhir, R.K. 1972. Strength and complete stress-strain relationships for concrete tested in uniaxial compression under different test conditions. *Materials and Structures* 5(6): 361-370.
- Teng, J. G., Huang, Y. L., Lam, L. & Ye, L. P. 2007. Theoretical model for fiber-reinforced polymer-confined concrete. *Journal of Composites for Construction*, ASCE 11(2): 201-210.
- Wu, H. L., Wang, Y. F., Yu, L., and Li, X. R. 2009. Experimental and Computational Studies on High-Strength Concrete Circular Columns Confined by Aramid Fiber-Reinforced Polymer Sheets. *Journal of Composites for Construction*, ASCE 13(2): 125-134.
- Yu, T., Teng, J. G., Wong, Y. L. & Dong, S. L. 2010a. Finite element modeling of confined concrete-I: Drucker-Prager type plasticity models. *Engineering Structures* 32(3): 665-679.
- Yu, T., Teng, J. G., Wong, Y. L. & Dong, S. L. 2010b. Finite element modeling of confined concrete-II: Plastic-damage model. *Engineering Structures* 32(3): 680-691.

Flexural Strengthening of Concrete Beams and Slabs

Numerical Analysis of Rectangular Reinforced Concrete Columns Confined with FRP Jacket under Eccentric Loading

M. Hajsadeghi (hajsadeghi_civil@yahoo.com)
MSc Candidate, Shahrood University of Technology, Shahrood, Iran

F.J. Alaei
Assistant Professor, Shahrood University of Technology, Shahrood, Iran

ABSTRACT The present paper is devoted to investigate the behavior of square RC columns confined with FRP wraps using ANSYS software. A total of four prisms of size 150mm×300mm×500mm and 210mm×210mm×500mm were simulated by the FE model and the results were compared with the experimental test results reported in literature. Very good agreement was found between the model results and the test results. Therefore, the model was validated. As predicted, it was found that the effectiveness of FRP jackets under eccentric loads is reduced in comparison with concentric loads. In the next step, the interaction diagrams of axial force and bending moment for columns confined with FRP wrap was obtained from the model results. They were compared with the interaction diagrams proposed by the design guideline of ACI 440.2R-08. It was found that the load carrying capacities resulted from the model are generally higher than those recommended by ACI 440.2R-08.

1 INTRODUCTION

Existing concrete structures may be found to perform unsatisfactorily for a variety of reasons. This could manifest itself by poor performance under service loading, in the form of excessive deflections and cracking, or there could be inadequate ultimate strength. Additionally, revisions in structural design and loading codes may render many structures previously thought to be satisfactory, noncompliant with current provisions. In the present economic climate, rehabilitation of damaged concrete structures to meet the more stringent limits on serviceability and ultimate strength of the current codes, and strengthening of existing concrete structures to carry higher permissible loads, seem to be a more attractive alternative to demolishing and rebuilding.

FRP materials as thin laminates or fabrics offer an ideal alternative for retrofitting of concrete structures. They generally have high strength to weight and stiffness to weight ratios and are chemically quite inert, offering significant potential for durable lightweight, cost effective and retrofit.

FRP composites are used as externally bonded reinforcement to concrete structures for essentially two purposes: to provide confinement to concrete subjected to compression (jacketing system), and to improve bending and/or shear strength of a reinforced concrete flexural member such as beam, slab, etc. In RC members under compression, longitudinal strains are produced. Considering Poisson effect, transverse strains

are also developed. Wrapping columns with FRP causes tensile stresses in confining members and applies pressure to concrete core. Confining columns significantly increases their load carrying capacity and ductility.

As shown in Figure 1, in circular and square columns confined with FRP wraps under concentric loading, the distribution of confining stresses on their sections are different. It can be seen that in circular sections the lateral confining stresses are uniformly distributed whereas in rectangular sections non-uniform lateral stresses are applied on the section. The corners of rectangular sections are confined in two directions; therefore, the strength of concrete located in these areas is higher than that of the other zones. In RC columns under eccentric loading, the distribution of lateral stresses varies from what shown in Figure 1.



Figure 1 Confining stress distribution in circular and square section under concentric loading

Saatcioglu et al. suggested a linear stress distribution for lateral compressive stresses induced by transverse reinforcement in the columns under eccentric loading. Based on their assumption the stress induced in concrete

varies linearly and its amount depends on its location in the section.

Parvin and Wang showed that the change of the compressive stresses due to FRP wrap is non-linear when eccentric load acts on columns. They also claimed that the efficiency of FRP wraps is intensively decreased when the eccentricity of the load is increased.

In the present article, first, the effect of confining stresses in rectangular columns wrapped with FRP is investigated using a Finite Element model (ANSYS Ver. 8). Then, using this model and varying the eccentricity of the applied load, the load carrying capacity of columns under different conditions of eccentric loading is evaluated. Finally, the interaction diagrams of axial load-bending moment proposed by ACI 440.2R-08 are compared with those resulted from the Finite element model.

2 FINITE ELEMENT MODELLING

In this study, a total of four prism specimens of size 150×300×500mm and 210×210×500mm were studied and modeled. The corner's radius of all columns was 40mm. Four 12mm steel bars and six 8mm stirrups were used as the longitudinal and transverse reinforcements of the specimens, respectively (see Figure 2).

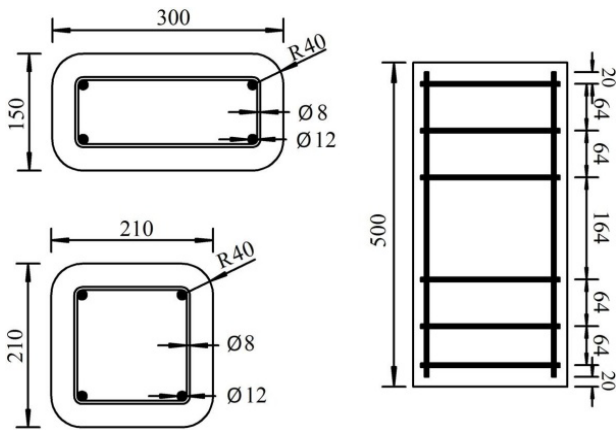


Figure 2 Specifications of columns (Dimensions are in mm unit)

The yield stress and strain of the main bars were 339MPa and 0.0017 and those of the stirrups were 476MPa and 0.0024, respectively. Two specimens were fully wrapped with 3 and the other two with 5 uni-directional CFRP layers with the thickness of 0.165 per ply. The details of each specimen can be found in Table 1. The cylindrical compressive strength, the modulus of elasticity and the Poisson's ratio of concrete were 26.4MPa, 24150MPa and 0.2, respectively. The mechanical properties of the CFRP are shown in Table 2.

There are many constitutive models for confined concrete as a pressure and constraint sensitive material. In this study the Drucker-Prager (DP) plasticity model was employed for modeling the non-linear behavior of

concrete, which assumes an elastic-perfectly plastic response. The DP model is a smooth circular cone along the hydrostatic axis in principal stress space. C is the cohesion of the material and ϕ is the internal friction angle of the material that those are used for defining the DP model. The values of cohesion and internal friction of concrete were selected to be 9.05MPa and 15 degrees, respectively.

Table 1 Finite element analysis column model

Model ID	Cross Section	Number of layers & Thickness of Wrap mm (in)
S-3	Square	3 - 0.495 (0.0195)
S-5	Square	5 - 0.825 (0.0325)
R-3	Rectangular	3 - 0.495 (0.0195)
R-5	Rectangular	5 - 0.825 (0.0325)

Table 2 Unidirectional CFRP material properties

Description	Coupon Test Data
Tensile Modulus of Elasticity	$E_x=230\text{GPa}$ (3, 3360Ksi) $E_y=12\text{GPa}$ (1740Ksi)
Tensile Strength	$f_{tu}^*=3430\text{MPa}$ (498Ksi)
Ultimate Rupture Strain	$\epsilon_{tu}=0.015$
Nominal Thickness	$t_f=0.165\text{mm/ply}$

In the present study the failure model of William-Warnke was used as failure criterion for concrete. Both cracking and crushing failure modes can be accounted for in it. The uni-axial tensile and compressive strengths are needed to define a failure surface for the concrete.

The bottom of the columns was restrained from displacement in x, y, and z directions. The symmetric condition was modeled on the two planes yz, and zx. The finite element modeling of rectangular specimens (containing, symmetric condition, boundary conditions, and meshing of model) are seen Figure 3.

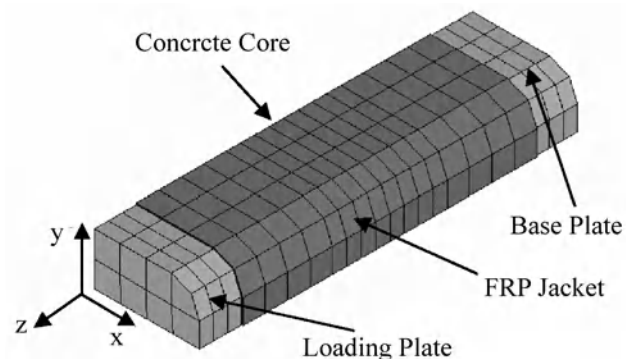


Figure 3 FE modeling of 1/4 rectangular specimens

Concrete, steel reinforcement (including longitudinal and transverse) and FRP were modeled using SOLID65, LINK8, and SHELL41 elements of ANSYS software, respectively. Any slip between concrete, steel

reinforcement and FRP was ignored. SOLID45 elements were used for the steel plates at the support and the loading areas as rigid bodies. Considering that FRP only resists tensile stresses, “tension-only” option of SHELL41 was activated. The loading of all specimens was controlled by force.

3 FAILURE CRITERIA

The maximum tensile strain observed in FRP wraps is usually lower than the value reported by manufacturers for tensile coupon tests. Generally, premature failures are related to several parameters such as material stiffness, lay-up technique, and radius of curvature throughout the cross section. To avoid the over-estimation of FRP strain capacities, a reduction factor of 48 percent was introduced to decrease the tensile rupture strain of FRP.

4 FINITE ELEMENT RESULTS AND DISCUSSION

To validate the proposed FE model, the test results [8] were compared with the model results. Good agreement was found between their results. In the following subsections the results of the FE model are presented and discussed.

4.1 Compressive stress distribution

In Figure 4 the contours of compressive stresses are shown at the mid-height of the rectangular columns under concentric loading. As it can be seen, the stress distribution over these sections is non-uniform and the level of non-uniformity is increased with the increasing of the number of layers. This phenomenon is caused by the shape of the cross section. In fact, at any location of the cross section different lateral pressure from FRP wrap is applied and therefore, the distribution of compressive stress becomes non-uniform.

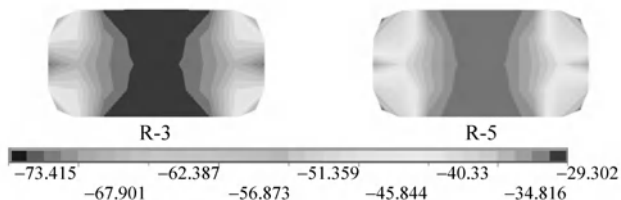


Figure 4 Contours of compressive stress in mid-height of rectangular columns under concentric loading

In all models, the maximum compressive stress occurs in the neighborhood of the corners and its minimum happens at the middle of the larger sides.

In Figure 5, the contours of the compressive stresses are shown for rectangular columns under the eccentric loads with $e/h=10\%$; in which, e is distance between load and plastic center and h is the dimension of the

section that perpendicular to the neutral axis. It can be observed that the level of non-uniformity of the stress distribution in this state is higher than that under concentric loading. It is evident that in this case in addition to the shape effect, the load is applied eccentrically. The maximum compressive stresses occur at the corners, close to the external load and away from the neutral axis, whereas the minimum stresses are observed along the sides away from the load and close to the neutral axis. Where the maximum compressive stresses occur, FRP wraps are active and provide efficient confinement to the section. In opposite areas, due to less lateral expansion, FRP wraps do not play an efficient role in confining application.

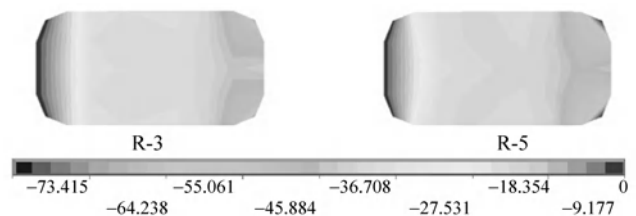


Figure 5 Contours of compressive stress in mid-height of rectangular columns under 10% eccentric loading

For better understanding of the effect of eccentricity on the compressive stresses, Figure 6 demonstrates the contours of the model S-3 under three load conditions: concentric load, 5% and 10% eccentric load. It can be observed that the more the eccentricity of the loading, the less confinement on the sides close to the neutral axis.

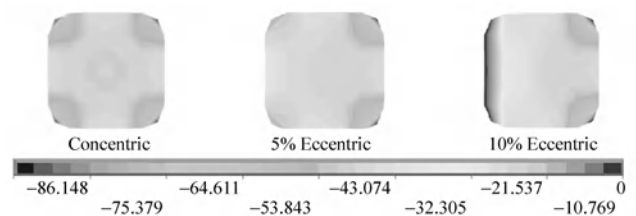


Figure 6 Contours of compressive stress in mid-height of S-3 column under different loading states

As be observed, compressive stress in 5% eccentric loading case, in closer corners to neutral axis has been decreased and with increasing eccentricity, in 10% eccentricity case compressive stress in these areas desire to zero. Lack of confining these areas is causes of lack sufficient transverse deformation of those.

4.2 Load carrying capacity

In Figure 7, the load carrying capacity of columns under concentric load and eccentric load (10% eccentricity) is compared. It is clear that the load carrying capacity of the columns under eccentric load is lower than that of concentric load. This reduction in the capacity has to be taken into account. As in practice, there is no column

under pure concentric loading and in design; a minimum eccentricity always has to be considered.

In Figure 7, the cross section, reinforcement ratio and the radius of corners in square and rectangular models are the same. However, in both concentric and eccentric loading cases, the effectiveness of confinement for square sections is higher than the rectangular ones. This difference is increased with the increasing of the number of layers.

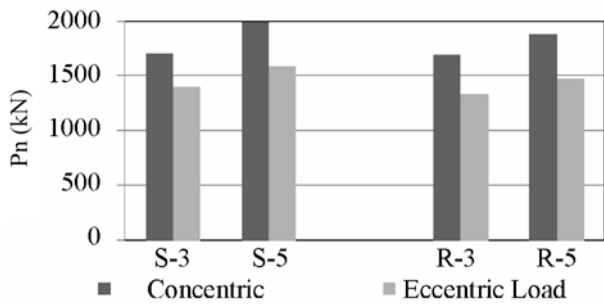


Figure 7 Load-carrying capacities of columns under concentric and 10% eccentric loading

4.3 Interaction diagrams

In the last step of this study, the interaction diagram of axial load-bending moment resulted from the FE models were compared with those proposed by ACI 440.2R-08. Figure 8 and Figure 9 show these diagrams for rectangular and square sections, respectively.

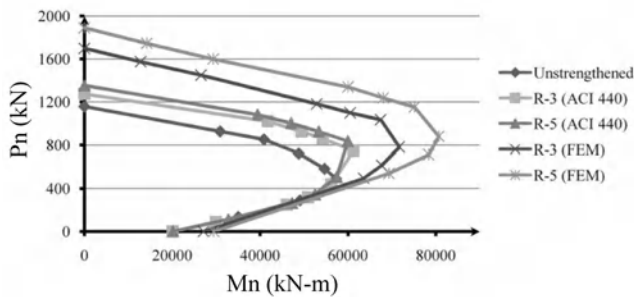


Figure 8 Interaction diagrams of rectangular columns

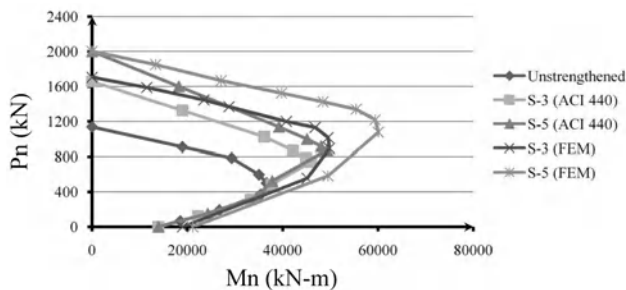


Figure 9 Interaction diagrams of square columns

Comparing these diagrams shows that there is a good agreement between the FE model and ACI results in the tension zones; while a considerable difference exists in some parts of compression zones. This issue is under investigation now and will be discussed in further publications.

5 CONCLUSIONS

The following conclusions can be drawn from this study:

- (1) FRP jackets can significantly enhance the load-carrying capacity of RC columns under concentric and eccentric loading.
- (2) In both loading states, concentric and eccentric, increasing the number of FRP wraps will increase the load-carrying capacity of columns.
- (3) In compression zone of interaction diagram, the value of load and moment proposed by ACI 440 are considerably lower than those resulted from FE models; while this difference is negligible in tension zone. Somehow this difference is very low in pure axial load for square specimens.

REFERENCES

Nanni, Amir. 1995. Concrete repair with externally bonded FRP reinforcement: examples from Japan; *J. Conc. Int.*, 97: 22-26.

Büyüköztürk, O. and Hearing, B. 1998. Failure behavior of pre-cracked concrete beams with FRP; *Journal of ASCE Compos Constr*, 2, 3: 138-144.

Saatcioglu, M., Salamat, A. H. and Razvi, S. R. 1995. Confined columns under eccentric loading; *Journal of ASCE of Structural Engineering*, Vol. 121, No. 11: 1547-1556.

Parvin, A., Wang, W. 2001. Behavior of FRP jacketed concrete columns under eccentric loading; *Journal of ASCE Compos Constr*, 5(3): 146-152.

Mirmiran, Amir, Zagers, Kenneth and Yuan, Wenqing. 2000. Nonlinear Finite Element Modeling of Concrete Confined by Fiber Composites; *Journal of Finite Element in Analysis and Design*, 35: 79-96.

Xiao, Y. and Wu, H. 2000. Compressive Behavior of Concrete Confined by Carbon Fiber Composites Jackets; *Journal of Material in Civil Engineering*, Vol. 12, No. 2: 139-146.

Fam, Amir Z., and Rizkalla, Sami H. 2001. Confinement Model for Axially Loaded Concrete Confined by Circular Fiber-Reinforced Polymer Tubes; *ACI Structural Journal*, Vol. 98, No. 4: 451-461.

Ilki, A., Peker, O., Karamuk, and E. Demir, C. Kumbasar, N. 2006. Axial Behavior of RC Columns Retrofitted With FRP Composites; *Journal of Materials in Civil Engineering*: 169-188.

Flexural Strengthening of Reinforced Concrete Beams with Textile Reinforced Concrete (TRC)

Si Larbi Amir (amir.si-larbi@univ-lyon1.fr) & Contamine Raphael & Ferrier Emmanuel & Hamelin Patrice
LGCIE Site Bohr, Université Claude Bernard Lyon1 INSA de Lyon, France

ABSTRACT Carbon-epoxy composite materials are of considerable interest for reinforcement, but they need to be improved and have constraints, particularly in terms of cost and criteria of sustainable development. Such alternatives as textile reinforced concrete (TRC) should be seriously considered as substitutes for traditional composite materials. It is in this background that this study aims to explore the feasibility and assess the mechanical performance of reinforced beams in bending. This work focuses on the mechanical feasibility of such solutions by comparing them with traditional solutions such as CFRP and NSM (deformation rate reinforcement, cracking density, ultimate load, degradation level... etc.) on the basis of an experimental campaign based on 5 beams tested under four point bending. Finally we will try to adapt, supplemented where appropriate, CFRP predictive models in the case of the TRC and assess their degree of relevance.

1 INTRODUCTION

The repair of structural elements by TRC is a relatively recent procedure, as research on this material began in the mid-90s (Ohno & Hannant 1994, Peled et al. 1994). Work done to characterise the composite focused on its tensile strength. Few studies concentrated on the use of TRC in the reinforcement and repair of structural elements (Triantafillou et al 2006, Brückner et al 2006). It therefore seemed important to evaluate the technological feasibility of the procedure and to quantify its mechanical performances (ultimate load, rigidity and level of work) by comparing them to more traditional solutions involving CFRP and NSM. To prepare other avenues of research, the use of TRC with embedded carbon rods was also studied.

2 EXPERIMENTAL APPROACH

2.1 Definition of specimen

This study involves a comparative analysis of the performance of five 2-metre beams, all containing the same iron framework (and being protected against failure by shearing force) and all subjected to four point bending (Figure 1). They were all made from the same mortar mix and had a compression resistance at 28 days of $30 \text{ MPa} \pm 2$ (average of 6 specimens). The retained instrumentation can be seen in Figure 2; in order to locate the neutral axis, it had 3 deformation gauges on the (compressed) top of the central part of the beam and on the steel tensile rebars. A displacement sensor (LVDT $\pm 10 \text{ mm}$) was placed at mid-span. The test was of static

monotone type with a loading speed of 5 kN/mm .

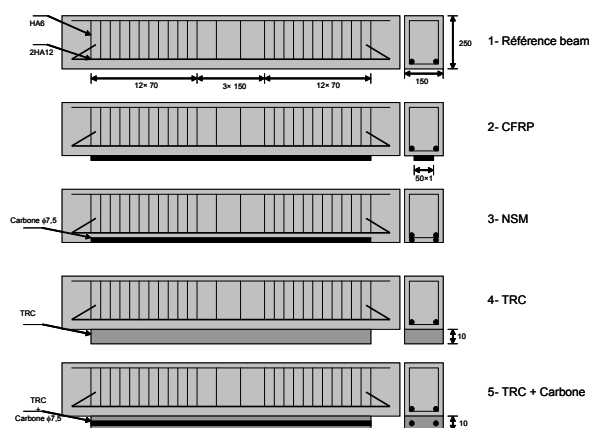


Figure 1 Reinforcing systems

All the reinforcement plates were bonded onto the tensile face of the beam with Sikadur30 (its properties are noted in Table 1. The properties of the CFRP plates and the carbon rods are noted in Table 1. The law of TRC behaviour obtained through characterisation in direct tension is presented in Figure 2.

Table 1 Properties of reinforcing materials

Constituent	Tensile strength (MPa)	Young's Modulus (MPa)	Ultimate deformation	Dimensions (mm)
CFRP	3100	165000	1.7%	50×1
Carbone rebars	2300	130000	1.8%	ø7.5
Sikadur30	30	12300	0.24%	–

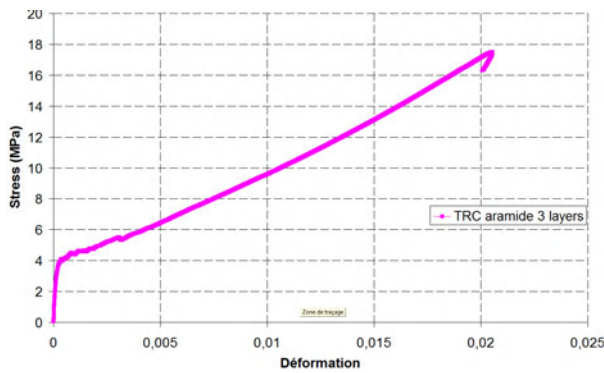


Figure 2 Tensile mechanical behaviour law of the TRC

2.2 Results

The load-deflection curves (Figure 3) indicate that the effect of TRC alone is not negligible and that it significantly increases the load at failure compared to the reference beam. It is also important to outline that its ductile behaviour is quite comparable to that of the reference beam. Incorporating two carbon rods in the TRC was seen to be very effective in terms of ultimate load (comparable to NSM) but was much less advantageous in terms of ductility. So it seems that, as long as the dimensions are adequate and that the work is done well, the reinforcement of beams that are subject to flexion with bonded plates of TRC is a conceivable and promising solution in terms of ultimate behaviour.

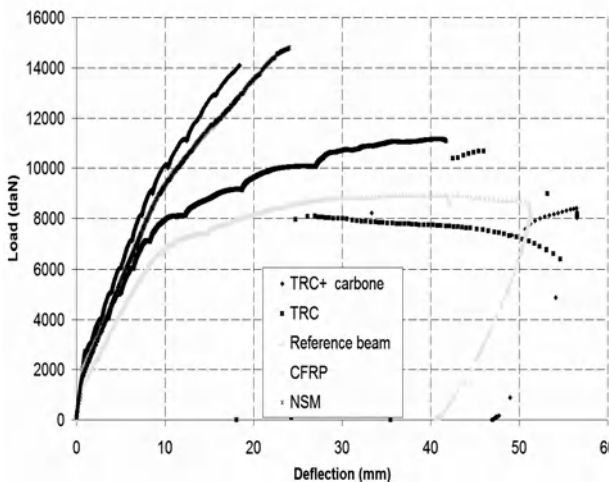


Figure 3 Global behaviour

The failure modes obtained (Figure 4) differ significantly and partly explain the variable levels of ductility. The failure obtained on the beam reinforced simply with a TRC plate is due to the advanced plasticity (Figure 5) of the steel (at +1.6%, very close to that of the reference beam, at 1.58%) linked to the clean break of the TRC in the central part (broken textile) which suggests a raised level of work in the TRC. The absence of failure by peeling-off could be explained by

the flexible character of the TRC conferred by the possibility of cracking easily, thus allowing a considerable and continuous stress redistribution. On the other hand, stiffening the reinforcement with two carbon rods resulted in failure by peeling-off, associated with a low level of work in the carbon rods. Failure of the same type is observed in NSM and CFRP beams.

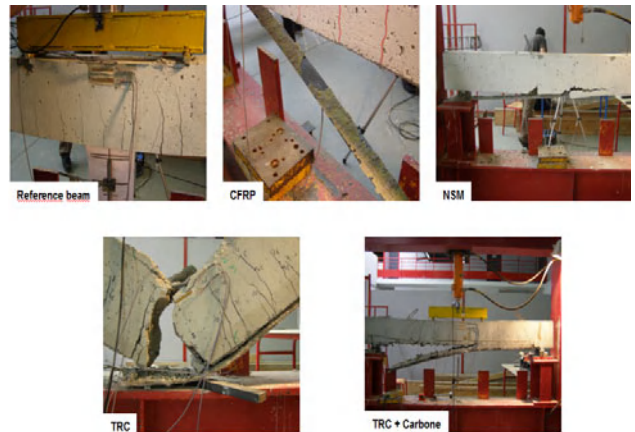


Figure 4 Failure modes

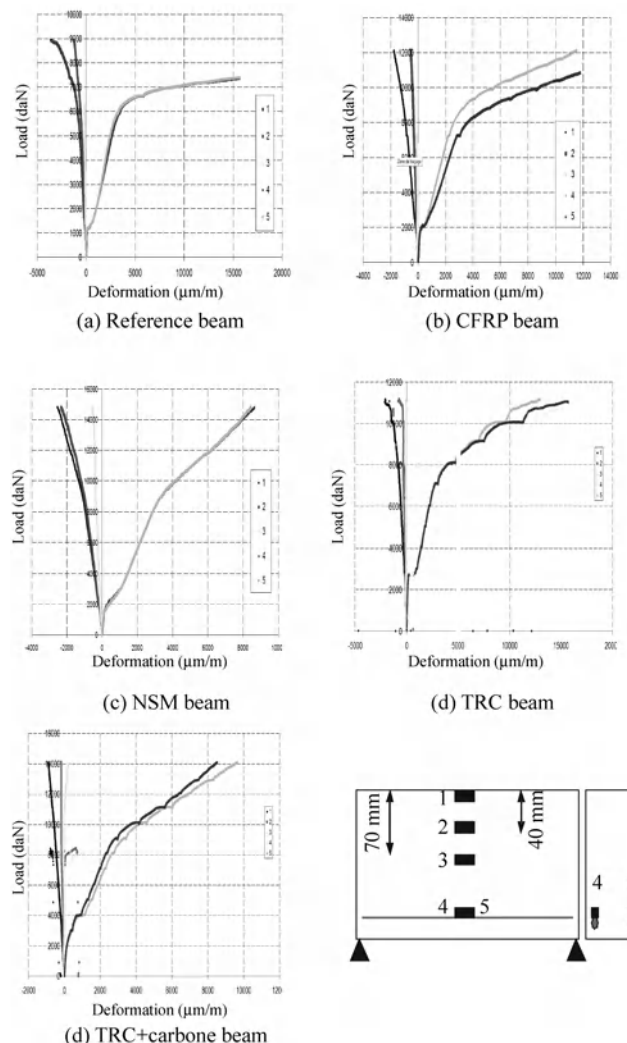


Figure 5 Material's deformation

In as much as it was established that Bernoulli's hypothesis on the flatness of the sections after deformation is valid, it is possible to determine the rigidity of experimental flexion EI_{exp} from the extreme deformation (of compressed concrete and of steel under tension) of the beam by the following relation:

$$EI_{exp} = M/\phi \quad (1)$$

Where $M = Fa/2$ and $\phi = (\epsilon_s + \epsilon_c)/d$

M : bending moment; ϕ : curvature; F : total load applied; a : distance between the point loading and the support; ϵ_c : concrete deformation in the upper strain gauge; ϵ_s : steel rebar deformation; d : useful height.

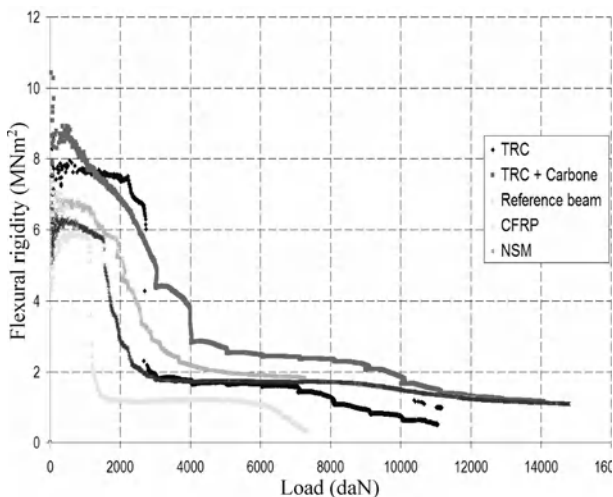


Figure 6 Beams rigidity evolution

The curves in Figure 4 show rigidity in function of load. The results clearly show the contribution of TRC before cracking begins; it is seen as an increase in flexional rigidity due to the increase in the resistant section of the beam. However, the initiation of cracking, which occurs noticeably later than on the reference beam (increasing from 1.1 tons to 2.4 tons), leads to a sudden drop in rigidity and the beam behavior is then similar to that of an NSM beam, that is to say its rigidity is superior to that of the reference beam, the result of a partial but effective bridging cracks. The difference, in flexional rigidity, between the reference beam and the

TRC beam was initially equal to 2 MN.m²; it is brought down to 0.5 MN.m² and stabilizes as from 3 tons of load, suggesting that the TRC is entirely cracked and that the textile reinforcement is alone, or nearly alone, in resisting the tensile force (with the steel). TRC + carbon shows itself, logically, to be very effective at all levels of load, providing the beam with a very sensitive surplus rigidity and making it very advantageous for service states.

3 CONCLUSION

This study has demonstrated the technological feasibility of the repair and/or reinforcement of beams subject to flexion by the bonding of TRC plates, and has established that this could be used as a complement to current solutions. It clearly appears that the bearing capacity can be significantly increased, that rigidity is consolidated and is comparable, up to certain point, to traditional solutions with a logically increased first-crack load due to the increased section of the beam. Also, the redistribution of forces in TRC, favoured by multicracking which makes the reinforcement more flexible, leads to ductile behaviour which contrasts favourably with the types of behaviour at failure of traditional solutions, and makes TRC attractive.

These are, of course, the first results, and further study is necessary. They are nevertheless very encouraging.

REFERENCES

- Ohno, S., Hannant, D. J., Modelling the Stress-Strain Response of Continuous fiber reinforced cement composites, *ACI Materials Journal*, 1994, Vol. 91, No.3, pp. 306-312.
- Peled, A., Bentur, A., Yankelevsky, D., 1994, Woven Fabric Reinforcement of Cement Matrix, *Advanced Cement Based Materials Journal*, Vol.1, pp. 216-223.
- Triantafillou TC, Papanicolaou CG. Shear strengthening of reinforced concrete members with textile reinforced mortar (TRM) jackets. *Materials and structures*, 2006;39(1):93-103.
- Brückner A, Ortlepp R, Curbach M. Textile reinforced concrete for strengthening in bending and shear. *Materials and structures*. 2006;39(8):741-748.

The Flexural Behavior of Beams Strengthened with FRP Grid and ECC

Ding Yi (ding-yi@tsinghua.org.cn), Chen Xiaobing & Chen Wenyong

China Jingye Engineering Corporation Limited, Beijing, China

ABSTRACT Engineered Cementitious Composite (ECC) is a new kind of random short fiber reinforced cementitious composite with ultra high ductility. Unlike common FRC, ECC is developed by optimizing the microstructure of the composite which exhibits tensile strain-hardening behavior with strain capacity more than 3%, yet the fiber content is typically 2% by volume or less. The flexural behavior of concrete beams reinforced with CFRP grid (named NEFMAC) and ECC is studied in this paper. The behavior of concrete beams reinforced with ECC-NEFMAC is compared with the behavior of a beam reinforced with steel and carbon fiber sheet. The research investigates their flexural behavior including pre-cracking state, cracking pattern and width, deflections, ultimate capacities and strains, and the mode of failure. The information obtained throughout this investigation is valuable for future field application and development of design guidelines for ECC and FRP grids.

1 INTRODUCTION

1.1 ECC

Engineered Cementitious Composite (ECC) is a new kind of random short fiber reinforced cementitious composite with ultra high ductility. Unlike common FRC, ECC is developed by optimizing the microstructure of the composite which exhibits tensile strain-hardening behavior with strain capacity more than 3%, yet the fiber content is typically 2% by volume or less. Due to the characteristic multiple cracking, ECC has lots of advantages on durability, safety, and sustainability, which can ravel out the limitation of concrete for its brittle behavior and low ductility, which are valuable for cementitious composites produce, roads and bridges construction and rehabilitation of old structures.

ECC is different from ordinary concrete most for its tensile and flexural properties. Figure 1 is a typical uniaxial tensile stress - strain curve of ECC. After the initial crack is generated, ECC into the plastic deformation stage, during which the strain - hardening process associated with micro-cracks continuously generated and developing showing great toughness. The ultimate tensile strain is more than 5%, which is almost 500 times of ordinary concrete. Restricted by crack bridging stress, the development of crack width always keeps a small range of values with the maximum crack width is smaller than 60 μ m. The Flexural behavior of ECC is usually tested by four-point bending test. The size of ECC specimen in Figure 2 is 304.8mm \times 76.2mm \times 12.2mm, and its ultimate deflection is 22mm which is 40 times of ordinary concrete.

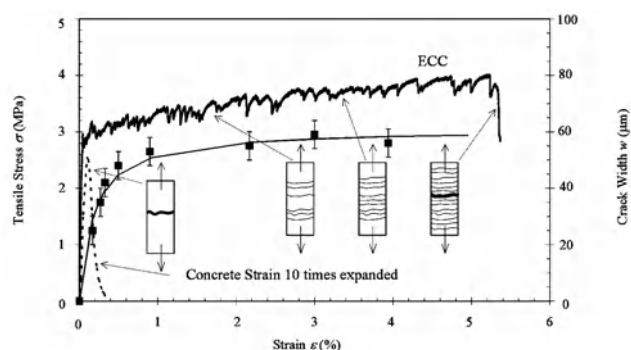


Figure 1 A typical tensile stress - strain curves and crack development of ECC

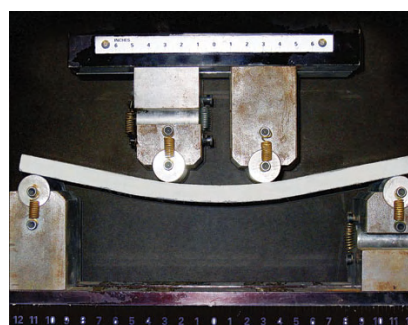


Figure 2 Four point bending test of ECC

1.2 FRP grid

FRP grid is usually fixed and bonded to work with original concrete by spraying a thin layer of concrete. Once the concrete cracked due to brittle and was broken, the bonding between reinforcement layer and original concrete may be invalid, and thus they may not work

together and cause structure damage. So it often requires the use of polymer cement mortar as a spray thin concrete to integrate FRP grid with original concrete. Considering the high strength and high toughness of ECC material, ECC/FRP grids working together may achieve good mechanical properties.

In this paper, the flexural behavior of concrete beams reinforced with FRP grid and ECC is studied to inspect its differences from beams reinforced with steel and carbon fiber sheet.

2 EXPERIMENTAL PROGRAMES

2.1 Materials

Three different repair materials, carbon fiber sheet, polymer cement mortar/FRP grid and ECC/FRP grid were used in this study.

A new type of CFRP grid named “NEFMAC (NEW Fiber Composite Material for Reinforcing Concrete)” was used here. Type C6-50 NEFMAC was selected, the nominal cross-sectional area of a single-limb of lattice bars is 17.5 mm^2 ; the space of lattice bars is 50mm.

The ECC mix comprised Portland Type 1 cement, water, silica sand with 0.1mm nominal grain size and 2% poly-vinyl-alcohol (PVA) fibers. These PVA fibers (PVA-REC 15) had length and diameter of 12mm and $39\mu\text{m}$. Its Young’s modulus was slightly lower than concrete due to lack of coarse aggregate in its composition. Uniaxial tensile tests were conducted to measure ECC mix’s strain capacity (Figure 3).

Table 1 Materials

Material	Type	Tensile strength (MPa)	Compressive strength (MPa)	Elastic modulus (MPa)
carbon fiber sheet	Toray 30	3500	/	2.1×10^5
CFRP grid	NEFMAC C6-50	1400	/	1×10^5
ECC	PVA-ECC	5.1	63 ± 2	/
polymer cement mortar	NEFCRETE	/	57 ± 2	/
concrete	C30	/	36 ± 2	/
rebar	HPB235	298	/	/

Table 2 Beams

No.	Reinforcement
S1	reinforced concrete beam as a reference
S2	reinforced with carbon fiber sheets on the underside
S3	reinforced with FRP grid and NEFCRETE on the underside
S4	reinforced with FRP grid and ECC on the underside

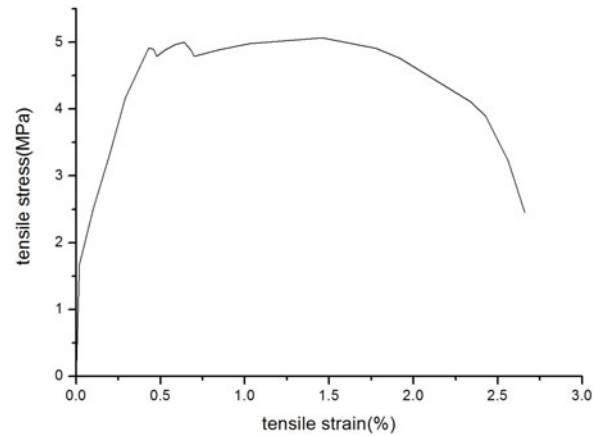


Figure 3 Tensile stress-strain curve of ECC

2.2 Specimen configuration

Four rectangular flat concrete beams were studied. They have the same size and reinforced rebar. The four point bending tests were carried out and the load and strain were recorded by sensors (S4 as a sample shown in Figure 4).

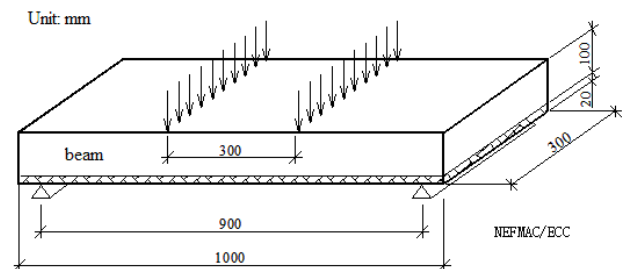


Figure 4 Beam S4 (S3)

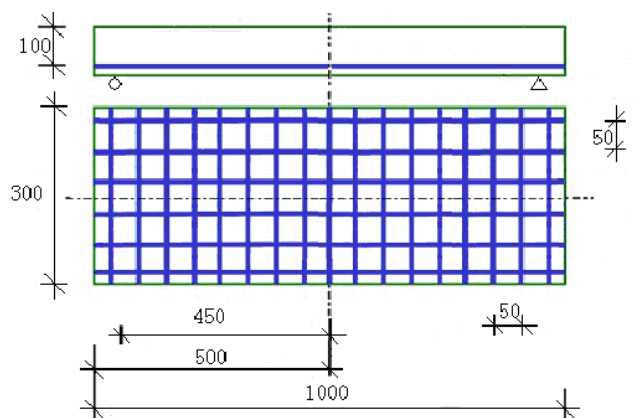


Figure 5 FRP grid installation diagram

3 EXPERIMENTAL RESULTS

3.1 Load-displacement relationships

Figure 6 shows the load-displacement relationships of the specimens. As a reference that reinforced with rebar, S1 had a minimum cracking load and ultimate load, and showed a typical reinforced beam bending failure.

Figure 7 shows the load-strain curve of rebar and carbon fiber sheet in S2. When the load reached 55kN, the end

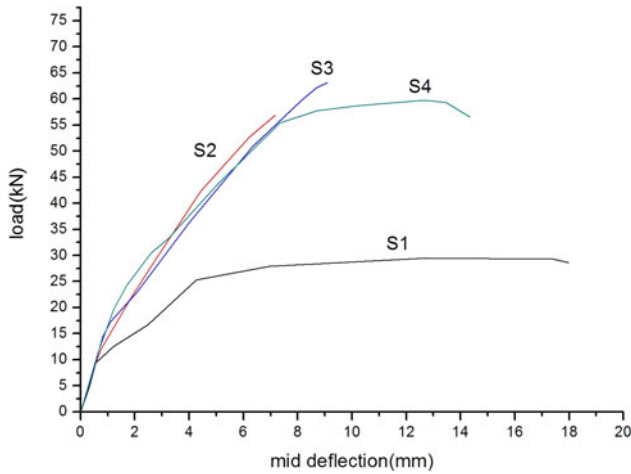


Figure 6 Load-displacement relationships of specimens

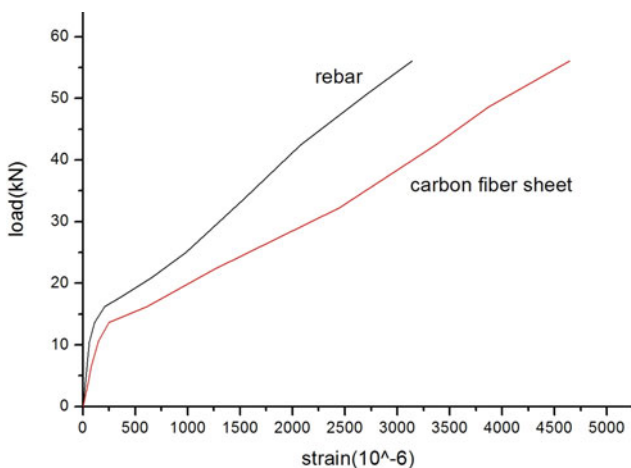


Figure 7 Load-strain curve of rebar & carbon fiber sheet in S2

of fiber sheet debonding due to inclined shear cracks, after which shear failure occurs. During the experiment, the maximum tensile strain of carbon fiber sheet was $4700\mu\epsilon$, while the ultimate tensile strain was $17,000\mu\epsilon$, showing the material strength capacity was not used fully. If the debonding did not occur, the ultimate load of S2 would be higher. No obvious sign was observed before failure, which showed a brittle debonding failure and shear failure.

Figure 8 shows the load-strain curve of rebar and FRP grid at mid-span in S3. When the load reached 40kN, micro shear cracks occurred on the side of concrete layer, slight debonding occurred between concrete and NEFCRETE, the two materials showed a tendency to debond off. The concrete layer showed a shear failure when the specimen was damaged, while the NEFCRETE layer remained relatively intact. The maximum tensile strain of FRP grid in the vertical position was $5400\mu\epsilon$, while the ultimate tensile strain was $14,000\mu\epsilon$. The failure model was similar to fiber sheet debonding failure in appearance, but more obvious signs were observed before specimen was damaged. Debonding between concrete and NEFCRETE continued for a long

time, the deflection of the specimen increased obviously from when the debonding began to the final failure.

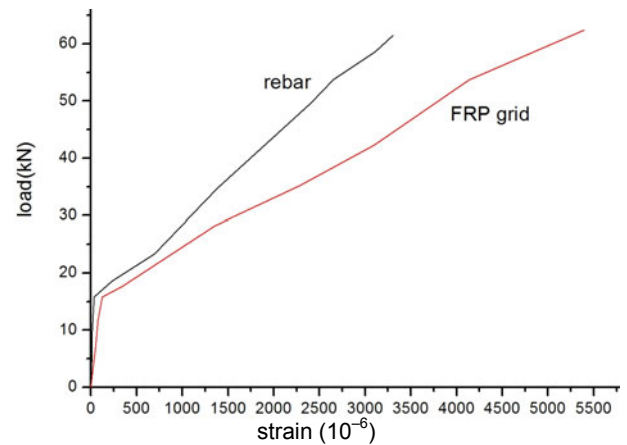


Figure 8 Load-strain curve of rebar & FRP grid in S3

Figure 9 shows the load-strain curve of rebar and FRP grid at mid-span in S4. When the load reached 34kN, micro cracks occurred for the first time on the underside of ECC, the crack width was less than 0.01mm, which showed that the tensile and crack-resistance properties were better than for concrete and NEFCRETE. The failure mode of S4 is similar to S3. ECC layer remained intact after the specimen was damaged, the cracks were many but tiny, the maximum crack width was only 0.1mm, and most of the crack widths were less than 0.05mm.

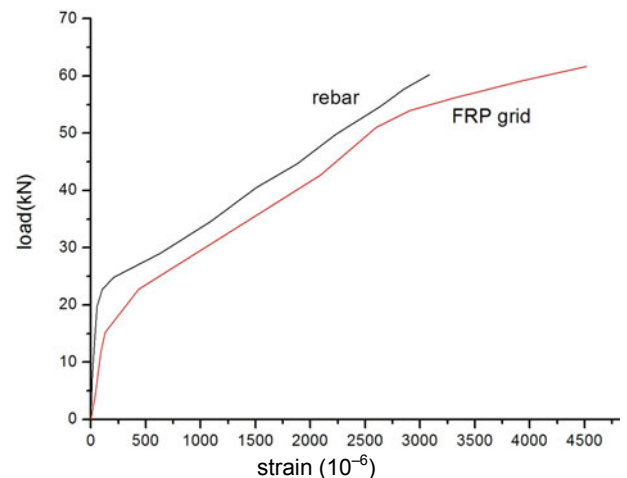


Figure 9 Load-strain curve of rebar & FRP grid in S4

3.2 Comparison between FRP grid and CFRP sheet

As shown in Figure 10, neither the carbon fiber sheet nor the FRP grid reached their ultimate strain capabilities, but only reached 27% ~ 40%. Debonding occurred in S2, S3 and S4 in different forms, but more obvious signs were observed before damage occurred in S3 and S4, so the FRP grid is relatively safer than carbon fiber sheet in beam reinforcement.

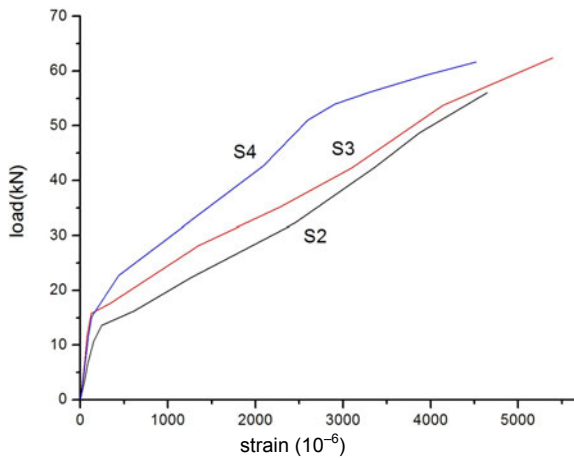


Figure 10 Load-strain curve of carbon fiber sheet and FRP grid

Overall, either from the load carrying ability or safety, FRP grid is superior to carbon fiber sheet as flexural reinforcement. If we can improve the bonding effect between extra cement-based materials and original concrete, to eliminate or delay the delaminating or debonding between reinforcement layer and original concrete layer, flexural reinforcement effect of FRP grid will further increase.

3.3 Comparison between ECC and NEFCRETE

As shown in Figure 11 and table 3, mechanical properties of ECC in flexural reinforcement were much

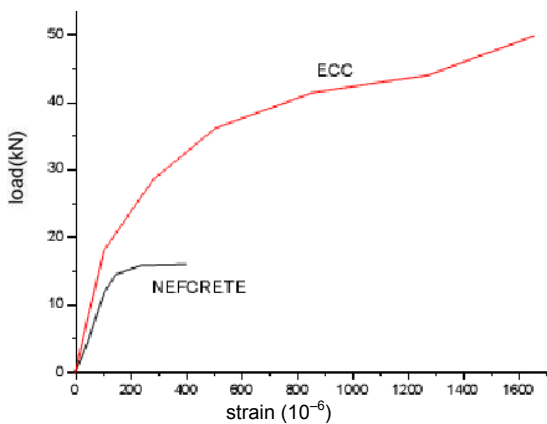


Figure 11 Load-strain curve of ECC and NEFCRETE

better than NEFCRETE. Due to the multiple crack of ECC, the deformation capability of ECC is higher than that of NEFCRETE. The crack control performance of ECC is also better than NEFCRETE which is shown in crack amount, crack width and the integrity after failure.

Table 3 Experiment results

No.x	Cracking load (kN)	Ultimate load (kN)	theoretical ultimate load (kN)	number of cracks on the underside	Crack width (mm)
S1	12	31	23	6	1.2~3.1
S2*	16	55.3	59	-	-
S3	16	63.2	60	24	0.2~0.8
S4	24	61.3	60	56	0.01~0.1

* As the underside of S2 specimen reinforced with carbon fiber sheets, it's difficult to observe the cracks on the underside.

4 DISCUSSION AND CONCLUSIONS

In this study, the behavior of concrete beams reinforced with ECC-FRP grid is compared with the behavior of a beam reinforced with steel and carbon fiber sheet.

The load carrying ability and safety of beams reinforced with FRP grid were better than carbon fiber sheet. The mechanical properties and crack-resistance property of ECC in flexural reinforcement were also significantly better than concrete and NEFCRETE. ECC/FRP grid system will show a better performance in flexural reinforcement.

REFERENCES

Victor C. Li., 2005. Engineered Cementitious Composites.
 Shuxin Wang, Victor C. L., 2003. Polyvinyl Alcohol Fiber Reinforced Engineered Cementitious Composites: Material Design and Performances.

Comparison of Different Repairing Techniques Used for Rehabilitation of Initially Cracked RCC Beams

Liaqat A. Qureshi (lqtqureshi@yahoo.com)

Department of Civil Engineering, University of Engineering & Technology, Taxila, Pakistan

Kamran A. Qureshi, Tahir Sultan & Jahangeer Munir

Department of Civil Engineering, Bahauddin Zakarya University, Multan, Pakistan

ABSTRACT This paper presents the comparison of different repairing techniques commonly used for cracked RCC beams. Five RCC beams (each 3 meter \times 225 mm \times 300 mm) designed as under-reinforced beams were cast, cured and tested by two-point loading. One beam was loaded up to failure and treated as “control beam”. Its failure load was noted and deflections were regularly measured by deflection gauges installed at middle and quarter points. Other four beams were loaded up to three-fourth of the failure load of control beam or otherwise up to the development of initial cracks. These beams were then repaired by using four different repair techniques i.e., ferrocement layer, section enlargement, cement grouting and epoxy injection. When repair process was over, the four repaired beams were tested again and loaded up to their ultimate loads. Again deflections were noted and overall performance of beams was examined. Results were analyzed and discussed to have a comparison between four methods used in terms of strength and ductility performance. However it was concluded that all patterns used were able to restore or enhance the original structural capacity of cracked sections of beams.

1 INTRODUCTION

The buildings which survive after intensive natural disasters like earthquake, flood, etc. are suffering from severe structural cracks. The rehabilitation and repair of these cracks in order to make these structures safe for daily use is a major problem. It has been proved that such deficiencies can be rectified within reasonable expenditure, which is a fraction of the cost of a completely new structure. Apart from the financial cost, considerable time saving results compared to discarding the existing members and building a new structure instead. With the advancement of technology based on new materials, which have superior mechanical properties and excellent resistance to damaging forces, many effective repairs and strengthening techniques have been developed. The final selection of a suitable and most effective method generally depends on simplicity, speed of application, structural performance and total cost.

The technical methods used in this research work are using ferrocement, section enlargement, epoxy injection and cement grouting techniques. These techniques are widely used to treat cracking problem in RCC members. The procedures adopted are well established in the literature (Emmons 1994, Allen & Edwards 1987, Raina 1993). The techniques had been chosen for their capability to either increase the structural capacity of members or to reinstate the initial capacity of the

sections. Furthermore, this study concentrates on the serviceability, strength and ductility performance for each of the repair techniques to establish their potential application in cracked reinforced concrete beams.

2 EXPERIMENTAL PROGRAM

All five beams were identical in X-section, length and materials. Cross-section of beams was 225 mm \times 300 mm and all beams were 3 meter long. Deformed steel of grade 40 for 3 # 4 bars was used as main reinforcement. # 4 stirrups were used @100 mm c/c up to 0.7 meter from each end. Concrete Mix. Proportion 1:2:4 (by weight) was used. Water cement ratio was kept as 0.50 and slump was measured as 38 mm (average). Average cube crushing strength at 28 days was recorded as 4258 psi (average).

2.1 Techniques used in retrofitting

2.1.1 Ferrocement layer

In this repair method, a concrete layer of 30 mm thickness was removed from the soffit of the beam manually using appropriate tools. The resulting surface was roughened to have a good bond between ferrocement layer and scratched surface (Irons 1987). The galvanized welded square mesh or equivalent (ASTM A-185), with a wire diameter 1.3 mm and spacing of 12 mm (0.5 inch) was used. It was used in two layers, one inside the skeleton

steel and other on the outside (Romualdi et al. 1998). The skeleton steel made up of 6 mm dia. bars was used. The skeleton steel was conforming to ASTM A-615 and A-616 or equivalents. For tying the mesh layers on the skeleton steel, annealed (soft) galvanized wire of 24 gauge was used (Paramasivam 1987). Cement mortar (cement to sand ratio is 1:2 with w/c ratio equal to 0.50) was applied and cured for 28 days.

2.1.2 Section enlargement

In this repair technique, the cracked beam was strengthened with providing an additional 50 mm thick RCC layer at the bottom. A number of holes were drilled up to a depth equal to the effective depth of beam on bottom side. Similar concrete mix and same reinforcement, fixed to shear connectors, was used to provide the supplementary 50 mm concrete layer and cured for 28 days before subjecting the beam to flexural testing.

2.1.3 Grout pouring technique

After subjecting the beams to three fourth of the failure load of controlled beam, two flexural cracks of 0.96 mm width each were visible between mid-point and three fourth of one beam. These cracks were widened up to 50 mm width and 30 mm in depth such that the main steel reinforcement was made visible. The exposed reinforcement and concrete surfaces were thoroughly cleaned, before grout is properly poured. The grout used is SikaGrout214 of a density 2.2 kg/lit. The mixing ratio exploited was 25 kg of grout to 4.6 kg of water. The specimen was allowed for 28 days curing and then subjected to flexural test.

2.1.4 Epoxy injection technique

In this repair method, Sikadur 30 was used to fix the injection nipples @ 250 mm c/c in position and to seal the cracks. The epoxy used to fill the crack was Sikadur 52, which is low viscosity epoxy, free flowing and fast curing injection resin based on 2-component solvent free epoxy resin. It has a density of 1.1 kg/lit, tensile strength of 25 N/mm² (7 days) and a compressive strength of 40 MPa at 20°C within 24 h. The viscosity of Sikadur 52 is equal to 290 and 130 cps at a temperature of 20 and 30°C, respectively. Sikadur 52 was pushed under pressure from one end of the crack until the material comes out from the next nipple. The whole process was repeated until the entire crack was filled with the epoxy material.

2.2 Testing of beams

First of all, beams were tested for flexural strength in a staining frame before strengthening. One dial gauge was installed at mid span to record the mid span deflection and two gauges were installed at quarter points to record deflection at those points. Two point loads were applied at the centre of beam and deflections recorded for each increment of load.

One beam was tested up to failure and designated as control beam. Other four beams were tested up to 3/4th of failure load of control beam. These beams were then removed from the testing frame and strengthened, by four already explained techniques. The strengthened beams, after curing, were tested again up to ultimate load and deflections noted. The results of beams strengthened with ferroceent layer, section enlargeent, grout filling and epoxy injection were designated as B₁, B₂, B₃, and B₄ respectively.

3 RESULTS AND DISCUSSION

3.1 Cracking and ultimate loads

Figure 1 shows the loads for different repaired as well as control beam at which initial cracking started. The entire repaired concrete beams crack at higher loads compared to the control beam. The repaired specimens using ferroceent (B₁), section enlargement (B₂), grout pouring (B₃), and epoxy injection (B₄) techniques show 11.54%, 20.55%, 21.47% and 20.05% increase in the cracking loads respectively as compared to control beam. Figure 2 shows

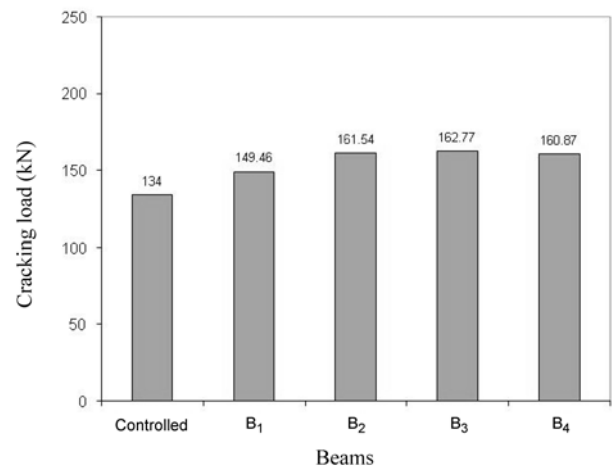


Figure 1 Cracking loads of controlled and strengthened beams

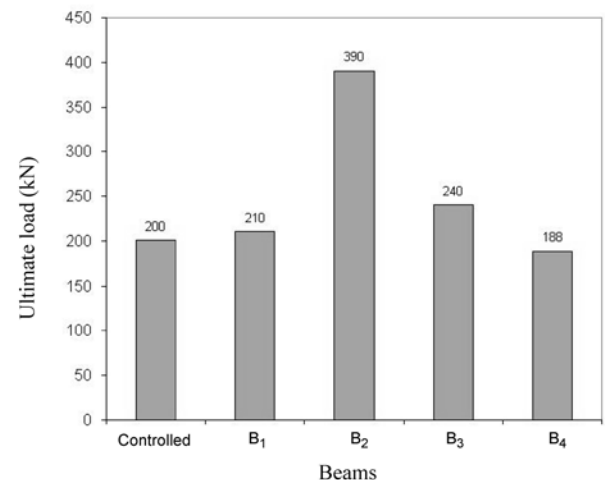


Figure 2 Ultimate loads of controlled and strengthened beams

the ultimate failure loads for controlled beam in first loading and other beams in second loading after retrofitting. All the repair techniques adopted have been proved to be able to restore the ultimate capacity of the cracked beams except in case of epoxy injection B₄. However, the drop in strength is only 6 % compared with the control beam. Moreover, there is no obvious increase in the ultimate load of the beam repaired by ferrocement layer compared to the control beam which is well in accordance with the conclusion reported by Al-Kubaisy & Zamin (2000).

3.2 Beam deflections

Figures 3-6 show load-deflections curves of B₁, B₂, B₃ and B₄ respectively, before and after repair. The deflections recorded at mid-span are used in these curves. All results reflect less deflection after repair, which is an indication of non-ductile behavior of the beams. Also load-deflection curve of control beam, shown in Figure 7, indicates more deflection at failure load i.e. 200 KN as compared to repaired beams at the same load value.

All beams show almost similar level of stiffness except beam repaired by section enlargement (B₂), where deflection has been considerably decreased due to extra stiffness of the additional layer of concrete at the

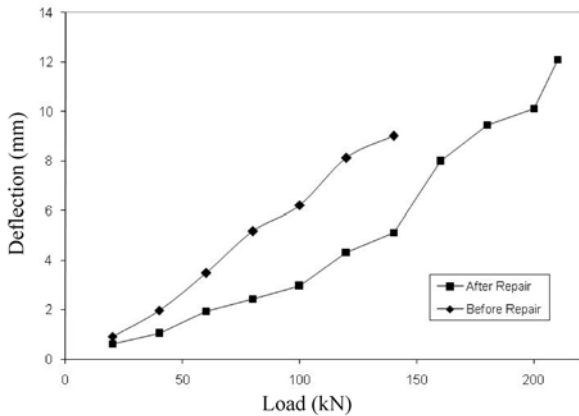


Figure 3 Load versus deflection graph for B₁

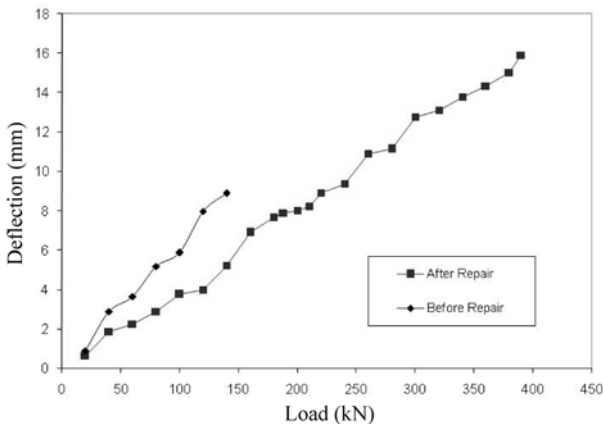


Figure 4 Load versus deflection graph for B₂

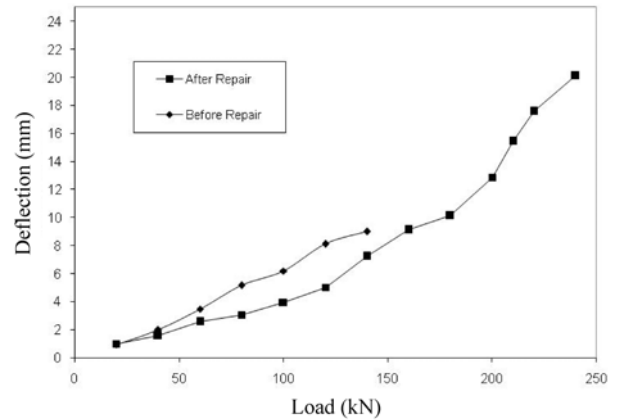


Figure 5 Load versus deflection graph for B₃

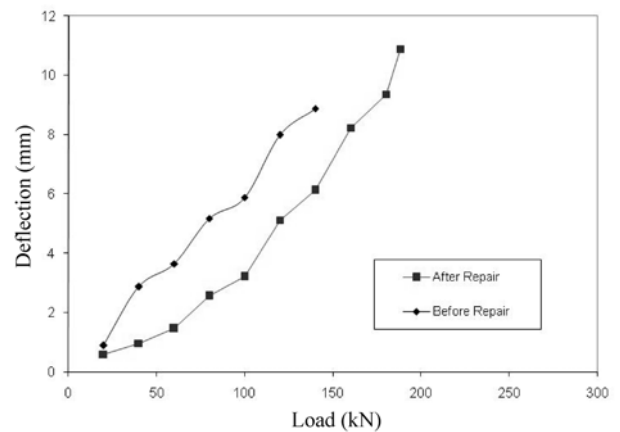


Figure 6 Load versus deflection graph for B₄

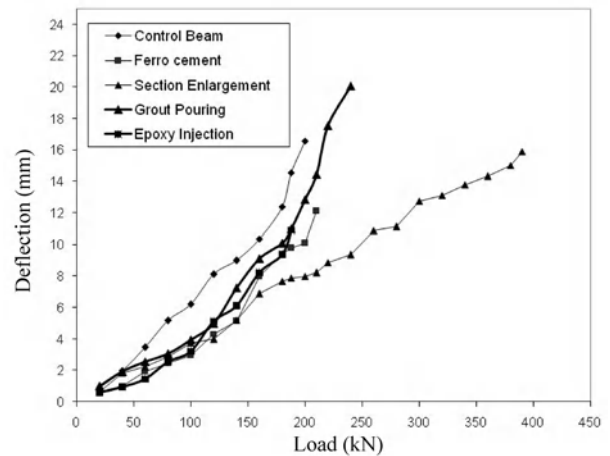


Figure 7 Comparison of load versus deflection graphs for strengthened beams and control beam

bottom. In this case the stiffness has been increased more drastically compared to other techniques. Coparison of deflection patterns for the control beam (B) and specimens B₂, B₄ and B₅ exhibits nearly similar initial stiffness. However, after three-fourth of the control beam's ultimate load, these beams exhibit different stage of ductility. The maximum deflections observed in B₁ (ferrocement) and B₄ (epoxy injection) are 26% to 35%

lower compared to the control slab, while grout filling technique (B₃) shows 20.31% increase in maximum deflection compared to the control beam (Figure 7).

On the other hand, beam repaired by section enlargement technique (B₂) exhibits different pattern of load–deflection curves compared to other techniques as shown in Figure 7. The maximum deflection recorded is almost same as in the control beam but observed at about twice the ultimate load. Moreover, non-ductile behavior in the load–deflection curve could be observed in this beam as compared to ductile behavior observed in the control beam (B). The results are again well in accordance with previously published data for cracked slabs (Razali et al. 2005).

3.3 Failure modes and mechanism.

The tests were continued until excessive deflection and/or extremely wide cracks were examined even though the beams did not completely and necessarily collapsed. Similar patterns of failure have been observed in the beams B₁, B₃ and B₄. Cracks initialized at the tension sides and increased in size with the loading continued.

In the control slab (B), the neutral axis position is moved upwards with the increasing strain until the strain attains its maximum value. Then, the steel bars are yielded leading fastly to compressive crushing of concrete. This is like a typical ductile failure observed in under-reinforced concrete sections. However, in the repaired beams, the ductility is not clearly observed as in the control slab. For B₂, in addition to the transverse cracks, horizontal crack had been formed between the original beam and the additional concrete layer due to shear. The failure patterns are similar to those observed in case of repair of initially cracked slab specimens (Razali et al. 2005)

4 CONCLUSIONS

(1) All repair techniques used in the research work are successfully effective to at least reinstate the structural capacity of cracked reinforced concrete beams.

(2) Initial cracking appears at higher loads compared to control beam.

(3) Ultimate failure loads of repaired beams are greater as compared to control beam except in case of epoxy injection technique.

(4) The repairs using grout filling, epoxy injection and ferrocement layers exhibit similar strength and ductility performance as that of control beam. In other words, these techniques can be confidently and securely used in the design of normal strength RCC concrete beams.

(5) The section enlargement technique is the most effective technique as far as ultimate load is concerned. The ductility performance for these beams, however, is less than that of the control beams.

(6) Both crack and ultimate loads for all beams prove that repaired beams have a high degree of integrity along with original beams.

REFERENCES

- Al-Kubaisy, M.A. & Zamin Jumaat, M. 2000. Flexural behaviour of reinforced concrete slabs with ferrocement tension zone cover. *Constr Build Mater* 14: 245-252.
- Allen, R.T.L. & Edwards, S.C. 1987. The repair of concrete structures, Blackie.
- Emmons, P.H. 1994. Concrete repair and maintenance. R.S. Means INC.
- Irons, M. 1987. Ferrocement for infrastructure rehabilitation, *Concrete Int Design Constr* 9: 24-28.
- Paramasivam, P. 1987. Laminated ferrocement for better repair, *Concrete Int. Design Constr* 9: 34-38.
- Raina, V.K. (2nd ed.) 1993. Concrete bridge Practice- Construction, Maintenance and Rehabilitation. New Delhi Tata McGraw Hill.
- Razali, M., Kadir, A. & Noorzaci J. 2005. Repair and structural performance of initially cracked reinforced concrete slabs. *Construction and Building Material J.* 19(8): 595-603.
- Romualdi, J.P., Lim, C.T.E. and Ong, K.C.G. 1998. Strengthening of RC beams with ferrocement laminates. *Cement Concrete Compos.* 20: 53-65.

Analysis on Mechanical Behavior of RC Beams Strengthened with Inorganic Adhesive CFRP Sheets

Xin Zhang¹⁻² (Zhangxin1964@163.com) & Shibin Li¹⁻² (lsbtj@163.com) & Liluan Yang¹ & Xiangfei Kong¹

1 College of Civil Engineering, Shandong Jianzhu University, Jinan, China 250014

2 Shandong Provincial Key Lab of Appraisal and Retrofitting in Building Structures, Jinan, China 250014

ABSTRACT The failure modes, ultimate states, flexural strength and shear capacity of reinforced concrete(RC) beams strengthened with inorganic adhesive carbon-fiber-reinforced-polymer(CFRP) sheets were separately discussed based the experimental results. The influences of CFRP sheet amount, anchor condition and steel reinforcement ratio on the flexural strength, and the effects of CFRP sheet amount, CFRP sheet layer, shear span/depth ratio and concrete strength on the shear capacity were analyzed. The results show that debonding failures are prevalent in the RC beams strengthened with inorganic adhesive CFRP sheets; the maximum effective tensile strain of the CFRP sheet is about 0.005; the flexural strength is increased due to the bottom CFRP sheets; the shear capacity is improved for the lateral U type CFRP sheets. Finally, practical calculation formulae for the flexural strength and shear capacity of RC beams strengthened with the inorganic adhesive CFRP sheets are established, which are found good agreement with test results with reasonable reliability.

1 GENERAL INSTRUCTION

The new strengthening technique of externally bonding fiber-reinforced-polymer(FRP) composite sheets to reinforced concrete(RC) structures was introduced into China in 1997. From then on, the technique was concerned by civil engineering fields and became increasingly research focus. Although many traditional methods could be adopted, the application of CFRP sheets impregnated with epoxy resin for RC structures strengthening or retrofitting had received considerable attention due to its light-weight, high-strength, high resistance against corrosion, quick and manageability on-site, easy fabrication and so on. After extensive research and promotion, the technique had now become a major method for strengthening RC structures. It was estimated that the FRP sheets used in structural strengthening total were about 600,000 m² in 2005. A series of experimental projects on the flexural and shear performance of RC beams strengthened with ordinary CFRP sheets were conducted at home and abroad to establish the design method for the RC beams strengthened with CFRP sheets(Wu 2000, Ye 2001, Deng 2001 et al.). The contribution of the CFRP sheet to the bearing capacity of RC members was determined by its strain development at the corresponding ultimate state, and a maximum allowable strain for ordinary CFRP sheets, equal to 2/3 the rupture strain of the CFRP, was proposed considering the elastic brittle material behavior of CFRP sheets. The flexural strength and

shear capacity of RC beams were efficiently improved after strengthened with ordinary CFRP sheets. But the general epibond utilized for affixing CFRP sheets had fire-proof and durability problems. Especially, the mechanical behaviors of epibond degenerate greatly when the environment temperature exceeds 80°C (Tadeu 2000). What's more, the epibond will become the burning resource after the environment temperature exceeds 600°C. The temperature of building fire disaster overpasses 1000°C easily, therefore, the application of CFRP sheets in building structures was limited by many standards(ACI 2002 and CECS 146 2003). Meanwhile, the epibond is not environment-friendly and costly, also the epoxy resin curing agent is deleterious. So, it was necessary to research and develop fire-resistance and environment-friendly adhesive for extending application scope of CFRP.

Magnesium Oxychloride Cement was one good kind of fire-resistant, environment-friendly and durable inorganic adhesive, which could be used to affix CFRP sheets for strengthening reinforced concrete structures (Zhao 2003, Li 2006). Besides, the resources for producing the inorganic adhesive are quite abundant and low-cost in China.

Six flexural strengthening beams and twelve shear strengthening beams bonded with inorganic adhesive CFRP sheets were separately tested in the literatures (Zhang 2010(a,b), Yang 2009 and Kong 2009). Based on the test results, the influence parameters on the flexural strength and shear capacity were analyzed and discussed,

and then practical calculation formulae for the flexural strength and shear capacity of the strengthening RC beams are established. The research results will be helpful for the practical design.

2 FAILURE MODES

2.1 Flexural strengthening

Debonding failures between concrete and CFRP sheets, especially middle flexural cracks debond, were concern in the RC beams strengthened with inorganic adhesive CFRP sheets, which might be caused by big deflection, low concrete strength, dense cracks, adhesive limitation or improper construction and so on. It was found that debonding failures could be deferred or avoided by adopting additional anchor measures, assuring construction quality and increasing section stiffness.

Flexural debonding failures could be divided into two conditions(Zhang 2010a):

(1) Middle flexural cracks debond

With the increase of external loads, the flexural cracks appeared near the middle. Then, the development of the cracks gave rise to debond between concrete and the CFRP sheet for the high interface shear stress. On occasion, the concrete was crushed. The failure model, as shown in Figure 1, was most prevalent in the tests.



Figure 1 The middle debonding failure picture

(2) End debonding failure

When the reinforcement ratio and the layer of CFRP was bigger, the end might took pace debond firstly, then the specimen failed. The failure model, as shown in Figure 2, was caused by end stress concentration, which could be effectively controlled by additional anchor measures.



Figure 2 The end debonding failure picture

The test results manifested that flexural strength of the strengthened beams was increased from 9% to 46% for the inorganic adhesive CFRP sheets.

2.2 Shear strengthening

All the specimens took place debond failure(Zhang 2010b). For the mezzo shear span/depth ratio strengthening beams, middle flexural cracks appeared initially. The diagonal shear cracks appeared later due to the confinement of U type CFRP sheets. The strain values of transverse reinforcement hoops and U type CFRP sheets increased greatly after the shear cracks occurred. With the increase of external loads, the transverse reinforcement hoops yielded, and some CFRP sheets uttered small crack, then the main diagonal shear cracks were extended and widened, and then the U type CFRP sheets partly debonded from concrete. Finally, the strengthening RC beam failed as shown in Figure 3.



Figure 3 The shear debonding failure pictures

The development of diagonal cracks was confined by the U type CFRP sheets development. So, besides 1-2 main diagonal shear cracks, there also were many thin and dense diagonal cracks. On the other hand, the shear force resisted by the U type CFRP sheets was mainly transferred by the truss mechanism just like that of transverse steel bars. The test results indicated that the crack load was improved little, but the shear capacity was increased from 8% to 45%.

Compared with general epibond CFRP sheets, the contribution of inorganic adhesive CFRP sheets was power. Because the magnesium oxychloride cement had poor osmosis and cohesiveness. But the inorganic adhesive satisfied engineering under better construction and anchor conditions.

3 INFLUENCE PARAMETERS ANALYSIS

3.1 Flexural strengthening

(1) The CFRP sheet amount It was controlled by the layer of CFRP sheet. It had few influences on crack loads, but had obvious effects on flexural strength and stiffness. The contribution of CFRP sheets on flexural strength was not in direct ratio with the layer because the debond became more easily with the layer increasing.

(2) The steel reinforcement The strengthening

effectiveness became better with the steel reinforcement ratio decreasing under proper steel reinforcement ratio. But the steel reinforcement ratio was smaller, the deflection was bigger, here, some measures should be taken to deferred or avoided debonding failures.

(3) The anchor condition debonding failures could be deferred by effective additional anchor conditions, such as U type CFRP sheets, but could not be completely avoided.

(4) Brief summary middle flexural cracks debond failures were general in the test. The CFRP sheets did not fractured along the tensile direction, but they snapped along the weak load direction after debond, and then they were divided into pieces. In addition, when the beams drew near failure, the CFRP sheets always uttered big crack, which sent out obvious break signs.

3.2 Shear strengthening

(1) The CFRP sheet amount more U type CFRP sheets gave rise to more shear capacity, because they just like that of transverse reinforcement partook shear force. Meanwhile, the development of diagonal shear cracks was confined by the U type CFRP sheets.

(2) The CFRP sheet layer under coequal CFRP sheet amount, the strengthening effectiveness was decreased with the layer increasing for stress concentration.

(3) The shear span/depth ratio the strengthening effectiveness was augmented with the increasing of shear span/depth ratio. As to the specimen with larger shear-span/depth ratio, the shear force was mainly transferred through the truss mechanism, which resulted in a larger effective tensile strain for CFRP sheets.

(4) Concrete strength The strengthening effectiveness was increased with concrete strength increasing, because the bond strength between CFRP sheets and concrete was directly affected by the tension strength of concrete.

4 BEARING CAPACITY ANALYSIS

4.1 Flexural strength

As to middle flexural debonding failures, the concrete near compression margin did not attain its ultimate compressive strain, for the corresponding compressive zone stress plot of concrete was not full, the flexural strength was lower than that calculated according to real material strength. The key problem for flexural strengthening with inorganic adhesive CFRP sheets was to determine the strain development degree of CFRP sheets at the ultimate state. According to the literatures (Ye 2007, Yang 2009), some suggested calculation formulae for flexural strength were given as below (rectangle section):

$$M \leq \omega f_c b x (h_0 - x/2) + E_{cf} \varepsilon_{fe,m2} A_{cf} (h - h_0) \quad (1)$$

$$\omega f_c b x = f_y A_s + E_{cf} \varepsilon_{fe,m2} A_{cf} \quad (2)$$

$$\omega = 0.7 + 0.3 \varepsilon_{fe,m2} / \varepsilon_{fe,m1} \quad (3)$$

$$\varepsilon_{fe,m2} = (0.8 / \sqrt{E_f t_f} - 0.16 / L_d) \beta_w f_t \quad (4)$$

$$\beta_w = \sqrt{(2.25 - b_{cf} / b) / (1.25 + b_{cf} / b)} \quad (5)$$

Where, M was the design value of bending moment; b was the width of control section; h was the height of control section; h_0 was the effective height of control section; x was the compressive zone height of concrete equivalent rectangle stress plot; A_s was the section area of longitudinal steel bars; A_{cf} was the section area of the CFRP sheet under specimens, which equaled to $n_{cf} t_{cf} b_{cf}$; n_{cf} was the layer, t_{cf} was the thickness of the CFRP; b_{cf} was the width of the CFRP sheet; f_c was the prism compressive strength design value of concrete; f_y was the tensile strength design value of longitudinal steel bars; E_{cf} was the elasticity module of the CFRP; $\varepsilon_{fe,m1}$ was the tensile strain corresponding to ultimate compressive strain of compression margin concrete, which was about 0.01 gained from the test results; $\varepsilon_{fe,m2}$ was the effective tensile strain corresponding to the middle flexural debonding failure, which should not be exceeded 0.005; f_t was the tensile strength design value of concrete; L_d was the length of CFRP sheet from the full use section to interruption position; β_w was the width influence coefficient; ω was a discount coefficient of concrete.

Therefore, the flexural strength of the RC beams strengthened with inorganic adhesive CFRP sheets could be easily calculated by the stated five formulae. The calculation values and test results were all listed in the Table 1, which were shown to be in good agreement. During the calculation process, all of strength values were the real testing results. For the flexural strengthening design, all strength values of materials adopted according to the design code of concrete structure (GB50010-2002).

Table 1 Comparison between calculation and test

Specimen	Test (kN·m)	Calculation (kN·m)	Calculation/Test
B I 3	26.58	27.23	0.98
B I 4	28.02	27.23	1.03
B I 5	32.00	32.56	0.98
B I 6	35.65	37.78	0.94
B II 2	46.07	42.54	1.08
B II 3	51.58	47.68	1.08

4.2 Shear capacity

Besides the requirements of GB50010-2002, the following suppositions should be satisfied. There was no relative slippage between CFRP and concrete; the mutual effects among CFRP, concrete and transverse steel hoop were not considered; the transverse steel hoops yielded before

debonding.

The shear capacity of RC beams strengthened with inorganic adhesive U type CFRP sheets could still be described as below(CECS 146 2003):

$$V_b \leq V_{\text{brc}} + V_{\text{bcf}} \quad (6)$$

$$V_{\text{brc}} = \frac{1.75}{1.0 + \lambda} f_t b h_0 + 1.0 f_{yv} \frac{A_{sv}}{s} h_0 \quad (7)$$

$$V_{\text{bcf}} = \varphi \frac{2n_{\text{cf}} w_{\text{cf}} t_{\text{cf}}}{(s_{\text{cf}} + w_{\text{cf}})} \varepsilon_{\text{cfv}} E_{\text{cf}} h_{\text{cf}} \quad (8)$$

Where, V_b was the design value of shear force; V_{brc} was the contribution of concrete and transverse steel hoops; V_{bcf} was the contribution of CFRP sheets; ε_{cfv} was the effective tensile strain corresponding the shear ultimate; φ was the effect coefficient of strengthening form, and for U type $\varphi = 0.85$; λ was the shear span/depth ratio of calculation section, and for concentration load $\lambda = a/h_0$, also it should lie between 1.5 and 3.0, finally for uniform loads $\lambda = 3.0$; n_{cf} was the layer of CFRP sheet; h_{cf} was the height of U type CFRP sheets; s_{cf} was the net space between CFRP sheet strips; t_{cf} was the thickness of one layer CFRP sheet; w_{cf} was the width of CFRP sheet. E_{cf} was elasticity module of CFRP sheet.

The key problem was to determine the tensile strain of the CFRP sheets corresponding to ultimate state. The effective tensile strain could be given as below (Hao 2004, Kong 2009):

$$\varepsilon_{\text{cfv}} = 0.30(0.32 + 0.19\lambda)\varepsilon_{\text{cfu}} \quad (9)$$

Where, ε_{cfu} was the rupture strain of CFRP.

Then, the shear capacity of the strengthening specimens could be easily calculated by the four formulae as given in Table 2.

Table 2 Comparison between calculation and test

Specimen	Test (kN·m)	Calculation (kN·m)	Calculation/Test
B-3-1	631.79	419.42	1.51
B-3-2	442.38	329.74	1.34
B-3-3	475.47	369.94	1.29
B-3-4	558.59	416.61	1.34
B-3-5	462.25	369.94	1.25
B-3-6	336.16	276.52	1.22

5 DISCUSSIONS AND CONCLUSIONS

For the limitation of the inorganic adhesive, the effective tensile strain of CFRP sheets was smaller than that of impregnated with epibond. But the inorganic adhesive has good durability as well as fire-resistance, also it was environmental-friendly and cheap. So the inorganic adhesive will have very good application fields.

The following conclusions can be drawn through mechanical analysis of RC beams strengthened with inorganic adhesive CFRP sheets:

(1) Debonding failure is common for the RC beams strengthened with inorganic adhesive CFRP sheets, which is brittle shear failures in nature. Some additional anchor measures must be taken to defer debonding failure in engineering.

(2) The flexural strength and stiffness of the RC beams strengthened with inorganic adhesive CFRP sheets are increased, because the bottom CFRP sheets partake flexure moment just like that of longitudinal reinforcement.

(3) The shear capacity of the RC beams strengthened with inorganic adhesive U type CFRP sheet strips are improved, because the U type CFRP sheet strips partake shear force just like that of transverse reinforcement, and also confine the development of diagonal shear cracks.

(4) The effectiveness of flexural strengthening is influenced by CFRP sheet amount, longitudinal reinforcement ratio, additional anchor conditions and so on.

(5) The direct contribution of U type CFRP sheets for the shear capacity of RC beams is affected by CFRP sheet amount, CFRP sheet layer, shear span/depth ratio as well as concrete strength.

(6) The maximum effective tensile strain of the inorganic adhesive CFRP sheet corresponding to flexural and shear strengthening is about 0.005.

(7) The established calculation formulae for the flexural strength and shear capacity of RC beams strengthened with inorganic adhesive CFRP sheets can be used to help practical design.

6 ACKNOWLEDGEMENT

This research project was supported by the Excellent and Youth and Middle Age Scientists Fund of Shandong Province (No. 03BS072).

REFERENCES

- Gang WU, Lin AN, Zhi-tao LV(2000). Experimental study on flexural behavior of RC beams strengthened by CFRP-sheet. *Building Structure*, 30(7):3-10. (in Chinese)
- Lie-ping YE, Wei CUI, Kong-guo HU, Qing-rui YUE(2001). Analysis and calculation of flexural strength of RC members strengthened with CFRP sheet. *Building Structure*, 31(3):3-5. (in Chinese)
- Zong-cai DENG(2001). Flexural strengthening of reinforced concrete beams with externally bonded composite laminates. *China Journal of Highway and Transport*, 14(2):45-51. (in Chinese)
- Yang-yu OU, Yi-hui HUANG, Zai-zi QIAN, Xiang-lin GU(2002). The analysis of flexural behavior of RC beams strengthened

- with GFRP sheet. *China Civil Engineering Journal*, 35(3): 1-6, 19. (in Chinese)
- Ming ZHAO, Hai-dong ZHAO, Yu ZHANG(2002). Experimental study on flexural RC members strengthened with CFRP fabrics. *Structural Engineers*, (2):52-58. (in Chinese)
- Wen-wei WANG, Guo-fan ZHAO(2004). Calculation of flexural capacity of RC beams strengthened with GFRP sheets. *Journal of Building Structures*, 25(3):93-98. (in Chinese)
- Su-yan WANG, Mei YANG(2006). Experimental study of flexural behavior of high-strength RC beams strengthened with CFRP sheets. *Building Science*, 22(5):34-38, 70. (in Chinese)
- Gang WU, Lin AN, Zhi-tao LV(2000). Experimental study on shear capacity of RC beams strengthened by CFRP-sheet. *Building Structure*, 30(7):16-20. (in Chinese)
- Zhuang TAN, Lie-ping YE(2003). Experimental research on shear capacity of RC beam strengthened with externally bonded FRP sheets. *China Civil Engineering Journal*, 36(11): 12-18. (in Chinese)
- Jian-fei Chen, Jin-guang Teng(2003). Shear capacity of fiber-reinforced polymer-strengthened reinforced concrete beams: fiber reinforced polymer rupture. *Journal of Structural Engineering, ASCE*. 129(5):615-625.
- Xin-zheng LU, Lie-ping YE, Jian-fei CHEN, Tian-hong LI(2006). Debonding failure strength in RC beams strengthened with FRP for shear. *Building Structure*, 36(9):31-36. (in Chinese)
- Tadeu A J B. and Branco F J F G(2000). Shear tests of steel plates epoxy-bonded to concrete under temperature. *Journal of Materials in Civil Engineering, ASCE*, 12(1):74-80.
- ACI.440.2R-02(2002) Guide for the Design and Construction of Externally Bonded FRP Systems for Strengthening Concrete Structures. Farmington Hills, Michigan: American Concrete Institute.
- CECS 146:2003(2003) Technical specification for strengthening concrete structures with CFRP laminate. Bei Jing: China Planning Press. (in Chinese)
- Ruo-hong ZHAO, Guang-jing XIONG(2003). Application potentials of fiber reinforced magnesium oxychloride cement in concrete strengthening. *Building Technique Development*, 30(5):60-61. (in Chinese)
- Zong-jin LI, Xin ZHANG(2006). Feasibility study of fiber reinforced inorganic paste. *Industrial Construction*, 36 (supplement):22-25.
- Xin ZHANG, Shi-bin LI, Li-luan YANG(2010). Experimental study on flexural behavior of RC beams strengthened with inorganic adhesive CFRP sheets. *Journal of Building Structures*, 31 (supplement 2):249-254. (in Chinese)
- Xin ZHANG, Shi-bin LI, Xiang-fei KONG(2010). Experimental research on shear performance of RC beams strengthened with inorganic adhesive CFRP sheets. *Journal of Building Structures*, 31(supplement2):255-260. (in Chinese)
- Lie-ping YE, Xin-zheng LU, Jin-guang TENG, Jian-fei CHEN (2007). Design models for debonding strength of RC beams strengthened with FRP sheets or plates. *Building Structure*, 37(12):79-82. (in Chinese)
- Li-luan YANG. (2009) Experimental study on flexural behavior of RC beams strengthened with CFRP by inorganic paste. Jinan: Shandong Jianzhu University. (in Chinese)
- Zhen HAO, Shuang-yin CAO, ZHAI Bao-xing, FANG Zhi-bao (2004). Analysis and calculation of shear behaviors for beams strengthened with externally bonded CFRP sheets. *Industrial Construction*, 34 (2): 81-84. (in Chinese)
- Xiang-fei KONG(2009). Study of shear behavior of RC beams strengthened with external CFRP U jackets by inorganic paste. Jinan: Shandong Jianzhu University. (in Chinese)

Experimental Study of Concrete Beams Strengthened with CFRP Sheets under Simulated Vehicles Loads

Wenwei Wang (wangwenwei@seu.edu.cn)

Department of Bridge Engineering, Southeast University, Nanjing, China

Guofan Zhao & Chengkui Huang

Department of Civil Engineering, Dalian University of Technology, Dalian, China

ABSTRACT Five reinforced concrete (RC) beams with epoxy-bonded carbon fiber reinforced polymer (CFRP) sheets were loaded symmetrically with sinusoidal dynamic loads simulating vehicles loads. One sustained loaded RC beam strengthened with externally bonded CFRP sheets and two control RC beams were experimentally investigated. Variables considered in this experimental program included compressive strength of the concrete, reinforcement ratio, bonded length, and load range. The experimental program included two parts: dynamic test and static test. Application of CFRP sheets to the bottom of five RC beams was conducted under dynamic loads and then the static test began after 174,000 dynamic cycles. The results demonstrate the feasibility of rehabilitating and strengthening damaged RC beams with CFRP sheets while the beams are under simulating vehicles loads. The static test program shows that the application of CFRP to RC beams results in increased strength and enhanced performance.

1 INTRODUCTION

The development of fiber-reinforced polymer (FRP) material, with a high-strength-to-weight ratio and excellent resistance to electrochemical corrosion, make it particularly suited for the repair of structurally deteriorated reinforced concrete (RC) structures. In recent years, considerable attention has been focused on the use of FRP for strengthening of RC beams under static and pseudo dynamic loads (Ahmed S. D. et al. 2002; Sergio F. B. et al. 2003; Triantafillou T. 1998; Wang W. 2003). In bridges engineering practice, there are many situations in which structures are under dynamic vehicles loads, such as truckloads. The characteristics of vehicles loads are different from those of static loads. Also, the performances of bond between CFRP sheets and RC beams will be different from those under static loads.

Some research work (Tang and Saadatmanesh 2003; Shahawy and Beitelaman 1999) has focused on RC beams strengthened with CFRP sheets under fatigue loads or impact loads, but there are no research works about RC beams strengthened with CFRP sheets under dynamic load simulating vehicles loads.

Tang and Saadatmanesh (2003) conducted tests to study the impact load effect on RC beams strengthened with CFRP sheets. Five beams were tested. Two beams strengthened with Kevlar laminates and two beams strengthened with carbon laminates. The test results showed that composites laminates significantly increased

the capacity of the concrete beams strengthened with Kevlar and carbon laminates and reduced the deflection and crack width.

Accelerated fatigue test were performed by Shahawy and Beitelaman (1999). Several specimens strengthened with various amounts of CFRP laminates system were tested. One specimen was fatigued for over half the expected fatigue life, then rehabilitated with CFRP, and fatigued again until failure. The results from the fatigue study indicated that fatigue life of RC beams can be significantly extended through the use the CFRP laminates.

This paper discusses the test results of RC beams strengthened with CFRP sheets and under dynamic loads simulating vehicles loads

2 RESEARCH SIGNIFICATION

The research presented in this paper is an attempt to investigate certain basic properties of RC beams strengthened with CFRP sheets under dynamic loads simulating vehicles loads, such as bond performance, failure mechanism, deflection, dynamic response, and distribution of stresses. The results can be utilized when RC beams are strengthened under vehicles loads.

3 EXPERIMENTAL PROGRAM

3.1 Test specimens

A total of 8 beams were tested. All beams have identical

rectangular cross-sections and the same size: 150mm×250mm×2700mm. Five beams were strengthened with one layer of CFRP sheet on the bottom face under simulated vehicles loads. Two beams were not strengthened and were used as control specimens. One beam strengthened with one layer of CFRP sheet under sustained loads. Figure 1 shows the design details of the test specimens and the beam cross-section. The test specimens are summarized in Table 1. Concrete with two grades of nominal compressive strength, labelled C30 and C40, respectively, were used. The flexural reinforcement consisted of 14mm and 22mm-diameter deformed bars. Two steel ratios ($\rho_s = A_s/bd$): 1.43% and 2.36% were used (Table 1). Two 8mm round bars with a sectional area of 100.5 mm² were used as

compression reinforcement (Table 1). Shear reinforcement consisted of 6mm-diameter round steel stirrups spaced at 100mm center-center (Figure 1). The beams were reinforced in this manner to prevent shear failure and to isolate the flexural behavior from shear behavior.

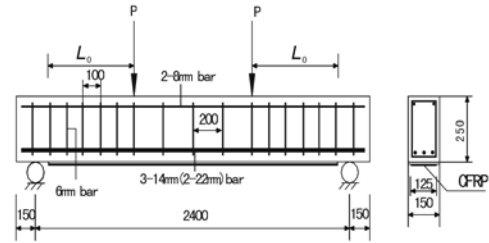


Figure 1 Details of test beams (unit: mm)

Table 1 Test specimens

Beam	Grade of concrete	CFRP	Length of CFRP (mm)	Bond length L_0 (mm)	Flexural tension reinforcement ratio ρ_s	Load (kN)		
						P_{min}	P_{max}	P_{min}/P_{max}
CL30	C30				three 14 mm deformed bars, 1.43%			
CL40	C40				two 22 mm deformed bars, 2.36%			
PL30-1	C30	1layer	2000	600	three 14 mm deformed bars, 1.43%	28	48	0.6
PL30-2	C30	1layer	2000	600	three 14 mm deformed bars, 1.43%	20	48	0.4
PL40-1	C40	1layer	1200	200	two 22 mm deformed bars, 2.36%	47	78	0.6
PL40-2	C40	1layer	1600	400	two 22 mm deformed bars, 2.36%	47	78	0.6
PL40-3	C40	1layer	2000	600	two 22 mm deformed bars, 2.36%	47	78	0.6
CFC40	C40	1layer	2000	600	two 22 mm deformed bars, 2.36%	47→78→47→	sustaining loading→bonding CFRP	

3.2 Material properties

The average 28-day concrete compressive strength was 40.3MPa for C30 and 48.9MPa for C40. The measured yield strength of the 8mm round rebar was 352.1MPa, and 14mm, and 22mm deformed rebar was 365.9MPa, and 366.5MPa, respectively. The CFRP material consisted of 125mm wide and 0.111mm thick carbon sheet externally bonded to the bottom face of RC beams using a two-part epoxy mixed at 2.5:1 ratio and cured at room temperature. Tensile strength, modulus, and elongation of the CFRP material were 3350MPa, 212GPa, and 1.58%, respectively. A summary of all the material properties is given in Table 2.

3.3 Testing procedure

For each beam, each longitudinal steel bar was instrumented with one electrical resistance strain gauge at midspan. In addition, each test beam with CFRP sheets was instrumented with two long strain gauges

(10cm length) at midspan before bonded to the bottom face of test beams. A total of three dial displacement gauges were used to measure midspan, and supporting points deflection. All specimens were tested in four-point bending over a 2.4m simple span in a 250kN MTS universal testing machine.

Table 2 Material properties

Material	Yield strength (MPa)	Yield strain
Steel	8mmbar	0.168
	14mmbar	0.183
	22mmbar	0.183
Concrete	C30	40.3*
	C40	48.9*
CFRP	3350*	1.58**

* Ultimate strength; ** Ultimate strain

As indicated in Table 1, Specimens CL30 and CL40 were control beams. Two control beams were tested to failure for evaluating crack, yield, and ultimate loads. The crack, yield, and ultimate loads of the control beam CL30 were 20kN, 90kN, and 95kN, respectively and CL40 were 24kN, 145kN, and 155kN, respectively. Application of the dynamic load was achieved by means of an electro hydraulic actuator that delivers a sinusoidal load ranging from 30% to 50% of the ultimate capacity loads of the control beams at a frequency of 1 Hz. To investigate the effect of load range on performance of bond between CFRP sheets and test beams, one specimen was tested under dynamic load ranging from 20% to 50% of the ultimate capacity loads of the control specimen CL30 at a frequency of 1 Hz (Table 1).

The surfaces of the beams were cleaned with acetone prior to bonding of the sheets. Then, the beams were laid on MTS universal testing machine and loaded with preestablished dynamic load range and frequency. One layer of epoxy was applied on the bottom face of the beam and the CFRP sheet was subsequently applied. The loads and strains were monitored with a SOMAT acquisition system that made it possible to monitor the test specimen throughout the investigation. The dynamic load was applied for a period of two days in order for the epoxy to dry. After that, a static test was conducted.

Beam CFC40 strengthened with one layer of CFRP sheet was a control beam under sustained loads. One cycle of load between 47kN and 78kN was applied, after which the load was held constant at 47kN for 48 hours to allow for application and curing of the CFRP sheet. The minimal loads of 20 kN, 28 kN, and 47 kN were selected to simulate permanent dead load effects, while the maximal load of 48 kN, 78 kN were selected to simulate vehicle load plus permanent dead load effects.

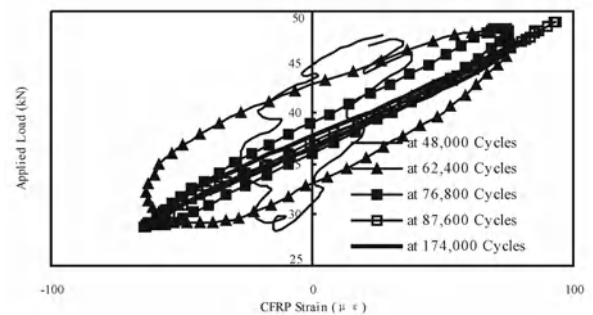
4 RESULTS AND DISCUSSION

4.1 Dynamic behavior

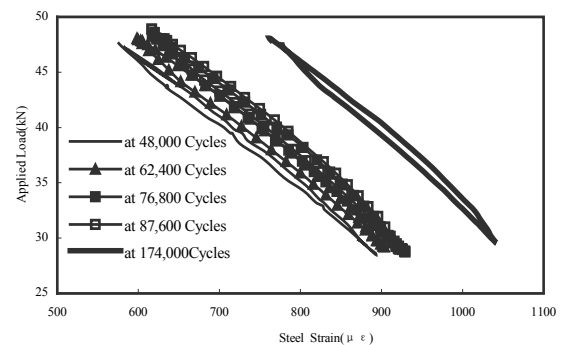
A total of five beams were tested under dynamic loads (Table 1). In all test specimens, the procedure of applying of CFRP sheets was conducted under dynamic loads, which simulated vehicles loads. All specimens were tested to 174,000 cycles and stopped prior to static tests.

Beams PL30-1 and PL30-2 were loaded statically beyond the crack loads up to the maximum level of the dynamic loads before commencing application of the dynamic loads cycles. The dynamic loads were interrupted after 48 hour, and further static tests were conducted to monitor the performance of the bond between the CFRP sheets and RC beams. The objective of the test was to study the effect of load range on the performance of bond between the CFRP sheets and RC beams.

Load-strain responses for the beam PL30-1 are shown in Figure 2. The strain of CFRP sheet was quite small and irregular at 13 hours, as shown in Figure 2 (a). It can be seen that the epoxy resin had not dried yet and the CFRP sheet can not carry the tensile forces. It is observed that the CFRP strain increased with the number of cycles increasing and the CFRP sheet began to carry the tensile forces gradually. At 24 hours, the relationship of strain of CFRP sheet and applied load was almost linear, as shown in Figure 2 (a). It shows that the epoxy resin had dried completely and the CFRP sheet can carry the tensile forces.



(a) Load-CFRP strain curves



(b) Load-steel strain curves

Figure 2 Load-strain curves for beam PL30-1

Figure 2 (b) shows the load-steel strain response at different hours. It can be seen that the relationship of steel strain and applied load was almost linear. The steel strain slightly increased between 48,000 cycles to 87,600 cycles. There is a relatively large shift in steel strain at 174,000 cycles, reflecting degradation of the specimen.

The specimens PL40-1, PL40-2, and PL40-3 were same in all respects except the bond length. The bond length of CFRP sheets for beam PL40-1, PL40-2, PL40-3 was 200mm, 400mm, and 600mm, respectively, as shown in Table 1. The objective of the test was to study the effect of bond length on the performance of bond between the CFRP sheets and RC beams. The beams, which were similar in all respects to beams PL30-1 and PL30-2, were tested to 17,400 cycles, during which the CFRP sheets was applied. The load-strain responses for

the beam PL40-1 was similar to beam PL30-1. The test beam strengthened with externally bonded CFRP sheet did not exhibit any delamination failure during the course of dynamic test, which demonstrate the bond length of CFRP sheet has a relatively small effect on the performance of bond between the CFRP sheet and RC beam.

The test results indicate that RC beams in service could be effectively rehabilitated with CFRP sheets. It is likely that the minimal bond length 200mm may be enough to avoid the delamination failure for RC beams strengthened with one layer of CFRP sheet but this is a subject for further investigation in more than one layer of CFRP sheet.

4.2 Static behavior

To verify the performance of bond between CFRP sheets and RC beams, the static tests were conducted.

Load-deflection responses for the beams under static loads are shown in Figure 3. For all strengthened beams, there was an increase in the load-carrying capacity when CFRP external sheets were added. For beams PL30-1 and PL30-2, ultimate flexural strength increases varying from 16.7% to 18.8% and for beams PL40-1, PL40-2, and PL40-3 from 11% to 16.1% were observed. The static test beams exhibited two failure modes. For the beams CL30, CL40, CFC40, PL30-2, PL40-1, PL40-2 and PL40-3, failures were by crushing of the concrete in the compression zone after tension steel yield. For the beam PL30-1, failure occurred by CFRP peeling off at the end of CFRP sheet after crushing of the concrete in the compression zone.

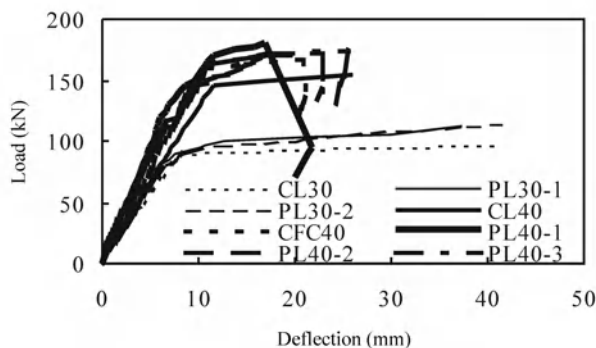


Figure 3 Load-deflection curves for all test beams

Beam CFC40, which was virgin before the CFRP sheet being applied, was strengthened with one longitudinal layer of CFRP sheet. After strengthening, as the additional loads applied, flexural cracks were initiated from the bottom of beams in the region of constant moment. As the applied loads were further increased, cracks propagated toward the upper of beam and failure of crushing of the concrete in the compression zone occurred.

For beams PL30-1, PL30-2, PL40-1, PL40-2, and PL40-3, some flexural cracks were formed in the region of constant moment when dynamic loads applied. Few diagonal cracks were formed in the region of shear span. In static test, with the applied loads increasing, some new flexural cracks were formed and the old flexural cracks widened and extended upward continuously. Similar to beam CFC40, as the applied loads were further increased, cracks propagated toward the upper of beam and failure of crushing of the concrete in the compression zone occurred.

For strengthened beams under static loads, no delamination failure has occurred. This indicates that the performance of bond between CFRP sheets and RC beams is satisfied. The use of CFRP sheet is an effective way of strengthening and rehabilitation under dynamic loads with different load range. It appears that the minimal bond length 200mm is enough to avoid the delamination failure.

5 CONCLUSIONS

(1) The study demonstrates the feasibility of using CFRP sheet in the rehabilitation and strengthening of RC beams with respect to dynamic performance.

(2) It is apparent from the static and dynamic test results that the bond performance between CFRP sheet and RC beams is satisfied at different load range and bond length.

(3) For beams strengthened with one layer of CFRP sheet, it seems that the minimal bond length 200mm should be enough to avoid the delamination failure. However, more tests should be done to support a definitive conclusion.

REFERENCE

- Ahmed S. D.et al. 2002. Carbon fiber-reinforced polymer wraps for corrosion control and rehabilitation of reinforced concrete columns. *ACI Material Journal*99 (2):129-136.
- Sergio F. B.et al. 2003. Increasing flexural capacity of reinforced concrete beams using fiber-reinforced polymer composites. *ACI Structural Journal*100 (1):36-46.
- Shahawy M., and Beitelman T.E. 1999. Static and fatigue performance of RC beams strengthened with CFRP laminates. *Journal of Structural Engineering, ASCE*125 (6):613-621.
- Tang T., and Saadatmanesh H. 2003. Behavior of concrete beams strengthened with fiber-reinforced polymer laminates under impact loading. *Journal of Composite for Construction, ASCE*7 (3):209-218.
- Triantafillou T. 1998. Shear strengthening of reinforced concrete beams using epoxy-bonded FRP composites. *ACI Structural Journal* 95(2):107-115.
- Wang W. 2003. Study on flexural behavior of reinforced concrete beams strengthened with fiber reinforced plastic. PhD thesis, *Dalian University of Technology*: China (in Chinese).

A Systematic Study of Rehabilitation of Reinforced Concrete T-beam Structures Using Externally Bonded FRP Composites

J. F. Davalos (julio.davalos@mail.wvu.edu), A. Chen (an.chen@mail.wvu.edu), I. Ray & A. Justice

Department of Civil and Environmental Engineering, West Virginia University, Morgantown, WV, USA

ABSTRACT This paper describes a synthesis of findings pertaining to rehabilitation of concrete T-beam bridges with externally bonded FRP composites from a Pennsylvania Department of Transportation District 3 (PennDOT D3) project, with the purpose of answering common questions of concern mainly by state Department of Transportation (DOT) engineers and officials. A method for selecting applicable candidate bridges for suitability of repair with externally bonded FRP composites is described. With this classification, a candidate bridge was selected for a contract repair project. Field and laboratory testing of existing and repaired bridge materials is described. Structural analysis was based on AASHTO specifications. Finite Element (FE) modeling was performed. Current ACI 440.2R-08 design guidelines were used. Supporting full-scale lab studies were conducted. Results were used to develop draft PennDOT design standards and construction specifications and to apply “lessons learned” to the design and constructability of nearly 1,000 concrete T-beam bridges in Pennsylvania, USA.

1 INTRODUCTION

Concrete highway bridges are continuously exposed to the deleterious effects of environmental attacks, leading to degradation of the material and corrosion of the reinforcing steel. Such degradation is exacerbated by the application of de-icing salts on highway bridges, and the freeze-thaw and wet-dry cyclic exposures causing accelerated ageing of the structure over time. Worldwide, concrete deterioration has motivated the development of new and innovative materials and methods for structural rehabilitation, since replacement of structures would be very costly and nearly prohibitive. In particular, over one hundred of T-beam bridges in Pennsylvania Department of Transportation (PennDOT) District 3 exhibit loss of concrete cover and reinforcing corrosion on the fascia beams due to weather, poor curb drain construction and minimal concrete cover. One solution for rehabilitation of concrete is to use Fiber-Reinforced Polymer (FRP) materials in the form of fabrics and laminates externally bonded to concrete structures to increase structural capacity and provide longer service-life. The application of this technology in practice has been highly successful (Bonacci and Maalej, 2000). Extensive review was provided in Davalos et al. (2005a and 2005b), which shows that past studies focused either on research in terms of analytical solutions and experimental investigations, or case-specific field applications. With the experience gained from these studies, especially the recent publication of ACI 440.2R-08 (2008), and urgent need from the bridge

industry, both the technology and market are ready for the wider application of this innovative repair and rehabilitation method in a more systematic way. Thus, West Virginia University (WVU) worked with PennDOT to conduct a comprehensive study on rehabilitation of concrete T-beam bridges with externally bonded FRP composites, which will be used for a rehabilitation program of nearly 1,000 concrete T-Beam bridges in Pennsylvania, USA. This paper describes a synthesis of findings pertaining to this project.

2 CLASSIFICATION OF CONCRETE BRIDGES

For the purpose of having criteria for visiting and inspecting a representative range of concrete bridges in the PennDOT-D3 inventory, the bridges were classified based on a weighted average of six characteristics (Mirmiran et al., 2004): age, span length, ADT/ADTT (Average Daily Traffic and Average Daily Truck Traffic), functional class of highway the bridge serves, the bridge capacity appraisal, and photographic indication of beam damage. For each of these characteristics, scores were assigned based on favorability for repair. Once a total score was calculated, the bridges were classified into three tentative groups, and then reclassified using field observations and more complete photographic data of damages. Class 1: Prime Candidate for Repair (Score of 70-100%). Class 2: Moderate Candidate for Repair (Score of 50-69%). Class 3: Low Candidate for Repair (Score of 0-49%). Bridges which did not show any

visible damage were ranked as 0 for the purpose of classification.

3 RECOMMENDATIONS FOR SELECTING CANDIDATE BRIDGES

Based on the above classification, the candidate bridges for FRP repair were to be selected from those either as Class 1 (Prime) or Class 2 (Moderate). Out of a total of 128 bridges, 57 scored 50% or greater, indicating that they are suitable candidates for FRP repair. Currently there is no analysis or design standard in any AASHTO (2002) documents to determine the type and amount of FRP required. The guidelines in ACI 440.2R-08 (2008) can be used as a basis for design, and this document can guide the designer through the process of analyzing and detailing surface bonded FRP.

Analysis, design and specification of the repair can be performed either by an outside consultant/contractor, or in-house by District personnel. Depending on the overall scope of work, the FRP-repair for candidate bridges may be defined at three levels: (1) Major, with all work contracted out; (2) Moderate, with combined outside contractor and in-house personnel; and (3) Minor, with all work accomplished in-house. The selection of candidate bridges should conform to this descending scale of FRP-repair work complexity, from Major to Moderate to Minor. This approach offers great potential for providing an efficient learning and training environment for District personnel, so that eventually, a Minor FRP-repair work of a candidate bridge can be accomplished entirely by District forces. Moreover, this approach can provide an opportunity to develop more specific design and construction guidelines and promote statewide acceptance of FRP rehabilitation.

4 FIELD ASSESSMENT OF SELECTED BRIDGE

A candidate bridge at Level-1 was selected for field implementation. This is a 13.7 m (45-ft) long single-span bridge with a total deck width of 8.2 m (26-ft 11-inch). The superstructure consists of six reinforced concrete girders monolithically cast with a 21.6 cm (8.5") deep deck plus a 6.4 cm (2.5") overlay. It can be assumed as simply-supported by the abutments. As shown in Figure 1, this bridge had extensive overall damage and had been considered for replacement. Two core samples were obtained from the bridge deck using a core drill; one at mid-span and one at the quarter-point. Each sample represented the entire depth of the deck. A single sample of beam reinforcing steel was cut from the bottom row of reinforcement on the fascia side of an external beam. This particular bar was chosen because it was completely exposed with no bond to the concrete. From a visual inspection, the external beams showed the

most damage with severe delamination and spalling along with several cracks. Interior beams showed less severe damage with some localized spalling or delamination.

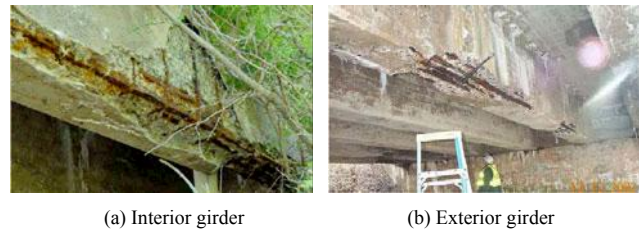


Figure 1 Selected bridge for Level-1 repair with FRP

5 EVALUATION OF IN-SITU MATERIALS AND FIELD SAMPLES

Concrete cylinders were obtained as deck core samples and tested in compression (ASTM C42). The average compressive strength was found to be 40 MPa (5783 psi). The fractured surfaces of the cylinders were tested for carbonation immediately after compression testing (Figure 2 (a)). The reagent turned dark pink throughout the cross section of the cylinders indicating that the deck concrete was not carbonated. A similar carbonation test was conducted on the freshly exposed surfaces of two concrete beam samples collected from the cover zone as shown in Figure 2(b) and (c). The phenolphthalein solution on beam samples was found to be completely colorless to a depth of 2.5 cm (1 inch) to 3.8 cm (1.5 inch), indicating thorough carbonation and lowering of pH below 9.0 near the concrete cover zone.

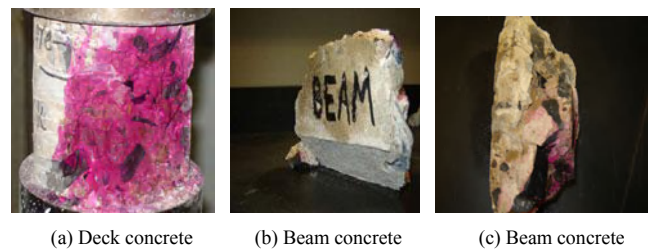


Figure 2 Carbonation test

Both SEM and EDX techniques were used to determine, respectively, the morphology and qualitative compositions of hydrated pastes in three concrete beam samples. SEM images showed the formation of calcite. EDX confirmed the formation of calcite mostly at the expense of Calcium Silicate Hydrate (C-S-H) gel (Figure 3).

Chemical analysis was performed for concrete powder samples, which were obtained from the beam and the two cores. The data showed that the beam sample had very low cement content compared to that of deck cores. The results indicated that, over time, much leaching of C-S-H gel and calcium hydroxide had occurred within the beam. The SEM-EDX and phenolphthalein tests indicated that carbonation and severe chloride attack

may have caused this leaching. The deck slab was in a relatively better condition, although there was some evidence of chloride attack.

The acid soluble chloride test was performed according to ASTM C1152. The quantities of acid soluble chloride by mass of cement in the beam specimen, core 1, and core 2 were calculated as 1.6%, 1.4%, and 0.19%, respectively. ACI 318 (2002) provides a maximum water soluble chloride ion limit to be 0.15%. The results showed that the concrete in the beam and core 1 had no protection against corrosion since their chloride threshold limit was grossly exceeded. The core 2 sample contained the least amount of chloride. The large quantities of chloride salt crystals and their reaction products (chloroaluminate) in core 1 and the beam indicated that their concrete was more porous than that of deck core 2. The confirmation of a higher porosity can also be seen in the results of the compression test since deck core 1 had a 25% lower compressive strength than deck core 2.

Reinforcing steel tension tests were performed according to ASTM Standard Test Methods for Tension Testing of Metallic Materials (ASTM E8). An extensometer (MTS) was used along with a data acquisition system to record load vs. strain throughout the test. This data was used to define the stress vs. strain curve. The average yield strength was 261 MPa (37 ksi) and the average ultimate strength was 441 MPa (64 ksi).

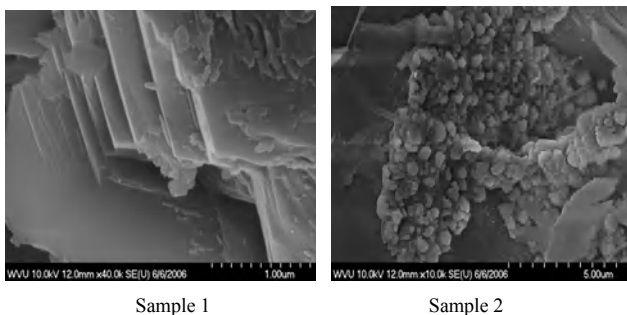


Figure 3 SEM images from beam samples

6 TESTING OF EXISTING BRIDGE

In order to investigate the response of the selected bridge under different loading conditions, a field test was conducted by applying tandem truck(s) on one or two lanes. The data acquired through field testing were compared to the results of the FE model in order to verify the accuracy of the model. Displacement transducers (LVDT) were used to obtain deflections of the reinforced concrete girders. Accelerometers were utilized to determine the natural frequency. All of the data were recorded at the mid-spans of the girders. Figure 4 shows the load cases and Figure 5 shows the instrumentation plan.

In order to observe the full response of the bridge

under loading, the trucks crossed the bridge at several different transverse locations. The locations were selected to maximize the deflections of the girders. The maximum deflection occurred when the truck's center of gravity was directly over the centerlines of the girders. There were a total of six dynamic load field tests. In the static tests, the truck moved at a crawl speed. In the dynamic tests, the truck travelled at 48 km/hr (30 mph) to 80 km/hr (50 mph) to excite the bridge when braking suddenly over the bridge. The data from the accelerometer showed that the natural frequency of the bridge was about 14.66 Hertz.

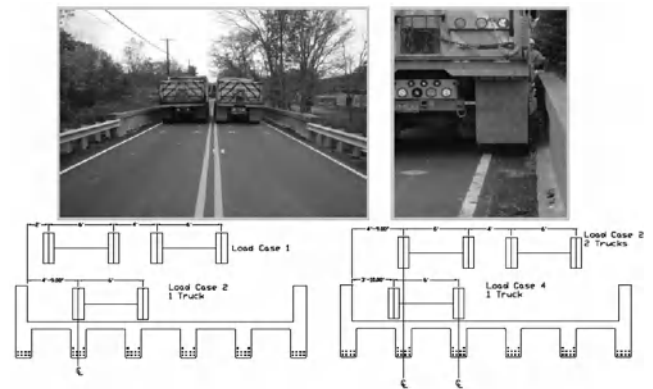


Figure 4 Load Cases

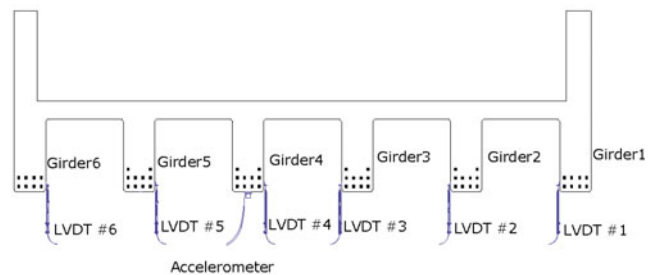


Figure 5 Cross-section setup of instrumentation plan

7 FINITE ELEMENT MODELING OF THE SELECTED BRIDGE

The selected bridge was analyzed for existing conditions. An FE model was built using the commercial program ABAQUS (2005). The information for the FE analysis was obtained from a combination of available design documents and field information gathered. The model was developed in order to determine current capacities of the bridge, to identify critical load conditions for field testing, and to compare predictions with field responses when actual test truck-loads were used. Subsequently, this model was calibrated using the field test results and modified as needed to increase its accuracy. The verification of the model permitted its confident use in designing the FRP reinforcement.

Figure 6 reports the analytical mid-span displacements relative to the most critical load case when the rear axle

of the truck was at the mid-span. The testing results are also shown in Figure 6 for comparison, where a good correlation can be observed.

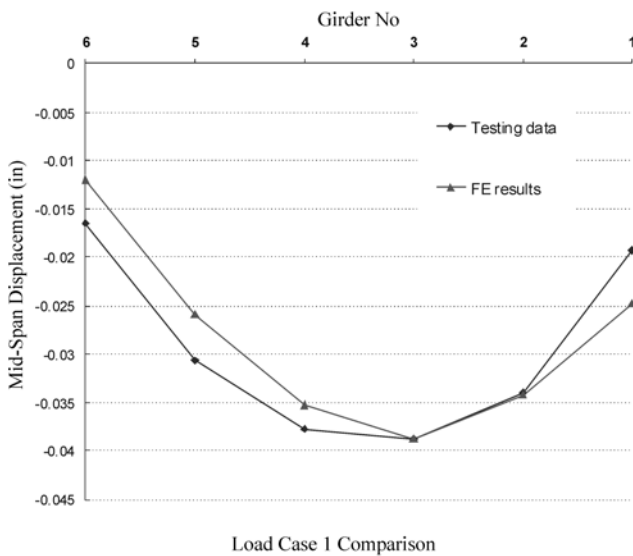


Figure 6 Mid-span displacement of girders

A dynamic analysis was also performed in order to determine the natural frequency of the bridge. This information provided added verification that the FE model and the actual bridge were yielding the same results and responding to loading in similar fashions. The natural frequency of the bridge was predicted to be 13.33 Hertz, which is about 10% lower than the test result (14.66 Hertz).

8 BRIDGE REPAIR

The FRP repair system was designed by the contractor and reviewed by WVU based on current ACI 440.2R-08 (2008) design guidelines. Initial FRP design was based on strengthening to replace a known area of corroded reinforcement. However, when the contractor removed the concrete from edge beams, they found that 20% of the tensile reinforcement and some of the diagonal shear bars and vertical stirrups as shown on the contract drawing were missing. The rest of the beams were thought to have the same missing reinforcement, although they were not exposed. Consequently, WVU initiated discussions on what design load should be used for FRP repair design calculations. Rather than being concerned with any discrepancies between original design plans/specifications and as-built conditions, WVU recommended using FRP strengthening to sustain a current AASHTO (2002) load, which is HS-20 for this bridge, based on the best evaluations of current conditions of the bridge, including details on material properties, such as concrete strength as per recommendations, steel section loss due to corrosion, etc. This methodology was accepted by PennDOT-D3. WVU

provided design loadings for all beams, based on which the contractor finished the design drawings.

The repair was done following ACI 546R and ICRI No. 03730 guidelines. The beams were either repaired with triple A concrete mix by using pumps or patched using bag repairing materials. Figure 7 shows the formwork for concrete repair. FRP strips were bonded using a typical dry application process, as shown in Figure 8.



Figure 7 Formwork for concrete repair



Figure 8 FRP strip installation

9 QUALITY CONTROL

WVU also assisted PennDOT D3 in overseeing the quality control of the repair and rehabilitation process, and evaluating the acceptability and adequate performance of the application. They monitored demolition of deteriorated concrete, concrete repair, FRP design, FRP installation, and acceptance testing and inspection. The quality of concrete repair materials, concrete-FRP, and also FRP laminates was evaluated.

10 POST-CONSTRUCTION LOAD TEST AND FINITE ELEMENT MODELING

The load testing on the repaired bridge was conducted using the same protocols as described above, except several loading cases were added because of the un-symmetric repair conditions. Deflection results for the repaired and un-repaired bridge for a typical load case are shown in Figure 9. It is important to note that all deflection values from testing of the un-repaired bridge were scaled up due to the weight difference of the trucks.

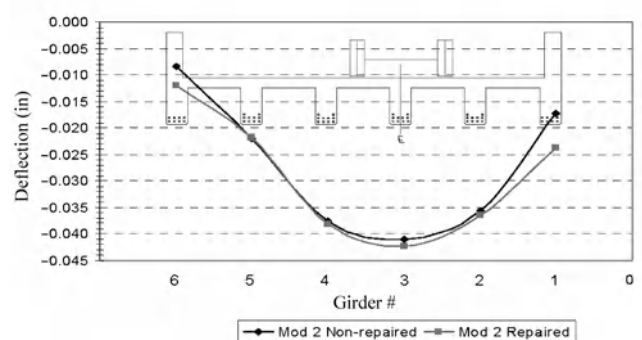


Figure 9 Case II repaired vs. un-repaired bridge mid-span deflection

The FE model as described above was modified to study the behavior of the concrete bridge repaired with FRP strips. The FRP strip was modeled using “Element-Based Surface,” and the surface based “TIE” constraint was used to couple the FRP strips and concrete surfaces. Figure 10 and Figure 11 report, respectively, the mid-span displacements and bottom strains from FE analysis for a typical load case, when the center of gravity of the PennDOT tandem truck was at mid-span. The testing results are also shown in these figures. The FE model predictions correlate well with the testing results. It is noted from Figure 11 that there is some localized effect for the strain on the girder which is directly under the wheel load, which cannot be represented by the FE model.

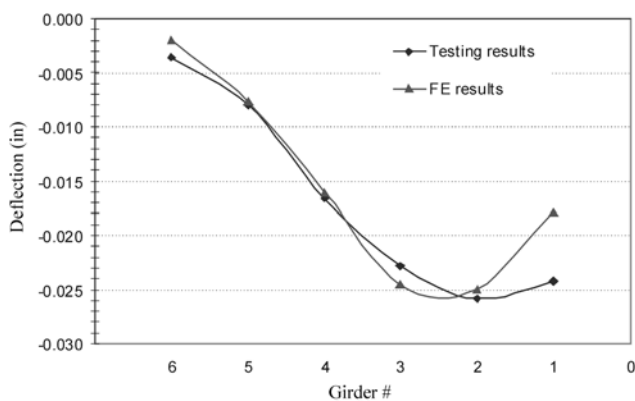


Figure 10 FE results for mid-span displacement

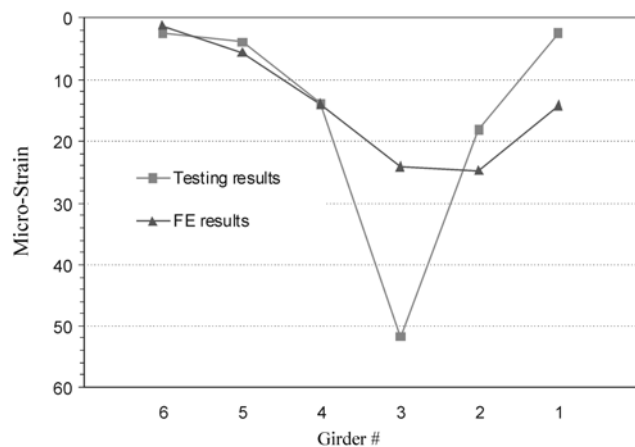


Figure 11 FE results for mid-span strain

A dynamic analysis was also performed in order to determine the natural frequency of the bridge. The natural frequency of the bridge was predicted to be 13.44 Hz for Mode 1. The Mode 1 natural frequency from field testing was 14.72 Hertz, which is about 9% higher than the predicted value.

It is concluded that, based on the loading factors from un-repaired and repaired bridges and design documents from the contractor, the moment and shear capacities of the repaired bridge increased. Overall, the stiffness of

the repaired bridge did not change much, as illustrated by both testing and FE analysis results.

11 SUPPORTING LAB-SCALE STUDY

Comprehensive testing and evaluation protocols were conducted at component level, with the purpose of simulating the ageing process by accelerated corrosion of the rebar using induced electric current. The distressed beam specimens due to rebar corrosion were retrofitted with FRP by effectively applying similar repair materials and procedures as in the field. The bending and fatigue tests of the repaired beam samples will serve to forecast the long-term performance of the field-repair and enhanced load-bearing capacity of the bridge structure.

This two-part study consisted of large-scale reinforced concrete beam specimens which were cast using chloride contaminated, low-strength, highly porous concrete, as determined from the evaluation of in-situ materials and field samples. The objectives of Part I were to compare two different concrete substrate repair methods and to study the long-term durability by inducing additional corrosion after repair. The objectives of Part II were to compare the performance of three distinct FRP anchorage schemes under both static and cyclic loading. Scheme 1 consisted of flexural FRP only, scheme 2 consisted of flexural FRP plus two strategically placed anchor stirrups, and scheme 3 consisted of flexural FRP plus eight evenly spaced anchor stirrups. In both Part I and Part II, an electrochemical accelerated corrosion technique was applied to the beams.

Part I consisted of 15 beams with dimensions of 15.2 cm × 20.3 cm × 274.3 cm (6x8x108 inch), which were divided into two groups (Ray et al. 2009; Parish 2008). In the first group, the concrete cover of the initially corroded beams was removed and the beams were patch-repaired along their entire length with polymer modified concrete (PMC). In the second group, the deteriorated concrete cover was not removed, but instead, all cracks were injected with epoxy, termed crack filled only (CFO). Figure 12 illustrates the setup of accelerated ageing system.

The results from Part I study demonstrated that the accelerated ageing process was highly successful in introducing level of corrosion, as shown in Figure 13, that is very similar to the condition observed in the field. Although it was expected that the polymer patch repaired beams (PMC) would outperform the crack-injected beams (CFO), the reverse was true for load capacity immediately after corrosion cycle I and repair. However, after a Corrosion Cycle II of repaired beams, those with polymer patch repair proved to be much more durable than crack-injected beams both in terms of strength and ductility. The accelerated corrosion process reduced specimen stiffness, as expected. However, the stiffness of the FRP-repaired beams was actually very close to

the stiffness of the corroded unrepaired beams, which verified the same observation in field testing results for the selected bridge. Overall, the PMC repair was superior to the crack-injection repair. Also, when coupled with FRP sheets, PMC produced more ductile failure and better durability.



Figure 12 Test setup **Figure 13** Typical deterioration

Part II consisted of 21 large-scale reinforced concrete beam specimens with dimensions of 15.2 cm×20.3 cm×198.1 cm (6 inch×8 inch×78 inch), which were cast using the same materials and subjected to the same accelerated corrosion as described in Part I (Parish 2008; Davalos and Parish et al. 2009). All load-deflection curves for the beams tested in static flexure were quite similar. This indicated that the anchorage scheme had little effect on newly repaired beams. However, based on the observations during the second corrosion phase of Part I, it can be concluded that more anchorage would be very beneficial to the long-term durability of an FRP repair system, as the concrete substrate and FRP-concrete bond is likely to deteriorate over time. More anchorage may add ductility to an FRP-repaired structure if concrete debonding begins to occur. Non-fatigued specimens tested in flexure failed via crack-induced debonding, where large v-shaped portions of concrete remained adhered to the FRP strips after debonding. These large v-shaped pieces of concrete were no longer observed on specimens subjected to fatigue and subsequently to static testing to failure.

12 DEVELOPING DRAFT GUIDELINES AND RECOMMENDATIONS

The culmination of this project resulted in practical guidelines and recommendations for the effective implementation of surface bonded FRP on concrete T-beam bridges in Pennsylvania. Two sets of guidelines were developed: (i) Guidelines for Project Selection and Management and (ii) Guidelines for Concrete T-beam Bridge Design and Construction.

13 CONCLUSIONS

Based on the repair contract, lab studies and post-construction load testing, it can be concluded that Externally Bonded FRP Composites are viable means to rehabilitate concrete T-beam bridges. The criterion developed for ranking the bridges into three categories was effective. The technical and cost-effective application

of externally bonded FRP was demonstrated for a Level-1 bridge repair. FRP strengthening should be designed to sustain a current AASHTO design load. The FE model can be used in designing the FRP reinforcement. Overall, the stiffness of the repaired bridge did not change much, as illustrated by both testing and FE analysis results, which was also verified by the lab-scale studies. Based on lab-scale studies, corrosion induced by the direct-current accelerated ageing technique resulted in deterioration of the laboratory specimens that was very similar to what was observed for bridges in the field. The anchorage scheme had little effect on newly repaired beams.

14 ACKNOWLEDGEMENTS

We gratefully acknowledge PennDOT District-3 for their financial and technical support. We appreciate the support from MAUTC, PTI at the Pennsylvania State University and WVU Research Corporation. We appreciate industry support for materials and advise from BASF, FYFE Co. LLC, Vector Corrosion Technologies, Arrow Concrete Co., and Sika Construction, USA.

REFERENCES

- Bonacci, J. F. and Maalej, M. 2000. Externally Bonded FRP for Service-life Extension of RC Infrastructure, *Journal of Infrastructure Systems*, ASCE, 6(1). pp. 41-51.
- Davalos, J.F., Parish, G., Chen, A., and Ray, I. 2009. Effect of FRP Wrapping Schemes for Beams Aged by Accelerated Corrosion and Strengthened with CFRP, Submitted to *Journal of Structural Engineering*, ASCE, under review.
- Davalos, J.F. Chen, A., Ray, I., Justice, A., and Anderson, M. 2009. District 3-0 Investigation of Fiber-wrap Technology for Bridge Repair and Rehabilitation (Phase-III), submitted to Pennsylvania Department of Transportation.
- Davalos, J.F. et al. 2005a. District 3-0 Investigation of Fiber-wrap Technology for Bridge Repair and Rehabilitation (Phase-I), submitted to Pennsylvania Department of Transportation.
- Davalos, J. F., Lin, C., Ray, I., and Brayack, D. 2005b. Applications of Externally Bonded Composites for Concrete Repair and Rehabilitation, Proceedings of the American Society for Composites 20th Technical Conference, Philadelphia, PA, September 7-9, 2005.
- Mirmiran A, Shahawy M, Nanni A, and Karbhari, V. 2004. NCHRP Report 514: Bonded Repair and Retrofit of Concrete Structures Using FRP Composites-Recommended Construction Specifications and Process Control Manual, Transportation Research Board, Washington, D.C. 2004.
- Parish, G. 2008. CFRP Repair of Concrete Beams Aged By Accelerated Corrosion, MSc Thesis, West Virginia University, Morgantown, WV.
- Ray, I., Parish, G., Davalos, J.F., and Chen, A. (2009). Effect of Concrete Substrate Repair Methods for Beams Aged by Accelerated Corrosion and Strengthened with CFRP, *Journal of Aerospace Engineering*, ASCE, to appear.

Basalt FRPs for Strengthening of RC Members

A. Serbescu (a.serbescu@shef.ac.uk), M. Guadagnini & K. Pilakoutas
Department of Civil and Structural Engineering, University of Sheffield, UK

A. Palmieri & S. Matthys
Magnel Laboratory for Concrete Research, Department of Structural Engineering, Ghent University, BE

ABSTRACT The use of FRPs to enhance the structural performance of RC members represents today's common practice. This is mainly due to their high strength to weight ratio, corrosion resistance or ease of application. However, given the current circumstances, the construction industry is in need of a more viable alternative to the commonly used glass and carbon fibres. Hence, the paper discusses two experimental programmes investigating the use of relatively new basalt fibres for strengthening of both compression and flexural members. Application of shear strips in strengthening of an RC beam (University of Sheffield) has shown that even a small amount of basalt FRPs can successfully increase the ultimate load capacity as well as provide anchorage and reduce the brittleness of plate end debonding. Testing of FRP confined concrete cylinders (Magnel Laboratory) has proven basalt to be 14% more effective than glass, yielding an average compressive strength increase of 84% when compared to the unconfined cylinders.

1 INTRODUCTION

The cost-effectiveness of FRP strengthening systems is one of the key aspects of their popularity within the construction industry. When compared to carbon, glass fibers are a cheaper alternative but their use is limited by their effectiveness and durability. Basalt fiber reinforced polymeric (BFRP) composites are becoming commercially available at a low cost and in view of the economical and environmental demands, may represent an alternative to the existing FRP systems.

Basalt fibers are a single component fibers obtained by melting solidified volcanic lava. The structural basalt fibers available on the market have higher failure strain than carbon fibers (fib, 2007) and a strength to weight ratio 1.5 times higher than that of glass. Although just few studies are available in the literature, manufacturers claim basalt fibers to be highly resistant to corrosive environments, such as salt and acid solutions and, especially alkalis (Sudaglass, 2008). In addition, the fibers exhibit high resistance to impact and high temperature loads and are an environment-friendly natural material. Basalt can be formed into continuous fibers adopting the same technology used for glass fibers. The production process however, requires less energy and the raw materials are widely available all around the world. This justifies the lower cost of basalt fibers compared to that of glass fibers. Basalt fibers are significantly cheaper than carbon fibres (BFCMTD, 2007) and their mechanical and physical properties make basalt FRPs ideal solution for a range of structural strengthening applications.

2 USE OF BASALT FIBRES FOR STRENGTHENING APPLICATIONS

2.1 Shear strengthening of RC beams

Basalt FRP wet lay-up strips were applied to enhance the shear capacity of an RC beam, referred here in as the tested beam. To enhance the quality of the shear strengthening procedure, the concrete surface was grinded and the beam edges rounded off to locally reduce the stress concentration that could induce rupture of the shear strips. The basalt woven strips were manually impregnated with epoxy resin before bonding them to the beam. Prior to shear strengthening, the tested beam was also strengthened in flexure using the same FRP solution (CFRP plate, $t_f=1.4\text{mm}$; $E_f=200\text{GPa}$; $f_{fk}=2590\text{MPa}$) as for the control beam (Pescic 2003). The beam was tested under four-point bending load (Figure 1). The load was applied in displacement control and three load cycles were performed (50 kN, 80 kN and 120 kN) before failure occurred at 170.5 kN. Table 1 shows the details of the tested beam and Table 2 presents the characteristics of the basalt fibres used in the study.



Figure 1 RC beam strengthened in shear with BFRP strips

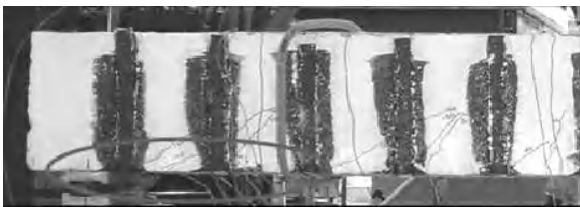
Table 1 Properties of RC beam

f_c (MPa)	$b \times h$ (mm)	L (mm)	Bottom steel	Top steel	Steel Shear links (mm)
35	150 × 250	2500	2 ϕ 20	2 ϕ 6	ϕ 6/125

Table 2 Properties of basalt fibres

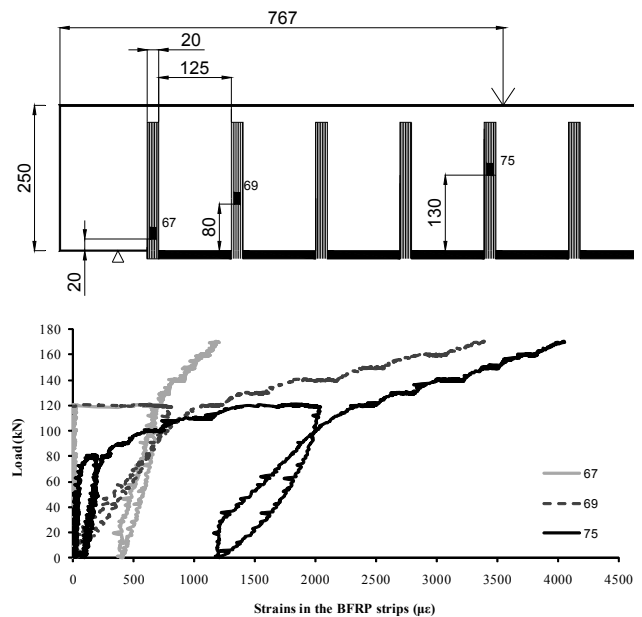
f_t (MPa)	E_t (GPa)	Strips shape	$b \times t$ (mm)	No. of strips	Spacing of strips (mm)
4850	90	U	20 × 1	7 × 2	125

Although a debonding type of failure still occurred, the ultimate load of the tested beam was increased by almost 40kN when compared to the control beam, which failed at 134kN. As can be seen in Figures 2 and 3, the failure mode of the control beam by sudden concrete cover separation, changed into a peeling off failure mode for the shear strengthened beam. The presence of the basalt shear strips contributed in enhancing the transfer of stresses between the FRP plate and the concrete, probably through friction as the tested beam was able to carry more load following the acoustic warning of debonding initiation. The control beam collapsed at a lower level than the yielding flexural capacity (157 kN) whilst the shear strengthened beam was able to exceed the yielding load.

**Figure 2** Rip-off failure of the control beam**Figure 3** Peel-off failure of the tested beam

The increase in capacity can be attributed to the presence of the transversally bonded U-strips which, not only increased the shear capacity of the section, thus delaying the initiation of the diagonal cracking process, but also contributed in decreasing the peeling stresses and consequently controlling the propagation of the debonding crack. It has to be mentioned that no debonding of the BFRP strips was observed. Their performance is presented in form of load versus strain diagram in Figure 4. The strain gauges mounted on the external shear BFRP strips (Figure 4 - top) recorded a

maximum strain value of 0.45% (Figure 4 - bottom), thus proving their efficiency up to that level.

**Figure 4** Strains developed in BFRP strips

2.2 Confinement of concrete cylinders

The comparative behavior of ten FRP confined concrete cylinders (five using basalt fibers and five using E-glass fibers) was experimentally investigated. The tested cylinders comprised FRP tubes filled with concrete. Filament winding technique was used to produce the tubes in 3 FRP layers. The first and the third layers were wound under a corner of 88 degrees with the rotation axis whilst the second under 56 degrees. Epoxy resin (type PC 5800) was used to produce the composite material by impregnation of fibers on the mould and manually. For technological purposes, the FRP tubes were made slightly cone-shaped (height of 300 mm and diameter of 160 mm for the upper side and 150 mm for the lower side). After hardening, the fiber reinforced cylinders were filled with concrete ($f_c=50$ MPa, $W/C=0.5$). The specimens were then tested in compression by applying axial loading monotonically under displacement control with a rate of 0.005 mm/s. To record the deformations, six strain gauges (three for the axial strain and three for transversal strain) were installed on the external surface of the tubes in the middle.

The mean experimental results on 5 cylinders for each FRP type and on 3 cylinders of unconfined concrete used as control specimens are reported in Table 3 in terms of confined strength f_{cc} and strengthening factor (the ratio between the average concrete strength of reinforced cylinders and unconfined ones).

Figures 5 and 6 show the axial stress plotted as a function of axial strain (drawn on the left side) and of

lateral strain (drawn on the right side) for basalt and glass confined cylinders, respectively.

Table 3 Confinement effects

Sample	f_{cc} (MPa)	$\zeta = f_{cc}/f_{co}$
Basalt	91.0	1.84
E-glass	84.1	1.70
Concrete	49.5	1.00

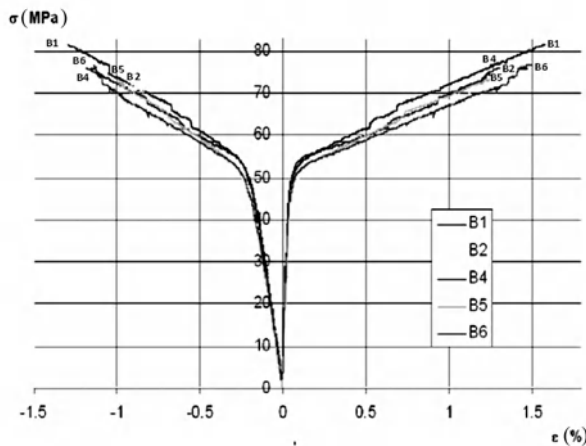


Figure 5 Stress-strain relationship of BFRP confined cylinders

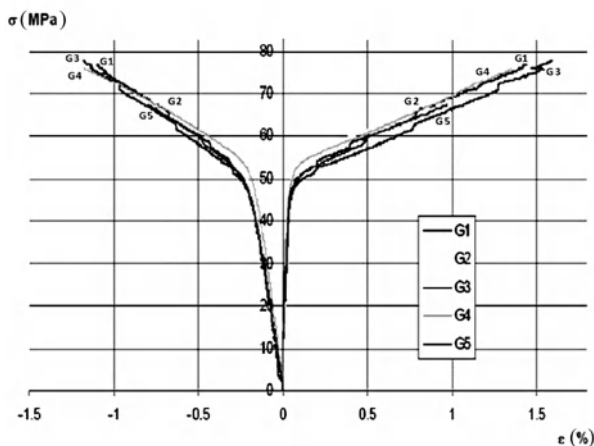


Figure 6 Stress-strain relationship of GFRP confined cylinders

For both materials, the curves are bilinear in nature with a small transition zone. In the first linear zone, concrete primarily takes the axial load; the slope of the confined concrete is the same as the slope for unconfined concrete. At stress levels near to the ultimate stress of the unconfined concrete, a transition zone to the second portion of the bilinear curve starts. This region corresponds to the stage at which concrete starts cracking and radially expanding, so that the FRP tube starts to show its full confining characteristics. As can be seen in Table 3, the experiments showed that basalt fiber reinforced cylinders provided substantial gain in strength: 84% of average compressive strength increase was recorded in comparison to the control specimens. In

addition, when compared to E-glass reinforced cylinders, basalt fiber cylinders are more effective ($\zeta=1.70$). Failure aspect of all composite specimens was characterized by fracture of the FRP tube with concrete bursting at half height of the cylinders.

3 CONCLUSIONS

The use of BFRP strips as external shear reinforcement for RC beams was shown to efficiently contribute to delaying plate end debonding failure and reducing the brittleness of the failure. Results from the experimental programme show that the shear capacity of the member strongly influences the anchorage debonding load. However, the amount of external FRP shear reinforcement to avoid debonding has to be optimized.

Confinement with BFRP was 14% more effective than that with GFRP in terms of compressive strength.

The experimental results on the use of basalt for strengthening application on both concrete columns, at Magnel Laboratory, and beams, at the University of Sheffield, confirm that basalt FRPs are a viable alternative to currently available FRP systems. As basalt fibres can only offer moderate strength increases, use of BFRP external reinforcement is recommended in applications where other FRP systems would lead to an uneconomic design and durability or heat resistance are critical. However, it's clear that further research is necessary to validate the effectiveness of basalt fibers.

4 ACKNOWLEDGEMENTS

The authors wish to acknowledge the companies Galen Ltd, Basaltex, Owens-Corning, ECC group and MagmaTech Ltd. UK for providing testing materials. Part of this work was financially supported by the European funded En-Core Research Training Network.

REFERENCES

- BFCMTD. 2007. *Basalt Fiber and Composite Materials Technology Development*, China <http://www.basaltfm.com/eng/fiber/info.html>, Access date: 20 June 2009.
- fib Bulletin No. 14. 2001. Design and use of externally bonded fibre reinforced polymers for reinforced concrete structures, *Federation International du Beton*.
- Lisakovski, A.N., Tsybulya, Y.L., & Medvedyev, A.A. 2001. Yarns of Basalt Continuous Fibers, *The Fiber Society Spring 2001 Meeting*, Raleigh, NC, May: 23-25.
- Palmieri A., Matthys S. & Tierens M. 2009. Basalt fibres: mechanical properties and applications for concrete structures, *Third International Conference on Concrete Repair*. Venice/Padua, Italy.
- Pesic, N. 2003. Analysis of reinforced concrete beams strengthened with externally bonded FRP reinforcement, *PhD thesis*, University of Sheffield, UK.

- Ramakrishnan, V. & Panchalan, R.K. 2005. A New Construction Material-Non-Corrosive Basalt Bar Reinforced Concrete. *ACI Journal Special publication*, Vol. 229, September 1: 253-270.
- Serbescu, A., Guadagnini, M. & Pilakoutas, K. 2008. Applicability of Basalt FRP in Strengthening of RC beams. *Fourth International Conference on FRP Composites in Civil Engineering*, Zurich, CH.
- Sim, J., Park, C. & Moon, D.Y. 2005. Characteristics of Basalt Fiber as a Strengthening Material for Concrete Structures. *Composites. Part B Engineering*, Vol. 36: 504-512.
- Sudaglass, 2008. Sudaglass Fibre Technology. <http://www.sudaglass.com>, Access date: 24 January 2009.
- Tierens, M. 2007. Verkennend onderzoek naar het gebruik van basaltvezels voor de versterking van betonconstructies (in Dutch) *master dissertation* (supervisor S.Matthys). Gent University, BE.

Load-Carrying Capacity of Flexural Reinforced PC Beams with Pretensioned AFRP Sheet

Y. Kurihashi (kuri@news3.ce.muroran-it.ac.jp), N. Kishi & A. M. Ali
CERU, College of Environmental Engineering, Muroran Institute of Technology, Muroran, Japan

H. Mikami
Technical Research Institute of Sumitomo-Mitsui Construction Co., Ltd., Nagareyama, Japan

ABSTRACT To develop a rational flexural reinforcing method for prestressed concrete (PC) beams with pretensioned Aramid Fiber Reinforced Polymer sheet (AFRPs), the new anchoring method is proposed. It is the concept of this method to rationally disperse the concentrated anchoring stress due to bonding the cross-directional AFRPs in the anchorage areas and to gradually relax the high strain caused at the ends of sheet due to applying the high-strain type epoxy-resin in the areas. Its applicability was confirmed by conducting static four-point loading test of the PC beams reinforced by means of the proposed method. From this study, following results were obtained: 1) applying the proposed anchoring method, predetermined pretensioning force of the sheet can be perfectly introduced into the beams without any mechanical anchoring devices; 2) the cracking and yielding loads, and the ultimate load of the PC beams can be upgraded due to bonding pretensioned AFRPs.

1 INTRODUCTION

Nowadays, continuous Fiber Reinforced Polymer sheet (FRPs) bonding method has been rapidly introduced for retrofitting and/or reinforcing existing reinforced concrete (RC) and prestressed concrete (PC) members. Usually, those FRPs will take the reinforcing effects after rebar yielding. Recently, pretensioned FRPs bonding method has been proposed to effectively increase the cracking and rebar yielding loads for flexural reinforced RC beams with FRPs. Also, an effective anchoring method for bonding pretensioned Aramid FRPs (AFRPs) for RC beams has been experimentally investigated by Kishi et al. (2009). The method may be more effective for PC members than RC ones. However, the reinforcing effects of the proposed method for PC beams have never been investigated so far.

From this point of view, under applying the proposed anchoring method for bonding pretensioned AFRPs, to

investigate load-carrying behavior of flexural reinforced PC beams with pretensioned AFRPs, static four-point loading test was conducted taking the ratio of the pretensioning force to the ultimate tensile capacity of the AFRPs (hereinafter, pretensioning force ratio) as variable.

2 EXPERIMENTAL OVERVIEW

2.1 Outline of specimens

Total four specimens listed in Table 1 were used for this study, in which pretensioning force ratio of AFRPs was taken as variable and control beam was prepared which is not reinforced with AFRPs. These specimens were designated using pretensioning force ratio n (%) such as Beam T n and control specimen was named as Beam N. Pretensioned AFRPs has 830 g/m² mass and 300 mm width. Its nominal load-carrying capacity is 1,176 kN/m.

Table 1 List of specimens

Specimen	Target pretensioning force ratio (%)	Actual pretensioning force ratio (%)	Actual introduced strain (μ)	Calculated flexural load-carrying capacity (kN)	Calculated shear load-carrying capacity (kN)	Shear-bending capacity ratio
N	–	–	–	87	297	3.41
T0	0	0	0	135	297	2.20
T20	20	20.5	3387	150	313	2.08
T40	40	36.1	6346	164	325	1.98

The beams have rectangular cross section of 220×300 mm (height \times width) and a clear span of 3.0 m. Layouts of the reinforcement, PC tendon, and AFRPs for reinforcing and/or dispersing concentrated anchoring stress are shown in Figure 1. Three PC tendons of 12.7 mm in nominal diameter are placed on the neutral axis of the section. Here, pretensioning force ratio of the PC tendon is 60 %. Also, each of the three steel rebars of 10 mm diameter are placed at the upper and lower fibers. Stirrups of 10 mm diameter are placed with intervals of 90 mm. Pre-tensioned AFRPs was bonded onto the tension-side surface of the beam leaving 80 mm between supporting point and the sheet end as shown in the bottom view of Figure 1.

In this study, in order to widely disperse the concentrated anchoring stress occurred near the ends of pretensioned AFRPs, before bonding pretensioned AFRPs, the cross-directional AFRPs was bonded on the concrete surface in the anchorage area, and a high-strain type epoxy-resin was used to relax the bond strain between pretensioned AFRPs and cross-directional one. A young's modulus of the resin is 1/60 times smaller than that of normal one and the strain capacity is 150%.

2.2 Outline of pretensioned AFRPs bonding method

Pretensioned AFRPs was bonded onto the tension-side surface of the PC beams as follows:

(1) Grit-blasting concrete surface of the PC beam to improve the bonding capacity and coating the whole bonding area with primer;

(2) Bonding the cross-directional AFRPs in the region of 430 mm from 30 mm inside the supporting points to widely disperse the concentrated anchoring stress around the ends of pretensioned AFRPs;

(3) Precasting AFRPs due to impregnating epoxy-resin and curing, after that, introducing a prescribed tension force in the sheet during one day for preventing relaxation;

(4) Applying epoxy-resin on the reinforcing area of the PC beam and high-strain type one in the anchorage area of 200 mm inside from the ends of sheet instead of normal one, introducing the prescribed tensioning force into the sheet, and bonding the sheet onto the surface of the beam with surcharging some pressure; and

(5) After 7-day curing, releasing the tension force surcharged at the ends of the sheet, and introducing the prestress into the PC beam.

2.3 Measuring items and material properties

In this experiment, four-point static loading tests were conducted using hydraulic jack. Measuring items are surcharged load, mid-span deflection (hereinafter, deflection), and axial strain distribution of pretensioned AFRPs. And, progress for cracking and sheet debonding was recorded by using digital camera. Tables 2 and 3 show the lists of material properties for AFRPs, reinforcement, and PC tendon, respectively. At the commencement of experiment, an average compressive strength of concrete was 72.5 MPa.

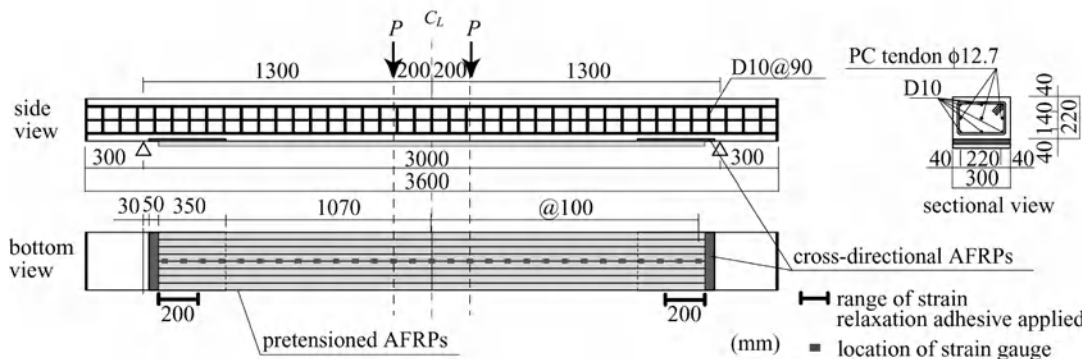


Figure 1 Layouts of reinforcement, PC tendon, and AFRPs

Table 2 Material properties of AFRPs (nominal value)

AFRPs	Mass (kg/m ²)	Nominal tensile capacity (kN/m)	Thickness (mm)	E-modulus (GPa)	Tensile strength (GPa)	Strain limit (%)
Pretensioned AFRPs	0.830	1176	0.572	118	2.06	1.75
Cross-directional AFRPs	0.435/0.435	588/588	0.286/0.286			

Table 3 Material properties of reinforcement and PC tendon

Nominal name	Material	E-modulus (GPa)	Yield strength (MPa)	Tensile strength (MPa)
D10	SD345	206	356	523
φ12.7	SWPR7BN	194	1783	1965

3 EXPERIMENTAL RESULTS

3.1 Strain distributions of AFRPs at introducing prestress into PC beam

Figure 2 shows axial strain distributions of AFRPs at introducing the prestress into PC beam due to releasing hydraulic jack after curing epoxy resin.

In this figure, the results at the points of 50 and 100 % introduced of predetermined prestress are shown. In this paper, the strain amplifier has been adjusted to zero level before releasing the tensioning force. Therefore, if the strains of the AFRPs were increased in the compression side, it implies that the prestress has not been perfectly introduced into the PC beam.

From this figure, it is observed that the strains in the whole area except anchorage zones are almost zero at 100% introduced of prestress. It means that the predetermined pretensioning force of the AFRPs has been perfectly transferred into the beam as prestress. At

the anchorage zone, it is observed that the strains are decreased in the compression side corresponding to the amount of introduced pretensioning force into AFRPs. Maximum compressive strains are occurred around the ends of sheet, and the strains are gradually decreased with leaving from the ends of sheet. From these results, it is confirmed that the prestress has been almost completely introduced into the beams by applying a proposed anchoring method.

3.2 Load-deflection relationship

The comparisons of load-deflection relationship between experimental and numerical results are shown in Figure 3. In this study, multi-section method was employed to analytically estimate the relationship assuming a plane conservation concept and perfect bond between concrete and AFRPs. The strain at compressive failure of concrete is assumed as 2756 μ based on Japan Concrete Standards (2007).

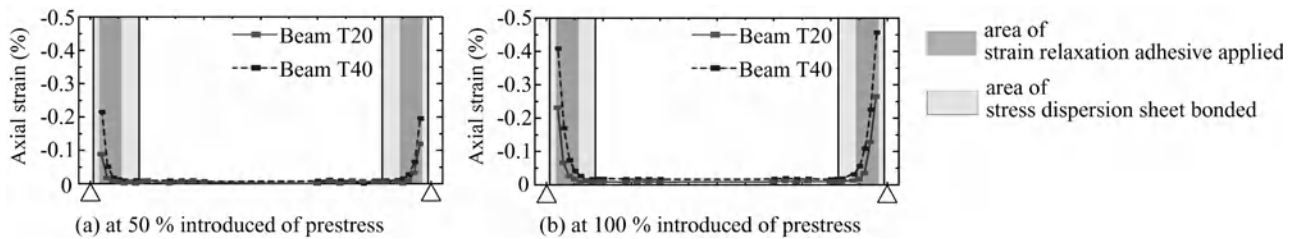


Figure 2 Strain distributions of AFRPs at introducing prestress into PC beam

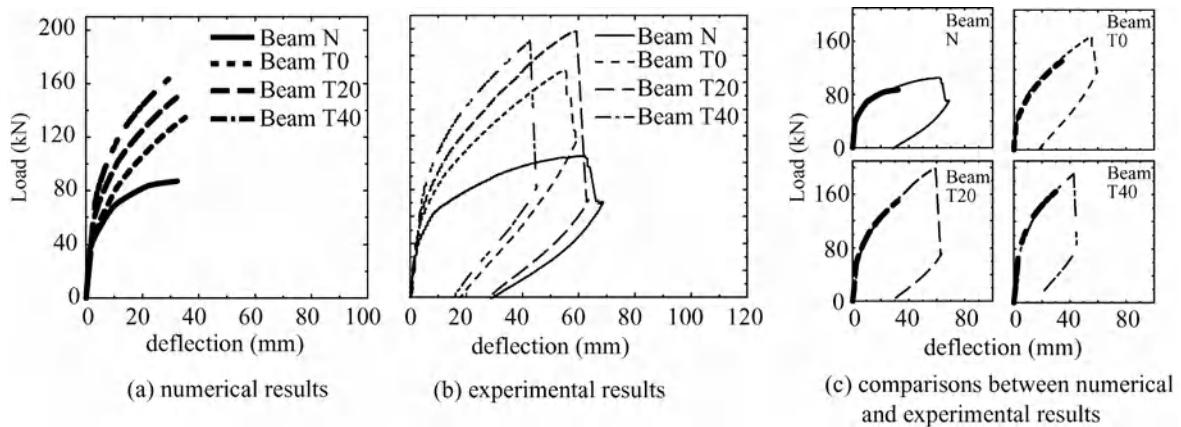


Figure 3 Comparisons load-deflection relationship between experimental and numerical results

From the numerical results, it is confirmed that: in the case of Beam N, (1) the stiffness is decreased due to the flexural cracks occurring at about 40 kN load and main rebar yielding at about 70 kN load; and (2) after that, deflection is increased keeping a constant small stiffness and then reaching the ultimate state at the loading level of 80 kN. In the case of Beam T0, even though cracking load is similar to that of Beam N, flexural stiffness after main rebar yielding becomes bigger than that in the case of Beam N.

In the cases of Beam T20/40, it is seen that the load in the region from crack-opening through the ultimate state

has a tendency to increase according to an increment of the introduced pretensioning force into the AFRPs. However, the deflection at the ultimate state has a tendency to decrease.

From the experimental results, it is observed that the loading levels at the crack-opening, main rebar yielding, and reaching the ultimate state are upgraded by introducing pretensioning force into the AFRPs as well as numerical results.

From these comparisons between experimental and numerical results, it is confirmed that the experimental results are in a good agreement with the numerical ones

for all specimens up to analytical ultimate state. Maximum load of each beam obtained from the experimental result is greater than that of numerical results. This means that the load-carrying capacity of the reinforced PC beams with pretensioned AFRPs can be better estimated by using multi-section method based on Japan Concrete Standards (2007).

3.3 Strain distributions of pretensioned AFRPs at analytical ultimate state

The comparisons of the strain distributions of the pretensioned AFRPs between experimental and numerical results at the analytical ultimate state are shown in Figure 4. The numerical results are estimated by using multi-section method mentioned above.

From these comparisons, it is observed that both experimental and analytical strain distributions are almost similar to each other in spite of the magnitude of

the predetermined pretensioning force ratio. This means that pretensioned AFRPs may be completely bonded to concrete surface up to the analytical ultimate level.

3.4 Behavior of PC beam at AFRPs being debonded

Figure 5 shows crack distributions on the side-surface of the beams at the ultimate state. From these figures, it is observed that in the cases of Beam T0/20, the pretensioned AFRPs is partially debonded due to peeling action of the critical diagonal crack (CDC) developed in the lower concrete cover near loading points. On the other hand, in the case of Beam T40, even though the flexural cracks are observed in equi-bending span, pretensioned AFRPs has never been debonded. This means that by reinforcing PC beams with pretensioned AFRPs, the peeling-off failure of the AFRPs may be rationally restrained due to the effects of the decompression moment.

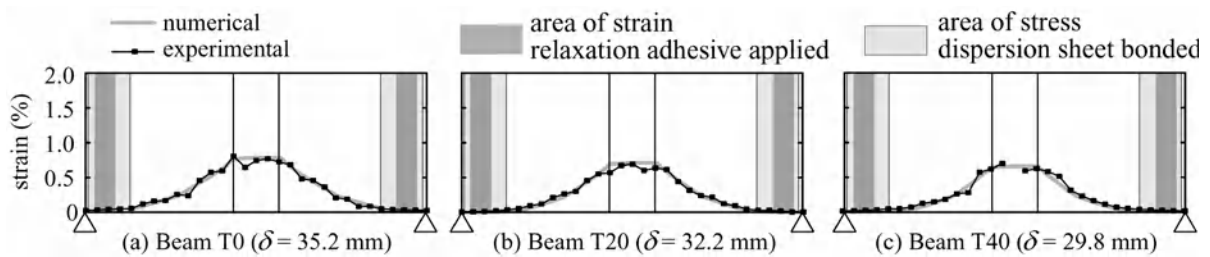


Figure 4 Comparisons of strain distributions of pretensioned AFRPs between experimental and numerical results at analytical ultimate state

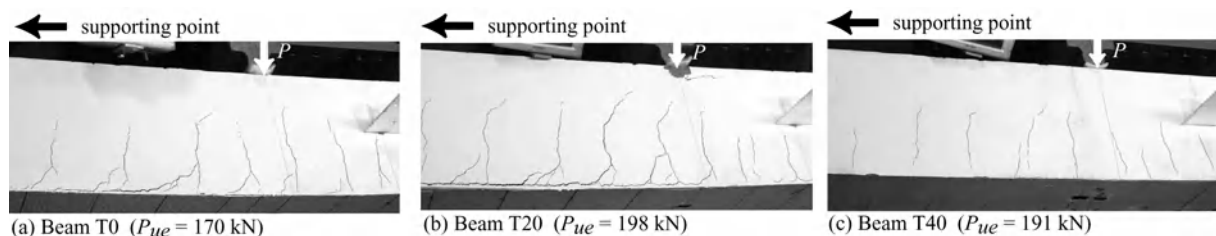


Figure 5 Failure behavior at ultimate state

4 CONCLUSIONS

In this paper, in order to develop a rational flexural reinforcing method for prestressed concrete (PC) beams with pretensioned Aramid Fiber Reinforced Polymer sheet (AFRPs), the new anchoring method was proposed. Its applicability was confirmed by conducting static four-point loading test with taking introduced pretensioning force ratio to the ultimate tensile capacity of the AFRPs as variable. The results obtained from this study are as follows:

(1) Applying the proposed anchoring method, predetermined pretensioning force into the sheet can be perfectly transferred to the beams without any anchoring devices;

(2) The cracking and rebar yielding loads, and the ultimate load of the PC beams can be rationally upgraded due to reinforcing with pretensioned AFRPs; and

(3) Reinforcing PC beams with pretensioned AFRPs, the peeling-off failure of the AFRPs may be rationally restrained due to the effects of the decompression moment.

REFERENCES

- Kishi, N., Mikami, H., Kurihashi, Y., and Ali, M. A. 2009. Load carrying behavior of Flexural Reinforced RC Beams with Pre-tensioned AFRP Sheet, *Proceedings of FRPRCS-9* (CD-ROM).
- Japan Concrete Standards 2007. *Structural performance verification*. JSCE. In Japanese.

Flexural Performance of RC Beams Strengthened with Prestressed AFRP Sheets: Part I. Experiments

Zong-cai Deng (dengzc@bjut.edu.cn) & Rui Xiao

College of Architecture and Civil Engineering, Beijing University of Technology, Beijing, China

ABSTRACT An experimental study of flexural performance of reinforced concrete beams (RC) using prestressed aramid fiber reinforced plastic (AFRP) sheets with permanent anchor was conducted. The number of AFRP sheet layers on beams varied from 1 to 3 and the prestress level varied from 0.45 to 0.65. Based on the experimental study of seven beams, the beams strengthened with prestressed AFRP sheets were compared with the beams strengthened with un-prestressed AFRP sheets in flexural properties of cracking moment, yield moment, ultimate moment and flexural stiffness. The experimental results show that, compared with the un-strengthened control beams, the flexural performance of beams strengthened with un-prestressed AFRP sheets were enhanced, and that of beams strengthened with prestressed AFRP sheets were further improved, validating the efficiency of prestressed AFRP sheet retrofit.

1 INTRODUCTION

Strengthening or retrofitting concrete structures using fiber reinforced polymer (FRP) sheets has become an increasingly popular strengthening technique for reinforced concrete (RC) structures. This is mainly due to several advanced features of the FRP materials, namely the high strength-to-weight ratio, good fatigue properties, excellent resistance to corrosion, quick and easy construction and low labor costs. Among different types of FRPs, carbon fiber reinforced plastic (CFRP) sheets have been used extensively to strengthen deteriorated concrete structures. CFRP sheets have some good mechanical properties, but some undesirable ones also, e.g. low shear and impact strength, relatively high brittleness, and high electric conductivity. Hence, aramid fiber reinforced plastic (AFRP) sheets have been considered in some engineering fields such as strengthening bridges, tunnels and building structures to replace CFRP sheets for its higher shear strength and impact strength than that of CFRP sheets, and AFRP sheets do not induce electromagnetic shield.

Using un-prestressed FRP sheets to strengthen RC flexural members, when the stress of longitudinal reinforcements achieves their yield strength, the tensile stress of FRP sheets does not exceed 20% of its ultimate tensile strength. As a result, the deformation and cracks of the strengthened structure members can not be effectively restrained (Triantafillou et al. 1991). The high tensile strength property of the FRP sheets can be made full use only after the steel bars yield; before the steel bars yield, FRP sheets improve the properties of the strengthened structure to a limited extent. Therefore,

un-prestressed FRP sheets do not significantly increase the initial cracking and the yield strength of the strengthened beam, i.e. un-prestressed FRP sheets do not improve the flexural and shear behaviors of the strengthened beam under service load. To this end, a more effective method for strengthening flexural members has been developed, that is prestressing FRP sheets. In this way, a greater portion of FRP's tensile capacity has been employed before the strengthened flexural member is subjected to any live load. Prestressed FRP sheets can support both dead and live loads carried by the structure, improve the serviceability of the structure, and provide excellent control of cracks by reducing crack widths and delaying the onset of cracking. Furthermore, prestressed FRP sheets may close some of the cracks in structures with preexisting cracks (fib Bulletin 14, 2001), thus improving durability by limiting the access of moisture into the concrete and adhesive layer. Finally, concrete beams strengthened with prestressed FRP sheets have higher ultimate strength than those beams strengthened with un-prestressed sheets (Triantafillou et al. 1992; Meier 1995; Wight et al. 2001; El-Hacha et al. 2004).

This paper focuses on applying prestressed AFRP sheets in strengthening RC beams with the method of applying a tensile force against the strengthened beam itself (Wight et al. 1995; Izumo et al. 1997; Wight et al. 2001; El-Hacha et al. 2004).

Experiments were carefully designed and conducted to study the flexural performance of RC beams strengthened with prestressed AFRP sheets. The theoretic study based on the experimental data is presented in Deng & Xiao 2010.

2 EXPERIMENTAL PROGRAM

2.1 Design of RC beams

Seven RC beams were constructed with the dimensions shown in Figure 1. All specimens were casted with a rectangular cross-section 120 mm wide and 180 mm high, and having a total length of 2300 mm. Tensile reinforcement of 226 mm² was provided by two 12 mm in diameter hot-rolled deformed bars and the reinforcement ratio was 1.05%. Compressive reinforcement of 57 mm² was provided by two 6 mm in diameter hot-rolled plain bars. Shear reinforcement consisted of 4 mm in diameter closed stirrups at a spacing of 60 mm center-to-center. The mechanical properties of all steel bars are listed in Table 1. The maximal size of aggregate in concrete was 20 mm. The same concrete mix ratio was used in all beams. The average compressive strength of the cube specimen was 31.7 MPa at 28 days. AFRP sheets used in the study were 0.193 mm thick and 100 mm wide, with a modulus of elasticity of 118 GPa and an ultimate tensile strength of 2060 MPa.

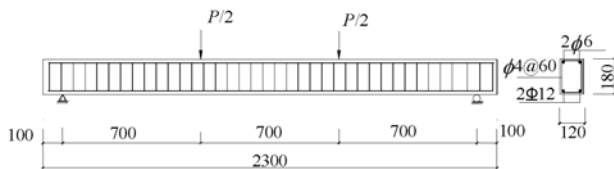


Figure 1 Geometry and reinforcement details for specimens

Table 1 Properties of steel bars

Steel Bar	Yield Strength (MPa)	Ultimate Strength (MPa)	Elongation Rate (%)	Elasticity Modulus (MPa)
8 [#] iron wire (Φ4)	326	438	27	2.03×10 ⁵
Φ6 Steel Bar	4299	550	12	2.02×10 ⁵
Φ12 Steel Bar	414	650	21	2.07×10 ⁵

2.2 Strengthening program

One beam of B0 was not strengthened and it served as the un-strengthened control beam to compare with the other six strengthened beams. One beam was strengthened with un-prestressed AFRP sheets, and the other five beams were strengthened with prestressed AFRP sheets. Strengthening details of beams are shown by the specimen code, e.g. a beam with code TBa-b, (i) if T=S, the beam is strengthened with un-prestressed AFRP sheets; (ii) if T=P, the beam is strengthened with prestressed AFRP sheets. The Roman numeral of “a” varied from I to III means layers of AFRP sheets varied from 1 to 3, and the number of “b” varied from 1 to 3 is the prestress level (the ratio between the tensile stress applied to AFRP sheets and their ultimate tensile strength) of 0.45, 0.55 and 0.65 respectively (“b” is null

if the beam is strengthened with un-prestressed AFRP sheets).

In order to avoid premature peeling failure at the ends of the un-prestressed AFRP sheets, two U-shaped AFRP strips were bonded next to the two ends of beams and cover the sheets. The width of AFRP strips was 100 mm and the space was 200 mm center-to-center for FRP strips. The construction program of strengthening beam using prestressed AFRP sheets (Figure 2) was that: the first, the two ends of AFRP sheets were attached to two anchors, and two permanent stationary barriers were installed to the ends of the beam; the second, the tensile surface of the strengthened beam was grinded and washed in order to ensure a good bonding interface, and then were coated with a concrete hardener primer. The primer was allowed to cure for some time until it hardened before applying the epoxy adhesive and the AFRP sheets to the beam. The third, the fixed end anchor of AFRP sheets was first fixed to one stationary barrier of the beam. The epoxy adhesive was applied by a brush to the tensile surface of the concrete beam in accordance with the manufacturer’s instruction. And then the jacking end anchor of AFRP sheets was placed in the other stationary barrier of the beam. The fourth, the movable jacking end anchor of AFRP sheets was attached by thread rods to a hydraulic jack that reacted against the beam, and then applied prestress to AFRP sheets by the hydraulic jack. When the desired prestress level was achieved, the jacking end anchor of AFRP sheets was fixed to the permanent stationary barriers of the beam. The data of stress was monitored by both strain gages adhered on the sheets and a load cell mounted at the jacking end of the stressing apparatus. The fifth, the epoxy adhesive was painted to the AFRP sheets. The anchorage system held the stressed sheets until the epoxy cured and the sheets were fully bonded to the beam.

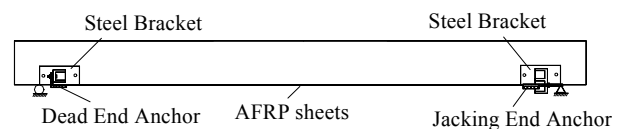


Figure 2 Strengthening beam by prestressed AFRP sheets

The anchorage system was kept permanently in place to avoid premature peeling failure at the ends of the sheets. The anchors at the ends of the prestressed AFRP sheets reduced the shear deformation occurring within the adhesive layer upon releasing the prestress force, thereby reduced the shear stresses transferred to the base of the concrete section and minimized the possibility of premature failure. The anchorage was also beneficial in controlling the effects of creep and shrinkage in the epoxy adhesive (El-Hacha et al. 2003).

2.3 Test setup

The beam was simply supported over a 2.1 m span loading system and loaded by four-point bend loading with two concentrated loads. Each load was applied at one-third of the span, as shown in Figure 1. The total load was applied gradually using a 300 kN capacity hydraulic jack.

2.4 Instrumentation

All beams were instrumented to measure the applied load, deflections and strains. Deflections at mid-span, one-third span of the beam, and the supports were measured using 5 linear variable displacement transducers (LVDTs). Electrical resistance strain gauges were installed at mid-span and at one-third span on the tensile reinforcement surface. An electrical resistance strain gauge was installed at mid-span on the AFRP sheet surface. Ten Electrical resistance strain gauges were installed at mid-span along the front and back faces of the beam to measure the strain distributions in concrete over the depth of the beam. The level of prestress and strains in the AFRP sheets were monitored during prestressing and the application of the external load up to failure. Readings of all LVDTs, strain gauges and load cells were recorded by an IMP data acquisition system. The cracking of the specimens was monitored during the experiment.

3 EXPERIMENTAL RESULTS AND ANALYSIS

3.1 Crack pattern and failure mode

During the loading process of the beams, crack formation followed a typical pattern. The first flexural crack occurred in the region of constant moment. Flexural cracks were symmetric around the mid-span of the beam. At a higher load, shear cracks were formed, but the stirrups (spacing of 60 mm) effectively controlled the shear cracks and prevented shear failure (Figures 3). The un-strengthened control beam failed in flexure by yielding of the tensile steel bars and then

local crushing of the compression concrete in the constant moment region (Figure 3(a)). Many cracks with small widths were observed on the strengthened beams when the ultimate load was attained, while on the un-strengthened control beam, fewer cracks with greater widths were observed. This can be explained by the fact that as the load increased, the strengthened beam deformed and the bonded sheets generated a tensile force so that the internal forces were balanced with much less deformation than in the un-strengthened control beam.

In this test, the failure of beam SB II with two layers of un-prestressed AFRP sheets occurred by local crushing of the compression concrete and at the same time the AFRP sheets' tensile ruptured after yielding of the flexural steel reinforcements (Figure 3(b)).

The failure mode for all prestressed strengthened beams is tensile rupture of the AFRP sheets at the section of the constant moment between the two loading points. Before the tensile rupture of the sheets, the strengthened beams retained a reserve capacity compared with the strength of the un-strengthened control beams. Before failure, the stress and strain levels were very high for AFRP sheets. When the sheets were at complete tensile failure, a large amount of strain energy was released. This resulted in the ruptured AFRP sheets dropping off quickly. After the experiment, it was observed that the AFRP sheets still adhered very well to the surface of the concrete beams, except the peeling off areas.

3.2 Bearing capacity

The measured flexural bearing capacities of test beams at the cracking moment, the yield moment and the ultimate moment are listed in Table 2, where 'moment' represents the constant moment between two point loads. Meantime, mid-span deflections are listed in the same table.

The results proved that, before the steel bars yield, bearing capacities of beams with un-prestressed sheets can be only enhanced to a limited extent. Nevertheless, those capacities of beams strengthened with prestressed AFRP sheets can be increased much more significantly than strengthened with un-prestressed AFRP sheets. Moreover, the higher the prestress level of the sheets is, the greater the cracking moment and the yield moment of the strengthened beam has.

3.3 Moment-deflection curve, stiffness and ductility

Moment versus mid-span deflection curves of the reinforced concrete beams are shown in Figures 4. Figure 4(a) shows the comparison curves among the beams un-prestressed and prestressed strengthened with two layers of AFRP sheet in different prestress levels and the un-strengthened control beam B0. Figure 4(b) shows the comparison curves among the beams strengthened in the

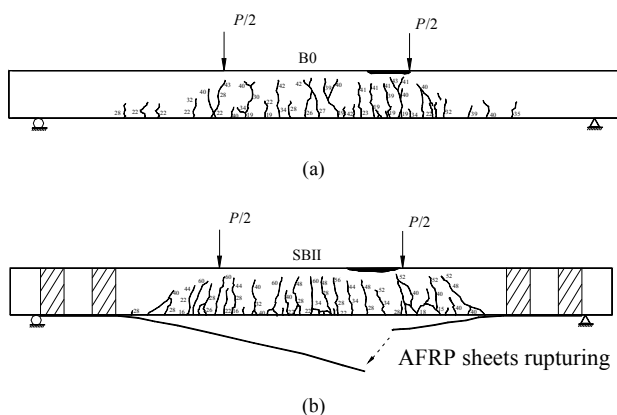


Figure 3 Failure modes of specimens

Table 2 Experimental results of bearing capacity and displacement for specimens

Beams	First Cracking			Yielding			Ultimate		
	Moment (kN·m)	Moment Relative value	Mid-span Deflection (mm)	Moment (kN·m)	Moment Relative Value	Mid-span Deflection (mm)	Moment (kN·m)	Moment Relative Value	Mid-span Deflection (mm)
B0	2.28	1.00	0.73	13.66	1.00	10.61	15.40	1.00	44.75
SB II	2.58	1.13	0.79	16.83	1.23	11.58	23.02	1.50	44.66
PSB I -2	4.89	2.14	1.61	18.84	1.38	12.55	19.81	1.29	17.25
PSB II -1	6.16	2.70	2.28	21.88	1.60	14.03	25.39	1.65	25.50
PSB II -2	8.07	3.54	3.15	23.72	1.74	14.76	26.40	1.71	24.52
PSB II -3	8.90	3.90	3.67	23.75	1.74	14.87	25.56	1.66	22.08
PSBIII-2	9.28	4.06	5.00	27.50	2.01	19.46	30.98	2.01	27.30

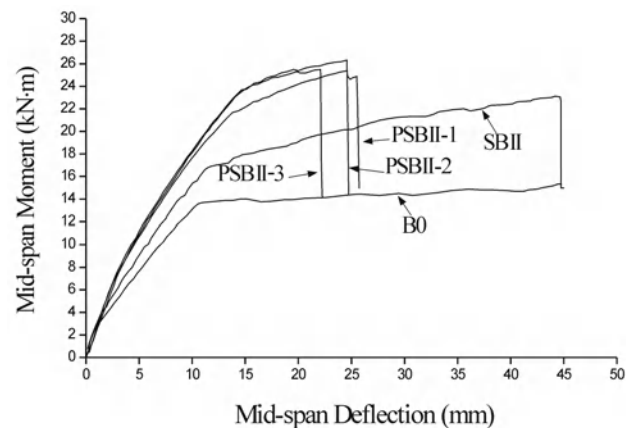
same prestress level, but with different layers of AFRP sheets and the un-strengthened control beam B0. During the application of external prestressing the AFRP sheets on beam PSBIII-2, cracks were seen on the top surface of the strengthened beams, which was due to large inverted camber deformation. Those cracks decreased the original stiffness of the strengthened beams. The decrease of original stiffness in beam PSBIII-2 was larger than that of beam PSB II -2 because the higher level of prestress caused worse cracking. This phenomenon can be seen in Figure 4(b).

Under a lower moment, the section moment is mainly supported by compressive concrete, tensile concrete, steel bars and AFRP sheets. Therefore, regardless of the number of layers and the prestress level of the sheets, the strengthening effects of AFRP sheets are relatively small, and the original stiffness of the un-strengthened control beam and the strengthened beams are almost the same. When the moment reaches the level of the cracking moment of the strengthened beams, the stress in concrete at tensile zone was transferred to the steel bars and the sheets, i.e. the tensile stress of AFRP sheets increases significantly. The flexural stiffness of the strengthened beams is significantly greater than the un-strengthened control beam. Increasing the number of layers of sheets greatly increases the magnitude of the flexural stiffness of the beams. In addition, the increased magnitude of the flexural stiffness of the prestressed strengthened beams is larger than that of the un-prestressed strengthened beams with same sheet layers.

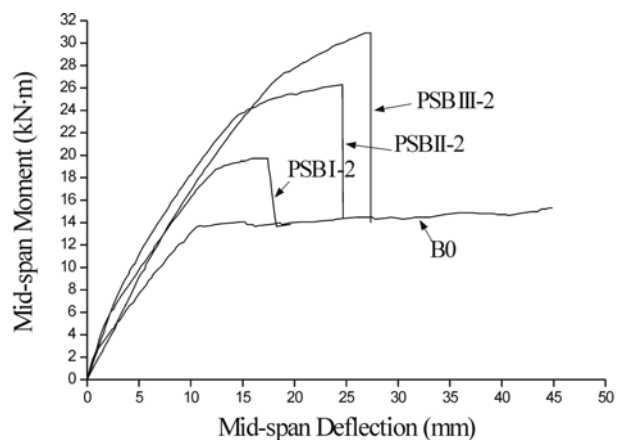
Because the ultimate strain is constant, the higher the prestress applied to the sheets, the less the remaining deformation capacity of the sheets will be, and the ductility of the strengthened beams will decrease accordingly. This phenomenon is shown in Figure 4(a).

It can be inferred from Figure 4(b), when the prestress level of the AFRP sheets is the same, the less the number of layers of the sheets is, the less the height of compression zone of concrete is. So, when the same

ultimate strains of AFRP sheets are achieved, the compressive strain (less than ultimate compressive strain) of edge concrete in compression zone is smaller for the strengthened beams using fewer layers of AFRP sheets, consequently flexural curvature of the beam is smaller, which means that the ductility of the beam is lower.



(a)



(b)

Figures 4 Comparisons of beams' load-deflection curves

3.4 The effects of the AFRP layers and prestress level of AFRP sheets

According to Table 2, in the same prestress level of

AFRP sheets, when the number of the prestressed AFRP sheet layers is gradually increased, the cracking moment of the strengthened beams is greatly increased, the yield moment and the ultimate moment are also increased, but the moment increasing magnitude is not always proportionate to the number of the AFRP sheet layers, and the operation of increasing AFRP sheet layers is much more effective for enhancing the cracking moment than yield and ultimate moments of beams strengthened with prestressed AFRP sheets.

It is also known from Table 2 that, with same layers of AFRP sheet, the cracking moment of the strengthened beams are all increased significantly following the increase of the prestress level. Where as, the yield moment is slightly increased and the ultimate moment is almost the same for all prestress levels.

4 CONCLUSIONS

From the experiments and analysis, it is concluded that:

Compared with the un-strengthened control beam, the cracking moment and yield moment of the beam strengthened with un-prestressed AFRP sheets are not increased significantly, and the incremental rate of the cracking moment is bigger than the yield moment in some sort. Nevertheless, the ultimate load is increased significantly.

Compared with the un-strengthened control beam, the cracking moment of the beam strengthened with prestressed AFRP sheets is increased significantly; the yield moment and ultimate moment are also increased, but not as prominent as cracking moment. Furthermore, the effect of the beam with prestressed AFRP sheets on increasing those moments is more obvious than that of the beam with un-prestressed AFRP sheets.

The original stiffness for the un-strengthened control beam and the prestressed strengthened beam is almost the same. However, after concrete cracking, the flexural stiffness of the prestressed strengthened beam is higher than that of the un-strengthened control beam.

Compared with the un-strengthened control beam, the ductility of the strengthened beam with un-prestressed AFRP sheet is almost same, but the ductility of the strengthened beam with prestressed AFRP sheet is decreased. Thus, the utilization of the prestressed AFRP sheet should be considered in some extent especially in seismic zones.

When the number of the prestressed AFRP sheet layers is increased, the bearing capacity is increased, but

the increasing magnitude is not always proportionate to the number of the AFRP sheet layers.

The cracking moment and yield moment of beams strengthened by pre-stressing AFRP sheet is increased with the pre-stress level; but the strengthening effect on the ultimate moment is in a limited extent.

5 ACKNOWLEDGEMENT

This research was supported by National Natural Science Foundation of China (50978006).

REFERENCES

- Deng Z. & Xiao R. 2010. Flexural performance of RC beams strengthened with prestressed AFRP sheets: Part II. Theoretical analysis. In *CICE 2010 - The 5th International Conference on FRP Composites in Civil Engineering*.
- El-Hacha, R., Wight, R. G. & Green, M. F. 2003. Innovative system for prestressing fiber-reinforced polymer sheets. *ACI Structural Journal*, 10 (3): 305-313.
- El-Hacha, R., Wight, R. W. & Green, M. F. 2004. Prestressed carbon fiber reinforced polymer sheets for strengthening concrete beams at room and low temperatures. *Journal of Composites for Construction*, 8 (1): 3-13.
- fib Bulletin 14. 2001. Externally bonded FRP reinforcement for RC structures. *Design and Use of Externally bonded Fibre Reinforced Polymer Reinforcement (FRP EBR) for Reinforced Concrete Structures*. International Federation for Structural Concrete, Lausanne, Switzerland.
- Izumo, K. M., Saeki, N., Asamizu, T. & Shimura, K. 1997. Strengthening reinforced concrete beams by using prestressed fiber sheets. In *Proc. 3rd Int. Symp. on Non-Metallic (FRP) Reinforcement for Concrete Structures (FRPRCS-3)*: 379-386.
- Meier, U. 1995. Strengthening of structures using carbon fiber/epoxy composites. *Constr. And Build. Mat.*, 9 (6): 341-351.
- Triantafillou, T. C. & Deskovic, N. 1991. Innovative prestressing with FRP sheets: mechanics of short-term behaviors. *Journal of Engineering Mechanics*, 117 (7): 1652-1672.
- Triantafillou, T. C., Deskovic, N. & Deuring, M. 1992. Strengthening concrete structures with prestressed fiber reinforced plastic sheets. *ACI Struct. J.*, 89 (3): 235-244.
- Wight, R.G., Green, M.F. & Erki, M.A. 1995. Post-strengthening concrete beams with prestressed FRP sheets. In *Proceedings of the Second International RILEM Symposium on Non-Metallic Reinforcement for Concrete Structures (FRPRCS-2)*: 568-575.
- Wight, R. G., Green, M. F. & Erki, M. A. 2001. Prestressed FRP sheets for post-strengthening reinforced concrete beams. *Journal of Composites for Construction*, 5 (4): 214-220.

Flexural Performance of RC Beams Strengthened with Prestressed AFRP Sheets: Part II. Theoretical Analysis

Zong-cai Deng (dengzc@bjut.edu.cn) & Rui Xiao

College of Architecture and Civil Engineering, Beijing University of Technology, Beijing, China

ABSTRACT The flexural performance of reinforced concrete beams (RC) strengthened by prestressed aramid fiber reinforced plastic (AFRP) sheets with permanent anchor have been tested and shown in companion paper (Deng & Xiao 2010). Based on sectional analysis, the formulas for calculating the bearing capacity of beams strengthened with prestressed AFRP sheets were established in this paper. By these formulas, the theoretic results of cracking, yield and ultimate moments and its corresponding deflections at these points were derived and compared with the experimental test results of beams. The comparison analysis show that, the analytical results of tested RC beams are in coincidence with the experimental results.

1 INTRODUCTION

The application of fiber reinforced polymer (FRP) sheets in civil engineering is developing rapidly and has become one of main popular techniques for strengthening and rehabilitating reinforced concrete (RC) structures in these years because of several advanced features of this kind of materials, e.g. the high strength-to-weight ratio, good fatigue properties, excellent resistance to corrosion, quick and easy construction and low labor costs.

Currently, the ultimate and serviceability behaviors of plated beams or slabs are understood; and design guides, codes and specifications about FRP strengthening systems were published in recent years (fib Bulletin 14 2001; JSCE 2001; TR 55 2004; ACI 440.2R-02 2002; Oehlers et al. 2008; CNR-DT 200/04 2005). In China, the code of GB50367-2006 issued in 2006 also illuminated the way of strengthening structure with FRP sheets. However, All of these design guides, codes or specifications do not regard the design of strengthening structure with prestressed FRP sheets because this technique is still in the premature stage.

In this paper, the formulas for calculating the flexural bearing capacity of beams strengthened with prestressed AFRP sheets were established based on the cross sectional analysis. By the calculation, analytical results of moments and deflection at critical points were obtained and compared with the experimental test results of beams. The comparison analysis show that the analytical results fit the experiment well.

2 THEORETICAL CALCULATIONS ON BEARING CAPACITY

2.1 Fundamental assumptions

According to the experimental results, fundamental assumptions are (1) strengthened concrete beam satisfies the plane cross-section assumption; (2) because the AFRP sheet is very thin, the distance between the centric of AFRP sheet and the top of beam is equal approximately to the height of beam; (3) the stress-strain relations of concrete are as follow:

$$\sigma_c = f_c \left[1 - \left(1 - \frac{\varepsilon_c}{\varepsilon_0} \right)^2 \right] \quad (\varepsilon_c \leq \varepsilon_0) \quad (1)$$

$$\sigma_c = f_c \quad (\varepsilon_0 < \varepsilon_c \leq \varepsilon_{cu}) \quad (2)$$

2.2 Prestressing Loss

In the process of applying prestress, the prestressing loss σ_{l1} due to the deformation of anchors can be calculated as below:

$$\sigma_{l1} = \frac{\alpha}{l} E_f \quad (3)$$

where α is the deformation amount of anchor; l is the length of tensile AFRP sheet; E_f is the elastic module of AFRP sheet.

The prestressing loss σ_{l2} due to the stress relaxation of AFRP sheet can be obtained by Quantrill & Holloway (1998) and Wight et al. (2001):

$$\sigma_{l2} = 0.15 \sigma_{con} \quad (4)$$

where σ_{con} is the control prestress applied to AFRP sheet.

The prestressing loss σ_{l3} due to concrete creep in pressure can be calculated as follow:

$$\sigma_{l3} = \alpha_{Efs} \frac{35 + 280 \frac{\sigma_{pc}}{f_{cu}}}{1 + 15 \rho_s} \quad (5)$$

where α_{Efs} is the elastic module ratio of the AFRP sheet to steel, $\alpha_{Efs} = E_f / E_s$; σ_{pc} is the compressive stress of concrete at the bottom, and considering only the prestressing loss σ_{l1} due to the anchor deformation at this time; f_{cu} is the compressive strength of cube specimen; ρ_s is the FRP's longitudinal reinforcement ratio in tensile region.

The total prestressing loss of AFRP sheet σ_l is:

$$\sigma_l = \sigma_{l1} + \sigma_{l2} + \sigma_{l3} \quad (6)$$

2.3 Stress analysis in the phase of construction

Based on the deformation coordination assumption of steel and concrete, the cross-section of steel reinforced concrete material can be converted to the section of single concrete material, as shown in Figure 1, α_E is the elastic module ratio of steel to concrete. With this conversion, the moment of inertia of transformed section could be derived.

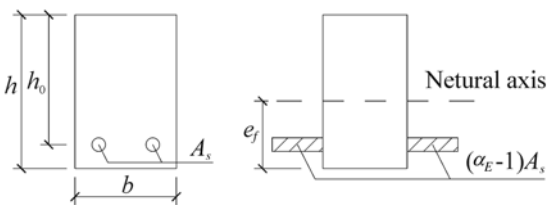


Figure 1 Section conversion section

After the control prestress applied to AFRP sheet was achieved, the AFRP sheet was fixed, and bonded to the concrete beam. Taking into account of the prestressing loss due to anchor deformation and material properties, the actual prestress of AFRP sheet σ_{f0} is:

$$\sigma_{f0} = \sigma_{con} - \sigma_l \quad (7)$$

The compressive prestress of concrete beam at the bottom σ_{pc} is:

$$\sigma_{pc} = \frac{\sigma_{f0} A_f}{A_0} + \frac{\sigma_{f0} A_f e_f}{I_0} y_0 \quad (8)$$

where A_f defines the total cross-section area of AFRP sheets; e_f is the eccentricity of prestressed AFRP sheet; A_0 is the area of transformed cross section; I_0 is the moment of inertia of transformed cross y_0 is the distance between the gravity of transformed section and the edge of concrete beam in compressive region.

2.4 Bearing capacity calculation in the phase of service

(1) Neutralization moment M_c

With the increase of external load, the compressive prestress of concrete at the bottom of the beam decreases gradually. When external load achieves some special value, the compressive prestress of concrete at the bottom became zero. The external moment is defined as neutralization moment.

$$M_c = \sigma_{pc} W_0 \quad (9)$$

where W_0 is the resisting moment of the transformed section. The strain of AFRP sheets is determined using the below equation:

$$\varepsilon_{f1} = \frac{\sigma_{con} - \sigma_l + \alpha_{Efc} \sigma_{pc}}{E_f} \quad (10)$$

(2) Cracking moment M_{cr}

$$M_{cr} = M_c + \gamma f_{tk} W_0 \quad (11)$$

where f_{tk} is the tensile strength standard value of concrete; γ is the plastic coefficient of the resisting moment of section, and calculated according to the code for concrete structural design of China (GB50010-2002).

(3) Yield moment M_y

Because of the combined action of the prestressed AFRP sheets, the compressive strain of concrete at the top is generally less than its ultimate compressive strain ε_{cu} when the tensile steel was justly yielded. The stress and strain conditions of concrete section are shown in Figure 2.

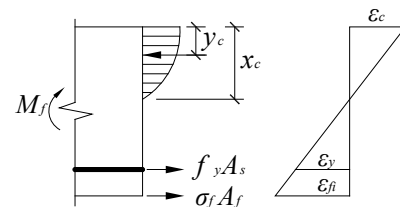


Figure 2 Distribution of strain and stress on the section at yielding

According to the geometrical relation of strain

$$\varepsilon_{f1} = \frac{h - x_c}{h_0 - x_c} \varepsilon_y \quad (12)$$

where h and h_0 are the depth and the effective depth of the beam respectively; ε_{f1} is the strain increment of AFRP sheet; x_c is the depth of the neutral axis.

The total strain of AFRP sheet ε_{f2} is

$$\varepsilon_{f2} = \varepsilon_{f1} + \varepsilon_{f1} \quad (13)$$

Based on the balance of force

$$C = f_y A_s + E_f \varepsilon_{f2} A_f \quad (14)$$

Based on the balance of moment

$$M_y = f_y A_s (h_0 - y_c) + E_f \varepsilon_{f2} A_f (h - y_c) \quad (15)$$

where C is the resultant pressure of concrete in compressive region obtained by integration:

$$C = \int_0^{x_c} b \sigma_c dx \quad (16)$$

where y_c is the distance between the application point of the resultant pressure of concrete in compressive region and the edge of concrete in compressive region, can be calculated as follow:

$$y_c = x_c - \frac{1}{C} \int_0^{x_c} x b \sigma_c dx \quad (17)$$

(4) Ultimate moment M_u

Boundary failure is defined as FRP failure and concrete crushing occurred at the same time, and its stress and strain conditions of section are shown in Figure 3.

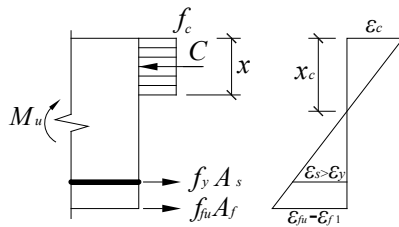


Figure 3 Distribution of strain and stress on the section at failure

Based on the balance of force

$$f_c b x = f_y A_s + f_{fu} A_f \quad (18)$$

where f_{fu} is the ultimate strength of the FRP sheet.

According to the geometrical relation of strain

$$x = \frac{0.8 \varepsilon_{cu}}{\varepsilon_{cu} + \varepsilon_{fu} - \varepsilon_{f1}} h \quad (19)$$

Alternating Equation (18) by Equation (19)

$$\rho_{fb} = \frac{0.8 f_c \varepsilon_{cu}}{f_{fu} (\varepsilon_{cu} + \varepsilon_{fu} - \varepsilon_{f1})} - \rho_s \frac{f_y}{f_{fu}} \quad (20)$$

where ρ_{fb} is the balanced AFRP sheet ratio. If $\rho_f > \rho_{fb}$, the failure of the strengthened concrete beam was occurred by the tensile rupture of AFRP sheets; otherwise, the failure of the strengthened beam was occurred by concrete crushing in compressive zone.

Based on the balance of moment

$$M_u = f_y A_s \left(h_0 - \frac{x}{2} \right) + f_{fu} A_f \left(h - \frac{x}{2} \right) \quad (21)$$

When $\rho_{fb} < \rho_f$, $\varepsilon_c < \varepsilon_{cu}$, the ultimate moment of M_u limited by ε_{fu} , so

$$C = f_y A_s + f_{fu} A_f \quad (22)$$

$$M_u = f_y A_s (h_0 - y_c) + f_{fu} A_f (h - y_c) \quad (23)$$

where C and y_c can be calculated by equation (16) and (17) respectively. And ε_{f2} equals to ε_{fu} for the equation of (13) at this time, hence

$$\varepsilon_c = \frac{x_c}{h - x_c} \varepsilon_{fu} \quad (24)$$

When $\rho_f < \rho_{fb}$, the ultimate moment of M_u controlled by ε_{fu} , according to the geometrical relation of strain

$$x = \frac{0.8 \varepsilon_{cu}}{\varepsilon_{cu} + \varepsilon_{fu}} h \quad (25)$$

where

$$\varepsilon_{fu} = \frac{h - x_c}{x_c} \varepsilon_{cu} \quad (26)$$

Based on the balance of force

$$f_c b x = f_y A_s + E_f \varepsilon_{f2} A_f \quad (27)$$

where x and ε_{f2} can be obtained by equation (25), (26) and (27), and according to the balance of moment

$$M_u = f_y A_s \left(h_0 - \frac{x}{2} \right) + E_f \varepsilon_{f2} A_f \left(h - \frac{x}{2} \right) \quad (28)$$

Table 1 Comparison of experimental and theoretic results of bearing capacity

Beam	Cracking Moment			Yielding Moment			Ultimate Moment		
	Theoretic value (kN·m)	Test Value (kN·m)	Relative error (%)	Theoretic alue (kN·m)	Test Value (kN·m)	Relative error (%)	Theoretic value (kN·m)	Test Value (kN·m)	Relative error (%)
B0	2.99	2.28	31.23	12.34	13.66	-9.69	13.01	15.40	-15.53
SB II	2.99	2.58	15.97	14.04	16.83	-16.55	24.83	23.02	7.86
PSB I -2	4.94	4.89	1.11	14.91	18.84	-20.83	19.75	19.81	-0.31
PSB II -1	6.01	6.16	-2.49	16.42	21.88	-24.96	25.08	25.39	-1.22
PSB II -2	6.90	8.07	-14.54	17.33	23.72	-26.92	25.20	26.40	-4.53
PSB II -3	7.77	8.90	-12.75	18.22	23.75	-23.29	25.34	25.56	-0.86
PSBIII-2	8.85	9.28	-4.65	19.59	27.50	-28.76	29.97	30.98	-3.25

The experimental and theoretic results of bearing capacity are listed in Table 1 (the naming code of the specimens is presented in Deng & Xiao 2010). It can be seen that the relative errors are controlled in acceptable arranges which indicates that the theoretic results of beams' bearing capacity meet the experiment results.

3 ANALYSIS OF DEFLECTION

Moment-curvature relationship could be derived by analyzing strain status at each cross section under different loads. Consequently, beams' deflection can be figured out. Due to limited space, the theoretical mid-span deflections at cracking, yield and ultimate moments are presented in Figure 4 and compared with test results (plotted in dash lines) but the calculation procedure is not elaborated in this paper.

From Figure 4, it is observed that the simulated mid-span load-deflection curves are in accordance with the test results, and there incremental and failure rules and orders conforms with test conclusions. So, it is deemed that the cross sectional analysis method is feasible for analyzing the flexural performance of beams strengthened with prestressed FRP sheets.

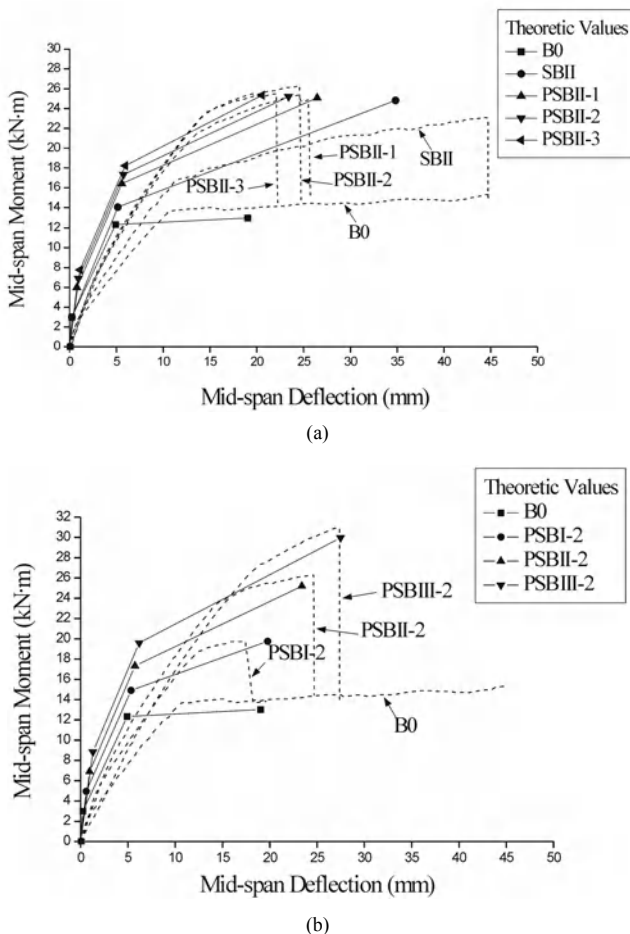


Figure 4 Comparisons of beams' mid-span load-deflection curves between test values and theoretic values

4 CONCLUSIONS

The theoretical calculation results of beams' bearing capacity compared with experimental results show that the relative errors are controlled in acceptable arranges, and the simulated mid-span load-deflection curves obey the experimental values. Hence, it is concluded that the cross sectional analysis method can be used for analyzing the flexural performance of beams strengthened with prestressed FRP sheets.

5 ACKNOWLEDGEMENT

This research was supported by National Natural Science Foundation of China (50978006).

REFERENCES

- ACI 440.2R-02. 2002. Guide for the Design and Construction of Externally Bonded FRP Systems for Strengthening Concrete Structures. ACI, Farmington Hills, MI, USA.
- CNR-DT 200/04. 2005. Instructions for design, execution, and control of strengthening interventions through fiber-reinforced composites. CNR, Rome.
- Deng Z. & Xiao R. 2010. Flexural performance of RC beams strengthened with prestressed AFRP sheets: Part I. Experiments. In *CICE 2010 - The 5th International Conference on FRP Composites in Civil Engineering*.
- fib Bulletin 14. 2001. Externally bonded FRP reinforcement for RC structures. *Design and Use of Externally bonded Fibre Reinforced Polymer Reinforcement (FRP EBR) for Reinforced Concrete Structures*. International Federation for Structural Concrete, Lausanne, Switzerland.
- GB50010-2002. 2002. *The code for concrete structural design*. (In Chinese)
- GB50367-2006. 2006. *The code for strengthening concrete structure*. (In Chinese)
- JSCCE. 2001. Recommendation for upgrading of concrete structures with use of continuous fiber sheets. Concrete Engineering Series 41, Japan Society of Civil Engineers, Tokyo.
- Oehlers D. J., Seracino R. & Smith S. 2008. Design guideline for RC structures retrofitted with FRP and metal plates: beams and slabs. Standards Australia HB 305 M.
- Quantrill, R. J. & Hollaway, L. C. 1998. The flexural rehabilitation of reinforced concrete beams by the use of prestressed advanced composite plates. *Composites Science and Technology*, 58: 1259-1275.
- TR 55. 2004. Design guidance for strengthening concrete structures using fiber composite materials (2nd Edition). The Concrete Society, Surrey, United Kingdom.
- Wight, R. G., Green, M. F. & Erki, M. A. 2001. Prestressed FRP sheets for post-strengthening reinforced concrete beams. *Journal of Composites for Construction*, 5 (4): 214-220.

Numerical Simulation on Flexural Reinforcing Effects of AFRP Sheet for Damaged RC Girders

N. Kishi (kishi@news3.ce.muroran-it.ac.jp) & M. Komuro

CERU, College of Environmental Engineering, Muroran Institute of Technology, Muroran, Japan

H. Mikami

Technical Research Institute of Sumitomo-Mitsui Construction, Co. Ltd, Nagareyama, Japan

ABSTRACT In order to rationally evaluate the reinforcing effects of Aramid fiber reinforced polymer (AFRP) sheet on damaged reinforced concrete (RC) girders, a 3D nonlinear FE analysis method was proposed. Here, firstly assuming the FRP sheet elements to be dummy, pre-analysis was conducted for numerically realizing the damaged situation of the girder. After that, the girder reinforced by bonding FRP sheet on the tension-side surface was analyzed by substituting the dummy elements into FRP sheet ones. In this analysis, the discontinuities of cracks, bond slip, and delamination of sheet were also considered by using interface elements. Its applicability was confirmed comparing with the experimental results.

1 INTRODUCTION

Nowadays, continuous fiber reinforced polymer (FRP) sheet has been sometimes applied for retrofitting and/or reinforcing existing reinforced concrete (RC) members. However, those design procedures have been established on the basis of the load-carrying behavior and debonding characteristics of the sheet for the members without any damages, even though the procedures are for designing the existing RC members. Therefore, in order to establish the rational design procedures for retrofitting/reinforcing the members with high reliability, it is important to investigate the reinforcing effects of the FRP sheet on the RC members suffered some damages. Those issues should be efficiently solved on the basis of the results obtained by cooperating with the experimental and analytical studies. Arduini et al. (1997) only tried to investigate those experimentally and numerically.

From this point of view, in this paper, the load-carrying behavior including debonding of FRP sheet of the flexural reinforced RC beams with Aramid FRP (AFRP) sheet was experimentally investigated, in which the girders were preloaded and cracked prior to bond the AFRP sheet on the tension-side surface. Also, proposing a numerical analysis method for this kind of RC girders and performing the numerical analysis, an applicability of the method was discussed comparing the experimental results.

In this paper, both smeared and discrete cracking models are applied. Specially, the discrete cracking model was applied for numerically reproducing the critical diagonal cracks, the diagonal cracks at the sheet-end,

and the lower concrete cover delamination. Also, numerically reproducing the damaged RC girders, pre-analysis is conducted prior to bond AFRP sheet on the tension-side surface of the girders. After unloading, adding AFRP sheet elements to the surface under the nodal displacements being stayed behind, the numerical analysis for reloading is conducted. In order to add the FRP sheet elements at reloading, the dummy elements with small stiffness have been prepared at preloading. Here, DIANA code (release 9.3) was used for this numerical analysis.

2 EXPERIMENTAL OVERVIEW

In this study, experimental results of seven RC specimens listed in Table 1 were used to confirm the applicability of the proposed numerical analysis method. Each girder is designated using two items: with/without reinforcing with AFRP sheet (N: without reinforcing; and S: with reinforcing); and preloading level L. Two digits following the notations "S" and "L" are number of laminated AFRP sheet piles and index for preloading level, in which L0 is the case of without preloading; L1 is the case at axial rebar reaching the yield stress; L2 is the case at the residual deflection at the mid-span reaching 4 % of the span length (=10.4 mm).

All specimens were designed as double reinforced RC girder with a rectangular cross section as shown in Figure 1. Each of the two deformed steel bars of 16 mm diameter were placed in the upper and lower fibers and stirrups of 10 mm diameter were placed at the intervals of 100 mm. After preloading, a 150 mm-wide

Table 1 List of experimental cases

Girder	No. of sheet piles	w/o preloading
N	–	–
S1-L0	1	Without
S1-L1	1	Level 1
S1-L2	1	Level 2
S2-L0	2	Without
S2-L1	2	Level 1
S2-L2	2	Level 2

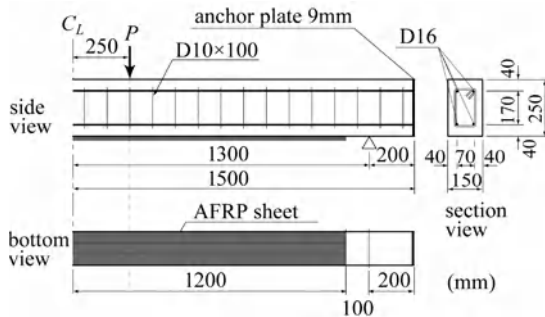


Figure 1 Specimen configuration and layout of FRP sheet

unidirectional AFRP sheet was bonded onto the tension-side surface of the girders leaving 100 mm between supporting point and the sheet end, in which its thickness and capacity are 0.286 mm and 588 kN/m, respectively.

At the commencement of experiment, the compressive strength of concrete was $f'_c = 29.5$ MPa and the yield strength of rebar was $f_y = 392$ MPa.

3 OUTLINE OF NUMERICAL ANALYSIS

3.1 Numerical analysis model

One quarter of each RC girder was three-dimensionally modeled for numerical analysis with respect to the two symmetrical axes. Figure 2 shows the mesh geometry of the Girder S1-L0 as an example. In this model, concrete, axial rebar, and FRP sheet were modeled using eight node solid elements and stirrups were modeled using embedded reinforced elements (DIANA 2008) assuming perfect bond between stirrup and concrete.

To limit the stress concentration occurring in the concrete elements around loading and supporting points, elastic steel plates $50 \times 75 \times 20$ mm in dimension were prepared for the numerical analysis and were modeled using eight nodes solid elements.

3.2 Modeling of geometrical discontinuities

In order to take into account geometrical discontinuities due to opening of dominant cracks, slipping of rebar, and debonding of AFRP sheet, those were considered using an interface element, which has pairs of overlapping nodes and zero thickness. Here, three stress-relative displacement models named as discrete cracking model, bond-slip model, and FRP sheet debonding model, were adopted in which those were applied by Kishi et al.

(2005). Here, the relations will be briefly outlined.

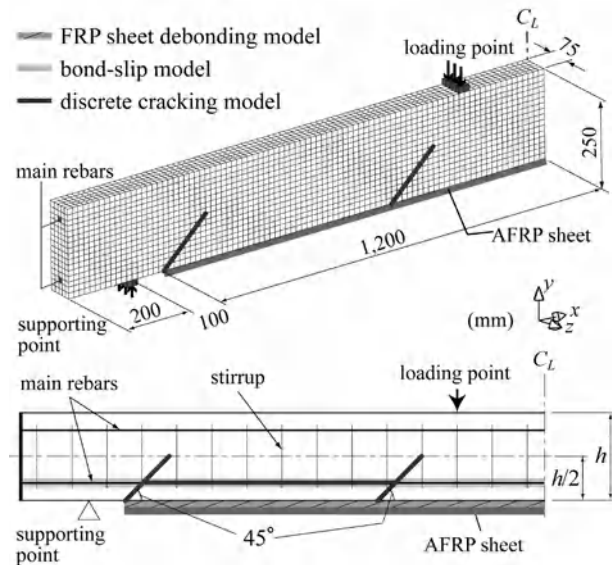
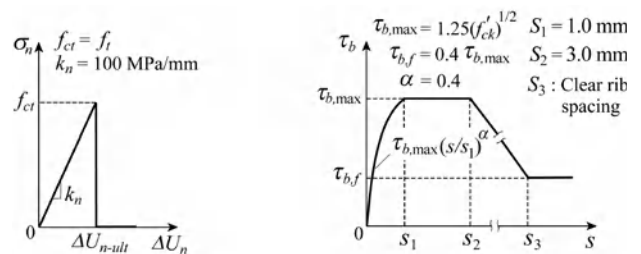


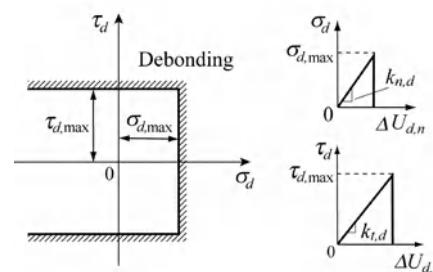
Figure 2 FE analysis model for Girder S1-L0

Figure 3(a) shows the relationship between normal stress and relative displacement between two surfaces of the interface elements in the discrete cracking model, in which ΔU_n is the relative displacement normal to the interface; f_{cr} is the ultimate tensile strength of the model, and k_n is the normal stiffness. Here, the ultimate tensile strength f_{cr} was assumed to be equal to the tensile strength of concrete f_t . the normal stiffness k_n was assumed to be 100 MPa/mm.



(a) Discrete cracking model

(b) Bond-slip model



(c) FRP sheet debonding model

Figure 3 Stress-relative displacement relations for interface elements

A bond-slip model was applied to the interface elements around the main rebar elements in the whole span to consider the slippage between rebar and concrete. The relationship between bonding stress τ_b and

relative displacement S was defined following to the CEB-FIP Model Code (CEB-FIP 1993), as shown in Figure 3(b).

Figure 3(c) shows a criterion of FRP sheet-debonding model based on the Coulomb friction concept. This model ignores an interaction between normal tensile stress σ_d and plane shear stress τ_d for simplicity. Those $\sigma_{d,max}$ and $\tau_{d,max}$ were assumed to be tensile strength of concrete f_t and the value given by Chajes et al. (1996), respectively. The value is formulated as:

$$\tau_{d,max} = 0.92 \sqrt{f'_c} \quad (1)$$

Girder N was analyzed without considering any geometrical discontinuities described here.

3.3 Procedures of numerical analysis for damaged RC girder

The load-carrying behavior of the RC girder which has been suffered damage and then was flexural reinforced by bonding AFRP sheet onto the tension-side surface, was analyzed following procedures:

(1) Applying a phase analysis procedure installed in DIANA code, dummy elements are prepared at the place of the RC girder where the AFRP sheet will be bonded;

(2) To numerically realize a damaged RC girder, numerical analysis is conducted for the girder subjected to load up to reaching a prescribed strain for the rebar and/or a prescribed deflection at the mid-span of the girder and then unloaded to zero level;

(3) Dummy elements are replaced with AFRP sheet elements; and

(4) Again numerical analysis is conducted for the flexural reinforced RC girder with AFRP sheet by applying displacement control method.

3.4 Modeling of materials

Stress-strain relationship of concrete is shown in Figure 4(a). For compression region, parabola-rectangle model was used up to the 0.35 % strain based on the specifications of Japan Concrete Standards (2002). In the post peak region, it was assumed that concrete linearly softens with the stiffness $E_{C1} = 0.05 E_c$ until $\sigma = -0.2 f'_c$. The von Mises yield criterion with associated plastic flow was applied to define the yield state. In the tension region, a linear tension-softening model was assumed. The ultimate tensile strain ε_{tu} was determined following the equation described in Figure 4(a), in which V is element volume; and G_f is tensile fracture energy estimated following the CEB-FIP Model Code (CEB-FIP 1993). The smeared crack model was applied to every concrete element to incorporate the effects of small cracks into the numerical analysis. Shear modulus of the element after cracking is assumed to be 1 % of the initial shear modulus G .

The stress-strain relationship for rebar and stirrup is defined by using a bilinear isotropic hardening model as shown in Figure 4(b). The plastic hardening modulus H'

is assumed to 1 % of elastic modulus E_s . Yielding of steel is estimated on the basis of von Mises yield criterion.

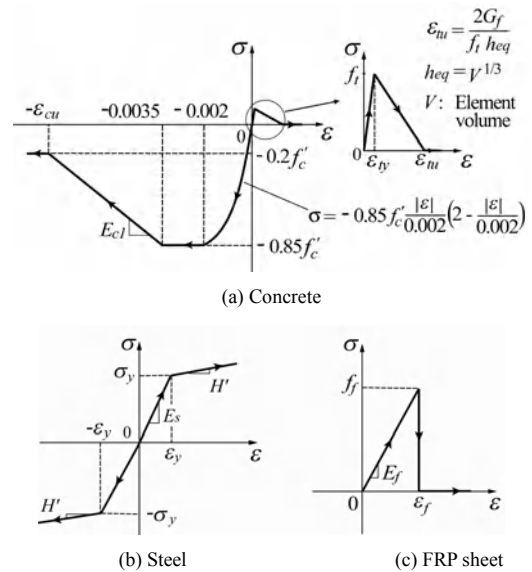


Figure 4 Stress-strain relationship of materials

AFRP sheet was assumed to be a linear elastic material until rupture and was treated as isotropic and homogeneous material as shown in Figure 4(c). Poisson's ratio of the sheet was assumed as 0.2.

4 NUMERICAL RESULTS AND DISCUSSION

Figure 5 shows the load and mid-span deflection (hereinafter deflection) curves for the Girder N and Girder S1-L0/1/2. From this figure, it is observed that the numerical results for all girders shown here are almost in good agreement with the experimental ones. However, the deterioration of the each load-carrying resistant of the girder after sheet delamination and/or rupture was underestimated by numerical analysis comparing with the experimental ones. It may be the reason that the numerical analysis method proposed here cannot better evaluate the delamination of concrete cover after the sheet debonding. This point will be a problem to be solved in the future. Also, it is confirmed that rebar yielding load and load-carrying capacity of the reinforced RC girders are clearly upgraded comparing with those of normal girder (Girder N).

The maximum load-carrying capacities for all girders considered here are listed in Table 2. From this table, it is seen that numerical results are within an error of 10 % referring to the experimental ones. Then, it is confirmed that the proposed numerical analysis method can better predict the maximum load-carrying capacity of the flexural reinforced RC girders with AFRP sheet after damaged. Maximum loads among each three girders for S1/2 are almost similar. Then, it is confirmed that the reinforcing effects of the AFRP sheet are similar

irrespective of the magnitude of damage level of the RC girders.

Figure 6 shows the comparisons between analytical and experimental results for the axial strain distribution of the AFRP sheet at the maximum load evaluated by numerical analysis in the cases of the Girder S1. From this

figure, it is observed that numerical results adequately evaluate the experimental results including the constant strain distribution in the equi-bending span. This means that the flexural reinforcing effects of the AFRP sheet for the damaged RC girders can be better predicted by using the proposed numerical analysis method.

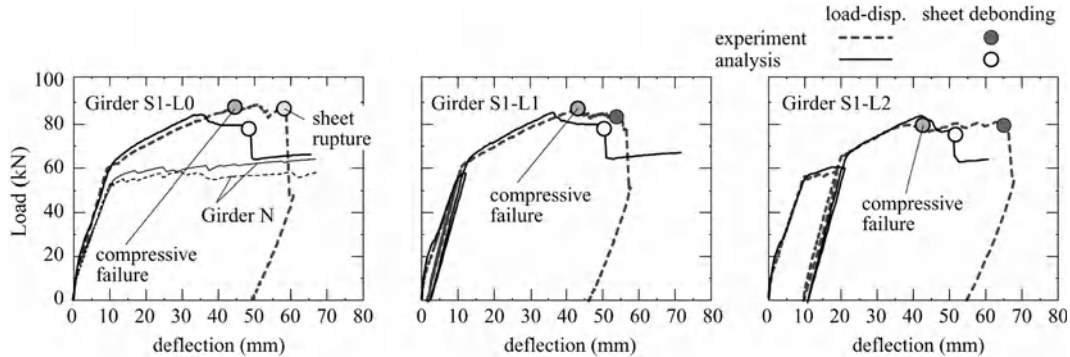


Figure 5 Comparison of load-deflection relationship and failure mode

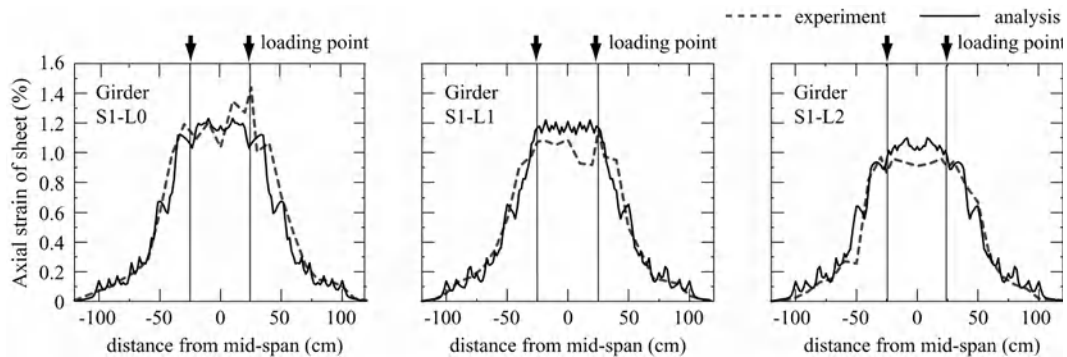


Figure 6 Comparison of axial strain distribution of AFRP sheet at analytical maximum load

Table 2 Comparison of max. load

Girder	Max. load (kN)		Ratio
	Analytical	Experimental	
N	54.0	53.5	1.01
S1-L0	83.6	89.0	0.94
S1-L1	84.5	87.4	0.97
S1-L2	83.0	81.0	1.02
S2-L0	92.0	102.6	0.90
S2-L1	89.7	94.5	0.95
S2-L2	89.3	95.4	0.94

5 CONCLUSIONS

(1) Assuming the FRP sheet elements to be dummy, pre-analysis was conducted for numerically realizing the damaged situation of the girder. Then, the damaged girder after reinforcing with AFRP sheet can be rationally analyzed replacing the dummy elements with the FRP sheet ones;

(2) Combining of smeared and discrete cracking models and considering bond-slip and FRP sheet delamination models, the load-carrying behavior and delamination of AFRP sheet can be roughly predicted;

(3) The rebar yielding load and load-carrying capacity of the existing RC girders can be rationally upgraded reinforced with AFRP sheet comparing with those of normal RC girder; and

(4) It is confirmed that those reinforcing effects of the AFRP sheet are almost similar irrespective of the magnitude of damage level of the girders.

REFERENCES

Arduini, M, and Nanni, A. 1997. Behavior of precracked RC strengthened with carbon FRP sheets. *Journal of CC, ASCE* 1(2): 63-70.

CEB-FIP model code 1993. *Design code*. Lausanne: Thomas Telford.

Chajes, M. J., Finch, W. W., Januszka T. F., and Thomson T. A. 1996. Bond and force transfer of composite material plates bonded to concrete. *ACI Structural Journal* 93(2): 208-217.

DIANA 2008. *User's manual –Nonlinear analysis*. Delft: TNO Building and Construction Research.

Japan Concrete Standards 2002. *Structural performance verification*. JSCE. In Japanese.

Kishi, N., Zhang G, and Mikami H. 2005. Numerical cracking and debonding analysis of RC beams reinforced with FRP sheet, *Journal of Composites for Construction* 9(6): 507-514.

A Study on the Applicability of ECE Technique on Chloride Contaminated Concrete Retrofitted with FRP Strips

Matthew Anderson

Graduate Research Assistant, Department of Civil and Environmental Engineering, West Virginia University, Morgantown, WV 26506-6103, USA

Indrajit Ray & An Chen (an.chen@mail.wvu.edu)

Research Associate Professors, Department of Civil and Environmental Engineering, West Virginia University

Julio Davalos (julio.davalos@mail.wvu.edu)

Benedum Distinguished Teaching Professor, Department of Civil and Environmental Engineering, West Virginia University

ABSTRACT The objective of this study is to evaluate whether the Electrochemical Chloride Extraction (ECE) technique, which has been proven to be an effective tool for removing chloride ions for regular concrete structures, can be effectively used for Fiber-Reinforced Polymer (FRP) repaired concrete structures. FRP retrofit for deteriorated concrete structures is a highly successful practice, but alone it does not address the corrosion at its source: accumulated chloride ions from environmental sources such as de-icing salts. A total of 28 beams were tested, with testing variables including intermittent vs. continuous ECE techniques, different FRP repairing schemes, and applying ECE before and after FRP repair. Parameters monitored during the study included chloride content, pH value around the steel, and current resistance and density. The effectiveness of ECE was determined by changes in chloride levels and the pH value around the steel.

1 INTRODUCTION

The corrosion of reinforcing steel due to ingress of chloride ions from de-icing salts is a primary source of deterioration in concrete bridges. The formation of corrosion products increases the internal steel volume, producing tensile stresses in the surrounding concrete which leads to cracking, spalling, and even delamination of structural components. In 2006, the Federal Highway Administration statistics showed that approximately one out of every 13 reinforced concrete bridges in the USA was structurally deficient. With the aid of governmental programs such as the American Recovery and Reinvestment Act of 2009, now is a crucial time for the rehabilitation of our nation's aging infrastructure. Many efficient repair technologies exist, and when properly implemented, they allow structurally deficient bridges to be restored rather than replaced, thus saving millions of dollars.

The application of Fiber-Reinforced Polymer (FRP) composites for retrofitting deteriorated concrete structures has been highly successful, but there are concerns with long-term performance and durability, particularly when chloride ions are still present for two possible reasons: (1) no chloride ion extraction is performed when a bridge is initially retrofitted; and (2) even if chloride

ions are initially extracted, they will again accumulate due to available sources such as continual application of de-icing salts. Naturally, leaving chlorides within concrete will exacerbate the onset of corrosion during the post-repair service life of the structure.

The most well-known technology available that addresses this problem directly is Electrochemical Chloride Extraction (ECE). ECE is a non-destructive corrosion mitigation mechanism applied to chloride-contaminated concrete structures. Rather than just masking the problem like other corrosion repairing technologies do, ECE functions to remove the chloride ions from contaminated concrete while simultaneously restoring the passivity of the embedded rebar. ECE utilizes an external direct current (DC) power source to drive the process, which essentially is the reverse of the current path during corrosion. To achieve the proper current paths for the process, the (-) lead is connected to the rebar, while the (+) lead is hooked to a temporary, externally-mounted anode. The temporary anode consists of steel or titanium mesh embedded in a conductive electrolyte media (most commonly fresh water mixed with cellulose fibers). The applied electricity creates a current moving from the rebar, through the concrete cover areas, to the externally mounted anode. The negatively charged chloride ions are repelled from the

reinforcing steel, traveling along current paths toward the externally-mounted anode. With the ECE setup, the chlorides will consume and corrode the anode as they are extracted from the concrete. A typical ECE project lasts for four to eight weeks, and is therefore a quick process with lasting effects.

It is desirable to study whether the ECE technique, which has proven to be an effective tool to remove chloride ions in regular concrete structures, can be effectively used in conjunction with FRP-repair, which is the objective of the current study at West Virginia University (WVU).

2 LITERATURE REVIEW AND BASIS FOR RESEARCH

2.1 Mixing chlorides into concrete cover

Swamy and McHugh (2006) performed ECE on 12 beams ($100 \times 165 \times 2300\text{mm}$) cast with uniformly distributed chlorides. They achieved 70-75% chloride removal in concrete cover zones, while only extracting 20-50% from the beam mid-sections. A major conclusion drawn from their work was that ECE is likely to be more efficient in real structures where most infiltrated chloride ions would remain in the concrete cover. Representatives from Vector Corrosion Technologies (2008) also indicated that ECE would be more effective if the chloride contamination was confined to the concrete cover, since the chlorides must be able to travel a current path between the steel and the exterior surface. Input from these sources directed our research work to introduce chlorides only within the cover zone of beam specimens, as explained further in the following section.

2.2 Methods of chloride extraction

ECE current cycle selection for this study was based on the findings of Elsener and Angst (2007). They stated that during ECE treatment the free chlorides in the pore solutions are transported along the electric current to the exterior anode, leaving only chemically bound chlorides within the concrete. The authors established a chemical equilibrium relationship between bound and free chlorides, stating that ECE becomes inefficient when the bound-free chloride relationship is far from equilibrium. To remedy the problem they used current “off” cycles during treatment (24 – 48 hr in this case), which allowed the system to re-establish equilibrium. After three on/off cycles, free chloride was completely removed, and much of the bound chloride was removed as well. The authors concluded that the use of current cycles is much more efficient than the standard constant current method. In a separate study, Elsener (2008) stated that a current cycle (two weeks on / one week off) would have eliminated the need for a second extraction to bring chloride levels down to 0.4% by weight of cement on a bridge project in Switzerland. Based on these findings, we adopted the

intermittent ECE cycles as outlined in the following section.

2.3 FRP wrapping scheme selection

Our concern was to define an FRP wrapping scheme for beams that would closely simulate a design typically used for actual bridges. Often the entire tension face of a beam is covered with a reinforcing strip, and the parameter under consideration is the spacing of the vertical shear-reinforcing “U-wraps.”

Parish (2008) identified the need for placing U-wraps across longitudinal FRP strips, in order to minimize debonding failure. He identified a critical section for flexural/shear failure beginning directly below the load and propagating at an angle 30-degrees from vertical down and away from the beam centerline. The U-wrap spacing in this study will be selected as uniformly distributed with U-wraps close enough to influence the chloride extraction results, but not placed too close for design practicality. With these considerations, in this research we will include three types of U-wrap anchorage spacing, using 101.6mm wide U-wraps. For the following three schemes (see Figure 1): (1) The center-to-center

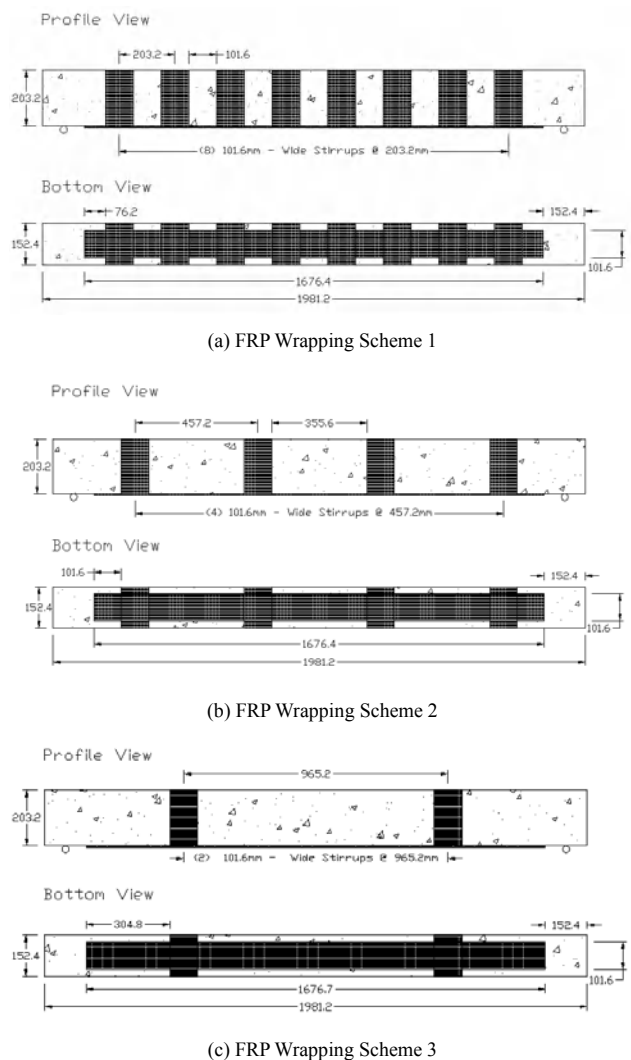


Figure 1 FRP U-wrap anchorage schemes (all dimensions in mm)

spacing, $s = 203.2\text{mm}$ for a total of 8 wraps (Figure 1(a)); (2) $s = 457.2\text{mm}$ for a total of 4 wraps; and (3) Only two wraps, strategically placed at the critical points for a four-point bending test (Figure 1c).

3 TESTING PROTOCOL

3.1 Materials

The current study involves casting twenty-eight $152.4 \times 203.2 \times 1981.2\text{mm}$ reinforced concrete beams with chlorides included within the concrete mix in the cover areas as mentioned above (Figure 2). This casting scheme was selected to closely simulate an actual environment while coping with time constraints that prevented us from corroding the beams by natural means (i.e. exposure to saltwater). The top concrete cover does not contain chlorides, on the basis that actual bridge beams are connected to and protected by a deck slab. The concrete mix was produced with a w/c ratio of 0.6 to produce weak, porous concrete similar to conditions found in deteriorated bridges. The beam size and reinforcement layout (shown in Figures 2 and 3) were selected to be the same as a previous study (Parish, 2008) in order to correlate the results.

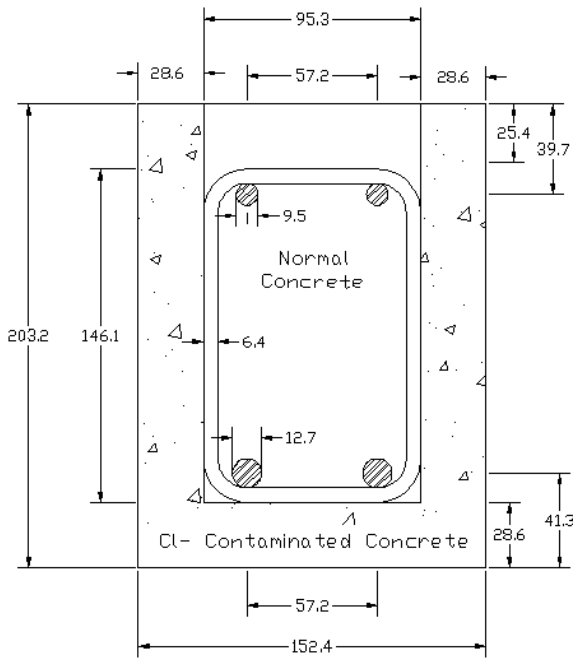


Figure 2 Beam cross-section (all dimensions in mm)

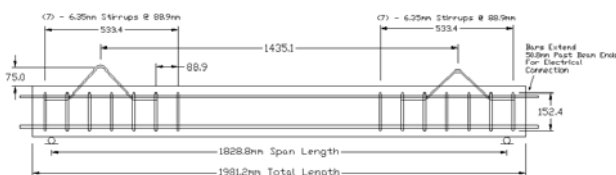


Figure 3 Beam specimen (profile dimensions) to show reinforcement layout (all dimensions in mm)

The exterior concrete was contaminated with 5% NaCl by weight of cement, added during mixing (Note: 5% NaCl corresponds to 3.03% Cl). Beams were removed from their forms after two days and moist-cured under wet burlap for 28 days before testing began.

A representative beam was selected to be used for concrete powder sample collection prior to testing; to serve as a baseline to compare with the ECE results. The samples were obtained using a drill with a 6.35mm diamond drill bit from extracted 50.8mm - diameter cores. The powder samples were used to perform a chloride content analysis following ASTM designation C 1152/C 1152M; Standard Test Method for Acid-Soluble Chloride in Mortar and Concrete. The results are shown in Figures 4 and 5:

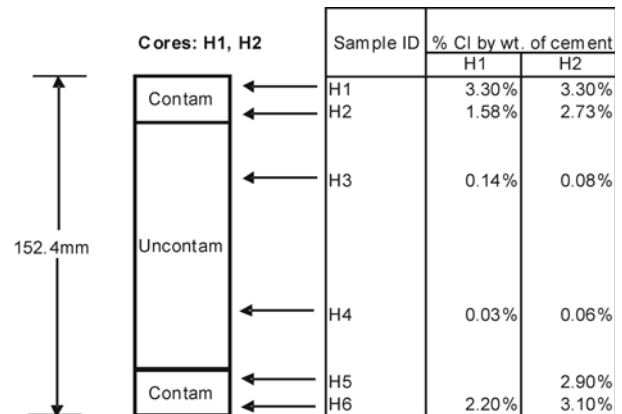


Figure 4 Chloride analysis results – horizontal cores H1 and H2

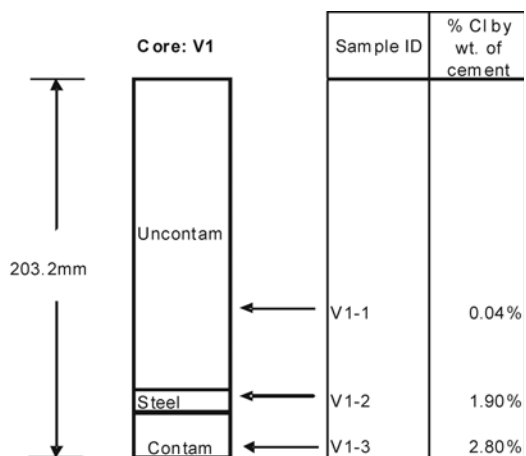


Figure 5 Chloride analysis results - vertical core

Data from the vertical cores also produced approximately the anticipated results, with similar relationships as the analyses for the horizontal cores: maximum chloride near the estimated 3.03% designed in the mix, with less near the interface and negligible amounts within the uncontaminated region.

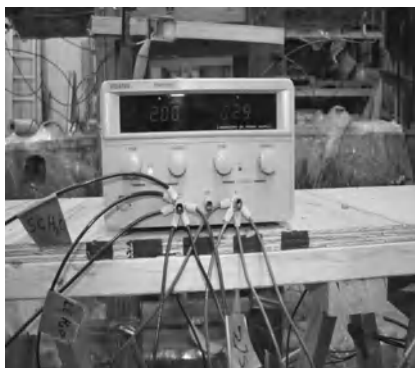
3.2 Actual testing plan

The test variables included various chloride extraction

time cycles, as well as varying FRP layout schemes. The information gathered on ECE techniques suggests applying a current density of 1 A/m^2 (of embedded steel) and terminating the process after a total of $600 \text{ A}^*(\text{hr/m}^2)$ has been achieved for each beam. Based on previous literature, chloride extraction cycles of continuous, short cycle (five days ON, two days OFF), and long cycle (12.5 days ON, 5 days OFF) were selected for the experiment. In addition to the varying current cycles, two different electrolyte materials were used. One type consisted of simply tap water, the other was tap water mixed with 5 g/L of calcium hydroxide. The electrolyte media was replenished daily using irrigation drip lines embedded in the anolyte media (wet cellulose fibers).



(a) Beam configuration details



(b) DC power supply

Figure 6 Photographs of test setup

Two unrepaired beams, as well as two beams of each of the three FRP layouts were designated for each current cycle: short, long, and continuous. Of each pair of beams, one received each type of electrolyte media. The plan resulted in a total of eight beams per current cycle, with testing totaling 24 beams between the three cycles. The remaining four beams were kept for baseline comparisons.

Rather than stopping at the recommended $600 \text{ A}^*(\text{hr/m}^2)$, the ECE process was continued for $900 \text{ A}^*(\text{hr/m}^2)$ to assess whether any added benefit would be achieved from additional current application. Concrete powder samples were collected using a hammer drill and 25.4mm masonry bit. Samples were collected near the end points of each beam, as well as from the midspan, from both the sides and bottom. At each sample location, two samples were taken: one from the concrete surface to 12.5mm depth and the other from 12.5mm depth to 25.4mm , through the entire contaminated cover zone. This way we could determine whether the extraction was more efficient at the level of the steel. Each sample was analyzed for chloride content and pH. Additional samples (one from the side, one from the bottom) were taken from each beam for X-ray diffraction testing. Samples were collected at approximately $300 \text{ A}^*(\text{hr/m}^2)$ during current OFF cycles for the intermittent ECE cycles, as well as at $600 \text{ A}^*(\text{hr/m}^2)$ and $900 \text{ A}^*(\text{hr/m}^2)$ for all six beams. The photographs in Figure 7 illustrate the test setup.

Figure 6(a) clearly shows the irrigation lines and beam configuration during the ECE process. The tank shown in front was periodically filled with calcium hydroxide and water, which was pumped by hand to send water to the three beams on the right side, aligned vertically. The remaining three beams on the left side of the picture were fed with water by a hose connected directly to a faucet. Figure 6(b) shows the DC power supply.

3.3 Results for unrepaired long and continuous cycle beams

Spots of brown, rusty staining were observed on samples in the electrolyte after only a few days of current, indicating that the ECE was working properly. Electrical continuity on all beams was routinely checked using a clamp meter capable of reading to the nearest 0.1A . Samples were analyzed following the ASTM procedure detailed above, and the results of the chloride analysis for unrepaired beams are reported in tables 1 through 4:

Tables 1 and 2 show data for sample locations bottom-middle (B-M), and bottom-end (B-E) for unrepaired beams subjected to the “Long” current cycle. Both locations were sampled directly beneath the reinforcing steel, and B-E samples were taken approximately 254mm from the beam end. Drill holes were patched with a commercial polymer-modified repair mortar before

resuming ECE. As shown, samples were taken at 300, 600, and 900 $A^*(hr/m^2)$ cumulative current densities at each location. The results show that ECE was highly effective in both locations, lowering chloride contents from the initial 3.03% by weight of cement down to 0.127% at the level of the steel at 900 $A^*(hr/m^2)$ for both electrolytes at the middle locations. The pH readings were generally slightly higher after chloride extraction.

Table 1 Chloride contents of unrepaired long cycle beams with tap water electrolyte

Sample ID	Current $A^*(hr/m^2)$	pH	% Cl	
			concrete	cement
H ₂ O - B-E - 0-12.5mm	300	12.30	0.154	0.921
H ₂ O - B-E - 12.5-25mm	300	12.39	0.148	0.881
H ₂ O - B-E - 0-12.5mm	600	12.31	0.110	0.656
H ₂ O - B-E - 12.5-25mm	600	12.33	0.074	0.444
H ₂ O - B-E - 0-12.5mm	900	12.31	0.067	0.402
H ₂ O - B-E - 12.5-25mm	900	12.39	0.074	0.444
H ₂ O - B-M - 0-12.5mm	300	12.30	0.138	0.825
H ₂ O - B-E - 12.5-25mm	300	12.36	0.129	0.767
H ₂ O - B-M - 0-12.5mm	600	12.29	0.067	0.402
H ₂ O - B-E - 12.5-25mm	600	12.26	0.053	0.317
H ₂ O - B-M - 0-12.5mm	900	12.26	0.043	0.254
H ₂ O - B-E - 12.5-25mm	900	12.25	0.021	0.127

Table 2 Chloride contents of unrepaired long cycle beams with calcium hydroxide electrolyte

Sample ID	Current $A^*(hr/m^2)$	pH	% Cl	
			concrete	cement
CaOH - B-E - 0-12.5mm	300	12.33	0.152	0.910
CaOH - B-E - 12.5-25mm	300	12.39	0.191	1.142
CaOH - B-E - 0-12.5mm	600	12.43	0.060	0.360
CaOH - B-E - 12.5-25mm	600	12.42	0.078	0.466
CaOH - B-E - 0-12.5mm	900	12.36	0.135	0.804
CaOH - B-E - 12.5-25mm	900	12.36	0.106	0.635
CaOH - B-M - 0-12.5mm	300	12.37	0.117	0.698
CaOH - B-M - 12.5-25mm	300	12.35	0.086	0.514
CaOH - B-M - 0-12.5mm	600	12.32	0.048	0.286
CaOH - B-M - 12.5-25mm	600	12.43	0.057	0.339
CaOH - B-M - 0-12.5mm	900	12.23	0.050	0.296
CaOH - B-M - 12.5-25mm	900	12.44	0.021	0.127

Tables 3 and 4 report the ECE results for side-middle (S-M) and bottom-middle (B-M) locations on continuous cycle unrepaired beams. Compared with initial chloride contents ECE was effective at each location. However, these beams show less benefit from continuing the process until 900 $A^*(hr/m^2)$ and also that extraction was much more efficient on the beam bottoms than on the

sides. Bottom areas likely experienced higher extractions since they were saturated with electrolyte at all times. The water tended to seep down the sides and collect at the bottom of each beam, providing a more electrically conductive environment.

Table 3 Chloride contents of unrepaired continuous cycle beams with tap water electrolyte

Sample ID	Current $A^*(hr/m^2)$	pH	% Cl	
			concrete	cement
H ₂ O - S-M - 0-12.5mm	600	12.20	0.124	0.741
H ₂ O - S-M - 12.5-25mm	600	12.28	0.132	0.789
H ₂ O - S-M - 0-12.5mm	900	12.28	0.131	0.783
H ₂ O - S-M - 12.5-25mm	900	12.39	0.152	0.910
H ₂ O - B-M - 0-12.5mm	600	12.35	0.172	1.024
H ₂ O - B-M - 12.5-25mm	600	12.49	0.074	0.444
H ₂ O - B-M - 0-12.5mm	900	12.44	0.067	0.402
H ₂ O - B-M - 12.5-25mm	900	12.53	0.110	0.656

Table 4 Chloride contents of unrepaired continuous cycle beams with calcium hydroxide electrolyte

Sample ID	Current $A^*(hr/m^2)$	pH	% Cl	
			concrete	cement
CaOH - S-M - 0-12.5mm	600	12.26	0.199	1.185
CaOH - S-M - 12.5-25mm	600	12.28	0.209	1.249
CaOH - S-M - 0-12.5mm	900	12.33	0.124	0.741
CaOH - S-M - 12.5-25mm	900	12.32	0.113	0.677
CaOH - B-M - 0-12.5mm	600	12.29	0.077	0.462
CaOH - B-M - 12.5-25mm	600	12.39	0.064	0.381
CaOH - B-M - 0-12.5mm	900	12.47	0.089	0.529
CaOH - B-M - 12.5-25mm	900	12.45	0.071	0.423

3.4 Conclusions

The testing is still ongoing. Based on limited results, it can be concluded that two types of concrete can be successfully combined into each beam, and based on chloride analysis results, the ECE testing protocol and laboratory methods have been proved successful.

REFERENCES

- AASHTO – Standard Specification for Electrochemical Chloride Extraction.
http://www.vector-corrosion.com/wordpress/wp-content/uploads/Re-alkalization/037_0001.PDF
 Davalos et al. 2009. *District 3-0 Investigation of Fiber-Wrap Technology for Bridge Repair and Rehabilitation (Phase-III)*. West Virginia University, Department of Civil and Environmental Engineering.
 Elsener, B. 2008. Long-term Durability of Electrochemical Chloride Extraction *Materials and Corrosion*, 59 (2): 91-97.

- Elsener, B., Angst, U. 2007. Mechanism of Electrochemical Chloride Removal. *Corrosion Science*, 59 (12): 4504-4522.
- Parish, G. 2008. *CFRP Repair of Concrete Beams Aged By Accelerated Corrosion*, MS Thesis, West Virginia University, Department of Civil and Environmental Engineering. i, 180-182.
- Swamy, R.N., McHugh, S. 2006. Effectiveness and Structural Implications of Electrochemical Chloride Extraction from Reinforced Concrete Beams. *Cement & Concrete Composites*, 28: 722-733.
- Sharp, et al. 2002. Electrochemical Chloride Extraction: Influence of Concrete Surface on Treatment PUBLICATION NO. FHWA-RD-02-107. Federal Highway Administration, Virginia Transportation Research Council.
<http://www.tfhrc.gov/structur/pubs/02107/01.htm#table5>.
- Vector Corrosion Technologies. 2008. College Park, MD: In-person conversation with Chris Ball and Rachel Stiffler.

Finite Element Modeling of RC Beams Strengthened in Flexure with Prestressed NSM CFRP Strips

Hamid Y. Omran & Raafat El-Hacha (relhacha@ucalgary.ca)
Department of Civil Engineering, University of Calgary, Calgary, Alberta, Canada

ABSTRACT This paper presents the results from Finite Element Modeling (FEM) of reinforced concrete (RC) beams strengthened in flexure with prestressed Near-Surface Mounted (NSM) Carbon Fiber Reinforced Polymer (CFRP) strips. A total of four large-scale (5.15 m long) RC beams tested at University of Calgary are modeled with ANSYS program. The beams are simply supported with rectangular cross section strengthened with CFRP strips, mounted in one groove in the concrete on the tension side of the beams, using various prestressing levels (0%, 20%, 40% and 60% of the ultimate tensile strength of the CFRP strip). The beams were tested under four-point bending. Comparison between numerical and experimental results shows a good correlation in terms of load-deflection curve at mid-span, strain profile along the CFRP strip at cracking, yielding and ultimate loads, and type of failure mode.

1 INTRODUCTION

During recent years, the conventional strengthening materials are being replaced by advanced composite materials such as Fiber Reinforced Polymer (FRP). The FRP reinforcement can be used more effectively if prestressed. Using Finite Element Modeling (FEM), Kang et al., (2005) evaluated the efficiency of reinforced concrete (RC) beams strengthened with non-prestressed NSM CFRP strips. However, the FEM of prestressed NSM CFRP reinforcement is relatively less known to date. This paper presents the results from FEM of RC beams strengthened in flexure with prestressed NSM CFRP strips. Four large-scale RC beams tested at University of Calgary are modeled with 3D ANSYS FEM package. This study mainly focuses on the effects of prestressing level on the load bearing capacity and ductility of RC beams strengthened with prestressed NSM CFRP strips in which the results of FE analysis are compared with experimental results.

2 NUMERICAL MODELING

2.1 Properties of the modeled beams

The beams are simply supported with rectangular cross section (200×400mm) strengthened with two CFRP strips, mounted in one groove pre-cut in the concrete cover on the tension side of the beams, using various prestressing levels (0%, 20%, 40% and 60% of the ultimate tensile strength of the CFRP strip). The beams were tested under static loading in four-point bending configuration (Gaafar, 2007). Geometry of the beams is depicted in Figure 1.

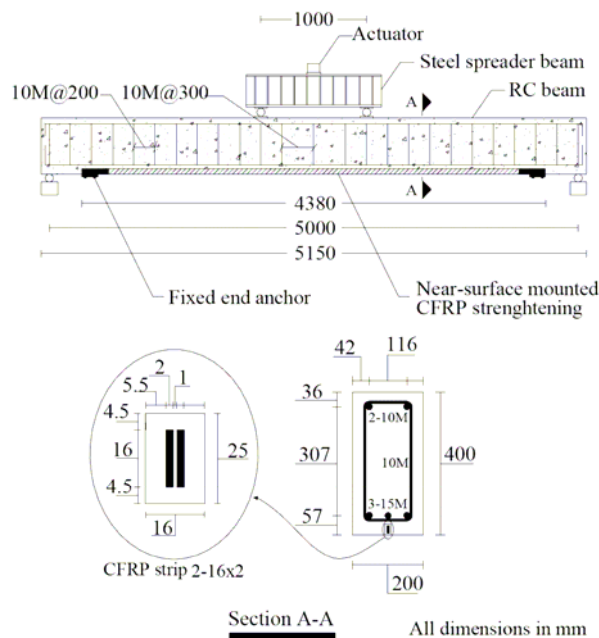


Figure 1 Geometry of the modeled beams

Table 1 represents the key points of stress-strain curve of reinforcing steel bars. Multi-linear elastic material model was defined for the steel bars, and a Poisson ratio of 0.3 was assumed.

Table 1 Key points of stress-strain curves of steel bars

	Strain	0.0025	0.025	0.04	0.06	0.1
10M bar	Stress (MPa)	500	505	547.5	588.5	610.5
	Strain	0.002375	0.025	0.04	0.06	0.1
15M bar	Stress (MPa)	475	475	530	560	608

The uniaxial concrete compressive strength of each beam is presented in Table 2. The Young modulus, uniaxial tensile strength, and Poisson ratio are assigned to $4500\sqrt{f'_c}$ MPa, $0.6\sqrt{f'_c}$ MPa, and 0.18 respectively. The considered material model for concrete is described by Omran et al., (2009). The CFRP strip had a Young modulus of 145GPa, a tensile strength of 2610 MPa, an ultimate strain of 1.8%, and a Poisson ratio of 0.35 with a linear-elastic behavior up to failure (Gaafar, 2007). In the model, to avoid mesh complexity, it is assumed that the dimension of CFRP is 5×16 mm instead of $2 \times 2 \times 16$ mm plus 1mm epoxy in-between (Figure 1). Therefore, a Young's modulus of 1160GPa, a tensile strength of 2088MPa, and an ultimate strain of 1.8% are assigned to the CFRP material in the model that produces the same axial stiffness of the CFRP in the test. The prestressing level as prestrain in CFRP strip corresponding to each beam is presented in Table 2. The epoxy adhesive had a Young modulus of 2400GPa, an ultimate tensile strength of 24MPa, and a Poisson ratio of 0.37. It is assumed that the epoxy adhesive has a linear-elastic behavior up to failure. Linear-isotropic material model was considered for the bolts, steel plates, and steel end anchor.

2.2 FE modeling

The models are 3D developed in the ANSYS commercial FEM package. All materials including concrete, longitudinal steel reinforcements, stirrups, CFRP strip, epoxy adhesive, bolts and end anchor were modeled using appropriate elements. Due to the symmetry in cross section and span, only one quarter of the beam was modeled. The Solid65 element was considered to model the concrete. This element has eight nodes with three degrees of freedom at each node, translations in the nodal x , y , and z directions with capability of plastic deformation, cracking in three orthogonal directions and crushing. The Link8 element was considered to model steel reinforcements. This element is a 3D spar element and it has two nodes with three degrees of freedom, translations in the nodal x , y , and z directions. This element is also capable of plastic deformation. The Solid45 element was used to model the epoxy adhesive, CFRP strip, end anchor and steel plates at the supports and under concentrated load for the beam. This element has eight nodes with three degrees of freedom at each node, translations in the nodal x , y , and z directions and is capable of assigning the initial stress. The Beam4 element was considered to model the bolts at the steel end anchor. This element has two nodes with six degrees of freedom at each node with capabilities of tension, compression, torsion and bending. By assigning the shear deflection constants this element is also capable to consider the shear effects. Fine mesh was mapped inside the groove to increase the accuracy of results, and there was no need to map fine mesh outside the groove to decrease the cost in terms of modeling time and solution time. Therefore, the surface-to-surface contact elements

were considered for interface between concrete and adhesive. The target surface (on concrete) was modeled with TARGE170 and the contact surface (on adhesive) was modeled with CONTA173. TARGE170 is capable to represent various 3D target surfaces for the associated contact elements. These elements can easily model complex shapes of rigid target. They must overlay the solid elements describing the boundary of the deformable target. CONTA173 is used to represent contact and sliding between 3D target surfaces and a deformable surface, defined by this element. The element is defined by four nodes and is applicable to 3D structural and coupled field contact analyses. Because no failure due to separation of epoxy from concrete was reported in the test by Gaafar (2007), the contact behavior was assigned to "bonded (always)". The meshed beam is depicted in Figure 2. To enforce the prestressing, control time, and increase the accuracy of results, the solution was performed with defining four load-steps: from beginning to prestressing, from prestressing to cracking, from cracking to yielding, and from yielding to ultimate.

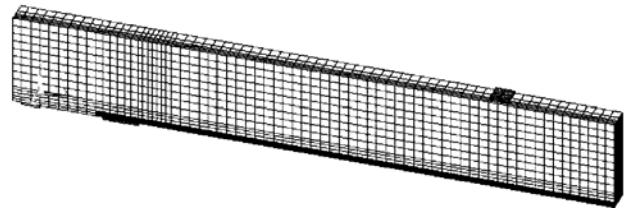
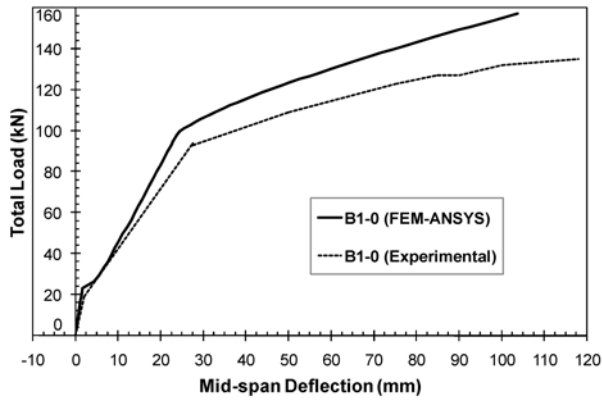


Figure 2 Meshed beam in ANSYS (1/4 of the tested beam)

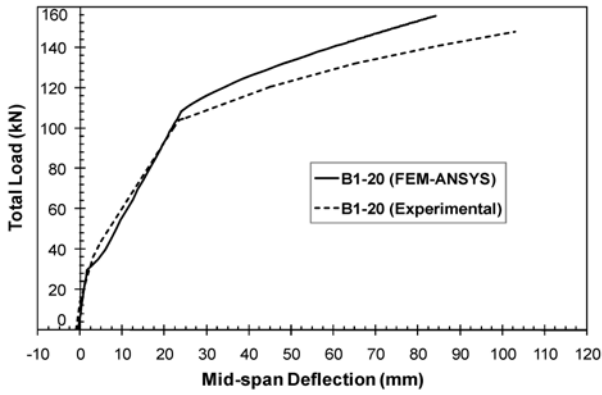
3 RESULTS

Figure 3 shows that the load-deflection curves of the modeled beams obtained from FE analysis are stiffer than the tested beams. This difference usually started after cracking on tension face and especially it appears in the plastic region of the curves which might be due to slight difference between material properties of the tested and modeled beams such as steel reinforcement and CFRP strip. Comparison between load-deflection values at cracking, yielding and ultimate, type of failure and ductility index (deflection at ultimate to deflection at yielding) obtained from FE analysis and test are presented in Table 2. Also, percentage of deference between FE and test results is calculated. For the modeled beams, the mode of failure is CFRP rupture same as the tested beams except B1-0 which failed due to concrete cover spalling during the test.

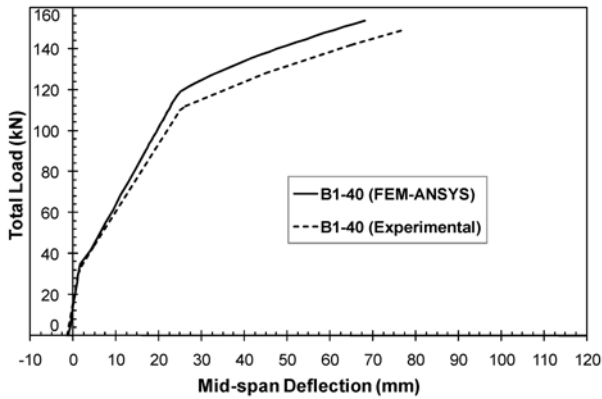
Because the CFRP rupture governs, the numerical ultimate load is in the same range for all beams. The numerical ultimate load slightly decreases when the prestress level increases. The ductility index decreases when the prestressing level increases. Maximum and minimum difference between FE and test ductility indices is 4.86% and 14.2%.



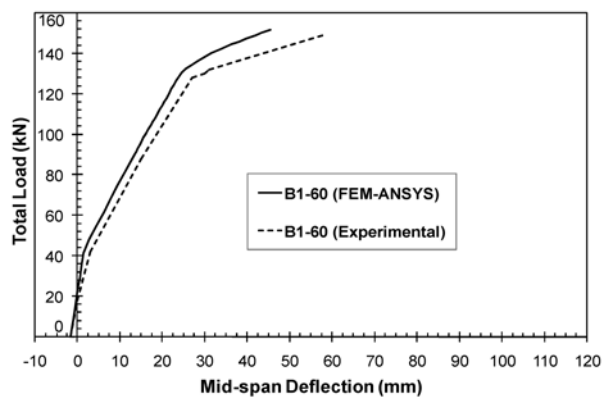
(a) Beam B1-0



(b) Beam B1-20

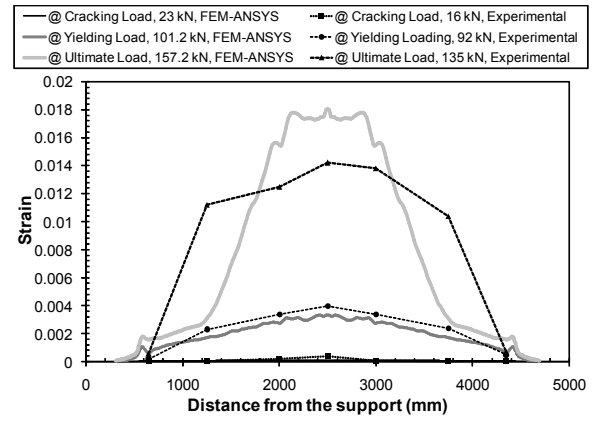


(c) Beam B1-40

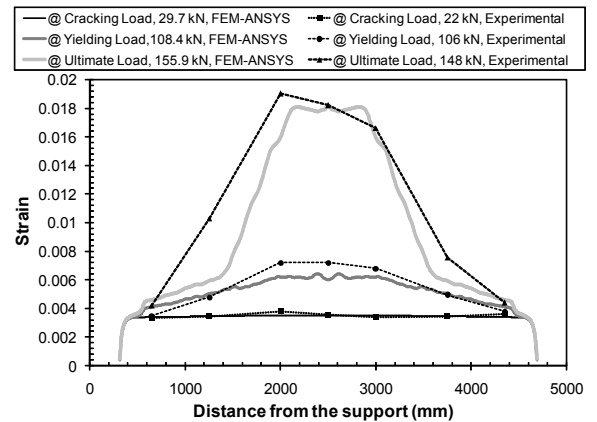


(d) Beam B1-60

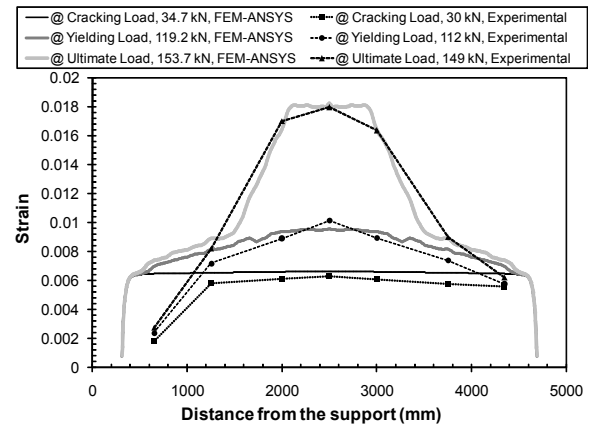
Figure 3 Comparison between experimental and numerical load-deflection curves



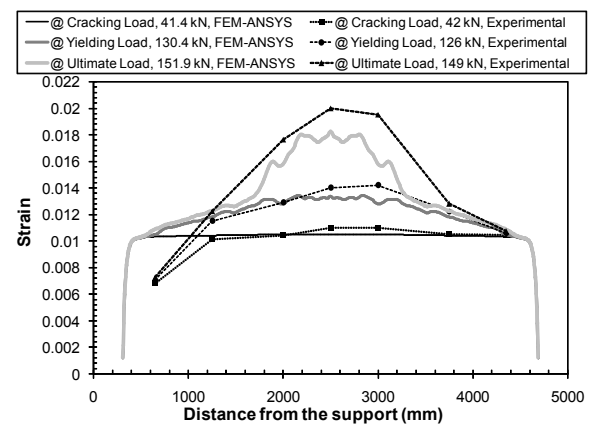
(a) Beam B1-0



(b) Beam B1-20



(c) Beam B1-40



(d) Beam B1-60

Figure 4 Strain profile along the length of the CFRP strip for all beams

Table 2 Key points of load-deflection curve of CFRP strengthened beams versus FE analysis

Beam ID#	f'_c (MPa)	Prestrain in CFRP	Results	Δ_o (mm)	P_{cr} (kN)	Δ_{cr} (mm)	P_y (kN)	Δ_y (mm)	P_u (kN)	Δ_u (mm)	μ	Type of failure
B1-0	46	0	Test	0.00	16.0	1.60	92.0	27.60	135.0	118.00	4.28	CCS
			ANSYS	0.00	23.0	1.58	101.2	25.48	157.2	103.65	4.07	FR
			Error %	0.00	43.75	1.09	10.00	7.68	16.44	12.16	4.86	—
B1-20	43	0.0034	Test	1.05	22.0	1.20	106.0	27.00	148.0	103.00	3.81	FR
			ANSYS	0.50	29.7	1.60	108.4	23.97	155.9	84.48	3.52	FR
			Error %	52.08	35.00	33.69	2.26	11.22	5.34	17.98	7.61	—
B1-40	39	0.0065	Test	1.40	30.0	1.10	112.0	26.30	149.0	77.00	2.93	FR
			ANSYS	1.00	34.7	1.57	119.2	25.13	153.7	68.07	2.71	FR
			Error %	28.50	15.75	43.01	6.43	4.46	3.15	11.59	7.46	—
B1-60	40	0.0104	Test	1.60	42.0	2.60	126.0	26.80	149.0	58.00	2.16	FR
			ANSYS	1.58	41.4	1.46	130.4	24.45	151.9	45.40	1.86	FR
			Error %	1.25	1.37	43.89	3.49	8.76	1.95	21.72	14.20	—

P_{cr} and Δ_{cr} = load and deflection at cracking

Δ_o = negative camber due to prestressing

μ = ductility index

P_y and Δ_y = load and deflection at yielding

CCS = Concrete cover spalling

P_u and Δ_u = load and deflection at ultimate

FR = CFRP rupture

Figure 4 shows a comparison between the FEM and the experimental results for the strain profile along the length of the CFRP strip for all beams at cracking, yielding and ultimate loads. At cracking and yielding loads, the predicted strain profile along the CFRP strip is in good correlation with the experimental values. For beam B1-0, at ultimate load, the strain profile from FEM is higher than the test, due to concrete cover spalling observed during the test as the CFRP did not reach its full capacity. For beam B1-20 and B2-40, the FEM strain profile at ultimate load is in a good correlation with the experimental curve. In beam B1-60, the failure was by CFRP rupture but the recorded ultimate strain of the CFRP is greater than the ultimate tensile strain of 1.8% obtained from the tension test by Gaafar (2007). Therefore, for beam B1-60, the FEM strain profile at ultimate is smaller than the experimental profile.

4 CONCLUSIONS

A 3D finite element model was proposed to estimate the behavior of RC beams strengthened in flexure with prestressed NSM CFRP strips. The model was validated with experimental results. According to this study, the following conclusions can be drawn:

(1) The proposed FE analysis procedure can be used to model the RC beams strengthened in flexure with

prestressed NSM CFRP strips. Currently, the verified FE model is used to perform a parametric study.

(2) Modeling the CFRP strip with Solid45 element that has the capability of assigning the initial stress is a reliable method to enforce the prestressing effect.

(3) The developed FE model can produce load-deflection curve and strain profile along the CFRP strip and estimate mode of failure satisfactorily.

PREFERENCES

- Gaafar, M. 2007. Strengthening of RC Beams Using Prestressed NSM FRP. MSc Thesis, *University of Calgary, Department of Civil Engineering*. Calgary, Canada.
- Kang, J.-Y., Park, Y.-H., Park, J.-S., You, Y.-J. & Jung, W.-T. 2005. Analytical Evaluation of RC Beams Strengthened with Near Surface Mounted CFRP Laminates. *The 7th International Symposium on FRP Reinforcement for Concrete Structures; Proc., Kansas City, MO, 5-9 November 2005*. USA: 779-794.
- Omran, H. Y., Zangeneh, P. & R. El-Hacha. 2009. Finite element modelling of steel-concrete composite beams strengthened with prestressed CFRP plates. *The Second International Conference of International Institute for FRP in Construction for Asia-Pacific Region; Proc., Seoul, 9-11 Dec. 2009*. South-Korea: 1-6.
- SAS. (2004). ANSYS 9 Finite Element Analysis System, SAS IP, Inc.

Advances of Finite Element Analysis for FRP Concrete Beams

Y.X. Zhang (y.zhang@adfa.edu.au) & Xiaoshan Lin

School of Engineering and Information Technology, The University of New South Wales, Australian Defence Force Academy, Canberra, ACT, 2600, Australia

ABSTRACT In this paper, the advances of finite element methods and analyses for FRP reinforced and strengthened concrete beams in last two decades are reviewed to present a state of the art of the research of numerical analysis and modelling of FRP composite concrete beams. Future research on finite element analysis of FRP composite beams is also presented.

1 INTRODUCTION

Due to the favorable material characteristics of fiber reinforced polymers (FRPs), such as high electrochemical corrosion resistance and high strength-to-weight ratio, they have increasingly been used to reinforce and strengthen new and existing damaged or deteriorated concrete infrastructures. The application of FRPs (typically glass FRPs and carbon FRPs) as internal reinforcements or external strengthening has been proved to be effective to improve the structural durability of concrete structures by numerous experimental studies and field applications. In particular, the FRP strengthening technique by bonding FRP plate to the tension regions of concrete structures is proving to be very competitive with regard to both structural performance and costs (Godat et al. 2007).

Concrete beams are very important structural components in civil engineering structures, and the investigation of the structural behavior of FRP reinforced/strengthened concrete beams has attracted lot of interests. Typically two forms of strengthening for RC beams using FRPs, i.e. flexural strengthening and shear strengthening, are often used. In flexural strengthening, a FRP laminate is externally bonded to the tension face of a concrete beam, and in shear strengthening, FRP laminates are bonded to the two sides of the beam. This review focuses only on the finite element analysis of concrete beam with flexural strengthening and with FRP as an internal reinforcement.

Debonding is one of the typical failure modes for both FRP internal reinforced and external strengthened concrete beams, and often compromise the effectiveness of the reinforcement or strengthening. For FRP reinforced concrete beams, debonding between concrete and the reinforcement rebar interface and debonding in the concrete substrate are frequently encountered during

experimental investigations. Experimental tests of FRP strengthened beams have identified a number of possible failure modes including tensile rupture of the composite laminate, debonding failure between the FRP laminate and the concrete substrate, concrete cover failure, and concrete crushing (ACI 2002). It has been demonstrated that debonding often prevents FRP-strengthened beams from attaining their ultimate flexural capacity (Brena et al. 2003, Thomsen et al. 2004). To accurately predict the ultimate load carrying capacities and capture the observed debonding failures, it is essential to understand the mechanics of the bond and failure and interfacial behavior between FRP and concrete. Thus a large number of research on finite element modeling of FRP concrete beam concentrated on the modeling of development of debonding and the interface behavior between the FRP and concrete although some papers also assumed perfect bonding between FRP and concrete.

Most of studies on FRP composite beams were carried out by experimental investigations due to the complexity of numerical modeling of concrete structures. It is well known that finite element method is one of the most versatile and powerful numerical modeling tools and have been employed successfully for nonlinear finite element analysis of RC structures including FRP composite concrete beams. In this paper, advances of finite element methods and analyses for FRP reinforced and flexibly strengthened concrete beams in the last two decades are reviewed to present a state of the art of the research of numerical analysis and modelling of FRP composite beams. Due to the limitation of the number of pages for the paper, only some typical papers published in key internal journals in English are included in this review and an exhausted list of the publication is beyond the scope of this paper. Future research on finite element analysis for FRP composite beams is also presented.

2 FINITE ELEMENT ANALYSIS OF FRP CONCRETE BEAMS

For an effective and accurate finite element analysis and modelling of FRP reinforced/strengthened concrete beams, a geometric model used to model the FRP composite beams, material models used to model the nonlinear material characteristics of concrete, concrete cracking and tension stiffening effects, and a bond-slip model to model the bedonding between FRP and concrete for the modelling of debonding failure play significant roles.

2.1 Geometric models

Various FEM-based geometric models have been proposed for finite element analysis and modeling of the behavior of FRP reinforced/strengthened RC beams, and generally they can be classified as 1-D models, 2-D models, 3-D models and layered shell models. In the layered shell models, the concrete is modeled by a series of layers and the rebar is usually treated as an smeared equivalent layer with stiffness only in the bar direction (Ebead & Marzouk 2005, Ferreira et al. 2001, Nitereka&Neale 1999, Takahashi 1997, Zhang & Zhu 2010). Perfect bonding was usually assumed in the layered finite element model. In the 1-D models, both the concrete and rebar and FRP sheet is modelled by a unified 1-D element (Faella et al. 2008). In the 2-D and 3-D models (Hoque et al. 2007), the rebar is usually modelled by one dimensional bar elements or truss element, the concrete is modeled by 2-D plane elements or 3-D solid elements, and the FRP sheet is usually modelled as plane element or shell element. To model debonding behavior, the interface between FRP and concrete is usually modelled using nonlinear spring elements.

2.2 Material models

To simulate the real response and the failure mechanisms of the FRP concrete beam, it is important to accurately model the crack propagation behavior in concrete, the bond-slip relationships between reinforcing bar and concrete, and interfacial bond behavior of FRP-concrete interface in addition to the constitutive behaviors of concrete, steel, and FRP sheets.

In most of the finite element analyses, the reinforcing steel was treated as a linear elastic-perfectly plastic material. The FRP sheets and the rebar were assumed to be linear elastic. Various nonlinear constitutive models were used to model the material characteristics of concrete. For concrete, cracking and propagation of cracks are important aspects of concrete behavior that considerably affects the overall response of concrete structures. Generally two approaches have been employed to model the concrete cracking, i.e. smeared crack approach and discrete crack approach. For a rational and accurate analysis of concrete structures, it is

often important to also include the postcracking resistance of concrete, thus an accurate tension stiffening model for FRP reinforced/strengthened concrete, such as the model developed by Nayal et al. (2006), should also be included.

2.3 Bond-slip models

For accurate numerical modelling of the debonding between FRP and concrete, an efficient mechanical characterization is required to model the FRP-to-concrete adhesive interface. Accurate and effective bond-slip models have been developed such as the bi-linear shear stresses-slip relationship (Holzenkaempfer 1994) and the accurate bond-slip models based on the predictions of a meso-scale finite element model (Lu et al. 2005).

3 FINITE ELEMENT ANALYSIS FOR FRP REINFORCED CONCRETE BEAMS

The deflections and stresses in concrete and rebars of perfectly bonded FRP reinforced concrete beams was predicted by a geometric and material nonlinear finite element analysis using a layered discretization of the laminate materials (Ferreira et al. 2001). The bond behaviour of FRP rebars with concrete was investigated by Achillides and Pilakoutas (2006) by modelling the concrete using 4-node plane square elements, FRP bars using 2-node square bar elements, and the interface between concrete and FRP bars using nonlinear spring elements. Rafi et al. (2007) analyzed some simply supported carbon FRP-reinforced concrete beams using a non-linear finite element model with the help of 2D isoparametric plane stress elements, in which the cracked concrete was considered as an orthotropic material and the crack formation was simulated as smeared cracks. The nonlinear response of concrete structures reinforced with internal and external FRPs was studied (Nour et al. 2007) by using a refined 3-D hypoelastic constitutive model for the nonlinear behavior of concrete. The reinforcing bar-concrete interaction was simulated implicitly using tension-stiffening factors modified according to the nature of reinforcement.

4 FINITE ELEMENT ANALYSIS FOR FRP STRENGTHENED CONCRETE BEAMS

4.1 FRP strengthened RC beams with perfect bonding

Hu et al. (2004) used 27-node solid elements to model the reinforced concrete beams, while FRPs were modelled by using 8-node shell elements. A fictitious crack approach was adopted by Wu and Davies (2003) to estimate the equivalent bridge effect of the fracture process zone of concrete for a beam subjected to three-point bending and externally reinforced with

unidirectional FRP plate near the bottom surface of the tensile zone. The rebar/concrete interface debonding of FRP-strengthened concrete beams with perfect bonding assumption between the concrete and FRP plate under fatigue load was investigated by Zhang and Shi (2008).

4.2 FRP strengthened RC beams with debonding

Arduini et al. (1997) examined the nonlinear behaviour and early concrete cover delamination and plate-end failure of FRP strengthened RC concrete beams using a smeared crack model for concrete. A 3-D elasto-plastic finite element analysis method was developed to simulate the load-carrying capacity of RC beams failed in the FRP sheet peel off mode (Kishi et al. 2005). The nonlinear behaviour of FRP-strengthened beams was examined using the smeared crack model for concrete, and the mixed mode of failure due to the combined shear and concrete cover delamination was addressed through modelling plate-end and shear crack discontinuities using the discrete crack approach (Pešić & Pilakoutas, 2003). Using a discrete crack model for concrete crack propagation and a bilinear bond-slip relationship with softening behavior to represent FRP-concrete interfacial behavior, Niu and Wu (2005) performed a nonlinear fracture mechanics-based finite element analysis to investigate the effects of crack spacing and interfacial parameters such as stiffness, local bond strength, and fracture energy on the initiation and propagation of the debonding. A 2-D frame finite element was presented by Barbato (2009) to estimate the load-carrying capacity of FRP strengthened RC beams. Wang and Zhang (2008) examined the debonding between the FRP plate and concrete using linear elastic Euler-Bernoulli's beam and a bilinear law for the modelling of the nonlinear bond-slip behaviour. Baky et al. (2007) used 2-D and 3-D models to simulate the FRP strengthened RC beams. In addition, Neale et al. (2006) investigated the load-deformation behaviour and debonding phenomenon of FRP strengthened concrete beams and slabs.

Great efforts have been made to model the interactive behavior between concrete and FRP. Qiao and Chen (2008) used a bilinear mode-I cohesive zone model to simulate the nonlinear cohesive fracture behavior of the FRP-concrete bonded interfaces in a three-point bending beam. Li et al. (2009) analyzed the interfacial stresses between the concrete and the FRP of RC beams strengthened with hybrid carbon fibres and glass fibres and the debonding process of the FRP sheets. Yang et al. (2004) studied the interfacial stress distribution and evaluated the effect of the structural parameters on the interfacial behavior in FRP-reinforced concrete hybrid beams. Intermediate crack debonding was simulated by a finite-element model based on the smeared crack

approach for concrete by Lu et al. (2007). Leung et al. (2006) determined the nonlinear softening behavior at FRP composite/concrete interface. In addition interfacial stresses in structural members bonded with a thin plate were predicted by Zhang and Teng (2010).

5 FRP COMPOSITE CONCRETE BEAMS UNDER ELEVATED TEMPERATURES

FRPs are susceptible to deterioration under elevated temperatures or fire conditions with mechanical and bond properties decreasing sharply at elevated temperatures. Although significant research has been conducted to investigate various aspects of the behavior of FRP RC beams, few studies on the performance of FRP concrete beams subjected to fire exposure have been reported. Among the few are the study of response of a reinforced RC beam in the entire range of loading up to collapse under fire (Kodur & Dwaikat 2008a,b), the nonlinear 3-D finite element model presented by Rafi et al. (2008) for the prediction of response and crack formation and propagation of steel and FRP reinforced concrete beams under a combined thermal and mechanical loading up to failure, the prediction of the fire behavior of FRP-strengthened RC beams by Gao et al. (2009), and the modeling of insulated CFRP-strengthened reinforced concrete T-beam exposed to fire (Hawileh et al. 2009).

6 FUTURE RESEARCH

According to the authors' investigation, very few research on the performance of the FRP concrete beams under fire condition, environmental effects, and dynamic loading have been reported so far. To better predict the structural and failure behavior of FRP concrete beams in the real environmental conditions, efforts listed below should be made in the future research.

- (1) Accurate and reliable predictions of the behavior of FRP concrete beams at high temperatures.
 - Further investigations on the material properties at elevated temperature, especially with respect to the strength and stiffness of FRP materials.
 - Interface damage behavior between FRP and concrete, such as debonding and etc.
 - More realistic material and bond models at elevated temperature.
- (2) Research on the tension stiffening stress-strain relationship for FRP reinforced/strengthened RC beams.
- (3) Long term structural performance under environmental effects, such as moisture, cycling temperature.
- (4) Structural performance under cyclic and dynamic loading.

REFERENCES

- Achillides Z. & Pilakoutas K. 2006. FE modelling of bond interaction of FRP bars to concrete. *Structural Concrete*, 7(1): 7-16.
- ACI 440.2R-02. 2002. Guide for the design and construction of externally bonded FRP systems for strengthening concrete structures. Reported by ACI Committee 440:21-22.
- Arduini, M., Di, Tommaso A, et al. 1997. Brittle failure in FRP plate and sheet bonded beams. *ACI Struct J* 94(4):363-370.
- Baky, Hussien Abdel, Ebead, Usama A., Neale, Kenneth W. 2007. Flexural and interfacial behavior of FRP-strengthened reinforced concrete beams. *Journal of Composites for Construction* 11(6): 629-639.
- Barbato, M. 2009. Efficient finite element modelling of reinforced concrete beams retrofitted with fibre reinforced polymers. *Computers and Structures* 87(3-4):167-176.
- Brena, S.F., Bramblett, R.M., et al. 2003. Increasing flexural capacity of reinforced concrete beams using carbon fibre-reinforced polymer composites. *ACI Structural Journal*, 100(1): 36-46.
- Ebead, U.A. & Marzouk, H. 2005. Tension-stiffening model for FRP-strengthened concrete two-way slabs. *Journal of Material and Structures/Materiaux et Constructions, RILEM, Paris*, 38: 193-200.
- Faella, C., Martinelli, E, Nigro, E. 2008. Formulation and validation of a theoretical model for intermediate debonding in FRP-strengthened RC beams. *Composites Part B: Engineering* 39(4):645-655.
- Ferreira, A. J. M., Camanho P. P., et al. 2001. Modelling of concrete beams reinforced with FRP re-bars. *Composite Structures* 53:107-116.
- Gao, Wanyang, Lu, Zhoudao, Hu, Kexu, 2009. Modeling the behavior of insulated FRP-strengthened reinforced concrete beams exposed to fire. *Key Engineering Materials* 400-402: 749-755.
- Godat, A., Neale K.W., Labossiere, P. 2007. Numerical modelling of FRP shear-strengthened reinforced concrete beams. *Journal of Composites for Construction, ASCE*, 11(6): 640-649.
- Hawileh, R.A., Naser, M., et al. 2009. Modeling of insulated CFRP-strengthened reinforced concrete T-beam exposed to fire. *Engineering Structures* 31(12):3072-3079.
- Holzenkaempfer. 1994. Ingenieurmodelle des verbundes geklebter bewehrung fur betonbauteile. Dissertation, TU Braunschweig [in German].
- Hoque, M., Rattanawangcharoen, N., et al. 2007. 3D nonlinear mixed finite-element analysis of RC beams and plates with and without FRP reinforcement. *Computers and Concrete* 4(2):135-156.
- Hu, Hsuan-The, Lin, Fu-Ming, Jan, Yih-Yuan, 2004. Nonlinear finite element analysis of reinforced concrete beams strengthened by fibre-reinforced plastics. *Composite Structures* 63: 271-281.
- Kishi, Norimitsu, Zhang, Guangfeng, Mikami, Hiroshi, 2005. Numerical cracking and debonding analysis of RC beams reinforced with FRP sheet. *Journal of Composites for Construction* 9(6):507-514.
- Kodur, V. K. R., Dwaikat, M. 2008a. A numerical model for predicting the fire resistance of reinforced concrete beams. *Cement & Concrete Composites* 30:431-443.
- Kodur, V. K. R., Dwaikat, M. 2008b. Flexural response of reinforced concrete beams exposed to fire. *Structural Concrete* 9(1):45-54.
- Leung, Christopher K.Y., Klenke, Marcus, et al. 2006. Determination of nonlinear softening behavior at FRP composite/concrete interface. *Journal of Engineering Mechanics* 132(5):498-508.
- Li, Li-juan, Guo, Yong-chang, et al. 2009. Interfacial stress analysis of RC beams strengthened with hybrid CFS and GFS. *Construction and Building Materials* 23(6):2394-2401.
- Lu, X.Z., Teng, J.G., Ye, L.P., Jiang, J.J. 2005. Bond-slip models for FRP sheets/ plates bonded to concrete. *Eng Struct* 27(6):920-937.
- Lu, X.Z., Teng, J.G., Ye, L.P., Jiang, J.J. 2007. Intermediate crack debonding in FRP-strengthened RC beams: FE analysis and strength model. *Journal of Composites for Construction* 11(2):161-174.
- Nayal, Rim, Rasheed, Hayder A. 2006. Tension stiffening model for concrete beams reinforced with steel and FRP bars. *Journal of Materials in Civil Engineering* 18(6):831-841.
- Neale, K.W., Ebead, U.A., et al. 2006. Analysis of the load-deformation behavior and debonding for FRP-strengthened concrete structures. *Advances in Structural Engineering* 9(6):751-763.
- Nitereka, C. & Neale, K.W. 1999. Analysis of reinforced concrete beams strengthened in flexure with composite laminates. *Canadian Journal of Civil Engineering* 26: 646–654.
- Niu, Hedong, Wu, Zhishen, 2005. Numerical analysis of debonding mechanisms in FRP-strengthened RC beams. *Computer-Aided Civil and Infrastructure Engineering* 20(5):354-368.
- Nour, Ali, Massicotte, Bruno, et al. 2007. Finite element modeling of concrete structures reinforced with internal and external fibre-reinforced polymers. *Canadian Journal of Civil Engineering* 34(3):340-354.
- Pešić, Ninoslav; Pilakoutas, Kypros, 2003. Concrete beams with externally bonded flexural FRP-reinforcement: Analytical investigation of debonding failure. *Composites Part B: Engineering* 34(4):327-338.
- Qiao, Pizhong, Chen, Ying, 2008. Cohesive fracture simulation and failure modes of FRP-concrete bonded interfaces. *Theoretical and Applied Fracture Mechanics* 49(2):213-225.
- Rafi, Muhammad Masood, Nadjai, Ali, Ali, Faris. 2007. Analytical modeling of concrete beams reinforced with carbon FRP bars. *Journal of Composite Materials* 41(22): 2675-2690.
- Rafi, Muhammad Masood, Nadjai, Ali, Ali, Faris. 2008. Finite element modeling of carbon fiber-reinforced polymer reinforced concrete beams under elevated temperatures. *ACI Structural Journal* 105(6):701-710.

- Takahashi, Y., Sato, Y., et al. 1997. Flexural behaviour of RC beams with externally bonded carbon fibre sheet. *Non-Metallic (FRP) Reinforcement for Concrete Structures*, Japan Concrete Institute, 1: 327–334.
- Thomsen, H., Spacone, E., et al. 2004. Failure mode analyses of reinforced concrete beams strengthened in flexure with externally bonded fibre-reinforced polymers. *Journal of Composites for Construction, ASCE*, 8(2):123–131.
- Wang, Jialai, Zhang, Chao, 2008. Nonlinear fracture mechanics of flexural-shear crack induced debonding of FRP strengthened concrete beams. *International Journal of Solids and Structures* 45:2916-2936.
- Wu, Z.J., Davies, J. M. 2003. Mechanical analysis of a cracked beam reinforced with an external FRP plate. *Composite Structures* 62(2):139-143.
- Yang, Q.S., Peng, X.R., Kwan, A.K.H. 2004. Finite element analysis of interfacial stresses in FRP-RC hybrid beams. *Mechanics Research Communications* 31(3):331-340.
- Zhang, L., Teng, J.G. 2010. Finite element prediction of interfacial stresses in structural members bonded with a thin plate. *Engineering Structures* 32(2): 459-471.
- Zhang, Rong, Shi, Zhifei, 2008. Numerical simulation of rebar/concrete interface debonding of FRP strengthened RC beams under fatigue load. *Materials and Structures/Materiaux et Constructions* 41(10):1613-1621.
- Zhang, Y.X., Zhu, Y. 2010. A new shear-flexible FRP-reinforced concrete slab element. *Composite Structures*, 92(3): 730-735.

Nonlinear Finite Element Analysis of Composite Steel/FRP-Reinforced Concrete Beams Using a New Beam Element

Xiaoshan Lin & Y.X. Zhang (y.zhang@adfa.edu.au)

School of Engineering and Information Technology, The University of New South Wales, Australian Defence Force Academy, Canberra, ACT, 2600, Australia

ABSTRACT In this paper, a simple and computation effective one-dimensional two-node beam element is developed based on the Timoshenko's beam functions and layered approach for nonlinear finite element analysis of structural behaviour of composite steel/FRP-reinforced concrete beams. Both geometric nonlinearity and material nonlinearity are accounted for in the nonlinear finite element model, and Timoshenko's composite beam functions are employed to represent the transverse displacement and rotation of the element. The agreement of the computed results for steel and FRP reinforced concrete beams with those obtained from experimental study and other numerical analysis demonstrate the efficiency and accuracy of the proposed element model.

1 INTRODUCTION

The use of fibre reinforced polymer (FRP) as internal reinforcing bars in concrete structures has become widespread in recent years. As a substitute of the traditional steel reinforcement, FRPs have many advantages, such as high strength-to-weight ratio, high electrochemical corrosion resistance and low thermal expansivity. FRP possesses different mechanical properties from steel bars, including elastic brittle behaviour and low elastic modulus. Hence, the investigation of structure performance of composite FRP-reinforced concrete members has become a critical issue.

During the past decades, a lot of experimental studies and theoretical analysis on the structural performance of composite FRP reinforced concrete beams have been conducted by many researchers. However, very few finite element models and analyses have been developed for accurate analysis of nonlinear structural behavior of FRP reinforced concrete beams. A two-dimensional layered degenerated shell element was developed and used to analyze deflections and stresses of FRP reinforced beams and shell structures with perfect bonding assumption by Ferreira et al. (2001). The reinforcing bars were implemented as an equivalent layer in the degenerated shell element with strength and stiffness characteristics in the bar direction only. Achillides and Pilakoutas (2006) analyzed the bond behaviour between FRP rebars and concrete by modelling the concrete using 4-node plane square elements, modelling the FRP bars using 2-node square bar elements, and modelling the interface between concrete and FRP bars using nonlinear spring elements with the

bond-slip curve of the springs. Rafi et al. (2007) analyzed some simply supported carbon FRP-reinforced concrete beams using a non-linear finite element model with the help of 2D isoparametric plane stress elements. They also developed nonlinear three-dimensional finite element model (Rafi et al. 2008) for the prediction of response and crack formation and propagation of steel and FRP reinforced concrete beams under a combined thermal and mechanical loading. In their 3-D model, 20-noded isoparametric three-dimensional solid brick elements with three translational degrees of freedom at each node were selected for FE discretization of concrete, and uniaxial bar elements were used to model reinforcing bars. Perfect bar-concrete bond was assumed and only tensile reinforcing bars were included in the model. Nour et al. (2007) used a refined 3-D hypoelastic constitutive model to study the nonlinear response of concrete structures reinforced with internal and external FRPs.

Most of the finite elements developed and used for finite element analysis and modelling of FRP reinforced concrete beams are 2-D models, 3-D models and layered shell elements. In 2-D and 3-D models, the concrete and the reinforcing bar have to be discretized individually using different elements, usually with 2-D or 3-D model modelling concrete and 1-D bar or truss element modelling the rebar, and these make the model and analysis not computation and cost effective.

In this paper, a 1-D two-node beam element is developed to predict load-deflection relationship of concrete beams reinforced with FRP and steel bars. The element is developed based on the Timoshenko's beam

functions (Zhang et al. 2007, Zhang & Zhu 2010), and a layered approach is used to model accurately the nonlinear behaviour of the concrete beams. Geometric nonlinearity caused by low elastic modulus of FRP is included in the new element. Due to the limitation of the page, the cracking progress will not be presented in this paper.

2 2-NODE COMPOSITE BEAM ELEMENT

The proposed two-node composite beam element and the cross section of composite beam element consisting of n concrete layers and smeared equivalent layers for the reinforcing bars are shown in Figure 1. There are only two degrees of freedom at each node, thus the element is very simple and computation effective.

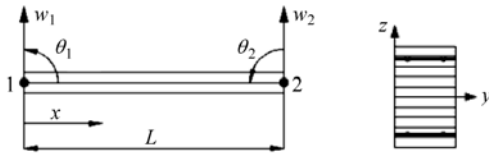


Figure 1 A two-node composite beam element and its cross section

2.1 Timoshenko's composite beam functions

Locking-free Timoshenko's composite beam functions (Zhang et al. 2007, Zhang & Zhu 2010) are utilized to represent the displacement and rotation in the proposed element. The formulas of deflection w and rotation θ for the composite beam element with length L , width b and height h are given as

$$w = (L_1 + \mu_e L_1 L_2 (L_1 - L_2)) w_1 + (L_1 L_2 + \mu_e L_1 L_2 (L_1 - L_2)) L / 2 \theta_1 + (L_2 + \mu_e L_1 L_2 (L_2 - L_1)) w_2 + (-L_1 L_2 + \mu_e L_1 L_2 (L_1 - L_2)) L / 2 \theta_2 \quad (1)$$

$$\theta = -\left(\frac{6L_1 L_2}{L}\right) \mu_e w_1 + L_1 (1 - 3\mu_e L_2) \theta_1 + \left(\frac{6L_1 L_2}{L}\right) \mu_e w_2 + L_2 (1 - 3\mu_e L_1) \theta_2 \quad (2)$$

where

$$L_1 = 1 - \frac{x}{L}, \quad L_2 = \frac{x}{L}, \quad \mu_e = \frac{1}{1 + 12\lambda_e}, \quad \lambda_e = \frac{Q_b}{Q_s L^2} \quad (3)$$

in which x is the coordinator along the beam, Q_b and Q_s are bending elastic constant and shear elastic constant respectively.

Assuming that the in-plane forces are zero and the in-plane displacements (u_0 v_0) in the mid-plane are zero, the displacement field takes the form of

$$u(x, z) = -z\theta(x) \quad (4)$$

$$w(x, z) = w_0(x) \quad (5)$$

Strain-displacement relationships are

$$\varepsilon_x = \frac{\partial u}{\partial x} = -z \frac{d\theta}{dx} \quad (6)$$

$$\gamma = \frac{\partial u}{\partial z} + \frac{\partial w}{\partial x} = \frac{\partial w}{\partial x} - \theta \quad (7)$$

where ε_x is axial strain, γ is shear strain, and $d\theta/dx$ is the slope of the neutral axis.

2.2 Strain and strain matrix

The element nodal displacement vector can be expressed as:

$$\{q^{(e)}\} = \begin{Bmatrix} q_1 \\ q_2 \end{Bmatrix} \quad \text{with} \quad \{q_i\} = \begin{Bmatrix} w_i \\ \theta_i \end{Bmatrix} \quad (i=1,2) \quad (8)$$

Hence, the element bending strain vector at neutral axis and shear strain vector are

$$\{\varepsilon_b\} = -\frac{d\theta}{dx} = [B_b] \{q^{(e)}\} \quad (9)$$

$$\{\gamma\} = [B_s] \{q^{(e)}\} \quad (10)$$

in which

$$[B_b] = \begin{bmatrix} \frac{6\mu_e}{L} \left(\frac{1}{L} - \frac{2x}{L^2} \right) \frac{3\mu_e + 1}{L} - 6\mu_e \frac{x}{L^2} \\ -\frac{6\mu_e}{L} \left(\frac{1}{L} - \frac{2x}{L^2} \right) - \frac{1 - 3\mu_e}{L} - 6\mu_e \frac{x}{L^2} \end{bmatrix} \quad (11)$$

$$[B_s] = \begin{bmatrix} -\frac{1}{L} + \frac{\mu_e}{L} & \frac{\mu_e}{2} - \frac{1}{2} & \frac{1}{L} - \frac{\mu_e}{L} & -\frac{1}{2} + \frac{\mu_e}{2} \end{bmatrix} \quad (12)$$

where $[B_b]$ is the curvature-displacement matrix, and $[B_s]$ is the shear strain-displacement matrix.

2.3 Material property

Material properties of the whole section of the element are

$$D_{bb} = b \sum_{i=1}^c E_{ci} t_{ci} Y_i^2 + b \sum_{j=1}^s E_{sj} t_{sj} Y_j^2 \quad (13)$$

$$D_{ss} = \kappa b \sum_{i=1}^c G_{ci} (z_{i+1} - z_i) \quad (14)$$

where

D_{bb} and D_{ss} : bending stiffness and transverse shear stiffness

b : breadth of beam element

c : number of concrete layers

s : number of the smeared reinforcing layers

κ : constant of the non-uniformity of the shearing stress, which is generally set to be 5/6

E_{ci} and E_{sj} : bending elastic modulus of the i^{th} concrete layer and the j^{th} reinforcement layer

G_{ci} : shear modulus of the i^{th} concrete layer

z_{i+1} and z_i : coordinates of the upper and lower surfaces of the i^{th} concrete layer in z direction

t_{ci} and t_{sj} : thickness of the i^{th} concrete layer and the j^{th}

reinforcement layer

Y_i and Y_j : distances from the centroid of the i^{th} concrete layer and j^{th} reinforcement layer to the neutral axis

2.3.1 Concrete model

The stress-strain curve of concrete under uniaxial compression shown in Figure 2(a) (Nitereka & Neale 1999) is used in the present model.

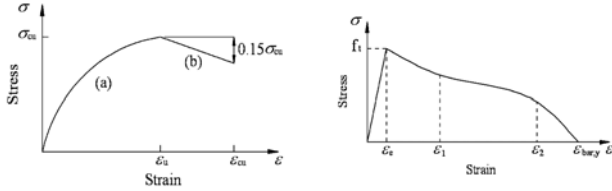


Figure 2 Stress-strain relationship of concrete in (a) compression and (b) tension

In the tension area, concrete is assumed to be isotropic and linear elastic before cracking. Once the maximum principal strain at Gauss points reaches the concrete ultimate tensile strain, crack occurs. After cracking, concrete becomes orthotropic. With regard to the tension stiffening effect between concrete and reinforcement after cracking, the constitutive relation curve of concrete is adopted as Figure 2 (b) (Nour et al. 2007).

2.3.2 Steel and FRP model

The reinforcing steel bars are modelled to be elastic-perfectly plastic in both tension and compression. FRPs are assumed to be linearly elastic until the tension stress reaches the material ultimate strength. After that, the stress within FRP reduces to zero immediately.

3 NONLINEAR FINITE ELEMENT FORMULATION

The nonlinear finite element analysis is carried out based on the Total Lagrangian approach. The strain vector due to large deflection of Timoshenko’s beam is

$$\{\varepsilon\} = \begin{Bmatrix} -z \frac{d\theta}{dx} \\ \frac{dw}{dx} - \theta \\ 0 \end{Bmatrix} + \begin{Bmatrix} \frac{1}{2} \left(\frac{dw}{dx} \right)^2 \\ 0 \end{Bmatrix} = \{\varepsilon_0\} + \{\varepsilon_i\} \quad (15)$$

where $\{\varepsilon_0\}$ and $\{\varepsilon_i\}$ are linear and nonlinear strain vectors respectively.

$$\{\varepsilon_i\} = \frac{1}{2} \left(\frac{dw}{dx} \right)^2 = \frac{1}{2} [C] \{q^{(e)}\} \bullet [C] \{q^{(e)}\} \quad (16)$$

$$[C] = \begin{bmatrix} -\frac{1}{L} + \mu_e \left(\frac{1}{L} - \frac{6x}{L^2} + \frac{6x^2}{L^3} \right) & \left(\left(\frac{1}{L} - \frac{2x}{L^2} \right) + \mu_e \left(\frac{1}{L} - \frac{6x}{L^2} + \frac{6x^2}{L^3} \right) \right) \frac{L}{2} \\ \frac{1}{L} + \mu_e \left(\frac{6x}{L^2} - \frac{1}{L} - \frac{6x^2}{L^3} \right) & \left(\left(\frac{2x}{L^2} - \frac{1}{L} \right) + \mu_e \left(\frac{1}{L} - \frac{6x}{L^2} + \frac{6x^2}{L^3} \right) \right) \frac{L}{2} \end{bmatrix}$$

hence

$$\delta\{\varepsilon\} = \delta(\{\varepsilon_0\} + \{\varepsilon_i\}) = ([B_0] + [B_i]) \delta\{q^{(e)}\} \quad (17)$$

in which $[B_0]$ is linear part of strain matrix, and $[B_i]$ is nonlinear part of strain matrix.

The unbalance force $\{\psi\}$ of the beam element can be expressed as

$$\{\psi\} = \int ([B_0] + [B_i])^T \{\sigma\} dx - \{R\} \quad (18)$$

where $\{R\}$ is the element equivalent nodal loadings, $\{\sigma\}$ is the inner stress matrix of the element. The tangential stiffness matrix of the element $[K_T]$ is

$$[K_T] = [K_0] + [K_i] + [K_\sigma] \quad (19)$$

where $[K_0]$ is the linear stiffness matrix, $[K_i]$ is large displacement matrix and $[K_\sigma]$ is the initial stress matrix, which are determined by the following equations:

$$[K_0] = \int [B_0]^T [D_i] [B_0] dx \quad (20)$$

$$[K_i] = \int ([B_0]^T [D_i] [B_i] + [B_i]^T [D_i] [B_0] + [B_i]^T [D_i] [B_i]) dx \quad (21)$$

$$[K_\sigma] = \int [C]^T N_x [C] dx \quad (22)$$

in which N_x is axial force of beam element, and $[D_i]$ is tangential modulus matrix.

$$[D_i] = \begin{bmatrix} b \sum_{i=1}^c E_{ct} t_{ct} + b \sum_{j=1}^s E_{st} t_{st} & b \sum_{i=1}^c E_{ct} t_{ct} Y_i + b \sum_{j=1}^s E_{st} t_{st} Y_j & 0 \\ b \sum_{i=1}^c E_{ct} t_{ct} Y_i + b \sum_{j=1}^s E_{st} t_{st} Y_j & D_{bb} & 0 \\ 0 & 0 & D_{ss} \end{bmatrix} \quad (23)$$

4 NUMERICAL EXAMPLES

The validation of the proposed model is examined by studying of two concrete beams which were reinforced with steel and FRP bars respectively.

4.1 A steel reinforced concrete beam

A steel reinforced concrete beam under three-point bending with overall length 1800mm tested by Karihaloo (1990) is computed firstly. The beam was 100mm wide and 150 mm high with a steel ratio of 0.75%. The compressive strength of concrete was 38MPa, and Young’s modulus was 30GPa. The total applied load versus mid-span deflection relationship is computed using the proposed 2-node model and the computed results are compared with those obtained from Ashour’s model and ABAQUS analysis (Ashour & Morley 1993) in Figure 3. It can be seen that the load-deflection curve obtained from the present model is in excellent agreement with that obtained from the Ashour’s model. As for the failure load of the beam, the result from the experimental investigation was 24.25 kN, 14.16 kN and 15.68 kN from

ABAQUS analysis and Ashour's model respectively, and 21.9 kN from the current model, which is much more closer to the test result.

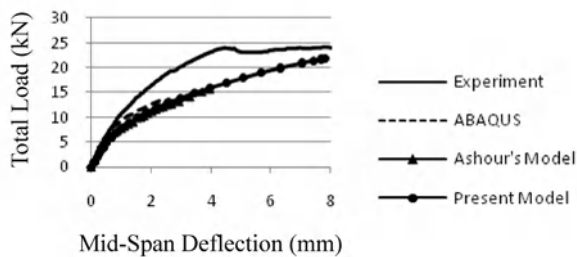


Figure 3 Load versus mid-span deflection of Beam 1

4.2 A FRP reinforced concrete beam

A FRP reinforced concrete beam tested by Barris et al. (2009) under four-point bending with 600mm shear span is computed by the present model. The beam has a total length of 2050mm, with a clear span 1800mm, a width of 40mm and a depth of 190mm. Two GFRP rebars with diameter of 16mm were used as longitudinal reinforcement in the bottom of the cross section. Ratios of reinforcement and effective depth-to-height were 1.78% and 0.85% respectively. Young's modulus and rupture tensile strength of GFRP were 64.152GPa and 995MPa. The compressive strength of concrete was 56.3MPa, and the modulus of elasticity was 26524MPa. The comparison of load-deflection relationship obtained from the proposed model, the experimental study and Eurocode 2 (Barris et al. 2009) are shown in Figure 4. It can be seen that the load-deflection curve obtained from the present model agrees well with the experimental data and the prediction given by Eurocode 2.

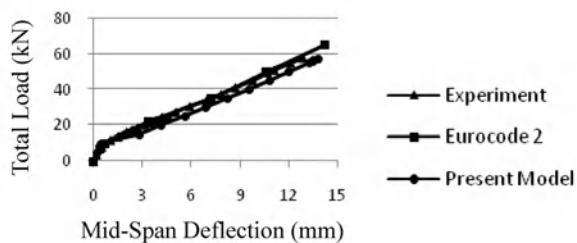


Figure 4 Load versus mid-span deflection of Beam 2

5 CONCLUSION

A 1-D two-node beam element is developed to investigate the flexural behaviour of concrete beams reinforced with FRP and/or steel bars in this paper. The proposed 1-D beam element is much simpler than 2-D and 3-D finite elements, which can save computation time and computational resources remarkably. Instead of being modelled separately, concrete and reinforcement are

modelled in one unified element in the new model by using layered approach, which simplifies modelling of structures. Analyses of concrete beams reinforced with FRP and steel bars, including material and geometric nonlinearities, were performed. The coincidence of the computed results from the proposed model with those obtained from other finite element model, experiments and ABAQUS analysis demonstrate the efficiency and accuracy of the model.

REFERENCES

- Achillides Z. & Pilakoutas K. 2006. FE modelling of bond interaction of FRP bars to concrete. *Structural Concrete*, 7(1): 7-16.
- Ashour, A.F. & Morley, C.T. 1993. Three-dimensional nonlinear finite element modelling of reinforced concrete structures. *Finite Elements in Analysis and Design* 15: 43-55.
- Barris, C., Torres, Ll., Turon, A., Baena, M. & Catalan, A. 2009. An experimental study of the flexural behaviour of GFRP RC beams and comparison with prediction models. *Composite Structures* 91: 286-295.
- Bischoff, Peter H. & Paixao, Richard 2004. Tension stiffening and cracking of concrete reinforced with glass fibre reinforced polymer (GFRP) bars. *Canadian Journal of Civil Engineering* 31: 579-588.
- Coronado, Carlos A. & Lopez, Maria M. 2006. Sensitivity analysis of reinforced concrete beams strengthened with FRP laminates. *Cement & Concrete Composites* 28: 102-114.
- Ferreira, A.J.M., Camanho, P.P., Marques, A.T. & Fernandes, A.A. 2001. Modelling of concrete beams reinforced with FRP re-bars. *Composite Structures* 53: 107-116.
- Karihaloo, B.L. 1990. Failure modes of longitudinally reinforced beams. *Int. Workshop on the Application of Fracture Mechanics to Reinforced Concrete*, Italy: 523-546.
- Nitereka, C. & Neale, K.W. 1999. Analysis of reinforced concrete beams strengthened in flexure with composite laminates. *Canadian Journal of Civil Engineering* 26: 646-654.
- Nour, Ali, Massicotte, Bruno, Yildiz, Emre & Koval, Viacheslav 2007. Finite element modeling of concrete structures reinforced with internal and external fibre-reinforced polymers. *Canadian Journal of Civil Engineering* 34: 340-354.
- Rafı, Muhammad Masood, Nadjai, Ali & Ali, Faris. 2007. Analytical modeling of concrete beams reinforced with carbon FRP bars. *Journal of Composite Materials* 41(22): 2675-2690.
- Rafı, Muhammad Masood, Nadjai, Ali & Ali, Faris. 2008. Finite element modeling of carbon fiber-reinforced polymer reinforced concrete beams under elevated temperatures. *ACI Structural Journal* 105(6):701-710.
- Zhang, Y.X., Bradford, M.A. & Gilbert, R.I. 2007. A layered shear-flexural plate/shell element using Timoshenko beam functions for nonlinear analysis of reinforced concrete plates. *Finite Elements in Analysis and Design* 43 (11): 888-900.
- Zhang, Y.X. & Zhu, Y. 2010. A new shear-flexible FRP-reinforced concrete slab element. *Composite Structures* 92 (3): 730-735.

Non-Bolted Anchorage Systems for CFRP Laminates Applied for Strengthening of RC Slabs

Ted Donchev (t.donchev@kingston.ac.uk) & Parviz Nabi

Department of Civil Engineering, Kingston University, London, UK

ABSTRACT The anchorage of carbon fibre reinforced polymer (CFRP) laminates used for improving bending capacity of RC slabs is one of the governing factors for their effectiveness. Many investigations are indicating that one of the main modes of failure for CFRP strengthened slabs and decks is via failure of the anchorage of the laminates. Existing systems for improving the anchorage via attaching steel bolts are effective but expensive and time consuming.

The proposed work is investigating the opportunity to use non-bolted anchorage systems which could achieve faster, easier and less expensive improvement of the anchorage in comparison with bolted anchorage systems. The attempt for developing new anchoring systems is based on the idea for redistribution of the stresses in the laminates and the adjacent concrete at the zone of the anchorage.

Four types of anchorage systems for CFRP laminates are used. The laminates are applied on reduced scale RC plinths loaded on bending and reflecting unidirectional strengthening of RC slabs. The results indicate opportunity to increase the anchoring capacity of the laminates using similar materials as for initial strengthening. Analysis of the experimental results and comparison with corresponding approaches suggested from other authors is offered.

1 BACKGROUND

Applying steel bolts is the classical approach for increasing anchoring capacity of CFRP laminates, used for strengthening of RC beams and slabs. Preferably they are designed to be chemically anchored and with sufficient length allowing the inner end of the bolt to reach beyond the layer of tensile reinforcement. As indicated from many authors (Hollway & Leeming, 1999, TR55, 2004) such approach leads to an increase in the strengthening capacity by about 25%. However the applicability of such type of bolted anchorage has been questioned by many construction companies and manufacturers of CFRP laminates. The doubts about the effectiveness of steel bolts anchoring are mainly due to a dramatic increase in the installation works which reduce the benefit of quick and easy installation of the laminates and increase both the time for full installation and the cost. Steel bolts in case of using traditional non-stainless steel are corroding, thus reducing the effect of lack of corrosion for laminates. In addition to the above, the effect of drilling through laminates after installation is decreasing locally the capacity of the laminates and could compromise the connection between laminate and concrete at the anchoring zone.

Having in mind the above problems an assumption could be made that there is a place for further improvement of the additional anchorage systems for CFRP laminates applied to reinforced concrete structural elements

loaded on bending. The aim of this research is to continue developing anchoring systems with minimized negative effects. Wide range of solutions has been considered.

The problem with corrosion of the bolts and opportunity for better connection between the bolts and the laminates could be solved by using of CFRP spike anchors. The latest development of the research with such type of additional anchorage is improving significantly the anchorage of CFRP strengthening system and is allowing wider application according to Kim and Smith (Kim & Smith, 2009).

Using similar type of materials and avoiding corrosion problems are obvious achievements of the proposed approach for improving the anchorage of laminates used for strengthening of RC beams via attaching FRP shear strips at the end of the laminates. The extensive research in this area (Khan & Naseem, 2008, Takashi, 2008) is producing promising results for future development and applications. A very interesting result for improved anchorage of CFRP strengthened beams is presented by Leung (Leung, 2006) and his opinion that the application of the additional anchorage on some distance from the edge of the laminates is in agreement with some results from this research.

Using self induced contact pressure is alternative approach which is a possible way for reducing the risk for delamination at the ends of externally bonded CFRP

laminates (Husemann & Budelmann, 2007). Some of the theoretical basis of this research is corresponding to the investigation employed in this paper.

Looking for reinforcing and improving mechanical properties of the concrete at the zones of anchoring of the laminates is other possible route for further improvement. Previous work in Kingston University (Donchev & Sifas, 2009) is an attempt for development in this direction.

The presented research is aiming at developing improved anchoring system based on attaching additional plates of CFRP laminates at the anchoring zone of main external reinforcement. It is expected to redistribute the stresses and to reduce their concentration at the end of the laminates. One of the benefits of this approach would be to use the same materials and technology as for initial installation of the laminates which would be less time consuming and less disruptive for the whole process of installation.

2 EXPERIMENTAL SET-UP

2.1 Preparing the RC samples

The aim of this experimental work is to model the behavior of slabs strengthened in one direction with CFRP laminates. The distance between the laminates is assumed as 300 mm. From this point of view the model of corresponding strip of the slab is accepted to be with 300 mm width and strengthened with single laminate at the middle. The test samples are six RC plinths with dimensions 150×300×1200 mm. Steel reinforcement is the same for all samples and consists of 4 longitudinal bars high yield steel 10 mm diameter and stirrups to keep longitudinal bars in position made of mild steel 6 mm diameter at 200 mm c/c. The concrete is designed with cubic strength 30 MPa and the strength is controlled via testing of 6 cubes 150×150×150 mm for each mix on 28th day. The mixing procedure is in accordance with BS188-125:1986. Both lintels and cubes are cured in curing room with controlled humidity of the air of 95% and temperature of 18°C for 28 days.

2.2 Strengthening of the plinths with CFRP laminates

After curing the samples are left for at least one week in room conditions to dry before applying the laminates to their surface and left another week after the application of the laminates to allow complete curing of the adhesive. The attached CFRP laminates are supplied by SBD Weber and are 50 mm wide and 1.2 mm thick. The length of the main longitudinal laminate is 800 mm and it is the same for all strengthened samples. The laminates are installed using structural adhesive EpoxyPlus supplied from SBD Weber. The application of the adhesive is according manufacturer's recommendations.

In total five samples with CFRP strengthening has been prepared. Two of them are control beams (B1 and

B2) with one longitudinal laminate attached, not having any additional anchorage at the end of the laminate. All other samples are using pieces of the same type of laminate (300 mm×50 mm×1.2 mm) attached at the end of the original laminate in means of improving the anchorage. The third one (B3) is with two additional pieces of laminates attached at each end of the laminate both of them oriented longitudinally and placed immediately next to the original laminate as indicated on Figure 1. The fourth sample (B4) is having additional anchorage in form of single strip of laminate attached at each end of the original laminate in transverse direction over the edge of the original laminate. The fifth sample (B5) is similar to the fourth one, but having two transverse pieces of laminate on each placed on 70 mm c/c.

The aim of various positioning of additional pieces of laminates is to allow for better distribution of the stresses at the end of the original laminate.

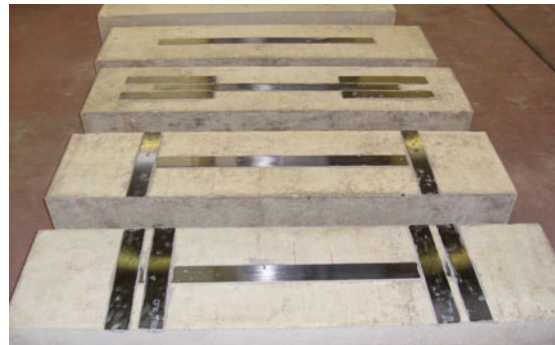


Figure 1 Plinths with additional anchorage. From top to bottom: B1(control beam), B3, B4 and B5

2.3 Loading and measuring equipment

Measuring equipment includes measuring of the deflection in the middle of the span and at both supports via dial gauges with precision 0.01 mm, the distribution of the strains at midspan via five Demec gauges with bases on 25 mm distance from each other and 150 mm length of the base and unidirectional electro-resistant strain gauges attached to the laminate at midspan and close to the ends of the laminates in longitudinal direction.

The loading scheme is representing loaded on bending simply supported beam. It includes roller supports on 1000 mm distance c/c and two symmetrically placed equal vertical forces on 200 mm from each other at midspan (Figure 2). The force is increased by increments of 5 kN allowing more than ten levels of loading for each of the beams. On each level of loading the load was held for 10 minutes before taking the readings.

3 EXPERIMENTAL RESULTS

3.1 Testing of the samples

The unstrengthened control sample is loaded till failure which in this case is by exceeding flexural capacity of

the plinth and failure after intensive cracking and yielding of the reinforcement. The ultimate capacity of this plinth is 55 kN.

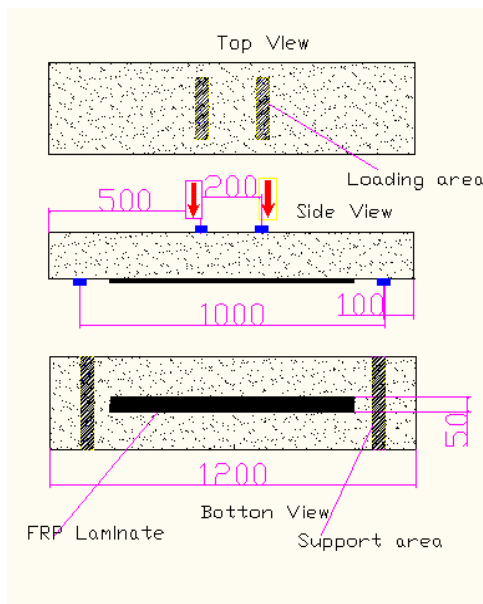


Figure 2 Testing equipment

Plinths B1 and B2 are strengthened with CFRP laminates, for both of them additional anchorage has not been applied. After exceeding the load of 65 kN for one of them and 70 kN for the other the beams were destructed. Failure mode is by delamination of the laminate at the end and progressing fast to midspan. The delamination is due to crack development beneath the surface of the concrete with a thin layer of concrete attached to the laminate.

Plinth B3 is with additional anchorage as longitudinally applied laminates very close to the laminate of the original strengthening, placed at both ends. The failure mode of this sample is via delamination of the end of the laminate with thin layer of concrete. The laminates at both ends of the original laminate remained attached to the concrete. Despite that they were separated from the original laminate due to the improved behavior and increased ultimate load is reasonable to assume that they contribute up to certain degree for improving of the anchorage. The ultimate load is 75 kN.

Plinth B4 is with additional anchorage as CFRP laminate attached in transverse direction at the end of the longitudinal laminate. The failure mode is by delamination as initial laminate and additionally attached one delaminated simultaneously (Figure 3).

The ultimate load in this case is 65 kN and this type of additional anchoring is not sufficiently effective. A possible reason for the low effectiveness could be the fact that the attached piece of laminate is at the edge of the original longitudinal CFRP laminate.

Plinth B5 is with additional anchorage employing two

pieces of laminate in transverse direction at each end. It appears that this way of improving the anchorage is most effective. The failure mode is similar to the previous case – simultaneous delamination. In this case the ultimate load is significantly higher (85 kN) and result is improving the anchorage with more than 20 %. Probable reason for higher effectiveness of B5 in comparison with B4 is the distribution of the delaminating stresses on better way and on wider area.



Figure 3 Delamination of the additional anchorage for B4

3.2 Comparison between different samples

As is indicated on Figure 5 most of the samples have slightly increased ultimate capacity. Most dramatic effect is observed for sample B5 which indicates the opportunity for sufficiently effective development of additional anchorage based on using the same type of CFRP laminates and structural adhesive as for the main strengthening system.

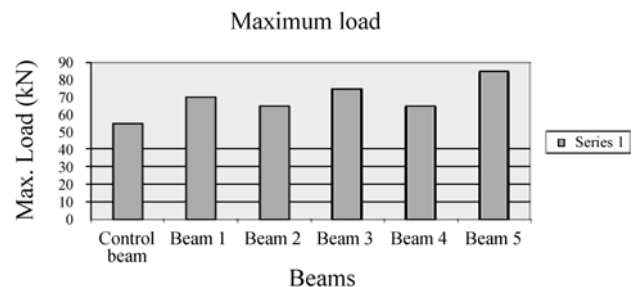


Figure 4 Comparison between the samples

Further research is planned to develop more effective application of this approach and more practical and detailed methodology.

4 CONCLUSIONS

- Application of additional laminates at the edges of laminates used for original strengthening as for B2, B3 and B5 could be used as additional anchorage.
- Application of one laminate in transverse direction (B4) overlapping existing longitudinal laminate is

less effective than positioning of two laminates in longitudinal direction (B3).

- Applying two laminates in transverse direction (B5) is found to be the most effective technique among the investigated approaches.
- The observed increase of the capacity of the beam when applying additional anchorage via two transverse laminates (B5) is more than 20%.

5 ACKNOWLEDGEMENTS

The authors would like to express their gratitude to SBD Weber for sponsoring the research with corresponding materials and Kingston University – London for allowing to use the laboratory equipment.

REFERENCES

- Hollway LC & Leeming M.B. 1999. *Strengthening of RC structures using externally bonded FRP composites in structural and civil engineering*. London: Woodhead Publishing.
- Design guidance for strengthening concrete structures using fibre composite materials*. TR55, 2004. Concrete Society UK, Second edition.
- Kim SJ and Smith ST. 2009. Shear strength and behaviour of FRP spike anchors in cracked concrete. *FRPRCS-9, Sydney, Australia, 13-15 July 2009*.
- Khan A.R. and Naseem N. 2008. Role of U-shaped anchorages on behaviour of RC beams strengthened by CFRP plates. *CICE2008, 22-24 July 2008, Zurich, Switzerland*.
- Takashi Y. 2008. Flexural strengthening of RC beams with CFRP sheets and U-jackets. *CICE2008, 22-24 July 2008, Zurich, Switzerland*.
- Leung CKY. 2006. FRP debonding from a concrete substrate: some recent findings against conventional belief. *Science Direct, Cement and Concrete Composites*.
- Husemann U and Budelmann H. 2007. Increase of the bond capacity of externally bonded CFRP plates on RC structures due to self-induced contact pressure. *FRPRCS-8, Patras, Greece, July 16-18, 2007*.
- Donchev T and Sifas D. 2009. Experimental Study of the Behavior of Various Non-Bolted Anchorages for CFRP Laminates. *FRPRCS-9, Sydney, Australia, 13-15 July 2009*.

Arching Action in Laterally Restrained GFRP Reinforced Slabs

G Tharmarajah (gtharmarajah01@qub.ac.uk), Susan E. Taylor, Desmond Robinson & David J. Cleland
School of Planning, Architecture and Civil Engineering, Queen's University Belfast, Belfast, U.K

ABSTRACT Expansive corrosion in steel reinforcement significantly reduces the design life and durability of concrete structures. Glass Fibre Reinforced Polymer (GFRP) reinforcement is a more durable alternative to steel reinforcement and has higher strength to weight ratio than steel. Replacing conventional steel with GFRP reinforcement can be highly beneficial. FRP reinforcement can be successfully used in laterally restrained slabs due to enhanced strength above the flexural capacity and increased stiffness as a result of arching action. This paper discusses the tests carried out on three full scale concrete slabs strips reinforced with GFRP bars.

1 INTRODUCTION

Concrete structures can be more durable and require less maintenance if the corrosion of the steel reinforcement can be prevented or a non corrosive alternative used instead. In the United Kingdom, repair cost due of concrete infrastructure exceeds £500 million/year (Broomfield et al. 2002) and much higher in the United States and Canada (Bedard 1992). Better quality concrete, steel protection methods such as epoxy coating, galvanizing have been practiced in the last decades in an effort to prevent the corrosion in steel reinforced structures (Clarke 1999). However, the efficiency of these methods raised concerns when corrosion was detected on epoxy coated steel reinforcement (Keesler & Powers 1988). FRP has been used in the aeronautical and marine engineering for some time and recently FRP was introduced to the construction industry as a non-corrosive durable reinforcement and is gaining acceptance.

Although FRP has been proved to be durable material, the perceived drawbacks such as brittle behaviour and low modulus of elasticity have raised concerns over the serviceability of the structure. The guidelines prepared for FRP reinforced construction (ACI 440.1R-06, 2006 etc.) provided recommendations such as over reinforcing the sections for concrete crushing failure and to provide adequate stiffness (ACI 440.1R-06, 2006). These guidelines are appropriate for simply supported slabs but are underestimating laterally restrained slabs such as deck slabs in beam and slab bridge structures where the benefits of arching action influence the stiffness and the failure mode of the slab (Rankin et al. 1991, Mufti & Newhook, 1998, Taylor, 2000).

The existence of arching action has been appreciated over fifty years (Ockleston, 1955). However, the beneficial use of this phenomenon was not yet been

fully utilised or implemented. BD 81/02 (HA), Canadian Highway Bridge Design Code and few other codes have incorporated the compressive membrane action into design guidelines.

It is considered that FRP reinforcement is suitable for laterally restrained slabs as they allow for the FRP reinforced slabs to achieve better serviceability and safe ultimate failure criteria. This project studies the influence of FRP reinforcement on the performance of laterally restrained slabs reinforced with different FRP parameters. The investigation shows that FRP can replace steel without compromising the strength and serviceability in laterally restrained slabs.

2 EXPERIMENTAL INVESTIGATION

2.1 Material properties

High strength concrete and GFRP reinforcement were used to construct these slabs. Control samples were taken at the time of testing to determine the material properties. A concrete mix, based on previous research (Taylor, 2000), was modified for the required strength and workability using trial mixes. The concrete mix details are provided in Table 1. The GFRP reinforcement was tested for its tensile strength and modulus of elasticity. The tests were carried out using an accurately calibrated tensile testing machine. It was found that the tested values of GFRP bars were around 70% of the manufacturer's reported strength (Table 2). This was due

Table 1 Concrete mix constituents (kg/m³ concrete)

Target strength (N/mm ²)	Cement	Super plasticizer	Tot. water	Aggregates		
				20 (mm)	10 (mm)	sand
60- 70	450	9	175	639	547	639

Table 2 GFRP material properties

Rebar	Tensile tests loading rate 0.2 kN/s		Manufacturer's reported loading rate 1 kN/s	
	Tensile strength (MPa)	Elastic modulus (GPa)	Tensile strength (MPa)	Elastic modulus (GPa)
GFRP	682	67.4	>1000	>60

to a different loading rate used in the tests. The loading rate of 0.2kN/s was considered more acceptable for a slab test rather a rapid tensile testing rate of 1.0kN/s used by the manufacturer.

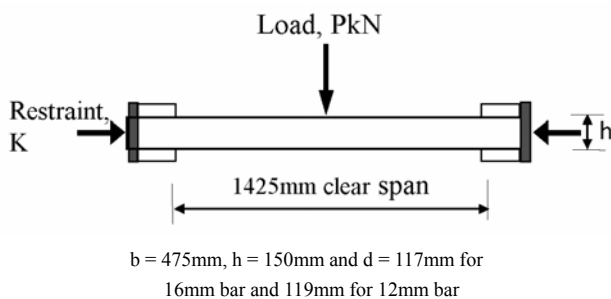
Table 3 Test slab details

Test slab	Reinforcement percentage (Both top and bottom layer)	Strain recorded on bars at 150 kN $\mu\epsilon$
SLAB 1	LRS - 0.6 % -12mm-125	1913
SLAB 2	LRS - No reinforcement	N/A
SLAB 3	LRS - 1.2 % -16mm-125	3886

Dimension (mm): 1765(H) \times 475(W) \times 150(T) for all slabs

2.2 Slab tests and procedures

Several slab tests were carried out to investigate the effect of different parameters on the performance of the laterally restrained slabs. The test set up is shown in Figure 1. A steel frame with known lateral stiffness was used to create the restraint condition (Figure 2). The lateral stiffness of the steel frame represented that in the

**Figure 1** Model Test Slab Set-up**Figure 2** Picture of a test arrangement

slab and beam bridge decks. The in-plane restrained slabs were tested to investigate serviceability behaviour and ultimate strength. In the FRP reinforced slabs, serviceability behaviour can be more significant than ultimate strength. Therefore, deflection of the slab, crack width development, strain on FRP bars and behaviour of the slab were observed in each test. Electrical resistant strain (ERS) gauges were embedded on the FRP bars to assess the strain development in both mid span and at the support location. The expansion of the steel frame was recorded using displacement transducers at the restrained faces. The mid-span deflection of the slab was recorded below the load using electronic transducers. Two test loads of about 40% of the predicted ultimate failure load were applied prior to the failure test. The loads were maintained for 5 minutes and unloaded incrementally and the recovery was measured. A vibrating wire strain gauge was installed perpendicular to the crack which formed during the test loads. The crack width was then measured using vibrating wire gauges for the test of the ultimate strength.

3 RESULTS AND DISCUSSION

Three slab test results are discussed in this paper. The summary of the test slabs is shown in Table 4.

Table 4 Test results

Test slab	Concrete strength (N/mm ²)	Effective depth (mm)	Failure load (kN)	Deflection at failure (mm)
SLAB 1	68.1	119	343.5	19.4
SLAB 2	72.6	N/A	296.7	11.4
SLAB 3	66.3	117	295.1	13.6

3.1 Stiffness of the slabs

The experimental results show that all the slabs have almost the similar stiffness as the load versus deflection behaviour follows the same line (Figure 3). This behaviour indicates that when the slab is laterally restrained, the concrete strength and concrete stiffness dominate the behaviour of the slab. Neither the reinforcement percentage nor the reinforcement stiffness has influences on the behaviour of the slab.

3.2 Behaviour of the slabs

A single crack formed directly below the line load at the soffit of all of the slabs. However, a few more cracks were observed in the slab 1 and slab 3 during the ultimate load test compare with slab 2. The crack expanded as the load increased with two other cracks appearing close to the restrained edge on the top face of the slab for all three tested slabs. The width of the primary crack on all slabs is shown in Figure 4. It shows that when the reinforcement percentage increases, the crack width

decreases. It should be noted that the slab with no reinforcement has some degree of crack control due to the compressive membrane action.

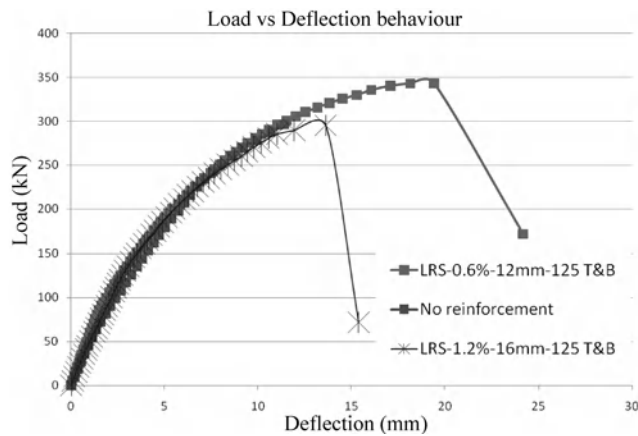


Figure 3 Load vs. deflection behaviour of three slabs



Figure 4 Crack width development on slabs

The failure of the unreinforced slab was a catastrophic collapse after concrete crushing. The other two slabs failed by concrete crushing but no catastrophic collapse was observed (Figure 5).

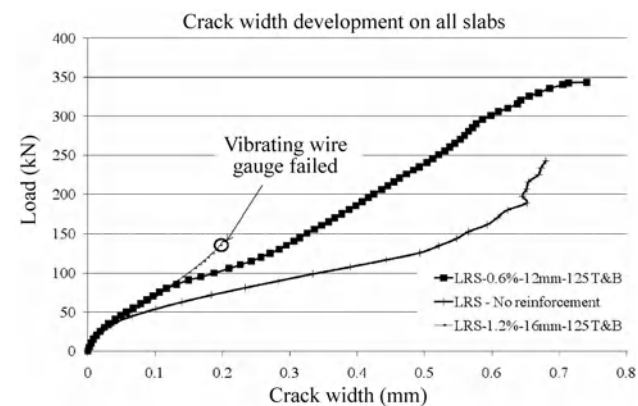


Figure 5 Typical failure mode of laterally restrained slab

It was interesting to note that the failure of the slab reinforced with 0.6% reinforcement was higher than the slab reinforced with 1.2% reinforcement. This was due to the higher concrete strength in slab 1, and caused a significant difference in the failure load (Table 4) and strain in the reinforcements. Table 3 shows that, the reinforcement in the slab 3 had a higher strain at the

same load level. Providing higher amount of reinforcement reduces the contribution from compressive membrane action due to a loss of arching in the slab.

3.3 Discussion

This research aimed at investigating the influence on the service behaviour and ultimate capacity of FRP reinforcement in laterally restrained slabs. The experimental investigation shows that even the unreinforced slab failed at a high load level. This highlights the strength enhancement due to arching action. Thus it proves that providing higher amount of reinforcement did not contribute towards higher failure load or serviceability. Designing a slab with optimum reinforcement percentage can ensure striking a balance load carried by arching action and that by flexural moment.

The arching action beneficially influences the mode of failure of the slab. The failure of the restrained slabs is always a concrete crushing at the mid span. The concrete crushing mode shows some plastic behaviour before the failure. Therefore, the concrete crushing failure is preferred in FRP reinforced slabs as FRP rupture could be catastrophic as FRP bars do not exhibit any plastic behaviour.

4 CONCLUSIONS

The following conclusions were drawn.

- (1) Restrained slabs can have substantial ultimate capacity even with zero reinforcement.
- (2) Although the unreinforced slab shows excellent ultimate strength capacity and stiffness, it results in large crack widths compared with the reinforced slabs.
- (3) It has been shown through these tests that the restraint can help to reduce reinforcement requirements in GFRP reinforced slabs. The GFRP reinforced slab reinforced with 0.6% reinforcement has show excellent serviceability and strength, better than to 1.2% GFRP reinforced slab.

5 ACKNOWLEDGMENT

The authors would like to gratefully acknowledge the support of Schock Bauteile GmbH, Germany for supplying the GFRP rebar and the technical staff at the university, K McDonald, W McRoberts, J Hunter and K McKnight.

REFERENCES

American Concrete Institute, 2006. ACI 440.1R-06 Guide for the Design and Construction of Concrete Reinforced with FRP Bars, *American Concrete Institute*.

Aftab A. Mufti and John P. Newhook, 1998. Punching Shear Strength of Restrained Concrete Bridge Deck Slabs, *ACI Structural Journal*, Vol. 95, No. 4.

Bedard, C., 1992. Composite reinforcing bars. Assessing their use

- in construction. *Concrete International*, 14(1), 55-59.
- Broomfield, J.P., Davies, K. and Hladky, K., 2002. The use of permanent corrosion monitoring in new and existing reinforced concrete structures. *Cement and Concrete Composites*, 24(1), 27-34.
- Canadian Highway Bridge Design Code (10th ed.), 2006., CAN/CSA-S6, *Canadian Standards Association*, Canada.
- Clarke, J.L., 1999. Fibre-reinforced plastic reinforcement for concrete. *Concrete (London)*, 33(1), 15-16.
- Highways Agency (UK), 2002. Use Of Compressive Membrane Action In Bridge Decks, *BD 81/02, Departmental Standard - The assessment of concrete highway bridges, Design Manual for Roads and Bridges*, Volume 3, Section 4, Part 20.
- Keesler, R.J. and Powers, R.G., 1988. Corrosion of epoxy coated rebars-Keys Segmental Bridge-Monroe County, Report No.88-8A, Corrosion Research Laboratory, *Florida Department of Transportation, Materials office, Gainesville*.
- Ockleston A.J. Load tests on a 3-storey RC building in Johannesburg. *Structural Engineer*, 1955, 33, 304-322.
- Rankin, G.I.B., Niblock, R.A., Skates, A.S. and Long, A.E., 1991. Compressive membrane action strength enhancement in uniformly loaded, laterally restrained slabs. *Structural engineer London*, 69(16), 287-295.
- Taylor, S.E., 2000. Compressive Membrane Action in High Strength Concrete Bridge Deck slabs, *Queen's University Belfast*, PhD Thesis.

Flexural Strengthening of RC Continuous Beams Using Hybrid FRP Sheets

Habib Akbarzadeh (h_akbarzadeh_b@yahoo.com)

Assistance Professor, Civil Engineering Department, Shomal University, Amol, Iran

A. A. Maghsoudi

Associate Professor, Civil Engineering Department, Kerman University, Kerman, Iran

ABSTRACT Due to linear stress–strain characteristics of FRP up to failure, the ductility of plated members and their ability to redistribute moment is less than that of unplated RC beams. Hybrid FRP laminates, which consist of a combination of either carbon and glass fibers, changes the behavior of the material to a non-linear behavior. Although many in situ RC beams are of continuous construction, there has been very little research into the behavior of such beams with external reinforcement. This paper presents an experimental program conducted to study the behaviour of RC two-span beams strengthened with hybrid carbon and glass reinforced polymer sheets (HCG). The program consists of a total of six continuous beams with overall dimensions equal to 250×150×6000 mm. The test results showed that using the HCG for strengthening the continuous RC beams lead to significantly increase of bearing capacity, ductility and moment redistribution ratio compared to strengthened beams with CFRP or GFRP.

1 INTRODUCTION

Externally bonding fiber reinforced polymer (FRP) sheets with an epoxy resin is an effective technique for strengthening and repairing the reinforced concrete (RC) beams under flexural loads. A large loss in beam ductility, however, occurs when FRP are used for flexural strengthening of RC beams, because these materials have dissimilar behavior to that of steel, that is, they exhibit a linear stress-strain behavior up to failure (Spadea et al. 2001, Toutanji et al. 2006 and Thomsen et al. 2004). Hybrid FRP laminates, which consist of a combination of either carbon and glass fibers or glass and aramid fibers have non-linear stress–strain behavior (Belarbi et al. 1999). Verification of research show that using the Hybrid FRP for strengthening RC simply supported beams cause to increase both of their capacity and ductility (Xiong et al. 2004, Hosny et al 2006 and Xiong et al. (2007)).

Although many in-situ RC beams are continuous construction, there has been very limited research into the behavior of such beams with external reinforcement (Akbarzadeh and Maghsoudi 2009a, b, Ashour et al. 2004, El-Refaie et al. 2003 and Grace et al. 2004, Liu et al. 2007 and Aiello et al. 2007). In addition, most design guidelines were developed for simply supported beams with external FRP laminates (ACI 440.2R 2008, JSCE 2001 and fib 2001). Ductility is even more important for statically indeterminate structures, such as continuous beams, as it allows for moment redistribution through

the rotations of plastic hinges. Moment redistribution permits the utilization of the full capacity of more segments of the beam.

Akbarzadeh and Maghsoudi (2009a, b), Ashour et al. (2004) and El-Refaie et al. (2003) found out that strengthening both the top surface at the negative moment and the beam soffit at positive moment region to be the most effective arrangement of the CFRP and GFRP laminates to enhance the load capacity, but ductility and moment redistribution are very low.

In this paper, the experimental behavior of six RC continuous (two-span) beams strengthened with externally bonded CFRP, GFRP and hybrid CFRP/GFRP (HCG) sheets along their negative and positive moment regions are investigated. The beams were loaded with a concentrated load at the middle of each span. Type of FRP (CFRP or GFRP or HCG) and lyres number of FRP were the main parameters investigated. The responses of the strengthened continuous beams were examined and discussed in terms of load-deflections, failure modes, moment and load capacity, moment redistribution and ductility.

2 EXPERIMENTAL PROGRAMS

Six large-scale continuous (two-span) beams (150×250×6000 mm) were tested to failure. Beams geometry and reinforcement as well as the loading and support arrangements are illustrated in Figure 1. Type of FRP (CFRP or GFRP or HCG) and lyres number of FRP

were the main parameters investigated as summarized in Table 1. Thickness each layer of CFRP and GFRP are 0.11 mm and 0.2 mm respectively. Width of each layer of CFRP sheet was 145 mm for SC1 and SC3; and 120 mm for SC1G1 and SC2G2. Width of each layer of GFRP sheet was 150 mm. The end anchorage system, consist of three or four plies of CFRP sheets was wrapped and bonded around the sides and the soffit or top of the concrete beams near the end of longitudinal FRP sheets (Figure 1).

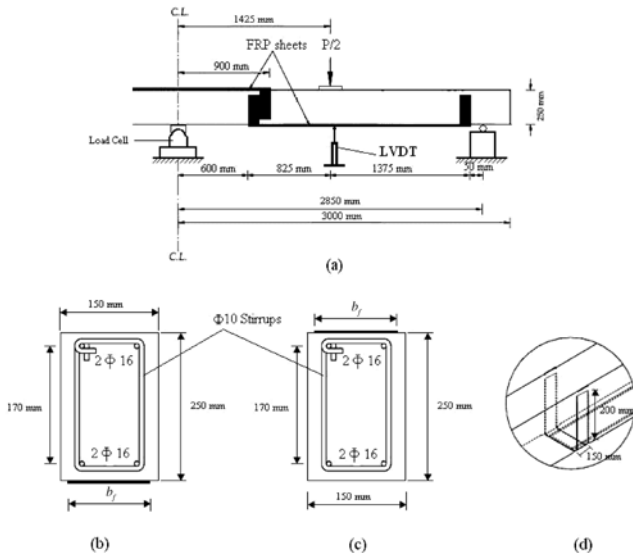


Figure 1 Test set-up and strengthened RC continuous beam details (a) longitudinal profile of beam (b) typical cross section of beam in sagging region (c) typical cross section of beam in hogging region (d) end anchorage system

The average concrete compressive strength (f'_c) for each beam is shown in Table 1. Yield stress of bars of diameter 16 mm is 412.5 MPa, and maximum tensile strength was 626.4 MPa. The modulus of elasticity of steel bars was 2×10^5 MPa. The Young's modulus (E_{fi}), ultimate tensile stress (f_{fi}) and ultimate strain of CFRP sheet are 242 GPa, 3800 MPa and 1.55%. Also, the Young's modulus (E_{fi}), ultimate tensile stress (f_{fi}) and ultimate strain of GFRP sheet are 73 GPa, 2250 MPa and 3.1% respectively. The properties of epoxies used for bonding the FRP sheets were obtained from the supplier and given in author's paper (Akbarzadeh and maghsoudi 2009a).

3 TEST RESULTS AND DISCUSSIONS

The beams were loaded with a concentrated load at the middle of each span. The obtained experimental results are presented and discussed subsequently in terms of the observed mode of failure, load-deflection, moment and load capacity, moment redistribution and ductility.

3.1 Failure mode and load -deflections responses

Three different failure modes were observed for tested

beams and given in Table 2. The results of test show that with increasing the number of FRP sheet layers will change the failure mode from tensile rupture to IC debonding of FRP sheets in continuous beams. Because of the beams were strengthened at both the sagging and hogging regions, beams have two failure level including first failure (maximum load) and comprehensive failure. The different typical of failure are shown in Figure 2.

Table 1 Details of the test specimens

Beam no.	f'_c (MPa)	Type of FRP	Sag. & hog. moment strengthening	
			No. layers	b_f (mm)
CB	74.2	-	0	-
SC1	74.6	CFRP	1	145
SC3	74.4	CFRP	3	145
SG3	79.7	GFRP	3	150
		CFRP	1	120
SC1G1	79.46	GFRP	1	150
		CFRP	2	120
SC2G2	79.34	GFRP	2	150

Table 2 Experimental results of tested beams including yield and ultimate load, deflection

Beam no.	Failure mode	P_y (kN)	ζ	(Δ_y) (mm)	P_u (kN)	λ	(Δ_u) (mm)	μ (Δ_u/Δ_y)
CB	FF	105	1	7.5	162	1	77.4	10.32
SC1	R-H [†]	110	1.05	7.5	190.6 [†]	1.18	26	3.47
	R-S ^{††}				183.3 ^{††}	1.13	33.6	4.48
SC3	ICD-H [†]	136	1.29	8.9	259.3 [†]	1.6	19.88	2.23
	ICD-S ^{††}				238 ^{††}	1.47	29.6	3.32
SG3	ICD-H [†]	157.3	1.49	9	222.6 [†]	1.37	26.6	2.96
	ICD-S ^{††}				180.6 ^{††}	1.11	52.7	5.85
SC1G1	R-H [†]	122.9	1.17	7.35	224.6 [†]	1.39	32.3	4.39
	ICD-S ^{††}				209.3 ^{††}	1.29	40.8	5.55
SC2G2	ICD-S [†]	138	1.31	7.4	264 [†]	1.63	44.18	5.97
	ICD-H ^{††}				216 ^{††}	1.33	65	8.78

[†] First failure, ^{††} Comprehensive failure

FF: Flexural failure, R-H: Rupture of FRP sheet at hogging region, R-S: Rupture of FRP sheet at sagging region, ICD-H: IC debonding at hogging region, ICD-S: IC debonding at sagging region.

The total applied load versus deflection at mid-span section of the beams is shown in Figure 3. As indicated in Figure 3, the beams did not lose their full load bearing capacity at the first failure, as the beams were strengthened at both the sagging and hogging regions. In other word, the beam can be reloaded after first failure and with bearing high deflection the comprehensive failure occurred. In the uncracked elastic stage, the same behavior was observed for all tested beams, indicating

very similar beams stiffness prior to concrete cracking. In the cracked preyield stage, the stiffness and yield load of the FRP strengthened beams were moderately larger than that of the control beam. However, significant decreases in beams stiffness was observed after yielding the tensile steel, but by increasing the number of FRP layers the loss in beams stiffness are reduced. The stiffness of SG3 is less than SC3 beam after yielding the tensile steel, it is because the elastic modulus of GFRP is much lower than CFRP sheets. Although stiffness of RC continuous beam strengthening with CFRP and GFRP is increased, but mid span deflection at first failure is decreased. But, both the stiffness after yielding load and mid span deflection at first failure significantly was increased by strengthening RC continuous beams with HCG compared to the strengthened beams with CFRP and GFRP.

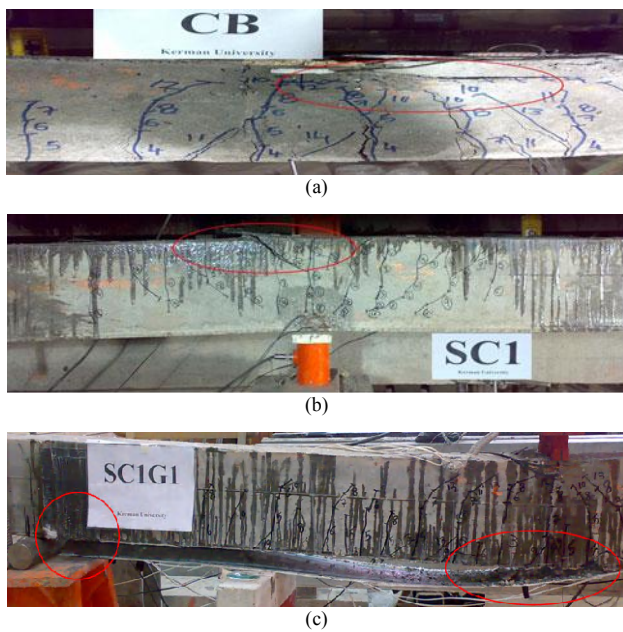


Figure 2 (a) Concrete crushing at mid-span (b) Rupture of CFRP sheets at hogging region (b) IC debonding of HCG sheets and rupture of end strap at sagging region

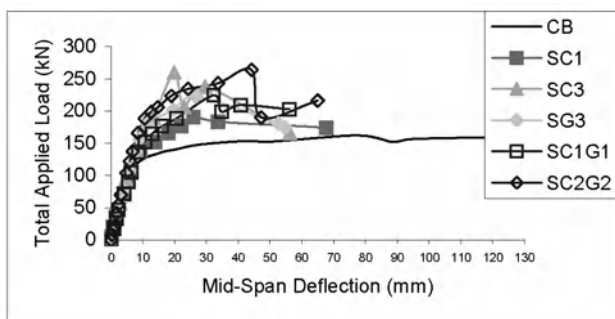


Figure 3 Total applied load-deflection responses of test beams

3.2 Enhancement of failure load

Table 2 summarizes the ultimate failure load, P_u (i.e., the sum of the two mid-span point loads at failure), the

ultimate load enhancement ratio (λ), which is the ratio of the ultimate load of an externally strengthened beam to that of the control beam, yielding load of tensile steel at central support (P_y) and the yielding load enhancement ratio (ξ), which is the ratio of yielding load of the strengthened beam to that of control beam.

The increase in the number of CFRP and HCG layers, the yield load of tensile steel at central support is only slightly increased.

As indicated in Table 2, the addition of one and three layers of CFRP sheet and three layers of GFRP sheet causes to increase the ultimate load capacity by 18%, 60% and 37%, respectively for beams SC1, SC3 and SG3 compared to the control beam, CB. While, use of the one and two layers of HCG sheet causes to increase the ultimate load capacity by 39% and 63%, respectively for beams SC1G1 and SC2G2. Also, after first failure, load enhancement for comprehensive failure was decreased by 13%, 47%, 11%, 29%, and 33%. By comparing the results of SC1 and SC1G1, it is found that nevertheless amount of CFRP in SC1G1 is lower than SC1, but load enhancement ratio of SC1G1 is twice SC1. Also, however ultimate load capacity of SC3 and SC2G2 is almost equal, but amount of CFRP in SC3 beam is higher than SC2G2 beam.

3.3 Enhancement of moment capacity

Total applied load versus the hogging and sagging bending moments for tested beams are plotted in Figure 4. The bending moment was calculated by equilibrium considerations of the beams using the measured central support reaction and mid-span applied load. The behavior of all beams at low load levels was essentially elastic. The behavior of beam SC3 was elastic until it failed at hogging or sagging region (first failure). While, for all other beams, as the applied load was increased, the bending moment tended to become non-linear.

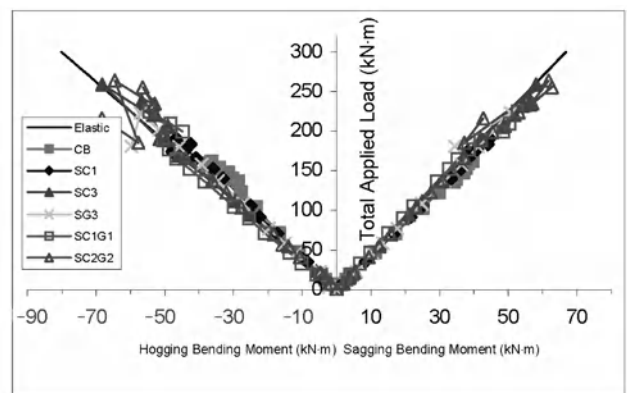


Figure 4 Total applied load versus bending moment of tested beams

The first failure resulted to increase the nonlinear behavior at beams comprehensive failure. The reason of this occurrence is reduction of stiffness at region of first failure.

Table 3 presents the failure moment, and the ultimate moment enhancement ratio χ , which is the ratio of ultimate moment of strengthened sections (central support and mid-span sections) to that of unstrengthened sections. As shown in Table 3, the addition of one and three layers of CFRP and GFRP sheet increases the ultimate moment capacity by 28%, 88% and 57% at central support and by 12%, 47%, and 28% at midspan, respectively for beams SC1, SC3 and SG3, while compared to the control beam, CB. But, use of the one and two layers of HCG sheet cause to increase the ultimate moment capacity by 50% and 78% at central

support and by 33% and 56% at mid span respectively for beams SC1G1 and SC2G2. Even after first failure, moment capacity at undamaged section is increased with reloading of beam. By comparing the ultimate load enhancement ratio of a strengthened beam and the moment enhancement ratio of a strengthened section at central support in the same beam (Table 3), it can be concluded that the latter was significantly higher than the former. It is also remained that, such conclusion is not valid for simply supported beams strengthened with external reinforcement where the moment and load enhancement ratios are always the same.

Table 3 Central support reaction, failure moments and moment redistribution of tested beams

Beam no.	P_u (kN)	R (kN)	Central support				Mid span			
			M_{exp} (kNm)	χ	M_e (kNm)	β (%)	M_{exp} (kNm)	χ	M_e (kNm)	β (%)
CB	162	106.5	36.33	1	43.28	16.06	39.54	1	36.07	-9.62
SC1	190.6 [†]	128.1	46.74	1.28	50.93	8.22	44.53	1.121	42.44	-4.92
	183.3 ^{††}	121.5	42.53	1.17	48.97	13.15	44.03	11	40.8	-7.92
SC3	259.3 [†]	177.4	68.26	1.88	69.28	1.51	58.14	1.47	57.73	-0.71
	238 ^{††}	158.83	56.76	1.56	63.59	6.83	56.41	1.43	52.99	-6.51
SG3	222.6 [†]	151.4	57.2	1.57	59.47	3.81	50.72	1.28	49.56	-2.34
	180.6 ^{††}	132.3	59.8	1.65	48.25	-23.94	34.41	0.87	40.21	14.42
SC1G1	224.6 [†]	150.6	54.58	1.50	60.01	9.05	52.72	1.33	50.01	-5.42
	209.3 ^{††}	138.6	48.38	1.33	55.92	13.48	50.37	1.27	46.6	-8.09
SC2G2	264 [†]	177.33	64.59	1.78	70.53	8.42	61.75	1.56	58.78	-5.05
	216 ^{††}	155.99	68.38	1.88	57.71	-18.49	42.75	1.08	48.09	11.10

R: Central support reaction

3.4 Moment redistribution

The moment redistribution ratio (β) given in Table 3 was calculated for the sagging and the hogging bending moment at mid span and at the central support at failure load. The ratio was calculated by:

$$\beta = \frac{M_e - M_{exp}}{M_e} \times 100\% \quad (1)$$

Where M_e is the value of the failure moment at central support and mid span based on the elastic analysis and M_{exp} is the experimental value of bending moment. As indicated in Table 3, beam CB had a moment redistribution ratio of 16.06% at central support and -9.62% at mid-span. The beams SC1, SC3, SG3, SC1G1 and SC2G2 had the moment redistribution ratio of 8.22%, 1.51%, 3.81%, 9.05 and 8.42 at central support and -4.92%, -0.71%, -2.34%, -5.42 and -5.05 at mid span respectively. Therefore, using the CFRP and GFRP for strengthening the continuous beam in both the sagging and hogging regions cause to increase load capacity, but moment redistribution significantly reduced. While, using the HCG for strengthening cause to increase the load capacity with high amount of moment redistribution. Therefore use the HCG need for ensuring of minimum

moment redistribution at continuous beam.

Tensile rupture or IC debonding failure of the FRP sheets at first failure resulted to increase the moment redistribution ratio appreciably at beams comprehensive failure, as indicated in Table 3. The reason of this occurrence is the stiffness lessening at hogging or sagging region after first failure.

3.5 Ductility

Ductility is more important for statically indeterminate structures, such as continuous beams, as it allows for moment redistribution through the rotations of plastic hinges. The ductility index (μ) in this study is obtained based on deflection computation, and is defined by Eq. (2):

$$\mu_{\Delta} = \frac{\Delta_u}{\Delta_y} \quad (2)$$

Where Δ_u is the midspan deflection at beam ultimate load, and Δ_y is the midspan deflection at yielding load of the tensile steel reinforcement at central support.

The midspan deflection at beam ultimate load (Δ_u) and yielding load (Δ_y), and the deflection ductility index (μ_{Δ}) are given in Table 2. As can be seen from Table 2 and experimental results of Ashour et al. 2004, El-Refaie et al. 2003, strengthening both the hogging

and sagging regions with CFRP laminate cause to increase significantly load capacity, but ductility of continuous beam is significantly decreased. Also using the GFRP for strengthening the beam (SG3) led to slightly increase the ductility. But, both the ductility and load capacity of beams strengthened with HCG is high.

For unstrengthened RC members, displacement ductility index, μ_{Δ} in the range of 3 to 5 is considered imperative for adequate ductility, especially in the areas of seismic design and the redistribution of moments (Maghsoudi and Akbarzadeh 2006). Therefore, assuming that an index value of 3 represents an acceptable lower bound to ensuring the ductile behavior of RC continuous beams strengthened with FRP sheet, it appears that, for the tested beams SC3, SG3 would not meet that requirement ($\mu_{\Delta} < 3$). While, using the HCG for strengthening RC continuous beam at both the sagging and hogging regions is a way for increasing significantly load capacity and ensuring the ductility.

4 CONCLUSIONS

The following conclusions can be drawn based on the test results:

(1) Both the stiffness after yielding load and mid span deflection at ultimate load was significantly increased by strengthening RC continuous beams with HCG compared to the strengthened beams with CFRP or GFRP.

(2) Behavior of the beams strengthening with HCG by increasing applied load tended to become non-linear compared to the strengthened beams with CFRP.

(3) Use of the HCG is needed for ensuring of minimum moment redistribution in continuous beams.

(4) Assuming that an index value of 3 represents an acceptable lower bound to ensuring the ductile behavior of RC continuous beams strengthened with FRP sheet, use of the HCG is a way for ensuring the minimum ductility.

REFERENCES

- ACI. 2008. *Guide for the design and construction of externally bonded FRP systems for strengthening concrete structures*. 440.2R-08, ACI Committee, 440, American Concrete Institute, Farmington Hills, Mich.
- Aiello, M.A., Valente, L., and Rizzo, A. 2007. Moment redistribution in continuous reinforced concrete beams strengthened with carbon-fiber-reinforced polymer laminate. *Mechanics of Composite Materials* 43(5): 453-466.
- Akbarzadeh, H., and Maghsoudi, A.A. 2009a. Experimental and analytical investigation of reinforced high strength concrete continuous beams strengthened with fiber reinforced polymer. *Materials and Design* 31: 1130-1147.
- Akbarzadeh, H., and Maghsoudi, A.A. 2009b. Experimental investigations and Verification of Debonding strain of RHSC Continuous Beams Strengthened in Flexure with Externally Bonded FRPs. *Materials and structures*, (In press).
- Ashour, A.F., El-Refaie, S.A., and Garrity, and S.W. 2004. Flexural strengthening of RC continuous beams using CFRP laminates. *Cement & Concrete Composite* 26: 765-775.
- Belarbi, A., Chandrashekhara, K., and Watkins, S. 1999. Performance evaluation of fibre reinforced polymer reinforcing bar featuring ductility and health monitoring capability. In: *Fourth international symposium on fiber reinforced polymers (FRP) for reinforced concrete structures*, Baltimore, Maryland, USA, ACI SP 188-29: 1-12.
- El-Refaie, S.A., Ashour, A.F., and Garrity, S.W. 2003. Sagging and hogging strengthening of continuous reinforced concrete beams using carbon fiber-reinforced polymer sheets. *ACI Structural Journal*, 100(4): 446-453.
- Fib. 2001. *Design and use of externally bonded FRP reinforcement (FRP EBR) for reinforced concrete structures*. Progress Rep. of fib EBR Group, Int. Concrete Federation.
- Grace, N.F., Ragheb, W.F., and Abdel-Sayed, G. 2004. Strengthening of cantilever and continuous beams using new triaxially braided ductile fabric. *ACI Structural Journal* 101(2): 237-244.
- Hosny, A., Shaheen, A., Abdelrahman, A., and Elafandy, T. 2006. Performance of reinforced concrete beams strengthened by hybrid FRP laminates. *Cement & Concrete Composites*, 28: 906-913.
- JSCE. 2001. *Recommendations for the upgrading of concrete structures with use of continuous fiber sheets*. Japanese Society of Civil Engineers, Concrete engineering, Series 41: Tokyo.
- Liu, I.S.T., Oehlers, D.J., and Seracino, R. 2006. Moment redistribution in FRP and steel-plated reinforced concrete beams. *Journal of Composites for Construction*, ASCE 10(2): 115-124.
- Maghsoudi, A.A., and Akbarzadeh, H. 2006. Flexural ductility of HSC members. *Structural Engineering and Mechanics* 24(2).
- Spadea, G., Swamy, R.N., and Bencardino, F. 2001. Strength and ductility of RC beams repaired with bonded CFRP laminates. *Journal of Bridge Engineering* 6(5): 349-355.
- Thomsen, H., Spacone, E., Limkatanyu, S., and Camata, G. 2004. Failure mode analyses of reinforced concrete beams strengthened in flexure with externally bonded fiber-reinforced polymers. *Journal of Composites for Construction*, ASCE, March/April: 123-131.
- Toutanji, H., Zhao, L., and Zhang, Y. 2006. Flexural behavior of reinforced concrete beams externally strengthened with CFRP sheets bonded with an inorganic matrix. *Engineering Structures* 28: 557-566.
- Xiong, G.J., Jiang, X., Liu, J.W., and Chen, L. 2007. A way for preventing tension delamination of concrete cover in midspan of FRP strengthened beams. *Construction and Building Materials* 21: 402-408.
- Xiong, G.J., Yang, J.Z., and Ji, Z.B. 2004. Behavior of reinforced concrete beams strengthened with externally bonded Hybrid carbon fiber-glass fiber sheets. *Journal of Composites for Construction*, ASCE, May/June: 275-278.

Comparative Study of Deflection Equations for FRP RC Beams

I. Vilanova(irene.vilanova@udg.edu), C. Barris, Ll. Torres, C. Miàs, M. Baena & V.O. García
Analysis and Advanced Materials for Structural Design (AMADE), University of Girona, Spain

ABSTRACT The mechanical and bond characteristics of Fibre Reinforced Polymers (FRP) used as internal reinforcement for Reinforced Concrete (RC) elements result in larger deflections and crack widths compared to the conventional steel RC elements. Consequently, serviceability requirements may govern the design of such members. In the last 20 years, several approaches and codes of practice have been published to predict the theoretical deflection of FRP RC elements.

This paper analyses and examines the experimental deflection results of 145 concrete beams reinforced with FRP bars tested by several researchers, and compares their values with the theoretical values of 10 different approaches and design codes. All of the beam specimens were tested under a four point bending configuration and presented different reinforcement ratios and mechanical and bond properties of the FRP bars.

The objective of the paper is to investigate the suitability of the different approaches at different states of loading under the serviceability range. A statistical analysis is performed to evaluate the goodness of fit of each approach. The influence of several parameters as the level of load, the reinforcement ratio, or the modular ratio is analyzed and compared.

1 INTRODUCCION

The design of FRP RC members may be governed by serviceability limit states due to the lower stiffness of FRP bars compared with steel reinforcement, which results in larger deflections.

Along the last two decades, several approaches to predict deflection of FRP RC elements have been developed.

This paper compares experimental results of the deflection of FRP RC beams found in the literature with 10 approaches from different authors and design codes and studies the suitability of these proposals.

2 EXISTING APPROACHES FOR THE CALCULATION OF DEFLECTIONS FOR FRP RC

The equation proposed by Branson (1977), and adopted in ACI 318R-05 (2005), has been widely used to calculate deflections of steel RC concrete members.

$$I_e = \left(\frac{M_{cr}}{M_a}\right)^3 I_g + \left[1 - \left(\frac{M_{cr}}{M_a}\right)^3\right] I_{cr} \leq I_g \quad (1)$$

Where M_{cr} = the cracking moment; M_a = applied moment; I_g = gross moment of inertia; and I_{cr} = cracking moment of inertia. A number of researchers has proposed adjustments to adapt it to experimental results of FRP RC members. Among them Benmokrane et al.

(1996) proposed Equation (2), Toutanji & Saafi (2000) proposed Equation (3), and Yost et al. (2003) proposed Equation (4).

$$I_e = \left(\frac{M_{cr}}{M_a}\right)^3 \frac{I_g}{7} + 0.84 \left[1 - \left(\frac{M_{cr}}{M_a}\right)^3\right] I_{cr} \leq I_g \quad (2)$$

$$I_e = \left(\frac{M_{cr}}{M_a}\right)^m I_g + \left[1 - \left(\frac{M_{cr}}{M_a}\right)^m\right] I_{cr} \leq I_g \quad (3)$$

$$I_e = \left(\frac{M_{cr}}{M_a}\right)^3 \beta I_g + \left[1 - \left(\frac{M_{cr}}{M_a}\right)^3\right] I_{cr} \quad (4)$$

In Equation (3), m is a coefficient depending on the reinforced ratio, and in Equation (4), β is a coefficient depending on the reinforcement ratio and the modular ratio (E_{FRP}/E_c). Other authors such as Faza & GangaRao (1992) (Eq. 5), and Bischoff (2007) (Eq.6) proposed a modified equivalent moment of inertia derived from curvatures.

$$I_m = \frac{23I_{cr}I_e}{8I_{cr} + 15I_e} \quad (5)$$

$$I_m = \frac{I_{cr}}{\left(1 - \left(1 - \frac{I_{cr}}{I_g}\right)\left(\frac{M_{cr}}{M_a}\right)^2\right)} \quad (6)$$

Regarding some of the existing design codes, ACI 440.1R-06 2006) adopted (Eq. 4), but with β depending on the reinforcement ratio and the balanced reinforcement ratio, whereas CSA S806-02 (2002) adopted Equation (8), and ISIS (2001) adopted Equation (9) proposing an equivalent moment of inertia derived from curvature methods.

$$\delta_{\max} = \frac{P_a}{24E_c I_{cr}} \left[3L^2 - 4a^2 - 8 \left(1 - \frac{I_{cr}}{I_g} \right) \left(\frac{M_{cr}}{M_a} \right)^3 a^2 \right] \quad (7)$$

$$I_e = \frac{I_g I_{cr}}{I_{cr} + \left[1 - 0.5 \left(\frac{M_{cr}}{M_a} \right)^2 \right] (I_g - I_{cr})} \leq I_g \quad (8)$$

In Equation (8), P = applied load, L = length of the beam, a = shear span; and E_c = concrete modulus of elasticity.

Eurocode 2 (CEN 2004), for steel RC members, proposes calculating the deflection of an element as an interpolation of the fully cracked (δ_2) and the uncracked (δ_1) conditions of the element (Eq. 10).

$$\delta_{\max} = \left(1 - \left(\frac{M_{cr}}{M_a} \right)^2 \right) \delta_2 + \left(1 - \left(1 - \left(\frac{M_{cr}}{M_a} \right)^2 \right) \right) \delta_1 \quad (9)$$

3 COMPARATIVE STUDY

In the following, results from tests on 145 RC beams (Abdalla 2002, Alsayed 1998, Al-Sunna et al. 2006, Barris et al. 2009, Bogdanovic 2002, Benmokrane et al. 1996, Cosenza et al. 1997, Duranovic et al. 1997, Larralde & Rodriguez 1992, Pecce et al. 1998, Saikia et al. 2007, Toutanji & Deng 2003, Yost et al. 2003) are compared with 10 existing approaches of deflection prediction. The objective of the study was to investigate the sensitivity and the goodness of fit of the different models to the mentioned database.

All the beams were tested under a static four-point bending test. The length of the beams ranged between 1500 and 3400 mm, being the concrete compressive strength between 27 and 96 MPa, and the modulus of elasticity of the rebars between 36 and 64 GPa. In some cases, due to lack of data, the modulus of elasticity and tensile strength of the concrete were adopted from the formulation of Eurocode 2 (CEN 2004), except when the concerned source paper suggested other expressions.

To evaluate the approaches three values of the moment ratio (M_a/M_{cr}) were adopted: 1.5, 3, and 5. For (M_a/M_{cr}) = 1.5 the value of the cracking moment was determinant to establish adequate comparisons. In the present study, M_{cr} was calculated from the mechanical properties of the materials. Due to a lack of space, this paper only shows the outcome of the moment ratio of 3; however, for a moment ratio of 5, similar results were

obtained.

In Figures 1 and 2, the different design codes and authors approaches are compared with the experimental results. It is observed that for a moment ratio of 1.5 (Figure 1), 85% of the studied beams give a deflection ratio, defined as the predicted deflection divided by the experimental one, between 0.25 and 2. Nevertheless, for a moment ratio of 3 (Figure 2) and also for 5 (not depicted), 92% of the beams show a deflection ratio between 0.6 and 1.7, giving less scattered results. Hence, as the moment ratio increases, all the studied approaches show a better fit to the deflection ratio with a smaller range of the depicted values.

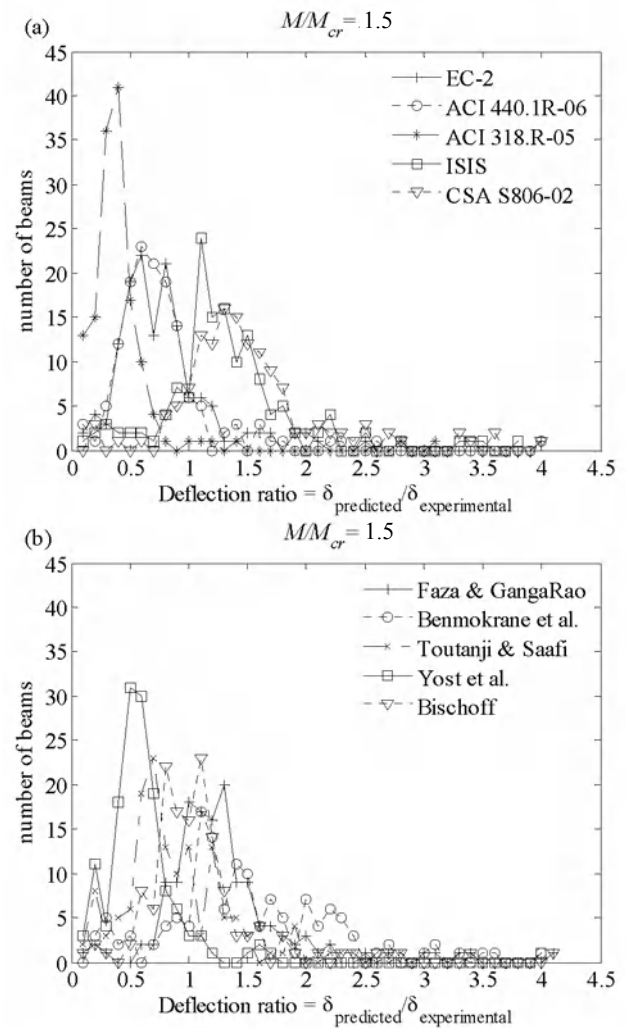


Figure 1 Deflection ratio for a moment ratio of 1.5 (a) Design codes (b) Authors proposals

In order to study the goodness of fit of the different theoretical expressions, the deflection ratio is statistically analyzed (Mota et al. 2006) depending on the parameter $n\rho$, being n the modular ratio and ρ the reinforcement ratio (Figures 3a, b). For a moment ratio of 1.5 (Figure 3a), the deflection ratio response varies from 0.25 to 3.20, depending on $n\rho$ and the considered theoretical approach. ISIS (2001), Bischoff (2007), Faza & GangaRao (1992)

approaches give the best prediction at this moment ratio, showing a deflection ratio value around 1. For this moment ratio, as the parameter $n\rho$ increases, the theoretical deflection tends to be overestimated. However, Yost et al. (2003), ACI 318.R-05 (2005), ACI 440.1R-06 (2006) and Eurocode 2 (CEN 2004) approaches show deflection ratios lower than the unity for any value of $n\rho$, underestimating the experimental deflection. For a moment ratio of 3 (Figure 3b), all the approaches except the ACI 318.R-05 (2005) (thought for steel RC) give a less scattered deflection ratio, with values ranging between 0.5 and 1.3. Nevertheless, most of them show a descending trend depending of the parameter $n\rho$, indicating that for high $n\rho$ values, these methods can underestimate deflections. This difference can be attributed to the fact that these approaches are designed for serviceability conditions, and therefore they use a linear stress-strain constitutive relationship for concrete and, also only account for deflection due to flexural effects (Al-Sunna et al. 2006, Barris et al. 2009).

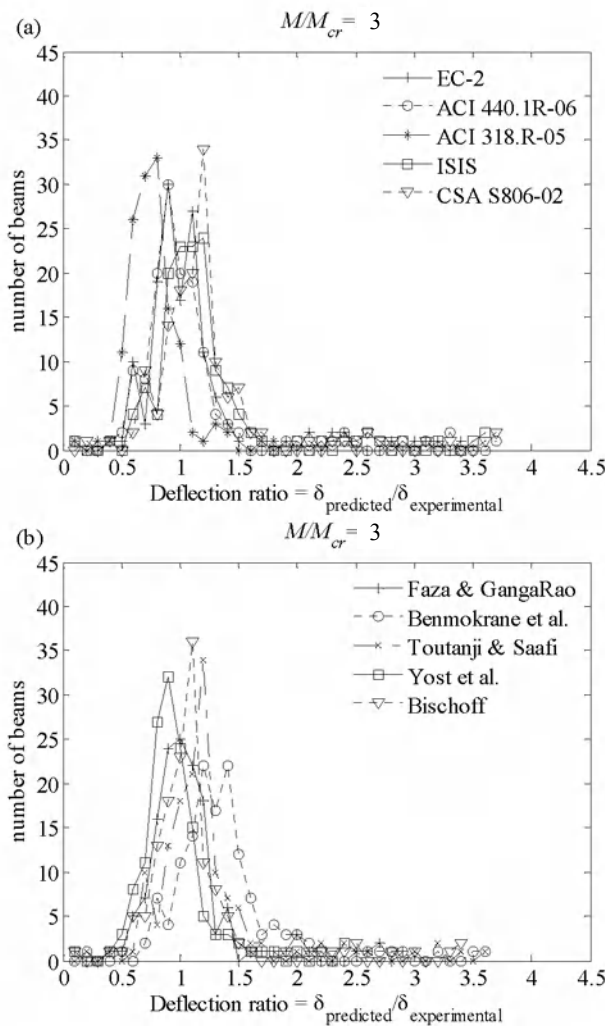


Figure 2 Deflection ratio for a moment ratio of 3 (a) Design codes (b) Authors proposals

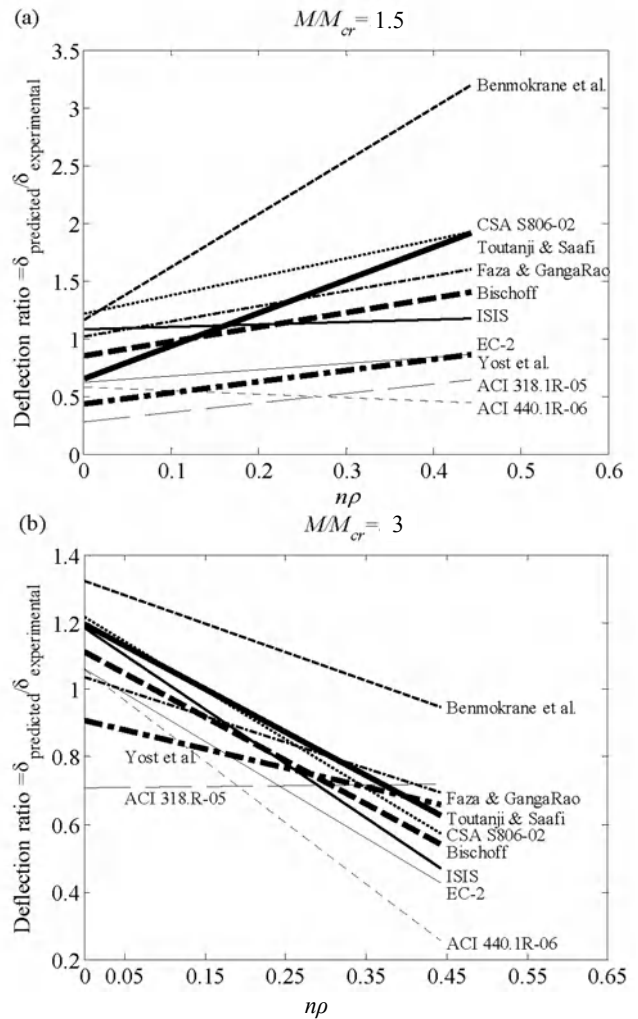


Figure 3 Deflection ratio depending on $n\rho$ (a) moment ratio of 1.5 (b) moment ratio of 3

Finally, Table 1 reports the mean value (μ), standard deviation (σ) and the variance (v) of the deflection ratio. It can be seen that for a moment ratio of 1.5, many approaches give a deflection ratio lower than the unity. It should be pointed out that this result may come from the difficulty in establishing the cracking moment. The

Table 1 Statistical analysis of the deflection ratio

Deflection ratio Approaches	$M/M_{cr} = 1.5$			$M/M_{cr} = 3$		
	μ	σ	v	μ	σ	v
EC-2	0.63	1.96	3.83	1.03	0.53	0.28
ACI 440.1R-06	0.57	2.37	5.62	1.01	0.57	0.32
ACI 318.R-05	0.30	0.93	0.86	0.71	0.25	0.06
ISIS	1.08	3.64	13.25	1.14	0.58	0.33
CSA S806-02	1.26	3.78	14.29	1.18	0.60	0.35
Faza & GangaRao	1.05	3.31	10.96	1.02	0.45	0.20
Benmokrane et al.	1.27	4.04	16.35	1.30	0.52	0.27
Toutanji & Saafi	0.72	2.23	4.90	1.16	0.55	0.30
Yost et al.	0.46	1.66	2.76	0.89	0.35	0.12
Bischoff	0.88	2.70	7.30	1.08	0.54	0.29

variation of results at this moment ratio is significantly bigger than that for a moment ratio of 3. At this moment ratio, all the approaches show accurate predictions.

4 CONCLUSIONS

From the analytical and statistical study presented in the paper, it is shown that most of the existing approaches to calculate deflections of FRP RC beams give safe predictions (not always accurate) for moment ratios of 3.0 and $n\rho$ values lower than 0.2, however, for lower moment ratios, and due to the dispersion of results, this conclusion is not proved.

In general, as the moment ratio increases, the approaches give less scattered results. The accuracy of the deflection ratio for a moment ratio of 1.5 is highly dependent on the cracking moment.

At a moment ratio of 3, almost all the approaches give results adjusted to the experimental data, with mean deflection ratios between 0.9 and 1.3.

5 ACKNOWLEDGEMENTS

The authors acknowledge the support provided by the Spanish Government (Ministerio de Educación y Ciencia), Project ref. BIA-2007-60222.

REFERENCES

- Abdalla, H.A. 2002. Evaluation of deflection in concrete members reinforced with fibre reinforced polymers (FRP) bars. *Composites Structures* 56 (02): 63-71.
- ACI 318-05. 2005. Building Code Requirements for Reinforced Concrete. ACI Committee 318, American Concrete Institute, Detroit, Michigan.
- ACI 440.1R-06. 2006. Guide for the Design and Construction of Concrete Reinforced with FRP Bars. ACI Committee 440, American Concrete Institute, USA.
- Alsayed, S.H. 1998. Flexural Behavior of concrete beams reinforced with GFRP bars. *Cement and Concrete Composites* 20(98): 1-11.
- Al-Sunna, R., Pilakoutas, K., Waldron, P. & Guadagnini, M. 2006. Deflection of GFRP Reinforced Concrete Beams. Proceedings of the 2nd FIB congress, Naples. Italy.
- Barris, C., Torres, Ll., Turon, A., Baena, M. & Catalan, A. 2009. An experimental study of the flexural behaviour of GFRP RC beams and comparison with prediction models. *Composites Structures* 91(09): 286-295.
- Benmokrane, B., Chaallal, O. & Masmoudi, R. 1996. Flexural response of concrete Beams reinforced with FRP reinforcing bars. *ACI Struct. J.* 91(2): 46-55.
- Bischoff, P.H. 2007. Rational model for calculation deflection of reinforced concrete beams and slabs. *Can. J. Civ. Eng.* 34: 992-1002.
- Bogdanovic, B. 2002. Deflection calculations of FRP-Reinforced concrete beams. 23.735 Use of composites Materials in Civil Engineering.
- Branson, D.E. 1977. Deformation of concrete structures. New York: McGraw-Hill.
- CEN 2004. Eurocode 2: Design of concrete structures - Part 1-1: General rules and rules for buildings. BS EN 1992-1-1, European Committee for Standardisation, Brussels.
- CSA 2002. S806-02: Design and Construction of Building Components with Fibre-Reinforced Polymers. Canadian Standards Association, Canada.
- Cosenza, E., Greco, C., Manfredi, G. & Pecce. M. 1997. Flexural behaviour of concrete beams reinforced with fibre reinforced plastic (FRP) bars. Non- Metallic (FRP) Reinforcement for Concrete Structures. Proceedings of the Third international Symposium, Vol. 2.
- Duranovic, N., Pilakoutas, K. & Waldron, P. 1997. Test on concrete beams reinforced with glass fibre reinforced plastic bars. Non- Metallic (FRP) Reinforcement for Concrete Structures. Proceedings of the Third international Symposium, Vol. 2.
- Faza, S.S., & GangaRao, H.V.S. 1992. Pre and post cracking deflection behaviour of concrete beams reinforced with fibre reinforced plastic rebars. Proc., Advanced Composites Materials in Bridges and Structures. Canadian Society for Civil Engineering, Sherbooke, Que., Canadian, 151-160.
- ISIS Canada. 2001. Reinforcing concrete structures with fibre reinforced polymers. Design manual N° 3 Manitoba, Canada ISIS Canada Corporation.
- Larralde, J. & Rodríguez, R.S. 1992. Nuevo tipo de refuerzo para hormigón. *Revista de obras publicas* N°. 3.315 Año 139.
- Mota, C., Almarin, S. & Svecova, D. 2006. Critical Review of Deflection formulas for FRP-RC members. *Journal of composites for construction*. ASCE J Compos Constr 3(10): 1090-1268.
- Pecce, M., Manfredi, G. & Cosenza, E. 1998. Experimental behaviour of concrete beams reinforced with glass FRP bars, *ECCM-8*, 227-234.
- Razaqpur, A.G., Svecova, D. & Cheung, M.A. 2000. Rational Method of calculation deflection of fibre reinforced polymer reinforced beams. *ACI Struct. J.* 97(1):175-184.
- Saikia, B., Kumar, P., Thomas, J., Nanjunda Rao, K. S. & Ramaswamy, A. 2007. Strength and serviceability performance of beams reinforced with GFRP bars in flexure. *Construction and Building Materials* 21(07): 1709-1719.
- Toutanji, H. & Deng, Y. (2003). Deflection and crack width prediction of concrete beams reinforced with glass FRP rods. *Construction and Building Materials* 17 (03): 69-74.
- Toutanji, H.A., & Saafi, M. 2000. Flexural behaviour of concrete beams reinforced with glass fibre reinforced polymers (GFRP) bars. *ACI Struct. J.* 97 (5): 712-719.
- Yost, J.R., Gross, P. & Dinehart, D.W. 2003. Effective moment of inertia for glass fibre reinforced polymer reinforced concrete beams. *ACI Struct, J.* 100 (6): 732-739.

Experimental Study on Deformation Recovery and Residual Strength of FRP RC Beams

M. H. Oh (s4mecca@gmail.com), S. N. Hong, T. W. Kim, J. Cui & S. K. Park

Department of Civil Environmental Engineering, Sungkyunkwan University, Suwon, Republic of Korea

ABSTRACT Many researches on behavior of the structures which were externally strengthened with FRPs have been conducted. However, researches on time-dependent behavior have not been conducted yet. In order to provide improved serviceability to reinforced concrete (RC) members strengthened with FRPs, the behavior of RC structures strengthened with FRPs under sustained loads should be investigated. This paper presents a series of long-term deflection, deformation-recovery and residual strength experiments. For the long-term experiments, three RC beams were fabricated and two of the beams were strengthened with a carbon FRP (CFRP) plate and a glass FRP (GFRP) plate respectively. The beams were placed under sustained load for about 550 days and unloaded. After unloading, static flexural experiments were carried out. As the result, CFRP showed better performance in terms of deflection and strains of rebars and CFRP plate. Moreover, CFRP showed higher deformation recovery and residual strength than the other beams.

1 INTRODUCTION

In the recent construction industry, there has been a wide use of reinforced concrete (RC) and these RC structures are in need of rehabilitation and strengthening as it gets old. In order to strengthen RC structures, various strengthening materials and methods have been used. Particularly, Fiber Reinforced Polymers (FRPs) have been considered to be an innovative material for application of the External Bonded Reinforcement and Near Surface Mounted Reinforcement. FRPs have many superior characteristics, such as corrosion resistance, high tensile strength-to-weight ratio, nonconductivity and design flexibility. Since the FRPs have not only mechanical superiority but also marketability, worldwide interest and application of the FRPs has arisen.

In order to investigate the behavior of the RC beams that had been externally strengthened with FRPs, various researchers such as Hamid & Allan (2001), Pham & Al-Mahaidi (2006), Wu et al. (2006) have carried out research works.

Unlike the static behavior of the FRPs, research works on the beams under sustained loads are extremely rare. Tan & Saha (2006) and Al Chami et al. (2009) carried out a series of experiments on the time-dependent behavior of CFRP and GFRP-strengthened concrete beams. Through the time-dependent experiments, there is no virtually improvement in terms of long-term deflection although FRP-strengthening is effective to increase the ultimate capacities of the beams.

For the creep recovery of prepacked aggregate

concrete, Abu & Abdul (1992) made twelve concrete cylinders and four creep specimens were loaded by sustained load, which were 40% of the ultimate strength. After 90 days, the specimens were unloaded to measure creep recovery.

In this paper, three RC beams, carbon FRP-strengthened beam, glass FRP-strengthened beam and normal RC beam were made. For investigating time-dependent behavior, deformation recovery and residual strength, long-term experiment and static flexural experiment were carried out.

2 EXPERIMENT

2.1 Parameters and dimensions of specimens

The experiment was carried out on three RC beams. Compression rebars were over-reinforced in order to prevent compression failure of the beams. Detail and test setup of the beams were shown in Figure 1. The parameters considered in this experiment were the types of FRPs. One beam was used as a control beam and two beams were externally strengthened with CFRP and GFRP plate respectively. The FRP plates were bonded underneath the beams in 2160mm lengths assuming the effective span length of 90%. The test parameters of the experiment are listed in Table 1.

2.2 Material properties

For the 28-day compressive strength of the concrete, average of three standard cylinder compressive tests were undertaken which has size of 100mm×200mm. Tensile tests were undertaken to obtain the yield strength and

Modulus of elasticity. Table 2 lists the material properties of concrete, steel and FRPs.

2.3 Experiment setup

In order to investigate the long-term behavior of the beams strengthened with CFRP and GFRP plates, all of the beams were loaded by a sustained load of 25kN for

about 550 days. For the measurement of strains, strain gauges were bonded to rebars and FRP plates. One dial gauge was installed at the mid-span to measure the deflection of the beams. The strains and deflections of the beams were obtained by using a data logger every day. The location of the gauges was shown in Figure 1.

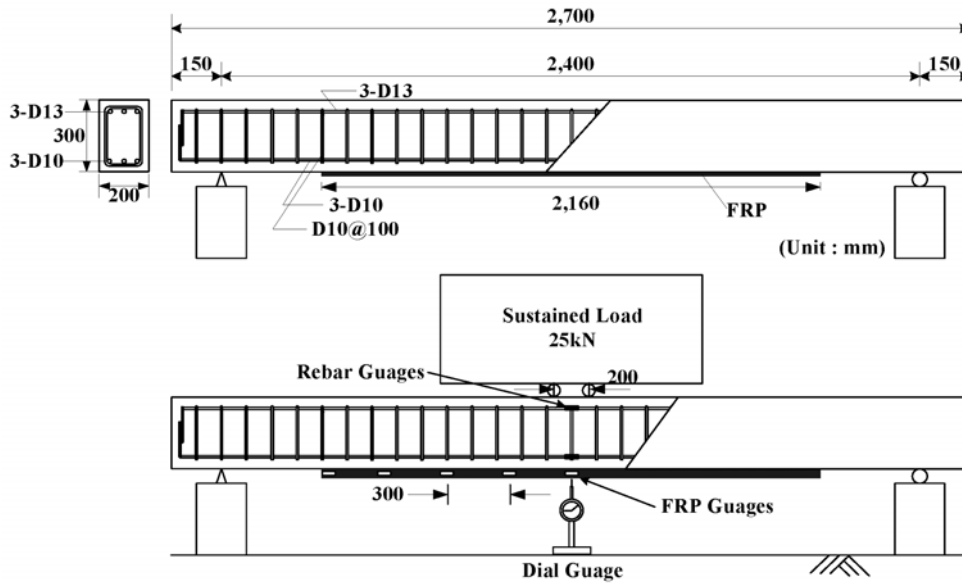


Figure 1 Detail and test setup of the beams

Table 1 Parameters of the experiments

Beams	Type of FRP	Amount of FRP	Strengthening Length (mm)
SNF	–	–	–
LCS	CFRP	1 Plate	2160
LGS	GFRP	1 Plate	2160

Table 2 Material properties (unit : MPa)

Type of Material	Concrete	Steel		FRP	
		D10	D13	CFRP	GFRP
Compressive Strength	25.7	–	–	–	–
Yield strength	–	457.2	466.2	–	–
Tensile Strength	–	766.3	679.3	3000	1000
Modulus of Elasticity	2.16 ×10 ⁴	2.01 ×10 ⁵	2.11 ×10 ⁵	1.65 ×10 ⁵	4.0 ×10 ⁴

After about 550 days, all beams were unloaded. In order to figure out the characteristics of deformation recovery of the beams, the strains and deflections were measured for about 60 days in the same way.

To estimate the residual strength of the beams, static flexural experiments were carried out by using a 1,000kN Universal Testing Machine(UTM). Each beam was loaded at the rate of 1mm/min and two linear

variable displacement transducers(LVDTs) were located at the mid-span of the beams.

3 RESULT AND DISCUSSION

3.1 Long-term experiments

In terms of the immediate deflection, the beams that were strengthened with CFRP and GFRP plates showed less deflection than that of SNF as shown in Figure 2. In particular, LCS, the beam with CFRP plate, showed the least immediate deflection compared with the other beams. The deflection of LCS was about 35% less than that of SNF. Thus it can be said that the beams externally strengthened with FRPs are superior to non-strengthened beam in terms of immediate deflection.

For about 550 days, the beams were located under the sustained load of 25kN. On the whole, it was indicated that LCS showed better time-dependent performance than the other beams. Comparing the total deflections on the last day of the long-term experiment, LGS and LCS showed 0.4% and 14% less deflections respectively than SNF did. For the time-dependent deflection, which is total deflection minus immediate deflection, no significant decrease in the time-dependent performance was indicated between SNF and LGS. It seems that the GFRP plate did not contribute to the long-term deflection control because its modulus of elasticity is lower than that of steel rebar.

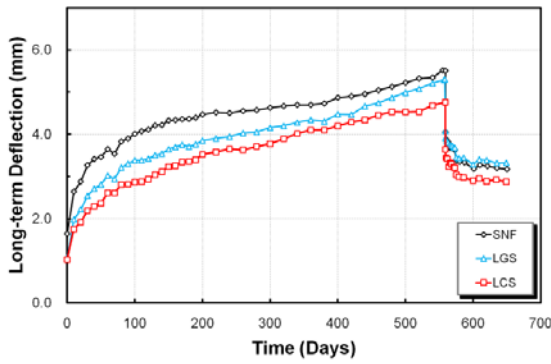


Figure 2 Long-term deflection at mid-span

Figure 3 shows changes in strains of tension rebars with the duration of time. For the immediate strains of tension rebars, the LCS indicated about 63% less strain than that of SNF. However, In terms of the time-dependent strain, which is excluding the immediate strain, three beams showed very similar performance. It can be said that the CFRP plate is very effective in resisting the tension force under the immediate load but FRPs are not so effective against a sustained load.

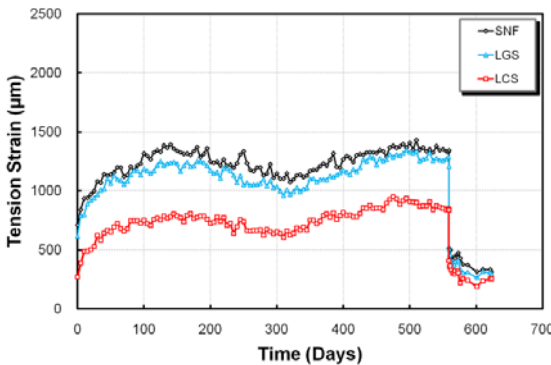


Figure 3 Tension strain at mid-span

Overall, the LCS showed less strain of FRP than LGS. For immediate strain of FRP, LCS showed about 51% less strain than LGS. In comparison of time-dependent strain, which excludes the immediate strain, LCS showed about 10% less strain than LGS. The strains of FRPs tend to decrease after 180 days and increase after 300 days. It is due to the change in temperature. The strains of FRPs with duration of time were shown in Figure 4.

3.2 Deformation recovery

For the deformation recovery experiment, all the beams were unloaded after about 550 days. The strains and deflections were measured for about 60 days. Table 3 shows the comparison of immediate deformation and immediate recovery of deformation. When the ratio of immediate deformation to immediate recovery of deformation is greater than 1, it means that the amount of the immediate deformation is greater than that of the

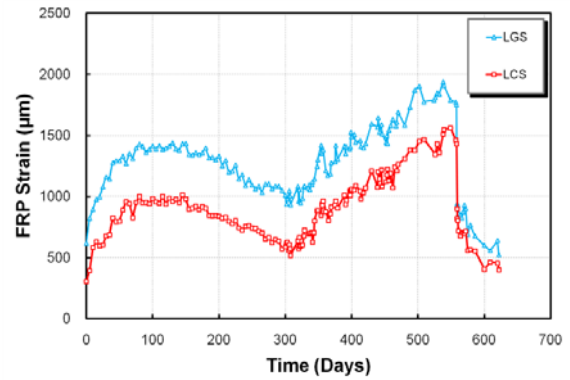


Figure 4 FRP strain at mid-span

immediate recovery of deformation. Unlike SNF, the strengthened beams showed the ratios less than 1. The ratios of immediate strain of FRP to immediate recovery of FRP seem to be resulted from the FRPs bonded to the bottom of the beams.

Table 3 Comparison of deformation recovery

(a)			
Beams	Immediate deflection ①	Immediate recovery of deflection ②	① / ②
SNF	1.642	1.445	1.136
LCS	1.020	1.124	0.907
LGS	1.070	1.226	0.873

(b)			
Beams	Immediate strain of tension rebar (µm) ①	Immediate recovery of tension rebar strain (µm) ②	① / ②
SNF	710	815	1.136
LCS	269	431	0.907
LGS	614	774	0.873

(c)			
Beams	Immediate strain of FRP (µm) ①	Immediate recovery of FRP strain (µm) ②	① / ②
SNF			1.136
LCS	305	533	0.907
LGS	617	813	0.873

In comparison of a net deformation recovery, excluding immediate recovery, the beams which had the most long-term deformation showed the most deformation recovery. Among SNF, LCS and LGS, SNF showed the most deformation recovery. On the other hand, LCS had the least deformation recovery. Thus, it can be said that deformation recovery is proportionate to long-term deformation.

3.3 Residual strength

In order to investigate the residual strength of the beams strengthened with FRPs, a static flexural experiment was carried out. Load-deflection curves of the beams are shown in Figure 5. As shown in the figure, LCS and

LGS were failed due to delamination. It appeared that the strengthened beams, LCS and LGS, had 21% and 7% higher load-carrying capacity than SNF did respectively. In addition, LCS had 15% higher load-carrying capacity than LGS did. Because of the material characteristics of FRPs, LCS, the beam with CFRP plate showed a better performance even though it showed a very brittle behavior. However, the beam with GFRP plate showed relatively ductile behavior. Figure 6 shows load-strain curves of CFRP plate and GFRP plate. Since the sustained load of 25kN was in the elastic range, the load of 25kN would not have an influence on the overall behaviors of the beams. Besides, initial stiffness of the beams showed quite linear elastic behavior. Because the sustained load was greater than a cracking load, concrete cracks had already occurred. Thus, tension rebars resisted tension force without contribution of concrete.

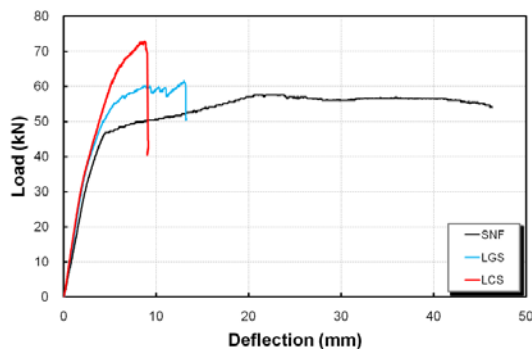


Figure 5 Load-deflection relationship

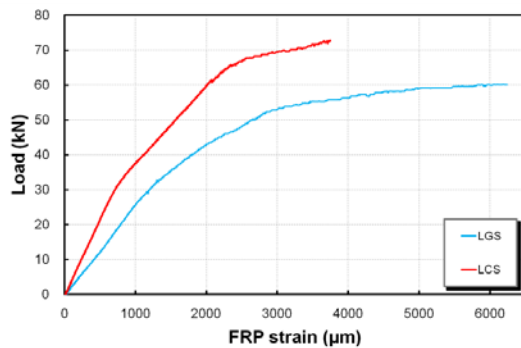


Figure 6 Load-strain relationship of FRPs

As shown in the Figures 6, delamination of CFRP occurred at a strain of 3743 μm which was only 19% of the ultimate strain. In case of GFRP, full capacity was not achieved either since the strain was 6236 μm which was only 25% of ultimate strain of GFRP plate when delamination occurred. Thus, it can be said that full capacity of FRP plates were not achieved through the external strengthening method. It was estimated that an

increase in load-carrying capacity was influenced by not only high modulus of elasticity of FRP but also bond characteristic.

4 CONCLUSIONS

Through the long-term experiment, deformation recovery and residual strength experiment, the following conclusions were reached.

(1) The beam with CFRP plate showed a better performance in terms of long-term deflection and residual strength.

(2) Although the strengthening materials were very effective in resisting immediate load, they did not affect the long-term deformation.

(3) There was a correlation between long-term deformation and deformation recovery. It can be said that deformation recovery is proportionate to long-term deformation.

(4) Even though all of the beams were loaded by a sustained load of 25kN, the beam strengthened with CFRP plate showed the most load-carrying capacity.

5 ACKNOWLEDGMENT

This work was supported by the R&D program (06 Construction innovation B05, NRG: Network Research Group) of the Korea Institute of Construction and Transportation Technology Evaluation Planning. (KICTTEP)

REFERENCES

- Abu, S.M. & Abdul, A. 1992. Creep recovery of prepacked aggregate concrete. *Journal of Materials in Civil Engineering*. Vol. 4(3): 320-325.
- Al Chami, G., Thériault, M., Neale Johnson, K.W. 2009. Creep behaviour of CFRP-strengthened reinforced concrete beams. *Construction and Building Materials*. Vol. 23(4): 1640-1652.
- Hamid, R. & Allan, H. 2001. Concrete beams strengthened with externally bonded FRP plates. *Journal of Composites for Construction*. Vol. 5(1): 44-56.
- Pham, H. & Al-Mahaidi, R. 2006. Experimental investigation into flexural retrofitting of reinforced concrete bridge beams using FRP composites. *Composite Structures*. Vol. 66(1-4): 617-625.
- Tan, K.H. & Saha, M.K. 2006. Long-term deflections of reinforced concrete beams externally bonded with FRP system. *Journal of Composites for Construction*. Vol. 10(6): 474-482.
- Wu, Z., Li, W., Sakuma, N. 2006. Innovative externally bonded FRP/concrete hybrid flexural members. *Composite Structures*. Vol. 72: 289-300.

Shear Strengthening of Concrete Beams

Influence of the Concrete Properties in the Effectiveness of the NSM CFRP Laminates for the Shear Strengthening of RC Beams

Salvador Dias (sdias@civil.uminho.pt) & Joaquim Barros

ISISE, University of Minho, Guimarães, Portugal

ABSTRACT The New Surface Mounted (NSM) technique was applied to increase the shear resistance of Reinforced Concrete (RC) beams. For this purpose, laminates of Carbon Fiber Reinforced Polymer (CFRP) were introduced into thin slits made on the concrete cover of the lateral faces of the beams to be strengthened. In the present paper the influence of concrete strength on the effectiveness of the NSM technique is assessed by an experimental program. From the obtained results it can be concluded that the NSM shear strengthening technique with CFRP laminates is still effective in RC beams with low concrete strength. However, as minimum is the concrete strength as less effective is the NSM technique.

1 EXPERIMENTAL PROGRAM

The influence of the concrete mechanical properties on the performance of the NSM technique using CFRP laminates for the shear strengthening of RC beams (Figure 1) is assessed by experimental research, which main features are presented in this publication.



Figure 1 NSM technique with CFRP laminates for the shear strengthening of RC beams

1.1 Test series and materials properties

Figure 2 presents the T cross section beam prototype used in the experimental program. The reinforcement systems were designed to assure that all the tested beams failed in shear. To localize shear failure in only one of the beam shear spans, a three point load configuration of a distinct length of the beam shear spans was selected. To avoid shear failure in the L_r beam span, steel stirrups $\phi 6@75\text{mm}$ were applied in this span. In terms of the shear reinforcement systems the differences between the tested beams were localized in the L_i beam span. Five arrangements of NSM CFRP laminates were used in RC beams that were manufactured with a concrete of a compressive strength at the age of beam tests of 39.7 MPa ($f_{cm} = 39.7$ MPa) and 18.6 MPa ($f_{cm} = 18.6$ MPa). The differences between the beams with $f_{cm} = 39.7$ MPa and the beams with $f_{cm} = 18.6$ MPa are restricted to the mode of preventing brittle spalling of the concrete cover

at the supports (Figure 2). To overcome the difficulties to bend $\phi 32$ mm longitudinal tensile bars, their ends were welded to steel plates in the beams with the lower concrete strength (Figure 2).

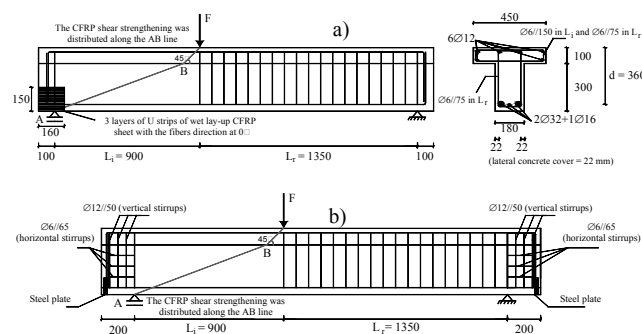


Figure 2 Geometry and steel reinforcements applied in all tested beams (dimensions in mm): a) beams with $f_{cm} = 39.7$ MPa and b) beams with $f_{cm} = 18.6$ MPa

For each type of concrete five arrangements of NSM CFRP laminates were applied in five RC beams with a percentage of steel stirrups of 0.10% ($\rho_{sw} = 0.10\%$), and in five RC beams with a percentage of steel stirrups of 0.17% ($\rho_{sw} = 0.17\%$). Three distinct inclinations of CFRP laminates (45° , 60° and 90°) were studied and, for inclined laminates, two levels of CFRP percentage (ρ_f) were analyzed (Table 1 and Figure 3). For both percentages of CFRP, the spacing of laminates for each inclination was obtained with the purpose that the shear strengthening contribution of the CFRP would be similar (Dias and Barros 2009).

The three point beam bending tests (Figure 2) were carried out using a servo closed-loop control equipment, taking the signal read in the displacement transducer,

placed at the loaded section, to control the test at a deflection rate of 0.01 mm/second.

The concrete compressive strength was evaluated at 28 days and at the age of the beam tests, carrying out direct compression tests with cylinders of 150 mm diameter and 300 mm height, according to EN 206-1 (2000). In the tested beams, high bond steel bars of 6, 12, 16 and 32 mm diameter were used. The values of their main tensile properties were obtained from uniaxial tensile tests performed according to the recommendations of EN 10002-1 (1990). The tensile properties of the CFK 150/2000 S&P laminates were characterized by uniaxial tensile tests carried out according to ISO 527-5 (1997). Table 2 includes the average values obtained from these experimental programs. According to this table, the

Table 1 Shear reinforcement configurations of the tested beams

Number of laminates	CFRP angle $[\theta_f]$ ^a (°)	CFRP spacing $[s_f]$ (mm)	CFRP percenta $ge [\rho_f]$ ^b (%)	Percentage of steel stirrups	
				$\rho_{sw} = 0.10\%$ ^c	$\rho_{sw} = 0.17\%$ ^d
2×4	45	275	0.08	2S-4LI45	4S-4LI45
2×4	60	243	0.07	2S-4LI60	4S-4LI60
2×7	90	114	0.13	2S-7LV	4S-7LV
2×7	45	157	0.13	2S-7LI45	4S-7LI45
2×6	60	162	0.11	2S-6LI60	4S-6LI60

^a Angle between the CFRP fiber direction and the beam axis; ^b The CFRP percentage was obtained from $\rho_f = (2a_f b_f) / (b_w s_f \sin \theta_f)$ being $a_f = 1.4$ mm and $b_f = 9.5$ mm the dimensions of the laminate cross section and $b_w = 180$ mm is the beam web width; ^c 2S-R is the reference beam without CFRP (Figure 3); ^d 4S-R is the reference beam without CFRP (Figure 3).

Table 2 Alues of the properties of intervening materials

Materials	Beams manufactured with the higher concrete strength				Beams manufactured with the lower concrete strength					
	Concrete ^a	$f_{cm} = 31.7$ MPa (at 28 days)				$f_{cm} = 15.9$ MPa (at 28 days)				
	$f_{cm} = 39.7$ MPa (age of beam tests)				$f_{cm} = 18.6$ MPa (age of beam tests)					
Steel	Tensile strength (MPa)	$\phi 6$	$\phi 12$	$\phi 16$	$\phi 32$	$\phi 6$	$\phi 12$	$\phi 16$	$\phi 32$	
	f_{sym} (yield stress)	542	453	447	759	539	453	429	734	
	f_{sum} (maximum stress)	594	591	566	902	595	581	563	885	
CFRP Laminates ^b	f_{fum} (MPa)	E_{fm} (GPa)			ϵ_{fum} (‰)	f_{fum} (MPa)	E_{fm} (GPa)			ϵ_{fum} (‰)
	2741.7	170.9	16.0	2847.9	174.3	16.3				

^a f_{cm} is the average value of the concrete compressive strength; ^b f_{fum} , E_{fm} and ϵ_{fum} are the maximum tensile strength, Young's modulus and maximum strain of the CFRP laminates.

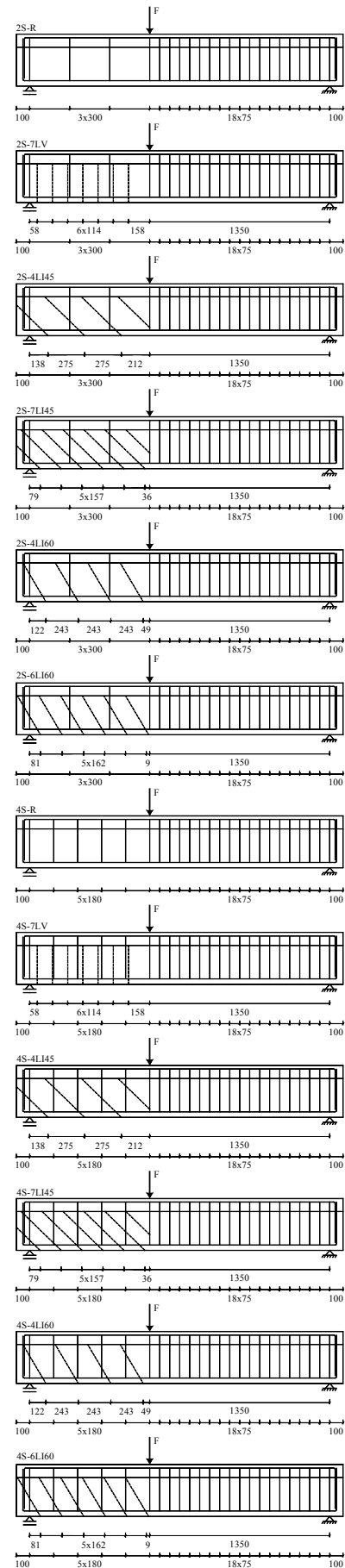


Figure 3 Localization of the steel stirrups (continuous line) and CFRP laminates (dashed line) (dimensions in mm)

properties of the steel and CFRP are similar in the two types of beams (beams with the higher and lower concrete strength). The MBrace Resin 220 (Degussa 2003) epoxy adhesive was used to bond the laminates to the concrete.

1.2 Discussion of tests results

The recorded force-displacement diagrams ($F-u$) in the loaded section obtained for the tested beams are reported in Figure 4.

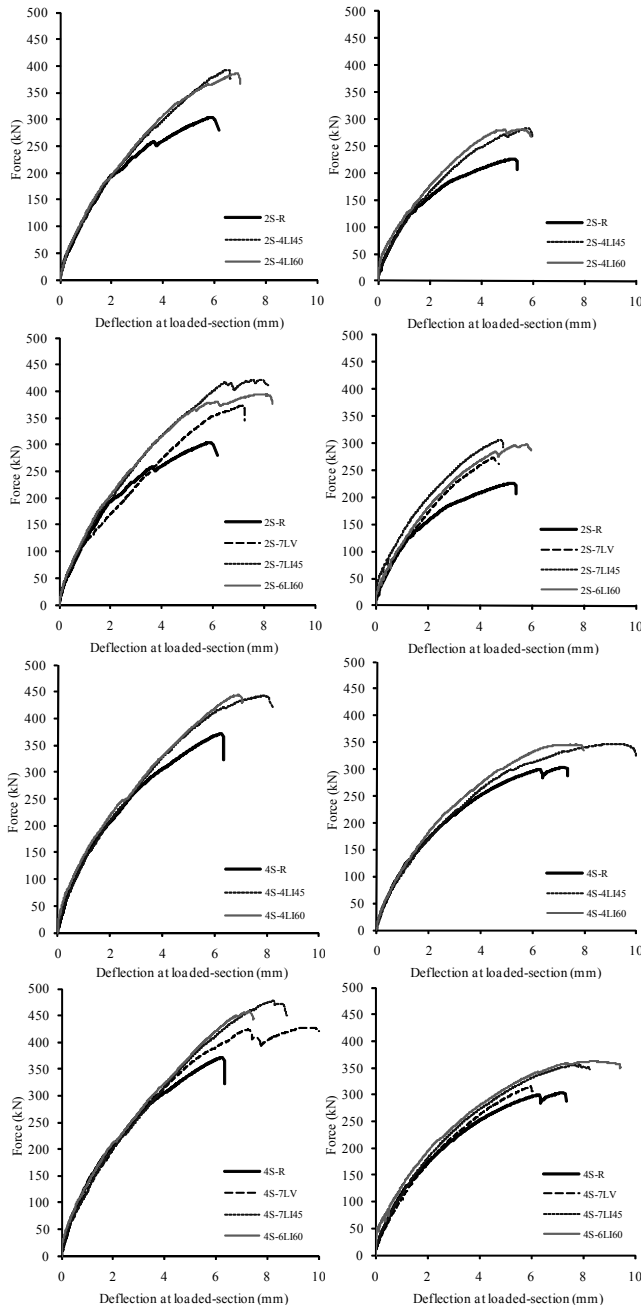


Figure 4 Force vs deflection at the loaded-section for the tested beams (left part: beams with $f_{cm} = 39.7$ MPa; right part: beams with $f_{cm} = 18.6$ MPa)

Up to critical diagonal crack (CDC) initiation the strengthened and its corresponding reference beam had similar $F-u$, regardless of the percentage of steel stirrups and the percentage and orientation of the CFRP. At CDC

initiation the load decay observed in the reference beams did not occur in the CFRP shear strengthened beams, revealing that the presence of the CFRP delayed the propagation of the shear crack. This results in an increase in the beam’s load carrying capacity.

The maximum load (F_{max}) and the corresponding deflection at loaded-section (u_{Fmax}) for all the tested beams are included in Table 3. The values of the $\Delta F_{max} / F_{max}^{ref}$ ratio (gain due to CFRP where $\Delta F_{max} = F_{max} - F_{max}^{ref}$ and F_{max}^{ref} is the maximum force of reference beam) for the beams with $f_{cm} = 39.7$ MPa and $f_{cm} = 18.6$ MPa are included in Table 3 and represented in Figure 5, being visible the increase of the NSM effectiveness with the increase of the concrete strength. According to the values into Table 3, the average value of the $\Delta F_{max} / F_{max}^{ref}$ ratio for NSM arrangements adopted in beams with higher and lower concrete compressive strength was 26.5% and 22.4%, respectively (the values regarding the 4S-7LV shear strengthening configuration was excluded for this analysis). Independently of the concrete strength and the percentage of existing steel stirrups, the inclined laminates were more effective than vertical laminates. An increase of the percentage of CFRP produced an increase of the shear strengthening contribution.

Table 3 Relevant results of the load capacity up to beam’s failure

	Beams	F_{max}	Gain	u_{Fmax}	Beams	F_{max}	Gain	u_{Fmax}
	($\rho_{sw} =$	(kN)	due to		($\rho_{sw} =$	(kN)	due to	
	0.10%)		CFRP	0.17%)		CFRP		
			(%)	(mm)			(%)	(mm)
$f_{cm} = 39.7$ MPa	2S-R	303.8	-	5.88	4S-R	371.4	-	6.25
	2S-4L145	392.8	29.3	6.45	4S-4L145	442.5	19.1	7.93
	2S-4L160	386.4	27.2	6.90	4S-4L160	443.8	19.5	6.91
	2S-7LV	374.1	23.1	7.17	4S-7LV	427.4	15.1	9.75
	2S-7L145	421.7	38.8	7.93	4S-7L145	478.1	28.7	8.26
	2S-6L160	394.4	29.8	7.87	4S-6L160	457.6	23.2	7.31
$f_{cm} = 18.6$ MPa	2S-R	226.5	-	5.29	4S-R	303.8	-	7.20
	2S-4L145	283.0	24.9	5.79	4S-4L145	347.2	14.3	9.28
	2S-4L160	281.6	24.3	5.57	4S-4L160	345.6	13.8	7.67
	2S-7LV	273.7	20.8	4.55	4S-7LV	315.2	3.8	5.98
	2S-7L145	306.5	35.3	4.79	4S-7L145	356.4	17.3	7.83
	2S-6L160	297.7	31.4	5.84	4S-6L160	362.3	19.3	8.36

In general the failure modes of the tested beams with CFRP have been influenced by the concrete strength, since at failure a certain concrete volume was attached to the laminates (concrete fracture). This justifies the better shear strengthening contribution of the CFRP in the beams with $f_{cm} = 39.7$ MPa. The failure modes of the beams with NSM laminates are also influenced by the percentage of the CFRP. In some beams with the higher percentage of CFRP a detrimental group effect (Figure 6) between neighboring laminates occurred that originated a separation of parts of the concrete cover, which had

already been observed in previous experimental programs (Barros and Dias 2006; Rizzo and De Lorenzis 2009; Dias and Barros 2009) and analytical research (Bianco et al. 2009).

Figure 5 also shows that the amount of existing steel stirrups plays a very important role on the effectiveness of the NSM shear strengthening technique with CFRP laminates. In fact, the effectiveness of the CFRP was higher in the beams with the lower percentage of steel stirrups analysed ($\rho_{sw} = 0.10\%$). According to Figure 5, for an increase from 0.10% to 0.17% in the percentage of steel stirrups in the L_i beam span (about 70%), the NSM strengthening effectiveness decreased in about 70% and 55% (the value regarding the solution with vertical laminates was excluded for this evaluation) for the beams with $f_{cm} = 39.7$ MPa and $f_{cm} = 18.6$ MPa, respectively. It emerges that a formulation for the prediction of the NSM shear strengthening contribution cannot neglect the percentage of existing steel stirrups.

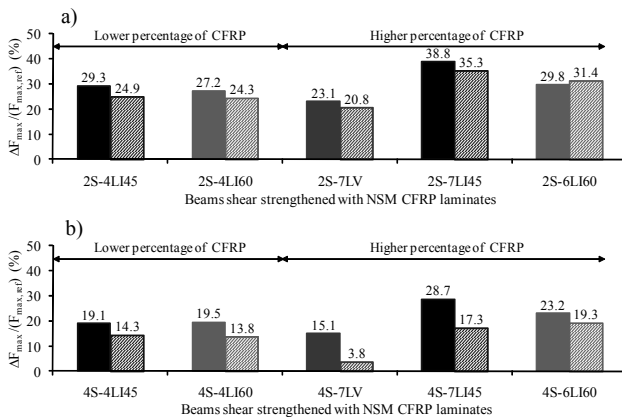


Figure 5 Concrete strength influence in the effectiveness of the NSM shear strengthening technique with CFRP laminates (left column: $f_{cm} = 39.7$ MPa; right column: $f_{cm} = 18.6$ MPa): a) beams with $\rho_{sw} = 0.10\%$; b) beams with $\rho_{sw} = 0.17\%$

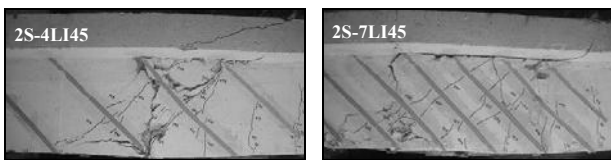


Figure 6 Influence of CFRP percentage on failure modes (beams with $f_{cm} = 18.6$ MPa)

2 CONCLUSIONS

The following conclusions can be obtained from the experimental results:

- The NSM CFRP laminates shear strengthening technique is still effective in beams of concrete with an average compressive strength of 18.6 MPa at the age of the tests, which can be considered as the lowest concrete strength class for structural purposes. The CFRP shear strengthening configurations provided an increase not only in terms of maximum load, but

also in terms of load carrying capacity after shear crack formation. The concrete strength has an important role on the effectiveness of the NSM shear strengthening technique, since this effectiveness decreases with the decrease of the concrete strength. In fact, when the same NSM CFRP laminates arrangements were applied in a group of beams of concrete compressive strength (f_{cm}) equal to 39.7 MPa and in another group of beams of $f_{cm} = 18.6$ MPa, the CFRP laminates were more effective in the former beams.

- Inclined laminates were more effective than vertical laminates and an increase of the percentage of laminates led to an increase of the shear capacity of the beams. A detrimental effect of the increase of the percentage of the existing steel stirrups exists in terms of the effectiveness of the NSM technique for the shear resistance of RC beams.
- An analytical formulation for the prediction of the NSM shear strengthening contribution should take into account the concrete mechanical properties, the percentage and orientation of the CFRP and the percentage of the existing steel stirrups.

3 ACKNOWLEDGEMENTS

The authors wish to acknowledge the support provided by the “Empreiteiros Casais”, Degussa, S&P® and Secil (Unibetão, Braga). The study reported in this paper forms a part of the research program supported by FCT, PTDC/ECM/73099/2006.

REFERENCES

- Barros, J.A.O. & Dias, S.J.E. 2006. Near surface mounted CFRP laminates for shear strengthening of concrete beams. *Journal of Cement and Concrete Composites* 28(3): 276-292.
- Bianco, V.; Barros, J.A.O.; Monti, G. 2009. Three dimensional mechanical model for simulating the NSM FRP strips shear strength contribution to RC beams. *Engineering and Structures Journal* 31(4): 815-826.
- Degussa Construction Chemicals Portugal. 2003. Technical Report MBrace Resin 220.
- Dias, S.J.E. & Barros, J.A.O. 2009. Performance of reinforced concrete T beams strengthened in shear with NSM CFRP laminates. *Engineering Structures* doi:10.1016/j.engstruct.2009.10.001.
- EN 206-1. 2000. Concrete - Part 1: Specification, performance, production and conformity. European standard, CEN: 69.
- EN 10002-1. 1990. Metallic materials - Tensile testing. Part 1: Method of test (at ambient temperature). European Standard, CEN: 35.
- ISO 527-5. 1997. Plastics - Determination of tensile properties - Part 5: Test conditions for unidirectional fibre-reinforced plastic composites. International Organization for Standardization (ISO): 9.
- Rizzo, A. & De Lorenzis, L. 2009. Behaviour and capacity of RC beams strengthened in shear with NSM FRP reinforcement. *Construction and Building Materials* 23: 1555-1567.

Experimental Tests on FRP Shear Retrofitted RC Beams

Camillo Nuti, Silvia Santini & Lorena Sguerri

Department of Structures, University of Roma Tre, Rome, Italy

ABSTRACT The paper presents the results of experimental tests on two reinforced concrete beams retrofitted by means of FRP strips. Both beams have been removed from the structure of one of the older r.c. buildings in Rome, built up at the beginning of XX century. The experimental tests are carried out in the Laboratory of the Department of Structures at the University of Roma Tre. Before retrofitting, preliminary tests are performed in order to evaluate the homogeneity and the mechanical characteristics of concrete, and elastic tests (shear/bending tests) in order to evaluate the original state of the beams. After retrofitting, failure tests (shear/bending tests) on the beams together with compressive tests on concrete and tension tests on rebars are carried out. All performed tests demonstrate the capability of repairing and retrofitting on r.c. structures of modest quality, moreover revealing some aspects due to the fragile behaviour of carbon fibers.

1 INTRODUCTION

Experimental tests on two existing beams, retrofitted by means of FRP strips, are carried out and discussed in the paper. Both beams have been removed from one of the older r.c. buildings in Rome built up in 1929, made of a 4 level frame with plan dimension of 75×36 meters.

In order to evaluate the original state of the beams, before retrofitting, some preliminary tests (Sonic Rebound method) have been performed.

After retrofitting, the beams have been subjected to loading until failure. In the paper results are described in terms of load bearing capacity and strain profile across section, with remarks on the strengthening contribution of FRP strips. In both beams, failure is due to shear, mainly as a consequence of lack of anchorage of longitudinal bars with subsequent rupture of FRP strips.

Performed tests demonstrate the capability of repairing and retrofitting interventions on r.c. structures of modest quality, moreover revealing some aspects due to the fragile behaviour of carbon fibres as well as the influence of the shear crack direction in relation to the unidirectional fibre.

Recently, some other authors have performed similar tests in order to show the efficiency of this kind of intervention (Carolin & Taljsten 2005, Guadagnini et al. 2006, Monti & Liotta 2007), but this is the first time that tests are carried out over beams extracted from real structures.

2 EXPERIMENTAL SETUP AND MATERIALS

2.1 Experimental setup and instrumentation

Tests were performed on two beams, named DB1 and

DB2, U strengthened in shear with externally bonded carbon fiber-reinforced plastics (CFRP) strips anchored in the web with an additional horizontal bar to prevent debonding. Both beams have also been strengthened in bending with longitudinal rebars placed along the lower side. Geometrical and reinforcing properties are summarized in Table 1. It is to point out that all existing rebars have no ribs and are protected with a very thin concrete cover while stirrups present a very random distribution.

Table 1 Geometrical and reinforcing properties of beams

	DB1	DB2
Total length	347 cm	389 cm
Experimental span	280 cm	310 cm
Section width	29 cm	29 cm
Section height	75 cm	75 cm
Existing rebars (inferior)	5φ10	6φ10
Retrofitting rebars	4φ16	4φ16
Stirrups	16φ6	15φ6
Stirrups step	15/30 cm	15/32 cm

Each beam was undertaken to both elastic and failure test. The beams were simply supported on rollers and were subjected to a three-point loading test. The total load at the midspan, was applied by means of a 1000 kN hydraulic actuator with small increments depending on the expected load capacity of the system.

A total of 24 linear position transducers have been used to register both vertical deflection in the midspan under the load and at the beam supports, diagonal deformations in the regions of expected critical shear cracks between the FRP strips along the shear span.

A total of 36 strain gauges are placed along all the FRP strips to check the local strains and to monitor the strain profile.

A complete description of the test setting together with instrumentation is given in Figure 1.

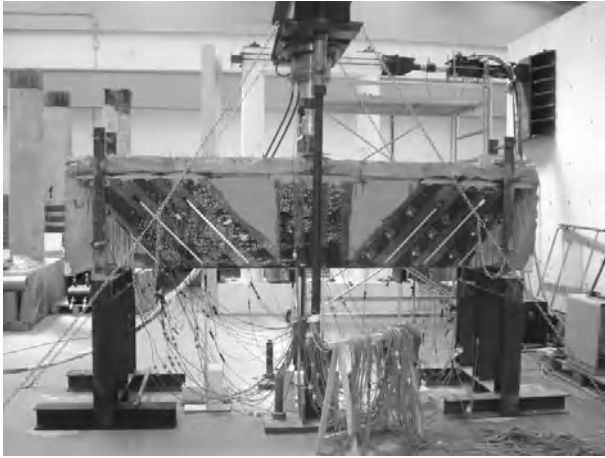


Figure 1 Test setting and instrumentation

2.2 Concrete

After completion of all experiments on retrofitted beams, customary direct tests on materials have been executed to evaluate their mechanical properties, giving for DB1 beam a mean value of cubic strength $R_{cu} = 14,70$ MPa and for DB2 $R_{cu} = 10,90$ MPa.

The compressive strength of concrete was evaluated by crushing 15 specimens obtained from core drilling on the two beams (diameter $\Phi = 94$ mm, height/diameter ratio $H/\Phi = 2.0$).

2.3 Steel Reinforcement

As for concrete, after completion of all experiments on retrofitted beams, 14 bar specimens (8 ϕ 6 from stirrups and 6 ϕ 10 from longitudinal reinforcement) have been taken from the reinforcement of as-built beams and subjected to direct tension tests. Afterwards, 4 specimens (ϕ 20 - FeB44k) from the bars provided to reinforce both beams in flexure, have been tested.

As expected, results of bars used in retrofitting are very homogeneous while results of tension test on original steel bars seems to be more scattered with minimum and maximum values of yielding and strength of: $f_{0.2\%,\min/\max} = 305$ MPa/630 MPa and $f_{\min/\max} = 430$ MPa/850 MPa.

3 FAILURE TESTS ON RETROFITTED BEAMS

3.1 Load-bearing capacity

During testing both of the strengthened beams failed in shear from one large diagonal crack. Failure occurred with complete debonding of composite nearly at the same load (around 425 kN) for both beams but with a quite different mode.

Failure of beam DB1 started from the left end of the beam as a result of a wide diagonal crack crossing the strips, probably due to the loss of anchorage of the longitudinal rebars close to the beam support (Figure 3), whereas failure of DB2 occurs, on the same side, with a wide crack started from a quarter of the span and a secondary crack started directly from the support (Figure 5). In this second case, longitudinal bars in flexure, passing over the support permitted a better anchorage.

The main phases of testing for both beams are presented in the following, with reference at the load versus displacement response in Figure 2 and Figure 4.

(1) Strips on the left of midspan start to debond from the beam bottom. For beam DB1 the phenomena occurred around 360 kN, whereas for DB2 it occurred around 300 kN. This last result match the experimental results by Carolin (2005) who observed that during loading of the beams to failure, when the load was approximately two-thirds or more of the failure load, a clicking sound was occasionally emitted from the beams. The occurrence of clicking increased in frequency as the beams were loaded closer to the maximum load-bearing capacity. Other than this, no significant warning signals preceded a sudden failure. Around 350 kN shear cracks on the left side become evident and at 400 kN the concrete repairing start to peel.

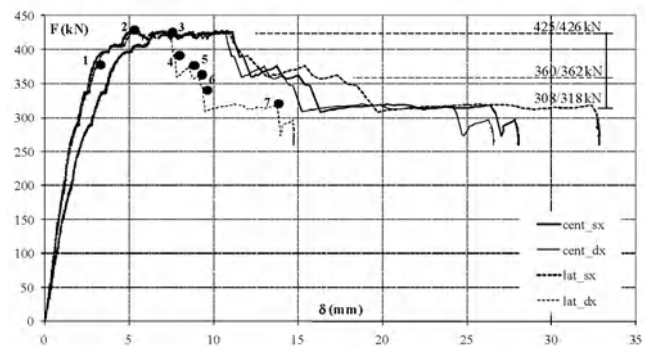


Figure 2 DB1: load – displacement graph with main phases of testing



Figure 3 DB1: failure

(2) Between 400 and 425 kN debonding for beam DB1 becomes more evident and progress until failure.

Deflection at midspan increases and diagonal shear cracks, already wide at 400kN, grow to be larger. A noticeable difference between displacement on the left support (hinge) and displacement on the right support (roller) have been observed. Diagonal displacements close to the left support vary between four and five times those on the right support. During loading of the beam to failure, the collapse mechanism tend to concentrate on the left side. Otherwise, for beam DB2 debonding becomes more evident at 427 kN and strips start to break. Diagonal displacements close to the left support are still small, about 2 mm.

(3,4,5,6,7) Post-peak behaviour of both beams is characterized by subsequent removal of remaining strips starting from the left support with increasing cracks up to failure.

The presence of several peak points on the load-displacement curves (Figure 2 and Figure 4) indicate the progressive rupture of the strips. More or less at 308 kN for DB1 and 221 kN for DB2 all frp strips are broken, shear cracks become more and more large until beam failure.

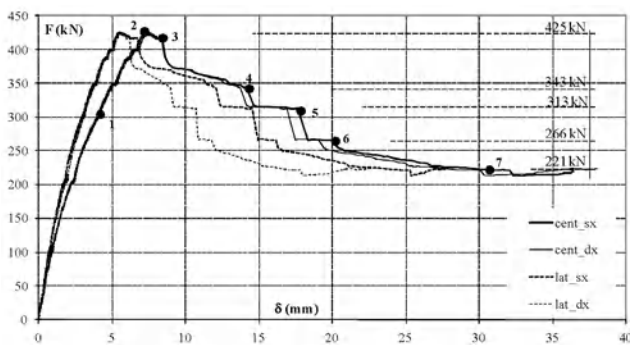


Figure 4 DB2: load – displacement graph with main phases of testing

3.2 Strain profile of FRP

In general, when a concrete structure is strengthened in shear, different failure modes can develop such as tensile failure in the fibre, anchorage failure for the composite sheet or strips or, more frequently, a combination of both.

In order to make out the strengthening behavior, three strain gauges were placed on each of the twelve diagonal strips in both beams.

The strains in the composite have been registered at three different height levels over the cross section in order to have the distribution of the strain field and to evaluate the corresponding stress level in the composite, assuming linear elastic behavior of FRP.

Strain profiles of both beams, have been drawn at different values of applied shear force, selected as follows: 0.25Pu (107 kN), equivalent to flexural cracking (from literature $P_{cr} = 0.24Pu$, on average); 0.50Pu (212 kN); 2/3Pu (212 kN), corresponding to debonding, as observed

also by Taljsten in his in experimental studies (2005); 0.85Pu (360 kN); 0.95Pu (400 kN); Pu (425 kN).

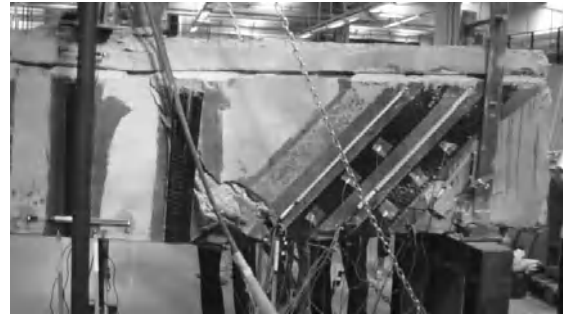


Figure 5 DB2: failure

Both beams failed in shear with complete debonding of the composite strips, which occurred more or less at the same load level (425,5 kN for DB1 and 427,5 kN for DB2).

Strain profiles, over the beam cross sections, remark that only a quarter of the strips reveals an effective contribution in shear resistance. All other strips shows premature debonding in proximity of the beam extrados.

Differently from steel stirrups, FRP strips do not seem to activate a truss resisting mechanism. Therefore the ultimate fiber fracture strain cannot be used in the same way as the yield strain for steel stirrups because of the nonuniform distribution of shear strains that act on the cross section. The design equations used in the main current design guidelines are based on a contribution of the FRP limited by the effective strain in the composite.

3.3 Strengthening contribution of FRP

Strain profiles allow to measure to what level the composite is stressed and also get an understanding of the contribution of composite strips to shear resistance of the beams.

Strains of DB1 beam (Figure 6) measured by strain gauges on FRP strips, corresponding to loading in the range 400 ÷ 425 KN are more or less equal to 0.3%. When load is close to collapse strains can reach peak values of 0.6%.

Given the linear elastic behaviour of CFRP strengthening with elastic modulus equal to 240 GPa, the strain limits above involve stress values around 720 MPa with peak of 1440 MPa.

The maximum FRP effective stress is given by *the effective debonding strength* $f_{fed} = 695$ MPa, based on *the debonding strength* $f_{fdd} = 715$ MPa, according to CNR design code, founded by assuming the strength of CFRP $f_f = 2400$ MPa and the cubic resistance of concrete cover used for strengthening $R_{cm} = 35$ MPa. Note that, in order to compare experimental results with predictions, mean values of material properties and unit value of partial factors are used.

For DB2 beam (Figure 7), strains measured by strain gauges on FRP strips at debonding, corresponding to

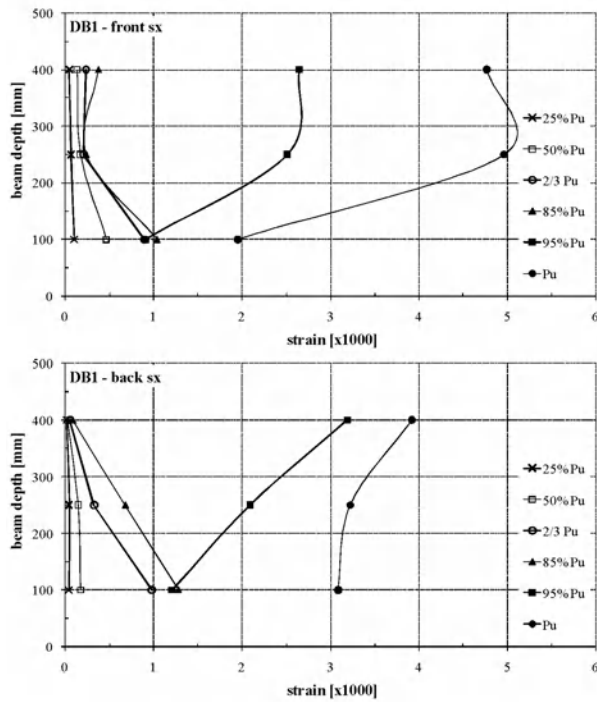


Figure 6 DB1: strain profiles along cross section on left side

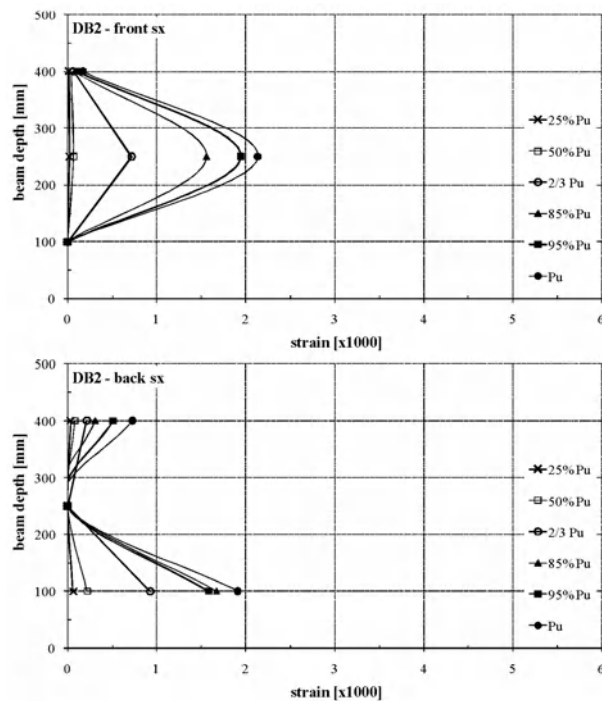


Figure 7 DB2: strain profiles along cross section on left side

loading in the range $400 \div 425$ kN, vary between 0.2% and 0.4% involving, on average, strains and stresses levels equivalent to those registered on DB1 beam.

As for the most tests from literature, strain gauge measures from DB1 and DB2 pointed out that strains at failure are quite low compared to the ultimate values given by suppliers of FRP products or by direct coupon tests.

4 CONCLUSIONS

For what concerns preliminary tests, investigations on materials have lighted up the low quality of concrete used to build up the two beams as well as the heterogeneity of the mechanical properties of original steel rebars.

For what concerns failure tests on beams, the observed collapse for both beams was given by a main diagonal crack occurring from the support with consequent debonding of FRP strips. In both beams, failure is due to shear, mainly as a consequence of lack of anchorage of longitudinal bars with subsequent rupture of FRP strips. The corresponding failure loads are 427.5 kN for DB1 beam and 425.5 kN for DB2, and the midspan mean deflections are respectively 6.48 and 7.25 mm.

To better understand the FRP effective contribution in terms of strength, it has been looked at the strain profile along the height of the beams. From test results it appears that only few strips give an effective contribution to the shear resistance. Most of them debond untimely and measured strains at failure are smaller than those obtained from qualification tests.

REFERENCES

- CNR-DT200/2004. Istruzioni per la progettazione, l'Esecuzione ed il Controllo di Interventi di Consolidamento Statico mediante l'uso di Compositi Fibrorinforzati.
- Carolin A., Taljsten, B. 2005. Experimental study of strengthening for increased shear bearing capacity. *Journal of Composite for Construction*. 9(6), 464-473.
- Guadagnini, M., Pilakutas K. & Waldron, P. 2006. Shear resistance of FRP RC beams: Experimental study. *Journal of Composite for Construction*. 10(6), 464-473.
- Monti, G. & Liotta, M. 2007. Tests and design equations for FRP strengthening in shear. *Construction and Building Materials*. 21, 799-809.

Influence of Transverse Steel on the Performance of RC T-Beams Strengthened in Shear with GFRP Strips

K. C. Panda (kishoriit@gmail.com) & S. V. Barai
Department of Civil Engineering, Indian Institute of Technology, Kharagpur, India

S. K. Bhattacharyya
Central Building Research Institute, Roorkee, India

ABSTRACT The need for structural rehabilitation of concrete structures all over the world is well established and a large amount of research is devoted in this area. Though a large volume of research is directed towards the flexural behaviour of beams, works on the effect of GFRP strips strengthened on shear are relatively sparse. The present paper focuses on the study of the effect of transverse steel on the performance against shear and modes of failure of simply supported RC T-beams strengthened in shear with GFRP strips. RC T-beams of 2.5 m span are cast at the structural laboratory of IIT, Kharagpur, and are tested with shear reinforcement and GFRP strips in U-shape around the web, and side bonded with orientation of the GFRP strips at 90° and 45° with the horizontal axis of the beam. All the beams are tested on a 300 T UTM. The experimental results clearly indicate the advantage of using externally applied epoxy bonded GFRP system to restore or increase the shear capacity of RC T-beams. It is also observed that the combination of configuration of GFRP strips and transverse steel is an important factor to gain the shear capacity and the ductility.

1 INTRODUCTION

The fiber reinforced polymer (FRP) strips or sheets are an excellent option for use as reinforcing material because of their high strength and stiffness-to-weight ratio, corrosion resistance, durability, non magnetic, non conductive, high resistance to chemical attack as well as ease of its installation. FRP composites are applied these days to many structural elements such as beam, column, slabs, joints, walls, domes, tanks, chimneys, pipes etc. The RC beams are strengthened in a variety of ways. FRP wraps covering the whole cross section of a beam, FRP U-jackets covering the two sides and tension face of a beam, and FRP plates placed on the two sides of the beam only.

The technique of strengthening reinforced concrete structures by externally bonded FRP strips or sheets was started about two decades back and has since attracted researchers around the world. The experimental studies on RC rectangular beam, strengthened with CFRP strips in shear have been carried out by several researchers (Chaallal et al. 1998; Triantafillou 1998; Khalifa et al. 1998; Zhang et al. 2005), CFRP and GFRP strips (Cao et al. 2005). Similarly, the experimental studies on RC T-beams, strengthened with CFRP strips have been contributed by (Khalifa et al. 2000). The researchers have shown that the shear strength of reinforced concrete beams may be substantially increased by bonding FRP strips as external shear reinforcement. Most of the

experimental works have been conducted by using CFRP as external shear reinforcement both for rectangular and T-beams, as compared with GFRP as external shear reinforcement. This paper presents an experimental study on the effect of transverse steel on the performance against shear and modes of failure of simply supported RC T-beams, externally strengthened in shear using epoxy bonded glass fiber reinforced polymer (GFRP) strips in different configurations and orientations.

2 EXPERIMENTAL PROGRAM

2.1 Test specimen

The experimental program consists of casting and testing of nine (9) simply supported RC T-beams of 2.5 m long. Nine beams are grouped in three categories with three beams in each category. In the first category, three beams are tested without any shear reinforcement. Stirrups as shear reinforcement are provided at the support and loading points to avoid any local shear failure. In the second category, three beams are tested with shear reinforcement. The stirrups are provided at a spacing of 200 mm. The beams in these two categories are treated as control specimen for comparison. In the third category, three beams are strengthened with GFRP strip in U-shape and side bonded at 45° and 90° to the longitudinal axis of the beam. The stirrups are also provided at a spacing of 200 mm for all the three beams.

2.2 Design of concrete beam

All the T-beams are 2.5 m long and designed to fail in shear. Based on the design, 2 Nos. 20 mm diameter Tor steel bars are used as flexural reinforcement (area 628.31 mm²) at the bottom, and 4 Nos. 8 mm diameter Tor steel bars are used in one layer at the top. Total six numbers of stirrups are provided, 2 Nos. at the support and 1 No. at the loading points to prevent any local failure. The control specimen details and dimensions are as shown in Figure 1.

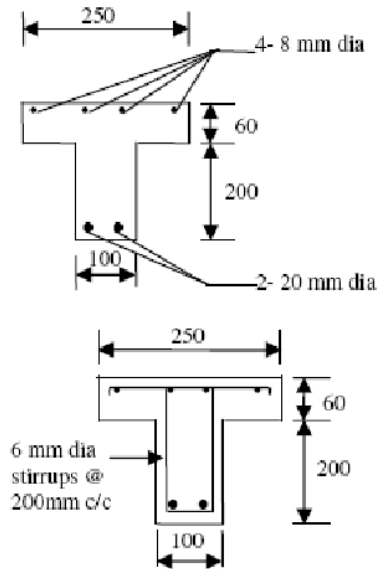


Figure 1 Details of control specimen

Ordinary Portland cement (OPC- 43 grade) and 12.5 mm down graded coarse aggregates are used for the preparation of concrete. The Mix design is carried out for M30 grade of concrete. Compression tests on cubes and cylinders are performed at 7 days and 28 days. The 28 days test results of cubes and cylinders are presented in Table 1. Steels of grade Fe 415 for longitudinal steel reinforcement and Fe 250 for transverse steel reinforcement are used as reinforcement in the experiment. The manufacturer standards and summary of test results are presented in Table 2. GFRP strip of thickness 0.36 mm is used for strengthening of beams the ultimate tensile strength measured is 160 MPa and the elastic modulus is 13.18 GPa.

Table 1 Test results of cubes and cylinders after 28 days

Specimen designation	No. of Beams	Mean cube compressive strength (MPa)	Mean cylinder compressive strength (MPa)
S0-0L	3	49.61	42.16
S200-0L	3	59.78	42.67
S200-1L-ST-S-90	1	53.62	37.83
S200-1L-ST-S-45	1	53.62	37.83
S200-1L-ST-U-90	1	53.62	37.83

Table 2 Mechanical properties of steel reinforcement used

Material	Diameter (mm)	Yield stress (MPa)	Ultimate stress (MPa)	Modulus of elasticity (GPa)	Yield strain (μ strain)
Tor steel	20	500	590	200	2500
Tor steel	8	503	646	180	2794
Mild steel	6	252	461	200	-

2.3 Strengthening schemes

The T-beams are strengthened with GFRP strip in the form of side bonded with orientation of the strips at 90° and 45° to the longitudinal axis of the beam and in U-shape orientation of the strip at 90° around the web of the T-beam. The details of the specimens are listed in Table 3.

Table 3 Details of test specimens

Specimen	Strengthening schemes
S0-0L	Control beam without transverse steel
S200-0L	Control beam with transverse steel (stirrups at a spacing of 200 mm c/c)
S200-1L-ST-S-90	With transverse steel @ 200 mm c/c + GFRP strip in the form of side bonded + 90° orientation
S200-1L-ST-S-45	With transverse steel @ 200 mm c/c + GFRP strip in the form of side bonded + 45° orientation
S200-1L-ST-U-90	With transverse steel @ 200 mm c/c + GFRP strip in the form of U-jacket + 90° orientation

2.4 Instrumentation

All specimens are tested as simple T-beams using two point loading with shear span to effective depth (a/d) ratio equal to 3.26. The tests are carried out using UTM at IIT Kharagpur. Figure 2 shows the details of the test setup. Five dial gauges are used for each test to monitor vertical displacements. One dial gauge is located at midspan of the beam. The other two are located below the loading points and another two are located at the center

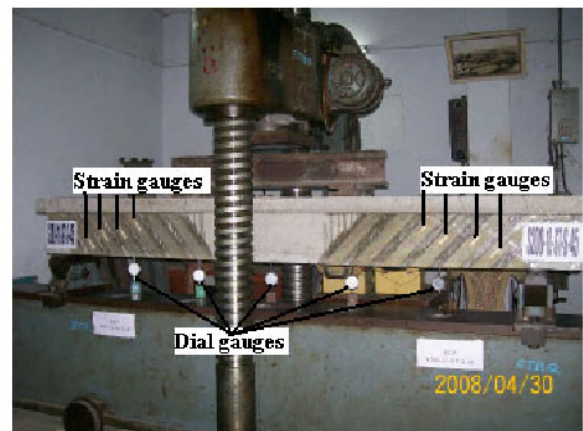


Figure 2 Test setup with dial gauge and strain gauge positions

of the shear zone on either side as shown in Figure 2. Two types of electrical strain gauges are used in the test; gauges BKNIC-10 are used on the surface of the longitudinal steel reinforcement and transverse steel, and gauges BKCT-30 are used on the side of the concrete surface and to the GFRP strip on the side of the strengthened T-beams.

3 ANALYSIS OF TEST RESULTS

Table 4 shows the experimental results of control and GFRP strips strengthened RC T-beams. Figure 3 shows the variation of midspan deflection with the applied load for the tested beams of S200 series. The modes of failure as observed in the experimental study are also indicated in Figure 4.

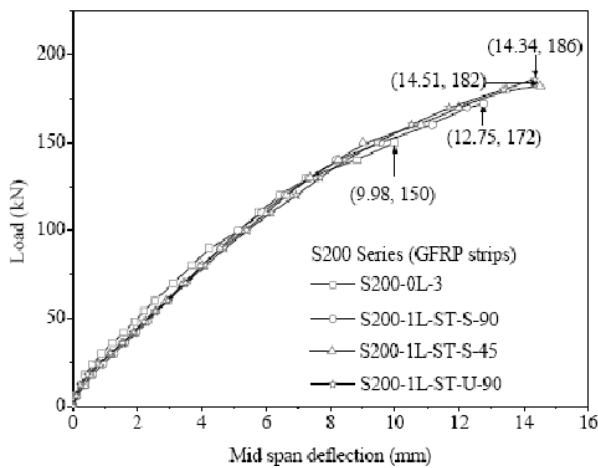


Figure 3 Load versus midspan deflection – Series S200

3.1 Strength

From Table 4 and Figure 3, it may be observed that for S200 series, the load at ultimate failure of S200-1L-ST-S-90, S200-1L-ST-U-90, and S200-1L-ST-S-45 specimens are 172 kN, 186 kN, and 182 kN respectively compared to 160 kN for control specimen S200-0L. This shows a gain of 7.5%, 16.25%, and 13.75% respectively on loads

Table 4 Experimental results of strengthened RC T-beams

Specimen Designation	Experimental results					
	Load at failure (kN)	$V_{n,test}$ (kN)	$V_{c,test}$ (kN)	$V_{s,test}$ (kN)	$V_{f,test}$ (kN)	$\frac{V_{f,test}}{V_{n,test,rif}} \times 100$ (%)
S0-0L	100	50	50	-	-	-
S200-0L	160	80	50	30	-	-
S200-1L-ST-S-90	172	86	50	30	6	7.50
S200-1L-ST-S-45	182	91	50	30	11	13.75
S200-1L-ST-U-90	186	93	50	30	13	16.25

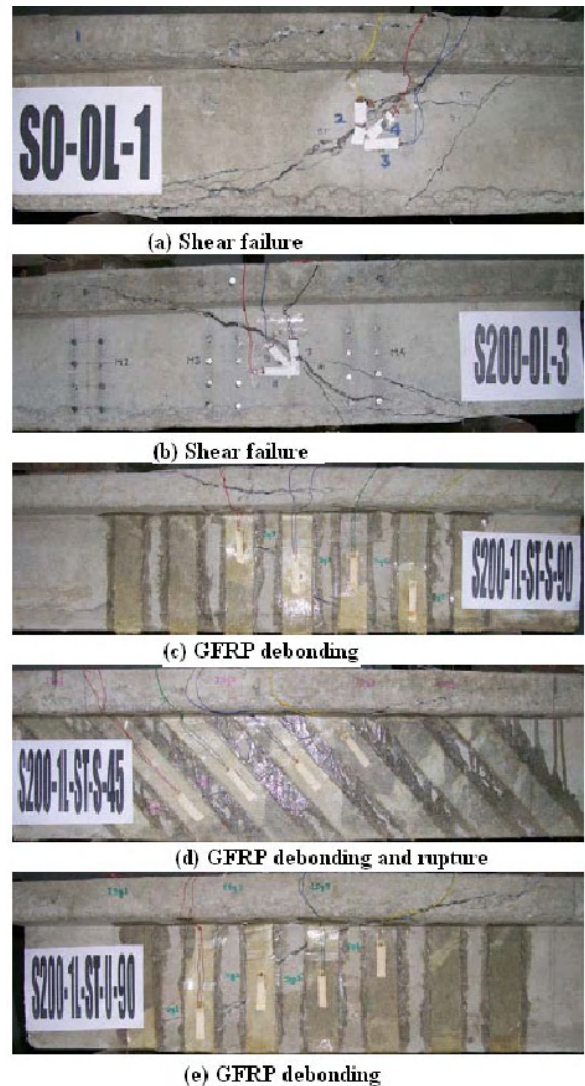


Figure 4 Modes of failure of control and strengthened beams

over control specimen. As expected with transverse steel reinforcement at 200 mm stirrups spacing, the beams strengthened with GFRP strips in U shape carry more loads than other.

3.2 Deflection

As observed from Figure 3, the deflection of control and strengthened specimens are almost equal up to 100 kN load. Thereafter, as load increases, the deflection in beams strengthened with GFRP strips is less in comparison to the control specimen for the same amount of load. The maximum deflection of beam strengthened with GFRP strip for S200-1L-ST-S-90, S200-1L-ST-S-45, and S200-1L-ST-U-90 is 12.75 mm, 14.51 mm, and 14.34 mm corresponding to the load of 172 kN, 182 kN, and 186 kN respectively, whereas in control specimen (S200-0L) the value is 9.98 mm corresponding to the load of 150 kN respectively. As expected the beam strengthened with GFRP strips in U-shape carry more load, whereas the beams strengthened with GFRP strips on side of the web of the T-beams in 45° to the longitudinal axis of the beam show more deflection than the other two.

3.3 Modes of failure

When beam S0-0L-1 and S200-0L-3 is loaded, it exhibited diagonal shear cracks at a load of 70 kN and 90 kN on both side of the shear spans respectively; the cracks started at the center of both shear spans. When specimen S200-1L-ST-S-90, S200-1L-ST-S-45 and S200-1L-ST-U-90 is loaded, the diagonal shear crack initiated at a load of 110 kN. As load increased, the width of the crack is also increased, until the load reached the ultimate strength of the control beam. The failure of the GFRP strips is caused mainly due to debonding of the GFRP strips in S200-1L-ST-S-90 and S200-1L-ST-U-90 specimens and due to both debonding and rupture of the GFRP strip from the concrete surface in S200-1L-ST-S-45 specimen.

4 CONCLUDING REMARKS

The test results clearly indicate that for strengthened RC T-beams in shear with U-shape and side bonded GFRP strips, increase the effectiveness by 7.5% to 16.25%.

The gain in shear capacity is significant in all the RC T-beams strengthened in shear with GFRP strips. As configuration and orientation is concerned, U-shape and side bonded with orientation of the strip at 45° to the longitudinal axis of the beam is more effective than side bonded with 90° orientations.

The modes of failure of strengthened RC T-beams in shear with U-shape and side bonded GFRP strips clearly indicate that, if the orientation of the strip is 90° to the longitudinal axis of the beam the failure is due to GFRP debonding. Whereas, for side bonded GFRP strips with orientation at 45° to the longitudinal axis of the beam the failure is due to both GFRP rupture and debonding.

The load-deflection graph clearly indicates that the

combination of transverse steel in strengthened RC T-beams in shear with GFRP strips have a significant effect on beams ductility. The RC T-beams, becomes more flexible and more deformable, in U-shape and side bonded with orientation of the GFRP strips at 45° to the longitudinal axis of the beam than 90° orientation.

As influence of transverse steel on GFRP strips is concerned, U-shape GFRP strips with transverse steel carry more load than the side bonded GFRP strips.

REFERENCES

- ACI 440.2R-02. (2002). Guide for the design and construction of externally bonded FRP systems for strengthening concrete structures. *ACI Committee 440*. Farmington Hills, Michigan. p. 45.
- Cao, S.Y., Chen, J.F., Teng, J.G., Hao, Z.& Chen, J. 2005. Debonding in RC beams shear strengthened with complete FRP wraps. *J. Compos. Constr.* 9(5): 417-428.
- Chaallal, O., Nollet, M.J. & Perraton, D. 1998. Shear strengthening of RC beams by externally bonded side CFRP strips. *J. Compos. Constr.* 2(2): 111-113.
- Khalifa, A., Gold, W.J., Nanni, A. & Aziz, A. 1998. Contribution of externally bonded FRP to shear capacity of RC flexural members. *J. Compos. Constr.* 2(4): 195-201.
- Khalifa, A., & Nanni, A. 2000. Improving shear capacity of existing RC T-section beams using CFRP composites. *Cement and Concrete Composites* 22: 165-174.
- Triantafillou, T.C. 1998. Shear strengthening of reinforced concrete beams using epoxy bonded FRP composites. *ACI Struct. J.* 95(2): 107-115.
- Zhang, Z. & Hsu, C.T.T. 2005. Shear strengthening of reinforced concrete beams using carbon-fiber-reinforced polymer laminates. *J. Compos. Constr.* 9(2): 158-169.

Shear Design Equations for Concrete Girders Strengthened with FRP

M. S. Murphy (msm9q3@mst.edu)

Department of Civil, Architectural, and Environmental Engineering, Missouri University of Science & Technology, Rolla, Missouri, USA

A. Belarbi (belarbi@uh.edu)

Department of Civil and Environmental Engineering, University of Houston, Houston, Texas, USA

D. Kuchma (kuchma@illinois.edu)

Department of Civil and Environmental Engineering, University of Illinois, Urbana, Illinois, USA

ABSTRACT Fiber Reinforced Polymer (FRP) systems have emerged as one of the most promising and widely accepted methods of strengthening concrete structures. FRP strengthening systems may consist of carbon (CFRP), glass (GFRP), or aramid (AFRP) fibers. The acceptance and utilization of such strengthening techniques depends on the availability of reliable design guidelines. Shear strengthening with externally bonded FRP is still under investigation and the results obtained thus far are scarce and sometimes controversial. In this study, predictions by the existing analytical models developed for externally bonded FRP shear reinforcements were evaluated and compared to experimental results available in the literature. The results of this investigation show that the models are not reliable for predicting the shear strengthening effect of externally bonded FRPs in a majority of cases. Results from full-scale testing and a comprehensive collection of data from the literature were used in the development and calibration of new design equations which give better predictions of the FRP contribution to shear resistance. This paper presents the results and final recommendations of this study.

1 EXPERIMENTAL PROGRAM

1.1 Background

The development of shear design equations for concrete members is a complex challenge that has traditionally relied heavily on semi-empirical methods. Adding FRP shear strengthening, with its specific design issues, adds another level of complexity. The difficulty in defining the FRP shear contribution arises from the anisotropic material characteristics of the composite combined with the wide variety of possible reinforcement configurations. The shear resistance mechanisms are further complicated by the bond characteristics between the FRP and concrete substrate. The effectiveness of FRP shear strengthening methods depends on the mode of failure. The general modes of failure for concrete members strengthened with externally bonded FRPs are debonding or rupture of the FRP depending on the anchorage conditions. These FRP-related shear design issues and lack of comprehensive analytical models were the main motivation for this research effort.

1.2 Current Analytical Models and Design Guidelines

Despite the limited number of experimental investigations,

a vast number of analytical models and design specifications have been proposed by various researchers for determining the FRP contribution to shear resistance. Two of the earliest suggested models were by Al-Sulaimani et al. (1994) and Chajes et al. (1995). These models were based on an experimentally determined limiting value of FRP shear strain or stress. Triantafillou (1998) was the first to propose that the FRP contribution to shear capacity be based on the computation of an effective FRP strain ($\epsilon_{frp,e}$). The effective FRP strain is the average strain that can be reached in the FRP before failure and is usually determined from curve fitting of experimental results. Several subsequent studies (Khalifa et al. 1998; Hutchinson and Rizkalla 1999; Khalifa and Nanni 2000; Triantafillou and Antonopoulos 2000; Chaallal et al. 2002; Pellegrino and Modena 2002; Zhang and Hsu 2005) followed this approach but developed their own expressions for determining the effective FRP strain. Chen and Teng (2003a and 2003b) conducted extensive experimental work investigating the effective stress distribution along externally bonded FRP shear reinforcement and developed two models which address the debonding and FRP rupture failure modes separately.

Their model uses stress distribution factors to account for the non-uniform stress distribution in externally bonded FRP shear reinforcements. Similar approaches were adopted by Carolin and Taljsten (2005) and Cao et al. (2005) in the development of their models. Other researchers have adopted completely different strategies which rely on mechanics based approaches rather than regression analysis. Malek and Saadatmanesh (1998) used the compression field theory as the basis for their model. Deniaud and Cheng (2001) proposed a model which combines the strip method and shear friction approach. Monti and Liotta (2005) developed closed-form equations based on mechanics rather than regression-based formulas. The model is obtained by defining the generalized constitutive law of an FRP layer bonded to concrete with consideration for the compatibility imposed by the shear crack opening and appropriate boundary conditions. Sim et al. (2005) suggested a model using plastic limit theory based on the study by Nielson and Braestrup (1975).

A few of these models have been developed into various specifications and codes of practice adopted around the world. ACI 440.2R-08: Guide for the Design and Construction of Externally Bonded FRP Systems for Strengthening Concrete Structures (ACI 440, 2008) is the most thorough and complete document developed to date. It has been developed based on the analytical model proposed by Khalifa et al. (1998) and ACI 318-08. The CAN/CSA S806-02 Canadian Building Code (CSA, 2002) is a formalized design code addressing externally bonded FRP reinforcement for concrete. The shear equations in CSA S806-02 are based on the simplified method of shear design used in the CSA A23.3-04 concrete design code and are restricted to the usual cases where the shear reinforcement including FRP is perpendicular to the longitudinal axis of beam. The CSA S6-06 Canadian Bridge Code also deals with shear strengthening of concrete using externally-bonded FRPs and specifies that the FRP shear strengthening system should consist of U-wraps anchored in the compression zone or complete wrapping of the cross-section. The design equations specified in this code are identical to the equations in ACI 440.2R-08. European fib-Bulletin 14 (fib-TG9.3 2001) represents a combination of guidelines and state-of-the-art reports and is based on the model proposed by Triantafillou and Antonopoulos (2000). Japanese researchers have also developed their own set of design guidelines for FRP strengthening (JSCE, 2001) which take a performance-based approach to the design of externally bonded FRP materials. ISIS Design Manual 4 (ISIS 2001) provides considerable guidance and a number of design examples for the use of externally bonded FRP based on CSA S6-06 and CSA S806-02. The Great Britain Technical Report 55 (Concrete

Society 2004) is similar to fib Bulletin 14 in its approach and scope; however, it addresses more practical construction issues associated with the use of externally bonded FRP materials.

2 PERFORMANCE OF EXISTING DESIGN METHODS

The diversity in approaches taken to develop the current design methods for FRP shear strengthening of concrete structures contributes to discrepancies in the estimated FRP shear contributions (V_f) by the various methods. Figure 1 shows the trend of the estimated FRP shear contributions by the various methods as a function of increasing axial rigidity ($\rho_f E_f$) of the FRP reinforcement for a particular concrete section. The vertical axis represents the calculated FRP contributions (V_f) which have been normalized with respect to the effective concrete section ($b_w d_f$). The horizontal axis represents the axial rigidity ($\rho_f E_f$) of the FRP reinforcements applied to the concrete section (i.e., a product of the reinforcement ratio and stiffness of the FRP reinforcement). The magnitude of the range in the calculated V_f values by the different models is indicative of the complexity of the resistance mechanisms, sensitivity of the type of strengthening provided with respect to the type of tests used for calibration of the models, and lack of maturity in the models.

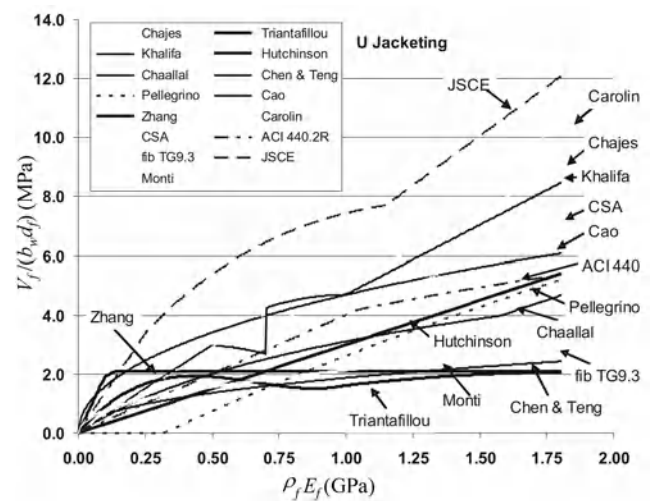


Figure 1 Comparison of FRP shear resistance estimated by various methods

3 DEVELOPMENT OF NEW DESIGN EXPRESSIONS

3.1 Design parameters

Experimental investigations in the literature illustrate that many factors affect the FRP contribution to shear resistance of a concrete member. The calibration of any analytical model must therefore deal with significant

uncertainties in other contributors to shear resistance as well as the deficiencies of the existing experimental databases. The most recognized factor affecting the effectiveness of externally bonded FRP shear reinforcement is the mode of failure. The two most common modes of failure that have been reported in the literature are rupture of the FRP and debonding of the FRP from the concrete substrate which is considered to include tearing of the outer concrete from its core. The mode of failure is strongly governed by the FRP attachment scheme. FRP rupture failure usually occurs when members are fully wrapped by the FRP reinforcement and in some cases where U-wrapping applications are employed, particularly when an anchorage system is used at the free ends. FRP debonding generally governs in members with side bonding and U-wrapping applications. The effectiveness of externally bonded FRP shear reinforcement has also been found to be influenced by the FRP stiffness, amount and orientation of this reinforcement, the rupture strength of the FRP, the adhesive resistance, type of anchorage, concrete strength, presence of shear cracking, presence and amount of steel shear reinforcement, shape of the section, and other factors.

3.2 Proposed FRP contribution to shear resistance

The total shear resistance of a reinforced concrete beam is generally expressed as a sum of the concrete contribution (V_c) and the steel shear reinforcement contribution (V_s). To be consistent with this structure, it is most common to account for the FRP shear reinforcement contribution (V_f) through the addition of a third term. The simplest and most widely accepted shear design methodology for evaluating the FRP contribution is the truss analogy based on the development of an effective strain in the FRP.

$$V_f = \frac{A_f f_{fe} d_f}{s_f} (\cot \theta + \cot \alpha) \sin \alpha \quad (1)$$

$$f_{fe} = E_f \varepsilon_{fe} \quad (2)$$

where A_f = cross-sectional area of FRP; f_{fe} = effective tensile stress in FRP sheet in the direction of the principal fibers; d_f = effective depth of FRP reinforcement; s_f = spacing of FRP strips; α = angle between principal direction of FRP sheets and the longitudinal axis of the beam; θ = shear crack angle; E_f = elastic modulus of FRP; and ε_{fe} = effective tensile strain of FRP.

Design methods based on this approach were found to give the most accurate predictions of the FRP shear contribution due to calibration of the effective FRP strain from experimental testing. As such, this methodology was adapted for development of new design methods based on finding best-fit empirical expressions from a comprehensive database of experimental results collected

from the literature and a full-scale experimental program. The effective FRP strain used in evaluating the FRP shear contribution was found to be best expressed by two separate design expressions due to the vast differences in effectiveness among the two predominant failure modes (i.e., debonding and FRP rupture). The most reasonable level of accuracy was achieved with the development of one expression for members in which sufficient anchorage is provided (FRP rupture failure mode) and a separate expression for members in which insufficient anchorage is provided (FRP debonding failure mode). Based on results from extensive statistical and reliability assessments, the following expressions are proposed for determining the effective FRP strain (ε_{fe}).

For fully-anchored FRP strengthening systems where shear resistance is expected to be controlled by FRP rupture failure:

$$\varepsilon_{fe} = R \varepsilon_{fu} \quad (3)$$

$$R = 0.143 (\rho_f E_f)^{-0.67} \leq 1.0 \quad \text{and} \quad \rho_f E_f \leq 2.07 \text{GPa} \quad (4)$$

where R = ratio of effective strain in the FRP sheet to its ultimate strain and ρ_f = FRP reinforcement ratio.

For un-anchored FRP strengthening systems where shear resistance is expected to be controlled by FRP debonding or other failure mode:

$$\varepsilon_{fe} = R \varepsilon_{fu} \leq 0.012 \quad (5)$$

$$R = 0.107 (\rho_f E_f)^{-0.67} \leq 1.0 \quad \text{and} \quad \rho_f E_f \leq 2.07 \text{GPa} \quad (6)$$

These expressions were found to yield an average strength ratio (bias) of 1.68 for the fully-anchored condition and 1.44 for the un-anchored condition when evaluated for the comprehensive database of test results. Similarly, coefficients of variation (COV) of 0.33 for the fully-anchored condition and 0.25 for the un-anchored condition were found.

4 RELIABILITY STUDY

After calibration of the proposed design equations, a reliability study was conducted to assess their performance. The large scatter in the test results of the comprehensive database considered prohibited the use of simplified approximate reliability index expressions and therefore, First Order Reliability Method (FORM) was used. Results of the reliability study showed that the proposed design expressions yield components that have a reliability index (β_r) in the range of 3.15 to 3.55. This range was deemed acceptable for strengthening applications where the design life is expected to be less than 75-years. Furthermore, the requirement for inspection and evaluation of a structure prior to strengthening reduce or eliminate many of the uncertainties and variables incorporated in this study.

5 CONCLUSIONS

None of the current models examined are able to provide reliable estimates of the FRP shear strengthening effect for all members in the database. This shows that the mechanisms of externally bonded FRP shear strengthening are still poorly understood. This is illustrated by the large differences in strength predictions by the models. Unfortunately, the types of members investigated for the calibration of these models do not adequately represent the types of members present in the field that would need FRP strengthening. Therefore, these models may not be reliable for estimating the FRP shear contribution of members outside the range of the experimental tests from which they were calibrated. The newly proposed design equations have been calibrated from a comprehensive database of test results collected worldwide including those of the full-scale testing done as part of this research. As such, these design equations are expected to give more reliable estimates of the shear increase due to FRP strengthening.

REFERENCES

- ACI Committee 318, Building Code Requirements for Structural Concrete and Commentary (ACI 318-08), American Concrete Institute, Farmington Hills, MI, 2008.
- ACI Committee 440, Guide for the Design and Construction of Externally Bonded FRP Systems for Strengthening Concrete Structures (ACI 440.2R-08), American Concrete Institute, Farmington Hills, MI, 2008.
- Al-Sulaimani, G.J., Shariff, A., Basanbul, I.A., Baluch, M.H. & Ghaleb, B.N. 1994. Shear Repair of Reinforced Concrete by Fiber Glass Plate Bonding. *ACI Structural Journal* Vol. 91 (No. 4): 458-464.
- CAN/CSA-S806-02, Design and Construction of Building Components with Fiber-Reinforced Polymer, Canadian Standard Association, Rexdale, Ontario, 2002.
- CAN/CSA-A23.3-04, Design of Concrete Structures for Buildings, Canadian Standards Association Rexdale, Ontario, Canada, 2004.
- CAN/CSA S6-6, Canadian Highway Bridge Design Code, Canadian Standard Association, Rexdale, Ontario, 2006.
- Cao, S.Y., Chen, J.F., Teng, J.G., Hao, Z. & Chen, J. 2005. Debonding in RC Beams Strengthened with Complete FRP Wraps. *Journal of Composites for Construction* Vol. 9 (No. 5): 417-428.
- Carolin, A. & Taljsten, B. 2005. Theoretical Study of Strengthening for Increased Shear Bearing Capacity. *Journal of Composites for Construction* Vol. 9 (No. 6): 497-506.
- Chaallal, O., Shahawy, M. & Hassan, M. 2002. Performance of Reinforced Concrete T-Girders Strengthened in Shear with Carbon Fiber-Reinforced Polymer Fabric. *ACI Structural Journal* Vol. 99 (No. 3): 335-343.
- Chajes, M.J., Jansuska, T.F., Mertz, D.R., Thomson, T.A. & Finch, W.W. 1995. Shear Strength of RC Beams using Externally Applied Composite Fabrics. *ACI Structural Journal* Vol. 92 (No. 3): 295-303.
- Chen, J.F. & Teng, J.G. 2003a. Shear Capacity of FRP Strengthened RC Beams: FRP Debonding. *Construction Building Materials* Vol. 17 (No. 1): 27-41.
- Chen, J.F. & Teng, J.G. 2003b. Shear Capacity of Fiber-Reinforced Polymer-Strengthened Reinforced Concrete Beams: Fiber Reinforced Polymer Rupture. *Journal of Structural Engineering* Vol. 129 (No. 5): 615-625.
- Concrete Society, Design Guidance on Strengthening Concrete Structures using Fibre Composite Materials: Technical Report 55, The Second Edition, The Concrete Society, London, 2004.
- Deniaud, C. & Cheng, J.J.R. 2001. Shear Behavior of Reinforced Concrete T-Beams with Externally Bonded Fiber-Reinforced Polymer Sheets. *ACI Structural Journal* Vol. 98 (No. 3): 386-394.
- fib-TG9.3, Design and Use of Externally Bonded Fiber Polymer Reinforcement (FRP EBR) for Reinforced Concrete Structures, Technical Report Prepared by EBR Task Group 9.3, Bulletin 14, Lausanne, 2001.
- Hutchinson, R.L. & Rizkalla, S.H. 1999. Shear Strengthening of AASHTO Bridge Girders Using Carbon Fiber Reinforced Polymer Sheets. *ACI Special Publications (SP-188)* Vol. 188: 945-958.
- ISIS Design Manual 4, Strengthening Reinforced Concrete Structures with Externally-Bonded Fiber Reinforced Polymers, Intelligent Sensing for Innovative Structures, Winnipeg, Canada, 2001.
- JSCE, Recommendations for Upgrading of Concrete Structures with Use of Continuous Fiber Sheets, Concrete Engineering Series 41, Japan Society of Civil Engineers, Tokyo, 2001.
- Khalifa, A., Gold, W., Nanni, A. & Abdel Aziz, M.I. 1998. Contribution of Externally Bonded FRP to Shear Capacity of RC Flexural Members. *Journal of Composites for Construction* Vol. 2 (No. 4): 195-202.
- Khalifa, A. & Nanni, A. 2000. Improving Shear Capacity of Existing RC T-Section Beams using CFRP Composites. *Cement & Concrete Composites* Vol. 22: 165-174.
- Malek, A.M. & Saadatmanesh, H. 1998. Ultimate Shear Capacity of Reinforced Concrete Beams Strengthened with Web-Bonded Fiber-Reinforced Plastic Plates. *ACI Structural Journal* Vol. 95 (No.4): 391-399.
- Monti, G. & Liotta, M. A. 2005. FRP-Strengthening in Shear: Tests and Design Equations. *SP-230-32, Proc. of the 7th Intern. Symp. on FRP for Reinforcement of Concrete Structures (FRPRCS-7)*: 543-562.
- Nielsen, M.P. & Braestrup, M.W. 1975. Plastic Shear Strength of Reinforced Concrete Beams. *Bygningssstatistiske Meddelelser* Vol. 46 (No. 3): 61-99.
- Pellegrino, C. & Modena, C. 2002. Fiber Reinforced Polymer Shear Strengthening of Reinforced Concrete Beams with Transverse Steel Reinforcement. *Journal of Composites for Construction* Vol. 6 (No. 2): 104-111.
- Sim, J., Kim, G., Park, C. & Ju, M. 2005. Shear Strengthening Effects with Varying Types of FRP Materials and Strengthening

- Methods. *Proc. of the 7th Intern. Symp. on FRP for Reinforcement of Concrete Structures (FRPRCS-7)*: 1665-1680.
- Triantafillou, T.C. 1998. Shear Strengthening of Reinforced Concrete Beams using Epoxy Bonded FRP Composites. *ACI Structural Journal* Vol. 95 (No. 2): 107-115.
- Triantafillou, T.C. & Antonopoulos, C.P. 2000. Design of Concrete Flexural Members Strengthened in Shear with FRP. *Journal of Composites for Construction* Vol. 4 (No. 4): 198-205.
- Zhang, Z. & Hsu, C.T. 2005. Shear Strengthening of Reinforced Concrete Beams Using Carbon-Fiber-Reinforced Polymer Laminates. *Journal of Composites for Construction* Vol. 9 (No. 2): 158-169.

The Shear Behavior of Beams Strengthened with FRP Grid

Wenyong Chen, Xiaobing Chen & Ding Yi

China Jing ye Engineering Corporation Limited, Beijing, China

ABSTRACT In this paper, the shear behavior of concrete beam reinforced with FRP grid is studied for the first time and is compared with the behavior of beams reinforced with steel and CFRP sheet respectively. The results show that the beams strengthened with FRP grid have good shear behavior both increasing shear capacity and controlling of crack width.

1 INTRODUCTION

1.1 FRP GRID

FRP grid is made from glass, aramid, or carbon fibers (or combinations of each) impregnated with an appropriate resin system, such as polyester, vinylester or epoxy to form a grid. It includes 2-Dimensional and 3-Dimensional FRP grid, which shows very good anchorage and mechanical interlock in concrete. Due to its resistance to corrosion and excellent resistance to alkalis, acids and chemicals, it does not require substantial cover and may instead of steel stirrups to solve the problems of steel corrosion in harsh environments. Its light weight facilitates ease and speed in construction, without loss in performance. Overseas, FRP grids have been used in tunnels, runways and aprons for airstrips/tarmacs, roads, buildings, channels, rehabilitation, and for general architectural elements. Also they can be applied as lightweight reinforcement in building fascia and curtain walls, which show the lower requirements for cover applications such as thinner and lighter panels^[1]. Furthermore, due to the non-magnetic properties, FRP grids are the excellent reinforcement material in hospitals and free-access floors, as well as in sensitive structures such as scientific laboratories and observatories. The fiber grid is protected by the polymer mortar which is used in conjunction with FRP grid, and to improve durability, enhance the performance of fire resistance^[2].

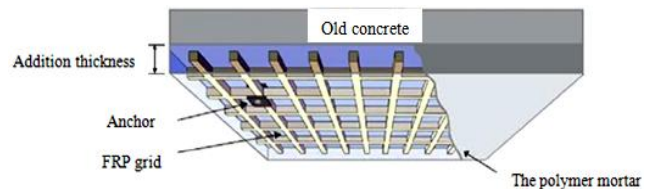


Figure 3 The figure of FRP grid reinforcement

1.2 ECC

ECC (Engineered Cementitious Composites), which is grouped in one of the fiber reinforced cementitious composites, shows pseudostrain hardening behavior with several percent tensile strain. Tensile strain capacity at a range of 3 to 5% has been demonstrated in ECC materials using polyethylene fibers and polyvinyl alcohol (PVA) fibers with fiber volume fraction no greater than 2%. The large strain is contributed by sequential development of multiple cracks, instead of continuous increase of the crack opening. The associated high fracture toughness and controlled crack width (typically below 100 μm [0.004 in]) make ECCs an ideal material to improve serviceability and durability of infrastructures. So, ECC has been applied to slope reinforcement, the dam's surface reinforcement, bridge connecting plate, seismic beams and other fields abroad.^[3]

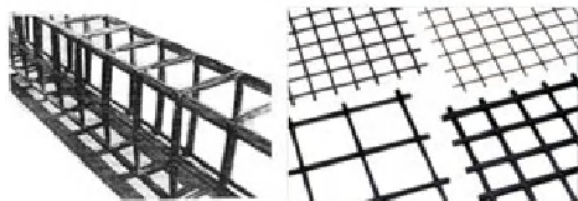


Figure 1 3D FRP grid

Figure 2 2D FRP grid

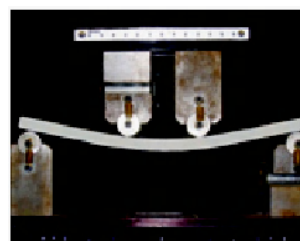


Figure 4 Four-point bending test of ECC

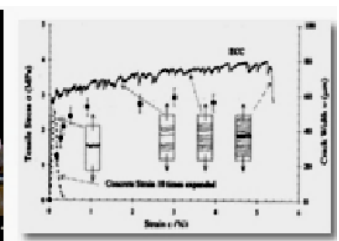


Figure 5 Typical tensile Stress-strain curve and crack width development in PE-ECC

2 TEST-UP

Four beams, which are reinforced concrete beam by steel (RC), strengthened concrete beam by FRP (FRP-RC), strengthened concrete beam by FRP grid and polymer mortar (FRP GRID & NC-RC), strengthened concrete beam by FRP grid and ECC (FRP GRID & ECC-RC), have been compared.

In the test, the concrete grade of strength is C40, the diameter of stirrup is 6mm and longitudinal bar's is 22mm. Fiber grid used in the test, which is called NEFMAC (New Fiber Composite Material for Reinforcing Concrete) in Japanese is C6-50 × 50 mm. The CFRP sheet is produced in TORAY, with 0.167m thickness. The polymer mortar conjunct with FRP grid is called NEFCRETE with a few of short glass fibers. The ECC has a high early strength, good interface bonding and good mobility characters. The material properties are showed in Table 1.

Table 1 Material properties

Material Type	Type	Modulus (MPa)	Compressive strength (MPa)	Yield Strength (MPa)	Ultimate Tensile Strength (MPa)
concrete	C40	30000	40.25	—	3
longitudinal bar	HPR335	200000	—	337.5	421.88
stirrup	HPR235	200000	—	250.1	312.5
ECC		19000	61.3	—	4.5
FRP GRID	C6-50	100000	—	—	1400
FRP	30 type	228000	—	—	3500

The dimensions and bar arrangements of the beam specimens are shown in Figure 6–9, All specimens were tested under a four-point load set-up, with loading rate of 0.4 KN/s. Load set-up is shown in Figure 10, and data acquisition equipment is shown in Figure 11.

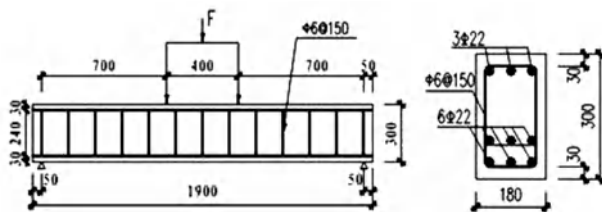


Figure 6 Dimension and bar arrangement of RC

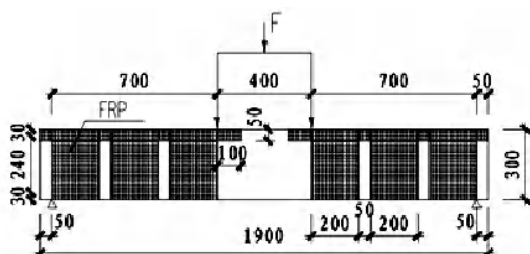


Figure 7 The figure of CFRP reinforce RC

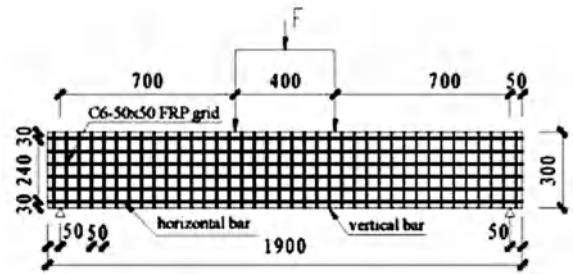


Figure 8 The figure of FRP grid reinforce RC

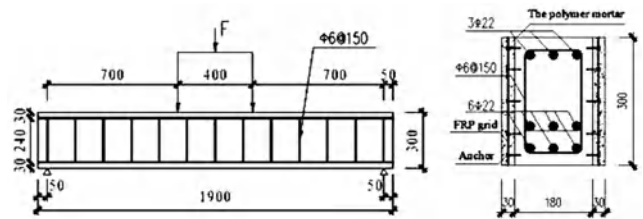


Figure 9 Dimension and bar arrangement of beam L3 and L4



Figure 10 Loading equipment

Figure 11 Data acquisition equipment

3 RESULT AND DISCUSSION

The results are shown in Table 2. In order to research the strengthening effective of reinforcement methods, the maximum deflection is defined, when the load dropped to 50% of the ultimate load.

Table 2 Test results of specimens

Specimen	B1	B2	B3	B4
	RC	FRP-RC	FRP GRID & NC-RC	FRP GRID & ECC-RC
Load at first crack (KN)	30	50	30	78
Ultimate load/KN	250	415.2	373	510.5
Deflection of the middle span (mm)	6.87	11.36	13.6	15.8
maximum Bending Crack wide (mm)	0.04	0.8	0.8	0.6
Shear crack wide (mm)	8	5	0.8	0.04
number Bending crack	3	4	4	13
Shear crack	4	16	48	50
Failure mode	S	S1	S1	S1

S: shear failure, S1: shear failure with debonding

From the phenomenon of Shear Failure, B1 has only one wide inclined crack, with the stirrups yielded. The surfaces of concrete of B2 appear two inclined cracks, with a large piece of carbon sheet debonding. B3 shows many inclined cracks in the end with debonding failure. In the case of the broken polymer mortar, anchor failure and debonding failure of FRP grid are occurred. The surface of ECC in B4 appears many small inclined cracks, which can remain at 0.08 mm until the end of concrete crushing. At the same time, some anchors are pulled out from the concrete, resulting in reinforcement layer debonding.



Figure 12 Shear failure of RC



Figure 13 Shear failure of FRP-RC



Figure 14 Shear failure of FRP GRID&NC-RC



Figure 15 Shear failure of FRP GRID&ECC-RC

As shown in Figure 16, the strengthening effect was significant. B4 shows biggest shear capacity and maximum mid-span deflection, which are 2.042 times and 2.16 times bigger than B1 respectively. The ultimate shear capacity of B3 is less than B2, but B3 shows better deflection performance. The debonding failure of B2 occurs suddenly, without sign. In this test, B3 doesn't show better ultimate

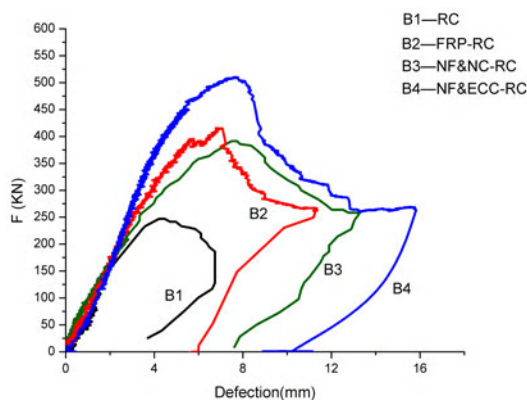


Figure 16 Load-deflection curves

shear capacity than B2, because the big cracks of Polymer mortar result in the loss of its restrain effect and FRP grid don't take enough effect. Figure 17 shows that with the same load, stirrup strain of four beams are different. When the load is 375kN, stirrup strain of B4 is 1000 μ m, stirrup strain of B3 is 4000 μ m, and stirrup strain of B2 is 2000 μ m. But the stirrup of B1 has already yield, when the load is 250kN. So, the FRP grid, FRP sheet and ECC all play the important role in strengthening beam and resisting shear force. Fiber grid has vertical and horizontal bars which can resist the force in both directions, so, they take a special advantage in the shear resist. Because of the effect of ECC, strain of horizontal and vertical bars of B4 are up to 3000 μ m, to 21.4% of ultimate strain. And B4 has more uniform stress distribution than the B3. In the B3, strain of horizontal bars is about 4000 μ m, to 28.6% of the ultimate strain, and strain of vertical bars is about 2000 μ m, to 14.3% of the ultimate strain.

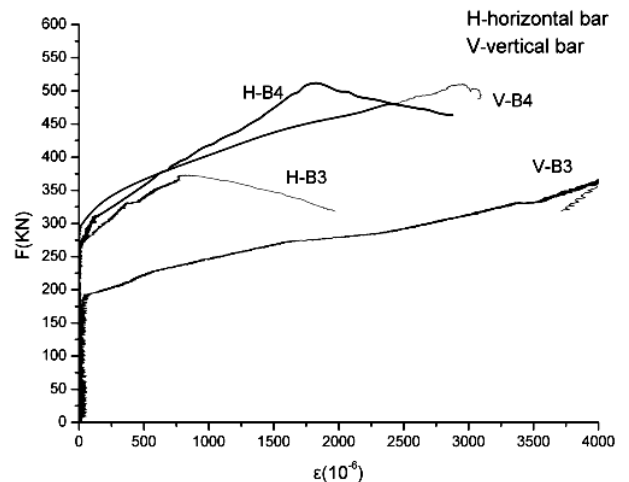


Figure 17 Load-strain curves of stirrup

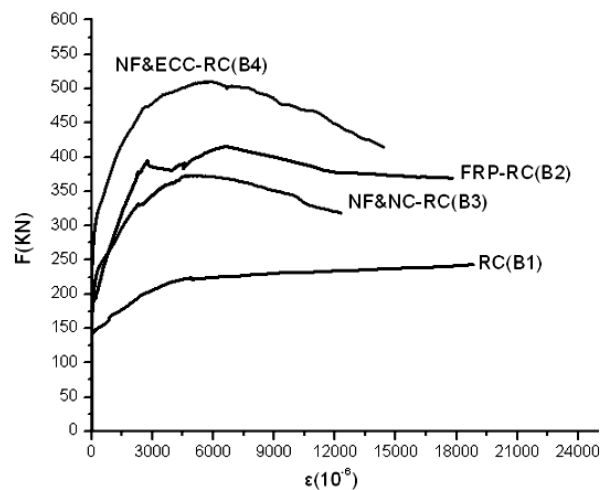


Figure 18 Load-strain curves of FRP bar in L3 and L4

As shown in Figure 19 and Figure 20, in the B4, anchors were pulled out from the original concrete. While in the

B3, anchors are mostly pulled out from the reinforced mortar layer. That means ECC and fiber grid strengthen method In the B4 can enhance the anchor effect, so that anchors and the strengthen system can work together to increase the shear capacity. In the B3, the layer of mortar reinforced appears many inclined cracks, which is about 0.8 mm width, showing a similar multi-cracking

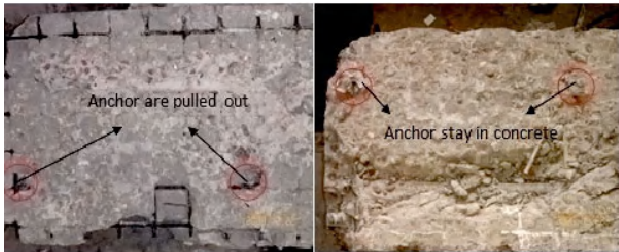


Figure 19 Failure of interface in L3



Figure 20 Failure of interfaces in L4

phenomenon, because of the grid restraining effect. But it does not have the strain-hardening properties. In the B4, ECC reinforcement layer appears many cracks, which is less than 0.16 mm width, showing stress-hardening characteristics, and strong controlling of the cracks.

Although the shear failures of B2, B3, and B4 are controlled by debonding, the shear capacity of B4 is 1.37 times bigger than B3 and 1.23 times of L2 respectively.

4 CONCLUSION

The shear strengthening system with fiber grid and ECC shows better performance in the shear capacity increasing, ductility increasing, anti-debond, crack width controlling, than in other strengthening systems (strengthened concrete beam by FRP, fiber grid strengthening system with the polymer mortar). The method may solve the defects of reinforcement by FRP sheet (poor fire resistance, temperature requirements), and also enhance the crack resistance, lower the ductility of shear failure and reduce other defects in the ordinary reinforced concrete.

The fibers of ECC, which are disorder and uniform distribution, can transform uniform the shear stresses in the complex stress zones. The properties of multiple-cracks and strain hardening exists in the whole shear resist process, controlling width of crack well and transforming shear stress more effectively. So, ECC have good shearing resistance properties.

Fiber bars of FRP grid are distributed in both directions. Obviously, vertical and horizontal bar can resist a large of the stress respectively. Although comparing with ultimate tensile strain of the grid, 30% utilization rate is not very high, The rate may be increased by improving the interface bonding effect and the anchoring devices.

The strengthening system by FRP grid and ECC is not indefinitely increasing shear capacity on concrete beams. When the width of cracks become too large or shear pressure of the beam fail, the bond of interface between ECC and concrete have been destroyed. This need to be well noticed in the design.

Efficiency of RC T-Section Beams Shear Strengthening with NSM FRP Reinforcement

Renata Kotynia (renata.kotynia@p.lodz.pl)

Department of Concrete Structures, Technical University of Lodz, Poland

ABSTRACT The paper analyzes an efficiency of a near-surface mounted (NSM) fiber reinforced polymers (FRP) technique for shear strengthening of reinforced concrete (RC) beams. A review of existing research shows that a number of experimental tests and engineering practice in this field is extremely limited. However, the first results have been very promising and aroused interest of the worldwide FRP community. Based on published test results, the paper provides a comparative study of failure modes, FRP strain efficiency and shear strength enhancement. The efficiency of the NSM shear strengthening is discussed in aspect of the following parameters: shape of the beam's cross-section, beam's dimensions, internal shear steel reinforcement percentage, type, cross-section, inclination and spacing of the NSM FRP reinforcement along the beam's axis and the concrete strength.

1 INTRODUCTION

A research attempt on the NSM FRP shear strengthening has been approved by a high efficiency of this technique in the flexure. The bending capacity of members strengthened with the NSM method demonstrated greater load capacity and rigidity, and in the ultimate failure state a controllable crack propagation, deflection increase, and more the FRP debonding, compared to an abrupt failure mode of EB RC members. Research on the shear NSM FRP strengthening started a few years ago, thus the number of experimental tests is very limited. The paper provides a review of existing research and shows an analysis of the NSM FRP effectiveness for the shear strengthening of RC structures, which attracts the FRP community attention of discussed problems.

2 SUMMARY OF EXISTING RESEARCH

Due to the author's knowledge, tests of RC beams strengthened for shear with the NSM reinforcement have been conducted so far in a few test programs.

A summary of existing experimental data of the T-section, shear strengthened RC beams is reported in Table 1. Due to a small cross-section of published the rectangular beams related to the scale effect (150 × 150mm, and 200 × 200mm), the analysis of shear strengthening effectiveness in those beams is not reliable. Moreover, a low degree of the longitudinal reinforcement of those members caused flexural failure, which is not analyzed in this paper.

Figure 1 shows a scheme of the strengthened beam with a description of all variable parameters considered

in the tests. The collected test programs (Table 1) consisted of 45 T-section beams. Single span, simply supported beams were tested in two static configurations: three and four point bending with the shear span to effective depth ratio a/d ranged from 2,5 to 3,0. In the most of tests, the shear strengthened region was localized in only one support, while the opposite one was strongly reinforced. However, in the beams carried out by Kotynia 2007, both shear spans were strengthened and tested one by one.

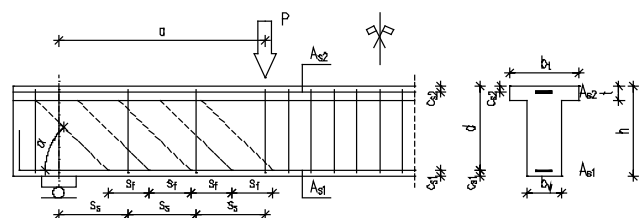


Figure 1 Scheme of NSM shear strengthened RC beam.

Generally, for NSM strengthening round bars, square and rectangular strips have been applied. For better FRP/concrete bond behavior they had various surfaces (smooth, sand-blasted, sand-coated, roughened, ribbed or spirally wound). Several types of the CFRP strips and bars differed in dimensions and elastic modulus collected in the paper were used in the research. The previous tests on NSM strengthened beams in flexure, indicated that though round bars require lower concrete cover thickness than the strips, they are susceptible to brittle FRP debonding. The narrow NSM strips maximize the ratio of confined surface-to-sectional area that provides higher strengthening effectiveness than bars.

Table 1 Characteristics of T cross-section beams

Beam ID	A_{sl}	ρ_{sl}	$b_w/h/b_t/t$	d_s/s_s	d_f/s_f $b_f/t_f/s_f$	α_f	c_{s1}/c_{s2}	A_f	E_f	f_c	V_{flex}	V_{test}	V_f	$\frac{V_{test}}{V_{test0}}$	Failure mode
	mm ²	%	mm	mm	mm	°	mm	mm ²	MPa	MPa	MPa	MPa	MPa	-	
De Lorenzis & Nanni 2001; a/d = 3,0; NSM strengthening system: CFRP round bars of $d_f=9,5$ mm diameter															
BV				-	-	-		-	-			90,3	-	1,00	S
B90-7				-	Ø 9,5/178	90						115,2	24,9	1,28	S
B90-5				-	Ø 9,5/127	90						127,7	37,4	1,41	S
B90-5A	1293	2,38	153 / 407 /	-	Ø 9,5/127	90		70,85	104,8			185,7	95,4	2,06	S
B45-7			281 / 102	-	Ø 9,5/178	45	50,8/40			31,0	165,5	165,5	75,2	1,83	D, F
B45-5				-	Ø 9,5/127	45						177,9	87,6	1,97	S
BSV				9,5/356	-	-						153,2	0,0	1,00	D, F
BS90-7A				9,5/356	Ø 9,5/178	90		70,85	104,8			206,8	53,6	1,35	S
Dias & Barros 2008; a/d = 2,53; NSM strengthening system: CFRP strips of 10 mm wide and 1.4 mm thick															
2S-R					-	-						189,0	-	1,00	S
2S-3LV					10/1,4/267	90						189,6	0,6	1,00	S
2S-5LV					10/1,4/160	90						214,2	25,2	1,47	S
2S-8LV					10/1,4/100	90						237,6	48,6	1,63	S
2S-3LI45	1874	2,92	180 / 400 /	6/300	10/1,4/367	45	44/24	14	166	31,1	296,6	196,8	7,8	1,35	S
2S-5LI45			450 / 100		10/1,4/220	45						230,4	41,4	1,58	S
2S-8LI45					10/1,4/138	45						229,2	40,2	1,57	S
2S-3LI60					10/1,4/325	60						224,4	35,4	1,54	S
2S-5LI60					10/1,4/195	60						235,2	46,2	1,61	S
2S-7LI60					10/1,4/139	60						243,6	54,6	1,67	S
Dias et al. 2007; a/d = 2,50; NSM strengthening system: CFRP strips of 10 mm wide and 1.4 mm thick															
2S-R'					-	-						135,9	-	1,00	S
2S-7LV					10/1,4/114	90						164,2	28,3	1,21	S
2S-4LI45				6/300	10/1,4/275	45						169,8	33,9	1,25	S
2S-7LI45					10/1,4/157	45						183,9	48,0	1,35	S
2S-4LI60					10/1,4/243	60						168,9	33,1	1,24	S
2S-6LI60	1809	2,79	180 / 400 /		10/1,4/162	60	40/25	14	166	18,6	455,9	178,6	42,7	1,31	S
4S-R			450 / 100		-	-						182,3	-	1,00	S
4S-7LV					10/1,4/114	90						189,2	6,9	1,04	S
4S-4LI45				6/180	10/1,4/275	45						208,3	26,0	1,14	S
4S-7LI45					10/1,4/157	45						213,8	31,6	1,17	S
4S-4LI60					10/1,4/243	60						207,4	25,1	1,14	S
4S-6LI60					10/1,4/162	60						217,4	35,1	1,19	S
Dias & Barros 2010; a/d = 2,50; NSM strengthening system: CFRP strips of 10 mm wide and 1.4 mm thick															
2S-R''					-	-						182,3	-	1,00	S
2S-4LV					10/1,4/180	90						202,4	20,2	1,11	S
2S-7LV					10/1,4/114	90						224,5	42,2	1,23	S
2S-10LV					10/1,4/80	90						238,5	56,2	1,31	S
2S-4LI45	1809	2,79	180 / 400 /	6/300	10/1,4/275	45	40/25	14	171	39,7	471,6	235,7	53,4	1,29	S
2S-7LI45			450 / 100		10/1,4/157	45						253,0	70,7	1,39	S
2S-10LI45					10/1,4/110	45						267,9	85,6	1,47	S
2S-4LI60					10/1,4/243	60						231,8	49,6	1,27	S
2S-6LI60					10/1,4/162	60						236,6	54,4	1,30	S
2S-9LI60					10/1,4/108	60						247,6	65,3	1,36	S
Kotynia 2007; a/d=2,54; NSM strengthening system: CFRP strips of 15 mm wide and 1.4 mm or 2.4 mm thick															
BI-1					-	-						112,0	-	1,00	S
BI-2/3A					15/1,4/210			21	170	39,0		208,3	96,3	1,66	S
BI-2/3B					15/2,4/360			36	163	39,0		176,6	64,6	1,58	S
BI-3/5A					15/2,4/210			36	163	38,5		212,6	100,7	1,69	S
BI-3/5B	1256	2,66	150 / 360 /	6/200	15/1,4/120	45	45/25	21	170	38,5	215,9	234,1	-	-	F
BI-4/7A			286 / 60		15/1,4/80			21	170	40,0		216,5	-	-	F
BI-4/7B					15/2,4/140			36	163	40,0		216,5	-	-	F
BI-s4/5A					15/1,4/120			21	170	41,9		220,9	-	-	F
BI-s4/5B					15/2,4/140			36	163	41,9		220,9	-	-	F

S = shear failure; F = flexural failure; D = CFRP debonding; A = anchorage of NSM bars in a beam's flange; s = steel stirrups cut; A_{sl}, ρ_{sl} = cross-section and percentage of longitudinal steel reinforcement; d_f, d_s = diameter of the CFRP and stirrup; $b_w/h/b_t/t$ = dimensions of the T-section (Figure 1); b_f, t_f = width and thickness of the FRP strip; c_{s1}, c_{s2} = distance between bottom and upper longitudinal steel bars from the bottom and upper beam's edge, respectively; V_{flex} = shear force at the support corresponding to the load bearing capacity; V_{test} = shear strength; V_f = FRP contribution to the shear strength

An effect of the NSM bar's anchorage in the beam's flange on the shear efficiency was investigated by De Lorenzis 2001. Problem of cutting the lateral arms of the steel stirrups during FRP installation was performed by Kotynia 2007 with promising test results. The influence of the existing steel stirrups percentage on the effectiveness of the NSM shear strengthening was studied by Dias et al. 2007.

The ultimate loads, FRP contribution to the shear strength, failure modes and shear strengthening efficiency, have been analyzed in aspect of the following variable parameters: ratio of steel transversal ρ_s and longitudinal ρ_{sl} reinforcement, type (GFRP and CFRP), shape (round bars and strips), cross-section A_f , inclination α_f (45° , 60° , 90°), NSM FRP spacing s_f along the longitudinal beam's axis and compressive concrete strength f_c .

2.1 Failure modes

The collected test results indicated appearance of three main shear failure mechanisms caused by debonding of CFRP reinforcement. The debonding proceeded by the loss of NSM/adhesive bond or by inclined shear cracking of surrounding concrete. That mode of failure may be avoided by anchoring of the composite bars in the flange of the T-shape beam or by reducing their spacing, which extends the bond length of the NSM bars, crossed by the shear crack. The second failure mechanism, resulted in the splitting of the concrete cover along the longitudinal steel reinforcement close to the support region occurred in beams with the low transversal steel reinforcement ratio, due to interaction between internal steel stirrups and NSM reinforcement. The NSM rods were not able to transfer tensile stress to longitudinal steel bars subjected to dowel forces, which led the concrete cover separation and loss of the NSM FRP anchorage. The third failure mode, typical for beams strengthened with NSM strips at a very small spacing, was characterized by the two-side debonding of a group of the NSM bars, together with detached concrete cover, from the core of the beam. Such a mode indicates a negative influence of the NSM spacing reduction, that may be prevented by anchoring of the FRP strips in the beam's flange. The fourth, theoretically possible failure mode, but not observed in any tests, is a rupture of the NSM FRPs crossed by the critical shear crack.

2.2 Deformability of strengthened beams

The NSM FRP strain are highly effected by the position of the strain gauges with reference to the shear crack. The maximal strain of CFRP round bars and rectangular strips registered during the test were in the range of $0.0023 \div 0.0029$ (for round bars), $0.003 \div 0.0045$ (for $15\text{mm} \times 1.4\text{mm}$ and $15 \times 2.4\text{ mm}$ strips) and $0.4 \div 0.006$ (for $10\text{mm} \times 1.4\text{mm}$ strips). The test results indicated that after cracking, the internal steel stirrups yielded and gave a full contribution to the shear capacity of the

NSM strengthened beam. The beams with low NSM spacing showed CFRP/concrete bond loss after shear cracking, which revealed gradual lateral concrete cover separation from the beam's core.

2.3 NSM CFRP contribution to the shear strength

A significant influence of the NSM composite reinforcement ratio, on the reduced FRP contribution to the shear strength V_f/b_{wd} , confirm Table 1 and diagrams presented in Figure 2. Classification of the test results for series differed in FRP inclination, type of the NSM reinforcement and transversal steel ratio allows to separate the influence of each investigated parameter on the shear NSM FRP strength.

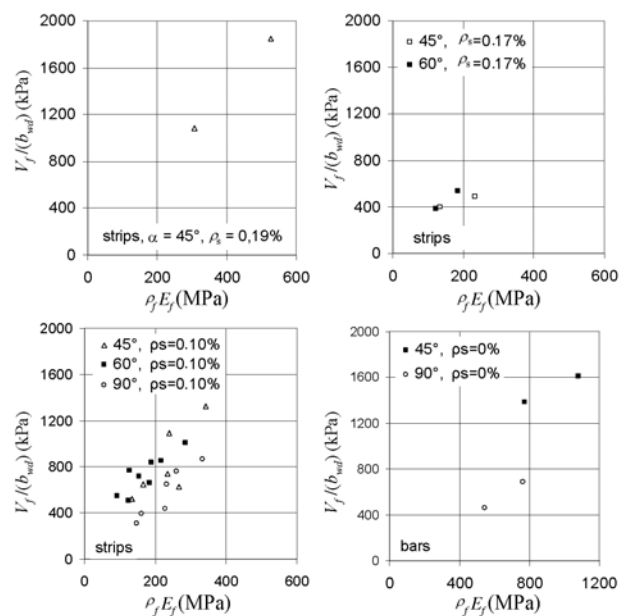


Figure 2 Influence of CFRP ratio and elasticity modulus on the reduced CFRP contribution to the shear strength

Figure 2 proves higher influence of the steel transversal ratio, than the NSM inclination angle on the FRP contribution to the shear strength. Based on the analysis of the FRP inclination on its shear contribution, indicates that the most effective was 45 degree NSM application, which was the most sufficient in the beams without internal steel stirrups, strengthened with the round bars. The shear strength should be considered with the account of both, the steel and FRP percentage with their elasticity modulus, $\rho_s E_s$ and $\rho_f E_f$, respectively.

$$\rho_s = \frac{2A_s}{b_w s_s}, \rho_f = \frac{2A_f}{b_w s_f \sin \alpha} \quad (1)$$

where: b_w = the width of the beam's web, s_f , s_s = the CFRP and steel spacing, A_f , A_s = cross-section of the CFRP and steel bars, α_f – inclination of the laminate, E_f , E_s = elasticity modulus of the CFRP and steel reinforcement.

The test results indicate decrease of the CFRP contribution with increase of its spacing s_f along the beam's axis. The drop rate is affected by the CFRP inclination and the internal steel ratio (Figure 3).

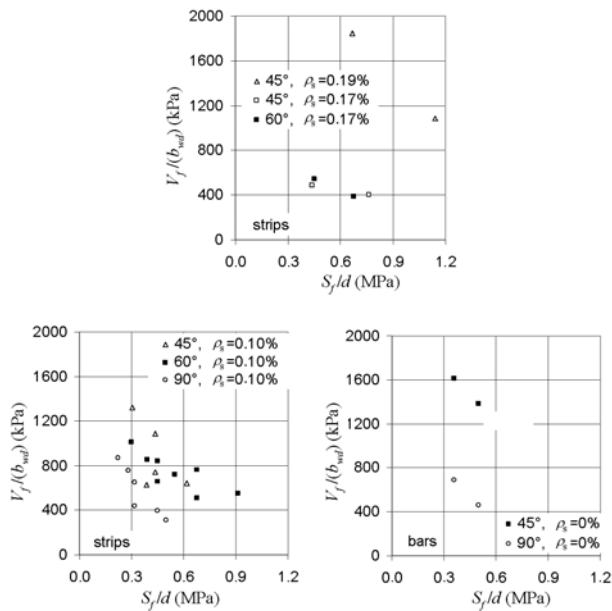


Figure 3 Effect of CFRP spacing on the reduced CFRP shear contribution

The shear strengthening ratio expressed by the ratio of the shear capacity between the strengthened and unstrengthened member (see Table 1)

$$\eta = V_{test}/V_{test0} \quad (2)$$

increases with reducing of the NSM FRP spacing, with increasing its cross-section area, with FRP inclination in respect of a beam's axis or with the FRP anchoring in the flange of the beam. However, reducing of the not anchored CFRP spacing below a certain limit value, may lead to debonding of the CFRP group. The effect of the strengthening sufficiently depends on the shear steel reinforcement ratio ρ_s , and for higher steel percentage, the shear strengthening ratio is less susceptible to changes of the NSM CFRP ratio ρ_f (Table 1).

Test data collected in Table 1 demonstrates a sufficient influence of the CFRP inclination on the shear strength, which in beams with 45 degree round bars, increased by average 56% compared to the beams strengthened with 90 degree bars. The lower influence of inclination of the rectangular strips, compared to round bars, was effected by five times smaller cross-section area of the first compared to the second. The highest strengthening effectiveness of 2.06 (in beams without the steel stirrups) was obtained due to anchoring of the NSM CFRP in the T-section flange.

Almost all tested beams had the concrete strength in the range from 31MPa to do 40MPa, except the series by Dias et al. 2007, where it was only 18,6MPa. Analysis

of the test results of Dias et al. 2007 and Dias & Barros 2010, referred two series of beams with the same transversal steel ratio ($\text{Ø}6$ every 300mm), identically strengthened and differed only in the concrete strength (Table 1) indicated a distinct effect of the concrete strength on the CFRP contribution to the shear strength (Figure 4). The increase in the concrete strength from 18.6MPa to 39.7 MPa, caused the increase in the CFRP contribution in the range from 47.4% to 57.5%.

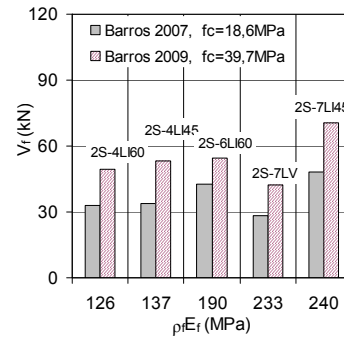


Figure 4 Effect of concrete strength on NSM CFRP contribution to the shear strength

3 CONCLUSIONS

Based on the analysis of the test results, the following conclusions may be drawn:

- The strengthening ratio is the most affected by the CFRP spacing, steel and CFRP percentage, NSM reinforcement inclination and NSM FRP anchorage in the flange of the beam;
- Cut of the steel stirrups during CFRP installation did not effected the shear strength;
- The maximal CFRP debonding strain ranged from 0,003 to 0,006 for the rectangular strips and above 0,002 for the round bars;
- The NSM CFRP contribution to the shear strength depends on the concrete strength;
- The increase in the CFRP ratio produces the increase in the shear strength, but the failure mode is highly influenced by the CFRP percentage, and reducing of the CFRP spacing may lead to the group CFRP debonding;
- The strengthening efficiency sufficiently depends on the shear steel percentage, and for higher steel ratio, the shear strengthening ratio is less susceptible to changes of the NSM CFRP percentage;

REFERENCES

De Lorenzis, L. & Nanni, A. 2001. Shear strengthening of reinforced concrete beams with near-surface mounted fiber-reinforced polymer rods. *ACI Struct J* 98(1):60-68.
 Dias, S.J.E. & Barros, J.A.O. 2008. Shear strengthening of T

- cross section reinforced concrete beams by near surface mounted technique. *J Compos Const* 12(3): 300-311.
- Dias, S.J.E. & Barros J.A.O. 2010. Performance of reinforced concrete T beams strengthened in shear with NSM CFRP. *Eng Struct* 32(2):373-384.
- Dias, S.J.E., Bianco, V. Barros, J.A.O. & Monti, G. 2007. Low strength T-cross section RC beams shear-strengthened by NSM technique. *Proc. Mat. App. Innov. per il Prog. in Zona Sis. Mitig. della Vulner. Strut.* Salerno, CD.
- Kotynia, R. 2007. Shear strengthening of RC beams with NSM CFRP laminates. *Proc. FRPRCS-8 International Symposium on Fiber Reinforced Polymer Reinforcement for Concrete Structures*, Patras, CD.

Mechanical Model to Simulate the NSM FRP Strips Shear Strength Contribution to RC Beams

Vincenzo Bianco (vincenzo.bianco@uniroma1.it)

Department of Structural Engineering and Geotechnics, Sapienza University, Rome, Italy

J.A.O. Barros

Department of Civil Engineering, University of Minho at Guimarães, Portugal

Giorgio Monti

Department of Structural Engineering and Geotechnics, Sapienza University, Rome, Italy

ABSTRACT A three dimensional mechanical model has been recently developed to simulate the Near Surface Mounted (NSM) Fibre Reinforced Polymer (FRP) strips shear strength contribution to Reinforced Concrete (RC) beams throughout the entire loading process, as function of the Critical Diagonal Crack (CDC) opening angle. It was developed by fulfilling equilibrium, kinematic compatibility and constitutive laws of both intervening materials and bond between them. It takes into consideration all of possible failure modes that can affect the behaviour, at ultimate, of a single NSM strip, namely: loss of bond (debonding), semi-conical concrete tensile fracture, rupture of the strip itself and a mixed shallow-semi-cone-plus-debonding failure. Besides, it allows the interaction among adjacent strips to be accounted for. The numerical results, in terms of both shear strength contribution and predicted cracking scenario are presented and compared with experimental evidence regarding some of the most recent experimental programs. From that comparison, a satisfactory level of prediction accuracy, regardless of the main parameters such as concrete mechanical properties, amount and inclination of strips, arises. The main findings, as well as the influence of some of the main intervening parameters, are shown.

1 INTRODUCTION

A model developed in Bianco (2008) and Bianco et al. (2009) is presented that predicts the NSM FRP strips contribution to the shear strength of an underdesigned RC beam. It assumes that each NSM strip may fail due to (Figure 1a): debonding, tensile rupture of the strip, concrete semi-conical fracture or mixed shallow semi-cone-plus-debonding. Phases undergone by bond by imposing an increasing end slip and representing the phenomena that occur, in sequence, within the adhesive layer, are plotted in Figure 1b. The beam is schematized as a prism divided in two parts by the Critical Diagonal Crack (CDC) that can be, in turn, thought as a plane (Figure 1c). After the insurgence of the CDC, the two parts of the web start moving apart by pivoting around the CDC tip (point E in Figure 1d) and the crossing strips oppose the crack widening by anchoring to the surrounding concrete where the force originating in the loaded section is transferred through bond. When the principal stresses transferred to the concrete exceed its mean tensile strength, it fractures along co-axial and successive semi-conical surfaces. When the spacing between adjacent strips is reduced, the fracture surfaces pertaining to each strip overlap

(Figure 1e). The concrete fracture capacity is evaluated taking into account this detrimental group effect. Moreover, when the spacing between adjacent strips is very small, the components of concrete mean tensile strength parallel to the CDC and orthogonal to the web faces, are balanced only from an overall point of view, but not locally on each web face, thus justifying the concrete cover spalling observed experimentally (Figure 3f).

2 SIMULATIONS OF EXPERIMENTAL TESTS AND PARAMETRIC STUDIES

The model proposed was applied to the RC beams tested by Dias et al. (2007) and by Dias and Barros (2008). The beams tested in those experimental programs were T-cross-section RC beams characterized by the same test set-up, the same amount of longitudinal reinforcement, the same kind of CFRP strips and epoxy adhesive and they differed for the mechanical properties of concrete. In fact, the former experimental program was characterized by a concrete mean compressive strength f_{cm} of 18.6 MPa while the latter by 31.1 MPa. Both series presented different configurations of NSM strips, in terms of both

inclination β and spacing s_f and the former program also included beams characterized by a different amount of existing steel stirrups. Those beams are characterized by the following common geometrical and mechanical parameters: $b_w=180$ mm ; $h_w=300$ mm ; $f_{fu}=2952$ MPa ; $E_f=166$ GPa ; $a_f=1.4$ mm ; $b_f=10.0$ mm (a_f ; b_f = strip cross section dimensions). The parameters characterizing the adopted local bond stress-slip relationship, being the average values of those obtained in a previous investigation (Bianco 2008) are: $\tau_0=2.0$ MPa ; $\tau_1=20.1$ MPa ; $\tau_2=9.0$ MPa ; $\delta_1=0.07$ mm ; $\delta_2=0.83$ mm ; $\delta_3=14.1$ mm.

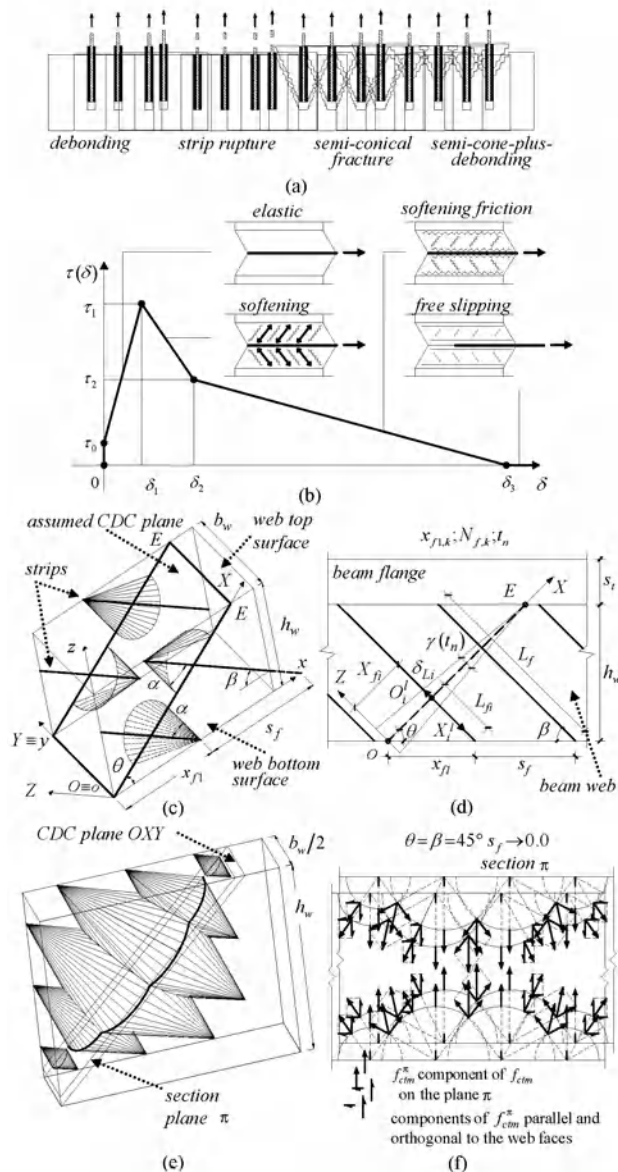


Figure 1 Main features of the mechanical model developed to predict the NSM FRP strips shear strength contribution: (a) assumed configurations at ultimate of an NSM FRP strip, (b) adopted local bond stress-slip relationship, (c) strengthened beam web and CDC occurred, (d) loading process of a shear strengthened beam, (e) interaction among adjacent strips, (f) section of the web by a plane parallel to the CDC plane

The CDC inclination angle θ adopted in the simulations plotted in Figure 2 is the one experimentally observed (Bianco 2009). The angle α was assumed equal to 28.5° , being the average of values obtained in a previous investigation (Bianco 2008) by back analysis of experimental data. The two parameters characterizing the loading process are: $\dot{\gamma}=0.01^\circ$ and $\gamma_{max}=1.0^\circ$ (Figure d). Concrete average tensile strength f_{ctm} was calculated from the average compressive strength by means of the formulae present in the CEB Fib Model Code 1990 resulting in 1.45 MPa and 2.45 MPa for the former and latter series of beams, respectively. Comparison between the numerical results and experimental recordings are plotted in Figure 2.

From that comparison, a satisfactory data-fitting performance of the proposed model, in terms of prediction of the peak NSM shear strength contribution $V_{f,k}^{max}$ arises, regardless of the different concrete mechanical properties, inclination of the strips, their spacing along the beam axis and amount of existing steel stirrups. It should be outlined that the difference between the peak value of V_f , obtained for the three different configurations, and consequently the dispersion of the numerical predictions with respect to the experimental recording, increases by reducing the spacing between adjacent strips (see Figure 2).

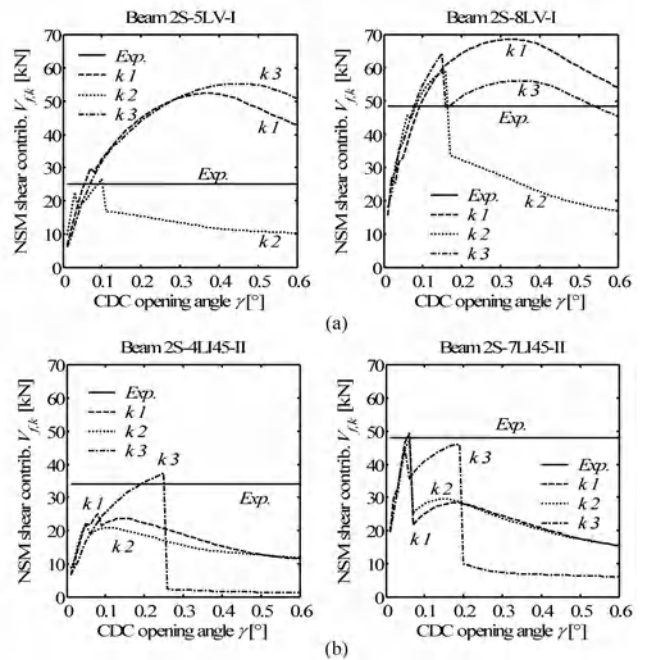


Figure 2 Comparison between numerical predictions and experimental recordings for: (a) some of the beams tested by Dias and Barros (2008) and (b) some of the beams tested by Dias et al. (2007)

The typical graph of shear strength contribution as function of the CDC opening angle $V_f[\gamma(t_n)]$ is characterized by abrupt decays corresponding to the strips' failure. The peculiar behavior of a RC beam

strengthened in shear by NSM technique can be easily explained referring to one of those beams as for instance the beam labeled 2S-7LI45-II (with 2 existing steel stirrups, 7 strips at 45°) whose cracking scenario, both numerically predicted and experimentally recorded, is reported in Figure 3.

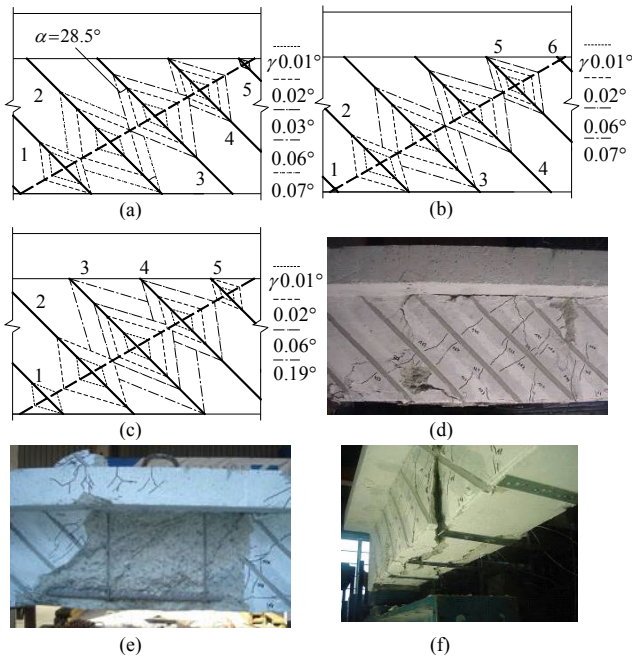


Figure 3 Cracking scenario regarding beam 2S-7LI45-II: numerical results for (a) the first $k = 1$, (b) second $k = 2$, and (c) third $k = 3$ geometrical configuration and (d-f) experimental post-test pictures

The first strips to fail are those characterized by shorter available bond lengths that generally fail in the first stages of the loading process, like for instance: the 1st ($\gamma = 0.02^\circ$) and the 5th ($\gamma = 0.03^\circ$) of the 1st configuration (Figure 3a); the 1st and 6th ($\gamma = 0.01^\circ$) and the 2nd ($\gamma = 0.02^\circ$) of the 2nd configuration (Figure 3b). Those failures are not so evident in the corresponding graph (Figure 2) since, in the first load steps, the contribution provided by the strips with larger available bond length is increasing and relatively much higher. When a strip fails at a higher stage of the loading process, the corresponding decay in the load carrying capacity is much more evident, like it happens, for instance: for the 2nd strip of the 1st configuration at $\gamma = 0.07^\circ$, the 3rd of the 2nd configuration at $\gamma = 0.07^\circ$ or the 3rd strip of the 3rd configuration at $\gamma = 0.19^\circ$. The first two are mixed shallow-semi-cone-plus-debonding failures and the third is characterized by a semi-conical concrete fracture that reaches the inner tip. After those failures, the corresponding graphs present a different trend: in the first two cases, a maximum relative follows while, in the third, the shear carrying capacity goes on diminishing in a smooth way. The former behavior is due to the fact that, when the last fracture occurs, that is the mixed failure of

the 2nd and 3rd strip respectively, the remaining strips still have a resisting bond length higher than the required transfer length and their contribution can still increase before gradual complete debonding follows. The latter is due to the fact that, when the 3rd central strip fails, the 2nd and the 4th had already failed by mixed failure so that the overall carrying capacity goes on diminishing until complete debonding of their left resisting bond lengths.

The numerical modeling strategy herein proposed also allows to carry out parametric studies to assess the influence of all of the involved parameters on the NSM shear strength contribution. Hereafter, for the sake of brevity, only a short parametric study is presented (Figure 4a-b) that aims at singling out, even by means of the comparison between numerical predictions and experimental recordings, the influence of the spacing for beams with strips at 60° and with two different concrete types. It arises that, as expected, the higher the concrete mechanical properties, the higher the shear carrying capacity, for the same value of spacing between adjacent strips.

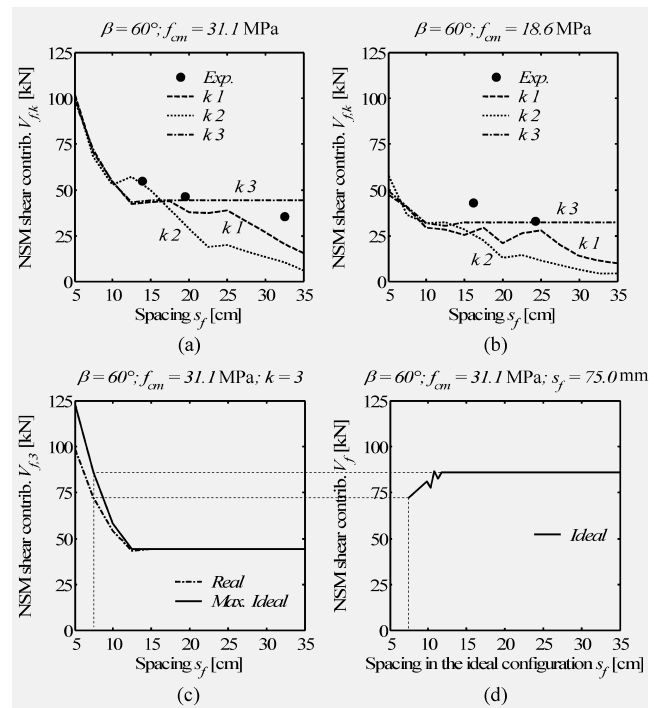


Figure 4 Comparison between numerical and experimental results: as function of the spacing between adjacent strips at 60° for concrete f_{cm} 31.1 MPa (a) and f_{cm} 18.6 MPa (b); group effect for the 3rd configuration (concrete f_{cm} 31.1 MPa and β 60°); (c) and ideal shear strength contribution for a system of NSM with spacing 75 mm (d)

It can also be gathered that, by reducing the spacing between adjacent strips, due to the increase of the number of strips effectively crossing the CDC, the shear strength contribution increases even if, as highlighted in Figure 4c for the 3rd configuration only (with $\beta = 60^\circ$; $f_{cm} = 31.1$ MPa), the smaller the spacing, the higher the

group effect. This latter can be defined as the decrease of shear strength contribution with respect to an ideal situation where the same system of strips, characterized by the real value of the spacing s_f , the same available bond lengths and the same imposed end slips, are instead spaced out, along the CDC, at such an extent that they do not interact any longer between each other. The corresponding increase in shear strength contribution increases up to a maximum ideal value, beyond which any further increase of the ideal spacing between adjacent strips does not produce any further increase in carrying capacity. That can be also gathered from Figure 4d, in which the ideal trend is plotted as function of the ideal spacing for the real configuration of strips at $s_f = 75$ mm.

The detrimental group effect increases by reducing the spacing between strips (Figure 4c).

3 CONCLUSIONS

The need to provide a rational explanation to the observed peculiar failure mode affecting the behavior, at ultimate, of RC beam strengthened in shear by the NSM technique led to the development of a comprehensive numerical model to simulate the NSM shear strength contribution throughout the loading process whose main features were herein presented. The comparison between the numerical predictions and the experimental recordings showed the high level of accuracy of the proposed model especially if one considers that: the model neglects the softening behavior of concrete in tension, the high scatter affecting concrete tensile strength and, on the contrary, the simplified and indirect way in which it was herein calculated.

The application of that model also let some complex phenomena to be pinpointed, such as the group effect between adjacent strips. Despite its relative complexity, the proposed model can be usefully applied to obtain useful information for designers interested in applying

such innovative technique. At the same time, it can be conveniently summarized into a simplified closed-form design formula for practitioners.

4 ACKNOWLEDGEMENTS

The authors of the present work wish to acknowledge the support provided by the “Empreiteiros Casais”, S&P®, degussa® Portugal, and Secil (Unibetão, Braga). The study reported in this paper forms a part of the research program “SmartReinforcement – Carbon fibre laminates for the strengthening and monitoring of reinforced concrete structures” supported by ADI-IDEIA, Project n° 13-05-04-FDR-00031. This work was also carried out under the auspices of the Italian DPC-ReLuis Project (repertory n. 540), Research Line 8, whose financial support is greatly appreciated.

REFERENCES

- Bianco, V. 2008. Shear strengthening of RC beams by means of NSM FRP strips: experimental evidence and analytical modeling. PhD Thesis, *Dept. of Struct. Engrg. and Geotechnics*, Sapienza University of Rome, Italy.
- Bianco, V., Barros, J.A.O. and Monti, G. 2009. Three dimensional mechanical model for simulating the NSM FRP strips shear strength contribution RC beams. *Engineering Structures*, 31(4): 815-826.
- Dias, S.J.E., Bianco, V., Barros, J.A.O., Monti, G. 2007. Low strength concrete T cross section RC strengthened in shear by NSM technique. *Workshop Materiali ed Approcci innovative per il Progetto in Zona Sismica e la Mitigazione della vulnerabilità delle Strutture*, University of Salerno, Italy 12-13 February.
- Dias, S.J.E., Barros, J.A.O. 2008. Shear Strengthening of T Cross Section RC Beams by Near Surface Mounted Technique. *Journal of Composites for Constructions*, ASCE, 12(3): 300-311.

Shear Strengthening of RC Beams by Means of NSM FRP Strips: Constitutive Law of a Single Strip

Vincenzo Bianco (vincenzo.bianco@uniroma1.it) & Giorgio Monti
Department of Structural Engineering and Geotechnics, Sapienza University, Rome, Italy

J.A.O. Barros
Department of Civil Engineering, University of Minho at Guimarães, Portugal

ABSTRACT The need to provide a rational explanation to the observed peculiar failure mode affecting the behaviour, at ultimate, of a Reinforced Concrete (RC) beam strengthened in shear by Near Surface Mounted (NSM) Fibre Reinforced Polymer (FRP) strips, led the authors to develop a comprehensive numerical model for simulating the NSM shear strength contribution to RC beams throughout the entire loading process as function of the Critical Diagonal Crack (CDC) opening angle. That model was respectful of equilibrium, kinematic compatibility and constitutive laws. Despite its high level of prediction accuracy, taking into account all of the possible failure modes, as well as the interaction among adjacent strips, that model resulted relatively complex to be easily implemented in a practitioners-addressed building regulations code. Yet, it can be conveniently simplified into a more user-friendly and closed-form design formula. Crucial point of that simplification is the development of a reliable constitutive analytical law providing the single strip strength as function of the imposed end slip. This paper presents the modelling strategy adopted to determine that constitutive law, as well as its final analytical expression.

1 INTRODUCTION

During the loading process of a RC beam strengthened in shear by NSM FRP strips, after the occurrence of the Critical Diagonal Crack (CDC), the two parts into which the beam web divides start moving apart and the crossing strips oppose this movement by anchoring to the surrounding concrete. Due to the imposed end slip $\delta_{Li}(t_n)$, the force originated in each NSM strip at the section crossing the CDC is transferred to the surrounding concrete through bond (Figure 1a). The local bond stress-slip relationship $\tau(\delta)$ simulating the mechanical phenomena occurring at the strip/adhesive interface, within the adhesive layer and at the adhesive/concrete interface, can be represented, in a simplified way (Bianco 2008, Bianco et al. 2009), by a bi-linear curve (Figure 1b). This curve envisages that, by imposing increasing end slips to the FRP strip, cracks form instantly within the adhesive layer, orthogonally to the (inclined) tension isostatics and along the interfaces. Stresses are transferred by friction along those micro-cracks. However, by imposing increasing end slips, those cracks progressively become smoother (softening friction phase) up to the point ($\delta_{Li} = \delta_i$) in which friction can no longer be mobilized and the strip is being pulled out without having to overcome any restraint left (free slipping phase). Even if bond is the main mechanism through which force present in the strip is transferred to

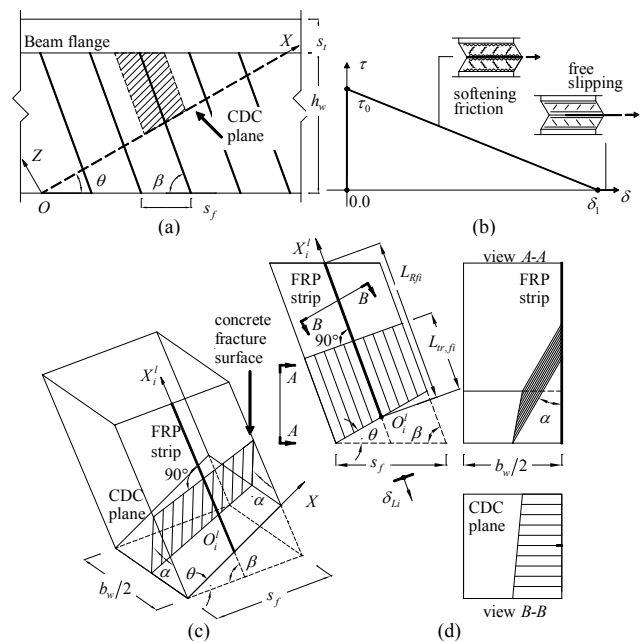


Figure 1 An NSM FRP strip: (a) web strengthened side, (b) local bond stress-slip relationship, (c) a single strip confined to a concrete prism, (d) sections of the concrete prism

the surrounding concrete, the behavior of an NSM FRP strip is more complex due to the interaction of bond with other phenomena such as concrete fracture and/or strip tensile rupture, and to the interaction among

adjacent strips and between these latter and the existing steel stirrups (Bianco 2008).

2 BOND-BASED CONSTITUTIVE LAW

The bond behavior of an NSM FRP strip subjected to an imposed end slip δ_{Li} can be modeled (Bianco et al. 2009) by fulfilling equilibrium, kinematic compatibility, constitutive laws of the intervening materials (FRP, adhesive and concrete) and the local bond stress-slip relationship (Figure 1(b)). In this way, it is possible to obtain closed-form analytical equations for both the bond-based constitutive law $V_{fi}^{bd}(L_{Rfi}; \delta_{Li})$ of a single strip and the corresponding bond transfer length $L_{tr,fi}^{bd}(L_{Rfi}; \delta_{Li})$ that are: the force that a strip of resisting bond length L_{Rfi} can transfer by bond, as function of δ_{Li} and the corresponding amount of L_{Rfi} along which bond is mobilized, respectively. Those analytical expressions, herein omitted for the sake of brevity (Bianco 2008), are plotted in Figure 2(a)–(c).

Those analytical expressions envisage, for a given L_{Rfi} , three phases, whose limits are function of the value assumed by L_{Rfi} with respect to the effective bond length L_{tr1} that is the value of resisting bond length beyond which any further increase of length does not produce any further increase of the maximum force transmissible by bond. Those phases can be singled out considering the progressive migration of the invariant distribution of shear stresses and slip (Figure 2(d)) from the loaded end towards the free one by increasing δ_{Li} . In the first phase, the force transmitted by bond stresses increases up to reaching the peak in correspondence of $\delta_{L1}(L_{Rfi})$ that is, for $L_{Rfi} < L_{tr1}$, the step in which the invariant distribution of bond stresses has reached the strip free end and, for $L_{Rfi} \geq L_{tr1}$, the step where $L_{tr,fi}^{bd} = L_{tr1}$. The second phase, for $L_{Rfi} < L_{tr1}$, is characterized by a decrease of V_{fi}^{bd} and a constancy of $L_{tr,fi}^{bd}$ while, for $L_{Rfi} \geq L_{tr1}$, V_{fi}^{bd} remains constant and equal to the peak V_1^{bd} and $L_{tr,fi}^{bd}$ goes on increasing up to $\delta_{L2}(L_{Rfi})$. In the third phase, the invariant distribution of bond stresses progressively abandons L_{Rfi} , whatever its value, resulting in a decrease of V_{fi}^{bd} up to zero and in a constant value of $L_{tr,fi}^{bd}$ that is equal to L_{Rfi} .

3 COMPREHENSIVE CONSTITUTIVE LAW

The comprehensive constitutive law $V_{fi}(L_{Rfi}; \delta_{Li})$ of the simple structural system constituted of an FRP strip near surface mounted on a prism of concrete is obtained by taking into consideration also the possibility of concrete fracture and tensile rupture of the strip itself during the loading process. In correspondence of each step (t_n) of the loading process, the system undergoes some modifications up to reaching the corresponding equilibrium configuration (q_e) (Figure 3).

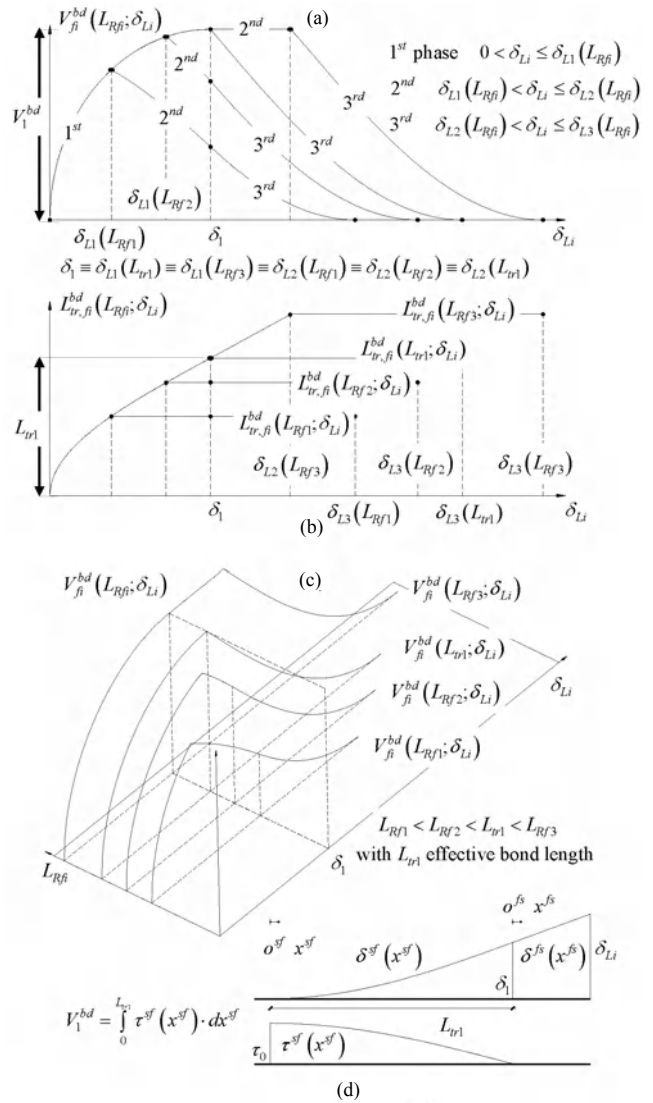


Figure 2 Bond-based constitutive law of a single NSM FRP strip: (a) $V_{fi}^{bd}(L_{Rfi}; \delta_{Li})$ and (b) $L_{tr,fi}^{bd}(L_{Rfi}; \delta_{Li})$ in a bi-dimensional representation, (c) $V_{fi}^{bd}(L_{Rfi}; \delta_{Li})$ in a tri-dimensional representation and (d) invariant distribution of bond stress and imposed end slip

At the generic iteration q_m of the t_n load step, the transfer length is given by (Figure 3a):

$$L_{tr,fi}(t_n; q_m) = L_{fi}^{cf}(t_{n-1}; q_e) + L_{tr,fi}^{bd}[L_{Rfi}(t_n; q_m); \delta_{Li}(t_n)] + \Delta L_{fi}^{cf}(t_n; q_m) \quad (1)$$

that is, the sum of $L_{fi}^{cf}(t_{n-1}; q_e)$ the cumulative depth of the concrete fracture as results from the equilibrium of the preceding t_{n-1} load step, the $L_{tr,fi}^{bd}[L_{Rfi}(t_n; q_m); \delta_{Li}(t_n)]$ bond-based necessary transfer length corresponding to the current value of the imposed end slip and the increment $\Delta L_{fi}^{cf}(t_n; q_m)$ of concrete fracture height at the current load step.

In correspondence of the q_m iteration of the t_n load step, if it happens that the concrete fracture capacity is smaller than the force transferred by bond, i.e.:

$$V_{fi}^{cf}[L_{tr,fi}(t_n; q_m)] < V_{fi}^{bd}[L_{Rfi}(t_n; q_m); \delta_{Li}(t_n)] \quad (2)$$

the bond transfer mechanism leaps forward towards the free end of the strip and the resisting bond length reduces accordingly, up to reaching equilibrium (Figure 3). The initial value of the resisting bond length reduces and the initial constitutive law modifies as indicated in Figure 3d for the general case in which, in correspondence of the last fracture and the contextual leap forwards, the value of the left amount of the initial resisting bond length is larger than the current value of the bond-based transfer length. In this case, in fact, concrete fracture acts just like a reducer of the initial resisting bond length and the point representative of the state of the system moves from one constitutive law to the other (Figure 3d). On the contrary, when the concrete fracture is very deep, there can be a drastic and abrupt reduction of the resisting bond length, to which corresponds a constitutive law as that indicated in Figure 4a. In the case (Figure 3) in which concrete fracture remains shallower and just acts like a reducer of the initial L_{Rfi} , the resulting constitutive law

is as depicted in Figure 4b. When, either following or not an initial concrete fracture, the rupture of the strip occurs, the resulting constitutive law is as depicted in Figure 4c. The analytical expressions of those constitutive laws are extensively supported on the ones of the bond based constitutive law (Bianco 2008).

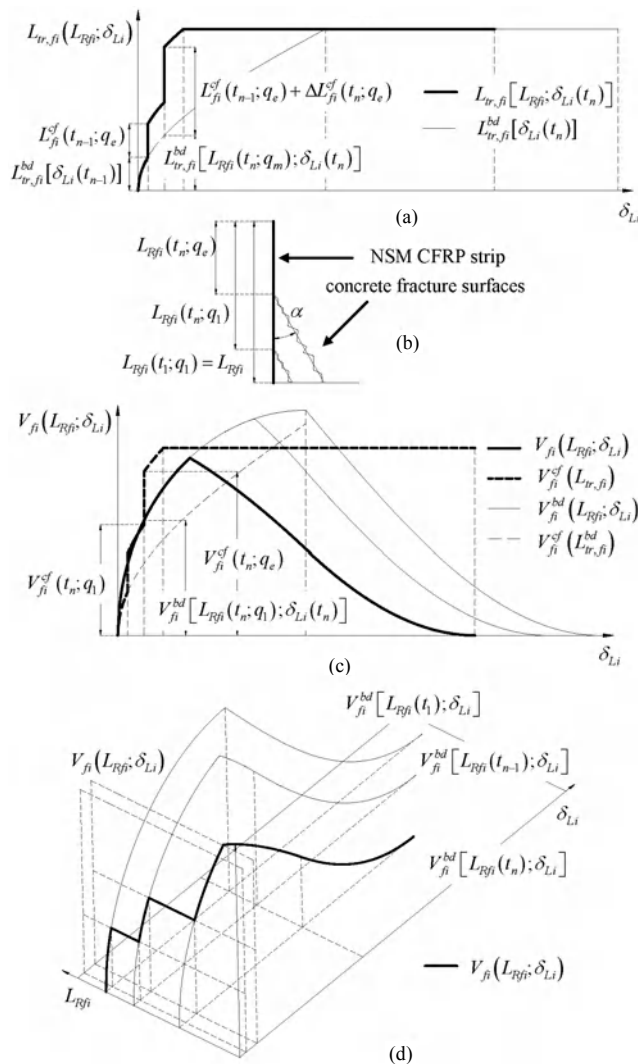


Figure 3 Comprehensive constitutive law of an NSM FRP strip: (a) transfer length, (b) section of the concrete prism, constitutive law in (c) a 2D and (d) in a 3D representation

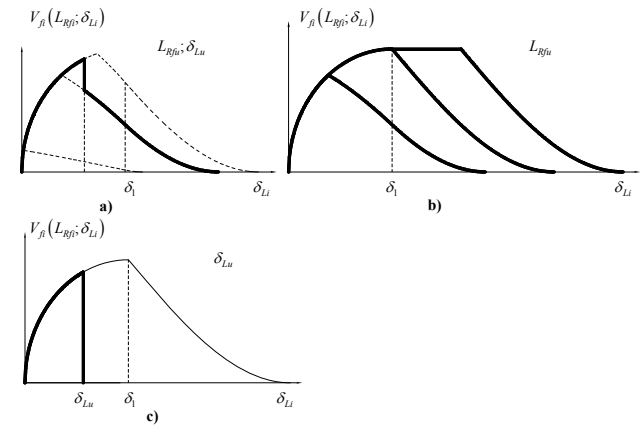


Figure 4 Comprehensive constitutive law of an NSM FRP strip confined within a prism of concrete: (a) deep concrete fracture, (b) superficial and/or absent concrete fracture, (c) strip tensile rupture

4 CONCLUSIONS

The correct definition of the bond-based constitutive law of an NSM FRP strip is the first step for the determination of the constitutive law of the structural system composed of an FRP strip near surface mounted on a concrete prism. Closed-form analytical equations for the bond-based constitutive law are obtained by assuming a simplified bi-linear local bond stress slip relationship and fulfilling equilibrium, kinematic compatibility and constitutive laws of the intervening materials. During the loading process of such a simple structural system as an NSM FRP strip confined to a concrete prism, in correspondence of each load step, the system undergoes some modifications that change the initial bond-based constitutive law. Nonetheless, the comprehensive constitutive law, which from an analytical standpoint does not present significant differences with respect to the bond-based one, can be determined by an iterative procedure searching for the equilibrium condition at each load step.

5 ACKNOWLEDGEMENTS

The authors of the present work wish to acknowledge the support provided by the “Empreiteiros Casais”, S&P®, degussa® Portugal, and Secil (Unibetão, Braga). The study reported in this paper forms a part of the research program “SmartReinforcement – Carbon fibre laminates for the strengthening and monitoring of reinforced concrete structures” supported by ADI-IDEIA, Project nº 13-05-04-FDR-00031. This work was also carried out under the auspices of the Italian DPC-ReLuis

Project (repertory n. 540), Research Line 8, whose financial support is greatly appreciated.

REFERENCES

- Bianco, V. 2008. Shear strengthening of RC beams by means of NSM FRP strips: experimental evidence and analytical modeling. PhD Thesis, *Dept. of Struct. Engrg. and Geotechnics*, Sapienza University of Rome, Italy.
- Bianco, V., Barros, J.A.O., Monti, G. 2009. Bond model of NSM-FRP strips in the context of the shear strengthening of RC beams. *ASCE Structural Journal*, 135(6): 619-631.

Size Effects in Reinforced Concrete Beams Strengthened with CFRP Straps

Levingshan Augustus Nelson (la275@cam.ac.uk) & Janet M. Lees
Engineering Department, University of Cambridge, Cambridge, UK

ABSTRACT A carbon fibre reinforced polymer (CFRP) strap system has been identified as a promising method for retrofitting existing reinforced concrete (RC) structures. The CFRP straps, which can be prestressed, act as additional transverse reinforcement and have been shown to increase the shear capacity of RC beams. Since the straps are unbonded, the strap strain consists of any initial prestrain plus an additional strain due to crack opening. Hence, in a retrofitted beam, there are two potential sources of size effects: within the base RC structure; and that inherent in the unbonded strap system. RC beams with low transverse reinforcement ratios have been found to exhibit a reduction in capacity with increasing depth. In strengthened beams, the crack opening strap strain decreases with increasing beam depth and the initial prestrain becomes of increasing importance. The potential interaction between the two sources of size effects presents difficulties when assessing the overall beam behaviour.

1 INTRODUCTION

An external unbonded CFRP strap system has been developed to increase the shear capacity of existing reinforced concrete (RC) beams. In this strengthening system, flexible CFRP straps are wrapped around a beam and act as external vertical shear links. The straps are not bonded to the concrete and can be prestressed to achieve the required level of shear enhancement (Lees et al 2002). Examples of CFRP strap strengthened beams can be found in Figure 1.

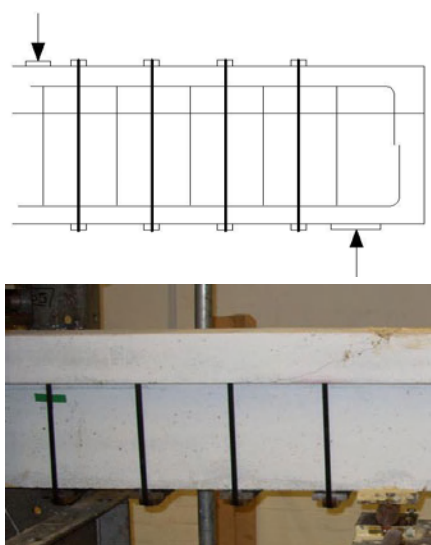


Figure 1 Reinforced concrete beams with CFRP straps

Experiments have shown that shear deficient reinforced concrete beams strengthened with CFRP straps can exhibit

a significantly higher shear capacity (Kesse & Lees 2007). Furthermore, the CFRP strengthening system can change the beam failure mode from a brittle shear to a ductile flexural failure, which is desirable in concrete structures. It has been identified that the stiffness of the CFRP straps, the strap prestress and the strap spacing are the major contributing factors in determining the level of shear enhancement. The initial strap prestress level has been found to be of particular importance in deeper beams (Stenger 2000) but of lesser importance in shallower beams (Kesse & Lees 2007). This then raises the question of the extent of size effects associated with CFRP strap strengthened concrete beams.

In a conventional steel reinforced concrete structure, the size effect is associated with a reduction in the concrete shear stress resistance as the beam depth increases. The size effect is felt to occur due to the quasi-brittle nature of concrete (Gustafsson & Hillerborg 1988). Therefore, in the retrofitted system, any size effect potentially arises from two different mechanisms: the size effect in the base reinforced concrete structure; and the size effect of the CFRP strap, which is related to the strain in the CFRP and is a function of the shear crack opening.

To investigate these mechanisms, size effects in baseline reinforced concrete structures with either no, or low percentages of, internal shear links will initially be considered. An existing semi-empirical size effect approach will then be used to explore how the influence of the strap prestress, which increases the normal forces across the crack faces, changes with increasing beam depth. It is important to understand these interactions in

order to effectively retrofit shear deficient concrete beams.

2 SIZE EFFECTS IN EXISTING STEEL REINFORCED CONCRETE BEAMS

2.1 Beams with longitudinal reinforcement

To investigate the size effect in longitudinal reinforced concrete beams without shear stirrups, Bentz & Buckley (2005) tested a series of rectangular beams with three different depths. The intention was to repeat a test series conducted by Bazant & Kazemi (1991). Figure 2 shows the specimen cross sections and the reinforcement details. The key variable was the depth of the specimen so the shear span and longitudinal reinforcement were scaled with the specimen depth. All the specimens were cast from the same concrete mix to ensure consistency and the maximum size of coarse aggregate was 10 mm. The longitudinal reinforcement had a nominal strength of 400 MPa but no yielding was observed.

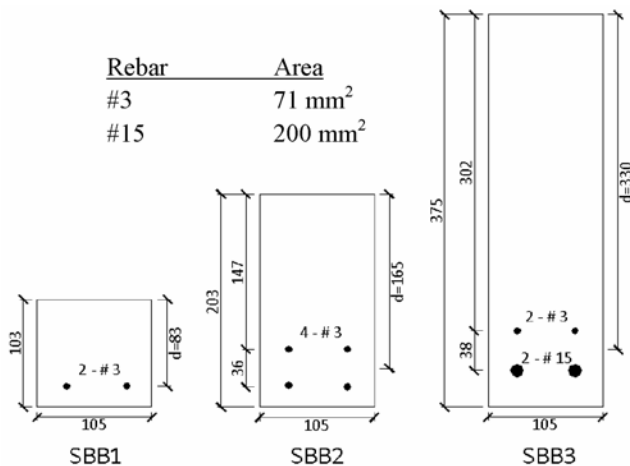


Figure 2 Cross sections of Bentz & Buckley's beams

The span to depth ratio was maintained as 3 for all the specimens and the specimens were tested under three point loading conditions. Table 1 summarises the span of the beams, the percentage of longitudinal reinforcement (ρ) and the concrete cylinder strength (f_c). Three beams were tested for each depth and the average failure loads and shear strengths are tabulated in Table 1.

Table 1 Beam properties and test results

Specimen	Span (mm)	% of steel reinforcement	Concrete strength (MPa)	failure load (kN)	Shear strength (N/mm ²)
SBB1	495	1.62	35.6	31.9	3.66
SBB2	990	1.61	34.3	59.3	3.42
SBB3	1980	1.59	36.1	83.7	2.42

Bentz & Buckley observed that the scaled up crack patterns of all beams were remarkably similar.

Based on these results, it can be seen that reinforced

concrete beams without stirrups show a reduction in shear strength as the beam depth increases. There have been several attempts to determine a size effect modification factor for reinforced concrete beams with only longitudinal reinforcement (e.g. Bazant & Kazemi 1991).

2.2 Beams with internal steel shear links

ACI committee 445 (1998) on shear and torsion suggests that the reason for the concrete size effect is the larger width of the diagonal shear cracks in larger beams. In an adequately transversely reinforced beam, the internal transverse reinforcement controls the crack width which reduces the size effect. Furthermore, it allows the concrete beam to rotate and to potentially reach its plastic limit. However, in a beam with minimal shear reinforcement, the stirrups reach their yield limit before the concrete reaches its ultimate shear capacity. Therefore, it has been concluded that a size effect still exists in a concrete beam with a minimum amount of transverse steel reinforcement (Bazant & Sun 1987). Of particular interest in strengthening applications is the transition point, where there is sufficient internal transverse steel such that the concrete size effect becomes insignificant.

Bazant & Sun (1987) developed a size effect equation based on the percentage of transverse steel reinforcement present in a concrete beam. The approach considers the summation of a concrete contribution λV_c , where the coefficient λ reflects a size dependency, and a steel contribution V_s where the additional shear resistance V_s is provided by the shear links. Bazant & Sun's size effect reduction factor (λ) is given as

$$\lambda = \frac{1}{\sqrt{1 + (h/25a_{agg}(1 + m\rho_v))}} \quad (1)$$

where ρ_v = the steel reinforcement ratio of transverse stirrups ($A_w/b s_w$); A_w is the area of the transverse steel, b is the beam width, s_w is the transverse reinforcement spacing, a_{agg} is the aggregate size, h is the beam height and m = a geometric constant for a given beam. The geometric constant is given as

$$m = 400 \left[1 + \tanh \left(2 \frac{s}{h} - 5.6 \right) \right] \quad (2)$$

where s = the shear span. It should be noted that this size effect reduction factor is empirical and was derived by curve fitting existing experimental results. As discussed, the size effect reduction factor λ is only used for the concrete contribution to the shear capacity. Assuming a maximum aggregate size of 10 mm and a shear span to beam height ratio of 3, the variation of λ with increasing beam depth has been plotted in Figure 3. Three different transverse reinforcement ratios have been considered; 0%, 0.1% and 0.2%.

It is of note that the expected reductions in capacity with increasing depth for a beam with no transverse

reinforcement ($\rho_v = 0\%$) are similar to the values observed in Table 1. Another feature is that even with $\rho_v = 0.1\%$, the reduction in the concrete contribution between a beam with a depth of say 300 mm and that of 1200 mm deep beam would be around 40%.

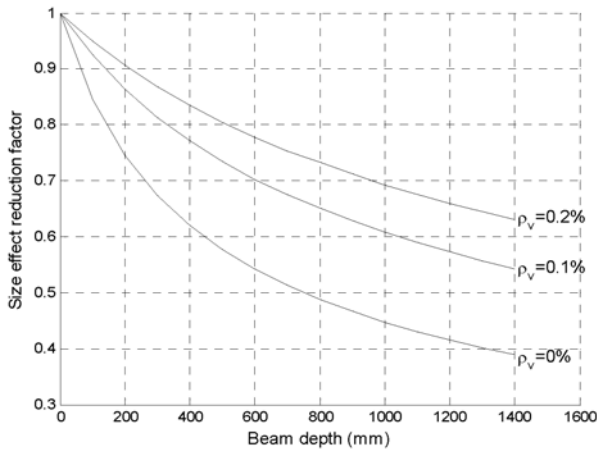


Figure 3 Size effect reduction factor

3 SIZE EFFECT IN CFRP STRAP STRENGTHENED SYSTEM

A CFRP strap acts like an unbonded prestress tendon. At a given load, the strap strain consists of two components; the initial prestrain and the additional strain due to the crack opening in the concrete encased between the strap supports. Any increase in strap strain also provides an additional transverse force across the crack face, which reduces the crack width and will influence the concrete contribution.

Many existing shear models based on conventional steel approaches do not include a connection between strain and crack opening since the internal transverse steel is generally assumed to yield. In the following, an initial model based on a shear friction approach will be used to investigate possible size effects in the strap system.

The shear friction model is based on the concept that shear is carried by aggregate interlock across a critical crack plane (Loov 1998). The aggregate interlock is enhanced in the presence of the longitudinal steel reinforcement across a crack and any transverse steel reinforcement contributes additional shear capacity. In the shear friction model the starting position of the crack and the crack angle θ are varied to find the critical crack plane associated with the minimum capacity of the beam.

Hoult & Lees (2009) modified the shear friction model to predict the shear capacity of retrofitted RC beams with CFRP straps. A simplified version of the modified shear friction equation is

$$V = 0.25 f_c k^2 b h \tan \theta + T_v + T_{FRP} \quad (3)$$

where T_{FRP} = CFRP strap contribution. V = shear force

carried by the beam; f_c = concrete strength; b = beam width; h = beam height; k = shear friction constant; θ = angle of crack; and T_v = transverse steel reinforcement contribution. Any internal steel reinforcement is assumed to yield at the final shear failure.

Of particular interest in the current work is the formulation for the shear contribution of the CFRP strap, T_{FRP} which depends on the crack width w :

$$T_{FRP} = A_{FRP} E_{FRP} \left(\varepsilon_{pre} + \frac{w}{h_{FRP} \cos \theta} \right) \quad (4)$$

where A_{FRP} = area of CFRP strap; E_{FRP} = elastic modulus CFRP strap; ε_{pre} = strain due to initial prestress; and h_{FRP} = unbonded strap length. To find the average crack width w associated with the average shear stress along the crack face, Hoult & Lees (2009) made reference to work by Collins et al (2007) and Walraven (1958) to develop an expression for the crack width opening for a given shear stress where:

$$w = \frac{1}{24} \left(\frac{0.18 \sqrt{f_c}}{0.25 f_c k^2 \tan \theta} - 0.3 \right) (a_{agg} + 16) \quad (5)$$

All the unknown parameters in Equations 4 and 5 are geometric and material properties. Furthermore, the size effect of the strap is related to the crack opening displacement.

To explore how the strap strain varies with beam depth, the case of a rectangular beam with a maximum aggregate size of 10 mm and a compressive strength of 40 MPa is considered. The shear friction coefficient k is taken as 0.5, the strap height is approximated as the beam height, and the crack angle is assumed to be 45°. The resulting variation of strap strain due to crack opening (the second term in Equation (4) is shown in Figure 3.

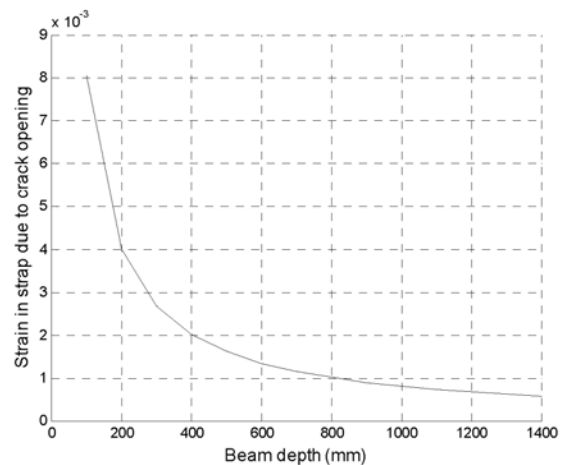


Figure 4 Strain in a CFRP strap due to crack opening

Figure 3 shows that the crack opening strain in the CFRP strap reduces dramatically with increasing beam depth up until a depth of around 500 mm. Thereafter, the

crack opening strain does not change significantly with increasing depth. This result helps to demonstrate why the level of initial prestrain is of particular importance in deeper beams. In beams with shallower depths (Kesse & Lees 2007), even if the initial prestrain is relatively low, a significant transverse force will be generated in the strap due to the strain due to crack opening. In larger beams (Stenger 2000), the crack opening displacement does not generate much elastic strain in the strap. Therefore, unless the strap is prestressed, the additional shear force carried by the strap is minimal.

4 INTERACTION BETWEEN CONCRETE AND CFRP STRAP SIZE EFFECTS

To determine the interaction between concrete and CFRP strap size effects it would be necessary to ascertain an appropriate size effect reduction multiplier for the concrete contribution term and a relationship between the crack width and beam depth.

As the additional CFRP straps increase the transverse reinforcement ratio it would be expected that their presence would cause a reduction in the concrete size effect. However, Bazant & Sun's concrete size effect reduction factor was developed using existing test data on beams with or without internal steel stirrups. So the inclusion of CFRP straps which are brittle-elastic and do not yield would mean that the load-sharing between any steel and CFRP straps would need to be taken into account. An additional challenge is how best to incorporate a concrete size effect into an overall shear formulation that also has a connection between strap strain and crack opening. Bazant & Sun's code formula for shear was developed based on the arch and composite action of longitudinally reinforced concrete beams and the theoretical basis for their size effect formula was derived using a fracture mechanics approach. In contrast, the shear friction approach assumes a single crack in the shear span and that the shear is resisted by friction between the crack faces. So the two models cannot be directly combined without due reflection on the differences between the approaches.

ACI committee 445 suggests that the crack opening displacement also changes with both the beam depth and the presence of internal steel reinforcement. In a CFRP strengthened system, a CFRP strap crossing the crack will induce a normal force across the crack. It can be noted that the crack width in Equation (5) does not depend explicitly on the height of the beam specimen although the clamping force and the crack angle will play a role.

In summary, the work of Bazant & Sun has given insight into the size effects in concrete beams with low ratios of transverse reinforcement. The modified shear friction approach has shown the connection between the crack opening strain and the beam depth. However, as

currently formulated, the approaches cannot be directly combined to predict the overall size effect of CFRP strengthened reinforced concrete beam. Further investigations are required to determine how these mechanisms depend on the beam depth, and the concrete and crack opening behavior, when both transverse steel and FRP reinforcement cross the crack.

5 CONCLUSIONS

The theoretical study suggests that that a RC beam with a low percentage of internal steel transverse reinforcement will show a size effect with increasing beam depth. In a RC beam strengthened with CFRP straps, there is potentially an additional size effect associated with the strengthening system. The size effect in the unbonded CFRP strap system comes from the crack opening displacement in the beam, where the crack width depends on the concrete properties and the beam dimensions. The inter-relationship between these mechanisms presents a challenge when developing predictive models.

6 ACKNOWLEDGEMENTS

The first author is grateful for the financial support provided by the Cambridge Commonwealth Trust.

REFERENCES

- ACI-ASCE Committee 445, 1998. Recent approaches to shear design of structural concrete, *Journal of Structural Engineering*, 1375-1417.
- Bazant, Z.P. & Kazemi, M.T., 1991. Size effect on diagonal shear failure of beams without stirrups, *ACI Structural Journal*, V. 88, No.3: 268-276.
- Bazant, Z.P., & Sun, H.H., 1987. Size effect in diagonal shear failure: Influence of aggregate size and stirrups, *ACI Material Journal*, V. 84, 259-272.
- Bentz, E.C. & Buckley, S. 2005. Repeating a classic set of experiments on size effect in shear of members without stirrups, *ACI Structural Journal*, V.102, No.6: 832-838
- Collins, M.P., Bentz, E.C., Sherwood, E.G. and Xie, L. 2007. An adequate theory for the shear strength of reinforced concrete structures, *Morley Symposium on Concrete Plasticity and its Application*, University of Cambridge, 75-93.
- Gustafsson, P.J. and Hillerborg, A. 1988. Sensitivity in shear strength of longitudinally reinforced concrete beams to fracture energy of concrete, *ACI Structural Journal*, V. 85, No.3: 286-294.
- Hoult, N.A. and Lees, J.M. 2009. Modelling of an unbonded CFRP strap shear retrofitting system for RC beams, *ASCE Journal of Composites for Construction*, V.13, No.4: 292-301.
- Kesse, G.K. and Lees, J.M. (2007) Experimental behaviour of reinforced concrete beams strengthened with prestressed CFRP shear straps, *ASCE Journal of Composites for Construction* V.11 No.4: 375-383

- Lees, J.M., Winistoerfer, A.U. and Meier, U. (2002) External prestressed CFRP straps for the shear enhancement of concrete, *ASCE Journal of Composites for Construction*, V.6, No.4, Nov., 249-256.
- Loov, R.E., 1998. Review of A23.294 simplified method of shear design and comparison with results using shear friction, *Canadian Journal of Civil Engineering*, V.25, No.3: 437-450
- Stenger, F. (2000) *Tragverhalten von Stahlbeton scheiben mit vorgespannter externer Kohlenstofffaser-Schubbewehrung*, PhD Dissertation Nr. 13991, ETH Zurich.
- Walther, R., 1958. The shear strength of prestressed concrete beam, *FIP: Third Congress, Berlin*, 80-100.

Shear Capacity of Flexural Strengthened Reinforced Concrete Structures with CFRP Materials

Wolfgang Finckh (finckh@mb.bv.tum.de) & Konrad Zilch

Department of concrete structures, Technische Universität München, Germany

ABSTRACT By enlarging the flexural capacity of reinforced concrete structures with externally bonded CFRP materials the shear behavior is also affected. To evaluate this effect shear tests on flexural strengthened reinforced concrete beams were carried out. Half of the tests were done with externally bonded CFRP-strips and the other half with near surface mounted reinforcement. Based on these tests and the EC2 approach for the shear force was checked.

1 INTRODUCTION

1.1 Principles

The shear failure of reinforced concrete structures is a non ductile failure and must be avoided. But the shear capacity of a reinforced concrete structure cannot be considered alone, the bending moment also has an influence on the shear capacity. Because of the higher strains in the CFRP reinforcement and the higher bending moments in strengthened reinforced concrete beams, the effects on the shear capacity have to be checked.

1.2 Former research work

In Germany (DIBt 2008) at the moment the shear capacity of a strengthened concrete beam is significantly reduced compared to an unstrengthened beam.

The model in the German design rules (DIBt 2008) is based on the theoretical model for the shear force from Schmidhuber (2004). This model is based on the thought that the ultimate strain in the bottom fiber of the concrete is much higher than in the unstrengthened reinforced concrete. This causes higher crack widths and a less aggregate interlock in the cracks. The aggregate interlock is one main bearing mechanism of the shear force transfer. Especially in the hogging region of 2-span beams it has an effect, because that is the region, where the maximum of the bending moment and the maximum of the shear force appear.

2 EXPERIMENTAL INVESTIGATION

2.1 Experimental program

To evaluate this model and to find a new approach six full scale shear test with two different strengthening techniques were carried out. All beams had an internal steel reinforcement (stirrups). Two beams were strengthened with near surface mounted reinforcement (NSM) and

four elements were tested with externally bonded CFRP-strips (EBR). In Table 1 the reinforcement and the concrete mixture of the six tests are listed. The properties of the concrete, the reinforcement and all other materials are given in chapter 3.

Table 1 Reinforcement of the full scale

Name*	C	TR	FRP	CR	SR
NSM 1	C1	3xD20	3xNSM	3xD20	D6@250
NSM-2	C2	3xD20	3xNSM	3xD20	D6@200
EBR-B-1	C2	3xD20	1x2xEBR1	3xD20	D6@200
EBR-S-1	C1	3xD16	2x2xEBR2	3xD16	–
EBR-S-2	C1	3xD16	2x2xEBR2	3xD16	–
EBR-S-3	C1	3xD16	2x2xEBR2	3xD16	–

* Name: C: Concrete mixture; TR: tensile reinforcement FRP: strengthening reinforcement; CR: compression reinforcement; SR: internal shear reinforcement (stirrups)

In the experimental program, both a slab as well as a beam cross section were tested. The different geometric properties of the testes are listed in Table 2 and are illustrated with Figure 1.

Table 2 Geometric properties of the tested beams

Name*	h (mm)	b (mm)	d1 (mm)	d2 (mm)	a _L (mm)	a (mm)	l ₀ (mm)
NSM 1	450	200	410	25	–	1250	3700
NSM-2	450	200	410	25	–	1250	3700
EBR-B-1	450	200	421	25	–	1250	3700
EBR-S-1	200	500	185	25	100	600	3700
EBR-S-2	200	500	185	25	–	600	3700
EBR-S-3	200	500	185	25	–	1500	3700

* Name: h: height; b: width; d1: internal lever arm; (TR) d2: internal lever arm (CR); a_L: gap between strip and bearing; a: shear span; l₀: span length

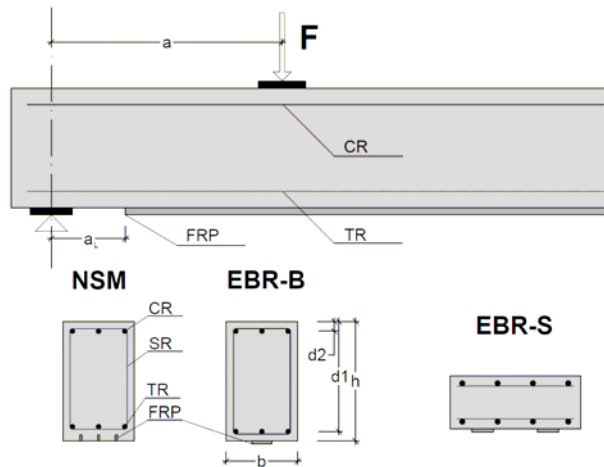


Figure 1 Geometric properties of the tests and of different cross sections used in the tests

The shear span was selected so that a shear failure occurs. An exception is test EBR-S-3, where a height strain in the FRP should be reached.

2.2 Materials

2.2.1 Concrete

For the experiments two different types of concrete were used, one low strength concrete and one high strength concrete. The concrete mixture is listed in table 3. The mixture has the peculiarity that only an 8 mm maximum aggregate size was used. Hence the aggregate interlock is small and the experimental results are on the save side.

Table 3 Concrete mixture

Setting	C1	C2
Raw material		
Cement*	CEM I 32.5 R	CEM I 42.5 R
Aggregate	0/8 from flint out of the Alps	
Concrete Admixtures	none	none
Concrete composition [kg/m ³]		
Water	210.00	210.00
Cement	338.71	437.50
Aggregate	1844.80	1758.44
Grading curve**	A/B 8	A/B 8
Properties		
W/C ratio	0.62	0.48
Flow diameter***	480	470
Density****	2340	2380

* According to CEN EN 197-1

** According to CEN EN 206-1

*** According to CEN EN 12350-5

**** According to CEN EN 12350-6

Because of the small size and the high strength of aggregates the cube and the cylinder compressive strength are almost the same. All necessary mechanical properties are listed in table 4. Especially the surface tensile strength is to be mentioned, which is one of the main parameter for the bond behavior of the EBR. The surface tensile

strength was evaluated on the bottom of the beams where the EBR was bonded.

Table 4 Concrete properties at the time of testing

		C1	C2
f_{cm}^*	(N/mm ²)	26.65	46.35
f_{cmcube}^*	(N/mm ²)	28.62	49.98
$E_{modulus}$	(N/mm ²)	26191	30105
$f_{ctm,surf}^{**}$	(N/mm ²)	2.76	3.63

* According to CEN EN 12390-3

** According to CEN EN 1542

2.2.2 Reinforcement steel

For internal reinforcement three different diameters of ribbed bars BSt 500B (according to DIN 488-1) were used. The small diameter was used for the shear reinforcement. All necessary mechanical properties are listed in table 5.

Table 5 Mechanical properties of the reinforcing steel

	D6	D16	D20
Diameter (mm)	6	16	20
Tensile strength (N/mm ²)	576.6	646.5	616.2
E Modules (kN/mm ²)	198.7	203.3	204.0
Yielding point (N/mm ²)	528.3	510.0	513.3

* Column dialog box in Format menu.

2.2.3 Strengthening materials

Mainly two different strengthening systems were used, NSM with CFRP-strips and EBR with CFRP-strips. For the NSM also a different adhesive was used than for the EBR. The two different strips of the EBR are nearly the same, but they have different width so they came out of a different charge. The mechanical properties are listed in Table 6.

Table 6 Properties of the strengthening systems

Setting	NSM	EBR1	EBR2
Width (mm)	20	50	100
Thickness (mm)	2	1.4	1.4
tensile strength (N/mm ²)	3200.6	3073.0	3121.4
E modulus* (kN/mm ²)	181,4	170.8	168.4
Adhesive** z	NSM	EBR	
Compressive strength	89.4	97.0	
Peel strength on steel	29.3	31.2	

* According to CEN EN 2561

** According to CEN EN 1504-4

2.3 Testing procedure and measurement

For all tests a three point bending test was carried out, with the shear span given in table 2. The load was applied with a deformation controlled hydraulic jack. The speed was depending on the stiffness of the structural element, so that there was constant increase of the force. In all tests the force was measured with a load cell. The deformation

was measured with both displacement transducer and optical deformation measurement of the whole side surface. The optical measurement has the advantage that every crack that appears can be measured continuously. To know the strains in the CFRP-strip six strain gages were put on the CFRP-strip. The whole measurement equipment and the testing procedure are shown in Figure 2.

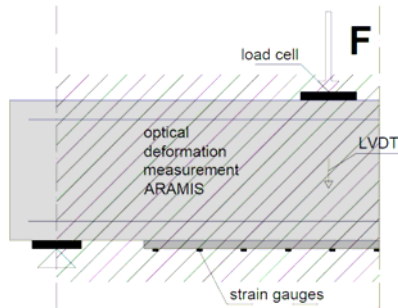


Figure 2 Measurement equipment for each test

2.4 Testing results

2.4.1 Slabs

The tests were made on slabs. In the test EBR-S-1 and EBR-S-2 a pure shear failure occurred. The test EBS-S-2 got a 9% higher load, because the CFRP strip was lead across the bearing.

On test EBR-S-3 the shear span was higher to get a higher strain in the CFRP strip. The CFRP strip was lead across the bearing as in test EBR S-2. So a higher strain could occur even if the CFRP strip debonds. The maximum strain in the CFRP strip was 7.17 mm/m. Although the strain was much higher than in the other tests the buckling load was 5% higher than in the test EBR S-2. But the failure mode was not a pure shear failure but a failure of concrete pressure.

The load deformation curves for the tests on slabs are plotted in Figure 3.

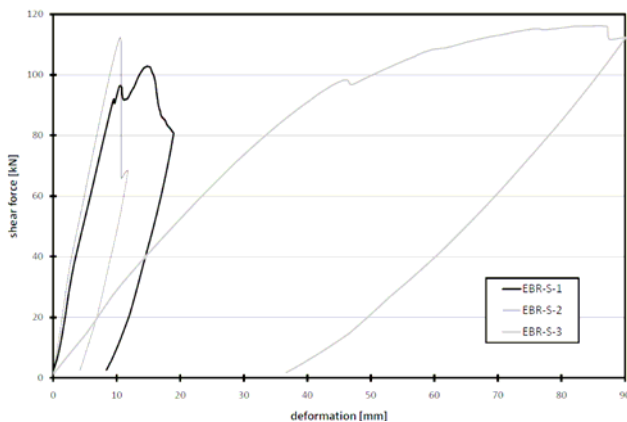


Figure 3 Load deformation curves of the test on slabs

2.4.2 Beams

Three tests were made on beams with internal shear reinforcement. In all tests a pure shear failure occurred

without debonding of the CFRP strip. All tests showed nearly the same behavior: the internal steel reinforcement crushed and a shear crack occurred. This is a really non ductile crush as the load deformation curves of the three beams plotted in figure 4 show.

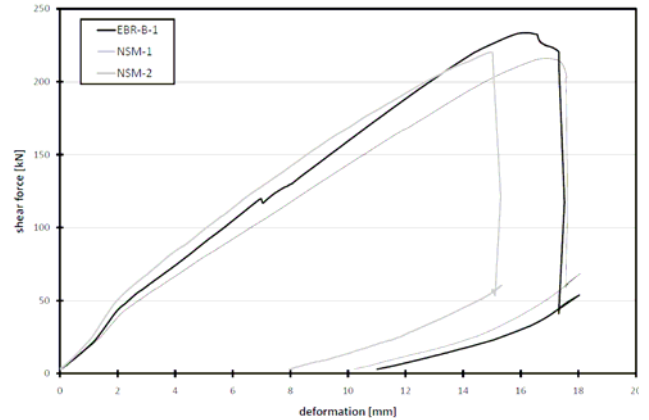


Figure 4 Load deformation curves of the test on beams

3 ANATIC MODELLING

3.1 Principles

In the following section the Eurocode 2 approach (CEN EN 1992-1-1) and the additional information of the national German annex (DIN EN 1992-1-1/NA) are described.

Only the necessary equations for a calculation of the buckling load of the tests are listed. The equations are also simplified for pure bending without additional compression force.

3.2 EC2 approach

3.2.1 Without shear reinforcement

For structural elements without shear reinforcement the resistance against a shear failure can be calculated with equation (1).

$$V_{Rd,c} = \left[C_{Rd,c} \cdot k \cdot \left(100 \cdot \rho_l \cdot f_{ck} \right)^{1/3} \right] \cdot b_w \cdot d \quad (1)$$

With $k = 1 + (200/d)^{0.5}$ as a factor for the internal lever arm and $C_{Rd,c}$ as a factor for the aggregate interlock. The recommended value for $C_{Rd,c} = 0.18/\gamma_c$ with γ_c as safety factor for the concrete.

There is also a minimum for $V_{Rd,c}$ but for the test equations (1) will always prevail.

3.2.2 With shear reinforcement

The design of structural elements with shear reinforcement is based on a truss model with reinforcement ties and concrete compression struts.

So the smaller value of the reinforcement ties $V_{Rd,s}$ and concrete compression struts $V_{Rd,max}$ must be selected. There is no test, in which the concrete compression strut $V_{Rd,max}$ will prevail. So for the calculation of the buckling

load only the equitation for reinforcement ties $V_{Rd,s}$ is needed.

$$V_{Rd,s} = \frac{A_{sw}}{s} \cdot f_{ywd} \cdot \cot \theta \quad (2)$$

For the calculation of $V_{Rd,s}$ the angel of the compression strut can be chosen according to equitation (3). The model is based on full plasticity so the angel can be chosen freely within the two boundaries.

$$1 \leq \cot \theta \leq 2.5 \quad (3)$$

3.3 EC2 with German national annex

One amendment of the German NAD is that the factor for the aggregate interlock $C_{Rd,c}$ is defined to $C_{Rd,c} = 0.15/\gamma_c$. Another change is that the angle of the compression strut must be calculated with equations(4) and cannot be selected free.

$$0,58 \leq \cot \theta \leq \frac{1,2}{1 - V_{Rd,cc} / V_{Ed}} \leq 3,0 \quad (4)$$

With the external force V_{ED} and the the empirical resistance for the concrete $V_{Rd,cc}$ which is back calculated out of many shear test.

$$V_{Rd,cc} = 0,24 \cdot f_{ck}^{1/3} \cdot b_w \cdot z \quad (5)$$

This calculation of the truss angle takes into account that the critical angle is in a narrow connection with the crack angle of the shear cracks.

3.4 Comparison with test results

For the comparison with the test results the equations (1) to (5) were calculated with the mean values of the building materials of tests without safety factors. The FRP reinforcement is neglected for the reinforcement ration in equation (1). So the mean values of the calculation can be compared with the single values of the test. Figure 5 shows the comparison of the test results with the calculation according to Eurocode 2 and to Eurocode 2 with amendment of the German NAD.

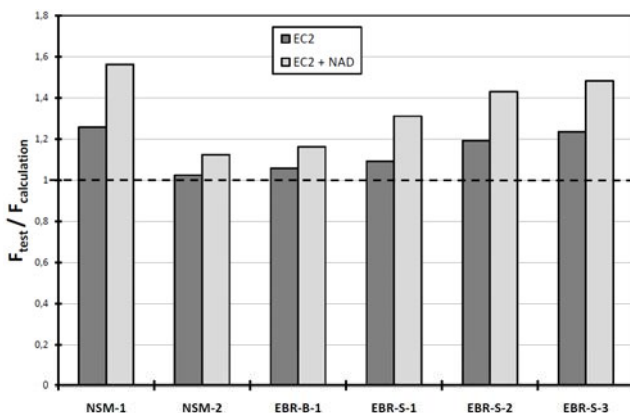


Figure 5 Comparison of the test results with the calculation according to Eurocode 2 and to Eurocode 2 with amendment of the German NAD

The comparison shows that all test results are higher than the calculated values. It also shows that the calculated values with amendment of the German NAD have a higher space for model uncertainties.

4 CONCLUSION

To check the influence of the flexural strengthening on the shear capacity of reinforced concrete elements six shear tests have been carried out. The test results have been compared with EC2 and EC2 with German NAD. The comparison showed that shear resistance can be calculated without hesitation using EC2 approach together with the German NAD. By calculating the shear resistance according only to EC2 caution is required, because the space between the test results and die EC 2 values is not very high.

REFERENCES

- DIBt (2008) Z-36.12-70, Verstärkung von Stahlbetonteilen durch mit dem Baukleber “StoPox SK14” schubfest aufgeklebte Kohlefaserlamellen “Sto S&P CFK Lamellen” nach DIN 1045-1:2008-08, (in German)
- DIN 488 -1 (2009) Reinforcing steels –Part 1: Grades, properties, marking
- DIN EN 1992-1-1/NA (2008) National Annex - Nationally determined parameter - Eurocode 2: Design of concrete structures - Part 1-1: General rules and rules for buildings, 2008
- EN 1002-1 (2001) Metallic materials - Tensile testing - Part 1: Method of testing at ambient temperature
- EN 12350-5 (2009) Testing fresh concrete - Part 5: Flow table test
- EN 12350-6 (2009) Testing fresh concrete - Part 6: Density
- EN 12390-3 (2009) Testing hardened concrete - Part 3: Compressive strength of test specimens
- EN 1504-4 (2005) Products and systems for the protection and repair of concrete structures - Definitions, requirements, quality control and evaluation of conformity - Part 4: Structural bonding
- EN 1542 (1999) Products and systems for the protection and repair of concrete structures - Test methods - Measurement of bond strength by pull-off
- EN 197-1 (2009) Part 1: Composition, specifications and conformity criteria for common cements
- EN 1992-1-1 Eurocode 2 (2004) Design of concrete structures - Part 1-1: General rules and rules for buildings
- EN 206-1 (2001) Concrete Part 1: Specification, performance, production and conformity
- EN 2561 (1995) Aerospace series - Carbon fibre reinforced plastics - Unidirectional laminates - Tensile test parallel to the fibre direction
- Schmidhuber, C. (2004) Neumodellierung des Schubtrageverhaltens mit CFK-Lamellen verstärkter Stahlbetonbauteilen, PHD-thesis, Technische Universität München (in German)
- Zilch, K.; Niedermeier, R.; Finckh, W. (2010) Praxisgerechte Bemessungsansätze für das wirtschaftliche Verstärken von Betonbauteilen mit geklebter Bewehrung, Querkrafttragfähigkeit, DAfStb –Heft 594, Beuth Verlag, Berlin (in German)

Strengthening of Concrete Columns, Walls and Frames

Emergency Retrofit for Damaged RC Columns by Fiber Belts Prestressing and Plywoods

N. Kyoda, T. Yamakawa, K. Nakada, P. Javadi
University of the Ryukyus, Okinawa, Japan

A. Nagahama
Daiwa House Industry Co., Ltd, Nara, Japan

ABSTRACT After a strong earthquake attacks to a building, damaged structural members such as columns should have sufficient vertical resistance to sustain gravity loads to rescue residents or move equipments. The rehabilitation of a damaged building is called “Emergency Seismic Retrofit” hereafter. Previous experimental investigations have demonstrated by utilizing high-strength steel bar prestressing or aramid fiber belt prestressing, seismic performances of shear-damaged RC columns significantly improved. In following the previous investigations on emergency seismic retrofit of shear-damaged RC columns, in this study a new approach is proposed regarding economic consideration and easy operation. In this method the polypropylene belts are used instead of aramid fiber belts, plywoods instead of steel plates, and customarily-fabricated ratchet buckles instead of specially-fabricated couplers. Experimental results exhibited efficiency of the pro-posed approach for emergency seismic retrofit of shear-damaged RC columns.

1 INTRODUCTION

Many kinds of seismic retrofit techniques have been researched and developed. An emergency seismic retrofit for earthquake-damaged buildings is important to prevent additional severe damage under aftershock and to rescue residents. To establish a quick and easy retrieval technique for damaged buildings in the high-seismic-risk areas, emergency seismic retrofit is considered as an urgent subject.

The authors have developed the emergency seismic retrofit technique for shear-damaged RC short columns after earthquake by using PC bar prestressing (Yamakawa & Miyagi 2005) or aramid fiber belt prestressing (Yamakawa et al. 2005).

In the above studies, thin steel plates are attached on the surfaces of the shear-damaged RC columns and external transverse reinforcement materials are prestressed through four corner pieces around the column. The vertical load sustaining capacity and the recovery of lateral force capacity can be verified easily through loading test. To establish the appropriate emergency seismic retrofit technique, it is required that the technique is simple and convenient, dry method without any heavy machinery, and applicable to columns with any shape and size. Therefore authors used the polypropylene (PP) belts are instead of aramid fiber belts, plywood instead of steel plates. Experimental results exhibited efficiency of the proposed approach for emergency seismic retrofit of shear-damaged RC columns.

2 TEST PLAN

The test specimens and their characteristics are shown in Table 1. The test specimens are RC short columns with a square cross-section of 250mm and a height of 500mm. The shear span to depth ratio of the columns is 1.0. The longitudinal reinforcement ratio is $p_g = 1.36\%$ and shear reinforcement ratio is $p_w = 0.08\%$. These column specimens are brittle shear failure type. The mechanical properties of materials used in the test specimens are shown in Table 2. The lashing belt device is a combination of ratchet buckle and polypropylene fiber belt. Prestressing is easily applied by ratchet buckle. The tensile load P and tensile strain ε relationships of aramid and polypropylene are illustrated in Figure 1. The pretension strain in belt is measured by strain gauges pasted on the belt that is impregnated partially with epoxy resin.

The details of emergency seismic retrofit are shown in Figure 2 and Photo 1. The lashing belts are applied in shear-damaged RC column at an interval of 65 mm through corner angles. These steel plates ($t=3.2\text{mm}$) or plywoods ($t=12\text{mm}$) are attached on the surfaces of the column by lashing belts prestressing. In the specimen retrofitted by plywood, the light-weight angles were installed at four corners to prevent the rubbing of belts at those zones. An emergency seismic retrofit was carried out under axial force of zero for safety. Figure 3 shows procedure of loading test. The specimens ER08S-CS, ER08S-CW were carried out under cyclic loading

Table 1 Details of retrofitted specimens

Specimen	Cyclic loading test		Axial compression test		
	ER08S-CS	ER08S-CW	ER08S-VS	ER08S-VW	ER08S-VW'
$M/(VD)=1.0$					
Damage level (Max. crack width)	IV (3mm)	IV (3mm)	IV (3mm)	IV (3mm)	IV (5mm)
polypropylene belt	2ply-@65mm				
Initial strain (Initial force)	0.50% (9.2kN)	0.46% (8.4kN)	0.48% (8.8kN)	0.56% (10.3kN)	0.56% (10.3kN)
Retrofitted by plate	Steel plate	Plywood	Steel plate	Plywood	Plywood
σ_B (MPa)	28.5		28.5	28.2	
Common details	Rebar : 12-D10 ($p_g = 1.36\%$), Hoop : 3.7 ϕ -@105 ($p_w = 0.08\%$), $N/(bD\sigma_B) = 0.2$.				

Notes: $M/(VD)$ = shear span to depth ratio, ply = a unit of numbering the layers of reinf. belt (cross sectional area: 2ply of polypropylene = 135.6mm², σ_B = cylinder strength, $N/(bD\sigma_B)$ = axial force ratio, In the specimen names, the letters denote as follows: C: cyclic loading, V: vertical loading, S: steel plate is used, W: plywood is used

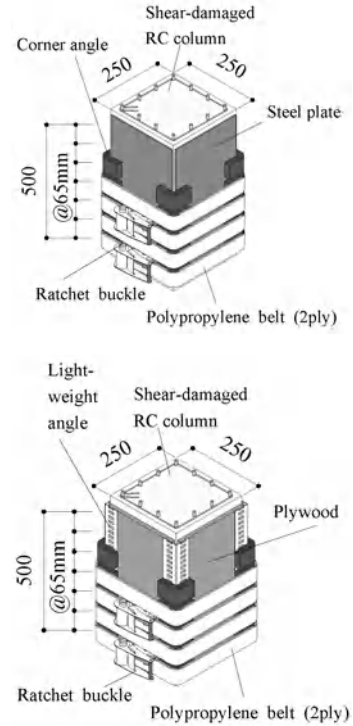


Figure 2 Details of emergency seismic retrofit

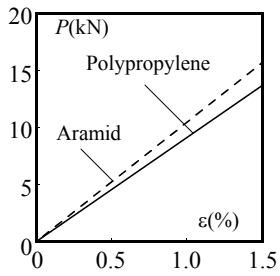


Figure 1 Tensile load P – tensile strain ϵ relationship



Photo 1 Retrofitted column specimen

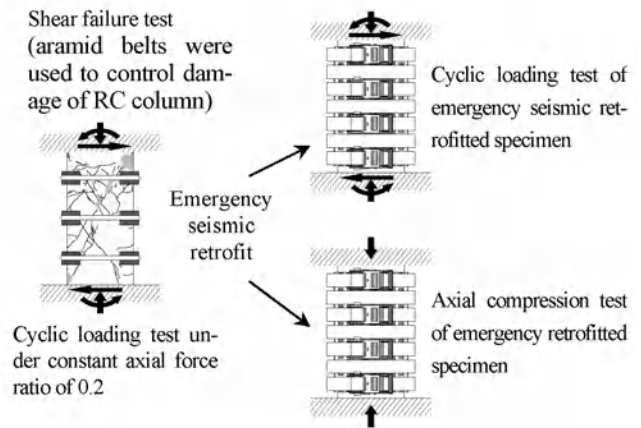


Figure 3 Procedure of loading test

and constant axial force ratio of 0.2, after emergency seismic retrofit. As shown in Figure 3, the specimens ER08S-VS, ER08S-VW, ER08S-VW' were subjected to the axial compression test after emergency seismic retrofit. The cyclic loading test was carried out in the range of drift angle $R=\pm 0.125\%$, $\pm 0.25\%$ at one cycle, $R=\pm 0.5\%$, $\pm 0.75\%$, $\pm 1.0\%$, $\pm 1.5\%$, $\pm 2.0\%$, $\pm 2.5\%$, $\pm 3.0\%$ at two successive cycles, and $R=4.0\%$, $\pm 5.0\%$ at one cycle. Figure 4 shows the test setup.

Table 2 Mechanical properties of materials

Reinforcement		A (mm ²)	E (GPa)	σ_y, σ_u^* (MPa)
Rebar	D10	71	201	355
Hoop	3.7 ϕ	11	188	617
Steel plate	$t=3.2\text{mm}$	-	218	366
Polypropylene	$t=3.00\text{mm}$	67.8	13.5	459*
Aramid	$t=0.57\text{mm}$	9.7	107	2381*

Notes : A = cross sectional area, E = Young's modulus of elasticity, σ_y = yield strength of steel, σ_u = ultimate tensile

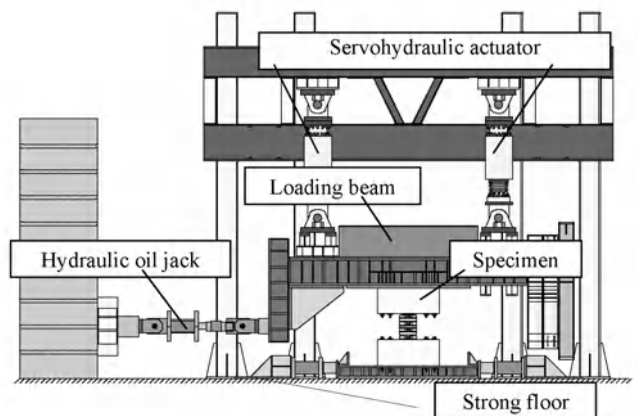


Figure 4 Test setup

3 TEST RESULTS

3.1 Shear failure test

The sound critical shear RC column specimens were damaged by cyclic loading test under constant axial force ratio of 0.2, before emergency seismic retrofit. Observed relationships between lateral force capacity V and the drift angle R of shear failure test specimens are illustrated in Figure 5. With observed cracking patterns on the depth sides of the columns after shear failure test, damage levels and maximum crack widths were estimated, as shown in Figure 6. In V - R graphs the broken line is flexural strength calculated by simplified flexural equation by AIJ (Architectural Institute of Japan) and the solid line is shear strength by AIJ (AIJ

1999). These specimens continued cyclic loading to $R = 1.5\%$ and reached to target damage, except specimen ER08S-CW because its damage suddenly increased at drift angle of $R = 0.5\%$. The damage levels based on the Japan Building Disaster Prevention Association's criterion were evaluated by crack width. As a result, in all specimens introduced damage level was level IV (width of crack = 3mm) (JBDPA 2002) but the damage of specimen ER08S-VW' was larger than other specimens (see Figure 6). There is no buckling of rebar in shear-failure test.

3.2 Cyclic loading test after emergency retrofit

The specimens ER08S-CS, ER08S-CW were tested under cyclic loading test and constant axial force (axial force ratio of 0.2), after emergency seismic retrofit. The relationships between the lateral capacity V and drift angle R are illustrated in Figure 7. The relationships of the average axial strain ε_v and drift angle R are also shown in Figure 7. The broken line is flexural strength which is calculated by simplified flexural equation by AIJ eq. used cylinder strength of concrete σ_B , and the solid line is flexural strength used confined damaged concrete strength f'_{cc} reached the maximum axial compression force after emergency seismic retrofit. The both specimens damage levels are level IV. The specimen ER08S-CS reached to the flexural strength by confined damaged concrete strength f'_{cc} at $R = 2.3\%$, and the deterioration of lateral capacity is due to P - δ effect. The specimen ER08S-CW which used plywoods also reached to flexural strength by f'_{cc} at $R = 0.6\%$. The sounds of plywoods breakage were beginning hearing at $R = 1.5\%$, and then the crack of plywoods was observed at $R = 3.0\%$, up to finishing test at drift angle of $R = 4.0\%$. The average axial strain proceeded due to brakeage of plywoods. The

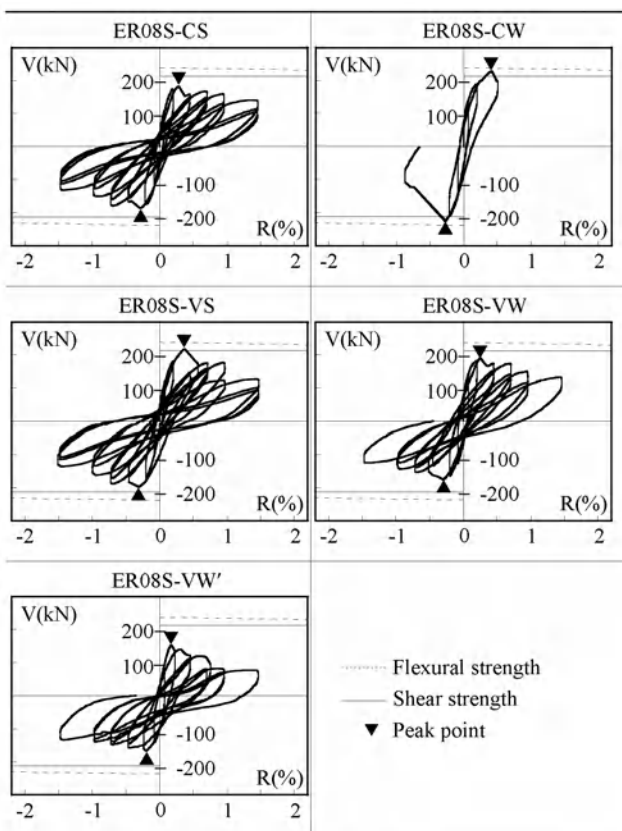
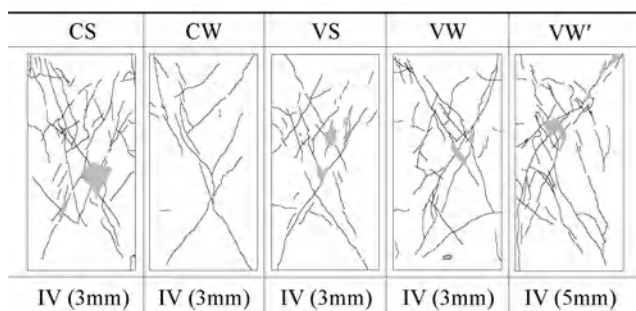


Figure 5 Measured V - R relationships (Shear failure test before emergency seismic retrofit)



IV: Damage level, (): Max. crack width (depth side).

Figure 6 Observed cracking patterns after shear failure test

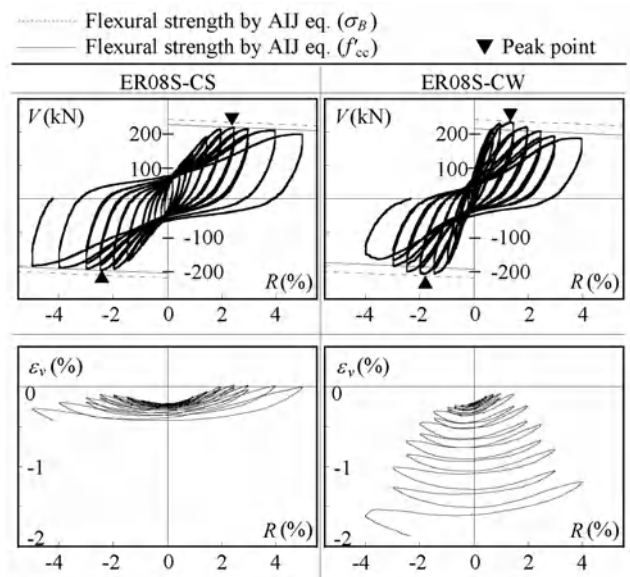


Figure 7 Measured V - R and ε_v - R relationships after emergency seismic retrofit

specimen ER08S-CW's cyclic loading is fewer than specimen ER08S-CS and the degree of damage is not the same as specimen ER08S-CS on shear-failure test. However, the lateral capacity recovered until shear-failure. It can be confirmed the improvement of ductility performance by active confinement effect which is one of this retrofit method features even if the plywoods were used. According to the past investigation results (Yamakawa & Miyagi 2005), attaching steel plates for shear-damaged RC column is effective, but plywood is not perfect to be adopted because its out-of-plane bending stiffness and strength is low.

3.3 Axial compression test after emergency retrofit

The specimens ER08S-VS, ER08S-VW, ER08S-VW' were subjected to axial compression test after emergency seismic retrofit. The relationships between axial capacity N and average axial strain ε_v are shown in Figure 8. The residual horizontal displacement due to shear failure test returned to zero. The axial compression capacities of specimens ER08S-VS, ER08S-VW, ER08S-VW' were $N=1570\text{kN}$, 1316kN , 1157kN , respectively. In the case of the same damage level, axial compression capacity of specimen ER08S-VS which used steel plates is higher than that of specimen ER08S-VW that used plywoods. The incremental strain of polypropylene belts in the axial compression test is shown in Figure 9. The incremental strains are calculated to deduct initial strain from strain at the maximum strength. In Figure 9, the passive incremental strain of polypropylene belt of the specimen ER08S-VS is higher than that of the specimen ER08S-VW, because there is a difference of out-of-plane bending stiffness and strength between steel plate and plywood,

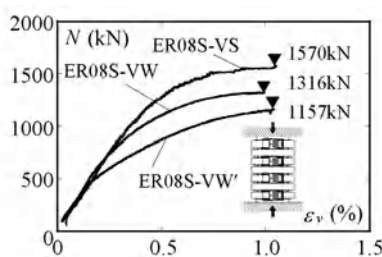


Figure 8 N - ε_v relationships after emergency seismic retrofit

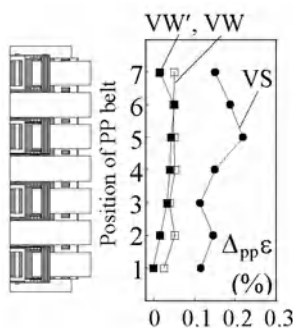


Figure 9 Measured belt incremental strain

so the steel plate has larger effectiveness of passive confinement than that of plywood. The confined damaged concrete strength f'_{cc} is derived by dividing axial capacity N_c by cross section ($f'_{cc}=N_c/(bD)$) which is used to deduct axial capacity N_s ($=302\text{kN}$) regarding yield strength of rebar from obtained axial compression capacity ($N_c=N-N_s$, see Figure 10). The relationships between the values of confined damaged concrete strength divided by cylinder strength σ_B and average axial strain ε_v are shown in Figure 10. The damaged concrete strength of damage level IV was $0.07\sigma_B$ (past investigation), the confined damaged concrete strength f'_{cc} with steel plate even using plywood increased. Specimen ER08S-VW and specimen ER08S-VW' are not able to get the passive confinement about that of specimen ER08S-VS due to crack into the plywoods. But its confined damaged concrete strength f'_{cc} increased to 7 times before retrofit by active confinement of this emergency seismic retrofit technique.

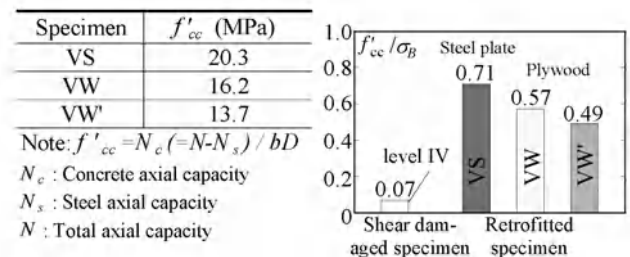


Figure 10 Damaged concrete strength of shear-damaged specimen and emergency seismic retrofitted specimens

4 CONCLUSIONS

An emergency seismic retrofit technique by lashing belts and plywoods instead of steel plates for shear-damaged RC columns is a quick and easy retrofitted method that recovered and increased the lateral and axial capacities of RC columns in emergency situations in the high-seismic-risk areas.

5 ACKNOWLEDGEMENTS

The investigation reported herein was carried out possible by a financial support of the Grant-in-aid for the Science Research (A), (20246091) by Japan Society for the Promotion of Science and a financial support of research by Japan Institute of Construction Engineering (JICE). The technical supports were provided by Ashimori Co., Ltd, Fibex Co., Ltd., and Hagiwara Industries Inc., in Japan.

REFERENCES

- Yamakawa, T and Miyagi, T. (2005). An Emergency Seismic Retrofit for Shear Damaged RC Short Columns Immediately After Earthquake Attack, IABSE SYMPOSIUM LISBON

- Structures and Extreme Events, 90, 108-109.
- Yamakawa, T., Banazadeh, M. and Fujikawa, S. (2005). Emergency Retrofit of Shear Damaged Extremely Short RC Columns Using Pre-tensioned Aramid Belts, *Journal of Advanced Concrete Technology (JCI)*, 3(1), 95-106.
- Architectural Institute of Japan (1999). Standard for Structural Calculation of Reinforced Concrete Structures –Based on Allowable Stress Concept. (in Japanese)
- The Japan Building Disaster Prevention Association (2002). Damage Level Assessment Criteria and Guidelines for Rehabilitation of Earthquake Damaged Reinforced Concrete Buildings.
- The Japan Building Disaster Prevention Association (2001). Standard and Guidelines for Seismic Evaluation and Retrofit of Existing RC Buildings. (in Japanese)

Seismic Retrofitting by FRP Jacketing and Prediction Method of Ultimate Deformation

T. Jirawattanasomkul, D. Anggawidjaja & T. Ueda

Department of Civil Engineering, Hokkaido University, Sapporo, Japan

ABSTRACT In this study, a method to predict the ultimate deformation is developed for reinforced concrete columns under seismic loading. The proposed sectional analysis or fiber model was combined with the truss mechanism approach in order to predict strength and deformation for both pre-peak and post-peak behavior. The proposed model is more effective at predicting the load deformation response of FRP-jacketed RC columns and shows that the fiber with a high rupture strain can provide good ultimate ductility.

1 INTRODUCTION

During the recent earthquakes, many existing reinforced concrete (RC) structures were destroyed due to the inadequacy of old seismic design, such as the failure of the Hanshin Expressway piers in Kobe, Japan. It is found that the main failure of columns was due to insufficient shear strength and ductility of structures. Therefore, improvement of seismic performance in such structures with consideration of shear capacity and ductility is vitally required. Currently, retrofitting of the structures by various materials such as steel, concrete, and Fiber-Reinforced Polymers (FRP) is one of the most practical schemes to enhance seismic resistance. Although steel jacketing and concrete jacketing have been successfully developed over the past decade to strengthen RC structures, the corrosion problem is a main disadvantage because it leads to increasing life cycle cost. Recently, the use of FRP retrofitting is becoming increasingly common, as FRP has no corrosion problem and higher durability. However, the disadvantage of FRP is its brittle nature due to low strain-to-failure so it tends to break at ultimate which can result in low ductility. To overcome the early breakage of the fiber and increase ductility, the jacketing with use of a new type of fiber with high fracturing strain, PET (Polyethylene Terephthalate) has been developed (Anggawidjaja, et al. 2006).

A method to predict the performance of RC columns at ultimate deformation is necessary to ensure the safety of reinforced concrete columns during extreme seismic events. Although many researchers have developed methods of predicting the ultimate deformation, these methods do not consider the shear and flexural deformations accurately. In reality, the concrete constitutive law obtained from flexural mechanisms influences the shear model due to the confinement effects, and likewise

shear deterioration directly influences flexural behavior. To address these deficiencies, the proposed model considers combined effects of shear and flexural deformations simultaneously. In this study, the shear deformation model is based on the truss mechanism that includes the effects of both tension stiffening and fiber confinement. The conventional fiber model is modified by applying parameters of confinement ratio and fracture strain of FRP together with shear effects to predict the flexural deformation. The shear and flexural deformations are combined with the pull-out deformations to obtain an accurate prediction of the total deformations of the columns.

2 ANALYTICAL MODEL

2.1 Flexural strength model

The traditional section analysis is widely used for the prediction of flexural strength of a reinforced concrete column. This analysis is performed on the column cross section by dividing the concrete area into a number of strips or fibers as shown in Figure 1 and assuming that plane sections remain plane at any load step.

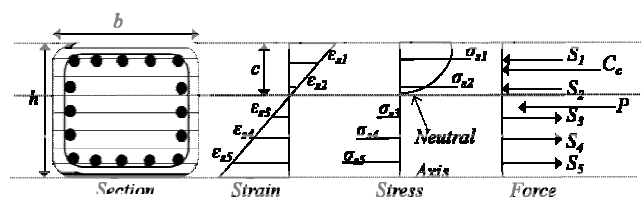


Figure 1 Section with strain, stress and force distribution

To calculate the flexural resisting capacity, the increments of strain in the extreme concrete compression fiber are given, and the strains across the depth of the

cross-section are obtained from compatibility conditions through the depth of the neutral axis. The location of the neutral axis is obtained from equilibrium shown by Equation 1, and the FRP-jacketed column was assumed to provide no flexural capacity enhancement since the fiber alignment is only in the horizontal direction.

$$P_{external} = \int_0^h \sigma_c b dy + \sum \sigma_{si} A_{si} \quad (1)$$

where, σ_c = stress in concrete

σ_{si} = stress in longitudinal reinforcement

A_{si} = area of longitudinal reinforcement

Due to the nonlinear stress-strain relationships of materials, it is necessary to develop an iterative procedure to calculate the depth of the neutral axis for each increment of the extreme fiber concrete compressive strain. The stress-strain relationships of concrete are based on confinement effects caused by transverse reinforcement and FRP-jacketing. Wang & Restrepo (2001) successfully developed the stress-strain relationship of concrete confined by both transverse steel and FRP reinforcement. However, this model can predict the behavior of concrete only in a pre-peak region. To extend to the post-peak region, the compressive fracture energy model proposed by Nakamura & Higai (1999) has been modified to consider the confinement effect as shown in Equation 2. It was found that $a = 0.86$ and $b = 2.25$ showed a good agreement in the case of column jacketed by PET.

$$G_f = 8.8(f'_{cc})^a + b \frac{f_l}{f'_{cc}} \quad (2)$$

To improve the accuracy in prediction of compressive strength of the confined concrete (f'_{cc}) under shear-flexure loading, the lateral pressures (f_l) should be evaluated by the transverse strain of concrete which is obtained from Poisson's ratio of concrete (ν) and axial strain (ϵ_x). Since the confinement effect occurs only in compression region which can be indicated by the neutral axis depth, the lateral confining pressure provided by both steel hoop and FRP jacket can be calculated by the simplified approach as in Figure 2. In section analysis, each element has different concrete's expansion based on Poisson's ratio and the biggest expansion is at the edge of square column in the compression region. In case of pure compression, the lateral confining pressure in x-direction (f_{lx}) is fully applied, while in case there is tension, the value of f_{lx} is averaged in every element.

The stress-strain relationships of materials are shown in Figure 3.

The load-deformation response of a specimen tested by Anggawidjaja, D. et al. (2006) is shown in Figure 4. Considering of the confinement effect in the stress-strain relationship of concrete, this sectional analysis (fiber model) can predict the load-deformation response in the

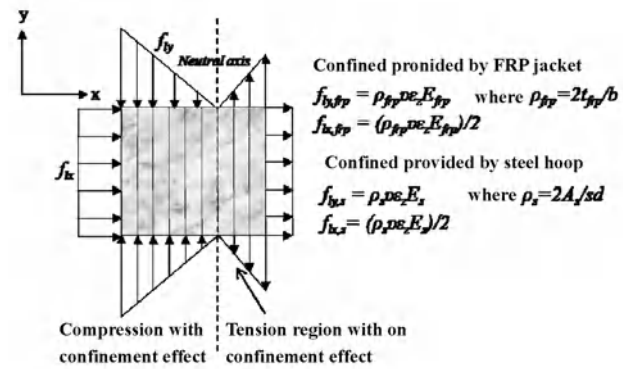


Figure 2 Proposed confining lateral pressure

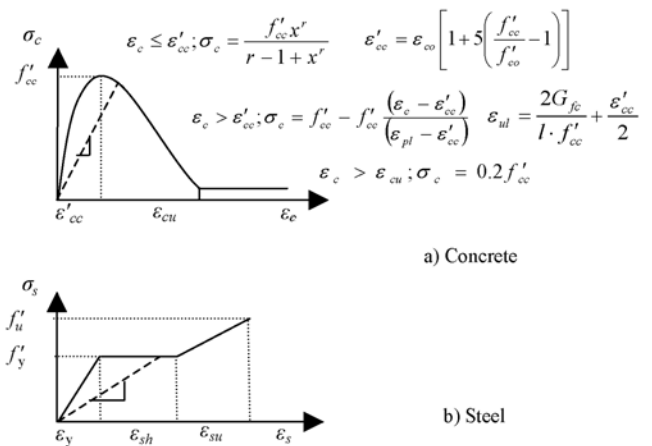


Figure 3 Constitutive laws and secant modulus

ascending region well. However, shear behavior is not taken into account in this approach, despite the fact that the post-peak of load-deformation response depends upon shear behavior, especially in columns subjected to flexural-shear forces. To include the effect of shear in this fiber model, a truss analogy approach is combined with section analysis in order to predict the structural-performance precisely.

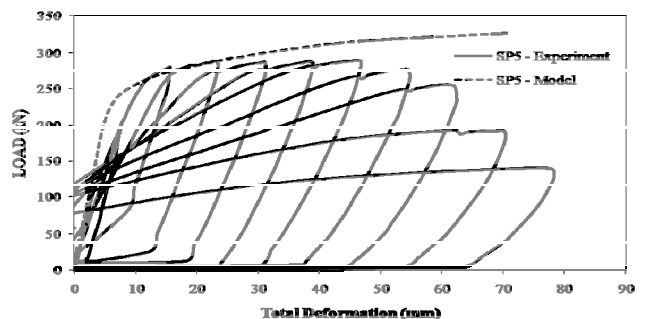


Figure 4 Load-deformation response of SP5 corresponding to flexural strength

2.2 Shear strength model

Evaluation of shear strength proposed by Sato et al. (1997) is mainly based on stiffness of both flexural and shear reinforcement. When the flexural reinforcement

reaches its yield stress, the reduction of flexural stiffness occurs and then a drop of potential shear capacity is observed. Moreover, the concrete compression zone is reduced as the neutral axis continues to move upward to the extreme compressive fiber after shear cracking. The potential shear capacity decreases further after yielding of shear reinforcement. This is because the contribution of concrete decreases further and the shear reinforcement contribution has no further increase.

After the intersection of the potential flexural and shear capacity curves, the descending part of load-deformation curve is controlled by the potential shear capacity as shown in Figure 5.

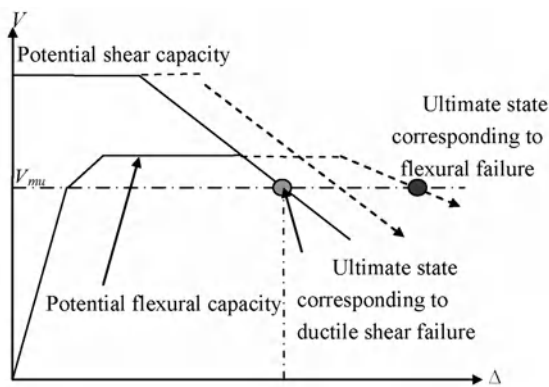


Figure 5 Flexural and shear potential capacity concept proposed by Anggawidjaja et al. (2006)

2.3 Prediction of Deformation

Total deformation of RC columns generally consists of three components which are flexural, shear and pull-out deformation. Although for simplicity these three deformations are considered to occur independently, they actually interact with each other. The flexural deformation can be obtained by integrating curvature along the column length as in Equation 3. This curvature is calculated from section analysis as discussed in the flexural behavior. However, the deformation obtained from this approach can predict well only the region prior to the shear cracking. Diagonal shear cracks cause the reduction in neutral axis depth and the increase in tension reinforcement stress by the tension shift (Ueda et al. 2002). The confinement effect by tie reinforcement and jacketing, which is considered in the flexural deformation model, on concrete strength may be considered in the shear deformation model.

$$\Delta_{flexure} = \int_0^l \int_0^l \phi dy dy \quad (3)$$

Shear deformation is neglected in the design process in many countries. However, shear deformation has been shown to remarkably influence the total deformation after shear cracking (JSCE 2002). In this study, the truss mechanism model for predicting shear deformation

proposed by Ueda et al. (2002) is extended to the post-yield range. In order to obtain an accurate prediction of the total deformations of the columns, the shear and flexural deformations are combined with the pull-out deformations which are calculated by Shima et al. model (1987).

3 MODEL VERIFICATION

3.1 Experimental Program (Anggawidjaja, et al. 2006)

In this study, five RC column specimens were tested under horizontal cyclic load and displacement control with an increment of $1\delta_y$ for each cycle. The constant vertical force of 1 MPa was applied at the top of the specimen as in Figure 6.

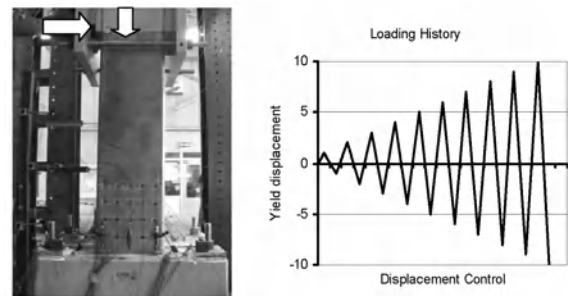


Figure 6 Experimental device and Loading history

The considered parameters were tension reinforcement ratio (ρ_t), fiber ratio (ρ_f) and shear span to depth ratio (a/d), while shear reinforcement ratio (ρ_w) was kept constant. The details of all specimens are shown in Table 1.

Table 1 Detail of specimens.

Item	Fiber	a (m)	a/d	ρ_t (%)	ρ_w (%)	ρ_f (%)
SP5	PET	1150	3.1	2.87	0.16	0.19
SP6	PET	1500	4	2.87	0.16	0.12
SP7	PET	1150	4	2.87	0.16	0.06
SP8	PET	1150	4	2.87	0.16	-
SP9	PET	1150	4	3.59	0.16	0.12
SP10	PET	1150	4	2.15	0.16	0.06

3.2 Strength-deformation relationship prediction

Based on the experimental results of SP6, the model to predict potential flexural and shear capacity of column with FRP jacketing showed good agreement as shown in Figure 7. However, in the descending part the model for potential shear capacity cannot predict well. In the potential shear capacity model, the concrete strength is assumed to increase due to the confinement effect. It is found, however, that the confinement effect is small in the descending part, in which the potential shear capacity is reducing. In the descending part, the compressive zone is reduced and this reduces the effectiveness of confinement.

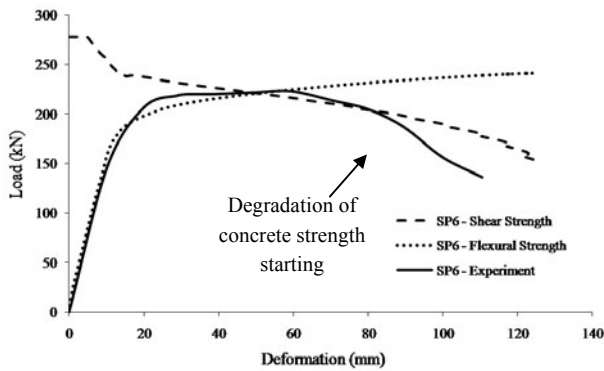


Figure 7 Load deformation and potential strength of SP6

3.3 Comparison of Analytical and Experimental Results

In Figure 8, the deformation component of SP6 was predicted. Flexural deformation occupied most of total deformation and pull-out deformation shows an important influence to total deformation. It seemed that shear deformation can be neglected at the early stage. However, after shear reinforcement yielding shear deformation increased significantly, especially at ultimate deformation.

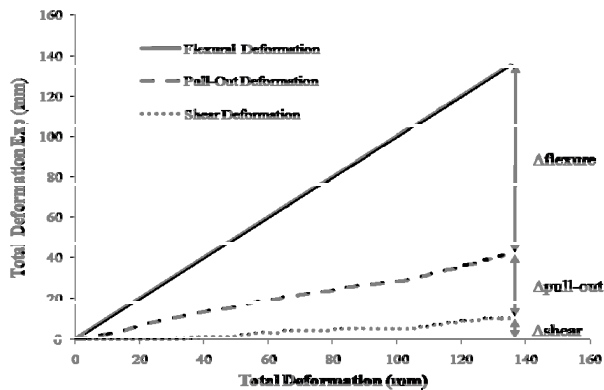


Figure 8 Deformation component of SP6

It was observed that for all specimens the ultimate deformation was mainly reached due to concrete crushing and buckling of longitudinal reinforcement. The experimental results have shown that there was no breakage of the high fracturing strain PET fibers. Thus, the performance of the structure was improved by FRP-retrofitting in terms of greater ductility.

For the specimen in which shear was dominant, SP5, with a small shear span, the ultimate deformation was due to the extensive shear cracking and eventually lead to flexure-shear failure. SP8 without FRP-retrofitting showed a sudden drop after buckling of longitudinal reinforcement, while SP6 which was jacketed by FRP shows a flexural failure and more ductility than that of SP8. This is great evidence to support that application of PET fibers improves ductility. In addition, the degradation of load-carrying capacity of FRP-jacketed specimens was prevented by the confinement provided by the PET fibers.

Verification of the proposed model with combination of fiber model and truss mechanism model was conducted. The analytical results can predict well and shows good agreement with the experimental results as shown in Figure 9.

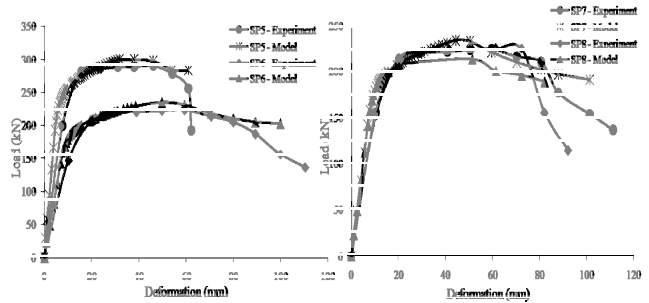


Figure 9 Analytical and experimental results of SP5-SP10

4 CONCLUSION

The analytical model for the ultimate of deformation of column, which consists of the potential flexure and shear model, is presented and its reliability is verified using an experimental program of square columns strengthened with PET sheet jacketing tested under reversed cyclic loading. The deformation from the experimental program well agrees with the analytical predictions. The proposed model shows that the fiber with high rupture strain can provide good ultimate ductility as the experimental fact indicates.

REFERENCE

Anggawidjaja, D. et al. 2006. Deformation Capacity of RC Piers Wrapped by New Fiber-Reinforced Polymer with Large Fracturing Strain. *Cement & Concrete Composites*, No.28/V-10: 914-927.

JSCE. 2002. Standard Specifications for Concrete Structures – 2002 ‘Structural Performance Verification’, JSCE Guidelines for Concrete, JSCE, No.3: 274 pages.

Nakamura, H. & Higai, T. 1999. Compressive Fracture Energy and Fracture Zone Length of Concrete. *JCI-C51E Seminar on Post-Peak Behavior of RC Structures Subjected to Seismic Loads, October 1999*, V-2: 2590-272.

Sato, Y. et al. 1997. Shear Strength of Reinforced and Prestressed Concrete Beams with Shear Reinforcement. *Concrete Library International of JSCE*, No.29: 233-247.

Shima, H. et al. 1987. Micro and Macro Models for Bond in Reinforced Concrete. *Journal of the Faculty of Engineering, The University of Tokyo*, No.2/V-39: 133-194.

Ueda, T. et al. 2002. Shear Deformation of Reinforced Concrete Beam. *JSCE Journal of Materials, Concrete Structures, Pavements*, No 711/V-56: 205-215.

Wang, Y. & Restrepo, J. 2001. Investigation of Concentrically Loaded Reinforced Concrete Column Confined with Glass Fiber-Reinforced Polymer Jackets. *ACI Structural Journal*, No.3/V-98: 377-385.

Seismic Performance of FRP-Confined Circular RC Columns

Z. Y. Wang & D. Y. Wang

School of Civil Engineering, Harbin Institute of Technology, Harbin, China

S. A. Sheikh & J. T. Liu

Department of Civil Engineering, University of Toronto, Toronto, Canada

ABSTRACT To investigate the seismic performance of FRP-confined circular RC columns with high axial compression ratio, six third-scaled columns confined with Carbon Fiber-reinforced Polymer (CFRP) at plastic hinge region and two control columns were tested under constant axial load and cyclic lateral force. The maximum axial compression ratio ($P/f'_c A_g$) was 0.65 and the shear span ratio was 3.5. Test results demonstrated marked improvement in the ductility and energy dissipation of the columns due to CFRP wrapping at plastic hinge region. The study also found that the contribution of hoops to confining effect should not be ignored under the condition of high axial compression ratio. To accurately simulate the seismic performance and obtain the hysteretic shear-deformation curves of FRP-confined columns, a nonlinear analytical procedure was developed using fiber model based on OpenSees (Open System for Earthquake Engineering Simulation). A stress-strain model which considers the confining effects of both the internal hoops and external CFRP jacketing was used. The analytical results indicated that inclusion of the both confining effects results in better simulation of the test results from this and other studies. But, if the axial compression ratio is less than 0.3, the analytical results are not affected even considering the contributions of hoops. The lateral loading capacity of columns begins to decrease when the axial compression ratio exceeds 0.6 and when the length of wrapped CFRP at the plastic hinge region exceeds 1.2D (D is the diameter of columns), the seismic performance could be improved to a level equivalent to fully wrapped columns.

1 INTRODUCTION

Reinforced concrete columns are critical structural member that withstand vertical compression and lateral seismic loading, but columns or piers with inadequate lateral confinement do not possess the necessary ductility to dissipate sufficient seismic energy and failures of key columns can trigger a catastrophic collapse of a structure (ACI Committee 440 2008). Therefore, there is an urgent need to upgrade the seismic ability of such deficient RC columns for the safety of existing structures in seismic regions around the world. In response to this need, the concept of the fiber-reinforced polymer (FRP) overlay technique was developed for the seismic retrofit of RC columns and had been proven to be an effective retrofitting technique to enhance the shear resistance or improve the ductility of columns.

Some experimental studies have been reported on the seismic behavior of FRP-confined columns, but in most cases, researchers concentrated on the piers under low axial load (Saadatmanesh et al. 1996, Sible et al. 1997, Xiao 1997). Limited research focused on columns with high axial compression ratio, despite high axial loads are common in existing buildings which need to be retrofitted (Sheikh & Yau 2002). On the other hand, to successfully

use the FRP overlay technique for retrofit of RC columns, the seismic behavior of FRP-confined column needs to be understood and accurately predicted. Although a number of finite element analysis studies have been conducted (Medhat & Hussein 2003, Lee 2006, Perera 2006), it is still not usual to simulate the hysteretic shear-deformation curves of FRP-confined columns subjected to constant axial load and cyclic lateral displacement. This study provides test data and relevant analysis on seismic behavior of deficient circular RC columns wrapped with CFRP under high axial load. Results can be used to develop design guidelines for retrofitting deficient columns with CFRP.

2 EXPERIMENTAL PROGRAM

2.1 Specimens and test setup

Eight reinforced concrete columns were constructed using typical lateral steel detailing from the Chinese 1989 design codes, which was equal to the pre 1971 design codes of ACI. Two RC columns were used as control specimens to evaluate the benefits of CFRP retrofitting and six another columns were retrofitted with CFRP at potential plastic hinge zone. Each specimen consisted of a circular column with 180 mm in diameter and 1260 mm in

length and two casts integrally stubs of dimensions 300×370×780 mm. The shear-span ratio of all specimens was 3.5 and the thickness of cover was 8 mm. Six longitudinal reinforcing bars with a diameter of 12 mm were evenly arranged in a circle and all longitudinal bars were completely extended into the stubs. The transverse reinforcements were 4 mm diameter hoops with a spacing of 60 mm (2.4 in.) at the two ends of specimens. The layout of specimen is shown in Figure 1 and the details of test specimens and material properties are given in Table 1.

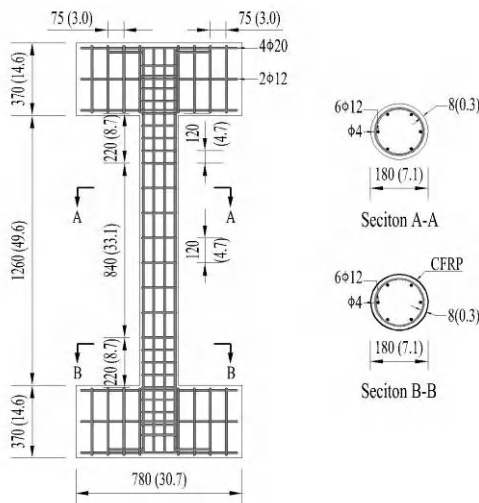


Figure 1 Specimens details (inch)

Table 1 The details of test specimens and material properties

Specimens	f'_c (MPa)	$P/f'_c A_g$	wrapping length (mm)	Retrofit detail
C1	54.8	0.45	—	Control
C2	71.2	0.45	—	Control
C1n1	54.8	0.45	200	4-layer
C1n2	54.8	0.55	320	4-layer
C1n3	54.8	0.65	320	4-layer
C2n2	71.2	0.45	200	4-layer
C2n2	71.2	0.55	320	4-layer
C2n3	71.2	0.65	320	4-layer
Materials	Longitudinal steel		Hoop	CFRP
Tensile strength	354 MPa		402 MPa	3430 MPa
Tensile modulus	1.98×10^5 MPa		2.01×10^5 MPa	2.3×10^5 MPa
Yield strain	0.00179		0.002	0.018

* f'_c is the cylinder compression strength of concrete; A_g is the gross area of circular column section.

Strain gages were placed on the longitudinal rebars, hoops and CFRP, respectively. The experiment was conducted by using a test frame specially designed to allow the top stub of columns to move only along horizontal direction and no rotation occurred, as shown

in Figure 2. Axial load was applied by hydraulic jack and rollers were placed under the jack to eliminate the frictional restraints and to ensure that axial load moved with the top stub of specimens in order to simulate P-Δ effect. Displacement control mode was used in the lateral displacement cycles until lateral load decreased to 80% of the maximum lateral loading capacity.

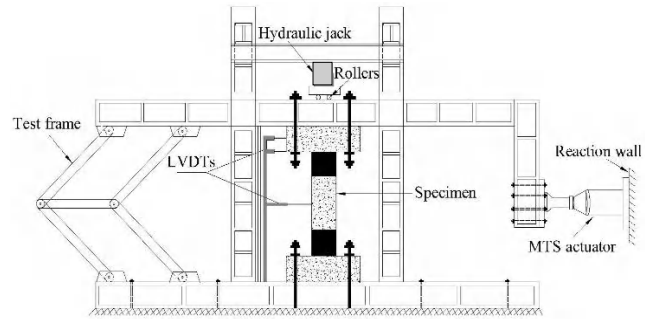


Figure 2 Test setup

2.2 Hysteretic lateral load-displacement curves

The hysteretic responses of all specimens are shown in Figure 3 and the envelope curves are plotted in Figure 4.

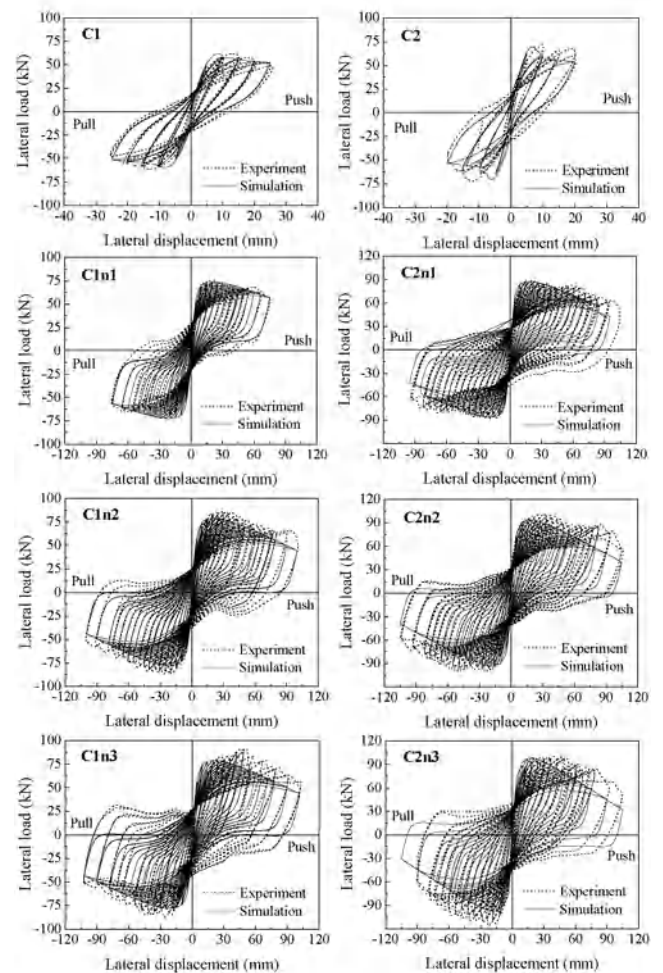


Figure 3 Hysteretic lateral load-displacement curves of all specimens

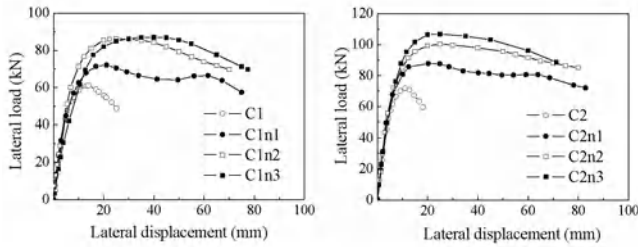


Figure 4 The envelope curves of all specimens

The effectiveness of strengthening deficient columns with CFRP is evaluated by comparing with the two control specimens. Both specimens C1 and C2 behaved in a very brittle manner and the energy dissipation capacity in each specimen was poor. However, the retrofitted columns showed the remarkable beneficial effects on strength, ductility and energy dissipation.

In Figure 4, comparing specimens C1 and C1n1, C2 and C2n1, it can be seen that the peak lateral load capacity increased 18% and 23%, and the ultimate displacement which is defined as the deflection on the softening branch where the lateral load drops to 80% peak lateral load enhanced 200% and 384%, respectively. With the increase of axial load, the peak lateral load of retrofitted columns was improved, but the ultimate displacement reduced.

2.3 Strain of hoop and CFRP

Figure 5 shows the tensile strain in hoops and CFRP versus drift ratio, which is the ratio of measured tip lateral displacement Δ to the length of columns H . It can be seen that the strain of hoop developed more rapidly in control columns. In the FRP-confined specimens, the strain of hoop were smaller than that of CFRP. It indicate that the confinement of CFRP is more effective than hoops. With the increase of drift ratio, the hoop yielded and its strain finally exceeded the control column in specimen C2n3. This show that the contribution of hoops to confining effect should not be ignored in retrofitted columns under high axial compression.

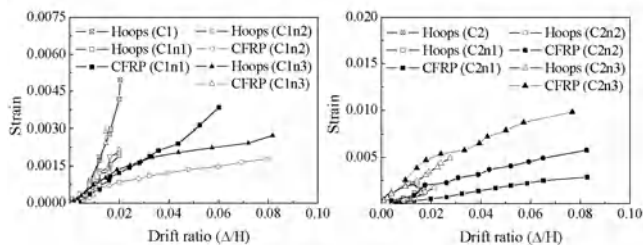


Figure 5 Strain of hoop and CFRP

3 FINITE ELEMENT ANALYSIS

3.1 Fiber model

An open source object-oriented nonlinear structural analysis software, OpenSees, was used for the seismic

analysis of CFRP-confined columns. The columns were analyzed using fiber model, as shown in Figure 6. The element type is non-linear beam-column element and fiber section consisted of cover, hoop-confined concrete, and CFRP-confined concrete.

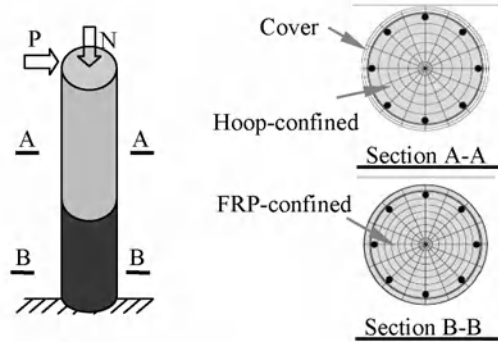


Figure 6 Sketch of fiber model used in OpenSees

3.2 Stress-strain relationship of materials

The different stress-strain relationships were used in corresponding fiber sections. The longitudinal reinforcement used Giuffrè-Menegotto-Pinto model and unconfined cover concrete used Kent-Park model, which the two model already included in OpenSees. The Mander model (Mander & Priestley 1988) was selected for hoop-confined concrete. A stress-strain model proposed by Mohamed (2006) which considers the confining effects of both the internal hoops and external FRP jacketing was used for FRP-confined concrete. The test cyclic compression stress-strain curve of FRP-confined concrete versus the relationship used in OpenSees was shown in Figure 7, which fully proved the accuracy of stress-strain relationships used in OpenSees.

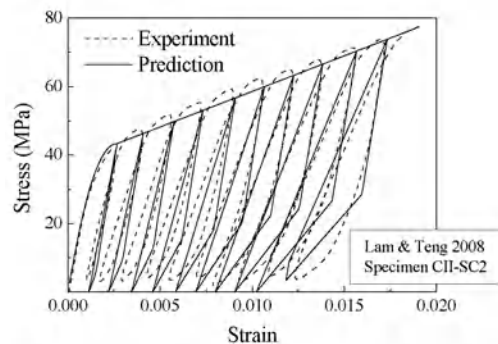


Figure 7 Test curve versus relationship used in OpenSees

3.3 Validation of finite element simulation

The validations of finite element simulation with the experimental data of this paper and other research are shown in Figure 3 and Figure 8, respectively. The simulation results have a good agreement with those test data. Besides, the contribution of hoops to confining effect was conducted by comparing the simulation with

results using ACI stress-strain model which didn't consider the effect of hoops. It is noted that the predictions were more accurate when consider the confinement of hoops. But, if the axial compression ratio is less than 0.3, the analytical results are not affected even considering the contributions of lateral hoops.

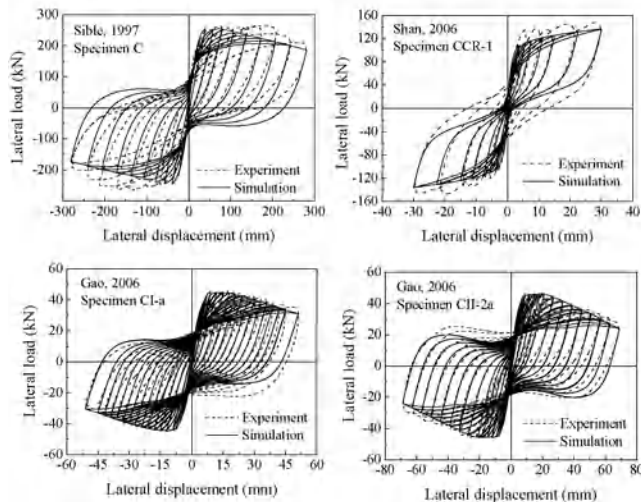


Figure 8 Validation of finite element simulation

4 PARAMETRIC ANALYSIS

4.1 Wrapping length of CFRP

Figure 9 shows influence of different CFRP wrapping lengths and layers on the lateral load-displacement response of CFRP-confined columns. It can be seen that if the length of wrapped CFRP at the plastic hinge region exceeds $1.2D$ (D is the diameter of columns), the seismic behavior could be improved to a level equivalent to the fully wrapped columns.

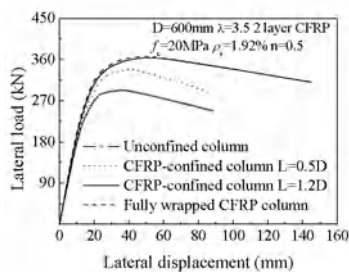


Figure 9 Influence of FRP wrapping length and layers

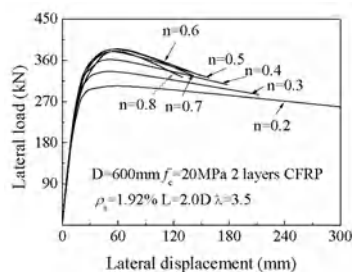


Figure 10 Influence of axial compression ratio

4.2 Axial load level

The influence of axial load levels on the lateral load-deformation response of FRP-confined columns is shown in Figure 10, in which $n=P/f'_c A_g$ is the axial compression ratio. It is found that with the increase of axial load, the peak lateral load capacity is improved, but the softening branch and the ultimate displacement decreases rapidly. The peak lateral load capacity of columns begins to decrease after the axial compression ratio exceeds 0.6. This shows the failure mode of FRP-confined columns start transferring from ductile failure to brittle failure.

5 CONCLUSIONS

The following conclusions can be drawn from this study.

- (1) Use of CFRP resulted in remarkable improvement in ductility, energy dissipation, and strength of the deficient lateral confinement RC columns;
- (2) The contribution of hoops to confining effect should not be ignored under high axial compression;
- (3) The peak lateral load capacity of columns begins to decrease when the axial compression ratio exceeds 0.6, which means the transformation of failure mode;
- (4) The length of wrapped CFRP at the plastic hinge region exceeds $1.2D$ (D is the diameter of columns), the seismic performance could be improved to a level equivalent to fully wrapped columns.

REFERENCES

- ACI Committee 440. 2008. Guide for the design and construction of externally bonded FRP systems for strengthening concrete structures. ACI 440.2R-08, Detroit, MI: American Concrete Institute.
- Gao, X. 2005. Research on cyclic behavior of circular RC columns confined with FRP jackets. PhD Thesis. Fu Zhou: Fuzhou University.
- Lam, L. & Teng, J. G. 2008. Stress-strain model for FRP-confined concrete under cyclic axial compression. *Engineering Structures* 10:1-14.
- Lee C. S. 2006. Modeling of FRP-jacketed RC columns subject to combined axial and lateral loads. San Diego: University of California.
- Mander, J. B. & Priestley, M. J. N. 1988. Theoretical stress-strain model for confined concrete. *Journal of Structural Engineering* 114(8):1805-1826.
- Medhat, A. Haroun. & Hussein, M. E. 2003. Numerical models for composite-jacketed reinforced concrete bridge columns. *Journal of Reinforced Plastics and Composites* 22(13):1203-1219.
- Mohamed, H. Harajli. 2006. Axial stress-strain relationship for FRP confined circular and rectangular concrete columns. *Cement & Concrete Composites* 28:938-948.
- Perera, R. 2006. A numerical model to study the seismic retrofit of RC columns with advanced composite jacketing. *Composites: Part B* 37:337-345.

- Saadatmanesh H. & Ehsani M. R. & Jin. L. M. 1996. Seismic Strengthening of Circular Bridge Pier Models with Fiber Composites. *ACI Structural Journal* 93(6):936-947.
- Sheikh, S. A. & Yau, G. 2002. Seismic behavior of concrete columns confined with steel and fiber-reinforced polymers. *ACI Structural Journal* 99(1):72-80.
- Sible F., & Priestley M. J. N. & Gilbert H., & Donato, I. 1997. Seismic retrofit of RC columns with continuous carbon fiber jackets. *Journal of Composites for Construction* 1(2):52-62.
- Xiao, Y. & Ma, R. 1997. Seismic retrofit of RC circular columns using prefabricated composite jacketing. *Journal of Structural Engineering October*:1357-1364.
- Shan B. 2006. Experimental studies on long-term behavior of FRP retrofitted RC columns with earthquake loading damage. PhD Thesis. Chang Sha: Hunan University.

Cyclic Behaviour of FRP Confined RC Rectangular Columns with High Aspect Ratio

A. Napoli (annapoli@unisa.it), B. Nunziata & R. Realfonzo

Department of Civil Engineering, University of Salerno, Fisciano (SA), Italy

ABSTRACT This paper presents an experimental study undertaken to investigate the seismic behavior of square and rectangular RC columns confined with FRP or strengthened with FRP wraps and longitudinal steel profiles. Test results aim to explore the influence on the column performance of relevant parameters, such as: concrete strength, longitudinal steel reinforcement of the member (smooth or deformed rebars), type of strengthening system (FRP confinement w/ or w/o steel profiles); axial load levels; number of FRP layers used for columns jacketing. In particular, results from tests on rectangular columns are reported herein.

1 INTRODUCTION

The use of Fiber Reinforced Polymer (FRP) materials for external confinement of under-designed RC columns has recently emerged as an attractive alternative to the traditional systems (i.e. systems made of steel or concrete jackets).

To date, a number of analytical and experimental studies have been performed to understand the behavior under axial compression of small scale concrete specimens confined with FRP materials. However, the effectiveness of the FRP confinement is not fully understood when large size members are tested under combined bending and axial load.

The main concerns are related to the reduced effectiveness of the FRP confinement when columns have cross section with high side ratio. It is noted that the Italian Guidelines DT200 (CNR 2004) discourage the use of FRP confinement for members with rectangular cross-section having a side ratio >2 if not otherwise proven by suitable experimental tests; this because these applications are not carefully validated by testing.

The experimental study presented herein addresses these knowledge gaps by investigating the performance of FRP confined RC columns having aspect ratio of about 2.3. Preliminary results of such tests can be found in a paper recently published by the authors (Napoli et al. 2009).

2 EXPERIMENTAL PROGRAM & TEST SETUP

2.1 The whole experimental program

A total of nine large scale RC specimens, with 300×700 mm cross section, 2500 mm long, were tested at the Laboratory of Structure of the University of Salerno

under constant axial load and cyclically reversed horizontal force.

These specimens are included in a larger test matrix comprising twenty-four 300×300 mm square members, 2200 mm long, whose results have been already detailed in Realfonzo & Napoli (2009).

Test specimens were representative of structural components belonging to gravity load designed (GLD) existing buildings; furthermore, some members were reinforced with smooth longitudinal steel rebars - commonly used in the past - and others with deformed ones. Details about the specimen configurations (geometry, longitudinal and transverse reinforcements, etc.) can be found elsewhere (Realfonzo & Napoli 2009; Napoli et al. 2009).

The average values of the mechanical properties of steel rebars, as obtained by tensile tests, are shown in Table 1, where: f_{sy} and ϵ_{sy} indicate the strength and strain at yielding; ϵ_{sh} is the strain at the onset of the steel hardening; f_{su} and ϵ_{su} are the ultimate strength and the corresponding strain.

2.2 Strengthening systems for rectangular columns

Focusing on the rectangular columns, two FRP strengthening systems were considered, namely "Type C" and "Type A1" (Figure 1a).

The "Type C" system consisted of an external confinement realized by wrapping members with unidirectional CFRP layers.

In the "Type A1" system, the FRP confinement was combined with four longitudinal steel angles placed at the member corners and glued to the concrete substrate by means of an epoxy adhesive; the angles ($80 \times 80 \times 6$ mm) were anchored to the concrete stub by means of steel connectors (see Figure 1b).

As provided by the suppliers, the employed CFRP plies were characterized by: an elastic modulus of 390 GPa; tensile strength and corresponding strain of 3000 MPa and 0.80 %, respectively. The thickness of the single layer was about 0.22 mm.

Table 1 Mechanical properties of the steel rebars

Type	f_{sy} (MPa)	ϵ_{sy} (%)	ϵ_{sh} (%)	f_{su} (MPa)	ϵ_{su} (%)
smooth	346	0.165	3.68	498	23.80
deformed	556	0.265	3.97	655	16.73

2.3 Test setup

Tests were conducted in displacement control by subjecting columns to a constant axial force and cyclically reversed horizontal force. A schematic of the test setup is shown in Figure 1c.

The axial load (N) – kept constant during each test – was applied before the horizontal load using a 2000 kN MOOG hydraulic actuator; in particular, two values of the normalized compression load “v”- respectively equal to 0.14 and 0.25 - were considered; “v” is given by:

$$v = \frac{N}{f_{cm} \cdot A_g} \quad (1)$$

where A_g is the column cross-section area; f_{cm} is the average cylinder compressive strength of the concrete.

The horizontal action, instead, was cyclically applied at 2050 mm from the column base by using a 500kN MTS hydraulic actuator, mounted to a reaction steel frame. An increment of the imposed horizontal displacement every three cycles was considered in order to evaluate the strength and stiffness degradation at repeated lateral load reversals.

During the tests, loads, strains, displacements and crack widths were accurately monitored.

Details on test setup and instrumentation, omitted herein for the sake of brevity, can be found in (Realfonzo & Napoli 2009; Napoli et al. 2009).

3 TEST RESULTS AND DISCUSSION

Table 2 summarizes the main data and results of the 9 tests performed on rectangular columns.

Each specimen is identified by a label which provides the following information: column number (from C25 to C33); steel reinforcement type (D=deformed; S=smooth); strengthening system (types “C” or “A1”), if any.

In addition, for each test the Table reports:

- the number of the FRP layers (2 or 4) used for column jacketing;
- the average cylinder compressive strength (f_{cm});
- the applied axial load (N) and its corresponding normalized value (v);
- the peak resistance in the two direction of loading (F_{max}^+ and F_{min}^-) and the corresponding tip displacement (Δ^+ and Δ^-);
- the maximum tip displacement of the column (Δ_{max}) measured at the conventional collapse (i.e. at the achievement of 10% strength degradation evaluated on the F- Δ curves);
- the peak values of the normalized bending moment (μ) in the two directions of loading (μ_{max}^+ and μ_{min}^-);
- lateral drift ratio “ δ_{max} ”, obtained by dividing the tip deflection of the column at the collapse (Δ_{max}) with the shear span ($L_s=2050$ mm).

The normalized flexural resistance is given by:

$$\mu = \frac{F \cdot L_s}{B \cdot H^2 \cdot f_{cm}} \quad (2)$$

where B and H are the width and the depth of the column cross section, respectively; F is the lateral force applied by the actuator.

From Table 2 can be observed that, despite the common belief on the reduced efficacy of the FRP confinement in case of high aspect ratio, tests performed by the authors highlighted a non negligible increase of ductility of the confined members, in particular when four layers are used to wrap the column.

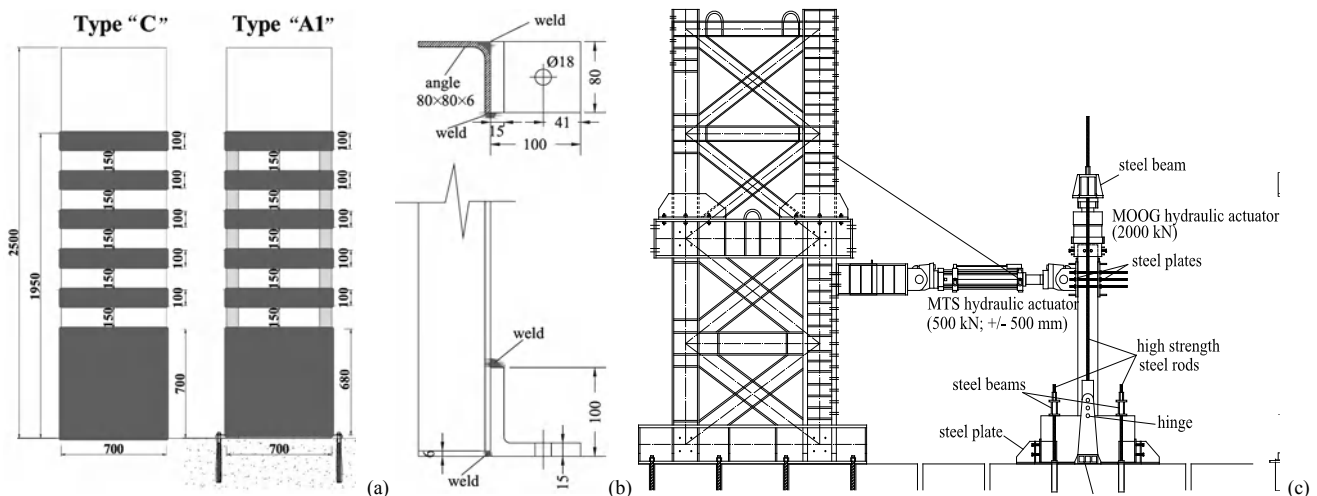


Figure 1 FRP strengthening systems (a); details of the anchorage in the Type A1 system (b); test setup (c)

Table 2 Test specimens: main data and test results

TEST	# FRP layers	f_{cm} (MPa)	N (kN)	ν	F_{max}^+ (kN)	Δ^+ (mm)	F_{max}^- (kN)	Δ^- (mm)	Δ_{max} (mm)	μ_{max}^+	μ_{max}^-	δ_{max} (%)
C25-S	–	12.1	635	0.25	161.67	29.43	158.08	22.25	43.46	0.19	0.18	2.12
C26-S-C	2	16.3	856	0.25	229.31	44.31	218.63	43.30	59.45	0.20	0.19	2.90
C27-S-C	4	13.1	688	0.25	202.09	52.29	215.49	59.29	73.59	0.22	0.23	3.59
C28-S-A1	4	13.8	725	0.25	302.04	89.76	303.90	89.79	101.27	0.31	0.31	4.94
C29-D	–	11.7	614	0.25	177.62	22.32	180.54	22.33	34.03	0.21	0.21	1.66
C30-D-C	2	22.6	1100	0.25	317.57	89.57	317.95	74.65	94.91	0.20	0.20	4.63
C31-D-C	4	15.0	787	0.25	293.27	89.32	280.56	66.51	84.05	0.27	0.26	4.10
C32-D-A1	4	11.7	614	0.25	319.33	66.75	320.90	66.83	69.91	0.38	0.38	3.41
C33-D-C	4	12.6	370	0.14	204.52	47.81	171.45	71.79	64.98	0.23	0.19	3.17

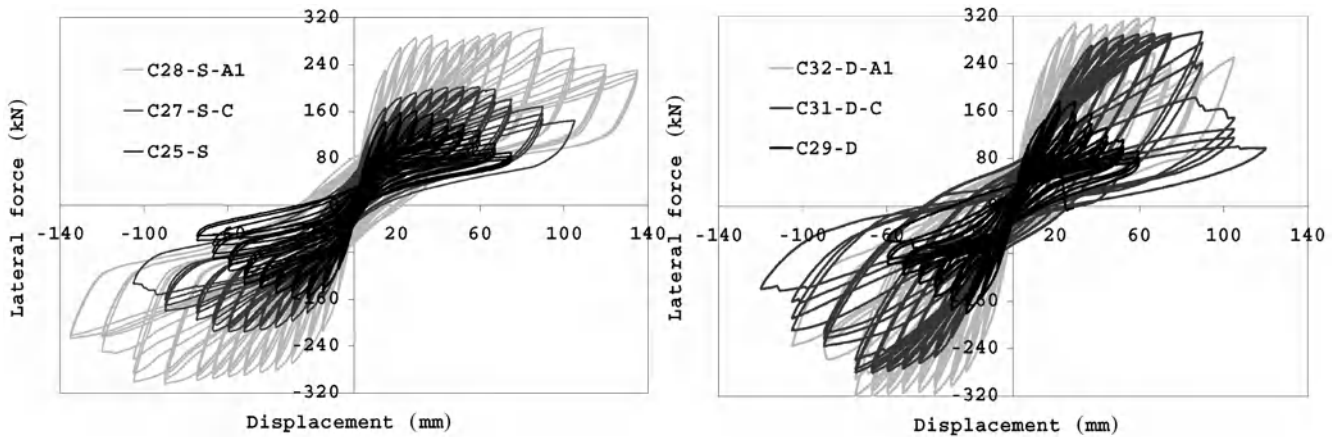


Figure 2 Load-displacement hysteretic curves

The positive effect of the FRP confinement on the column performances is more evident in case of higher axial load level ($\nu=0.25$).

Furthermore, as already observed for square members (Realfonzo & Napoli 2009), a significant increase of flexural strength is evidenced when the FRP confinement is associated with the use of steel angles connected to the foundation.

Figure 2 shows some lateral force-tip displacement cyclic curves relative to rectangular specimens reinforced with smooth or deformed steel rebars and subjected to the higher value of axial load ($\nu=0.25$).

Regardless of the type of steel reinforcement (smooth or deformed), the curves relative to FRP confined members are characterized by lower strength degradation when compared with those of the unconfined members. The latter, once the maximum flexural strength is attained, are not able to undergo significant deflection without considerable reduction of the strength, so that the conventional collapse is achieved at low values of displacement.

In the case of columns strengthened with both FRP wrapping and steel angles (system type “A1”), the flexural strength degradation is affected by the occurrence of the steel connector pullout from the concrete stub. At that time, in fact, the contribution of the anchored angles abruptly becomes negligible.

As already observed for square members (Realfonzo & Napoli 2009), also in the case of rectangular columns a non negligible “pinching effect” characterized the cyclic behavior of columns reinforced with smooth rebars, so that a lower energy dissipation capacity is attributed to these members.

This is clearly confirmed from Figure 3 where some hysteretic cycles at equal displacement amplitude, recorded in case of FRP confined columns reinforced by using smooth (test C27) and deformed steel rebars (test C31), are shown.

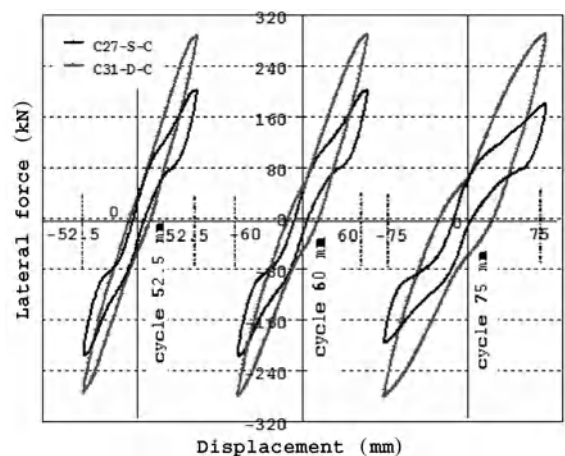


Figure 3 Shape of hysteresis loop

3.1 Dimensionless μ - δ curves

The performances of the tested members can be better compared through the peak values of the normalized bending moment " μ ".

In fact, using normalized values for the flexural strength allows to by-pass the dependence of test results on concrete strength, thus providing a more accurate comparison.

The experimental μ - δ envelopes are plotted in Figure 4. The comparative analysis clearly shows the benefits produced by the FRP confinement mainly when four layers are used to wrap the column.

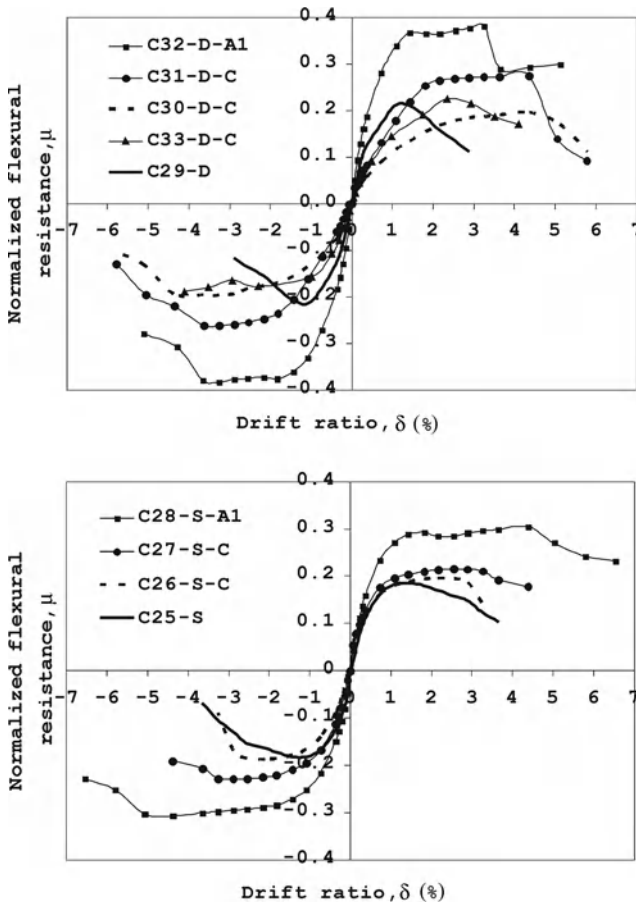


Figure 4 Dimensionless μ - δ envelopes

Furthermore, the dimensionless curves show that columns strengthened also with steel angles reached higher level of strength. It has to be underlined that at the collapse of anchor system the behaviour of these columns becomes very similar to that of FRP confined members (compare tests C32 and C31).

3.2 Chord rotation vs drift ratio curves

The crack pattern exhibited during tests by FRP confined columns, w/ or w/o steel angles, mainly was characterized by the opening of cracks out of the wrapped regions; a dominant crack located at the column-stub interface was always observed.

The type of longitudinal steel rebars and the level of

axial load have both a strong influence on the evolution of these cracks and consequently on column cyclic responses.

The rotation at the base of the specimens (local deformation parameter) versus the drift ratio (global deformation parameter) θ - δ curves for some FRP confined columns are shown in Figure 5.

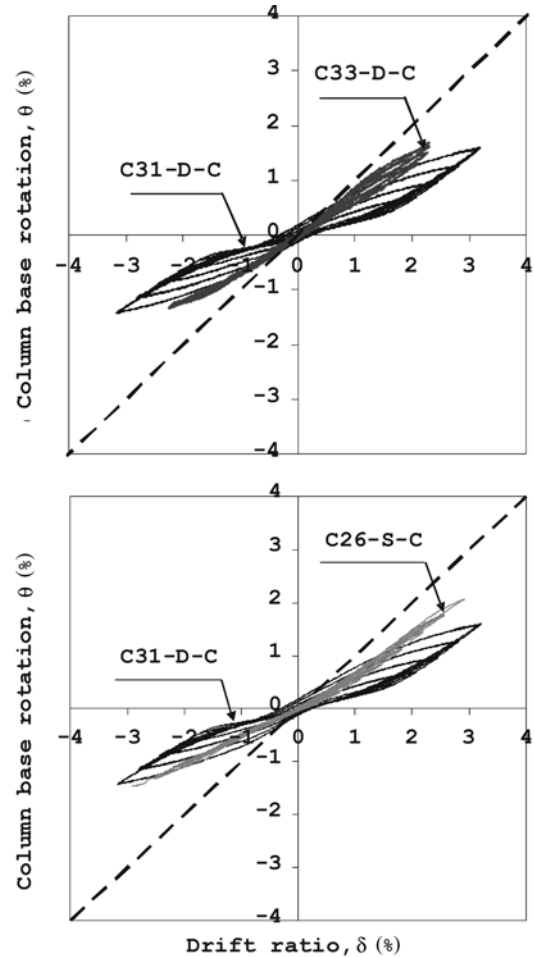


Figure 5 Comparison of θ - δ curves

In particular Figure 5a shows the dependence of the response on the axial load level for two columns reinforced by deformed steel rebars.

It can be observed that under $v=0.14$ (test C33) the rotation at the base nearly coincides with the drift ratio. This implies that the rotation capacity of the member is slightly influenced by the flexural contribution, while the deformation component due to the rigid rotation at the base is dominant.

Under $v=0.25$ (test C31), instead, the slope of the θ - δ curves significantly reduces as the flexural contribution to the rotation capacity becomes relevant.

The influence of the longitudinal steel reinforcement type is instead shown in Figure 5b; the Figure depicts the cyclic response of columns reinforced with smooth (test C26) and deformed rebars (test C31) and subjected to the same axial load level.

From the Figure it can be observed that, due to the lower bond of the smooth rebars, the contribute due to the rigid rotation exhibited by column C26 is much greater than that observed for column C31.

4 CONCLUSIONS

In this paper, results from cyclic tests performed on RC rectangular (300×700 mm) columns strengthened with FRP systems have been discussed.

Despite the high side ratio, it has been shown that the FRP confinement leads to a non negligible ductility enhancement of the columns.

REFERENCES

- CNR. 2004. Guide for the design and construction of externally bonded FRP systems for strengthening existing structures. *Technical Document CNR-DT 200/2004*, Italian National Research Council, Rome, Italy.
- Napoli, A., Nunziata, B. & Realfonzo, R. 2009. Cyclic behaviour of rectangular reinforced concrete columns strengthened with FRP systems. In *Proc. of XIII National Congress ANIDIS*, Bologna, June 28-July
- Realfonzo, R. & Napoli, A. 2009. Cyclic behavior of RC columns strengthened by FRP and steel devices. *Journal of Structural Engineering*, 135(10): 1164-1176.

Numerical Simulation of FRP-Jacketed RC Columns Subjected to Cyclic Loading

J.G. Teng¹ (cejgteng@polyu.edu.hk), J.Y. Lu^{1,2}, L. Lam¹ & Q.G. Xiao¹

1. Department of Civil and Structural Engineering, The Hong Kong Polytechnic University, Hong Kong, China

2. Key Laboratory of Concrete and Prestressed Concrete Structures of the Ministry of Education, College of Civil Engineering, Southeast University, Nanjing 210096, China

ABSTRACT This paper presents a study that forms part of an ongoing project on the seismic retrofit of reinforced concrete (RC) structures with fibre-reinforced polymer (FRP). In this study, a stress-strain model for FRP-confined concrete subjected to cyclic loading was implemented into OpenSees to support the performance-based design of FRP jackets for the seismic retrofit of RC columns/structures. Initial results from the numerical column model for two test columns show that the predicted responses are in close agreement with the test responses.

1 INTRODUCTION

The performance-based seismic design approach as presented in ATC-40 (ATC 1996), FEMA-356 (ASCE 2000) and FEMA-440 (ATC 2005) is becoming widely accepted in structural engineering practice, particularly in the seismic assessment and retrofit of structures. In this approach, the performance of a structure under seismic actions is commonly estimated by the performance point (e.g. ATC 1996) or the target displacement (e.g. ASCE 2000), and a push-over analysis of the structure is an essential key step. The popular open-source program "Open System for Earthquake Engineering Simulation" (OpenSees), developed at the University of California, Berkeley, offers a good programming platform for the numerical simulation of the seismic behaviour of structures. OpenSees allows the introduction of new materials and elements as well as the updating of material constitutive models based on the latest research.

While the seismic retrofit of RC columns may be achieved using various methods, lateral confinement with fibre-reinforced polymer (FRP) jackets has become a popular choice due to the effectiveness and ease of the method. Confinement of concrete by FRP jackets improves the ductility and hence the energy dissipation capacity of RC columns significantly. Despite the popularity of the method, an accurate numerical model for the seismic performance of FRP-jacketed RC columns does not seem to have been developed. This deficiency has been due to the lack of an accurate stress-strain model for FRP-confined concrete subjected to cyclic loading until the recent publication of such a model by Lam and Teng (2009). The two recent studies on the seismic performance analysis of concrete-filled FRP tubes (Zhu et al. 2006)

and FRP-wrapped RC columns (Mosalam et al. 2007) respectively using OpenSees suffer from this deficiency.

This paper presents a study that forms part of an ongoing project on the seismic retrofit of RC structures with FRP at The Hong Kong Polytechnic University (PolyU). This project has been motivated by the expectation that many of the concrete buildings in Hong Kong designed without consideration of seismic risks will need to be seismically retrofitted in the foreseeable future. In this study, the model of Lam and Teng (2009) was extended to include the tensile behaviour of FRP-confined concrete and was implemented in OpenSees. This paper presents this implementation as well as the initial results obtained using this numerical column model.

It should be noted that axial stresses and axial strains are simply referred to as stresses and strains for brevity in this paper unless otherwise specified. In addition, compressive stresses and strains are taken to be positive.

2 STRESS-STRAIN MODELS

2.1 FRP-confined concrete in compression

In this study, the stress-strain model proposed by Lam and Teng (2009) for FRP-confined concrete in cyclic compression was adopted to describe the compressive behaviour of FRP-confined concrete. In this model, the boundary of the hysteretic responses of FRP-confined concrete in cyclic compression (i.e., the envelope curve) is represented by a monotonic model previously proposed by them (Lam and Teng 2003). Expressions for the unloading and reloading paths of FRP-confined concrete within the compressive stress-strain domain (ε_c and σ_c , where ε_c and σ_c are the strain and stress of concrete, respectively) were developed by Lam and Teng (2009)

(see Figure 1). They also developed equations for predicting the plastic strain ϵ_{pl} and stress deterioration under cyclic loading, accounting for the effects of loading history. Details are available in Lam and Teng (2009).

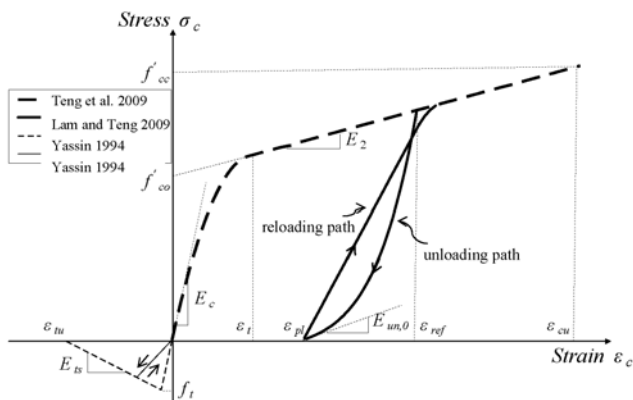


Figure 1 Stress-strain model for FRP-confined concrete

It must be noted that a typographical error exists in Equation 22 of Lam and Teng (2009) and the correct equation is given below:

$$\epsilon_{ret,env} = \frac{E_c - B}{2A + \frac{(E_c - E_2)^2}{2f'_{co}}} < \epsilon_i \quad (1)$$

where $\epsilon_{ret,env}$ is the strain in concrete at which the reloading path meets the envelop curve, A and B are coefficients defining the reloading path, E_c is the modulus of elasticity of unconfined concrete, f'_{co} is the compressive strength of unconfined concrete, E_2 is the slope of the linear second portion of the envelope curve, and ϵ_i is the strain in concrete at which the parabolic first portion of the envelope curve meets the linear second portion. Both E_2 and ϵ_i are defined in Lam and Teng (2003).

Teng et al. (2009) have recently published an improved version of the Lam and Teng (2003) monotonic stress-strain model, which predicts the compressive strength f'_{cc} and ultimate axial compressive strain ϵ_{cu} of FRP-confined concrete more closely. This improved version (Teng et al. 2009), instead of the original version (Lam and Teng 2003), was adopted to define the envelope curve in this study (see Figure 1).

2.2 FRP-confined concrete in tension

A model proposed by Yassin (1994) for unconfined concrete which is referred to as Concrete02 in OpenSees (2009) was used to represent the tensile behaviour of FRP-confined concrete in this study. A deficiency of Yassin’s (1994) model is that it omits the effect of compressive deterioration on the tensile modulus of concrete. As a result, whenever the concrete enters the tension zone ($\sigma_c < 0$), the initial tensile modulus is equated to the initial elastic modulus E_c (see Figure 2), as if the concrete has not been subjected to prior loading-induced deterioration.

To overcome the above deficiency, Yassin’s model needs to be modified so that the tensile modulus of concrete is equal to E_c only when it is loaded from the origin. When entering the tension zone along an unloading path at a point with $\sigma_c = 0$ and $\epsilon_c > 0$, the tangent modulus of concrete at this point, $E_{un,0}$, is assumed to be the same as the slope of the unloading path at the same point (see Figure 2). The definition of $E_{un,0}$ is given in Lam and Teng (2009).

The uniaxial stress-strain model for FRP-confined concrete covering cyclic behaviour in both compression and tension as described above was implemented into Version 2.10 of OpenSees (2009) as a new material model named “FrpConfinedConcrete”. This material module can be invoked in numerical simulations with OpenSees as a dynamic-link library (DLL) file.

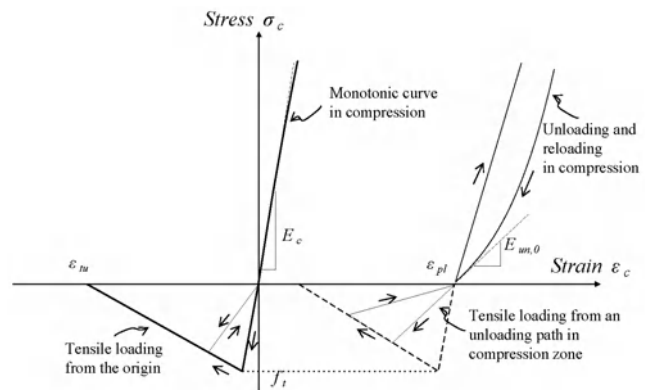


Figure 2 Stress-strain model for FRP-confined concrete in tension

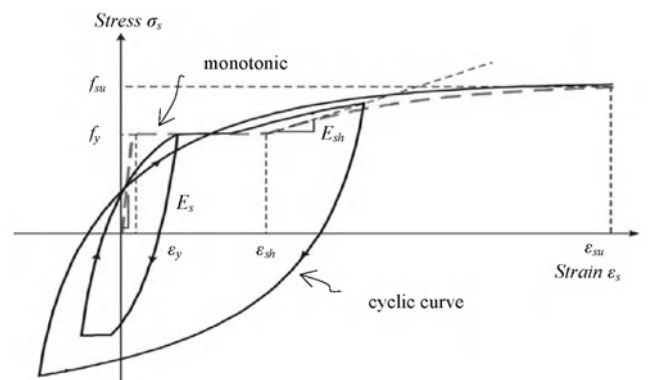


Figure 3 Stress-strain model for reinforcing steel

2.3 Steel reinforcement

Version 2.10 of OpenSees (2009) offers three stress-strain models for steel reinforcement. Compared to the other two models named “Steel01” and “Steel02” which feature either a simple or a smoothed bilinear monotonic stress-strain curve as the envelope curve, the model “ReinforcingSteel (RS)” is more suitable for use in nonlinear analysis of RC members using a fiber-based cross-section discretization (Heo and Kunnath 2009). A schematic of the model is given in Figure 3. This model was adopted in the present study to represent the hysteretic behaviour of steel reinforcement.

3 ANALYSIS OF FRP-JACKETED RC COLUMNS

3.1 Test columns

Two of the columns tested by Haroun et al. (2003), namely CS-R1 and CS-R2, are considered herein. The columns had a diameter of 610 mm and a clear height of 2440 mm, each reinforced with 20 deformed longitudinal steel bars of 19.1 mm in diameter and steel hoops of 6.4 mm in diameter at 127 mm spacing. The clear cover to the steel hoops was 19 mm. The thicknesses of the carbon FRP (CFRP) jackets were different within and outside the two potential plastic hinge regions (915 mm in length) at the top and the bottom. Key information of the columns is given in Table 1.

Both columns were tested under double bending, by the application of a constant axial compression load of 654 kN using prestressing bars and cyclic lateral loads. Failure of both columns was by jacket rupture within the plastic hinge regions, followed by the crushing of concrete.

Table 1 Details of the two test columns (Haroun et al. 2003)

Description	Column	
	CS-R1	CS-R2
Thickness of Plastic hinge zone	0.671	0.671
FRP (mm) Outside plastic hinge zone	0.503	0.470
Properties of Elastic modulus (GPa)	231.7	230.3
FRP Ultimate tensile strain	0.0180	0.0193
Unconfined concrete strength (MPa)	40.82	39.23
Yield strength of steel Longitudinal bars (MPa)	299.3	299.3
Transverse	210.3	210.3

3.2 Numerical simulation

The “NonlinearBeamColumn” element available in OpenSees (2009), which is a force-based nonlinear beam-column element and considers the spread of plasticity, was used in the present numerical simulations. Five Gauss-Lobatto integration points are defined along each element. The discretization of the column section is shown in Figure 4. The confinement provided by the transverse steel reinforcement, and the buckling and bond-slip behaviour of the longitudinal reinforcement are not considered. For defining the backbone curve of the steel reinforcement, the strain at the initiation of strain hardening ϵ_{sh} was taken as 14 times of the yield strain, the ultimate stress f_{su} was taken as 1.5 times of the yield strength f_y , and the corresponding strain was taken as ϵ_{sh} plus 0.14, according to the information provided in Haroun et al. (2003). The initial slope of the strain hardening portion E_{sh} is 2,138 MPa, determined based on the approach of Dhakal and Maekawa (2002).

The numerical simulations were conducted with displacement control. Unloading/reloading cycles were

initiated at the same lateral displacements as recorded in the tests. The analyses were terminated when the ultimate strain of FRP-confined concrete ϵ_{cu} was first reached by the extreme compression fibre of the column. The value of ϵ_{cu} was determined using the improved Lam and Teng model (Teng et al. 2009), with the jacket hoop rupture strain taken to be equal to the ultimate tensile strain of the FRP obtained from flat coupon tests (Table 1).

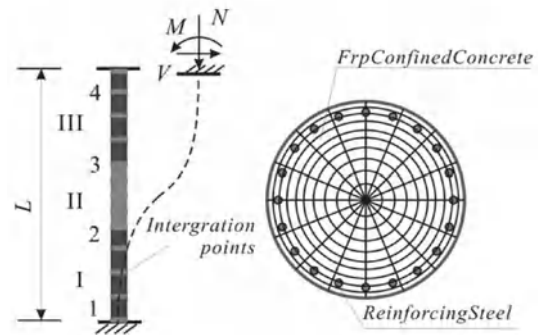


Figure 4 Numerical model for FRP-jacketed columns

3.3 Numerical results

It can be observed from Figure 5 that the numerical simulations predicted the responses of columns CS-R1 and CS-R2 reasonably well, although only the envelope curve of the hysteretic responses is available from the test

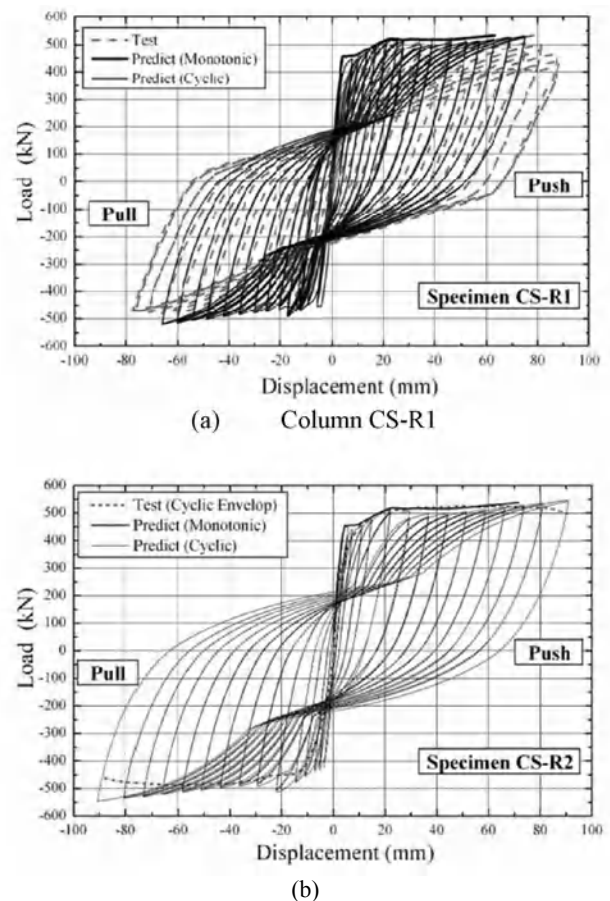


Figure 5 Test and predicted responses of FRP-jacketed RC columns

of column CS-R2 (Haroun et al. 2003). The predicted maximum displacements from cyclic analysis are significantly larger than those from pushover analysis. This may be attributed to the isotropic hardening of the longitudinal steel bars under cyclic loads.

One important point to note is that in the present numerical simulations, the ultimate axial strain of FRP-confined concrete was predicted by assuming that the hoop rupture strain of the FRP jacket is the same as the material ultimate tensile strain of the FRP obtained from coupon tests (Haroun et al. 2003). This assumption is likely to have overestimated the ductility of the column (Teng et al. 2009), even though the predicted ductility is still less than that observed in the test for column CS-R1. This discrepancy may have been due to the effects of buckling and bond-slip behaviour of the longitudinal reinforcement which were not considered in the simulations.

4 CONCLUDING REMARKS

A numerical column model has established by implementing a stress-strain model for FRP-confined concrete in cyclic loading into OpenSees. Numerical results for two FRP-confined RC test columns have been obtained using the numerical model and have been shown to be in close agreement with the test results.

Future work will be focused on the inclusion of the buckling and bond-slip behaviour of the longitudinal steel reinforcement in the numerical column model. The definition of the ultimate condition of FRP-jacketed columns also needs further attention.

5 ACKNOWLEDGEMENTS

The authors are grateful for the financial support provided by the Hong Kong Research Grants Council and The Hong Kong Polytechnic University.

REFERENCES

American Society of Civil Engineers (ASCE) 2000. *Prestandard and Commentary for the Seismic Rehabilitation of Buildings*.

- Report No. FEMA 356, Federal Emergency Management Agency: Washington, DC, USA.
- Applied Technology Council (ATC) 1996. *ATC-40 Seismic Evaluation and Retrofit of Concrete Buildings, Volume 1*. Report No. SSC 96-01, Seismic Safety Commission, State of California, USA.
- Applied Technology Council (ATC) 2005. *Improvement of Nonlinear Static Seismic Analysis Procedures*. Report No. FEMA 440, Federal Emergency Management Agency: Washington, DC, USA.
- Dhakal R.P. & Maekawa K. 2002. Path-dependent cyclic stress-strain relationship of reinforcing bar including buckling. *Engineering Structures* 24: 1383-1396.
- Haroun, M.A., Mosallam, A.S., Feng, M.Q. & Elsanadedy, H.M. 2003. Experimental investigation of seismic repair and retrofit of bridge columns by composite jackets. *Journal of reinforced Plastics and Composites* 22(14): 1243-1268.
- Heo, Y.A. & Kunnath, S.K. 2009. Sensitivity to constitutive Modeling in fiber-based discretization of reinforced concrete members for performance-based seismic evaluation. *Advances in Structural Engineering* 12(1): 37-51.
- Lam, L. & Teng, J.G. 2009. Stress-strain model for FRP-confined concrete under cyclic axial compression. *Engineering Structures* 31: 308-321.
- Lam, L., & Teng, J.G. 2003. Design-oriented stress-strain model for FRP-confined concrete. *Construction and Building Materials* 17(6-7): 471-489.
- Mosalam, K.M., Talaat, M. & Binici, B. 2007. A computational model for reinforced concrete members confined with fiber reinforced polymer lamina Implementation and experimental validation. *Composites Part B-Engineering* 38: 593-613.
- OpenSees 2009. *Open System for Earthquake Engineering Simulation*. Pacific Earthquake Engineering Research Center, University of California, Berkeley, <http://opensees.berkeley.edu>.
- Teng, J.G., Jiang, T., Lam, L. & Luo, Y.Z. 2009. Refinement of a design-oriented stress-strain model for FRP-confined concrete. *Journal of Composites for Construction*, ASCE 13: 269-279.
- Yassin, M.H.M. 1994. *Nonlinear Analysis of Prestressed Concrete Structures under Monotonic and Cyclic Loads*. PhD thesis, University of California, Berkeley, California, USA.
- Zhu, Z., Ahmadb, I. & Mirmirana, A. 2006. Fiber element modeling for seismic performance of bridge columns made of concrete-filled FRP tubes. *Engineering Structures* 28: 2023-2035.

Concrete Column Shape Modification with FRP and Expansive Cement Concrete

Zihan Yan (yanzh214@yahoo.com)

Department of Engineering Services, California Department of Transportation, Sacramento, USA

Chris P. Pantelides

Department of Civil and Environmental Engineering, University of Utah, Salt Lake City, USA

Jeffrey B. Duffin

Department of Engineering Services, California Department of Transportation, Sacramento, USA

ABSTRACT Fibre Reinforced Polymer (FRP) composites are an effective material for confining circular concrete columns. FRP confinement for square and rectangular columns is less effective due to stress concentrations at the sharp corners and loss of the membrane effect. Shape modification using post-tensioning of FRP shells through expansive cement concrete is described. In the field, shape modification can be achieved by utilizing pre-fabricated FRP shells as the permanent forms. An analytical model is briefly introduced to predict results of the experiments regarding the enhanced stress-strain behaviour of FRP-confined concrete. The confinement model and shape modification technique with FRP shells and expansive cement concrete are used in simulations of seismic rehabilitation of square columns for existing reinforced concrete bridges and are compared to in-situ tests of square columns with bonded FRP jackets.

1 INTRODUCTION

Externally bonded FRP composite jackets can provide effective confinement for circular concrete columns (Karbhari et al. 1997). However, FRP confinement is much less effective in increasing the axial compressive strength of square and rectangular columns compared to circular columns (Rochette and Labossière 2000, Pessiki et al. 2001) due to stress concentrations at the corners and ineffective confinement at the flat sides. The presence of steel ties limits rounding of the corner radius in existing square or rectangular columns. Lower confinement effectiveness for square/rectangular columns results in softening behavior and premature FRP composite rupture; therefore, the inherent high tensile strength of FRP composite materials cannot be fully utilized.

One approach for improving the effectiveness of FRP jackets for rectangular columns is to use prefabricated (non-bonded) FRP composite shells with expansive cement concrete. A prefabricated elliptical/oval/circular FRP shell may be used as stay-in-place formwork for casting additional expansive cement concrete around the square or rectangular cross-section to achieve shape modification. Expansive cement normally consists of a Portland cement and a calcium-sulfoaluminate anhydrite component.

The mechanism of expansive cement concrete can be used with FRP composite shells for confinement: when expansive cement concrete is applied to prefabricated FRP shells, expansion of the grout is restrained by the FRP shell, thus creating a post-tensioning effect which confines the original concrete core as well as the expansive grout. It is apparent that this post-tensioning effect would increase the confinement behavior of FRP shells and change the confinement action from “passive” to “active”.

Experiments were conducted to investigate the shape modification effect on large concrete specimens, and analytical model for developing the axial stress-strain relationship of shape-modified columns is briefly described. The confinement model and shape modification technique with FRP shells and expansive cement concrete are used in simulations of seismic rehabilitation of square columns for existing reinforced concrete bridges and are compared to actual in-situ tests of square columns with bonded FRP jackets.

2 EXPERIMENTAL PROGRAMS AND RESULTS

2.1 Experimental program

The experiments involved FRP-jacketed specimens bonded for the full specimen height, as well as shape-modified

specimens confined with FRP. Two FRP composite systems, a Carbon Fiber Reinforced Polymer (CFRP) system and a Glass Fiber Reinforced Polymer (GFRP) system were used. Three groups of specimens: square specimens (S-type), rectangular specimens with an aspect ratio of 2:1 (R2-type) and 3:1 (R3-type), respectively. All specimens were 914 mm high; no steel reinforcement was used inside the specimens. Each group included an unconfined (baseline) specimen, two specimens with the original square or rectangular cross-section confined by bonded CFRP or GFRP jackets and two shape-modified specimens using prefabricated CFRP or GFRP shells with expansive cement concrete. For S-type the shape-modified cross-section was circular, and for R2-type and R3-type it was elliptical, as shown in Figure 1.

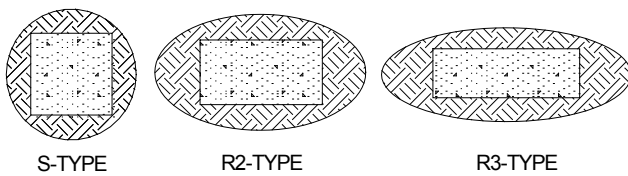


Figure 1 Cross-sections of shape-modified specimens: S-Type (square to circle); R2-Type (2:1 rectangle to ellipse); R3-Type (3:1 rectangle to ellipse)

Table 1 lists the details of all specimens. The specimens are identified using a three-code scheme. The first part is the shape of the column (Square or Rectangular), and the aspect ratio of the rectangular cross-section (2:1 or 3:1). The second part indicates the type of FRP composite (CFRP or GFRP) and the number of FRP layers (2 or 6, respectively). The third part denotes the type of material used to achieve shape modification; expansive cement concrete is denoted as (E) and (0) denotes no shape modification.

Table 1 Dimensions of column specimens

Specimen	Original cross-section (mm)	Modified cross-section ($B_j \times D_j$)* (mm)
S-C2-0	279×279	-
S-G6-0	279×279	-
R2-C2-0	203×381	-
R2-G6-0	203×381	-
R3-C2-0	152×457	-
R3-G6-0	152×457	-
S-C2-E	279×279	406×406
S-G6-E	279×279	406×406
R2-C2-E	203×381	635×387
R2-G6-E	203×381	660×362
R3-C2-E	152×457	775×279
R3-G6-E	152×457	762×298

* Denote major axis length (B_j) and minor axis length (D_j)

Regular and expansive cement concrete were used in this experimental program. Regular concrete was used to cast the original square or rectangular specimens; expansive cement concrete was used to perform shape modification. The mix design of expansive cement concrete was investigated by Yan et al. (2006). The 28-day compressive strength of the original concrete specimens was 15 MPa. For the shape-modified specimens, unconfined concrete strength f'_{co} was calculated by obtaining a mean value as:

$$f'_{co} = f'_{co1} \cdot \frac{A_o}{A} + f'_{co2} \cdot \frac{A_f}{A} \quad (1)$$

where f'_{co1} = unconfined concrete strength of square or rectangular specimens; f'_{co2} = unconfined strength of expansive cement concrete obtained from cylinder compression tests, which was 10 MPa; A_o = area of square or rectangular cross-section; A_f = area of expansive cement concrete; A = total area of shape-modified cross-section. Using this method f'_{co} is calculated to be 13 MPa for specimens with expansive cement concrete.

Two FRP composite materials were used to confine the concrete columns. One was SikaWrap Hex 103C which is a high strength, unidirectional carbon fiber fabric with epoxy resin. The other was Aquawrap G-06, which is a unidirectional pre-impregnated glass fiber fabric with urethane resin. The material properties were determined from tensile coupon tests per ASTM Standard D3039 (2001). The properties of the two FRP composite systems were: (1) for the CFRP composite, which was cured with epoxy resin, tensile strength was 1220 MPa, tensile modulus was 87 GPa, and ply thickness was 1.0 mm; and (2) for the GFRP composite, which was cured with urethane resin, tensile strength was 228 MPa, tensile modulus was 17 GPa, and ply thickness was 1.6 mm; for both FRP composite systems, the ultimate tensile strain was 1.4%. All concrete specimens were subjected to uniaxial compression until failure. The load was applied using displacement control at a constant rate of 1.3 mm/min.

2.2 Experimental results

For FRP-confined square/rectangular columns without shape modification, failure started with concrete crushing followed by fracture of the FRP composite jacket at a corner. Failure was brittle due to the corner and flat side effects, which eliminate membrane action of the FRP jacket and result in ineffective confinement except at the diagonals and the four corners. Failure of shape-modified specimens with non-bonded FRP shells and expansive cement concrete was fracture of the FRP shell and cracking of the expansive cement concrete. Fracture of the FRP shell extended over the specimen height, demonstrating extensive participation of the FRP shell in confinement. At the end of the test, vertical and diagonal cracks were observed in the expansive cement

concrete, but the original concrete column cross-section was protected. These specimens achieved a higher compressive strain compared to FRP-bonded specimens. Specimens with a smaller aspect ratio reached a higher axial strength. GFRP-confined specimens failed less explosively and at a higher hoop strain than CFRP-confined specimens.

Axial strain was measured using the average of two linear variable displacement transducers; axial stress was computed by dividing the axial compression load by the total cross-sectional area. CFRP-confined square specimen S-C2-0 showed limited hardening behavior and CFRP-confined rectangular specimen R3-C2-0 demonstrated softening behavior; a drop of axial stress was observed after the initial axial strength was reached, and the degree of softening increased with aspect ratio. For shape-modified specimens, the stress-strain curves show ascending branches without softening behavior. Improvement of compressive strength and ultimate strain capacity is significant for shape-modified square columns S-C2-E since their modified shape was circular; improvement was less significant for rectangular columns, especially the sections with the higher aspect ratio as the section becomes a flatter ellipse. A summary of the experimental results in terms of ultimate compressive strength f'_{cc} and corresponding compressive strain ϵ'_{cc} is given in Table 2. Stress-strain curves are not presented herein due to the page limitations. More details of the experimental results are described elsewhere (Yan et al. 2006).

Table 2 Main experimental results for column specimens

Column Designation	f'_{cc} (MPa)	f'_{cc} / f'_{co}	ϵ'_{cc} (mm/mm)
S-C2-0	26	1.72	0.0100
S-G6-0	22	1.45	0.0031
R2-C2-0	24	1.63	0.0045
R2-G6-0	22	1.48	0.0040
R3-C2-0	22	1.46	0.0046
R3-G6-0	22	1.48	0.0036
S-C2-E	49	3.71	0.022
S-G6-E	44	3.35	0.021
R2-C2-E	27	2.22	0.011
R2-G6-E	31	2.32	0.018
R3-C2-E	26	2.08	0.008
R3-G6-E	23	1.74	0.006

3 ANALYTICAL MODEL

3.1 Dilatancy behavior of shape-modified columns

In this study, the dilatancy behavior of FRP-confined concrete is represented by the volumetric strain versus axial strain relationship. Volumetric strain ϵ_v is defined as the FRP area strain in the two transverse orthogonal

directions minus the axial strain in the concrete column ϵ_c :

$$\epsilon_v = 2\epsilon_j - \epsilon_c \quad (2)$$

where ϵ_j is defined as the FRP hoop strain for circular cross-sections or average FRP hoop strain for elliptical cross-sections. Figure 6 shows the volumetric strain versus axial strain relations for shape-modified specimens with expansive cement concrete. Since the FRP shell was already post-tensioned prior to axial loading through chemical post-tensioning, the amount of radial expansion was smaller compared to bonded FRP jackets. Therefore, the axial strain was larger than the hoop area strain, $2\epsilon_j$; this reveals that the axial strain was dominant in the volumetric strain versus axial strain curve. This dilatancy behavior is extremely important for shape-modified FRP specimens with expansive cement concrete because in this case the FRP confinement becomes “active” instead of “passive”.

The authors suggest the relationship between volumetric strain and axial strain is approximately linear and α is the slope of a straight line that is:

$$\epsilon_v = -\alpha\epsilon_c \quad (3)$$

where α is determined by the FRP effective confinement ratio f_{lu} / f'_{co} and is proposed as (Yan & Pantelides 2006):

$$\alpha = 0.26 + 0.428 \frac{f_{lu}}{f'_{co}} \quad (4)$$

The effective confinement ratio f_{lu} / f'_{co} is defined as the ratio of the ultimate FRP confining pressure f_{lu} at rupture of the FRP jacket to the unconfined concrete strength f'_{co} , where f_{lu} is:

$$f_{lu} = \frac{1}{2} \rho_{FRP} E_j k_\epsilon \epsilon_{fu} \quad (5)$$

where ρ_{FRP} = FRP volumetric ratio; E_j = elastic modulus of FRP composite; k_ϵ = FRP jacket efficiency factor; and ϵ_{fu} = ultimate FRP tensile strain obtained from material coupon tests. In Eq. (5), k_ϵ is used to account for the reduction factor of the FRP ultimate hoop strain compared to the material coupon tests and depends on the aspect ratio of the cross-section. Since the FRP composite shells are already post-tensioned prior to axial loading, k_ϵ is smaller than that of the corresponding bonded FRP jackets. Based on this study, k_ϵ was found to be in the range of 0.30 and 0.50 for circular non-bonded FRP shells, and a value of 0.40 is recommended; for elliptical cross-sections, k_ϵ is controlled by the aspect ratio as (Yan et al. 2006):

$$k_\epsilon = 0.15 \left[1 + \left(\frac{B_j}{D_j} \right)^{-0.65} \right] \frac{B_j}{D_j} \geq 1.5 \quad (6)$$

3.2 Axial stress versus axial strain relationship

The Popovics (1973) model and a modified Willam-Warnke (Willam & Warnke 1975, Yan et al. 2006) model

were used for developing the analytical stress-strain relationship for shape-modified specimens with expansive cement concrete. Considering that the confining pressure provided by FRP shells varies continuously and exhibits an approximately linear behavior until failure; the analytical FRP-confined concrete model was implemented based on an incremental approach (Yan & Pantelides 2006) to account for the variable FRP confining pressure by which the axial loading was divided into a number of steps. This incremental approach also utilizes the specific dilatancy behavior of shape-modified columns with expansive cement concrete. The model predictions agree well with the experimental results (Yan & Pantelides 2006).

4 SIMULATION OF SEISMIC RETROFIT FOR SHAPE MODIFIED SQUARE COLUMNS

To investigate the advantage of shape modification, the confinement model and shape modification technique with FRP shells and expansive cement concrete are used in a simulation of seismic rehabilitation of square columns for existing reinforced concrete bridges and are compared to actual in-situ tests of square columns with bonded FRP jackets. The details of a typical bridge bent of the South Temple Bridge in Salt Lake City consisting of three columns and a cap beam are shown in Figure 2. The vertical steel reinforcement of the 914 mm square columns consisted of 16-#10 bars (32 mm diameter) with #4 confinement ties (13 mm diameter) at 305 mm on center. A seismic retrofit utilizing bonded CFRP jackets (Pantelides et al. 2007) was implemented in the field as shown in Figure 3 and the bent was tested in-situ with a hydraulic actuator that applied a quasi-static load at the bent cap level as shown in Figure 2. The CFRP composite rehabilitation consisted of confinement layers at the top and bottom of the columns, diagonal and horizontal CFRP sheets at the joints and CFRP straps at

the joints. As shown in Figure 3, each column top has six layers for the first 0.91 m, three layers for the next 0.41 m, and two layers for the next 0.41 m; each column bottom has fourteen layers for the first 0.91 m, three layers for the next 0.41 m, and two layers for the next 0.41 m.

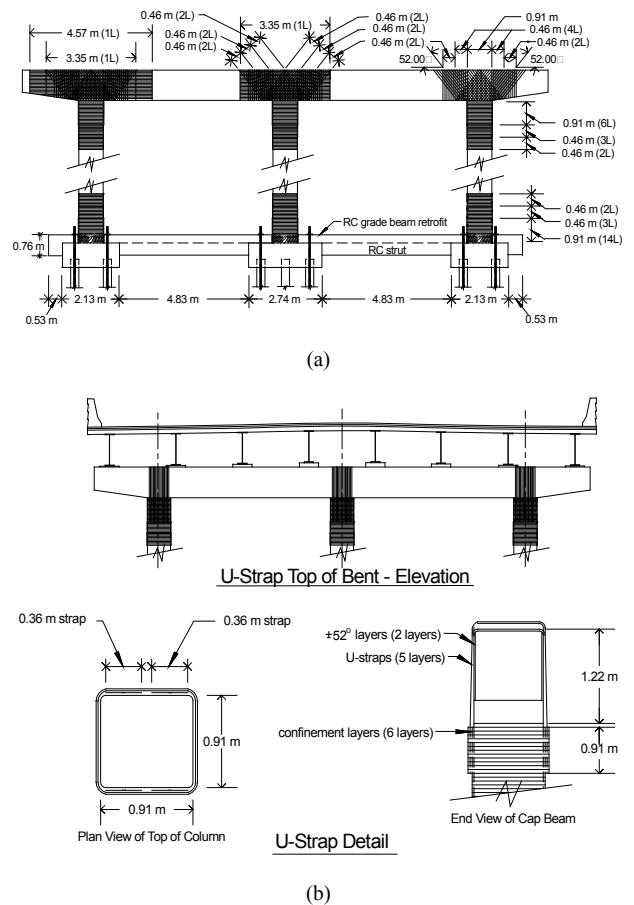


Figure 3 CFRP composite retrofit design of typical bent at South Temple Bridge: (a) ankle wrap, zero layers in the cap beam and column jackets, (b) U-strap details (xL = no. of layers)

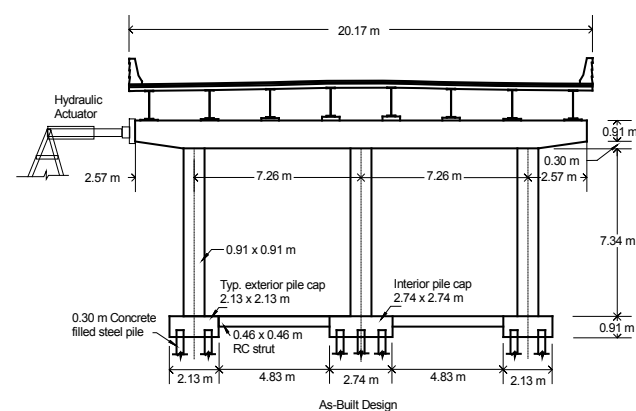


Figure 2 Dimensions and test layout of typical bridge bent at South Temple Bridge in Salt Lake City

The analytical pushover curve for the bridge bent with columns confined with bonded CFRP jackets is shown in Figure 4; this pushover curve has been verified with the test results (Pantelides et al. 2007). The alternative CFRP composite retrofit of the bent is simulated here using shape modification and the same number of CFRP layers in a circular shell filled with expansive cement concrete for each top and bottom 1.83 m length of the columns. The shape modified column for the top and bottom 1.83 m of each column has a circular shape of 1.52 m diameter. For comparison purposes, the expansive cement concrete is assumed to be the same material used in the present experimental program. The CFRP composite material properties used for obtaining the push-over curve for the bridge bent with the bonded CFRP-jacketed columns are used in the present analysis; the tensile strength of the CFRP composite was 720 MPa, the tensile modulus was 70 GPa, and the ultimate

tensile strain was 0.009 mm/mm. Due to the insufficient amount of transverse steel reinforcement in the column, the confinement effect from the transverse steel was not considered for developing the stress-strain relations. The resulting analytical curve is also shown in Figure 4. It is clear from this simulation that the columns confined with CFRP composites show a significant increase in shear and displacement capacity compared to reinforced concrete columns. In this simulation case, it is also noted that for the case of rehabilitation with shape modification and a CFRP shell with expansive cement concrete, the shear capacity of the bridge bent would be increased by approximately 15% compared to the regular retrofit method of the bonded CFRP jacket by using a wet layup.

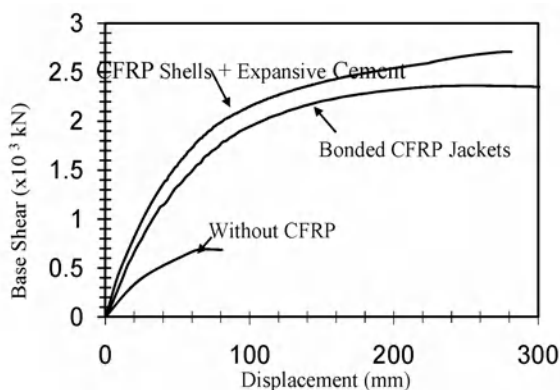


Figure 4 Comparison of pushover curves for bridge bent for columns without CFRP jackets, for columns with bonded CFRP jackets, and for shape modified columns with CFRP shells and expansive cement concrete

5 CONCLUSIONS

Shape modification using expansive cement concrete and prefabricated FRP composite shells can restore the membrane effect; in addition, it can change FRP confinement from passive to active which is induced by the unrestrained expansion of the grout before the column is loaded. Shape-modified columns with expansive cement concrete achieved a higher axial strength for modified square and rectangular columns compared to original columns with the same number of FRP composite layers. The non-bonded FRP jacket can be used as a stay-in-place form to save construction time and the significant expense of formwork. In addition, the difference in cost between expansive and Portland cement is small compared to the total cost of the retrofit.

For lightly or moderately FRP-confined square or rectangular columns, shape modification can modify the stress-strain behavior from softening to hardening and achieve a higher axial strength and strain. The optimal column cross-sectional shape for FRP confinement is

circular. For columns with a rectangular cross-section, especially those with a large aspect ratio, change to a circular cross-section requires a higher cost and significant enlargement of the foundation. Therefore, for strengthening rectangular columns by shape modification, the influence of factors such as: (a) volume increase, (b) increase in surface area, (c) foundation enlargement, and (d) material cost increase need to be considered to obtain an optimal solution.

6 ACKNOWLEDGEMENT

The authors would like to thank Professor Lawrence D. Reaveley of the University of Utah for his constructive suggestions. The authors acknowledge financial support provided by the Utah Department of Transportation, contribution of FRP composite materials from Sika Inc. and Air Logistics, and contribution of Type K cement and Komponent from CTS Company. The authors also acknowledge Gavin Fitzsimmons for his assistance with the bridge application example in this article.

REFERENCES

- Karbhari, V.M. & Gao, Y. 1997. Composite jacketed concrete under uniaxial compression-verification of simple design equations. *Journal of Materials in Civil Engineering ASCE* 1997; 9(4): 185-193.
- Rochette, P. & Labossière, P. 2000. Axial testing of rectangular column models confined with composites. *Journal of Composites for Construction ASCE* 2000; 4(3): 129-136.
- Pessiki, S., Harries, K.A., Kestner, J.T., Sause, R., Ricles J.M. 2000. Axial behavior of reinforced concrete columns confined with FRP jackets. *Journal of Composites for Construction ASCE* 2001; 5(4): 237-245.
- Yan, Z., Pantelides, C.P., Reaveley, L.D. 2006. Fiber-reinforced polymer jacketed and shape-modified compression members: I-experimental behavior. *ACI Structural Journal* 2006; 103(6): 885-893.
- American Society for Testing Materials (ASTM). 2001. Standard Test Method for Tensile Properties of Polymer Matrix Composite Material. *ASTM Standards*, 15.03, ASTM D3039, West Conshohocken, PA.
- Yan, Z. & Pantelides, C.P. 2006. Fiber-reinforced polymer jacketed and shape-modified compression members: II-model. *ACI Structural Journal* 2006; 103(6): 894-903.
- Popovics, S. 1973. Numerical approach to the complete stress-strain relation for concrete. *Cement Concrete* 1973;3(5): 583-599.
- Willam, K.J. & Warnke, E.P. 1975. Constitutive model for the triaxial behavior of concrete. *Proceedings of International Association for Bridge and Structural Engineering* 1975; 19: 1-30.
- Pantelides, C.P., Duffin, J.B., Reaveley, L.D. 2007. Seismic strengthening of reinforced-concrete multicolumn bridge piers. *Earthquake Spectra EERI* 2007; 23(3): 635-664.

Flexural Behavior of Concrete Columns Strengthened with Near Surface Mounted FRP Bars

F. Danesh (danesh@kntu.ac.ir)

Associate professor, Department of Civil Engineering, KNT University of technology, Tehran, Iran

B. Baradaran Noveiri (baharakbn@gmail.com)

Msc. Student, Department of Civil Engineering, KNT University of technology, Tehran, Iran

ABSTRACT Using composite materials for repairing and strengthening of concrete structures, specifically reinforced concrete (RC) columns, has continuously increased during past few years. Fiber reinforced polymer (FRP) is one of the different types of these materials, which can be used by either wrapping or near surface mounted (NSM) methods, in order to improve the confinement effects and the flexural capacity of RC columns. In this study, concrete column specimens, strengthened with near surface mounted FRP bars, were modeled in computer program, using finite element analysis. The behaviors of these columns were then analyzed under monotonic and cyclic lateral loads with constant axial compressive loads. The analytical results were compared to the results obtained from experimental observations on specimens with the same geometry and loading conditions and they were in good agreement. Since the anchorage of FRP bars in column's foundation is an important factor to prevent premature failure, an additional parametric study on the specimens was done to find the optimal development length of FRP reinforcement in the foundation.

1 INTRODUCTION

Near surface mounted (NSM) reinforcement involves cutting grooves into the concrete cover and bonding rebar inside the grooves through the use of appropriate filler (typically epoxy resin or cement-based mortar). The idea of NSM reinforcement was born in Europe for steel rebar in the late 1940s (Asplund 1949), but it was only recently when more hi-tech materials, such as FRPs and high quality epoxies, become available, that the technique was given substantial attention by the research community and practitioners [Bournas & Triantafillou 2008].

This technique was successfully used to upgrade the flexural capacity of reinforced concrete (RC) piers. Flexural strengthening and testing to failure of the piers were carried out on a bridge that was scheduled for demolition during the spring of 1999. Three of the four piers of the bridge were strengthened with different configurations using FRP rods and jackets. The flexural strengthening was achieved using NSM carbon FRP rods that were anchored into the footings [Alkhrdaji & Nanni 1999].

The first systematic study on NSM-based flexural strengthening of RC columns under simulated seismic loading was presented by Bournas and Triantafillou [Bournas & Triantafillou 2008]. Their investigation addressed column strengthening with NSM carbon or glass fibers, as well as stainless steel rebars. Another

innovative aspect in that study was the combination of NSM reinforcement with local jacketing, which comprised the recently developed textile-reinforced mortar (TRM) confining system, described by Triantafillou et al. (2006) and Bournas et al. (2007) [Triantafillou et al. 2006, Concrete... – Bournas et al. 2007, Textile-Reinforced...].

The obtained experimental results from a recent study by Barros et al. (2008) involved strengthening RC columns subjected to axial compression and lateral cyclic loading with NSM CFRP strips indicate that the proposed strengthening technique is very promising for increasing the load carrying capacity of concrete columns failing in bending. However, as was expected, the energy absorption capacity of the tested RC columns was not improved by this technique, since it did not provide significant concrete confinement [Barros et al. 2008].

The aim of this paper is to investigate the flexural behavior of reinforced concrete columns strengthened with NSM technique. In order to reach this goal, a three dimensional model of RC column subjected to monotonic and cyclic lateral with constant axial compressive load was created in computer program. The column was then strengthened with FRP bars to observe the effects of NSM strengthening method on increasing the flexural capacity of column. To prevent FRP bars from debonding, the bars were continued in the foundation and finally their optimal development length was found.

2 FINITE ELEMENT MODELING

For this study a finite element model of RC column was chosen to allow comparison between the result obtained from experimental work and the analytical one which is described below. The geometry, material, boundary conditions and loadings are similar to those used in previous experimental works [Sarafraz & Danesh 2010].

2.1 Geometry and model

The concrete column assembly being analyzed is depicted in Figure 1 and Figure 2. The height of column is 100 cm. The foundation and cap beam were also modeled to apply the boundary condition and loads (Figure 2).

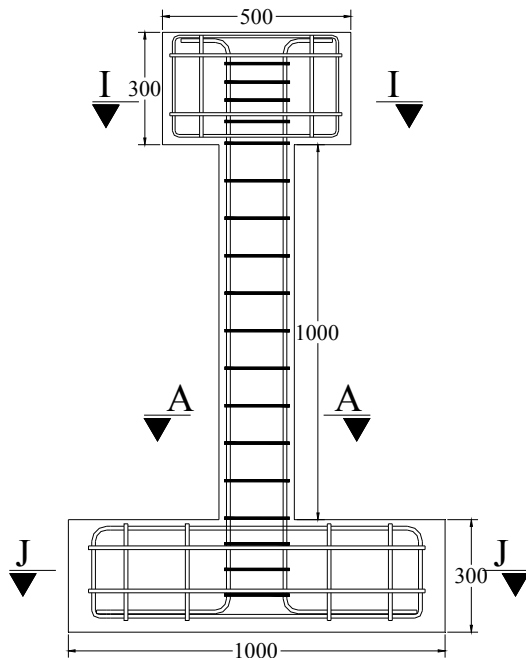


Figure 1 Geometry of modeled specimen (dimensions in mm)

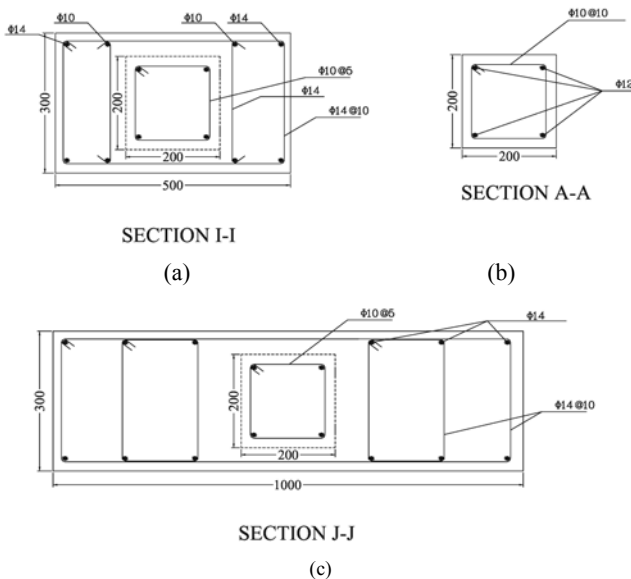


Figure 2 Cross sections of cap beam, column and foundation (dimensions in mm)

The column, foundation and cap beam were modeled with continuum elements (8-node linear brick element - C3D8). Rebar and stirrup were modeled using truss elements (3-node quadratic displacement elements - T3D2) which were embedded in concrete elements.

2.2 Material

Concrete damaged plasticity material model was applied to concrete elements for the assessment of the structural stability and damage of concrete columns subjected to cyclic lateral loading. It assumes that the main two failure mechanisms are tensile cracking and compressive crushing of the concrete material. The evolution of the yield (or failure) surface is controlled by two hardening variables, ϵ_t^{-pl} and ϵ_c^{-pl} (which refers to tensile and compressive equivalent plastic strains), linked to failure mechanisms under tension and compression loading, respectively. The material properties used in this study are summarized in Table 1.

Linear kinematic hardening model which is a bilinear model for steel was assumed for rebar and stirrup. The column has reinforcement ratio of 0.01.

CFRP rebar were supposed to have linear elastic behavior up to failure. The rupture strain of CFRP is 1.7%. For strengthening the column a CFRP bar with diameter of 12mm is used at each side of it.

Table 1 Summary of material properties

Concrete	Compressive strength (MPa)	20
	Yield strength (MPa)	400
Steel	Elasticity modulus (MPa)	200000
	Tensile strength (MPa)	2000
CFRP rebar	Elasticity modulus (GPa)	72
	Ultimate strain (%)	1.7

2.3 Boundary condition and loading

Concrete elements have three degrees of freedom (u_x, u_y, u_z). The boundary condition was applied to nodes on the bottom of the foundation to constrain the motion of the foundation in the x, y and z-directions.

A constant axial compressive load of 200 kN (which corresponds to an axial load ratio of 0.25) was applied on the top elements of cap beam in the area of 200×200 mm. This was followed by a cyclic (or monotonic) lateral displacement load applied to the cap beam.

3 LAYOUT OF ANALYSIS

The analysis program consisted of seven columns models. A description of the specimens follows next. One

specimen was analyzed without retrofitting as Control. The experimental observation on this specimen is also available from previous studies [Sarafraz & Danesh 2010]. The results obtained from analysis were compared to the experimental work to verify the computer modeling and analytical results.

The other specimens were strengthened with four CFRP bars at each side of the column. In order to investigate the effect of development length of CFRP bars into the foundation on the flexural capacity and plastic length of column, the development length of CFRP bars into the foundation varied from zero (no anchorage) to 250 mm in these six specimens.

4 RESULTS

4.1 Verification

In control specimen analysis, the loading condition was similar to the load condition in experimental work. In other words a cyclic lateral and a constant axial compressive load were applied to the specimen and it was analyzed until failure. The base shear force-displacement curve obtained from analysis and experimental work for control specimen can be compared in Figure 3.

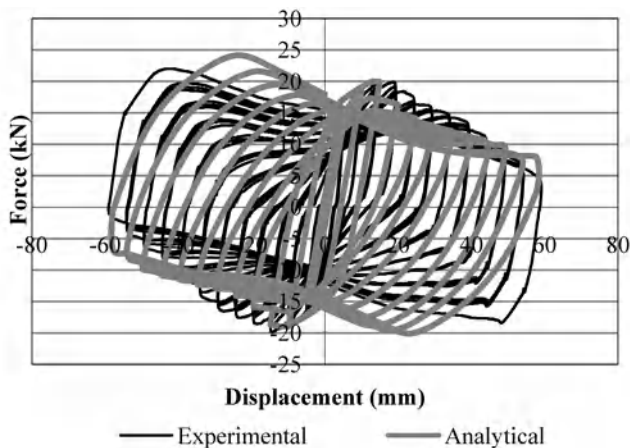


Figure 3 Force-displacement curves for control specimen subjected to cyclic lateral and constant compressive axial load

It can be seen that the maximum strength of two curves are equal but the experimental control column shows a more flexible behavior as compared to the analytical one. However, the observed difference in between experimental and analytical curves in this study was not significant. Since there wasn't any cyclic test on steel and concrete in experimental work, their stress-strain properties might be different from those assumed and these differences could be the causes of various flexibilities of the above curves.

4.2 Improving the flexural capacity of strengthened column

In order to see the effect of NSM strengthening technique on improving flexural capacity of column the control

specimen was analyzed under monotonic increasing lateral load and constant axial compressive load. The corresponding force-displacement curves were compared to the specimen which was strengthened with NSM CFRP bars and analyzed under the same loading condition. The development length of CFRP bars in this specimen was 10cm. Force-displacement curves obtained from analysis are shown in Figure 4. The flexural capacity of strengthened column increased 25% over the control specimen.

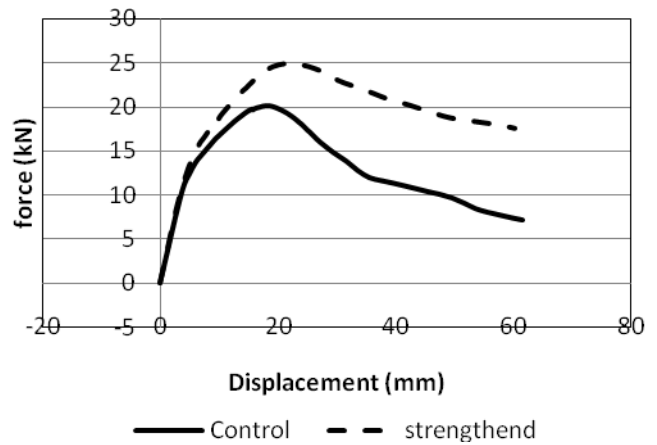


Figure 4 Force-displacement curves for strengthened and Control specimens

4.3 Optimal development length of CFRP bars in foundation

To investigate the effect of development length of CFRP bars into the foundation on flexural capacity and plastic length of column, six specimens strengthened with CFRP bars with different development length were analyzed under monotonic increasing lateral load and constant axial compressive load. Since the experimental work [Sarafraz & Danesh 2010] on specimens strengthened with NSM rebar indicated that the failure modes of strengthened columns are crushing the concrete, in this investigation the NSM rebars were modeled using embedding in the concrete elements And it is assumed that the failure modes of NSM FRP strengthened RC columns are crushing the concrete but not FRP debonding. Figure 5 presents the force-displacement curves of these specimens.

The graph above suggests that increasing development length of CFRP bars in foundation up to 15 cm, enhanced the flexural capacity of specimens, but there were no significant differences between specimens with 15, 20 and 25 cm development length of CFRP bars.

Table 2 illustrates the plastic length of columns for different development length.

It is indicated that the increasing development length of CFRP bars up to 15 cm in foundation resulted in the

enhancement of plastic length of columns and increasing the length more than 15 cm had no significant effect.

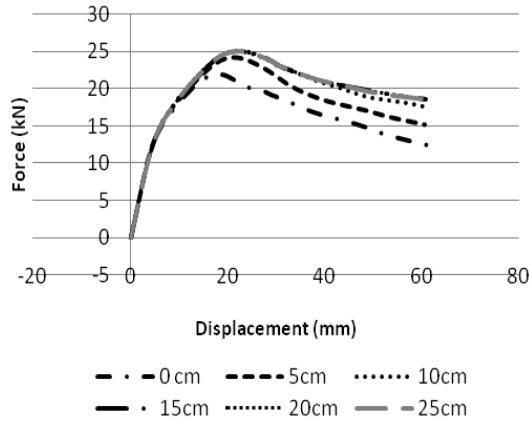


Figure 5 Shear base force-displacement curves of strengthened specimens with NSM CFRP bars with different development length

Table 2 Summary of material properties

Development length of CFRP bars (cm)	Plastic length of column (cm)
0	12.5
5	17.5
10	22.5
15	27.5
20	27.5
25	27.5

5 CONCLUSION

The present study was designed to determine the effect of NSM strengthening technique for columns. The obtained analytical results indicated that this technique is promising for increasing the load carrying capacity of concrete columns that fail in bending. Anchoring the

CFRP bars in the foundation is a very important factor to prevent premature debonding and to increase the flexural capacity and plastic length of columns. The results of this investigation show that increasing development length of CFRP bars up to a specific length (which may be $12.5d_b$) into foundation enhances the plastic length and flexural capacity of columns and increasing the length more than 15 cm had no significant effects.

REFERENCES

- Alkhrdaji, T. & Nanni, A. 1999, Flexural strengthening of bridge piers using FRP composites, ASCE Structures Congress 2000, Philadelphia, PA, M.Elgaaly, Ed., May 8-10, CD version, #40492-046-008, 8 pp.
- Barros, J. A.O., Varmaa, R. K., Sena-Cruz a, J. M. & Azevedo, A. F.M., 2008, Near surface mounted CFRP strips for the flexural strengthening of RC columns: Experimental and numerical research, *Engineering Structures*, 30 (2008) 3412-3425.
- Bournas, D.A. & Triantafillou, T.C. , 2008. Flexural strengthening of RC columns with near surface mounted FRP or stainless steel reinforcement: experimental investigation, The 14th World Conference on Earthquake Engineering, October 12-17, 2008, Beijing, China, p.2.
- Bournas, D. A., Lontou, P. V., Papanicolaou, C. G. & Triantafillou, T. C. ,2007, Textile-Reinforced Mortar (TRM) versus FRP Confinement in Reinforced Concrete Columns. *ACI Structural Journal*, 104:6, 740-748.
- Guide for the Design and Construction of Concrete Reinforced with FRP Bars Reported by ACI Committee 440, American concrete institute.
- Sarafraz, M. & Danesh, F., 2010, Flexural Strengthening of RC columns with NSM rods. PhD thesis, University of KNT, Tehran, Iran.
- Triantafillou, T. C., Papanicolaou, C. G., Zissimopoulos, P. & Laourdekis, T., 2006, Concrete Confinement with Textile-Reinforced Mortar Jackets. *ACI Structural Journal*, 103:1, 28-37.

Use Near Surface Mounted FRP Rods for Flexural Retrofitting of RC Columns

Mehdi Sarafraz (mehdi_sarafraz@yahoo.com) & Fakhreddin Danesh

Civil Engineering Faculty, K.N.Toosi University of Technology, Tehran, Iran

ABSTRACT Near surface mounted (NSM) fiber-reinforced polymer (FRP) reinforcement is one of the latest and most promising strengthening techniques for reinforced concrete (RC) structures. This technique based on bonding carbon or glass fiber reinforced polymer (CFRP or GFRP) bars (rods or laminate strips) into pre-cut grooves on the concrete cover of the elements to strength. In this work, a strengthening technique based on near surface mounted (NSM) carbon fiber rods is used to improve the flexural capacity of columns subjected to bending and compression. We describe the strengthening technique and report the experimental results in the strengthening process. The results obtained in series of reinforced concrete columns, subjected to combined constant axial compression and lateral cyclic loading, show that a significant increase on the load carrying capacity and flexural resistance can be achieved by using the NSM technique.

1 INTRODUCTION

Many concrete structures are in need of strengthening due to new seismic codes requirements, structural deficiencies due to errors in calculation or plan execution, adaptation of a structure for a different function, and/or poor construction practices.

Retrofitting of reinforced concrete columns is of paramount importance in the rehabilitation of existing structures (Park 2001). The most common traditionally methods for repair and retrofit of RC columns are concrete and steel jacketing. However, these systems may not be very practical due to undesirable section enlargement or construction constraints.

In recent years, Fiber-reinforced polymer (FRP) composite jackets are increasingly used for strengthening and retrofitting of reinforced concrete columns. The main advantages of the FRP system for strengthening of RC columns include lightweight, noncorrosive and high-tensile strength of the FRP and these in turn provide a more flexible and economical technique than traditional techniques. The FRP jackets however provide lateral confinement to concrete columns that can improve compression strength, shear strength, and ductility of the member, but it may not sufficiently improve flexural capacity (Saadatmanesh and Ehsani 1994; Saadatmanesh, Ehsani and Jin 1996; Seible and Priestley 1997; Mirmiran and Shahawy 1998; Teng, Chen, Smith, and Lam 2002; Wu, Liu, and Wang, L. 2008).

In this work a strengthening technique, consists of FRP rods embedded in grooves made on the surface of the concrete and bonded in place with epoxy paste, is used

to increase the flexural resistance of RC columns failing in bending. This technique is termed near surface mounted (NSM). NSM requires no surface preparation work and after cutting the slit, requires minimal installation time compared to the externally bonded reinforcing (EBR) technique (Hassan and Rizkalla 2004; De Lorenzis and Nanni 2002; El-Hacha and Rizkalla 2004; Barros, Ferreira, Fortes and Dias 2006).

To investigate the applicability and effectiveness of this technique, a test program was carried out. Flexural strengthening was achieved by inserting NSM rods on two opposite sides of the columns. The columns were tested to failure by applying constant axial compressive and cyclic lateral loading. The behavior of strengthened columns and their failure modes are discussed and conclusions are drawn.

2 EXPERIMENTAL PROGRAM

2.1 Specimens

Three column specimens of an approximately 1/3 scale were tested. Figure 1 shows the cross-sections of specimens. The columns with bottom and top reinforced concrete blocks were used to anchor the specimens to the reaction frame and applied the lateral and axial loads at the top of the columns, respectively. The column height of all specimens was 1000 mm and the original cross-section was 200 mm in width and depth. Four longitudinal reinforcement bars with 14 mm diameter were placed around the section sides (reinforcement ratio: 1.53%). The transverse reinforcement hoops were 10 mm diameter with spacing of 100 mm for all specimens.

The following denominations are adopted: CN for non-strengthened column; CS2 for column strengthened with 2 GFRP NSM rods; CS4 for column strengthened with 4 GFRP NSM rods. Also, for anchoring the NSM rods in bottom reinforced concrete block, a hole with 100 mm length in bottom block was created and the NSM rods placed in the hole. The 100 mm development length in concrete block is enough.

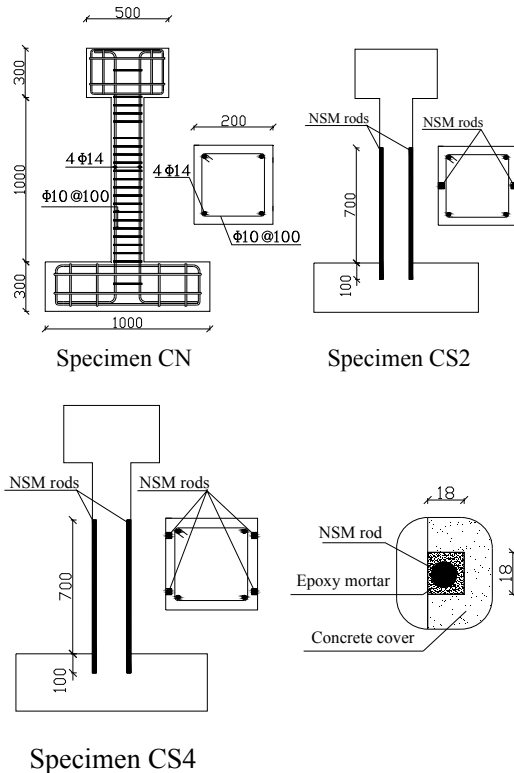


Figure 1 Dimensions, details of reinforcement and NSM strengthening for the specimens (Unit; mm)

2.2 Material properties

The nominal concrete strength was 21 MPa. Columns were fabricated using steel with nominal yield stress of 400 MPa. The average measured yield stress of the 14 mm diameter longitudinal reinforcing bars was 410 MPa and the average measured yield stress of the 10 mm diameter transverse reinforcing bars was 380 MPa.

The mechanical properties of the NSM rods, CFRP jacketing and epoxy pastes were provided by the manufacturer and given in Table 1.

Table 1 Properties of the NSM materials

type	Tensile strength (MPa)	Tensile modulus (GPa)	Ultimate strain (%)
NSM	760	40.8	1.6
mortar	27.6	3	1

2.3 Test setup and loading protocol

The test set-up consisted of a reaction frame supporting

the lateral and vertical hydraulic actuator. Figure 2 shows the test setup and details of the loading system. Specimens were constructed on a stiff base block to simulate rotational fixity of the columns. A pantograph system was installed to restrain the top fixed end of the test column against rotation.

Prior to the application of lateral load, the column was first loaded with a constant axial compressive force of 200 kN using a 500 kN actuator centered on the top block of the specimens. This axial load corresponded approximately to 25% of the ultimate axial load carrying capacity. Under a sustained constant axial force, the 250 kN servo controlled actuator applied the horizontal load to the test specimen in a displacement control mode in accordance with the predetermined loading history of Figure 3.

For all specimens, the lateral cyclic displacement level was selected as multiples of $0.5\Delta_y$. Three full cycles were applied at each load or displacement level before proceeding to the next predetermined level. The yield deflection Δ_y for control specimen was defined as the displacement at the top of the column when first yielding of the longitudinal bars occurs. From the analytical and numerical simulations for control specimen, it was verified that the steel yield initiation occurred for a lateral deflection of about 10 mm at the level of the horizontal actuator. For comparison between specimens, the yield displacement was assumed equal to the measured displacement of the control specimen at the calculated yield load.

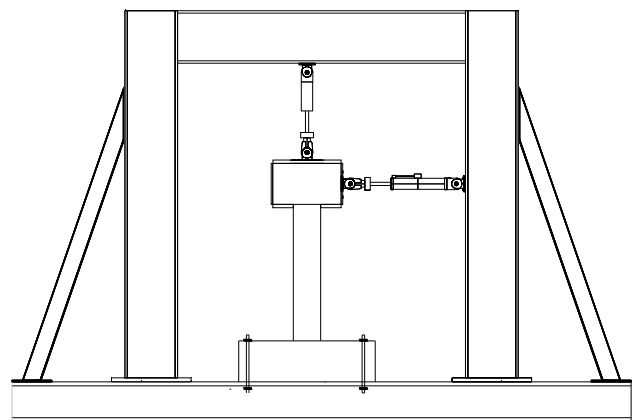


Figure 2 Test set-up

2.4 Instrumentation

Linear variable displacement transducers (LVDTs) were used to record the horizontal displacements of the column as well as any vertical movement of the footing.

Strains in the longitudinal reinforcement and NSM rods were measured using strain gauges. For each specimen, two strain gauges were placed on each of the four corner longitudinal bars and located at the bottom and 1/3 height of each bar.

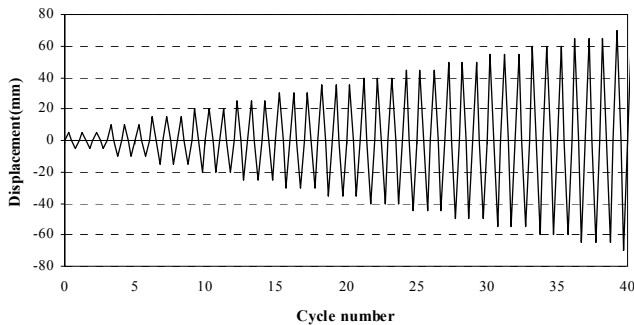


Figure 3 Loading history for the cyclic test

3 EXPERIMENTAL RESULTS

3.1 Failure modes and crack patterns

The tests were done according to the procedures described in Section 2.3. Observations during the first test in column CN indicated that the first crack was formed at the tension side at 0.65% drift ratio. Drift ratio was calculated dividing the measured displacement at the center of the top block by the distance to the top face of the base block. The position of the first crack was about 100 mm distance from the base of column. The cracks were widened during the subsequent cycles at the same displacement. At the 1.0% cent and 1.5% drift levels, new cracks appeared and continued to widen. As the lateral displacement reached a value of 1.8% of drift, the specimen reached to the maximum capacity of lateral resistance strength. At 2.3% drift level, the cover concrete experienced extensive spalling. At this stage, the Buckling of longitudinal bars was accomplished with the crushing of the concrete. The column lost its stability and severely damaged when the lateral displacement reached 5.4% drift. The test was ended with crushing of the concrete, buckling of longitudinal reinforcements.

The column CS2 was subjected to the same loading program as described for column CN. This Column was tested to investigate the effect of NSM rod for flexural strengthening of column. The first cracking occurred when the specimen was subjected to a drift level of 1%. The lateral resistance reached the maximum value at the displacement of about 2.1% of drift. After some cracking near peak load, the bearing capacity of the column started decreasing. When the lateral drift reached 2.4%, spalling of concrete occurred in the column. The test stopped when the displacement reached 5% of drift, because the specimen had lost approximately 50% of its ultimate lateral load resistance capacity. the debonding of NSM FRP rods did not occurred In this specimen.

The column CS4 was subjected to the same loading program as described for column CN and CS2. The behavior and performance of column CS4 was similar to

the column CS2. The first cracking occurred when the specimen was subjected to a drift level of 1.1%. The lateral resistance reached the maximum value at the displacement of about 2.2% of drift. The test was deliberately stopped at about 50% of ultimate lateral load resistance capacity. At this time, the drift ratio was 5.4%. the debonding of NSM FRP rods did not occurred In this specimen.

3.2 Force-displacement relationship

Table 2 lists the main load–displacement parameters of all the specimens reported in this paper. The lateral load–displacement relationships for the three columns are plotted in Figure 4. The displacement is related to the top of the column. The lateral load is adjusted to include the contribution of the horizontal component of inclined axial load.

Figure 4(a) shows that column CN reached a maximum lateral displacement of 59 mm, which corresponds to a drift ratio of 5.4% before its failure. Figure 4(b) shows that specimen CS2 reached a maximum lateral displacement of 54 mm, which corresponds to approximately 50% decrease in ultimate lateral load resistance capacity of column. Figure 4(c) shows that specimen CS4 reached a maximum lateral displacement of 59 mm, which corresponds to approximately 50% decrease in ultimate lateral load resistance capacity of column.

In unstrengthened column (specimen CN), a pronounced pinching effect occurred (narrowing of the hysteretic diagrams), indicating that these columns had reduced capacity to dissipate energy. In the strengthened columns this pinching effect was even more pronounced since, due to the increase of the flexural carrying capacity provided by the NSM rods.

Table 2 Summary of Test Results

Specimen	Positive peak point		Negative peak point	
	F_{peak}^+ (kN)	Δ_{peak}^+ (mm)	F_{peak}^- (kN)	Δ_{peak}^- (mm)
CN	19.65	19	19.2	19
CS2	26.4	23	26.1	22.8
CS4	34.6	23.5	34.2	23.1

By comparing the lateral load– displacement curve, it is cleared that a significant increase in the maximum lateral load capacity of the columns CS2 and CS4 was observed. Increase of lateral load capacity in column CS4 was 76% and in column CS2 was 34%. So the increase of the ultimate lateral load capacity was larger in column with higher NSM ratio.

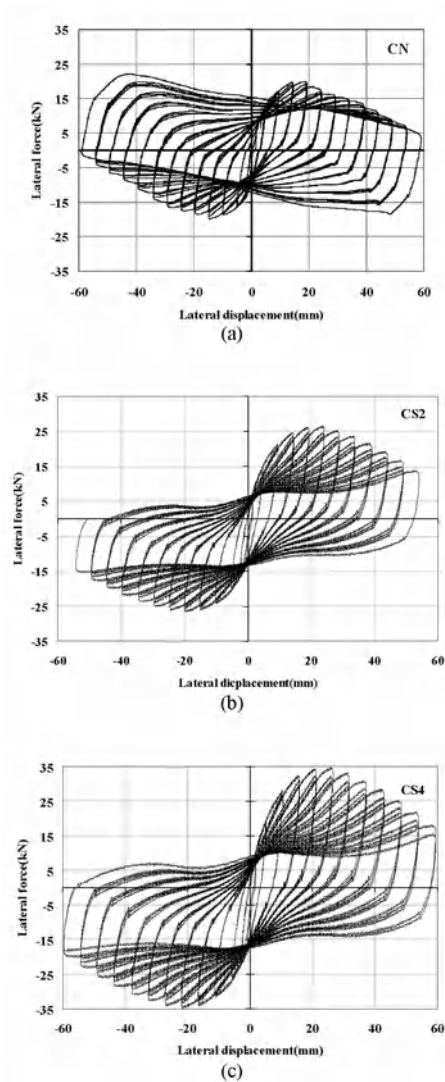


Figure 4 Comparison between the lateral force–displacement relationships for the specimens

4 CONCLUSIONS

A new method of strengthening based on embedding NSM rods into the grooves on the cover of concrete to retrofit RC columns has been developed in this paper. Three columns subjected to axial compression and lateral cyclic loading were tested to examine the effect of this technique.

Laboratory outcomes highlighted that the proposed strengthening technique can enhance the flexural capacity of RC column subjected to combine axial and lateral loading.

REFERENCES

- De Lorenzis L, Nanni A 2002. Bond between NSM fiber-reinforced polymer rods and concrete in structural strengthening. *ACI Structural Journal* 99:123-132.
- El-Hacha R, Rizkalla SH. 2004. Near-surface-mounted fiber-reinforced polymer reinforcements for flexural strengthening of concrete structures. *ACI Structural Journal* 101:717-726.
- Hassan T, Rizkalla S .2004. Bond mechanism of near-surface-mounted fiber-reinforced polymer bars for flexural strengthening of concrete structures. *ACI Structural Journal* 101:830-839.
- Barros J et al. 2006. Assessing the effectiveness of embedding CFRP laminates in the near surface for structural strengthening. *Construction and Building Materials* 20: 478-491.
- Mirmiran A et al .1998. Effect of column parameters on FRP-confined concrete. *Journal of Composite for construction* 2:175-185.
- Park, R. 2001. Improving the resistance of structures to earthquakes. *Bulletin of the New Zealand Society for Earthquake Engineering* 34:1-39.
- Parretti R, Nanni A. 2004. Strengthening of RC members using near surface mounted FRP composites: design overview. *advance in structural engineering* 7: 469-483.
- Saadatmanesh H, Ehsani MR. 1994. Strength and ductility of concrete columns externally reinforced with fiber composite straps. *ACI Structural Journal* 91: 434-447.
- Saadatmanesh H et al.1996. Seismic strengthening of circular bridge pier models with fiber composites., *ACI Structural Journal* 93: 639-647.
- Seible F et al. 1997. Seismic retrofit of RC columns with continuous carbon fiber jackets. *Journal of Composite for construction* 1:52-62.
- Teng J et al.2002. *FRP-Strengthened RC Structures*. John Wiley and Sons Chichester.
- Wu Y et al. 2008. Experimental Investigation on Seismic Retrofitting of Square RC Columns by Carbon FRP Sheet Confinement Combined with Transverse Short Glass FRP Bars in Bored Holes. *Journal of Composite for construction* 12: 53-60.

Effect of FRP Strengthening on the Behavior of Shear Walls with Opening

M. Asfa (Asfa.mohammad@gmail.com)

Graduate Student of Structural Eng., Yazd University, Yazd, Iran

D. Mostofinejad

Department of Civil Engineering, Isfahan University of Technology (IUT), Isfahan, Iran

N. Abdoli

Department of Civil Engineering, Yazd University, Yazd, Iran

ABSTRACT In recent decades, Fiber Reinforced Polymer (FRP) strengthening of concrete members is known as a unanimously acceptable method. An example of a proper application of this method is strengthening of shear walls with openings using FRP strips around them, especially at corners with high stress concentration, where FRP strips keep cracks closed and prevent brittle shear failure to the edges. The efficiency of FRP strengthening on shear walls and around the openings was examined in the current study using finite element (FE) software (ABAQUS). Available laboratory test results on concrete shear walls under lateral loads were used to calibrate the software and verify its application. Then, boundaries of the openings in the wall strengthened with FRP composites in different configurations and nonlinearly were analysed. The results showed considerable effectiveness of FRP strengthening on the overall behaviour of the walls with opening.

1 INTRODUCTION

Shear walls are structures which provide resistance against lateral loads. In some cases, due to the architecture and installation needs, creating opening in the walls is inevitable. The openings divide solid wall into two or more separate walls that are connected to each other by special beams called coupled beams, depending on the strength and stiffness of the beams, the performance of separated walls changes to a solid one to some extent. Creating openings leads to severe loss of shear and flexural resistance. In recent decade FRP was used for shear, bending and in some cases twisting strengthening of beams and columns. Today, because of easy installation, high strength to weight ratio and resistance to corrosion, use of fibers in the RC walls and slabs due to the existing opening are also prevalent. These fibers can prevent diagonal cracks and brittle failure around the openings.

In the field of coupled wall FRP strengthening, Meftah (2007a), using a numerical method, verified the effect of fiber reinforced polymer on the seismic behavior improvement of coupled walls. He applied flexural reinforcement on piers in bottom, middle and top the of wall's piers. It was concluded that the greatest effect in reducing the lateral displacement is to strengthen bottom of the wall and close to foundation. He also changed parameters such as FRP thickness and strengthened area

of a damaged coupled wall, to evaluate the effect of FRP flexural retrofitting on frequency of first seven seismic modes on a 20 floors coupled shear wall. The results showed that increasing the two parameters leads to increasing the frequency of the wall (Meftah 2007b). Nagy (2007) also, studied the shear and flexural FRP strengthening effect on several damaged coupled walls, with different opening arrangements, under cyclic loading. They concluded that the load bearing capacity of all samples before damages is recovered. Antoniadis (2007) also retrofitted 11 models of coupled walls using FRP, after loading them up to failure. They evaluated the FRP effect on energy dissipation and lateral displacement of the wall. Dimitri (2009) investigated the FRP strengthening effect on the prefabricated panels with cut-out openings, before and after applying load. The results showed that, fiber reinforcements increased the load bearing capacity of both damaged and undamaged walls.

In this paper, verification of software finite element modeling, using existing laboratory test has been investigated. And then, effect of proposed FRP retrofitting method on a shear wall with opening has been studied. By sticking FRP strips around the opening of coupled walls, an effective way to improve overall behavior of the wall and reducing damages has been developed in this method.

2 STUDY PROCESS

For software calibration, two experimental models including a FRP strengthened beam (Harries 2007) and a coupled shear wall (Lu & Chen 2005) are verified. Then, FRP strengthening effect around openings of the coupled wall is investigated. The coupled wall is designed based on the high-rise building codes in China JGJ-391 (1991). It is a scaled model of five floors coupled wall and was tested under gravitational and lateral load.

According to ACI-318 (2005), if the ratio of the coupled beam length to its height is less than 2, using diagonal reinforcement is required. The ratio in the studied wall is 1.6 and therefore, applying diagonal reinforcement in the coupled beams is necessary and the wall needs retrofitting.

In this study, the wall behavior, in two cases, with the diagonal bars in coupled beam according to ACI-318 and excluding them is verified and then the latter is retrofitted using proposed methods and compared with the other walls in order to verify the efficiency of retrofitting methods, to improve the wall behavior.

3 MODEL SPECIFICATION

The characteristics of the beam and shear wall including dimensions with the type and arrangement of existing reinforcement are shown in Figure 1 and 2, respectively. Also reinforcement specification of coupled beam, according to the ACI-318, is illustrated in Figure 3.

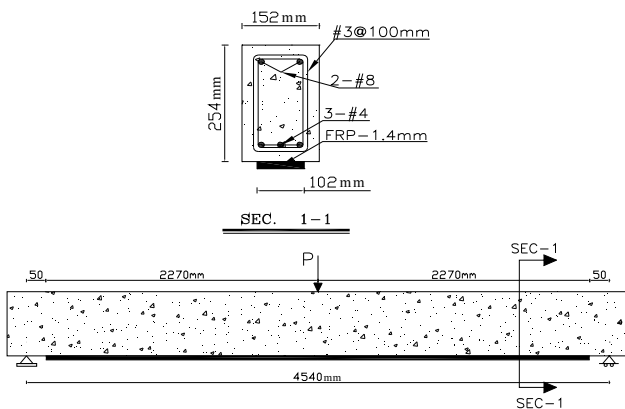


Figure 1 Parameters of the FRP strengthened beam (Harries 2007)

4 MATERIALS STRENGTH

4.1 Beam

The beam includes #4, #6 steel bars with the yield stress of 429MPa. The 28-day cylindrical compressive strength and Young's modulus of concrete is 23.3 and 22680MPa respectively. FRP strip thickness is 1.4mm with elasticity modulus of 155GPa and tensile strength of 2800MPa.

4.2 Coupled wall

As shown in Figure 2, the wall steel reinforcements include $\Phi 4$, $\Phi 6$ and $\Phi 8$ with the yield stress of 796.9,

311.3 and 278.3MPa, respectively. The 28-day cylindrical compressive strength, tensile strength and Young's modulus of concrete were measured 35, 2.63 and 31100MPa respectively. Thickness of FRP layers is 0.16mm with elasticity modulus of 230GPa and tensile strength of 3500MPa.

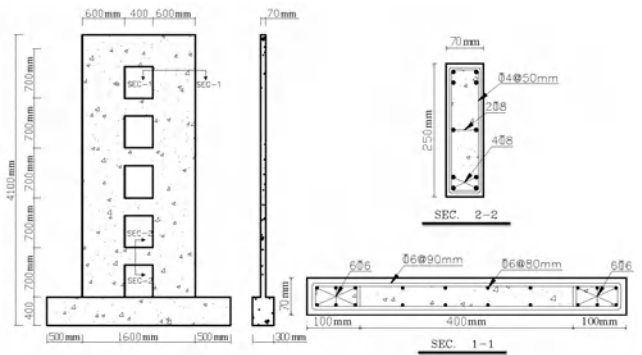


Figure 2 Parameters of the coupled wall (Lu & Chen 2005)

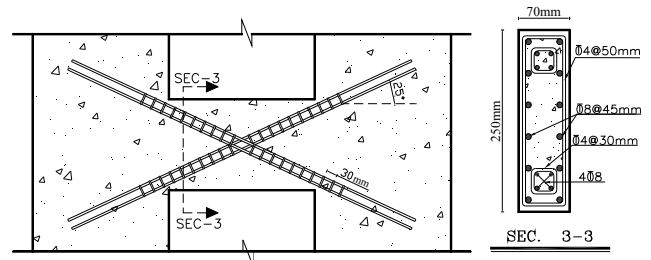


Figure 3 Parameters of the coupled beam with diagonal bars according to the ACI-318

5 FINITE ELEMENT PROCESS

5.1 Elements

For this study analysis, ABAQUS software which can solve linear and nonlinear FE problems is used.

For concrete, bar and FRP layer modeling, 8 node cubic elements (C3D8), 2 node rod element (T3D2) and 4 node Shell element (S4) are used, respectively.

5.2 Boundary conditions

For simulation of restraint in software, the degree of freedoms are limited according to the type of restraints. Because of the symmetry in the geometry and loading condition, in order to reduce the analysis time and prevent out-of-plane displacement, a quarter of beam and half of the wall is modeled by applying symmetrical boundary conditions.

Wall loadings include first, a total 200kN vertical load on the wall piers and then applying the lateral load gradually up to wall failure through an upper beam attached to the wall top.

As illustrated in Figure 1, beam loading is applied at mid span monotonically.

5.3 Materials specification

Steel is introduced as an elastic-plastic material to the

software and a completely linear and elastic material is defined for FRP. Concrete is defined using the Concrete Damage Plasticity option which exists in software library. This model is defined according to the Lubliner (1989) studies and was developed by Lee & Fenves (1998). In this model the development of yield surface is controlled by two strain-hardening variables, one in tension and the other in pressure (Habbit et al. 2008).

Compressive stress-strain curve of concrete should be obtained from test result, but if it was not available, equation introduced by various researchers, can be used. In the current study, Hognestad equation in which the relationship of stress-strain is defined according to concrete compressive strength, strain related to maximum stress or, elastic modulus of the concrete (MostofiNejad 2009), is used.

Effects associated with steel-concrete interface, such as bond-slip or dowel action, are approximately introduced to the concrete by applying strain-hardening characteristic in tension to the concrete material. This characteristic simulates load transfer from concrete to the reinforcement through cracks.

After concrete cracking under tensile stress, the stiffness of concrete does not reach to zero at once and it still transmits shear force, due to aggregate inter-locking and friction (Habbit et. al. 2008).

In this study a complete bond between FRP and concrete is considered in the models and debonding is controlled according to the ACI-440.2R (2002), it limits the FRP strain to a specified extent for preventing FRP debonding.

6 COMPARISON OF THE EXPERIMENTAL AND SOFTWARE MODELING RESULT

Figures 4 & 5 present experimental and analytical diagram of load-displacement of the beam and coupled wall respectively. The failure mode of the beam is FRP debonding and then flexural failure, and for the wall is flexural-shear mode. Obviously, the results are in good agreement with each other for both failure modes and load-displacements curve, expressing that the software modeling results are reliable.

To evaluate the primary effect of diagonal bars in coupled beam on wall behavior, they were implemented in the coupled beam of the studied wall according to ACI-318 and nonlinearly analyzed. In Figure 6, the obtained results from software analysis of wall with diagonal bars and without them were compared. The results showed that diagonal bars in coupled beam increased ultimate load bearing capacity about 22 percent from the 145kN to 185kN and they also increased the ultimate failure strain up to 32 percent from 34mm to 50mm. Generally, this type of bars improved the overall behavior of the shear wall.

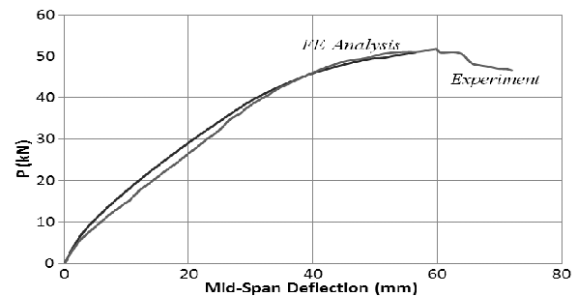


Figure 4 Comparison of load-displacement diagram of beam, from software FE test and experimental result

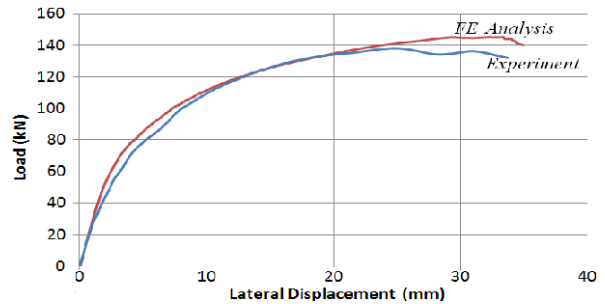


Figure 5 Comparison of lateral load-displacement diagram of wall, from software FE test and experimental result

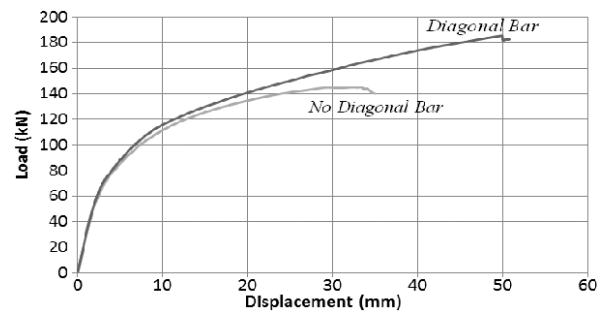


Figure 6 Comparison of lateral load-displacement diagram, from software FE test of walls with and without diagonal bar

7 FRP RETROFITTING OF WALL

As depicted in Figure 7, three different methods for FRP retrofitting of wall are presented as follows:

- a) Connection of FRP sheets around opening corners justified at the angle of 45° in 3 layers (Cw-45).

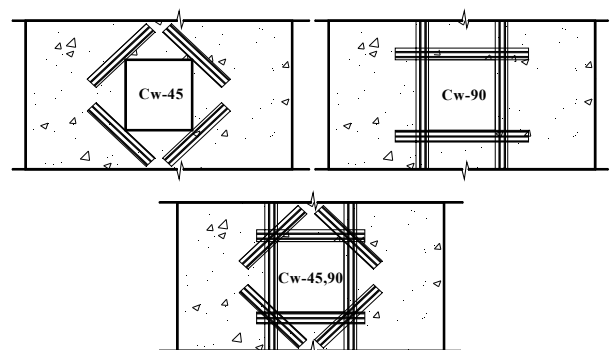


Figure 7 FRP Retrofitting method, used in this study

b) Connection of FRP sheets parallel to the opening edges at the angles of zero and 90° in 2 layers (Cw-90).

c) A shape combination of two previous methods, in 1 and 2 layers (Cw-45,90).

To compare the efficiency of retrofitting methods, in all cases the volume of FRP sheets are considered the same (324 cm^3 on each side of the wall). In Table 1, the FRP sheet dimensions are presented.

Table 1 Dimensions of FRP Layers for wall strengthening

Type	Horizontal strip mm	45° strip mm	Vertical layers* mm
a	–	500×75×0.48	–
b	800×75×0.32	-	3150×75×0.32
c	650×75×0.32	500×75×0.16	3150×75×0.16

* This layer is extended 3150mm from 275mm above the foundation level to the 175mm above the top opening of wall.

8 RESULTS

Figure 8 presents load-displacement diagram from FE analysis of FRP reinforced walls, compared with unretrofitted walls in both cases, with diagonal bar (SWD) and without it (SW). As expected, the diagrams' slopes in the linear region are in excellent agreement, indicating that the strengthening method does not affect the shear walls stiffness in linear region and before the onset of considerable cracks. In non-linear region, however, the curves' slopes change based on their strengthening case. All of the studied wall models failed in a flexural-shear mode with no FRP debonding.

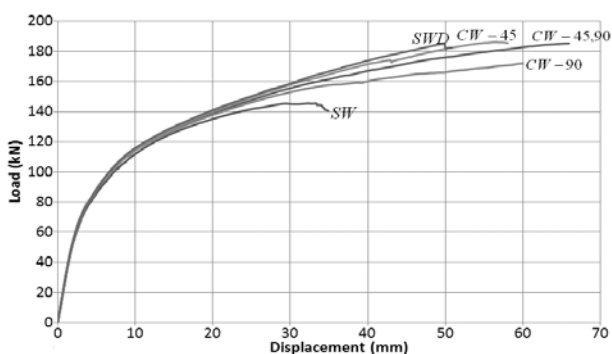


Figure 8 Lateral Load-Displacement diagram of walls with different type of strengthening method

9 CONCLUSION

Among the FRP strengthened walls, the Cw-45 gained the most stiffness, while the highest ductility was belonged to Cw-45,90. In terms of efficiency of FRP strengthening methods, generally all the techniques increased the strength and ductility of the coupled wall. However, the most efficient method in compensation of lack of diagonal bar was Cw-45 which increased the ultimate load bearing

capacity to 186kN, while this amount for Cw-45,90 and Cw-90 were 185kN and 171kN, respectively. It can be concluded that using FRP strips at the angle of 45° in the corners of the opening can keeps cracks closed and thus increases the stiffness and ultimate load bearing capacity. On the other hand, vertical and horizontal FRP strips on the coupled beam and around the wall openings increase the ductility of coupled wall. Therefore, the combination of diagonal, vertical and horizontal FRP layers (Cw-45,90), leads to an efficient strengthening method that improves the overall wall behavior.

REFERENCES

- ACI Committee 318. 2005. Building Code Requirements for Structural Concrete (ACI 318-05). *American Concrete Institute*, Farmington Hills.
- ACI Committee 440.2R 2002. Guide for the Design and Construction of Externally Bonded FRP Systems for Strengthening Concrete Structures.
- Antoniades, K.K., Thomas, N. & Kappos, A.J. 2007. Evaluation of hysteric response and strength of repaired R/C walls strengthened with FRPs. *Engineering Structures* 29: 2158-2171.
- Demeter, I., Nagy-György, T., Stoian, V., Dăescu, C. & Dan, D. 2009. Precast RC wall panels with cut-out openings retrofitted by CFRP composites. *NOVI SAD*.
- Harries, K.A., Reeve, B., & Zorn, A., 2007. Experimental evaluation factors affecting monotonic and fatigue behavior of FRP concrete bond in RC beams, *ACI Structural Journal*, 104-S62, Nov-Dec.
- Hibbit, Karlsson & Sorensen Inc. 2008. ABAQUS theory manual, user manual and example manual. Version 6.8, Providence, RI.
- Lee, J & Fenves, GL. 1998. Plastic-damage model for cyclic loading of concrete structures. *J Eng Mech* 124(8).
- Lu, X. & Chen, Y. 2005. Modeling of Coupled Shear Walls and Its Experimental Verification, *Journal of Structural Engineering*, 131(1).
- Lublinter, J., Oliver, J., Oller, S & Onate E. 1989, A plastic-damage model for concrete, *Int J Solids Struct*, 25(3): 229-326.
- Meftah, S. A., Yeghnem, R., Tounsi, A. & Adda Bedia, E. A. 2007a. Seismic behavior of RC coupled shear walls repaired with CFRP laminates having variable fibers spacing. *Construction and Building Materials Structures*. 21.
- Meftah, S. A., Yeghnem, R., Tounsi, A. & Adda Bedia E. A. 2007b. Lateral stiffness and vibration characteristics of damaged RC coupled shear walls strengthened with thin composite plates, *Building and Environments*. 42.
- Ministry of Construction. 1991, Code for design and construction of reinforced concrete high-rise buildings. *JGJ 3-91*. *Chinese Building Industry Press*, Beijing (in Chinese).
- MostofiNejad, D. 2009. Reinforced Concrete Structures. Vol.1. 14th ed. Esfahan: Arkane Danesh.
- Nagy-Gyorgy, T., Stoian, V., Dan, D., Dăescu, C., Diaconu, D., Sas, G. & Mosoarca M. 2007. Research Results on RC Walls and Dapped Beam Ends Strengthened with FRP Composites. *FRPRCS-8, Patras, Greece*.

Seismic Assessment of FRP-Retrofitted RC Frames Using Pushover Analysis Considering Strain Softening of Concrete

S.S. Mahini (smahini@une.edu.au)

Department of Engineering, The University of New England, Armidale, NSW 2351 Australia

S.A. Hadigheh

Department of Civil Engineering, Yazd University, Yazd, Yazd, Iran

M.R. Maheri

Department of Civil Engineering, Shiraz University, Shiraz, Fars, Iran

ABSTRACT Seismic actions cause unacceptable levels of damage in existing RC buildings. Existing buildings designed to earlier codes have insufficient lateral resistance, exhibit lower strength and ductility, which induce a global failure mechanism to the structure. Under these circumstances, “weak-column strong-beam” behaviour dominated the buildings which may lead to the formation of local hinges in the column and so strengthening becomes necessary. In this paper, seismic behaviour of retrofitted RC frames using FRP at joints and steel braces are investigated. For this, moment curvature of the FRP-retrofitted joints are captured by FE analysis considering strain softening of concrete and then pushover analysis for all frames are carried out. Ductility, behaviour factor and performance points of two, four and eight stories frames are then evaluated. The results show that FRP-retrofitting technique can better improve the seismic performance of eight storey frame than steel braces but in low-rise frames, both techniques are beneficial.

1 INTRODUCTION

Reinforced concrete (RC) structures which were designed and constructed based on the old codes often suffer from seismic loads due to insufficient energy dissipation, rapid strength deterioration and improper hinging mechanisms. This deficient behavior comes from inadequate reinforcement detailing which leads to excessive drifts and damages and finally structural collapse. On the other hand, observations from past earthquakes indicate that the performance of reinforced concrete structures which were designed only for gravity loads have poor behavior under seismic actions due to limited ductility and insufficient lateral load-carrying capacity. In fact, such structures do not satisfy the “*weak beam-strong column*” principle and therefore leads to brittle soft-storey or column sideway collapse mechanisms during strong ground motions (Zou et al. 2007). Attempts have been made to modify the engineering notions and the codes’ regulation in order to upgrade these insufficient behaviors to ensure the safety of structures. For example in existing structures, several strategies such as rehabilitation, repairing and retrofitting schemes can be used (Mukherjee & Joshi 2005).

In recent years, strengthening of RC buildings using steel braces has been examined. This strengthening system is easier for construction and has lower costs than other

shear resisting elements such as concrete and masonry shear walls or a rigid frame system (Maheri & Sahebi 1997). Steel bracing systems have been used in Mexico and Japan to strengthen the non-ductile RC buildings (Ghobarah 2003).

Fiber reinforced materials have been examined for retrofitting of the existing RC buildings. Past studies (Balsamo et al. 2005, Mahini et al. 2004 and 2010 and Zou et al. 2007) have shown that the load carrying capacity and serviceability of existing structures can be increased by using FRP sheets. Mahini et al. (2008) showed that seismic performance of the existing RC frames retrofitted at joints by FRP sheets is better than the retrofitted frames by steel braces systems.

In this research, performance of the retrofitted RC ordinary moment resisting frames at joints by FRP sheets (called web-bonded system) and also steel braces is studied considering strain softening of concrete. For this purpose, an exterior joint of an eight-storey building tested by Mahini et al. (2004 and 2010) under monotonic loads is simulated in ABAQUS finite element software (Hibbit, Karlsson, & Sorensen Inc. 2007) before and after retrofitting by CFRP web-bonded system. The ABAQUS results showed good correlation with experiments. Moment- rotation relations of the joints were captured by ABAQUS and then were employed in pushover

analysis (nonlinear static analysis) of the frames using SAP2000 software (Computers and Structures Inc. CSI, 2007) in order to investigate the seismic behavior of the plain and the retrofitted frames.

Following this study, seismic behavior of two and four stories frames retrofitted with FRP web-bonded at the joints and also with steel braces was investigated. These retrofitting techniques were evaluated through performance parameters such as ductility, the behavior factor and performance points.

2 EXPERIMENTAL PROGRAM

The prototype was designed according to Australian Concrete Code (AS3600 2001). Figure 1 shows the 1/2.2 scaled down specimens' details tested by Mahini and Ronagh (2010). The number, length and thickness of FRP layers for two specimens are tabulated in Table 1.

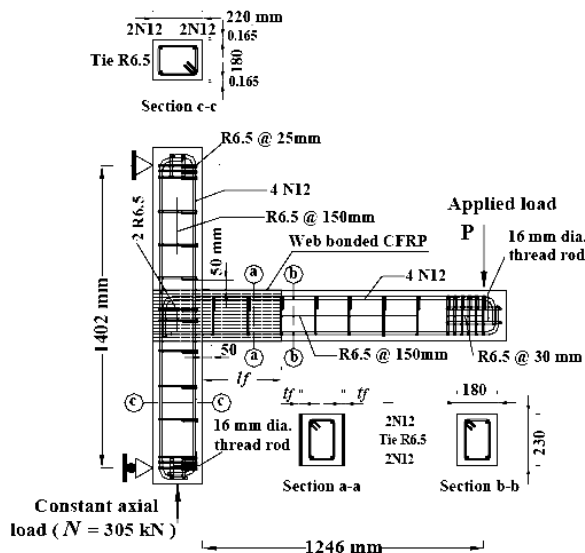


Figure 1 Details of the selected joint

Table 1 Geometry of FRP layers

Specimen	l_f (mm)	No. of plies	t_f (mm)
CSM0	—	—	—
RSM1	350	1	0.165
RSM2	200	3	0.495

Cross-sectional dimensions of beams and columns were 180 by 230 mm and 180 by 220 mm respectively. Four N12 rebars ($\phi=12$ mm) were used for both the column vertical reinforcement and the beam longitudinal reinforcement. R6.5 bars ($\phi=6.5$ mm) were used for stirrups with a spacing of 150mm in both column and beam. The length of beam and column were 1246 and 1402 mm, respectively. The concrete had a compressive strength of 40.8 and 47.2 MPa for plain (CSM0) and retrofitted Specimens (RSM1, and RSM2) respectively.

Yield strength of the main steel reinforcements, N12 and the stirrups R6.5 were around 500 MPa and 382 MPa. Carbon Fibre Reinforced Plastic (CFRP) sheets that were used in all experiments were uni-directional with an ultimate stress of $f_{fr} = 3900$ MPa, ultimate strain of 0.0155 mm/mm and a constant modulus of 240 GPa. A monotonic load was applied on the beam's tip to investigate the load-displacement relations of the specimens. A constant load equals to 305 kN was applied on the columns to consider the gravity loads of upper stories.

Test results showed that for plain specimen (CSM0), the steel yielding occurred at the column's face and cracks formed at the joint core and the column's face. The ultimate load for this specimen was about 24.6 kN with displacement of 70 mm. The maximum load, which measured for RSM1 and RSM2 were 24.7 kN and 21.12 kN respectively. RSM1 exhibited a brittle sudden failure due to FRP rupture at the column face whereas RSM2 failed in a ductile manner in which cracks relocated from column's face to the end of the FRP sheets.

3 NUMERICAL PROGRAM

To verify the finite element results with the experiments, specimens tested by Mahini and Ronagh (2010) were modeled in ABAQUS.

The behavior of concrete under monotonic load was modeled by concrete damaged plasticity. In this modeling, compressive behavior of concrete can be introduced in terms of yield stress versus inelastic strain. Hognestad stress-strain relation was used to define the uniaxial compressive stress of concrete. The behavior of concrete after cracking under tensile stresses can be represented by tension stiffening to define the strain-softening behavior of cracked concrete. In addition, to define the softening behavior of concrete after cracking, cracking displacement method of ABAQUS was used. Stress-strain curve of steel under tension or compression was idealized by three straight lines. The Tsai-Wu theory (Hibbitt, Karlsson, & Sorensen Inc. 2007) was used to introduce the failure surface of FRP composite to the software. To define the interaction between concrete and steel reinforcement, embedded region constraint was used. In order to achieve an accurate result, displacement control regime was applied at the beam's tip.

In this analysis, continuum 8-node linear brick elements (C3D8R) with three degrees of freedom per node and reduced integration were used to model the concrete. Two-node linear 3-D trusses (T3D2), which can only carry axial loads through their centerline as compressive or tensile loads, was used to model steel reinforcement. The T3D2 elements use quadratic interpolation for displacement and have only transitional degrees of freedom at each node. Quadratic eight-node shell elements with six degrees of freedom per node (S8R) were used

to model FRP sheets. Experimental and numerical load-displacement curves of FRM1 are represented in Figure 2.

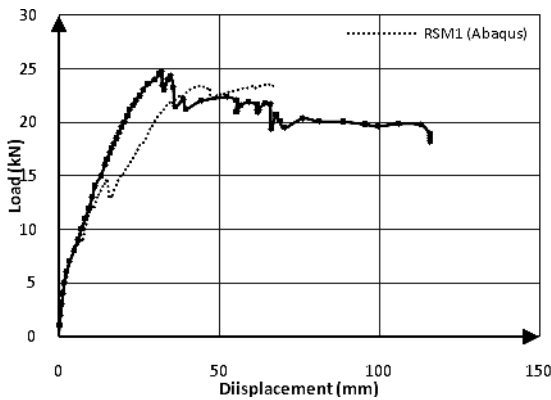


Figure 2 Comparison between experimental and analytical results of RSM1

4 BEHAVIOR OF FRP RETROFITTED EIGHT-STORY FRAME

To study the influence of FRP retrofitting technique at the joints of the eight storey RC frames, the frame’s joints before and after retrofitting tested by Mahini et al. (2004) were analyzed using ABAQUS and then pushover analysis for the plain and retrofitted frames were carried out using SAP2000 software. For this, mass source of building is assumed to be equal to Dead loads plus 0.2 Live loads according to Iranian seismic code; standard No. 2800 (2005). The P-delta effect is taken into account during pushover analysis. Flexural moment hinges and force-moment hinges were assumed for beams and columns respectively. Link property was used to introduce the behavior of joints to SAP2000. For this purpose, moment-rotation curves of the plain and retrofitted specimens obtained from ABAQUS were employed.

Base shear-roof displacement curve of original and retrofitted frames are represented in Figure 3. This figure indicates that this retrofitting technique can increase the maximum base shear and lateral load-carrying capacity of frame.

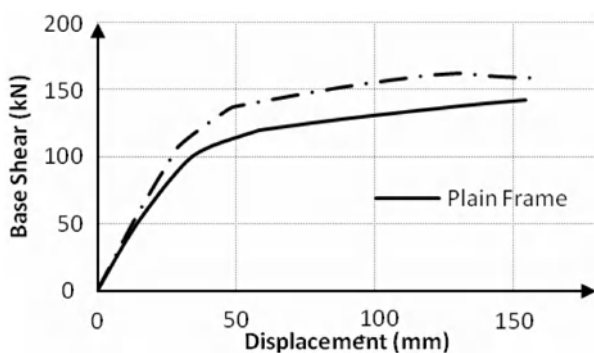


Figure 3 Base shear-roof displacement of plain and retrofitted frames

Basically, the behavior factor, R , consists of three different values; the ductility reduction factor, R_{μ} , overstrength factor, R_s and allowable stress factor, Y . R_{μ} is determined by a relation which is presented by Miranda and Bertero (1994). Because of the using ultimate strength method, the allowable stress factor, Y , is assumed unity and R_s can be obtained by Equation 1.

$$R_s = V_y / V_s \tag{1}$$

By comparing the frames behavior before and after retrofitting, it is found that the over-strength and the behavior factors of the retrofitted frame increases about 24.81% and 10.66%, respectively and ductility reduction factor decreases to 11.39% (see Table 2).

Table 2 Seismic performance parameters of 8 storey frames

Frame	R_s	R	Performance Point (S_d, S_a)
Plain	1.29	7.13	-
Retrofitted	1.61	7.89	(12.27, 0.126g)
Increase (%)	24.8	10.66	-

5 BEHAVIOR OF LOW-RISE STORIES FRAMES RETROFITTED BY STEEL BRACES AND FRP

To study the seismic behavior of low-rise buildings retrofitted by FRP materials and steel braces, pushover analysis was performed for two and four stories frames and the seismic parameters of these frames were compared.

The beams’ length is 4 m and the height of each storey is 3 m (Figure 4). Compressive strength of concrete and yield stress of steel reinforcements was assumed to be 40 MPa and 340 MPa respectively. For all sections, minimum and maximum values of steel reinforcements were checked based on Iranian Concrete Code (ABA 2005). Gravity loads assumed equal to Dead load (2200 kg/m) with 0.2 Live load (1400 kg/m) based on Iranian codes. Equivalent static earthquake lateral loads on the frames were calculated using design response spectrum of the Iranian seismic code (2005). It was assumed that frames are located in a high earthquake zone.

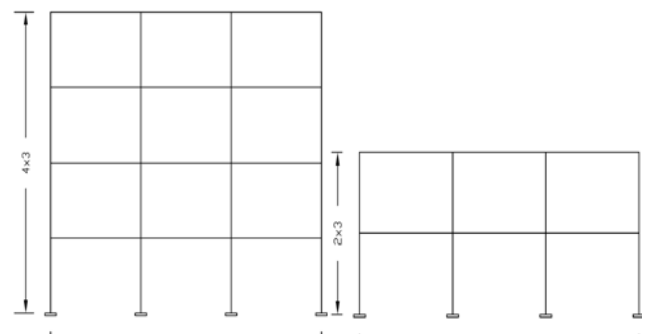


Figure 4 Geometry of the two and four stories frames

Braces were placed in the middle bay of the frame from the first to last floor uniformly. Firstly, 75% of lateral loads ($0.75V$) were applied to 2 and 4 stories frames to design plain concrete frames but after adding X-steel braces to the frames, 100% of lateral loads, V were applied. Therefore, members of braces were designed to undergo 25% lateral loads. Members of X-braces were designed according to AISC-LRFD 93 for 25% share of lateral loads. Load combinations of ACI318-99 (1999) were used to design frames by SAP2000 program.

5.1 Performance parameters of frames

Pushover analysis was carried out on 2 and 4-storey frames before and after retrofitting by FRP materials and X-steel braces (see Table 3). According to this table, by using X-steel braces, period of frames reduces. In addition, the behavior factor of frames which retrofitted by FRP are higher than plain and the retrofitted frames by braces. The differences between R factor of frames retrofitted by FRPs and X-steel braces are 14.2% and 3.63% for 2- and 4-storey frames respectively. As is seen, by increase of frame's storey, this difference reduces.

According to capacity spectrum method of ATC-40 (1996), performance points of plain and retrofitted of 2 and 4-storey frames were extracted from base shear-roof displacement curves. After nonlinear static analysis, capacity and demand spectra of frames are plotted in the same coordinate and the intersect point represents the performance point of frames (Table 3). According to this table, both FRP retrofitting technique and X bracing system can improve the seismic performance of the frames. However, the FRP-retrofitting of the 4-storey frame failed to upgrade the frame to and satisfy the life-safety performance demand of the selected Iranian design earthquake, indicating insufficient thickness of the FRP sheets.

Table 3 Seismic performance parameters of 2 and 4-storey frames

Storey	Frame	T	R	Performance point
2	Plain	0.44	4.02	(4.00, 0.36g)
	FRP-Retrofitted	0.44	4.99	(3.79, 0.38g)
	X braces	0.2	4.37	(1.00, 0.70g)
4	Plain	0.56	4.54	(2.66, 0.27g)
	FRP -Retrofitted	0.56	5.14	N.A.
	X braces	0.25	4.96	(0.92, 0.66g)

6 COCLUSION

In this paper, performance assessment factors of the plain and retrofitted RC frames with FRPs at joints or X bracing systems were obtained using pushover analysis according to ATC-40. Moment-curvature relations of the joints were captured by ABAQUS and then were used in this analysis. Based on the results, the behaviour factor

was increased by 10.66% when 8 storey frame was retrofitted by two layers of FRP. However, ductility ratio of the retrofitted structure was reduced by 11.71%. It was shown that the behavior factor and the maximum base shear of retrofitted low-rise frames are higher than the plain frames. Therefore, both FRP and X braces can improve the seismic performance of the existing low-rise RC frames.

REFERENCES

- ABA. 2005. Iranian concrete code. Report No. 120, Islamic Republic of Iran Management and Planning Organization.
- ACI318. 1999, 2005. Building code requirements for structural concrete. American Concrete Institute.
- AS3600. 2001. Australian standard on concrete structures. Standards Australia International Ltd, Sydney, NSW, Australia.
- ATC. 1996. Seismic evaluation and retrofit of concrete buildings. ATC-40, Applied Technology Council, Redwood City.
- Balsamo et al. 2005. Seismic behavior of a full-scale RC frame repaired using CFRP laminates. *Engineering Structures* 27: 769-780.
- Computers and Structures Inc. CSI. 2007. SAP2000 software. Non-linear version 11.0.0, Berkeley, California, USA.
- Ghobarah, A. 2003. Seismic rehabilitation of RC frames using steel brace system. Sixth International Conference on Civil Engineering (ICCE), Isfahan, Iran : 43-50.
- Hibbitt, Karlsson, & Sorensen Inc. 2007. ABAQUS theory manual, users manual and example manual. Version 6.7.
- Maheri, M.R. & Sahebi, A. 1997. Use of steel bracing in reinforced concrete frames. *Engineering Structures*, Vol. 19, No. 12: 1018-1024.
- Mahini, S.S., Ronagh, H.R., and Niroomandi, A. 2008. Performance Based Assessment of FRP-Retrofitted Existing RC Frames. Proceedings of Fourth International Conference on FRP Composites in Civil Engineering (CICE08) 22-24 July 2008, Zurich, Switzerland Empa, Duebendorf, Paper 6.B.6. p.6 (CD-ROM).
- Mahini S.S. and Ronagh, H.R. 2009. Numerical modelling of FRP strengthened RC beam-column joints. *Structural Engineering & Mechanics*, 32(5): 649-665.
- Mahini, SS. & Ronagh, H.R. 2010. Strength and ductility of FRP web-bonded RC beams for the assessment of retrofitted beam-column joints. *Composite structures*, 92(6): 1325-1332.
- Miranda, E. & Bertero, VV. 1994. Evaluation of strength reduction factors for earthquake-resistant design. *Earthquake Spectra* 10(2): 357-379.
- Mukherjee, A. & Joshi, M. 2005. CFRP reinforced concrete beam-column joints under cyclic excitation. *composite structures*, 70: 185-199.
- Ohishi, H. et al. 1988. A seismic strengthening design and practice of an existing reinforced concrete school building in Shejuoka City. Proc. 9th World Conf. on Earthquake Engineering, Japan, Vol. III.
- Standard No. 2800, 2005. Iranian code of practice for seismic resistant design of buildings. Building and Housing Research Center, Third edition.
- Zou et al. 2007. Optimal performance- based design of FRP jackets for seismic retrofit of reinforced concrete frames. *Composites: Part B* 38: 584-597.

Seismic Performance Analysis of FRP Reinforced Concrete Frame Structure

Yaping Peng (cea_pengyp@ujn.edu.cn), Ming Ma, Guang Dong

School of Civil Engineering and Architecture, University of Jinan, Jinan, China

ABSTRACT Based on the experimental study for seismic performance of FRP reinforced concrete beam-column joints, two-storey two-span plane frames were taken for examples, in which the static elastoplastic analysis (the pushover method) was carried on the joints of the FRP strengthened concrete frames, and then the comparative analysis was made on seismic performance of RFP strengthened frame structure through the calculated pushover curve, the distribution of plastic hinges, the target displacement and other parameters. The result showed that effective reinforcement for the beam-column joints may obviously improve overall seismic performance of frame structures.

1 INTRODUCTION

In the recent great earthquake, many reinforced concrete frame structures were greatly damaged, particularly those structures not considering earthquake resistance in design or in accordance with the old specifications were badly damaged, the main damage reason is integrally insufficient horizontal shear strength and limited ductility in these structures, for which relatively simple techniques and methods with high efficiency are required to be used for their repair and reinforcement of earthquake resistance.

According to many studies in recent years, the effectiveness of the technique attaching FRP sheets on the surface of reinforced concrete structure as reinforcement have been proved, which has been widely used in the engineering practices. At present, most studies focus on the evaluation and analysis on the effect of FRP reinforcement in the individual members, the design of the engineering reinforcement also starts from the requirement of the bearing capacity of partial or individual member to provide the directional reinforcement for the areas with insufficient capacity, and even the improvement of ductility is considered, it also mainly starts from the aspect of concept design. While better seismic performance of the integral reinforced concrete structure should be realized by the composition of the members as well as the reasonable matching of all members on their bearing capacity, rigidity and ductility, so as to create a reasonable damage form, for which it is required to make deep study on the integral working performance of the FRP reinforced concrete members, however, there is not enough study has been done in this respect currently.

For analysis on integral reinforcement of frame structure for earthquake resistance, it is firstly required to determine the reasonable and effective FRP attachment

methods, secondly achieve correct understanding of and analysis on the bearing capacity, rigidity and deterioration of frame structures after reinforcement, and finally carry out reasonable evaluation on the overall seismic performance of the structures, to find out the relatively economical reinforcement methods with high efficiency.

2 SEISMIC REINFORCEMENT OF FRAME STRUCTURES WITH FRP

When frame structure is under the horizontal seismic action, moment at the ends of the member is relatively large, named with plastic hinges. This is the potential energy consumption mechanism of the structure in the earthquake, critical to the structure distributed at the ends of the beam-column. Since reasonable presence mechanism and rotation capacity of plastic hinges will directly determine the seismic performance of the frame structure, strengthening frame structure should observe the following rules, (1) ensure sufficient shearing strength in the core areas of the joints, (2) avoid the position shift of plastic hinges due to partial adjustment of rigidity arising from strengthening, so as to ensure that plastic hinges remain at the ends of the members, (3) observe the principle of strong column and weak beam, to realize the column-hinge damage mechanism, and (4) most reasonable matching of bending reinforcement and shearing reinforcement, to fully ensure rotational capacity of the plastic hinges.

The reinforcement of frame structures should be highlighted from reasonable matching between the bending and shearing strengths at the core areas of joints, in order to realize the beam-hinge damage mechanism. Therefore, should be laid upon the strengthening of the joints first, to achieve good seismic performance of the

frame structure from their bending and shearing strengths at the ends of beam-columns and the core areas of possible joints.

The author raised an effective strengthening method of the strengthened concrete joints. Experimental study on beam-column side joints reinforced with FRP under cyclic loading has shown that this reinforcement method has improved the seismic performance of these joints. Based upon the study, this paper continues the analysis the effect for the application of this FRP reinforcement method on the strengthened concrete frame structures with capacity spectrum method, and evaluation on the seismic performance of FRP-strengthened concrete frame structures of various types in case of the rare earthquake under the condition of given requirements for prevention.

3 SEISMIC PERFORMANCE TEST OF FRP STRENGTHENED BEAM-COLUMN JOINTS

Four test members of T-shape side joints were prepared, one is used for reference and the other three are used for FRP strengthening. The reference member is numbered as J-1, the member reinforced with glass fiber is numbered as GRJ-1, the member reinforced with both 0° carbon fiber and glass fiber is numbered as HRJ-1, and the member reinforced with $\pm 45^\circ$ mixed fiber is numbered as HRJ-2 (where the direction of fiber yarns enveloping fiber 1 in the joint area has the included angle of 45° with horizontal axial line of the beam). The winding mode of reinforced fibers is shown in Figure 1.

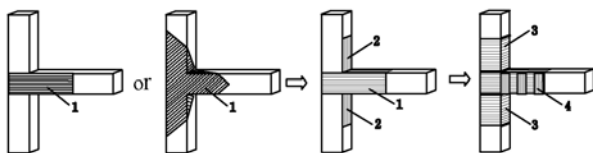


Figure 1 Sketch of T-joints reinforced with FRP

(1—anchoring fiber in the core area of the joints; 2—bending and anchoring fiber in beam-column; 3—shearing and anchoring fiber at the column end; 4—shearing and anchoring fiber at the beam end)

During the test, the fixed axial force on the columns, and the cyclic load of compressive and tensile strength on the beam ends, are applied with the pattern of mixed control of force and displacement. Refer to Figure 2 for

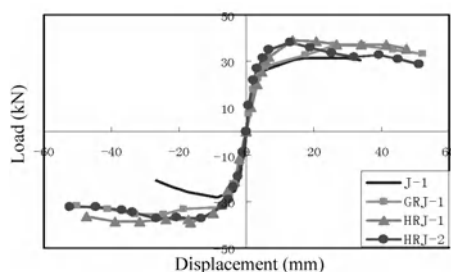


Figure 2 Envelopes curve

the envelopes curve about hysteresis loop of displacement at beam ends. The members after strengthening have been obviously improved on their bearing capacity, ductility and energy consumption.

4 MODELS OF FRP STRENGTHENED FRAME STRUCTURE

The test model of two-storey two-span frame shown in Figure 3 is taken for analysis, with the section of middle beam in the frame $150\text{mm} \times 250\text{mm}$, two 12mm longitudinal reinforced bars (HRB335) respectively at the upper and lower parts, column section $150\text{mm} \times 180\text{mm}$, and three 12mm longitudinal reinforced bars (HRB335) respectively at both sides of the column along the frame, and it was placed with C20 concrete. Every joint in the frame is reinforced with FRP, for which the attachment method of fiber strengthening is as shown in Figure 1 above, where the fiber strip 1 for the middle joint is horizontally attached at both sides of the joint. The unreinforced frame is numbered as KJ-1, with the other three FRP strengthened frames are named as GRKJ-1, HRKJ-1 and HRKJ-2 accordingly.

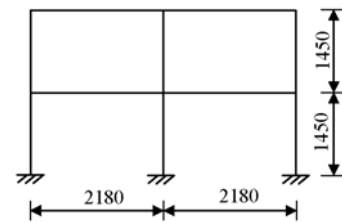


Figure 3 Schematic diagram for frame

SAP2000V14 software is used for the Pushover static elastoplastic analysis, in which the modeling is based upon the frame pole unit, the constitutive relations of concrete and reinforced bars followed the regulations in the GB50010-2002 specification, and moment-rotation relationship of the measured results in the test of joints can be converted into curves of frame model, then plastic hinge property could be defined according to the relations between moment and curvature in SAP2000. The M3 plastic hinges were designed at the beam ends, that is, taking no consideration of the influence of axial force on the bending resistance of the section; and PMM plastic hinges were designed at the column ends.

The progressive loading model from the frame top is used with 0.15g, which is designed as the basic acceleration during analysis.

5 CAPACITY SPECTRUM ANALYSIS AND SEISMIC PERFORMANCE EVALUATION

5.1 Capacity spectrum method

For capacity spectrum method, the Pushover analysis is made on the structure to obtain the relation curve between

shearing strength and the displacement of control point, and transform the curve to find out the capacity spectrum curve, in which longitudinal coordinate is taken as acceleration spectrum and horizontal coordinate as displacement spectrum, the designed response spectrum under the damping ratio corresponding to the predicted maximum displacement response is used to express the earthquake demand curve of the structure, while the displacement corresponding to the intersection point of capacity spectrum curve and the demand curve is the required target displacement. Capacity spectrum method is based upon displacement performance. Since the software SAP2000 integrates demand spectra of ATC-40, it can be applied to current specifications in China through parameter transformation, and can automatically transform the curves obtained from Pushover analysis into the capacity spectrum, based on which the performance point (target displacement) will be automatically solved from the equivalentization of standard demand spectrum.

5.2 Development of plastic hinges

The plastic hinges of three FRP strengthened frames have the similar development process. The development and distribution of KJ-1 and GRKJ-1 plastic hinges are shown in Figure 4. ATC-40 classifies the possible states of the structure after being struck by the earthquake into IO (Immediate Occupancy), LS (Life Safety) and SS (CP) (Structure Stability), where B means the presence of plastic hinge, and C refers to the collapse point.

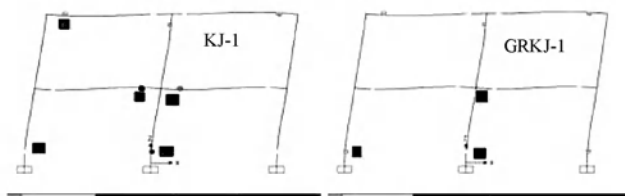


Figure 4 Development and distribution of plastic hinges in the frame

Seen from Figure 4, the development sequence of plastic hinge is from beam to column, bottom layer to top layer, and central joints to the side joints, and that all the frame structures can realize the damage from the beam-hinge yield mechanism of strong column and weak beam type with good performance in energy consumption. The plastic hinge at the central joint in the bottom layer of KJ-1 reached the collapse point C, and the plastic hinge at the foot of the central column was also developed to the LS status, and could not meet the requirements for earthquake resistance, and therefore strengthening measures had to be taken on plastic hinges. While for GRKJ-1, all plastic hinges were developed to IO (Immediate Occupancy), in which they would not affect integral performance of the structure if they may be

repaired as soon as possible, and the good strengthening effect may be achieved so as to greatly improve the seismic performance.

5.3 Push-over curve

Push-over curves calculated for the frames are shown in Figure 5, where the top layer of the frame is taken as the loading control point and the ultimate displacement is fixed at the position where Push-over curve shows obvious falling. Seen from the comparative analysis, the ultimate displacement for the control point of FRP strengthened frame has been greatly improved, and the ductility of the frame is also significantly improved, and the ultimate bearing capacity is also increased by various degrees.

Compared with the unstrengthened frame KJ-1, GRKJ-1 has been most greatly improved in its ultimate deformation capacity by about 45%, while the ultimate deformation capacity of HRKJ-1 and HRKJ-2 is improved by 40% and 32% respectively. This is because of the functions of FRP strengthened system to make the concrete in the ends and the core areas of the beam-column joints in the frames into the restrained concrete, so that its ultimate compressive strain has been greatly improved, in particular, the ductility of the members determined by the rotational capacity of plastic hinges at the beam ends is also greatly improved. With varying FRP strengthening methods, the ultimate bearing capacity of the strengthened frames has also been greatly improved. In addition, various strengthened frames have basically the same results with that of the joints in the improvement of ductility and bearing capacity. The comparative analysis on the Push-over curves of various analysis frames has shown that strengthening the combination unit of the joints is critical to the integral seismic performance of the frame structure, and the strengthening effect will have direct influence on the extent of improvement of overall seismic performance of the frames. It is feasible to improve the overall seismic performance of the frames based on the joint strengthening.

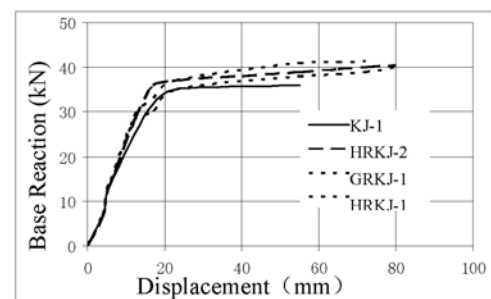


Figure 5 Comparison of push-over curves for the frames

5.4 Performance point and target displacement

Target displacement of the structure means the maximum

displacement that the structure would possibly achieve in an earthquake (generally refers to the top point displacement), the software SAP2000 may automatically transform the curves obtained from Push-over analysis into the capacity spectrum curve and based on this, the performance point (target displacement) will be automatically solved from the equivalentization of standard demand spectrum. After the determination of the performance point, the displacement of control point on its corresponding Push-over curve is the target displacement, and the performance point for displacement analyzed in this article is shown in Figure 6.

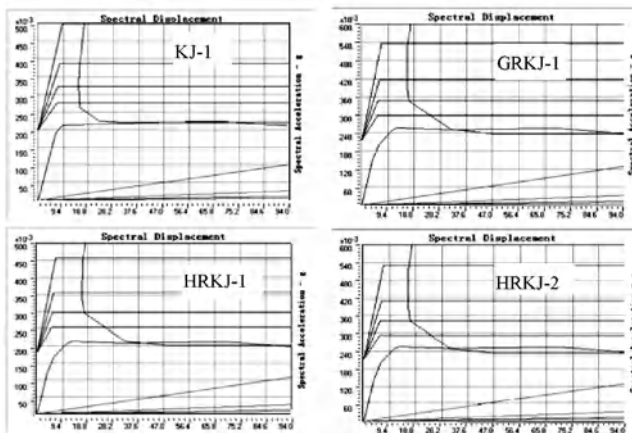


Figure 6 Performance points of frame displacement in analysis with capacity spectrum method

Table 1 Analysis on target displacement of frames

Item No.	Target displacement d (mm)	Interlayer displacement angle	Ultimate displacement D(mm)	d/D
KJ-1	57.2	1/51	55	> 1
GRKJ-1	36.6	1/79	80	45.8%
HRKJ-1	41.9	1/69	72	58.2%
HRKJ-2	38.6	1/75	77	50.1%

From analysis on the results in Table 1, it can be seen that all the inter-layer displacement angles corresponding to the target displacement of various strengthened frames are smaller than 1/50, complying with the requirements in current specification GB50011-2001 for earthquake resistance and meeting the requirements of maximum deformation in earthquake. The allowable value of inter-layer displacement angles in the unstrengthened frame is 1/50, which means that the frames show insufficient reserve of ductility, and that target displacement is larger than the ultimate displacement. Target displacement at the dropping section of Pushover curve means the

presence of the yielding member in the frame structure, and cannot meet the demand on its ductility in case of earthquake with fortification intensity for the rarely happening earthquake, when the frame should be strengthened for earthquake resistance so as to improve its ductility. All the inter-layer displacement angles of frames reinforced with various FRP are far less than 1, and all the target displacements are smaller than the ultimate displacement, the capacity demand ratio parameter d/D is far less than 1, which is only 45.8% in GRKJ-1, which means the strengthened frame maintains relatively large reserve of ductility under such earthquake intensity with fortification, and shows good seismic performance.

6 CONCLUSIONS

(1) In this article, better effect of strengthening has been achieved on the basis of the application of FRP strengthening method for beam-column joints of plane frame structures;

(2) Compared with the unstrengthened frames, the seismic performance of the FRP strengthened frames in three different types was greatly improved and increased;

(3) By comprehensive analysis on target displacement obtained from Push-over curve and capacity spectrum method, FRP strengthened frame structure presents greater ductility improvement degree than the improvement of the ultimate bearing capacity, and is more applicable to seismic strengthening, particularly, GFRP showed more outstanding strengthening effect.

REFERENCES

- Balsamo, A. & Colombo A. et al. 2005. Seismic behavior of a full-scale RC frame repaired using CFRP laminates. *Engineering Structures* 27:769-780.
- Jiang Weiguo & Chen Zhongfan. et al. 2009. Analysis on Seismic Performance of FRP strengthened RC Frames. *Earthquake Resistant Engineering and Retrofitting* 31(1): 91-96+69
- Ludovico, M.D. & Prota, A. et al. 2008. Seismic strengthening of an under-designed RC structure with FRP. *Earthquake Engineering and Structural Dynamics* 37:141-162.
- Peng Yaping & Wang Tiecheng. et al. 2006. Research on seismic performance of concrete beam-column joints reinforced with FRP. *Building Structure* 36(9): 28-30.
- Sokkary, H. El. & Galal, K. 2009. Analytical investigation of the seismic performance of RC frames rehabilitated using different rehabilitation techniques. *Engineering Structures* 31:1955-1966.
- Ye Lieping & Feng Peng. 2006. Applications and development of fiber - reinforced polymer in engineering structures. *China civil engineering journal* 39(3): 24-36.

The Anchorage Behavior of FRP EBR in the Plastic Zone of RC Beams

Francesca Ceroni (ceroni@unisannio.it), Marisa Pecce & Fabio A. Bibbò

Department of Engineering, University of Sannio, Benevento, Italy

ABSTRACT In this paper the bond behavior of external FRP reinforcement anchored in an high stressed zone of RC beams has been investigated under monotonic and cyclic actions. The detailed study of the experimental strain distributions along the FRP strengthening has evidenced a progressive damage of bond at increasing the cycles and the influence of steel yielding propagation under both monotonic and cyclic load histories.

1 INTRODUCTION

The behaviour of structures under cyclic loads can regard two different types of performances: a very high number of cycles applied in the elastic field concerns the fatigue strength, while a low number of cycles in the post-elastic field is significant of the seismic response of the structure.

Experimental results on Reinforced Concrete (RC) members externally strengthened with FRP laminates/sheets subjected to cyclic loads are few and usually refer to fatigue behaviour (Aidoo et al., 2004; Kim & Heffernan, 2008). The effect of cyclic loads on bond behaviour at the FRP-concrete interface hasn't been much investigated by experimental tests yet, since a suitable test set-up is difficult to realize especially when reversed loads are applied. Bond tests under cyclic loads without reversing loads (Nigro et al., 2008; Mazzotti & Savoia, 2007) showed that the debonding force is not affected by cycles, even if a light degrade of the interface bond stresses occurred.

Some bending tests on RC beams externally strengthened with CFRP sheets were realized in the past by the Authors (Ceroni & Pecce, 2005) performing a low number of cycles before and after the elastic field with and without load sign inversion. The experimental results evidenced a reduction of the end debonding load of about 10-15% respect to similar beams subjected to monotonic loads; furthermore buckling phenomena of fibres stressed in compression were observed (Budelmann & Husemann, 2005). In these tests debonding occurred at the end of the FRP reinforcement, where the bending moment was low and the stresses in the concrete far from the plastic field. On the contrary, if the FRP reinforcement is anchored in a zone where a plastic hinge forms, the bond behaviour can be significantly affected by both the damage of the concrete surface and the excursions of concrete and steel in the plastic field.

Thus, in this paper the first results of a new experimental program are presented. Three point bending tests have been carried out on RC beams where the ends of the FRP external reinforcement were anchored close to both a low and high moment area in order to investigate the effect of the plasticization of the materials and the degradation of the concrete surface on the bond behaviour.

2 THE EXPERIMENTAL PROGRAM

The experimental program concerns five three point bending tests on RC beams having cross section 400 mm×200 mm and span of 3.8 m; internal steel reinforcements are symmetrical in tension and compression and are made of 4 bars with diameter 14 mm (reinforcement percentage $\rho_s = 0.91\%$).

The mean compressive cubic strength of concrete, evaluated by experimental tests on cubes with side 150 mm, is 35.8 MPa. The mean values of yielding and ultimate stress of the steel bars, evaluated by three tensile tests, are 543 MPa and 629 MPa, respectively. The external reinforcement is made of one layer of Carbon FRP sheet having width of 200 mm (ratio FRP-to-concrete width 0.5) and applied according to the configuration of Figure 1a, symmetrically on both top and bottom sides of the beam. Tensile strength and Youngs' modulus of the CFRP sheet given by the manufacturer are 4800 MPa and 230 GPa.

The deflection at the mid-span was measured by an inductive transducer; several strain gauges were applied on the FRP reinforcement according to the general scheme of Figure 1a. The load was applied under displacement control by an hydraulic jack connected to the beam by a steel frame made of two stiff plates and four bars crossing the beam outside (Figure 1b).

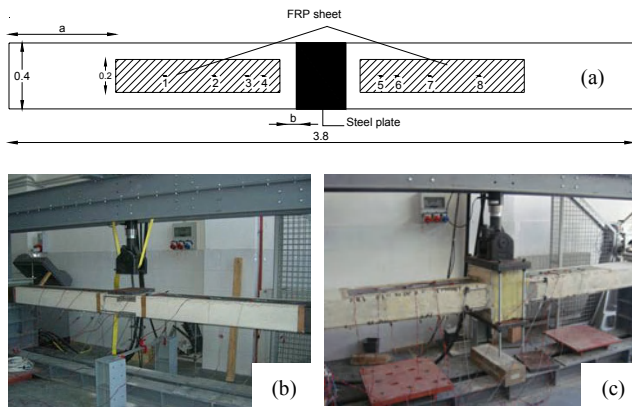


Figure 1 a) Strengthening scheme; b) Testing configuration of beams A1-A2; c) Final testing configuration for beams A3-A4

This strengthening and loading lay-out is aimed to investigate the bond behavior at the concrete/reinforcement interface under cyclic loads in high stressed zones where a plastic hinge can form and the concrete surface can be damaged. Thus, this set-up allows to apply high cyclic loads to the FRP reinforcement and provides to solve the difficulty of realizing bond tests under inverted cyclic actions. In this way the end-debonding failure can be investigated both when the end of the FRP reinforcement is anchored in a maximum moment zone (section B, Figure 2) and in a very low or zero moment zone (section A, Figure 2). Two actual examples of this condition could be the anchorage of inferior FRP reinforcements close to the middle support of continuous beams or the free end of reinforcement used to strengthen beams in hogging moment areas (cantilever or hyper-static schemes). In both cases one end of the reinforcement is subjected to a very high moment, while the other one is in a low moment area (as the section B and A of Figure 2, respectively). Furthermore the cyclic loads add the effect of sign changing of the bending moment. In fact, under seismic actions, high positive and negative bending moments can be cyclically applied to the FRP reinforcement when is anchored close to an intermediate support of an RC frame or when it is used as flexural strengthening of RC columns and its end is not anchored in the beam-column joint.

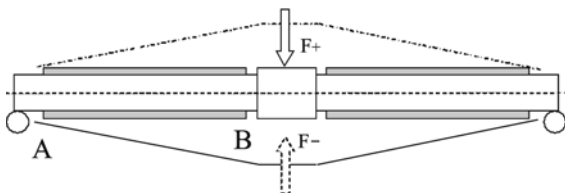


Figure 2 Lay-out of the loading test set-up

A first experimental test on a strengthened beam (beam A2) showed an insufficient propagation of the plastic hinge out of the loaded zone (corresponding to the steel plate in Figure 1a), so that the FRP ends were not

influenced by concrete plasticization. Hence the specimen configuration was changed: in particular an enlargement of the mid-span zone was realized by adding a supplementary concrete volume wrapped with FRP sheets (+100 mm on the top and bottom sides of the beam for a width of 300 mm straddle the mid-span, Figure 1c). This modification was aimed to increase the strength of the mid-span zone, move the formation of the plastic hinge out of the loaded area and shift it as close as possible to the ends of the reinforcement. In order to achieve this last intent, the reinforcement was glued just at the end of the enlarged mid-span zone ($b \approx 0$, Figure 1a); moreover the distance from the supports, a , has been increased from 100 mm to 740 mm (Figure 1a) because no end debonding was observed in the previous test and the aim of the test is the study of the bond behaviour at the other end of the FRP reinforcement placed in an high moment area.

Finally the tested beams were:

- (1) Beam A1: the reference not strengthened specimen monotonically tested;
- (2) Beam A2: the first strengthened beam tested according to an ineffective configuration (Figure 1b);
- (3) Beam A2bis: the beam A2 modified with the enlargement of the mid-span zone and aimed to verify the reliability of the new configuration;
- (4) Beam A3: the strengthened beam monotonically tested according to the final configuration (Figure 1c);
- (5) Beam A4: the strengthened beam (Figure 1c) equal to A3 and subjected to a cyclic load history fixed basing on the load-deflection curve of the beam A3:
 - monotonic loading (0.10 mm/s) until a deflection of 24.5 mm corresponding to 47 kN that is about the 85% of steel yielding load (55 kN);
 - 10 cycles (0.75 mm/s) in the range +24.5 mm and -24.5mm;
 - monotonic loading up to 47 mm corresponding to +58 kN that is an intermediate condition in the plastic field branch of steel after yielding;
 - 10 cycles (0.75 mm/s) between +47 mm and -47 mm;
 - monotonic loading up to 100 mm corresponding to +53 kN that is an intermediate condition in the softening branch of the load-displacement curve of the beam A3;
 - cycles (1.00 mm/s) between +100 mm and -100 mm until the beam failure.

In the following the only results of beams A1, A3 and A4 are discussed since the beam A2 was used to assess the testing procedure.

3 EXPERIMENTAL RESULTS

3.1 Failure mode and load – displacement relations

In Table 1 the theoretical and experimental values of the bending moment corresponding both to the yielding of steel bars (M_y) and the failure (M_{max}) are reported. The

theoretical values are calculated neglecting the external reinforcement since it is interrupted at the mid-span. Moreover, the theoretical and experimental values for the beams with the enlarged mid-span section (A3 and A4) are referred to the first regular section out of the enlarged zone (at 150 mm from the centre). The inferior and superior concrete covers (c_{inf} and c_{sup}) are not the same for all beams, so that the theoretical values are different. For beam A4, loaded cyclically, both negative and positive bending moments are listed.

For all beams the scatter between experimental and theoretical moments is negligible (maximum 9% for beam A4 probably due to cyclic degrade). Beams A1 and A3 failed for crushing of the compressed concrete with steel bars yielded; in Figure 3 the comparison between the moment-deflection relationships of beams A1 and A3 is plotted. In beam A3 the failure occurred at the first section close to the enlarged mid-span (Figure 4a) where the FRP reinforcement started detaching due to the wide opening of cracks after the steel yielding.

Table 1 Experimental and theoretical values of strength

Beams	c_{inf} (mm)	c_{sup} (mm)	$M_{y,th}$ (kN·m)	$M_{y,exp}$ (kN·m)	$M_{max,th}$ (kN·m)	$M_{max,exp}$ (kN·m)
A1	4.0	5.5	50.8	51.8	56.7	55.2
A3	4.5	5.5	49.1	48.7	54.8	53.5
A4 ⁺	4.5	5.5	49.1	48.8	54.8	51.4
A4 ⁻	5.5	4.5	44.4	44.3	49.8	45.4

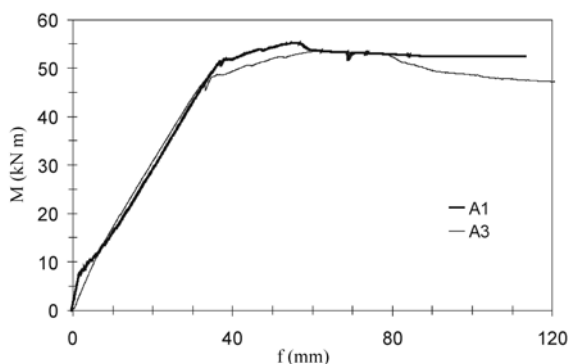


Figure 3 Experimental moment vs. deflection for beams A1 & A3

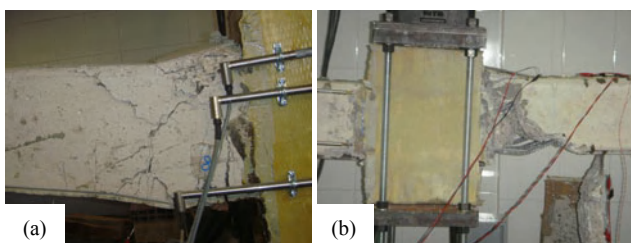


Figure 4 Failed sections: a) beam A3; b) beam A4

In Figure 5 the load-deflection curves of beams A3 and A4 are compared showing that the monotonic curve is a good envelope of the cyclic ones. Moreover for the

beam A4 the following results were observed:

- after the first series of 10 cycles the residual deflection is practically zero, while it becomes relevant (about 16.5 mm) after the second series of cycles;
- the difference between the positive and negative behaviour, observed during the first series of cycles, is gained during the second series (± 47 mm that correspond to -51 and $+54$ kN). The experimental negative yielding and maximum loads are about 10% lower than the positive ones, as the theoretical values too (see Table 1);
- the third series of cycles is realized when the steel bars are in an advanced plastic field, so that the residual deflection is relevant (about 67 mm);
- after the first cycle of the last series the loading capacity dropped off to 40% due to the failure of the section close to the mid-span because of the FRP debonding and the buckling of steel bars (Figure 4b).

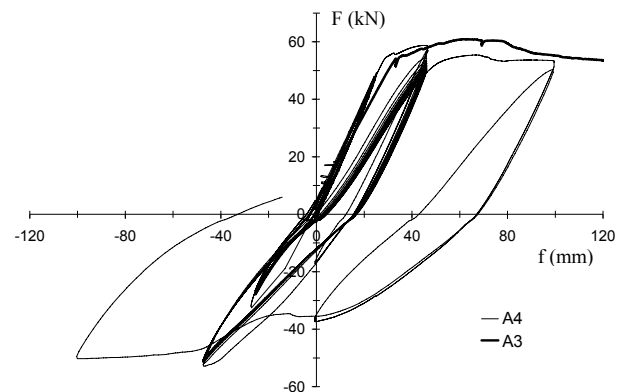


Figure 5 Experimental load vs. deflection for beams A3 & A4

3.2 Strain distributions in the FRP reinforcement

Experimental strain distribution along the FRP reinforcement at several load levels for the beam A3 (Figures 6) shows that the peak values are attained in the central part of the reinforcement: this means the presence of a transfer length at both ends.

Moreover, when the steel bars begin yielding (≈ 50 kN) in the sections close to the mid-span the strains become constant or decrease, while in the more distant ones the strains continue to increase as load raises. This behaviour evidences a degradation of bond in the most stressed part of the beam close to the mid-span because of the superficial damage of concrete and the wide opening of cracks after the steel yielding. However these phenomena were not sufficient to cause the detachment of the FRP reinforcement in the beam A3 also at advanced failure conditions (Figure 4a). On the contrary debonding happened in the beam A4 (Figure 4b) due to the higher damage level induced in the concrete by the cyclic actions.

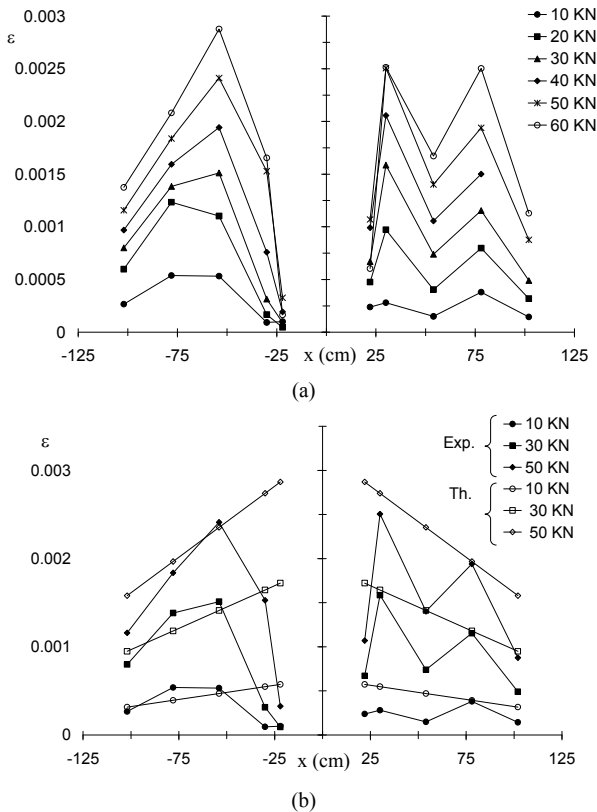


Figure 6 Strain distribution along the CFRP sheet in beam A3. (a) experimental values; (b) comparison with theoretical values

The comparison (Figure 6b) between the experimental and theoretical strains (given by the Naviers' formula under the hypothesis of plane section) at loads lower than steel yielding (50 kN) confirms that at both ends the experimental values are lower than the predicted ones. The two FRP sheets interrupted at the mid-span are able to sustain stresses comparable with the theoretical ones at a distance from the ends of 250 – 300 mm that, thus, is the effective transfer length.

In order to follow the degradation phenomena under the cycling actions, the strains measured in correspondence of the maximum positive displacement at the end of each cycle are graphed in Figures 7 for the strain gauges glued on the left inferior FRP sheet; the strains are normalized to the value measured at the beginning of the first cycle and plotted versus the number of cycles. In particular Figure 7a refers to the 1st series of cycles in the elastic field, Figure 7b refers to the 2nd series after the steel yielding, and Figure 7c refers to the last 4 cycles before the complete failure. The strain gauges 4 and 3 are close to the mid-span (200 and 300 mm), the no. 2 is glued about at the centre of the sheet (550 mm), and the no. 1 is placed at about 800 mm from the mid-span (Figure 1a).

The strains measured by gauges 1 and 2 have a negligible reduction ($\varepsilon/\varepsilon_1 \approx 1$) during the 1st series of cycles (Figure 7a), while in the 2nd and 3rd ones they decrease quite proportionally to the applied load. The

maximum positive load remains constant during the 1st series and reduces of about 15% and 70%, respectively at the end of the 2nd and 3rd series. By the contrast, the strains measured close to the mid-span (gauges 3 and 4) show sensible variations that are larger than the load decrease: the reduction is about 5% at the end of the 1st series and 25% and 60%, respectively, after the 2nd series. Finally during the last 4 cycles the strains of gauge 3 reduce of 80%, quite as the load, while the strains of the gauge 4 become negative, despite the tension stresses in the reinforcement (Figure 7c).

Therefore, the observed reduction of strain is as larger as the gauges are close to the mid-span, while, if they are far from the mid-span, the strains decrease proportionally to the load. This phenomenon is due not only to the degradation of bond under the cyclic actions, particularly evident in the most stressed zones in the elastic field too (Figure 7a), but also to the steel yielding propagation. When steel yields in the first not strengthened section the moment can not increase anymore, differently from the adjacent strengthened sections where the moment can increase thanks to the FRP reinforcement. Therefore, the loading scheme (simply supported beam) requires a lower moment in the more distant strengthened sections, so that the section equilibrium causes a reduction of stresses in the FRP reinforcement. This phenomenon has been observed also in the strain distribution of the beam A3 (monotonically loaded) after the steel yielding.

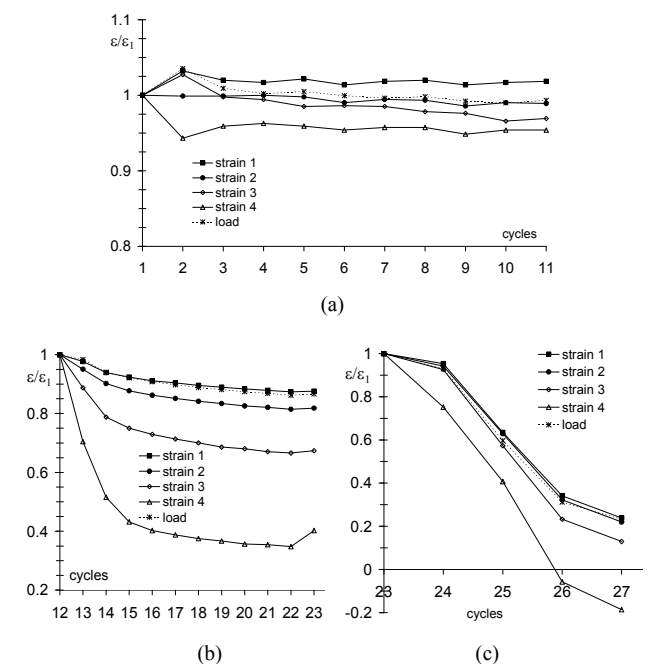


Figure 7 Normalized experimental strain in the FRP during the cycles: (a) first series; (b) second series; (c) third series

4 CONCLUSIONS

This paper presents the first results of bending tests on RC beams strengthened with CFRP sheets aimed to

study the bond behaviour of the external reinforcement in a high stressed area where concrete and steel can plasticize under both monotonic and cyclic actions. An evident effect of the cycles was observed that usually is negligible when the end of the FRP reinforcement is in a low stressed zone of the beam.

The damage of bond is evidenced by the reduction of the strains in the external reinforcement that occurred especially after the steel yielding under monotonic loads and was amplified under cyclic actions. Hence, the effect of damage of concrete on bond behaviour should be considered for application in seismic areas. However further tests will be carried out to better assess these first observations and to study the effect of anchorage systems to avoid or delay the debonding under cyclic actions.

REFERENCES

- Aidoo, J., Harries, K.A., Petrou, M. 2004. Fatigue behavior of Carbon fiber Reinforced Polymer–Strengthened Reinforced Concrete, *J. of Comp. Constr.*, 8 (6), 501-509.
- Budelmann, H., Husemann U. 2005. Effect of repeated live loads on the bond capacity of externally bonded CFRP-plates, *Composites in Constructions CCC 2005*, July, Lyon, France.
- Ceroni, F., Pecce, M. 2006. Monotonic and cyclic performance of RC Beams Strengthened with FRP sheets, *2nd Int. fib Congress*, 5-8 June, Naples, Italy, CDROM.
- Kim, Y.J., Heffernan, P.J. 2008. Fatigue Behavior of Externally Strengthened Concrete Beams with Fiber-Reinforced Polymers: State of the Art, *J. Comp. Constr.*, 12 (3), 246-256.
- Nigro, E., Di Ludovico, M., Bilotta, A. 2008. FRP- Concrete Debonding: experimental Tests under Cyclic Actions, *14th World Conf. on Earthquake Engin.*, Beijing, China, CDROM.
- Mazzotti, C., Savoia, M. 2007. FRP-concrete bond behaviour under cyclic debonding force, *APFIS 2007*, S.T. Smith ed., Int. Inst. for FRP in Construction.

Application of FRP for Punching Shear Retrofit of Concrete Slab-Column Connections

Maria Anna Polak (polak@uwaterloo.ca)

Department of Civil and Environmental Engineering, University of Waterloo, Waterloo, Canada

Nicholas Lawler

Design Engineer, Structural Design Inc. Ann Arbor, Mi. USA

ABSTRACT Fibre reinforced plastic, FRP, shear bolt system has been recently developed at the University of Waterloo, Canada. The system can be used to protect existing reinforced concrete slabs against brittle and sudden punching shear failure. The retrofit procedure requires drilling small holes in a slab around the perimeter of a column, inserting bolts into the holes and anchoring the bolts at both external surfaces of the slab. Many existing reinforced concrete slabs had been built without any shear reinforcements. Also, many of these slabs are in corrosive environments, e.g. in parking garages where the use of de-icing salts accelerates reinforcement corrosion and concrete deterioration. Therefore, FRP is an ideal material to be used for such retrofit. The challenge, however, has been the development of mechanical end anchorages for FRP rods that is efficient, aesthetic, cost effective, and that can be applied on-site. In the presented research six isolated slab-column specimens were constructed representing interior slab-column connections in a continuous flat plate slab system. The specimens were subjected to simulated gravity and gravity plus seismic loadings. A new anchorage technique for the FRP rods was developed, which is based on crimping the rod ends with the aluminum fittings. Using this approach, fairly large loads can be resisted by the end-fittings. The developed FRP bolts worked very well improving the performance of the slab-column connections and showing the benefits of using FRP in punching shear retrofit of reinforced concrete slabs.

1 INTRODUCTION

Corrosion of reinforced concrete infrastructure is a major problem especially in cold weather countries where use of deicing salts accelerate corrosion of steel reinforcement causing cracking and deterioration of concrete.

Flat reinforced concrete slabs supported on columns are common in construction of parking garages and buildings. These slabs are subject to high transverse stresses concentrated at the slab-column connections, which can lead to a nonductile, sudden and brittle punching shear failures. The most efficient method for ensuring adequate punching shear strength and ductility of such connections is to provide properly designed transverse reinforcement, however many existing slabs do not have such reinforcements. The steel shear bolt developed at the University of Waterloo can be effectively applied to existing slabs to strengthen the connections, both in gravity loading, and lateral cyclic loading (Adetifa and Polak 2005, Bu and Polak 2009). However, the steel bolts, exposed to the environmental conditions pose a problem of corrosion and thus a non-corrosive repair solution was needed.

Fibre Reinforced Polymer (FRP) reinforcements do not corrode under high salt levels like traditional steel.

Research by the ISIS Canada Research Network has shown that FRP reinforcements are strong, reliable, and practical for use in many different types of structural applications and retrofits (Neale, 2008).

This paper focuses on the newly developed strengthening technique for punching shear in flat plate slabs using FRP reinforcement. Several options were investigated namely, an off-the-shelf glass fibre reinforced polymer (GFRP) threaded nut and rod product, and two different types of GFRP used with aluminum fittings. A new crimping anchorage technique for the FRP rod was developed. Six isolated slab-column specimens representing interior slab-column connections in a continuous flat plate slab system were tested. To allow direct comparisons, the specimens were identical to the specimens previously tested (Adetifa and Polak 2005, Bu and Polak 2009) and retrofitted with steel bolts.

2 DEVELOPMENT OF FRP SHEAR BOLTS

Punching shear failure is a result of a formation of a truncated cone of cracks forming around the column area of a slab. Therefore, shear bolts must overcome tensile forces which are opening the shear cracks inside the slab. In this retrofit procedure small diameter holes

are drilled through the slab, around the column area, in a predetermined pattern to ensure crossing of the shear cracks by the drilled holes (Figure 1). The bolts are inserted in the holes and tightened against the slab surfaces (Lawler 2008, Adetifa and Polak 2005). The essential component of the bolt is the anchorage against the slab's surfaces; in previous work on steel bolts it was achieved by a forged head on one end and a washer and a nut on the other threaded end of the bolt.

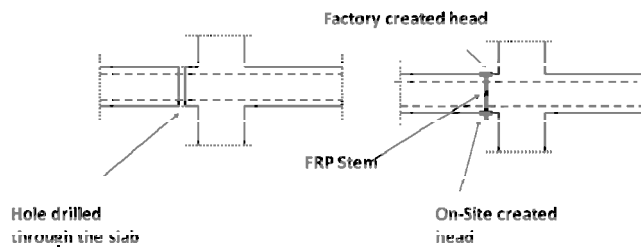


Figure 1 Installation of shear bolts in existing slabs

The development of the FRP bolt required developing adequate anchorage for the FRP rod. FRP bar is a one-dimensional, engineered material with fibers aligned along the bar ensuring very high longitudinal tensile strength. FRP product exists on the market which has a thread, intended to be used with washers and nuts. (e.g. Strongwell Ltd.). Threading FRP weakens the tensile strength of the FRP bar.

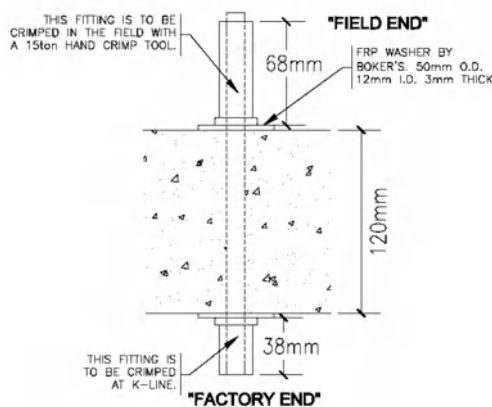


Figure 2 Schematic of FRP bolt with crimped ends.

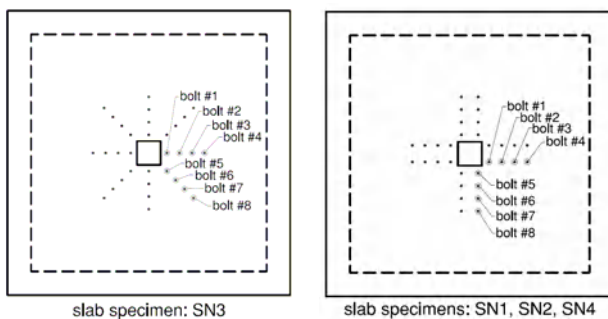


Figure 3 Plan view of the specimens tested in concentric punching showing orthogonal and radial patterns of FRP Bolts

Mechanical crimping has been used for many years to attach aluminum fittings to electrical insulators. Crimping electrical insulators is done primarily in a factory, using industrial presses, under well controlled conditions. By compressing the end fitting, the stress is transmitted through the metal to the GFRP providing a frictional bond between the two materials. This technique seemed promising and it was used to create end anchorages used in this research. The retrofit method must be practical for use on construction sites. Therefore, one end of the FRP bolt can be crimped in a factory but the other end must be installed on site, after the bolt is inserted into the predrilled holes. For this purpose a portable crimping device was used.

3 EXPERIMENTAL PROGRAM

Six isolated slab-column interior connection specimens, SN1, SN2, SN3, SN4, SN5 and SN6 of dimensions 1800×1800×120 mm were tested; the SN1-SN4 specimens under static vertical load, while SN5 and SN6 were subjected to constant gravity load of 160kN and increasing lateral drifts. The test frame is described in detail by Bu and Polak (2009). The slabs were supported on 25 mm thick neoprene pads attached to a horizontal frame located underneath the vertical frame. Simple supports were placed at the in-plane distances of 1500 x 1500 mm, which represent the lines of contraflexure in a continuous slab-column structural system (Lawler, 2008). Corners were restrained from lifting for SN1-SN4. The line normal to lateral load application was restrained from lifting for SN5 and SN6. The specimens were loaded in displacement controlled mode through column stubs. The load cell attached to the 150 kip actuator was used to apply vertical loads and the specimen displacements were measured using displacement transducers. Horizontal displacements (SN5 and SN6) were applied at the column stubs, 565mm from the slab top and bottom faces

The specimens were designed to ensure punching failure, before application of the shear bolt strengthening reinforcement. Flexural reinforcement was identical to the previously tested slabs by Adetifa and Polak (2005). For the tension mat, 10M bars at 100 and 90 mm centers were used for the bottom and top tension layers (two orthogonal directions), respectively. 10M bars at 200mm, both layers, were used for the compression mat. The concrete cover in both tension and compression zones was 20mm. The slab SB1 (Adetifa and Polak 2005) was considered a control specimen without any shear reinforcement.

The specimens were retrofitted with either four (SN1-SN4, tested in concentric punching, Figure 3), five (SN5 tested in gravity and lateral pseudo-seismic loading) or six (SN6 tested as SN5 but with two 150×150 mm openings next to the column in the direction of lateral

loading) peripheral rows of GFRP bolts. SN1 was retrofitted with 12.5mm diameter GFRP bolts by Strongwell Industries (Type 3, Lawler 2008). Strongwell produce a product known as a Fibrebolt, a fiberglass stud and a nut system to be used for fastening non-structural lightweight fixtures. The bolts are threaded over their entire length, and have fiberglass nuts that are used in conjunction with the threaded rods. Slab SN2 was retrofitted using 12mm diameter GFRP smooth (Type 1) rods with crimped aluminum ends. Slab SN3 was retrofitted with Type 1 bolts in a radial pattern recommended by Eurocode 2. Slab SN4 was retrofitted with ComBar reinforcement with aluminum crimped ends (Type 2). ComBAR is manufactured by Schöck Canada. These are GFRP bars with the specially designed ribbing for better bond with concrete. Slabs SN5 and SN6 were reinforced with Type 1 bars (Lawler 2008)

4 EXPERIMENTAL OBSERVATIONS

4.1 Load versus displacement

Load versus central vertical displacement curves have been created based on the experimental data for specimens SN1, SN2 and SN3, and SN4 (Figure 4). Slab SN1 (type 3 bolts) failed in a sudden punching mode at a maximum load of 199kN. The specimen experienced a sudden and rapid drop in stiffness at the maximum load, which was accompanied by failure of the shear bolts in tension. Slab SN2 (Type 1 bolts) failed in flexural/punching mode at a maximum load of 280kN. After reaching a peak load, the specimen sustained the load with increasing deflections until punching occurred at large deformations. The test was stopped after substantial drop in post-peak load was observed. Slab SN3 (type 2 bolts in radial pattern) failed in flexure at a maximum load of 310kN. After reaching a peak load, the specimen continued to sustain the load. Unlike the two previous tests (SN1 and SN2), no significant reduction of strength was observed during the test. This connection behaved very ductile, and the test had to be stopped as the deformation reached the limit of the testing apparatus. Slab SN4 failed in flexure at a maximum load of 332kN. After reaching a peak load, the strength that the specimen could resist reduced, but maintained at a constant load until no more additional load could be added.

Figure 5 and 6 show the hysteresis plots for SN5 and SN6, respectively. There are two plots in Figure 5, the test was restarted after the hydraulic system failure and sudden overloading of the specimen. The specimen did not fail due to this overload, however, the stiffness of the connection decreased, and continued to degrade with the loading. The test was finally stopped when the connection could not sustain any further increases in loading. Testing of SN6 was not interrupted by unexpected events and

the specimen sustained large drifts. Few observations should be noted. Both connections, SN5 and SN6 sustained similar maximum loads as unreinforced for shear but otherwise identical connections tested previously by Bu and Polak (2009). The difference in the behaviour was that the unreinforced connections failed abruptly after attaining the maximum load while the SN5 and SN6 connections continued to deform and sustain load. Also, the connections showed very little pinching in their hysteretic behaviour. Thus even thou the connection sustained lower loads (than the connections reinforced with steel bolts) their energy dissipation (area under the hysteretic curve) was very good. In seismic events the amount of energy dissipated through a structural connection is an important factor. It should be noted that the identical connections reinforced with steel bolts (Bu and Polak 2009) sustained higher lateral loads but experienced pinching, which reduced the dissipated energy. The reason for lower lateral loads and no pinching of SN5 and SN6 is possibly the fact that FRP bolts were installed not very tightly against slab surfaces allowing the internal shear cracks to form and dissipate energy through friction during the reversed cyclic loading.

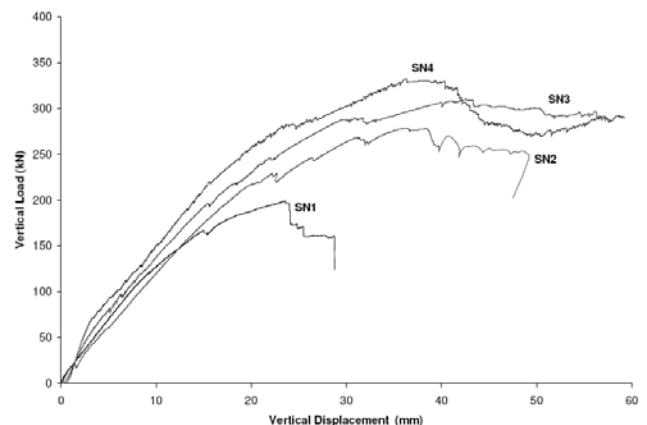


Figure 4 Load vs. displacement for slabs tested in concentric static loading

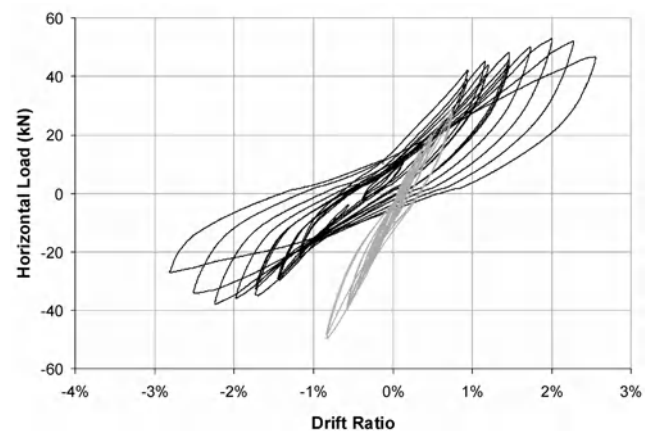


Figure 5 Lateral Load vs. Drift Ratio, SN5 (Type 1 bolts)

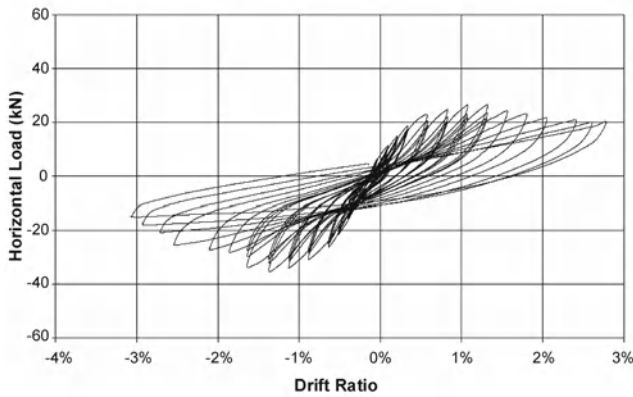


Figure 6 Lateral load vs. drift ratio, SN6 (type 1 bolts, 2 openings)

4.2 Load versus bolt strains

Figure 7 illustrates strains in Bolt #1 and Bolt #2, in the four specimens tested in static loading. In SN4, Bolt #1 recorded consistent strains until approximately 270kN loading. At this load the strain gauge stopped functioning properly; possibly a punching crack formation damaged it. In SN2 and SN3 the Bolts #1 behaved similarly until approximately 150kN of loading when the Bolt #1 in SN2 experienced little strain increase with the increase in load; possibly indicating slipping of the aluminum fitting. At 220kN a large increase in strain on Bolts #1 can be observed in SN2; when the bolt started to restrain the formation of the punching cone. Bolt #1 in SN3

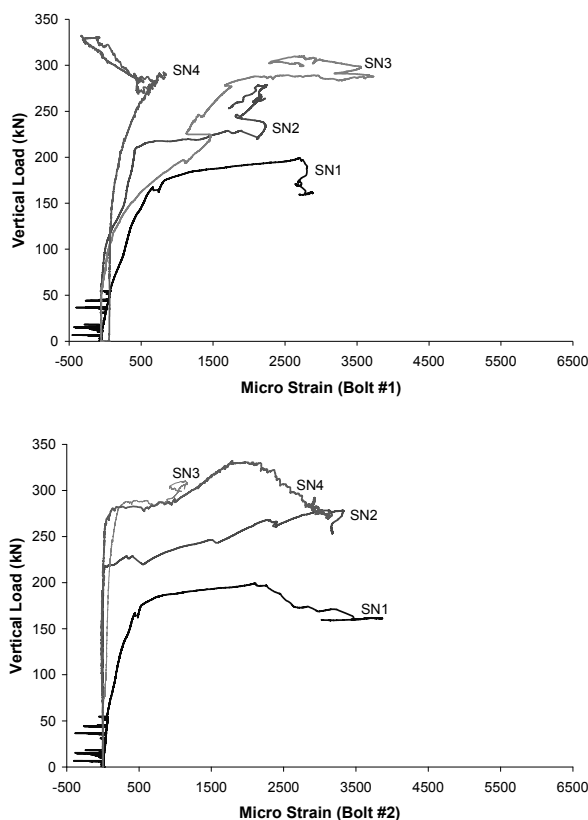


Figure 7 Vertical Load vs. Strain in Shear Bolts #1 and #2

sustained a greater load and more strain than SN2. Some slip of the crimped connection is visible on the plot (reduction in strain at the given load), however the crimp was able to sustain load up to 300kN. The strains in SN3 and SN4 in Bolt #2 were very similar. The bolts did not become active until about 270kN, at which point they both had an increase in strain. Bolt #2 in SN2 experienced a strain increase at the lower load of approximately 230kN. As the crimping process was being improved with each test, the crimps were likely not as strong in SN2 as in SN3 and SN4. Therefore, the punching cone in SN2 formed at a lower load, and activated the shear bolts at lower loads. SN1 experienced a sudden increase in strain at the lowest load of approximately 170kN.

From the strain analysis of Figure 7 it seems that formation of punching cone in SN1 happened at around 170 kN, in SN2 at 220 kN and in SN3 and SN4 at around 270 kN.

5 CONCLUSIONS

The presented research shows that FRP rods work well as a retrofit method provided the anchorage is strong enough to carry tensile forces opening the internal shear cracks. The retrofitted slabs were able to sustain higher load and higher ultimate deflections.

Crimping aluminum fittings to the FRP rods was found to be a feasible way to provide anchorage for this type of application. This shows promise that further development of the crimping and installation procedures of the GFRP shear bolt system can result in a practical solution for punching shear retrofit of reinforced concrete slabs in corrosive environments.

REFERENCES

- Adetifa, B., and Polak, M.A. 2005. Retrofit of Slab Column Interior Connections Using Shear Bolts. *ACI Structural Journal*. 102(2), 268-272.
- Bu, W., Polak, M.A. 2009. Seismic Retrofit of RC Slab-Column Connections using Shear Bolts. *ACI Structural Journal* 106(4), 514-522.
- Bu, W., 2008. Punching Shear Retrofit Method Using Shear Bolts for Reinforced Concrete Slabs Under Seismic Loading. *PhD Thesis, Department of Civil and Environmental Engineering, University of Waterloo*.
- Lawler, N.D., 2008. Punching Shear Retrofit of Concrete Slab-Column Connections with GFRP Shear Bolts. Masters Thesis, *Department of Civil and Environmental Engineering, University of Waterloo*.
- Neale, K., 2008. "Manual No. 4-Strengthening Reinforced Concrete Structures with Externally-Bonded Fibre Reinforced Polymers (FRPs)." *ISIS Canada*.
- Strongwell Coporation. 2002 "Section 11 – Fibrebolt Studs and Nuts". *Product Guide, Bristol: Strongwell Corporation*, 1-11.

Strengthening of Steel Structures

Beam-to-Column Connection of a Precast Concrete Frame Strengthened by NSM CFRP Strips

T. de C. C. S. da Fonseca (tfonseca@sc.usp.br), S. F. de Almeida, J. B. de Hanai

Department of Structural Engineering, University of São Paulo (USP), São Carlos, Brazil

ABSTRACT This paper presents results of experimental tests of a concrete frame with emphasis on the connections strengthening assessment. The tests were conducted in a small scale frame composed of precast columns and beam. Initially there were pinned connections between the beam and columns. The frame was loaded in two points of the beam until a beam cracking had been observed. The connections were strengthened by embedding CFRP strips in the lateral concrete cover. The frame was loaded again until failure which had occurred by splitting concrete edge in the connection region. It was observed that the strengthened connection exhibited semi-rigid behavior and provided significant reduction in the beam midspan deflection.

1 INTRODUCTION

Over the last decades the strengthening by embedding FRP strips in concrete cover has become more popular, some guidelines to design the strengthening are being developed and more ways to apply this technique are emerging. In this paper the application of this technique to the strengthening of beam-to-column connections in precast frames is evaluated. Specifically, the aim is to assess the improvement of the connection capacity to transfer bending moment.

Precast concrete structures can present unsatisfactory global behavior evidenced by either excessive lateral displacements or vibration, or excessive vertical deflections. In either monolithic or precast deficient structures, the rehabilitation is usually performed at their beams or columns. Certainly for most cases such procedure is the easiest to follow. However if the subject to be corrected is related to the global behavior of the structure, the strengthening of the connections between beams and columns should be considered. Marin & El Debs (2009) affirm that the global stability of precast multi-storey structures can be obtained by improving the stiffness of the beam-to-column connections. They have shown through numeric simulation that the use of semi-rigid beam-to-column connections makes the construction of up to six-storey buildings with precast skeletal structures possible in terms of global stability. For such buildings with pinned beam-to-column connections a referential limit is twelve meters in height.

2 EXPERIMENTAL TEST

2.1 Specimen

A small scale specimen was used in this study. The

specimen is a plane assemblage of two precast columns and one beam. The beam was connected to the columns by pinned connections. This type of connection is widely used in low-rise building structures of precast concrete and is formed by support cushions and dowels. The geometric characteristics of the model are presented in Figure 1.

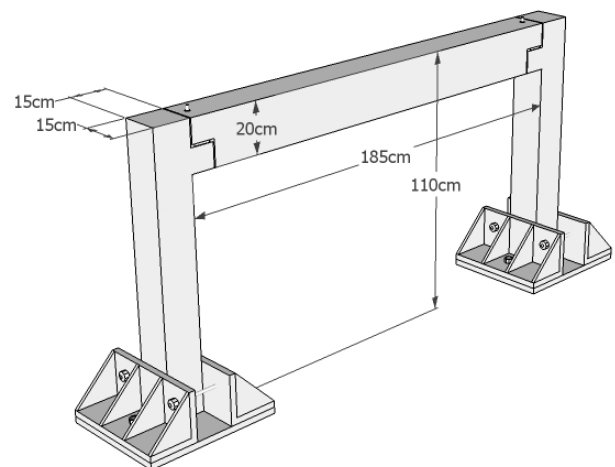


Figure 1 Specimen with metallic devices in column bases

2.2 Properties of materials

In the first set of tests, the beam and columns had a concrete cylinder compressive strength of 37 MPa, tensile strength (obtained by diametral compression test) of 3 MPa and a concrete Young's modulus of 31 GPa. Support cushions of natural rubber NR 1087 with Shore Hardness 70 A manufactured by ORION were used. The CFRP strips used for the strengthening have a cross-section of 2×16 mm and area of 32 mm². The strip

tensile strength guaranteed by manufacturer is 2.1 GPa and the tensile modulus is 130 GPa. The ultimate strain of the strip specified by manufacturer is 1.7%. The measured tensile strength of 1.6 GPa was determined in the laboratory, as well as the tensile modulus of 116 GPa and the ultimate strain of 1.3%. The adhesive chosen to glue CFRP strips was Sikadur® 330. The manufacturer guarantees tensile strength of 30 MPa and tensile modulus of 4500 MPa.

2.3 Preparation of specimen

The columns and beam were cast in wood molds and remained curing for two days. In the base of each column mold a metallic plate that composes the metallic device was coupled and longitudinal reinforcement bars were anchored in that by nuts and washers. The elements were air-dried in laboratory environment and then removed from the molds. The columns were erected and fixed on the structural floor of the laboratory by metallic devices. The support cushions were placed on the corbels and then the beam edges were supported over the cushions. Finally the spaces between the corbel and the beam were fulfilled with grout. The specimen with this configuration was used for the first two loading stages.

After these stages, the beam-to-column connections were strengthened by the procedure as follows. Four slits were made in each connection region, two located at 3 cm from the specimen top and two located at 3 cm from the beam bottom. These slits were made with a standard concrete saw, with 0.5 cm width and 1.8 cm depth along 50 cm in the lateral concrete cover, as it is shown in Figure 2. The slits were washed and then air-dried in laboratory environment. The dust in the slits was removed with compressed air and the slits were fulfilled with resin. The strips previously cleaned with alcohol and daubed

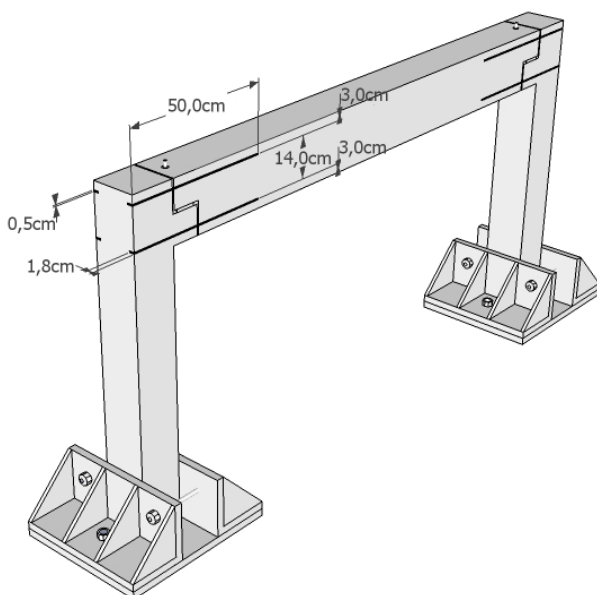


Figure 2 Specimen with strengthened connections

with resin were introduced in the slits. They were then pressed into the slits to force the epoxy adhesive to flow between the CFRP and the slit borders. The exceeding resin was removed with a trowel to finish the strengthening procedure. The model with strengthened beam-to-column connections was used for the third and fourth loading stages.

2.4 Test setup, instrumentation and procedure

The specimen was fixed on the structural floor of the laboratory by metallic devices in the columns bases. An actuator hung in an auxiliary frame was used to apply the loading, which was distributed for two points in the beam. The test setup and instrumentation are illustrated in Figure 3.

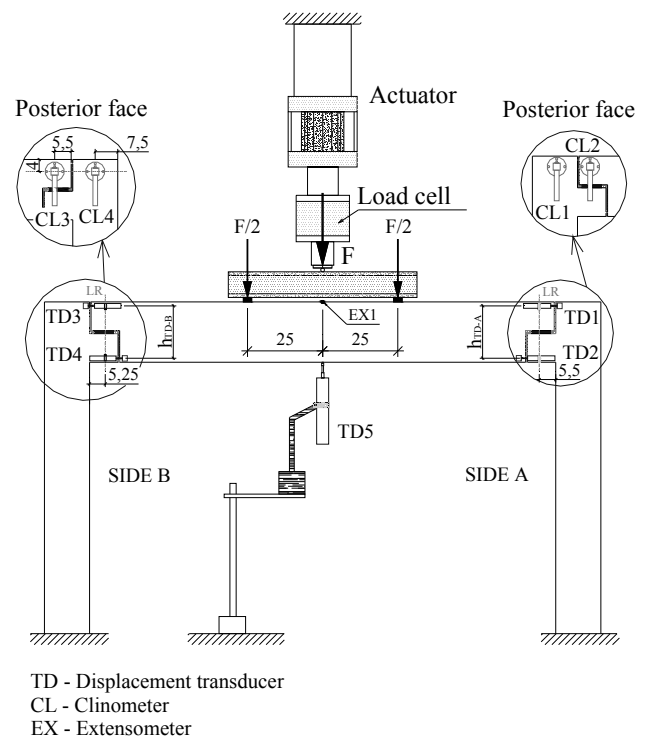


Figure 3 Test setup and instrumentation

Five displacement transducers were used, one of them (TD5) to measure the vertical displacement in the beam midspan and the others to measure horizontal relative displacements between the beam and columns in the connection regions (TD1-4). These measurements allowed indirectly assessing the connection rotation. Additionally, four clinometers (CL1-4) were used to obtain the connection rotation. Details of the position of these measure instruments are presented in Figure 3.

An electric extensometer was fixed on the top face of the beam centered in the span (EX1). Other extensometers were placed in the reinforcement of the sections subjected to higher efforts.

The test was divided into two parts. In the first one, the specimen had pinned connections and in the second

it had strengthened connections. Monotonically increasing loads were applied at a rate of 0,005 mm/s under displacement control of the actuator piston. In the first part of the test two loading-unloading cycles were carried out. In the first cycle, a force of 35 kN (nominal value) was reached and in the second, 55 kN. At this point of the test the cracking at the bottom of the beam midspan region was clearly identified, as well as the interface separation between the grout and the concrete of the connection regions. Then the test was paused and the beam-to-column connections were strengthened, as already described at Section 2.3. The same setup test was again assembled and the second part of the test was initiated with one loading-unloading cycle until the force had reached 41 kN. Afterwards, the specimen was loaded until failure which occurred when the total force was 94 kN.

2.5 Results

The failure occurred in one of the connections regions (SIDE A in Figure 3) and involved the concrete edge splitting at the column top (Figure 4). The strain in the CFRP strip at failure was 5.3 ‰, which was very distant from its ultimate strain (1.7%).

The splitting of the edge was observed in bond tests in other researches, e. g. Lorenzis & Teng (2006), and is supposed to occur when the strip is bonded close to the edge. Blaschko (2003) suggests that the distance between the strip and the edge should be either not shorter than 30 mm or the maximum aggregate size. Kang et al. (2005) affirm that this distance should be longer than 4 cm. In this test a 3 cm distance was adopted, mainly due to the specimen dimensions. The premature splitting could be facilitated by the limited length available for embedding the strips in columns, which is also related with the specimen's dimensions. The beam showed a usual crack pattern at failure. The longitudinal steel reinforcement of the beam presented maximum strain of 2.8‰.



Figure 4 Connection region after failure

The bending moment x rotation curve was traced for stiffness evaluation and is presented in Figure 5. The

transducer (TD1-4) measurements were used to calculate the connections rotation. The methodology proposed by Catoia (2007) was used to calculate the bending moments at the connections. It is based on the equivalence between the moment bending x curvature relationship in the beam for two conditions: frame with pinned beam-to-column connection (simple supported beam) and frame with semi-rigid connections. Figure 5 also shows a bi-linear approach adopted for the behavior of the connection. The last measurements were taken disregarded in this approach as the splitting process had already started for those data. The gradient of the two linear stages gives the initial and final connection stiffnesses (k).

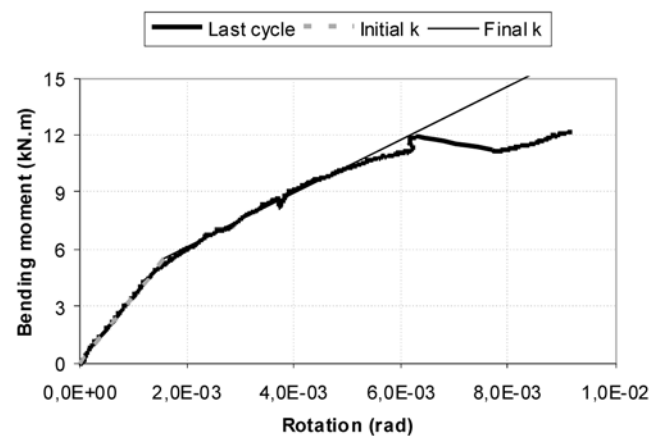


Figure 5 Bending moment versus rotation for the last loading stage

The connection stiffness for the initial stage was 3500 kN.m/rad (initial k) and for the second stage 1400 kN.m/rad (final k). The value of initial k classifies the connection as semi-rigid with medium flexural strength according to the proposal of Ferreira et al. (2002).

Figure 6 shows the total load x midspan deflection curves for all loading cycles. It is interesting to notice that comparing the first loading stage (P_35) with the second (P_55) a decreasing in the initial inclination is

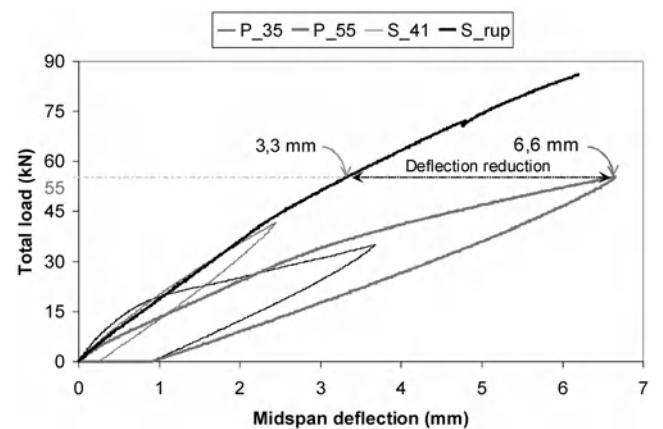


Figure 6 Total load versus midspan deflection for the four loading stages

observed, probably due to a decrease in the beam stiffness. Comparing the first loading with the loadings made in the structure with strengthened connections (S_41 and S_rup) allows noting that the initial inclination is almost reestablished. Another interesting consequence of the strengthening is the reduction in the midspan beam deflection, illustrated in Figure 6. A reduction of approximately 50% is observed to the force of 55 kN, considering the curve for the last loading stage (S_rup) and the curve of the second loading stage (P_55).

3 CONCLUSIONS

The strengthening was effective in the increase of connection stiffness. After strengthened the connection could be even classified as semi-rigid with medium flexural strength.

The connection strengthening provided a significant reduction in the midspan beam deflection.

The premature failure with the fragile splitting of the edge observed when the strips presented only 30% of their ultimate strain is undesirable. However, it can be emphasized that it is certainly related to the distance between the strips and concrete edges. Additionally, it could be related to the limited length available for embedding the strips in columns. Both conditions could be changed if the tests were made with real scaled specimens.

4 ACKNOWLEDGEMENTS

The authors would like to acknowledge the financial support given by the São Paulo Research Foundation (FAPESP).

REFERENCES

- Blaschko M. 2003. Bond behavior of CFRP strips glued into slits. In: Proceedings FRPRCS-6. World Scientific. 205-214, Singapore.
- Catoia, B. 2007. Comportamento de vigas protendidas pré-moldadas com ligações semi-rígidas. Master thesis. Universidade Federal de São Carlos. São Carlos.
- De Lorenzis, L. & Teng, J.G. 2006. Near-surface mounted FRP reinforcement: An emerging technique for strengthening structures, *Composites Part B: Engineering* 38: 119-143.
- Ferreira, M. A et al. 2002. Modelo teórico para projeto de ligações semi-rígidas em estruturas de concreto pré-moldado. In: Congresso Brasileiro do Concreto, 44. Belo Horizonte.
- Kang, J. Y. et al. 2005. Analytical Evaluation of RC Beams Strengthened with Near Surface Mounted CFRP Laminates. In: 7th international symposium – Fiber-reinforced polymer reinforcement for concrete structures (FRPRCS – 7), 779-794. Kansas City.
- Marin, M. C. & El Debs, M. K. 2009. Análise do limite do número de pavimentos em estruturas usuais de múltiplos pavimentos em concreto pré-moldado. In: 2º Encontro Nacional de Pesquisa-Projeto-Produção em Concreto Pré-Moldado. São Carlos.

Treatment of Steel Surfaces for Effective Adhesive Bonding

J.G. Teng (cejgteng@polyu.edu.hk), D.Fernando, T. Yu & X.L. Zhao

Department of Civil and Structural Engineering, The Hong Kong Polytechnic University, Hong Kong, China

ABSTRACT In the FRP strengthening of steel structures, cohesion failure in the adhesive is the preferred mode of debonding failure at FRP-to-steel interfaces so that the design theory can be established based on the properties of the adhesive. In this paper, results from a systematic experimental study are presented to examine the effects of steel surface treatment and adhesive properties on the adhesion strength between steel and adhesive. The test results show that adhesion failure can be avoided if the steel surface is grit-blasted prior to bonding and the treated surface can be characterised using three key surface parameters.

1 INTRODUCTION

When steel structures are strengthened with adhesively bonded FRP laminates, debonding failure between the steel and the FRP may occur in the following modes: (a) within the adhesive (cohesion failure); (b) at the physical interfaces between the adhesive and the adherends (adhesion failure); (c) a combination of adhesion failure and cohesion failure. If adhesion failure controls the strength of FRP-strengthened steel structures, then the interfacial bond strength depends on how the steel surface and FRP surface are treated as well as the bond capability of the adhesive. As adhesion failure depends on surface treatment and the degree of surface treatment, especially to the steel substrate, is difficult to control precisely on site, the development of a design theory becomes much more involved. This important issue has not previously been given adequate attention. Teng et al. (2009) have recently recommended that in FRP-strengthened steel structures, debonding should occur within the adhesive layer in the form of cohesion failure, and a proper surface treatment procedure coupled with the use of an appropriate adhesive should ensure that such cohesion failure is critical and adhesion failure is suppressed.

In an FRP-to-steel interface, adhesion failure is much more likely to occur at the steel/adhesive interface than at the FRP/adhesive interface. In the published literature, the treatment and characterization of steel surfaces has received significant research attention (Baldan 2004; Harris and Beevers 1999; Mays and Huthcinson 1992). The most popular methods for steel surface treatment include solvent cleaning and mechanical abrasion through grit blasting or using other tools (e.g. sand papers, wire brushes, abrasive pads and wheels, and needle guns) (Baldan 2004; Hollaway and Cadei 2002). Solvent cleaning removes contaminants on the surface (e.g.

grease, oil and water) but does not change the surface properties. Mechanical abrasion aims to roughen the surface and to remove the weak surface layer (e.g. oxide layer) which is chemically inactive (Baldan 2004; Harris and Beevers 1999). Among various mechanical abrasion approaches, grit blasting appears to be the most effective (Harris and Beevers 1999; Hollaway and Cadei 2002; Schnerch 2005) and is recommended by existing guidelines (Cadei et al. 2004; Schnerch et al. 2007).

To better understand the effect of a particular surface treatment procedure, it is also important to characterize the surface to evaluate its bonding capability. A steel surface is often characterized by its three main properties (Amada and Satoh 2000; Gent and Lin 1990; Harris and Beevers 1999; Lavaste et al. 2000): surface energy, surface chemical composition and surface roughness/topography. All three properties significantly affect the adhesion strength.

While many studies (Baldan 2004; Gent and Lin 1990; Mays and Huthcinson 1992) exist on the surface preparation of various materials (e.g. steel, aluminum and ceramic) for adhesive bonding, research focusing on the effects of surface preparation methods and adhesive properties on the adhesion strength between steel and adhesive is rather limited. This paper therefore presents a systematic experimental study to correct this deficiency within the context of FRP strengthening of steel structures.

2 EXPERIMENTAL PROGRAM

Two series of tests were conducted, namely, butt-joint tensile tests and single-lap shear tests. Each series of tests included sixty specimens covering four different adhesives and five different surface preparation methods; three identical specimens were tested for each combination of adhesive and surface preparation method. The four adhesives are commonly available commercial products

which may be used in the FRP-strengthening of steel structures (Table 1). The adhesive thickness was carefully controlled to be 1 mm in all cases. The five surface preparation methods include: (1) solvent wiping; (2) hand grinding after solvent wiping; (3)-(5) grit blasting after solvent wiping using 0.5 mm grits, 0.25 mm grits and 0.125 mm grits respectively [referred to as methods (1) to (5) respectively]. The 0.5 mm grits and 0.125 mm grits were the so-called white alumina grits (Teng et al. 2010), while the 0.25 mm grits were the so-called brown alumina grits (Teng et al. 2010); the main content of both types of grits is Al_2O_3 but the latter has a larger percentage of SiO_2 .

A butt-joint specimen consisted of two mild steel circular rods (25 mm in diameter and 52.5 mm in length), with their ends bonded together using an adhesive (ASTM C633 2001). A single-lap shear test specimen consisted of two mild steel coupons (each of 80 mm × 25 mm × 2 mm) bonded together with a lap zone of 25 mm × 12.5 mm (ASTM D3165 2000). In the preparation of specimens, the test steel surfaces were subjected to appropriate treatment, followed by the removal of fine abrasive dust arising from the preparation process (for hand ground and grit blasted specimens) using a vacuum head. Adhesive bonding was then carried out within 24 hours to minimize surface contamination during air exposure (Schnerch 2005). Afterwards, the specimens were left for curing at room temperature for 14 days before testing. All tests were conducted with a displacement control at a rate of 1.2 mm/min.

In addition to the butt-joint specimens and the single-lap shear test specimens, three small rectangular coupons were prepared using each of the five surface preparation methods for surface characterization. A VCA (video contact angle) device was used to measure the contact angle from which the surface energy was evaluated. A SEM/EDX (scanning electron microscopy/energy dispersive x-ray) system was used to measure the surface chemical composition while a profilometer was used to measure the surface roughness & topography. Again, these measurements were completed within 24 hours after surface preparation. More details of the experimental program are available in Teng et al. (2010).

3 RESULTS AND DISCUSSIONS

3.1 Surface characteristics

Various parameters have been proposed to represent the surface roughness/topography among which the so-called fractal dimension D appears to be the most popular (Amada and Satoh 2000; Packham 2003). The fractal dimension is normally found using the “box counting method” (Amada and Satoh 2000), and a larger fractal dimension generally means a rougher topography. The fractal dimensions for all the five surface preparation methods

are given in Figure 1, where each point represents the average value obtained from three specimens subjected to the same surface treatment. Figure 1 shows that the fractal dimensions of the three grit-blasting methods are larger than those for the other two surface preparation methods, and method (1) (i.e. solvent wiping) leads to the lowest D among the five methods. Among the three grit blasting methods, finer grits appear to produce a rougher surface (i.e. a higher D).

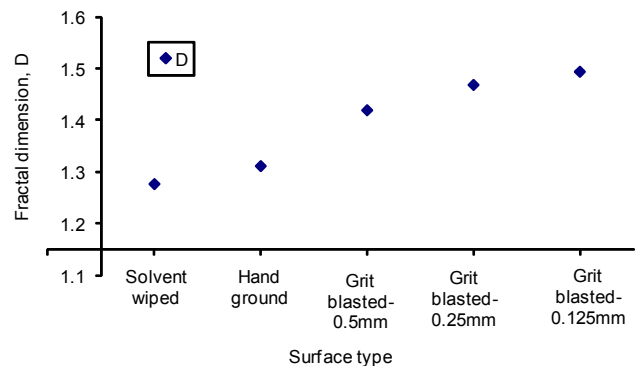


Figure 1 Fractal dimension

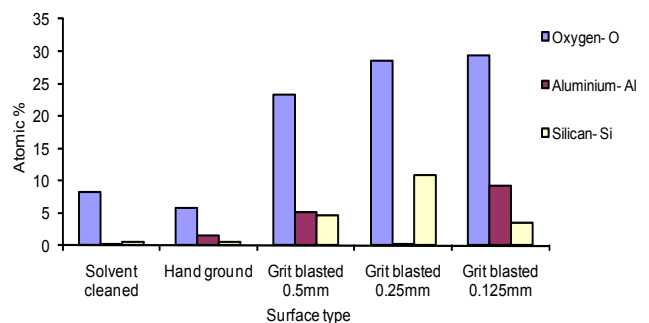


Figure 2 Chemical composition

Surface treatment can change the chemical composition of the surface by removing the weak surface layer (e.g. the oxide layer) and/or introducing grit or other residues to the surface. Figure 2 shows the atomic percentages of various foreign atoms (i.e. atoms other than C and Fe) for the five surface preparation methods examined in this study. Again, the results in Figure 2 are average values from three nominally identical specimens for each surface preparation method. Compared with method (1) (i.e. solvent wiping), method (2) (i.e. hand grinding) led to a smaller oxygen percentage but introduced additional aluminium atoms. This is believed to be due to the partial removal of the weak oxide layer and the introduction of Al_2O_3 residues from the sand paper used for hand grinding. Similarly, grit blasting introduced a large amount of Al_2O_3 residues and/or SiO_2 residues although it was expected to be more effective in removing the weak oxide layer. The amount of grit residues was found to be much more than that introduced by the hand grinding process, as a high pressure was used in the grit blasting

process which pressed more grits deeply into the surface. It was also noted that when finer grits were used, a larger amount of grit residues was introduced. The obvious higher silicon percentage for method (4) (i.e. grit blasting with 0.25 mm grits) was due to the use of brown alumina grits instead of white alumina grits as used in the other two grit blasting methods; the former had a larger percentage of SiO₂.

Figure 3 shows the average surface energy calculated from the measured contact angles. The surface energy depends on several factors, with the surface chemical composition and the surface roughness/topography being the two important ones (Baldan 2004; Harris and Beevers 1999). Examination of Figure 1 together with Figure 3 indicates that a surface with a larger fractal dimension also has a larger surface energy, implying that these two quantities are related. By contrast, the surface chemical composition (Figure 2) does not seem to have a clear effect on the surface energy although some previous studies have shown that the existence of more aluminium and silicon atoms may increase the surface energy (Adams et al. 1997).

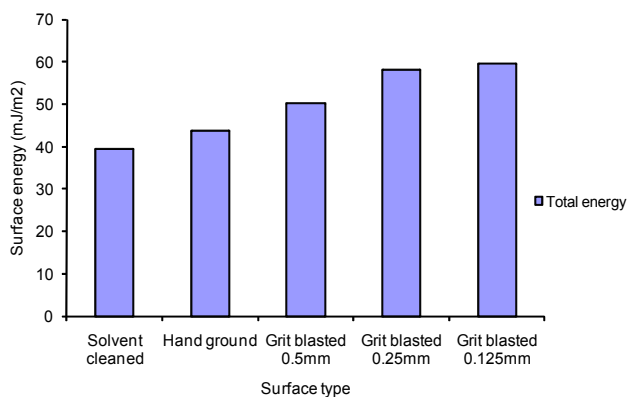


Figure 3 Surface energy

It was found that the characteristics of surfaces were closely similar when grit-blasted using the same grits, which offers the possibility of developing a standard surface preparation procedure.

3.2 Adhesion strength

Table 1 presents the ultimate loads of all butt-joint specimens and their corresponding failure modes. The results of single-lap shear tests are summarized in Table 2. These two tables show that pure adhesion failure occurred in most solvent wiped specimens, but such failure can be avoided if the steel surface is grit-blasted prior to bonding. The ultimate loads of hand ground specimens are generally higher than those of the corresponding solvent wiped specimens, but are lower than those of the corresponding grit-blasted specimens.

Almost all hand-ground specimens and some grit-blasted specimens suffered a combined adhesion and cohesion failure. The ultimate load of this combined

failure mode is expected to depend on both the adhesion strength between steel and adhesive and the cohesion strength of the adhesive. All grit-blasted specimens of the single-lap shear test series with Sika 330 or Araldite 2015 as the bonding adhesive failed in the combined failure mode and the average ultimate load from three nominally identical specimens was the smallest when the largest grits (i.e. 0.5 mm) were used. The use of 0.25 mm grits and 0.125 mm grits, however, led to similar ultimate loads. This observation indicates the importance of using sufficiently fine grits in grit blasting.

Table 1 Results of the butt-joint tensile tests

Adhesive	specimen No.	Ultimate load (kN)				
		Solvent-wiped	Hand-ground	Grit-blasted		
				0.125m m grit	0.25mm grit	0.5mm grit
Sika 30	I	0.85 #	9.33 #*	12.1 *	11.3 *	12.0 *
	II	1.50 #	10.1 #*	12.5 *	11.4 *	11.2 *
	III	2.10 #	9.80 #*	12.3 *	12.3 *	14.3 *
Sika 330	I	2.57 #	11.2 #*	14.7 *	13.3 *	14.0 *
	II	3.40 #	11.4 #*	15.8 *	12.8 *	14.6 *
	III	3.10 #	10.7 #*	17.8 *	12.4 *	16.0 *
Araldite 2015	I	3.94 #	9.60 #*	12.1 *	10.8 #*	12.7 *
	II	3.50 #	12.4 #*	12.6 *	10.9 #*	13.2 *
	III	3.20 #	11.1 #*	11.6 *	12.9 *	12.6 *
Araldite 420	I	9.61 #	12.2 #*	21.0 *	17.4 *	18.4 *
	II	11.6 #	16.0 #*	21.7 *	17.9 *	19.7 *
	III	9.90 #	12.2 #	21.6 *	16.7 *	17.9 *

#= adhesion failure, *= cohesion failure, #*= combined adhesion and cohesion failure

Table 2 Results of the single-lap shear tests

Adhesive	specimen No.	Ultimate load (kN)				
		Solvent wiped	Hand ground	Grit blasted		
				0.125m m grit	0.25mm grit	0.5mm grit
Sika 30	I	2.91 #*	3.31 #*	4.43 *	4.97 *	4.08 *
	II	2.81 #	3.87 #*	4.44 *	4.32 *	4.43 *
	III	2.38 #	3.39 #*	4.81 *	4.76 *	5.08 *
Sika 330	I	3.66 #	4.72 #*	5.74 #*	6.09 #*	5.48 #*
	II	3.88 #	4.73 #*	5.60 #*	5.46 #*	5.30 #*
	III	3.45 #	4.93 #*	5.70 #*	5.47 #*	5.79 #*
Araldite 2015	I	2.86 #*	2.73 #*	4.09 #*	4.37 #*	3.54 #*
	II	1.88 #	2.48 #*	3.82 #*	4.04 #*	3.77 #*
	III	2.85 #*	2.89 #*	4.13 #*	4.04 #*	3.50 #*
Araldite 420	I	3.67 #	5.23 #*	5.62 *	5.70 *	5.42 #*
	II	3.04 #*	5.30 #*	6.65 *	5.15 *	5.40 *
	III	3.56 #	5.11 #*	5.39 *	6.01 *	5.45 #*

#= adhesion failure, *= cohesion failure, #*= combined adhesion and cohesion failure

Examined together with Figures 1 and 3, Tables 1 and 2 reveal that the adhesion strength generally increases with the fractal dimension and the surface energy until the two reach certain values (1.47 for the fractal dimension and 55 mJ/m² for the surface energy in the present study). This is easy to understand as an increase in the fractal dimension leads to stronger mechanical bonding while an increase in the surface energy generally enhances the wettability of the surface which in turn enhances the bonding. However, Hitchcock et al. (1981) argued that an overly rough surface (i.e. an overly high fractal dimension) may also have negative effects on bonding capability as it may restrict the spreading of adhesive over the surface. This explains the similar ultimate loads of grit-blasted specimens using 0.125 mm grits and 0.25 mm grits, which may be the result of the two counteracting effects of an increased fractal dimension.

It should also be noted that some previous studies (e.g. Adams et al. 1997) have shown that the chemical composition of a surface can affect the adhesion strength, but among the cases examined in the present study, this effect is not clearly seen. Further studies are needed if the chemical composition of a surface is significantly different from those examined in this study.

Tables 1 and 2 also show that the ultimate loads for different adhesives are quite different, even for the same surface preparation method. In particular, Table 1 shows that Araldite 420 led to a much larger adhesion strength than the other three adhesives, indicating the excellent bonding capability of this adhesive. The differences in adhesion strength among the four adhesives are believed to depend significantly on their different chemical compositions among other factors; more in-depth investigations into this aspect are beyond the scope of this study.

4 CONCLUSIONS

The bond strength between steel and adhesive is a key issue in the FRP strengthening of steel structures. This paper has presented a systematic experimental study on the effects of steel surface treatment and adhesive properties on the adhesion strength between steel and adhesive. These tests have shown that if a suitable adhesive is used together with appropriate surface treatment by grit-blasting, adhesion failure between steel and adhesive can be avoided. These tests have also shown that the characteristics of a surface grit-blasted using the same grits are closely similar, which offers the possibility for developing a standard surface preparation procedure.

5 ACKNOWLEDGEMENT

The authors are grateful for the financial support from the Hong Kong Polytechnic University.

REFERENCES

- ASTM C633. 2001. Standard test method for adhesion or cohesion strength of thermal spray coatings, ASTM C633.
- ASTM D3165. 2000. Standard test method for strength properties of adhesives in shear by tension loading of single-lap-joint laminated assemblies, ASTM D3165.
- Adams, R.D., Comyn, J. & Wake, W.C. 1997. Structural adhesive joints in engineering, Chapman and Hall, London, UK.
- Amada, S. & Satoh, A. 2000. Fractal analysis of surfaces roughened by grit blasting. *Journal of Adhesion Science and Technology*, 14(1): 27-41.
- Baldan, A. 2004. Adhesively-bonded joints and repairs in metallic alloys, polymers and composite materials: Adhesives, adhesion theories and surface pretreatment. *Journal of Materials Science*, 39(1): 1-49.
- Cadei, J.M.C., Stratford, T.J., Hollaway, L.C. & Duckett, W.G. 2004. Strengthening metallic structures using externally bonded fibre-reinforced polymers- C595, CIRIA, London.
- Gent, A.N. & Lin, C.W. 1990. Model studies of the effect of surface-roughness and mechanical interlocking on adhesion. *Journal of Adhesion*, 32(2-3): 113-125.
- Harris, A.F. & Beevers, A. 1999. The effects of grit-blasting on surface properties for adhesion. *International Journal of Adhesion and Adhesives*, 19(6): 445-452.
- Hitchcock, S.J., Carroll, N.T. & Nicholas, M.G. 1981. Some effects of substrate roughness on wettability. *Journal of Materials Science*, 16(3): 714-732.
- Hollaway, L.C. & Cadei, J. 2002. Progress in the technique of upgrading metallic structures with advanced polymer composites. *Progress in Structural Engineering and Materials*, 4(2): 131-148.
- Lavaste, V., Watts, J.F., Chehimi, M.M. & Lowe, C. 2000. Surface characterisation of components used in coil coating primers. *International Journal of Adhesion and Adhesives*, 20(1): 1-10.
- Mays, G.C. & Huthcinson, A.R. 1992. Adhesives in civil engineering, Cambridge University Press, New York.
- Packham, D.E. 2003. Surface energy, surface topography and adhesion. *International Journal of Adhesion and Adhesives*, 23(6): 437-448.
- Schnerch, D. 2005. Strengthening of steel structures with high modulus carbon fiber reinforced polymer (CFRP) materials, PhD Thesis, North Carolina State University, Raleigh (NC).
- Schnerch, D., Dawood, M., Rizkalla, S. & Sumner, E. 2007. Proposed design guidelines for strengthening of steel bridges with FRP materials. *Construction and Building Materials*, 21(5): 1001-1010.
- Teng, J.G., Yu, T. & Fernando, D. 2009. FRP composites in steel structures, Proceedings of the Third International Forum on Advances in Structural Engineering, Shanghai, China.
- Teng, J.G., Fernando, D., Yu, T. & Zhao, X.L. 2010. Preparation and characterization of steel surfaces for adhesive bonding, in preparation.

Effect of Surface Preparation on the Strength of FRP-to-Mild Steel and FRP-to-Stainless Steel Joints

S.J. Kim, S.T. Smith (stsmith@hku.hk) & B. Young

Department of Civil Engineering, The University of Hong Kong, Hong Kong, China

ABSTRACT A detailed understanding of the strength and behaviour of the bond between fibre-reinforced polymer (FRP) composites to metals is an ongoing field of research. The many different geometrical and material parameters make for extensive research demands. This paper in turn reports a series of tests on the shear strength and behaviour of FRP-to metal joints in which the main test parameters, which have received limited attention to date, consists of (i) type of metal (i.e. non-galvanised mild steel and stainless steel), and (ii) surface preparation technique (i.e. different mechanical abrasion methods). All specimens are loaded in displacement control which enables the failure process to be followed and identification of different failure modes to be made. The results enable the effectiveness of different surface preparation techniques upon the bond of FRP to different types of metals to be made.

1 INTRODUCTION

Externally bonded fibre-reinforced polymer (FRP) composites can strengthen metallic members (Hollaway and Teng 2008). For example, Silvestre et al. (2008) showed the load-carrying capacity of cold-formed steel lipped channel columns strengthened by FRP to be enhanced by up to 20% above control specimens. The effectiveness of the strengthening is, however, largely dependent upon the quality of the bond between the two materials. In particular, understanding the effect of different surface preparation techniques, in addition to the effect of such techniques on different metals, are two important issues which have received limited attention to date.

In adhesively bonded FRP-to-FRP joints, failure has been classified into seven distinct modes (ASTM D5573-99 2005) namely; (i) adhesive failure (ADH), (ii) cohesive failure (COH), (iii) thin-layer cohesive failure (TLC), (iv) fibre-tear failure (FT), (v) light-fibre-tear failure (LFT), (vi) stock-break failure (SB), and (vii) mixed failure (any combination of two or more failure modes). Further subdivision produces *interfacial failure* (i.e. ADH, TLC, FT and LFT), *cohesive failure* (i.e. COH), *adherent failure* (i.e. SB) and *mixed failure*. Such a classification system does not yet exist for FRP-to-metal joints.

A commonly reported FRP-to-metal joint failure mode is *interfacial failure* (e.g. Xia and Teng 2005, Zhao and Zhang 2007). In such joints, the preparation of the surface of the metal is an important parameter which requires further investigation.

A series of tests is reported in this paper on the shear strength and behaviour of single-lap FRP-to-metal joints.

The main test variables are (i) surface preparation, and (ii) type of metal. The results enable the most suitable surface preparation techniques to be determined for two different metals. In addition, the test results will also enable the future development and calibration of analytical models. A much more detailed account of the tests can be found in Kim et al. (2010).

2 EXPERIMENTAL DETAILS

2.1 Test set-up and details of test specimens

The single-lap shear test set-up utilised in this study is shown in Figure 1. In order to minimise bending of the

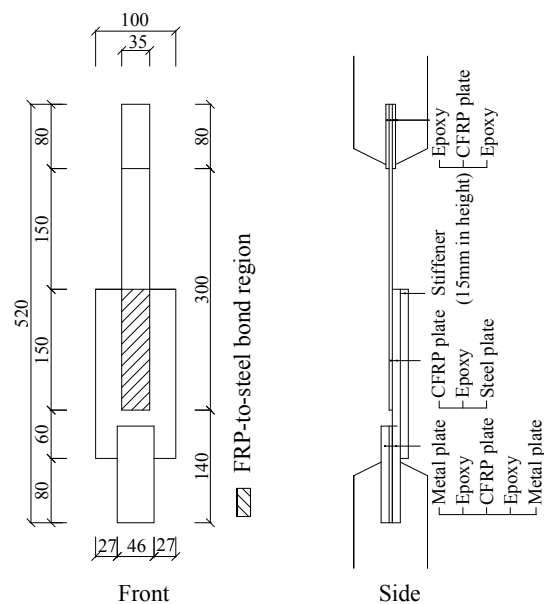


Figure 1 Test set-up

test specimens, the metal plate was stiffened. The flexural rigidity ratio of the stiffened metal plates to FRP was over 13,000 which resulted in minimal bending of the metal plates during testing. The two main test parameters were (i) four different types of surface preparation techniques, and (ii) two different types of metals. The total number of test specimens was twenty-four (i.e. three identical test specimens for each of the eight test permutations). The properties of the two different metals (i.e. mild steel and stainless steel) are fully described in Section 2.2. The four different surface techniques of (i) solvent wiping, (ii) light sanding, (iii) grinding, and (iv) needling, are described in detail in Section 2.3.

A constant adhesive thickness was maintained by adhering small plastic prisms of equal size to the metal substrate prior to bonding of the FRP. Post-test measurements revealed an average adhesive thickness of 1.3 mm and standard deviation of 0.1 mm. A long bond length of FRP (i.e. 150 mm) and slow loading rate (0.2 mm/min) was utilised in order to capture the full failure process of the joints.

2.2 Materials

All metal plates were nominally 9 mm thick. Three coupons were averaged to produce yield strengths of 322 MPa and 426 MPa and elastic moduli of 212 GPa and 178 GPa for the mild and stainless steels, respectively. Five FRP coupons (nominal thickness of 1.4 mm) were tested and averaged to produce an elongation at rupture of 1.47%, tensile strength of 3,367 MPa and elastic modulus of 230 GPa. Five dog-bone shaped epoxy adhesive samples were tested and averaged to produce an elongation at rupture of 0.36 %, tensile strength of 27 MPa and elastic modulus of 8,886 MPa.

2.3 Surface preparation

The four different surface preparation techniques considered in this study were (i) no treatment (denoted as NT), (ii) sanding of the metal surface with fine sandpaper attached to an electric sander (i.e. 220 grit sandpaper comprising an average particle diameter of 68 μm) (denoted as SF), (iii) grinding of the metal surface with a 11000 rpm 840w electric angle grinder fitted with a metal grinding wheel (denoted as GR) and (iv) needling of the metal surface with a pneumatically powered needle scaler containing 26 \times 2.8 mm diameter needles (denoted as NS). Prior to application of the FRP to all prepared surface, the surfaces were cleaned by wiping with a solvent (i.e. an aromatic and oxygenated solvent). The time which elapsed from the beginning of the surface preparation treatment to the application of the FRP was limited to 3 hours. Such limitation of time was primarily on account of minimising the oxidised layer that formed on the surface of the mild steel. Note that the stainless steel did not contain any form of protective coating.

For preparation by sanding (i.e. SF), the electric sander was applied for 3 minutes with new sandpaper used for each specimen. Of the three minutes, one minute was devoted to sanding parallel to the longitudinal axis of the plate and then one minute for $\pm 45^\circ$ to the longitudinal axis. The grinding and needling techniques were also applied for 3 minutes for each specimen although in no specific manner. In the case of grinding, an optimal surface preparation was achieved when the base metal was exposed. Optimal needling occurred when the complete bond surface was affected. In the case of sanding (i.e. SF), a very small portion of the mild steel oxide layer was removed (Figure 2b). In the case of grinding, the bare steel was exposed (Figure 2c) for the mild steel although the surface texture was the same for both mild steel and stainless steel. The needling left minor impressions on the surface for both mild steel and stainless steel and partially removed the oxide layer from the mild steel (Figure 2d).

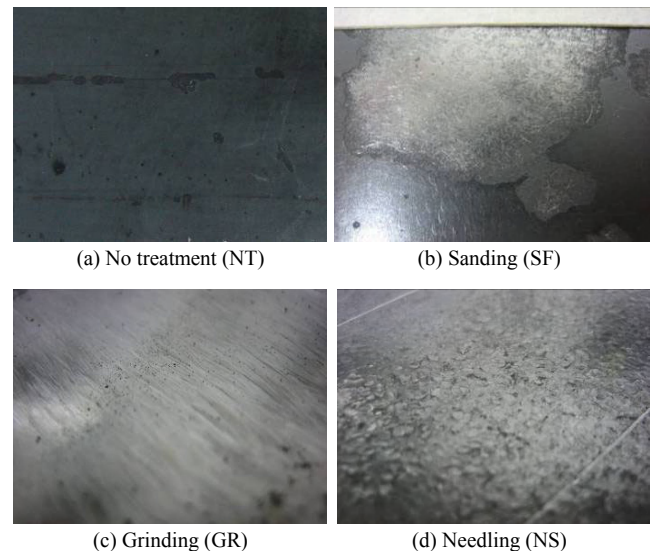


Figure 2 Surface preparation techniques

3 TEST RESULTS

A summary of the measured adhesive thickness and FRP plate dimensions in addition to the failure loads and failure modes are provided in Table 1.

3.1 Failure modes

All specimens failed by debonding which generally occurred in a sudden manner. The failure sequence involved initial cracking between the FRP and metal at the loaded plate end (Figure 3a) which then propagated toward the plate end (Figure 3b). The modes of failure can be categorised into two main categories (i.e. *Modes 1* and *2*) as per the following. One of the failure modes is further sub-divided.

Mode 1: Adherend failure in oxidised layer

Mode 2A: Thin-layer cohesive failure in metal-to-adhesive interface

Mode 2B: Thin-layer cohesive failure in FRP-to-adhesive interface

Mode 2C: Mixed thin-layer cohesive failure

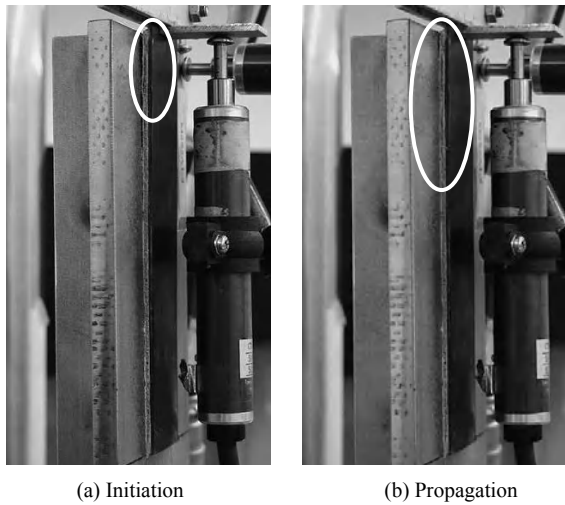


Figure 3 Debonding crack (SS-NS-2)

Table 1 Test results

Specimen*	Adhesive Thickness# (mm)	FRP		P _u (kN)	Failure Mode
		Width# (mm)	Length# (mm)		
MS-NT-1	1.5	36.0	150.7	28.0	Mode 1
MS-NT-2	1.4	36.0	150.3	22.9	Mode 1
MS-NT-3	1.3	36.0	150.6	30.4	Mode 1
MS-SF-1	1.3	35.7	150.3	32.5	Mode 1
MS-SF-2	1.4	35.4	152.3	31.5	Mode 1
MS-SF-3	1.4	36.3	150.7	35.9	Mode 1
MS-GR-1	1.2	35.1	152.0	33.0	Mode 2B
MS-GR-2	1.5	35.7	151.0	34.5	Mode 2B
MS-GR-3	1.3	35.2	150.2	33.8	Mode 2B
MS-NS-1	1.2	35.4	151.2	31.7	Mode 2B
MS-NS-2	1.4	36.1	151.4	31.7	Mode 2B
MS-NS-3	1.3	34.8	153.6	36.2	Mode 2B
SS-NT-1	1.3	35.1	151.4	35.5	Mode 2A
SS-NT-2	1.5	35.6	151.6	33.4	Mode 2A
SS-NT-3	1.3	36.2	152.1	37.5	Mode 2A
SS-SF-1	1.4	35.9	150.9	35.8	Mode 2B
SS-SF-2	1.3	35.8	150.5	41.3	Mode 2B
SS-SF-3	1.4	34.9	150.6	37.4	Mode 2B
SS-GR-1	1.5	34.7	149.8	34.8	Mode 2C
SS-GR-2	1.4	35.9	151.6	37.0	Mode 2C
SS-GR-3	1.4	35.4	151.3	35.0	Mode 2C
SS-NS-1	1.2	36.2	150.3	32.2	Mode 2A
SS-NS-2	1.3	36.1	150.7	31.0	Mode 2A
SS-NS-3	1.3	35.0	151.3	33.0	Mode 2A

*MS (Mild steel)/SS (Stainless steel), NT (No treatment)/SF (Sanding)/GR (Grinding)/NS (Needling) # Measured dimension

Mode 1

All six mild steel specimens with sanded surfaces or

surfaces with no preparation failed in a Mode 1 manner (Figure 4). Figure 4a shows the failure interface to be located either purely in the oxidised layer-to-base metal interface or in combination with the adhesive-to-oxidised layer (Figure 4b).

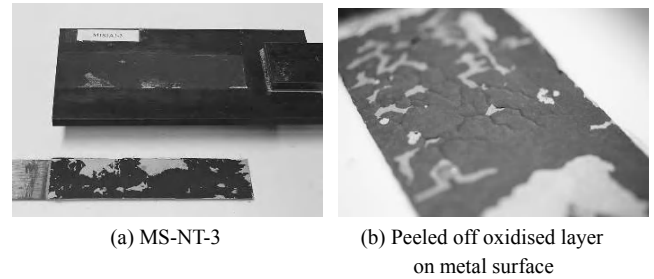


Figure 4 Mode 1 failure

Mode 2A

Mode 2A failure occurred in all six stainless steel specimens prepared by needling or with no treatment. For these specimens, the epoxy was completely removed (Figure 5a) with a very thin layer adhesive (herein referred to as a *light-dusting*) remaining attached to the metal surface (Figure 5b).

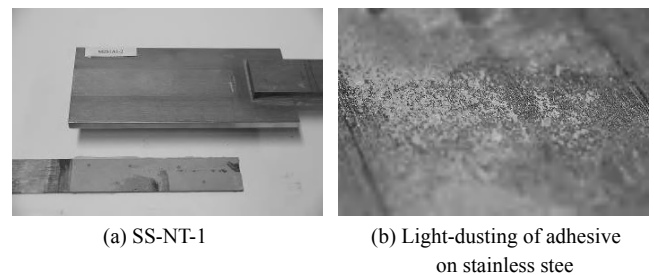


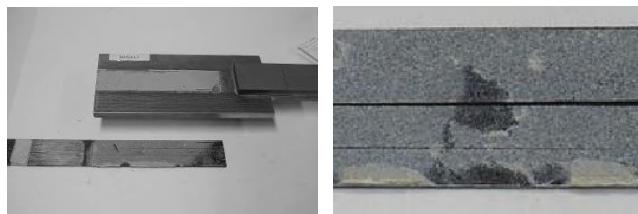
Figure 5 Mode 2A failure

Mode 2B

All mild steel specimens prepared with grinding or needling failed in a Mode 2B manner while the stainless steel specimens prepared with sanding also failed in the same manner. Similar to Mode 2A failures, all specimens exhibited near complete delamination (> 90% of the bond region) of the FRP plate from the adhesive (Figure 6a) with a light-dusting of adhesive remaining attached to the FRP surface (Figure 6b). A very small portion of adhesive (< 10 %) remained attached to the metal in the stainless steel specimens; in such cases the adhesive detached from the metal substrate (Figure 6b). In some cases, splitting of the FRP plates along the fibre direction was observed post-debonding failure.

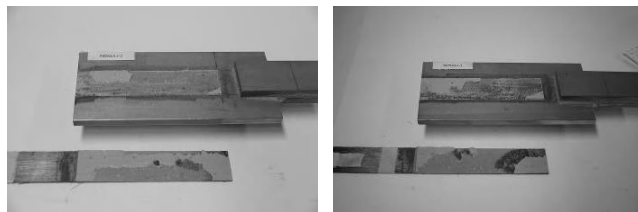
Mode 2C

This failure mode was observed in all three stainless steel specimens prepared by grinding. The failure interfaces were located in both the metal- and FRP-to-adhesive layers (Figure 7). A light-dusting of adhesive was observed on the failure surfaces.



(a) SS-SF-2

(b) Light-dusting of adhesive on FRP plate

Figure 6 Mode 2B failure

(a) SS-GR-2

(b) SS-GR-3

Figure 7 Mode 2C failure

3.2 Effect of surface preparation techniques

The effect of the different methods of surface preparation upon the stainless steel joints was much more obvious than the mild steel joints (Figure 8). The weak oxidised layer inherent in mild steel was the important contributing factor making the results less sensitive to the surface preparation method. Grinding was marginally the most optimal on average.

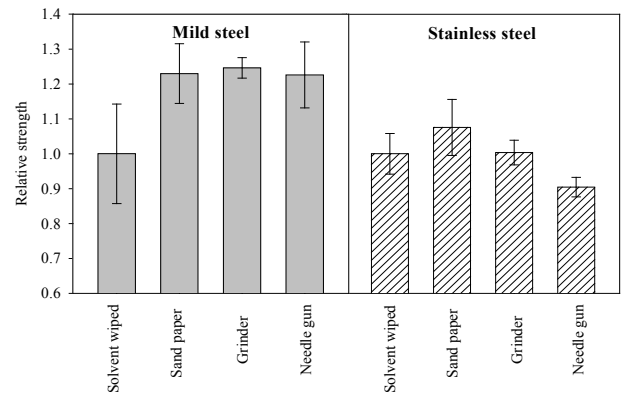
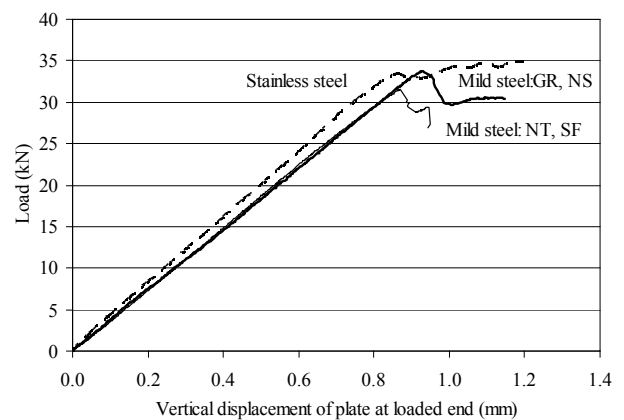
As the rate of oxidation of stainless steel is well below that of mild steel, the former did not suffer from the same fate as the latter. As a result, Figure 8 reveals the optimal method of preparation for stainless steel is via sanding although there is a deal of scatter in the results. It would appear that the surface damage caused by the needle gun severely affects the strength of the bond for FRP-to-stainless steel. The strength of FRP-to-mild steel joints was superior to FRP-to-stainless steel joints.

3.3 Load-displacement response

Figure 9 shows typical load-displacement responses for both mild steel and stainless steel specimens. Typical responses for each of the four different surface preparation techniques for mild steel yielded slightly different behaviours, while all stainless steel specimens yielded approximately the same behaviour. Stainless steel exhibited a peak load plateau.

4 CONCLUSIONS

The fundamental behaviour and strength of FRP-to-metallic joint assemblies, in which different metals have been prepared with different surface preparation techniques, have been reported. The most suitable preparation methods for mild-steel and stainless steel was grinding and sanding respectively. In addition, four distinct failure modes were observed. In the case of mild-steel, it is important to minimise the time allowed for oxidation to occur.

**Figure 8** Relative strength enhancements (relative to solvent wiped specimens)**Figure 9** Load-displacement response

5 ACKNOWLEDGEMENT

The authors are grateful to the assistance provided by Mr Joel LIU (2009-10 undergraduate final year project student of the University of Hong Kong).

REFERENCES

- ASTM D5573-99 (2005) Standard Practice for Classifying Failure Modes in Fiber-Reinforced-Plastic (FRP) Joints, American Society for Testing and Materials (ASTM), USA.
- Hollaway, LC & Teng, JG 2008. Strengthening and rehabilitation of Civil Infrastructures using Fibre-reinforced Polymer (FRP) Composites, Woodhead Publishing, UK.
- Kim, SJ, Smith ST, & Young B 2010. Effect of mechanical surface preparation on the strength and behaviour of FRP-to-mild steel and FRP-to-stainless steel joints, in preparation.
- Silvestre, N, Young, B & Camotim, D 2008. Non-linear behaviour and load-carrying capacity of CFRP-strengthened lipped channel steel columns, Eng. Struct., 30(10), 2613-2630.
- Xia, SH & Teng, JG 2005. Behaviour of FRP-to-steel bonded joints, Proceeding, Third International Symposium on Bond Behaviour of FRP in Structure (BBFS 2005), Hong Kong, 7-9 December, pp. 419-426.
- Zhao, XL & Zhang, L 2007. State-of-the-art review on FRP strengthened steel structures, Eng. Struct., 29(8), 1808-1823.

Modeling of Steel Beams Strengthened with CFRP Strips Including Bond-Slip Properties

Yail J. Kim (jimmy.kim@ndsu.edu)

Department of Civil Engineering, North Dakota State University, ND, USA

Kent A. Harries (kharries@pitt.edu)

Department of Civil and Environmental Engineering, University of Pittsburgh, PA, USA

ABSTRACT This paper presents a modeling approach to predict the flexural behavior of steel beams strengthened with carbon fiber reinforced polymer (CFRP) strips. The beams, W150×18, are simply supported and monotonically loaded until failure occurs. To examine the effect of CFRP-strengthening, selected beams are intentionally damaged by creating a notch at the tension flange. A three-dimensional finite element analysis is conducted, including bond-slip properties at the CFRP-steel interface. The CFRP-strengthening results in improved load-carrying capacity of the damaged beam and reduces strain localization near the damage.

1 INTRODUCTION

Carbon fiber reinforced polymer (CFRP) composites have been widely used for strengthening concrete structures. Uniaxial CFRP sheets/strips are bonded to the tensile soffit of deteriorated members to improve structural performance, primarily load-carrying capacity (Bakis et al. 2002, Teng et al. 2003). The well-known benefits of CFRP-strengthening include high strength and stiffness to weight ratios, excellent durability, fatigue resistance, and reduced long-term maintenance expenses (Kim and Heffernan 2008). The application of CFRP composites has been recently extended to strengthening metallic structures (Harries and El-Tawil 2008). Nozaka et al. (2005) studied the effect of CFRP-bond length on the strength-gain of steel beams strengthened with CFRP strips, including various types of adhesives and bonding schemes. An optimum bond length for the CFRP strip was determined to provide the maximum increase in the load-capacity of steel beams. The importance of bond-stress distribution along the CFRP-steel interface was addressed. Xia and Teng (2005) studied the behavior of CFRP plates bonded to the surface of steel members, based on a simple shear pull-off test. Test parameters included adhesive type and thickness. The test specimens exhibited either a cohesive failure of the adhesives or an adhesive failure at the steel interface, both effectively resulting in delamination of the CFRP plates. An empirical bond-slip model was proposed to predict the interfacial behavior of CFRP plates bonded to a steel substrate. Shaat and Fam (2008) conducted an experimental program to examine the flexural behavior of damaged steel beams

strengthened with CFRP sheets. The strengthened beams recovered their undamaged load-carrying capacity although the bond length of the CFRP substantially influenced the strength capacity. Debonding of the CFRP sheets was the dominant limit state of the strengthening system. Harries and Webb (2009) reported on the behavior of CFRP-steel interface based on a fracture mechanics perspective. Notched four-point bending specimens were used to determine the fracture characteristics of the interface and the propagation of bond failure. CFRP-bonding schemes influenced the energy release rate of the CFRP-steel interface. Linghoff et al. (2009) conducted an experimental study related to the bond behavior of CFRP laminates when used for steel members. The significance of surface preparation was discussed. Stress concentrations at the cut-off point of the CFRP were reported to be a critical factor influencing the bond performance.

Previous research has highlighted CFRP-strengthening as promising for steel beams provided adequate bond is obtained. Most of the existing research, however, is concerned with experimental investigations. Numerical studies that can provide additional insights into the behavior of steel members strengthened with CFRPs require further attention, including developing bond-slip properties of CFRP-steel interface. The present study is part of a complementary experimental and analytical investigation examining the static and fatigue behavior of steel beams strengthened with CFRP strips. A preliminary modeling approach for the static behavior is presented in this paper.

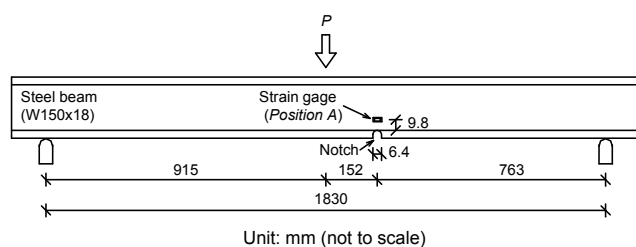
Table 1 Beam details

Beam	Notch	CFRP	Ultimate load (kN)		Failure mode ^a	
			Exp	FEA	Exp	FEA
A	No	No	102	113	S	Y
B	Yes	No	82	98	S	Y
C	Yes	Yes	85	123	S	R

^a S = stability failure; Y = yielding; R = CFRP rupture

2 BEAM DETAILS

Three W150×18 (US designation: W6×12) steel beams were tested in simple midpoint flexure as shown in Figure 1. Tests included an undamaged control (A), damaged (B), and strengthened (C) beam as shown in Table 1. To simulate the damage, Beams B and C were notched at the tension flange, as shown in Figure 1. The notch was offset from midspan so that the direction of debonding was fixed thus minimizing instrumentation needs (Harries et al. 2010). A single 50 mm wide and 1.4 mm thick CFRP strip was bonded on the bottom of the tension flange of Beam C using an epoxy adhesive to improve the flexural behavior of the notched beam. The CFRP strip had a tensile strength of 2,800 MPa and tensile modulus of 155 GPa. The steel beam had a yield strength of 393 MPa. The two-part epoxy adhesive, applied in a 1 mm thick glue line, had a tensile strength of 25 MPa and modulus of 4.5 GPa. A displacement transducer was installed at midspan of the beams and an electric foil strain gage was bonded at the root of the notch to provide critical strains of the test beams (*Position A* in Figure 1). All of the beams were monotonically loaded until failure occurred. Details of the experimental program are found in Harries et al. (2010).

**Figure 1** Overview of test beam

3 MODELING APPROACH

A nonlinear three-dimensional finite element analysis (FEA) model was developed using the general-purpose software ANSYS to predict the flexural behavior of steel beams. The following describes details of the modeling approach.

3.1 Material modeling

A bilinear stress-strain relationship having a yield strength of 393 MPa and an elastic modulus of 200 GPa was used to model the steel beams. A Poisson's ratio of 0.3

was assumed. The CFRP strip was modeled as having a linear stress-strain relationship to rupture ($f_{u-cfrp} = 2,800$ MPa) with a Poisson's ratio of 0.27.

3.2 Bond-slip model

The constitutive behavior of CFRP-steel interface was modeled based on Xia and Teng (2005). The bilinear interface model represents the behavior the epoxy adhesive:

$$\tau_f = 0.8f_{ta} \quad (1)$$

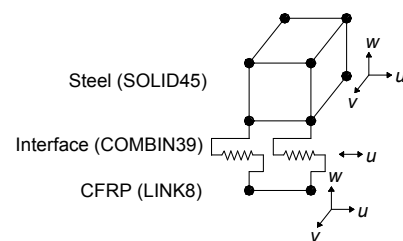
$$\delta_l = \frac{\tau_f t_a}{G_a} \quad (2)$$

$$\delta_f = 62 \left(\frac{f_{ta}}{G_a} \right)^{0.56} \frac{t_a^{0.27}}{\tau_f} \quad (3)$$

where τ_f is the local bond strength; f_{ta} is the tensile strength of the adhesive; t_a is the thickness of the adhesive; G_a is the shear modulus of the adhesive; and δ_l and δ_f are the slip values at the peak stress and at zero stress after complete softening of the bond stress, respectively. The units of the model are in *N* and *mm*.

3.3 Elements

Three-dimensional structural solid elements (SOLID45) were used to represent the steel beam. This element has eight nodes with three translational degrees of freedom per node. The unidirectional CFRP strips were modeled with three-dimensional spar elements (LINK8). The spar element has two nodes with three translational degrees of freedom per node. The LINK8 element is able to represent uniaxial tension and compression behavior with a uniform stress along the element. The CFRP-steel interface was modeled with nonlinear spring elements (COMBIN39). This element enforces longitudinal capability (i.e., tension and compression) and thus no bending resistance is available. The interface element had no initial distance between nodes. Slip between the two nodes was generated when the element was subjected to tension or compression forces.

**Figure 2** Formulation of interface element

One node of the interface element was connected to a steel element and the other node was connected to a CFRP element, as schematically shown in Figure 2. Eqs. 1 to 3 were incorporated into the interface element. The translational degree of freedom of the interface element

was associated with the relative displacement of the CFRP and steel elements so that longitudinal bond-slip responses were simulated. Prior to the application of the interface element for steel beams, the predicted response of the interface was compared to the bond-slip model (Eqs. 1 to 3), as shown in Figure 3. The predicted bilinear bond-slip response agreed well with the theoretical model.

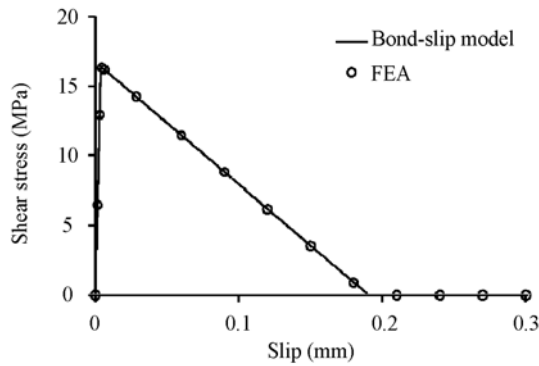


Figure 3 Validation of the interface element

3.4 Geometry and boundary condition

Figure 4 shows a constructed FEA model. A fine mesh was formulated to avoid mesh convergence issues, including an element size ranging from 6 mm to 38 mm (0.3% to 1.8% of the beam length). Simply-supported conditions were modeled by constraining appropriate nodes, as shown in Figure 4. Load was incrementally applied until failure of the beam occurred. Environmental and thermal effects were not considered.

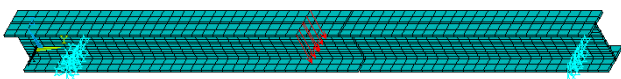


Figure 4 Constructed FEA model (Beam B)

4 POSTPROCESSING

4.1 Load-displacement response

Figure 5 shows the load-displacement response of the steel beams. The CFRP-strengthening improved the load-carrying capacity of the damaged beam. For example, the strengthened beam with a notch (Beam C) showed an increase of 8.1% and 20.4% in the ultimate load when compared to the control (Beam A) and the notched (Beam B) beams, respectively. A noticeable difference in flexural stiffness of the beams was not observed prior to yielding of the beams (Figure 5). This is attributed to the fact that the notch was not located at the critical section and the CFRP-strengthening was passive in nature (no prestress). The predicted behavior of Beams A and B had failure in yielding of the steel section, whereas Beam C failed due to the rupture of the CFRP strip, as shown in Table 1.

It must be noted that the experimentally tested beams were intended as control specimens for a study of fatigue behavior and thus were not substantially braced; all eventually failed due to lateral torsional buckling. Nonetheless, both Beams B and C exhibited significant plastic behavior at the root of the notch (strains in excess of 1% prior to the strain gage failing) and the CFRP of Beam C debonded prior to the ultimate capacity of the beam being achieved (Harries et al. 2010).

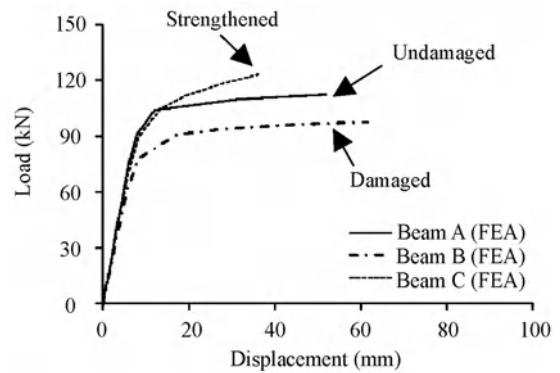


Figure 5 Load-displacement response

4.2 Strain localization near the notch

The strain development at the root of the notch (Position A in Figure 1) is shown in Figure 6. The local plasticity near the notch considerably affected the strain response. For example, the strain at the root of the notch in Beam B at a load of 60 kN (typical service load taken as 60% of ultimate capacity) was over 12 times greater than at the same location in Beam A. Additionally, Beam B was clearly exhibiting local inelastic behavior at this location while Beam A remained entirely elastic. This observation emphasizes that small damage in a steel beam may cause significant stress concentrations that could accelerate the deterioration, particularly in the presence of fatigue loads or harsh environmental conditions (i.e., stress corrosion). The CFRP-strengthening reduced the strain localization of the notched beam. Beam C showed a decrease of 50% in the strain at 60 kN when compared to Beam B, as shown in Figure 6.

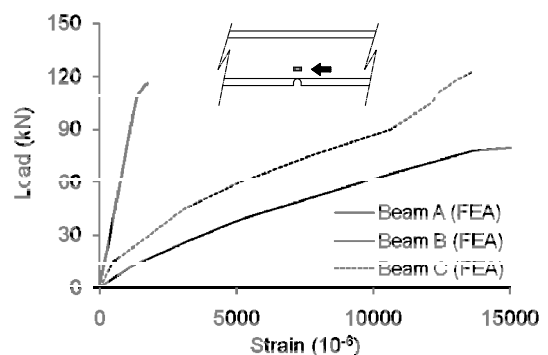


Figure 6 Strain development at root of notch

4.3 Strain development of CFRP strips

Figure 7(a) shows a strain profile along the CFRP strip of Beam C at the service load of 60% of ultimate capacity. The strain envelope follows the moment gradient of the beam in three-point bending, except for the strain concentration at the notch. The strain at the notch was almost 5 times greater than the strain at midspan (Figure 7a). This concentration reflects the product of the local change in section properties and the stress concentration factor associated with the presence of the notch. A gradual increase in the CFRP strains was observed near the notch until the CFRP ruptured, as shown in Figure 7(b).

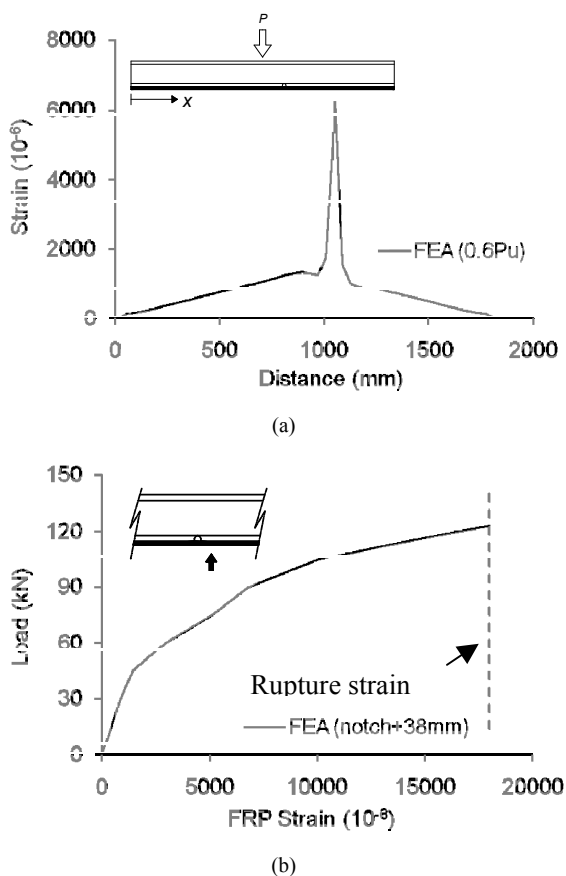


Figure 7 FRP strains in Beam C: (a) along beam span; (b) near notch

5 SUMMARY AND CONCLUSIONS

This paper has presented a modeling approach to predict the flexural behavior of steel beams strengthened with CFRP strips. Structural damage was intentionally created by notching selected beams. Three-dimensional FEA models were developed, including bond-slip properties at the CFRP-steel interface. The CFRP-strengthening

resulted in a 26% improvement in load-carrying capacity of the notched beam. The stress-intensifying effect of the notched beam was significantly reduced due to the presence of the CFRP.

6 ON-GOING WORK

The research is currently continuing to examine the behavior of steel beams strengthened with CFRP strips subjected to static and fatigue loads, including numerical parametric studies.

REFERENCES

- Bakis, C.E., Bank, L.C., Brown, V.L., Cosenza, E., Davalos, J.F., Lesko, J.J., Machida, A., Rizkalla, S.H., and Triantafillou, T.C. 2002. Fiber-reinforced polymer composites for construction: State-of-the-art review, *ASCE Journal of Composites for Construction*, 6(2): 73-87.
- Harries, K.A. and El-Tawil, S. 2008. Review of Steel-FRP Composite Structural Systems *Proceedings of the 5th International Conference on Composite Construction*, Colorado.
- Harries, K.A. and Webb, P. 2009. Experimental assessment of bonded FRP-to-steel interfaces, *Structures and Buildings*, 162(4), 233-240.
- Harries, K.A., Richard, M.J., and Kim, Y.J. 2010. Fatigue behaviour of CFRP retrofitted damaged steel beams, *International Conference on Structural Faults and Repair*, Edinburgh, Scotland, UK.
- Kim, Y.J. and Heffernan, P.J. 2008. Fatigue behavior of externally strengthened concrete beams with fiber-reinforced polymers: State of the art, *ASCE Journal of Composites for Construction*, 12(3): 246-256.
- Linghoff, D., Haghani, R., and Al-Emrani, M. 2009. Carbon-fibre composites for strengthening steel structures, *Thin-walled Structures*, 47: 1048-1058.
- Nozaka, K., Shield, C.K., and Hajjar, J.F. 2005. Effective bond length of carbon-fiber-reinforced polymer strips bonded to fatigued steel bridge I-girders, *ASCE Journal of Bridge Engineering*, 10(2): 195-205.
- Shaat, A. and Fam, A. 2008. Repair of cracked steel girders connected to concrete slabs using carbon-fiber-reinforced polymer sheets, *ASCE Journal of Composites for Construction*, 12(6): 650-659.
- Teng, J.G., Chen, J.F., Smith, S.T., and Lam, L. 2003. Behavior and strength of FRP-strengthened RC structures: a state-of-the-art review, *Structures and Buildings*, ICE, 156(1): 51-62.
- Xia, S.H. and Teng, J.G. 2005. Behaviour of FRP-to-steel bonded joints, *Proceedings of the International Symposium on Bond Behaviour of FRP in Structures*: 411-418.

Temperature Effect on Adhesively Bonded CFRP and Steel Double Strap Joints

Tien C Nguyen, Yu Bai (yu.bai@eng.monash.edu.au), Xiao-Ling Zhao & M.R Bambach
Department of Civil Engineering, Monash University, Melbourne, Australia

Riadh Al-Mahaidi
Faculty of Engineering and Industrial Sciences, Swinburne University of Technology Hawthorn, Melbourne, Australia

ABSTRACT Steel/CFRP double-strap joints adhesive-bonded by epoxy were tested in tension under different temperatures ranging between 20°C and 60°C. Effective bond length was experimentally determined at 20°C first. Specimens, varied with the effective, half and twice the effective bond length and with one or three carbon fibre layers, were examined under the specified temperature range. It was found that the ultimate load and the joint stiffness of all specimens decreased significantly at temperatures near to T_g . Based on the kinetic modeling of glass transition of adhesive, a mechanism-based model was proposed to describe the strength and stiffness degradation of steel/CFRP double strap joints at elevated temperatures, and the modeling results were validated by the corresponding experimental measurements. In addition, it demonstrated that the effective bond length is increased with temperature.

1 INTRODUCTION

Intensive research has been performed on FRP strengthened steel structures to investigate their mechanical behaviors at ambient condition (Zhao & Zhang 2006), while temperature effect on strength and stiffness degradation of these structures has not been well clarified. Particularly for adhesively bonded steel/CFRP double strap joints, in the few studies that have been conducted (Yang et al. 2005, Colombi et al. 2006, Al-Shawf et al. 2009), no mechanism-based models were established to link the degradation of strength and stiffness of the adhesive to that of the joint. In addition, the relationship between effective bond length and temperature has not been identified.

On the other hand, thermo-mechanical models using temperature-dependent FRP mechanical properties have been proposed by several researchers such as Gibson et al. (2006), Cao et al. (2009) and Bai et al. (2008, 2009). However, these models were used to predict the change in the mechanical properties of FRP materials alone under different temperatures. It is not clear whether these models could however be applied directly to the FRP strengthened steel structures in which the adhesive between the steel and the FRP is highly sensitive to temperature.

In this study, a series of adhesively bonded steel/CFRP double strap joints were tested in tension at different temperatures between 20°C and 60°C. Based on the kinetic description of the glass transition of the structural adhesive, a mechanism-based model was used to predict the joint stiffness and strength degradation at elevated

temperatures. The modeling results compared well with the experimental data. In addition, the tendency of temperature-dependent effective bond length was derived from the proposed model.

2 EXPERIMENTAL PROGRAM

2.1 Material properties

The materials of the joints studied were CFRP, adhesive and steel plates. The CFRP was of type CF130 with E-modulus of 240 GPa and nominal tensile strength of 3800 MPa based on the manufacturer's specifications. The adhesive was two-part epoxy Araldite 420 with tensile strength and tensile modulus of 32 MPa and 1900 MPa respectively. The adhesive glass transition temperature (T_g) was determined as 41.7°C (Al-Shawf et al. 2009). The yield stress of steel was found as 359 MPa using coupon tests.

2.2 Test specimens

More than 40 adhesively bonded steel/CFRP double-strap joints were prepared. The two surfaces of steel plates (180 mm length, 50 mm width and 5 mm thickness) were sandblasted and cleaned with acetone to remove grease, oil and rust. Each specimen was fabricated from two steel plates joined together using CFRP with Araldite 420 epoxy (Figure 1). Two different fibre layouts were investigated, being one layer (Type 1) and three layers of CFRP (Type 2). Araldite 420 epoxy was used between steel surface and CFRP and between the layers of CFRP, and each adhesive layer had an average thickness of 0.28 mm.

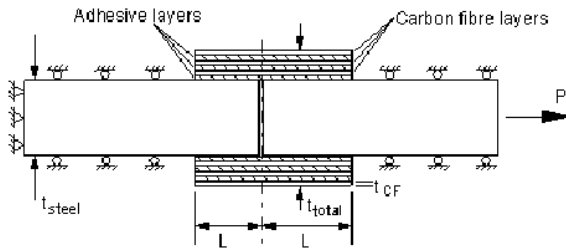


Figure 1 Schematic view of a double strap joint test

The first test series was to determine the effective bond length at ambient condition (20°C). Specimens with different bond lengths ranging between 10 mm and 100 mm (Figure 2), after being cured for 10 days at room temperature as per the manufacturer’s instructions, were tested until failure. The load carrying capacity against the bond length is plotted in Figure 2. The figure clearly shows that for each type of specimen, there was a certain value of bond length, beyond which no significant increase in load capacity occurred. This bond length is defined as effective bond length. The effective bond lengths of specimens having one and three layers of CFRP were found as around 30 mm and 60 mm respectively (see Figure 2).

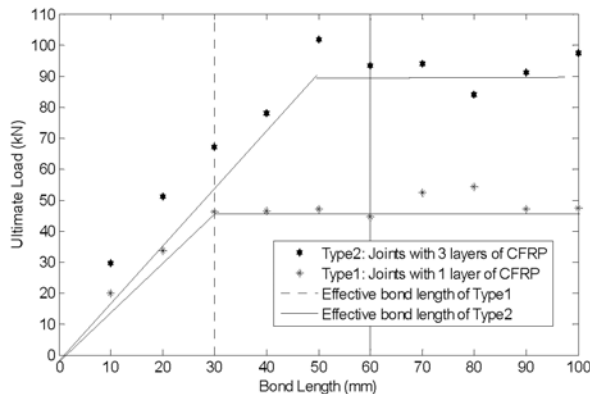


Figure 2 Effective bond lengths at 20°C

Then in the second series, specimens with the effective, half and twice the effective bond lengths of Type 1 and Type 2 were fabricated. All specimens were also cured for ten days at room temperature. After that, this second series was tested to failure at 20°C, 30°C, 40°C, 45°C, 50°C, 55°C and 60°C. A test matrix is shown in Table 1.

Table 1 Matrix test of the second series

Specimen ID	30°C	40°C	45°C	50°C	55°C	60°C
BL15Type1*	-	x	-	-	-	x
BL30Type1	x	x	x	x	x	-
BL60Type1	-	x	x	x	x	x
BL50Type2	-	x	x	x	x	-
BL100Type2	x	x	x	x	x	-

*BL15Type1 means Type 1 specimen with 15mm bond length.

2.3 Thermal and mechanical load setup

The required thermal soaking time determined by Alshawaf (2009) for the same BL100Type2 joint was 45 to 60 minutes. In the current work, each specimen was put in the environmental chamber to reach its targeted temperature for 90 minutes to ensure the entire specimen was saturated with same temperature. It was then tested in tension to failure with constant displacement rate of 2 mm/min.

3 RESULTS AND DISCUSSION

3.1 Temperature effects on joint stiffness

Figure 3 shows the load-displacement curve of the BL60Type1 specimens at different temperatures as an example. The slope of the curves was found to decrease as temperature increased, indicating that the joint stiffness decreased with temperature. The stiffness of each joint at different temperatures was normalized by that at 20°C and plotted in Figure 4.

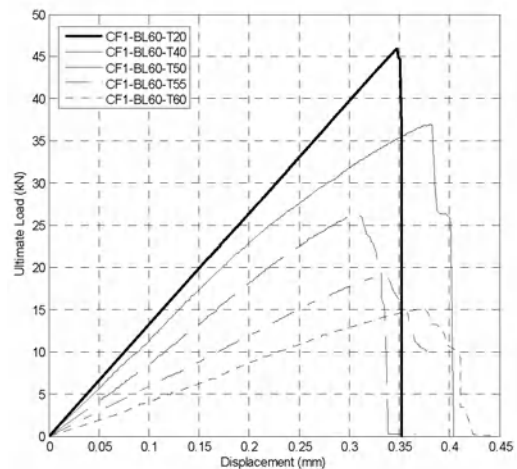


Figure 3 Load-displacement curves of BL60Type1 joints

To compare the degradation of the joint stiffness with that of the adhesive, the result of a dynamic mechanical analysis (DMA) on the same adhesive was also plotted in Figure 4. The figure shows that the normalized joint stiffness degraded similarly to that of the adhesive. This demonstrates that the reduction in stiffness of the steel/CFRP composite double strap joints under elevated temperatures was caused by that of the adhesive.

3.2 Temperature effects on joint strength and effective bond length

The ultimate tensile loads of two series of joints at different temperatures are summarized in Figures 2 and 5. These figures show: (1) With the same number of carbon layers, the joints with longer bond length (less than effective value) have higher ultimate load at a given temperature. (2) With the same bond length, the joints with more layers of carbon fibre could carry higher tensile load. (3) The

ultimate loads of all joints degraded when subjected to elevated temperatures. At 20°C, the ultimate tensile load of Type1 and Type2 joints were 45 kN and 90 kN respectively. At 40°C, these values dropped by up to 20%, except for the BL100Type2 joints with longest bond length which remained close to their initial ultimate load. This observation may imply a effective bond length at 40°C greater than 60 mm (the effective bond length at 20°C). As a result, although the bond strength decreased, increasing the bond length may compensate for the bond strength loss and maintain the ultimate load.

At 60°C, the residual strength of all joints was only between 5% and 20% of their initial value. The ultimate load reduction of the double strap joints is attributed to the shear strength reduction of the epoxy between steel and CFRP and the change of effective bond length. When subjected to elevated temperatures, the shear strength reduces significantly (Bai et al. 2008), and the effective bond length also changes.

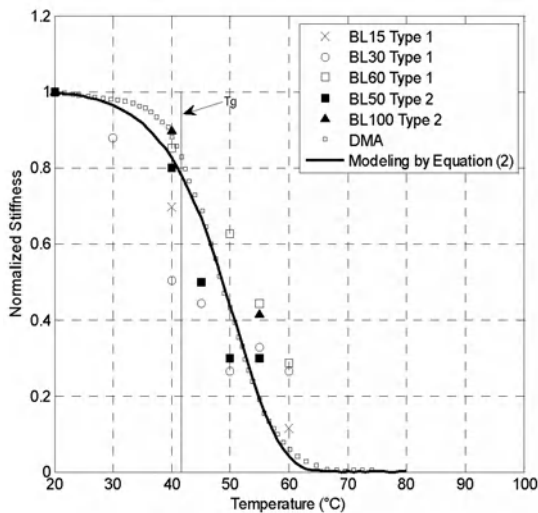


Figure 4 Normalized stiffness degradation

4 MODELING OF STIFFNESS AND STRENGTH DEGRADATION

4.1 Modeling of joint stiffness

A mechanism-based model proposed by Bai et al. (2008, 2009) to describe the mechanical properties of polymer across the glass transition is applied in the current work. In this model, the conversion degree of the glass transition α_g is presented by the following Arrhenius equation:

$$\frac{d\alpha_g}{dT} = \frac{A_g}{\beta} \exp\left(\frac{-E_{A,g}}{RT}\right) (1 - \alpha_g) \quad (1)$$

where $E_{A,g}$ = the constant activation energy for glass transition, T = the temperature, β = the heating rate, R = the universal gas constant (8.314 J/mol.K). Based on Coats-Redfern method (Coats & Redfern, 1964), the kinetic parameters were calculated as $A_g = 1.32 \times 10^{18} \text{ min}^{-1}$

and $E_{A,g} = 115365 \text{ J/mol}$. Substituting the kinetic parameters into Equation 1, the conversion degree of the glass transition can be calculated; and the mechanical properties of the adhesive material (as a mixture of material states before and after glass transition) can be described by the rule of mixture (Bai et al. 2008, 2009):

$$C_m = C_{initial}(1 - \alpha_g) + C_{end}\alpha_g \quad (2)$$

where C_m = the temperature-dependent material properties (E-modulus, shear strength and shear modulus), $C_{initial}$ = the properties at initial state (ambient condition), C_{end} = the properties at final state, being zero because the DMA test revealed that after glass transition E-modulus of the epoxy was negligible. The normalized modeling E-modulus degradation is plotted in Figure 4 and compared well with the DMA results. A good agreement also demonstrates that this model is able to describe the stiffness degradation of the steel/CFRP double strap joints at elevated temperatures.

4.2 Modeling of joint strength

The temperature-dependent modulus model in Section 4.1 can be integrated into the modified Hart-Smith model (Liu et al. 2005) for CFRP/steel double strap joints to predict the joint strength degradation.

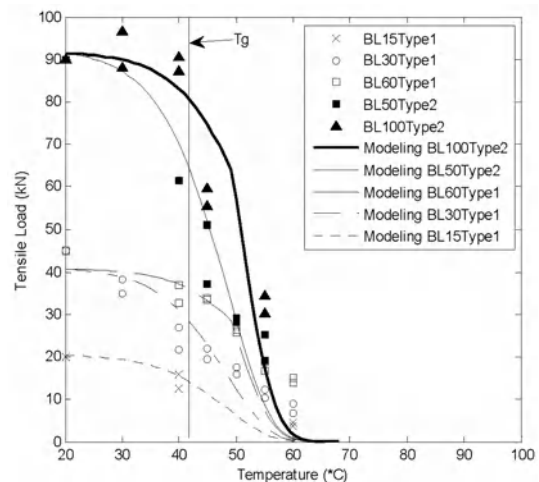


Figure 5 Experimental results and model prediction of the ultimate load

The ultimate load carrying capacity per unit width, P_{ult} , is less of P_i and P_o :

$$P_i = \sqrt{\left[2\tau_p t a \left(\frac{1}{2} \gamma_e + \gamma_p \right) \cdot 2E_i t_i \left(1 + \frac{E_i \cdot t_i}{2 \cdot E_o \cdot t_o} \right) \right]} \quad (3)$$

$$P_o = \sqrt{\left[2\tau_p t a \left(\frac{1}{2} \gamma_e + \gamma_p \right) \cdot 4E_o t_o \left(1 + \frac{2E_o \cdot t_o}{E_i \cdot t_i} \right) \right]} \quad (4)$$

where τ_p = the adhesive shear strength, G_a = the adhesive shear modulus. E and t = the E-modulus and thickness respectively. Subscripts i and o represent inside and

outside adherends, respectively. The thickness of outside adherend is the total thickness of CFRP layers and adhesive layers between CFRP layers. Elastic (γ_e) and plastic (γ_p) adhesive shear strains were calculated as $\gamma_e = \tau_p / G_a$ and $\gamma_p = 3 \gamma_e$. The joint ultimate load is:

$$P = b(L/L_e)P_{ult} \text{ if } L < L_e \text{ or } P = bP_{ult} \text{ if } L \geq L_e \quad (5)$$

where, L_e = the effective bond length determined by Equation 6, b is the steel plate width.

$$L_e = \frac{\sigma_{ult} \cdot t_i}{\tau_p} + \frac{2}{\sqrt{\frac{G_a}{t_a} \left(\frac{1}{E_o t_o} + \frac{2}{E_i t_i} \right)}} \quad (6)$$

where σ_{ult} = the ultimate tensile strength of the inside adherend.

At a given temperature, the parameters required in Equations 3-6 can be calculated from Equation 2 given their initial values at ambient condition. Note that temperatures in this current work (max. 60°C) was not high enough to have obvious effects on E-modulus of steel and CFRP. Thus they can be assumed as constants.

Knowing τ_p and G_a from Equation 2, Equation 6 describes the temperature-dependent effective bond length. The modeling curve in Figure 6 shows that the effective bond length increases with temperature. This result is also supported by the observation in Section 3.2 and the improvement of ultimate load at 40°C of BL100Type2 compared with that of BL50Type2 (Figure 5). This means that the effective bond length of Type2 joints at 40°C has to be greater than 50 mm (as the effective bond length at 20°C), otherwise the ultimate loads of BL100Type2 and BL50Type2 would be similar. Further experimental work is to validate not only such a tendency, but also the exact values of effective bond length as predicted in Figure 6.

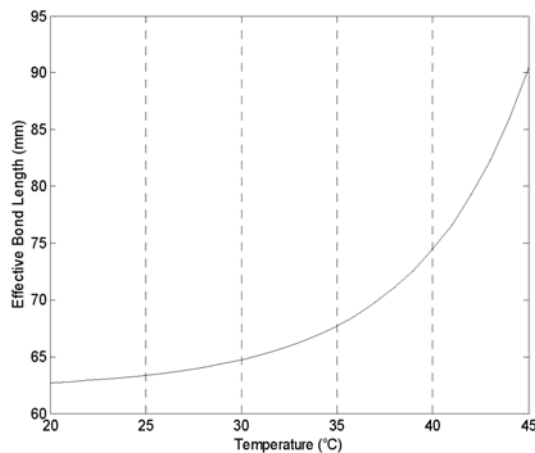


Figure 6 Prediction of the effective bond length

The prediction of joint ultimate load with different numbers of carbon fibre layers and bond lengths at different temperatures was calculated from Equation 5,

considering the effective bond length L_e from Figure 6. The results were plotted in Figure 5, and well compared to the experimental results.

5 CONCLUSIONS

In this study, experimental tests revealed that the stiffness and strength of steel/CFRP double strap joints reduced significantly at elevated temperatures, while the effective bond length was found to increase with temperature. In addition a mechanism-based model to describe the joint stiffness and strength degradation at elevated temperatures was proposed and validated by the experimental results. The models are able to predict the joint stiffness and strength degradation, and describe the increase of effective bond length with temperature.

6 ACKNOWLEDGEMENT

The authors would like to thank Mr. Kevin Nievaart for experimental assistances, and Mr. Haydar Faleh for providing the DMA result.

REFERENCES

- Al-Shawaf A., Al-Mahaidi R., Zhao X-L. 2008. Effects of elevated temperature on bond behavior of high modulus CFRP/steel double strap joints. *Australian Journal of Structural Engineering* 10(1).
- Bai Y. and Keller T., 2009. Modeling of mechanical response of FRP composites in fire. *Composite: Part A* 40: 731-738.
- Bai Y., Keller T., Vallee T., 2008. Modeling of stiffness of FRP composites under elevated and high temperatures. *Composite Science and Technology* 68: 3099-3106.
- Cao, S., Wu, Z., Wang, X. 2009. Tensile properties of CFRP and hybrid FRP composites at elevated temperatures. *Journal of Composite Materials* 43(4).
- Coats, A.W., Redfern J.P., 1964. Kinetic parameters from thermogravimetric data. *Nature* 201: 68-69.
- Colombi, P., Fava, G. & Poggi, C. 2006. Durability of steel members strengthened by CFRP strip under mechanical and environmental loadings, CICE 2006, Miami, FL, USA, IIFC.
- Gibson A.G, Wu Y-S, Evans J.T, Mouritz A.P. 2006. Laminate theory analysis of composites under load in fire. *J Compos Mater* 40(7): 639-58.
- Liu HB, Zhao XL, Al-Mahaidi R, Rizkalla S. 2005. Analytical bond models between steel and normal modulus CFRP. In: 4th international conference on advances in steel structures. 1545-52.
- Yang, Y.X., Yue, Q.R., Peng, F.M. 2005. Experimental Research on the Bond Behavior of CFRP to Steel, in *International Symposium on Bond Behaviour of FRP in Structures-BBFS-2005*, Chen, J.F & Teng, J.G (editors), Hong Kong, China, International Institute for FRP in Construction.
- Zhao, X.L. & Zhang, L. 2006. State-of-the-art review on FRP strengthened steel structures. *Engineering Structures* 29(8): 1808-1823.

Repairing Method for the Steel Members by CFRP Strand Sheets

Y. Hidekuma (y-hidekuma@nick.co.jp), A. Kobayashi & A. Tateishi
Nippon Steel Composite Co., Ltd., Technical Development Dept., Tokyo, Japan

M. Nagai & T. Miyashita
Nagaoka University of Technology, Department of Civil and Environmental Engineering, Niigata, Japan

ABSTRACT The steel structure is corroded by various mechanisms, and thus its performance decreases. As a repairing method of the corroded steel member, a method in which carbon fiber sheets is bonded to the steel member with glue has been studied. In recent years, as more efficient repairing method using FRP materials, the strand sheet method which has high mass per unit area has been developed. The purpose of this study is to propose the repairing method for corroded steel member by using the strand sheets. In order to confirm a reinforcing effect, the tensile and flexural tests using steel plates and girders reinforced with strand sheets were performed. Test results showed effectiveness of strand sheets for the reinforcement of the steel members.

1 INTRODUCTION

Steel structures are corroded by various mechanisms, and their performance decreases due to corrosion. As a repairing method for corroded steel members with a reduced cross-sectional area, a method to bond the carbon fiber sheets with resin to the steel member was developed. This is known as an efficient and economical method for repairing because no heavy equipment is necessary at work site. As for common reinforcing method, the continuous fiber sheets and FRP (Fiber Reinforcement Plastics) strips are being used. However, there are some demerits using these materials. When using continuous fiber sheets, adhesion defects may occur caused by poor impregnation of resin. When also using FRP strips, the delamination may occur at lower load because of bonding shear stress concentration at its tips.

In recent years, to solve these problems, the FRP strand sheet which consists of bunch of individually hardened continuous fiber strands was developed. The adhesion defects do not occur by using the CFRP strand sheets, because it is impregnated with resin and hardened at factory beforehand. Furthermore, the CFRP strand sheets can reduce the number of layers of a sheet compared to continuous fiber sheets because of its high mass per unit area. The purpose of this study is to propose the repairing method for steel members by using CFRP strand sheets. In order to clarify a reinforcing effect and delamination property of CFRP strand sheets bonded to steel members, the tensile and flexural tests of steel reinforced with CFRP strand sheets, continuous fiber sheets and FRP strips were performed.

2 OUTLINE OF TESTS

2.1 Tensile tests

As shown in Figure 1, CFRP strand sheets, conventional CFRP sheets, and CFRP plates were bonded to both sides of steel plate (yield strength: 385 N/mm²). The simple tensile tests of the reinforced steels were performed until the applied load reaches the yield load of the steel (200 kN). The experimental parameter and properties of each material are shown in Table 1 and Table 2. The strains in CFRP and steel were measured and delamination between CFRP and steel was observed. In order to reduce the stress concentration, each layer was dislocated 25 mm and laminated with a step.

2.2 Flexural tests

CFRP strand sheets and continuous fiber sheets were chosen as reinforcement for flexural tests since the delamination did not occur in tensile tests. These sheets were bonded to upper and lower flanges of two H-shaped steel girders of named A and B (yield stress: 315 N/mm²), which are subjected to uniform bending as shown in Figure 2. The four-point bending tests were performed until yield load of steel (1200 kN). The deflection and strain in CFRP/steel were measured, and also delamination between CFRP and steel was observed.

3 RESULTS AND DISCUSSIONS

3.1 Tensile tests

The delamination between the CFRP and the steel occurred at 30-60% of yield load of the steel in specimens which were reinforced with CFRP plates. On the other hand, in case of specimens which were reinforced with CFRP

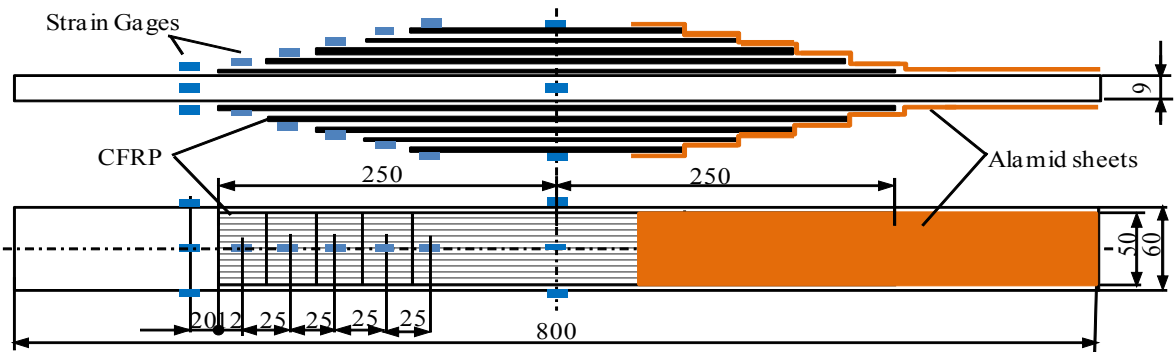


Figure 1 Specimen for tensile tests

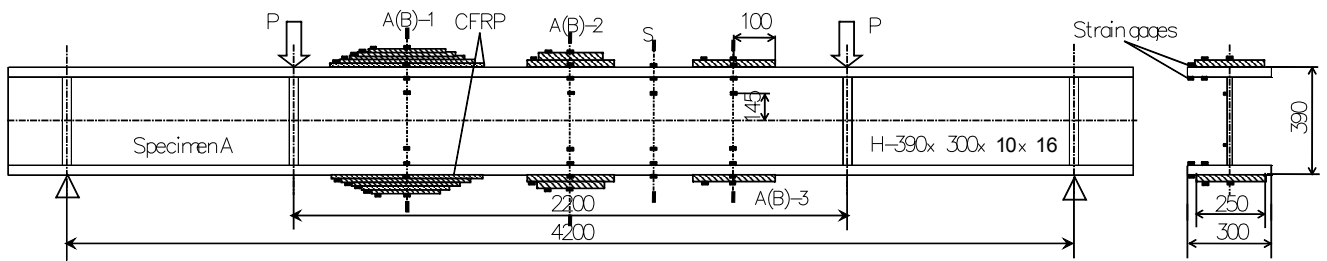


Figure 2 Specimen for flexural tests

Table 1 Properties of CFRP

Type		CF Sheet	CFRP Strand Sheets			CFRP Plate		
		CFHM300	SSHT600	SSHM600	SSHM900	PLHT20	PLHM20	PLHM40
Mass per unit area	g/m ²	314	600	628	910	-	-	-
Thickness t	mm	0.143	0.333	0.286	0.429	2.0	2.0	4.0
Elastic modulus E	GPa	682	245	724	710	165	450	450
Tensile stiffness Et	kN/mm	97.5	81.6	207	305	330	900	1800

Table 2 Parameter of tests

	No.	Laminate constitution	
		CFRP type	Number of ply
Tensile	1-1	SSHT600	5
	1-2	SSHM600	1
	1-3	SSHM600	3
	1-4	SSHM600	5
	1-5	SSHM900	1
	1-6	SSHM900	3
	1-7	SSHM900	5
	1-8	PLHT20	1
	1-9	PLHM20	1
	1-10	PLHM40	1
	1-11	CFHM300	6
	1-12	CFHM300	10
Flexural	A-1	CFHM300	5
	A-2	SSHM600/900	1/1(Total 2)
	A-3	SSHM900	1
	B-1	SSHM600	5
	B-2	SSHM900	5
	B-3	SSHM900	2

strand sheets and CFRP sheets, no delamination occurred. Figure 3 and Figure 4 show the relationship between load

and strain of No.1-7 without delamination and No.1-9 with delamination. The load mentioned here is divided by yield load of steel. As measuring strain, a value of strain gages at unreinforced part, steel in reinforced part, tip of CFRP and center of CFRP were indicated in these figure. In the figure, the calculated value of composite cross section consisting of CFRP and steel was shown. The tensile rigidity was calculated by the following formulas.

$$\frac{P}{\epsilon} = E_s \cdot A_{s+cf} \tag{1}$$

$$A_{s+cf} = A_s + \frac{E_{cf}}{E_s} \cdot A_{cf} \tag{2}$$

where

P: tensile force

ε: strain at reinforced steel

E_s, E_{cf}: elastic modulus of steel and CFRP

A_{s+cf}: reduced cross-sectional area

A_s, A_{cf}: cross-sectional area of steel and CFRP

From these results, it was found that the experimental value agree - - s well with the calculated value until delamination occurs. In other specimens, the same results were obtained.

Table 3 Results of tensile tests

No.	Type	CFRP Number of laminates	Stiffness $E_{cf}A_{cf}$ kN	Tensile stiffness		Achievement ratio E_{ms}/E_{cal}	Initial delamination P_{ip}/P_y	Complete delamination P_{fp}/P_y
				Calculated E_{cal} kN	Measurement E_{ms} kN			
1-1	SSHT600	5	40790	139586	136883	98.1%	>100%	>100%
1-2	SSHM600	1	20706	118930	127951	107.6%	>100%	>100%
1-3	SSHM600	3	62118	160646	163296	101.7%	>100%	>100%
1-4	SSHM600	5	103530	202159	200788	99.3%	>100%	>100%
1-5	SSHM900	1	30460	129019	130938	101.5%	>100%	>100%
1-6	SSHM900	3	91380	190446	185047	97.2%	>100%	>100%
1-7	SSHM900	5	152300	251015	236971	92.5%	>100%	>100%
1-8	PLHT20	1	33000	132250	132661	100.6%	59%	82%
1-9	PLHM20	1	90000	189123	204596	113.7%	33%	49%
1-10	PLHM40	1	180000	278990	267588	95.9%	34%	35%
1-11	CFHM300	6	58512	157496	151926	96.5%	>100%	>100%
1-12	CFHM300	10	97520	196149	167067	86.4%	>100%	>100%

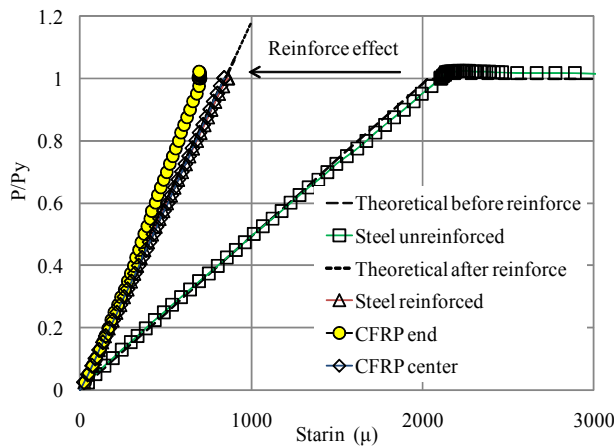


Figure 3 Load - strain diagram of No.1-7

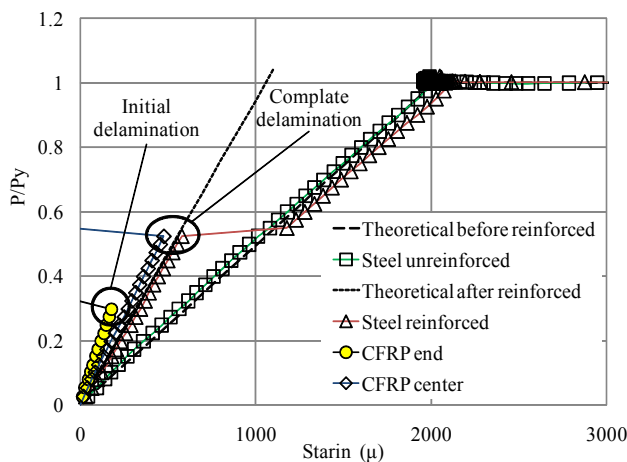


Figure 4 Load - strain diagram of No.1-9

Table 3 shows the comparison between experimental and calculated value of tensile stiffness. In this table, tensile stiffness of CFRP ($E_{cf}A_{cf}$) was calculated with elastic modulus, cross-sectional area and number of layered CFRP. A calculated whole tensile stiffness ($E_{cal}A_{cal}$) was given by adding the tensile rigidity of steel to tensile stiffness of CFRP ($E_{cf}A_{cf}$). A experimental whole tensile stiffness ($E_{ms}A_{ms}$) is calculated with load and

strain between $P/P_y=0.2$ and $P/P_y=0.6$ of steel in reinforced part. In No.1-9 and No.1-10, the load and strain between $P/P_y=0.1$ and $P/P_y=0.5$ and between $P/P_y=0.05$ and $P/P_y=0.25$ were used because the delamination of CFRP plate occurred. The new findings from Table 3 are given in the followings.

3.1.1 Tensile stiffness

In each specimen, the experimental whole tensile stiffness agrees well with calculated stiffness. In No.1-12, the ratio of the experimental value to the calculated one is lower than others. It is thought that the force which transfers from steel to CFRP is not enough due to short outermost layer. Although more than 200 mm length of outermost layer is necessary for getting the enough ratio of the experimental value to the calculated value, which was known from the past research, the length of outermost layer of No.1-12 turned out to be 50 mm only.

3.1.2 Delamination

Form Figure 4, in case of specimen reinforced with CFRP plate, it was found that the delamination occurred before yield of steel from tip of CFRP and then the delamination grows to center. In No.1-8, initial delamination load was 57 % of yield load of steel. That of No.1-9 was 32 % and that of No.1-10 was 30 %. The complete delamination load of No.1-8 was 82 %, that of No.1-9 was 52 %, and that of No.1-10 was 35 %. Hence, when the elastic modulus and thickness of CFRP plate are higher, the delamination load becomes lower. It is considered that delamination occurred because of the higher bonding shear stress concentration at interface between steel and CFRP plate.

On the other hand, no delamination occurred until yield load of steel in case of continuous fiber sheets and CFRP strand sheets. It is thought that the bonding shear stress concentration has been reduced with lower tensile rigidity per one layer and laminated CFRP with a step.

3.2 Flexural tests

In both tensile and compressive sides, the strains of steel

at reinforced part were reduced compared with that of the unreinforced part. The delamination of CFRP sheets also did not occur in all cases until the applied load reaches yield load of steel.

Figure 5 shows the relationship between load and strain located web-side surface of flange of specimen A. The load mentioned here was divided by yield load of steel. In the figure, the calculated value of composite cross section of CFRP sheets and steel was given. The tensile stiffness was calculated by the following formulae.

$$\varepsilon_i = \frac{M}{E_s \cdot I_{s+cf}} \cdot y_i \tag{5}$$

$$I_{s+cf} = I_s + \frac{E_{cf}}{E_s} (I_{cf} + A_{cf} \cdot e_{cf}^2) \tag{6}$$

where

ε_i : strain of optional location

M : bending moment

E_s, E_{cf} : elastic modulus of steel and CFRP

I_{s+cf} : reduced geometrical moment of inertia

I_s, I_{cf} : geometrical moment of inertia of steel and CFRP

A_{cf} : cross-sectional area of CFRP

y_i : distance from neutral axis to optional location

e_{cf} : distance from neutral axis to centroid of CFRP

From Figure 5, it is found that the reinforcing effect of section A-1 where conventional carbon fiber sheets were bonded and section A-2 where CFRP strand sheets were bonded, in which both have the same total mass per unit area, is nearly the same. In addition, they are equal to the calculated value obtained from composite cross section.

Figure 6 shows the relationship between load and strain of specimen B. The higher total mass per unit area of CFRP sheet, the higher reinforcing effect is obtained. Furthermore, they are equal to the calculated value from composite cross section.

In Table 4, the experimental reduction ratio of strain at $P/P_y=0.6$ and $P/P_y=0.9$ and calculated reduction ratio of composite cross section are given. The ratio of the experimental value to the calculated one is also shown in Table 4. In all cases, the ratio of the experimental reduction ratio to the calculated one is more than 90 %. It is found that the strain of steel reinforced by CFRP sheets can be calculated using composite cross section.

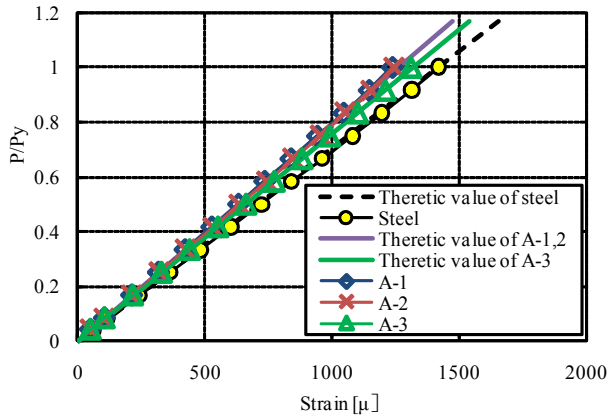
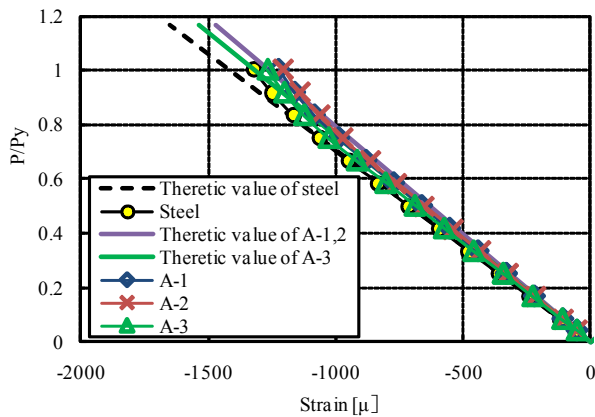


Figure 5 Load - strain diagram of specimen A

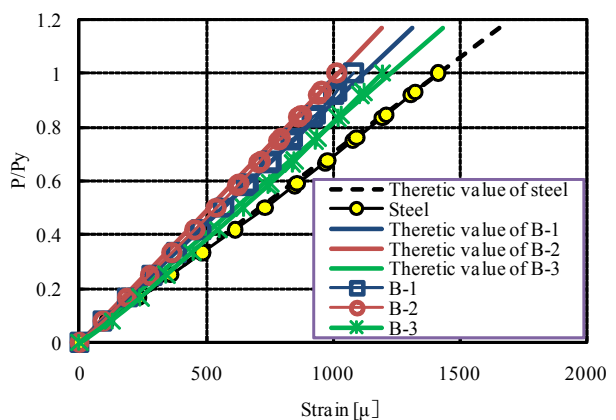
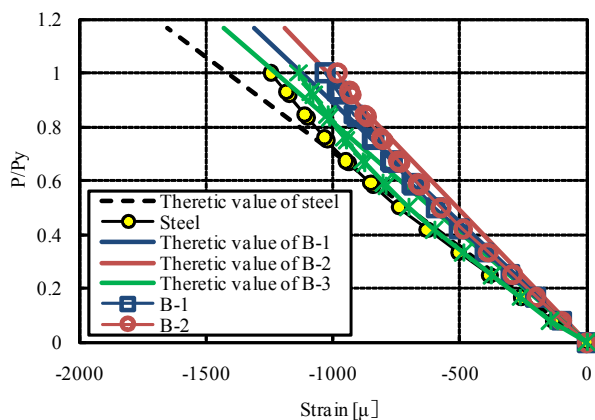


Figure 6 Load - strain diagram of specimen B

Table 4 Reduction ratio of strain

(a) Tensile side					
	Reduction ratio of strain (%)			Achievement ratio	
	Measurement R_{exp}		Calculated R_{cal}	R_{exp}/R_{cal} (%)	
	$P/P_y=0.6$	$P/P_y=0.9$		$P/P_y=0.6$	$P/P_y=0.9$
A-1	11.3	12.0	10.9	103	110
A-2	10.2	11.4	11.4	90	100
A-3	6.7	7.1	7.1	94	99
B-1	20.2	23.2	20.7	98	112
B-2	24.6	27.8	27.9	88	100
B-3	13.2	17.2	13.3	99	130

(b) Compressive side					
	Reduction ratio of strain (%)			Achievement ratio	
	Measurement R_{exp}		Calculated R_{cal}	R_{exp}/R_{cal} (%)	
	$P/P_y=0.6$	$P/P_y=0.9$		$P/P_y=0.6$	$P/P_y=0.9$
A-1	6.9	10.9	10.9	63	100
A-2	8.3	12.2	11.4	73	107
A-3	8.0	12.0	7.1	113	168
B-1	17.3	25.3	20.7	83	122
B-2	20.5	28.7	27.9	73	103
B-3	11.0	21.6	13.3	83	163

4 CONCLUSION

The results obtained from this research are summarized in the followings.

From tensile tests, it is clarified that no delamination occur until yield load of steel when continuous fiber sheets and CFRP strand sheets are used as reinforcement, but delamination occur at 30-60 % of yield load when CFRP plate is used. It is also shown that the CFRP reinforced steel can be dealt with as composite cross section.

From flexural tests, it is clarified, as is the same case with conventional continuous fiber sheets, when CFRP strand sheets which have high mass per unit area are used. that the no delamination occur until the applied load reaches the yield load of steel. Furthermore, it is clarified that steel reinforced by CFRP strand sheets can be designed as composite cross section.

REFERENCES

- H Sugiura, A Kobayashi, N Inaba, A Honma, K Ohgaki and M Nagai, 2009. A Proposal of Design and Construction Method of Repair for Corroded Steel Member by Carbon Fiber Sheets, *Journal of Construction Management and Engineering*, JSCE, vol.65, No.1, 106-118.

Temperature Effects in Adhesively Bonded FRP Strengthening Applied to Steel Beams: Experimental Observations

Tim J Stratford (Tim.Stratford@ed.ac.uk) & Luke A Bisby

The Institute for Infrastructure and Environment, The University of Edinburgh, Scotland, UK

ABSTRACT FRP plates can be used to strengthen a steel beam in flexure, but this method relies critically upon the adhesive used to bond the FRP plate to the existing steel member. When the temperature of the strengthened beam is increased, differential thermal expansion occurs between the steel and FRP. In addition, the glass transition temperature of a typical two-part ambient-cure epoxy adhesive is typically between about 50°C and 65°C, and the stiffness and strength of the adhesive will decrease at temperatures somewhat below the glass transition temperature. This paper reports tests conducted on steel beams strengthened with CFRP plates and ambient-cure epoxy adhesive. Load was applied to the beams in four-point bending, and the temperature of the strengthening was then increased until failure occurred. Slip deformations were directly observed across the adhesive joint, giving an indication of the performance of the strengthening at elevated temperatures. The consequences of this preliminary study upon the design of externally-bonded FRP strengthening for steel structures are discussed.

1 INTRODUCTION

Properly designed and installed FRP strengthening often requires less installation equipment and time than other strengthening techniques (such as bonded steel plates or bolted strengthening solutions). Consequently, FRP strengthening is an increasingly popular method to extend the life of steel and cast iron structures (CIRIA 2004).

To enable easy installation, two-part ambient-cure epoxy resins are commonly used to bond the FRP to the existing structure without the need for elevated temperature curing. These ambient-cure epoxies soften at low glass-transition temperatures of typically 50-65°C (Concrete Society 2004), which are similar to the temperatures considered during the design of steel bridges in the UK (Highways Agency 2001).

Research into the elevated temperature performance of bonded FRP strengthening has concentrated upon the *high* temperatures present during a fire (e.g.: Kodur, Bisby & Green 2007); this paper investigates *warm* temperatures (< 100°C). It presents results from a preliminary experimental study conducted on CFRP strengthened steel beams, the aims of which were to:

- Establish how an FRP plate bonded beam is affected by warm temperatures.
- Study slip deformation across the adhesive joint under warm conditions.

1.1 Thermal effects in bonded strengthening

Two thermal effects act when a plated beam is heated:

- differential expansion between the CFRP plate and the metal; and

- glass transition of the adhesive, which reduces the strength and of stiffness of the adhesive.

Differential thermal expansion causes high shear stresses across the adhesive joint. Elastic bond stress analysis predicts that for a typical bridge strengthening scheme, the thermal shear and peel stresses can be greater than those due to traffic loading (Denton 2001, Stratford and Cadei 2005).

However, the implications of differential thermal expansion and the glass transition of the adhesive are not obvious. The reduction in adhesive strength at elevated temperatures is accompanied by a reduction in the adhesive stiffness and an increase in deformation capacity, both of which could be beneficial to the overall strength of the adhesive connection.

1.2 Epoxy adhesive at elevated temperatures

Figure 1 shows the glass transition for the epoxy bonding adhesive used in the present tests. This is a 2-part, ambient-cure adhesive, sold specifically for plate bonding applications. The reduction in stiffness with temperature shown in the figure was obtained by dynamic mechanical analysis (DMA) of five adhesive samples. The specimens (15×10×1mm) were tested in a double cantilever configuration, hence Figure 1 plots normalised flexural stiffness; however, this is also the variation in adhesive shear stiffness with temperature. The tests were conducted after 15 days ambient cure (whereas the manufacturer specifies full cure after 5 days at 25°C).

At 40°C, the adhesive stiffness has reduced to 94% of its ambient value, a change that would normally be

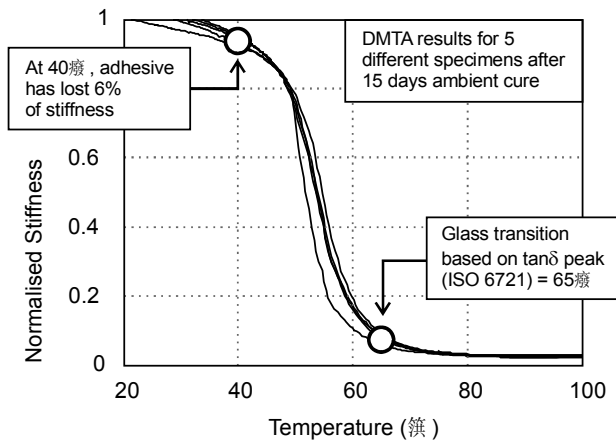


Figure 1 Measured loss in stiffness of the epoxy bonding adhesive through the glass transition

considered significant for structural design. The glass transition, however, is not normally characterised in full, but by single temperature, T_g . The definition of T_g varies depending upon the phenomenon being tested (Ludwig et al. 2008). ISO 6721 (2002) defines the glass transition temperature for DMA as the peak in the $\tan\delta$ curve, which is the ratio of the loss modulus to the storage modulus (simplistically, the ratio of plastic deformation to elastic deformation). This gives $T_g = 65^\circ\text{C}$, for which the adhesive stiffness has reduced to less than 10% of its ambient value.

2 EXPERIMENTAL ARRANGEMENT

Six steel I-beams were strengthened using pultruded CFRP plates and the ambient cure epoxy adhesive characterised in Figure 1. The beams were loaded in inverted 4-point bending, as shown in Figure 2. The cross-sectional dimensions and material properties are shown in Figure 3.

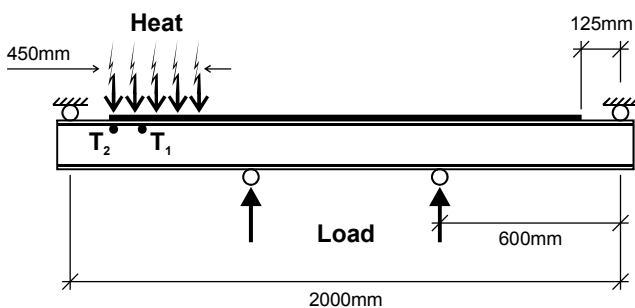


Figure 2 The test arrangement

The end of the strengthening plate was heated from above using a silicone rubber electrical heating pad, the temperature of which was controlled according to a thermocouple on the surface of the plate. The temperature of the flange of the steel beam was measured using two further thermocouples located at the end of the plate (T_2) and 160mm from the end of the plate (T_1). These temperatures are assumed to be representative of the

temperature of the adhesive, due to the high thermal conductivity of the steel.

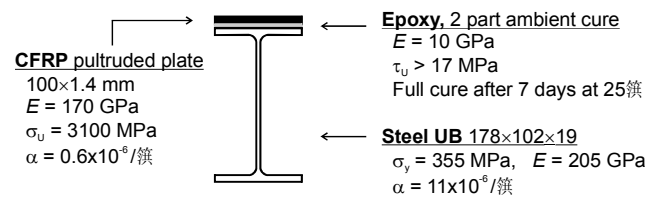


Figure 3 Cross-section dimensions and material properties of the strengthened beams. (The material properties for the adhesive and CFRP plate are from the manufacturer’s data sheet)

Table 1 summarises the tests conducted. The capacities of the strengthened beam (1) and unstrengthened beam (7) were found at ambient temperature. Test 6 failed prematurely due to air voids in the bondline, so does not represent the true strengthened capacity of the beam.

Beams 2 to 5 were loaded to above their unstrengthened capacity. This load was held constant whilst the temperature in the adhesive was increased until failure occurred, as shown schematically in Figure 4. Each of the two ends of beams 4 and 5 were tested separately (tests 4a, 4b; 5a, 5b).

Table 1 Details of experimental program and headline results.

ID	Load (kN)	Temperature T_2 ($^\circ\text{C}$)	Comment
1	190.0	Ambient	Capacity of a strengthened beam (l.t. buckling)
6	(155.6)	Ambient	Premature failure due to poor bonding
7	140.4	Ambient	Capacity of an unstrengthened beam (l.t. buckling)
2	150	65	Plate debonding failure
3	160	not available	Data acquisition error
4a	170	74	Plate debonding failure.
4b	170	74	Plate debonding failure.
5a	180	60	Plate debonding failure.
5b	180	64	Plate debonding failure.

High resolution digital images were recorded at 10 second intervals during the tests, for later analysis to establish the deformation across the adhesive joint. The images focused upon the heated end the plate, where the side of the CFRP, adhesive and beam flange had first been painted with a high-contrast texture, as shown in Figure 5.

The images were analysed using a bespoke image-processing algorithm (White et al. 2003) that tracks the movement of patches of pixels. The relative horizontal displacement of pairs of patches in the CFRP plate and flange of the beam allowed the slip (shear displacement) across the adhesive joint to be determined (Figure 5).

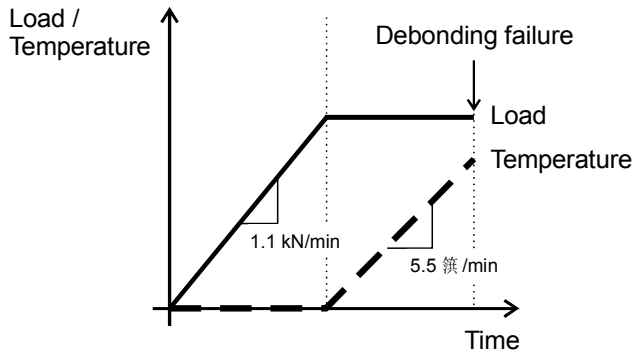


Figure 4 Schematic loading and heating history

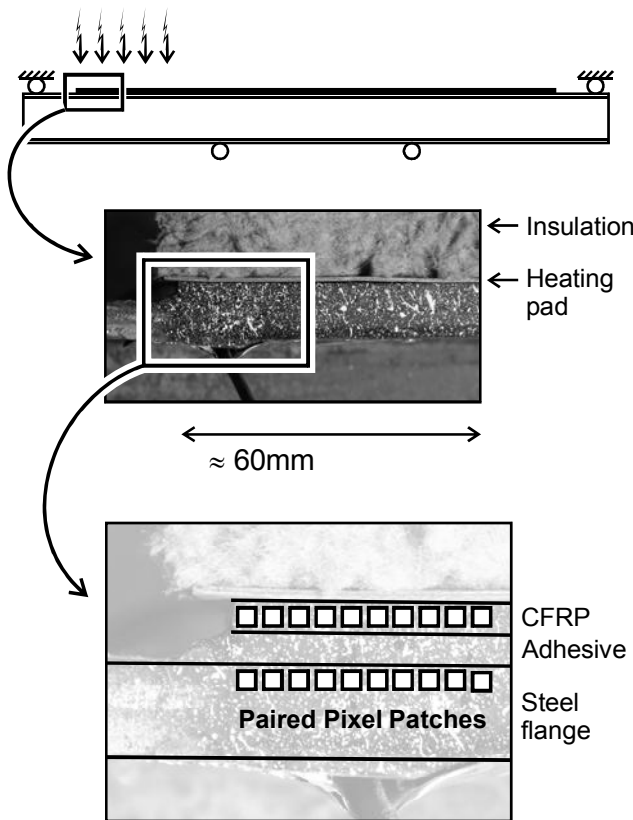


Figure 5 Measurement of slip displacement across the adhesive joint by digital image analysis

3 RESULTS

Table 1 summarises the key results from the tests. The strengthening failed adhesively at the adhesive-steel interface in every case, resulting in debonding of the plate from the beam along the 450mm heated length. Failure of the adhesive joint was followed by lateral-torsional buckling of the steel beam, as for the unstrengthened beam at ambient temperature.

Figure 6 plots the failure temperature and applied load for the tests, showing the temperature at both thermocouples. There is no discernible trend between the failure temperature and applied load. All tests failed after 25 to 30 minutes of heating.

The temperature at the plate end (T_2) is lower than the temperature within the plate (T_1) due to conduction into the unheated steel beam towards the supports (Figure 2). Debonding failure usually initiates at the stress concentration at the end of the plate, thus T_2 is more representative of the failure temperature.

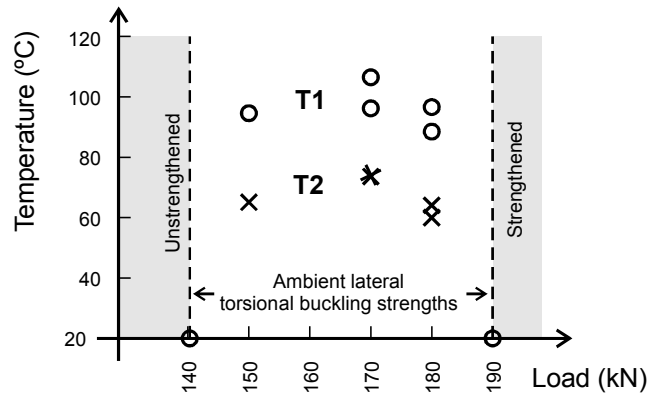


Figure 6 Reduction in beam strength due to temperature

The plate-end slip displacements obtained using image analysis are plotted in Figure 7 for all tests. Significant slip deformation occurred from 40 °C, and this slip increased to failure. The slips recorded by the last image before failure were in the range 0.16 to 0.23mm; the actual failure slip will have been slightly higher as the last image was taken up to 10 seconds before debonding occurred.

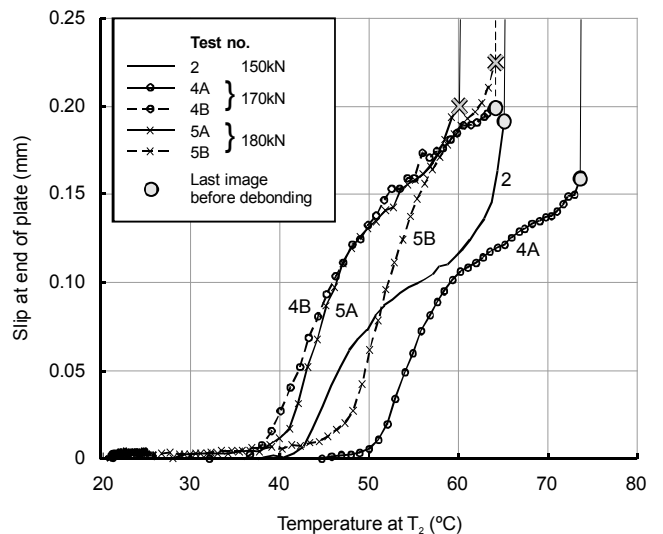


Figure 7 Plate end slip variation with temperature for all tests

An example of the complete output from the image analysis is shown in Figure 8 for Test 5B. This plots the slip displacement with position from the plate end and against temperature. Slip occurs along the whole of the observed length of the adhesive joint, with little variation in slip along the beam.

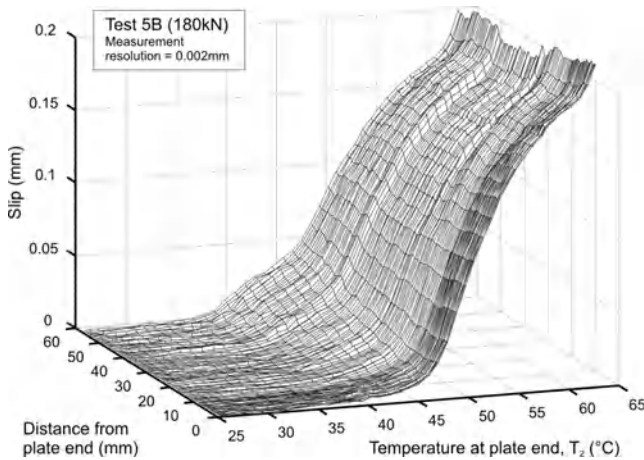


Figure 8 Slip distribution variation for Test 5B

4 DISCUSSION

Significant adhesive joint slip occurred from around 40°C, well before the plate debonded from the steel beam (Figures 7 & 8). This slip behaviour follows the glass transition response of the adhesive shown in Figure 1. Debonding occurred at a plate end temperature of around 65°C, the ISO 6721 glass transition temperature; however, it should be noted that Test 5a failed at 60°C (Table 1).

The significance of the slips observed prior to failure is not obvious. A linear-elastic analysis of bond stress (Stratford & Cadei 2005) using the ambient material properties supplied by the manufacturer (Figure 3) predicts that the shear strength of the adhesive is reached at a slip displacement ≈ 0.005 mm, and that this slip is localised at the end of the plate. This elastic slip is only slightly greater than the measurement resolution of the image analysis method and so is not visible in Figure 8.

The glass transition that occurs when the strengthened beam is heated results in a weaker adhesive; however, the adhesive is also less stiff and has a greater deformation capacity. Thus, load is transferred between the strengthening plate and the flange of the beam over a longer bond length than at ambient temperature.

Close examination of Figure 8 reveals that the slip *increases* with distance from the end of the plate for $T_2 \approx 45^\circ\text{C}$. This is probably because the adhesive temperature increases away from the plate end (as noted above), and is further into the glass transition.

5 CONCLUSIONS

The test results presented in this paper demonstrate that the strength of an FRP-plated steel beam can be

significantly reduced by warm temperatures ($\approx 65^\circ\text{C}$). Significant irrecoverable slip deformation occurs across the adhesive joint prior to failure (from $\approx 40^\circ\text{C}$) due to the glass transition of the adhesive.

It is not straightforward to predict the consequences of the adhesive glass transition upon the strengthened beam. The increased deformation capacity and reduced stiffness of the adhesive at elevated temperatures allow stress redistribution along the length of the strengthening. Consequently, greater load can be transferred between the plate and beam than is suggested by the reduction in strength of the adhesive through the glass transition.

6 ACKNOWLEDGEMENTS

The experiments were undertaken by Cameron Gillespie and Martin Moran for their MEng theses. The authors gratefully acknowledge the support of the School of Engineering at the University of Edinburgh, which is part of the Edinburgh Research Partnership in Engineering and Mathematics.

REFERENCES

- CIRIA (2004). Strengthening metallic structures using externally bonded fibre-reinforced polymers. C595, CIRIA, London, UK.
- Concrete Society (2004), Design Guidance for Strengthening Concrete Structures using Fibre Composite Materials, Technical Report 55, 2nd Edition, The Concrete Society, Camberley, UK.
- Denton SR. 2001. Analysis of stresses developed in FRP plated beams due to thermal effects. 1st International Conference on FRP Composite in Civil Engineering: 527-536.
- Highways Agency. 2001. BD37/01: Loads for Highways Bridges. Design Manual for Roads and Bridges. The Stationary Office Ltd., London, UK.
- ISO 6721-1:2002. Plastics. Determination of dynamic mechanical properties. General principles. BSI, London, UK.
- Kodur, V.K.R., Bisby, L.A. and Green, M.F. 2007. Preliminary guidance for the design of FRP-strengthened concrete members Bonded Fibre Reinforced Polymer Strengthening exposed to fire, Journal of Fire Protection Engineering, 17(5):5-26.
- Ludwig C., Knippers J., Hugi E., and Ghazi Wakili K. 2008. Damage of flexural loaded composite beams subjected to fire. 4th International Conference on FRP Composite in Civil Engineering: 527-536.
- Stratford T. and Cadei J. 2005. Elastic analysis of adhesion stresses for the design of a strengthening plate bonded to a beam, Construction and Building Materials, 20:34-45.
- White D.J., Take W.A. and Bolton M.D. 2003. Soil deformation measurement using particle image velocimetry (PIV) and photogrammetry. Geotechnique 53 7:619-631.

Experimental Study on Bond Behaviour between UHM CFRP Laminate and Steel

Chao Wu, Xiao-Ling Zhao (ZXL@eng.monash.edu.au)

Department of Civil Engineering, Monash University, Clayton, VIC 3800, Australia

Riadh Al-Mahaidi

Faculty of Engineering and Industrial Sciences, Swinburne University of Technology, Hawthorn, VIC 3122, Australia

Wen Hui Duan

Department of Civil Engineering, Monash University, Clayton, VIC 3800, Australia

ABSTRACT The technique of strengthening steel structures with carbon fibre reinforced polymer (CFRP) has attracted growing attention in research field as well as in practice. A newly developed CFRP laminate with a modulus of 460GPa makes it possible to increase the elastic behaviour of strengthened steel structures. A series of tension tests were carried out with double-strap joints using different types of adhesives and bond lengths. Full range bond behaviour including bond strength, effective bond length, stress distribution and derived bond-slip relations at different locations along the bond line are presented in this paper.

1 INTRODUCTION

Traditional methods of retrofitting steel structures like drilling holes at the ends of cracks, bolting splices over damaged areas, attaching steel plates to faces and introducing post-tensioning suffered from some inherent drawbacks like further corrosion threat, residual stresses from welding, rise of local stresses, adding extra weights and most importantly, labour consuming thus increasing maintenance cost (Hamilton et al. 2009, Bakis et al. 2002, Schnerch 2005). This has lead researchers to look at alternative techniques. The use of carbon fibre reinforced polymer (CFRP) composites has attracted much attention over the past two decades. A number of investigations covering various aspects of CFRP retrofitting have been carried out (Hollaway 1993, 2001, Bakis et al. 2002, Fawzia et al. 2006, Zhao & Zhang 2007).

The high strength-to-weight ratio of CFRP makes it possible to use less materials and labour to carry out this technology. In addition, CFRP has high resistance to corrosion and environmental degradation as well as high fatigue life (Hamilton et al. 2009, Alsayed et al. 2000, Teng et al. 2002).

The ultimate load carrying capacity and post-elastic stiffness of strengthened steel structures were greatly increased by externally attached CFRP (Buyukozturk et al. 2004). However, the elastic stiffness was not improved very much due to the relatively low value of axial stiffness of the CFRP material as measured by its modulus times the cross sectional area. A newly developed CFRP laminate with a modulus of 460GPa makes it possible to

increase the elastic behaviour of retrofitted steel structures. Before its wide application in retrofitting steel structures, the bond behaviour between this ultra high modulus CFRP (UHM CFRP) laminate and steel needs to be fully investigated.

In the present study, a series of tension tests were carried out with double-strap joints. Different adhesives were used in order to compare their effectiveness when used for bonding UHM CFRP laminate with steel. The strain distribution along CFRP and shear stress distribution within CFRP-to-steel interface were established. Effective bond length was obtained and bond slip relations were derived.

2 MATERIALS

MBRACE UHM LAMINATE is a newly developed CFRP laminate with a modulus of 460GPa. Two types of two-part epoxies were selected to investigate their suitability for bonding the UHM CFRP and steel. The CFRP material properties and those of the adhesives are listed in Table 1. Hot rolled structural steel HA300 was

Table 1 Manufacturer specified material properties of UHM CFRP laminate and adhesives

	CFRP	Araldite 420	Sikadur 30
Tensile strength	1500 MPa	32.0 MPa	33.0 MPa
Tensile modulus	460 GPa	1.9 GPa	12.8 GPa
Ultimate strain	0.3-0.4%	4%	0.30%
Fibre content	0.71	/	/

used. Its minimum yield strength is 300MPa. The steel plates' width and thickness of (20mm) were chosen in a way that would result in CFRP breakage or debond prior to yielding of steel.

3 MEASUREMENT OF MATERIAL PROPERTIES OF MBRACE UHM LAMINATE

Tensile tests were conducted to verify the material properties from the manufacturer. Three tensile tests were conducted separately. The length and width of the specimen were 400mm and 52 mm, respectively. At the two ends of CFRP sample, aluminum plates were attached to grip the laminate to the jaws of the test machine. Two strain gages were fixed on one side to measure the longitudinal strain and another strain gage was fixed on the other side to record the transverse strain.

The stress vs. strain curves are shown in Figure 1. Measured properties are summarized in Table 2. It is evident that they agree well with manufacturer specified values.

Table 2 Measured Material properties of UHM CFRP

	Test measured	Manufacturer specified
Tensile strength	1607. MPa	1500 MPa
Tensile modulus	479 GPa	460 GPa
Elongation at break	0.36%	0.3-0.4%
Poisson's ratio	0.36	/

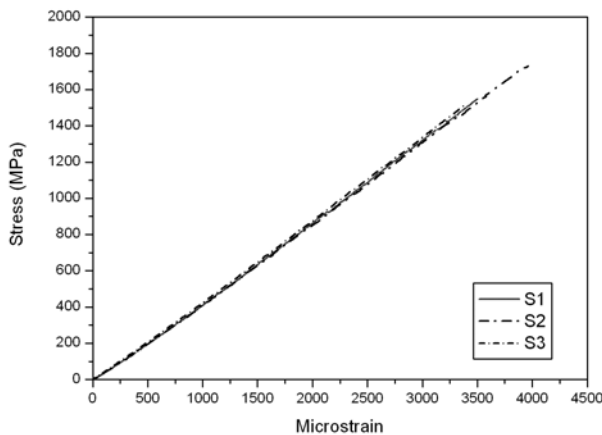


Figure 1 Stress vs strain relationship of CFRP specimens

4 SPECIMEN PREPARATION, INSTRUMENTATION AND TEST PROCEDURE

4.1 Specimen preparation

The steel surface was prepared to increase the bond quality between CFRP and steel. Sandblasting was used to remove all rust, paint, and primer from the steel surface along the bond length. Acetone was used to clean the surface immediately before the adhesive application. Thin coat of adhesive was applied uniformly on steel

surfaces. The whole specimen was then cured at room temperature for at least one week.

Two steel plates with a dimension of 300mm×50mm×20mm were connected by the CFRP laminate on each side. The CFRP laminate was 52mm wide and 1.45 mm thick. CFRP sheets were used to wrap the other end of the specimen to force the failure happen only on the controlled end.

4.2 Instrumentation

Several strain gauges were attached to specimens with the longest bond length. Figure 2 shows the location of each gauge. Strain gauges were placed at the short side of the bonded CFRP to capture the longitudinal strain development along the CFRP and the steel plate. All strain gauges were applied along the CFRP and steel plate at 30mm intervals.

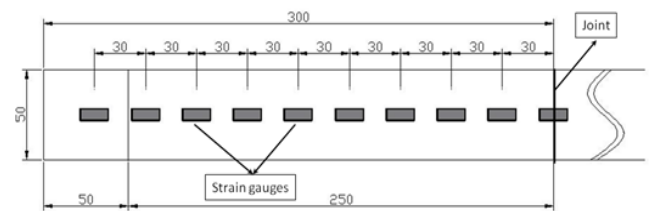


Figure 2 Location of strain gauges

4.3 Test procedure

Each specimen was loaded in a Baldwin Universal Testing machine. The test procedure consisted of monotonically applied tensile displacements at constant speed and recording the accompanying strain data. The test was continued until failure of the specimen.

5 TEST RESULTS

5.1 Bond strength and failure modes

The failure modes and ultimate loads obtained in the tests are presented in Table 3. The failed specimens are shown in Figure 3.

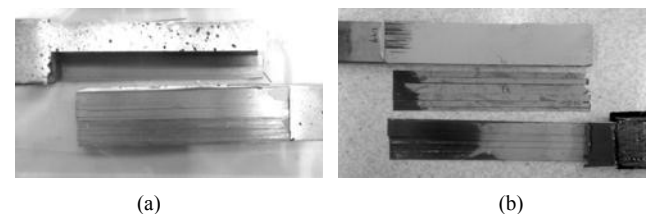


Figure 3 Typical failure mode of Araldite specimen: (a) Araldite specimen; (b) Sikadur specimen

For specimens with Araldite 420 adhesive, the failure mode for shorter specimens was mainly CFRP delamination. For specimens with Sikadur 30 adhesive, the failure mode was mainly cohesive failure. The results indicated that for Araldite specimens, the adhesive and the CFRP-

to-adhesive and the adhesive-to-steel interfaces are stronger than interfaces between fibres and the resin matrix within the CFRP laminate.

Table 3 Test results

Specimen label	t (mm)	l (mm)	Pu (kN)	Failure mode
A-20-260	0.39	250	275	CFRP rupture
A-20-250	0.38	260	267	CFRP rupture
A-20-120	0.36	120	271	CFRP delamination
A-20-100	0.31	100	251	CFRP delamination
A-20-50	0.36	50	137	CFRP delamination
A-20-30	0.35	30	72.97	CFRP delamination
S-20-250-1	0.45	250	155	Cohesive failure
S-20-250-2	0.42	250	147	Cohesive failure
S-20-100	0.40	100	148	CFRP delamination & Cohesive failure
S-20-80	0.35	80	158	Cohesive failure
S-20-50	0.43	50	136	Cohesive failure
S-20-30	0.34	30	58.51	Cohesive failure

* "A, S" refer to the adhesive type; "20" refers to the steel thickness, the second number refers to the bond length and the third number refers to the specimens with same bond length. "t" refers to the adhesive thickness. The terms of failure modes are adopted from (Zhao & Zhang 2007), including (a) steel and adhesive interface failure; (b) cohesive failure (adhesive layer failure); (c) CFRP and adhesive interface failure; (d) CFRP delamination (separation of some carbon fibers from the resin matrix); (e) CFRP rupture and (f) steel yielding. The schematic view of failure modes is shown in Figure 8.

Figure 4 shows the bond strength and bond length relationship for all specimens. It can be seen that the effective bond lengths for Araldite 420 and Sikadur 30 are about 110 mm and 75mm respectively.

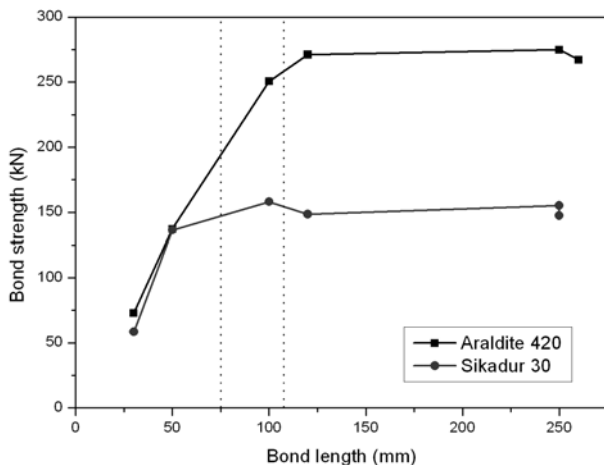


Figure 4 Bond strength and Bond length relationship

5.2 Strain distribution along CFRP

Strain distributions at different distances away from the joint along CFRP laminate are shown in Figure 5. The strain distributions are plotted at different load levels. It is clear from the figure that strain generally decreases with the distance away from the joint.

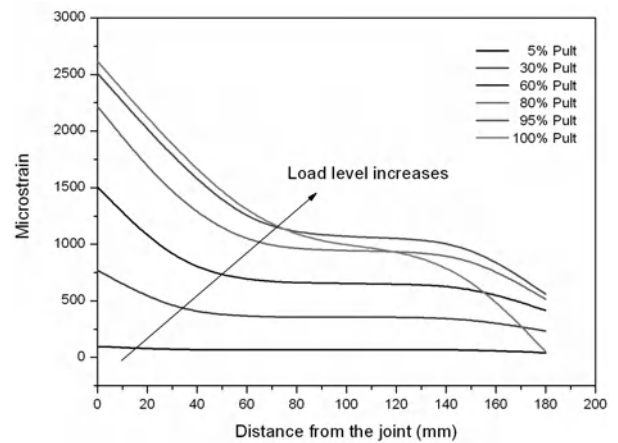


Figure 5 Strain distribution along CFRP laminate

5.3 Shear stress distribution along CFRP-to-steel interface

The average experimental shear stress away from the steel joint was calculated from the readings of strain gauges mounted on the surface of the CFRP laminate (Yuan et al. 2004). The calculated shear stress distributions at different load levels for specimens A-2-250 are plotted in Figure 6.

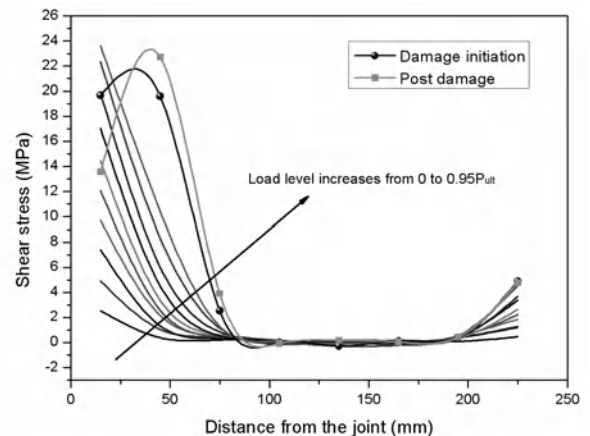


Figure 6 Shear stress distribution of S-20-250

5.4 Bond-slip curves

Local slips were calculated by integrating measured strain distribution along the bond length. This local slip is the relative displacement between the CFRP laminate and the steel plate.

The bond-slip curves at different locations of the same interface are consistent (Xia & Teng 2005). The local bond-slip relationships at 45mm from the specimen joint of A-20-260 and 15mm from the joint of S-20-250 are shown in Figure 7.

The softening part of A-20-260 could not be established due to the sudden failure of the specimen and the damage of the strain gauges. To obtain this data, longer bond lengths will be considered in future testing. The maximum shear stress and initial slip for the Araldite

and Sikadur specimens are approximately 26/24MPa and 0.09/0.052mm.

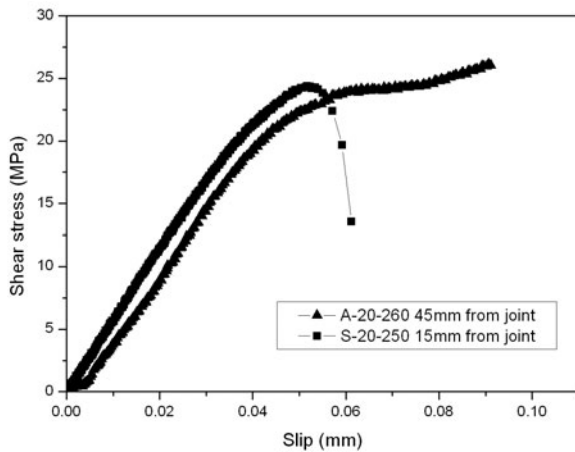


Figure 7 Typical bond-slip curves of A-20-260 and S-20-250

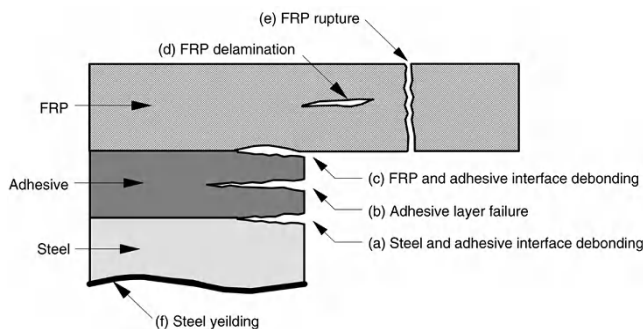


Figure 8 Schematic view of failure modes (Zhao & Zhang 2007)

6 CONCLUSIONS

This paper has presented an experimental study into the bond behaviour of a newly developed UHM CFRP laminate bonded to steel plates. Results from a series of double-strap joint tests have been discussed to understand the effects of the different adhesives and the CFRP bond length on bond behaviour. The results and discussions presented in the paper allow the following conclusions to be made:

(1) For different adhesives used (Araldite 420/Sikadur 30), the bond strength of the double strap joints increased with the bond length. After certain bond length (effective bond length) was reached, the bond strength became constant.

(2) The failure mode for Araldite specimens was mainly CFRP delamination before the effective bond length was reached and the failure mode changed to CFRP rupture afterward. The failure mode for all Sikadur specimens was mainly cohesive failure.

(3) The effective bond length was around 110mm for Araldite 420 and 75mm for Sikadur 30.

(4) The combination of UHM CFRP laminate and

Araldite 420 could achieve higher bond strength than that with Sikadur 30.

7 ACKNOWLEDGEMENT

The project was sponsored by an ARC Discovery Grant. Tests were conducted at Monash Civil Engineering Laboratory.

REFERENCES

- Alsayed, S.H., Al-Aalloum, Y.A. and Almusallam, T.H. 2002. Fibre-reinforced polymer repair materials-some facts. Proceedings of the Institution of Civil Engineers.
- Bakis, C.E., Bank, L.C., Brown, V.L., Cosenza, E., Davalos, J.F., Lesko, J.J., Machida, A., Rizkalla, S.H. and Triantafillou, T.C. 2002. Fiber-Reinforced Polymer Composites for Construction-State-of-the-Art Review. *Journal of Composites for Construction* 6(2): 73.
- Buyukozturk, O., Gunes, O. and Karaca, E. 2004. Progress on understanding debonding problems in reinforced concrete and steel members strengthened using FRP composites. *Construction and Building Materials* 18(1): 9-19.
- Fawzia, S., Al-Mahaidi, R. and Zhao, X.L. 2006. Experimental and finite element analysis of a double lap shear connection between steel plates and CFRP. *Composite Structures*, 75(1-4): 156-162.
- Hamilton, H.R., Benmokrane, B., Dolan, C.W. and Sprinkel, M.M. 2009. Polymer Materials to Enhance Performance of Concrete in Civil Infrastructure. *Polymer reviews* 49(1).
- Hollaway, L.C. 1993. *Polymer composites for civil and structural engineering*. London, Chapman & Hall.
- Hollaway, L.C. 2001. *Advanced polymer composites and polymers in the civil infrastructure*. Oxford (UK), Elsevier.
- Moy, S. 2001. *ICE Design and Practice Guides-FRP composites life extension and strengthening of metallic structures*. London (UK), Thomas Telford Publishing.
- Schnerch, D. 2005. Use of high modulus carbon fibre reinforced polymers (CFRP) for strengthening steel structures.
- Teng, J.G., Chen, J.F., Smith, S.T. and Lam, L. 2002. *FRP strengthened RC structures*. West Sussex (UK), John Wiley and Sons Ltd.
- Tumialan, G., Nanni, A., Ibell, T. and Fukuyama, H. 2002. FRP composites for strengthening civil infrastructure around the world. *SAMPE Journal* 38(5): 9-15.
- Xia, S.H. and Teng, J.G. 2005. Behaviour of FRP-to-steel bonded joints. *Bond Behaviour of FRP in Structures: Proceedings of the International Symposium BBFS 2005*: 419-426.
- Yuan, H., Teng, J.G., Seracino, R., Wu, Z.S. and Yao, J. 2004. Full-range behavior of FRP-to-concrete bonded joints. *Engineering Structures* 26(5): 553-565.
- Zhao, X. L. and Zhang, L. 2007. State-of-the-art review on FRP strengthened steel structures. *Engineering Structures* 29(8): 1808-1823.

Static Behavior of Tension Steel Plate Strengthened with Pre-Stressed CFRP Laminates

Huawen Ye(hbha2000@163.com) & Shizhong Qiang

School of Civil Engineering, Southwest Jiaotong University, Chengdu, China

Christian König & Robin Plum

Institute for Rehabilitation of Buildings and Structures, University of Braunschweig, Braunschweig, Germany

Thomas Ummenhofer

Research Center for Steel, Timber and Masonry, Karlsruhe Institute of Technology, Karlsruhe, Germany

ABSTRACT An experimental and analytical study was conducted to investigate the static performance of steel plates strengthened with pre-stressed CFRP (carbon fiber-reinforced polymer) in uni-axial tension. A linear elastic theoretical model was presented to predict the stress distribution of reinforced specimens. Static testing was performed on the double edge notched specimens strengthened by CFRP laminates at different pre-stressing levels. The theoretically predicted results were in good agreement with the experimental results. The results show that pre-stressed CFRP laminates had a large impact on the specimen's strength but resulted only in a moderate increase of its stiffness. An eccentricity due to pre-stressing was observed leading to bending effects which result in a non-uniform stress distribution. The test results indicated that the long-term pre-stress losses due to static and fatigue loading were slight because of the excellent mechanical properties of CFRP laminates. Therefore, the total pre-stress losses could be simplified as the short-term pre-stress losses with considering a safe factor.

1 INTRODUCTION

CFRP materials used in strengthening and rehabilitation of metallic structures provide an excellent solution for short-term and long-term retrofits. This specialized application combines the benefits of passive bonded CFRP laminate systems with the advantages due to external pre-stressing like improvements in the serviceability and ultimate strength of the damaged steel structure. Recent experiences in the USA [1], the UK [2] and Switzerland [3] showed that there is a great potential for CFRP materials to be used in the retrofiting of steel structures. Hollaway and Cadei [2], Xiao-Ling Zhao [4] and Shaat [5] presented state-of-the-art articles on the retrofit of steel structures using FRP. They mainly studied the static behavior of steel structures reinforced by FRP with focuses on the installation and serviceability and durability of steel members retrofitted with FRP.

Triantafillou [8] investigated the static behavior of steel girders strengthened with pre-stressed CFRP plates and analyzed the effective pre-stress in the CFRP plate. Täljsten [6] theoretically and experimentally investigated the static and fatigue behavior of notched steel plates strengthened with pre-stressed and non pre-stressed CFRP laminates. The results showed a more significant improvement after reinforcement with the pre-stressed

CFRP laminates compared to the non pre-stressed CFRP. The reasonably accurate estimate of the pre-stress loss is one of the critical problems in the application of pre-stressed CFRP laminates. In the available literature review, no measured values could be found for the pre-stress loss. Deng Jun [7] and Zhao Qilin [9] investigated the pre-stress loss due to elastic shortening of the girder reinforced by pre-stressed CFRP laminates in theory.

The objective of this paper is to investigate pre-stressed CFRP laminates for improvement of the static performance of steel structures, including bending effect, stress distribution and estimation of pre-stress losses.

2 THEORETICAL ANALYSIS

The theoretical formulations of a steel plate bonded with double symmetric reinforcements using pre-stressed CFRP laminates presented in [10] are restated as follow,

$$\sigma_c = \frac{T}{A_s \frac{E_s}{E_c} + A_c} + \frac{\sigma_p}{1 + \frac{E_c A_c}{E_s A_s}} \quad (1)$$
$$\sigma_s = \frac{T - A_c \sigma_p}{A_s + \frac{E_c}{E_s} A_c}$$

where σ_c = laminate stress; σ_s = steel stress, T = tension load, σ_p = initial pre-stress, E_c , E_s , A_c and A_s are the elastic moduli and section areas of laminate and steel, respectively.

3 EXPERIMENTAL PROGRAM

Small-scale double-edge-notched steel plates strengthened with pre-stressed CFRP laminates were tested and strain gages G1 and G2 were used to measure the stress in the middle of the CFRP in both sides and G3 and G4 were applied on the steel plate, shown in Mild steel with grade S355 according to EC was used for the specimens. The CFRP laminates having a cross-section of nominally 1.4mm by 50mm and the two-component epoxy adhesive “S&P Resin 220” were provided by the S&P Clever Reinforcement Company. They were applied with a length of 800mm on each side of the specimens. The CFRP laminates were pre-stressed prior to bonding in order to introduce compressive stresses in the cracked plate and were anchored at their ends using steel plates connected with high strength pre-stressed bolts. The metallic surface was well prepared by grit blasting. Table 1 and 2 summarize the main geometric parameters and material properties in this analysis. An earlier study [3] indicated that the load transmission through the adhesive layer became secondary due to the end anchorages. For simplification the adhesive properties were not determined but used from previous study [11] and also were not experimentally verified.

Table 1 Geometric and mechanical properties

Materials	Steel	Adhesive	CFRP
Length (mm)	1200	800	800
Width(mm)	150	50	50
Thickness(mm)	10	2	1.4
Properties	$E_s=210\text{GPa}$, $\nu_s=0.3$	$E_a=2.7\text{GPa}$, $\nu_a=0.35$	$\nu_c=0.2$

Table 2 Configuration of specimens

Specimen	Prestress(MPa)	E_c (GPa)
A1		
A2	-	-
A3		
B1		
B2	0	205
B3		
C1		165
C2	600	165
C3		205
D1		205
D2	1000	165
D3		205
E1		205
E2	1200	205

According to different pre-stress levels, the specimens were divided into five configurations: A, B, C, D, and E, as shown in Table. The pre-stress level was controlled by the initial pre-stress. Configuration A was the reference specimen, which was un-reinforced.

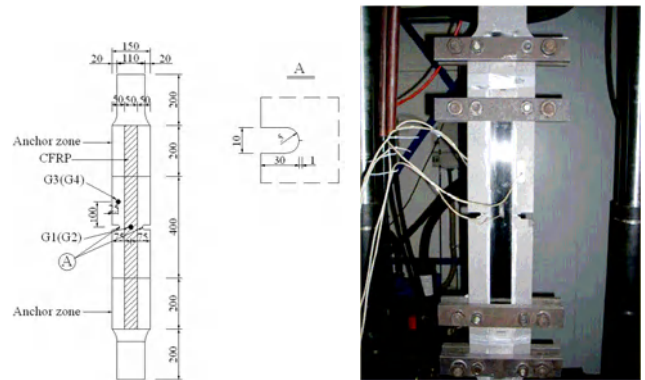


Figure 1 Geometry of the specimen and test setup

4 DISCUSSION OF STATIC TEST RESULTS

4.1 Stress-load relationship

The static test was conducted to study the stress distribution of the specimens. Table 3 shows the measured steel and laminate stresses and the results predicted by Eq.(1) under an applied load of 200kN. The comparison of the analytical and measured stresses shows a very good correlation. Eq.(1) provided an accurate estimation of stresses for the specimens. The steel stress level was decreased to 15%–50% of the stress level of the bare steel specimen after strengthening with pre-stressed CFRP laminates.

The stress distribution of the non-pre-stressed and un-reinforced specimens was uniform while the measured values for specimens with pre-stressed CFRP laminates show a gradient in the stress distribution through the steel thickness. For these specimens a bending effect occurred due to misalignment of the steel specimens.

Figure2 shows the stress-load relationship of steel and laminate stresses which exhibited a linear elastic behavior. The stress-load diagram was not recorded up to failure of each test. The increment of approximately 9% (see Table 1) in the elastic stiffness can be calculated by using a standard transformed section. Therefore the slope of the stress-load relationship lines changed slightly for all specimens. There was no difference in stiffness improvement between non pre-stressed and pre-stressed CFRP laminates.

The external compression decreased the tensile stress in the steel plate to a large amount. (The yield strength of bare steel specimen A was 320kN. According to Eq.(1), the yield strength increases to 536kN after reinforcement by CFRP with a pre-stress level of 1200MPa. A 67.5% increase in the yield strength was obtained. It could be concluded that the ultimate capacity of the specimen after reinforcement increases significantly.

Table 3 Measured and predicted stress values (MPa)

(a)					
Specimen	Prestress	Measured CFRP stress			Predicted results
		G1	G2	Average	
A3	-	-	-	-	-
B3	0	144.4	142.8	143.6	175.4
C1		703.2	676.5	689.8	
C2	600	629.1	668.2	690.2	686.3
C3		670.4	711.6	691	
D2	1000	1053.4	1047.6	1050.5	1043.4
D3		1019.7	1055.3	1037.5	1052.4
E1	1200	1240.5	1191.3	1215.9	
E2		1162.4	1207.5	1185	1228.1

(b)					
Specimen	Prestress	Measured steel stress			Predicted results
		G3	G4	Average	
A3	-	137.6	132.4	135	133.3
B3	0	130	124	127	123
C1		93.2	63.2	78.2	
C2	600	56.8	89.2	73	72.3
C3		70.8	85.2	78	
D2	1000	26	46	36	37.5
D3		12.8	66.8	39.8	36.9
E1	1200	43.2	13.2	28.2	19.7
E2		7.6	26.8	17.2	

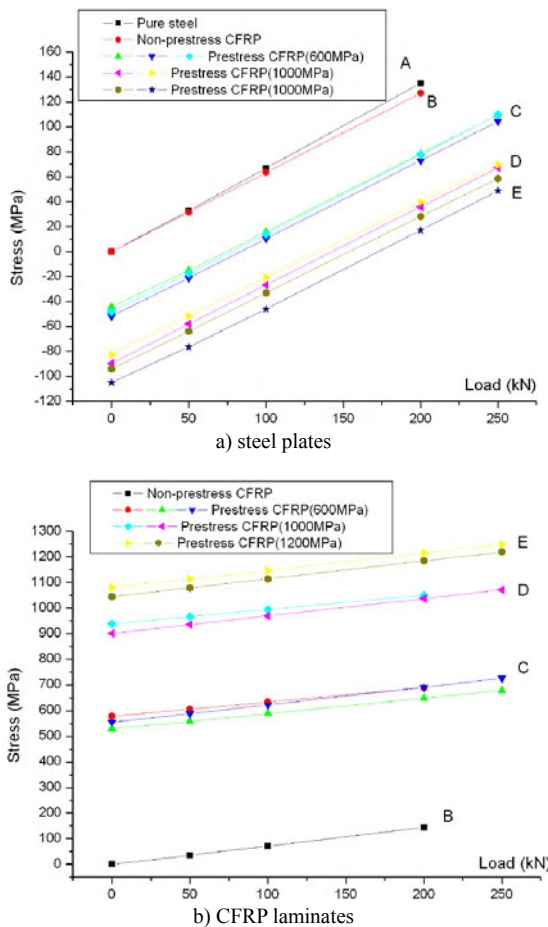


Figure 2 Stress-load relationship

At the same time, the stress level in the CFRP laminates increases up to 1300MPa (approximately 40% of its ultimate strength), nearly nine times higher than the non pre-stressed specimen with 150MPa (approximately 5% of its ultimate strength). By applying a pre-stress to the laminate the material can be used much more efficiently.

4.2 Bending effect

In practice the pre-stress eccentricity was caused by the positioning deviation in fabrication and misalignment of the steel plate. This results in bending stresses which were negligible in the case of non pre-stressed symmetric reinforcements.

Table 4 summarizes the steel compressive stresses after the pre-stressed CFRP laminates were anchored in the test. The results show a significant difference between the measured stress values of the two steel surfaces. The bending stress was computed as half the compression difference between the two surfaces of the steel plate. It changed the stress distribution through the steel thickness significantly for several specimens. The analysis which based on the average steel stress would overestimate the static and fatigue performance due to this non-uniform stress distribution, especially when a high pre-stress level is introduced.

Table 4 Measured bending stresses (MPa)

Specimen	Pre-stress	Compression			Bending stress
		G3	G4	Average	
C1		-42.8	-46.0	-44.4	1.6
C2	600	-71.2	-32.4	-51.8	19.4
C3		-42.8	-53.6	-48.2	5.4
D2	1000	-80.4	-98.8	-89.6	9.2
D3		-111.6	-53.2	-82.4	29.2
E1	1200	-76.0	-112.0	-94.0	18
E2		-117.6	-92.4	-105.0	12.6

4.3 Creep of CFRP in pre-stressing process

Creep deformation of CFRP occurs as a result of long term exposure to a high stress level. The thermal expansion coefficient of CFRP material is very small (approximately $10^{-6}/^{\circ}\text{C}$) and the temperature during the tests remained stable, so the effect of temperature change can be ignored in this analysis. The strain of the CFRP laminates was measured at an interval of 2 days while the pre-stressing force was kept constant. ϵ_p denotes the instantaneous strain after pre-stressing and δ denotes the increasing strain after 2 days of pre-stressing. Table 5 records the test results of the creep ratio (δ/ϵ_p) of the CFRP laminates. The results show that a minor decrease in the pre-stress occurred after 2 days. The calculated creep ratios are lower than 3%. The low creep of pre-stressed CFRP laminate shows that its mechanical properties were stable,

however long-term creep behaviors under practical conditions need further investigations.

Table 5 Creep of pre-stressed CFRP laminates

Specimen	Pre-stress (MPa)	Creep ratio ($\delta/\varepsilon_p \times 100\%$)	
		G1	G2
C2	600	2.42	2.89
C3		1.12	0.88
D2	1000	2.14	2.06
D3		1.00	0.54
E1	1200	0.79	1.20
E2		0.99	0.93

4.4 Pre-stress loss

Reasonably accurate estimate of the pre-stress losses is one of the critical problems in the application of pre-stressed CFRP laminates. If pre-stress losses are overestimated, the tensile strength of CFRP could be exceeded at critical sections under full service loads and fracture might occur. On the other hand, underestimated pre-stress loss leads to a decrease or failure of the reinforcement. Therefore, a reasonably accurate estimate of pre-stress loss is indispensable.

Table 6 summarizes the pre-stress loss ratios which were defined as the ratio of the pre-stress loss and the initial pre-stress in the CFRP laminates. The results show that the pre-stress loss ratio was approximately equal to the respective stiffness ratio ($\eta = (E_s A_s + \Sigma E_c A_c) / E_s A_s$). This means that the pre-stress loss due to elastic shortening of the composite structure accounts for the largest amount of the total instantaneous loss. The pre-stress loss due to deformation of the mechanical gripping and slipping of the anchors with high strength bolts is slight and can be neglected in the calculation.

The experimental results show that the total pre-stress loss is mainly covered by the short-term losses due to elastic shortening. The long-term pre-stress losses due to static and fatigue loading were of secondary importance because of the excellent mechanical properties of CFRP laminates as only a minor creep ratio was observed in the test. Therefore, it is recommended that the total pre-stress losses could be simplified as the short-term pre-stress losses multiplied by a safe factor.

Table 6 tested pre-stress loss of the specimens

Specimen	Stiffness ratio (%)	Effective stress (MPa)	Initial pre-stress (MPa)	Prestress loss ratio (%)
C1	7.3	553.20		7.8
C2	7.3	529.20	600	11.8
C3	9.1	544.20		9.3
D2	7.3	922.00	1000	7.8
D3	9.1	895.00		10.5
E1		1083.60	1200	9.7
E2	9.1	1078.80		10.1

5 CONCLUSION

The experimental and analytical study was conducted to investigate the static behavior of tension steel plates strengthened with pre-stressed carbon fiber-reinforced polymer. A simple linear elastic model was used to predict the stress distribution of reinforced specimens. Static testing of tension specimens was performed on 13 double edge notched specimens. Theoretically predicted results were in good agreement with the experimental results.

The experimental and theoretical results show that CFRP laminates had a large impact on strength (doubling of the strength of the section is not uncommon), but only resulted in a moderate increase of stiffness (approximately 10% increase). The introduction of compressive stresses to the steel specimens due to reinforcement with pre-stressed CFRP decreased the steel stress level at static loading significantly. The pre-stress eccentricity due to bending effects caused by imperfections of the steel specimens leads to a non-uniform stress distribution. An analysis based on the average stress would overestimate the static and fatigue performance of the pre-stressed reinforcement and therefore bending effects have to be considered.

The total pre-stress loss was observed to be dependent mainly on the short-term losses due to elastic shortening. The long-term pre-stress losses due to static and fatigue loading were slight because of the excellent mechanical properties of the CFRP laminates showing only small creep deformation. The total pre-stress losses can be simplified as the short-term pre-stress losses multiplied by a safe factor.

REFERENCES

- M.Tavakkolizadeh, H.Saadatmanesh. Fatigue strength of steel girders strengthened with carbon fiber reinforced polymer patch. *Journal of Structural Engineering*, ASCE 2003; 129(2):186-196.
- L.C. Hollaway, J.Cadei. Progress in the technique of upgrading metallic structures with advanced polymer composites. *Progress in Structural Engineering and Materials* 2002; 4(2):131-148.
- A.Bassetti, A.Nussbaumer, M.A.Hirt. Crack repair and fatigue extension of riveted bridge members using composite materials. In: *Bridge engineering conference, ESE-IABSE-FIB*. 2000: 227-238.
- Xiao-Ling Zhao, Lei Zhang. State-of-the-art review on FRP strengthened steel structures. *Engineering Structures*. 29 (2007) 1808-1823.
- A.Shaat, D.Schmerch, A.Fam, S.Rizkalla. Retrofit of steel structures using Fiber-Reinforced Polymers (FRP): State-of-the-art. *Transportation research board (TRB) annual meeting*. 2004. CD-ROM (04-4063).
- B.Täljsten et.al. Strengthening of old metallic structures in fatigue with prestressed and non-prestressed CFRP laminates. *Construction and Building Material*. 2008:1-13.

- Deng Jun, Huang Yan-pei. The load-carrying capacity of steel beam strengthened by prestressed CFRP plates and prestressing loss of CFRP plates. *Railway Engineering*. 2007(10):4-7.
- T.C.Triantafillou, and N.Deskovic. Innovative Prestressing with FRP Sheets, Mechanics of Short-term Behavior. *Journal of Engineering Mechanics*, ASCE, 1991, 117(7): 1653-1672.
- Zhao Qi-lin,Wang Jing-quan,Jin Guangqian. Analysis of the reverse-arch prestressed technique and the improved bearing capacity for steel structure strengthened by carbon-fiber. *Steel structure*. 2002, 3(17):51-53.
- Ye Huawen. Experimental study of static and fatigue behavior of tension steel plate strengthened with prestressed CFRP laminates. Ph.D dissertation. Southwest Jiaotong University, Chengdu, China, 2009.
- J.F.Chen, J.G.Teng. Anchorage Strength Models for FRP and Steel Plates Bonded to Concrete. *Journal of Structural Engineering*, 2001, 127(7):784-791.

Fatigue Life Prediction of Steel Beams Strengthened with a Carbon Fibre Composite Plate

Jun Deng (jdeng@gdut.edu.cn)

Faculty of Civil and Transportation Engineering, Guangdong University of Technology, Guangzhou, China

ABSTRACT There are many applications in metallic beams strengthened with a bonded carbon fibre reinforced polymer (CFRP) plate in recent years. The fatigue performance of the retrofitted beams in a bridge must be considered. In this study, steel beams strengthened with a bonded CFRP plate were tested under fatigue loading. Both crack-free fatigue life and crack propagation life were considered. In accordance with the test results, the relationship between the peak interfacial stresses and the cyclic number to crack initiation in the bonding layer was obtained to predict the crack-free fatigue life. The relationship between the CFRP peeling rate and the energy release rate was obtained to predict the crack propagation life. In addition, based on the findings obtained from the previous and present studies on adhesive bonding in the retrofitted beams, some design suggestions for steel beams strengthened by bonded CFRP plates are proposed.

1 INTRODUCTION

FRP strengthening is becoming an attractive technique for extending the life of metallic structures, especially in cases where there are severe access constraints, with associated high costs and installation time. To date, using CFRP to upgrade metallic structures was focused on strengthening beams in building or bridges (Miller et al. 2001, Holloway & Cadei 2002 and Dodds 2003).

But this application requires a number of considerations, in which the structural adhesive bonding is a very important issue. Buyukozturk et al. (2004) indicated that the potential of brittle debonding failures is an important concern regarding the effectiveness and safety of a bonded structure. Smith and Teng (2001), Denton (2001) and Mukhopadhyaya and Swamy (2001) investigated the interfacial stresses in the retrofitted beam and indicated the bonding is the weakest link in metallic strengthening due to the high stress concentration. The fatigue performance of metallic beams with CFRP bonded plates was investigated by Miller et al. (2001), El Tawil et al. (2001) and Nikoukar (2004). However, the method and technique are not sophisticated in failure criteria based on the calculated stresses and to predict the debonding failure and fatigue life. CIRIA report C595 (Cadei et al. 2004) indicated that further research and testing are required in most aspects of externally bonded FRP strengthening of metallic structures.

As a further development of the author's study (Deng et al. 2004, Deng & Lee 2007a, b, c), this paper presents a theoretical and experimental study on the fatigue performance of the adhesive bonding in steel beams

strengthened with a CFRP plate, as shown in Figure 1. Two equations are given to predict the crack free life and crack propagation life of the retrofitted beams, respectively. Moreover, based on the findings obtained from the previous and present studies on adhesive bonding in the retrofitted beams, some design suggestions for steel beams strengthened by bonded CFRP plates is proposed.

2 EXPERIMENTAL DETAILS

2.1 Test specimens

Ten small-scale steel beams strengthened with CFRP plates were tested. The steel beams used were 1.2 m long 127×76UB13. The steel had a design strength of 275 MPa and a Young's modulus of 205 GPa. The flange surface that received the CFRP plate was sand blasted to SA2½ industry standard and the plate was attached to it within four hours. The CFRP plates used were 3 mm thick and 400 mm long, which were fabricated from 0.3 mm thick unidirectional epoxy prepreg. The adhesive used was a two-part thixotropic epoxy resin epoxy adhesive (Sikadur-31 Normal), with a Young's modulus of 8 GPa, a shear modulus of 2.6 GPa and a tensile strength of 29.7 MPa (data provided by the manufacturer). It was mixed with 1% by weight 1 mm diameter ballotini to ensure a uniform bond thickness.

2.2 Test set-up and instrumentation

The fatigue tests were carried out in a servo-hydraulic Dennison test machine with a maximum capacity of 200 kN, using a three-point bending setup. The clear

span was 1.1 m and the loading point was at mid-span, as shown in Figure 1. The specimens were supported on two rollers, which allowed the specimens to behave in a simply supported manner, but were restrained from any sideways movement. The loading block had two steel plates, each with a counter seat, and a roller in the between.

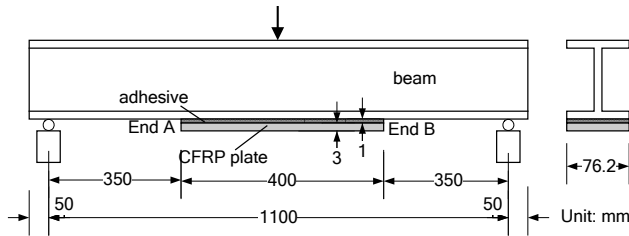


Figure 1 Geometry of the retrofitted beam

One of the ten beams was first tested under static load, by displacement control at a rate of 0.5 mm/second, to determine the failure load, which then governed the maximum load applied to the other nine beams under fatigue loading condition. The failure load obtained for this beam was 135 kN. This load can be used to obtain the maximum principal interfacial stress σ_n of 80.4 MPa ($\sigma_{n,u}$) at the end of CFRP plate. σ_n was calculated by combining the maximum shear stress τ_{max} and the maximum normal stress σ_{max} using the following equation:

$$\sigma_n = \frac{\sigma_{max}}{2} + \sqrt{\left(\frac{\sigma_{max}}{2}\right)^2 + \tau_{max}^2} \quad (1)$$

In this equation both σ_{max} and τ_{max} were calculated using the analytical solution proposed by the authors (Deng et al. 2004). The discontinuity at the ends of the CFRP plate creates a stress concentration, σ_n was therefore the governing fatigue stresses. The other nine beams were tested under fatigue loading, with a maximum centrally applied load P equal to between 40 kN and 125 kN. These loads convert to a range for σ_n of 23.8 MPa to 74.4 MPa, as shown in Table 1.

To investigate the phenomenon of crack initiation and propagation, two 2 mm long strain gauges were mounted at the ends of the bottom of the CFRP plate. The authors (Deng & Lee 2007a) pointed out that the crack initiates when the strain range (the difference of the strain under the maximum load and minimum load of the same cycle) measured by the strain gauges decreases close to zero. The crack initiation lives N_1 of ends A and B are recorded in Table 1. After crack initiation, the crack propagation was monitored visually using a magnifying glass, and the length of the crack with the associated number of cycles were noted. The test was stopped when crack propagation passed the middle of the specimen or when the crack stopped growing, which means that the CFRP plate had lost its strengthening effect and the specimen failed.

Table 1 Specimen test details and results

	P (kN)	σ_n (MPa)	N_1	
			End A	End B
F135	135	80.4	/	/
F125	125	74.4	3	/
F90	90	53.6	700	600
F70	70	41.7	3000	4000
F55-1	55	32.8	17000	45000
F55-2	55	32.8	16000	15000
F50	50	29.8	300000	350000
F40-1	40	23.8	/	/
F40-2	40	23.8	/	/
F70s	70	41.7	6400	7000

2.3 Test procedure

A minimum load of 5 kN was applied so as to ensure firm contact between the beam and the supports. Loading was applied sinusoidally, with a frequency of 1 (for specimens F125, F90 and F70) to 2 Hz (for specimens F55, F50 and F40).

3 S-N CURVE AND CRACK FREE LIFE

Before crack initiation, theoretical analysis (Deng et al. 2004) shows that the maximum principal interfacial stress is constant. The curves for the maximum principal interfacial stresses σ_n (and the normalized maximum interfacial stresses ($\sigma_n / \sigma_{n,u}$)) versus the log of crack free life N_1 is presented in Figure 2. The relationship is approximately linear and regression analysis produced the following best-fit equation (correlation coefficient, $R^2 = 0.954$):

$$\sigma_n = 78.62 - 4.19 \ln N_1 \quad (2)$$

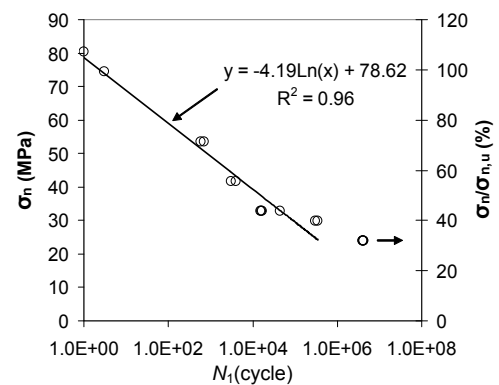


Figure 2 S-N curve

It has been established by the authors (Deng et al. 2004) that the bonded strength of retrofitted metallic beams is not influenced by the size and material properties of the metallic beams or the CFRP plates. Therefore, this S-N curve can be applied generally as long as the same adhesive is used.

Specimens F40-1 and F40-2 did not fail even after four million cycles. Furthermore, the variation of the strain at the end of plates are very small after 3 million cycles in F40-1 and after 2 million cycles in F40-2, which indicates that the specimens are not likely to fail in fatigue. Therefore, the fatigue threshold for the tested beams is 40kN, with a corresponding threshold stress 23.8 MPa for the adhesive. This threshold limit is about 30% ultimate failure stress 80.4 MPa under static load.

4 CRACK PROPAGATION LIFE

The crack initiation and propagation in all the specimens were similar except for specimen F125. The load range on this specimen was too high and caused it to debond suddenly at one end after only 30 cycles. For all the plates that had debonded, cracking started from the middle of the spew fillet and then propagated to the interface between the steel beam and the adhesive at an angle of 45 degrees. Then the crack grew along the interface and stopped eventually. There was always a short length of adhesive remaining uncracked and bonding the plate to the beam. The curves of the crack length a versus the number of cycles N (not including the crack free life) of specimens F55-1 and F55-2 are presented in Figure 3. The crack propagation rate da/dN can be obtained from the curves.

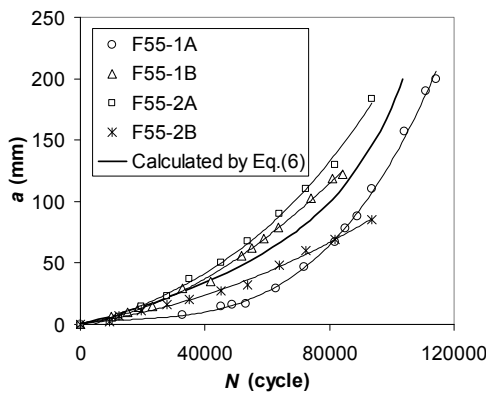


Figure 3 a - N curves

In accordance with Paris Law, the relationship between the crack propagation rate da/dN and the energy release rate G can be expressed as:

$$\frac{da}{dN} = D(G_{\max})^n \quad (3)$$

where G_{\max} is the maximum energy release rate during one fatigue cycle, D and n are the empirical coefficients, which can be determined by experimental data. Guidance CIRIA C595 [8] provides an equation to calculate the energy release rate G of strengthened beams:

$$G = \frac{M^2}{2b} \left[\frac{1}{(EI)_s} - \frac{1}{(EI)_1} \right] \quad (4)$$

where M is the applied bending moment on the beam at plate end or the crack front, b the width of adhesive layer, $(EI)_1$ and $(EI)_s$ the section bending stiffness of beam strengthened with the FRP plate and the plain beam, respectively. Since the beam is under three-point bending, M is given as:

$$M = \frac{1}{2} p(l_0 + a) \quad (5)$$

where p is the concentrated load, l_0 (350 mm) the distance from the supports to the plate end. Submitting (4) (5) into (3) gives:

$$N = \frac{(-2n + 1)^{-1}(l_0 + a)^{-2n+1} + C}{D \left[\frac{1}{4} p^2 \left(\frac{1}{(EI)_s} - \frac{1}{(EI)_1} \right) \right]^n} \quad (6)$$

Considering the boundary condition $N=0$ when $a=a_0$,

$$C = -(-2n + 1)^{-1}(l_0 + a_0)^{-2n+1} \quad (7)$$

Assuming the initial crack length $a_0 = E_a G_{\max} / (\pi \sigma_n^2)$, submitting G_{\max} and σ_n into this equation gives $a_0 = 0.24$ mm. When the crack crosses the middle of the beam, i.e. $a = L_p/2$, the fatigue crack propagation life N_2 can be obtained from Eq. (6).

The curves for the log of the crack propagation rate da/dN versus the log of the energy release rate G is presented in Figure 4. The relationship is approximately linear and regression analyses produce the following best-fit equation (with a correlation coefficient, $R^2 = 0.7896$):

$$\log(da/dN) = 2.753 \log(G_{\max}) - 11.718 \quad (8)$$

Therefore, the empirical coefficients D and n in Eq. (3) are $10^{-11.7}$ and 2.75, respectively.

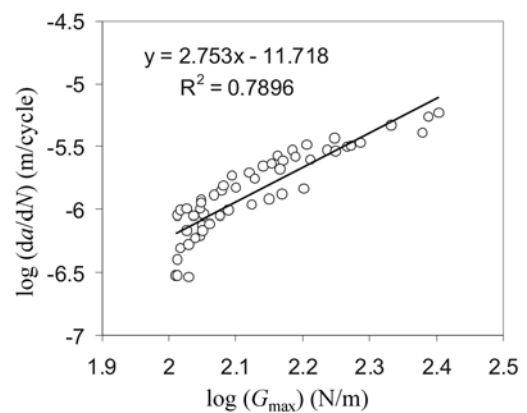


Figure 4 $\log(G_{\max}) \sim \log(da/dN)$

To validate the predication equation of the crack propagation life (Eq. (6)), the curves for the crack length a and the number of cycles N (not including the crack free life) of specimen F70 obtained from the test are compared to the corresponding predicated results calculated by Eq. (6) in Figure 5. It shows that the agreement is good.

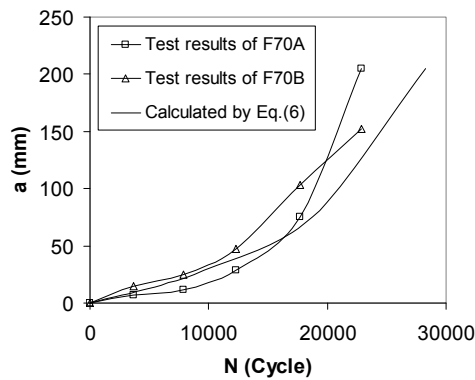


Figure 5 a - N curves of F70

5 DESIGN SUGGESTIONS

The following design suggestions are given in accordance with the findings obtained from the previous and present studies.

(1) Use details to reduce the maximum adhesive stresses

Adhesives with low elastic modulus are suggested to reduce the maximum adhesive stresses. Taper is suggested to reduce the maximum adhesive stresses as well. The natural spew fillet at the end of plate is suggested to be retained in fabrication, but its effect on the reduction on stress concentration should not be considered in design.

(2) Fatigue limit of the bonded joint in reinforced beams

To avoid fatigue crack initiation in the adhesive at the end of the plate, the maximum adhesive stresses must be limited. The S - N curve investigated in this study shows the fatigue limit is 30% of the ultimate static failure stress.

(3) Curtailment of plate length

The strength and the stiffness of reinforced beams are not influenced by the plate length. Therefore, the plate length is determined by the maximum allowable adhesive stresses.

Except for the thermal effect, the maximum adhesive stresses are influenced by the applied bending moment and the applied shear force, especially the former. Therefore, to curtail the plate length, the plate ends should be located in an area of low applied bending moment.

Implementation of any details such as tapers and spew fillets to reduce the stress concentrations is suggested.

(4) Monitor reinforced beams

Backface-strain technique is suggested to be used to monitor the deterioration of the adhesive and crack initiation at the plate end, especially for beams under fatigue load.

6 SUMMARY

In this paper, the fatigue testing of small-scale steel beams bonded with a 400 mm long CFRP plate is reported. An S - N curve was plotted from the test results. The fatigue limit, i.e. the threshold, of the S - N curve is about 30% of the ultimate static failure stress, which validates the fatigue limit suggested by the CIRIA Design Guidance (Cadei et al. 2004). In accordance with Paris Law, a crack

propagation life prediction equation is derived. The empirical coefficients are determined by the experimental data. The agreement between the experimental data and the analytical results confirms the validity of the prediction equation. The fatigue load range will affect the fatigue life, but its significance is much less than the magnitude of the maximum load in the load range. Furthermore, based on the results obtained, the design suggestions were introduced for adhesive bonding of the retrofit beams.

7 ACKNOWLEDGEMENT

This work was supported by the National Natural Science Foundation of China through Grant 50808085.

REFERENCE

- Buyukozturk, O., Gunes, O., Karaca, E. 2004. Progress on understanding debonding problems in reinforced concrete and steel members strengthened using FRP composites, *Construction and Building Materials*, 18(1):9-19.
- Cadei, J. M. C., Stratford, T. J., Hollaway, L. C., Duckett, W.G. 2004. *Strengthening metallic structures using externally bonded fibre-reinforced polymers - C595*. London: CIRIA.
- Deng, J., Lee, M. M. K., Moy, S. S. J. 2004. Stress analysis of steel beams reinforced with a bonded CFRP plate, *Composite Structures*, 65(2):205-215.
- Deng, J., Lee, M.M.K. 2007a. Behaviour under static loading of metallic beams reinforced with a bonded CFRP plate, *Composite Structures*, 78(2):232-242.
- Deng, J., Lee, M. M. K. 2007b. Fatigue performance of metallic beams strengthened with a bonded CFRP plate, *Composite Structures*, 78(2): 222-231.
- Deng, J., Lee, M. M. K. 2007c. Effect of plate end and adhesive spew geometries on stresses in retrofitted beams bonded with a CFRP plate, *Composites: Part B*, doi:10.1016/j.compositesb.2007.05.004.
- Denton, S.N. 2001. Analysis of stresses developed in FRP plates beams due to thermal effects, *Proceeding of the Conference on Composites in Civil Engineering*. Hong Kong: 527-536.
- Dodds, N. 2003, Strengthening a bridge using carbon fibre reinforced plates, *The Structural Engineer*, 81(5):117-9.
- El Tawil, S., Ogunc, C., Okeil, A., Shahawy, M. 2001. Static and fatigue analyses of RC beams strengthened with CFRP laminates, *Journal of Composites for Construction*, 5(4):258-267.
- Hollaway, L.C., Cadei, J. 2002. Progress in the technique of upgrading metallic structures with advanced polymer composites, *Progress in Structural Engineering and Materials*, 4(2):131-148.
- Miller, T. C., Chajes, M.J., Mertz, D.R., Hastings, J.N. 2001. Strengthening of steel bridge girder using CFRP plates, *Journal of Bridge Engineering*, 6(6):514-522.
- Mukhopadhyaya, P., Swamy, N. 2001. Interface shear stress: A new design criterion for plate debonding, *Journal of Composites for Construction*, 5(1):35-43.
- Nikoukar, F. 2004. *Strengthening of metallic structures using carbon fibre composite plates*, PhD thesis, University of Southampton.
- Smith, S.T., Teng, J.G. 2001. Interfacial stresses in plated beams, *Engineering Structures*, 23(7):857-871.

Tests on CFRP Repaired Welded Thin-Walled Cross-Beam Connections

Zhi-Gang Xiao (zhigang.xiao@sci.monash.edu.au)

School of Applied Sciences and Engineering, Monash University, Churchill, VIC 3842, Australia

Xiao-Ling Zhao

Department of Civil Engineering, Monash University, Clayton, VIC 3800, Australia Changjiang Professor, Tongji University, Shanghai, China

Le-Wei Tong

Department of Building Structures, Tongji University, Shanghai, China

ABSTRACT Cracked cross-beam connections made of thin-walled rectangular hollow sections (RHS) are repaired with carbon fibre reinforced polymer (CFRP) composites and constant amplitude fatigue experiments are conducted on the repaired specimens. In the previous pilot test on a T-connection of square hollow sections (SHS), early debonding happened in the corner region due to peeling effect. In this study, circumferential or transverse restraining CFRP patches are applied in the corner region which prevent early debonding and lead to significant increase in fatigue life. Furthermore, the addition of strengthening steel plates has further increased the flexural stiffness and fatigue life of the cracked specimens.

1 INTRODUCTION

OneSteel's DuraGal thin-walled sections are produced by cold-forming and in-line galvanizing. Because of beneficial properties such as high-strength and corrosion protection, DuraGal sections are used in the road transportation industry, agricultural equipment and recreation structures. In most of the applications, welded DuraGal connections may be subjected to repeated or cyclic loading and therefore, as with other welded steel connections, are prone to fatigue failure. Most of DuraGal sections have a thickness less than 4 mm, and are not covered by existing research on fatigue of cold-formed steel hollow sections (Zhao et al 2000). Mashiri et al (2005b) reported fatigue behaviours of welded cross-beam connections made of rectangular hollow sections (RHS) and angles, i.e. RHS-to-angle cross-beam connections. Fatigue behaviours of other types of DuraGal cross-beam connections such as RHS-to-RHS and RHS-to-channel are reported by Mashiri & Zhao (2005a).

Carbon fibre reinforced polymer (CFRP) composites have advantages over traditional construction materials which include high strength, ease and speed of application, corrosion resistance, and ability to conform to irregular surfaces (Nadauld & Pantelides, 2007) and have been used quite successfully in concrete and masonry structures, especially for repair and strengthening. However, for metallic structures, although extensive research has been conducted, field application has not yet gained a wide

potential (Fam et al 2006, Zhao & Zhang 2007). Jiao & Zhao (2004), Haedir et al (2006), and Fawzia et al (2007) strengthened circular hollow sections with CFRP, while Fam et al (2006), Nadauld & Pantelides (2007), and Pantelides et al (2003) repaired aluminium overhead sign structures using CFRP or glass fibre reinforced polymer (GFRP) composites. However, little research effort has been made on repairing RHS-to-RHS cross-beam connections with fibre reinforced polymer composites.

In cross-beam connections, fillet welded joints are normally used to connect the two hollow section members, and fatigue cracks usually initiate at the weld toe on the surface of one member that is subjected to significant cyclic tensile stress, as shown in Figure 1. In this research, through repairing and experimenting on a limited number of specimens, an effective way of

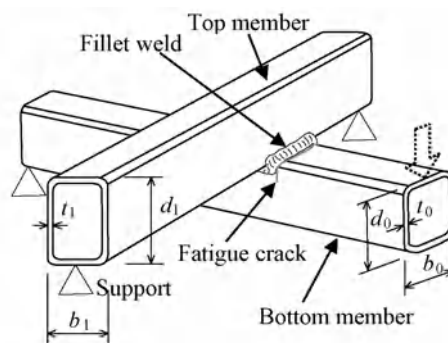


Figure 1 Schematic of test specimen

repairing cracked cold-formed thin-walled RHS-to-RHS cross-beam connections and restoring their fatigue resistance capacity is found.

2 TEST SPECIMENS

Three tested specimens of RHS-to-RHS cross-beam connections, i.e. S4R1L2A, S5R1L2A, and S1R1L1A, are selected for CFRP strengthening. They were fatigue-tested to failure with a constant amplitude bending load by Mashiri & Zhao (2005a). The minimum yield strength and the minimum tensile strength are 450 and 500 MPa, respectively. The configuration and dimensions of test specimens are shown in Figure 1 and Table 1. GMAW fillet welds were used to join the RHS bottom and top members (Mashiri & Zhao 2005a).

Under the bending load shown in Figure 1, fatigue cracks initiated along the weld toe on the surface of bottom member at the two corners where the stress concentration is high. The fatigue cracks then coalesced and broke the whole tensile face of the bottom member. In the meantime, the other end of the cracks deviated from the weld toe on the side surfaces of the bottom member and propagated into the parent metal, as shown in Figure 1. Fatigue failure was defined when the whole surface crack length had reached a size equal to the width of the bottom member, b_0 , plus twice the size of weld leg length, and the number of loading cycles at this time was taken as the final fatigue life (Mashiri & Zhao 2005b). The three specimens with the crack length on side surfaces (webs) of bottom member being less than one-third of the member depth, i.e. $1/3 d_0$, are selected for strengthening. Their dimensions and original fatigue lives are shown in Table 1.

In addition to the RHS-to-RHS cross-beam specimens, a SHS-to-SHS T-connection tested by Mashiri et al (2002) with an in-plane bending load, D3D1L3B, was chosen for a pilot test to investigate the method of applying CFRP. Early debonding was found in the pilot test which results in an insignificant extension of fatigue life after repairing. Refer to Xiao et al. (2008) for details of the pilot test.

Table 1 Cracked RHS-to-RHS specimens for CFRP strengthening

Specimen	Bottom member $d_0 \times b_0 \times t_0$ (mm)	Top member $d_1 \times b_1 \times t_1$ (mm)	N (kilo-cycles)
S4R1L2A	35×35×3	75×50×3	180
S5R1L2A	35×35×1.6	75×50×3	12.7
S1R1L1A	50×50×3	75×75×3	872

3 CFRP APPLICATION

3.1 Materials and surface preparation

The CFRP used is a normal modulus one in the CF MBrace family, MBrace CF130, with an elastic modulus of 240 GPa and an ultimate tensile strength of 3800 GPa;

the adhesive used to join the CFRP sheets is a two-part epoxy adhesive, Araldite 420, which has a lap shear strength of 37 MPa (Fawzia et al 2007).

Surfaces of the brace and chord are sandblasted and cleaned with acetone over the bonding area before applying CFRP. Such preparation creates a lightly abraded surface which gives a better key to adhesives than a galvanized DuraGal surface does.

3.2 Stop holes

To arrest the crack or impede its progress, stop holes of 5 mm in diameter were drilled at the ends of the crack after surface preparation. Though big stop holes will help decrease the stress concentration, a drill of 5 mm in diameter was used due to the dimension limitation of the bottom member.

3.3 CFRP application

Five steps are involved in the CFRP application process. In Step 1, CFRP sheets are applied over the tensile surface of bottom member across the fatigue crack. After 3 days' cure, four layers of CFRP sheets are applied over the other three surfaces of the bottom member (Step 2). Further three days later, in Step 3, a CFRP sheet of 90 mm wide is wrapped 3 rounds around the bottom member at each end of CFRP patches applied in Steps 1 and 2. In Step 4, CFRP sheets are applied over the top member surface adjacent to the crack, and after 3-day's curing, in Step 5, CFRP sheets are wrapped 3 rounds around the top member over Step 4 sheets. Refer to Xiao et al. 2008 for details of CFRP application. A finished specimen is shown in Figure 2.

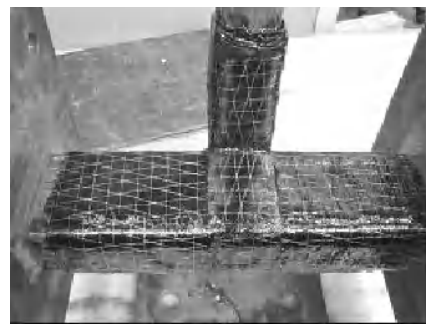


Figure 2 CFRP-repaired cross-beam

4 EXPERIMENTS ON S4R1L2A AND S5R1L2A

Constant amplitude fatigue experiments are conducted on the repaired S4R1L2A and S5R1L2A in the same loading conditions as in the original S4R1L2A and S5R1L2A tests, respectively. The stress ratio is 0.1 for both experiments, and the maximum pushing force is 2.0 kN for S4R1L2A and 1.35 kN for S5R1L2A. Figure 3 shows the repaired S4R1L2A mounted on the test rig. The bottom member is mounted vertically in the rig with one end connected to the loading arm and the other

bolted to the testing rig. The top member is bolted to the rig at both ends. Pressured air is used to drive the loading arm, and the maximum and minimum loads are monitored by a load cell exciter and controlled by adjusting the maximum and minimum air pressure valves. A break detector is set in the control circuit to stop the fatigue test automatically when the displacement at the loading end of the bottom member is larger than a preset limit. The displacement at the loading end of the bottom member is measured each time the experiment is inspected and the number of loading cycles is recorded.



Figure 3 S4R1L2A mounted on the test rig

The displacement at the loading end of the bottom members is shown in Figure 4. Three distinctive stages can be identified from the displacement curves of S4R1L2A and S5R1L2A. In Stage 1, the slope is small and the displacement increase is relatively quick which suggests that the CFRP is not fully engaged. Stage 1 ends at a life of about 133.5 kilocycles and a displacement of 6.5 mm or so for S4R1L2A, and at 145 kilocycles and 7.5 mm for S5R1L2A. In Stage 2, the relatively large slope indicates a slow increase in deformation, which suggests the full engagement of CFRP sheets. Stage 2 ends at about 429.6 kilocycles and 10 mm displacement for S4R1L2A, and at about 506.7 kilocycles and 9 mm displacement for S5R1L2A. From this point onward, the test enters into Stage 3 with a rapid increase in deformation and less increase in fatigue life, until the

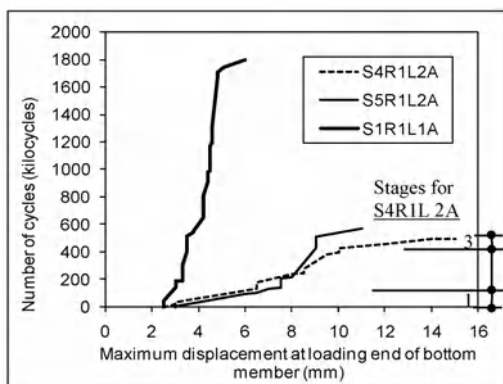


Figure 4 Maximum displacement at the loading end of bottom member vs. number of cycles

break detector was finally triggered after 60-70 kilocycles of loading in this stage. For clarity, these stages are shown only for S4R1L2A in Figure 4.

During the whole process, debonding was not observed, nor the breaking of CFRP patches. For S4R1L2A, the extended fatigue life at the end of Stage 1 (133.5 kilocycles) is 75.3% of the original life (180 kilocycles, Table 1), while that at the end of Stage 2 (429.6 kilocycles) is 238.7% of the original life. The extended fatigue life of S5R1L2A is even more significant in comparison with its original life.

5 EXPERIMENT ON S1R1L1A

In the previous experiments on RHS-to-RHS cross beam connections, the CFRP application method prevented early debonding effectively and extended the fatigue life of the repaired significantly. However, due to the inability of the restraining sheets to cover the small corner area close to the crack, debonding may still happened very early in this region and failed to bring a full engagement of CFRP at the initial stage. The other factor contributing to the softness of the repaired connections is the small stiffness of the CFRP sheets in comparison with the original 3 mm or 1.6 mm steel plate.

To overcome the weakness of the above mentioned CFRP-repairing method, an L-shaped steel plate is used to strengthen the repair, Figure 5a. The thickness of the plate is 3 mm and the width 40 mm, and the L-plate is cold formed from a flat plate with a fillet of 10 mm to confirm the cracked corner of CFRP-repaired S1R1L1A. A holding plate is also used to hold the short leg of the L-plate onto the CFRP-applied surface of the top member. The repair of S1R1L1A with CFRP is the same with the previous two cross-beam members, except with Step 3 strips shown in Section 3.3 being postponed until the strengthening steel plates having been attached. As with the surface treatment of previous specimens, the surfaces of the strengthening steel plates are sandblasted and cleaned with acetone before being attached to CFRP sheets or to each other. One week after steel plates being attached, Step 3 CFRP strips in Section 3.3 are applied to wrap Step 1 strips and the L-plate. CFRP sheet is also wrapped 4 rounds at the ends of the holding plate over the top member to hold the holding plate to the top member. The photo of the finished cross-beam connection is shown in Figure 5b.

As with the other repaired cross-beam connections, constant amplitude fatigue experiments are conducted on S1R1L1A with a cyclic pushing force applied at one end of the bottom member. The stress ratio is 0.1 and the maximum force is 4 kN. The stress ratio and the cyclic loading are the same as the original S1R1L1A experiment. The curve of the fatigue life versus the displacement at the loading end of the bottom member is shown in Figure 4.

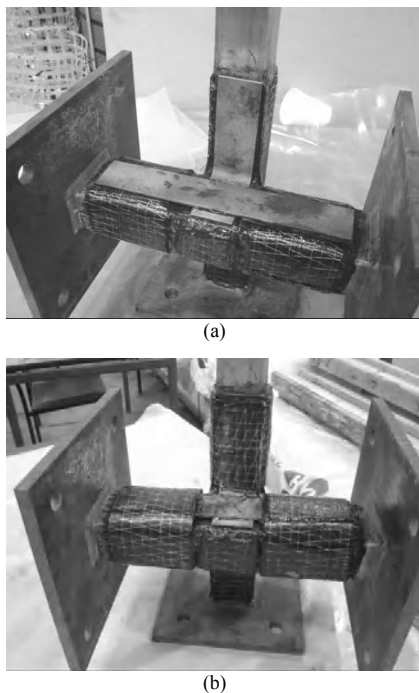


Figure 5 Strengthening cracked S1R1L1A with CFRP sheets and steel plates (a) attaching an L-plate and a holding plate; (b) finished specimen

Being different from the previous two specimens, significant stiffness (slope) change has not shown until 1700 kilocycles when the displacement reached 4.8 mm, which indicates the full engagement of CFRP sheets since the beginning of the experiment. From this point onward, the repaired specimen lost its stiffness and the displacement increased drastically to about 6.0 mm before triggering the break detector, which indicates the failure stage of the specimen that may have been accompanied by the debonding of CFRP though having not been observed through the experiment. If we define the number of cycles before the abrupt slope change stiffness loss, i.e. 1700 kilocycles, as the final fatigue life, the extension of fatigue life after strengthening is roughly twice larger than the original fatigue life of 872 kilocycles (Table 1), i.e. $1700/872=1.95$.

6 CONCLUSIONS

By applying circumferential wrapping CFRP strap and transverse covering CFRP patches to S4R1L2A and S5R1L2A, early debonding is prevented successfully along the major bonding length in the repaired RHS-to-RHS cross-beam connections, and the extension of fatigue life is significant in comparison with the pilot test. However, the repaired specimens are relatively soft at the initial stage which indicates the lack of full engagement of CFRP at the beginning. The reason for this might be attributed to the uncovered corner region around the cracked section by the transverse or circumferential covering strap.

During the repair of S1R1L1A, an L-shaped plate confirming to the corner and a holding plate are added. The combination of strengthening steel plates with CFRP patches led to a significant increase in both the flexural stiffness of the cracked connection and its fatigue life, which proved to be an effective method of retrofitting cracked thin-walled RHS-to-RHS cross-beam connections.

REFERENCES

- Fam, A., Witt, S., & Rizkalla, S. 2006. Repair of damaged aluminum truss joints of highway overhead sign structures using FRP. *Construction and Building Materials* 20: 948-956.
- Fawzia, S., Al-Mahaidi, R., Zhao, X.L., & Rizkalla, S. 2007. Strengthening of circular hollow steel tubular sections using high modulus CFRP sheets. *Construction and Building Materials* 21(4): 839-845.
- Haedir, J., Bambach, M., & Zhao, X.L. 2006. Bending strength of CFRP-strengthened circular hollow steel sections, In: *The Proceedings of 3rd International Conference on FRP Composites in Civil Engineering*, Miami, USA.
- Jiao, H. & Zhao, X.L. 2004. CFRP strengthened butt-welded very high strength (VHS) circular steel tubes. *Thin-Walled Structures* 42(7): 963-978.
- Mashiri, F.R., Zhao, X.L. & Grundy, P. 2002. Fatigue tests and design of welded T-connections in thin cold-formed square hollow sections under in-plane bending. *Journal of Structural Engineering* 128(11): 1413-1422.
- Mashiri, F.R. & Zhao, X.L. 2005a. *Fatigue Behaviour of DuraGal Cross-Beam Welded Connections, OneSteel Market Mills Project, Interim Report No. 04/05*, Department of Civil Engineering, Monash University, Clayton, Australia, 63pp.
- Mashiri, F.R. & Zhao, X.L. 2005b. Fatigue behaviour of welded thin-walled RHS-to-Angle cross-beams under bending. In M.G. Stewart & B. Dockrill (eds), *Structural Engineering-Preserving and Building into the Future, Australian Structural Engineering Conference (ASEC2005)*: 11-14. Newcastle, Australia.
- Nadauld, J.D. & Pantelides, C.P. 2007. Rehabilitation of cracked aluminium connections with GFRP composites for fatigue stresses. *Journal of Composites for Construction* 11(3): 328-335.
- Pantelides, C.P., Nadauld, J. & Cercione, L. 2003. Repair of cracked aluminum overhead sign structures with glass fiber reinforced polymer composites. *Journal of Composites for Construction* 7(2): 118-126.
- Xiao, Z.G., Zhao, X.L. & Mashiri, F.R. 2008. Fatigue experiments on CFRP repaired welded thin-walled RHS-to-RHS cross-beam connections. In *Proceedings of the Tenth International Symposium on Structural Engineering for Young Experts*: 971-980. Changsha, China.
- Zhao, X.L., Herion, S., Packer, J.A., Puthli, R.S., Sedlacek, G., Wardenier, J., Weynand, K., van Wingerde, A.M., & Yeomans, N.F. 2000. *Design Guide for Circular and Rectangular Hollow Section Welded Joints under Fatigue Loading*. Verlag TÜV Rheinland, Cologne, Germany.
- Zhao, X.L. & Zhang, L. 2007. State-of-the-art review on FRP strengthened steel structures. *Engineering Structures* 29(8): 1808-1823.

Fatigue Behavior of CFRP Repaired Non-Load Carrying Cruciform Welded Joints

Tao Chen (t.chen@tongji.edu.cn) & Xianglin Gu

Department of Building Engineering, Tongji University, Shanghai, China

Xiaoling Zhao

Department of Civil Engineering, Monash University, Clayton, VIC 3800, Australia Changjiang Professor, Tongji University, Shanghai, China

ABSTRACT In recent years, large amount of research has been conducted on carbon fibre reinforced polymer (CFRP) strengthening of steel members. There is very limited work on CFRP strengthening of welded connections. This paper reports an experimental study on the use of CFRP sheets to rehabilitate non-load carrying cruciform welded joints subjected to fatigue loading. Failure modes and corresponding fatigue lives were recorded during tests. Thereafter, series of numerical analyses were performed to understand the effects of weld toe radius, layer of CFRP sheets and Young's modulus of reinforced materials on local stress concentration at weld toe. It was found that fatigue life of such welded connections can be enhanced by CFRP sheets. A para-metric study was also carried out. It was found that the weld toe radius and the number of CFRP layers are the key parameters influencing the stress concentration factors of such joint.

1 INTRODUCTION

Fatigue cracking is usually observed for steel structures through their life cycles. And they are often attributed to the cracks emanating from welded joints, which are assumed as weak parts for steel structures (Maddox 1991). Generally, stop holes, welding repair or steel plate attachment etc. are adopted to prolong fatigue life. However, these may raise new problems such as difficulties in manufacturing complex shapes of steel plate with heavy weight, requirement of electrical equipment and additional defects introduced by welding or drilling etc. Carbon fibre reinforced polymer (CFRP) has been successfully applied to retrofitting deficient concrete and masonry structures for their high strength, durability, light weight and ease of installation. Nevertheless, research on using CFRP to strengthen steel structures is still in the exploratory stage.

Earlier research indicated that CFRP retrofitting to steel structures can decrease stress intensity factor at fatigue crack tip that can reduce crack growth rate, thereby extending fatigue lives of damaged steel members (Fam et al. 2006, Dawood et al. 2007). Recent state-of-the-art studies (Wan & Guo 2006, Zhao & Zhang 2007) have comprehensively summarized the research on using fibre reinforced polymer (FRP) for strengthening steel structures. However, most contents are focused on steel members and discussions on welded joints are limited. Artificial defects were adopted to study crack initiation

and propagations in steel plates (Colombi 2005, Liu et al. 2009). Inaba et al (2005) used glass fibre reinforced polymer (GFRP) to retrofit non-load-carry cruciform welded joints subject to fatigue loading. No artificial defects were introduced for welded joints because fatigue crack initiated at the spot with the largest stress concentration factor. It was found that GFRP can bear part of the load and polymer adhesive can improve local shape of weld toe, which reduces the stress concentration at weld toe and thereby improve fatigue performance. However, the effect of weld toe radius on stress concentration was not reported. Zhang et al. (2004) also conducted fatigue test on cruciform welded joints. Test results indicate significant improvement (up to 318%) of fatigue life for specimens bonded with CFRP. Only limited parameters were varied in the testing program. The objective of this study is to investigate the CFRP strengthening method for non-load carrying cruciform through laboratory tests and numerical analysis. Several parameters, such as weld toe radius, layers of CFRP sheet and modulus of strengthening materials were considered.

2 EXPERIMENTAL PROGRAM

2.1 Configuration of the test specimens

Mild carbon steel (Q345) conforming to Chinese Standard GB 50017-2003 in the form of rolled plates of 8mm thickness was used as the base material throughout the

investigation. The mechanical properties and chemical composition of the plate are presented in Tables 1 and 2, respectively. Cruciform specimen consists of a main plate (340mm×80mm) and two longitudinal attachments (70mm×40mm), as shown in Figure 1. They were fabricated using CO₂ gas shield fillet welding and kept in the as-welded condition.

Table 1 Measured mechanical property of steel

Material	Yield stress (MPa)	Ultimate strength (MPa)	Elongation (%)	Young's Modulus (MPa)
Q345	359	521	24.3	2.04×10^5

Table 2 Chemical compositions of steel (mass %)

Material	C	Si	Mn	P	S
Q345	0.16	0.40	1.27	0.026	0.014

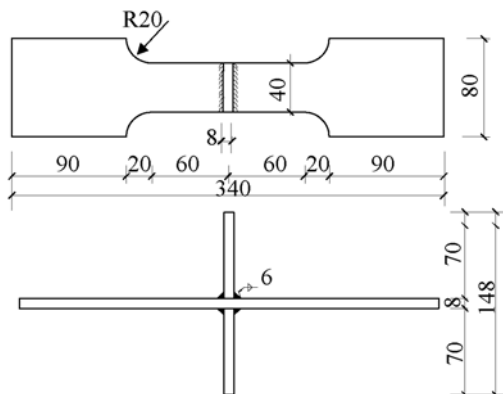


Figure 1 Geometry configurations of non-load carrying cruciform (dimensions are in mm)

Retrofitting material was CFRP sheet (CFC2-2) with its property details listed in Table 3. Several specimens were ground with sand paper and cleaned by acetone. Thereafter, one or three CFRP layers, 120×40mm each, were applied using wet lay-up method to the joint surfaces as shown in Figure 2. The surfaces were finally finished using polymer adhesive and left to cure in room temperature.

Weld toe geometry, which consists of weld toe radius and flank angle, was obtained by using silicon imprint technique (Mashiri et al 2001) before the fatigue testing. Statistical results show that the average toe radius is 1.67mm and the average flank angle is 45.9°.

Table 3 Properties of CFRP sheet

Type	Thickness (mm)	Tensile strength (MPa)	Longitudinal modulus (MPa)	Elongation at break (%)
CFC2-2	0.167	4180	2.50×10^5	1.7

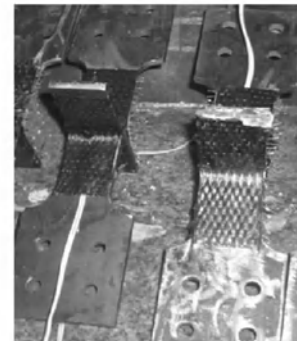
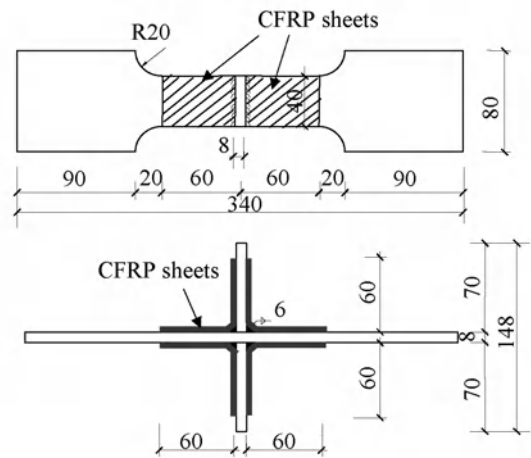


Figure 2 Specimen strengthened with CFRP sheets (dimensions are in mm)

Table 4 Loading cases and test results

Specimen	Stress range (MPa)	Fatigue life $\times 10^3$	Failure pattern
AW-1	216	300*	-
AW-2	180	209	Base material
SF1-1	216	230	Weld toe
SF1-2	180	450	Base material
SF3-1	216	190	Weld toe

* Stopped due to equipment malfunction when cycles attained 300,000. AW-1 did not fail.

2.2 Experimental results

Constant amplitude fatigue tests were conducted on the machine CS-500 at room temperature. The load ratio R ($=\sigma_{\min}/\sigma_{\max}$) for all axial tension loading levels is kept constant at 0.1. Loads were applied sinusoidally at a frequency of 6 Hz. The specimens were tested with two loading levels, which are 216MPa and 180MPa, as listed in Table 4. In the first column, AW denotes specimens without CFRP. SF1 and SF3 denote specimens bonded with one layer and three layers of CFRP sheets respectively.

During the tests, two types of failure modes were observed, which are fracture at weld toe (as shown in Figure 3) and fracture at main plate away from weld. Total fatigue lives for the five specimens have been

plotted in Figure 4. Arrow indicates the specimen did not fail. The E-class line (for non load-carrying type fillet welded joint) specified in JSSC (Japanese Society of Steel Construction) was also plotted in Figure 4. All the test data points are above.

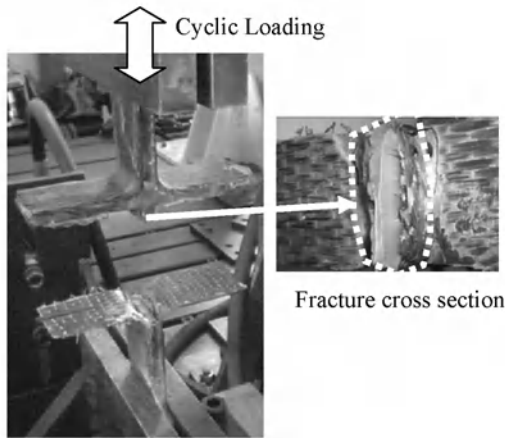


Figure 3 Fatigue failure mode at weld toe

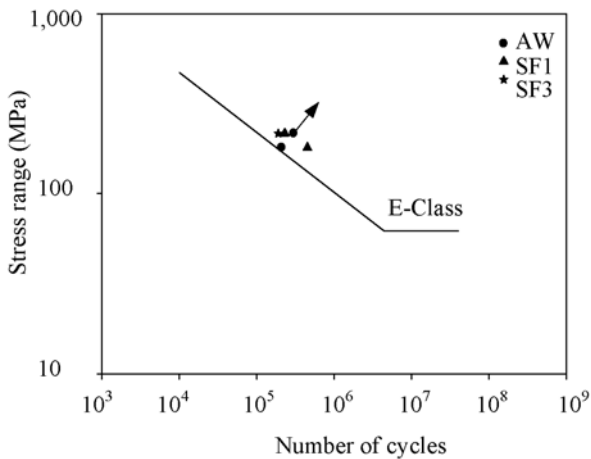


Figure 4 Fatigue test results

E-class line. More fatigue tests are needed in order to recommend a fatigue class for CFRP strengthened non-load carrying cruciform joint.

Life of specimen SF1-2 with one layer of CFRP sheet is more than twice life of specimen AW-2 without CFRP. Both specimens fractured at main plate. By comparing two specimens fractured at weld toe, it was found that the life of specimen SF1-1 with one layer of CFRP sheet is longer than specimen SF3-1 with three layers of CFRP sheets. Comparison failed to reflect the increment of CFRP sheet amount on improvement of fatigue performance. Preliminary analysis indicates that this may due to the influence of weld toe geometry. A detailed discussion will be presented in following session that deals with effect of weld toe radius on fatigue life. More fatigue tests are needed to classify this issue.

3 NUMERICAL ANALYSIS

3.1 Finite element models

Finite element (FE) models were built based on the geometry of tested specimens using the ANSYS software package. One quarter plane strain model was adopted due to symmetric configuration and loading, as shown in Figure 5. Thickness of adhesive was measured as 0.55mm. Slip was not considered during modeling.

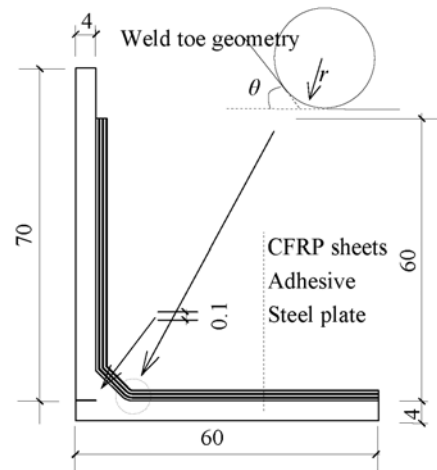


Figure 5 Geometry configurations of finite element model (dimensions are in mm)

FE models were meshed by controlling element size. The dimension is kept below 0.5mm for edge lines and length is kept less than one tenth of weld toe radius near weld toe region. Material properties of steel were inputted referring to Table 1 and Poisson’s ratio was assumed as 0.3. Modulus of adhesive was taken as 3000MPa and Poisson’s ratio was also assumed as 0.3 according to Yue et al. (2009). Other material parameters were taken from Table 3.

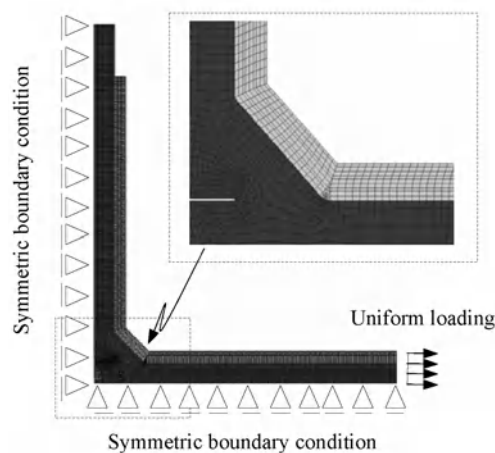
Symmetric boundary condition was applied to left side and lower side of models. In order to acquire stress concentration directly at weld toe, uniform loading were applied to right end that can introduce 1MPa stress at main plate without CFRP sheets. Same loading level was also applied to other models with CFRP sheets. Various parameters, which are weld toe radius, layers of CFRP sheets, modulus of adhesive and CFRP sheet, were considered by performing linear elastic analyses on 20 cases. Details are listed in Table 5. Figure 6 illustrates an example of FE model (Case 3).

3.2 Numerical analysis results

Numerical results demonstrated that stress concentrated at weld toe, which tally with the fatigue crack appearance at weld toe. The maximum principle stress near weld toe is regarded as stress concentration factor since a nominal stress of 1 MPa was applied in base plate for specimen without CFRP. These values of maximum principle stress were tabulated in the last column of Table 5.

Table 5 Numerical analysis cases

Case	Weld toe radius (mm)	Adhesive modulus (MPa)	CFRP modulus $\times 10^3$ (MPa)	Layers of CFRP sheets	Stress Concentration factor
1	1.0	3000	2.5	0	2.27
2	1.0	3000	2.5	1	2.13
3	1.0	3000	2.5	3	2.01
4	1.0	2000	2.5	3	2.06
5	1.0	4000	2.5	3	1.97
6	1.0	5000	2.5	3	1.94
7	1.0	6000	2.5	3	1.91
8	1.0	3000	2.0	3	2.03
9	1.0	3000	3.0	3	1.99
10	1.0	3000	4.0	3	1.96
11	1.0	3000	5.0	3	1.93
12	0.5	3000	2.5	0	2.68
13	0.5	3000	2.5	1	2.50
14	0.5	3000	2.5	3	2.35
15	2.0	3000	2.5	0	1.84
16	2.0	3000	2.5	1	1.74
17	2.0	3000	2.5	3	1.64
18	3.0	3000	2.5	0	1.65
19	3.0	3000	2.5	1	1.56
20	3.0	3000	2.5	3	1.48

**Figure 6** Finite element model (Case 3)

By comparing Case 1-3, Case 12-14, Case 15-17 and Case 18-20, it can be observed that stress concentration factor decreased in the range between 10.1%-12.6% with the increment amount of CFRP sheets. Stress concentration factor of Case 18 is reduced by 27.5% comparing to Case 1 when weld toe radius change from 1mm to 3mm. But the plate stress remains same. Influence of adhesive modulus on stress concentration was studied by Case 3-7. Little variation (about 7.3%) was observed although stress concentration factor decreases with the increment of adhesive modulus. When it comes to the modulus of CFRP sheets, same trend was found by referring to Case 3, Case 8-11 with a variation about 4.9%. Based on aforementioned discussion, it can be concluded that

weld toe radius and the number of CFRP layers are key parameters influencing the stress concentration factor.

4 CONCLUDING REMARKS

In this study, fatigue life of CFRP sheet retrofitting non-load carrying cruciform welded joints was investigated. Both experimental study and numerical analysis were conducted. CFRP strengthening increased the fatigue life of such joint. The weld toe radius and the number of CFRP layer are key parameters influencing the stress concentration factor. More fatigue tests are needed in order to produce a fatigue design class.

5 ACKNOWLEDGMENTS

This work was supported by National Natural Science Foundation of China (Grant Number 50808139), Shanghai Municipal Education Commission and Shanghai Education Development Foundation ("Chen Guang" project, Grant Number 09CG16). We would like to thank Mr. DAI, Y. and Ms. Zang, X.M. for preparing the test specimens.

REFERENCES

- Colombi, P. 2005. Plasticity induced fatigue crack growth retardation model for steel elements reinforced by composite patch. *Theoretical and Applied Fracture Mechanics* 43: 63-760.
- Dawood, M., Rizkalla, S. & Sumner, E. 2007. Fatigue and overloading behavior of steel-concrete composite flexural members strengthened with high modulus CFRP materials. *Journal of Composite for Construction* 11(6): 659-669.
- Fam, A., Witt, S. & Rizkalla, S. 2006, Repair of damaged aluminum truss joints of highway overhead sign structures using FRP. *Construction and Building Materials* 20: 948-956.
- Inaba, N., Tomita, Y., Shito, K., Suzuki, H. & Okamoto, Y. 2005. Fundamental study on a fatigue strength of a cruciform welded joint patched a glass fiber reinforced plastic. *Doboku Gakukai Ronbunshuu, JSCE VI-68(798)*: 89-99. (in Japanese)
- Liu, H.B., Al-Mahaidi, R. & Zhao, X.L. 2009. Experimental study of fatigue crack growth behaviour in adhesively reinforced steel structures. *Composite Structures* 90: 12-20.
- Maddox, S.J. 1991. *Fatigue strength of welded structures*. Abington Publishing: Cambridge.
- Mashiri, F.R., Zhao, X.L. & Grundy, P. 2001. Effects of weld profile and undercut on fatigue crack propagation life of thin-walled cruciform joint. *Thin-Walled Structures*, 39(3): 261-285.
- Wan, H.Y., Guo, F. 2006. The current situation and prospect on steel structure strengthened with CFRP. *Journal of Anhui Institute of Architecture & Industry* 14(6): 1-4. (in Chinese)
- Yue, Q.R., Zhang, N., Peng, F.M. & Zheng, Y. 2009. *Research and application of steel structures strengthened with CFRP*. China Building Industry: Press Beijing. (in Chinese)
- Zhang, N., Yue, Q.R., Yang, Y.X., Hu, L.Q., Peng, F.M., Cai, P., Zhao, Y., Wei, G.Z. & Zhang, Y.S. 2004. Research on the fatigue tests of steel structure member reinforced with CFRP. *Industrial Construction* 34(4): 19-21, 30. (in Chinese)
- Zhao, X.L. & Zhang, L. 2007. State-of-the-art review on FRP strengthened steel structures. *Engineering Structures* 29: 1808-1823.

Tests on CFRP Strengthened Aluminium RHS Subject to End Bearing Force

Xiao-Ling Zhao (ZXL@eng.monash.edu.au), Phaon Phiphat

Department of Civil Engineering, Monash University, Clayton, VIC 3800, Australia

ABSTRACT Web crippling of thin-walled members is often observed at loading or reaction points where concentrated forces exist. This paper reports an investigation on using CFRP (carbon fiber reinforced polymer) strengthening technique to improve the web crippling capacity of aluminium RHS (rectangular hollow section). Several types of strengthening technique were adopted in this project. They include applying CFRP plates outside or/and inside the RHS. A series of laboratory tests were conducted. Significant increase in load carrying capacity was obtained. The test results are also compared with those for cold-formed steel RHS strengthened by CFRP.

1 INTRODUCTION

Web crippling of thin-walled members is often observed at loading or reaction points where concentrated forces exist (e.g. Packer 1984, Zhao and Hancock 1992, 1995, Young and Hancock 2001, Hancock et al 1994, Zhou et al 2009). Using CFRP (carbon fiber reinforced polymer) to strengthen steel members was found to be an efficient method (Hollaway and Cadei 2002, Shaat et al 2004, Cadei et al 2004, Zhao and Zhang 2007). Previous work has been conducted to strengthen RHS (rectangular hollow section), LSB (lightsteel beam) and open sections (e.g. channel and I-section) subject to concentrated forces (Zhao et al 2006, Zhao and Al-Mahaidi 2009, Zhao 2009). This paper reports an investigation on using CFRP strengthening technique to improve the web crippling capacity of aluminium RHS. Several types of strengthening technique were adopted in this project. They include applying CFRP plates outside or/and inside the RHS. A series of laboratory tests were conducted. Significant increase in load carrying capacity was obtained. The test results are also compared with those for cold-formed steel RHS strengthened by CFRP.

2 SPECIMENS

Nine different sizes of aluminium rectangular and square hollow sections are chosen for the testing program. The section ID and nominal section dimensions are given in Table 1 where d is the depth, b is the width and t is the thickness of the section. The external corner radius (r_{ext}) only exists for section S3 whereas no rounded corners

exist for the rest of the sections. The CFRP reinforcement plates used for strengthening the aluminium sections were MBrace S&K laminate 150/2000 with a nominal modulus of elasticity of 165GPa, a nominal ultimate tensile strength of 2700MPa and nominal thickness of 1.2mm. Adhesive used to bond the CFRP to the sections was Araldite 420.

Table 1 Section ID and dimensions

Section ID	Nominal dimensions ($d \times b \times t$) in mm	r_{ext} (mm)
R1	80 × 50 × 3	N/A
R2	100 × 50 × 3	N/A
R3	150 × 50 × 3	N/A
R4	200 × 50 × 3	N/A
S1	50 × 50 × 3	N/A
S2	100 × 100 × 3	N/A
S3	100 × 100 × 6	12.33

Several types of strengthening technique are adopted in the testing program as shown in Figure 1. The specimen length is 500 mm. The fiber direction of the CFRP plate is vertical to the longitudinal axis of the section. One layer of CFRP was applied. Each specimen is given a label to define the section and the type of strengthening. For example R3T3 refers to rectangular hollow section R3 (defined in Table 1) with Type 3 strengthening (CFRP on the inner web alone). The specimen labels are listed in Table 2.

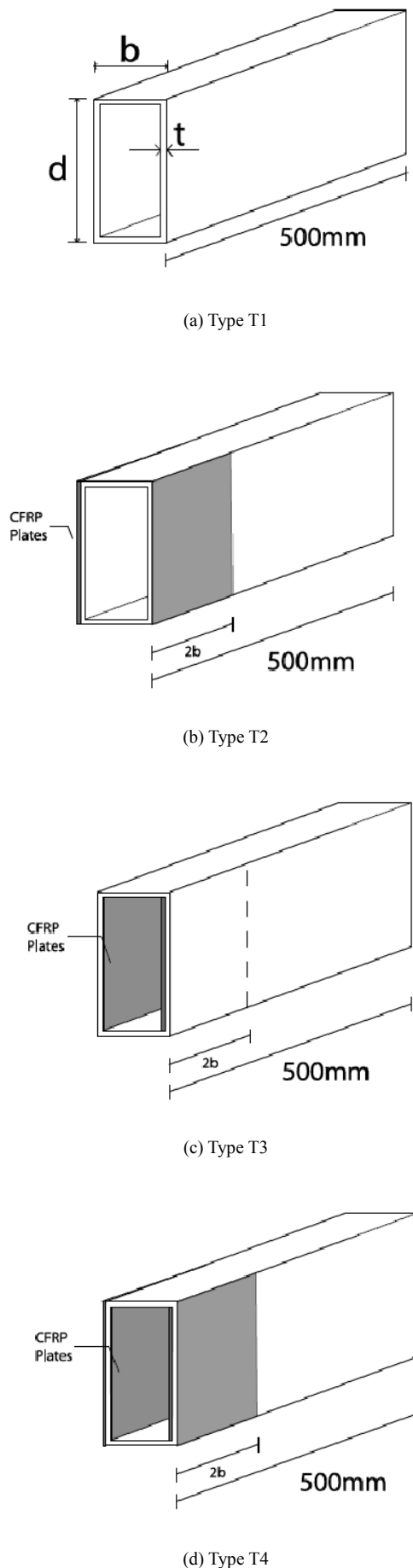


Figure 1 Types of strengthening technique

Table 2 Specimen labels and test results

Specimen label	d/t	P_{max} (kN)	Observed failure mode
R1T1	26.22	51.8	Buckling
R1T2	26.22	77.1	Buckling
R1T3	26.22	104.4	Buckling
R1T4	26.22	159.2	Yield
R2T1	33.58	49.9	Buckling
R2T2	33.58	74.7	Buckling
R2T3	33.58	110.1	Buckling
R2T4	33.58	193.0	Yield
R3T1	51.54	37.4	Buckling
R3T2	51.54	61.8	Buckling
R3T3	51.54	77.0	Buckling
R3T4	51.54	150.5	Yield
R4T1	67.75	31.2	Buckling
R4T2	67.75	51.4	Buckling
R4T3	67.75	63.6	Buckling
R4T4	67.75	149.5	Yield
S1T1	17.37	57.6	Buckling
S1T2	17.37	70.9	Buckling
S1T3	17.37	107.3	Buckling
S1T4	17.37	125.3	Yield
S2T1	32.06	53.4	Buckling
S2T2	32.06	80.8	Buckling
S2T3	32.06	98.1	Buckling
S2T4	32.06	133.4	Yield
S3T1	16.23	115.2	Yield
S3T2	16.23	118.4	Yield
S3T3	16.23	141.1	Yield
S3T4	16.23	152.3	Yield

3 TEST SET UP AND PROCEDURES

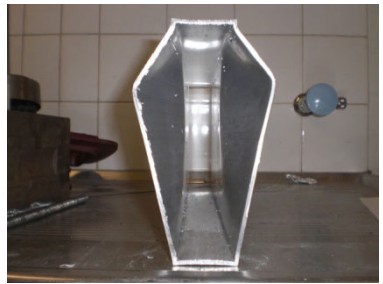
The procedures to prepare the CFRP plate strengthened specimens are similar to those described by Zhao et al 2006. All tests were performed in a 500kN capacity Baldwin Universal testing machine. The loading rate was 1mm/min. All specimens were tested under a 50mm bearing length. String pots located on either side of the specimen were used to record the amount of deformation occurring during loading. The loading arrangement and supporting conditions are the same as those for RHS and lightsteel beam (Zhao et al 2006, Zhao and Al-Mahaidi 2009). A typical test set up is shown in Figure 2.



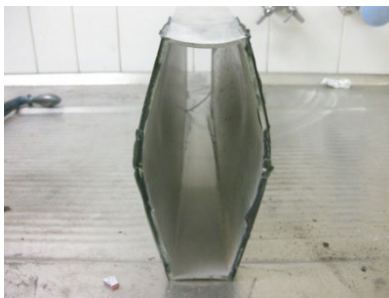
Figure 2 Typical test set up

4 TEST RESULTS

The failure modes are shown in Figure 3 for each type. Web buckling is clearly shown in Figure 3 (a) for a bare RHS section. Figure 3 (b) demonstrates that less web buckling occurs due to CFRP strengthening from outside. Less web buckling was also observed for Type T3 where the inward buckling occurs. Yielding of the section starts to occur when CFRP plates were applied on both sides (see Type T4 in Figure 3 (d)).



(a) Type T1



(b) Type T2



(c) Type T3



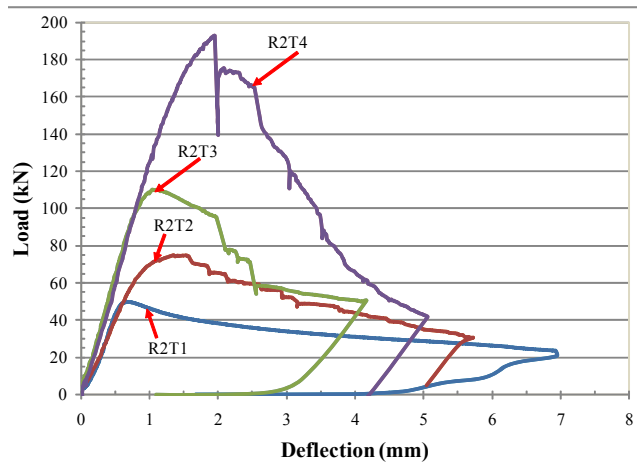
(d) Type T4

Figure 3 Typical failure modes

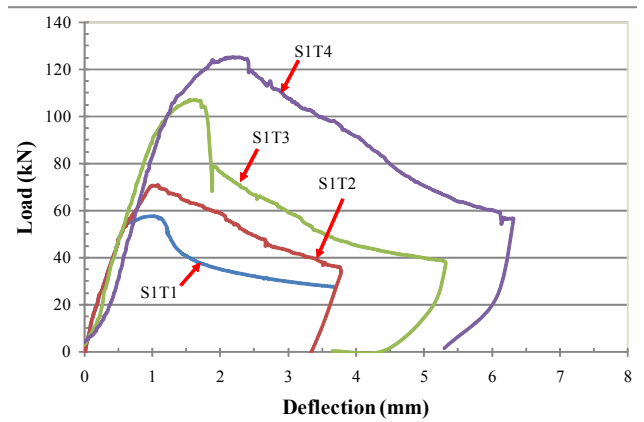
Typical load versus deformation curves are presented in Figure 4. It can be seen from Figure 4 that significant increase in load carrying capacity and ductility was obtained due to CFRP strengthening. The ultimate load carrying capacity is listed in Table 2 for each specimen.

The load carrying capacity of strengthened specimens (Type T2, Type T3 and Type T4) is compared in Figure 4 with that of reference specimens (Type T1). For Type T2 (CFRP applied on the outer web) the increase is about 50%. For Type T3 (CFRP applied inside the web) the increase is about 100%. More increase (over 350%) is gained for Type T4 (CFRP applied on both sides of the web).

The increase in load carrying capacity for aluminium RHS sections strengthened using Type T2 and Type T4 is compared with that for cold-formed RHS sections reported in Zhao et al 2006. The same CFRP plates and adhesives were used in both testing programs. When the CFRP is applied on the outside of the web the increase is similar. However, much more increase is achieved for aluminium sections. This is most likely due to the fact that the elastic modulus of CFRP plate is much higher than that of aluminium.



(a) R2 section



(b) S1 section

Figure 4 Typical load versus deformation curves

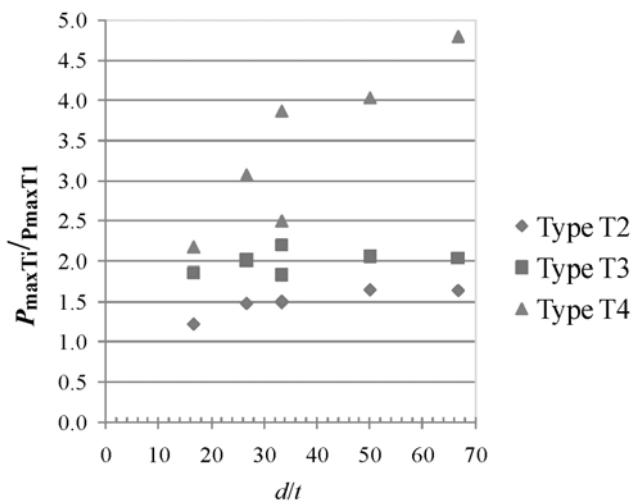


Figure 5 Increase in load carrying capacity for aluminium sections

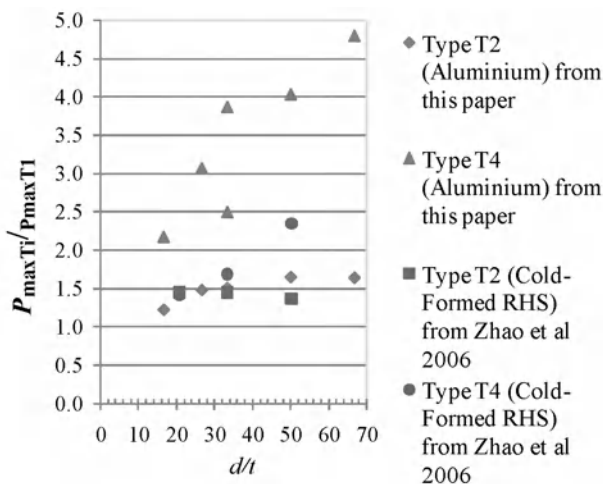


Figure 6 Comparison of increase in load carrying capacity for aluminium RHS sections and cold-formed RHS sections

5 CONCLUSIONS

This paper has presented an experimental study on CFRP strengthened aluminium rectangular hollow sections subject to end bearing force. Twenty eight tests were conducted on different types of strengthening techniques. The CFRP strengthening significantly reduced the web buckling. The increase in load carrying capacity has been found to be up to 50%, 100% and 350% for Type T2, Type T3 and Type T4 respectively. More increase has been found for aluminium RHS compared with cold-formed steel RHS especially when the CFRP is applied on both sides of the web. More research is needed to derive design formulae for strengthened aluminium RHS subject to end bearing force.

6 ACKNOWLEDGEMENT

The authors gratefully acknowledge the financial support provided by the Australian Research Council. The authors wish to thank Mr. Kevin Nievaart and Mr. Long Goh for their assistance in carrying out the experimental testing.

REFERENCES

- Cadei J.M.C., Stratford T.J., Hollaway L.C., Duckett W.G. 2004. C595 - Strengthening metallic structures using externally bonded fibre-reinforced composites, London: CIRIA.
- Hancock, G.J., Sully, R.M. and Zhao, X.L. 1994. Hollow flange beams and RHS sections under combined bending and bearing, *Proceedings of sixth International Symposium on Tubular Structures*, Melbourne, 47-54.
- Hollaway, LC and Cadei, J. 2002. Progress in the technique of upgrading metallic structures with advanced polymer composites. *Progress in Structural Engineering and Materials* 4(2): 131-148.
- Packer, J.A. 1984. Web crippling of rectangular hollow sections. *Journal of Structural Engineering*, ASCE 110(10): 2357-2373.
- Shaat, A., Schnerch, D., Fam, A., and Rizkalla, S. 2004. Retrofit of steel structures using fiber-reinforced polymers (FRP): State-of-the-art, *Transportation Research Board (TRB) Annual Meeting*. Washington, CD-ROM (04-4063).
- Young, B. And Hancock, G.J. 2001. Design of cold-formed channels subjected to web crippling. *Journal of Structural Engineering*, ASCE 127(10): 1137-1144.
- Zhao, X.L. 2009. Tests on CFRP strengthened open sections subjected to end bearing forces, *Asia Pacific Conference on FRP in Structures*, Seoul, Korea, December.
- Zhao, X. L. and Zhang, L. 2007. State-of-the-art review on FRP strengthened steel structures. *Engineering Structures* 29(8): 1808-1823.
- Zhao, X.L. and Hancock, G.J. 1992. Square and rectangular hollow sections subject to combined actions. *Journal Structural Engineering*, ASCE 118(3): 648-668.
- Zhao, X.L. and Hancock, G.J. 1995. Square and rectangular hollow sections under transverse end bearing force. *Journal of Structural Engineering*, ASCE 121(9): 1323-1329.
- Zhao, X.L. and Al-Mahaidi, R. 2009. Web buckling of lightsteel beams strengthened with CFRP subjected to end-bearing force, *Thin-Walled Structures* 47(10): 1029-1036.
- Zhao, X.L., Fernando, D. and Al-Mahaidi, R. 2006. CFRP strengthened RHS subjected to transverse end bearing force, *Engineering Structures* 28(11): 1555-1565.
- Zhou, F., Young, B. and Zhao, X.L. 2009. Tests and design of aluminum tubular sections subjected to concentrated bearing load, *Journal of Structural Engineering*, ASCE 135(7): 806-817.

Lateral Torsional Buckling of Steel I-Beam Retrofitted Using FRP Sheets: Analytical Solution and Optimization

M. Z. Kabir (mzkabir@aut.ac.ir) & A. E. Seif

Department of civil engineering, Amirkabir University of Technology (Tehran Polytechnic), Tehran, Iran

ABSTRACT This paper presents an analytical investigation on lateral stability of steel metal beam which is retrofitted using FRP patch. The methodology is based on implementing total potential energy and Rayleigh Ritz method. The laminate theory including first order shear deformation is included in this study. The linear elasticity solution is considered for determining of buckling critical load. The compound beam is assumed a simply supported under pure bending. Some combinations of FRP sheets on single or both sides of flanges and web are applied as different cases of section retrofitting in order to investigate the effectiveness of strengthening pattern on the lateral torsional buckling of the metal beam. The FRP sheet can be extended to the total or partial length, full or partial patch, of the beam. In each case, parametric study with variation of fiber orientation is examined to find out the optimum fiber direction for design purposes. The results of this study would be benefitted for retrofitting of existing steel bridges which many of them are exposed to the harsh environment.

1 INTRODUCTION

There are some traditional methods to strengthen the steel members such as welding or using adhesively bonding steel plates, yet using FRP sheets is newest method which is applied and appears to be an excellent solution. For an I-beam, FRP sheets can be attached to the flanges and web to develop its capacity and stability.

The analytical solutions were widely presented for steel beams with different cross-sections, loads and boundary conditions. This study intends to present an analytical solution for predicting of lateral-torsional buckling load of simply supported I-section beam retrofitted using FRP sheets.

2 KINEMATICS

The buckling deformation of the section can considered as U and V in X and Y directions, and rotation ϕ_z about axial beam Z axis. The shear strains are also denoted by γ_{xz} and γ_{yz} . In the first order shear deformation theory which assumes transverse normal does not remain perpendicular to the mid-surface after deformation, the rotations about X and Y axis based on right-hand rule are $\phi_x = \gamma_{yz} - V'$ and $\phi_y = -(\gamma_{xz} - U')$ where prim denotes derivation with respect to Z . Then, the displacement fields on each element are obtained as those of mid-plane.

The energy criterion is used to determine the lateral-torsional buckling load of a beam based on internal strain energy and external work of load. Since U_i and W_e represent the internal strain energy and the external work of load, the total potential energy will be $\Pi = U_i - W_e$.

Using matrix form, the internal strain energy of the beam is given by summation of strain energy in each element as:

$$U_i = \frac{1}{2} \int_0^L \int_S (f \cdot \chi^T) dS dZ \quad (1)$$

where, $f = \{ N, M, Q \}$ and $\chi = \{ e, \beta, e_o \}$ are forces and displacement fields, in which, N and M are in-plane forces and moments and Q indicates out of-plane shear forces; the parameters e, β and e_o are relevant to in-plane and out of-plane strains and curvatures. Supposing that in-plane lateral forces and moments are zero, the reduced constitutive relations for hybrid element consisted of metal and composite patch are:

$$\begin{Bmatrix} N \\ M \end{Bmatrix} = \begin{bmatrix} A^* & B^* \\ B^* & D^* \end{bmatrix} \cdot \begin{Bmatrix} e \\ \beta \end{Bmatrix} \quad (2a)$$

$$\{Q\} = [A_o] \cdot \{e_o\} \quad (2b)$$

Rewriting Equation 1 will lead to strain energy of beam in terms of section stiffness.

$$U_i = \frac{1}{2} \int_0^L \left[I_y (U_b'')^2 + I_x (V_b'')^2 + I_\phi (\phi'')^2 + 2I_{xy} (V_b'' U_b'') + 2I_{x\phi} (V_b'' \phi'') + 2I_{y\phi} (U_b'' \phi'') + G_x (U_s')^2 + G_y (V_s')^2 + G_\phi (\phi')^2 + 2G_{x\phi} (U_s' \phi') + 2G_{y\phi} (V_s' \phi') + 2H_x (V_b'' U_s') + 2H_y (U_b'' V_s') + 2H_\phi (\phi'' \phi') + 2H_{xy} (V_b'' V_s') + 2H_{yx} (U_b'' U_s') + 4H_{x\phi} (V_b'' \phi') + 4H_{y\phi} (U_b'' \phi') \right] dz \quad (3)$$

Apart from that, the potential of external load can be obtained from Sherbourne & Kabir (1995).

$$W = \int_0^L [M(z)(V_b'' + \phi U_b'') - Q(z)(\gamma_{yz} + \phi \gamma_{xz})] dz \quad (4)$$

where, $M(z)$ and $Q(z)$ represent the internal bending moment and shear force of beam due to external loads. By minimizing the total potential energy for a simple I-beam subjected to uniform moment, the buckling moment is obtained as:

$$M_{ocr} = -\frac{\pi^2}{L^2}(I_{y\phi} - \eta_{y\phi}) \pm \frac{\pi}{L} \sqrt{(I_y - \eta_y) \left(\frac{\pi^2}{L^2}(I_\phi - \eta_\phi) + (G_\phi - \mu_\phi) \right)} \quad (5)$$

$$\eta_y = \frac{I_{xy}^2}{I_x}, \quad \eta_\phi = \frac{I_{x\phi}^2}{I_x}, \quad \eta_{y\phi} = \frac{I_{xy} I_{x\phi}}{I_x} \quad (6a, 6b, 6c)$$

$$\mu_\phi = \frac{G_{x\phi}^2}{G_x} + \frac{G_{y\phi}^2}{G_y} \quad (7)$$

in which, μ_ϕ refers to shear rigidities and η generates the coupling terms I_{xy} and $I_{x\phi}$. It is seen by neglecting the shear terms, the relation (5) is simplified to the standard form as derived in Timoshenko & Gere (1961). By defining the notation M_{os} as the critical moment of metal section, then the buckling load increasing factor is determined by $k_m = (M_{ocr}/M_{os} - 1)$ which will be discussed later on.

3 SECTION OPTIMIZATION

In this section, a simply supported I-beam with the length of $L = 4000$ mm under uniform moments, as shown in

(Figure 1) is used with fourteen cases of section retrofitting schemes (Figure 2).

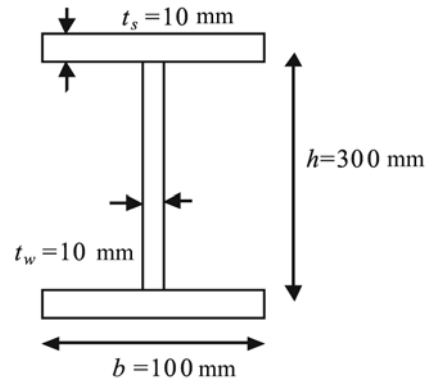


Figure 1 Steel I-beam (dimensions)

The proposed parametric study in this paper applies for each case in which FRP patch is used through the beam length and fiber angle of FRP patch with $[+\theta / -\theta]$ laminate sequences. It is changed separately for the flanges and the web.

The proposed cases in Figure 3 show the optimum fiber angle of flanges and web. Results show that the fiber angles 0° and 45° , respectively, for flanges and web make maximum increasing in buckling load.

To compare the efficiency of different retrofitting schemes, the special ratio R is defined for each case as $R = k_m / k_s$; this parameter shows the superior retrofitting manner. There are two dimensionless factors k_m and k_s are buckling load increasing factor as defined in previous section and the area ratio of FRP patch to metal which is given in (Figure 2), respectively. The consequences of this investigation are plotted in (Figure 4).

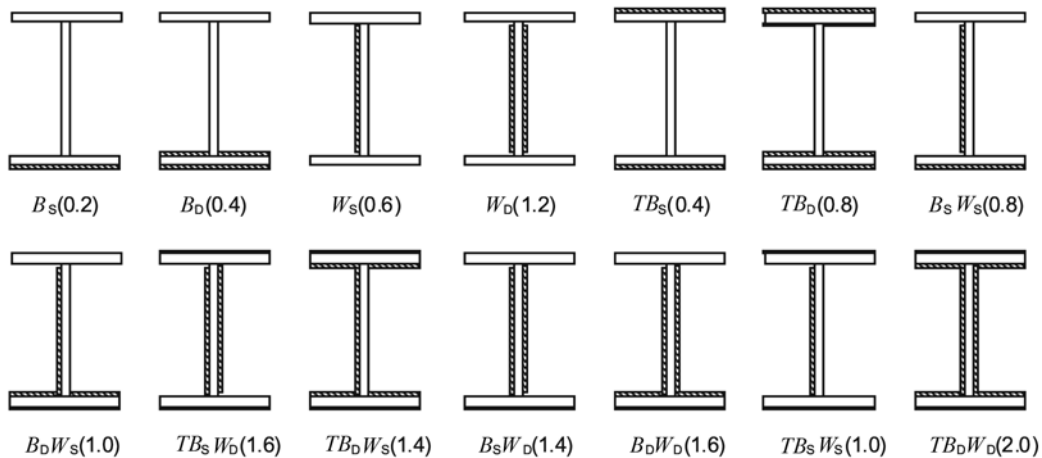


Figure 2 Fourteen cases of section retrofitting schemes. Values in the parenthesis are the area ratio of FRP patch to metal named k_s

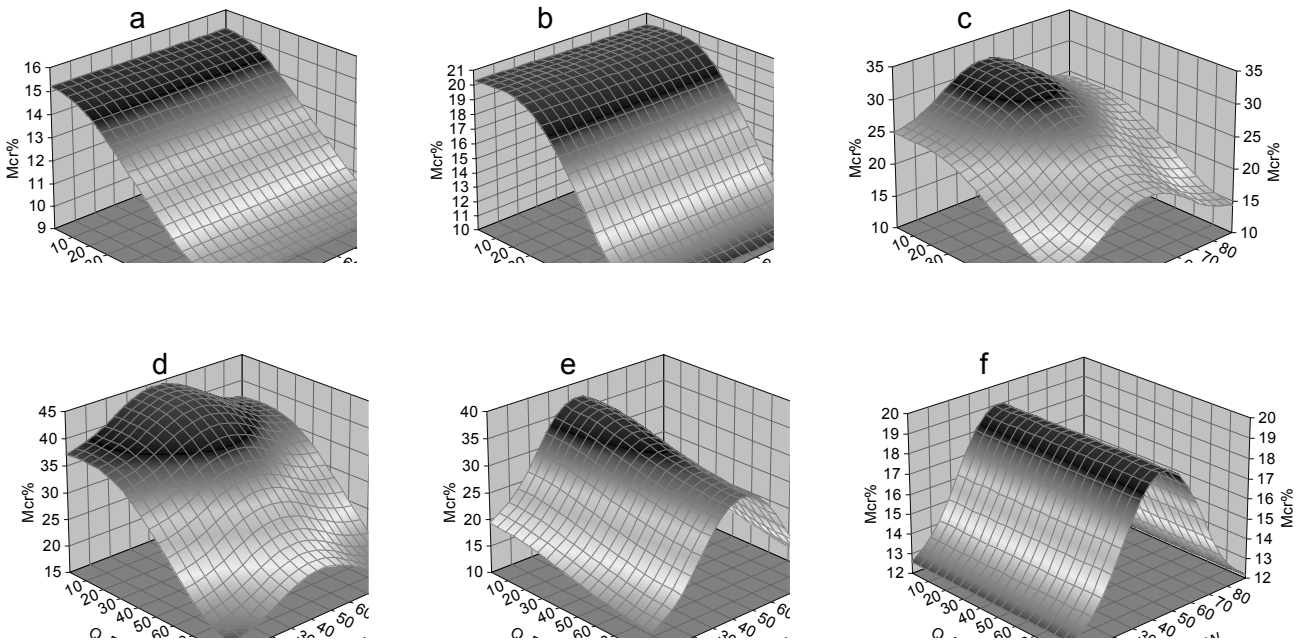


Figure 3 Increasing percentage in the buckling load versus patches fiber angle of flanges Q_F and the web Q_W ; a) Case B_S similarly for TB_S and $TB_S W_S$; b) Case B_D similarly for TB_D ; c) Case $B_D W_S$ similarly for $B_S W_S$, $B_D W_D$, $TB_D W_D$ and $TB_D W_D$; d) $TB_D W_S$; e) Case $B_S W_D$; f) Case W_S similarly for W_D

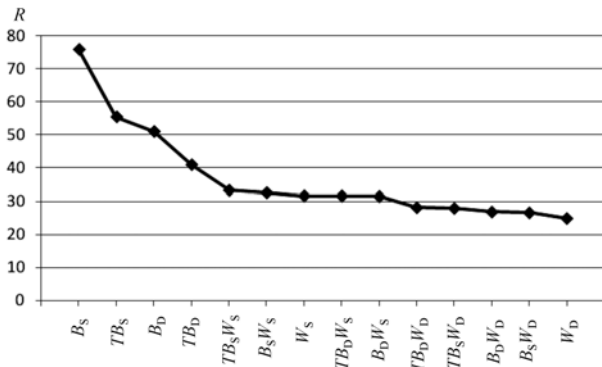


Figure 4 Optimization factor R ordered for fourteen cases of section retrofitting

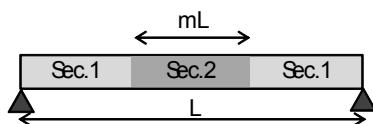


Figure 5 Simple beam with two types of retrofitting

4 PATCH LENGTH OPTIMIZATION

In this section, two parts of beam were retrofitted with two different types see Figure 5. Since the length of beam is L , section type 1 and 2 does have length of $(1 - m) L$ and $(m) L$ respectively and one new factor can be defined as $k_f = (1 - m) k_{s1} + m k_{s2}$; where k_{s1} and k_{s2} are section retrofitting factor related to section 1 and 2. Thus, this time, the optimization factor is $R = k_m / k_f$ with the previous definition of k_m and the point is to get

the coefficient m related to the maximum optimization factor R . The investigation results for two types of loading consist of one central point load and uniform distributed load applied to a simply supported which are plotted in Figure 6. It is important to note that for each type of loading the internal moment at the center of beam is used to calculate the factor k_m . In related figures, section retrofitting combinations are written in Sec1-Sec2 format and maximum value at each curve is marked with solid marker and related value of m is written near that.

According to the results, for both types of loading, the B_S-B_D and TB_S-TB_D gives the maximum R factor with $m = 0.3$. The cases W_D-B_S , W_D-B_D , W_D-TB_S and W_D-TB_D are laid in the second rank. It means that the web should not preferably be retrofitted at center regions of beam.

5 CONCLUSION

This study uses an analytical solution based on the energy method to give the critical value for the lateral-torsional buckling analysis for a retrofitted I-beam using FRP sheets. Investigating fourteen types of section retrofitting with various fiber angles of FRP patches, shows that fiber angles 0° and 45° respectively for patches on flanges and the web, gives maximum buckling capacity. Based on the numerical results, for a simply supported I-beam subjected to uniform moment, when patches are used constantly through the length, applying patches to both flanges, name B_S , TB_S , B_D and TB_D respectively gives the maximum optimization factor R . Finally, some

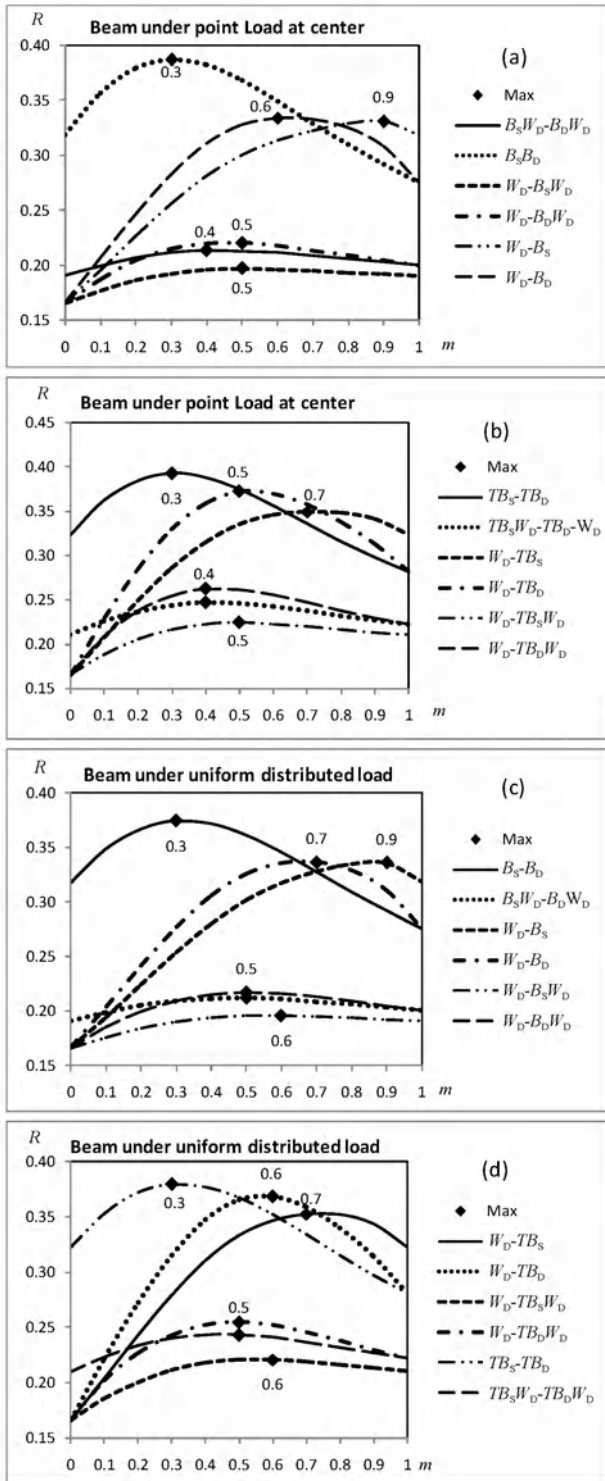


Figure 6 Optimization factor R versus the length coefficient m (defined in Figure 5) for simple beam subjected to one central point load (a, b) and uniform distributed load (c, d)

inspects on applying different retrofitting partially to the length show that the best method is using B_D or TB_D on 0.3 of length at center respectively with B_S or TB_S on remained length. Also, it was shown that it is better to retrofit the web at a region near supports.

REFERENCES

Bazant, Z.P. & Cedolin, L. 2003. Stability of structures: elastic, inelastic, fracture, and damage theories. New York: Dover publication, Inc.

El Damatty, A.A., Abushagur, M. & Youssef, M.A. 2005. Analytical prediction of the linear and nonlinear behavior of steel beams rehabilitated using FRP sheets. Applied Composite Materials 12: 309-325.

Karbhari, M.K. & Seible, F. 2000. Fiber Reinforced Composites – Advanced Materials for the Renewal of Civil Infrastructure. Applied Composite Materials 7: 95-124.

Lee, J. & Kim, S.E. 2002. Lateral-torsional buckling analysis of thin-walled laminated channel-section beams. Composite Structures 56: 391-399.

Lee, J. & Lee, S. 2004. Flexural-torsional behavior of thin-walled composite beams. Thin-Walled Structures 42: 1293-1305.

Photiou, N.K., Holloway, L.C. & Chryssanthopoulos M.K. 2006. Strengthening of an artificially degraded steel beam utilising a carbon-glass composite system. Construction and Building Materials 20: 11-21.

Popov, I.P. 1961. Engineering mechanics of solids. ISBN 964-6904-14-6.

Qiao, P., Zou, G. & Davalos, J.F. 2003. Flexural-torsional buckling of fiber-reinforced plastic composite cantilever I-beams. Composite Structures 60: 205-217.

Sherbourne, A.N & Kabir, M.Z. 1995. Shear strain effects in lateral-torsional strain of thin-walled Fibrous composite beams. Journal of Engineering Mechanics 121: 640-647.

Silvester, N., Young, B. & Camotim, D. 2008. Non-linear behavior and load-carrying capacity of CFRP-strengthened lipped channel steel columns. Engineering Structures doi:10.1016/j.engstruct.2008.02.010.

Teng, J.G. & Hu, Y.M. 2007. Behaviour of FRP-jacketed circular steel tubes and cylindrical shells under axial compression. Construction and Building Materials 21: 827-838.

Timoshenko, S.P. & Gere, J.M. 1961. Theory of elastic stability. New York: McGraw-Hill,

Youssef, M.A. 2006. Analytical prediction of the linear and nonlinear behaviour of steel beams rehabilitated using FRP sheets. Engineering Structures 28: 903-911.

Experimental Study on Behavior of FRP Anti-Buckling Strengthening Steel Members

Sawulet. Bekey

College of Architecture Engineering, Xinjiang University, Urumqi 830008, China

Feng Peng & Ye Lieping

Department of Civil Engineering, Tsinghua University, Beijing 100084, China

ABSTRACT This paper puts forward a thought of a FRP (Fiber Reinforced Polymer) anti-buckling strengthening of steel members. Through compression tests of 14 specimens, the influence of slenderness ratio, binding (filled or not filled), fillers, as well as connection methods to the core steel compression performance was studied. The results show that the reinforcement changes the ultimate failure mode of the specimen, and increases the ultimate bearing capacity and ductility to varying degrees. It is worthy of further research and has the value of promotion in practice.

1 INTRODUCTION

1.1 Engineering Application of FRP materials

Fiber Reinforced Polymer/Plastic (FRP), a proper mixture of fibers and matrix materials and formed with a certain composite processing technology, is a new kind of high performance nonmetal material. From 1940s, FRP has been widely used in various fields such as aeronautics and astronautics, shipping, chemical engineering, medicine and mechanics, etc. In virtue of the advantages of light weight, high strength, corrosion resistance, easy construction and easy molding, FRP has been applied to civil engineering in recent years, and has become a supplement for traditional building materials like concrete and steel. It has been an important and hot direction to apply FRP to various constructions properly. Some major types of FRP are as follows: Carbon Fiber (CFRP), Glass Fiber (GFRP), Aramid Fiber (AFRP) and Basalt Fiber (BFRP).

1.2 Putting forward FRP anti-buckling strengthening of steel members

There are a lot of axial compression members like steel truss rods, space grid rods and columns, etc. There are two kinds of failure modes of axial compression members in steel structures: buckling and yielding. Buckling is the main failure mode of the two, which happens frequently in steel structures. The sudden instability of steel members could lead to a rapid change in structure geometry, after which the whole structure will lose bearing capacity totally and collapse. In the history of engineering all around the world, the accident caused by compressive rod failure is nothing new. For instance, in 1907, Quebec Bridge in Canada collapsed when under construction.

9000 tons of steel structures dropped into the river and 75 people died. It is the buckling failure of compressive bottom-chord in the cantilever that caused this accident. In 1960, a single-story spherical shell of 90m in diameter collapsed for the reason of buckling in Bucharest, the capital of Romania. In 1978, a space grid (plane dimension of 92m×110m) of Hartford Gymnasium in America collapsed because of the buckling of the compressive rod as well. In 1988 in Taiyuan, a plane space grid (13.2m×17.99m) collapsed brittlely due to continuous buckling of the compressive rod. In 1992 in an exhibition centre in Shenzhen, the steel compressive flank rod of a space grid buckled because of the heavy weight of rain water. At the beginning of 2008 in South China, plenty of power transmission towers fell down in the snow disaster. These engineering accidents, for the same reason of buckling failure of the compressive steel rod, caused severe economic losses and heavy casualties.

In recent years, China's steel structure industry develops fast. Whereas, with people's lack of experience or excessive pursuit of economy, there has been many unsafe structures with low stability capacity, some even lead to instable failure accidents; meanwhile, a number of structures lack for enough bearing capacity due to increasing imposed load, corrosion damage, construction mistake and so on. With the gradually increasing scale of China's steel structure industry, the need of steel structure strengthening will be larger and larger.

Under the snow disaster in south China in 2008, some power transmission steel towers suffered instable failure due to shortage of compressive rod stiffness. Later in the same year, some towers were damaged in 5-12 Wenchuan earthquake. From these facts we know that some tensile

rods and compressive rods of the existing buildings need for seismic reinforcement (the increasing load, etc.) and stability reinforcement (the shortage of stability bearing capacity). Therefore large quantities of steel transmission towers need for reinforcement. Meanwhile, most of them locate in the field, where we would encounter inconvenient traffic condition and lack of appropriate strengthening methods, so we have an urgent need for simple, light-material and effective strengthening techniques.

Metal members under axial compression or both compression and bending will probably buckle when destructed, that is to say, long and thin components would be instably destructed under a relatively low load. They lose bearing capacity prior to yielding without taking full use of materials' strength capacity. When load or safety requirement increases, we can improve components' bearing capacity through anti-buckling reinforcement.

At present, the primary methods of steel structure reinforcement in practice are: to replace components, to decrease load, to change the structure system, to increase component cross-section areas, to use prestress cable and so on. These methods have their own limits, as follows: some will cause new problems to the structure like partial failure, residual stress, etc.; some have difficulties in meeting requirements when under construction or in use, for example, unable to be demounted, no fire present and increasing use of steel. These lead to difficulties in application promotion and inconvenience in on-site reinforcement of existing structures or operation in the field.

So this paper introduces FRP anti-buckling reinforcement and puts forward a new thought, which is light-weight and convenient, about FRP anti-buckling reinforcement for steel members. We will loop fiber fabrics partially around the tube, which is composed of FRP pultruded profiles or longitudinal fiber fabrics, and fill the space between the FRP tube and the steel structure with light weight materials like slight-expansive bubbly mortar or bamboo splints. Thereby, the stiffness and bearing capacity of the members will be increased, of which we can take advantage to reinforce tower rods, columns, truss rods, space grid rods and braces whose failure mode is controlled by stability capacity. The figure of FRP anti-buckling reinforcement for steel members is shown in Figure 1, in which 1 represents reinforced steel members. This technique fits different kinds of cross-sections; Figure 2 is fillers; Figure 3 is FRP pultruded profile or FRP fabric strengthening layer around outside; Figure 4 is the partially FRP strengthening layer. When necessary, additional strengthening is needed at the centre and the end of the component.

Three construction methods of FRP and light weight filler anti-buckling reinforcement are as follows:

(1) Put solid light-weight materials including bamboo, wood or polyurethane foam around the reinforced com-

ponent to form a solid cross-section, such as round, oval, square, etc. Then cover filling materials with FRP profiles, and wrap FRP strengthening fabrics around them to constrain internal filling materials and reinforced components.

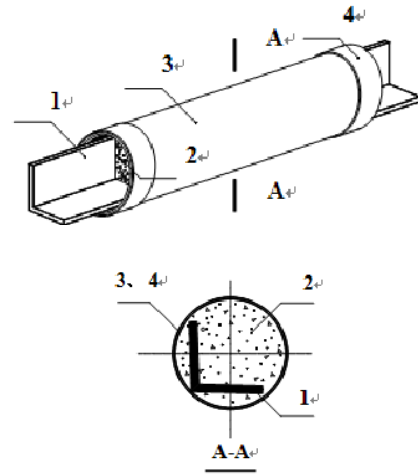


Figure 1 Diagram of FRP anti-buckling strengthening steel members

(2) Put solid light-weight materials including bamboo, wood or polyurethane foam around the reinforced component to form a solid cross-section, such as round, oval, square, etc. Then wrap FRP fabrics around filling materials to constrain internal filling material and reinforced components.

(3) Put prefabricated FRP profiles around the steel component, and fill the space between them with filling materials including polyurethane foam or expansive mortar, which can be completely or incompletely filled. And finally wrap FRP profiles with FRP strengthening fabrics.

External constraints are composed of FRP profiles, wrapping FRP fabrics, variety filling materials like foam slight-expansion mortar or bamboo, which have a certain bending capacity, torsion capacity and splitting capacity at the end part. Usually after loaded, components will first experience little wave low-level buckling mode. Due to external constraints inhibiting the lateral deformation of low-level buckling, reinforced components tend to experience higher-level buckling mode where components will have a higher bearing capacity; A higher-level buckling mode means more half-wave, increasing the number of action points where the external constraint inhibits the buckling deformation of the internal component; If the external constraint has enough loop stiffness and strength, and have a certain longitudinal bending stiffness, the external load will not stop increasing until the axial stress of all points in the whole cross-section reaches yield point.

Usually GFRP (glass fiber reinforced composite material) with relatively low price would meet reinforcement needs. When high strength capacity is required, we can use a small amount of superior-performance but relatively

expensive CFRP (carbon fiber reinforced composite material), so as to be economical. Meanwhile, for high requirements of fire protection, we could use slight-expansion foam mortar as the filling materials to improve fire resistance ability of the core steel. And for power transmission towers or other outdoor structures, we mainly use bamboo splints to reduce on-site wet work and facilitate the construction. Compared with other reinforcement, this method has the following advantages:

(1) Convenient and fast construction, no formwork is needed, no fire is induced, no need for lifting equipments, and little effect on the production and use;

(2) Light additional weight, little effect on the original structure;

(3) Improvement of corrosion resistance;

(4) Flexible reinforcement method, either profiles casing or fabrics wrapping, applicable for diverse cross-sections, insignificant increase of the outline size of the components;

(5) Remarkable improvement of bearing capacity and ductility in the process of failure;

(6) Can be simultaneously used with other FRP reinforcement for steel structures such as anti-fatigue reinforcement, flexural reinforcement, shear reinforcement, and joints reinforcement;

(7) To make use of the abundant bamboo resources in China so as to contribute to sustainable development;

(8) Existing experimental research shows that, the weakness of FRP surface-pasting reinforcement for steel components is the adhesive between the FRP and the steel, that is, suffering interface exfoliation failure. However, according to the FRP anti-buckling reinforcement method presented in this paper, there's no need for FRP to connect with steels with surface paste, so interface exfoliation failure would never occur.

This reinforcement method is different from traditional ones. It increases the buckling bearing capacity of the components by providing external constraints and reasonably enlarging the cross-section. The validity has been shown experimentally in this paper. We have worked on an axial compressive test on the equilateral angle through FRP anti-buckling reinforcement, the results show that: for the reinforced angle of universal slenderness ratio, the compressive bearing capacity could be increased by 71% ~ 186%.

2 THE OVERVIEW OF FRP ANTI-BUCKLING REINFORCEMENT FOR STEEL MEMBERS TEST

2.1 Design of specimen

There are 3 important factors affecting bearing capacity and failure mode: slenderness ratio, constraint condition and end connection condition. In the test, 4 groups (different slenderness ratio, end connection condition) of

altogether 14 specimens were tried in three reinforcement plans, they are, core steel → external GFRP tube; core steel → bamboo casing → external longitudinal wrapping GFRP fabrics → local lateral GFRP at the centre and the end; core steel → external GFRP tube → high-strength non-shrinkage grout materials between the steel and GFRP tube. Details are shown in Table 1.

The length of the specimen is determined by the slenderness ratio (the ratio of elements effective length to the radius of gyration of the cross-section) of the steel compressive rod. The slenderness ratio requirement " $\lambda \leq 1$ " has been satisfied. We adopts "L-shaped" section, which has been commonly used in practical projects such as power tower, for the cross-section of the core steel, and two ways of joint connections, pinned end condition and non-pinned end condition. The inhibiting buckling members will only provide necessary anti-buckling constraints for the core steel rather than the limit of both lateral (cross-section direction) and longitudinal (length direction) stretching or shrinkage. The polyethylene film is used as a non-bonded structure between the core section of the core steel and external constraints, and no-stress-transfer (non-bonded) contact is adopted between the core steel and external filling materials as far as possible, so as that the external filling material only serves as constraints for the core steel.

2.2 Loading Protocol

We use monotonically and continuously loading protocol shown in Figure 2.

2.3 Test Measurement Protocol

In order to monitor force status and analyse loading mechanism, three displacement transducers are set on the specimen, two horizontally and one vertically. We also put 6 strain gauges on the surface of the core steel and 4 on the FRP tube. The measurements are: bearing capacity, load-displacement curves, the strain of the core steel and the FRP tube. The measurement protocol is shown in Figure 3. The load of hydraulic actuator is measured by transducers. All of the data are measured and monitored by IMP system.

3 ANALYSIS OF FAILURE CHARACTERISTICS AND MODES

In B1 series, the difference between B1-RT ($P_u=39.03\text{kN}$) and B1-T ($P_u=38.43\text{kN}$) is that, there is no GFRP fabric wrapping at the centre of the FRP tube, where the component have enough bearing capacity when the specimen failed ultimately. There is little difference of failure mode or ultimate bearing capacity between them, and compare to control specimen B1 ($P_u=27.51\text{kN}$), the ultimate bearing capacity are 41.88% and 39.70% higher. The ultimate bearing capacities of B1-TF ($P_u=47.08\text{kN}$) and B1-WF ($P_u=47.88\text{kN}$) are almost the same, which

Table 1 Parameters of the specimen

Specimen No.	Angle Size (mm)	Component length (mm)	Specimen reinforcement method	Slenderness	Notes
B1	L23×2	650	control specimen without reinforcement		
B1-RT	L23×2	650	GFRP tube outside (Ø38×3, length 600mm) at the end of the GFRP tube, 5-layer GFRP fabrics wrapping		
B1-T	L23×2	650	GFRP tube outside (Ø38×3, length 600mm) at the centre and end of the GFRP tube, 5-layer GFRP fabrics wrapping	141	
B1-TF	L23×2	650	GFRP tube outside (Ø38×3, length 600mm) at the centre and end of the GFRP tube, 5-layer GFRP fabrics wrapping filling the tube with high-strength non-shrinkage grout materials		non-pinned end conditions
B1-WF	L23×2	650	bamboo outside the steel core 10-layer GFRP fabrics wrapping around at the centre and end of the GFRP tube, 5-layer GFRP fabrics wrapping		
B2	L25×2	650	control specimen without reinforcement		
B2-T	L25×2	650	GFRP tube outside (Ø41×3, length 600mm) at the centre and end of the GFRP tube, 5-layer GFRP fabrics wrapping	141	
B2-TF	L25×2	650	GFRP tube outside (Ø41×3, length 600mm) at the centre and end of the GFRP tube, 5-layer GFRP fabrics wrapping filling the tube with high-strength non-shrinkage grout materials		
B3	L34×2.5	775	control specimen without reinforcement		
B3-T	L34×2.5	775	GFRP tube outside (52×2.5, length 725mm) at the centre and end of the GFRP tube, 5-layer GFRP fabrics wrapping	110	
B3-TF	L34×2.5	775	GFRP tube outside (52×2.5, length 725mm) at the centre and end of the GFRP tube, 5-layer GFRP fabrics wrapping filling the tube with high-strength non-shrinkage grout materials		pinned end conditions
B4	L34×2.5	1000	control specimen without reinforcement		
B4-T	L34×2.5	1000	GFRP tube outside (52×2.5, length 950mm) at the centre and end of the GFRP tube, 5-layer GFRP fabrics wrapping	141	
B4-TF	L34×2.5	1000	GFRP tube outside (52×2.5, length 950mm) at the centre and end of the GFRP tube, 5-layer GFRP fabrics wrapping filling the tube with high-strength non-shrinkage grout materials		

Notes: 1. The width of the GFRP fabrics at the center and end of the GFRP tube is equal to the outside diameter of the GFRP tube;

2. Radius of gyration adopts the reference value. Therefore the actual slenderness ratio is bigger than the calculation value. So we take the radius of gyration of L25×2 angle as the one of L23×2 angle in calculation.

are 71.14% and 74.05% higher than B1. Filling materials of the core steel have played a significant role in lateral constraints. The failure condition is shown in Figure 4 (a).

B2 series has basically the same effect as batch B1. B2 has higher ultimate bearing capacity than B1 because of the larger cross-section of the core steel. The ultimate bearing capacities of B2-T ($P_u=41.09\text{kN}$) and B2-TF ($P_u=51.83\text{kN}$) are 15.07% and 45.14% higher than the control specimen B2 ($P_u=35.71\text{kN}$). The photo-graphs show the failure condition in Figure 4 (b).

In comparison with B3 ($P_u=40.23\text{kN}$), the ultimate bearing capacity of B3-T ($P_u=57.50\text{kN}$) is 42.93% higher. Because of the sudden destruction after local instability, the ultimate bearing capacity of B3-TF ($P_u=50.62\text{kN}$) only increases 25.83% compared with B3, which relates to unideal end connection of the specimen. Too small space between the specimen end and the end plate limits free rotation of the specimen. The photographs show the failure condition in Figure 4 (b).

The ultimate bearing capacities of B4-T ($P_u=46.01\text{kN}$) and B4-TF ($P_u=66.72\text{kN}$) are 97.21% and 185.98% higher than that of the control specimen B2 ($P_u=23.33\text{kN}$).

In general, the failure mode of reinforced specimen has been changed from overall bending failure to local buckling failure at the end part. When the loading is removed, the elastic deformation of the control specimen (B1, B2 and B4), which experienced overall bending failure, recovered partially. The bearing capacity and ductility of reinforced specimen are improved, especially for the specimen filled with grout materials. Figure 5 shows the load - displacement curve in details.

4 CONCLUSIONS

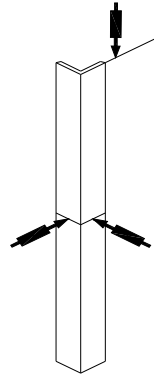
Through theoretical analysis and loading test of 14 specimens, we can draw initial conclusions as follows:

(1) The failure mode of reinforced specimens has been changed (all specimens after reinforcement were damaged because of local buckling at the end).

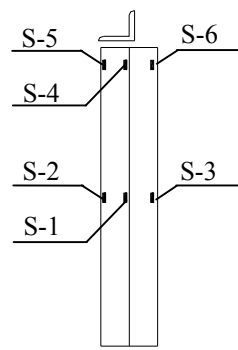


Figure 2 A view of test setup

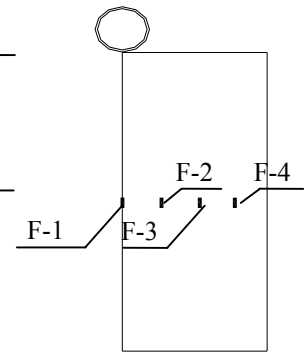
Displacement transducer



(a) displacement transducer



(b) strain gauge-angle



(c) strain gauge-FRP tube

Figure 3 Test measurement protocol



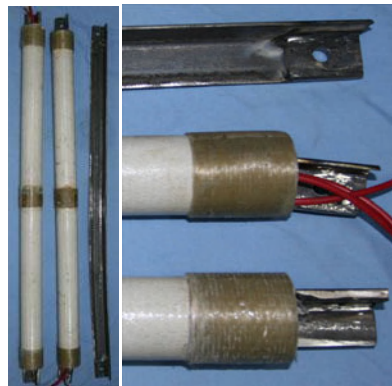
(a) B1 series (whole & end)



(b) B2 series (whole & end)



(c) B3 series (whole & end)



(d) B4 series (whole & end)

Figure 4 Photos of failure modes of specimens

(2) There is an improvement of bearing capacity and ductility of the reinforced specimen, which represents a large-scale advancement of deformability.

(3) The failure mode of reinforced specimens shows that the transition section and connecting section need to be strengthened. Only if the non-yielding constraint part and non-yielding no-constraint part keep elastic when destructed, can the steel core work effectively.

(4) When we carry through FRP anti-buckling reinforcement, we could enhance FRP fabrics at the centre and the end of the steel members. That will be an effective way of construction to avoid local failure.

(5) The equipments of FRP anti-buckling reinforcement for steel members are simple, and the technique is convenient and feasible, which can be a reference in engineering practice.

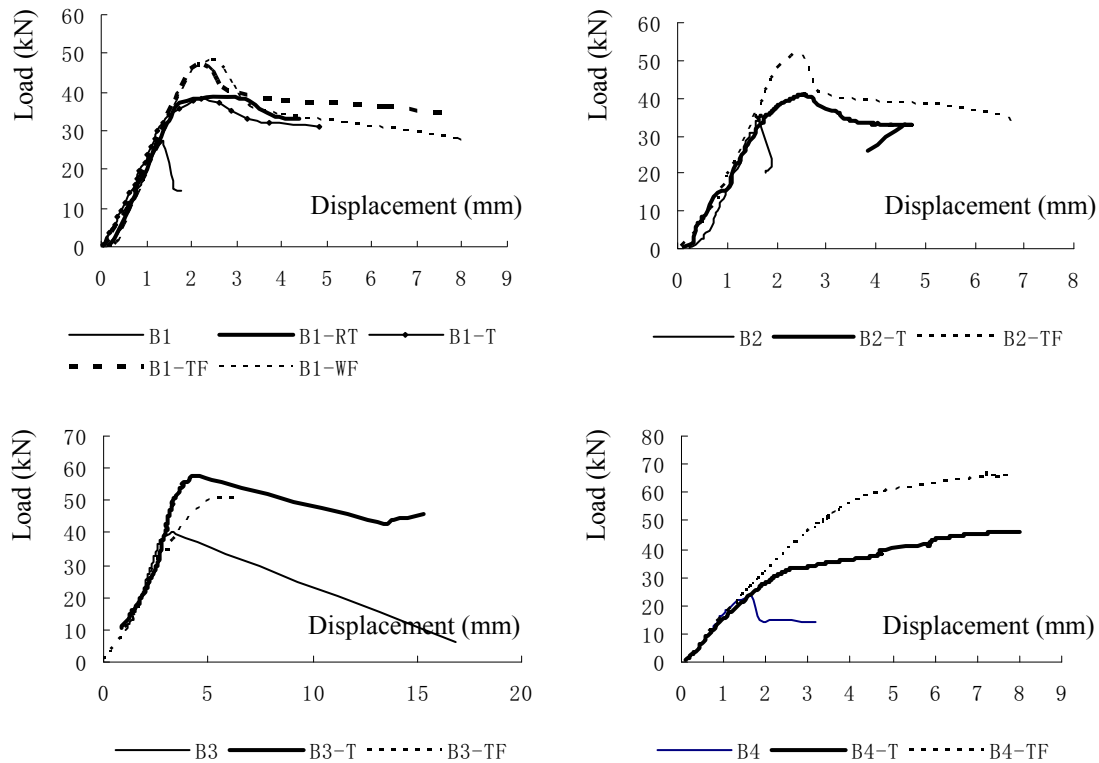


Figure 5 Comparison of the load-displacement curves

REFERENCE

- Ye Lieping, Feng Peng. Applications and development of fiber reinforced polymer in engineering structures [J]. China civil engineering journal, 2006, 39(3): 24-3. (In Chinese)
- Zhou Yun. Design and application of Buckling-Restrained Braces [M]. Beijing: China Architecture & Building Press.
- Cheng Guangyu, Ye Lieping, XU Xiuzhen, etc. Experimental researches on buckling-restrained brace [J]. Journal of Building Structure, 2008, 29(1): 31-39. (In Chinese)
- Cheng Guangyu, Ye Lieping, CUI Hongchao. Study on the design method of buckling-restrained brace [J]. Journal of Building Structure, 2008, 29(1): 40-48. (In Chinese)
- Qian Hongtao, Zhu Hongmin, Deng Xuesong. Progress in research and application on buckling restrained brace [J]. Journal of Disaster Prevention and Mitigation Engineering, 2007, 24(4): 225-233. (In Chinese)
- Gao Xiangyu, Du Haiyan, ZhangHui, etc. Experimental study on seismic performance of buckling-restrained brace made of Q235hot-rolled steel in China [J]. Journal of Building Structure 2008, 38 (3): 91-95. (In Chinese)
- Li Yan, Wu Bin, Wang Qianying, etc. An experimental study of anti-buckling steel damping-braces [J]. China civil engineering journal, 2006, 39(7): 9-14. (In Chinese)
- GB 50135-2006, Code for design of high-rising structures [S]. Beijing: China Architecture and Building Press, 2006. (In Chinese)
- Ekin Ekiz, Sherif EI-Tavil. Restraining steel brace buckling using a carbon fiber-reinforced polymer composite system: Experiments and computational simulation [J]. Journal of Composites for Construction, 2008, 12 (5): 562-569.
- Qian Peng. Research on FRP and FRP-aluminum alloy composite members under axial force [D]. Department of Civil Engineering Tsinghua University, 2006. (In Chinese)
- Cheng Guangyu. Study on energy-based seismic design methodology and application in steel braced frames [D]. Department of Civil Engineering Tsinghua University, 2007. (In Chinese)
- Ning Ma, Bin Wu, Junxian Zhao, etc. Full scale test of all-steel buckling restrained brace (C). The 14th World Conference on Earthquake Engineering, Beijing China, 2008.
- Zheng Yun, Ye Lieping, Yue Qingrui. Progress in research on steel structures strengthened with FRP [J]. Journal of Industrial Construction, 2005, 35 (8): 20-25. (In Chinese)
- Zhao X L, Zhang L. State-of-the-art review on FRP strengthened steel structures. ENGINEERING STRUCTURES, 2007, 29 (8): 1808-1823.
- Liu X D, Nanni A, Silva P F. Rehabilitation of compression steel members using FRP pipes filled with non-expansive and expansive light-weight concrete. ADVANCES IN STRUCTURAL ENGINEERING, 2005, 8(2): 129-142.

Effects of FRP Reinforcements on the Buckling and Reduced Stiffness Criteria of Compressed Steel Cylinders

Seishi Yamada (yamada@ace.tut.ac.jp), Krishna Kumar Bhetwal, Masayuki Yanagida & Yukihiro Matsumoto
Department of Civil Engineering, Toyohashi University of Technology, Toyohashi, Japan

ABSTRACT FRP laminated reinforced steel cylinders under compression have been studied in this paper. The effects of the thickness and fibre orientation of reinforcements as well as initial geometric imperfections on the buckling load carrying capacity and the associated buckling modes have been made clear through three kinds of analytical procedures; the conventional linear eigenvalue buckling analysis, the reduced stiffness buckling analysis and the fully nonlinear numerical experiments. These multiple treatments suggest obtaining valuable information for the design of FRP based hybrid structural elements having the complex buckling collapse behavior.

1 INTRODUCTION

For environmental issues, conventional civil structures have faced on the sustainable retrofit requirements. An alternative reinforcement using FRP would be much anticipated to apply on steel structure members on account of long-life usage. In this paper the reinforcement of steel cylindrical shell piers or tanks with CFRP has been dealt with, however, it has been well-known that the cylindrical shell is much affected by initial geometric imperfections (Yamada & Croll, 1999). In addition, the mechanical behavior of FRP shells is much dependent upon the fibre orientation. In this paper, the effects of reinforcement on the buckling collapse loads have been made clear using the conventional linear buckling theory, the reduced stiffness method (RSM) and the fully nonlinear numerical experiments.

2 METHOD OF ANALYSIS

As shown in Figure 1, a shell having length L , radius of curvature R , thickness t , is adopted and axial load P is adopted here. The coordinate of shell is taken as x, y and z and the corresponding displacement on the middle surface is adopted as u, v and w , respectively. The adopted simply supported boundary condition is

$$w = 0, \quad \partial^2 w / \partial x^2 = 0, \quad \partial u / \partial x = 0, \quad v = 0 \quad \text{at } x = 0, L \quad (1)$$

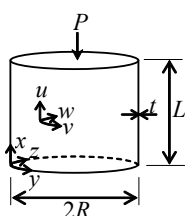


Figure 1 A cylindrical shell

As shown in Figure 2, an anisotropic orthogonal thin plate is considered in which x - y denotes the coordinate of thin cylindrical shell and 1-axis denotes the coordinates along fibre direction. Also, θ is taken as angle of fibre orientation with respect to x -axis. In this paper, material constants are obtained adopting Halpin-Tsai equation (Jones, 1999) as:

$$\begin{aligned} E_1 &= E_F V_F + E_P V_P \\ \mu_{12} &= \mu_F V_F + \mu_P V_P, & \mu_{21} &= \frac{E_2}{E_1} \mu_{12} \\ E_2 &= \frac{1 + \xi \eta_2 V_F}{1 - \eta_2 V_F} E_P, & \eta_2 &= \frac{E_F / E_P - 1}{E_F / E_P + \xi} \\ G_{12} &= \frac{1 + \xi \eta_{12} V_F}{1 - \eta_{12} V_F} G_P, & \eta_{12} &= \frac{G_F / G_P - 1}{G_F / G_P + \xi} \end{aligned} \quad (2)$$

where subscript F and P relate to fibre and polymer, respectively, V_F and V_P as volume fraction for fibre and polymer, respectively, E_1 as elastic coefficient and μ_{12} and μ_{21} as poison's ratios. Referring to Jones (1999), the elastic coefficient normal to the fibre E_2 is calculated taking $\xi = 1 + 40 V_F^{10}$ and the shear elastic coefficient G_{12} is obtained by using $\xi = 2$.

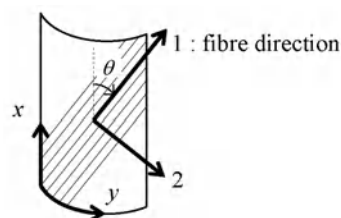


Figure 2 Definition of θ

From the reference (Yamada & Croll, 1999), displacement functions are taken as bi-harmonic function u, v and w , can be written as:

$$\begin{aligned} u &= u_{i,j} \cos(iy/R) \cos(j\pi x/L) \\ v &= v_{i,j} \sin(iy/R) \sin(j\pi x/L) \\ w &= w_{i,j} \cos(iy/R) \sin(j\pi x/L) \end{aligned} \quad (3)$$

where $u_{i,j}$, $v_{i,j}$ and $w_{i,j}$ are amplitudes; i and j are respectively the circumferential full-wave number and the longitudinal half-wave number.

The strains of an arbitrary point ($\bar{\varepsilon}_x, \bar{\varepsilon}_y, \bar{\varepsilon}_{xy}$) may be divided as the membrane strain components ($\varepsilon_x, \varepsilon_y, \varepsilon_{xy}$) and the bending strain components ($\kappa_x, \kappa_y, \kappa_{xy}$) defining that the superscript d and dd are strain components for first and second order of each displacement.

$$\begin{aligned} \bar{\varepsilon}_x &= \varepsilon_x + z\kappa_x, \quad \bar{\varepsilon}_y = \varepsilon_y + z\kappa_y, \quad \bar{\varepsilon}_{xy} = \varepsilon_{xy} + z\kappa_{xy} \\ \varepsilon_x &= \varepsilon_x^d + \varepsilon_x^{dd}, \quad \varepsilon_y = \varepsilon_y^d + \varepsilon_y^{dd}, \quad \varepsilon_{xy} = \varepsilon_{xy}^d + \varepsilon_{xy}^{dd} \\ \kappa_x &= \kappa_x^d, \quad \kappa_y = \kappa_y^d, \quad \kappa_{xy} = \kappa_{xy}^d \end{aligned} \quad (4)$$

The strain-displacement relationships (Yamada & Croll, 1999) are of the DMV-type as:

$$\begin{aligned} \varepsilon_x^d &= \frac{\partial u}{\partial x}, \quad \varepsilon_y^d = \frac{\partial v}{\partial y}, \quad \varepsilon_{xy}^d = \frac{1}{2} \left(\frac{\partial u}{\partial y} + \frac{\partial v}{\partial x} \right) \\ \varepsilon_x^{dd} &= \frac{1}{2} \left(\frac{\partial w}{\partial x} \right)^2, \quad \varepsilon_y^{dd} = \frac{1}{2} \left(\frac{\partial w}{\partial y} \right)^2, \quad \varepsilon_{xy}^{dd} = \frac{1}{2} \frac{\partial w}{\partial x} \frac{\partial w}{\partial y} \\ \kappa_x^d &= -\frac{\partial^2 w}{\partial x^2}, \quad \kappa_y^d = -\frac{\partial^2 w}{\partial y^2}, \quad \kappa_{xy}^d = -\frac{\partial^2 w}{\partial x \partial y} \end{aligned} \quad (5)$$

The constitutive relation for general anisotropic laminated plates is well-known to be able to be written by dividing the components as the following equation (Vinson, J.R & Sierakowski, R.L. 1986).

$$\begin{Bmatrix} n_x \\ n_y \\ n_{xy} \\ m_x \\ m_y \\ m_{xy} \end{Bmatrix} = \begin{bmatrix} A_{11} & A_{12} & 0 & B_{11} & B_{12} & 0 \\ A_{12} & A_{22} & 0 & B_{12} & B_{22} & 0 \\ 0 & 0 & A_{66} & 0 & 0 & B_{66} \\ B_{11} & B_{12} & 0 & D_{11} & D_{12} & 0 \\ B_{12} & B_{22} & 0 & D_{12} & D_{22} & 0 \\ 0 & 0 & B_{66} & 0 & 0 & D_{66} \end{bmatrix} \begin{Bmatrix} \varepsilon_x \\ \varepsilon_y \\ 2\varepsilon_{xy} \\ \kappa_x \\ \kappa_y \\ 2\kappa_{xy} \end{Bmatrix} \quad (6)$$

Since the present paper adopts symmetric lamination, all the components of B_{ij} are equal to zero. To provide the systematic framework for the interpretation of buckling behavior and for convenient analytical modeling, the principle of total potential energy is adopted to formulate the equations of equilibrium. Then, the linear buckling analysis for initially perfect shells can be obtained by energy components of equation as:

$$\delta \Pi_2 = \delta \left[U_{2mm} + U_{2bb} + P_c \frac{\partial (V_{2m}^x + V_{2m}^y)}{\partial P} \right] = 0 \quad (7)$$

where P_c = linear buckling load; U_{2bb} and U_{2mm} = bending and membrane energies, respectively; V_{2m}^x and V_{2m}^y = linearized membrane energies.

On the other hand, the RSM can be introduced for predicting the reduction due to imperfections. The RSM is based upon the observation that it is the components of the initial membrane stiffness, or energy that are lost

in the unstable postbuckling of shells (Croll 2006). This risk membrane energy has been eliminated by linear buckling analysis (Sosa, et al., 2006). Yamada & Croll (1999) on RSM for axial compressed cylinders has shown that U_{2bb}, U_{2mm} and V_{2m}^y in Eq.7 are positive, while V_{2m}^x is negative. That is, V_{2m}^x contributes the destabilizing component in the buckling and the following equation can be adopted here,

$$\delta \left[U_{2bb} + P_c^* \left(\frac{\partial V_{2m}^x}{\partial P} \right) \right] = 0 \quad (8)$$

On the other hand, for fully nonlinear experiments the displacement functions u, v and w shown in Eq.9 can be adopted as the linear sum of bi-harmonic functions which satisfy the boundary condition of Eq. 1.

$$\begin{aligned} u &= \sum_{i=0,b,2b,3b}^{J_u} \sum_j u_{i,j} \cos(iy/R) \cos(j\pi x/L) \\ v &= \sum_{i=b,2b,3b}^{J_v} \sum_j v_{i,j} \sin(iy/R) \sin(j\pi x/L) \\ w &= \sum_{i=0,b,2b}^{J_w} \sum_j w_{i,j} \cos(iy/R) \sin(j\pi x/L) \end{aligned} \quad (9)$$

The present nonlinear experiments need to use the initial imperfection w^0 as shown in Eq.10; its circumferential wave number b varies, while its axial half wave number f is adopted to be of single mode $f=1$.

$$w^0 = w_{b,f}^0 \cos(by/R) \sin(f\pi x/L) \quad (10)$$

3 RESULTS AND DISCUSSION

To illustrate the behavior of reinforced shells, the geometric parameters are adopted as $t_s = 4\text{mm}$ for only steel wall thickness, $L/R = 0.512$, $R/t_s = 405$, $E_s = 205\text{GPa}$, $E_F = 235\text{GPa}$, $\mu_s = 0.3$, $\mu_F = 0.3$ and $\mu_P = 0.34$. The adopted lamination in the present study is shown in Figure 3 having outer and inner plane reinforced by the CFRP material. The parametric experiments with CFRP plates having total thickness 0, 1, 2 and 4 mm in varying angle of fibre orientation have been carried out to predict the effect of reinforcement.

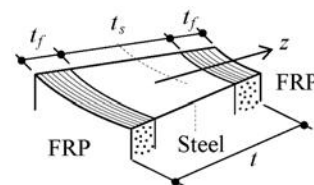


Figure 3 Lamination of steel and FRPs

In Figures 4 and 5 the linear buckling loads are shown by upper spectrum of curves; the horizontal axis indicating the circumferential full-wave number i . The linear buckling loads with varying longitudinal half-wave number j are defined as $P_{cm,j}$. Then the corresponding

circumferential full-wave number is obtained as, $i_{cm}(j)$. After that, its RS critical load associated with, $i_{cm}(j)$ ($\cong 2$) for axi-symmetric shell buckling), is calculated as $P_{cm,j}^*$. Consequently, from all the calculated $P_{cm,j}^*$, the minimum value can be selected as defining the RS criterion P_{cm}^* as depicted on Figures 4 and 5. Figure 4 for isotropic steel cylinders indicates $P_{cm}=12.47$ MN for $j=1,2,3,4,\dots$ associating with *Koitor circle* (Koiter, 1963), but $P_{cm}^*=3.385$ MN for mode $(i_{cm}, j_{cm}) = (13.7, 1)$. On the other hand, Figure 5 for $t_f = 4$ mm reinforced orthotropic cylinders indicates $P_{cm} = 17.56$ MN for $(i_{cm}, j_{cm}) = (13.1, 5)$ and $P_{cm}^* = 6.88$ MN for $(i_{cm}, j_{cm}) = (11.1, 1)$.

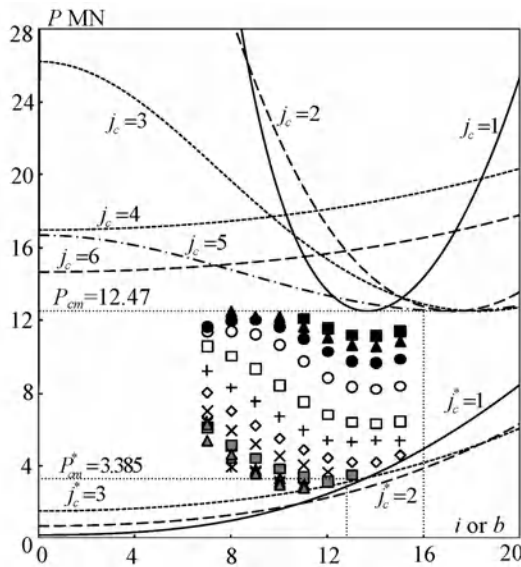


Figure 4 Buckling load spectra for $t_f=0$

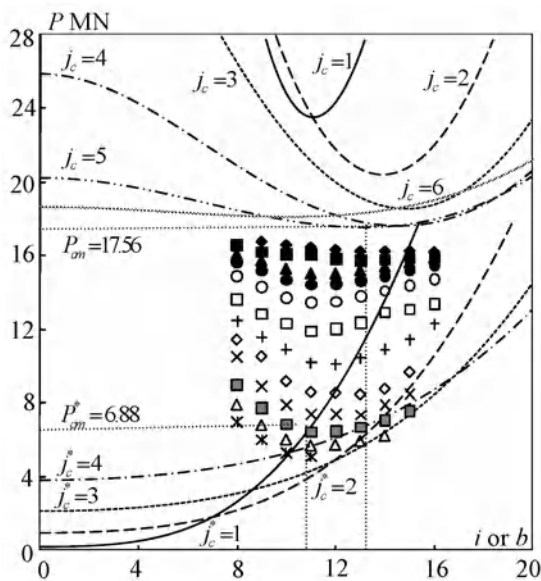


Figure 5 Spectra for $t_f=4$ mm and $\theta=90^\circ$

In Figure 6, the heavy solid line represents the minimum linear buckling load P_{cm} , the thinner solid line the RS critical load P_{cm}^* . The linear buckling load P_{cm} becomes optimum at an angle of fibre orientation 35° and as the

results of nonlinear numerical experiments for angle of fibre orientation $20^\circ, 35^\circ$ and 70° , the imperfect shell buckling loads (P^N) and the RS critical loads are approximately the same for the imperfection amplitude $w_{b,1}^0 = (1.0 \sim 1.2) \times t_s$.

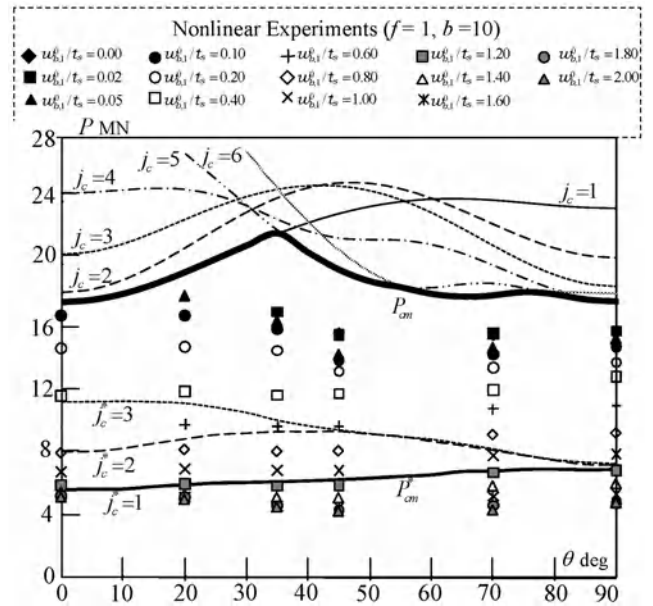


Figure 6 Effects of fibre orientation for $t_f=4$ mm

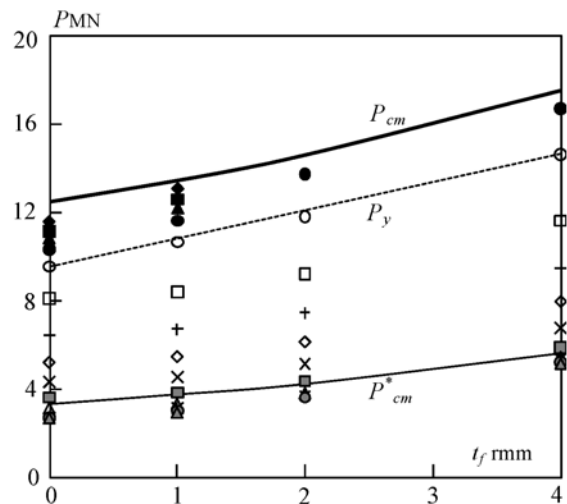


Figure 7 Various buckling criteria for $\theta=0^\circ$

Figures 7 and 8 represent the relationship between buckling loads and the thickness of fibre t_f for angle of fibre orientation $\theta=0^\circ$ and 90° . The heavy solid line denotes the linear buckling P_{cm} , the dotted line denotes the steel yield load P_y , which has been obtained from $\sigma_y=235$ N/mm² and E_S ; the slight solid line is the RS P_{cm}^* . In the case of $\theta=0^\circ$, the cylinders having $w_{b,1}^0/t_s < 0.2$, the steel wall is expected to yield first ($P_{cm} \geq P^N \geq P_y$). But the elastic buckling for $w_{b,1}^0/t_s > 0.2$ is shown to occur first ($P^N < P_y$) as suggested in Figure 7. In the case of $\theta=90^\circ$, P_y increases a little as t_f increases, then the more large imperfection amplitudes are needed

for the occurrence of elastic buckling. However, the result $P_{cm}^* < P_y$ by RS analysis suggests that the elastic buckling for moderately large imperfect shells in the use of practical civil engineering structures will occur first rather than material damage induced collapse.

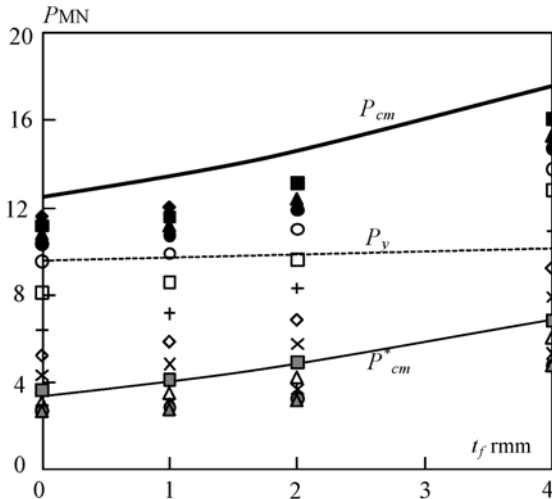


Figure 8 Various buckling criteria for $\theta = 90^\circ$

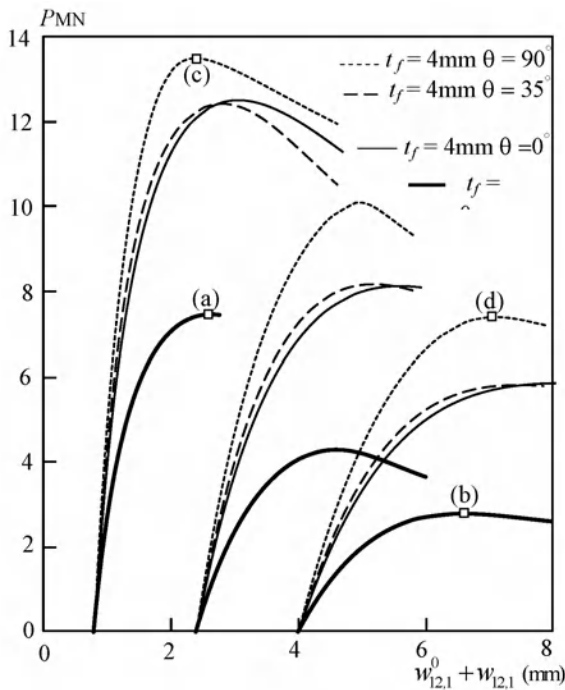


Figure 9 Load-deflection curves

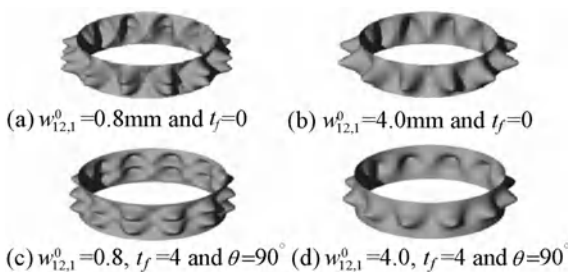


Figure 10 Incremental displacement modes for $t_f = 4\text{mm}$

Figure 9 shows the present numerical experimental examples of load-deflection curves in the case of circumferential full-wave number $b = 12$ in adopted imperfection; the imperfection amplitudes are 0.8mm, 2.4mm and 4.0mm. The heavy solid lines are of no reinforced condition. The slight solid lines denotes for reinforcement $t_f = 4\text{mm}$ having $\theta = 0^\circ$, similarly, broken lines for $\theta = 35^\circ$ and dotted lines for $\theta = 90^\circ$ for $t_f = 4\text{mm}$ reinforced condition. Figure 10 shows the incremental displacement as the buckling modes for linear buckling analysis in the case of the imperfection amplitude $w_{12,1}^0 = 0.8\text{mm}$ and 4.0mm. From this figure, it can be understood that the axial wavelength becomes longer when initial imperfection amplitude increases and there is little influence of reinforcement in the present numerical experimental models.

Table 1 Critical loads given by the associated axial half-wave and circumferential full wave numbers

t_f	$\theta = 0^\circ$						$\theta = 90^\circ$					
	Linear			RS			Linear			RS		
i_{cm}	j_{cm}	P_{cm}	i_{cm}^*	j_{cm}^*	P_{cm}^*	i_{cm}	j_{cm}	P_{cm}	i_{cm}^*	j_{cm}^*	P_{cm}^*	
0	17.2	4	12.47	13.7	1	3.35	17.2	4	12.5	13.7	1	3.35
1	17.2	4	13.44	13.7	1	3.78	16.8	4	13.4	13.0	1	4.03
2	13.6	1	14.59	13.6	1	4.24	14.0	5	14.6	12.3	1	4.86
4	13.4	1	17.52	13.4	1	5.61	13.1	5	17.6	11.1	1	6.88

4 CONCLUSION

In this paper, CFRP laminated reinforced steel cylinders under compression have been considered and the linear buckling analysis and the innovative RS critical analysis and the fully nonlinear numerical experiments have been carried out and the comparison among these various analytical results has been discussed. It has been shown that the initial imperfection sensitivity is very dependent upon the lamination and the angle of fibre orientation. Buckling load carrying capacity increases from 40%~100% for the lamination thickness $t_f = 4\text{mm}$, but this amount and the associated buckling mode vary in accordance with the angle of fibre orientation.

REFERENCES

Croll, J.G.A 2006. Stability in shells, *Nonlinear Dynamics*, Vol.43, 17-28.

Koiter, W.T. 1963. The effect of axisymmetric imperfections on the buckling of cylindrical shells under axial compression, *Koninkl. Ned Akad. Wetenschap., Proc., B*, Vol.66, 265-279.

Jones, R.M. 1999. *Mechanics of Composite Materials*, 2nd Ed., Taylor & Francis.

Sosa, E.M., et al. 2006. Computation of lower-bound elastic buckling loads using general-purpose finite element codes, *Computers and Structures*, Vol.84, 1934-945.

Vinson, J.R & Sierakowski, R.L. 1986. *The Behavior of Structural Composed of Composite Materials*, Martinus Nijhoff Publishers.

Yamada, S. & Croll, J.G.A. 1999. Contributions to understanding the behavior of axially compressed cylinders, *Journal of Applied Mechanics*, ASME, Vol.66, 299-309.

Numerical Simulation of Prestressed CFRP Plate Strengthened Steel-Concrete Composite Girders

Pouya Zangeneh, Hamid Y. Omran, & Raafat El-Hacha (relhacha@ucalgary.ca)

Department of Civil Engineering, University of Calgary, Calgary, Alberta, Canada

ABSTRACT This paper presents the results of Finite Element (FE) modeling of flexural behavior of steel-concrete composite girders strengthened with prestressed Carbon Fiber Reinforced Polymer (CFRP) plate. To the best knowledge of the authors, this is the first numerical modeling of such application with prestress available in the literature. The level of prestressing that is used to validate the model is 12% of the ultimate tensile strength of the CFRP plate and it is based on the results of an experimental study conducted at University of Calgary on the same large-scale beam tested in bending under monotonic static loading. Comparison shows a very good agreement between the numerical and the experimental results. After validation of the model, a parametric study using different prestressing levels is conducted and the effects of increasing the prestress level on ductility index, yield and ultimate loads are presented.

1 INTRODUCTION

The use of Fiber Reinforced Polymers (FRPs) in concrete structures has grown widely since 1970s. Because of their special properties such as high-strength-to-weight ratio, corrosion resistance, etc... FRPs have got their way to steel structures as well. The cost of FRPs is between 4 and 20 times of steel in terms of unit volume. However, each 2 kg of FRPs materials is equivalent to 47 kg of steel in terms of equal strength (Hollaway & Cadei 2002).

Many researchers investigated the advantages of using FRPs in retrofitting and strengthening of steel structures in various ways. Such investigation included the repair of artificially damaged beams with FRP materials (Al-Saidy et al. 2004), strengthening of over loaded and undamaged steel structures (Tavakkolizadeh & Saadatmanesh 2003). Recently, Ragab (2007) tested investigated the efficiency of various FRP materials to strengthen steel-concrete composite beams. These materials include CFRP sheets, intermediate modulus CFRP plates, high modulus CFRP plates, ultra high modulus CFRP plates and Steel Fiber Reinforced Polymer sheets. Aly (2007) investigated the effect of prestressing in strengthening steel-concrete composite beams using CFRP and SFRP with different prestressing levels.

Rizkalla et al. (2008) reported that prestressing the strengthening material dramatically improve the efficiency of this system. The effect of prestressing was compared with nonprestressed strengthened steel beams (Schnersch et al. 2005).

There was not so much effort in numerically modeling of FRP strengthened steel. Fawzia et al., (2006) numerically modeled series of double strap joints in tension to investigate the bond characteristics between the FRP, epoxy and the steel. Colombi and Poggi (2006) tested four 2.5 meter long strengthened steel beams in three points bending configuration then validated the test with a 2D finite element model.

To the best knowledge of the authors there is no record in the literature of full 3D numerical modeling of prestressed FRP for strengthening steel-concrete composite girders. The objective of this research is to develop a 3-D FE model and validate it with the experimental results, and conduct a parametric study. Three beams were strengthened with prestressed CFRP plate were modeled using 3-D FE package ANSYS and validated with the experimental results obtained by tested by Aly (2007) (Omran et al., 2009). In this paper, using the validated model, a parametric study was conducted on one of these beams.

2 EXPERIMENTAL PROGRAM AND MATERIAL PROPERTIES

Similar steel-concrete composite girders tested by Ragab (2007) using non-prestressed CFRP plate were tested by Aly (2007) using prestressed CFRP plate. The beams were 6000mm long (Figure 1) and tested under four point bending configuration with different prestress levels and FRP materials. The steel beams were W200×19 (G40.21-M350W) hot rolled section with a yield stress, ultimate

stress, Young’s Modulus and ultimate strain determined from the tension tests were 352MPa, 454.3MPa, 200GPa, and 0.1085, respectively (Aly, 2007). The reinforced concrete slab was 56 mm thick and 435mm wide, with a designed target compressive strength of 40MPa. The actual concrete compressive strength was reported as 47.92MPa, with modulus of elasticity and modulus of rupture are 31150.9MPa and 4.15MPa as determined according to (CSA A23.3-04, 2004). The Poisson ratio of the concrete was taken as 0.18 for all the models. The cross section of the steel welded wire mesh was 13.3mm², with the Modulus of elasticity, yield and ultimate stresses of 200GPa, 400MPa, and 410MPa, respectively. As determined from the tension tests, the CFRP plate has a Young modulus, tensile strength and ultimate tensile strain of 153752 MPa, 2565 MPa and 0.0177, respectively (Ragab, 2007). The beam investigated in this study was strengthened with one layer of CFRP plate with 1.2mm thickness and 80mm width. The CFRP plate was prestressed to 12% of its ultimate tensile strength equivalent to 307MPa initial stress or total prestressing force of 30kN. The epoxy used to bond the CFRP plate to the bottom steel flange had a Modulus of elasticity of 4500MPa, with a tensile strength of 24MPa and Poisson ratio of 0.37 as reported by the manufacturer.

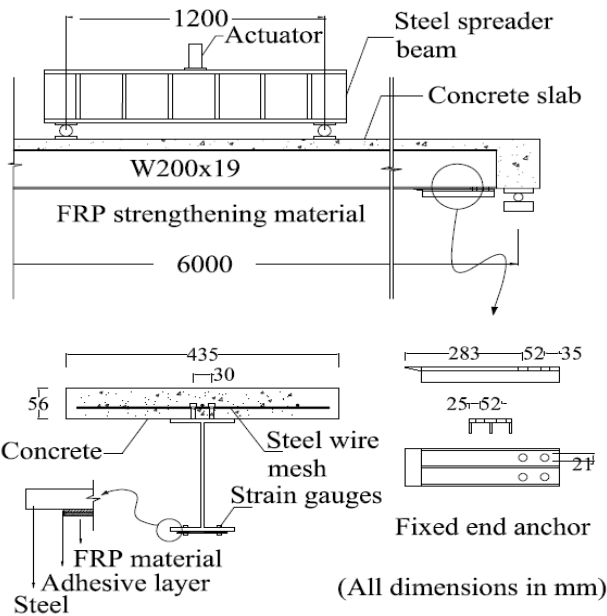


Figure 1 Geometry of the modeled beams

3 FINITE ELEMENT MODELING

The 3-D finite element modeling was carried using ANSYS software (SAS 2004). Modeling the prestress is one of the important objectives of this research. The model has been managed to reflect the effect of prestressing as close as possible by choosing different types of elements and with extensive trial and error procedure. Prestressing is performed by assigning initial

stress on the steel beam represented by Solid45 element. Due to the symmetry of the beam and the testing system about the longitudinal and normal axes, for reducing the computational effort and hence increasing the accuracy, only 1/4 of the actual beam was modeled (Figure 2).

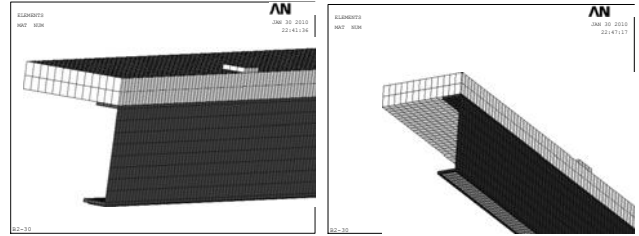


Figure 2 Final 3D FE model of one fourth of the actual beam with total number of 12510 elements

All materials have been assumed to be isotropic and homogenous, since the strengthening materials are only being utilized in the axis of their fibers. Due to the sufficient number of shear connectors used to connect the concrete slab to the steel top flange perfect bond between the concrete and the steel was assumed. This assumption has also been taken into account for the interfaces between the CFRP plate and adhesive and steel since no slippage or debonding has been observed in during the test.

The Solid65 element was used to properly model the concrete; this element is capable of cracking and crushing but for proper modeling of concrete a multi-linear behavior for concrete has been defined. A simplified multi-linear stress strain curve for concrete has been adopted (MacGregor 1992). The schematic diagram of this multi-linear stress strain curve with the properties of the modelled beam (designated as B2-30 in the test) is shown in Figure 2.

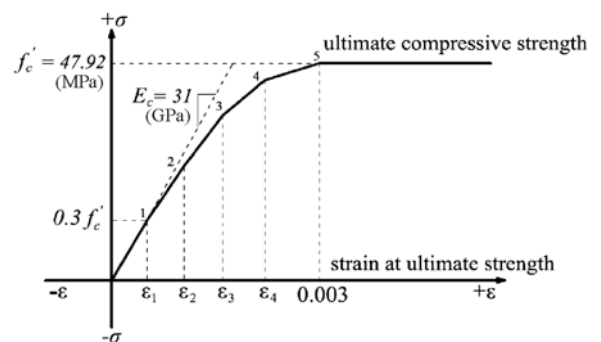


Figure 3 Multi-linear concrete stress-strain curve with properties of the beam B2-30

Steel, CFRP and adhesive layer as well as steel anchorage system have been modeled with Solid45 element with their material properties. Steel has been considered to be a multi-linear material with much lower modulus of elasticity after yielding, to account for

the strain hardening. The CFRP plate was modeled as linear elastic material until failure. Steel wire mesh has been modeled with Link8 element. Loading was applied in three steps, i) from release point to the initial prestress force, ii) from prestressing to yielding, and iii) and from yielding to failure. This resulted in sufficient accuracy needed at in the nonlinear stage of modeling. The failure criteria have been specified by the material properties, either the CFRP plate reaches its ultimate tensile strength or the concrete reaches strain of 0.003 first.

4 RESULTS

Figure 4 shows a comparison between the load midspan deflection from the FE model and the experimental result. The effect of self-weight has been investigated and shows a slight difference as expected which can be neglected. The model shows perfect agreement with the experiment. The negative deflection at zero loads represents the upward camber due to prestressing. Table 1 shows the cardinal points of the load deflection curves of the beam. The small % of error especially for the ultimate load shows that the model is valid. The maximum error observed is for the ultimate deflection as expected since the deflection measurements might not be accurate at that point. The failure mode is the same between the model and experiment. It should be noted that the validation of the model has been verified with 5 other experimental tests (Omran et al. 2009). Figure 5 shows good correlation of strain profile along the length of the beam between the FE model and the experimental results.

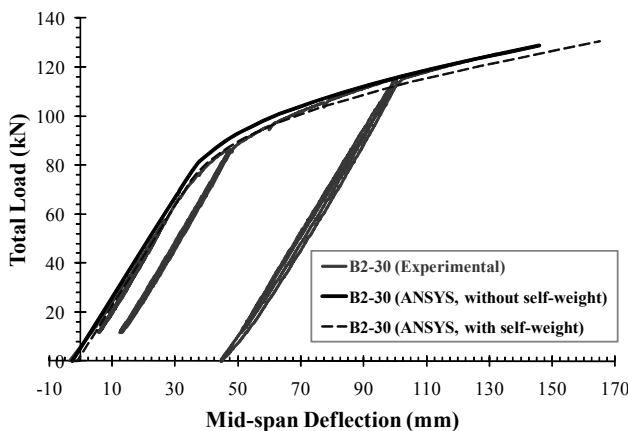


Figure 4 Load deflection curve of the CFRP modeled beam

Table 1 Cardinal point of the FE model results v.s experiment

Beam	Method	Δ_o (mm)	P_y (kN)	Δ_y (mm)	P_u (kN)	Δ_u (mm)	Failure
	Test [†]	-3.38	78.3	37.78	125.2	132.59	CC*
B2-30	ANSYS	-2.64	77.9	35.65	128.8	145.87	CC
	Error %	21.8	0.4	5.64	2.9	10.02	

P_y and Δ_y = load and deflection at yielding *CC: concrete crushing
 P_u and Δ_u = load and deflection at ultimate [†]Aly (2007)

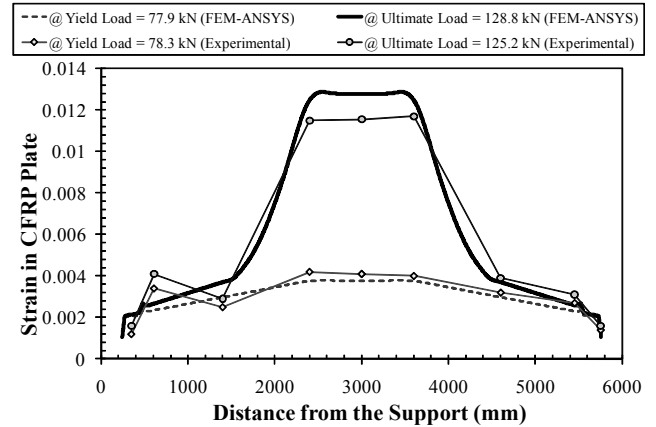


Figure 5 Strain profile along the length of CFRP plate for B2-30

5 PARAMETRIC STUDY

Based on the validated model, a parametric study was conducted to investigate the behavior of the strengthened beams with 5 different prestressing levels taken as percentage of the ultimate tensile strength of the CFRP material and compared to un-strengthened beam. For the purpose of this study the concrete strength of all the beams was assumed to be 40MPa with the modulus of elasticity and modulus of rupture equal to 28460MPa and 3.79MPa, respectively. The results are presented in Table 2 and Figure 6. The load deflection curve of the modeled beams tends to rich higher yield and ultimate load as the prestress level increases, while the ultimate deflection decreases gradually (Figure 6). However, the area under the curves, which represents the amount of energy absorption, remained almost constant (average value of 13334kN.m with a -1.0 to 1.3% error between all curves). This is attributed to the fact that the camber the beams experience due to the prestressing force, shifts the curves to the left as the prestressing force increases which decreases with the ultimate deflection (Figure 6). The parametric study showed that as the prestressing level increases the ductility index decreases (Figure 7), while the yield and ultimate loads increase (Figure 8). The improvement in the yield load was more pronounced than the ultimate load. The ductility of the unstrengthened beam is almost the same as the nonprestressed strengthened beam and the variation of the ductility index between the modeled beams with different prestressing level is insignificant.

Table 2 Results of the parametric study

Beam ID	P_i (kN)	Δ_o (mm)	P_y (kN)	Δ_y (mm)	P_u (kN)	Δ_u (mm)	μ
B0-000	N/A	0	68.0	36	93.7	149	4.10
B2-000	0	0	72.8	37	122.0	151	4.11
B2-200	7.8	1.73	76.7	37	124.3	147	3.96
B2-400	15.6	3.46	81.7	38	127.3	145	3.79
B2-600	23.4	5.20	83.2	37	129.3	139	3.75
B2-800	31.2	6.93	86.8	37	132.4	137	3.70

P_i initial prestress level (Percentage of CFRP ultimate strength)
 μ = ductility index, calculated as Δ_u/Δ_y

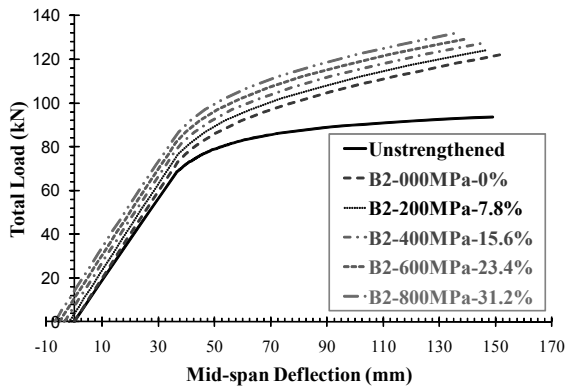


Figure 6 Load midspan deflection from the parametric study with different % of prestressing vs. the un-strengthened beam

Therefore, if someone is looking at determining the optimum prestressing level in order to maintain the beam’s original ductility before strengthening and at the same time taking advantage of the prestressing effect applied to the system, will find that this corresponds to a prestressing level equal to zero. Therefore, increasing the prestressing level does not have an impact on the ductility index, while it significantly increases the yield and ultimate loads.

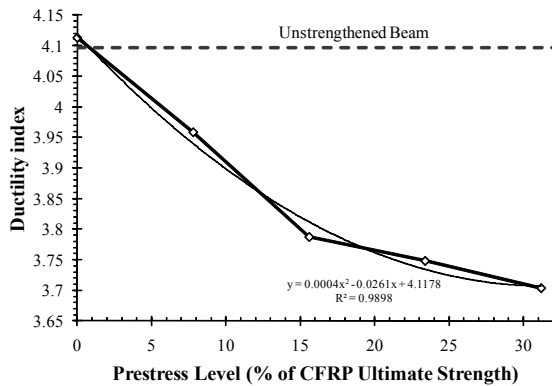


Figure 7 Variation of the ductility index vs. prestressing level

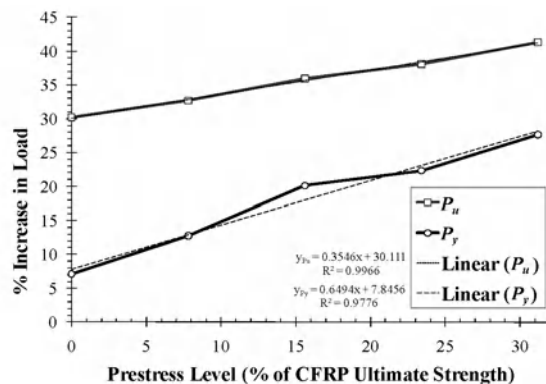


Figure 8 Variation of the percentage of increase in ultimate and yield loads vs. the prestressing level

6 CONCLUSIONS

A FE model for predicting the flexural behavior of steel-concrete composite beams strengthened with prestress

CFRPs was developed and validated with the experimental results. Prestressing effect has been modeled properly with initial stress being assigned on the bottom flange of the steel beam along with the reported combination of elements. A parametric study was conducted using the validated FE model. Results showed increase in the ultimate and yield loads as the prestressing percentage increases, whilst the ductility index tends to decrease. However, the amount of energy absorption remained almost constant, independent of the prestressing level. Further studies are undergoing on different prestressing levels, various amounts and types of FRP materials.

REFERENCES

Al-Saidy, A.H., Klaiber, F.W. & Wipf, T.J. 2004, Repair of Steel Composite Beams with Carbon Fiber-Reinforced Polymer Plates, *Journal of Composites for Construction*, vol. 8, no. 2, pp. 163-172.

Aly, M. 2007, *Strengthening of steel-concrete composite girders using prestressed fiber reinforced polymer*, University of Calgary (Canada).

Canadian Standards Association 2004, *Design of Concrete Structures CSA A23.3-04*, Canadian Standards Association, Toronto, ON, Canada.

Colombi, P. & Poggi, C. 2006, An experimental, analytical and numerical study of the static behavior of steel beams reinforced by pultruded CFRP strips, *Composites Part B: Engineering*, Vol. 37, No. 1, pp. 64-73.

Fawzia, S., Al-Mahaidi, R. & Zhao, X. 2006, Experimental and finite element analysis of a double strap joint between steel plates and normal modulus CFRP, *Composite Structures*, Vol. 75, No. 1-4, pp. 156-162.

Hollaway, L.C. & Cadei, J. 2002, Progress in the technique of upgrading metallic structures with advanced polymer composites, *Progress in Structural Engineering and Materials*, Vol. 4, No. 2, pp. 131-148.

MacGregor, J.G. 1992, *Reinforced Concrete Mechanics and Design*, Prentice-Hall Inc, Englewood Cliffs, NJ, USA.

Omrán, H.Y., Zangeneh, P. & R. EL-Hacha, R., Finite element modelling of steel-concrete composite beams strengthened with prestressed CFRP plate, *Asia Pacific Conference on FRP in Structures*, Seoul, Korea, Dec. 9-11, 2009, CD-Rom 6p.

Ragab, N. 2007, *Strengthening of steel-concrete composite girders using various advanced composite materials*, University of Calgary (Canada).

Rizkalla, S., Dawood, M. & Schnerch, D. 2008, Development of a carbon fiber reinforced polymer system for strengthening steel structures, *Composites Part A: Applied Science and Manufacturing*, Vol. 39, No. 2, pp. 388-397.

SAS 2004, *ANSYS 9 Finite Element Analysis System manual*, SAS IP, Inc. SAS IP, Inc.

Schnerch, D., Dawood, M., Sumner, E. & Rizkalla, S. Behavior of steel-concrete composite beams strengthened with unstressed and prestressed high-modulus CFRP strips, *Fourth Middle East Symposium on Structural Composites for Infrastructure Applications*, Alexandria, Egypt, May 20-23, 2005, 13p.

Tavakkolizadeh, M. & Saadatmanesh, H. 2003, Strengthening of steel-concrete composite girders using carbon fiber reinforced polymers sheets, *Journal of Structural Engineering*, Vol. 129, No. 1, pp. 30-40.

Experimental Study on Fatigue Behavior of I-Steel Beam Strengthened with Different FRP Plates

Gang Wu (g.wu@seu.edu.cn) & Haiyang Liu & Zhishen Wu & Haitao Wang

International Institute for Urban Systems Engineering, Southeast University, Nanjing, 210096, China

ABSTRACT Fatigue experiments of eight I-steel beams strengthened with different fiber reinforced polymer (FRP) plates are presented in this paper. The experimental results show that, (1) under the principle of equivalent axial tensile stiffness of different types of FRP plates, the fatigue life of strengthened steel beam could be increased by 3.33-5.26 times over un-strengthened steel beam, while the fatigue life of steel beam strengthened with welding steel plate increased by 1.74 times; (2) Application of FRP plates can significantly reduce the crack growth rate, prolong the fatigue life and even change the fatigue failure mode of I-steel beams compared with welding steel plates; (3) The CFRP plate with high modulus was found to be the most efficient strengthening way; (4) It was also observed that the interfaces treating method and the plate configuration have considerable influence on the fatigue life.

1 INTRODUCTION

Due to the light weight, high strength, good durability, excellent fatigue performance and convenient construction, fiber reinforced polymer (FRP) is widely used for the repair and strengthening of concrete structures and bridges. In recent years, some researchers have also investigated the use of bonded carbon FRP materials for the repair and strengthening of steel structures and bridges. Most studies were focused on static capacity of strengthened members, and researches on fatigue behavior are very limited especially comparative researches on fatigue behavior of steel beams strengthened with different materials. Tavakkolizadeh & saadatmanesh (2003) studied fatigue strength of 21 notched specimens made of S127×4.5 A36 steel beams. The steel beams were tested under four point bending with the loading rate of between 5 and 10 Hz and different constant stress ranges between 69 and 379 MPa. The results showed that the CFRP patch not only tends to extend the fatigue life of a detail more than three times, but also decreases the crack growth rate significantly. Researches conducted by Liu et al. (2009) illustrated that the double-sided repair scheme increased the fatigue life by 2.2-2.7 times over un-patched steel plates when normal modulus CFRP sheets were used, and by 4.7-7.9 times when high modulus CFRP sheets were used. The high modulus CFRP sheets were found to be much more efficient. Bond width has a considerable influence on the crack growth life. Furthermore the parameters of patch thickness, patch length and patch configuration had more influence on single-sided repairs than on double-sided repairs. Bassetti et al. (2000) reported that prestressing CFRP patches prior to installation

can help promote crack-closure effects and further prolong the fatigue life of cracked steel members.

Steel-basalt fiber reinforced polymer (BFRP) composite plate (SBFCP), a novel type of hybrid composite plate composed by steel wire and BFRP was proposed by our research group with high modulus and low cost (Liu, 2010). And there is no study on the fatigue behavior of I-steel beams strengthened with SBFCP in the past and comparative studies on fatigue behavior of I-steel beams strengthened with different type of FRP plates is still very limited. Hence, the principal aim of the work reported in this paper is to investigate the fatigue performance of I-steel beams strengthened with high modulus CFRP, high strength CFRP, SBFCP and welding steel plate under the principle of equivalent axial tensile stiffness.

2 SPECIMEN DESIGN

Mechanical properties of the strengthening material used in this study can be seen in Table 1, in which the SBFCP was handmade products. The SBFCP plates with 165 mm width and 4.8 mm thickness, which consists of basalt FRP sheets and 0.5 mm diameter steel wires. High modulus CFRP plates with 50 mm width and 2 mm thickness, and high strength CFRP plates with 50 mm width and 1.4 mm thickness were used. A two-component epoxy resin was used for the bonding reinforced material. The mixing ratio of the epoxy was 3 parts resin to one part hardener by weight.

The I-steel beams used were 3000 mm long and HT350×175 hot rolled sections. Steel cover plates with a width of 240 mm and a thickness of 12 mm were welded to the upper surface of upper flange. The properties for

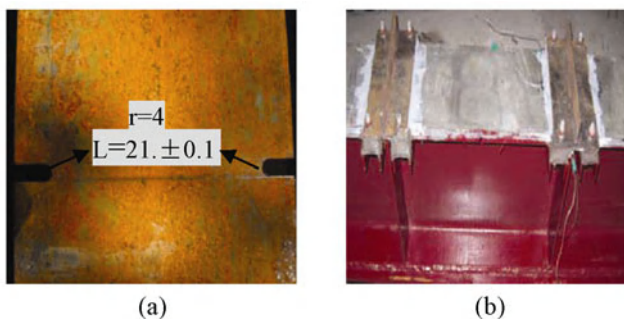
Table 1 Mechanical Properties of Materials

Material	The modulus of elasticity (GPa)	Elongation (%)	Ultimate strength (MPa)	Yield strength (MPa)
SBFCP	108.3	2.24	1789	–
High strength CFRP	145	1.70	2123	–
High modulus CFRP	436.4	0.334	1540	–
Adhesive	2.63	1.5	31.7	–
Steel	199	–	441	330

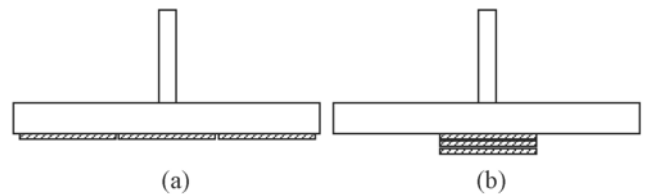
Table 2 Speimens and Main test results of beams

Specimen numbers	Strengthening material	$\Delta \sigma$ (MPa)	N_i	α_i	N_f	α_f
F-0	Without strengthening	141.9	120,000	1.00	156,000	1.00
F-STE	Steel	105.6	170,000	1.42	272,000	1.74
F-SBF1	SBFCP	107.3	200,000	1.67	520,000	3.33
F-HMC	High modulus CFRP	98.8	325,000	2.71	820,000	5.26
F-HSC1	High strength CFRP	105.0	240,000	2.00	626,000	4.01
F-SBF2	SBFCP	107.3	290,000	2.42	700,000	4.49
F-HSC2	High strength CFRP	124.1	40,000	0.33	770,000	4.94
F-HSC3	High strength CFRP	125.5	13,000	1.08	172,000	1.10

steel plate are listed in Table 1. Both edges of the tension flange at midspan were cut by a blade to create two U-shape notches as shown in Figure 1(a). The length of the notches was kept at 21.8 mm with ± 0.1 mm tolerance. Anchors were used at the end of FRP plates and location of loading points to avoid debonding of FRP plates suddenly. Anchors are shown in Figure 1(b).

**Figure 1** (a) Notches in tension flange (b) Schematic of anchors

All strengthened plates were cut to the length of 2000 mm. One layer of high modulus CFRP plate was bonded on the surface of tension flange, according to equivalent axial tensile stiffness of different types of FRP plates, two layers of SBFCP plate and four layers of high strength CFRP were designed. The six specimens with equivalent axial tensile stiffness and the two additional specimens were shown in Table 2. The surface of SBFCP plates used in F-SBF2 was rough while that of F-SBF1 was smooth. F-HSC2 and F-HSC3 were strengthened with the same three plates but different plate configuration (Figure. 2).

**Figure 2** Plate configuration: (a) F- HSC3 (b) F- HSC2

The four-point bending tests were performed using a MTS testing machine with capacity of 1,000 kN. The clear span was 2800 mm and the loading points were 500 mm apart as shown in Figure 3. Then the fatigue testing of all specimens was conducted under the cyclic loads with the maximum of 200 kN and the minimum of 40 kN. A constant amplitude sine wave of 240 times/min frequency with stress ratio of 0.2 was applied.

3 EXPERIMENTAL RESULTS

The experimental results of all specimens are listed in Table 2. $\Delta \sigma$ means the stress range of tension flange calculated by the tests. N_i and N_f mean the crack initiation life and the fatigue life, respectively. α_i and α_f mean the the crack initiation life increase ratio and the fatigue life increase ratio, respectively.

3.1 Failure modes

Two different failure modes were observed in this experimental program (Figure 4). The failure modes for F-STE and F-0 were identical, which illustrated that the I-steel beam was fractured the moment the tension flange

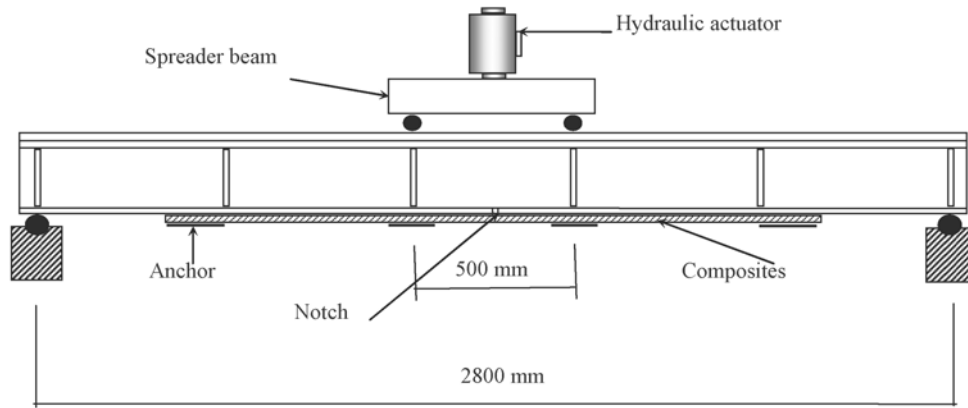


Figure 3 Schematic of loading setup

had completely cracked and failed to carry the extra cycles. The failure modes for all strengthened beams with FRP plates were similar, but different those of F-0 and F-STE. The crack always initiated from the tip of one of the U-shaped notches, and then started to move toward the web. With the increasing of the number of cycles, the crack also initiated from the tip of the other notch and then also started to move toward the web. The beams were able to carry a few extra cycles even after the tension flange had completely cracked, eventually debonding failure happened at the interfaces in-between the fibers or the composites /steel interfaces.

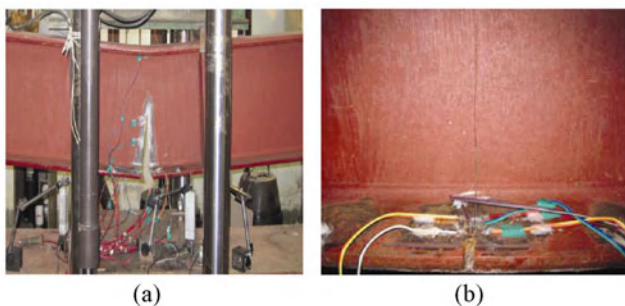


Figure 4 Typical failure of steel beam: (a) F-STE (b) F-HMC

3.2 Fatigue life

Comparison on the propagation of fatigue cracks was shown in Figure 5. From the Table 3 and Figure 5, it can be found that, compared with the welding steel plates, application of FRP plates shows the better effectiveness on preventing fatigue propagation and extending the fatigue life of steel beam. The FRP repair scheme increases the crack initiation life by 1.67-2.71 times and the fatigue life by 3.33-5.26 times over the un-strengthened beams, and the high modulus CFRP is most effective in all used FRP plates. As shown in Figure 5, the use of welding steel plate can reduce crack growth rate only when the fatigue crack propagates from 0 mm to 20 mm. Once the crack length is beyond 20 mm, the welding steel plates would fail to prevent the fatigue crack propagation, and the crack growth rate of the specimen

F-STE is approximately equal to that of specimen F-0. Application of composites can reduce the crack growth rate until the failure of specimens.

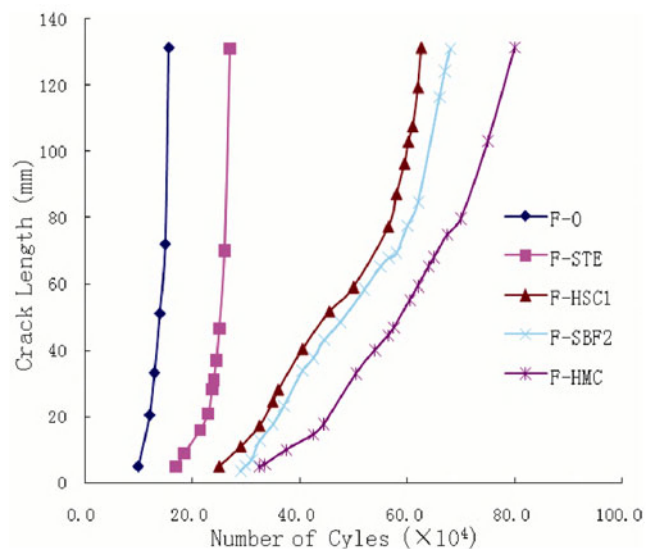


Figure 5 Expansion curve of the fatigue cracks

3.3 Effect of interface treatment

F-SBF1 is identical to F-SBF2 except for the surface of SBFCP used. However the fatigue life increase ratios are 3.33 and 4.49, respectively. It is evident that the roughness of SBFCP has a considerable effect on extending the fatigue life. The reason is that the better roughness the surface has, the better interfaces in-between composites or composites/steel are. The influence of number of composites layers on the fatigue life was investigated by comparison of the results obtained from specimens of F-SBF2 and F-HMC. Under the principle of equivalent tensile stiffness, specimens of F-SBF2 and F-HMC have different layers, yet the fatigue life increase ratio is 4.49 and 5.26 respectively. It indicates that high modulus CFRP plate is much more efficient due to fewer layers which result in smaller number of interfaces. Therefore it is concluded that the interface treatment have a significantly effect on the fatigue life.

3.4 Effect of plate configuration

Two specimens, F-HSC2 and F-HSC3, were designed to study the effect of plate configuration. They both were strengthened with three high strength CFRP plates, but they had different plate configuration as shown in Figure 2. The experimental results show that the fatigue life increase ratio of F-HSC2 is approximately 4.5 times greater than that of F-HSC3. Note that the breakdown of electricity supply lead to the crack initiation uncommonly when the cycles were 40,000. Therefore, in the fielding application, a proper plate configuration had better be chosen to make full use of the FRP plates.

3.5 Effect of different strengthened materials

As shown in Table 3 and Figure 5, under the principle of equivalent axial tensile stiffness of different types of FRP plates, I-steel beam perform different fatigue behavior. Compared with the welding steel plates, FRP plates have more advantages as below: (1) postponing the time of fatigue crack initiation; (2) reducing the crack growth rate; (3) changing the fatigue failure mode of I-steel beams. However, different FRP plates also show different effectiveness on preventing fatigue crack propagation and extending the fatigue life of I-steel beams. The high modulus CFRP plate is most effective and the high strength CFRP plate has a worst effect among the FRP plates. It is because that the steel beam strengthened with high modulus CFRP plate needed only one layer of plates while the steel beam strengthened with high strength CFRP plates needed four layers of plates under the principle of equivalent axial tensile stiffness, and interfacial stress transfer is more effective when the high modulus CFRP plates were used.

4 CONCLUSIONS

This paper has reported on the experimental investigations of I-steel beams strengthened with different FRP plates. The following conclusions can be gotten:

(1) Under the principle of equivalent axial tensile stiffness, the fatigue life of strengthened I-steel beams was increased from 3.33 to 5.26 times over un-strengthened beam, while the fatigue life of welding steel plate strengthened steel beam was increased by 1.74 times. It

is evident that application of FRP plates substantially reduces crack growth rate and prolongs the fatigue life compared with welding steel plates, especially when the high modulus CFRP were used.

(2) Compared to welding steel plate, the use of composites can change the fatigue failure modes of I-steel beams. The failure modes for F-STE and F-0 were identical, which illustrated that the I-steel beam was fractured the moment the tension flange had completely cracked and failed to carry the extra cycles. The failure modes for all strengthened beams with FRP plates were similar, and the steel beams were able to carry a few extra cycles even after the tension flange had completely cracked, eventually debonding failure happened at the interfaces in-between the fibers or the composites /steel interfaces.

(3) The interface treatment has an effect on the fatigue life. SBFCP plates with rouge surface can prolong the fatigue life more effectively than SBFCP plates with smooth surface do.

(4) The plate configuration has considerable influence on the fatigue life. Under the principle of equivalent axial tensile stiffness, the fatigue life increase ratio of F-HSC2 is approximately 4.5 times greater than that of F-HSC3.

REFERENCES

- Tavakkolizadeh, M. and Saadatmanesh, H. (2003). Fatigue Strength of Steel Girders Strengthened With Carbon Fiber Reinforced Polymer Patch, *Journal of Structural Engineering*, Vol. 129, No.2, pp. 186-196.
- Liu Hongbo, AL-Mahaidi Riadh, Zhao Xiaolin (2009). Experimental study of fatigue crack growth behavior in adhesively reinforced steel structures, *Composite Structures*, pp. 12-20.
- Bassetti, A, Nussbaumer, A, and Hirt, M. A (2000). Crack repair and fatigue life extension of riveted bridge members using composite materials, *Bridge Engineering Conference 2000: Past Achievements, Current Practice, Future technologies*, Egypt, pp. 227-237.
- Liu Haiyang (2010). Experimental Study on Fatigue Property of Steel Beam Strengthened with Novel Materials, *Mater Degree Thesis of Southeast University*, 2010.

Strengthening of Masonry and Timber Structures

Experimental Study on Seismic Behavior before and after Retrofitting of Masonry Walls Using FRP Laminates

Asal Salih Oday (odaycivileng@yahoo.com), Li Yingmin & Mohammad Agha Houssam
College of Civil Engineering, Chongqing University, Chongqing, China

ABSTRACT Masonry buildings are the most common and seismically vulnerable structures in the rural areas of China. However, 2008 Sichuan earthquake has showed that failure of masonry walls is one of the major causes of material damage and loss of human life due to seismic events. Therefore, this work presents an experimental program that investigates in-plane seismic behaviour of common types of shale masonry shear walls before and after retrofitting using fibre-reinforced polymers (FRP). The motivation of the present work is associated with the important influence that the FRP introduce as an effective and affordable retrofitting technique for masonry members. To achieve this goal, a total of four half-scale shale masonry walls, two walls with door opening and the other two are solid, were subjected to combined uniformly distributed constant vertical load and incrementally increased in-plane lateral load. This paper analyzed the general behaviour of the shear walls before and after retrofitting based on lateral load-top displacement curves and the action of the FRP laminates to masonry shear walls. The test results indicated that the FRP system remarkably increases the lateral load capacity of retrofitted walls. Moreover, during the later loading stages, FRP Sheets were effective in enhancing the stiffness of retrofitted walls.

1 INTRODUCTION

Masonry buildings are the most common and seismically vulnerable structures in the rural areas of China. 2008 Sichuan earthquake has showed that failure of masonry walls is one of the major causes of material damage and loss of human life due to seismic events.

Previous researchers have shown that CFRP laminates are effective in increasing the in-plane and out-of-plane strength of masonry walls (Ehsani et al., 1999; Hamoush et al., 2001; Albert et al., 2001). Little investigation on the use of externally FRP laminates as in-plane shear reinforcement of masonry walls with opening has been reported. Some experimental results (Schwegler, 1995; Priestley & Sieble, 1995; Laursen et al., 1995) have shown that masonry walls externally reinforced with FRP and subjected to in-plane shear have large increase of strength and load deformation capacity. Others (Valluzi et al., 2002; Santa Maria et al., 2004) reported that masonry panels externally reinforced with FRP and subjected to diagonal compression have between 15 and 70% increase of strength.

In terms of shear strength a diagonal configuration was more efficient than a grid configuration. As for the lateral loads, no difference in the response between monotonic and cyclic loading was found (Santa Maria et al., 2004).

In this paper, quasi-static experimentation was employed in the test investigation of the masonry walls. Four

half-scale brick masonry walls, two with door opening and others are solid walls, were subjected to combined uniformly distributed constant vertical load and incrementally increased in-plane lateral load. The damaged walls were retrofitted using CFRP laminates with epoxy injection and retested. The walls were tested at the Laboratory of Civil Engineering College in Chongqing University, P.R. China. It is hoped that these experiments will make a contribution to better understanding of the seismic behavior of masonry walls before and after retrofitting in earthquake prone areas.

2 EXPERIMENTAL PROGRAM

2.1 Test specimens and material properties

The testing program is composed of 4 confined masonry walls, scaled 1:2, with different structural column. Two groups have been considered, assuming solid and perforated shear walls. Thus, solid walls BCW-1 confined with two RC tie columns, and BC1W-1 confined with two hollow block tie columns filled with RC were used. Walls with door opening (BCW-2, BC1W-2) were also confined with two RC tie-columns and two hollow blocks tie-columns filled with RC, respectively. The tie-columns and beams sizes are 240mm×240mm and 240mm×120mm, respectively. The columns and beam reinforcement consists of 4Φ10mm bars with average yield strengths 240 MPa and with Φ6.5@100/200mm stirrups. Two 1m long horizontal tie-bars Φ6.5mm/500mm vertical spacing

were used to improve the structural integrity between the tie-columns and the brick wall. The walls were constructed using a double piece of 240mm×115mm×53mm solid bricks with M5 type mortar. The cubic compressive strength of the mortar were 3, 10.3, 3.4, 4.8, and for the concrete in tie-columns 16.9, 18.5, 16.8, and 25.1 MPa for specimens BCW-1, BC1W-1, BCW-2, and BC1W-2, respectively. Figure 1 shows the dimensions and structural details of these walls.

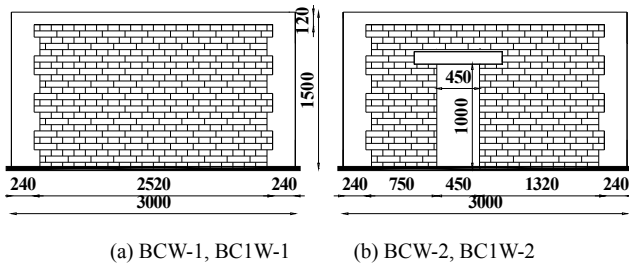


Figure 1 Layouts of specimens

The specimens were tested twice; first they were tested till a predefined degree of damage; then these damaged specimens were retrofitted using CFRP laminates on both sides of the walls with epoxy injection and were retested. Figure 2 shows the FRP laminates distribution of these retrofitted walls.

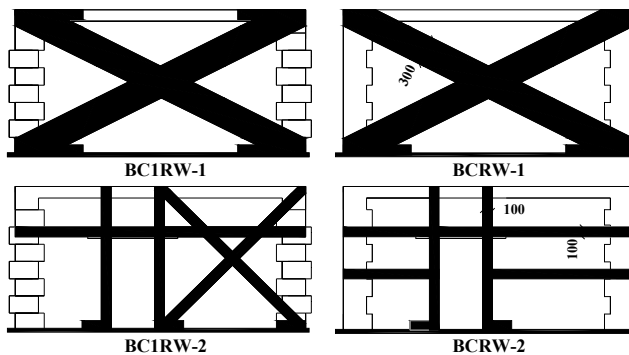


Figure 2 FRP laminates Distribution

The experimental vertical stress was 0.5 MPa for all test specimens. The CFRP laminates used in this research was CXS-200 type with 3632 MPa tensile strength and 225 GPa elastic modulus. The epoxy resin includes three components: epoxy putty, epoxy resin (CH-4A) and epoxy resin adhesive (CH-1A). Each component consists of Part A and Part B. In this study, the mixing ratio (part A: part B) was 3:1 by volume for all specimens.

2.2 Loading Devices and Test Method

All specimens were tested under increased cyclic lateral load and 0.5 MPa vertical stresses. The loading devices and test setup are shown in Figure 3. An identical boundary condition was used in all tests. The walls were loaded vertically by two point loads applied to the loading

beam attached to the top of the masonry panel. Horizontal load was applied to the beam along its centerline. The loads were applied manually using hydraulic jacks and hand pumps. The applied vertical and horizontal forces were measured by the loading cells. The specimens can be considered cantilever walls, i.e. fixed at the base and free at the top. The lateral displacement was measured by a linear variable displacement transducer (LVDT), which was used to measure the top lateral displacement of the test panel. During the experiment, force and displacement measurements were always taken from the loading cell and LVDT whether in displacement control mode or in force control mode. During all the tests, the vertical load was maintained constant by readjusting the vertical jack, whereas the lateral loading was cycled based on mixed lateral force/displacement control mode.

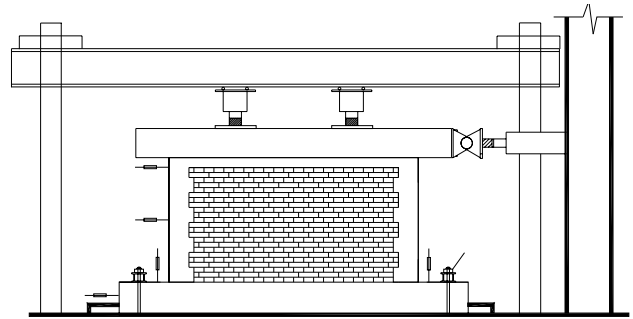


Figure 3 Test setup and loading devices

3 EXPERIMENTAL RESULTS

3.1 Hysteretic behavior, response envelopes

The hysteresis envelope loops of all walls specimens are presented in Figures 4-7. Also, comparisons of the hysteresis loops envelopes of reference specimens and the corresponding retrofitted specimens are presented in Figures 8, 9. Retrofit configurations enhanced the lateral resistance by factors of 1.19, 1.39, 1.25, and 1.27 for BCW-1, BC1W-1, BCW-2, and BC1W-2, respectively. Table 1 shows the average loads of the first cracks, the maximum horizontal load and the average failure load with their corresponding displacements.

3.2 Cracks patterns

The final cracks patterns for all tested walls are depicted in Figure 10, where it can be observed that they are typical diagonal tension shear patterns on the references walls. It is also worth mentioning that the shear crack penetrated the confining columns and beams elements. The retrofitted walls showed several spread cracks, with small width. For these repaired and retested specimens, cracks began from the place where cracks had occurred in the former test. When the FRP sheets crossing the cracks peeled off and broke with scary sound, the load resistant capability of specimen decreased abruptly.

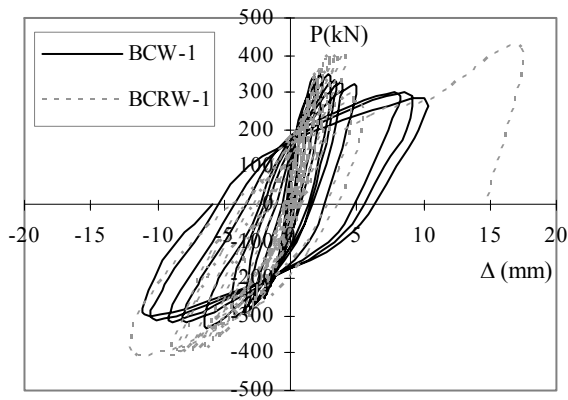


Figure 4 Hysteresis loop of Walls BCW-1 & BCRW-1

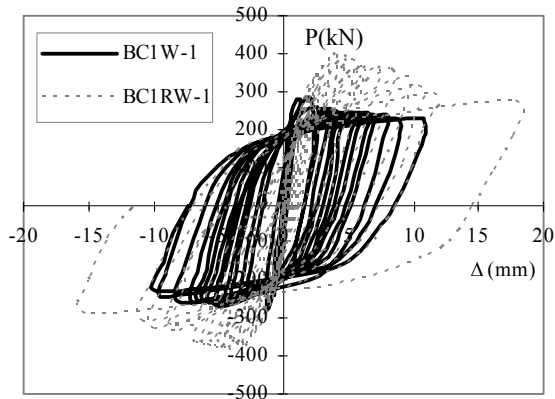


Figure 5 Hysteresis loop of Walls BC1W-1 & BC1RW-1

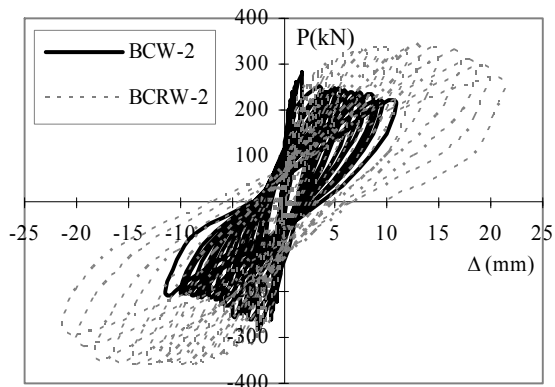


Figure 6 Hysteresis loop of Walls BCW-2 & BCRW-2

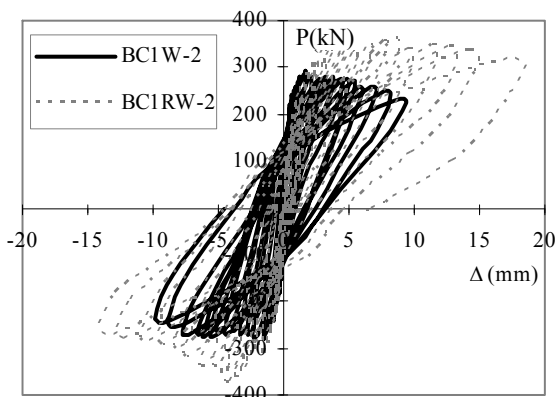


Figure 7 Hysteresis loop of Walls BC1W-2 & BC1RW-2

Table 1 Average loads and corresponding displacements

Specimen	First crack		Peak Point		Failure (0.85 Peak)	
	Displ. Δ_c (mm)	Load P_c (kN)	Displ. Δ_u (mm)	Load P_u (kN)	Displ. Δ_f (mm)	Load P_f (kN)
BCW-1	0.60	201.5	4.36	342.00	6.03	290.70
BCRW-1	1.30	210.0	6.40	405.78	8.13	345.00
BC1W-1	0.55	220.0	1.69	282.00	8.10	239.50
BC1RW-1	1.04	150.0	4.00	390.00	8.85	331.60
BCW-2	0.54	200.0	2.14	280.00	6.27	238.00
BCRW-2	0.88	200.0	12.77	349.15	19.81	296.80
BC1W-2	0.40	180.0	1.63	287.50	9.08	244.40
BC1RW-2	1.20	260.0	6.39	365.65	13.70	310.83

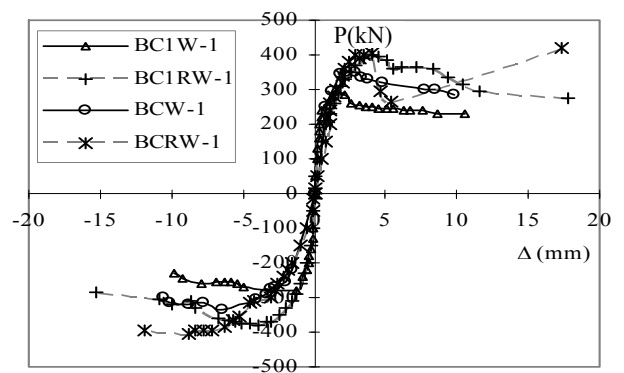


Figure 8 Hysteresis envelopes Comparison of solid walls

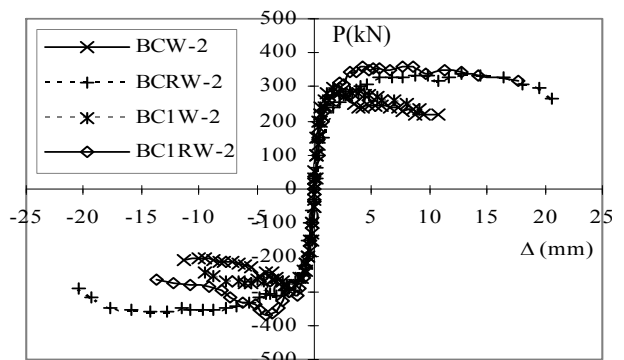


Figure 9 Hysteresis envelopes comparison of perforated walls

3.3 Stiffness degradation

In order to assess the level of damage, stiffness degradation is calculated and presented in this section. Figures 11 and 12 present the stiffness degradation comparison of references and retrofitted wall specimens. It could be seen that the lateral stiffness was not constant but decreased with increased lateral deformation.

Reference walls had a little higher stiffness at the loading stages before yielding, but this initial stiffness decreased faster than in the retrofitted wall, because the CFRP system has restricted the development of the cracks. It is clear that CFRP strips could increase the wall stiffness of masonry shear walls in the later stage of loading. Mechanical stiffness curves indicate that there

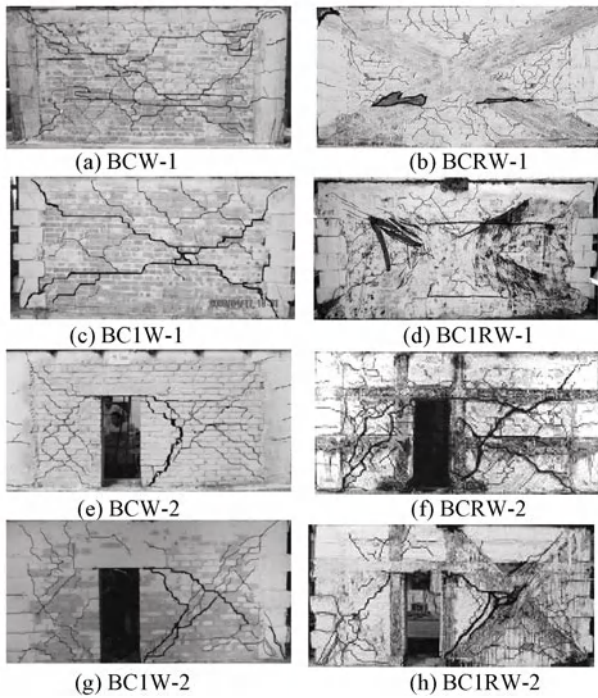


Figure 10 Final cracks patterns of tested walls

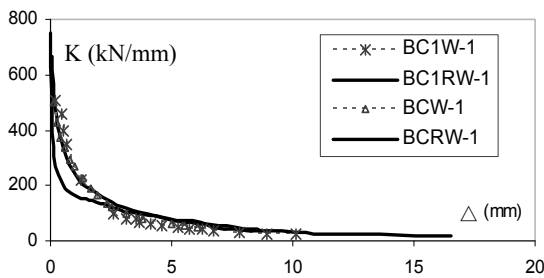


Figure 11 Stiffness Degradation of solid walls

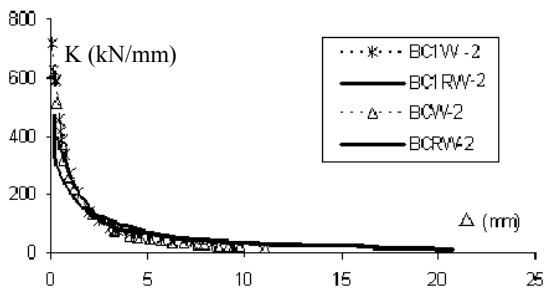


Figure 12 Stiffness degradation of perforated walls

is negligible effect of amount and layout of CFRP reinforcement on the stiffness of the walls retrofitted by CFRP sheets and epoxy injection. It is evident that the effect of CFRP Sheets in increasing the wall stiffness is small.

4 CONCLUSIONS

FRP retrofitted masonry walls were tested under cyclic horizontal load and constant uniform vertical stress. The behavior of walls during the testing was studied based on their lateral load versus top displacement response, failure mode, cracking patterns and stiffness degradation. The results were compared to the reference masonry walls. It was shown that CFRP along with epoxy resin injection retrofitting technique is effective and reliable. It has increased the in-plane strength and improved the stiffness of masonry shear walls in the later stage of loading. Retrofitted walls had a higher first crack load compared with the reference walls. The action of this technique restricted the development of the major diagonal cracks and improved the integrity of the walls with opening.

REFERENCES

Albert M.L., Elwi A.E., & Cheng J.J.2001. Strengthening of unreinforced masonry walls using FRPs, *Journal of Composites for Construction* 5 (2): 76-184.

Ehsani M.R., Saadatmanesh H.,& Al-Saidy A.1999. Behavior of retrofitted URM walls under simulated earthquake loading, *Journal of Composites for Construction* 3 (3): 134-142.

Hamoush S.A., McGinley M.W., Mlakar P.,Scott D., & Murray K. 2001. Out-of-plane strengthening of masonry walls with reinforced composites, *Journal of Composites for Construction*; 5 (3):139-145.

Laursen P.T., Seible F., Hegemier G.A., & Innamorato D.1995. Seismic retrofit and repair of masonry walls with carbon overlays, *Non/Metallic (FRP) Reinforcement for Concrete Structures, RILEM*: 616-627.

Priestly M.J.N., & Sieble F. 1995. Design of seismic retrofit measures for concrete and masonry structures, *Construction and Building Materials* 9 (6): 365-377.

Santa Maria H., Duarte G., & Garib A. 2004, Experimental investigation of masonry panels externally strengthened with CFRP laminates and fabric subjected to in-plane shear load, *13th World Conference on Earthquake Engineering Vancouver, B.C., Canada*.

Schwegler G.1995. Masonry construction strengthened with fiber composites in seismically endangered zones, *Proceedings of the Tenth European Conference on Earthquake Engineering, Viena, Austria, I*: 467-476.

Valluzzi M.R., Tinazzi D., & Modena C. 2002. Shear behavior of masonry panels strengthened by FRP laminates, *Construction and Building Materials* 16(7): 409-416.

Strengthening of Masonry Structures Using FRP – Experimental Research

J. Witzany, T. Cejka & R. Zigler

Department of Building Structures, Faculty of Civil Engineering, Czech Technical University in Prague, Czech Republic

ABSTRACT The article deals with the problems of the failure mechanism and the load-bearing capacity of masonry barrel vault structures and masonry columns strengthened with fabric of carbon fibres. The executed experimental research of the effect of strengthening segmental barrel vaults and masonry columns by carbon fabric showed a prominent growth in the ultimate bearing capacity and ductility of barrel vault structures and masonry columns. The application of carbon fabric (CFRP) in the vault area exposed to tensile stresses limited not only the appearance and development of characteristic tensile cracks at these vault cross-sections, but also significantly increased the vault stability against buckling. The position of strengthening elements - the carbon fabric (CFRP) - affected the failure mechanism of the masonry vaults and masonry columns.

1 INTRODUCTION, MECHANISM OF MASONRY VAULT COLLAPSE

The barrel vault failure process is characterized by a phase where the vault becomes a structurally definite structure with most frequently two to four hinges. At this phase, local failure of the area around the cross-sections in which imperfect line hinges are created gradually occurs. The vault failure process as a rule includes two prominent mechanisms – local as well as overall changes in the vault system's shape (stability criterion) and the vault masonry disintegration due to the effect of tensile and compressive normal stresses exceeding gradually the load-bearing capacity of the vault cross-sections in which hinges have been created (load-bearing capacity criterion) (Figure 1).

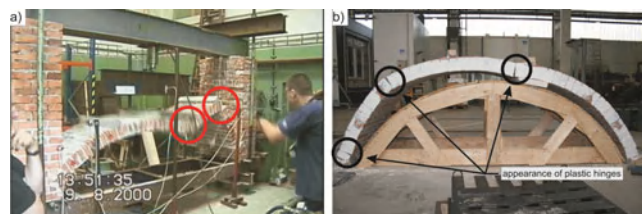


Figure 1 The process of failure and successive collapse of barrel vault (span 3.0 m) a) vault collapse due to stability loss by buckling; b) appearance of tensile cracks and plastic hinges

The total failure – vault collapse – is usually the result of these two mutually interrelated parallel processes. Both of these processes are simultaneous and cannot be separated from each other.

The vault failure prior to the reaching of the vault

cross-section ultimate bearing capacity in compression is seriously affected by initial shape imperfections, heterogeneous masonry characteristics or the asymmetry of load, barrel vaults with higher rises being more sensitive to the respective imperfections.

The vault failure resulting from its loss of stability caused by shape or geometric deflections due to insufficient stability of supports or load asymmetry occurs under loads in which the ultimate bearing capacity of the vault cross-section in compression is not utilized.

Insufficient rigidity of supports in relation to horizontal shift causes a significant decrease in the vault load-bearing capacity and vault failure. The magnitude of horizontal forces in the vault imposts grows with the decrease in the vault rise. Horizontal shift of supports may, in such cases, seriously affect total deformations and the vault failure.

Vault investigation, as a rule, starts at points notorious for creating hinges, i.e. places where e.g. crushing or buckling of surface layers arises and where tensile cracks appear. By comparing these “theoretical” points with the points of existing failures on the investigated vault, the cause or causes of these failures may be determined with some probability so that an effective method of the vault rehabilitation or reconstruction may be designed.

In existing masonry vaults, the central line usually deviates from the thrust line – the vault shape is not completely in accordance with the thrust line given by exerted load. Therefore, the cases of vault failure after reaching the ultimate bearing capacity of the full vault cross-section in compression are relatively rare.

2 EXPERIMENTAL RESEARCH OF MASONRY BARREL VAULT STRENGTHENING

Experimental research of segmental barrel vaults in a 1:1 scale was aimed at obtaining new knowledge about the failure mechanism and load-bearing capacity of strengthened vaults in relation to their rise and strengthening method.

The strengthening by carbon fabric was performed on the vault extrados and intrados, at areas of presumed tensile stresses and appearance of tension cracks that were specified by the FEM-based numerical computation, at width identical to the vault width and an anchoring length of ca 150 mm in areas of pushed vault cross-sections (Figure 2).



Figure 2 The barrel vault strengthened with CFRP in the area of tensile stresses

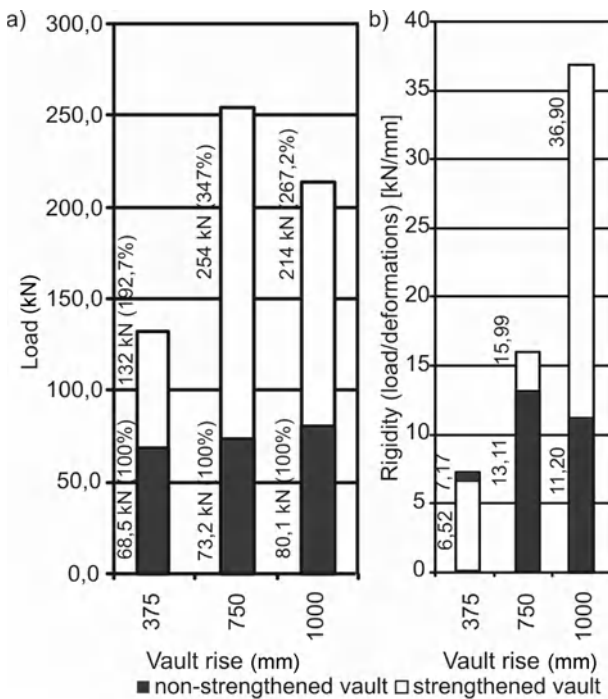


Figure 3 a) Experimentally determined ultimate bearing capacity of barrel masonry vaults with different vault rise; b) rigidity of non-strengthened and strengthened vaults

The analysis of the results of experimental research of strengthened segmental masonry barrel vaults by carbon fabric showed that the ultimate bearing capacity of segmental masonry barrel vaults strengthened by carbon

fabric (CFRP), symmetrically loaded by two vertical loads at thirds of the vault span reached values of ca 190%-350% of the ultimate bearing capacity of non-strengthened masonry vaults (Figure 3a).

The strengthening segmental masonry barrel vaults by carbon fabric (CFRP) shows increased rigidity and decreased deformation, see Figure 3b).

The effect of strengthening was not so visibly demonstrated in segmental barrel vaults with the central angle of 60°, which do not include areas of so-called critical cross-sections (Figure 4). In the case of these vaults strengthened by carbon fabric (CFRP) in the extent of ca 1/3 of the arch length on the vault intrados at the crown and on the vault extrados, the failure of the these vaults

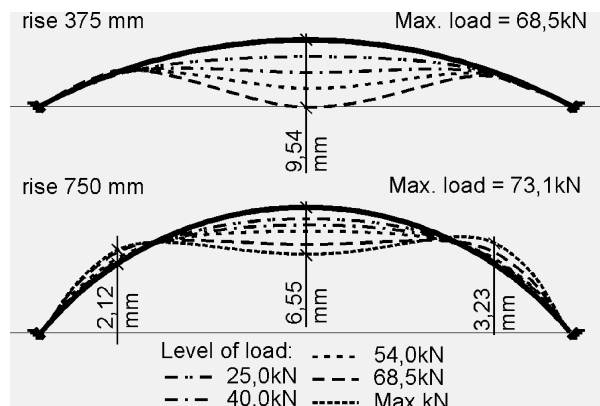


Figure 4 Experimentally measured deformation of barrel vault structure

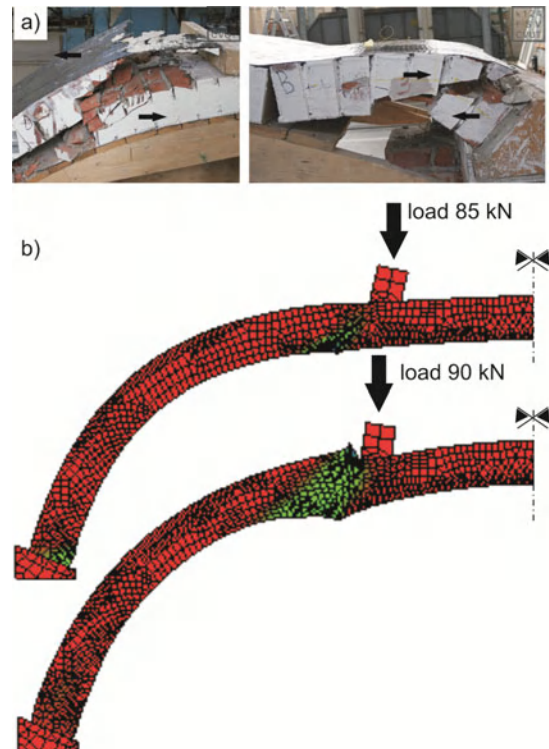


Figure 5 Shear failure of vault strengthened on both sides by carbon fabric a) vault rise 0.75m and 0.375m, span 3.0m; b) non-linear numerical analysis of vault with rise 1m

was caused by the appearance of a prominent inclined shear crack accompanied by the shift of vault cross-sections at the point where the anchoring of carbon fabrics installed on the vault extrados and intrados overlapped (Figure 5).

The limit deformation and the ultimate bearing capacity of these vaults strengthened by carbon fabric amounted to values of ca 1,5 to 2,9 of limit deformations and ultimate bearing capacity of non-strengthened masonry barrel vaults.

The failure mechanism of vaults with the area of hazardous cross-sections (i.e. fault vault with more than 120° central angel) is characterized by a progressive growth in horizontal vault deformations in areas of hazardous cross-sections (Figure 6). Figure 6 shows mainly the growth in the horizontal component of vault deformation in cross-sections situated ca in 1/3 of the rise under increased vault load.

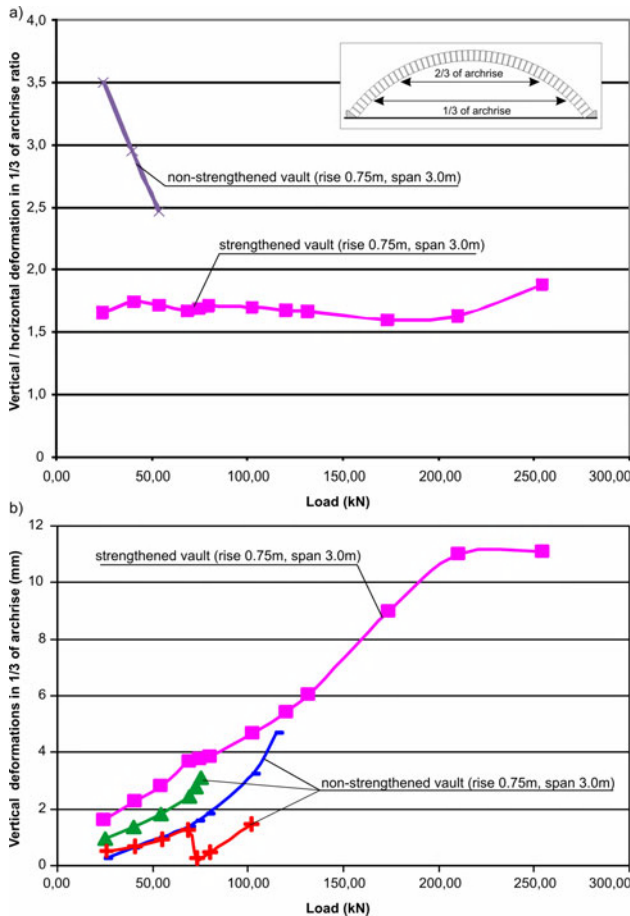


Figure 6 a) Dependence of vertical and horizontal deformation ratio on load; b) horizontal deformation of non-strengthened segmental vaults and vaults strengthened by carbon fabric

The barrel vaults with the central angle more than 120° strengthened by carbon fabric (CFRP) showed, due to vault strengthening in the area of hazard cross-sections (prevention of vault failure by its stability loss) under identical load, total values of vertical and horizontal

deformations lower (approximately 20%-70%) than the values of deformations of non-strengthened vaults (Figure 7).

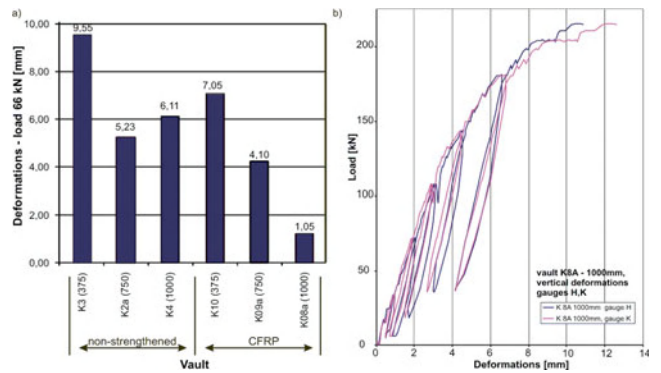


Figure 7 a) Vertical deformations of non-strengthened segmental vaults and vaults strengthened by carbon fabric; b) characteristic working diagrams of vaults strengthened by carbon fabric $L \times \delta_{y(x)}$

The application of carbon fabric (CFRP) in vaults with the central angel greater than 120°, in areas where tensile cracks arise, limited the occurrence and development of these characteristic tensile cracks and, at the same time, raising the vault stability (Figure 8).

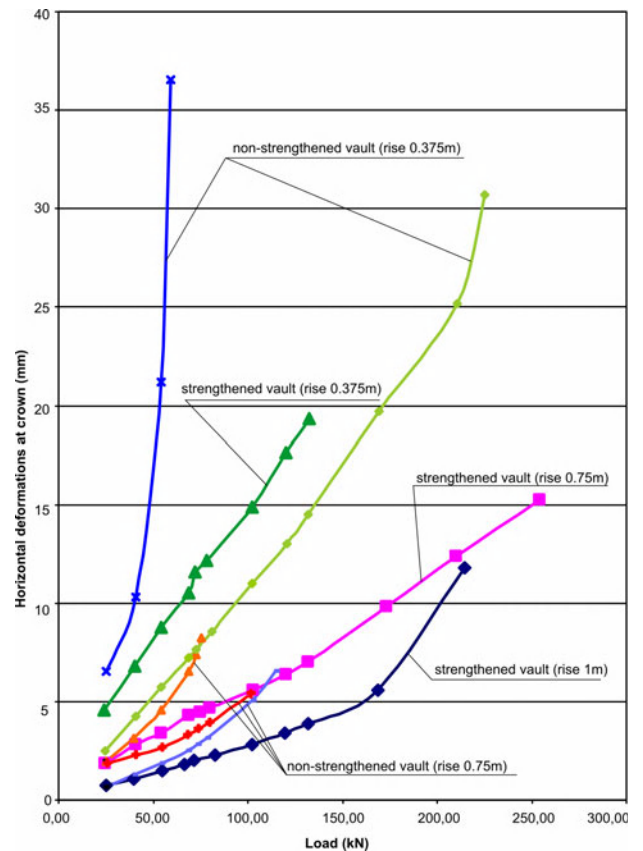


Figure 8 Vertical deformation of non-strengthened segmental vaults and vaults strengthened by carbon fabric

The effectiveness of vault strengthening in the area of tensile stress appearance preceding tensile cracks in

non-strengthened vaults is documented by the stress time pattern in carbon fabric. Figure 9 shows a gradual growth in stresses in carbon fabric during the vault loading procedure at the phase of the vault masonry disintegration.

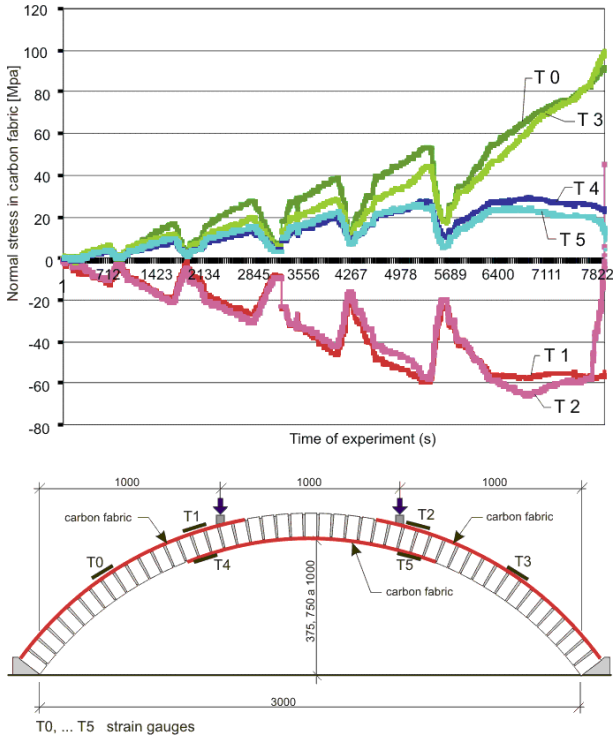


Figure 9 Normal stresses in carbon fabric

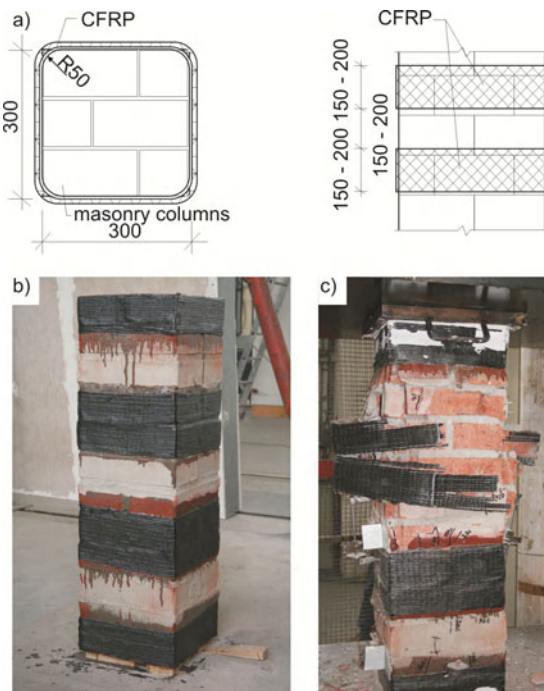


Figure 10 a) Scheme of strengthening of masonry column; b) strengthening masonry column with carbon fabric; c) total failure - strengthened column collapse - cause by the effect of transversal tensile stress

The failure mechanism of masonry columns is characterized by tensile crack appearance due to the effect of transversal tensile stresses, which leads to smaller load bearing capacity than the ultimate load bearing capacity of masonry. The experimental research of the strengthening of masonry columns with carbon fabric showed prominent effect of CFRP on reduction of characteristic tensile cracks and thus on significant increase of load bearing capacity of these structures (Figure 10).

3 CONCLUSION

The executed experimental research of the effect of strengthening segmental barrel vaults by carbon fabric showed a prominent growth in the ultimate bearing capacity and ductility of barrel vault structures.

In the case of vault strengthening, not only the increased ultimate bearing capacity of the strengthened vault cross-section, but, at the same time, also the consequences of potential increased loadability of the strengthened vault on the growth of horizontal forces in the supports must be assessed (Figure 11).

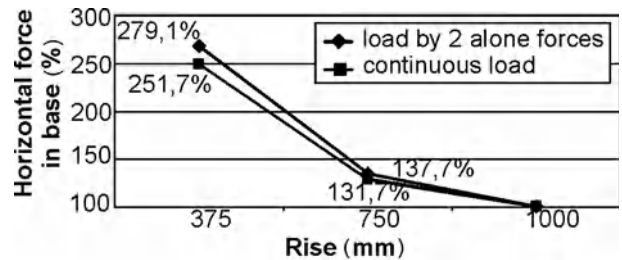


Figure 11 The influence of vault rise on horizontal forces at the vault base

Experimental research of masonry barrel vault strengthening will continue during this year and the last experimental and theoretical results will be presented on this conference.

The paper was written with support from Research Plan MSM 6840770001 “Reliability, optimization and durability of building materials and structures”.

REFERENCES

Witzany, J. et al.: Partial report Research of Masonry Vault Structures, VZ MSM 6840770001 *Reliability, optimization and durability of building materials and structures* (research project, in Czech), 2006-2009.

Witzany, J. et al.: Masonry Barrel Vault Structures; In: *Stavební ročenka 2006* (Structural yearbook, in Czech), Jaga Bratislava, pp. 76-92, ISBN 80-8076-024-1.

Witzany, J. et al.: Experimental research of masonry vaults strengthening; In: *International Conference Structural Faults + Repaire*, 2008, Edinburgh, Scotland, UK, ISBN 0-947644-62-7.

Improvement of Transverse Connection of Masonry Walls through AFRP Bars

M. Menegotto, G. Monti, S. Salvini, M. Vailati

Department of Structural and Geotechnical Engineering, Sapienza Università di Roma, Rome, Italy

ABSTRACT An innovative method to connect existing orthogonal masonry walls through aramidic FRP bars is presented. The proposed technique has the objective of mobilizing and maximizing the collaboration of intersecting structural elements, thus increasing the overall strength and stiffness of masonry buildings under horizontal forces. The method was experimentally tested to prove its applicability and effectiveness.

1 INTRODUCTION

When retrofitting existing masonry buildings, it may be convenient to exploit the contribution of all walls against horizontal forces, by enhancing their mutual connection degree.

To this purpose, a non-invasive method for connecting orthogonal walls with aramidic FRP bars was developed and tested.

T-shaped wall joints between a main “web” wall and a “flange” wall are connected by inserting thin AFRP (aramid) bars at $\pm 45^\circ$ through small holes in the flange wall near the intersection, and anchoring them on the outer faces of both walls, respectively.

With such connectors, a combined action is obtained on a T-shaped cross-section wall with larger flexural capacity.

The objective of the work is to quantify the effectiveness of the strengthening and to relate its basic design parameters to the overall capacity increase.

2 TESTING SET-UP

The tests described below have been carried out at the Department of Structural and Geotechnical Engineering, Sapienza University of Rome, Italy.

The configuration of the testing equipment with the wall is shown in figure 1.

The boundary condition are:

$$F_v = \sigma_0 \cdot t \cdot d$$

$$u_{v1} = u_{v2} = 0$$

$$u_h = \text{imposed}; F_h = \text{measured.}$$

Figure 2 shows a typical wall configuration; in other tests to be carried out, the wall slenderness will be doubled to emphasize the flexural behavior and to maximize the interface sliding.

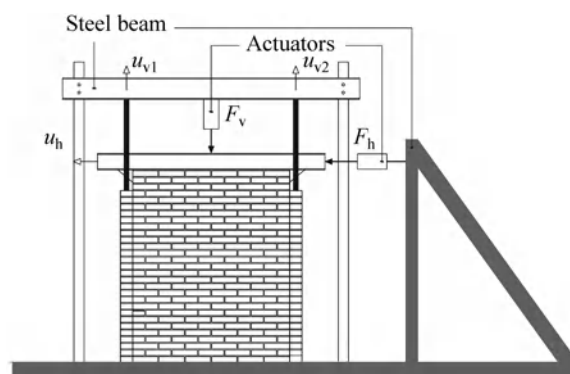


Figure 1 Configuration of testing machine and walls

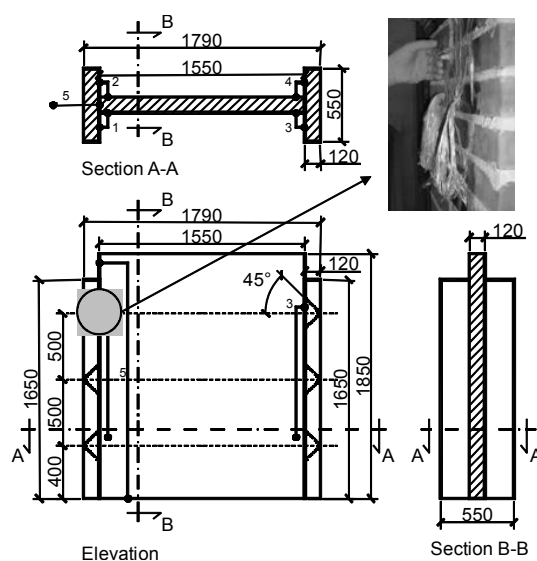


Figure 2 Displacement transducers on a masonry wall prototype. At top right the anchorage detail of the bars

3 MATERIALS

Clay bricks with premixed mortar were used to build the walls, while aramid FRP bars were used to connect them.

The walls mean mechanical properties were:

- Compression strength $f_m = 6.00$ MPa
- Shear strength $\tau_0 = 1.38$ MPa
- Young's modulus $E = 2700$ MPa
- Shear modulus $G = 900$ MPa

and for the connection system:

- Tensile strength $f_{y,d,c} = 1400$ MPa
- Young's modulus $E_{d,c} = 60000$ MPa
- Total tensile strength
- in configuration 1 $R_{T,1} = 32$ kN
- Total tensile strength
- in configuration 2 $R_{T,2} = 16$ kN

In configuration 1 the spread of the anchorage terminal lays on the bar axis, while in configuration 2 they are arranged at 90° (see figure 3).

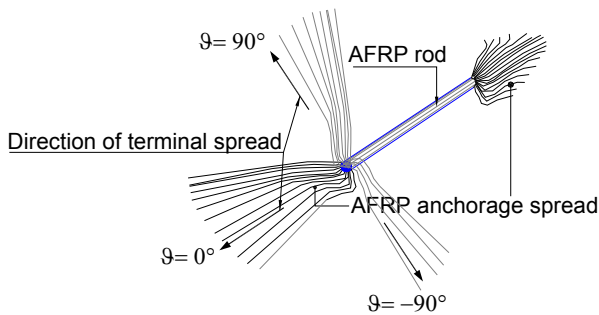


Figure 3 Configuration of system connection

4 CONNECTING THE WALLS

The link between web and flange walls is realized in few simple steps, as see in figure 4:

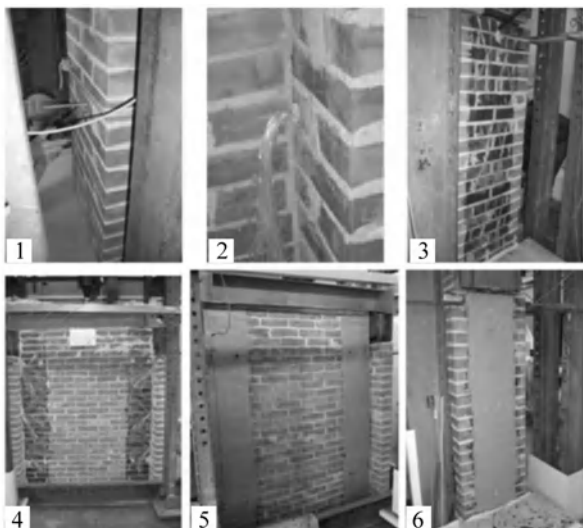


Figure 4 Realization phases of the connections between flange and wall

Phase 1: drilling holes from the outer face of the flanges, tangent to the central wall faces;

Phase 2: passing the bars through the flanges and fixing them in the hole with mortar;

Phases 3 and 4: glueing the fanned bar ends to the surface of both walls;

Phases 5 and 6: applying aramid sheets with vinylester resin to cover and strengthen the anchorages.

The bars have diameter 5.5 mm and are made of reinforced polymer with aramid fibers ($1.0-3.5 \cdot 10^5$ fibers), while the crossing holes through the flange have diameter 7 mm.

5 TESTS RESULTS

The walls specimens consist of one web wall and two flange walls at its ends. They are instrumented as shown in figure 2.

Transducers 1, 2 and 3, 4 measure the relative displacement between wall and flanges, while transducer 5 measures the horizontal displacement between foundation and wall head. The following graphs show the global effects of this strengthening method.

Figure 5 shows the comparison at the first cycle between unstrengthened and strengthened wall. In the strengthened one, the improved collaboration between orthogonal walls gives rise to a stiffness increase.

For low horizontal forces, the curves are practically coincident; when passing 30% of the unstrengthened wall failure load, the connections begin to change the system response.

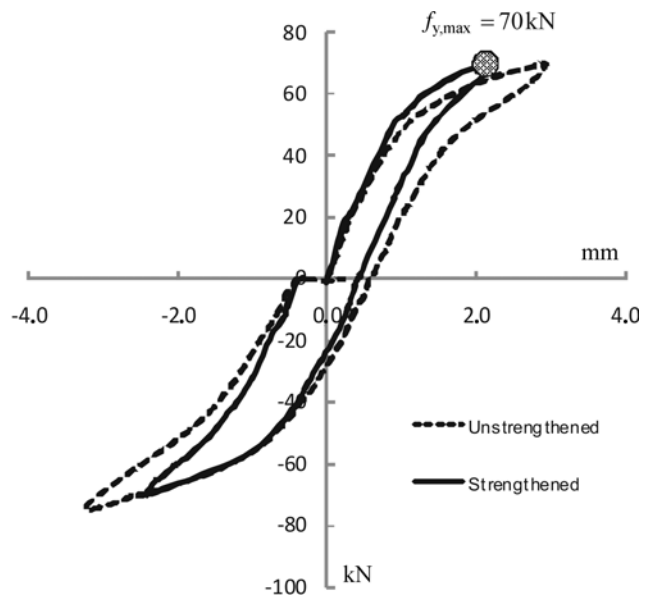


Figure 5 Comparison between strengthened and unstrengthened wall at the first cycle

This delay is due to the absence of pretensioning in the bars. In fact, a strut-and-tie mechanism with the bars cannot be mobilized before reaching a minimum force value.

In figure 6, the difference in terms of relative displacement between web-wall and flanges can be observed: for

the unstrengthened configuration it is 0.31 mm, while in the other one it is 0.02 mm.

The smaller displacement in the strengthened case is ascribed to the mode of application of the bars.

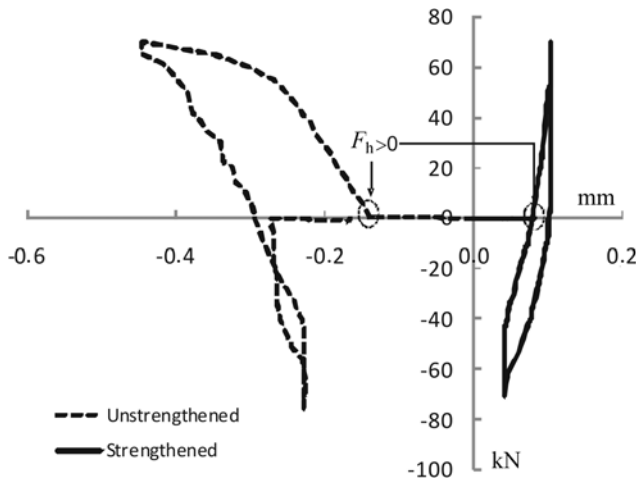


Figure 6 Vertical stiffness of the wall

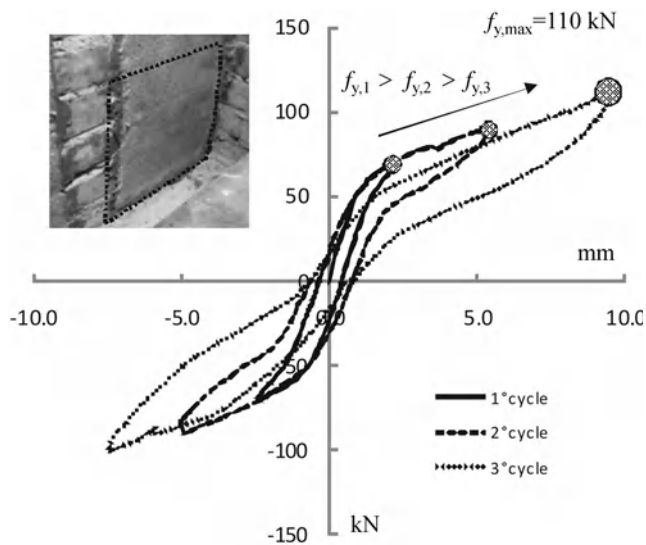


Figure 7 Cyclic behavior of the strengthened wall: at top left a detail of collapse due of crushing the masonry

Initially, the contacting surfaces slip relatively one to each other. When the bars start being pulled, they provide their contribution by imposing compatibility of the displacements between both surfaces. At this stage, the tests show a significant increase of resistance and ductility, as shown in figure 7.

As observed from the tests performed, the strengthening effectiveness strongly depends on the correct application of the bars. In order to make the most of material mechanical properties, the bars are inserted at $\pm 45^\circ$, in dependence of the direction of shear force at the top of the wall. For a plane tension state of shear, the maximum tensile force is inclined at 45° with respect to the vertical. The tensional state is shown in Figure 8.

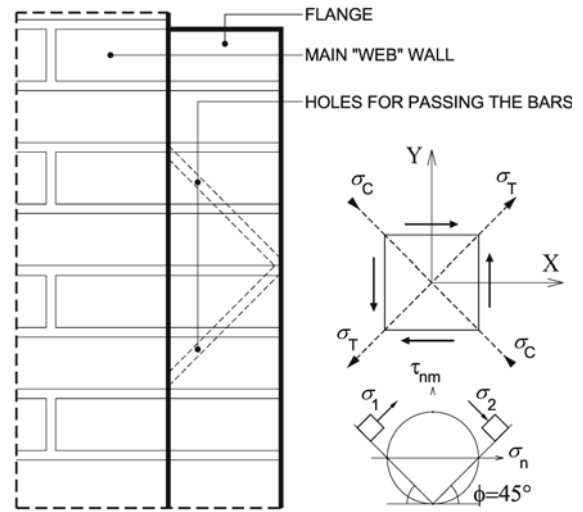


Figure 8 Shear transfer mechanism between main “web” wall and flange

Two effects can be observed when reaching the ultimate limit state:

- Detachment of aramid sheet, covering the bars’ anchor, from the wall;
- Loss of the wall verticality.

6 COMPARISON WITH THE ANALYTICAL SOLUTION

The stiffness obtained from the experimental results is compared with the analytical model proposed by Tomažević (1999):

$$K_e = \frac{G \cdot A_w}{1.2 \cdot h \cdot \left[1 + \alpha \cdot \frac{G}{E} \cdot \left(\frac{h}{l} \right)^2 \right]} \quad (1)$$

Figure 9 contains the comparison between analytical and experimental stiffness.

It can be seen that eq. 1 accurately predicts the elastic experimental stiffness, while a 50% reduction gives a good estimate of the ultimate displacement.

The wall capacity is assessed by considering the two possible failure mechanisms (circolare n.617 2009, DM 14 gennaio 2008) that may develop, flexural and diagonal shear, respectively:

$$f_{yF} = \frac{\left[\frac{l^2 t \sigma_0}{2} \cdot \left(1 - \frac{\sigma_0}{0.85 \cdot f_m} \right) \right]}{H_0} \quad (2)$$

$$f_{yV} = l \cdot t \cdot \frac{1.5 \cdot \tau_0}{b} \cdot \sqrt{1 + \frac{\sigma_0}{1.5 \cdot \tau_0}} \quad (3)$$

The prevailing collapse mechanism is the one with lower capacity.

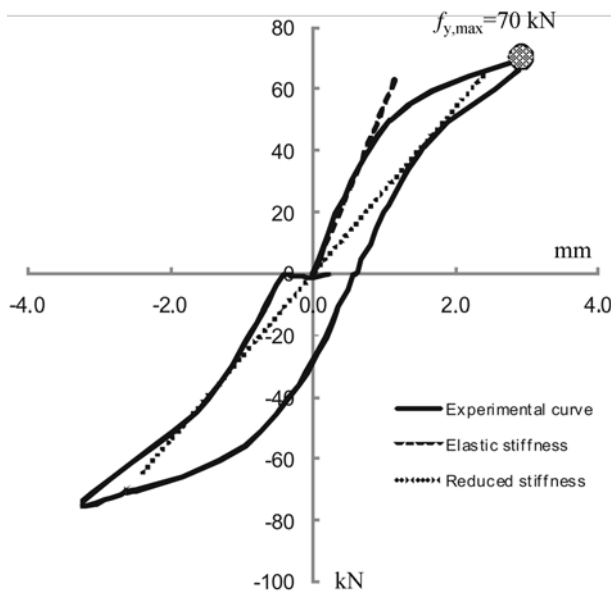


Figure 9 Comparison between stiffness and peak strength at first cycle

Table 1 contains the parameters used to calculate the stiffness (1) and the forces (2) and (3).

Table 1 Calculation parameters to evaluate the wall capacity

h (mm)	l (mm)	t (mm)	A_w (mm)	α	G (MPa)	E (MPa)	f_m (MPa)	τ_0 (MPa)	σ_0 (MPa)
1850	1550	120	$\frac{1.86 \cdot 10^5}{10^5}$	0.83	900	2700	6.00	1.38	0.97

where h = height wall; l = length wall; t = thickness wall; A_w = transverse area of wall; α = factor dependent of boundary condition (0.83 or 3.33 in case of cantilever); G = shear modulus; E = Young's modulus; f_m = mean compression strength; τ_0 = mean shear strength; σ_0 = mean normal tension on the total section area; H_0 = point along the wall where the moment change sign; b = factor depending of wall slenderness, and it can be take $1 \leq b = h/l \leq 1.5$.

For the case at hand, the capacities are:

$$f_{yF} = 64.6 \text{ kN}$$

$$f_{yV} = 390.8 \text{ kN}$$

and the failure is of flexural type.

The experimental test on unstrengthened walls exactly show this behavior, for a horizontal force equal to 70 kN, very close to the analytically predicted value. Figure 10 shows the crack pattern, compatible with a flexural failure mechanism.

Comparing the performance of the strengthened and unstrengthened wall, the following ratios are obtained:

- Strength ratio $\rho_R = 1.57$
- Ultimate displacement ratio $\rho_D = 3.20$

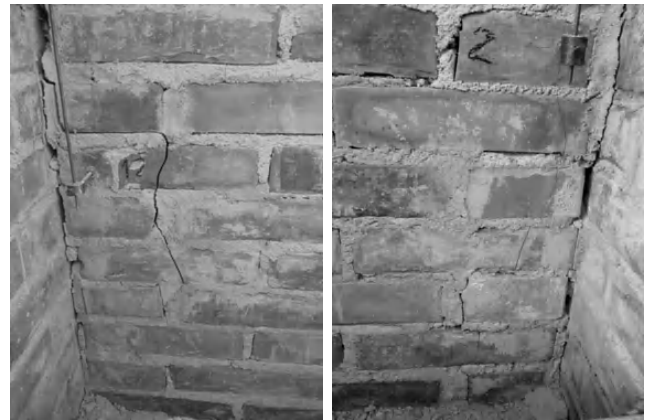


Figure 10 Crushing of masonry in unstrengthened wall: left and right side near foundations

It is important to notice that the connections were able to maximize the capacity of all available elements with only 6 bars active out of a total of 24, because only one flange contributes to the stiffness in each direction (24/2) and only the bars in one direction (+45° or -45°, alternatively) are under tension (12/2).

7 CONCLUSIONS

The tests helped interpreting and describing the effects of the connections on the overall wall behavior. In the adopted geometrical configurations, the strength increase is about 60%, while the ductility increase is about 200%. Horizontal shear capacity is not particularly influenced by the connections, because the flanges give a low contribution. It is noticed that the connections also improve the out-of-plane stiffness (against overall overturning).

Future tests will allow to study and define analytical models able to quantify strength, stiffness and ultimate displacement in the strengthened configuration.

8 ACKNOWLEDGEMENTS

The authors thank the SACEN company of Naples, Italy, for providing and applying the NAILTEX aramidic bars.

REFERENCES

- Circolare n. 617 C.S.LL.PP 2009. Istruzioni per l'applicazione delle nuove norme tecniche per le costruzioni di cui al decreto ministeriale 14 gennaio 2008. *Supplemento ordinario n. 27 alla Gazzetta Ufficiale 26 febbraio 2009.*
- DM 14 Gennaio 2008. Nuove norme tecniche per le costruzioni. *Gazzetta Ufficiale della Repubblica Italiana 4 febbraio 2008.*
- Tomazević, M. 1999. *Earthquake resistant design of masonry buildings*. Series on Innovation in Structures and Construction, vol.1. London: Imperial College Press.

FRP-to-Softwood Joints: Experimental Investigation

J. Wan & S.T. Smith (stsmith@hku.hk)

Department of Civil Engineering, The University of Hong Kong, China

P.Z. Qiao

Department of Civil and Environmental Engineering, Washington State University, USA

ABSTRACT A proper understanding of the interfacial behaviour between timber and bonded fibre-reinforced polymer (FRP) composites will assist in the rational and optimal design of FRP strengthening works for timber structures. To enhance this understanding, a series of single-lap FRP-to-timber joint shear tests are reported herein in which the strength of the bond between the FRP and timber is examined. The shear tests are conducted on softwood (Pine) which has been strengthened with carbon FRP with the main test variables being the FRP bond length and the growth characteristics of the timber. Extensive strain gauging of the FRP has enabled the onset and propagation of debonding cracks to be monitored. An effective bond length is identified, however, the results also show that timber is a variable material which requires continued investigation.

1 INTRODUCTION

Timber has been used as a construction material in civil infrastructure (Breyer et al. 2007) throughout the world for several millennia and it is still a popular construction material to this day. Degradation of timber due to mechanical and environmental loadings, as well as the need for the timber to withstand higher loads, can require the timber to be strengthened or repaired. The external bonding of fibre-reinforced polymer (FRP) composites offers a viable solution. A lack of understanding of the bond strength and behaviour of FRP to the timber substrate is, however, hindering the safe and rational design of FRP strengthening.

Tests on the bond strength and behaviour of FRP-to-timber are limited. The majority of testing has involved the use of the called modified block-shear test of ASTM D905-03 (2003) (e.g. Davalos et al. 2000, Crews and Smith 2006). This test gives the shear strength of the bond as an average bond stress over the bonded length, however, the surface of the FRP is sandwiched between two pieces of timber. Such positioning does not make it possible to easily monitor the surface of the FRP. Claisse et al.'s (2007) study appears to be one of the few on double-lap FRP-to-timber joint shear specimens in which the surface of the FRP is exposed.

This paper reports the results of a series of tests on single-lap FRP-to-timber joints. These tests form part of a much larger test program at The University of Hong Kong concerned with the strengthening of timber with FRP. For the tests reported herein, Pine (softwood) and carbon FRP (wet lay-up) sheets are the materials of choice, with the two primary test variables being (i) length of

bonded FRP, and (ii) timber growth characteristics. All test specimens are instrumented with an extensive array of electric resistance strain gauges which help shed light on the interfacial behaviour of the joints. A much more detailed account of the tests reported herein can be found in Wan et al. (2010).

2 EXPERIMENTAL DETAILS

The test set-up is shown in Figure 1 and a schematic of a typical joint is shown in Figure 2.

In total, 52 joint tests were conducted (Wan et al. 2010). Seven different lengths of FRP were investigated with at least seven identical specimens prepared and tested for each length. The lengths L_{frp} were 15 mm, 30 mm, 60 mm,

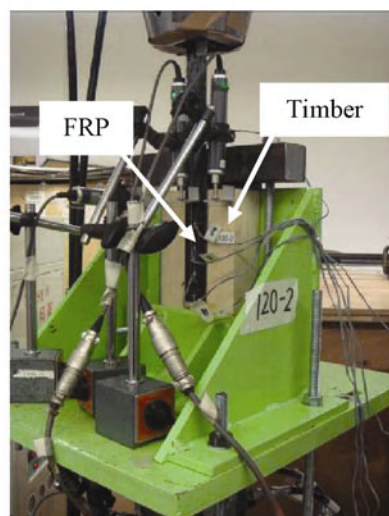


Figure 1 Test set-up

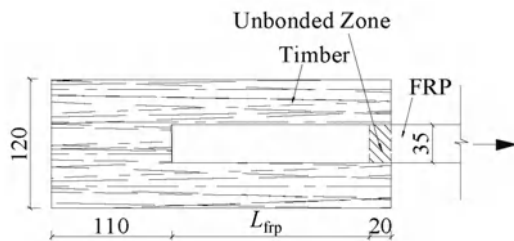


Figure 2 Joint schematic (timber thickness = 50 mm)

90 mm, 120 mm, 150 mm and 180 mm. Pine (softwood) was used and every attempt was made to select test pieces which were relatively free of growth defects such as knots. In some instances small growth defects were, however, present and the effect of such defects is discussed in Section 3. The moisture content of the timber, up to a depth of 8 mm, was measured with a hand-held digital wood moisture tester prior to application of the FRP and was found to be on average 9.5 %. All FRP plates were formed in a wet lay-up procedure from two layers of carbon fibre sheet of nominal thickness 0.166 mm (per sheet).

The surface of the timber was prepared in the following manner prior to bonding of the FRP: (i) sanding of the timber with 120 grit sandpaper, and (ii) cleaning of the prepared surface by spraying with compressed air and then wiping with acetone. Sanding consisted of sweeping the sandpaper back and forward 15 times along the longitudinal axis of the timber (i.e. direction of grain) and also at 45 degrees to the direction of grain. The FRP was then applied to either the A side or B side of the timber as shown in Figure 3. Side A was the side located closest to the pith of the timber. In this case, the annual growth rings were inclined to the edge of the timber and the FRP face. The Side B annual growth rings were oriented predominantly parallel to the edge of the timber. At least three test specimens were prepared and tested for both A and B side bonded FRP.

The properties of two-layered flat FRP coupon tests of 35 mm width (i.e. the same width and number of fibre sheet layers as the plates used to strengthen the timber joints) were 231 GPa (modulus of elasticity), 2768 MPa (tensile strength) and 1.2 % (rupture strain). Preliminary testing of the compressive and tensile properties of the timber produced relatively consistent elastic moduli on average of about 13.5 GPa.

The two longitudinal linear variable differential transformers (LVDT 1 and 2), shown in Figure 4, enabled relative slip between the loaded end of the bonded FRP and adjacent timber to be measured. LVDT 3 confirmed the lateral deflection to be suitably low at an average displacement of about 0.3 mm. Electric resistance strain gauges of 10 mm gauge length were installed on the surfaces of all FRP plates at 10 mm from the bond line of the loaded end and then at 30 mm centres. Load was

applied monotonically by displacing the ram of the universal testing machine at a constant rate of 0.3 mm/min.

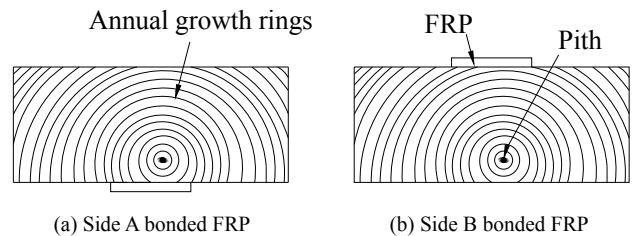


Figure 3 Timber growth characteristics and FRP bonding schemes

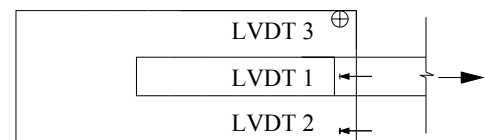


Figure 4 Instrumentation

3 EXPERIMENTAL RESULTS

3.1 Failure modes

All specimens failed by debonding at the interface of the FRP and timber substrate and predominantly in the timber. Debonding initiated at the loaded end of the bonded FRP and propagated to the far end. The condition of the debonded surface of the FRP, however, varied. For example, the results for three of the 120 mm bond length specimens are shown in Figure 5. Figures 5(a) and 5(b) show typical failed Side A and Side B specimens, respectively. Side B failures were mainly in the timber, while Side A failures were less often in the timber, for two main reasons: (i) younger wood away from the pith is less dense than older wood closer to the pith, and (ii) the inclination of the annual growth rings. These two factors are, however, intertwined because the growth ring pattern in relation to the cut edge of the timber is a function of the location of the pith. Interlaminar failure between the annual growth rings is particularly evident in Figure 5(b). Figure 5(c) shows a Side A specimen which contains a small knot in the bonded area. This specimen (120A-1) recorded the highest failure load for all 120 mm bond length specimens and this can be attributed to the knot. The knot did not contribute to the highest joint strength in all cases though.

3.2 Load versus slip

Figure 6 shows typical load versus slip relationships for specimens with short (30B-1) and long (150B-2) bond lengths in which the slip is based on the LVDT measurements. In all cases, the relationship is predominantly linear until debonding occurs. For the shorter bond length specimens, the entire plate debonded quite rapidly once the maximum load was reached. For the longer bond length specimens, a peak load plateau sometimes existed.

The peak load plateau began when the FRP started debonding and finished once the FRP had completely debonded. These curves would suggest that once debonding initiates, then there is little to no increase in joint strength. This in turn introduces the concept of an effective bond length in FRP-to-timber joints in which the bond strength will not increase once a certain bonded length of FRP has been reached.

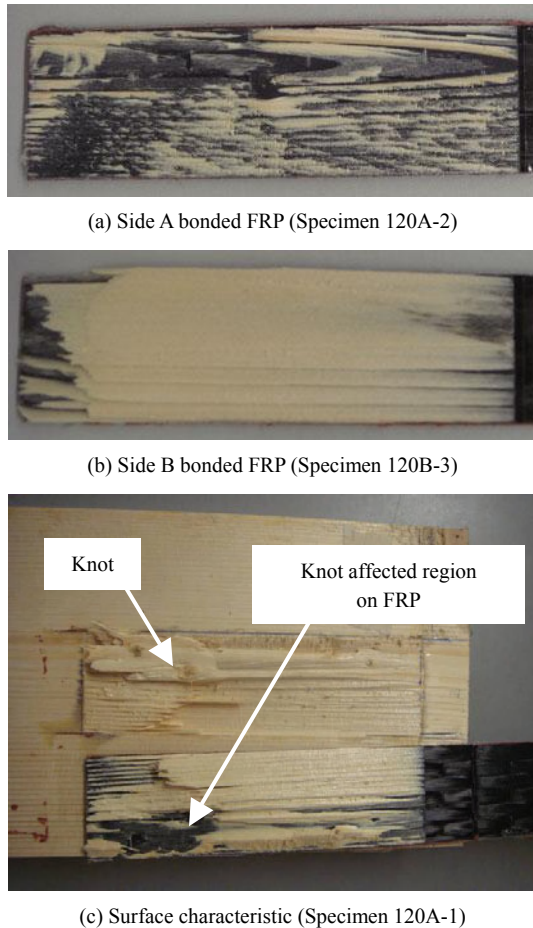


Figure 5 Debonded FRP surface condition

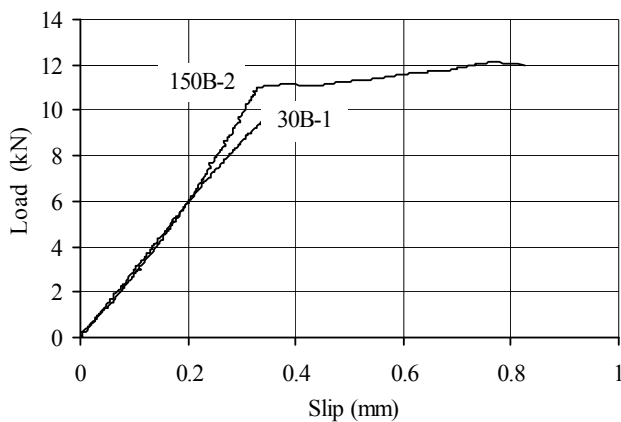


Figure 6 Typical load versus slip responses

3.3 Failure load versus bond length

Figure 7 shows the relationship between failure load and

bond length. The data points have been differentiated by Side A or Side B bonded FRP. All joints failed by debonding. The bond strength of the joint for Side B bonded FRP is clearly the lowest for each bond length. The amount of scatter in bond strength of Side A bonded FRP is evident. Such variation can be attributed to the timber characteristics such as location of the pith, inclination of the annual growth rings, and local defects.

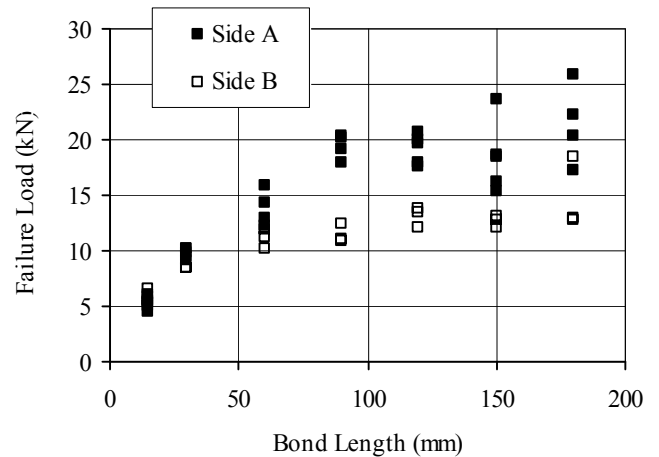


Figure 7 Failure load versus bond length

3.4 Load versus strain

Figure 8 presents typical distributions of strain along the length of bonded FRP. Specimen 150B-2 is selected and this is the same specimen exhibiting the peak load plateau in Figure 6. At the low load ranges of responses in Figure 8, the first 70 mm or so of FRP plate nearest to the loaded end is providing most of the resistance. Debonding of the FRP initiates at a load and slip of approximately 11.0 kN and 0.33 mm (based on LVDT readings), respectively. This combination of load and slip represents the approximate start of the sharp change in slope observed in Figure 6. At approximately the same load (11.1 kN) but at a larger slip of 0.41 mm, Figure 8 shows the debonding crack to have propagated to the strain gauge located at 10 mm from the loaded end of the joint. This propagation is evident from the relatively constant strain at the first two strain gauges at 0 mm and 10 mm from the loaded end (note that the 0 mm strain gauge was positioned at 40 mm from the bonded end of the FRP towards the grips of the universal testing machine). The strain distribution for the last recorded load and slip just prior to complete debonding of the plate is also shown in Figure 8. The extensive debonding of the plate is evident from the large and reasonably constant strains.

4 DISCUSSION

4.1 Effective bond length

Figure 7 reveals the effective bond length for the Side B results to be about 90 mm. The effective bond length for

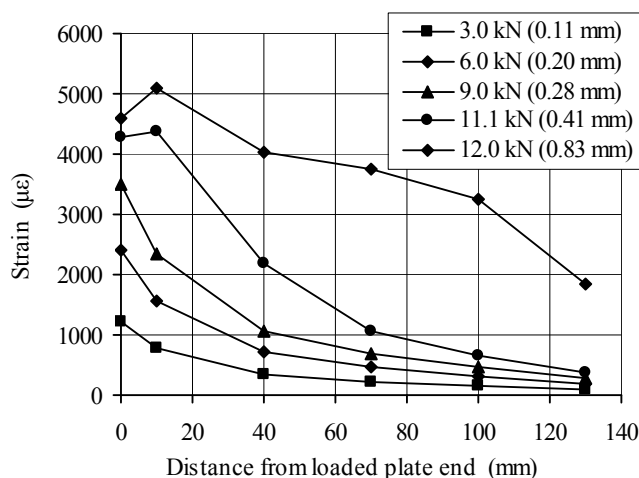


Figure 8 Load versus strain for specimen 150B-2

the Side A specimens is not as obvious due to the large scatter of results. For design it is recommended to use the lower bound Side B results until more testing has been undertaken. While the bond strength has the potential to be much larger (i.e. depending on the cut of the timber), it is much less predictable.

4.2 Inclination of annual growth rings

For all of the Side B bonded FRP specimens, the FRP was predominantly tangential (i.e. parallel) to the annual growth rings. For all the Side A specimens, the growth rings were predominantly oriented perpendicular to the FRP. The strength of the timber at the FRP-to-timber interface proved the weakest for Side B specimens. This weakness was also demonstrated by the debonded surface of the FRP in which a large portion was covered in thick timber of up to 5 mm thickness (Figure 5(b)). The amount of timber remaining attached to the debonded surface of the Side A bonded FRP was on occasions considerably less (i.e. Figure 5(a)).

4.3 Location of pith

The effect of the pith is only evident in the Side A bonded FRP results. The following observations can, however, be made. The radius of curvature of the growth rings in the immediate vicinity of the pith was smallest, thus leading to rings intersecting the FRP plate in a more

perpendicular manner. In addition, the denser older wood in the immediate vicinity of the pith contributes to higher bond strength. This is particularly evident in the large range of the results for the 120 mm and 180 mm bond length specimens.

5 CONCLUSIONS

A series of tests has been reported on the bond strength and behaviour of FRP-to-timber softwood joints. The results were found to be heavily influenced by the growth characteristics of the timber such as annual growth ring inclination to the bonded faces as well as the location of the pith. Knots were also found to affect the results. The existence of an effective bond length was confirmed and a lower bound bond strength was evident when the FRP was bonded to surfaces predominantly tangential (parallel) to the annual growth rings.

6 ACKNOWLEDGEMENTS

Financial support provided by GRF Incentive Award HKU 10208970 (09-10) is gratefully acknowledged.

REFERENCES

- ASTM D 905-03 2003. *Strength Properties of Adhesive Bonds in Shear by Compression Loading*, American Society for Testing and Materials (ASTM), PA, USA.
- Breyer, DE, Fridley, KJ, Cobeen, KE & Pollock, DG 2007. *Design of Wood Structures-ASD-LRFD*, McGraw Hill, USA.
- Claisse, PA, Davis, TJ & Masse, B 2007. Fatigue testing of glass/epoxy joints in timber up to the endurance limit, *Construction and Building Materials*, 21: 139-149.
- Crews, K & Smith, ST 2006. Tests on FRP-strengthened timber joints, *Proceedings, 3rd International Conference on FRP Composites in Civil Engineering, CICE 2006*, Miami, FL, USA, 677-680.
- Davalos, J.F., Qiao, PZ & Trimble, BS 2000. Fiber-reinforced composite and wood bonded interfaces: Part 1. durability and shear strength, *Journal of Composites Technology and Research*, 22(4): 224-231.
- Wan, J, Smith, ST & Qiao, PZ. Bond strength and behaviour of FRP-to-softwood joints, in preparation.

Author Index

Note:**Volume I pages 1-482****Volume II pages 483-954****A**

Abbas, S. 381
 Abdoli, N. 837
 Abdul-Razzak, A.A. 419
 AbduRahman, B. 279
 Abu Bakar, B.H. 419
 Ahmed, E. 287
 Aidoo, J. 504
 Akbarzadeh, H. 739
 Akgun, D. 622
 Alae, F.J. 658
 Alessandri, S. 634
 Ali, A.M. 695
 Al-Mahaidi, R. 317, 877, 890
 Almansour, H. 152
 Alves, J. 368
 Ammar, H.H. 562
 An, F.C. 499
 An, Z.O. 224
 Anderson, M. 712
 Anggawidijaja, D. 806
 Aravinthan, T. 139, 376, 447, 478
 Asfa, M. 837
 Aubagnac, C. 385
 Awad, Z.K. 478
 Ayub, T. 533
 Ayudhya, B.I.N. 585

B

Baena, M. 271, 352, 744
 Bai, Y. 405, 877
 Bakis, C.E. 33, 397
 Baky, A. 626
 Banbach, M.R. 877
 Bank, L.C. 115
 Barai, S.V. 763
 Barbeta, G. 271
 Barbezat, M. 348, 423
 Barris, C. 271, 744
 Barros, J.A.O. 755, 781, 785
 Bekey, S. 919

Belarbi, A. 767
 Benmokrane, B. 279, 287
 Benzarti, K. 385
 Bhattacharyya, S.K. 763
 Bhetwal, K.K. 925
 Bi, Q.W. 576
 Bianco, V. 781, 785
 Bibbò, F.A. 849
 Bijlaard, F.S.K. 360
 Bisby, L.A. 423, 443, 595, 599, 886
 Boroujeni, S.T. 646
 Boscato, G. 127, 131
 Bouazza, A. 317
 Bro, W. 504

C

Cai, W.H. 313
 Cairns, J. 512
 Cao, S.Y. 499
 Cao, Y.B. 529
 Carey, N.L. 81
 Carrigan, L. 317
 Cejka, T. 943
 Ceroni, F. 849
 Chakrabarti, A. 607
 Chakraborty, A. 156, 228
 Chapeleau, X. 73
 Chataigner, S. 385, 537
 Chen, A. 177, 468, 557, 562, 685, 712
 Chen, A.R. 197
 Chen, C.H. 202
 Chen, D. 185, 191
 Chen, G.D. 460
 Chen, G.M. 485
 Chen, H.S. 525
 Chen, J.F. 45, 485, 494, 512, 595
 Chen, T. 907
 Chen, W.Y. 668, 772
 Chen, X.B. 668, 772
 Cheng, L. 610
 Cheng, L.T. 85
 Cheung, M. 152
 Cho, J.R. 211
 Cho, K. 211, 215
 Chung, W. 224
 Cleland, D.J. 735
 Contamine, R. 77, 665

Cournée, S. 73
Cui, J. 748

D

da Fonseca, T.de C.C.S. 858
Dai, H. 301, 304
Dai, J.G. 428, 529
Dai, L. 197
Danesh, F. 829, 833
Daugevičius, M. 642
Davalos, J.F. 177, 468, 557, 562, 685, 712
David, B. 452
de Almeida, S.F. 858
de Castro, J. 95
de Hanai, J.B. 858
Demers, M. 626
Demir, C. 622
Deng, J. 899
Deng, Z.C. 699, 704
Dias, S. 755
Ding, L.N. 589, 650
Ding, Y. 668, 772
Donchev, T. 731
Dong, G. 845
Drissi-Habti, M. 73, 264
Duan, W.H. 890
Duffin, J.B. 824
Dulude, C. 287

E

Eftekhari, M.R. 490
El-Gamal, S. 279, 287
El-Hacha, R. 185, 191, 638, 718, 929
El-Mogy, M. 283
El-Ragaby, A. 283, 330, 368
El-Salakawy, E. 283, 330, 368
Eveslage, T. 504

F

Fahmy, M.F.M. 325
Fam, A. 164, 237
Fan, H.F. 197
Fang, H. 123
Feng, P. 160, 173, 202, 919
Fernando, D. 865
Ferrier, E. 344, 452, 537, 541, 665
Finckh, W. 517, 794

Flood, J.P. 397
Foley, C.M. 207, 464
Fujita, S. 168

G

Gao, D.Y. 296
Gao, W.Y. 428
Garcia, V.O. 744
Ge, C. 219
Ge, Q. 499
Ge, W.J. 301, 304
Godat, A. 521
Gu, X.L. 907
Guadagnini, M. 691
Guo, X.Y. 341

H

Hadigheh, S.A. 841
Haido, J.H. 419
Hajrasouliha, M.J. 545
Hajsadeghi, M. 658
Hale, M. 164
Hamelin, P. 77, 344, 452, 541, 665
Hao, Q.D. 248, 292
Harries, K.A. 504, 873
Hasaballa, M. 330
Haskett, M. 37
He, J. 197
He, X.J. 397
Heiza, Kh.M. 433
Helal, M.A. 433
Hidekuma, Y. 881
Hojatkashani, A. 508
Holschemacher, K. 252, 256
Hong, S.N. 748
Houssam, M.A. 939
Hu, Y.M. 595
Huang, C.K. 681
Huang, P.Y. 337, 341
Hugi, E. 405
Hwash, M. 308

I

Ilki, A. 622
Imani, F.S. 557, 562
Ishihama, T. 103, 111
Islam, M.M. 376

J

Jaipurkar, A. 397
 Jamaji, R. 456
 Jang, H. 224
 Javadi, P. 801
 Jayaprakash, J. 419
 Jiang, X. 360
 Jin, F.F. 173
 Jin, Q.X. 53
 Jing, W.J. 57
 Jirawattanasomkul, T. 806
 Justice, A. 685

K

Kabir, M.Z. 508, 915
 Karunasena, W. 139
 Käseberg, S.F. 252, 256
 Keller, T. 20, 91, 95, 405
 Khan, A.R. 533, 630
 Khennane, A. 156, 228
 Kim, B.S. 211, 215
 Kim, S.J. 869
 Kim, S.T. 211, 215
 Kim, T.W. 748
 Kim, Y.J. 873
 Kishi, N. 695, 708
 Kitayama, N. 168
 Kivi, M.P. 646
 Knippers, J. 107, 308
 Kobayashi, A. 881
 Kolstein, H. 360
 Komuro, M. 708
 Kong, X.F. 676
 König, C. 894
 Kotynia, R. 567, 776
 Kuchma, D. 767
 Kurihashi, Y. 695
 Kyoda, N. 801

L

Labossière, P. 521
 Lam, L. 654, 820
 Lawler, N. 854
 Lees, J.M. 789
 Leo, B. 156
 Leung, C.K.Y. 53
 Li, F. 525

Li, H. 65, 69, 260, 356
 Li, J.B. 460
 Li, S.B. 676
 Li, S.Q. 595
 Li, X.Q. 494
 Li, Y.M. 939
 Li, Z.W. 337
 Liang, S.T. 313
 Lim, B.K. 415
 Limam, A. 344
 Lin, X.S. 722, 727
 Liu, H.Y. 933
 Liu, J.T. 810
 Liu, W.Q. 119, 123
 Liu, Y.Q. 197
 Llorens, M. 352
 Lopez, M.M. 397
 Lou, W.J. 202
 Lovo, V. 614, 634
 Lu, J.Y. 820
 Lu, Y. 494
 Lucas, W. 37
 Ludwig, C. 405
 Luo, J.L. 260

M

Ma, J.X. 85
 Ma, M. 845
 Ma, Y.S. 390
 Mady, M. 330
 Maeda, K. 148, 168
 Maghsoudi, A.A. 739
 Maheri, M.R. 841
 Mahini, S.S. 841
 Mahmoud, A.M. 562
 Manalo, A. 139
 Manshadi, B.D. 91, 95
 Martinelli, E. 548
 Marty, C. 385
 Mashrik, M.A. 638
 Matsui, T. 148
 Matsumoto, Y. 925
 Matthys, S. 401, 572, 691
 McCarthy, M.J. 115
 Meekum, U. 135
 Meier, U. 348
 Menegotto, M. 947

Mercier, J. 537
 Miàs, C. 271, 352, 744
 Michel, L. 541
 Mikami, H. 695, 708
 Min, K.H. 275, 410
 Miyashita, T. 881
 Mohamed Ali, M.S. 37
 Monti, G. 614, 634, 781, 785, 947
 Morozov, E.V. 228
 Mostofinejad, D. 490, 545, 837
 Mottram, J.T. 99
 Muhamad, R. 37
 Mukdadi, O.M. 562
 Müller, R. 348
 Munir, J. 672
 Murphy, M.S. 767
 Mutsuyoshi, H. 103, 111, 148
 Myers, J.J. 81

N

Nabi, P. 731
 Nagahama, A. 801
 Nagai, M. 881
 Nakada, K. 801
 Nakamura, H. 148, 168
 Napoli, A. 548, 815
 Narayanamurthy, V. 512
 Neale, K.W. 521, 626
 Nelson, L.A. 789
 Nguyen, D.H. 103, 111
 Nguyen, T.C. 877
 Nishizaki, I. 372, 474
 Nisticò, N. 614, 634
 Noveiri, B.B. 829
 Nunziata, B. 815
 Nuti, C. 759

O

Oday, A.S. 939
 Oehlers, D.J. 37
 Oh, M.H. 748
 Omran, H.Y. 718, 929
 Oppe, M. 107
 Oskouei, A.V. 646
 Ou, J.P. 248, 292

P

Palmieri, A. 401, 572, 691

Pan, J.L. 499
 Panda, K.C. 763
 Pantelides, C.P. 824
 Park, S.K. 748
 Park, S.Y. 211, 215
 Pecce, M. 849
 Peng, Y.P. 845
 Phiphat, P. 911
 Pilakoutas, K. 691
 Plum, R. 894
 Plunkett, J.D. 177
 Polak, M.A. 854

Q

Qi, Y.J. 160
 Qiang, S.Z. 894
 Qiao, P.Z. 951
 Qiu, X.M. 85
 Quayyum, S. 581
 Quiertant, M. 344, 385, 537
 Quon, C. 610
 Qureshi, K.A. 672
 Qureshi, L.A. 672

R

Raikar, K.R. 456
 Ramadass, S. 321
 Ray, I. 177, 557, 562, 685, 712
 Realfonzo, R. 548, 815
 Reinaldy, R. 603
 Rizkalla, S. 589, 650
 Robinson, D. 735
 Rteil, A. 381, 581
 Russo, S. 127, 131

S

Sadone, R. 537
 Salvini, S. 947
 Sami, Q. 541
 Santini, S. 634, 759
 Sarafraz, M. 833
 Sasaki, I. 372, 474
 Savardekar, S.K. 456
 Scheffers, C.A. 603
 Seif, A.E. 915
 Seliem, H.M. 650
 Sentry, M. 317

Serbescu, A. 691
 Sguerri, L. 759
 Sheikh, S.A. 810
 Shin, H.O. 275
 Shiroki, K. 103, 111
 Si Larbi, A. 77, 541, 665
 Sirimanna, C.S. 376
 Smith, S.T. 13, 553, 869, 951
 Sri Ravindrarajah, R. 603
 Stratford, T.J. 599, 886
 Stutz, A. 423
 Sultan, T. 672

T

Taerwe, L. 401
 Tamužs, V. 642
 Tan, Y. 219
 Tao, Y. 45
 Tateishi, A. 881
 Taylor, S.E. 735
 Teng, J.G. 26, 428, 485, 595, 654, 820, 865
 Terrasi, G.P. 348, 423
 Tharmarajah, G. 735
 Thomas, J. 321
 Tomlinson, D.G. 237
 Tong, L.W. 903
 Torres, L. 271, 352, 744
 Tran, K. 638
 Triantafillou, T. 3
 Tu, Y.M. 301, 304, 313
 Turon, A. 271, 352

U

Ueda, T. 806
 Ummenhofer, T. 894
 Ungkoon, Y. 585

V

Vailati, M. 947
 Vantaram, A. 177
 Vassilopoulos, A.P. 91, 95
 Vilanova, I. 352, 744

W

Wan, B.L. 207, 464
 Wan, C. 610
 Wan, J. 951
 Wan, L. 123

Wang, D.Y. 810
 Wang, H. 576
 Wang, H.T. 933
 Wang, H.Y. 341
 Wang, W.W. 61, 681
 Wang, X. 243
 Wang, Y.F. 390
 Wang, Y.L. 85, 248, 292
 Wang, Y.S. 219
 Wang, Z.Y. 810
 Watanabe, T. 168
 Wei, Y.Y. 618
 Witzany, J. 943
 Woltman, G.D. 237
 Wong, Y.L. 26
 Wu, C. 890
 Wu, C.L. 460
 Wu, G. 57, 232, 325, 589, 933
 Wu, J.Y. 65, 69
 Wu, Y.F. 364, 618
 Wu, Z.S. 57, 232, 243, 325, 589, 933

X

Xian, G.J. 65, 69, 260, 356
 Xiao, B. 65, 356
 Xiao, Q.G. 654, 820
 Xiao, R. 699, 704
 Xiao, Y. 144
 Xiao, Z.G. 903
 Xiao, Z.L. 296
 Xie, J.H. 337
 Xue, W.C. 219

Y

Yaginuma, K. 148
 Yahiaoui, A. 626
 Yamada, S. 925
 Yamakawa, T. 801
 Yan, D.M. 460
 Yan, Z.H. 824
 Yanagida, M. 925
 Yang, J.M. 275, 410
 Yang, L.L. 676
 Yang, M.H. 415
 Yang, W. 61
 Ye, H.W. 894
 Ye, L.P. 160, 173, 919

Yoo, D.Y. 410
Yoon, Y.S. 275, 410
Young, B. 869
Yu, T. 26, 654, 865
Yun, Y.C. 364

Z

Zafar, N.S. 630
Zafari, B. 99
Zangeneh, P. 929
Zhang, H.W. 553
Zhang, J.W. 301, 304, 313
Zhang, P. 232
Zhang, X. 676
Zhang, Y.K. 296
Zhang, Y.X. 722, 727
Zhao, F. 202
Zhao, G.F. 681
Zhao, Q.L. 525
Zhao, X.L. 865, 877, 890, 903, 907, 911
Zheng, X.H. 337
Zhou, D. 119, 123
Zhou, H. 337, 341
Zhou, Q. 144
Zhou, Z.L. 341
Zhu, B. 119
Zhu, H. 232
Zhu, H.T. 296
Zhuge, Y. 478
Zigler, R. 943
Zilch, K. 517, 794
Zile, E. 642